SPECTRA
Computer Code Manuals

Volume 3 - Verification and Validation

Version 24-02

M.M. Stempniewicz

Arnhem, February 2024

K6223/24.277594 MSt-2402

author : M.M. Stempniewicz reviewed : E.A.R. de Geus

1323 page(s) approved : J.J. Meulenbrugge

Spectra-Vol3.doc

Contents

Abstract

SPECTRA (**S**ophisticated **P**lant **E**valuation **C**ode for **T**hermal-hydraulic **R**esponse **A**ssessment) is a fully integrated system analysis code, that models thermal-hydraulic behaviour of Nuclear Power Plants, including reactor cooling system, emergency and control systems, containment, reactor building, etc. of various reactor types, like BWR, PWR, HTR. It can also be used to assess thermal-hydraulic response of non-nuclear plants, for example cooling systems of chemical reactors.

The full documentation of SPECTRA consists of the following four volumes:

- Volume 1: Program Description
- Volume 2: User's Guide
- Volume 3: Verification and Validation
- Volume 4: Code Structure, Development, Hardware and Software Requirements

Volume 3 of the SPECTRA Code Manuals contains Verification and Validation of the SPECTRA code. Verification and validation (V&V) is performed following the recommendations set by the American Nuclear Society (ANS) guidelines for the verification and validation of scientific and engineering computer programs for the nuclear industry, ANSI/ANS-10.4-1987.

The SPECTRA Manuals are freely available in internet and are also supplied together with the SPECTRA code. The Volume 3 of the Code Manuals is provided in the file **Spectra-Vol3.pdf**.

Explanation of names and abbreviations

CF	Control Function
CV	Control Volume
DIA	Diagnostics file
ICF	Initial Condition File
IT	Isotope Transformation
JN	CV Junction
MP	Material Properties
OUT	Output file
OX	Metal Oxidation
PLT	Plot file
RK	Reactor Kinetics
RT	Radioactive Particle Transport
SC	1-D Solid Heat Conductor
SPECTRA	**S**ophisticated **P**lant **E**valuation **C**ode for **T**hermal-hydraulic **R**esponse **A**ssessment
TC	2-D Solid Heat Conductor
TF	Tabular Function
TFD	Tabular Function Data file
TR	Thermal Radiation

1 Introduction

SPECTRA (**S**ophisticated **P**lant **E**valuation **C**ode for **T**hermal-hydraulic **R**esponse **A**ssessment) is a fully integrated system analysis code, that models the thermal-hydraulic behaviour of Nuclear Power Plants, including reactor cooling system, emergency and control systems, containment, reactor building, etc. of various reactor types, like BWR, PWR, HTR. It can also be used to assess thermal-hydraulic response of non-nuclear plants, for example cooling systems of chemical reactors. The structure of SPECTRA is shown in Figure 1-1.

The full documentation of SPECTRA consists of the following four volumes:

- Volume 1: Program Description
- Volume 2: User's Guide
- Volume 3: Verification and Validation
- Volume 4: Code Structure, Development, Hardware and Software Requirements

Volume 3 of the SPECTRA Code Manuals contains Verification and Validation of the SPECTRA code. Verification and validation (V&V) is performed following the recommendations set by the American Nuclear Society (ANS) guidelines for the verification and validation of scientific and engineering computer programs for the nuclear industry, ANSI/ANS-10.4-1987 [1].

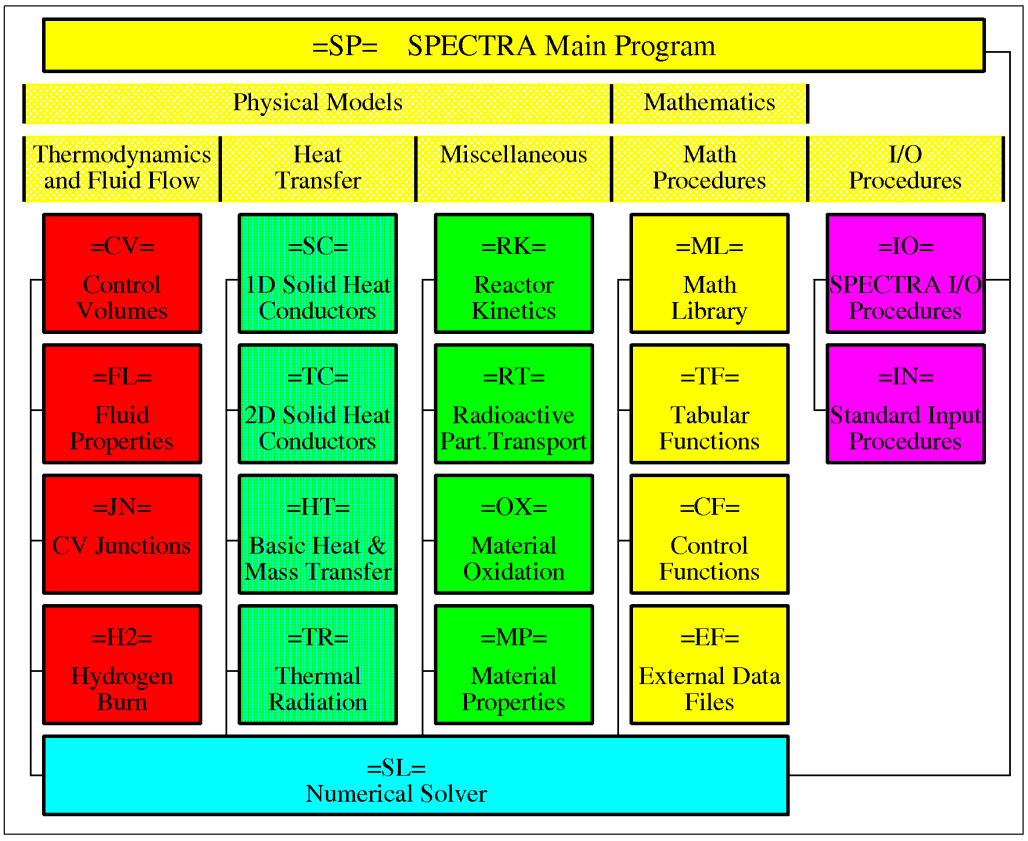

Figure 1-1 SPECTRA code structure.

1.1 Definitions

Following reference [1] the meaning of the terms verification and validation is as follows.

- **Validation.** The process of testing a computer program and evaluating the results to ensure compliance with specified requirements.

- **Verification.** The process of evaluating the products of a software development phase to provide assurance that they meet the requirements defined by the previous phase.

The above definitions can be given in a simpler form, as (see reference [1]):

- **Verification** can be considered to be the proof or demonstration that the computer program instructions correctly represent the program/procedure design and that the program/procedure design correctly represents the mathematical model.

- **Validation** is a demonstration that the verified computer program and by inference its mathematical models are an adequate representation of the natural phenomena.

1.2 Overview of V&V

Reference [1] distinguishes the following phases of software development:

- **Initiation Phase**, when a decision is made to develop a computer program to solve a certain problem. The problem is often documented in a report called Statement of Problem.
- **Requirements Definition Phase**, during which the requirements that the program must satisfy are specified.
- **Design Phase**, when the logical structure, information flow, processing steps, data structures, and other aspects of a computer program are defined.
- **Coding Phase**, when the developer implements the program design by coding it in a programming language.
- **Integration and Testing Phase**, when program components are integrated into an overall program.
- **Installation Phase**, during which the program is installed in its operational environment and the program documentation is updated to completely and accurately describe the program.
- **Operation and Maintenance Phase**, during which the program is modified as necessary to correct problems and changing requirements.

Reference [1] specifies the V&V activities for the different phases, including checklists:

- **Initiation Phase**, no specific activities.

- **Definition Phase** ([1], section 5), including Checklists 5-1 - Verification of Requirements, and Checklist 5-2 - Verification of Test Plan. Checklist 5-1 contains questions related to sponsor-developer interactions. Some of the questions from Checklist 5-1 are not applicable because SPECTRA was developed internally in NRG, there is no clear sponsor-developer interaction. In the case of SPECTRA the Statement of Problem is simply to "provide a well-documented and user-friendly tool for simulations of thermal-hydraulic phenomena occurring in nuclear as well as non-nuclear power plants during normal and abnormal (accident) conditions". The Statement of Problem for the current version of the code is stated below, in section 1.3.1. The requirement specification that matches this statement of the problem is given in section 1.3.2. The requirements defined in Checklists 5-2 are fulfilled - see section 1.3.3. Since SPECTRA covers very wide range of phenomena, a large number of tests is required. Consequently it is not possible to define general acceptance criteria, but the acceptance criteria are set for each test individually.

- **Design Phase** ([1], section 6), including Checklist 6-1 - Verification of Design, and Checklist 6-2 - Verification of Program Documentation. The SPECTRA documentation is written according to the ANS standard (reference [2]). The requirements set in Checklists 6-1 and 6-2 are fulfilled - see SPECTRA code manuals, Volume 1 and 2. Since Volume 3 presents only verification of the program itself, the verification of design and documentation is not addressed here.

- **Coding Phase** ([1], section 7), including Checklist 7-1 - Verification of Source Code. The SPECTRA code is written according to the programming practices set in the ANS standard (reference [3]). The requirements set in Checklists 7-1 are fulfilled - see SPECTRA code manuals, Volume 4.

- **Integration and Testing Phase** ([1], section 8), including Checklists 8-1 - Verification of Program Integration, Checklists 8-2 - Program Validation, and Checklist 8-3 - Verification of Test Results. The requirements set in Checklist 8-1 are fulfilled - see SPECTRA code manuals, compilation batch file, listings produced during compilation and linking. The requirements set in Checklists 8-2 and 8-3 are fulfilled - see Chapters 2, 3, 4 below. If the acceptance criteria set for a given test in the design phase (see above) were not met, then the part of coding responsible for the discrepancy was identified, and improved.

- **Installation Phase** ([1], section 9), including Checklist 9-1 - Verification of the Installation Package. SPECTRA compilation and installation is very easy and user friendly. All requirements set in Checklists 9-1 are fulfilled - see SPECTRA code manuals, installation guidelines, as well as the compilation batch file and the base set of test cases.

- **Operation and Maintenance Phase** ([1], section 10). During the operation and maintenance phase modifications are made to the SPECTRA code. The modifications involve addition of new capabilities, correction of errors or deficiencies found during operation, and improvement in user-friendliness. The V&V activities for program modifications are the same as those carried out in parallel with program development.

1.3 Description of SPECTRA V&V Activities

1.3.1 Statement of Problem

In case of SPECTRA the Statement of Problem is simply to "provide a well-documented and user-friendly tool for simulations of thermal-hydraulic phenomena occurring in nuclear as well as non-nuclear power plants during normal and abnormal (accident) conditions". Such had been the statement of problem for the Version 1.00 of the code. The Statement of Problem for the current version of the code is given as: SPECTRA must provide a well-documented and a user-friendly tool for simulations of thermal-hydraulic phenomena occurring in nuclear as well as non-nuclear power plants during normal and abnormal (accident) conditions. The program must be capable of simulating design accidents as well as an early stage of severe accident, including fuel oxidation, hydrogen generation, as well as eventual threats from hydrogen burn, fission product release and transport. The modelling of the refill phase must be enhanced by introducing multi-dimensional heat conduction model. It must be possible to model the nuclear reactor kinetics, including the effect of poisons, such as xenon and samarium, on reactivity, and also space-dependent effects. The kinetics model must be applicable to the flowing fuels (molten salt reactors). The user-friendliness must be enhanced by incorporating a free numbering scheme for all components.

1.3.2 Requirement Specification

The requirement specifications that arise from the statement of problem given above, are:

- A general 2-D transient heat conduction package is required.
- A metal oxidation package is required, capable of computing the oxidation of Zircaloy and steel in a hot steam environment, as well as an oxidation of any material in such environment via user defined reaction kinetics coefficients.
- A hydrogen burn package is required, capable of computing ignition limits, and simulate slow deflagrations, fast turbulent deflagrations and detonations, within the limits imposed by the general code structure.
- A reactor kinetics package accompanied by an isotope transformation package to track poisons and other isotopes is required. A space independent, point reactor kinetics as well as space-dependent nodal kinetics. Furtheremore, the kinetics model for flowing flowing fuels (molten salt reactors) must be able to model the important phenomena: drift of delayed, neutron precursors, transport of fission products throughout the primary system, migration of fission product to struactures and gas spaces.
- The fluid property package must extend to high temperatures that may be encountered during oxidation (~3000 K).
- It must be possible to include additional gases, on top of the six built-in gases, with thermophysical properties specified by the user in the input deck.
- It must be possible to use alternative fluids (liquid metals, molten salts, etc.), with thermophysical properties specified by the user in the input deck.
- A fission product release and transport models applicable for variety of reactor types is required.
- An extended input/output package is required, to facilitate input and output data to be given using free (i.e. non-consecutive) numbers.

These are additions to the SPECTRA Version 1.00, for which the requirement specification consisted of:

- A control volume package, with extensive sub-volume physics: water level tracking, bubble and droplet tracking in a CV.
- A junction package capable of transporting all CV components: atmosphere, pool, bubbles and droplets.
- A fluid property package that is able to deal with water and gas mixtures including steam and the most commonly encountered gases, such as nitrogen oxygen, hydrogen, helium, and carbon dioxide.
- A general heat transfer package that is able to model heat and mass transfer including surface boiling, non-equilibrium boiling (flashing), condensation in presence of non-condensable gases and non-equilibrium condensation (fogging).
- A general thermal radiation package, based on net enclosure with (or without) participating gas.
- Generic mathematical functions (tabular and control functions), capable to model algebraic and differential equation sets, suitable for modelling the control system providing boundary conditions, etc.
- A general input/output package(s), capable of providing extensive diagnostics of input data. Every input entry must be checked for acceptable range; default values must be available; error and warning messages must be clear.

1.3.3 Test Plan

The SPECTRA test plan consists of the following four steps.

- Every subroutine must be separately tested. This is often done by a specifically designed "driver" program - a program that supplies required input parameters and stores the results of tests in a format convenient for plotting or other post-processing. The testing must cover the full possible range of input parameters. In this way correctness of coding of the mathematical models into subroutines is assured.
- Every model (subroutine or group of subroutines) must be tested from the program level, that means preparing the input deck, performing SPECTRA runs. In this way correctness of integration of the model as well the input and output procedures, diagnostics messages, etc., is assured.
- Separate effect tests must be performed using specific test problems, involving multiple, but limited number of models, for which analytical solutions, graphical data, or experimental results are available.
- The SPECTRA code must be validated using available measurement data, International Standard Problems (ISP), comparisons with other codes, etc.

The testing is performed by the developer, except for the validation runs, which are performed by variety of analysts. The acceptance criteria are defined individually for each test, as described in section 1.4.

1.4 Overview of Verification and Validation Runs

This section presents a short overview of the SPECTRA Verification and Validation. It should be noted that Volume 3 deals only with V&V of the SPECTRA program itself, so it is narrower that V&V defined in reference [1], and discussed in section 1.2 and 1.3. Reference [1] discusses not only verification of the program, but also verification of the documentation and the coding. The documentation and coding of SPECTRA are discussed in Volumes 2 and 4, rather than Volume 3.

Volume 3 of the code manuals contains results of verification and validation runs and comparisons of the calculated results with available data. The V&V on SPECTRA was performed in four steps, described below. According to the ANS definitions of the terms verification and validation (see section 1.1), the first two steps (1, 2) belong to the verification of the program, while the next two steps (3, 4) belong to the program validation. The first two steps belong to the definition phase (Checklist 5-2, see section 1.2) and the coding phase (Checklist 7-1 - see section 1.2), while the next two steps belong to the integration and testing phase (Checklist 8-1, 8-2, 8-3 - see section 1.2).

- *Subroutine Testing*. Every subroutine, or group of subroutines responsible for calculation of a certain physical phenomenion, was verified independently before it was inserted into the code. This task was done using short "driving programs". These programs contain calls to the desired subroutines with appropriate input parameters, and print the results. The obtained results are then compared with hand calculations, graphs available in literature, etc. Two- or three-dimensional graphs are made to verify continuity of the calculated results. This involves calling subroutine thousands of times to make graphs and visually verifying their qualitative correctness. Of course only several selected values are checked using hand calculations. Whenever possible graphs produced by the driving programs are compared with graphs available in literature. Full references to the literature data, including section number, figure number or page number, are given. A detailed description of the results of this verification effort is presented in Chapter 2.

- *Model Testing.* Each subroutine, or group of subroutines responsible for calculation of a certain physical phenomenion, was verified from the program level, that means preparing the input deck, performing SPECTRA calculations, and comparing results with available graphs, hand calculations, etc. A detailed description of the results of this verification effort is presented in Chapter 2.

- *Separate Effects Tests*. V&V on the code was performed using specific test problems, involving multiple but limited number of models, for which analytical solutions, graphical data, or experimental results are available. This group of tests is referred to as separate effect tests. Sometimes the separate effect tests were very similar to tests performed within step (described above). For example, the tests of 1-D transient heat conduction performed within step were nearly the same as those performed within step , the difference being only the boundary conditions. While in the verification process of subroutine testing (step) the boundary conditions were supplied using the simplest possible method (tabular functions), in the separate effect tests different methods of supplying boundary conditions and the influence on results were studied. A detailed description of the results of this V&V effort is presented in Chapter 3.

- *Integral System Tests*. V&V on the code was performed using available measurement data, International Standard Problems (ISP), comparisons with other codes, etc. This group of validation tests is referred to as the integral system tests. A detailed description of the results of this validation effort is presented in Chapter 4.

A short overview of the separate effect tests and a list of the integral system tests are provided in sections 1.4.1 and 1.4.2.

1.4.1 Separate Effect Tests

About 300 separate effect tests were performed within the SPECTRA V&V activities. The results of these test runs were compared with:

- *Analytical solutions*. Analytical solutions are typically available only for steady state conditions or for simple transient conditions. The acceptance criteria for those tests are typically very strict: there should be no observable discrepancies. This means the agreement of at least 6 decimal places (typical length of numbers in SPECTRA printouts). In case of simplifications in the model representation the acceptance criteria are less strict in the areas where the simplifications affects the solution. For example, transient temperature response of a semi-infinite plate may be calculated from an analytical expression that can be found in handbooks of heat transfer. A SPECTRA simulation model for such cases was set up to represent as closely as possible the case being analyzed. As a necessary simplification, the semi-infinite plate had to be represented in the model by a plate with a finate thickness and a certain boundary condition at the end of the modeled domain. The deviations from the ideal model near the end of the modeled domain are discussed (section 3.5.4).

- *Other codes*. For a large number of separate effect tests, results from other codes were used for validation of the SPECTRA results. Typically RELAP5, MELCOR, TRAC-BF1 were used, depending on the analyzed problem. The acceptance criteria are less strict, because different codes use different solution techniques, modeling approach, etc. The acceptance criteria are also different for different types of tests. Some codes are more suitable for tests involving certain phenomena than others. For example, for tests involving thermal radiation heat transfer MELCOR is a better tool, while for cases involving two-phase flows RELAP5 or TRAC-BF1 are a better choice. Whenever possible two codes were used to validate SPECTRA results.

- *Experimental data*. Whenever possible SPECTRA simulations of the separate effect tests were compared to experimental data. The acceptance criteria depend of the kind of test; they are more strict for simple tests and less strict for more complex tests, involving multiple phenomena. Experiments, such as for example the Berkeley single tube condensation tests, MIT condensation tests, etc., were used to validate performance of the SPECTRA code. Because it would be very difficult to find experimental data to cover all phenomena modeled in the SPECTRA code, the validation with other codes (described under the previous bullet point) is an important part of SPECTRA verification.

1.4.2 Integral System Tests

Analysis of Integral System Tests (IST) is the main part of code validation. While analyses of the separate effect tests allow to build up confidence in specific models in the code, analyses of the integral system tests allow to build up confidence in the code itself. Analysis of IST is an continuous process that is realized within the NRG R&D Program, sponsored by the Dutch government.

The following list gives a brief overview of the experimental integral system tests, which were used for the validation of the SPECTRA code.

- **PWR plants**

  Hydrogen distribution in PWR containment, HDR E11.2 test - comparisons with experiment.

  Hydrogen distribution in PWR containment, NUPEC M-4-3, M-7-1 tests (International Standard Problem No. 35, ISP-35), comparison with experimental measurement data and other code (MAAP-4).

- **BWR plants**

  Building Condenser (BC) performance and long-term containment behavior of the SWR-1000 (Siedewasserreaktor, evolutionary Boiling Water Reactor, designed by Siemens) - PANDA BC Tests. Comparison with experimental measurement data and the computer code CFX

  Passive Containment Cooling System (PCCS) performance of the SBWR (Simplified Boiling Water Reactor designed by General Electric), PANDA PCC Tests. Comparison with the computer codes MELCOR, RELAP, TRAC-BF1, TRACG.

  Passive safety systems performance and long-term containment behavior of the scaled down ESBWR - PANDA Tests (International Standard Problem No. 42, ISP-42), comparison experimental measurement data and computer codes CATHARE, CONTAIN, COCOSYS, GOTHIC, RALOC, RBIC, RELAP5.

- **HTR/PBMR plants**

  ACACIA, comparison with the computer codes OCTOPUS/PANTHERMIX.

  NACOK, comparison with expriment and computer code TINTE and THERMIX/REACT

  HTR-PM, comparison with other code TINTE.

- **Liquid Metal Reactors**

  EBR-II, comparison with experiment and other codes SASSYS-1/SAS4A, SAC-CFR, THACS, CATHARE, SIMMER-III, FRENTIC, NETFLOW++, RELAP5-3D, MARS-LMR, SOCRAT-BN, TRACE, ANSYS-CFX.

  ASTRID, comparison with other codes: TRACE, CATHARE, SIM-SFR, SAS-SFR, ATHLET, SPECTRA, SAS4A.

ESFR, comparison with other codes: CATHARE, RELAP5, TRACE, SIM-SFR, SAS-SFR, MAT4-DYN.

LEADER, comparison with other codes: SAS-LFR, RELAP, TRACE, CFX, SIMMER.

- **Molten Salt Reactors**

  Molten Salt Reactor Experiment (MSRE) comparison with measured data.

- **Research reactors**

  HFR Petten Reactor comparison with RELAP5 and measured data.

- **Chemical Reactors**

  Analyses of emergency shutdown scenario in a Hypothetical Multi-Tubular Reactor, comparison with RELAP5.

2 Verification of Individual Packages (Subroutine Testing)

Detailed description of the subroutine testing is provided in the Volume 4 of the code manuals: "Subroutine Description". Here, results of some tests, selected as potentially more interesting for the code user, are shown.

2.1 Verification of the Fluid Property Package

2.1.1 Gas Properties

The properties of pure substances, tabulated in the gas property data tables, are discussed in section 2.1.1.1. Properties of gas mixtures are discussed in sections 2.1.1.3, 2.1.1.4, and 2.1.1.5. These sections present the properties, which are not calculated using a simple mass averaging rule - viscosity, thermal conductivity, and diffusion coefficient. Verification of the agreement among three different subroutines, that are used to obtain gas properties, is discussed in section 2.1.1.6.

2.1.1.1 Gas Property Data Tables

Verification of the data from the gas property data tables was performed by plotting the data points for selected pressures and comparison of the plotted values with tabulated data, shown in: [10], [11], [12], [13].

Eight pressure points were selected to plot the data from the gas property data tables. These are: 1, 2, 5, 10, 25, 50, 100 and 150 bar. The values from the data tables are plotted using the temperature scale from 0°C to 2800°C (273 K to 3073 K). For each gas four graphs are shown, each graph gives of the following properties:

- Compressibility, defined as: $Z = pv/RT$. The value of compressibility is a measure of deviation of the gas density from the density given by the ideal gas equation of state.
- The constant volume specific heat, $c_v(T)$. In case of steam the internal energy is shown instead of the specific heat ratio. This is because steam properties are generated without using specific heat. The steam internal energy data table is obtained directly, while in case of all other gases the internal energy data tables are obtained by integrating the specific heat.
- Dynamic viscosity.
- Thermal conductivity.

H_2

Hydrogen properties are shown in Figure 2-1. It may be observed that in the range of parameters considered, hydrogen behaves very much like a perfect gas. Deviation from the perfect gas equation of state is below 11% in the considered range of parameters. Almost no influence of pressure on the thermal properties is observed.

He

Helium properties are shown in Figure 2-2. Helium, like hydrogen, behaves like a perfect gas. Deviation from the perfect gas equation of state is below 8% in the considered range of parameters. Almost no influence of pressure on thermal properties is observed.

H_2O

Steam properties are shown in Figure 2-3. The compressibility of steam decreases close to the saturation line. In the subcooled steam range the density was extrapolated in such way that the compressibility smoothly levels with increasing subcooling. A similar extrapolation in the subcooled range was applied for the thermal conductivity. In case of internal energy and viscosity a simple linear extrapolation of properties in subcooled range is used. For practical application the extrapolated values are not important, since subcooled steam will quickly condense and only very small subcooling may be encountered. Nevertheless the data points in the data tables had to be filled. This was done to obtain reasonable and safe extrapolated properties, so that, should a significant subcooling ever been encountered, the property calculating subroutines should not fail in calculating the state and the obtained values should be in reasonable agreement with the values expected based on observations.

N_2

Nitrogen properties are shown in figures Figure 2-4. Deviation from the perfect gas equation of state is, for the considered range of parameters, up to about 7%. Some small influence of pressure on viscosity and thermal conductivity is observed, specifically for low temperatures.

O_2

Oxygen properties are shown in figures Figure 2-5. Deviation from the perfect gas equation of state is the largest for temperatures close to 0°C. At this temperature the maximum deviation is slightly almost 10%. The influence of pressure on viscosity and thermal conductivity is similar to that observed for nitrogen.

CO_2

Carbon dioxide properties are shown in Figure 2-6. Deviation from the perfect gas equation of state is quite large for low temperatures. Above ~500 K (~230°C) the deviation does not exceed 10%, but below that temperature it becomes larger. The influence of pressure on viscosity and thermal conductivity is significant especially below ~500 K.

The calculated values were compared to the tabulated data in literature. In case of H_2, N_2, O_2 and CO_2 the tables from [10] and [11] were used for verification. In case of He the tables from [11] and [12] were used for verification. In case of H_2O the tables from [13] were used for verification. It was concluded that the data shown in the figures agrees well with the tabulated data.

The graphs were generated using a FORTRAN program which calls fluid property subroutines from SPECTRA =FL= package and stores results in columns convenient for plotting. The program is provided in **\Z-TESTS\FL\GAS-T.FOR**.

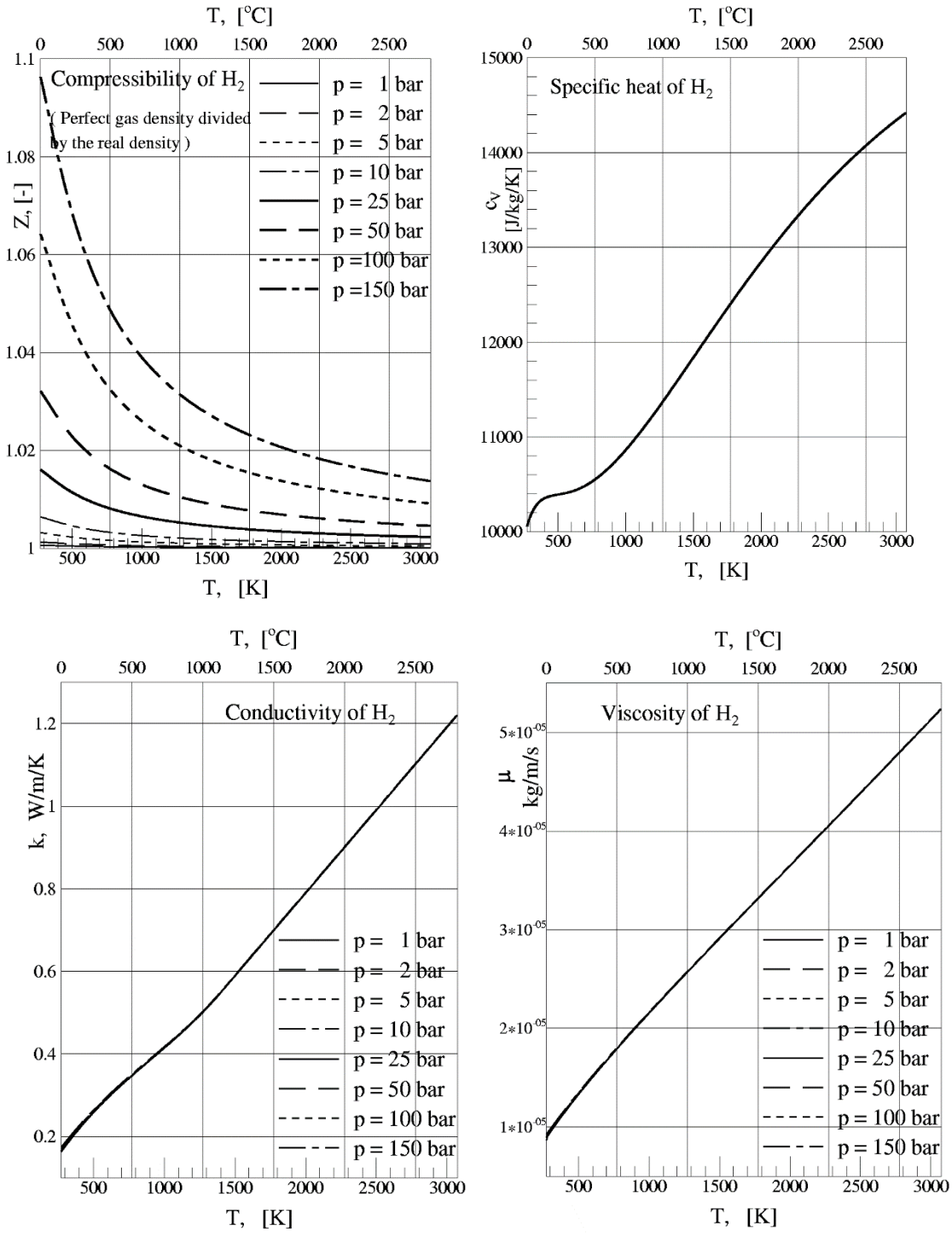

Figure 2-1 Properties of H_2.

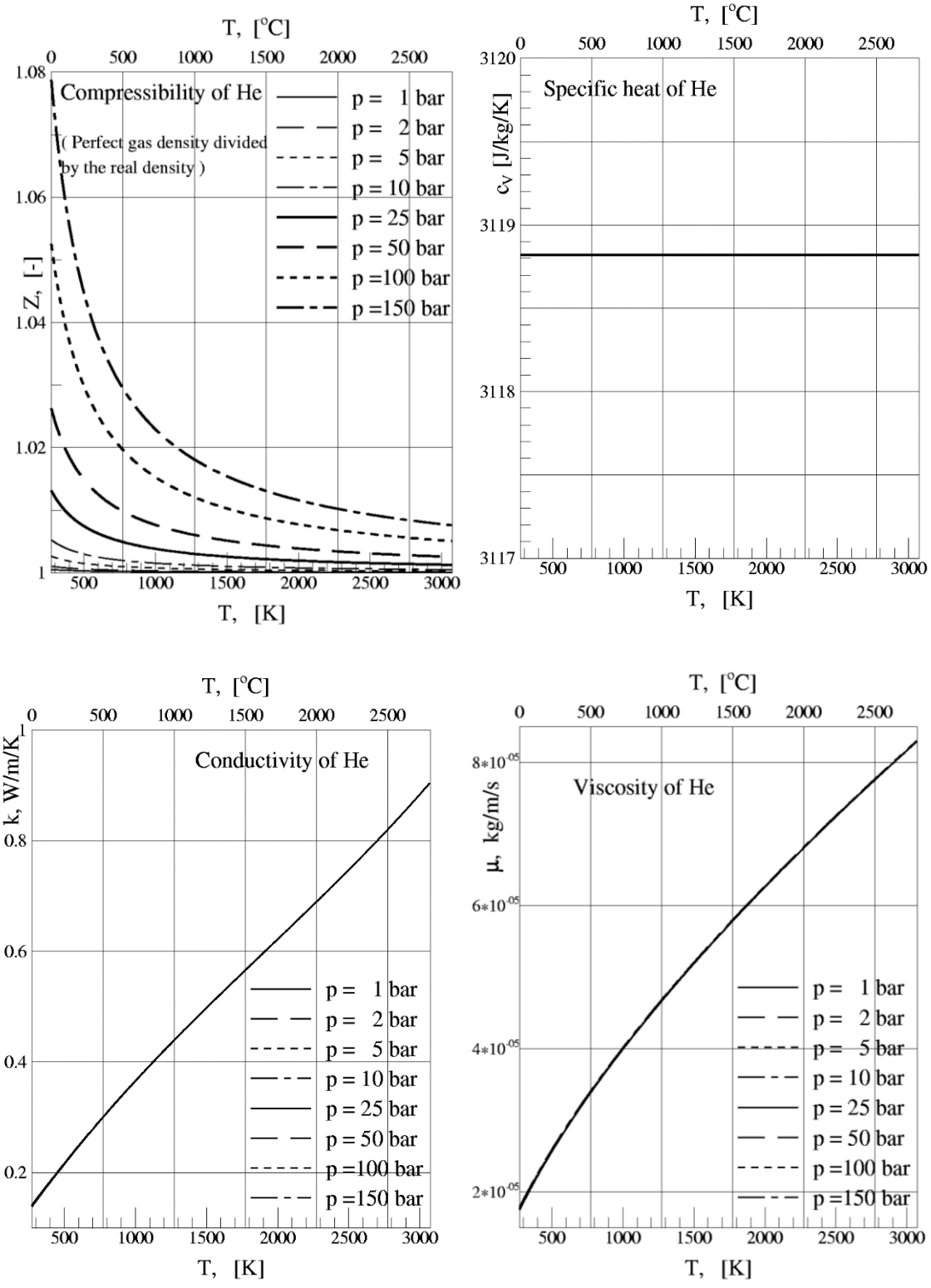

Figure 2-2 Properties of He.

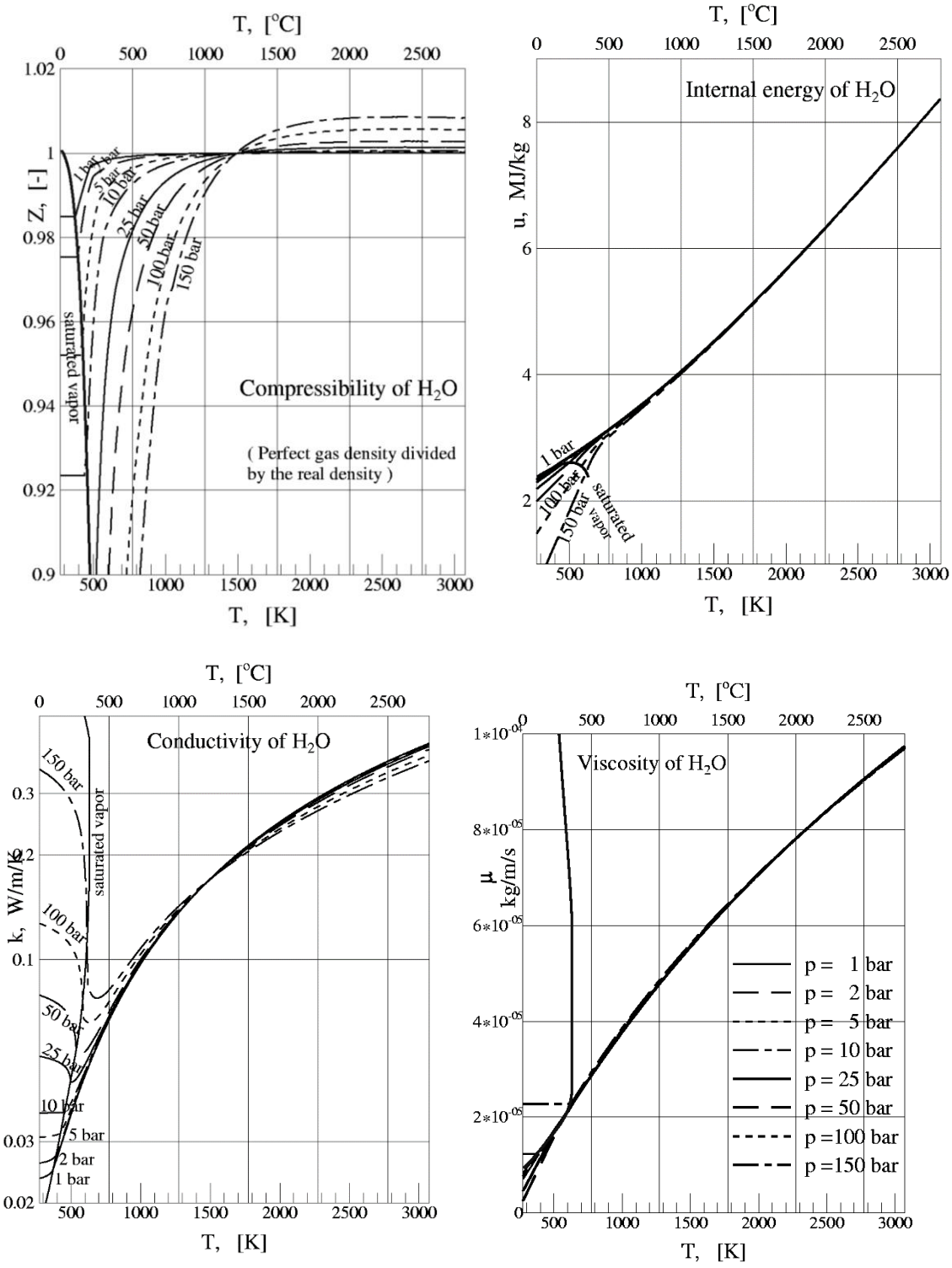

Figure 2-3 Properties of H_2O.

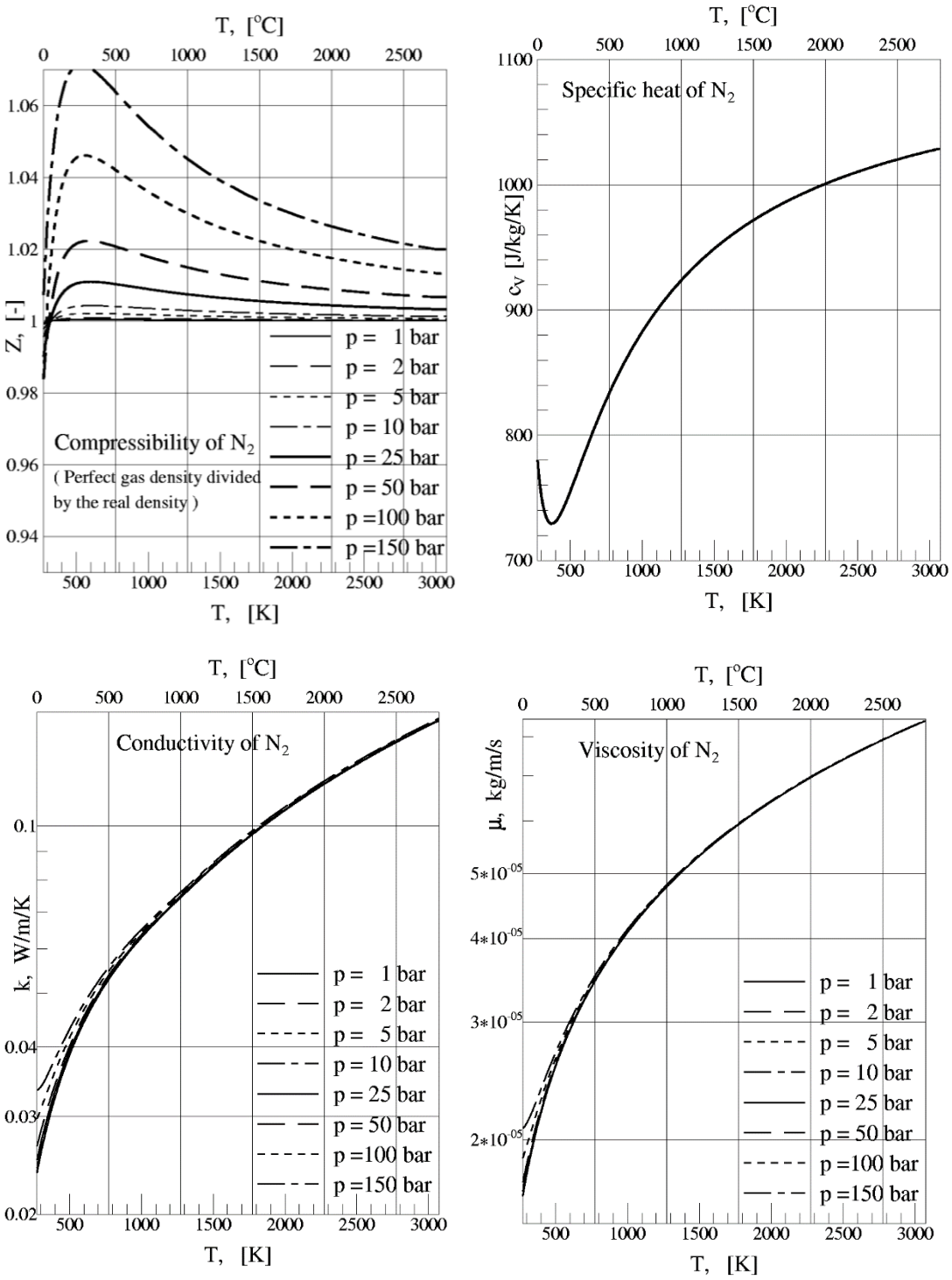

Figure 2-4 Properties of N_2.

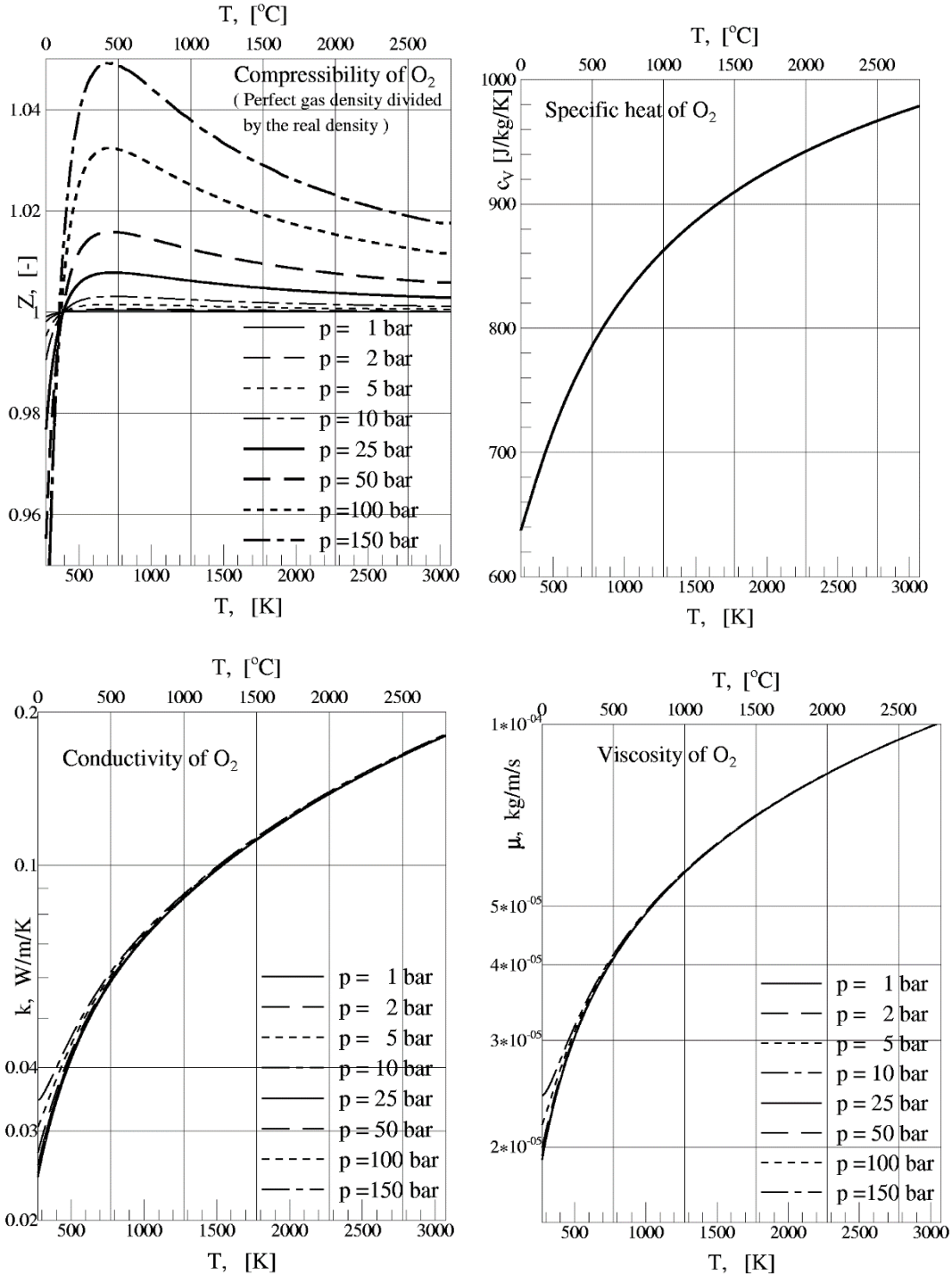

Figure 2-5 Properties of O_2.

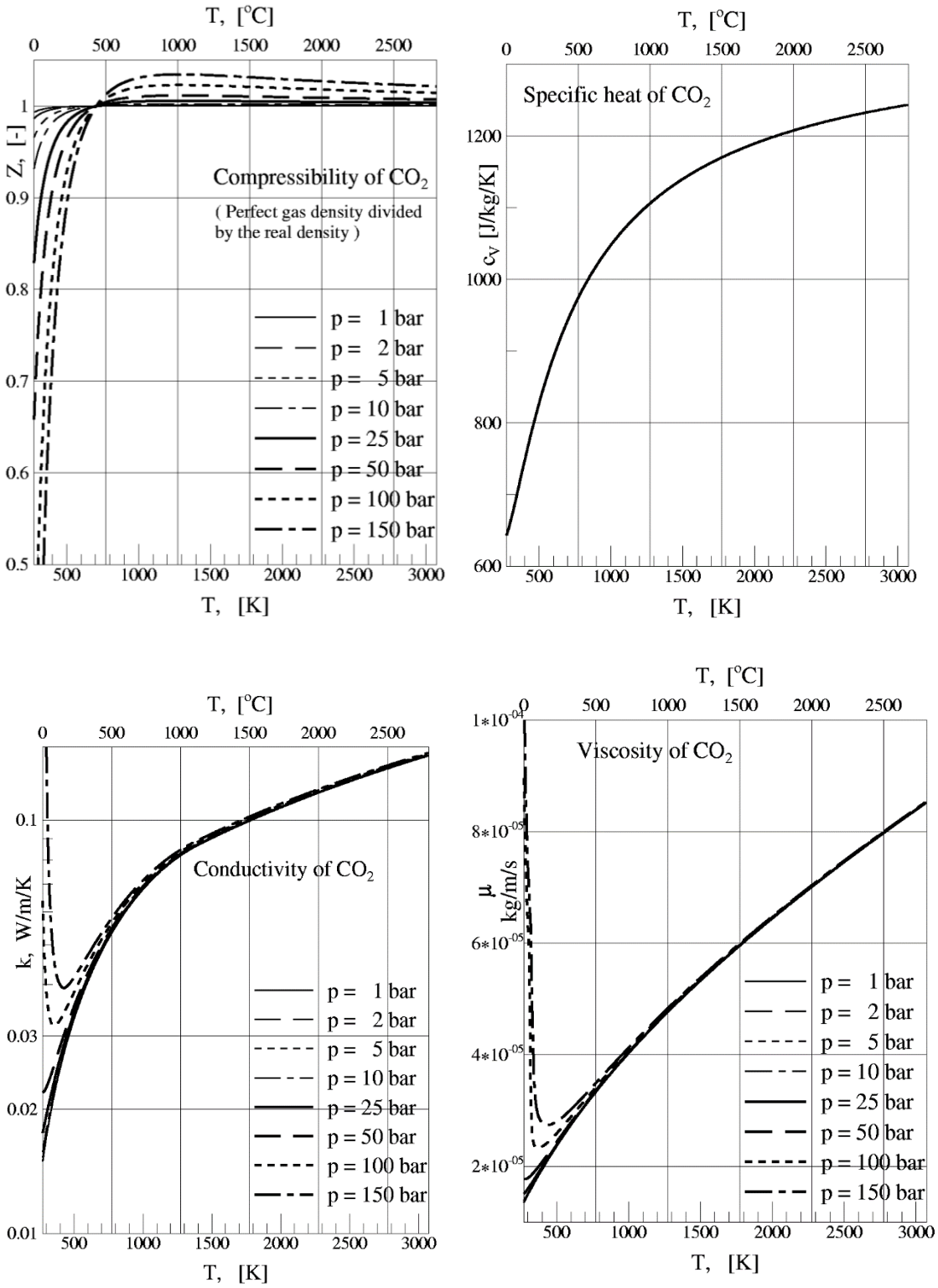

Figure 2-6 Properties of CO_2.

2.1.1.2 Thermal Conductivity of Helium

Thermal conductivity of gases is calculated using the method recommended by Reid et al. [25], with conductivity is obtained from the following formula (Volume 1):

$$k_{p=0}(T) = A + BT + CT^2 + DT^3$$

It was found out that the method describe above does not provide a sufficient accuracy in case of Helium. Therefore, for this gas, the formula from KTA rules [137] is used. The formula is:

$$k(p,T) = 2.682 \cdot 10^{-3} \cdot (1 + 1.123 \cdot 10^{-8} \cdot p) \cdot T^{0.71 \cdot (1 - 2 \times 10^{-9} \cdot p)}$$

The improvement of accuracy of this formula, compared to the formerly used formula is discussed below.

Table 2-1 shows comparison of He conductivities obtained from the new (KTA) and the old (Reid et al.) methods. The difference is up to 5.5%.

Table 2-2 shows comparison of the new and the old method with data. It is seen that the new method gives on the average, slightly better agreement with data. The average error is:

- new: 1.5 %
- old: 4.4 %

Finally, it is noted that for the calculation of He thermal conductivity the same reference is used by the MELCOR code. However, in MELCOR a pressure independent version of this equation is used, obtained for $p = 0.1 \times 10^6$ Pa.

$$k(p,T) = 2.682 \cdot 10^{-3} \cdot (1 + 1.123 \cdot 10^{-3}) \cdot T^{0.71 \cdot (1 - 2 \times 10^{-4})}$$

Therefore, the values in SPECTRA and MELCOR are not identical, although they are very similar. The differences are shown in Table 2-3. It is seen that in the considered range of parameters, the relative difference is up to 2.5%.

Table 2-1 He conductivities obtained from the new (KTA) and the old (Reid et al.) methods

P(bar)	1			20			40			60			80			100		
T (K)	kNEW	kOLD	d(%)	kNEW	kOLD	d(%)	kNEW	kOLD	d(%)	kNEW	kOLD	d(%)	kNEW	kOLD	d(%)	kNEW	kOLD	d(%)
300.	0.154	0.148	4.2	0.155	0.148	4.5	0.156	0.148	4.8	0.156	0.149	5.1	0.157	0.149	5.3	0.158	0.150	5.5
350.	0.172	0.165	4.1	0.173	0.165	4.4	0.174	0.166	4.8	0.174	0.166	5.0	0.175	0.166	5.3	0.176	0.167	5.5
400.	0.189	0.182	3.8	0.190	0.182	4.1	0.191	0.183	4.4	0.191	0.183	4.7	0.192	0.183	5.0	0.193	0.183	5.2
450.	0.205	0.199	3.3	0.206	0.199	3.7	0.207	0.199	4.0	0.208	0.199	4.3	0.209	0.200	4.5	0.209	0.200	4.7
500.	0.221	0.215	2.9	0.222	0.215	3.2	0.223	0.215	3.5	0.224	0.216	3.8	0.225	0.216	4.0	0.225	0.216	4.2
550.	0.237	0.231	2.4	0.238	0.231	2.7	0.239	0.232	3.1	0.239	0.232	3.3	0.240	0.232	3.5	0.241	0.232	3.7
600.	0.252	0.247	2.0	0.253	0.247	2.3	0.254	0.247	2.6	0.254	0.248	2.8	0.255	0.248	3.0	0.256	0.248	3.1
650.	0.267	0.263	1.5	0.267	0.263	1.8	0.268	0.263	2.1	0.269	0.263	2.3	0.270	0.263	2.5	0.270	0.263	2.6
700.	0.281	0.278	1.1	0.282	0.278	1.4	0.283	0.278	1.6	0.284	0.278	1.9	0.284	0.279	2.0	0.285	0.279	2.1
750.	0.295	0.293	0.7	0.296	0.293	1.0	0.297	0.293	1.2	0.298	0.293	1.4	0.298	0.294	1.6	0.299	0.294	1.7
800.	0.309	0.308	0.3	0.310	0.308	0.6	0.311	0.308	0.8	0.311	0.308	1.0	0.312	0.308	1.1	0.312	0.309	1.2
850.	0.322	0.322	-0.0	0.323	0.323	0.2	0.324	0.323	0.4	0.325	0.323	0.6	0.325	0.323	0.7	0.326	0.323	0.8
900.	0.336	0.337	-0.3	0.337	0.337	-0.1	0.338	0.337	0.1	0.338	0.337	0.3	0.339	0.337	0.4	0.339	0.338	0.4
950.	0.349	0.351	-0.6	0.350	0.351	-0.4	0.351	0.351	-0.2	0.351	0.352	-0.1	0.352	0.352	0.0	0.352	0.352	0.1
1000.	0.362	0.365	-0.9	0.363	0.365	-0.7	0.363	0.365	-0.5	0.364	0.366	-0.4	0.365	0.366	-0.3	0.365	0.366	-0.3
1050.	0.375	0.379	-1.2	0.375	0.379	-1.0	0.376	0.379	-0.8	0.377	0.379	-0.7	0.377	0.380	-0.6	0.377	0.380	-0.6
1100.	0.387	0.393	-1.4	0.388	0.393	-1.2	0.389	0.393	-1.1	0.389	0.393	-1.0	0.390	0.393	-0.9	0.390	0.393	-0.9
1150.	0.400	0.406	-1.7	0.400	0.406	-1.5	0.401	0.407	-1.3	0.402	0.407	-1.2	0.402	0.407	-1.2	0.402	0.407	-1.2
1200.	0.412	0.420	-1.9	0.413	0.420	-1.7	0.413	0.420	-1.6	0.414	0.420	-1.5	0.414	0.420	-1.4	0.414	0.420	-1.4
1250.	0.424	0.433	-2.1	0.425	0.433	-1.9	0.425	0.433	-1.8	0.426	0.433	-1.7	0.426	0.433	-1.7	0.426	0.433	-1.7
1300.	0.436	0.446	-2.3	0.437	0.446	-2.1	0.437	0.446	-2.0	0.438	0.446	-2.0	0.438	0.446	-1.9	0.438	0.447	-1.9
1350.	0.448	0.459	-2.5	0.448	0.459	-2.3	0.449	0.459	-2.2	0.449	0.459	-2.2	0.450	0.459	-2.2	0.450	0.460	-2.2
1400.	0.459	0.472	-2.7	0.460	0.472	-2.5	0.461	0.472	-2.4	0.461	0.472	-2.4	0.461	0.472	-2.4	0.461	0.472	-2.4
1450.	0.471	0.485	-2.8	0.472	0.485	-2.7	0.472	0.485	-2.6	0.473	0.485	-2.6	0.473	0.485	-2.6	0.472	0.485	-2.6
1500.	0.483	0.498	-3.0	0.483	0.498	-2.9	0.484	0.498	-2.8	0.484	0.498	-2.8	0.484	0.498	-2.8	0.484	0.498	-2.8
1550.	0.494	0.510	-3.2	0.495	0.510	-3.1	0.495	0.510	-3.0	0.495	0.510	-3.0	0.495	0.510	-3.0	0.495	0.511	-3.1
1600.	0.505	0.523	-3.4	0.506	0.523	-3.3	0.506	0.523	-3.2	0.506	0.523	-3.2	0.506	0.523	-3.2	0.506	0.523	-3.3
1650.	0.516	0.535	-3.5	0.517	0.535	-3.4	0.517	0.535	-3.4	0.517	0.535	-3.4	0.517	0.535	-3.4	0.517	0.536	-3.5
1700.	0.527	0.548	-3.7	0.528	0.548	-3.6	0.528	0.548	-3.6	0.528	0.548	-3.6	0.528	0.548	-3.6	0.528	0.548	-3.7
1750.	0.538	0.560	-3.9	0.539	0.560	-3.8	0.539	0.560	-3.8	0.539	0.560	-3.8	0.539	0.560	-3.8	0.539	0.560	-3.9
1800.	0.549	0.572	-4.0	0.550	0.572	-4.0	0.550	0.572	-3.9	0.550	0.573	-4.0	0.550	0.573	-4.0	0.549	0.573	-4.1

Table 2-2 Comparison of the new and the old method with data

Comparison of the new and old method with experiment

P(bar)	1			100		
T (K)	kNEW	kOLD	kSRC	kNEW	kOLD	kSRC
300.	0.154	0.148	0.147 - 0.157	0.154	0.148	0.158 - 0.162
1500.	0.483	0.498	0.479 - 0.479	0.483	0.498	0.480 - 0.483

Error estimations

P(bar)	1			100		
T (K)	dNEW(%)	dOLD(%)	Exp-ave.	dNEW(%)	dOLD(%)	Exp-ave.
300.	1.28	-2.79	0.152	-3.52	-7.54	0.160
1500.	0.74	3.87	0.479	0.28	3.34	0.481

Average error: dNEW-AVE = 1.5 %
dOLD-AVE = 4.4 %

Table 2-3 He conductivities in SPECTRA and MELCOR

P(bar)	1			20			40			60			80			100		
T (K)	kSPE	kMEL	d(%)	kSPE	kMEL	d(%)	kSPE	kMEL	d(%)	kSPE	kMEL	d(%)	kSPE	kMEL	d(%)	kSPE	kMEL	d(%)
300.	0.154	0.154	0.0	0.155	0.154	0.6	0.156	0.154	1.1	0.156	0.154	1.6	0.157	0.154	2.1	0.158	0.154	2.5
350.	0.172	0.172	0.0	0.173	0.172	0.5	0.174	0.172	1.0	0.174	0.172	1.5	0.175	0.172	1.9	0.176	0.172	2.3
400.	0.189	0.189	0.0	0.190	0.189	0.5	0.191	0.189	1.0	0.191	0.189	1.4	0.192	0.189	1.8	0.193	0.189	2.1
450.	0.205	0.205	0.0	0.206	0.205	0.5	0.207	0.205	0.9	0.208	0.205	1.3	0.209	0.205	1.7	0.209	0.205	2.0
500.	0.221	0.221	0.0	0.222	0.221	0.4	0.223	0.221	0.8	0.224	0.221	1.2	0.225	0.221	1.5	0.225	0.221	1.8
550.	0.237	0.237	0.0	0.238	0.237	0.4	0.239	0.237	0.8	0.239	0.237	1.1	0.240	0.237	1.4	0.241	0.237	1.7
600.	0.252	0.252	0.0	0.253	0.252	0.4	0.254	0.252	0.7	0.254	0.252	1.1	0.255	0.252	1.3	0.256	0.252	1.5
650.	0.267	0.267	0.0	0.267	0.267	0.4	0.268	0.267	0.7	0.269	0.267	1.0	0.270	0.267	1.2	0.270	0.267	1.4
700.	0.281	0.281	0.0	0.282	0.281	0.3	0.283	0.281	0.7	0.284	0.281	0.9	0.284	0.281	1.1	0.285	0.281	1.3
750.	0.295	0.295	0.0	0.296	0.295	0.3	0.297	0.295	0.6	0.298	0.295	0.9	0.298	0.295	1.1	0.299	0.295	1.2
800.	0.309	0.309	0.0	0.310	0.309	0.3	0.311	0.309	0.6	0.311	0.309	0.8	0.312	0.309	1.0	0.312	0.309	1.1
850.	0.322	0.322	0.0	0.323	0.322	0.3	0.324	0.322	0.5	0.325	0.322	0.8	0.325	0.322	0.9	0.326	0.322	1.1
900.	0.336	0.336	0.0	0.337	0.336	0.3	0.338	0.336	0.5	0.338	0.336	0.7	0.339	0.336	0.9	0.339	0.336	1.0
950.	0.349	0.349	0.0	0.350	0.349	0.3	0.351	0.349	0.5	0.351	0.349	0.7	0.352	0.349	0.8	0.352	0.349	0.9
1000.	0.362	0.362	0.0	0.363	0.362	0.2	0.363	0.362	0.5	0.364	0.362	0.6	0.365	0.362	0.7	0.365	0.362	0.8
1050.	0.375	0.375	0.0	0.375	0.375	0.2	0.376	0.375	0.4	0.377	0.375	0.6	0.377	0.375	0.7	0.377	0.375	0.8
1100.	0.387	0.387	0.0	0.388	0.387	0.2	0.389	0.387	0.4	0.389	0.387	0.5	0.390	0.387	0.6	0.390	0.387	0.7
1150.	0.400	0.400	0.0	0.400	0.400	0.2	0.401	0.400	0.4	0.402	0.400	0.5	0.402	0.400	0.6	0.402	0.400	0.6
1200.	0.412	0.412	0.0	0.413	0.412	0.2	0.413	0.412	0.4	0.414	0.412	0.5	0.414	0.412	0.5	0.414	0.412	0.6
1250.	0.424	0.424	0.0	0.425	0.424	0.2	0.425	0.424	0.3	0.426	0.424	0.4	0.426	0.424	0.5	0.426	0.424	0.5
1300.	0.436	0.436	0.0	0.437	0.436	0.2	0.437	0.436	0.3	0.438	0.436	0.4	0.438	0.436	0.4	0.438	0.436	0.5
1350.	0.448	0.448	0.0	0.448	0.448	0.2	0.449	0.448	0.3	0.449	0.448	0.4	0.450	0.448	0.4	0.450	0.448	0.4
1400.	0.459	0.459	0.0	0.460	0.459	0.2	0.461	0.459	0.3	0.461	0.459	0.3	0.461	0.459	0.4	0.461	0.459	0.3
1450.	0.471	0.471	0.0	0.472	0.471	0.1	0.472	0.471	0.3	0.473	0.471	0.3	0.473	0.471	0.3	0.472	0.471	0.3
1500.	0.483	0.483	0.0	0.483	0.483	0.1	0.484	0.483	0.2	0.484	0.483	0.3	0.484	0.483	0.3	0.484	0.483	0.3
1550.	0.494	0.494	0.0	0.495	0.494	0.1	0.495	0.494	0.2	0.495	0.494	0.3	0.495	0.494	0.3	0.495	0.494	0.2
1600.	0.505	0.505	0.0	0.506	0.505	0.1	0.506	0.505	0.2	0.506	0.505	0.2	0.506	0.505	0.2	0.506	0.505	0.2
1650.	0.516	0.516	0.0	0.517	0.516	0.1	0.517	0.516	0.2	0.517	0.516	0.2	0.517	0.516	0.2	0.517	0.516	0.1
1700.	0.527	0.527	0.0	0.528	0.527	0.1	0.528	0.527	0.2	0.528	0.527	0.2	0.528	0.527	0.1	0.528	0.527	0.1
1750.	0.538	0.538	0.0	0.539	0.538	0.1	0.539	0.538	0.1	0.539	0.538	0.2	0.539	0.538	0.1	0.539	0.538	0.0
1800.	0.549	0.549	0.0	0.550	0.549	0.1	0.550	0.549	0.1	0.550	0.549	0.1	0.550	0.549	0.1	0.549	0.549	-0.0

2.1.1.3 Viscosity of a Gas Mixture

The viscosity of a gas mixture is calculated by the subroutine GASMTP, using the method of Wilke [14]. Verification of the subroutine is performed by comparison of the calculated values with experimental data for the H_2-CO_2 mixture.

For the H_2-CO_2 mixture, at atmospheric pressure and temperature of 23°C, experimental data is shown in [15] (pages 2-118, 2-119) for pure gases and the mixture containing 41.3 % (mole fraction) of H_2. The values are shown in Table 2-4. The calculated values were generated using a FORTRAN program provided in **\Z-TESTS\FL\GASMIX-T.FOR**. In order to compile the program it must be first moved to the directory \Z-EXE\.

Table 2-4 Comparison of calculated viscosity with experimental data.

H_2 fraction	Viscosity, kg/m/s		Relative error
	Experiment	Calculated	
0.0%	1.493×10^{-4}	1.464×10^{-4}	–1.9%
41.3%	1.506×10^{-4}	1.497×10^{-4}	–0.6%
100.0%	8.91×10^{-5}	9.39×10^{-5}	+5.4%

The viscosity of H_2-CO_2 mixture was calculated for the whole range of possible compositions, from 0 % to 100 % of H_2, using the subroutine GASEQT. GASEQT calculates viscosity by a call to the subroutine GASMTP. Within GASMTP the viscosities of pure substances are obtained from the gas property data tables, GASDAT. Then the method of Wilke is used to obtain the value for mixture.

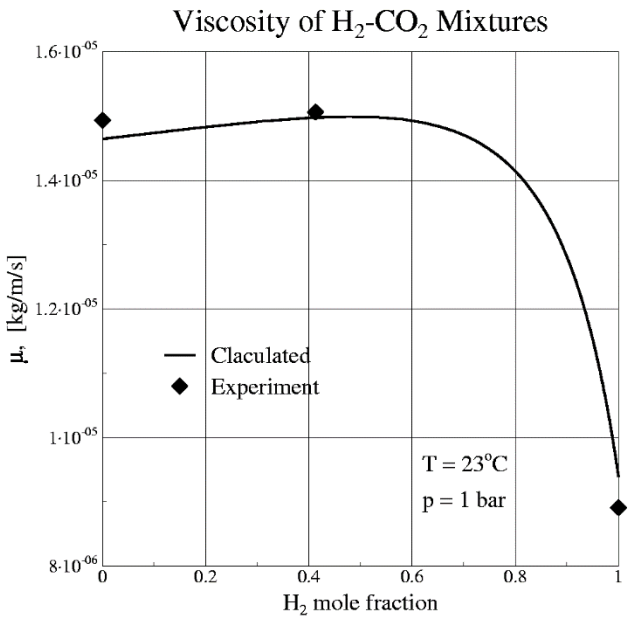

Figure 2-7 shows calculated and experimental viscosity of H_2-CO_2 mixture. The agreement is good. The pure substances values were generated using the method of Chung et al. for low pressures, with the correction of Richtenberg for high pressures. These methods are known to give an error of a few percent. Thus the discrepancies observed for pure substances are acceptable. For the mixture a correct trend is observed - the viscosity first increases with increasing hydrogen content, passes a maximum at about 40-50 % hydrogen fraction, and then decreases. The calculated values were generated using a FORTRAN program provided in **\Z-TESTS\FL\GASMIX-T.FOR**. In order to compile the program it must be first moved to the directory \Z-EXE\.

Figure 2-7 Viscosity of H_2-CO_2 mixtures.

2.1.1.4 Thermal Conductivity of a Gas Mixture

The thermal conductivity of a gas mixture is calculated by the subroutine GASMTP, using the method of Wassiljewa [18], modified by Mason and Saxena [19]. Verification of the subroutine is performed by comparison of the calculated values with experimental data for the H_2-CO_2 mixture.

For the H_2-CO_2 mixture, at atmospheric pressure and temperature of 0°C, experimental data is shown in [15] (page 2-126) for pure gases and the mixture containing 50.0% (mole fraction) of H_2. The values are shown in Table 2-5. The calculated values were generated using a FORTRAN program provided in **\Z-TESTS\FL\GASMIX-T.FOR**. In order to compile the program it must be first moved to the directory \Z-EXE\.

Table 2-5 Comparison of calculated viscosity with experimental data.

H_2 fraction	Thermal conductivity, cal/cm/s/K		Relative error
	Experiment	Calculated	
0.0%	3.60×10^{-5}	3.57×10^{-5}	–0.8%
50.0%	1.35×10^{-4}	1.39×10^{-4}	+2.9%
100.0%	4.04×10^{-4}	3.89×10^{-4}	–3.7%

The conductivity of H_2-CO_2 mixture was calculated for the same compositions, using the subroutine GASEQT. GASEQT calculates conductivity by a call to the subroutine GASMTP. Within GASMTP the viscosities of pure substances are obtained from the gas property data tables, GASDAT. Then the method of Wassiljewa, Mason and Saxena, is used to obtain the value for mixture.

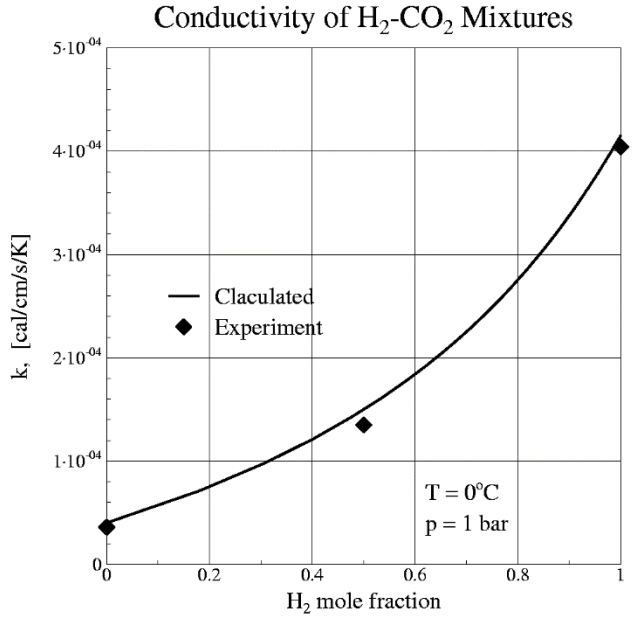

Figure 2-8 shows the calculated and experimental conductivity of the H_2-CO_2 mixture, using the same units as those used in [15]. To obtain these units the calculated values, in SI units, were divided by the conversion factor, equal to: 418.6. The calculated values were generated using a FORTRAN program provided in **\Z-TESTS\FL\GASMIX-T.FOR**. In order to compile the program it must be first moved to the directory \Z-EXE\.

Figure 2-8 Thermal conductivity of H_2-CO_2 mixtures.

2.1.1.5 Diffusion Coefficient

The diffusion coefficient for a gas mixture is calculated by the function DIFCM. DIFCM uses DIFCB to calculate binary diffusion coefficients. Verification of the models used by DIFCM and DIFCB is performed by comparing results of the function DIFCM with experimental data and with the correlations applied in MELCOR 1.8.3 [20].

Comparison with Experimental Data

Experimental diffusion coefficients for several different gases in air at 1 bar, 0°C, are given in [24] (page F-62). The conditions for those experiments were: pressure of 1 bar, temperature of 8°C for steam diffusion in air and 0°C for other gases. The experimental value for N_2-CO_2 at 1 bar, 590 K, is shown in [25] (section 11-3, page 583). All these values are reproduced in Table 2-6.

The function DIFCM was used to calculate diffusion coefficients for the same conditions. In case of diffusion in air the following air composition (mass fractions) was assumed:

- N_2: 0.77,
- O_2: 0.22.

The concentration of the diffusing gas was assumed to be 1% (the actual value of this concentration does not affect the results).

The results of the calculations are shown in Table 2-6. The agreement with experimental values is good. The largest discrepancy (about 7.6%) is observed in case of H_2-air mixture. The calculated values were generated using a FORTRAN program provided in **\Z-TESTS\FL\DC-T.FOR**. In order to compile the program it must be first moved to the directory \Z-EXE\.

Table 2-6 Comparison of calculated diffusion coefficients with experimental data.

Gas mixture	Diffusion coefficient, (m^2/s)		Relative error
	Experiment	Calculated	
CO_2-air (0ºC)	0.139×10^{-4}	0.141×10^{-4}	+7.4%
H_2-air (0ºC)	0.634×10^{-4}	0.682×10^{-4}	+7.6%
O_2-air (0ºC)	0.178×10^{-4}	0.179×10^{-4}	+0.6%
H_2O-air (8ºC)	0.239×10^{-4}	0.236×10^{-4}	–1.3%
N_2-CO_2-air (590 K)	0.520×10^{-4}	0.542×10^{-4}	+4.2%

Comparison with Correlations in MELCOR

The binary diffusion coefficients are computed in MELCOR using two different methods depending on which package requires the information. The CVH (Control Volume Hydrodynamics) package uses the equations shown below. The RN (Radionuclide) package uses the Chapman-Eskong method (see [20], Material Property package, section 7.2). The method applied for the CVH Package is used here for comparison.

The MELCOR CVH Package uses two correlations, which give binary diffusion coefficients for the steam-air and steam-hydrogen mixtures. The correlations are ([20], Material Package, section 7.1).

$$D = 4.7931\times10^{-5}\,\frac{T^{1.90}}{p} \qquad for\ steam-air$$

$$D = 6.6064\times10^{-4}\,\frac{T^{1.68}}{p} \qquad for\ steam-H_2$$

where: D - diffusion coefficient, (m^2/s),
T - temperature, (K),
p - pressure, (Pa).

Those correlations were used to produce the data for pressures 0.1×10^6 Pa and 1.0×10^6 Pa and temperatures up to 1000 K.

The function DIFCM was used to calculate diffusion coefficients for the same pressure and temperature values. For comparison with the MELCOR steam-air correlation the following mass fractions of gases were assumed:

- H_2O: 0.01,
- N_2: 0.77,
- O_2: 0.22.

For comparison with the steam-hydrogen case, the mass fractions 0.5, 0.5 were used for steam and hydrogen. (For the two-component mixture the actual values of concentrations may be arbitrary because they are never used in calculations).

Comparison of the results obtained by the function DIFCM with the results obtained with the correlation applied in MELCOR 1.8.3 is shown in Figure 2-9 and Figure 2-10. The values are in very good agreement for temperatures below 1000 K. In case of the steam-air mixture the correlations applied in MELCOR give a little higher values of diffusion coefficients than DIFCM in the high temperature region (Figure 2-9). In case of the steam-hydrogen mixture the reverse is true (Figure 2-10).

The comparison shows that results of the equations used by MELCOR and the subroutine DIFCM are in very good agreement. The method used to calculate the binary diffusion coefficient (Fuller's method is preferred over the correlations used by MELCOR because of its generality - it allows computing diffusion coefficients for many different gases (see [25], table 11.1).

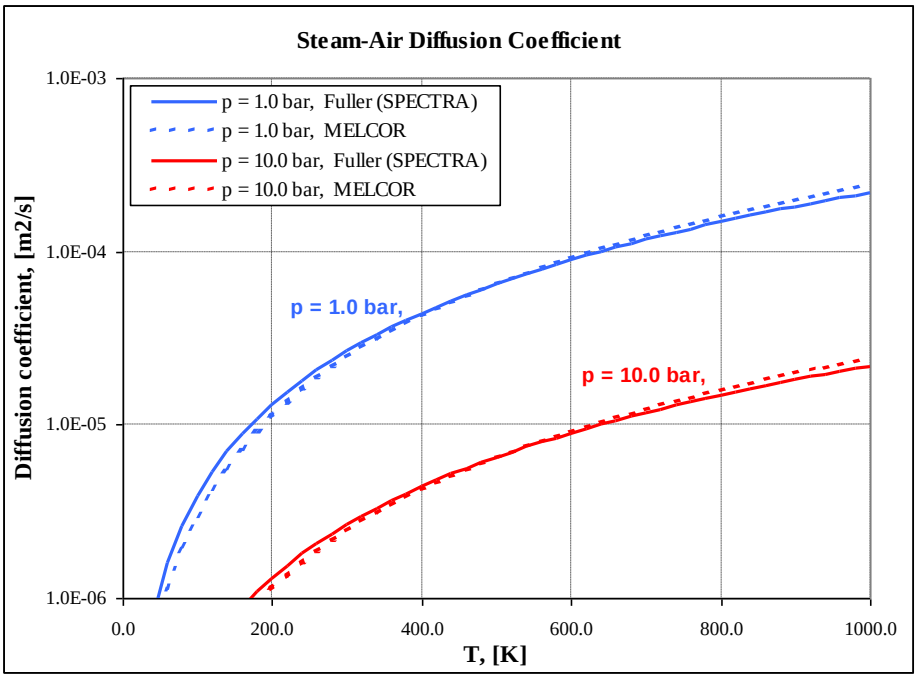

Figure 2-9 Comparison of steam-air diffusion coefficients.

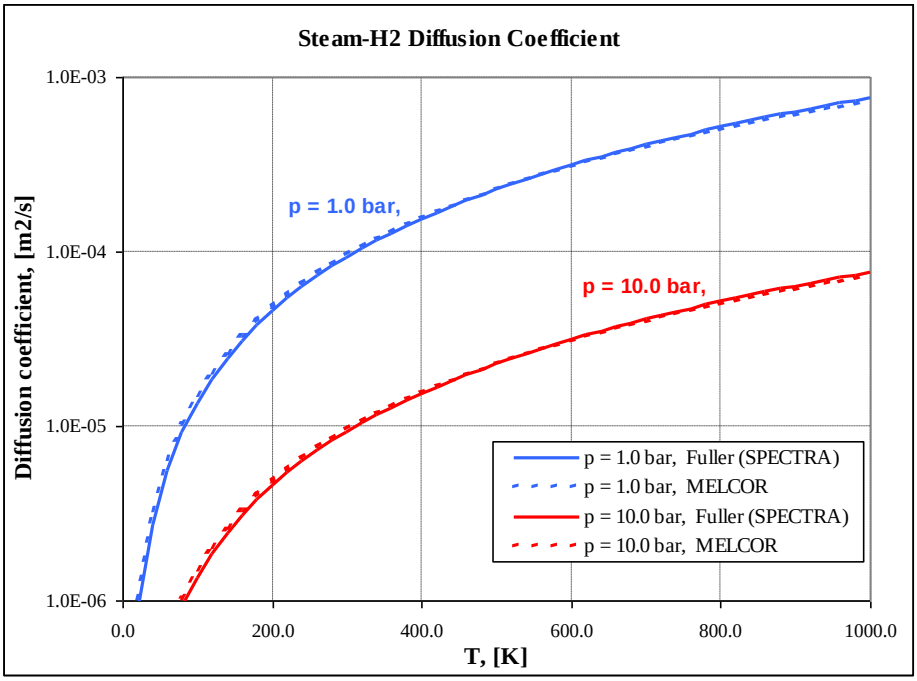

Figure 2-10 Comparison of steam-H_2 diffusion coefficients.

Comparison with Correlations of Luijten et al.

A method of calculating binary diffusion coefficients for dilute condensable vapors has recently been presented by Luijten et al. [26]. For steam-nitrogen and steam-helium mixtures the following correlations are recommended:

$$D = 1.13\times10^{-5}\,\frac{T^{2.159}}{p} \qquad for\ steam-N_2$$

$$D = 4.35\times10^{-3}\,\frac{T^{1.338}}{p} \qquad for\ steam-He$$

where: D - diffusion coefficient, (m^2/s),
T - temperature, (K),
p - pressure, (Pa).

The results of the above correlations are compared with the correlation of Fuller and with experimental data in Figure 2-11 and Figure 2-13. The figures are reproduced from [26]. The temperature range covered by this comparison is 200 - 400 K. The correlation of Luijten gives better agreement with experimental data for temperatures of about 250 K. For higher temperatures, 300 - 375 K, both correlations give very similar results.

The function DIFCM was used to calculate diffusion coefficients for the same temperature range. Results are shown in Figure 2-12 and Figure 2-14. For comparison also the correlations of Luijten et al. are shown in those figures. The diffusion coefficients calculated by DIFCM are in agreement with the "Fuller" results plotted in Figure 2-12 and Figure 2-14. Since the function DIFCM uses the Fuller method, this fact only confirms correctness of the implementation of the Fuller method in the coding.

Although Luijten correlation gives better agreement with the experimental data presented in Figure 2-12 and Figure 2-14, the Fuller method is used by the subroutines calculating diffusion coefficient. The Fuller method is preferred because it is more general (see comparison with MELCOR correlations, above). The advantage of the Luijten correlations is clear only in the seldom used, “freezing” region (for temperatures around 250 K). For the temperatures between 300 and 375 K both methods give very similar results. The correlations of Luijten et al. are valid only up to 375 K (see [26]), while Fuller's method is appropriate also for higher temperatures (see [25], table 11-2).

The values presented in Table 2-6, as well as Figure 2-9, Figure 2-10, Figure 2-12, and Figure 2-14, were generated using a FORTRAN program provided in **\Z-TESTS\FL\DC-T.FOR**. In order to compile the program it must be first moved to the directory \Z-EXE\.

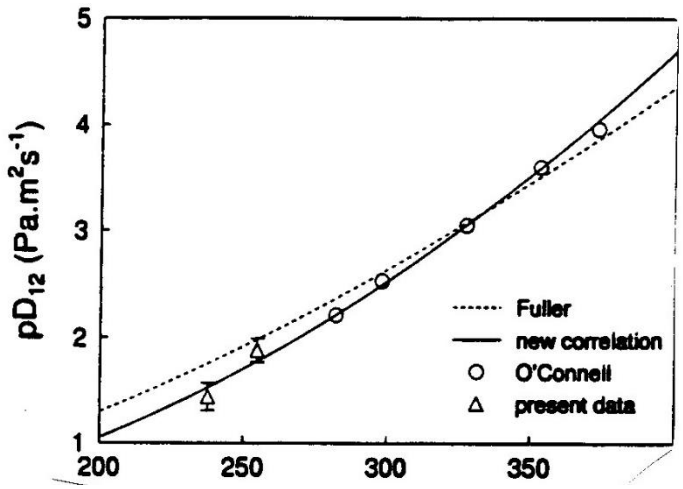

Figure 2-11 Steam-N_2 diffusion coefficient,
measurement and correlations of Fuller and Luijten [26].

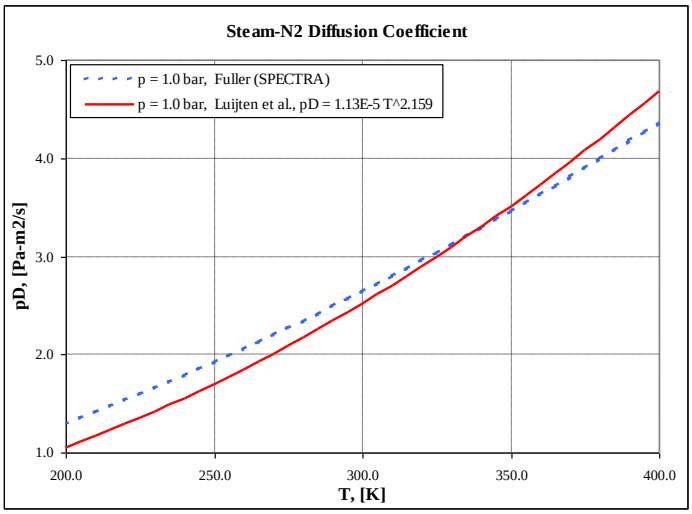

Figure 2-12 Steam-N_2 diffusion coefficient,
results of DIFCM and correlation of Luijten [26].

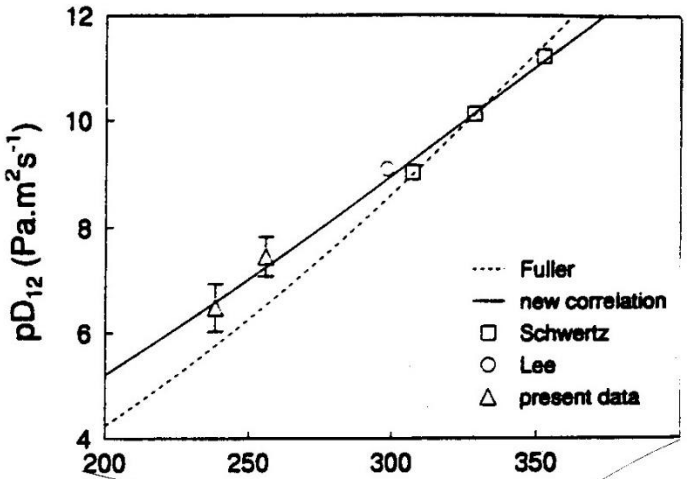

Figure 2-13 Steam-He diffusion coefficient, measurement and correlations of Fuller and Luijten.

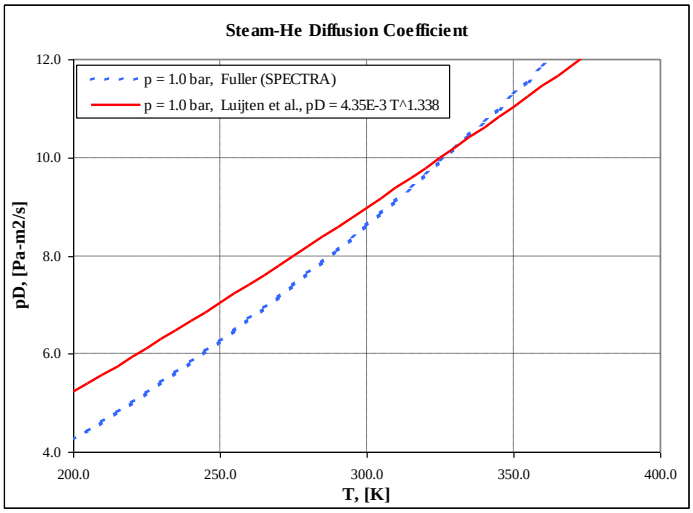

Figure 2-14 Steam-He diffusion coefficient, results of DIFCM and correlation of Luijten.

2.1.1.6 Tests of Different Subroutines Calculating Gas Properties

Five subroutines are available for calculating the properties of a gas mixture: GASEQV, GASEQT, GASEQU, GASEQC, and GASEQP. Each calculates properties based on different input parameters, listed below.

	Subroutine	*Input parameters*		
-	GASEQT:	pressure,	temperature,	mass fractions.
-	GASEQV:	specific volume,	internal energy,	mass fractions.
-	GASEQU:	pressure,	internal energy,	mass fractions.
-	GASEQC:	specific volume,	temperature,	mass fractions.
-	GASEQP:	partial pressures,	temperature.	

In case of GASEQP and GASEQC the properties are obtained by straightforward interpolation of data tabulated in the data tables. Thus those subroutines are the fastest. In case of the other subroutines a short iteration is needed to obtain partial pressures consistent with input mass fractions.

To check the agreement among the results of the three subroutines a testing program was written, which uses random numbers to define the input properties. The following procedure is applied:

- Mass fractions are assumed using random number generator for all gases and then normalizing fractions to 1.0.
- A total pressure is assumed using random numbers and the range between PLLIM and PULIM.
- A temperature is assumed using random numbers from the range between TLLIM and TULIM. If the gas temperature is more than 20 K subcooled (the gas temperature is more than 20 K below the saturation temperature at the steam partial pressure) then the test is abandoned.
- With the above parameters GASEQT is used to calculate all properties (Set 1).
- All other subroutines are called using the parameters calculated by GASEQT. Thus four more sets of properties (Set 2 - 5) are generated.
- Each property from Sets 2 - 5 is compared to the corresponding value in Set 1. Relative differences are calculated.
- If any of the relative differences exceeds 10^{-5}, a warning message is written to the output file. If any of the relative differences exceeds 10^{-2}, calculations are stopped.

Several ranges of parameters were considered. In the Case No. 1 the nearly the full size of the gas property data tables was tested (T: 273.2 - 3070.0 K; p: 1.0×10^{0} - 2.10×10^{7} Pa). The maximum relative error was relatively large (~10^{-3}). All tests with rather large error were occurring near the upper limits of the tabulated data (T~3070.0 K; p~2.10×10^{7} Pa). If the tested limits are slightly narrowed, then the relative error becomes much smaller - see Table 2-7.

Based on the tests the fluid property limits were set in the code to be somewhat narrower than the tabulated space. The upper limits were decreased by about 0.1%, compared to the maximum values in the gas property data tables (T: 3070.0 K $\rightarrow$ 3067 K; p: 2.10×10^{7} Pa $\rightarrow$ 2.09×10^{7} Pa). With respect to the lower temperature limit, the water properties additionally restrict the lower temperature limit.

The temperature and pressure limits set for the SPECTRA code are therefore equal to (compare Volume 1 and Volume 2):

- Temperature: T: 273.2 - 3067.0 K
- Pressure: p: 1.0×10^{0} - 2.09×10^{7} Pa

Table 2-7 Results of gas properties testing (500,000 random tests for each case).

Case No.	Temperature and pressure limits	Maximum relative error
1	T: 273.2 - 3070.0 K; p: 1.0×10^{0} - $2.100\times10^{+7}$ Pa	4.5×10^{-2}
2	T: 273.2 - 3067.0 K; p: 1.0×10^{0} - $2.100\times10^{+7}$ Pa	4.5×10^{-3}
3	T: 273.2 - 3070.0 K; p: 1.0×10^{0} - $2.090\times10^{+7}$ Pa	4.5×10^{-5}
4	**T: 273.2 - 3067.0 K; p: 1.0×10^{0} - $2.090\times10^{+7}$ Pa**	**6.9×10^{-7}**

A tests of steam properties was made using 1.0 bar pressure and a temperature of 373.15 K (100ºC). The results are compared below to the steam tables.

	GASEQT	GASEQV	GASEQP	**Steam tables [13]:**
T =	3.73150E+02	3.73150E+02	3.73150E+02	
P =	1.00000E+05	1.00000E+05	1.00000E+05	
V =	1.69647E+00	1.69647E+00	1.69647E+00	**1.674** (=1/0.5975)
U =	2.50626E+06	2.50626E+06	2.50626E+06	**2.508E6** (=2.675E6-1.0E5/0.5975)
H =	2.67591E+06	2.67591E+06	2.67591E+06	**2.675E6**
R =	4.61525E+02	4.61525E+02	4.61525E+02	-
CV =	1.60400E+03	1.60400E+03	1.60400E+03	-
CP =	2.06553E+03	2.06553E+03	2.06553E+03	-
VS =	1.22664E-05	1.22664E-05	1.22664E-05	**1.228E-5**
TC =	2.50739E-02	2.50739E-02	2.50739E-02	**2.509E-2**
PR =	1.01047E+00	1.01047E+00	1.01047E+00	**1.000**

The tests were performed using a FORTRAN program provided in **\Z-TESTS\FL\GASMIX-T.FOR**. In order to compile the program it must be first moved to the directory \Z-EXE\.

2.1.2 Water Properties

The properties of water are calculated by two different subroutines:

- WATERT - calculates water properties using pressure and temperature as input arguments.
- WATERU - calculates water properties using pressure and internal energy as input arguments.

While the first method is quite straightforward, the second requires an internal iteration to calculate the properties. The iteration continues until the desired convergence is achieved (relative error between the assumed and the calculated internal energy is less than 10^{-9}). The second method is more useful in practice. Since it is the internal energy, which is obtained from the energy balance, the second method allows obtaining quickly all properties for the new energy.

The tests of water properties consist of two types. First, the subroutine WATERT was called using several different values of temperatures and pressures. The output was compared to the data shown in steam/water tables [13]. Second, a random test was performed, similar to that performed for the gas properties, described in section 2.1.1.6.

The first tests were made for two different temperatures, one for low temperature (303.15 K, 30ºC), and one for high temperature (623.15 K, 350ºC). The saturated liquid properties were tested by setting the pressures to values slightly above saturation. The influence of pressure is only taken into account in case of enthalpy and internal energy. In contrast to SPECTRA Version 1.00, the present code version does not take into account the influence of pressure on water density. This influence was skipped in order to eliminate small phantom flows in non-symmetrical loops (see Volume 1). The results are shown below.

```
    T  3.03150E+02
         WATERT      WATERU       REL.DIF.        Steam tables [13]:
    P  4.25000E+03
   UL  1.25666E+05  1.25666E+05  0.00000E+00        125.666E3 (=125.67E3-4245.5/995.61)
 PSAT  4.24550E+03  4.24550E+03  4.70461E-12       4245.5
   HL  1.25670E+05  1.25670E+05  0.00000E+00        125.67E3
   VL  1.00441E-03  1.00441E-03  2.20206E-14          1.00441E-3 (=1/995.61)
 RHOL  9.95610E+02  9.95610E+02  2.20383E-14        995.61
BETAL  3.04778E-04  3.04778E-04  2.20556E-14           -
VISCL  7.98000E-04  7.98000E-04  1.58568E-12        798.0E-6
TCONL  6.15400E-01  6.15400E-01  1.88525E-13        615.4E-3
  CPL  4.18210E+03  4.18210E+03  1.10911E-14          4.182E3 (5.423*615.4E-3/798.0E-6)
  PRL  5.42300E+00  5.42300E+00  1.78536E-12          5.423
SIGMA  7.12000E-02  7.12000E-02  1.59439E-13         71.2E-3

    T  6.23150E+02
         WATERT      WATERU       REL.DIF.
    P  1.66000E+07
   UL  1.64165E+06  1.64165E+06  0.00000E+00        164.165E3(=1670.4E3-165.21E5/574.7)
 PSAT  1.65210E+07  1.65210E+07  2.56221E-11        165.21E+5
   HL  1.67054E+06  1.67054E+06  2.47948E-13      1,670.4E+3
   VL  1.74004E-03  1.74004E-03  1.43417E-11          1.74E-3 (1./574.7)
 RHOL  5.74700E+02  5.74700E+02  1.43417E-11        574.7
BETAL  7.05210E-03  7.05210E-03  4.29539E-11           -
VISCL  6.57000E-05  6.57000E-05  1.54878E-11         65.7E-6
TCONL  4.47800E-01  4.47800E-01  9.49838E-12        447.8E-3
  CPL  1.01283E+04  1.01283E+04  5.58398E-11         10.128E3 (=3.67*447.8E-3/65.7E-6)
  PRL  1.48600E+00  1.48600E+00  4.98505E-11          1.486
SIGMA  3.67000E-03  3.67000E-03  1.04805E-10          3.67
```

The random tests were performed for temperatures between 273.2 K and 645 K and pressures between saturation and $1.499\times10^{+7}$ Pa). The results are shown in Table 2-8. Relative error is very small.

The tests were performed using a FORTRAN program provided in **\Z-TESTS\FL\WATER-T.FOR**. In order to compile the program it must be first moved to the directory \Z-EXE\.

Table 2-8 Results of water properties testing (1,000,000 random tests).

Case No.	Temperature and pressure limits	Maximum relative error
1	T: 273.2 - 645.0 K; p: $p_{sat}(T)$ - 2.09×10^{7} Pa	1.18×10^{-7}

2.2 Verification of the Control Volume Package

2.2.1 Terminal Velocity of Bubbles - Default Model

Bubble terminal velocity is calculated by the subroutine VBUBBF, which uses five correlations, valid for five bubble dimension regions.

- Region 1: Hadamard and Rybczynski correlation. Bubble velocity is proportional to the bubble diameter squared: $v \sim D^2$.
- Region 2: Peebles and Garber correlation, velocity is proportional to: $v \sim D^{1.28}$.
- Region 3: Peebles and Garber correlation, velocity is proportional to: $v \sim D^{0.5}$.
- Region 4: Zuber correlation, velocity is independent of D.
- Region 5: Davies and Taylor correlation, velocity is proportional to: $v \sim D^{0.5}$.

Results are shown in Figure 2-15. In Regions 1 - 4 the terminal velocity depends on gas/liquid properties. Region 5 is independent of gas/liquid properties. Detailed description of all correlations is provided in Volume 1.

Bubble terminal velocity data is shown in Figure 2-16. The figure was obtained from [169]. Comparison of Figure 2-16 and Figure 2-17 shows that the bubble velocities calculated by the subroutine VBUBBF are in good agreement with the data. Note that Region 1, Hadamard and Rybczynski correlation is not visible in Figure 2-17.

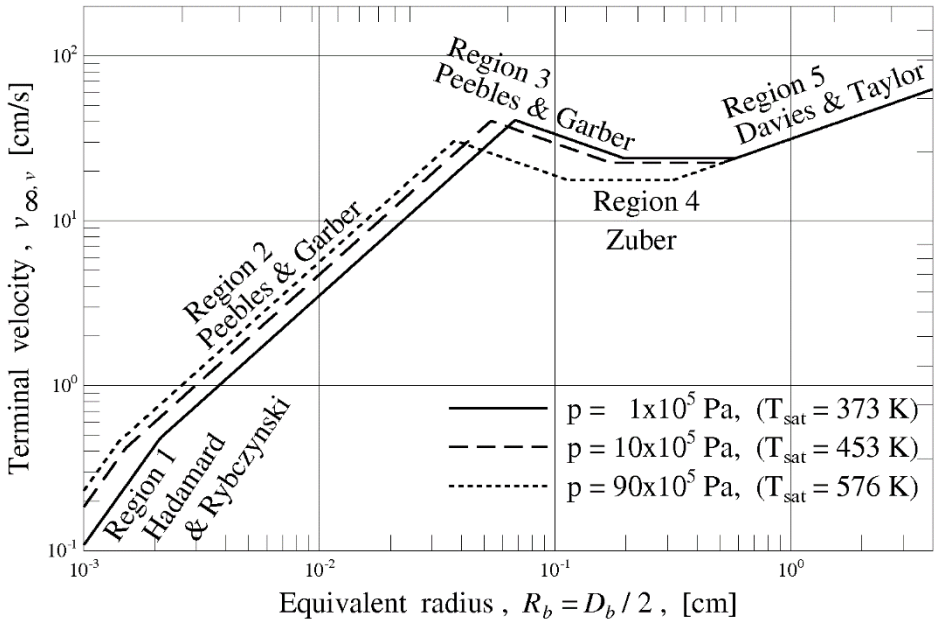

Figure 2-15 Terminal velocity of bubbles, results of subroutine VBUBBF

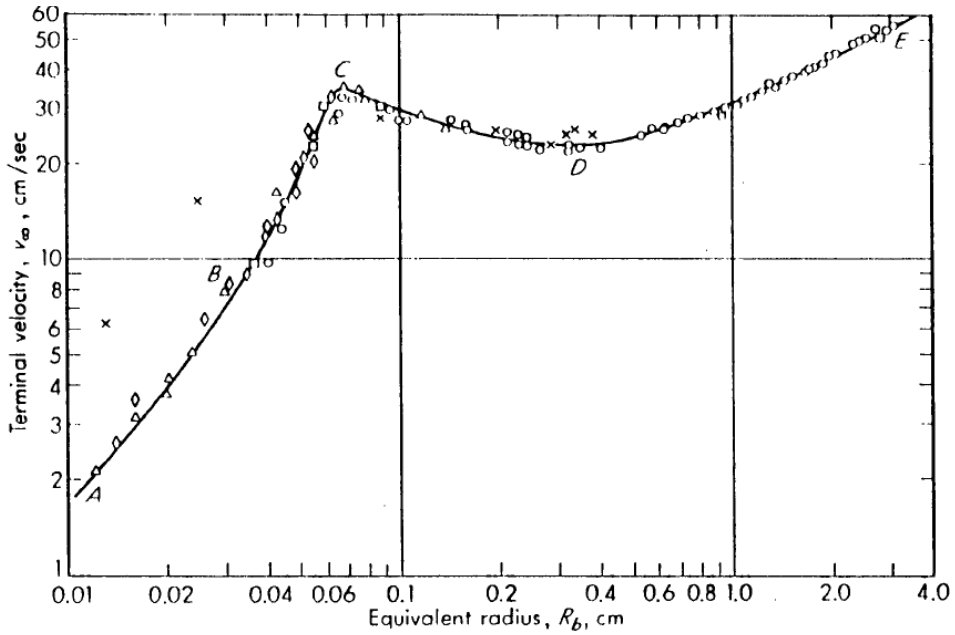

Figure 2-16 Terminal velocity of bubbles [169]

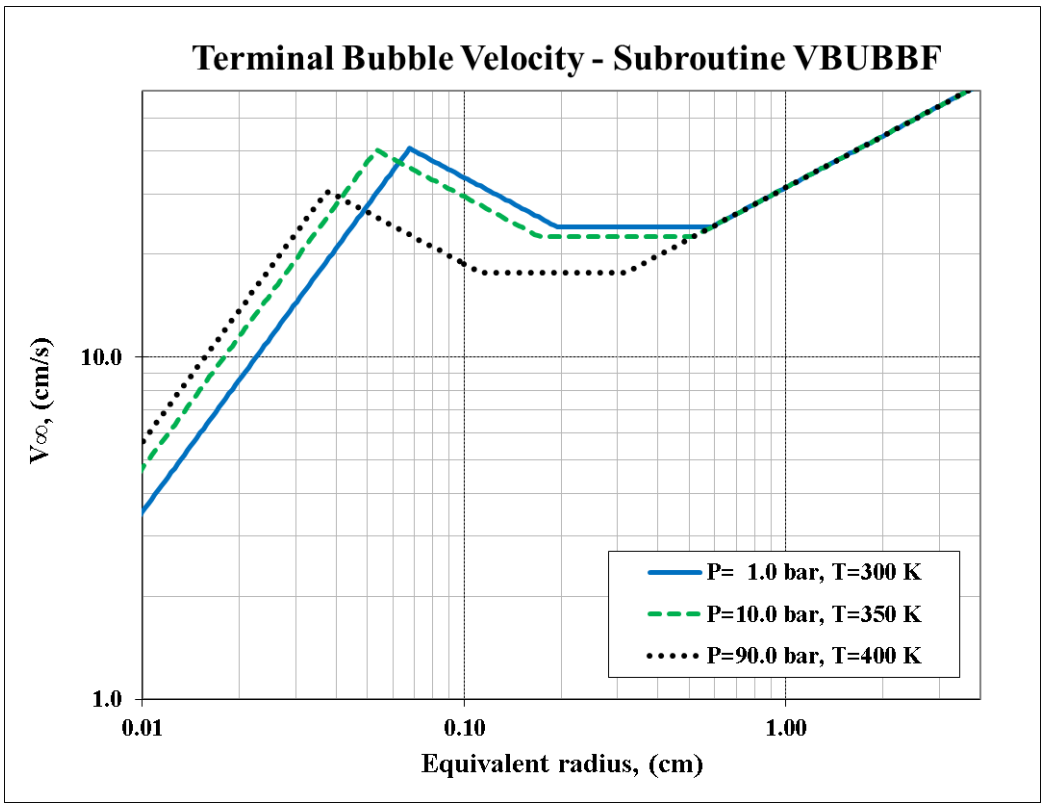

Figure 2-17 Terminal velocity of bubbles, results of subroutine VBUBBF

2.2.2 Terminal Velocity of Droplets - Default Model

Terminal droplet velocity is calculated by the subroutine VDRPDF, which uses three correlations, valid for three droplet dimension regions. Results are shown in figure 1.4.4.

- Region 1: Hadamard and Rybczynski correlation, velocity proportional to: $v \sim D^2$.
- Region 2: Wallis, velocity is proportional to: $v \sim D^{0.5}$. In this region the droplet velocity depends on the drag coefficient, C_D, Three ranges are distinguished:
  - Re < 30 $C_D \sim 1/Re^{0.8}$
  - 30 < Re < 1000 $C_D \sim 1/Re^{0.4}$
  - 1000 < Re $C_D \sim$ const.
- Region 3: Levich correlation, velocity is independent of D.

In all three ranges the terminal velocity depends on the gas/liquid properties. Detailed description of all correlations is provided in Volume 1.

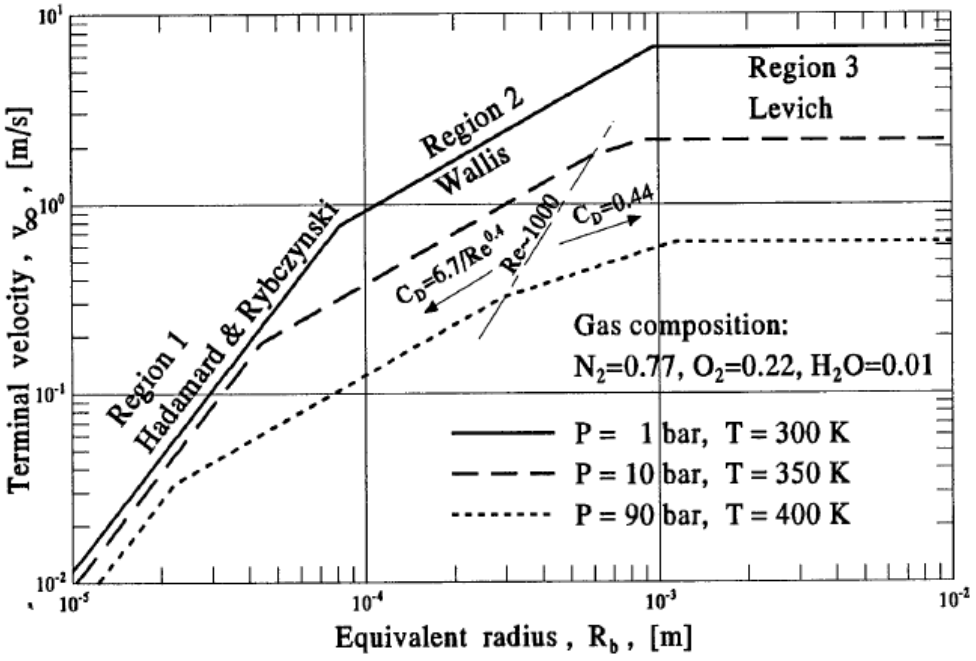

Figure 2-18 Terminal velocity of droplets, results of subroutine VDRPDF

2.2.3 Terminal Velocity of Particles - Alternative Correlation

The alternative correlation for particle terminal velocity may be applied in two ways:

- Drag coefficient, C_D, calculated using five correlations, valid for different Re:
  - Re < 30 $C_D \sim 1/Re^{0.8}$
  - 30 < Re < 1,000 $C_D \sim 1/Re^{0.4}$
  - 1,000 < Re < 10,000 $C_D \sim 1/Re^{0.1}$
  - 10,000 < Re<100,000 $C_D \sim Re^{0.06}$
  - 100,000 < Re $C_D \sim$ const.
- Drag coefficient, C_D, defined by the user.

Test calculations were performed for both cases. Results of the case with five built-in correlations, calculated by the subroutine VDCIFL, are shown in Figure 2-20. For comparison, results of the default correlation for droplets, shown in section 2.2.2, are shown in Figure 2-19.

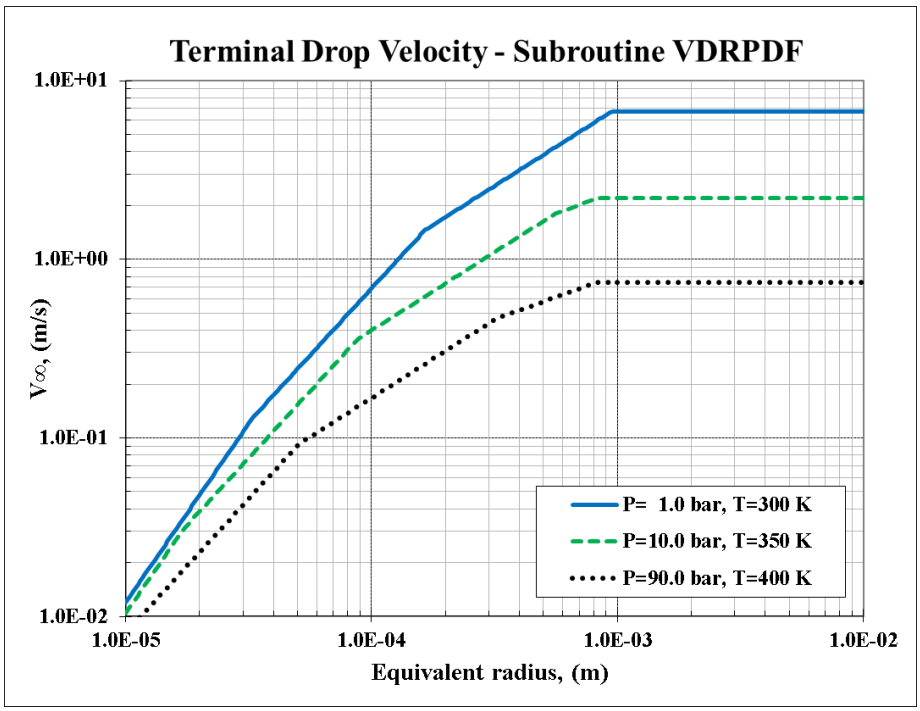

Figure 2-19 Default correlation for droplets

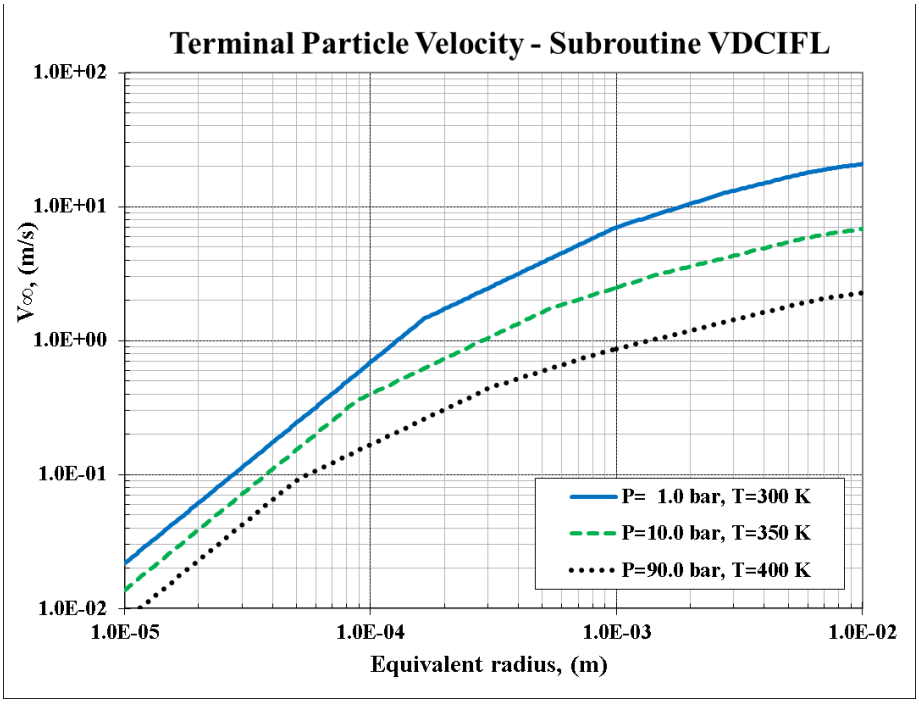

Figure 2-20 Alternative correlation applied to droplets, C_{small} = 0.0

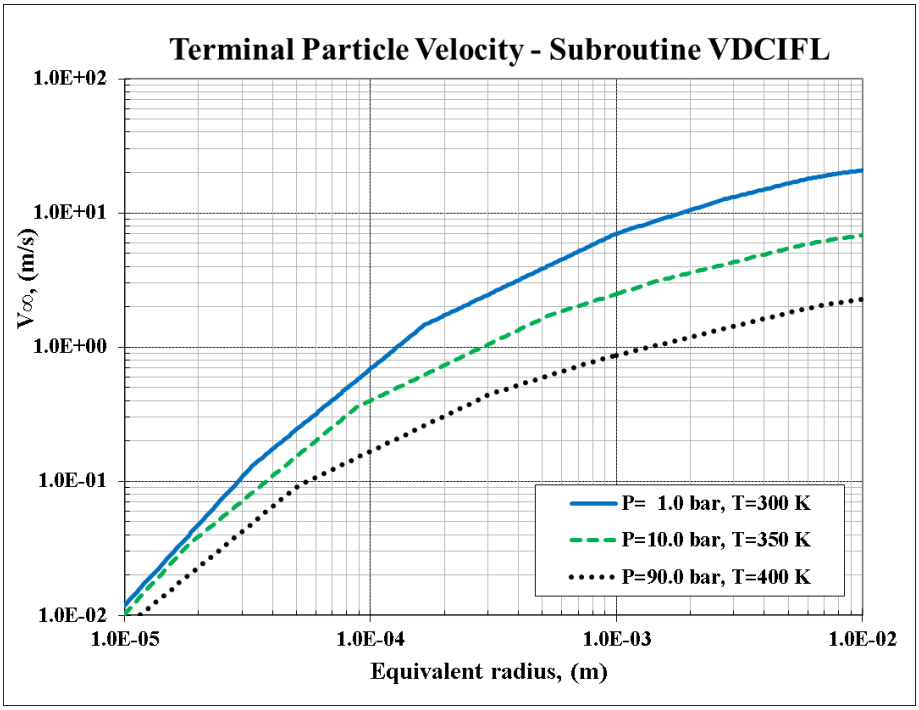

Figure 2-21 Alternative correlation applied to droplets, C_{small} = 1.0

Figure 2-20 shows results obtained using purely the drag coefficient correlation (C_{small} = 0.0). The correlation valid for very small particles is:

$$v_\infty = \frac{1}{18} \cdot \frac{D_p{}^2 g(\rho_f - \rho_p)}{\eta_f} \cdot C_{small}$$

This correlation is applicable for very small particles, $D_p < \sim 10^{-4}$ m. The best estimate value of C_{small} is 1.0. Results obtained using this value are shown in Figure 2-21. Comparison of Figure 2-21 and Figure 2-20 shows that the effect of the small particle correlation is seen only for $D_p \sim 10^{-5}$ m.

Results of the case with user-defined C_D, calculated by the subroutine VDCIFO, are shown in Figure 2-22. This figure shows results obtained using purely the drag coefficient correlation (C_{small} = 0.0). As verification, one point was calculated by hand: R_p=10^{-2} m (→ D_p=0.02 m), p=1.0 bar, T=300 K (→ ρ_f = 1.148 kg/m^3 - air, ρ_p = 996.5 kg/m^3 - water):

$$v_\infty = \left(\frac{4/3}{C_D} \cdot \frac{D_p g(\rho_p - \rho_f)}{\rho_f} \right)^{0.5} = \left(\frac{4/3}{1.0} \cdot \frac{0.02 \times 9.81 \times (996.5 - 1.148)}{1.148} \right)^{0.5} = 15.06$$

The value obtained from the test program (Figure 2-22) is 15.06 m/s.

Figure 2-23 shows results obtained with C_{small} = 1.0. Comparison of Figure 2-23 and Figure 2-22 shows that the effect of the small particle correlation is seen only for D_p smaller than ~3×10^{-5} m (90 bar) to ~10^{-4} m (1 bar).

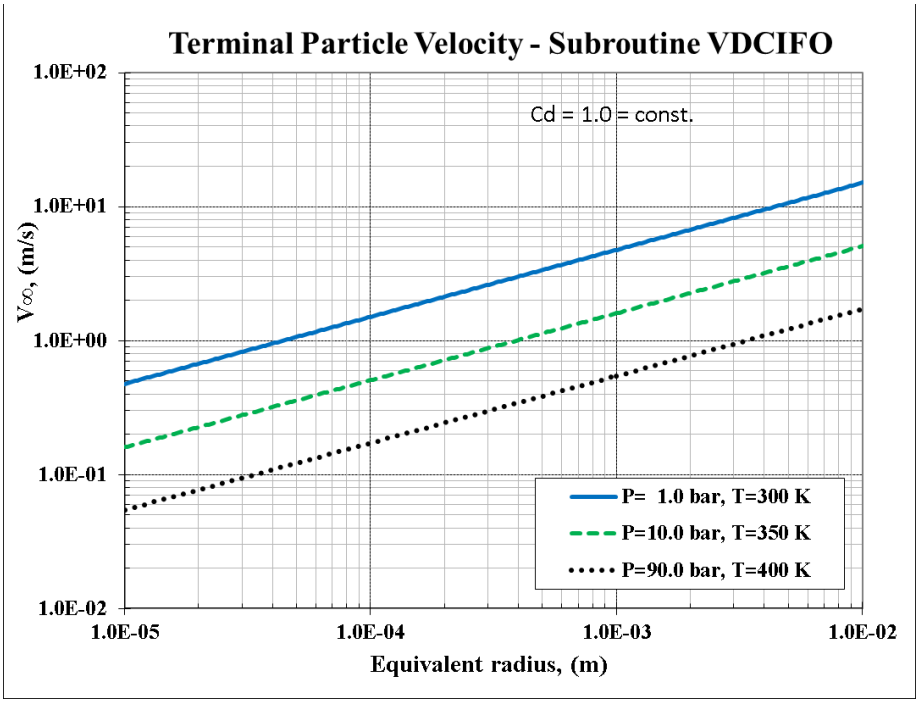

Figure 2-22 Alternative correlation with C_D = 1.0 = const., C_{small} = 0.0

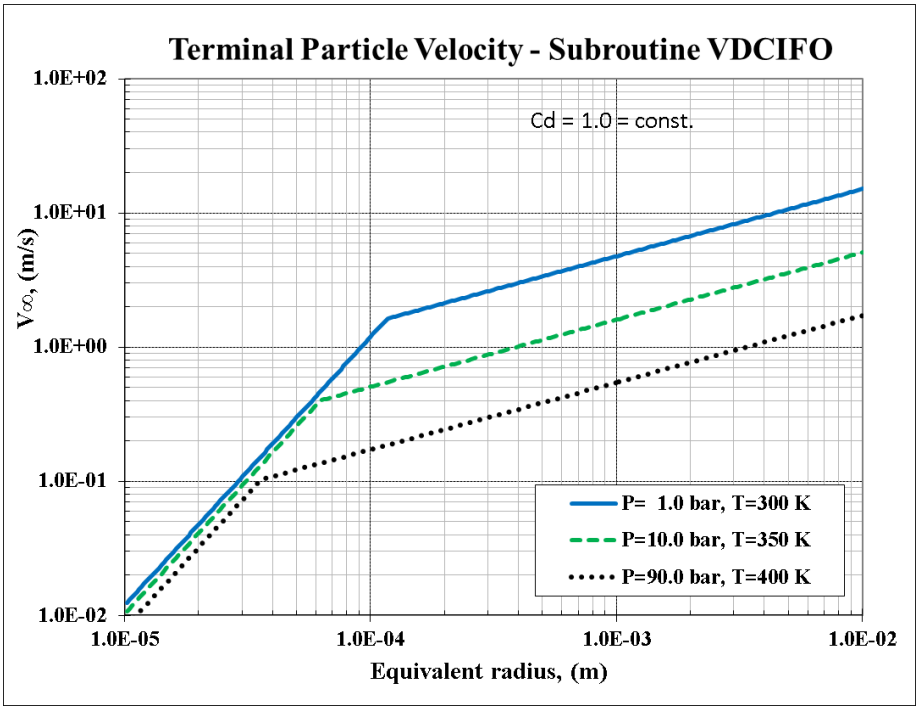

Figure 2-23 Alternative correlation with C_D = 1.0 = const., C_{small} = 1.0

2.3 Verification of the Junction Package

2.3.1 Critical Flow

The critical flow is calculated using a simplified method based on the Moody model. Approximation formulas are used to calculate the critical mass flux for a two-phase or a single-phase mixture.

The critical mass flux obtained using the correlations applied in SPECTRA are compared to other models and to experiments in this section. The comparison is performed in three steps:

- The approximation formulas, used by the subcooled water and superheated steam subroutines (GCSUB, GCSUP), are compared to the source data for the model - critical flow tables from RELAP-4 (see Volume 1, section "Subcooled Liquid Critical Flow"). This comparison is shown in section 2.3.1.1. This comparison shows how well the relatively simple approximation formulas represent the exact values of the source model. The approximation formula for the two-phase region is compared to the original model data later, in section 2.3.1.3.

- The two available models: GC2PSW - 2-phase steam-water mixture, and GC2PMC - 2-phase multi-component mixture, are compared in section 2.3.1.2. The model GC2PMC is more general but slightly slower and requires more arguments. It is shown in section 2.3.1.2 that if the gas phase consists of pure steam both models give approximately the same results.

- The results of the model are compared with the experimental data and the results of other models in section 2.3.1.3.

2.3.1.1 Comparison of Approximation Formulae with the Source Tables

As described in Volume 1, SPECTRA uses approximation formulae to approximate the tabular data from RELAP-4. Comparison of the approximation formulas with the source data of the model is given in this section.

The data tables in RELAP are produced using British units. The SPECTRA subroutines are written entirely in SI units. To make the comparison plots the RELAP data tables were converted to the SI units using the following conversion factors:

- pressure: Psia $\rightarrow$ Pa : $6.8947\times10^{+3}$,
- enthalpy: Btu/lb $\rightarrow$ J/kg : $2.3256\times10^{+3}$,
- mass flux: lb/ft^2/s $\rightarrow$ kg/m^2/s : $0.45359 / 0.3048^2$.

The subcooled liquid approximation formulas (used by the function GCSUB) are compared to the appropriate tabular values ((RELAP, 1976), subroutine DATZ) in Figure 2-24.

The superheated steam approximation formula (used by the function GCSUP) is compared to the appropriate tabular values ((RELAP, 1976), subroutine DATB) in Figure 2-25.

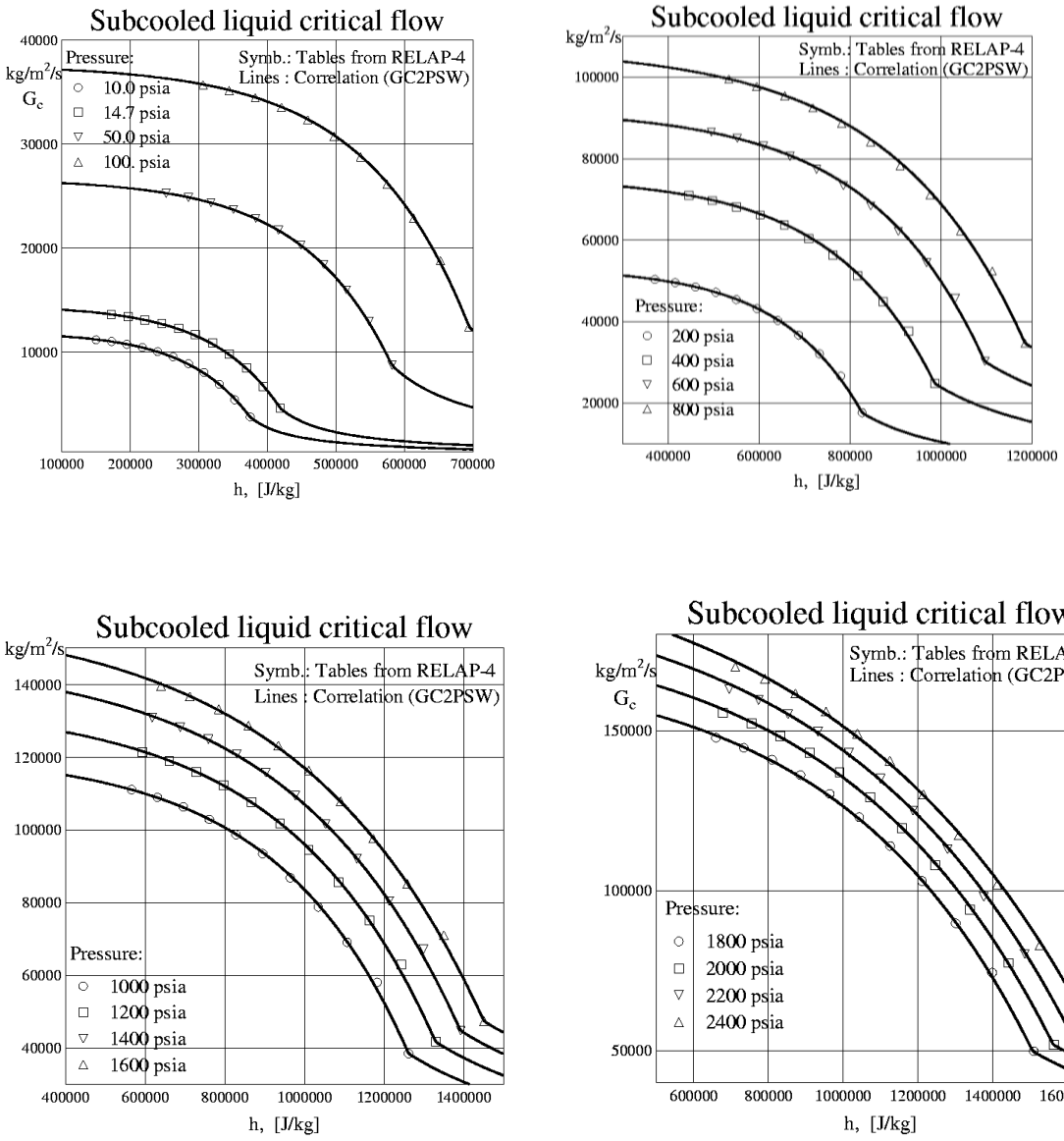

Figure 2-24 Subcooled critical flow model - comparison with RELAP4 data tables.

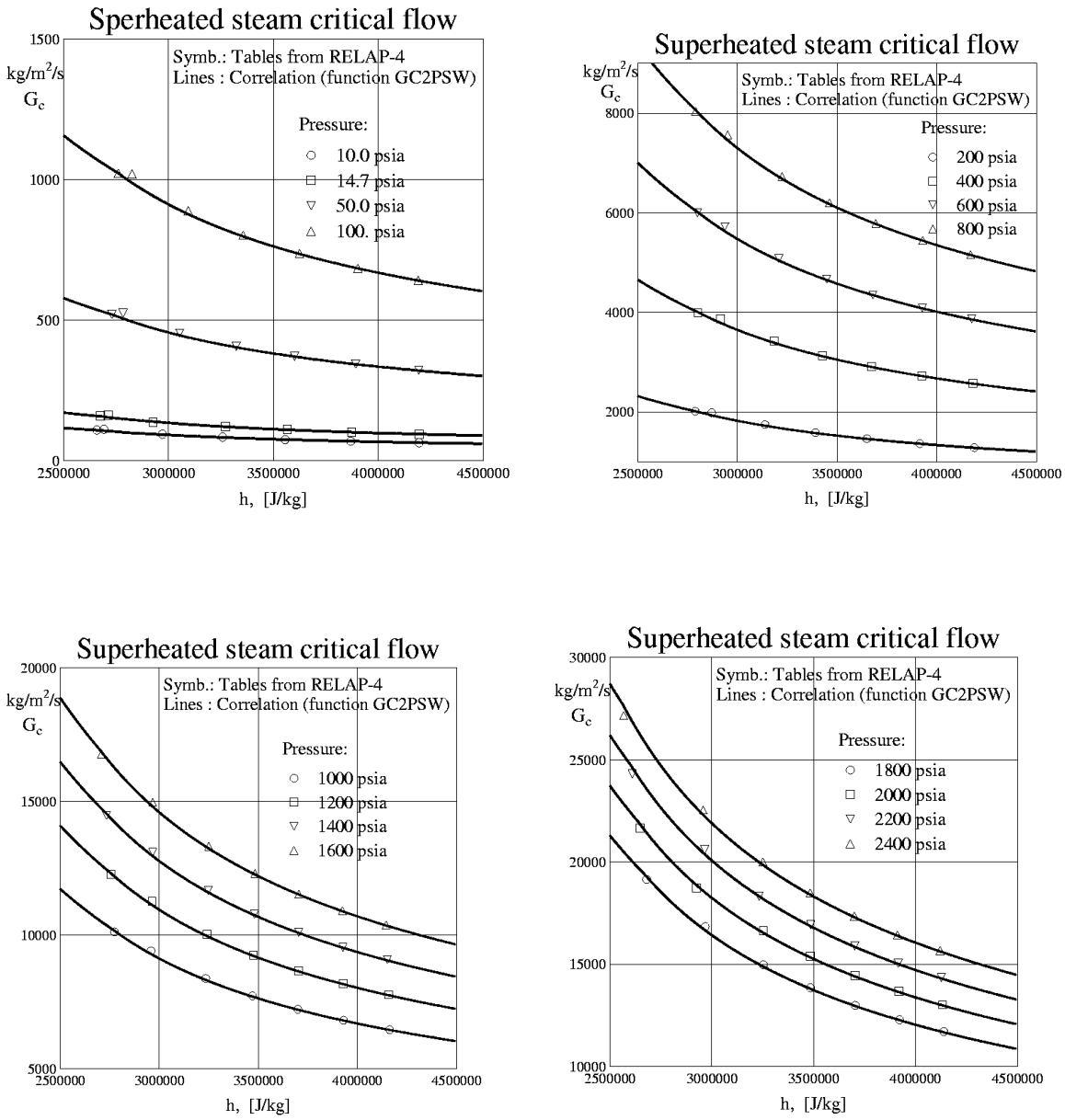

Figure 2-25 Superheated steam critical flow model - comparison with RELAP4 data tables.

The approximation formulae, in spite of their simplicity, represent quite well the data points. The relative differences are given in Table 2-9. The average relative differences for the whole subcooled range and superheated range are equal to 0.5 % and 0.64 % respectively.

Table 2-9 Average relative differences between the correlation and values from RELAP-4.

Pressure range	Subcooled region	Superheated region
10 - 100 psia (6.895×10^4 - 6.895×10^5 Pa)	0.35 %	1.01 %
200 - 800 psia (1.379×10^5 - 5.516×10^6 Pa)	0.66 %	0.56 %
1000 - 1600 psia (6.895×10^6 - 1.103×10^7 Pa)	0.47 %	0.45 %
1800 - 2400 psia (1.241×10^7 - 1.655×10^7 Pa)	0.51 %	0.55 %
10 - 2400 psia (6.895×10^4 - 1.655×10^7 Pa)	0.50 %	0.64 %

The differences are very small compared to the expected error of the model prediction. Experiments confirm that the critical flow depends on the local values of slip and on thermal non-equilibrium ([27], section 3.4.1, page 190). It is very difficult to take those factors into account. Theories are often in contradiction with experimental data ([28], section 11.4.3.2, figure 11.8). Because of that the models for the two-phase critical flow have moderate accuracy. Therefore the differences of order of 1 % between the results of the approximation formulas and the exact values from the RELAP-4 tables have no practical meaning.

The correlations have good extrapolation properties. In the subcooled range the critical mass flux, G_c, slowly increases with increasing subcooling (decreasing enthalpy). In the superheated range the correlation approaches the perfect gas model with increasing superheat (see section 2.3.1.2).

The graphs for subcooled critical flow (Figure 2-24) and the average relative differences (Table 2-9) were generated using the driver program GCSUBTT. The program is provided in \Z-TESTS\JN\GCSUB-T.FOR. The graphs for superheated critical flow (Figure 2-25) and the average relative differences (Table 2-9) were generated using the driver program GCSUPTT. The program is provided in \Z-TESTS\JN\GCSUP-T.FOR.

2.3.1.2 Comparison of Steam-Water Model with Multi-Component Model

As described in Volume 1, two models are available, coded as the functions (see Volume 1, "Critical Flow of a Gas Mixture"):

- GC2PSW - 2-phase, steam-water mixture. In the superheated steam region the model uses approximation formula. This model is simpler to use since it only requires 2 input parameters: pressure and enthalpy. The applicability is restricted to steam-water mixtures. Current SPECTRA version does not use this model.

- GC2PMC - 2-phase, multi-component mixture. For the gas phase the perfect gas model is used to calculate critical mass flux. The advantage of GC2PMC is that it can be applied for mixture of steam with non-condensable gases. Current SPECTRA version uses only this model.

If the gas phase consists of pure steam both models should give approximately the same results.

To check the agreement of both models in the superheated steam range the critical mass flux was calculated using both functions GC2PSW and GC2PMC. Calculations were performed for four different pressures, for temperature ranges between the saturation temperature and 3070 K. The required input parameters (enthalpy, density, specific heats) were calculated using the gas property subroutine GASEQP. The results are shown in Figure 2-26. Both models give very similar results for temperatures below about 1500 K. It should be remembered that the developed correlation ($G_{c,steam}=Cp/(h-h_0)^{1/2}$, see Volume 1) was developed based on the data from RELAP-4, which contains tables up to about 1000 K. Thus for high temperatures the correlation is extrapolated beyond its original range of application. The correlation is not used by current SPECTRA version and is shown here only as an extra verification of the critical flow model.

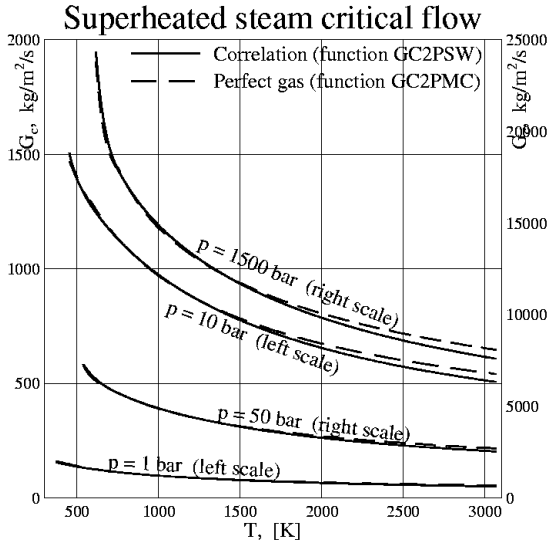

Figure 2-26 Comparison of the critical flow, correlation based on RELAP-4 data and the ideal gas model.

Comparison of results calculated for different gas mixtures is shown in Figure 2-27, showing the results obtained with both models (GC2PSW and GC2PMC) for: water-H_2 mixture, water-steam mixture and water-O_2 mixture. The plots were made for pressures, p, from 1 bar to 150 bar and qualities, X, from –0.3 to +1.5. The quality is defined as:

$$X = \frac{h - h_f}{h_g - h_f}$$

where: h enthalpy, J/kg,
h_f saturated liquid enthalpy, J/kg,
h_g saturated vapor enthalpy, J/kg.

In case of water-hydrogen and water-oxygen mixtures the gas properties, needed by the function GC2PMC, ρ_{gas}, c_p, ν_v, were calculated by the gas property subroutine GASEQP, using the following arguments:

Critical flow, water-H_2 and water-steam systems

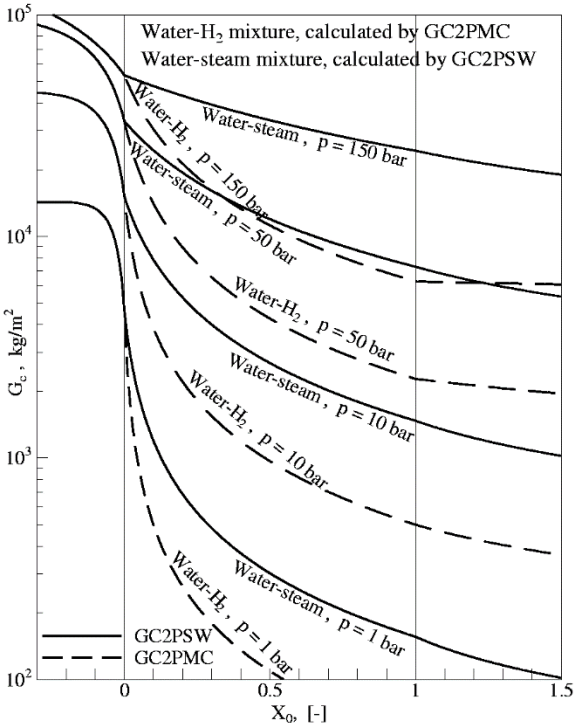

Critical flow, water-O_2 and water-steam systems

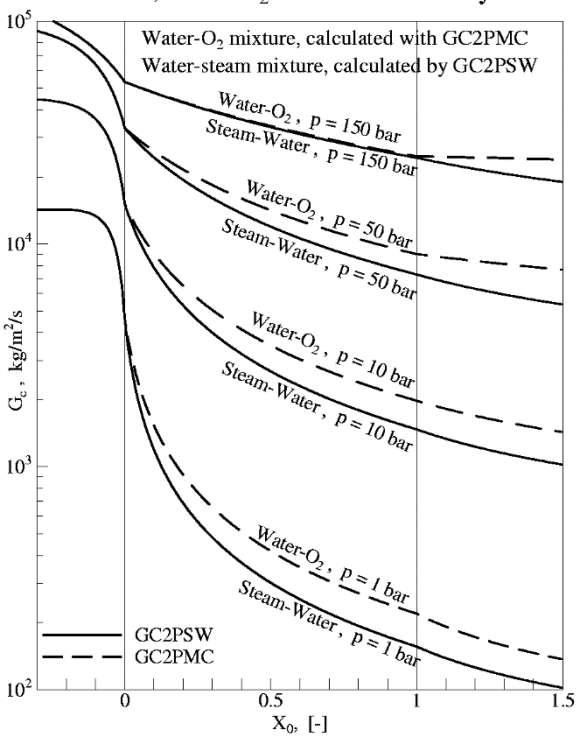

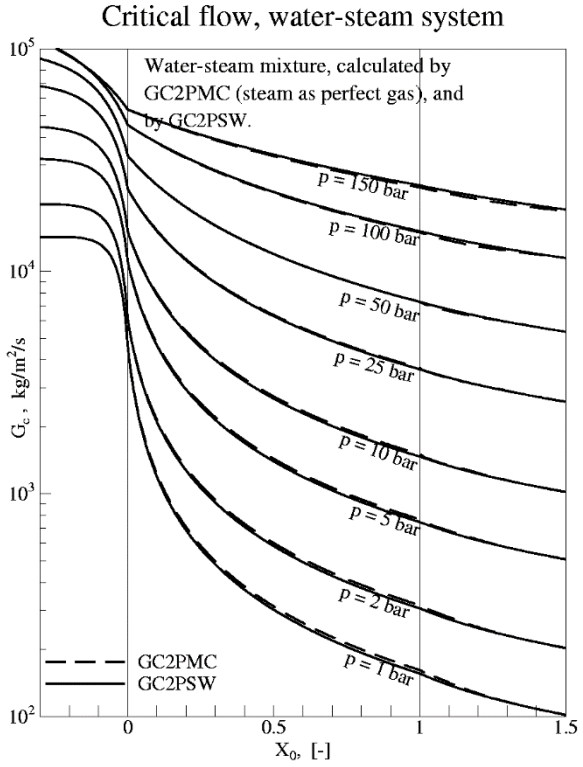

Figure 2-27 Critical flow comparisons for water-H_2, water-steam and water O_2 mixtures.

- $X < 1.0$: pressure and the saturation temperature,
- $X > 1.0$: pressure and this temperature for which the steam enthalpy would be equal to: $h = h_f + X(h_f - h_g)$. In other words, the quality in Figure 2-27 is based on the enthalpy of steam at the same temperature as the gas temperature.

Results shown in Figure 2-27 show that:

- For subcooled liquid both models are identical (both are using the same function GCSUB in this region).

- For a single-phase gas flow, the critical mass flux is lower for H_2 than for steam, while it is higher for O_2 than for steam. For perfect gases the critical flow is approximately proportional to the square root of the molecular weight, thus for heavier gases the critical flow is larger.

- The interpolation rule proposed by Gauntt et.al. [20] for the two phase region, $0 < X < 1$, provides a convenient way of calculating the critical mass flux in this region for any composition of the gas phase.

- Both models give approximately the same results if gas phase consists of pure steam (same as Figure 2-26, but now plotted for wider range of parameters).

The SPECTRA graphs presented in this section were generated using the program GCRITT. The program is provided in \Z-TESTS\JN\GCRIT-T.FOR.

2.3.1.3 Comparisons with Other Models and Experimental Data

Comparison with other models and experimental data is based on experiments made with steam-water mixture. It has been shown in section 2.3.1.2 above, that for the steam-water mixture both models GC2PMC and GC2PSW give almost identical result. Therefore for the comparisons shown in this section the function GC2PSW was used. This allows using only pressure and enthalpy as the input variables and thus eliminates the necessity of using gas property subroutines (involving relatively long compilation times).

Comparison of several critical flow models with experimental data was performed by Ardron and Furness [29]. Figure 2-28 and Figure 2-30 are reproduced from this paper. The figures show critical flow results obtained using the following theoretical models:

- Homogeneous-Equilibrium [30],
- Moody [31],
- Starkman [32],
- Homogeneous-Frozen [33],
- Henry-Fauske [33].

Experimental data points are from the following experiments:
- Maneely, [30],
- Friedrich, [34],
- Starkman, [32],
- Sozzi and Sutherland, [35].

Comparison of available data on the steam-water mixture critical flow rates, performed by Ardron et.al., has shown that the critical flow models in common use agree with observations only in a

restricted range of thermodynamic and geometric conditions ([29], page 263). It was pointed out that the worst discrepancies appear in the prediction of low quality flows in pipes of $L/D < 12$. The influence of the length to diameter ratio is very important in this region.

For very short pipes ($L/D = 0$) the critical flow rate approaches the Bernoulli flow. The Moody or Henry-Fauske models give lower critical flow rate values (Figure 2-32, left).

For very long pipes ($L/D = 40$) the experimental values are well predicted by homogeneous-equilibrium model. Moody and Henry-Fauske models give larger critical flow rates in this case.

For large vessels a consistent overestimation of the critical flow calculated by the Moody model, for qualities above 1 %, has been observed and measured. The Moody multiplier, C_M, has been defined as the ratio between the observed flow rate to that obtained from the Moody theory ([29], page 262).

Reported values of Moody multipliers for a large number of published blowdown experiments are listed in table 1 in [29]. C_M has been always found to be less than unity. The values shown in [29] are between 0.60 and 0.85, with the average value of about 0.70.

In SPECTRA both the influence of *L/D* and the Moody multiplier are taken into account. The Moody multiplier is an input parameter with the default value of 0.70 (Volume 2, input record 210XXX). The influence of *L/*D is calculated by a separate function: FGCLD, based on *L* and *D* entered in the input data.

Figure 2-29 and Figure 2-31 show the critical flow rates using the Moody multiplier, C_M, of 0.70, for the same conditions as those shown in Figure 2-28 and Figure 2-30 respectively. Also the base model - the approximation of the Moody model - is shown. The latter is calculated by simply putting both Moody multiplier, C_M, and *L/D* multiplier, $f_{L/D}$, equal to 1.0.

It may be observed that the Moody model lines in Figure 2-29 and Figure 2-31 are very close to the corresponding lines in Figure 2-28 and Figure 2-30. This is a confirmation of the correctness of the approximation formula used to represent Moody model in the two-phase region.

The calculated results (denoted by symbols in Figure 2-29 and Figure 2-31) are close to the experimental results shown in Figure 2-28 and Figure 2-30. The differences are about 10 - 15 % for the pressure of 500 psia and up to 20 - 25 % for the pressure of 900 psia. Rather large scatter of experimental data in the latter case is observed.

Figure 2-32, right shows the critical flow rates calculated using the Moody multiplier: $C_M = 0.70$. Note that since the values are those of saturated liquid both GC2PMC and GC2PSW will give identical results (see Figure 2-27). Therefore the name of the base model in Figure 2-32 is denoted as: GC2P(MC/SW). In fact the values shown in the figure were calculated using GC2PSW, for the sake of convenience.

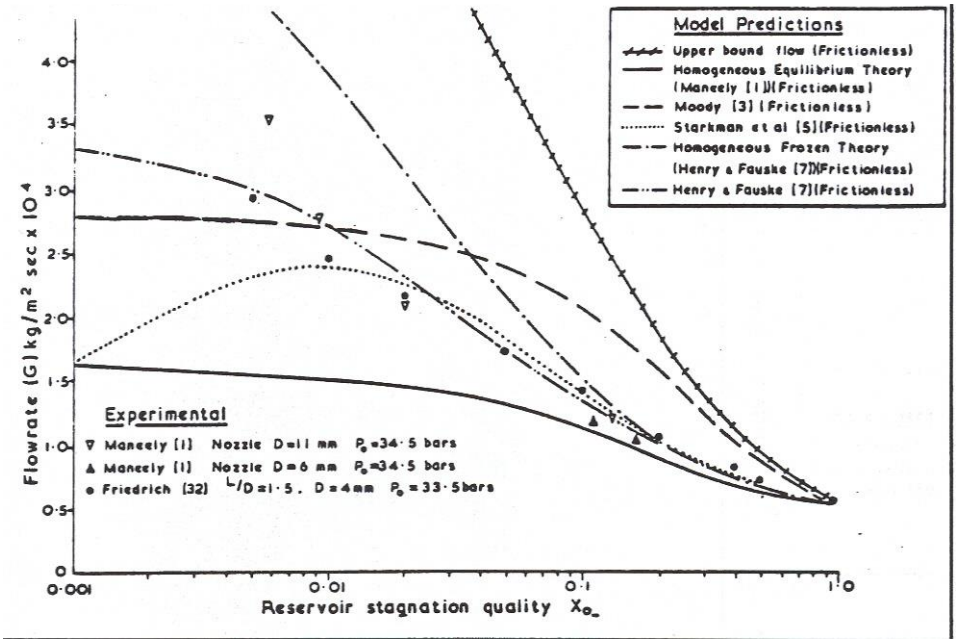

Figure 2-28 Comparison of critical flow models with data, p=500 psia (34.5×10^5 Pa) [29].

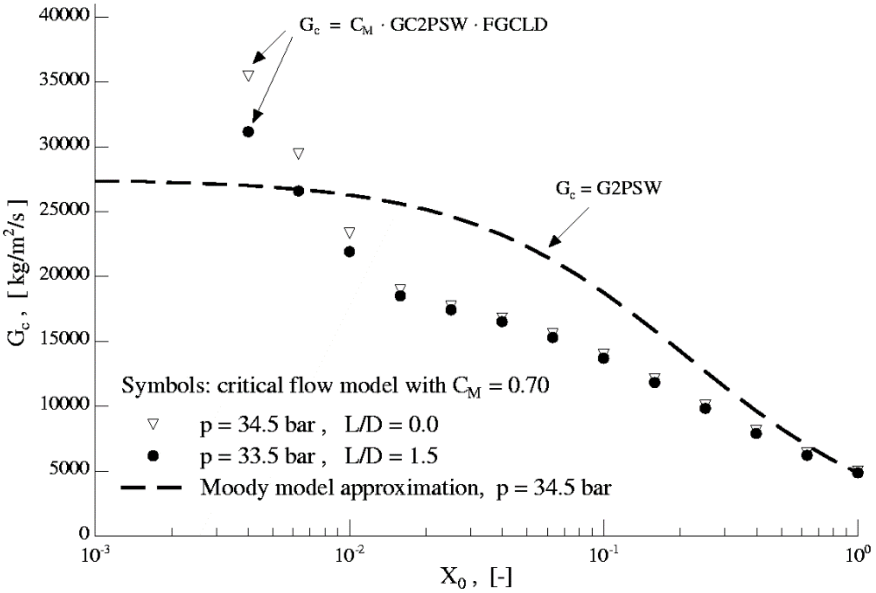

Figure 2-29 Comparison of critical flow models with data, p=500 psia (34.5×10^5 Pa), functions GC2PSW, FGCLD.

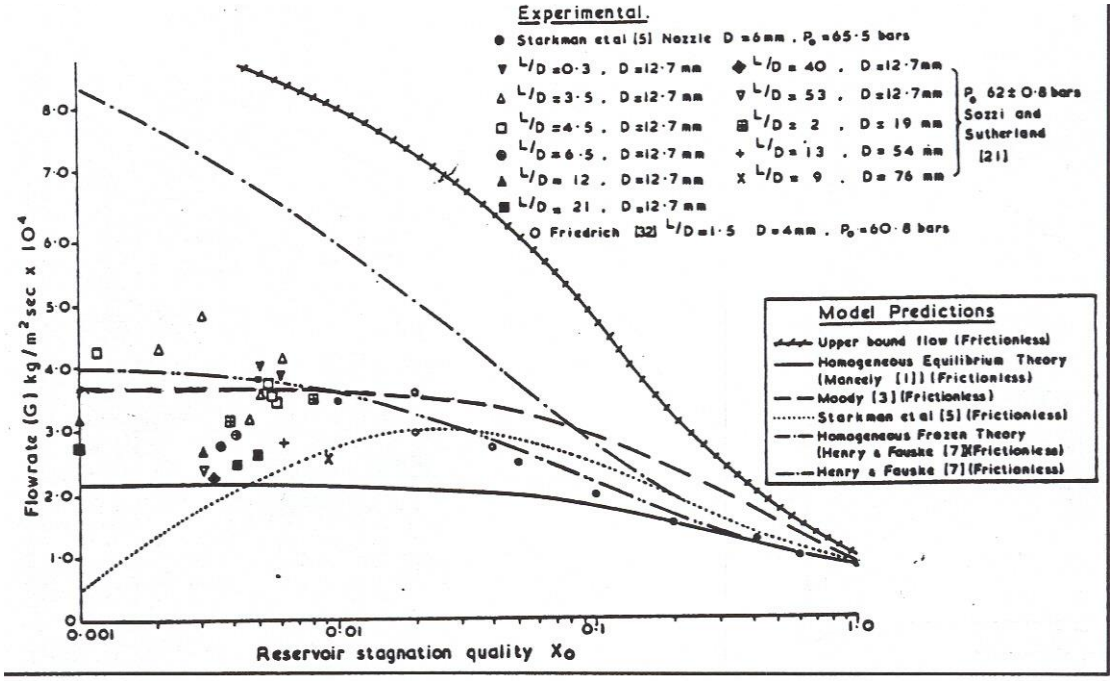

Figure 2-30 Comparison of critical flow models with data, *p*=900 psia (62.0×10^5 Pa) [29].

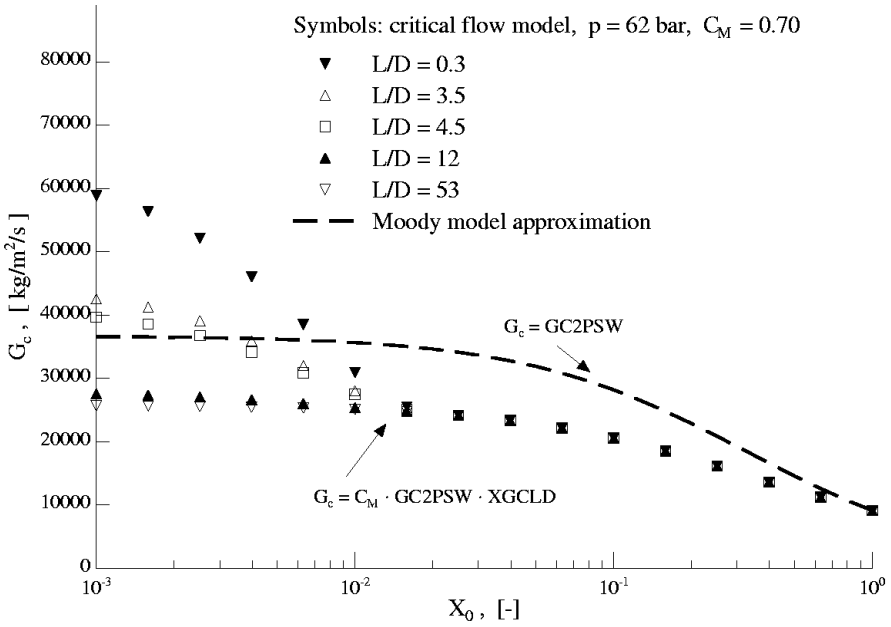

Figure 2-31 Comparison of critical flow models with data, *p*=500 psia (62.0×10^5 Pa), functions GC2PSW, FGCLD.

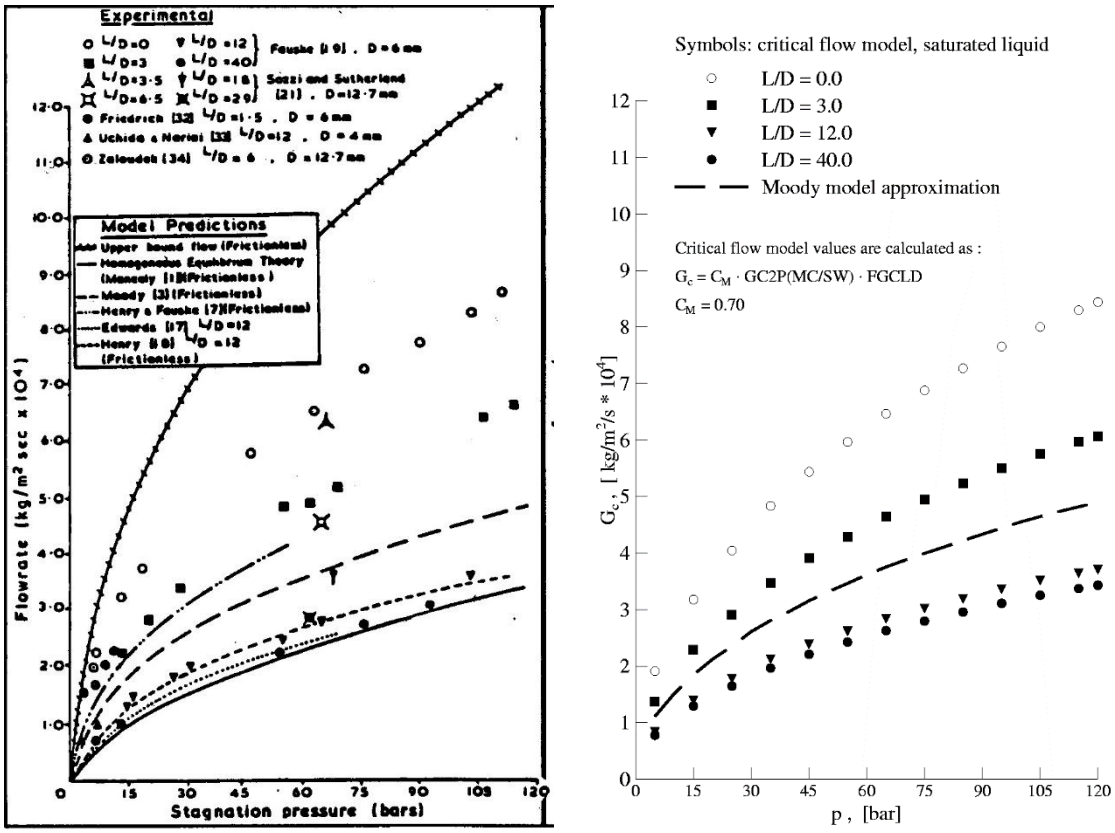

Figure 2-32 Critical flow rate of saturated water, experimental data [29] (left), and SPECTRA model (right).

Values shown in Figure 2-32 right should be compared to the experimental data shown in the left figure. The following experimental data is shown in this figure:

- Fauske, for *L/D* = 0, 3, 12, 40, [36].
- Sozzi and Sutherland, for *L/D* = 3.5, 6.5, 18, 29, [35].
- Friedrich, for *L/D* = 1.5, [34].
- Uchida and Nariari, for *L/D* = 12, [37].
- Zaloudek, for *L/D* = 6, [38].

Generally values calculated by the model applied in SPECTRA are in good agreement with all experiments. Agreement with Fauske data is very good for *L/D* equal to 12 and 40. For small *L/D* (0 and 3) the calculated values are slightly below the experimental data points, relative differences being up to about 10 %. Results reported by Sozzi and Sutherland give generally somewhat larger mass fluxes than Fauske. Therefore the difference between the calculated and the experimental values is somewhat larger for those experiments.

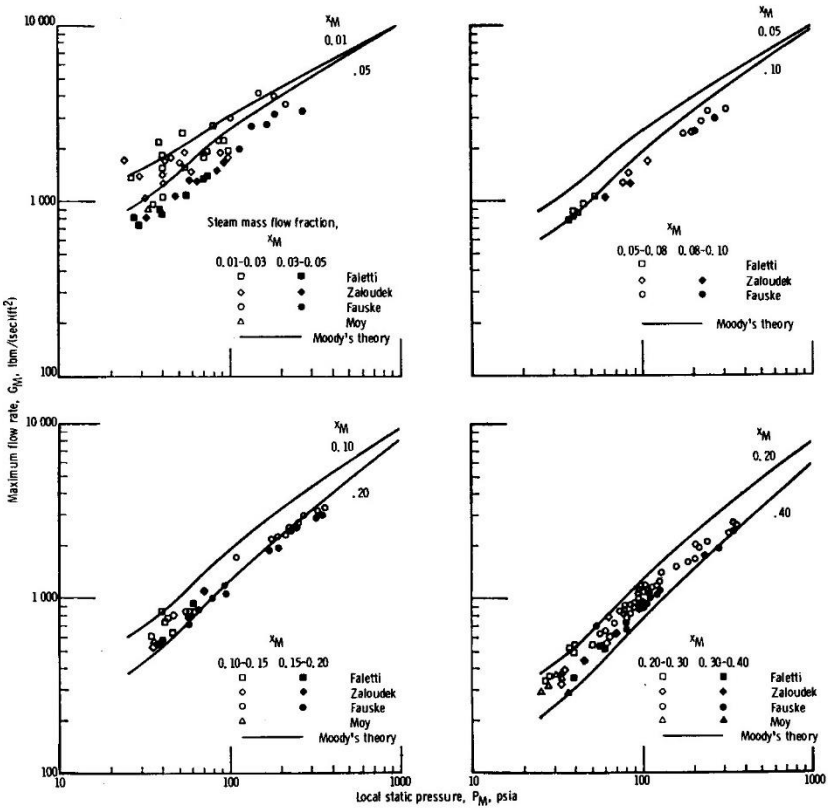

Figure 2-33 Critical flows - data of Faletti, Zaloudek, Fauske, Moy [28].

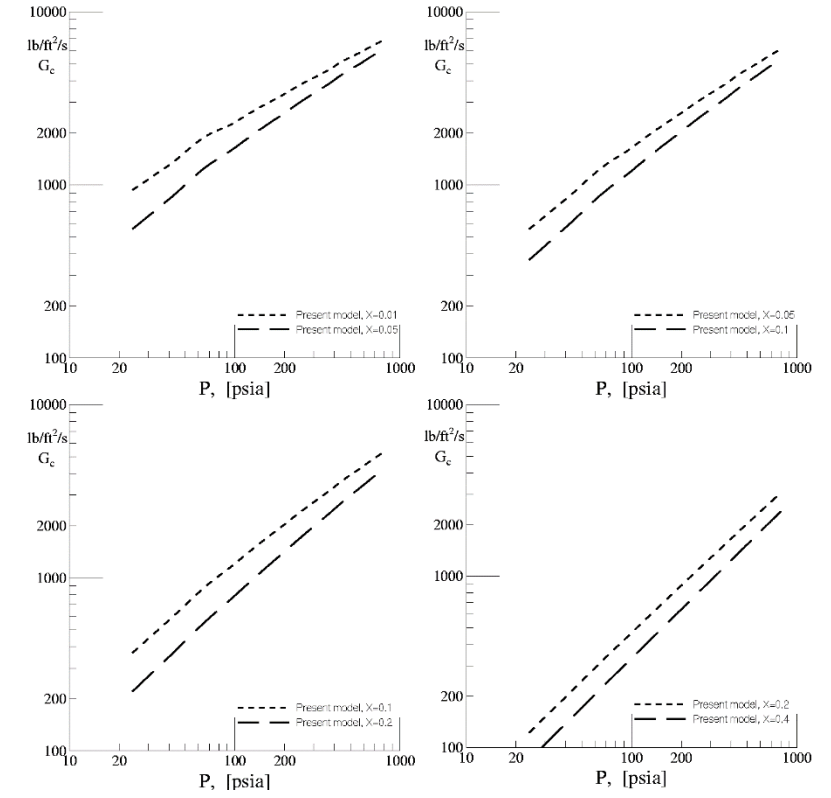

Figure 2-34 Critical flows - subroutine GC2PSW.

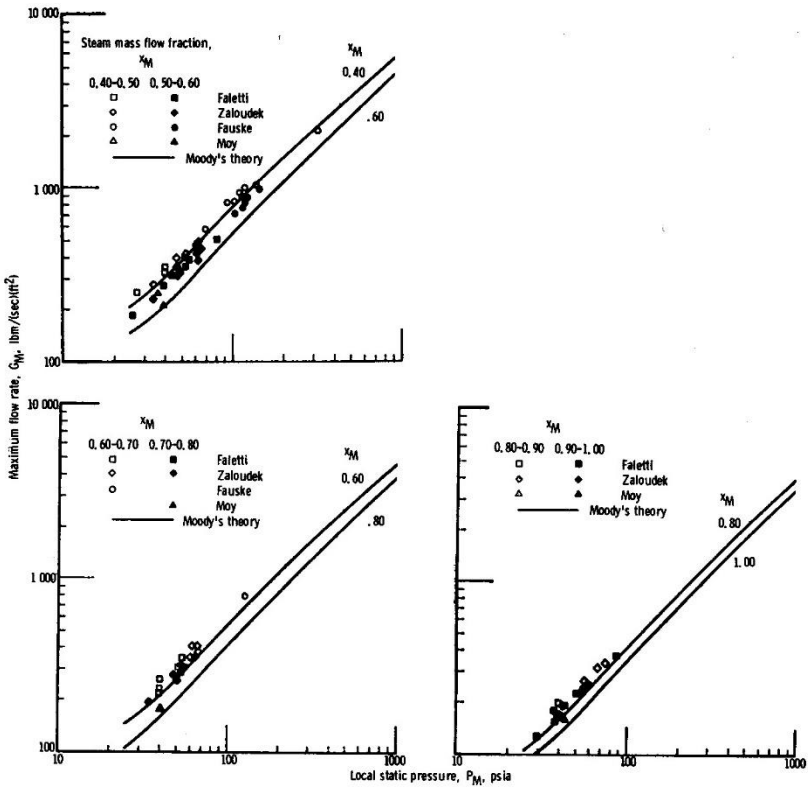

Figure 2-35 Critical flows - data of Faletti, Zaloudek, Fauske, Moy [28].

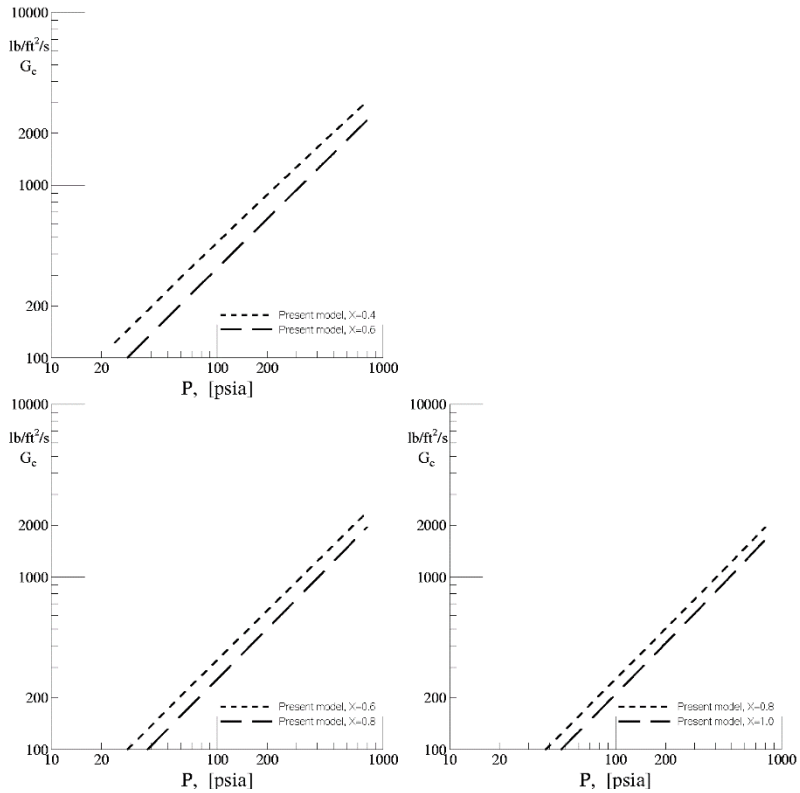

Figure 2-36 Critical flows - subroutine GC2PSW.

Results of the experimental data of Faletti, Zaloudek, Fauke and Moy together with predictions of the Moody model, are shown in Figure 2-33 and Figure 2-35. The figures are reproduced from [28], fig. 11-4. Results of GC2PSW subroutine (no Moody multiplier, no *L/D* multiplier) are shown in Figure 2-34 and Figure 2-36. Surprisingly enough the Moody lines, shown in Figure 2-33 and Figure 2-35 are clearly higher than the lines calculated by the subroutine GC2PSW, which of course represents the Moody model. It is not clear why this discrepancy is observed. Results shown in Figure 2-28, Figure 2-29, Figure 2-30, and Figure 2-31, show that results of GC2PSW are in very good agreement with the Moody model. For example, at 500 psia and quality of 0.01 the critical flow is about 27,000 kg/m^2/s (Figure 2-28, Figure 2-29 - the dashed line in both figures). The data in Figure 2-35 indicate that at these conditions critical flow is above 7,000 lbm/ft^2/s = 34,160 kg/m^2/s. It is therefore concluded that there is something wrong with the data in Figure 2-33 and Figure 2-35 are those results are not disregarded in the critical flow verification.

The review of critical flow models, performed by Ardron et.al., lead to the conclusion that all experimental data were bounded from below by the homogeneous-equilibrium model (HEM), and from above by the non-evaporating flow limit ([29], page 264). Figure 2-37 is given to compare the base model applied in SPECTRA with the "lower bound model" - HEM. Figure 2-37, left, reproduced from [39], gives the homogeneous-equilibrium model results. Figure 2-37, right, gives the results of the base model applied in SPECTRA (no Moody multiplier, no *L/D* multiplier).

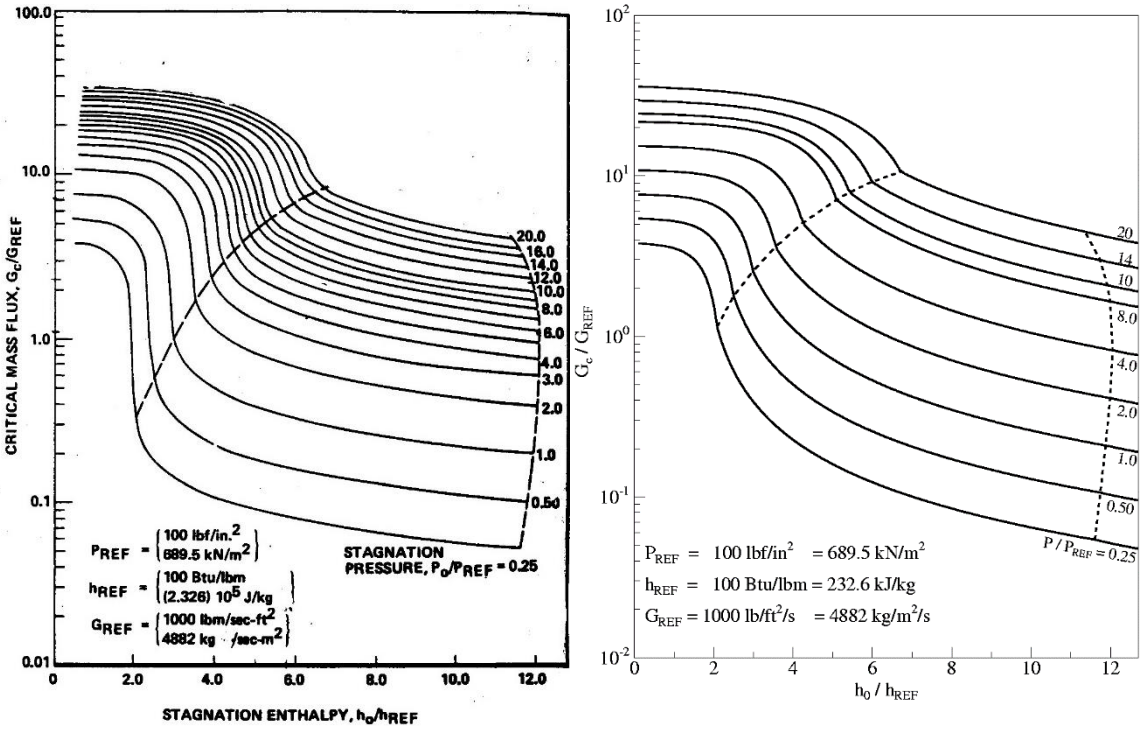

Figure 2-37 Critical flow - HEM -left: [39] figure 9-11a, right: results of GC2PSW.

For highly subcooled liquid both models give very similar values. Near the saturated liquid line the homogeneous-equilibrium model gives clearly lower values. The difference decreases with increasing quality. At the saturated vapor line both models again give very similar results.

The SPECTRA graphs presented in this section were generated using the program GCRITT. The program is provided in \Z-TESTS\JN\GCRIT-T.FOR.

2.3.1.4 Conclusions

The two-phase critical flow model, prepared for SPECTRA, has a wide range of application. It may be applied for two-phase, steam-water mixtures, or multi-component mixtures. The pressure range is up to 1.65×10^7 Pa, so it is wider than the pressure range in the Fluid Property Package (1.499×10^7 Pa bar -section 2.1.1). In case of steam-water mixture the model is valid from highly subcooled water to highly superheated steam. In case of multi-component mixture the upper limit on temperature is set by the Fluid Property Package as 3067.0 K.

The model is relatively simple and fast. It may therefore easily be applied in any engineering calculations performed with the use of a computer. The results of the model are in good agreement with experimental data. The discrepancies between the calculated and observed mass fluxes are for most experimental data ±10 %. Incidentally the discrepancies are up to 25 - 30 %. Only in case of data presented in Figure 2-33 and Figure 2-35 the discrepancies are larger, but this data has been disregarded for reasons described in section 2.3.1.3.

2.3.2 Friction Factors

2.3.2.1 Friction Factor Models

The following models are available to calculate wall friction factor:

1 The model based on Colebrook-White formula, which gives friction factor in case of non-uniform roughness (typical commercial pipes). The model is coded as the function FFWNR.

2 The model based on Nikuradse formula, which gives friction factor in case of uniform roughness (an artificial sand roughness, [40]). The model is coded as the function FFWUR.

3 Simplified model that calculates friction factor with smaller accuracy, but is significantly faster because there is no need to iterate to obtain the friction factor. The model is coded as the function FFWSM.

On top of these three models, there are two approximations of the Colebrook-White formula, derived by Beluco-Camano and by Churchill. These are discussed in the next section.

Verification of the models used by FFWNR and FFWUR is performed by comparing results of these functions with the graphs shown in [40]. Verification of the function FFWSM is performed comparing its results with the results of the other two functions.

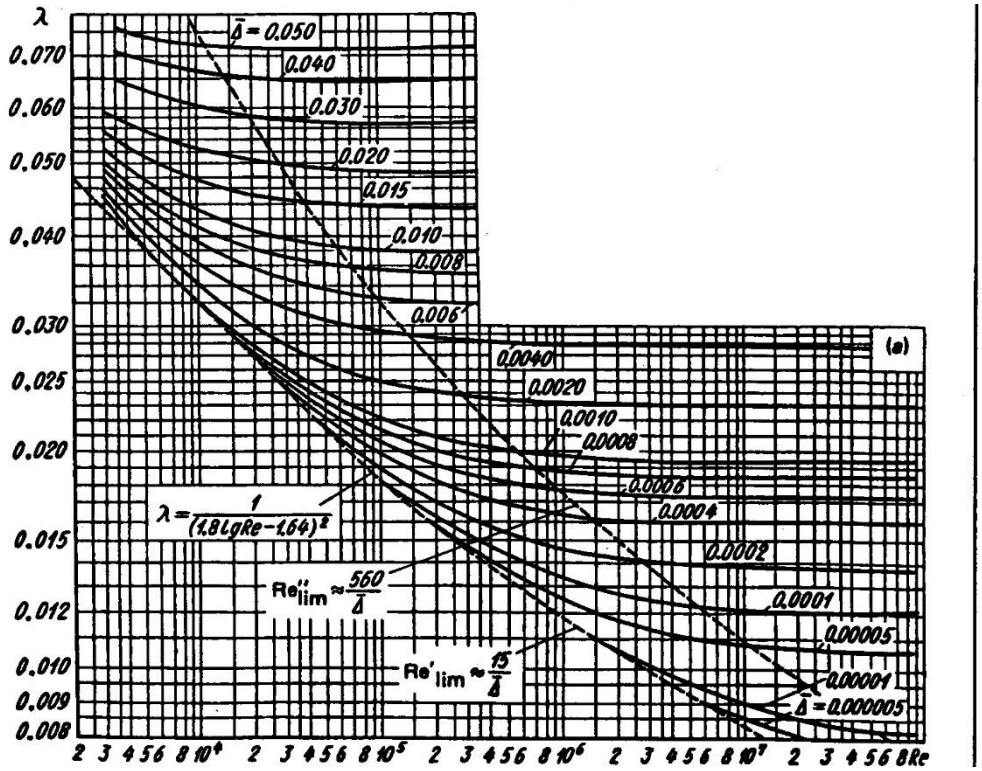

Figure 2-38 Friction factors, non-uniform roughness, reproduced from [40]

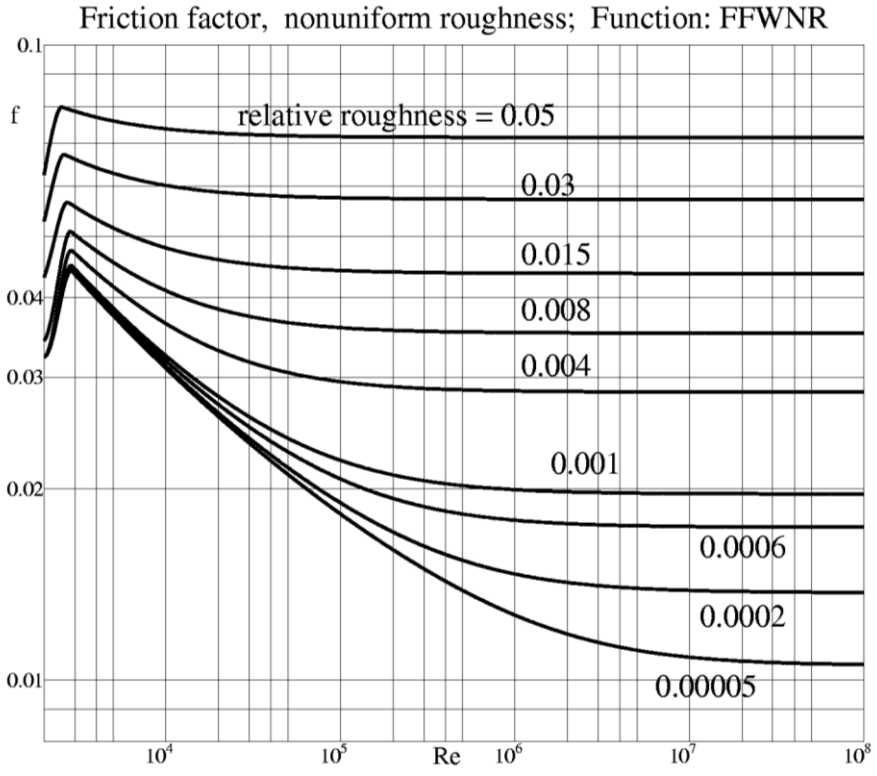

Figure 2-39 Friction factors, non-uniform roughness, function FFWNR

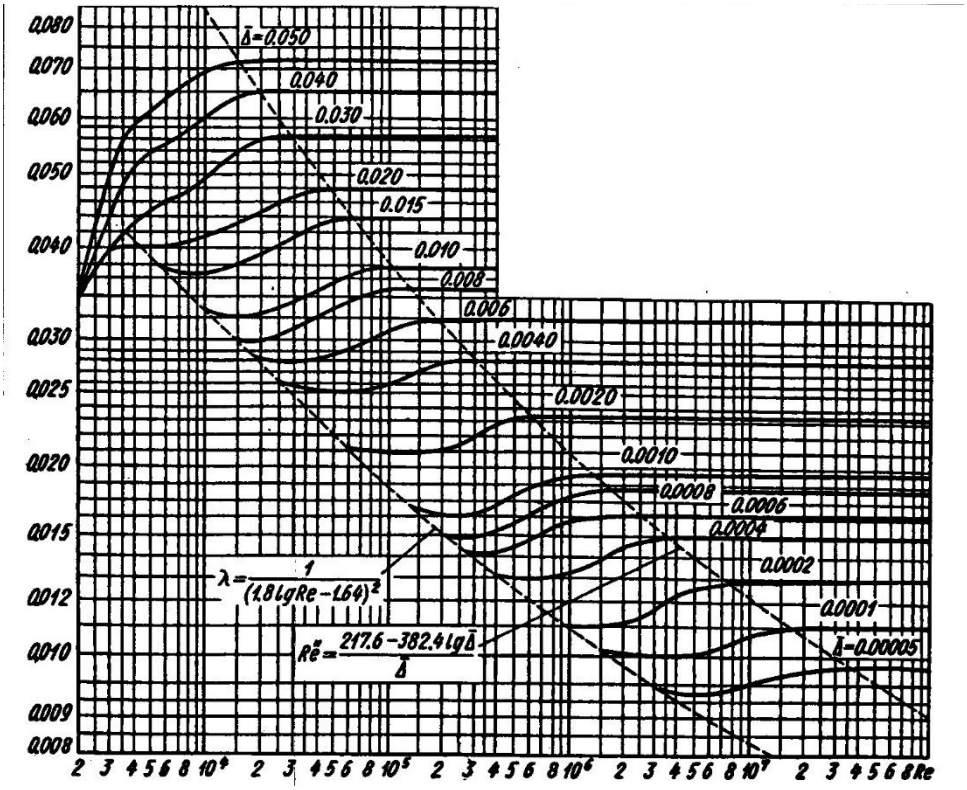

Figure 2-40 Friction factors, uniform roughness, reproduced from [40]

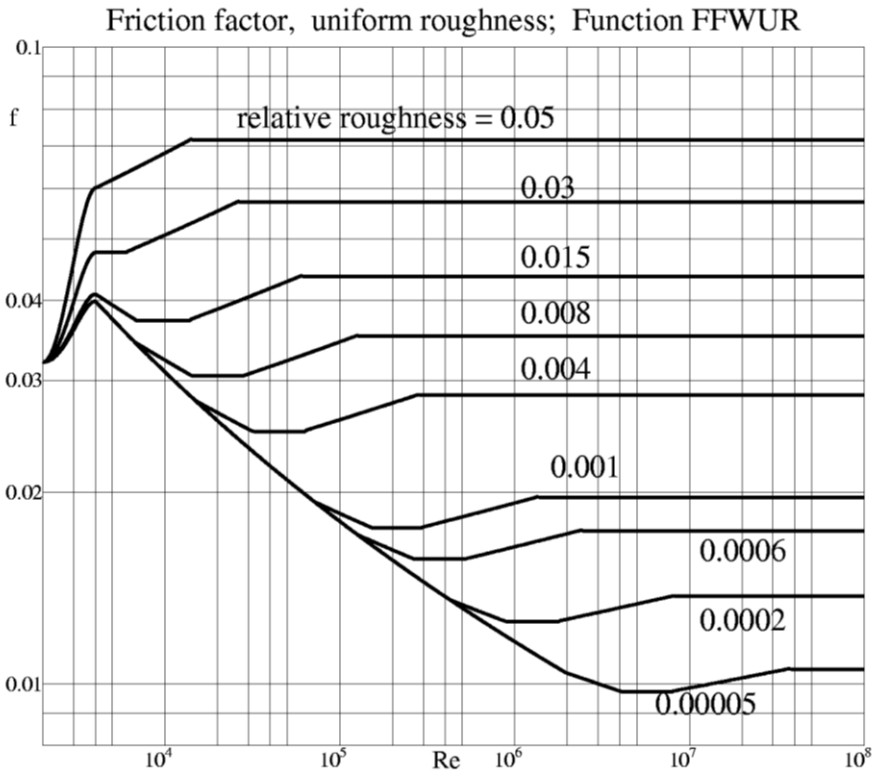

Figure 2-41 Friction factors, uniform roughness, function FFWUR

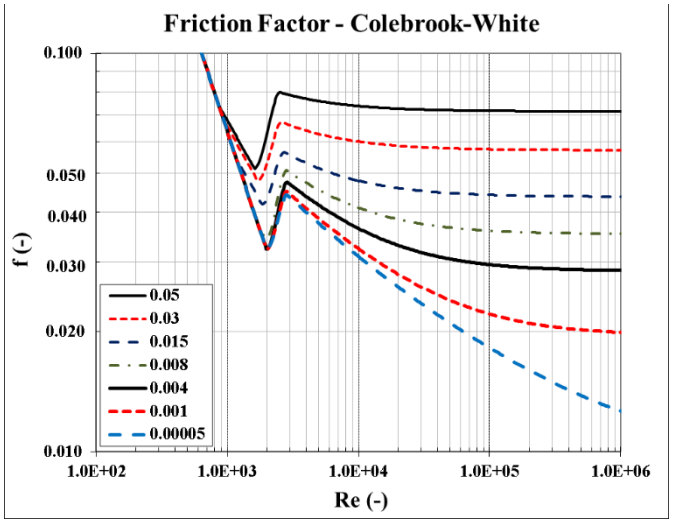

Figure 2-42 Friction factor, non-uniform roughness, Colebrook-White formula

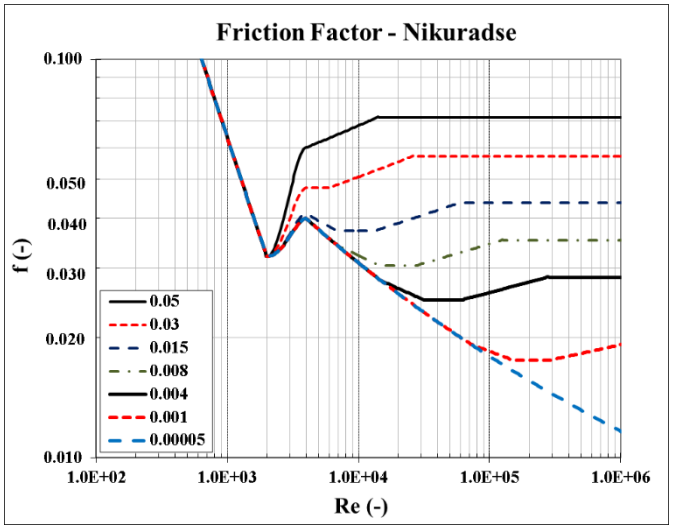

Figure 2-43 Friction factor, uniform roughness, Nikuradse formula

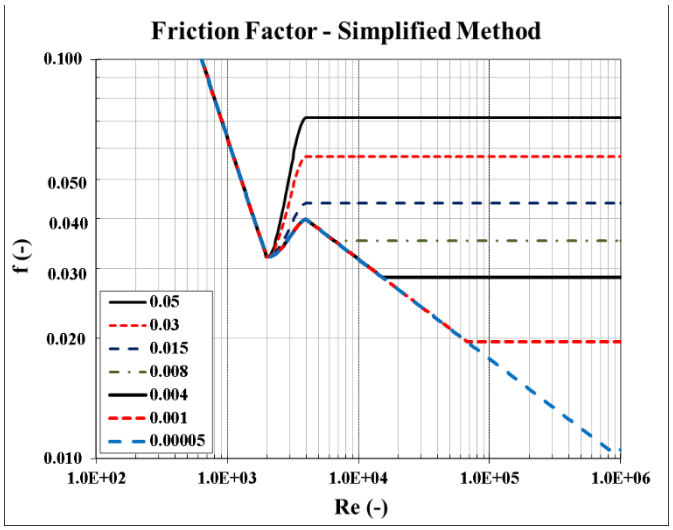

Figure 2-44 Friction factor, simplified model

For non-uniform roughness the friction factors are presented in [40], section 2-1, diagram 2-4. These data are reproduced in Figure 2-38. Results obtained with function FFWNR for selected values of roughness, e, are shown in Figure 2-39. Results are in agreement.

For uniform roughness the friction factors are presented in [40], section 2-1, diagram 2-2. These data are reproduced in Figure 2-40. Results obtained with function FFWNR for selected values of roughness, e, are shown in Figure 2-41. Results are in agreement.

Results of the simplified model for calculating friction factor, function FFWSM, are compared to the results of the functions FFWNR and FFWUR in Figure 2-42, Figure 2-43, and Figure 2-44. FFWSF is in agreement with FFWNR and FFWUR in the first part of laminar range and in the stabilized turbulent region. In the transition between those two regions FFWSM results are somewhere between the results of those functions.

The graphs shown in Figure 2-39, Figure 2-41, Figure 2-42, Figure 2-43, and Figure 2-44 were generated using the program FFT. The program is provided in \Z-TESTS\JN\FF-T\FF-T.FOR.

2.3.2.2 Non-Uniform Roughness - Approximations of the Colebrook-White Formula

The Colebrook-White formula requires iteration, since the friction factor depends on itself:

$$f_{wall} = \left[2\log_{10}\left(\frac{2.51}{\mathrm{Re}\sqrt{f_{wall}}} + \frac{e}{3.7} \right) \right]^{-2}$$

Several approximations of the Colebrook-White formula have been developed and published in open literature, for example [205]. Below two approximations are discussed. In each case only the turbulent correlation (Colebrook-White) is replaced by the approximation. The laminar and transition models are the same.

- Beluco and Camano approximation [205]:

$$f_{wall} = \left[2\log_{10}\left(\left(\frac{5.9802}{\mathrm{Re}} \right)^{0.9695} + \left(\frac{e}{3.7315} \right)^{1.0954} \right) \right]^{-2}$$

  The friction factor calculated based on the Beluco and Camano approximation in the turbulent range (function FFWNB) is shown in Figure 2-46. For comparison, the results based on the Colebrook-White are shown in Figure 2-45. Calculations performed for the range of Reynold numbers $10^2 \le \mathrm{Re} \le 10^8$ and relative roughness $0.05 \le e \le 0.00005$ showed that the average relative difference between the Beluco-Camano formula and the Colebrook-White formula is:

$$\delta = 0.08\%$$

  The agreement is excellent and the correlation is significantly faster in numerical calculations, therefore it is the default correlation in SPECTRA.

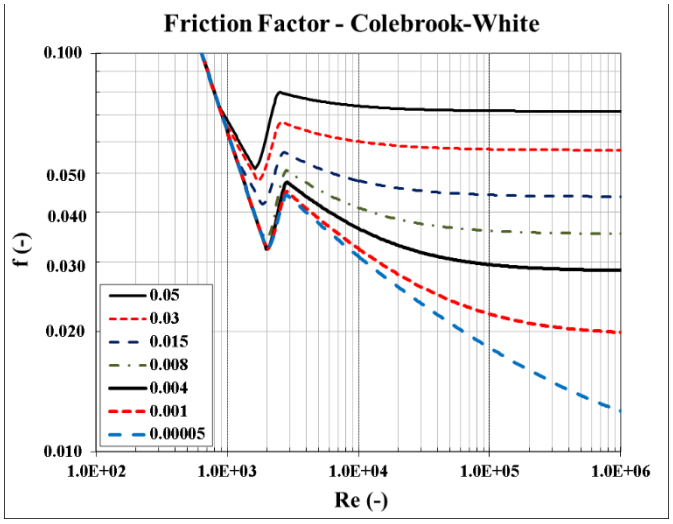

Figure 2-45 Friction factor, non-uniform roughness, Colebrook-White formula

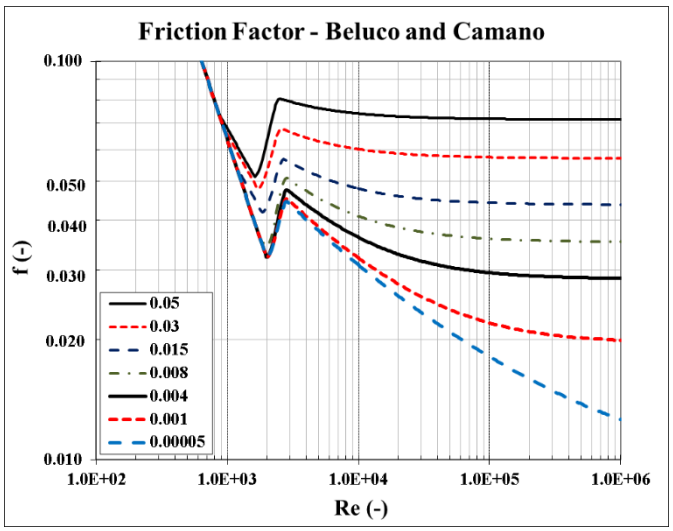

Figure 2-46 Friction factor, non-uniform roughness, Beluco and Camano formula

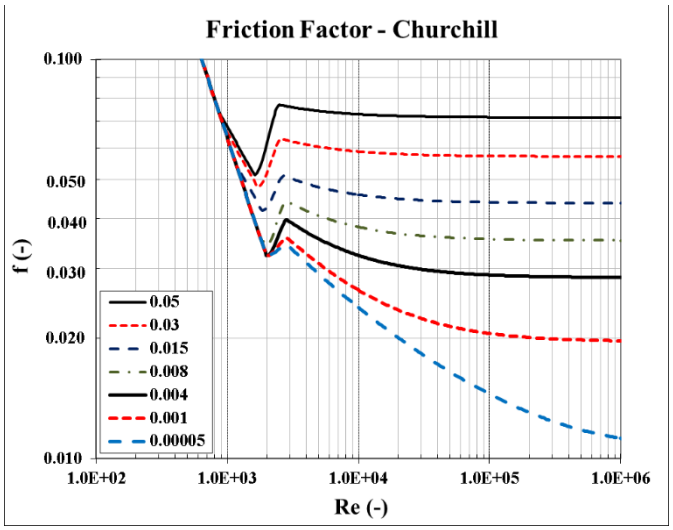

Figure 2-47 Friction factor, non-uniform roughness, Churchill formula

- Churchill approximation is [205]:

$$f_{wall} = \left[2\log_{10}\left(\frac{5.74}{\mathrm{Re}} + \frac{e}{3.7} \right) \right]^{-2}$$

The friction factor calculated based on the Churchill approximation in the turbulent range (function FFWNH) is shown in Figure 2-47. For comparison, the results based on the Colebrook-White are shown in Figure 2-45. Calculations performed for the range of Reynold numbers $10^2 \leq \mathrm{Re} \leq 10^8$ and relative roughness $0.05 \leq e \leq 0.00005$ showed that the average relative difference between the Churchill formula and the Colebrook-White formula is:

$$\delta = 4.7\%$$

The disagreement is worse in the range of Reynolds numbers $2000 \leq \mathrm{Re} \leq 10{,}000$ and small relative roughness. This approximation is clearly not as good as the previous one, but since it is frequently used in engineering applications, it is available in SPECTRA.

The graphs shown in Figure 2-45, Figure 2-46, and Figure 2-47 were generated using the program FFT. The program is provided in \Z-TESTS\JN\FF-T\FF-T.FOR.

2.3.3 Two-phase Friction Factor Multiplier

The two-phase friction factor multiplier is calculated using the Hancox-Nicoll correlation [41], and alternative Levy correlation. The Hancox-Nocoll correlation has been selected as a default correlation because it gives relatively good representation of experimental data over a wide range of conditions. It has been found that Hancox-Nicoll correlation gives generally better agreement with experiments than the Lockhart-Martinelli [43], Martinelli-Nelson [44], Baroczy [45] and Chisholm [46] correlations.

Verification of the Hancox-Nicoll model (coded as function F2PHN), is performed in two steps. First, the results of the function are compared with the plots in original article. Second, the results of the function are compared with experimental data. Verification of the Levy correlation (coded as function F2PLE), is performed by comparing the results of Levy with Hancox-Nicoll, for the same experiments.

2.3.3.1 Comparison with the Original Article

Function F2PHN has been used to reproduce the results shown in [41] (figure 1 in [41] - reproduced in Figure 2-48, left). It was found out that the equation presented in the article (equation 20 in [41]) gives incorrect results. This mistake has already been found and corrected in [47] (see section 6.2.6.1 in [47]). The same correction was made in F2PHN. Results obtained with the corrected formula are shown in Figure 2-48, right. The results are in agreement with the results presented in the original article.

2.3.3.2 Comparison with Experimental Data

Figure 2-49 shows experimental data from CISE Laboratory, Milan (reproduced from [27], chapter 2, figure 4). Figure contains also lines obtained using Martinelli-Nelson and Thom correlations. Results obtained using function F2PHN are plotted in Figure 2-50. Generally the results are in good agreement with experiments. The influence of mass flux on the friction multiplier is a little weaker in calculated results than observed in experiments. For low mass flux (1145 kg/m^2/s) calculated results are consistently below the experimental data points.

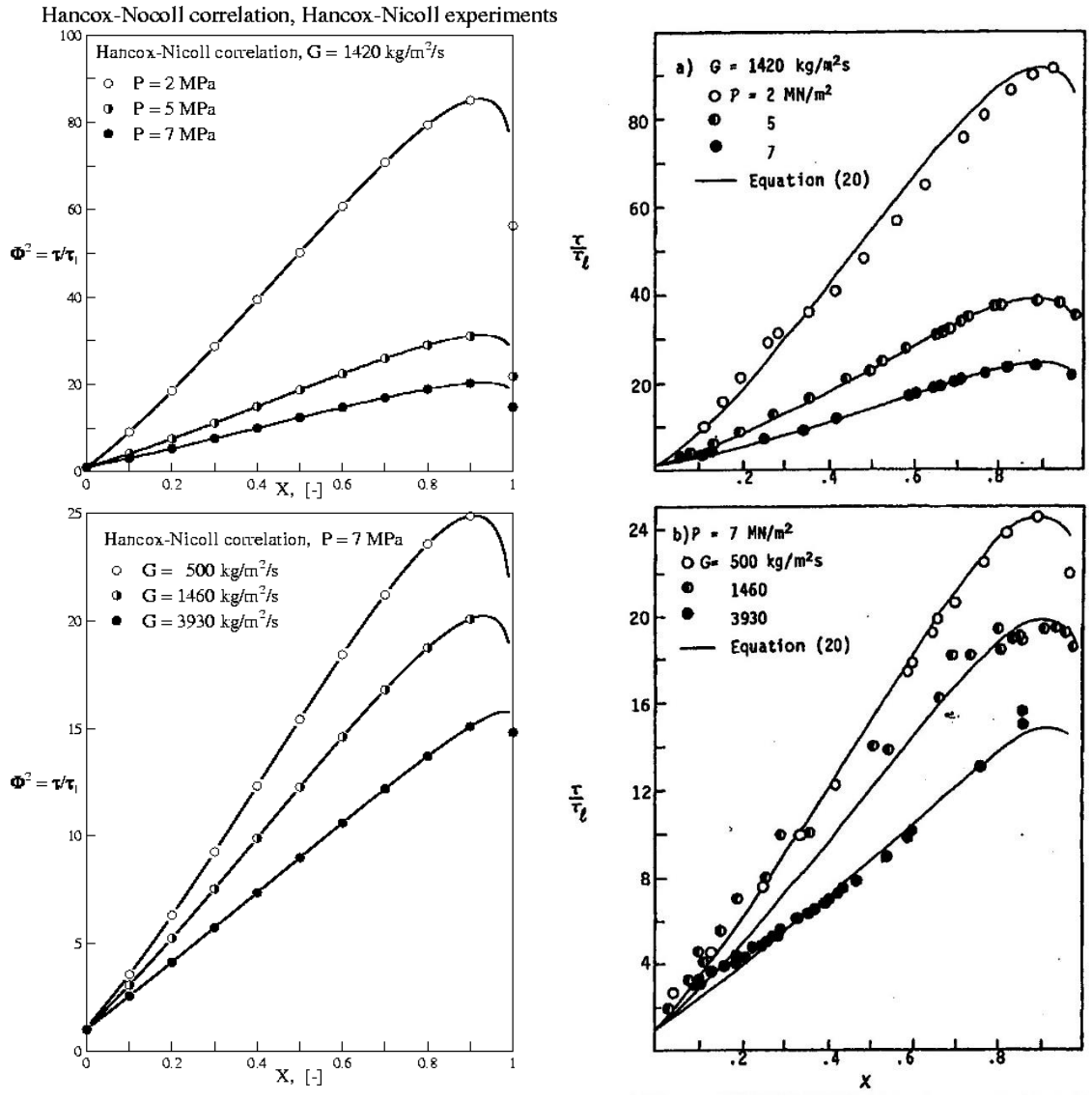

Figure 2-48 Hancox-Nicoll correlation, left: [41], right: function F2PHN.

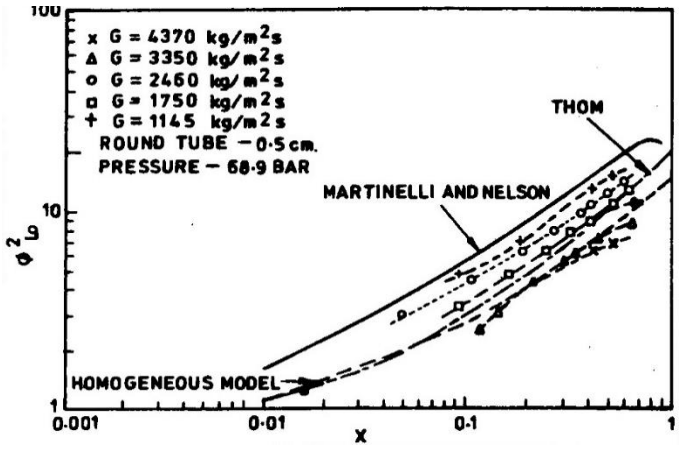

Figure 2-49 Experimental data from CISE Laboratories, Milan [27].

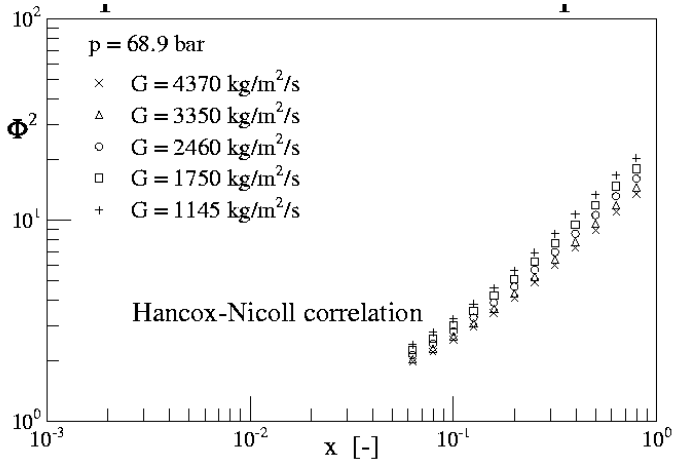

Figure 2-50 Results of F2PHN.

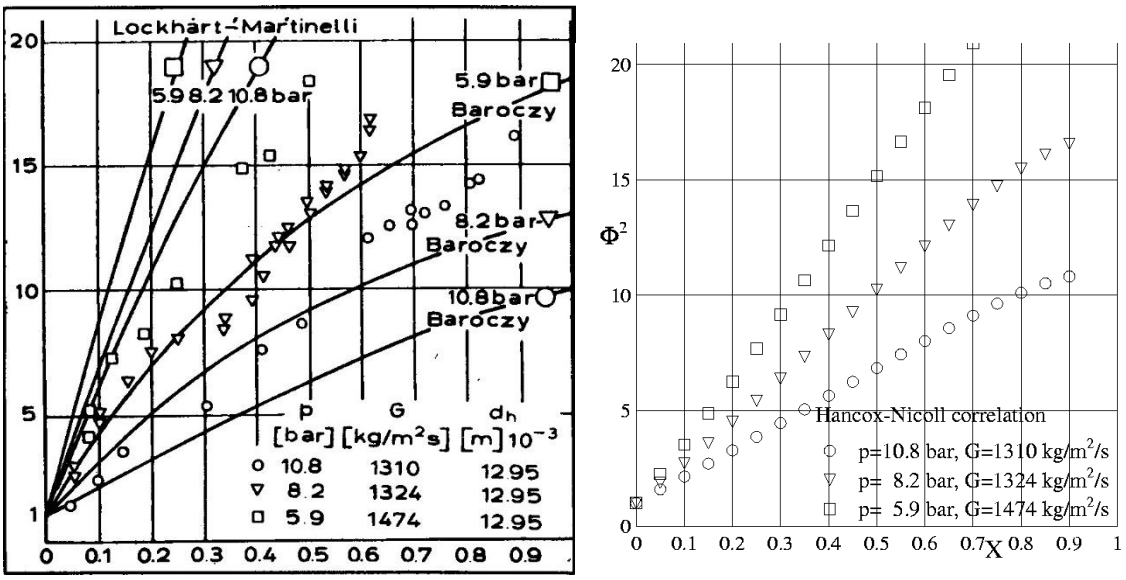

Figure 2-51 Left: experimental data compiled by Friedel [49], right: results of F2PHN.

Figure 2-51 (left) shows experimental data compiled by Friedel [49] (reproduced from [48], chapter 11, figure 12). Figure contains also lines obtained using Lockhart-Martinelli and Baroczy correlations. Results obtained using function F2PHN are plotted in Figure 2-51 (right). Calculated results are consistently below the experimental data points but closer to the experimental data points than the results of Baroczy correlation, which gives lowest multipliers (Figure 2-51, left). The Lockhart-Martinelli lines give clearly too high multipliers (Figure 2-51, left).

The graphs shown in Figure 2-48, Figure 2-50, and Figure 2-51 were generated using the program F2PT. The program is provided in \Z-TESTS\JN\F2P-T.FOR.

2.3.3.3 Comparison of Hancox-Nicoll and Levy Correlations

Comparison of Hancox-Nicoll and Levy correlations is shown in Figure 2-52. Calculations were performed using conditions of the Hancox-Nicoll data [41] and CISE data [27]. Experimental results are reproduced above, in Figure 2-48 and Figure 2-49.

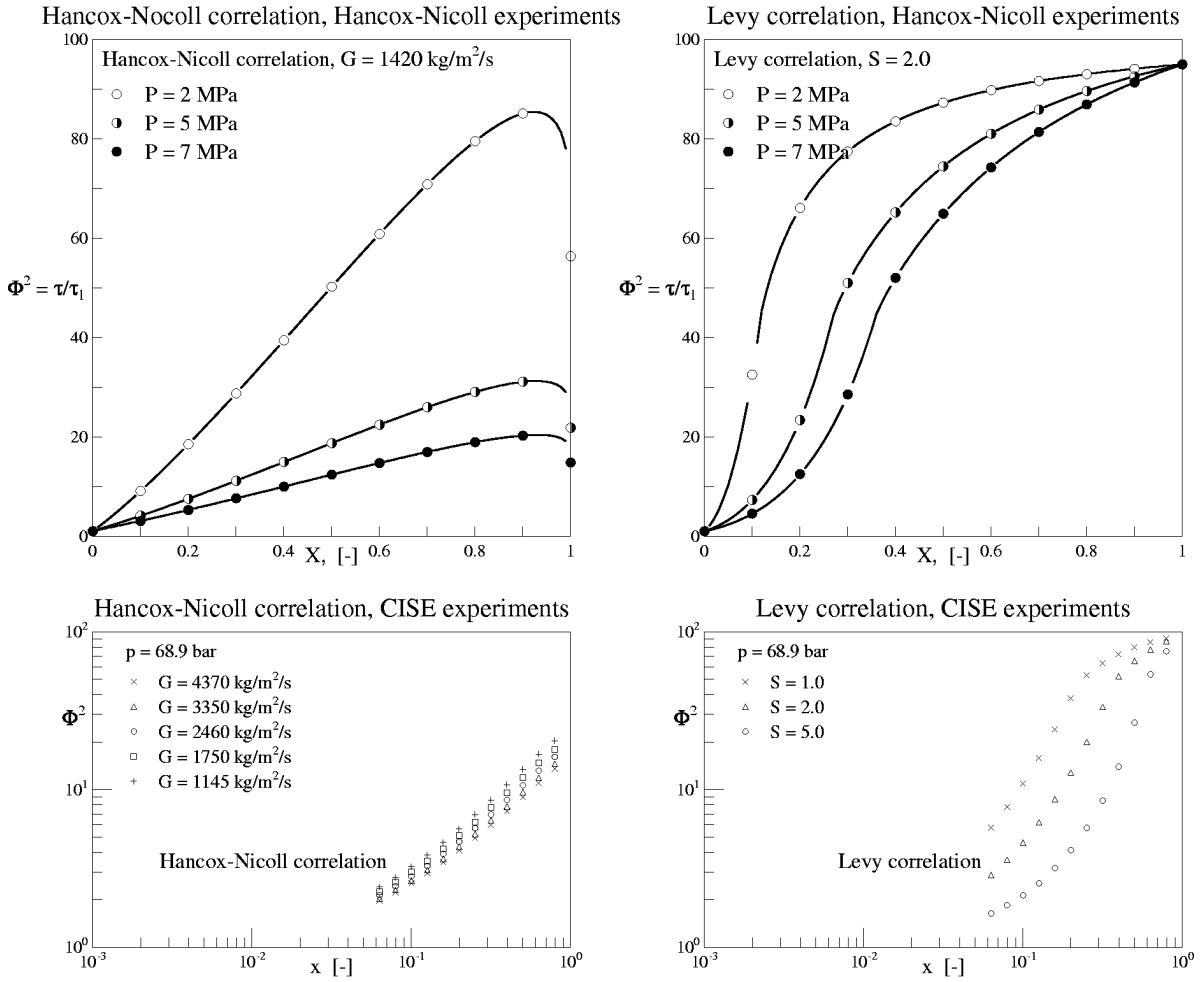

Figure 2-52 Comparison of Hancox-Nicoll (left) and Levy (right) correlation for the Hancox-Nicoll data (above) and CISE data (below).

Figure 2-52 shows results obtained with Hancox-Nicoll (left graphs), and Levy (right graphs). The Levy uses void fraction rather than quality. For comparison graphs the void fractions were calculated from the quality using the slip factor, *S*, of 2.0 for the Hancox-Nicoll data. For the CISE data results obtained with three slip factors, namely S = 1.0, 2.0 and 5.0 are shown (the mass flux, *G*, is not used in the Levy correlation, therefore only one line is obtained for all mass fluxes).

Generally it may be observed that Levy correlation provides higher friction multiplier than the Hnacox-Nicoll correlation, specifically in the high quality region. It should be remembered that in the Levy correlation implemented in SPECTRA a "damping factor" was used in the high quality region (see Volume 1). In the original correlation $\Phi^2 \rightarrow \infty$, when $\alpha \rightarrow 1.0$.

2.3.4 Tests of the Pump/Compressor Model

The pump/compressor model testing consists of two groups of tests. As a first step, the maps are produced using simple model configuration, with pump/compressor running at different speeds. The volumetric flow and pressure head are then plotted against each other. In this way the shape of pump/compressor maps are visualized for different input values of the pump/compressor model parameters. This part is described in section 2.3.4.1, and it is intended mainly as an illustration and verification of the influence of the input parameters on the maps. As a second step, the behavior of the pump/compressor model is investigated for several cases for which the solution is known. Those cases are presented in section 2.3.4.2.

2.3.4.1 Pump/Compressor Maps

The influence of the constant C_P (see Volume 2) on the pump/compressor map is shown in Figure 2-53.

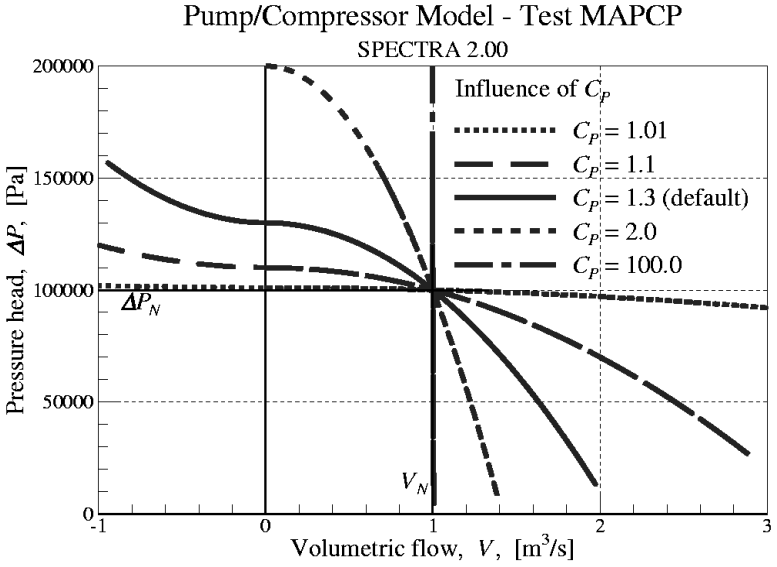

Figure 2-53 Influence of C_P on pump/compressor map.

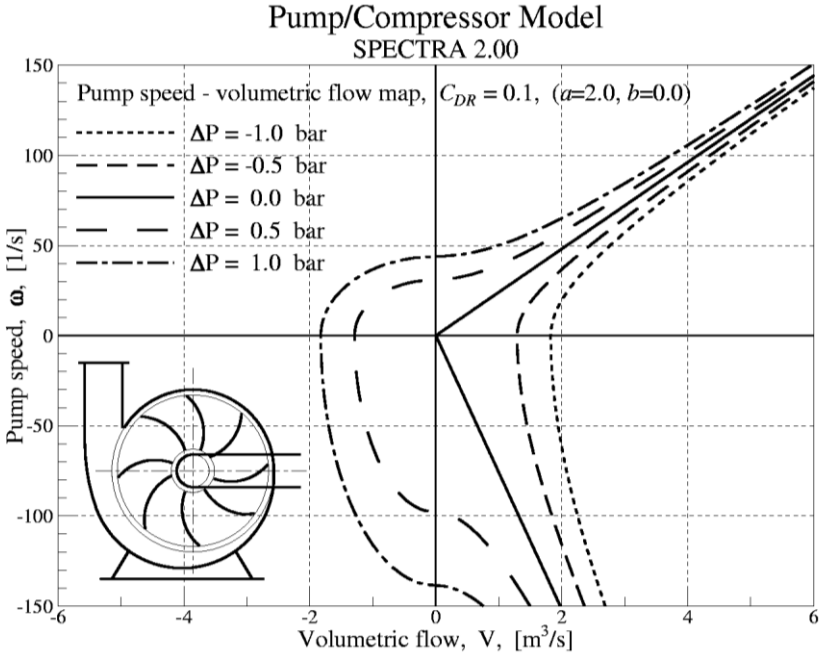

Figure 2-54 Influence of the parameter C_{DR} on the pump maps. C_{DR} =0.1 (typical centrifugal pump).

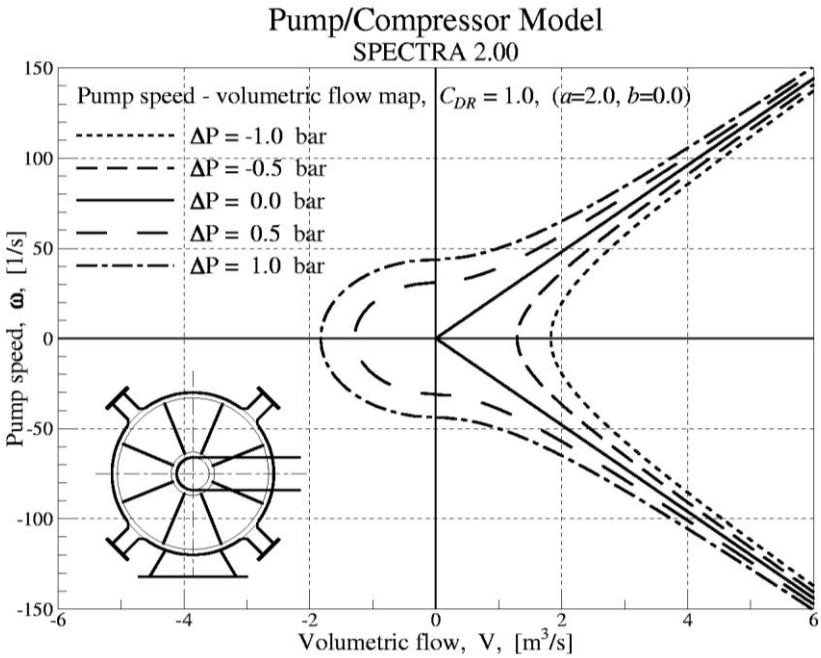

Figure 2-55 Influence of the parameter C_{DR}, on the pump maps. C_{DR} =1.0 (theoretical centrifugal “pump”).

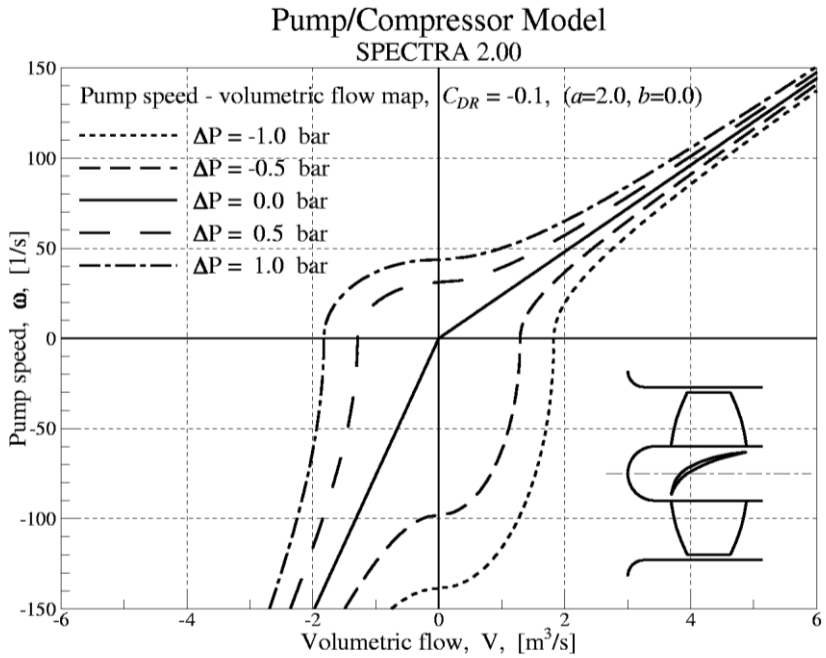

Figure 2-56 Influence of the parameter C_{DR}, on the pump maps. C_{DR} =–0.1 (typical axial pump).

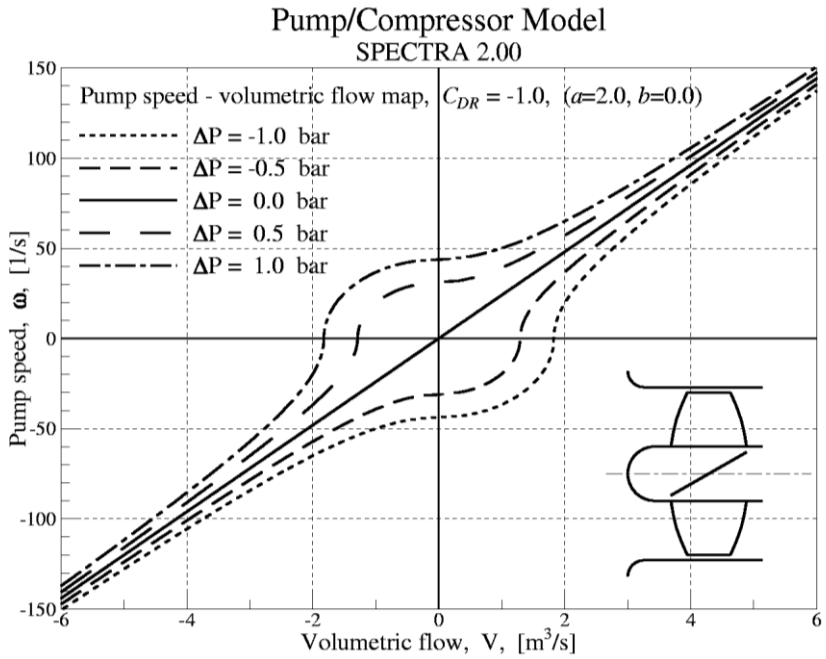

Figure 2-57 Influence of the parameter C_{DR}, on the pump maps. C_{DR} =–1.0 (theoretical axial “pump”).

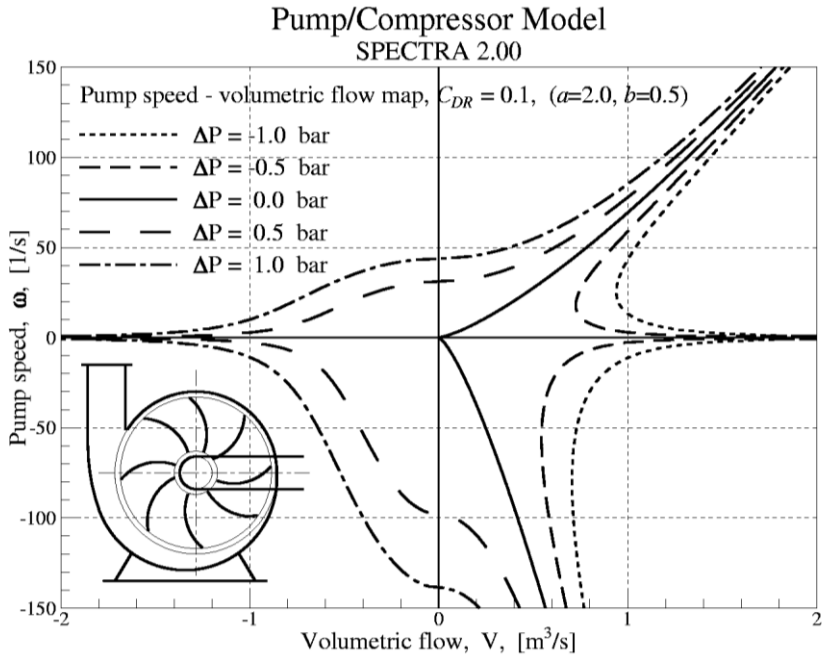

Figure 2-58 Influence of the parameter C_{DR}, on the pump maps. C_{DR} =0.1 (a=2.0, b=0.5).

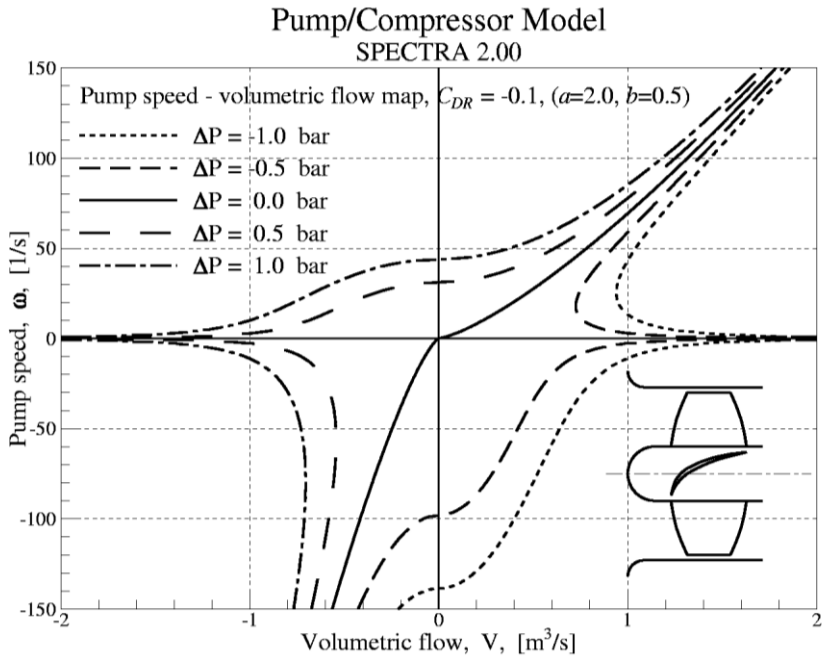

Figure 2-59 Influence of the parameter C_{DR}, on the pump maps. C_{DR} =–0.1 (a=2.0, b=0.5).

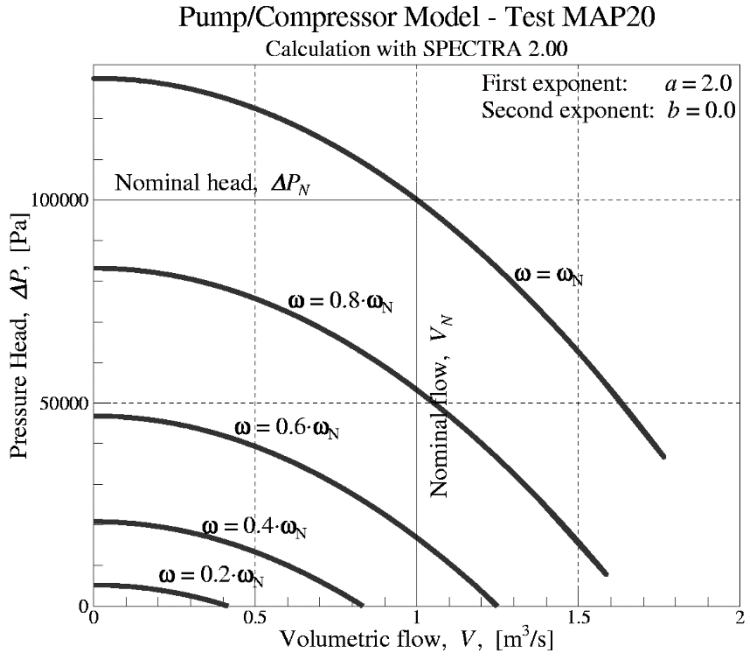

Figure 2-60 Influence of exponents on map, *a*=2.0, *b*=0.0 (Type 1 pump).

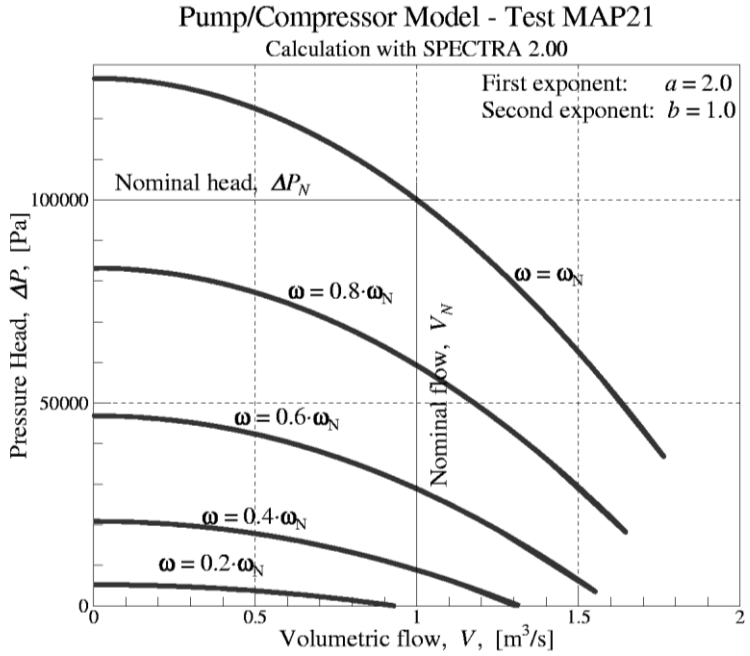

Figure 2-61 Influence of exponents on map, *a*=2.0, *b*=1.0 (default for Type 2 pump).

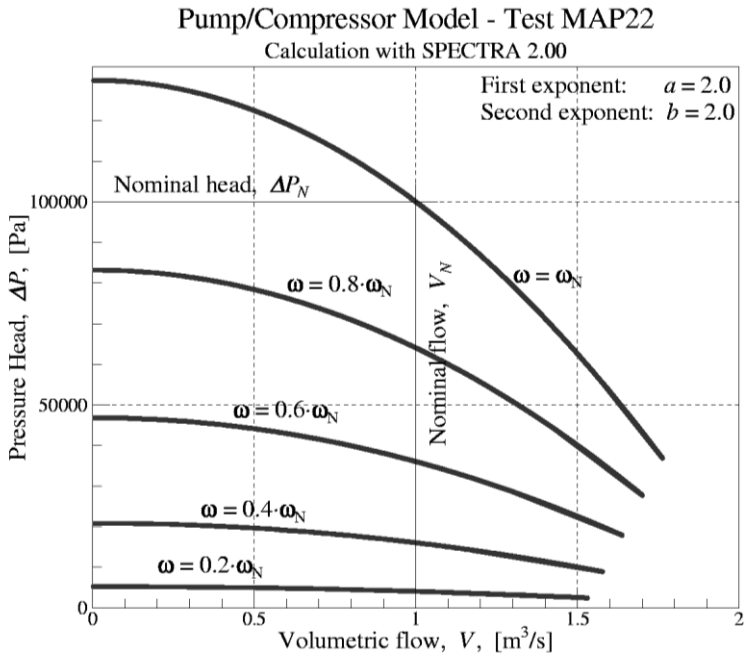

Figure 2-62 Influence of exponents on map, *a*=2.0, *b*=2.0.

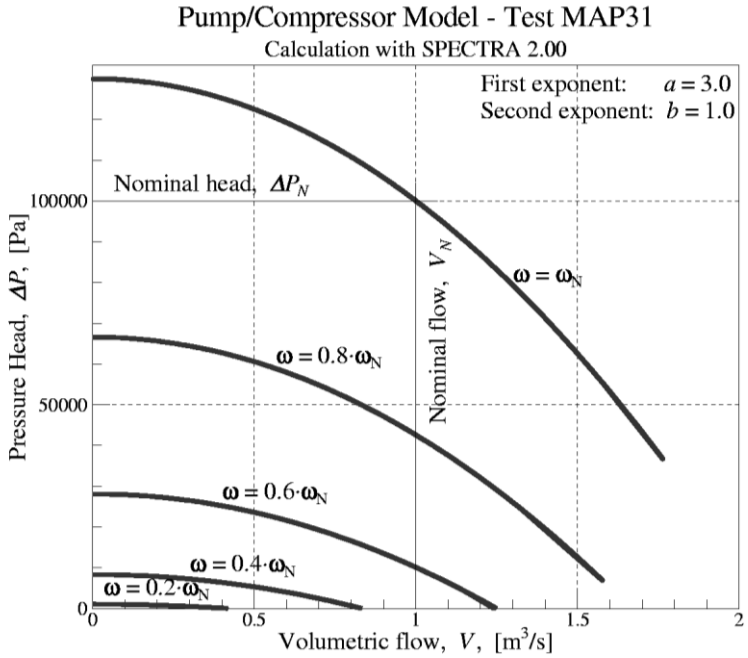

Figure 2-63 Influence of exponents on map, *a*=3.0, *b*=1.0.

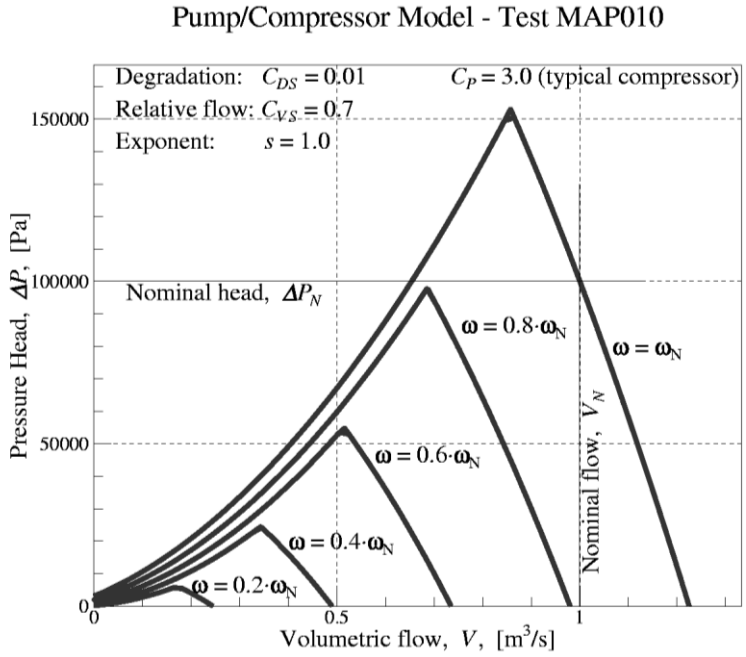

Figure 2-64 Influence of surge parameters on map, C_{DS}=0.01, C_{VS}=0.7 (C_P=3.0 - typical compressor).

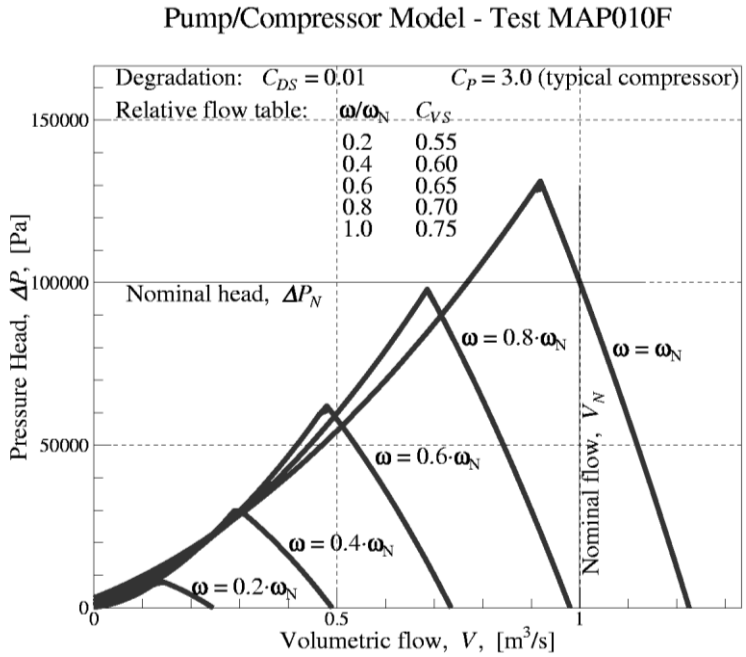

Figure 2-65 Influence of surge parameters on map, C_{DS}=0.01, C_{VS}=f(ω) (C_P=3.0 - typical compressor).

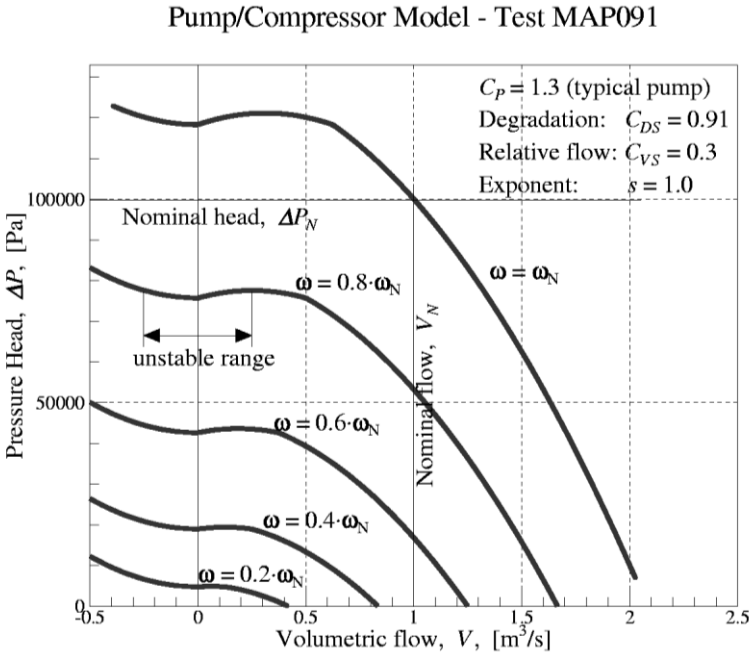

Figure 2-66 Influence of surge parameters on map, C_{DS}=0.91, C_{VS}=0.3, s=1.0 (C_P=1.3 - typical pump).

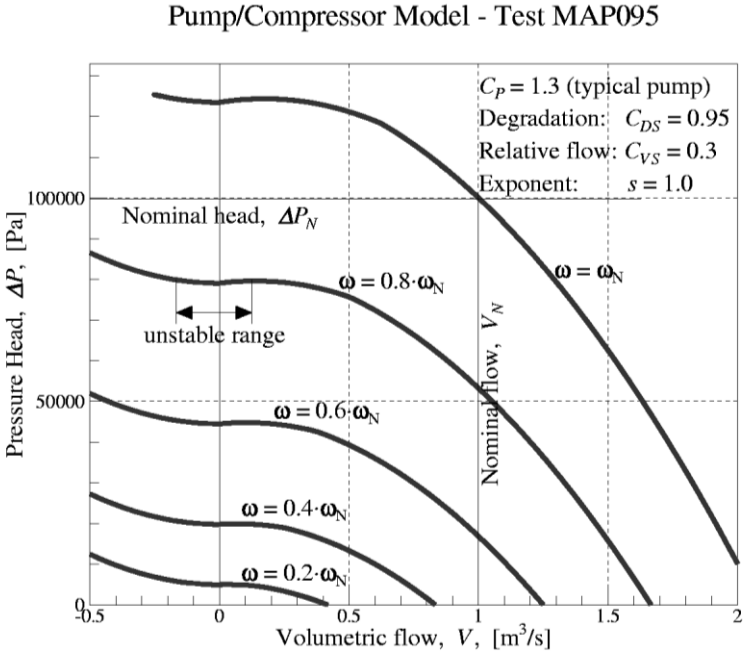

Figure 2-67 Influence of surge parameters on map, C_{DS}=0.95, C_{VS}=0.3, s=1.0 (C_P=1.3 - typical pump).

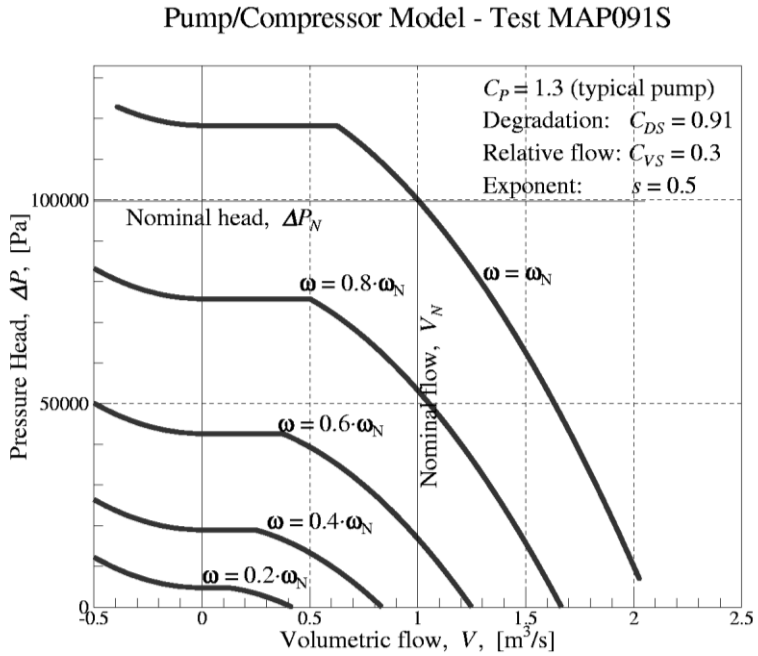

Figure 2-68 Influence of surge parameters on map, C_{DS}=0.91, C_{VS}=0.3, s=0.5 (C_P=1.3 - typical pump).

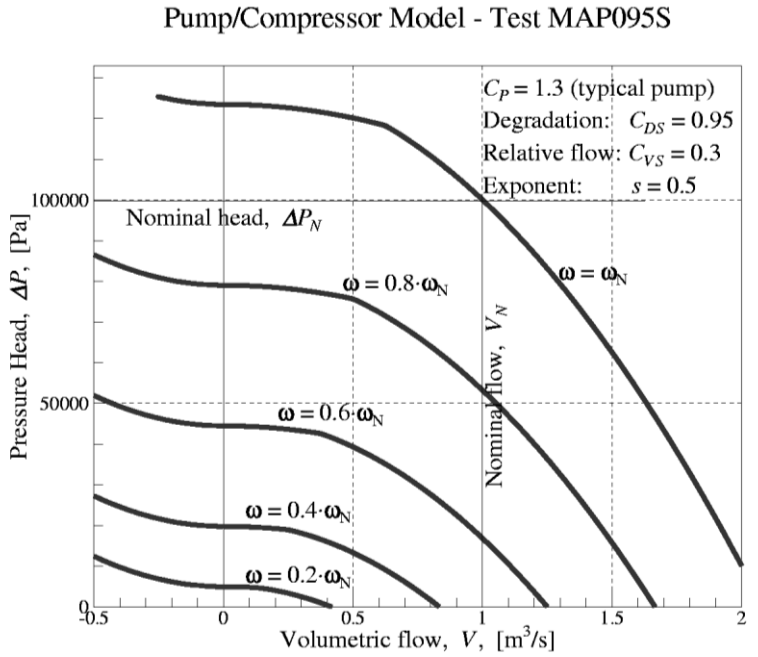

Figure 2-69 Influence of surge parameters on map, C_{DS}=0.95, C_{VS}=0.3, s=0.5 (C_P=1.3 - typical pump).

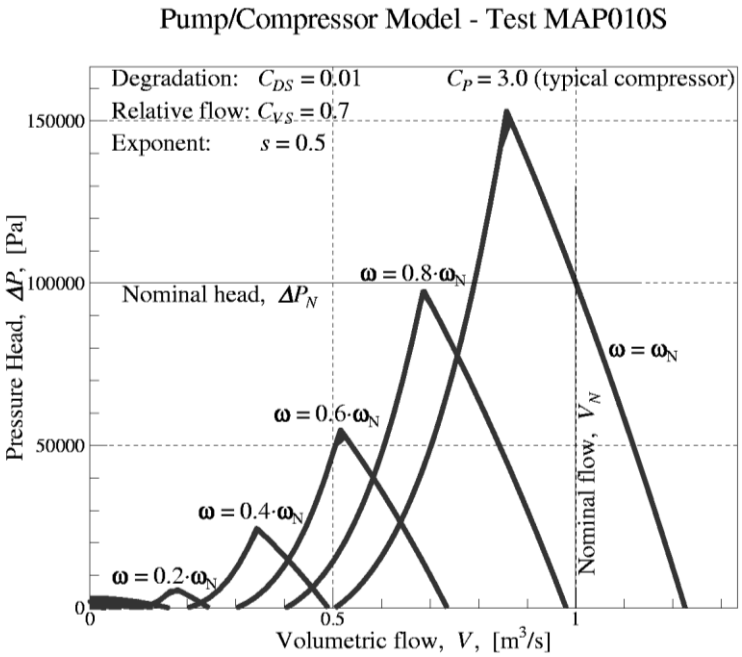

Figure 2-70 Influence of surge parameters on map, C_{DS}=0.01, C_{VS}=0.7, s=0.5 (C_P=3.0 - typical compressor).

The influence of the reverse speed degradation factor, C_{DR} , on the pump/compressor map is illustrated in Figure 2-54 through Figure 2-59.

The influence of the exponents *a, b,* on the pump/compressor maps is shown in Figure 2-60 through Figure 2-63.

The influence of the surge parameters C_{VS}, C_{DS}, s, on the pump/compressor maps is shown in Figure 2-64 through Figure 2-70.

A detailed discussion of the influence of the input parameters on the pump/compressor maps is given in the Volume 2 of the SPECTRA Code Manuals (Appendix A).

2.3.4.2 Pump/Compressor Tests PUMP-A

The PUMP-A test investigates the pump/compressor model in SPECTRA. Verification is done by comparing results with RELAP-5 / MOD-3.2 [50]. The model consists of a water reservoir and a pool. The reservoir is sufficiently large to ensure practically constant parameters during the test. The water level in the reservoir is 10 m. The bottom of the pool is located at the elevation of 20 m. The pool is connected with the reservoir by a pipe with a flow area of 0.1 m^2. The pump is located near the bottom of the reservoir. The model is visualized shown in Figure 2-71 and Figure 2-72. SPECTRA and RELAP input decks are provided in \Z-INPUTS\JN\PUMP.

For the present comparison the built-in RELAP pump was used. The input entry defining the pump map was set to –1, which means the Bingham type pump was used. The following nominal parameters were assumed:

nominal pressure head:	ΔP_N	$= 1.0\times10^5$ Pa
nominal volumetric flow	V_N	$= 1.0$ m^3/s
nominal speed	ω_N	$= 50.0$ s^{-1}

Note that in SPECTRA the pump speed is defined in revolutions per second, while in RELAP in radians per second. Therefore, strictly speaking, the nominal speed in RELAP should be entered as equal to $50\times2\pi = 314.16$. Since only the relative speed, $\omega(t)/\omega_N$, is important in the calculations, the value of 50.0 was used in both input decks and the value of $\omega(t)/\omega_N$ was defined consistently in both inputs. The pump speed, $\omega(t)$, was defined as follows.

for $t < 10.0$ s	$\omega(t) = 0.0$
for $10 < t < 20.0$ s	linear increase from zero to the nominal speed, $\omega(t) = \omega_N$
for $20 < t$	constant speed, equal to the nominal, $\omega(t) = \omega_N$

The constants defining pump map were determined in a few test runs as:

the first constant:	C_P	$= 1.4$
limit for the low flow degradation:	C_{VS}	$= 0.15$
low flow degradation factor:	C_{DS}	$= 0.975$

The necessary condition for stable pump map is (see Volume 2, Appendix A):

$$C_{DS} \geq 1 - C_{VS}^2$$

For the present case $1 - (C_{VS})^2 = 0.9775$, so it is very close to the stability limit. As shown in Volume 2, the above condition is not sufficient for the map stability. When the default value of the exponent s is used (s=1.0), the map has still a small unstable region, shown in Figure 2-67. To obtain stable map one has to set the exponent to 0.5 - compare Volume 2, Appendix A. This value gives the map shown in Figure 2-69.

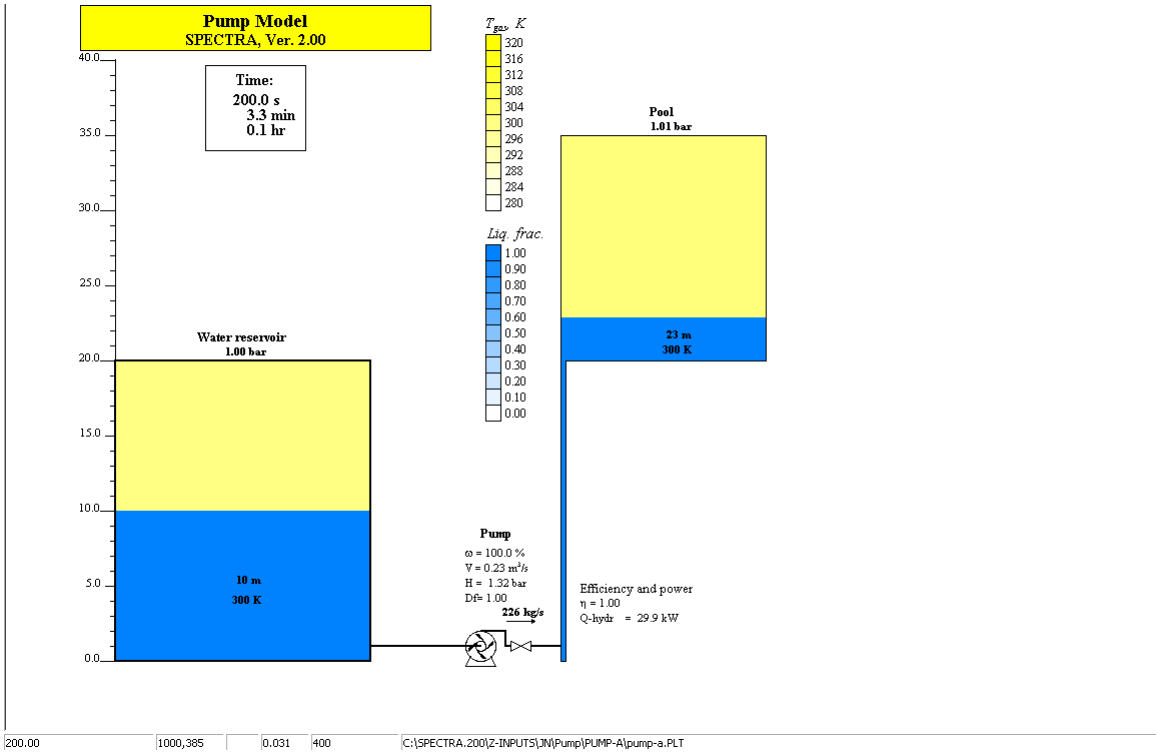

Figure 2-71 Test of pump model, Run PUMP-A - *s*=0.5 (stable), SPECTRA.

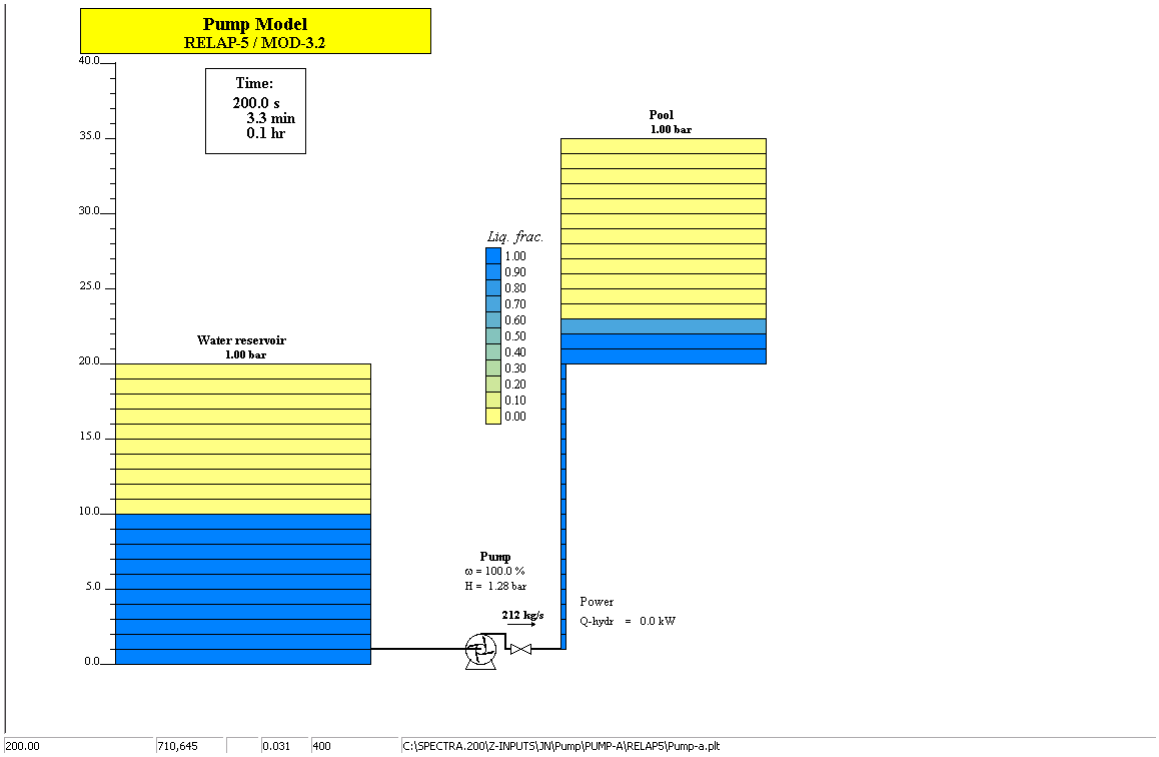

Figure 2-72 Test of pump model, Run PUMP-A, RELAP-5 / MOD-3.2.

Two SPECTRA runs were performed. In the first case (PUMP-A) the exponent *s* was set to 0.5. SPECTRA input deck is provided in \Z-INPUTS\JN\PUMP\PUMP-A. In the second case (PUMP-A1) the exponent *s* was set to the default value of 1.0. In the run PUMP-A the pump map is very similar to that shown in Figure 2-67. In the run PUMP-A1 the pump map is very similar to that shown in Figure 2-69.

At the start of the calculations the water level in the pipe is in equilibrium with the reservoir (10 m). At 10 s the pump is started and is kept running at the nominal speed till the end of the test. The water is pumped until the water level in the pool is so large that the pump head becomes insufficient, and the mass flow decreases to zero. The mass flow decreases to zero at about 350 s - Figure 2-73, Figure 2-74, and Figure 2-77. The visualization pictures (Figure 2-71 and Figure 2-72) show the state of the system at 200 s.

Results of the RELAP run and the SPECTRA run with the stable pump map (PUMP-A) are in good agreement - see Figure 2-73 through Figure 2-76. The flow decreases to zero and remains practically at zero after about 500 s. It is seen from Figure 2-74 and Figure 2-76 that the Bingham pump has a stable map, best represented in SPECTRA by the exponent $s = 0.5$.

For comparison results of the PUMP-A1 run are presented in Figure 2-77 and Figure 2-78. The map has a small unstable region (see Figure 2-67), resulting from the exponent *s* being equal to 1.0. As a consequence the flow is oscillating, which is clearly visible in Figure 2-77.

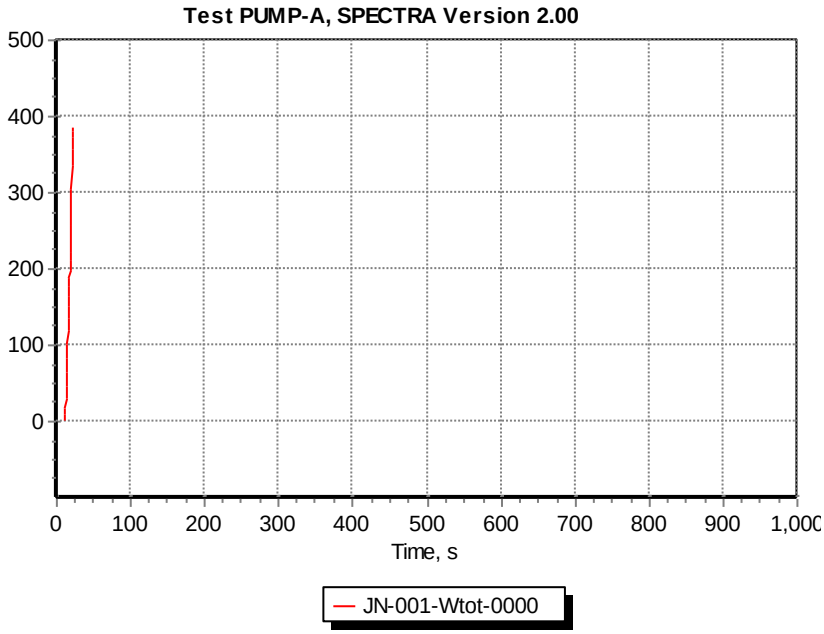

Figure 2-73 Mass flow rate, Run PUMP-A - s=0.5 (stable), SPECTRA.

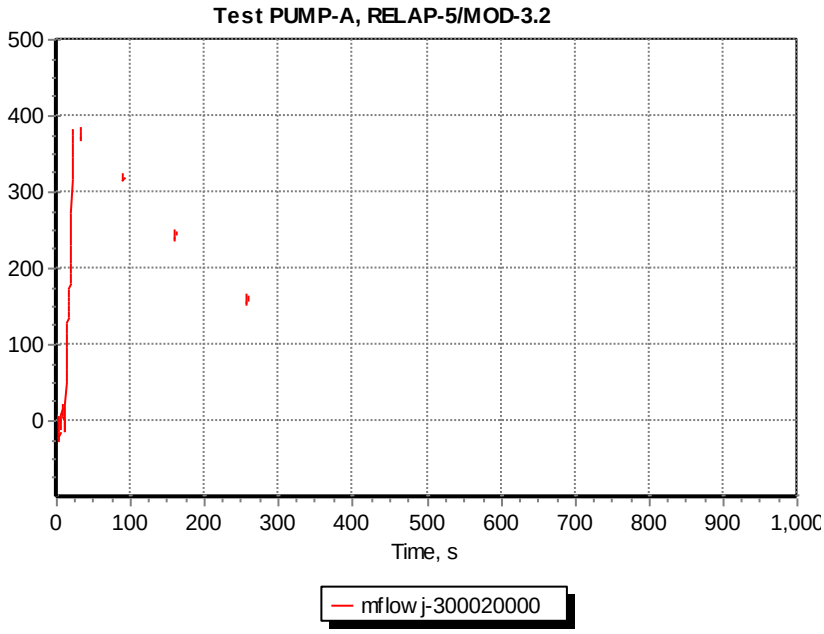

Figure 2-74 Mass flow rate, Run PUMP-A, RELAP-5 / MOD-3.2.

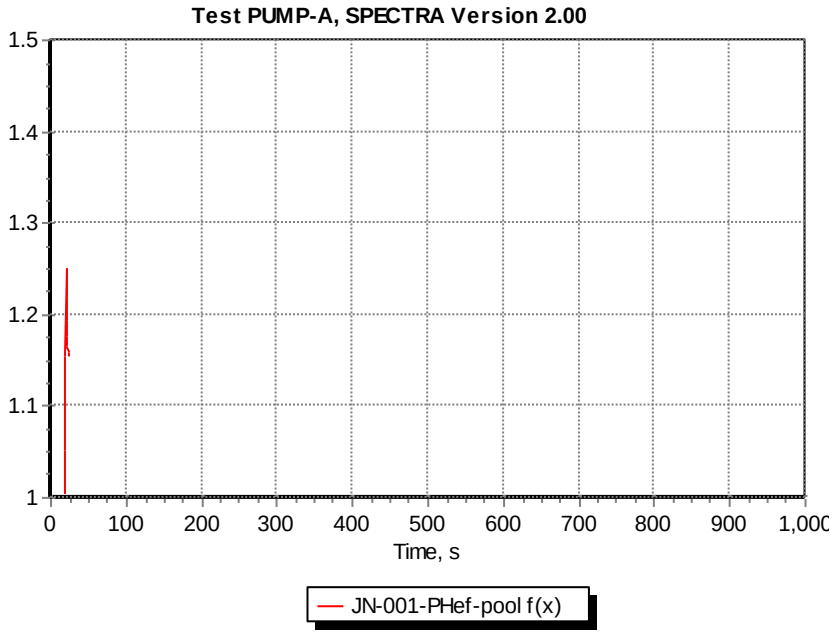

Figure 2-75 Pressure head, Run PUMP-A - *s*=0.5 (stable), SPECTRA.

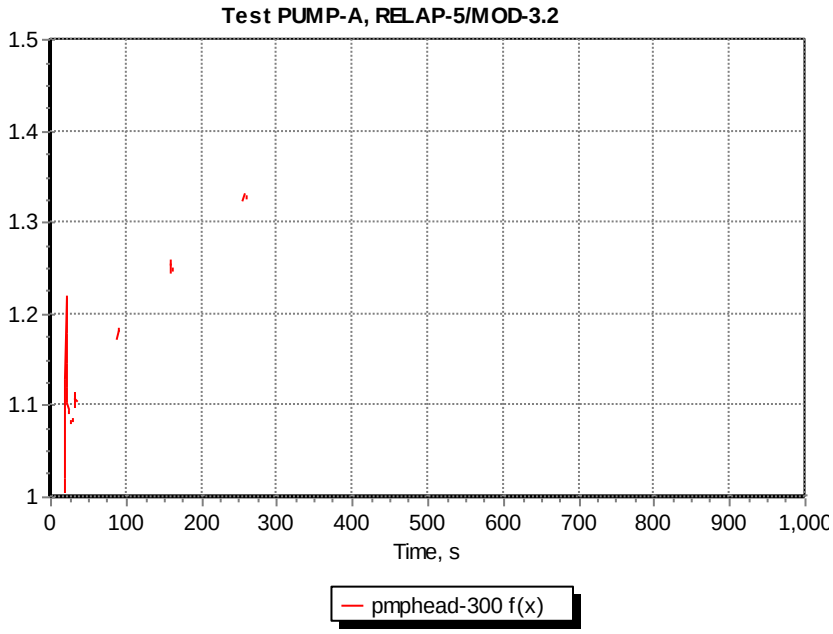

Figure 2-76 Pressure head, Run PUMP-A, RELAP-5 / MOD-3.2.

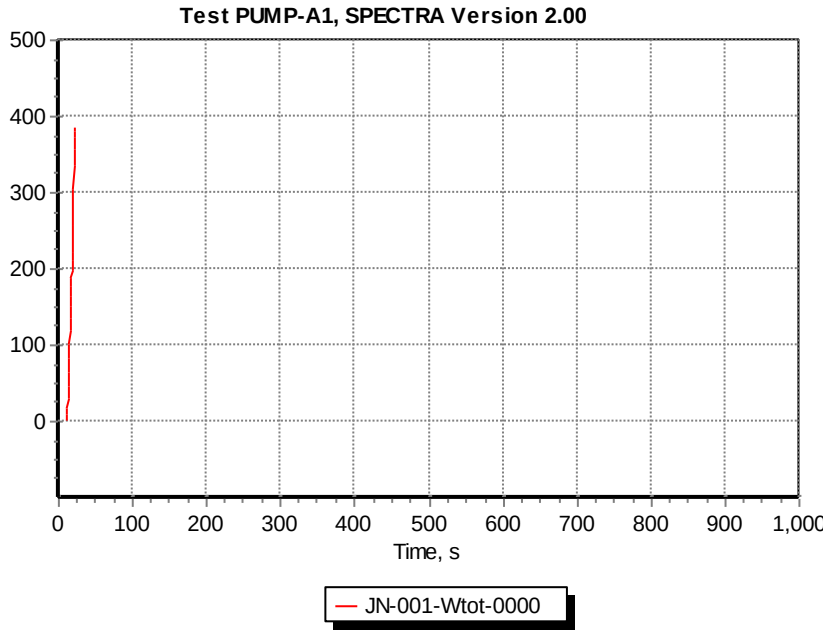

Figure 2-77 Mass flow rate, Run PUMP-A1 - *s*=1.0 (unstable), SPECTRA.

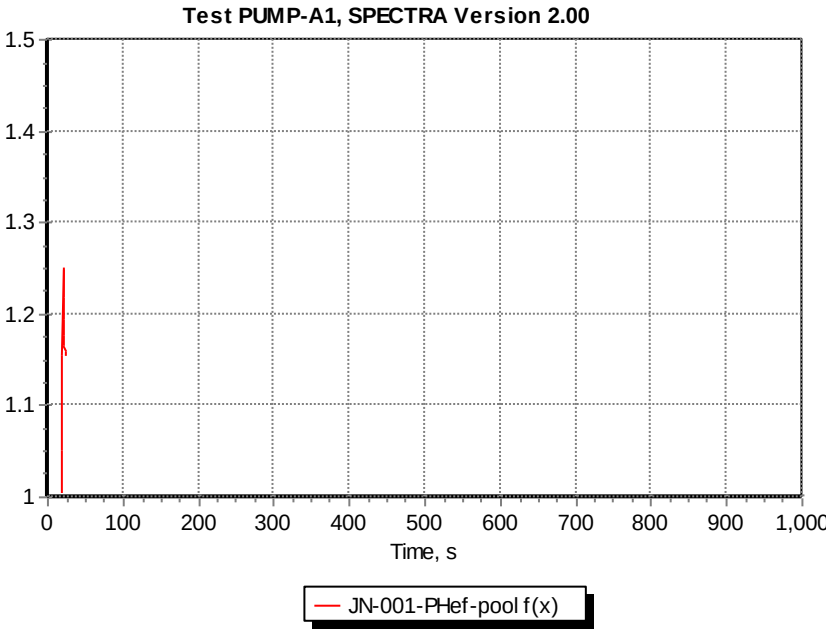

Figure 2-78 Pressure head, Run PUMP-A1 - *s*=1.0 (unstable), SPECTRA.

2.3.4.3 Pump/Compressor Tests PUMP-B

The PUMP-B test investigates the pump/compressor model in SPECTRA. Verification is done by comparing results with RELAP-5 / MOD-3.2 [50]. The model is exactly the same as PUMP-A. The only difference between the present case and the PUMP-A case is the pump speed. For the present test the pump was stopped after 400 seconds. Thus, the pump speed for the test PUMP-B was defined as:

for $t < 10.0$ s	$\omega(t) = 0.0$
for $10 < t < 20.0$ s	linear increase from zero to the nominal speed, $\omega(t) = \omega_N$
for $20 < t < 400$ s	constant speed, equal to the nominal, $\omega(t) = \omega_N$
for $400 < t < 410.0$ s	linear decrease from the nominal speed, $\omega(t) = \omega_N$, to zero
for $410 < t$	$\omega(t) = 0.0$

The exponent s = 0.5 was used. SPECTRA input deck is provided in \Z-INPUTS\JN\PUMP\PUMP-B.

The RELAP model is very similar to the model applied for the case PUMP-A. One modification was made, because of the observation that in RELAP gas bubbles are carried down into the pipe at the time when the water level reaches the lowest cell of the pool. This fact results in degradation of the pump performance when the lowest pool cell is still nearly full of water; thus when the water level in the pool is nearly 1.0 m. To prevent this behavior one small cell (0.03 m high) was added at the bottom of the pool. This cell is not visible in the visualization picture, shown in Figure 2-80. RELAP input deck is provided in \Z-INPUTS\JN\PUMP\PUMP-B.

The visualization pictures (Figure 2-79 and Figure 2-80) show the state of the system at 500 s, shortly after the pump was stopped. The time dependent graphs are shown in Figure 2-81, Figure 2-82, Figure 2-83, and Figure 2-84.

Results of the RELAP run and the SPECTRA run are in good agreement when the pump speed is positive. When the pump is stopped, the RELAP model gives higher pressure head than the SPECTRA model - see Figure 2-83 and Figure 2-84. Consequently the mass flow is somewhat lower (in terms of the absolute values) in RELAP than in SPECTRA - see Figure 2-81 and Figure 2-82. This is also visible in the visualization pictures - at 500 s the flow is equal to –402 kg/s in SPECTRA (Figure 2-79), and –340 kg/s in RELAP (Figure 2-80).

This difference indicates that in RELAP the pressure head lines are somewhat steeper in the negative (reverse) flow range than in SPECTRA. The present pump/compressor model in SPECTRA does not allow the user to change the slope of the pressure head in the negative flow range. Therefore the user cannot obtain closer match between the SPECTRA and the RELAP model. This fact is not very important, since in practical cases check valves are present behind the pumps, so negative flows through the pumps are prohibited.

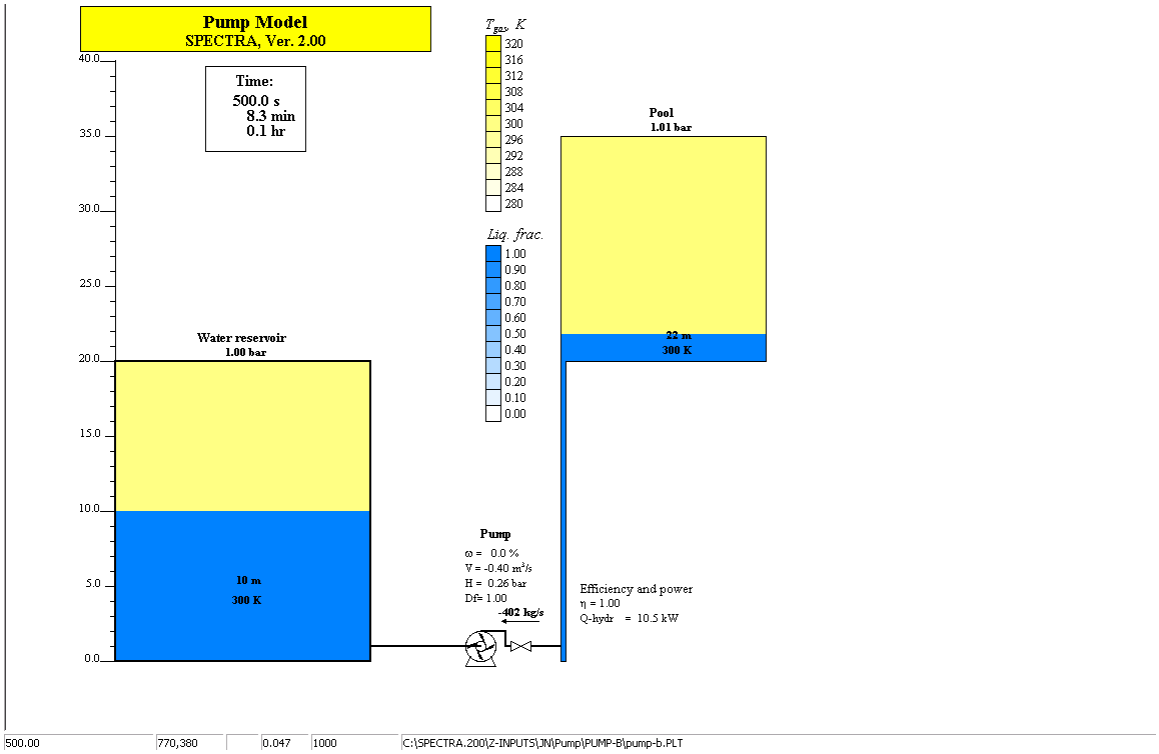

Figure 2-79 Test of pump model, Run PUMP-B - *s*=0.5, SPECTRA.

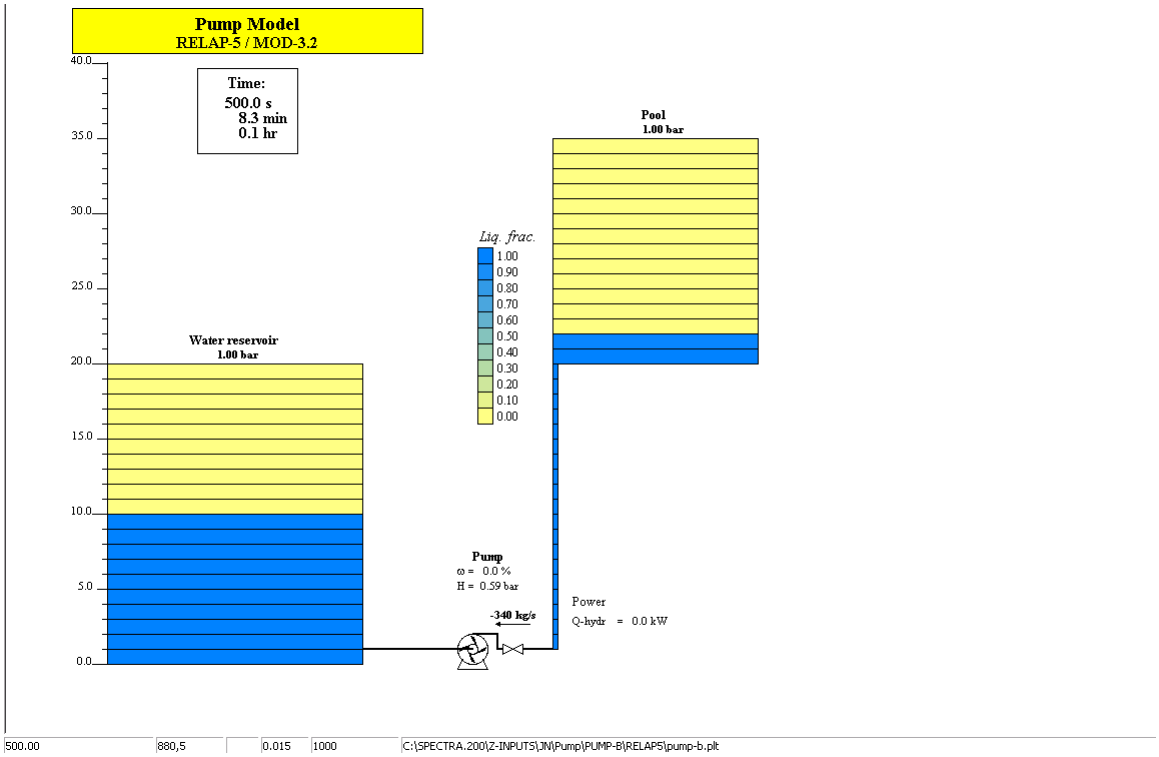

Figure 2-80 Test of pump model, Run PUMP-B, RELAP-5 / MOD-3.2.

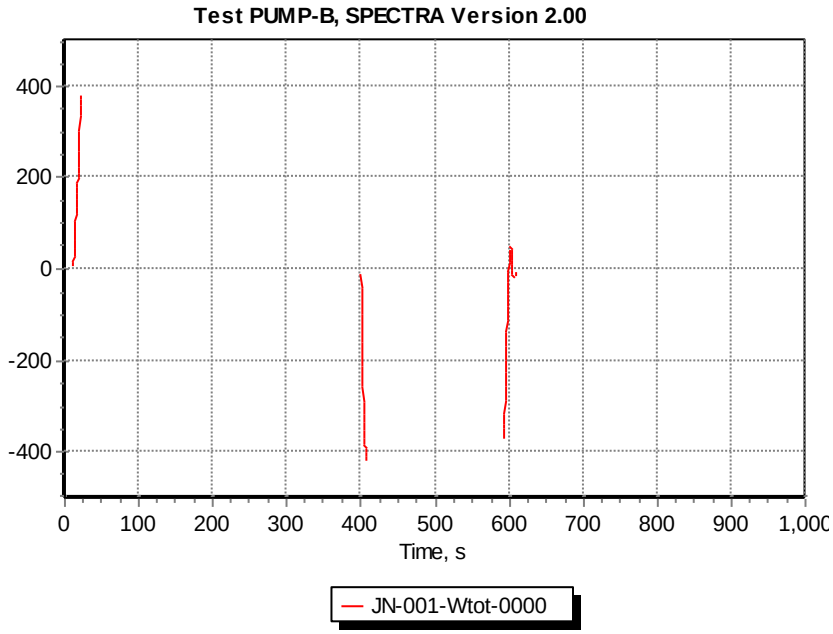

Figure 2-81 Mass flow rate, Run PUMP-B - *s*=0.5, SPECTRA.

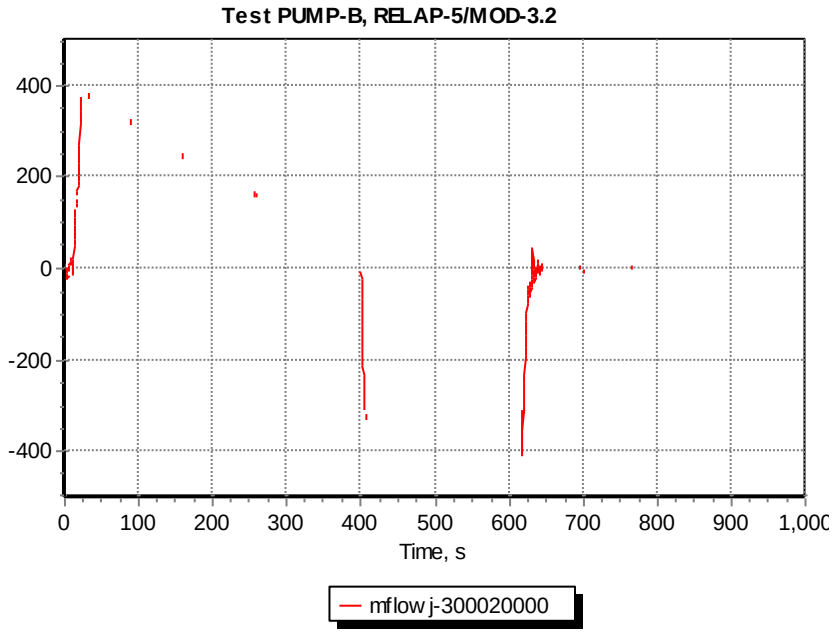

Figure 2-82 Mass flow rate, Run PUMP-B, RELAP-5 / MOD-3.2.

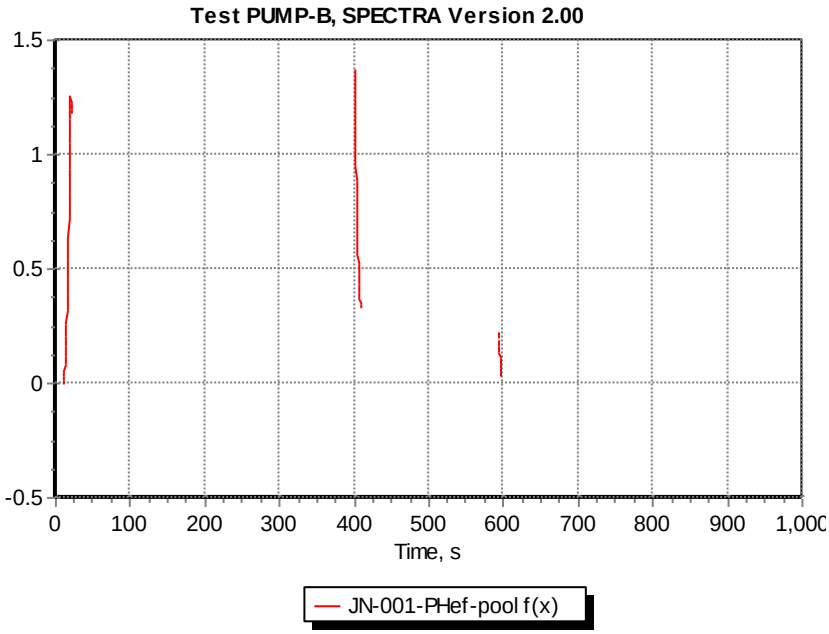

Figure 2-83 Pressure head, Run PUMP-B - *s*=0.5, SPECTRA.

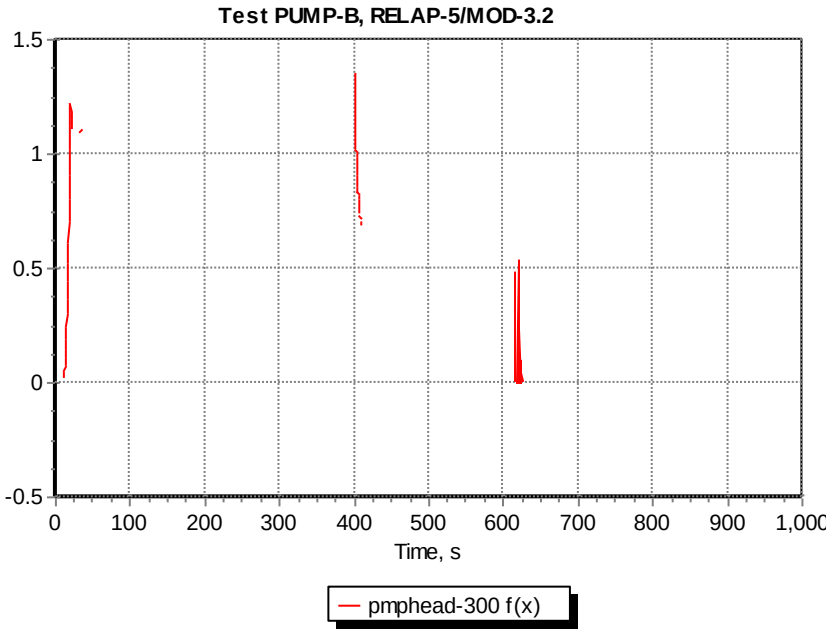

Figure 2-84 Pressure head, Run PUMP-B, RELAP-5 / MOD-3.2.

2.4 Verification of the Heat and Mass Transfer Models

2.4.1 Heat and Mass Transfer from Wall and Pool Surface

Verification of the three subroutines which calculate the wall-to-pool heat and mass transfer, the wall-to-atmosphere heat and mass transfer, and the pool-to-atmosphere heat and mass transfer, is given in sections 2.4.1.1, 2.4.1.2, and 2.4.1.3, respectively.

2.4.1.1 Wall-to-Pool Heat and Mass Transfer

The subroutine HTWLPL, calculating wall-to-pool heat transfer, considers the following mechanisms of heat transfer: natural and forced convection, nucleate, transition boiling and film boiling. Two boiling heat transfer models are available, the pool boiling and the forced convective boiling. Verification of models is performed in two steps.

First, the two different models, available for boiling heat transfer calculation, are shown and discussed. Second, results of the two models are compared with experimental data.

- *Discussion and comparison of the wall-to-pool heat transfer models*

Two different models are available for calculations of boiling heat transfer:

"Pool boiling curve"
Based on Rohsenow correlation for nucleate boiling and Zuber correlation for critical heat flux (see Volume 1). Applied for external flows (I_{CFC} = +1, - see Volume 2).

"Forced convective boiling curve"
Based on Chen correlation for nucleate boiling and a combination of USSR Academy of Sciences critical heat flux tables with Zuber correlation for critical heat flux (Volume 1). Applied for internal flows (I_{CFC} = –1, - Volume 2). Results obtained with the pool boiling and the forced convective boiling models are shown in Figure 2-85 and Figure 2-86. Qualitatively the heat transfer coefficient is very similar for both models. When wall temperature is below saturation temperature (T_{sat} = 373 K) the heat is transferred through natural convection or forced convection. Heat transfer coefficient depends on wall temperature for natural convection and on flow velocity (Reynolds number) for forced convection.

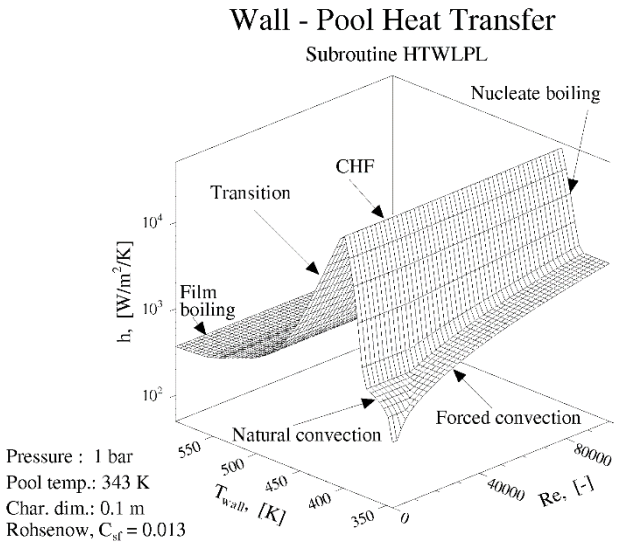

Figure 2-85 Wall-to-pool heat transfer coefficient - pool boiling model

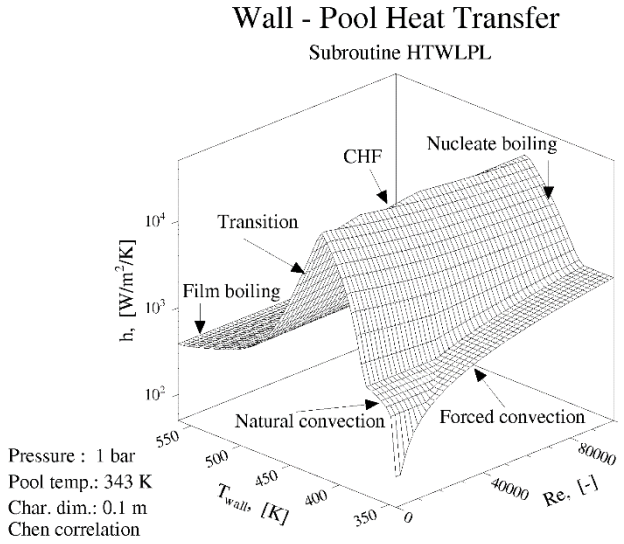

Figure 2-86 Wall-to-pool heat transfer coefficient - forced convective boiling model

Above the saturation temperature boiling becomes significant. Heat transfer coefficient increases with increasing wall temperature. This increase is faster in case of pool boiling, where the heat transfer coefficient, h, is proportional to $(T_{wall} - T_{sat})^2$. In case of convective boiling h is approximately proportional to $(T_{wall} - T_{sat})$.

The critical heat flux (CHF) is independent of flow (Reynolds number) in case of pool boiling. In case of convective boiling the dependence of CHF on Reynolds number is visible, although rather weak. Data in Figure 2-85 was obtained for saturated boiling (X=0). In case of subcooled boiling or two-phase flow ($X > 0$) the influence of flow on CHF is more visible. Film boiling is identical in both models. Transition boiling is very similar.

The data shown in Figure 2-85 and Figure 2-86 was generated using a FORTRAN program, which is provided in **\Z-TESTS\HT\WP\WP-T.FOR**. Note: in order to compile the program, it must be first moved to the directory: **\Z-TESTS**.

- *Comparison with experimental data*

Comparison with experimental data is given in several parts.

- Results of both models are compared to the Bergles-Rohsenow, forced convective and pool boiling experiments.

- Results of both models are compared to the Rohsenow-Clark, forced convective boiling experiments.

- Transition boiling and film boiling heat transfer coefficients are compared with experimental data reproduced from Delhaye et al. [48].

- Influence of surface and application of Rohsenow constant C_{sf}, to reproduce the influence of surface on boiling is shown, based on Hsieh-Hsu experiments.

Forced convective and pool boiling - Bergles and Rohsenow experiments

Figure 2-87 shows results of Bergles and Rohsenow experiments [51]. Figure has been reproduced from Collier [52] (figure 5.16).

Results calculated using the pool boiling model and the convective boiling model are shown in Figure 2-88. In case of convective boiling the subcooling applied for calculations was taken as the average of the subcooling range, shown in Collier, [52]. The value of the surface constant, C_{sf}, has been set to 0.013.

Generally the calculated results are in agreement with experiments. In case of convective boiling the calculated values are consistently below the experimental data. The difference is most visible in case of highe wall superheats. The very large heat flux obtained in experiments (almost 20 MW/m^2) can not be reproduced in calculations because the critical heat flux is typically well below that value (generally below 10 MW/m^2 .

Forced convective boiling - Rohsenow and Clark experiments

Figure 2-87 left shows results of Rohsenow and Clark experiments [53]. Figure has been reproduced from [52] (figure 5.14). The experiments were performed using electrically heated nickel tube. Water was flowing inside the tube with the velocity of 6.1 m/s. Fluid temperature varied from 193°C to 271°C. For nickel the appropriate value of C_{sf} is 0.006 (Volume 1, Chapter 7).

Figure 2-87 right shows results obtained using the "pool boiling curve", with the Rohsenow boiling correlation and the Rohsenow constant C_{sf} equal to 0.006. Since the constant C_{sf} for water-nickel was established based on these experiments, the fit is almost perfect.

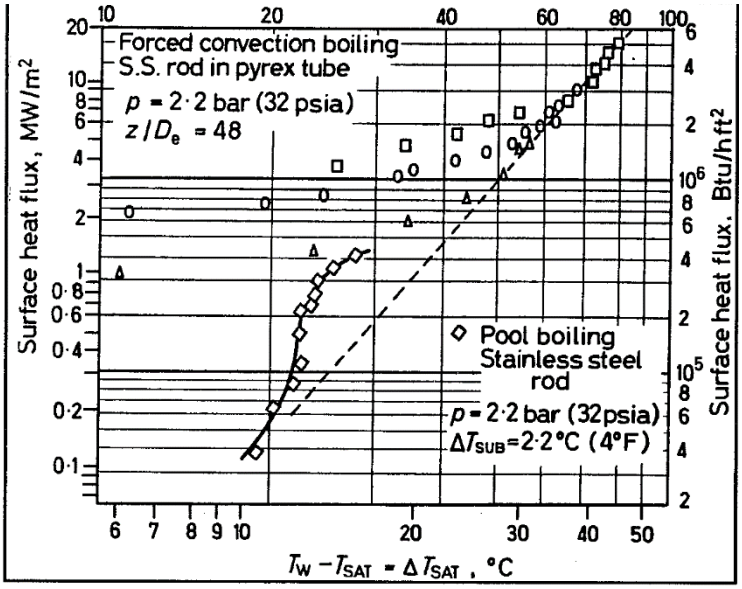

Figure 2-87 Bergles-Rohsenow experiments - reproduced from [52]

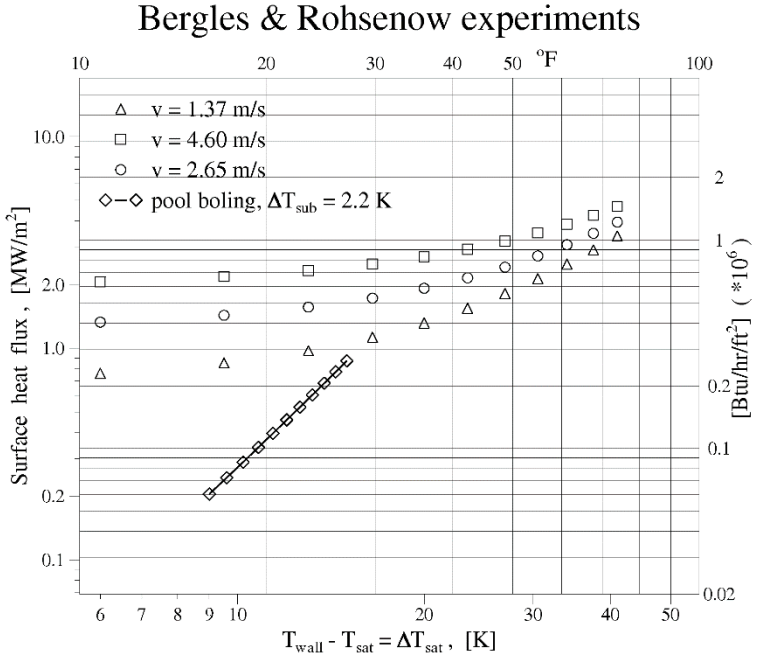

Figure 2-88 Bergles-Rohsenow experiments - SPECTRA results

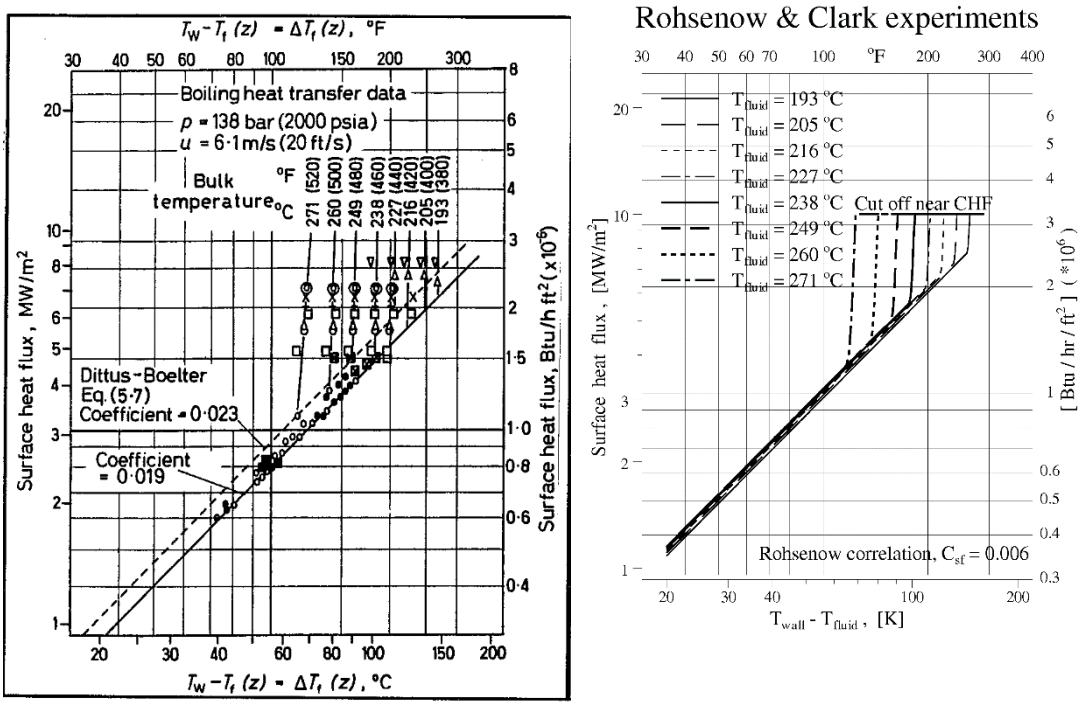

Figure 2-89 Rohsenow-Clark experiments, left: data [52], right: pool boiling model, Rohsenow, C_{sf} = 0.06

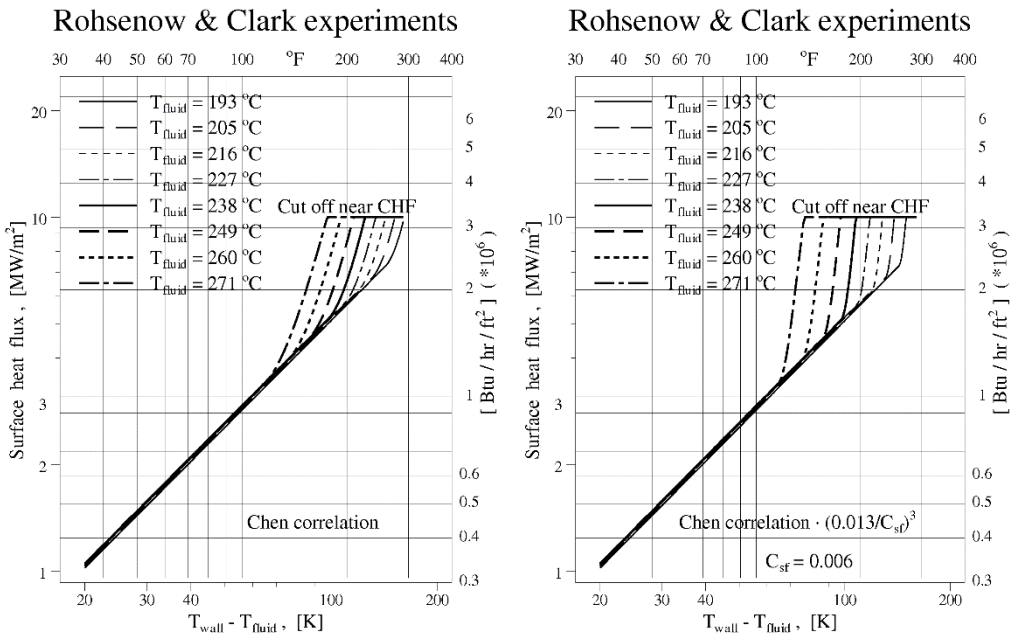

Figure 2-90 Rohsenow-Clark, left: convective boiling (Chen) right: convective boiling (Chen)×(0.013/C_{sf})^3, C_{sf} = 0.06

Since the Rohsenow-Clark experiments were performed with forced flow inside a tube the more appropriate model to use is the "convective boiling curve" with the Chen boiling correlation. Figure 2-88 left shows results obtained using the convective boiling model. The calculated heat flux at boiling conditions is clearly below the experimental points (lines are shifted to the right and less steep).

To obtained better results with the Chen correlation the following reasoning was made:

- It was hypothesized that the influence of surface can be introduced into Chen correlation in a similar manner as it is present in the Rohsenow correlation. In Rohsenow correlation the heat flux is proportional to C_{sf}^3 (Volume 1, Chapter 7). The same dependance was assumed for the Chen correlation.
- The reference value of C_{sf} was assumed as 0.013 - the value appropriate for water boiling on stainless steel surface (Volume 1, Chapter 7). Consequently the Chen boiling correlation is multiplied by the ratio: $(0.013/C_{sf})^3$:

$$h_{boil} = h_{Chen}\left(\frac{0.013}{C_{sf}}\right)^3$$

Results of Chen boiling correlation modified by the multiplier $(0.013/C_{sf})^3$, with the value of C_{sf} taken again as 0.006, are shown in Figure 2-88 right. Results are in very good agreement with experiments near the incipience of boiling (low heat fluxes). At high heat fluxes calculated values are shifted somewhat to the right, indicating that the increase of heat flux with wall superheat is somewhat too slow. In case of Chen correlation the heat flux is approximately proportional to the wall superheat squared (Volume 1, Chapter 7), while in Rohsenow correlation it is proportional to the wall superheat to the power of three (Volume 1, Chapter 7).

Because the Rohsenow-Clark experiments could be reproduced rather well by Chen correlation with the Rohsenow constant, C_{sf}, this constant is applied not only for pool boiling model but also for convective boiling model. Default value of C_{sf} is 0.013 (Volume 2). If this value is used, the original Chen correlation is applied in convective boiling. Use of other value will result in multiplying of the Chen boiling correlation by the ratio: $(0.013/C_{sf})^3$.

Transition boiling and film boiling - experimental data from Delhaye et al. [48]

Figure 2-91 shows experimental results of transition and film boiling. Figure has been reproduced from [48] (chapter 14, figure 12).

Figure 2-92 shows results of calculations. The film boiling results are in agreement with experiments. The behavior of the transition boiling indicates that the minimum film boiling point is too low. The calculation of the minimum film boiling point involves many uncertainties. Since the post-CHF modes of heat transfer typically are not interesting for containment calculations the present model is considered as a sufficient approximation.

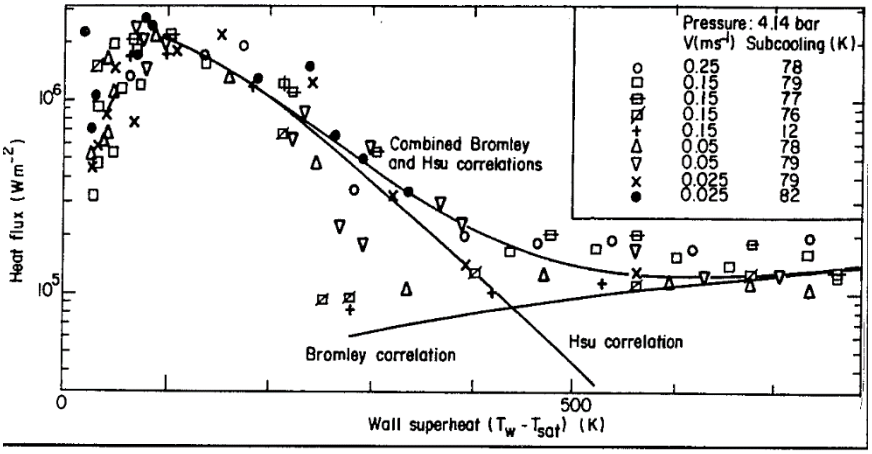

Figure 2-91 Transition and film boiling, reproduced from [48]

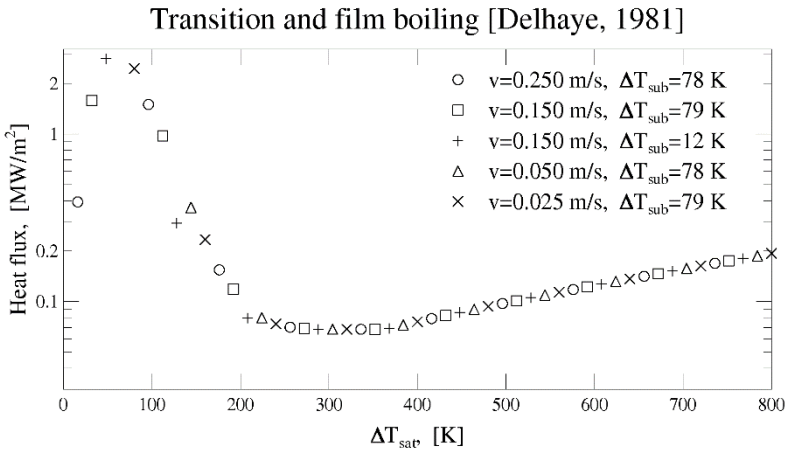

Figure 2-92 Transition and film boiling, results of calculations

Influence of surface - Hsieh-Hsu Experiments

The possibility of use of the Rohsenow constant C_{sf} to simulate experimental data of boiling on different surfaces is illustrated using Hsieh and Hsu experiments. Hsieh and Hsu investigated pool boiling of different fluids (water, R-114, R-134a) on plain and rib-roughened tubes [54]. Only the results obtained with water are discussed here.

The boiling tube is shown in Figure 2-93. The dimensions of ribs are:

- distance between centers of ribs, p = 39.4 mm
- rib width W = 15 mm
- rib height H = 4 mm
- diameters: d_1 = 27 mm, d_2 = 19 mm

Five tube types were used: smooth tube and four ribbed tubes, for which the angle, θ, varied from 30° to 90°, as shown in Table 2-10.

Measured heat fluxes are shown in Figure 2-94 for all five tube types. Several trial and error calculations were performed using the pool boiling model and different constants C_{sf}. A set of five constants was established that allows to reproduce relatively well the experimental data. The values of constants are shown in Table 2-10. The heat fluxes calculated using those constants are shown in Figure 2-95.

Table 2-10 Values of constant C_{sf} used to simulate the Hsieh and Hsu experiments

Tube number	Kind	θ	C_{sf}
1	Smooth	-	0.021
2	Rib	90°	0.013
3	Rib	60°	0.010
4	Rib	45°	0.020
5	Rib	30°	0.011

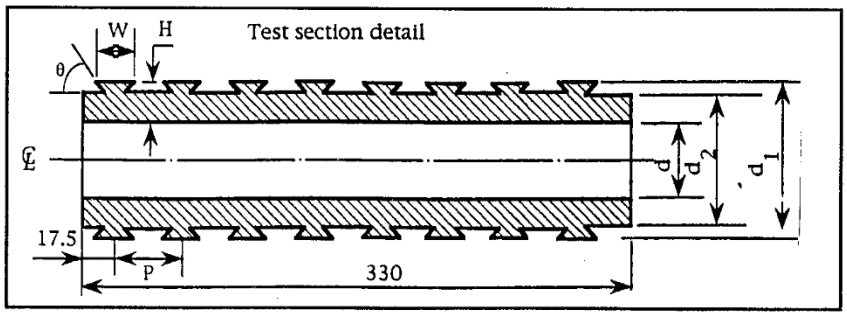

Figure 2-93 Test tube (figure reproduced from [54])

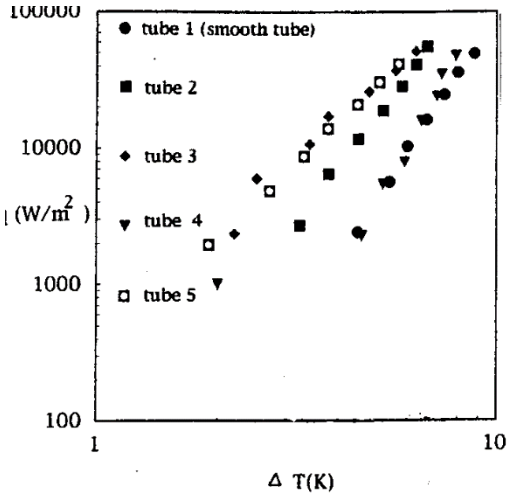

Figure 2-94 Hsieh and Hsu experiments, (figure reproduced from [54])

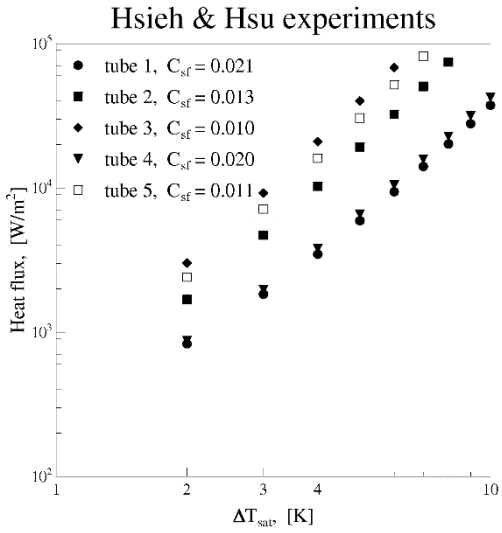

Figure 2-95 Hsieh and Hsu experiments, results of calculations

This example shows that selection of appropriate fluid-surface constant, C_{sf}, allows to obtain relatively good agreement with experiments for different surface types. Unfortunately the data of Hsieh and Hsu could not be correlated to form some general dependence of C_{sf} on, for example rib angle.

2.4.1.2 Wall-to-Atmosphere Heat and Mass Transfer

The subroutine HTWLAT, calculating wall-to-atmosphere heat transfer, considers the following mechanisms of heat transfer: natural convection, forced convection and condensation. As a qualitative verification, the results of HTWLAT are plotted using 3-D graphs. Calculations were performed for p=1 bar, T_{gas}=330 K, steam partial pressure of p_{H2O}=0.1 bar, gas velocities ranging from 0 to 2.5 m/s, and the wall temperatures from 300 to 350 K. The saturation temperature at the steam partial pressure is approximately 319 K.

Figure 2-96 shows the heat transfer coefficient and the condensation mass flux. If the wall temperature is below the steam saturation temperature (319 K) steam condensation occurs. The condensation heat transfer coefficient is about 200 W/m^2/K. This rather low condensation heat transfer coefficient is caused by large noncondensable gas fraction.

For wall temperatures above saturation, the heat is transferred through natural and forced convection. The natural convection heat transfer increases with the wall-gas temperature difference. Since the wall is vertical the natural convection is approximately the same for negative temperature differences as it is for positive temperature differences.

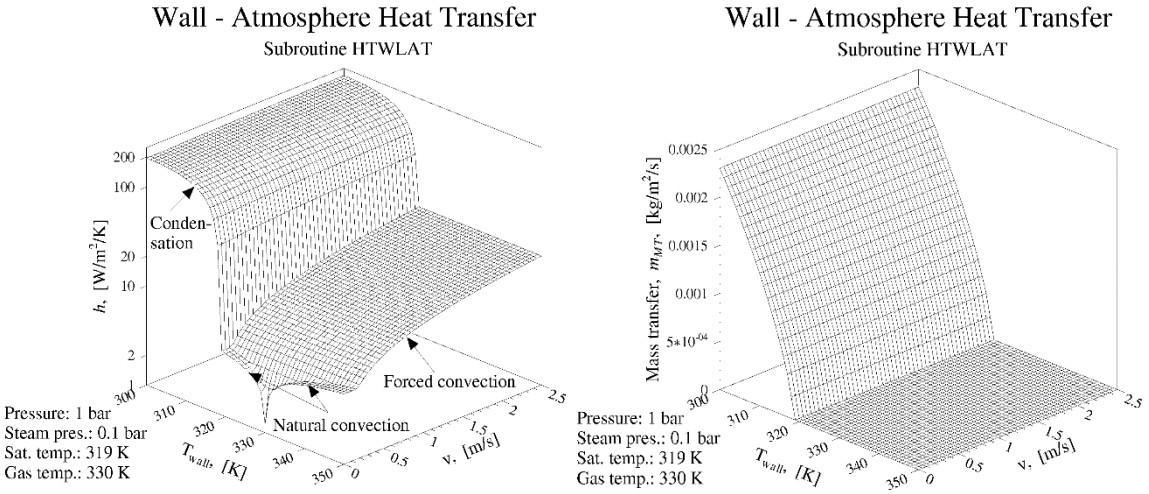

Figure 2-96 Left: wall-to-atmosphere heat transfer coefficient, right: mass transfer flux

2.4.1.3 Pool-to-Atmosphere Heat and Mass Transfer

The subroutine HTPLAT, calculates the convective heat transfer and the mass transfer (condensation or evaporation) from the pool surface. As a qualitative verification, the results of HTWLAT are plotted using 3-D graphs. Calculations were performed for p = 1 bar, T_{gas} = 330 K, steam partial pressure p_{H2O} = 0.1 bar. The saturation temperature at the steam partial pressure is approximately 319 K. Calculations were performed for the pool-gas relative velocities ranging from 0 to 2.5 m/s, and the pool surface temperatures from 300 to 350 K.

Figure 2-97, left, shows the calculated convective heat flux. In case of forced convection the calculated heat flux for negative pool-gas temperature differences is approximately equal to the heat flux for positive pool-gas temperature differences with changed sign (symmetry around 330 K for high velocities). In contrast to the forced convection the natural convection is only "efficient" when the pool temperature is above the gas temperature ("hot pool"). When the pool temperature is below the gas temperature ("cold pool"), natural convection is limited by the thermal stratification of the gas near the pool surface.

Figure 2-97, right, shows calculated mass transfer flux. When the pool temperature is above the steam saturation temperature (319 K) the mass flux is positive - water evaporates from the pool surface. When the pool temperature is below steam saturation temperature the mass flux is negative - steam condenses on the pool surface. Note that evaporation occurs even when the pool temperature is below the gas temperature ($319 < T_{pool} < 330$). In this range the evaporation rate is small especially for low pool-gas relative velocities.

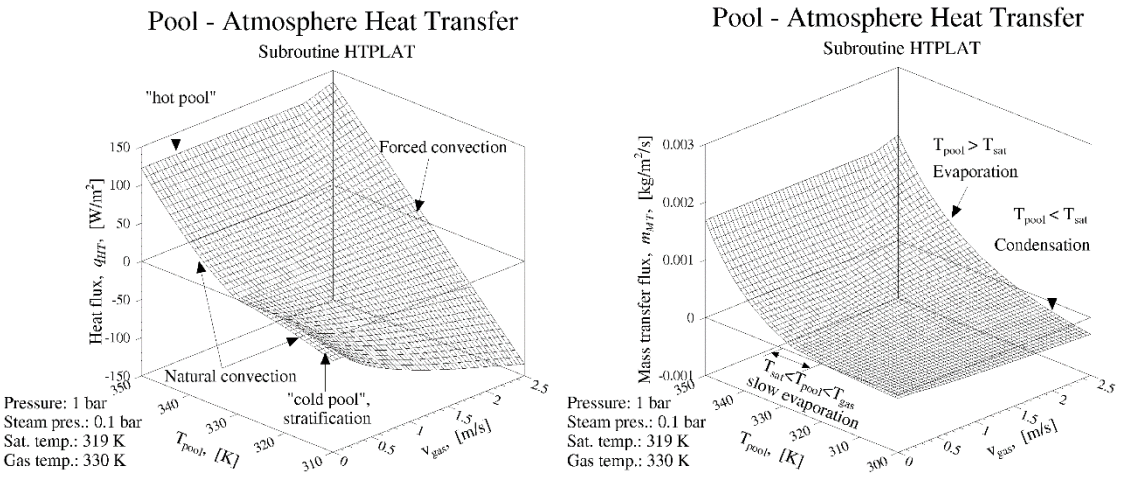

Figure 2-97 Left: pool-to-atmosphere heat transfer coefficient, right: mass transfer flux

As a quantitative verification, a simple test case from [16] is considered. In the example problem 9.8 of [16], the heat and mass transfer from a pool surface to air are calculated. The pool temperature is 330 K; the gas temperature is 300 K; the relative humidity is 15 %. The results given in [16] are: convective heat flux 180 W/m^2, latent heat loss is 1640 W/m^2. The values calculated using the subroutine HTPLAT are: 177 W/m^2 and 1520 W/m^2 respectively. The results are in good agreement, differences are caused by different fluid property data and somewhat different method of calculating the mass transfer flux.

2.5 Verification of Thermal Radiation

This section presents the verification of the thermal radiation subroutines. Graphs shown in this section were generated by FORTRAN programs that use the appropriate SPECTRA subroutines to calculate the values to be plotted. The first part, shown in section 2.5.1, gives verification of the radiative properties of gases. In the next section, 2.5.2, the radiative properties of solid materials are discussed.

2.5.1 Radiative Properties of Gases

The radiative properties of gases are discussed in this section for the two gases for which internal models of emissivity and absorptivity are built into SPECTRA. These are

- H_2O
- CO_2

Other gases are assumed to be transparent for the thermal radiation; unless the user defines the gas emissivity and absorptivity using a general correlation (see Volume 1). Typically gases other than H_2O and CO_2 are very weak absorbers/emitters, and the default treatment is justified. However in special cases one may wish to define gas emissivity because of expected radiation of for example dust particles that may be present in the gas atmosphere. Such example is provided in section 3.8. Below, verification of the built-in models for the H_2O and CO_2 are presented.

- Section 2.5.1.1 provides a discussion on the emissivity of steam.
- Section 2.5.1.2 provides a discussion of the CO_2 emissivity.

The sections 2.5.1.1 and 2.5.1.2 discuss emissivities at atmospheric pressure and low steam partial pressure. For other conditions correction factors are used. These correction factors are discussed in the following sections:

- Section 2.5.1.3 provides a discussion on the correction factor for steam.
- Section 2.5.1.4 provides a discussion on the correction factor for CO_2.

For a gray gas the emissivity (and absorptivity) is equal to 1.0 for a very thick gas layer. In reality the absorptivity and emissivity of the gas are never equal to 1.0 (see Volume 1). Therefore a concept of maximum emissivity is imposed on the gray gas model available in SPECTRA. Verification of the maximum emissivity model is shown in section 2.5.1.5.

Finally, section 2.5.1.6 presents the verification of the model used to calculate the correction factor for the spectral overlap of H_2O and CO_2.

2.5.1.1 Emissivity of H_2O

For the total emissivities of H_2O and CO_2 useful charts were prepared some years ago by Hottel, Egbert and others. The validity of these charts remains unchanged and no important additions are required to the data ([15], page 15-75). The model used in SPECTRA to calculate the emissivity of steam is verified by comparing the calculated data with the charts prepared by Hottel, et. al.

The Hottel data for steam emissivity [17] at low steam pressure and atmospheric total pressure is shown in Figure 2-98, left. This figure was reproduced from [21], where the data is presented in SI units.

The emissivity of H_2O is calculated by the function EKSH2O, which uses the Kostowski correlation, valid for low steam pressure and atmospheric total pressure. This function was used to generate tabular data for plotting. The data generated using the function EKSH2O is shown in Figure 2-98, right. The values calculated by Kostowski correlation are very close to the Hottel data. The Kostowski correlation has been selected from several as the one giving the closest representation of the Hottel data.

The data shown in Figure 2-98, right, was generated using a FORTRAN program, which is provided in **\Z-TESTS\RT\EMIS-T.FOR**. Note: in order to compile the program, it must be first moved to the directory: **\Z-TESTS**.

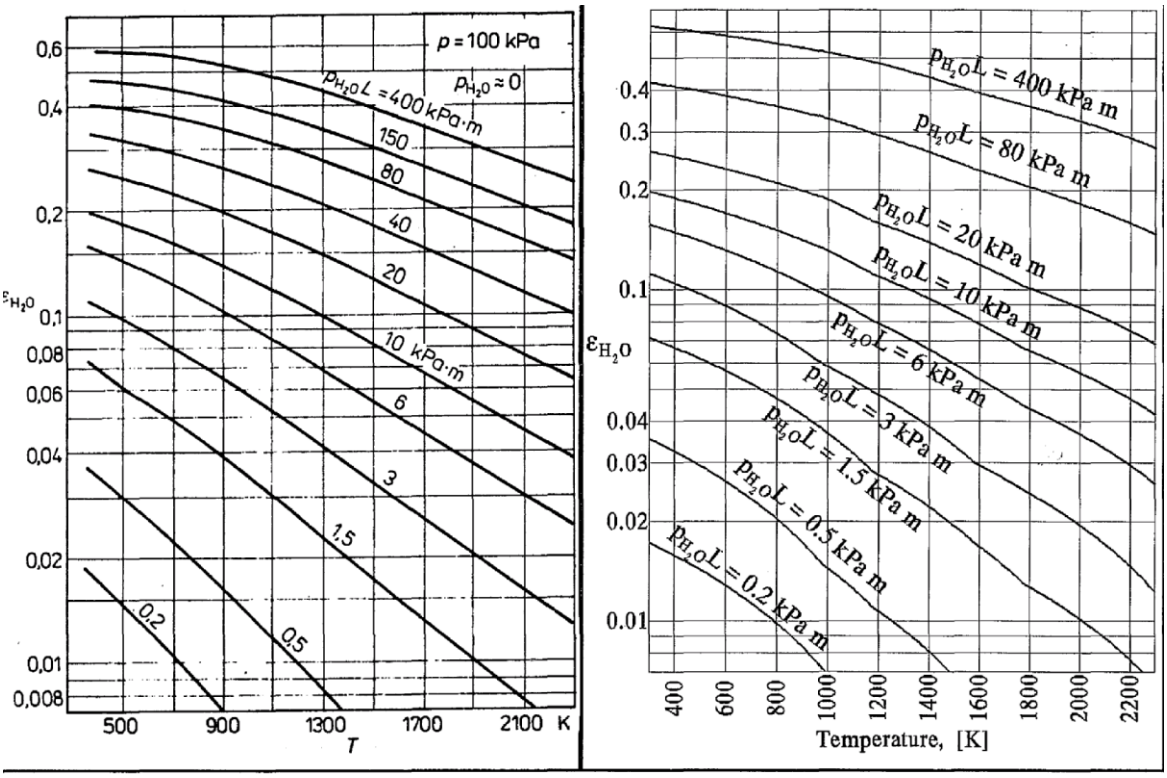

Figure 2-98 H_2O emissivity, left - Hottel data, right - subroutine EKSH2O

2.5.1.2 Emissivity of CO_2

For the total emissivities of H_2O and CO_2 useful charts were prepared some years ago by Hottel, Egbert and others. The validity of these charts remains unchanged and no important additions are required to the data ([15], page 15-75). The model used in SPECTRA to calculate emissivity of CO_2 is verified by comparing the calculated data with the charts prepared by Hottel, et. al.

The Hottel data for CO_2 emissivity [17] at atmospheric total pressure is shown in Figure 2-99, left. This figure was reproduced from [21], where the data is presented in SI units.

The emissivity of CO_2 is calculated by the function EKSCO2, which uses the Kostowski correlation, valid for low CO_2 pressure and atmospheric total pressure. This function was used to generate tabular data for plotting. The data generated using the function EKSCO2 is shown in Figure 2-99, right. The values calculated by Kostowski correlation are very close to the Hottel data. The Kostowski correlation has been selected from several as the one giving the closest representation of the Hottel data.

The data shown in Figure 2-99, right, was generated using a FORTRAN program, which is provided in **\Z-TESTS\RT\EMIS-T.FOR**. Note: in order to compile the program, it must be first moved to the directory: **\Z-TESTS**.

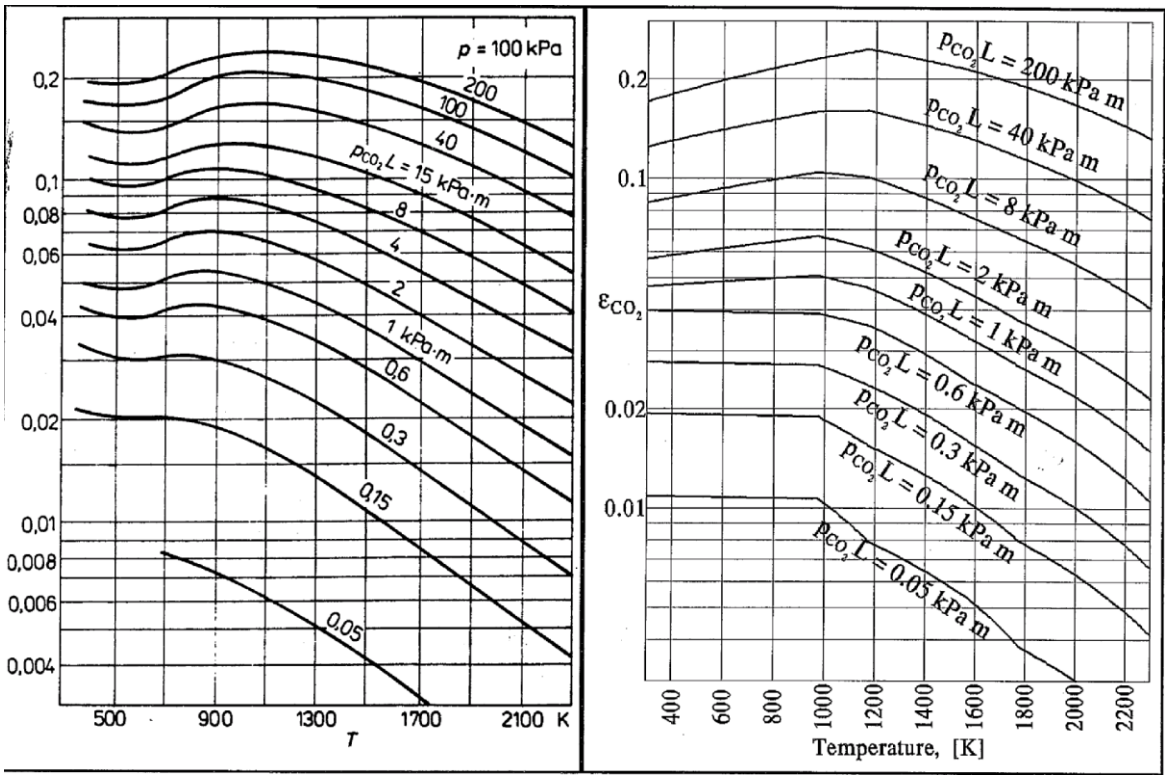

Figure 2-99 CO_2 emissivity, left - Hottel data, right - subroutine EKSCO2

2.5.1.3 Pressure Correction Factor for H_2O

The function EKSH2O calculates the emissivity for low steam partial pressure and atmospheric total pressure. When the conditions are different the correction factor C_H must be used. The values of the correction factor are shown in Figure 2-100. This figure was reproduced from [21], where the data is presented in SI units.

The correction factor is calculated by the function PCFCH which uses the correlation developed for SPECTRA ([6] and Volume 1). This function was used to generate tabular data for plotting. The data generated using the function PCFCH is shown in Figure 2-101. Comparison of plots shows that the function PCFCH gives a good representation of the Hottel data.

The data shown in Figure 2-101 was generated using a FORTRAN program, which is provided in **\Z-TESTS\RT\EPCF-T.FOR**. Note: in order to compile the program, it must be first moved to the directory: **\Z-TESTS**.

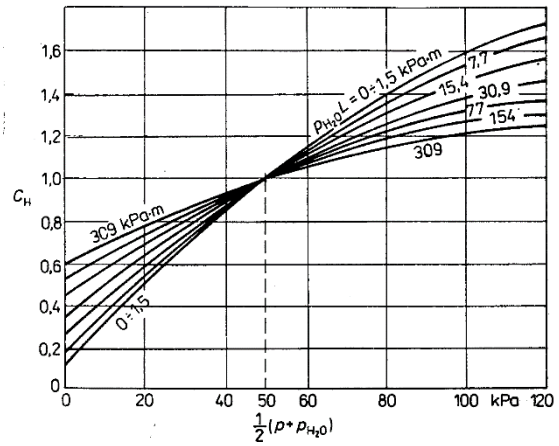

Figure 2-100 Pressure correction factor for H_2O - Hottel data

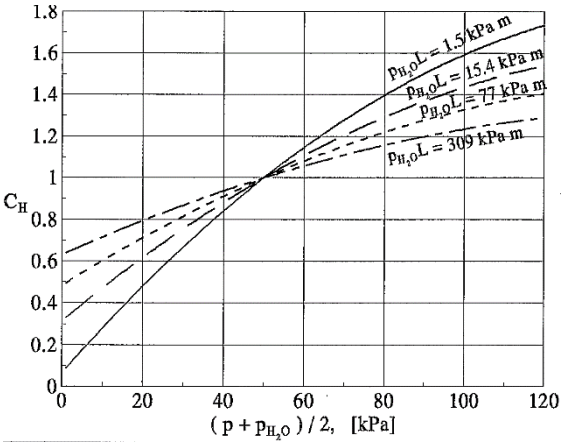

Figure 2-101 Pressure correction factor for H_2O - subroutine PCFCH

2.5.1.4 Pressure Correction Factor for CO_2

The function EKSCO2 calculates the emissivity for atmospheric total pressure. When the pressure is different the correction factor C_C must be used. The values of the correction factor are shown in Figure 2-102. This figure was reproduced from [21], where the data is presented in SI units.

The correction factor is calculated by the function PCFCC which uses the correlation developed for SPECTRA ([6] and Volume 1). This function was used to generate tabular data for plotting. The data generated using the function PCFCH is shown in Figure 2-103. Comparison of plots shows that the function PCFCC gives a good representation of the Hottel data.

The data shown in Figure 2-103 was generated using a FORTRAN program, which is provided in **\Z-TESTS\RT\EPCF-T.FOR**. Note: in order to compile the program, it must be first moved to the directory: **\Z-TESTS**.

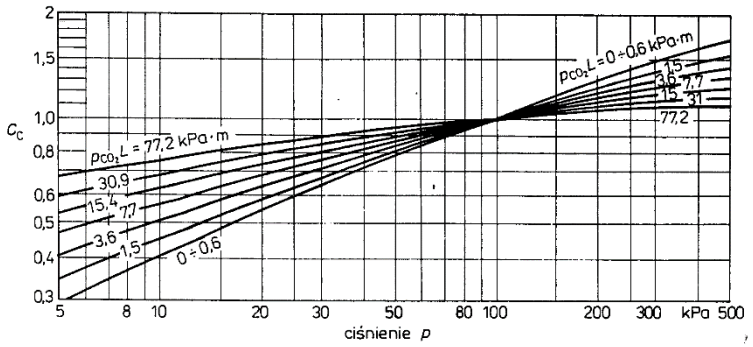

Figure 2-102 Pressure correction factor for CO_2 - Hottel data

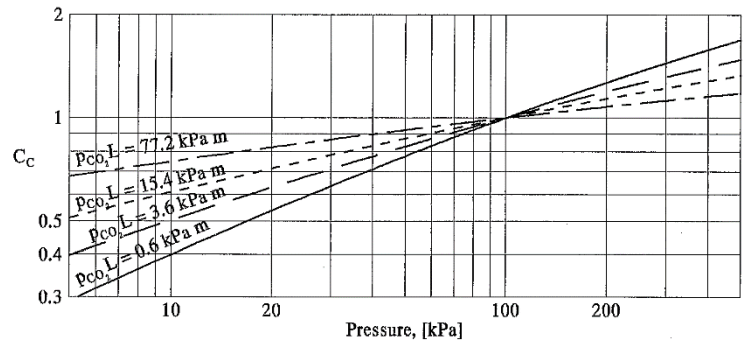

Figure 2-103 Pressure correction factor for CO_2 - subroutine PCFCH

2.5.1.5 Maximum Emissivity of H_2O and CO_2

Maximum emissivities (for very large optical length, $pL \rightarrow \infty$) for H_2O and CO_2 are shown in [21]. The values are shown in Figure 2-104 (reproduced from [21], figure 6-15).

The values of the maximum emissivity are calculated by the functions EMXH2O and EMXCO2. Results of these functions are shown in Figure 2-105. Comparison of the plots shows that the functions EMXH2O and EMXCO2 give a good representation of the data presented in reference [21].

The data shown in Figure 2-104 was generated using a FORTRAN program, which is provided in **\Z-TESTS\RT\EMAX-T.FOR**. Note: in order to compile the program, it must be first moved to the directory: **\Z-TESTS**.

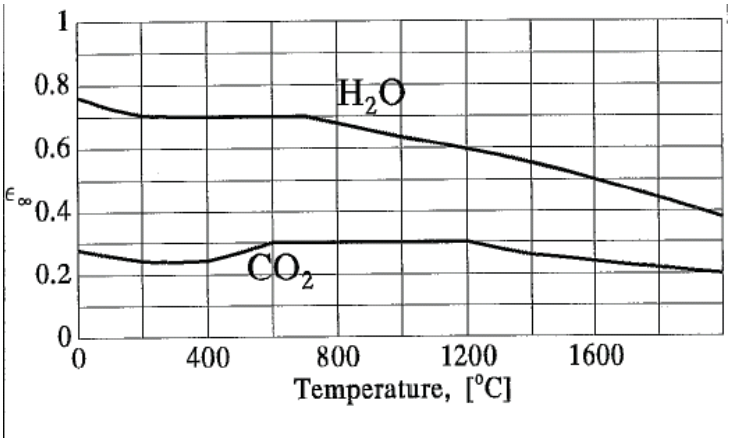

Figure 2-104 Maximum emissivity of H_2O and CO_2 - Kostowski data

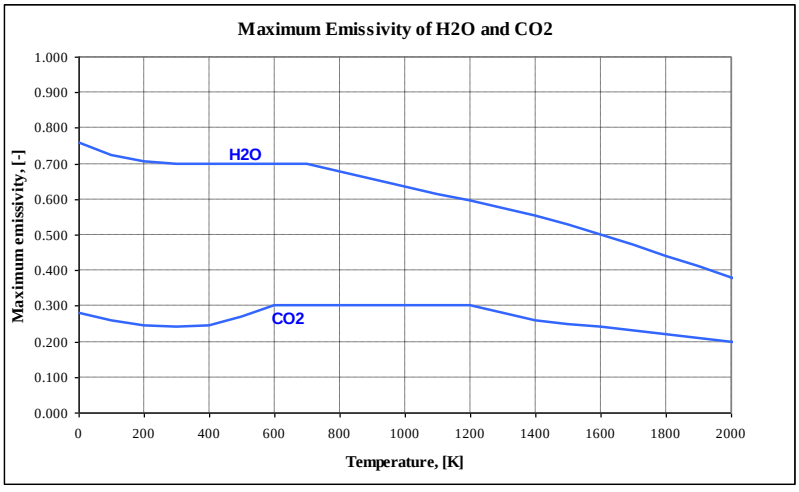

Figure 2-105 Maximum emissivity of H_2O and CO_2 - EMXH2O, EMXCO2

2.5.1.6 Emissivity Correction for Spectral Overlap of H_2O and CO_2

The emissivity correction for spectral overlap is shown in form of graphs in [17], [21]. The graphs shown in [21] are given in SI units and are reproduced in Figure 2-106.

The correction for overlapping is calculated by the function DEMISS which uses the correlation developed for SPECTRA ([6] and Volume 1). This function was used to generate tabular data for plotting. The data generated using the function PCFCC is shown in Figure 2-107. Comparison of the plots shows that the function PCFCC gives a good representation of the Hottel data.

Note that a correlation for spectral overlap has been developed by Leckner [23]. The Leckner correlations are used for example in MELCOR and CONTAIN codes. However, review of correlations showed that the Leckner correlations do not provide much better accuracy than a simple gray gas expression ($\Delta\varepsilon_g = \varepsilon_{H2O} \times \varepsilon_{CO2}$). Figure 2-108 shows results of the correlation used by SPECTRA (called here MST model - top row) the gray gas (middle row) and the Leckner model (bottom row). When the MST correlation is applied, an upper limit is used that is set by the gray gas model: $\Delta\varepsilon_g \leq \varepsilon_{H_2O} \cdot \varepsilon_{CO_2}$. The limit is active at high temperatures, which may be seen in Figure 2-108; for *T*=1253 K, "MST Model" and "Gray Gas model" are identical.

Comparison of Figure 2-107, Figure 2-108 with Figure 2-106 shows that the correlation applied in SPECTRA, provides the best match to the Hottel data. Figure 2-107 and Figure 2-108 were generated using a FORTRAN program provided in: **\Z-TESTS\TR\DEMIS-T.FOR**.

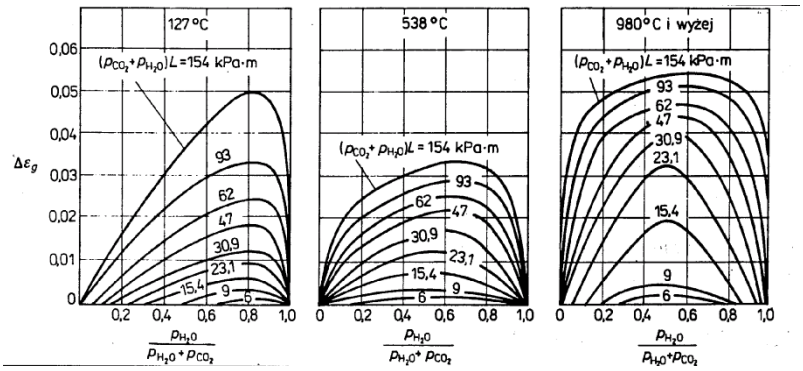

Figure 2-106 H_2O and CO_2 spectral overlap correction factor - Hottel data

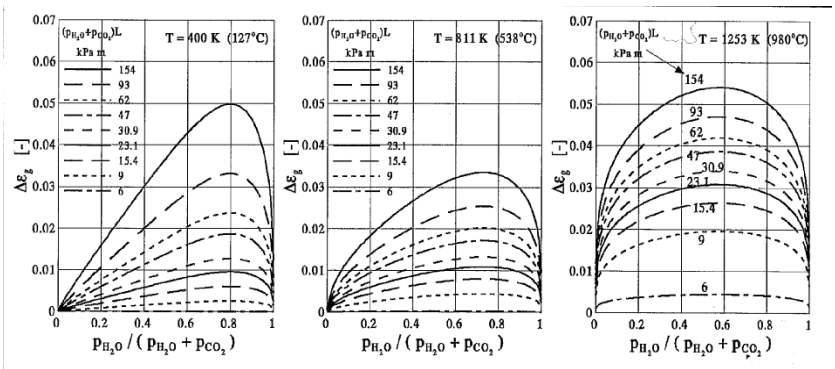

Figure 2-107 H_2O and CO_2 spectral overlap correction factor - results of subroutine DEMISS

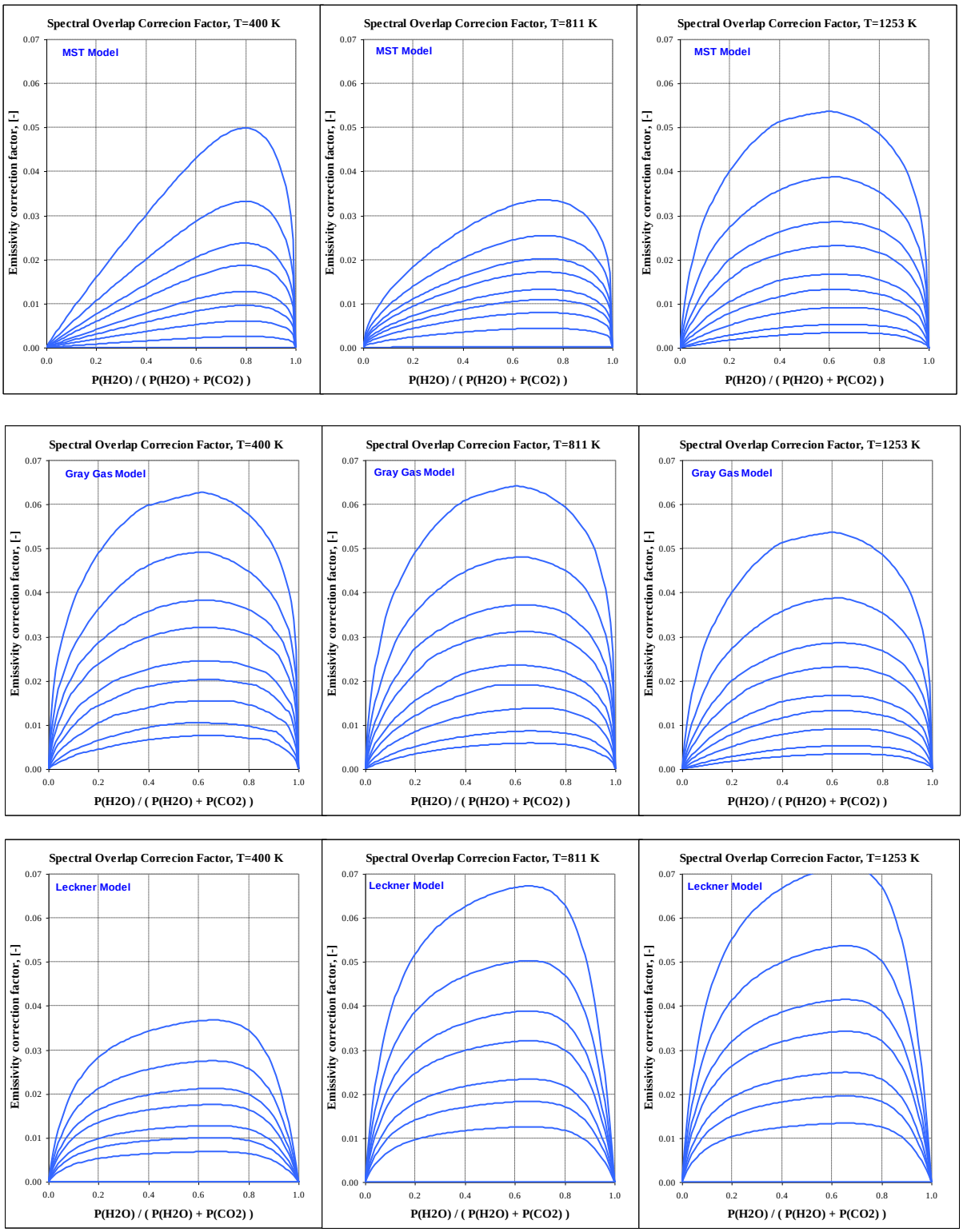

Figure 2-108 Emissivity correction: MST model (top), gray gas model (middle), Leckner (bottom)

2.5.2 Radiative Properties of Solids

The spectral emissivities of gold are shown in figure 7 in [15] (page 15-18). Based on that figure the band emissivity data was prepared, dividing the total spectrum range of interest into seven bands, as shown in Table 2-11.

The data shown in Table 2-11 was used as input to the function TSEMIS to calculate the total surface emissivity for gold for temperatures between 250 and 1250 K. The calculated values are shown in Figure 2-109. The total emissivity of gold for the same temperature range is shown in [22] (table 2.1, page 144). The values are reproduced in Figure 2-109 for comparison. The agreement is good.

The data shown in Figure 2-109 was generated using a FORTRAN program, which is provided in **\Z-TESTS\RT\TSEM-T.FOR**. Note: in order to compile the program, it must be first moved to the directory: **\Z-TESTS**.

In practical cases there is no need to use the function TSEMIS to calculate the total emissivity because the total emissivities obtained from experiments are available in literature for many materials. Spectral emissivities are in fact much more difficult to find.

Table 2-11 Band emissivities of gold

Band number	1	2	3	4	5	6	7
Band upper boundary, (μm)	0.6	1.0	2.0	4.0	6.0	8.0	1000
Band emissivity, (-)	0.620	0.100	0.035	0.030	0.025	0.020	0.020

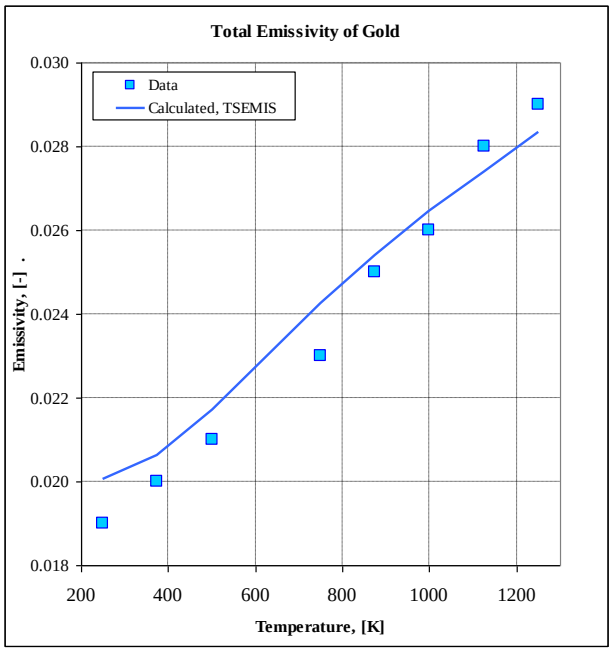

Figure 2-109 Total emissivity of gold - data and results of TSEMIS

2.6 Verification of the Material Oxidation Package

2.6.1 Zr Oxidation by H_2O

Two models are available for steam-Zr reaction (see Volume 1):

- A combination of Cathcart (low temperatures) and Urbanic-Heidrich (high temperatures)
- Urbanic-Heidrich.

Additionally any other model (for example Baker-Just) may be easily incorporated into calculations, applying the user-defined oxidation model, where the reaction coefficients are specified in the input deck (see Volume 2).

The two models are compared in Figure 2-110. Above the transition point (T≈1800 K, or 10,000/T≈5.5) Urbanic-Heidrich coefficients are used and the results are exactly the same. Below the transition point the reaction coefficients from Cathcart give somewhat lower reaction rate at low temperatures, and somewhat higher at high temperatures.

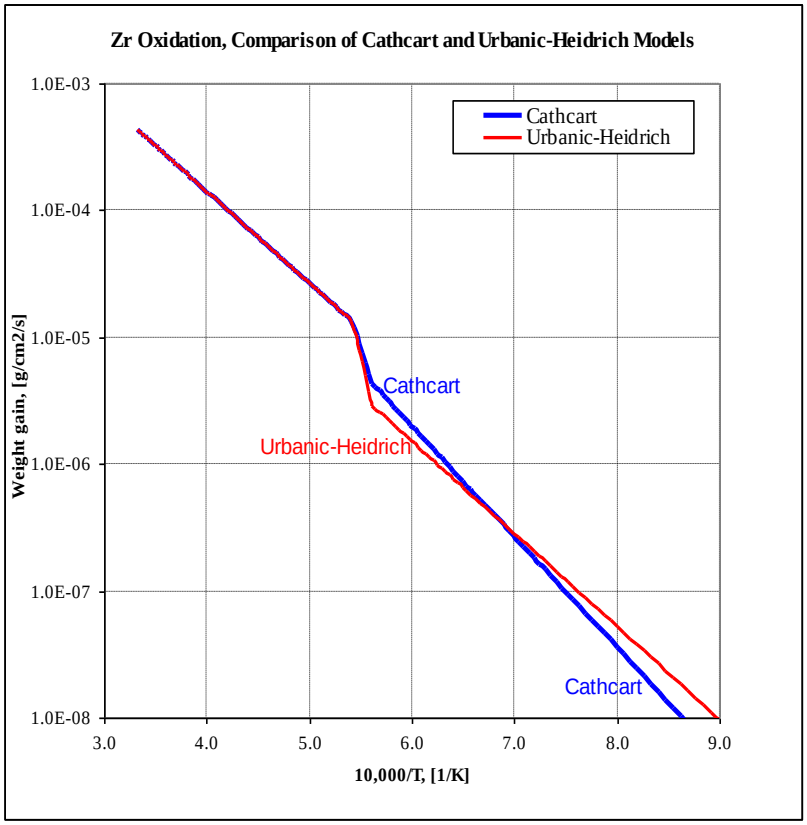

Figure 2-110 Comparison of the built-in Zr-H_2O oxidation models.

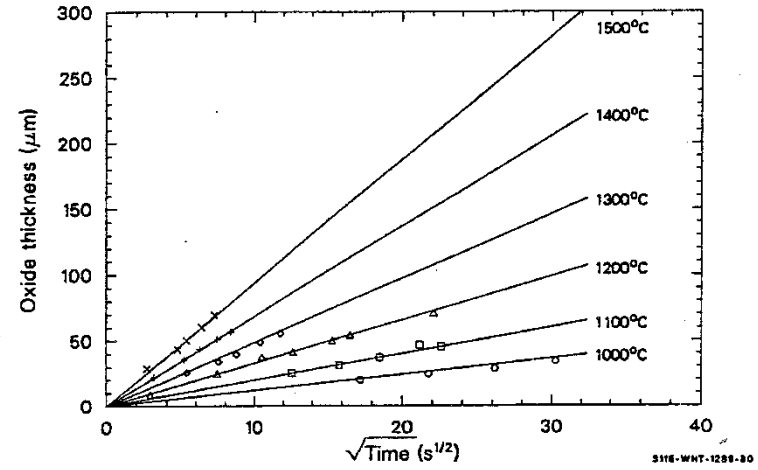

Figure 2-111 Zr oxidation by H_2O – reproduced from [56] (figure 4-66).

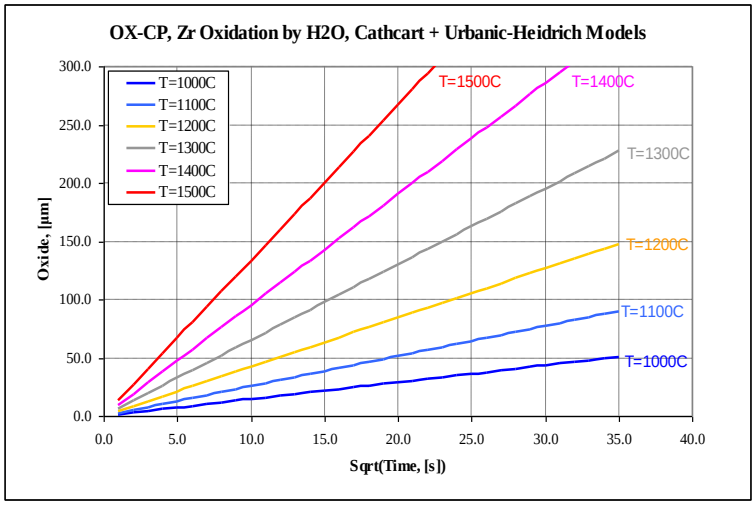

Figure 2-112 Zr oxidation by H_2O – SPECTRA model 1 (Cathcart + Urbanic-Heidrich).

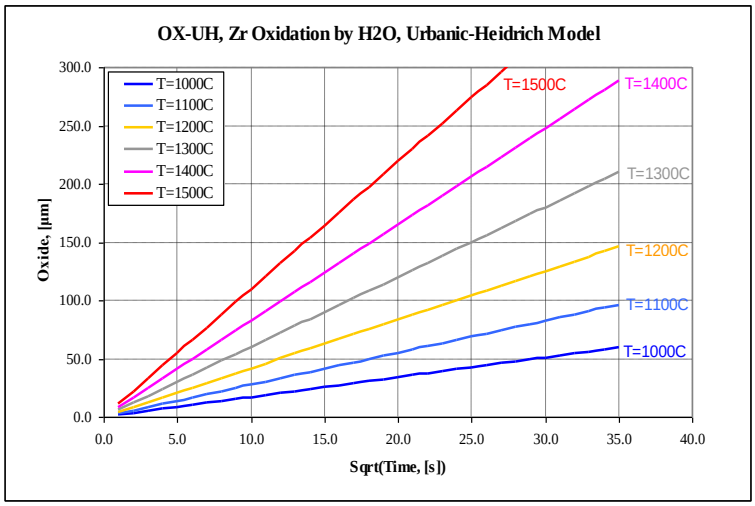

Figure 2-113 Zr oxidation by H_2O – SPECTRA model 2 (Urbanic-Heidrich)

Experimental data on Zr oxidation by H_2O, as well as correlation lines of the Urbanic-Heidrich model, are shown in Figure 2-111, reproduced from [56]. The results of two models available in SPECTRA are shown in Figure 2-112 Figure 2-113. The FORTRAN program to generate those graphs is provided in **\Z-TESTS\OX\OX-T.FOR**. The SPECTRA models provide somewhat higher oxide thickness. Note that the lines in Figure 2-111 are obtained using the Cathcart model, so it could be expected that the SPECTRA results obtained with the Cathcart model (Figure 2-113) are exactly the same. Explanation of the difference is provided below.

The original model provides reaction coefficients for three parameters:

- Reacted mass (or weight gain),
- Oxide layer thickness, and
- Alpha layer thickness.

In SPECTRA only the equation for reacted mass is used (expressed in kg of Zr reacted per unit surface area per second – see Volume 1). This equation is important to properly compute the masses of consumed steam and generated hydrogen, as well as the generated heat. The layer thickness on the other hand is a parameter that is not very important for calculations – the geometrical changes of Solid Heat Conductors are not modelled anyway within the SC/TC package. Therefore the oxide thickness is estimated in the model from:

$$t_{ox} = \frac{M_{Zr}}{\rho_{Zr}} \cdot \sigma_{ox}$$

where:
M_{Zr} mass of Zr reacted, (kg)
ρ_{ox} density of unreacted Zr, (kg/s)
σ_{ox} volumetric growth upon oxidation, estimated as 1.5 ([62], page 446)

In conclusion, the oxide thickness printed by SPECTRA are just estimations, based on the assumption of 50% volumetric growth during oxidation. Therefore the oxide layer thickness is not the same as in the correlations provided in literature.

2.6.2 Zr Oxidation by O_2

Figure 2-119 shows comparison of the steam and oxygen reactions. The steam reaction is calculated from the Cathcart model, while the oxygen reaction from the Benjamin model. The oxygen reaction is roughly twice faster than the steam reaction. The FORTRAN program to generate this graph is provided in **\Z-TESTS\OX\OX-T.FOR**.

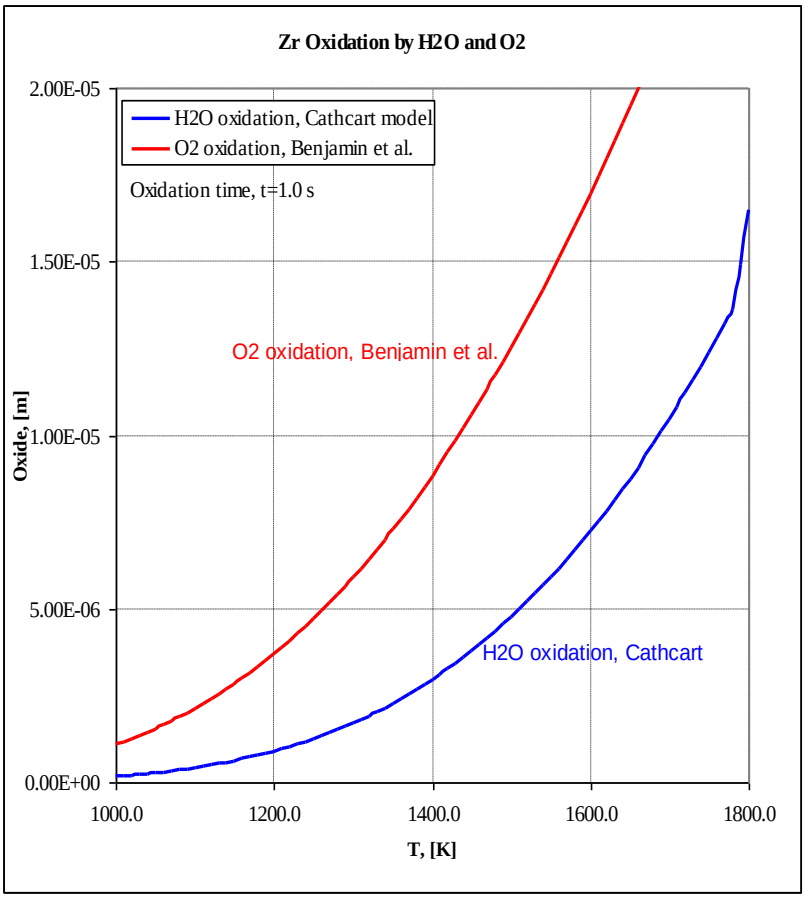

Figure 2-114 Zr oxidation by O_2 and H_2O, SPECTRA built-in models

2.6.3 Steel Oxidation by H_2O

Results of the subroutine calculating steel oxidation by steam are compared to the externally computed values, plotted in reference [56], in Figure 2-115 through Figure 2-118. The FORTRAN program to generate those graphs is provided in **\Z-TESTS\OX\OX-T.FOR**. Good agreement is observed in both reaction heat and oxide thickness. Note that, as in case of Zr oxidation, the original model provides coefficients for both reacted mass and layer thickness, while in SPECTRA only reacted mass is calculated.

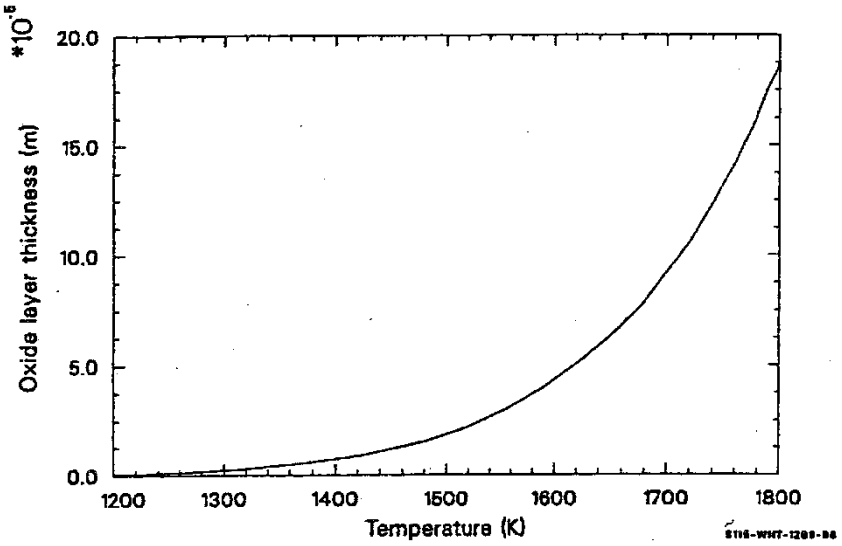

Figure 2-115 Steel oxidation by H_2O – reproduced from [56] (figure 6-9).

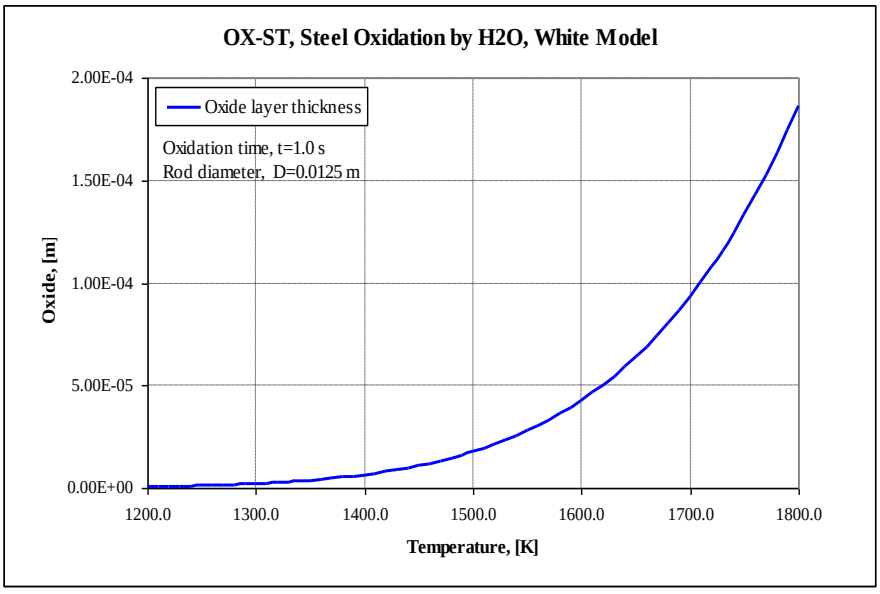

Figure 2-116 Steel oxidation by H_2O – SPECTRA built-in model.

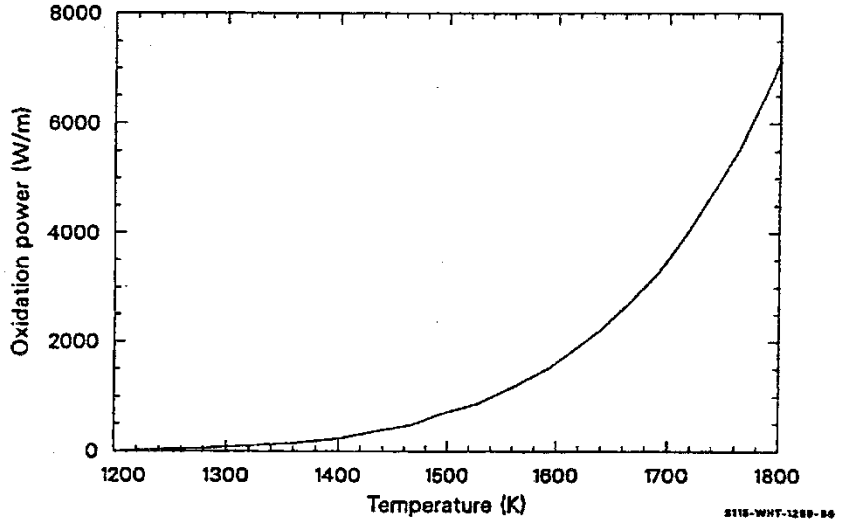

Figure 2-117 Steel oxidation by H_2O – reproduced from [56] (figure 6-7).

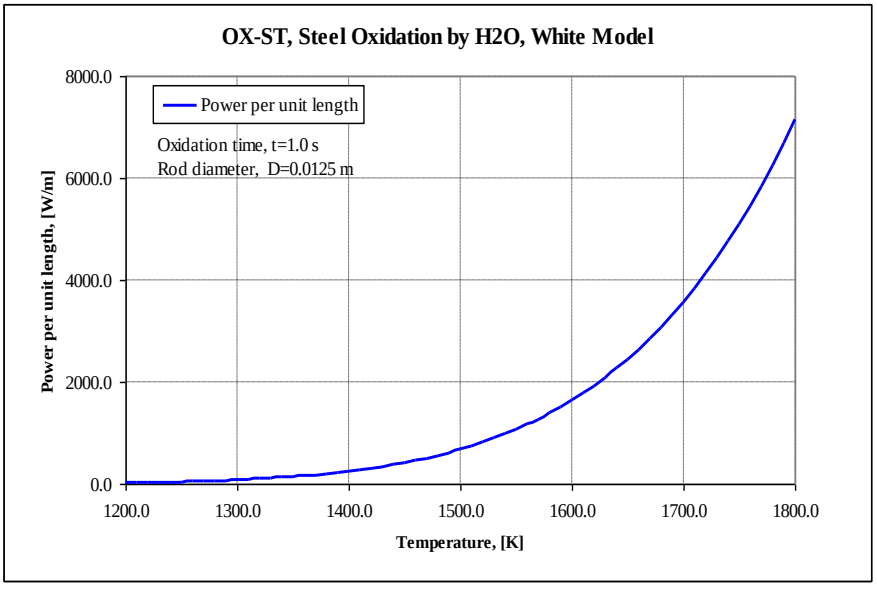

Figure 2-118 Steel oxidation by H_2O –SPECTRA built-in model.

2.6.4 Steel Oxidation by O_2

There is no built-in model for steel oxidation by O_2. However, a data from Nanni et al., reference [60], was used to estimate reaction coefficients, *A* and *B* (see Volume 1). The reaction kinetics is:

$$\frac{dm^2}{dt} = A \exp\left[\frac{B}{T}\right] = 2.3\times10^{10} \exp\left[\frac{43350}{T}\right]$$

Figure 2-119 shows comparison of the steam and oxygen reactions. The FORTRAN program to generate this graph is provided in **\Z-TESTS\OX\OX-T.FOR**. The steam reaction is calculated from the White model, while the oxygen reaction from a user-defined model, with reaction coefficients shown above. The oxygen reaction is roughly 1.5 times faster than the steam reaction.

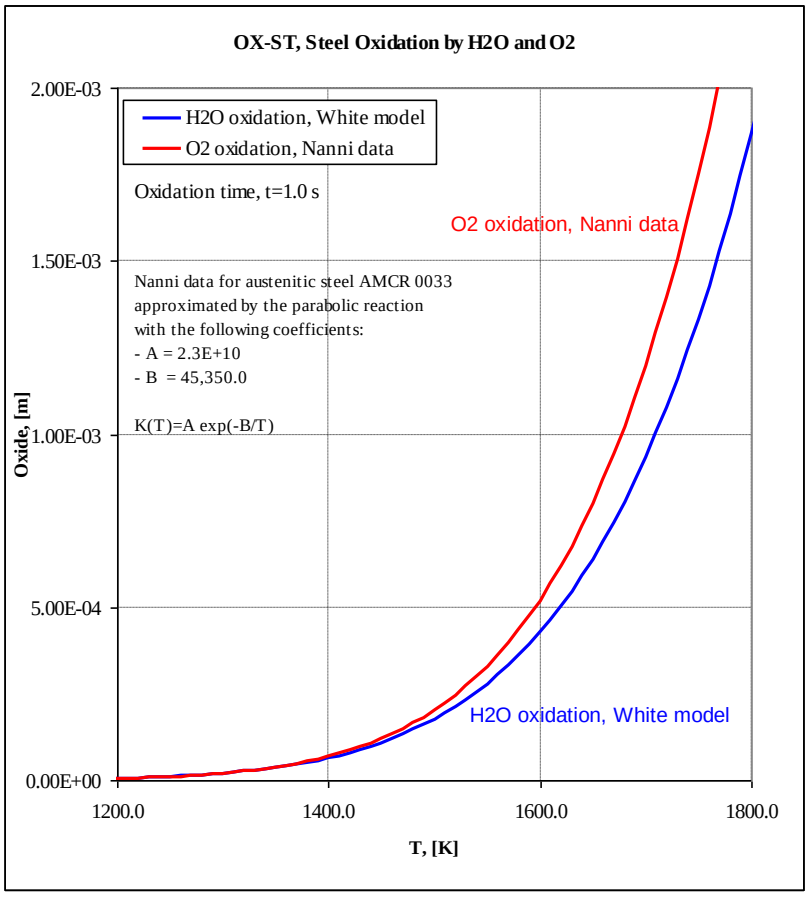

Figure 2-119 Steel oxidation by H_2O (built-in model) and O_2, (user-defined model)

2.6.5 Graphite Oxidation by O_2

Graphite oxidation model is based on Roes work [61]. Results are compared to the graph shown in [61], in Figure 2-120 and Figure 2-121. The FORTRAN program to generate those graphs is provided in **\Z-TESTS\OX\OX-T.FOR**. Results are in good agreement.

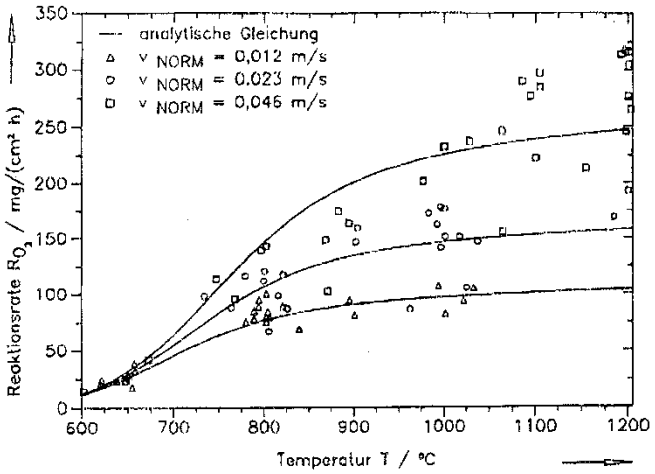

Figure 2-120 Graphite oxidation by O_2 –reproduced from [61] (fig. 5.5).

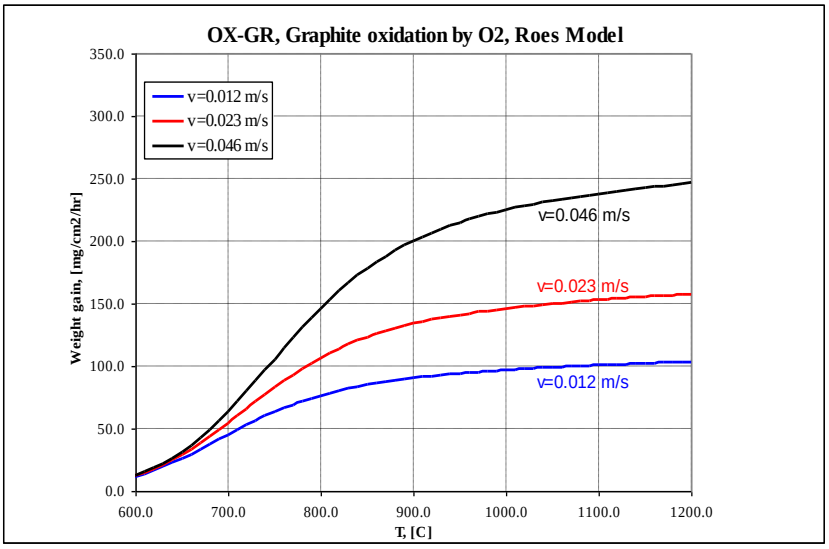

Figure 2-121 Graphite oxidation by O_2 –SPECTRA built-in model.

2.6.6 User-Defined Oxidation Model

The user-defined model was verified by comparing its results of all built-in models. To test each model, the user-defined coefficients for this model were defined identical to the coefficients in the appropriate built-in model. The FORTRAN program used to perform the comparison is provided in **\Z-TESTS\OX\OX-COMP.FOR**.Results of the user-defined and the built-in models were identical. Note that the built-in models have slightly different calculation procedure. For example, the Zr or steel oxidation models are governed by temperature only, $K=K_T(T)$, so the velocity- and the pressure-dependent terms are not present. The user-defined model is always using the full kinetics formula, $K(T,v,p)$.

2.7 Verification of the Hydrogen Burn Package

This section provides verification of individual subroutines from the Hydrogen Burn Package. Subroutines responsible for the calculation of gas flammability limits, ignition limits, flame velocities, etc. are tested separately. The alternative models are compared to the base models. The results are described in sections 2.7.1, 2.7.2, and 2.7.3.

2.7.1 Flammability Limits

The model used to calculate flammability is described in detail in Volume 1. The model distinguishes three burn modes: slow deflagration, fast turbulent deflagration, and detonation. Each mode is assigned a code number and a plot variable MODEH2 may be used to plot the current mode. The meaning of the values are:

- MODEH2=0 : inflammable gas mixture
- MODEH2=1 : flammable gas mixture, slow deflagration expected upon ignition
- MODEH2=2 : flammable gas mixture, fast turbulent deflagration expected upon ignition
- MODEH2=3 : flammable gas mixture, detonation expected upon ignition

To check the flammability limits the value of the variable MODEH2 was plotted in 3-D graphs, for a wide range of parameters. The FORTRAN program used to generate the graphs is provided in **\Z-TESTS\H2\MODE\MODE-T.FOR**. Note: in order to compile the program, it must be first moved to the directory: **\Z-TESTS**. Figure 2-122 through Figure 2-125 show the lower and the upper flammability limits, for steam fractions of 0% and 20%, and for the default as well as alternative models for the detonation and fast turbulent deflagration limits. A list of all plots is shown in Table 2-12.

Table 2-12 Flammability limits - figure numbers

Model	Flammability limit			
	Lower		Upper	
	H_2O frac.= 0.00	H_2O frac.= 0.20	H_2O frac.= 0.00	H_2O frac.= 0.20
Default	Figure 2-122 top	Figure 2-123 top	Figure 2-124 top	Figure 2-125 top
σ criterion	Figure 2-122 mid	Figure 2-123 mid	Figure 2-124 mid	Figure 2-125 mid
λ criterion	Figure 2-122 bot	Figure 2-123 bot	Figure 2-124 bot	Figure 2-125 bot

Figure 2-122 show that for a dry gas mixture (x_{H2O} = 0.0) the default fast turbulent deflagration criterion is somewhat more conservative than the σ criterion, specifically at high temperatures. On the other hand, the default criterion gives less conservative estimation of the detonability limit at temperatures above about 350 K than the λ criterion. In case of gas mixture with 20% steam, the λ criterion for detonation is clearly less conservative than the default criterion, as seen in Figure 2-123. Of course the λ criterion uses one additional variable: characteristic dimension, *D*, so these findings may not be true for *D* very different than that for which the bottom were made, namely *D*=10.0 m.

Figure 2-124 show that for dry gas mixture (x_{H2O} = 0.0) detonation occurs without "previous warnings" on the high hydrogen concentration side. This is because all three lines, determining the deflagration limit, the fast deflagration limit, and the detonation limit, meet at the zero steam concentration, as shown in Volume 1. It should be noted that the lines meet exactly in that point only if the default model is consistently used. If the σ or the λ criteria are used, then different modes are possible in some regions, as seen in Figure 2-124 bottom.

Figure 2-125 show that for 20% steam (x_{H2O} = 0.2) the default fast turbulent deflagration criterion is somewhat less conservative than the σ criterion on the high hydrogen side. On the other hand, the default criterion gives more conservative estimation of the detonability limit than the λ criterion.

Summarizing, it may be said that:

- Both thee default and the alternative criteria give similar results.
- The σ-criterion is likely to give less conservative results than the default model on the low hydrogen fraction side (typically encountered in practice), and more conservative on the high hydrogen fraction side.
- The λ-criterion is likely to give more conservative results than the default model for low steam fractions and less conservative for the high steam fractions.

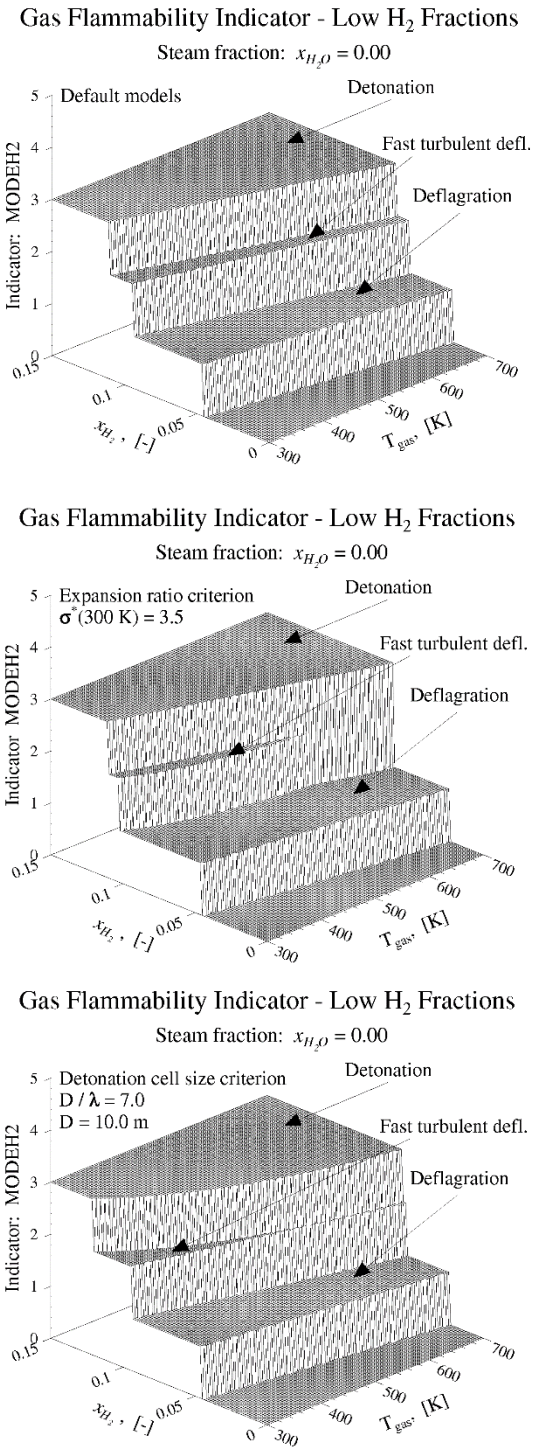

Figure 2-122 Flammability limits, low H_2 fracions, H_2O fraction 0.00, top = default models, middle = σ-criterion, bottom = λ-criterion

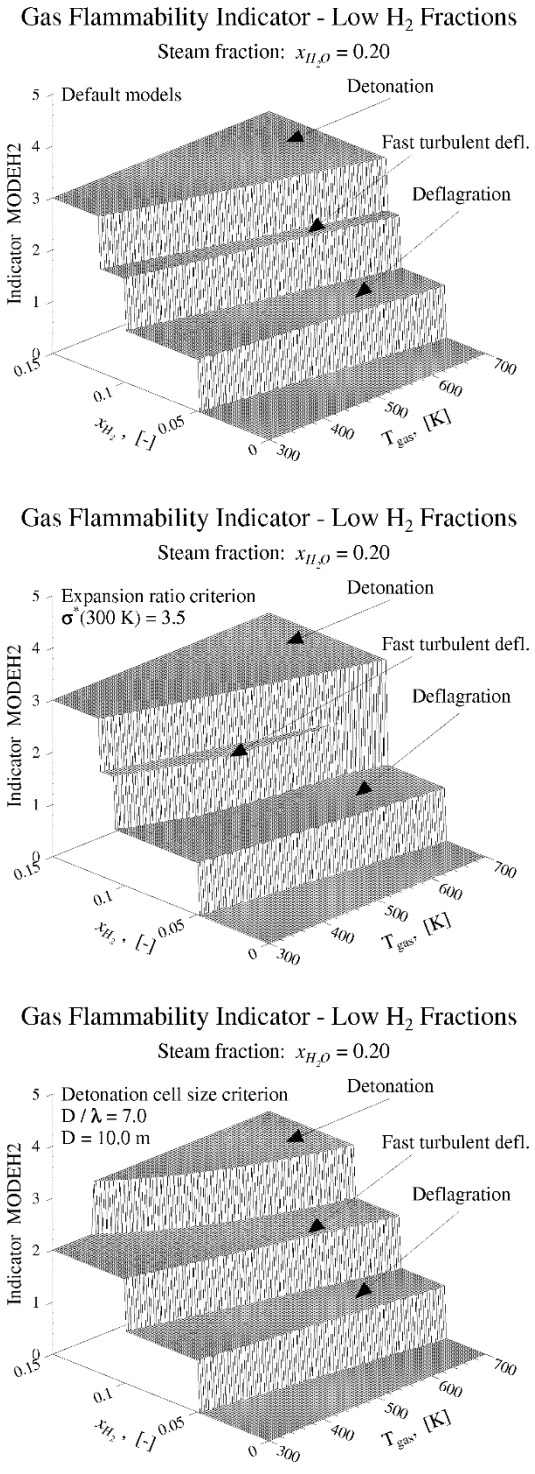

Figure 2-123 Flammability limits, low H_2 fracions, H_2O fraction 0.20, top = default models, middle = σ-criterion, bottom = λ-criterion

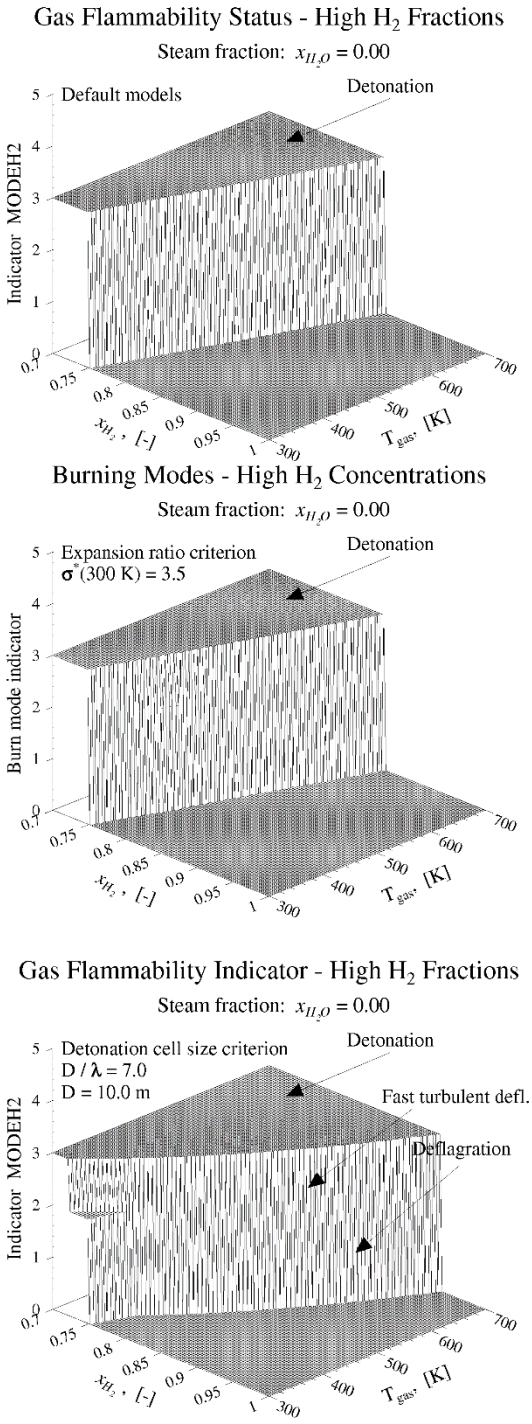

Figure 2-124 Flammability limits, high H_2 fracions, H_2O fraction 0.00, top = default models, middle = σ-criterion, bottom = λ-criterion

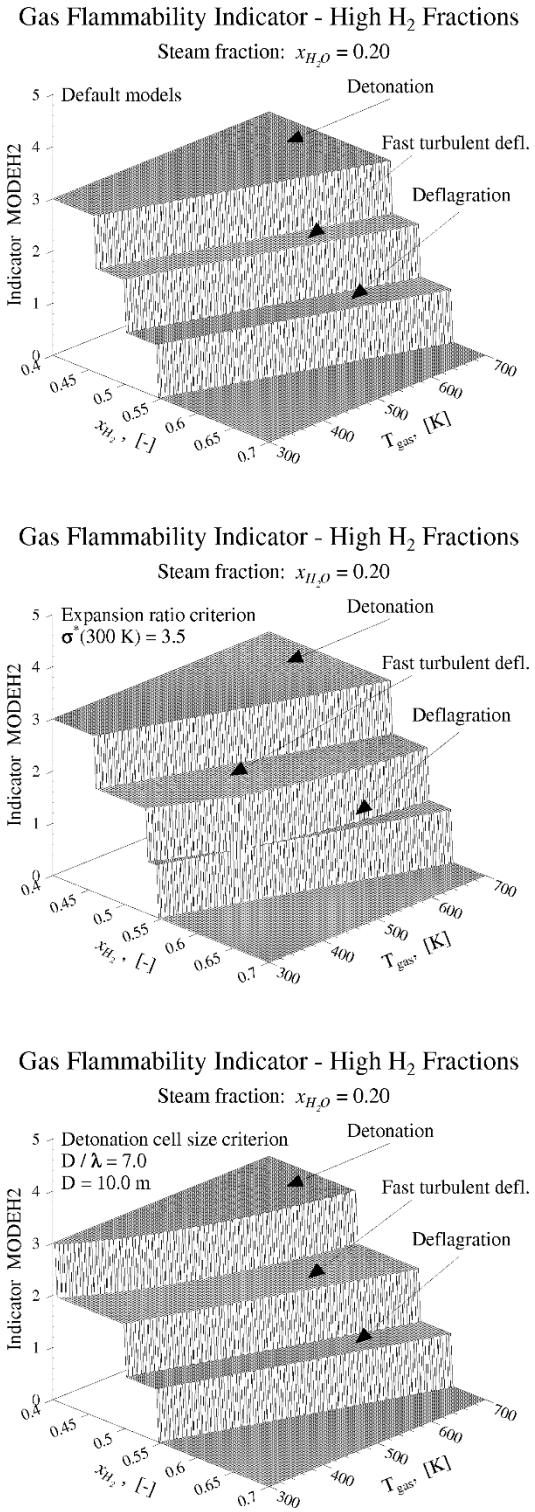

Figure 2-125 Flammability limits, high H_2 fracions, H_2O fraction 0.20, top = default models, middle = σ-criterion, bottom = λ-criterion

2.7.2 Ignition Limits

The model used to calculate ignition is described in detail in Volume 1. If, at any time of the calculation the ignition criteria are satisfied, then the hydrogen burn is initiated. The burn mode indicator, IBRNH2, becomes equal to the gas flammability at the moment of ignition (IBRNH2=MODEH2). The meaning of the variable IBRNH2 is as follows:

- IBRNH2=0 : no burn
- IBRNH2=1 : slow deflagration in progress
- IBRNH2=2 : fast turbulent deflagration in progress
- IBRNH2=3 : detonation in progress

To check the ignition calculation procedure the value of the variable IBRNH2 was plotted in 3-D graphs for a wide range of parameters. The FORTRAN program used to generate the graphs is provided in **\Z-TESTS\H2\IGN\IGN-T.FOR**. Note: in order to compile the program, it must be first moved to the directory: **\Z-TESTS**. Figure 2-126 through Figure 2-129 show the burn indicator for steam fractions of 0% and 20%, and for the default as well as alternative models for the detonation and fast turbulent deflagration limits.

Figure 2-126 and Figure 2-127 show the gas burn indicator, for a dry hydrogen-air gas mixture at 1 bar pressure, calculated using the default models, as well as the alternative models, with the value of σ^*(300 K)=3.5, and critical value of D/λ=7.0.

It is seen that ignition occurs at temperatures of about 700 - 730 K (430 - 460°C). The alternative models give somewhat less conservative results, that is the fast turbulent deflagration and detonation occur at somewhat higher hydrogen fractions than in the default model. This is because the default model has been set up to give possibly the most conservative (yet realistic) results.

Figure 2-128 and Figure 2-129 show the gas burn indicator, for a hydrogen-air-steam mixture at 1 bar pressure and 20% steam volume fraction. Again, calculations were performed using the default models, as well as the alternative models, with the value of σ^*(300 K) =3.5, and critical value of D/λ=7.0.

In case of 20% steam fraction the ignition occurs at quite higher temperatures than in case of dry mixtures. The ignition temperatures are about 750 - 800 K (480 - 530°C). The alternative models give less conservative results, most clearly visible for the detonation limit. As already stated in section 2.7.1, the λ criterion is clearly less conservative in case of high steam fractions.

2.7.3 Flame Velocities

Subroutines calculating flame velocities for slow deflagrations, fast turbulent deflagrations, and detonations have been tested by comparing results of the particular subroutine with the literature data upon which the model was based. The FORTRAN program used to generate the graphs is provided in **\Z-TESTS\H2\VDFL-T.FOR**. Graphs are presented in Volume 1.

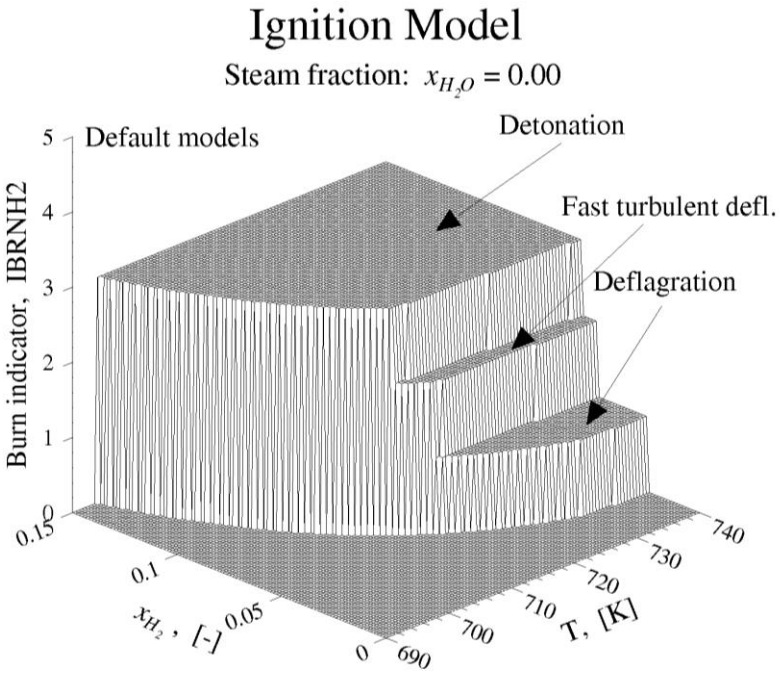

Figure 2-126 Hydrogen burn indicator, steam fraction 0.0%, default models

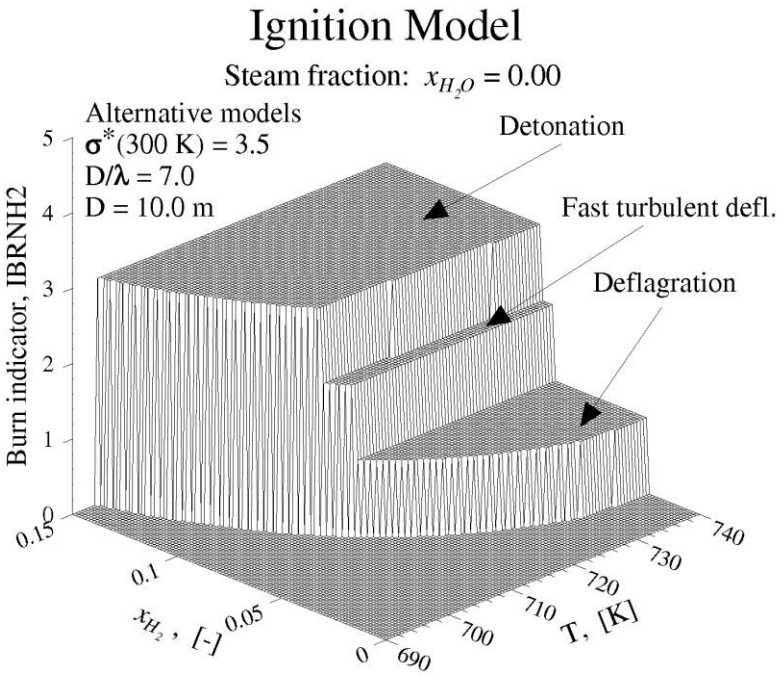

Figure 2-127 Hydrogen burn indicator, steam fraction 0.0%, alternative models

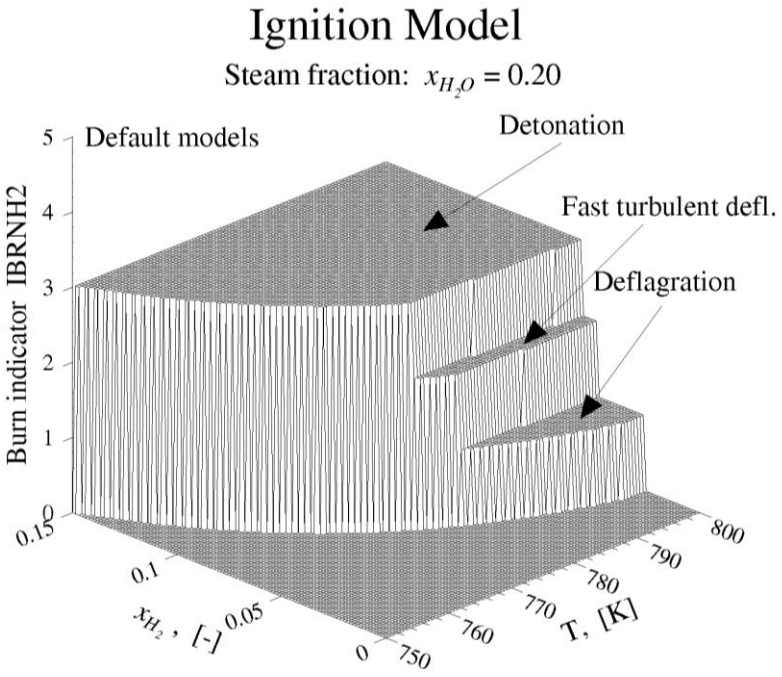

Figure 2-128 Hydrogen burn indicator, steam fraction 20.0%, default models

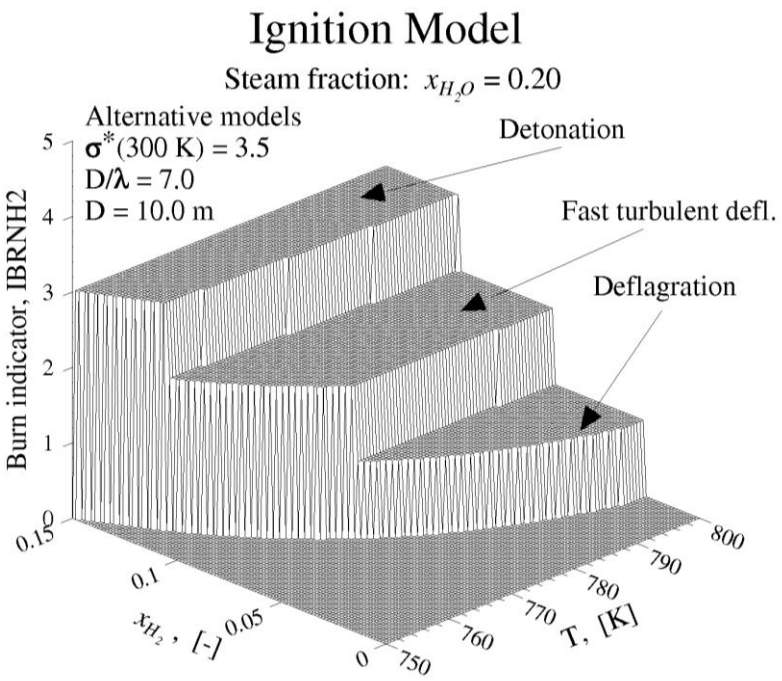

Figure 2-129 Hydrogen burn indicator, steam fraction 20.0%, alternative models

2.8 Verification of the Radioactive Particles Transport Package

2.8.1 Gravitational Deposition

The gravitational settling is important for relatively large particles. The deposition velocities, as calculated by the SPECTRA subroutine VDGRAV, are shown in Figure 2-130. The testing program is provided in **\Z-TESTS\RT\GRAV.FOR**. The results were checked by hand calculations. For $d_p = 10^{-4}$ m, particle density of 1000 kg/s, the gravitational deposition velocities obtained by the subroutine VDGRAV (file VDGRAV.OUT) are:

- T = 300 K, $v_{D,grav}$ = 0.299 m/s
- T = 700 K, $v_{D,grav}$ = 0.164 m/s
- T = 1000 K, $v_{D,grav}$ = 0.130 m/s

Calculations were performed for air at atmospheric pressure, resulting with the gas viscosity of:

- T = 300 K, $\mu_g = 1.824\times10^{-5}$ kg/m-s
- T = 700 K, $\mu_g = 3.337\times10^{-5}$ kg/m-s
- T = 1000 K, $\mu_g = 4.218\times10^{-5}$ kg/m-s

The number are checked by hand calculations. For this particle diameter $Kn \sim 0.001$, and the Cunningham correction factor, C_m, is practically equal to 1.0 (to be precise, it is equal to 1.002, 1.005 and 1.007 for 300 K, 700 K, and 1000 K respectively). The gravitational deposition velocity is equal to:

$$v_{D,grav} = \frac{1}{18}\frac{\rho_p d_p^2 g\, C_m}{\mu_g \chi}$$

- T = 300 K, $$v_{D,grav} = \frac{1000\cdot\left(10^{-4}\right)^2\cdot 9.81}{18\cdot 1.824\times10^{-5}}\cdot 1.002 = 0.299$$

- T = 700 K, $$v_{D,grav} = \frac{1000\cdot\left(10^{-4}\right)^2\cdot 9.81}{18\cdot 3.337\times10^{-5}}\cdot 1.005 = 0.164$$

- T = 1000 K, $$v_{D,grav} = \frac{1000\cdot\left(10^{-4}\right)^2\cdot 9.81}{18\cdot 4.218\times10^{-5}}\cdot 1.007 = 0.130$$

The calculated numbers are in agreement with the values obtained from VDGRAV.

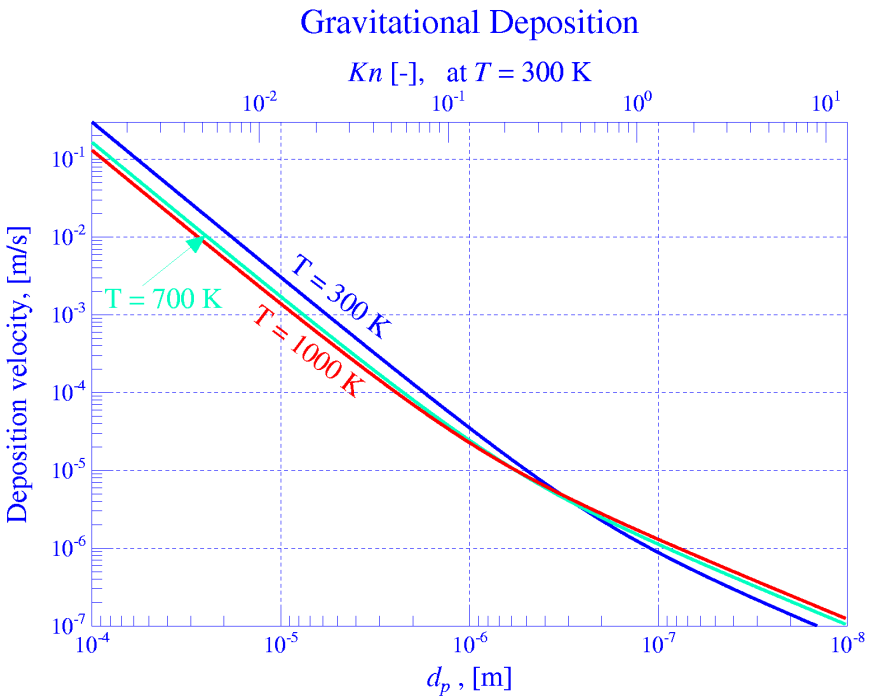

Figure 2-130 Gravitational deposition velocities.

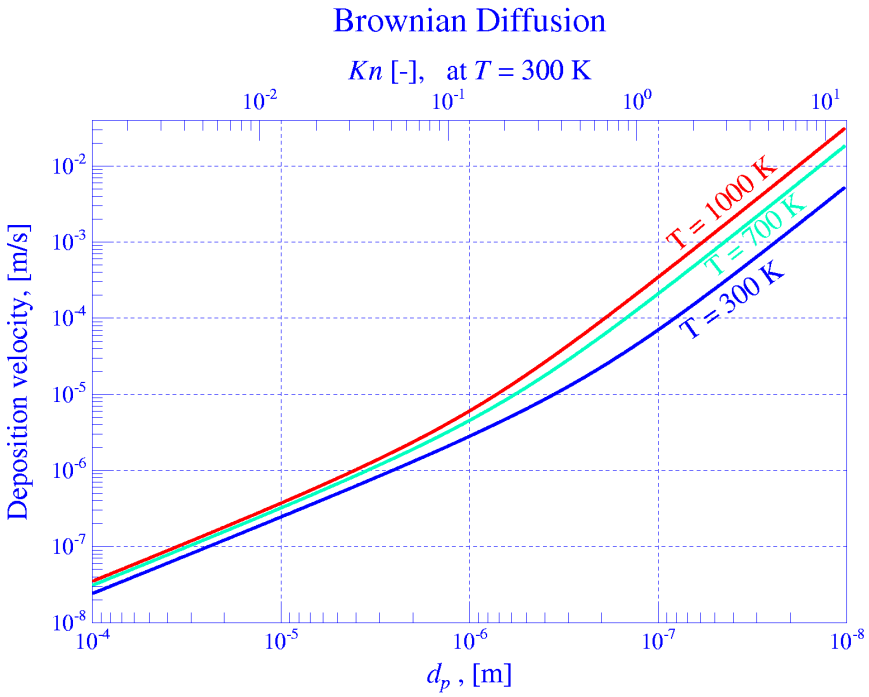

Figure 2-131 Brownian deposition velocities.

2.8.2 Brownian Diffusion

The Brownian diffusion is important for very small particles. The deposition velocities, as calculated by the SPECTRA subroutine VDBRWN, are shown in Figure 2-131. The testing program is provided in **\Z-TESTS\RT\BROWN.FOR**. The results were checked by hand calculations. For d_p = 10^{-4} m, particle density of 1000 kg/s, the gravitational deposition velocities obtained by the subroutine VDBRWN (file VDBRWN.OUT) are:

- T = 300 K, $v_{D,Brown} = 2.41\times10^{-8}$ m/s
- T = 700 K, $v_{D,Brown} = 3.09\times10^{-8}$ m/s
- T = 1000 K, $v_{D,Brown} = 3.50\times10^{-8}$ m/s

Calculations were performed for air at atmospheric pressure, resulting with the gas viscosity of:

- T = 300 K, $\mu_g = 1.824\times10^{-5}$ kg/m-s
- T = 700 K, $\mu_g = 3.337\times10^{-5}$ kg/m-s
- T = 1000 K, $\mu_g = 4.218\times10^{-5}$ kg/m-s

The number are checked by hand calculations. For this particle diameter Kn ~ 0.001, and the Cunningham correction factor, C_m, is practically equal to 1.0 (to be precise, it is equal to 1.002, 1.005 and 1.007 for 300 K, 700 K, and 1000 K respectively). The Brownian deposition velocity is equal to:

$$D_C = \frac{k_B T}{3\pi\mu_g d_p} C_m$$

$$v_{D,Brown} = \frac{D_C}{\delta_{BL}}$$

The results depend on the choice of the diffusion boundary layer thickness, δ_{BL}. The results shown in Figure 2-131 were obtained using the default value of δ_{BL} of 10^{-5} m. The hand calculations are shown below.

- T = 300 K:

$$D_C = \frac{1.38\cdot10^{-23}\cdot300}{3\pi\cdot1.824\cdot10^{-5}\cdot10^{-4}}\cdot1.002 = 2.41\cdot10^{-13}$$

$$v_{D,Brown} = \frac{2.41\cdot10^{-13}}{10^{-5}} = 2.41\cdot10^{-8}$$

- T = 700 K:

$$D_C = \frac{1.38\cdot10^{-23}\cdot700}{3\pi\cdot3.337\cdot10^{-5}\cdot10^{-4}}\cdot1.005 = 3.09\cdot10^{-13-8}$$

$$v_{D,Brown} = \frac{3.09\cdot10^{-13}}{10^{-5}} = 3.09\cdot10^{-8}$$

- T = 1000 K:

$$D_C = \frac{1.38 \cdot 10^{-23} \cdot 1000}{3\pi \cdot 4.218 \cdot 10^{-5} \cdot 10^{-4}} \cdot 1.007 = 3.50 \cdot 10^{-13-8}$$

$$v_{D,Brown} = \frac{3.50 \cdot 10^{-13}}{10^{-5}} = 3.50 \cdot 10^{-8}$$

The calculated numbers are in agreement with the values obtained from VDBRWN. Comparison of the Brownian diffusion deposition velocities with the other deposition velocities shows that this mechanism has very small contribution to the overall deposition. Therefore it seems that accurate calculation of the diffusion boundary layer thickness is not necessary.

2.8.3 Thermophoresis

Two correlations are available in SPECTRA for the thermophoretic deposition, the Brock correlation [70], and the He and Ahmadi correlation [71]. Results of both correlations, as calculated by the SPECTRA subroutines VDTRM1, VDTRM2, VDTRM3, are compared in Figure 2-133. Temperature difference of ΔT=1.0 K was used. The testing program is provided in:

\Z-TESTS\RT\THERMO.FOR.

Several deposition correlations were compared in [73] - Figure 2-132. It was concluded that He and Ahmadi correlation gives the most accurate predictions for Knudsen numbers, $0.1 < Kn < 20$. The Brock correlation is valid for Kn up to about 0.1. The Kn number of 20 corresponds to the particle diameters of ~2×10^{-8} m, while the Kn number of 0.1 corresponds to the particle diameters of ~4×10^{-6} m - Figure 2-132.

The default SPECTRA model (see Volume 1) consists of both correlations. The Brock correlation is used for $Kn < 0.1$. The He and Ahmadi correlation is used for $Kn > 0.2$. An interpolation zone, $0.1 < Kn < 0.2$, is provided to ensure smooth transition from one correlation to another. Results obtained with the default correlation are shown in Figure 2-134.

It is interesting to note that the Brock correlation is applied in the MELCOR code, however the constant in the correlation is slightly different. In SPECTRA there is a constant multiplier of $2C_s$ = 2.34 (where C_s =1.17, see Volume 1). In MELCOR this multiplier is equal to 3/2 = 1.5 [20] (the corresponding C_s value is 0.75). Therefore the Brock correlation, as implemented in MELCOR, gives the thermophoretic deposition velocities of about 64% (1.5/2.34) of the values obtained in SPECTRA. Comparison of Brock correlation, obtained using default coefficients from MELCOR, with He-Ahmadi correlation is shown in Figure 2-135.

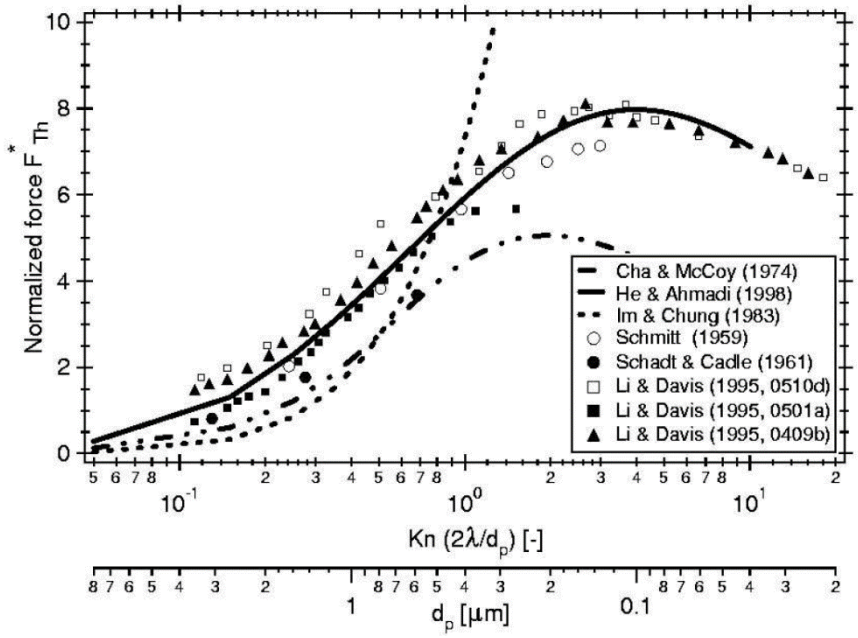

Figure 2-132 Comparison of the thermophoresis correlations [73]

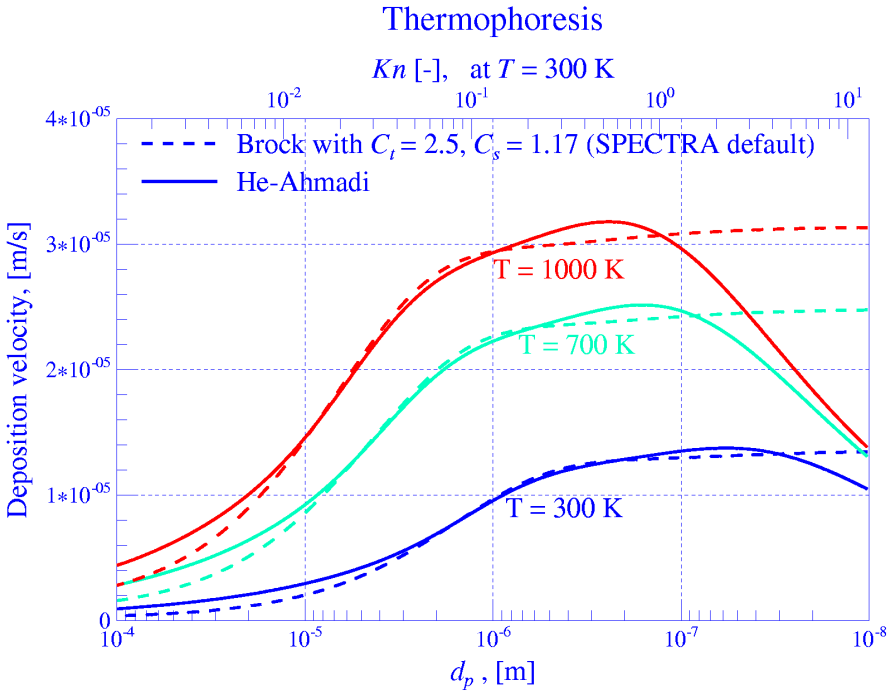

Figure 2-133 Comparison of the thermophoresis correlations.

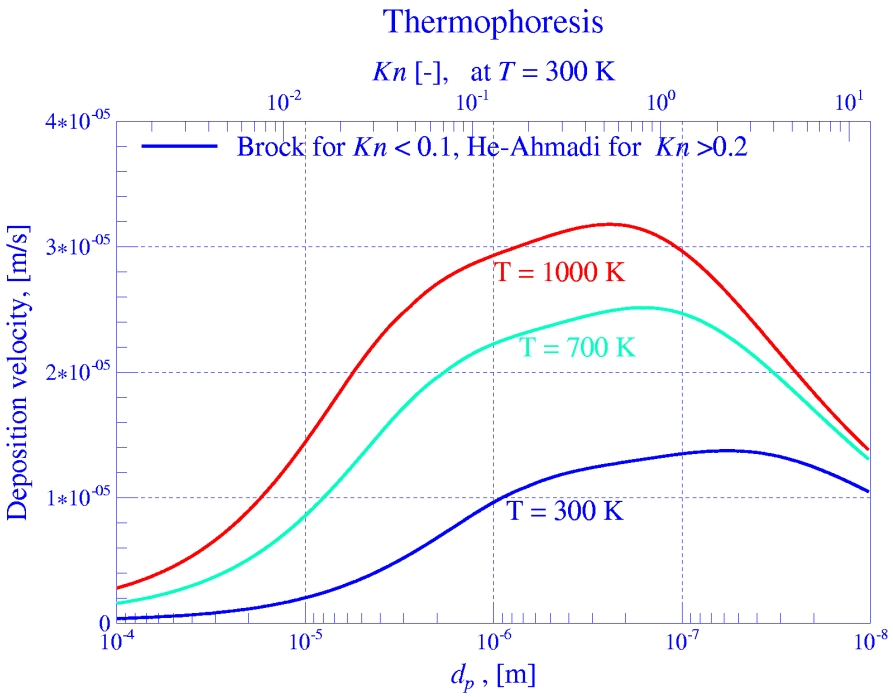

Figure 2-134 Default thermophoresis correlation, Brock for *Kn*<0.1, He & Ahmadi for *Kn*>0.2.

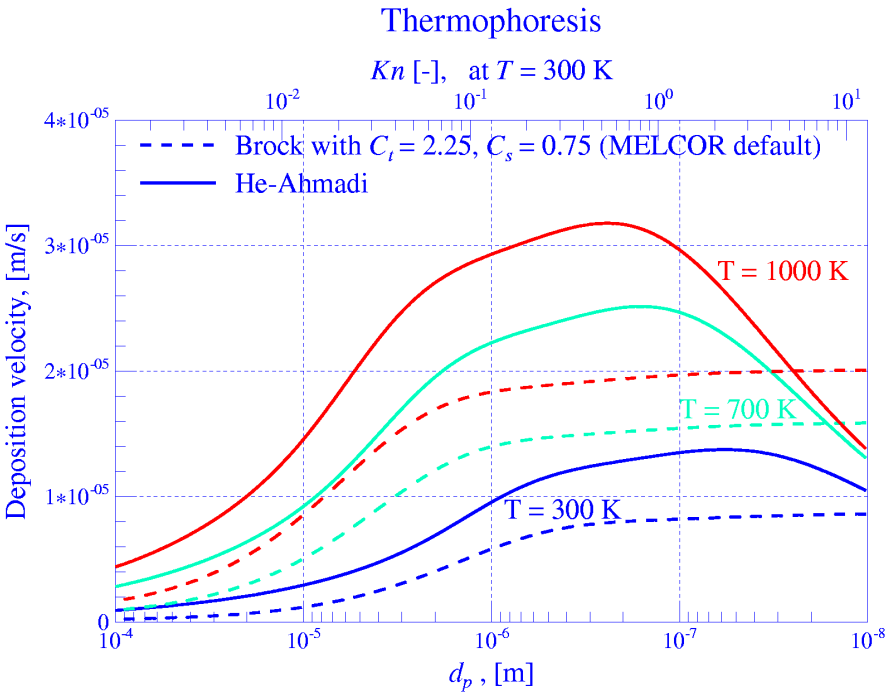

Figure 2-135 Comparison of the thermophoresis correlations, Brock with MELCOR defaults.

2.8.4 Diffusiophoresis

When water condenses on (evaporates from) a structure surface or pool surface, composition gradients will exist in the adjacent gas, which will affect aerosol deposition on the surface [20]. Two related mechanisms produce these gradients. First, a net molar flux of gas toward (away from) the condensing (evaporating) surface will exist, and this net flux, commonly called the Stefan flow [79], will tend to move aerosol particles with it. Second, differences in the momentum transfer by molecular impacts on opposite sides of the particle will tend to drive the particle into the direction decreasing concentration of the heavier constituent. In SPECTRA, as in MELCOR [20], the term diffusiophoresis is used to represent the net result of both effects. Note that when the non-condensable gas is heavier than steam (for example air), the differential molecular impact effect opposes the Stefan flow (which dominates the net result); the effects are in the same direction if the non-condensable gas is lighter than steam (for example helium).

Two models are available in SPECTRA to calculate the diffusiophoretic deposition.

- *Model 1*. In the first model the differential molecular impact effect is included in case of both condensation and evaporation.

- *Model 2*. In the second model the differential molecular impact effect is included only in case of condensation (MELCOR model - see [20], RN Reference Manual, section 2.4.2.2).

The testing program is provided in **\Z-TESTS\RT\DIFF.FOR**. Results of the diffusiophoretic deposition velocity, as calculated by the SPECTRA Model 1 (subroutine VDDIF1), are shown in Figure 2-136, for steam-air mixture, and in Figure 2-137 for steam-helium mixture.

It is seen that in the condensation regime the differential molecular impact effect opposes the effect of Stefan flow and decreases the overall deposition velocity in case of steam-air mixture (the net deposition velocities are below 0.2 m/s for W= –0.2 - Figure 2-136), while it enhances the deposition velocity in case of steam-helium mixtures (the net deposition velocities are ~2 m/s for W= –0.2 - Figure 2-137).

In the evaporation region the effect is less visible, nevertheless the differential molecular impact effect still opposes the effect of Stefan flow in case of steam-air mixture (the net deposition velocities are ~ –0.25 m/s for W=0.2 - Figure 2-136), while it enhances the effect of Stefan flow in case of steam-helium mixtures (the net deposition velocities are ~ –0.6 m/s for W=0.2 - Figure 2-137).

Note that in case of evaporation the deposition velocity is negative. This is correct because the individual deposition velocities are not used, but the sum of all deposition velocities is calculated first. Then if the sum is smaller than zero, it is truncated to zero.

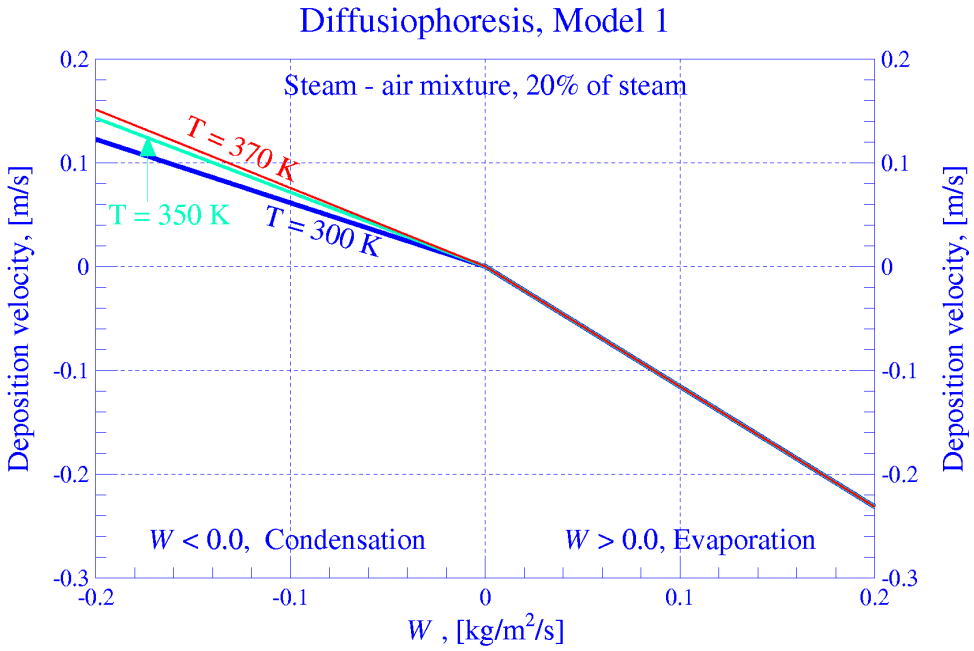

Figure 2-136 Diffusiophoretic deposition velocities, steam-air mixture, Model 1.

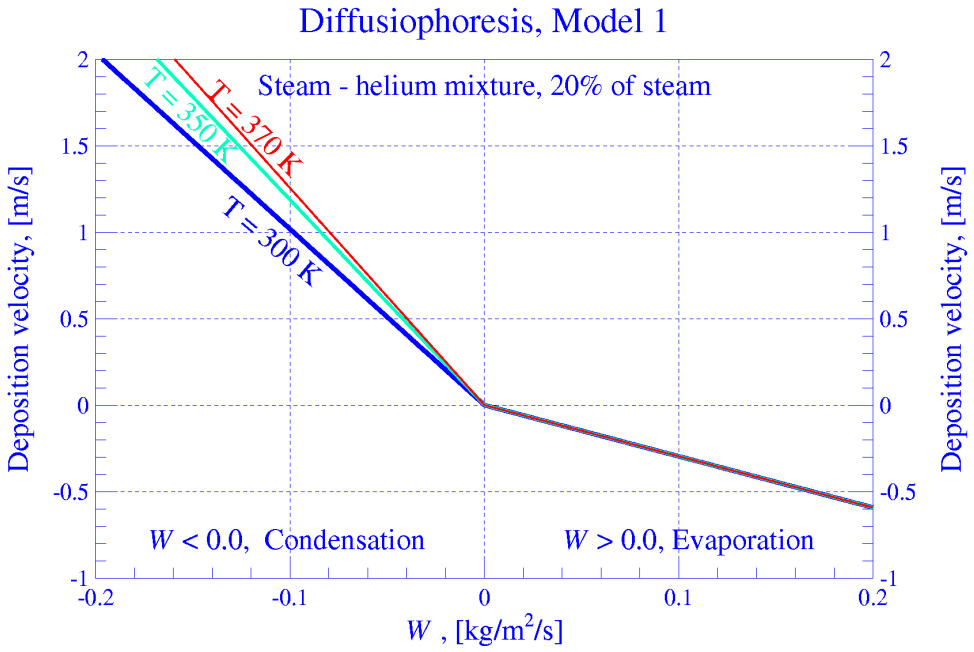

Figure 2-137 Diffusiophoretic deposition velocities, steam-helium mixture, Model 1.

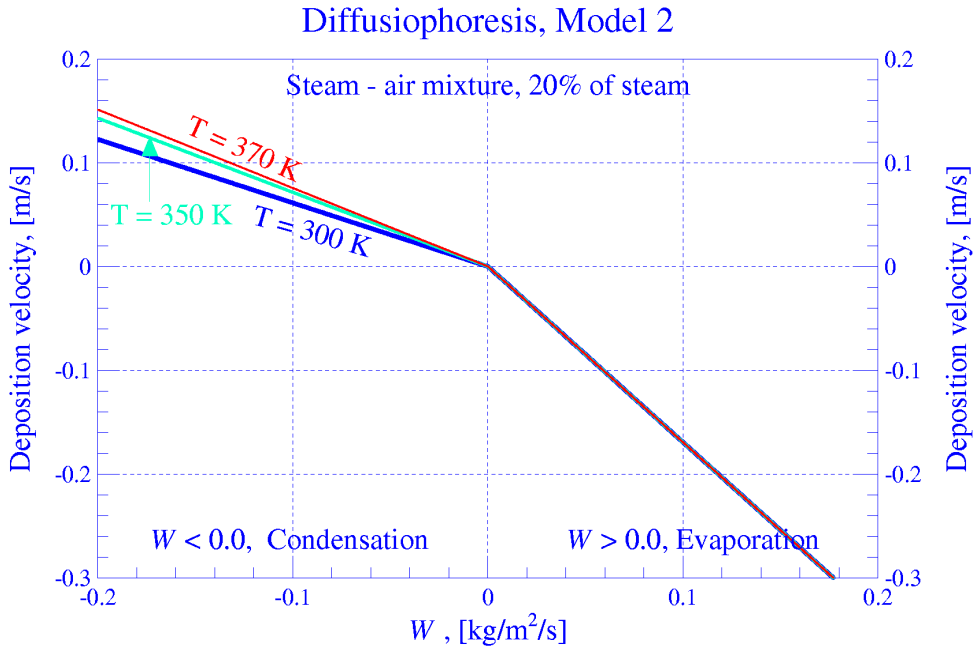

Figure 2-138 Diffusiophoretic deposition velocities, steam-air mixture, Model 2.

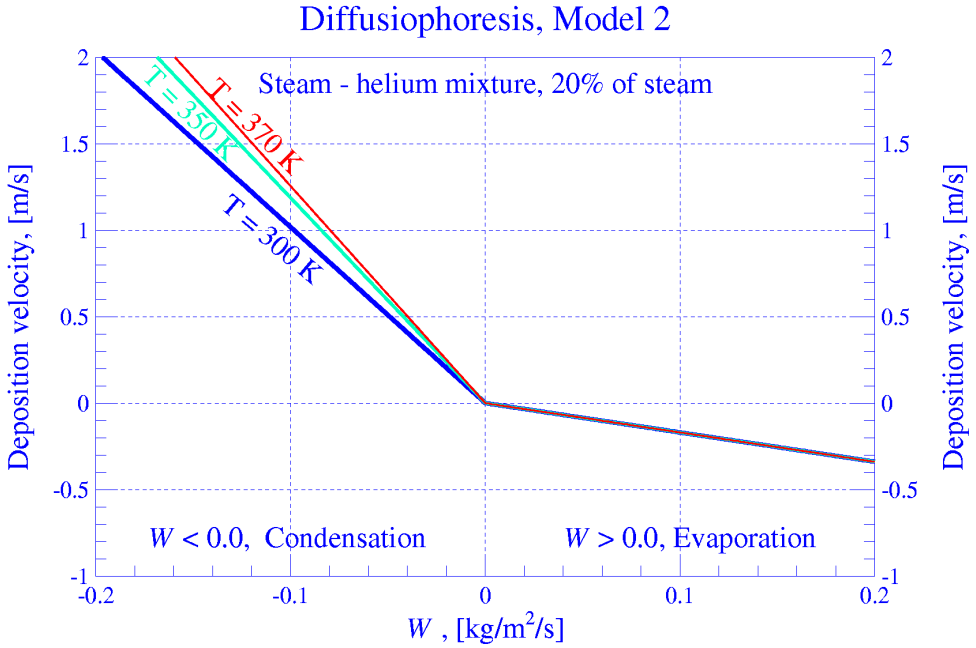

Figure 2-139 Diffusiophoretic deposition velocities, steam-helium mixture, Model 2.

For example, assume there is intensive evaporation from the pool surface, which gives the diffusiophoretic deposition velocity of –0.1 m/s. The particles have diameters of 10^{-4} m, and the gravitational deposition velocity is equal to 3×10^{-3} m/s (Figure 2-130). Brownian deposition can be neglected for such large particles (Figure 2-131). Furthermore it is assumed that other deposition mechanisms can be neglected. The total deposition velocity is:

$$v = v_{grav} + v_{diff} = 0.003 - 0.1 = -0.997$$

Since the number is negative, it will be set to zero, and the total deposition velocity at the pool surface will be equal to zero in this case. If the individual deposition velocities were truncated to zero, then there would be always small gravitational deposition on the pool surface, no matter how intensive evaporation is observed. This would not be realistic.

Results of the diffusiophoretic deposition velocity, as calculated by the SPECTRA Model 2 (subroutine VDDIF2), are shown in Figure 2-138, for steam-air mixture, and in Figure 2-139 for steam-helium mixture.

It is seen that in contrast to the Model 1 results the Model 2 gives in the evaporation range the same deposition velocities for the steam-air mixture as for steam-helium mixture (the deposition velocity is about –0.35 m/s for the evaporation rate of 0.2 kg/m^2/s). This is a consequence of omitting the differential molecular impact effect in the Model 2. Model 1 is a default model in SPECTRA. Model 2 is intended for eventual comparisons with MELCOR.

2.8.5 Turbulent Deposition

Results of the turbulent impaction deposition velocity, as calculated by the SPECTRA subroutine VDTURB, are shown in Figure 2-140 through Figure 2-143. The testing program is provided in **\Z-TESTS\RT\TURB.FOR**. Measurement data is shown in Figure 2-144. Figure 2-140 shows the deposition velocities (m/s) versus the particle diameter (m) for the temperatures 300, 700, and 1000 K. The dimensionless particle relaxation times τ_P^+, corresponding to the particle diameters at T = 300 K is shown at the top axis. The results shown in this figure were obtained using dry air, and the gas velocity of 10 m/s. The friction factor of f = 0.02 was used for the calculations.

Figure 2-141 shows the deposition velocities for different gas velocities: 1, 10 and 50 m/s. Again, the dimensionless particle relaxation times τ_P^+ are shown at the top axis, here for the velocity of 10 m/s. The results shown here were obtained for dry air at T = 300 K.

Figure 2-142 and Figure 2-143 show the same data as Figure 2-140 and Figure 2-141, but this time plotted using the dimensionless parameters. The dimensionless deposition velocities v^+_{dep}, are plotted versus the dimensionless particle relaxation time, τ_P^+. The particle diameters corresponding to the particle relaxation time, τ_P^+, for T = 300 K and v = 10 m/s, are shown in Figure 2-142 and Figure 2-143 respectively. The dimensionless parameters are defined as follows:

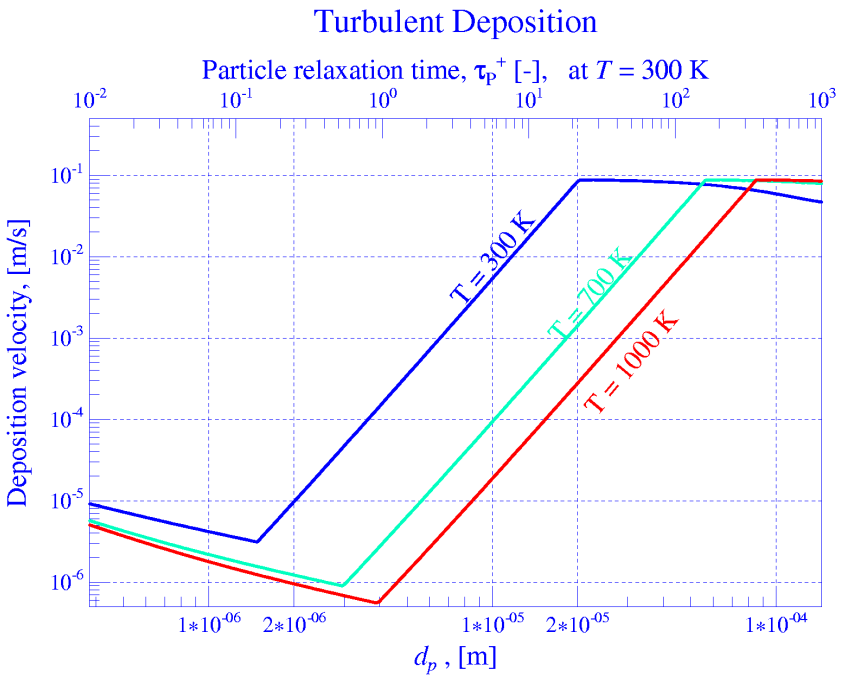

Figure 2-140 Turbulent deposition velocities, v_g = 10 m/s, T = 300, 700, 1000 K.

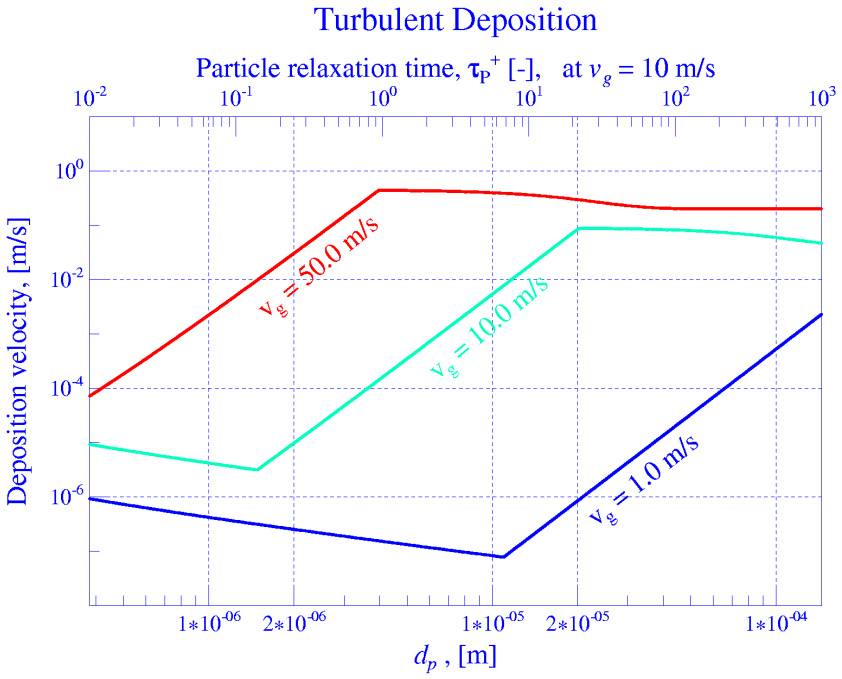

Figure 2-141 Turbulent deposition velocities, T = 300 K, v_g = 1, 10, 50 m/s.

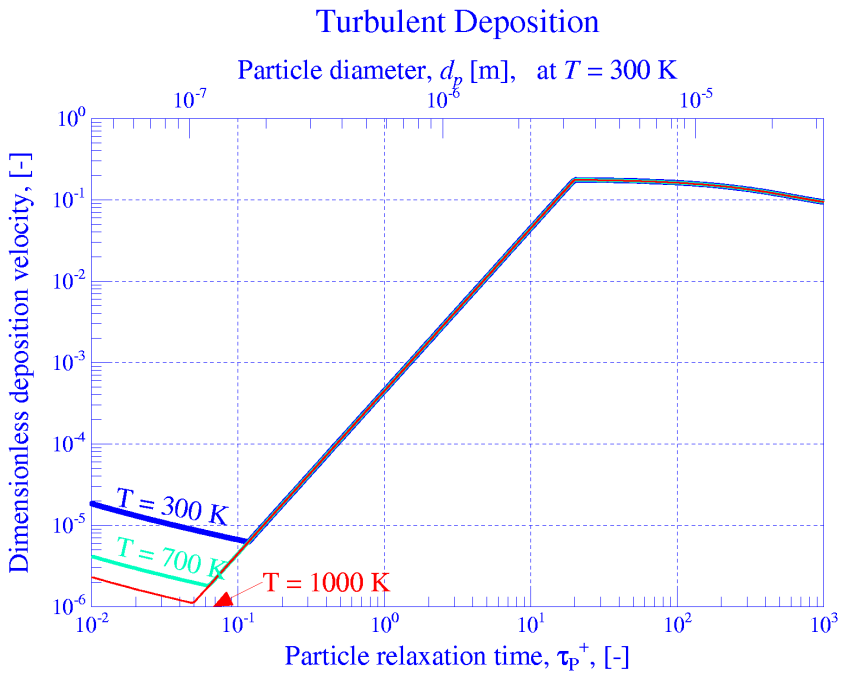

Figure 2-142 Dimensionless turbulent deposition velocities, v_g = 10 m/s, T = 300, 700, 1000 K.

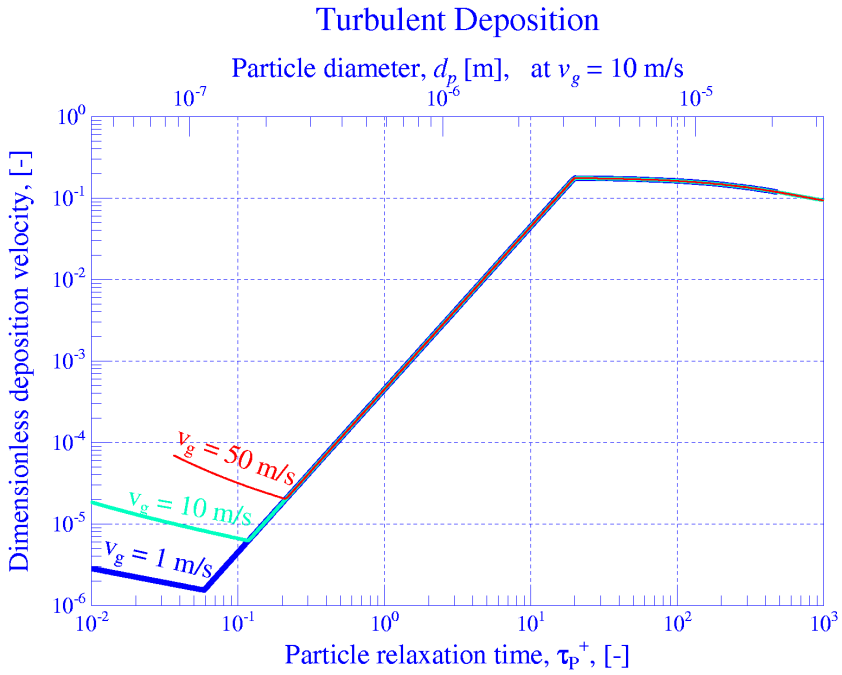

Figure 2-143 Dimensionless turbulent deposition velocities, T = 300 K, v_g = 1, 10, 50 m/s.

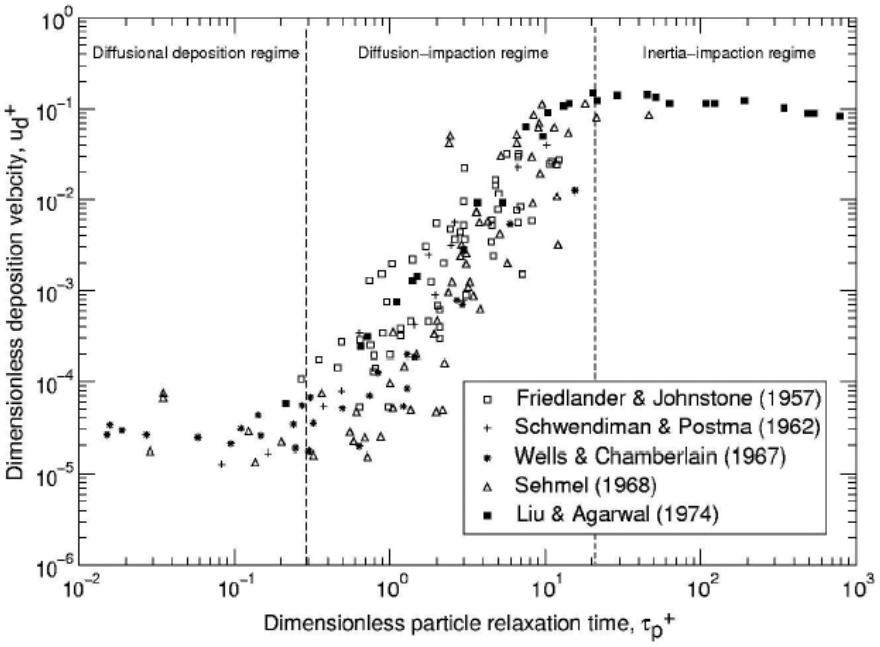

Figure 2-144 Dimensionless turbulent deposition velocities, [74].

- Dimensionless deposition velocity:

$$v_{dep}^{+} = \frac{v_{dep}}{u^{*}}$$

where u^* is the friction velocity, given by: $(f/8)^{1/2}\, v$, with f being the friction factor and v being the gas velocity.

- Dimensionless particle relaxation time, τ_p^+:

$$\tau_p^{+} = \frac{1}{144}\frac{\rho_p \rho_g d_p^2 f v^2}{\mu_g} C_m$$

Experimental data is shown in Figure 2-144. The model as coded (Figure 2-142 and Figure 2-143) well represents the measured values.

2.8.6 Collision Efficiency

Three models are available in SPECTRA to calculate the collision efficiency (needed for the gravitational coagulation kernel). These are:

- Fuchs model [75], approximate formula, developed for the diameter ratios smaller than 1.0 (see [72], section 4.3).
- Fuchs model [75], exact formula (see [72], section 4.3).
- Pruppacher and Klett model [76].

The testing program is provided in **\Z-TESTS\RT\CE.FOR**. The results, as obtained from the subroutine COLEFF, are compared to the experimental data [77] (reproduced from [78], figure 12) in Figure 2-145. The simple approximation formula of the Fuchs model gives the best agreement with the experimental data. Therefore this is the default model in SPECTRA (see Volume 2).

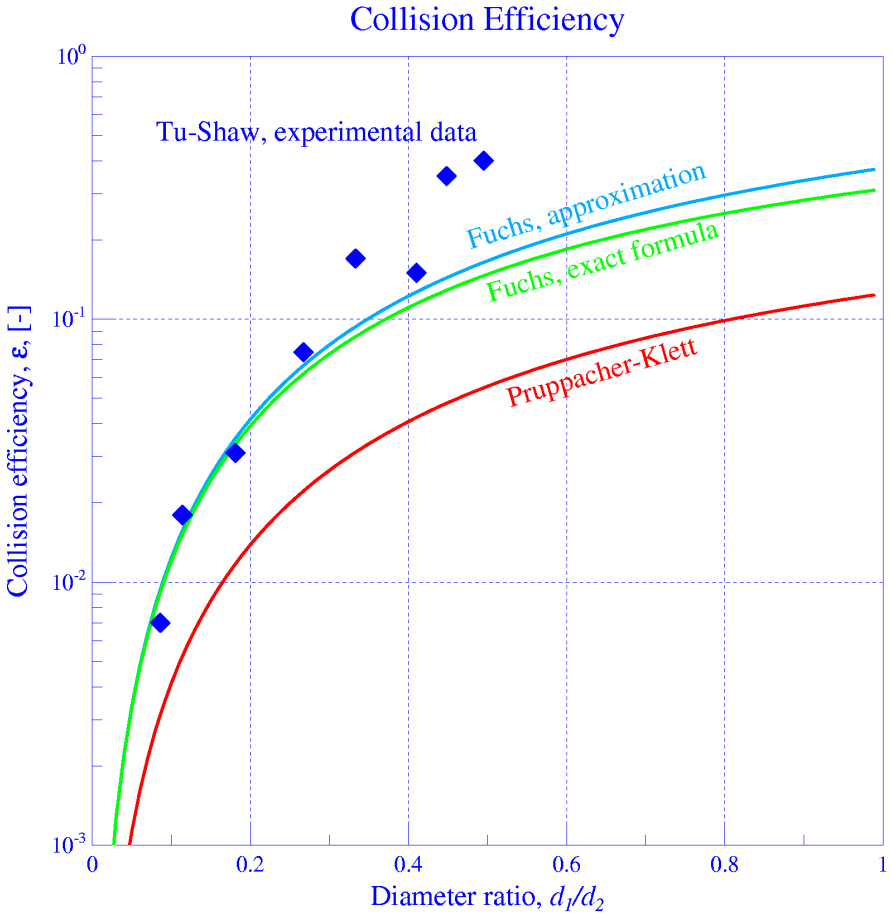

Figure 2-145 Comparison of the collision efficiency models with experimental data.

2.8.7 Gravitational Coagulation

The gravitational coagulation is calculated in SPECTRA using one of the three available models to calculate the collision efficiency

The gravitational coagulation kernel, as calculated by the subroutine CKGRAV, is shown in Figure 2-146. The testing program is provided in **\Z-TESTS\RT\CKGRAV.FOR**. The calculations were performed for dry air at atmospheric temperature and pressure. The dimension of the first colliding particle was varied from 10^{-8} m to 10^{-4} m. The diameter of the second particle was 10^{-6} m. The coagulation kernel decreases to zero when both particles have the same diameter (10^{-6} m) because in such case the gravitational settling velocities are the same.

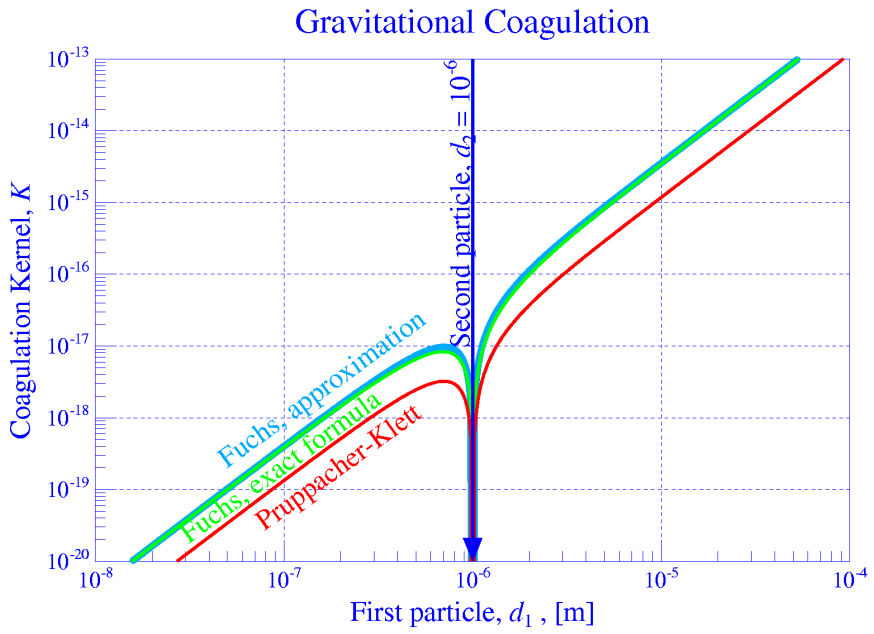

Figure 2-146 Gravitational coagulation – comparison of models, $d_2 = 10^{-6}$ m.

2.8.8 Brownian Coagulation

Three models are available in SPECTRA to calculate the Brownian coagulation. These are:

- Diffusion model ([72], section 4.2.1, equation 4.27). The diffusion model is valid for large particles and therefore is not recommended for general application.
- Slip flow model ([72], section 4.2.3, equation 4.45).
- Fuchs model [75] ([72], section 4.2.4, equation 4.55).

The Brownian coagulation kernel, as calculated by the subroutine CKBRWN, is shown in Figure 2-147, Figure 2-148, and Figure 2-149. The testing program is provided in **\Z-TESTS\RT\CKBROWN.FOR**. The calculations were performed for dry air at atmospheric temperature and pressure. The dimension of the first colliding particle was varied from 10^{-8} m to 10^{-4} m. The diameter of the second particle was equal to 10^{-7} m (Figure 2-147), 10^{-6} m (Figure 2-148), and 10^{-5} m (Figure 2-149).

It is seen that all models give very similar results for particle diameters > ~10^{-6} m (Figure 2-148 and Figure 2-149). The diffusion model gives smaller coagulation kernel than the two other models if one of the particles is smaller than ~10^{-6} m.

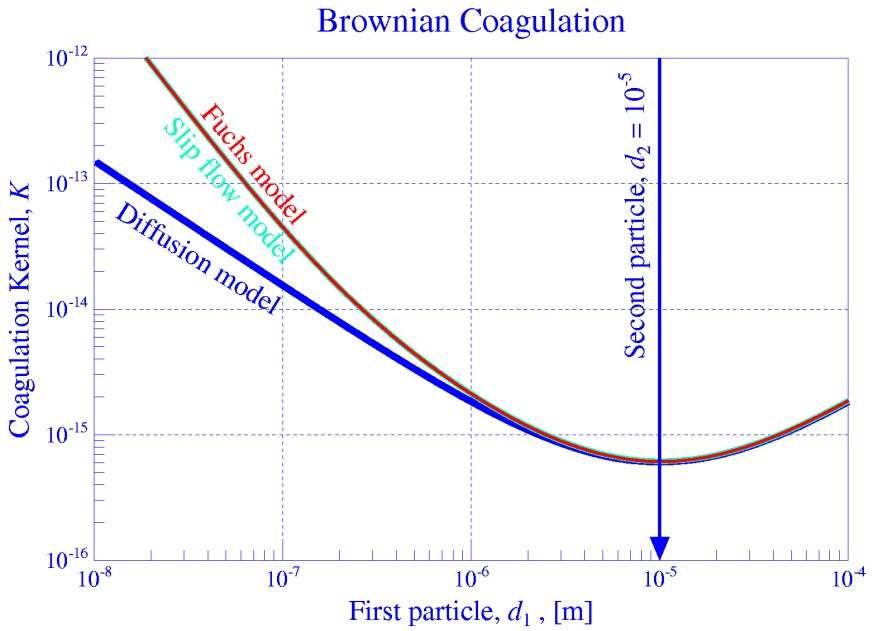

Figure 2-147 Brownian coagulation – comparison of models, $d_2 = 10^{-7}$ m.

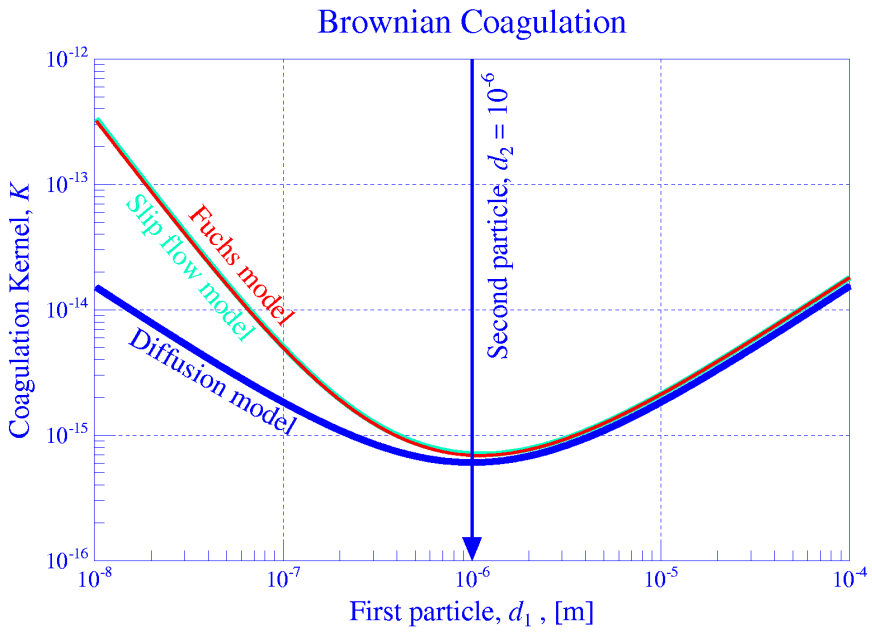

Figure 2-148 Brownian coagulation – comparison of models, $d_2 = 10^{-6}$ m.

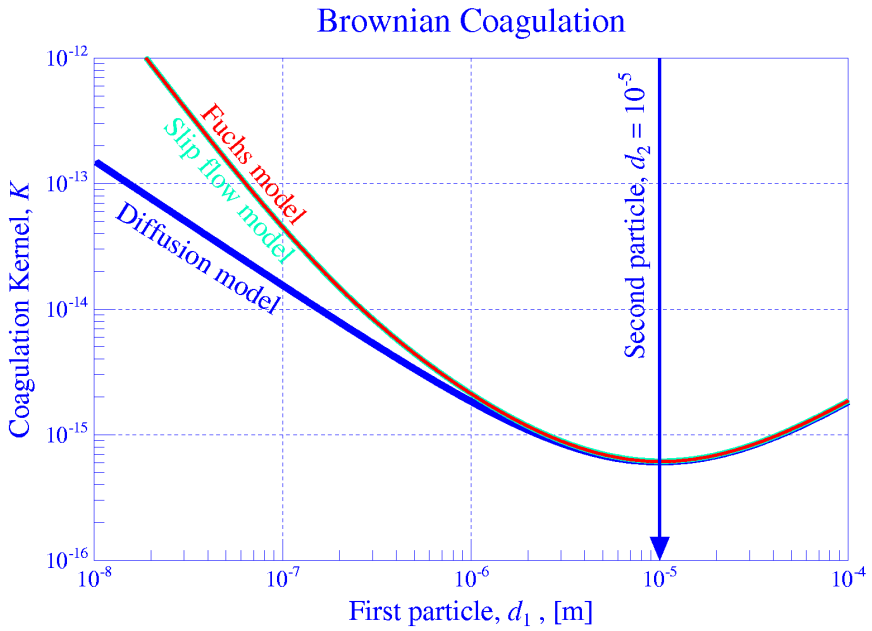

Figure 2-149 Brownian coagulation – comparison of models, $d_2 = 10^{-5}$ m.

2.8.9 Turbulent Coagulation

The turbulent coagulation depends on the user-defined turbulence dissipation rate, ε_T. The value may be defined in the input deck. The default value is 0.001 (same as in MELCOR).

The coagulation kernels calculated for ε_T = 0.001 are shown in Figure 2-150. The testing program is provided in **\Z-TESTS\RT\CKTURB.FOR**. The data is plotted for the dimension of the first colliding particle was varied from 10^{-8} m to 10^{-4} m. The diameter of the second particle was 10^{-7} m, 10^{-6} m, and 10^{-5} m.

The turbulence dissipation rate, as coded in SPECTRA depends on the Reynolds number. In the turbulent region ($Re > Re_{tur}$) the input value of ε_T is used in the laminar region ($Re < Re_{lam}$) the value is zero, and therefore the turbulent coagulation does not occur. In the transition region a third order, smooth interpolation is performed. The values of ε_T versus the Reynolds number are shown in Figure 2-151.

The laminar and turbulent region boundaries are defined by the user. The default values are:

- Re_{lam} = 2200.
- Re_{tur} = 10000.

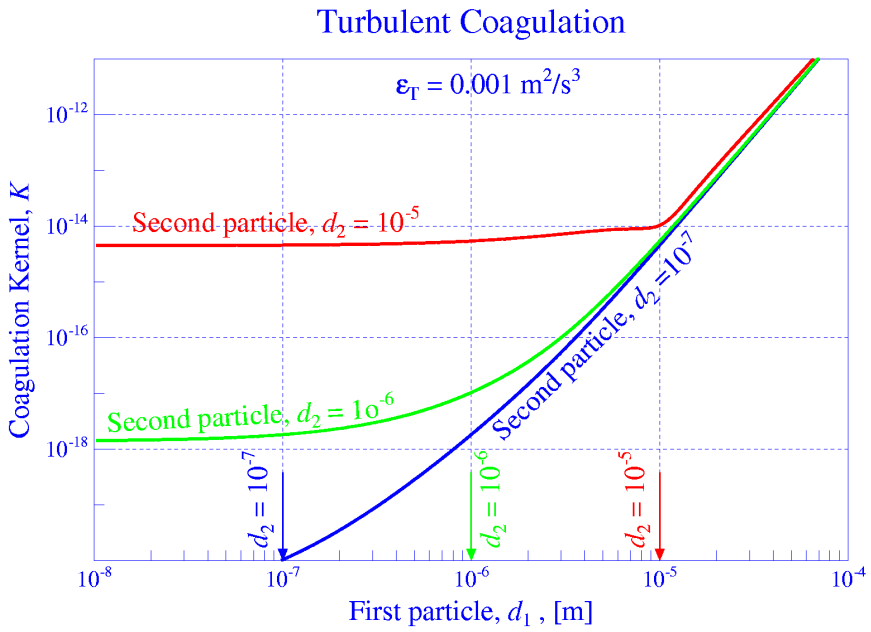

Figure 2-150 Turbulent coagulation – results obtained for turbulent flow.

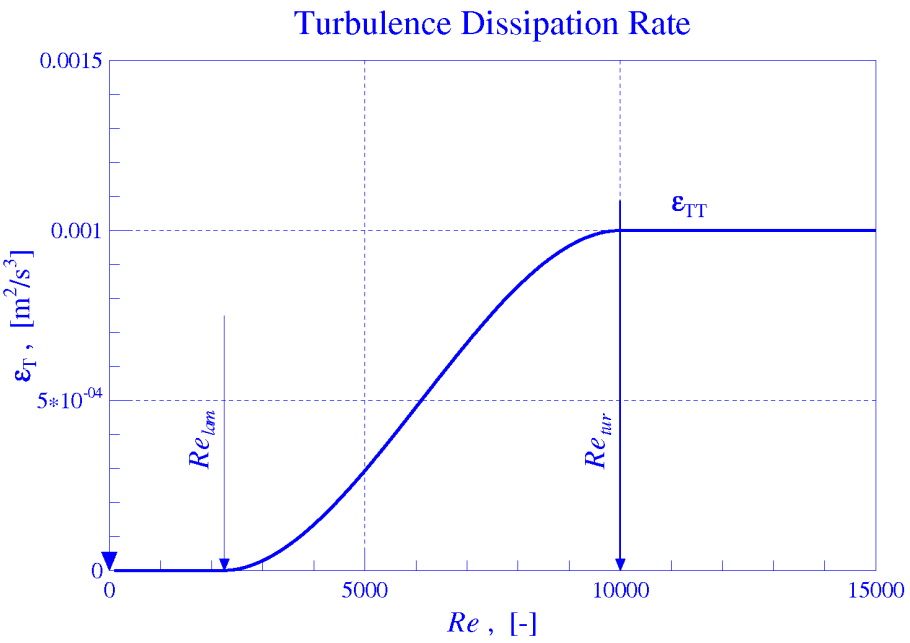

Figure 2-151 Turbulence dissipation rate.

2.8.10 Filter Model

A glass fiber filter model is available in SPECTRA. The model is based on [79]. The tests of the filter model were compared with the results shown in [79].

The testing program is provided in **\Z-TESTS\RT\FILTER.FOR**. The calculations were performed using the following filter data:

- Solidity, $\alpha = 0.05$
- Thickness, $t = 0.001$ m
- Fiber diameter, $d_f = 2.0 \times 10^{-6}$ m

The results are shown in Figure 2-152, Figure 2-153, Figure 2-154, and Figure 2-155. A good agreement between the values calculated by the subroutine EFILTR and the data from [79] is observed.

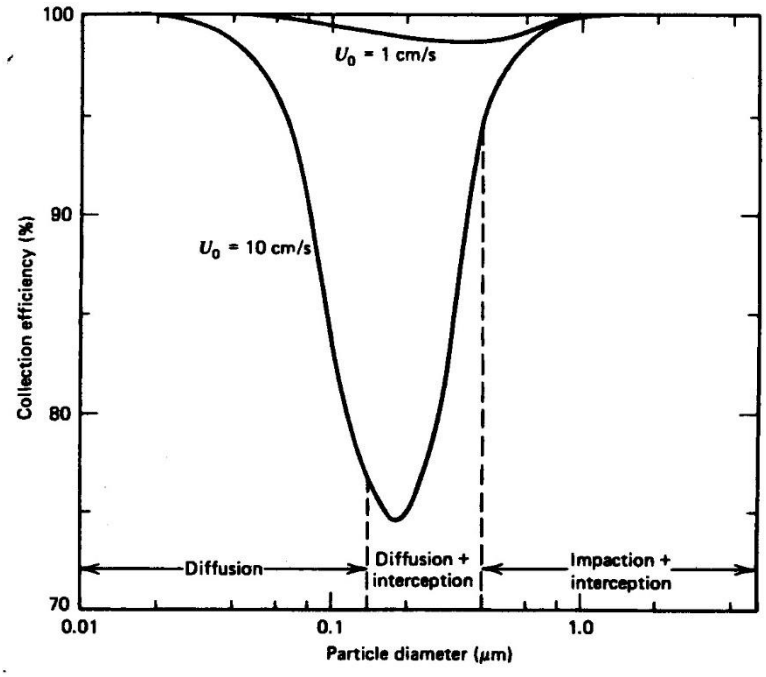

Figure 2-152 Filter efficiency data (reproduced from [79]).

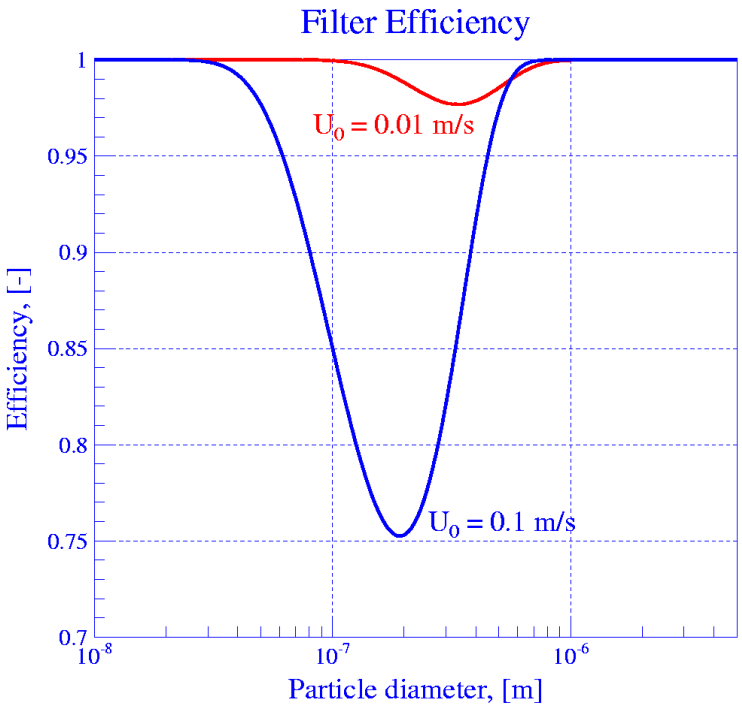

Figure 2-153 Filter efficiency data as calculated by the subroutine EFILTR.

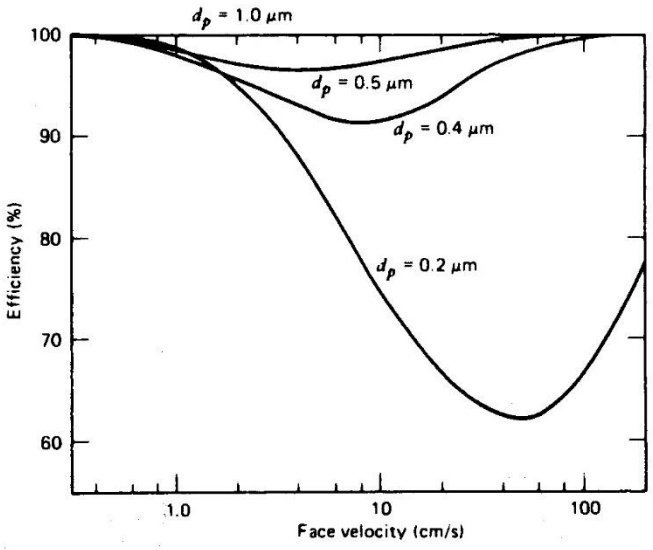

Figure 2-154 Filter efficiency data (reproduced from [79]).

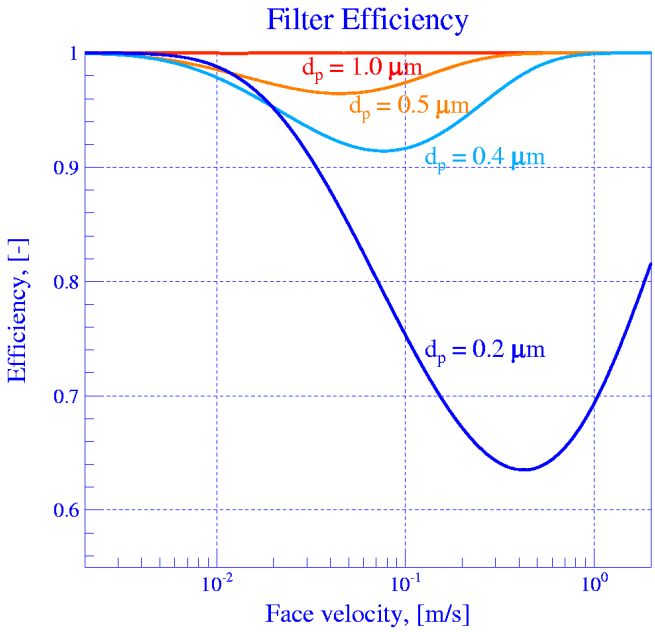

Figure 2-155 Filter efficiency data as calculated by the subroutine EFILTR.

2.8.11 Pool Scrubbing Model

A correlation is available in SPECTRA to calculate the pool scrubbing efficiency. The correlation is (see Volume 1):

$$E_{PS} = A \cdot (1 - \exp[-B \cdot D_p])$$

In the formula the *A*, *B* are user-defined coefficients, and D_p is the particle diameter, (m). The default values of the user-defined coefficients are $A = 0.8$ and $B = 0.5 \times 10^6$ (m^{-1}) (see Volume 2). The testing spreadsheet is provided in **\Z-TESTS\RT\PScrubbing.xls.**

The influence of particle diameter on the pool scrubbing efficiency is shown in [89] Figure 32. Results of SPARC and BUSCA codes are shown. The more conservative (smaller pool scrubbing) results of BUSCA are used. The values of *DF* and the corresponding pool scrubbing efficiencies are given in Table 2-13. The pool scrubbing efficiency values are shown in Figure 2-156 (square markers).

Results of the correlation are included in this figure for $A = 1.0$ and three values of the coefficient *B*, 0.5×10^6, 1.0×10^6, 2.0×10^6. The value of $B = 1.0 \times 10^6$ gives good match to the source data, and is used as a default value.

The default value of the coefficient *A* is conservatively taken as 0.8, while the best estimate value is 1.0, as is seen in Figure 2-157. The conservatism in efficiency calculation was applied because pool scrubbing is not calculated in a mechanistic way, but a very simple correlation is used instead.

Table 2-13 Pool scrubbing efficiency versus particle diameter, [89], Figure 32.

D_p (μm)	Value	
	DF	$E_{PS} = 1 - 1/DF$
0.1	1.3	0.23
1.0	2.5	0.60
2.0	7.0	0.86
4.0	45.0	0.98
6.0	300.0	1.00
8.0	2000.0	1.00

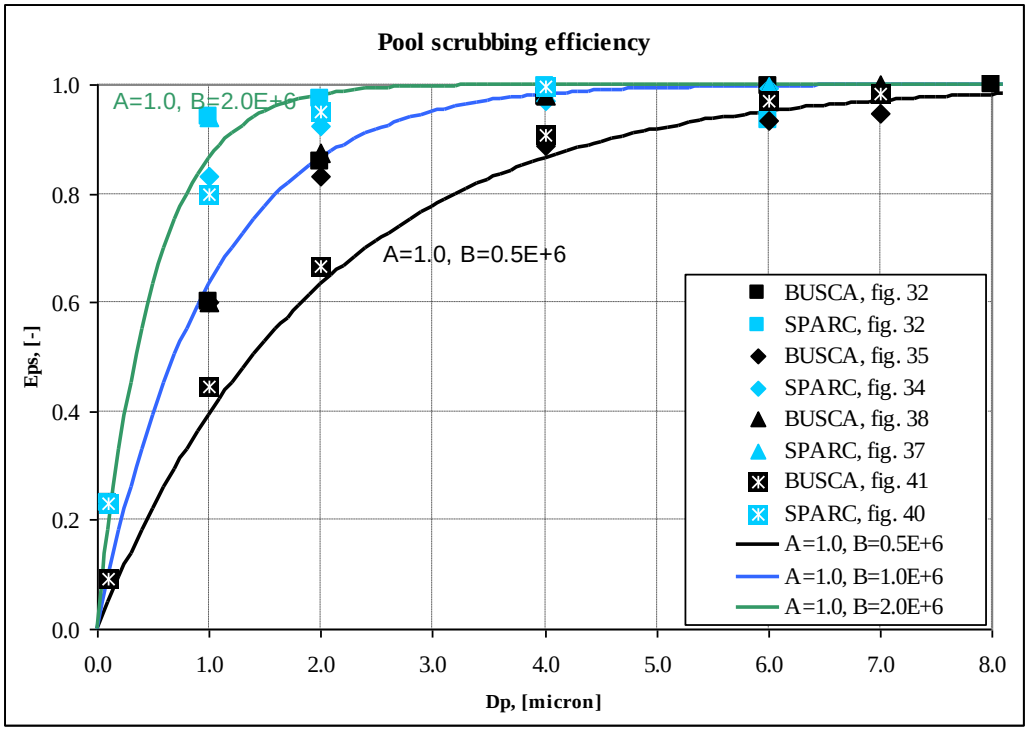

Figure 2-156 Pool scrubbing efficiency - data [89], and influence of the coefficient *B*.

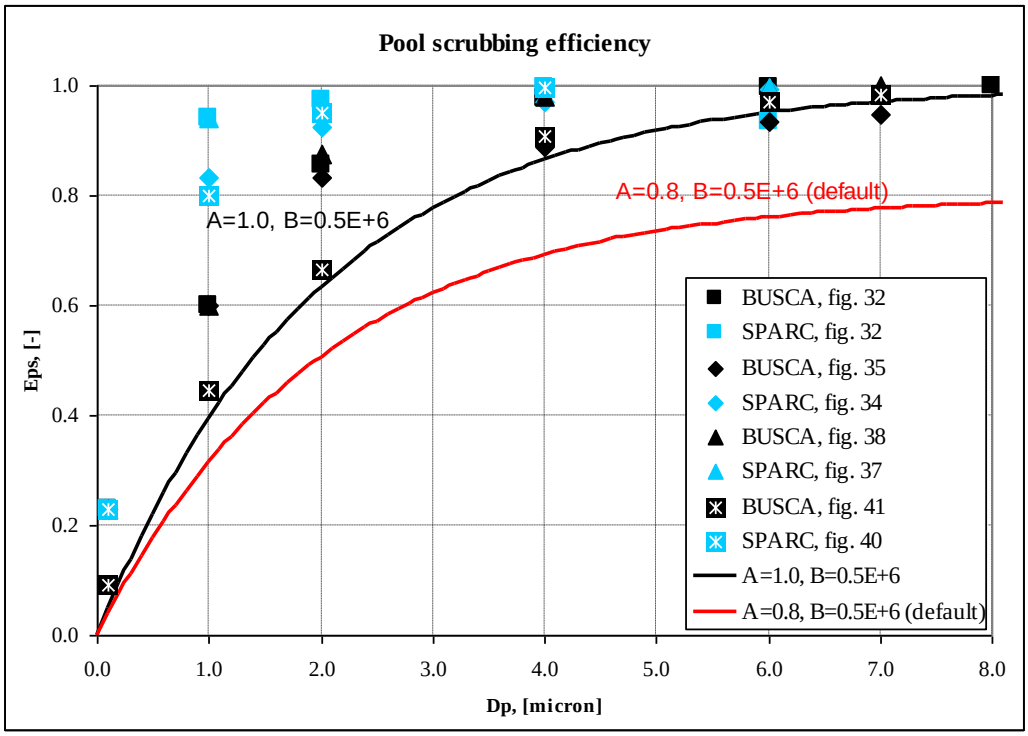

Figure 2-157 Pool scrubbing efficiency - data [89], and influence of the coefficient *A*.

2.8.12 Mechanistic Resuspension Model

Three models (sets of subroutines), available within the mechanistic resuspension model, are described. These are the lognormal distribution, the adhesion force calculation, and the drag/lift force calculation.

- **Lognormal distributions**

The lognormal distributions calculated by SPECTRA subroutines for different mean adhesion force and adhesive spread are shown in Figure 2-159 and Figure 2-161. Results shown in Figure 2-159 show distribution functions for the mean value of $<F_a>$=0.1 and the adhesive spread factors of σ_a = 1.25, 3.0, and 6.0. Results shown in Figure 2-161 show distribution functions for the mean value of $<F_a>$=1.0 and the adhesive spread factors of σ_a = 1.2, 2.0, and 4.5. The choice of unis is important for the shape of functions and the functions. Therefore if a user-defined distribution is entered, the adhesive force is expressed in relative units (see Volume 2), which means $<F_a>$=1.0.

Note that with increasing adhesive spread factor the peak value is shifted towards smaller values. The mean value is nevertheless always the same. This is because the lines represent the fraction per unit adhesion force and in the logarithmic scale the unit force on the left-hand side is smaller than on the right-hand side. Results shown in Figure 2-159 are verified by comparing with results of MathCAD (stored in the directory **Z-INPUTS\RT\Res-Ed**) shown in Figure 2-158.

The lognormal distributions are integrated within SPECTRA in order to calculate particle fractions within a finite number of the adhesion force sections (F_a-sections). Default number of F_a-sections is 51. Figure 2-160 and Figure 2-162 show the particle fractions (normalized to one) for 51 F_a-sections, for the distribution functions shown in Figure 2-159 and Figure 2-161. Note that the distribution expressed in particle fractions (relative number of particles) per single F_a-section is symmetrical around the mean value, independently of the adhesive spread σ_a.

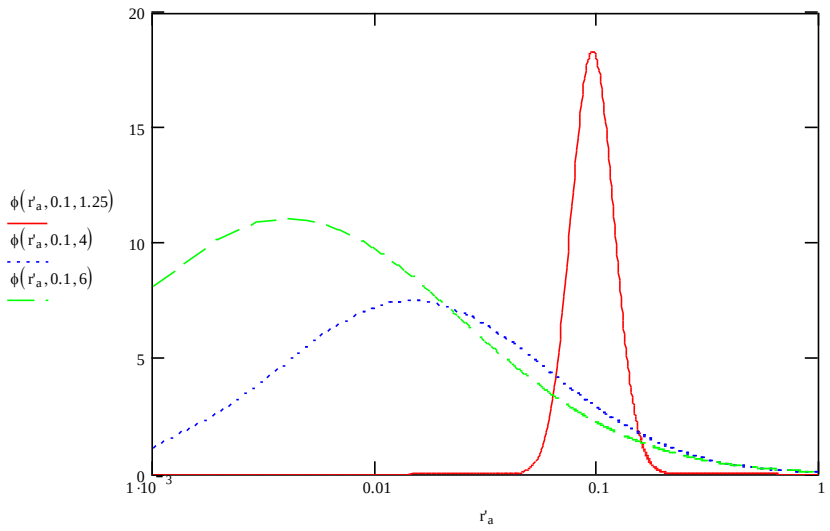

Figure 2-158 Lognormal distribution functions, (1/N), $<F_a>$=0.1, MathCAD results.

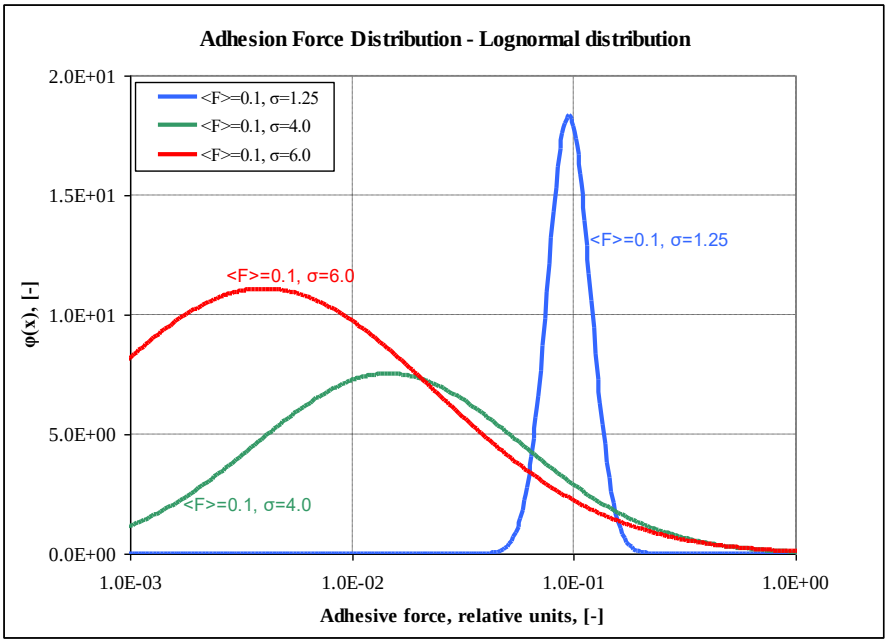

Figure 2-159 Lognormal distribution functions, (1/N), <F_a>=0.1, SPECTRA.

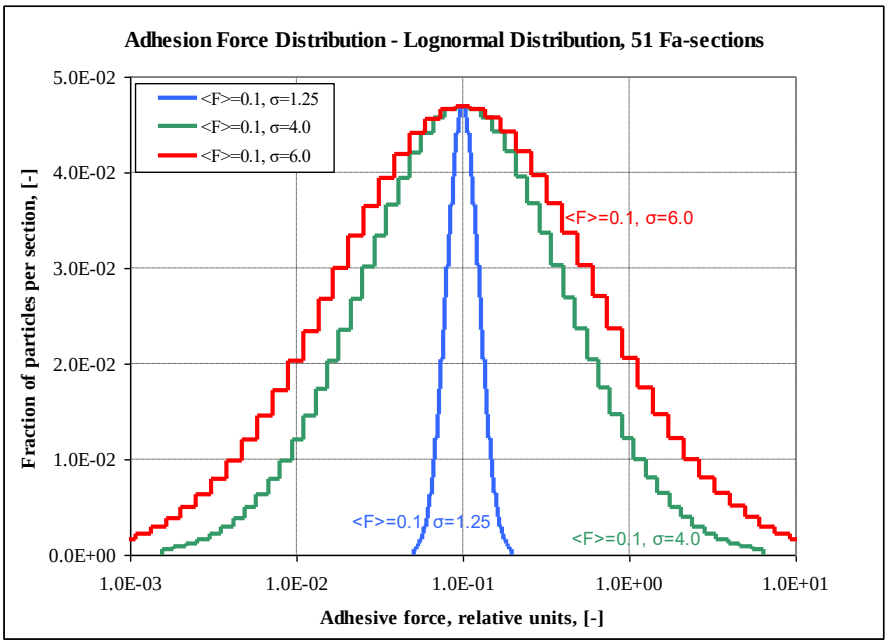

Figure 2-160 Particle fractions per F_a-section, (-), <F_a>=0.1, SPECTRA.

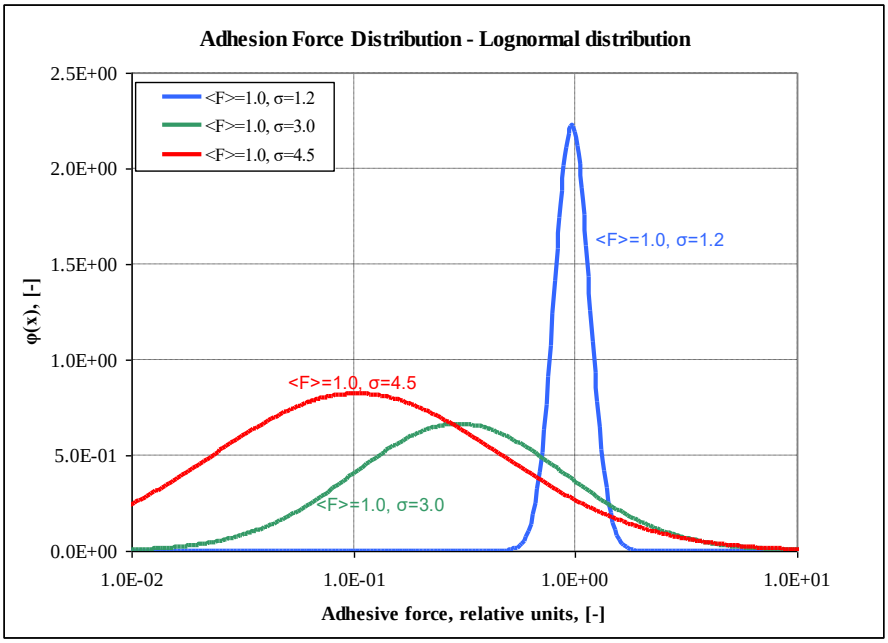

Figure 2-161 Lognormal distribution functions, (1/N), <F_a>=1.0, SPECTRA

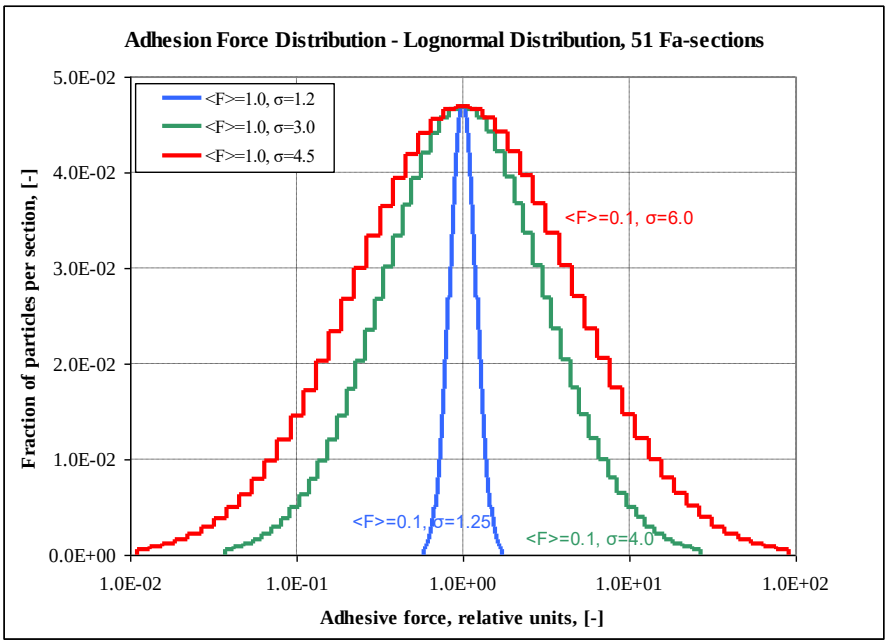

Figure 2-162 Particle fractions per F_a-section, (-), <F_a>=1.0, SPECTRA.

- **Adhesion force calculations**

Adhesion forces calculated by the CÆSAR code [85] are shown in Figure 2-163. CÆSAR predicts that the particle-surface adhesive force is proportional to the particle diameter and inversely proportional to the surface roughness.

In SPECTRA the following correlation is used:

$$F_{a,1} = \frac{A_1}{R^{x_1}} D_{eff,1}$$

In order to be consistent with the observation from CÆSAR (adhesive force is inversely proportional to the surface roughness), the power x_1 must be equal to 1.0. Figure 2-164 shows results obtained with the following values:

- $A_1 = 5.0\times10^{-10}$, $x_1 = 1.0$

These are the default coefficients (see Volume 2). Results agree well with the values calculated by CÆSAR ([85]).

Note that in SPECTRA the value of roughness R has an internal limit of a minimum of 10^{-9}. Thus the "smooth surface" line is obtained for $R=10^{-9}$. With the value of $A_1 = 5.0\times10^{-10}$ the proportionality coefficient in the adhesion force is equal to:

$$\frac{A_1}{R^{x_1}} = \frac{5.0\times10^{-10}}{(1.0\times10^{-9})^1} = 0.5$$

For smooth surfaces the literature (see [86], [87]) gives the following formulae for the adhesion:

$$F_a = \pi \cdot \Delta\gamma \cdot D_p \qquad \text{for small hard particles}$$

$$F_a = \frac{3}{4}\pi \cdot \Delta\gamma \cdot D_p \qquad \text{for large soft particles}$$

$\Delta\gamma$ is the adhesive surface energy, (J/m^2). The value of $\Delta\gamma$ used in [86] is 0.15 J/m^2. Therefore:

$$F_a = 0.47 \cdot D_p \qquad \text{for small hard particles}$$

$$F_a = 0.35 \cdot D_p \qquad \text{for large soft particles}$$

To obtain exactly the same values in SPECTRA, the following values should be used:

- $A_1 = 4.7\times10^{-10}$, for for small hard particles.
- $A_1 = 3.5\times10^{-10}$, for for large soft particles.

The default value, $A_1 = 5.0\times10^{-10}$, is sufficiently quite close to those values for most practical applications.

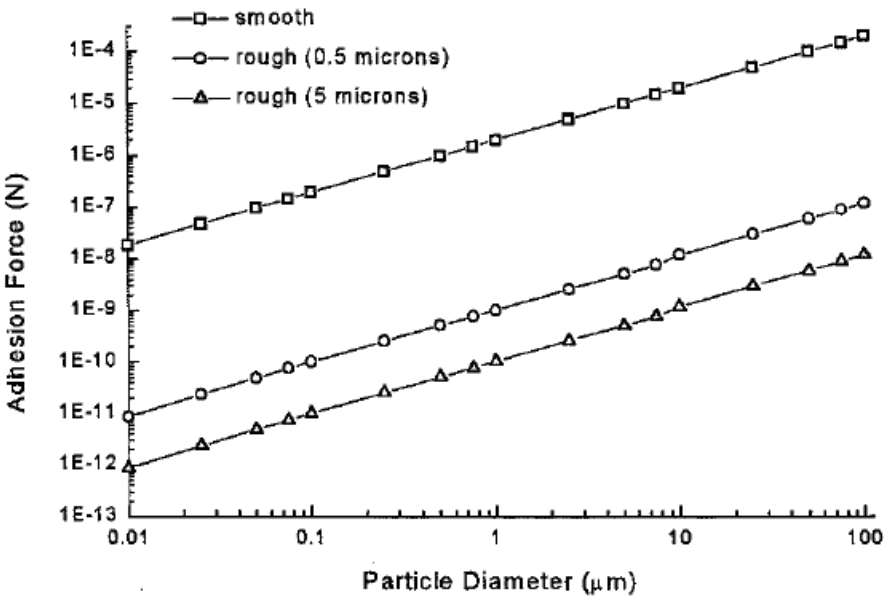

Figure 2-163 Adhesive force of SnO_2 particles to a steel surface [85].

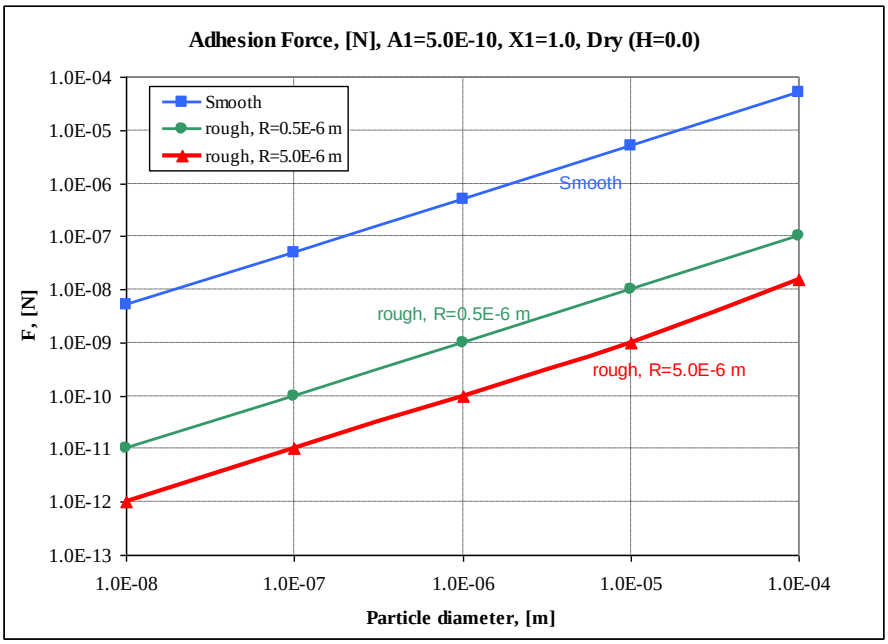

Figure 2-164 Adhesive force, $A_1 = 5.0\times10^{-10}$, $x_1 = 1.0$, $H = 0.0$ (dry).

The observation from CÆSAR (adhesive force is inversely proportional to the surface roughness), results in very rapid decrease of the adhesion forces with roughness. Figure 2-163 and Figure 2-164 show that the adhesion force decreases by four orders of magnitude if the roughness is 5.0×10^{-6} m. Surfaces of typical commercial pipes have a roughness of ~1.0×10^{-5} m, so the adhesion force will be even smaller.

The user may decrease the effect of roughness by changing the value of the power x_1. A value smaller than 1.0 will result in decreasing the effect of the surface roughness for the adhesion force. As an example the value of $x_1 = 0.5$ is used. When x_1 is set to 0.5, the user must "calibrate" the constant A_1 in order to have the same value for a smooth surface. The value of $A_1 = 1.5\times10^{-5}$ provides a good adhesion force for a smooth surface:

$$F_{a,1} = \frac{A_1}{R^{x_1}} D_{eff,1} = \frac{1.5\times10^{-5}}{\left(10^{-9}\right)^{0.5}} D_{eff,1} = 0.47 \cdot D_{eff,1}$$

Therefore another practically useful set of coefficients is:

- $A_1 = 1.5\times10^{-10}$, $x_1 = 0.5$

Results obtained with these values are shown in Figure 2-165. The reduction of adhesive forces is in such case only two orders of magnitude for the same roughness of 5.0×10^{-6} m.

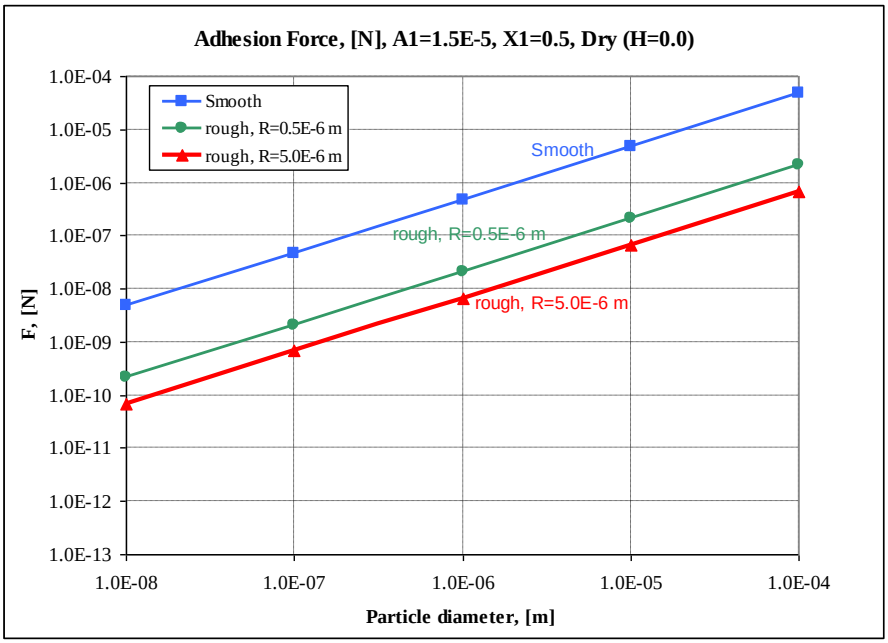

Figure 2-165 Adhesive force, $A_1 = 1.5\times10^{-5}$, $x_1 = 0.5$, $H = 0.0$ (dry).

Note that the user defines not only the model coefficients (A_1, x_1) but also the surface roughness (R) for each resuspension model individually. Therefore any desired adhesion force may be easily achieved and the correlation itself is presently not very useful. It has been put in the code for the future, when more data on adhesion force become available. In such case it will be possible to have recommended values of (A_1, x_1) for typical surfaces. The surface roughness, R, which is typically a well-known parameter characterizing a surface, will remain the only required user-parameter. Thus it will be possible to minimize the user effort and to reduce the possibility of wrong input values.

The discussion above was limited to the cases when surface asperity did not affect the result. The effective diameter was simply equal to the particle diameter:

$$D_{eff,1} = D_p$$

Below the influence of surface asperities is shown. The effective diameter is given by (see Volume 1):

$$D_{eff,1} = \frac{1}{\frac{1}{x_{p,1} D_p} + \frac{1}{x_{as,1} 2r_{as}}}$$

$x_{p,1}$ and $x_{as,1}$ are user-defined multipliers. With this definition qualitatively good results are obtained for the asymptotic cases:

$$F_a \sim \begin{cases} r_{as} & if \quad r_{as} << D_p \\ D_p & if \quad r_{as} >> D_p \end{cases}$$

Results shown in Figure 2-166 and Figure 2-167 show adhesion forces for the asperity radius of 10^{-7} m, and the default values of the user-defined multipliers (see Volume 1 and 2):

- Asperity radius: $r_{as} = 10^{-7}$ m, $x_{p,1} = 1.0$ and $x_{as,1} = 3.0$.

The same two cases are considered as these shown in Figure 2-164 and Figure 2-165, namely:

- (A_1, x_1) = (5.0×10^{-10}, 1.0)
- (A_1, x_1) = (1.5×10^{-5}, 0.5)

Figure 2-166 and Figure 2-167 show that when the particle diameter becomes large, the adhesion force does not depend on the particle diameter (lines become horizontal). In this region the adhesion force is governed by the asperity radius, $r_{as} = 10^{-7}$ m. This region is indicated in the figure with the comment "**asperity effect**". In the first case, (A_1, x_1) = (5.0×10^{-10}, 1.0), the gravity effect becomes visible on the right-hand side of the picture. In the no-asperity effect cases, the forces in this region were so large (~10^{-8} Figure 2-164, ~10^{-6} Figure 2-165) that the gravity force was not visible. In the present case the gravity force (~10^{-9} for the large particles) becomes visible in the right-hand side of the figure. This region is indicated in the figure with the comment "**gravity effect**".

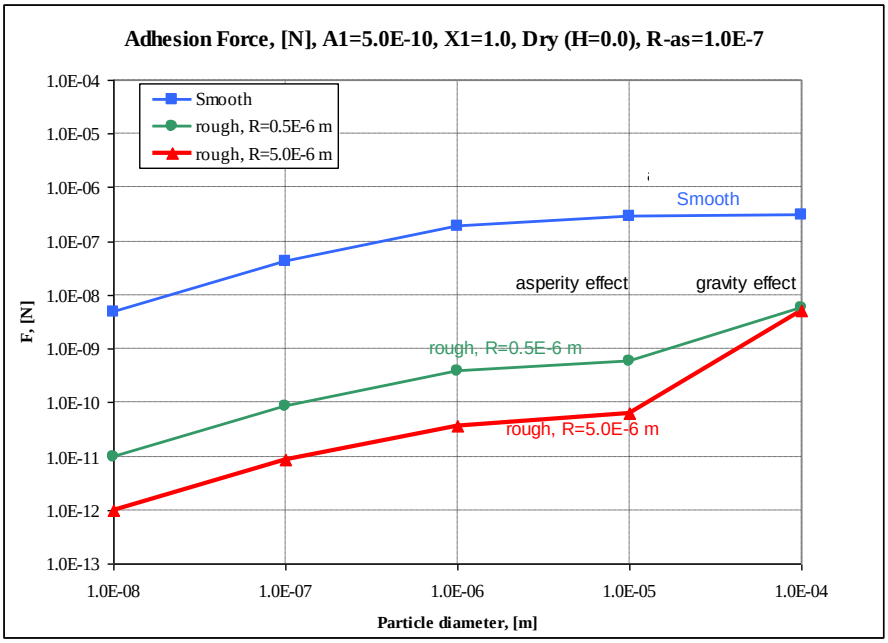

Figure 2-166 Adhesive force, $A_1 = 5.0\times10^{-10}$, $x_1 = 1.0$, $H = 0.0$, $\langle r_{as}\rangle = 1.0\times10^{-7}$.

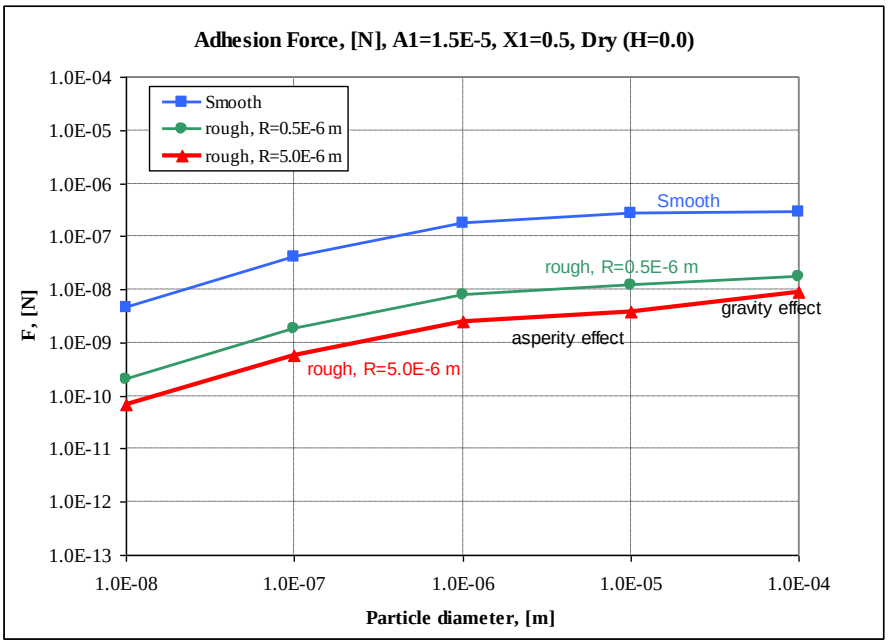

Figure 2-167 Adhesive force, $A_1 = 1.5\times10^{-5}$, $x_1 = 0.5$, $H = 0.0$, $\langle r_{as}\rangle = 1.0\times10^{-7}$.

So far all considered cases were the "dry" cases, with the relative humidity, H, set to zero. The influence of humidity is discussed below.

The effect of relative humidity is taken into account in SPECTRA using the following formula (see Volume 1):

$$F_{a,2} = A_2 \cdot f(H) \cdot \sigma \cdot D_{eff,2}$$

A_2 is a user-defined constant, with a default value of 6.28 (=2π), $f(H)$ is given by:

$$f(H) = \begin{cases} 0.0 & if \quad H = 0.0 \\ (3-2X)X^2 & if \quad 0.0 < H < 0.9 \\ 1.0 & if \quad H \geq 0.9 \end{cases}$$

and:

$$D_{eff,2} = \frac{1}{\frac{1}{x_{p,2}D_p} + \frac{1}{x_{as,2}2r_{as}}}$$

Maximum humidity effect is obtained when the relative humidity is $H > 0.9$. Two cases are shown in Figure 2-168 and Figure 2-169, obtained with $H = 1.0$. Default values are used for the multipliers.

- Asperity radius: $r_{as} = 10^{-7}$ m, $x_{p,2} = 1.0$ and $x_{as,2} = 1.0$.

The same two cases are considered as these shown in Figure 2-166 and Figure 2-167, namely:

- $(A_1, x_1) = (5.0\times10^{-10}, 1.0)$, $r_{as} = 10^{-7}$ m
- $(A_1, x_1) = (1.5\times10^{-5}, 0.5)$, $r_{as} = 10^{-7}$ m

Figure 2-168 and Figure 2-169 show that the force caused by adsorbed liquid dominates for large roughness. Practically the same results are obtained with $R = 0.5\times10^{-6}$ m as with $R = 5.0\times10^{-6}$ m, which means that the roughness-independent term is dominating. The asperities still have an effect, through the effective diameter. For large particle diameters the lines becomes horizontal, which means that the adhesion force does not depend on the particle diameter. In this region the adhesion force is governed by the asperity radius, $r_{as} = 10^{-7}$ m. This region is indicated in the figure with the comment "**asperity effect**". The gravity effects are not visible in this case, because the force due to humidity is very large compared to the gravity force.

It is also interesting to note that with the humidity term both figures look very similar. This means that the uncertainties involved in the definition of the parameters (A_1, x_1) and the surface roughness, R, become practically meaningless when the humid force appears.

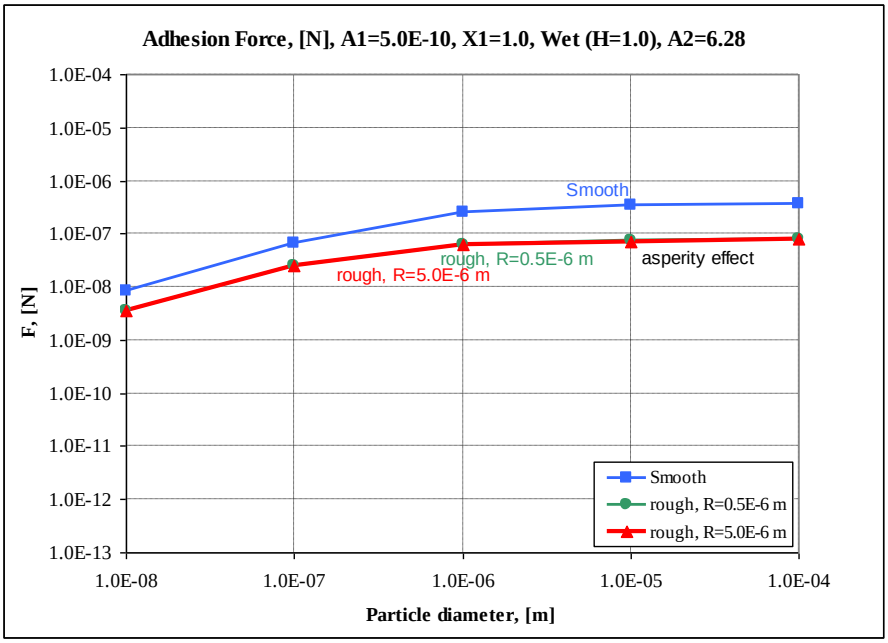

Figure 2-168 Adhesive force, $A_1 = 5.0\times10^{-10}$, $x_1 = 1.0$, $H = 1.0$, $\langle r_{as}\rangle = 1.0\times10^{-7}$,

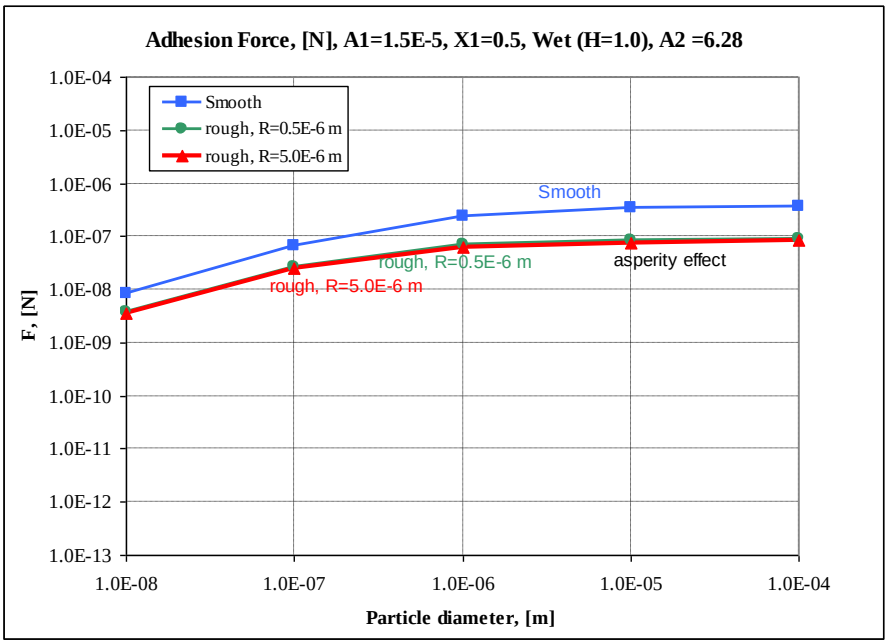

Figure 2-169 Adhesive force, $A_1 = 1.5\times10^{-5}$, $x_1 = 0.5$, $H = 1.0$, $\langle r_{as}\rangle = 1.0\times10^{-7}$.

So far all considered cases were no net electric charge was considered. If the net electric charge is present in the particles, the adhesion force caused by the electrostatic forces is given by (see Volume 1):

$$F_{a,3} = A_3 \cdot \frac{q^2}{[\min(x_E R, D_p)]^2}$$

where A_3 is a user-defined constant, with a default value of 9.0×10^9 ($=K_E$), and q is a user-defined net electric charge for the particle. If the user wishes to take the electrostatic force into account, a useful expression for the average number of charges in a particle with diameter D_p at an equilibrium charge is given by (see Volume 1)

$$n = 2.37 \cdot \sqrt{D_p \times 10^6} = 2.37\times10^3 \cdot \sqrt{D_p}$$

The electric charge is n times the charge of electron (1.6×10^{-19} C). Therefore the electric charge may be estimated as:

$$q = 3.8\times10^{-16} \cdot \sqrt{D_p}$$

The cases without the humid forces were calculated, to avoid the dominating force, which would make it practically impossible to see any effect of the electric charge. It was found out that the even in absence of humidity, the effect of the electric charge is practically invisible for the equilibrium charge. Therefore the charge was increased to 10-fold the equilibrium charge. Two cases are shown in Figure 2-170 and Figure 2-171.

Figure 2-168 and Figure 2-169, obtained with H = 1.0. Default values are used for the multipliers.

- 10-fold the equilibrium charge:

$$q = 3.8\times10^{-15} \cdot \sqrt{D_p}$$

The same two cases are considered as these shown in Figure 2-166 and Figure 2-167, namely:

- $(A_1, x_1) = (5.0\times10^{-10}, 1.0)$, $r_{as} = 10^{-7}$ m
- $(A_1, x_1) = (1.5\times10^{-5}, 0.5)$, $r_{as} = 10^{-7}$ m

Figure 2-170 and Figure 2-171 show the effect of the electric charge with 10-fold the equilibrium charge. Influence of the electrostatic field is visible by comparing this figure to Figure 2-166 and Figure 2-167. The effect is visible for large particles on a smooth surface and small particles on a rough surface.

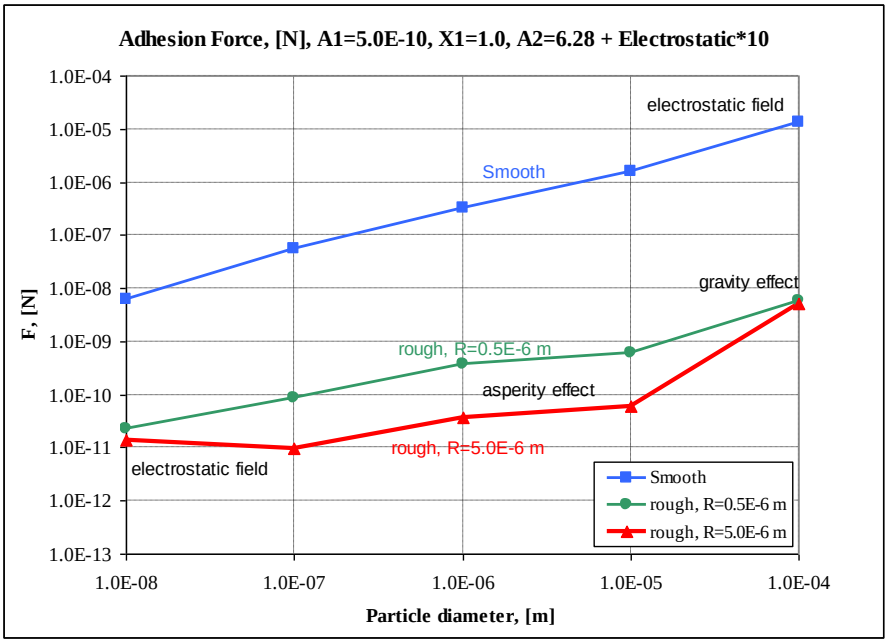

Figure 2-170 Adhesive force, $A_1 = 5.0\times10^{-10}$, $x_1 = 1.0$, $\langle r_{as}\rangle = 1.0\times10^{-7}$, electric charge.

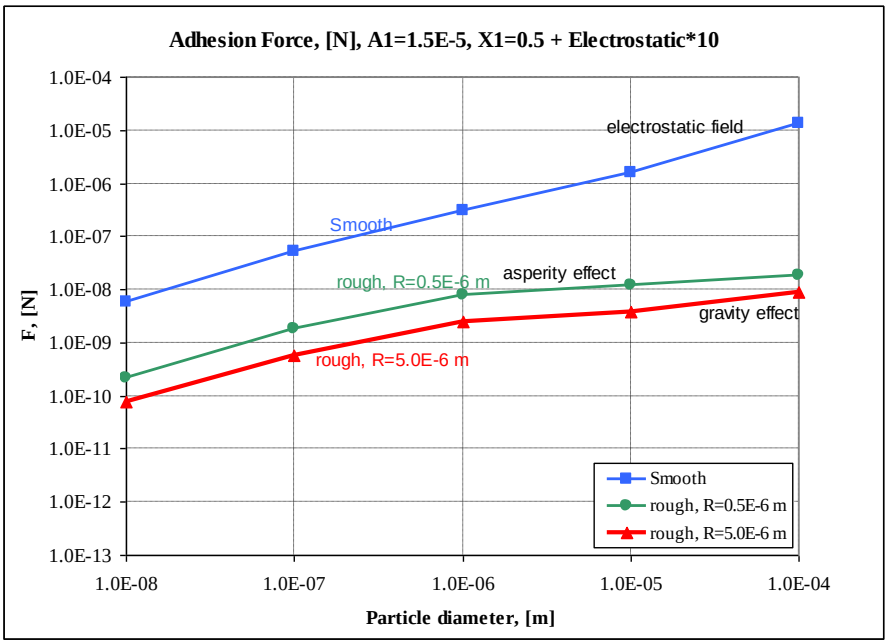

Figure 2-171 Adhesive force, $A_1 = 1.5\times10^{-5}$, $x_1 = 0.5$, $\langle r_{as}\rangle = 1.0\times10^{-7}$, electric charge.

- **Drag force calculations**

Two models are available in SPECTRA for the drag force calculation. The first model calculates drag force for a particle in a bulk flow. The formula (see Volume 1)

$$F_{d,b} = C_D \cdot \frac{\pi}{8} \cdot \rho_g \left(D_p V_g\right)^2$$

uses the drag coefficient, C_D. The drag coefficient as calculated by SPECTRA is shown in Figure 2-173. For comparison a graph with the drag coefficient is reproduced from reference [79] in Figure 2-172. This model is not used by the Radioactive Particle Package.

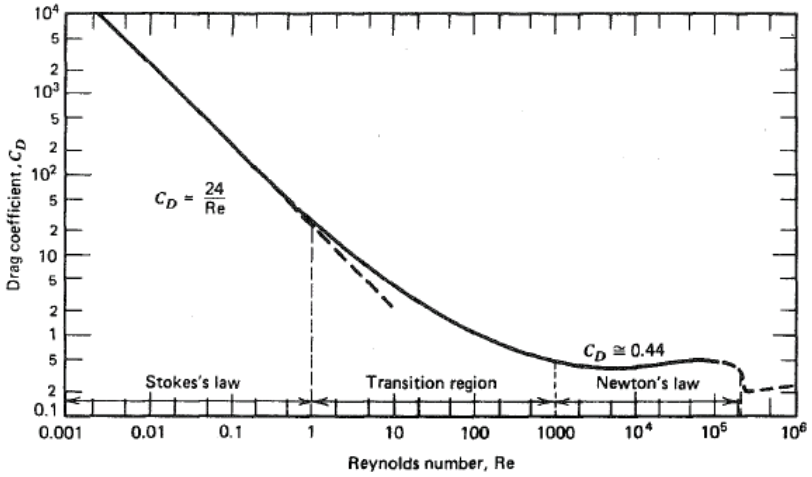

Figure 2-172 Drag coefficient, reproduced from [79].

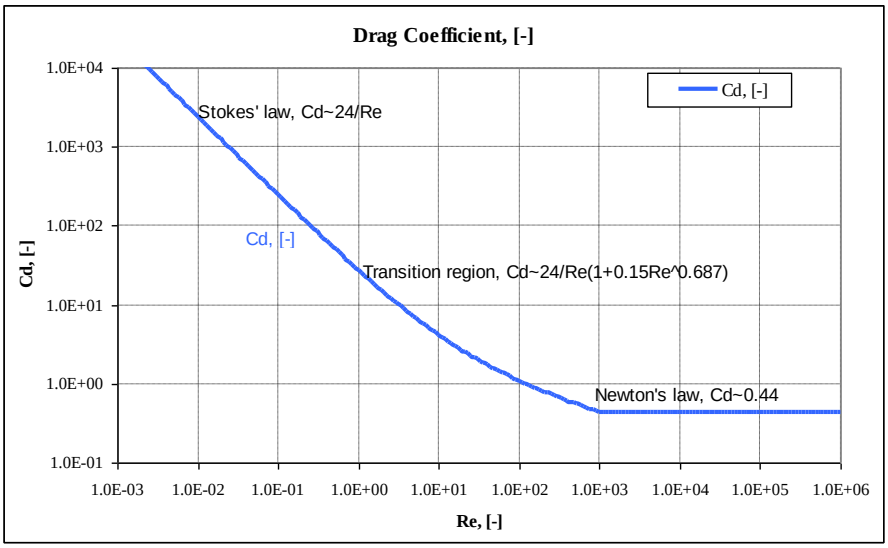

Figure 2-173 Drag coefficient.

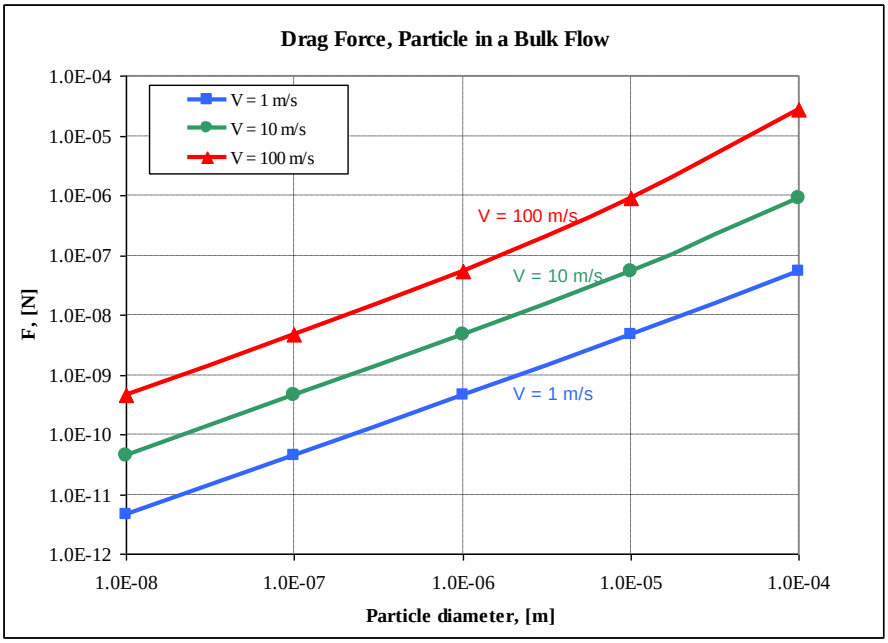

Figure 2-174 Drag force, particle in a bulk flow.

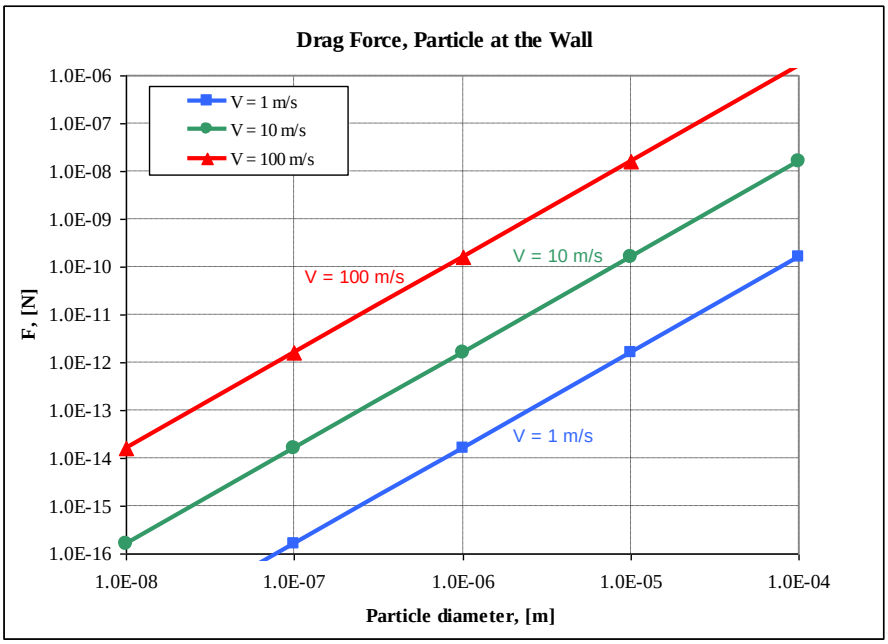

Figure 2-175 Drag force, particle in at the wall.

For particles deposited on a wall the drag force is given by (see Volume 1):

$$F_d = X_d \cdot 8.0 \cdot \frac{\mu_g^2}{\rho_g} \cdot \left(D_p^+\right)^2$$

$$D_p^+ = \sqrt{\frac{f}{8}} \cdot \frac{\rho_g}{\mu_g} \cdot D_p \cdot \left|V_g\right| \cdot \chi$$

Results of the drag force acting on a particle in a bulk flow and particle at a wall are shown in Figure 2-174 and Figure 2-175. It is seen that a particle at the wall is several orders of magnitude smaller for the same gas velocity. This is quite understandable, since the particle in a bulk flow experiences the full gas velocity, while the particle deposited at the wall experiences only a small velocity ("friction velocity", u_τ):

$$u_\tau = \sqrt{\frac{f}{8}} \cdot \left|V_g\right|$$

- **Lift force calculations**

The lift force is calculated from the expressions of Soltani and Hall (see Volume 1):

- Expression of Soltani, applied for $D^+ < 8.34525$:

$$F_{L,Soltani} = X_L \cdot 0.975 \cdot \frac{\mu_g^2}{\rho_g} \cdot \left(D_p^+\right)^{3.0}$$

- Expression of Hall, applied for $D^+ > 8.34525$:

$$F_{L,Hall} = X_L \cdot 4.215 \cdot \frac{\mu_g^2}{\rho_g} \cdot \left(D_p^+\right)^{2.31}$$

Both expressions are compared in Figure 2-176. The expression of Soltani gives lower forces for small dimensionless diameters, D_p^+, while the expression of Hall gives lower forces for large dimensionless diameters, D_p^+. The exact value at the point where both lines crosses is equal to: $(4.215 / 0.975)^{1/(3-2.31)} = 8.34525$. This is the transition point from one expression to another in SPECTRA. In this way a smooth curve is obtained.

Resulting lift forces are shown in Figure 2-177. It is clearly seen that the lift forces are a couple of orders of magnitude lower than the drag forces (see Figure 2-175).

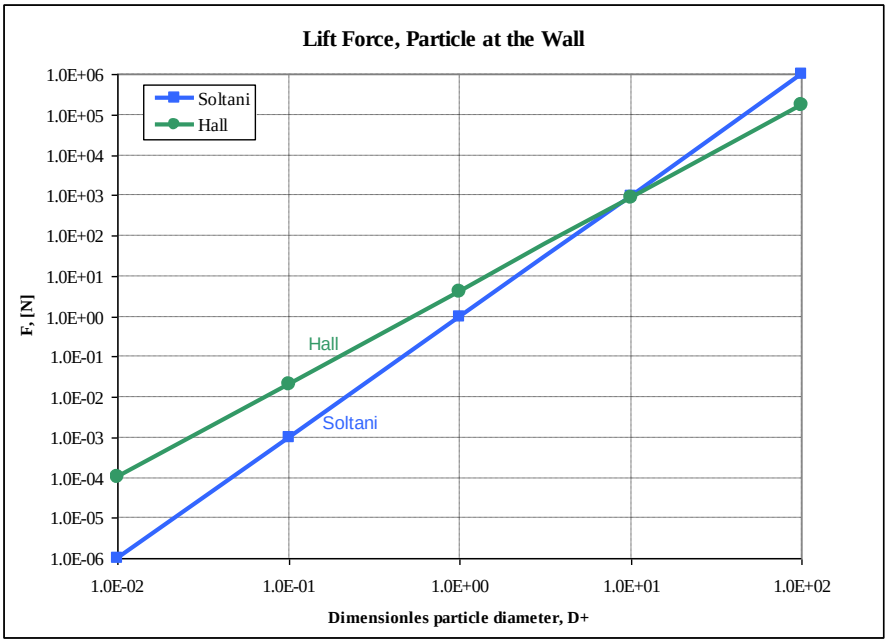

Figure 2-176 Lift force, comparison of Hall and Soltani models.

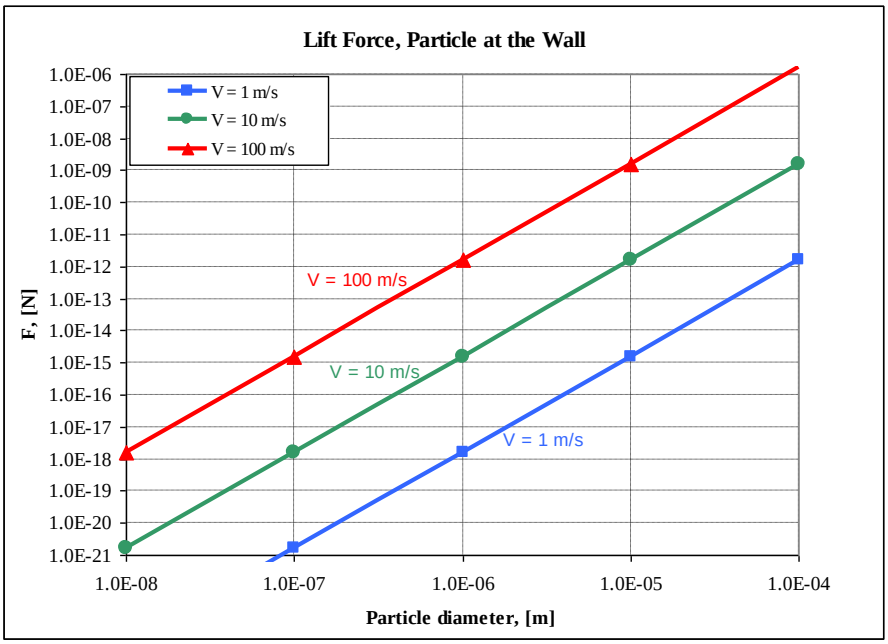

Figure 2-177 Lift force, particle in at the wall.

2.8.13 LWR Fission Product Release Models

Two alternative models for fission product release are available for LWR:

- CORSOR-M model [81].
- ARSAP model [82].

Results of both models with the default (built-in) model coefficients are shown in Figure 2-178 through Figure 2-182. The testing program is provided in **\Z-TESTS\RT\FP-rel.FOR**.

Note that in case of the CORSOR-M model the model coefficients have been modified for several release classes, as described in Volume 1. The original CORSOR-M coefficients are shown in Table 2-14, while the SPECTRA default coefficients are shown in Table 2-15. The rationale for modifying the CORSOR-M release coefficients is discussed in Volume 1. Results obtained with the original coefficients are shown using dashed lines in Figure 2-179, Figure 2-181, and Figure 2-182.

Table 2-14 Release coefficients, original CORSOR-M data [81].

Release class	Member Elements	$\boldsymbol{A}$, (s^{-1}), ($=k_0$ / 60.0)	$\boldsymbol{B}$, (K^{-1}), ($=Q$ / R)
1	Xe, Kr	2.00×10^{5} / 60.0 = 3.333×10^{3}	63.8 / R = 32108.7
2	Cs, Rb	2.00×10^{5} / 60.0 = 3.333×10^{3}	63.8 / R = 32108.7
3	Ba, Sr	2.95×10^{5} / 60.0 = 4.917×10^{3}	100.2 / R = 50427.8
4	I, Br	2.00×10^{5} / 60.0 = 3.333×10^{3}	63.8 / R = 32108.7
5	Te, Se	2.00×10^{5} / 60.0 = 3.333×10^{3}	63.8 / R = 32108.7
6	Ru, Rh, Pd	1.62×10^{6} / 60.0 = 2.700×10^{4}	152.8 / R = 76899.8
7	(Mo)	0.0	0.0
8	Zr	2.67×10^{8} / 60.0 = 4.450×10^{6}	188.2 / R = 94715.7
9	Y	0.0	0.0
10	(U)	1.46×10^{7} / 60.0 = 2.433×10^{5}	143.1 / R = 72018.1
11	Sb	0.0	0.0
12	(Sn)	5.95×10^{3} / 60.0 = 9.917×10^{1}	70.8 / R = 35631.6

Table 2-15 Release coefficients, SPECTRA default.

Release class	Member Elements	$\boldsymbol{A}$, (s^{-1}), ($=k_0$ / 60.0)	$\boldsymbol{B}$, (K^{-1}), ($=Q$ / R)
1	Xe, Kr	2.00×10^{5} / 60.0 = 3.333×10^{3}	63.8 / R = 32108.7
2	Cs, Rb	2.00×10^{5} / 60.0 = 3.333×10^{3}	63.8 / R = 32108.7
3	Ba, Sr	9.50×10^{6} / 60.0 = 1.583×10^{5}	100.2 / R = 50427.8
4	I, Br	2.00×10^{5} / 60.0 = 3.333×10^{3}	63.8 / R = 32108.7
5	Te, Se	2.00×10^{5} / 60.0 = 3.333×10^{3}	63.8 / R = 32108.7
6	Ru, Rh, Pd	2.00×10^{10}/ 60.0 = 3.333×10^{8}	152.8 / R = 76899.8
7	(Mo)	3.00×10^{4} / 60.0 = 5.000×10^{2}	65.0 / R = 32712.6
8	Zr	2.67×10^{8} / 60.0 = 4.450×10^{6}	188.2 / R = 94715.7
9	Y	0.0	0.0
10	(U)-	1.46×10^{7} / 60.0 = 2.433×10^{5}	143.1 / R = 72018.1
11	Sb	7.90×10^{3} / 60.0 = 1.317×10^{2}	61.4 / R = 30900.9
12	(Ag)	7.90×10^{3} / 60.0 = 1.317×10^{2}	61.4 / R = 30900.9

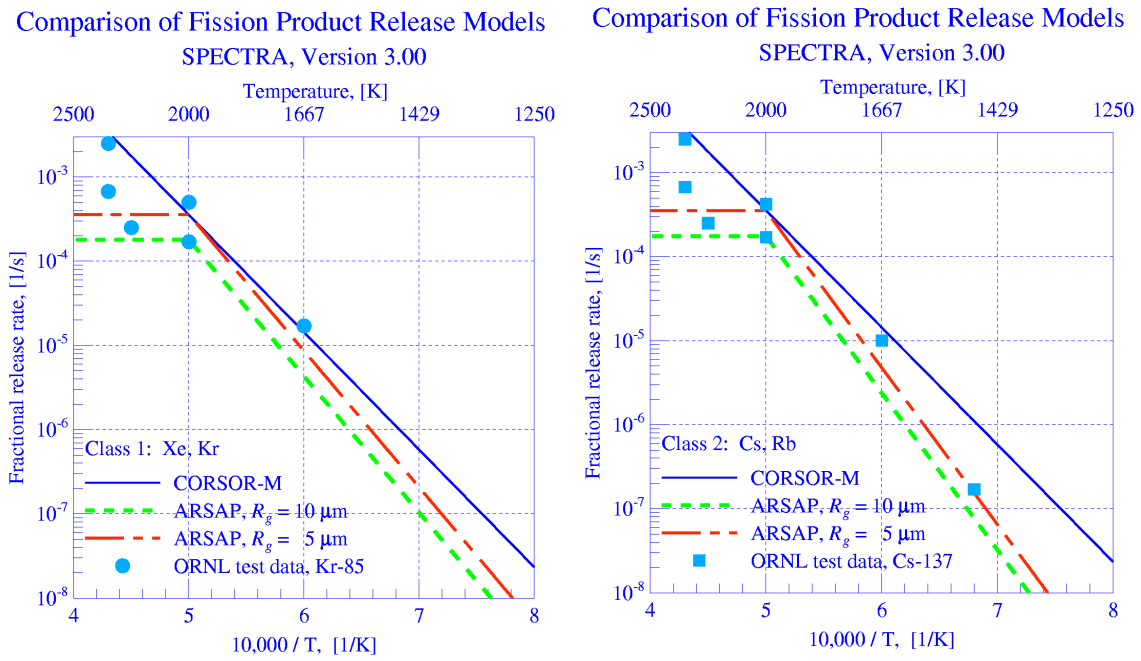

Figure 2-178 Fission product release models, Class 1 (Xe, Kr) and 2 (Cs, Rb).

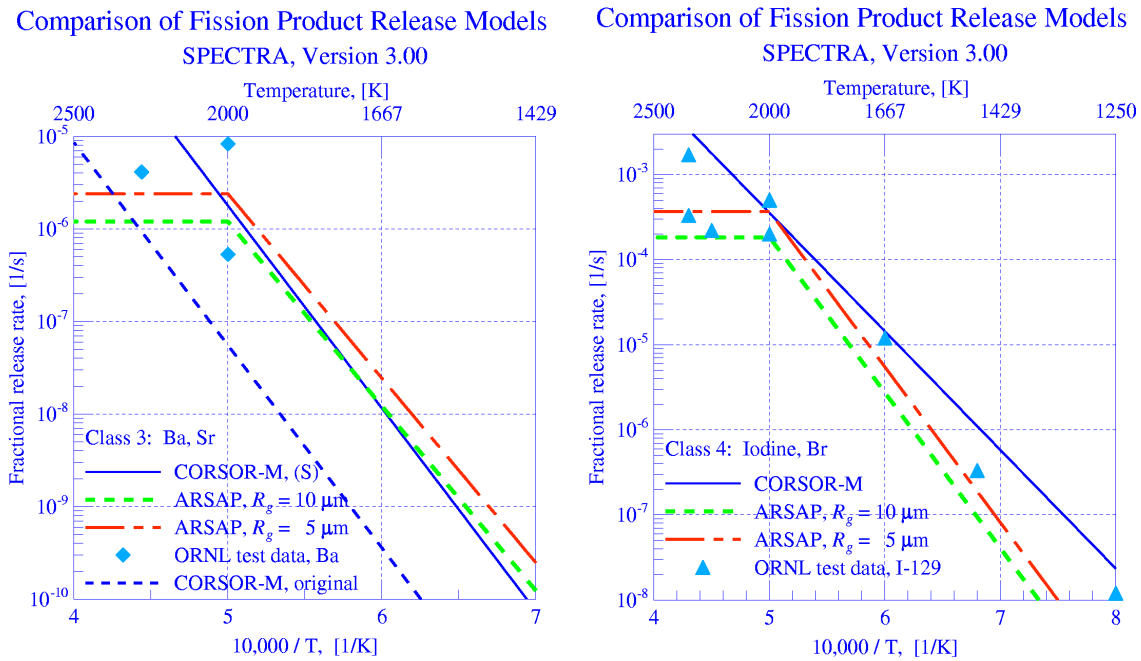

Figure 2-179 Fission product release models, Class 3 (Ba, Sr) and 4 (I, Br).

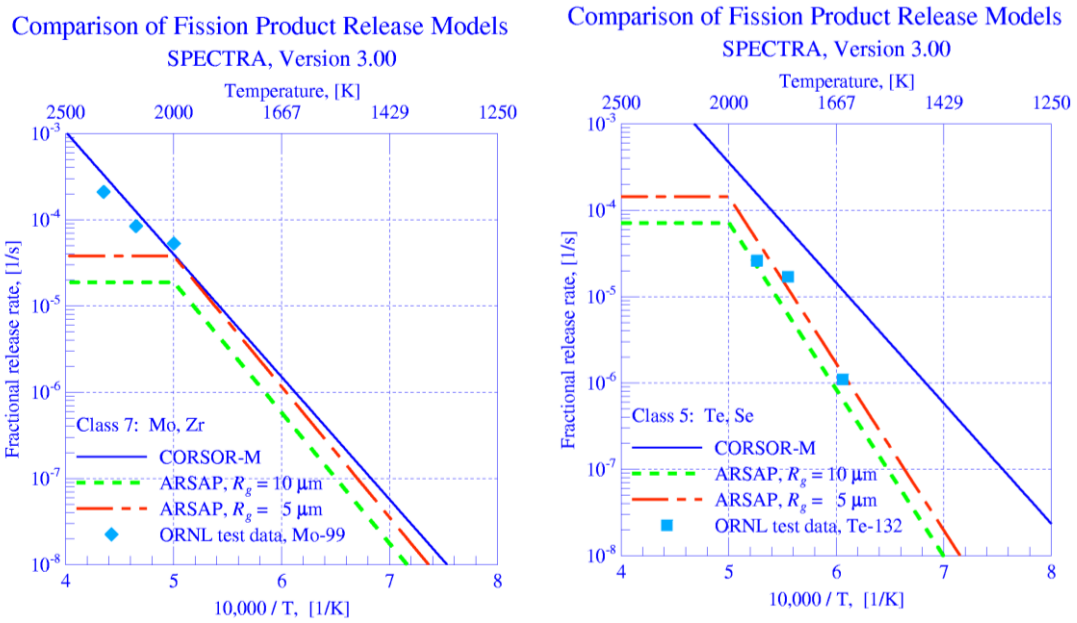

Figure 2-180 Fission product release models, Class 5 (Te, Se) and 7 (Mo, Zr).

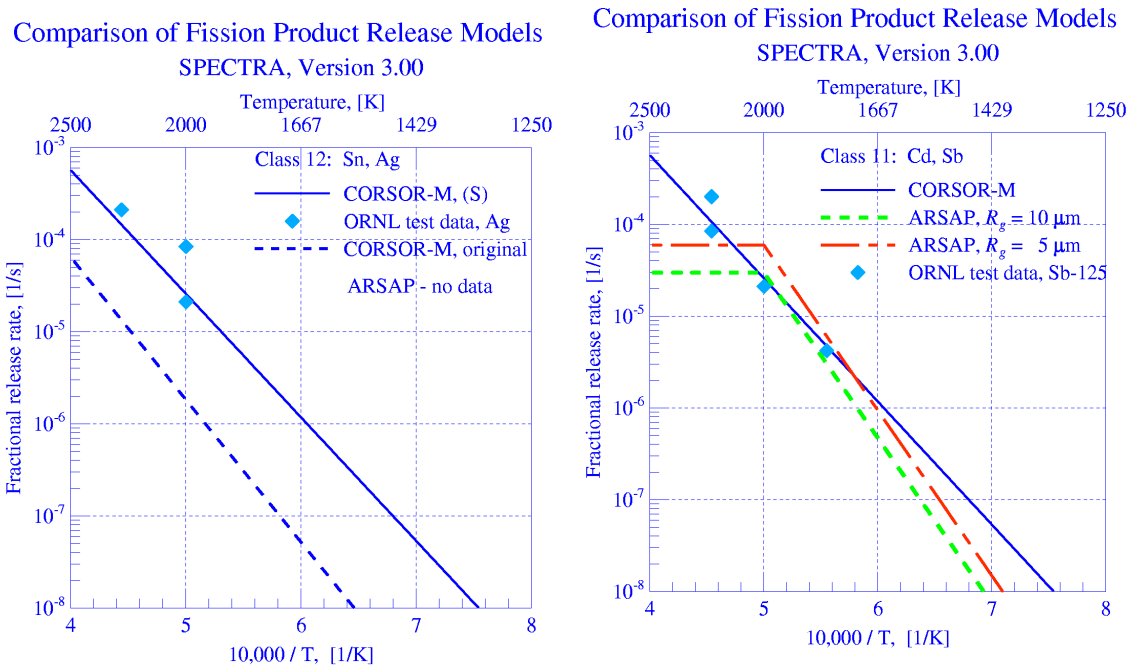

Figure 2-181 Fission product release models, Class 11 (Cd, Sb) and 12 (Sn, Ag).

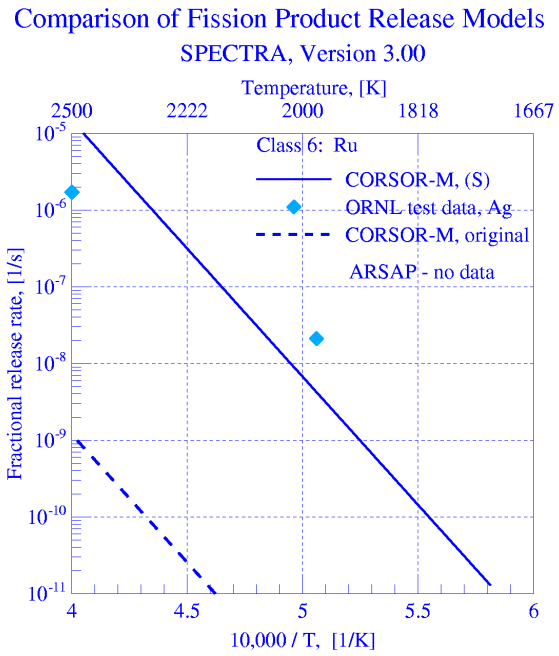

Figure 2-182 Fission product release models, Class 6 (Ru).

It is seen in Figure 2-178 through Figure 2-182 that the results of both CORSOR-M and ARSAP model are in agreement with the ORNL test data [83]. For the release classes 8, 9, and 10 the release rates are very small, and therefore the results are not plotted for these classes.

2.8.14 HTR Fission Product Release Model

Within the HTR-FPR model, a correlation has been developed that determines the particle failure versus temperature. The correlation is discussed in Volume 1. The correlation is coded in the subroutine FTRISO. A testing program, provided in \Z-INPUTS\RT\FP-Release\HTR\Model-Support\FTRISO-T\FTRISO-T.FOR, is used to obtain the release fractions calculated by the subroutine FTRISO for different temperatures and burn-ups. The values are compared to the values obtained from the correlation (calculated in the Excel file: \Z-INPUTS\RT\FP-Release\HTR\Model-Support\HTR-Release-Fractions.xlsx). The values obtained for one temperature point (1600°C = 1873.15 K) are shown below.

	T (°C)	B = 1.0 (80,000 MWd/t)	B = 0.5 (40,000 MWd/t)	B = 0.0 (0.0 MWh/t)
correlation:	1600.0	8.013E-04	6.912E-04	5.589E-04
FTRISO:	1600.0	8.013E-04	6.913E-04	5.589E-04

The results of the subroutine FTRISO give practically identical results as the correlation.

2.8.15 Fission Product Vapor Pressures

The general formula used to compute the fission product vapor pressure is [20]:

$$\log_{10}(P'[mmHg]) = -\frac{A'}{T} + B' + C'\log_{10}(T)$$

where: P - saturation pressure, (mm Hg)
A', B', C' coefficients,
T - temperature, (K)

In SPECTRA the SI units are used; therefore the formula is converted to:

$$\log_{10}(P) = -\frac{A}{T} + B + C\log_{10}(T)$$

where: P - saturation pressure, (Pa)
A, B, C coefficients, up to 3 sets of coefficients are used
T - temperature, (K)

Conversion to the SI units is quite simple: $B = B' + \log_{10}(10^5/750) = B' + 2.125$ (A and C remain unchanged: $A=A'$, $C=C'$). The fission product vapor equations, as applied in SPECTRA (SI units) for 13 vapor classes (the first 12 classes the same as the release classes, and the 13-th class of CsI), are shown in Table 2-16. The coefficients for all classes except for the Class 1 were obtained from [20]. Class 1 (noble gases) is always a vapor; therefore the coefficients were set to give a constant vapor pressure of 10^{10} Pa. (B=10.0, A=C=0.0). The vapor pressures are shown in Figure 2-182 and Figure 2-183. The testing program is provided in **\Z-TESTS\RT\FP-rel.FOR**.

Table 2-16 Fission product vapor pressures, SI units.

Class		A		B		C		T-lim	
1:	log(P) = -	0.0	/ T +	10.00	-	0.00 log(T) ,	T >	273.0	
2:	log(P) = -	9400.0	/ T +	23.71	-	3.75 log(T) ,	T >	390.0	(600.0)
	log(P) = -	6870.8	/ T +	10.12	-	0.00 log(T) ,	T >	1553.0	
3:	log(P) = -	7836.0	/ T +	8.57	-	0.00 log(T) ,	T >	422.0	(1000.0)
4:	log(P) = -	3578.0	/ T +	19.84	-	2.51 log(T) ,	T >	273.0	(298.0)
	log(P) = -	3205.0	/ T +	25.79	-	5.18 log(T) ,	T >	387.0	
	log(P) = -	2176.9	/ T +	9.77	-	0.00 log(T) ,	T >	457.0	
5:	log(P) = -	13940.0	/ T +	25.63	-	3.52 log(T) ,	T >	534.0	(298.0)
6:	log(P) = -	33200.0	/ T +	12.73	-	0.00 log(T) ,	T >	1460.0	(1500.0)
7:	log(P) = -	32800.0	/ T +	11.80	-	0.00 log(T) ,	T >	1504.0	(1500.0)
8:	log(P) = -	21570.0	/ T +	10.87	-	0.00 log(T) ,	T >	1032.0	(1500.0)
9:	log(P) = -	21800.0	/ T +	10.80	-	0.00 log(T) ,	T >	1046.0	(1000.0)
10:	log(P) = -	32110.0	/ T +	14.00	-	0.00 log(T) ,	T >	1338.0	(1500.0)
11:	log(P) = -	13730.0	/ T +	10.55	-	0.00 log(T) ,	T >	666.0	(1000.0)
12:	log(P) = -	15400.0	/ T +	10.28	-	0.00 log(T) ,	T >	758.0	(1000.0)
13:	log(P) = -	10420.0	/ T +	21.82	-	3.02 log(T) ,	T >	436.0	(600.0)
	log(P) = -	9678.0	/ T +	22.48	-	3.52 log(T) ,	T >	894.0	
	log(P) = -	7303.9	/ T +	9.71	-	0.00 log(T) ,	T >	1553.0	

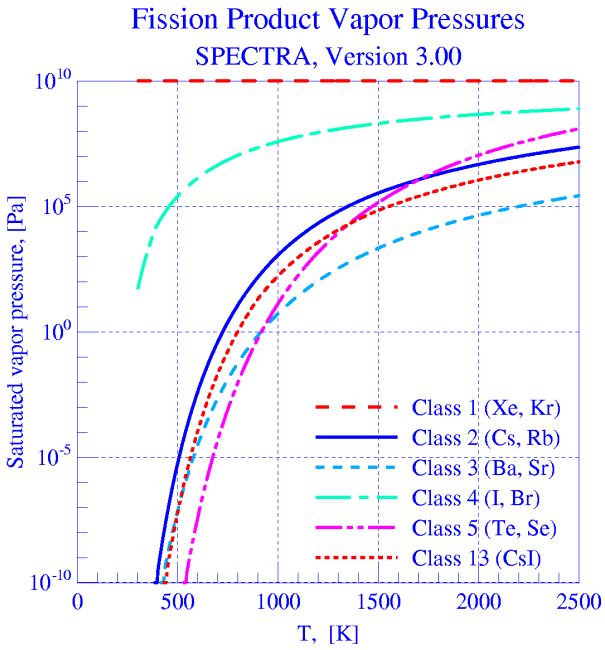

Figure 2-183 Fission product vapor pressures, classes 2 – 5 and 13 (CsI).

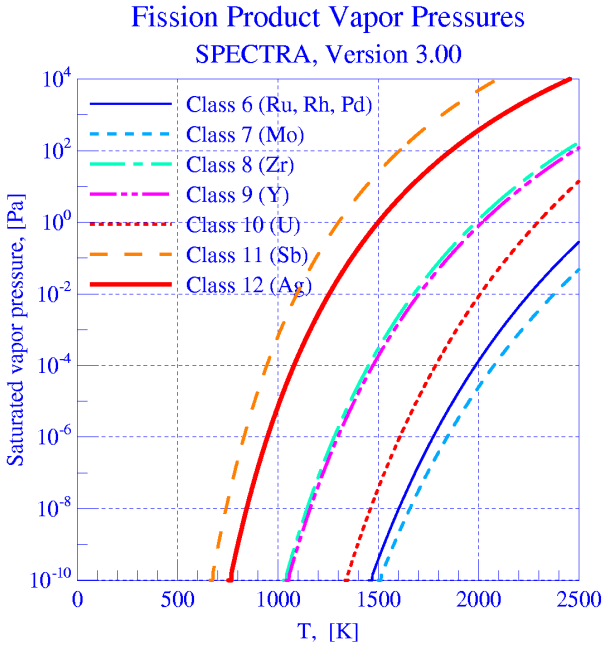

Figure 2-184 Fission product vapor pressures, classes 6 – 12.

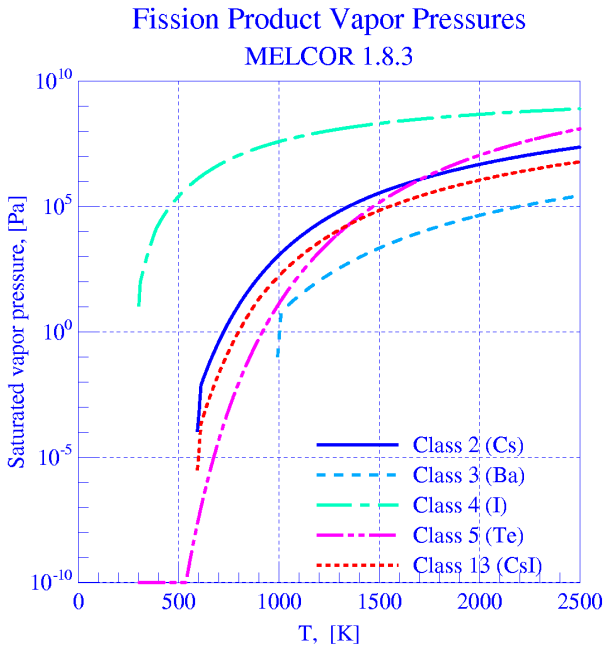

Figure 2-185 Vapor pressures, classes 2 – 5 and 13 – $T_{lim}(1)$ from [20].

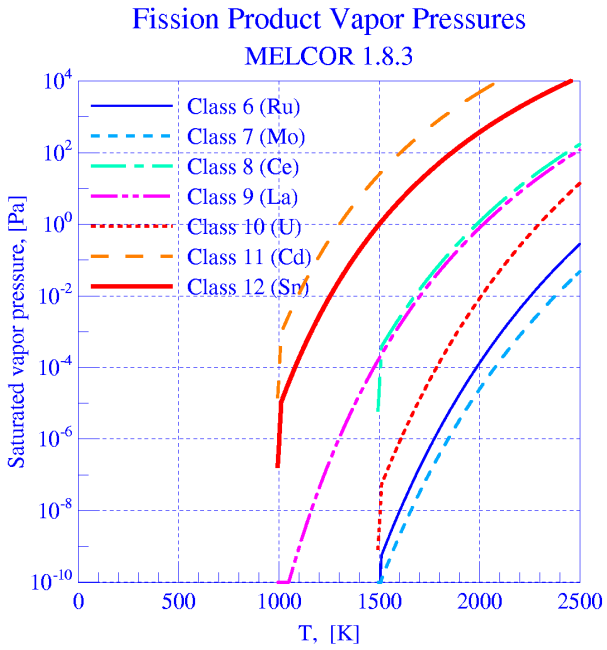

Figure 2-186 Vapor pressures, classes 6 – 12 – $T_{lim}(1)$ from [20].

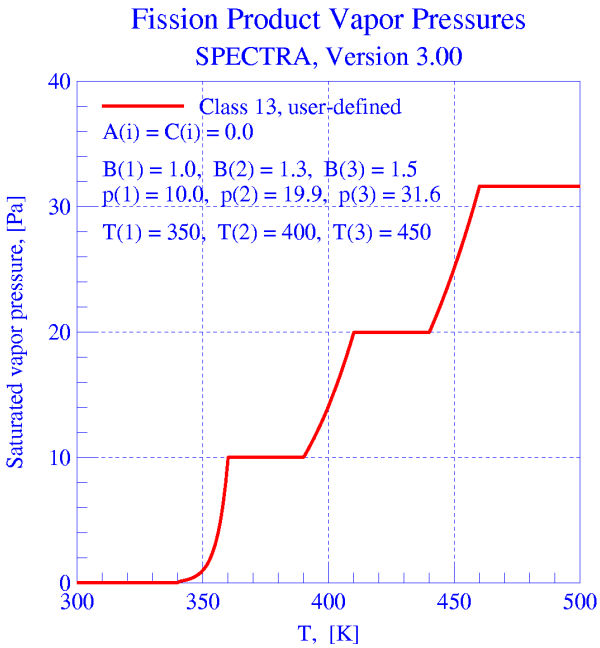

Figure 2-187 Fission product vapor pressure, example of a user-defined class.

The limiting temperatures for the first sets were modified compared to the data from [20]. They were set to the values for which $P = 10^{-10}$ Pa. This was done to minimize discontinuities at this temperature. The discontinuities are seen in Figure 2-185 and Figure 2-186, which were made using the original values of the limiting temperatures from [20]). The original limiting temperatures from reference [20] are printed in Table 2-16 in brackets, behind the actually used temperatures.

As an example of the interpolating scheme a simple function has been built, using three sets that provide a constant value within each set:

- Set 1: $A = 0.0$, $B = 1.0$, $C = 0.0$, $T_{lim} = 350.0$ $P(T)$=10.0
- Set 2: $A = 0.0$, $B = 1.3$, $C = 0.0$, $T_{lim} = 400.0$ $P(T)$=19.9
- Set 3: $A = 0.0$, $B = 1.5$, $C = 0.0$, $T_{lim} = 450.0$ $P(T)$=31.6

Resulting pressure is shown in Figure 2-187. The interpolation is linear with respect to the exponent, X, so the actual vapor pressure, which is equal to 10^X, is not linear. The function $P(T)$ is however continuous. Summarizing, the applied interpolation scheme assures that the vapor pressure function is always continues, independently of the value of the coefficients and the limiting temperatures, which are entered by the user.

2.8.16 Alternative Sorption Model - Gnielinski Correlation

As an alternative Sherwood number correlation may be used. In such case the Sherwood number is calculated from the following correlation, the Gnielinski correlation [96] may be used. The correlation is:

$$Sh = \frac{r \cdot (Re - 1000) \cdot Sc}{1 + 12.7 \cdot \sqrt{r} \cdot (Sc^{2/3} - 1)} \cdot \left(1 + \left(\frac{d}{x}\right)^{2/3}\right) \cdot \left(\frac{Sc_{gas}}{Sc_{wall}}\right)^{0.11}$$

where:

$$r = (1/8) \cdot (1.82 \cdot \log_{10}(Re) - 1.64)^{-2}$$

Sc_g and Sc_w are the Schmidt numbers at the gas temperature, T_{gas}, and the wall temperature, T_{wall} , respectively, d is the hydraulic diameter and x is the distance from tube entrance. For practical purposes half of the flow length can be used. In the implementation used in RADAX the ratio of Schmidt numbers is replaced by the temperature ratio. The same approach is taken in SPECTRA:

$$Sh = \frac{r \cdot (Re - 1000) \cdot Sc}{1 + 12.7 \cdot \sqrt{r} \cdot (Sc^{2/3} - 1)} \cdot \left(1 + \left(\frac{d}{x}\right)^{2/3}\right) \cdot \left(\frac{T_{gas}}{T_{wall}}\right)^{y}$$

In the RADAX code the value of y is taken as 0.45. Comparison of the results of $(Sc_g/Sc_w)^{0.11}$ and $(T_g/T_w)^y$ obtained with the value of y = 0.45 is shown in Figure 2-188.

The following values were used for calculations:

- Gas temperature: T_g = 900 K
- Gas pressure: $p_g = 9.0 \times 10^6$ Pa
- Gas composition: helium
- Wall temperatures: $0.5\ T_g < T_w < 2.0\ T_g$

The Schmidt number was calculated from:

$$Sc(T) = \frac{\mu_g(T)}{\rho_g(T) \cdot D_{C,g}(T)}$$

Here μ_g is the dynamic viscosity of gas, ρ_g is the density of gas, and $D_{C,g}$ is the diffusion coefficient of gas, The diffusion coefficient was calculated from the Chapman-Enskog correlation:

$$D_C = A_D \cdot \frac{T_g^{B_D}}{p}$$

with $A = 1.0 \times 10^{-3}$ and $B = 1.5$, as the values appropriate for I, Cs, Ag in He, (see Volume 1).

The testing program is provided in **\Z-TESTS\RT\GNIEL.FOR**. Note: in order to compile the program, it must be first moved to the directory: \Z-EXE\.

The results obtained with the value of y used in RADAX, $y = 0.45$ are shown in Figure 2-188. It was found out by trial and error that a better representation is obtained using $y = 0.015$ - see Figure 2-189. Therefore this value is chosen as a default value in SPECTRA (see Volume 2, Word 28, record 895YXX).

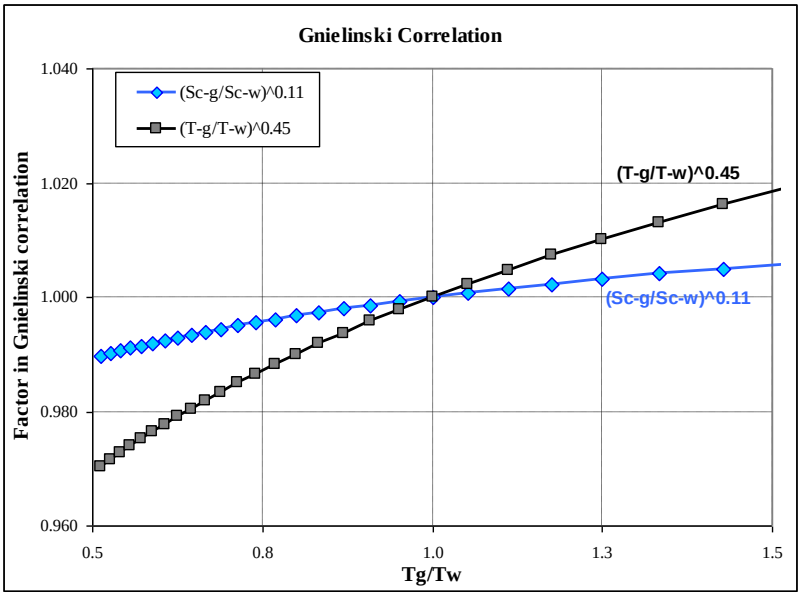

Figure 2-188 Comparison of correction factors $(Sc_g/Sc_w)^{0.11}$ and $(T_g/T_w)^{0.45}$

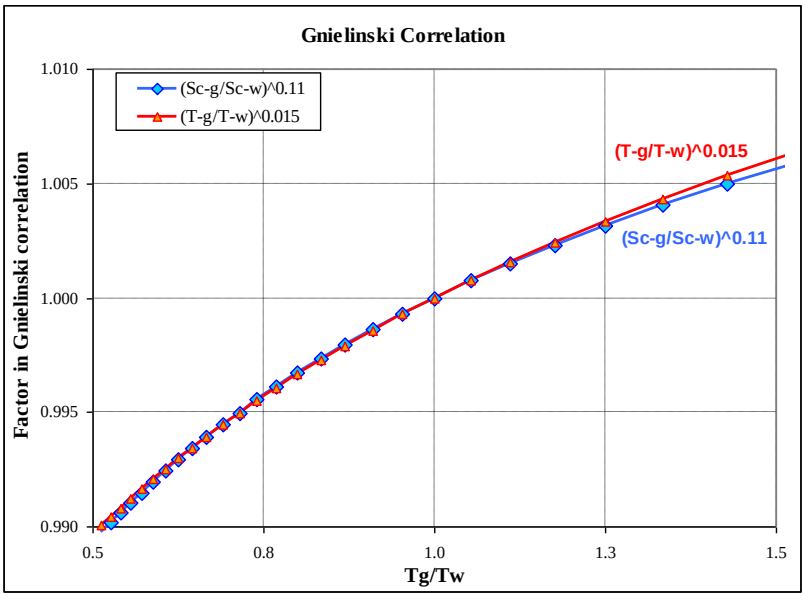

Figure 2-189 Comparison of correction factors $(Sc_g/Sc_w)^{0.11}$ and $(T_g/T_w)^{0.015}$

2.8.17 Inertial Impaction Correlations

2.8.17.1 Langmuir-Blodgett and Modified Langmuir-Blodgett Correlation

Langmuir and Blodgett (L-B) correlation. The L-B correlation was developed for a single sphere. The correlation is:

$$\eta = \eta_{\max} \cdot \frac{Stk^2}{(Stk + C_{LB})^2}$$

C_{LB} constant (=0.25, see [119], eq. 3)
η_{max} maximum value of collection efficiency (=1.0)
Stk Stokes number, (-)

Modified Langmuir and Blodgett correlation. The modified correlation is defined as follows:

$$\eta = \eta_{\max} \cdot \begin{cases} \dfrac{0.25}{C_{LB}} \cdot Stk & for \quad Stk < C_{LB} \\ \dfrac{Stk^2}{(Stk + C_{LB})^2} & for \quad Stk > C_{LB} \end{cases}$$

Both correlations are in SPECTRA calculated within the subroutine CELABL. Comparison of both correlations is shown in Figure 2-190. The comparison was made using the testing program, provided in **\Z-TESTS\RT\LB-T.FOR**.

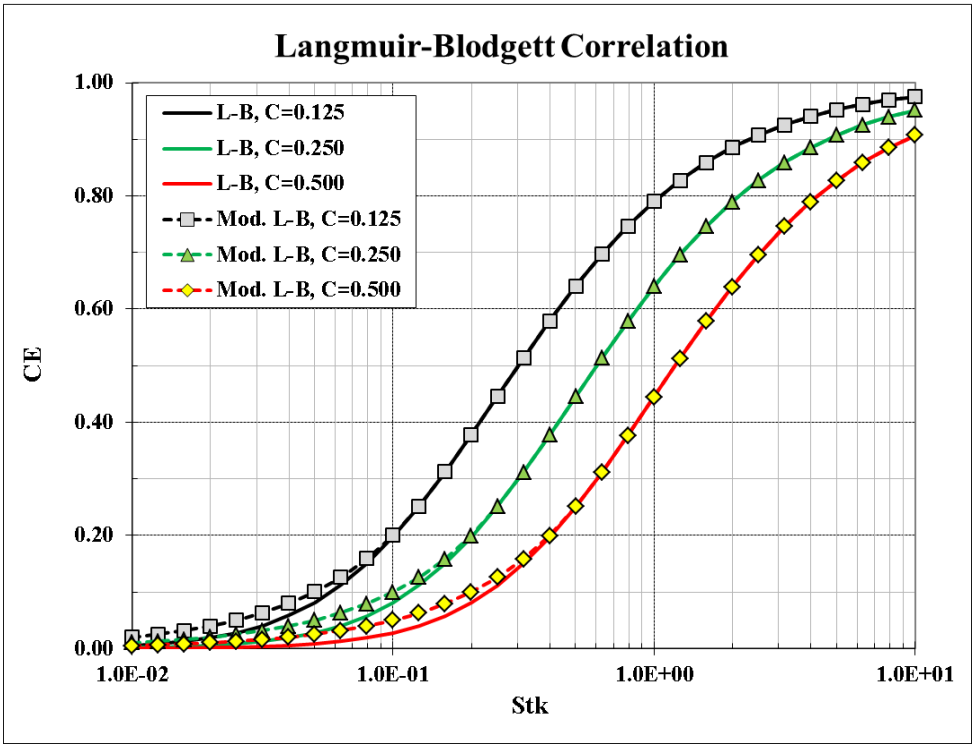

Figure 2-190 Modified versus original Langmuir and Blodgett correlation

In the modified correlation, the collection efficiency η is in the low *Stk* range ($Stk < C_{LB}$), proportional to the Stokes number, $\eta \sim Stk$. The Stokes number is defined as:

$$Stk = \frac{\rho_p \cdot v_\infty \cdot d_p^2}{9 \cdot \mu_f \cdot D_{bubb}}$$

ρ_p particle density, (kg/m^3)
v_∞ particle-to-bubble relative velocity, (m/s)
d_p particle diameter, (m)
μ_f liquid viscosity, (kg/m/s)
D_{bubb} bubble diameter, (m)

In the low *Stk* range the modified correlation gives somewhat higher collection efficiency than the original L-B correlation. The difference is quite small, smaller than the scatter of the source data ([119], figure 1). The difference is important only for small values of the Stokes number. For example, for *Stk*=0.03, the L-B correlation gives η=0.01 and the modified correlation η=0.03, so the relative difference is quite large in this region. The modified correlation gives much better agreement with the experimental data for the Static Column experiments, as shown in section 3.12.56. It is also in qualitative agreement with the new correlation developed for SPECTRA and discussed in the following section.

2.8.17.2 Correlation Based on Data of Yoon & Lutrell and Afruns & Kitchener

The following correlation has been developed specifically for use in the SPECTRA code, based on the data of Yoon & Lutrell [172] for coal particles and Afruns & Kitchener [173] for quartz particles. The data, (copied from [174], figure 9.5) is shown in Figure 2-191. The correlation is:

$$\eta = Min\left(\eta_{\max}, A \cdot \frac{d_p^{\,2}}{D_b} \right)$$

Performed calculations showed that best agreement is obtained with A = 13,000. The lines obtained with A = 13,000 are shown in Figure 2-192 (red lines, yellow markers). It was found that, due to the scatter of data, values between $9{,}000 \le A \le 17{,}000$ can be justified. The values obtained with A = 9,000 are shown in Figure 2-192. The values obtained with A = 17,000 are shown in Figure 2-193.

The correlation is calculated by the subroutine CEYLAK. Comparisons of data with the calculated values are shown in Excel file located in: **\Z-INPUTS\RT\IN-IM\IN-IM.xlsx.**

In the new correlation, the collection efficiency is expressed as:

$$\eta = A \cdot \frac{d_p^{\,2}}{D_b}$$

The Stokes number is defined as:

$$Stk = \frac{\rho_p \cdot v_\infty}{9 \cdot \mu_f} \cdot \frac{d_p^{\,2}}{D_b}$$

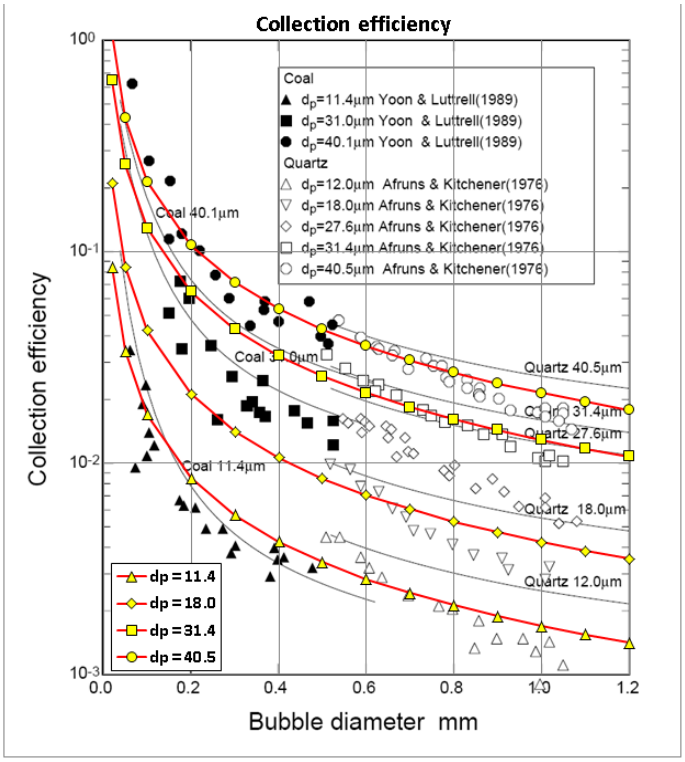

Figure 2-191 New correlation, A = 13,000 (middle)

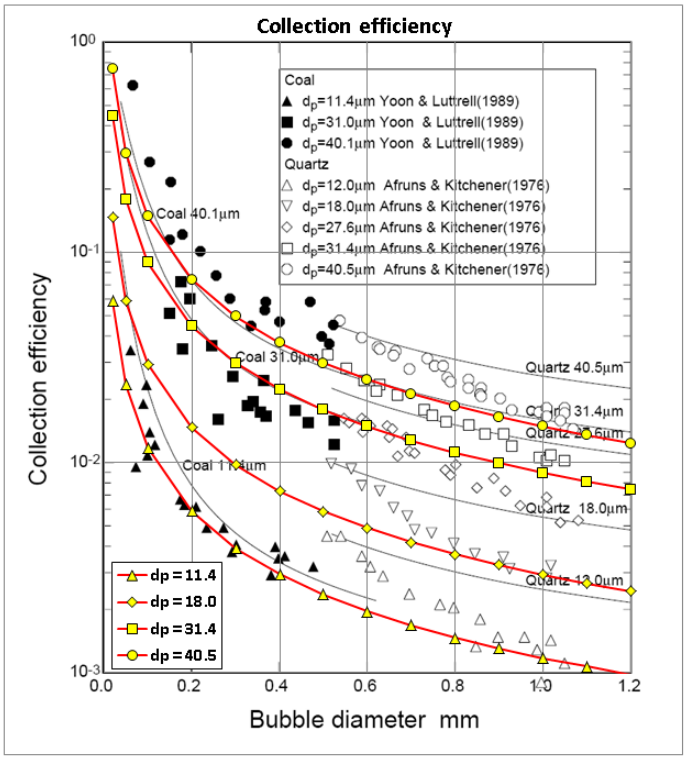

Figure 2-192 New correlation, A = 9,000 (minimum)

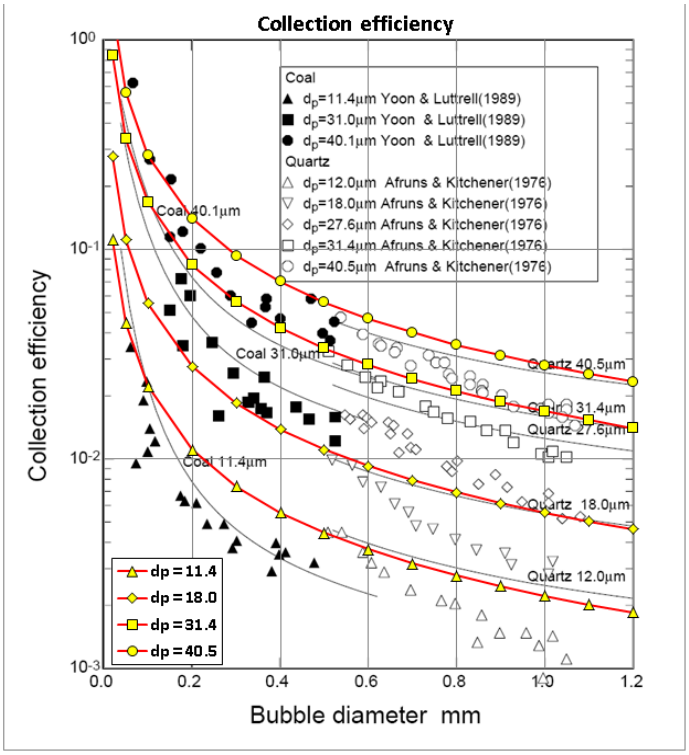

Figure 2-193 New correlation, A = 17,000 (maximum)

Therefore in this correlation $\eta \sim Stk$. This observation was the main motivation of modifying the Langmuir and Blodgett correlation in the low Stokes number range (section 2.8.17.1). The modified L-B correlation, as well as the new correlation, give better agreement with measured data than the original L-B correlation in case of Static Column experiments (section 3.12.56, see the effect of modification in the L-B correlation - Figure 3-1093).

In case of Static Column experiments, the particle density is ρ_p = 10,280 kg/m^3, bubble velocity was ranging from 0.03 to 0.06 m/s: $v_\infty \sim 0.05$ m/s, fluid viscosity is $\mu_f = 3.3\times10^{-3}$ kg/m-s. Therefore:

$$A = \frac{\rho_p \cdot v_\infty}{9 \cdot \mu_f} \approx \frac{10280 \cdot 0.05}{9 \cdot 3.3 \cdot 10^{-3}} = 17{,}300$$

As shown in section 2.8.17.1, a good agreement between calculated and measured data was obtained using A = 17,000.

2.9 Verification of the Mathematical Library

Verification of procedures from the Math Library is given in the following five sections:

- Interpolating procedures - section 2.9.1
- Differentiating and integrating procedures - section 2.9.2
- Linear equation set solution procedures - section 2.9.3
- Real roots of quadratic and cubic equation - section 2.9.4
- Bessel functions - section 2.9.5

2.9.1 Interpolation

A table consisting of nine data points is used for verification of YINTP1. The data points are shown in Figure 2-194. The values calculated with the functions YINTP1 and YINTPC (identical) are shown in Figure 2-194 using a solid line. The results are correct. For the reasons mentioned in Volume 1 the function YINTP1 does not perform extrapolations but keeps the end point values beyond the range of tabulated data. Thus a horizontal line is obtained to the left of the first data point and to the right of the last data point.

For verification of YINTP3 the same table is used as for YINTP1. The tabulated data points are shown in Figure 2-195. The values calculated with the function YINTP3 are shown in Figure 2-195 using a solid line. For comparison results of the subroutine SPLINT ([97], section 3.3) are shown. The results are of both procedures are very similar. YINTP3 requires less memory and is somewhat easier to use. In contrast to SPLINT, YINTP3 does not perform extrapolations, but keeps the end point values beyond the data range. This is done for the reasons mentioned in Volume 1.

The execution speed of interpolating procedures was tested using an array of 100,000 data pairs. 1,000,000 interpolations were performed using either "random" arguments x or the same x. Calculations were performed using Pentium, 1.73 GHz computer. The results are shown in Table 2-17.

Apart from the interpolating procedures: YINTP1, YINTPC and YINTP3, discussed above, two subroutines are available within the code, that allow to locate the interpolation points - FINDI1 and FINDIC. These subroutines have been verified by comparison with results of similar subroutine: LOCATE, available within the "Numerical Recipes in FORTRAN" [97]. The execution speed of these subroutines was tested using the same array (100,000 data pairs). 1,000,000 interpolations were performed using either "random" arguments x or the same x.

The tests described above were performed using a FORTRAN program, which is provided in **\Z-TESTS\ML\INT-T.FOR**. In order to compile the program, it must be first moved to the directory: **\Z-TESTS**.

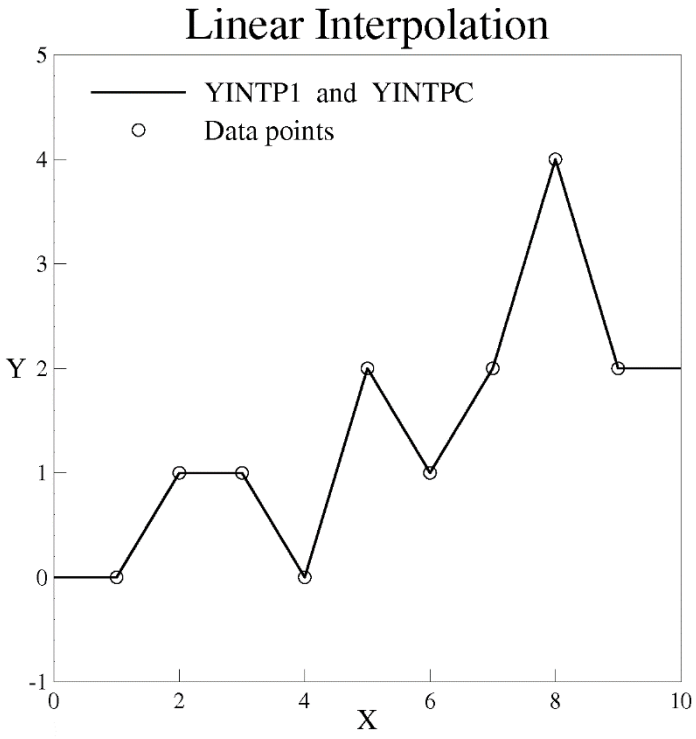

Figure 2-194 Linear interpolation

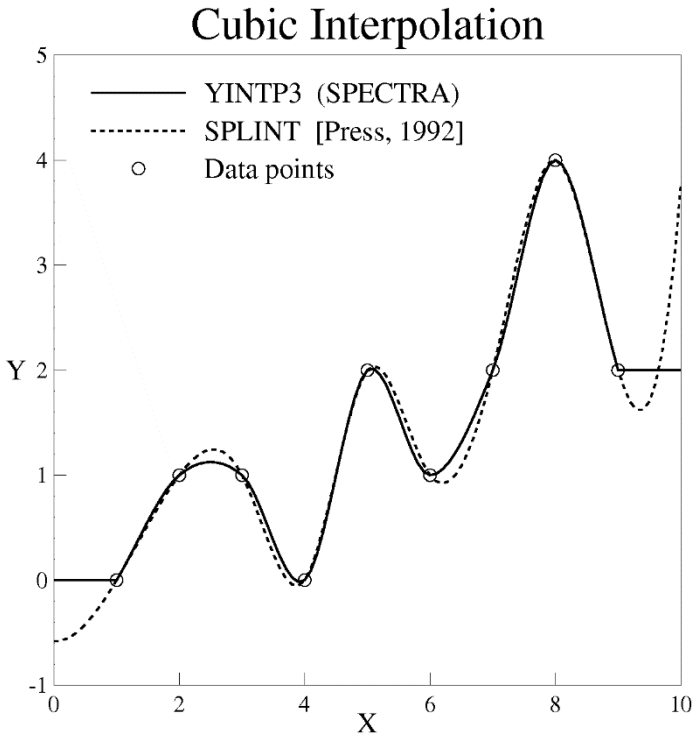

Figure 2-195 Cubic interpolation

Table 2-17 Comparisons of execution speed of interpolating procedures

Interpolation	Procedure	CPU, (s)	Relative CPU	
Linear	YINTP1, "random" *x*	0.62	100%	
	YINTP1, the same *x*	0.03	5%	
	YINTPC, "random" *x*	0.50	80%	
Cubic	YINTP3, "random" *x*	0.78	125%	100%
	YINTP3, the same *x*	0.03	5%	4%
	SPLINT, "random" *x*	0.66	105%	84%

Table 2-18 Comparison of execution speeds of locating procedures

Procedure	CPU, (s)	Relative CPU
FINDI1	0.59	100%
FINIC	0.52	87%
LOCATE	0.77	129%

2.9.2 Differentiation and Integration

A table consisting of nine data points is used for verification of differentiating procedures. The data points are shown in Figure 2-196. The values of derivative, calculated by the functions DERTB1 and DERTBC (identical), are shown in Figure 2-196 using dots. The results are correct. Beyond the data range ($x < 1$ and $x > 9$) the derivative is equal to zero. This is consistent with the interpolating functions: YINTP1 and YINTPC, which do not perform extrapolations but keep the end point values beyond the range of tabulated data.

The same data table was used for verification of integrating procedures. The following integrals were calculated:

$$I_2 = \int_{-1}^{x} y(x)dx$$

$$I_2 = \int_{2}^{x} y(x)dx$$

where $y(x)$ is the integrated function, given by the tabulated data points.

The calculated integrals which are functions of x (the upper integration boundary) are shown in Figure 2-196. The difference between the first and the second integral is equal to 3.5 - which is equal to the value of the integral taken from –1 to 2. The correctness of the obtained value is easily checked by hand calculations.

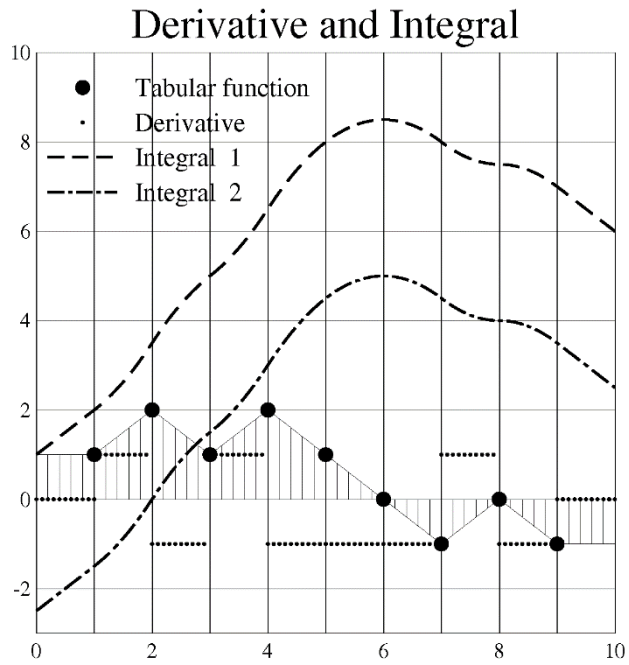

Figure 2-196 Derivative and integral of a tabulated function

The execution speed of differentiating and integrating procedures was tested using an array of 100,000 data pairs. The derivative was calculated 1,000,000 times using either "random" arguments *x* or the same *x*. The integral was calculated 100 times using integration boundaries that cover the range of independent variable of the whole table. Calculations were performed using Pentium, 1.73 GHz computer, using a FORTRAN program, which is provided in **\Z-TESTS\ML\DI-T.FOR**. In order to compile the program, it must be first moved to the directory: **\Z-TESTS**. The results are shown in Table 2-19.

Table 2-19 Comparisons of execution speed of differentiating and integrating procedures

	Procedure	CPU (s)	Relative CPU
Derivative (1,000,000 tests)	DERTB1, "random" *x*	0.61	100%
	DERTB1, the same *x*	0.03	5%
	DERTBC, "random" *x*	0.48	80%
Integral (100 tests)	XINTB1	0.28	100%
	XINTBC	0.23	83%

2.9.3 Real Roots of Quadratic and Cubic Equations

Verification of subroutine ROOT2 is performed by calculating real roots of the following three equations:

$$(a) \quad x^2 - 1 = 0$$

$$(b) \quad x^2 + 1 = 0$$

$$(c) \quad x^2 - 2x + 1 = 0$$

As shown in Figure 2-197 the equation (*a*) has two real roots, equation (*b*) has none. Equation (*c*), which may be written as: $(x - 1)^2 = 0$, has a double real root at x=1.0.

The values of x_1 and x_2, calculated with ROOT2 are shown in Table 2-20. The correctness of the calculated values (when $|x_i| < 10^{99}$) may be checked by substitution of x_1 and x_2 into the equations.

It should be noted that the calculated roots always fulfill the condition: $x_1 \le x_2$. This allows easier selection between the calculated roots in practical applications.

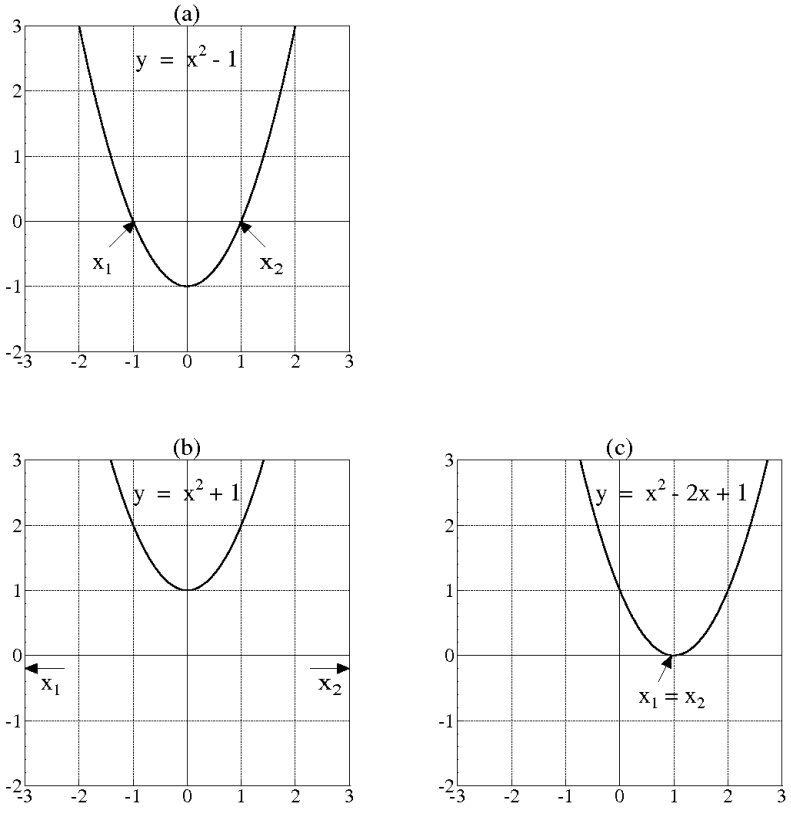

Figure 2-197 Quadratic functions used to verify ROOT2

Table 2-20 Results of ROOT2

Equation	x_1	x_2
$x^2 - 1 = 0$	–1.0	1.0
$x^2 + 1 = 0$	-10^{99}	10^{99}
$x^2 - 2x + 1 = 0$	1.0	1.0

Verification of subroutine ROOT3 is performed by calculating real roots of the following five equations:

$$(a) \quad x^3 - x = 0$$
$$(b) \quad x^3 - x + 1 = 0$$
$$(c) \quad x^3 - x - 1 = 0$$
$$(d) \quad x^3 - x^2 = 0$$
$$(e) \quad x^3 - 3x^2 + 3x - 1 = 0$$

As shown in Figure 2-198 the equation (*a*) has three real roots, equation (*b*) has only one, which is located on the left arm of the parabola. Similarly equation (*c*) has one real root, but in this case located on the right arm of the parabola. Equation (*d*), which may also be written as: $x^2(x - 1) = 0$, has a double root at $x = 0$, and another root at $x = 1$. Equation (*e*), equivalently written as: $(x - 1)^3 = 0$, has a triple root at $x = 1$.

The values of x_1, x_2 and x_3, calculated with ROOT3 are shown in Table 2-21. The correctness of the calculated values (when $|x_i| < 10^{99}$) may be checked by substitution of x_1, x_2 and x_3 into the equations. The values of order of 10^{-16} represent the zero, to the accuracy of the double precision (REAL*8) number.

It should be noted that the calculated roots always fulfill the condition: $x_1 \le x_2 \le x_3$. This allows easier selection between the calculated roots in practical applications.

A FORTRAN program to perform tests of quadratic and cubic equation is provided in **\Z-TESTS\ML\ROOT-T.FOR**. In order to compile the program, it must be first moved to the directory: **\Z-TESTS**.

Table 2-21 Results of ROOT3

Equation	x_1	x_2	x_3
$x^3 - x = 0$	–1.0	4×10^{-16}	1.0
$x^3 - x + 1 = 0$	–1.32472	10^{99}	10^{99}
$x^3 - x - 1 = 0$	-1.0^{99}	-1.0^{99}	1.32472
$x^3 - x^2 = 0$	2×10^{-16}	2×10^{-16}	1.0
$x^3 - 3x^2 + 3x - 1 = 0$	1.0	1.0	1.0

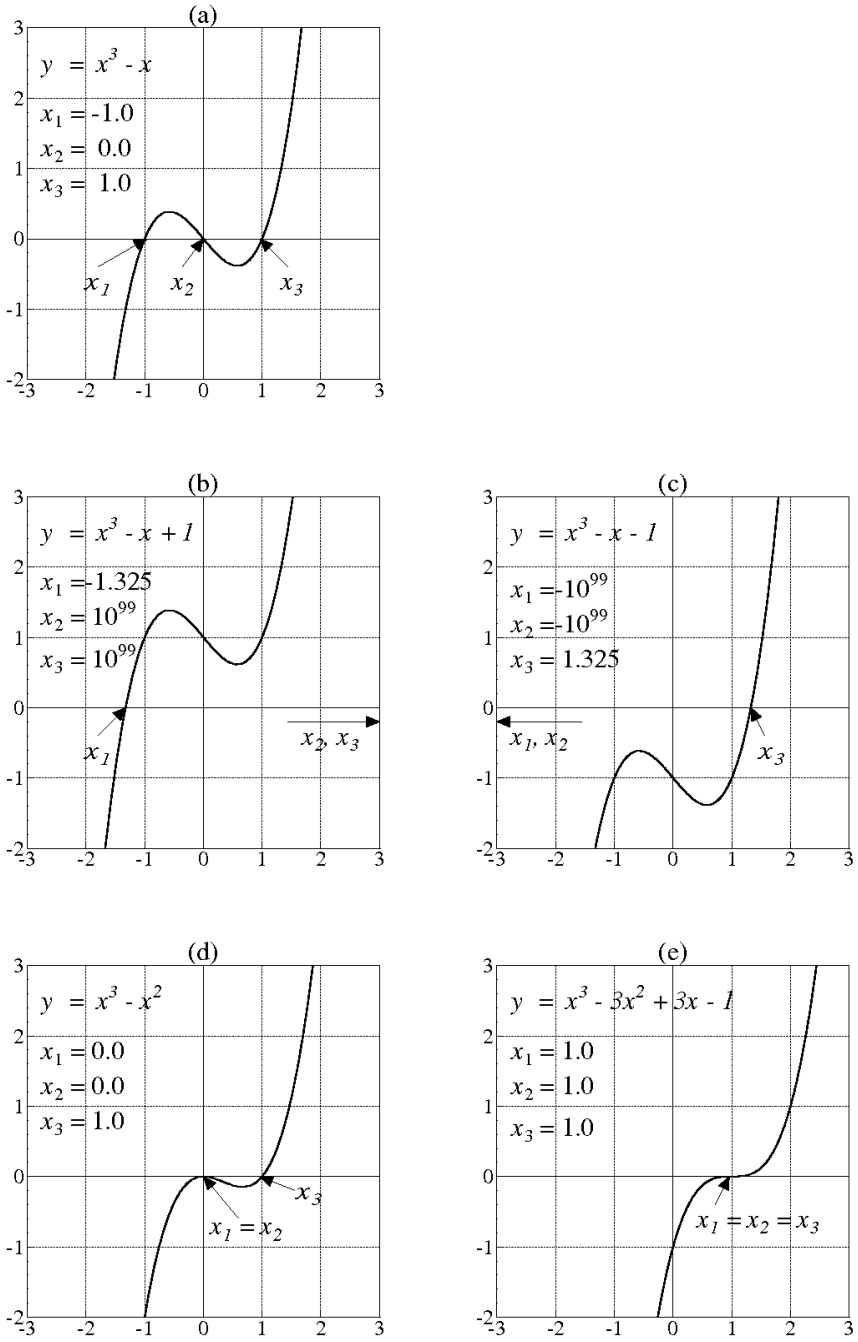

Figure 2-198 Cubic functions used to verify ROOT3

2.9.4 Linear Equation Set (Matrix) Solvers

The linear equation set solution procedures consist of the following subroutines:

- For full matrices: subroutines LUDCMP and LUBKSB, [97]
- For 3-diagonal matrices: TRIDAG, [97]
- For sparse matrices: LINBCG [97]
- For band diagonal matrices: BANDEC and BANBKS, [97], for symmetrical bands: GAUSSB [98].

The procedures for solution of full matrix and 3-diagonal matrix are based on the method called LU decomposition. Another method of solving linear equations is the Gauss elimination. Comparison of the LU decomposition method and the Gauss method is shown in Table 2-22. The procedures using the Gauss elimination method, used for comparison runs, were adapted from [98] (GAUSS) and [99] (GAUSS3). It is seen that the LU decomposition method is somewhat faster than the Gauss elimination. Both methods give very accurate solutions. The maximum relative error was smaller than 10^{-13}.

An important type of matrix is a sparse matrix. Iterative methods are typically used to solve sparse matrices. Subroutine LINBCG solves a sparse matrix using bi-conjugate gradient method. Comparison of the standard LU decomposition method with the bi-conjugate gradient method is shown in Table 2-23. It is seen that the bi-conjugate gradient method is very useful if the matrix consists of only few per cent of nonzero elements. If the matrix contains ten or more per cent of nonzero elements, the gain on the execution time is rather small. Thus for such systems the LU decomposition method should be preferred, since it gives better accuracy (see Table 2-23). Moreover it was observed that in some cases LINBCG fails to calculate accurate solution. Therefore this matrix solver is not used in the current SPECTRA version. It was used in Versions 1.00 and 2.00 for solving gas and liquid flows in junctions.

A FORTRAN program to test the matrix solvers is provided in **\Z-TESTS\ML\MATR-T.FOR** (full and 3-diagonal matrix tests) and **MTRX-T.FOR** (sparse matrix tests). In order to compile these programs they must be first moved to the directory: **\Z-TESTS**.

Table 2-22 Comparison of execution speed of linear algebraic equation solvers

Matrix type	No. of equations	Procedure	Solution type	Maximum relative error	CPU (%)
Full	100	LUDCMP LUBKSB	LU decomposition	3×10^{-12}	100%
		GAUSS	Gauss elimination	6×10^{-13}	205%
3-diagonal	1000	TRIDIAG	LU decomposition	3×10^{-16}	100%
		GAUSS3	Gauss elimination	2×10^{-16}	130%

Table 2-23 Comparison of execution speed of linear algebraic equation solvers

Matrix type	No. of equations/ /% of nonzero elements	Procedure	Solution type	Maximum relative error	CPU (%)
Band matrix, band width=5 (five nonzero elements in a row)	200 / 2.5%	LUDCMP LUBKSB	LU decomposition	2×10^{-14}	100%
		LINBCG	Bi-conjugate gradient	4×10^{-8}	~10%
	400 / 1.25%	LUDCMP LUBKSB	LU decomposition	5×10^{-14}	100%
		LINBCG	Bi-conjugate gradient	9×10^{-8}	~1%

2.9.5 Bessel Functions

The procedures calculating Bessel functions were implemented from [97]. Correctness of this implementation is performed by plotting results obtained with the implemented functions and comparing with graphs reproduced from [97].

Figure 2-199 and Figure 2-200 show Bessel functions: J_n and Y_n. Figure 2-200 is copied from [97] (figure 6.5.1). Calculated values are shown in Figure 2-199. Figure 2-201 and Figure 2-202 show modified Bessel functions: I_n and K_n. Figure 2-202 is copied from [97] (figure 6.6.1). Calculated values are shown in Figure 2-201. It is seen that the calculated values of Bessel functions are correct.

A FORTRAN program to test calculations of the Bessel functions is provided in **\Z-TESTS\ML\BESSEL-T.FOR** In order to compile the program it must be first moved to the directory: **\Z-TESTS**.

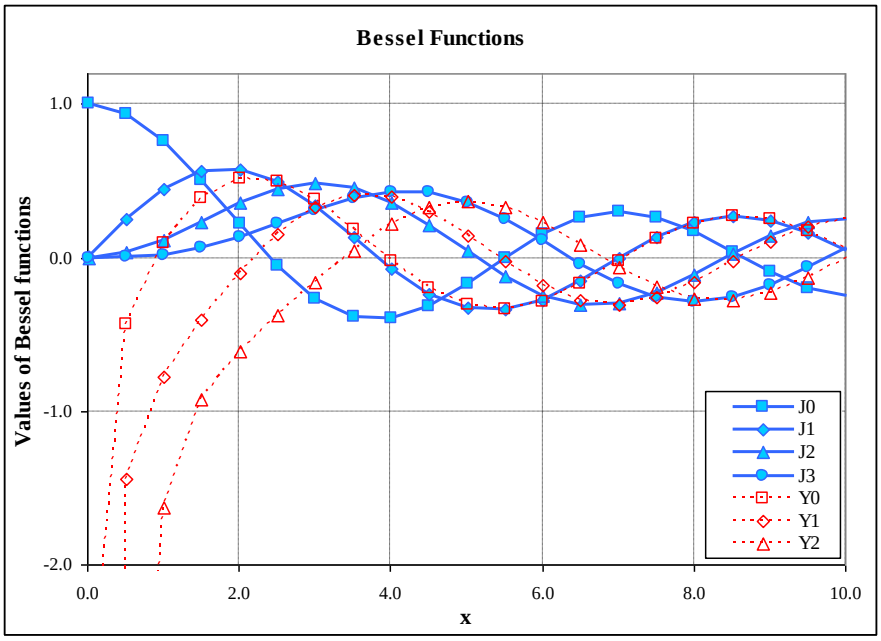

Figure 2-199 Bessel functions, SPECTRA

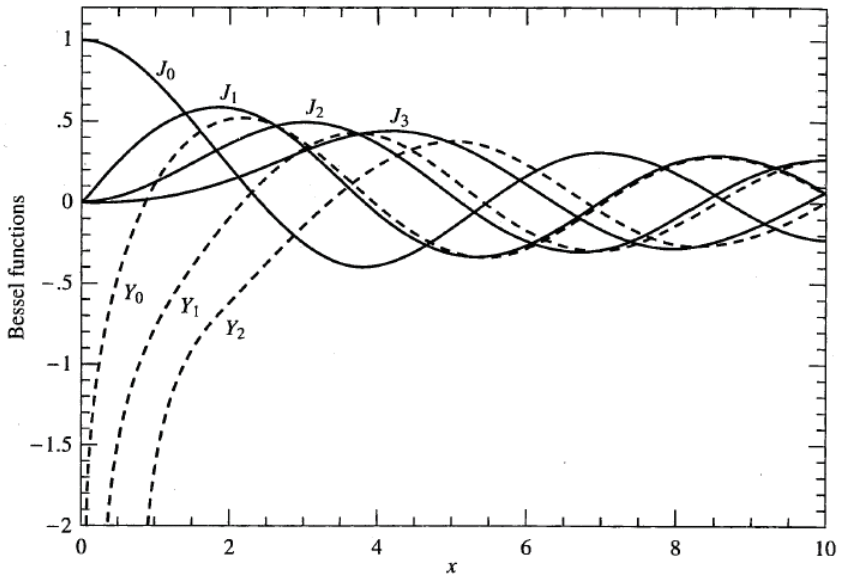

Figure 2-200 Bessel functions, [97]

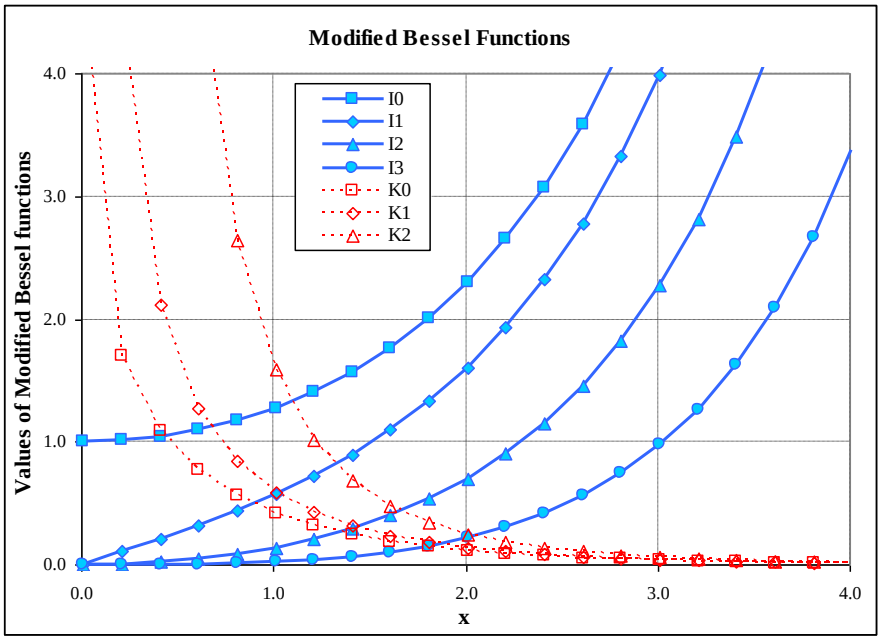

Figure 2-201 Modified Bessel functions, SPECTRA

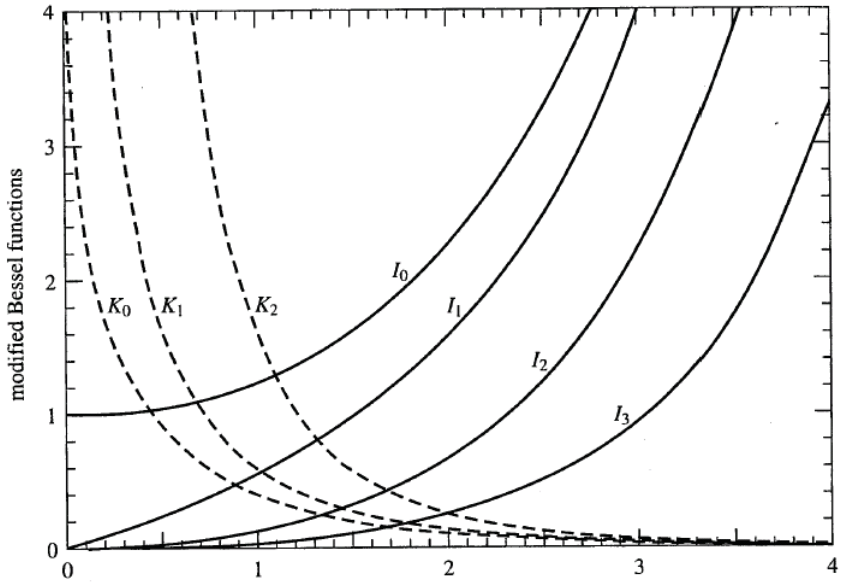

Figure 2-202 Modified Bessel functions, [97]

2.9.6 Utility Functions

The function DNLEXP calculates exp(x) using the FORTRAN double precision function DEXP(X). A separate function was built to calculate the exponent for the reason of computational efficiency, as explained below.

For very large negative arguments the value of function is very close to zero:

$$\exp(x) \to 0.0 \quad for: \quad x \to -\infty$$

The function DEXP(X) takes quite some time to calculate the value for $x \to -\infty$. In SPECTRA calculations exp($-\infty$) are quite frequent, for example in case of particle resuspension the characteristic exponent for weakly-bound particles are very large (resulting in immediate resuspension). In such case FORTRAN takes quite some time in order to obtain the value which is equal to zero with a very good accuracy. A similar problem arises for a very small absolute arguments:

$$\exp(x) \to 1.0 \quad for: \quad x \to 0.0$$

Again, the solution is known with a very good accuracy while FORTRAN takes quite some time to arrive at a value which is just slightly different that one.

The SPECTRA exponent function, DNLEXP(X), has been defined as follows:

$$DNLEXP(x) = \begin{cases} 1.0 & for: \quad |x| < 10^{-5} \\ 0.0 & for: \quad x < -60.0 \\ 1.426 \times 10^{26} & for: \quad x > +60.0 \\ DEXP(x) & for: \quad other\ x \end{cases}$$

A FORTRAN program to test the speed of DNLEXP is provided in **\Z-TESTS\ML\UTIL-T.FOR** In order to compile the program it must be first moved to the directory: **\Z-TESTS**. The results are shown below:

```
                                        TOTAL CPU    CPU / TEST      %

  DEXP( 1.00E-09) = 1.00000E+00 :  CPU =  4.68750E-01  4.68750E-08   100.0
 DNLEXP( 1.00E-09) = 1.00000E+00 :  CPU =  6.25000E-02  6.25000E-09    13.3

  DEXP(-1.00E+09) = 0.00000E+00 :  CPU =  6.26992E+01  6.26992E-06   100.0
 DNLEXP(-1.00E+09) = 0.00000E+00 :  CPU =  6.25000E-02  6.25000E-09     0.1

  DEXP( 6.00E+01) = 1.14315E+26 :  CPU =  1.03125E+00  1.03125E-07   100.0
 DNLEXP( 6.00E+01) = 1.14200E+26 :  CPU =  7.81250E-02  7.81250E-09     7.6

  DEXP( 1.00E+00) = 2.71828E+00 :  CPU =  1.00000E+00  1.00000E-07   100.0
 DNLEXP( 1.00E+00) = 2.71828E+00 :  CPU =  1.15625E+00  1.15625E-07   115.6
```

The performed CPU tests showed that:

- For $x \rightarrow -\infty$ ($x = -10^9$) the gain in speed is of three orders of magnitude (a factor of 1000).
- For $|x| \rightarrow 0.0$ ($x = 10^{-9}$) the gain is about an order of magnitude (a factor of 10).
- For $x \rightarrow +\infty$ ($x = 60$) the gain is about an order of magnitude (a factor of 10).
- For other x the FORTRAN function is used and the calculations are slower by about 15% because of the checks that need to be made for the three above mentioned conditions before the DEXP function can be called.

Comparison of CPU time consumption is shown in Figure 2-203. Note that for $x = -10^9$ DEXP takes about 60 times more time than for a "decent" value of $x = 1.0$.

In a summary, the gain is between one and there orders of magnitude for very large and very small values of $|x|$, while the price to pay is only about 15% slower calculations in case of other values of x.

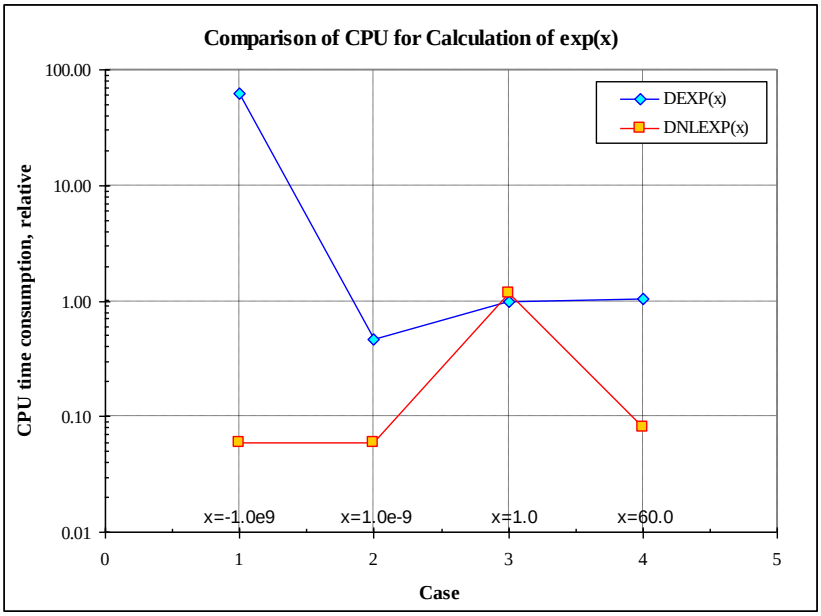

Figure 2-203 Comparison of CPU time for calculation of exponent

3 V&V of the Program - Separate Effect Tests (SET)

Separate Effect Tests are a relatively simple test cases that serve to demonstrate correct functioning of certain class of models, for example, condensation, boiling, convection, etc. SET allow to asses specific models much better than integral system tests (IST), because the latter are characterized by an interplay of multiple physical phenomena and therefore cannot serve as a sufficient proof that individual phenomena are modeled correctly.

Several SET analyzed with SPECTRA are identical to those of MELCOR (e.g. saturated liquid depressurization problem, hydrogen adiabatic expansion, establishment of flow, cooling of a structure in a fluid) and RELAP (e.g. gap model validation PBF-LOC11 tests, FLECHT-SEASET forced reflood test). Those tests were analyzed with SPECTRA as well as MELCOR or RELAP, using an automated export of SPECTRA input to MELCOR or RELAP input format (these tests also serve as verification of the automatic export procedures).

3.1 Tests Related to CV and Junctions

3.1.1 Saturated Liquid Depressurization Problem

The Saturated Liquid Depressurization Problem (SLDP) is described in the MELCOR Assessment Manual [142]. A volume containing saturated water at high pressure is connected to another volume containing only a low-pressure, steam atmosphere by a flow path and a solid heat conductor. The flow path connecting these volumes is opened at time zero and the system is allowed to come into pressure and thermal equilibrium. The solid heat conductor, which thermally equilibrates the two volumes, must have low enough heat capacity to be negligible in the energy balances. The initial conditions are listed in Table 3-1. The theoretical solution is copied from [142], where the derivation of theoretical equations can be found. The theoretical values are shown in Table 3-2.

Table 3-1 Initial conditions for the Saturated Liquid Depressurization Problem [142]

Parameter	Volume 1	Volume 2
Pressure [MPa]	7.999	0.01
Temperature [K]	568.23	568.23
Water mass [kg]	72240	0
Steam mass [kg]	0	152.57
Void fraction	0	1

SPECTRA model was created based on the data in Table 3-1. The nodalization can be seen in Figure 3-3. Two versions of the input deck were prepared:

- heterogeneous CV, MELCOR-type Control Volumes (IHOMCV=1, default value)
- homogenous CV, RELAP-type Control Volumes (IHOMCV=2)

The SPECTRA input files are located in:

\Z-INPUTS\JN\SLDP

For comparison, a model for MELCOR 1.8.6 was generated using the automated export option (IEXPSL=2). Two versions of the input deck were prepared:

- non-equilibrium Control Volumes (ICVTHR = 2, default value)
- equilibrium Control Volumes (ICVTHR = 1)

The MELCOR input files are located in:

\Z-INPUTS\JN\SLDP\MELCOR

Since no precise geometry data was available, several issues have been solved, as described below.

- ***Volumes***. The volumes were guessed using pressure, temperature, and mass data. The volumes are 100 m^3 for the liquid volume and 4000 m^3 for the gas volume. With these volumes and the initial pressure and temperature as in Table 3-1, the initial masses are:
  - CV-100: SPECTRA: 72,238 m^3, MELCOR: 72,242 m^3, reference: 72,240 m^3
  - CV-200: SPECTRA: 152.9 m^3, MELCOR: 152.6 m^3, reference: 152.6 m^3

- ***Flow area***. The flow area of the flow path between CV-100 and CV-200 determines the speed with which pressures equilibrate. The value used in [142] is unknown. An arbitrary value of $A = 0.02$ m^2 was assumed.

- ***Area and heat capacity of the solid structure***. The solid structure is present in order to equilibrate conditions in both Control Volumes. The surface area of the solid structure determines the speed with which temperatures equilibrate. The structure must have a relatively large surface area and a relatively small heat capacity. The following values were assumed: $A = 10^6$ m^2, wall thickness = 2×10^{-4} m, volumetric heat capacity = 10^{-8} J/m^3-K ($\rho = 10^{-4}$ kg, $c_p = 10^{-4}$ J/kg-K). This gives the total heat capacity of $V\times\rho\times c_p = 2\times10^{-6}$ J/-K.

Since the flow area and the heat transfer area are not the same as in [142], the transient behavior is not comparable with the results presented in [142]. This is not important because the theoretical solution is obtained for the end results and only these are important for this test.

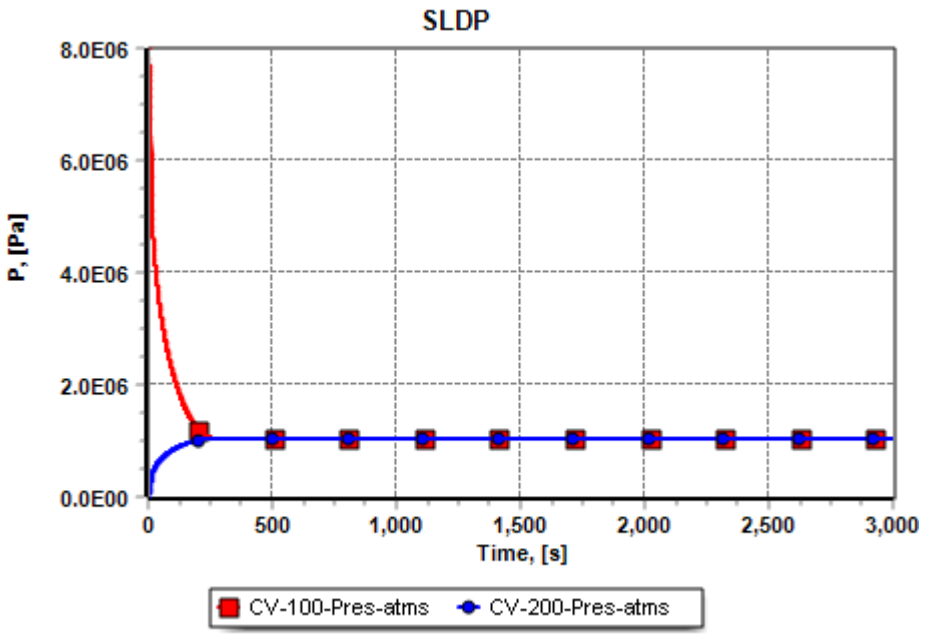

Figure 3-1 SLDP, pressure versus time, SPECTRA

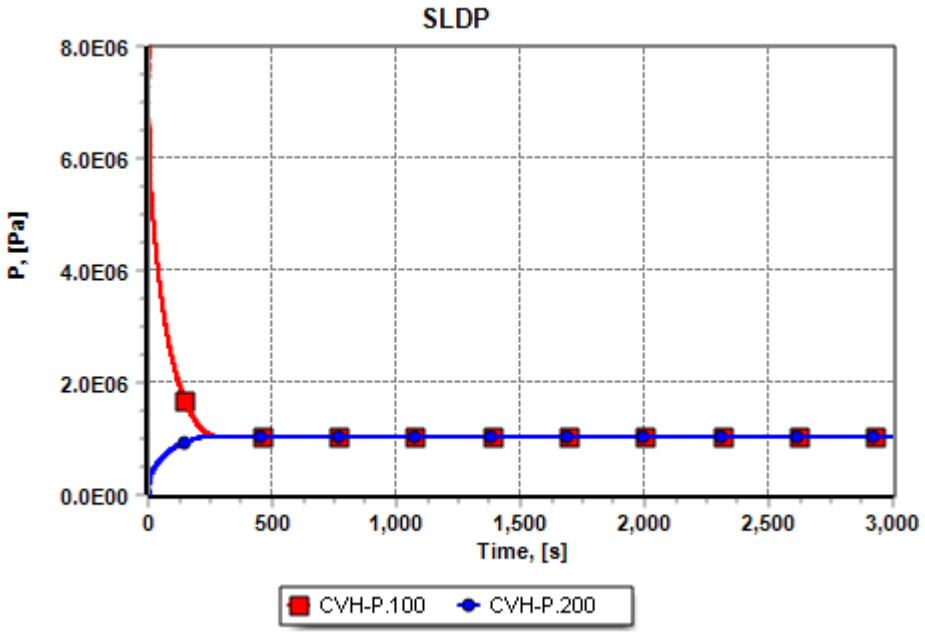

Figure 3-2 SLDP, pressure versus time, MELCOR

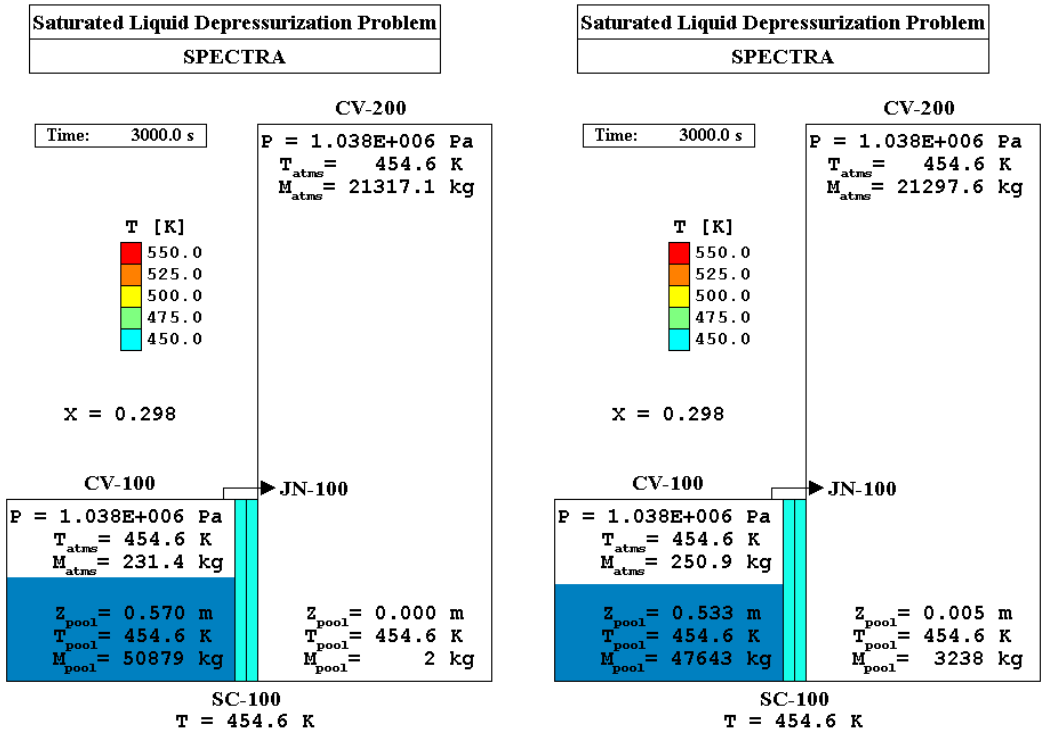

Figure 3-3 SLDP, final state, SPECTRA left: heterogeneous, right: homogeneous

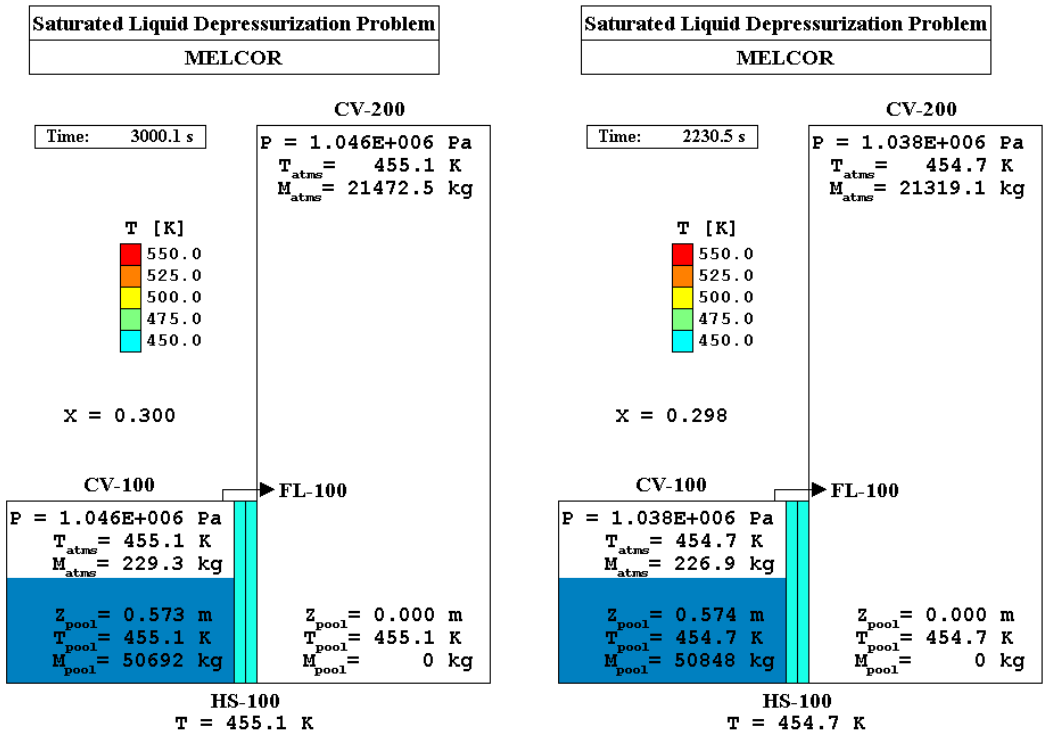

Figure 3-4 SLDP, final state, MELCOR 1.8.6, left: non-equilibrium, right: equilibrium.

SPECTRA results are shown in Figure 3-1 and Figure 3-3. Both heterogeneous and homogeneous models give the same pressure, temperature and quality. The mass distribution among the Control Volume is somewhat different.

MELCOR results are shown in Figure 3-2 and Figure 3-4. Results of the equilibrium model are closer to the theoretical values and also closer to the results reported in [142].

The end-results obtained for SLDP are compared in Table 3-2. The results are in very good agreement with the theoretical solution. The SPECTRA and MELCOR results are in good agreement.

Table 3-2 Comparison of end-results obtained for SLDP

		MELCOR		SPECTRA	
Case	Theory (*)	Non-equil.	Equil.	Hetero.	Homo.
Pressure [MPa]	1.037	1.046	1.038	1.038	1.038
Temperature [K]	454.7	455.1	454.7	454.6	454.6
Quality	0.297	0.300	0.298	0.298	0.298

(*) Copied from MELCOR Assessment Problems, SAND2015-6693 R, August 2015

3.1.2 Hydrogen Adiabatic Expansion

The Hydrogen Adiabatic Expansion Problem (HAEP) is described in the MELCOR Assessment Manual [142]. The problem consists of two control volumes that are pressurized with hydrogen such that the pressure in the first volume is greater than that in the second volume. At time zero, a flow path is opened between the two control volumes, and hydrogen from the higher-pressure control volume expands into the lower-pressure control volume until the two pressures equilibrate. Six cases were analyzed, according to the specifications given in Table 3-3.

Table 3-3 Initial conditions for the Saturated Liquid Depressurization Problem [142]

Case No.	Volume 1 (m^3)	Volume 2 (m^3)	T(I=2) (K)	P(1) (Pa)	P(2) (Pa)	Flow Area (m^2)	Loss Coeff.
1	1000.	1000.	300.	2.0e5	1.0e5	0.05	2.0
2	1000.	1000.	300.	5.0e5	1.0e5	0.05	2.0
3	100.	1000.	300.	2.0e5	1.0e5	0.05	2.0
4	10000.	1000.	300.	2.0e5	1.0e5	0.05	2.0
5	1000.	1000.	300.	2.0e5	1.0e5	50.0	2.0
6	1000.	1000.	300.	2.0e5	1.0e5	0.05	0.1

Theoretical solution, valid for an ideal gas, is presented in [142]. The equations are:

$$T_1 = T_{10} \cdot \left(\frac{m_1}{m_{10}} \right)^{\gamma - 1} \qquad P_1 = P_{10} \cdot \left(\frac{m_1}{m_{10}} \right)^{\gamma}$$

$$T_2 = \frac{m_{20} \cdot T_{20}}{m_2} + \frac{m_{10} \cdot T_{10}}{m_2} \cdot \left[1 - \left(\frac{m_1}{m_{10}} \right)^{\gamma} \right] \qquad P_2 = P_{20} + P_{10} \cdot \frac{V_1}{V_2} \cdot \left[1 - \left(\frac{m_1}{m_{10}} \right)^{\gamma} \right]$$

T_N temperature (K) in volume N
T_{N0} initial temperature (K) in volume N
P_N pressure (Pa) in volume N
P_{N0} initial pressure (Pa) in volume N
m_N mass (kg) of hydrogen in volume N
m_{N0} initial mass (kg) of hydrogen in volume N
V_N volume (m^3) of volume N
γ ratio of specific heats for hydrogen

SPECTRA model was created based on the data in Table 3-3. The nodalization can be seen in Figure 3-5. Two versions of the input deck were prepared:

- Volumes are filled with the built-in hydrogen gas. In such case, hydrogen is treated as real gas, with virial equation of state (see Volume 1).

- Volumes are filled with a user-defined gas. Hydrogen properties were defined in the input. In such case, the gas is treated as an ideal gas.

The theoretical solution, shown above, was defined in the input using appropriate Control Functions. The SPECTRA input files are located in:

\Z-INPUTS\JN\HAEP

Six Cases were analyzed. Results of the Case 1 are shown in Figure 3-5 through Figure 3-10. The end-state is shown in Figure 3-5 and Figure 3-6 for the real gas and ideal gas cases, respectively. Only very small differences in the results are observed. The theoretical solutions are slightly different in Figure 3-5 and Figure 3-6 because of different mass distribution.

The time-temperature behavior in the case of built-in H_2 is shown in Figure 3-7 and Figure 3-8. A discrepancy between SPECTRA and the theoretical solution is because the latter is valid for an ideal gas. The discrepancy is very small because H_2 is very close to the ideal gas (small molecules, low intermolecular forces). The time-temperature behavior in the case of user-defined H_2 is shown in Figure 3-9 and Figure 3-10. The results are practically identical.

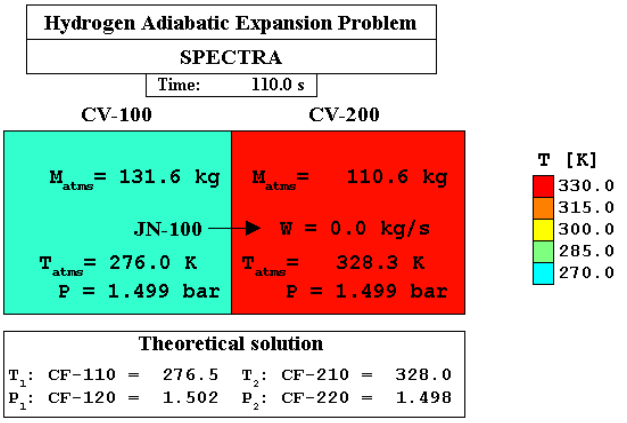

Figure 3-5 HAEP, end-state, built-in H_2 (real gas)

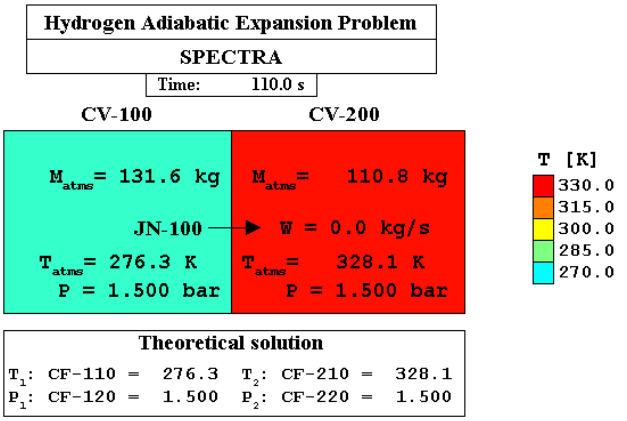

Figure 3-6 HAEP, end-state, user-defined H_2 (ideal gas)

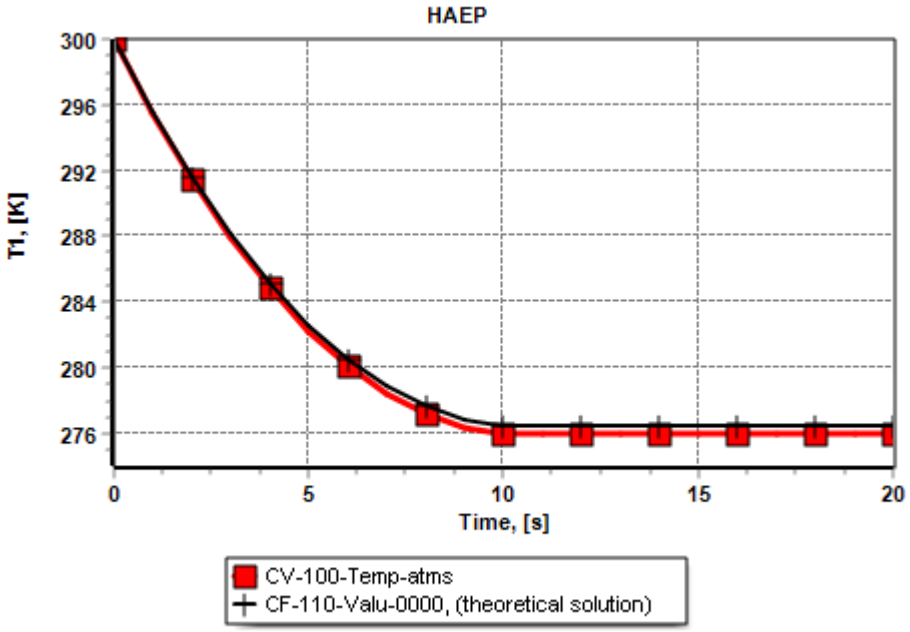

Figure 3-7 HAEP, Temperature in CV-100, built-in H_2 (real gas)

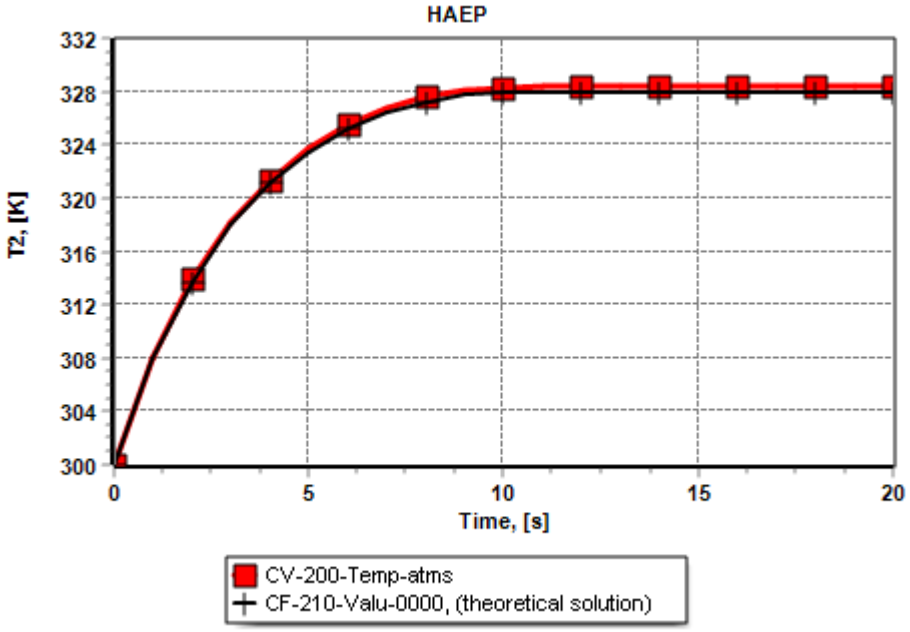

Figure 3-8 HAEP, Temperature in CV-200, built-in H_2 (real gas)

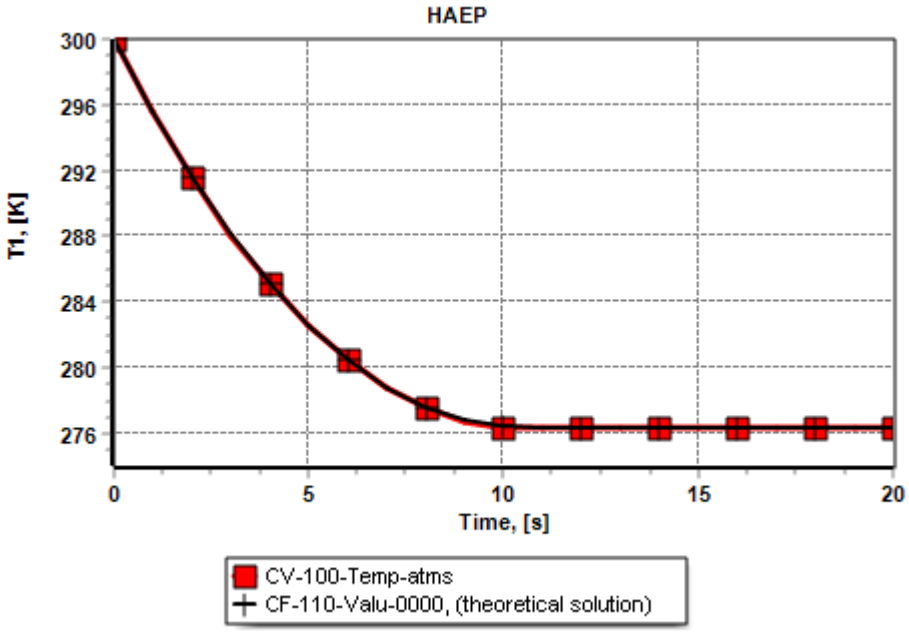

Figure 3-9 HAEP, Temperature in CV-100, user-defined H_2 (ideal gas)

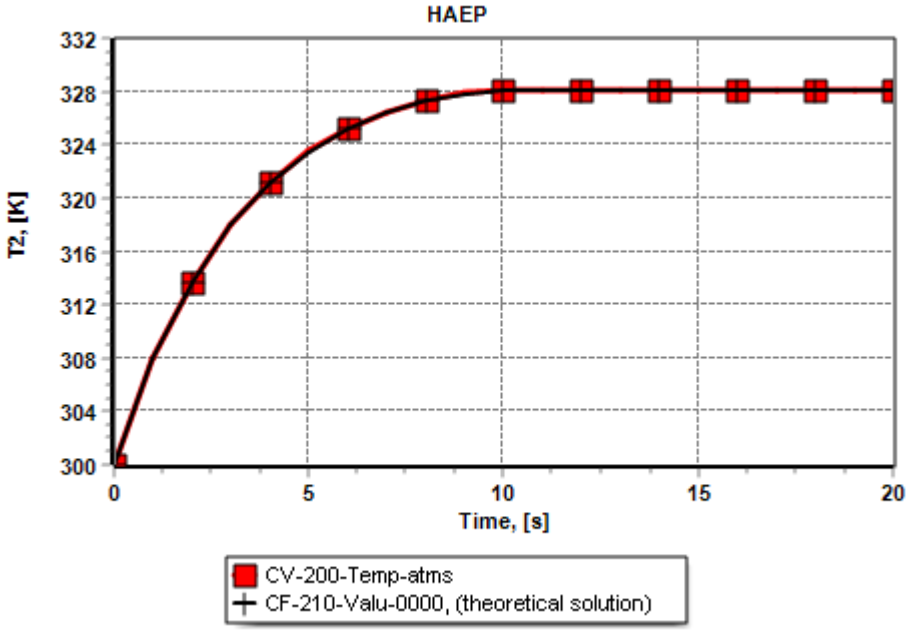

Figure 3-10 HAEP, Temperature in CV-200, user-defined H_2 (ideal gas)

3.1.3 Establishment of Flow

The Establishment of Flow Problem (EFP) is described in the MELCOR Assessment Manual [142]. The model consists of two control volumes and one flow path. One control volume represents a reservoir partly filled with liquid water, while the other control volume models the surrounding environment. Both volumes are specified to have constant parameters (time-independent), to prevent any undesired change of conditions. A junction, connecting the two volumes, represents the pipe in which the flow is being established. The problem is initialized with zero flow, but with an open flow area at $t = 0$ seconds. A total of twenty cases were considered, with dimensions and initial conditions as specified in Table 3-4. The minimum velocity for critical flow calculations (VMCFJN) was set to a large value (1000.0 m/s), to avoid choking in the calculation. The asymptotic flow velocity, v_∞, established in the pipe is given by [142]:

$$v_\infty = \sqrt{\frac{2gDH}{fL}} = \sqrt{\frac{2gH}{f(L/D)}}$$

L pipe length, (m)
f pipe friction factor, (-),
g gravity constant, (m/s^2)
H head of liquid in the reservoir, (m)

SPECTRA model was created using arbitrary data for volumes and junction, keeping the correct water height in each case. The nodalization can be seen in Figure 3-11. The theoretical asymptotic velocity was defined in the input using Control Functions. Five cases were analyzed, with different method of calculating friction factors (see section 2.3.2 and Volume 1):

- Non-uniform roughness - Colebrook-White formula in the turblent flow regime
- Uniform roughness - Nikuradse formula in the turblent flow regime
- Simplified method - Blasius formula in the turblent flow regime
- Non-iterative approximation of Colebrook-White - Beluco-Camano
- Non-iterative approximation of Colebrook-White - Churchill

The SPECTRA input files are located in: **`\Z-INPUTS\JN\EFP.`** For comparison, a model for MELCOR 1.8.6 was generated using the automated export option (IEXPSL=2). The MELCOR input files are located in: **`\Z-INPUTS\JN\EFP\MELCOR\`**

Table 3-5 presents the asymptotic flows calculated by SPECTRA and MELCOR 1.8.6. Table also shows the theoretical solution. The theoretical solution, as well as the results of MELCOR 2.1 are copied from [142]. The values are valid for the friction factor, *f*, obtained from the Colebrook-White formula, which is the formula used in MELCOR [107]. It is concluded that:

- The Colebrook-White formula provides the best agreement with the MELCOR values.
- The Beluco-Camano formula gives better approximation of Colebrook-White than the Churchill formula.

Figure 3-11 and Figure 3-12 show the end results obtained for the Case A.

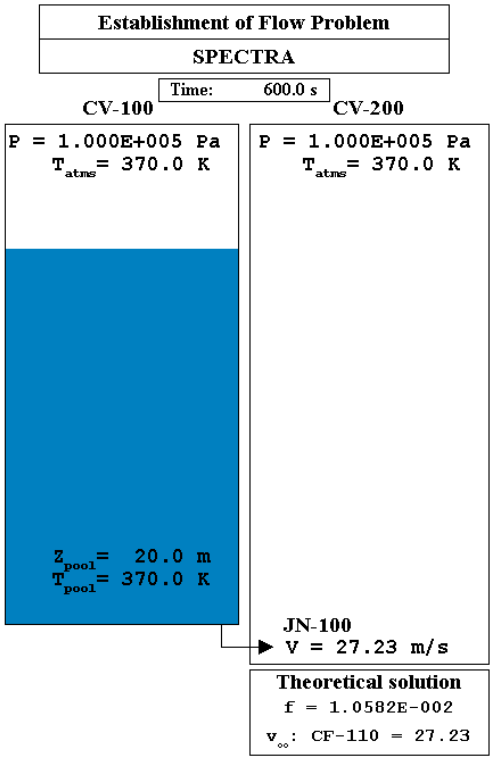

Figure 3-11 EFP, end-state, Case A, SPECTRA

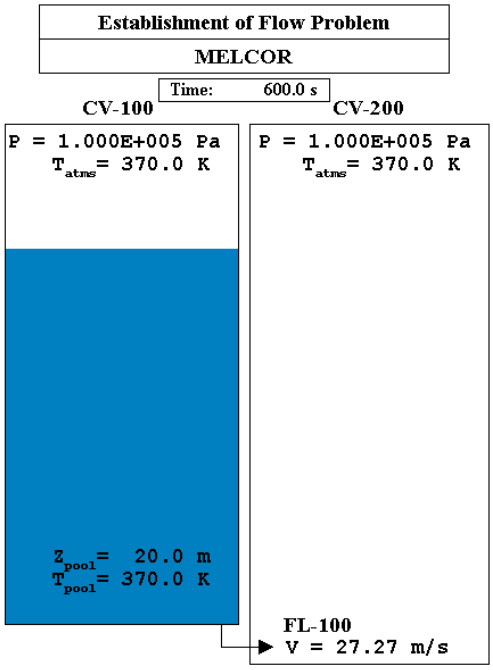

Figure 3-12 EFP, end -state, Case A, MELCOR

Table 3-4 Specifications for Flow Establishment Analyses [142]

Case	T [K]	Head [m]	Rough. [m]	D [m]	L [m]
A	370	20	5.0E-05	1.0	50
B	370	100	1.0E-06	2.0	10
C	300	5	1.0E-03	0.1	5000
D	300	1000	3.0E-02	2.0	50
E	300	5	1.0E-06	0.2	5000
F	300	5	1.0E-06	0.2	3000
G	300	5	1.0E-06	0.2	1000
H	300	5	1.0E-06	0.2	100
I	300	5	1.0E-06	0.2	10
J	300	5	1.0E-06	0.2	2.5
K(*)	300	20	5.0E-05	1.0	5000
L	300	20	5.0E-05	0.2	5000
M	300	5	5.0E-05	1.0	50
N	300	5	5.0E-05	1.0	5000
O	300	5	5.0E-05	0.6	50
P	300	5	5.0E-05	0.4	50
Q	300	500	1.0E-04	0.01	10
R	300	100	1.0E-04	0.01	10
S	300	20	1.0E-04	0.01	10
T	300	5	1.0E-04	0.01	10

(*) Table 2.8 in MELCOR Assessment Problems gives 5.0E-4 m for K through P
This is a mistake, the results in Table 2.9 are for 5.0E-5 m

Table 3-5 Asymptotic Velocities for Flow Establishment

		MELCOR		SPECTRA				
Case	Theory (*)	2.1 (*)	1.8.6	Colebrook	Nikuradse	Blasius	Beluco	Churchill
A	27.23	27.27	27.27	27.23	27.29	27.28	27.21	27.27
B	269.8	269.9	269.9	269.9	277.5	272.1	268.9	271.7
C	0.221	0.222	0.222	0.221	0.242	0.228	0.221	0.225
D	134.0	134.1	134.1	134.0	134.1	134.0	134.0	134.0
E	0.471	0.469	0.469	0.471	0.472	0.476	0.472	0.543
F	0.625	0.623	0.623	0.626	0.627	0.637	0.627	0.720
G	1.149	1.146	1.146	1.151	1.153	1.194	1.150	1.316
H	4.063	4.057	4.057	4.067	4.088	4.449	4.057	4.583
I	14.12	14.11	14.11	14.13	14.33	16.44	14.07	15.50
J	29.59	29.60	29.60	29.61	30.34	32.89	29.47	31.79
K	2.618	2.614	2.614	2.619	2.813	2.728	2.617	2.697
L	0.955	0.951	0.951	0.956	1.019	1.045	0.958	1.011
M	13.51	13.57	13.57	13.51	13.94	13.64	13.50	13.61
N	1.271	1.273	1.272	1.271	1.348	1.346	1.271	1.334
O	9.954	9.996	9.996	9.957	10.385	10.086	9.948	10.052
P	7.793	7.824	7.824	7.796	7.796	7.796	7.796	7.796
Q	16.02	16.02	16.02	16.02	16.09	16.09	16.02	16.06
R	7.127	7.124	7.124	7.127	7.241	7.195	7.126	7.164
S	3.152	3.151	3.151	3.152	3.367	3.218	3.153	3.187
T	1.547	1.550	1.550	1.547	1.735	1.609	1.548	1.579

(*) Copied from MELCOR Assessment Problems, SAND2015-6693 R, August 2015

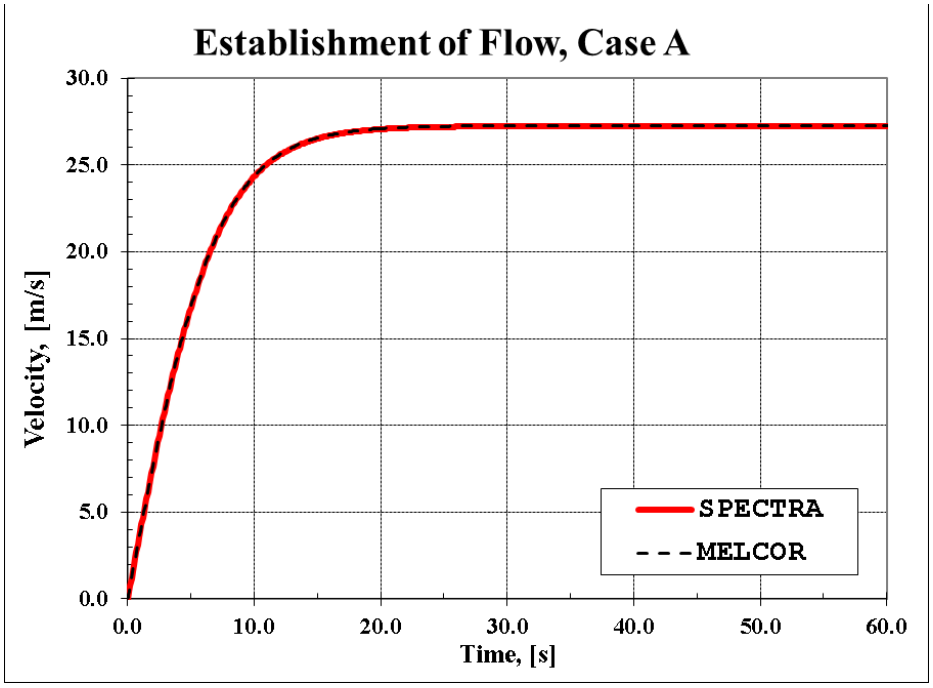

Figure 3-13 EFP, velocity in JN-100, Case A

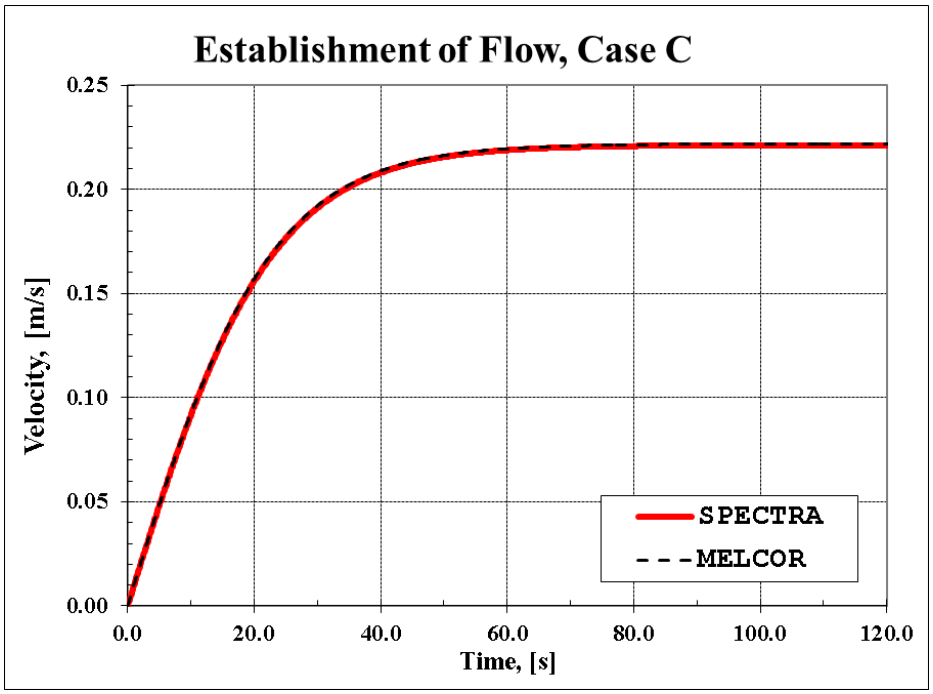

Figure 3-14 EFP, velocity in JN-100, Case C

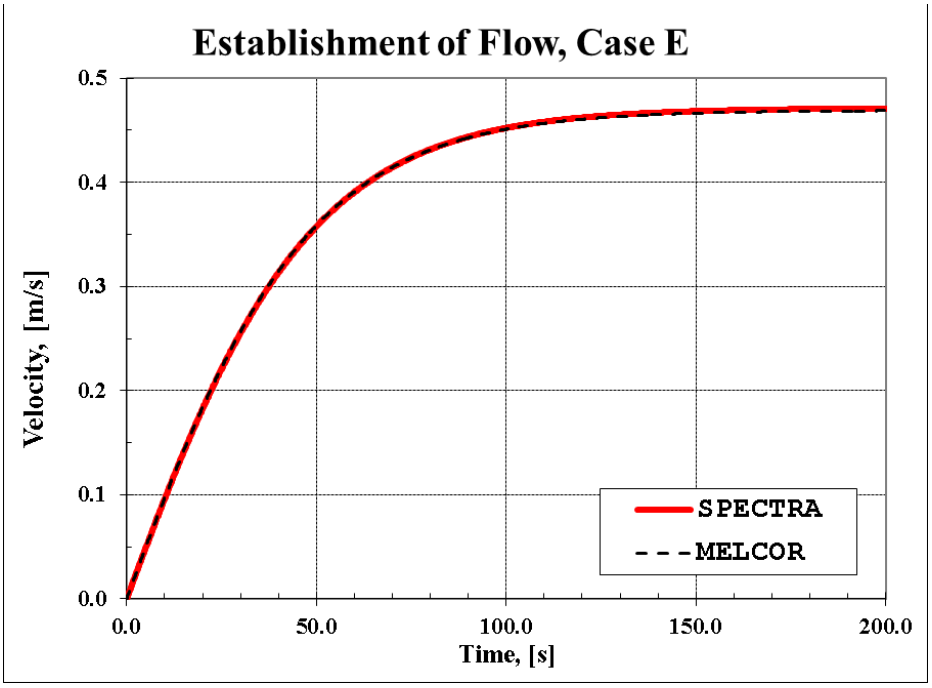

Figure 3-15 EFP, velocity in JN-100, Case E

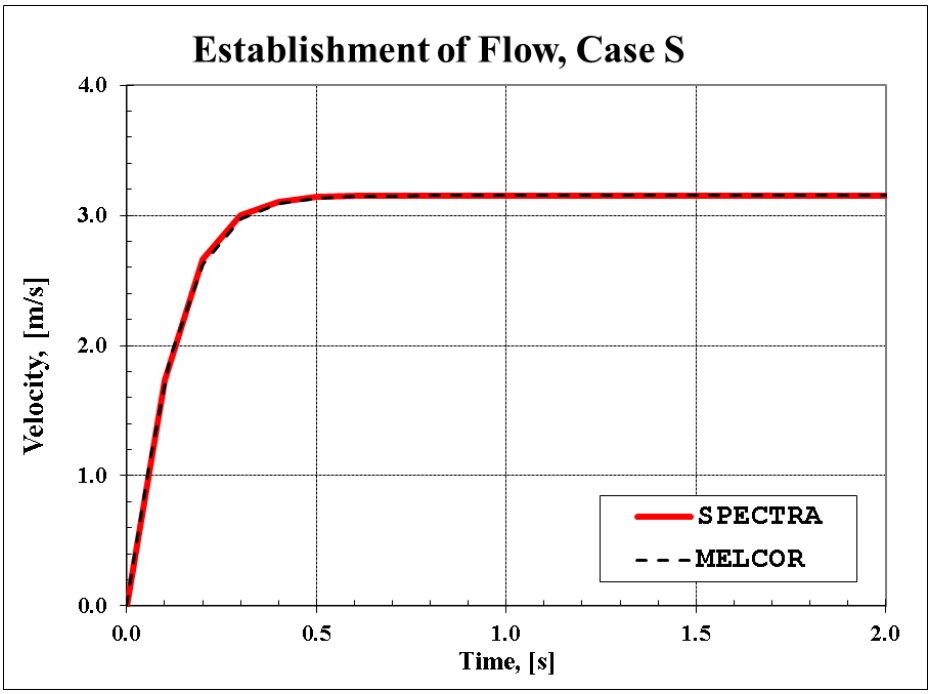

Figure 3-16 EFP, velocity in JN-100, Case S

Figure 3-13 through Figure 3-16 show the comparison of the time-dependent velocity predicted by SPECTRA to those obtained from MELCOR for four of the cases: A, C, E, and S (the same as presented in [142]). Each case shows a very good agreement between the codes. Agreement of MELCOR with theoretical solution has been demonstrated in [142].

All the calculations presented above were performed using time step of 0.01 s. In Figure 3-17, the dependence of the solution on time step is shown for Case S. This calculation shows that when the time step is on the order of the relaxation time, the error is small. Even when the time step is large, the asymptotic velocity is well calculated. The same results are obtained for time-independent Control Volumes (ITYPCV=1) and normal CVs with large volume (VOLTCV=1000.0 m^3).

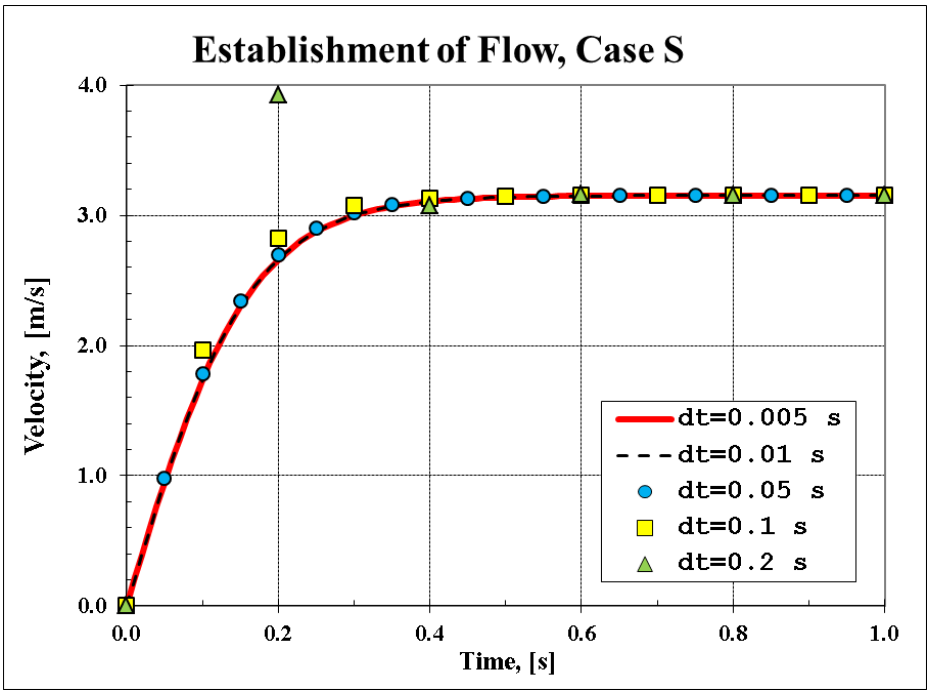

Figure 3-17 EFP, time step sensitivity, Case S

3.1.4 Tests of Pipes with Different Inclinations

This test illustrates the use of the Control Volume flow area input parameters, AHORCV and AVERCV. The geometry considered is a pipe with different inclinations. The pipe geometry is:

- Diameter, $D = 0.1$ m
- Flow area, $A = \pi D^2 / 4 = 0.0078$ m^2
- Length, $L = 1.0$ m

A constant flow of 0.089 kg/s of air at room temperature and pressure ($T = 300$ K, $p = 1.0\times10^5$ Pa) is pushed through the pipe. Three cases are considered:

- Horizontal pipe
- Vertical pipe
- 45-degree inclined pipe. For this case two methods are used:
    - Vertical junctions (the flow through the connecting junctions is treated as vertical)
    - Horizontal junctions

In each case the junction flow area is set to the true flow area of the pipe, i.e. 0.0078 m^2. The volume of CV is equal to $V = L\ \pi D^2 / 4 = 0.0078$ m^3, and is of course the same in all cases. The Control Volume height and the flow areas are different for each case.

- Horizontal pipe:
  Height of CV (HSEGCV): $H = D = 0.1$ m
  Horizontal cross section (AHORCV): $A_h = V / H = V / D = 0.078$ m^2
  Vertical cross section (AVERCV): $A_v = \pi D^2 / 4 = 0.0078$ m^2

- Vertical pipe:
  Height of CV (HSEGCV): $H = L = 1.0$ m
  Horizontal cross section (AHORCV): $A_h = \pi D^2 / 4 = 0.0078$ m^2
  Vertical cross section (AVERCV): $A_v = V / D = 0.078$ m^2 (rough est.: $D{\cdot}H = 0.1$ m^2)

- Inclined pipe (α = angle between the pipe axis and a horizontal plane):
  Height of CV (HSEGCV): $H = L\ \sin(\alpha{=}45^\circ) = 0.707$ m
  Horizontal cross section (AHORCV): $A_h = \pi D^2 / 4 / \sin(\alpha{=}45^\circ) = 0.011$ m^2 ($= V / H$)
  Vertical cross section (AVERCV): $A_v = \pi D^2 / 4 / \cos(\alpha{=}45^\circ) = 0.011$ m^2

The input file is located in: `Z-INPUTS\CV\PIPE\PIPE-Ver-1.SPE`. The results are shown in Figure 3-18. The figure shows the Junction velocities, the Control Volume horizontal and vertical velocities, calculated by SPECTRA, as well as the Control Volume total velocity, equal to:

$$v_{CV} = \sqrt{v_{hor}^2 + v_{ver}^2}$$

A short discussion of the presented results is shown below.

- For the horizontal CV the horizontal velocity is the same as the junction velocity, v = 9.89 m/s. The vertical velocity is zero.
- For the vertical CV the vertical velocity is the same as the junction velocity, v = 9.89 m/s. The horizontal velocity is zero. (*Note: the flow is upwards, therefore the vertical velocity sign is negative. For the atmosphere and the droplet flow within a CV a positive velocity is downwards, which is needed for the drift flux model calculating the droplet velocity. Similarly for the pool and the bubble flow within a CV a positive velocity is upwards, which is needed for the drift flux model calculating the bubble velocity.*)
- For the inclined pipes the total velocity is 7.01 m/s for both the case with the vertical and the horizontal junctions. The CV velocity should be of course the same as for horizontal or vertical pipes, therefore it is concluded that with the present definition of the CV flow area for horizontal and vertical flow the resulting CV velocity is incorrect.

The obtained results are summarized below.

- Horizontal pipe: v_{CV} = 9.81 m/s = v_{JN}
- Vertical pipe: v_{CV} = 9.81 m/s = v_{JN}
- Inclined pipe: v_{CV} = 7.01 m/s ≈ v_{JN} sin(45°) - incorrect.

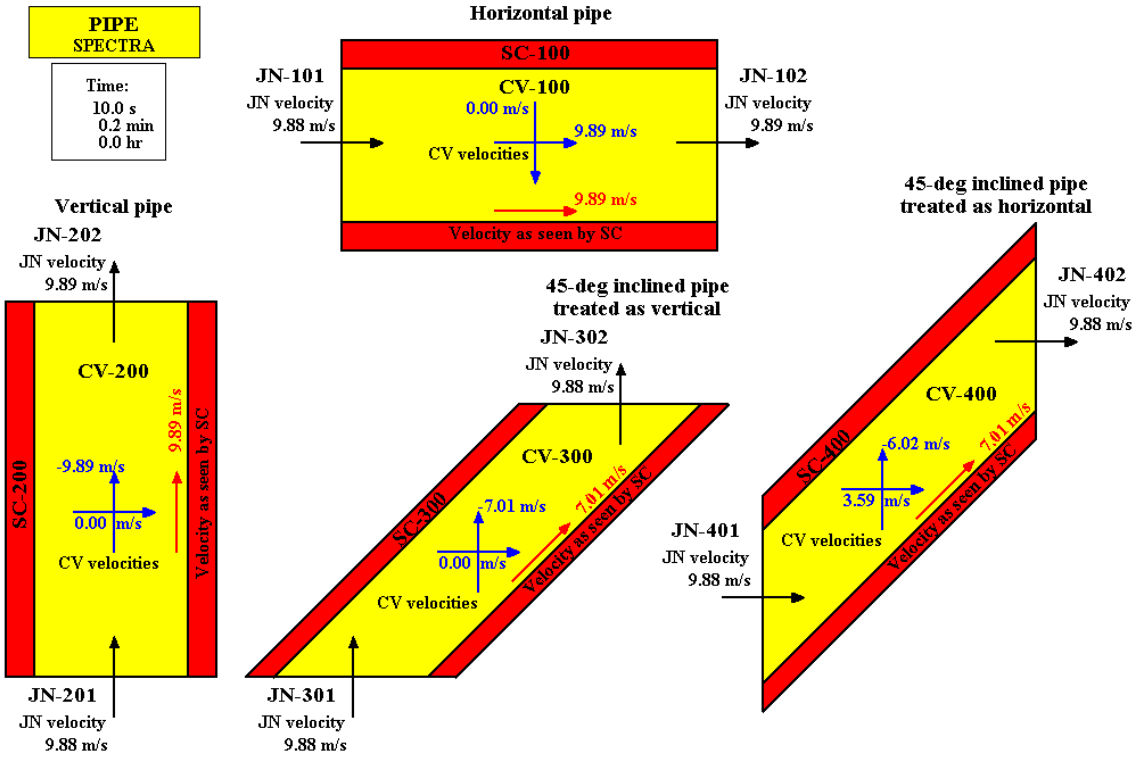

Figure 3-18 Pipes with different inclination - Version 1

In the second run the CV flow areas were in each case set to the pipe flow area of $A = \pi D^2 / 4 = 0.0078$ m^2. The input file is located in: `Z-INPUTS\CV\PIPE\PIPE-Ver-1.SPE`. The results are shown in Figure 3-19. In this case the CV velocity is always correctly calculated as 9.89 m/s. The results obtained for both Version 1 and Version 2 are summarized in the Table 3-6.

The results presented above lead to the conclusion that for the 1-D flow within a pipe the **CV flow areas for both horizontal and vertical flow should be entered as the same and equal to the flow area in the main flow direction**. This recommendation is contradictory to the recommendation made in the earlier SPECTRA versions, when the user was encouraged to enter the true flow area for horizontal and vertical direction. The previous recommendation leads to too low gas velocities in inclined pipes, which is affecting the heat transfer in such pipes. The new recommendation is clearly stated in the Volume 2. Furthermore, the current code version gives a warning message if AHORCV is not equal to AVERCV.

Table 3-6 Summary of the results

Flow direction	Version 1, "old" input			Version 2, "new" input		
	CV flow area		Velocity, v_{CV} , m/s	CV flow area		Velocity, v_{CV} , m/s
	Horizontal	Vertical		Horizontal	Vertical	
Horizontal	$\frac{1}{4}\pi D^2$	V / H	9.89	$\frac{1}{4}\pi D^2$	$\frac{1}{4}\pi D^2$	9.89
Vertical	V / H	$\frac{1}{4}\pi D^2$	9.89	$\frac{1}{4}\pi D^2$	$\frac{1}{4}\pi D^2$	9.89
Inclined	$\frac{1}{4}\pi D^2/\sin(\alpha)$	$\frac{1}{4}\pi D^2/\cos(\alpha)$	7.01	$\frac{1}{4}\pi D^2$	$\frac{1}{4}\pi D^2$	9.89

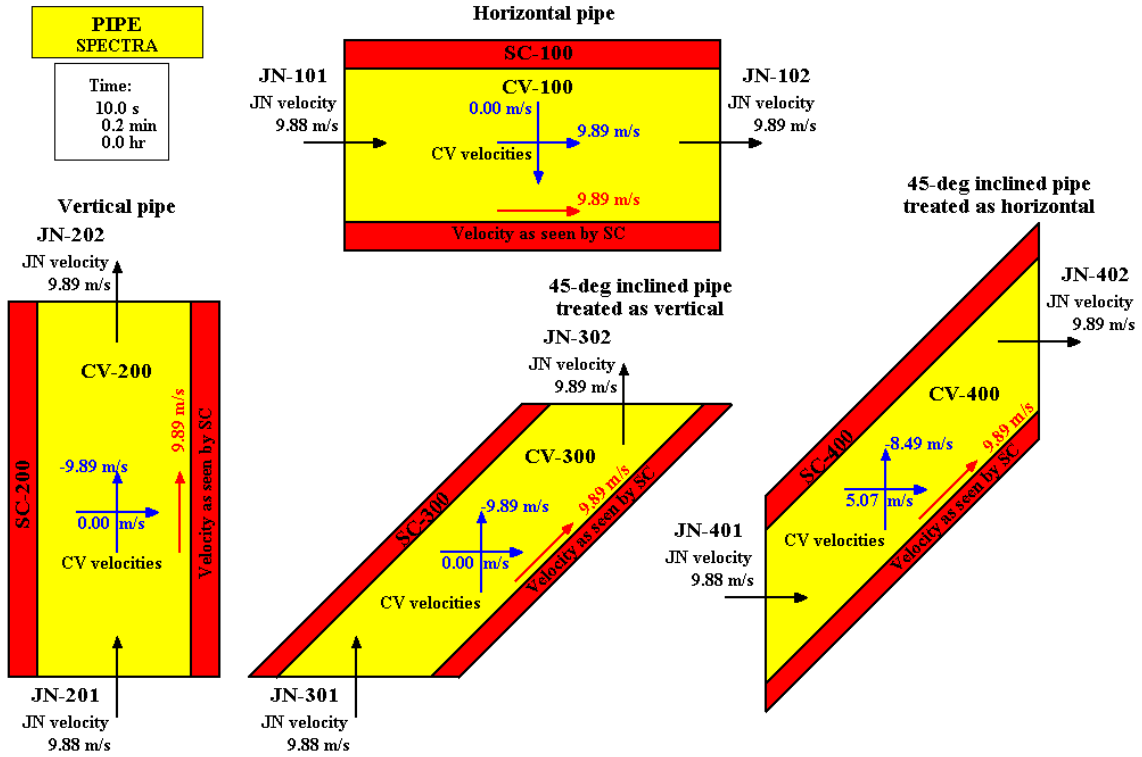

Figure 3-19 Pipes with different inclination - Version 2

3.1.5 Discharge Test

A simple model is set up to test a discharge of water from a water storage tank through an opening (a hole in the tank wall) and a short pipe. Here the word "short" means that the friction loss in the pipe is small compared to the local pressure losses at the pipe entrance and exit. The purpose of the present test is three-fold:

- Firstly, to compare the discharge rate through a sharp-edged opening in the vessel and through a short pipe of the same cross section area.
- Secondly, to verify if the results obtained using a "normal" junction and a valve junction are identical.
- Finally, to verify the results by performing code-to-code comparison. Results obtained by SPECTRA and RELAP5 are compared.

3.1.5.1 Assumptions

The following assumptions are made:

- The tank pressure is 1.0×10^5 Pa. The water level is 10 m. The water temperature is 300 K. The opening is on the tank side wall at the bottom of the tank. With these conditions the pressure at the elevation of the opening is 1.97×10^5 Pa. The conditions in the tank are constant.
- The environment pressure is constant and equal to 1.0×10^5 Pa.
- The flow area of the opening is 0.01 m^2.
- The flow area of the discharge pipe is 0.01 m^2.
- Only the local resistance factors due to the area change are used. The friction resistance is neglected.

3.1.5.2 Model

The following resistance factors are used:

- The resistance factor for the opening is defined using the value appropriate for a sharp-edged orifice (Idelchik [40], Equation 4-4 on page 151 or Diagram 4-11 on page 168):

$$K = \left(1 + 0.707 \cdot \sqrt{1 - \frac{A_0}{A_1}} - \frac{A_0}{A_2}\right)^2$$

Here A_0 is the flow area of the opening, A_1 is the flow area of the tank, and A_2 is the flow area outside the tank. For the case when $A_0 \ll A_1$, $A_0 \ll A_2$ the formula reduces to:

$$K = (1 + 0.707)^2 = 2.9$$

This value is in good agreement with experimental data, which gives K equal to 2.7 ÷ 2.8 ([40], page 154).

- The resistance factors for the discharge pipe are defined using the values for a sudden contraction and sudden expansion. These are:

  - Contraction ([40], Diagram 4-9):

$$K = 0.5 \cdot \left(1 - \frac{A_0}{A_1}\right)^n$$

    Here A_0 is the flow area of the pipe, A_1 is the flow area of the tank, and n is an exponent, equal to 1 ([40], page 149) or 3/4 ([40], page 151 and page 167, Diagram 4-9). For the case when $A_0 \ll A_1$ the formula reduces to:

$$K = 0.5$$

    independently of the exponent n. Note that the same value is obtained from the formula for an orifice by substituting $A_0 / A_1 = 0$ and $A_0 / A_2 = 1$. This leads to the K-factor of: $K = (1.0 + 0.707 - 1.0)^2 = 0.5$.

  - Expansion ([40], equation 4-1, page 145):

$$K = \left(1 - \frac{A_0}{A_2}\right)^2$$

    Here A_0 is the flow area of the pipe while A_2 is the flow area downstream the pipe. For the case when $A_0 \ll A_2$ the formula reduces to:

$$K = 1.0$$

    Note that the same value is obtained from the formula for an orifice by substituting $A_0 / A_1 = 1$ and $A_0 / A_2 = 0$: $K = (1.0 + 0.707 \times 0.0 - 0.0)^2 = 1.0$.

3.1.5.3 Analyzed Cases - SPECTRA

Two sets of calculations are performed with SPECTRA:

- In the first set the "normal" (always open) junctions are used to represent all flow paths.

- In the second set valve junctions are used to represent all flow paths. The valves are closed for the first 10 seconds of calculations and then open for the remaining time. The total calculation time is 100 s.

Within each set two cases are considered:

- A sharp edged opening is represented by JN-110 (see Figure 3-20, top), with a local loss factor of 2.9. In order to minimize the friction resistance the friction length is set to a small value (0.01 m).

- A short pipe is represented by JN-210, JN-220 and CV-220 (see Figure 3-20, bottom). The local loss factors of 0.5 and 1.0 are used at the entrance and exit respectively, to represent a sudden contraction and the sudden expansion. In order to minimize the friction resistance the friction length is set to a small value (0.01 m).

Input decks for these calculations are located in:

- `Z-INPUTS\JN\DISCH\SPECTRA\DISCH.SPE` normal junctions
- `Z-INPUTS\JN\DISCH\SPECTRA\DISCH-V.SPE` Valve junctions

3.1.5.4 SPECTRA Results

SPECTRA results are presented in Figure 3-20 (flow paths represented by "normal" junctions) and Figure 3-21 (flow paths represented by valves). The resulting mass flows are:

- Sharp-edged opening: W = 82 kg/s
- Short pipe: W = 113 kg/s

The following remarks can be made:

- The flow rate through a sharp edged opening is smaller than the flow rate through the pipe. This is a consequence of the larger resistance factor of the opening.

- The results obtained using "normal" junctions and fully open valves are the same.

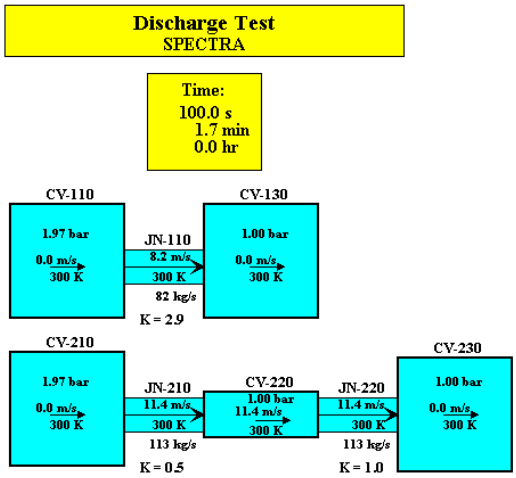

Figure 3-20 Discharge test, SPECTRA, "normal" junctions

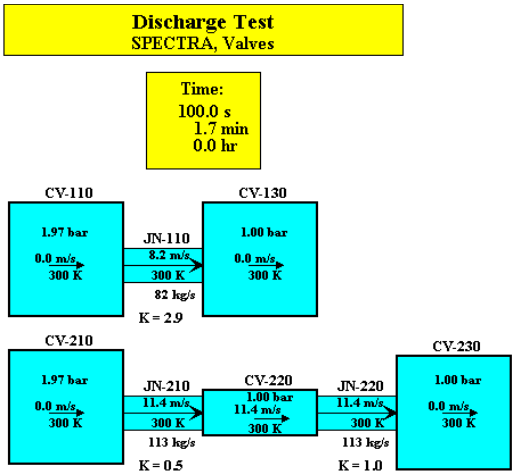

Figure 3-21 Discharge test, SPECTRA, valve junctions

3.1.5.5 Analyzed Cases - RELAP

Three sets of calculations are performed with RELAP:

- In the first set the "normal" (always open) junctions with user-defined loss factors are used to represent all flow paths.

- In the second set the "normal" (always open) junctions with the loss factors calculated by the code using the abrupt area change model are used. One has to keep in mind that when the abrupt area change model is activated, the user-defined loss factors must be set to zero. Otherwise the local resistance will be double counted, as the code adds the user-defined *K*-factors to the ones obtained from the abrupt area change model - see RELAP User's Guide [55]

- In the third set valve junctions are used to represent all flow paths. The valves are closed for the first 10 seconds of calculations and then open for the remaining time. The total calculation time is 100 s. With the valve junctions the abrupt area change must be used. Therefore results of this set are compared to the results of the second set.

Within each set two cases are considered:

- A sharp-edged opening is represented by JN-110 (see Figure 3-22, top), with a local loss factor of 2.9 applied in the first set. In the next two sets the loss factors are of course calculated by the code. In order to minimize the friction resistance the friction length is set to a small value (0.01 m).

- A short pipe is represented by JN-210, JN-220 and CV-220 (see Figure 3-22, bottom). The local loss factors applied for the first set are 0.5 and 1.0 at the entrance and exit respectively, to represent a sudden contraction and the sudden expansion. In order to minimize the friction resistance the friction length is set to a small value (0.01 m).

Input decks for these calculations are located in:

- `Z-INPUTS\JN\DISCH\RELAP\DISCH.SPE` User-defined *K*-factors
- `Z-INPUTS\JN\DISCH\RELAP\DISCH-1.SPE` Code-calculated *K*-factors
- `Z-INPUTS\JN\DISCH\RELAP\DISCH-V.SPE` Valve junctions

3.1.5.6 RELAP5 Results

RELAP5 results are presented in Figure 3-22, Figure 3-23, and Figure 3-24. The user-defined loss factors applied for the calculations and the code-calculated loss factors, taken from the RELAP output, are summarized in Table 3-7. It is seen that the RELAP calculated values are in agreement with the theoretical values, although they are slightly smaller in cases of the sharp edged opening and the contraction. The resulting mass flows are shown in Table 3-8.

The following remarks can be made:

- The flow rate through a sharp edged opening is smaller than the flow rate through the pipe. This is a consequence of the larger resistance factor of the opening.

- The results obtained using "normal" junctions with the code-calculated resistance factors and fully open valves are identical. Note that when the valves are applied the user must select the option with the resistance factors are calculated by the code.

Table 3-7 Loss factors - theoretical and calculated by RELAP5

Case	Loss factors	
	Ref. [40]	RELAP5
Sharp-edged opening	2-7 ÷ 2.9	2.60
Contraction	0.5	0.39
Expansion	1.0	1.00

Table 3-8 Mass flow rates calculated by RELAP5

Case	Discharge flow (kg/s)	
	User-defined loss factors	Abrupt area change model
Sharp-edged opening	82	86
Short pipe	113	118

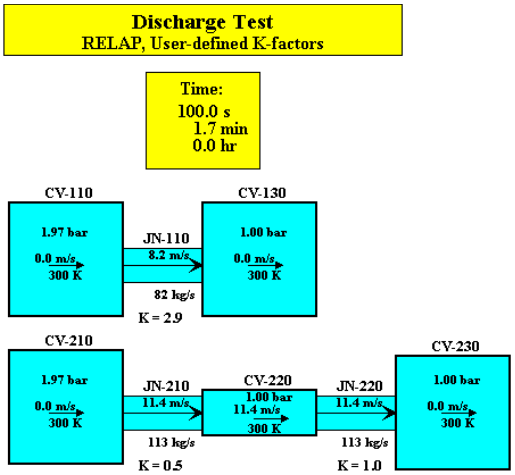

Figure 3-22 Discharge test, RELAP5, “normal” junctions with user-defined loss factors

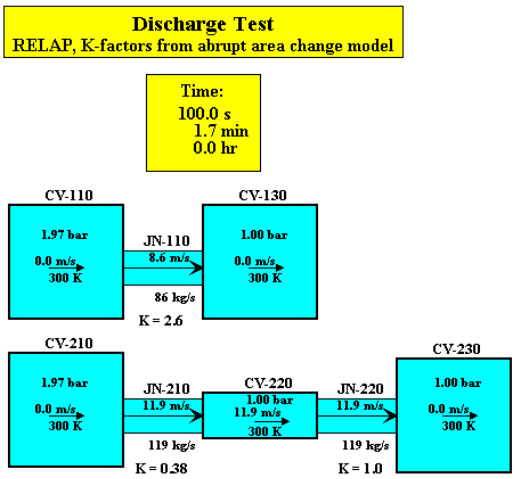

Figure 3-23 Discharge test, RELAP5, “normal” junctions with abrupt area change model

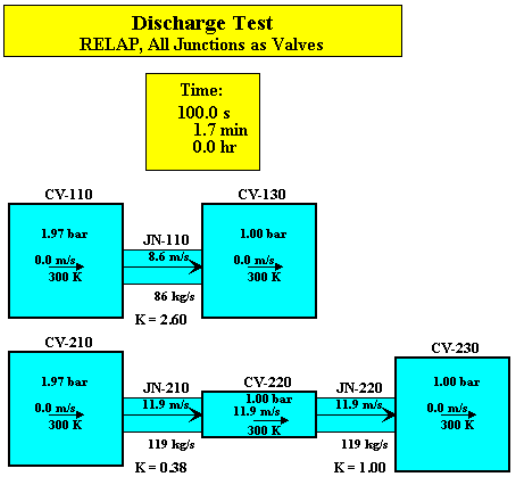

Figure 3-24 Discharge test, RELAP5, valve junctions with abrupt area change model

3.1.5.7 Summary and Conclusions

The results are summarized in Table 3-9. Results of the present test lead to the following conclusions:

- The discharge rate through a sharp-edged opening (hole) is slower than through a short (frictionless) pipe of the same cross section area. This is a consequence of larger resistance of the sharp edged opening ($K \approx 2.6 \div 2.9$) compared to the overall resistance of the pipe (contraction + expansion, $K \approx 1.4 \div 1.5$).

- The results obtained using "normal" junctions and valve junctions are the same when the same loss factors are used. This is true for both SPECTRA and RELAP5.

Table 3-9 Summary of the calculated results

Case	Discharge flow, (kg/s)		
	SPECTRA *K*: user-defined	RELAP5 *K*: user-defined	RELAP5 *K*: abrupt area ch.
Sharp-edged opening	82	82	83
Short pipe	113	113	118

3.1.6 Bubble Velocity Test

Velocity of gas bubbles injected into water and liquid lead (alternative fluid) is studied in this test. The code results are compared to the measured data presented in [170] showing data for liquid lead, copper and tin, as well as water following Uno and Kintner. The data for lead, copper and tin are quite similar, therefore only liquid lead is modeled here. The input files are located in:
\Z-INPUTS\CV\V-vs-D

The input model consists of 10 identical Control Volumes. Each CV contains fluid at prescribed conditions:

- water at: $T = 293$ K, $p = 1.0$ bar,
- liquid Lead at: $T = 630$ K, $p = 1.0$ bar.

Gas bubbles are created by tabular mass source at the bottom of each CV. The mass sources are as follows.

- Air is injected into water.
- Argon is injected into liquid Lead.

In order to study the bubble velocity for different bubble sizes, the bubble diameter was defined by the user (DBWFCV record 158XXX) rather than left to be calculated by the code.

3.1.6.1 Default Correlation Set

Results obtained with the default set of correlations for the bubble terminal velocity are shown in Figure 3-25 for the wide range of Reynolds numbers. In Figure 3-27 the calculated results are superimposed on the graph from [170], showing measured data for liquid Tin (Sn), Lead (Pb), and Copper (Cu), as well as correlation of Uno and Kinter for H_2O. In case of Argon - Lead bubbles, the data from [170] show clearly higher velocities than those calculated by the default model.

3.1.6.2 Alternative Correlation, Input C_D(Re→∞)

In the earlier versions of SPECTRA (June 2018 and earlier) only one set of correlations was available to calculate bubble velocity. At the same time no model was available for vertical velocity of particles in liquids. In the new code version there is an alternative correlation that may be applied for bubbles, droplets and particles suspended in the pool. The model is based on drag coefficient. The set of correlations for the drag coefficient was extended from three to five correlations. The value of drag coefficient for Re→∞, $C_{D,Re\to\infty}$, can be defined by the user in input. To add to the flexibility, the drag coefficient may also be tabulated by the user for the whole range of Reynolds numbers, $C_D = f$(Re) (this is discussed in the next section).

The alternative correlation was used with the following drag coefficients

- Air in H_2O: $C_{D,Re\to\infty} = 2.6$
- Ar in Pb: $C_{D,Re\to\infty} = 1.8$

The values of $C_{D,Re\to\infty}$ were assumed based on data in [170] - Figure 3-29. Results are shown in Figure 3-26. In Figure 3-28 the calculated results are superimposed on the graph from [170]. The agreement obtained for Ar-Lead bubbles is very good.

3.1.6.3 Alternative Correlation, Input $C_D = f$(Re)

Finally, the alternative correlation is used with the drag coefficient tabulated for the whole range of Reynolds numbers. The tabulated values were selected as:

- Re = 3,000 $C_D = 1.0$
- Re = 15,000 $C_D = 2.0$

These values were used to approximately math the data from [170] - Figure 3-29. The Ar-Lead data is marked by triangles. The tabulated data is shown as a red solid line, superimposed on the original graph from [170]. Note that SPECTRA keeps the end-point values beyond the tabulated range, which is shown in Figure 3-29.

In Figure 3-30 the calculated results are superimposed on the graph from [170]. The agreement obtained for Ar-Lead bubbles is very good.

The present calculations show that the model is very flexible. By applying appropriate data in input, the user can model accurately the bubble velocity, if sufficient data exist.

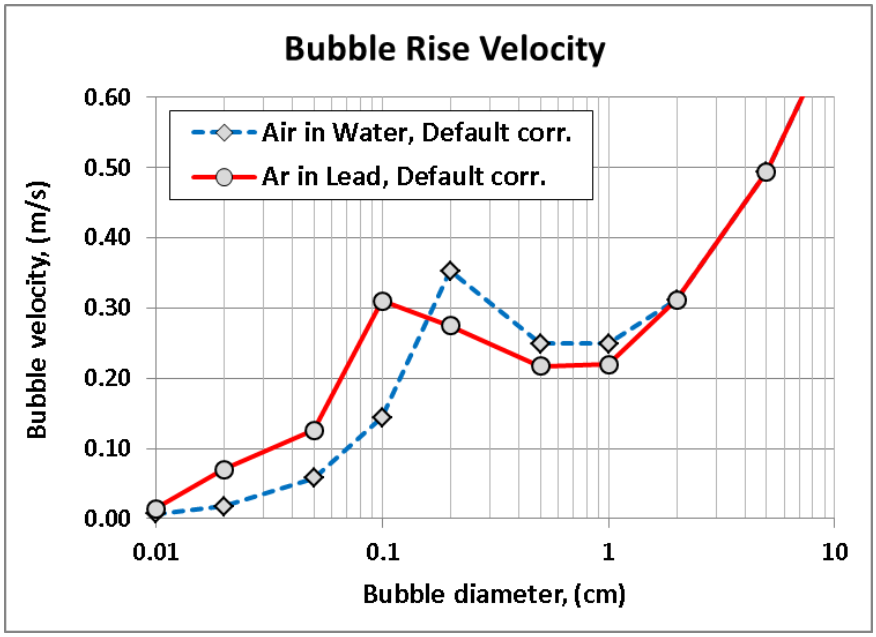

Figure 3-25 Bubble velocity, default correlation

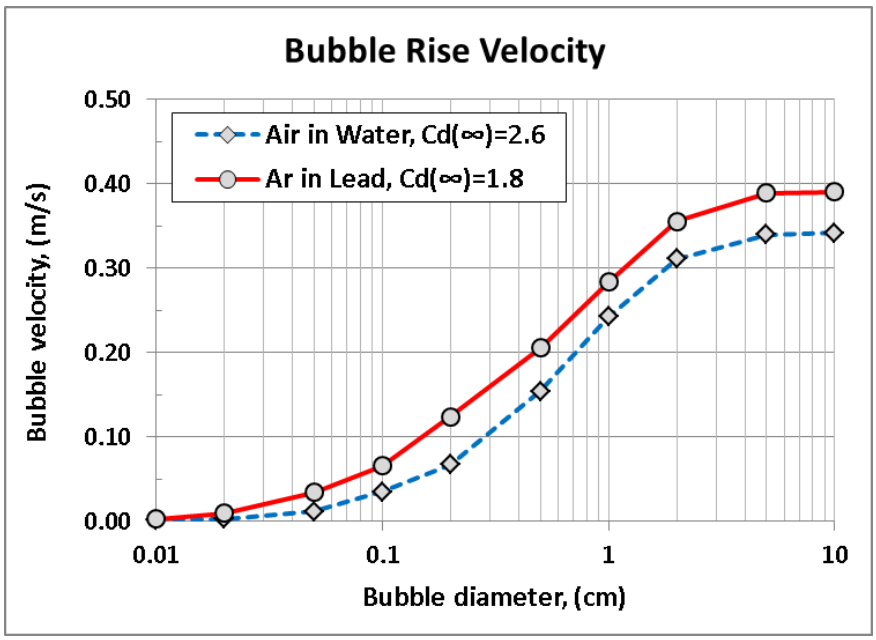

Figure 3-26 Bubble velocity, alternative correlation

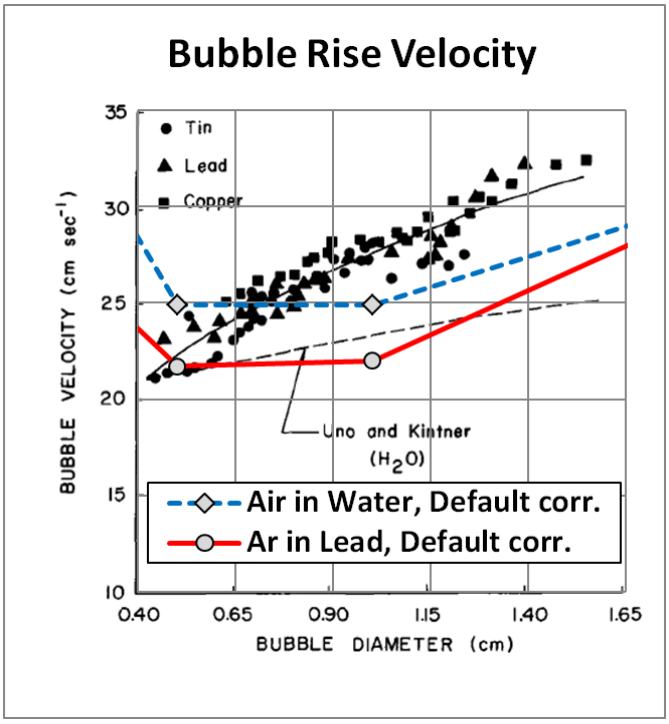

Figure 3-27 Bubble velocity, data [170] and default correlation

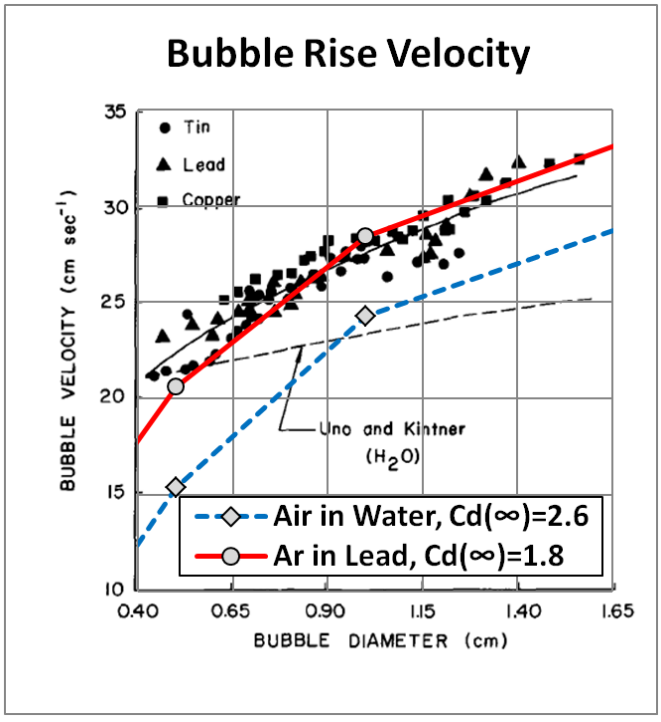

Figure 3-28 Bubble velocity, data [170] and alternative correlation, $C_D(\mathrm{Re}\rightarrow\infty)$ = const.

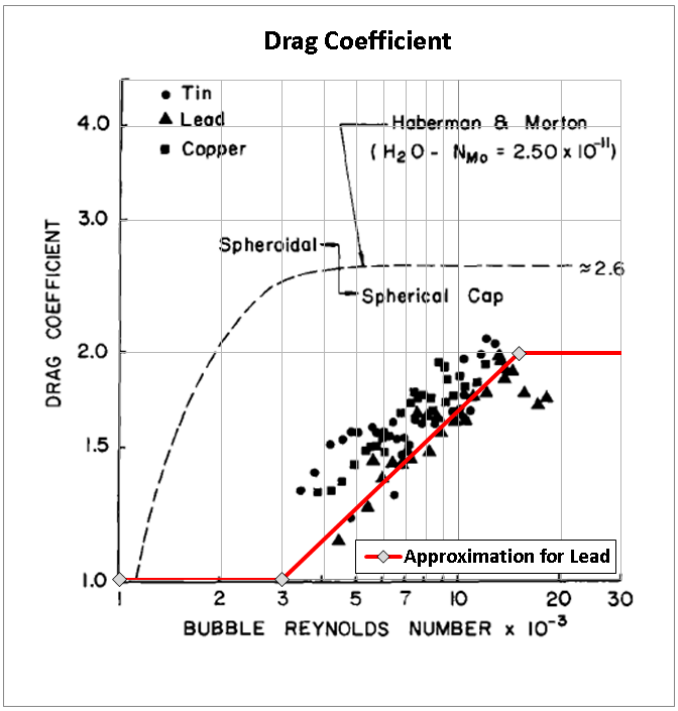

Figure 3-29 Drag coefficient, data [170] and tabular approximation, $C_D = f(\mathrm{Re})$

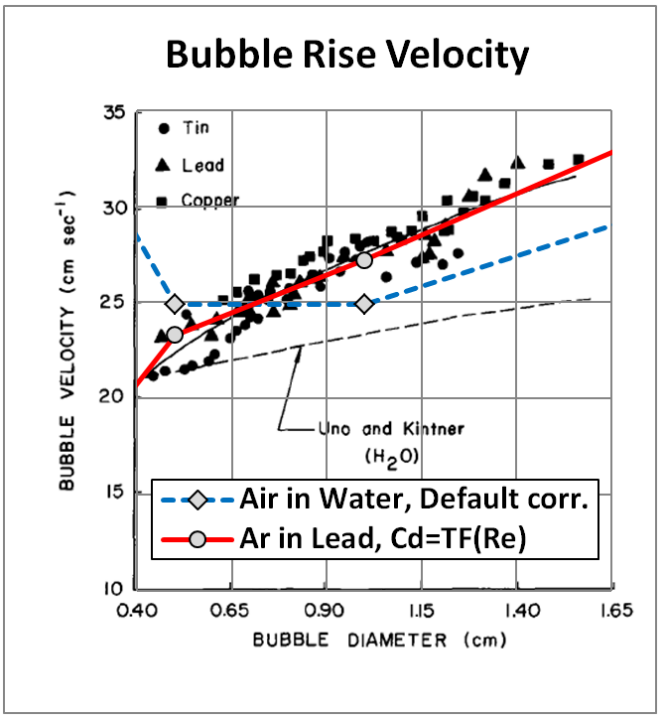

Figure 3-30 Bubble velocity, data [170] and alternative correlation, tabulated $C_D = f(\mathrm{Re})$

3.1.7 Diffusion Tests

This section discusses transport of gases from one Control Volume to another by diffusion. The model needs to be activated by the user (see Volume 2, IDIFJN). Transport is based on differences in gas concentrations in the neighboring Control Volumes. Transport by diffusion is important only if there is no flow or very small flow through a junction. If the diffusion model is turned on, the code calculates the transfer of gases through the connecting junction using the diffusion equation (see Volume 1):

$$J_i = \frac{\Delta C_i}{R_i}$$

$$R_i = \frac{L_{from}}{D_{i,from}} + \frac{L_{to}}{D_{i,to}}$$

J_i volumetric flux of gas *i*, (m/s)
D_i diffusion coefficient of gas *i* in the mixture of gases, (m^2/s)
C_i molar concentration of gas *i* in the mixture of gases, (-)
ΔC_i difference in concentration of gas *i* in the connected Control Volumes:
$\Delta C_i = C_i$('from-CV') – C_i('to-CV')
L_{from} diffusion lengths in the 'from-CV' (input parameter X1DFJN)
L_{to} diffusion lengths in the 'to-CV' (input parameter X2DFJN)

This section describes diffusion test cases and verification of results based on analytical solutions. A simple model is set up for diffusion verification. The model consists of two Control Volumes (1.0 m^3 each) connected by a single Junction (flow area of 1.0 m^2). The nodalization is shown in Figure 3-31.

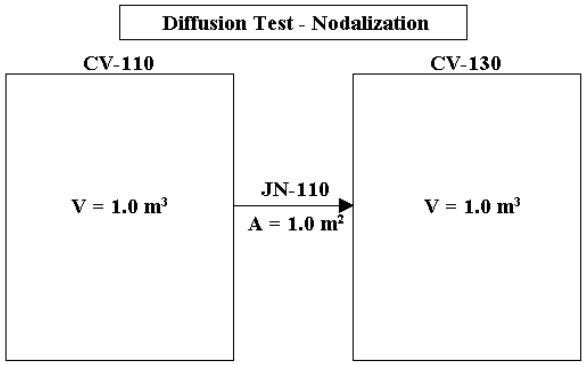

Figure 3-31 Nodalization applied for the diffusion tests

The same initial temperature (T=300 K) and pressure (p=1.0×10^5 Pa) are defined in both volumes. Two test cases are considered:

- ***Diffusion test 1***. CV-110: 100% He, CV-130: 100% O_2
- ***Diffusion test 2***. CV-110: 50% H_2, 50% He, CV-130: 50% N_2, 50% O_2

The input files are located in: \Z-INPUTS\JN\DIFF. The tests are discussed below.

- ***Diffusion test DIFF-1***

  The results obtained for this test are shown in Figure 3-32, Figure 3-33, Figure 3-34, and Figure 3-35.

  Figure 3-32 (a) shows the initial conditions. Since the pressures are the same, there will be no flow through JN-110 and in absence of diffusion, the conditions in both CVs will stay the same. This was checked in the run DIFF-1-0.SPE. A very small flow was observed for a very short time (caused by different densities) and the pressures stabilized quickly at values only slightly different than defined initially, namely CV-110: P = 9.99970371E+04 Pa, CV-130: P = 1.00002492E+05 Pa (file DIFF-1-0.ICF). With these values flow through JN-110 is zero all the time. This is important because one of the aspects that needs to be checked whether the diffusion process does not cause any undesired, phantom flows.

  Once perfectly stable initial conditions were defined, the test case with the diffusion model active (DIFF-1.SPE) was run. Calculations were performed until stable conditions were reached (t = 50,000 s ≈ 14 h). Time dependent graphs are shown in Figure 3-33, Figure 3-34, and Figure 3-35. The end-state of the system is shown in Figure 3-32 (b).

  Correctness of the end-state is clear, since the gas mixtures have identical compositions in both volumes. Correctness of the numerical scheme is seen in Figure 3-33, as there is no flow through JN-110 throughout the whole diffusion process. The velocities were practically zero throughout the test ($|v| < 10^{-9}$ m/s).

  As a last step of the verification the correctness of the time-dependent gas concentrations is checked against a theoretical solution. The change of volume of Helium in CV-110 is governed by:

$$\frac{dV_{He,CV-110}}{dt} = A_{JN-110} \cdot J_{He}$$

  or:

$$V_{CV-110} \frac{dC_{He,CV-110}}{dt} = D_{He-O2} \cdot \frac{C_{He,CV-130} - C_{He,CV-110}}{L_{JN}}$$

$V_{CV\text{-}110}$	volume of CV-110, (m^3)
$D_{He\text{-}O2}$	diffusion coefficient for mixture of He and O_2, (m^2/s)
$C_{He,CV\text{-}110}$	molar concentration of He in CV-110, (-)
$C_{He,CV\text{-}130}$	molar concentration of He in CV-130, (-)
L_{JN}	diffusion length (=friction length) of the junction JN-110, (m)

  A similar equation may be written for O_2. The following equations are obtained:

$$\frac{dC_{He,CV-110}}{dt} = \frac{A_{JN-110} \cdot D_{He-O2}}{V_{CV-110} \cdot L_{JN}} \cdot \left(C_{Hr,CV-130} - C_{Hr,CV-110}\right)$$

$$\frac{dC_{O2,CV-110}}{dt} = \frac{A_{JN-110} \cdot D_{O2-He}}{V_{CV-110} \cdot L_{JN}} \cdot \left(C_{O2,CV-130} - C_{O2,CV-110}\right)$$

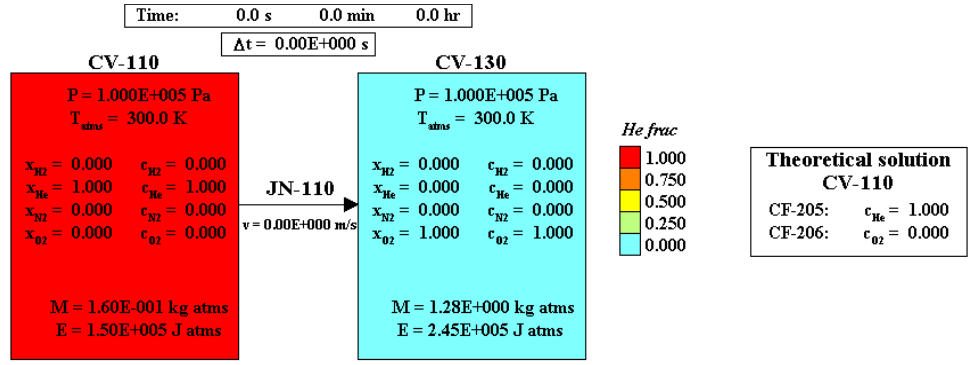

(a) initial state (t = 0.0 s)

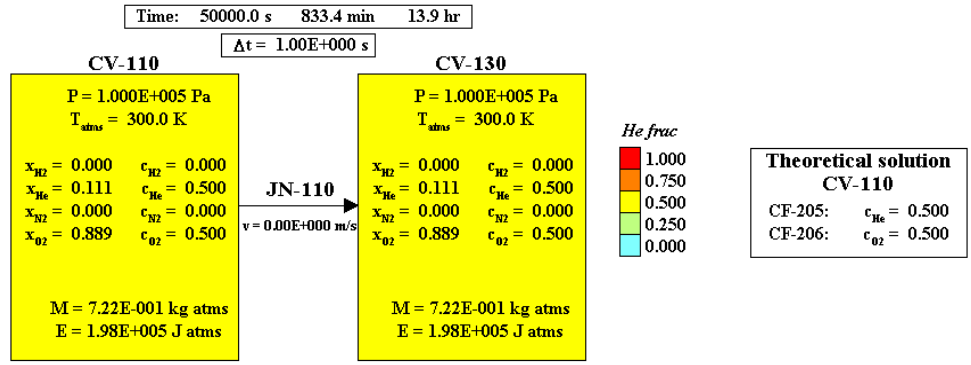

(b) final state (t = 50,000 s)

Figure 3-32 Diffusion test DIFF-1 - mixing of He and O_2

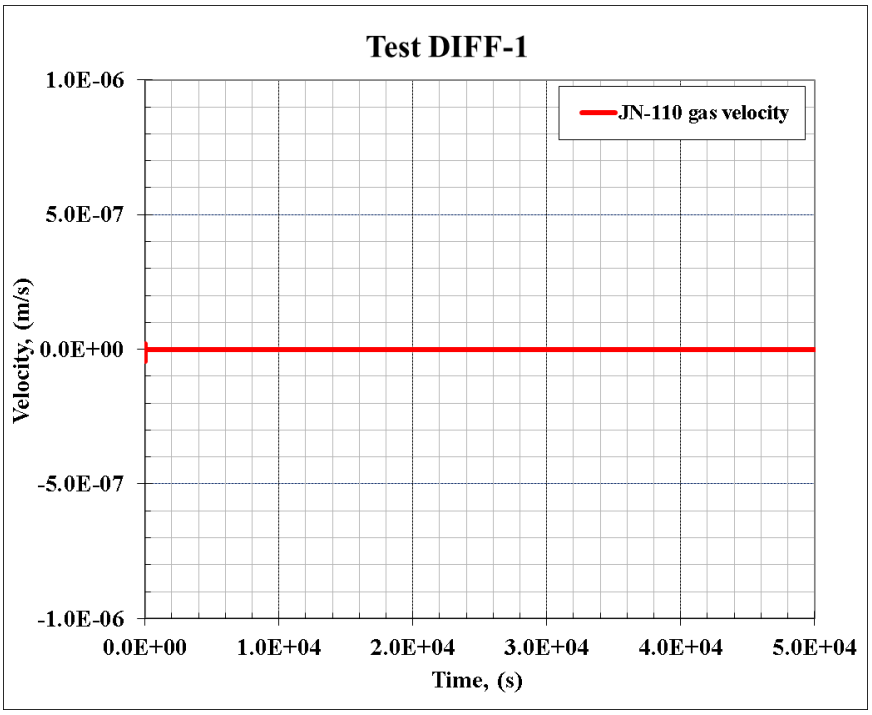

Figure 3-33 Diffusion test DIFF-1 - gas velocity in the junction

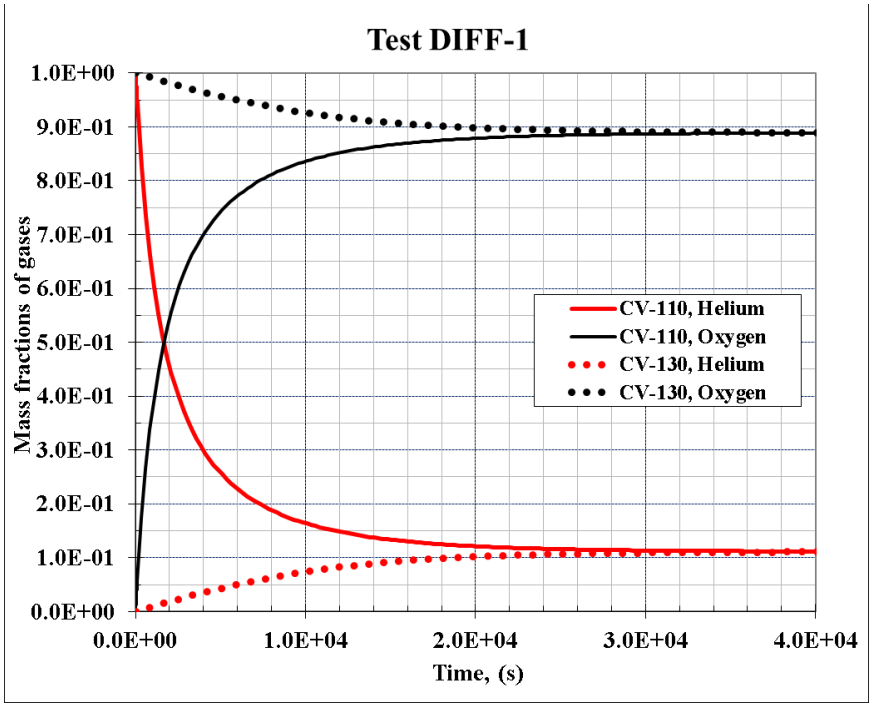

Figure 3-34 Diffusion test 1 - mass fractions of gases

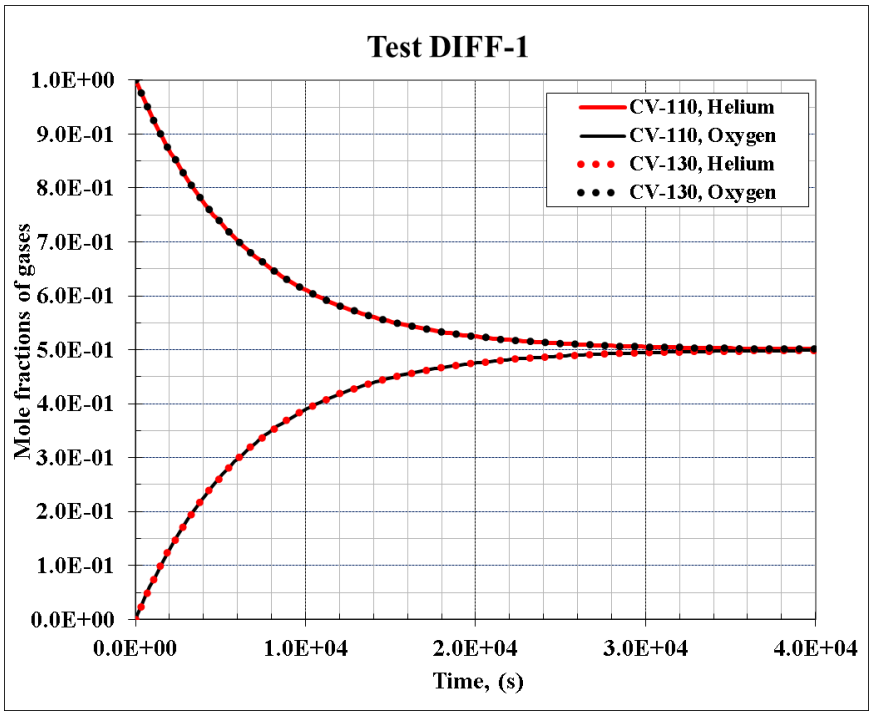

Figure 3-35 Diffusion test DIFF-1 - mole fractions of gases

Theoretical solution of the above equations with appropriate boundary conditions are (for simplicity, the subscripts CV-110 and JN-110 are dropped):

$$C_{He} = 0.5 \cdot \exp\left(-\frac{2A_{JN} D_{He-O2}}{V_{CV} \cdot L_{JN}} \cdot t \right) + 0.5$$

$$C_{O2} = -0.5 \cdot \exp\left(-\frac{2A_{JN} D_{O2-He}}{V_{CV} \cdot L_{JN}} \cdot t \right) + 0.5$$

In order to perform verification of the computed values, an automated verification was set-up using Tabular Functions and Control Functions, defined as follows:

- CF-201 = $D_{He\text{-}O2} = D_{O2\text{-}He} = 7.533 \times 10^{-5}$
- CF-202 = $-2 \times A_{JN} \times D_{He\text{-}O2} \times t / V_{CV} / L_{JN}$ =
  = $-2 \times 1.0 \times$ CF-201 $\times t / 1.0 / 1.0$
  = $-2 \times$ CF-201 $\times t$
- CF-205 = $C_{He,\text{CV-110}}$ = $0.5 \times \exp(\text{CF-202}) + 0.5$
- CF-206 = $C_{O2,\text{CV-110}} = -0.5 \times \exp(\text{CF-202}) + 0.5$

The diffusion coefficient for the He-O_2 mixture at 300 K and 1.0 bar pressure is calculated from the method of Blanc and Fuller. The value is 7.533×10^{-5} m^2/s (see \Z-INPUTS\JN\DIFF\DIFF-1-Graphs.xlsx). Comparison of calculated concentrations with the theoretical values is shown in Figure 3-36. The agreement is very good.

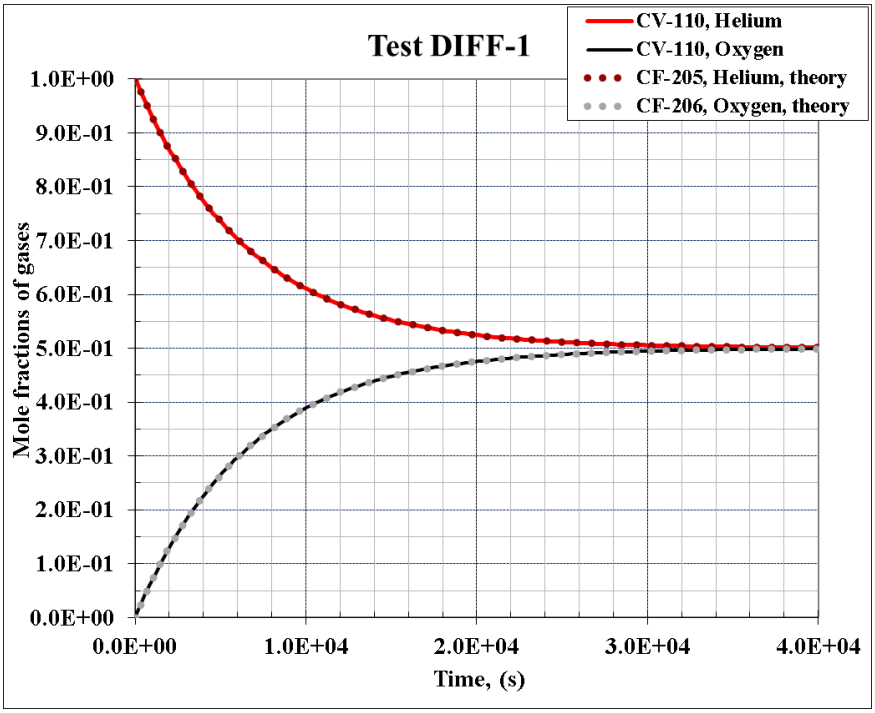

Figure 3-36 Diffusion test DIFF-1 - verification using theoretical expressions

- ***Diffusion test DIFF-2***

  The results obtained for this test are shown in Figure 3-37, Figure 3-38, Figure 3-39, and Figure 3-40. Figure 3-37 (a) shows the initial conditions. Again the initial pressures were set to exactly stable values in a short run with the diffusion model disabled (DIFF-1-0.SPE). This is important because one of the aspects that needs to be checked is whether the diffusion process does not cause any undesired, phantom flows.

  Once perfectly stable initial conditions were defined, the test case with the diffusion model active (DIFF-2.SPE) was run. Calculations were performed until stable conditions were reached (t = 100,000 s ≈ 28 h). Time dependent graphs are shown in Figure 3-38, Figure 3-39, and Figure 3-40. The end-state of the system is shown in Figure 3-37 (b).

  Correctness of the end-state is clear, since the gas mixtures have identical compositions in both volumes. Correctness of the numerical scheme is seen in Figure 3-38, as there is no flow through JN-110 throughout the whole diffusion process. The velocities were practically zero throughout the test ($|v| < 10^{-9}$ m/s).

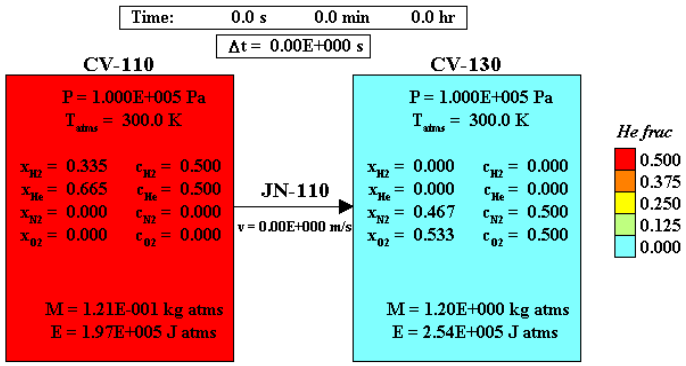

(a) initial state (t = 0.0 s)

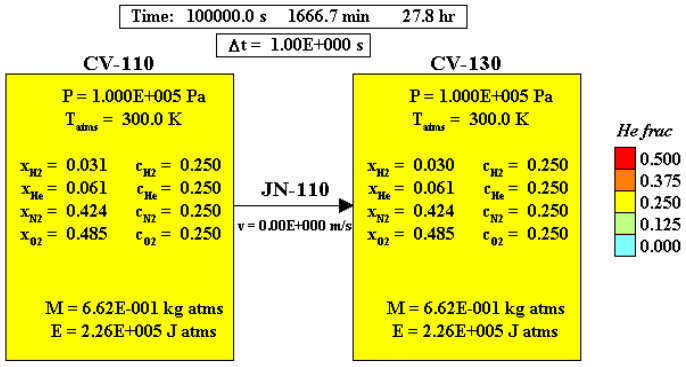

(b) final state (t = 100,000 s)

Figure 3-37 Diffusion test DIFF-2 - mixing of H_2/He and N_2/O_2

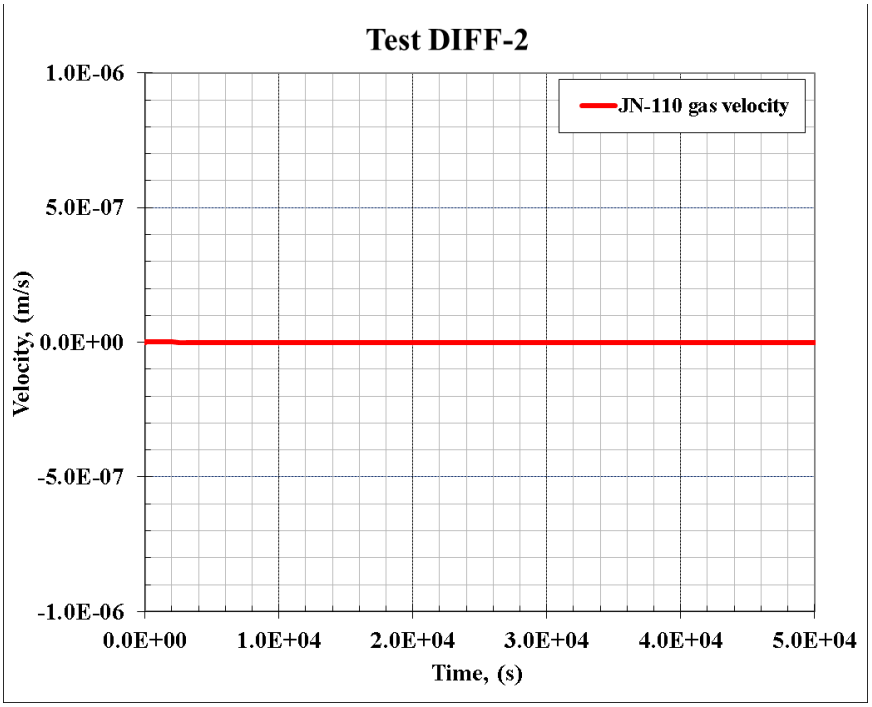

Figure 3-38 Diffusion test DIFF-2 - gas velocity in the junction

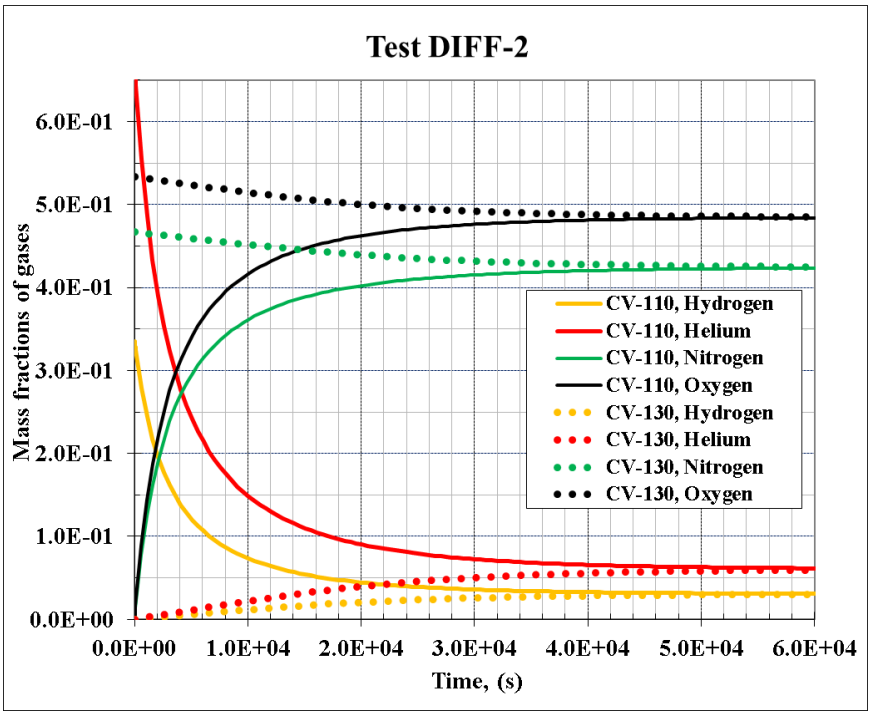

Figure 3-39 Diffusion test DIFF-2 - mass fractions of gases

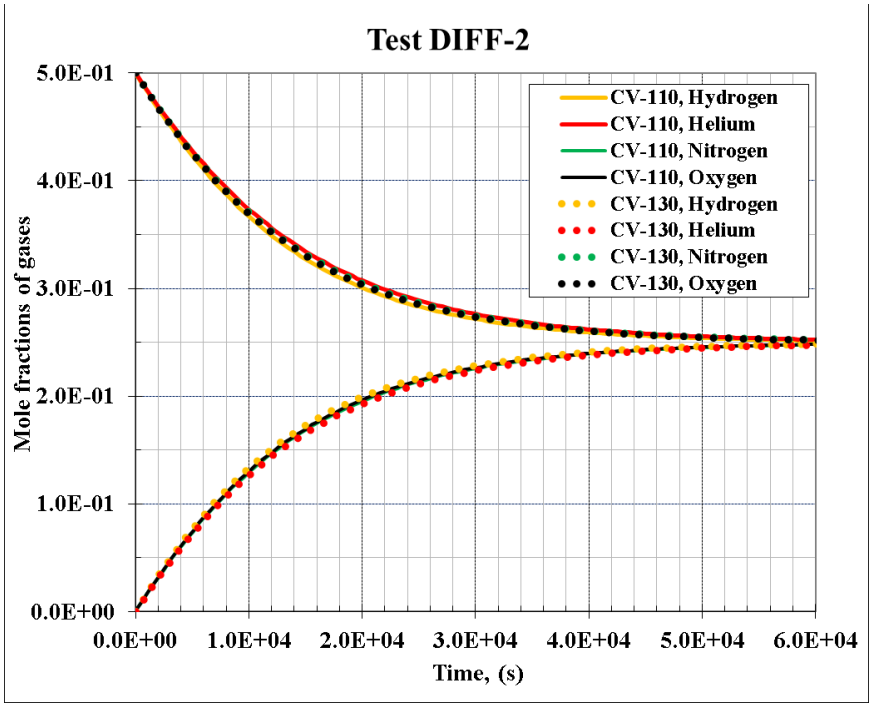

Figure 3-40 Diffusion test DIFF-2 - mole fractions of gases

3.1.8 Diffusion Tests for Fission Product Vapors

The previous section was discussing diffusion of gases, defined in the FL Package, present in the atmosphere of Control Volumes. This section discusses similar transport of fission product vapors. Again, the diffusion model needs to be activated by the user (input parameter IDIFJN, see Volume 2). Additionally the diffusion volume, Σ (input parameter SGFPRT) must be defined for each isotope that is diffusing. The diffusion volumes for different gases are shown in Volume 1. The diffusion volume is needed to calculate the binary diffusion coefficients (described in Volume 1). If the diffusion model is turned on, the code calculates the transfer of gases through the connecting junction using the diffusion equation (see Volume 1):

$$J_i = \frac{\Delta C_i}{R_i}$$

$$R_i = \frac{L_{from}}{D_{i,from}} + \frac{L_{to}}{D_{i,to}}$$

J_i volumetric flux of gas *i*, (m/s)
D_i diffusion coefficient of gas *i* in the mixture of gases, (m^2/s)
C_i molar concentration of the isotope vapor *i* in the CV gas mixture, (-)
ΔC_i difference in concentration of gas *i* in the connected Control Volumes:
$\Delta C_i = C_i$('from-CV') – C_i('to-CV')
L_{from} diffusion lengths in the 'from-CV' (input parameter X1DFJN)
L_{to} diffusion lengths in the 'to-CV' (input parameter X2DFJN)

This section describes diffusion test cases and verification of results based on analytical solutions. A simple model is set up for diffusion verification. The model consists of two Control Volumes (1.0 m^3 each) connected by a single Junction (flow area of 1.0 m^2). The nodalization is shown in Figure 3-41.

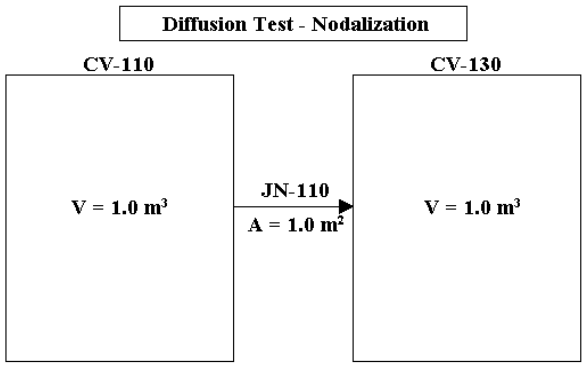

Figure 3-41 Nodalization applied for the diffusion tests

The same initial temperature (T=300 K) and pressure (p=1.0×10^5 Pa) are defined in both volumes. Both volumes are assumed to be filled with Helium. A relatively small amount (0.005263 kg) of the Xe-131 (isotope defined as FP-211) was placed in CV-110. The reason for selecting this particular initial mass is explained below. Three cases are considered. These are described below.

- ***Diffusion test DIFF-Xe-1***.
  Input file is provided in DIFF-Xe-1.SPE (diffusion model on) and DIFF-Xe-1-0.SPE (diffusion model off). The results of DIFF-Xe-1.SPE are shown in Figure 3-42 and Figure 3-43. Figure 3-42 shows the initial and the final state. Figure 3-43 shows the time-dependent masses of isotope 211 in CV-110 and CV-130. In this case Xe-131 is treated as trace-specie; i.e. the mass of Xe in the CV atmosphere is assumed to be negligible. Consequently, the Xe gas concentrations in the CV gas space cannot be plotted (the value is always 0.0 - Figure 3-42).

- ***Diffusion test DIFF-Xe-2***.
  Input file is provided in DIFF-Xe-2.SPE (diffusion model on) and DIFF-Xe-2-0.SPE (diffusion model off). In this case the Xe mass in the RT Package is linked to the Xe mass in the FL/CV Package using the input record 897001, which defines the list of RT isotopes (in this case only Xe-131) that corresponds to the user-defined gas 7 (Xe):

```
*
*        Xe isotopes -> Xe gas (user-defined gas number 07)
*        Gas No.     Isotopes:  Xe-131
897001       07                    211   *
*
```

  Additionally the mass sources referring to this list are present for CV-110 and CV-130. Consequently, the diffusion of Xe-131 (isotope FP-211 in RT) may be also observed as the Xe gas (gas No. 7 in CV) concentrations change. The initial mass of Xe-131 (0.005263 kg) was selected to get the initial volume fraction of Xe equal to 0.001.

  The results of DIFF-Xe-2 are shown in Figure 3-44 and Figure 3-45. Figure 3-44 shows the initial and the final state. Figure 3-45 shows the time-dependent masses of isotope 211 in CV-110 and CV-130.

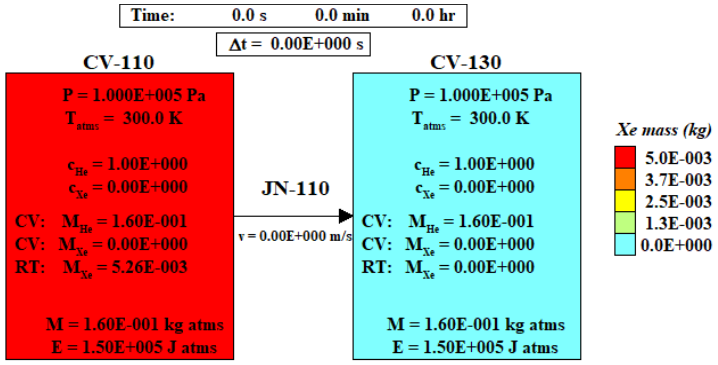

(a) initial state (t = 0.0 s)

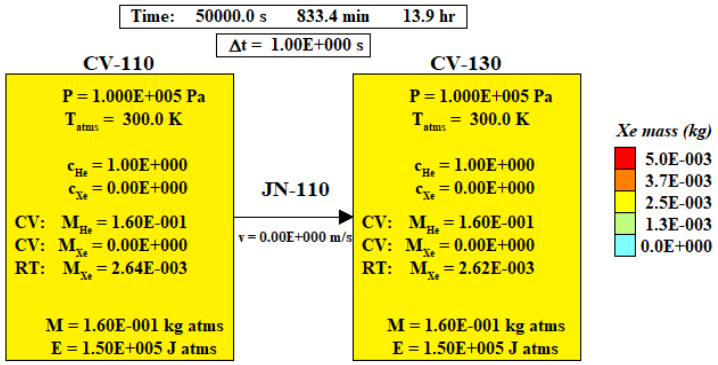

(b) final state (t = 50,000 s)

Figure 3-42 Diffusion test DIFF-Xe-1

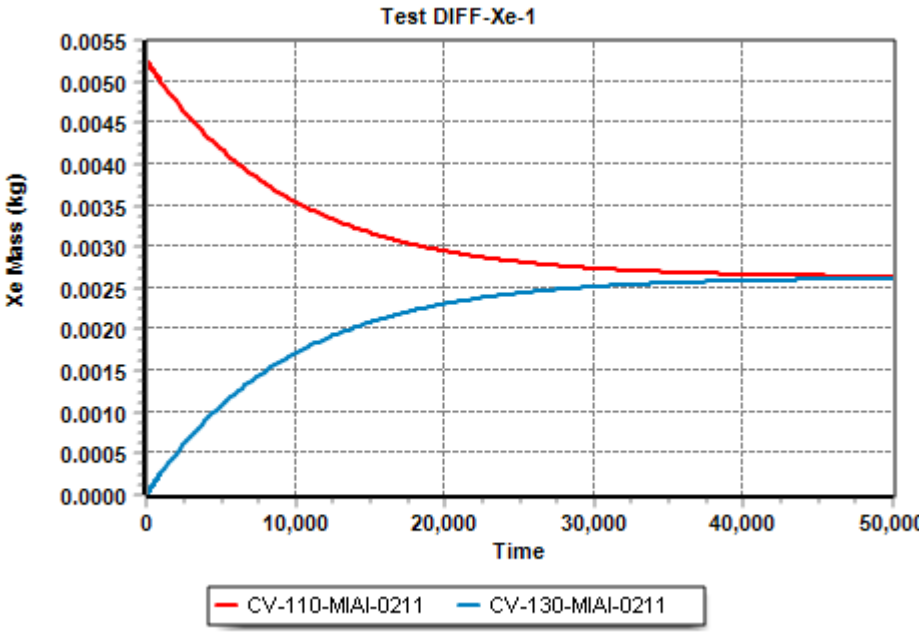

Figure 3-43 Diffusion test DIFF-Xe-1 - mass of Xe-131

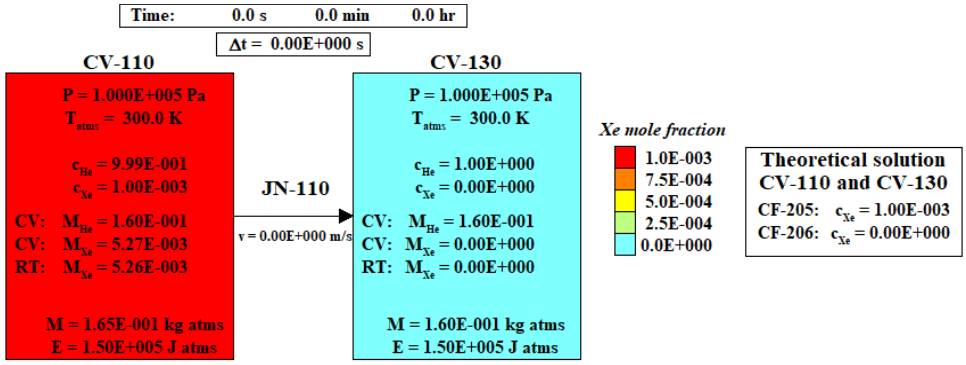

(a) initial state (t = 0.0 s)

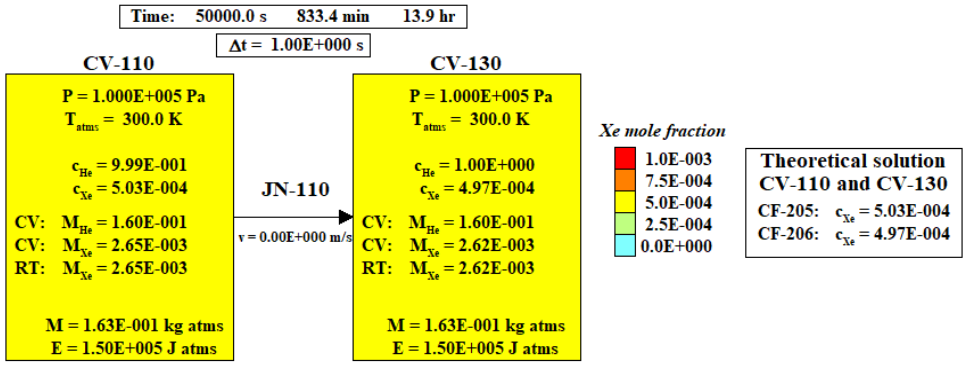

(b) final state (t = 50,000 s)

Figure 3-44 Diffusion test DIFF-Xe-2

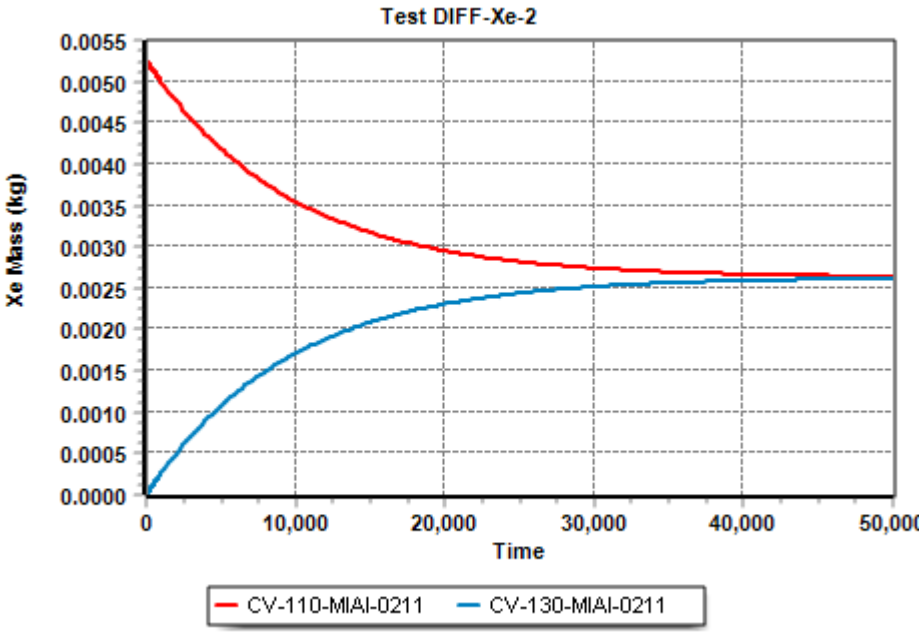

Figure 3-45 Diffusion test DIFF-Xe-2 - mass of Xe-131

The correctness of the time-dependent gas concentrations is for this case checked against a theoretical solution. The change of volume of Xe in CV-110 is governed by:

$$\frac{dV_{Xe,CV-110}}{dt} = A_{JN-110} \cdot J_{Xe}$$

or:

$$V_{CV-110} \frac{dC_{Xe,CV-110}}{dt} = D_{Xe-He} \cdot \frac{C_{Xe,CV-130} - C_{Xe,CV-110}}{L_{JN}}$$

$V_{CV\text{-}110}$	volume of CV-110, (m^3)
$D_{Xe\text{-}He}$	diffusion coefficient for Xe in He, (m^2/s)
$C_{Xe,CV\text{-}110}$	molar concentration of Xe in CV-110, (-)
$C_{Xe,CV\text{-}130}$	molar concentration of Xe in CV-130, (-)
L_{JN}	diffusion length of the junction JN-110, (m)

A similar equation may be written for CV-130. The following equations are obtained:

$$V_{CV-110} \frac{dC_{Xe,CV-110}}{dt} = D_{Xe-He} \cdot \frac{C_{Xe,CV-130} - C_{Xe,CV-110}}{L_{JN}}$$

$$V_{CV-130} \frac{dC_{Xe,CV-130}}{dt} = D_{Xe-He} \cdot \frac{C_{Xe,CV-110} - C_{Xe,CV-130}}{L_{JN}}$$

Theoretical solution of the above equations with appropriate boundary conditions is:

$$C_{Xe,110} = 0.0005 \cdot \exp\left(-\frac{2A_{JN} D_{Xe-He}}{V_{CV} \cdot L_{JN}} \cdot t \right) + 0.0005$$

$$C_{Xe,130} = -0.0005 \cdot \exp\left(-\frac{2A_{JN} D_{Xe-He}}{V_{CV} \cdot L_{JN}} \cdot t \right) + 0.0005$$

In order to perform verification of the computed values, an automated verification was set-up using Tabular Functions and Control Functions, defined as follows:

- CF-201 = $D_{Xe\text{-}He} = 5.27\times10^{-5}$
- CF-202 = $-2 \times A_{JN} \times D_{Xe\text{-}He} \times t / V_{CV} / L_{JN}$ =
  = $-2 \times 1.0 \times$ CF-201 $\times t / 1.0 / 1.0$
  = $-2 \times$ CF-201 $\times t$
- CF-205 = $C_{Xe,CV\text{-}110}$ = 0.0005 × exp(CF-202) + 0.0005
- CF-206 = $C_{Xe,CV\text{-}130}$ = –0.0005 × exp(CF-202) + 0.0005

The diffusion coefficient for the Xe-He mixture at 300 K and 1.0 bar pressure is calculated from the method of Blanc and Fuller. The value is $D_{Xe\text{-}He} = 5.277\times10^{-5}$ m^2/s (see \Z-INPUTS\JN\DIFF-FP\DIFF-Xe-2-Graphs.xlsx). Comparison of calculated concentrations with the theoretical values is shown in Figure 3-46. The agreement is very good.

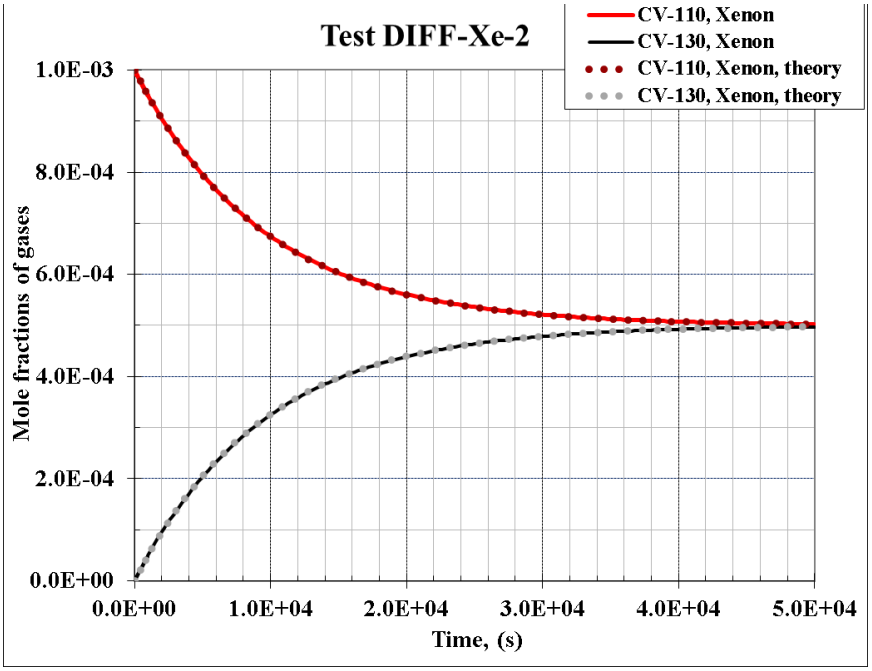

Figure 3-46 Diffusion test DIFF-Xe-2 - verification using theoretical expressions

- ***Diffusion test DIFF-Xe-2-FL***.
  Input file is provided in DIFF-Xe-2-FL.SPE. This case is similar to the case DIFF-Xe-2 (input file DIFF-Xe-2-FL.SPE). The initial volume fraction of Xe in CV-110 is again 0.001. However, in this case the RT Package is disabled. Consequently, this is a "classical" gas diffusion case, similar to the test analyzed in the previous section.

  The results of DIFF-Xe-2-FL are shown in Figure 3-47 and Figure 3-48. Figure 3-47 shows the initial and the final state. Figure 3-48 shows the time-dependent concentrations of Xe (FL gas number 7) in CV-110 and CV-130. The results of DIFF-Xe-2-FL are compared to the results of DIFF-Xe-2. The results are practically identical. This shows that the gas diffusion and the isotope diffusion give the same results.

  It should be remembered that the two calculations compared in Figure 3-48 are verifying two different diffusion mechanisms:
  - DIFF-Xe-2-FL: diffusion of gases present in CV atmosphere (defined in FL).
  - DIFF-Xe-2: diffusion of isotopes (defined in RT). In this case the Xe gas concentrations within CV simply follow the concentration of the RT isotope and the CV gas transport is overruled by the fact that Xe is linked to the RT isotope.

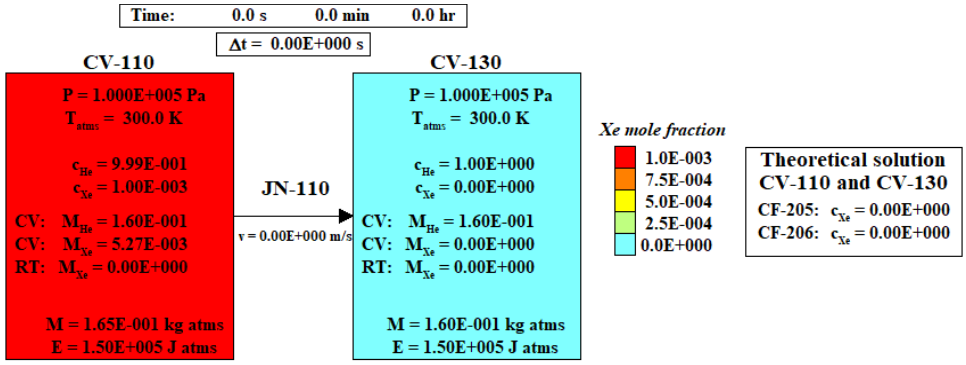

(a) initial state (t = 0.0 s)

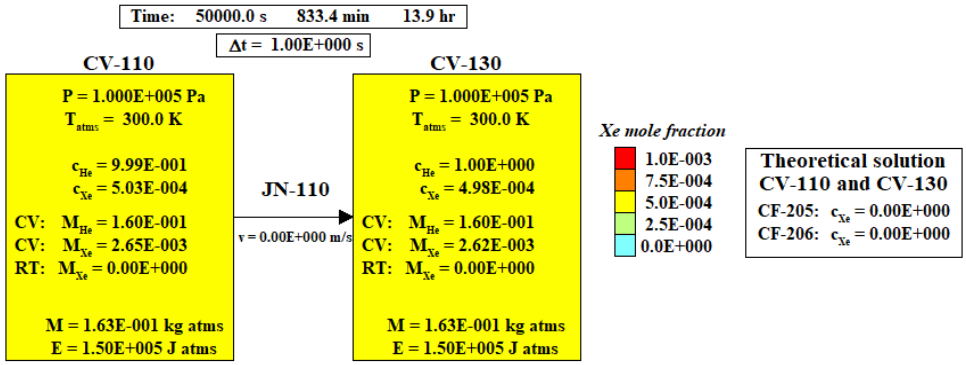

(b) final state (t = 50,000 s)

Figure 3-47 Diffusion test DIFF-Xe-2-FL

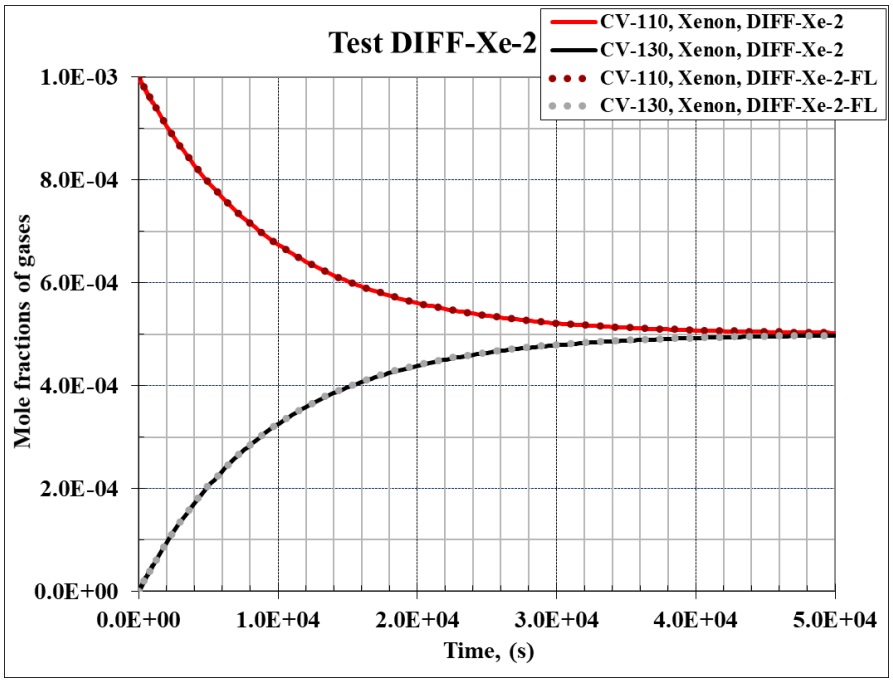

Figure 3-48 Concentrations of Xe (gas No.7), DIFF-Xe-2 and DIFF-Xe-2-FL

3.2 Valve Tests

3.2.1 Valve Test - Motor Valve, Check Valve and Serial Valve

Models for two types of valves are available:

- Motor valve - valve open fraction defined by a user-defined tabular or control function
- Check valve - valve opening and closing is determined by pressure differences.

The user may wish to apply both motor and check valve in the same junction. In such case the valves are assumed to be located one behind the other. Such combination is referred to as a serial valve. The effective open fraction of a serial valve is equal to the minimum of the two motor and the check valve. The present test case shows the performance of a motor valve, a check valve, and a serial valve. The test consists of two Control Volumes, CV-100 and CV-200 (Figure 3-49). Pressure in CV-200 is kept constant at 1.0 bar. Pressure in CV-100 changes from 2.0 bar down to 1.0 bar and then back to 2.0 bar, as shown in Figure 3-50. The input file for the serial valve test is located in:
`Z-INPUTS\JN\VALVE\SerVlv.SPE`

Three valves are used:

- Motor valve, JN-101. The valve is controlled by a user-defined function, TF-101. The valve is initially closed starts opening at 10, is fully open between 20 and 50 s, and closes from 50 to 60 s, as shown in Figure 3-51.
- Check valve, JN-102. Opening pressure difference of ΔP_{open} = 0.5 bar. Closing pressure difference of ΔP_{close} = 0.4 bar.
- Serial valve, JN-103. This valve is a combination of valves JN-101 and JN-102.

Calculations were performed for 50 seconds. Results are shown in Figure 3-51. When the closing setpoint is reached the serial valve starts closing from its current position, therefore it is closed somewhat faster than the check valve. This discrepancy between a serial and a check valve should be kept in mind but is not very important in practice.

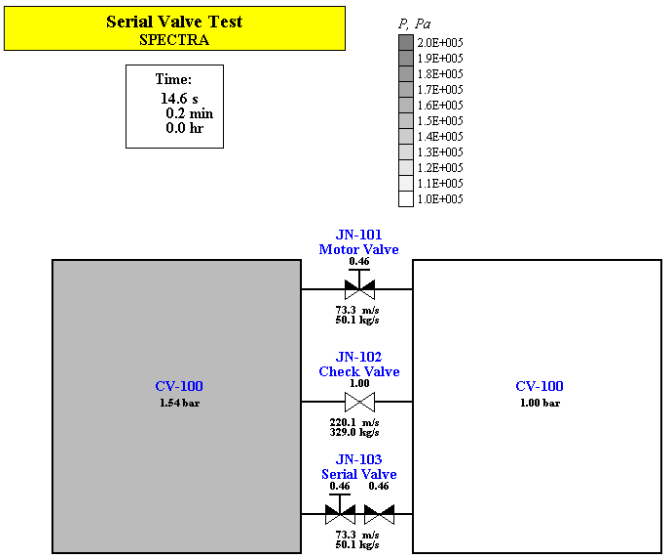

Figure 3-49 Serial Valve Test.

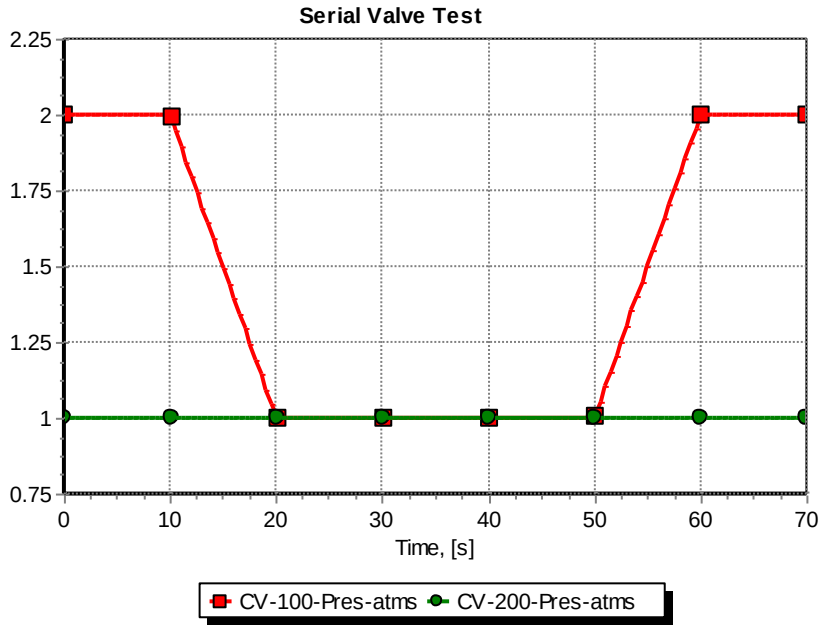

Figure 3-50 Pressures - Serial Valve Test

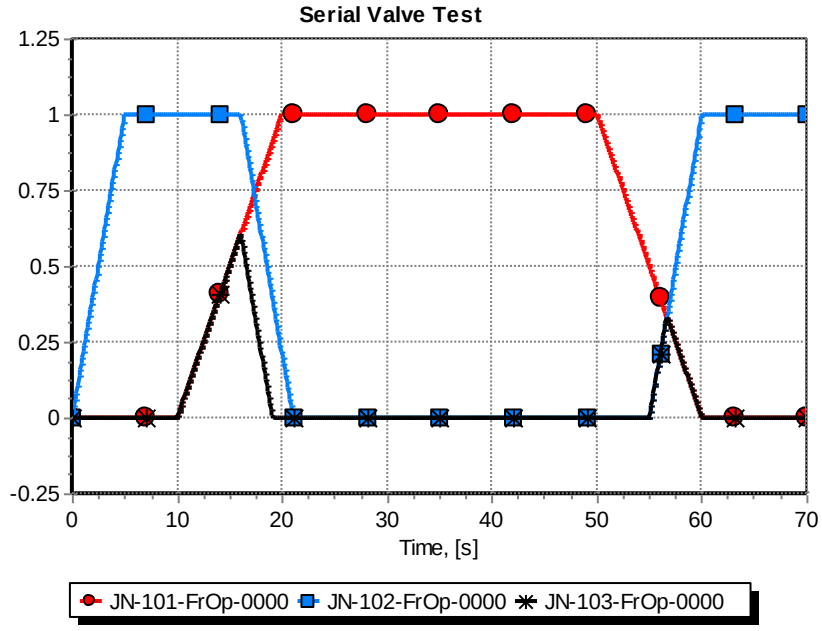

Figure 3-51 Valve open fractions - Serial Valve Test

3.2.2 Valve Test - Pressure Loss Coefficient for a Butterfly Valve

In general the pressure loss coefficient of a valve changes with the valve open fraction. Sometimes the change is so significant that it is important to include a variable loss coefficient in the computational model.

The present example shows possible ways of modelling a variable pressure loss coefficient for a valve. A butterfly valve is considered. Reference [40] gives the loss coefficients for a butterfly valve in a tube with a circular cross section (Diagram 9-16 in [40]). The pressure loss coefficients appropriate for a thin plane disk (Curve 2 in Diagram 9-16) versus the valve angular position, $K_{Idel}(\theta)$, are shown in Table 3-10.

Table 3-10 Butterfly valve data

θ°	0	10	20	30	40	50	60	70
A/A_0	1.00	0.826	0.658	0.500	0.357	0.234	0.134	0.0603
K_{Idel}	0.30	0.52	1.54	4.50	11.0	29.0	108.0	625.0
K	0.30	0.355	0.667	1.13	1.40	1.59	1.94	2.27

The loss factors given in [40], K_{Idel}, are related to the velocity in a fully open channel, which means the pressure loss is given by:

$$\Delta p = K_{Idel} \frac{\rho v_0^2}{2}$$

Here v_0 is the fluid velocity for a fully open valve (area of A_0). In SPECTRA the loss coefficient is always used with the current fluid velocity, v, and thus with the current flow area, A:

$$\Delta p = K \frac{\rho v^2}{2}$$

To obtain values of K-factor related to the current valve flow area one must multiply the values of K_{Idel} by the area ratio squared: $(A/A_0)^2$. For a given angle, θ, the valve open area is given by: $A=A_0\times(1-\sin\theta)$. Therefore the loss factors related to the current flow area are given by the formula: $K=K_{Idel}\times(1-\sin\theta)^2$. The values of K, calculated from the above formula, are shown in Table 3-10 below K_{Idel} .

There are two ways in which a variable loss coefficient can be modelled:

- Approximation curve, using the loss coefficient K_0 and valve coefficient C_V: $K = f(K_0, C_V)$
- Tabulated values versus valve open fraction: $K = K_0 \times TF(A/A_0)$

The first method was available in earlier SPECTRA versions. The second method allows a more general way of defining variable loss coefficient for a valve. Both methods were used in the present example test case.

The test consist of two Control Volumes; one is kept at 2.0 bar pressure, the other at 1.0 bar pressure. Calculations were performed for 50 seconds. The valves are modelled by JN-101 and JN-102. They open at 10 - 20 s and re-close at 30 - 40 s. The approximation curve is used for JN-101; the tabulated data is used for JN-102.

- Approximation curve, JN-101

  The value of K_0, needed for SPECTRA input, is equal to the loss factor for the fully open valve, thus 0.30. It has been found using a trial and error procedure, that a value of C_V=7.0 represents well the K values. Therefore:

  $$K_0 = 0.30 \qquad C_V = 7.0$$

  and

  $$K_V = K_0 \left[C_V + \left(1 - C_V \right) \frac{A_V}{A_0} \right] = 0.3 \left[7.0 - 6.0 \frac{A_V}{A_0} \right]$$

  Those values were applied for JN-101. Resulting line is shown in Figure 3-52.

- Tabulated values versus valve open fraction: $K = K_0 \times TF(A/A_0)$, JN-102

  With this option the K-factors may be tabulated exactly as desired (shown in Table 3-10). The following values were used:

  $K_0 = 1.0$
  K/K_0, tabulated as shown below:

A/A_0	1.00	0.826	0.658	0.500	0.357	0.234	0.134	0.0603
K/K_0	0.30	0.355	0.667	1.13	1.40	1.59	1.94	2.27

  The values were tabulated for JN-102. Resulting line is shown in Figure 3-53.

The input file is located in:
`Z-INPUTS\JN\VALVE\Butterfly-Valve.SPE`

The test setup and results obtained at t = 35 s is shown in Figure 3-55. The valve open fraction and the valve loss coefficients are shown in Figure 3-54. For a fully open valve both models give the same value of K = 0.3. For closed valve the approximation gives K = 2.1, while the tabulated value gives K = 2.27 (as always in SPECTRA the end-point value is used outside the tabulated range, so K = 2.27 for $A/A_0 \geq 0.0603$).

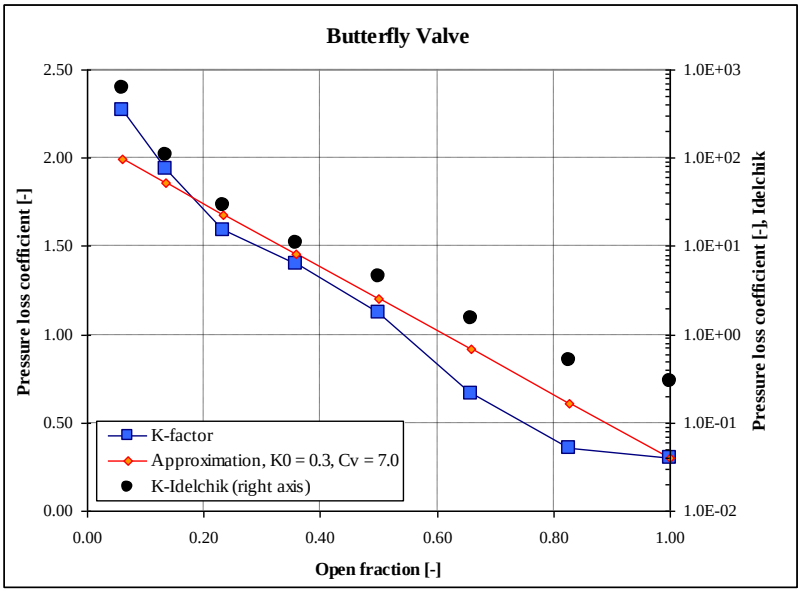

Figure 3-52 Butterfly valve - pressure loss: K_0 = 0.3, C_V = 7.0 (JN-101).

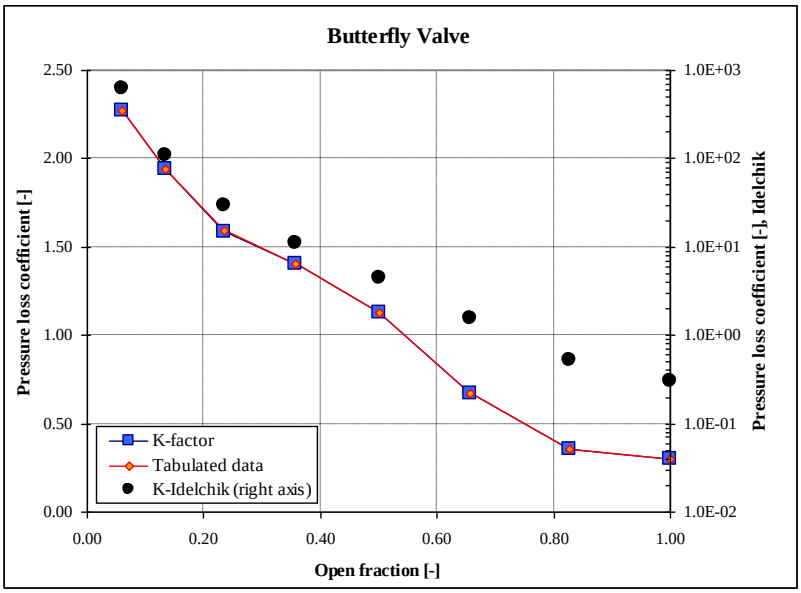

Figure 3-53 Butterfly valve - pressure loss: tabulated data (JN-102).

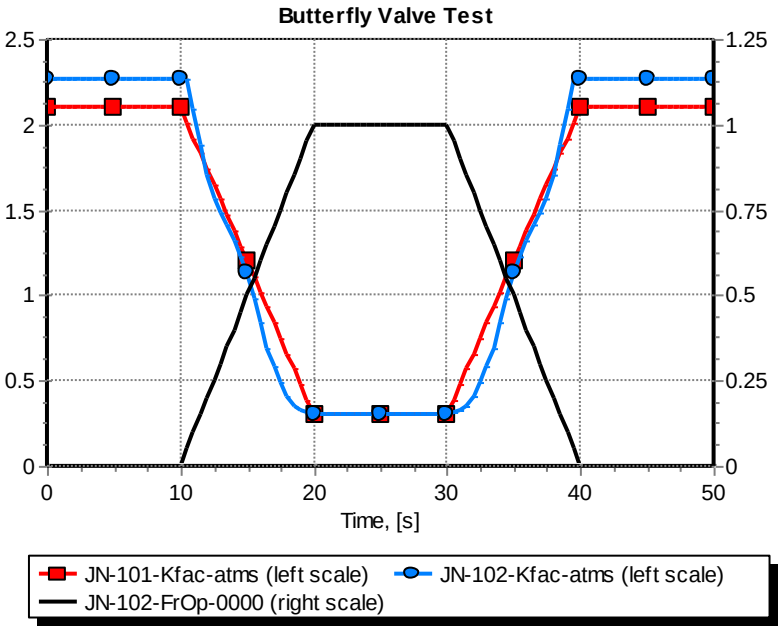

Figure 3-54 Butterfly valve - loss factors and open fraction.

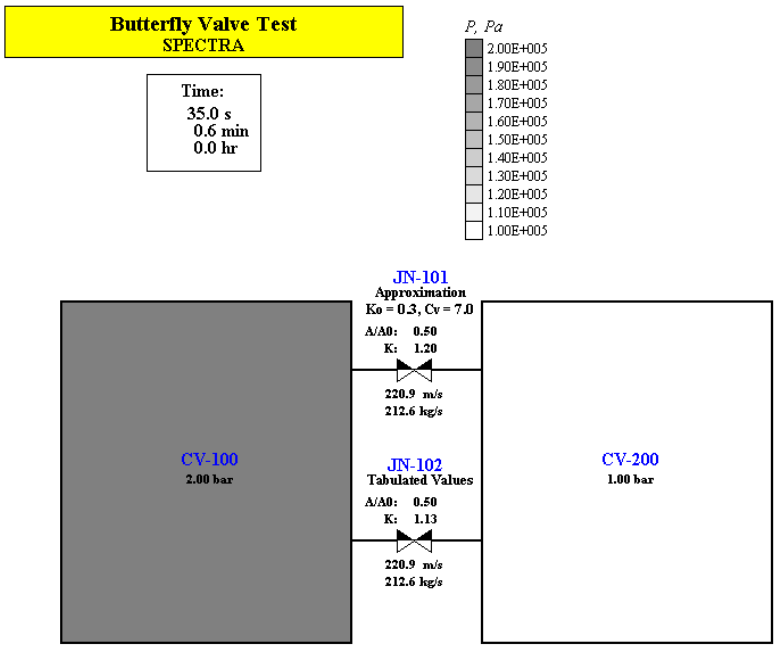

Figure 3-55 Butterfly Valve Test

3.3 ORNL THTF Tests

3.3.1 Introduction

ORNL THTF tests have been selected as one of the Separate Effect Tests (SET) to verify code capability to predict two-phase mixture flow and level swell in a tube bundle.

The two-phase mixture level swell is a phenomenon important to a small break loss-of-coolant-accident (SBLOCA) in a PWR. In fact, the extent of core uncovery following a SBLOCA strongly depends not only on the core liquid inventory, but also on the core void fraction distribution. It is thus essential to well predict the mixture level swell. The void fraction distribution is also important to simulate correctly the steam generator secondary side.

3.3.2 Description of the THTF Tests

The experiments were performed in the Thermal Hydraulic Test Facility (THTF), an electrically heated, PWR thermal hydraulic test loop, shown in Figure 3-56. Two sets of experiments were run; the first to obtain both void fraction and uncovered core heat transfer data (tests 3.09.10 I through N) and the second to obtain only void fraction data (tests 3.09.10 AA through FF) [4], [5].

The core of the THTF is a 64-rod bundle with a 3.66-m heated length (see Figure 3-57 and Figure 3-58). The bundle has an axially and radially uniform power profile, and internally heated Fuel Rod Simulators (FRS) (Figure 3-58). Unheated rods are in positions normally occupied by control rod guide tubes in a PWR. The rod diameter and the pitch are typical of a 17 x 17 fuel assembly. The void fraction was measured at different levels of the test section.

The measured values include for most tests both inlet and outlet flows. Since those are the steady-state tests, both numbers should be the same. The measured values show quite large discrepancies. For example, in case of test K the inlet flow is 0.137 kg/s, while the outlet flow is 0.193 (see reference [4], page 128). The discrepancy is about 30%. In the Nuclear Technology paper [5] the outlet flows were used (although some small discrepancies between the outlet flows in [4] and published in [5] exist). Therefore it is surmised that the outlet flow measurements were considered more accurate, and those values were taken in the present analysis. The tests conditions are presented in Table 3-11 and Table 3-12.

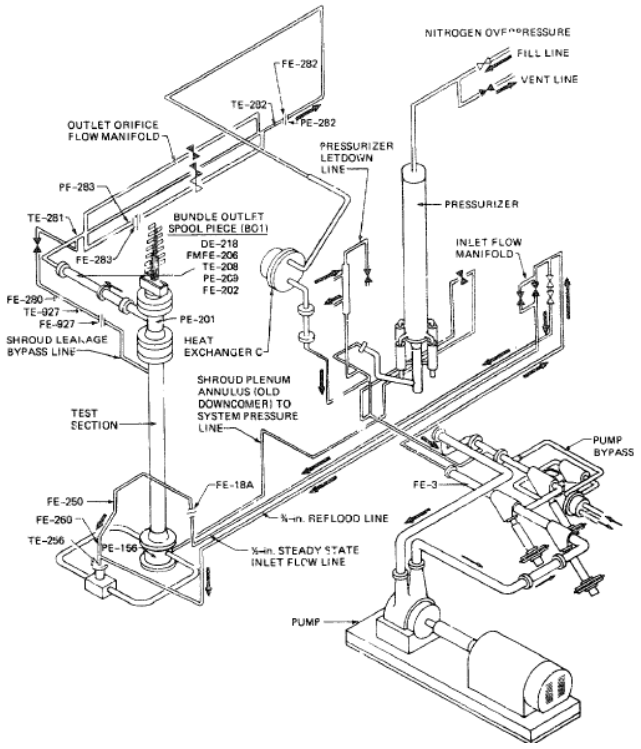

Figure 3-56 View of the THTF – reproduced from (2).

Table 3-11 THTF uncovered bundle tests - test conditions [4].

Test	p (bar)	T_{inlet} (K)	G (kg/m^2/s)	W (kg/s)	Q (kW)	Q_{loss} (%) / (kW)
3.09.10I	45.0	473	27.9	0.185	487	2% / 10 kW
3.09.10J	42.0	480	12.7	0.079	234	5% / 12 kW
3.09.10K	40.0	466	3.1	0.019	70	18% / 13 kW
3.09.10L	75.2	461	29.1	0.181	476	2% / 10 kW
3.09.10M	69.6	474	12.6	0.079	225	4% / 9 kW
3.09.10N	70.8	473	4.6	0.029	104	16% / 17 kW

Table 3-12 THTF void fraction tests - test conditions [4].

Test	p (bar)	T_{inlet} (K)	G (kg/m^2/s)	W (kg/s)	Q (kW)	Q_{loss} (%) / (kW)
3.09.10AA	40.4	451	21.2	0.130	279	2% / 6 kW
3.09.10BB	38.6	458	9.4	0.059	141	3% / 4 kW
3.09.10CC	35.9	468	7.0	0.044	71	3% / 2 kW
3.09.10DD	80.9	453	19.7	0.120	283	3% / 8 kW
3.09.10EE	77.2	456	10.9	0.068	140	4% / 6 kW
3.09.10FF	75.3	451	4.8	0.030	71	9% / 6 kW

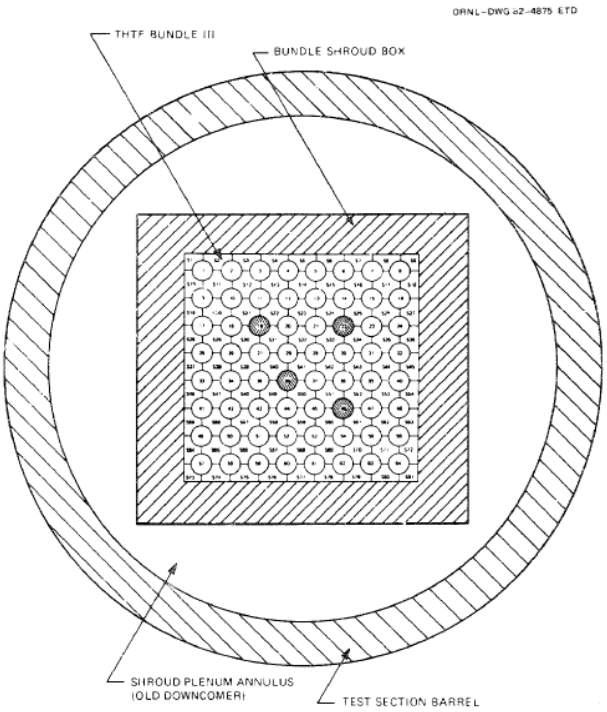

Figure 3-57 Cross section of the THTF test section – reproduced from (2).

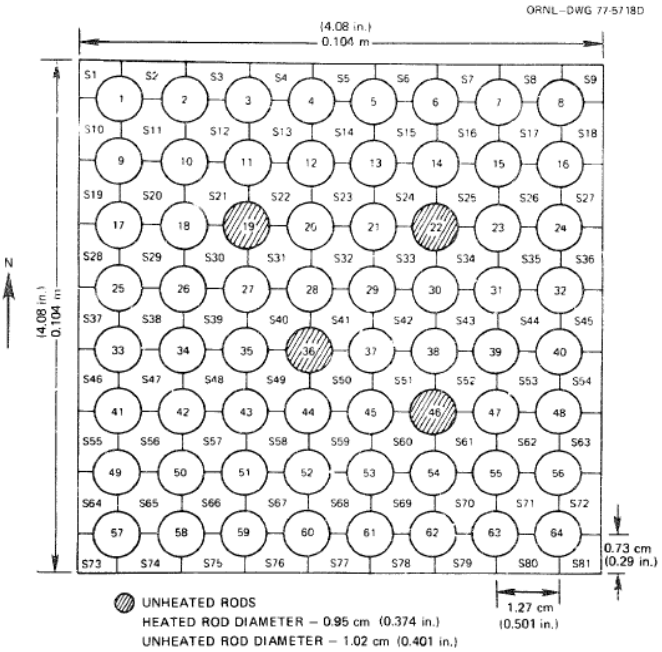

Figure 3-58 Cross-section of the THTF Bundle 3 – reproduced from (2).

3.3.3 SPECTRA Model of the THTF

Nodalization used for RELAP5/MOD3.3 calculations is shown in Figure 3-59. The model geometry and the main modeling assumptions are discussed below.

The core test section is simulated by ten Control Volumes, CV-101 through CV-110. It is divided into 10 axial cells, in order to well simulate the core uncovery. The nodalization is finer at the top of the core than at the bottom. The flow area of the test section is equal to:

$$A = 0.104^2 - 60 \times \frac{\pi}{4} \times 0.0095^2 - 4 \times \frac{\pi}{4} \times 0.0102^2 = 0.006236$$

The hydraulic diameter and junction diameter are equal to 0.01096 m. It is equal to $4A/P_w$ where A represents the cross section of the core flow path at the rod bundle location without the grid spacer, and P_w the total wetted perimeter, calculated as:

$$P_w = 4 \times 0.104 + 60 \times \pi \times 0.0095 + 4 \times \pi \times 0.0102 = 2.3349$$

The boundary conditions are specified in the inlet and outlet components. The inlet temperature is imposed in the CV-010. The test pressures are imposed in the CV-050. The inlet flow is imposed in the JN-003. The applied values are taken from Table 3-11 and Table 3-12.

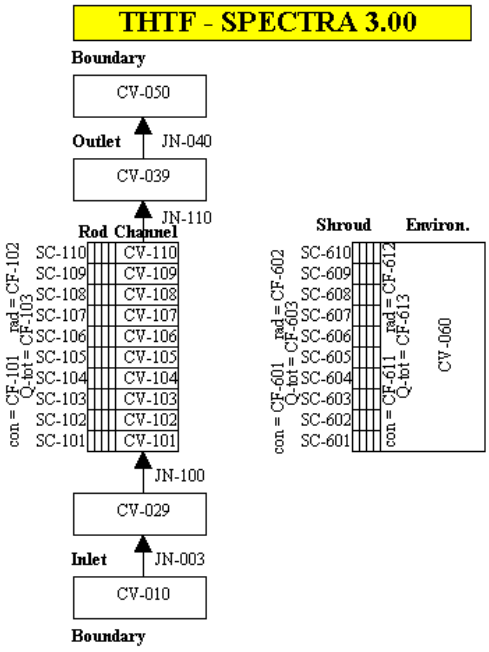

Figure 3-59 SPECTRA model of the THTF.

The fuel rods are simulated using Solid Heat Conductors SC-101 through SC-110, with the left boundary representing the rod center line, with an adiabatic boundary, and the right boundary representing the outside of the cladding connected to a corresponding CV. The additional input parameter, required for this boundary condition is the pitch-to-diameter ratio, *P/D*. The value was set to 1.27/0.95 (see Figure 3), which is equal to 1.33684. The heat transfer hydraulic diameter (or heated equivalent diameter D_h) is input as 0.01393 m, and is calculated as $4A/P_h$, where P_h denotes the heated perimeter, calculated as:

$$P_h = 60 \times \pi \times 0.0095 = 1.7907$$

The heated bundle height of a single rod, i.e. 3.658 m, is considered as the natural circulation length of the heat structure right boundary.

Five radial mesh points delimit the 4 intervals of different material compositions (boron nitride, Inconel-600, boron nitride and stainless steel). The total core power is specified as a source, and the internal source multipliers are input such to model a uniform axial power profile. This means, for each axial section the power fraction is equal to the length of this section divided by the total length of the rod bundle. All the power is distributed in the Inconel-600 interval.

The 4 unheated rods are simulated exactly the same way by SC-201 through SC-210, with no internal power source.

Finally, the SC-601 through SC-610 represent the shroud wall. These structures transfer heat to the corresponding CV at the left boundary. The heat transfer hydraulic diameter is set to the hydraulic diameter 0.01069 m. At the right surface the heat transfer coefficient is calculated using a tabular function. The value of the heat transfer coefficient was adapted for each test to approximately match the heat loss, specified in the experimental data (reproduced in Table 3-11 and Table 3-12). The external heat transfer coefficients assumed for each test are given in Table 3. Generally the heat losses are higher for the uncovered bundle tests (left column) than the void fractions tests because of higher temperatures.

Th input files are located in **\Z-ANALYSES\PWR\THTF**. Results are shown below. Figure 3-60 through Figure 3-77 presents comparison of the calculated results with the experimental values. Figure 3-78 through Figure 3-80 includes comparison with RELAP5 results.

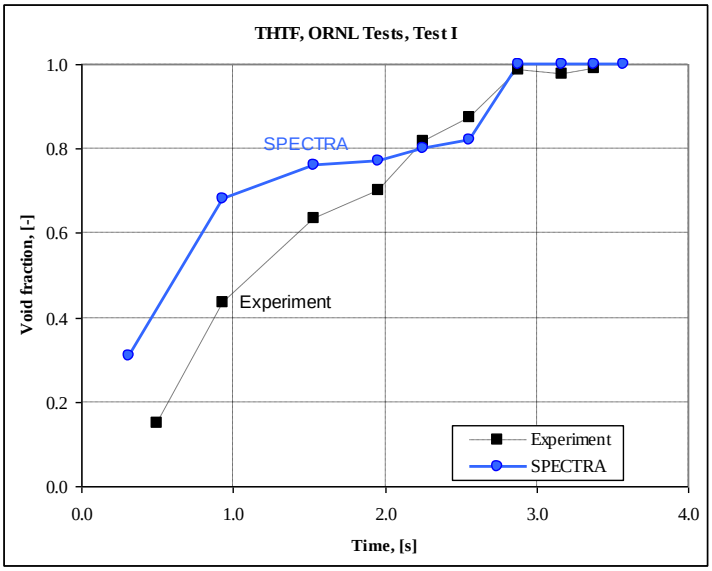

Figure 3-60 Void fractions, ORNL test I.

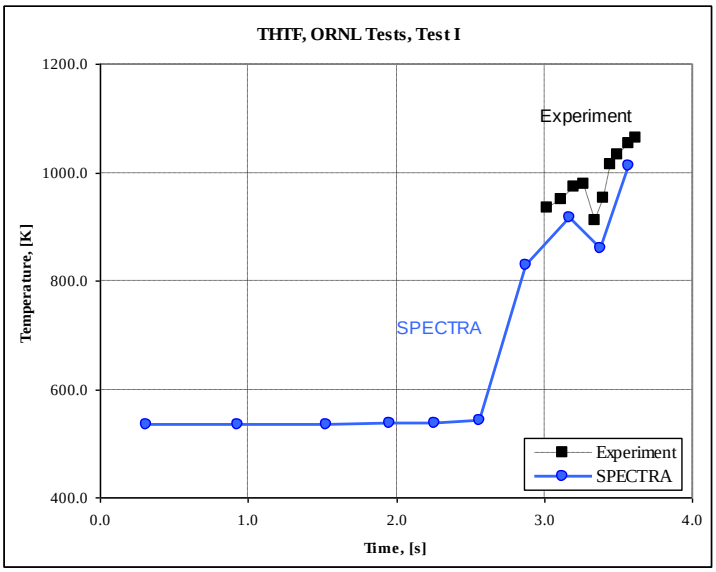

Figure 3-61 Rod surface temperatures, ORNL test I.

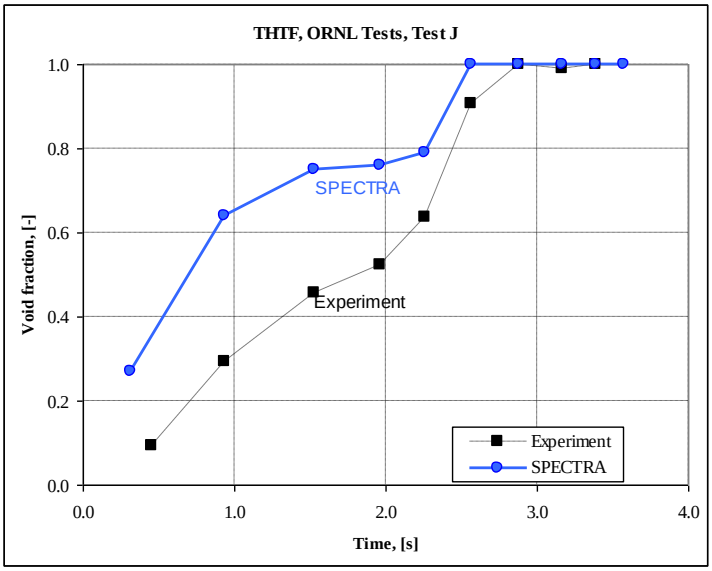

Figure 3-62 Void fractions, ORNL test J.

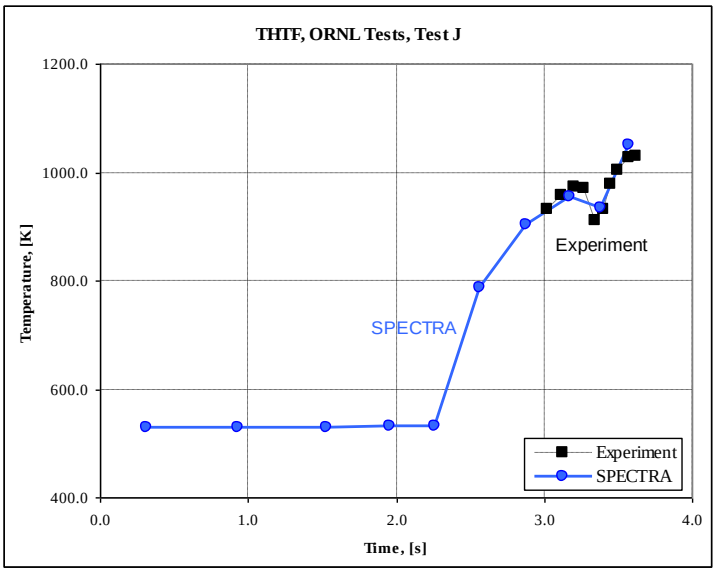

Figure 3-63 Rod surface temperatures, ORNL test J.

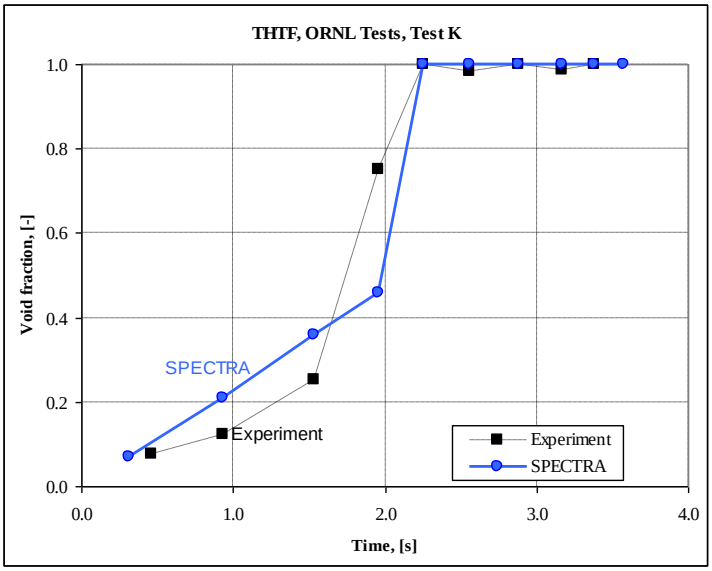

Figure 3-64 Void fractions, ORNL test K.

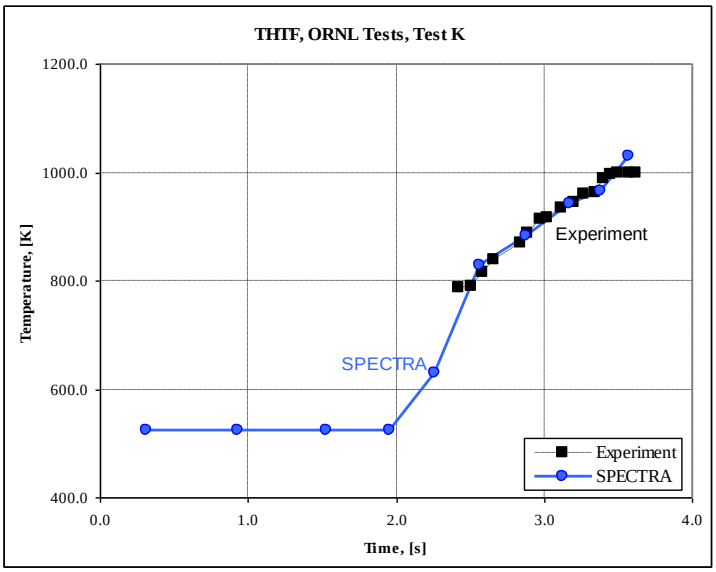

Figure 3-65 Rod surface temperatures, ORNL test K.

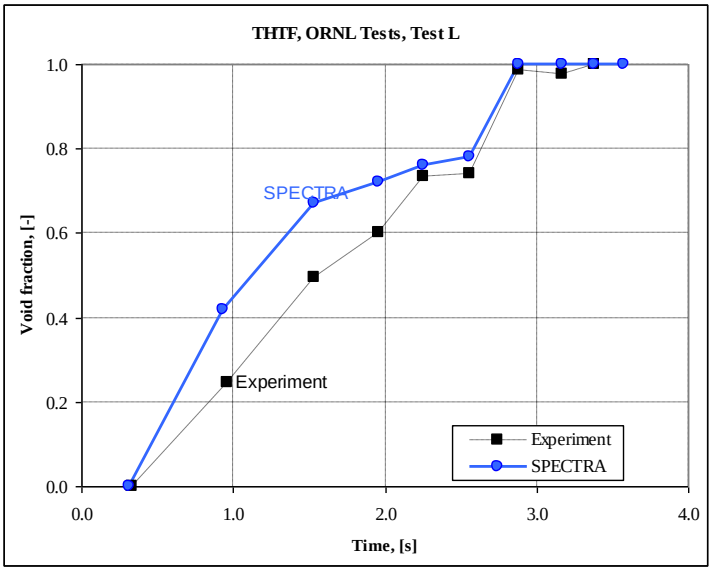

Figure 3-66 Void fractions, ORNL test L.

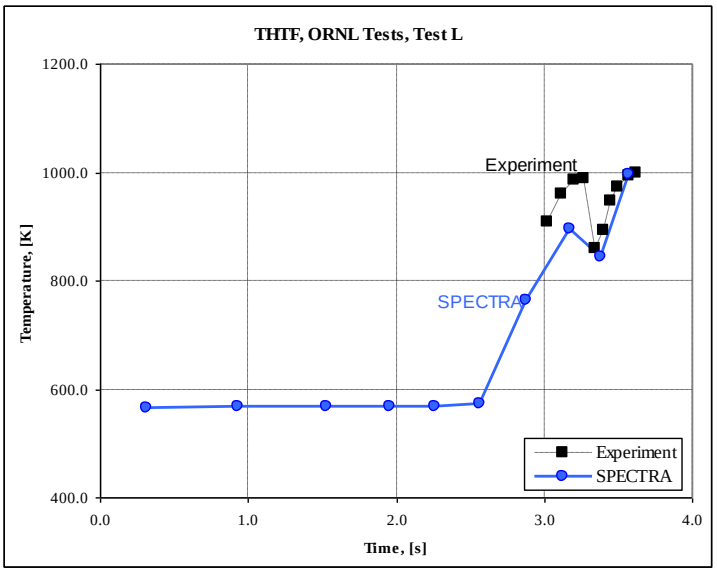

Figure 3-67 Rod surface temperatures, ORNL test L.

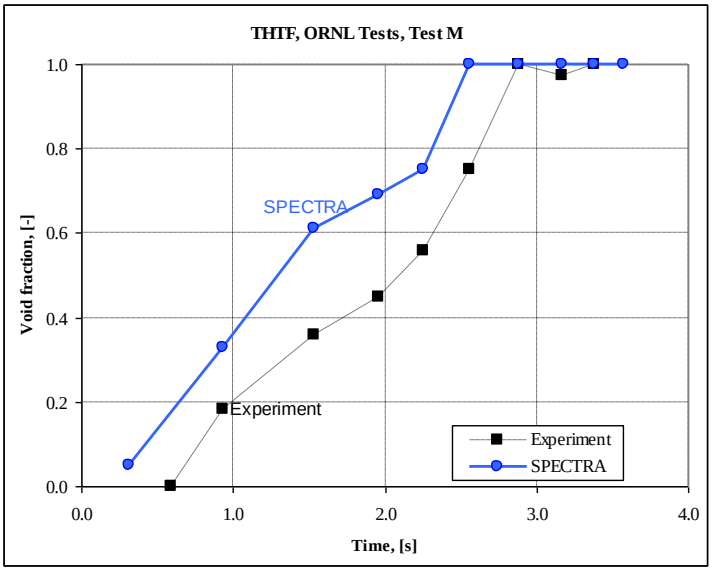

Figure 3-68 Void fractions, ORNL test M.

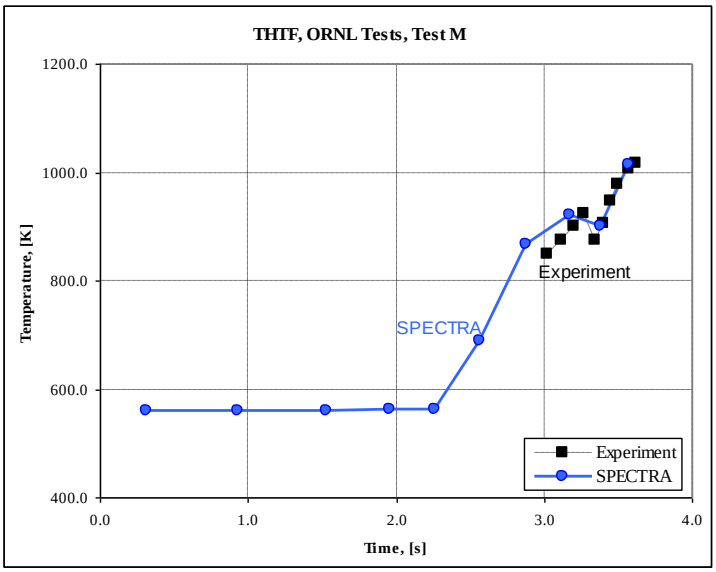

Figure 3-69 Rod surface temperatures, ORNL test M.

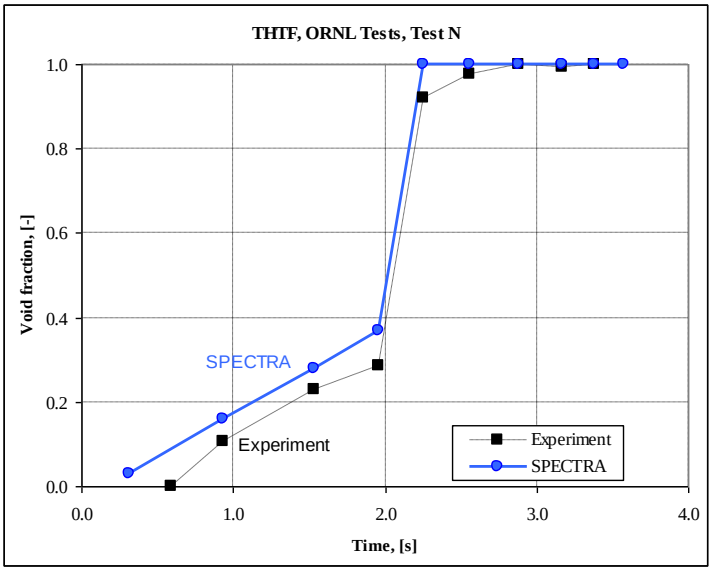

Figure 3-70 Void fractions, ORNL test N.

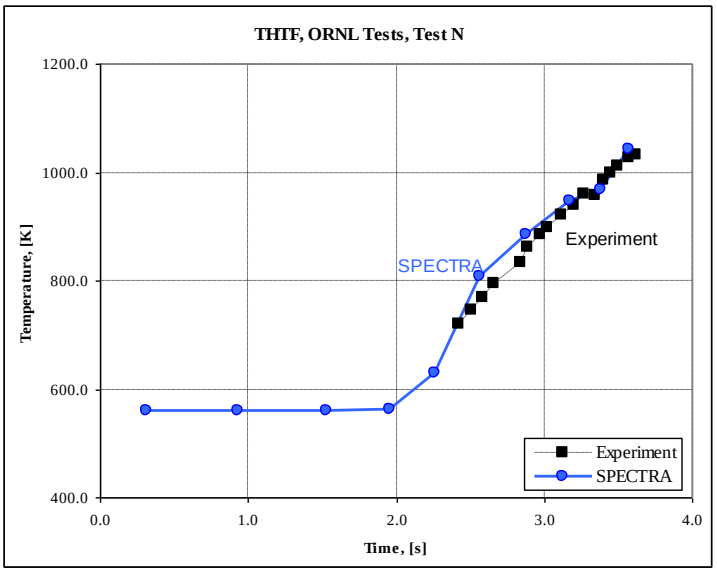

Figure 3-71 Rod surface temperatures, ORNL test N.

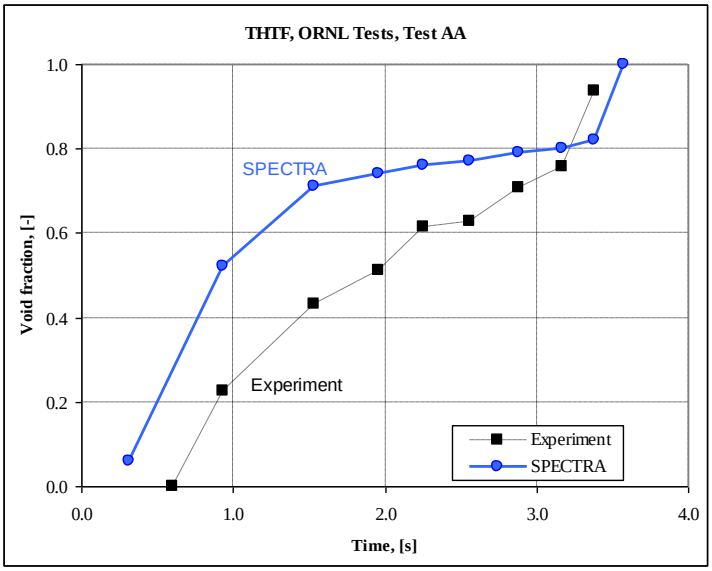

Figure 3-72 Void fractions, ORNL test AA.

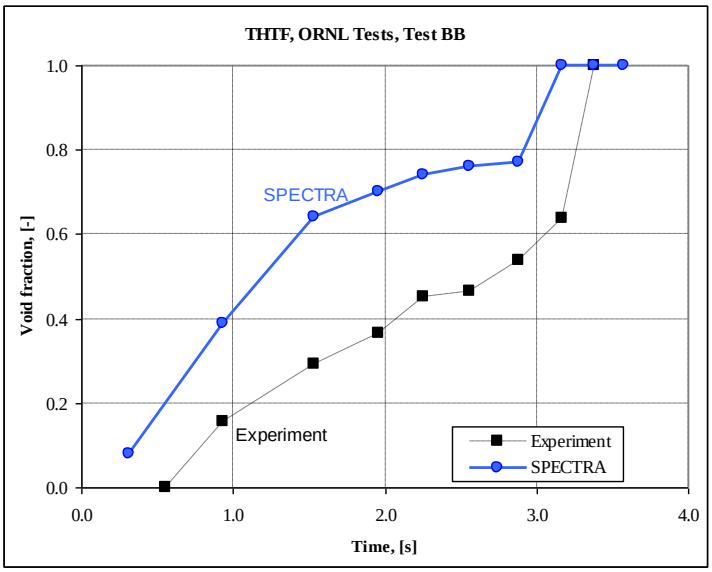

Figure 3-73 Void fractions, ORNL test BB.

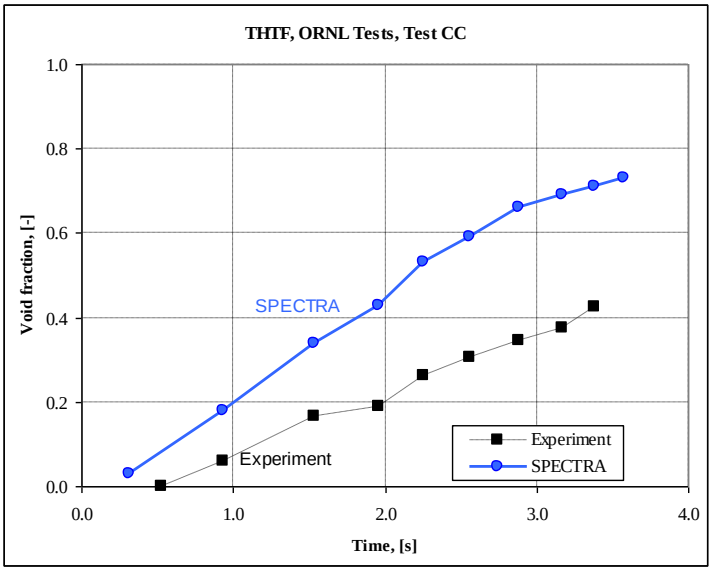

Figure 3-74 Void fractions, ORNL test CC.

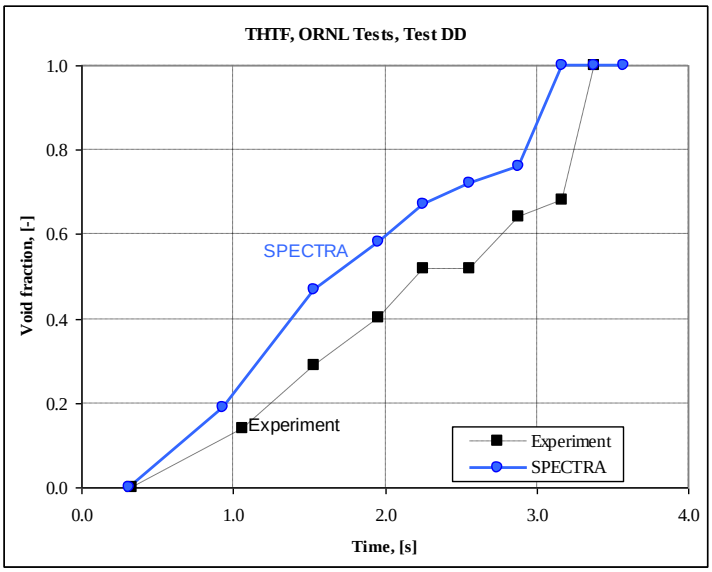

Figure 3-75 Void fractions, ORNL test DD.

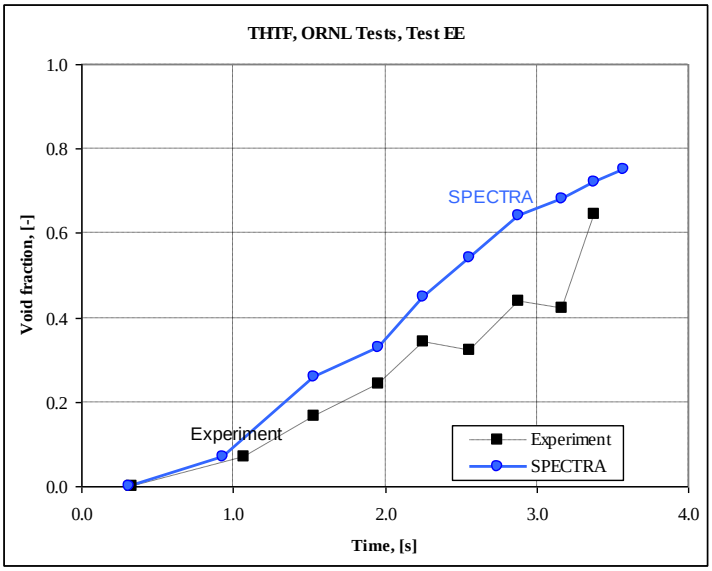

Figure 3-76 Void fractions, ORNL test EE.

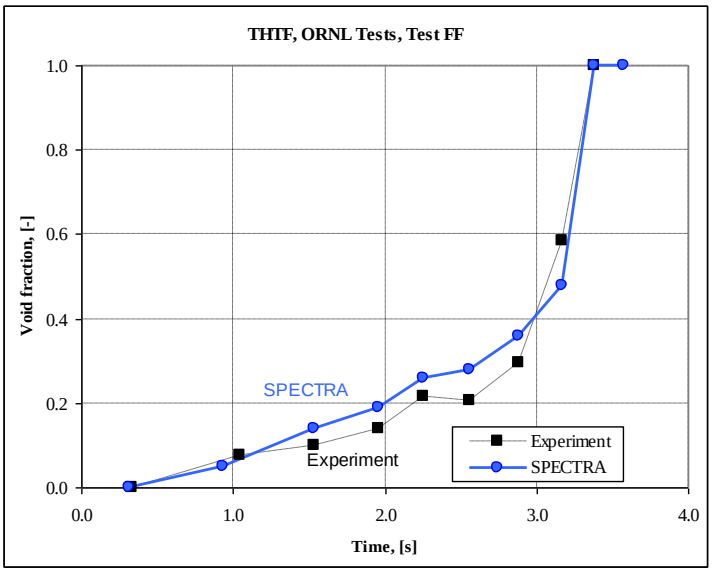

Figure 3-77 Void fractions, ORNL test FF.

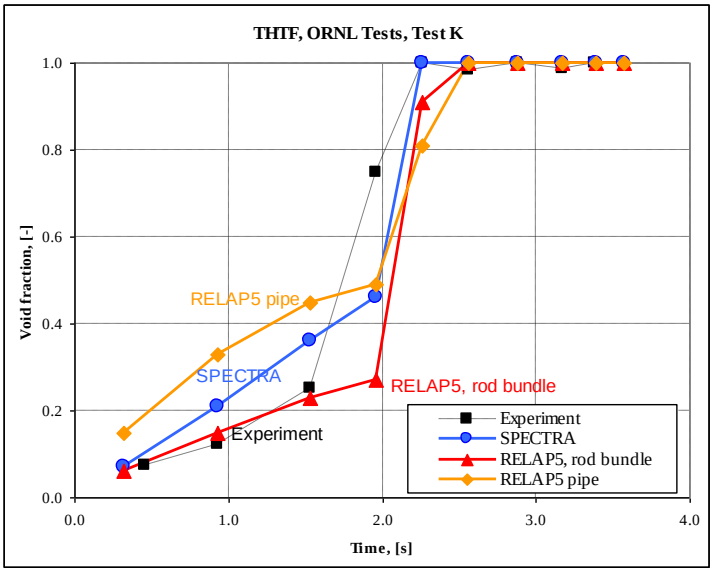

Figure 3-78 Void fractions, ORNL test K, comparisons with RELAP5.

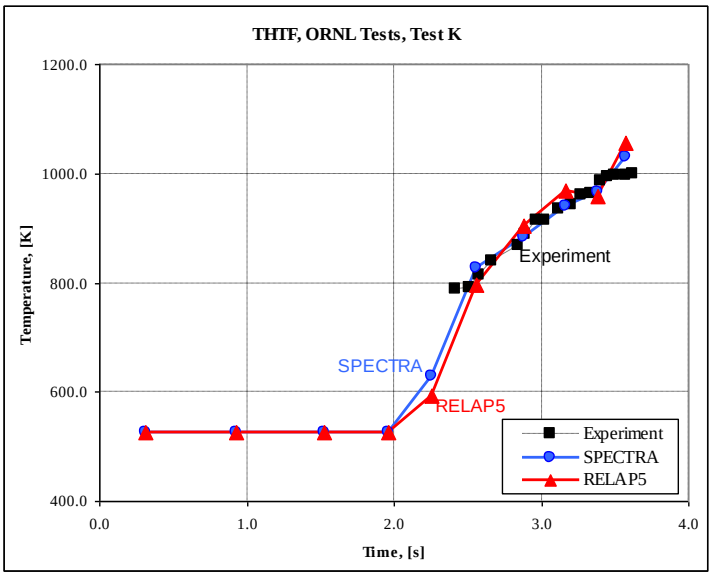

Figure 3-79 Temperatures, ORNL test K, comparisons with RELAP5.

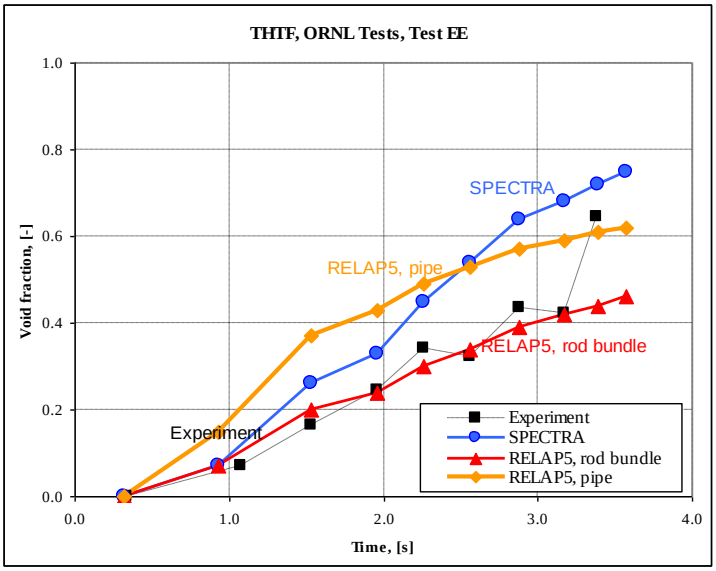

Figure 3-80 Void fractions, ORNL test EE, comparisons with RELAP5.

3.4 Fluid Properties

3.4.1 Fluid Property Test Run

A simple input file, defining two Control Volumes, is used to test the results of the Fluid Property Package. The initial conditions are:

- CV-001 - pure steam at 1.0 bar and 373.15 K (100°C).
- CV-002 - water/air at 1.0 bar and 303.15 K (30°C). The gas composition is: 50% humidity, oxygen and nitrogen volume fractions of 21% and 79% in dry air.

The input file is provided in `\Z-INPUTS\FL\FL.SPE`. A printout of the fluid properties is provided below. Results are compared to available data in sections 2.1.1.6 (steam properties) and 2.1.2 (water properties).

- CV-001 - pure steam at 1.0 bar and 373 K

```
=CV=  CV-001,   THERMODYNAMIC DATA AT TIME :  1.00000E+00 (s)

Quantity         Units    Atms-Gas
---------------  -----   -----------
Pressure,        Pa      1.00000E+05
Temperature,     K       3.73000E+02
Sat. Temp.,      K       3.72757E+02
Sat. Pressure    Pa      1.00816E+05
Volume           m3      1.00000E+00
Mass             kg      5.89216E-01
Energy           J       1.47651E+06
Vert.  Velocity  m/s     0.00000E+00
Horiz. Velocity  m/s     0.00000E+00

=CV=  CV-001,   FLUID PROPERTY DATA AT TIME :  1.00000E+00 (s)

Quantity         Units    Atms-Gas
---------------  -----   -----------
Specific Volume  m3/kg   1.69717E+00
Density          kg/m3   5.89216E-01
Internal Energy  J/kg    2.50588E+06
Enthalpy         J/kg    2.67560E+06
Viscosity        kg/m/s  1.22664E-05
Conductivity     W/m/K   2.50635E-02
Cp               J/kg/K  2.06653E+03
Cv               J/kg/K  1.60500E+03
R                J/kg/K  4.61525E+02
Prandtl Number   -       1.01139E+00
Expansion coef.  1/K     2.68097E-03
Diffusion coef.  m2/s    1.00000E-03

=CV=  CV-001,   ATMOSPHERE GAS COMPOSITION AT TIME :  1.00000E+00 (s)

   GAS              MASS          MASS        PRESSURE       VOLUME
 No.  Id.            kg          FRACTION        Pa          FRACTION
 --   ---         -----------   -----------   -----------   -----------
  3   H2O         5.89216E-01   1.00000E+00   1.00000E+05   1.00000E+00
                  -----------   -----------   -----------   -----------
  Totals:         5.89216E-01   1.00000E+00   1.00000E+05   1.00000E+00

  Relative humidity  (-) :     9.91903E-01
```

- CV-002 - water/air at 1.0 bar and 303.15 K(30°C)

=CV= CV-002, THERMODYNAMIC DATA AT TIME : 1.00000E+00 (s)

Quantity	Units	Atms-Gas	Atms-Drop	Pool-Liq	Pool-Bub
Pressure,	Pa	1.00000E+05	0.00000E+00	1.00000E+05	0.00000E+00
Temperature,	K	3.03000E+02	0.00000E+00	3.03000E+02	0.00000E+00
Sat. Temp.,	K	2.91316E+02	0.00000E+00	3.72757E+02	0.00000E+00
Sat. Pressure	Pa	4.21321E+03	0.00000E+00	4.21321E+03	0.00000E+00
Volum. Fraction	-	1.00000E+00	0.00000E+00	1.00000E+00	0.00000E+00
Mass Fraction	-	1.00000E+00	0.00000E+00	1.00000E+00	0.00000E+00
Volume	m3	5.00000E-01	0.00000E+00	5.00000E-01	0.00000E+00
Mass	kg	5.68035E-01	0.00000E+00	4.97828E+02	0.00000E+00
Energy	J	1.44717E+05	0.00000E+00	6.22475E+07	0.00000E+00
Vert. Velocity	m/s	0.00000E+00	0.00000E+00	0.00000E+00	0.00000E+00
Horiz. Velocity	m/s	0.00000E+00	0.00000E+00	0.00000E+00	0.00000E+00

=CV= CV-002, FLUID PROPERTY DATA AT TIME : 1.00000E+00 (s)

Quantity	Units	Atms-Gas	Atms-Drop	Pool-Liq	Pool-Bub
Specific Volume	m3/kg	8.80227E-01	0.00000E+00	1.00436E-03	0.00000E+00
Density	kg/m3	1.13607E+00	0.00000E+00	9.95655E+02	0.00000E+00
Internal Energy	J/kg	2.54767E+05	0.00000E+00	1.25038E+05	0.00000E+00
Enthalpy	J/kg	3.42790E+05	0.00000E+00	1.25139E+05	0.00000E+00
Viscosity	kg/m/s	1.83524E-05	0.00000E+00	8.00628E-04	0.00000E+00
Conductivity	W/m/K	2.60134E-02	0.00000E+00	6.15159E-01	0.00000E+00
Cp	J/kg/K	1.02673E+03	0.00000E+00	4.18218E+03	0.00000E+00
Cv	J/kg/K	7.36288E+02	0.00000E+00	4.17883E+03	0.00000E+00
R	J/kg/K	2.90439E+02	0.00000E+00	0.00000E+00	0.00000E+00
Prandtl Number	-	7.24356E-01	0.00000E+00	5.44310E+00	0.00000E+00
Expansion coef.	1/K	3.30033E-03	0.00000E+00	3.03595E-04	0.00000E+00
Diffusion coef.	m2/s	2.69597E-05			0.00000E+00
Surface tension	N/m		0.00000E+00	7.12235E-02	

=CV= CV-002, ATMOSPHERE GAS COMPOSITION AT TIME : 1.00000E+00 (s)

GAS No.	Id.	MASS kg	MASS FRACTION	PRESSURE Pa	VOLUME FRACTION
3	H2O	7.36694E-03	1.29692E-02	2.10660E+03	2.10660E-02
4	N2	4.30038E-01	7.57062E-01	7.73358E+04	7.73358E-01
5	O2	1.30631E-01	2.29969E-01	2.05576E+04	2.05576E-01
Totals:		5.68035E-01	1.00000E+00	1.00000E+05	1.00000E+00

Relative humidity (-) : 5.00000E-01

3.4.2 User-Defined Gases Test 1

This test provides a verification of a single user-defined gas. A simple input, defining two Control Volumes with pressure and temperature defined as functions of time, is used for this test.

- CV-100 Helium, molar weight of M_w = 4.0,
- CV-200 user-defined gas. An artificial gas with "easy-to-check" properties:
  - M_w = 8.345, resulting in gas constant R = 1000.0 J/kg-K
  - Σ = 10.0
  - c_p = 2000 J/kg-K, reference parameters: T_{ref} = 0.0 K, u_{ref} = 0.0 J/kg-K
  - $\mu = 3\times10^{-5}$ kg/m-s at T=300 K, $\mu = 4.0\times10^{-5}$ kg/m-s at 400 K
  - k = 0.03 W/m-K at T=300 K, k = 0.04 W/m-K at 400 K

CV-200 is the test volume. CV-100 serves only as a reference volume with a built-in gas. The following conditions are present in both Control Volumes:

- Pressure, $p = 1.0\times10^6$ Pa
- Temperature: linear increase from T = 300.0 K to T = 400.0 K

The input file is provided in `\Z-INPUTS\FL\UD-GAS-1.SPE`. Results are shown in Figure 3-81 (T = 300 K) and Figure 3-82 (T = 400 K). It is seen that the computed parameters are in agreement with the definitions. The intermediate values (between 300 and 400 K) are linear interpolations, which can be seen in time-dependent graphs, such as Figure 3-83.

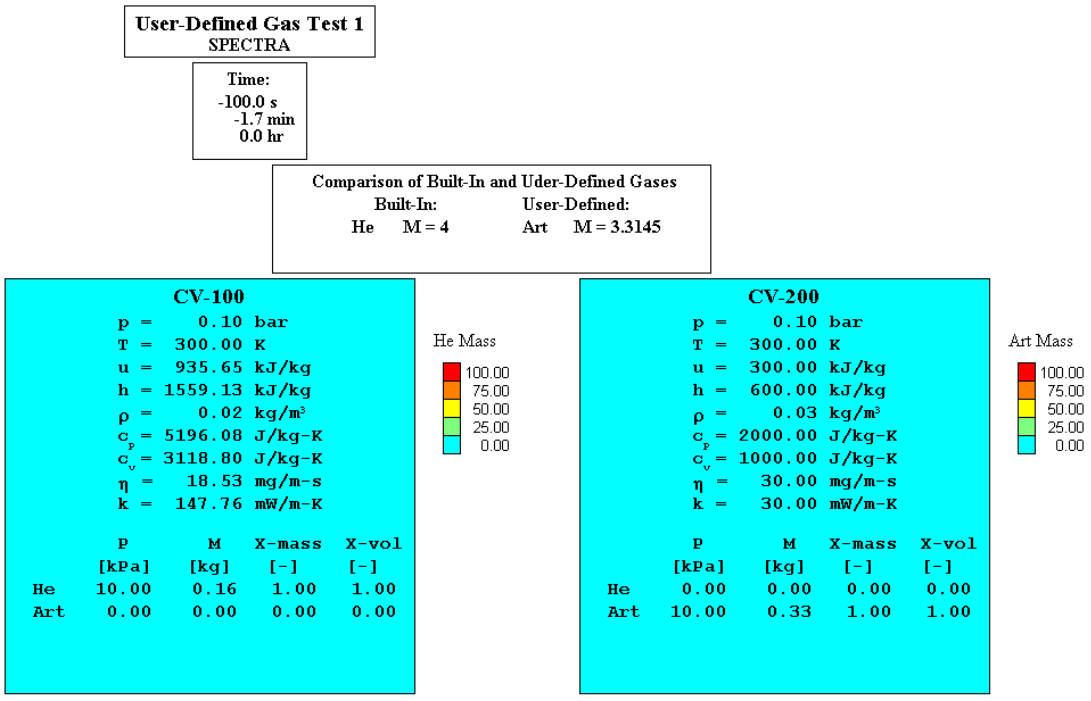

Figure 3-81 Results of the user-defined gas test 1, T= 300 K

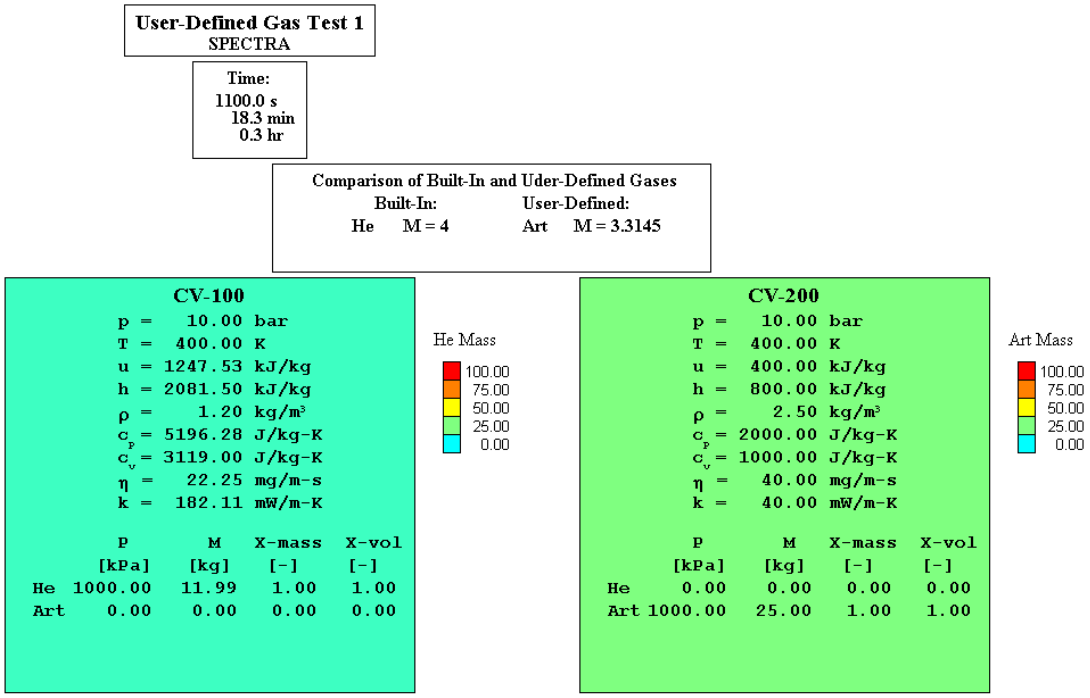

Figure 3-82 Results of the user-defined gas test 1, T= 400 K

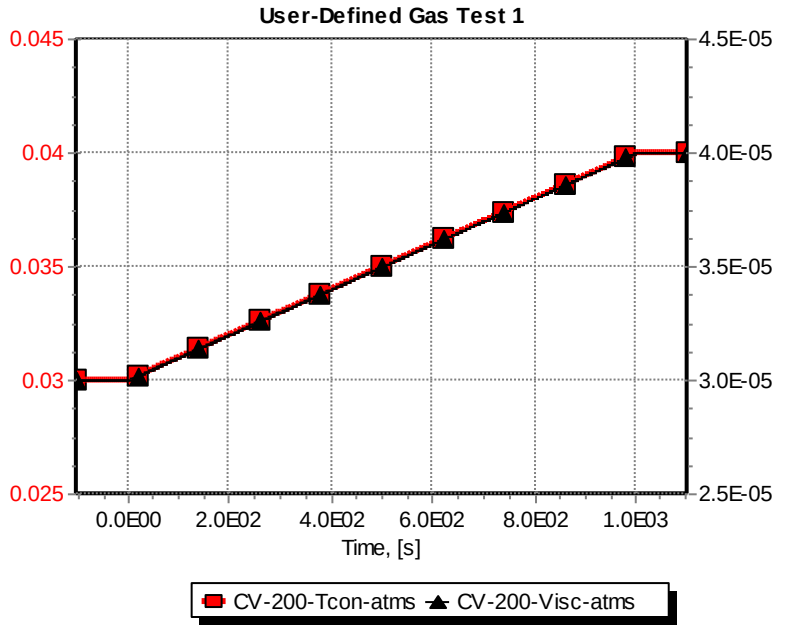

Figure 3-83 Time-dependent graph of conductivity and viscosity - gas test 1

3.4.3 User-Defined Gases Test 2

This test provides a verification of the user-defined gas properties for a mixture of gases. A simple input, defining two Control Volumes with pressure and temperature defined as functions of time, is used for this test.

- CV-100 Mixture of O_2 (M_w = 16.0) and CO_2 (M_w = 44.0)
- CV-200 user-defined CO (M_w = 20.0) and Ar (M_w = 40.0)

The data for CO and Ar was obtained from the Handbook of Chemistry and Physics [125]. The reference parameters were assumed as T_{ref} = 0.0 K, u_{ref} = 0.0 J/kg-K. CV-200 is the test volume. CV-100 serves as a reference volume with a mixture of gases with similar molar weights. The following conditions are present in both Control Volumes:

- Pressure, linear increase from $p = 0.1\times10^5$ Pa to $p = 10.0\times10^5$ Pa
- Temperature: T = 300.0 K

The input file is provided in `\Z-INPUTS\FL\UD-GAS-2.SPE`.

Results are shown in Figure 3-84, Figure 3-85, Figure 3-86, and Figure 3-87. For the reference volume (CV-100) the gases of similar molar weights were selected. The internal energy reference point for the user-defined gases was selected as (0.0, 0.0); the same as is the case with the built-in gases. Therefore the properties of the gas mixture in the test volume (CV-200) are expected to be similar as in the reference volume (CV-100), which is indeed the case - Figure 3-84 and Figure 3-85.

The time dependent graphs, Figure 3-86 and Figure 3-87, show a small pressure dependency of the conductivity and viscosity in for the gas mixture in the reference volume (CV-100), since the built-in gas properties are tabulated versus temperature and pressure (see Volume 1, description of built-in gases). In the test volume (CV-200) conductivity and viscosity of the gas mixture are constant independently of the pressure, since the user-defined gas properties are tabulated versus temperature only (see Volume 1, description of user-defined gases).

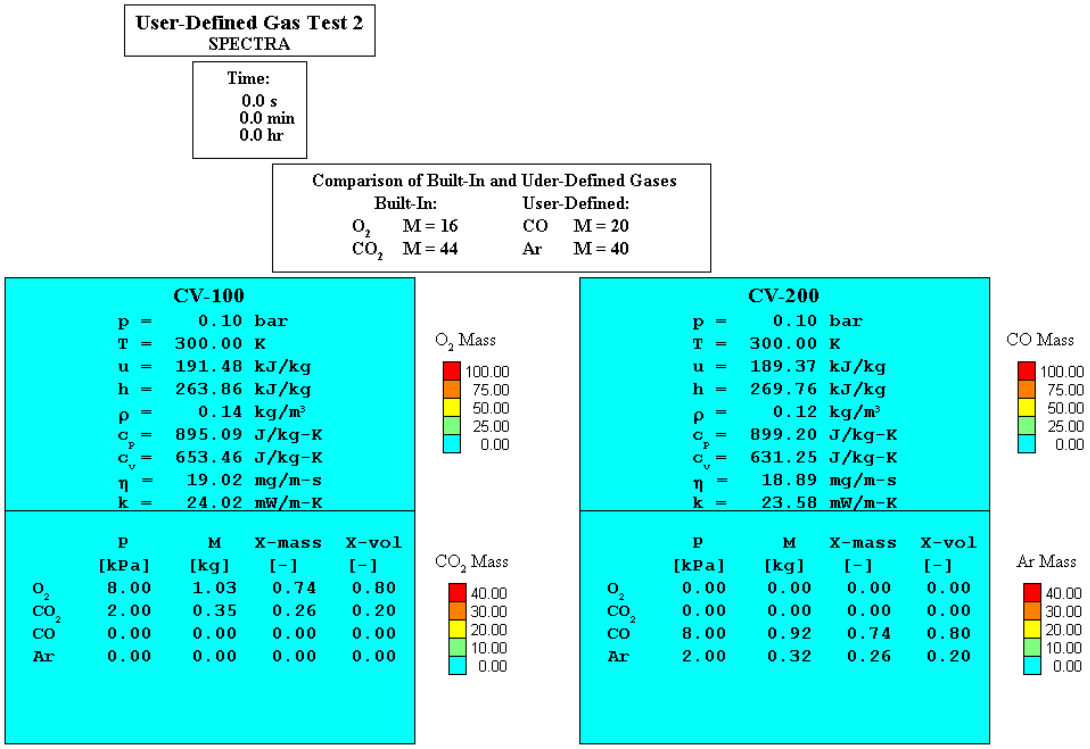

Figure 3-84 Results of the user-defined gas test 2, p = 0.1 bar

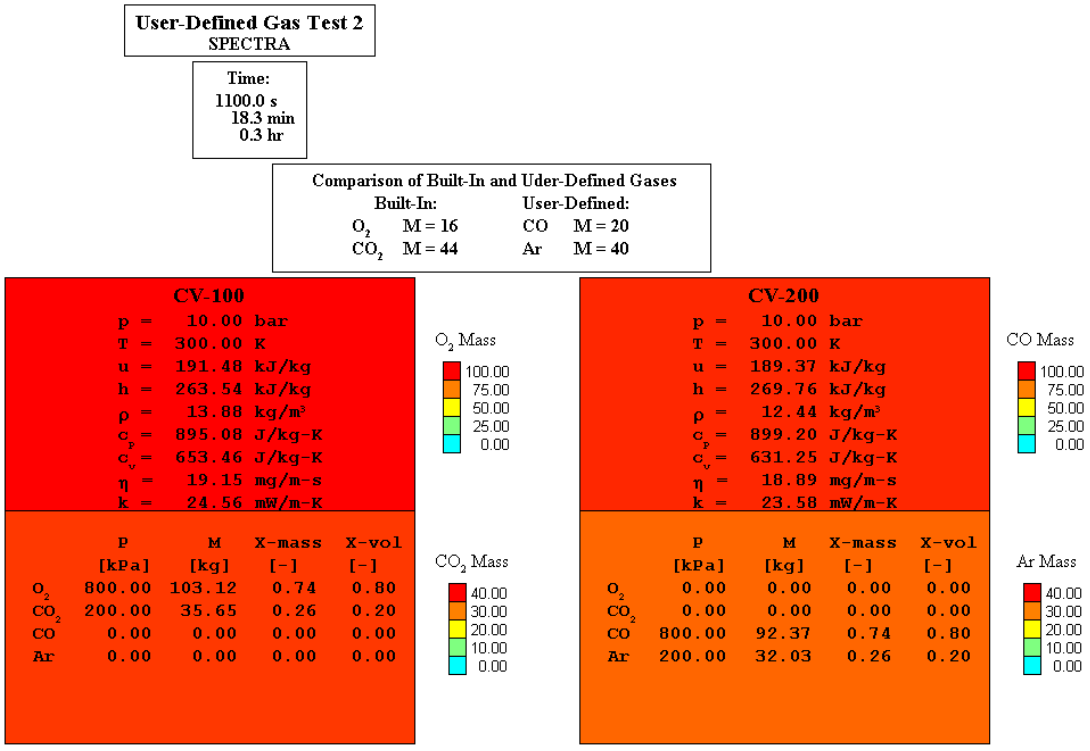

Figure 3-85 Results of the user-defined gas test 2, p = 10.0 bar

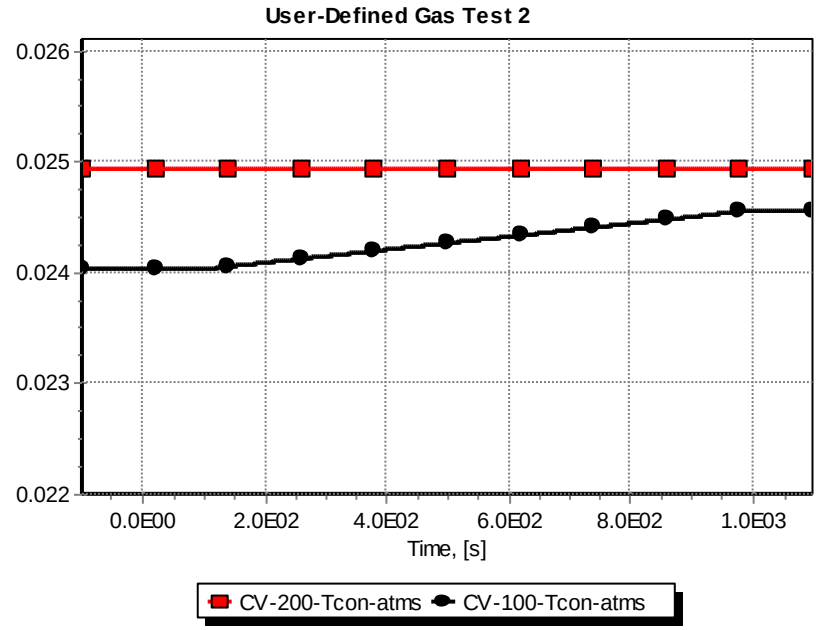

Figure 3-86 Thermal conductivity, user-defined gas test 2

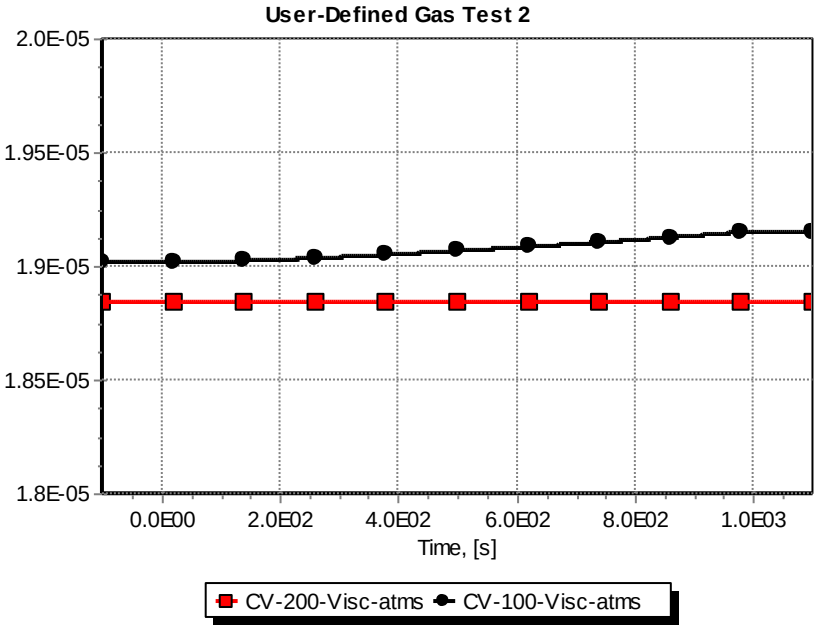

Figure 3-87 Viscosity, user-defined gas test 2

3.4.4 Liquid Lead Loop Test

One test case is provided to illustrate the user-defined fluid properties. It is a liquid lead loop test. The model consists of two loops:

- Primary loop, with liquid lead as coolant
- Secondary loop, with pressurized water as coolant

Modeling of the primary and the secondary loops is described in sections 3.4.4.1 and 3.4.4.2. Sections 3.4.4.3 and 3.4.4.4 show how the properties of liquid lead were obtained and what heat transfer correlations are used for liquid lead. Section 3.4.4.5 describes how the EDF Package is used to run the two loops in synchronized run. Finally, section 3.4.4.6 shows the calculated results.

3.4.4.1 Model - Loop 1

The Loop 1 consists of (see Figure 3-80, left half):

- Reactor vessel, modeled by CV-110, CV-120, CV-130, and SC-100, which represents the "reactor core". The right surface of SC-100 is transferring heat to CV-120. For the left surface of SC-100 the following boundary conditions are used:
    - Heat transfer coefficient, h = TF-101 = 10^9 (W/m-K)
    - Fluid temperature: T_f = TF-102, equal to 700 (K)

- Primary side of the intermediate heat exchanger, HEX-INT, modeled by CV-210, CV-220, CV-230, and SC-200 which represents the plates of the intermediate heat exchanger. The left side of these plates convect heat to CV-220. For the right surface of SC-200 the following boundary conditions are used:
    - Heat transfer coefficient, h = TF-201 = 10^9 (W/m-K)
    - Fluid temperature: T_f = TF-202, defined in EDF (section 3.4.4.5)

The Loop 1 pressure is 1.0 bar. The boundary temperatures are selected in such a way that the temperatures in the lead loop are above about 600 K, which is the lower limit (freezing limit) for this fluid.

The input file is located in: `Z-INPUTS\FL\LEAD-SYNCH\LOOP-1-Pb.ATT`

3.4.4.2 Model - Loop 2

The Loop 2 consists of (see Figure 3-80, right half):

- Secondary side of the intermediate heat exchanger, HEX-INT, modelled by CV-310, CV-320, CV-330, and SC-300 which represents the plates of the intermediate heat exchanger. The right side of these plates convects heat to CV-320. For the left surface of SC-300 the following boundary conditions are used:
  - Heat transfer coefficient, h = TF-301 = 10^9 (W/m-K)
  - Fluid temperature: T_f = TF-302, defined in EDF (section 3.4.4.5)
- Primary side of the ultimate heat sink heat exchanger, HEX-ULT, modelled by CV-410, CV-420, CV-430, and SC-400 which represents the plates of the ultimate heat exchanger. The left side of these plates convects heat to CV-420. For the right surface of SC-300 the following boundary conditions are used:
  - Heat transfer coefficient, h = TF-401 = 10^9 (W/m-K)
  - Fluid temperature: T_f = TF-402, equal to 550 (K)

The Loop 2 pressure is 200.0 bar. The boundary temperatures are selected in such a way that the temperatures in the water loop are below about 640 K, which is the upper limit (boiling) for this fluid.

The input file is located in: `Z-INPUTS\FL\LEAD-SYNCH\LOOP-2-Pb.ATT`

3.4.4.3 Fluid Properties of Liquid Lead (Loop 1)

A FORTRAN program with properties of liquid lead has been created, based on approximation formulae for the following properties of liquid lead [113].

- Saturation pressure, (Pa) ([113], section 2.8.1):

$$p_{sat}(T) = 6.5715 \times 10^9 \cdot \exp\left(-\frac{22{,}247.0}{T}\right)$$

  Here T is temperature, (K). The values obtained from the above correlation and the data are shown in Figure 3-88.

- Enthalpy of saturated liquid, (J/kg) ([113], section 3.2):

$$h_{liq}(T) = h_0(T_{melt}) + \Delta h(T - T_{melt})$$

  Here h_0 is the enthalpy at the melting point, T_{melt}, and Δh is the enthalpy change from the melting temperature to the temperature T. These values of h_0 and T_{melt}, expressed in (J/mol) and Δh isotherms are given by:

$$h_0(T_{melt}) = -5.13300\times10^{-4}\cdot T_{melt}^2 + \\ +3.03623\times10^{1}\cdot T_{melt} - \\ -4.67191\times10^{3}$$

$$\Delta h(T-T_{melt}) = 3.3756\times10^{+1}\cdot(T-T_{melt}) - \\ -3.1310\times10^{-3}\cdot(T-T_{melt})^2 + \\ +5.7614\times10^{-7}\cdot(T-T_{melt})^3$$

Finally the value of enthalpy should be expressed in (J/kg). Therefore the value given by the above formulae is multiplied by 1000 and divided by the molar weight of lead, equal to 207.2 kg/kmol. The values obtained from the above correlation and the data are shown in Figure 3-89.

- Density of saturated liquid, (kg/m^3) ([113], section 2.10.1):

$$\rho_{liq}(T) = 1.1367\times10^{4} - 1.1944\cdot T$$

The values obtained from the above correlation and the data are shown in Figure 3-90.

- Specific heat of saturated liquid, (J/kg-K) ([113], section 2.13.1):

$$c_p(T) = 175.1 - 4.961\times10^{-2}\cdot T + \\ +1.985\times10^{-5}\cdot T^2 - \\ -2.099\times10^{-9}\cdot T^3 - \\ -1.524\times10^{6}\cdot T^{-2}$$

The values obtained from the above correlation and the data are shown in Figure 3-91.

- Thermal conductivity, (W/m-K) ([113], section 2.17.1):

$$k_{liq}(T) = 9.2 + 0.011\cdot T$$

The values obtained from the above correlation and the data are shown in Figure 3-92.

- Viscosity of saturated liquid, (kg/m/s) ([113], section 2.15.1):

$$\eta_{liq}(T) = 4.55\times10^{-4}\cdot\exp\left(\frac{1069}{T}\right)$$

The values obtained from the above correlation and the data are shown in Figure 3-93.

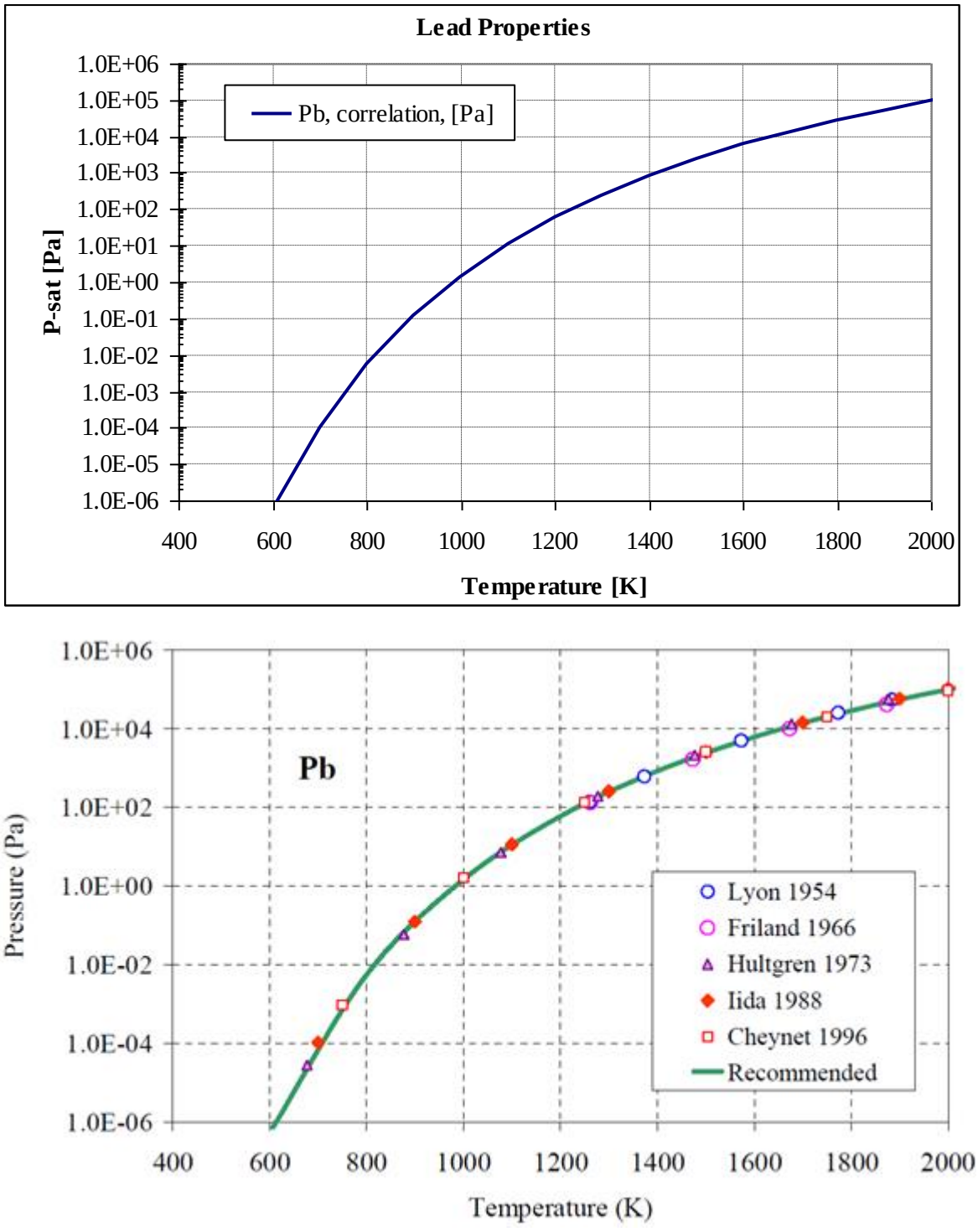

Figure 3-88 Saturation pressure, liquid lead, above: corelation, below: data [113]

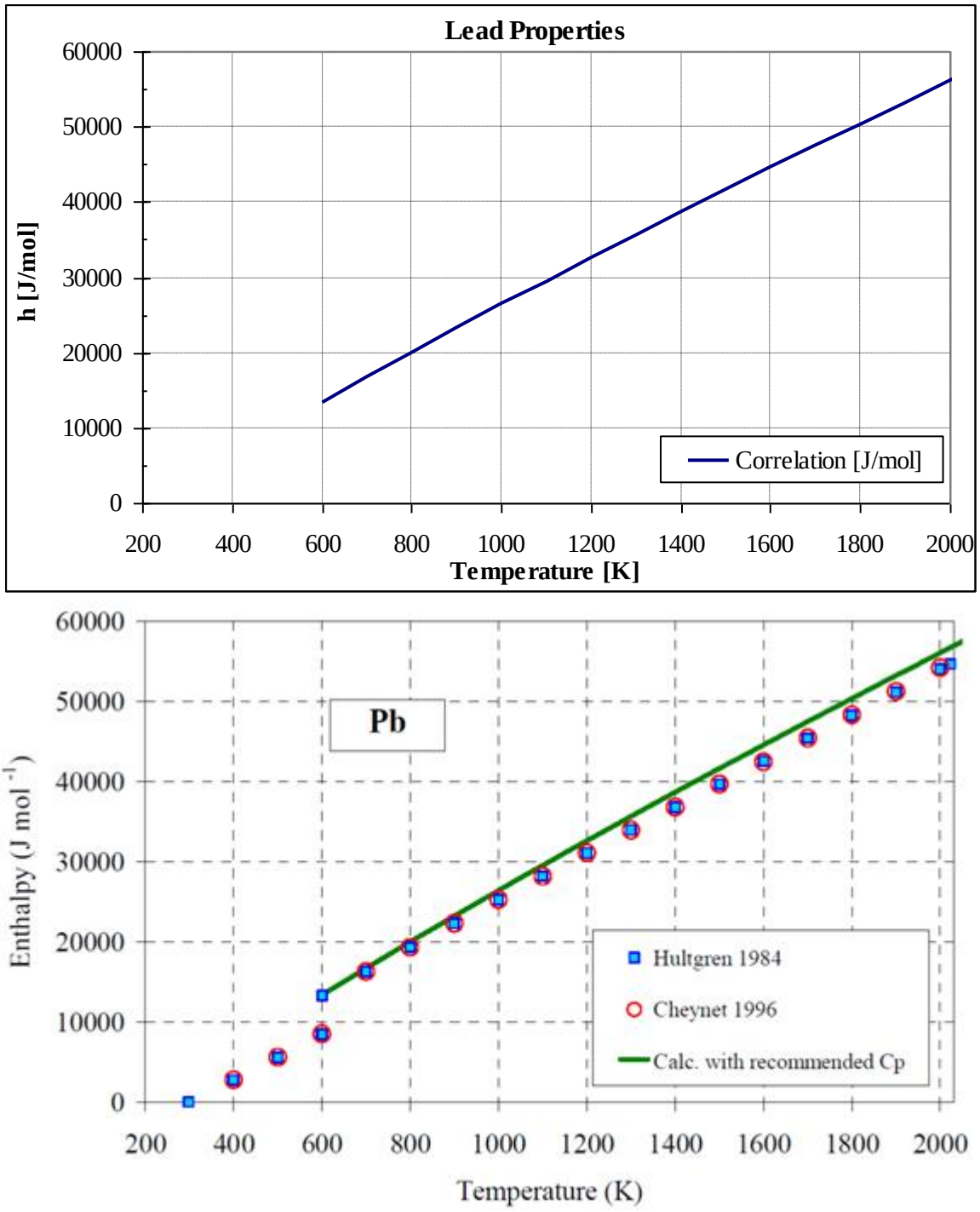

Figure 3-89 Enthalpy, liquid lead, above: corelation, below: data [113]

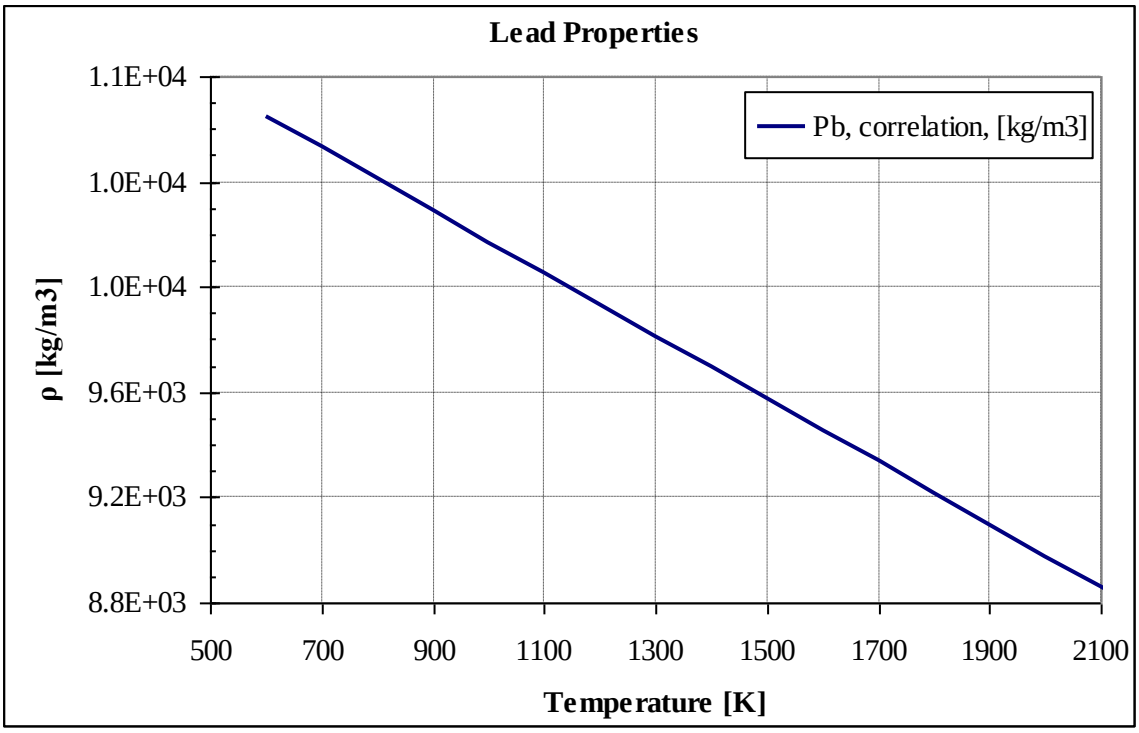

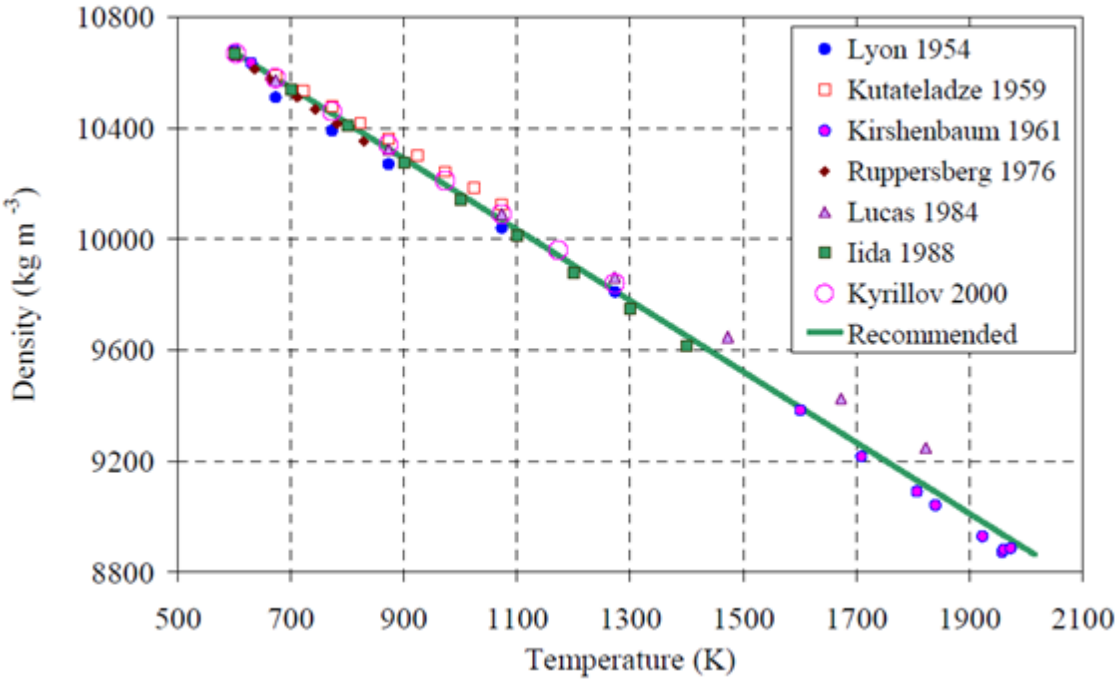

Figure 3-90 Density, liquid lead, above: corelation, below: data [113]

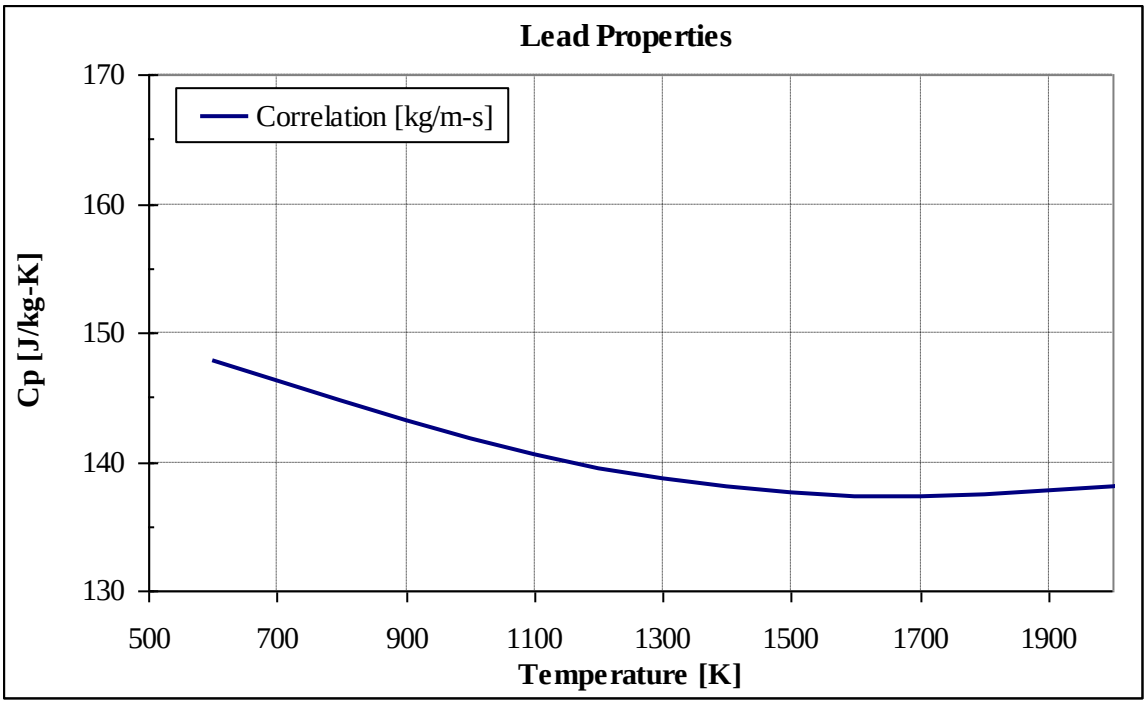

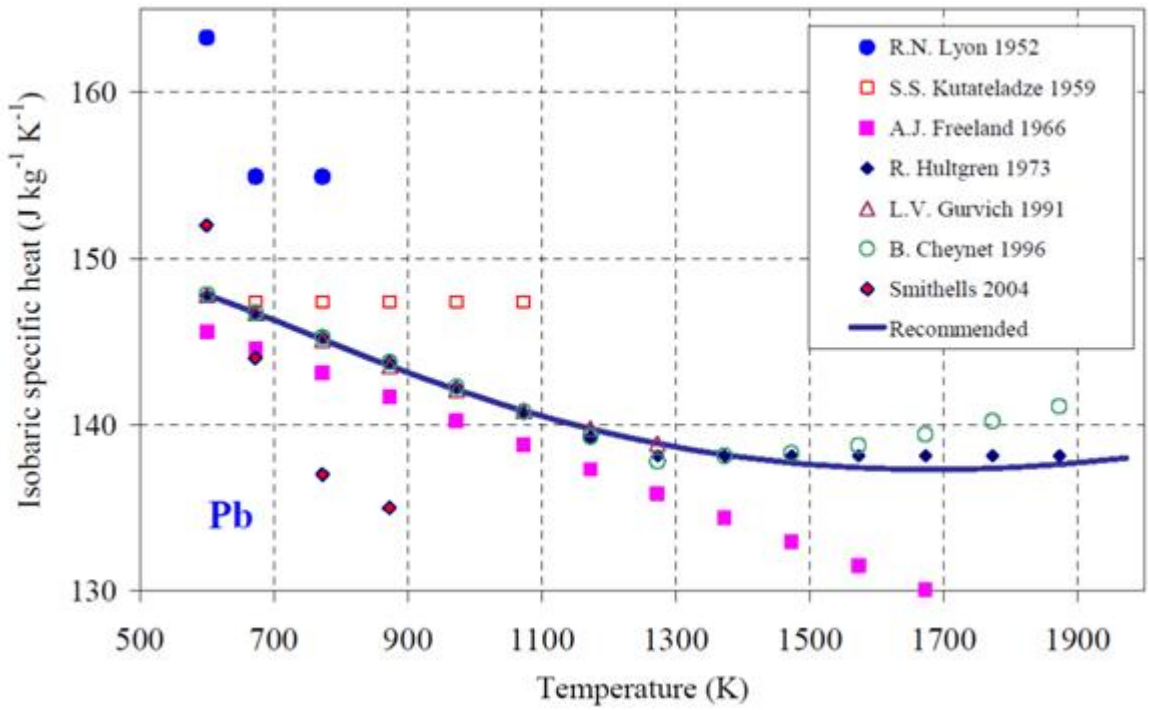

Figure 3-91 Specific heat, liquid lead, above: corelation, below: data [113]

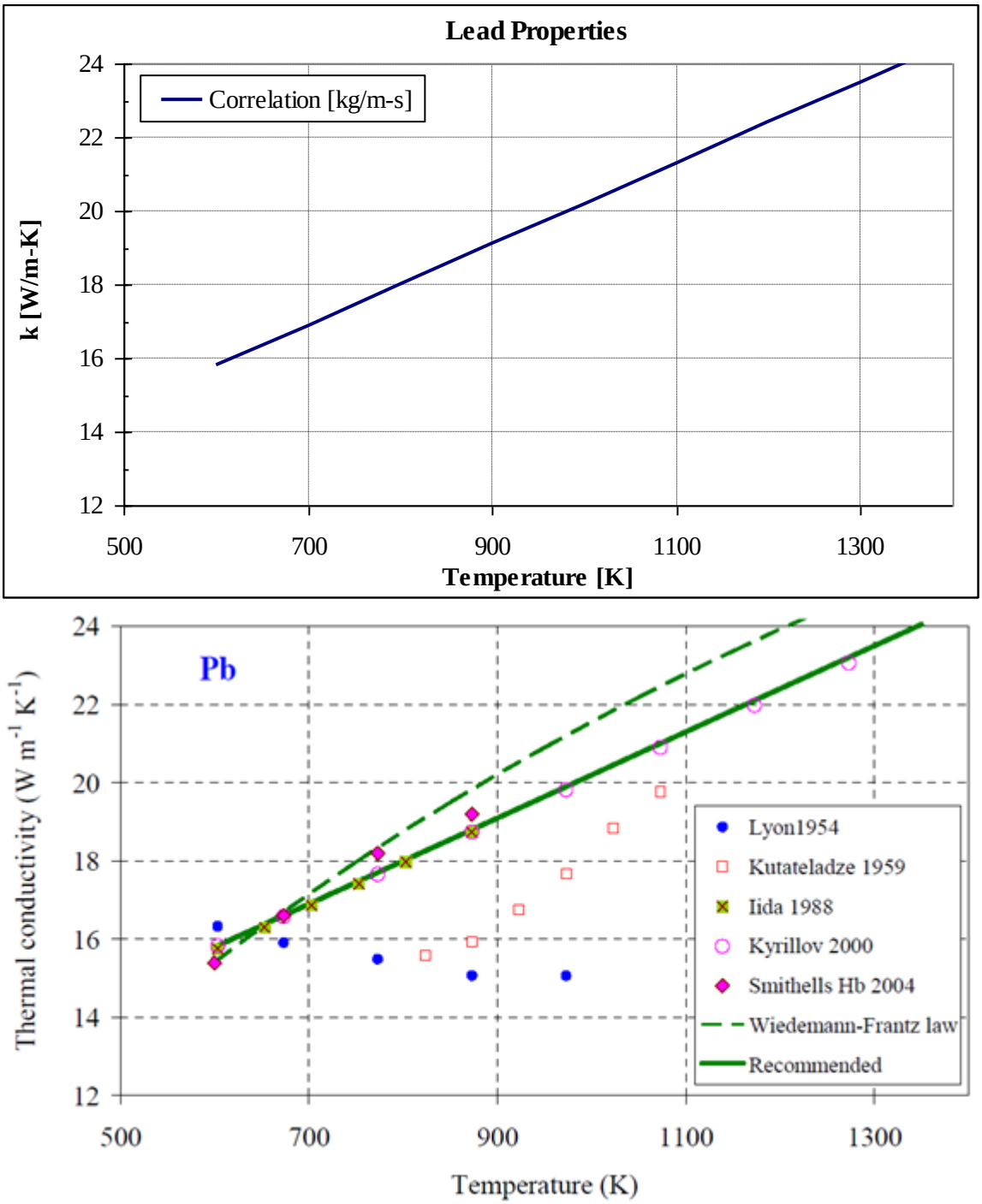

Figure 3-92 Thermal conductivity, liquid lead, above: corelation, below: data [113]

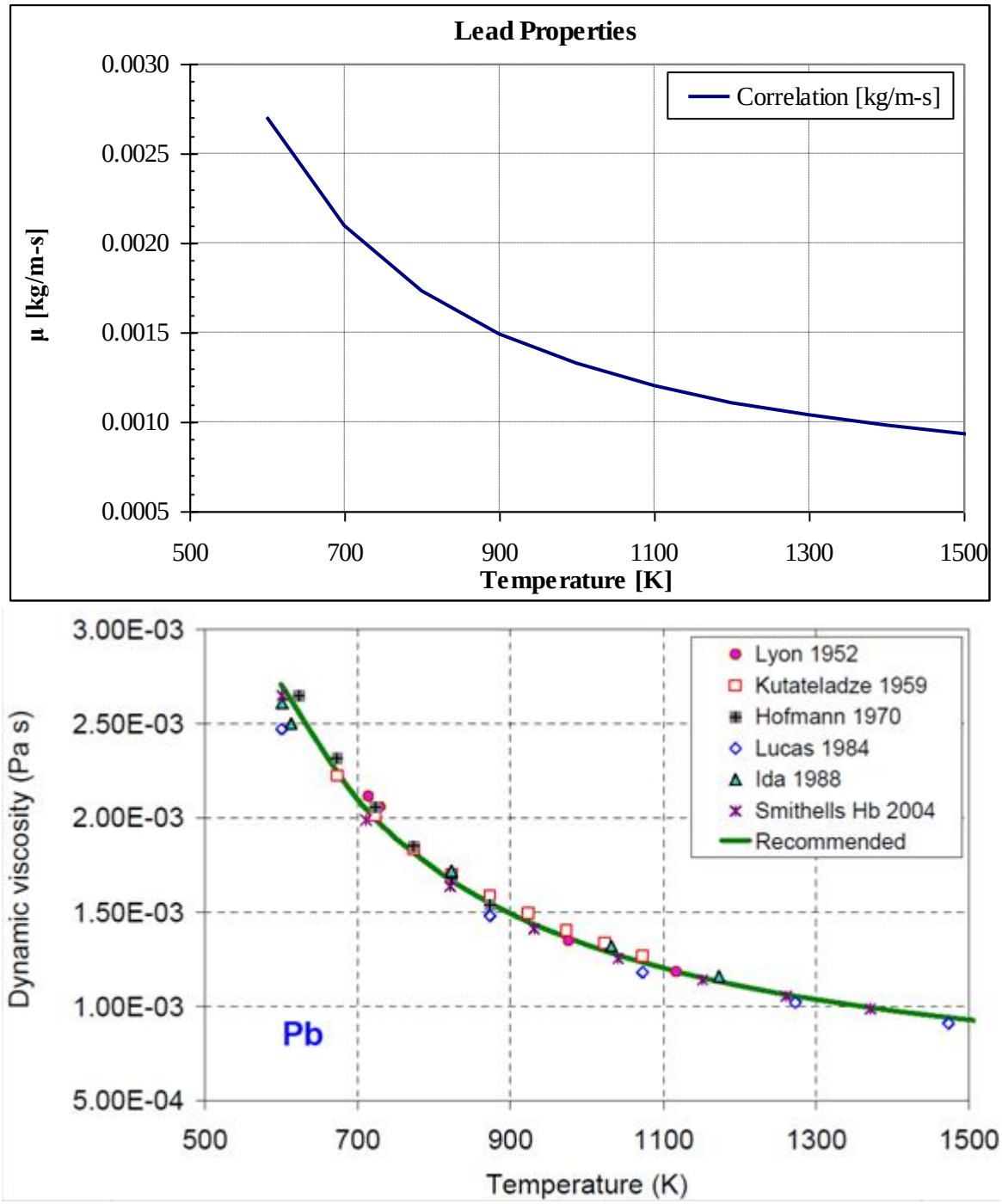

Figure 3-93 Viscosity, liquid lead, above: corelation, below: data [113]

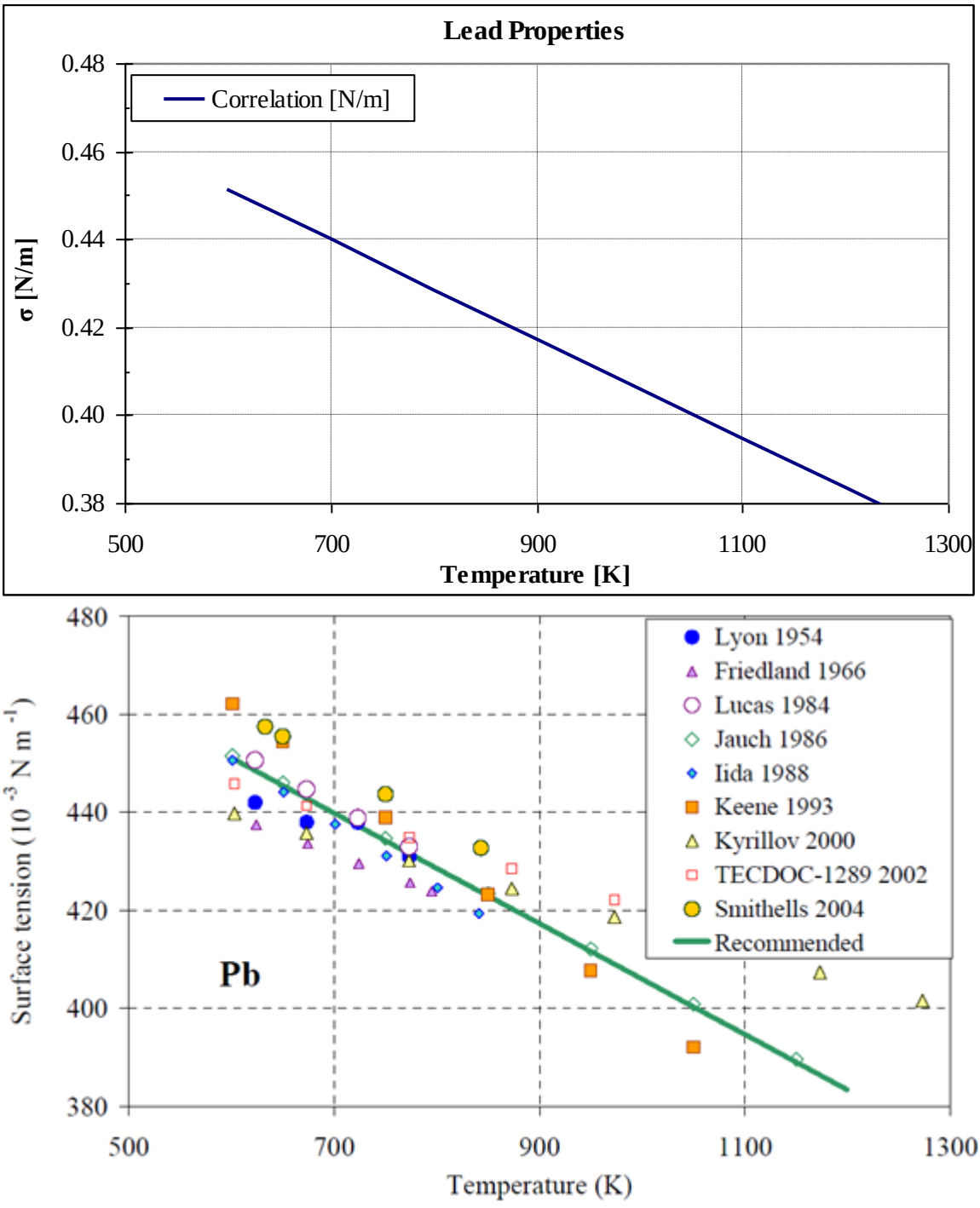

Figure 3-94 Surface tension, liquid lead, above: corelation, below: data [113]

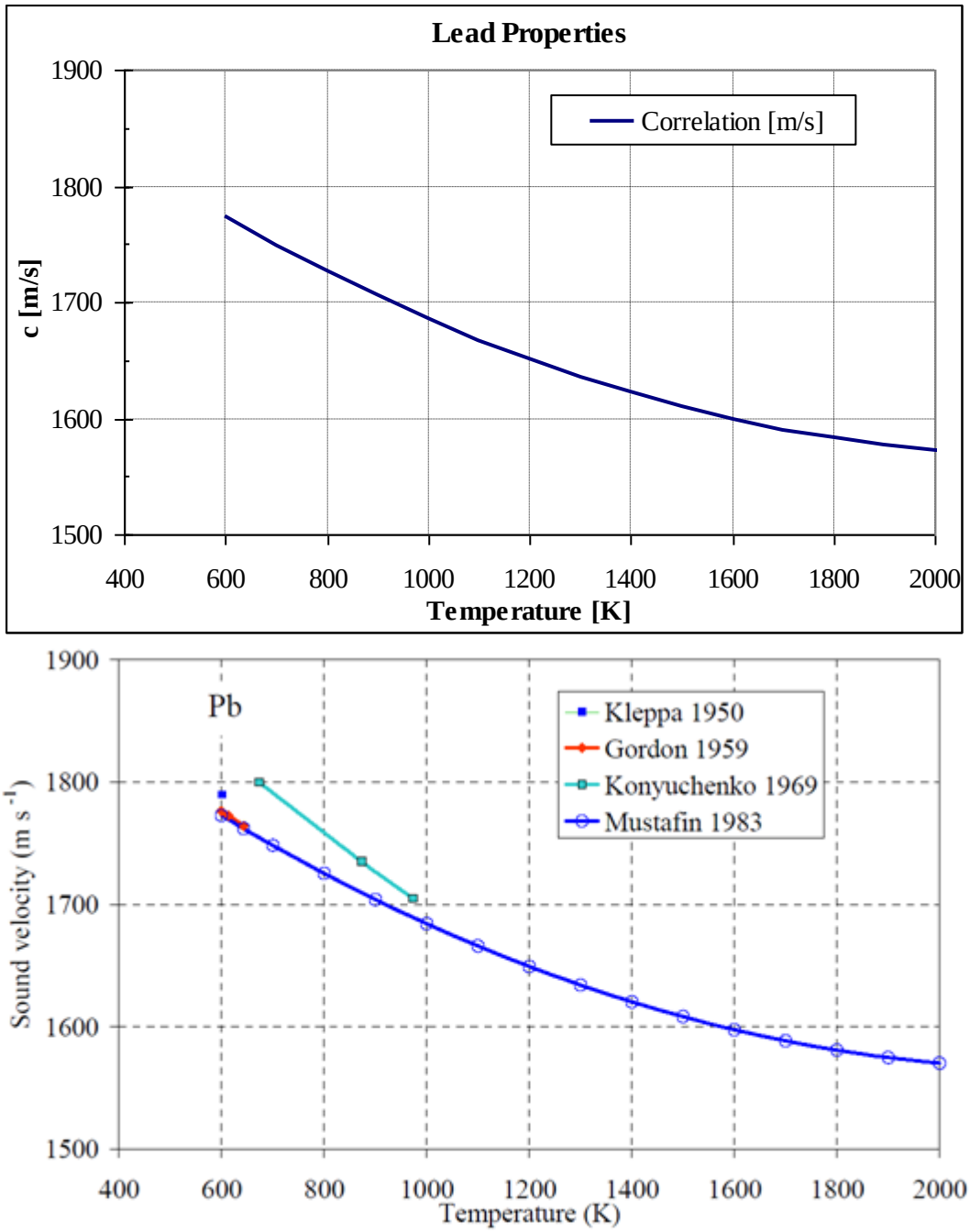

Table 2.12.2. Sound velocity in the molten bismuth

Figure 3-95 Sound velocity, liquid lead, above: corelation, below: data [113]

- Surface tension, (N/m) ([113], section 2.9.1):

$$\sigma(T) = 0.519 - 1.13 \times 10^{-4} \cdot T$$

The values obtained from the above correlation and the data are shown in Figure 3-94.

- Speed of sound, (m/s) ([113], section 2.12.1):

$$c(T) = 1951.75 - 0.3423 \cdot T + 7.635 \times 10^{-5} \times T$$

The values obtained from the above correlation and the data are shown in Figure 3-95.

A set of functions computing the lead properties from the above equations is located in:
`Z-GENS\FL\LEAD\LEAD.FOR`

The program to generate tables of liquid lead properties is located in:
`Z-GENS\FL\LEAD\LEAD-G.FOR`

The program generates two files that may be used directly by SPECTRA. These are:

`LEAD-K.ATT` The file contains tabulated properties versus temperature expressed in Kelvins
`LEAD-C.ATT` The file contains tabulated properties versus temperature expressed in ˚C

In order to activate the liquid lead the user must attach one of these files with the ATTACH statement, for example:

```
ATTACH LEAD-K
```

For the Loop 1 the liquid lead is defined by attaching the LEAD-K file. An example input is provided as:
`Z-GENS\FL\LEAD\LEAD-Q.SPE`

3.4.4.4 Heat Transfer Correlations for Liquid Lead (Loop 1)

A set of heat transfer correlations, recommended in [113] has been defined by specifying the coefficients shown in Table 3-13 (the correlations and the coefficients for different geometries are discussed in Volume 1).

Table 3-13 Correlation coefficients for liquid lead

Geometry	A_0	A_1	B_1	C_1	A_2	B_2	C_2	D_2	A_3	B_3	C_3	D_3
Rectangular	5.60	0.019	0.775	0.775	-	-	-	-	-	-	-	-
Cylindrical	3.66	0.620	0.5	0.333	$3.923 \cdot 10^{-4}$	0.625	0.0	0.8	0.543	0.0	–0.667	–0.25
Spherical	-	-	-	-	-	-	-	-	-	-	-	-

For the rectangular geometry the correlation for multiple plates is used:

$$Nu = 5.60 + 0.019 \cdot Re^{0.775} \cdot Pr^{0.775}$$

For cylindrical geometry an appropriate correlation is defined here, although it is done only for illustration purposes because both the reactor and the heat exchangers are made of plates so they will be using the rectangular geometry correlation.

For the spherical geometry no correlation is defined, which means that the correlation applicable for the cylindrical geometry would be used if such structures were present in the model.

The default option is used, with the heat transfer calculated from the forced convective set of correlations applicable for liquid metal (shown above), and the natural convection correlations are not used.

3.4.4.5 Synchronization of Loop 1 and 2 (EDF)

Since liquid metal and water cannot be used simultaneously in one SPECTRA job, the Loop 1 and Loop 2 must be run in parallel using the synchronized option available within the EDF Package. (Example of synchronized runs are shown in sections 3.17.4 and 3.17.5.)

The interface between the two loops is the intermediate heat exchanger INT-HEX. The two independent runs need to exchange the following information:

- Loop 1:
  - HEX-INT right surface temperature needs to be obtained from the Loop 2
  - HEX-INT left surface temperature needs to be given to the Loop 2

- Loop 2:
  - HEX-INT left surface temperature needs to be obtained from the Loop 1
  - HEX-INT right surface temperature needs to be given to the Loop 1

Therefore the EDF data include:

- Loop 1:
  - Write-EDF file: `LOOP-1-Pb.DAT`. SC-200, node 1 (left) temperature is written to this file
  - Read-EDF file: `LOOP-2-Pb.DAT`. Value of TF-202 is read from this file. As shown in section 3.4.4.1 the right fluid temperature for SC-200 is defined by this TF. Since the value obtained from the Loop 2 is the wall temperature, one needs to make sure that the wall temperature is equal to the fluid temperature, given by TF-202. This is ensured by using a very large number for the heat transfer coefficient - see section 3.4.4.1.

  The input file is located in: `Z-INPUTS\FL\LEAD-SYNCH\LOOP-1-Pb.SPE`

- Loop 2:
  - Write-EDF file: `LOOP-2-Pb.DAT`. SC-300, node 4 (right) temperature is written to this file
  - Read-EDF file: `LOOP-1-Pb.DAT`. Value of TF-302 is read from this file. As shown in section 3.4.4.2 the left fluid temperature for SC-300 is defined by this TF.

Since the value obtained from the Loop 1 is the wall temperature, one needs to make sure that the wall temperature is equal to the fluid temperature, given by TF-302. This is ensured by using a very large number for the heat transfer coefficient - see section 3.4.4.2.

The input file is located in: `Z-INPUTS\FL\LEAD-SYNCH\LOOP-2-Pb.SPE`

3.4.4.6 Results

Results are shown in Figure 3-96. The left side of the picture shows results for the Loop 1, while the right side of the picture shows results for the Loop 2. The Loop 1 and Loop 2 results are separated by vertical dashed line.

For the interfacing structure, SC-200, the left and right side values are available from both models, to check if the synchronization is correct. The left/right side temperatures are 611 K / 607 K, which is seen on both Loop 1 and Loop 2 results. The data transfer is performed explicitly, at the beginning of the time step. Therefore the interfacing values are not identical. They are lagging by one synchronization step (equal to the maximum time step) in the present case equal to Δt_{max}=0.01 s. This is seen in the heat fluxes:

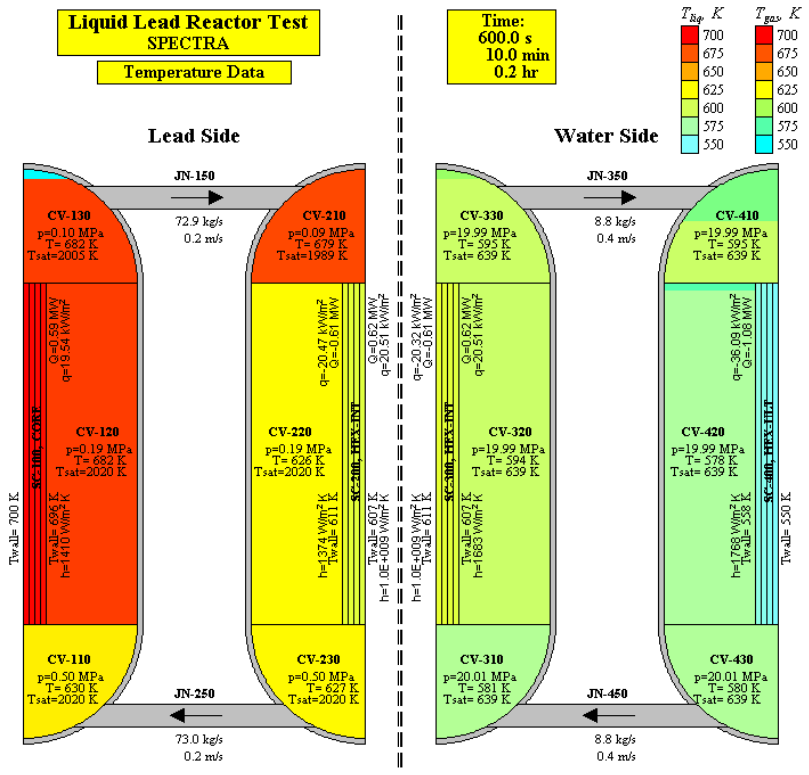

Figure 3-96 Liquid lead loop. Synchronized run with liquid lead (loop 1) and water (loop 2)

- Loop 1 (left / right): 20.47 kW/m^2 / *20.51* kW/m^2
- Loop 2 (left / right): *20.32* kW/m^2 / 20.51 kW/m^2

The values printed in italics are the values which were obtained from the EDF files so they are lagging by 0.01 s.

It is seen that the natural circulation in the primary loop (lead loop) is large - more than 70 kg/s. On the secondary loop the natural circulation flow is much smaller, about 9 kg/s. The results are qualitatively correct. Quantitative verification and validation of the liquid metal package is being performed and documented in a separate report.

3.4.5 Heat Transfer Correlations for Alternative Fluid

The present test provides verification of the user-defined heat transfer correlation for alternative liquids. The test consists of CV-801, filled with liquid lead at $p = 1.0\times10^5$ Pa, $T = 650$ K. The thermal conductivity is equal to:

$$k = 16.35 \text{ W/m-K}$$

Seven 1-D Solid Heat Conductors are defined, SC-801 through SC-807, with internal heat source (10 kW) and different geometries (geometry is shown in Table 3-14). The characteristic dimension is assumed to be:

$$D = 0.1 \text{ m}$$

Seven heat transfer correlations are defined, which give Nusselt numbers from 1.0 to 7.0. The corresponding heat transfer coefficient was calculated from:

$$h = Nu \cdot \frac{k}{D}$$

The calculations are provided in `\Z-INPUTS\FL\Correlations.XLS`. The values of the Nusselt number and the heat transfer coefficients are shown below.

- Correlation No. 1: $Nu = 1.0$ $h = 0.16$ kW/m^2-K
- Correlation No. 2: $Nu = 2.0$ $h = 0.33$ kW/m^2-K
- Correlation No. 3: $Nu = 3.0$ $h = 0.49$ kW/m^2-K
- Correlation No. 4: $Nu = 4.0$ $h = 0.65$ kW/m^2-K
- Correlation No. 5: $Nu = 5.0$ $h = 0.82$ kW/m^2-K
- Correlation No. 6: $Nu = 6.0$ $h = 0.98$ kW/m^2-K
- Correlation No. 7: $Nu = 7.0$ $h = 1.14$ kW/m^2-K

The correlations are selected got each surface as shown in Table 3-14. On the right surfaces the default selection is applied, which is (see Volume 2):

- Rectangular geometry: Correlation No. 1
- Cylindrical geometry: Correlation No. 2
- Spherical geometry: Correlation No. 3

Table 3-14 Selection of correlations on SC surfaces

SC number	Geometry	Correlation selection	
		Left surface	Right surface
SC-801	rectangular	1	default
SC-802	cylindrical	2	default
SC-803	spherical	3	default
SC-804	rectangular	4	default
SC-805	cylindrical	5	default
SC-806	spherical	6	default
SC-807	rectangular	7	default

The input file is provided in `\Z-INPUTS\FL\Correlations.SPE`. Calculations were performed for a sufficiently long time (t = 1000 s) to obtain stationary conditions. Results are shown in Figure 3-97. It is seen that the correlations are properly selected on each surface, i.e.:

Left surface:	1	2	3	4	5	6	7	(user-defined)
Right surface:	1	2	3	1	2	3	1	(default)

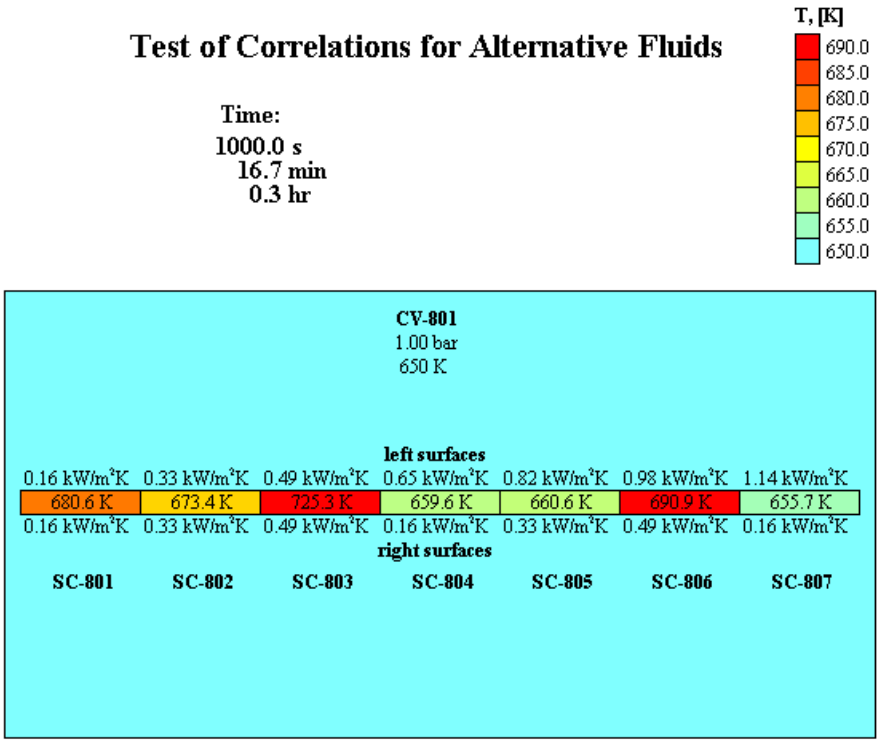

Figure 3-97 Results of the “Correlations” test

3.5 1-D Solid Heat Conductors

Sections 3.5.1 and 3.5.4 present verification cases for conduction heat transfer in 1-D Solid Conductors. Verification is performed by comparing calculated results against analytical solutions. Section 3.5.6 presents results of a test for a simple radiation model and verification by comparisons with analytical solution. Section 3.5.7 shows test of a heat exchanger and comparison with numerical results obtained with other codes (RELAP, MELCOR).

3.5.1 Steady State Conduction Tests for 1-D Solid Heat Conductors

Conductor with internal heat source, constant thermal conductivity

- *Theory*

The steady state conduction in a heat conductor with internal heat source is considered for three geometries: rectangular, cylindrical, and spherical. The left surface of the rectangular conductor is assumed to be insulated. The cylinder and sphere are assumed to be solid (the inner radius is equal to zero). The right surface of the conductors is transferring heat by convection. The heat transfer coefficient and the fluid temperature at the right surface are constant. The internal heat source is assumed to be uniformly distributed throughout the conductor. The thermal conductivity of conducting material is assumed to be constant.

The theoretical solutions of heat conduction equation result in the following steady state temperature distribution inside the conductors of rectangular, cylindrical and spherical shapes (see [102], equations: 2.21a on page 32, 2.24a on page 34 for plate and cylinder, for sphere see [15], equation 149 on page 3-111):

$$T(x) - T_R = \frac{q}{\alpha \cdot k} \cdot \left(x_R^2 - x^2 \right)$$

$T(x)$	temperature at the distance x from the left boundary, (K)		
T_R	right surface temperature, (K)		
q	internal heat source density, (W/m^3)		
k	thermal conductivity, (W/(m-K))		
x_R	right surface coordinate, (m)		
α	constant dependent on geometry:	rectangular:	$\alpha = 2$
		cylindrical:	$\alpha = 4$
		spherical:	$\alpha = 6$

The temperature difference between left and right surface of the conductor is obtained substituting zero for the value of x:

$$T_L - T_R = \frac{q \cdot x_R^2}{\alpha \cdot k}$$

T_L left surface temperature, (K)

Since in steady state the total amount of heat must be removed by conduction the right side temperature may be obtained from the following relation:

$$A_R h_R \left(T_R - T_{fluid}\right) = V \cdot q$$

A_R	-	right side surface area, (m^2)
h_R	-	right side heat transfer coefficient, ($W/(m^2K)$)
T_{fluid}	-	fluid temperature, (K)
V	-	total volume of the conductor, (m^3)

This leads to the following expression for temperature difference between the right surface of the conductor and the fluid:

$$T_R - T_{fluid} = \frac{q \cdot (V / A_R)}{h_R}$$

The values of (V/A_R) depend on the conductor geometry, and are shown below.

- Rectangular geometry: (V/A_R) = x_R
- Cylindrical geometry: (V/A_R) = $x_R/2$
- Spherical geometry: (V/A_R) = $x_R/3$

The conductor dimension, x_R, is equal to the thickness of a rectangular conductor, and the radius of a cylinder and a sphere. The following data were assumed for calculations:

thermal conductivity:	k	=	1	(W/(mK))
internal heat source density:	q	=	2×10^6	(W/m^3)
conductor dimension:	x_R	=	10^{-2}	(m)
heat transfer coefficient:	h_R	=	200	($W/(m^2K)$),
fluid temperature:	T_{fluid}	=	300	(K).

With the data shown above the values of left and right side temperatures were calculated using the relations shown above. The values of the volume-to-surface ratios and the resulting wall-to-fluid temperature difference, and finally the right surface temperature itself, are shown in the first three rows of Table 3-15. The values of: $q\ x_R^2 / (\alpha\ k)$ and the left surface (cylinder centerline, sphere center) temperatures are shown in the last two rows. The theoretical temperature distribution was calculated for this case by a FORTRAN program, located in:
`\Z-INPUTS\SC\T-CON\T-CON-THEORY.FOR`

Table 3-15 Conduction test parameters

Geometry	Rectangular	Cylindrical	Spherical
(V/A_R), (m)	10^{-2}	0.5×10^{-2}	0.3333×10^{-2}
$T_R - T_{fluid}$, (K)	100.0	50.0	33.33
T_R, (K)	400.0	350.0	333.3
$q\ x_R^2 / (\alpha\ k)$, (K)	100.0	50.0	33.33
T_L, (K)	500.0	400.0	366.76

- *SPECTRA Calculations*

The input data for all conduction problems were prepared as a single input data file with several conductors. The input file for the calculations is stored in:
`\Z-INPUTS\SC\T-CON\T-CON.SPE`
For the test cases described in this section the conductors SC-0011, SC-002, and SC-003 are used, which represent the rectangular, the cylindrical, and the spherical geometry, respectively.

The material property data were defined in the material property input records. The material No. 1 (k = 1.0 W/m-K, ρ = 1000 kg/m^3, c_p = 100 J/kg-K) was used for all conductors SC-001, SC-002, and SC-003.

For the rectangular geometry case the conductor SC-001 is used. The surface area of this conductor was set 1.0 m^2. The internal power source is equal to the product of the power density (2 MW/m^3) and the volume of the conductor (10^{-2} m^3). The total thickness of the conductor (10^{-2} m) was divided into 11 cells. Thickness of the internal cells is 10^{-3} m, while the boundary cell thickness id 0.5×10^{-3} m. This is the most natural approach in SPECTRA where the boundary nodes are "half nodes" with respect to the location of the temperature measurement point (see Volume 1). With this approach there is an equal distance between the neighboring nodes. In the present case the node-to-node distance is 10^{-3} m.

The heat source was uniformly distributed over all cells. The initial temperatures of all cells were set to 300 K. The left surface of the conductor is assumed to be insulated; the right surface is using tabular functions: TF-001 and TF-002 for the convective heat transfer coefficient (TF-001 = 200.0 (W/m^2-K)) and fluid temperature (TF-002 = =300.0 (K)), respectively.

For the cylindrical geometry case the conductor SC-002 is used. The length of this conductor was set 1.0 m. The internal power source is equal to the product of the power density (2 MW/m^3) and the volume of the conductor ($\pi\times(10^{-2})^2\times1.0$ m^3). The total thickness of the conductor (10^{-2} m) was divided into 11 cells as in SC-001, using the same approach as above. The heat source was uniformly distributed aver all cells. The initial temperatures of all cells were set to 300 K. Left surface of the conductor is assumed to be insulated, right surface is using tabular functions TF-001 and TF-002 for convective heat transfer coefficient and fluid temperature respectively.

For the spherical geometry case the conductor SC-003 is used. The internal power source is equal to the product of the power density (2 MW/m^3) and the volume of the conductor ($4/3\times\pi\times(10^{-2})^3$ m^3). The total thickness of the conductor (10^{-2} m) was divided into 11 cells as in SC-001. The heat source was uniformly distributed aver all cells. The initial temperatures of all cells were set to 300 K. Left surface of the conductor is assumed to be insulated, right surface is using tabular functions TF-001 and TF-002 for convective heat transfer coefficient and fluid temperature respectively.

The time steps used for calculations were:

$0 < t < 20$ s:	Δt = 0.1 s
$20 < t < 200$ s:	Δt = 1.0 s
$200 < t < 2000$ s:	Δt = 10.0 s

The small time step and frequent outputs for the first 20 s are necessary for the transient tests (see section 3.5.4) which are calculated simultaneously with the steady state tests. For the steady state only the stable values are needed. Those are taken at the end of calculations (t = 2000.0 s)

Results of the steady state tests with internal heat source are shown in Figure 3-98, Figure 3-99, and Figure 3-100. Figure 3-99 shows visualization picture of the rectangular heat conductor (SC-001) at the end of the calculated period (taken at 2000 s), well after the results become stable (about 50 s - see Figure 3-98). Figure 3-100 shows the temperature of the conductors SC-001, SC-002, and SC-003, calculated by SPECTRA and theoretical values obtained from the formula:

$$T(x) - T_R = \frac{q}{\alpha \cdot k} \cdot \left(x_R^2 - x^2 \right)$$

Results obtained with the code are in perfect agreement with the theoretical results.

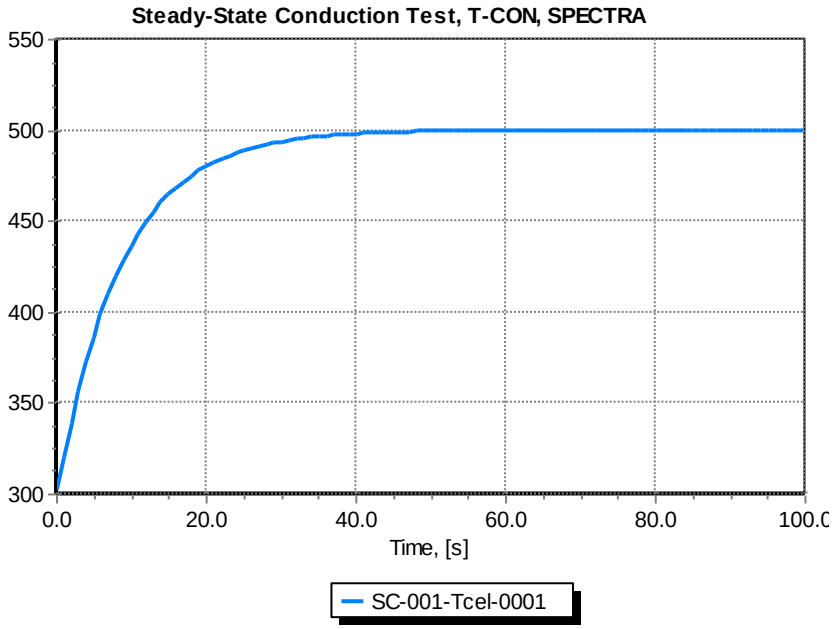

Figure 3-98 Steady state conduction test - left node (0001) of SC-001 (rectangular).

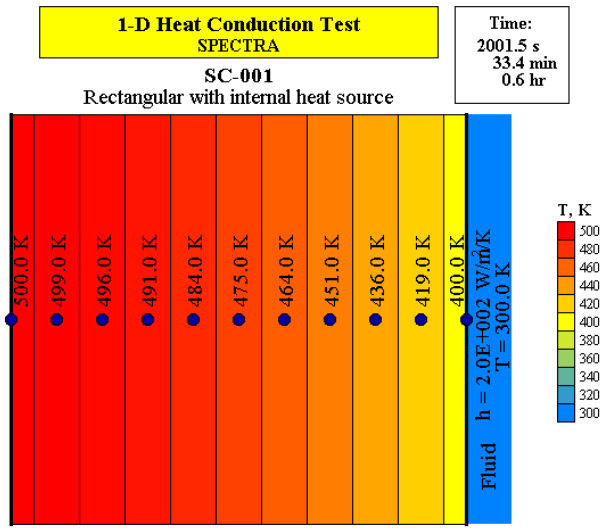

Figure 3-99 Steady state conduction tests - rectangular with internal heat source.

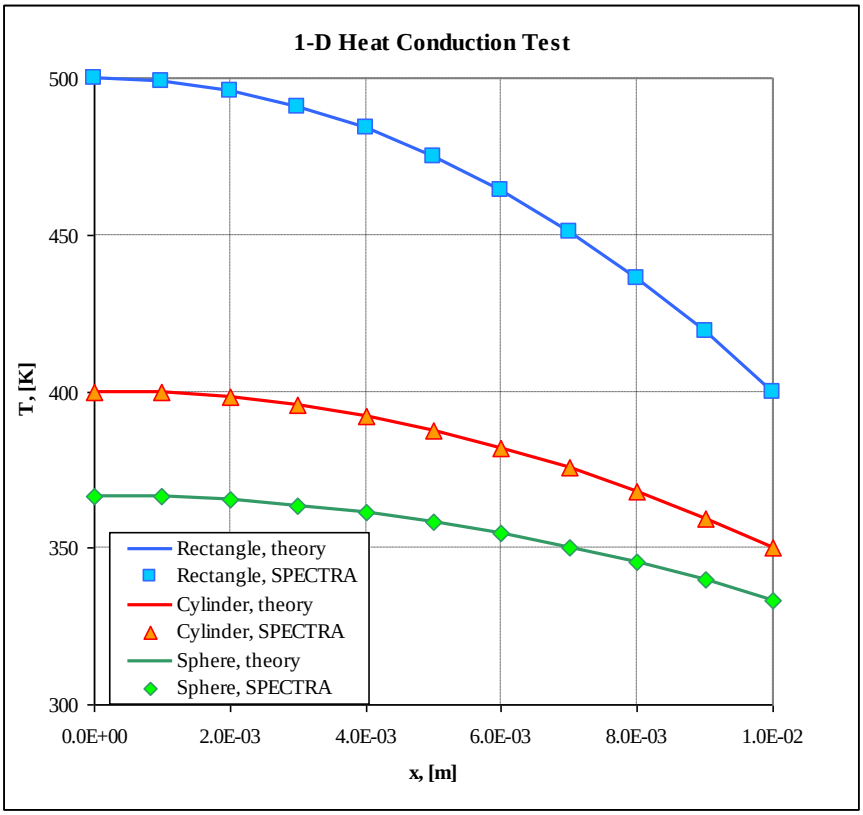

Figure 3-100 Steady state conduction tests - internal heat source.

Conduction with variable thermal conductivity

- Theory

The steady state conduction in a conductor with variable thermal conductivity is considered for two different geometries: rectangular and cylindrical. The left and right surface temperatures are known. The thermal conductivity is linearly dependent on local temperature as:

$$k = k_0 \cdot (1 + a_0 T)$$

The theoretical solutions for rectangular and cylindrical geometries result in the following steady state temperature distribution inside the conductors:

- Rectangular geometry ([15], pages 3-104, 3-105, equation 112)

$$T(x) = \frac{\sqrt{(1+a_0 T_L)^2 - [(1+a_0 T_L)^2 - (1+a_0 T_R)^2] \cdot \frac{x}{D}} - 1}{a_0}$$

- Cylindrical geometry ([15], pages 3-104, 3-105, equation 11)

$$T(r) = \frac{\sqrt{(1+a_0 T_L)^2 - [(1+a_0 T_L)^2 - (1+a_0 T_R)^2] \cdot \frac{\ln(r/R_L)}{\ln(R_R/R_L)}} - 1}{a_0}$$

$T(x)$ temperature at the distance x from the left boundary of rectangular conductor, (K)
$T(r)$ temperature at radius r of cylinder, (K)
D thickness of the conductor, (m)
T_L left (inside) surface temperature, (K)
T_R right (outside) surface temperature, (K)
R_L left (inner) radius of the cylinder, (m)
R_R right (outer) radius of the cylinder, (m)

The following data were assumed for calculations:

-	rectangular conductor thickness:	D	= 0.01 (m)
-	cylinder inner radius:	R_L	= 0.01 (m)
-	cylinder outer radius:	R_R	= 0.01 (m)
-	left (inside) temperature:	T_L	= 300 (K)
-	right (outside) temperature:	T_R	= 500 (K)
-	conductivity coefficient:	k_0	= 1.0 (1/K)
-	conductivity coefficient:	a_0	= 0.01 (1/K)

Therefore the thermal conductivity is equal to: $k = 1.0 \cdot (1+0.01 \cdot T)$. Note that the value of k_0 does not appear in the solution, so any number may be used. The theoretical temperature distribution was calculated for this case by a FORTRAN program, located in:
`\Z-INPUTS\SC\T-CON\T-CON-THEORY.FOR`

- SPECTRA Calculations

The input data for all conduction problems were prepared as a single input data file with several conductors. The input file for the calculations is stored in:
`\Z-INPUTS\SC\T-CON\T-CON.SPE`
For the test cases described in this section the conductors SC-004 and SC-005 are used, which represent the rectangular and the cylindrical geometry, respectively.

The material property data were defined in the material property input records. The material No. 2 was used for both conductors SC-004 and SC-005. The conductivity was defined using two points:

T = 0.0 K	$k = 1.0 \cdot (1 + 0.01 \cdot 0.0)$	= 1.0 W/m/K
T = 900.0 K	$k = 1.0 \cdot (1 + 0.01 \cdot 900.0)$	= 10.0 W/m/K

This is in agreement with the equation defining thermal conductivity shown above. Other material properties (ρ = 1000 kg/m^3, c_p = 100 J/kg-K) are rather meaningless for this test (they only determine how fast the temperatures become stable (i.e. how long calculations are needed).

For the rectangular geometry case the conductor SC-004 is used. The surface area of this conductor was set 1.0 m^2. The total thickness of the conductor (10^{-2} m) was divided into 11 cells with equal distance between the neighboring nodes, which means thickness of 0.5×10^{-3} m of the boundary cells and the thickness of 10^{-3} m of the internal cells. The initial temperatures of all cells were set to 300 K. The left and right side boundary conditions were defined using tabular functions. TF-005 defines the heat transfer coefficient, TF-002 and TF-004 the left and right fluid temperature. The heat transfer coefficient was set to a large number (10^{99}) to ensure that the conductor surface temperature is the same as the fluid temperature.

For the cylindrical geometry case the conductor SC-005 is used. The length of the cylinder was set 1.0 m. The total thickness of the conductor (10^{-2} m) was divided into 11 cells with equal distance between the neighboring nodes. The initial temperatures of all cells were set to 300 K. The left and right side boundary conditions were defined using tabular functions. TF-005 defines the heat transfer coefficient, TF-002 and TF-004 the left and right fluid temperature. The heat transfer coefficient was set to a large number (10^{99}) to ensure that the conductor surface temperature is the same as the fluid temperature.

The time steps used for calculations were:

$0 < t < 20$ s:	Δt = 0.1 s
$20 < t < 200$ s:	Δt = 1.0 s
$200 < t < 2000$ s:	Δt = 10.0 s

The small time step and frequent outputs for the first 20 s are necessary for the transient tests (see section 3.5.4) which are calculated simultaneously with the steady state tests. For the steady state only the stable values are needed.

Results are shown in Figure 3-101 and Figure 3-102. Figure 3-101 shows visualization picture of the rectangular heat conductor (SC-004) at the end of the calculated period (taken at 2000 s), well after the results become stable (about 100 s). Figure 3-102 shows the temperature of the conductors SC-004 and SC-005, calculated by SPECTRA and theoretical values obtained from the theoretical formulae. Results obtained with the code are in perfect agreement with the theoretical results.

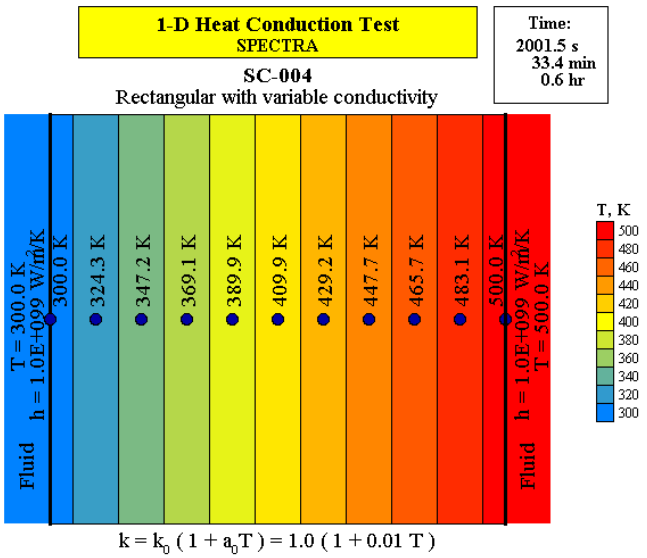

Figure 3-101 Steady state conduction tests - variable conductivity.

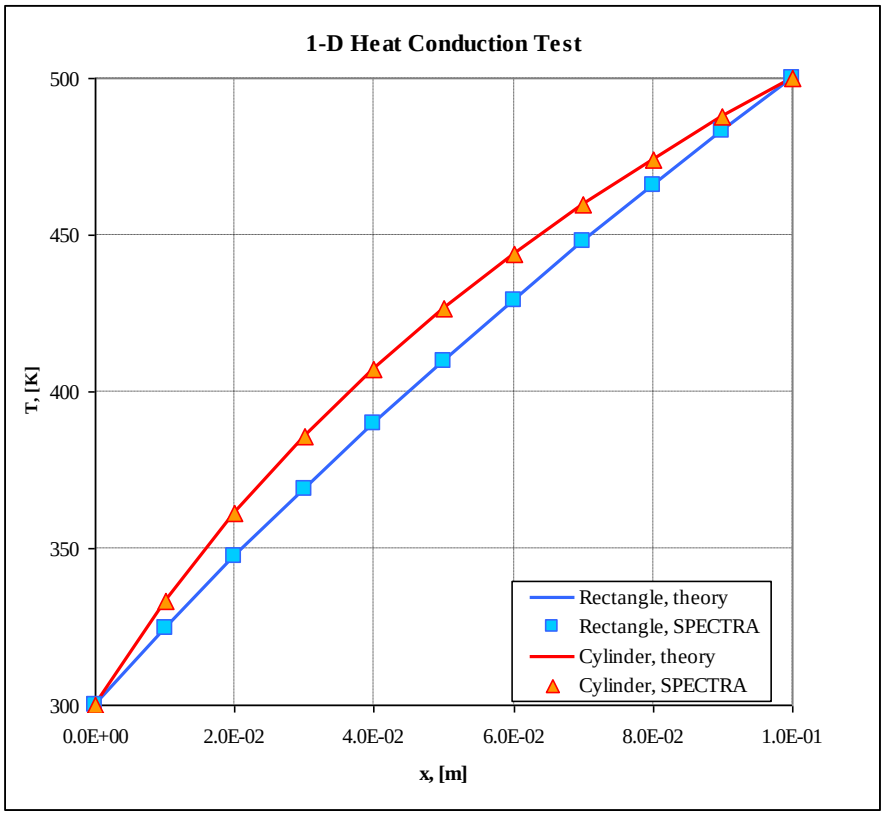

Figure 3-102 Steady state conduction tests - variable conductivity.

3.5.2 Integration Methods 1 and 2 - Uniform Power, Comparison with MELCOR

As described in Volumes 1 and 2, two alternative numerical integration methods are available for the 1-D Solid Heat Conductors:

- Method 1: Temperature nodes are located at cell-centers (used in earlier SPECTRA versions - before May 2018).
  A disadvantage of this method is less accurate stationary state temperature distribution in case of a coarse nodalization.
- Method 2: Temperature nodes at cell-edges (used in MELCOR, RELAP, etc.).
  An advantage is an accurate stationary state temperature distribution even in case of a very coarse nodalization.

The Method 1 was used in earlier SPECTRA versions. An advantage of this method is that it may be treated as a special case of the 2-D Solid Heat Conductor, and therefore direct comparison between 1-D and 2-D solutions is possible - see sections 3.6.1, 3.6.2.

The Method 2 is used in most system codes, for example MELCOR, RELAP, TRACE, therefore application of this method allows easier code-to-code comparisons. Furthermore, it provides more accurate stationary state results, independently of the number of nodes used. This will be illustrated in the next section.

This and the next section present comparison of steady state results obtained for three geometries, rectangular, cylindrical, and spherical. The wall thickness, as well as the radius of the cylinder and the sphere, are equal to 0.01 m. The analyzed cases are very similar to those listed in Table 3-15. The only difference is the surface heat transfer coefficient has been set to a large value ($h = 10^9$ W/m^2-K), so that the surface temperature is practically equal to the "fluid" temperature, 300 K. The temperature drop over the wall is equal to: $q\, x_R^2 / (\alpha\, k)$ = 100.0 K, 50.0 K, 33.3 K for the rectangular, cylindrical, and spherical geometries respectively (Table 3-15). The maximum temperatures are therefore equal to:

- rectangular geometry: 400.0 K,
- cylindrical geometry: 350.0 K,
- spherical geometry: 333.3 K.

The input data files for the calculations are stored in:

```
\Z-INPUTS\SC\T-CON\Power-Uniform
```

In each analyzed geometry, 10 mesh cells are used. This means that the number of temperature nodes is 10 in case of Method 1 and 11 in case of Method 2. Results of the two integration methods are in each case compared to the results obtained with the MELCOR code [107].

The stationary state results are shown in Figure 3-103 through Figure 3-111. Figure 3-103, Figure 3-104, and Figure 3-105 show results obtained for rectangular geometry. Figure 3-106, Figure 3-107, and Figure 3-108 show results obtained for cylindrical geometry. Figure 3-109, Figure 3-110, and Figure 3-111 show results obtained for spherical geometry. All results are in very good agreement.

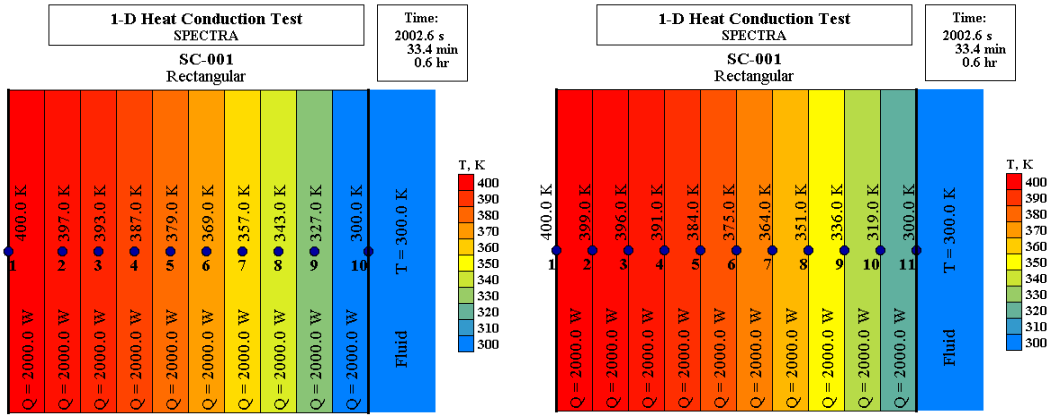

Figure 3-103 Uniform power, rectangular geometry, SPECTRA, left: Method 1, right: Method 2

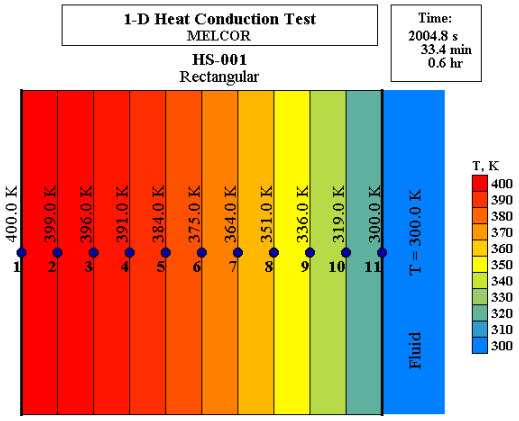

Figure 3-104 Uniform power, rectangular geometry, MELCOR

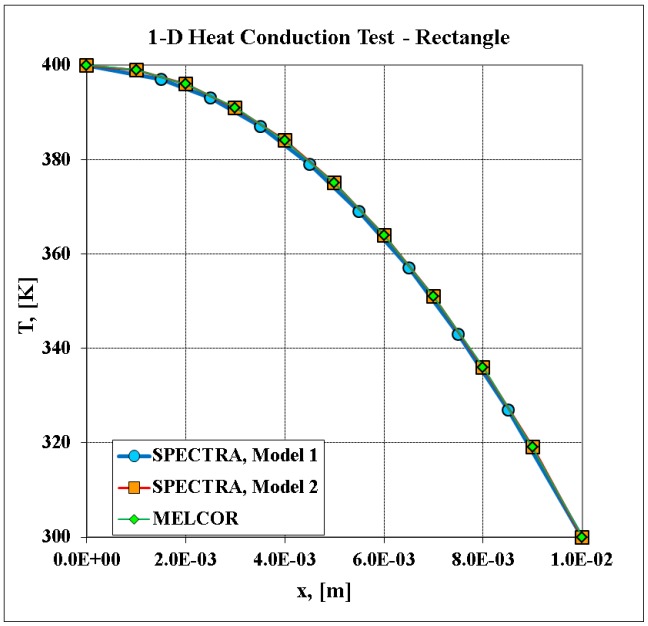

Figure 3-105 Uniform power, rectangular geometry

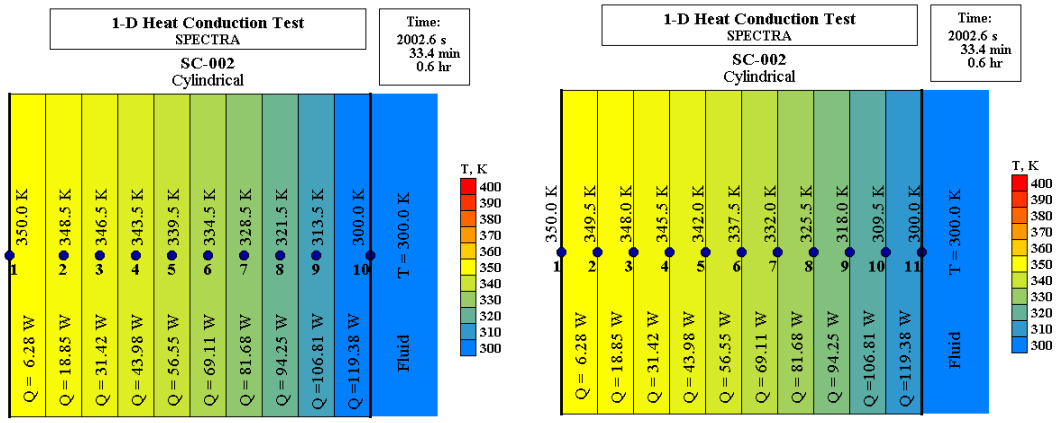

Figure 3-106 Uniform power, cylindrical geometry, SPECTRA, left: Method 1, right: Method 2

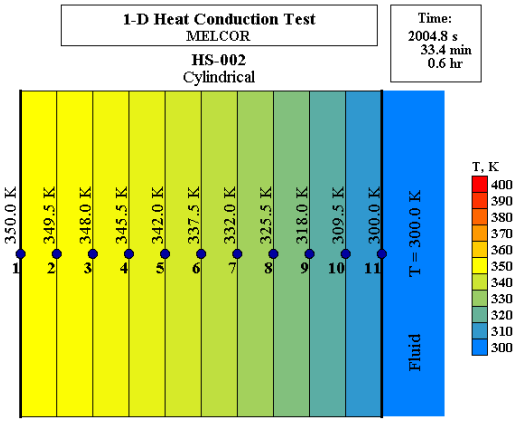

Figure 3-107 Uniform power, cylindrical geometry, MELCOR

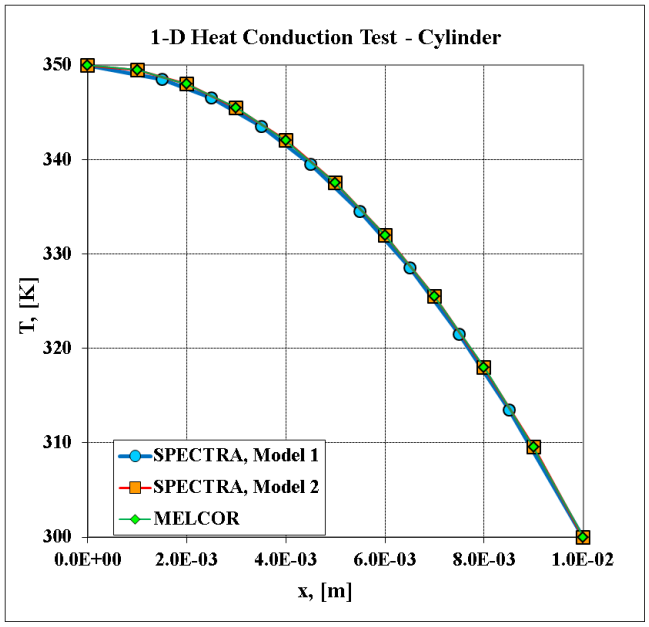

Figure 3-108 Uniform power, cylindrical geometry

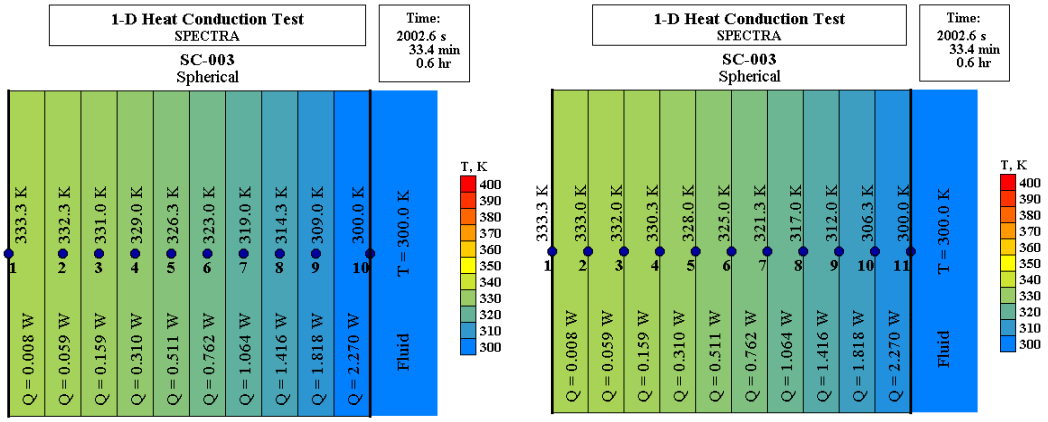

Figure 3-109 Uniform power, spherical geometry, SPECTRA, left: Method 1, right: Method 2

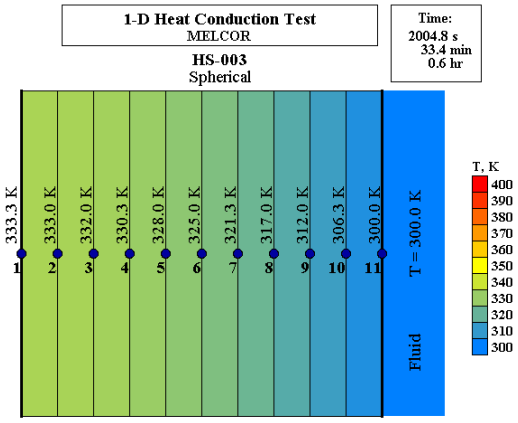

Figure 3-110 Uniform power, spherical geometry, MELCOR

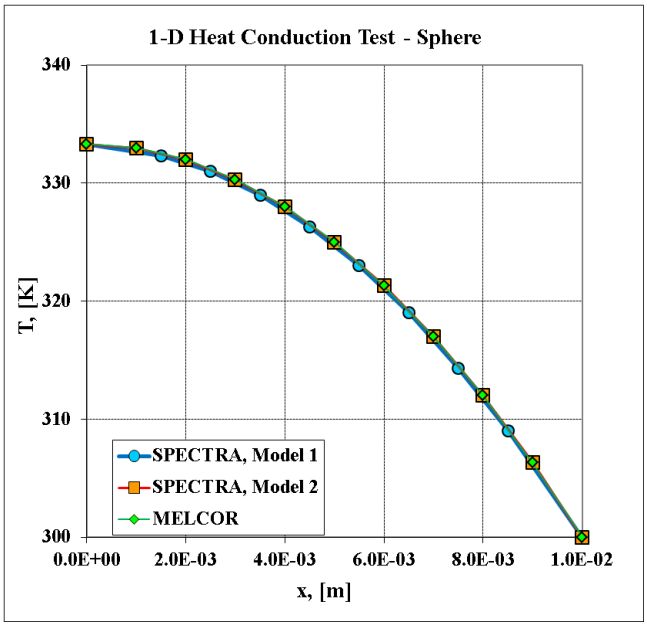

Figure 3-111 Uniform power, spherical geometry

3.5.3 Integration Methods 1 and 2 - Non-uniform Power, Comparison with MELCOR

This test is very similar to the test presented in the previous section. This time the structures are twice thicker. The left half is identical to the previous test, with the same power generation. The right side has no internal power generation. For simplicity, a high conductivity material (k = 99,999 W/m-K) was applied in the right side. Therefore the temperature in the right hand side of the structures is practically constant and equal to 300 K. The temperature distribution in the left hand side of the structures should be the same as in the previous section. The maximum temperatures are therefore equal to:

- rectangular geometry: 400.0 K,
- cylindrical geometry: 350.0 K,
- spherical geometry: 333.3 K.

The input data files for the calculations are stored in:

`\Z-INPUTS\SC\T-CON\Power-Nonuniform`

In each analyzed geometry, 10 mesh cells are used. The single cell size is equal to 0.002 m, twice larger than in the previous case. Results of the two integration methods are in each case compared to the results obtained with the MELCOR code [107].

The stationary state results are shown in Figure 3-112 through Figure 3-120. Figure 3-112, Figure 3-113, and Figure 3-114 show results obtained for rectangular geometry. Figure 3-115, Figure 3-116, and Figure 3-117 show results obtained for cylindrical geometry. Figure 3-118, Figure 3-119, and Figure 3-120 show results obtained for spherical geometry.

As can be seen, the maximum temperature in steady state is correctly calculated by Method 2 (and in MELCOR, which uses the same method). In case of Method 1, an error is introduced at the boundary where the power source changes from a certain positive value to zero. The temperature profile changes from parabolic to linear and this is not accounted for in the Method 1.

The error is more clearly visible in an “extreme” case, where the power-generating part is represented by two cells only (single cell size of 0.005 m). Results are shown in Figure 3-121, Figure 3-122, and Figure 3-123. In this case the temperature overestimation is larger.

Generally, the solutions obtained with both methods will be very similar to each other if sufficiently detailed nodalization is applied. If the user wishes to apply relatively coarse nodalization of structures, the Method 2 is recommended. It may be set for the entire model using the global activator NIMGSC (see Volume 2).

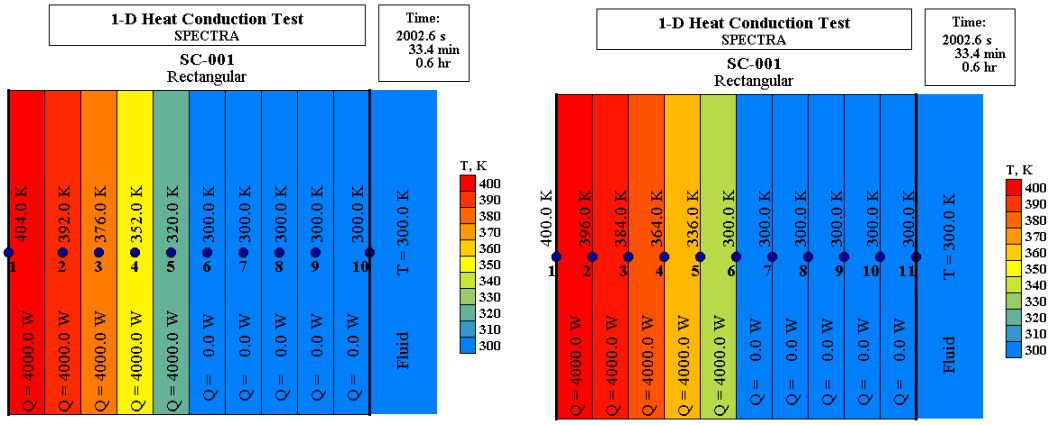

Figure 3-112 Non-uniform power, rectangular, SPECTRA, left: Method 1, right: Method 2

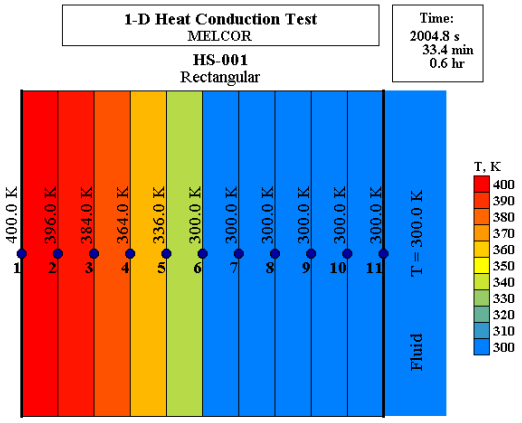

Figure 3-113 Non-uniform power, rectangular, MELCOR

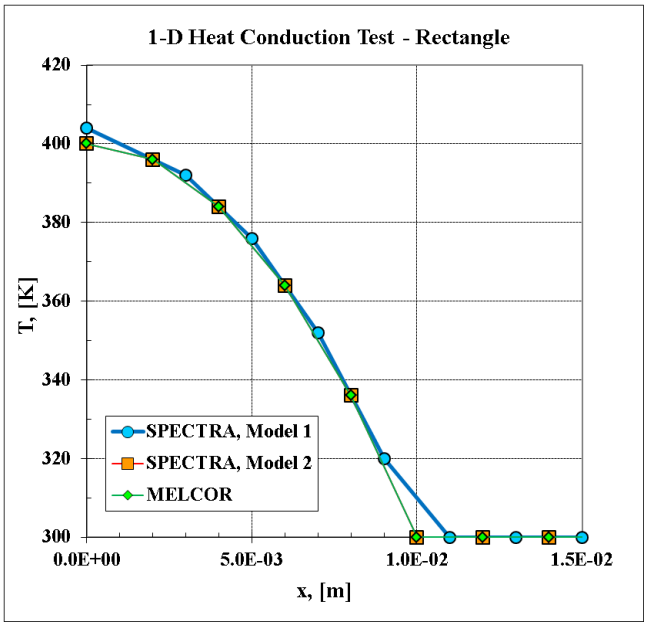

Figure 3-114 Non-uniform power, rectangular geometry

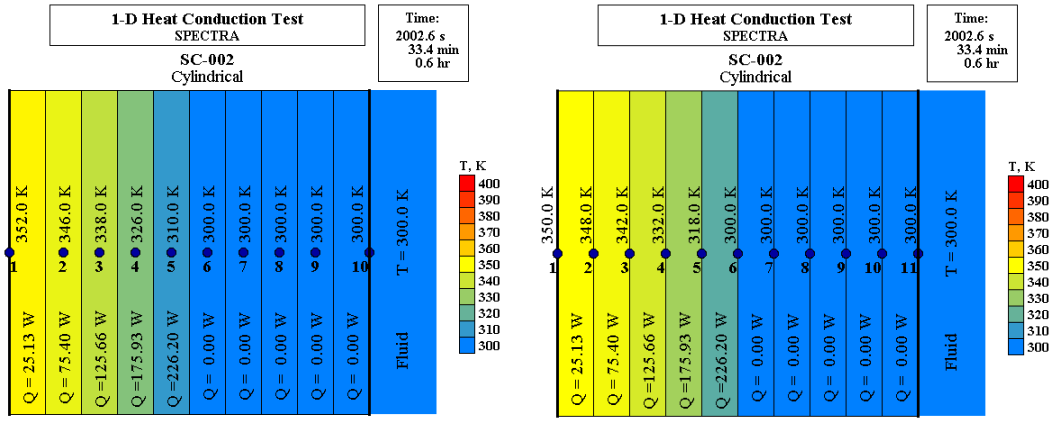

Figure 3-115 Non-uniform power, cylindrical, SPECTRA, left: Method 1, right: Method 2

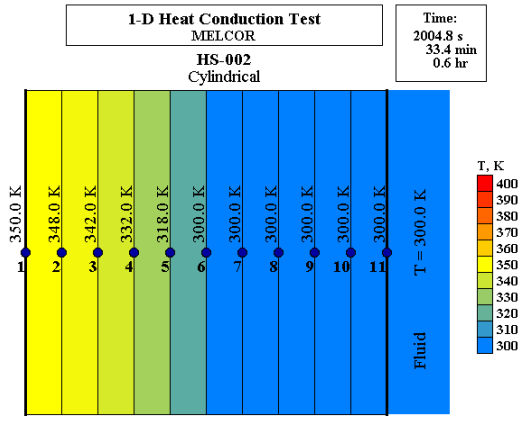

Figure 3-116 Non-uniform power, cylindrical, MELCOR

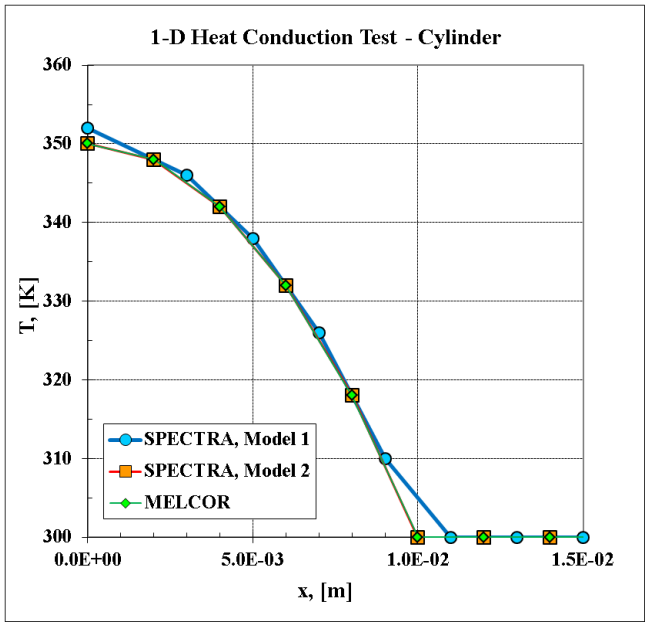

Figure 3-117 Non-uniform power, cylindrical geometry

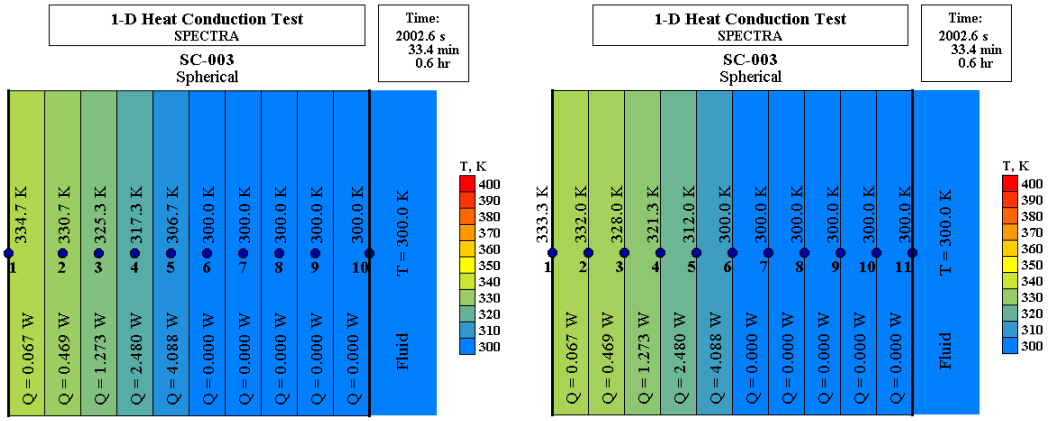

Figure 3-118 Non-uniform power, spherical, SPECTRA, left: Method 1, right: Method 2

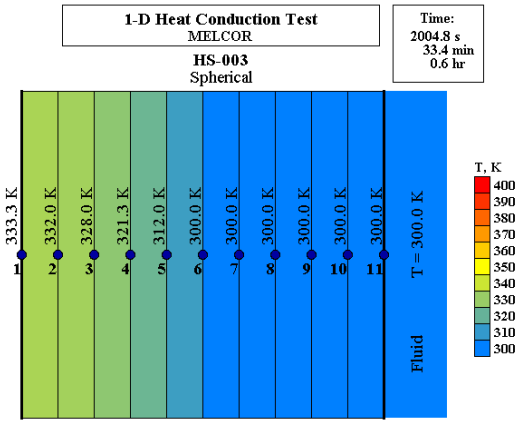

Figure 3-119 Non-uniform power, spherical, MELCOR

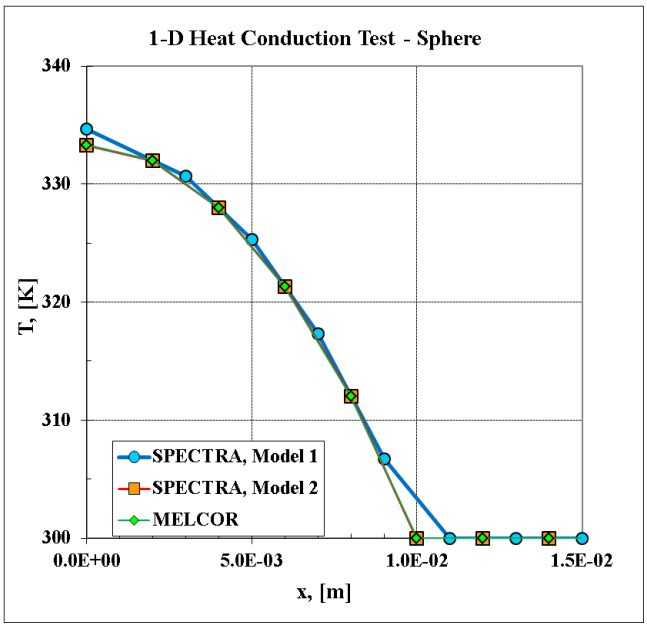

Figure 3-120 Non-uniform power, spherical geometry

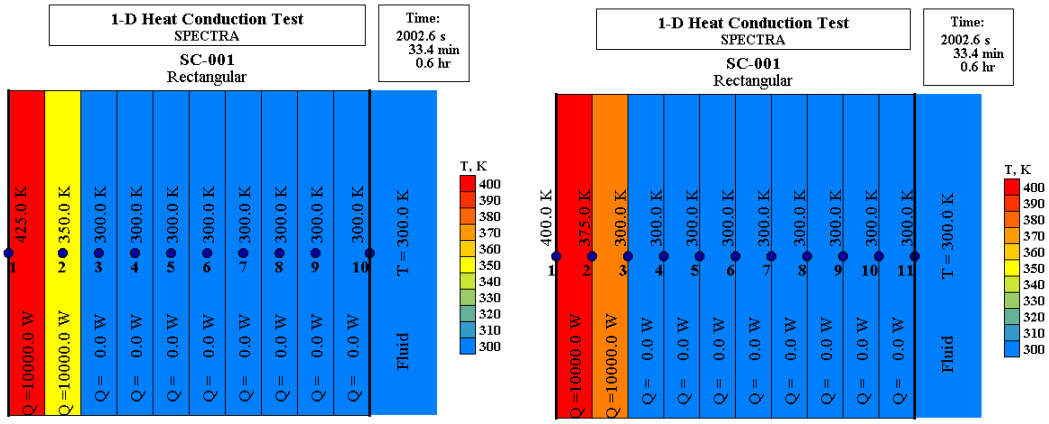

Figure 3-121 “Extreme” case, rectangular, SPECTRA, left: Method 1, right: Method 2

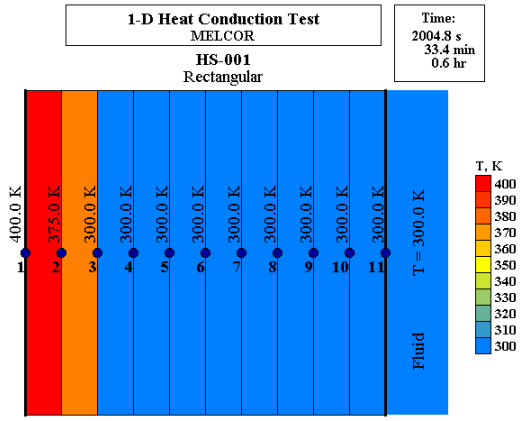

Figure 3-122 “Extreme” case, rectangular, MELCOR

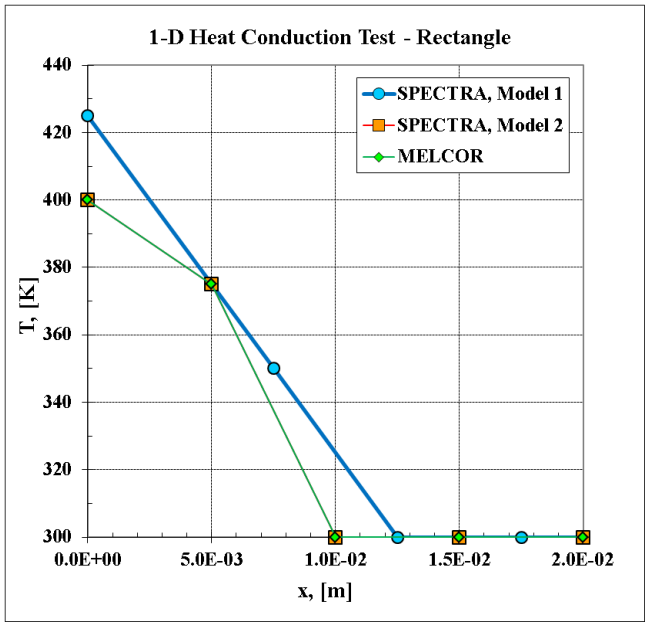

Figure 3-123 “Extreme” case, rectangular geometry

3.5.4 Transient Conduction Tests for 1-D Solid Heat Conductors

Slab heated at one side

- Theory

The transient conduction in a slab with step change of boundary surface temperature for the rectangular geometry is considered. The initial temperature of the conductor is 300 K. The left surface temperature is equal to 400 K.

The theoretical solution is obtained for a semi-infinite slab. It results in the following temperature distribution inside the conductor (see [15], eq. 55, page 3-61):

$$T(x,t) = T_0 + (T_w - T_0) \cdot erfc\left(\frac{x}{2\sqrt{at}}\right)$$

$T(x,t)$ temperature, (K), at the location x (m) from the left boundary, at the time t, (s)
T_0 initial temperature of the conductor, (K)
T_w wall surface temperature, (K)
a thermal diffusivity ($k/\rho/c_p$), (m^2/s)

The following data were assumed for calculations:

-	initial temperature:	T_0	=	300 K
-	wall surface temperature:	T_w	=	400 K
-	thermal diffusivity:	a	=	5×10^{-7} m^2/s

The theoretical temperature distribution was calculated for this case by a FORTRAN program, located in `\Z-INPUTS\SC\T-CON\T-CON-THEORY.FOR`.

- SPECTRA Calculations

The input data for all conduction problems were prepared as a single input data file with several conductors. The input file for the calculations is stored in:
`\Z-INPUTS\SC\T-CON\T-CON.SPE`
For the test case described in this section the conductor SC-006 is used.

The material property data were defined in the material property input records. The material No. 3 was used for SC-006 (k = 1.0 W/m-K, ρ = 2000 kg/m^3, c_p = 1000 J/kg-K, therefore $a = k/\rho c_p = 5\times10^{-7}$ m^2/s).

The surface area of the conductor was set 1.0 m^2. Theoretical solution is valid for semi-infinite conductor. For computation purposes the thickness of the conductor must be set to a finite number. The thickness of the conductor was set to 10^{-2} m. The numerical solution should be in agreement with theory when the thermal penetration depth is smaller than the conductor thickness.

The total thickness of the conductor (10^{-2} m) was divided into 21 cells of distance between the neighboring nodes, which means thickness of 0.00025 m of the boundary cells and 0.0005 m of the internal cells. The initial temperatures of all cells were set to 300 K.

Left surface of the conductor is using tabular functions TF-005 and TF-003 for the convective heat transfer coefficient and the fluid temperature respectively. The heat transfer coefficient was set to a large number (10^{99}) to ensure that the conductor surface temperature is the same as the fluid temperature. The right side boundary is assumed to be insulated.

The time steps used for calculations were:

$0 < t < 20$ s:	$\Delta t =$ 0.1 s
$20 < t < 200$ s:	$\Delta t =$ 1.0 s
$200 < t < 2000$ s:	$\Delta t =$ 10.0 s

For this test the first 20 s of transient calculations are used. The remaining part of the transient is necessary for the steady state tests (see sections 3.5.1) which are calculated simultaneously with the transient tests.

Figure 3-124 through Figure 3-127 show the temperatures at times 1.0, 5.0, 10.0, and 20.0 s. Comparison of the calculated results with the analytical solution is shown in Figure 3-128. The calculated values are in good agreement with the theoretical values, except near the right boundary, at $t = 20$ s. At that time temperature has penetrated into the right side of the conductor and the analytical solution, obtained for a semi-infinite slab becomes a bad approximation of the real geometry in the region close to the right boundary.

In order to verify the influence of the applied time step on the solution, the present test case was recalculated (only the period of $0 < t < 20$ s) using the time steps of:

- $\Delta t = 1.0$ s
- $\Delta t = 5.0$ s
- $\Delta t = 10.0$ s

Results are shown in Figure 3-129, Figure 3-130, and Figure 3-131. Obviously, with the increasing time step the solution becomes less accurate. With $\Delta t = 1.0$ s the solution is still quite accurate, but with $\Delta t = 5.0$ s and $\Delta t = 10.0$ s the discrepancies become visible. Nevertheless even with large time steps the numerical solution is still very good qualitatively, as a result of implicit numerical scheme.

In the present case there is a very rapid temperature change at the beginning of the transient near the left boundary, where the temperature suddenly increases by ~100 K. In the practical cases the temperature variations are less rapid and therefore the influence of time step is less visible. Therefore it is concluded that the sensitivity of the conduction solution to the applied time step is small.

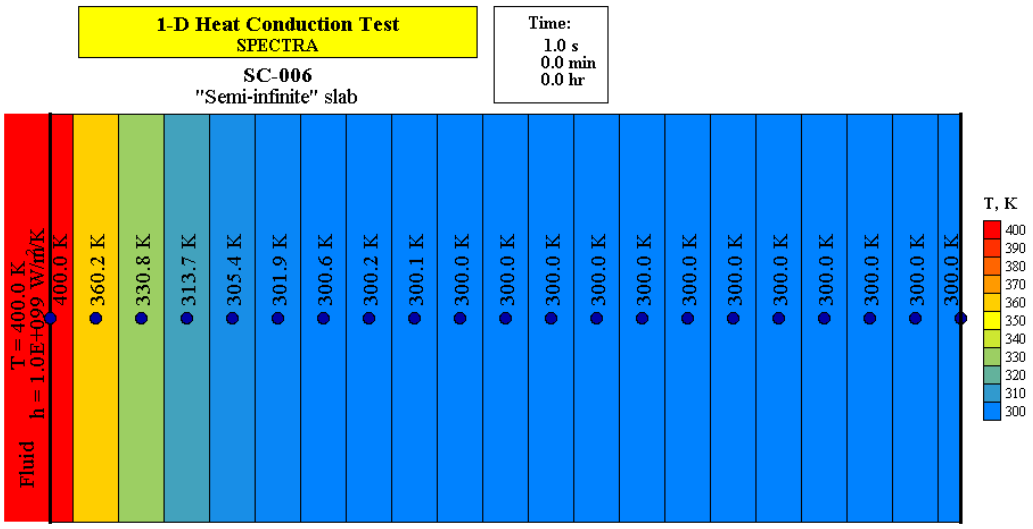

Figure 3-124 Transient conduction, slab heated from one side, SPECTRA, t = 1 s

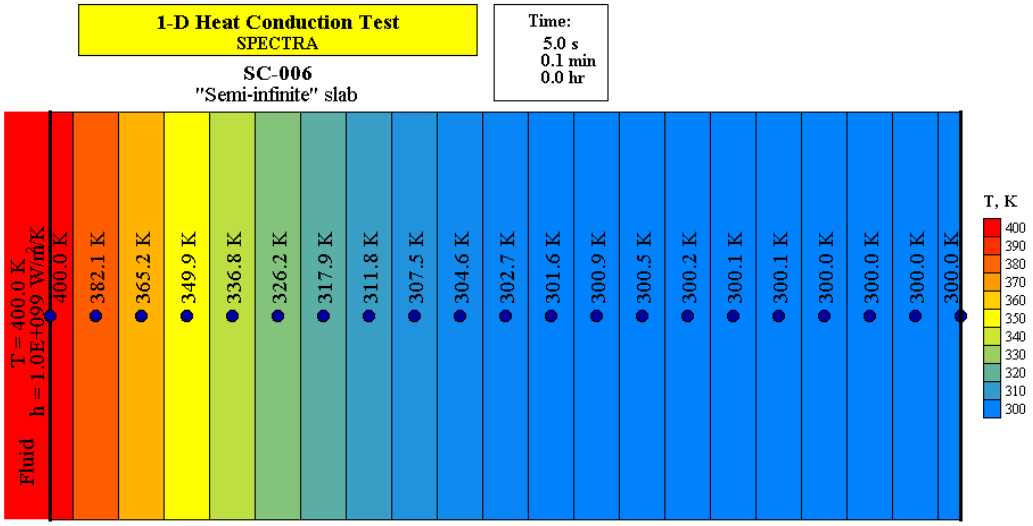

Figure 3-125 Transient conduction, slab heated from one side, SPECTRA, t = 5 s

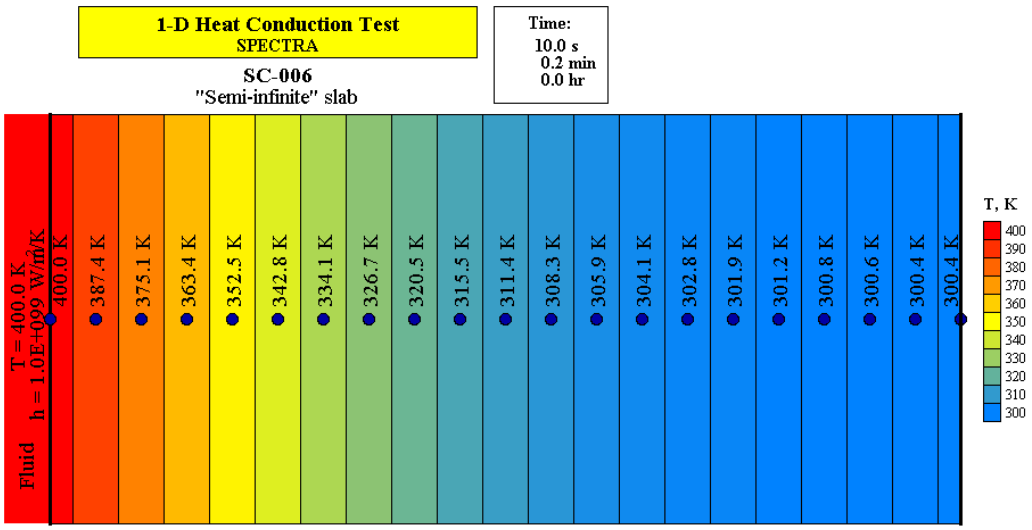

Figure 3-126 Transient conduction, slab heated from one side, SPECTRA, t = 10 s

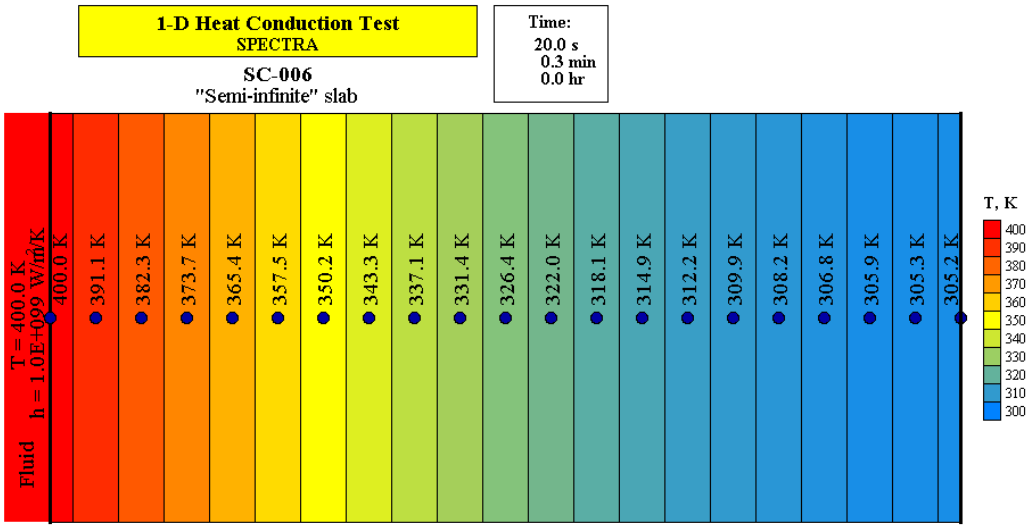

Figure 3-127 Transient conduction, slab heated from one side, SPECTRA, t = 20 s

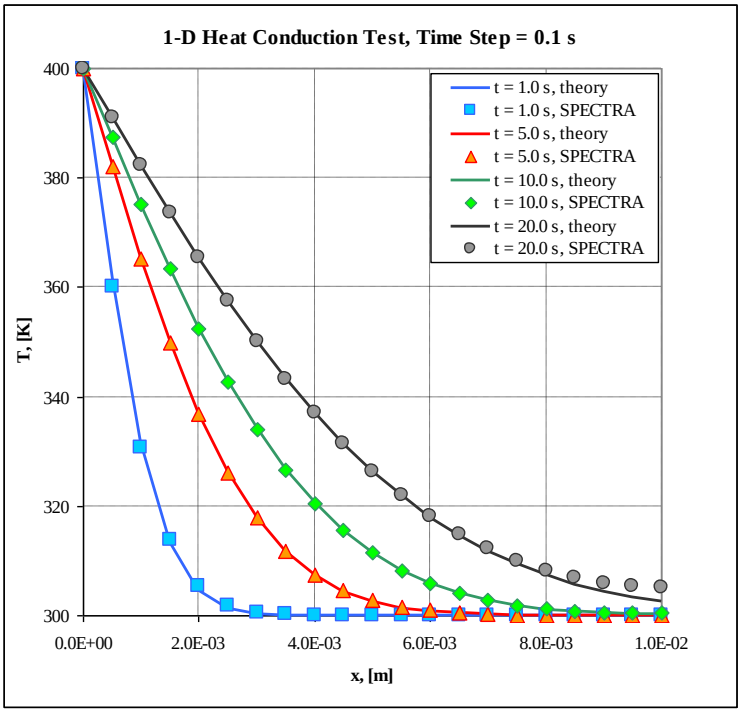

Figure 3-128 Slab heated from one side, SPECTRA and analytical solution.

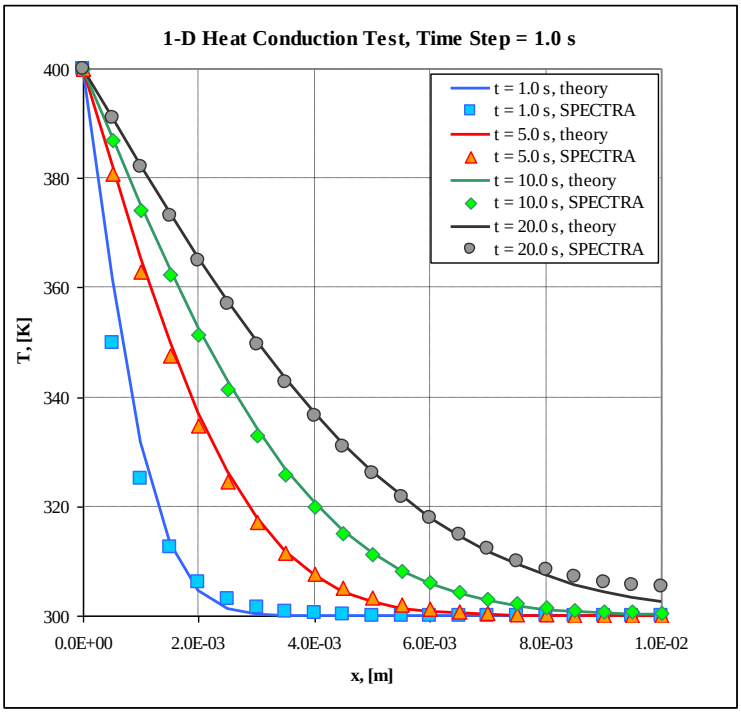

Figure 3-129 Slab heated from one side, SPECTRA time step of 1.0 s.

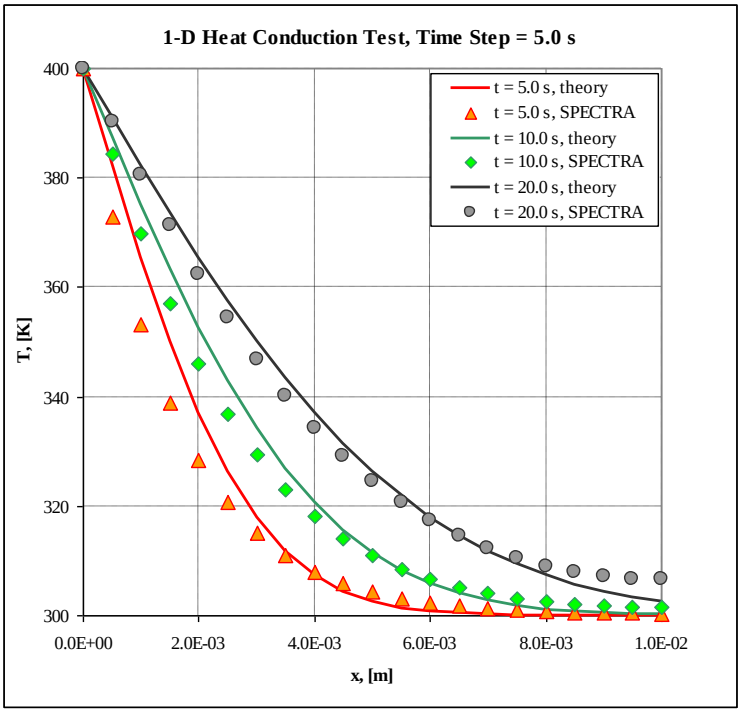

Figure 3-130 Slab heated from one side, SPECTRA time step of 5.0 s.

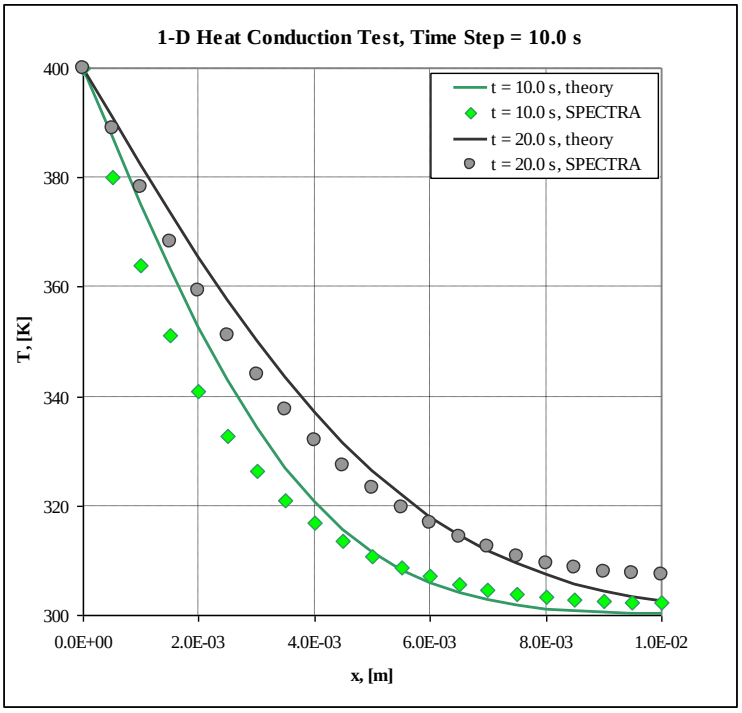

Figure 3-131 Slab heated from one side, SPECTRA time step of 10.0 s.

- Comparison of Method 1 and 2

A similar test was set up for comparison of method 1 and 2 for the case when material properties vary with temperature, in particular to verify the correctness of the definition of the average thermophysical properties, which for Method 2 were defined (see Volume 1) as:

$$k_i = k\,(\tfrac{1}{2}\cdot T_i + \tfrac{1}{2}\cdot T_{i+1})$$
$$\rho_i = \rho\,(\tfrac{3}{4}\cdot T_i + \tfrac{1}{4}\cdot T_{i+1})$$
$$c_{p,i} = c_p\,(\tfrac{3}{4}\cdot T_i + \tfrac{1}{4}\cdot T_{i+1})$$

For the test case described in this section the conductor SC-006 is used. Temperature-dependent material property data were defined for the material No. 3 as follows:

T (K)	k (W/m-K)	ρ (kg/m^3)	c_p (J/kg-K)
300.0	1.0	2000	1000
400.0	2.0	1000	500

The input file for the calculations is stored in:
`\Z-INPUTS\SC\T-CON\1-vs-2`

The results are shown in Figure 3-132 and Figure 3-133. The results of both methods are practically identical. This is best seen in Figure 3-132. Figure 3-133 show that the values for the boundary nodes are nearly identical (left: 400.0 K, right: 315.7 and 315.9 K). The values printed for the internal other nodes are different because the location of the internal nodes are different.

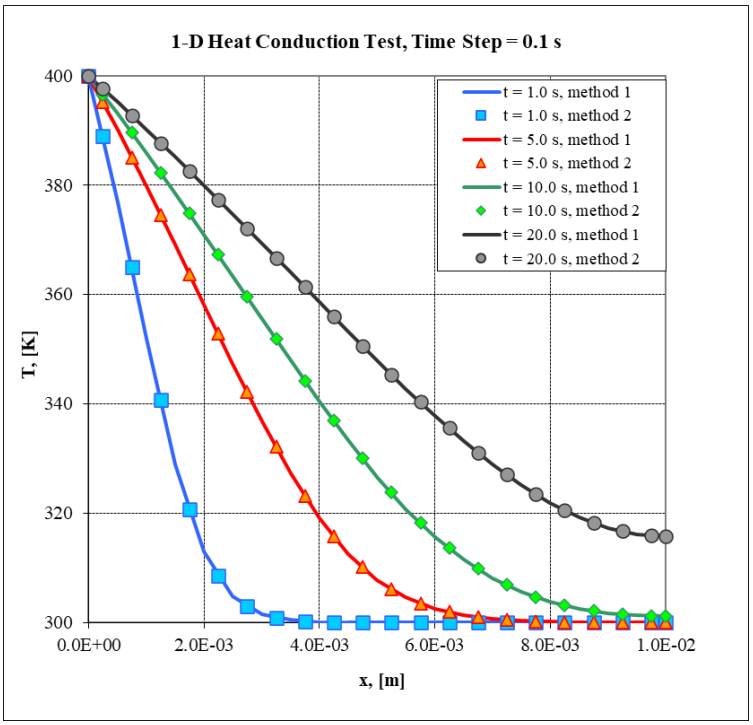

Figure 3-132 Slab heated from one side, comparison of Method 1 and 2

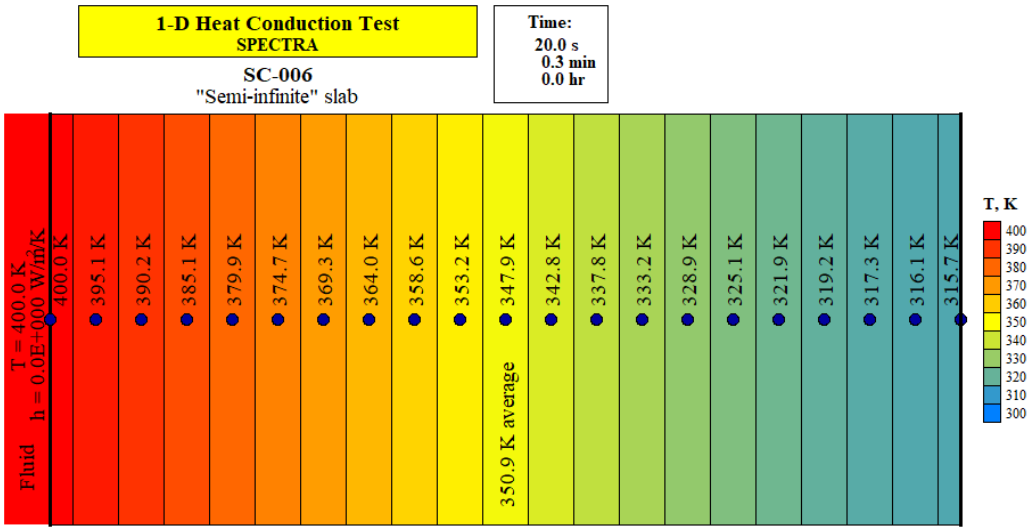

(a) Method 1

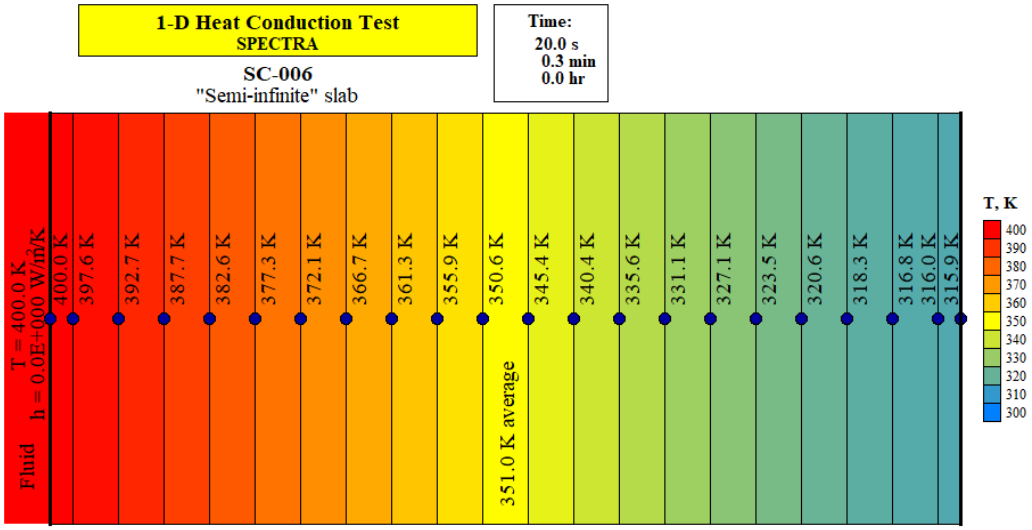

(b) Method 2

Figure 3-133 Slab heated from one side, comparison of Method 1 and 2

Slab heated from both sides

- Theory

The transient conduction in a slab with step change of temperature at both boundary surfaces is considered. The initial temperature of the conductor is 300 K. At time equal to zero the left and right surface temperature is set to 400 K.

The theoretical solution of heat conduction equation results in the following temperature distribution inside the conductor (see [16], section 3.4.3, page 169):

$$T(x,t) = T_w + (T_0 - T_w) \cdot \sum_{n=1}^{\infty} A_n \cdot \exp\left(-\lambda_n^2 \cdot Fo\right) \cdot \cos\left(\lambda_n \frac{x}{L}\right)$$

where:

$$A_n = \frac{2 \cdot \sin(\lambda_n)}{\lambda_n + \sin(\lambda_n) \cdot \cos(\lambda_n)}$$

and

$$\lambda_n = \left(n - \frac{1}{2}\right) \cdot \pi$$

$T(x,t)$ temperature, (K), at the location x (m) from the left boundary, at the time t, (s)
T_0 initial temperature of the conductor, (K)
T_w wall surface temperature, (K)
Fo Fourier number, equal to: at/L^2, $t \geq 0.0$
a thermal diffusivity ($k/\rho/c_p$), (m^2/s)
L half of the slab thickness, (m), $-L \leq x \leq +L$

The above solution is obtained for an infinitely large heat transfer at the surface. A general solution is obtained by solving the following transcendental equations:

$$\cot(\lambda) = \frac{\lambda}{Bi}$$

Here Bi is a Biot number, equal to hL/k where h is the heat transfer coefficient and k is the thermal conductivity. For $h \rightarrow \infty$ $1/Bi \rightarrow 0.0$ and therefore the equation becomes $\cot(\lambda) = 0.0$. This equation has the roots $\lambda_n = (n - ½) \cdot \pi$, as shown above.

The following data were assumed for calculations:

-	initial temperature:	T_0	=	300 K
-	wall surface temperature:	T_w	=	400 K
-	thermal diffusivity:	a	=	5×10^{-7} m^2/s

The theoretical temperature distribution was calculated for this case by a FORTRAN program, located in `\Z-INPUTS\SC\T-CON\T-CON-THEORY.FOR`.

- SPECTRA Calculations

The input data for all conduction problems were prepared as a single input data file with several conductors. The input file for the calculations is stored in:
`\Z-INPUTS\SC\T-CON\T-CON.SPE`.

For the test case described in this section the conductor SC-007 is used. The dimensions nodalization and material properties are the same as those applied for SC-006 (slab heated from one side, described above).

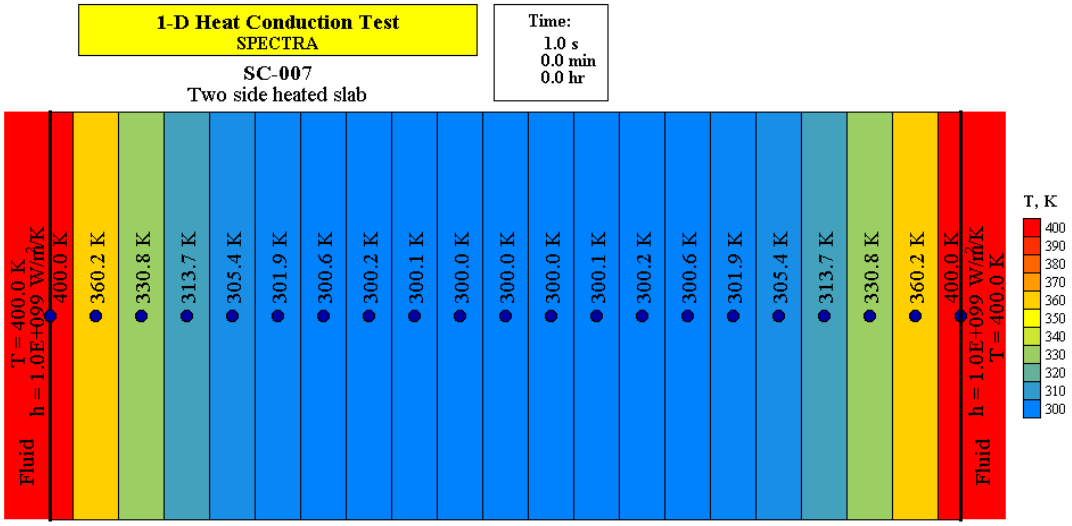

Figure 3-134 Transient test - slab heated from both sides, SPECTRA, t = 1.0 s

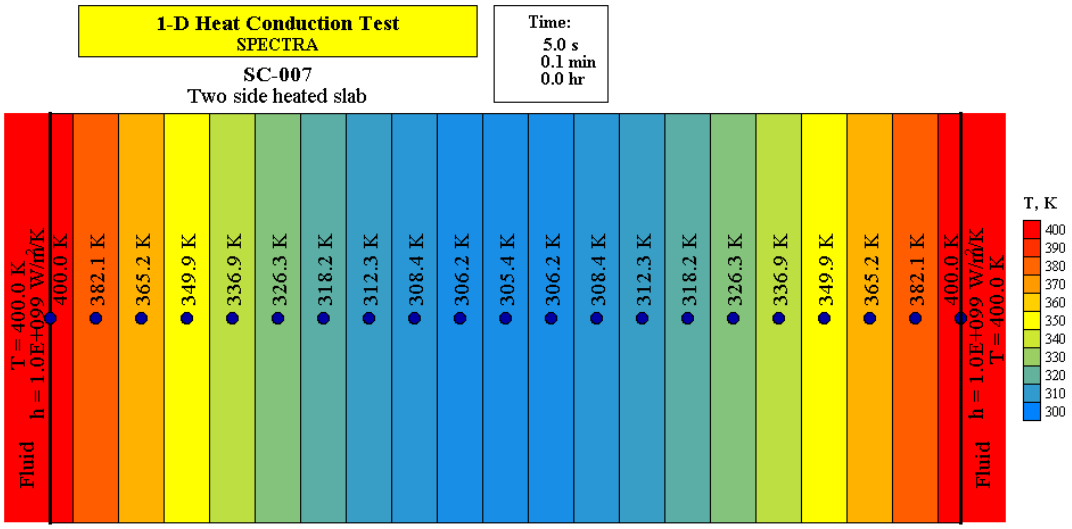

Figure 3-135 Transient test - slab heated from both sides, SPECTRA, t = 5.0 s

In this test both left and right surfaces of the conductor are using tabular functions TF-005 and TF-003 for the convective heat transfer coefficient and the fluid temperature respectively. The heat transfer coefficient was set to a large number (10^{99}) to ensure that the conductor surface temperature is the same as the fluid temperature.

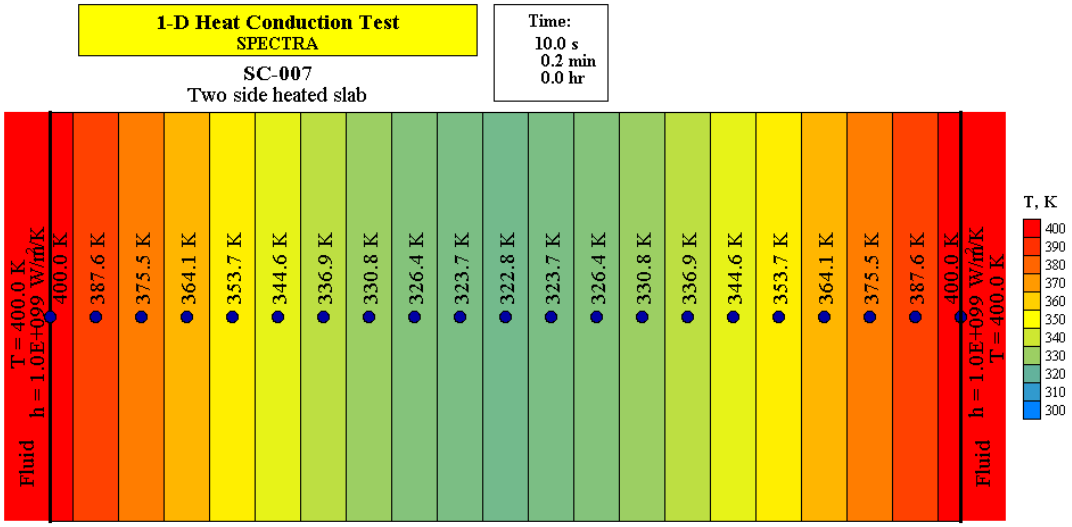

Figure 3-136 Transient test - slab heated from both sides, SPECTRA, t = 10.0 s.

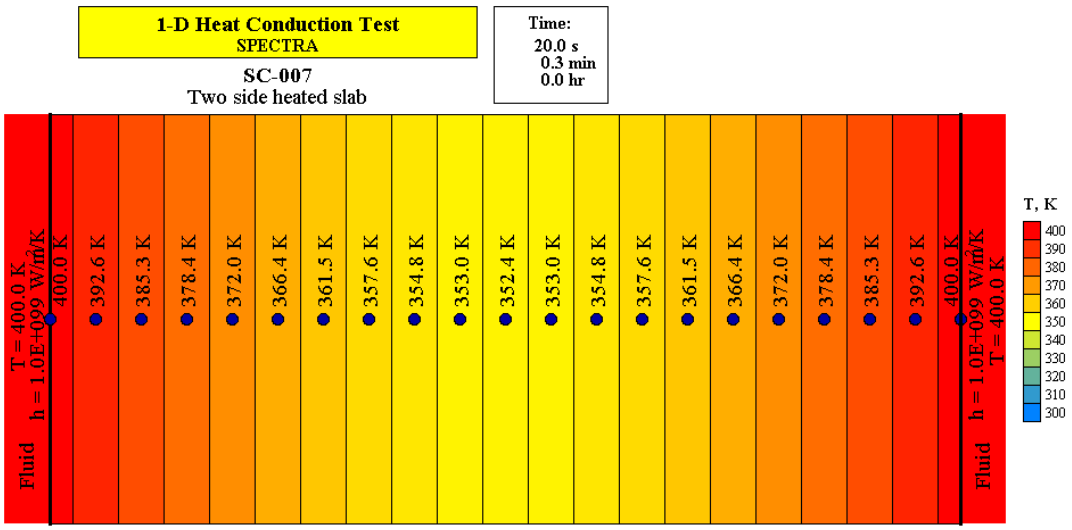

Figure 3-137 Transient test - slab heated from both sides, SPECTRA, t = 20.0 s.

The time steps used for calculations were:

$0 < t < 20$ s:	$\Delta t =$ 0.1 s
$20 < t < 200$ s:	$\Delta t =$ 1.0 s
$200 < t < 2000$ s:	$\Delta t =$ 10.0 s

For this test the first 20 s of transient calculations are used. The remaining part of the transient is necessary for the steady state tests (see sections 3.5.1) which are calculated simultaneously with the transient tests.

Figure 3-134 through Figure 3-137 show the temperatures at times 1.0, 5.0, 10.0, and 20.0 s. Comparison of the calculated results with the analytical solution is shown in Figure 3-138. The calculated values are in excellent agreement with the theoretical values

In order to verify the influence of the applied time step on the solution, the present test case was recalculated (only the period of $0 < t < 20$ s) using the time steps of:

- $\Delta t = 5.0$ s
- $\Delta t = 10.0$ s

Results are shown in Figure 3-139 and Figure 3-140. The conclusions are the same as those reached in case of the slab heated from one side described above; the sensitivity of the conduction solution to the applied time step is small.

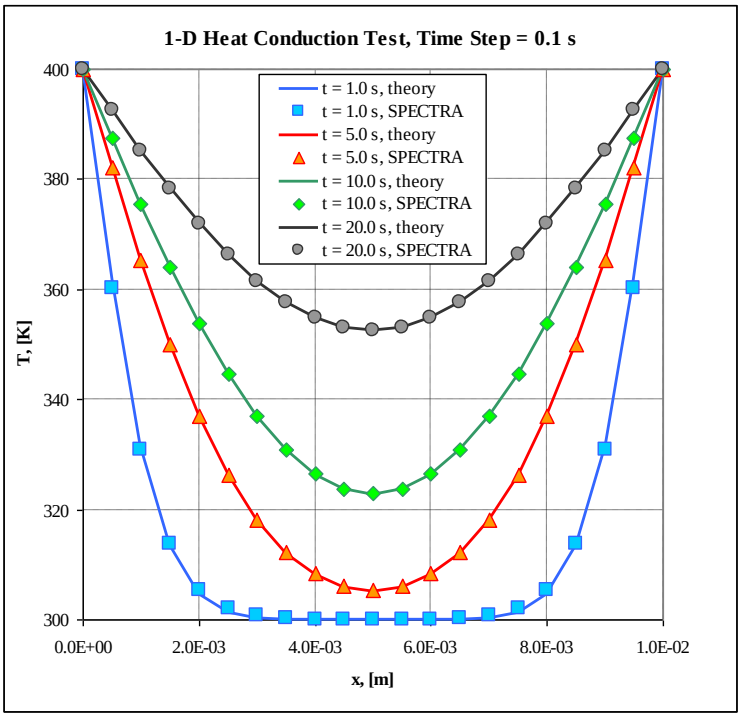

Figure 3-138 Transient test - slab heated from both sides.

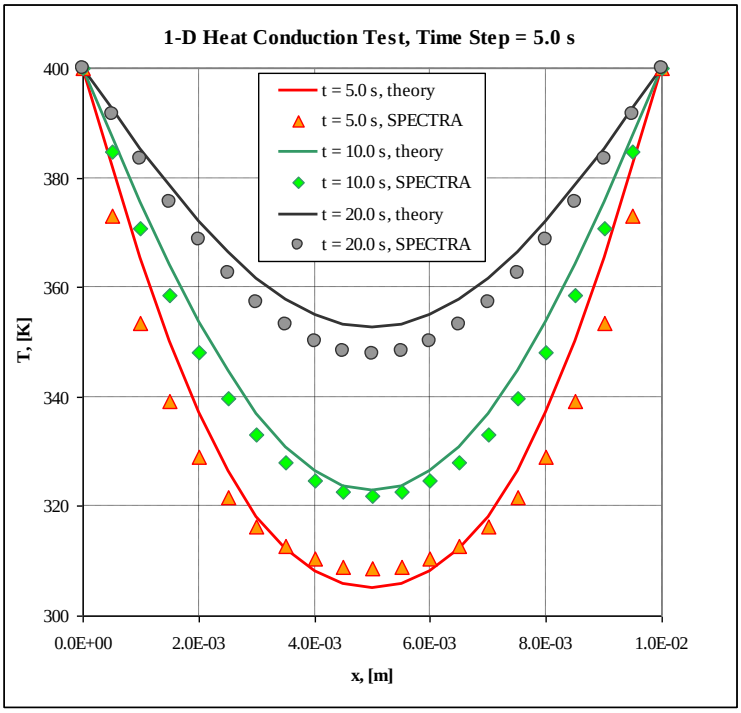

Figure 3-139 Slab heated from both sides, SPECTRA time step of 5.0 s.

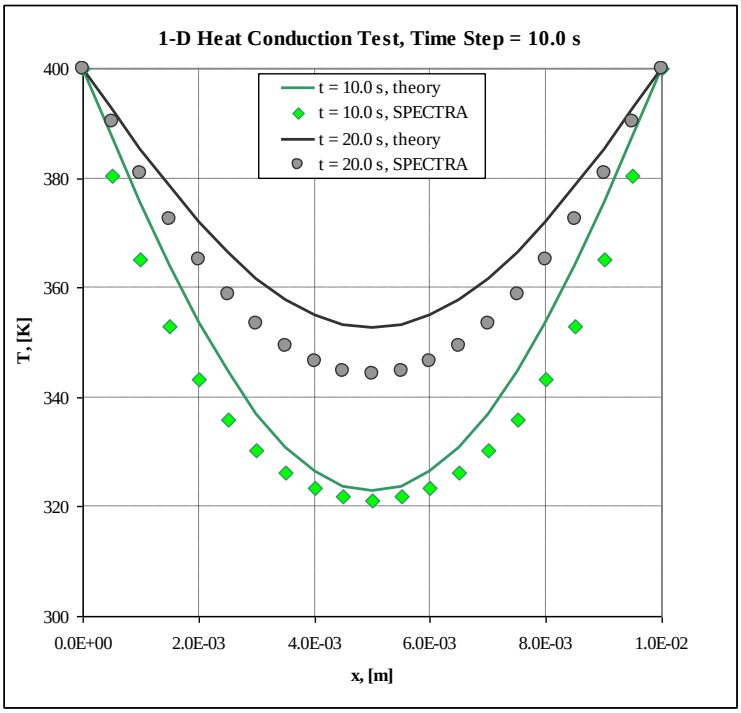

Figure 3-140 Slab heated from both sides, SPECTRA time step of 10.0 s.

3.5.5 Cooling of a Structure in Fluid

The Cooling of a Structure by Fluid (CSF) problem is described in the MELCOR Assessment Manual [142]. Two uniform structures (one rectangular and one cylindrical) with constant thermal properties and constant surface heat transfer coefficients are considered. These structures, initially at T_i = 1,000 K, were immersed in a fluid at T_f = 500 K. Table 3-16 gives values of the various thermal properties of the material in these structures, as well as other parameters used in these calculations that were used in [142]. For the current calculations the same values were used, with the exception of thermal conductivity, which is discussed below.

Table 3-16 Specification of the CSCF problem [142]

Parameter	Value
Thermal Conductivity	50.0 W/m-k
Density	1.0 kg/m^3
Specific Heat Capacity	1500.0 J/kg-K
Surface heat transfer coefficient	50.0W/m^2-K
Structure initial temperature	1000.0 K
Fluid temperature	500.0 K
Rectangular slab thickness	0.1 m
Rectangular slab surface area	1.0m^2
Cylindrical slab radius	0.1m
Cylindrical slab height	1.0m

The analytical solution for the temperature of a lumped (uniform temperature) structure that is immersed in a fluid is given by [142]:

$$T = T_f + (T_i - T_f) \cdot \exp\left(-\frac{hA}{c_p V} t \right)$$

T uniform temperature (K)
T_f temperature (K) of fluid
T_i initial temperature (K) of the solid
h heat transfer coefficient (W/m^2-K)
c_p volumetric heat capacity (J/m^3-K)
V volume (m^3) of the solid
A surface area (m^2) of the solid
t time (s)

SPECTRA model was created based on the data in Table 3-16. Two versions of the input deck were prepared, using two alternative methods concerning the location of nodes in a 1-D Solid Heat Conductor:

- Method 1, nodes at cell centers
- Method 2, nodes at cell edges

The theoretical solution, shown above, was defined in the input using appropriate Control Functions. Both rectangular and cylindrical geometry was analyzed. The SPECTRA input files are located in:

\Z-INPUTS\SC\CSF

For comparison, a model for MELCOR 1.8.6 was generated using the automated export option (IEXPSL=2). The MELCOR input file is located in:

\Z-INPUTS\SC\CSF\MELCOR

Results obtained with all parameters as given in Table 3-16 are shown in Figure 3-141 and Figure 3-142. The figures give temperatures obtained at 1.0 second into the transient. It is seen that the temperatures in the solid are not entirely uniform. Therefore it is difficult to compare with theoretical solution, which is valid for a uniform temperature in the structure.

In order to obtain a case that is more comparable to the theoretical solution, the thermal conductivity of the material was changed from $k = 50$ W/m^2-K to a large number, namely $k = 9999$ W/m^2-K. Results are shown in Figure 3-143 and Figure 3-144. It is seen that the structures have now uniform temperature and this temperature agrees well with the analytical solution.

Figure 3-145 and Figure 3-146 show the time-dependent graphs. It is seen that the SPECTRA results agree very well with the theoretical results. Results shown here are obtained for the rectangular geometry. Exactly the same results are obtained for the cylindrical structures.

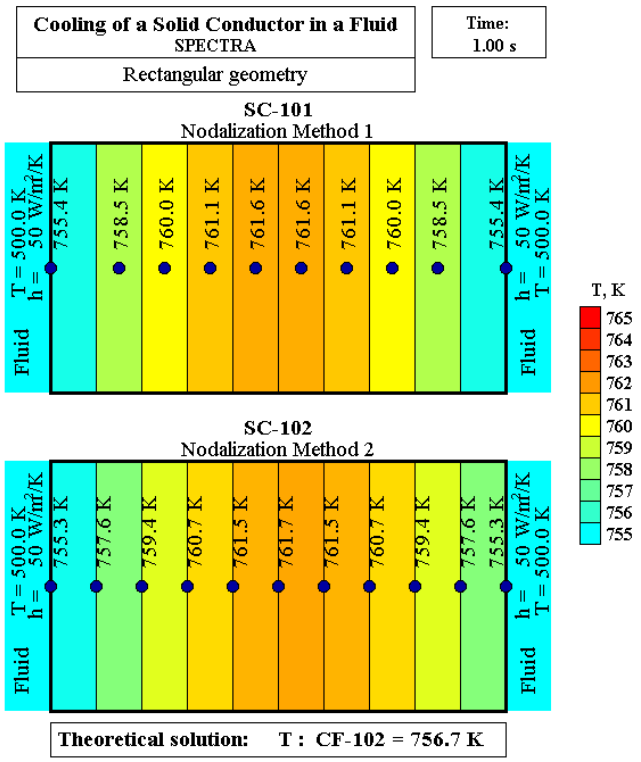

Figure 3-141 CSF problem at t = 1.0 s, k = 50 W/m^2-K, SPECTRA

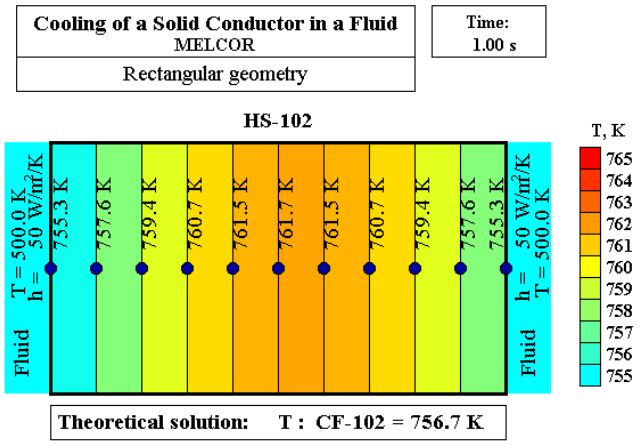

Figure 3-142 CSF problem at t = 1.0 s, k = 50 W/m^2-K, MELCOR

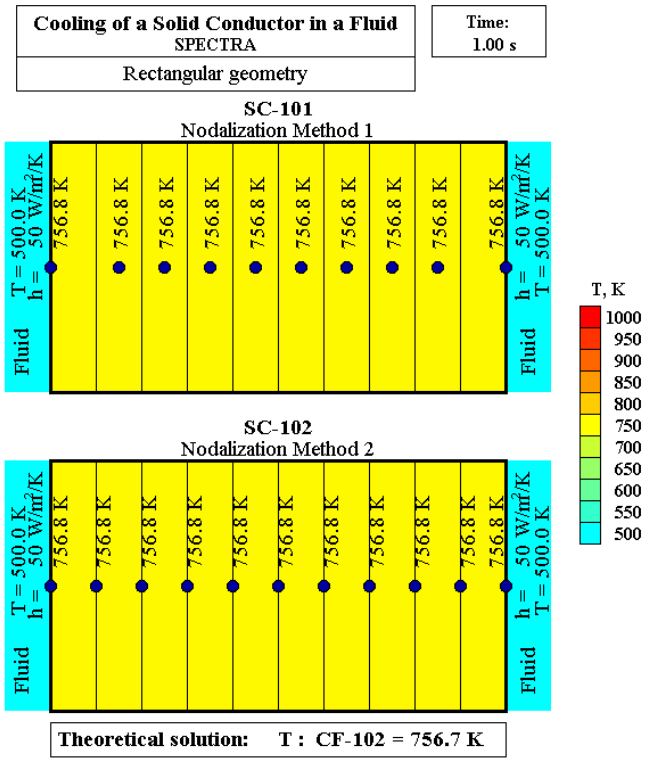

Figure 3-143 CSF problem at t = 1.0 s, k = 9999 W/m^2-K, SPECTRA

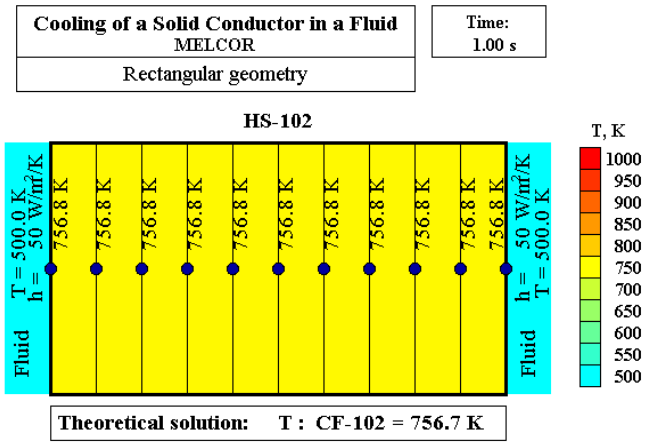

Figure 3-144 CSF problem at t = 1.0 s, k = 9999 W/m^2-K, MELCOR

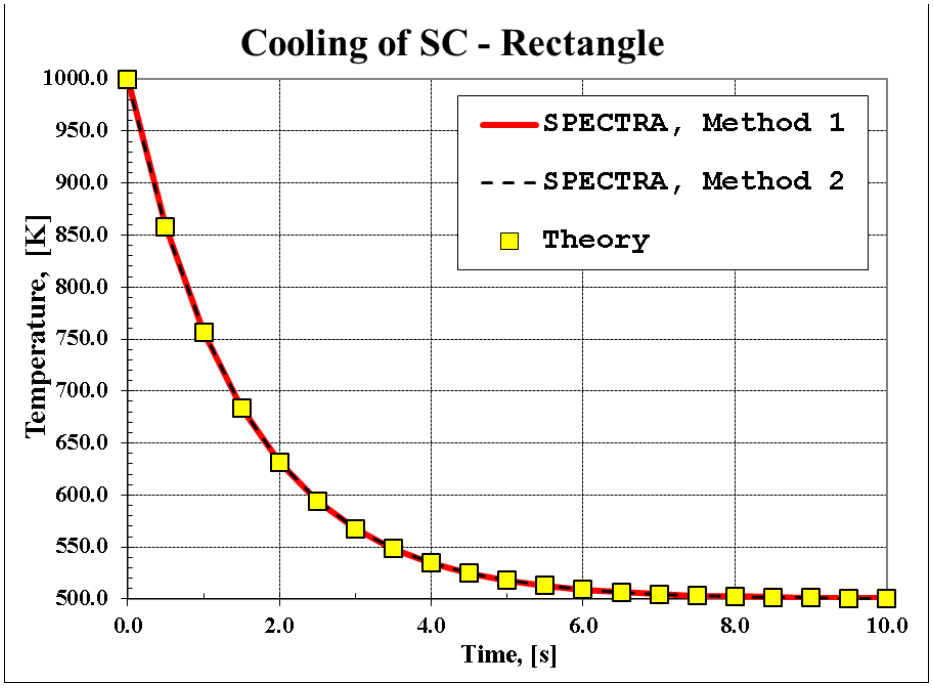

Figure 3-145 CSF problem, temperature history, k = 9999 W/m^2-K, SPECTRA

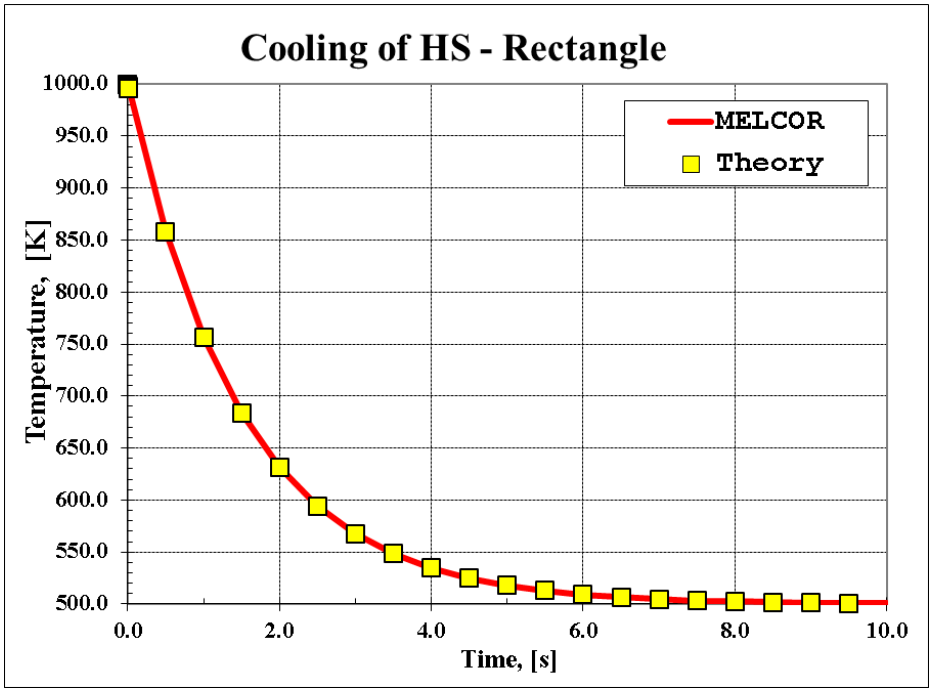

Figure 3-146 CSF problem, temperature history, k = 9999 W/m^2-K, MELCOR

3.5.6 Two Radiating Surfaces - Test of Structure-to-Gas Radiation Model

A simple structure-to-gas radiation model available in the Solid Heat Conductor Package calculates radiative heat exchange between the wall surface and the surrounding gas. The gas is assumed to be opaque (gas emissivity and absorptivity are equal to one). For such cases the radiative heat flux is given by:

$$q = \sigma \cdot \varepsilon_w(T_w) \cdot \left(T_w^4 - T_g^4\right)$$

where σ is the Stefan-Boltzmann constant ($\sigma = 5.67\times10^{-8}$ W/m^2/K^4), $\varepsilon_w(T_w)$ is the wall emissivity (assumed to be a function of the wall temperature), T_w, T_g are the wall and the gas temperatures respectively. The assumption of gas opacity is taken for modelling consistency. Gas emissivity could be introduced into the above equation by replacing the wall emissivity, $\varepsilon_w(T_w)$, by an effective wall-gas emissivity, defined as:

$$\varepsilon_{wg} = \frac{1}{\frac{1}{\varepsilon_w(T_w)} + \frac{1}{\varepsilon_g(T_g)} - 1}$$

Here $\varepsilon_g(T_g)$ is the gas emissivity at given gas temperature. Such method is used for example in the MELCOR code, Heat Structure Package [20]. This approach may be criticized, as follows.

If the detailed net enclosure model or the structure-to-structure model is not used, In absence of the model of the direct wall-to-wall radiation, the radiative heat exchange can be correctly modelled only if the atmosphere is opaque. In any other case, that means if the gas emissivity and absorptivity are smaller than one, then the use of the effective emissivity is approximately correct only in case of hot gas radiating to relatively cold walls, for example in case of burning chamber.

In cases when there is no internal energy source in the gas then, because of the relatively low heat capacity of gas, the gas temperature equilibrates quickly with the temperatures of the surrounding walls. In such case the gas acts mainly as a screen between radiating walls, and radiative exchange between the walls is minimal in case of opaque atmosphere, and increases with decreasing gas emissivity (see section 3.8.2.3, Table 3-49). Use of the effective emissivity will result in the radiative exchange being maximal in case of opaque atmosphere, and decreasing with decreasing gas emissivity (Figure 3-147), so the effect contradictory to that observed in reality. Therefore it is concluded that when the simplified radiation model is used, the best one can do is to assume opaque atmosphere:

$$\varepsilon_g(T_g) = 1.0$$

which leads to:

$$\varepsilon_{wg} = \varepsilon_w(T_w)$$

Further discussion is provided in section 3.8.2.3.

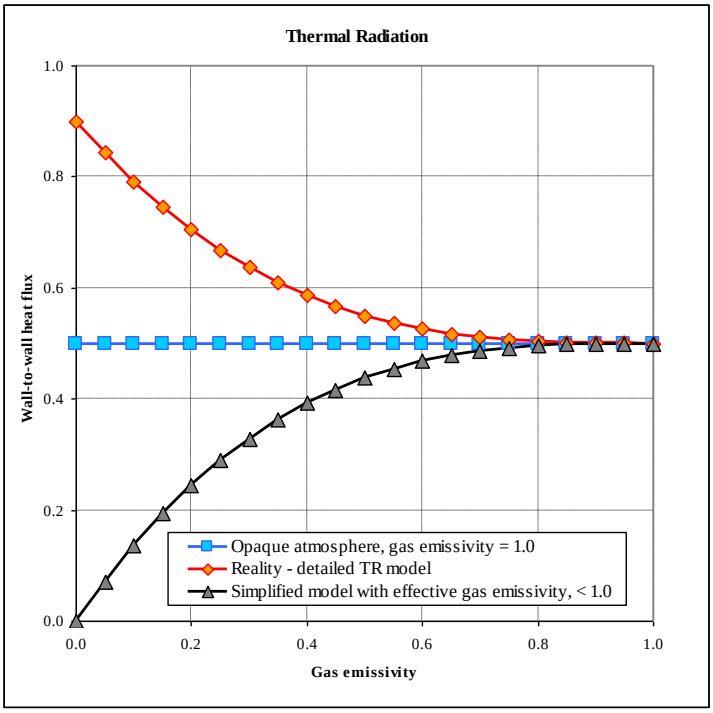

Figure 3-147 Influence of gas emissivity on radiation heat flux.

For verification of the simple radiation model the following test case has been selected. The selected test has also been analyzed using the elaborate Thermal Radiation model (see section 3.8.2.3).

Simplified Radiation Model Test - Theory

The system consists of two flat parallel radiating surfaces and a gas space between them. A more detailed description is given in section 3.8.2.3. The theoretical solution is ([21], section 7.1, equations 7.16, 7.17):

$$q = \sigma \cdot \varepsilon_{1-2} \cdot \left(T_1^4 - T_2^4\right)$$

where $\varepsilon_{1\text{-}2}$ is the effective emissivity given by:

$$\varepsilon_{1-2} = \left(\frac{1}{\varepsilon_1} + \frac{1}{\varepsilon_2} - 1 + \frac{\varepsilon_g}{2 - \varepsilon_g} \right)^{-1}$$

In case of the simplified radiation model the gas emissivity, ε_g, is by definition equal to 1.0 (as explained above). The emissivities of the surfaces 1 and 2, ε_1 and ε_2, are assumed to be equal to 0.5.

Therefore:

$$\varepsilon_{1-2} = \left(\frac{1}{0.5} + \frac{1}{0.5} - 1 + \frac{1.0}{2-1.0} \right)^{-1} = 0.25$$

The heat flux is:

$$q = 5.67 \times 10^{-8} \cdot 0.25 \cdot \left(1000^{4} - 400^{4} \right) = 13.81 \times 10^{3}$$

Therefore the theoretical heat flux is equal to 13.81 kW/m^2.

SPECTRA Calculations

The SPECTRA model is shown in Figure 3-148. Two Solid Heat Conductors (SC-001 and SC-002) exchange radiative heat with the atmosphere of Control Volume CV-001. The temperatures of SC-001 and SC-002 are held constant by tabular boundary conditions, at 1000 K and 400 K respectively.

The conduction effects were minimized by selecting very small thickness of both conductors (0.02 mm) and very large material conductivity (1000 W/m-K). Surface emissivities of SC-001 and SC-002 were set to 0.5. To avoid convective heat transfer, the default convective heat exchange models have been replaced by tabular heat transfer coefficient, with the value of zero.

Input deck for this test is provided in:
`\Z-INPUTS\SC\S-RAD\2RG1-S.SPE`

Calculations were performed for long period (3600 s = 1 hour) to obtain stable conditions. The resulting heat flux was identical to the value obtained in section 3.8.2.3 for the case ε_g = 1.0, namely: q = 13.81 kW/m^2.

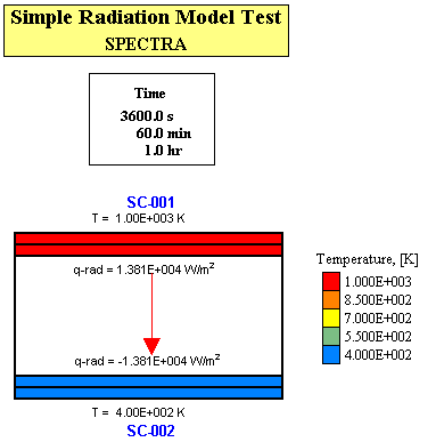

Figure 3-148 Two radiating surfaces with gas

Further verification of two simple radiation models: structure-to-gas and structure-to-structure, and comparison with the detailed net enclosure models is shown in section 3.8.2.4.

3.5.7 Heat Exchanger

3.5.7.1 Analysis of a Steady State Performance

A counter flow liquid-to-liquid heat exchanger is modeled. It is assumed to consist of a tube bundle, with N = 10,000 horizontal tubes. The tube inner diameter is D_i = 0.02 m; the tube thickness is t = 0.005 m. The total length of the tubes is L = 3.0 m. The tubes are assumed to be made of stainless steel, SS-304. The thermophysical properties of this material are shown in Table 3-17. The primary and secondary side inlet parameters are:

- Primary side (inside the tubes):
  - Inlet temperature: 280.0 K
  - Pressure: 1.0×10^5 Pa
  - Inlet flow: 200.0 kg/s

- Secondary side (outside the tubes):
  - Inlet temperature: 370.0 K
  - Pressure: 1.0×10^5 Pa
  - Inlet flow: 200.0 kg/s

Three cases are considered with different tube nodalization

- 3-node model: the tubes are divided into 3 sections, each 1.0 m long.
- 6-node model: the tubes are divided into 6 sections, each 0.5 m long.
- 12-node model: the tubes are divided into 12 sections, each 0.25 m long.

As a verification of SPECTRA results, calculations are performed with two other codes, MELCOR, Version 1.8.3 and RELAP5/MOD3.2. Input decks for these calculations are located in:

- MELCOR: `\Z-INPUTS\SC\HEX\MELCOR\hex.gen, hex.cor`
- RELAP: `\Z-INPUTS\SC\HEX\RELAP\hex.inp`
- SPECTRA `\Z-INPUTS\SC\HEX\SPECTRA\HEX.SPE`

Table 3-17 Properties of stainless steel, SS-304 [101].

Property	Temperature	Value
k, (W/m^{2}K)	300.0	13.5
	800.0	23.0
	1300.0	32.0
ρ, (kg/m^3)	300.0	7800.0
	800.0	7600.0
	1300.0	7350.0
c_p, (J/kgK)	300.0	410.0
	500.0	450.0
	800.0	500.0
	1300.0	550.0

Calculations were performed for 300 s. At this time results are completely stable. Results are shown in Figure 3-150, Figure 3-151, and Figure 3-152. The power transferred by the heat exchanger depends on the number of nodes that are being used. The more nodes the higher power. An accurate power transfer would be obtained if the number of nodes is very large. This of course is not a practical solution. With an increasing number of nodes one has to use smaller time steps (because of the courant limit), therefore the computational time increases approximately proportional to N^2. In order to avoid the necessity of using a large number of nodes, SPECTRA has a Temperature Averaging (TA) model.

Use of the Temperature Averaging concept is shown in Figure 3-149 (b) and (d). A more detailed description is provided in Volume 1. In a nutshell when the scheme is used, the boundary fluid temperatures that the conducting structure "sees" are equal to the average of the temperature in the given control volume (equal to the temperature of the fluid leaving the control volume), and the temperature of the fluid entering this control volume - Figure 3-149 (b).

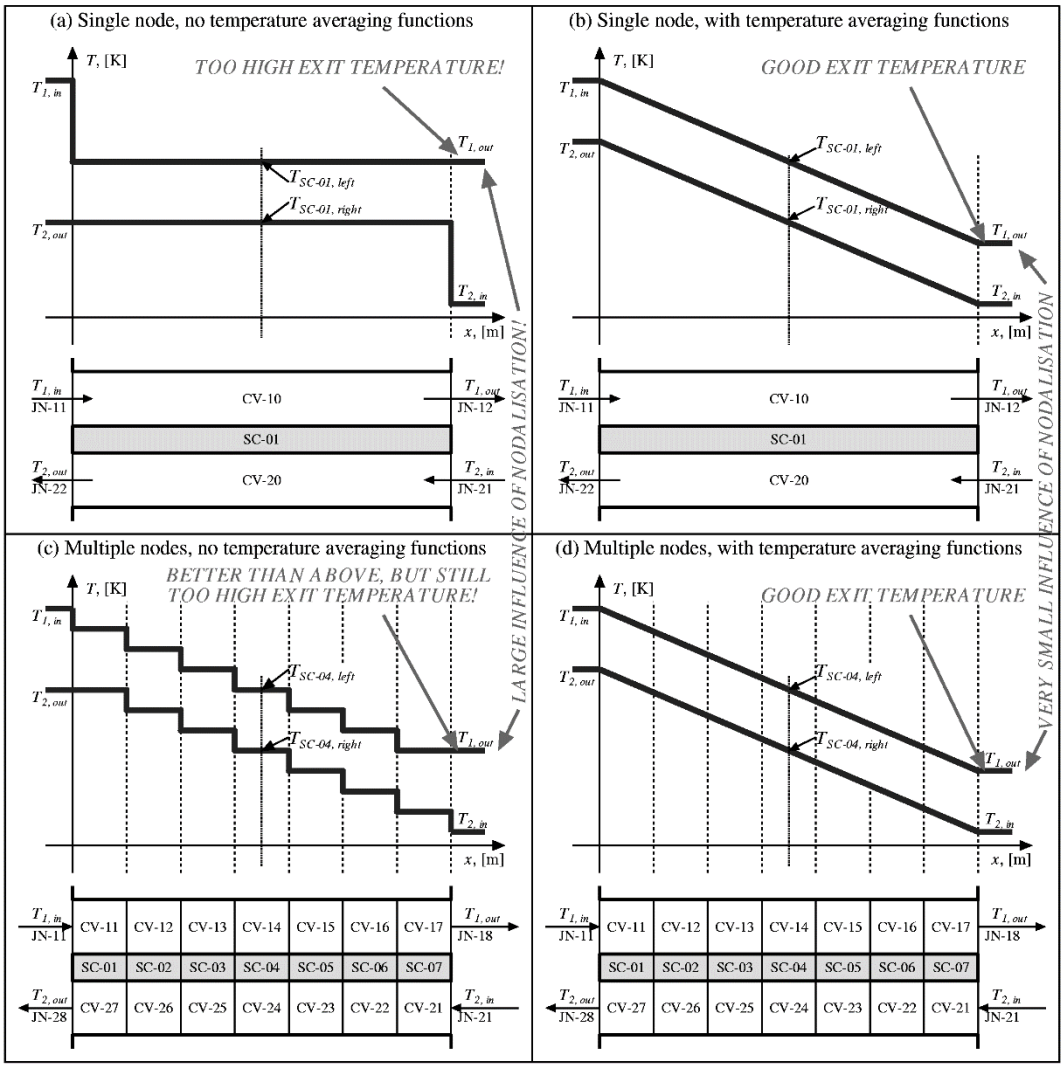

Figure 3-149 Counter flow heat exchanger modelling

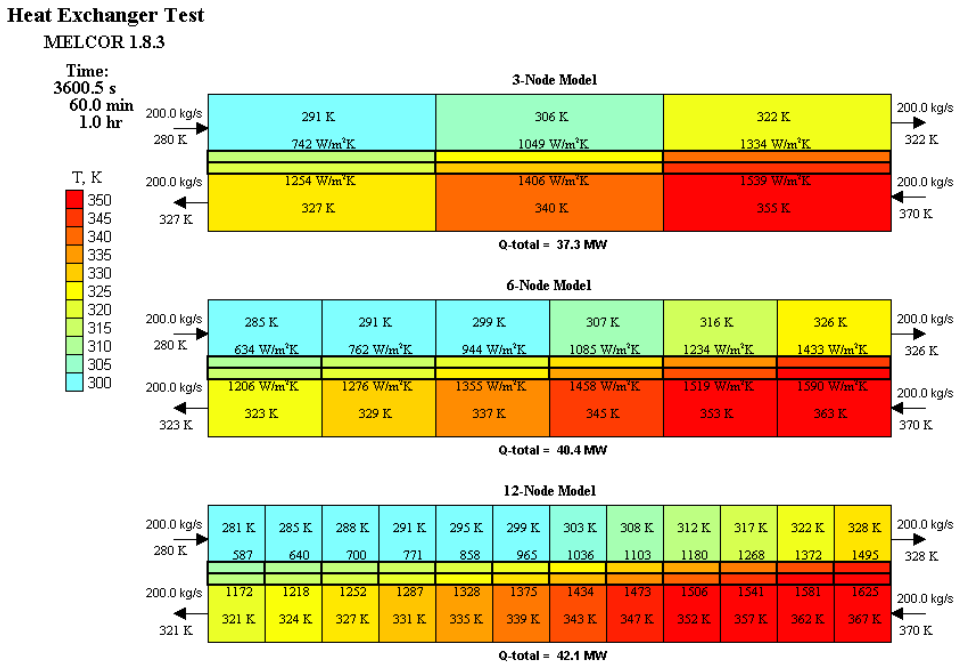

Figure 3-150 Counter flow heat exchanger - MELCOR results

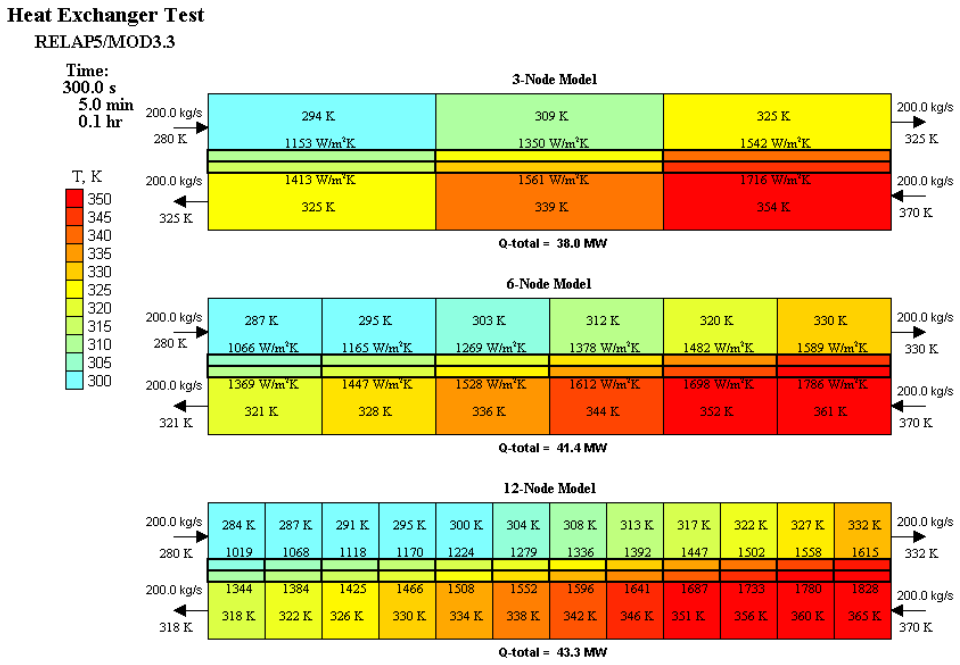

Figure 3-151 Counter flow heat exchanger - RELAP results

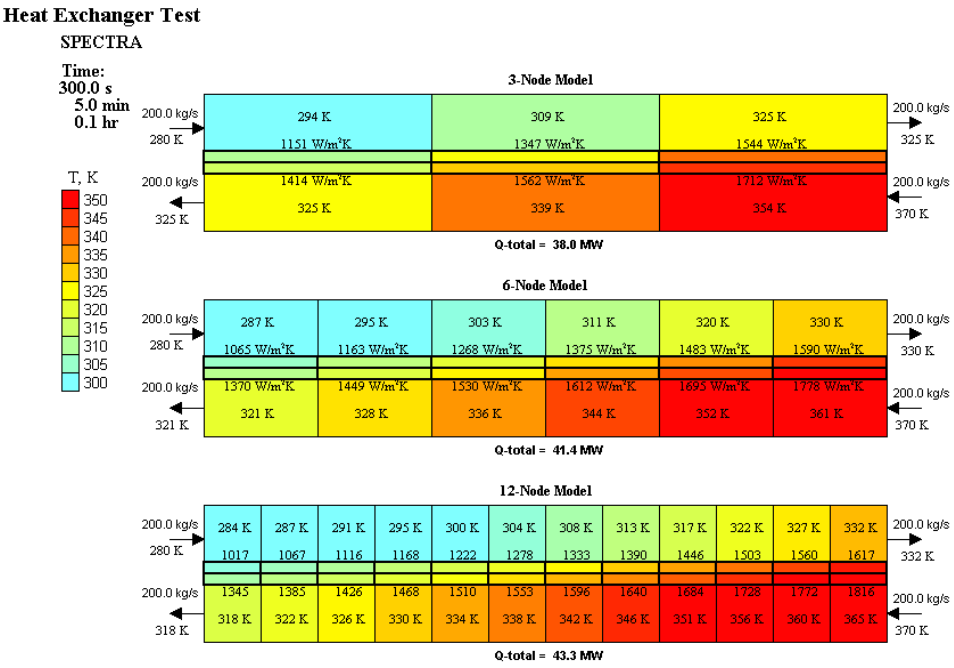

Figure 3-152 Counter flow heat exchanger - SPECTRA results

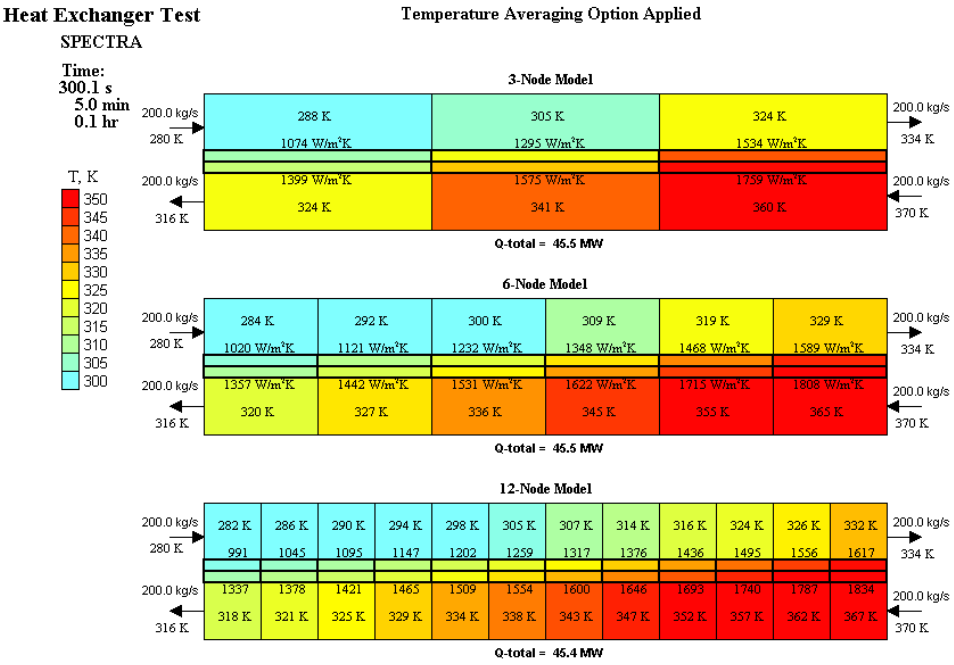

Figure 3-153 Counter flow heat exchanger - SPECTRA with Temperature Averaging

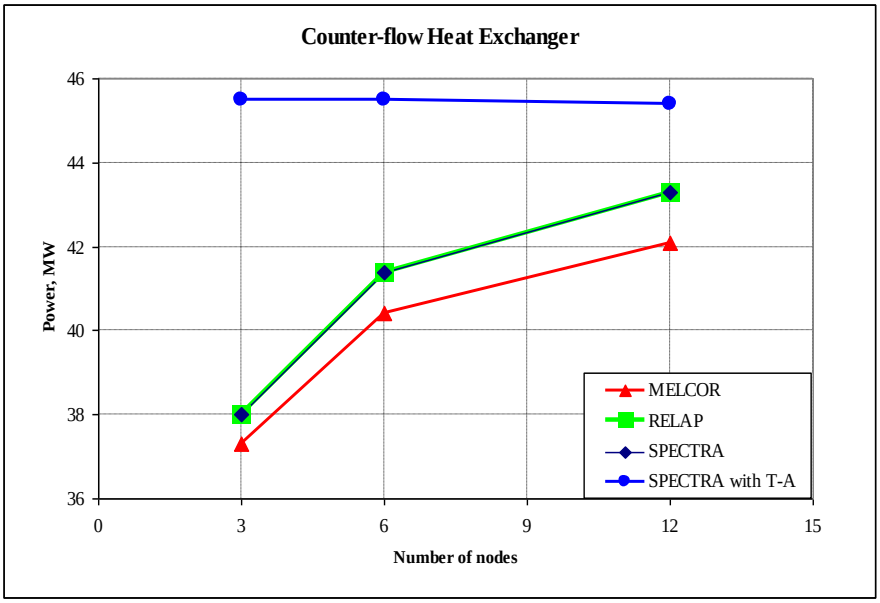

Figure 3-154 Summary of the results obtained with MELCOR, RELAP, and SPECTRA

Table 3-18 Summary of the results obtained with MELCOR and RELAP

Number of nodes	MELCOR		RELAP	
	Power	Error	Power	Error
3	37.3 MW	17.8%	38.0 MW	16.3%
6	40.4 MW	11.0%	41.4 MW	8.8%
12	42.1 MW	7.3%	43.3 MW	4.6%

Table 3-19 Summary of the results obtained with SPECTRA

Number of nodes	SPECTRA		SPECTRA with T-A	
	Power	Error	Power	Error
3	38.0 MW	16.3%	45.5 MW	0.02%
6	41.4 MW	8.8%	45.5 MW	0.02%
12	43.3 MW	4.6%	45.4 MW	0.00%

A new the case was prepared with the temperature averaging activated . The input deck is stored in `Z-INPUTS\SC\HEX\SPECTRA\HEX-TA.SPE`. Results are shown in Figure 3-153. Practically the same power is obtained for all three nodalizations.

3.5.7.2 Summary

The results are summarized in Figure 3-154, Table 3-18, and Table 3-19. The most accurate result (SPECTRA with T-A, 12 nodes) is taken as a reference value for the error estimation. Thus, the "exact" solution is: 45.4 MW.

Results of SPECTRA without the temperature averaging are very similar to the RELAP results (Figure 3-154). In MELCOR the power is lower because the heat transfer coefficients are lower than in RELAP and SPECTRA: 1000 - 1800 W/m^{2}K in RELAP and SPECTRA, and 600 - 1600 W/m^{2}K in MELCOR. This fact is caused by the use of different correlation for the heat transfer coefficient in MELCOR than in RELAP/SPECTRA. A separate set of calculations were performed with the same model using a higher mass flow, 500 kg/s instead of 200 kg/s. The files are located in `\Z-INPUTS\SC\HEX-500`. The results are summarized in Figure 3-155. In this case the power calculated by MELCOR is somewhat higher than that from RELAP/SPECTRA.

3.5.7.3 Conclusions and Recommendations

The temperature-averaging concept (T-A) in SPECTRA provides a good way to obtain accurate results with relatively small amount of nodes in steady state conditions. Further verification is needed for the transient conditions.

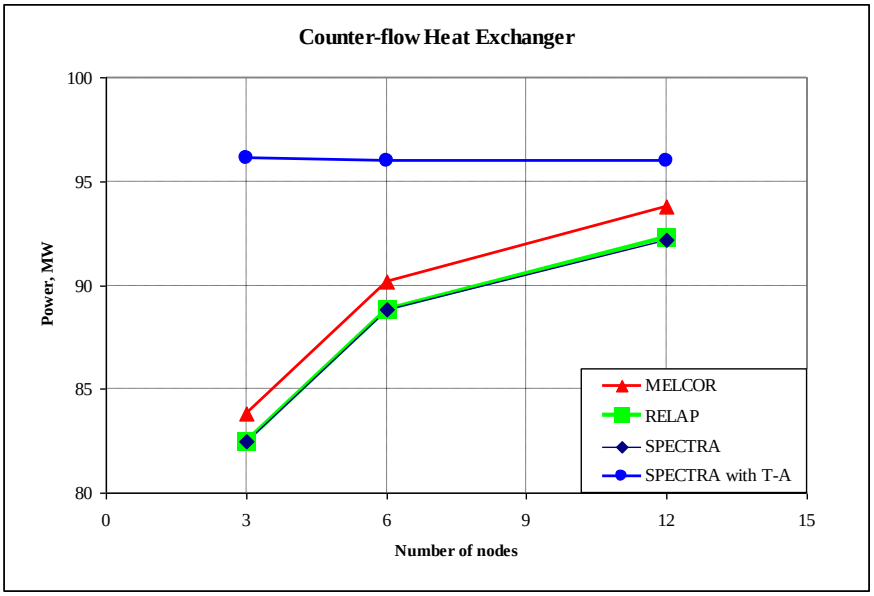

Figure 3-155 Summary of the results obtained for 500 kg/s

3.5.8 Failure Analysis for a 1-D Structure - Inconel 600

This section presents results of a creep failure test performed for a 1-D Solid Heat Conductor. The geometrical data is taken from the cylindrical structure with variable thermal conductivity, SC-005, section 3.5.1. The boundary conditions were set to 800 K and 1000 K on the left and the right side respectively. The failure data of Inconel-600 has been applied (see Volume 1). The data is listed in Table 3-20. The stress was defined using Control Function CF-935. A constant stress of 100 MPa (10^8 Pa) has been applied. The creep rupture is calculated using the default option, which uses the SC maximum temperature for the creep calculation. In the present case the maximum temperature is equal to the right boundary temperature, namely 1000 K.

Table 3-20 Failure model data for Inconel-600

Constants	Inconel-600
A	54,086
B	4,968.5
C	9.44
T_M	1644.0
$\sigma_{U,lowT}$	7.3×10^8
$t_{U,highT}$	634.0

SPECTRA input file is provided in:
`\Z-INPUTS\SC\FAILURE\FAILURE-1.SPE`

Calculations were performed for 100,000 s. Results are shown in Figure 3-156, Figure 3-157, and Figure 3-158. Creep rupture was calculated to occur at t = 79,068 s.

Verification is performed using hand calculations. The Larson-Miller parameter is equal to:

$$LMP = A - B \cdot \log_{10}(\sigma) =$$
$$= 54086 - 4968.5 \cdot \log_{10}(10^8) = 14338$$

The time to rupture is obtained from:

$$\log_{10}(t_r) = \frac{LMP}{T} - C =$$
$$= \frac{14338}{1000} - 9.44 = 4.898$$

Therefore:

$$t_r = 10^{4.898} = 79{,}068$$

This is in agreement with the calculated value - see Figure 3-156, Figure 3-157, Figure 3-158.

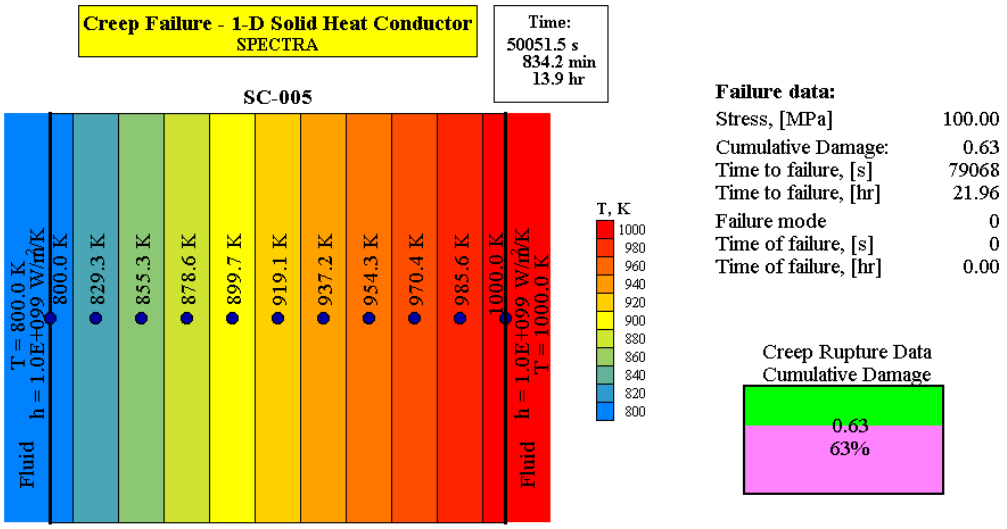

Figure 3-156 Failure analysis for 1-D Structure - values at 50,000 s

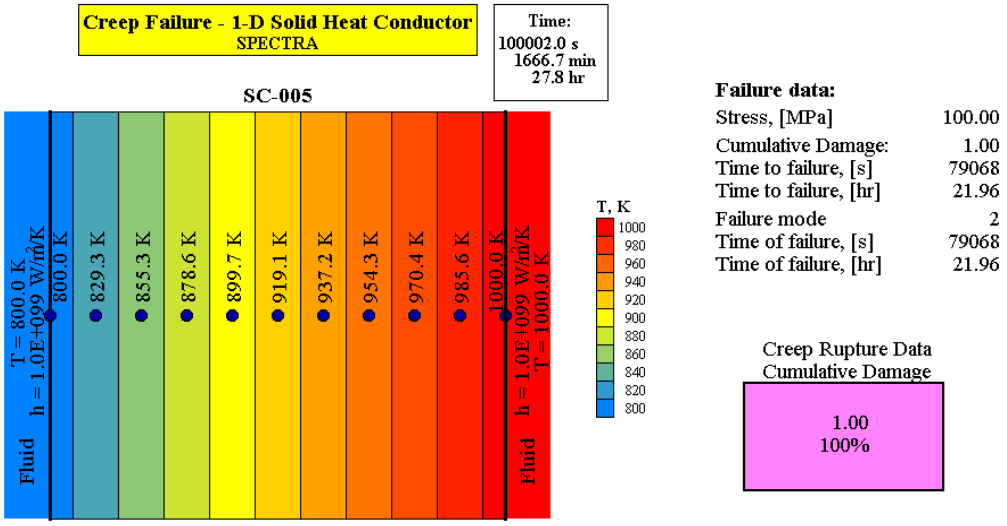

Figure 3-157 Failure analysis for 1-D Structure - values at 100,000 s

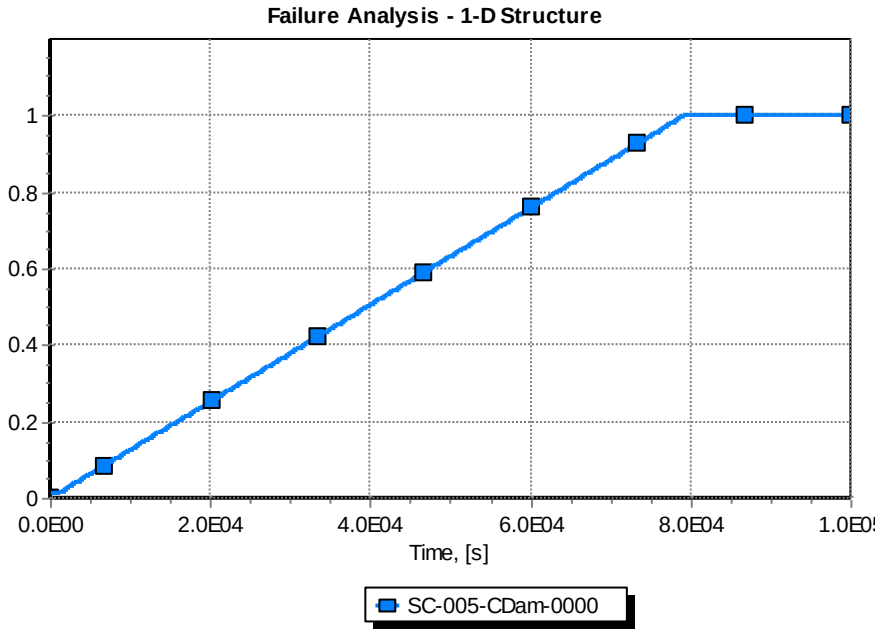

Figure 3-158 Failure analysis for 1-D Structure - cumulative damage versus time

3.5.9 Failure Analysis for a 1-D Structure - Steel 22 NiMoCr 37

This section presents results of a creep failure test performed for a 1-D Solid Heat Conductor. The geometrical data and boundary conditions are the same as in previous section. The failure data of steel 22 NiMoCr 37 has been applied. The creep data for this steel is given in reference [128]. The time to rupture is obtained from ([128], equation 1):

$$\log_{10}(t_r / t_0) = \frac{LMP}{T} - C'$$

Here C' is constant, equal to $C' = 21.0$ and t_0 is reference time, equal to 1 hr [128]. Since t_r has to be expressed in seconds (SI), then $t_0 = 3600$ s. Substituting the value for t_0, time to rupture may be written as:

$$\log_{10}(t_r) = \frac{LMP}{T} - C$$

with $C = 21.0 - \log_{10}(3600) = 17.44$. The Larson-Miller parameter dependence on stress is given by ([128], equation 2):

$$LMP = 5.049 \times 10^3 \times [6.078 - \log_{10}(\sigma / \sigma_0)]$$

Here *LMP* is the Larson Miller parameter, in Kelvins and σ_0 is reference stress, equal to 1 N/mm^2 [128]. Since σ has to be expressed in Pa (SI), then $\sigma_0 = 10^6$ Pa. Substituting the value for σ_0, *LMP* may be written as:

$$LMP = 6.0982 \times 10^4 - 5{,}049 \times 10^3 \times \log_{10}(\sigma)$$

or:

$$LMP = A - B \cdot \log_{10}(\sigma)$$

with: $A = 6.0982 \times 10^4$
$B = 5.049 \times 10^3$

The melting temperature is T_M = 1700 K ([129], section 2.2). The low temperature ultimate strength is 584 MPa ([129], table 2.1-3). The ultimate strength at high temperatures is tabulated in [129], table 2.1-3 - the values are shown here in Figure 3-159. The properties of steel 22 NiMoCr 37 are summarized in Table 3-21. The creep lines are shown in Figure 3-159. The Larson-Miller correlation, defined as shown above, is plotted for the 1 and the 10 hours creep failure. The high temperature ultimate strength data is approximated by a creep line with t_r = 100 s.

Table 3-21 Failure model data for steel 22 NiMoCr 37

Constants	22 NiMoCr 37
A	60,982
B	5,049
C	17.44
T_M	1700.0
$\sigma_{U,lowT}$	5.84×10^8
$t_{U,highT}$	100.0

SPECTRA input file is provided in:
`\Z-INPUTS\SC\FAILURE\FAILURE-1-A.SPE`

The applied stress was 10^8 Pa, the maximum temperature was 1000 K. Calculations were performed for 2000 s. Results are shown in Figure 3-160. Creep rupture was calculated to occur at t = 1413 s.

Verification is performed using hand calculations. The Larson-Miller parameter is equal to:

$$LMP = A - B \cdot \log_{10}(\sigma) =$$
$$= 60982 - 5049.0 \cdot \log_{10}(10^8) = 20590$$

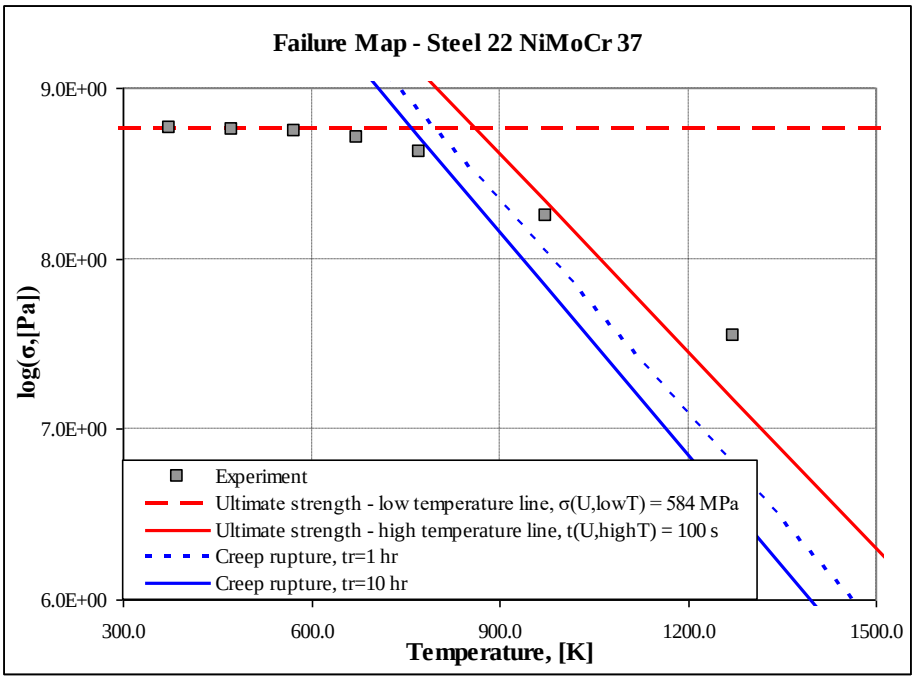

Figure 3-159 Failure properties of steel 22 NiMoCr 37

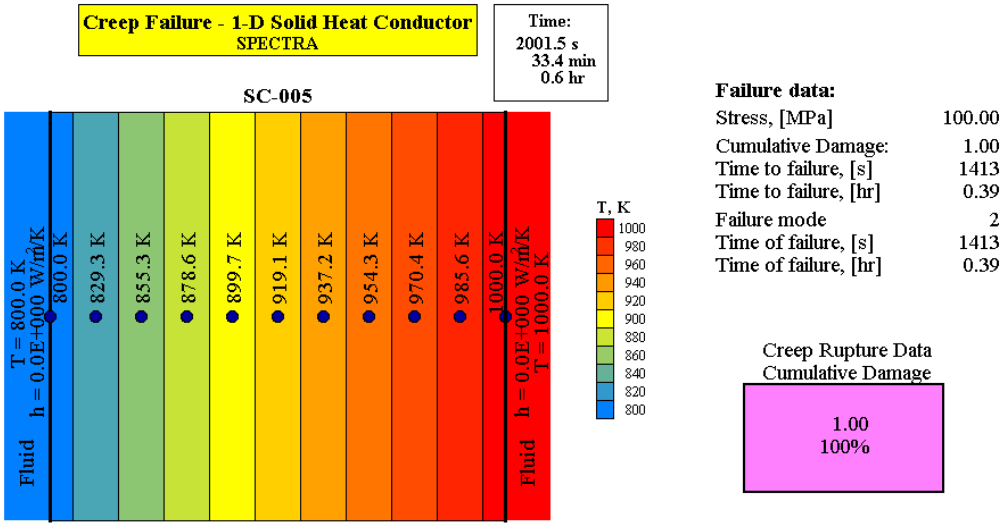

Figure 3-160 Failure analysis for 1-D Structure - values at 2000 s

The time to rupture is obtained from:

$$\log_{10}(t_r) = \frac{LMP}{T} - C =$$

$$= \frac{20590}{1000} - 17.44 = 3.146$$

Therefore:

$$t_r = 10^{3.146} = 1400$$

This is in agreement with the calculated value - see Figure 3-160.

3.5.10 Failure Analysis for a 1-D Structure - Incoloy 800HT

This section presents results of a creep failure test performed for a 1-D Solid Heat Conductor. The geometrical data and boundary conditions are the same as in previous section. The failure data of Incoloy 800 has been applied. The creep data for this material is given in reference [130]. The Larson-Miller parameter is equal to:

$$LMP = T \cdot (22.93 + \log_{10} t_r) \cdot 10^{-3}$$

Here T is temperature in Rankine, t_r is time to rupture in hours. The creep rupture strength line is shown in [130], Figure 7, reproduced here in Figure 3-161. The line was approximated by:

$$\log_{10}(\sigma) = 4.475 - 0.0725 \cdot LMP$$

Here σ is stress in ksi. The usual relation between stress and Larson-Miller parameter is given as:

$$LMP = A - B \cdot \log_{10}(\sigma)$$

Here A and B are material constants and σ is stress in Pa. The above equation is written for the SI units. It has to be remembered that reference [130] uses English units, with stress expressed in ksi and Larson-Miller parameter in ºF. For use in SPECTRA, the equation has to be converted to SI units. This is done as follows. First, the equation written in English units (using the sign ' to signify English unit):

$$LMP' = A' - B' \cdot \log_{10}(\sigma')$$

The constants in English units are obtained from Figure 3-161 and are equal to:

B' = 1/0.0725 = 13.79
A' = 4.475×13.79 = 61.72

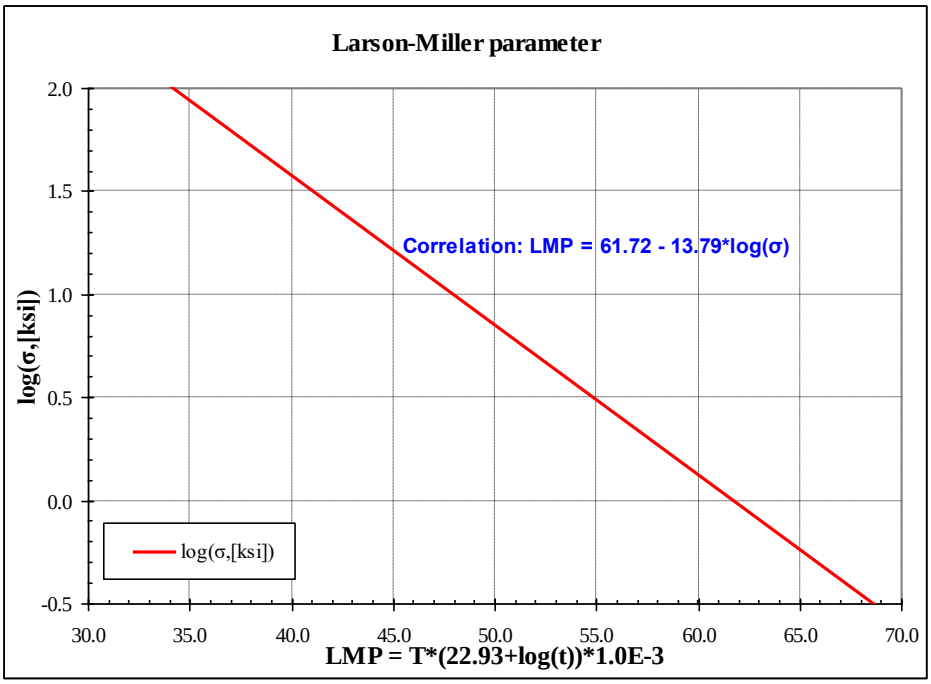

Figure 3-161 Creep rupture correlation for Incoloy 800HT

Next, the values have to be converted to the SI units. Conversion from Rankine to Kelvins and from hours to seconds means that when the formula is expressed in SI units $LMP = 1000/1.8 \times LMP'$ and $C = C' - \log_{10}(3600) = C' - 3.56$. One ksi is 1000 psi. Since 1 bar = 14.504 psi, 1 ksi is equal to $1000/14.504 \times 10^5 = 6.89465 \times 10^6$ Pa. Therefore when the Pa are used for stress, then: $A'' = A' + B' \times \log_{10}(6.89 \times 10^6) = A' + B' \times 6.8385$. The value of A'' is now converted to account for different units of stress. Now it has to be converted still to account for different temperature units and for the presence of the factor 10^{-3} in the original formula for LMP. Therefore: $A = A'' \times (1000/1.8)$. For the same reason the factor B' must be multiplied by the factor 1000/1.8. Therefore: $B = B' \times (1000/1.8)$. Therefore for the SI units the coefficients must be converted as follows:

$$A = (A' + B' \times 6.8385) \times (1000 / 1.8)$$
$$B = B' \times (1000 / 1.8)$$
$$C = C' - 3.56$$

The formulae in English units:

$LMP' = 61.72 - 13.79 \times \log_{10}(\sigma')$
$LMP' = T'(22.93 + \log_{10}(t_r'))(10^{-3})$

converted to SI units become:

$A = (61.72 + 13.79 \times 6.8385) \times (1000/1.8) = 86694$
$B = 13.79 \times (1000/1.8) = 7663$
$C = 22.93 - 3.56 = 19.37$

$$LMP = 86694 - 7663 \times \log_{10}(\sigma)$$
$$LMP = T \times (19.37 + \log_{10}(t_r))$$

The ultimate strength experimental data for Incoloy 800HT is shown in Figure 3-162. The figure shows the ultimate strength data and the creep data for 10,000 hours and 100,000 hours creep, obtained from [130]. The Larson-Miller correlation defined as shown above, is plotted for the 10,000 and the 100,000 hours creep failure. The correlation represents well the creep data. As expected, the high temperature ultimate strength data is well matched by a creep line for low rupture time, in this case the line for t_r = 300 s was used.

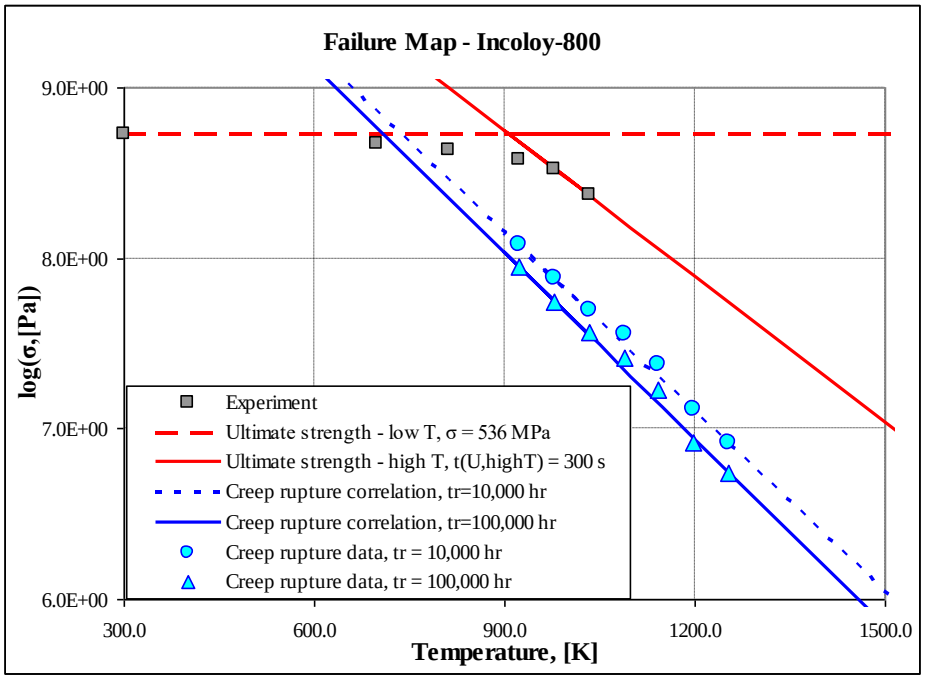

Figure 3-162 Failure properties of Incoloy 800HT

SPECTRA input file is provided in:
`\Z-INPUTS\SC\FAILURE\FAILURE-1-B.SPE`

The applied stress was 10^8 Pa, the maximum temperature was 1000 K. Calculations were performed for 1.2E+6 s. Results are shown in Figure 3-163. Creep rupture was calculated to occur at t = 1.047×10^6 s.

Verification is performed using hand calculations. The Larson-Miller parameter is equal to:

$$LMP = A - B \cdot \log_{10}(\sigma) =$$
$$= 86694 - 7663 \cdot \log_{10}(10^8) = 25390$$

The time to rupture is obtained from:

$$\log_{10}(t_r) = \frac{LMP}{T} - C =$$

$$= \frac{25390}{1000} - 19.37 = 6.02$$

Therefore:

$$t_r = 10^{6.02} = 1.047 \times 10^6$$

This is in agreement with the calculated value - see Figure 3-163.

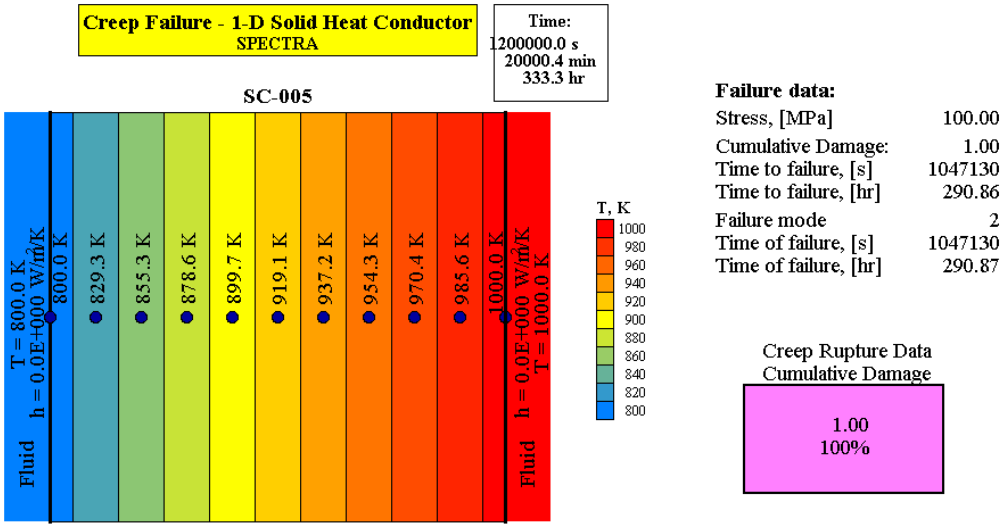

Figure 3-163 Failure analysis for 1-D Structure - values at 1,200,000 s

3.5.11 Failure Analysis for a 1-D Structure - Incoloy 800

Data on Incoloy 800 is obtained from [131]. The reference does not provide Larson-Miller parameter, only creep strength as a function of creep rate ([131], Figure 7). This data is compared to the same data for Incoloy 800HT ([130], Figure 5). Based on this comparison the data for Incoloy-800 is estimated using the data for Incoloy 800HT and a "correction factor" estimated by comparing the above mentioned figures. It was found out that reducing the factor *A* from 86694 to 85500 while keeping *B* and *C* the same, one obtains the desired effect. This may be seen by comparing Figure 4 and Figure 5 with the corresponding figures in literature ([131], Figure 7 and [130], Figure 5, respectively). Figure 3-164 and Figure 3-165 were made using the assumption that the fracture strain is 2%. This value was obtained based on reference [132].

Creep correlation for Incoloy 800 is compared to the creep correlation for Incoloy 800HT in Figure 6. The Incoloy 800 has clearly lower creep properties. For example, at T = 1200 K, the value of $\log_{10}(\sigma)$ for the alloy 800 is about 6.8, while it is 7.0 for the alloy 800HT. This means the stress is σ = 6.3 MPa and 10 MPa respectively. The strength of the alloy 800 is only about 60% of that of 800HT. Alloy 800 is not normally used for applications that require optimum creep-rupture properties. In those cases, Incoloy alloys 800H or 800HT should be used [131].

SPECTRA input file is provided in:
`\Z-INPUTS\SC\FAILURE\FAILURE-1-C.SPE`

The applied stress was 10^8 Pa, the maximum temperature was 1000 K. Calculations were performed for 80,000 s. Results are shown in Figure 3-167. Creep rupture was calculated to occur at t = 66,989 s.

Verification is performed using hand calculations. The Larson-Miller parameter is equal to:

$$LMP = A - B \cdot \log_{10}(\sigma) =$$
$$= 85500 - 7663 \cdot \log_{10}(10^8) = 24196$$

The time to rupture is obtained from:

$$\log_{10}(t_r) = \frac{LMP}{T} - C =$$
$$= \frac{24196}{1000} - 19.37 = 4.83$$

Therefore:

$$t_r = 10^{4.83} = 6.699 \times 10^4$$

This is in agreement with the calculated value - see Figure 3-167.

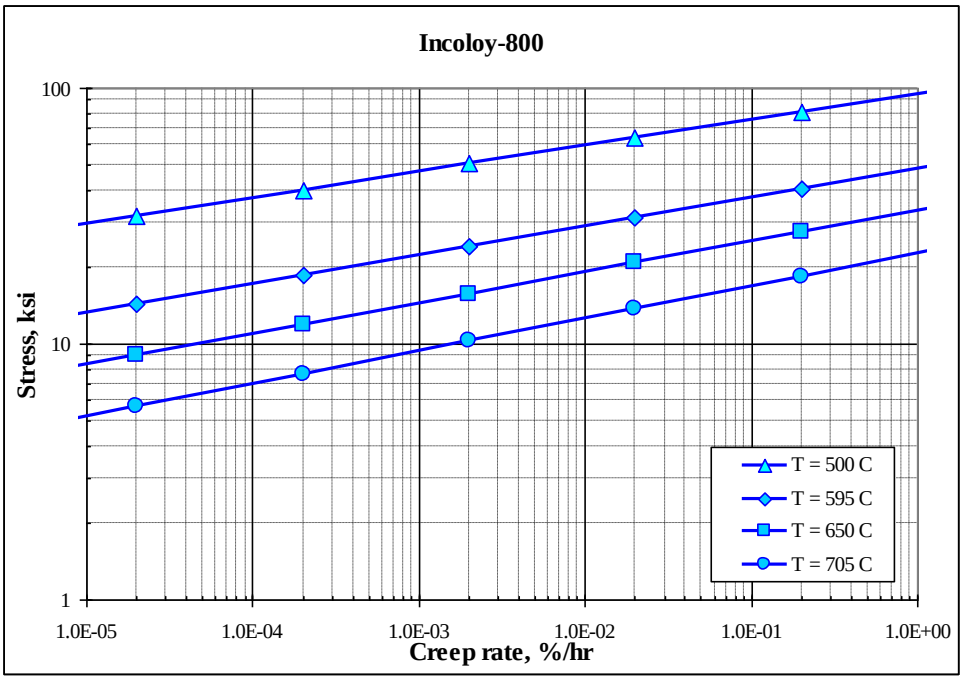

Figure 3-164 Creep strength for Incoloy 800

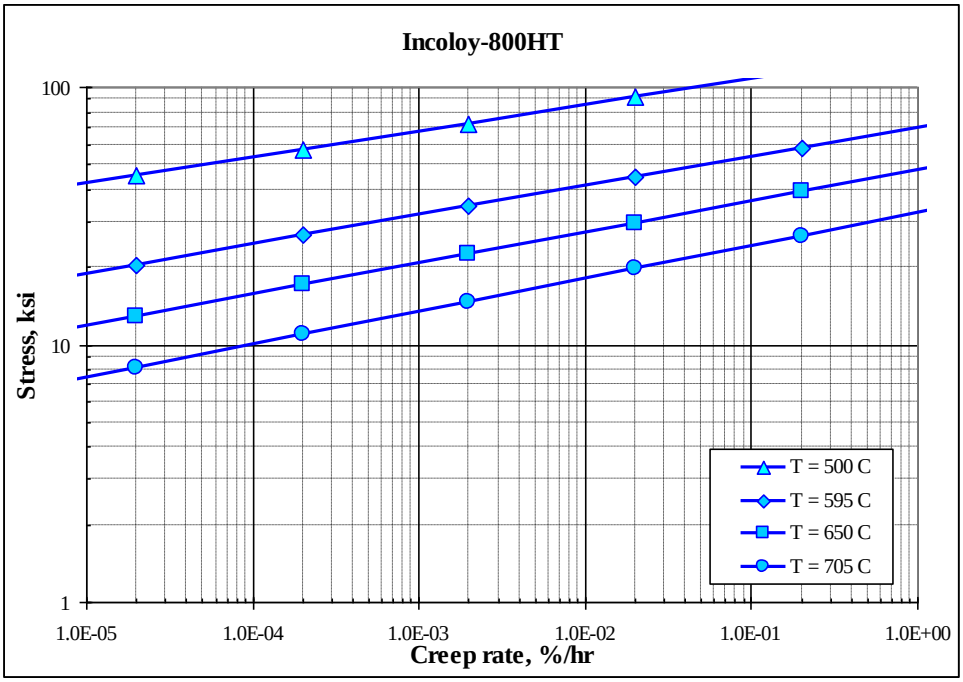

Figure 3-165 Creep strength for Incoloy 800HT

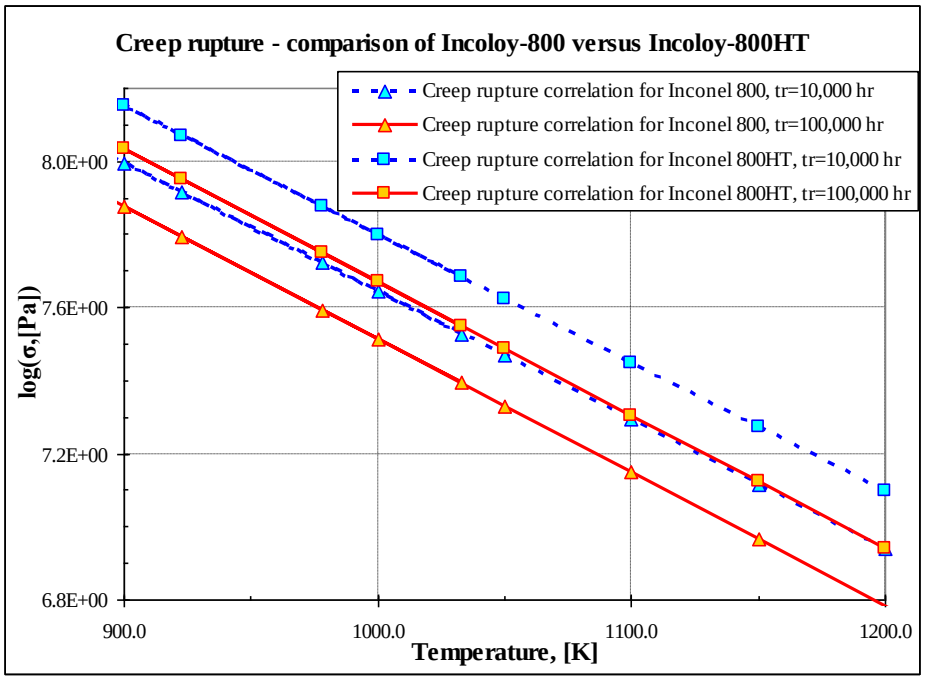

Figure 3-166 Creep rupture - comparison of Incoloy 800 and Incoloy 800HT

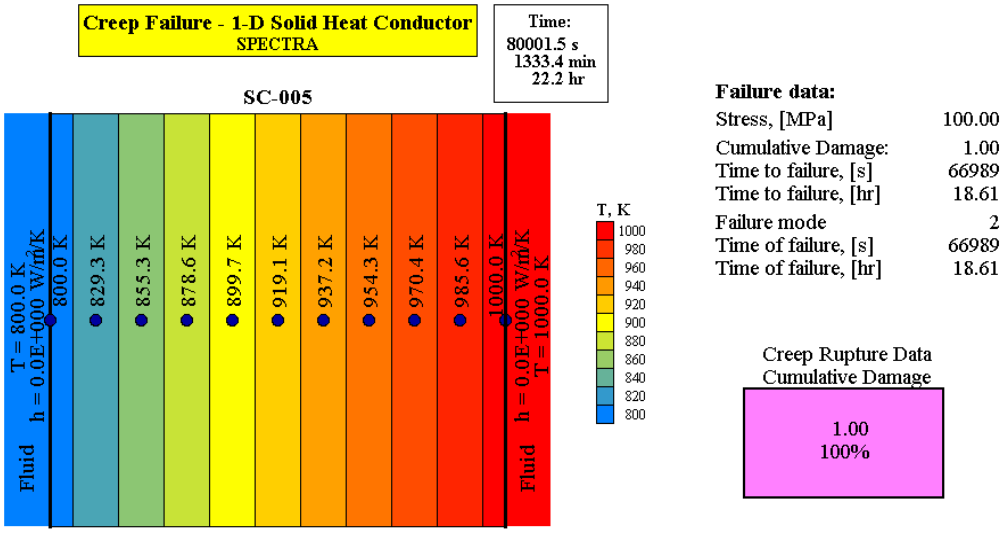

Figure 3-167 Failure analysis for 1-D Structure - values at 80,000 s

3.5.12 Gap Model, 1-D Model, Qualitative Verification

For the present test a simple reactor core is modelled. The core consists of one hot rod and one average rod, representing 1000 identical rods (multiplicity of 1000). Both hot and average rods are represented by five 1-D Solid Heat Conductors in the axial direction (Figure 3-168). The hot rod is represented by SC-101 through SC-105. The average rod is represented by SC-201 through SC-205. The fuel regions and the common fuel regions are in such case defined as follows:

- Fuel regions (total reactor core):
  SC-101, SC-102, SC-103, SC-104, SC-105, SC-201, SC-202, SC-203, SC-204, SC-205

- Common fuel regions:
  - Common region 1 (hot rod):
    SC-101, SC-102, SC-103, SC-104, SC-105
  - Common region 2 (average rod):
    SC-201, SC-202, SC-203, SC-204, SC-205

The hot rod and the average rod, shown in Figure 3-168, are made of 6 nodes. Nodes 1 - 4 represent the fuel, node 5 represents the gap, and node 6 represents the cladding.

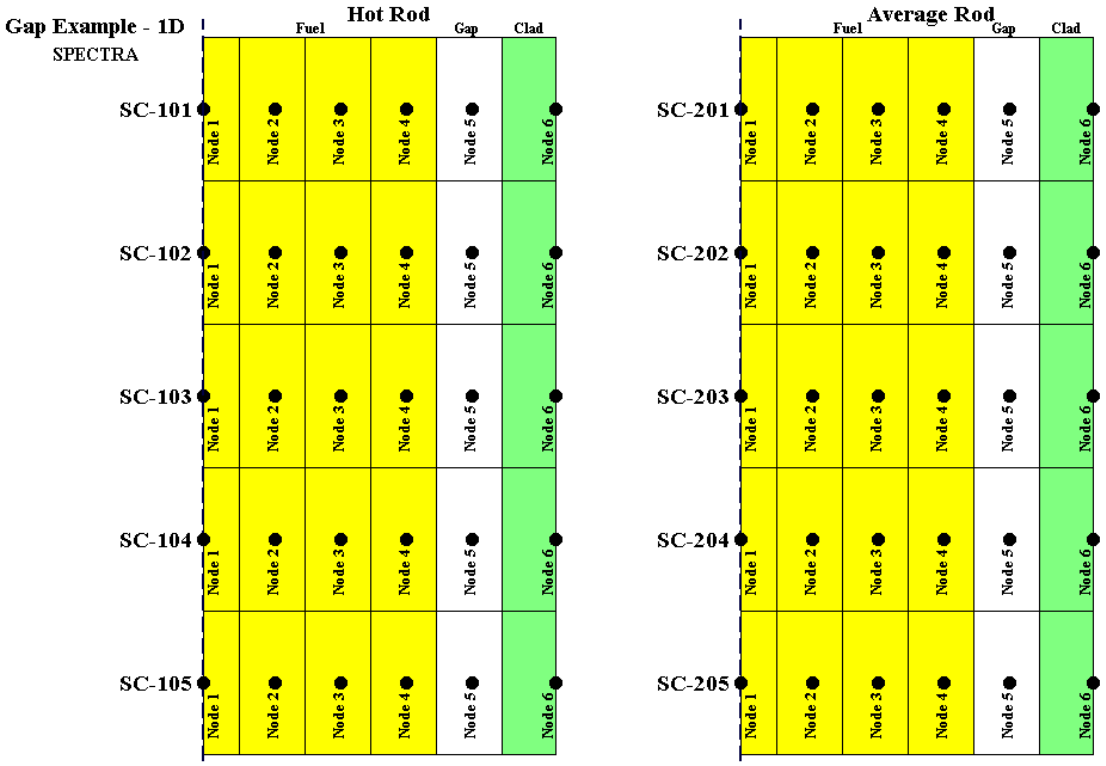

Figure 3-168 Nodalization for gap test, 1-D model

The internal power generation is 2000 W per single SC (0.5 m long) for the hot rod, and 1000 W per single SC for the average rod. Since the length of each SC is 0.5 m, the linear power density is 4 kW/m for the hot rod and 2 kW/m for the average rod. The power density is constant in the axial direction. The relative power density in the radial direction is taken as 1.0 in the fuel nodes (1 - 4) and 0.01 in the gap and cladding nodes (5, 6).

The gap is modelled using all default parameters, that means thermal radiation and gas conduction are considered. The solid conduction is ignored.

The purpose of the present test is to provide a qualitative verification of the gap model and check the consistency of the solution for different fuel regions, represented by different SC-s.

SPECTRA input file is provided in:
`\Z-INPUTS\TC\GAP\Verification\GAP-Method-1\GAP-Example-1D-const.SPE`

Results are provided in Figure 3-169. The gap heat transfer coefficient is 368 W/m^2-K for the hot rod and 308 W/m^2-K for the average rod. Since all axial segments are identical, all gaps give the same heat transfer coefficient. The gaps in the hot rod give higher heat transfer coefficient because of the higher temperature and consequently, higher thermal radiation. The results are consistent and sufficient for the present purpose of qualitative verification of the gap model. Quantitative verification is shown in the following section.

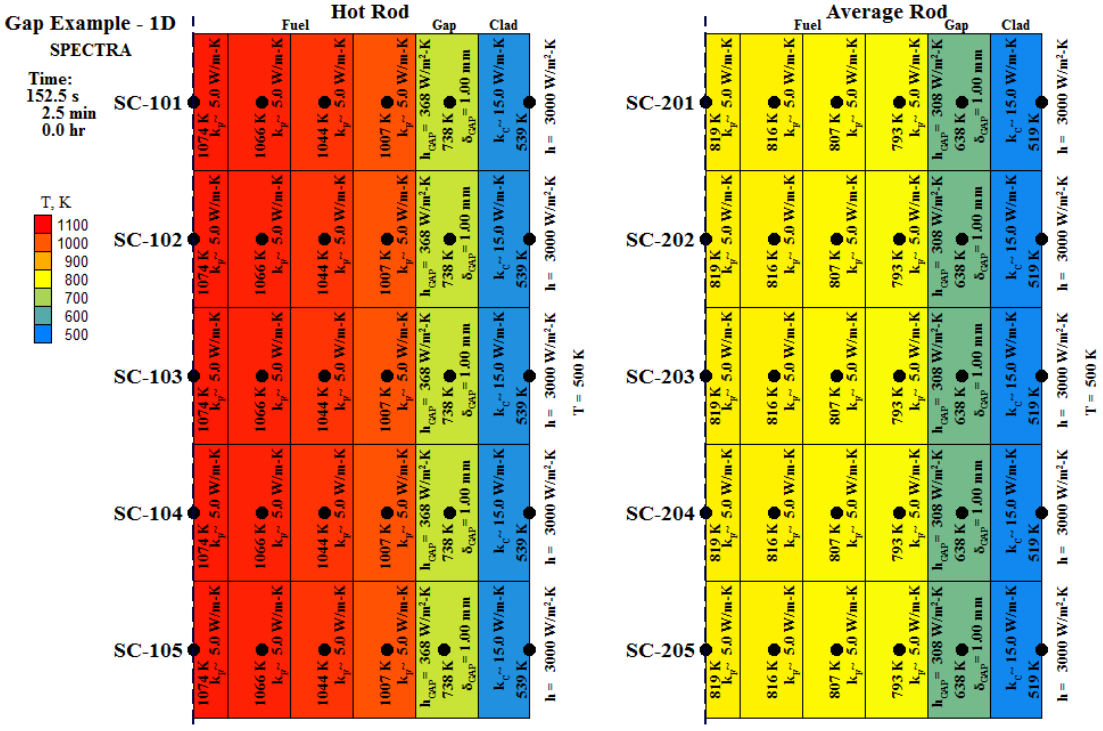

Figure 3-169 Results of gap test, 1-D model

3.5.13 Gap Model, 1-D Model, Quantitative Verification

The present test is a quantitative verification of the gap model results. Five 1-D Solid Heat Conductors are used; all of them are defined as a common fuel region:

- Fuel regions:
  SC-101, SC-102, SC-103, SC-104, SC-105

- Common fuel regions:
  - Common region 1:
    SC-101, SC-102, SC-103, SC-104, SC-105

The gap is filled with a user-defined gas with a molar weight equal to the weight of Xenon (131.3 kg/kmol). The thermal conductivities of fuel and cladding are set to constant values of 5 and 20 W/m-K respectively, to provide easy verification. The gas filling the gap is a user-defined gas with a constant thermal conductivity of 0.01 W/m-K, to provide easy verification. The gap model is different in each of the five Solid Heat Conductor, as described below. The SPECTRA input file is provided in:
`\Z-INPUTS\TC\GAP\Verification\GAP-Method-1\GAP-Test.SPE`

- SC-101
  No radiation ($\varepsilon_f = \varepsilon_c = 0.0$), no roughness effect ($C_d = 0.0$), no "temperature jump" ($C_j = 0.0$), no solid conduction ($p_a = 0.0$). In absence of radiation and solid conduction, only the gas conduction term remains. The heat transfer coefficient of the gap is:

$$h_{gap} = h_c = \frac{k_g}{d_{gap} + d_{\min} + (g_f + g_c)}$$

  Since $C_d = 0.0$, the term with roughness $d_{\min} = C_d\ (r_f + r_c) = 0.0$. Since $C_j = 0.0$, the "temperature jump" is equal to zero: $(g_f + g_c) = 0.0$. Therefore the expression for the heat transfer coefficient reduces to:

$$h_{gap} = \frac{k_g}{d_{gap}}$$

  In the present test a constant gas conductivity of 0.01 W/m-K was used. The gap thickness was assumed to be 1 mm: $d_{gap} = 0.001$ m. Therefore $h_{gap} = 10.0$ W/m^2-K. The SPECTRA calculated value for SC-101, shown in Figure 3-170, is 10.0 W/m^2-K, in agreement with the hand calculation.

- SC-102
  No radiation ($\varepsilon_f = \varepsilon_c = 0.0$), no roughness ($C_d = 0.0$), temperature jump of Xenon and default value of $C_j = 0.0247$, no solid conduction ($p_a = 0.0$). In this case the heat transfer coefficient of the gap is equal to:

$$h_{gap} = h_c = \frac{k_g}{d_{gap} + (g_f + g_c)}$$

The temperature jump for Xenon is (see Volume 1):

$$(g_f + g_c) = C_j \cdot \frac{k_g \cdot \sqrt{T_g}}{p_g \cdot a_{Xe} \cdot M_{Xe}^{-1/2}}$$

with:

$$a_{Xe} = 0.740 - 2.5 \times 10^{-4} \cdot T_g$$

The accommodation coefficient is calculated for the gas temperature taken from code output (T_g = 2004 K - Figure 3-170):

$$a_{Xe} = 0.740 - 2.5 \times 10^{-4} \cdot 2004 = 0.239$$

The jump distance is calculated for the gas temperature and pressure taken from code output (T_g = 2004 K, p = 6.68×10^5 Pa, file GAP-Test.OUT):

$$(g_f + g_c) = 0.0247 \cdot \frac{0.01 \cdot \sqrt{2004}}{6.68 \times 10^5 \cdot 0.239 \cdot 131.3^{-1/2}} = 7.94 \times 10^{-7}$$

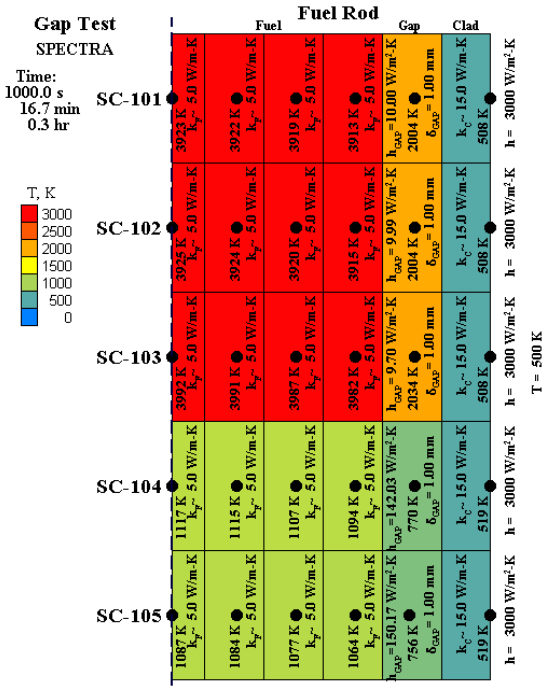

Figure 3-170 Results of the gap test

Finally, the heat transfer coefficient is equal to:

$$h_{gap} = \frac{0.01}{0.001 + 7.94 \times 10^{-7}} = 9.99$$

The SPECTRA calculated value for SC-102, shown in Figure 3-170, is 9.99 W/m^2-K, in agreement with the above number.

- SC-103
  No radiation ($\varepsilon_f = \varepsilon_c = 0.0$), with roughness of 10^{-5} m for fuel and cladding, default value of $C_d = 1.5$, temperature jump of Xenon and default value of $C_j = 0.0247$, no solid conduction ($p_a = 0.0$). In this case the heat transfer coefficient of the gap is equal to:

$$h_{gap} = h_c = \frac{k_g}{d_{gap} + d_{\min} + (g_f + g_c)}$$

The jump distance is calculated for the gas temperature and pressure taken from code output (T_g = 2034 K, $p = 6.68 \times 10^5$ Pa, file GAP-Test.OUT):

$$a_{Xe} = 0.740 - 2.5 \times 10^{-4} \cdot 2034 = 0.2315$$

$$(g_f + g_c) = 0.0247 \cdot \frac{0.01 \cdot \sqrt{2038}}{6.68 \times 10^5 \cdot 0.2315 \cdot 131.3^{-1/2}} = 8.25 \times 10^{-7}$$

$$d_{\min} = 1.5 \cdot (1.0 \times 10^{-5} + 1.0 \times 10^{-5}) = 3.0 \times 10^{-5}$$

Finally, the heat transfer coefficient is equal to:

$$h_{gap} = \frac{0.01}{0.001 + 3.0 \times 10^{-5} + 8.25 \times 10^{-7}} = 9.70$$

The SPECTRA calculated value for SC-103, shown in Figure 3-170, is 9.70 W/m^2-K, in agreement with the above number.

- SC-104
  Same as above but with thermal radiation ($\varepsilon_f = \varepsilon_c = 1.0$). In this case the heat transfer coefficient of the gap is equal to:

$$h_{gap} = h_r + h_c$$

The gas conduction is calculated similarly as shown above for SC-103. The jump distance is calculated for the gas temperature and pressure taken from code output (T_g = 770.0 K, $p = 6.68 \times 10^5$ Pa, file GAP-Test.OUT):

$$h_c = \frac{k_g}{d_{gap} + d_{\min} + (g_f + g_c)} = \frac{0.01}{0.001 + 3.0 \times 10^{-5} + 2.15 \times 10^{-7}} = 9.71$$

The thermal radiation is calculated using the node temperatures of fuel, cladding and gap, taken from the code output (T_{fuel} = 1094 K, T_{gap} = 770 K, T_{clad} = 519 K). The surface temperatures of fuel and cladding are obtained from (see Volume 1):

$$T_f = T_{gap} + X_{fuel} \cdot (T_{fuel} - T_{gap})$$
$$T_c = T_{gap} + X_{clad} \cdot (T_{clad} - T_{gap})$$

$$X_{fuel} = \frac{R_{gap}}{R_{gap} + R_{fuel}} = \frac{\delta_{gap} / k_{gap}}{\delta_{gap} / k_{gap} + \delta_{fuel} / k_{fuel}}$$
$$X_{clad} = \frac{R_{gap}}{R_{gap} + R_{clad}} = \frac{\delta_{gap} / k_{gap}}{\delta_{gap} / k_{gap} + \delta_{clad} / k_{clad}}$$

The node thickness of fuel gap and cladding are assumed to be 0.001 m. Therefore the values needed to calculate resistances left and right of the fuel and cladding surfaces (see Figure 3-171 and description in Volume 1) are equal to: $\delta_{fuel} = \delta_{gap} = 0.0005$ m, $\delta_{clad} = 0.001$ m.

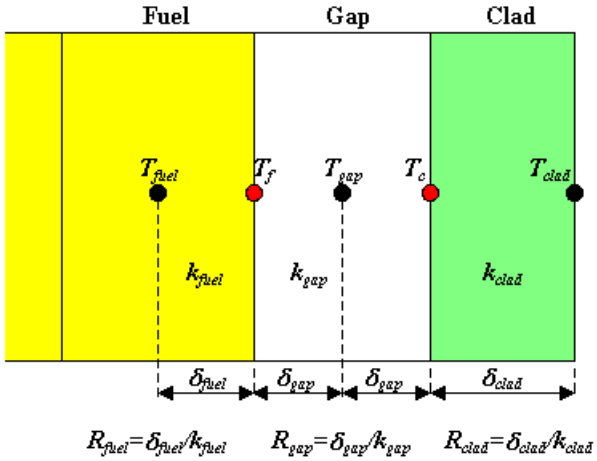

Figure 3-171 Fuel and cladding surface temperature calculation

The thermal conductivity of fuel and cladding is 5 and 20 W/m^2-K respectively. The thermal conductivity of gap (code output) is equal to 0.14 W/m^2-K (Figure 3-170). The interpolation factors are therefore equal to:

$$X_{fuel} = \frac{0.0005 / 0.14}{0.0005 / 0.14 + 0.0005 / 5} = 0.9728$$
$$X_{clad} = \frac{0.0005 / 0.14}{0.0005 / 0.14 + 0.001 / 20} = 0.9862$$

The surface temperatures of fuel and cladding are equal to:

$$T_f = 770 + 0.9728 \cdot (1094 - 770) = 1085.5$$
$$T_c = 770 + 0.9862 \cdot (519 - 770) = 522.8$$

The thermal radiation term is equal to (see Volume 1, the fuel and cladding surface emissivities are assumed equal to 1.0):

$$h_r = \sigma \cdot \left(T_f^2 + T_c^2\right) \cdot \left(T_f + T_c\right) =$$
$$= 5.67 \times 10^{-8} \cdot (1085.5^2 + 522.8^2) \cdot (1085.5 + 522.8) = 132.36$$

Finally, the heat transfer coefficient is equal to:

$$h_{gap} = 132.36 + 9.71 = 142.07$$

The SPECTRA calculated value for SC-104, shown in Figure 3-170, is 142.03 W/m^2-K, in agreement with the analytical solution above.

- SC-105
  The same as above, but with solid conduction present due to fuel-cladding contact. The apparent interfacial pressure is assumed to be equal to the internal gas pressure in the gap, p = 6.68×10^5 Pa, file GAP-Test.OUT. The Meyer hardness of cladding is tabulated as shown below.

T (K)	H_c (Pa)
298	1950×10^6
373	1410×10^6
473	1010×10^6
573	800×10^6
673	710×10^6
773	650×10^6
873	500×10^6
973	350×10^6
1073	200×10^6
1173	50×10^6

The Meyer hardness defined by the above table is compared to the data for Zircaloy in Figure 3-172.

The hand calculation of all three terms, gas conduction, thermal radiation, and solid conduction, is described below.

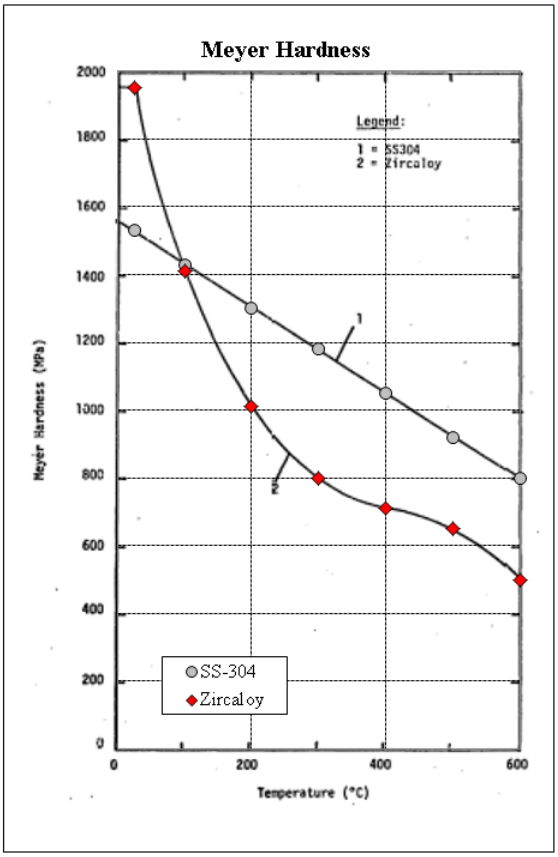

T [K]	T [°C]	SS-304	Zircaloy
298	25	1530	1950
373	100	1430	1410
473	200	1300	1010
573	300	1180	800
673	400	1050	710
773	500	920	650
873	600	800	500
973	700	*680*	*350*
1073	800	*560*	*200*
1173	900	*440*	*50*

Figure 3-172 Meyer hardness of Zircaloy, left: data, right: table

- Gas conduction

$$h_c = \frac{k_g}{d_{gap} + d_{\min} + (g_f + g_c)} = \frac{0.01}{0.001 + 3.0\times10^{-5} + 2.78\times10^{-7}} = 9.71$$

- Thermal radiation

$$X_{fuel} = \frac{0.0005/0.15}{0.0005/0.15 + 0.0005/5} = 0.9709$$

$$X_{clad} = \frac{0.0005/0.15}{0.0005/0.15 + 0.001/20} = 0.9852$$

$$T_f = 758 + 0.9709 \cdot (1066 - 758) = 1057.0$$

$$T_c = 758 + 0.9852 \cdot (519 - 758) = 522.5$$

$$h_r = \sigma \cdot \left(T_f^2 + T_c^2\right) \cdot \left(T_f + T_c\right) =$$

$$= 5.67\times10^{-8} \cdot (1055.0^2 + 522.5^2) \cdot (1055.0 + 522.5) = 123.98$$

- Solid conduction

$$k_s = 2 \cdot \frac{k_f \cdot k_c}{k_f + k_c} = 2 \cdot \frac{5 \cdot 20}{5 + 20} = 8.0$$

$$r_t = \sqrt{\frac{r_f^2 + r_c^2}{2}} = \sqrt{\frac{(1.0 \times 10^{-5})^2 + (1.0 \times 10^{-5})^2}{2}} = 1.0 \times 10^{-5}$$

$$h_s = C_s \cdot \frac{k_s}{\sqrt{r_t}} \cdot \left(\frac{p_a}{H_c} \right)^n = 11.89 \cdot \frac{8.0}{\sqrt{1.0 \times 10^{-5}}} \cdot \left(\frac{5 \times 10^5}{902.9 \times 10^6} \right)^1 = 16.66$$

The heat transfer coefficient is equal to:

$$h_{gap} = h_r + h_c + h_s = 123.98 + 9.71 + 16.66 = 150.34$$

The SPECTRA calculated value for SC-105, shown in Figure 3-170, is 150.17 W/m^2-K, in agreement with the analytical solution above.

All hand calculations presented in this section are stored in:
`\Z-INPUTS\TC\GAP\Verification\GAP-Method-1\GAP-Test.XLS`

3.5.14 Gap Model Quantitative Verification, Comparison of Method 1 and Method 2

This chapter presents comparison of the gap model results obtained with the numerical method 1 and 2 (section 3.5.2, 3.5.3). The results of Method 1 are discussed in detail in the previous section. Here only the results of both methods are compared.

The SPECTRA input file for the Method 2 is provided in:
`\Z-INPUTS\TC\GAP\Verification\GAP-Method-2\GAP-Test.SPE`

Results of Method 1 and 2 are compared in Figure 3-173. It is seen that both methods give very similar results. Since the surface temperatures of fuel and cladding are directly available in Method 2, this method is considered as slightly more accurate than the Method 1 where the surface temperatures are obtained by interpolations.

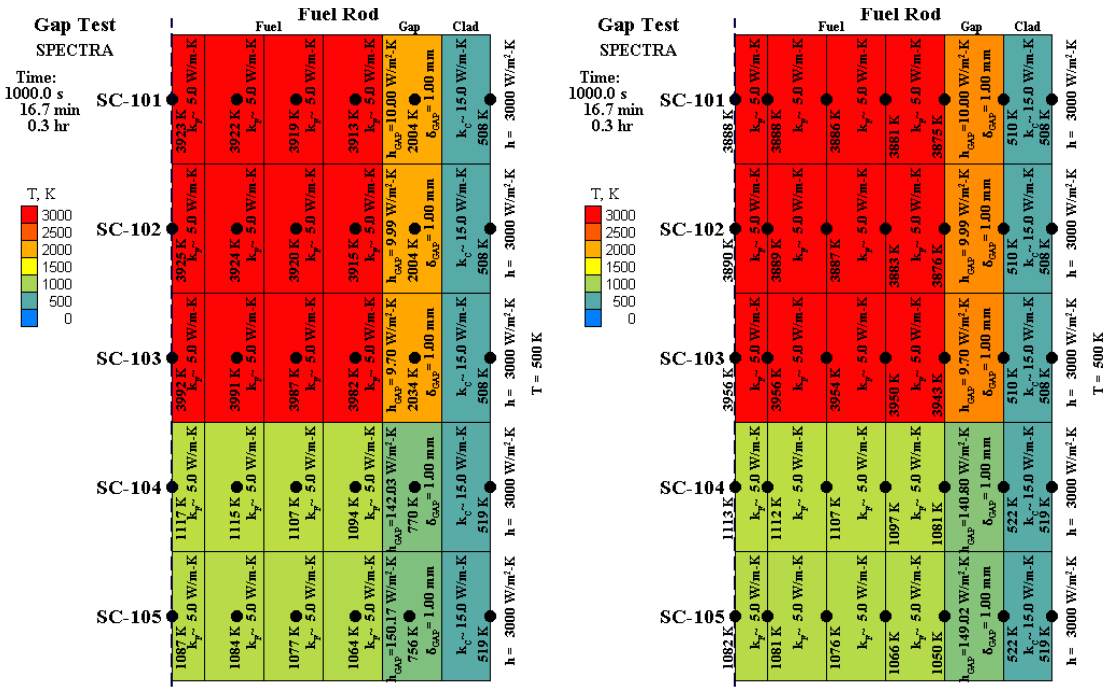

Figure 3-173 Results of the gap test, left: Method 1, right – Method 2

3.5.15 Gap Model, Centerline Shift Verification

SPECTRA results obtained for different centerline shifts, between 0.0 (fuel in the center) to 1.0 (fuel touching the cladding) - Figure 3-174, are compared to RELAP results. Nodalization of the SPECTRA and RELAP models are shown in Figure 3-175 and Figure 3-176, respectively.

All calculations are stored in:
`\Z-INPUTS\TC\GAP\Verification\GAP-Centerline-shift\`

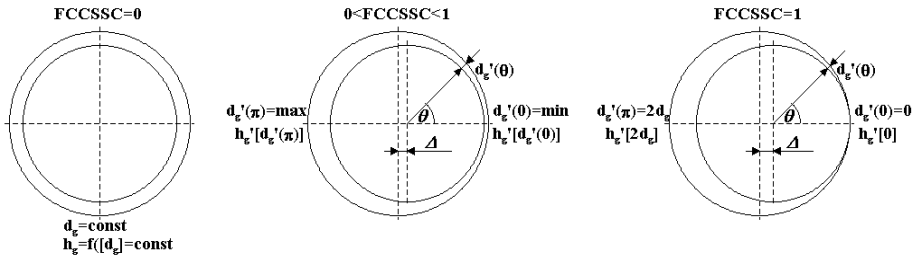

Figure 3-174 Centerline shift verification - comparison with RELAP

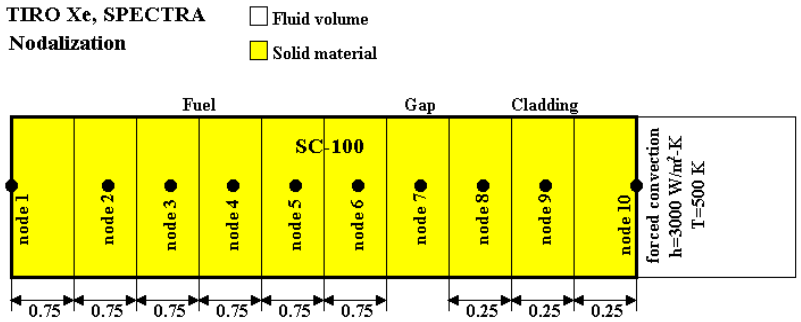

Figure 3-175 Nodalization for SPECTRA

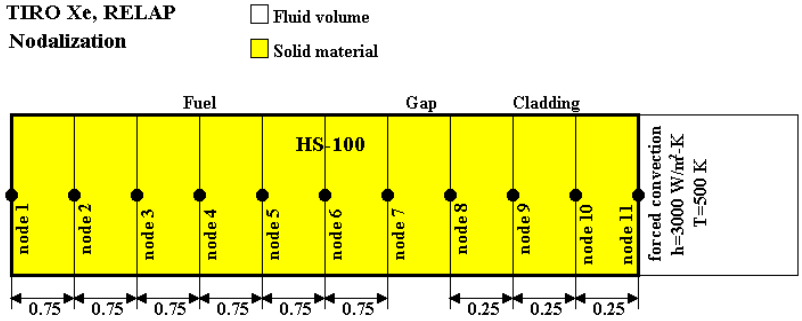

Figure 3-176 Nodalization for RELAP

Calculations were performed using four different gases in the gap:

- Helium
- Nitrogen
- Krypton
- Xenon

Results are shown in Figure 3-177 through Figure 3-182 and summarized in Table 3-22. Results obtained for Helium gas are shown in Figure 3-177 and Figure 3-178 for zero centerline shift, and in Figure 3-179, Figure 3-180 for maximum centerline shift. SPECTRA and RELAP results are in very good agreement.

All results obtained for different gases filling the gap, are shown in Figure 3-181 (Helium), Figure 3-182 (other gases), and summarized in Table 3-22. SPECTRA and RELAP results are in good agreement.

Table 3-22 Gap conductance, *h* (W/m^2-K) - effect of centerline shift

Shift	He		N2		Kr		Xe	
	SPECTRA	RELAP	SPECTRA	RELAP	SPECTRA	RELAP	SPECTRA	RELAP
0.0	2043.0	2005.0	386.0	397.0	159.0	185.0	110.0	133.0
0.5	2287.0	2239.0	433.0	441.0	177.0	202.0	122.0	143.0
0.9	3483.0	3383.0	681.0	674.0	278.0	294.0	188.0	200.0
1.0	4692.0	4537.0	982.0	962.0	408.0	419.0	279.0	280.0

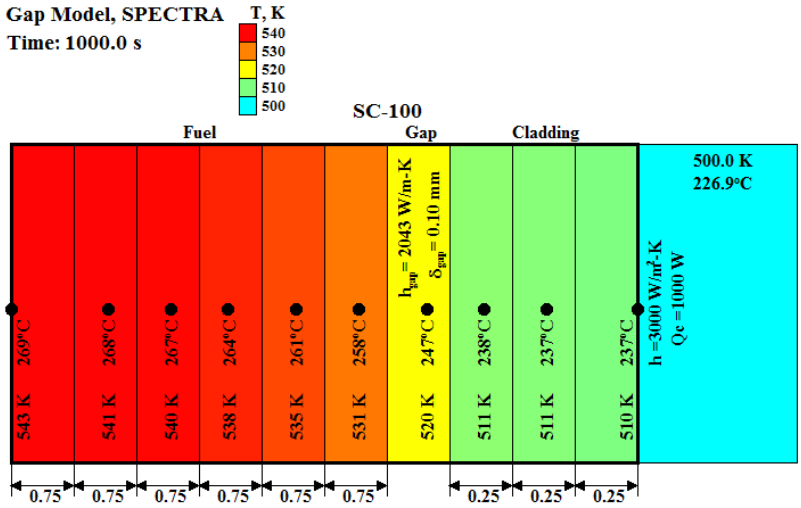

Figure 3-177 Results for Helium gap, centerline shift = 0.0, SPECTRA

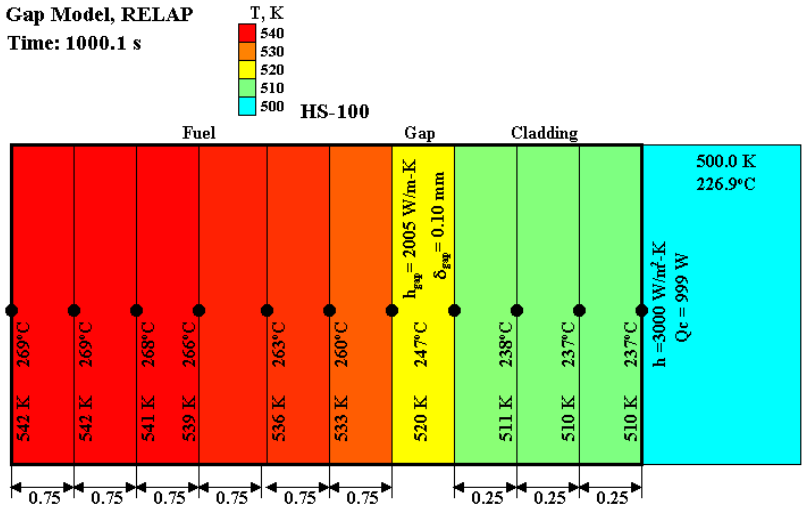

Figure 3-178 Results for Helium gap, centerline shift = 0.0, RELAP

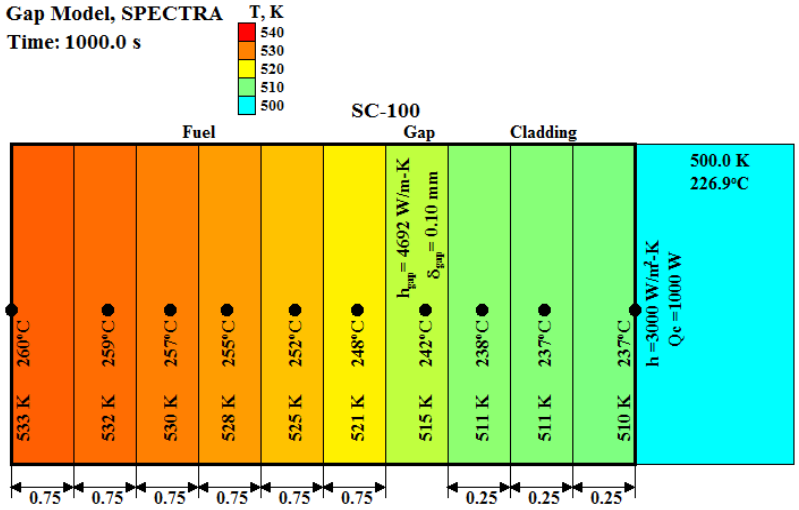

Figure 3-179 Results for Helium gap, centerline shift = 1.0, SPECTRA

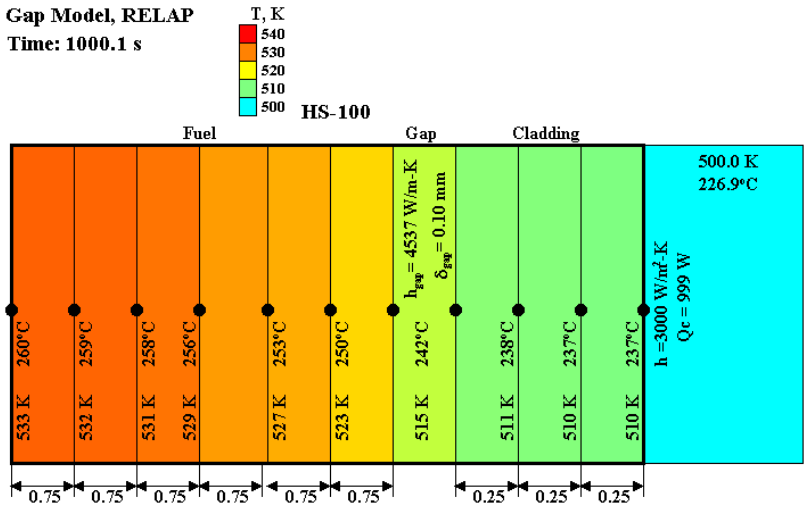

Figure 3-180 Results for Helium gap, centerline shift = 1.0, RELAP

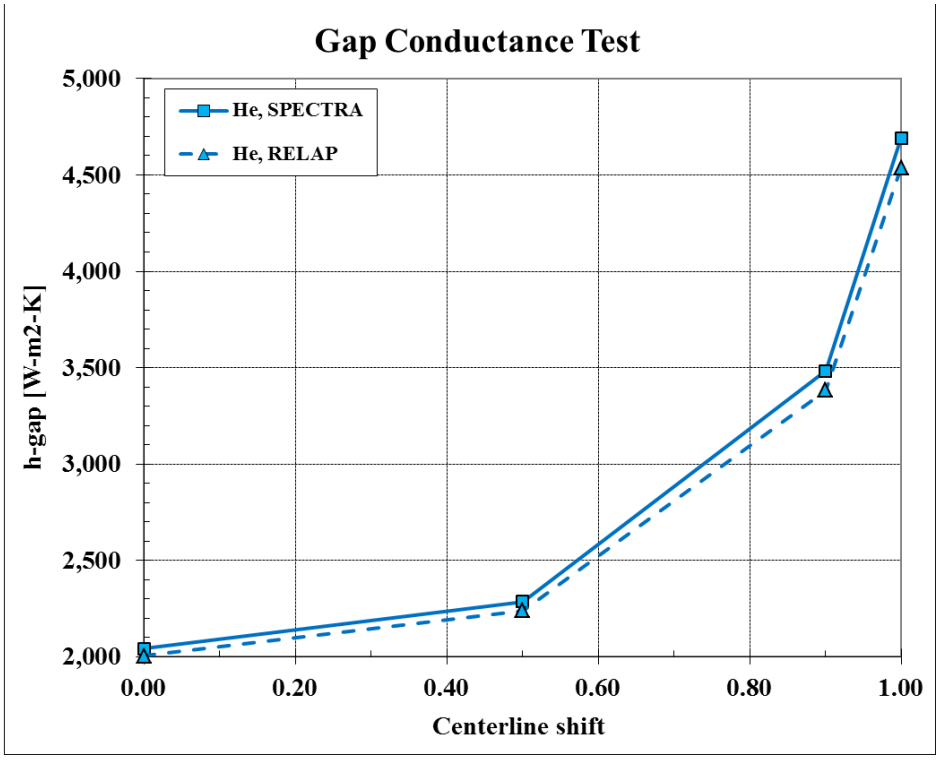

Figure 3-181 Gap conductance, *h* (W/m^2-K), effect of centerline shift, Helium gas

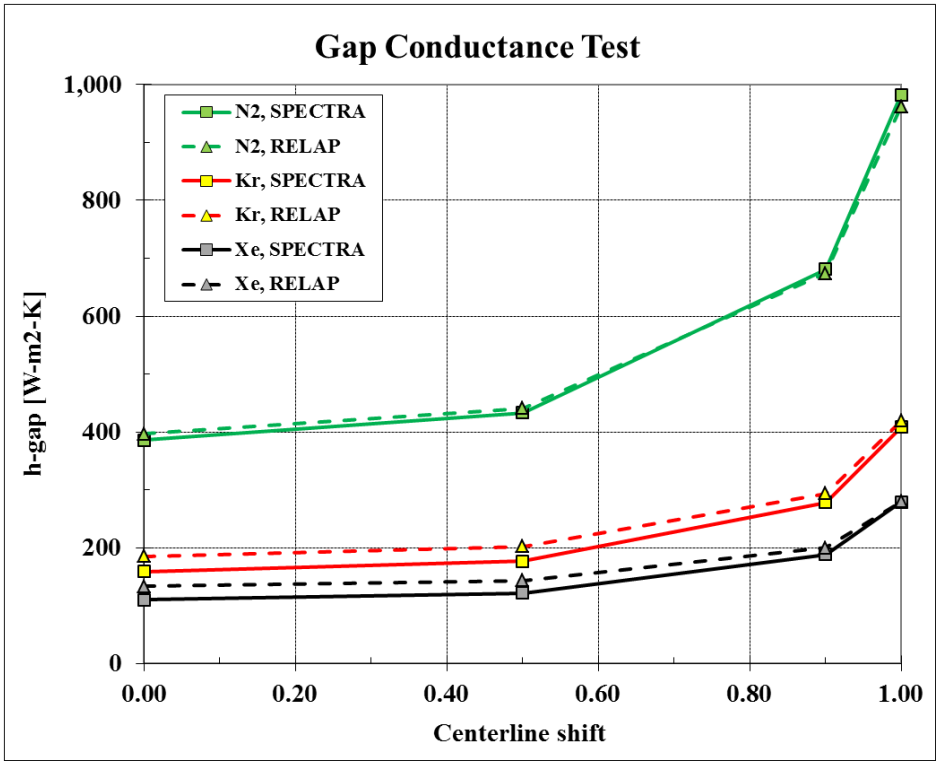

Figure 3-182 Gap conductance, *h* (W/m^2-K), effect of centerline shift, other gases

The SPECTRA results for He-filled gap have changed somewhat compared to the earlier code version, during the code modification of July 4, 2018. There the He conductivity calculation has been changed. The new formula is:

$$k(p,T) = 2.682 \cdot 10^{-3} \cdot (1 + 1.123 \cdot 10^{-8} \cdot p) \cdot T^{0.71 \cdot (1 - 2 \times 10^{-9} \cdot p)} .$$

The modification is described in section 2.1.1.2. Because of this modification the He gap results are somewhat different than before. Figure 3-183 shows the results obtained with the earlier code versions (up to and including the version of May 2018). It is seen that the agreement with RELAP was better for these particular tests. Nonetheless the new He conductivity has better accuracy. Comparison with a number of experimental data showed improvement of the accuracy from 4.4% to 1.5% average error.

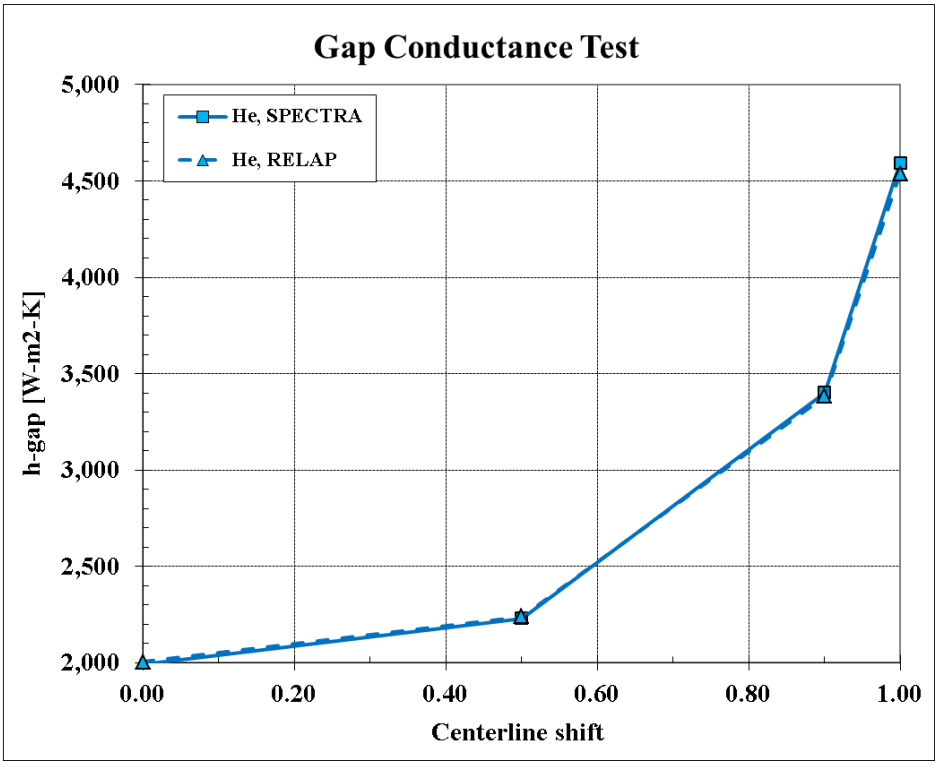

Figure 3-183 Gap conductance, *h* (W/m²-K), effect of centerline shift, Helium gas code version May 2018 or earlier

3.5.16 Gap Model Validation – PBF-LOC11C Tests

Steady-state average centerline temperature data from the Power Burst Facility (PBF) Test LOC-11C [140] were used to evaluate the dynamic gap conductance model. Similar validation was performed in the past for the RELAP5 code and the results are described in [138]. Figure 3-184 shows RELAP results. Two RELAP5-calculated results are given, one with and one without the gap deformation model. The calculated values using the gap conductance model are about 0 to 100 K higher than the data. However, the calculation without using the gap conductance model yields temperatures much higher than the data. In particular, the differences are about 500 to 700 K in the high power region. The reduction of centerline temperatures with the gap conductance model is primarily due to thermal expansion of UO_2, which reduced the gap size and increased the gap conductance. The dynamic gap conductance model in RELAP5 can significantly improve the simulation of nuclear reactor transients where the gap size has a significant effect on the transient [138].

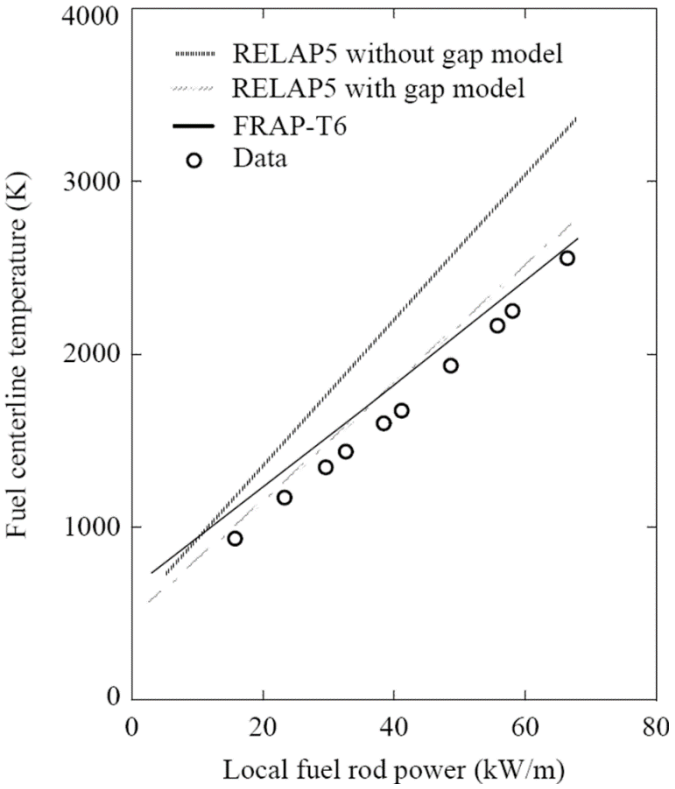

Figure 3-184 Maximum fuel *T* (K), PBF-LOC-11C tests, RELAP5 [138]

The main input parameters, used in the current model, are listed in Table 3-23. Default values were assumed for the gap model parameters, including the surface emissivities and roughness. The parameters assumed for the dynamic gap expansion model are shown in Figure 3-185 and Figure 3-186 (see Volume 1). The cladding creepdown was neglected.

Table 3-23 PBF Test LOC-11C data

Parameter	Value
Pellet diameter	9.3 mm
Cladding outside diameter	10.72 mm
Cladding inside diameter	9.50 mm
Gap thickness, cold state	0.10 mm
Helium pre-pressurization	2.41 MPa
Coolant temperature	596 K
Coolant pressure	15.3 MPa

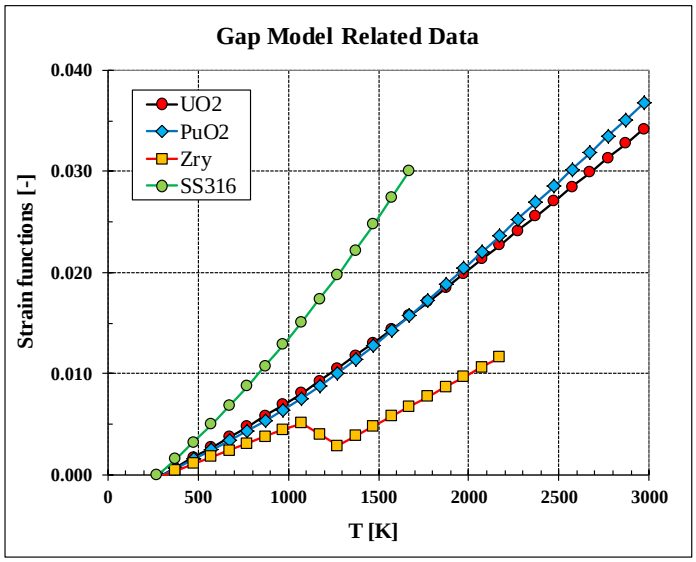

T [K]	UO2	PuO2	Zry	SS316
273.0	0.000	0.000	0.000	0.000
373.0	7.301E-04	6.571E-04	4.348E-04	1.580E-03
473.0	1.731E-03	1.559E-03	1.107E-03	3.248E-03
573.0	2.736E-03	2.467E-03	1.779E-03	5.004E-03
673.0	3.754E-03	3.394E-03	2.451E-03	6.847E-03
773.0	4.792E-03	4.356E-03	3.123E-03	8.778E-03
873.0	5.860E-03	5.367E-03	3.795E-03	1.080E-02
973.0	6.965E-03	6.438E-03	4.467E-03	1.290E-02
1073.0	8.109E-03	7.576E-03	5.140E-03	1.510E-02
1173.0	9.293E-03	8.784E-03	4.020E-03	1.738E-02
1273.0	1.052E-02	1.006E-02	2.900E-03	1.975E-02
1373.0	1.178E-02	1.140E-02	3.870E-03	2.220E-02
1473.0	1.307E-02	1.279E-02	4.840E-03	2.475E-02
1573.0	1.440E-02	1.424E-02	5.810E-03	2.738E-02
1673.0	1.574E-02	1.573E-02	6.780E-03	3.010E-02
1773.0	1.711E-02	1.726E-02	7.750E-03	
1873.0	1.850E-02	1.882E-02	8.720E-03	
1973.0	1.990E-02	2.041E-02	9.690E-03	
2073.0	2.132E-02	2.202E-02	1.066E-02	
2173.0	2.274E-02	2.364E-02	1.163E-02	
2273.0	2.416E-02	2.527E-02		
2373.0	2.559E-02	2.691E-02		
2473.0	2.703E-02	2.856E-02		
2573.0	2.846E-02	3.021E-02		
2673.0	2.989E-02	3.185E-02		
2773.0	3.132E-02	3.349E-02		
2873.0	3.275E-02	3.513E-02		
2973.0	3.417E-02	3.677E-02		

Figure 3-185 Gap model data for frequently used materials - strain function (Volume 1)

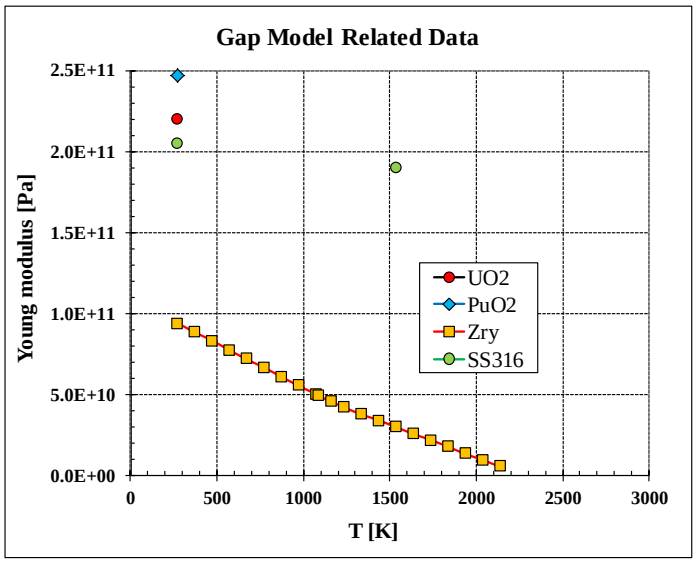

T [K]	UO2	PuO2	Zry	SS316
273.0	2.200E+11	2.470E+11	9.385E+10	2.050E+11
373.0			8.838E+10	
473.0			8.290E+10	
573.0			7.743E+10	
673.0			7.195E+10	
773.0			6.648E+10	
873.0			6.100E+10	
973.0			5.553E+10	
1073.0			5.005E+10	
1090.0			4.912E+10	
1165.0			4.550E+10	
1240.0			4.188E+10	
1340.0			3.783E+10	
1440.0			3.378E+10	
1540.0			2.973E+10	1.900E+11
1640.0			2.568E+10	
1740.0			2.163E+10	
1840.0			1.758E+10	
1940.0			1.353E+10	
2040.0			9.480E+09	
2140.0			5.430E+09	
2240.0				
2340.0				
2440.0				
2540.0				
2640.0				
2740.0				
2840.0				

Figure 3-186 Gap model data for frequently used materials - Young modulus (Volume 1)

The following cases were calculated with SPECTRA:

- No dynamic gap expansion model, gap size = 0.1 mm = const.
- Dynamic gap expansion, no centerline shift
- Dynamic gap expansion, maximum centerline shift

For comparison the following cases were calculated with the recent RELAP version: RELAP5/3.3jz:

- Dynamic gap expansion, no centerline shift
- Dynamic gap expansion, maximum centerline shift

Calculations are stored in: `\Z-INPUTS\TC\GAP\Verification\GAP-PBF-LOC-11C\`
The following computational procedure was applied. The power was changed in steps and a sufficient time (1000 s) was given to obtain stationary state after each power step. The power density and the gap size are shown in Figure 3-189 (SPECTRA) and Figure 3-190 (RELAP5). Results obtained with the dynamic gap expansion model and maximum centerline shift are shown in the visualization pictures Figure 3-187 (SPECTRA) and Figure 3-188 (RELAP). All results are shown in Figure 3-191 (left) and Figure 3-192 (left). The result show the same tendency as observed in [138]. The main observations are:

- Dynamic gap expansion model significantly improves results.
- Centerline shift improves results further. The effect of centerline shift becomes smaller at higher power because at that time the gap is nearly closed (Figure 3-189, Figure 3-190)

In conclusion, the dynamic gap conductance model can significantly improve the simulation of nuclear reactor transients where the gap size has a significant effect on the transient. The maximum temperatures were overestimated with the present gap model parameters. In a sensitivity run, the surface roughness was changed from the default values (3.3×10^{-6} for fuel, 1.78×10^{-6} for cladding) to a very small number (10^{-7} m, files in: `\Z-INPUTS\TC\GAP\Verification\GAP-PBF-LOC-11C-smooth\`). The reason for choosing this parameter is explained in the sensitivity analysis, presented below. Results are shown in Figure 3-191 (right) and Figure 3-192 (right). The agreement with experiment is somewhat better. A good agreement between the two codes is observed in all cases.

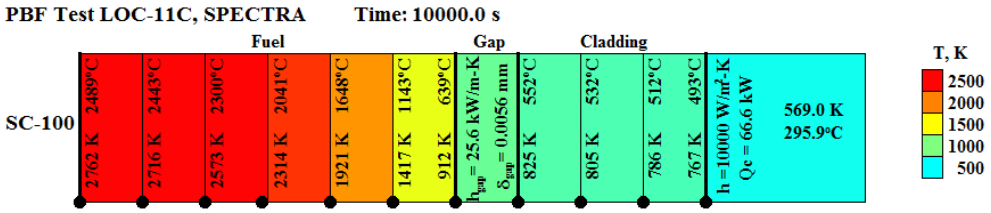

Figure 3-187 SPECTRA, dynamic gap expansion, maximum centerline shift, maximum power

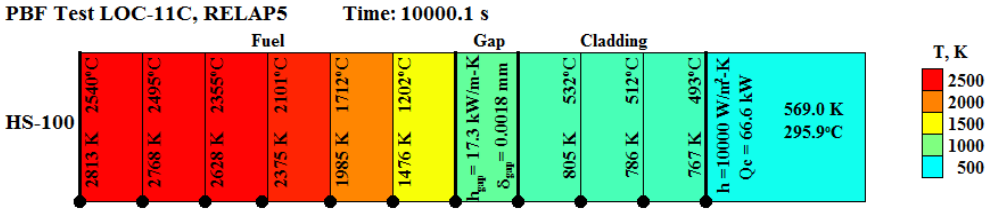

Figure 3-188 RELAP5, dynamic gap expansion, maximum centerline shift, maximum power

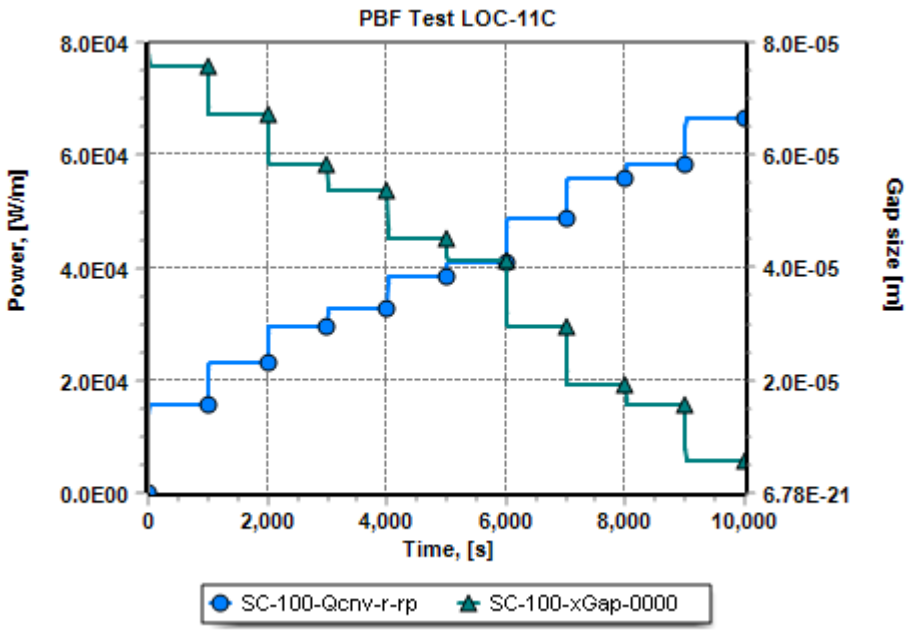

Figure 3-189 Power and gap width, SPECTRA, dynamic gap expansion, centerline shift=1

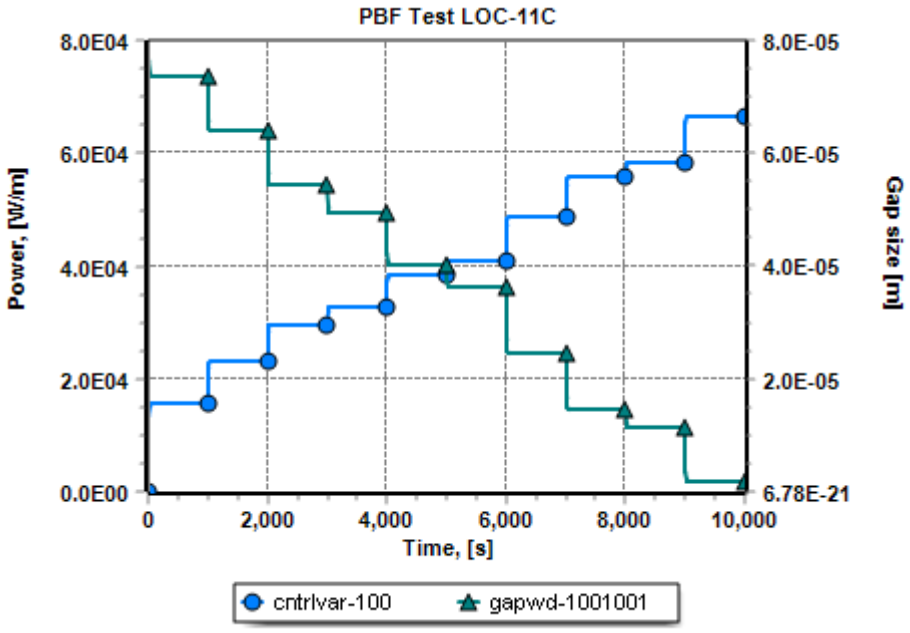

Figure 3-190 Power and gap width, RELAP5, dynamic gap expansion, centerline shift=1

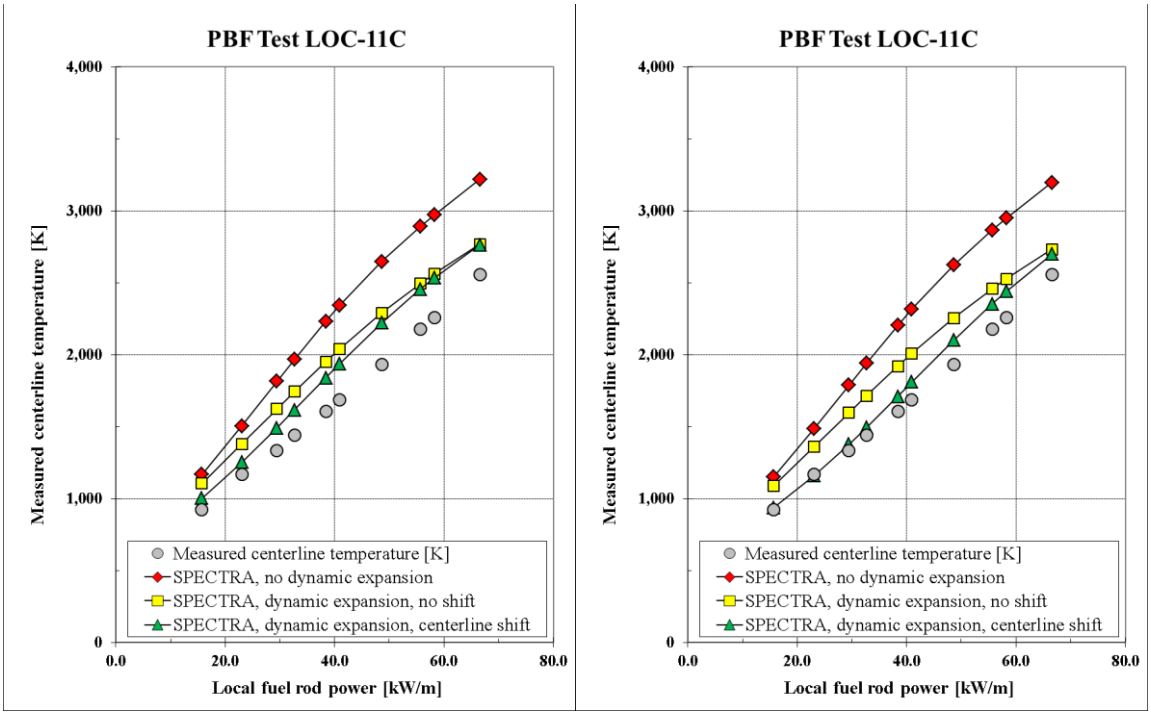

Figure 3-191 Maximum fuel *T* (K), PBF-LOC-11C tests, SPECTRA, left: default, right: smooth

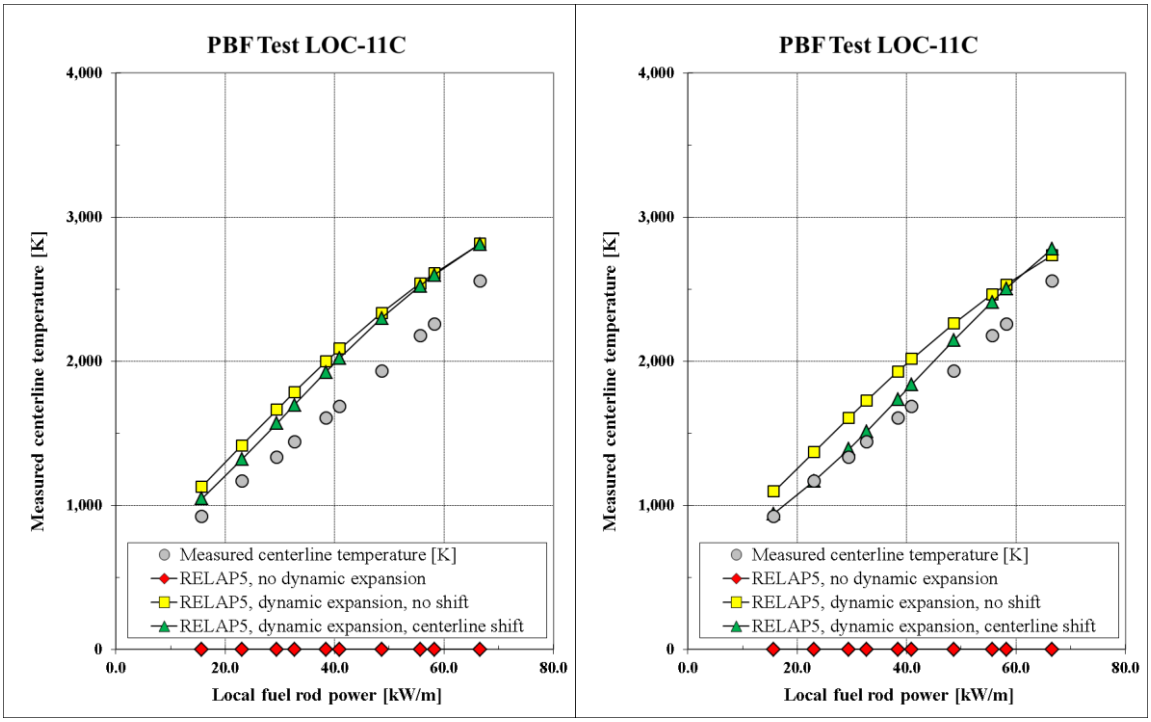

Figure 3-192 Maximum fuel *T* (K), PBF-LOC-11C tests, RELAP5, left: default, right: smooth

- **Sensitivity**

A number of sensitivity runs were performed in order to find which parameters have the most significant effect on the gap conductance. The results are shown in Table 3-24 and Table 3-25.

In the first step, a constant gap size was used (=0.1 mm - Table 3-23), to show the effect of a change of a single parameter. The results are shown in Table 3-24. The table shows the base case value, the values used in sensitivity calculations and the gap conductance values obtained for each case. The relative change of parameters is defined as the difference between the base value and the sensitivity value divided by the maximum of the two. As a base case, the case with the highest power is selected (66.6 kW - Figure 3-187, Figure 3-189). The parameter variation was selected based on engineering judgment. In case of emissivity, the difference between the base value and the maximum physical value (1.0) is used. In case of roughness, an order of magnitude is used. In case of the parameter C_d, the minimum and maximum values recommended in literature (0.6 and 3.2 - see Volume 1) are used. In case of contact pressure, p_a, the values of 10^5 and 10^6 Pa are used. It is seen in Table 3-24 that the parameters that have the largest effect on the results are:

- fuel and cladding surface roughness, together with the parameter C_d ,
- gas present in the gap,
- centerline shift (this is also shown in section 3.5.15).

In the second step, the sensitivity runs were performed using the dynamic gap expansion model. The results are shown in Table 3-25. There are two additional cases, to investigate the contact pressure calculation. In order to obtain clear contact pressure, the initial gap size was reduced from 0.1 mm (Table 3-23) to 0.05 mm. Calculations were performed assuming zero contact pressure (Case 18) and the formula shown in Volume 1 (Case 19). The contact pressure and its effect on gap conductance are quite significant. Generally the same observations are made as in Table 3-24, however there are few differences worth noting.

- In case of different gas, the net effect is somewhat smaller than in the case with constant gap size. If the low conductivity gas (Kr, Xe) is used, the gap conductance is much smaller compared to He-filled gap, which leads to higher fuel temperatures. Consequently the fuel expansion is larger and the gap size becomes smaller. Therefore the total effect is somewhat smaller than in the previous case, when constant gap size was used.
- In case of centerline shift, the effect is much smaller than in the case with constant gap size. In the high power case the gap is almost closed - Figure 3-189 and Figure 3-190. Therefore the centerline shift plays very small role.

The results of sensitivity runs may be summarized as follows.

- Fuel and cladding surface roughness has significant effect on the gap conductance. The surface roughness is used together with the parameter C_d. (values recommended in literature range from 0.62 to 3.2).
- Gas composition has significant effect on gap conductance because of differences in thermal conductivities of different gases.
- Centerline shift may in some circumstances have a significant effect on gap conductance (this is also shown in section 3.5.15).
- Solid conduction may have a significant effect on gap conductance, depending on the value of apparent interfacial contact pressure. If the pressure is low and moderate

Since the surface roughness has a large effect on gap conductance, this parameter was used in the sensitivity calculations shown in Figure 3-191 (right) and Figure 3-192 (right).

Table 3-24 Sensitivity calculations - constant gap size

Case	Parameter	Parameter Value			Gap Conductance			dY/dX
		Base case	Sensitivity	dX, %	Base case	Sensitivity	dY, %	
1	Emissivity, fuel	0.800	0.600	-25%	8.53	8.50	-0.4%	0.014
2			1.000	20%		8.56	0.4%	0.018
3	Emissivity, cladding	0.900	0.800	-11%	8.53	8.52	-0.1%	0.011
4			1.000	10%		8.54	0.1%	0.012
5	Roughness, fuel	3.30E-06	3.30E-07	-90%	8.53	12.16	29.9%	-0.332
6			3.30E-05	90%		3.66	-57.1%	-0.634
7	Roughness, cladding	1.78E-06	1.78E-07	-90%	8.53	9.98	14.5%	-0.161
8			1.78E-05	90%		4.58	-46.3%	-0.515
9	Cd	1.500	0.620	-59%	8.53	12.18	30.0%	-0.511
10			3.200	53%		6.15	-27.9%	-0.525
11	Cj	0.0247	0.0222	-10%	8.53	8.58	0.6%	-0.058
12			0.0272	9%		8.48	-0.6%	-0.064
13	Gas He -> Kr	0.340	0.023	-93%	8.53	1.57	-81.6%	0.875
14	Gas He -> Xe		0.015	-96%		1.42	-83.4%	0.872
15	Centterline shift	1.000	0.000	-100%	8.53	3.85	-54.9%	0.549
16	Pa	0.000	1.00E+04	100%	8.53	8.53	0.0%	0.000
17			1.00E+06	100%		8.59	0.7%	0.007

Table 3-25 Sensitivity calculations - dynamic gap expansion model

Case	Parameter	Parameter Value			Gap Conductance			dY/dX
		Base case	Sensitivity	dX, %	Base case	Sensitivity	dY, %	
1	Emissivity, fuel	0.800	0.600	-25%	25.58	25.56	-0.1%	0.003
2			1.000	20%		25.60	0.1%	0.004
3	Emissivity, cladding	0.900	0.800	-11%	25.58	25.58	0.0%	0.000
4			1.000	10%		25.59	0.0%	0.004
5	Roughness, fuel	3.30E-06	3.30E-07	-90%	25.58	36.84	30.6%	-0.340
6			3.30E-05	90%		7.25	-71.7%	-0.796
7	Roughness, cladding	1.78E-06	1.78E-07	-90%	25.58	30.21	15.3%	-0.170
8			1.78E-05	90%		10.85	-57.6%	-0.640
9	Cd	1.500	0.620	-59%	25.58	36.90	30.7%	-0.523
10			3.200	53%		17.48	-31.7%	-0.596
11	Cj	0.0247	0.0222	-10%	25.58	25.72	0.5%	-0.054
12			0.0272	9%		25.45	-0.5%	-0.056
13	Gas He -> Kr	0.340	0.023	-93%	25.58	5.23	-79.6%	0.853
14	Gas He -> Xe		0.015	-96%		4.49	-82.4%	0.863
15	Centterline shift	1.000	0.000	-100%	25.58	24.23	-5.3%	0.053
16	Contact pressure, Pa	0.000	1.00E+04	100%	25.58	25.58	0.0%	0.000
17			1.00E+06	100%		25.63	0.2%	0.002
18(*)	Contact pressure, Pa	0.000			38.44			
19(*)	calculation(**)		8.37E+07	100%		43.09	10.8%	0.108

(*) The initial gap size for Cases 18 and 19 is half of the value used in other cases

(**) Case 19 contact pressure is calculated internally

3.5.17 Gap Model Validation – Garnier and Begej Tests

The Garnier and Begej tests are described in [139]. The test data includes gap conductance values for a given plane separation distance, as well as theoretical results obtained using the expression derived by Kennard. The Kennard expression gives gap conductance as the ratio of gas conductivity over the sum of the "ideal" separation distance, D_{mp}, and the temperature jump distances, g_1, g_2. The gap model in SPECTRA may be used here with the gap size equal to the separation distance and the term with surface roughness C_d ($r_f + r_c$) set to zero.

- **He-filled gap, separation distance 5.9 µm**

Figure 3-193 shows results obtained for Helium-filled gap and the separation distance of 5.9 µm. The data from [139] include the measured data and the "Kennard" expression. On top of these data SPECTRA results are superimposed. The SPECTRA "Kennard" lines are obtained assuming C_d = 0.0. An additional term is the solid conduction term. For most Garnier and Begej experiments the cladding and fuel are reported to be at light contact, with p_a ~1300 Pa. The solid conduction term was used assuming p_a = 1300 Pa. As will be shown below (Table 3-27) this gives negligible contribution to the gap conductance (<0.06 W/m^2-K). The results are in good agreement with the Kennard lines from [139]. The values are clearly lower than the measured values.
Calculations are stored in: `\Z-INPUTS\TC\GAP\Verification\GAP-GB-He-5_9`

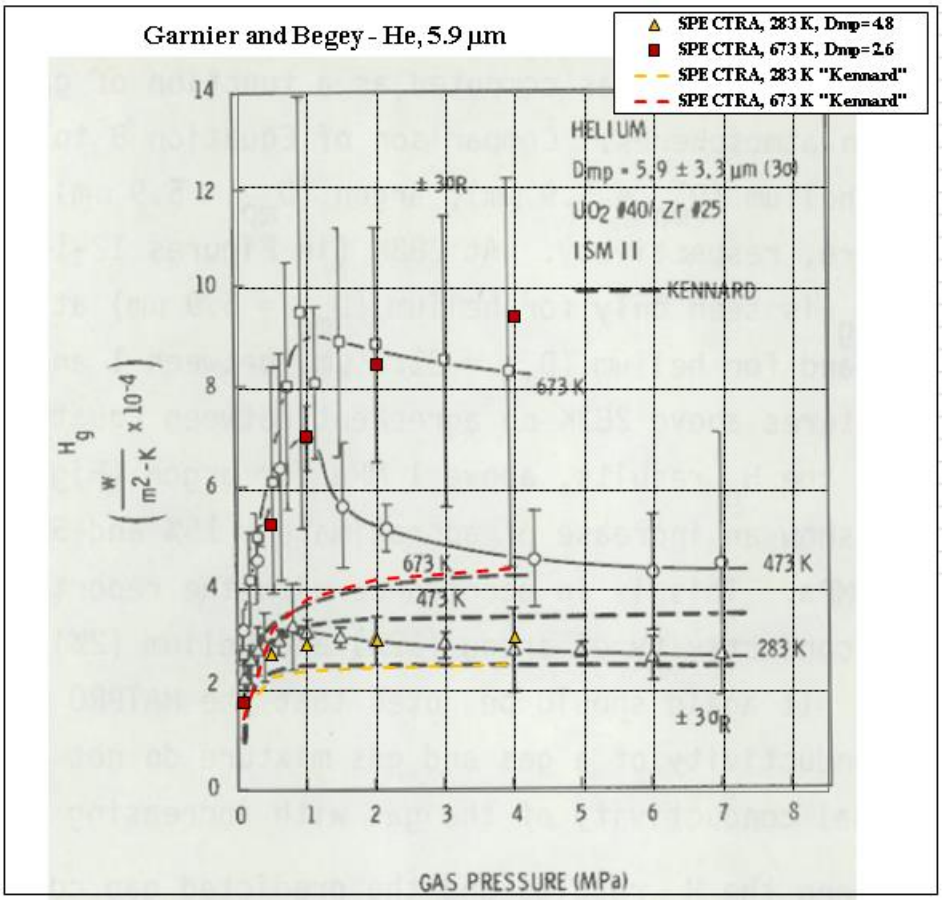

Figure 3-193 Gap conductance, h (W/cm^2-K), Garnier and Begej tests, He, 5.9 µm

Sensitivity calculation was performed using the separation distance. The source data gives 5.9 ± 3.3 μm. This means a minimum value of 2.6 μm. It was found by trial and error that a good match to experiment was obtained using the separation distance of 4.8 μm and 2.6 μm for the 283 and 673 K cases respectively - Figure 3-193. The value of 4.8 = 5.9 – 1.1 μm lies well within the measurement error: 1.1 < 3.3 μm. The value of 2.6 = 5.9 – 3.3 μm lies at the edge of the measurement error of 3.3 μm.

Another sensitivity calculation was performed using the solid conduction term. The source data mentions "light contact, 1300 N/m²". With this value of p_a, the solid contact term is practically zero. In order to obtain higher gap conductance a significantly larger p_a, must be used. It was found by trial and error that values of $p_a = 1.0\times10^8$ and 5.0×10^8 give good match to experimental values - Figure 3-194. Clearly these values are many orders of magnitude larger than the 1300 Pa reported by Garnier and Begley.

Calculations are stored in: `\Z-INPUTS\TC\GAP\Verification\GAP-GB-He-5_9-pa`

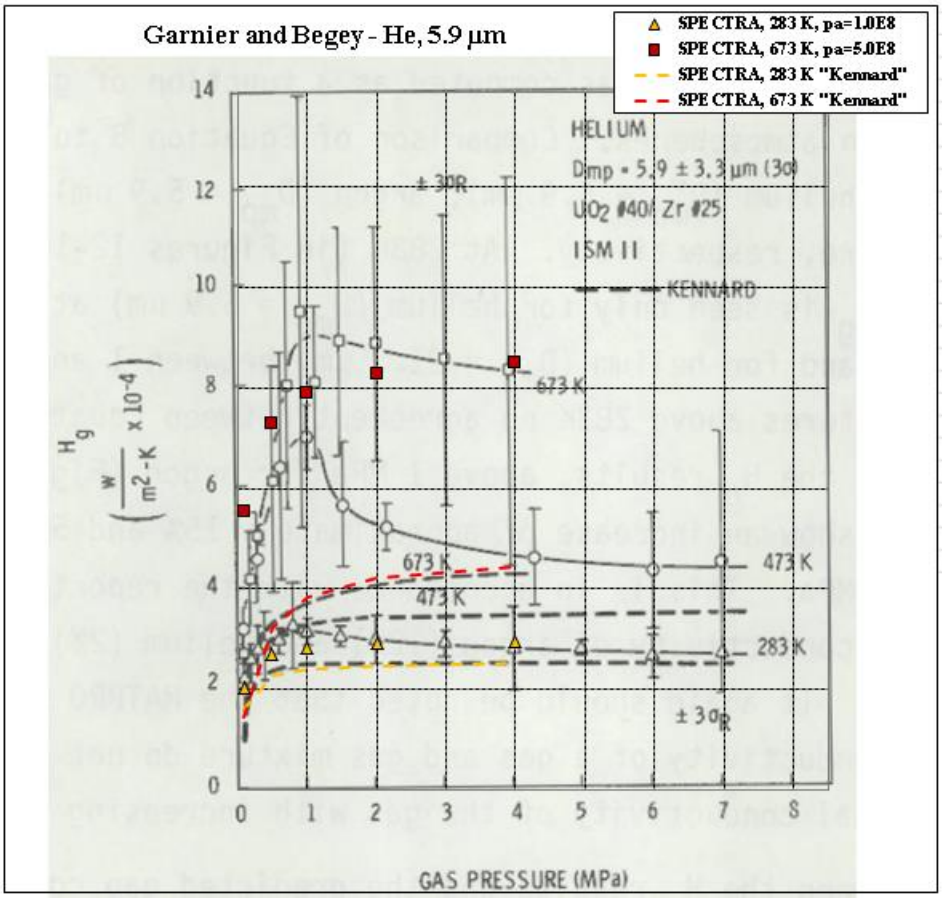

Figure 3-194 Gap conductance, h (W/cm²-K), Garnier and Begej tests, He, 5.9 μm, C_j=0.0

In order to verify the solid conduction model, the calculated solid conduction values were compared to the data reported by Lanning and Hall [141]. The results are shown in Table 3-26. The solid conduction term in SPECTRA, which is based on the Ross and Stoute model, gives very similar results to the results reported by Lanning and Hall as the "Ross and Stoute" results and also quite similar to the experimental results, although at very low contact pressures (p_a/H = 0.00015) the model clearly underestimates the gap conductance. This is not important for the present case. The values obtained for the T=283 K case are shown in Figure 3-195, Figure 3-196 and Table 3-27. For p_a = 1300, p_a/H = 0.000001, the gap conductance term is very small (<0.06 W/m^2-K) and any error has no practical consequences. For $p_a = 10^8$, p_a/H = 0.051, the gap conductance term is ≈4400 W/m^2-K. This is in the range 0.014 < p_a/H < 0.071, where relatively good accuracy is obtained from the model - Table 3-26.

In conclusion, the results of experiments could be well matched if we assume the apparent interfacial pressure of order of 10^8 Pa. This is far larger than the reported "light contact, ~1300 N/m^2". Therefore it is concluded that a more likely explanation of the measured values is the error in the separation distance measurement, given in the source report as ±3.3 μm. The experimental results were reasonably well reproduced by using a separation distances of 4.8 = 5.9 – 1.1 μm for the 283 K case and 2.6 = 5.9 – 3.3 μm, as shown in Figure 3-193.

Table 3-26 Verification of the solid conduction in gap model, based on [141]

	R 1-1	R 1-7	1-1	1-5	3-1	3-5	D 1-7
Model constant, Cs	11.89	11.89	11.89	11.89	11.89	11.89	11.89
average conductivity, Km [m]	11.2	11.2	7.8	7.8	7.8	7.8	7.8
Pa/H [-]	0.00015	0.00015	0.014	0.071	0.014	0.071	0.005
roughness, fuel [micron]	1370	16	100	100	24	24	290
roughness, clad [micron]	940	6	48	48	18	18	120
roughness, fuel [m]	1.370E-05	1.600E-07	1.000E-06	1.000E-06	2.400E-07	2.400E-07	2.900E-06
roughness, clad [m]	9.400E-06	6.000E-08	4.800E-07	4.800E-07	1.800E-07	1.800E-07	1.200E-06
average roughness, rt [m]	1.175E-05	1.208E-07	7.843E-07	7.843E-07	2.121E-07	2.121E-07	2.219E-06
SPECTRA, W/m2-K	**6**	**57**	**1,466**	**7,435**	**2,819**	**14,297**	**311**
SPECTRA, W/cm2-K	**0.00058**	**0.0057**	**0.147**	**0.743**	**0.282**	**1.430**	**0.031**
R&S [Lanning&Hall], W/cm2-K	**0.00060**	**0.0050**	**0.140**	**0.640**	**0.210**	**1.000**	**0.023**
rel. difference	**0.03**	**0.15**	**0.05**	**0.16**	**0.34**	**0.43**	**0.35**
exp. [Lanning&Hall], W/cm2-K	**0.0800**	**0.4200**	**0.120**	**0.700**	**0.032**	**1.000**	**0.660**
rel. difference	**0.99**	**0.99**	**0.22**	**0.06**	**7.81**	**0.43**	**0.95**

Table 3-27 Verification of solid conduction term in the gap model, He, 5.9 μm, T=298 K

	Case: He, 5.9 micron	
Pa [Pa]	**1300.0**	**1.00E+08**
T [K]	283	283
conductivity, fuel [m]	9	9
conductivity, clad [m]	17	17
average conductivity, Km [m]	11.8	11.8
Meyer hardness, H [Pa]	1.95E+09	1.95E+09
Pa/H [-]	0.000001	0.051
roughness, fuel [m]	3.30E-06	3.30E-06
roughness, clad [m]	1.78E-06	1.78E-06
average roughness, rt [m]	2.651E-06	2.651E-06
solid conduction: h, W/m2-K	**0.057**	**4407.3**
	difference:	**4407.2**
code output, SC-101: h, W/m2-K	**16030**	**20460**
case: GAP-GB-5_9-pa	difference:	**4430.0**

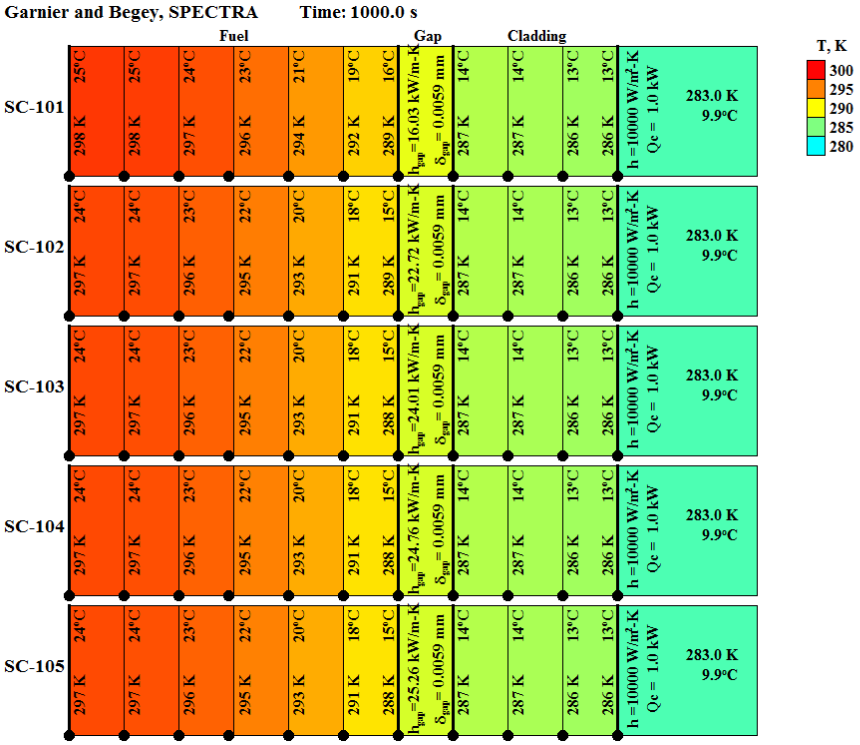

Figure 3-195 Garnier and Begej test, He, 5.9 µm, *T*=283 K, SPECTRA p_a = 1300 Pa

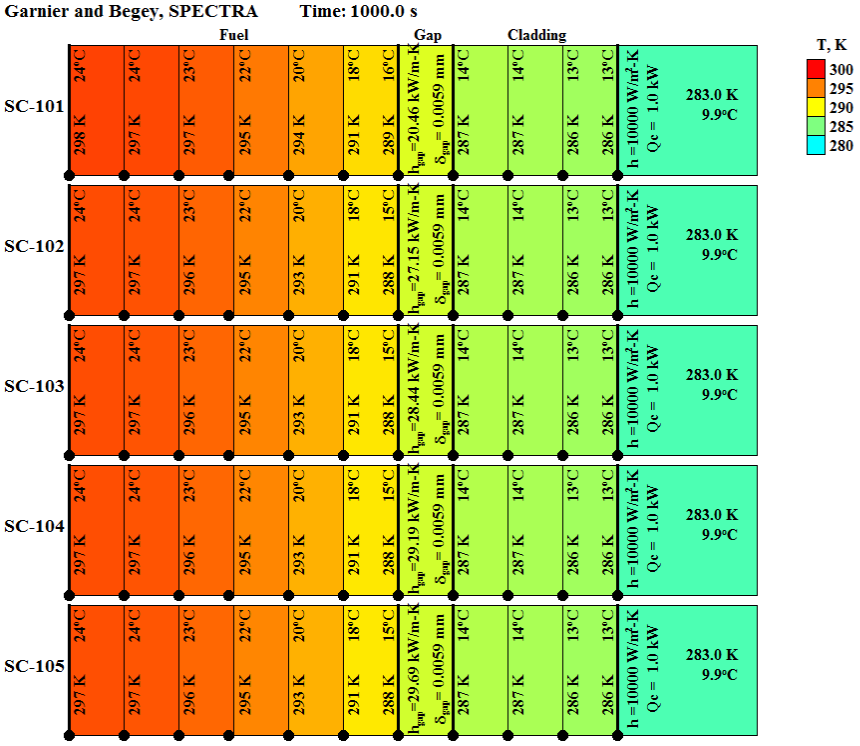

Figure 3-196 Garnier and Begej tests, He, 5.9 µm, *T*=283 K, SPECTRA p_a = 10^8 Pa

- **Ar-filled gap, separation distance 5.9 µm**

Figure 3-197 shows results obtained for Argon-filled gap and the separation distance of 5.9 µm. Again the source data, reference [139] gives gap conductance values for a given plane separation distance, as well as theoretical results obtained using the Kennard expression.

As in case of the He-filled gap, the gap model was used here with the gap size equal to the separation distance and the term with surface roughness C_d (r_f + r_c) set to zero. SPECTRA results are superimposed on the source data in Figure 3-197. The SPECTRA "Kennard" lines are obtained assuming C_d = 0.0 and p_a = 1300 Pa. The results are in good agreement with the Kennard lines from [139]. The values are clearly lower than the measured values.

Sensitivity calculations were performed using the separation distance. The source data gives 5.9 ± 3.3 µm. This means a minimum value of 2.6 µm. It was found by trial and error that a good match to experiment was obtained using the separation distance of 3.0 µm - Figure 3-197. The value 3.0 = 5.9 – 2.9 µm lies within the measurement error: 2.9 < 3.3 µm.

Calculations are stored in: `\Z-INPUTS\TC\GAP\Verification\GAP-GB-Ar-5_9`

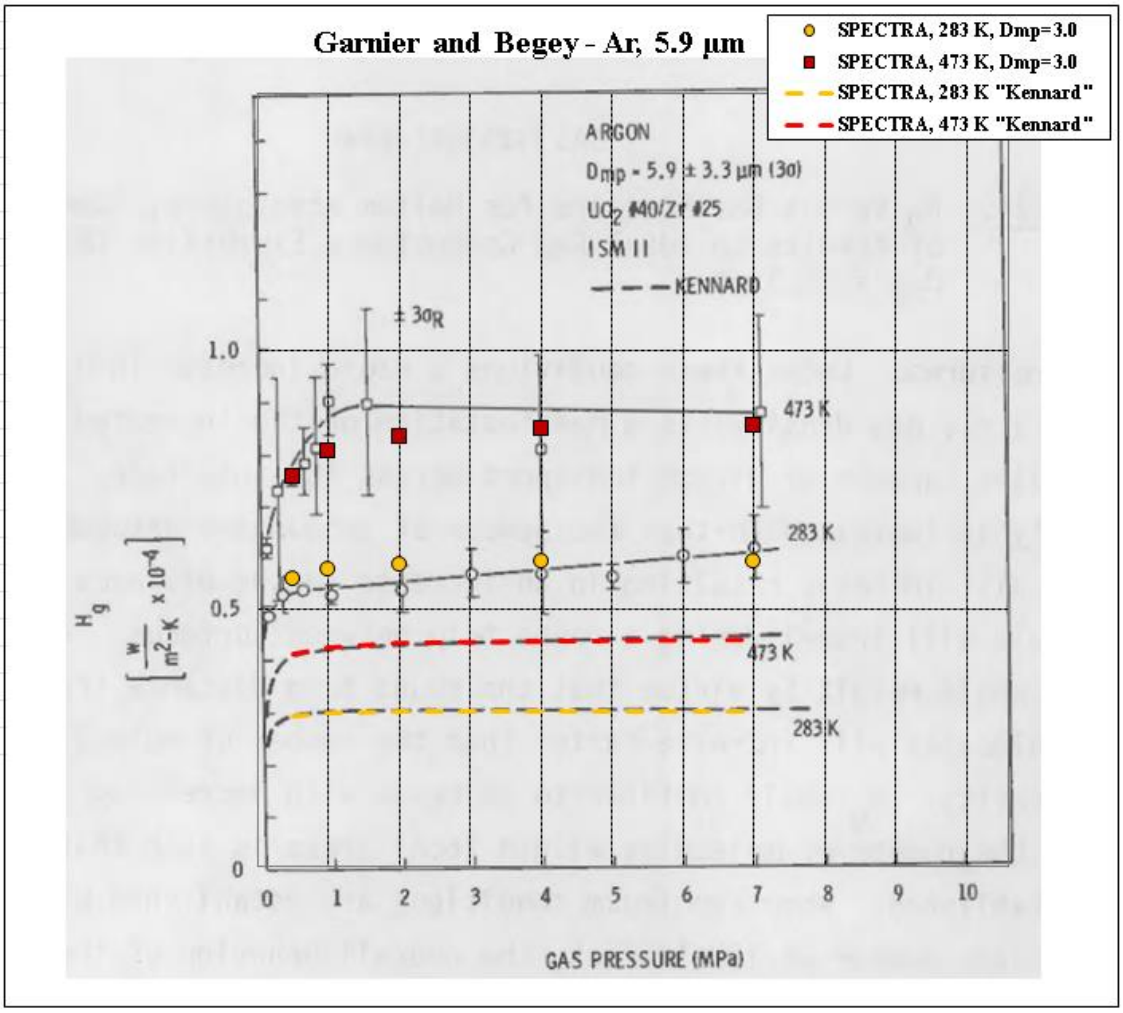

Figure 3-197 Gap conductance, *h* (W/cm²-K), Garnier and Begej tests, Ar, 5.9 µm

- **He-filled gap, separation distance 21.3 µm**

Figure 3-198 shows results obtained for Helium-filled gap and the separation distance of 21.3 µm. Again the source data, reference [139] gives gap conductance values for a given plane separation distance, as well as theoretical results obtained using the Kennard expression.

As before, the gap model was used here with the gap size equal to the separation distance and the term with surface roughness C_d ($r_f + r_c$) set to zero. SPECTRA results are superimposed on the source data in Figure 3-198. The SPECTRA "Kennard" lines are obtained assuming $C_d = 0.0$ and $p_a = 0.0$ Pa. The results are in good agreement with the Kennard lines from [139]. The values are clearly lower than the measured values.

Sensitivity calculations were performed using the separation distance. The source data gives 21.3 ± 4.1 µm. The value of 21.3 – 4.1 = 17.2 µm was tried first. The results for 283 K were enveloped by the values obtained with 21.3 and 17.2 µm - Figure 3-198. However, for 673 K the obtained conductance was still too low. The separation distance was further reduced by trial and error to obtain a good match to experiment. The value that had to be used was 9.0 µm = 21.3 – 12.3 µm - Figure 3-198. The difference in separation distance of 12.3 µm is far larger than the reported measurement error of 4.1 µm. For this test the relatively large separation distance, D_{mp} = 21.3 µm, basically precludes any significant contact pressure [139]. Therefore no attempt was made to include contact pressure in sensitivity calculations. It has to be concluded that it was not possible to reproduce the measured value for the 673 K case.
Calculations are stored in: `\Z-INPUTS\TC\GAP\Verification\GAP-GB-He-21_3`

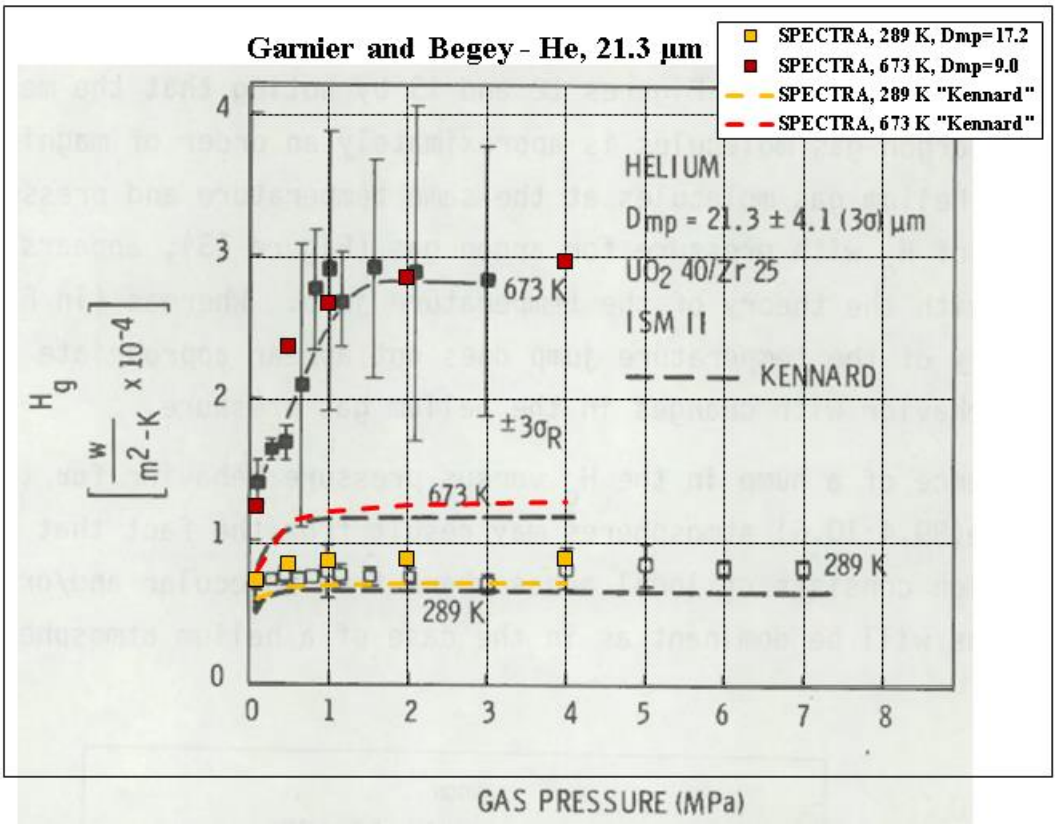

Figure 3-198 Gap conductance, h (W/cm^2-K), Garnier and Begej tests, He, 21.3 µm

3.5.18 Summary of the Gap Model Verification and Validation

The Verification and Validation of the gap models consists of several steps

- Comparisons with analytical solutions for the simplest cases
- Comparison with other code
- Comparisons with experiment

Verification of the centerline shift is performed by comparison with RELAP5 model. Altogether 16 runs were performed using different centerline shifts and different gases inside the gap. A very good agreement with RELAP-calculated values was obtained. It was observed that the centerline shift may have a significant impact on the gap conductance; the gap conductance may change by a about factor of 2 due to the centerline shift.

Validation was performed by comparing the calculated results with measurement values. The validation runs were performed for PBF-LOC11C tests [140] and Garnier and Begej tests [139]. In case of PBF-LOC11C tests calculations were performed with SPECTRA and RELAP5. In case of both codes a similar overestimation of the fuel maximum temperature was obtained. A good code-to-code agreement was observed. In case of the Garnier and Begej tests, a good agreement was obtained for all cases except one (21.3 μm, 673 K).

Furthermore, a number of sensitivity runs, described in section 3.5.16, were performed in order to find which parameters have the most significant effect on the gap conductance. The following observations were made:

- Fuel and cladding surface roughness has significant effect on the gap conductance. The surface roughness is used together with the parameter C_d. (values recommended in literature range from 0.62 to 3.2).
- Gas composition has significant effect on gap conductance because of differences in thermal conductivities of different gases.
- Centerline shift may in some circumstances have a significant effect on gap conductance (this is also shown in section 3.5.15).
- Solid conduction may have a significant effect on gap conductance, depending on the value of apparent interfacial contact pressure.
- Fuel and cladding surface emissivities have rather small effect on the gap conductance, at least in the typical temperature range.

3.5.19 Axial Conduction and Direct Contact Conduction in 1-D Structures

The tests presented below provide a qualitative and quantitative verification of the axial conduction and the direct contact conduction in 1-D Solid Heat Conductors. The following tests are considered:

- AXIAL-00 axial heat transfer in 1-D structures
- DIRECT-11 combination of direct contact and axial heat transfer in 1-D structures
- PBR-IC direct contact conduction application for reflector/inlet pipes of Pebble Bed Reactor (PBR).
- PBR-k-eff application of direct contact conduction to model an effective bed conductance for the pebble bed core, and the PMR uses an effective radial conductivity for conduction through the fuel compacts, graphite blocks, and gaps between graphite blocks.
- PMR-k-eff application of direct contact conduction to model an effective radial conductivity for conduction through the fuel compacts, graphite blocks, and gaps between graphite blocks in prismatic modular reactors (PMR).

Descriptions of these tests are given below.

3.5.19.1 Axial Conduction Tests, AXIAL-00

This section shows how to use the axial conduction model and provides verification of the calculated results by comparing with exact solution obtained from 2-D Solid Heat Conductors. The SPECTRA input files are located in:
`\Z-INPUTS\SC\AXIAL\AXIAL-00\`

The test cases are considered for rectangular, cylindrical, and spherical geometries. The input files are:
`AXIAL-00-REC.SPE`
`AXIAL-00-REC-Exact.SPE`
`AXIAL-00-CYL.SPE`
`AXIAL-00-CYL-Exact.SPE`
`AXIAL-00-VESSEL.SPE`

- AXIAL-00-REC, AXIAL-00-REC-Exact

The test case consists of three 1-D Solid Heat Conductors, SC-210, SC-220, SC-230, all of them rectangular geometry. An internal heat source of 10 kW is defined for SC-220. The left surfaces of the SC-s are insulated; the right surfaces transfer heat using a tabulated boundary conditions h = 5000 W/m^2-K, T = 300 K. Each SC has a surface area of 1.0 m^2. The axial length (not an input for this geometry) is assumed to be 0.1 m. Axial heat transfer is activated with axial length equal to 0.05 m. Results (stationary state) are shown in Figure 3-199 and Figure 3-200 (right side). Verification is performed in two ways:

- Consistency of heat flux (Figure 3-199) is checked using the printed node temperatures. Calculations are provided in the file AXIAL-00-REC.XLS. The computed values of heat power were identical to that printed in SPECTRA output file as the internal heat source for SC-210 and SC-230. For these SCs the true internal heat source is zero, therefore the value printed by the code as the "internal source" is solely due to the applied axial conduction model.

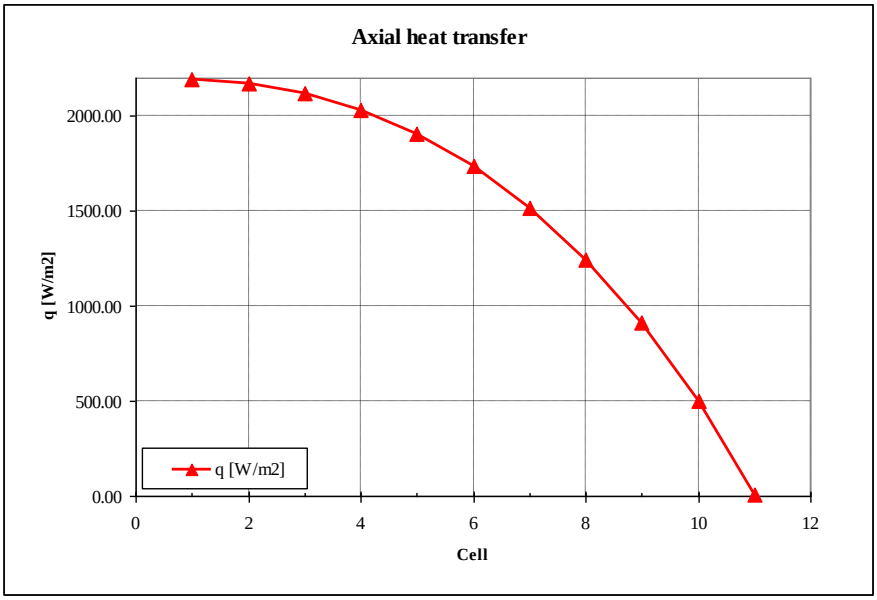

Figure 3-199 Results of test AXIAL-00-REC

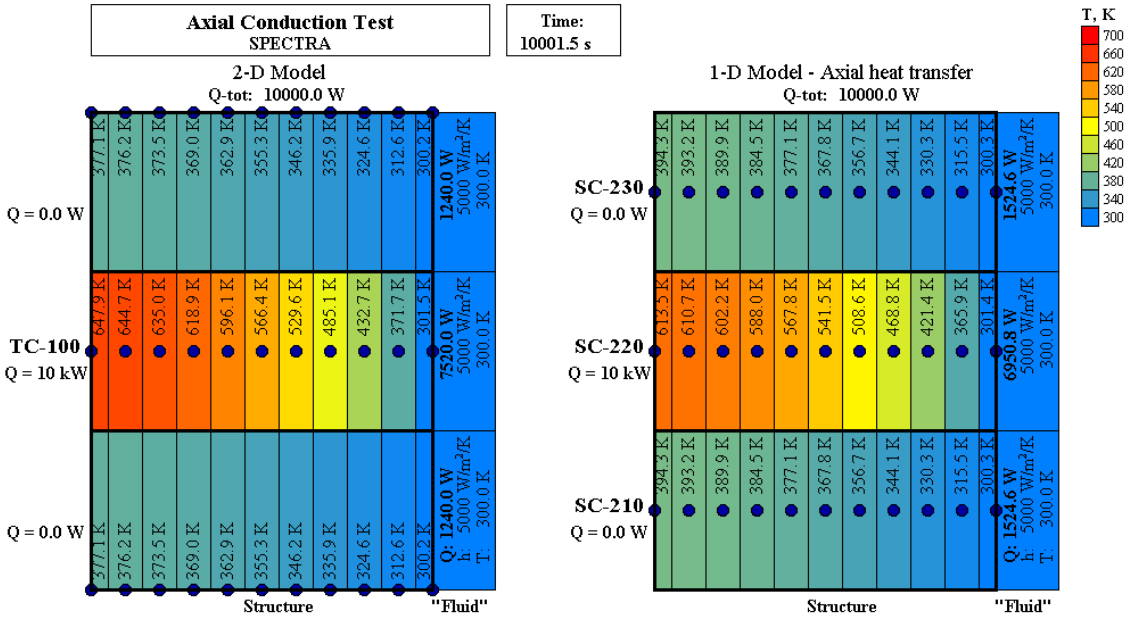

Figure 3-200 Results of test AXIAL-00-REC

- As verification, a 2-D model has been set up using TC-100. The results are shown in Figure 3-200 (left side). The temperatures calculated by the 2-D model are somewhat different than in the 1-D structures, due to differently located nodes. In the 2-D structures the nodes are, as always, located at the surface. Therefore the conduction resistance is larger than in the 1-D model.

In order to have exactly the same solution the SC model was redefined by defining the axial lengths as:

- L_i = 0.05 m for SC-220
- L_j = 0.10 m for SC-210 and SC-230

Both transfers to SC-210 and 230 are defined for SC-220:

```
*       SC    i j L-i  L-j     h     A1    A2
390220 1 210 0 0 0.05 0.10  210   1.0    2.0 *  Axial transfer to SC-210, contact h = TF-210
390220 1 230 0 0 0.05 0.10  210   1.0    2.0 *  Axial transfer to SC-230, contact h = TF-210
```

It should be remembered that for the rectangular geometry the area for axial heat transfer is obtained from:

$$A_i = \Delta x_{cell} \times width$$
$$width = A_{SC,i} / (2L_i)$$

Here A_{SC} is the surface of the rectangular SC, *width* is the width of SC, which is assumed to be equal to the surface area divided by twice the conduction length, L_i. Therefore, when a length is artificially increased from 0.05 to 0.10 m, to put the nodes at the edges, simultaneously the area multiplier is set to 2.0. Results are shown in Figure 3-201. The results obtained in the 1-D model (Figure 3-201 right side) are identical to the results obtained in the 2-D model (Figure 3-201 left side).

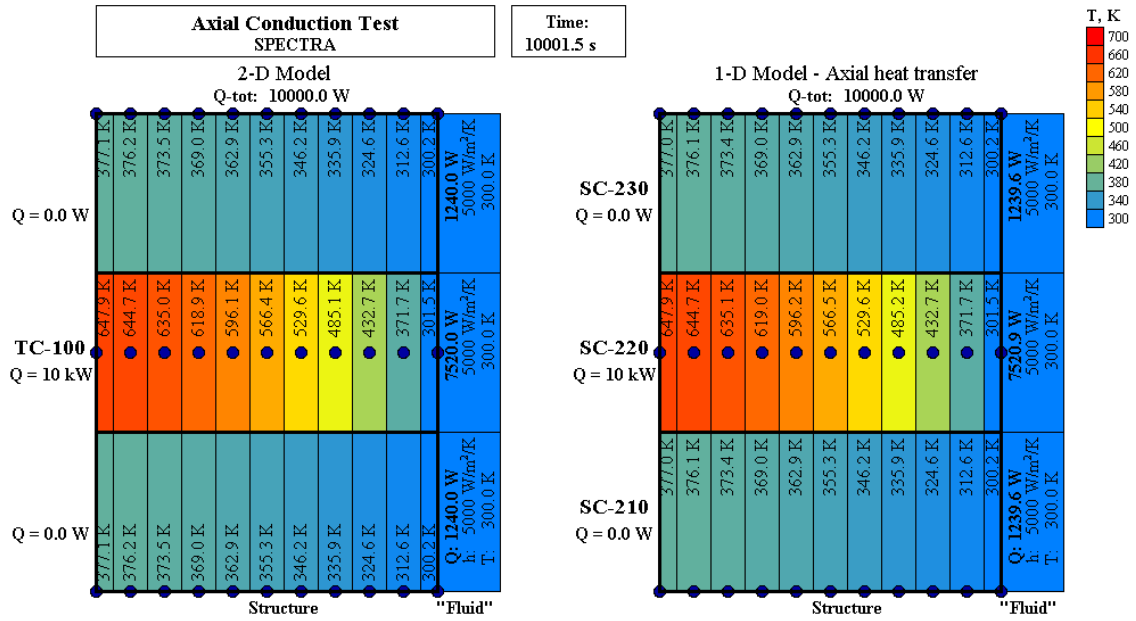

Figure 3-201 Results of test AXIAL-00-REC-Exact

- AXIAL-00-CYL, AXIAL-00-CYL-Exact

The present tests are the same as described above, but in this case SC-210, SC, 220, and SC-230, are cylindrical structures. The values are set to 0.05 and 0.10 m in the tests AXIAL -00-CYL and AXIAL-00-CYL-Exact respectively:

AXIAL-00-CYL:

```
*       SC   i j L-i  L-j    h
390220 1 210 0 0 0.05 0.10  210 *  Axial transfer to SC-210, contact h = TF-210
390220 1 230 0 0 0.05 0.10  210 *  Axial transfer to SC-230, contact h = TF-210
```

AXIAL-00-CYL-Exact:

```
*       SC   i j L-i  L-j    h
390220 1 210 0 0 0.10 0.10  210 *  Axial transfer to SC-210, contact h = TF-210
390220 1 230 0 0 0.10 0.10  210 *  Axial transfer to SC-230, contact h = TF-210
```

In case of axial conduction in cylindrical geometry the axial heat transfer area is clearly defined by the cylinder geometry, which means the conduction lengths are not used to determine the conduction area. Therefore, in contrast to AXIAL-00-REC-Exact, there is no need to define the area multipliers:

The code will issue a warning message that the axial length is different than half of the cylinder length for SC-210 and SC-230, but the values are accepted for calculations.

Results are shown in Figure 3-202. The results obtained in AXIAL-00-CYL are shown in Figure 3-202 (a). The results obtained in AXIAL-00-CYL-Exact are shown in Figure 3-202 (b).

The results obtained in the 1-D model - Figure 3-202 (b) right side, are identical to the results obtained in the 2-D model - Figure 3-202 (b) left side.

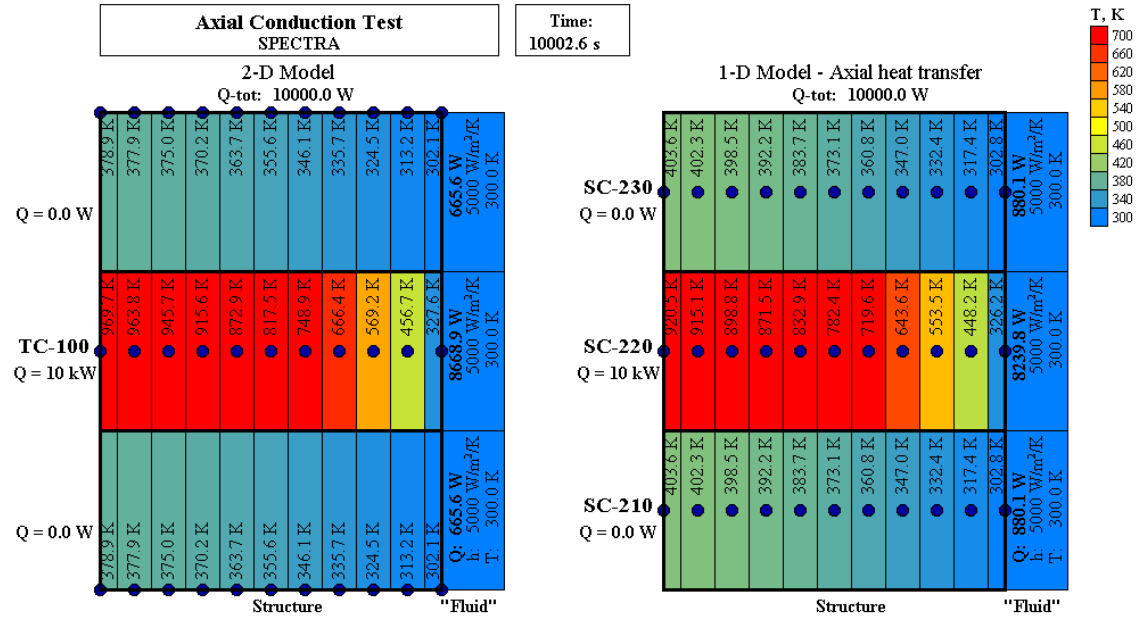

(a)

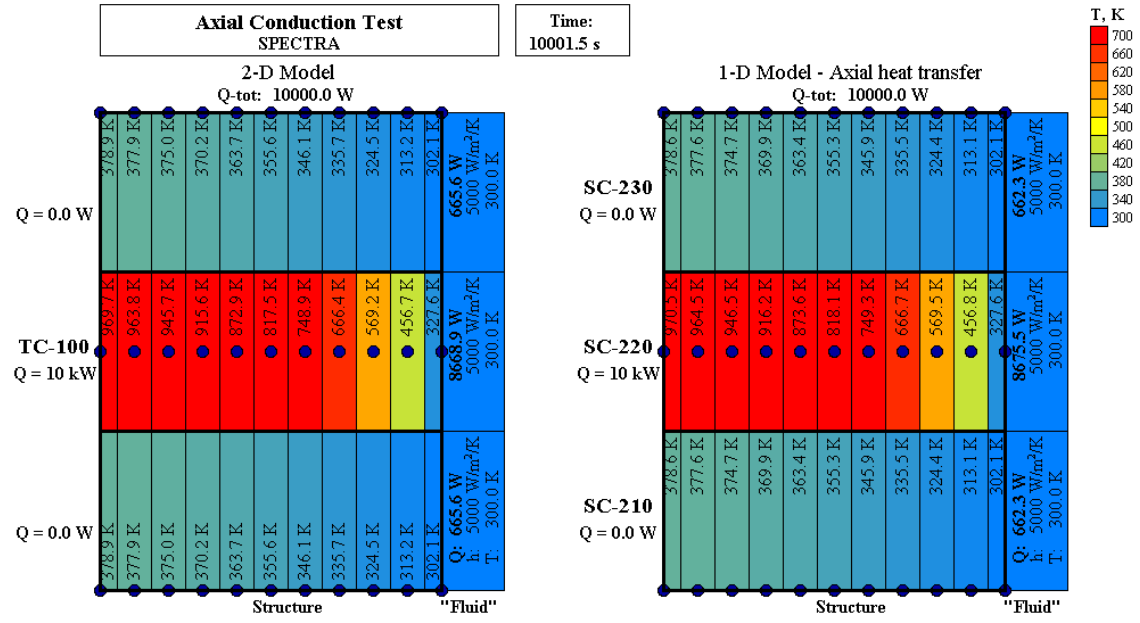

(b)

Figure 3-202 Results of (above) AXIAL-00-CYL, (below) AXIAL-00-CYL-Exact

- AXIAL-00-Vessel

The present test shows axial conduction in a vessel-type geometry. SC-110 and SC-210 are cylindrical structures. SC-120 and SC-220 are spherical structures with multiplier of 0.5 to signify a hemisphere. The length of cylinders is 1.0 m. The inner radius of both cylinders and spheres is 1.0 m. The axial conduction length within a cylinder is set to half-length, 0.5 m. The axial conduction length within a sphere is assumed equal to 1/16 of the circumference, = $\pi/8$ × inner radius of the sphere = 0.393 m. The input deck defining axial conduction is shown below.

```
*       SC    i j  L-i  L-j    h    A-frac
390220 1 210 0 0 0.393 0.50  210   1.0 *  Axial heat transfer to SC-210, contact h = TF-210
```

Results are shown in Figure 3-203. The results obtained with axial conduction (Figure 3-203 right side) are compared to the results obtained without axial conduction (Figure 3-203 left side).

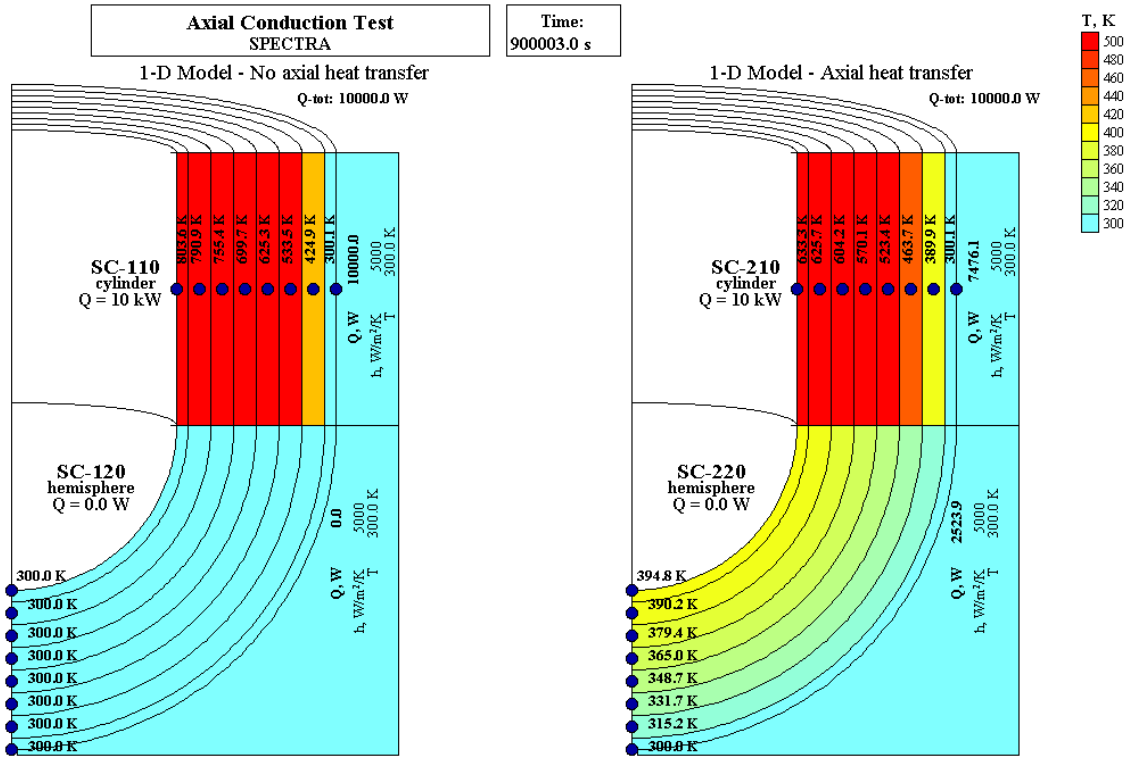

Figure 3-203 Results of test AXIAL-00-Vessel

3.5.19.2 Direct Contact Conduction Tests, DIRECT-11

This section shows how to use the direct contact model and provides a verification of the calculated temperature distribution using an exact solution. The SPECTRA input files are located in:
`\Z-INPUTS\SC\AXIAL\DIRECT-11\`

The test cases are considered for rectangular, cylindrical, and spherical geometries. The input files are: DIRECT-11-REC.SPE, DIRECT-11-CYL.SPE, DIRECT-11-SPH.SPE. Below only the results of DIRECT-11-REC.SPE are shown. The test case consists of three pairs of 1-D Solid Heat Conductors:

- SC-110 and SC-120
- SC-210 and SC-220
- SC-310 and SC-320

A heat source is present in the "right" structures: SC-120, SC, 220, and SC-320. Direct contact is modeled for the second and the third pair:

```
*       SC   i j  L-i  L-j    h  A1 A2
390220 1 210 1 1 0.0  0.0   210   0.0  *  Axial heat transfer to SC-210, contact h = TF-210
390320 1 310 1 1 0.0  0.0   230   0.0  *  Axial heat transfer to SC-310, contact h = TF-230
```

The contact heat transfer coefficients are set to:

- TF-210 = 10 (W/m^2-K) - a "small" heat transfer coefficient.
- TF-230 = 1000 (W/m^2-K) - a "large" heat transfer coefficient.

The area of contact is calculated automatically by the code. The value must be checked by the user and, if needed, must be modified by using the area multipliers A1AXSC, A2AXSC. In the present case, the output file contains the following printout:

```
Heat transfer area, all cells :   A = 1.20000E+00 [m2]
Total, including multiplicity :   A = 1.20000E+00 [m2]
Individual cells
SC-220  0001  TO  SC-210  0001:   A = 1.20000E+00 [m2]
```

The surface area of every rectangular SCs was set to 1.2 m^2. This is also the area picked by default by the code. The area is correct and does not need to be modified.

As a verification of the last case, a single solid conductor is used, SC-400. The results of SC-400 correspond to the case with infinitely large contact heat transfer coefficient. The value of the contact heat transfer coefficient for the third case is large enough to compare the results with SC-400.

Calculations were performed until stationary state was reached. Results are shown in Figure 3-204 and Figure 3-205. Figure 3-204 shows visualization of stationary state results. Figure 3-205 shows temperature profiles. The results for the pair SC-310 and SC-320 are practically identical to the results of SC-400, which is a verification of the direct contact model results for this case. It is seen in Figure 3-204 and Figure 3-205 that the node locations in the central part are somewhat different - the pair has double node in the center, while the verification SC-400 has the temperature nodes at cell-centers. The calculated temperatures are nonetheless in very good agreement, as seen in Figure 3-205.

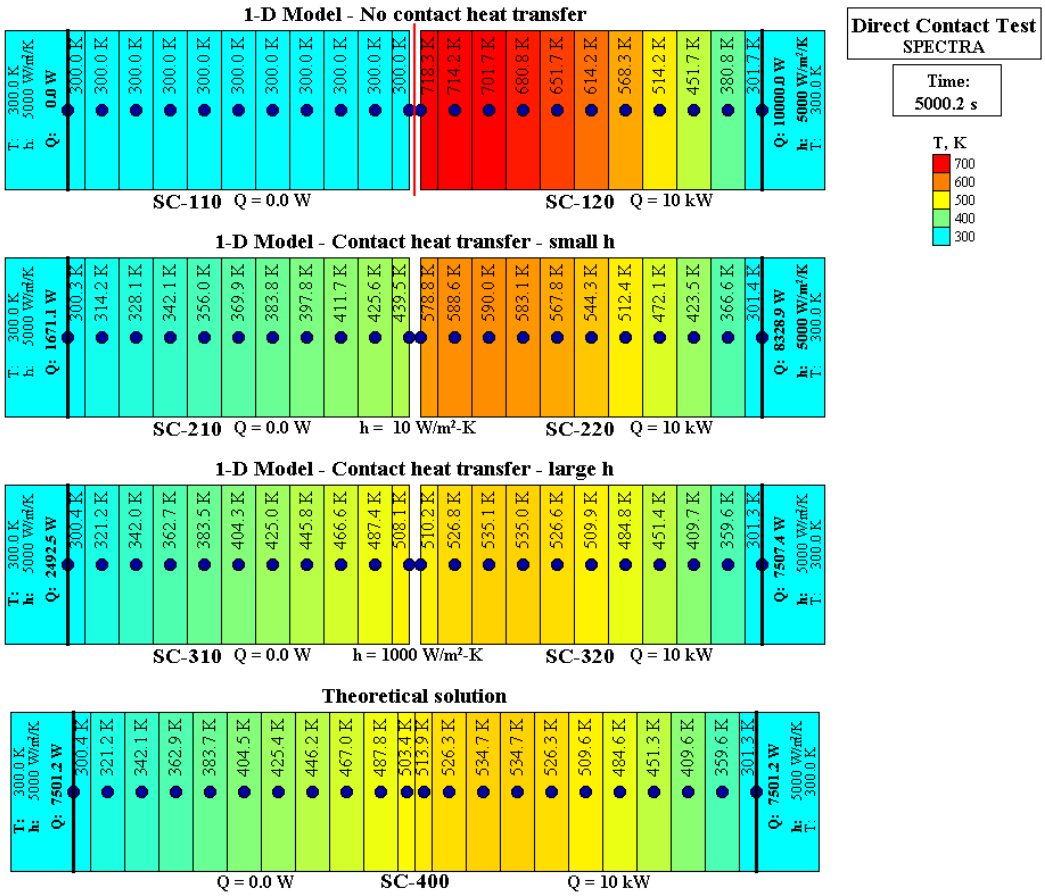

Figure 3-204 Results of test DIRECT-11-REC

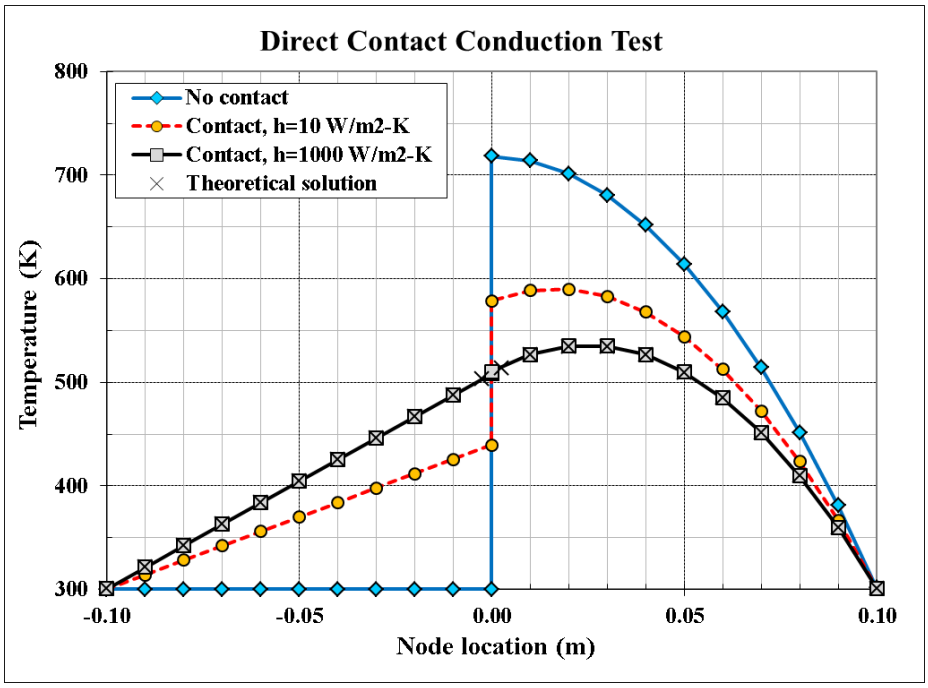

Figure 3-205 Results of test DIRECT-11-REC

3.5.19.3 Direct Contact Tests, PBR-IC

This section shows how to use the direct contact model to approximate a multidimensional heat transfer. The SPECTRA input files are located in:
\Z-INPUTS\SC\AXIAL\PBR-IC\

The test case represents the geometry of a graphite reflector of a Pebble Bed Reactor with inlet channels passing through. The inner and outer temperatures of the reflector (SC-120 - Figure 3-207) are set by appropriate tabular functions to 900 K and 500 K respectively. The space in the immediate vicinity of the cooling channels is represented by SC-130 with an appropriate multiplicity, to represent all "cooling channels". The size of the "immediate vicinity" has to be chosen somewhat arbitrary. In the present examples 3 nodes were used. Four cases were analyzes with a single node size of 0.01, 0.02, 0.04, and 0.06 m, which means the total radius of R = 0.03, 0.06, 0.12, and 0.18 m. The reflector nodes are 0.20 m each, so even with the 6 cm nodes, the outer node of SC-130 "sees" (and is linked to) a single node (node 5) of SC-120. The input deck is:

```
*       SC   i j  L-i  L-j    h  A1 A2
390130 1 120 3 5 0.01  0.00  200 0  0 *  Axial heat transfer to SC-120, contact h = TF-200
```

The outer node (number 3) of SC-130 is linked to the node 5 of SC-120. A large value (10,000 W/m^2-K) is used for the contact heat transfer (TF-200).

The area of contact is calculated automatically by the code. The value must be checked by the user and, if needed, must be modified by using the area multipliers A1AXSC, A2AXSC. In the present case, the output file contains the following printout:

```
Heat transfer area, all cells :   A = 1.44513E+00 [m2]
Total, including multiplicity :   A = 2.89027E+01 [m2]
Individual cells
SC-130  0003  TO  SC-120  0005:   A = 1.44513E+00 [m2]
```

The total area is 10.053 m^2. The value should be equal to the outer surface of the outer cell of SC-130: $A = 2\,\pi\,(R_0 + R)\,H\,N = 2\,\pi\times(0.05+018)\times1.0\times20 = 28.9027$. Here R_0 is the radius of the cooling channel, H is the height (assumed as 1.0 m) and N is the number of identical structures in the circumference (assumed as 20). The area is in this case correct and need not to be modified. As will be shown in the following two sections, this is not always the case and for some more complex geometries the user must calculate appropriate area multipliers.

Results are shown in Figure 3-206 and Figure 3-207. Visualizations of stationary state results are shown in Figure 3-206. Temperature profiles in the reflector are shown in Figure 3-207. Results for the smallest R and the largest R are different but similar and clearly different from the case when the direct contact is not modeled. In such case 100% of heat is lost through the outer reflector. When inlet channels are modeled, only ~20% is lost through the outer reflector; ~80% is lost to the channels. The exact value depends on R: 87% for R=0.03, 84% for R=0.06, 80% for R=0.12, 78% for R=0.18.

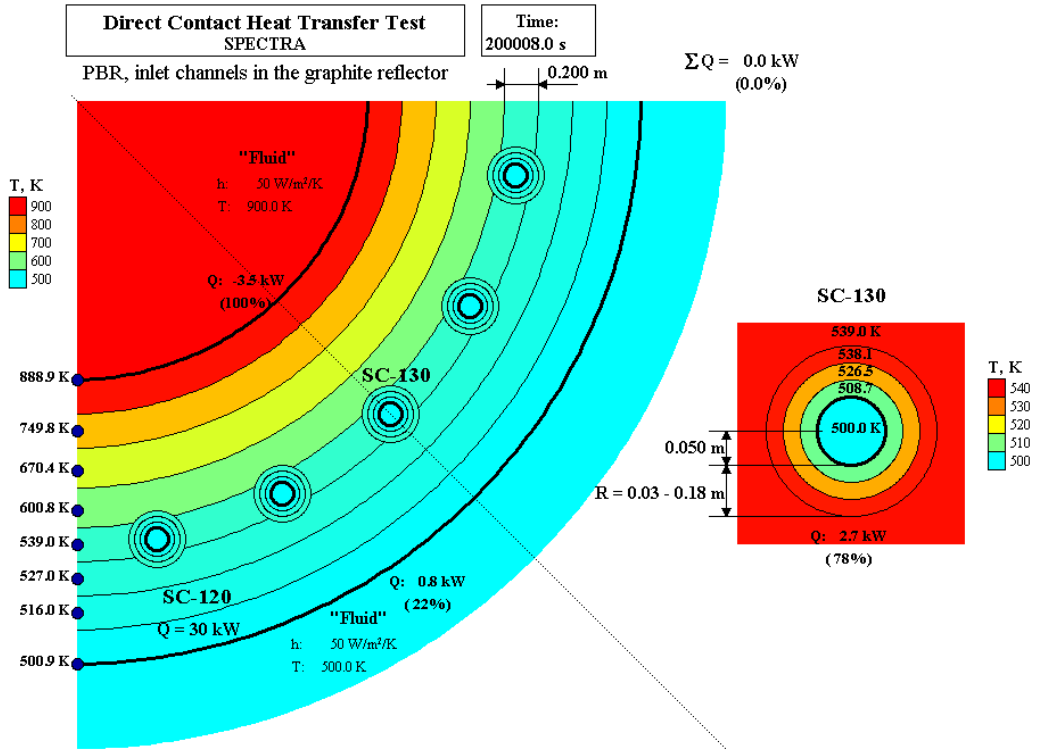

(a) Direct contact model, R = 0.18 m
78% of heat enters the inlet channels, 22% is lost from the reflector outer surface

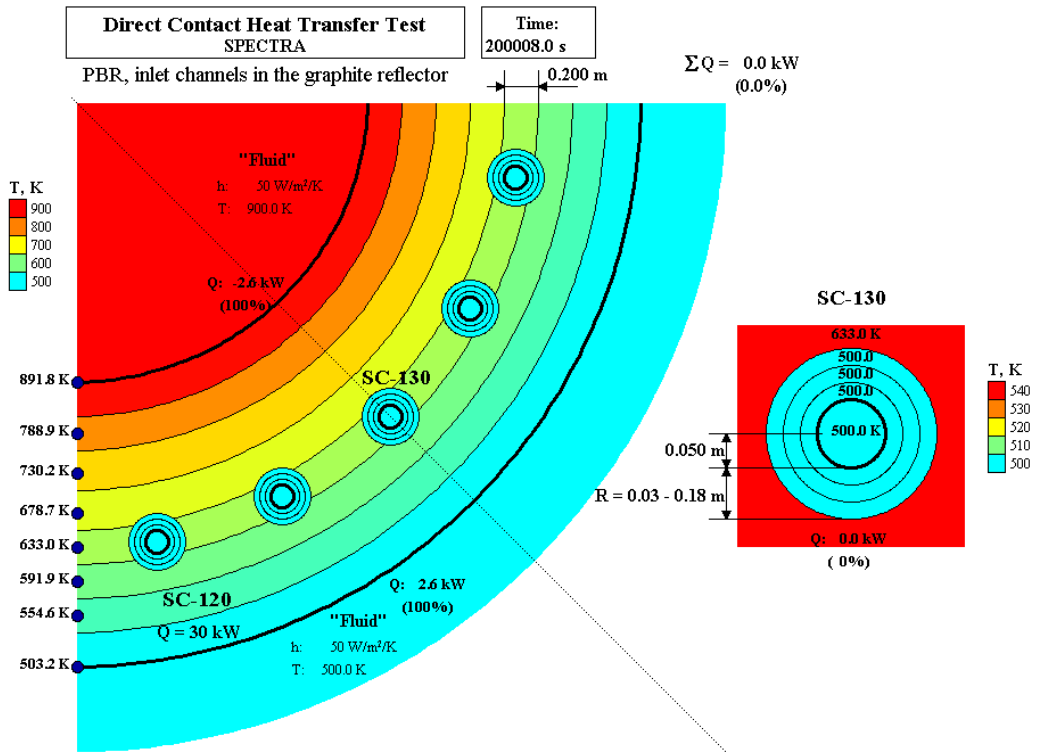

(b) No direct contact model: 100% of heat lost from the reflector outer surface

Figure 3-206 Results of test PBR-IC

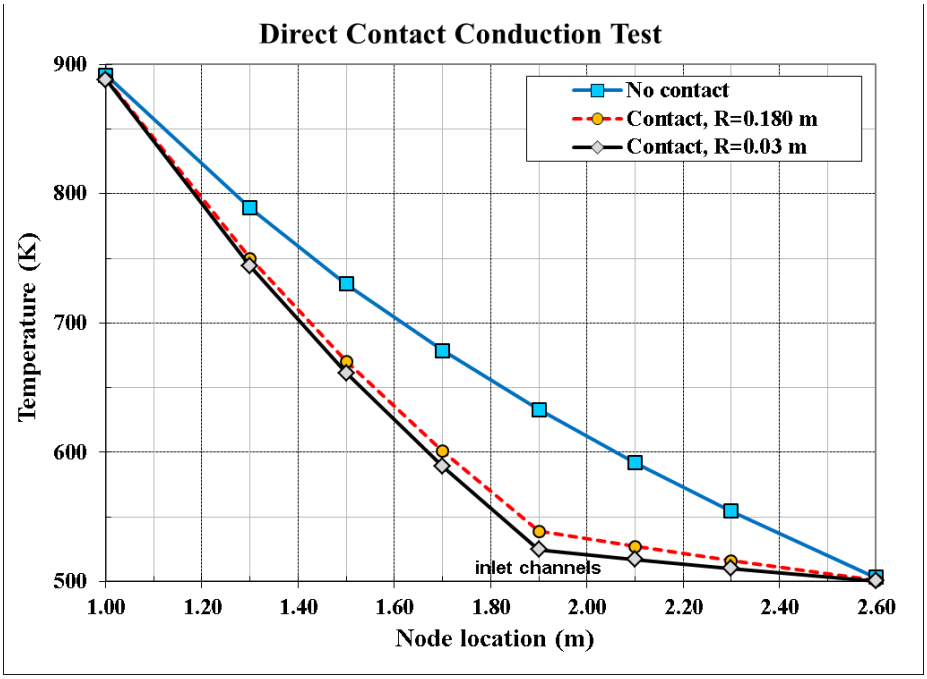

Figure 3-207 Results of test PBR-IP

3.5.19.4 Pebble Bed Tests, PBR-k-eff

This example shows how to build a model of a pebble bed reactor and provides a verification of the calculated temperature distribution using theoretical solution. The SPECTRA input files are located in: `\Z-INPUTS\SC\AXIAL\PBR-k-eff\`

A simple "pebble bed" is built. There are four rings of pebbles, each 0.5 m thick. The pebble bed porosity is assumed to be 0.39. The number of pebbles (identical spherical 1-D solid heat conductors) in each ring is set using appropriate multipliers (shown in Figure 3-209). Two cases are considered.

- No forced cooling. The generated heat must be removed radially to the reflector (shroud). This is achieved by using a tabulated heat transfer coefficient on the surface of pebbles and setting it to zero. For this case the power was assumed to be 1.0 W per pebble.
- Forced cooling. For this case the power was assumed to be 200.0 W per pebble. The tabulated heat transfer coefficient on the surface of pebbles was assumed to be equal to 100 W/m^2-K. The coolant flowing around the pebbles is assumed to have a constant temperature of 500 K (the same as the shroud outer temperature).

When modeling a pebble bed reactor, the user must first define an effective conductivity of the pebble bed. Effective conductivity of pebble bed may be calculated from Zehner-Schlunder and Robold correlations. This was done for example in analyses described in [178]. Figure 3-208 shows the effective conductivity as a function of temperature. More details are provided in: \PBR-k-eff\Effective-Conductivity.xlsx and \PBR-k-eff\Doc. The user needs to define an artificial material whose thermal conductivity is equal to the effective conductivity of the pebble bed. The density and specific heat of this material are not used in calculations and any number may be entered.

Next, the structures representing pebbles must be linked using the direct contact model. For the considered example, the (preliminary) input deck is:

```
*       SC    i j   L-i    L-j    k    A1  A2 Mh  M1  M2 L1 L2
390100 1 200  6 6  0.500  0.250  902  0.0 0.0  1 902 902 0  0
390200 1 300  6 6  0.250  0.250  902  0.0 0.0  1 902 902 0  0
390300 1 400  6 6  0.250  0.250  902  0.0 0.0  1 902 902 0  0
390400 1 500  6 1  0.250  0.000  902  0.0 0.0  1 902 000 0  0
```

The conduction lengths in pebbles are taken as center-to-center of the pebble node. For the reflector, the conduction length is zero, since the heat coming from the pebbles is deposited on the inner surface of the reflector. The material defining the effective pebble bed conductivity is MP-902. For the sake of easy verification of the calculated results the conductivity was here set to a constant value of 30 W/m^2-K and not the values obtained from the correlation (Figure 3-208).

Next, the area of heat transfer must be set. The default values, calculated by the code, are printed in the output file. For example, in case of transfer from SC-100 to SC-200 the output is:

```
Heat transfer area, all cells :   A = 4.52389E-02 [m2]
Total, including multiplicity :   A = 5.74896E+02 [m2]
Individual cells
SC-100  0006  TO  SC-200  0006:   A = 4.52389E-02 [m2]
```

The actual value is obtained as $2\pi RH = 2\pi \times 0.5 \times 1.0 = 3.14159$ m^2. The required multiplier is 5.46463E-03. All values and multipliers were calculated in \PBR-k-eff\PBR-k-eff.xlsx and are shown in Table 3-28. The final input deck is therefore:

```
*       SC    i j   L-i    L-j    k       A1           A2       Mh  M1  M2 L1 L2
390100 1 200  6 6  0.500  0.250  902  5.46463E-03 5.46463E-03  1 902 902 0  0
390200 1 300  6 6  0.250  0.250  902  6.55724E-03 6.55724E-03  1 902 902 0  0
390300 1 400  6 6  0.250  0.250  902  7.02571E-03 7.02571E-03  1 902 902 0  0
390400 1 500  6 1  0.250  0.000  902  9.36761E-03 9.36761E-03  1 902 000 0  0
```

Finally, the area printed in the output file needs to be checked. The values printed in case of transfer from SC-100 to SC-200 are:

```
Heat transfer area, all cells :   A = 2.47214E-04 [m2]
Total, including multiplicity :   A = 3.14159E+00 [m2]
Individual cells
SC-100  0005  TO  SC-200  0005:   A = 2.47214E-04 [m2]
```

This shows that the total area is correct. Calculations were performed until stationary state was reached. Results obtained for the first case (only radial transfer) are shown in Figure 3-209 (A). Figure shows temperatures and ring-to-ring temperature differences. In order to check the results, the temperature differences were calculated in \PBR-k-eff\PBR-k-eff.xlsx. The values are shown in Table 3-29. The agreement between the SPECTRA stationary-state values (Figure 3-209 A) and the theoretical values of ΔT, calculated in excel (Table 3-29) is very good.

Figure 3-209 (B) shows the results obtained for the second case (forced cooling). In this case most of the heat is transferred from the pebble surface to the "coolant" (here replaced by suitable Tabular Functions). Only minor part is transfer radially. The ring-to-ring temperature differences are very small.

Finally one needs to keep in mind that one of two available options must be selected by the user:

- The transferred heat is added (subtracted) to (from) the cell specified by the user (L1AXSC=0, L2AXSC=0)
- The transferred heat is uniformly distributed over all cells (L1AXSC=1, L2AXSC=1)

Table 3-28 Direct contact input - area multipliers (file: PBR-k-eff.xlsx)

	TRUE	SPECTRA (tot.)	Multiplier
0->1	3.14159	5.74896E+02	5.46463E-03
1->2	6.28319	9.58206E+02	6.55724E-03
2->3	9.42478	1.34147E+03	7.02571E-03
3->4	12.56637	1.34147E+03	9.36761E-03

Table 3-29 Theoretical temperature differences (file: PBR-k-eff.xlsx)

Q	dx-1	dx-2	ΔT
4236.1	0.50	0.25	33.7
16944.4	0.25	0.25	44.9
38125.0	0.25	0.25	67.4
67777.8	0.25	0.00	44.9

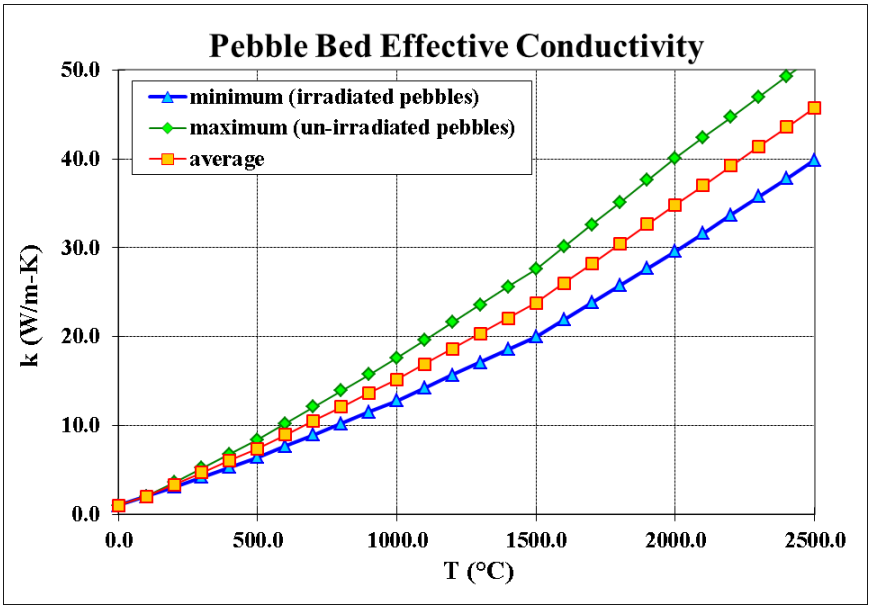

Figure 3-208 Effective conductivity - Zehner-Schlunder and Robold correlations

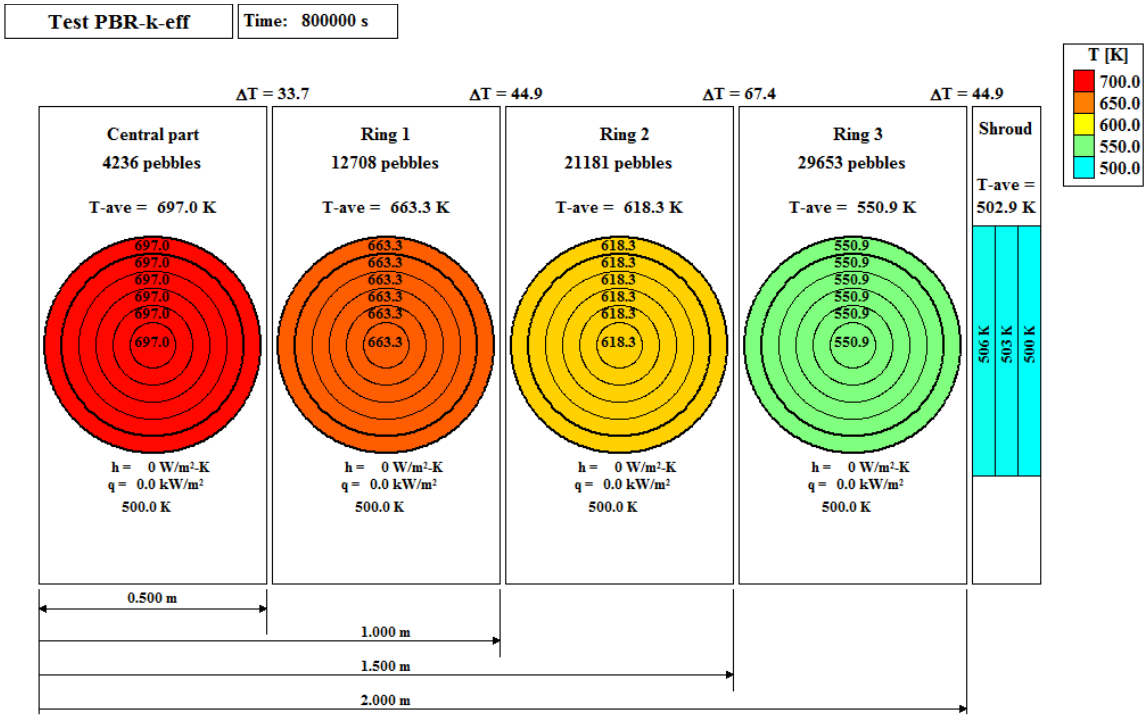

(A) no forced cooling - radial heat transfer only

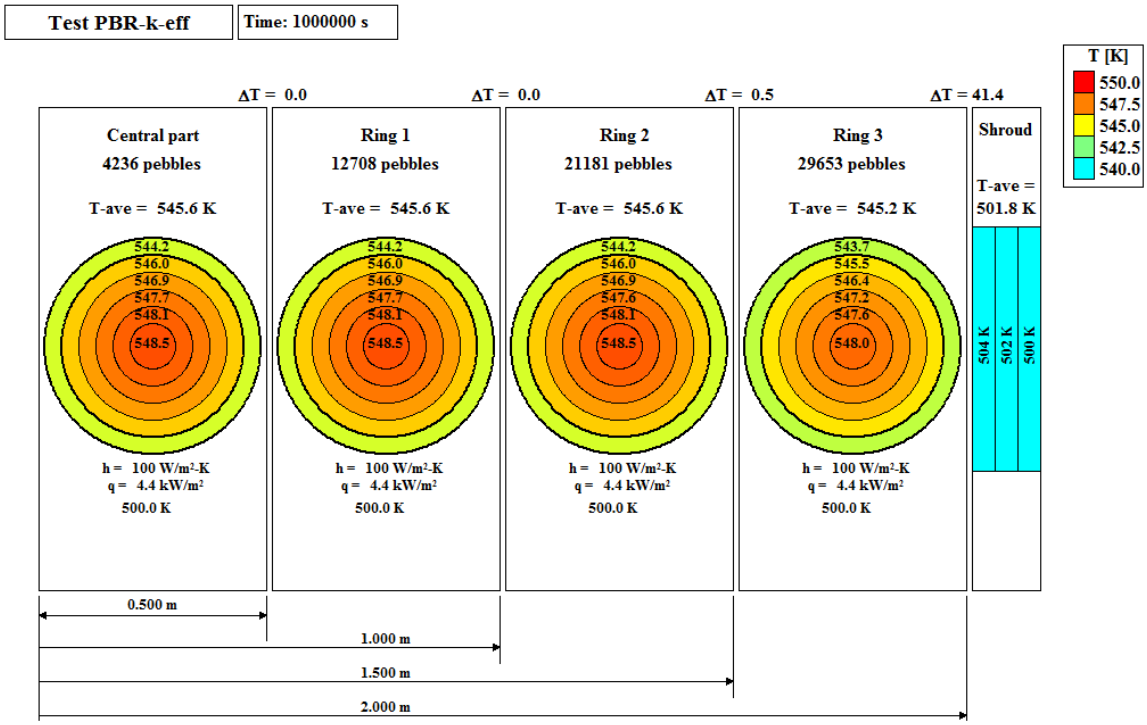

(B) forced cooling

Figure 3-209 Results of test PBR-k-eff

In case of reflector (shroud) the heat must be transferred to the inner cell, therefore L2AXSC must be equal to zero:

```
*       SC    i j   L-i    L-j    k       A1           A2       Mh  M1  M2 L1 L2
390400 1 500  6 1  0.250  0.000  902  9.36761E-03 9.36761E-03  1 902 000 0  0
```

However for the pebbles the user may select the uniform heating option. The input deck will be (input file \PBR-k-eff\PBR-k-eff-1.SPE):

```
*       SC    i j   L-i    L-j    k       A1           A2       Mh  M1  M2 L1 L2
390100 1 200  6 6  0.500  0.250  902  5.46463E-03 5.46463E-03  1 902 902 1  1
390200 1 300  6 6  0.250  0.250  902  6.55724E-03 6.55724E-03  1 902 902 1  1
390300 1 400  6 6  0.250  0.250  902  7.02571E-03 7.02571E-03  1 902 902 1  1
390400 1 500  6 1  0.250  0.000  902  9.36761E-03 9.36761E-03  1 902 000 1  0
```

The results are practically the same because the power temperature difference over a pebble is very small (power per pebble only 1.0 W). The effect of this option will be more visible in case of the prismatic block reactor, discussed in the next section.

Direct input of heat transfer area

The discussion above illustrated the input procedure for earlier versions of SPECTRA, where two area multipliers A1AXSC and A2AXSC had to be used to determine the heat transfer area. In the current SPECTRA version the user may define the area directly, using the input parameter AXAXSC. In such case the multipliers A1AXSC and A2AXSC are ignored by the code. For the current case the following input:

```
*       SC    i j   L-i    L-j    k     A1AXSC       A2AXSC     Mh  M1  M2 L1 L2
390100 1 200  6 6  0.500  0.250  902  5.46463E-03 5.46463E-03  1 902 902 0  0
390200 1 300  6 6  0.250  0.250  902  6.55724E-03 6.55724E-03  1 902 902 0  0
390300 1 400  6 6  0.250  0.250  902  7.02571E-03 7.02571E-03  1 902 902 0  0
390400 1 500  6 1  0.250  0.000  902  9.36761E-03 9.36761E-03  1 902 000 0  0
```

can be replaced by:

```
*       SC    i j   L-i    L-j    k     A1AXSC       A2AXSC     Mh  M1  M2 L1 L2  AXAXSC
390100 1 200  6 6  0.500  0.250  902  0.00000E-00 0.00000E-00  1 902 902 0  0   3.14159
390200 1 300  6 6  0.250  0.250  902  0.00000E-00 0.00000E-00  1 902 902 0  0   6.28319
390300 1 400  6 6  0.250  0.250  902  0.00000E-00 0.00000E-00  1 902 902 0  0   9.42478
390400 1 500  6 1  0.250  0.000  902  0.00000E-00 0.00000E-00  1 902 000 0  0  12.56637
```

Here the true heat transfer areas, shown in Table 3-28, are entered directly. The input files are located in `\Z-INPUTS\SC\AXIAL\PBR-k-eff\AXAXSC`. Comparison of output files from this directory with the outputs of the earlier analysed where A1AXSC and A2AXSC were used (present in `\Z-INPUTS\SC\AXIAL\PBR-k-eff`) showed practically no difference.

3.5.19.5 Prismatic Block Test, PMR-k-eff

This example shows how to build a model of a prismatic block reactor and provides a verification of the calculated temperature distribution using theoretical solution. The SPECTRA input files are located in: `\Z-INPUTS\SC\AXIAL\PMR-k-eff\`

A simple "prismatic block" is built. There are four rings of prismatic blocks, each has the size of 0.36 m. The number of blocks (identical solid heat conductors) in each ring is: 1 for the central Fuel Assembly, 6 in ring 1,18 in ring 2 and 24 in ring 3 (shown in Figure 3-211). Two cases are considered.

- No forced cooling. The generated heat must be removed radially to the reflector (shroud). This is achieved by using a tabulated heat transfer coefficient on the surface of blocks and setting it to zero. For this case the power was assumed to be 500.0 W per block.
- Forced cooling. For this case the power was assumed to be 10,000.0 W per block. The tabulated heat transfer coefficient on the surface of blocks was assumed to be equal to 100 W/m^2-K. The coolant is assumed to be flowing around the blocks and have a constant temperature of 500 K (= the shroud outer temperature). In reality cooling is present inside the blocks, which in this case is neglected. In a more advanced modeling this would be achieved by linking each cell of the block with an appropriate cooling channel, in a similar way as it was done in case of cooling channels passing through the reflector blocks, shown in section 3.5.19.3, Figure 3-206.

When modeling a prismatic block reactor (PMR), the user must first define an effective conductivity of the pebble bed. The effective conductivity may be calculated from Tanaka-Chisaka correlation [179]. The Tanaka and Chisaka expression for discontinuous and continuous solid systems is used to obtain the effective radial conductivity of the graphite blocks in the PMR, including the effects of the coolant channels and fuel compacts. The Tanaka-Chisaka expression is:

$$k_{eff} = k_s \cdot \left\{ A + (1-A) \cdot \frac{\ln[1 + 2 \cdot B \cdot (k_{por} / k_s - 1)]}{2 \cdot B \cdot (1 - k_s / k_{por})} \right\}$$

where: A = 2 (1 – ε) / (2 + ε)
B = (1 – ε) / 3
ε = porosity.
k_s = thermal conductivity of solid (continuous) material (W/m-K),
k_{por} = thermal conductivity of pores (discontinuous) material (W/m-K).

For the case of helium gas as the pore material, the pore conductivity, k_{por}, should be modified by adding an effective radiative conductivity to the helium gas conductivity: $k_{por} = k_{He} + k_{rad}$. The radiative conductivity can be written as:

$$k_{rad} = 4 \cdot \varepsilon_r \cdot \sigma \cdot T^3 \cdot D$$

where: k_{rad} = radiative conductivity (W/m-K),
ε_r = emissivity in pores (channels walls),
σ = Stefan-Boltzmann constant (W/m^2-K^4),
D = effective diameter of pores (m).

The effect of the discontinuous material on the continuous material appears in the Tanaka-Chisaka equation as an effective porosity, and only the volume ratios of discontinuous to continuous material are necessary to define an effective porosity. Hence, all that is required are the volume ratios of

features in the block. If the fuel compacts are assumed to have the same thermal conductivity as the graphite, then the ratio of the coolant channel volume to the volume of block + fuel channel defines the effective porosity in the block. The coolant conductivity, the conductivity of graphite, and the porosity define the effective block conductivity. The thermal resistance of the gaps between blocks is then added to come up with an effective radial conductivity. The effective radial block conductivity then can be expressed as :

$$k_{er} = \frac{1}{\frac{1}{h_{gap} \cdot D_{blk}} + \frac{1}{k_{blk}}}$$

where: k_{er} = Effective radial block conductivity (W/m-K),
h_{gap} = Gap heat transfer coefficient (W/m^2-K),
D_{blk} = Effective radial diameter of a block (m),
k_{blk} = Effective radial conductivity (=k_{eff} from the Tanaka-Chisaka model) (W/m-K).

Two versions were prepared. One with constant gap heat transfer coefficient, h_{gap} = 500 (W/m^2-K) and one with the gap heat transfer coefficient estimated using the same expression as the pore material.

$$h_{gap} = (k_{He} + 4 \cdot \varepsilon_r \cdot \sigma \cdot T^3 \cdot \delta_{gap}) / \delta_{gap}$$

Figure 3-210 shows the effective conductivity as a function of temperature for this case. More details are provided in: \PMR-k-eff\Effective-Conductivity.xlsx and \PMR-k-eff\Doc.

Next, the structures representing prismatic blocks must be linked using the direct contact model. For the considered example, the (preliminary) input deck is:

```
*       SC    i j   L-i    L-j    k    A1  A2 Mh  M1  M2 L1 L2
390100 1 200  5 5  0.189  0.189  902  0.0 0.0  1 902 902 0  0
390200 1 300  5 5  0.189  0.189  902  0.0 0.0  1 902 902 0  0
390300 1 400  5 5  0.189  0.189  902  0.0 0.0  1 902 902 0  0
390400 1 500  5 1  0.189  0.000  902  0.0 0.0  1 902 000 0  0
```

The conduction lengths are taken as center-to-center of the blocks, assuming an effective radius (blocks are represented by cylindrical solid heat conductors with the same cross section area as the area of hexagons). For the reflector, the conduction length is zero. The material defining the effective conductivity is MP-902. For the sake of easy verification of the calculated results the conductivity was here set to a constant value of 10 W/m-K and not the values obtained from the correlation (Figure 3-210).

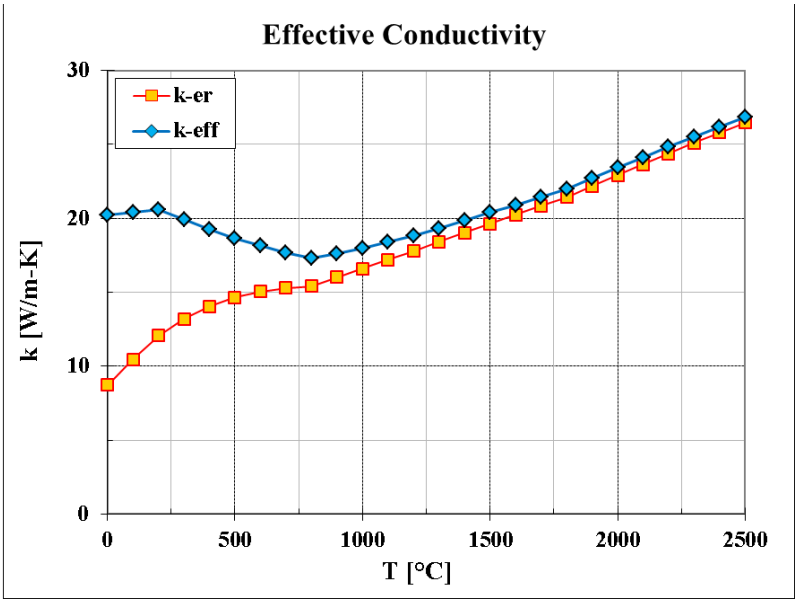

Figure 3-210 Effective conductivity - Tanaka-Chisaka correlation

Next, the area of heat transfer must be set. The default values, calculated by the code, are printed in the output file. For example, in case of transfer from SC-100 to SC-200 the output is:

```
Heat transfer area, all cells :   A = 1.18752E+00 [m2]
Total, including multiplicity :   A = 7.12513E+00 [m2]
Individual cells
SC-100  0005  TO  SC-200  0005:   A = 1.18752E+00 [m2]
```

The actual value is obtained as $2\pi RH = 2\pi \times 0.375 \times 1.0 = 1.187522023$ m^2. The required multiplier is 1.66667E-01. All values and multipliers were calculated in \PMR-k-eff\PMR-k-eff.xlsx and are shown in Table 3-30. The final input deck is therefore:

```
*       SC    i j   L-i    L-j    k       A1          A2       Mh  M1  M2 L1 L2
390100 1 200  5 5  0.189  0.189  902  1.66667E-01 1.66667E-01  1 902 902 0  0
390200 1 300  5 5  0.189  0.189  902  1.66667E-01 1.66667E-01  1 902 902 0  0
390300 1 400  5 5  0.189  0.189  902  2.08334E-01 2.08334E-01  1 902 902 0  0
390400 1 500  5 1  0.189  0.000  902  2.91667E-01 2.91667E-01  1 902 000 0  0
```

Finally, the area printed in the output file needs to be checked. The values printed in case of transfer from SC-100 to SC-200 are:

```
Heat transfer area, all cells :   A = 1.97921E-01 [m2]
Total, including multiplicity :   A = 1.18752E+00 [m2]
Individual cells
SC-100  0005  TO  SC-200  0005:   A = 1.97921E-01 [m2]
```

This shows that the total area is correct. Calculations were performed until stationary state was reached. Results obtained for the first case (only radial transfer) are shown in Figure 3-211 (A). Figure shows temperatures and ring-to-ring temperature differences. In order to check the results, the temperature differences were calculated in \PMR-k-eff\PMR-k-eff.xlsx. The values are shown in Table 3-31. The agreement between the SPECTRA stationary-state values (Figure 3-211 A) and the theoretical values of ΔT, calculated in Excel (Table 3-31), is very good. Some small differences re explained below.

Table 3-30 Direct contact input - area multipliers (file: PMR-k-eff.xlsx)

	TRUE	SPECTRA (tot.)	Multiplier
0->1	1.187522023	7.12513E+00	1.66667E-01
1->2	3.562566069	2.13754E+01	1.66667E-01
2->3	5.937610115	2.85005E+01	2.08334E-01
3->4	8.312654161	2.85005E+01	2.91667E-01

Table 3-31 Theoretical temperature differences (file: PMR-k-eff.xlsx)

Q	dx-1	dx-2	ΔT
500	0.189	0.189	15.9
3500	0.189	0.189	37.1
12500	0.189	0.189	79.6
24500	0.189	0	55.7

Figure 3-211 (B) shows the results obtained for the second case (forced cooling). In this case most of the heat is transferred from the block surface to the "coolant" (here replaced by suitable Tabular Functions). Only minor part is transfer radially. The ring-to-ring temperature differences are very small.

Finally one needs to keep in mind that one of two available options must be selected by the user:

- The transferred heat is added (subtracted) to (from) the cell specified by the user (L1AXSC=0, L2AXSC=0)
- The transferred heat is uniformly distributed over all cells (L1AXSC=1, L2AXSC=1)

In case of reflector (shroud) the heat must be transferred to the inner cell, therefore L2AXSC must be equal to zero:

```
*       SC    i j   L-i    L-j    k       A1          A2       Mh  M1  M2 L1 L2
390400 1 500  5 1  0.189  0.000  902  2.91667E-01 2.91667E-01  1 902 000 0  0
```

However for the blocls the user may select the uniform heating option. The input deck will be (input file \PMR-k-eff\PMR-k-eff-1.SPE):

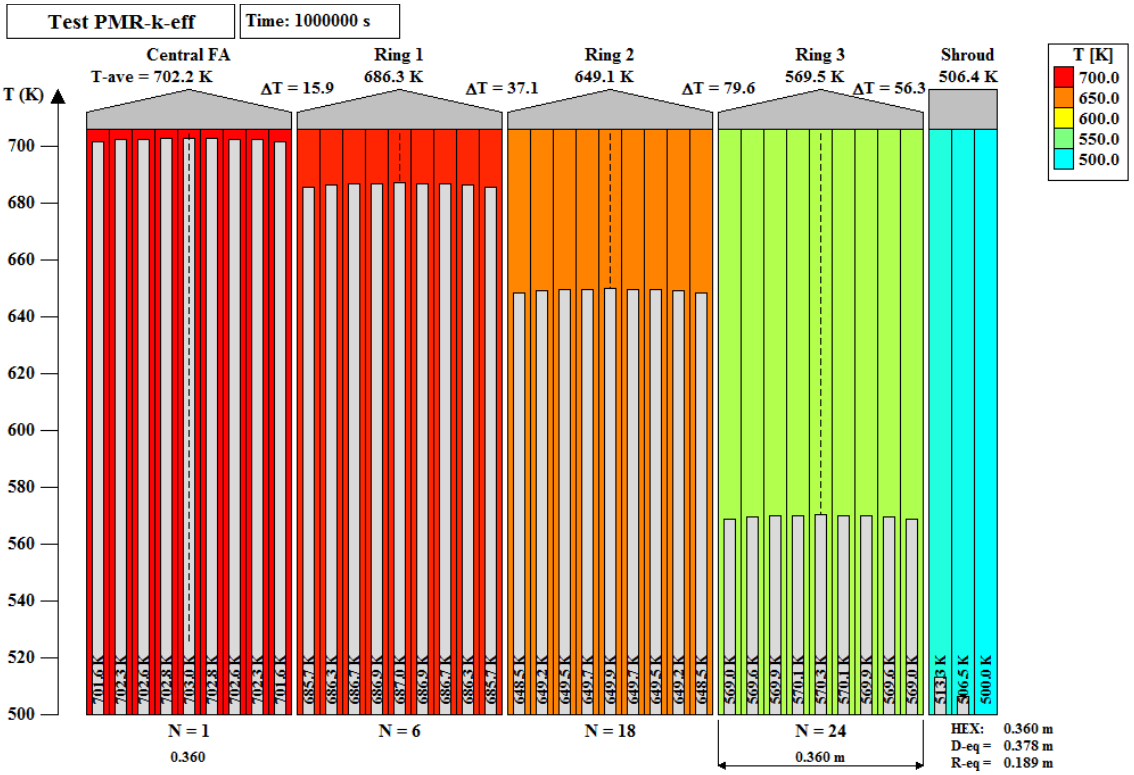

(A) no forced cooling - radial heat transfer only (option 0)

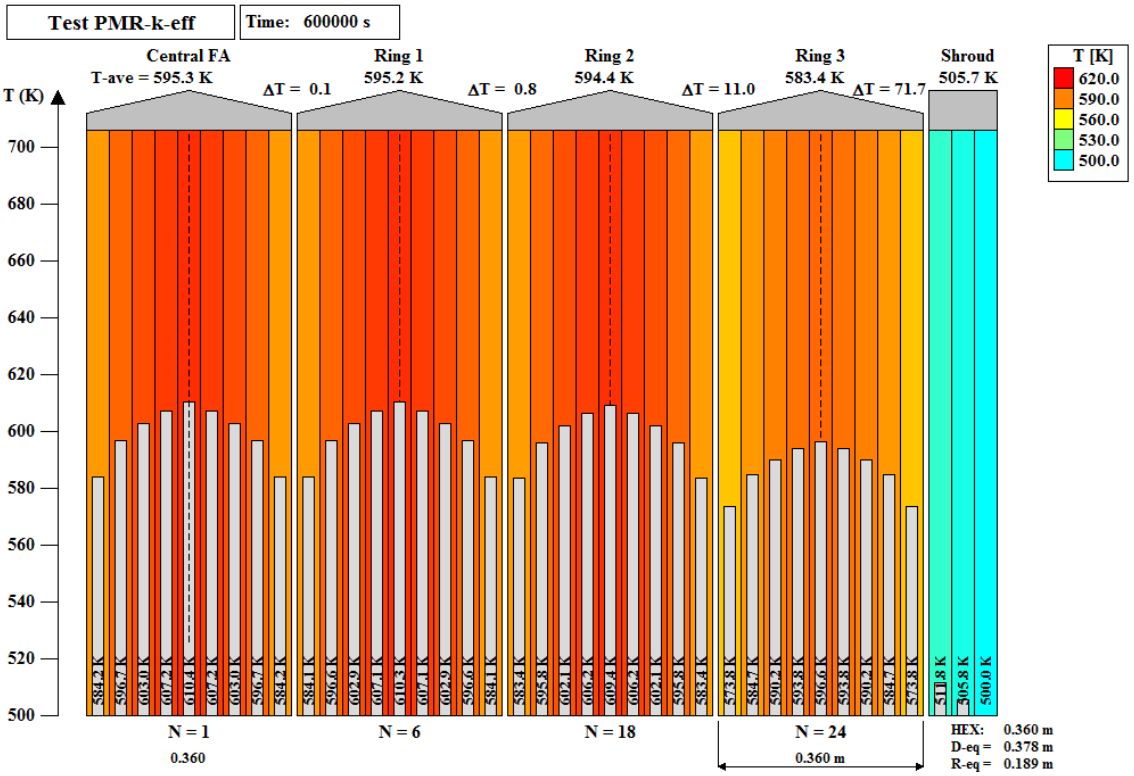

(B) forced cooling

Figure 3-211 Results of test PMR-k-eff

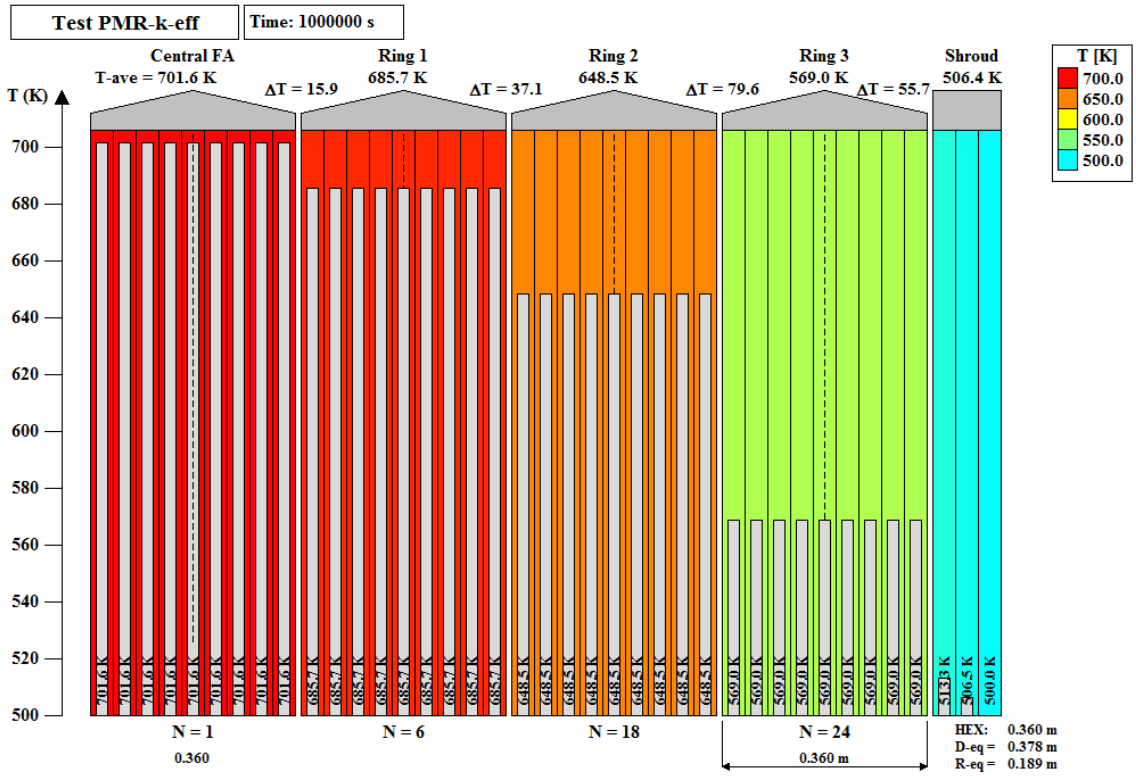

(A) no forced cooling, option 1

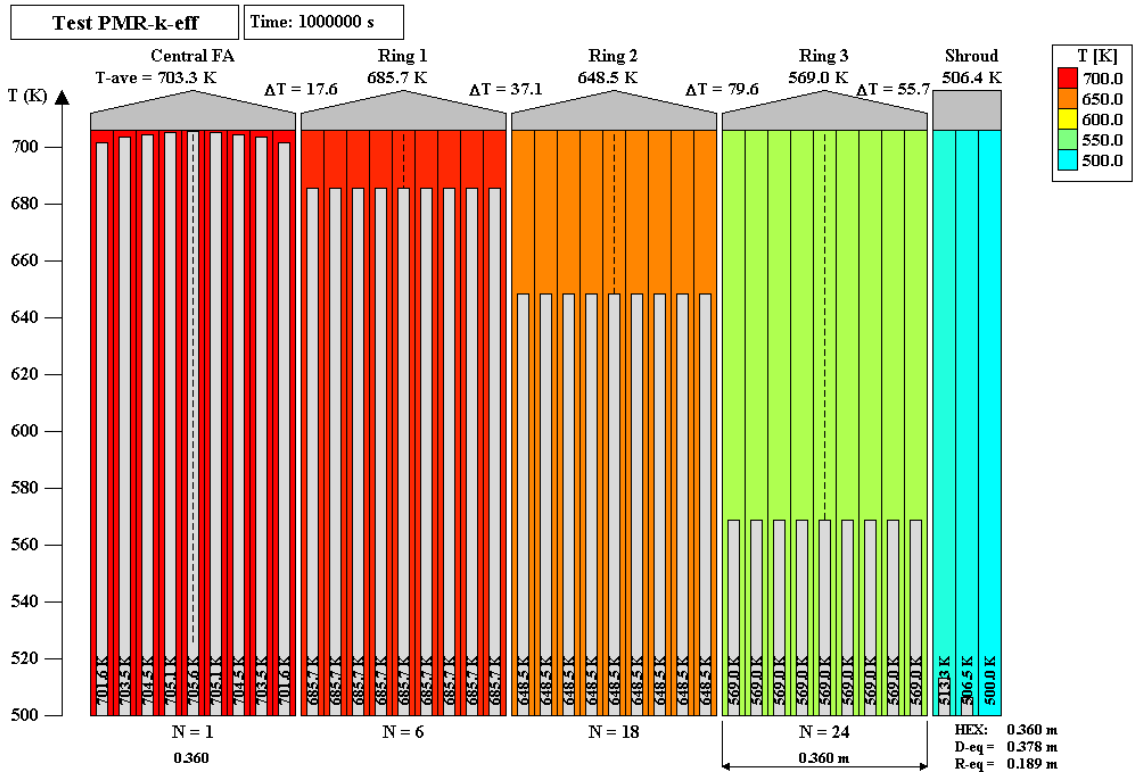

(B) no forced cooling, option 0 in central ring, 1 in other rings

Figure 3-212 Results of test PMR-k-eff

```
*       SC    i j   L-i    L-j    k       A1          A2       Mh  M1   M2 L1 L2
390100 1 200   5 5  0.189  0.189  902  1.66667E-01 1.66667E-01  1 902 902 1  1
390200 1 300   5 5  0.189  0.189  902  1.66667E-01 1.66667E-01  1 902 902 1  1
390300 1 400   5 5  0.189  0.189  902  2.08334E-01 2.08334E-01  1 902 902 1  1
390400 1 500   5 1  0.189  0.000  902  2.91667E-01 2.91667E-01  1 902 000 1  0
```

Results are shown in Figure 3-212 (A). The temperature distribution inside blocks is flat as the heat is uniformly added to / removed from all the cells, in contrast to the previous case, Figure 3-211 (A), where the heat is added to / removed from the outer cells. The agreement between the calculated values (Figure 3-212 A) and the theoretical values of ΔT, calculated in excel (Table 3-31), is excelent for this case. This shows that the small difference observed in Figure 3-211 (A) was caused by the non-uniform temperature distribution inside the blocks. This option is more realistic for the blocks other than the central block, where the heat is indeed lost from the outer surface of the block represented by SC-100. Therefore the most realistic modeling of the blocks is:

```
*       SC    i j   L-i    L-j    k       A1          A2       Mh  M1   M2 L1 L2
390100 1 200   5 5  0.189  0.189  902  1.66667E-01 1.66667E-01  1 902 902 0  1
390200 1 300   5 5  0.189  0.189  902  1.66667E-01 1.66667E-01  1 902 902 1  1
390300 1 400   5 5  0.189  0.189  902  2.08334E-01 2.08334E-01  1 902 902 1  1
390400 1 500   5 1  0.189  0.000  902  2.91667E-01 2.91667E-01  1 902 000 1  0
```

Results of this case are shown in Figure 3-212 (B). The temperature distribution is flat, except for the central FA. In order to obtain correct temperature difference between the center and the surface of the central FA, the material for this FA was set to MP-902. Strictly speaking, this material should be the pure Tanaka-Chisaka correlation without the effect of gap (blue line in Figure 3-210), since there is no gap between the center and the surface of the central FA. In this case a constant effective conductivity of 10 is used.

Direct input of heat transfer area

The discussion above illustrated the input procedure for earlier versions of SPECTRA, where two area multipliers A1AXSC and A2AXSC had to be used to determine the heat transfer area. In the current SPECTRA version the user may define the area directly, using the input parameter AXAXSC. In such case the multipliers A1AXSC and A2AXSC are ignored by the code. For the current case the following input:

```
*       SC    i j   L-i    L-j    k     A1AXSC      A2AXSC    Mh  M1   M2 L1 L2
390100 1 200   5 5  0.189  0.189  902  1.66667E-01 1.66667E-01  1 902 902 0  0
390200 1 300   5 5  0.189  0.189  902  1.66667E-01 1.66667E-01  1 902 902 0  0
390300 1 400   5 5  0.189  0.189  902  2.08334E-01 2.08334E-01  1 902 902 0  0
390400 1 500   5 1  0.189  0.000  902  2.91667E-01 2.91667E-01  1 902 000 0  0
```

can be replaced by:

```
*       SC    i j   L-i    L-j    k     A1AXSC      A2AXSC    Mh  M1   M2 L1 L2  AXAXSC
390100 1 200   5 5  0.189  0.189  902  0.00000E-00 0.00000E-00  1 902 902 0  0  1.187522023
390200 1 300   5 5  0.189  0.189  902  0.00000E-00 0.00000E-00  1 902 902 0  0  3.562566069
390300 1 400   5 5  0.189  0.189  902  0.00000E-00 0.00000E-00  1 902 902 0  0  5.937610115
390400 1 500   5 1  0.189  0.000  902  0.00000E-00 0.00000E-00  1 902 000 0  0  8.312654161
```

Here the true heat transfer areas, shown in Table 3-30, are entered directly. The input files are located in `\Z-INPUTS\SC\AXIAL\PMR-k-eff\AXAXSC`. Comparison of output files from this directory with the outputs of the earlier analysed where A1AXSC and A2AXSC were used (present in `\Z-INPUTS\SC\AXIAL\PMR-k-eff`) showed practically no difference.

3.5.20 Pebble Bed Effective Conductivity- HTTU Tests

3.5.20.1 HTTU Test Facility and Test Description

This section provides a verification of the pebble bed model based on the data from the HTTU test facility. The HTTU test facility and test results are provided in [200]. The HTTU test facility is shown in Figure 3-213, Figure 3-214, Figure 3-215. The test section consisted of approximately 25,000 machined graphite spheres containing no nuclear fuel, with an outer diameter of 60 mm. The spheres were randomly packed within an annular core configuration bounded by inner and outer graphite reflectors. The diameter of the inner reflector was 600 mm and of the outer reflector 2300 mm, while the height of the bed was 1200 mm.

The inner reflector contained a set of heater elements/electrodes while the outer reflector was enclosed within a water-cooled jacket. This means that a temperature gradient could be imposed in the radial direction through the bed while the heat transfer rate was measured and energy balances could be ascertained. In an effort to limit the heat transfer in the axial direction, the bed was well-insulated at the top and bottom ends.

The darker colored spheres in Figure 3-215 indicate the approximate position of spheres that were fitted with thermocouples in order to measure the temperature distributions through the bed at different levels.

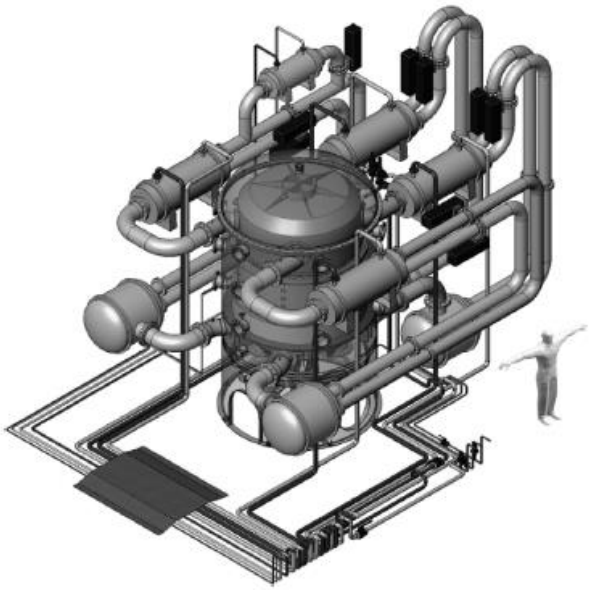

Figure 3-213 HTTU test facility [200]

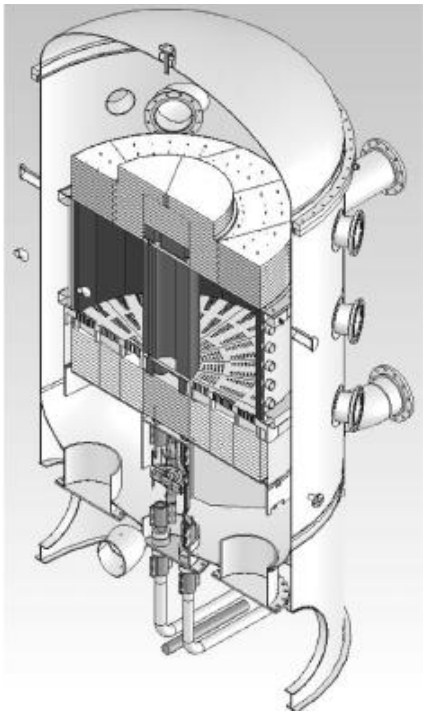

Figure 3-214 Cross section of HTTU [200]

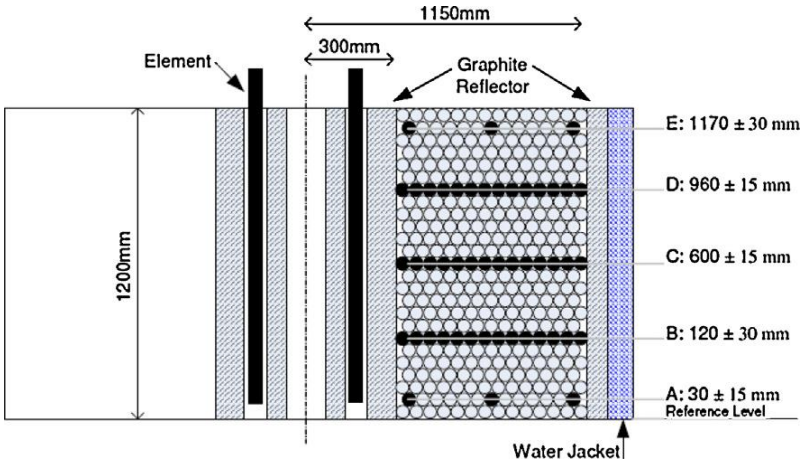

Figure 3-215 HTTU test section [200]

The so-called near-vacuum tests were conducted with the inside of the vessel filled with nitrogen gas at an absolute pressure of 10 kPa. This pressure was determined via simulation as the level at which the effects of natural convection are negligible. For the first set of tests the surface temperature of the inner reflector was maintained at approximately 1200°C and the inlet and outlet water temperatures of the water jacket at 25°C and 35°C respectively. In this case the power input to the electrodes was roughly 82 kW [200].

For the second set of tests the surface temperature of the inner reflector was maintained at approximately 600°C, with the same inlet and outlet water temperatures of the water jacket as previously. The power input to the electrodes was roughly 20 kW [200].

3.5.20.2 Model

The nodalization of the SPECTRA model of HTTU is shown in Figure 3-216. The pebble bed model consists of 10 rings and 10 axial sections. Four reflectors (inner, outer, lower, and upper) are included in the model. The heat source is present in the inner reflector. The cooling at the water jacket is modeled using appropriate boundary conditions. The heat losses in the lower and the upper reflectors are taken into account.

A constant pressure (10^4 Pa) is kept at CV-100 that is connected to the pebble gas volumes by JN-110, as shown in Figure 3-216. For clarity, the JN numbers are not shown in the nodalization diagram.

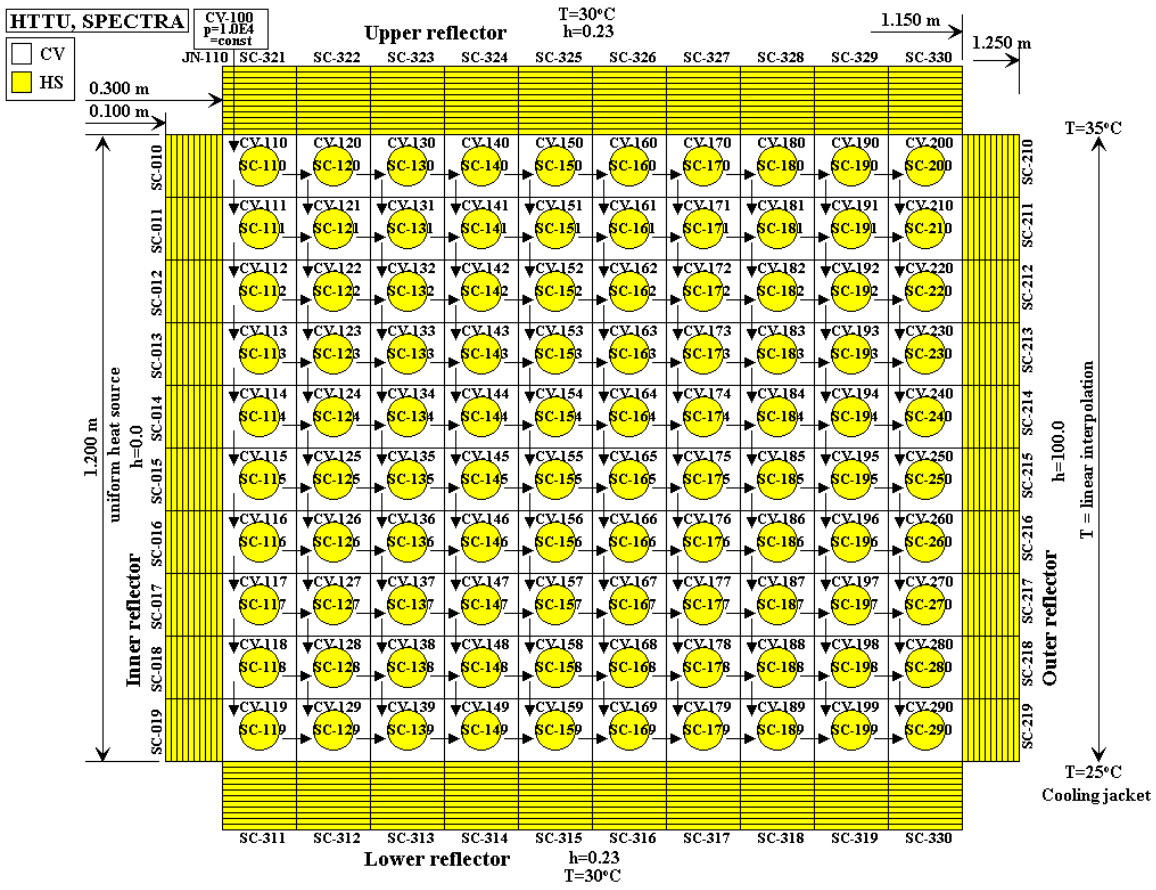

Figure 3-216 Nodalization of HTTU

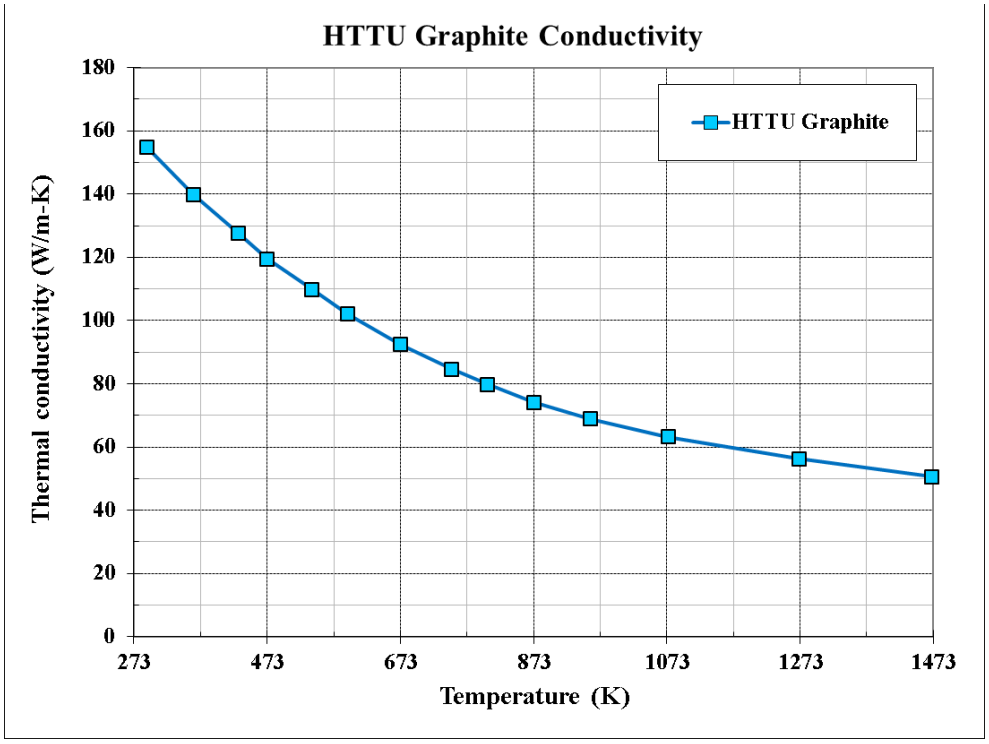

Figure 3-217 Thermal conductivity of HTTU graphite

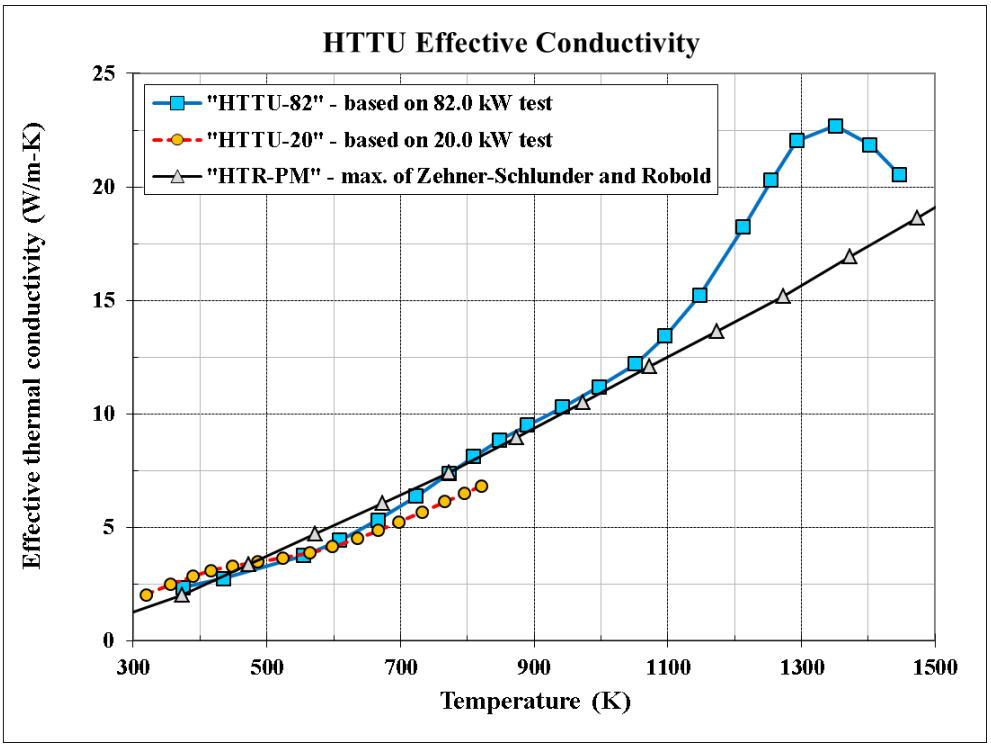

Figure 3-218 Effective conductivity of HTTU

The boundary conditions at the water jacket are assumed as follows. The local fluid temperatures were obtained by linear interpolation between the inlet and outlet temperatures, obtained from the source data (25°C and 35°C respectively). The heat transfer coefficient on the outer surface of the outer reflector was assumed as 100 W/m^2-K (the value was selected based on the measured outer reflector temperature data).

The heat transfer coefficients and the lower and upper reflector were modeled using a constant temperature and heat transfer coefficient of 0.23 W/m^2-K - Figure 3-216. The value was obtained in a trial and error to get a good agreement with the source data [200]:

- 82 kW: 1.07 kW total heat loss
- 20 kW: 0.36 kW total heat loss

The measured electrical power source was equal to 82.77 kW for the 82 kW test and 20.03 kW for the 20 kW test. However, the heat input to the pebble bed was lower due to heat removed via the stem coolers. The net heat input was 66.4 kW for the 82 kW test and 12.22 kW for the 20 kW test. These values were applied as a heat source for the inner reflector.

The number of pebbles in each node was calculated using the pebble bed porosity factor of 0.39. The values are shown below.

	Pebble multiplicity per node										
Ring	1	2	3	4	5	6	7	8	9	10	Total
No.	118	148	177	207	236	265	295	324	353	383	2506

Total number of pebbles for 10 identical axial levels is equal to: 2505×10 = 25,060. The source data gives the value of approximately 25,000; the agreement is very good.

Thermal conductivity of the graphite was digitized from figure 26 of [200]. The obtained thermal conductivity values are shown in Figure 3-217.

The effective conductivity of the pebble bed was modeled using the structure-to-structure direct heat transfer model, discussed in section 3.5.19.4. The effective conductivity was defined as MP-903. The effective conductivity was digitized from figures 22 and 24 of [200]. The values are shown in Figure 3-218. Reference [200] show values obtained based on the results of the 82 kW test and the 20 kW test. The results obtained in two experiments are somewhat different. The authors of [200] propose the following explanation of this fact.

"*In the 82 kW tests the temperature gradient is approximately −1400°C/m while for the 20 kW tests it is approximately −630°C/m. At the steeper temperature gradient the effective conductivity is higher. The authors believe that the difference in the effective conductivity can indeed be attributed to the difference in the macro temperature gradient. This obviously also implies that in general the effective thermal conductivity is not only a function of the temperature, but also of the macro temperature gradient at the point of interest. This deviates from conventional wisdom since none of the existing models for effective thermal conductivity addresses the macro temperature gradient.*"

The influence of temperature gradient on the effective conductivity is an interesting observation, but currently cannot be incorporated in the calculations (the effective conductivity is a function of temperature only). For the current analysis the curve obtained based on the 82 kW test was used. The curve was digitized and tabulated as MP-903. Those results are marked as "**HTTU-82**". Additionally, calculations were performed using the correlations of Zehner-Schlunder and Robold, which were applied in SPECTRA analyses of the HTR-PM reactor [178]. Those results are marked as "**HTR-PM**". The effective conductivity obtained from the Zehner-Schlunder and Robold correlations is shown in Figure 3-218. The values are somewhat lower than "HTTU-82". It has to be remembered that the "HTR-PM" values were obtained for the fuel pebbles, containing TRISO particles, while in HTTU pure graphite was used.

In each case, the structure-to-structure heat transfer model with an appropriate effective conductivity correlation ("HTTU-82" or "HTR-PM"), was activated for both horizontal and vertical directions. The convection on the reflector inner surfaces was disabled because this heat transfer is already taken into account in the effective conductivity correlation.

Calculations were performed in each case until stationary conditions were reached in the system. In order to accelerate the approach to steady state, the option to reduce heat capacity of solid material (CREDSL) was used. The heat capacity of all solid materials in the model was reduced by a factor of 1000 (CREDSL=0.001). With this value, the temperatures were practically constant (within 0.1 K) after approximately 1000 s. The total run time was selected as twice that, 2000 s. The SPECTRA input files are located in: `\Z-INPUTS\SC\AXIAL\HTTU\`.

3.5.20.3 Results

The results are shown in Figure 3-219 through Figure 3-222. Figure 3-219 and Figure 3-220 show the visualization pictures of the results obtained for the 82 kW and the 20 kW tests respectively. It may be seen that the heat losses through the lower and upper reflector match well the test data:

- 82 kW: 0.52 + 0.52 = 1.04 kW total
- 20 kW: 0.19 + 0.18 = 0.37 kW total

Figure 3-221 and Figure 3-222 show the temperatures in the middle level. There is a good agreement between the measured and calculated values for both 82 kW and 20 kW tests. The difference between the "HTR-PM" and the "HTTU-82" correlations is rather small, except for the high temperature region ($T \approx 1200$°C), where HTR-PM gives temperatures higher by about 70°C.

It can be observed that temperature gradient near the outer surfaces is larger in experimental data compared to the SPECTRA-calculated values. In SPECTRA, the effective conductivity correlation is used that was developed based on average (bulk) pebble bed porosity. In reality, porosity near walls is generally larger than the bulk porosity, which reduces local effective thermal conductivity. It is concluded that the results may be improved by using different effective conductivity near walls. Calculation of the effective conductivity near the walls would require knowledge of the porosity in this region.

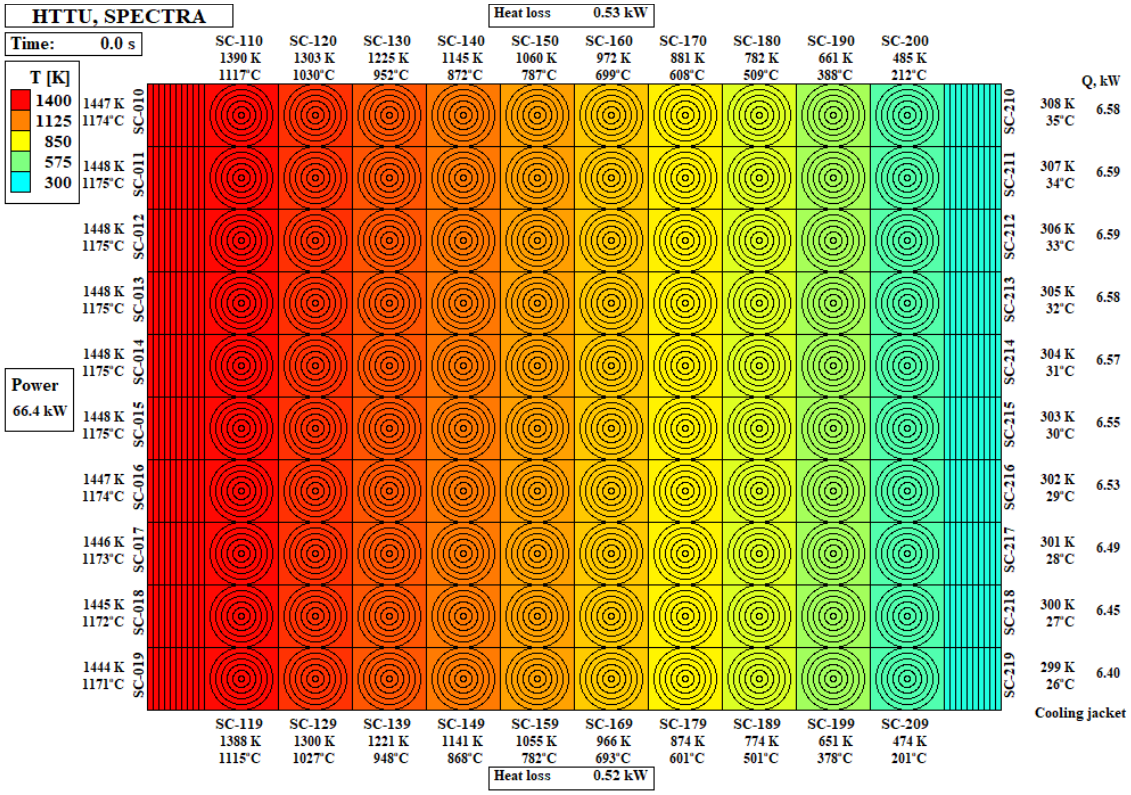

Figure 3-219 Results, 82 kW test, “HTTU-82” correlation

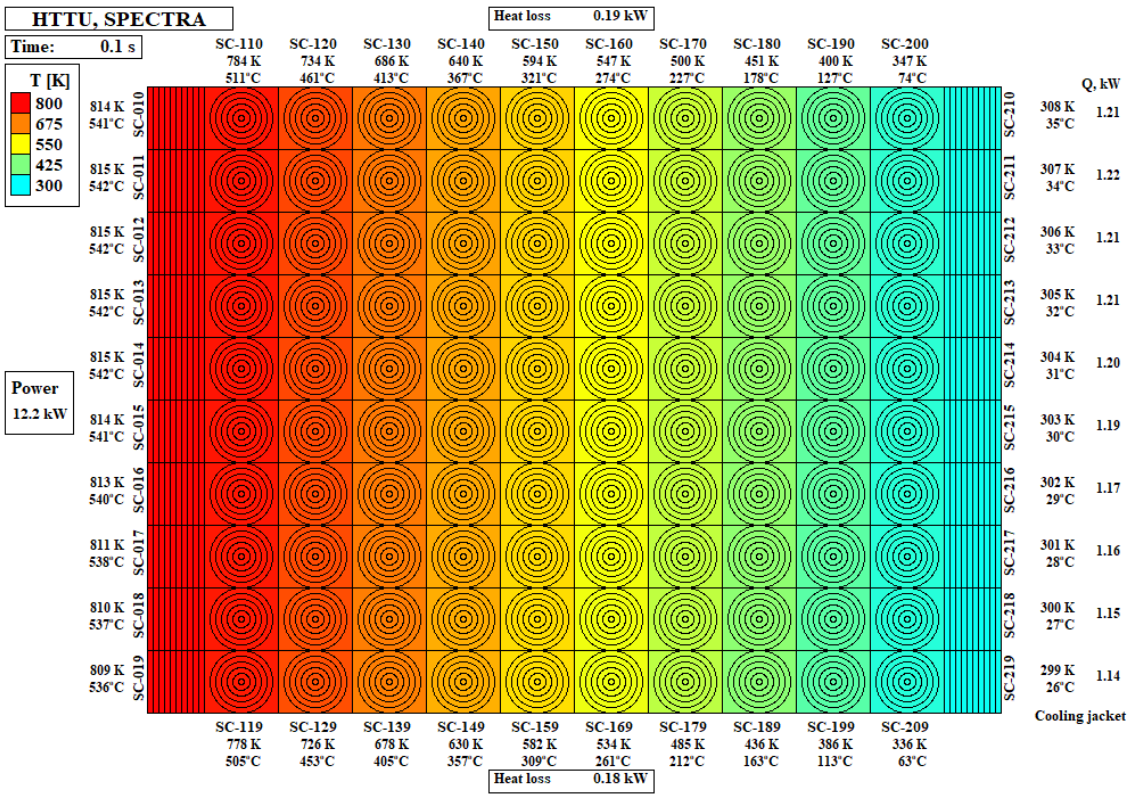

Figure 3-220 Results, 20 kW test, “HTTU-82” correlation

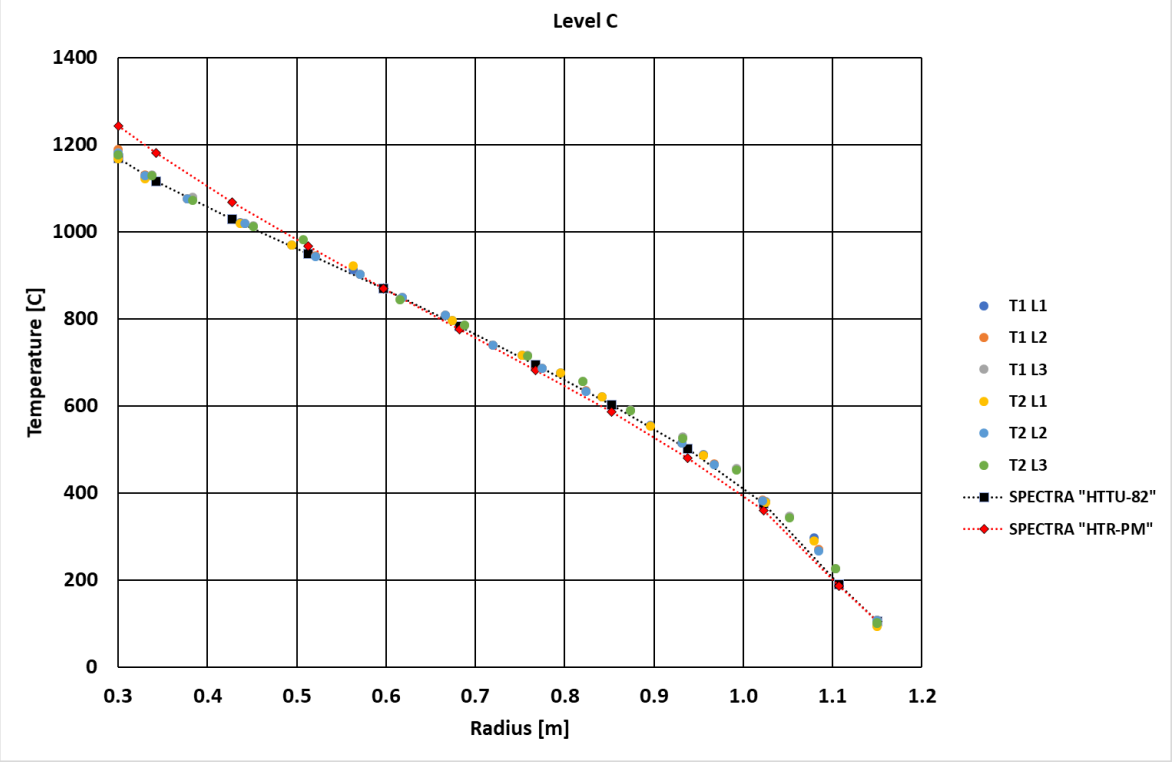

Figure 3-221 HTTU calculated versus measured temperatures, 82 kW test 10-node model

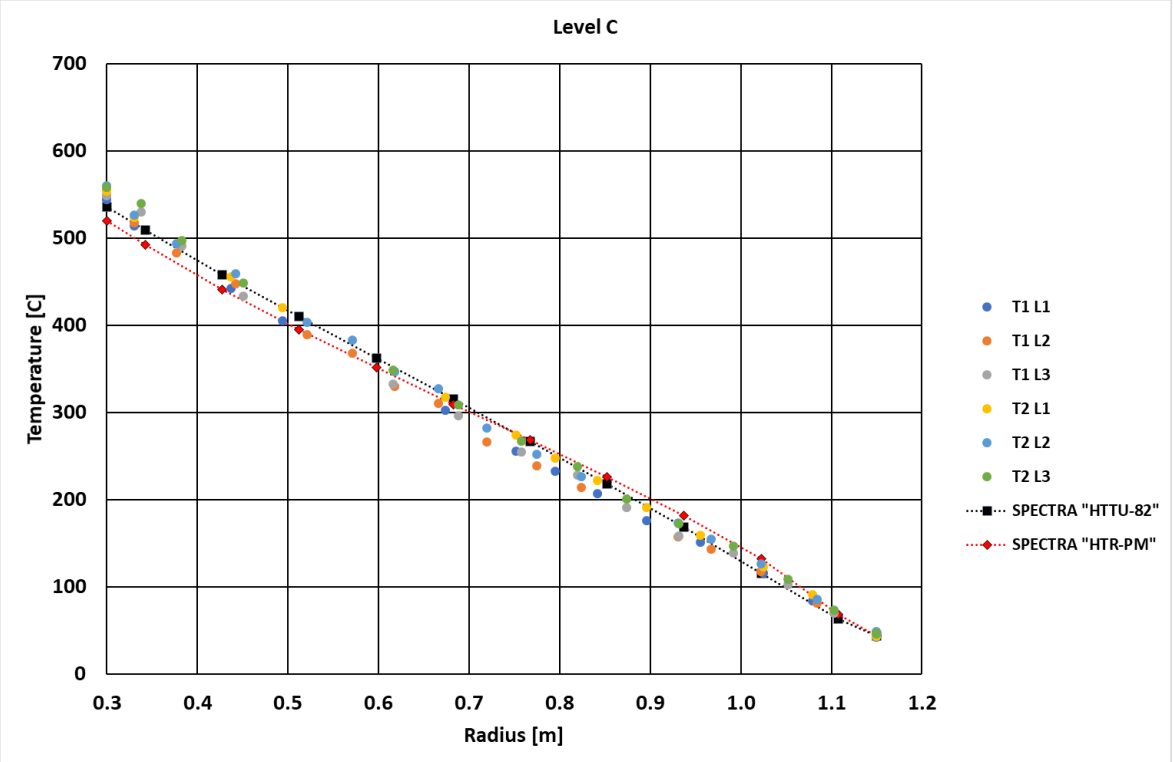

Figure 3-222 HTTU calculated versus measured temperatures, 20 kW test 10-node model

Next, nodalization sensitivity was checked. A coarse nodalization was used, with 5 radial rings representing the pebble bed (the axial nodalization was kept the same). The nodalization scheme is shown in Figure 3-223. The numbers of pebbles in each ring are shown below.

	Pebble multiplicity per node					
Ring	1	2	3	4	5	Total
No.	266	384	501	619	736	2506

Figure 3-224 and Figure 3-225 show the temperatures in the middle level. It is seen that the agreement is still good. The difference in the regions near the wall is more visible. The maximum temperatures are however practically the same in the 5-node model as in the 10-node model.

	Maximum temperature ("HTTU-82")	
	82 kW test	20 kW test
10-node	1168°C	535°C
5-node	1169°C	528°C
Difference	1°C	7°C

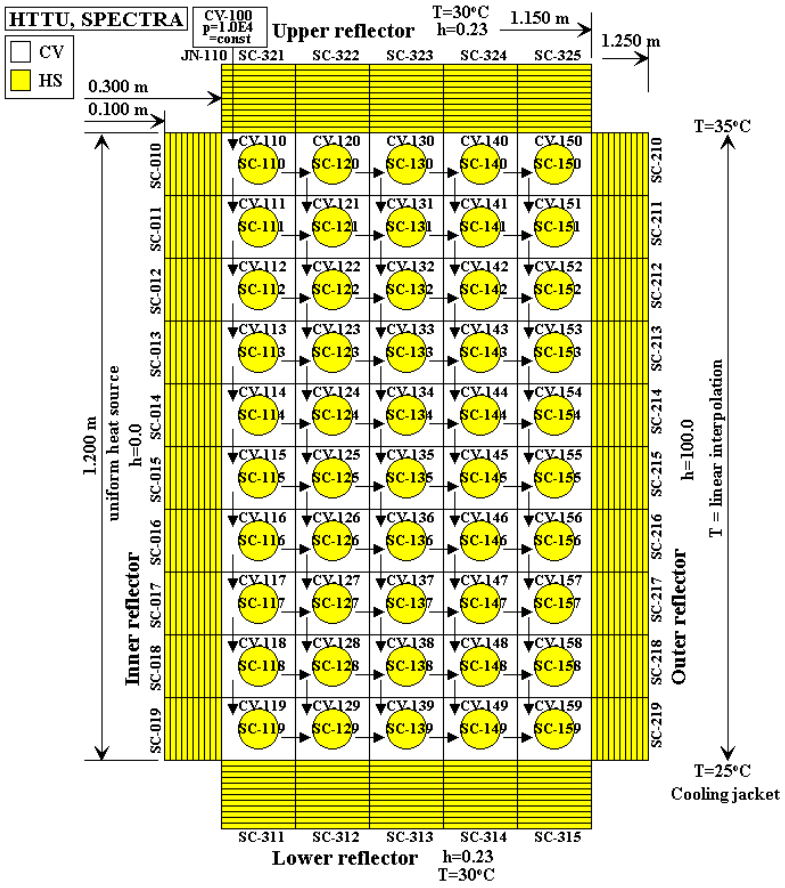

Figure 3-223 HTTU nodalization for the 5-node pebble model

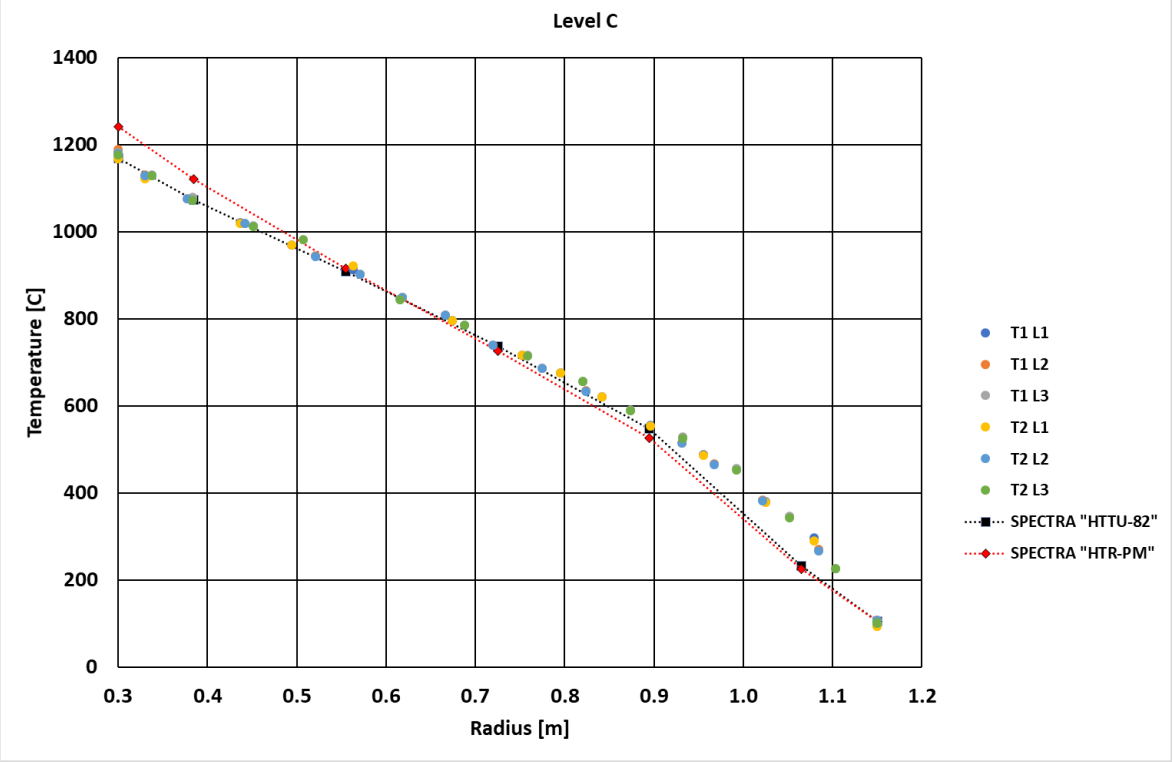

Figure 3-224 HTTU calculated versus measured temperatures, 82 kW test 5-node model

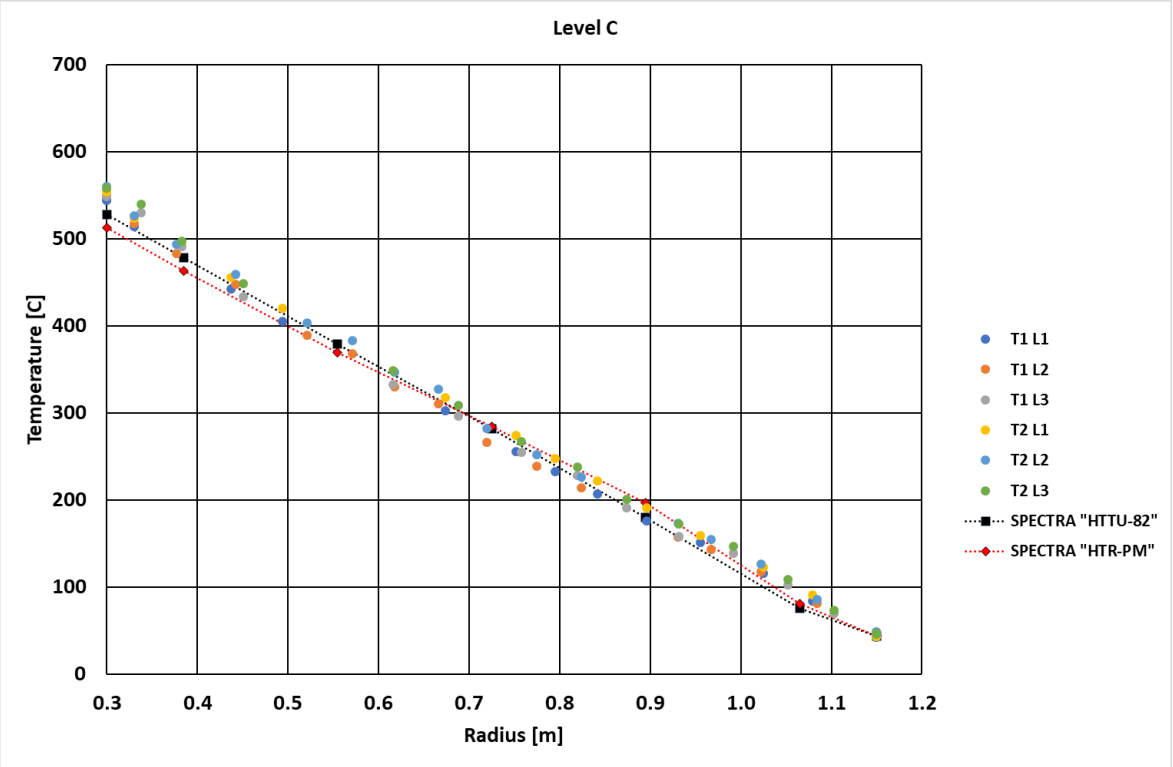

Figure 3-225 HTTU calculated versus measured temperatures, 20 kW test 5-node model

3.5.20.4 Conclusions

The main conclusions from the analysis of the HTTU experiments are as follows.

- A good agreement was obtained, using both “HTTU-82” and “HTR-PM” correlations for the effective conductivity.
- The calculated results may be improved by using different effective conductivity near walls. Calculation of the effective conductivity near the walls would require knowledge of the porosity in this region.

3.5.21 Solid Heat Conductors with Size Change during Transient

This section presents examples and numerical verification of the model of a SC with size change. When the model is applied, the size (both left and right surface area) of a SC may be controlled by a Tabular or a Control Function. The function defines a fraction of the nominal surface area that is available for heat transfer. The value obtained from the Tabular or Control Function is internally limited to the range between 10^{-3} and 1.0. The model may be applied in the following situations:

- SC surfaces are convecting heat,
- simple radiation-model between the surface and gas is used,
- structure-to-structure radiation model is used.

The model cannot be used if the SC is a member of the detailed radiation model network, because the radiation view factors do not change in time. Test cases and numerical verification are presented below. A very simple test, described below, was set up for verification of the SC size change model.

- The test consists of the "hot" SC (with internal heat source: Q = 20,000 W) and the "cold" SC, cooled on the outer side.

- Each test consists of three cases:
  - First reference case, with the surface area of both hot and cold SC equal to 1.0 m^2, to match the starting situation of the tested case.
  - Tested case, with one of the surfaces (hot or cold) changed from 1.0 m^2 to 0.5 m^2 during the calculations. In each case the area is controlled by the Tabular Function TF-900.
  - Second reference case, with the surface of one SC is equal to 1.0 m^2, and other SC is equal to 0.5 m^2, to match the final situation of the tested case.

- Each of the possible situation is tested, i.e.:
  - convection to gas - a constant heat transfer coefficient of h = 1000 W/m^2-K is assumed for simplicity,
  - radiation to gas - wall emissivity of ε_w = 0.90 was used; at the same time convection was eliminated by setting: h = 0.0 W/m^2-K,
  - wall-to-wall radiation - wall emissivities of ε_w = 0.90 were used; at the same time convection was eliminated by setting: h = 0.0 W/m^2-K.

The cases where the size of the cold SC is varied are shown in section 3.5.21.1. The cases where the size of the hot SC is varied are shown in section 3.5.21.2. The input files for these tests are stored in `\Z-INPUTS\SC\SC-Area-Change`

3.5.21.1 Size Change of the "Cold" Structure

Results are shown in Figure 3-226 through Figure 3-230. Figure 3-226, Figure 3-227, and Figure 3-228 show results of the case with convection on the surfaces. Figure 3-229 shows the case with radiation to gas. Figure 3-230 shows the case with wall-to-wall radiation. The input file for these tests is stored in `\Z-INPUTS\SC\SC-Area-Change\AREA-cold.SPE`

- **Convection**

Figure 3-226 shows the time dependent values of the surface area of the cold SC-012 and the temperature of the hot SC-011. When the surface area of the cold SC-012 changes from 1.0 to 0.5, the temperature of the hot SC-011 increases from 416 K to 436 K. The temperature increases because the area of the cooling surface decreases.

Figure 3-227 shows the values obtained at t = 1000 s (stable situation at SC-012 area of 1.0 m^2) while Figure 3-228 shows the values obtained at t = 2000 s (stable situation at SC-012 area of 0.5 m^2). It is seen that the values obtained at t = 1000 s are identical to those obtained in the "left" reference case, while the values obtained at t = 2000 s are identical to those obtained in the "right" reference case. Consistency of the obtained values is checked by hand calculations. The convective heat transfer is given by (see Volume 1):

$$Q_c = A \cdot q_c = A \cdot h \cdot \left(T_w - T_g\right)$$

or:

$$\frac{q_c}{h} = \frac{Q_c}{A \cdot h} = \left(T_w - T_g\right)$$

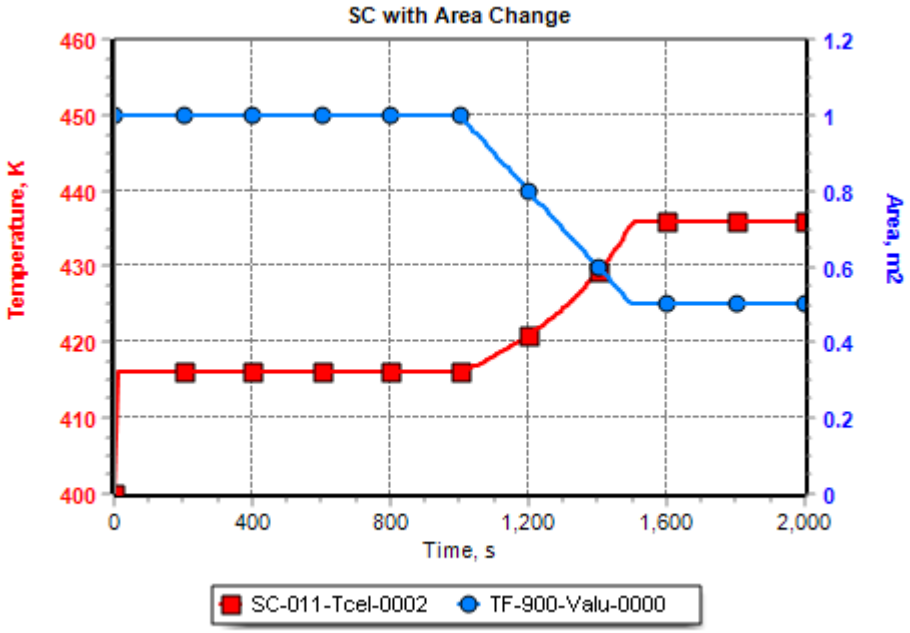

Figure 3-226 "Cold" SC with area change - convection to gas

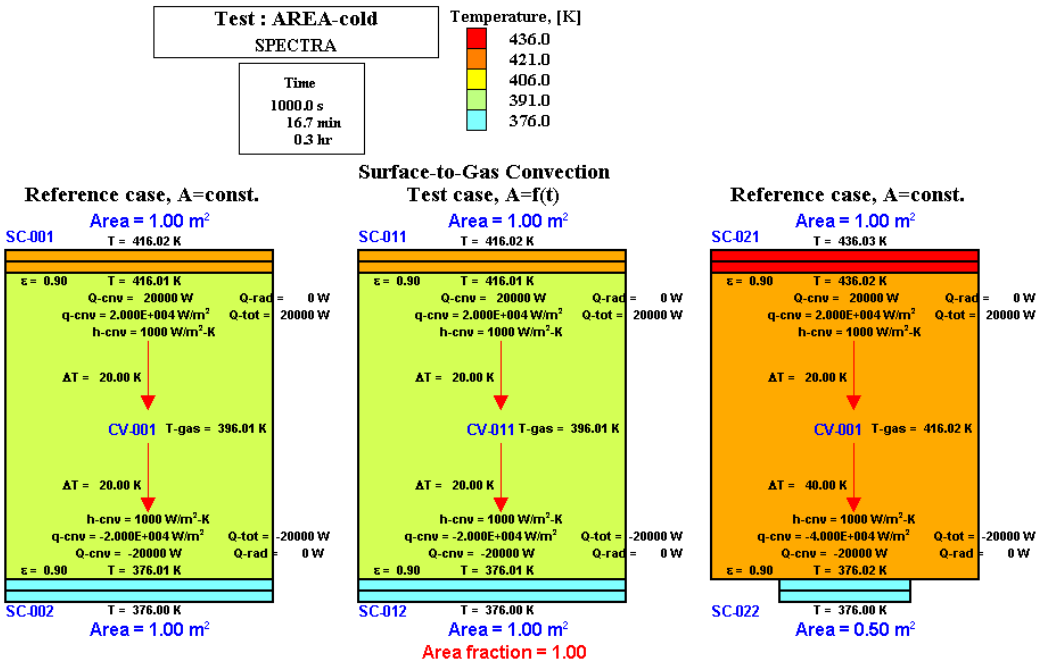

Figure 3-227 “Cold” SC with area change - convection to gas, t = 1000 s

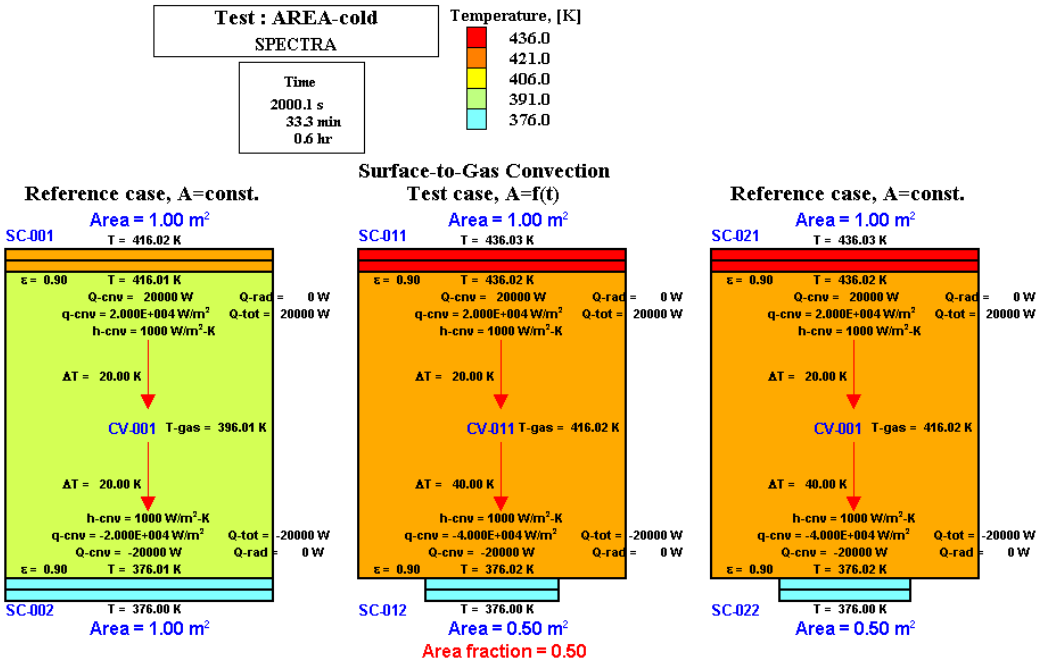

Figure 3-228 “Cold” SC with area change - convection to gas, t = 2000 s

The theoretical values are:

- SC-011: $\frac{q_c}{h} = \frac{20{,}000}{1000} = \frac{Q_c}{A \cdot h} = \frac{20{,}000}{1.00 \times 1000} = \left(T_w - T_g\right) = 20$ K
- SC-012: $\frac{q_c}{h} = \frac{40{,}000}{1000} = \frac{Q_c}{A \cdot h} = \frac{20{,}000}{0.50 \times 1000} = \left(T_w - T_g\right) = 40$ K

Calculations are shown in `\Z-INPUTS\SC\SC-Area-Change\SC-Area-Change.xlsx`. The values agree with those calculated by the code, as seen in Figure 3-228.

- **Radiation to gas**

Figure 3-229 shows the values obtained at t = 2000 s (stable situation at SC-112 area of 0.5 m^2). It is seen that the values obtained at t = 2000 s are identical to those obtained in the "right" reference case. Consistency of the obtained values is checked by hand calculations. The radiative heat transfer is given by (see Volume 1):

$$q_r = \sigma \cdot \varepsilon_w \cdot \left(T_w^4 - T_g^4\right)$$

The theoretical values are:

- SC-111: $q_r = 5.67 \times 10^{-8} \cdot 0.90 \cdot \left(1045.72^4 - 946.88^4\right) = 20{,}001$ W/m^2-K
- SC-112: $q_r = 5.67 \times 10^{-8} \cdot 0.90 \cdot \left(946.88^4 - 376.02^4\right) = 40{,}001$ W/m^2-K

Calculations are shown in `\Z-INPUTS\SC\SC-Area-Change\SC-Area-Change.xlsx`. The values agree with those calculated by the code, as seen in Figure 3-229.

- **Structure-to-structure radiation**

Figure 3-230 shows the values obtained at t = 2000 s (stable situation at SC-212 area of 0.5 m^2). It is seen that the values obtained at t = 2000 s are identical to those obtained in the "right" reference case. Consistency of the obtained values is checked by hand calculations. The radiative heat transfer is given by (see Volume 1):

$$\varepsilon_{1-2} = \left(\frac{1}{\varepsilon_1} + \frac{A_1}{A_2} \cdot \left(\frac{1}{\varepsilon_2} - 1\right)\right)^{-1} \qquad q_{1-2} = \varepsilon_{1-2} \cdot \sigma \cdot \left(T_1^4 - T_2^4\right)$$

$$q_{2-1} = \varepsilon_{1-2} \cdot \sigma \cdot \left(T_2^4 - T_1^4\right) \cdot \frac{A_1}{A_2}$$

The theoretical values are:

$$\varepsilon_{1-2} = \left(\frac{1}{0.9} + \frac{0.50}{1.00} \cdot \left(\frac{1}{0.90} - 1\right)\right)^{-1} = 0.8571$$

- SC-211: $q_r = 5.67 \times 10^{-8} \cdot 0.8571 \cdot \left(958.21^4 - 376.02^4\right) = 40{,}000$ W/m^2-K
- SC-212: $q_r = 5.67 \times 10^{-8} \cdot 0.8571 \cdot \left(958.21^4 - 376.02^4\right) \cdot 0.50 / 1.00 = 20{,}000$ W/m^2-K

Calculations are shown in `\Z-INPUTS\SC\SC-Area-Change\SC-Area-Change.xlsx`. The values agree with those calculated by the code, as seen in Figure 3-230.

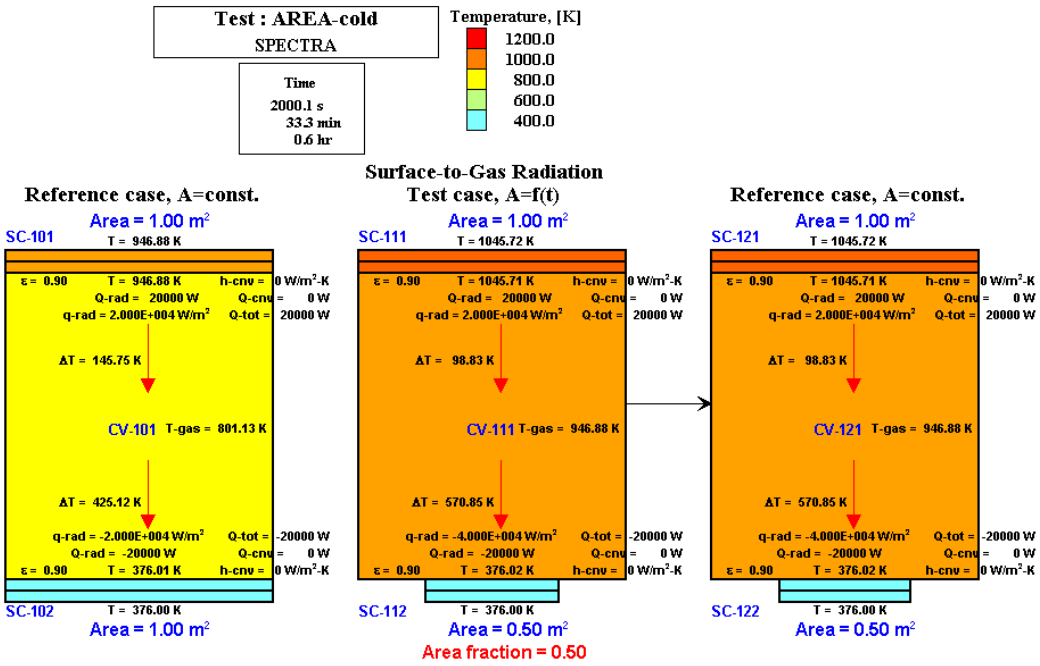

Figure 3-229 “Cold” SC with area change - radiation to gas, t = 2000 s

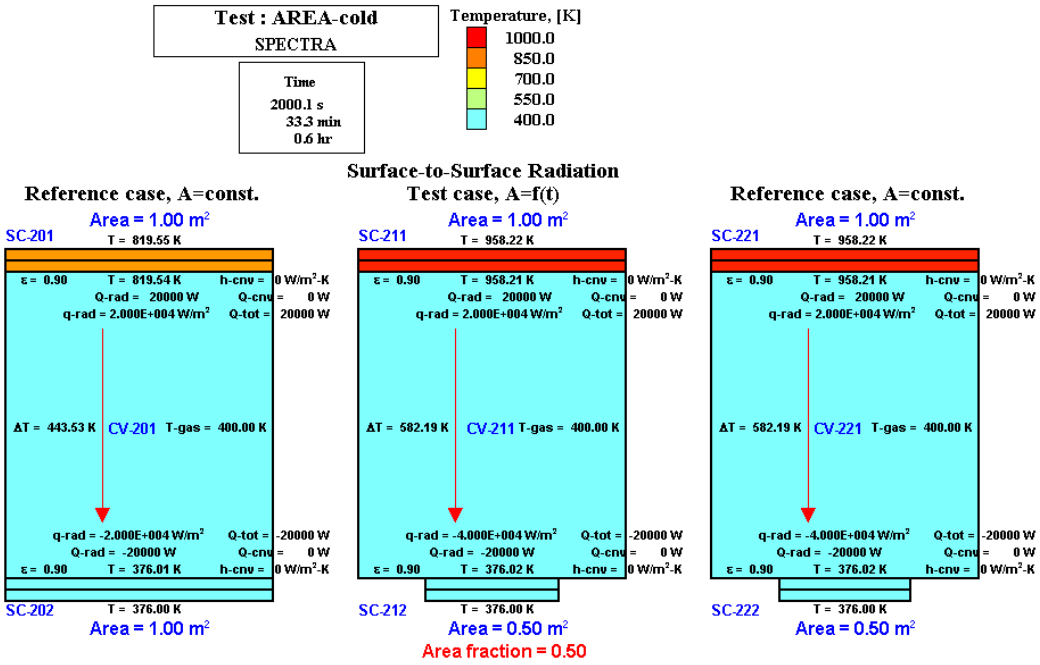

Figure 3-230 “Cold” SC with area change - structure-to-structure radiation, t = 2000 s

3.5.21.2 Size Change of the "Hot" Structure

Results are shown in Figure 3-231 through Figure 3-235. Figure 3-231, Figure 3-232, and Figure 3-233 show results of the case with convection on the surfaces. Figure 3-234 shows the case with radiation to gas. Figure 3-235 shows the case with wall-to-wall radiation. The input file for these tests is stored in `\Z-INPUTS\SC\SC-Area-Change\AREA-hot.SPE`

- **Convection**

Figure 3-231 shows the time dependent values of the surface area of the cold SC-012 and the temperature of the hot SC-011. When the surface area of the hot SC-012 changes from 1.0 to 0.5, the temperature of the hot SC-011 decreases from 416 K to 406 K. In this case the area is reduced for the hot SC containing the heat source. In this case, the heat source strength is automatically reduced when the area is reduced. Consequently, the temperature of the hot surface decreases.

Figure 3-232 shows the values obtained at t = 1000 s (stable situation at SC-011 area of 1.0 m^2) while Figure 3-233 shows the values obtained at t = 2000 s (stable situation at SC-011 area of 0.5 m^2). It is seen that the values obtained at t = 1000 s are identical to those obtained in the "left" reference case, while the values obtained at t = 2000 s are identical to those obtained in the "right" reference case. Consistency of the obtained values is checked by hand calculations. The convective heat transfer is given by (see Volume 1):

$$Q_c = A \cdot q_c = A \cdot h \cdot \left(T_w - T_g\right)$$

or:

$$\frac{q_c}{h} = \frac{Q_c}{A \cdot h} = \left(T_w - T_g\right)$$

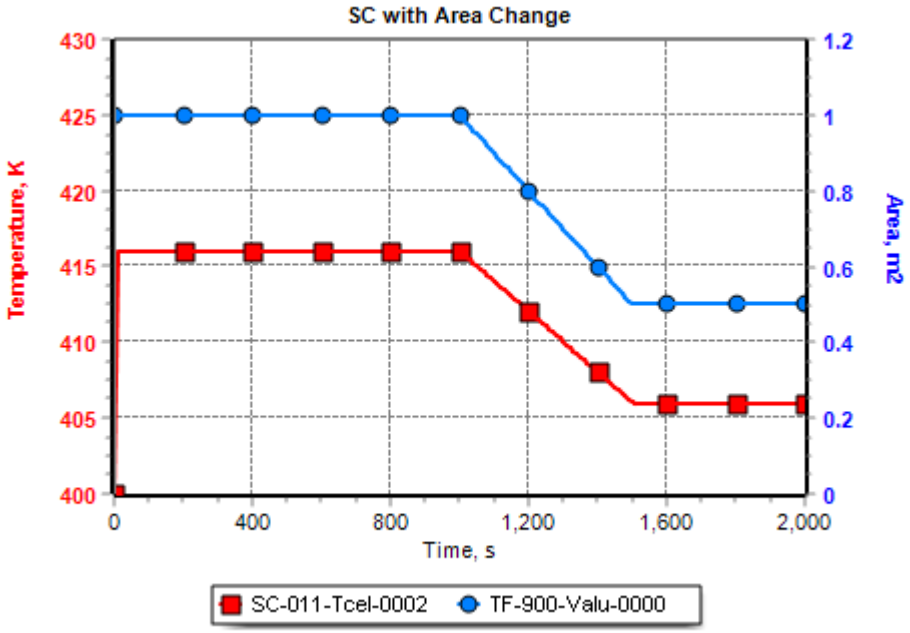

Figure 3-231 "Hot" SC with area change - convection to gas

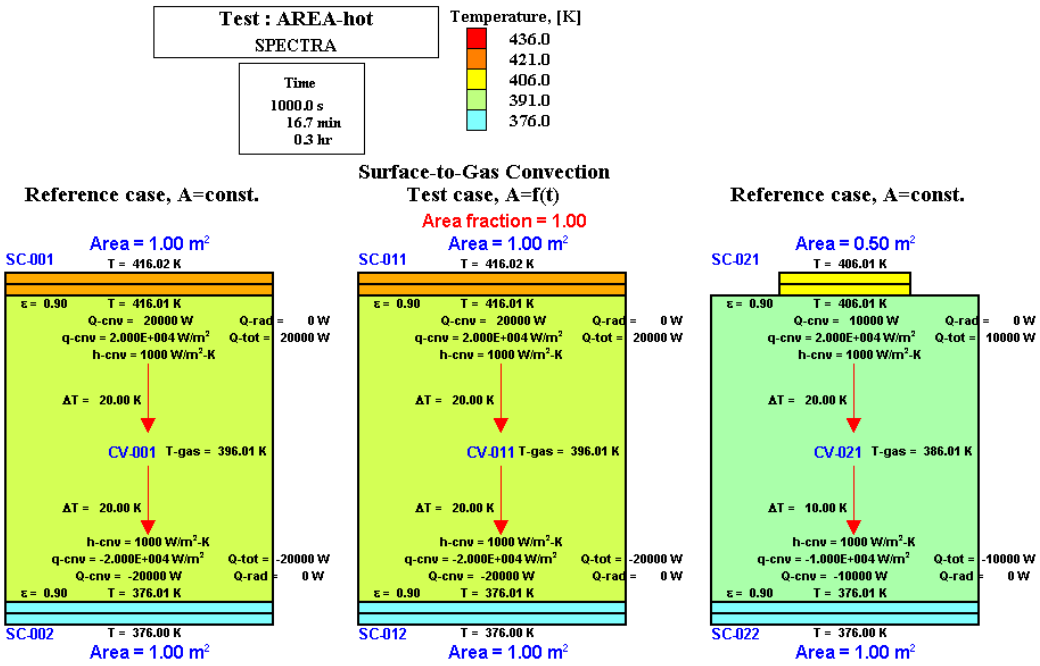

Figure 3-232 “Hot” SC with area change - convection to gas, t = 1000 s

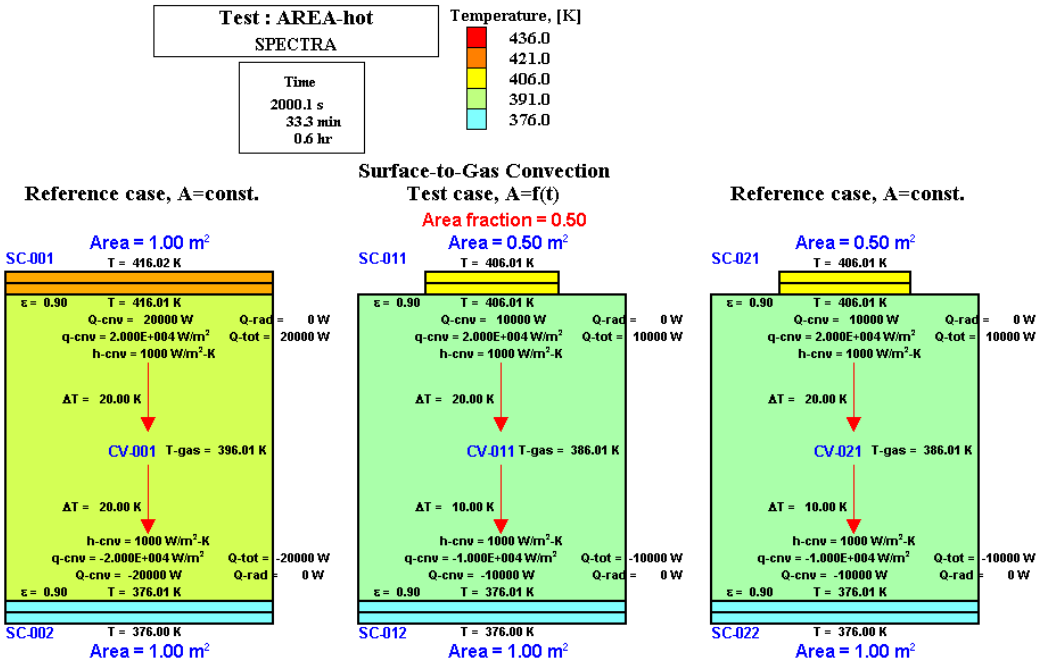

Figure 3-233 “Hot” SC with area change - convection to gas, t = 2000 s

The theoretical values are:

- SC-011: $$\frac{q_c}{h}=\frac{20{,}000}{1000}=\frac{Q_c}{A\cdot h}=\frac{10{,}000}{0.50\times 1000}=\left(T_w-T_g\right)=20 \text{ K}$$
- SC-012: $$\frac{q_c}{h}=\frac{10{,}000}{1000}=\frac{Q_c}{A\cdot h}=\frac{10{,}000}{1.00\times 1000}=\left(T_w-T_g\right)=10 \text{ K}$$

Calculations are shown in `\Z-INPUTS\SC\SC-Area-Change\SC-Area-Change.xlsx`. The values agree with those calculated by the code, as seen in Figure 3-233.

- **Radiation to gas**

Figure 3-234 shows the values obtained at t = 2000 s (stable situation at SC-111 area of 0.5 m^2). It is seen that the values obtained at t = 2000 s are identical to those obtained in the "right" reference case. Consistency of the obtained values is checked by hand calculations. The radiative heat transfer is given by (see Volume 1):

$$q_r=\sigma\cdot\varepsilon_w\cdot\left(T_w^4-T_g^4\right)$$

The theoretical values are:

- SC-111: $q_r=5.67\times10^{-8}\cdot0.90\cdot\left(882.99^4-681{,}69^4\right)=20{,}001$ W/m^2-K
- SC-112: $q_r=5.67\times10^{-8}\cdot0.90\cdot\left(681.69^4-376.01^4\right)=10{,}000$ W/m^2-K

Calculations are shown in `\Z-INPUTS\SC\SC-Area-Change\SC-Area-Change.xlsx`. The values agree with those calculated by the code, as seen in Figure 3-234.

- **Structure-to-structure radiation**

Figure 3-235 shows the values obtained at t = 2000 s (stable situation at SC-211 area of 0.5 m^2). It is seen that the values obtained at t = 2000 s are identical to those obtained in the "right" reference case. Consistency of the obtained values is checked by hand calculations. The radiative heat transfer is given by (see Volume 1):

$$\varepsilon_{1-2}=\left(\frac{1}{\varepsilon_1}+\frac{A_1}{A_2}\cdot\left(\frac{1}{\varepsilon_2}-1\right)\right)^{-1}$$

$$q_{1-2}=\varepsilon_{1-2}\cdot\sigma\cdot\left(T_1^4-T_2^4\right)$$

$$q_{2-1}=\varepsilon_{1-2}\cdot\sigma\cdot\left(T_2^4-T_1^4\right)\cdot\frac{A_1}{A_2}$$

The theoretical values are:

$$\varepsilon_{1-2}=\left(\frac{1}{0.9}+\frac{0.50}{1.00}\cdot\left(\frac{1}{0.90}-1\right)\right)^{-1}=0.8571$$

- SC-211: $q_r=5.67\times10^{-8}\cdot0.8571\cdot\left(810.49^4-376.01^4\right)=20{,}000$ W/m^2-K
- SC-212: $q_r=5.67\times10^{-8}\cdot0.8571\cdot\left(810.49^4-376.01^4\right)\cdot0.50/1.00=10{,}000$ W/m^2-K

Calculations are shown in `\Z-INPUTS\SC\SC-Area-Change\SC-Area-Change.xlsx`. The values agree with those calculated by the code, as seen in Figure 3-235.

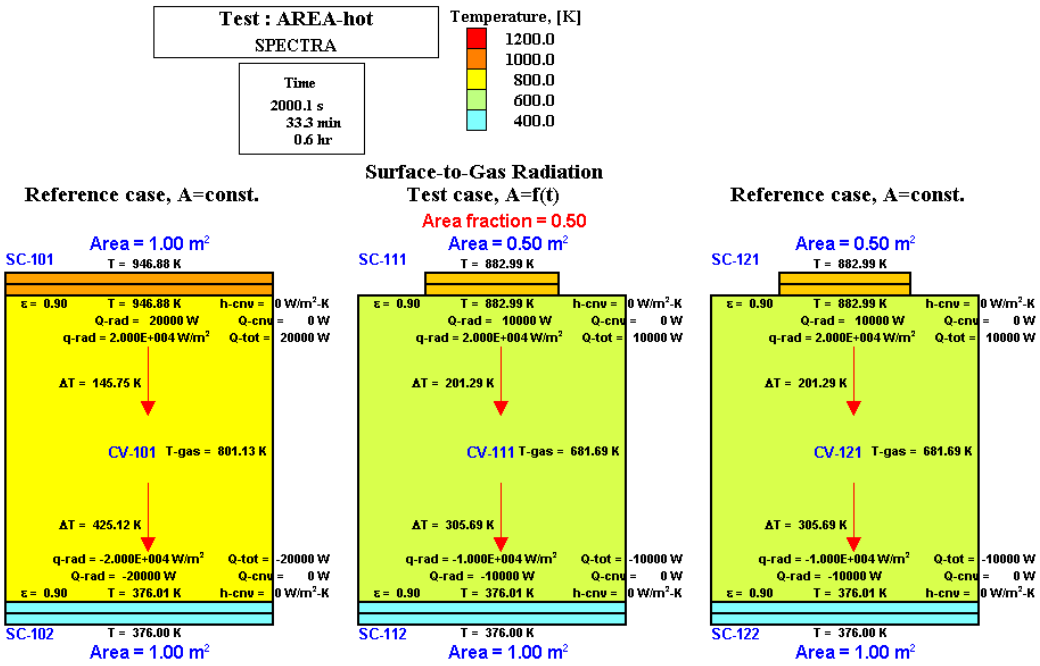

Figure 3-234 "Hot" SC with area change - radiation to gas, t = 2000 s

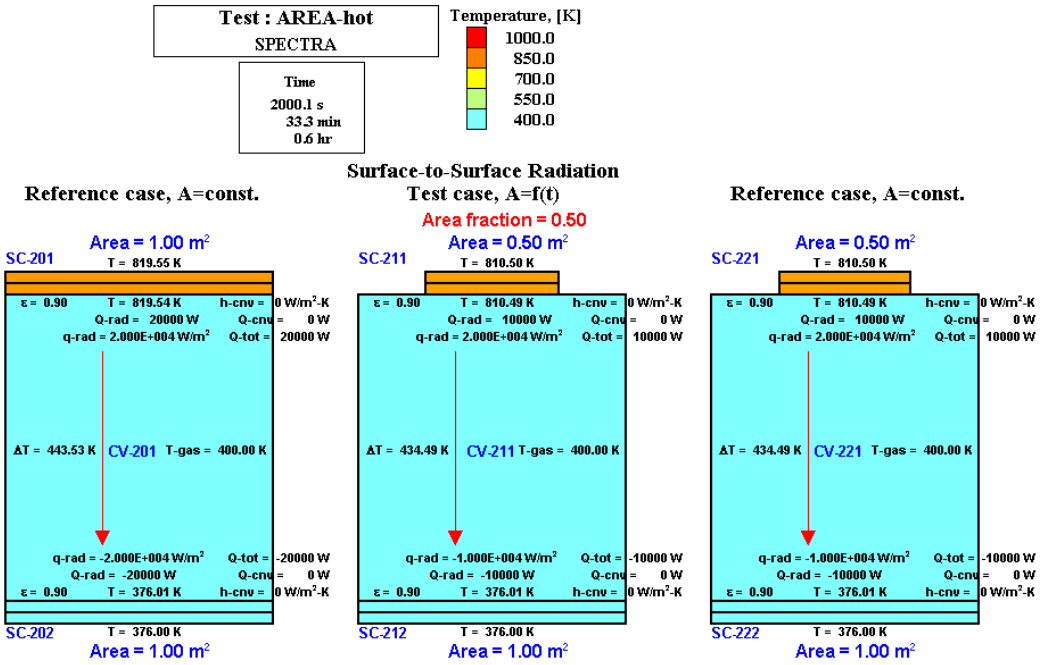

Figure 3-235 "Hot" SC with area change - structure-to-structure radiation, t = 2000 s

3.6 2-D Solid Heat Conductors

3.6.1 1-D Steady State Conduction Tests for a 2-D Solid Heat Conductor

As a first set of tests for 2-D Solid Heat Conductors the 1-D conduction tests, described in section 3.5.1, were repeated.

Conductor with internal heat source, constant thermal conductivity

A model was built for a 2-D Solid Heat Conductors TC-001 and TC-002 corresponding to the 1-D conductors SC-001 and SC-002, described in section 3.5.1. TC-001 is nodalized the same as SC-001 in the *x*-direction. This means the cell half-thickness of 5.0×10^{-4} m. In the *y*-direction it is divided into 11 cells with the cell half-thickness of 0.05 m.

- 5.0×10^{-4} m for the *x*-direction
- 5.0×10^{-2} m for the *y*-direction

The total size of TC-001 in the *y*-direction is 1.0 m. The length of TC-001 was set to 1.0 m, so that the total area of heat transfer is 1.0 m^2, the same as for SC-001.

The cylindrical structure TC-002 was built in the same way as TC-001, i.e. 11 cells with a half-width of 0.05 m were applied. The boundary conditions for both TC-001 and TC-002 were specified in such a way that these 2-D structures should behave exactly the same as the corresponding 1-D structures, SC-001 and SC-002.

Note that the 2-D conduction model is in SPECTRA available only for rectangular and cylindrical geometries. Therefore a 2-D structure corresponding to the spherical SC-003 from section 3.5.1 cannot be built.

Input deck for this test is provided in `\Z-INPUTS\TC\T-CON\T-CON.SPE`. Results obtained for t = 10 s are shown in Figure 3-236 and Figure 3-238. The results of the corresponding 1-D structures are shown in Figure 3-237 and Figure 3-239. It is seen that the 2-D results are identical to the 1-D results. It has been verified that results are identical for all other time points.

Conduction with variable thermal conductivity

A model was built for a 2-D Solid Heat Conductors TC-004 and TC-005 corresponding to the 1-D conductors SC-004 and SC-005, described in section 3.5.1.

Input deck for this test is provided in `\Z-INPUTS\TC\T-CON\T-CON.SPE`. Results obtained for t = 10 s are shown in Figure 3-240 and Figure 3-242. The results of the corresponding 1-D structures are shown in Figure 3-241 and Figure 3-243. It is seen that the 2-D results are identical to the 1-D results. It has been verified that results are identical for all other time points

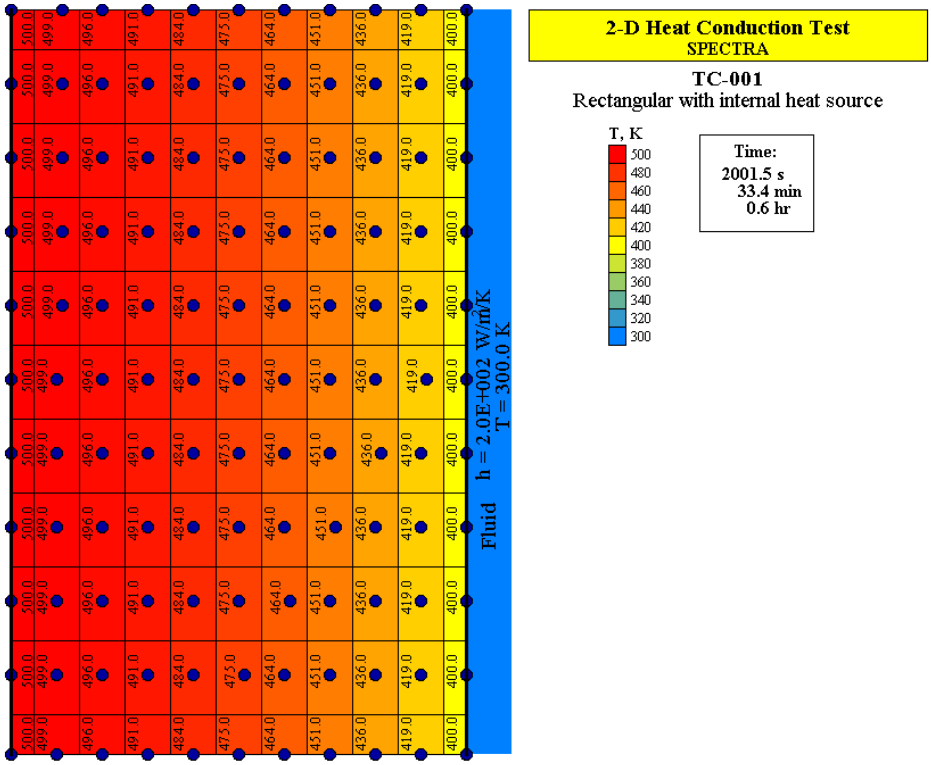

Figure 3-236 2-D conduction tests - rectangular with internal heat source.

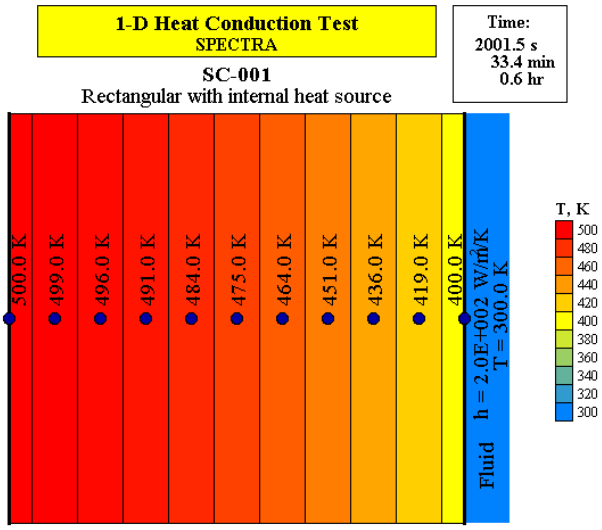

Figure 3-237 1-D conduction tests - rectangular with internal heat source.

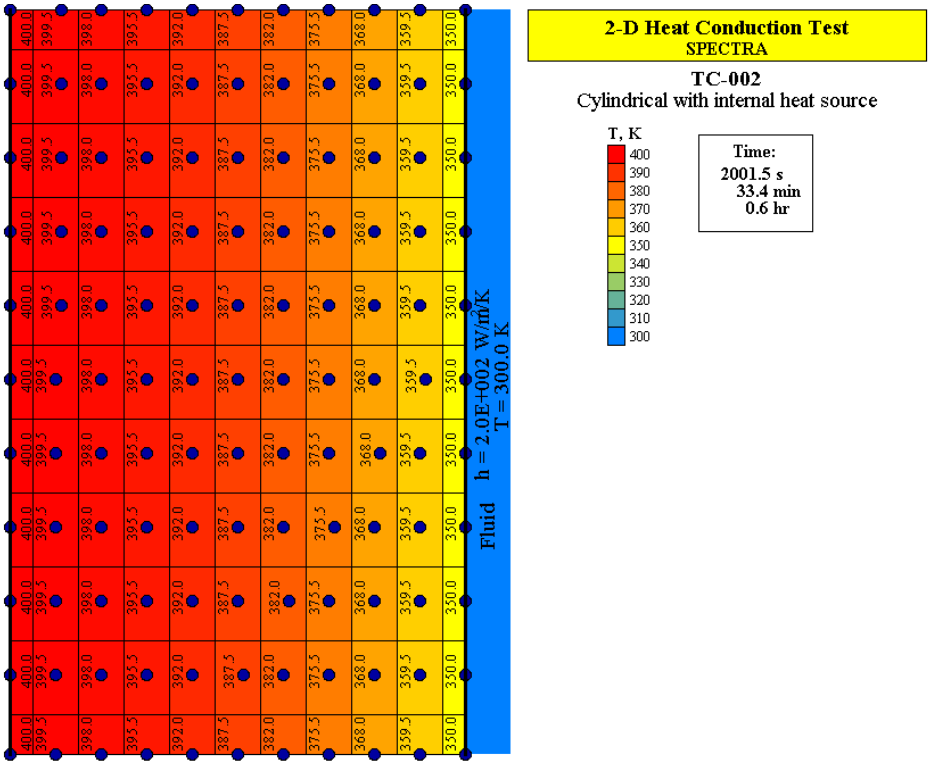

Figure 3-238 2-D conduction tests - cylindrical with internal heat source.

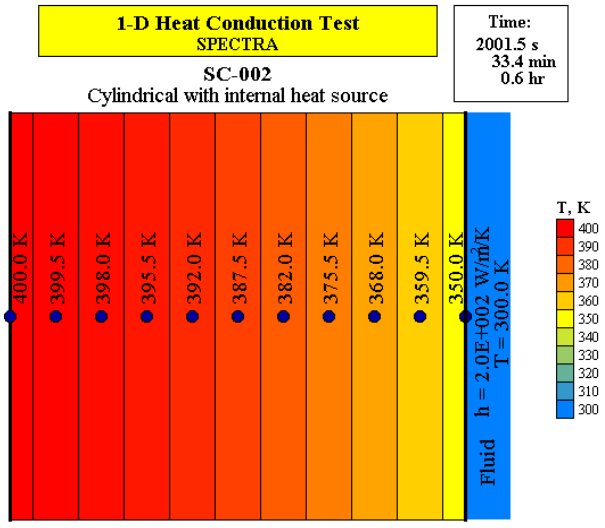

Figure 3-239 1-D conduction tests - cylindrical with internal heat source.

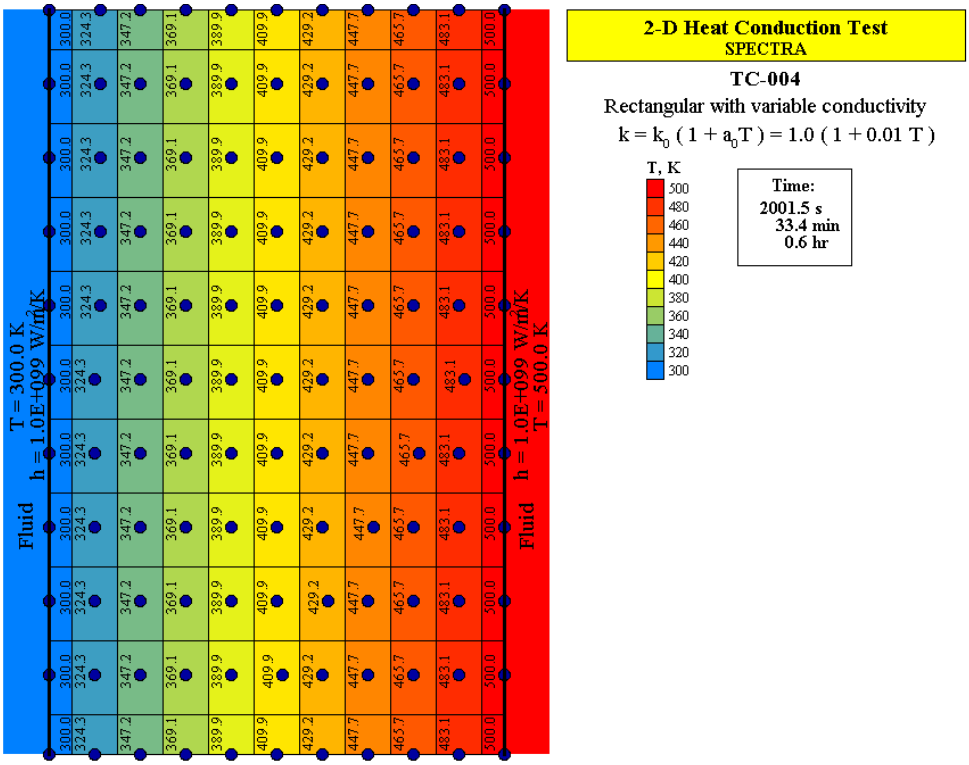

Figure 3-240 2-D conduction tests - rectangular with variable conductivity.

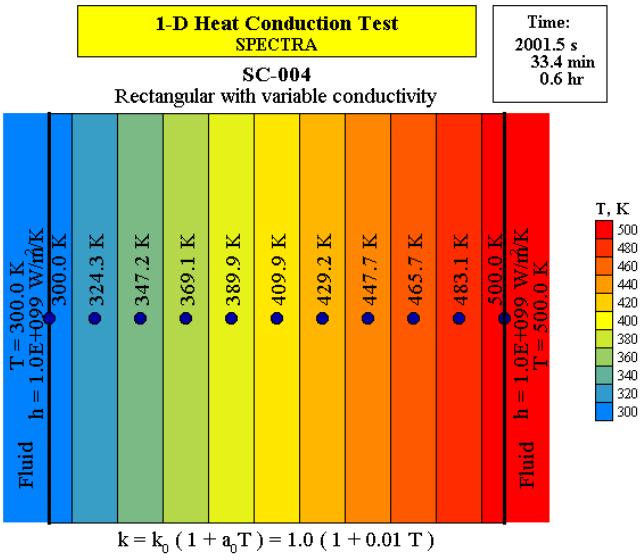

Figure 3-241 1-D conduction tests - rectangular with variable conductivity.

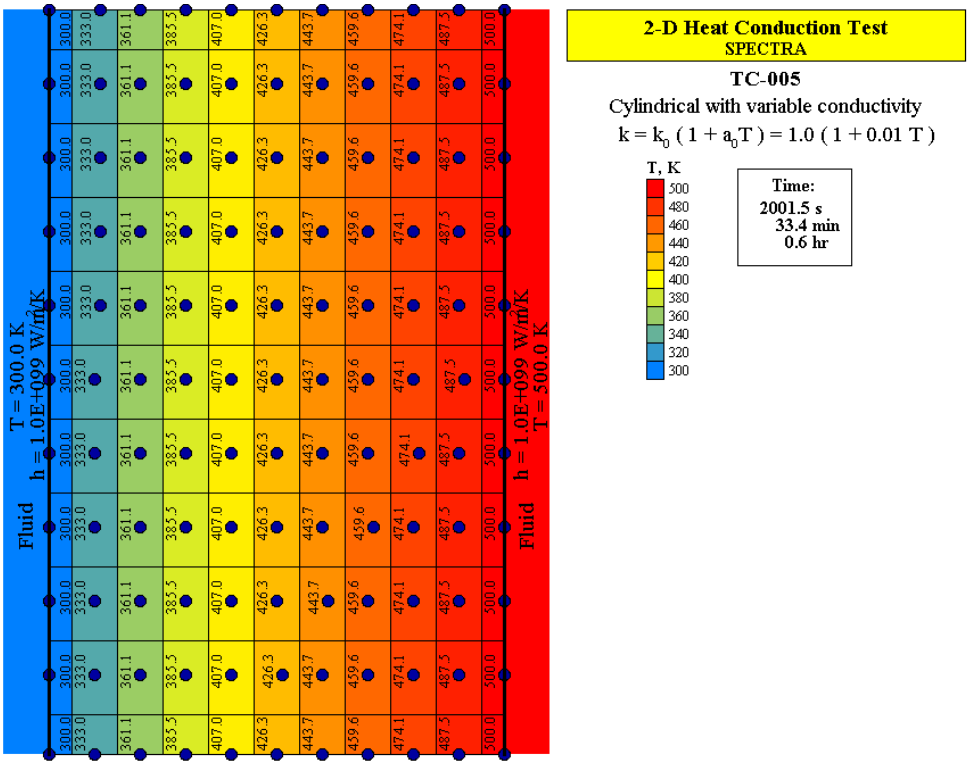

Figure 3-242 2-D conduction tests - cylindrical with variable conductivity.

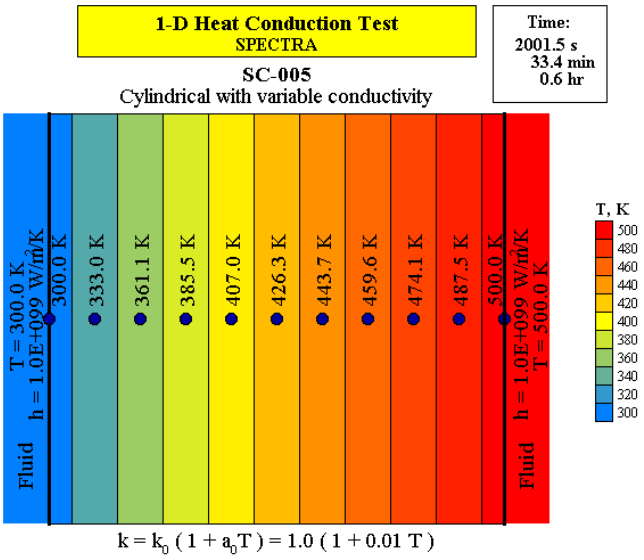

Figure 3-243 1-D conduction tests - cylindrical with variable conductivity.

3.6.2 1-D Transient Conduction Tests for a 2-D Solid Heat Conductor

As a second set of tests for 2-D Solid Heat Conductors the transient 1-D conduction tests, described in section 3.5.4, were repeated.

Slab heated from one side

A model was built for a 2-D Solid Heat Conductor TC-006 corresponding to the 1-D conductor SC-006, described in section 3.5.4.

TC-006 is nodalized the same as SC-006 in the *x*-direction. This means the 21 cells with a half-thickness of 2.5×10^{-4} m. In the *y*-direction it is divided into 11 cells with the cell half-thickness of 0.05 m.

- 2.5×10^{-4} m for the *x*-direction
- 5.0×10^{-2} m for the *y*-direction

The total size of TC-006 in the *y*-direction is 1.0 m. The length of TC-006 was set to 1.0 m, so that the total area of heat transfer is 1.0 m^2, the same as for SC-006.

Input deck for this test is provided in `\Z-INPUTS\TC\T-CON\T-CON.SPE`. Results obtained for t = 10 s are shown in Figure 3-244. The results of the corresponding 1-D structures are shown in Figure 3-245. It is seen that the 2-D results are identical to the 1-D results. It has been verified that results are identical for all other time points.

Slab with both sides heated

A model was built for a 2-D Solid Heat Conductor TC-007 corresponding to the 1-D conductor SC-007, described in section 3.5.4.

TC-007 is nodalized the same as SC-007 in the *x*-direction. This means the 21 cells with a half-thickness of 2.5×10^{-4} m. In the *y*-direction it is divided into 11 cells with the cell half-thickness of 0.05 m.

- 2.5×10^{-4} m for the *x*-direction
- 5.0×10^{-2} m for the *y*-direction

The total size of TC-007 in the *y*-direction is 1.0 m. The length of TC-007 was set to 1.0 m, so that the total area of heat transfer is 1.0 m^2, the same as for SC-007.

Input deck for this test is provided in `\Z-INPUTS\TC\T-CON\T-CON.SPE`. Results obtained for t = 10 s are shown in Figure 3-246. The results of the corresponding 1-D structures are shown in Figure 3-247. It is seen that the 2-D results are identical to the 1-D results. It has been verified that results are identical for all other time points.

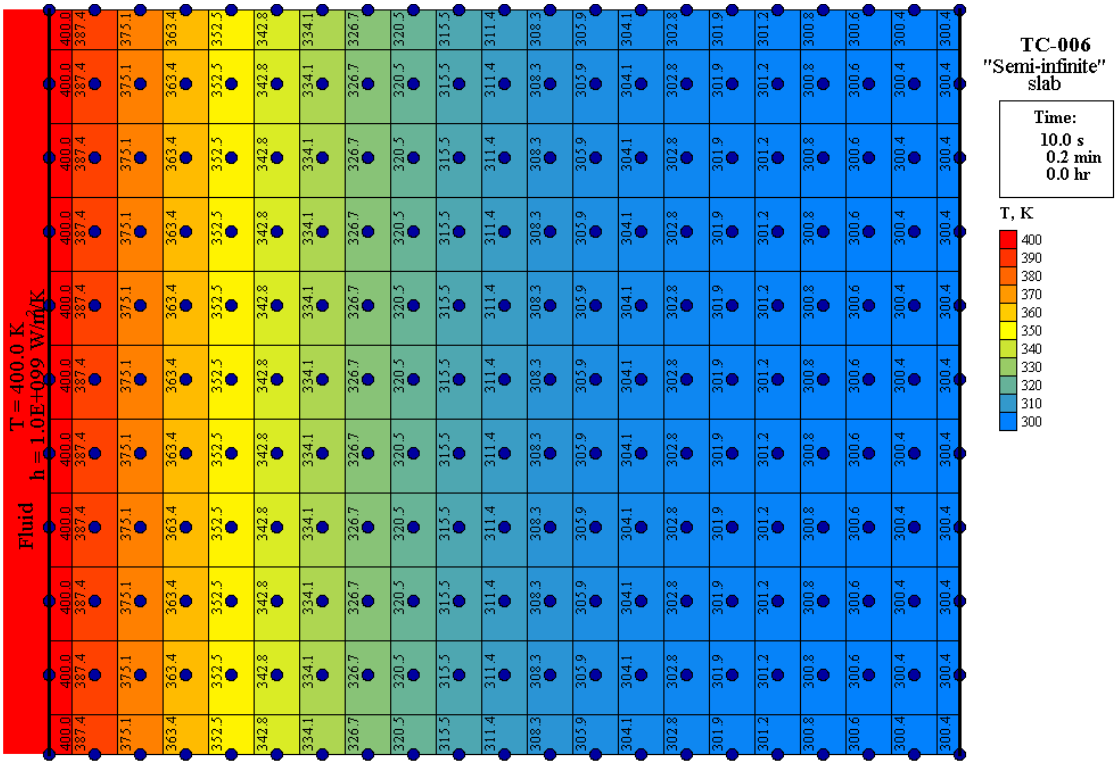

Figure 3-244 2-D conduction test, slab heated from one side, t = 10.0 s.

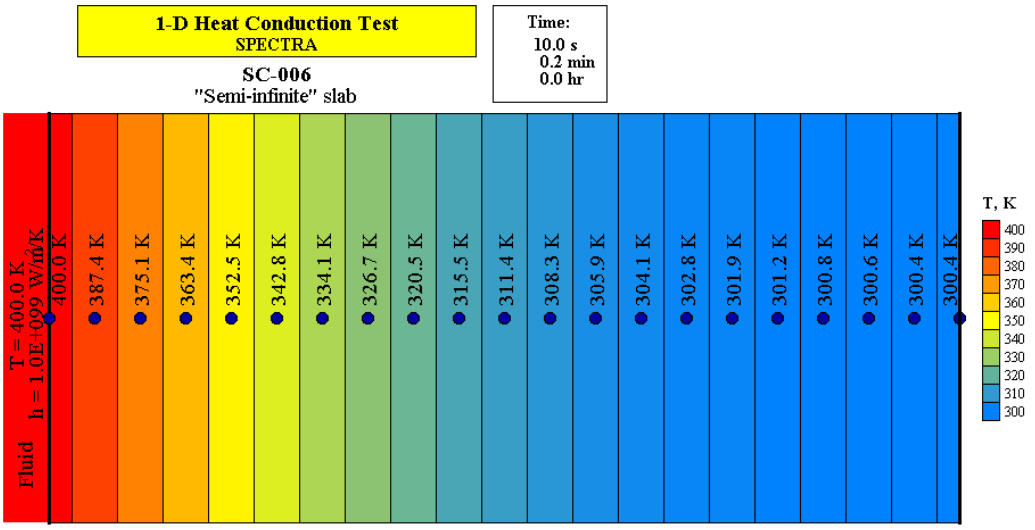

Figure 3-245 1-D conduction test, slab heated from one side, t = 10.0 s.

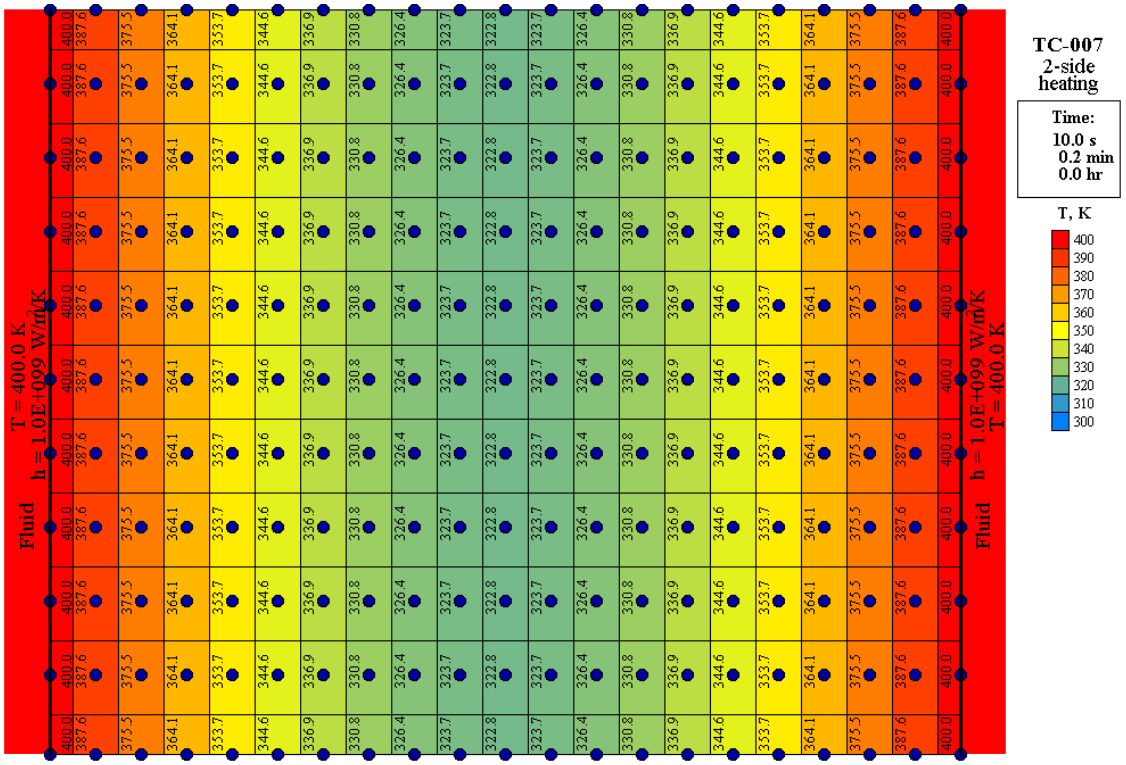

Figure 3-246 2-D conduction test, slab with both sides heated, t = 10.0 s.

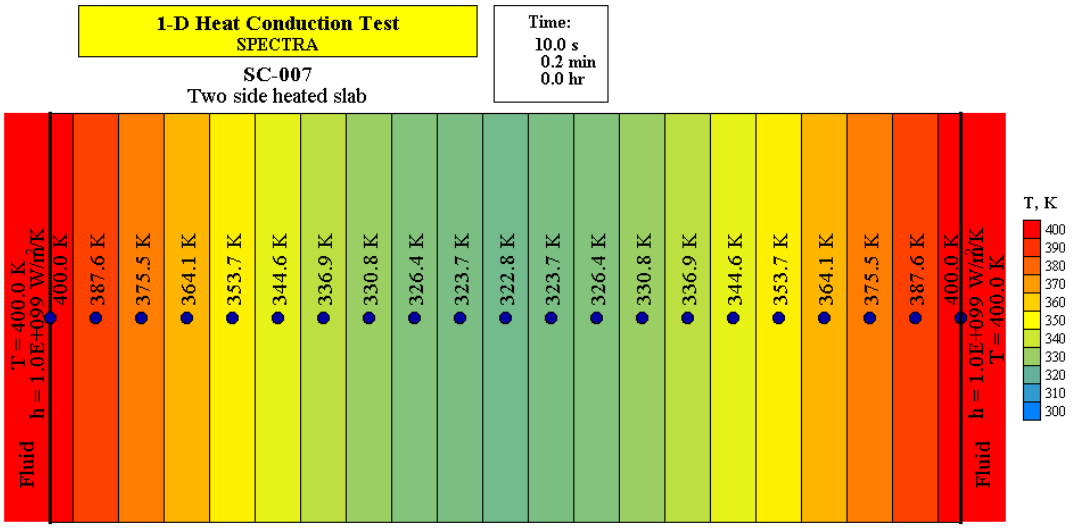

Figure 3-247 1-D conduction test, slab with both sides heated, t = 10.0 s.

3.6.3 2-D Steady-State Conduction Tests for a 2-D Solid Heat Conductor

The previous sections showed that when the 2-D model is applied to 1-D heat conduction problems it gives exactly the same results as the 1-D conduction model (at a considerably higher consumption of the processor time of course). This section presents results of a real 2-D conduction test case.

Test case for 2-D Conduction

- Theory

A steady state conduction in a rectangular plate, shown in Figure 3-248. The plate dimensions in x and y directions are a and b respectively. The boundary temperature is T_s at the top edge (y=b), and T_0 at all other boundaries.

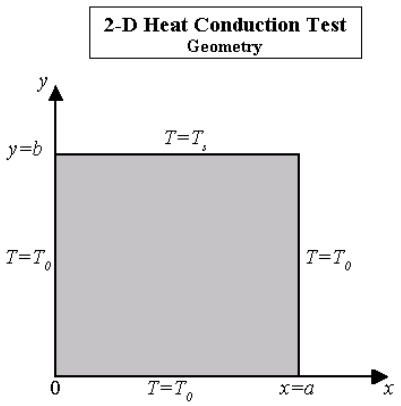

Figure 3-248 Geometry of 2-D conduction test case.

The theoretical solution of heat conduction equation results in the following temperature distribution inside the conductor (see [16], section 3.3, eq. 3-30):

$$T(x,y) = T_0 + (T_s - T_0) \cdot \sum_{n=1}^{\infty} A_n \cdot \sin\left(n\pi \frac{x}{a}\right) \cdot \sinh\left(n\pi \frac{y}{a}\right)$$

where:

$$A_n = \frac{2 \cdot [1-(-1)^n]}{n\pi \cdot \sinh\left(n\pi \frac{b}{a}\right)}$$

$T(x,y)$ temperature, (K), at the location (x, y)
T_0 side and bottom boundary temperature, (K), at x = 0, x = a, y = 0
T_s top boundary temperature, (K), at y = b
a size of the plate in the x-direction, (m)
b size of the plate in the y-direction, (m)

The following data were assumed for calculations:

- T_0 = 300 K
- T_s = 400 K
- a = 0.1 m
- b = 0.1 m

The theoretical solution has been calculated by a FORTRAN program that computes the sum of the infinite series with a sum termination criterion set at 10^{-20} on the absolute value of the n-th element of the series and 10^{-10} on the relative contribution (absolute value of the n-th element of the series, divided by the total value). The series was found to converge quite slowly for some particular locations in the slab and few hundred elements of the series had to be calculated. Independently of the described above criteria, a minimum number of 200 elements was imposed, just to be sure that sufficient number of elements of the series has been used.

The program to calculate the theoretical solution is provided in:
`\Z-INPUTS\TC\T-CON\T-CON-THEORY.FOR`

Results are shown in Figure 3-249. The values in the upper row should be 400.0 K and there are values of 399.2 K close to the corners; therefore it is concluded that an inaccuracies of up to about 0.8 K may be expected from the theoretical solution. At the corners the solution gives 300 K.

- SPECTRA Calculations

The input data for all conduction problems were prepared as a single input data file with several conductors. The input file for the calculations is stored in:
`\Z-INPUTS\TC\T-CON\T-CON.SPE`

For the test case described in this section the conductors TC-010 and TC-011 are used. The material property data were defined in the material property input records. The material No. 1 was used (k = 1.0 W/m-K, ρ = 1000 kg/m^3, c_p = 100 J/kg-K).

The dimensions are 0.1×0.1 m. The applied nodalization is:

- 11 cells, each with a half-width of 5.0×10^{-3} m for the x-direction
- 11 cells, each with a half-width of 5.0×10^{-3} m for the y-direction

The boundary conditions were specified using Tabular Functions TF-005 for the heat transfer coefficient, while TF-002 and TF-003 fluid temperatures. The heat transfer coefficient was set to a large number (10^{99}) to ensure that the conductor surface temperature is the same as the fluid temperature. The "top" surface temperature, T_s, is specified using TF-003 (equal to 400 (K)), while the temperature T_0, is specified using TF-002 (equal to 300.0 (K)).

Boundary condition definition presents a certain problem at the upper left and the upper right corners. The corner cells should ideally have two boundary temperatures: T_0 for the vertical part and T_s for the horizontal part. This however is not possible in SPECTRA, since only one boundary condition may be applied for a single cell. There is an option however to apply the boundary condition to one part only (vertical or horizontal) and keep the other part adiabatic. Therefore there are two possibilities to define boundary conditions at the corner cells:

- Method 1 “cold corners”: use T_0 on the vertical part, insulate the horizontal part
- Method 2 “hot corners”: use T_s on the horizontal part, insulate the vertical part

Both methods were applied. The first method was applied for TC-010. Additionally a new Solid Conductor, TC-011, was created, identical to TC-010 but with the second option for the boundary condition definition at the corner cells.

The time steps used for calculations were:

$0 < t < 20$ s:	$\Delta t =$ 0.1 s
$20 < t < 200$ s:	$\Delta t =$ 1.0 s
$200 < t < 2000$ s:	$\Delta t =$ 10.0 s

Results of SPECTRA calculations are shown in Figure 3-250 (case with “cold corners” - TC-010) and Figure 3-251 (case with “hot corners” - TC-011). It is seen that apart from the corner node temperatures themselves, temperatures in all other nodes are identical for TC-010 and TC-011. Therefore it is concluded that the accuracy of the solution is not affected by the assumption made to specify the boundary conditions at the corners. The calculated results are in good agreement with the theoretical solution. When the top nodes are not taken into account, the largest discrepancy is 0.7 K (367.5 K - Figure 3-250 versus 368.2 K - Figure 3-249). For the top nodes the largest discrepancy is 0.8 K, but in this case it is clearly the theoretical solution that gives an inaccurate number (the value should be 400.0 because of the boundary condition). It is concluded that the SPECTRA results are in agreement with theoretical solution within the accuracy of the theoretical solution.

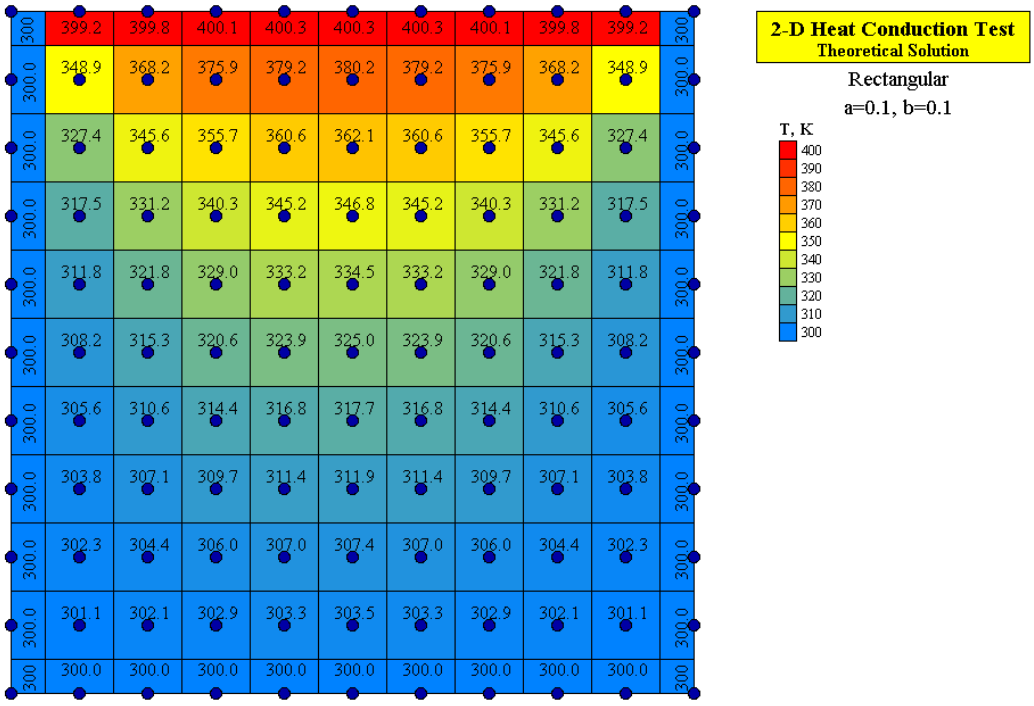

Figure 3-249 2-D condution case - theoretical solution

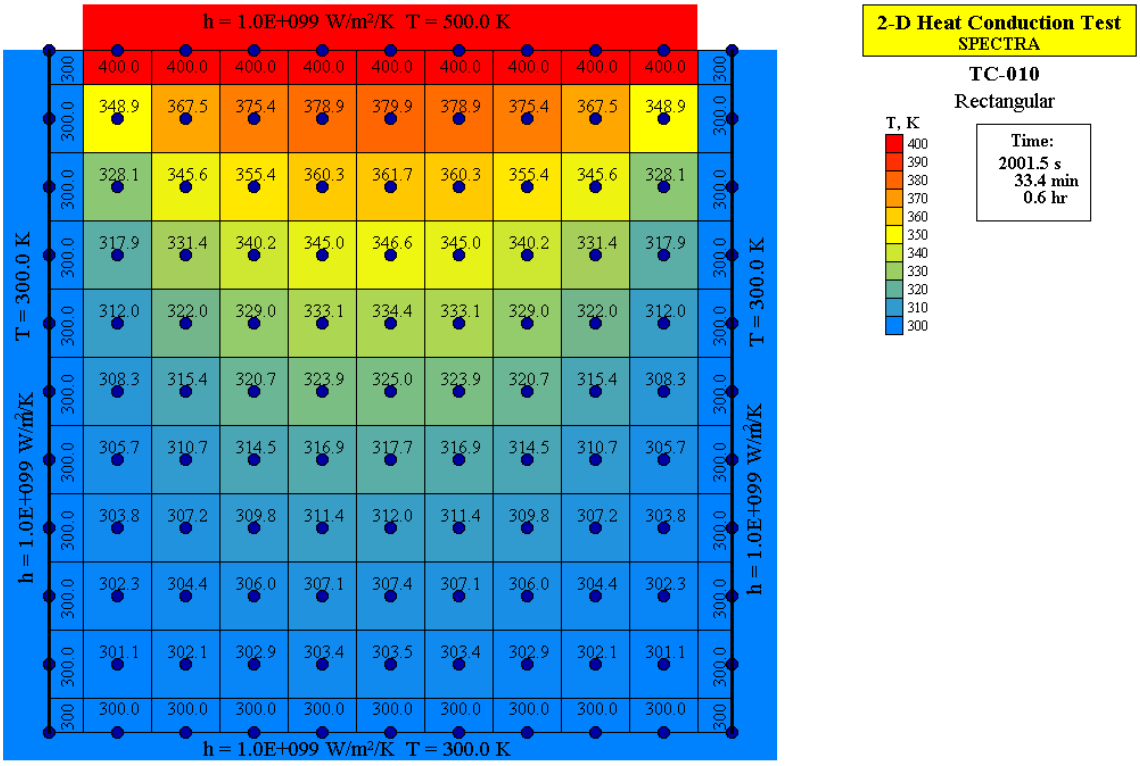

Figure 3-250 2-D conduction test - SPECTRA, - “cold corners”.

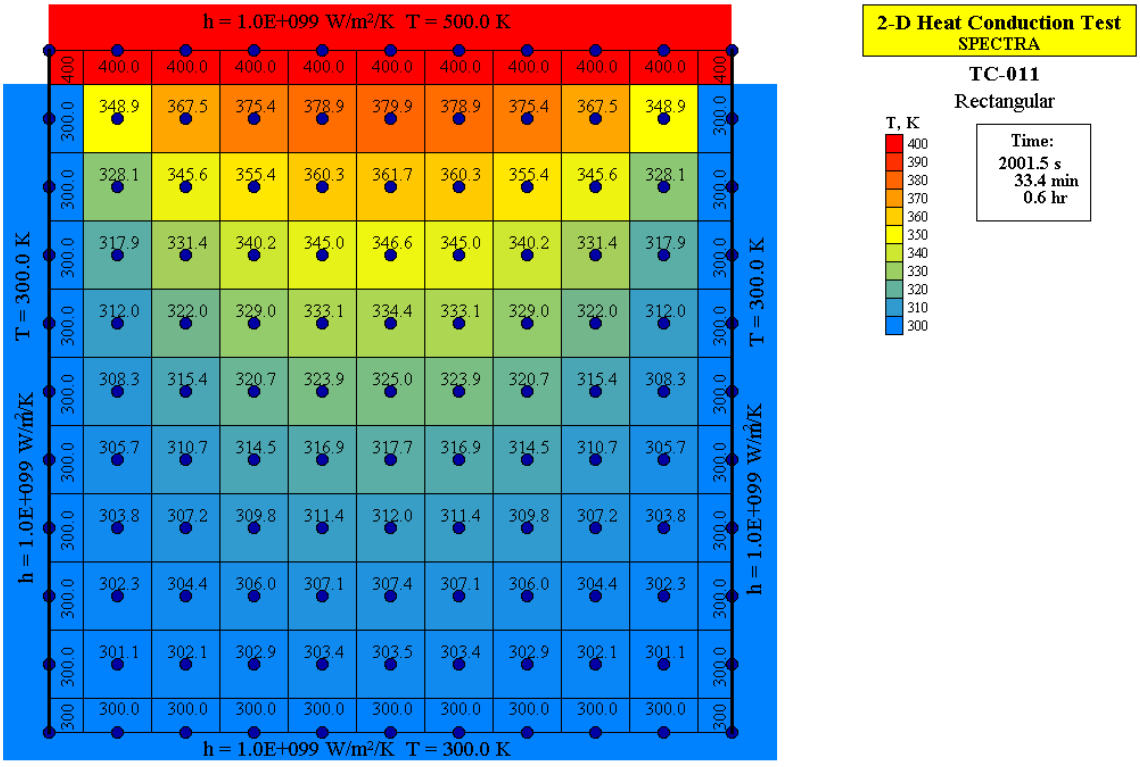

Figure 3-251 2-D conduction test - SPECTRA, - “hot corners”.

3.6.4 2-D Transient Conduction Tests - "Sterilization of a Vegetable Can"

An example of a 2-D transient conduction is presented in [16], section 3.4.4, Example 3.11. The example is called "sterilization of a vegetable can". A can of vegetables 10 cm in diameter and 8 cm high (Figure 3-252) is to be sterilized by immersion in a saturated steam at 105°C. The initial temperature is 40°C. The requested value is the minimum temperature in the can after 80 min (4800 s).

The material properties are: k = 0.676 W/m-K
ρ = 967 kg/m^3
c_p = 4200 J/kg-K

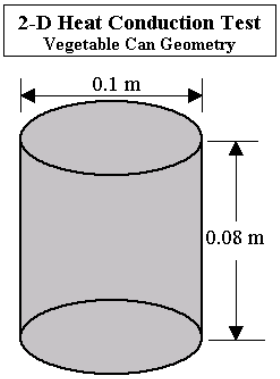

Figure 3-252 Geometry of 2-D conduction test case.

The theoretical solution, presented in [16], is based on approximation where solution for a 2-D structure is obtained as a product of functions valid for 1-D geometries, an infinite cylinder with the diameter of D = 0.1 m, and an infinite plate with the thickness of H = 0.08 m.

The functions for 1-D geometries are obtained from charts, for Bi = 1000. In order to be in agreement with the theoretical approach, the corresponding heat transfer coefficients were applied in SPECTRA. The heat transfer coefficients are:

Cylinder with 5 cm radius $$h = Bi \cdot \frac{k}{R} = 1000 \cdot \frac{0.676}{0.05} = 13{,}520$$

Slab with 4 cm half-width $$h = Bi \cdot \frac{k}{L/2} = 1000 \cdot \frac{0.676}{0.04} = 16{,}900$$

The theoretical solution gives: T_{min} = 98.3°C = 371.5 K (see [16], p. 182). Note that this is only an approximation and not an exact value.

SPECTRA model has been prepared using TC-012 with material properties defined as material 4. The applied nodalization is:

- 11 cells, each with a half-width of 2.5×10^{-3} m for the *r*-direction
- 9 cells, each with a half-width of 5.0×10^{-3} m for the *z*-direction

The boundary conditions were specified using Tabular Functions:

TF-006 = 378 boundary temperature
TF-007 = 10^{10} heat transfer coefficient on the outer surface

The input file for the calculations is stored in:
`\Z-INPUTS\TC\STERIL\STERIL.SPE`

Results are shown in Figure 3-253 and Figure 3-254. The minimum temperature (cell 0005 of TC-012) is shown together with the hot steam temperature in Figure 3-253. Results for all cells obtained for t = 4800 s are shown in Figure 3-254. The minimum temperature is 376.1 K (102.9°C).

In order to check the time step sensitivity calculations were performed with 3 different time steps:

- Δt = 0.1 s (input file: \STERIL.SPE)
- Δt = 1.0 s (input file: \STERIL-1.SPE)
- Δt = 10.0 s (input file: \STERIL-10.SPE)

As a check for nodalization sensitivity the calculations were repeated with finer nodalization:

- 21 cells, each with a half-width of 1.25×10^{-3} m for the *r*-direction
- 17 cells, each with a half-width of 2.5×10^{-3} m for the *z*-direction

The input file is \STERIL-NOD.SPE. Calculations with the finer nodalization were performed using the time step of 1.0 s. All results are summarized in Table 3-32. The calculations give the value of 371.8 ±0.1 K. The discrepancy between the calculated and the analytical result is about 5 K. Since the numerical values are quite consistent, with discrepancy only ±0.1, it is concluded that the approximation used for analytical solution is responsible for the discrepancy. In order to verify this statement an independent calculation is needed. It will be performed in the future.

Table 3-32 Results of the sterilization test.

	T_{min} , °C	T_{min} , K
Analytical solution	98.3°C	371.5 K
SPECTRA, Δt = 0.1 s	98.6°C	371.8 K
SPECTRA, Δt = 1.0 s	98.6°C	371.8 K
SPECTRA, Δt = 10.0 s	98.6°C	371.8 K
SPECTRA, Δt = 1.0 s, fine nodalization	98.7°C	371.9 K

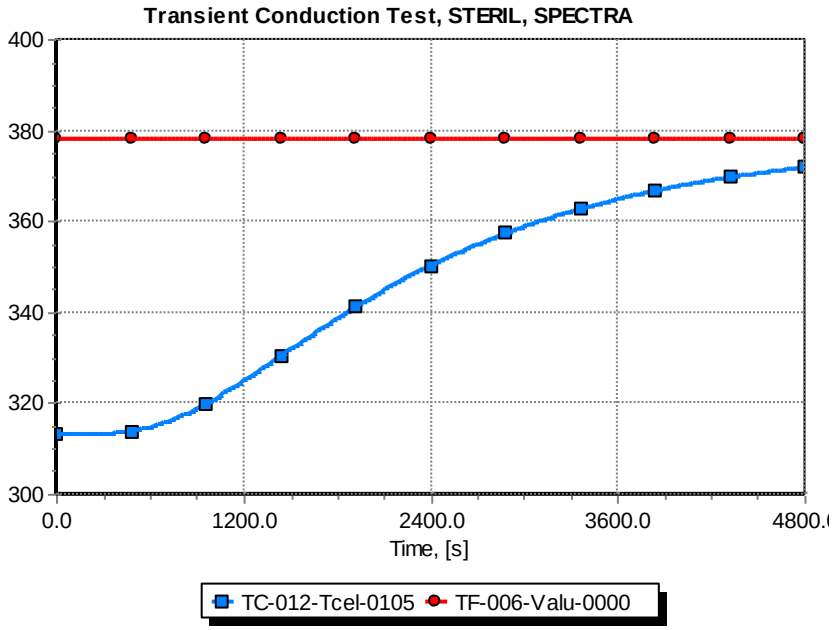

Figure 3-253 Sterilization of a vegetable can, T_{min} (cell 0005) and steam temperature (TF-006).

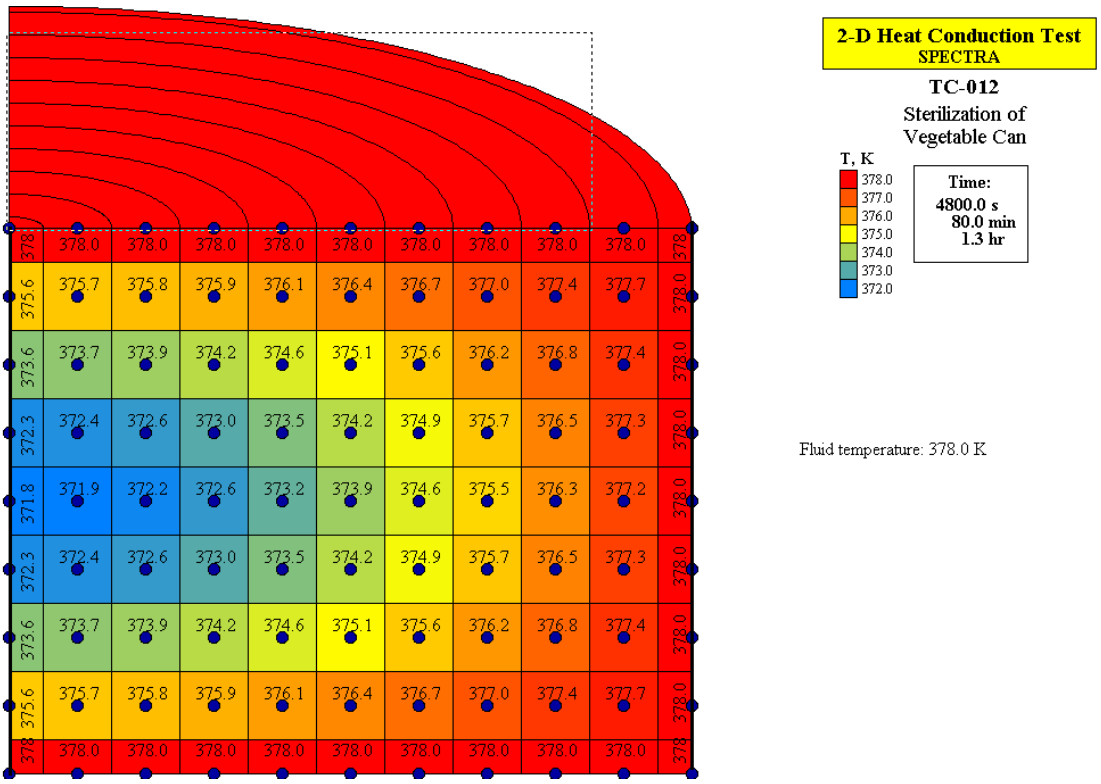

Figure 3-254 Sterilization of a vegetable can, t = 4800 s (80 min).

3.6.5 2-D Transient Conduction Tests - "Boiling Egg"

The "boiling egg" test is very similar to the previous test, only the geometrical details are somewhat different. A solid cylinder, height H, and radius R, has a uniform density, specific heat, and conductivity. It is initially at uniform temperature, T_0. At time t = 0.0 s the temperature of the boundary of the cylinder is raised to a higher temperature, T_b. One needs to calculate the temperatures at specified locations (R_i, Z_i). The test data is shown in Table 3-33. The calculation period is 7200 s.

Table 3-33 Test specification

Geometry	
H	0.48 m
R	0.12 m
Properties	
k	166.7 W/m^{2}K
ρ	8000 kg/m^3
c_p	10478.75 J/kgK
Temperatures	
Initial temperature, T_0	773.15 K (500.0°C)
Boundary temperature, T_b	1773.15 K (1500.0°C)
Measurement	
Location 1:	r = 0.0453 m, z = 0.115 m
Location 2:	r = 0.0453 m, z = 0.405 m
Location 3:	r = 0.1051 m, z = 0.115 m
Location 4:	r = 0.1051 m, z = 0.405 m

In the present test definition the measurement locations are not "reasonable". A "reasonable" location is for example center point of the cylinder, one half, one quarter, etc. of the length and height. In such case one may use a natural nodalization, with equal node distances in the radial direction and equal distances in the axial direction (although in general the axial distance will differ from the radial distance).

With the measurement point defined for this test it is not possible to find an equidistant mesh that would allow to obtain nodes exactly at the requested locations. This problem may be overcome in two ways:

- One may built a uniform mesh (equal distances between nodes) and estimate temperatures at the desired location by using the data from the four closest nodes and performing interpolations.
- One may built a nonuniform mesh in which will provide a node at each requested location.

This section shows a comparison of results obtained using both methods.

- Model 1 - uniform mesh, with node to node distances of 0.012 m in the radial direction and 0.06 m in the axial direction. Temperatures at the desired locations are obtained by bi-linear interpolations from the four closest nodes. The interpolations are performed using Control Functions. The interpolated values are available as CF-103, CF-203, CF-303, and CF-403 for the measurement locations 1, 2, 3, and 4, respectively.

- Model 2 - nonuniform mesh. The nodes are located exactly at the requested measurement points. The mesh cells sizes are different. It was decided to use three regions with equidistant cells:
    - Left (upper) boundary - first measurement point: Δr=0.0056625, Δz=0.028750
    - First measurement point - second point: Δr=0.0058360, Δz=0.027969
    - Second point - right (lower) boundary: Δr=0.0057450, Δz=0.037500

The input decks for these calculations are located in: \Z-INPUTS\TC\EGG, with:

- EGG-Uniform.SPE - Model 1,
- EGG-Nonuniform.SPE - Model 2.

Results are shown in Figure 3-255 through Figure 3-258, and summarized in Table 3-34. Results obtained at t = 500 s are shown in the visualization pictures in Figure 3-255 and Figure 3-256. The time dependent graphs are shown in Figure 3-257 and Figure 3-258.

As seen in Figure 3-255 and Figure 3-256 and Table 3-34, both methods gave very similar results. The reference data (analytical solutions) are shown in Table 3-34.

Table 3-34 The “boiling egg” test - results at t = 500 s

		***R* = 0.0453**		***R* = 0.1051**	
		T, (K)	Rel.Diff, (%)	*T*, (K)	Rel.Diff, (%)
***Z* = 0.115**	Uniform mesh	974	1.0%	1575	0.2%
	Non-uniform m.	964		1572	
***Z* = 0.405**	Uniform mesh	1000	–5.8%	1582	–0.9%
	Non-uniform m	1062		1597	

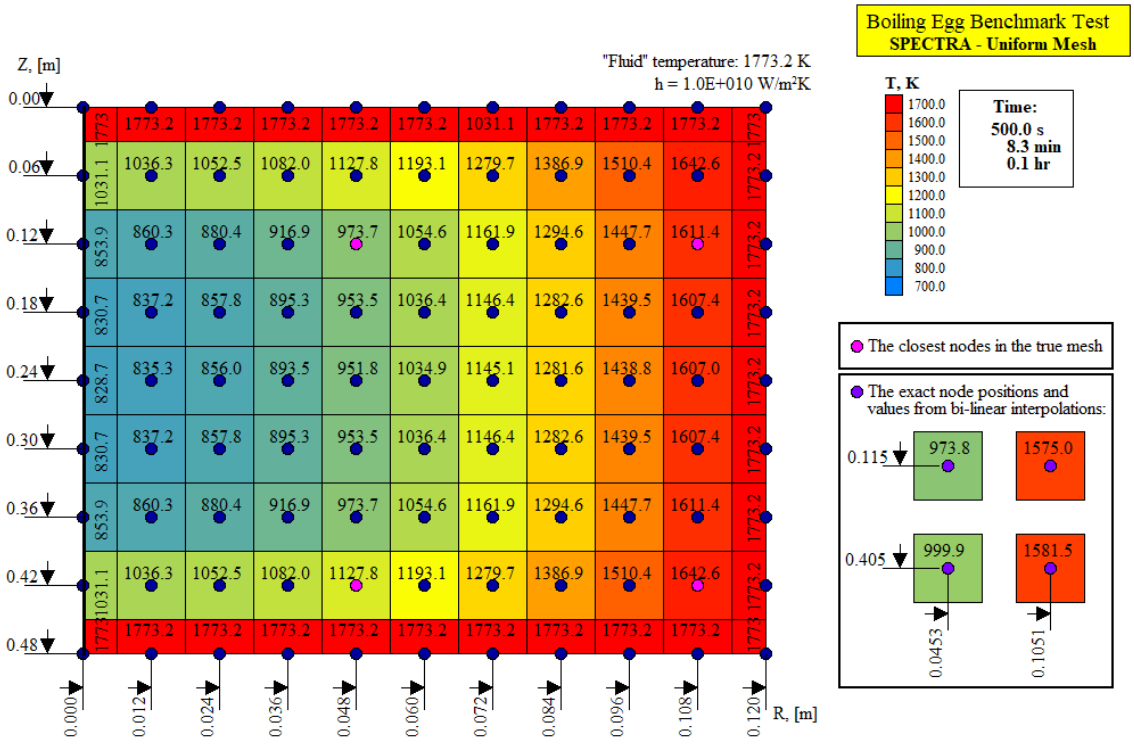

Figure 3-255 “Boiling egg”, uniform mesh, t = 500 s

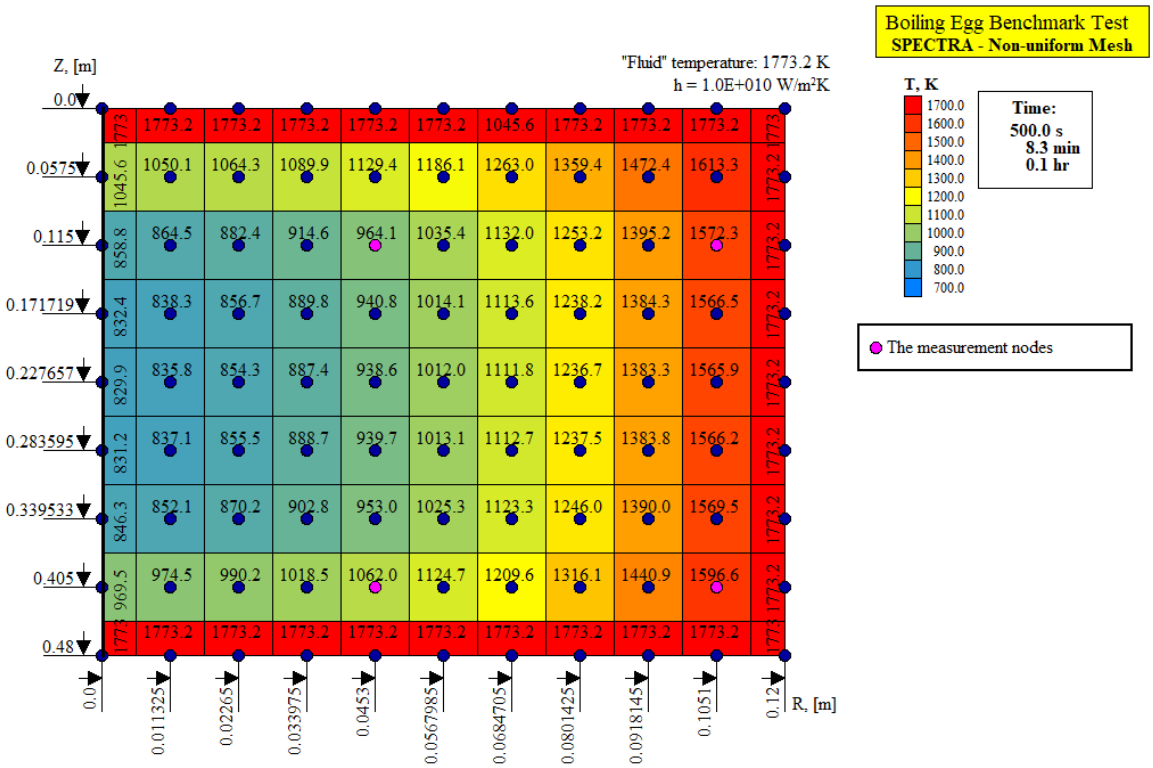

Figure 3-256 “Boiling egg”, non-uniform mesh, t = 500 s

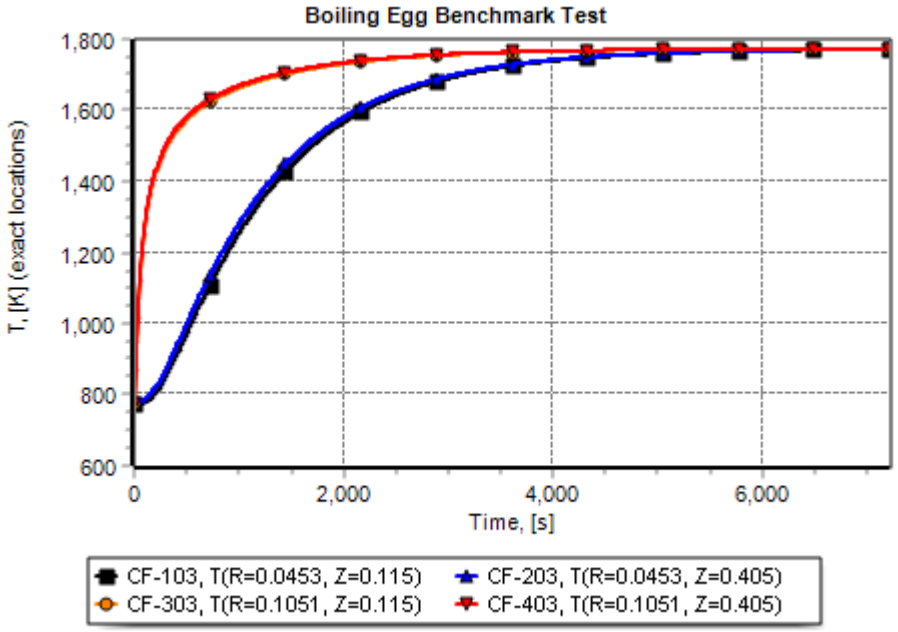

Figure 3-257 “Boiling egg”, uniform mesh, interpolated temperatures

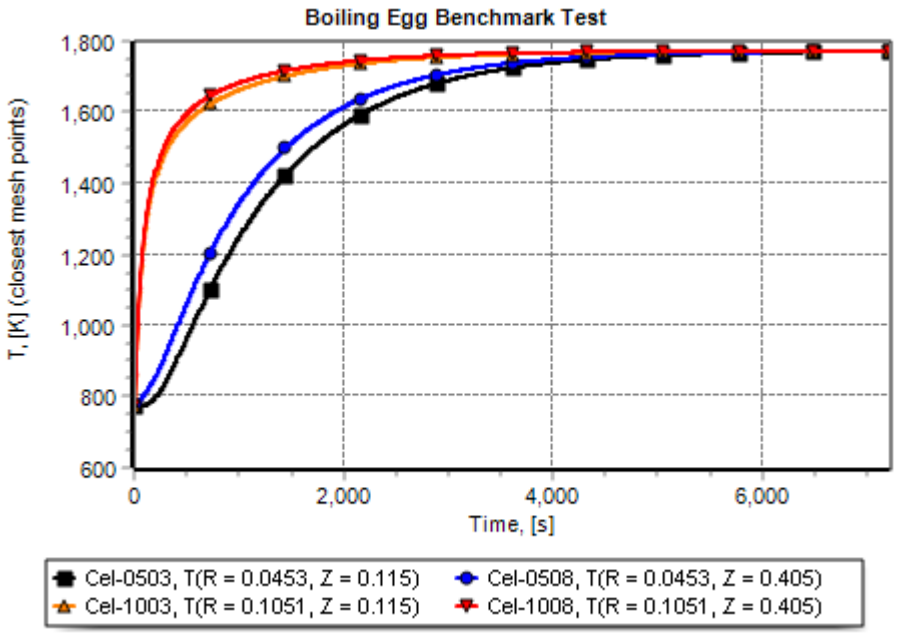

Figure 3-258 “Boiling egg”, nonuniform mesh, nodes at the desired locations

3.6.6 Fins and Spines

3.6.6.1 Comparison between 1-D and 2-D Model

A simple test has been prepared for testing the fin model available for the 1-D Solid Heat Conductors. A flat wall 8 mm with fins 12 mm long and 4 mm thick is used. The finned wall is assumed to be a part of a heater. On the hot side the fluid temperature is assumed to be 90°C (363 K) with a high heat transfer coefficient is 3000 W/m^{2}K (forced convection conditions). On the cold (finned) side a temperature of 15°C (288 K) is assumed with a low heat transfer coefficient, 20 W/m^{2}K (natural convection conditions).

Three cases are analyzed, two with fins and one without fins:

- Case 1: Aluminum fins - both wall and fins are made of aluminum.
- Case 2: Steel fins - both fins and wall are made if steel.
- Case 3: No fins - the aluminum wall without fins is used for this case.

The thermophysical properties of aluminum and steel were assumed using the data from material property handbooks for the Al and stainless steel SS-304. The values are shown in Table 3-35.

For comparison of the results obtained with the 1-D model with extended surfaces (fins), a 2-D model was built with a true geometry. Three 1-D and three 2-D structures are used in the model, as shown in Table 3-36. The boundary conditions are provided using Tabular Functions TF-001 (=3000.0), TF-002 (=363.0), TF-003 (=20.0), and TF-004 (=288.0). The input file for the calculations is stored in `\Z-INPUTS\TC\FINS\FINS.SPE`.

Results are shown in Figure 3-259 through Figure 3-262. The stationary state is shown in the visualization picture in Figure 3-259. Three time dependent graphs, Figure 3-260, Figure 3-261, and Figure 3-262, show comparison of the 1-D and 2-D results for the three cases.

In the current SPECTRA version the heat capacity of fins is taken into account by enlarging the heat capacity of the boundary cell (see Volume 1). In the previous versions of SPECTRA the heat capacity was neglected. The user may still activate this option by setting a constant conductivity of fins in the records 323XXX, 324XXX (see Volume 2).

Table 3-35 Material properties used for the fin test

Property	Aluminum	Steel
k, (W/m^{2}K)	180.0	13.0
ρ, (kg/m^3)	4800.0	7800.0
c_p, (J/kgK)	892.0	410.0

Table 3-36 1-D and 2-D structures used in the fin test

Case	1-D structures	2-D structures
1. Aluminum fins	SC-001	TC-001
2. Steel fins	SC-002	TC-002
3. No fins	SC-003	TC-003

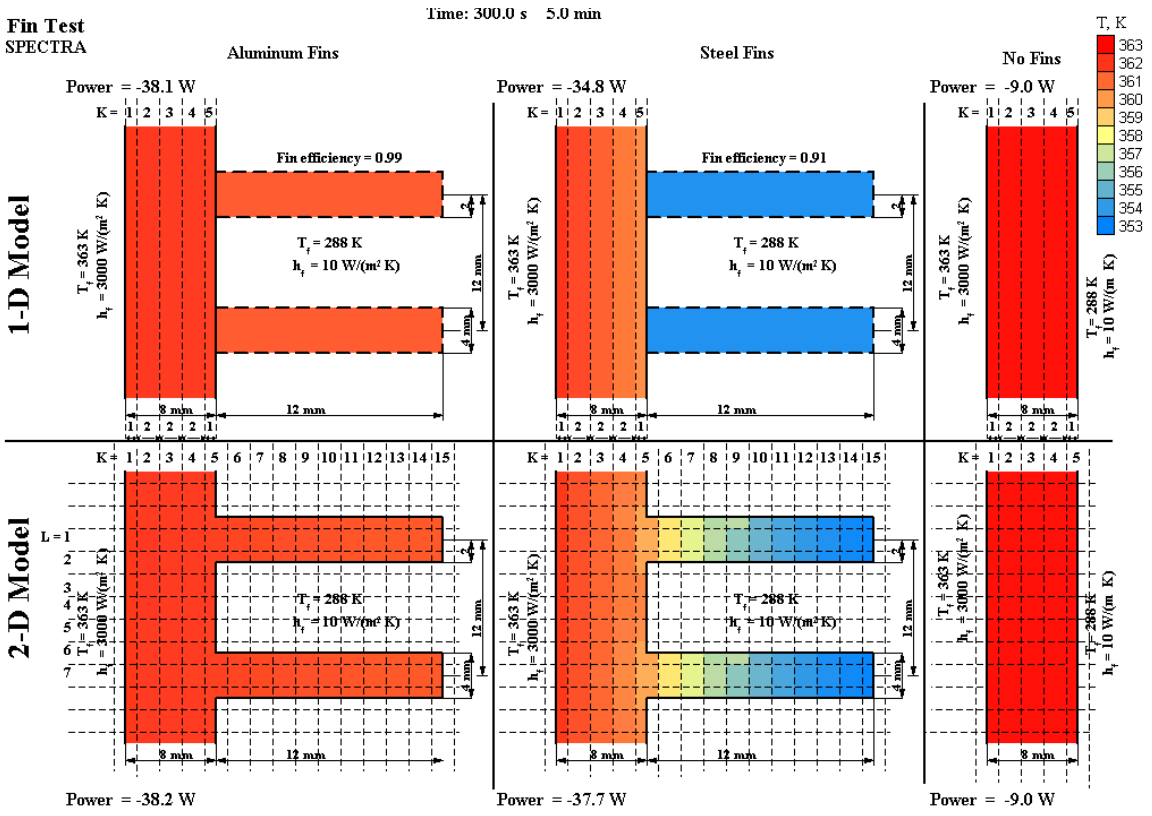

Figure 3-259 Fin test - comparison of 1-D fin model results with 2-D fins

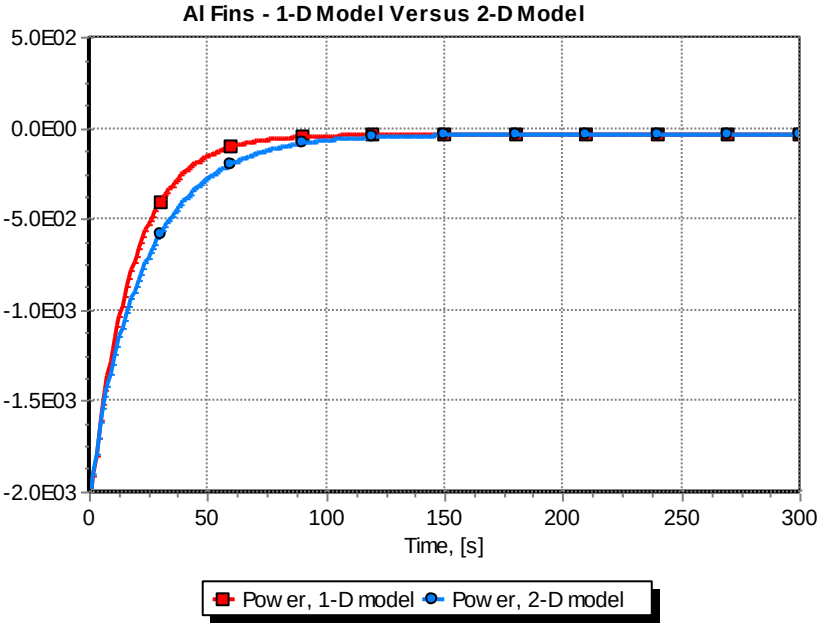

Figure 3-260 Fin test - aluminum fins

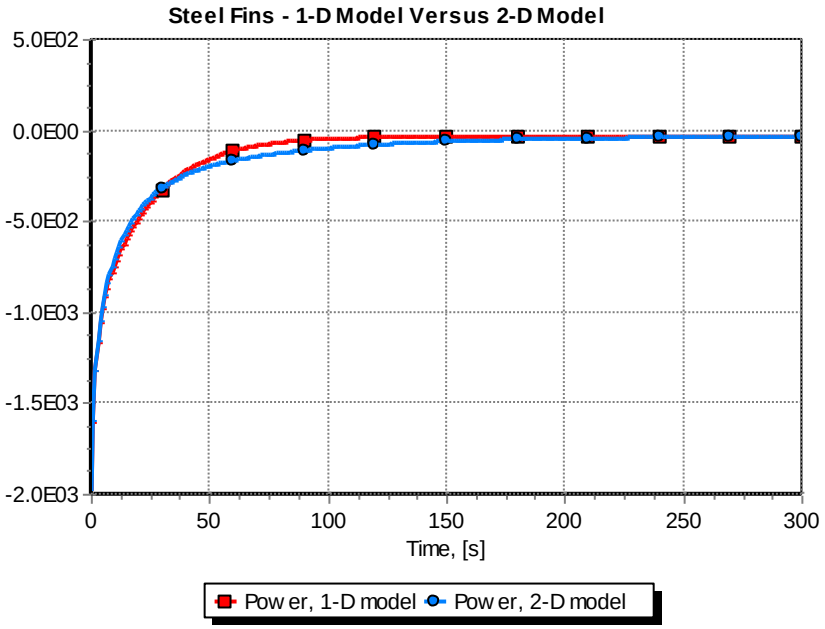

Figure 3-261 Fin test - steel fins

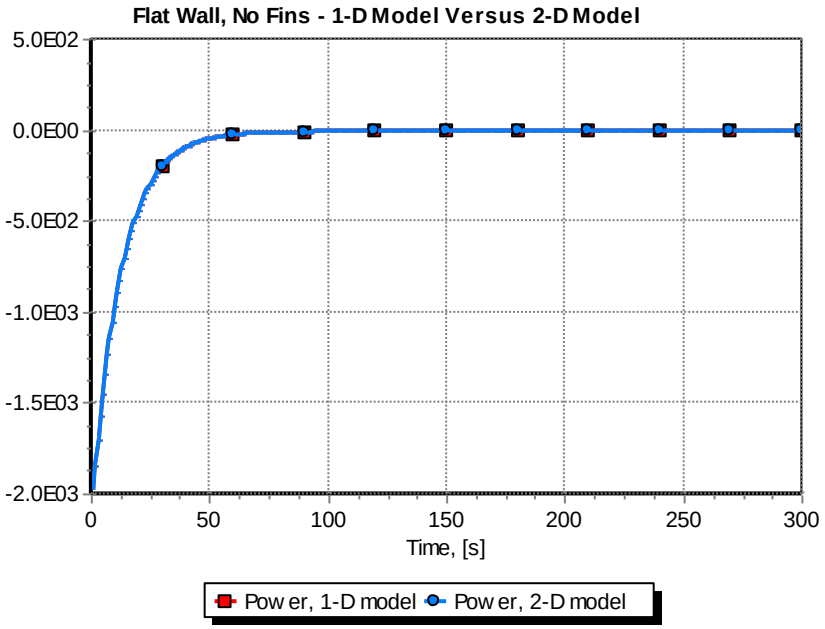

Figure 3-262 Fin test - flat wall without fins

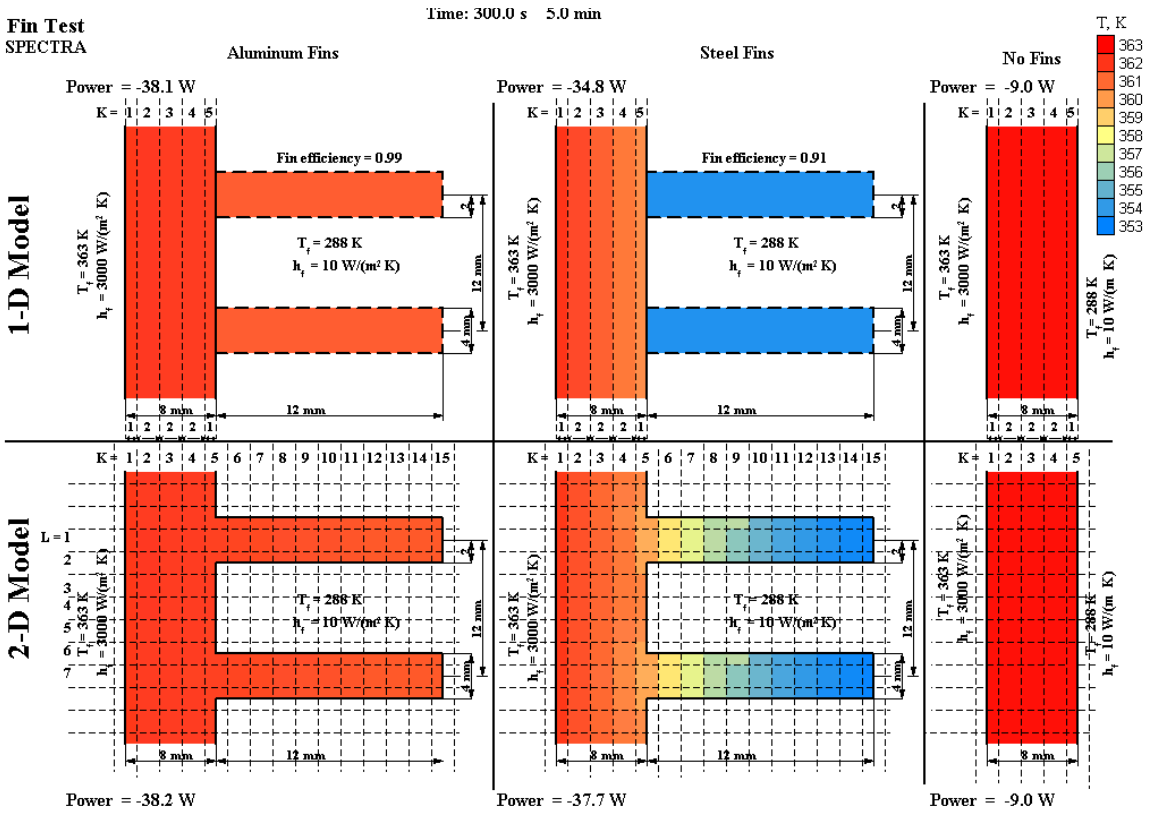

Figure 3-263 Fin test - 1-D fin model with no heat capacity (earlier SPECTRA versions)

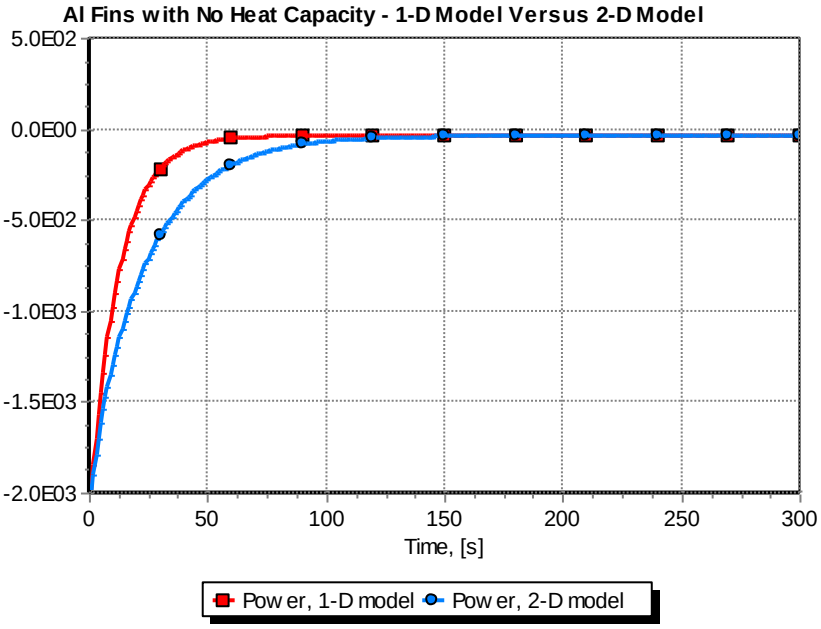

Figure 3-264 Fin test - aluminum fins, no heat capacity (earlier SPECTRA versions)

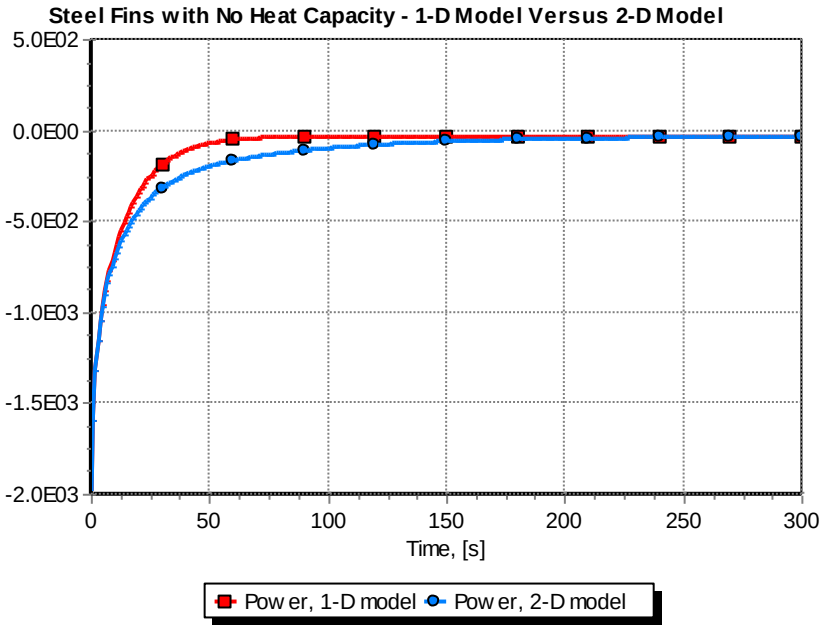

Figure 3-265 Fin test - steel fins, no heat capacity (earlier SPECTRA versions)

For comparison a zero heat capacity model was prepared. The input file for the calculations is stored in `\Z-INPUTS\TC\FINS\FINS-0.SPE`. Results are shown in Figure 3-263, Figure 3-264, Figure 3-265. The stationary state results are of course the same. In the transient graphs the lack of heat capacity is clearly visible as the lines becomes stable in the 1-D model faster than in the 2-D model. When the heat capacity is taken into account the transient results of the 1-D and the 2-D models are very similar (Figure 3-260, Figure 3-261), but of course not identical. Even with the same heat capacity, in the 1-D model the heat is transferred directly to/from the boundary cell, while in the 2-D model (and reality) it takes some time for the heat to flow along the fins.

The results are summarized in Table 3-37. In the case of aluminum fins the agreement between the 1-D and the 2-D model is very good. In the case of steel fins, the discrepancy is close to 8%. In this case the fin efficiency is relatively low. In the case without fins the 1-D model and the 2-D model are in fact the same and give identical results, which is shown by the present test.

It is concluded that the 1-D model with extended surfaces give very good results when the fin efficiency is high. Those are the practical cases because that's how the fins are being designed.

Table 3-37 Fin test - the heat power transferred through the wall

Case	1-D model	2-D model	Relative difference
Aluminum fins	38.1 W	38.2 W	0.3%
Steel fins	34.8 W	37.7 W	7.6%
No fins	9.0 W	9.0 W	0.0%

3.6.6.2 Fins on Cylindrical and Flat (Rectangular) Walls

The fin model is tested for rectangular and cylindrical geometries. The geometries are:

- Rectangular (SC-001 and SC-011). The surface are of 1.0 m^2 is assumed. Fins are present on both sides.
- Cylindrical (SC-002 and SC-012). The inner radius of 1.59155 m and the cylinder length of 0.1 m are assumed. The corresponding surface area is 1.0 m^2 on the left surface. Fins are present on both sides.

An internal heat source of 200 kW is defined for each SC. Two fin materials are considered:

- Steel fins (SC-001 and SC-002).
- Al fins (SC-011 and SC-012).

The fin dimensions are the same as in the previous test. The fin length is 12 mm for both sides. The input file for the calculations is stored in `\Z-INPUTS\TC\FINS\FINS-CYL.SPE`. The results are shown in Figure 3-266. Since the fin length is small compared to the cylinder radius, the results obtained for the cylindrical walls are expected to be very similar to the results obtained for the rectangular walls. This is clearly seen in Figure 3-266.

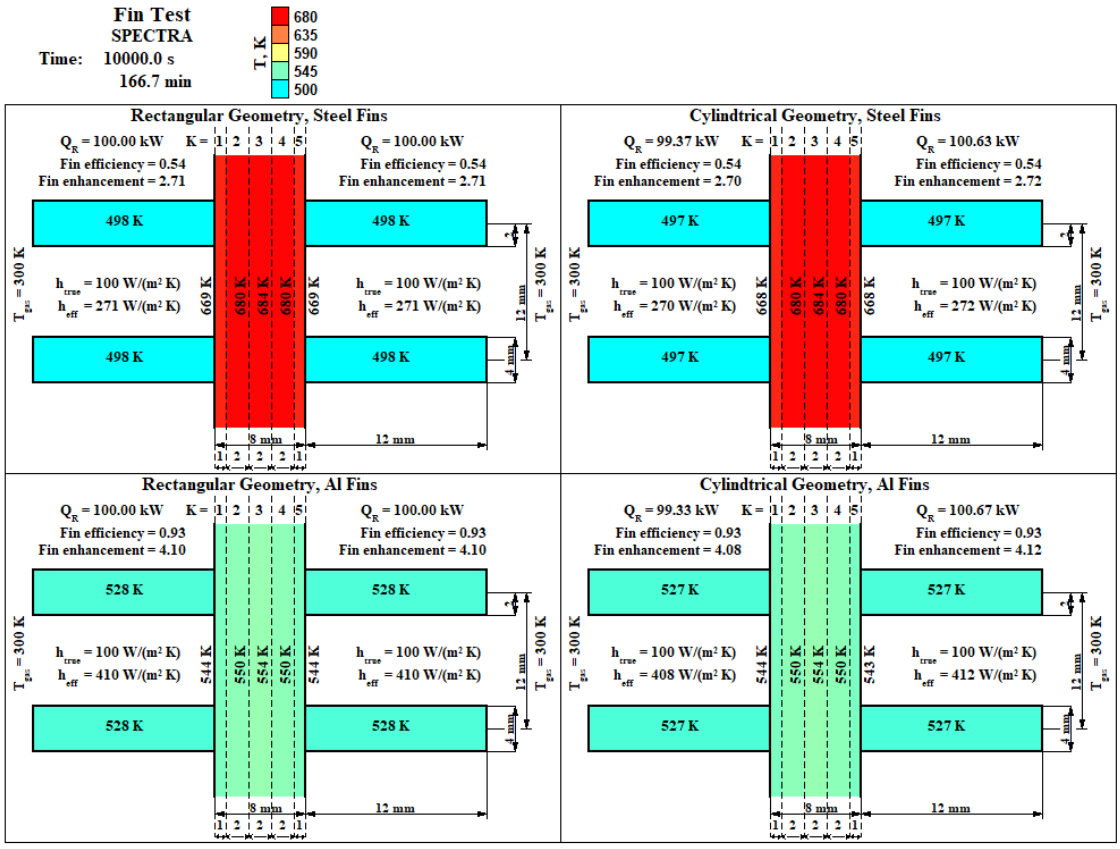

Figure 3-266 Fin test - fins on cylindrical and rectangular walls

3.6.7 Heat Exchanger - Comparison between 1-D and 2-D Model

3.6.7.1 Model

A counter flow gas-to-gas heat exchanger is modeled. It is assumed to consist of a tube bundle, with N = 10,000 horizontal tubes. The tube inner diameter is D_i = 0.02 m. The total length of the tubes is L = 3.0 m. The wall material is assumed to be stainless steel SS-304, with the following properties: k = 13.5 W/m^{2}K, ρ = 7800 kg/m^3, c_p, =410.0 J/kg-K. In the present test only the stationary results are compared. In order to obtain the stationary state fast, the specific heat was set to a small value by multiplying it by a factor 10^{-6}, therefore for the present test c_p, =410.0×10^{-6} J/kg-K was applied. With this heat capacity all parameters were stable already after about 20 s. All calculations were performed for the model time of 50.0 s.

The primary and secondary side inlet parameters are:

- Primary side (inside the tubes):
  - Inlet temperature: 300.0 K
  - Pressure: 1.0×10^5 Pa
  - Inlet flow: 10.0 kg/s
  - Gas composition: x_{N2} = 0.8, x_{O2} = 0.2 (dry air)

- Secondary side (outside the tubes):
  - Inlet temperature: 900.0 K
  - Pressure: 1.0×10^5 Pa
  - Inlet flow: 10.0 kg/s
  - Gas composition: x_{N2} = 0.8, x_{O2} = 0.2 (dry air)

The purpose of the present test is to investigate influence of the axial heat conduction in the case with a large temperature difference between the inlet and the outlet of the heat exchanger. In the present case the temperature difference is 900 – 300 = 600 K. Three cases are considered with different wall thickness:

- "THIN" wall case: wall thickness, t = 0.0002 m (0.2 mm)
- "MID" wall thickness case: wall thickness, t = 0.002 m (2 mm)
- "THICK" wall case: wall thickness, t = 0.02 m (2 cm)

As a verification of SPECTRA results, calculations are performed with RELAP5/MOD3.2. Input decks for these calculations are located in:

- RELAP: `\Z-INPUTS\TC\HEX\RELAP\`
  - `HEX-THIN.INP` the thin wall case
  - `HEX-MID.INP` the middle wall thickness case
  - `HEX-THICK.INP` the thick wall case

- SPECTRA `\Z-INPUTS\TC\HEX\SPECTRA-NoTA\`
  - `HEX-THIN.SPE` the thin wall case
  - `HEX-MID.SPE` the middle wall thickness case
  - `HEX-THICK.SPE` the thick wall case

As shown in several test calculations the most accurate results for a heat exchanger are obtained using the Temperature Averaging (**TA**) concept (see section 3.5.7). Therefore a set of SPECTRA runs listed above, was repeated with the TA active. The file locations are:

- SPECTRA with TA `\Z-INPUTS\TC\HEX\SPECTRA-TA\`
  - `HEX-THIN.SPE` the thin wall case
  - `HEX-MID.SPE` the middle wall thickness case
  - `HEX-THICK.SPE` the thick wall case

Both RELAP and SPECTRA models were set up using a 12-node division of the heat exchanger tubes; the length of each node is 0.25 m.

3.6.7.2 Comparison of the RELAP and SPECTRA Results

RELAP and SPECTRA results are shown in Figure 3-267 through Figure 3-272 and summarized in Figure 3-273, Table 3-38, and Table 3-39. The RELAP results are obtained with the 1-D conduction model, therefore are compared to the 1-D results from SPECTRA in Table 3-38. There is a difference of 1 - 3% between the codes. The individual results, such as heat transfer coefficients and local temperatures are very similar (Figure 3-267 through Figure 3-272). The difference in the power is most likely caused by different fluid properties. Comparing Figure 3-267 and Figure 3-268 one sees that the hot gas cools down more in RELAP than in SPECTRA. This is contradictory to the heat exchange, which is higher in SPECTRA than in RELAP. Those facts indicate that there is some discrepancy between the air heat capacity in RELAP and SPECTRA. Because the local heat transfer coefficients are very similar, the agreement between RELAP and SPECTRA is considered satisfactory.

Figure 3-273 shows summary of the heat power. It is seen that the power increases with increasing wall thickness. This seems to be a paradox; it is caused by increased heat transfer area of the outside tube surfaces. In the present case the heat transfer coefficients are quite low and the effect of the heat transfer area is large. The low heat transfer is caused by relatively low pressure and flows applied in this test.

The influence of the axial heat conduction is shown in Table 3-39. For the thin wall case no influence is observed. A small influence is observed for the thick wall case. Therefore it is concluded that the axial heat conduction is not very important even with the applied temperature gradient of 200 K/m.

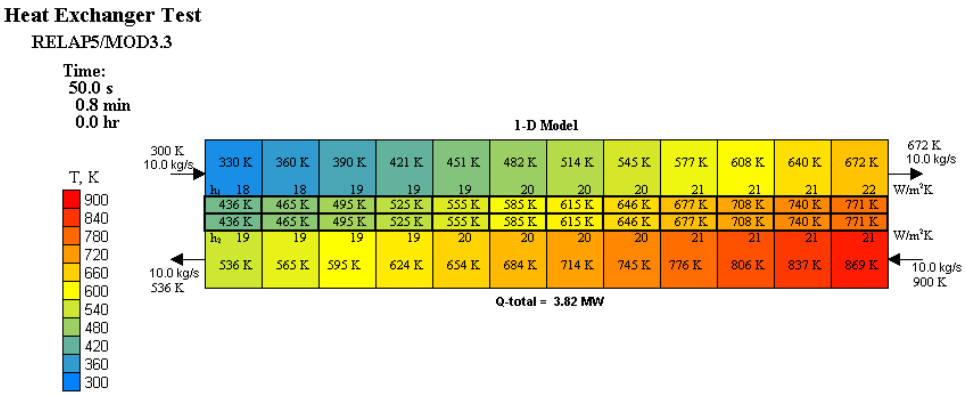

Figure 3-267 Counter-current heat exchanger, thin walls, RELAP5

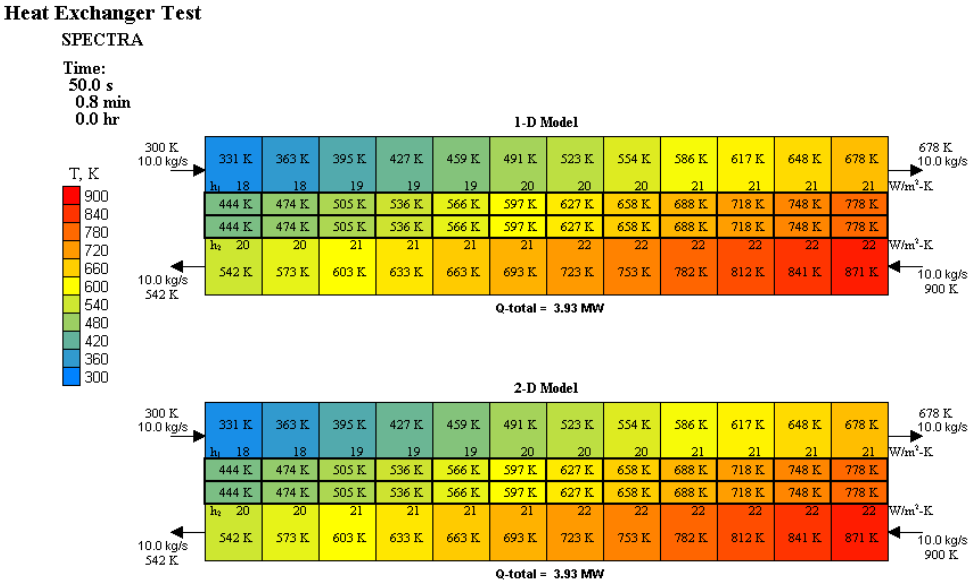

Figure 3-268 Counter-current heat exchanger, thin walls, SPECTRA

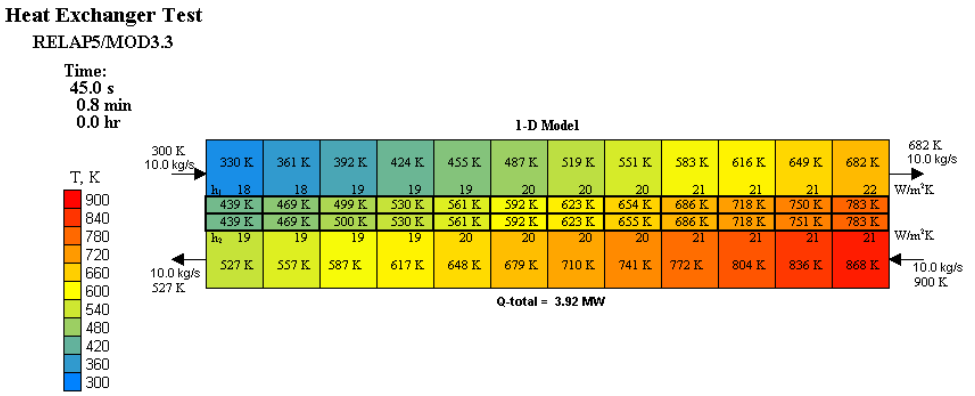

Figure 3-269 Counter-current heat exchanger, middle wall thickness, RELAP5

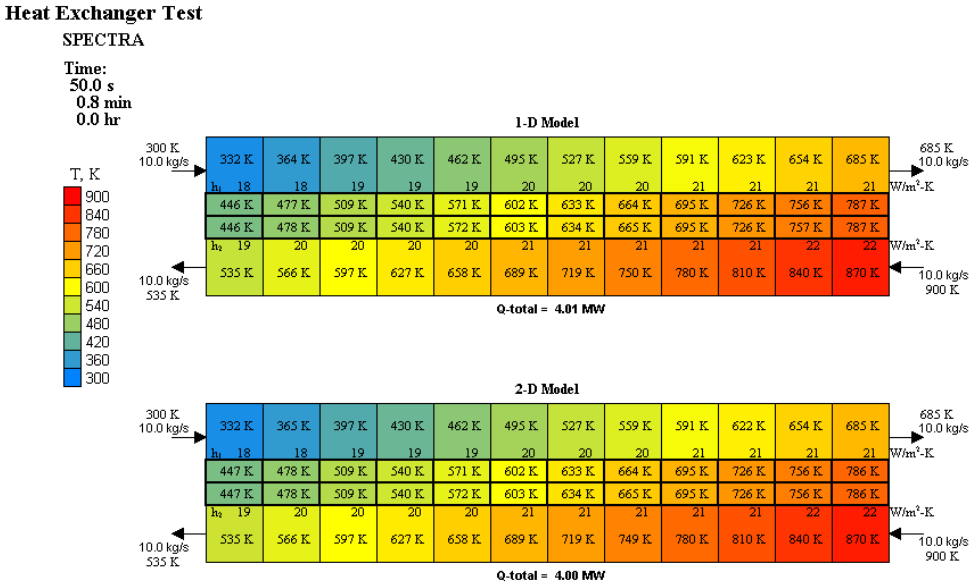

Figure 3-270 Counter-current heat exchanger, middle wall thickness, SPECTRA

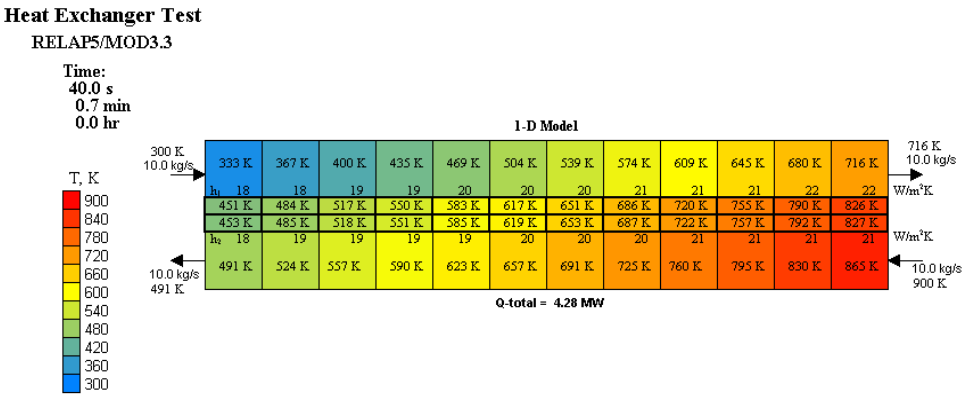

Figure 3-271 Counter-current heat exchanger, thick walls, RELAP5

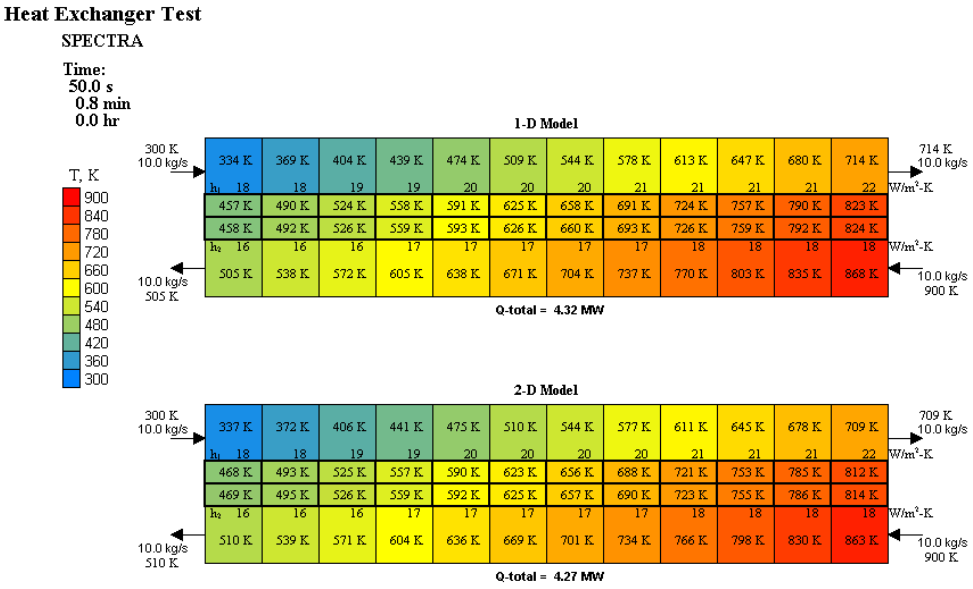

Figure 3-272 Counter-current heat exchanger, thick walls, SPECTRA

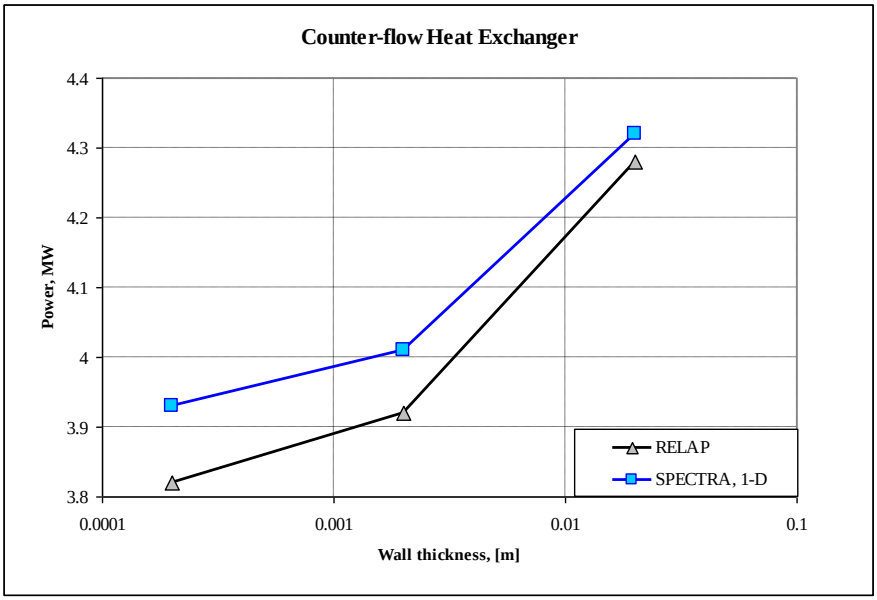

Figure 3-273 Summary of results - comparison of RELAP and SPECTRA results

Table 3-38 Summary of results - comparison of RELAP and SPECTRA results

Case, *t*, (m)	Total power, MW		Relative difference, %
	RELAP	SPECTRA, 1-D	
THIN, 0.0002 m	4.28	4.32	0.9
MID, 0.002 m	3.92	4.01	2.2
THICK, 0.02 m	3.82	3.93	2.7

Table 3-39 Summary of results - influence of axial conduction

Case, *t*, (m)	Total power, MW		Relative difference, %	Influence of axial conduction
	1-D	2-D		
THIN, 0.0002 m	3.93	3.93	0.0	none
MID, 0.002 m	4.01	4.00	0.2	very small
THICK, 0.02 m	4.32	4.27	1.2	small

3.6.7.3 SPECTRA Results with Temperature Averaging

Results obtained using the Temperature Averaging are shown in Figure 3-274 through Figure 3-276 and summarized in Figure 3-277 and Table 3-40. The power is higher than in the cases without TA, which is to be expected based on the results shown in section 3.5.7. The effect of the axial conduction is practically the same as in the cases without TA: for the thin wall case no influence is observed. A small influence is observed for the thick wall case. Therefore it is concluded that the axial heat conduction is not very important even with the applied temperature gradient of 200 K/m

Table 3-40 Summary of results - influence of axial conduction

Case, *t*, (m)	Total power, MW		Relative difference, %	Influence of axial conduction
	1-D	2-D		
THIN, 0.0002	4.15	4.15	0.0	none
m	4.24	4.23	0.2	very small
MID, 0.002 m	4.60	4.54	1.3	small
THICK, 0.02 m				

3.6.7.4 Summary

The results are summarized as follows:

- Satisfactory agreement is observed between RELAP and SPECTRA. The local heat transfer coefficients are very similar in both codes. There is a discrepancy of 1 - 3% in the total power. It was found out that this discrepancy is caused by differences in fluid (air) properties in the two codes.
- The influence of axial heat conduction is small for the thick walls (2 cm), very small for the middle walls (2 mm), and practically none for the thin wall case (0.2 mm). Those results are obtained for the axial temperature gradient of 200 K/m. This is not an extremely large value. For example, in case of the PBMR recuperator the temperature gradient is ~400 K/0.5 m = 800 K/m.

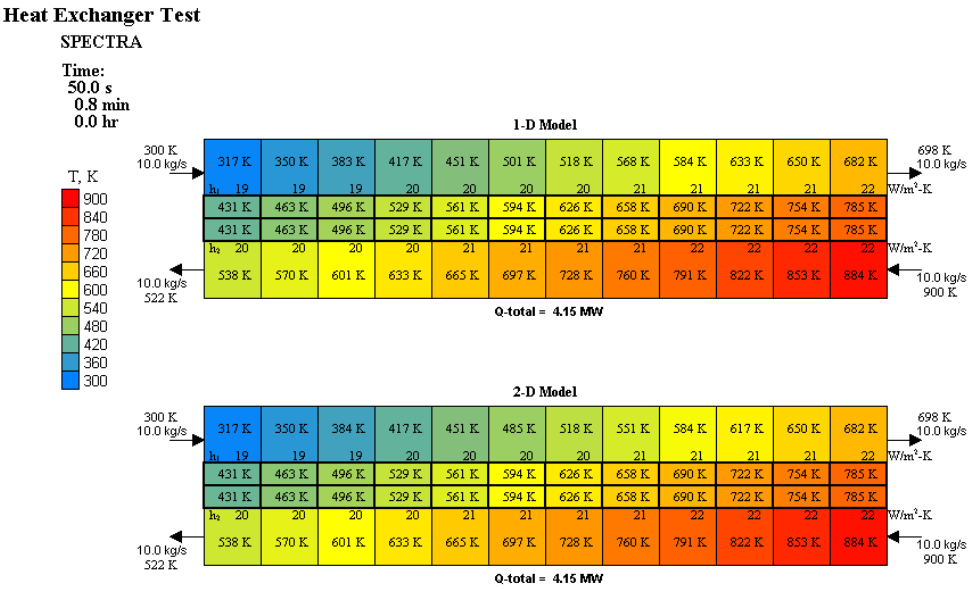

Figure 3-274 Counter-current heat exchanger, thick walls, SPECTRA with TA

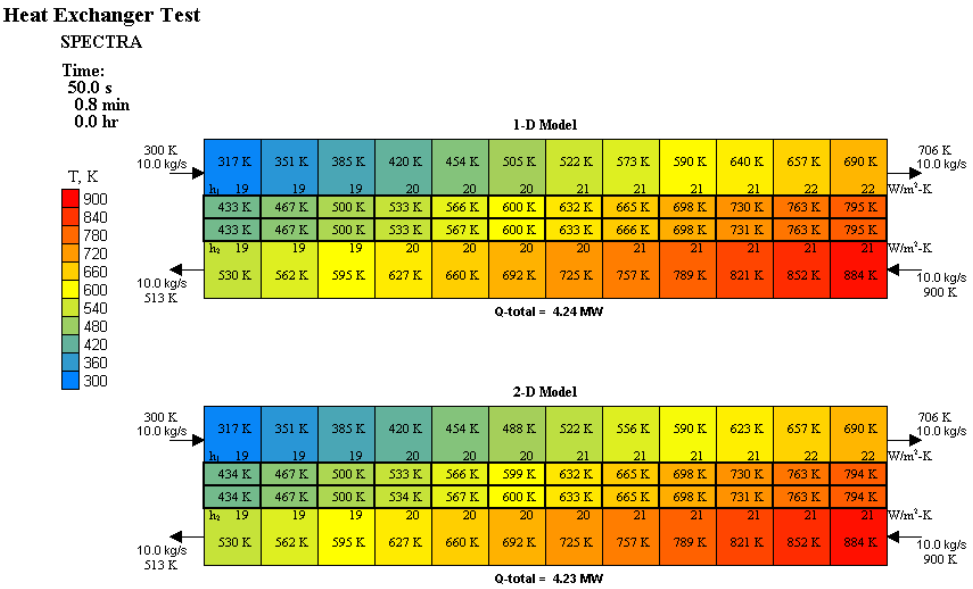

Figure 3-275 Counter-current heat exchanger, middle wall thickness, SPECTRA with TA

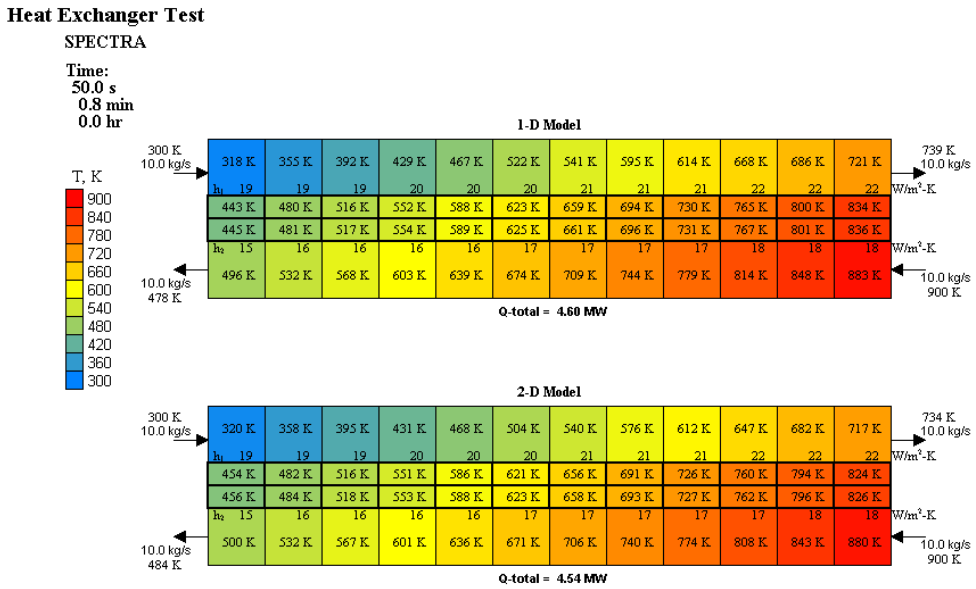

Figure 3-276 Counter-current heat exchanger, thin walls, SPECTRA with TA

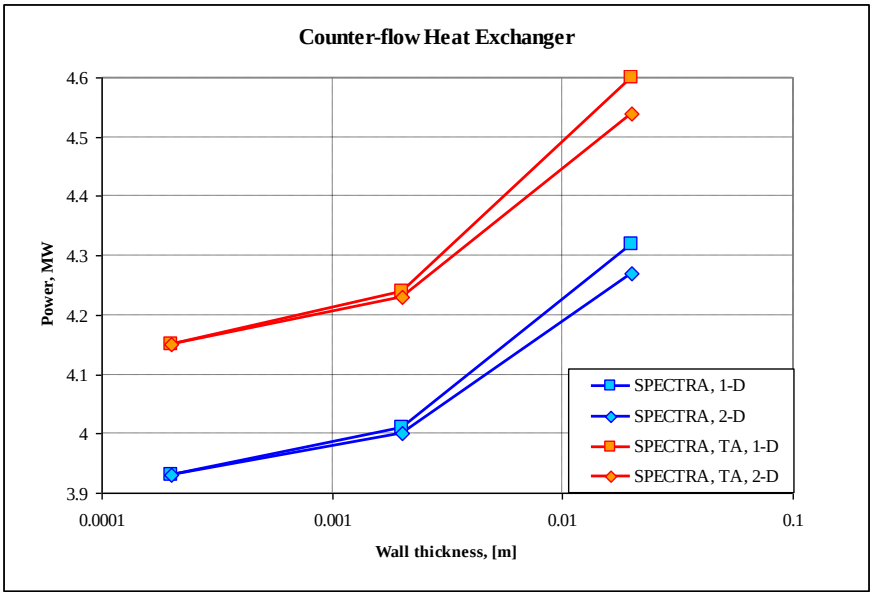

Figure 3-277 Summary of results - influence of axial conduction

3.6.8 Reflood Test FLECHT SEASET

Analysis of the FLECHT SEASET reflooding tests [143], [144], will be performed in the future.

3.6.9 ECN Reflood Test

3.6.9.1 Test Facility

In 1985, the Energy Research Center of the Netherlands (ECN) conducted reflood experiments representing a 36 rod-bundle of standard 15x15 PWR fuel design with an axially uniform power profile [145]. The ECN test facility consists of a pressurized water supply accumulator and injection line, two carry-over tanks connected to the upper plenum and a blowdown tank for steam condensation. The test section is shown in Figure 3-278. The 36 rod-bundle is located inside a rectangular housing. The bundle consists of 32 electrically heated rods and 4 unheated rods which are used to place the instrumentations. An axially uniform power profile is applied. The rods can be set at different power levels to establish a radially non-uniform initial wall temperature profile. The rods have a heated length of 3 m and an outer diameter of 10.7 mm.

A total of 48 experiments have been performed under a certain range of test conditions and parameters, as shown in Table 3-41. Seven tests are described in reference [145] and those tests were used for the current validation. The tests are presented in Table 3-42.

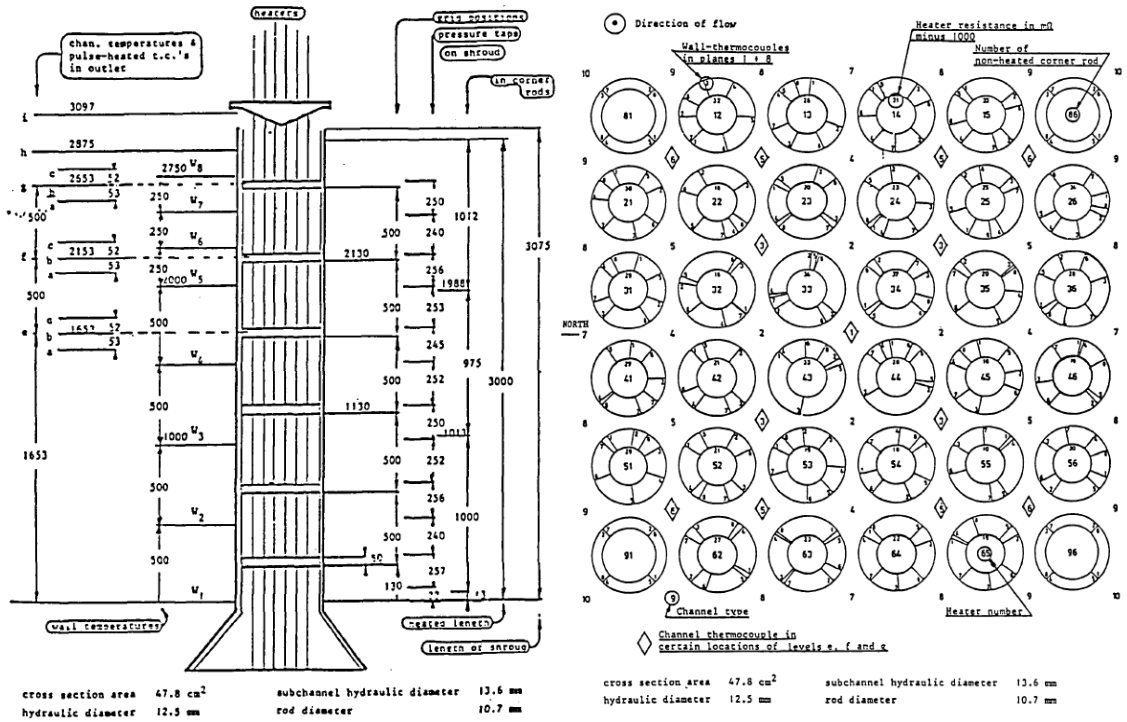

Figure 3-278 ECN test facility [145]

Table 3-41 ECN tests - range of test conditions [145]

Initial heater rod wall temperature	200°C - 850°C
Power	1.7 - 5 W/cm²
Bundle outlet pressure (upper plenum pressure)	.2 - .6 MPa
Flooding rates:	
Constant	1.4 - 8.0 cm/sec
Variable in steps	3.0 - 0.9 cm/sec
Coolant subcooling	20°C - 80°C

Table 3-42 ECN tests - initial and operating conditions [145]

EXP	P	T_{in}	t	v_{in}	Wall temperature (K) level							t	Power	Power
	(MPa)	(K)	(s)	(m/s)	2	3	4	5	6	7	8	(s)	(W)	(W/cm^2)
3216	0.2	313	0 4.9 5.0 805.0	0 0 .15486 .014356	450	459	463	473	473	449	449	0 14.5 17.5 587.5	426.0 426.0 114805.3 115736.9	 3.56 3.59
3224	0.2	373	0 4.9 5.0 1192.5	0 0 .014371 .014193	475	469	467	473	473	467	452	0 13.5 17.5 965.0	475 475.0 113668.6 115347.2	 3.52 3.57
4100	0.2	373	0 7.4 7.5 1000.0	0 0 .080549 .080549	899	893	893	873	865	863	846	0 17.0 20.5 398.0	8962.0 8962.0 114336.6 115819.2	 3.54 3.59
4106	0.2	373	0 7.4 7.5 1000.0	0 0 .023222 .023222	860	863	867	868	870	870	850	0 6.0 11.0 781.0	6505.0 6505.0 112308.7 114510.7	 3.48 3.55
4120	0.2	313	0 5.9 6.0 1000.0	0 0 .081754 .081754	849	851	859	857	860	859	841	0 13.0 16.0 131.5	6558.0 6558.0 113832.5 115350.4	 3.53 3.57
4138	0.2	373	0 7.9 8.0 1000.0	0 0 .02349 .02349	1105	1105	1114	1118	1122	1121	1095	0 14.0 19.0 409.0 799.0	18806.0 18806.0 112584.2 114032.4 114973.0	 3.49 3.53 3.56
4149	0.4	393	0 5.9 6.0 200.0 380.0 766.0	0 0 .023123 .023267 .023275 .023273	1082	1085	1104	1116	1115	1115	1083	0 10.0 14.0 574.0	10390.0 10390.0 112502.3 114565.7	 3.49 3.55

3.6.9.2 Model

The SPECTRA model and analysis results are described in detail in the publicly available report [146]. The model nodalization of the ECN facility is shown in Figure 3-279. It was decided to apply basically the same nodalization as the one that was used in the earlier RELAP5 analysis (described in [145], nodalization sensitivity of the RELAP5 model was checked within the a separate activity [146]). Most of the test section is represented by Control Volumes of 0.25 m height. Three CV-s at the bottom and one CV at the top of the test section have twice smaller height (0.125 m).

The solid structures (SC-s) in SPECTRA do not have a moving mesh option that is available in RELAP5; therefore the user must ensure that sufficiently small axial nodes are applied for reflood. Sensitivity study was performed using the axial nodes of all SC-s of:

- Case 1: H=0.125 m (height of the smallest CV)
- Case 2: H=0.0625 m (1/2 of the smallest CV)
- Case 4: H=0.03125 m (1/4 of the smallest CV)

It was concluded that the Case 4 gives sufficiently accurate results and this model was used to perform calculations (and is shown in Figure 3-279). Therefore each of the 0.125 m long CV has 4 SC-s and each 0.25 m long CV has 8 SC-s. Axial conduction is activated for all SC-s, SC-301 through SC-404.

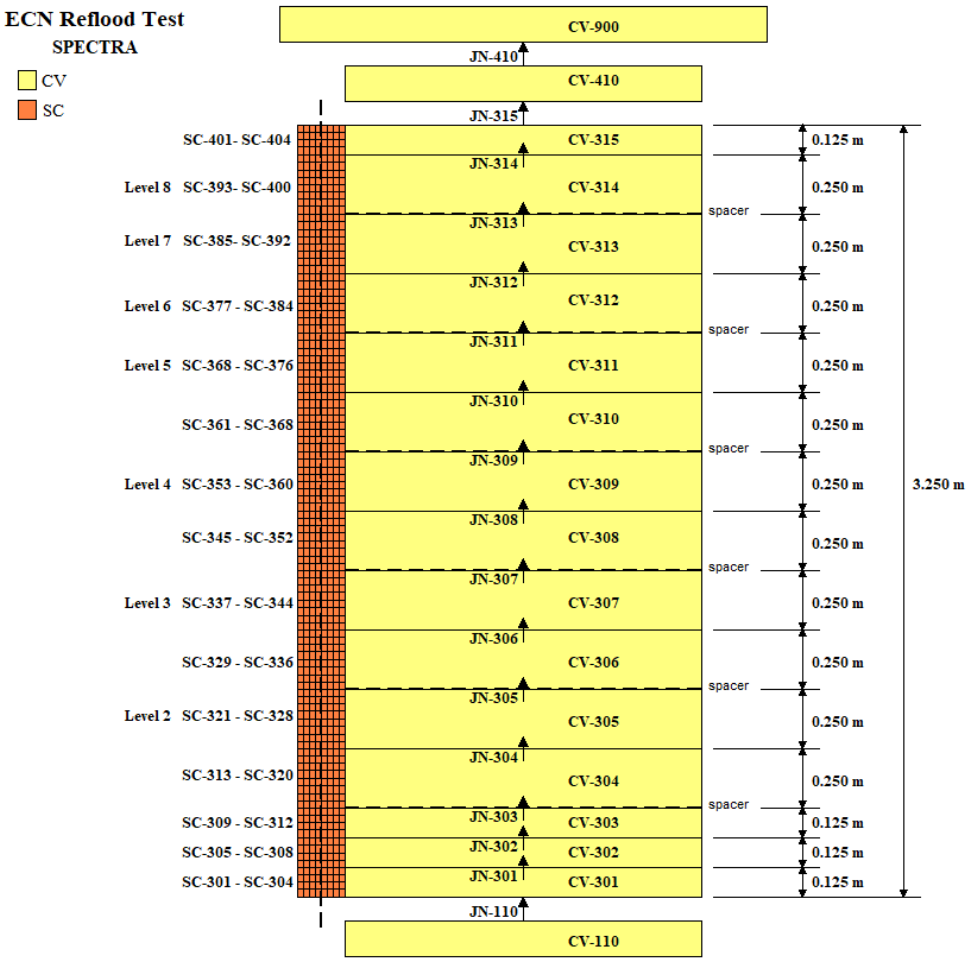

Figure 3-279 Nodalization of the SPECTRA model [146]

3.6.9.3 Results

The discussion of the results is limited here to the results in the lower part of the bundle (levels 2, 3, 4). A broader discussion is provided in [146]. Seven tests were analyzed:

- Test 3216, Figure 3-280
- Test 3224, Figure 3-281
- Test 4100, Figure 3-282
- Test 4106, Figure 3-283
- Test 4120, Figure 3-284
- Test 4138, Figure 3-285
- Test 4149, Figure 3-286

For all tests, figures (a) show the results obtained with the default settings. In all analyzed cases, the rewetting is too slow, compared to the measured data. Figures (b) show the results obtained with the constant in Berenson minimum film boiling correlation changed to $C_{MFB} = 0.25$ (input parameter CMFBSC). Since the default value is 0.127, this means an increase by nearly a factor of 2. With the modified constant C_{MFB}, the agreement with experiment is clearly better.

As shown in [146], further improvement of the rewetting time may be obtained by changing other model parameters, such as:

- critical void fraction for film boiling, α_1, (input parameter VFL0HT),
- boiling hysteresis parameter, C_{hyst}, (input parameter CBH0HT).

Summarizing, the default model settings give conservative (too slow) rewetting. With modified film boiling constant, $C_{MFB} = 0.25$, the agreement is better but clearly the current results are not perfect and it is recommended to continue the work on rewetting tests in the future.

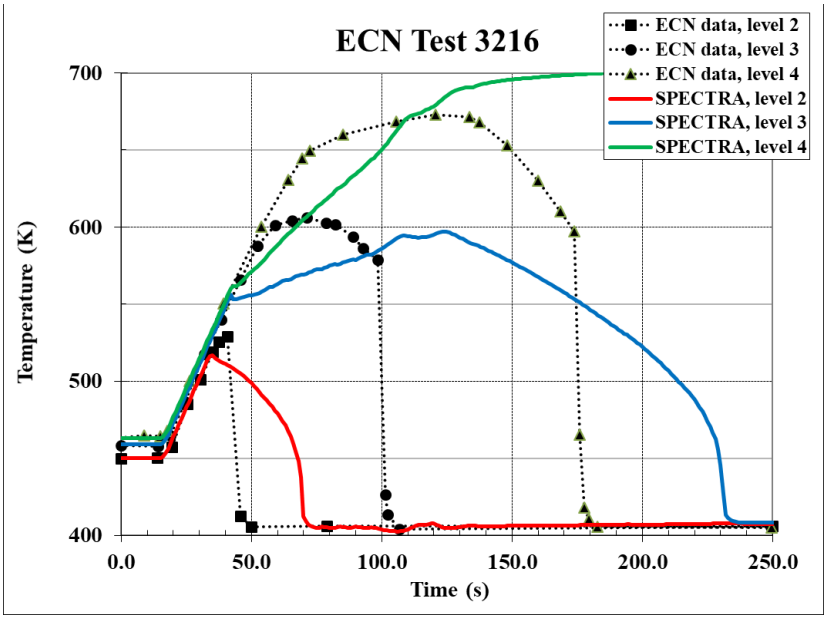

(a) default parameters (C_{MFB}= 0.127)

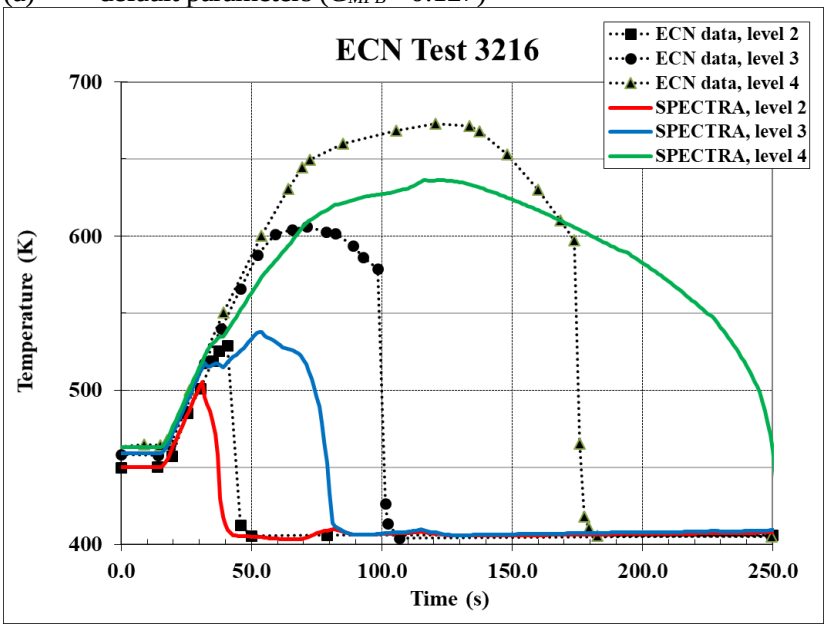

(b) C_{MFB}= 0.25

Figure 3-280 Test 3216, (a) all defaults, (b) C_{MFB}= 0.25

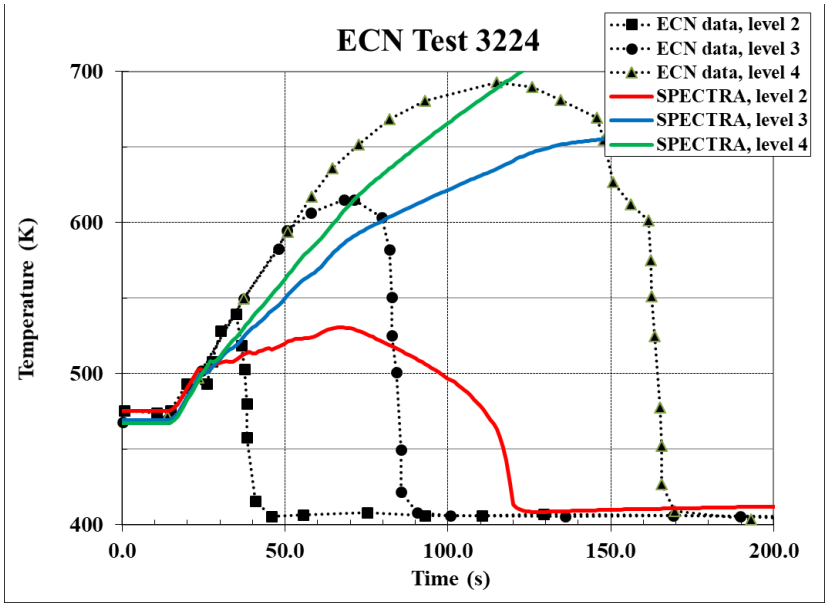

(a) default parameters (C_{MFB}= 0.127)

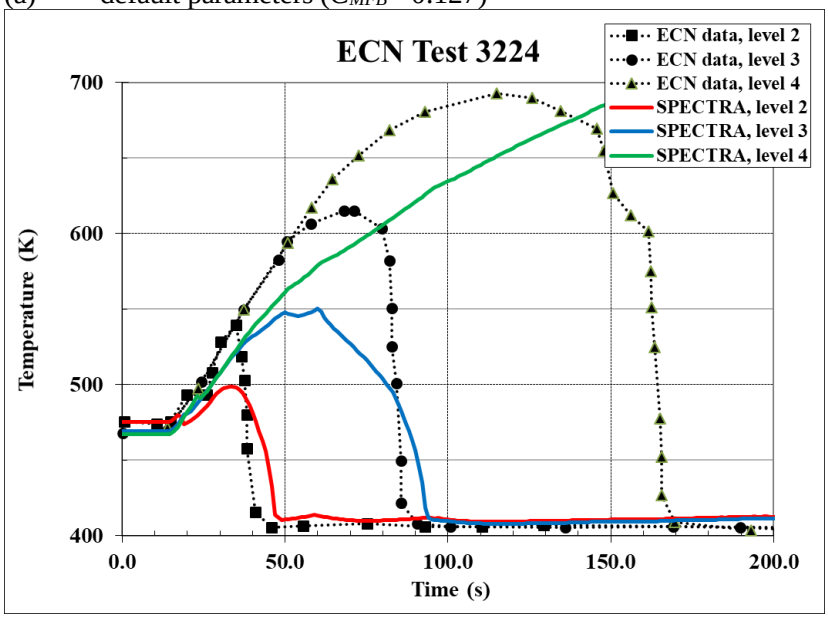

(b) C_{MFB}= 0.25

Figure 3-281 Test 3224, (a) all defaults, (b) C_{MFB}= 0.25

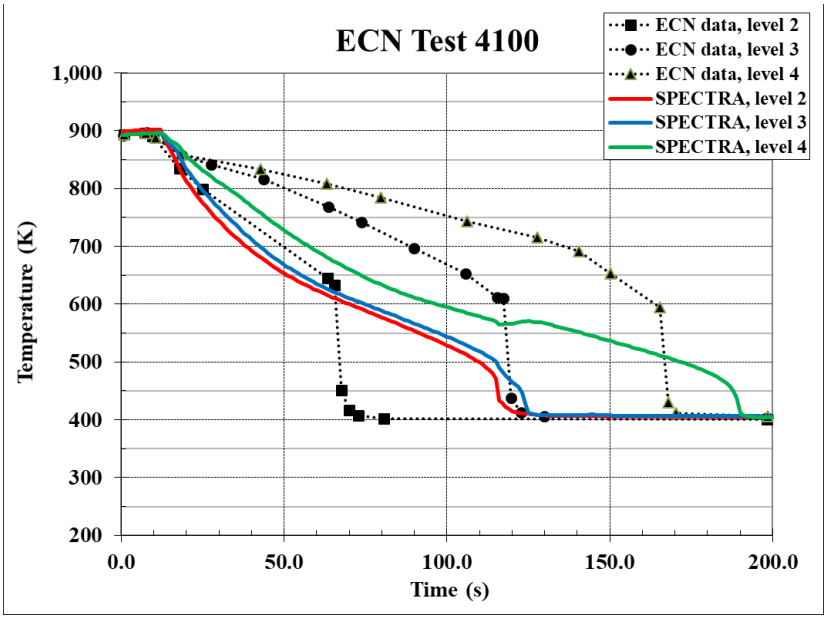

(a) default parameters (C_{MFB}= 0.127)

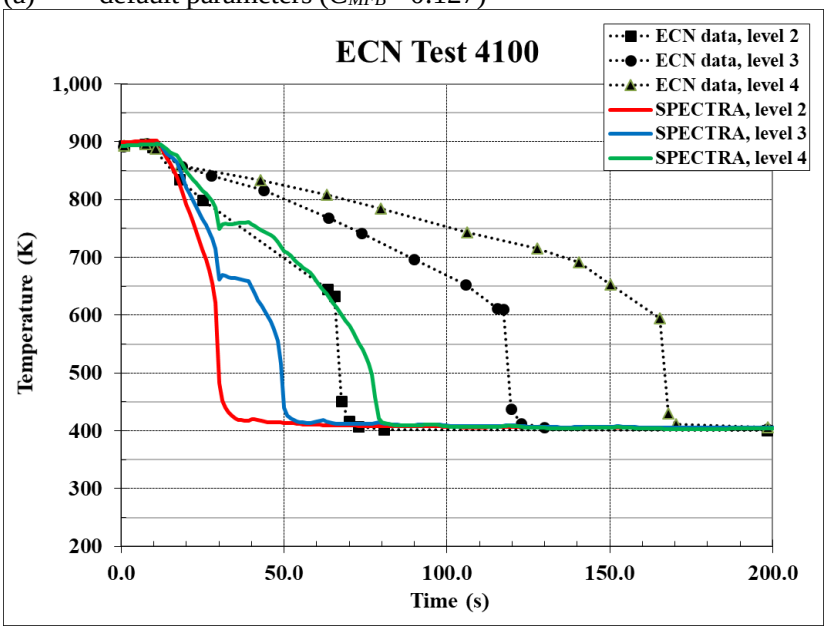

(b) C_{MFB}= 0.25

Figure 3-282 Test 4100, (a) all defaults, (b) C_{MFB}= 0.25

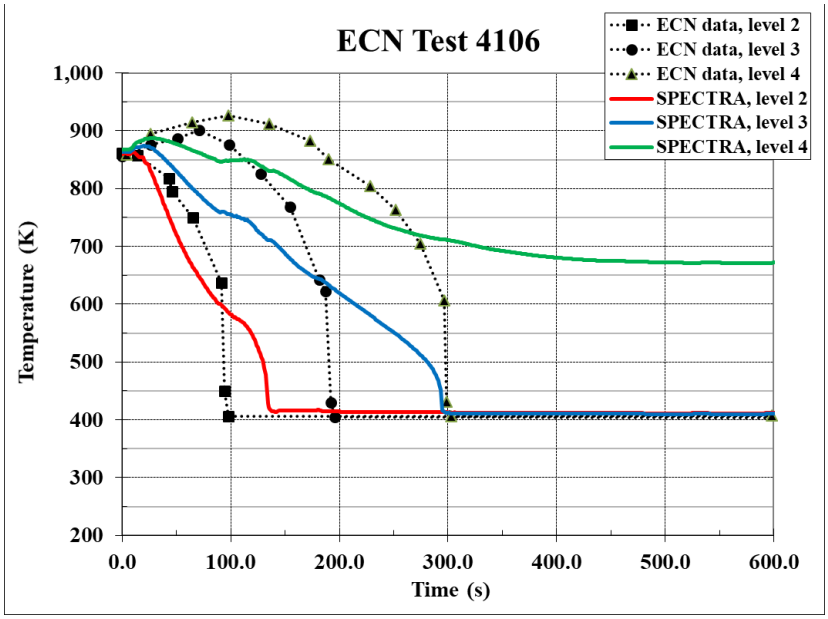

(a) default parameters (C_{MFB}= 0.127)

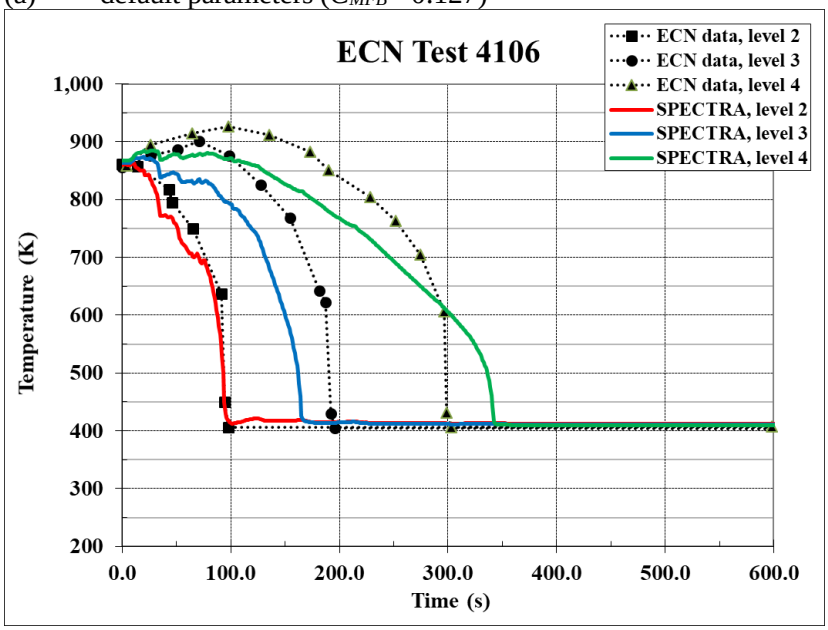

(b) C_{MFB}= 0.25

Figure 3-283 Test 4106, (a) all defaults, (b) C_{MFB}= 0.25

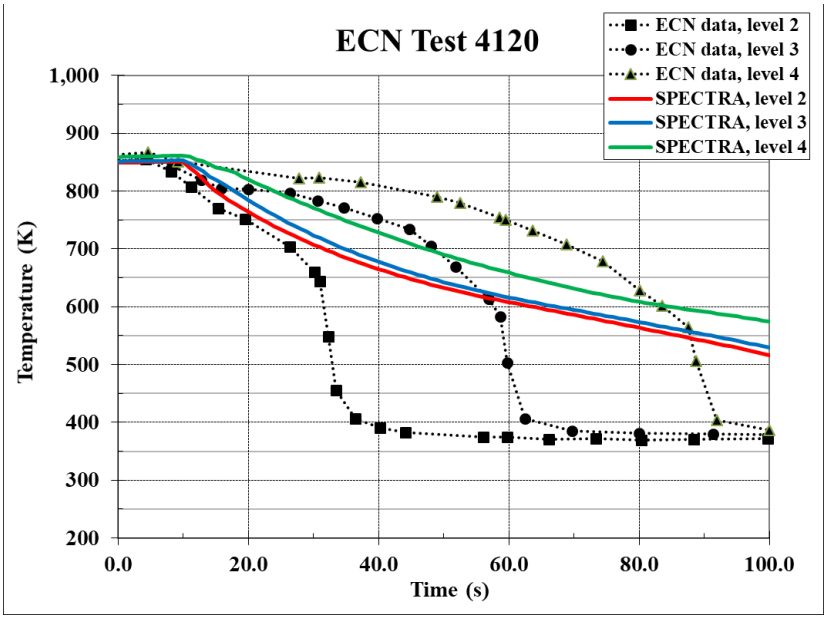

(a) default parameters (C_{MFB}= 0.127)

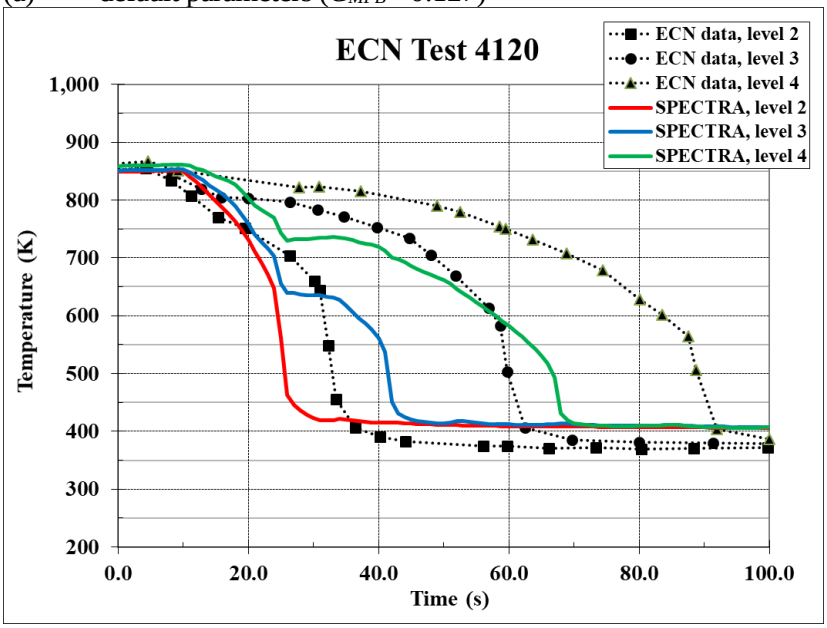

(b) C_{MFB}= 0.25

Figure 3-284 Test 4120, (a) all defaults, (b) C_{MFB}= 0.25

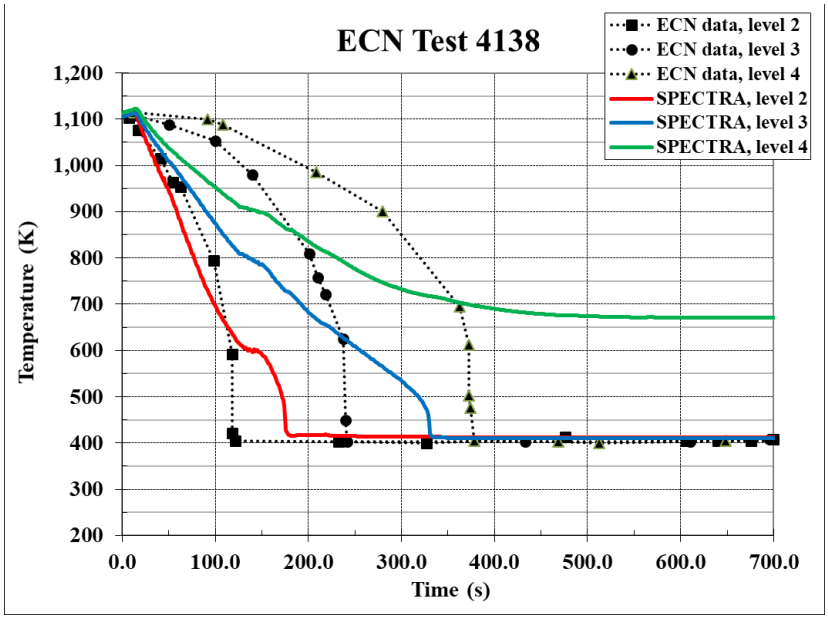

(a) default parameters (C_{MFB}= 0.127)

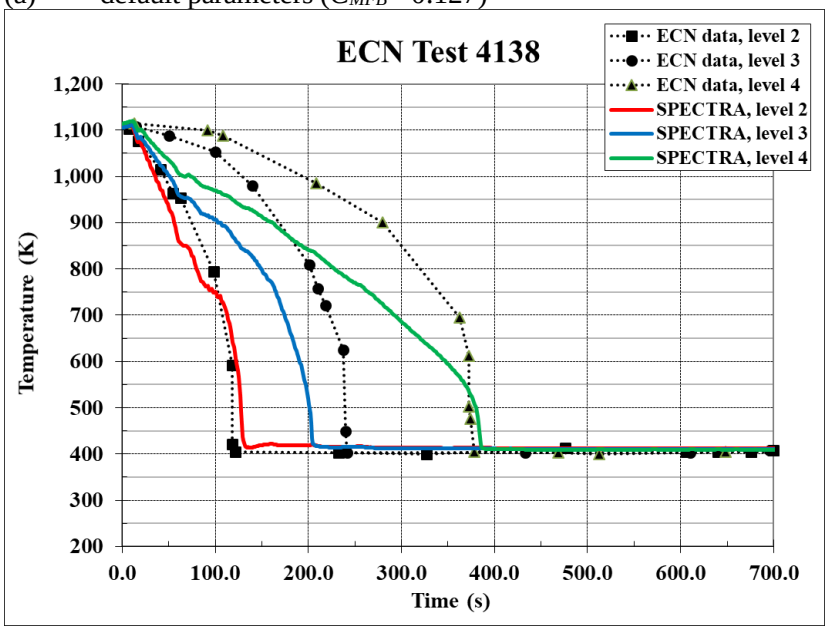

(b) C_{MFB}= 0.25

Figure 3-285 Test 4138, (a) all defaults, (b) C_{MFB}= 0.25

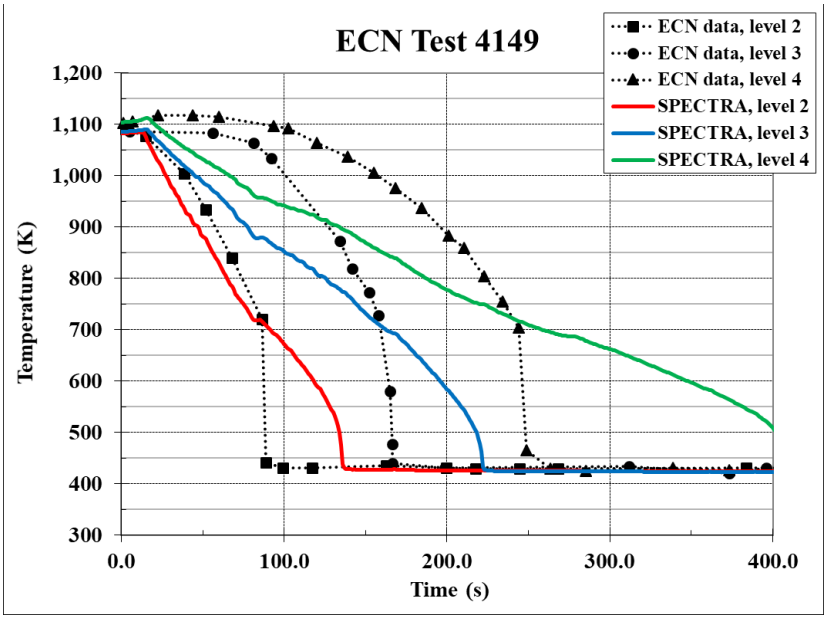

(a) default parameters (C_{MFB}= 0.127)

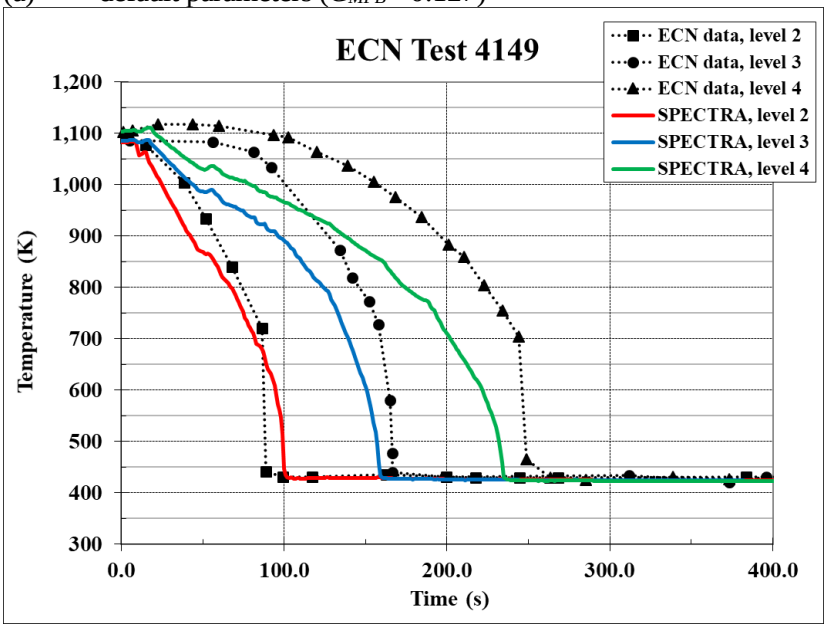

(b) C_{MFB}= 0.25

Figure 3-286 Test 4149, (a) all defaults, (b) C_{MFB}= 0.25

3.6.10 Failure Analysis for a 2-D Structure

This section presents results of a creep failure test performed for a 2-D Solid Heat Conductor. The geometrical data is taken from the cylindrical structure with variable thermal conductivity, TC-005, section 3.6.1. The boundary conditions were set to 800 K and 1000 K on the left and the right side respectively. The failure data of Inconel-600 has been applied (see Volume 1). The data is listed in Table 3-43. The stress was defined using Control Function CF-935. A constant stress of 100 MPa (10^8 Pa) has been applied. The creep rupture is calculated using the default option, which uses the maximum temperature for the creep calculation. In the present case the maximum temperature is equal to the right boundary temperature, namely 1000 K.

Table 3-43 Failure model data for Inconel-600

Constants	Inconel-600
A	54,086
B	4,968.5
C	9.44
T_M	1644.0
$\sigma_{U,lowT}$	7.3×10^8
$t_{U,highT}$	634.0

SPECTRA input file is provided in `\Z-INPUTS\TC\FAILURE\FAILURE-2.SPE`. Calculations were performed for 100,000 s. Results are shown in Figure 3-287, Figure 3-288, and Figure 3-289. Creep rupture was calculated to occur at t = 79,068 s.

Verification is performed using hand calculations. The Larson-Miller parameter is equal to:

$$LMP = A - B \cdot \log_{10}(\sigma) =$$
$$= 54086 - 4968.5 \cdot \log_{10}(10^8) = 14338$$

The time to rupture is obtained from:

$$\log_{10}(t_r) = \frac{LMP}{T} - C =$$
$$= \frac{14338}{1000} - 9.44 = 4.898$$

Therefore:

$$t_r = 10^{4.898} = 79{,}068$$

This value is in agreement with the calculated value - see Figure 3-287, Figure 3-288, Figure 3-289.

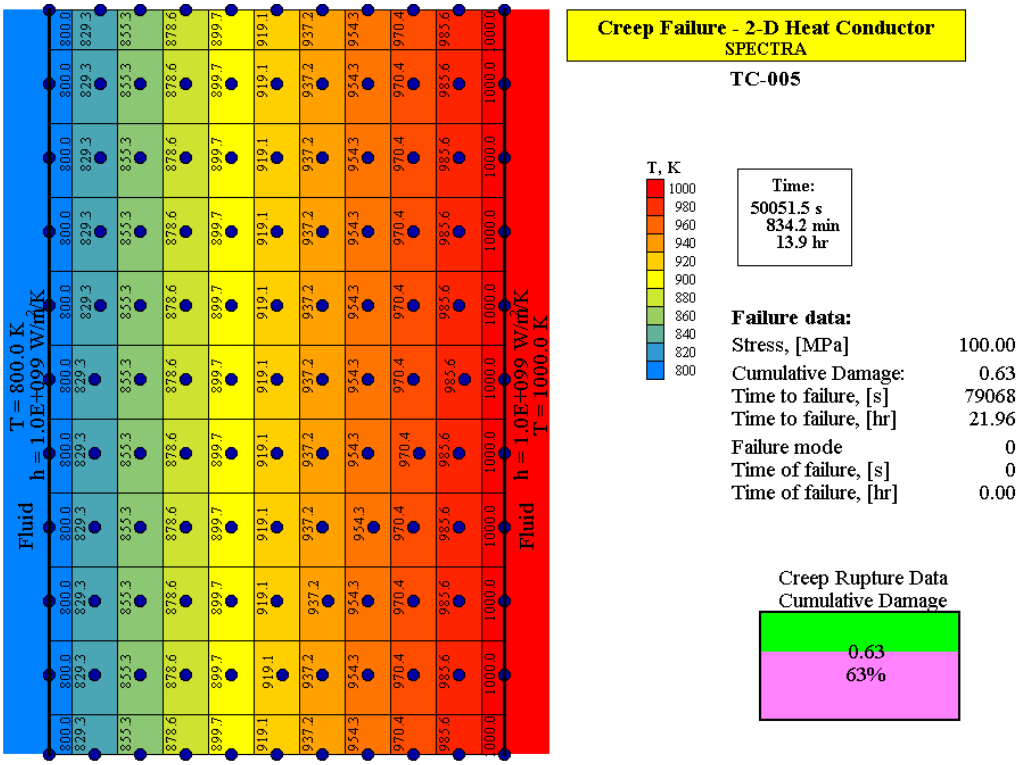

Figure 3-287 Failure analysis for 2-D Structure - values at 50,000 s

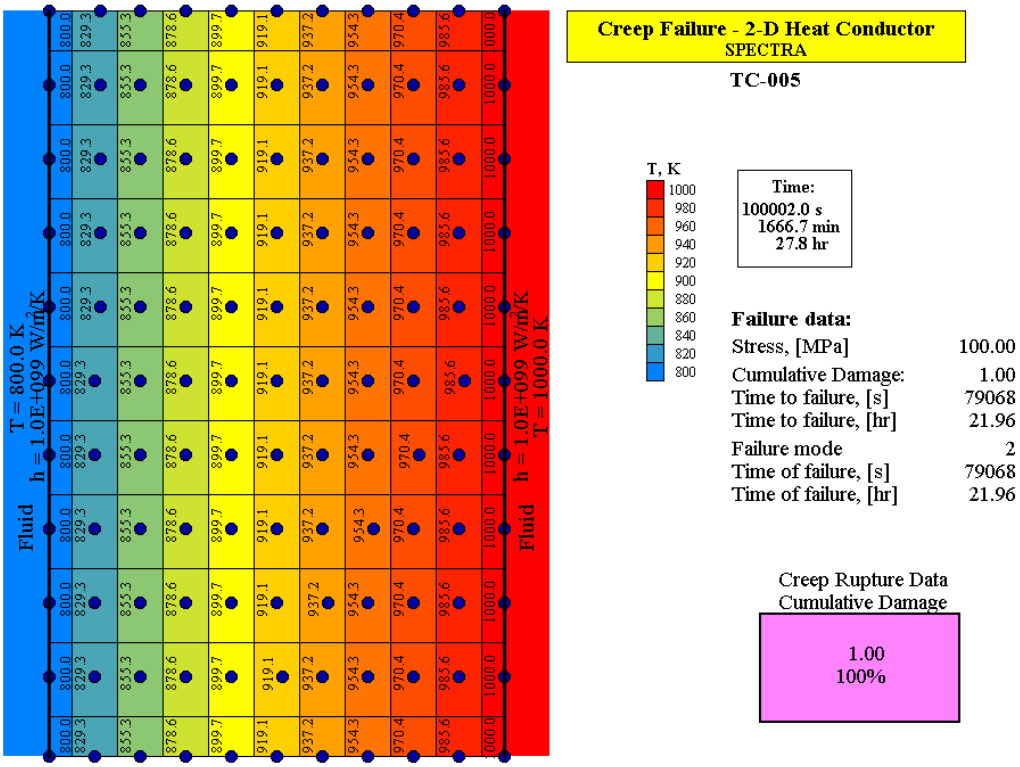

Figure 3-288 Failure analysis for 2-D Structure - values at 100,000 s

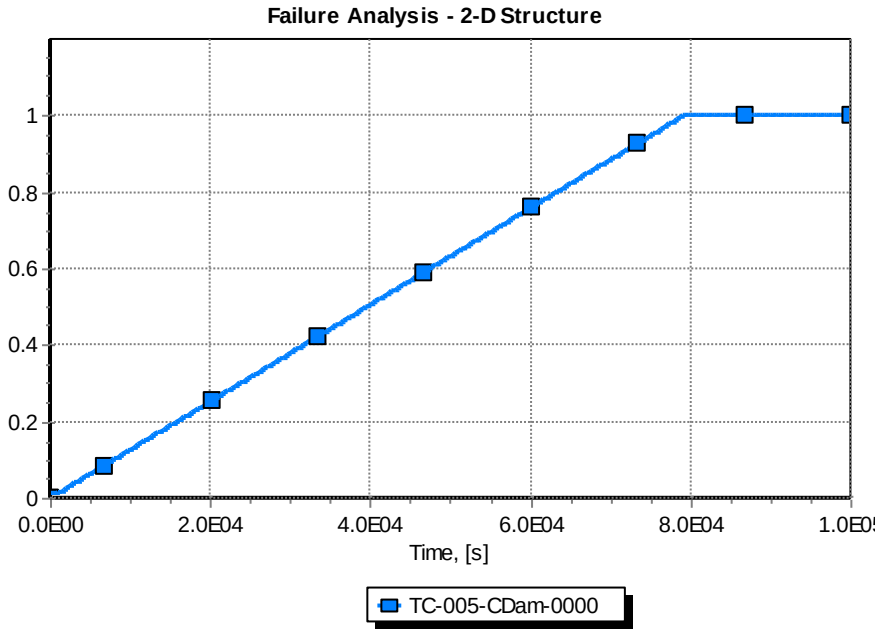

Figure 3-289 Failure analysis for 2-D Structure - cumulative damage versus time

3.6.11 Gap Model, Comparison of 2-D and 1-D Results

A reactor core is modelled. The core consists of one hot rod and one average rod (Figure 3-290). The hot rod is represented by TC-100. The average rod is represented by TC-200. The fuel regions and the common fuel regions are in such case defined as follows:

- Fuel regions (total reactor core):
  TC-100, TC-200

- Common fuel regions:
  - Common region 1 (hot rod):
    TC-100
  - Common region 2 (average rod):
    TC-200

The hot rod and the average rod, shown in Figure 3-290, are made of 5 axial nodes and 6 radial nodes. The radial nodes 1 - 4 represent the fuel, the node 5 represents the gap, the node 6 represents the cladding. The internal power generation is 10000 W for TC-100 and 5000 W for TC-200. Since the axial length of each TC is 2.5 m, the linear power density is 4 kW/m for the hot rod and 2 kW/m for the average rod. The power density is constant in the axial direction. The relative power density in the radial direction is 1.0 in the fuel nodes (1 - 4) and 0.01 in the gap and cladding nodes (5, 6). The gap is modelled using all default parameters, that means thermal radiation and gas conduction are considered. The solid conduction is ignored.

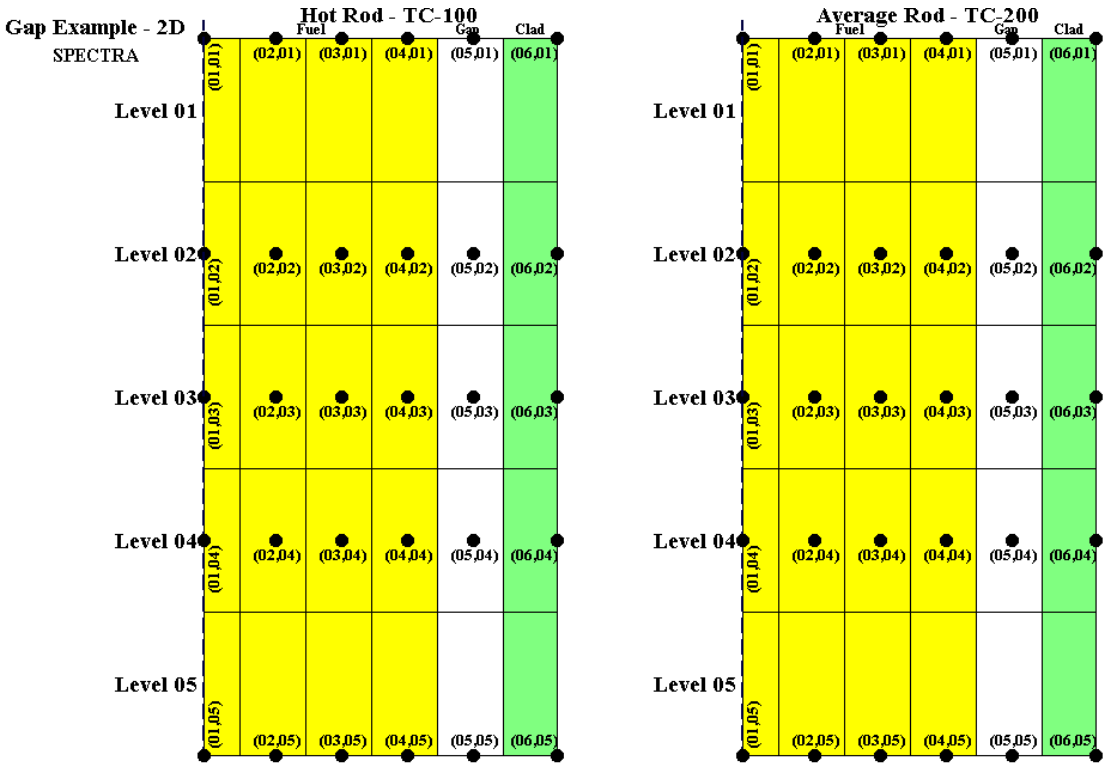

Figure 3-290 Nodalization for gap test, 2-D model

The present model is a 2-D version of the model discussed in section 3.5.12. The purpose of the present test is to compare gap results obtained with a 2-D model to those obtained with a 1-D model. Since the model is uniform in the axial direction, there is no heat transfer in the axial direction and the results of the 1-D model and the 2-D model should be identical.

SPECTRA input file is provided in:
`\Z-INPUTS\TC\GAP\GAP-Example-2D.SPE`

Results of the 2-D model are provided in Figure 3-292. For comparison the results of the 1-D model (section 3.5.12) are reproduced here in Figure 3-291. It is seen that both results are identical. The gap heat transfer coefficient is 368.2 W/m^2-K for the hot rod and 307.0 W/m^2-K for the average rod.

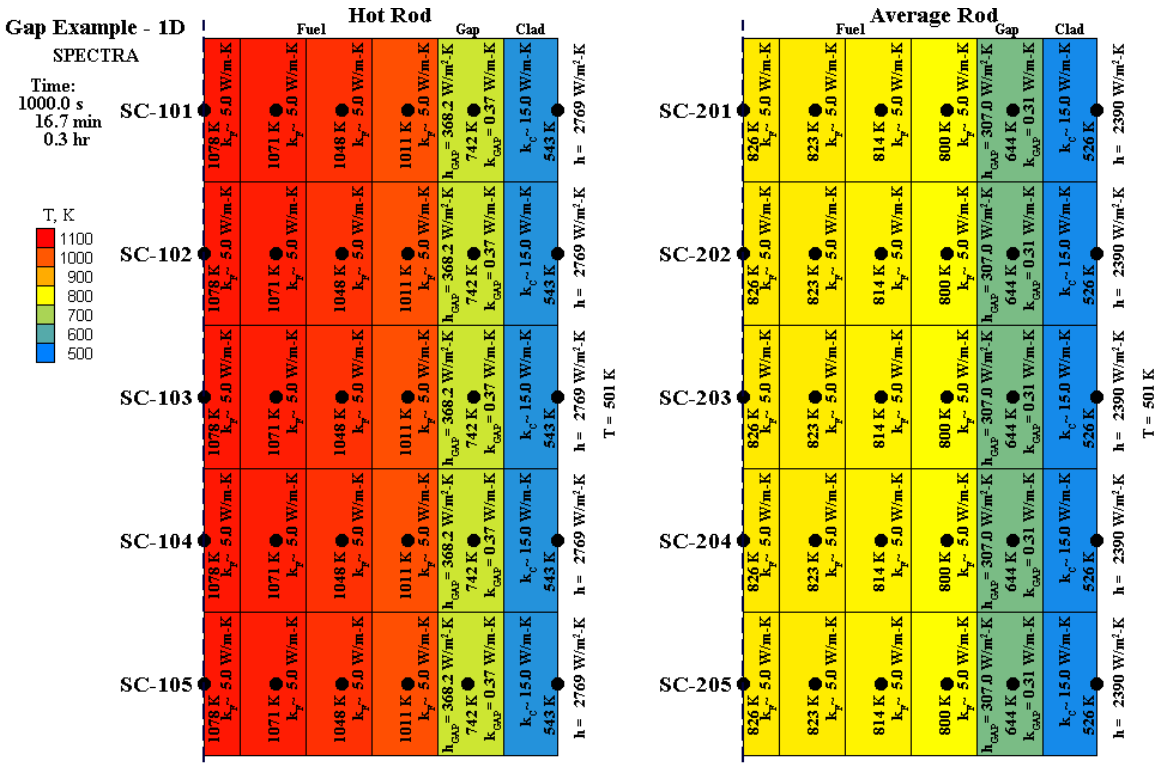

Figure 3-291 Results of gap test, 1-D model

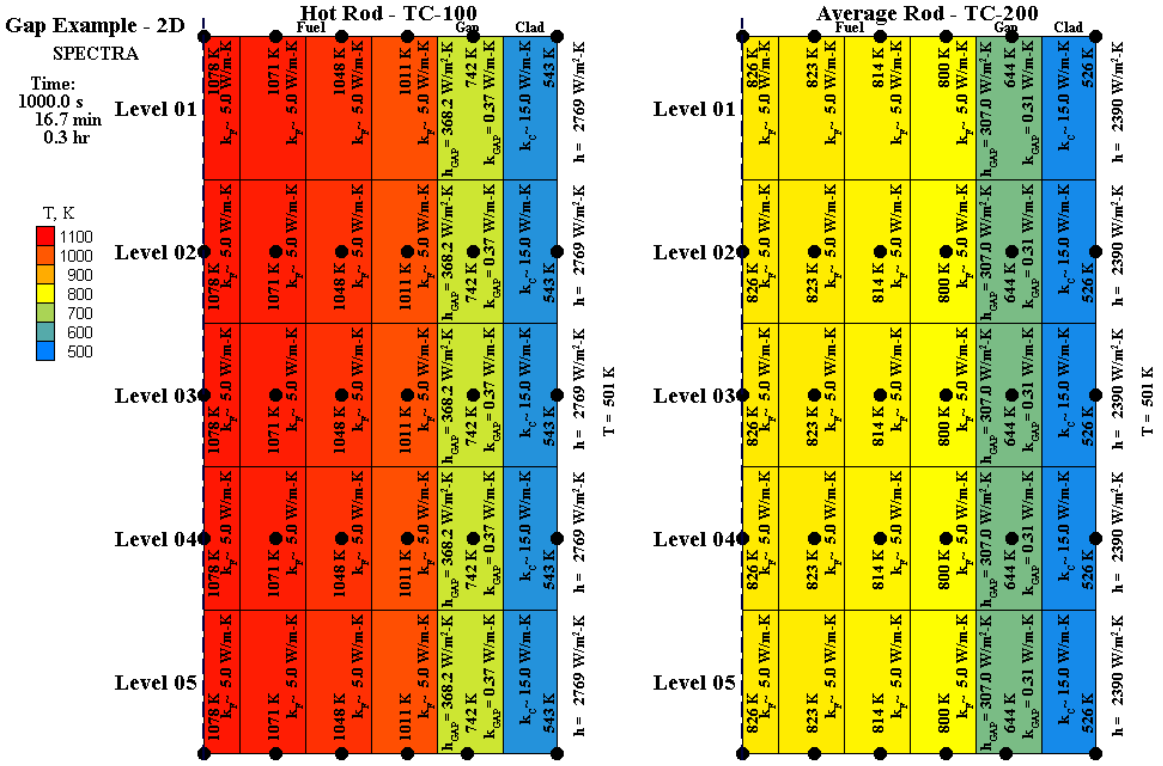

Figure 3-292 Results of gap test, 2-D model

3.6.12 Gap Model, Comparison of 2-D and 1-D Results for the Reflood Test

The present test is a qualitative verification of 1-D and 2-D models in transient conditions. The purpose of the test is to compare gap results obtained with a 2-D model to those obtained with a 1-D model for the Reflood test, discussed in section 3.6.8. Since the axial conduction is important in this case, the 1-D and the 2-D model give different results. Nonetheless, since the same gap model is applied in the 2-D and the 1-D structure, the gap results should be similar. The purpose of the present test is to perform a qualitative check if the gap results are similar in the 1-D and 2-D models. The SPECTRA input file is provided in:
`\Z-INPUTS\TC\GAP\GAP-Reflood.SPE`

The results obtained at the end of calculations are shown in Figure 3-293. It is seen that the gap heat transfer coefficients are similar for the 1-D and the 2-D model. The results are very similar at the bottom (level 1, h_{GAP} = 140 and 145 W/m^2-K for the 1-D and 2-D models respectively) and in the middle and upper levels (levels 10 to 20 from the bottom - h_{GAP} = 257 and 256 W/m^2-K for the 1-D and 2-D models respectively at the level 20). In the vicinity of the quench front (levels 2 - 3 from the bottom) the 1-D and 2-D results are most different for in this region the axial conduction has the largest effect (h_{GAP} = 254 and 190 W/m^2-K for the 1-D and 2-D models respectively at the level 3).

Since the results are similar and the area with the largest differences can be explained from physical basis, the qualitative verification of the model is considered successful.

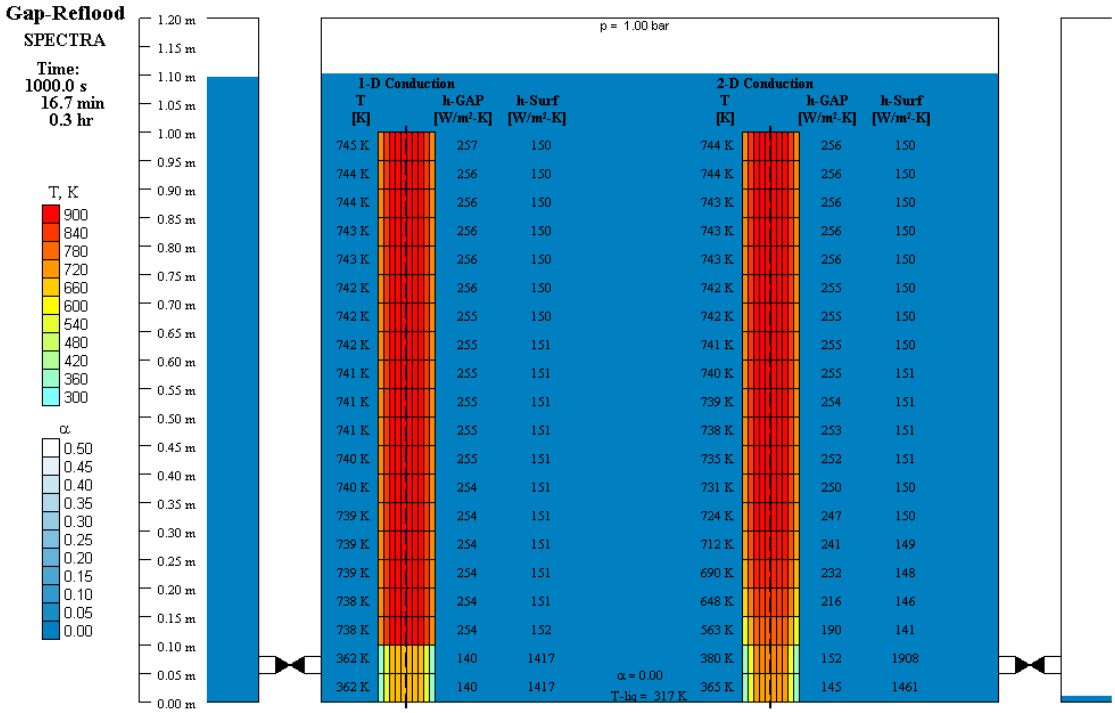

Figure 3-293 Results of Gap-Reflood test.

3.7 Heat and Mass Transfer

3.7.1 Berkeley Condensation Tests

In Berkeley experiments condensation inside a vertical tube was investigated for pure steam, steam-air and steam-helium mixtures [103]. Out of large number of experiments performed several were selected for the purpose of testing the condensation model available in SPECTRA. The selected tests are listed below.

- Pure steam
  - Run 1.1-1
  - Run 1.1.5
- Steam-air mixtures
  - Run 2.1-4 (inlet air mass fraction = 0.042)
  - Run 2.1-7 (inlet air mass fraction = 0.100)
  - Run 2.1-8 (inlet air mass fraction = 0.147)
  - Run 2.1-13 (inlet air mass fraction = 0.396)
- Steam-He mixtures
  - Run 5.1-1 (inlet He mass fraction = 0.003)
  - Run 5.1-7 (inlet air mass fraction = 0.163)

SPECTRA model was created based on the data of Kuhn, Schrock and Petersen [103] and the final report from the University of California, UCB-NE-4201, Rev. 2 (1994). The nodalization can be seen in Figure 3-3. The SPECTRA input files are located in: **\Z-INPUTS\HT\Berkeley**

For comparison, a model for RELAP5 was generated using the automated export option (IEXPSL=3). The RELAP5 input files are located in: **\Z-INPUTS\HT\Berkeley\RELAP**

Results are shown in the following figures:

- Pure steam
  - Run 1.1-1 Figure 3-294 and Figure 3-295
  - Run 1.1.5 Figure 3-296 and Figure 3-297
- Steam-air mixtures
  - Run 2.1-4 Figure 3-298 and Figure 3-299
  - Run 2.1-7 Figure 3-300 and Figure 3-301
  - Run 2.1-8 Figure 3-302 and Figure 3-303
  - Run 2.1-13 Figure 3-304 and Figure 3-305
- Steam-He mixtures
  - Run 5.1-1 Figure 3-306 and Figure 3-307
  - Run 5.1-7 Figure 3-308 and Figure 3-309

The condensation efficiency (fraction of steam that is condensed) calculated by SPECTRA and RELAP are compared to the measured values in Figure 3-310 for the steam-air tests and in Figure 3-312 for the steam-He tests. All results are summarized in Table 3-44.

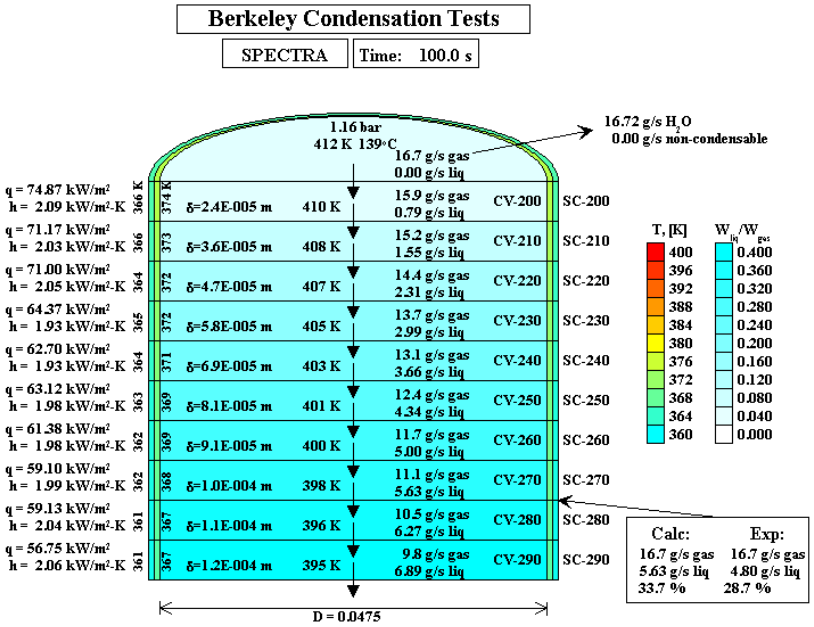

Figure 3-294 Berkeley test 1.1-1, SPECTRA

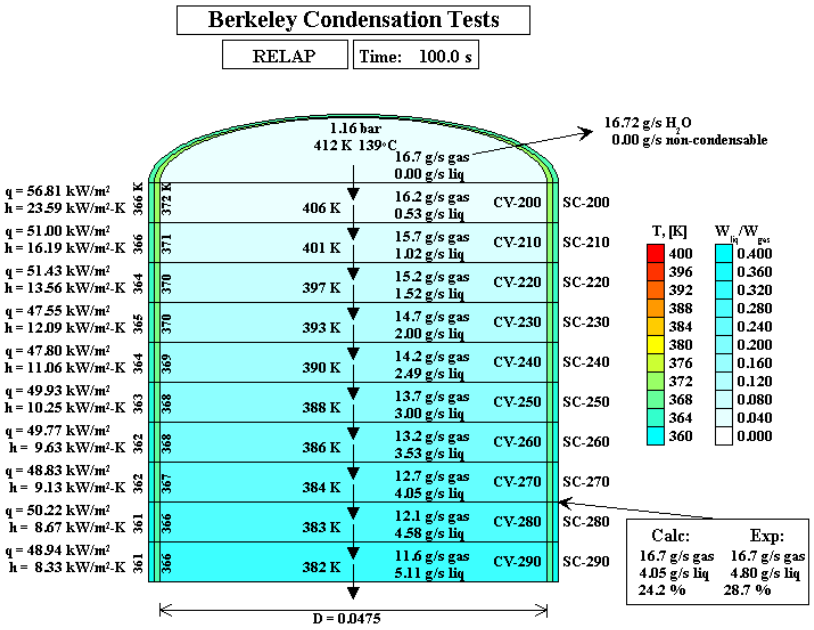

Figure 3-295 Berkeley test 1.1-1, RELAP5

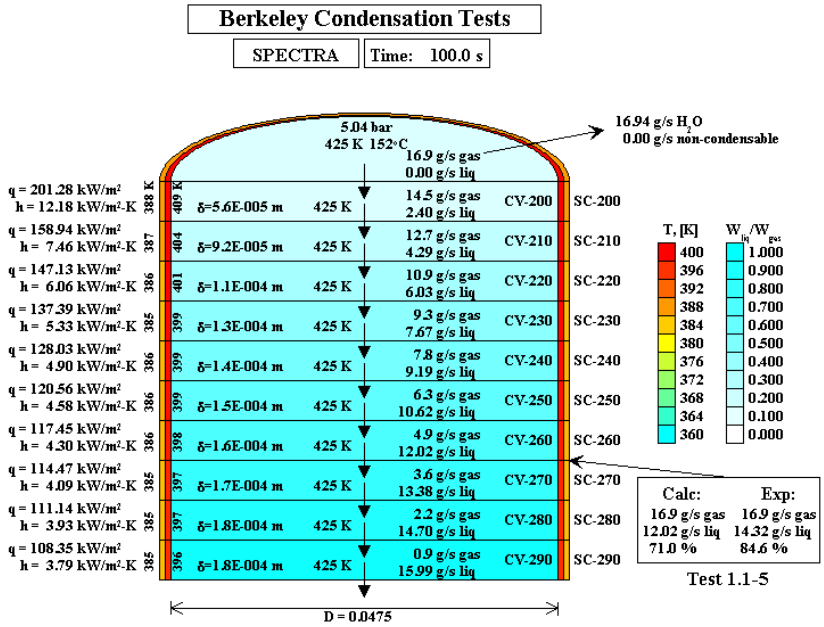

Figure 3-296 Berkeley test 1.1-5, SPECTRA

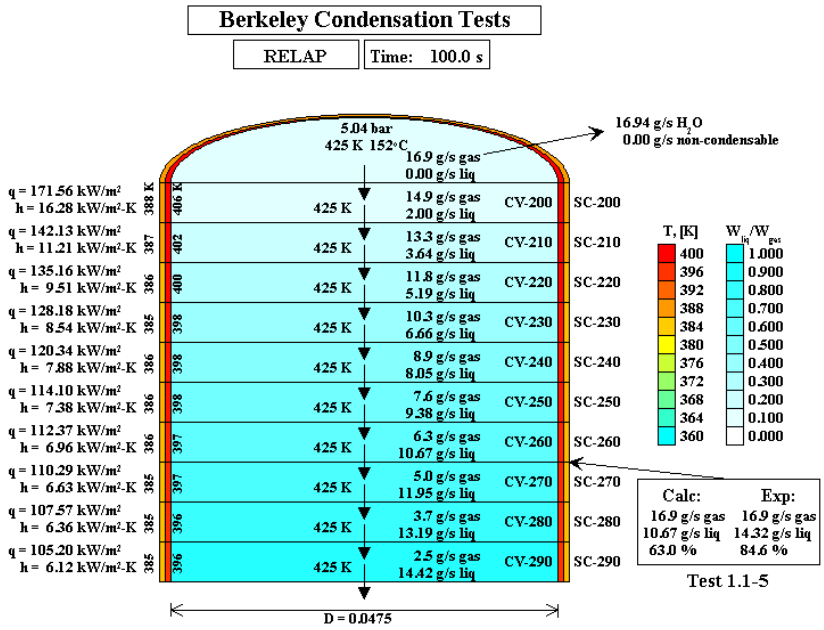

Figure 3-297 Berkeley test 1.1-5, RELAP5

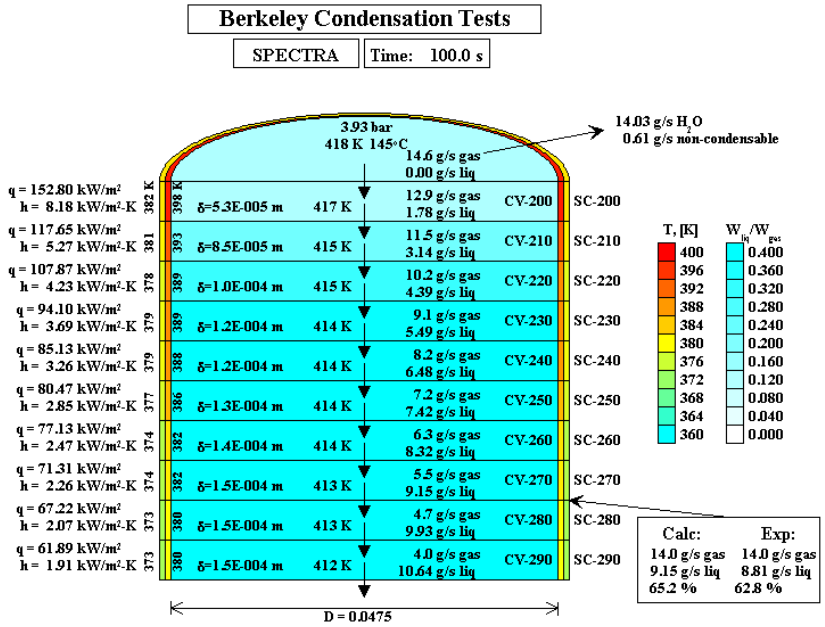

Figure 3-298 Berkeley test 2.1-4, SPECTRA

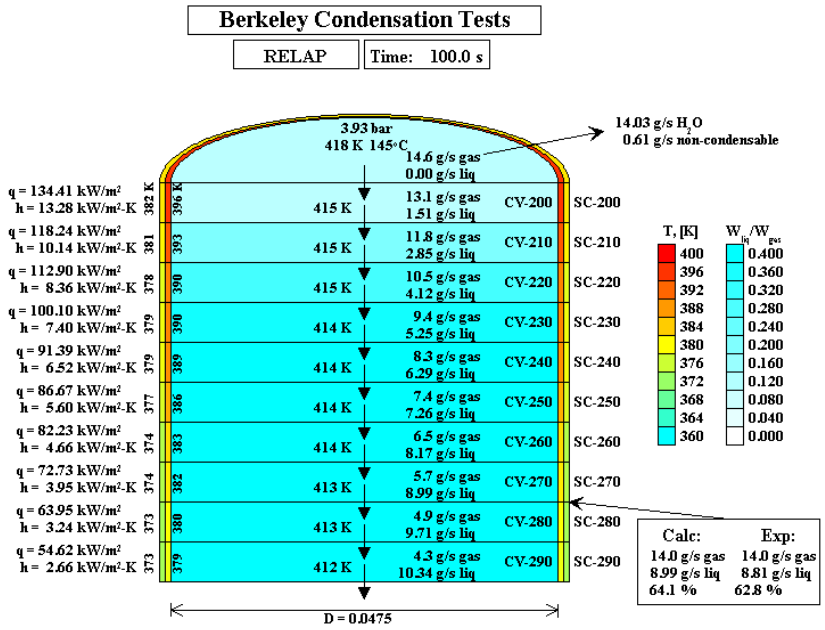

Figure 3-299 Berkeley test 2.1-4, RELAP5

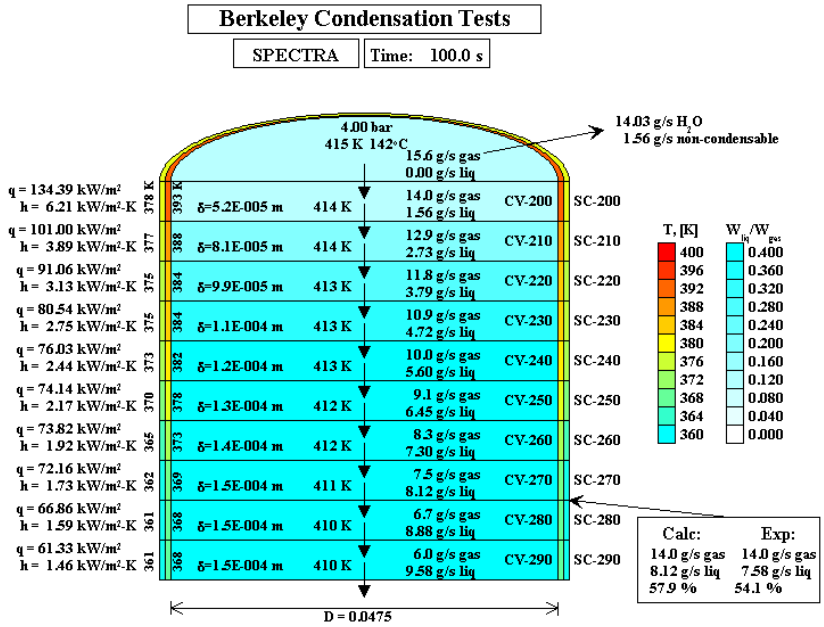

Figure 3-300 Berkeley test 2.1-7, SPECTRA

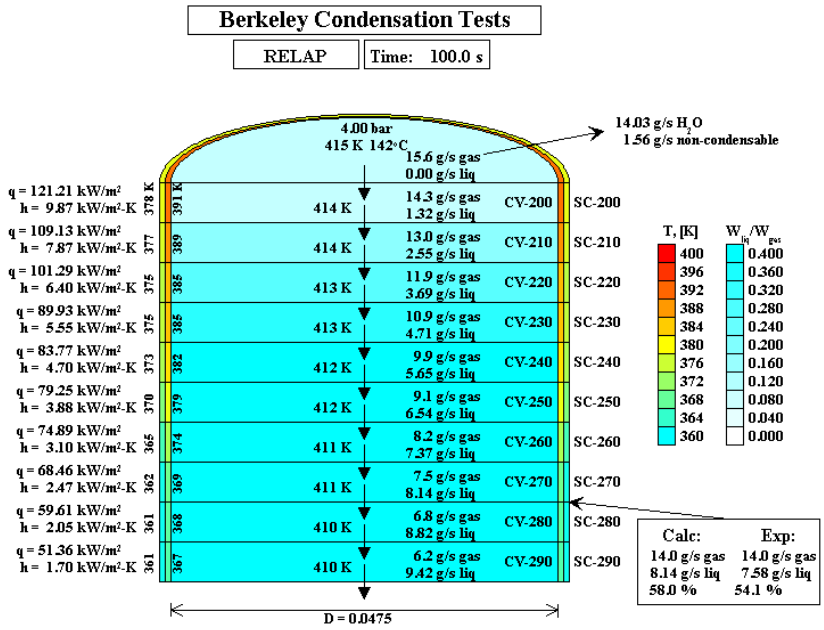

Figure 3-301 Berkeley test 2.1-7, RELAP5

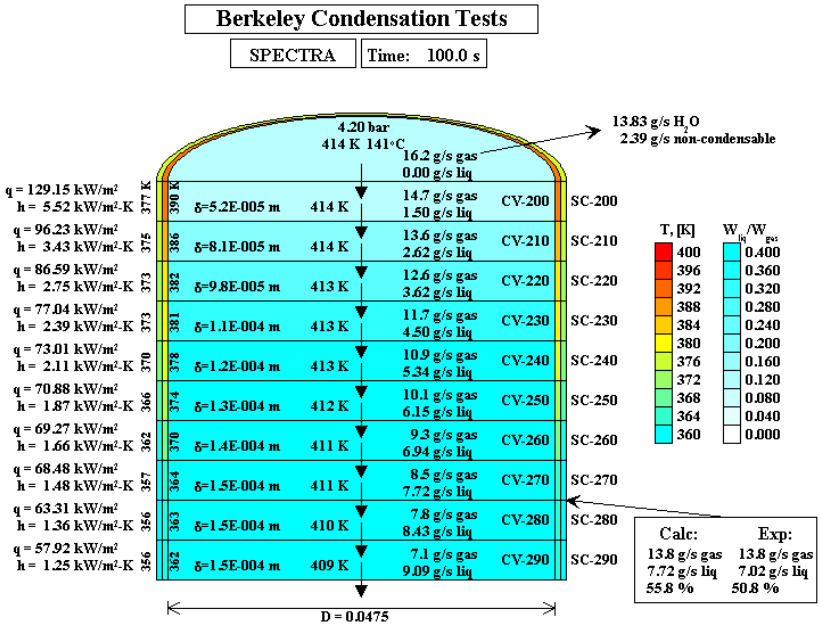

Figure 3-302 Berkeley test 2.1-8, SPECTRA

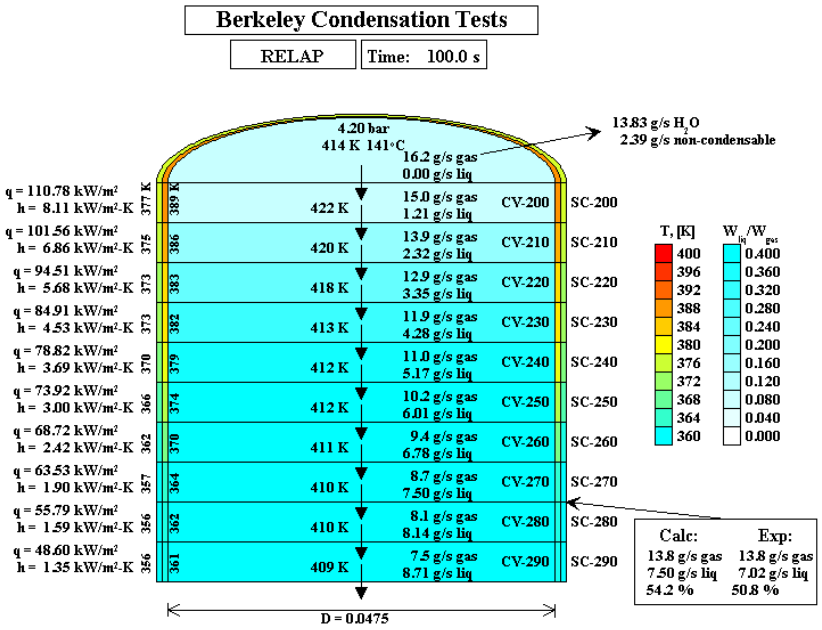

Figure 3-303 Berkeley test 2.1-8, RELAP5

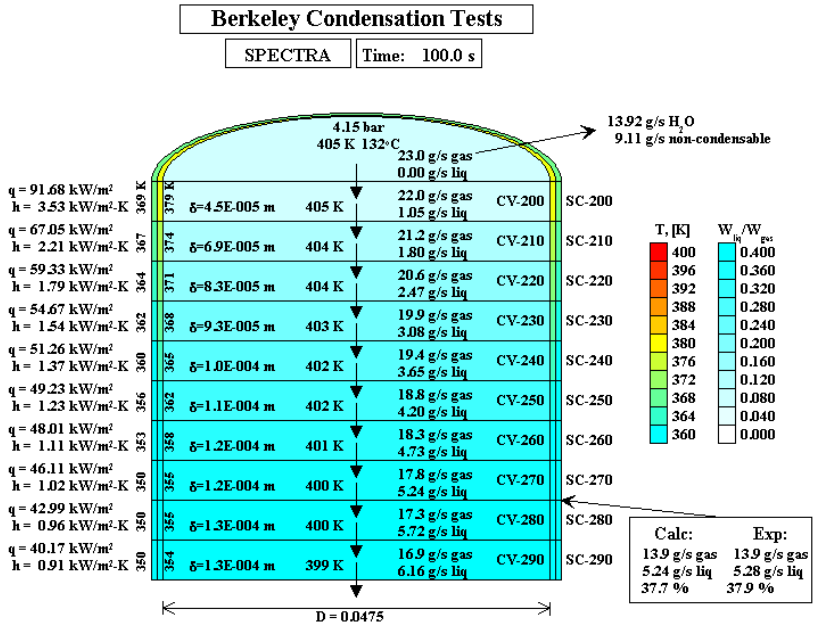

Figure 3-304 Berkeley test 2.1-13, SPECTRA

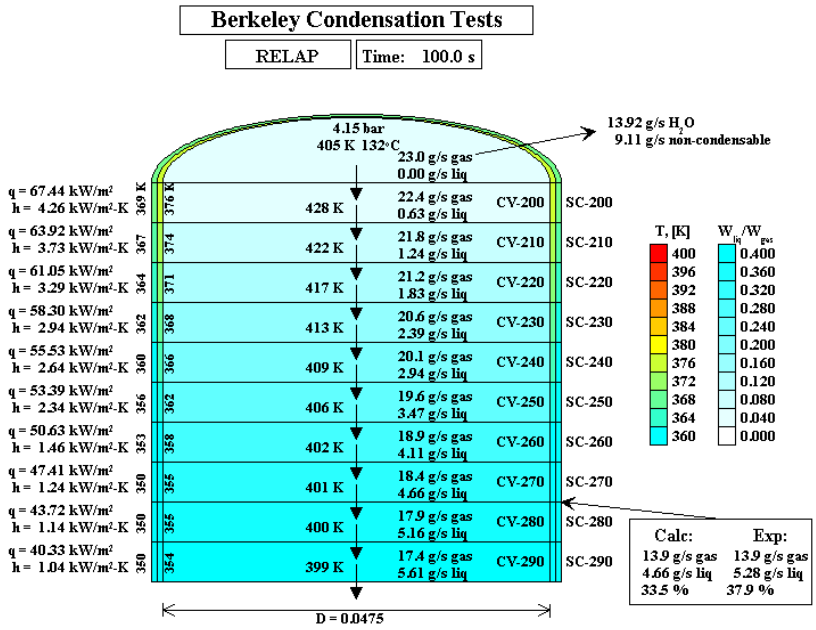

Figure 3-305 Berkeley test 2.1-13, RELAP5

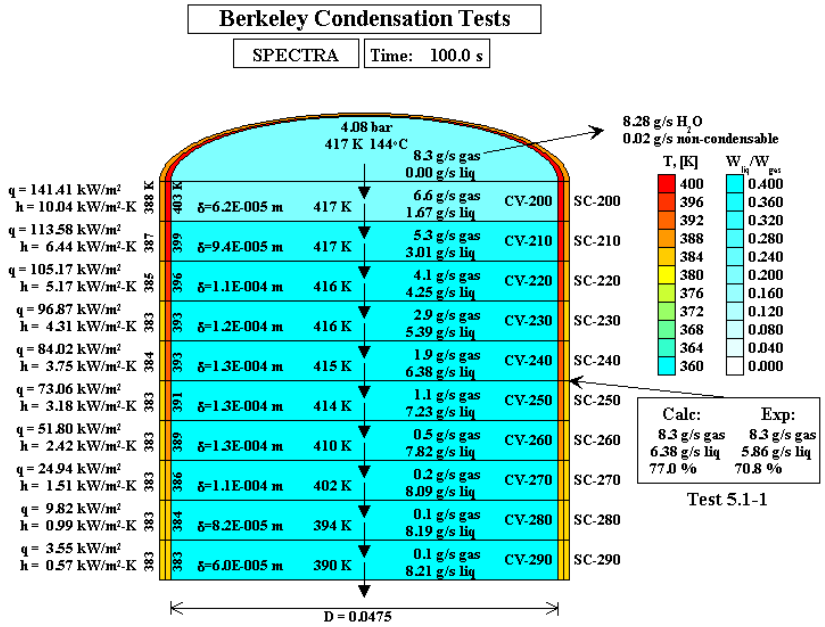

Figure 3-306 Berkeley test 5.1-1, SPECTRA

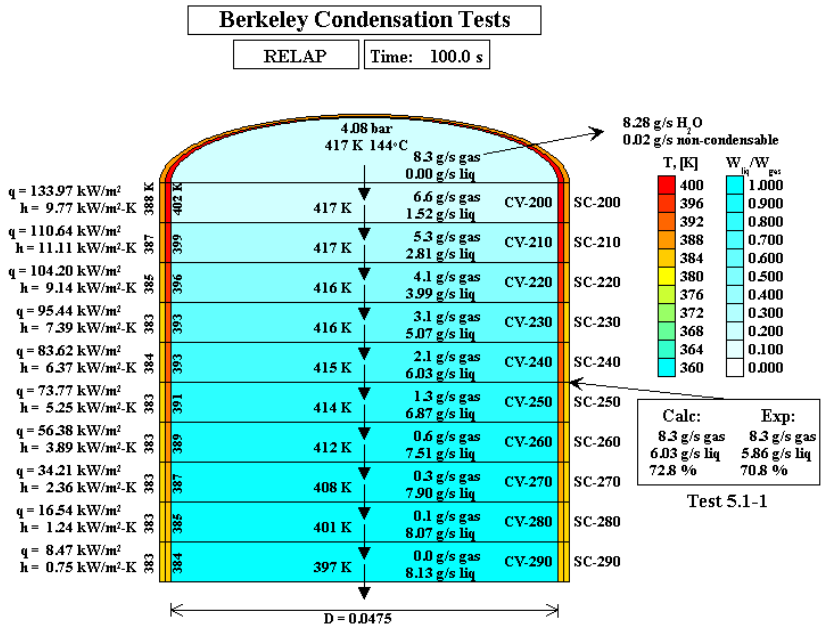

Figure 3-307 Berkeley test 5.1-1, RELAP5

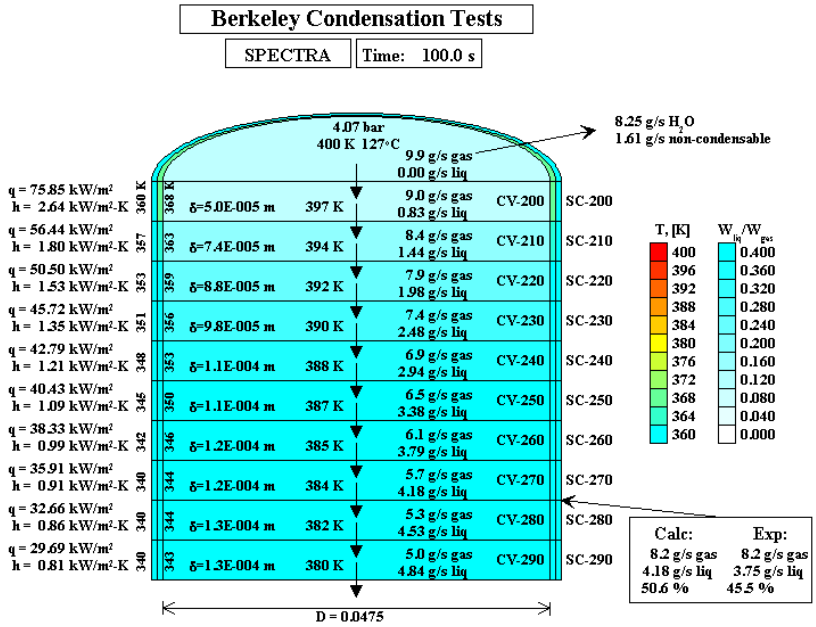

Figure 3-308 Berkeley test 5.1-7, SPECTRA

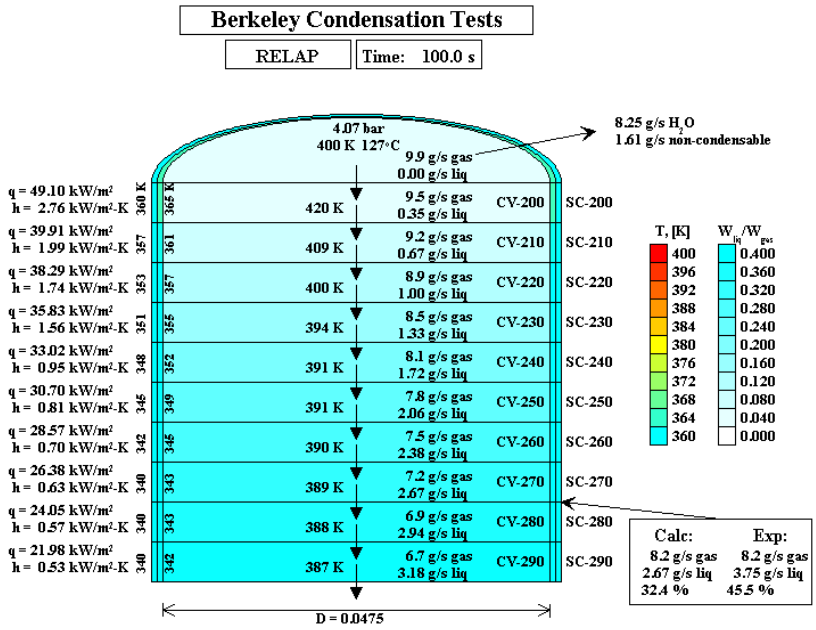

Figure 3-309 Berkeley test 5.1-7, RELAP5

The primary goal of using these tests is to perform sensitivity study with different models for non-condensable gas degradation factors. For each test a calculation was performed using:

- KSP correlation
- Ogg correlation
- Modified Ogg correlation

Results obtained with different correlations are compared to the measured values in Figure 3-311 for the steam-air tests and in Figure 3-313 for the steam-He tests. Table 3-45 shows test results for the steam-noncondensable and comparison of SPECTRA results obtained with three different correlations for the non-condensable gases, KSP, Ogg, and Modified Ogg.

It is concluded that a good agreement with measured data was obtained with both SPECTRA as well as RELAP for the Berkeley single tube condensation tests. Generally, the best agreement was obtained when the KSP correlation was used. The KSP correlation overestimates the condensation rate while the Ogg and the Modified Ogg correlations consistently give values lower than measured.

Table 3-44 Berkeley single tube condensation tests

	Fraction of steam condensed, η, %		
Test	**Experiment**	**SPECTRA**	**RELAP5**
1.1-1	28.7	33.7	24.2
1.1-5	84.6	71.0	63.0
2.1-4	62.8	65.2	64.1
2.1-7	54.1	57.9	58.0
2.1-8	50.8	55.8	54.2
2.1-13	37.9	37.7	33.5
5.1-1	70.8	77.0	72.8
5.1-7	45.5	50.6	32.4

Table 3-45 Berkeley single tube condensation tests, steam-non-condensable tests

	Fraction of steam condensed, η, %			
Test	**Experiment**	**KSP**	**Ogg**	**Modified Ogg**
2.1-4	62.8	62.5	54.8	54.8
2.1-7	54.1	57.9	47.9	47.9
2.1-8	50.8	55.8	43.9	43.9
2.1.13	37.9	37.7	29.1	27.3
5.1-1	70.8	77.0	68.0	68.0
5.1-7	45.5	50.6	45.7	32.4

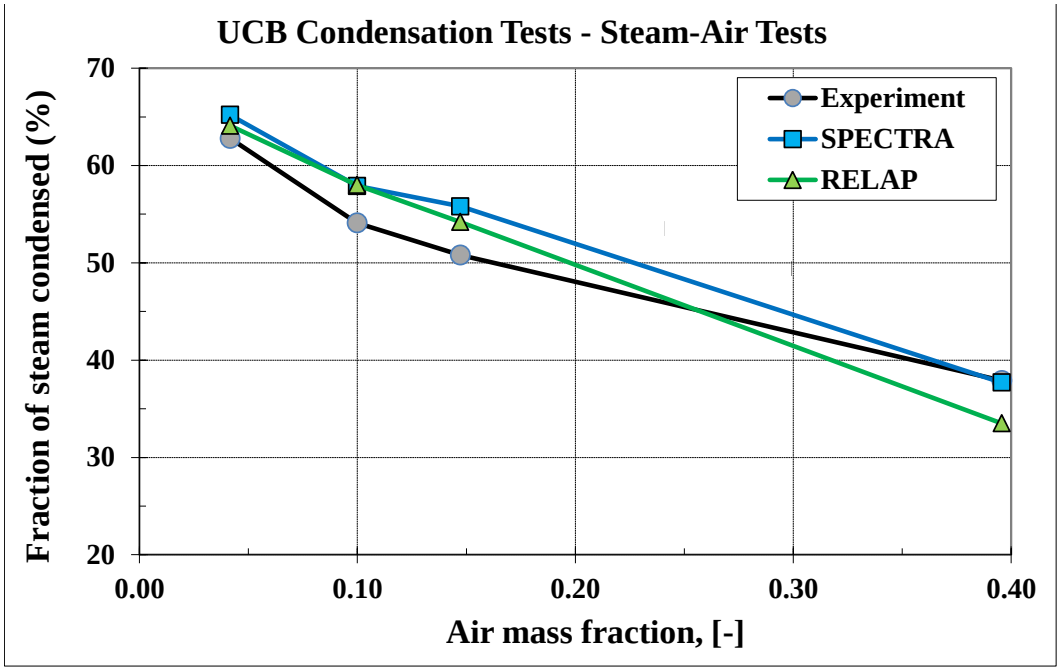

Figure 3-310 Berkeley condensation tests - Steam-Air Tests

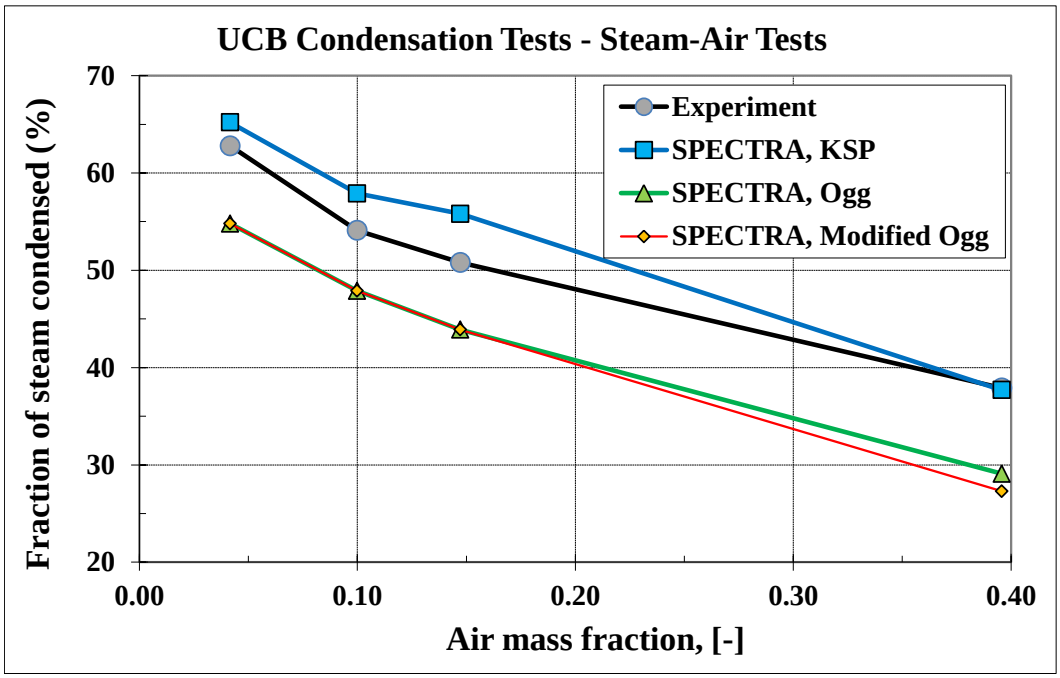

Figure 3-311 Berkeley condensation tests - Steam-Air Tests

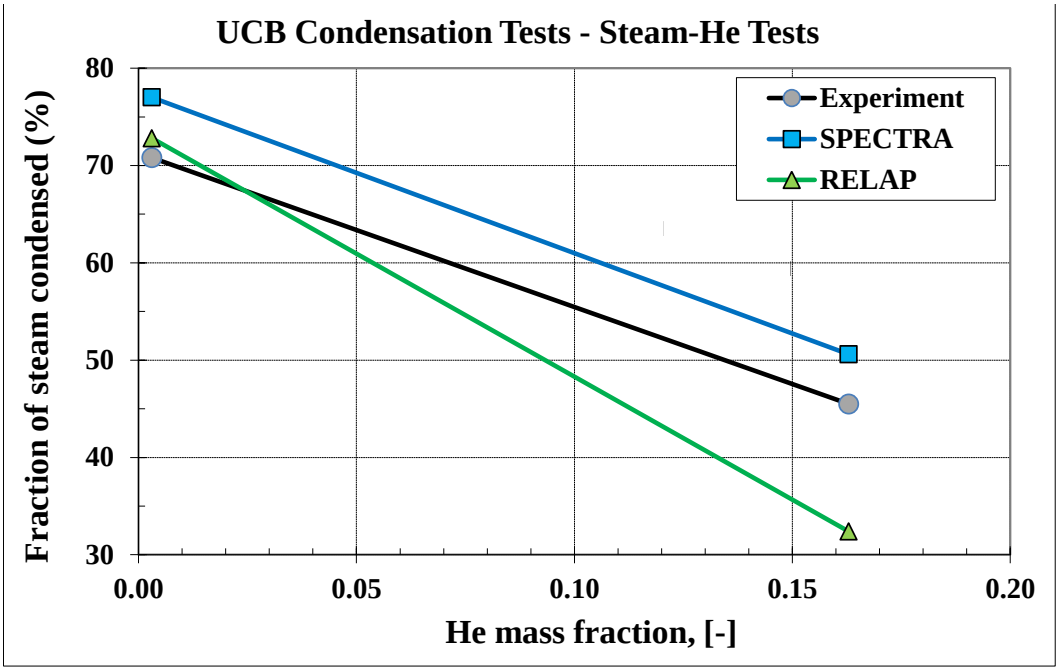

Figure 3-312 Berkeley condensation tests - Steam-He Tests

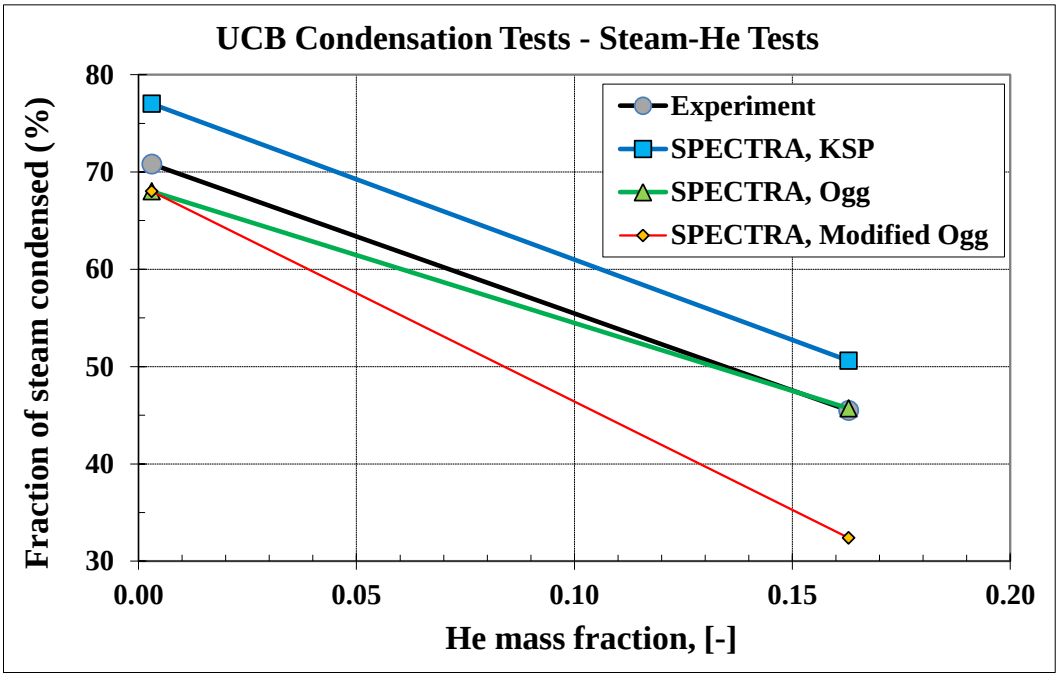

Figure 3-313 Berkeley condensation tests - Steam-He Tests

3.7.2 MIT Condensation Tests

Experimental results of condensation on the outside surface of a vertical tube is presented by Dehbi et al. [104]. The experimental test section consisted of a 3.5 m long water cooled copper tube enclosed in a large pressure vessel. Known amounts of noncondensable gases were admitted inside the vessel while steam was produced at the bottom of the vessel by a set of heaters with a total capacity of 36 kW. The pressure vessel was fully insulated so that the heat produced by steam condensation was entirely removed by the coolant. The results are reproduced in Figure 3-314.

The following values were applied for calculations:

- Tube length, L = 3.5 m
- Pressures, p: 1.5, 3.0, 4.5 bar
- Air mass fractions, x_{air}: 0.2 - 0.9
- Wall subcooling: $\Delta T_{sat} = T_{sat} - T_{wall}$ = 30 K ([104], page 24)

The saturation temperature, T_{sat}, was calculated in each case as a saturation temperature for steam partial pressure p_{steam}, $T_{sat} = f(p_{steam})$. The steam partial pressure was calculated as:

$$p_{steam} = p \cdot \frac{x_{steam} / M_{steam}}{x_{steam} / M_{steam} + x_{air} / M_{air}}$$

p_{steam} steam partial pressure, (Pa)
p total pressure, (Pa)
x_{steam} steam mass fraction, (-)
x_{air} air mass fraction, (-)
M_{steam} molar weight of steam, (kg/kg-mole)
M_{air} molar weight of air, (kg/kg-mole)

The saturation temperatures and the wall temperatures were calculated by a FORTRAN program, located in `\Z-INPUTS\HT\MIT\MIT.FOR`. This program calculates T_{sat} and T_{wall} for different pressures and air mass fractions, using the above formula. The obtained values were used in SPECTRA input decks, discussed below.

Calculations were performed using three correlations for noncondensable gases:

- KSP, input file: `\Z-INPUTS\HT\MIT\MIT-KSP.SPE`
- Ogg, input file: `\Z-INPUTS\HT\MIT\MIT-Ogg.SPE`
- Modified Ogg, input file: `\Z-INPUTS\HT\MIT\MIT-Ogg-Mod.SPE`

In SPECTRA input files all experiment, characterized by a different pressure and air mass fraction, are included in a single input file. The input data for each experiment consists of a single Control Volume (CV) and a single 1-D Solid Heat Conductor (SC). For convenience the resulting condensation heat transfer coefficient is stored as a Control Function (CF). The CV, SC, and CF numbers for each experiment are listed in Table 3-46. The same numbering scheme is adopted in each of the three input files, listed above.

Table 3-46 MIT condensation tests - numbering scheme for SPECTRA inputs

Air fraction X_{air}	Pressure, p		
	1.5 bar	3.0 bar	4.5 bar
0.2	CV / SC / CF - 101	CV / SC / CF - 201	CV / SC / CF - 301
0.3	CV / SC / CF - 102	CV / SC / CF - 202	CV / SC / CF - 302
0.4	CV / SC / CF - 103	CV / SC / CF - 203	CV / SC / CF - 303
0.5	CV / SC / CF - 104	CV / SC / CF - 204	CV / SC / CF - 304
0.6	CV / SC / CF - 105	CV / SC / CF - 205	CV / SC / CF - 305
0.7	CV / SC / CF - 106	CV / SC / CF - 206	CV / SC / CF - 306
0.8	CV / SC / CF - 107	CV / SC / CF - 207	CV / SC / CF - 307
0.9	CV / SC / CF - 108	CV / SC / CF - 208	CV / SC / CF - 308

The resulting heat transfer coefficients are shown in Figure 3-315, Figure 3-316, and Figure 3-317. The Modified Ogg correlation (Figure 3-315) best reproduces the experimental results. The influence of pressure is somewhat smaller than that shown in Figure 3-314, but the same trend (increase of HTC with pressure) is observed.

The Ogg correlation (Figure 3-316) gives clearly higher HTC than experiment for air mass fractions between 0.4 and 0.9. The KSP correlation (Figure 3-317) overpredicts the condensation heat transfer coefficient for the whole range of noncondensable gas fraction.

The correlation proposed by in [104] is reproducing quite accurately the experimental data, as may be seen in figure 6.5.8. It was initially intended to implement it into SPECTRA as an optional model. However, the deficiency of this correlation is that it is not sufficiently general. It cannot be applied for very small air fractions because the value of the logarithm becomes very large. For certain range of helium mass fraction it was found to give negative heat transfer coefficient. Applied for the Berkeley experimental results it significantly underpredicts the heat transfer coefficient (factor of two or three). Because of those difficulties, and also because the MIT data could be rather well reproduced by the Modified Ogg correlation, the correlation from [104] was not implemented as an optional model into SPECTRA.

3.7.3 Summary of the Condensation Test Results

The condensation test results are summarized as follows:

- The condensation inside tubes (Berkeley tests) are reproduced best when the KSP correlation is applied.
- The condensation on the outside tube surface (MIT tests) are reproduced best when the Modified Ogg correlation is applied.
- Among the three available correlations the Modified Ogg correlation, gives the most conservative (lowest heat transfer coefficient) values in the whole range of noncondensable gas fractions.

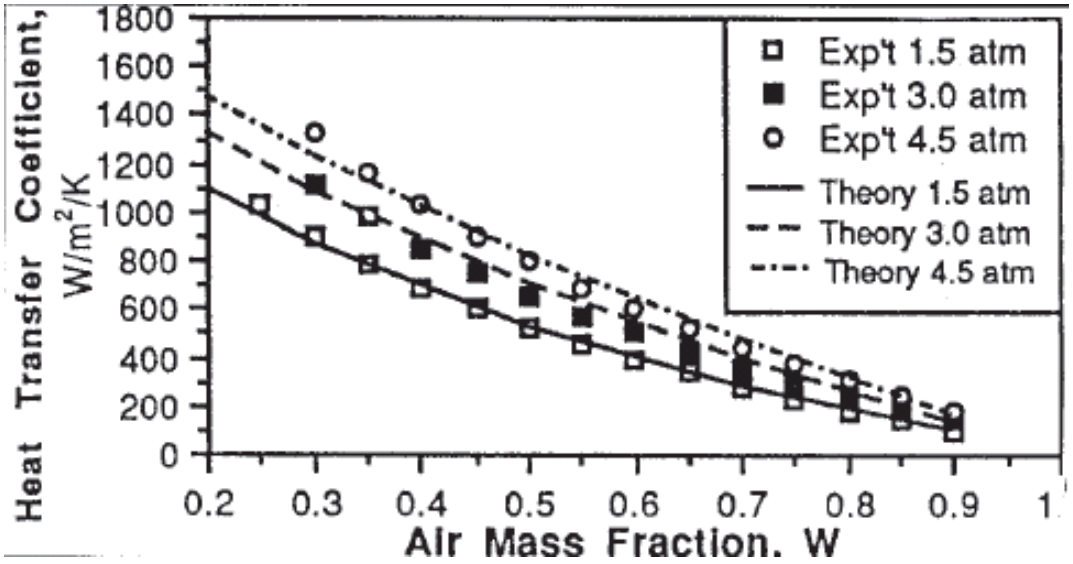

Figure 3-314 MIT test results [104]

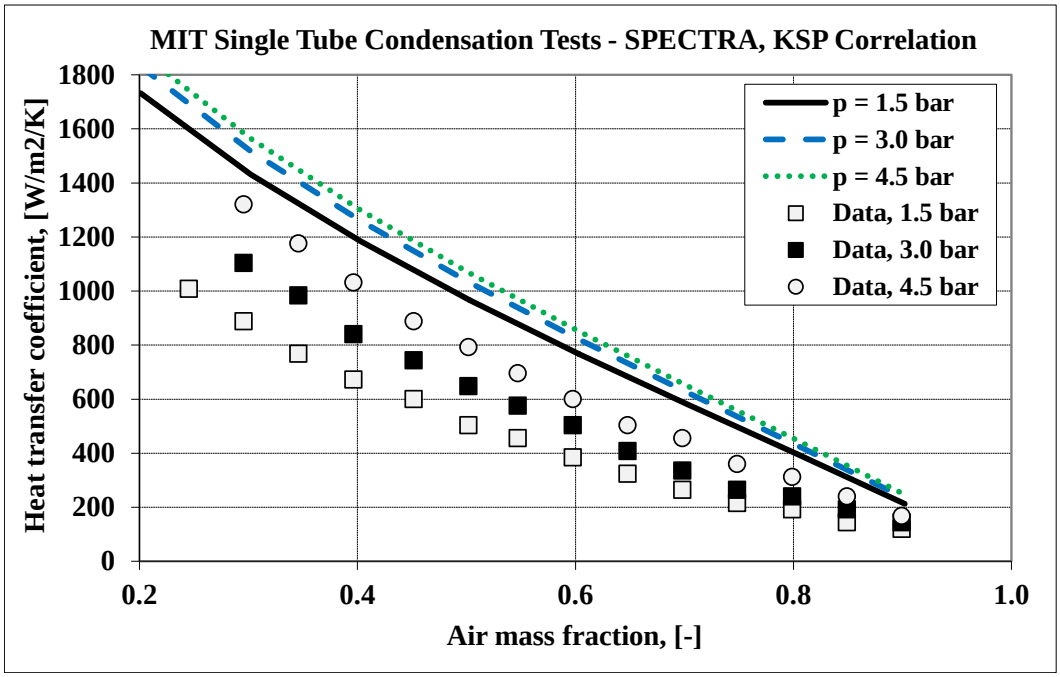

Figure 3-315 MIT tests, SPECTRA results, Modified Ogg correlation.

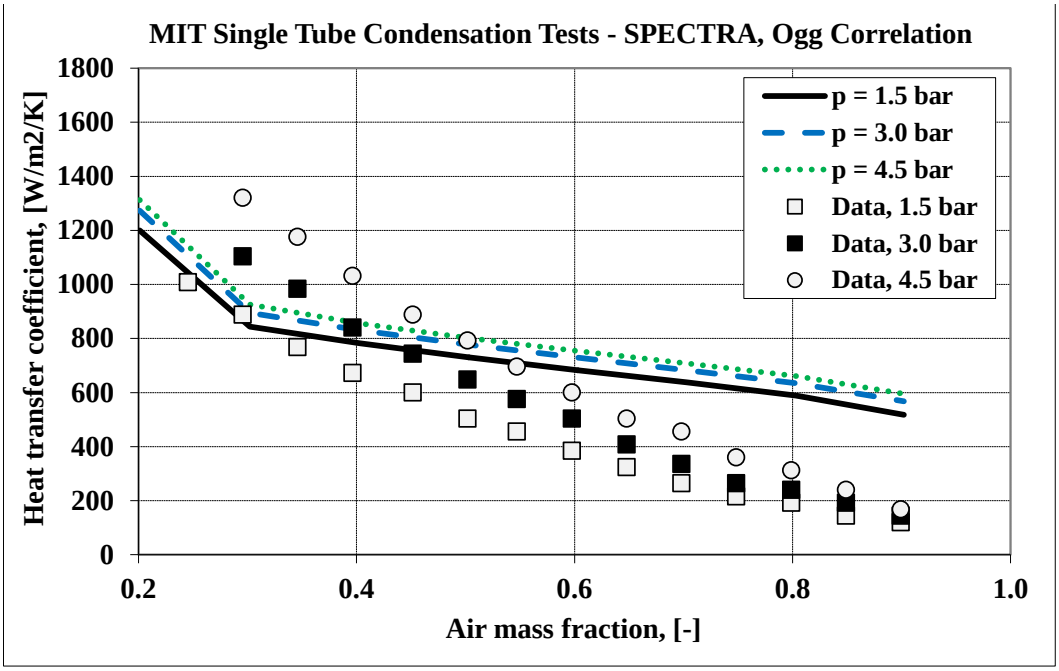

Figure 3-316 MIT tests, SPECTRA results, Ogg correlation.

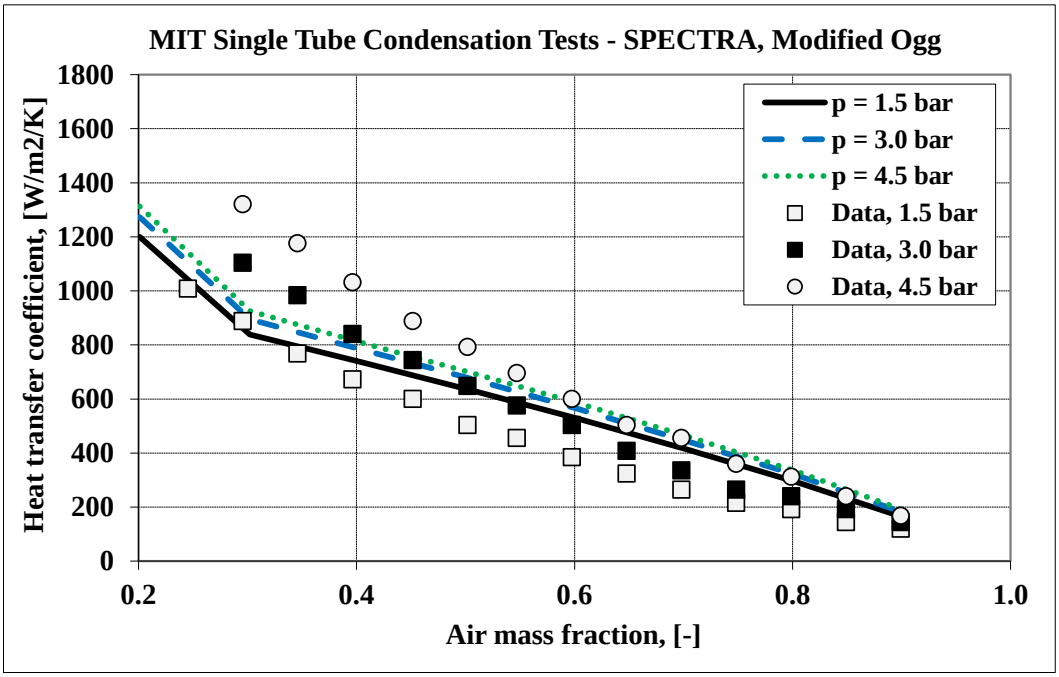

Figure 3-317 MIT tests, SPECTRA results, KSP correlation.

3.8 Thermal Radiation

The verification of radiant heat exchange models is given in this chapter. Section 3.8.1 describes the verification runs of the radiation model with non-absorbing/non-emitting gas. The verification of the radiation model with participating gas is given in section 3.8.2.

3.8.1 Radiative Heat Exchange in a Non-absorbing/Non-emitting Medium

Two test cases are considered for verification of the radiating heat exchange model in case of no gas participation (the model is selected by MODRAD=1 in the radiation input data - Volume 2). These are:

- Heat exchange between two surfaces separated by a screen (sections 3.8.1.1, 3.8.1.2).
- Heat exchange among five surfaces with a configuration of a Christiansen system (section 3.8.1.3)

3.8.1.1 Two Radiating Surfaces Separated by a Screen

The system consists of two flat parallel surfaces, separated by a screen (Figure 3-318). The effective emissivity for radiant heat exchange between surfaces 1 and 2 is given by ([21], section 3.4):

$$\varepsilon_{1-2} = \left(\frac{1}{\varepsilon_1} + \frac{1}{\varepsilon_2} + \frac{2}{\varepsilon_{scr}} - 2 \right)^{-1}$$

Here ε_1 and ε_2 are the emissivities of the surfaces 1 and 2, ε_{scr} is the emissivity of the screen surfaces.

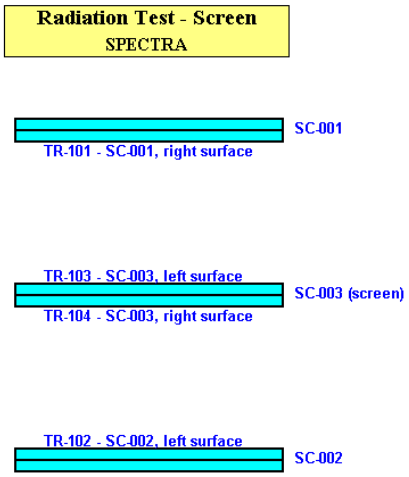

Figure 3-318 Two radiating surfaces and secreen - SPECTRA model

The radiant heat flux exchanged between surfaces 1 and 2 in stable conditions is equal to [21]:

$$q_{1-2} = \varepsilon_{1-2} \cdot \sigma \cdot \left(T_1^4 - T_2^4\right)$$

where σ is the Stefan-Boltzmann constant (equal to 5.67×10^{-8} W/m^2/K^4), T_1 and T_2 are temperatures of the surfaces 1 and 2.

The model used to represent the system described above is shown in Figure 3-318. Three Solid Conductors (SC-001 through SC-003) were used to represent the surfaces and the screen. Radiating system 1 with four radiating surfaces (TR-101 through TR-104) was used. The radiation mode without gas participation was selected for this system. The radiating surfaces were associated with the SC surfaces, as shown in Figure 3-318. The temperatures of SC-001 and SC-002 were held constant by tabular boundary conditions at 1000 K and 400 K respectively. The conduction resistance was minimized by selecting a very small thickness of all conductors (0.02 mm, 2 nodes, 0.01 mm each) and a large material conductivity (100.0 W/m/K). Other material properties were set to values appropriate for steel (ρ = 7000 kg/m^3, c_p = 500 J/kg-K). The emissivities of surfaces 1 and 2 were set to 0.5. The screen emissivity (applied on both sides of SC-003) was varied from 0.1 to 1.0.

The input decks are located in:

- `\Z-INPUTS\TR\Screen\Screen-01.SPE` - screen emissivity of ε_{scr} = 0.1
- `\Z-INPUTS\TR\Screen\Screen-05.SPE` - screen emissivity of ε_{scr} = 0.5
- `\Z-INPUTS\TR\Screen\Screen-10.SPE` - screen emissivity of ε_{scr} = 1.0

Calculations were performed for a sufficiently long period (500 s) to obtain stable conditions. Results are shown in Figure 3-319, Figure 3-320, Figure 3-321, and summarized in Table 3-47. There are no differences between the theoretical and calculated results within at least four decimal places.

Table 3-47 Results for two surfaces separated by a screen

Screen emissivity	Theoretical values		Calculated values
ε_{scr}	ε_{1-2}	q_{1-2} (kW/m^2)	q (kW/m^2)
0.10	0.0454545	2.511	2.511
0.50	0.1666667	9.208	9.208
1.00	0.2500000	13.81	13.81

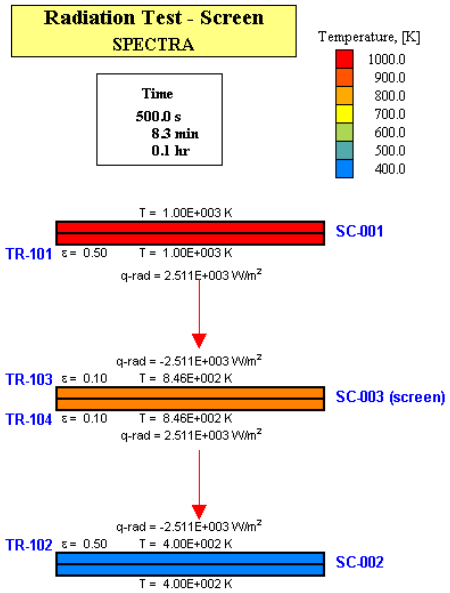

Figure 3-319 Two radiating surfaces and screen - results for $\varepsilon = 0.1$

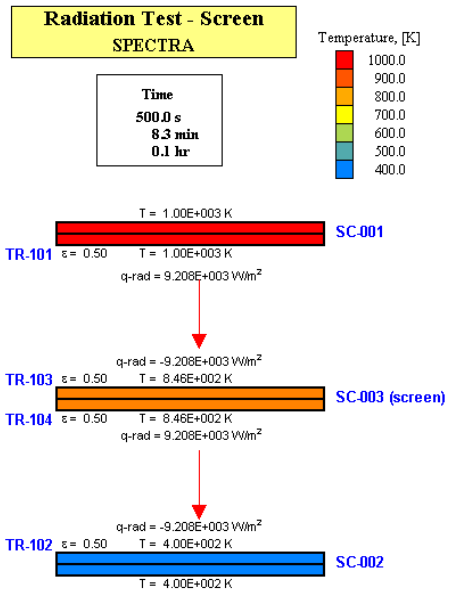

Figure 3-320 Two radiating surfaces and screen - results for $\varepsilon = 0.5$

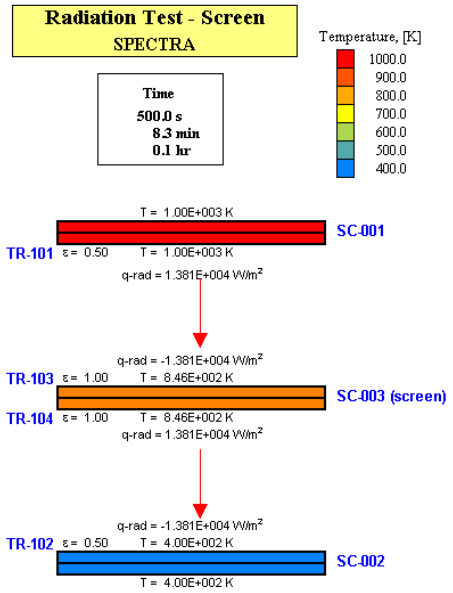

Figure 3-321 Two radiating surfaces and screen - results for $\varepsilon = 1.0$

3.8.1.2 Effective Emissivity of Two Radiating Surfaces Separated by a Screen

This section shows how the presence of a screen can be taken into account in a simplified way, by specifying effective emissivity of the radiating surfaces. In this case the screen does not need to be modeled as a separate Solid Heat Conductor, which may sometimes be very convenient. The test consists of two radiating surfaces separated by a screen. Two cases are considered.

(A) True case, the screen is modeled as a separate SC (SC-115 - Figure 3-322).
(B) Simplified case, the screen is not modeled; the effective emissivity is used instead.

The effective emissivity is obtained from the following reasoning. In the case (A), two surfaces separated by a screen, the effective emissivity is given by (see previous section):

$$\varepsilon_{1-2} = \left(\frac{1}{\varepsilon_1} + \frac{1}{\varepsilon_2} + \frac{2}{\varepsilon_{scr}} - 2 \right)^{-1}$$

If all emissivities are equal, $\varepsilon_1 = \varepsilon_2 = \varepsilon_{scr} = \varepsilon_A$:

$$\varepsilon_A = \left(\frac{4}{\varepsilon_A} - 2 \right)^{-1}$$

In the case (B), two surfaces with no screen in between, the effective emissivity is given by:

$$\varepsilon_{1-2} = \left(\frac{1}{\varepsilon_1} + \frac{1}{\varepsilon_2} - 1 \right)^{-1}$$

If both emissivities are equal, $\varepsilon_1 = \varepsilon_2 = \varepsilon_B$:

$$\varepsilon_{1-2} = \left(\frac{2}{\varepsilon_B} - 1 \right)^{-1}$$

Suppose that all emissivities are equal. If both situations are to be equivalent, the effective emissivities must be equal in both cases (A) and (B):

$$\left(\frac{4}{\varepsilon_A} - 2 \right)^{-1} = \left(\frac{2}{\varepsilon_B} - 1 \right)^{-1}$$

After simple transformations we get:

$$\varepsilon_B = \frac{2\varepsilon_A}{4 - \varepsilon_A}$$

If the true emissivity in the case (A) is equal to $\varepsilon_A = 0.9$, then the effective emissivity in the case (B) is equal to $\varepsilon_B = 0.581$. The effective emissivity is in both cases equal to $\varepsilon_{1\text{-}2} = 0.409$.

Both cases (A) and (B) are modeled using the simple structure-to-structure radiation model (see section 3.8.2.4). The input deck is located in: `\Z-INPUTS\TR\2R-Screen\`. The stationary state results are shown in Figure 3-322. It is seen that in both cases the heat flux is the same and equal to $q = 23.0$ kW/m^2. The correctness is easily checked as:

$$q_{1-2} = \varepsilon_{1-2} \cdot \sigma \cdot \left(T_1^4 - T_2^4 \right) = 0.409 \cdot 5.67 \times 10^{-8} \cdot \left(1000^4 - 300^4 \right) = 23.0 \times 10^3$$

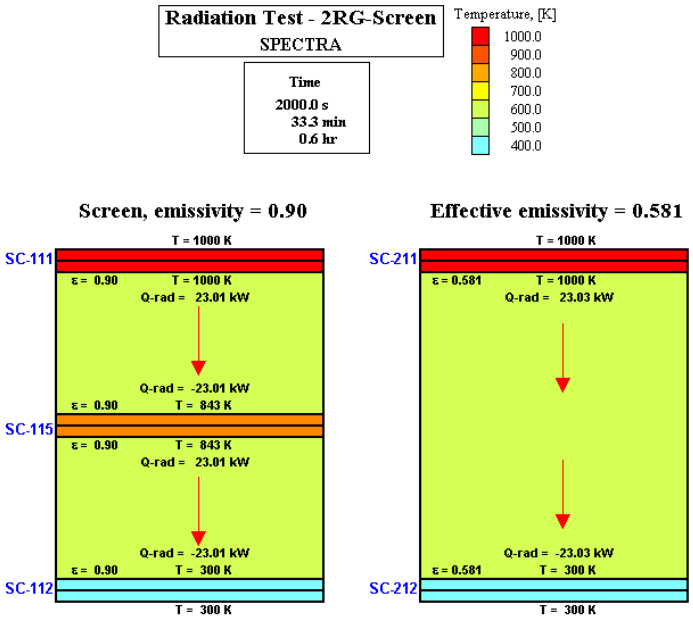

Figure 3-322 Two radiating surfaces and screen

3.8.1.3 Five Radiating Surfaces - Christiansen System

For the second test a "Christiansen system" was selected. This system consists of an inner, convex surface, and an outer surface. The effective emissivity for radiant heat exchange between the inner and the outer surfaces is given by ([21], section 3.1):

$$\varepsilon_{Ch} = \left(\frac{1}{\varepsilon_{in}} + \frac{A_{in}}{A_{out}} \cdot \left(\frac{1}{\varepsilon_{out}} - 1 \right) \right)^{-1}$$

where A_{in}, A_{out} are the areas of the inner surface and outer surface and ε_{in}, ε_{out} are the surface emissivities. The radiant heat fluxes emitted from the inner and outer surfaces in stable conditions are equal to [21], section 3.1):

$$q_{in-out} = \varepsilon_{Ch} \cdot \sigma \cdot \left(T_{in}^4 - T_{out}^4 \right)$$

$$q_{out-in} = \varepsilon_{Ch} \cdot \sigma \cdot \left(T_{out}^4 - T_{in}^4 \right) \cdot \frac{A_{in}}{A_{out}}$$

The following model was built for SPECTRA, that falls into the Christiansen system type. Five structures are applied as shown in Figure 3-323.

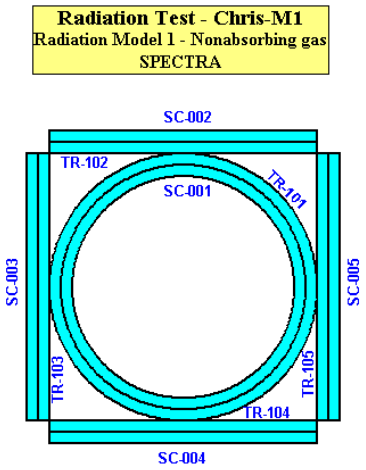

Figure 3-323 Five surfaces test case (Christiansen system)

The internal (convex) surface is modelled by a single, cylindrical Conductor (SC-001) with radius equal to: R = 1.0 m. The external surface is modelled using four rectangular Conductors (SC-002 through SC-005), with the SC width equal to: W = 2.0 m. Five radiating surfaces (TR-101 through TR-105) were associated with the SC surfaces, as shown in Figure 3-323. Note that temperatures of all rectangular conductors must be identical for the system to behave according to the Christiansen formula. The cylindrical conductor (SC-001) is held at 1000 K by a tabular boundary condition at the inner side.

Conductors SC-002 through SC-005) are held at 400 K by similar boundary conditions. The conduction resistance was minimized by selecting a very small thickness of all conductors (0.02 mm, 2 nodes, 0.01 mm each) and a large material conductivity (100.0 W/m/K). Other material properties were set to values appropriate for steel (ρ = 7000 kg/m^3, c_p = 500 J/kg-K).

The view factors were calculated using the Hottel's string rule (see [16], section 6.3.2, figure 6.10). For two surfaces shown in Figure 3-324 (a) the view factor from surface 1 to 2, F_{1-2}, is computed by summing the lengths of the crossed strings (ab + bd), then subtracting the summed length of the uncrossed strings (ad + bc), and then dividing by twice the arc length of the surface 1:

$$F_{1-2} = \frac{(ac+bd)-(ad+bc)}{2L_1}$$

This method, applied to a one half of the considered system, shown in Figure 3-324 (b), will give:

- length of crossed strings: $L_C = (\pi R/2+R) + (R+\pi R/2) = \pi R + 2R$
- length of uncrossed strings: $L_U = R + R = 2R$
- arc lengths: $L_1 = \pi R$
  $L_2 = 2R$

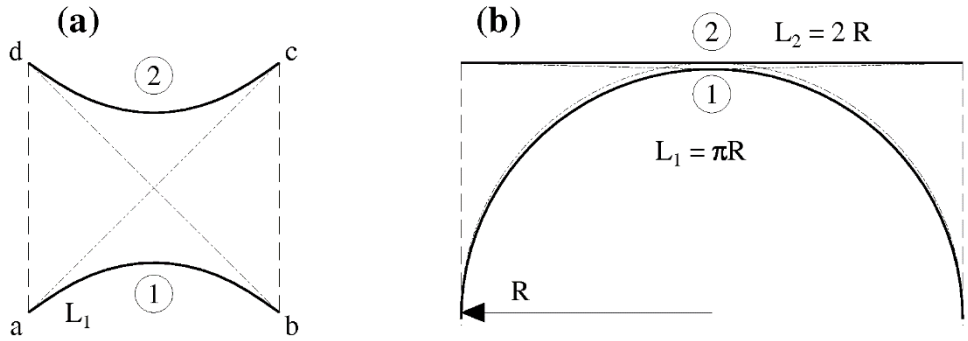

$F_{1->2}$ =
= [(ac + bd) - (ad + bc)] / (2·L_1)

F_{1-2} = [(πR + 2R) - (2R)] / (2·πR) = 1/2
F_{2-1} = [(πR + 2R) - (2R)] / (2·2R) = π/4

Figure 3-324 Calculation of view factors using Hottel's string method.

The view factors are equal to:

$$F_{1-2} = \frac{L_C - L_U}{2L_1} = \frac{(\pi R + 2R) - (2R)}{2(\pi R)} = \frac{1}{2}$$

$$F_{2-1} = \frac{L_C - L_U}{2L_2} = \frac{(\pi R + 2R) - (2R)}{2(2R)} = \frac{\pi}{4}$$

The string method is very useful in view factors calculations and was therefore applied here as an example of the procedure rather than out of a real necessity (for the present case the view factors can be obtained simpler, using only the symmetry and closure relations).

The real view factor from 1 to 2 is twice smaller than the calculated above, since only one half of the surface 1 was taken into account in Figure 3-324 (b) (in other words, L_1 is in fact equal to $2\pi R$ rather than πR). Thus the view factor F_{1-2} is 1/4 (which can be also deduced from symmetry). The same values will of course be appropriate for F_{1-3}, F_{1-4}, and F_{1-5}. Using the calculated F_{1-2} and the symmetry, one obtains: $F_{k-1} = \pi/4$ for: $k > 1$.

Finally the view factors F_{2-3}, etc. are calculated using closure relation:

$$F_{2-1} + F_{2-3} + F_{2-5} = 1.0$$

Using the fact that due to symmetry $F_{2-5} = F_{2-3}$ the value of F_{2-3} is obtained as:

$$F_{2-3} = \frac{1}{2} \cdot (1 - F_{2-1}) = \frac{4-\pi}{8}$$

The full matrix of view factors is:

$$F = \begin{bmatrix} 0 & \frac{1}{4} & \frac{1}{4} & \frac{1}{4} & \frac{1}{4} \\ \frac{\pi}{4} & 0 & \frac{4-\pi}{8} & 0 & \frac{4-\pi}{8} \\ \frac{\pi}{4} & \frac{4-\pi}{8} & 0 & \frac{4-\pi}{8} & 0 \\ \frac{\pi}{4} & 0 & \frac{4-\pi}{8} & 0 & \frac{4-\pi}{8} \\ \frac{\pi}{4} & \frac{4-\pi}{8} & 0 & \frac{4-\pi}{8} & 0 \end{bmatrix}$$

The view factors must be entered in SPECTRA with good accuracy, to avoid energy error (see Volume 1). The code checks the consistency of the view factors (closure and reciprocity relations) within 8 decimal places. In the current example the view factors were entered with 9 decimal places accuracy:

$$\frac{\pi}{4} = 7.85398163 \times 10^{-1}$$
$$\frac{4-\pi}{8} = 1.07300918 \times 10^{-1}$$

The following data were used for calculations:

- Radius, R = 1.0 m
- Temperatures: cylinder: T = 1000 K, rectangular walls: T = 400 K
- Emissivities: cylinder: ε = 0.6, rectangular walls: ε = 0.4

The input deck is provided in `\Z-INPUTS\TR\Chris\Chris-M1.SPE`. Calculations were performed for a sufficiently long period (500 s) to obtain stable conditions. Results are shown in Figure 3-325 and Table 3-48. There are no differences between the theoretical and calculated results within at least four decimal places.

Table 3-48 Results of the Christiansen system test

Theoretical values			Calculated values	
ε_{Ch} (-)	Surface	q (kW/m^2)	Structure	q (kW/m^2)
0.351523	$q_{in\text{-}out}$	+19.42	SC-001	+19.42
	$q_{out\text{-}in}$	–15.25	SC-002 - 005	–15.25

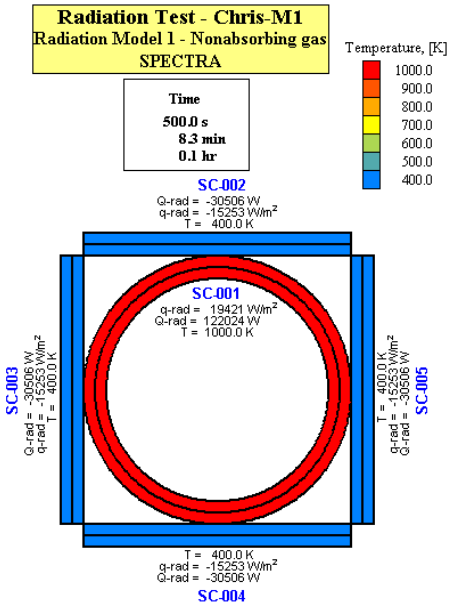

Figure 3-325 SPECTRA results for the Christiansen system test

3.8.2 Radiant Heat Exchange in an Enclosure with Participating Gas

The verification of the radiation model with a participating gas was performed in two steps. As a first step the two tests for the non-absorbing/non-emitting gas model, shown in section 3.8.1.1 and 3.8.1.3, were calculated using the model with a participating gas. Results are shown in sections 3.8.2.1 and 3.8.2.2. As a second step the test case described in section 3.8.2.3 was calculated.

3.8.2.1 Two Radiating Surfaces with Participating Gas

The test described in section 3.8.1.1 was recalculated using the radiation model with a participating gas. A single Control Volume (CV-001) was added, filled initially with hot (600 K) steam. The radiating surfaces were connected to CV-001, which means the corresponding SC-s are transferring heat by convection to CV-001.

The radiation model 2 was applied and the radiation beam lengths (assumed equal to 1.0 m) were added. The input file is provided in `\Z-INPUTS\TR\Screen\Screen-M2.SPE`.

Results are shown in Figure 3-326. Because steam absorbs/emits radiation, there are two heat transfer mechanisms: radiation and convection. The net radiation absorption is equal to about 1.99 kW. In stationary conditions this heat is "returned" to the structures by convection. The net convective heat is 0.987 kW + 0.016 + 0.016 –3.008 ≈ –1.99 kW. The radiation fluxes are of course different from the values shown in section 3.8.1.1.

In order to make the results the same as in section 3.8.1.1, the convective heat transfer was eliminated by replacing the default heat transfer correlations by a tabular convective heat transfer coefficient. The TF-006 with the value of 0.0 was used on all radiating surfaces thus eliminating convection completely. Additionally the radiation absorption in gas was minimized by setting a very small value (10^{-10} m) for the radiation beam length.

The input file is provided in `\Z-INPUTS\TR\Screen\Screen-M2-A.SPE`. Results are shown in Figure 3-327. During the initial phase the gas participates of course, by absorbing radiation. However, as soon as stationary conditions are reached the absorption in gas decreases to practically zero. The radiation fluxes are the same as those obtained in section 3.8.1.1.

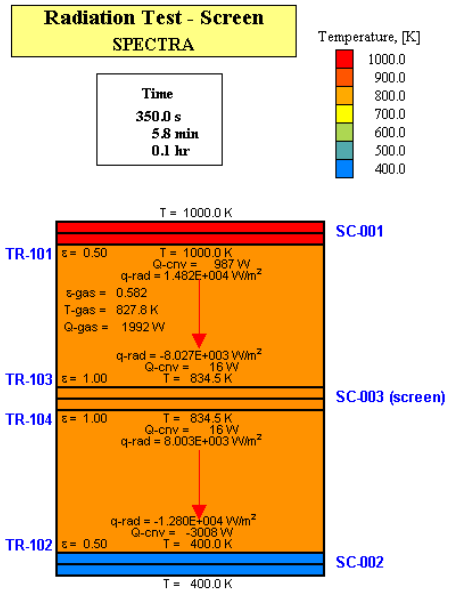

Figure 3-326 Screen test - radiation model with participating gas

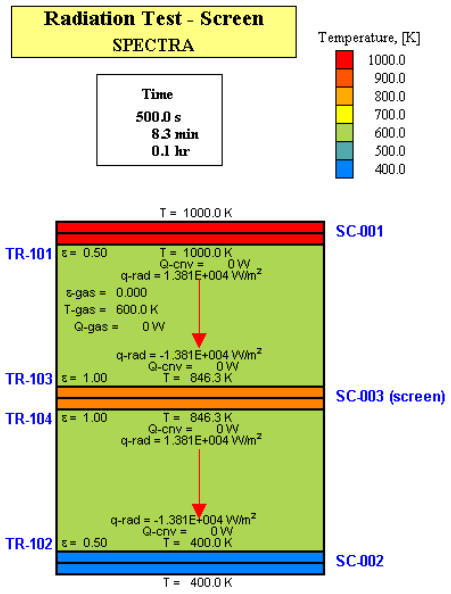

Figure 3-327 Screen test - radiation model with participating gas, convection disabled

3.8.2.2 Five Radiating Surfaces - Christiansen System

The test described in section 3.8.1.3 was recalculated using the radiation model with a participating gas. A single Control Volume (CV-001) was added, filled initially with hot (600 K) steam - Figure 3-328. The radiating surfaces were connected to CV-001, which means the corresponding SC-s are transferring heat by convection to CV-001.

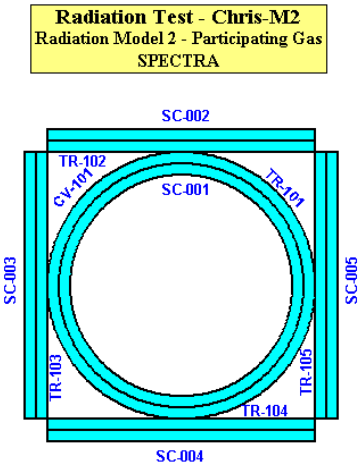

Figure 3-328 Five surfaces test case (Christiansen system)

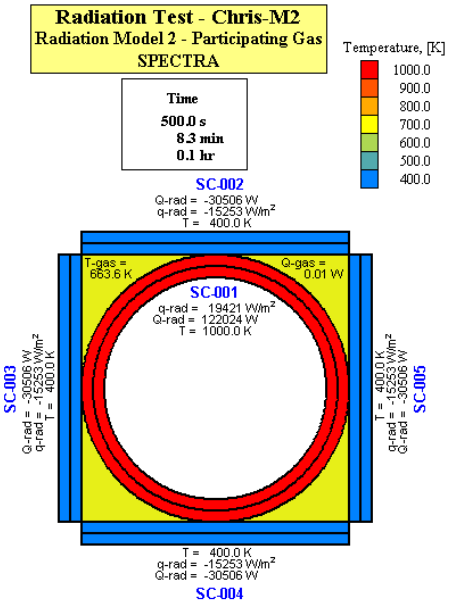

Figure 3-329 SPECTRA results for the Christiansen system test

As shown in the previous section with this model the convection and radiation to gas changes the radiation fluxes. In order to make the results the same as those obtained with the model with non-absorbing and non-emitting gas, the radiation beam lengths are set to a very small number (10^{-10} m) in order to minimize the radiation absorption in gas.

The input file is provided in `\Z-INPUTS\TR\Screen\Screen-M2-cnv.SPE`. Results are shown in Figure 3-329. The absorption of radiation in the gas is minor and the heat fluxes are practically the same as those shown in section 3.8.1.3.

3.8.2.3 Two Radiating Surfaces with Participating Gas

The system consists of two flat parallel surfaces with an absorbing/emitting gas filling the space between the surfaces (Figure 3-330). The effective emissivity for radiant heat exchange between surfaces 1 and 2 is given by ([21], section 7.1):

$$\varepsilon_{1-2} = \left(\frac{1}{\varepsilon_1} + \frac{1}{\varepsilon_2} - 1 + \frac{\varepsilon_g}{2 - \varepsilon_g} \right)^{-1}$$

Here ε_1 and ε_2 are the emissivities of the surfaces 1 and 2, ε_g is the gas emissivity. The radiant heat flux exchanged between surfaces 1 and 2 in stable conditions is equal to [21]:

$$q_{1-2} = \varepsilon_{1-2} \cdot \sigma \cdot \left(T_1^4 - T_2^4 \right)$$

where σ is the Stefan-Boltzmann constant (equal to 5.67×10^{-8} W/m^2/K^4), T_1 and T_2 are temperatures of the surfaces 1 and 2. The model shown in Figure 3-330 was used to represent the system described above.

Two Solid Conductors (SC-001 and SC-002) with associated radiating surfaces (TR-101 and TR-102) were used to represent the surfaces. The temperatures of SC-001 and SC-002 were held constant by tabular boundary conditions, at 1000 K and 400 K respectively. The conduction effects were minimized by selecting a very small thickness of both conductors (0.02 mm) and a large material conductivity (100.0 W/m/K). Other material properties were set to values appropriate for steel (ρ = 7000 kg/m^3, c_p = 500 J/kg-K). The emissivities of surfaces 1 and 2 were set to 0.5. A single Control Volume (CV-1) filled with steam represents the gas space between the surfaces. The default models to calculate steam emissivity and absorptivity were overruled using input parameters (Volume 2) to obtain emissivity and absorptivity equal to a desired constant.

To avoid convective heat transfer, the default convective heat exchange models have been replaced by a tabular heat transfer coefficient, with the value of zero. Calculations were performed using gas emissivities (and absorptivities) of: 0.0, 0.5, and 1.0. The input decks are provided in:

- `\Z-INPUTS\TR\2RG\2RG-00.SPE` - gas emissivity of ε_g = 0.0
- `\Z-INPUTS\TR\2RG\2RG-05.SPE` - gas emissivity of ε_g = 0.5
- `\Z-INPUTS\TR\2RG\2RG-10.SPE` - gas emissivity of ε_g = 1.0

Calculations were performed for a sufficiently long period (500 s) to obtain stable conditions. Results are shown in visualization pictures in Figure 3-331, Figure 3-332, Figure 3-333. Summary of calculated results is given in Table 3-49 and Figure 3-334. There are no differences between the theoretical and calculated results within four decimal places.

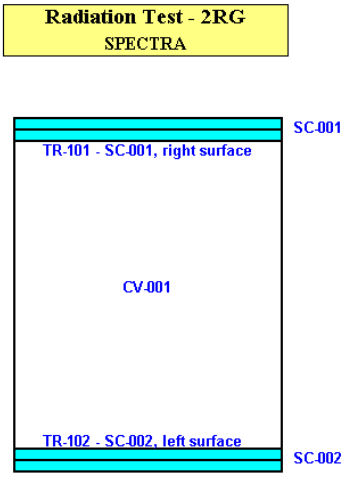

Figure 3-330 Two radiating surfaces and gas - nodalization

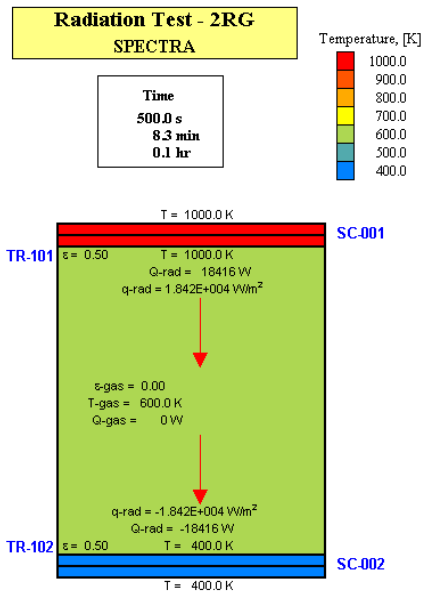

Figure 3-331 Two radiating surfaces and gas - results for ε_g = 0.0

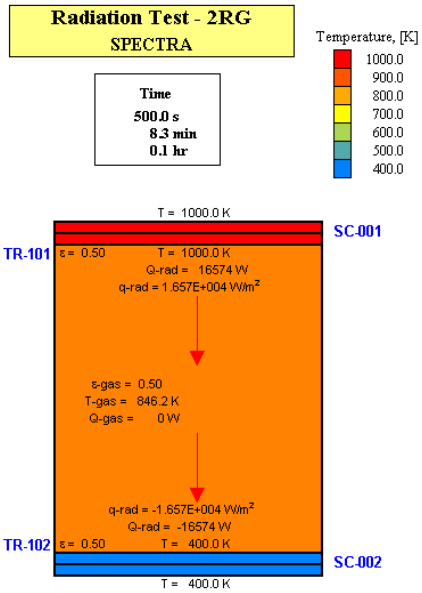

Figure 3-332 Two radiating surfaces and gas - results for ε_g = 0.5

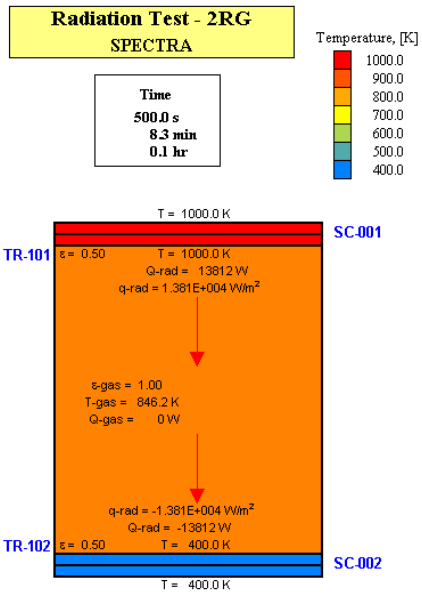

Figure 3-333 Two radiating surfaces and gas - results for ε_g = 1.0

Table 3-49 Radiation heat flux for two surfaces with gas

Gas emissivity ε_g	Theoretical values		Calculated values q (kW/m^2)
	ε_{1--2}	q_{1--2} (kW/m^2)	
0.00	0.3333	18.42	18.42
0.50	0.3000	16.57	16.57
1.00	0.2500	13.81	13.81

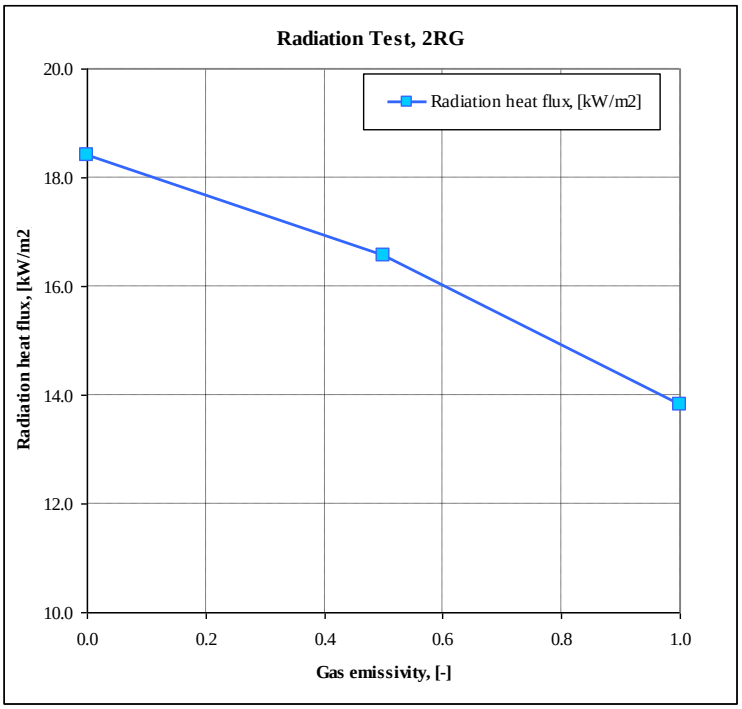

Figure 3-334 Radiation heat flux for two surfaces with gas

As shown in Figure 3-334 the smallest radiation flux is observed in case of ε_g = 1.0 (opaque atmosphere). If the gas emissivity is smaller the heat flux increases. This effect is opposite to the one that would be observed if the gas emissivity was taken into account in the simplified radiation model (see section 3.5.6). Therefore, as described in section 3.5.6, when the simplified radiation model is used, the best one can do is to assume gas emissivity of 1.0.

3.8.2.4 Simple Structure-to-Gas and Structure-to-Structure Radiation Models

This section presents comparison of two simple radiation models with the detailed net enclosure model:

- Structure-to-gas radiation comparison with net enclosure model with ε_g=1.0
- Structure-to-structure radiation comparison with net enclosure model with ε_g=0.0

The SPECTRA input files are located in:

\Z-INPUTS\TR\2RG-Simple

The model consists of radiating pairs of surfaces. The surface area of radiating surfaces is assumed as 1.0 m^2 (except for one case, described at the end of this section), the surface emissivity is assumed as ε = 0.9. Calculations were performed for a sufficiently long time to obtain stationary state: 2000 s. The applied time step was Δt = 1.0 s. Two versions were prepared:

- **Fixed structure temperatures**. In this case the surface temperatures are fixed by using appropriate boundary conditions and the stationary state flux is the result of the test. The cold surface temperature is equal to T_c = 400 K. The following four value are used for the hot surface temperature:
  - T_h = 500 K
  - T_h = 700 K
  - T_h = 900 K
  - T_h = 1100 K

Input and output files are located in:
\Z-INPUTS\TR\2RG-Simple\Q-vs-T\SPECTRA

- **Fixed power**. In this case the power source in the hot structure is fixed by using appropriate energy source. The cold surface temperature is fixed as T_c = 400 K by using appropriate boundary condition. The temperature of the hot surface in stationary state is the result of the test. The following four value are used for the power source:
  - q = 1 kW/m^2
  - q = 10 kW/m^2
  - q = 20 kW/m^2
  - q = 40 kW/m^2

Input and output files are located in
\Z-INPUTS\TR\2RG-Simple\T-vs-Q\SPECTRA

For comparison, a model for MELCOR 1.8.6 was generated using the automated export option (IEXPSL=2). Since MELCOR plot parameters do not include radiation flux, it is not possible to check the output of the case Q-vs-T (Q cannot be plotted or looked up in the output file). Therefore only the case T-vs-Q is discussed here. It was observed that numerical instability may occur between radiating surfaces if too large time step is used. The time step of Δt = 0.01 s was used in all MELCOR calculations, which ensured stable solution.

The MELCOR input files are located in:
\Z-INPUTS\TR\2RG-Simple\T-vs-Q\MELCOR

Results obtained for the case T-vs-Q, q = 20 kW/m^2, are shown in Figure 3-335 and Figure 3-336. Figure 3-335 shows results for ε_g = 1.0. Results of the simple structure-to-gas model (SC-111, SC-112) are practically identical to the results of the net enclosure model (SC-101, SC-102). Results of structure-to-gas model in MELCOR (HS-111, HS-112) are very similar to SPECTRA. Small differences are caused by the differences in the convective heat transfer; the convective heat transfer coefficient calculated for this case (stagnant fluid) is higher in MELCOR due to different correlation for natural convection.

Figure 3-336 shows results for ε_g = 0.0. Results of the simple structure-to-structure model (SC-211, SC-212) are practically identical to the results of the net enclosure model (SC-201, SC-202). Results of structure-to-structure model in MELCOR (HS-211, HS-212) are very similar to SPECTRA. Small differences are caused by the differences in the convective heat transfer.

Figure 3-337 shows SPECTRA results obtained for the case Q-vs-T, for the hot surface temperatures between 500 K and 1100 K. The heat fluxes obtained in the simplified model are practically identical to the results obtained with the net enclosure model.

Figure 3-338 shows SPECTRA and MELCOR results obtained for the case T-vs-Q, for the hot surface heat fluxes between 1.0 kW/m^2 and 40.0 kW/m^2. Results of structure-to-structure model in MELCOR (HS-211, HS-212) are very similar to SPECTRA. Small differences are caused by the differences in the convective heat transfer.

In order to eliminate the small differences due to convective heat transfer, the input model was modified. The convective heat transfer was minimized by using a tabular heat transfer coefficient. The heat transfer coefficient was set to a very small value: 10^{-9} W/m^2-K. Input and output files are located in: **\Z-INPUTS\TR\2RG-Simple\T-vs-Q-no-conv**

Results are shown in Figure 3-339 and Figure 3-340. MELCOR and SPECTRA results are practically identical when the convective heat transfer is eliminated. Results obtained with the net enclosure model (not shown in Figure 3-338 and Figure 3-340), are identical to the results of the simple structure-to-gas and structure-to-structure models, which can be seen in Figure 3-335 and Figure 3-336. Therefore it is concluded that the simple structure-to-gas and structure-to-structure radiation models work correctly.

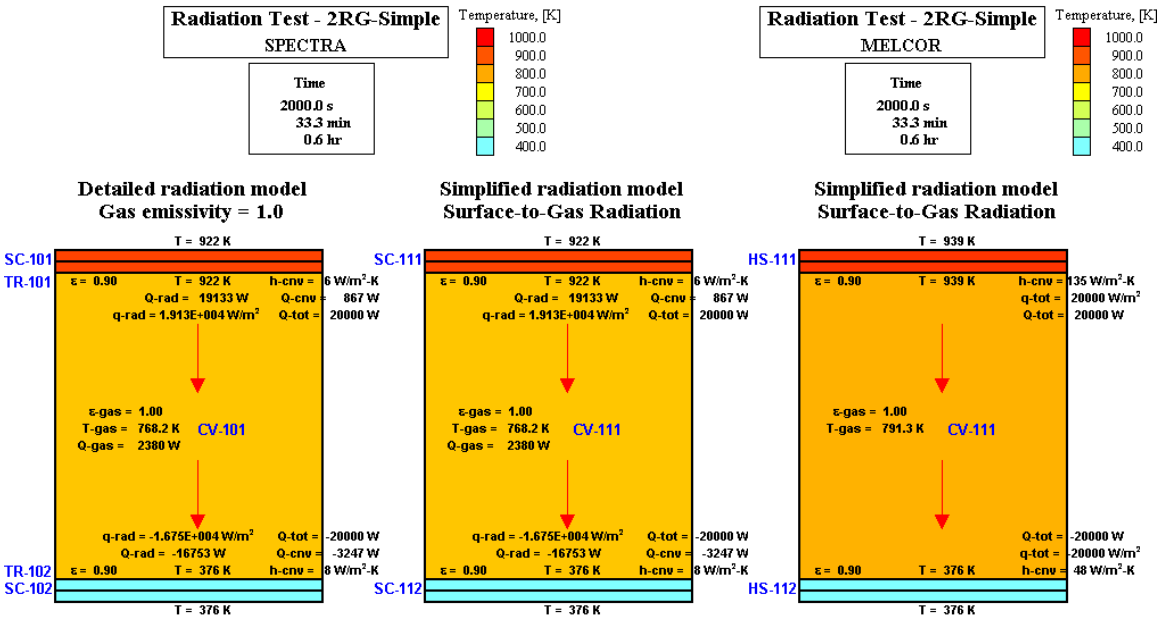

Figure 3-335 Radiation test with gas emissivity ε_g = 1.0, q = 20 kW/m²
left: SPECTRA: net enclosure and structure-to-gas model
right MELCOR structure-to-gas model

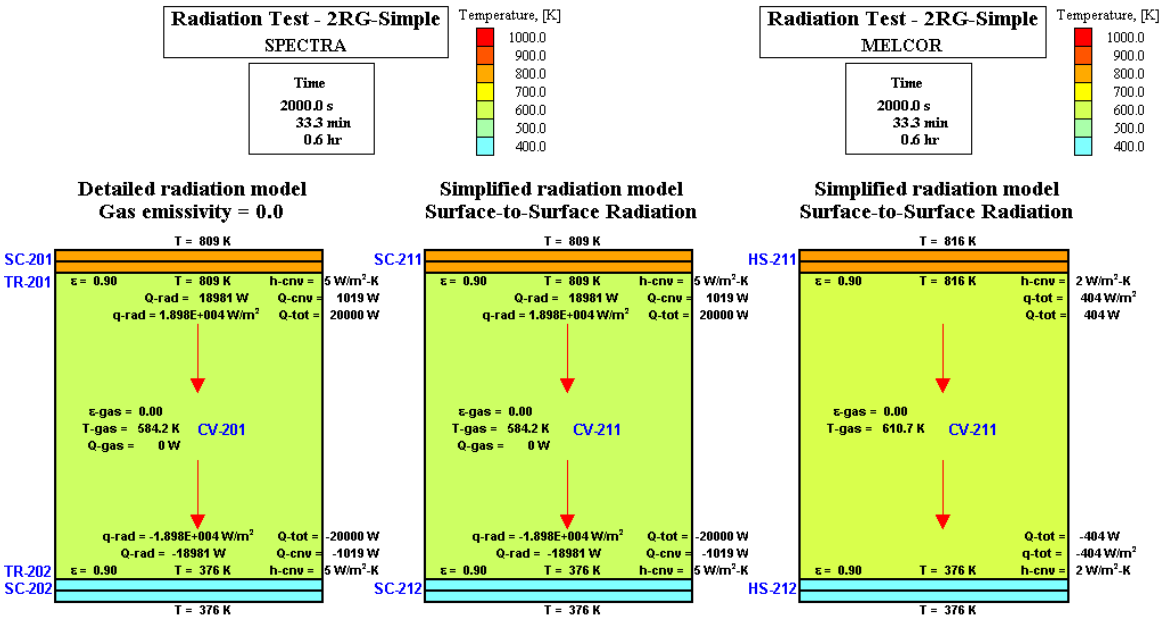

Figure 3-336 Radiation test with gas emissivity ε_g = 0.0, q = 20 kW/m²
left: SPECTRA: net enclosure and structure-to-structure model
right MELCOR structure-to-structure model

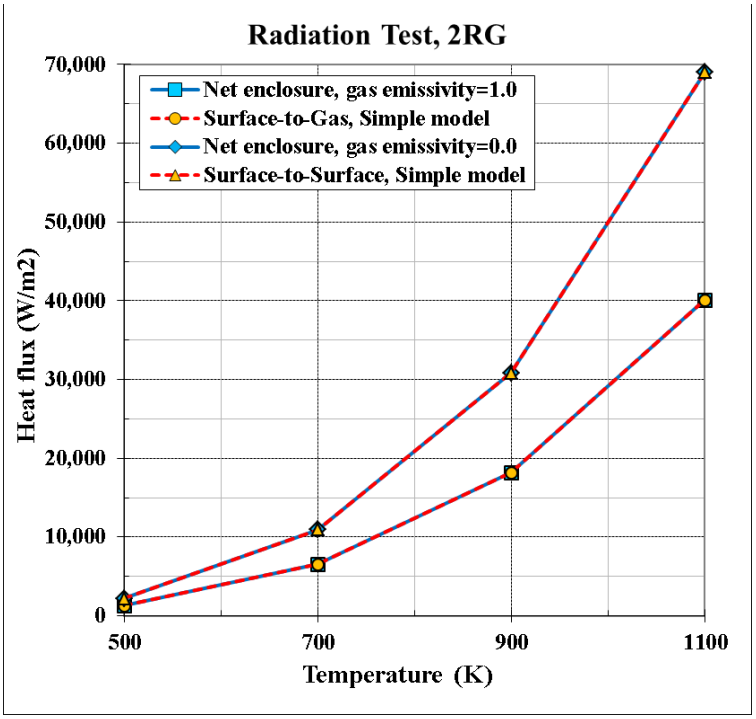

Figure 3-337 Simple structure-to-gas and structure-to-structure models versus net enclosure

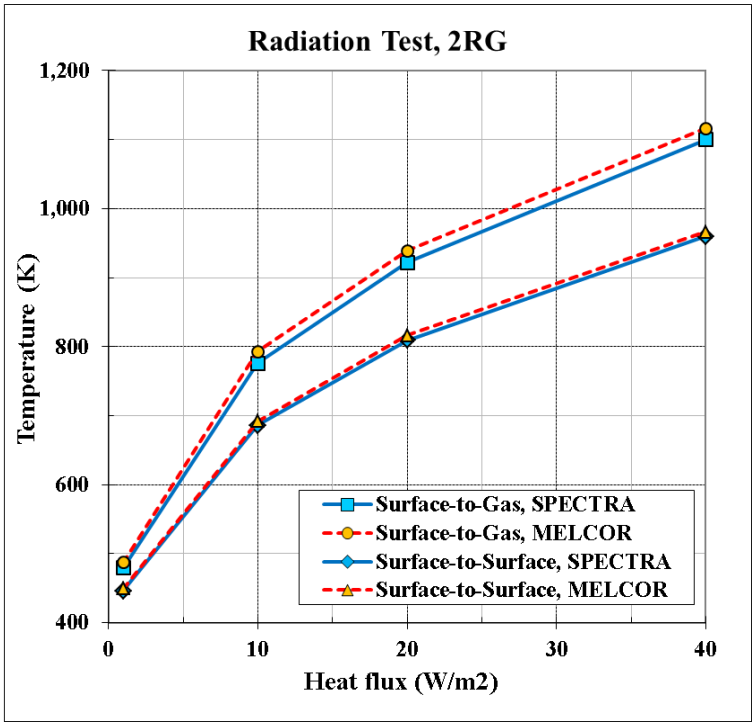

Figure 3-338 Simple structure-to-gas and structure-to-structure models versus MELCOR

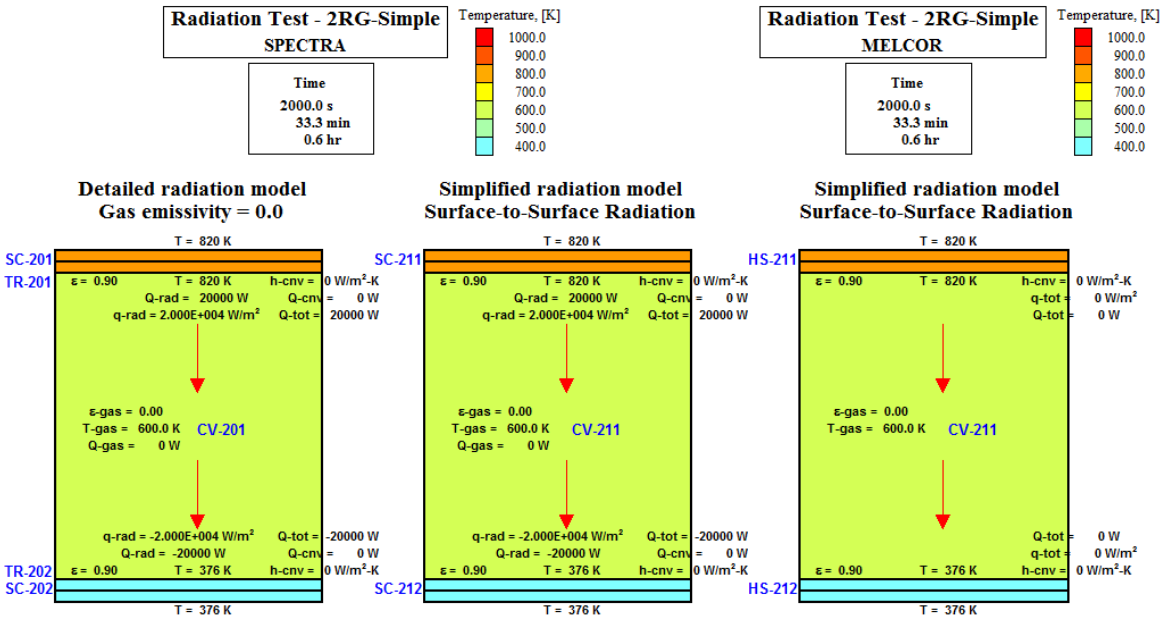

Figure 3-339 Radiation test with gas emissivity ε_g = 0.0, q = 20 kW/m², convection eliminated
left: SPECTRA: net enclosure and structure-to-structure model
right MELCOR structure-to-structure model

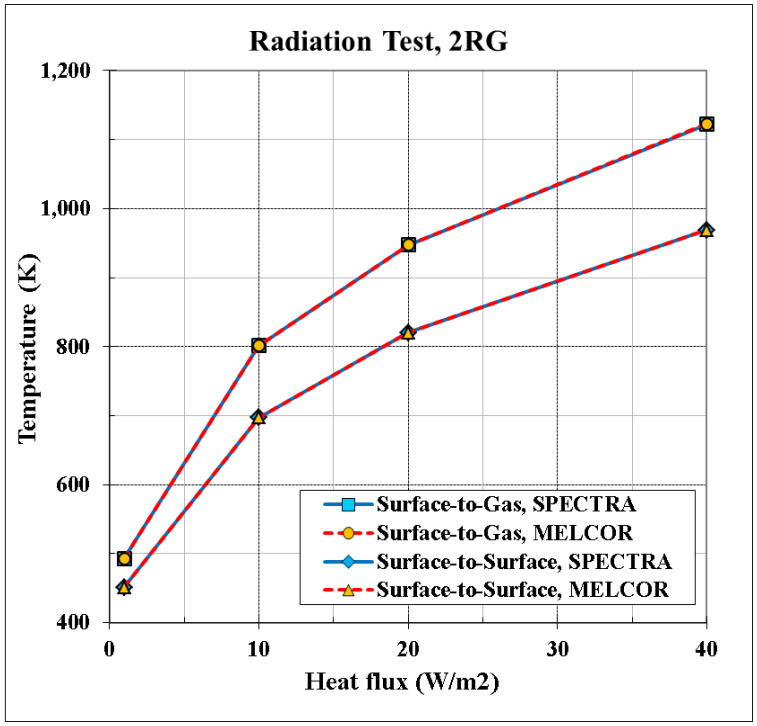

Figure 3-340 Structure-to-gas and structure-to-structure models versus MELCOR convection eliminated

Finally, a case with different surface areas and view factors is checked. The radiating surfaces areas are assumed as follows:

- Hot surface: $A_1 = 1.0\ m^2$
- Cold surface: $A_2 = 2.0\ m^2$
- View factor $F_{1-2} = 0.5$

The power source for the hot structure is set to 20 kW/m^2. For comparison, the detailed net enclosure model is created. The view factor matrix is obtained as follows. The view factor F_{1-1} is obtained from the closure relation: $F_{1-1} = 1 - F_{1-2} = 1.0 - 0.5 = 0.5$. The view factor F_{2-1} is obtained from the reciprocity relation: $F_{2-1} = F_{1-2} \times A_1/A_2 = 0.5 \times 1.0/2.0 = 0.25$. The view factor F_{2-2} is obtained from the closure relation: $F_{2-2} = 1 - F_{2-1} = 1.0 - 0.25 = 0.75$. The final view factor matrix for the net enclosure model is as follows:

$$F_{i-j} = \begin{vmatrix} 0.50 & 0.50 \\ 0.25 & 0.75 \end{vmatrix}$$

Results are shown in Figure 3-341. Both methods give identical temperature of the hot surface in stationary state. SPECTRA and MELCOR give identical results. These results show that the structure-to-structure radiation model works correctly.

Note: the heat fluxes are not plotted in MELCOR - in absence of convection the wall heat flux is always zero. However, the wall temperatures show that the radiation model in MELCOR gives identical results as the two radiation models in SPECTRA.

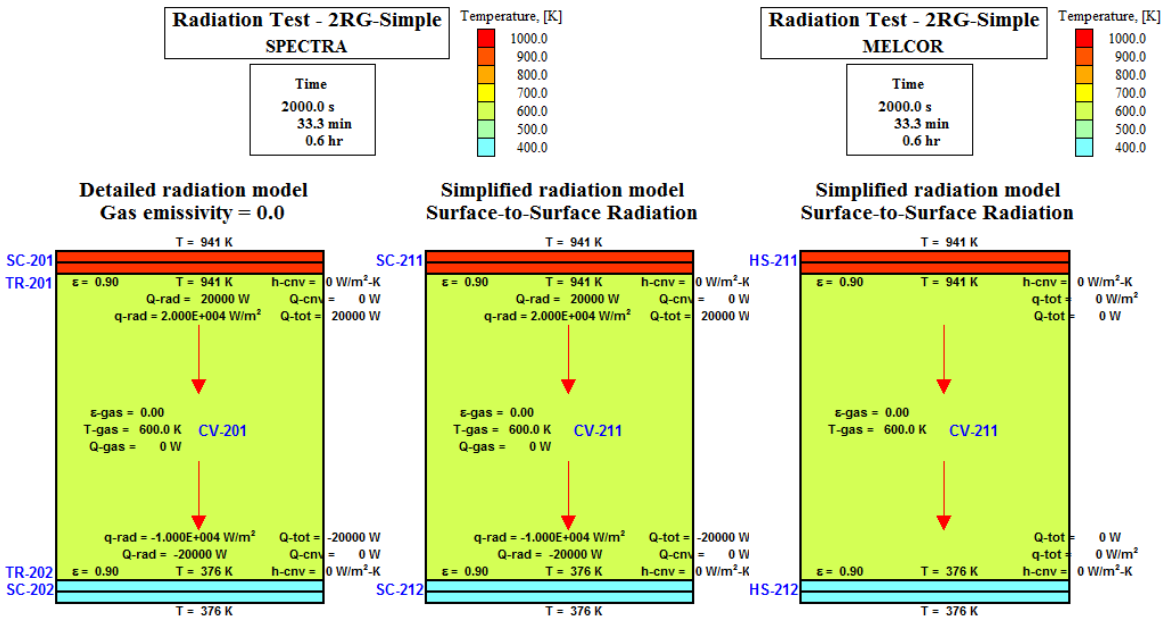

Figure 3-341 Radiation test, $\varepsilon_g = 0.0$, $F_{1-2} = 0.5$, $A_1 = 1.0\ m^2$, $A_2 = 2.0\ m^2$, convection eliminated
left: SPECTRA: net enclosure and structure-to-structure model
right MELCOR structure-to-structure model

3.8.2.5 Radiation to Pool

A "pool option" may be activated for one of the SC surfaces forming the radiation enclosure. The pool option is available only for 1-D Solid Heat Conductors. The structure with the pool option must be a floor of the Control Volume. The radiative flux is deposited at the SC surface in absence of a pool, or at the pool surface if a pool is present. A transition zone is defined (0, 10^{-3} m), in which the radiative fluxes are interpolated between the SC surface and the pool surface. The emissivity of the pool surface is assumed to be constant, equal to 0.96.

The system used to verify the model consists of four flat surfaces with an absorbing/emitting gas filling the space among the surfaces (Figure 3-342). The pool option is activated for the radiating surface TR-102. The fluid volume is a 1.0 m high, 1.0 m^3 CV. A small amount of water (0.1 m) is present initially. The initial temperature of the fluid and structures is close to saturation (372 K). The gas space is initially filled with dry air. The "back side" of the roof (SC-101) is heated up by specifying a boundary temperature of 700 K and a heat transfer coefficient of 100.0 W/m^2-K. All other structures are assumed to be insulated on their "back sides". A junction (JN-100) is provided, which leads to a constant parameter volume (CV-200 - "the environment") in order to keep the pressure constant and allow slow evaporation of the water pool.

The input deck is provided in:`\Z-INPUTS\TR\Pool\Pool.SPE`. Calculations were performed for 60,000.0 s. Results are shown in visualization pictures in Figure 3-343, Figure 3-344, Figure 3-345, and time dependent graphs in Figure 3-346, Figure 3-347, Figure 3-348, Figure 3-349. The following transient behavior is observed. Due to evaporation from the pool surface, the gas space is quickly filled with steam. There is a long period (about 55,000 s - Figure 3-346) during which the water pool evaporates. During this period the radiation from the hot roof is distributed among the two vertical surfaces and the pool surface. For example, at 50,000 s, shortly before the pool is totally evaporated, the radiation from the roof is 3944 W (Figure 3-344). The walls receive 954 W each; the rest $3944 - 2\times954 = 2036$ W, is absorbed by gas (826 W) and the pool surface (1211 W). Note that the radiation flux of TR-102 is 0.0; the radiation heat is absorbed by the pool and not by the structure SC-102.

When the pool is evaporated, the radiation from the roof causes all structures to heat up quickly (Figure 3-347). During this period there is a "normal" radiation in an enclosure formed by four radiating surfaces and the gas.

The radiation flux which is calculated for the floor (TR-102) is deposited in the pool as long as the pool level is more than 0.001 m. At about 54,000 s the pool level is decreased to 0.001 m (Figure 3-348). From this moment the radiation flux is interpolated between the pool and the structure SC-102 (Figure 3-349). At about 55,000 s the pool is completely evaporated and the full radiation heat is deposited on the surface of SC-102 (Figure 3-349). The sign convention in SPECTRA gives a positive heat flux when radiation is emitted from a surface, and when it is absorbed by gas or liquid. Therefore the sign was changed in the radiation flux shown in Figure 3-349.

The purpose of this test is to demonstrate the radiation to pool and to verify the calculated values and the calculation scheme in the interpolation zone. The consistency of the calculated radiation fluxes is easily checked by hand calculations, as shown above. The correctness of the interpolation scheme is verified by comparing values shown in Figure 3-348 and Figure 3-349.

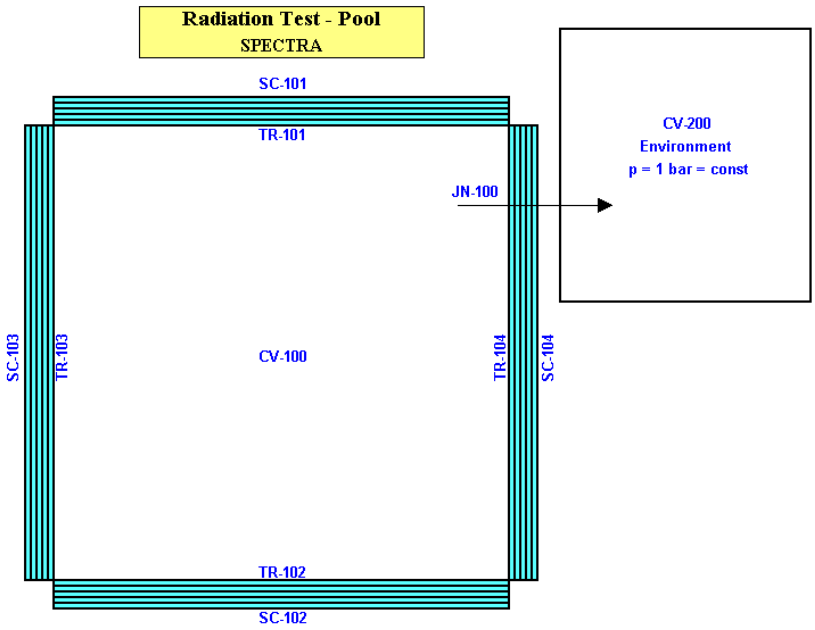

Figure 3-342 Radiation to pool - nodalization

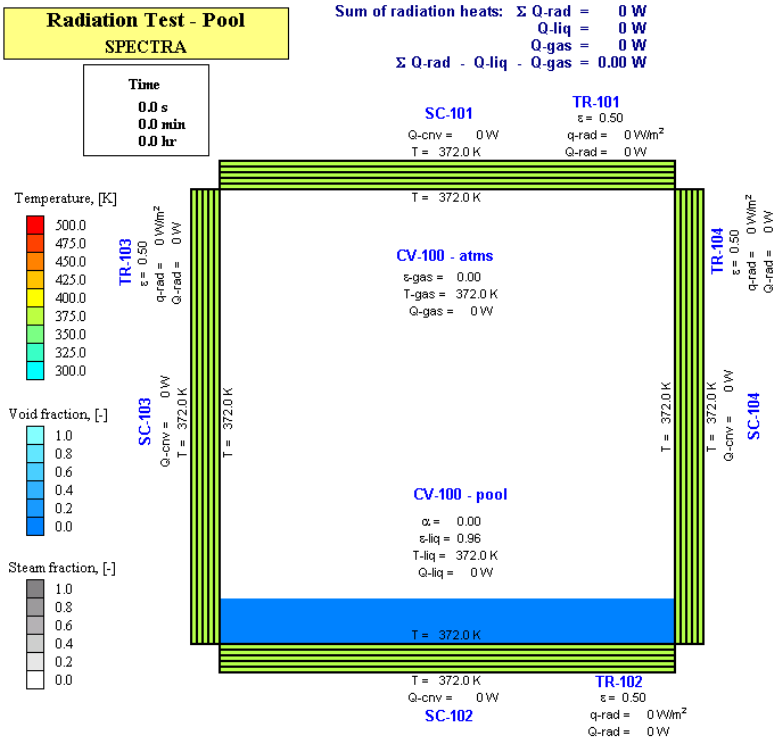

Figure 3-343 Radiation to pool, t = 0.0 s - start of the calculations

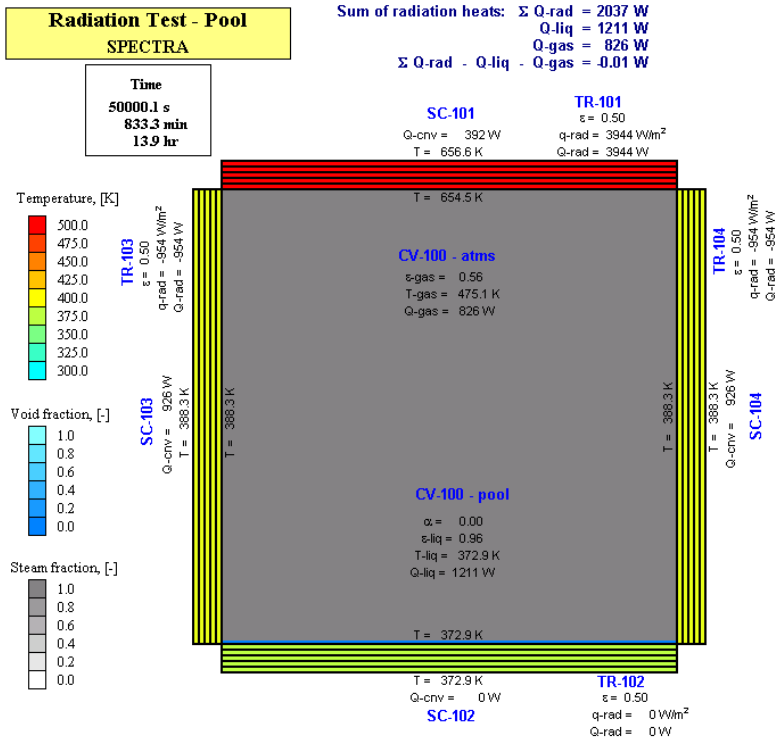

Figure 3-344 Radiation to pool, *t* = 50,000.0 s - soon before the pool is evaporated

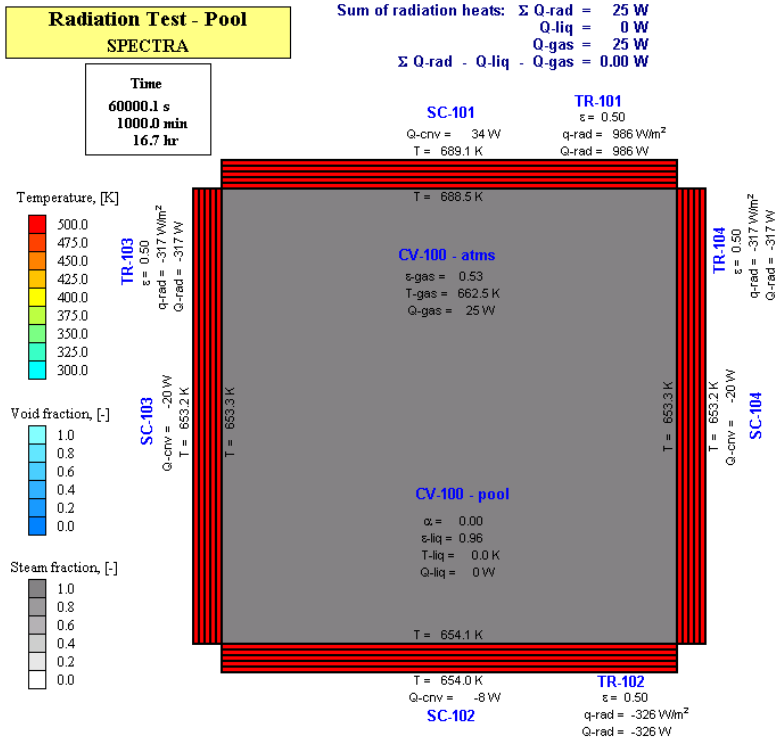

Figure 3-345 Radiation to pool, *t* = 60,000.0 s - soon after the pool is evaporated

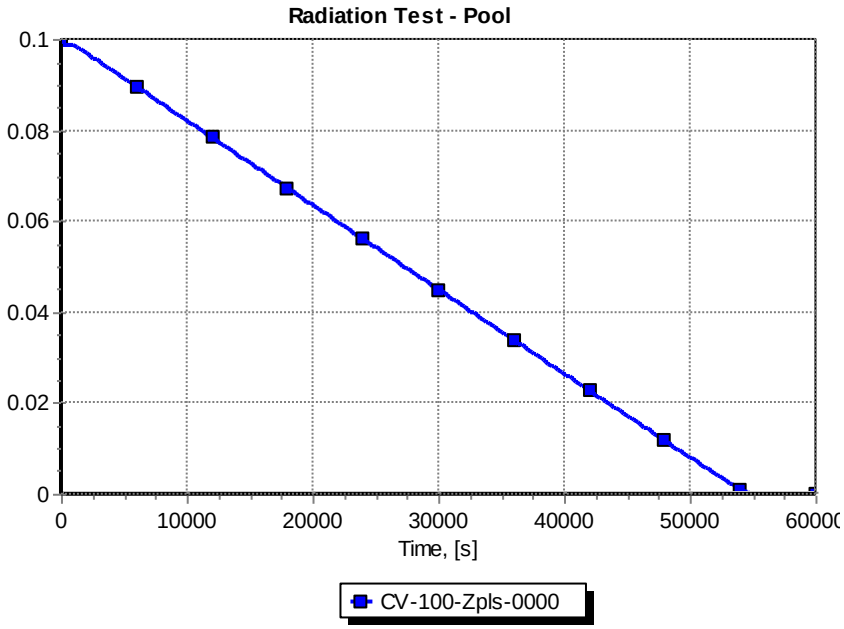

Figure 3-346 Radiation to pool - water level

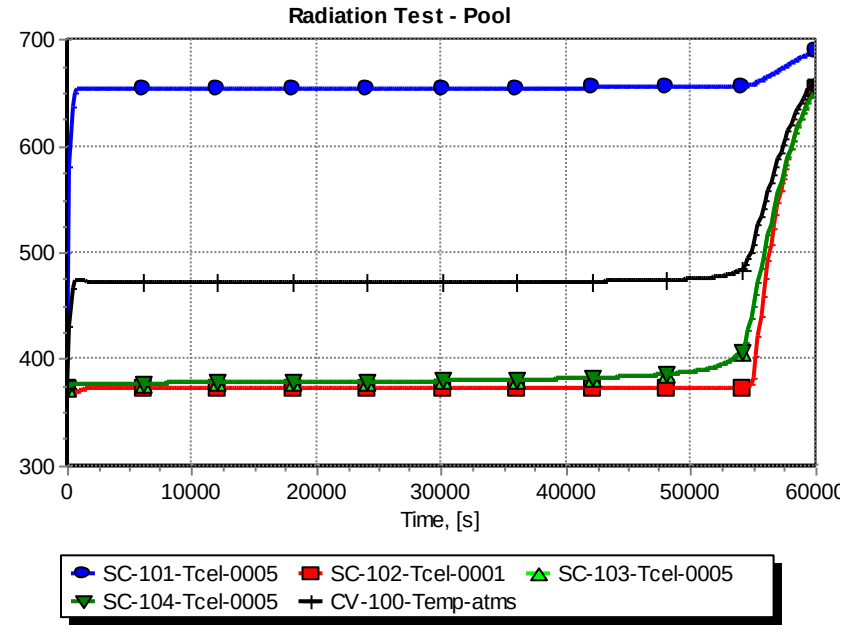

Figure 3-347 Radiation to pool - surface temperatures

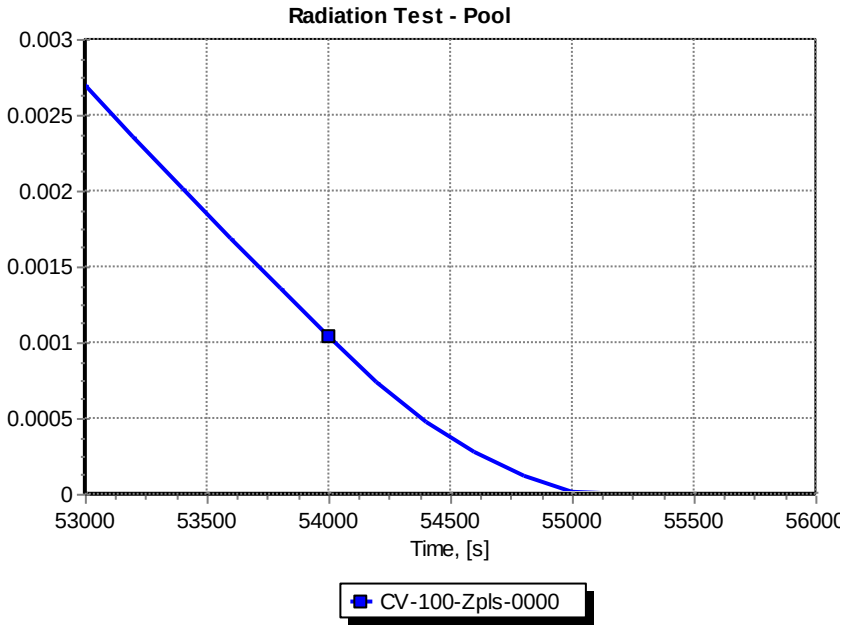

Figure 3-348 Radiation to pool - water level in CV-100 (around ~55,000 s)

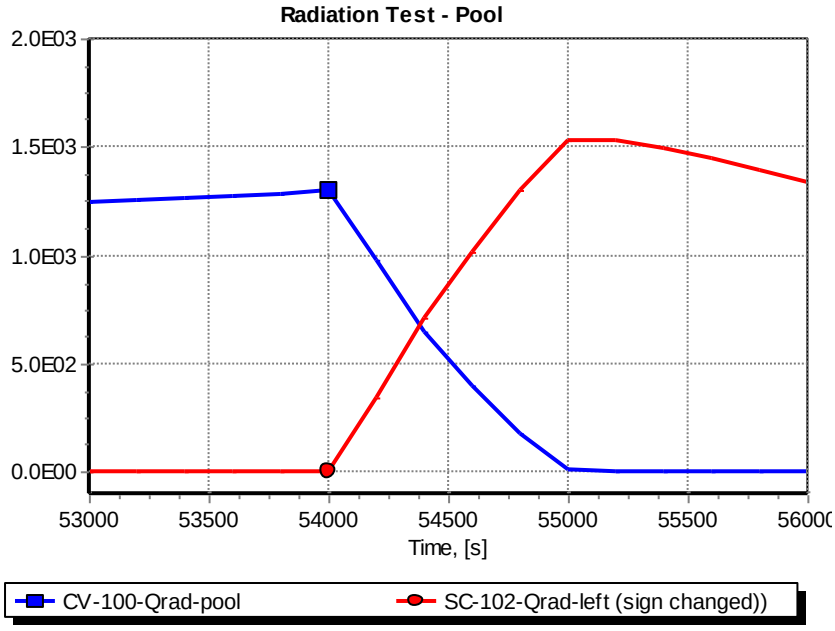

Figure 3-349 Radiation to pool - radiation heat to the CV-100 pool and the SC-102 surface

3.8.2.6 Radiation Beam Passing Several Control Volumes

It is possible to build a model where a radiation beam passes through several Control Volumes, on its way between surfaces *i* and *j*. For each of these CV's user must specify a path length, $L_{i\to j,\,k}$. The sum of all individual path lengths must be equal to the overall beam length on path between surfaces *i* and *j*:

$$\sum_k L_{i\to j,k} = L_{i\to j}$$

The system used to verify the model consists of two flat surfaces with an absorbing/emitting gas filling the space (Figure 3-350). The structure on the left, SC-101, is continuously heated by specifying the following boundary conditions on the "back side": a fluid temperature of 700 K and heat transfer coefficient of 10^6 W/m^2-K. The structure on the right, SC-102, is continuously cooled by specifying the following boundary conditions: a fluid temperature of 300 K and a heat transfer coefficient of 10^6 W/m^2-K.

The gas space is modelled using three Control Volumes (Figure 3-350). For the present test these volumes are isolated, i.e. there are no junctions that would allow gas flow and mixing. This is done to allow easier verification of the model results. The radiation path length is assumed to be 3.0 m, 1.0 m in each CV. The volumes are filled with:

- CV-101: dry air (non-absorbing/non-emitting gas)
- CV-102: air with 100% humidity (absorption/emission by steam)
- CV-103: air with 100% humidity (absorption/emission by steam)

The input deck is provided in: `\Z-INPUTS\TR\MultipleCV\MultipleCV.SPE`. Calculations were performed for a time sufficiently long to obtain stable conditions (3600.0 s). Results are shown in the visualization picture in Figure 3-351.

Volume CV-101 does not participate in the radiation heat transfer, as it is filled with a non-absorbing/non-emitting gas (dry air). This is visible in Figure 3-351, as the gas emissivity, ε_{gas}, and the absorbed radiation heat, Q_{gas} are equal to zero. The gas in CV-101 is heated only by convection from the surface of SC-101. Therefore the gas temperature in the stable conditions is practically equal to the structure surface temperature (700 K).

Both CV-102 and CV-103 are filled with radiating gas. In CV-102 radiation is the only heat transfer mechanism. Therefore the gas temperature stabilizes at the value (574.1 K) at which the radiation heat is zero. CV-103 on the other hand exchanges heat by both radiation and convection to SC-102. The gas temperature stabilizes at the level for which the absorbed radiation is convected to the cold SC-102 (1105 W - Figure 3-351). The sum of the radiation fluxes,
Q(TR-101) + Q(TR-102) = 4751 – 3646 = 1105 W, balances the gas absorption, which is a good check of the overall energy balance.

The purpose of this test is to demonstrate the multiple CV radiation model and to verify the calculated values. Consistency of the calculated radiation fluxes is easily checked by hand calculations, as shown above.

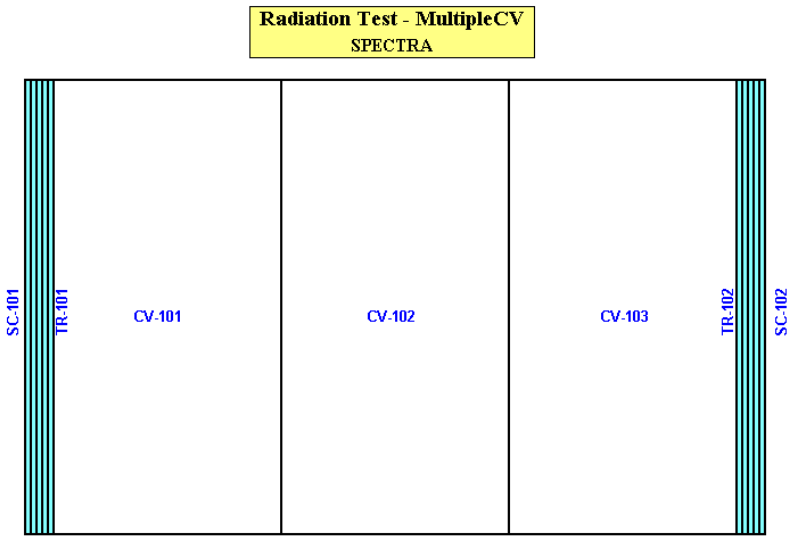

Figure 3-350 Multiple CV test - nodalization

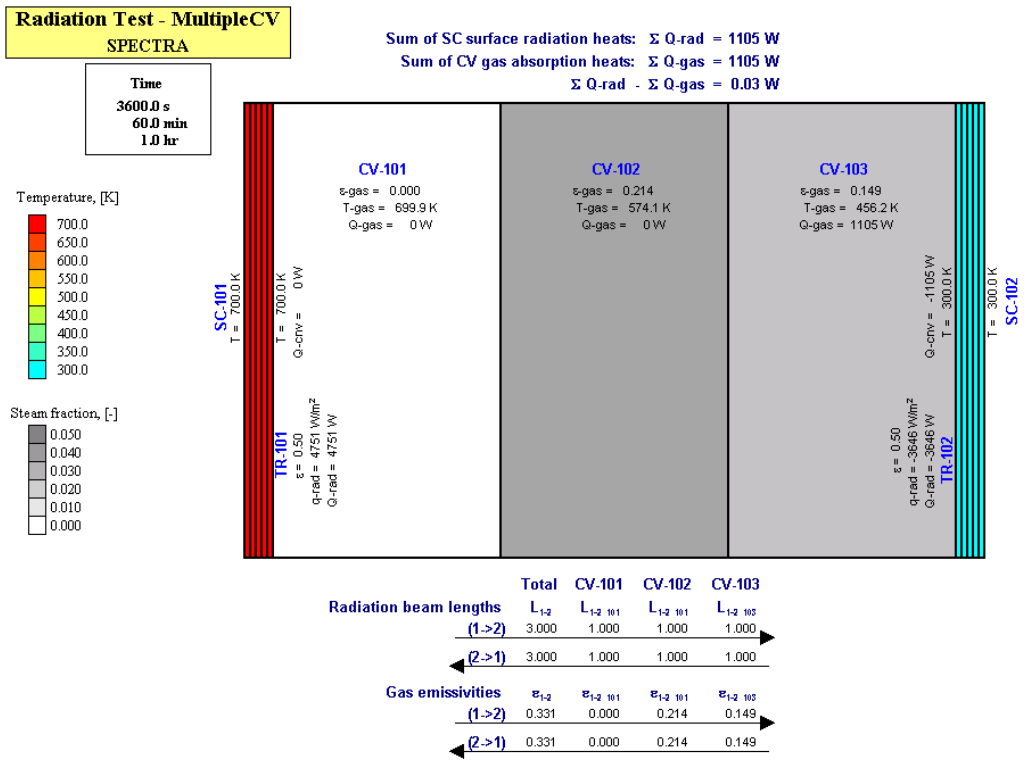

Figure 3-351 Multiple CV test - results

When the multiple CV radiation path is defined, the user must be careful that exactly the same path is defined for both directions. The part of the input shown below shows the definition used in the above example. The radiation paths $L_{1\to2}$ and $L_{2\to1}$ are defined in exactly the same way.

```
*       Beam Lengths (individual CV-s),  L(i->j, through k)
*
*         \  k:   1         2         3
*    i  j \   CV   L    CV   L    CV   L
531101 02     101 1.0   102 1.0   103 1.0
531102 01     101 1.0   102 1.0   103 1.0
```

In fact it is easier for the user to define just one of these radiation paths. The code will automatically assume the return path to be exactly the same. If both forward and reverse paths are specified, the code checks consistency of the forward and reverse paths in the following way:

- The Control Volumes must be the same for the path $L_{i\to j}$ and $L_{j\to i}$. If this is not the case, it is an input error. No calculations are performed; the program terminates writing an appropriate error message.
- The sum of all individual path lengths must be equal to the beam length on the path between surfaces *i* and *j*. The individual beam lengths in each Control Volume should, generally speaking, be the same, so $L_{i\to j,k} = L_{j\to i,k}$. However, if this is not the case, it is still a correct input, although a warning message is given in the diagnostics file. The reason why different individual beam lengths are accepted for calculations is explained below.

If the gas emissivity is close to 1.0, one may argue that practically all radiation is absorbed in the vicinity of the radiating structure and it is more realistic to apply very small radiation lengths for the CVs far away from the structure. In order to illustrate such case the model discussed above is modified as follows:

- Volumes were filled with a radiating gas (p=10^5 Pa), for which emissivity is defined using a general correlation:

$$\varepsilon = 1 - \exp(-10^{-5} \cdot pL)$$

  This expression gives a large emissivity for L~1.0 m and a small one for L~ 0.01 m.

- Two cases were defined:
  - Uniform lengths, $L_{1\to2}$ = (1.01, 1.01, 1.01) = $L_{2\to1}$
  - Nonuniform lengths $L_{1\to2}$ = (3.01, 0.01, 0.01), $L_{1\to2}$ = (0.01, 0.01, 3.01)

  In both cases the total lengths 3.03 m. In the second case the radiation absorption/emission occurs mainly in the vicinity of radiating surfaces. The input decks for these cases are provided in:
  `\Z-INPUTS\TR\MultipleCV\L-uniform.SPE and \L-nonuniform.SPE`.

Results are shown in Figure 3-352, and Figure 3-353. Qualitatively the model behaves as expected. In the nonuniform case the gas emissivity is ~1.0 in the vicinity of the radiating surface and ~0.01 in other volumes. The gas temperature is higher near the hot surface (Figure 3-353). Quantitative verification is difficult and therefore it is not sure if the results can be improved by playing the "nonuniformity trick". Nevertheless this option is available in the program, if for no other reason then at least to allow the user to perform sensitivity calculations.

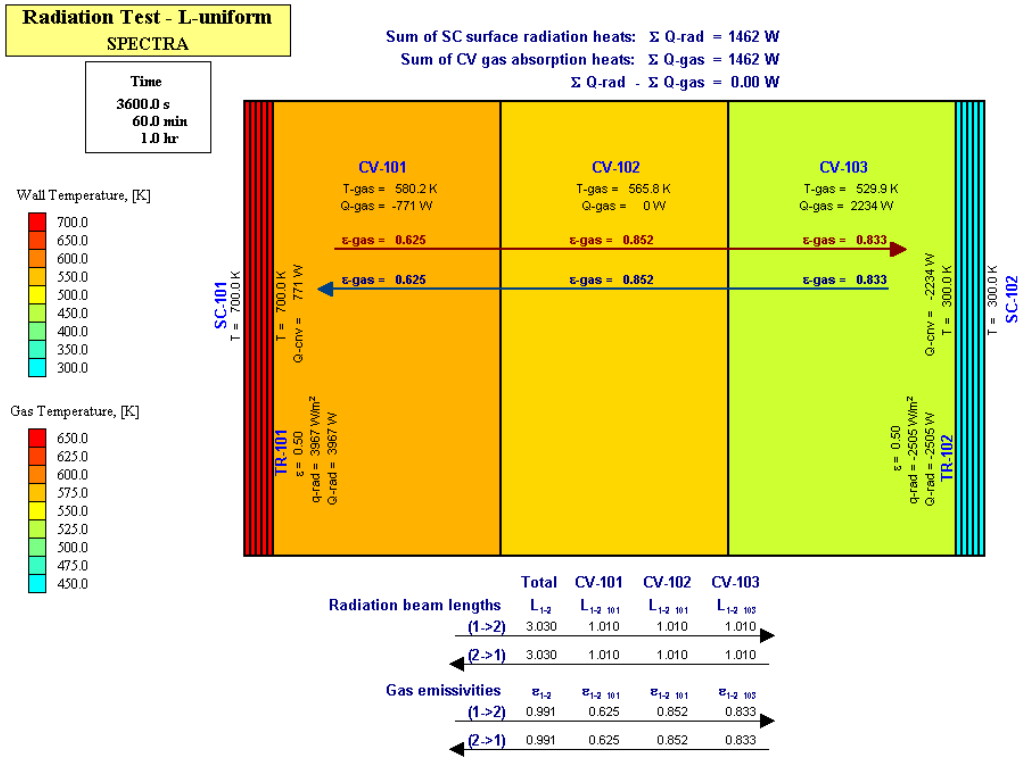

Figure 3-352 Uniform beam lengths ($L_{i\to j,\,k} = L_{j\to i,\,k}$)

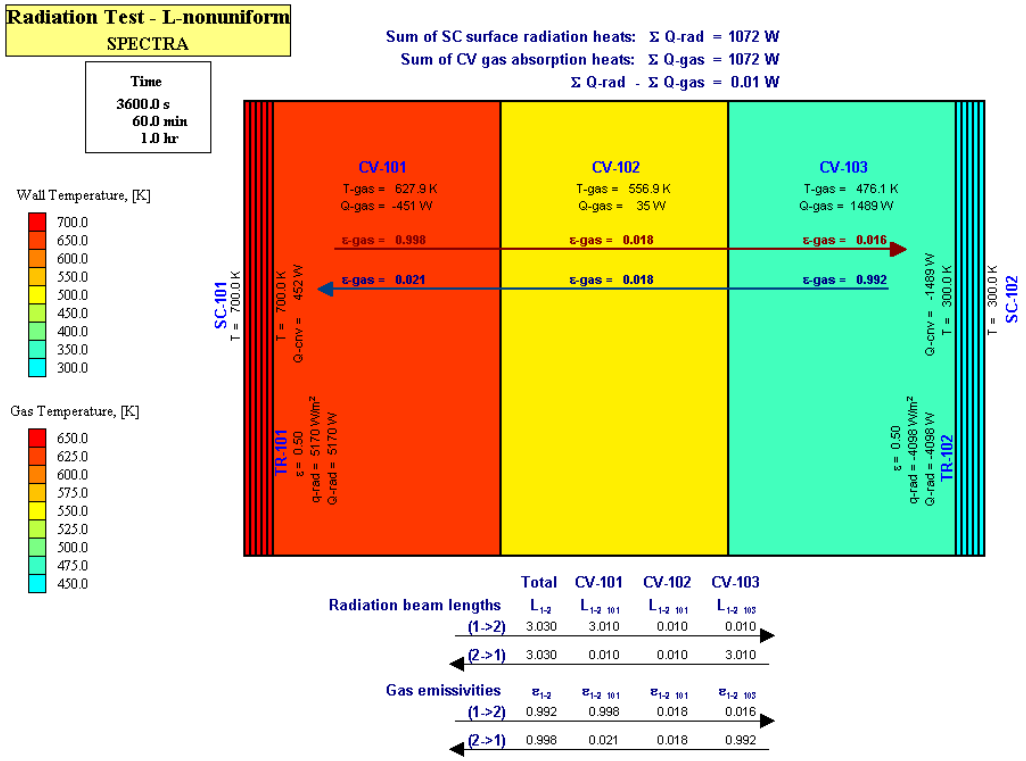

Figure 3-353 Nonuniform beam lengths ($L_{i\to j,\,k} \neq L_{j\to i,\,k}$)

3.8.2.7 Aerosol Emissivity Test

The aerosol emissivity, ε_{aer}, is calculated from (see Volume 1):

$$\varepsilon_{aer} = 1 - \exp\left[- L \cdot \sum_{i=1}^{N_{size}} n_i \cdot \sigma_i \right]$$

The cross section for radiation absorption, σ_i, may be temperature-dependent:

$$\sigma_i = \left(\frac{\pi D_i^2}{4} \right) \cdot (a_{aer} + b_{aer} T^{c_{aer}})$$

a_{aer}, b_{aer}, c_{aer}	user-defined constants
T	temperature of gas / aerosol particles, K
D_i	diameter of the aerosol particles from the size section i, (m)

In the example shown below the following values of the model constants are used:

- a_{aer} = 1.0
- b_{aer} = 0.0
- c_{aer} = 0.0

Furthermore only a single aerosol size section is used. In such case the aerosol emissivity is equal to:

$$\varepsilon_{aer} = 1 - \exp\left[- L \cdot n_1 \cdot \left(\frac{\pi D_1^2}{4} \right) \right]$$

The system used to verify the model consists of two flat surfaces with a non-absorbing/non-emitting gas filling the space (helium is used) - see Figure 3-354. The structure on the left, SC-101, is continuously heated by specifying the following boundary conditions on the "back side": a fluid temperature of 700 K and a heat transfer coefficient of 10^6 W/m^2-K. The structure on the right, SC-102, is continuously cooled by specifying the following boundary conditions: fluid temperature of 300 K and a heat transfer coefficient of 10^6 W/m^2-K.

An aerosol source is defined using a Tabular Function. A single aerosol size section, with diameter of 1.44×10^{-6} m, is used. In order to eliminate the eventual presence of other aerosol sizes due to coagulation, only one aerosol size section was defined for the model. The aerosol source versus time was defined as follows:

- t = 0 - 600 s — no aerosol source
- t = 600 - 1800 s — aerosol source strength of 5.0×10^{-7} kg/s
- t = 1800 - 3600 s — aerosol source strength of 5.0×10^{-6} kg/s

The input deck is provided in: `\Z-INPUTS\TR\Aerosol\Aerosol.SPE`. Calculations were performed for 3600.0 s. Results are shown in visualization pictures in Figure 3-355, Figure 3-356, Figure 3-357, and time-dependent graphs in Figure 3-358, Figure 3-359, Figure 3-360.

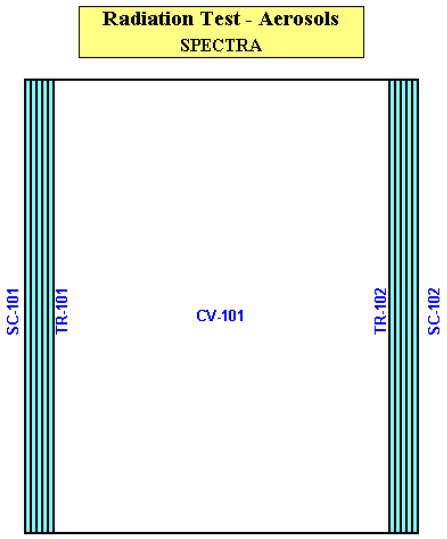

Figure 3-354 Aerosol emissivity test - nodalization

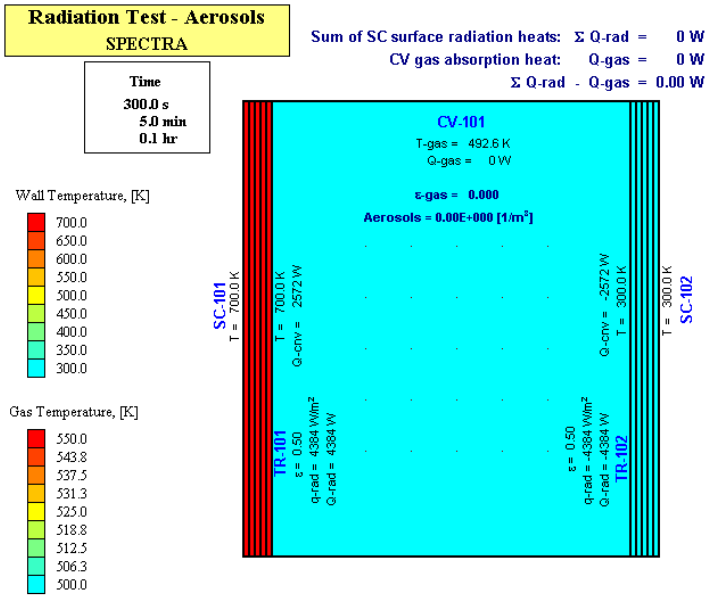

Figure 3-355 Aerosol emissivity test - results at *t* = 600.0 s, no aerosols

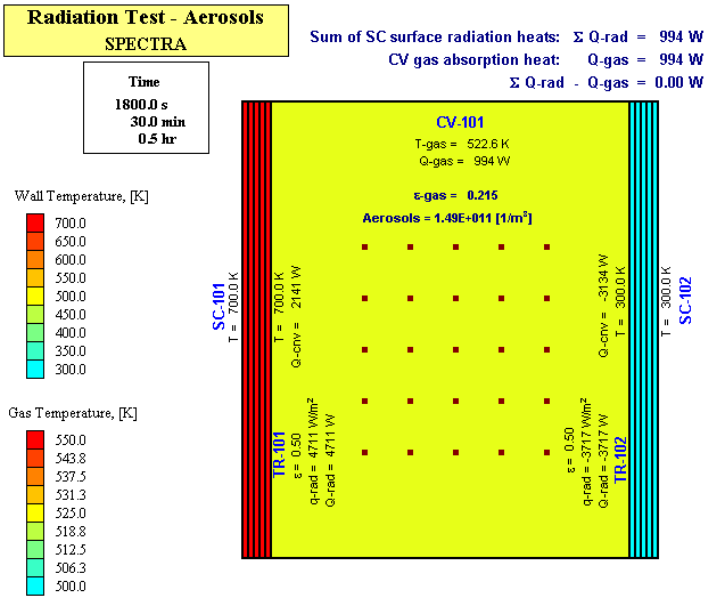

Figure 3-356 Aerosol emissivity test - results at *t* = 1800.0 s, small amount of aerosols

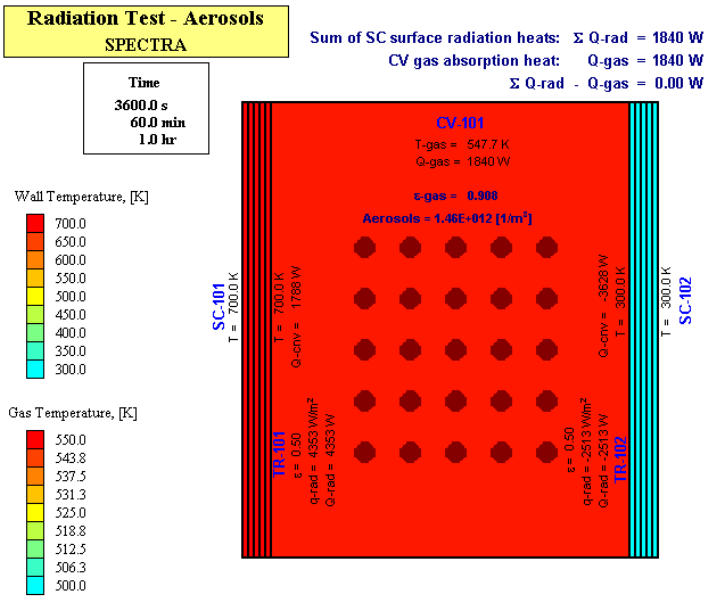

Figure 3-357 Aerosol emissivity test - results at *t* = 3600.0 s, large amount of aerosols

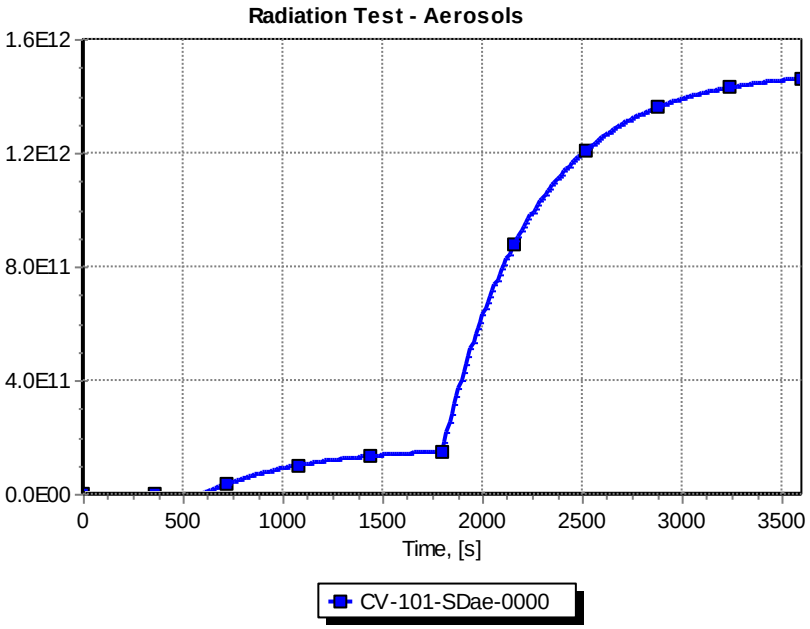

Figure 3-358 Aerosol emissivity test - aerosol density, *n* (1/m^3)

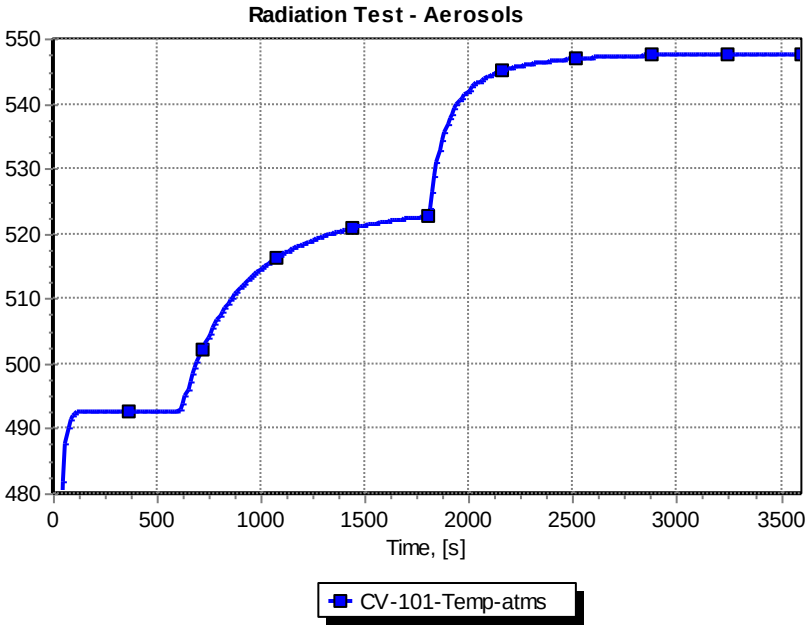

Figure 3-359 Aerosol emissivity test - temperature of gas/aerosol mixture

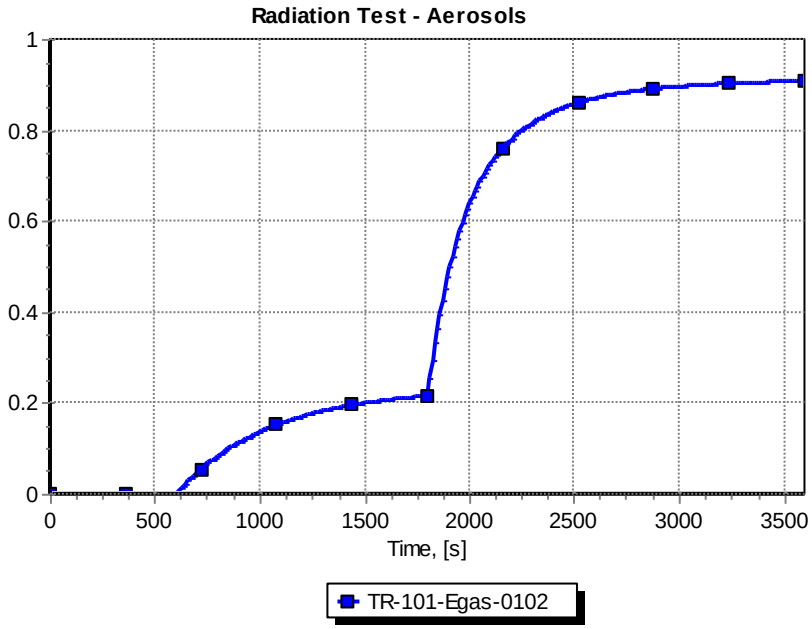

Figure 3-360 Aerosol emissivity test - emissivity of gas/aerosol mixture, ε (-)

Pure helium, which is present for the first 600 s, does not radiate, therefore the gas emissivity is zero and the gas temperature is low (Figure 3-355). The gas emissivity (for simplicity the term "gas emissivity" is used here, although strictly speaking one should use "emissivity of the gas-aerosol mixture") increases (Figure 3-360) with increasing aerosol concentration (Figure 3-358). The gas temperature increases (Figure 3-359) when the gas becomes participating in the radiant heat transfer. The calculated gas emissivity may be verified by hand calculations, taking into account that with the emissivity of helium equal to zero, the emissivity of helium/aerosol mixture is equal to the emissivity of the aerosols.

- t = 1800 s, $n = 1.49\times10^{11}$, ε = 0.215 (Figure 3-358):

$$\varepsilon_{aer} = 1 - \exp\left[-1.0 \cdot 1.49\times10^{11} \cdot \left(\frac{\pi \cdot (1.44\times10^{-6})^2}{4}\right)\right] = 0.215$$

- t = 3600 s, $n = 1.46\times10^{12}$, ε = 0.908 (Figure 3-360):

$$\varepsilon_{aer} = 1 - \exp\left[-1.0 \cdot 1.46\times10^{12} \cdot \left(\frac{\pi \cdot (1.44\times10^{-6})^2}{4}\right)\right] = 0.907$$

The purpose of this test is to demonstrate the use of the radiation model for a gas / aerosol mixture and to verify the calculated values. The correctness of the calculated gas emissivities for different aerosol concentrations is demonstrated by hand calculations, shown above.

3.9 Verification of the Reactor Kinetics Package

Verification of the point kinetics model is given in section 3.9.1. Verification of the isotope transformation model is given in section 3.9.2. These sections present relatively simple "separate effect" tests.

3.9.1 Point Reactor Kinetics

Verification of the point reactor kinetics model is performed by comparing the results obtained from the SPECTRA code, with analytical solutions for two simple test cases, and with numerical solutions obtained with the RELAP5 code for somewhat more complex cases. The simple cases and the comparison with analytical solutions are described in sections 3.9.1.1 and 3.9.1.2. Comparisons with RELAP5 are described in sections 3.9.1.3 and 3.9.1.4.

3.9.1.1 Step Change of Reactivity - Comparison with Analytical Solution

As a first test a simple case was selected, with only one group of delayed neutron precursors. A step reactivity change is considered; both positive and negative reactivities are analyzed. An analytical solution of such case may be found in many handbooks of reactor theory, for example [57], [58].

Suppose a reactor is initially at steady state condition (reactivity equal to zero), at power P_0. At t=0 the reactivity is changed suddenly to a value of ρ. If only one group of delayed neutron precursor is taken into account, then the point kinetics equations can easily be solved analytically. The reactor power at time t, $P(t)$, is given by (see [57], equation 6-40, [58], equation 7.5.11):

$$P(t) = P_0 \cdot \left[\frac{\beta}{\beta - \rho} \cdot \exp\left(\frac{\lambda \rho}{\beta - \rho} t \right) - \frac{\rho}{\beta - \rho} \cdot \exp\left(- \frac{\beta - \rho}{\Lambda} t \right) \right]$$

P power, (W)
t time, (s)
P_0 initial power, (W)
ρ reactivity, (-)
β delayed neutron yield fraction, (-)
λ decay constant of delayed neutron precursor, (1/s)
Λ prompt neutron generation time, (s)

Reactivity is frequently expressed in dollars. A reactivity of one dollar means that the reactor is prompt critical, that means the absolute reactivity ρ is equal to β. The relation between the reactivity in dollars (R), and the dimensionless reactivity (ρ) is therefore:

$$R[\$] = \frac{\rho}{\beta}$$

Taking that into account, the above equation may be written as:

$$P(t) = P_0 \cdot \left[\frac{1}{1-R} \cdot \exp\left(\frac{\lambda R}{1-R} t \right) - \frac{R}{1-R} \cdot \exp\left(-\frac{\beta(1-R)}{\Lambda} t \right) \right]$$

The following data were assumed for calculations: P_0 = 1000 W, β = 0.0075, λ = 0.08 s^{-1}, Λ = 0.001 s. Two cases are considered, with a step change of reactivity at t=0, equal to:

- $\Delta\rho$ = +0.0025 ΔR = +1/3 \$
- $\Delta\rho$ = –0.0025 ΔR = –1/3 \$

SPECTRA input decks for these calculations are provided in:

- `\Z-INPUTS\RK\STEP\STEP-1.SPE` - positive reactivity change, ΔR = +1/3 \$
- `\Z-INPUTS\RK\STEP\STEP-2.SPE` - positive reactivity change, ΔR = –1/3 \$

The results of SPECTRA calculations and those obtained from the theoretical formulae shown above, are shown in Figure 3-361. The values calculated by SPECTRA are in good agreement with the theoretical solution.

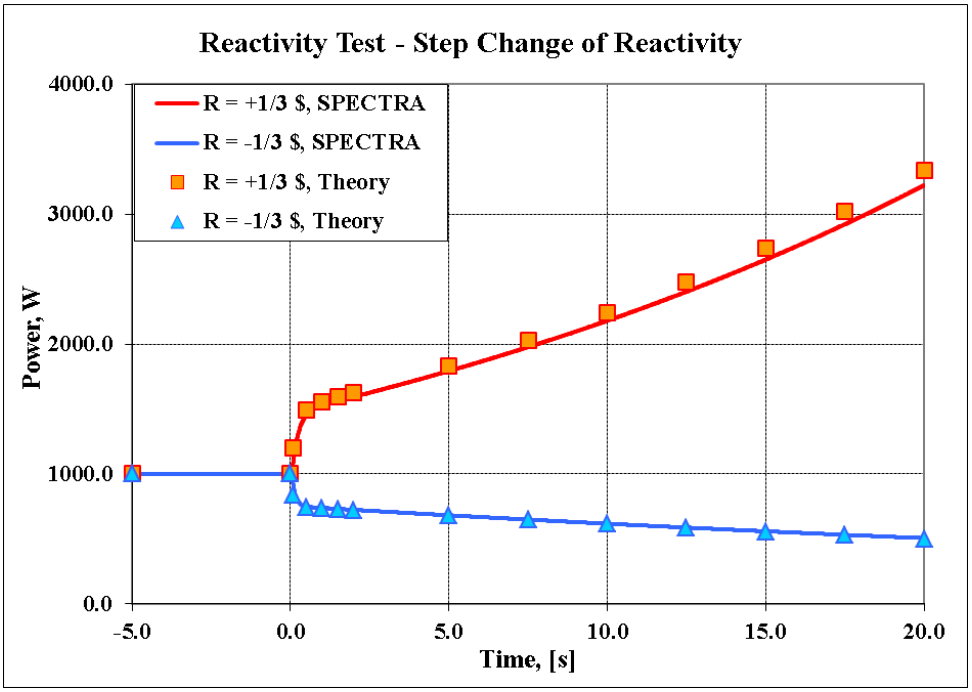

Figure 3-361 Reactor power, test cases STEP-1 and STEP-2

3.9.1.2 Reactor Start-up with a Neutron Source

Reactor start-up is typically performed using an external neutron source. With the neutron source present, the reactor can be brought up to power with negative reactivity, and thus in a relatively safe manner.

The example presented in this section is a start-up test of a reactor, 5 m^3 in size, using an external neutron source of strength of 10^{11} neutrons per second. The reactivity is changed first from –0.5 \$ to –0.2 \$ at 10.0 s. Reactivity is further increased to –0.1 \$ at 2000 s. Finally, reactivity is increased to –0.05 \$, at 3000 s. The neutron flux and reactor power are measured when stable values are reached. Since there is a simple relation between the stable reactor power and reactivity, this power measurement may in a real reactor be used to "calibrate" the control rod reactivity. SPECTRA input deck for the present calculation is provided in:
`\Z-INPUTS\RK\START-UP\START-UP.SPE`

As a verification stable values of the reactor power, neutron flux, and precursor concentrations are calculated by hand from the point kinetics equations, which are (see Volume 1):

$$\frac{dn(t)}{dt} = \frac{\rho(t)-\beta}{\Lambda} n(t) + \sum_i \lambda_i C_i(t) + S_V(t)$$
$$\frac{dC_i(t)}{dt} = \frac{\beta_i}{\Lambda} n(t) - \lambda_i C_i(t)$$

where S_V is the source of neutrons per cubic volume (1/m^3-s), other symbols are explained in detail in Volume 1. If the source is constant ($S_V(t) = S_V$ = const.), the stable conditions can be calculated by setting the derivatives to zero. Therefore:

$$0 = \frac{\rho(t)-\beta}{\Lambda} n_\infty + \sum_i \lambda_i C_{i,\infty} + S_V$$
$$0 = \frac{\beta_i}{\Lambda} n_\infty - \lambda_i C_{i,\infty}$$

The stable values of neutron and precursor concentrations were assigned an infinity subscript in the above equations. The above system can be easily solved by summing the equations for all precursors and then substituting into the equation for neutron concentration. The final values are:

$$n_\infty = -\frac{S_V \cdot \Lambda}{\beta \cdot R} = \frac{S_V \cdot \Lambda}{\beta \cdot |R|}$$
$$C_{i,\infty} = \frac{\beta_i}{\lambda_i \cdot \Lambda} n_\infty$$

The neutron concentration, and therefore the reactor fission power, is proportional to the neutron source strength and to the inverse of reactivity. The reactivity of course must be negative (R<0.0), otherwise no stable solution is possible.

In the example problem presented here the default model parameters were used, this means (see Volume 2): $\Lambda = 7\times10^{-5}$ s, $\beta = 6.5\times10^{-3}$. The volumetric source is equal to: $S_V = S/V = 10^{11}/5.0 = 2.0\times10^{10}$. The stable neutron concentrations should therefore be equal to:

- at $|R|$ = 0.20 \$: $n_\infty = 2.0\times10^{10} \times 7.0\times10^{-5} / 6.5\times10^{-3} / 0.20 = 1.077\times10^{9}$
- at $|R|$ = 0.10 \$: $n_\infty = 2.0\times10^{10} \times 7.0\times10^{-5} / 6.5\times10^{-3} / 0.10 = 2.154\times10^{9}$
- at $|R|$ = 0.05 \$: $n_\infty = 2.0\times10^{10} \times 7.0\times10^{-5} / 6.5\times10^{-3} / 0.05 = 4.308\times10^{9}$

The results of SPECTRA calculations are shown in time dependent graphs in Figure 3-362 through Figure 3-365 and visualization pictures in Figure 3-366. The time dependent graphs are presented to show a general trend of calculated parameters, but it would be difficult to verify the calculated data based on the graphs. Therefore the data is taken from the visualization picture. The values of neutron concentrations taken from Figure 3-366 are equal to:

- at t = 1990.0 s: $n(t) = 1.077\times10^{9}$ error: (1.077–1.077)/1.077×100% = 0.00%
- at t = 2990.0 s: $n(t) = 2.151\times10^{9}$ error: (2.154–2.151)/2.154×100% = 0.14%
- at t = 9990.0 s: $n(t) = 4.307\times10^{9}$ error: (4.308–4.307)/4.308×100% = 0.02%

The SPECTRA values agree very well with the analytical solution. Similarly the precursor concentrations can be checked by using the precursor data (see default precursor values in Volume 2). For example, in case of precursor group 1, $\beta_1 = 2.2\times10^{-4}$, $\lambda_1 = 1.24\times10^{-2}$. Therefore, for the end conditions (t=10,000 s) $C_{1,\infty} = 2.2\times10^{-4} / 1.24\times10^{-2} / 7.0\times10^{-5} \times 4.308\times10^{9} = 1.092\times10^{12}$, in agreement with the SPECTRA printed value, which in this case was equal to 1.092×10^{12} - Figure 3-366.

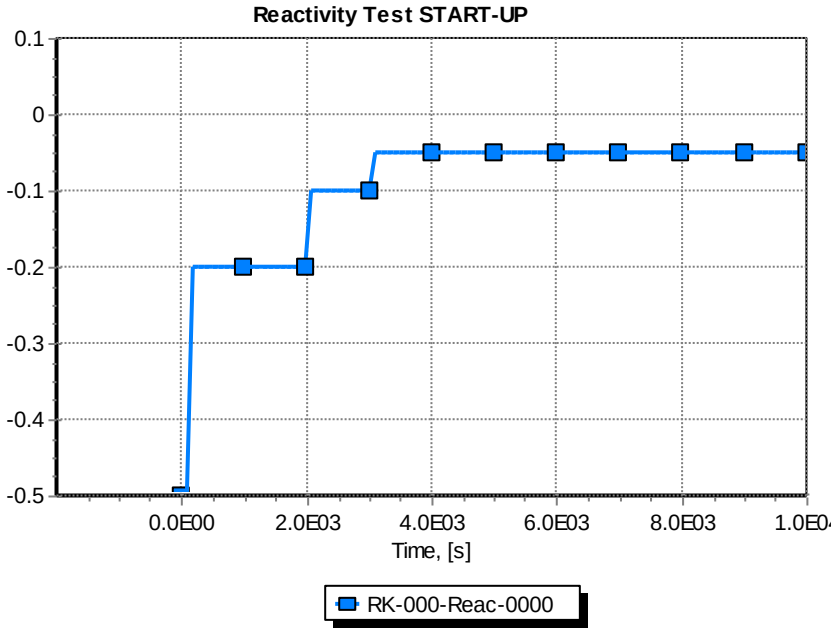

Figure 3-362 Reactivity, Test START-UP

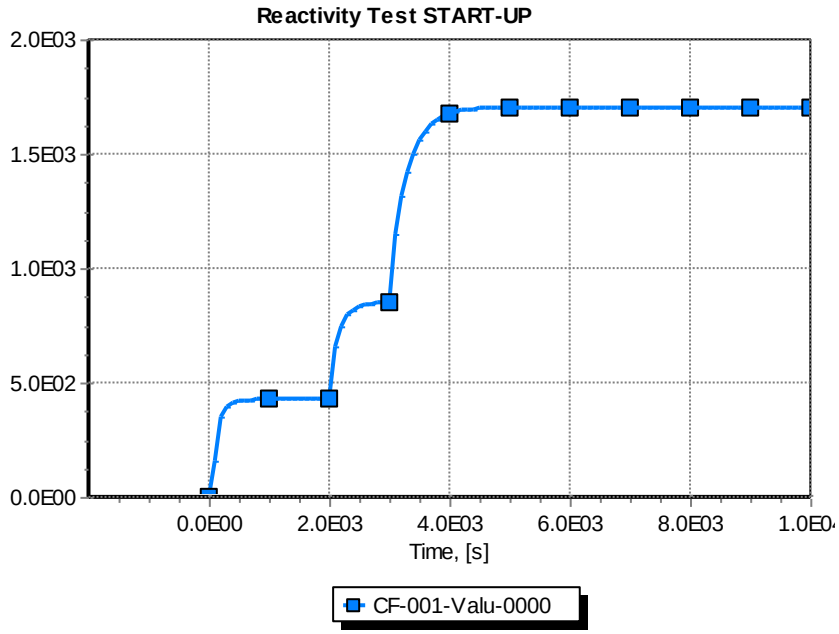

Figure 3-363 Reactor power, Test START-UP

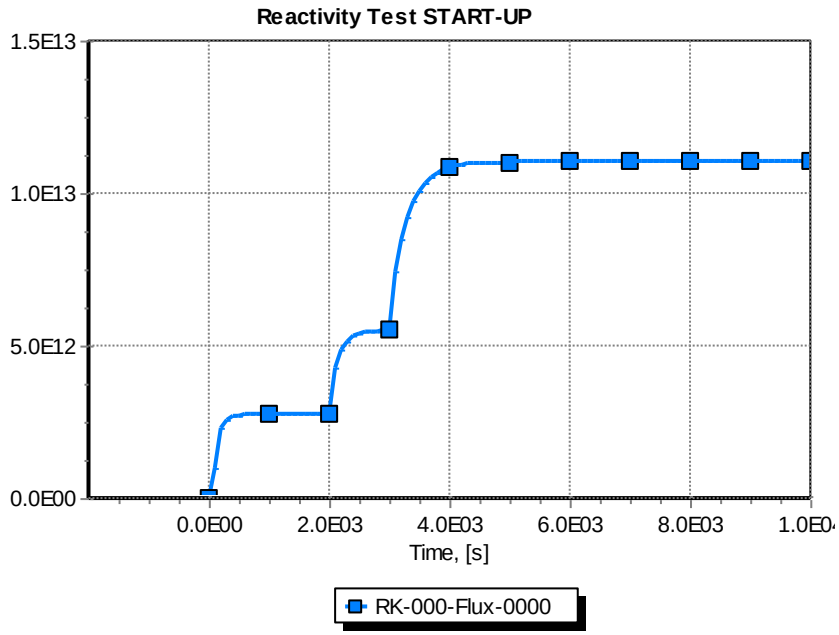

Figure 3-364 Neutron flux, Test START-UP

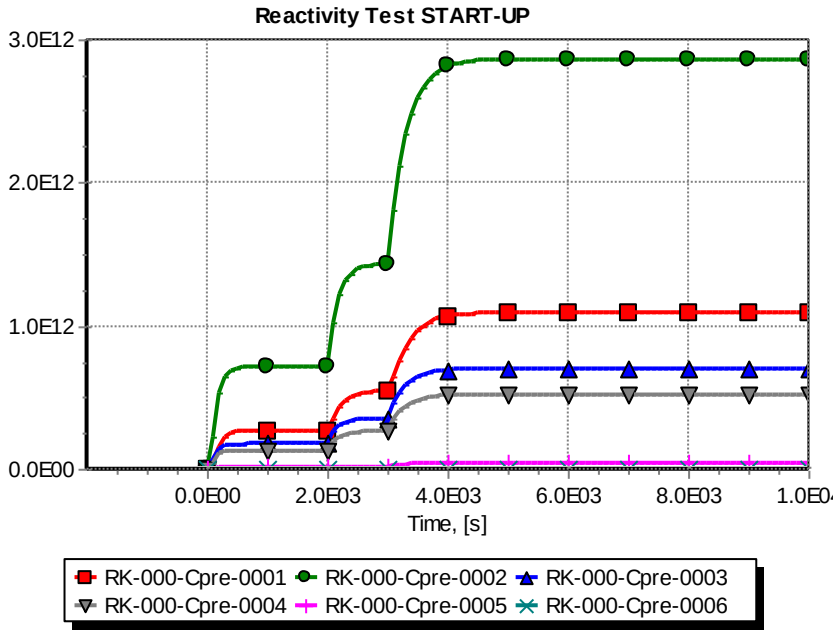

Figure 3-365 Precursor concentrations, Test START-UP

Reactivity Test START-UP
SPECTRA

Time: 1990.3 s 33.2 min 0.6 hr

Reactor Core Power Data	
Total core power, W	426.0
Fission power, W	426.0
Decay power, W	0.0

Reactivity Data	
Toatal reactivity, $	-0.20
Thermal feedback, $	0.00
Isotope feedback, $	0.00
Fuel temperature, K	0
Moderator temperature, K	0
Control rod 1 reactivity, $	0.30
Control rod 2 reactivity, $	0.00
Control rod 3 reactivity, $	0.00
Control rod total, $	0.30

Neutron Data	
Neutron density, [1/m³]	1.077E+009
Neutron flux, [1/m²-s]	2.757E+012
Neutron source, [1/s]	1.000E+011

Delayed Neutron Precursors	
Group 1, [1/m³]	2.729E+011
Group 2, [1/m³]	7.162E+011
Group 3, [1/m³]	1.760E+011
Group 4, [1/m³]	1.314E+011
Group 5, [1/m³]	1.012E+010
Group 6, [1/m³]	1.380E+009

Reactivity Test START-UP
SPECTRA

Time: 2990.3 s 49.8 min 0.8 hr

Reactor Core Power Data	
Total core power, W	850.9
Fission power, W	850.9
Decay power, W	0.0

Reactivity Data	
Toatal reactivity, $	-0.10
Thermal feedback, $	0.00
Isotope feedback, $	0.00
Fuel temperature, K	0
Moderator temperature, K	0
Control rod 1 reactivity, $	0.30
Control rod 2 reactivity, $	0.10
Control rod 3 reactivity, $	0.00
Control rod total, $	0.40

Neutron Data	
Neutron density, [1/m³]	2.151E+009
Neutron flux, [1/m²-s]	5.507E+012
Neutron source, [1/s]	1.000E+011

Delayed Neutron Precursors	
Group 1, [1/m³]	5.446E+011
Group 2, [1/m³]	1.430E+012
Group 3, [1/m³]	3.516E+011
Group 4, [1/m³]	2.624E+011
Group 5, [1/m³]	2.022E+010
Group 6, [1/m³]	2.757E+009

Reactivity Test START-UP
SPECTRA

Time: 9990.3 s 166.5 min 2.8 hr

Reactor Core Power Data	
Total core power, W	1703.6
Fission power, W	1703.6
Decay power, W	0.0

Reactivity Data	
Toatal reactivity, $	-0.05
Thermal feedback, $	0.00
Isotope feedback, $	0.00
Fuel temperature, K	0
Moderator temperature, K	0
Control rod 1 reactivity, $	0.30
Control rod 2 reactivity, $	0.10
Control rod 3 reactivity, $	0.05
Control rod total, $	0.45

Neutron Data	
Neutron density, [1/m³]	4.307E+009
Neutron flux, [1/m²-s]	1.103E+013
Neutron source, [1/s]	1.000E+011

Delayed Neutron Precursors	
Group 1, [1/m³]	1.092E+012
Group 2, [1/m³]	2.864E+012
Group 3, [1/m³]	7.040E+011
Group 4, [1/m³]	5.253E+011
Group 5, [1/m³]	4.048E+010
Group 6, [1/m³]	5.519E+009

Figure 3-366 Test START-UP - reactor kinetics data at t = 1990, 2990, and 9990 s

3.9.1.3 Reactivity Feedback - Doppler Effect

For the test presented in this section a simple model was set up in SPECTRA and RELAP5. The reactor volume is represented by a single Control Volume and a single 1-D Sold Heat Conductor (Figure 3-367). The initial power is 1.0 kW, the initial reactivity is 0.0. Reactivity is increased using control rods at three time points, t=0.0 s, t=100 s, and t=200 s. At each of these points the reactivity is increased by 0.05 $ over the time period of 0.1 s. The reactivity feedback is entered as independent reactivity tables (format 1 in SPECTRA - see Volume 2, and "separabl" format in RELAP5 - see [55]). The fuel temperature reactivity (the Doppler reactivity) is entered as follows:

T_{fuel} =	300.0 K	R = 1.0 $
T_{fuel} =	800.0 K	R = 0.9 $
T_{fuel} =	1300.0 K	R = 0.8 $
T_{fuel} =	1800.0 K	R = 0.7 $

The feedback from the moderator temperature and the moderator density are ignored in this test (the full reactivity feedback is analyzed in the next test). With only the Doppler reactivity feedback the results are easier to compare, because there is no influence of fluid flow models, which are different in the two codes. The Doppler reactivity depends only on the heat conductor temperature, and as the conduction models are practically the same in the two codes, it is expected that results should be nearly identical. In order to obtain a very similar surface heat transfer coefficient in both codes, internal flow forced convection to gas is used for this case, with the hydraulic diameter assumed equal to 0.1 m. The gas inlet temperature is 800 K, and mass flow is 1.0 kg/s.

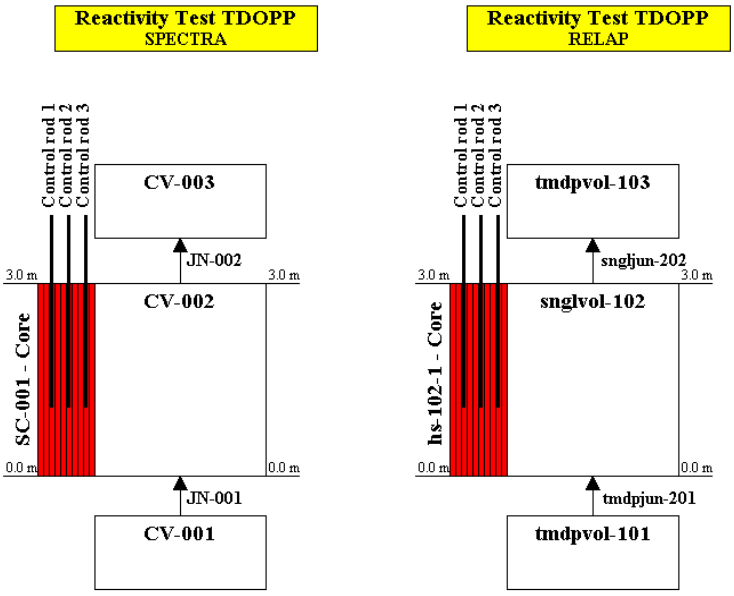

Figure 3-367 Test TDOPP - nodalization for SPECTRA (left) and RELAP (right)

SPECTRA input is provided in `\Z-INPUTS\RK\TDOPP\TDOPP.SPE`. The RELAP input deck is provided in `\Z-INPUTS\RK\TDOPP\RELAP5\TDOPP.INP`. The results of SPECTRA and RELAP calculations are compared in visualization pictures in Figure 3-368, Figure 3-369, and Figure 3-370, as well as time dependent graphs in Figure 3-371, Figure 3-372, and Figure 3-373. When a positive reactivity is inserted (0 - 200 s, Figure 3-371), the reactor power increases from the initial 1.0 kW to about 200 kW at about 400 s (Figure 3-372). As a result of the large power the fuel temperature increases. A significant increase of the fuel temperature is observed from about 400 s (Figure 3-373). The increase of the fuel temperature causes a decrease of reactivity (Figure 3-371). At 657 s the reactivity becomes negative and the reactor power starts to decrease.

Figure 3-368 through Figure 3-373 show a very good agreement between SPECTRA and RELAP. This is because the models important for this test are very similar in both codes. The heat transfer coefficients are calculated from the Dittus-Boelter correlation. This is a default forced convection model in RELAP5. In SPECTRA the Dittus-Boelter is used for internal flow cases, while the Bennet correlation is used for external flows. Bennet gives about 60% higher heat transfer coefficient than Dittus-Boelter. For the conductor geometry applied in this case - single flat plate - SPECTRA assumes by default an external flow. This default setting was overruled in the TDOPP.SPE input deck, and an internal flow was imposed at the SC-001 right boundary surface.

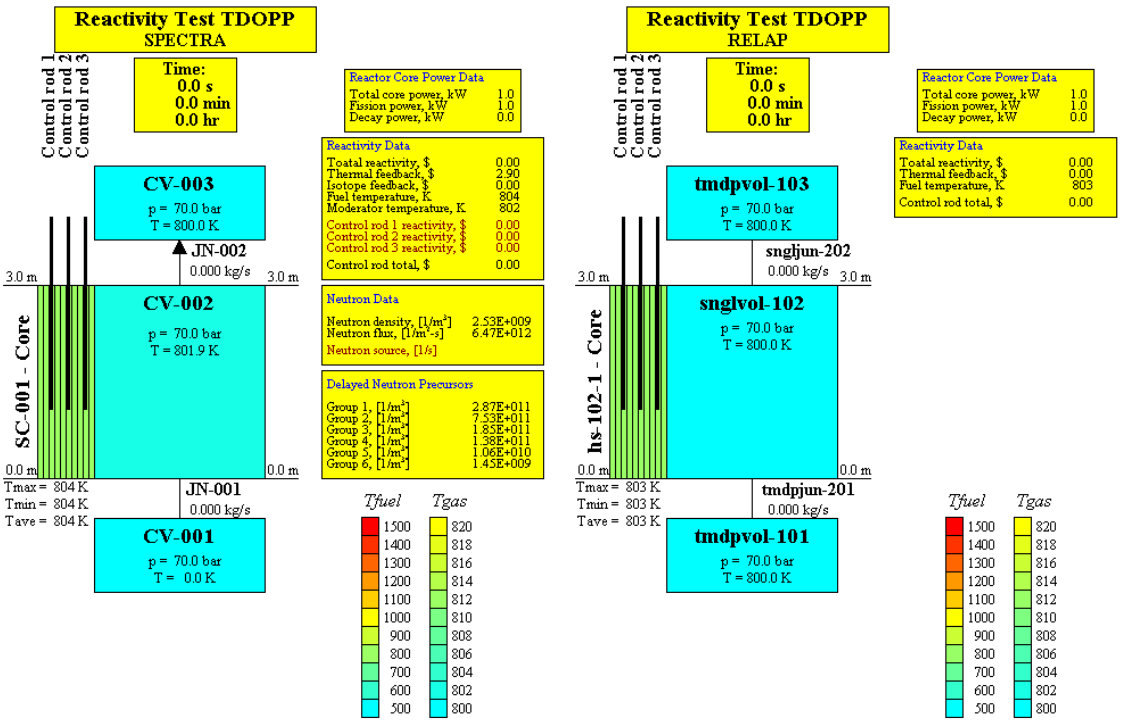

Figure 3-368 Test TDOPP, *t* = 0.0 s, SPECTRA (left) and RELAP (right)

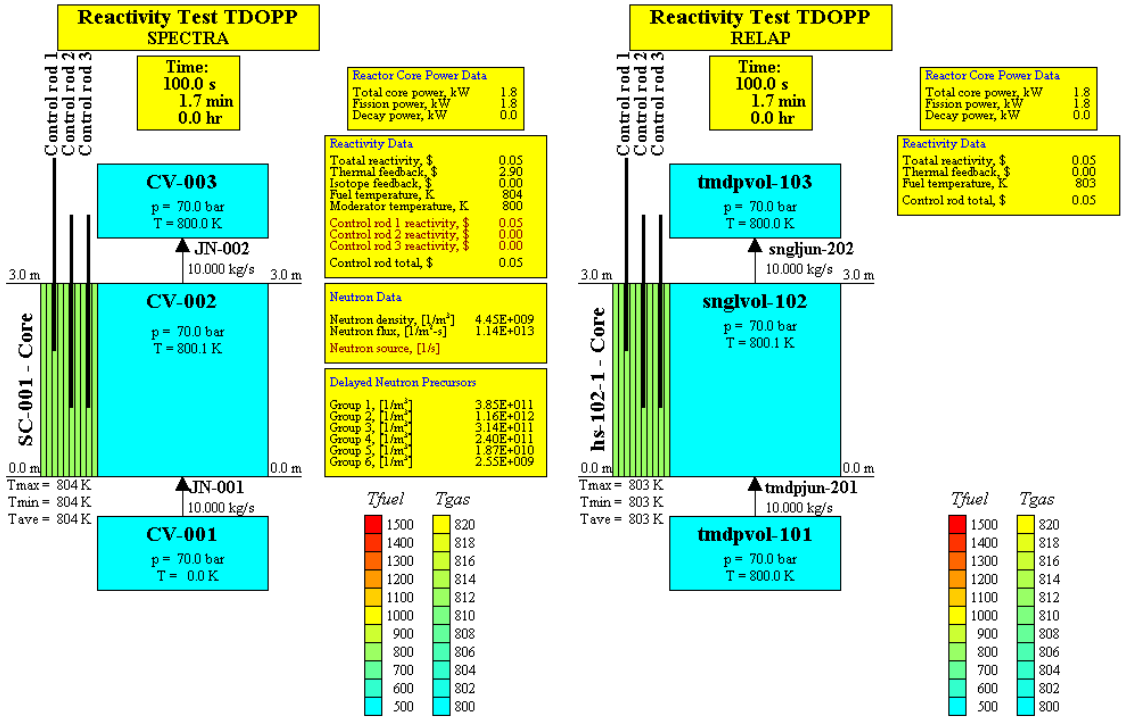

Figure 3-369 Test TDOPP, *t* = 100.0 s, SPECTRA (left) and RELAP (right)

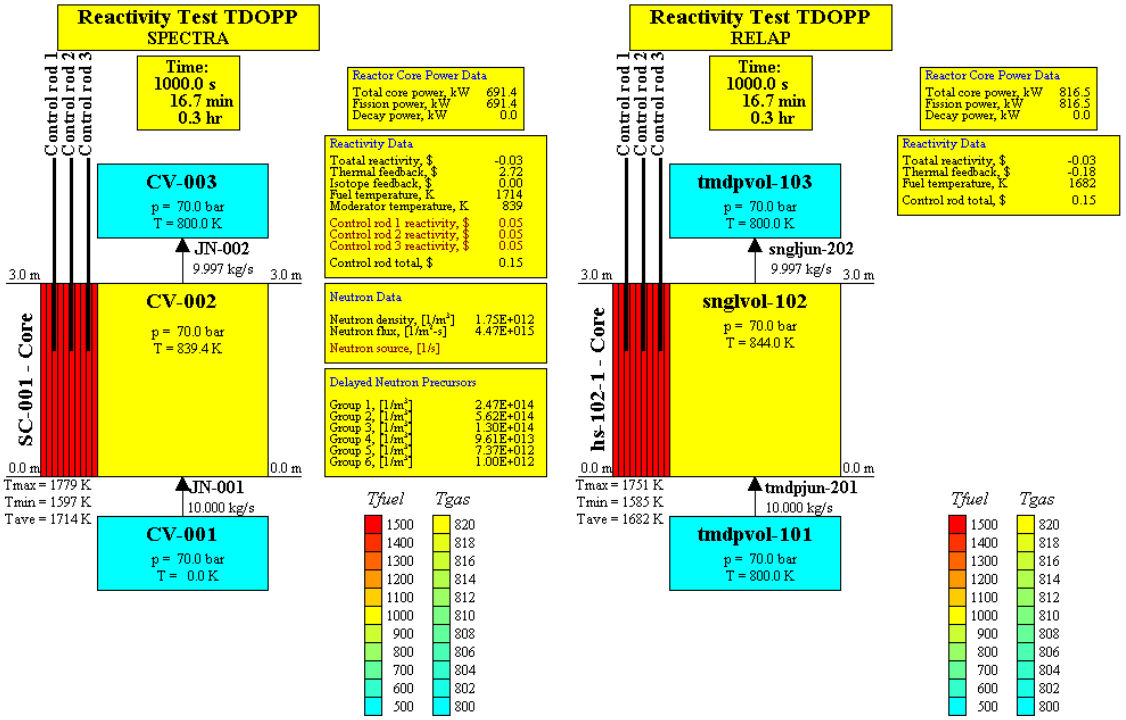

Figure 3-370 Test TDOPP, *t* = 1000.0 s, SPECTRA (left) and RELAP (right)

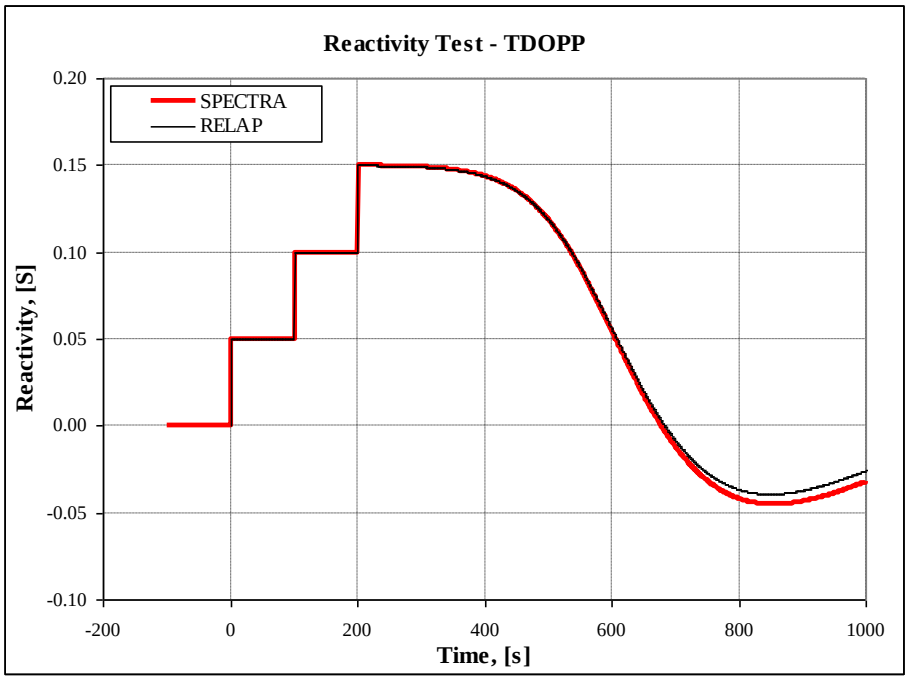

Figure 3-371 Reactivity, Test TDOPP

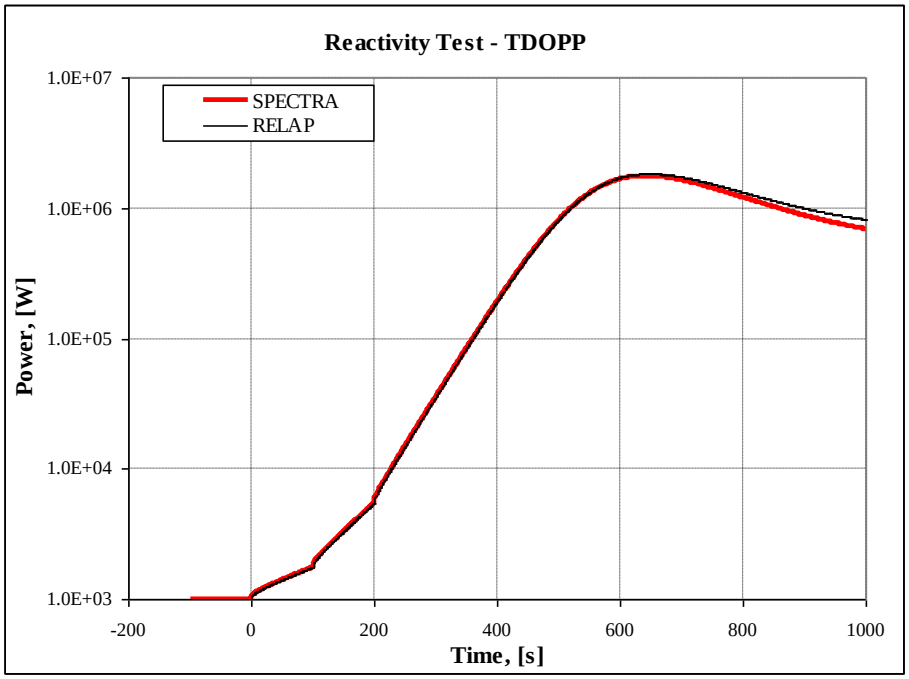

Figure 3-372 Power, Test TDOPP

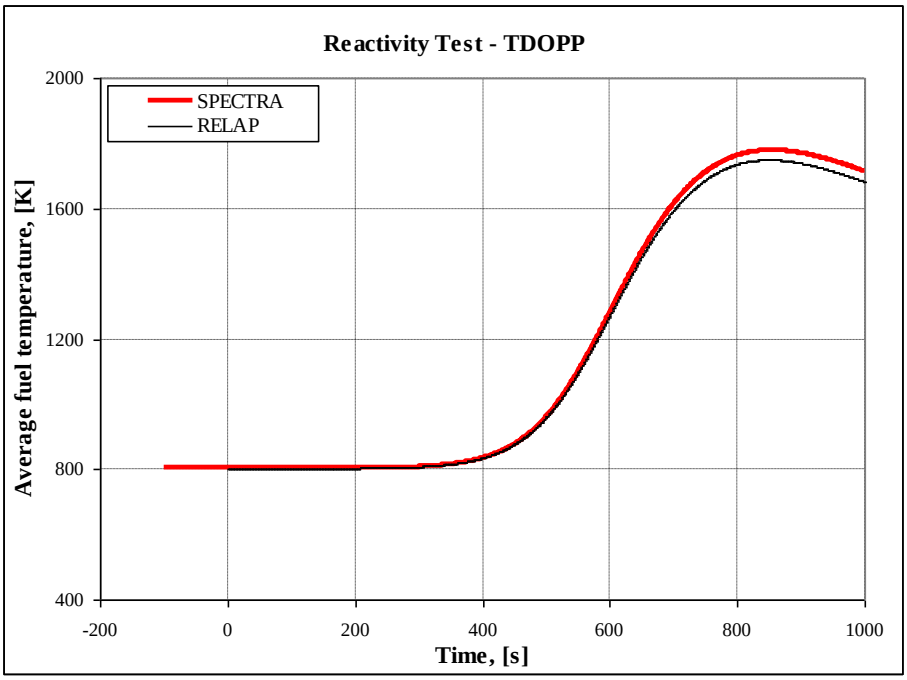

Figure 3-373 Average fuel temperature, Test TDOPP

3.9.1.4 Full Reactivity Feedback - Comparison with RELAP

In this reactor kinetics test a full reactivity feedback is considered, including the fuel temperature, the moderator temperature, and the void fraction. The reactor is represented by a 1-D Solid Heat Conductor immersed in a water pool (Figure 3-374). The total height of the "reactor vessel" is 6.0 m; the initial water level is 3.1 m; the "reactor core" height is 3.0 m. The initial pool level was established somewhat above the top of the core to avoid any core uncovery during calculations, which would have a drastic effect on the reactivity. There is no refilling; the vessel flows through JN-001 and tmdpjun-101 were set to zero.

In SPECTRA the "reactor vessel" is represented by a single CV, which is consistent with the approach to Control Volume modelling in SPECTRA (see Volume 1). In RELAP the "vessel" is represented by a pipe, consisting of 3 cells - Figure 3-374, right. Initially it was attempted to use only 2 cells, with a division at 3.0 m, and the initial void fraction in the upper cell of $\alpha = 2.9/3.0$. With this modelling it was observed that some gas from the upper cell would occasionally penetrate down to the lower cell, which had a strong impact on reactivity.

To avoid this gas ingression, an intermediate cell, 0.1 m in height, and initially filled with water, was included in the model. This prevents the gas ingression into the core volume.

One important comment should be made here. In order to avoid the gas ingression the user might be tempted to set the initial water level relatively high, say, close to 6.0 m. In this case the initial void fraction in the RELAP upper cell would be equal to $\alpha \sim 0.0$, and the gas ingression would not occur. However, in such case there would be a relatively large amount of water above the core, which in RELAP would not be heated up. If the same water level was consistently entered in the SPECTRA input deck, then the pool temperature rise would be significantly slower in SPECTRA (whole pool heated) than in RELAP. This RELAP5 result comes from a "1-dimensional" representation of the vessel. This fact is often overlooked by users of codes such as RELAP, which tend to apply "1-dimensional model" of a vessel. To obtain realistic results, two parallel stacks of interconnected cells (pipe components) should be used in the RELAP model. This would enable water circulation, and heat up of the whole pool. Note that in this case the same should be done in SPECTRA: two parallel CVs should be used to allow natural circulation of the pool. In the present example this was avoided, to keep the models simple, and easily comparable.

The initial reactor power for the present test is 1.0 kW. Reactivity is increased using control rods at three time points, t = 0.0 s, t = 100 s, and t = 200 s. At each of these points the reactivity is increased by 0.05 $. The time needed for each reactivity increase is 0.1 s.

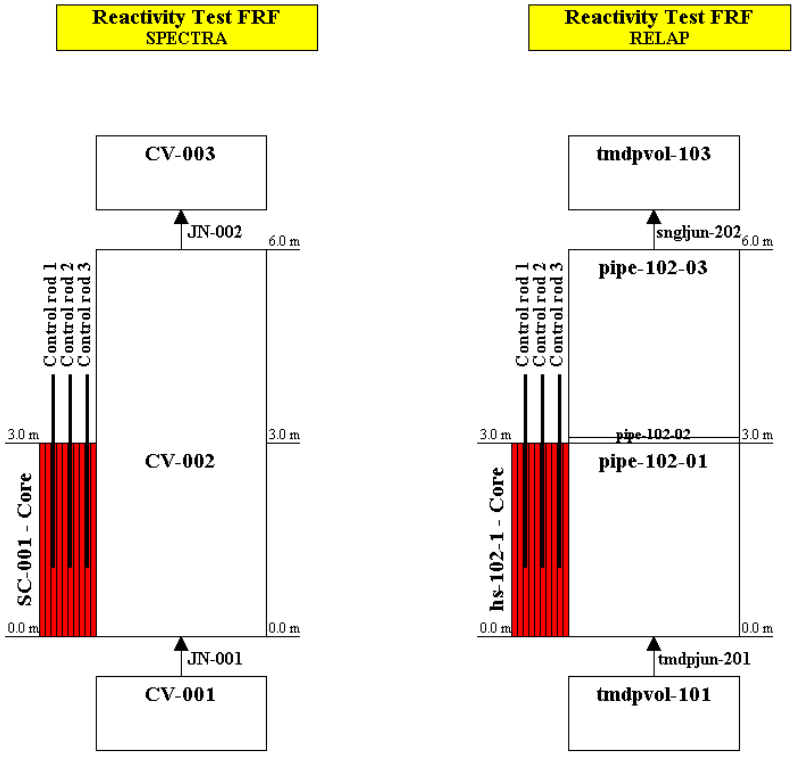

Figure 3-374 Test FRF - nodalization for SPECTRA (left) and RELAP (right)

The reactivity feedback is entered as full reactivity tables (format 2 in SPECTRA - see Volume 2, and "table3a" format in RELAP5 - see [55]). Roughly speaking, a change of void fraction by 25% results in a reactivity change of about 1.0 $; a change of fuel temperature by 300 K results in a reactivity change of 0.1 $; a change of moderator temperature by 200 K results in a reactivity change of 0.1 $. The above values were assumed based on data for typical commercial reactors ([57], table 14-2). It is expected that, with the rather strong void reactivity, the void fraction would have the most striking effect of the results.

SPECTRA input is provided in `\Z-INPUTS\RK\FRF\FRF.SPE`. The RELAP input deck is provided in `\Z-INPUTS\RK\FRF\RELAP5\FRF.INP`. The results of SPECTRA and RELAP calculations are compared in visualization pictures in Figure 3-375 and Figure 3-376, as well as time dependent graphs in Figure 3-377, Figure 3-378, Figure 3-379, and Figure 3-380.

When a positive reactivity is inserted (0 - 200 s - Figure 3-377), the reactor power increases. The initial increase is relatively slow; significant increase starts at about 350 s. At 500 s the power is close to 1.0 MW (Figure 3-378). As a result of the large power, the fuel temperature increases (Figure 3-379). Since initially the pool is about 50 degrees subcooled, there is no void in the reactor until about 550 s (Figure 3-380).

Voids appear at approximately the same time in SPECTRA and RELAP, but in SPECTRA the void fraction increase is slower than in RELAP. SPECTRA predicts quick bubble collapse (at 550 s the pool is still about 50 degrees subcooled!. As a consequence, in RELAP the reactivity is somewhat lower in the period 550 - 800 s (Figure 3-377) and the power increases to about 2.5 MW, while in SPECTRA to about 3.4 MW (Figure 3-378).

At about 800 s the pool temperature approaches saturation, which is accompanied by a sudden increase in void fraction, as a fully developed boiling is established. In SPECTRA this void fraction increase is faster than in RELAP. Consequently there is a steeper reactivity decrease at this time in SPECTRA (Figure 3-377). In both codes the fully developed boiling results in significantly negative reactivities, and power decrease.

The transient is practically terminated at about 1500 s. Stationary conditions are created in both codes, with nucleate boiling in the core, core void fractions of about 2.5% (Figure 3-380), and reactivity practically equal to zero (Figure 3-377).

Figure 3-375 through Figure 3-380 show relatively good agreement between SPECTRA and RELAP5, considering that the two-phase models are very different in those two codes. The point reactor kinetics model in SPECTRA are therefore considered as verified.

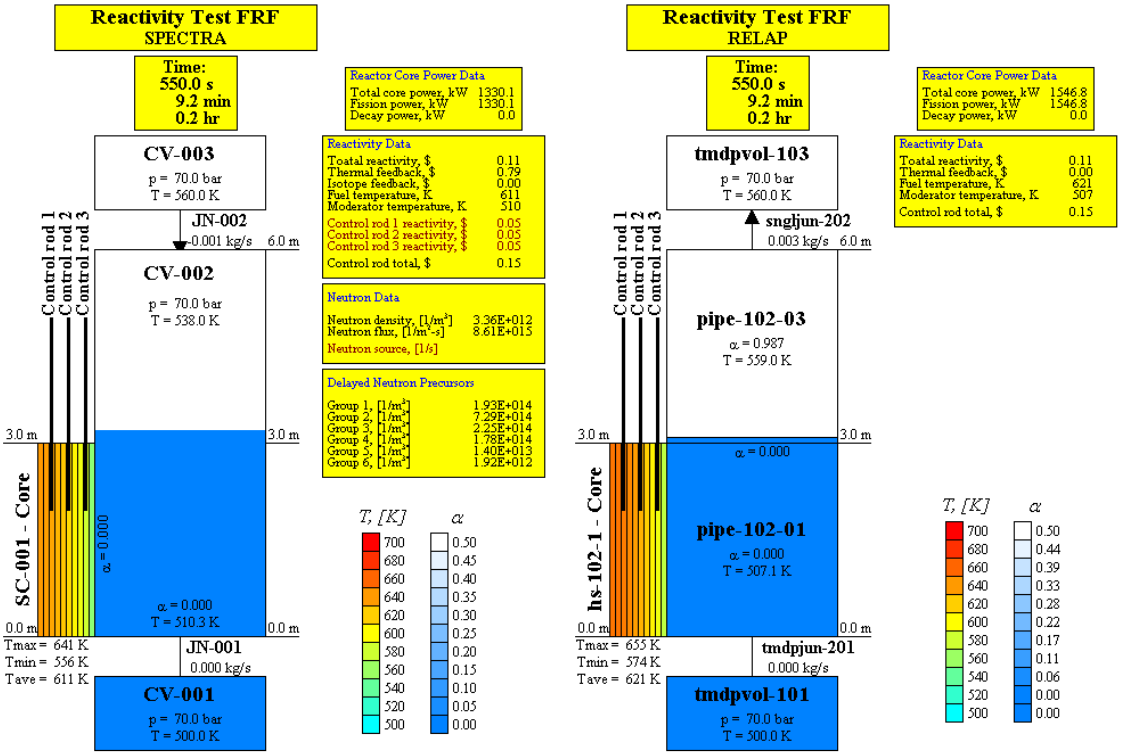

Figure 3-375 Test FRF, *t* = 550.0 s, SPECTRA (left) and RELAP (right)

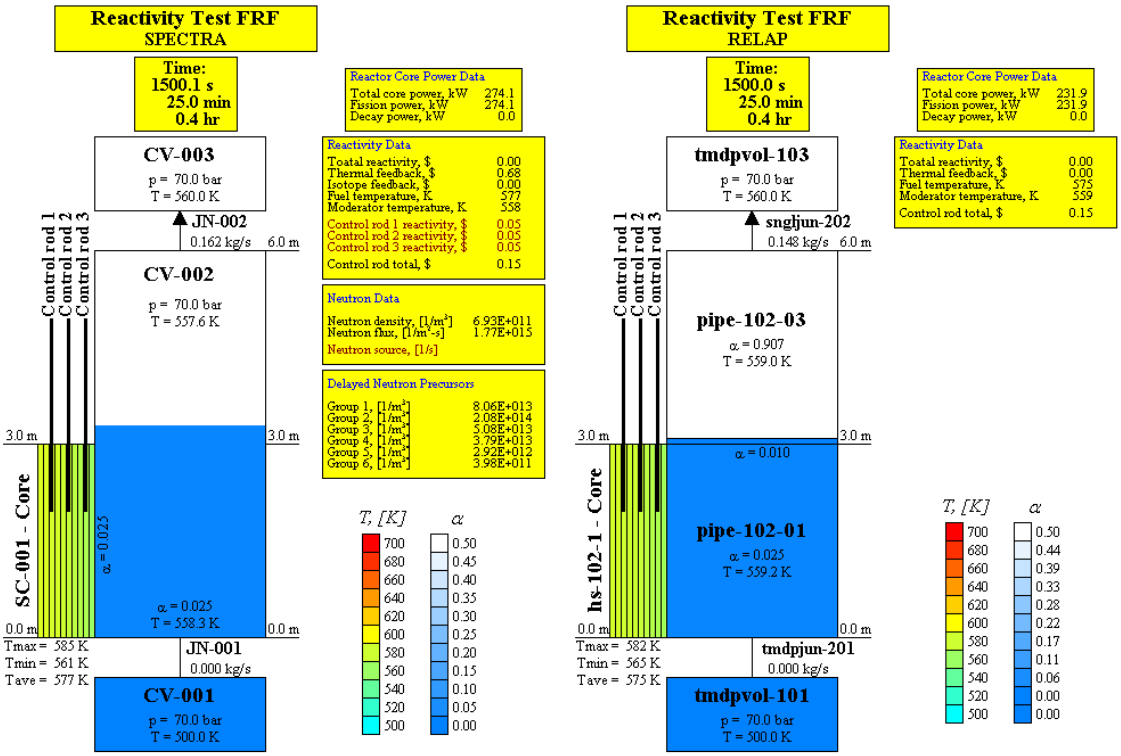

Figure 3-376 Test FRF, *t* = 1500.0 s, SPECTRA (left) and RELAP (right)

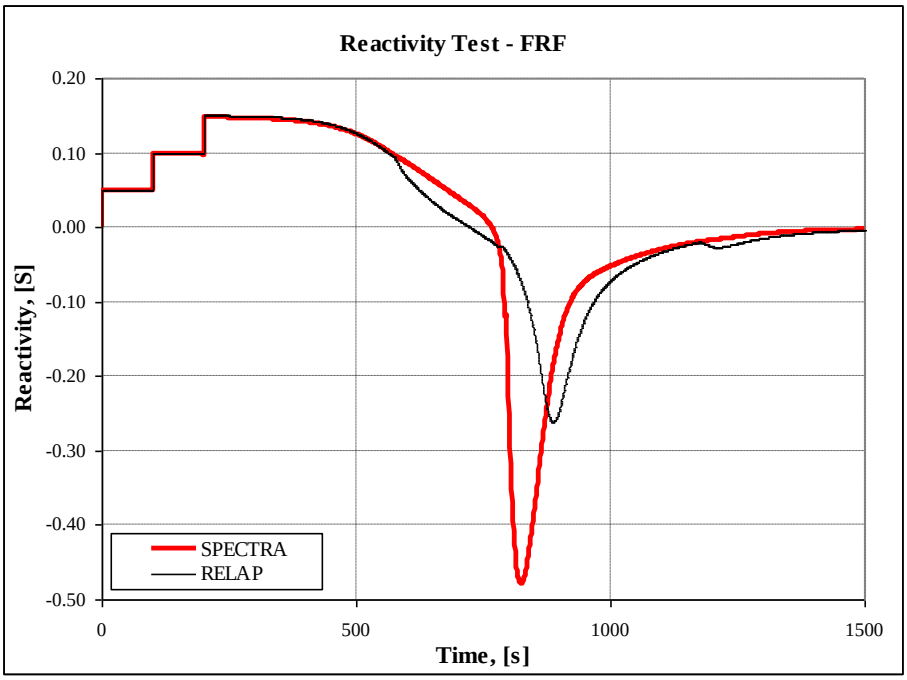

Figure 3-377 Reactivity, Test FRF

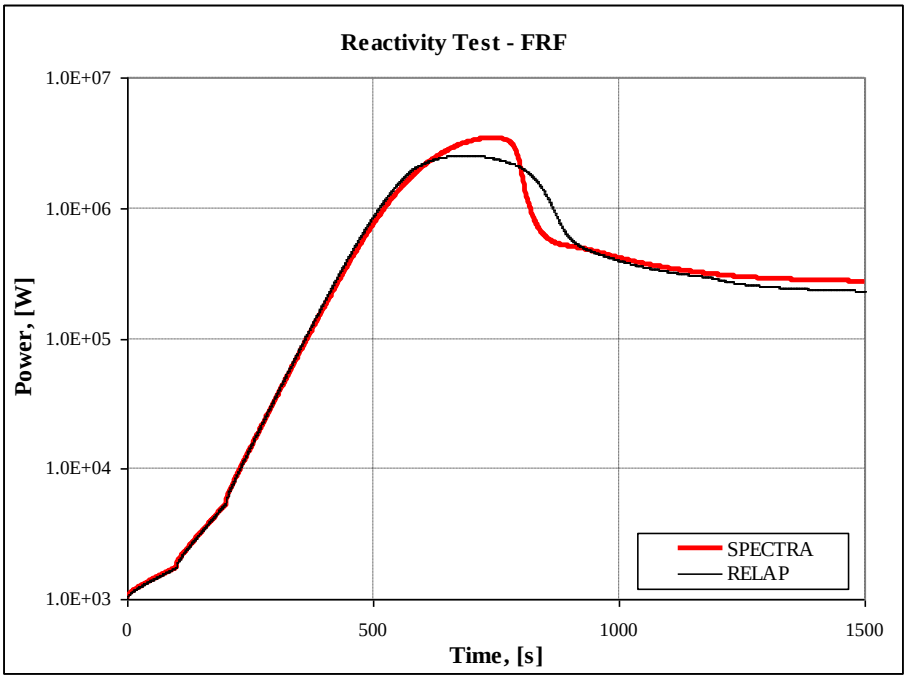

Figure 3-378 Power, Test FRF

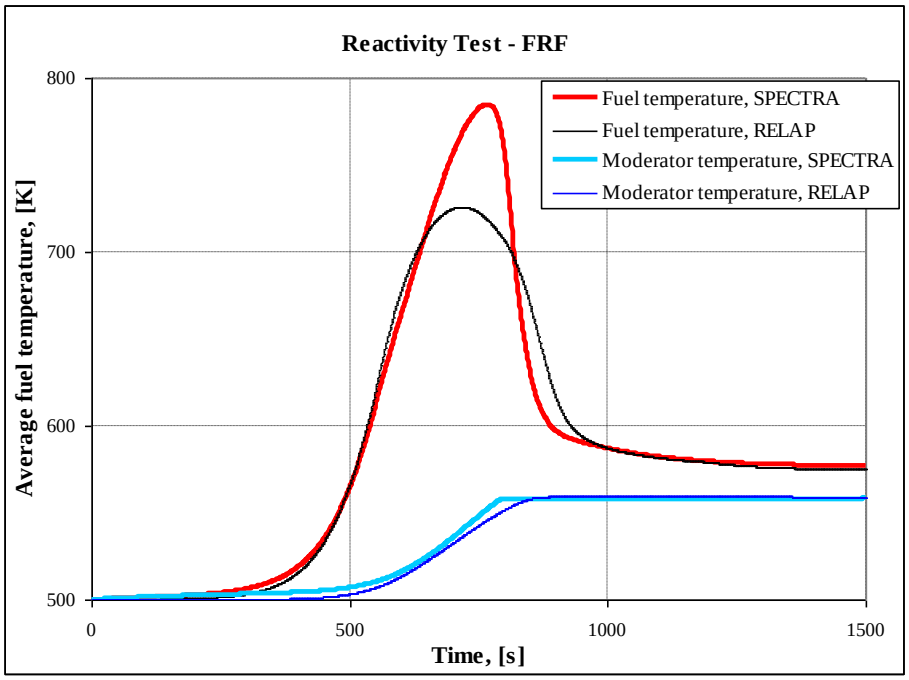

Figure 3-379 Fuel and moderator temperature, Test FRF

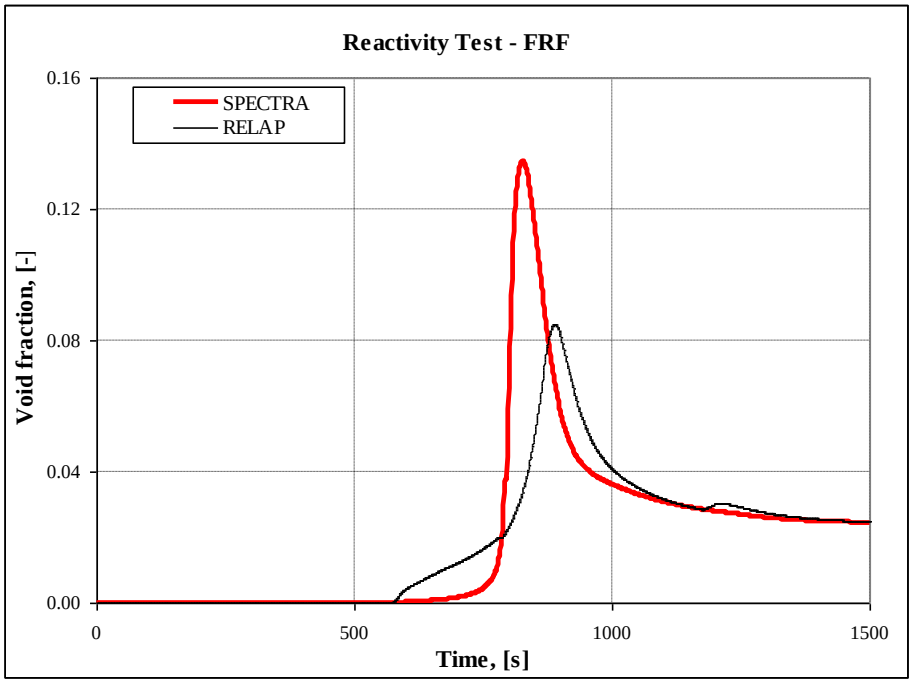

Figure 3-380 Void fraction, Test FRF

3.9.2 Isotope Transformation

Verification of the isotope transformation model is performed by comparing the results obtained from the SPECTRA code with analytical solutions for several simple test cases. The simple cases and comparison with analytical solutions are described in this section. A more complex analyses, and comparisons with the results obtained with the PANTHER code are described below in Chapter 4.

3.9.2.1 Xenon Poisoning Test - Comparison with Analytical Solution

Xenon 135 is important for reactor operation because it has a very large cross section for neutron capture. A simplified decay chain for ^{135}Xe is shown in Figure 3-381. In case of an abrupt reactor shutdown from stationary conditions, the isotope concentrations can be calculated analytically, as shown below.

A simplified Xe chain is considered (see [57], figures 15-1, 15-2). The equilibrium concentrations of iodine and xenon during reactor stationary operation are given by (see [58], equation 6.3.13):

$$N_I(\infty) = \frac{\gamma_{f,I}\Sigma_f\Phi}{\lambda_I}$$

$$N_{Xe}(\infty) = \frac{\gamma_{f,Xe}\Sigma_f\Phi}{\lambda_{Xe} + \sigma_{c,Xe}\Phi}$$

$N_i(\infty)$ equilibrium concentration of isotope i, (1/m^3)
$\gamma_{f,i}$ fission yield of isotope i
Σ_f macroscopic fission cross section (1/m)
Φ neutron flux, (1/m^2-s),
λ_i decay constant of isotope i, (1/s)
$\sigma_{c,i}$ microscopic cross section for neutron capture for isotope i, (m^2)

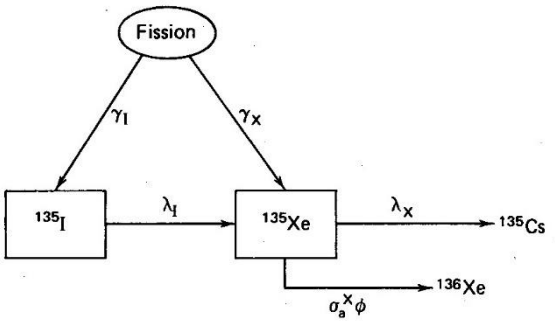

Figure 3-381 Simplified decay chain for ^{135}Xe [57]

The concentrations following abrupt reactor shutdown are given by (see [58] equation 6.3.15):

$$N_I(t) = N_I(\infty) \cdot \exp(-\lambda_I t) \frac{\gamma_{f,I} \Sigma_f \Phi}{\lambda_I}$$

$$N_{Xe}(t) = N_{Xe}(\infty) \cdot \exp(-\lambda_{Xe} t) + N_I(\infty) \cdot \frac{\lambda_I}{\lambda_I + \lambda_{Xe}} \cdot \left[\exp(-\lambda_{Xe} t) - \exp(-\lambda_I t)\right]$$

Here t is time in seconds.

SPECTRA input deck for this test is provided in `\Z-INPUTS\RK\XE\XE.SPE`. The input contains data for a simplified ^{135}Xe chain, shown in Figure 3-381. The half-lives of ^{135}I and ^{135}Xe are equal to 6.58 hr and 9.17 hr respectively ([57], figure 15-1). This means: $\lambda_I = 2.93 \times 10^{-5}$ s^{-1}, and $\lambda_{Xe} = 2.01 \times 10^{-5}$ s^{-1}.

The yield fractions from fission of ^{235}U are: γ_I = 6.32%, and γ_{Xe} = 0.26% ([59], table 8). The absorption cross section for ^{135}Xe is 2.722×10^6 barn ([59], table 4). The fission cross section for ^{235}U is 505 barn ([59], table 4).

Six isotopes are defined for the SPECTRA calculation:

- ^{235}U (note that at least one fissile isotope must be present)
- ^{238}U
- ^{135}I
- ^{135}Xe
- ^{135}Cs
- ^{136}Xe

There is only one fissile nuclide - ^{235}U. The fuel is assumed to be composed of ^{235}U and ^{238}U, with an enrichment of 2%. This means the ratio of ^{238}U to ^{235}U is equal to:

$$\frac{N_{U-238}}{N_{U-235}} = \frac{1-e}{e} = \frac{1-0.02}{0.02} = 49.0$$

Calculations were performed for times from 0.0 s to 200,000 s (55.5 hours). In the time period from 0.0 s to 0.1 s a large negative reactivity was inserted, –9.99 $, to shutdown the reactor. Results of the SPECTRA calculations are compared with the analytical solution in Figure 3-383, Figure 3-384, and Figure 3-385. Results obtained at t = 36,000 s = 10 hr (about the time of maximum Xe concentration) are shown in visualization picture in Figure 3-382

Figure 3-383 shows the concentrations of iodine and xenon, calculated by SPECTRA and from the formulae shown above. The calculated values agree very well with the analytical solutions. A detailed comparison of the numbers shows that the discrepancies are within about 1.0%. The differences come from a fact that in SPECTRA it takes some time to decrease the neutron flux to zero. This is mainly due to the influence of delayed neutron precursors.

The neutron flux is shown in Figure 3-384. The initial neutron flux is equal to: $\Phi = 6.47\times10^{17}$ (1/m^2-s). It takes about 180 s (3 minutes) to decrease the flux to about 1/1000 of its initial value, and about 700 s (12 minutes) to decrease the flux to about $1/10^6$ of its initial value. These times are still small, compared to the typical times for Xe buildup, which are of order of tens of hours. Therefore the concentrations calculated by SPECTRA are almost identical to the theoretical concentrations, obtained with the assumption that the neutron flux decreases to zero instantaneously at time = 0.0 s.

The xenon reactivity is shown in Figure 3-385. SPECTRA calculates the reactivity due to a "poisonous" isotope i ($\sigma_{c,\,i} > 0.0$, $\sigma_{f,\,i} = 0.0$), from the following formula (see Volume 1):

$$R_i = -\frac{C_{R,i}}{\beta}\cdot\frac{1}{\nu P_{FNL}P_{TNL}}\cdot\frac{\sigma_{c,i}}{\Sigma_{f,0}}\cdot N_i$$

R_i reactivity due to isotope *i*, ($)
$C_{R,i}$ reactivity worth of isotope *i*, (-)
β sum of all delayed neutron group yield fractions
ν number of neutrons generated per fission, (-)
P_{FNL} fast non-leakage probability, (-)
P_{TNL} thermal non-leakage probability, (-)
$\sigma_{c,\,i}$ microscopic cross section for neutron capture for isotope *i*, (m^2)
N_i concentration of nuclides of isotope *i*, (1/m^3)
$\Sigma_{f,\,0}$ initial macroscopic fission cross section (1/m)

Default values of all parameters were used in the present example. That means (see Volume 2):

- $C_{R,i}$ = 1.0
- P_{FNL} = 0.97
- P_{TNL} = 0.99
- $\sigma_{c,\,Xe}$ = 2,722,000 barn = 2.722×10^{-22} m^2
- ν = 2.5
- β = 0.0065

Using these values the xenon reactivity was calculated by “hand” (Excel was used), using the xenon concentrations obtained from the theoretical solution, $N_{Xe}(t)$. The values obtained from SPECTRA and from the hand calculation are compared in Figure 3-385. Both results are practically identical.

Reactivity Test Xe
SPECTRA

Time:
36000.0 s
600.0 min
10.0 hr

Reactor Core Power Data

Total power, W	1.08E-009
Fission power, W	1.08E-009
Decay power, W	0.00E+000

Reactivity Data

Toatal reactivity, $	-18.65
Thermal feedback, $	0.00
Isotope feedback, $	77.32
Fuel temperature, K	0
Moderator temperature, K	0
Control rod 1 reactivity, $	-9.99
Control rod 2 reactivity, $	
Control rod 3 reactivity, $	
Control rod total, $	-9.99

Neutron Data

Neutron density, [1/m^3]	2.73E-003
Neutron flux, [1/m^2-s]	6.99E+000
Neutron source, [1/s]	

Delayed Neutron Precursors

Group 1, [1/m^3]	6.09E+000
Group 2, [1/m^3]	1.60E+001
Group 3, [1/m^3]	3.93E+000
Group 4, [1/m^3]	2.93E+000
Group 5, [1/m^3]	2.26E-001
Group 6, [1/m^3]	3.08E-002

Xenon Data

	I-135	Xe-135
N, [1/m^3]	4.86E+020	7.13E+020
R, [$]	0.00	-12.44
ΔR, [$]	0.00	-8.66

Figure 3-382 Xenon poisoning test, values at the time maximum Xe concentration

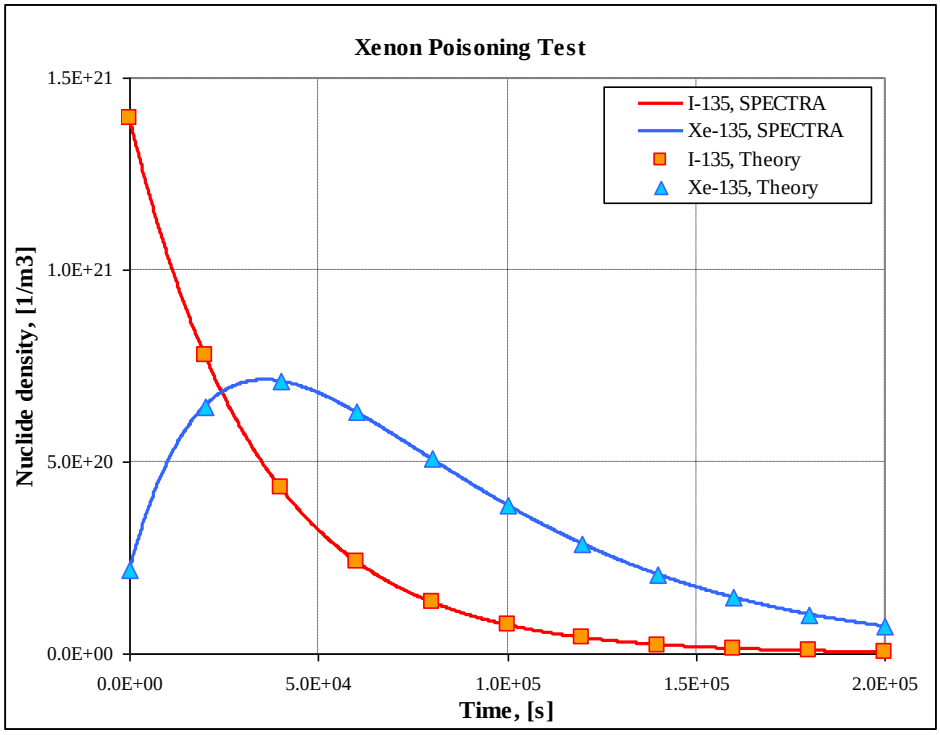

Figure 3-383 Nuclide density, Xenon poisoning test

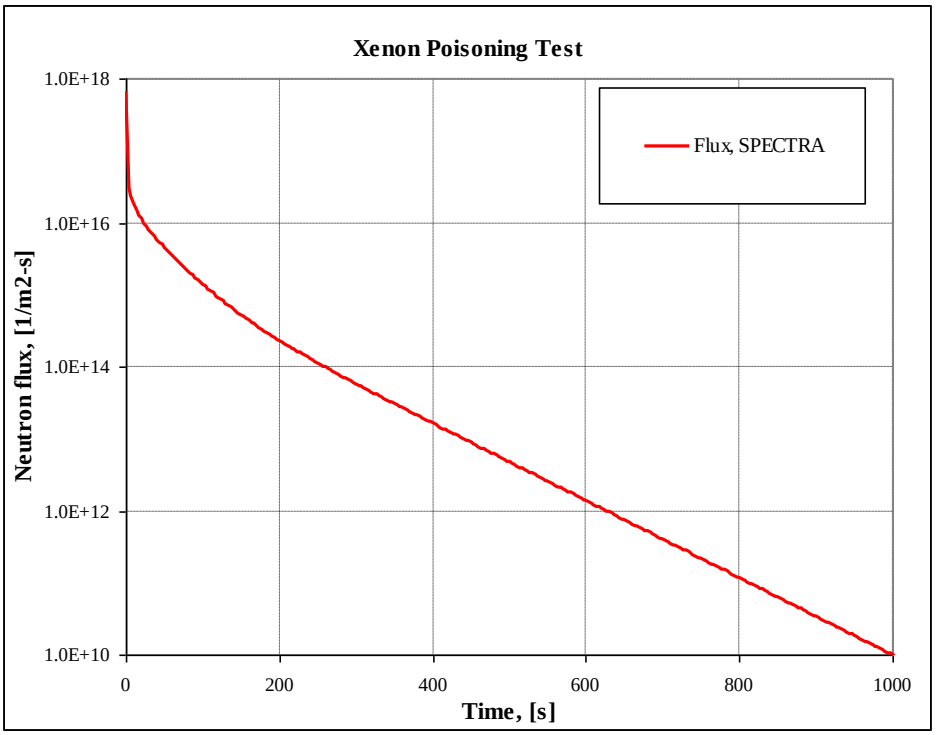

Figure 3-384 Neutron flux, Xenon poisoning test

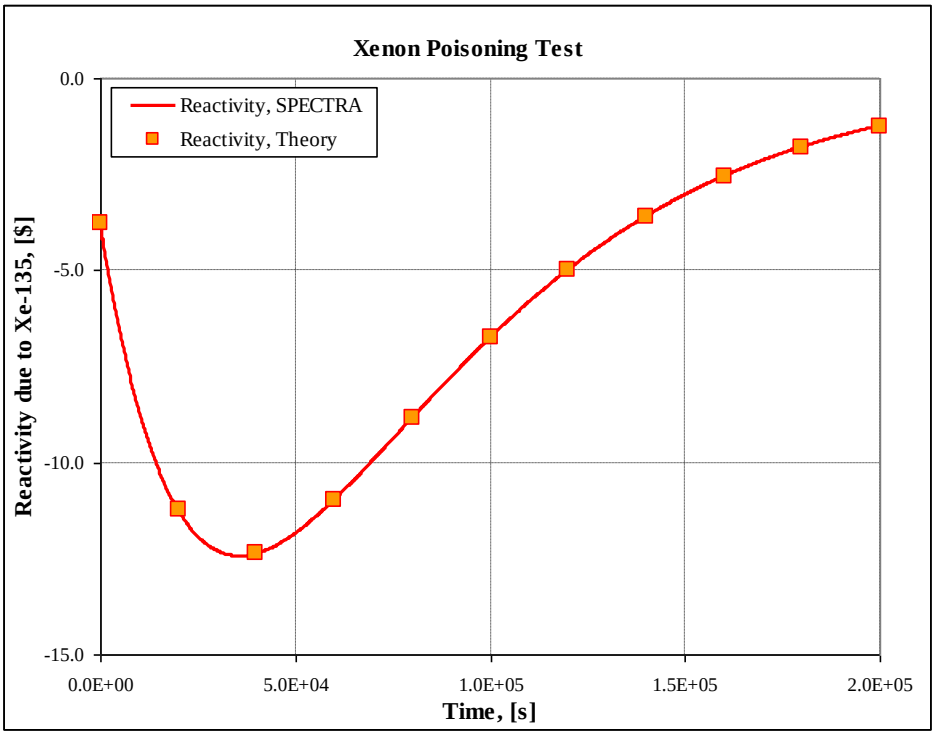

Figure 3-385 Reactivity change due to ^{135}Xe, Xenon poisoning test

3.9.2.2 Simple Fuel Unloading Test - R1

Four simple tests, R1, R2, R3, and R4, are shown to demonstrate the use of the loading and removal functions. Initially the core consists of U-235 only. There is no neutron flux, so the isotope change is caused only by loading/removal functions. In test R1 a negative loading function number 1, $R^F(1)$, was used, defined as follows:

- $t < 5000$ s $\quad R^F(1) = 0.0$
- $t > 5000$ s $\quad R^F(1) = -1.0\times10^{-4}$

This means that starting from the time of t = 5,000 s U-235 was being removed from the core with a constant removal rate, equal to $R = 1.0\times10^{-4}$ (1/s). SPECTRA input deck for this test is provided in `\Z-INPUTS\RK\RELOAD\R1.SPE`. Figure 3-386 shows the average concentration of U-235 in the core (1/m^3). In 15,000 s the fuel disappears totally from the core. The time to fully unload the core is easily checked, since it is equal to the inverse of the absolute value of the loading rate function. For times t > 15,000 s the loading function is still negative but the U-235 concentration doesn't change, since no fuel is left in the core (the program has a built-in limit to prevent concentrations from becoming negative).

Physically this test represents a process of removing the fuel assemblies, one by one, until the core is empty. Of course such removal of the fuel elements has consequences, for example a change in the non-leakage probabilities that cannot be taken into account in the model. In practice one should only analyze cases in which relatively few elements are being removed or added to the core. The present test (and the tests below) serves only as an illustrative case for the loading/removal functions.

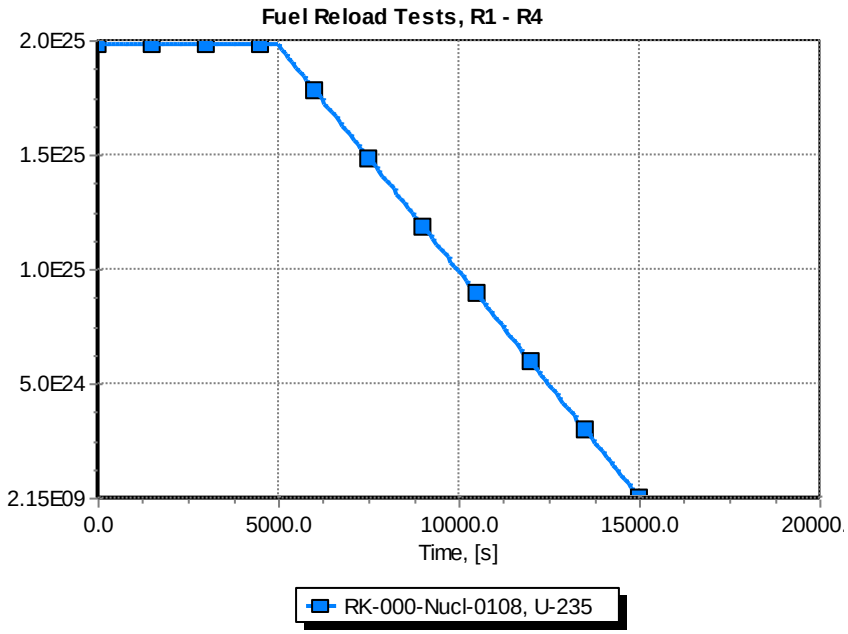

Figure 3-386 Concentrations of U-235 in the core - simple fuel unloading test R1

3.9.2.3 Simple Fuel Unloading Test - R2

Four simple tests, R1, R2, R3, R4, are shown to demonstrate the use of loading and removal functions. Initially the core consists of U-235 only. There is no neutron flux, so the isotope change is caused only by loading/removal functions. In test R2 a removal function, R^R, was used, defined as follows:

- $t < 5000$ s $\quad R^R = 0.0$
- $t > 5000$ s $\quad R^R = 1.0\times10^{-4}$

This means that starting from the time of t = 5,000 s U-235 was being removed from the core proportionally to the removal rate of 1.0×10^{-4} (1/s), and to the actual U-235 concentration, since the optional multiplier on U-235 concentration (Volume 2) was not used. SPECTRA input deck for this test is provided in `\Z-INPUTS\RK\RELOAD\R2.SPE`. Figure 3-387 shows the average concentration of U-235 in the core ($1/m^3$). The theoretical solution is:

$$N(t) = N_0 \cdot \exp[-R^R (t - t_0)]$$

where $N(t)$ is the actual concentration, N_0 is the initial concentration, t is time, t_0 is the time when removal begins. In 10,000 s the concentration should decrease to e-1=0.368 of the initial value. This is in agreement with code result, which gives $N_0 = 4.359\times10^{25}$, and $N(t{=}15{,}000) = 1.604\times10^{25}$.

Physically this test represents a process in which assemblies are picked randomly, removed from the core, and replaced by dummy assemblies, which contain no U-235.

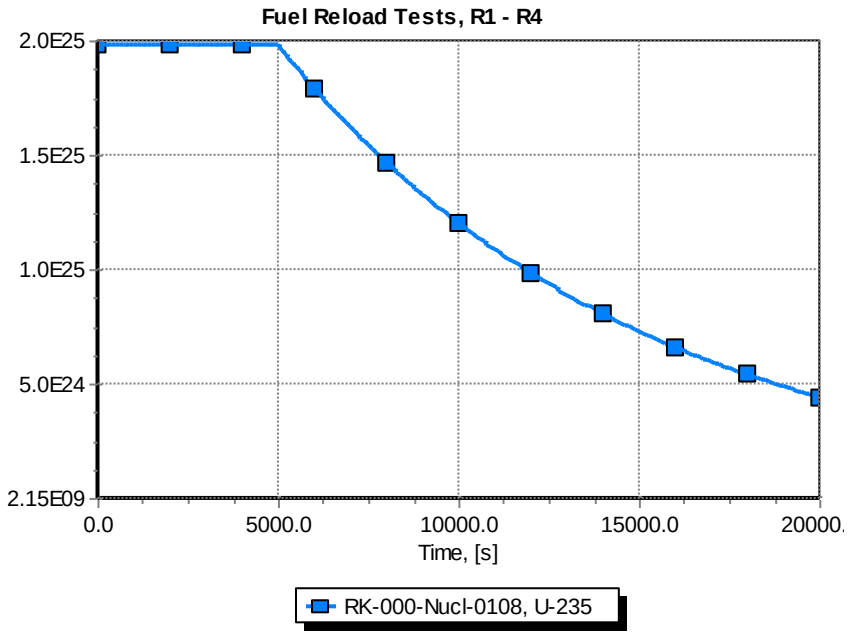

Figure 3-387 Concentrations of U-235 in the core - simple fuel unloading test R2

3.9.2.4 Simple Fuel Reloading Test - R3

Four simple tests, R1, R2, R3, R4, are shown to demonstrate the use of loading and removal functions. Initially the core consists of U-235 only. There is no neutron flux, so the isotope change is caused only by loading/removal functions. In test R3 two loading functions, $R^F(1)$, $R^F(2)$, were used, defined as follows:

- $t < 5000$ s $\quad R^F(1) = 0.0 \quad R^F(2) = 0.0$
- $5000 < t < 15000$ s $\quad R^F(1) = -1.0\times10^{-4} \quad R^F(2) = 1.0\times10^{-4}$
- $15000 < t$ $\quad R^F(1) = 0.0 \quad R^F(2) = 0.0$

The isotope composition of the loading function 1 was 100% U-235. The isotope composition of the loading function 2 was 50% U-235, 50% U-239. SPECTRA input deck for this test is provided in `\Z-INPUTS\RK\RELOAD\R3.SPE`. Figure 3-388 shows the average concentrations of U-235 and Pu-239 in the core ($1/m^3$).

Physically this test represents a process in which assemblies are removed one by one, and replaced by assemblies with fuel consisting of 50% uranium and 50% plutonium. At 15,000 s all uranium assemblies have been removed and therefore the loading functions are set to zero. The user should always take care that the loading functions represent correctly the physical process. This is specifically important in case when negative loading functions are used. The program will internally prevent concentrations from becoming negative, but other constraints may sometimes be important (like in the present case), that cannot be detected by the program.

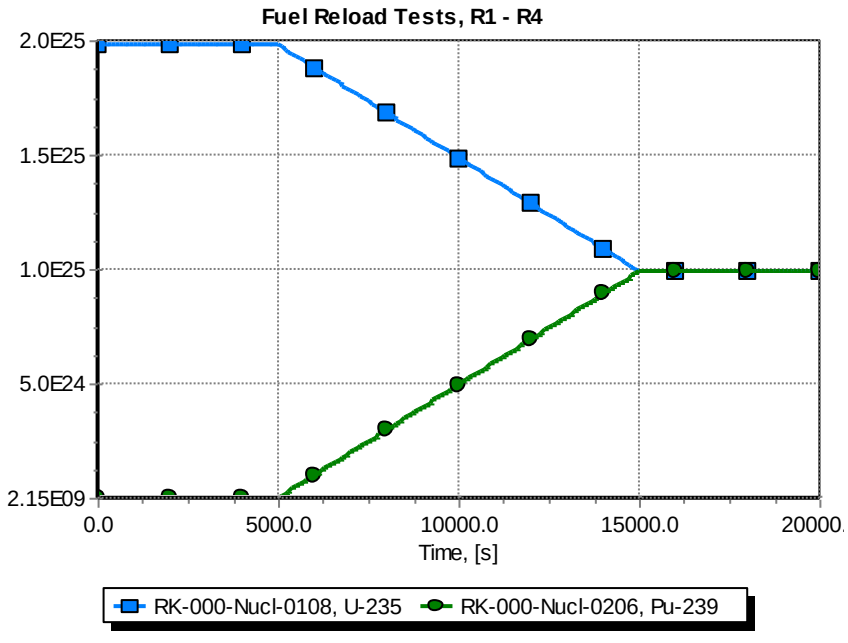

Figure 3-388 Concentrations of U-235 and Pu-239 in the core - simple fuel unloading test R3

3.9.2.5 Simple Fuel Unloading Test - R4

Four simple tests, R1, R2, R3, R4, are shown to demonstrate the use of loading and removal functions. Initially the core consists of U-235 only. There is no neutron flux, so the isotope change is caused only by loading/removal functions. In the test R4 one removal function, R^R, and one loading function, $R^F(1)$, were used, defined as follows:

- $t < 5000$ s $\quad R^R = 0.0 \quad R^F(1) = 0.0$
- $t > 5000$ s $\quad R^R = 1.0\times10^{-4} \quad R^F(1) = 1.0\times10^{-4}$

The isotope composition of the loading function 1 was 50% U-235, 50% U-239. For the removal function the isotope composition is the current core composition, since the optional multipliers on core composition (Volume 2) were not used. SPECTRA input deck for this test is provided in `\Z-INPUTS\RK\RELOAD\R4.SPE`. Figure 3-389 shows the average concentrations of U-235 and Pu-239 in the core ($1/m^3$).

Physically this test represents a process in which assemblies are picked randomly, removed from the core, and replaced by assemblies with fuel consisting of 50% uranium and 50% plutonium. In contrast to the previous case (R3), this process can go on forever, so it was not stopped at 15,000 s.

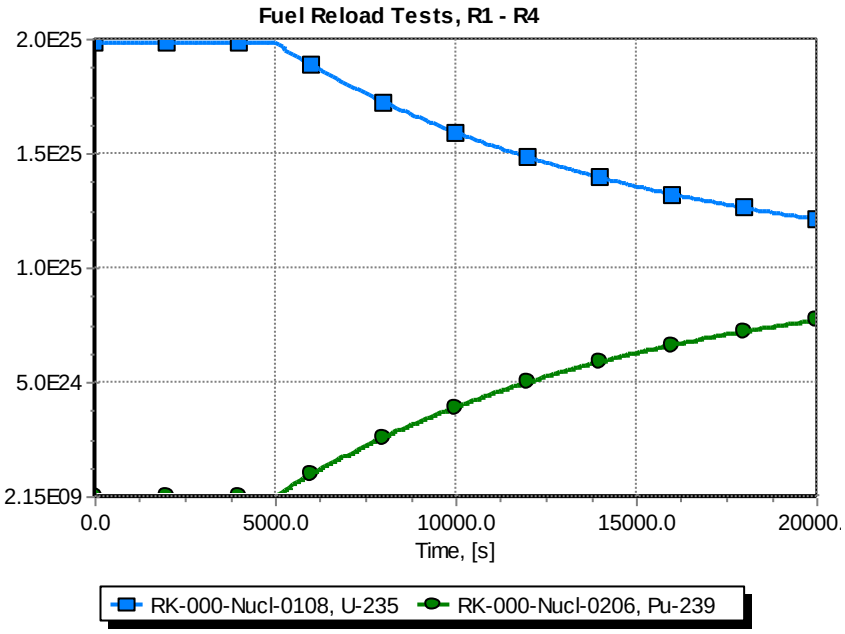

Figure 3-389 Concentrations of U-235 and Pu-239 in the core - simple fuel unloading test R4

3.9.2.6 Decay Heat Test, ^{235}U Fuel

The decay heat producers are represented in SPECTRA by 11 groups of "isotopes", similarly as in the RELAP code. The decay constants and fission yields of these groups were established based on literature data from and comparisons with the ANS standard (see Volume 1). Verification of the model is shown in this section and the next section.

In the present section calculations are performed using U-235 fuel. The initial reactor power is assumed to be 100 MW (10^8 W). The initial fission power is 93.43 MW. The number was obtained in a trial and error method, to give the total power of 100 MW for this case. The reactor is shutdown at t = 0.0 by inserting a large negative reactivity (–9.99 $). A relative reactor power, equal to the total reactor power divided by 10^8 W, is plotted. The SPECTRA results are compared to the decay heat obtained from the ANS standard.

SPECTRA input deck for this test is provided in `\Z-INPUTS\RK\DH\DH-U235.SPE`. The input deck for the ANS decay heat calculation is provided in `\Z-INPUTS\RK\DH\U235.DHC`. Note that the *.DHC files contain data for the DHC-ANS program; it means they should be "opened with" the DHC-ANS.EXE code, provided in `\Z-UTIL\DHC-ANS\DHC-ANS.EXE`.

Comparison of the decay heat calculated by SPECTRA, with the decay heat curves obtained from the ANS standard is shown in Figure 3-390. The behavior is very similar.

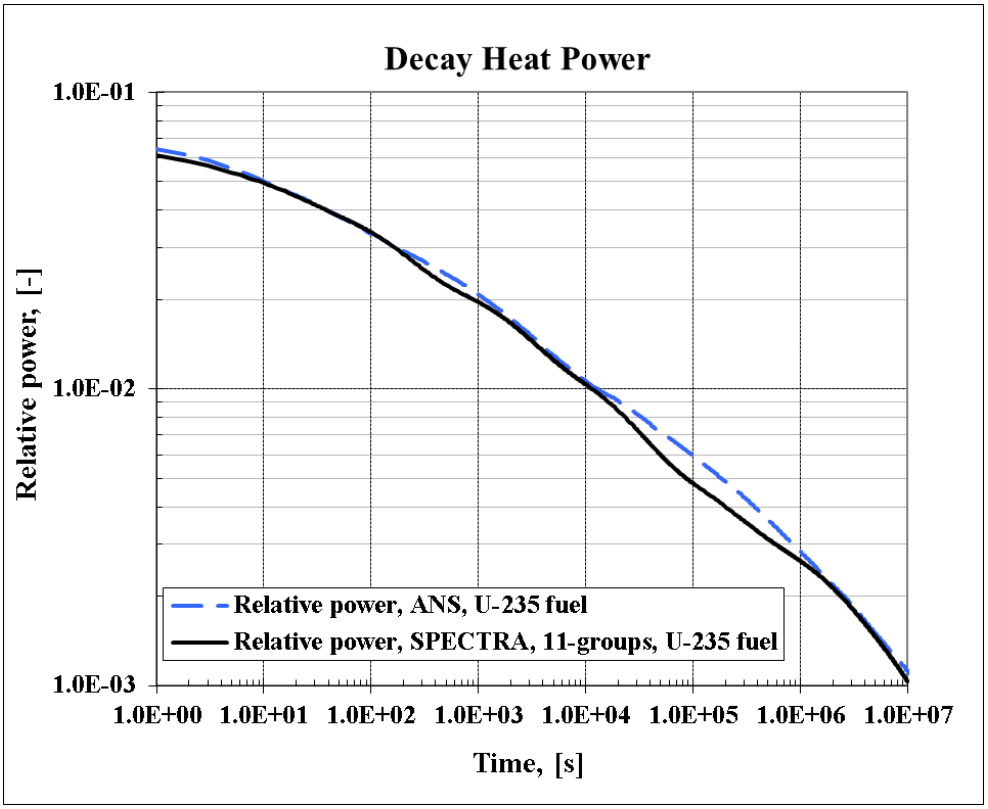

Figure 3-390 Comparison of decay heat for ^{235}U fuel, ANS and SPECTRA 11 groups

3.9.2.7 Decay Heat Test, ^{239}Pu Fuel

The decay heat producers are represented in SPECTRA by 11 groups of "isotopes", similarly as in the RELAP code. The decay constants and fission yields of these groups were established based on literature data from and comparisons with the ANS standard (see Volume 1). Verification of the model is shown in this section and the previous section.

In the present section calculations are performed using Pu-239 fuel. The initial reactor power is assumed to be 100 MW (10^8 W). The initial fission power is 94.43 MW. The number was obtained in a trial and error method, to give the total power of 100 MW for this case. The reactor is shutdown at t = 0.0 by inserting a large negative reactivity (–9.99 $). A relative reactor power, equal to the total reactor power divided by 10^8 W, is plotted. The SPECTRA results are compared to the decay heat obtained from the ANS standard.

SPECTRA input deck for this test is provided in `\Z-INPUTS\RK\DH\DH-Pu239.SPE`. The input deck for the ANS decay heat calculation is provided in `\Z-INPUTS\RK\DH\Pu239.DHC`. Note that the *.DHC files contain data for the DHC-ANS program; it means they should be "opened with" the DHC-ANS.EXE code, provided in `\Z-UTIL\DHC-ANS\DHC-ANS.EXE`.

Comparison of the decay heat calculated by SPECTRA, with the decay heat curves obtained from the ANS standard is shown in Figure 3-391. The behavior is very similar.

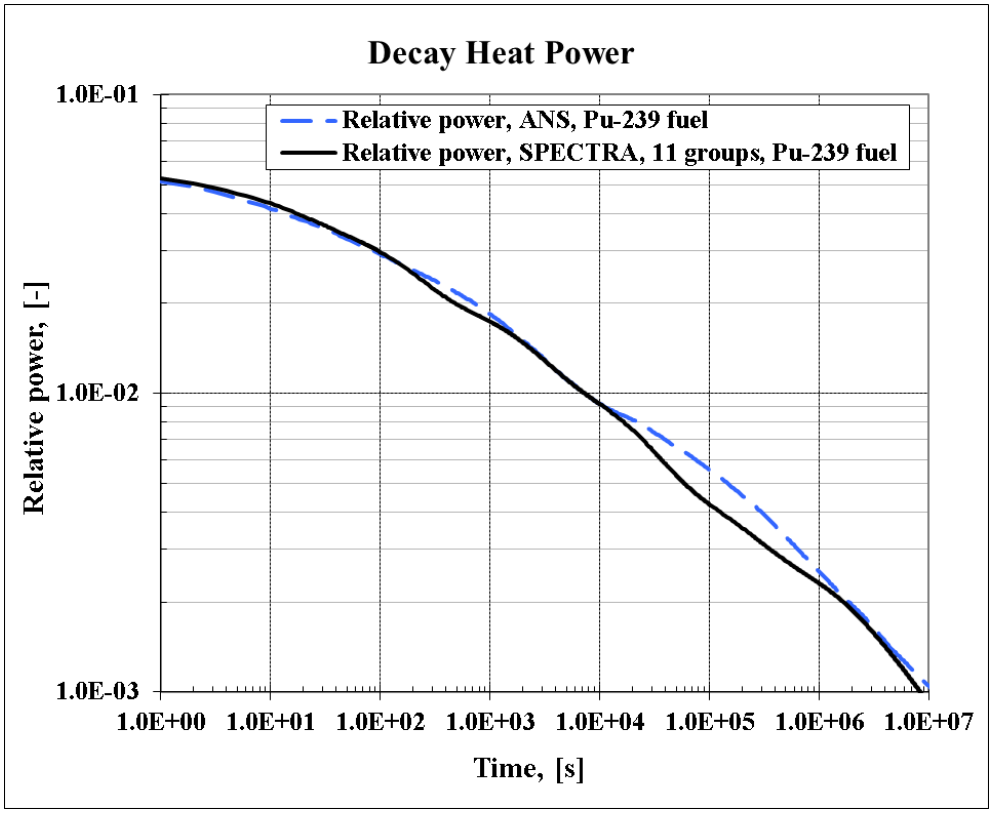

Figure 3-391 Comparison of decay heat for ^{239}Pu fuel, ANS and SPECTRA 11 groups

Comparison of ANS decay heat curves for the U-235 and Pu-239 fuels is shown in Figure 3-392 and Figure 3-393. The U-235 fuel gives somewhat higher decay heat.

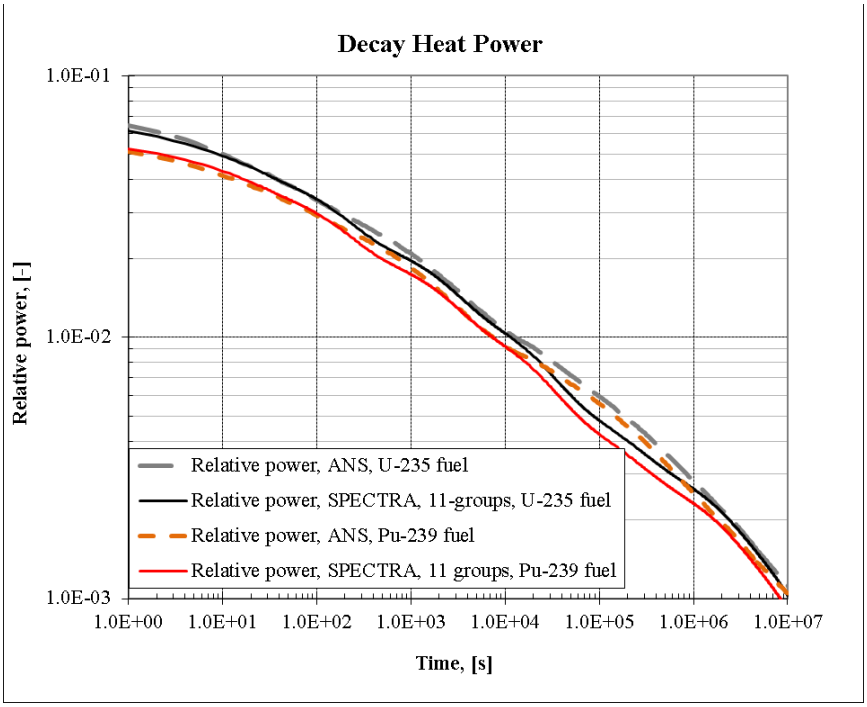

Figure 3-392 Comparison of ANS decay heat curves for ^{235}U and ^{239}Pu fuels

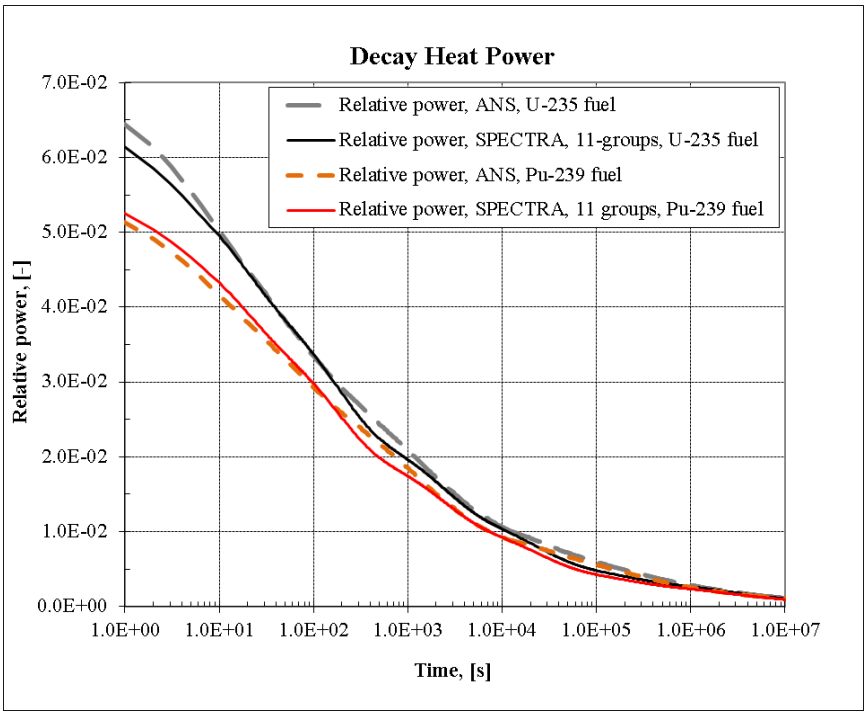

Figure 3-393 Comparison of ANS decay heat curves for ^{235}U and ^{239}Pu fuels

3.9.2.8 DNP-1 Test

The test DNP-1 provides verification of the concentration of delayed neutron precursors (DNP), in particular the case where the DNP yield fractions depend on the fissile isotope. SPECTRA input decks and support files are provided in \Z-INPUTS\RK\DNP-1\.

The DNP data is obtained from [207] (see also Volume 1, section "Delayed Neutron Precursors"). The calculation of yield fractions is shown in the Excel file: DNP-1.xlsx, which is provided in the folder \Z-INPUTS\RK\DNP-1\. The yield fractions are compared with the published data for the HTR fuel for U-235 and MSR data for U-235 and Pu-239 fuels. The values are shown in Table 3-50.

Table 3-50 Delayed neutron precursor data

Group i	Decay constant λ_i, (1/s)	Yield fractions, β_i		
		U-235	U-233	Pu-239
1	1.24667E-02	2.145E-04	8.580E-05	6.930E-05
2	2.82917E-02	1.001E-03	4.004E-04	3.234E-04
3	4.25244E-02	5.915E-04	2.366E-04	1.911E-04
4	1.33042E-01	1.281E-03	5.122E-04	4.137E-04
5	2.92467E-01	2.151E-03	8.606E-04	6.951E-04
6	6.66488E-01	5.850E-04	2.340E-04	1.890E-04
7	1.63478E+00	5.265E-04	2.106E-04	1.701E-04
8	3.55460E+00	1.495E-04	5.980E-05	4.830E-05
	sum:	6.500E-03	2.600E-03	2.100E-03

Two input decks are defined:

- DNP-U235 fuel consists initially of U-235 only,
- DNP-Pu239 fuel consists initially of Pu-239 only.

The DNP input data is defined as follows:

- The main yield fractions (BTDNRK) are defined as those for U-235.
- The individual data (BIDNRK) is defined for U-233 and Pu-239 (Pu-241 values are assumed as the same as for Pu-239).

```
*        DELAYED NEUTRON DATA            individual yields (BIDNRK)
*        BTDNRK (-)    DCDNRK (1/s)      U-233      U-235  U-239  Pu-239     Pu-241
770001   2.145E-04     1.24667E-02       8.580E-05  0      0      6.930E-05 6.930E-05
770002   1.001E-03     2.82917E-02       4.004E-04  0      0      3.234E-04 3.234E-04
770003   5.915E-04     4.25244E-02       2.366E-04  0      0      1.911E-04 1.911E-04
770004   1.281E-03     1.33042E-01       5.122E-04  0      0      4.137E-04 4.137E-04
770005   2.151E-03     2.92467E-01       8.606E-04  0      0      6.951E-04 6.951E-04
770006   5.850E-04     6.66488E-01       2.340E-04  0      0      1.890E-04 1.890E-04
770007   5.265E-04     1.63478E+00       2.106E-04  0      0      1.701E-04 1.701E-04
770008   1.495E-04     3.55460E+00       5.980E-05  0      0      4.830E-05 4.830E-05
```

The test is a reactivity insertion. The "control rod" reactivity is defined in dollars, using the main yield fractions as the definition of dollar (see Volume 2). In this case this means that 1 $ = 6.5E-3 (or 650 pcm). The assumed transient scenario is an insertion of 214 pcm, which for the U-235 input deck corresponds to 0.33 $ while for the Pu-239 input deck to 1.02 $ (see DNP-1.xlsx) - Figure 3-394.

Calculations are performed until a new stationary state is reached at higher power and temperature, due to the assumed negative reactivity feedbacks:

- fuel: –50 $ / 10000 K,
- moderator: –500 $ / 10000 K.

The stationary state results are verified by comparing the SPECTRA results with the results of theoretical formula. The stationary state DNP concentrations are equal obtained from

$$\frac{dC_i(t)}{dt} = \frac{\beta_i(t)}{\Lambda} n(t) - \lambda_i C_i(t) = 0$$

which means:

$$C_i(t) = \frac{\beta_i(t)}{\Lambda \lambda_i} n(t)$$

The transient is relatively short; stationary state is reached after a few hundred seconds. The total run time of 2000 s was selected. During this time, the fuel composition practically does not change, so $\beta_i(t)$ = const.

As an additional verification, the following test was set up:

- DNP-Pu239-check

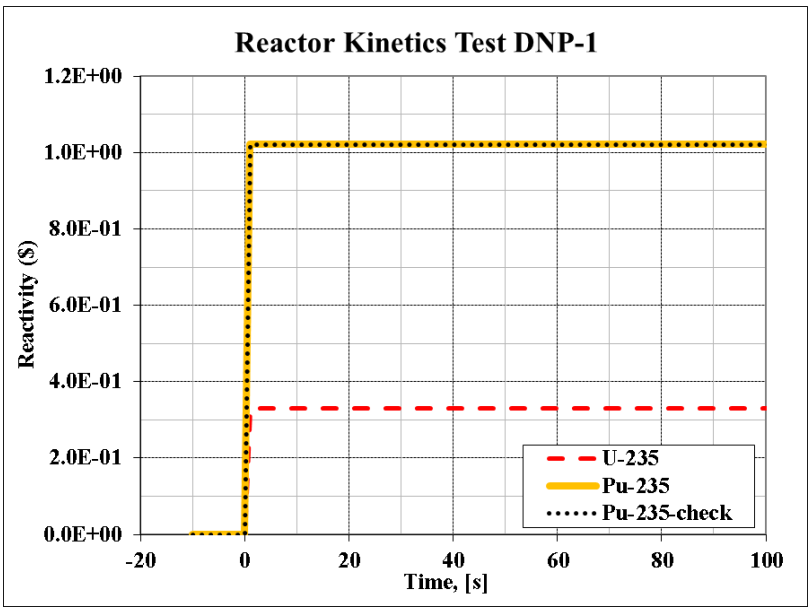

Figure 3-394 Test DNP-1, reactivity insertion

In this case, the DNP data was defined for Pu-239 only:

```
*        DELAYED NEUTRON DATA
*        BTDNRK (-)    DCDNRK (1/s)
770001   6.930E-05     1.24667E-02
770002   3.234E-04     2.82917E-02
770003   1.911E-04     4.25244E-02
770004   4.137E-04     1.33042E-01
770005   6.951E-04     2.92467E-01
770006   1.890E-04     6.66488E-01
770007   1.701E-04     1.63478E+00
770008   4.830E-05     3.55460E+00
```

Therefore the one dollar reactivity is in this case equal to 2.1E-3 (or 210 pcm). The reactivity insertion and the feedback coefficients were recalculated for this case as shown in DNP-1.xlsx. The reactivity insertion is equal to 1.02143 $. The feedback coefficients are

- fuel: –154.76 $ / 10000 K
- moderator: –1547.6 $ / 10000 K

With such definitions, the results of DNP-Pu-239-check should be the same as the results of DNP-Pu239. The results are shown in Figure 3-394 through Figure 3-399 and Table 3-51. Figure 3-394 shows the reactivity insertion. Figure 3-395 shows the total reactivity. Figure 3-396 shows the fission power. Figure 3-397 and Figure 3-398 show the concentrations of DNPs of group 1 and 8. In case of Pu-239 fuel the reactivity insertion is more than one dollar and therefore the power increase is much more rapid than in the case of U-235 fuel. The case DNP-Pu239 and DNP-Pu239-check give practically the same results.

Figure 3-399 shows the values of DNP-U235 and DNP-Pu239 cases at the end of the calculations. The DNP concentrations are much smaller in the case of Pu-239 fuel. The results are compared to the theoretical solutions in Table 3-51. The theoretical calculations are provided in DNP-1.xlsx. The results are in very good agreement. The current DNP yield fractions are not plottable, therefore could not be included in Figure 3-399, but are printed in the output file, as shown below.

- Printout of DNP, case DNP-U-235 at the end of the calculations (t = 2000 s):

```
Group     Concentration    Yield
 No.         [1/m3]         [-]
  1        6.40326E+11   2.14500E-04
  2        1.31674E+12   1.00100E-03
  3        5.17656E+11   5.91500E-04
  4        3.58332E+11   1.28100E-03
  5        2.73709E+11   2.15100E-03
  6        3.26654E+10   5.85000E-04
  7        1.19857E+10   5.26500E-04
  8        1.56522E+09   1.49500E-04
                         -----------
    TOTAL D.N.P. YIELD:  6.50000E-03
```

- Printout of DNP, case DNP-Pu239 at the end of the calculations (t = 2000 s):

```
Group     Concentration    Yield
 No.         [1/m3]         [-]
  1        2.06874E+11   6.93000E-05
  2        4.25408E+11   3.23400E-04
  3        1.67243E+11   1.91100E-04
  4        1.15723E+11   4.13700E-04
  5        8.84494E+10   6.95100E-04
  6        1.05534E+10   1.89000E-04
  7        3.87230E+09   1.70100E-04
  8        5.05686E+08   4.83000E-05
                         -----------
    TOTAL D.N.P. YIELD:  2.10000E-03
```

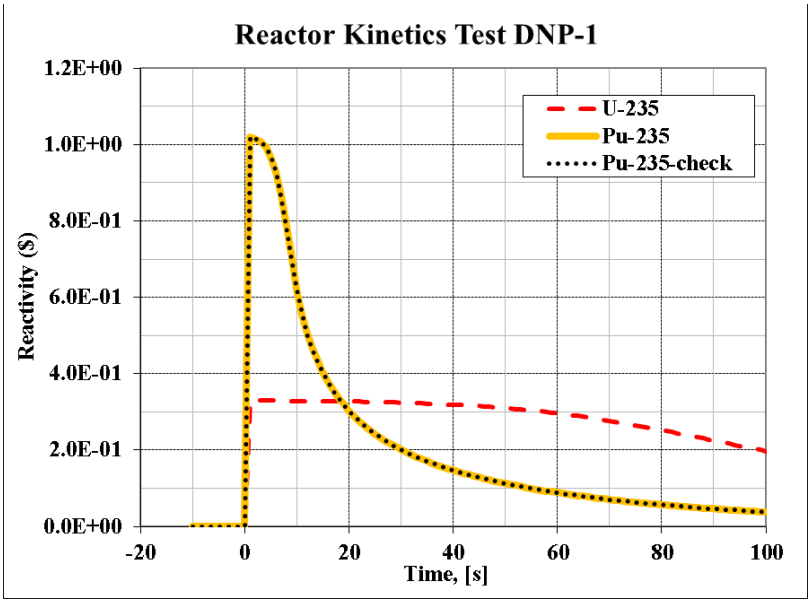

(a) short term

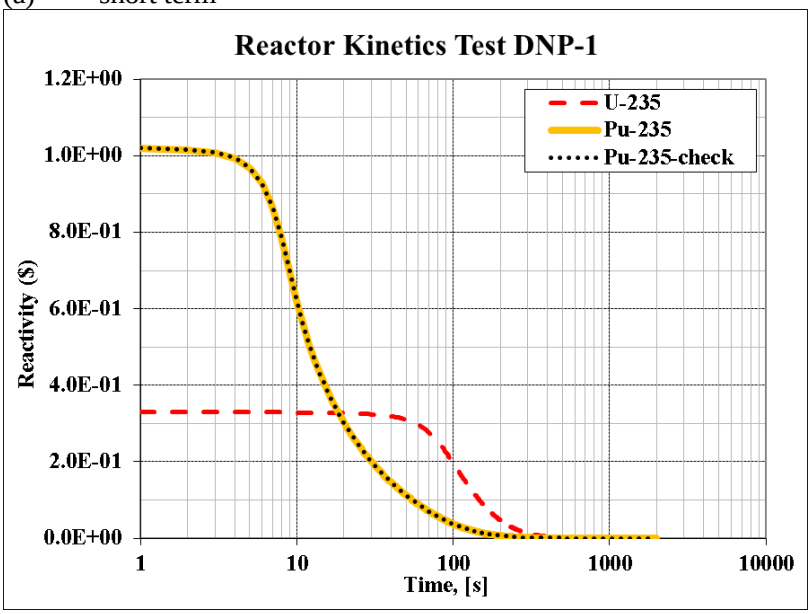

(b) long term

Figure 3-395 Test DNP-1, total reactivity

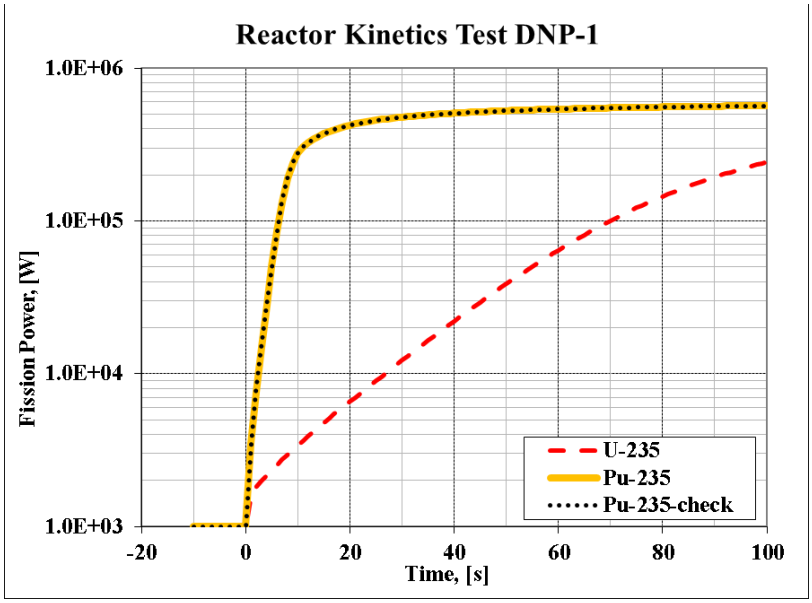

(a) short term

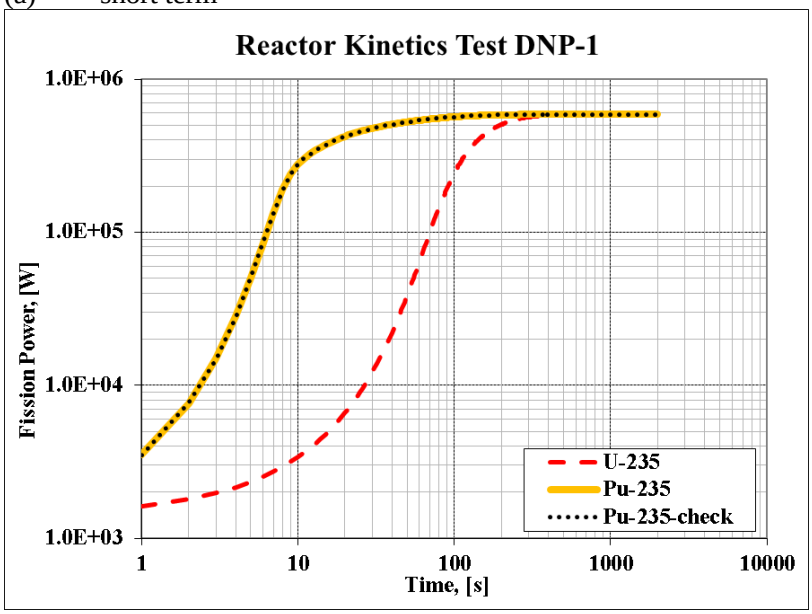

(b) long term

Figure 3-396 Test DNP-1, fission power

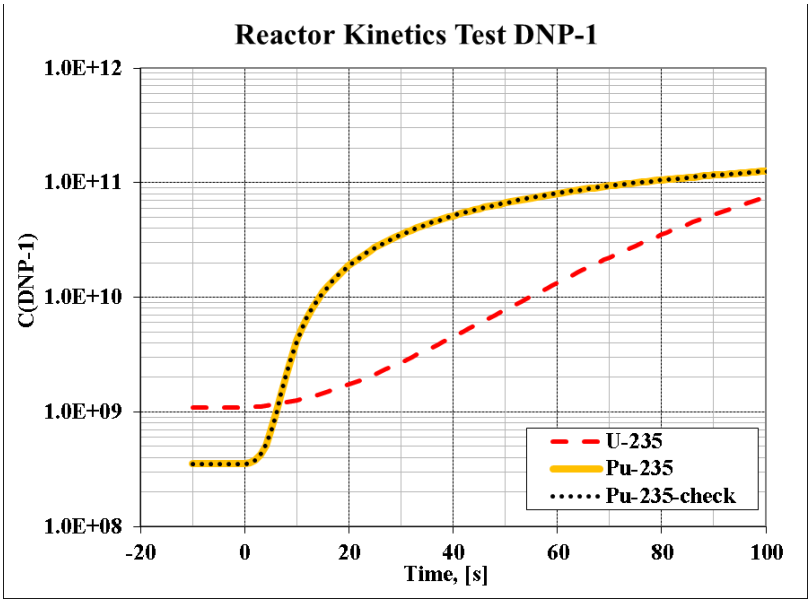

(a) short term

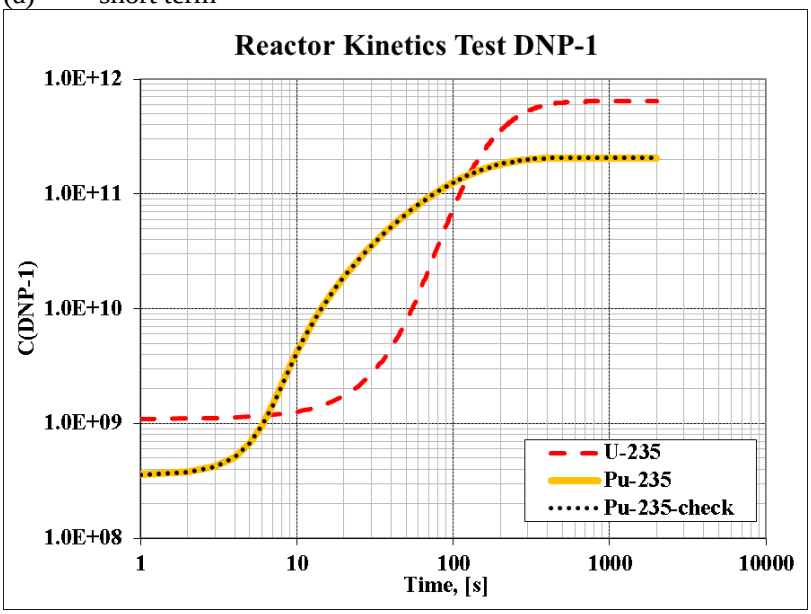

(b) long term

Figure 3-397 Test DNP-1, concentrations of DNP group 1

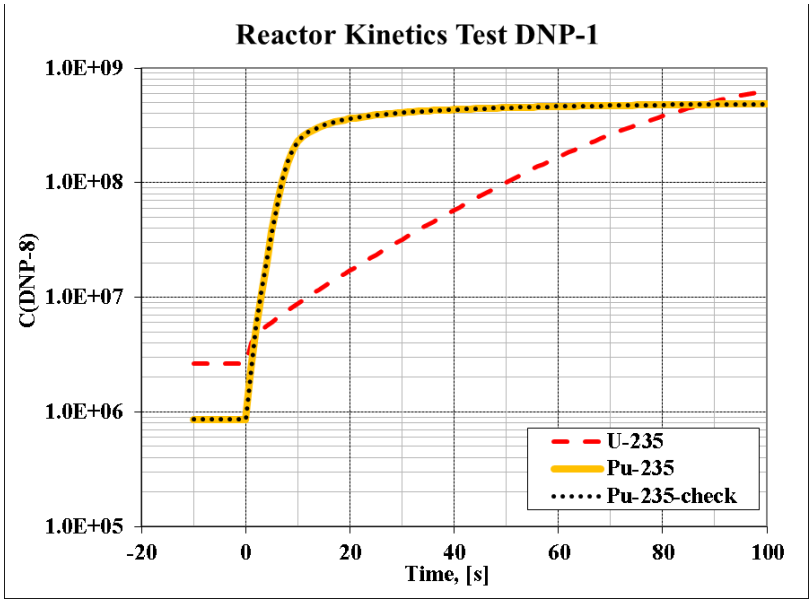

(a) short term

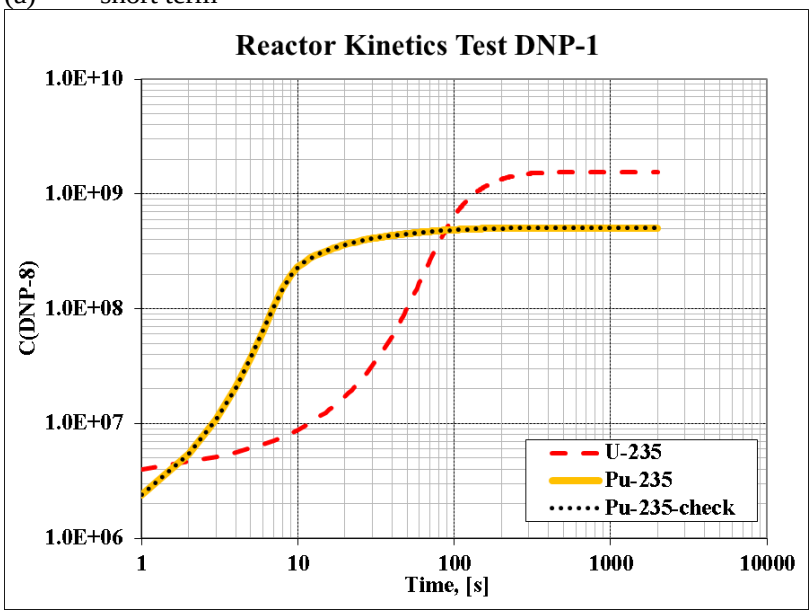

(b) long term

Figure 3-398 Test DNP-1, concentrations of DNP group 8

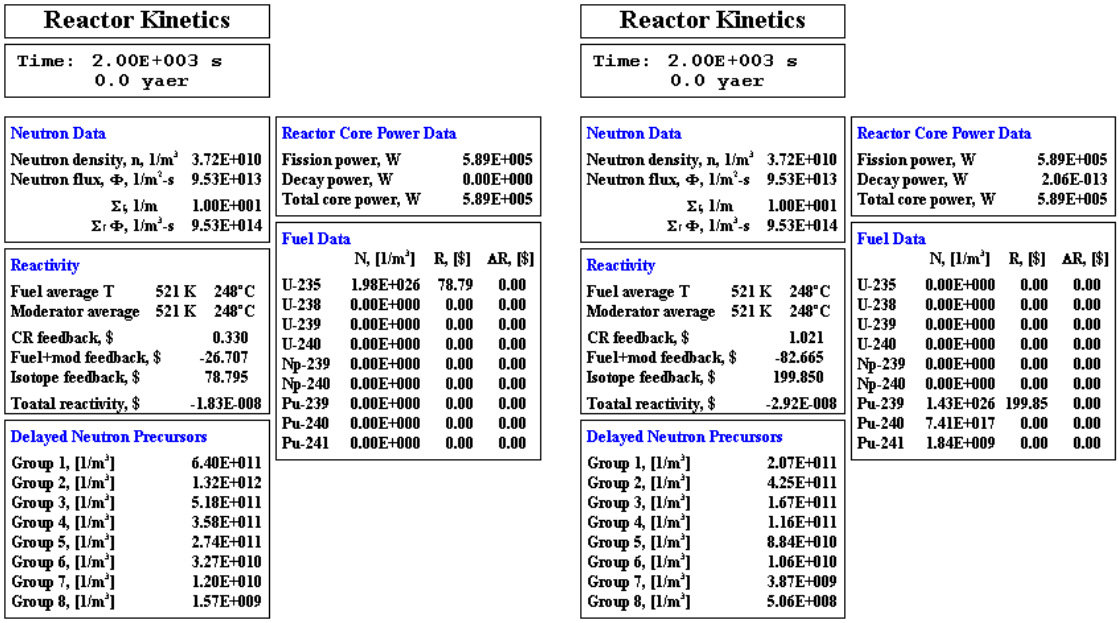

Reactor Kinetics

Time: 2.00E+003 s
0.0 yaer

Neutron Data

Neutron density, n, 1/m³	3.72E+010
Neutron flux, Φ, 1/m²-s	9.53E+013
Σt, 1/m	1.00E+001
Σf Φ, 1/m³-s	9.53E+014

Reactivity

Fuel average T	521 K	248°C
Moderator average	521 K	248°C
CR feedback, $		0.330
Fuel+mod feedback, $		-26.707
Isotope feedback, $		78.795
Toatal reactivity, $		-1.83E-008

Delayed Neutron Precursors

Group 1, [1/m³]	6.40E+011
Group 2, [1/m³]	1.32E+012
Group 3, [1/m³]	5.18E+011
Group 4, [1/m³]	3.58E+011
Group 5, [1/m³]	2.74E+011
Group 6, [1/m³]	3.27E+010
Group 7, [1/m³]	1.20E+010
Group 8, [1/m³]	1.57E+009

Reactor Core Power Data

Fission power, W	5.89E+005
Decay power, W	0.00E+000
Total core power, W	5.89E+005

Fuel Data

	N, [1/m³]	R, [$]	ΔR, [$]
U-235	1.98E+026	78.79	0.00
U-238	0.00E+000	0.00	0.00
U-239	0.00E+000	0.00	0.00
U-240	0.00E+000	0.00	0.00
Np-239	0.00E+000	0.00	0.00
Np-240	0.00E+000	0.00	0.00
Pu-239	0.00E+000	0.00	0.00
Pu-240	0.00E+000	0.00	0.00
Pu-241	0.00E+000	0.00	0.00

Reactor Kinetics

Time: 2.00E+003 s
0.0 yaer

Neutron Data

Neutron density, n, 1/m³	3.72E+010
Neutron flux, Φ, 1/m²-s	9.53E+013
Σt, 1/m	1.00E+001
Σf Φ, 1/m³-s	9.53E+014

Reactivity

Fuel average T	521 K	248°C
Moderator average	521 K	248°C
CR feedback, $		1.021
Fuel+mod feedback, $		-82.665
Isotope feedback, $		199.850
Toatal reactivity, $		-2.92E-008

Delayed Neutron Precursors

Group 1, [1/m³]	2.07E+011
Group 2, [1/m³]	4.25E+011
Group 3, [1/m³]	1.67E+011
Group 4, [1/m³]	1.16E+011
Group 5, [1/m³]	8.84E+010
Group 6, [1/m³]	1.06E+010
Group 7, [1/m³]	3.87E+009
Group 8, [1/m³]	5.06E+008

Reactor Core Power Data

Fission power, W	5.89E+005
Decay power, W	2.06E-013
Total core power, W	5.89E+005

Fuel Data

	N, [1/m³]	R, [$]	ΔR, [$]
U-235	0.00E+000	0.00	0.00
U-238	0.00E+000	0.00	0.00
U-239	0.00E+000	0.00	0.00
U-240	0.00E+000	0.00	0.00
Np-239	0.00E+000	0.00	0.00
Np-240	0.00E+000	0.00	0.00
Pu-239	1.43E+026	199.85	0.00
Pu-240	7.41E+017	0.00	0.00
Pu-241	1.84E+009	0.00	0.00

Figure 3-399 Test DNP-1, end-results (t=2000 s), left: U-235, right Pu-239

Table 3-51 DNP concentrations, U-235 and Pu-239 - theoretical solution

		U-235	Pu-239	Equilibrium concentrations		
Group	λi	βi	βi	Group	U-235	Pu-239
1	1.24667E-02	2.14500E-04	6.93000E-05	1	6.40E+11	2.07E+11
2	2.82917E-02	1.00100E-03	3.23400E-04	2	1.32E+12	4.25E+11
3	4.25244E-02	5.91500E-04	1.91100E-04	3	5.18E+11	1.67E+11
4	1.33298E-01	1.28100E-03	4.13700E-04	4	3.58E+11	1.16E+11
5	2.92467E-01	2.15100E-03	6.95100E-04	5	2.74E+11	8.84E+10
6	6.66488E-01	5.85000E-04	1.89000E-04	6	3.27E+10	1.06E+10
7	1.63478E+00	5.26500E-04	1.70100E-04	7	1.20E+10	3.87E+09
8	3.55460E+00	1.49500E-04	4.83000E-05	8	1.57E+09	5.06E+08
	total:	**6.50000E-03**	**2.10000E-03**			

A similar analysis was made where the initial reactivity was defined instead of the step change of reactivity. The input files are stored in \Z-INPUTS\RK\DNP-1\Initial\. Again, three cases were analyzed, U-235, Pu-239 and Pu-239-check. The results are practically identical to the current results and therefore are not discussed here.

3.9.2.9 DNP-2 Test

The test DNP-2 provides verification of the concentration of delayed neutron precursors (DNP), in particular the case where the DNP yield fractions depend on the fissile isotope. SPECTRA input decks and support files are provided in \Z-INPUTS\RK\DNP-2\.

The DNP data is the same as described in the test DNP-1. In the DNP-1 test the individual DNP yield fractions were not essential for calculations, as the fuel composition was practically constant in the analyzed time frame and DNP yields appropriate for given fuel could be defined for each case (as was done for the test Pu-239-check). In the current test a long term behavior is analyzed, where the yield fractions do change in time.

A long term behavior (10 years) is analyzed. The reactor power is kept constant at 100 MW. The initial fuel composition (Σ_f, U-235 enrichment) is assumed in such a way that the consumption of U-235 is approximately compensated by the production of Pu-239 from U-238, and therefore a long term operation is possible without fuel reload. Two input decks are defined:

- DNP-2-1: DNP data for U-235,
- DNP-2-2: Individual DNP data shown in the DNP-1 test (Table 3-50).

The results are shown in Figure 3-400 through Figure 3-406 and Table 3-52. Figure 3-400 shows the concentrations of U-235 and Pu-239. Figure 3-401 shows the reactor power, which is practically constant at 100 MW. Figure 3-402 shows the macroscopic fission cross section, equal to (see Volume 1):

$$\Sigma_f = \sum_i \sigma_{f,i} N_i(t)$$

where $\sigma_{f,i}$ is a microscopic cross section for fission, (m^2), for isotope i. and $N_i(t)$ is a concentration ($1/m^3$) of the fissile isotope i. The initial value of Σ_f is assumed to be 10.0 (1/m). The value is approximately constant because U-235 is in time being replaced by Pu-239. Figure 3-403 shows the neutron flux. The value is approximately constant because the macroscopic fission cross section is constant.

Figure 3-404 and Figure 3-405 show the concentrations of DNP groups 1 and 8 respectively. In the case DNP-2-1, the DNP yields are constant and therefore the DNP concentrations are approximately constant with constant neutron flux/concentration. In the case DNP-2-2, the DNP concentrations are slowly decreasing in time as more fission is caused by Pu-239, which has about three times smaller DNP yield than U-235.

Figure 3-406 shows the values of DNP-2-1 and DNP-2-2 cases at the end of the calculations. The DNP concentrations are much smaller in the case of DNP-2-2. The results are compared to the theoretical solutions in Table 3-52. Theoretical calculations are provided in DNP-2.xlsx. Since the fuel concentration changes are very slow, stationary-state values of DNP concentrations are used:

$$C_i(t) = \frac{\beta_i(t)}{\Lambda \lambda_i} n(t)$$

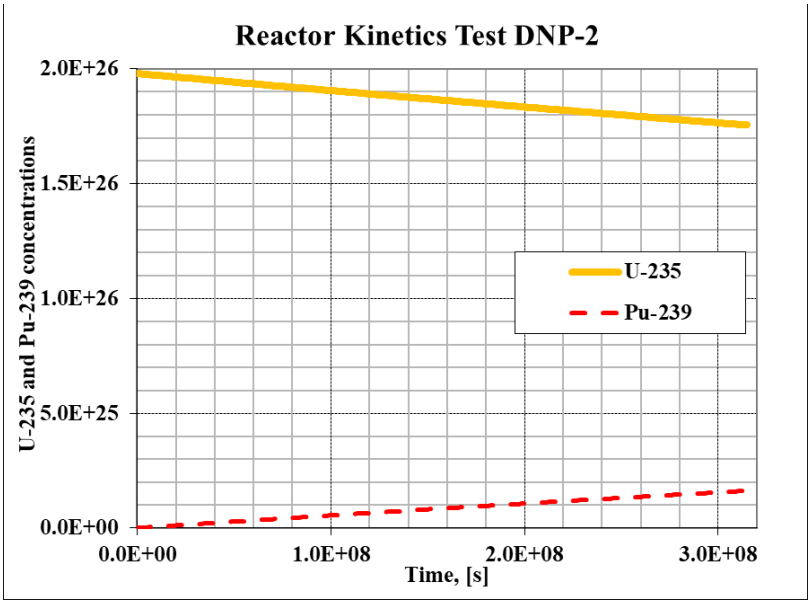

Figure 3-400 Test DNP-2, concentrations of U-235 and Pu-239

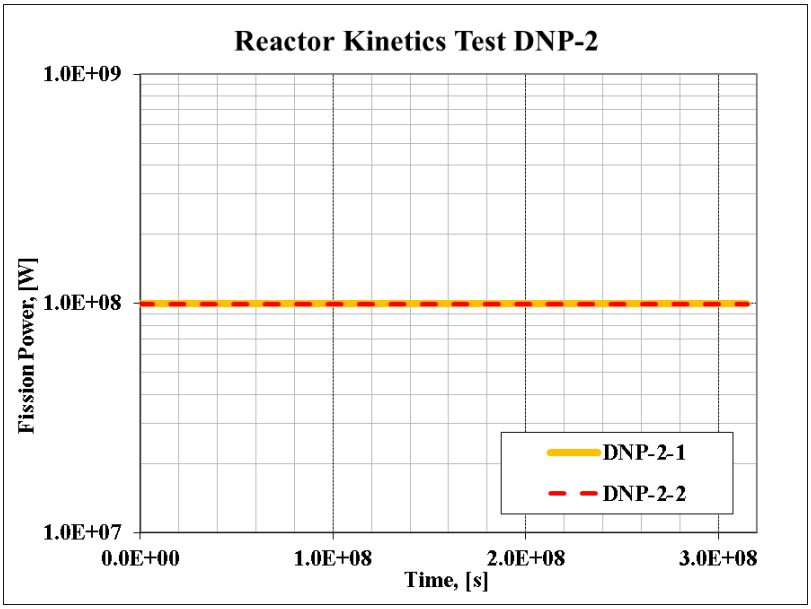

Figure 3-401 Test DNP-2, fission power

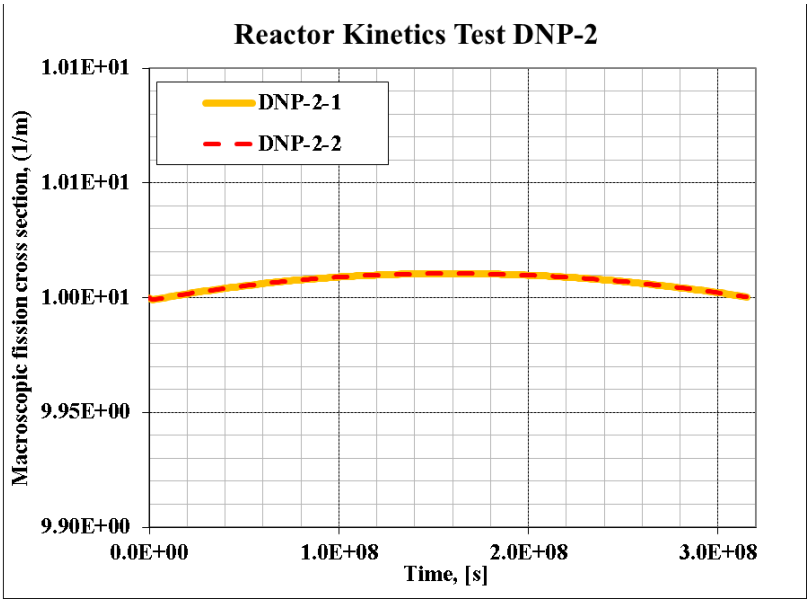

Figure 3-402 Test DNP-2, macroscopic fission cross-section

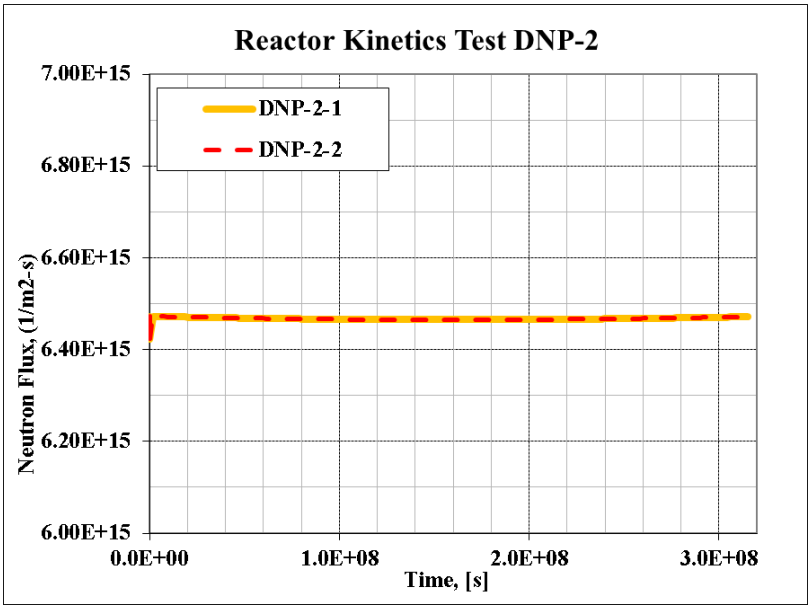

Figure 3-403 Test DNP-2, neutron flux

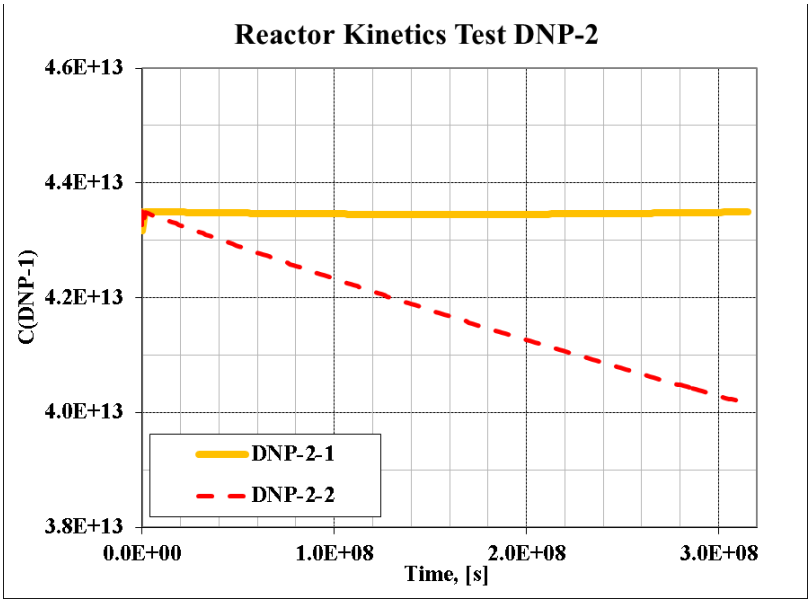

Figure 3-404 Test DNP-2, concentrations of DNP group 1

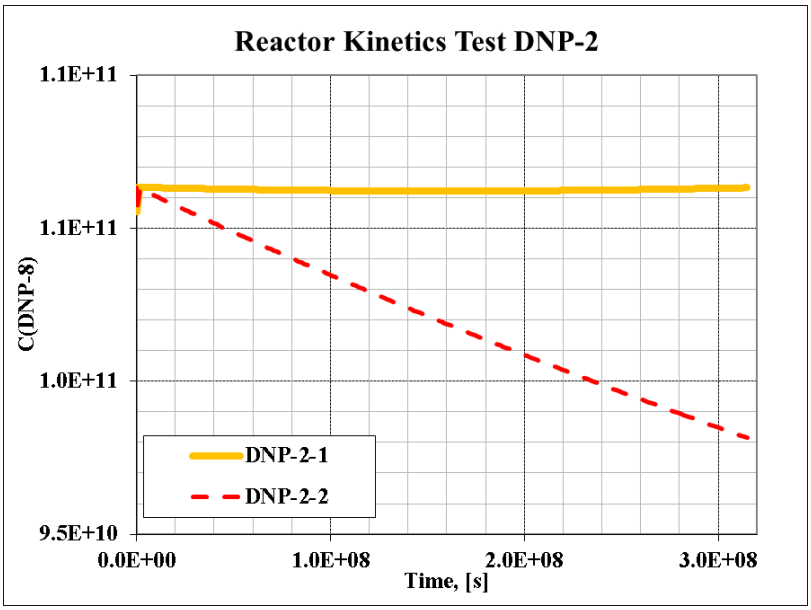

Figure 3-405 Test DNP-2, concentrations of DNP group 8

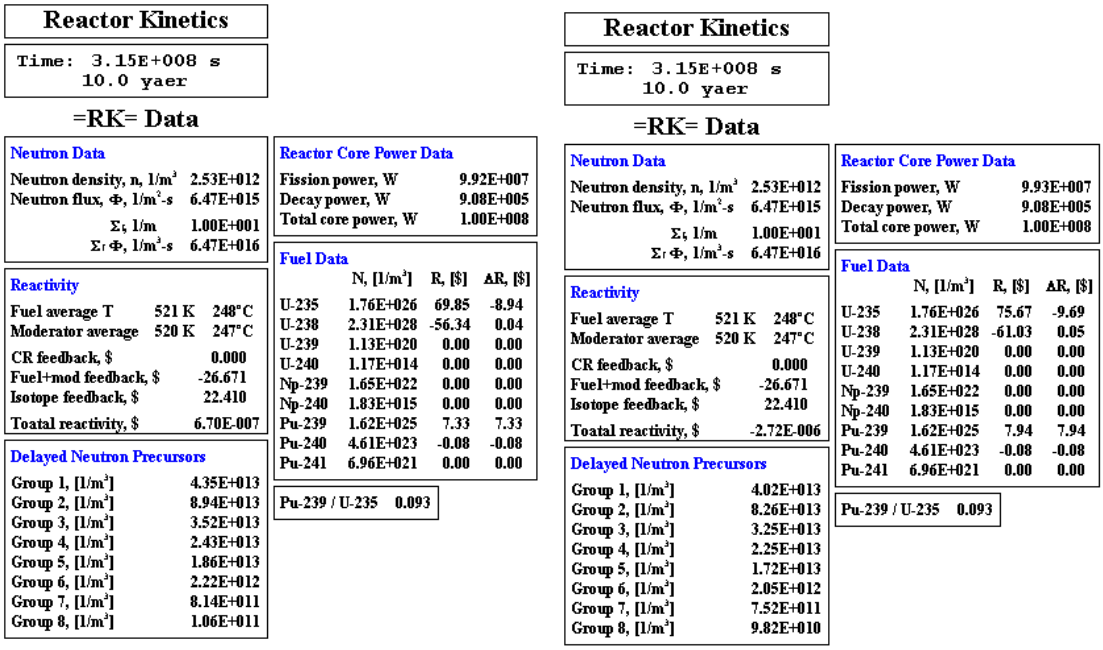

Reactor Kinetics

Time: 3.15E+008 s
10.0 yaer

=RK= Data

Neutron Data

Neutron density, n, 1/m³	2.53E+012
Neutron flux, Φ, 1/m²-s	6.47E+015
Σₜ, 1/m	1.00E+001
Σₜ Φ, 1/m³-s	6.47E+016

Reactivity

Fuel average T	521 K	248°C
Moderator average	520 K	247°C
CR feedback, $		0.000
Fuel+mod feedback, $		-26.671
Isotope feedback, $		22.410
Toatal reactivity, $		6.70E-007

Delayed Neutron Precursors

Group 1, [1/m³]	4.35E+013
Group 2, [1/m³]	8.94E+013
Group 3, [1/m³]	3.52E+013
Group 4, [1/m³]	2.43E+013
Group 5, [1/m³]	1.86E+013
Group 6, [1/m³]	2.22E+012
Group 7, [1/m³]	8.14E+011
Group 8, [1/m³]	1.06E+011

Reactor Core Power Data

Fission power, W	9.92E+007
Decay power, W	9.08E+005
Total core power, W	1.00E+008

Fuel Data

	N, [1/m³]	R, [$]	ΔR, [$]
U-235	1.76E+026	69.85	-8.94
U-238	2.31E+028	-56.34	0.04
U-239	1.13E+020	0.00	0.00
U-240	1.17E+014	0.00	0.00
Np-239	1.65E+022	0.00	0.00
Np-240	1.83E+015	0.00	0.00
Pu-239	1.62E+025	7.33	7.33
Pu-240	4.61E+023	-0.08	-0.08
Pu-241	6.96E+021	0.00	0.00

Pu-239 / U-235 0.093

Reactor Kinetics

Time: 3.15E+008 s
10.0 yaer

=RK= Data

Neutron Data

Neutron density, n, 1/m³	2.53E+012
Neutron flux, Φ, 1/m²-s	6.47E+015
Σₜ, 1/m	1.00E+001
Σₜ Φ, 1/m³-s	6.47E+016

Reactivity

Fuel average T	521 K	248°C
Moderator average	520 K	247°C
CR feedback, $		0.000
Fuel+mod feedback, $		-26.671
Isotope feedback, $		22.410
Toatal reactivity, $		-2.72E-006

Delayed Neutron Precursors

Group 1, [1/m³]	4.02E+013
Group 2, [1/m³]	8.26E+013
Group 3, [1/m³]	3.25E+013
Group 4, [1/m³]	2.25E+013
Group 5, [1/m³]	1.72E+013
Group 6, [1/m³]	2.05E+012
Group 7, [1/m³]	7.52E+011
Group 8, [1/m³]	9.82E+010

Reactor Core Power Data

Fission power, W	9.93E+007
Decay power, W	9.08E+005
Total core power, W	1.00E+008

Fuel Data

	N, [1/m³]	R, [$]	ΔR, [$]
U-235	1.76E+026	75.67	-9.69
U-238	2.31E+028	-61.03	0.05
U-239	1.13E+020	0.00	0.00
U-240	1.17E+014	0.00	0.00
Np-239	1.65E+022	0.00	0.00
Np-240	1.83E+015	0.00	0.00
Pu-239	1.62E+025	7.94	7.94
Pu-240	4.61E+023	-0.08	-0.08
Pu-241	6.96E+021	0.00	0.00

Pu-239 / U-235 0.093

Figure 3-406 Test DNP-2, end-results (t=10 years), left: DNP-2-1, right: DNP-2-2

Table 3-52 DNP concentrations, DNP-2-0 and DNP-2 - theoretical solution

		DNP-2-1	DNP-2-2	Equilibrium concentrations		
Group	λi	βi	βi	Group	DNP-2-1	DNP-2-2
1	1.24667E-02	2.145E-04	1.9801E-04	1	4.35E+13	4.02E+13
2	2.82917E-02	1.001E-03	9.2406E-04	2	8.94E+13	8.26E+13
3	4.25244E-02	5.915E-04	5.4603E-04	3	3.52E+13	3.25E+13
4	1.33298E-01	1.281E-03	1.1825E-03	4	2.43E+13	2.24E+13
5	2.92467E-01	2.151E-03	1.9857E-03	5	1.86E+13	1.72E+13
6	6.66488E-01	5.850E-04	5.4003E-04	6	2.22E+12	2.05E+12
7	1.63478E+00	5.265E-04	4.8603E-04	7	8.14E+11	7.52E+11
8	3.55460E+00	1.495E-04	1.3801E-04	8	1.06E+11	9.82E+10
	total:	6.500E-03	6.0004E-03			

The current fission yields are given by (see Volume 1, delayed neutron precursors):

$$\beta_i(t) = \frac{\sum_{j \in fis} \sigma_{f,j}\ N_j(t)\ \beta_{j \to i}}{\sum_{j \in fis} \sigma_{f,j}\ N_j(t)}$$

All theoretical calculations from the above formulae are shown in the Excel file DNP-2.xlsx. The concentrations of fissile isotopes, N_j, for U-235 and U-239 are taken from SPECTRA output files. The other fissile isotopes have negligible effect. The theoretical results, shown in Table 3-52 are in very good agreement. The current DNP yield fractions are not plottable, therefore could not be included in the visor picture in Figure 3-399, but are printed in the output files. Below the printouts of the 10-year values for DNP-2.

- Printout of DNP, case DNP-2, 10-year values:

```
 =RK=  DATA FOR   8 DELAYED NEUTRON PRECURSORS

       Node No.:  1
   Group     Concentration    Yield
    No.         [1/m3]         [-]
     1        4.01529E+13   1.98012E-04
     2        8.25689E+13   9.24057E-04
     3        3.24607E+13   5.46034E-04
     4        2.24696E+13   1.18252E-03
     5        1.71636E+13   1.98568E-03
     6        2.04835E+12   5.40033E-04
     7        7.51589E+11   4.86030E-04
     8        9.81504E+10   1.38008E-04
                            -----------
       TOTAL D.N.P. YIELD:  6.00037E-03
```

3.9.3 Point Reactor Kinetics for Circulating Fuel

Verification of the point reactor kinetics model for circulating fuel is performed as follows:

- For a non-flow situation the solution of the circulating fuel is compared to the results of the standard point kinetics model, as well as analytical solutions, if available. It is checked that the same results are obtained.
- For a flow situation, no direct comparison is possible, as there is no similar tool available and it is not possible to obtain analytical solutions even for a simplified case. For such cases only qualitative verification is possible.
- For one case a verification of the isotope transport is performed by comparing SPECTRA results with results obtained with a CFD code: FLUENT 15. The isotope source, obtained from the SPECTRA point kinetics, is provided to FLUENT as an external source. Concentrations of isotopes in several selected positions are compared.

The non-flow simple cases and the comparison with analytical solutions are described in sections 3.9.3.1, 3.9.3.2, 3.9.3.3, 3.9.3.6, 3.9.3.8, and 3.9.3.9. Results of the flow tests are discussed in sections 3.9.3.4, 3.9.3.5, and 3.9.3.7. Comparison with CFD is shown in section 3.9.3.10. Section 3.9.3.11 shows power behavior during fuel dump. Section 3.9.3.12 provides a discussion about alternative ways of modeling fission products in circulating fuel. Section 3.9.3.13 provides a discussion on defining reactor volume. Finally, section 3.9.3.16 shows a summary of all verification tests performed for the circulating fuel model.

3.9.3.1 Step Change of Reactivity - Non-flow Case

As a first test a simple case was selected, with only one group of delayed neutron precursors. A liquid core with no flow is defined. Results are compared to the standard point kinetics, discussed in section 3.9.1.1, as well as a theoretical solution.

A step reactivity change is considered; both positive and negative reactivities are analyzed. An analytical solution of such case may be found in many handbooks of reactor theory, for example [57], [58]. Suppose a reactor is initially at steady state condition (reactivity equal to zero), at power P_0. At t=0 the reactivity is changed suddenly to a value of ρ. If only one group of delayed neutron precursor is taken into account, then the point kinetics equations can easily be solved analytically. The reactor power at time t, $P(t)$, is given by (see [57], equation 6-40, [58], equation 7.5.11):

$$P(t) = P_0 \cdot \left[\frac{\beta}{\beta - \rho} \cdot \exp\left(\frac{\lambda \rho}{\beta - \rho} t \right) - \frac{\rho}{\beta - \rho} \cdot \exp\left(- \frac{\beta - \rho}{\Lambda} t \right) \right]$$

P power, (W)
t time, (s)
P_0 initial power, (W)
ρ reactivity, (-)
β delayed neutron yield fraction, (-)
λ decay constant of delayed neutron precursor, (1/s)
Λ prompt neutron generation time, (s)

In SPECTRA reactivity is expressed in dollars. The relation between the reactivity in dollars (R), and the dimensionless reactivity (ρ) is: $R\ (\$) = \rho / \beta$. Taking that into account, the above equation may be written as:

$$P(t) = P_0 \cdot \left[\frac{1}{1-R} \cdot \exp\left(\frac{\lambda R}{1-R} t \right) - \frac{R}{1-R} \cdot \exp\left(-\frac{\beta(1-R)}{\Lambda} t \right) \right]$$

The following data were assumed for calculations: P_0 = 1000 W, β = 0.0075, λ = 0.08 s^{-1}, Λ = 0.001 s. Two cases are considered, with a step change of reactivity at t=0, equal to:

- $\Delta\rho$ = +0.0025 ΔR = +1/3 \$
- $\Delta\rho$ = –0.0025 ΔR = –1/3 \$

A circulating fuel kinetics model is used with no flow. Calculations were performed for times from 0.0 s to 20 s. Results are compared to the standard point kinetics, discussed in section 3.9.2.1, as well as the analytical solution.

SPECTRA input decks for these calculations are provided in:

- `\Z-INPUTS\RK\STEP\CIR\STEP-1.SPE` - positive reactivity change, ΔR = +1/3 \$
- `\Z-INPUTS\RK\STEP\CIR\STEP-2.SPE` - positive reactivity change, ΔR = –1/3 \$

The results of the standard point kinetics, and the circulating fuel model calculations and those obtained from the theoretical formulae shown above, are shown in Figure 3-407. As expected, the results of the circulating fuel model are identical to the results of the standard point kinetics. The SPECTRA results are in agreement with the theoretical solution.

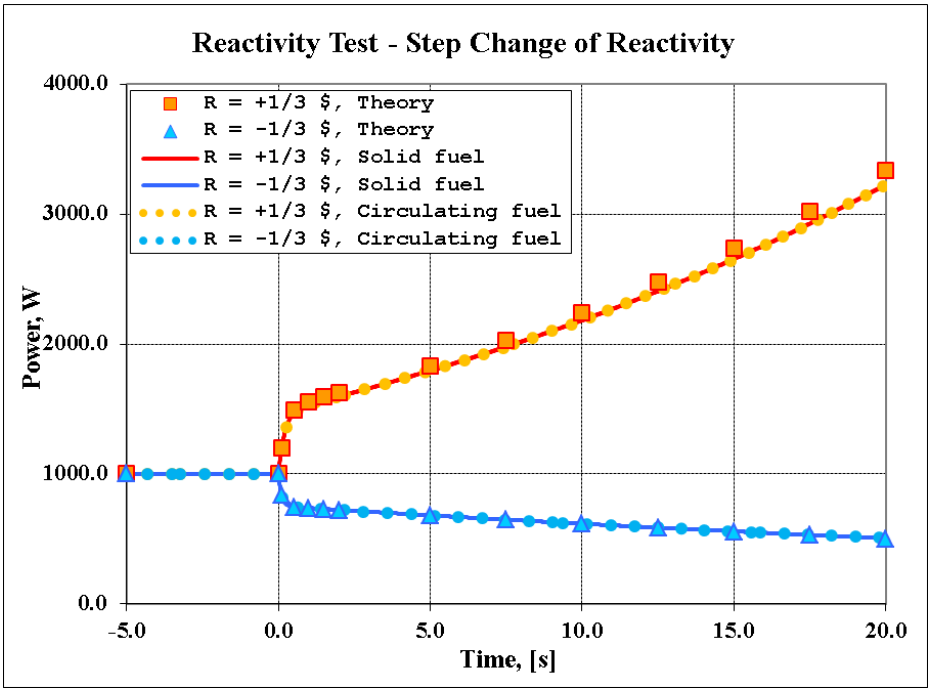

Figure 3-407 Reactor power, test cases STEP-1 and STEP-2

3.9.3.2 Reactor Start-up with a Neutron Source - Non-flow Case

The test case presented in this section is a start-up test of a reactor using an external neutron source. The source strength is assumed to be 10^{11} neutrons per second. The reactivity is increased in steps, first to –0.2 $ at 10.0 s, next to –0.1 $ at 2000 s, and finally to –0.05 $, at 3000 s. The reactivity history is shown in Figure 3-408. The neutron density is measured when stable values are reached.

SPECTRA input deck for the present calculation is provided in:
`\Z-INPUTS\RK\START-UP\CIR\START-UP-CIR.SPE`
The comparison input, containing standard reactor kinetics model is provided in:
`\Z-INPUTS\RK\START-UP\START-UP.SPE`

A liquid core with no flow is defined. Results are compared to the standard point kinetics, discussed in section 3.9.1.2, as well as a theoretical solution. Results are shown in Figure 3-409. As expected, the results obtained with the kinetics model for the circulating fuel are identical to those obtained with the standard point kinetics model.

As verification, the stable values of the reactor power, neutron flux, and precursor concentrations are calculated by hand from the point kinetics equations, which are (see Volume 1):

$$\frac{dn(t)}{dt} = \frac{\rho(t)-\beta}{\Lambda} n(t) + \sum_i \lambda_i C_i(t) + S_V(t)$$
$$\frac{dC_i(t)}{dt} = \frac{\beta_i}{\Lambda} n(t) - \lambda_i C_i(t)$$

where S_V is the external source of neutrons per cubic volume (1/m^3-s), other symbols are explained in detail in Volume 1. If the source is constant ($S_V(t) = S_V$ = const.), the stable conditions can be calculated by setting the derivatives to zero. Therefore:

$$0 = \frac{\rho(t)-\beta}{\Lambda} n_\infty + \sum_i \lambda_i C_{i,\infty} + S_V$$
$$0 = \frac{\beta_i}{\Lambda} n_\infty - \lambda_i C_{i,\infty}$$

The stable values of neutron and precursor concentrations were assigned an infinity subscript in the above equations. The above system can be easily solved by summing the equations for all precursors and then substituting into the equation for neutron concentration. The final values are:

$$n_\infty = -\frac{S_V \cdot \Lambda}{\beta \cdot R} = \frac{S_V \cdot \Lambda}{\beta \cdot |R|}$$
$$C_{i,\infty} = \frac{\beta_i}{\lambda_i \cdot \Lambda} n_\infty$$

The neutron concentration, and therefore the reactor fission power, is proportional to the neutron source strength and to the inverse of reactivity. The reactivity of course must be negative (R<0.0), otherwise no stable solution is possible.

In the example problem presented here the default model parameters were used, this means (see Volume 2): $\Lambda = 7\times10^{-5}$ s, $\beta = 6.5\times10^{-3}$. The volumetric source is equal to: $S_V = S/V = 10^{11}/5.0 = 2.0\times10^{10}$. The theoretical values of the stable neutron concentrations are therefore equal to:

- at $|R|$ = –0.20 \$: $n_\infty = 2.0\times10^{10} \times 7.0\times10^{-5} / 6.5\times10^{-3} / 0.20 = 1.077\times10^{9}$
- at $|R|$ = –0.10 \$: $n_\infty = 2.0\times10^{10} \times 7.0\times10^{-5} / 6.5\times10^{-3} / 0.10 = 2.154\times10^{9}$
- at $|R|$ = –0.05 \$: $n_\infty = 2.0\times10^{10} \times 7.0\times10^{-5} / 6.5\times10^{-3} / 0.05 = 4.308\times10^{9}$

The results are compared with the results of the theoretical solution in Table 3-53. The calculated values agree very well with the analytical solution.

Table 3-53 Results of the start-up test and comparison with theoretical solution

Time, (s)	Reactivity (\$)	Stable neutron concentration, n_∞		
		Circulating fuel model	Standard point kinetics model	Theoretical solution
1990	–0.20	1.077×10^{9}	1.077×10^{9}	1.077×10^{9}
2990	–0.10	2.151×10^{9}	2.151×10^{9}	2.154×10^{9}
9990	–0.05	4.308×10^{9}	4.307×10^{9}	4.308×10^{9}

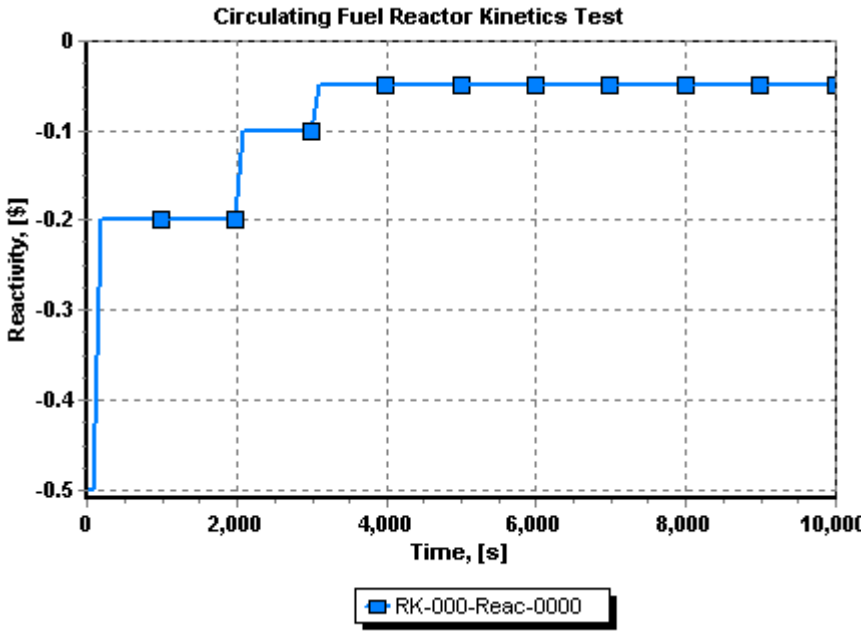

Figure 3-408 Reactivity, Test START-UP

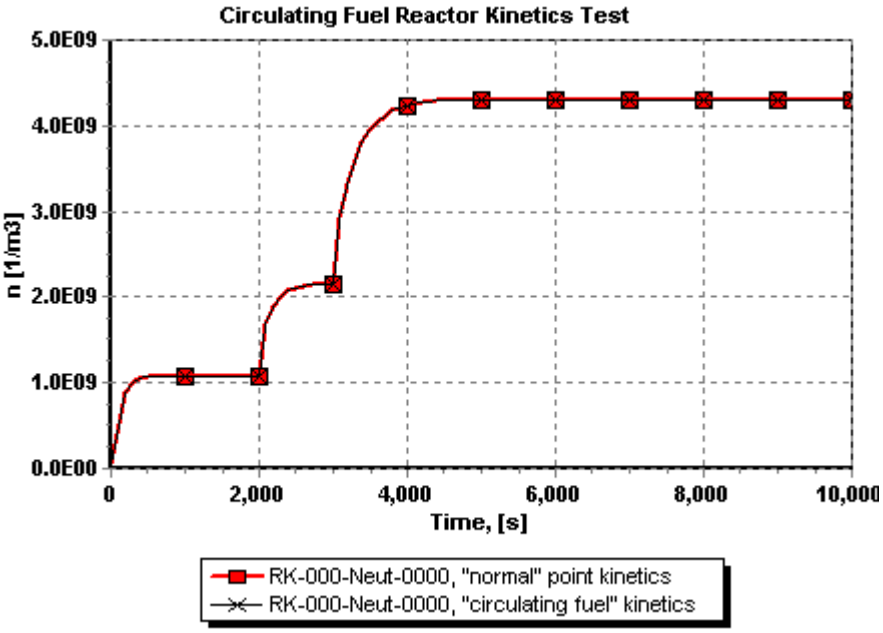

Figure 3-409 Neutron concentrations, Test START-UP

3.9.3.3 Doppler Reactivity Feedback, Non-flow Case

The test presented in this section investigates reactivity feedback from fuel temperature (Doppler effect). A simple model was set up. The reactor volume is represented by a single Control Volume (Figure 3-410). The initial power is 1.0 kW, the initial reactivity is 0.0. Reactivity is increased using control rods at three time points, t=0.0 s, t=100 s, and t=200 s. At each of these points the reactivity is increased by 0.05 $ over the time period of 0.1 s. The reactivity feedback table is assumed as follows:

T_{fuel} = 800.0 K R = 3.0 $
T_{fuel} = 1300.0 K R = 0.0 $

The temperature feedback coefficient is $(\partial R/\partial T) = -3/500 = -0.006$ $/K. The fluid is assumed to be molten salt FLiBe. The initial temperature is assumed as 800 K. The liquid volume is constant and equal to 1.0 m^3. Fuel temperature is defined as the liquid (pool) temperature in CV-001, with weighting factor of 1.0. There is no flow considered for this test.

SPECTRA input is provided in:
`\Z-INPUTS\RK\TDOPP\CIR-NonFlow\TDOPP-CIR.SPE`.
The comparison input, containing standard reactor kinetics model is provided in
`\Z-INPUTS\RK\TDOPP\CIR-NonFlow\TDOPP.INP`.

The results of standard point kinetics and circulating fuel kinetics model are compared in Figure 3-412, Figure 3-413, and Figure 3-414. When a positive reactivity is inserted, the neutron density increases from the initial 2.53×10^{9} ($1/m^3$) (corresponding power 1.0 kW - Figure 3-410) to 1.02×10^{13} ($1/m^3$) (corresponding power 4074.3 kW - Figure 3-411) at 675 s.

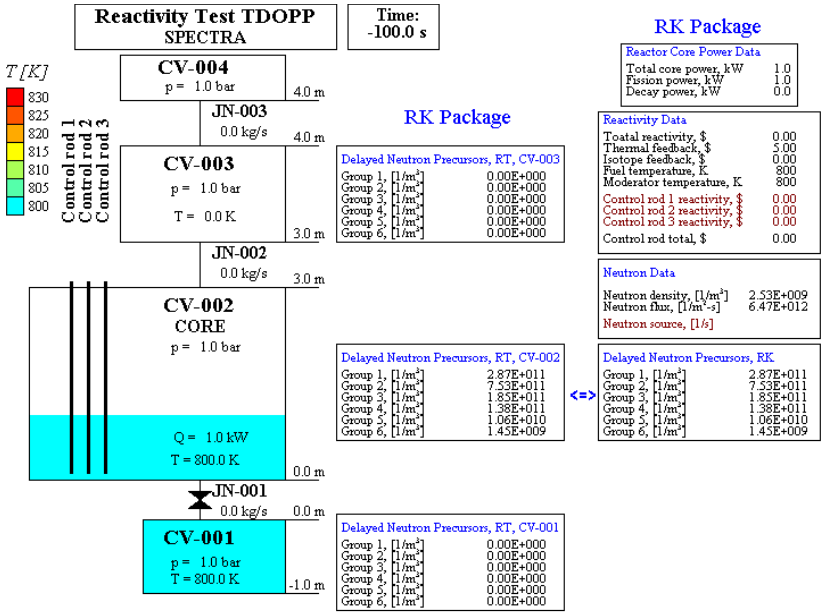

Figure 3-410 Test TDOPP\Cir-NonFlow - initial state

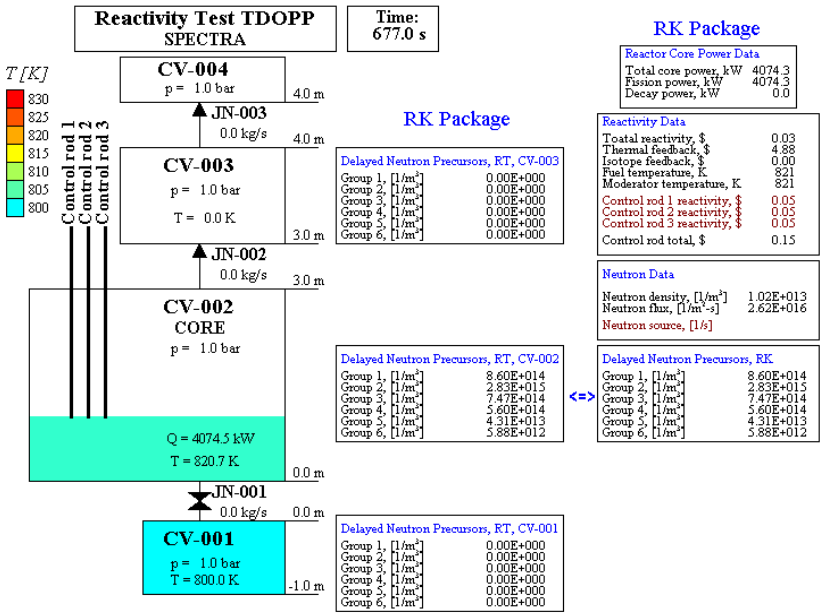

Figure 3-411 Test TDOPP\Cir-NonFlow, t = 675 s (maximum neutron concentration).

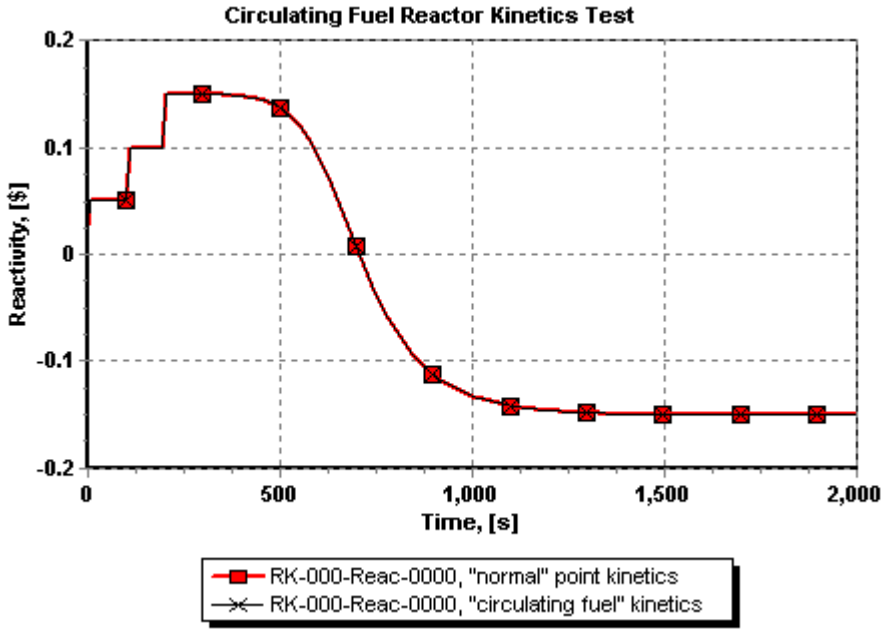

Figure 3-412 Reactivity, test TDOPP\Cir-NonFlow

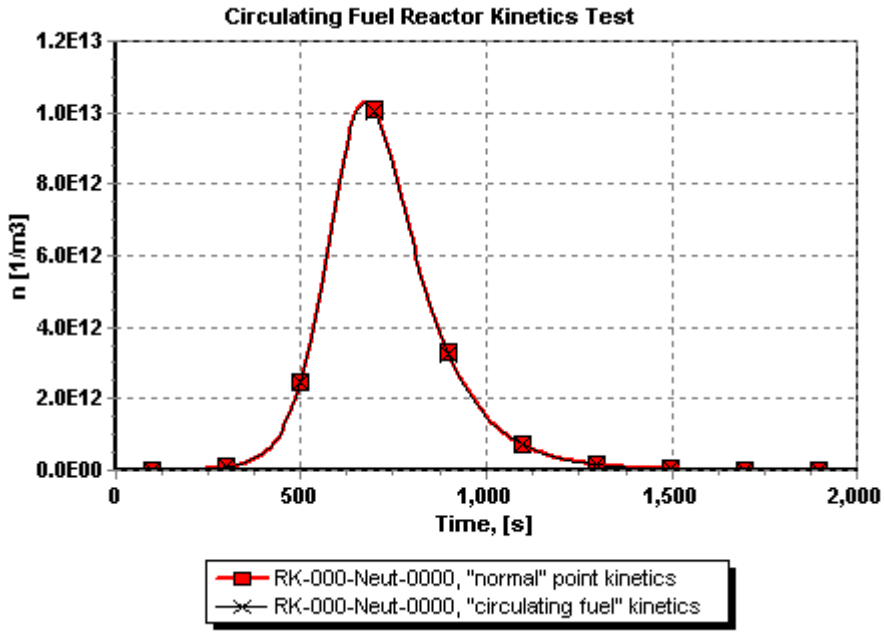

Figure 3-413 Neutron density, test TDOPP\Cir-NonFlow

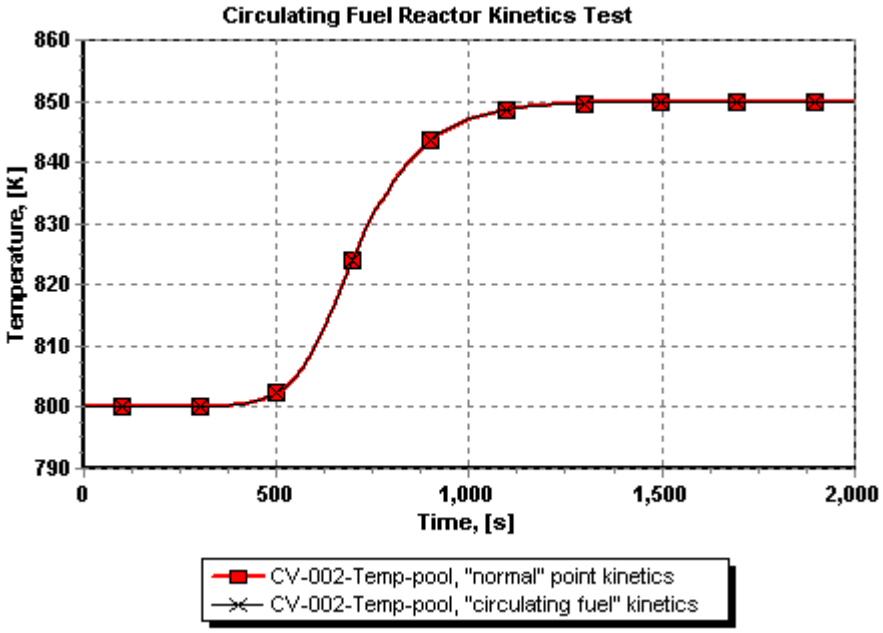

Figure 3-414 Fuel temperature, test TDOPP\Cir-NonFlow

As a result of the large power the fuel temperature increases. A significant increase of the fuel temperature is observed from about 400 s (Figure 3-414). The increase of the fuel temperature causes a decrease of reactivity (Figure 3-412). At 675 s the reactivity becomes negative and the reactor power starts to decrease.

Figure 3-412, Figure 3-413, and Figure 3-414 show very good agreement between the standard point kinetics and the circulating fuel kinetics. Figure 3-410 and Figure 3-411 shows exact correspondence between the concentrations in the Reactor Kinetics Package (RK) and the concentrations in CV-002, according to the RT Package.

During the transient the temperature increases by 50 K - Figure 3-414, while the reactivity decreases by 0.30 $ - Figure 3-412. This result can be verified by a hand calculation. The thermal feedback coefficient is equal to: $(\partial R/\partial T) = -0.06$ \$/K. The temperature corresponding to the reactivity change is:

$$\Delta T = \frac{\Delta R}{|\partial R / \partial T|} = \frac{0.3}{0.006} = 50$$

3.9.3.4 Doppler Reactivity Feedback, Flow Case

For the present test, a very similar model is used as in the previous test. The difference is that in the present test a flow of liquid is forced through the core. A constant mass flow of 100 kg/s is used. Again, the solution obtained with the circulating fuel model is compared to the standard point kinetics model. However, in this case the circulating fuel solution cannot be the same as the result of the standard point kinetics. SPECTRA input is provided in:
`\Z-INPUTS\RK\TDOPP\CIR-Flow\TDOPP-CIR.SPE`.
The comparison input, containing standard reactor kinetics model is provided in
`\Z-INPUTS\RK\TDOPP\CIR-Flow\TDOPP.INP`.

Calculations are performed until steady state conditions are reached. Results are shown in Figure 3-415, Figure 3-416, Figure 3-417, Figure 3-418, and Figure 3-419. In case of the standard point kinetics, the reactivity at the stationary state is zero (Figure 3-415) and the temperature is 25 K higher than the inlet temperature (Figure 3-417), which follows from:

$$\Delta T = \frac{\Delta R}{\left|\partial R / \partial T\right|} = \frac{0.15}{0.006} = 25$$

In case of circulating fuel, the stable reactivity is positive: ~0.06 $ (Figure 3-415, Figure 3-418). This is caused by the removal of the delayed neutron precursors (DNP) from the core volume (CV-002). The removed DNPs are seen in CV-003 (Figure 3-418). At the same time there are no DNPs in the inlet fluid (Figure 3-418), therefore there is a net loss of the neutron source from the DNPs. Due to loss of the DNPs, the stable values of neutron concentration (Figure 3-416) and temperature (Figure 3-417) are lower than in the standard point kinetics.

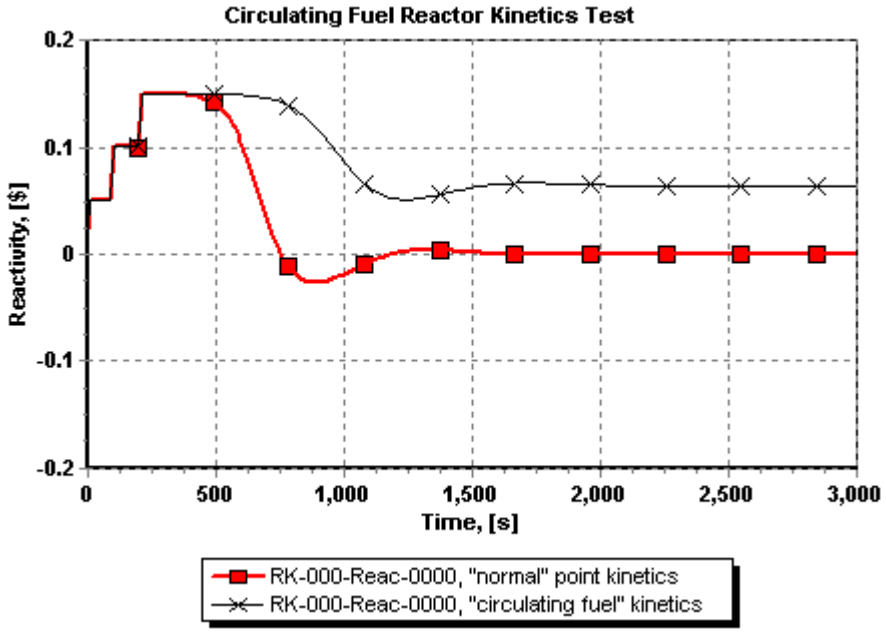

Figure 3-415 Reactivity, test TDOPP\Cir-Flow

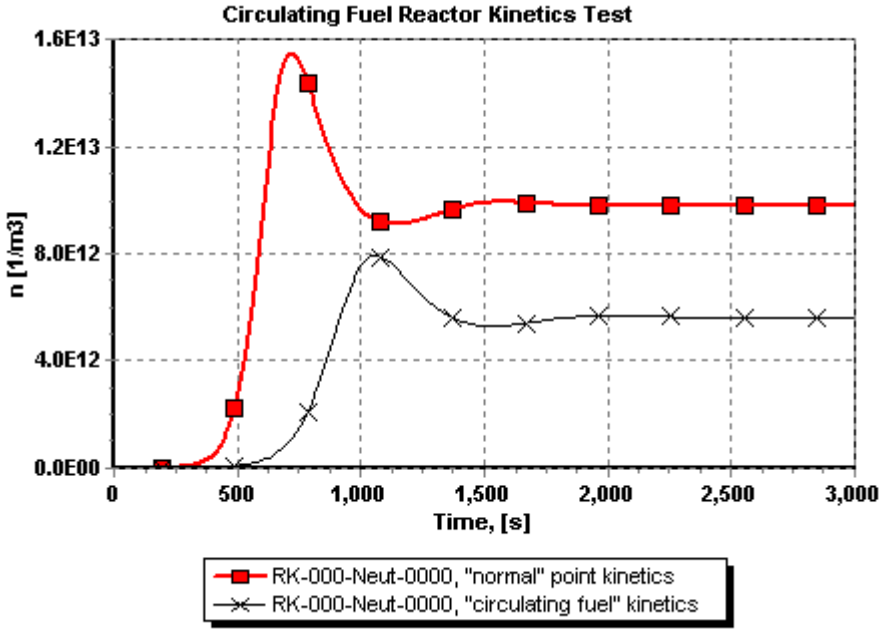

Figure 3-416 Neutron density, test TDOPP\Cir-Flow

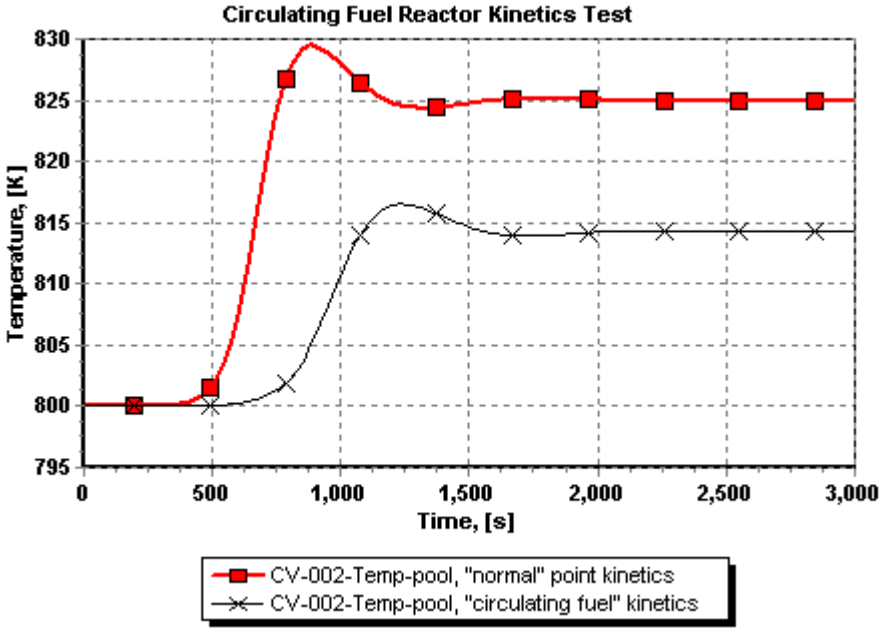

Figure 3-417 Fuel temperature, test TDOPP\Cir-Flow

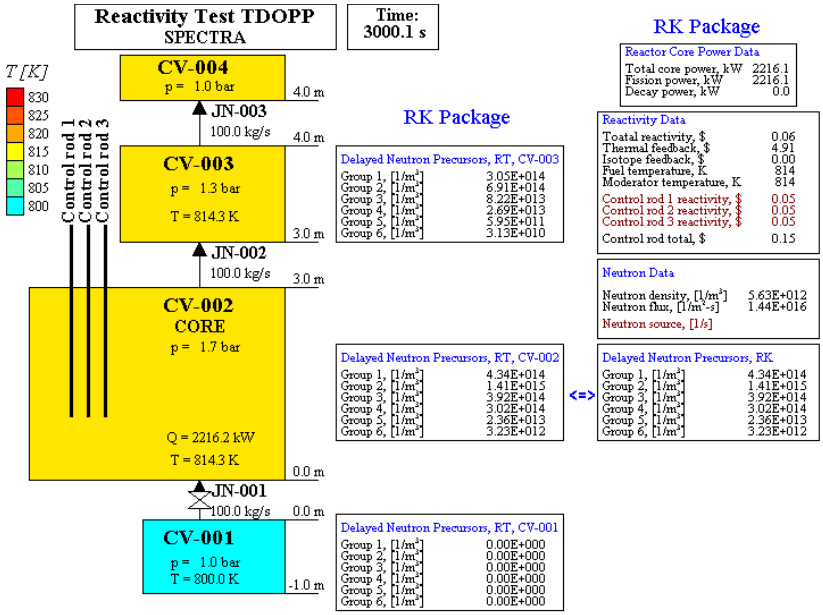

Figure 3-418 Test TDOPP\Cir-Flow, circulating fuel, final state

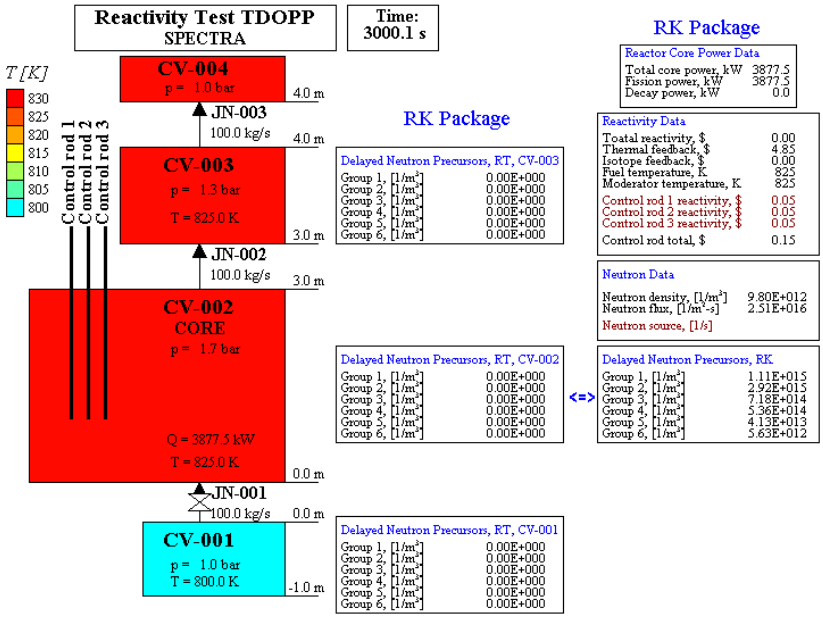

Figure 3-419 Test TDOPP\Cir-Flow, standard point kinetics, final state

Concentration of the DNP group 1 in CV-003 is similar as in CV-002 (Figure 3-418). This group decays slowly ($T_{1/2}$= 55.9 s). Group 6 on the other hand is decaying fast ($T_{1/2}$= 0.23 s), therefore the concentration that is seen in CV-003 is much lower.

3.9.3.5 Multiple-CV Core Tests

This section presents test cases performed using a core composed of multiple Control Volumes. The salt is assumed to be FliBe. Four cases are considered:

- Only Delayed Neutron Precursor (DNP) isotopes - non-flow case
- Only Delayed Neutron Precursor (DNP) isotopes - flow case
- All Isotope Transformation (IT) model isotopes - non-flow case
- All Isotope Transformation (IT) model isotopes - flow case

A reactivity insertion is considered. A total of 0.15 $ reactivity is inserted into the core during 200 seconds, in three steps: at t=0.0 s, t=100.0 s, and t=200.0 s. Each time the reactivity is increased by 0.05 $. The transient is the same as analyzed in sections 3.9.3.3, 3.9.3.4. The difference is a multiple-CV core model and non-uniform power profile in the present case.

Only DNP Isotopes - Non-Flow Case

In this case only the delayed neutron precursors (DNP) are considered. The Isotope Transformation model (IT) is not used. The fluid is stagnant. The input deck is located in:
`\Z-INPUTS\RT\Cir-fuel\Multiple\Multiple-NonFlow\`
The cases considered include:

- Standard point kinetics (input file MULTIPLE.SPE)
- Circulating fuel, (input file MULTIPLE-CIR.SPE)

Results are shown in Figure 3-420 and Figure 3-421. As expected for this non-flow case, the results obtained with the circulating fuel kinetics are identical to the results obtained with the standard point kinetics model. This verifies the circulating model results for this test.

Only DNP Isotopes - Flow Case

In this case only the delayed neutron precursors (DNP) are considered. The Isotope Transformation model (IT) is not used. The fluid mass flow is 10 kg/s (corresponding velocity in the core region is about 0.003 m/s). The input deck is located in:
`\Z-INPUTS\RT\Cir-fuel\Multiple\Multiple-Flow\`
The cases considered include:

- Standard point kinetics (input file MULTIPLE.SPE)
- Circulating fuel, (input file MULTIPLE-CIR.SPE)

Results are shown in Figure 3-422 and Figure 3-423. Qualitatively this case is similar to the case discussed in section 3.9.3.4, as can be seen comparing Figure 3-423 to Figure 3-416. The circulating fuel kinetics gives lower final power than the standard point kinetics model because of the drift of DNPs out of the core.

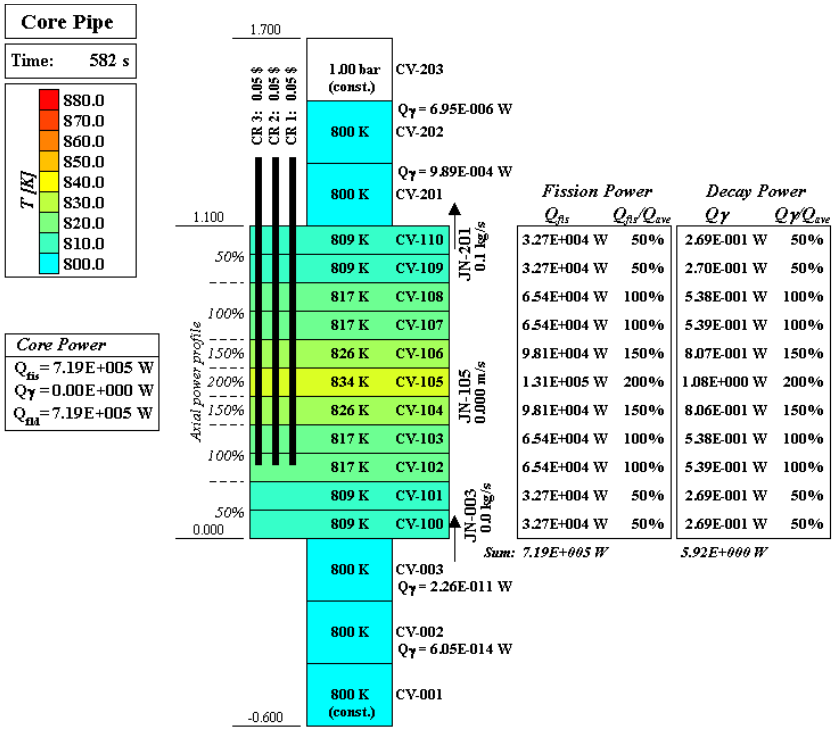

Figure 3-420 Test \Multiple-NonFlow\MULTIPLE-CIR, t=582 s (maximum core power)

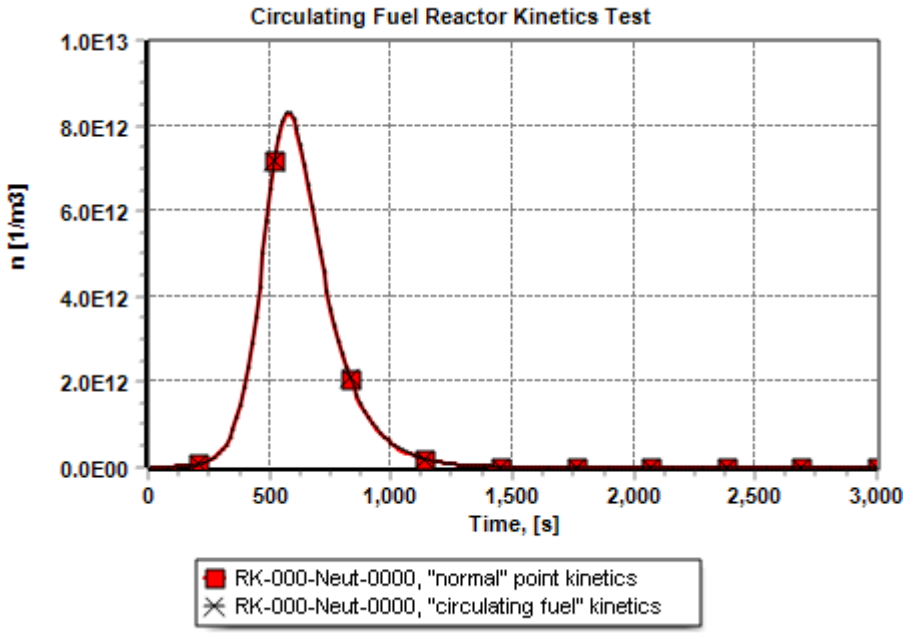

Figure 3-421 Neutron density, tests:
\Multiple-NonFlow\MULTIPLE and \Multiple-NonFlow\MULTIPLE-CIR

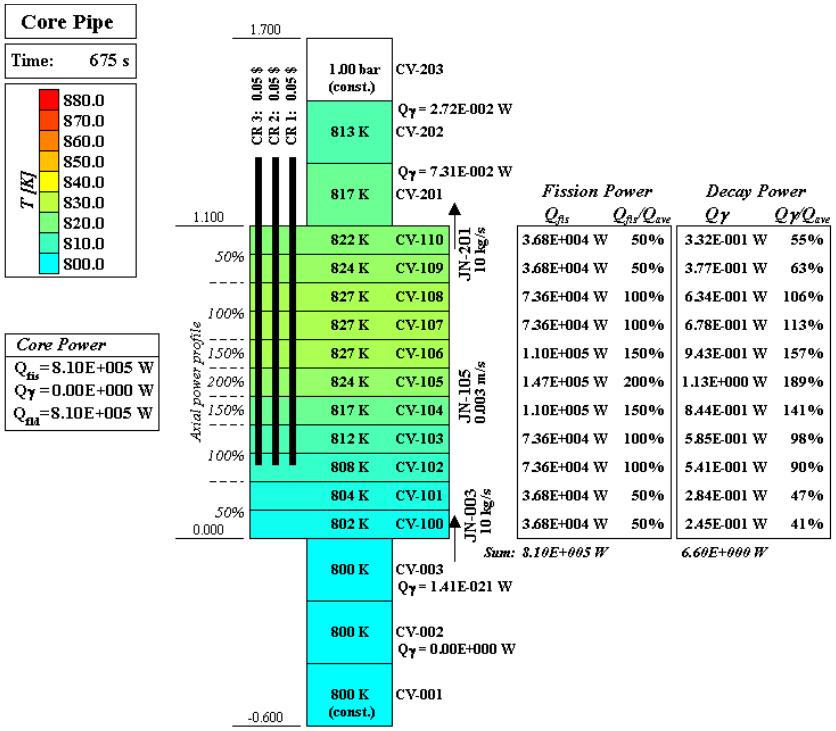

Figure 3-422 Test \Multiple-Flow\MULTIPLE-CIR, t=675 s (maximum core power)

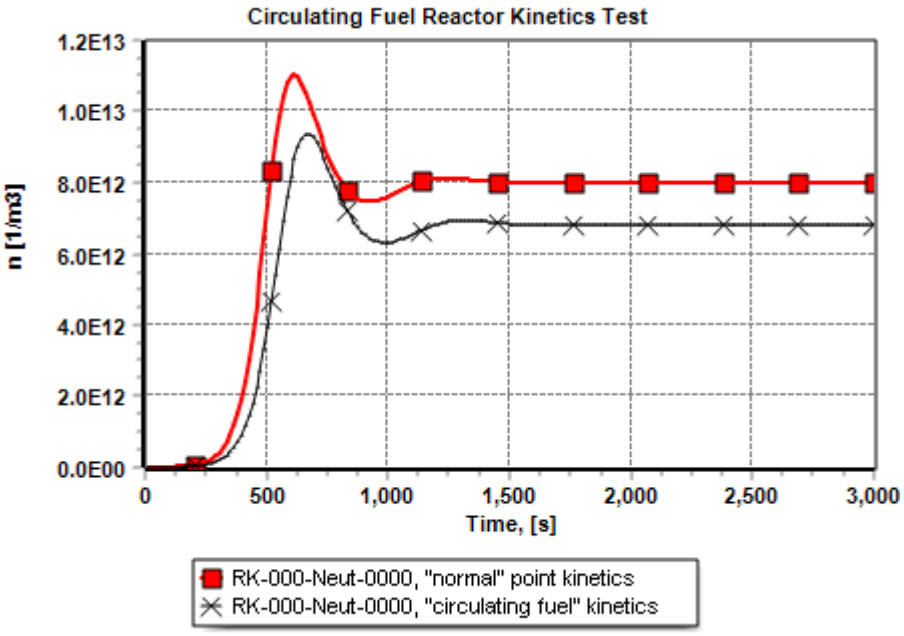

Figure 3-423 Neutron density, tests:
\Multiple-Flow\MULTIPLE and \Multiple-Flow\MULTIPLE-CIR

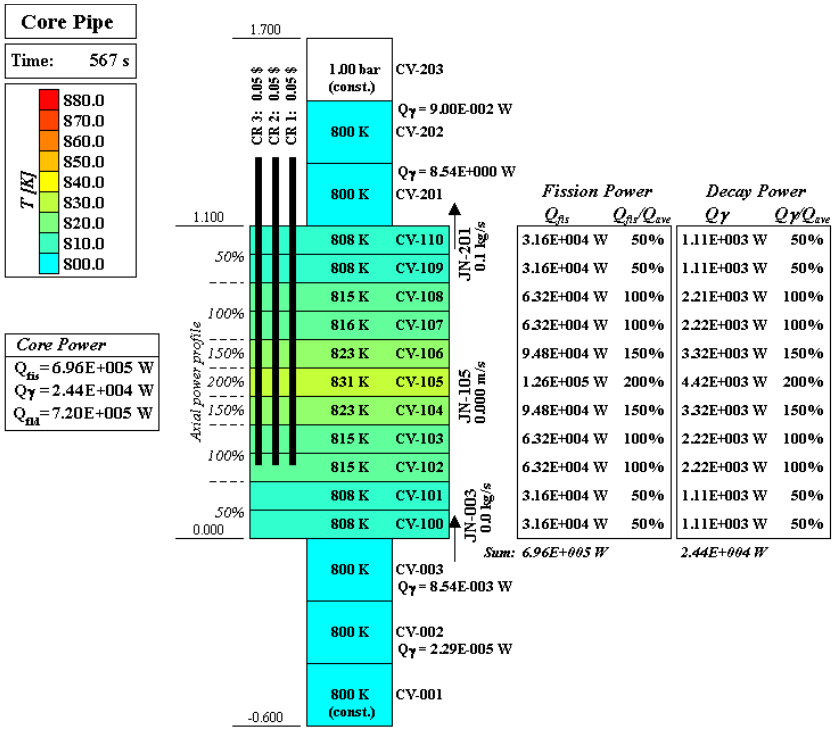

Figure 3-424 Test \Multiple-DH-NonFlow\MULTIPLE-CIR, t=567 s (maximum core power)

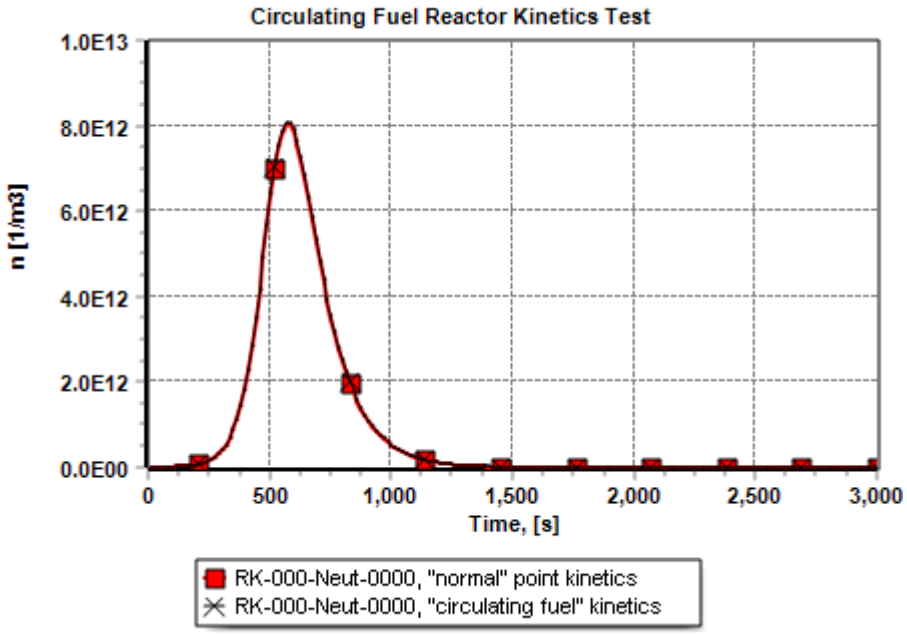

Figure 3-425 Neutron density, tests:
\Multiple-DH-NonFlow\MULTIPLE and \Multiple-DH-NonFlow\MULTIPLE-CIR

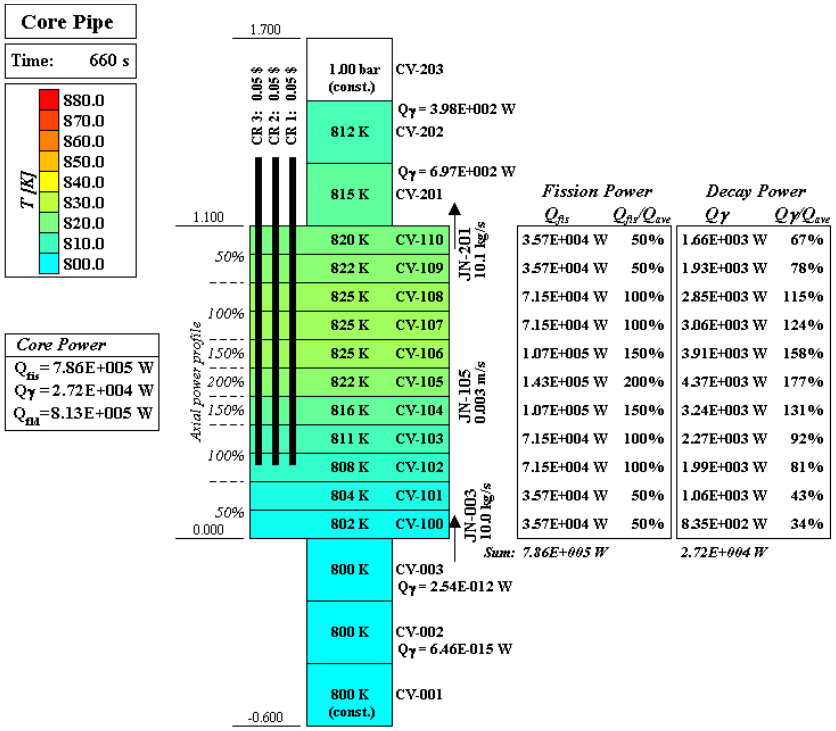

Figure 3-426 Test \Multiple-DH-Flow\MULTIPLE-CIR, t=660 s (maximum core power)

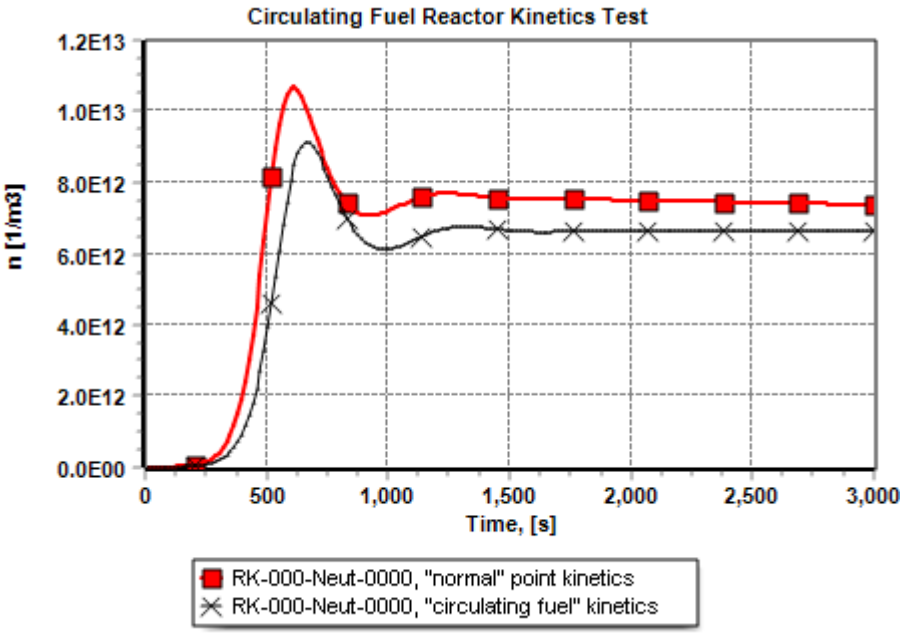

Figure 3-427 Neutron density, tests:
\Multiple-DH-Flow\MULTIPLE and \Multiple-DH-Flow\MULTIPLE-CIR

All IT Isotopes - Non-Flow Case

In this case not only the delayed neutron precursors (DNP) are considered, but all isotopes, as used by default by the Isotope Transformation (IT) model within the Reactor Kinetics Package. The fluid is stagnant. The input deck is located in:
`\Z-INPUTS\RT\Cir-fuel\Multiple\Multiple-DH-NonFlow\`
The cases considered include:

- Standard point kinetics (input file MULTIPLE.SPE)
- Circulating fuel, option IREIRK=2 (input file MULTIPLE-CIR.SPE)

For this run a non-default value of IREIRK was used. The reason is explained below (see "Effect of IREIRK). Results are shown in Figure 3-424 and Figure 3-425. As expected for this non-flow case, the results obtained with the circulating fuel kinetics are identical to the results obtained with the standard point kinetics model. This verifies the circulating model results for this test.

All IT Isotopes - Flow Case

In this case not only the delayed neutron precursors (DNP) are considered, but all isotopes, as used by default by the Isotope Transformation (IT) model within the Reactor Kinetics Package. The fluid mass flow is 10 kg/s (corresponding velocity in the core region is about 0.003 m/s). The input deck is located in:
`\Z-INPUTS\RT\Cir-fuel\Multiple\Multiple-DH-Flow\`
The cases considered include:

- Standard point kinetics (input file MULTIPLE.SPE)
- Circulating fuel, option IREIRK=2 (input file MULTIPLE-CIR.SPE)

For this run a non-default value of IREIRK was used. The reason is explained below (see "Effect of IREIRK). Results are shown in Figure 3-426 and Figure 3-427. Qualitatively this case is similar to the case discussed in section 3.9.3.4, as can be seen comparing Figure 3-427 to Figure 3-416. The circulating fuel kinetics gives lower final power because of the drift of DNPs out of the core.

Effect of IREIRK

For the cases with isotopes: Multiple-DH-NonFlow and Multiple-DH-Flow, a non-default value of IREIRK=2 was used. With this value the reactivity effect from isotopes is ignored. The results are more comparable to the stationary fuel solution. The results obtained with the default value of IREIRK=1, which means reactivity effect from isotope concentrations are taken into account, are compared to the cases with IREIRK=2 in Figure 3-428 and Figure 3-429. The neutron concentrations are clearly different.

In the case Multiple-DH-NonFlow the power peak is lower (Figure 3-428). This is mainly due to depletion of U-235, caused by sudden power peak. In the case Multiple-DH-NonFlow the power shape is quite different (Figure 3-429). Initially this is due to removal of the neutron poisons, mainly Sm-149.

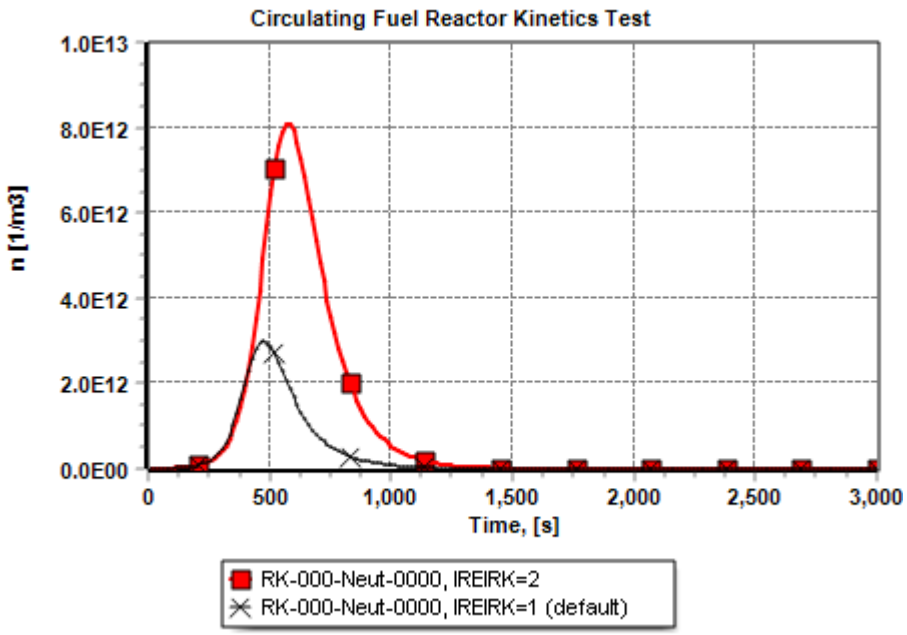

Figure 3-428 Neutron density, influence of IREIRK, tests:
\Multiple-DH-NonFlow\MULTIPLE-CIR and MULTIPLE-CIR-IREIRK-1

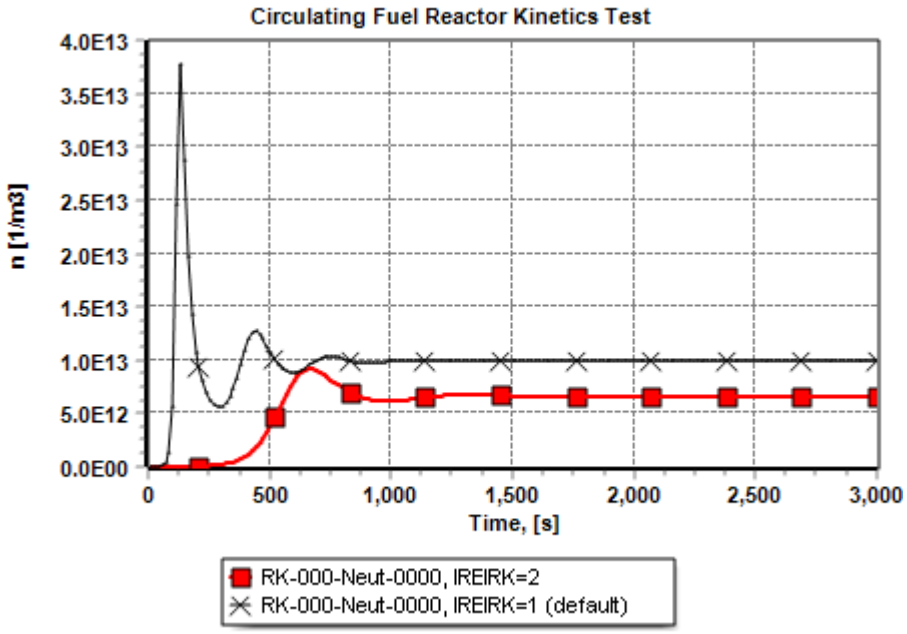

Figure 3-429 Neutron density, influence of IREIRK, tests:
\Multiple-DH-Flow\MULTIPLE-CIR and MULTIPLE-CIR-IREIRK-1

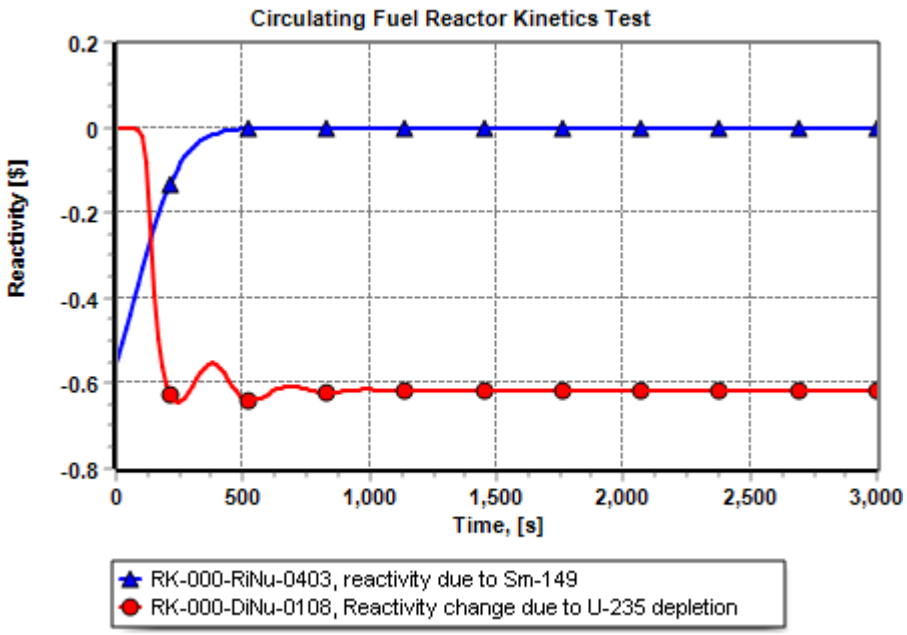

Figure 3-430 Reactivity due to Sm-149 and U-235 depletion, test: \Multiple-DH-Flow\MULTIPLE-CIR-IREIRK-1

The fission products are initially present only in the core (see discussion about the parameter IDSORK, below). When the flow is started, the Sm-149 is removed from the core and the corresponding reactivity effect is shown in the Figure 3-430 (there is a similar effect of Xe-135, but it is much smaller due to low initial Xe-135 at the low power). Depletion of U-235 plays role in the longer term. The reactivity effect from U-235 depletion is shown in Figure 3-430.

Effect of IDSORK

The initial distribution of isotopes, including delayed neutron precursors, is determined by the input parameter IDSORK. All tests described above were performed with default value of 3, which gives best approximation for an initially stagnant fuel. With this option:

- fuel isotopes have the same density in all Control Volumes of the primary system (user-defined CV group),
- fission products are initially distributed only in the core volumes, with density proportional to the fuel weighting factors.

For a sensitivity, all tests were done with IDSORK=2, which gives best approximation for an initially flowing fuel. With this option:

- all isotopes (fuel and fission products) have the same density in all Control Volumes of the primary system (user-defined CV group).

Input file for this test is MULTIPLE-CIR-IDSO. Practically no differences in the results were observed for the case MULTIPLE-CIR-IDSO and the case MULTIPLE-CIR. This is because the reactivity effect is not taken into account in both these runs, so any differences in the behavior of isotopes does not affect the main results, such as reactor power, temperatures, etc.

It is more interesting to study the effect of the parameter IDSORK on a case where the effect of isotopes on reactivity is taken into account, namely for IREIRK=1 (Figure 3-429 and Figure 3-430). For such comparison, the test MULTIPLE-CIR-IDSO-IREIRK-1 was set up, with:

- IREIRK = 1 (reactivity from isotope changes taken into account)
- IDSORK = 2

This case is again compared to the case MULTIPLE-CIR, where reactivity change from isotope concentration changes is not taken into account.

Results are shown in Figure 3-431 and Figure 3-432. In case of IDSORK = 2, the initial concentrations of all isotopes are the same in the entire loop. Therefore at time t = 0.0 s, when the flow starts, there is no "flushing" of poisons out of the core region, which was causing reactivity increase in the case with IDSORK = 3 (Figure 3-430). Consequently, there is no reactivity change from poisons (Figure 3-432). The main reactivity change is from the Uranium depletion, at the moment of a sudden power peak (~ 600 s. This negative reactivity feedback causes the power to be lower than in the case MULTIPLE-CIR (Figure 3-431).

It is important to notice that in the case MULTIPLE-CIR-IDSO-IREIRK-1 the power is lower than in the "no isotope feedback" case (Figure 3-431), while in the case MULTIPLE-CIR-IREIRK-1 the power is higher than in the "no isotope feedback" case (Figure 3-429). These examples illustrate the importance of proper selection of the initial conditions.

An important conclusion from the examples presented in this section is:

> ***For each individual case the user should pick most appropriate initial conditions option (IDSORK) and still perform steady state calculations, because neither option provides perfect initialization of all isotopes. Choice of a more appropriate option allows to reach steady state faster.***

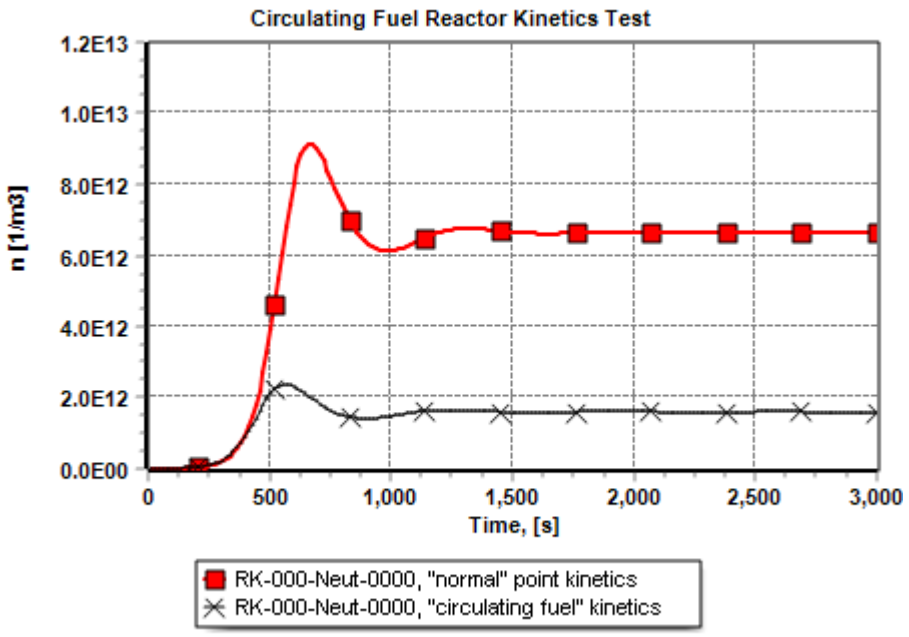

Figure 3-431 Neutron density, influence of IDSORK, tests:
\Multiple-DH-Flow\MULTIPLE-CIR and MULTIPLE-CIR-IDSO-IREIRK-1

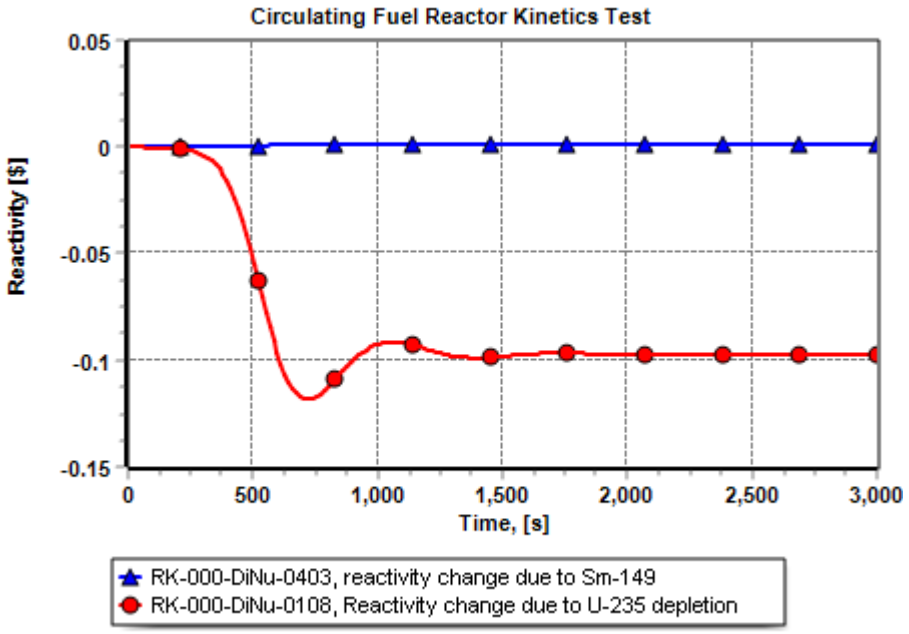

Figure 3-432 Reactivity due to Sm-149 and U-235 depletion, test:
\Multiple-DH-Flow\MULTIPLE-CIR-IDSO-IREIRK-1

3.9.3.6 Xenon Poisoning Test - Non-flow Case

A simple reactor shutdown test is considered to investigate the poisoning from Xe-135. The volume of reactor is assumed to be 5.0 m^3. The core consists of a single Control Volume and no flow is occurring. The reactor is assumed to be initially at 100 MW power (corresponding neutron density of $n = 2.53\times10^{14}$ ($1/m^3$)). At the start of the test ($t = 0.0$ s) a large negative reactivity is inserted, –9.99 $, to shutdown the reactor. The changes of concentrations of Xe-135 and the reactivity effect are investigated. All built-in chains, including the Xenon chain, are activated in the RK Package and mapped to the RT Package. The fuel is assumed to consist of U-235.

A circulating fuel kinetics model is used with no flow. Calculations were performed for times from 0.0 s to 200,000 s (55.5 hours). Results are compared to the standard point kinetics, discussed in section 3.9.2.1, as well as the analytical solution.

SPECTRA input deck for this test is provided in:
`\Z-INPUTS\RK\XE\CIR\XE-CIR.SPE`.
The comparison input, containing standard reactor kinetics model is provided in:
`\Z-INPUTS\RK\XE\CIR\XE.SPE`.

Results are shown in Figure 3-434, Figure 3-435, and Figure 3-436. As expected, the results of the circulating fuel model are identical to the results of the standard point kinetics. The SPECTRA results are in good agreement with the theoretical solution. The theoretical solution is obtained from (see [58] equation 6.3.15):

$$N_I(t) = N_I(\infty)\cdot\exp(-\lambda_I t)\frac{\gamma_{f,U\to I}\Sigma_f\Phi}{\lambda_I}$$

$$N_{Xe}(t) = N_{Xe}(\infty)\cdot\exp(-\lambda_{Xe}t) + N_I(\infty)\cdot\frac{\lambda_I}{\lambda_I+\lambda_{Xe}}\cdot\left[\exp(-\lambda_{Xe}t)-\exp(-\lambda_I t)\right]$$

$$N_I(\infty) = \frac{\gamma_{f,U\to I}\Sigma_f\Phi}{\lambda_I}$$

$$N_{Xe}(\infty) = \frac{\gamma_{f,U\to Xe}\Sigma_f\Phi}{\lambda_{Xe}+\sigma_{c,Xe}\Phi}$$

N_i concentration of isotope i, ($1/m^3$),
λ_i decay constant of isotope i, (1/s),
$\gamma_{f,j\to i}$ yield fraction of isotope i from fission of isotope j ,
Σ_f macroscopic fission cross section (1/m),
Φ neutron flux (one-group) ($1/m^2$-s),
$\sigma_{c,i}$ microscopic cross section for neutron capture of isotope i, (m^2),
t time, (s).

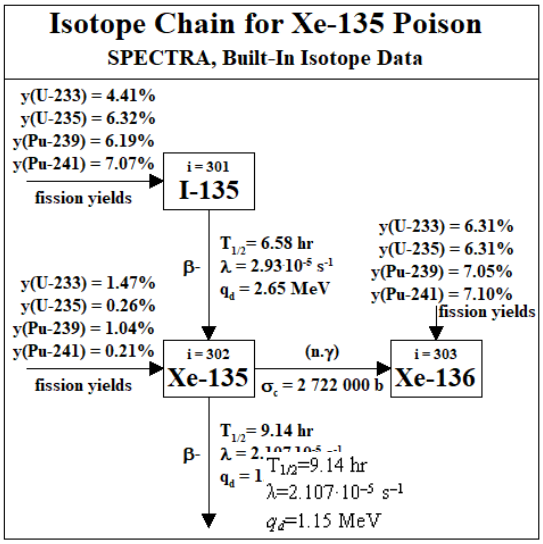

Figure 3-433 Xenon chain data (see Volume 1)

The decay constants, fission yield fractions, absorption cross sections, are shown in Figure 3-433. Using the above formulations, the concentrations of I-135 and Xe-135 were calculated by "hand" (Excel was used). The values obtained from the circulating fuel model and the standard point kinetics model agree very well with the "hand calculation", as seen in Figure 3-434.

The reactivity effect of Xenon is obtained from the following formula (see Volume 1):

$$R_{Xe} = -\frac{1}{\beta} \cdot \frac{1}{\nu P_{FNL} P_{TNL}} \cdot \frac{\sigma_{c,Xe}}{\Sigma_f} \cdot N_{Xe}$$

ν number of neutrons generated per fission, (-)
P_{FNL} fast non-leakage probability, (-)
P_{TNL} thermal non-leakage probability, (-)
$\sigma_{c,\,i}$ microscopic cross section for neutron capture for isotope i, (m^2)
N_i concentration of nuclides of isotope i, ($1/m^3$)
$\Sigma_{f,\,0}$ initial macroscopic fission cross section (1/m)

The following values were used in the present example:

- P_{FNL} = 0.97
- P_{TNL} = 0.99
- ν = 2.5

The Xenon reactivity was calculated by "hand" (Excel was used), using the above formula and the Xenon concentrations obtained from the theoretical solution, $N_{Xe}(t)$. The values obtained from the circulating fuel model and the standard point kinetics model agree very well with the "hand calculation", as seen in Figure 3-435. Figure 3-436 shows values of all parameters at the end of the calculations: t = 200,000 s. The figure is used to check the consistency between the RK and the RT Packages.

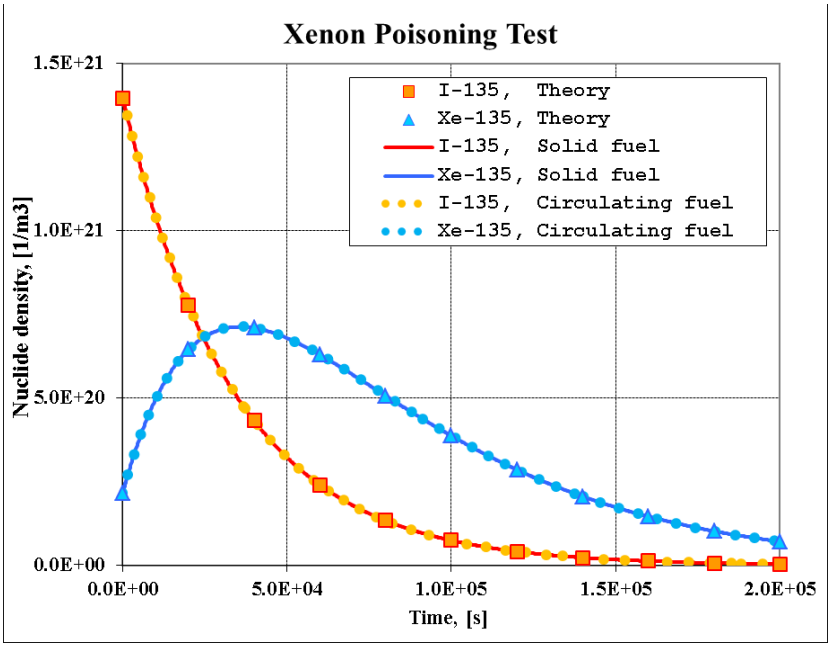

Figure 3-434 Nuclide density, Xenon poisoning test

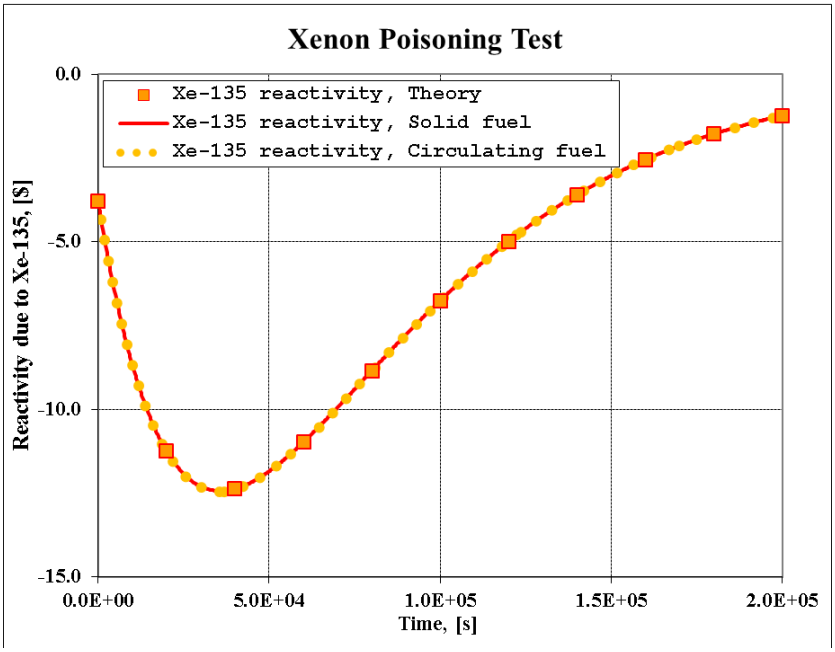

Figure 3-435 Reactivity change due to ^{135}Xe, Xenon poisoning test

Reactor Kinetics | Time: 200000.0 s 55.56 hr

=RK= Data		=RT= Data	
Neutron Data			
Neutron density, n, 1/m³	1.47E-002		
Neutron flux, Φ, 1/m²-s	3.75E+001		
Neutron source, S, 1/s			
Reactivity Data			
Toatal reactivity, $	-7.77E+000		
Control rod, $	-9.990		
Fuel+mod feedback, $	3.000		
Isotope feedback, $	40.907		
Volume change feedback, $	0.000		
Reactor Core Power Data, RK		**Reactor Core Power Data, RT**	
Fission power, W	5.80E-009		
Decay power, W	4.29E+005	Decay power, W	4.29E+005
Total core power, W	4.29E+005		
Core, RK		**Core, RT**	
Active core volume, m³	5.00E+000	Active core volume, m³	4.99E+000
Delayed Neutron Precursors - RK		**Delayed Neutron Precursors - RT**	
Group 1, [1/m³]	1.46E+001	Group 1, [1/m³]	1.46E+001
Group 2, [1/m³]	3.83E+001	Group 2, [1/m³]	3.83E+001
Group 3, [1/m³]	9.42E+000	Group 3, [1/m³]	9.42E+000
Group 4, [1/m³]	7.03E+000	Group 4, [1/m³]	7.03E+000
Group 5, [1/m³]	5.42E-001	Group 5, [1/m³]	5.42E-001
Group 6, [1/m³]	7.38E-002	Group 6, [1/m³]	7.38E-002

Decay Heat Isotope Data - RK

	N, [1/m³]	q, [W/m³]
Group 1	5.08E+000	3.45E-012
Group 2	4.30E+001	9.52E-012
Group 3	6.91E+002	1.79E-011
Group 4	9.36E+003	2.23E-011
Group 5	7.30E+004	1.33E-011
Group 6	5.18E+017	9.57E+000
Group 7	8.78E+021	1.80E+004
Group 8	1.43E+023	3.15E+004
Group 9	5.72E+023	2.29E+004
Group 10	1.02E+024	1.16E+004
Group 11	3.97E+024	1.16E+003

Decay Heat Isotope Data - RT

	N, [1/m³]	Q, [W]
Group 1	5.06E+000	1.72E-011
Group 2	4.30E+001	4.75E-011
Group 3	6.91E+002	8.93E-011
Group 4	9.36E+003	1.11E-010
Group 5	7.30E+004	6.63E-011
Group 6	5.18E+017	4.78E+001
Group 7	8.78E+021	8.99E+004
Group 8	1.43E+023	1.57E+005
Group 9	5.72E+023	1.14E+005
Group 10	1.02E+024	5.78E+004
Group 11	3.97E+024	5.78E+003

Poison Data - RK

	N, [1/m³]	R, [$]	ΔR, [$]
I-135	3.99E+018	0.00	0.00
Xe-135	7.11E+019	-1.24	2.54
Sm-149	2.66E+021	-1.05	-0.39

Poison Data - RT

	N, [1/m³]
I-135	3.99E+018
Xe-135	7.11E+019
Sm-149	2.66E+021

Fuel Data - RK

	N, [1/m³]	R, [$]	ΔR, [$]
U-233	0.00E+000	0.00	0.00
U-235	1.98E+025	78.90	0.10
U-238	9.72E+026	-35.69	-0.05
Pu-239	2.34E+017	0.00	0.00
Pu-241	0.00E+000	0.00	0.00

Fuel Data - RT

	N, [1/m³]
U-233	0.00E+000
U-235	1.98E+025
U-238	9.72E+026
Pu-239	2.34E+017
Pu-241	0.00E+000

Figure 3-436 Xenon poisoning test, values of all parameters at the end of the test (*t*=200,000 s)

3.9.3.7 Xenon Poisoning Test - Flow Case

In order to verify the flow of delayed neutron precursors, a simple loop is considered. The loop layout is shown in Figure 3-437. All the dimensions are shown in the picture. The fluid considered is the FLiBe salt based on ternary FLiBe salt properties in [134]. The Xe data was assumed the same as in the non-flow test, discussed in section 3.9.3.6. The reactor is assumed to be initially at 100 MW power (corresponding neutron density of $n = 2.53\times10^{14}$ (1/m^3)). At the start of the test ($t = 0.0$ s) a large negative reactivity was inserted, –9.99 $, to shutdown the reactor. The changes of concentrations of Xe-135 and the reactivity effect are investigated. All built-in chains, including the Xenon chain, are activated in the RK Package and mapped to the RT Package. The fuel is assumed to consist of U-235.

A circulating fuel kinetics model is used with a flow of 20 kg/s. Calculations were performed for times from -10.0 s to 200,000 s (55.5 hours). Results are compared to the standard point kinetics (non-flow case), discussed in section 3.9.3.6.

SPECTRA input deck for this test is provided in:
`\Z-INPUTS\RT\Cir-fuel\Loop\Xe\Xe-CIR.SPE`.
The comparison input, containing standard reactor kinetics model is provided in:
`\Z-INPUTS\RK\XE\CIR\XE.SPE`.

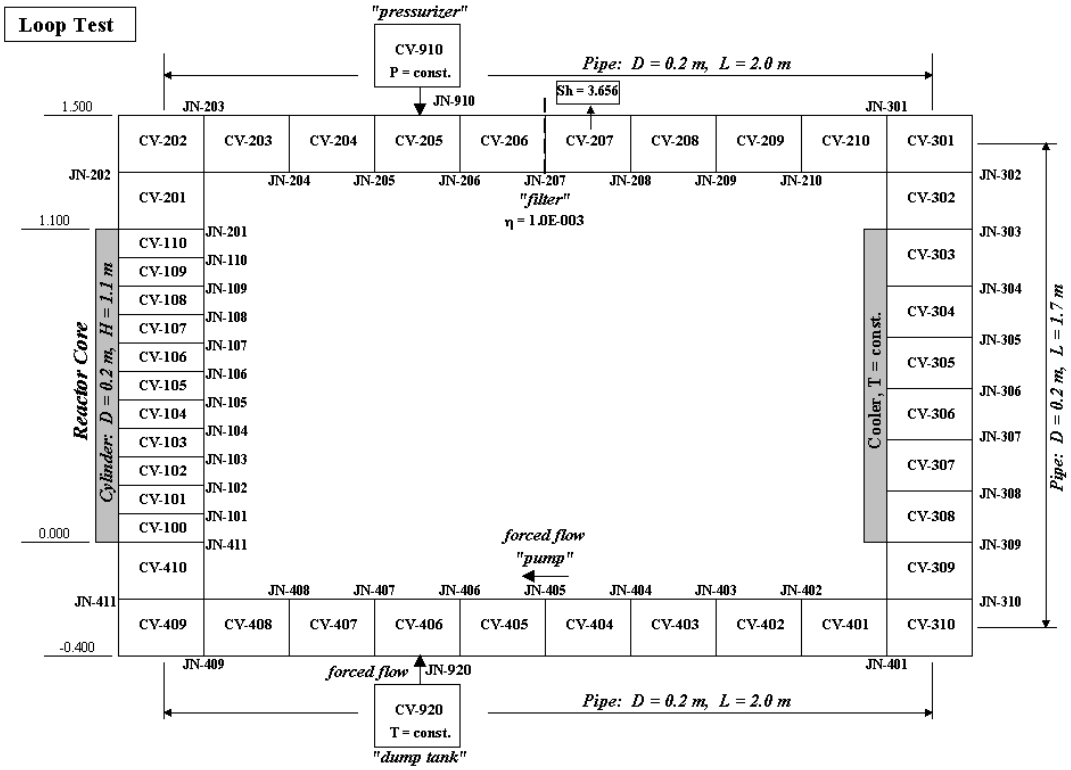

Figure 3-437 Xe poisoning test - loop layout and nodalization for SPECTRA

Circulating fuel versus solid fuel

Results are shown in Figure 3-438 and Figure 3-439. In case of circulating fuel concentrations of Iodine and Xenon are much smaller than in case of solid fuel. This is caused by larger volume where isotopes decay. In case of solid fuel the volume where isotopes decay is the same as the volume where they are being produced (core volume). In case of circulating fuel, the volume where isotopes decay is the whole loop. In the present case we have:

- Volume of the core: $V_{core} = 11 \times 0.1 \times \pi \times 0.2^2/4 = 11 \times 3.14\text{E-}3\ m^3 = 0.0345\ m^3$.
- Volume of the loop: $V_{loop} = 0.2198\ m^3$ (code output, CV group 1).

The volume ratio is 0.0345 / 0.2198 = 0.157. In case of solid fuel the initial (stationary state) concentrations are:

- I-135: 1.4E21 (Figure 3-438)
- Xe-135: 2.2E20 (Figure 3-438)

In case of circulating fuel the initial (stationary state) concentrations are:

- I-135: 2.2E20 (Figure 3-438)
- Xe-135: 1.4E19 (Figure 3-438)

In case of I-135, the concentration in circulating fuel is equal to the concentration in solid fuel multiplied by the volume ratio. 1.4E21 × 0.157 = 2.2E20. This is because I-135 is produced in core volumes (uniform power density assumed) and decays in the total loop volume. This simple hand calculation serves as a verification of the I-135 concentration in the circulating fuel.

In case of Xe-135, verification is not as easy. The solid concentration multiplied by the volume ratio is 2.2E20 × 0.157 = 3.4E19. The actual concentration is 1.4E20. Part of Xe-135 is produced by fission in the core, but majority is produced as a daughter product of I-135, i.e. in the entire loop (fission yield of Xe-135 is only 0.26%, while I-135 is 6.32% - Figure 3-433). Furthermore, Xe-135 removal is not only due to decay but also due to neutron absorption in the core. In the end it is not easy to verify the Xe-135 concentration. A "trick" here is to observe that if there was no Xe-135 decay, the Xe-135 removal was by the neutron capture only, the Xe-135 removal would occur in core volume only, V_{core} . The production on the other hand occurs in the entire loop, as it is due to I-135 decay (direct fission yield is small and can be neglected). In such case the production is governed by loop volume and removal by core volume, opposite as in the case of I-135.. Since the I-135 concentrations are decreased by the volume ratio, the Xe-135 concentrations should increase by the volume ratio, with the reference value of I-135, so in the end should become identical to the solid fuel value. This was verified in a separate run, where the decay constant for Xe-135 was set to zero (input file Xe-CIR-NoDecay). The Xe-135 concentration was in this case 2.4E20, very similar to the solid fuel value. The agreement is increased further by removing the direct fission yield (input file Xe-CIR-NoDecay-NoYield). In such case the calculated value of Xe-135 concentration is 2.3E20.

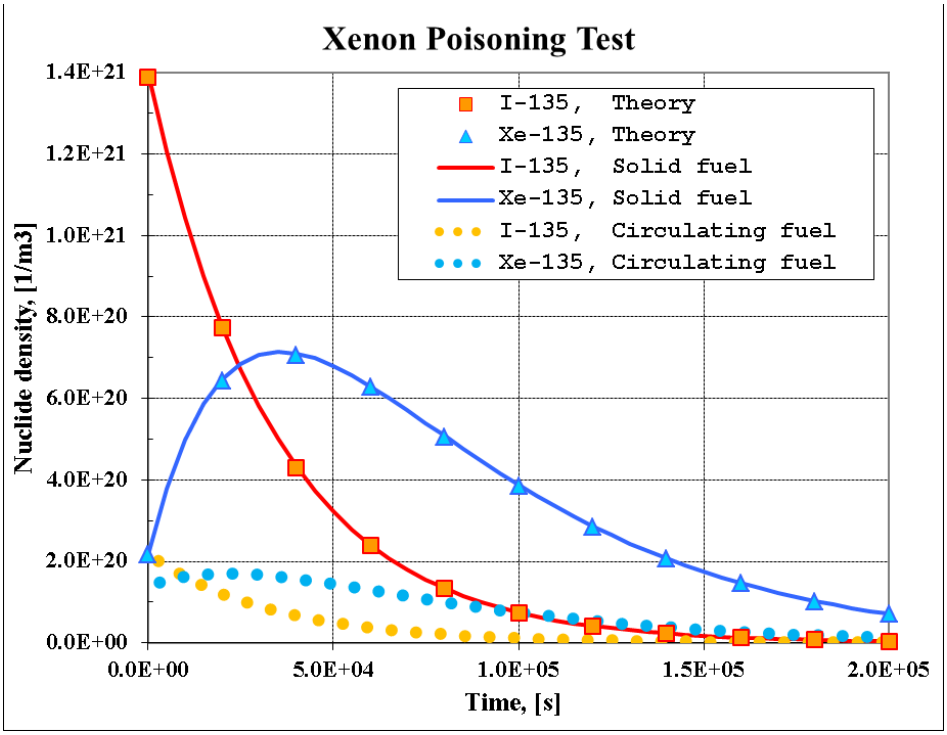

Figure 3-438 Xe-135 density, comparison of solid fuel and circulating fuel case

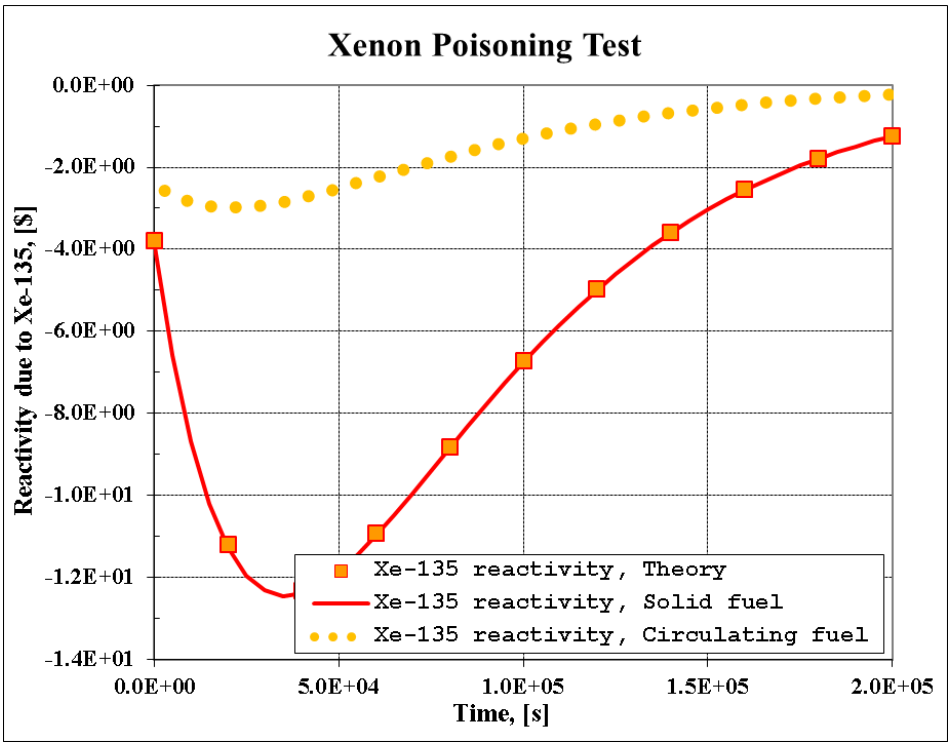

Figure 3-439 Xe-135 reactivity, comparison of solid fuel and circulating fuel case

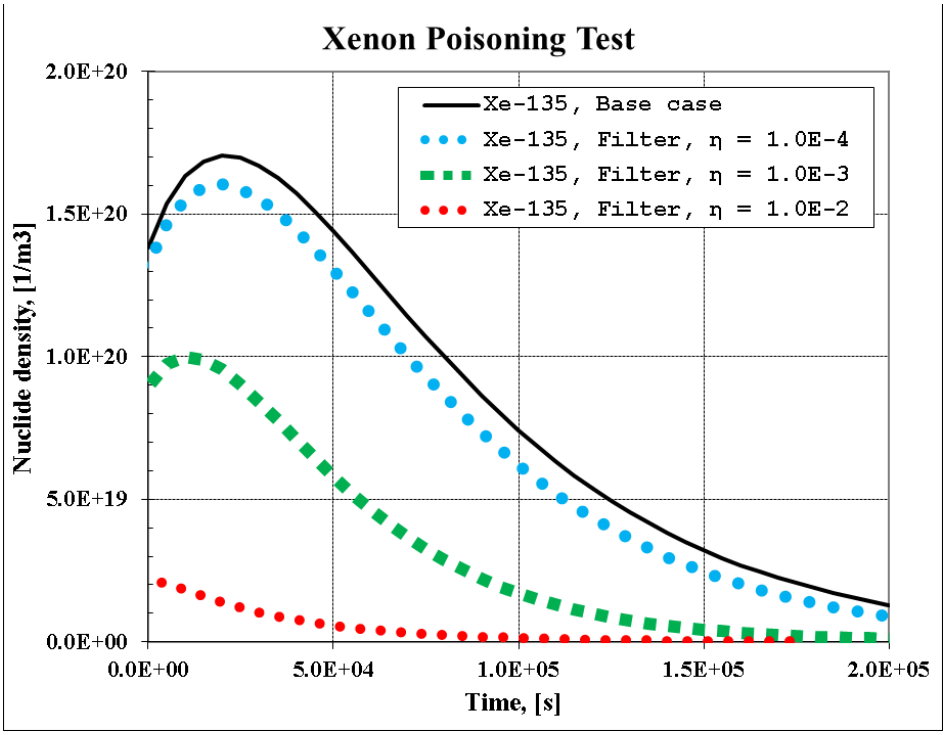

Figure 3-440 Xe-135 density, circulating fuel, influence of Xe filter

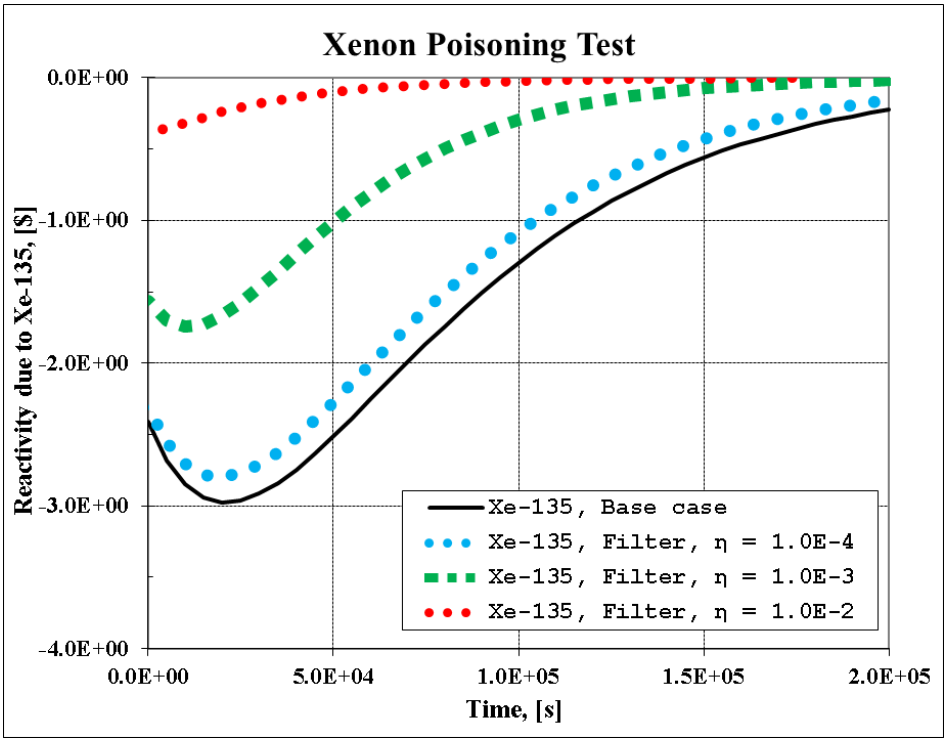

Figure 3-441 Xe-135 reactivity, influence of Xe filter

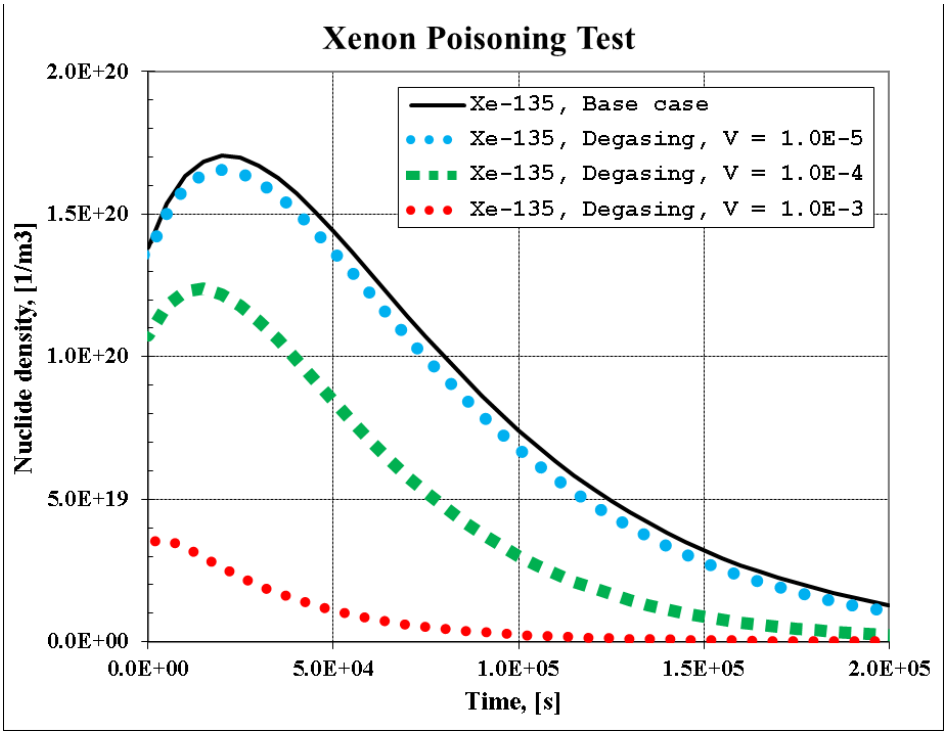

Figure 3-442 Xe-135 density, influence of mass transfer

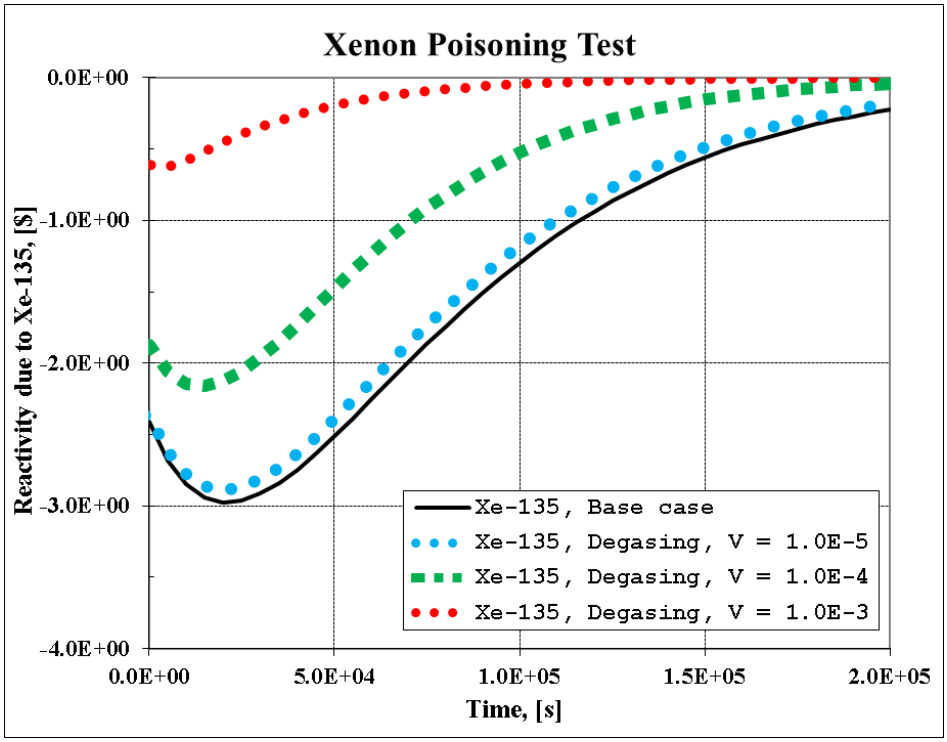

Figure 3-443 Xe-135 reactivity, influence of mass transfer

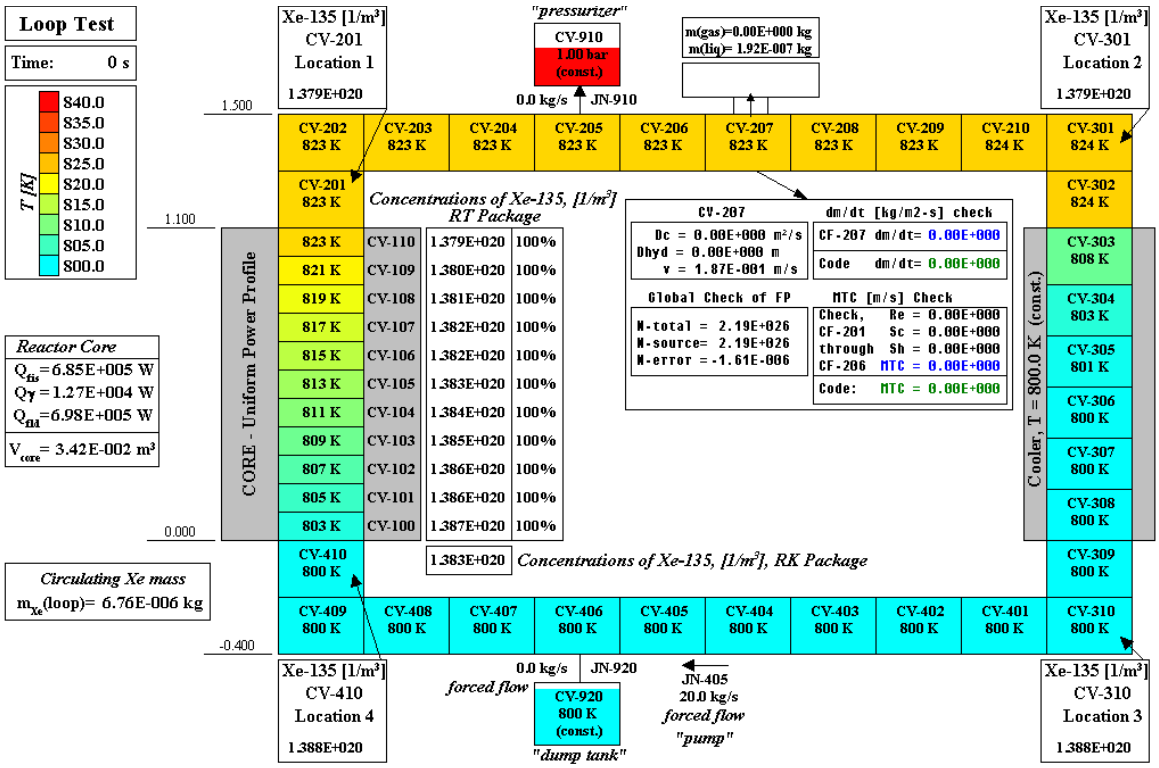

Figure 3-444 Xe-135 test, no liquid-gas transfer

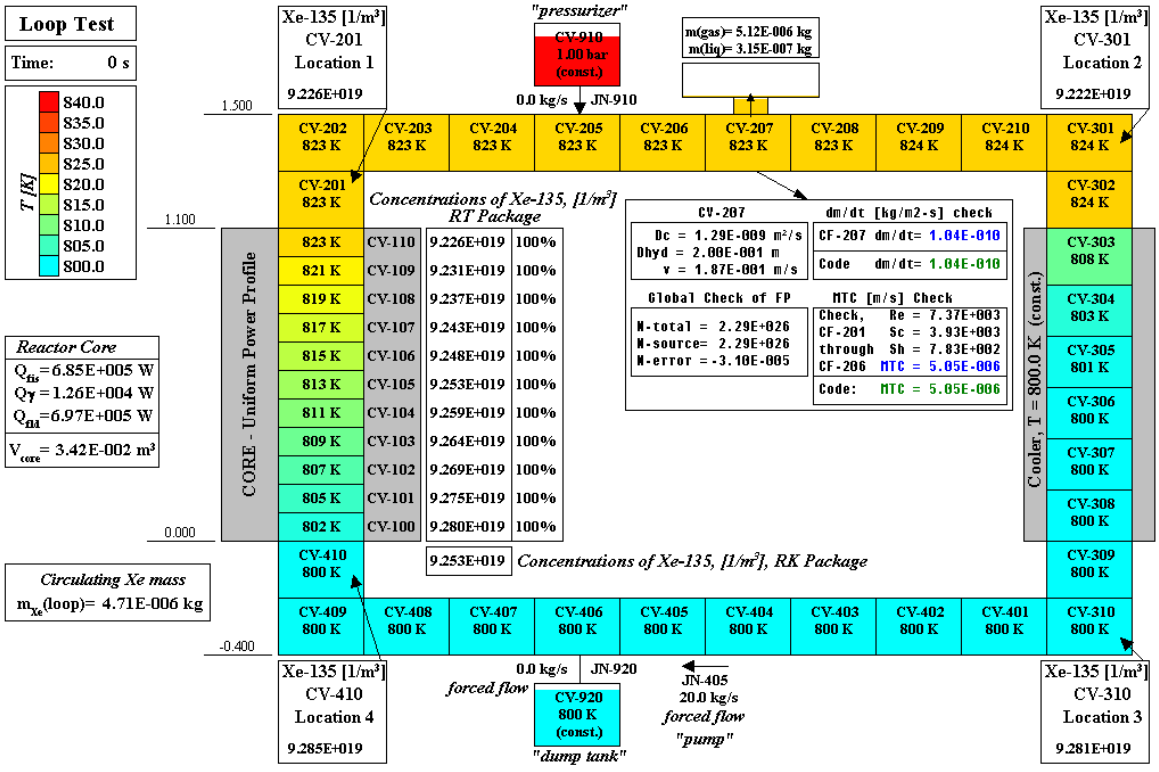

Figure 3-445 Xe-135 test, Sh number correlation for liquid-gas transfer

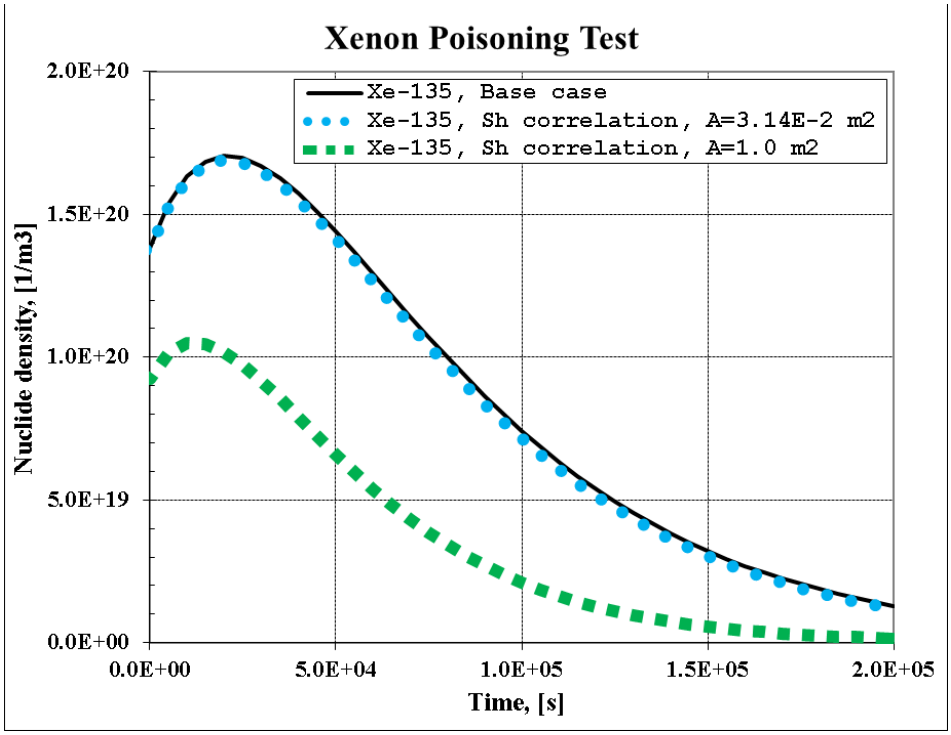

Figure 3-446 Xe-135 density, influence of mass transfer

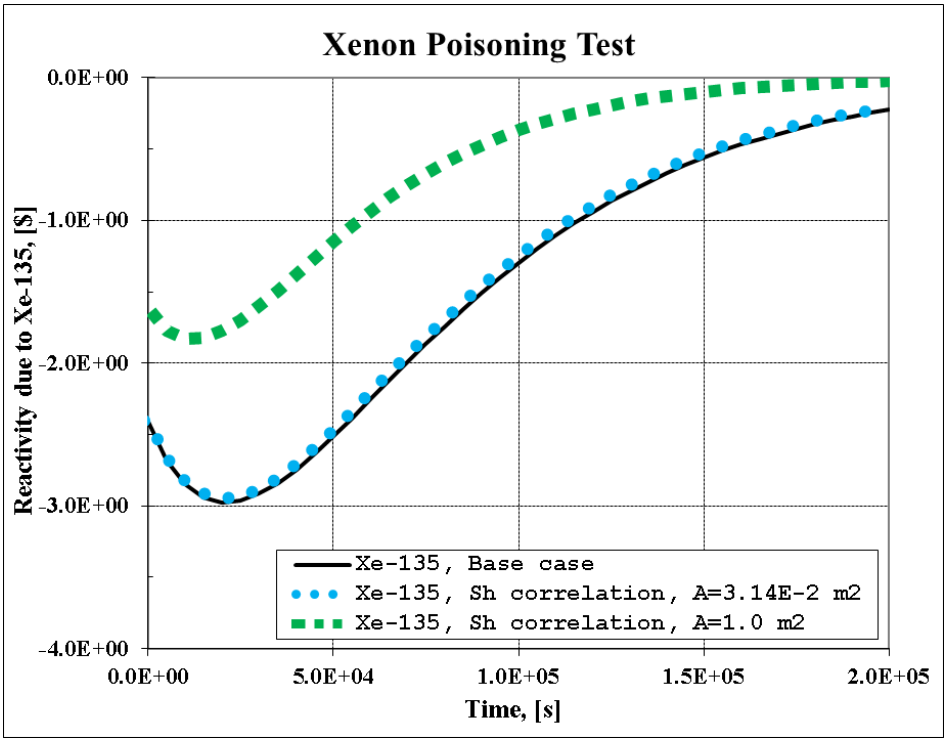

Figure 3-447 Xe-135 reactivity, influence of mass transfer

Influence of isotope filter

Influence of the filter is shown in Figure 3-440 and Figure 3-441. For this case an isotope filter is assumed to be located in JN-207 (Figure 3-437). Three cases are considered, with filter efficiencies of $\eta = 10^{-4}$, 10^{-3} and 10^{-2}. The Xe-135 concentrations decrease with increasing filter efficiency, which is a qualitative verification of the mode.

Influence of pool-gas mass transfer

Influence of pool gas mass transfer is shown in Figure 3-442 and Figure 3-443. For these calculations a constant mass transfer coefficient was assumed in CV-207 (Figure 3-437). The Xe-135 is transported in CV-207 from liquid to the gas space at the top of CV-207 (surface area of 3.14E–2.m^2). Three cases are considered, with mass transfer coefficients of $V = 10^{-5}$, 10^{-4} and 10^{-3} m/s. The Xe-135 concentrations decrease with increasing mass transfer coefficient, which is a qualitative verification of the mode.

Mass transfer coefficient from Sherwood calculations

Here the test case is very similar to the previous one, except that the mass transfer coefficient is calculated by the heat and mass transfer analogy (Sherwood number correlation). For a forced convective flow, we have:

$$Sh = 0.023\ Re^{0.8}\ Sc^{0.4}$$

Here *Re* is the Reynolds number, *Sc* is the Schmidt number, *Sh* is the Sherwood number. The mass transfer coefficient (m/s) is obtained as: $Sh \times D_C / D_{FC}$, where D_{FC} is the characteristic dimension for forced convection (hydraulic diameter = 0.127 m), D_C, is the diffusion coefficient, equal to 1.29×10^{-9} m^2/s (based on [136]).

Calculations were performed for 200,000 s of steady state (from –200,000 to 0.0 s) and 200,000 s of shutdown transient. Results are shown in visualization pictures for stationary state Figure 3-444, Figure 3-445, and time dependent graphs Figure 3-446, Figure 3-447.

In order to perform verification of the computed values, an automated verification was set-up using Tabular Functions and Control Functions, defined as follows:

- TF-200 = $D_C = 1.29\times10^{-9}$
- TF-201 = D_{FC} = 0.199949 m
- CF-201 = $Re = v \times D_{FC} \times \rho / \eta$ =
  = SC-207-Vfld-l-pl × TF-201 × CV-207-Dens-pool / CV-207-Visc-pool
- CF-202 = $Sc = v / \rho / D_C$ =
  = CV-207-Visc-pool / CV-207-Dens-pool / TF-200
- CF-203 = $Re^{0.8}$ = CF-201$^{0.8}$
- CF-204 = $Sc^{0.4}$ = CF-202$^{0.4}$
- CF-205 = $Sh = 0.023\ Re^{0.8}\ Sc^{0.4}$ =
  = 0.023 × CF-203 × CF-204
- CF-206 = mass transfer coefficient, *MTC* (m/s) = $Sh \times D_C / D_{FC}$ =
  = CF-205 × TF-200 / TF-201
- CF-207 = Sorption mass transfer rate (kg/m^2-s) = $MTC \times M_{Xe\text{-}135} / V_{pool}$ =
  = CF-206 × CV-207-MIPi-0132 / CV-207-Volm-pool

Here $M_{Xe\text{-}135}$ / V_{pool} is the average density of Xe-135 in the pool, $M_{Xe\text{-}135}$ is the mass of Xe-135 in the pool (kg), and V_{pool} is the pool volume (m^3).

Figure 3-445 shows the calculated values at 0.0 s, when stationary state is reached. The mass transfer coefficient is not directly available from SPECTRA plot parameters, however it can be constructed from the following plot parameters:

- Pool-atmosphere mass transfer rate (kg/s) isotope 132 (Xe-135) in CV-207:
  CV-207-FmPA-0132 (plot pointers: 8 / 207 / 164 / 132)
- Pool surface area in CV-207, (m^2)
  CV-207-A_IN-pl>a (plot pointers 1 / 207 / 68 / 1)
- No. of nuclides of isotope 132 (Xe-135) in the pool of CV-207, ($nucl/m^3$)
  CV-207-NIPi-0132 (plot pointers: 8 / 207 / 167 / 132)

The mass transfer divided by interface surface area and by nuclide density must be multiplied by (Avogadro/Molar weight), which may be taken from the SPECTRA output for Xe-135:

i	Isotope	Mass in the core (kg)	Molar weight (kg/kmol)	Beta- -fraction (-)	Gamma- -fraction (-)	Fission Yield (-)	Avogadro / / Molar w. (1/kg)
...							
132	Xe-135	1.66354E-06	1.35000E+02	5.00000E-01	5.00000E-01	2.60000E-03	**4.46074E+24**

The value obtained in such a way is given in Figure 3-445 as “Code: MTC = 5.05E-6”. The value obtained from the automated check is shown in Figure 3-445 as “CF-206: MTC = 5.05E-6”. Both values are in agreement.

The mass transfer rate (kg/m^2-s) is not available as plot parameter, however it may be constructed as a ratio of the following parameters:

- Pool-atmosphere mass transfer rate (kg/s) of isotope 132 (Xe-135) in CV-207:
  CV-207-FmPA-0132 (plot pointers: 8 / 207 / 164 / 132)
- Pool-atmosphere surface area, (m^2)
  CV-101-A_IN-pl>a (plot pointers: 1 / 101 / 68 / 1)

The value is given in Figure 3-445 as “Code: dm/dt = 1.04E-10”. The value obtained from the automated check (CF-207) is shown in Figure 3-445 as “CF-207: dm/dt = 1.04E-10”. Both values are in agreement.

3.9.3.8 Decay Heat Test, ^{235}U Fuel - Non-flow Case

The decay heat test with U-235 fuel. The initial reactor power is assumed to be 100 MW (10^8 W). The reactor is shutdown at t = 0.0 by inserting a large negative reactivity (–9.99 $). The resulting reactor power is plotted. A circulating fuel kinetics model is used with no flow. Calculations were performed for times from 0.0 s to 10,000 s. Results are compared to the standard point kinetics, discussed in section 3.9.2.6.

SPECTRA input deck for this test is provided in:
`\Z-INPUTS\RK\DH\CIR\DH-U235-CIR.SPE`.
The comparison input, containing standard reactor kinetics model is provided in:
`\Z-INPUTS\RK\DH\CIR\DH-U235.SPE`.

The results of standard point kinetics and circulating fuel kinetics model are compared in Figure 3-448. As expected, the results obtained with the kinetics model for the circulating fuel are identical to those obtained with the standard point kinetics model.

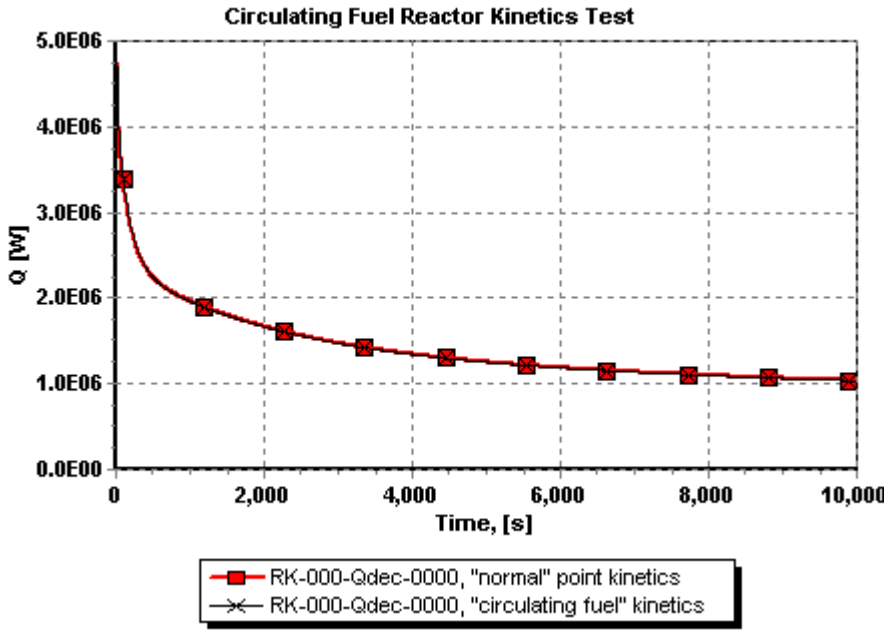

Figure 3-448 Comparison of decay heat for ^{235}U fuel

3.9.3.9 Decay Heat Test, ^{239}Pu Fuel - Non-flow Case

The decay heat test with Pu-239 fuel. The initial reactor power is assumed to be 100 MW (10^8 W). The reactor is shutdown at t = 0.0 by inserting a large negative reactivity (–9.99 $). The resulting reactor power is plotted. A circulating fuel kinetics model is used with no flow. Calculations were performed for times from 0.0 s to 10,000 s. Results are compared to the standard point kinetics, discussed in section 3.9.2.7.

SPECTRA input deck for this test is provided in:
`\Z-INPUTS\RK\DH\CIR\DH-PU239-CIR.SPE`.
The comparison input, containing standard reactor kinetics model is provided in:
`\Z-INPUTS\RK\DH\CIR\DH-PU239.SPE`.

The results of standard point kinetics and circulating fuel kinetics model are compared in Figure 3-449. As expected, the results obtained with the kinetics model for the circulating fuel are identical to those obtained with the standard point kinetics model.

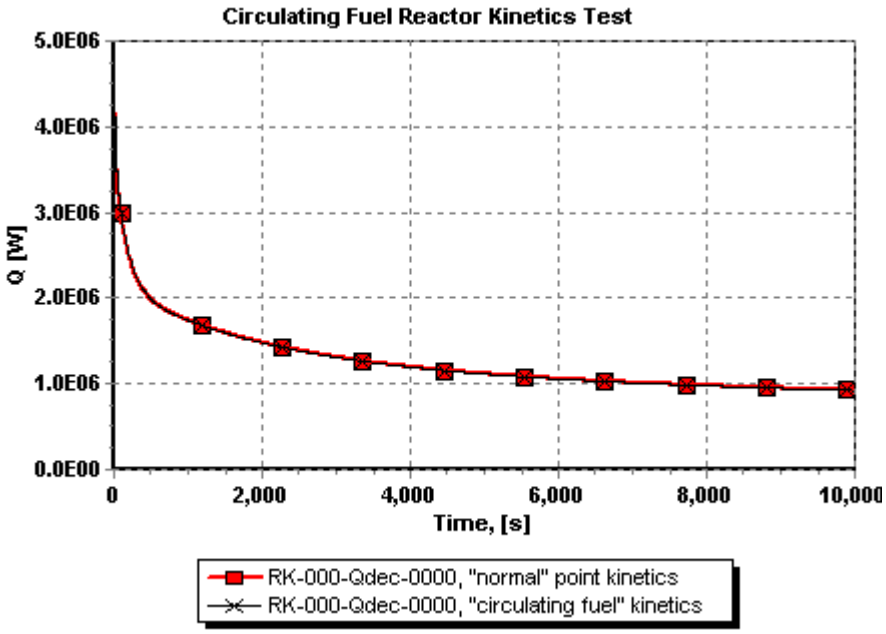

Figure 3-449 Comparison of decay heat for ^{239}Pu fuel

3.9.3.10 Delayed Neutron Precursor Drift - Comparison with CFD

In order to verify the flow of delayed neutron precursors, a simple loop is considered. The loop layout is shown in Figure 3-450. All the dimensions are shown in the picture. The nodalization was based on 0.1 m nodes for the core volumes and 0.2 m nodes elsewhere. The fluid considered is the FLiBe salt based on ternary FLiBe salt properties in [134]. The following data was assumed for the delayed neutron precursors (DNP):

	Yield		Decay	Half-life
Group No.	Absolute (1/fis)	Relative (-)	Constant (1/s)	T(1/2) (s)
1	2.20000E-04	3.38462E-02	1.24000E-02	5.58990E+01
2	1.42000E-03	2.18462E-01	3.05000E-02	2.27261E+01
3	1.27000E-03	1.95385E-01	1.11000E-01	6.24457E+00
4	2.57000E-03	3.95385E-01	3.01000E-01	2.30281E+00
5	7.50000E-04	1.15385E-01	1.14000E+00	6.08024E-01
6	2.70000E-04	4.15385E-02	3.01000E+00	2.30281E-01
	---	---		
Sum:	6.50000E-03	1.00000E+00		

The following simplifying assumptions were made:

- Uniform axial reactor power and uniform generation of the delayed neutron precursors in the core was assumed.
- Practically isothermal conditions were obtained by applying a very low initial power (1 W).

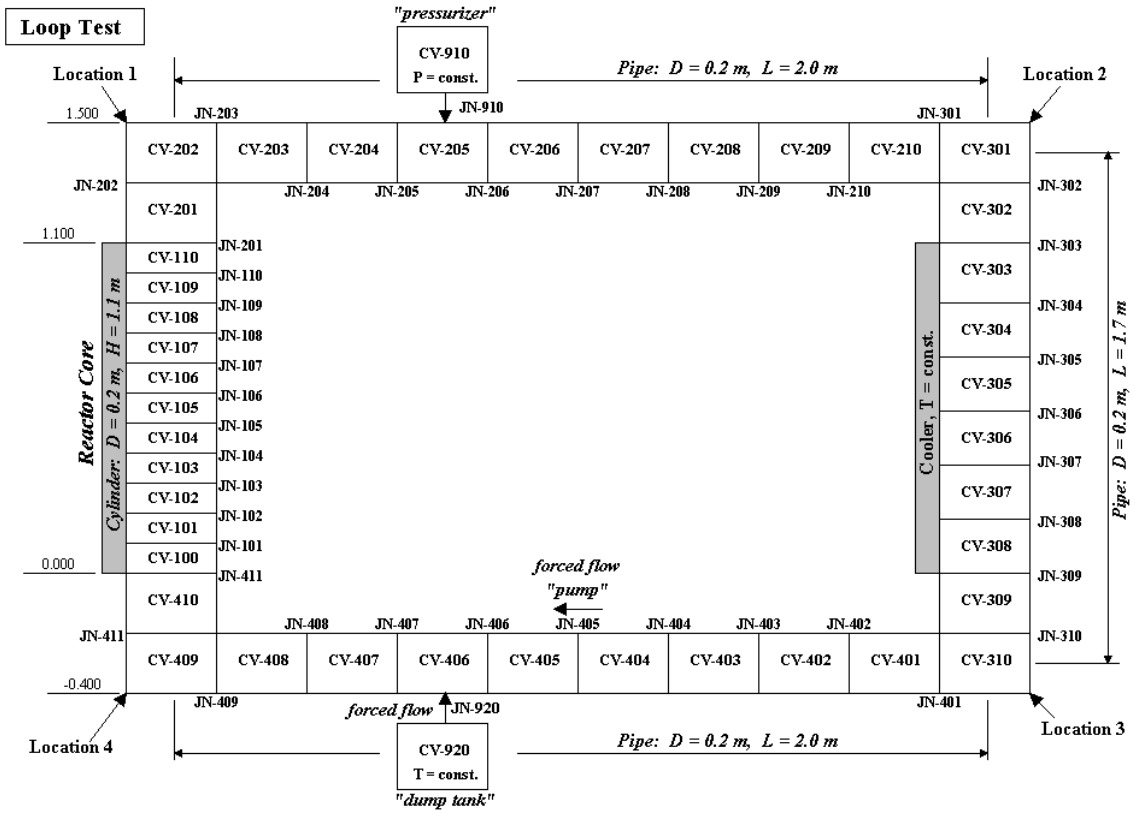

Figure 3-450 Loop circulation test - loop layout and nodalization for SPECTRA

SPECTRA input deck for this test is provided in:
`\Z-INPUTS\RT\Cir-fuel\Loop\Loop-low-power-uniform\LOOP-CIR.SPE`

The results of the CFD calculations are stored in:
`\Z-INPUTS\RT\Cir-fuel\Loop\Loop-low-power-uniform\CFD`

The considered transient is as follows. The reactor is initially at 1.0 W power and no flow. A short period (20.0 s) of stationary state at these conditions is simulated. It was checked that during this period the concentrations of DNP (uniform across the core) are identical to those obtained from the standard point kinetics model.

At time equal to t = 20.0 s, a forced flow of the fluid is initiated. The mass flow through the loop is assumed to increase linearly to from 0.0 to 10.767 kg/s during 10.0 s and is kept at that value for the rest of the test. The fluid velocity corresponding to this flow is 0.100 m/s. With the applied speed, a full circulation around the loop takes about 74 seconds. The path outside the core takes about 63 s. The long-life groups have a chance to make a full circle (group 1 has half-life of 55.9 s); while the short-life, once drifted out of the core are practically completely lost (group 5 has half-life of 0.23 s).

During the considered test, the delayed neutron precursors drift out of the core leads to a reduction of power, as well as a reduction of the generation rate of delayed neutron precursors. Concentrations of the DNPs are monitored in four characteristic points, the "corners" of the loop.

SPECTRA results are shown in Figure 3-451 through Figure 3-457. Figure 3-451 shows the decreasing reactor power due to loss of DNPs. The power temporarily increases when the DNPs make a full circle around the loop. Figure 3-452 shows the source rates (in atoms per second) of the delayed neutron precursors. Since uniform power distribution is assumed, the source is identical in all core volumes (CV-100 through CV-110). Figure 3-453 shows the state of the system at t = 0.0 s, with DNPs present only in the core (uniform concentrations) and zero outside the core (in the monitored points). Figure 3-454 shows the state of the system at t = 200.0 s, with DNPs present in the entire loop. The short-life groups (5, 6) are however zero in the third and the fourth monitoring point, because these groups have decayed before reaching the points.

As an independent verification of the DNPs drift calculated by SPECTRA, a confirmatory calculation is performed using the CFD code FLUENT 15. The source of DNPs, calculated by the point kinetics model in SPECTRA is used as a time-dependent external source of particles. The primary goal of CFD simulation is to verify the particle (delayed neutron precursor) transport model in the SPECTRA system code. For that reason, a series of CFD simulations starting from the most simplified model, where the loop is simplified with a straight periodic pipe, and gradually built a complex model, which predicts better realistic 3D effects and mixing in the primary loop of a molten salt reactor.

Each CFD numerical model consisted of reactor core, pipes and the pump. Molten salt transports DNPs throughout the entire system; hence an exponential decay for 6 different groups of DNPs is implemented in the core, the pipes and the pump. DNPs are generated only in the reactor core, thus the source terms are specified for each group of DNP in the reactor core. Production of DNPs in the reactor core is varying in time during the analyzed flow start-up transient; the DNP sources have been provided by SPECTRA calculations, as obtained from the reactor kinetics model.

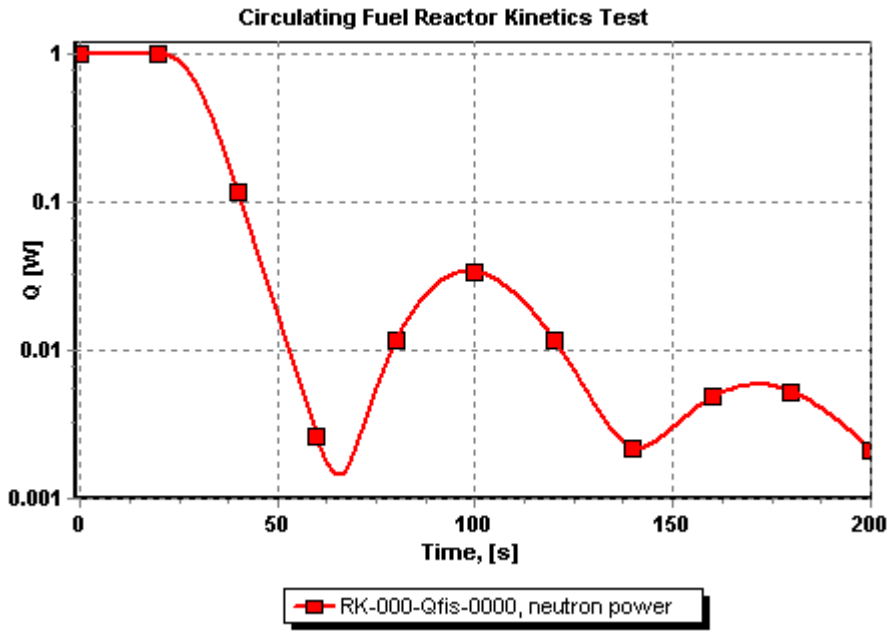

Figure 3-451 Loop circulation test - fission power

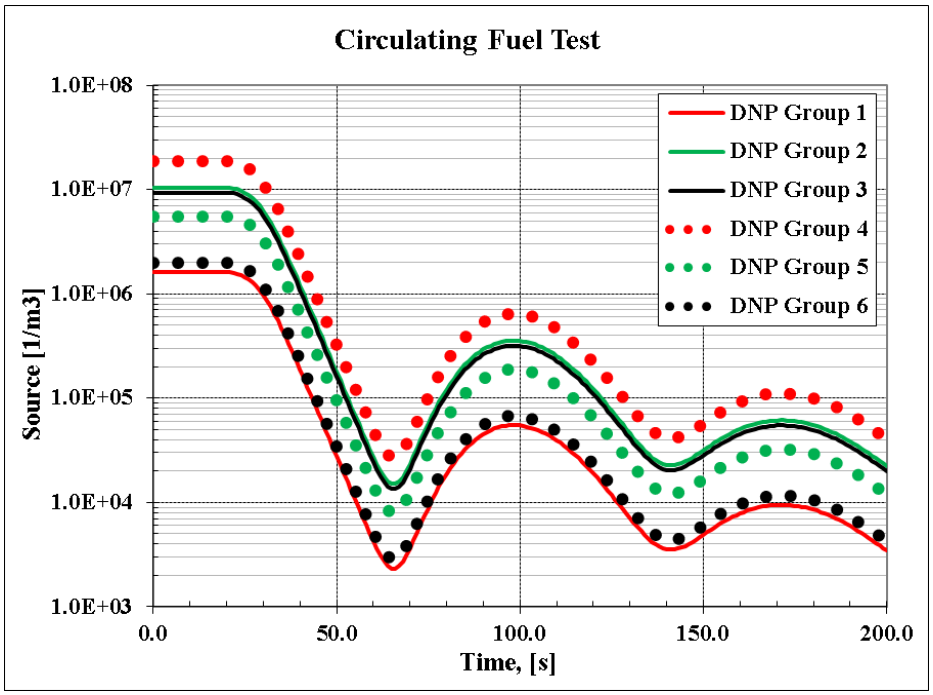

Figure 3-452 Loop circulation test - DNP sources in the core (CV-105)

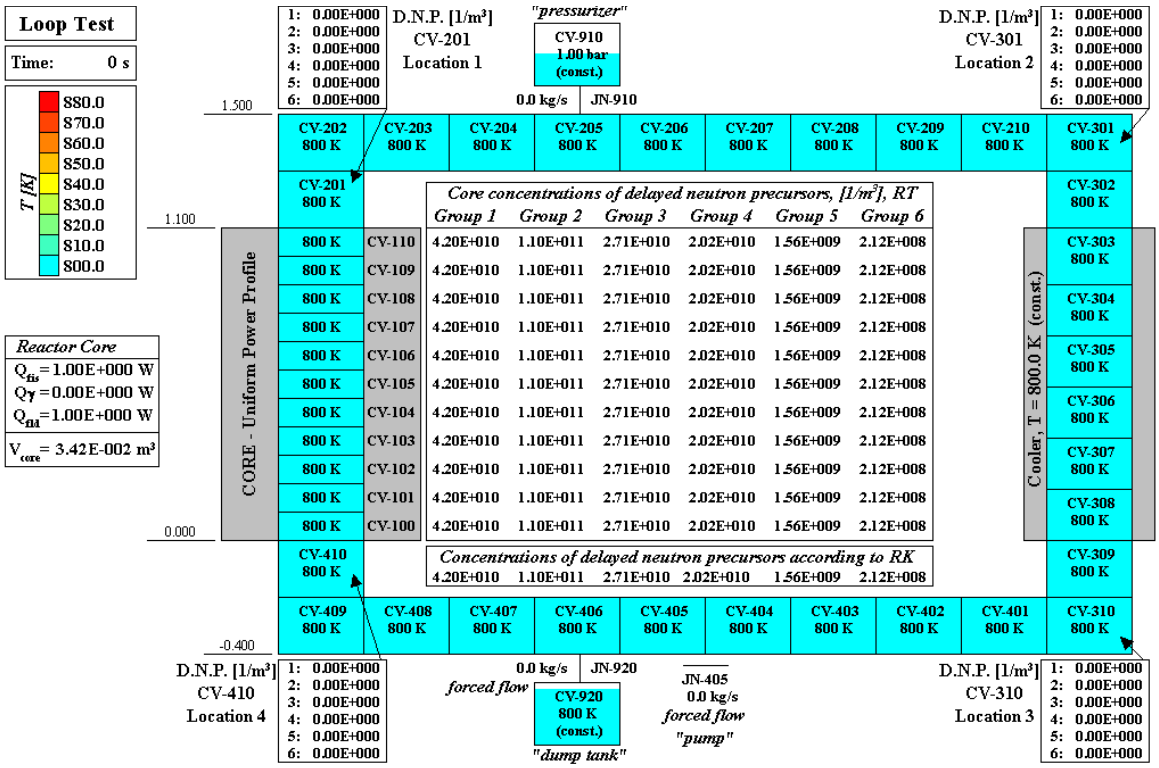

Figure 3-453 Loop circulation test - delayed neutron precursor concentrations at t = 0.0 s

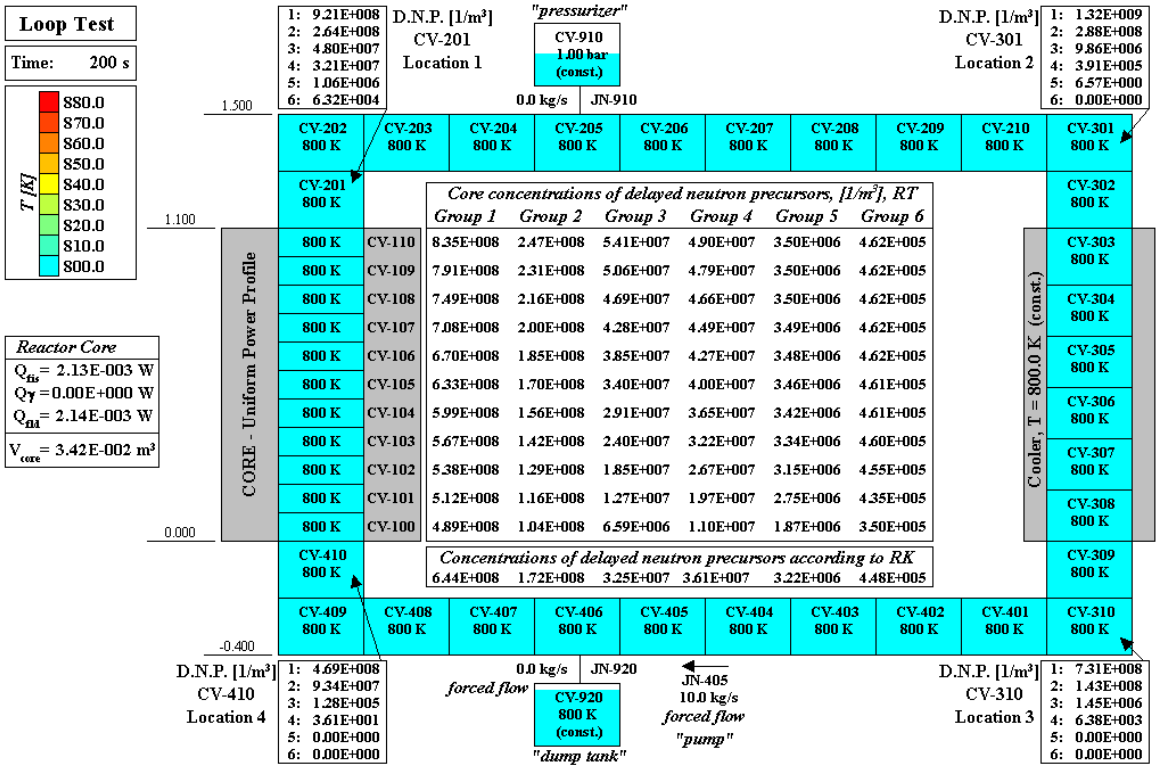

Figure 3-454 Loop circulation test - delayed neutron precursor concentrations at t = 200 s

Six CFD simulations were performed:

- Case 1: modeling assumptions are: coarse mesh, 1-st order numerical schemes for DNPs
- Case 2: coarse mesh, 2-nd order numerical schemes
- Case 3: fine mesh, 2-nd order numerical schemes
- Case 4: fine mesh, 2-nd order numerical schemes, viscous effects included
- Case 5: fine mesh, 2-nd order numerical schemes, viscous effects and bends included
- Case 6: as Case 5 but with turbulence model included

In Cases 1-4, the loop is modelled with a straight circular pipe with periodic boundary conditions. Cases 1 and 2 apply a coarse mesh, which consist of 836 cells and has a similar streamwise discretization as the SPECTRA model. Second order spatial and temporal discretization was used in all cases except for Case 1, which applies first order upwind discretization for DNP transport equations. Fine meshes with about 47,000 cells are applied in the Cases 3 - 6. Case 3 applies slip wall boundary condition (i.e. zero shear at walls) whereas Case 4 applies no-slip boundary condition, which includes viscous effects of the walls. Case 5 and 6 are performed in a closed loop rather than a periodic pipe, therefore they take into account mixing effects in the pipe bends. The flow is laminar in all simulations except in the Case 6, which applies turbulence model. The k–ω *SST* turbulence model was used, where k is the turbulence kinetic energy and ω is the specific rate of dissipation of k into internal thermal energy. Below, the SPECTRA results are compared to the results obtained with CFD for the above mentioned cases.

- **Case 1**

SPECTRA results are compared to the Case 1 obtained with CFD. Figure 3-456 shows concentrations of the DNPs in the four monitoring points of the loop. Figure 3-457 shows concentrations of the DNPs in the core. An increase of the DNP group 1 concentrations is clearly seen after 60 s; the time needed for this isotope to make a full circle. A good agreement is obtained for this case.

- **Case 2**

SPECTRA results are compared to the Case 2 obtained with CFD. Figure 3-458 shows concentrations of the DNPs in the four monitoring points of the loop. Figure 3-459 shows concentrations of the DNPs in the core.

- **Case 3**

SPECTRA results are compared to the Case 3 obtained with CFD. Figure 3-460 shows concentrations of the DNPs in the four monitoring points of the loop. Figure 3-461 shows concentrations of the DNPs in the core.

- **Case 4**

SPECTRA results are compared to the Case 4 obtained with CFD. Figure 3-462 shows concentrations of the DNPs in the four monitoring points of the loop. Figure 3-463 shows concentrations of the DNPs in the core.

- **Case 5**

SPECTRA results are compared to the Case 5 obtained with CFD. Figure 3-464 shows concentrations of the DNPs in the four monitoring points of the loop. Figure 3-465 shows concentrations of the DNPs in the core.

- **Case 6**

SPECTRA results are compared to the Case 6 obtained with CFD. Figure 3-466 shows concentrations of the DNPs in the four monitoring points of the loop. Figure 3-467 shows concentrations of the DNPs in the core.

Summary

With fine CFD mesh, the numerical diffusion is smaller and the peaks are more pronounced. The agreement becomes worse. However, when the flow model is more realistic with viscous effects, turbulence and pipe bends the solution becomes again similar to the results of the system code. For the realistic Case 6, peaks in CFD are still more pronounced than in SPECTRA, but the difference is not as large as in the idealized Cases 2 - 5. The agreement was further improved by using finer nodalization in SPECTRA, with all nodes 0.1 m long. The fine nodalization is shown in Figure 3-455. Results obtained with this nodalization are compared to the Case 6 obtained with CFD in Figure 3-468 and Figure 3-469. The comparison shows good agreement.

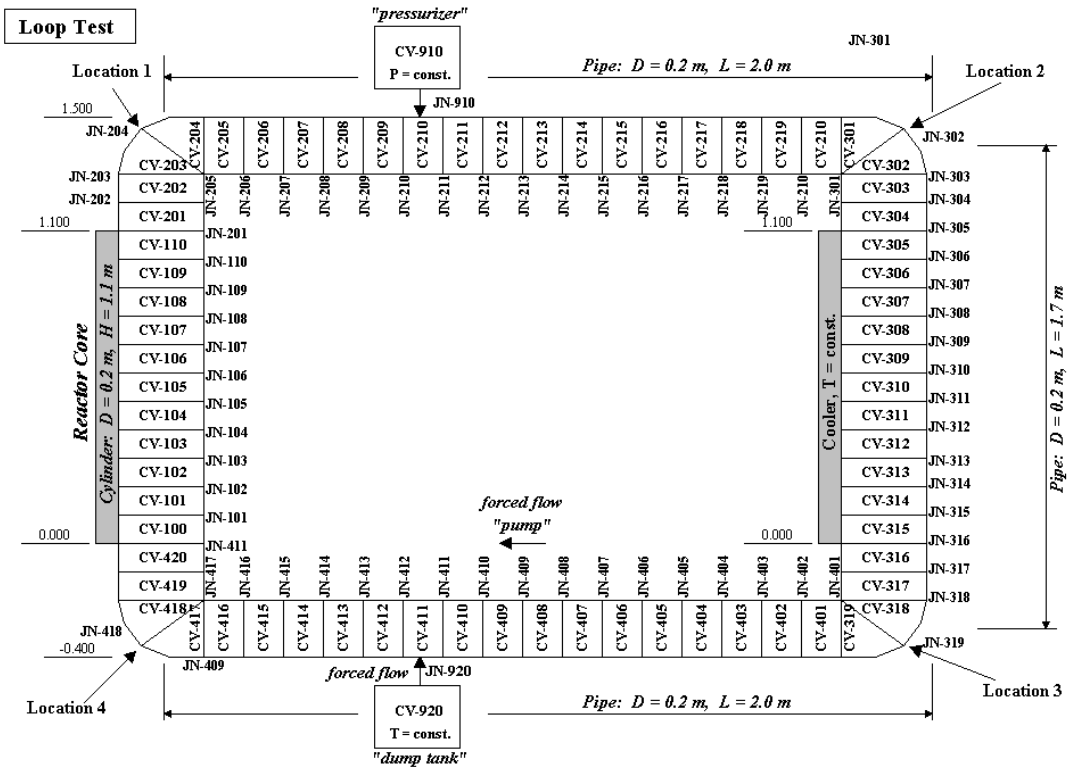

Figure 3-455 Re-fined nodalization for SPECTRA

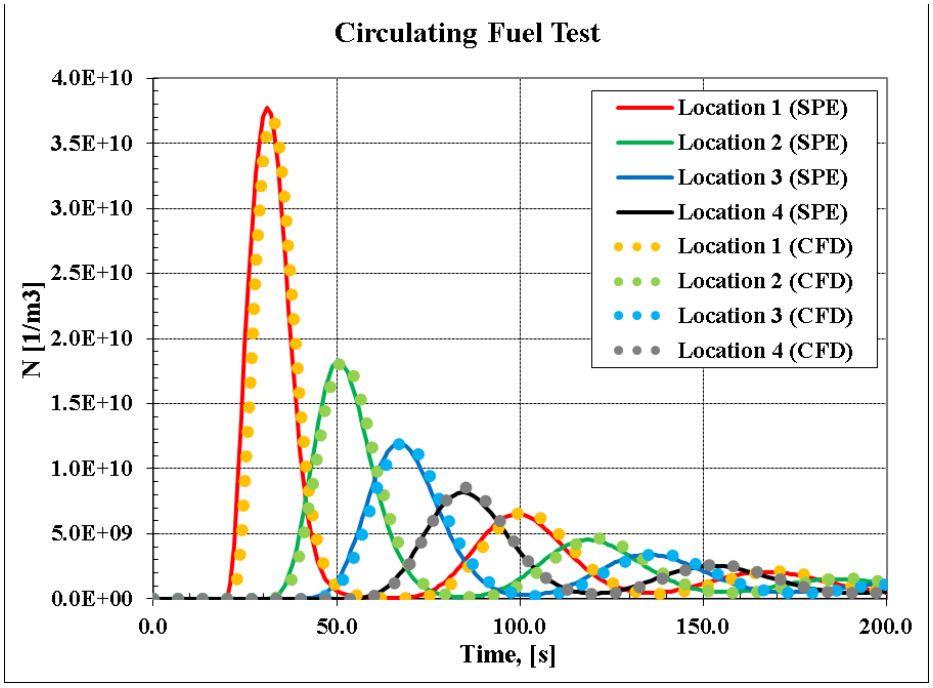

Figure 3-456 Loop circulation test - DNP Group 1 concentrations in the loop, **Case 1**

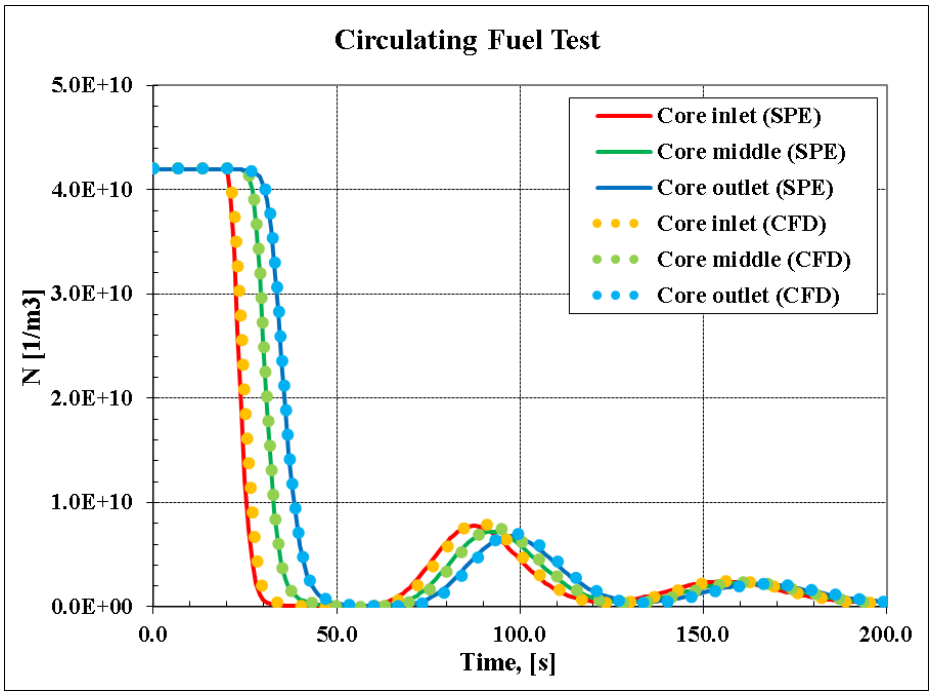

Figure 3-457 Loop circulation test - DNP Group 1 concentrations in the core, **Case 1**

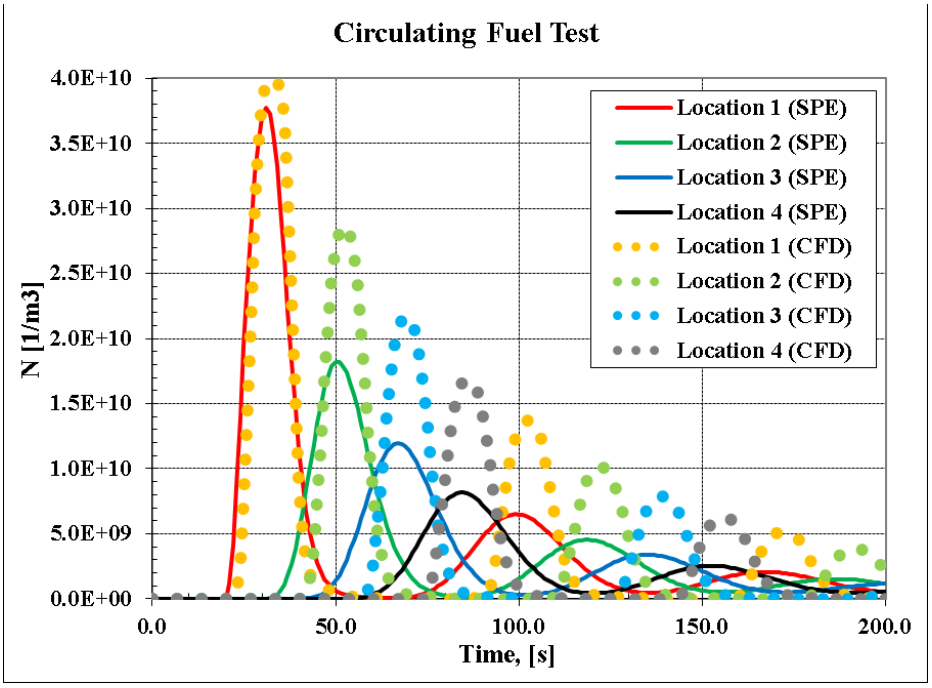

Figure 3-458 Loop circulation test - DNP Group 1 concentrations in the loop, **Case 2**

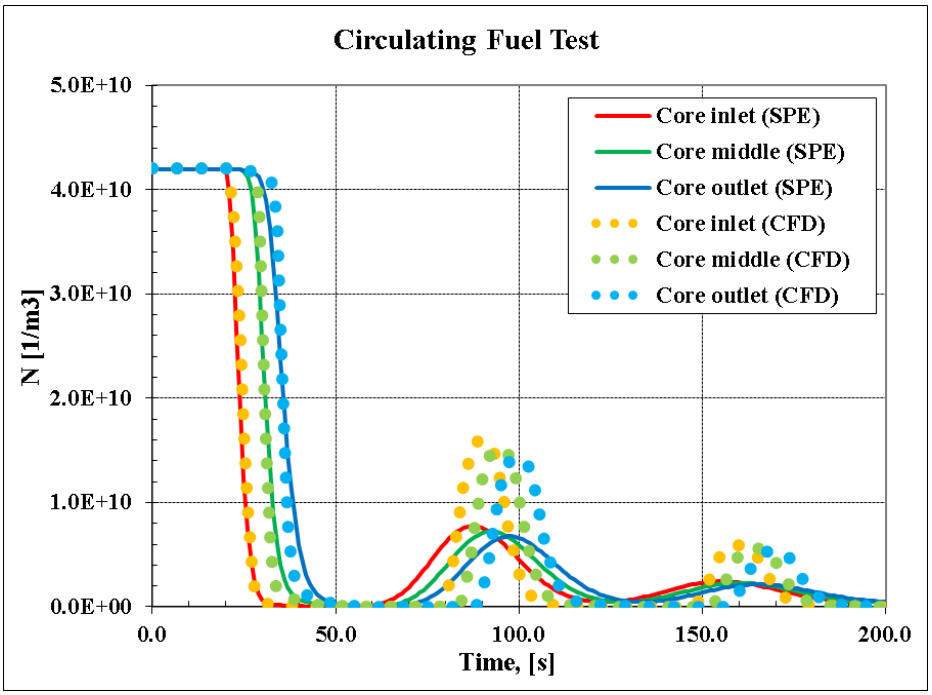

Figure 3-459 Loop circulation test - DNP Group 1 concentrations in the core, **Case 2**

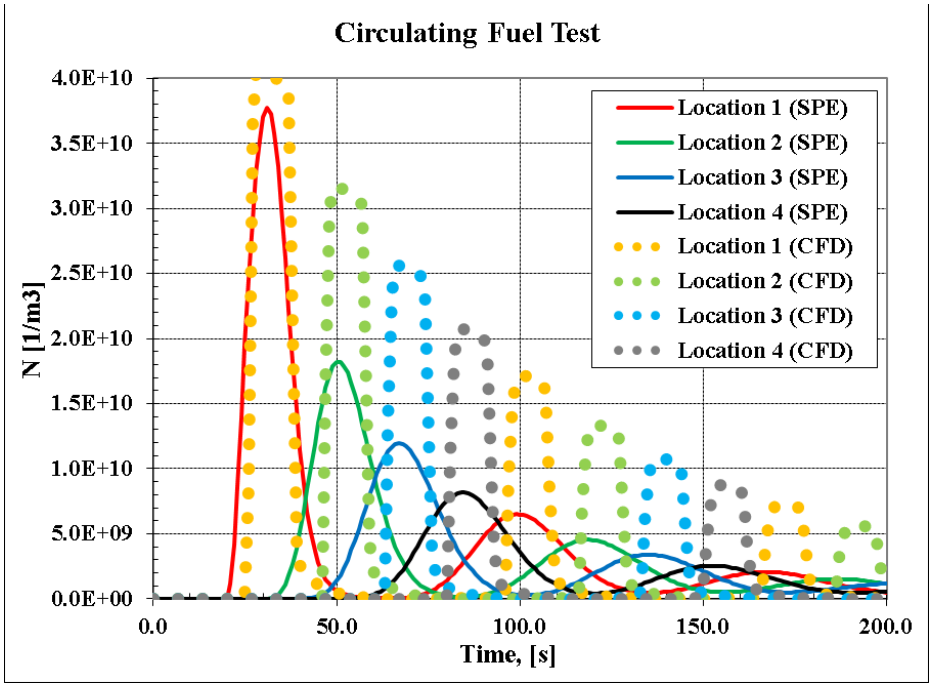

Figure 3-460 Loop circulation test - DNP Group 1 concentrations in the loop, **Case 3**

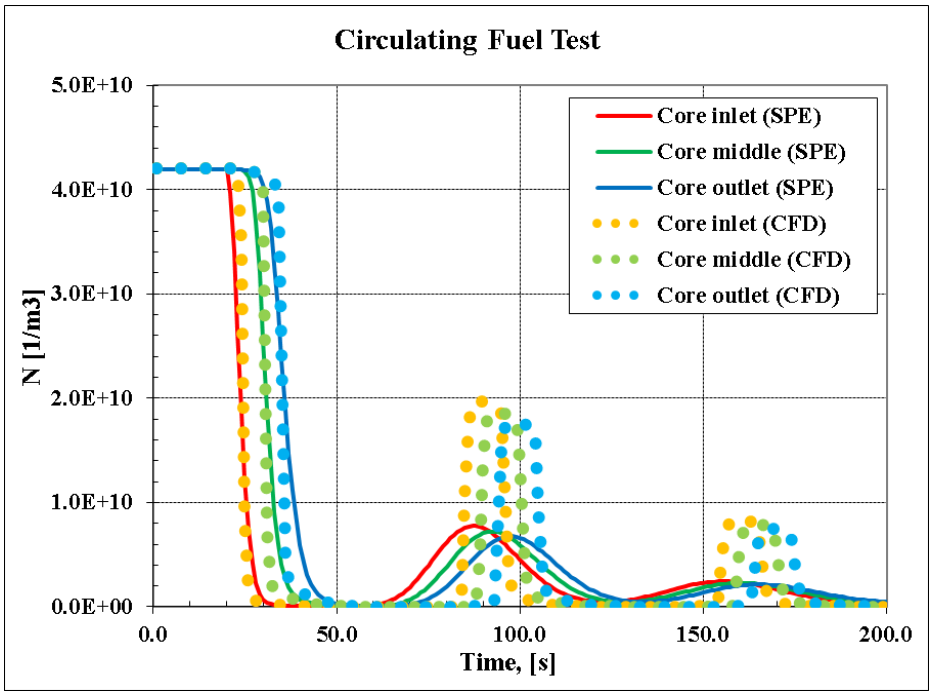

Figure 3-461 Loop circulation test - DNP Group 1 concentrations in the core, **Case 3**

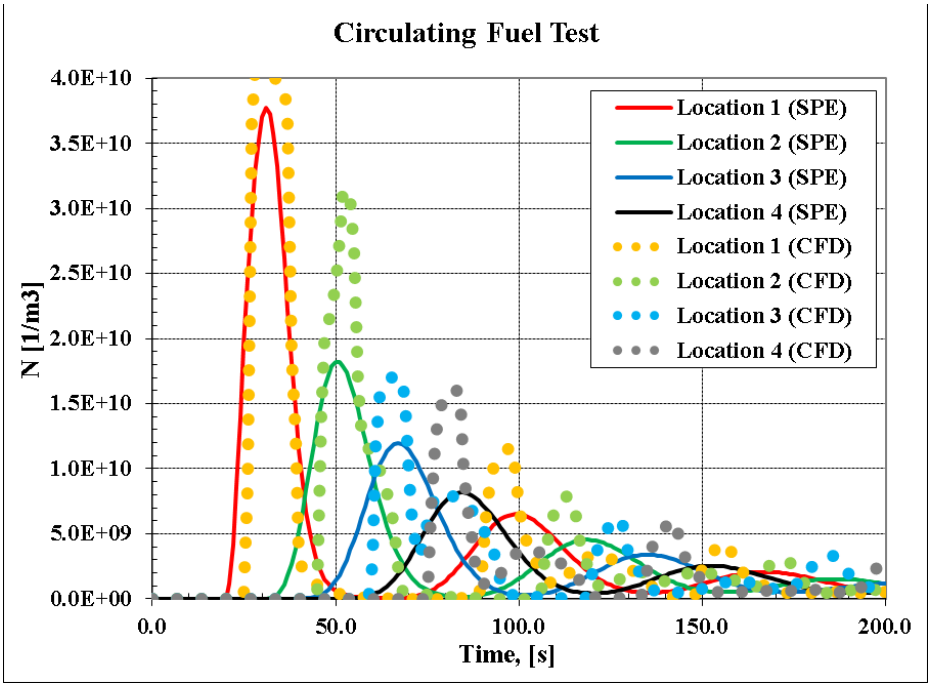

Figure 3-462 Loop circulation test - DNP Group 1 concentrations in the loop, **Case 4**

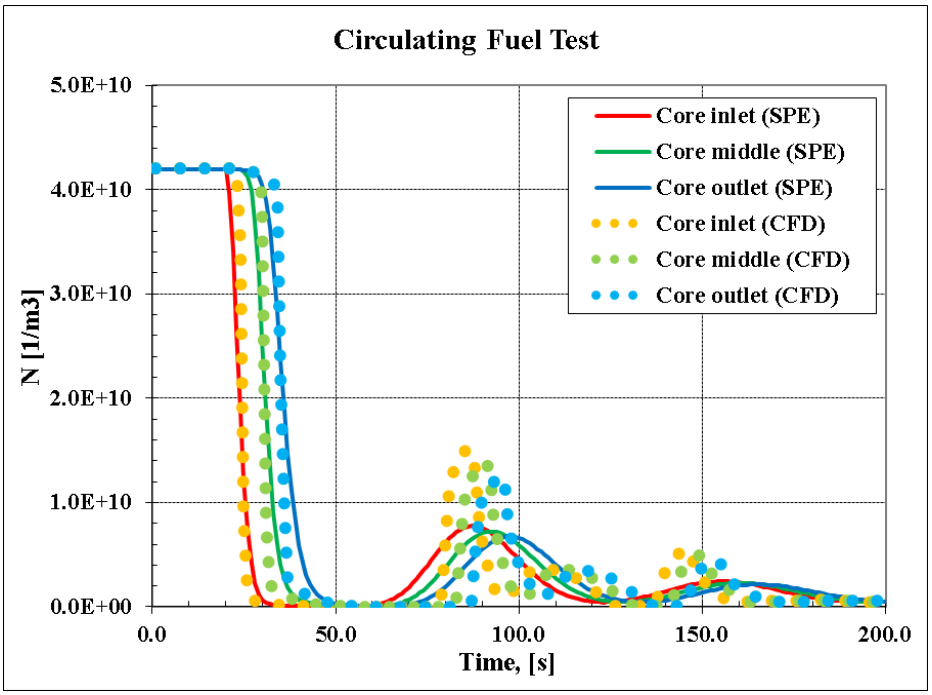

Figure 3-463 Loop circulation test - DNP Group 1 concentrations in the core, **Case 4**

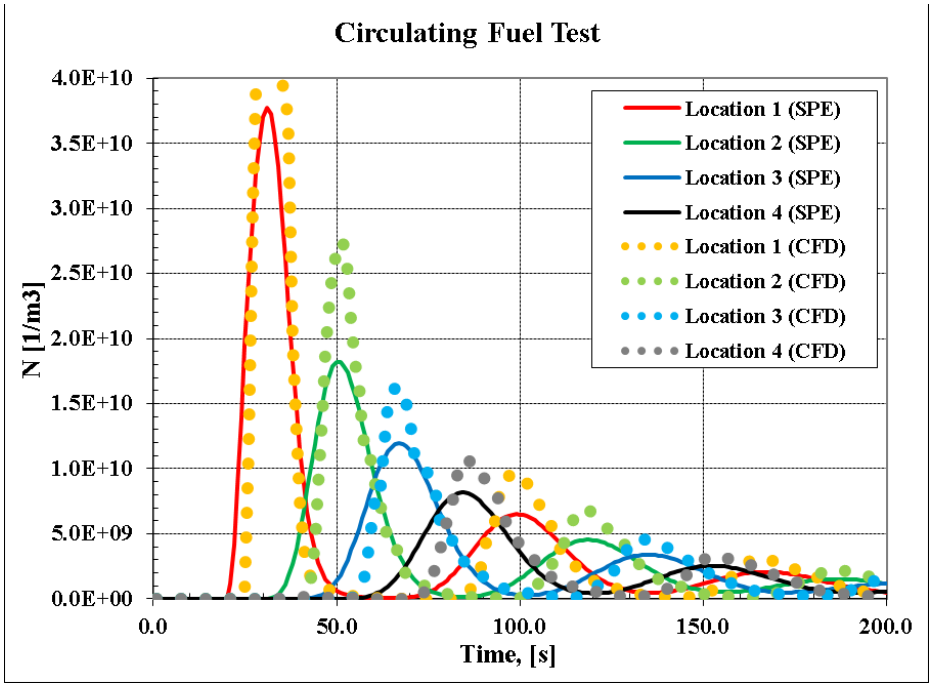

Figure 3-464 Loop circulation test - DNP Group 1 concentrations in the loop, **Case 5**

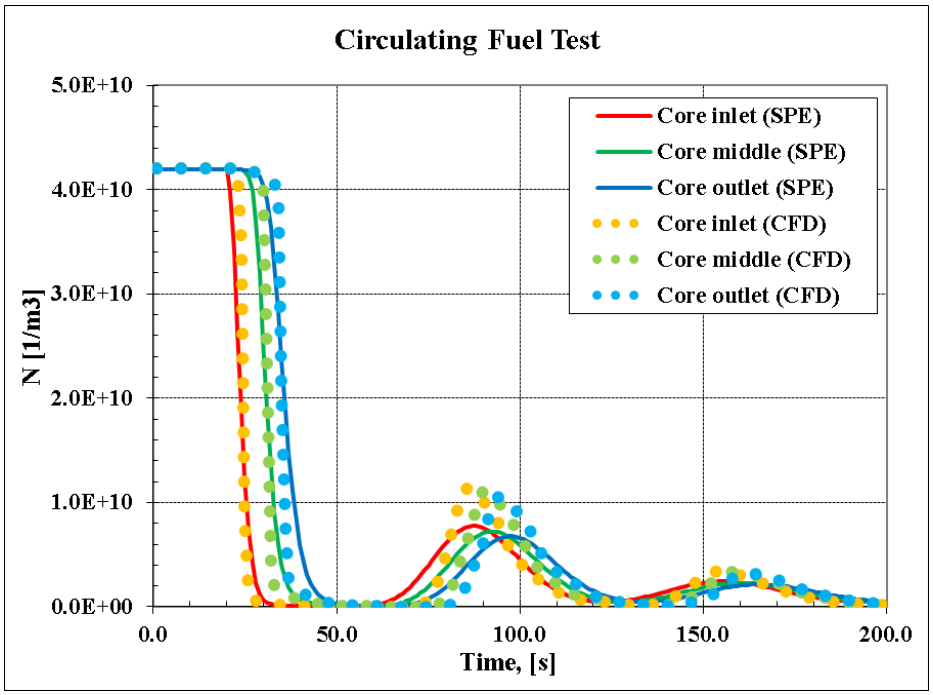

Figure 3-465 Loop circulation test - DNP Group 1 concentrations in the core, **Case 5**

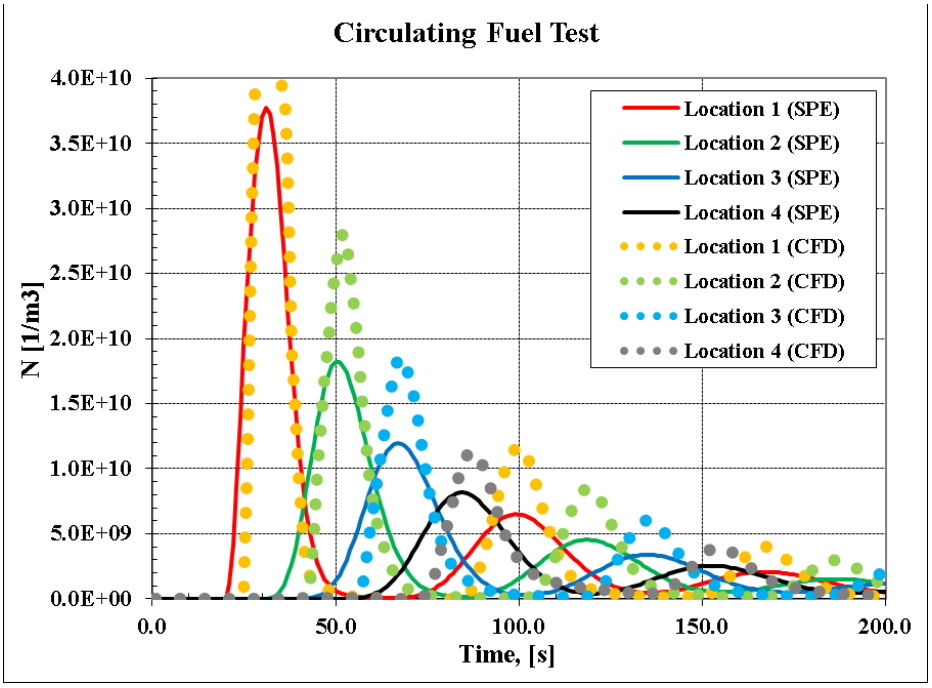

Figure 3-466 Loop circulation test - DNP Group 1 concentrations in the loop, **Case 6**

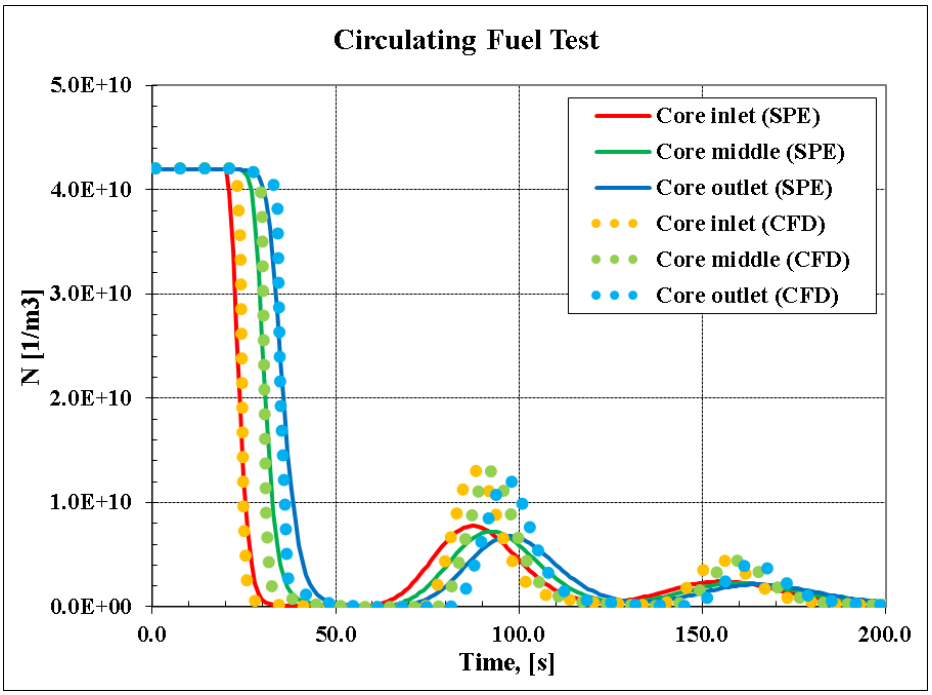

Figure 3-467 Loop circulation test - DNP Group 1 concentrations in the core, **Case 6**

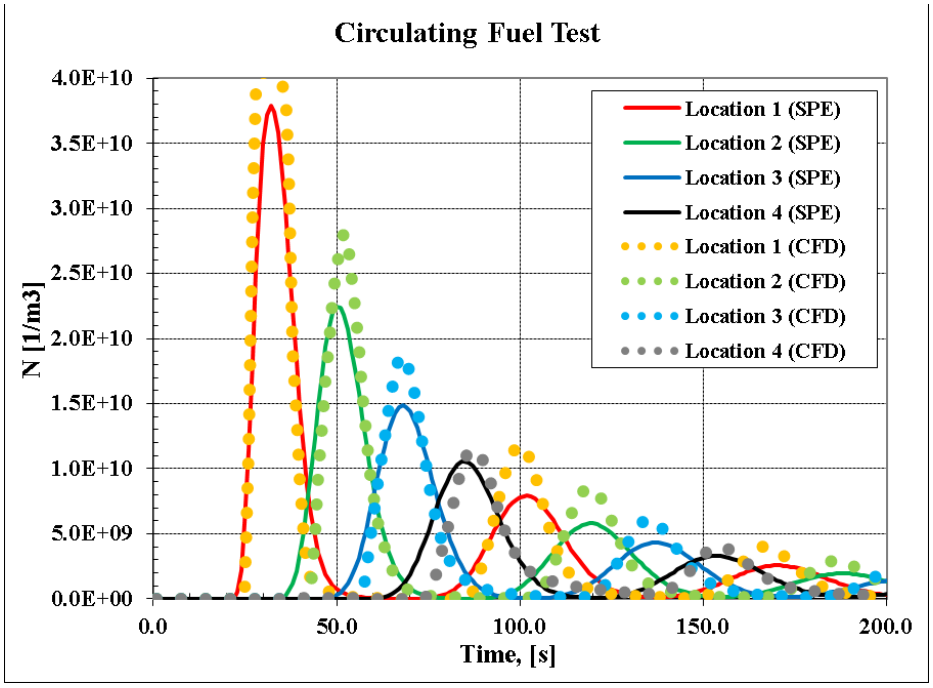

Figure 3-468 Loop circulation test - DNP Group 1 concentrations in the loop, **Case 6, re-fined SPECTRA nodalization**

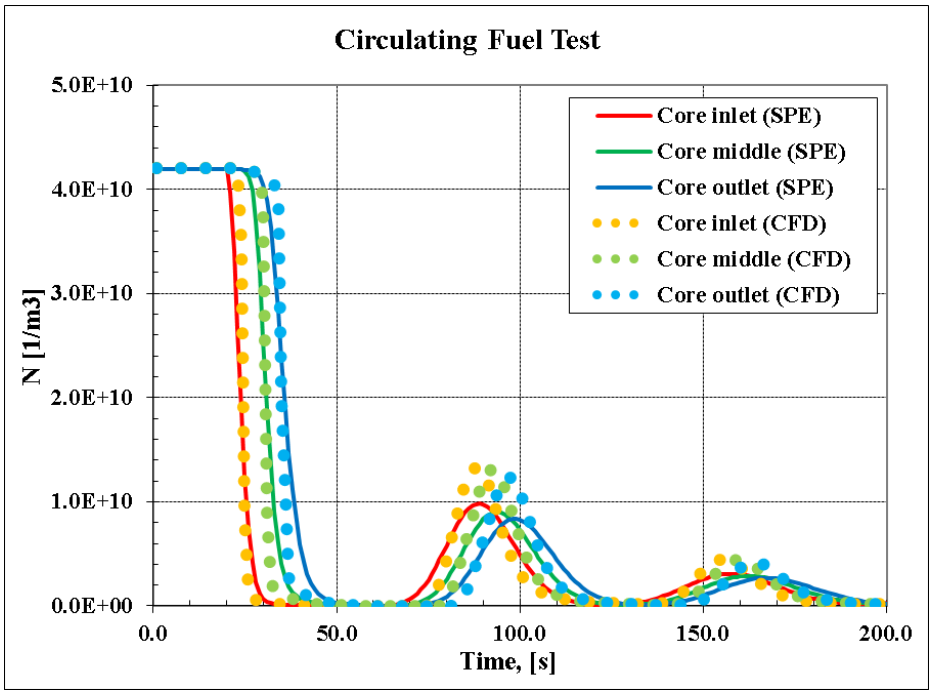

Figure 3-469 Loop circulation test - DNP Group 1 concentrations in the core, **Case 6, re-fined SPECTRA nodalization**

3.9.3.11 Power Behavior During Fuel Dump

The present section shows tests of fuel dump. In such case the molten salt / fuel mixture flows out of the core region, where the chain fission reaction is possible, into a lower region, where the chain reaction is not possible. A simple model is set up, with Control Volume CV-101, the "core" volume, where the chain reaction is possible, and CV-201, the "dump" volume, where chain reaction is not possible.

Several cases are considered, starting from the simple case, where only delayed neutron precursors are present and no reactivity change is considered, next including the reactivity feedback from changing liquid level and, finally, including other fission products.

Simple Case - Delayed Neutron Precursors Only

In this case only the delayed neutron precursors (DNP) are considered. The Isotope Transformation model (IT) is not used. The initial power is set as 10^6 W. At t=0.0 s the valve JN-101 opens and the salt mixture flows down to CV-201. The input deck is located in:

`\Z-INPUTS\RT\Cir-fuel\Dump\CV-power-source-no\Dump-NoIT`

Results are shown in Figure 3-470 through Figure 3-474. The power source is automatically reduced by the code, proportional to the amount of liquid in the core. Figure 3-471 shows that the generated power is proportional to the liquid level in the core. The mass of DNPs decreases as well, as seen in Figure 3-472. Note that the reactivity is all the time zero and the specific power (neutron density) is constant - Figure 3-470.

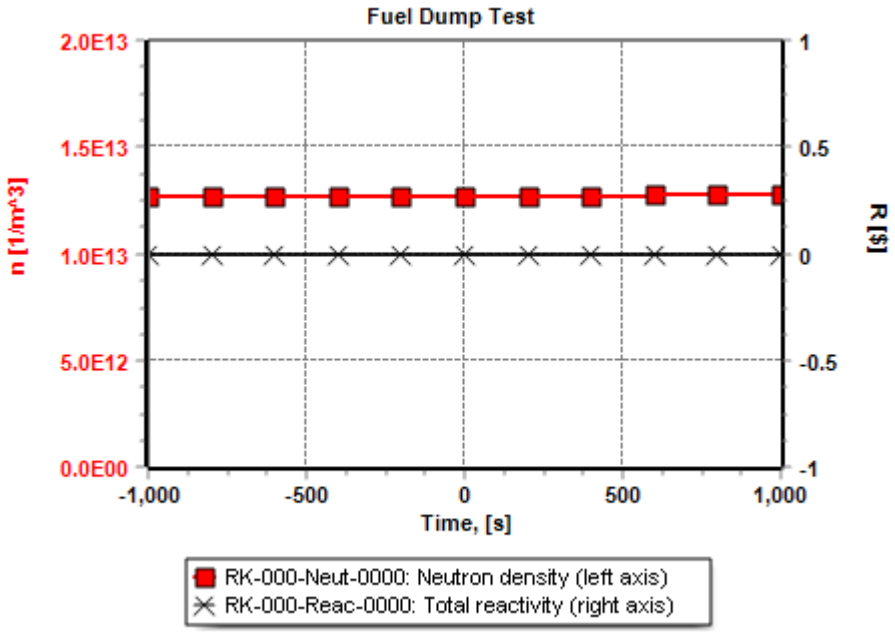

Figure 3-470 Fuel dump - simple case, reactivity and neutron density

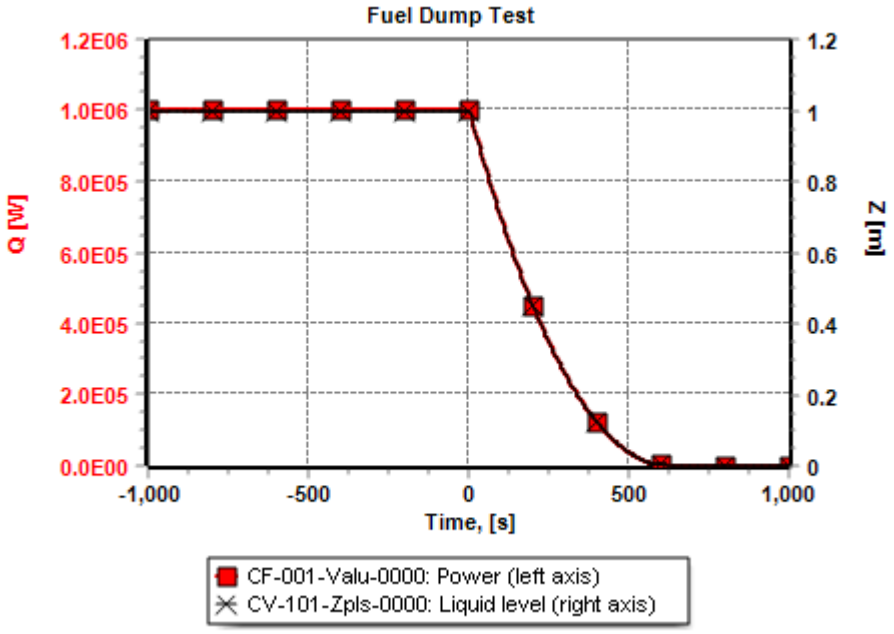

Figure 3-471 Fuel dump - simple case, power and liquid level

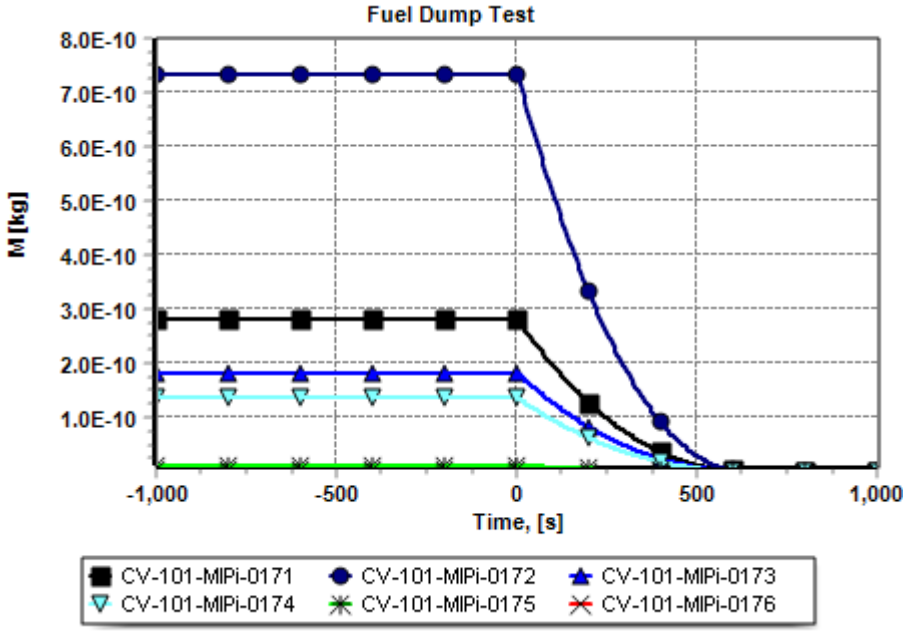

Figure 3-472 Fuel dump - simple case, DNP concentrations in CV-101

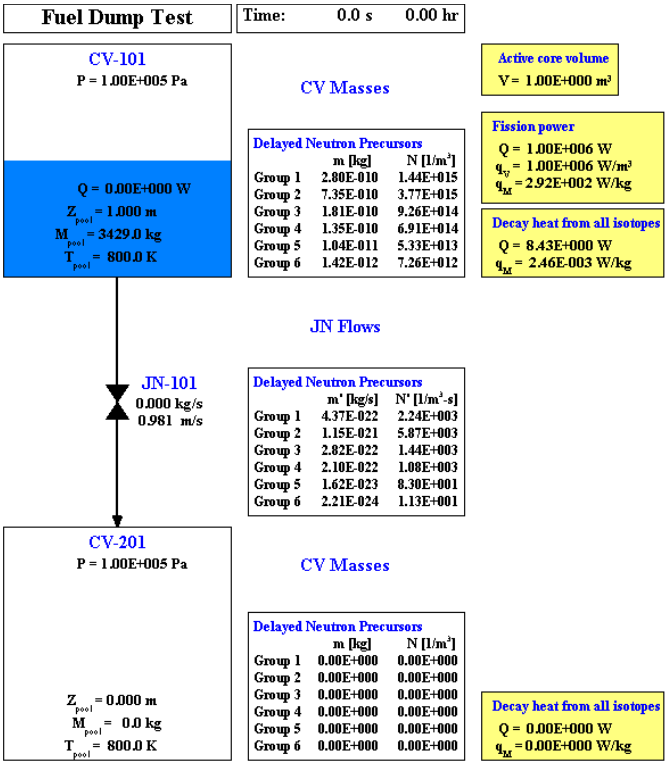

Figure 3-473 Fuel dump - simple case, t = 0.0 s

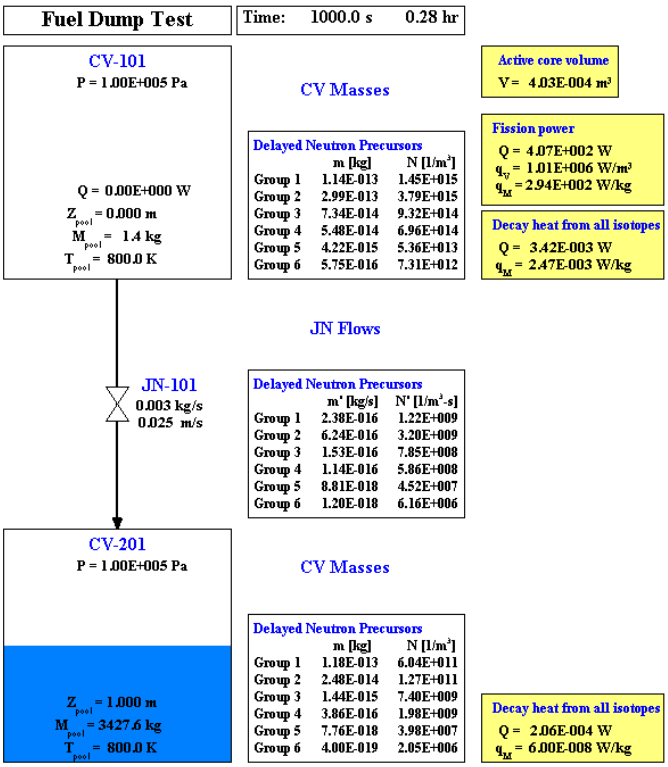

Figure 3-474 Fuel dump - simple case, t = 1000.0 s

In the model, the power calculated by the reactor kinetics model is ignored as a CV heat source. This simplification is made to obtain steady state without a need of modeling a cooling system. An analogical model where the heat source is taken into account is presented in:

`\Z-INPUTS\RT\Cir-fuel\Dump\CV-power-source-yes\Dump-NoIT`

In this case there is a slow temperature increase during the steady state period ($-1000.0 < t < 0.0$ s). Consequently there is a slow level increase due to thermal expansion of the fluid. Other results are very similar.

Reactivity Feedback

In this case again only the delayed neutron precursors (DNP) are considered. Compared to the previous case a reactivity feedback from core volume change is taken into account. It is assumed that the reactivity decreases linearly from 0 to –1.0 $ when the liquid level decreases from initial level to zero. As in the previous case, the initial power is set as 10^6 W. At t=0.0 s the valve JN-101 opens and the salt mixture flows down to CV-201. The input deck is located in:

`\Z-INPUTS\RT\Cir-fuel\Dump\CV-power-source-no\Dump-NoIT-Volume-feedback-1`

Results are shown in Figure 3-475 through Figure 3-477. The total reactivity decreases due to volume change reactivity from 0.0 to –1.0 $ (Figure 3-475). The total power (Figure 3-476) and the DNP masses (Figure 3-477) decrease faster than in the previous case because the specific power (neutron density) decreases (Figure 3-475), while in the previous case it remained constant.

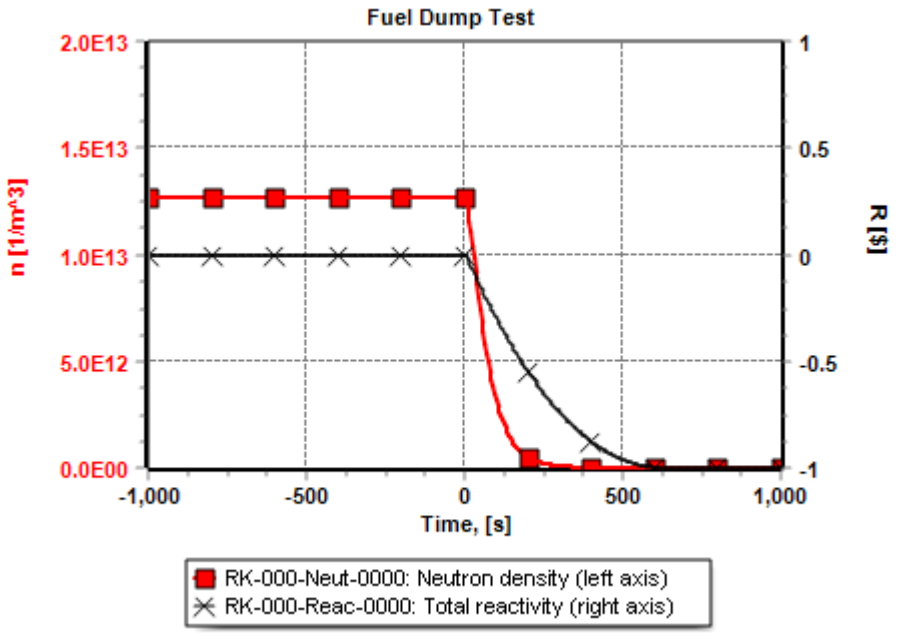

Figure 3-475 Fuel dump - reactivity feedback, reactivity and neutron density

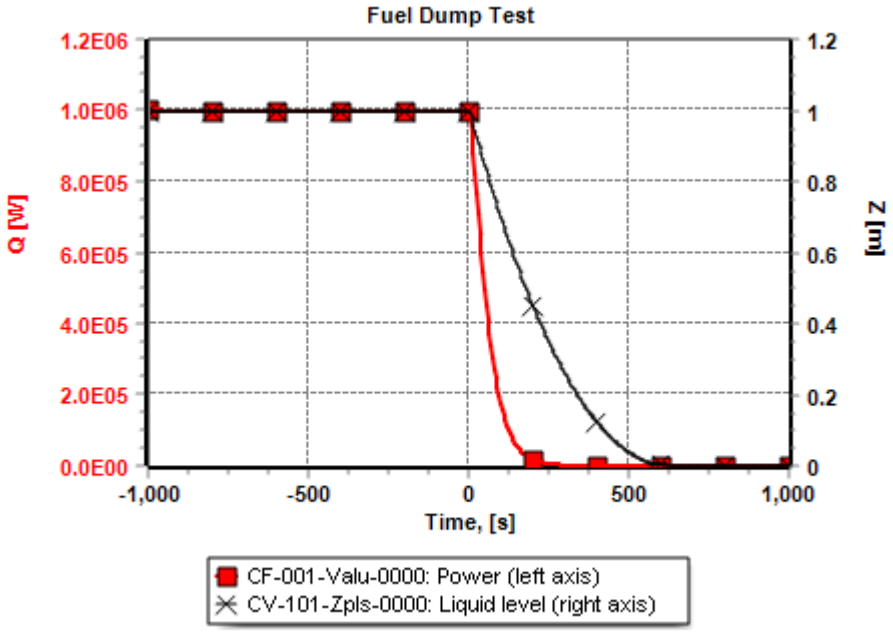

Figure 3-476 Fuel dump - reactivity feedback, power and liquid level

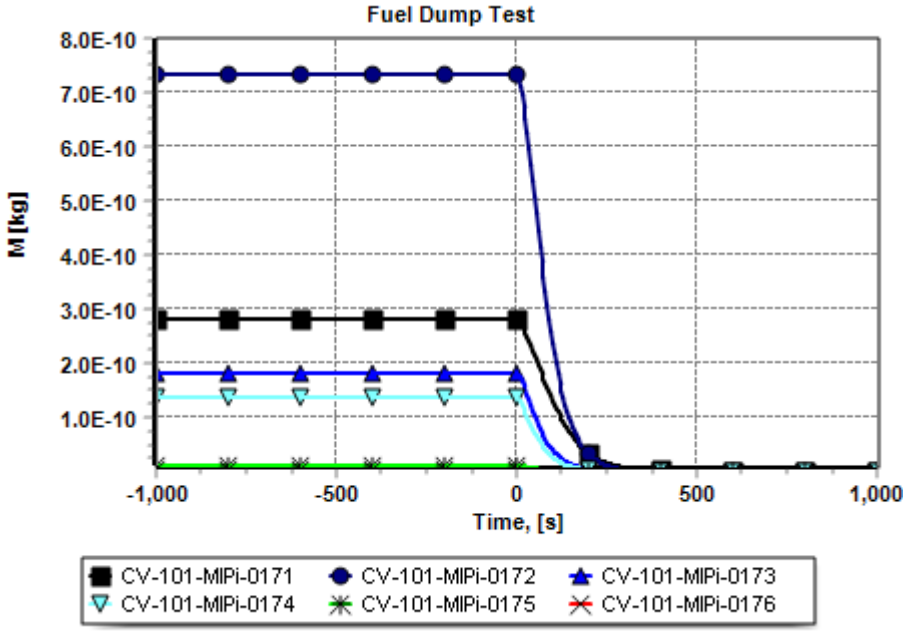

Figure 3-477 Fuel dump - reactivity feedback, DNP concentrations in CV-101

All IT Isotopes

In this case not only the delayed neutron precursors (DNP) are considered, but all isotopes, as used by default by the Isotope Transformation (IT) model within the Reactor Kinetics Package. In this case a control system is needed, otherwise small changes of isotope concentrations, mainly Xe-135, would cause slow power decrease during a steady-state period, prior to fuel dump. A simple Automatic Power Control (APC) system has been designed to keep the fission power at the desired level (934 kW, corresponding total power of about 1.0 MW). The same reactivity feedback is considered as in the previous case: the reactivity decreases linearly from 0 to –1.0 $ when the liquid level decreases from initial level to zero. The total initial power (fission + decay) is 10^6 W. At t=0.0 s the valve JN-101 opens and the salt mixture flows down to CV-201. The input deck is located in:

`\Z-INPUTS\RT\Cir-fuel\Dump\CV-power-source-no\Dump-IT`

Results are shown in Figure 3-478 through Figure 3-482. Figure 3-478 shows the reactor power and reactivity due to APC and due to core volume change. The Automatic Power Control inserts slowly reactivity during steady state to compensate a slow build-up of poisons and keep the power constant.

The total power (Figure 3-479) and the DNP masses (Figure 3-480) decrease faster than the liquid level because the neutron density decreases due to feedback from decreasing core volume (Figure 3-478). Figure 3-481 shows the state of the system at the start of the transient, Figure 3-482 at time t = 1000.0 after start of the fuel dump. These results are very similar to the results of the previous case (Figure 3-476, Figure 3-477). As an “added value” of this test, the isotopes such as poisons, decay heat producers, are tracked; their behavior can be seen in Figure 3-481 and Figure 3-482.

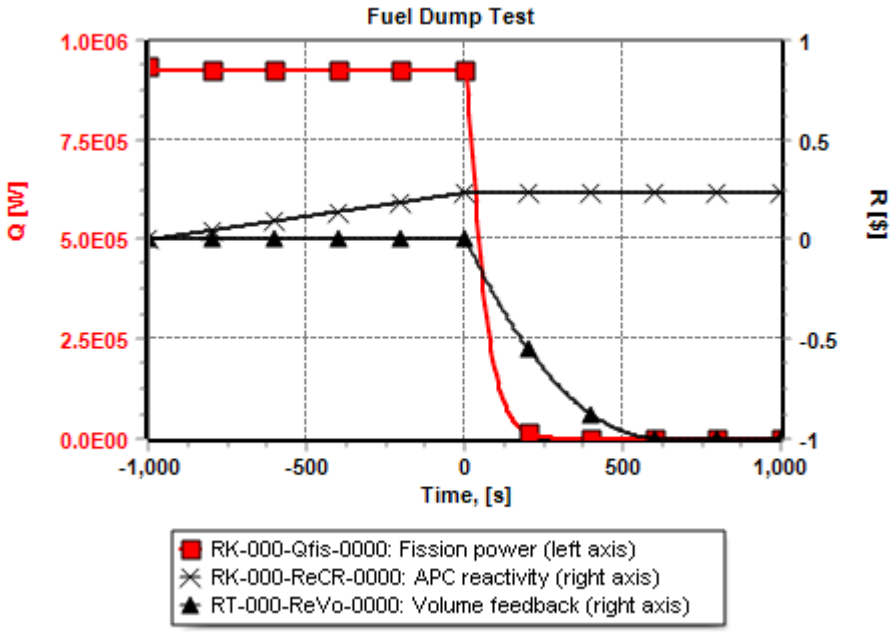

Figure 3-478 Fuel dump - all IT isotopes, reactivity and neutron density

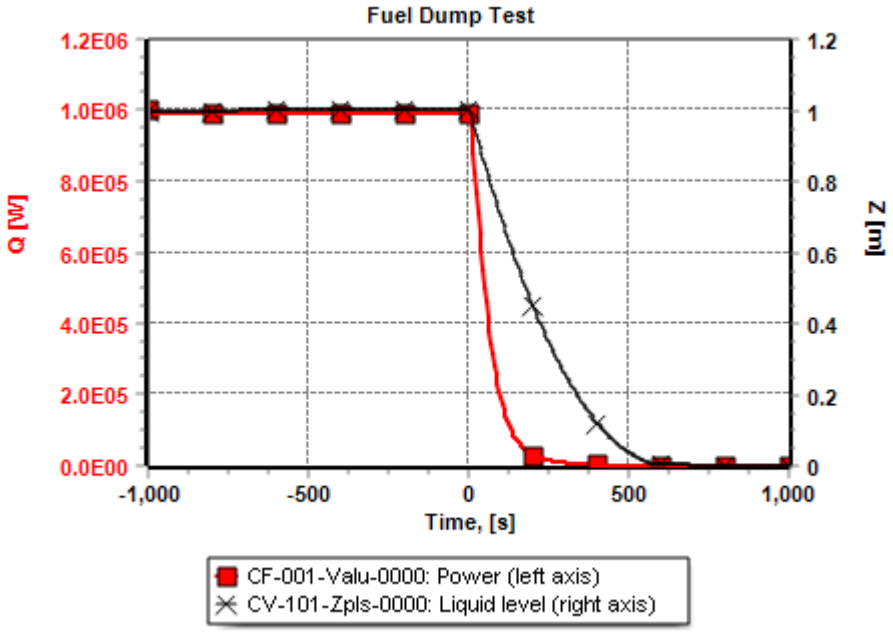

Figure 3-479 Fuel dump - all IT isotopes, power and liquid level

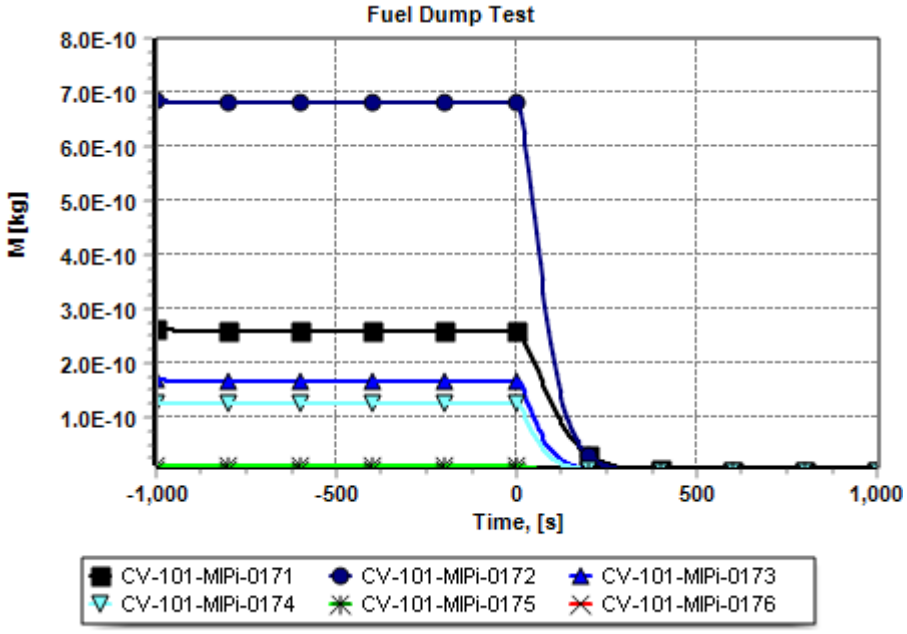

Figure 3-480 Fuel dump - all IT isotopes, DNP concentrations in CV-101

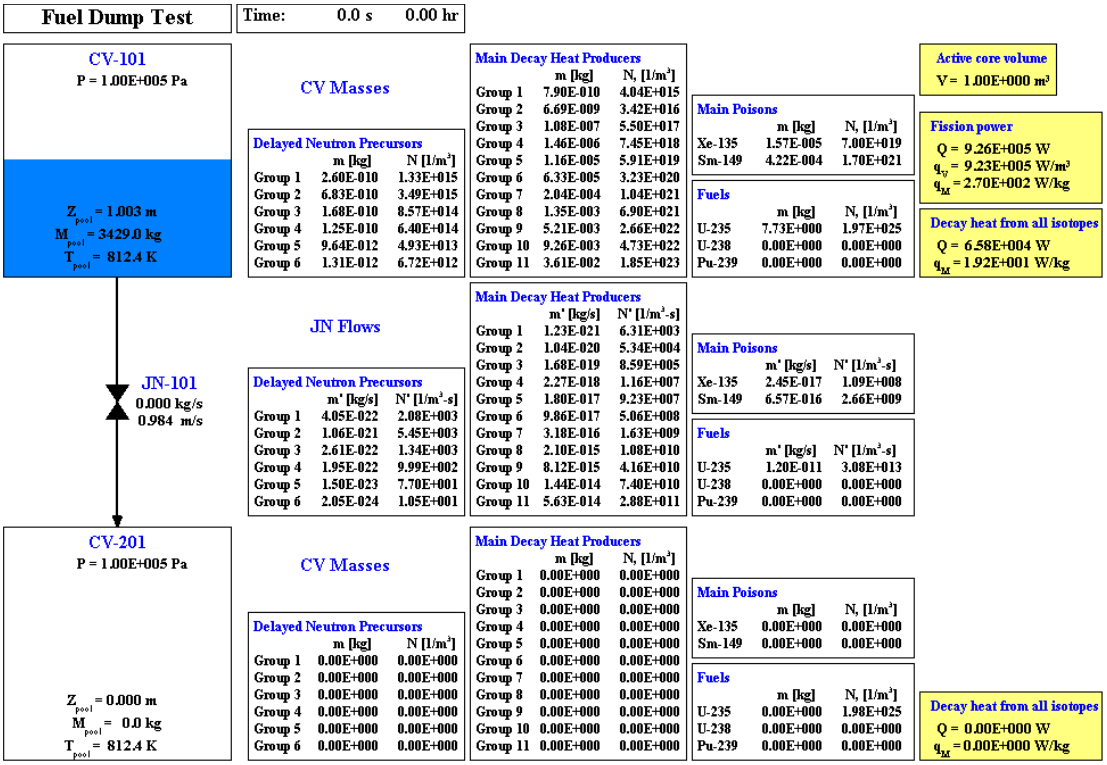

Figure 3-481 Fuel dump - all IT isotopes, t = 0.0 s

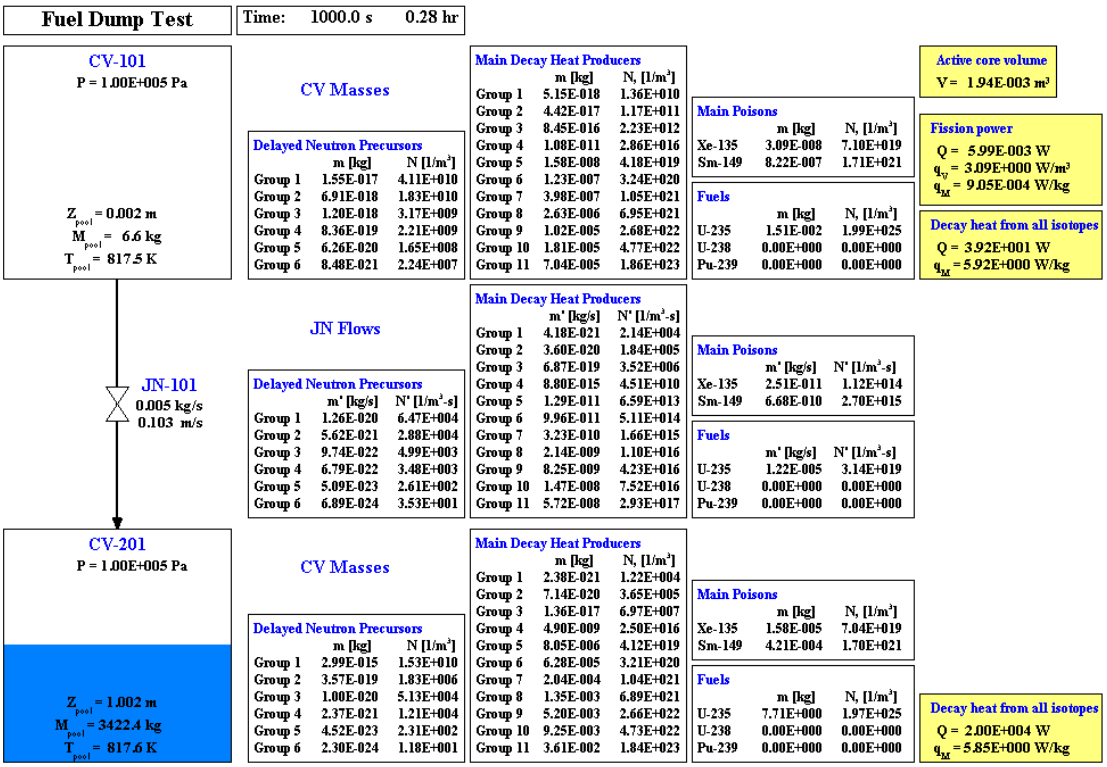

Figure 3-482 Fuel dump - all IT isotopes, t = 1000.0 s

3.9.3.12 Analyzing Fission Product Behavior in Circulating Fuels

When a user wishes to analyze behavior of a fission product decay chain that is not a part of the RK Package, there are two alternative ways to do that.

- ***Method 1***. The decay chain can be defined in the RK Package as a user-defined chain and then mapped to the RT Package. This way the calculation procedure will be exactly the same as used for the delayed neutron precursors and the default chains of the RK Package.

- ***Method 2.*** The user may activate the option to calculate the source of the isotopes within RT Package (non-mapped from the RK) on the same way as those mapped from the RK Package. The source is calculated by the code as:

$$S_i = \gamma_{f,i} \cdot \sum_{k \in fis} \sigma_{f,k} N_k \Phi - \sigma_{a,i} N_i \Phi + \sum_{j \neq i} \sigma_{a,j} N_j \Phi \gamma_{a,j \to i}$$

Here Φ is the neutron flux (1/m^2-s), N_k is the concentration (1/m^3) of isotope k, $\sigma_{f,k}$ is the fission cross section of isotope k, $\sigma_{a,j}$ is the neutron capture (non-fissile absorption) cross section of isotope j, $\gamma_{f,i}$ is the average yield fraction of isotope i from fission of all fissile isotopes, $\gamma_{a,j \to i}$ is the yield fraction of isotope i due to neutron capture by isotope j.

In such case the isotope chain is present only in the RT Package and the calculation procedure is somewhat different but the results are almost exactly the same as in method 1.

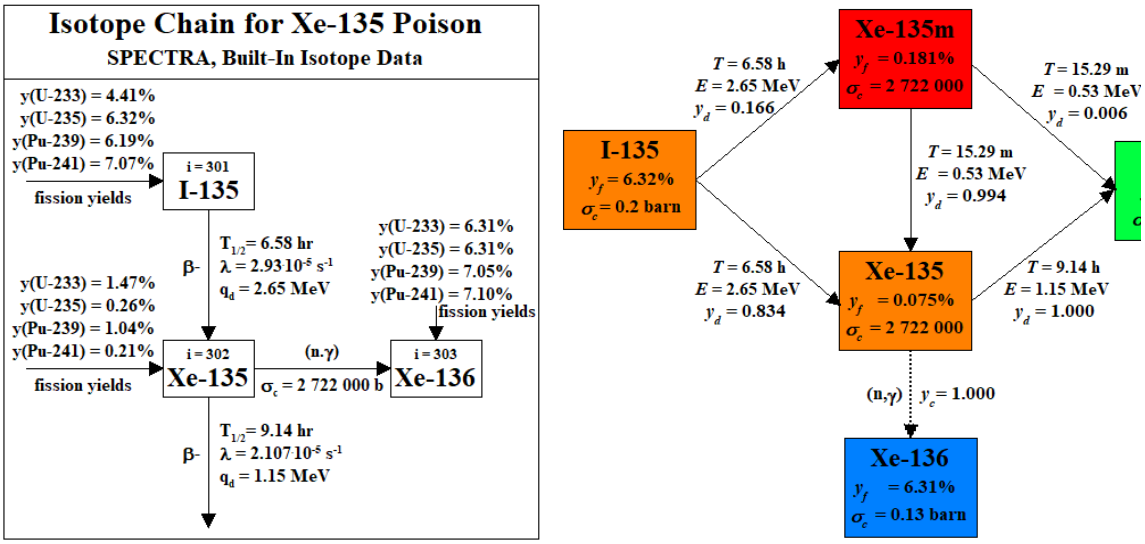

Figure 3-483 Decay chain M_W = 135,
left: RK Package see Volume 1, "Description of the Built-in Isotope Library"
right: RT Package, see Volume 1, "Isotope Chains (Decay Chains)"

One difference is related to the fission yields. In the RK Package, the fission yield may be different for each fissile isotope, as the yield fraction is given as $\gamma_{f,k\to i}$: yield fraction of isotope *i* from fission of a nuclide of isotope *k*. In contrast, the RT Package uses only one yield fraction for each isotope, $\gamma_{f,i}$, and the user must make sure that the value appropriate for given fuel is used. For example, the RK Package contains different I-135 yield fractions for U-233, U-235, Pu-239 and Pu-241 - Figure 3-483, left. The RT Package uses a single yield fraction, with a default value of 6.32%, appropriate for the U-235 fission - Figure 3-483, right.

As an example, let's consider chain 137, which is one of the built-in chains for the RT Package. The chain is shown in Figure 3-484. The two methods are shortly described below. A more detailed description is provided in Volume 3.

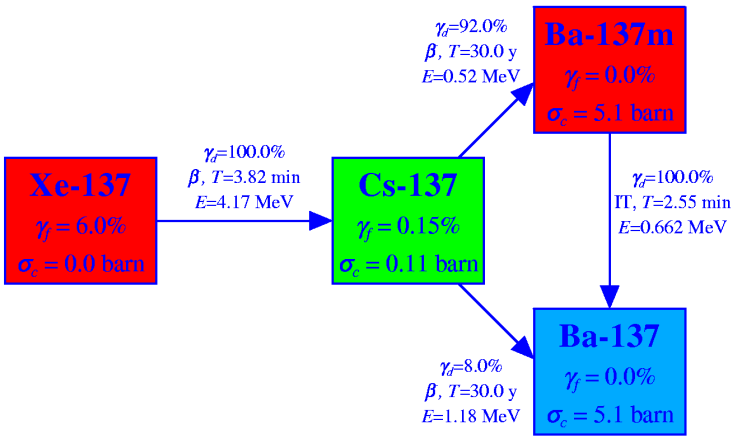

Figure 3-484 Decay chain, M_w = 137

- ***Method 1***

  ✓ ***Step 1***. The decay chain is defined in the RK Package as a user-defined chain, using records 741XXX, 742XXX, 743XXX. At the same time, the built-in chain 137 is NOT activated in the RT Package.

```
*      Additional chain, Chain 137
I05701 Xe-137    *  Isotope No. 701
I05702 Cs-137    *  Isotope No. 702
I05703 Ba-137m   *  Isotope No. 703
I05704 Ba-137    *  Isotope No. 704
*
*      Decay       Decay
*      constant    heat           Yield fractions
*      (1/s)       (W)            Isot. Yield   Isot. Yield
741701 3.02408E-03 6.68034E-13    702   1.00                *  Xe-137 -> Cs-137
741702 7.32667E-10 9.17626E-14    703   0.92    704   0.08   *  Cs-137->Ba-137m, ->Ba-137
741703 4.53020E-03 1.06052E-13    704   1.00                *  Ba-137m-> Ba-137
*
```

```
*      Absorption
*      cross section   Yield fractions
*      (barn)          Isot. Yield
742701 0.0000                          *  Xe-137
742702 0.1100                          *  Cs-137
742703 5.1000                          *  Ba-137m
742704 5.1000                          *  Ba-137
*
*      Fission         Yield fractions
*      cross section   (1)             (2)
*      (barn)          Isot. Yield   Isot. Yield
743108  505.0          701   0.06    702   0.0015  *  U-235
```

- ✓ ***Step 2***. The user-defined chain is mapped to the RT Package using IMAPRK ($h \neq 0$).

```
* ---- CIRCULATING FUEL
*      CIR-FUEL MAPPING IDSORK ICVGRK IVRERK IREIRK XFULRK IRTSRK
748000    2     11111111    2      0     0      0      0.0    0      *  Circulating fuel,
*               map all built-in chains + user chain
```

- ✓ ***Step 3***. The values of molar weight as well as the vapor classes, which are not a part of the RK, are defined within the RT Package using records 880XXY, 885XXY, 886XXY. Those values are not defined within the RK Package and during the mapping process they receive default values, molar weight of 235/2=117.5 and vapor class 9. (Note that this is only necessary in case of a user-defined RK chain. In case of the built-in chains, for example Xe-135 chain, these parameters are correctly defined during mapping.)

```
*      Adjust values of the chain mapped from the RK Package
*
880181 0.0  137.0  * Molar weight (default value = 235.0/2=117.5)
880182 0.0  137.0
880183 0.0  137.0
880184 0.0  137.0
*
885181  1  *  release class Xe-137 (default class = 9, La)
885182  2  *  release class Cs-137
885183  3  *  release class Ba-137m
885184  3  *  release class Ba-137
*
886181  1  *  vapor class Xe-137 (default class = 9, La)
886182  2  *  vapor class Cs-137
886183  3  *  vapor class Ba-137m
886184  3  *  vapor class Ba-137
```

- ***Method 2.***

  - ✓ ***Step 1***. The built-in chain 137 is activated in the RT Package.

```
*      M    Built-in                ISRGRT     AMFPRT
880000 0    0001000000  0 0 0 0 0 0 0      0   -1.0 * 137 built-in chain, no error corr.
```

  - ✓ ***Step 2***. The option to calculate the RT isotope source in the circulating fuel is activated by setting IRTSRK to 2

```
*      CIR-FUEL MAPPING IDSORK ICVGRK IVRERK IREIRK XFULRK IRTSRK
748000    2     1111111    2      0      0      0      0.0    2      *  Circulating fuel,
*          map all built-in chains, use non-mapped RT isotopes
```

SPECTRA input decks for these tests are provided as follows:

- The input decks for Method 1: XE-CS-RK.SPE, LOOP-RK
- The input decks for Method 2: XE-CS-RT.SPE, LOOP-RT

The input decks are located in:
`\Z-INPUTS\RT\Cir-fuel\Loop\Xe-Cs-Nonuniform`

Additionally, a version with uniform power generation is provided in:
`\Z-INPUTS\RT\Cir-fuel\Loop\Xe-Cs-Uniform`

Results of both methods obtained for the non-uniform power case are compared in Figure 3-485, Figure 3-486, Figure 3-487, Figure 3-488, showing stationary state in a simple test loop. The concentrations of Cs-137 and Ba-137, as well as the source strengths in the core are practically identical in both methods. The Ba-137 sources are negative because there is no source of this isotope from fission ($\gamma_f = 0.0$) and the source includes only the negative neutron caption term: $-\sigma_{a,i} N_i \Phi$.

Results of both methods obtained for the uniform power case are compared in Figure 3-489, Figure 3-490, Figure 3-491, Figure 3-492, showing stationary state in a simple test loop. Again, the concentrations of Cs-137 and Ba-137, as well as the source strengths in the core are practically identical in both methods. The source strengths are identical for each core volume for this uniform power test.

In both uniform and non-uniform cases, the concentrations of the fission products are very similar. The concentrations are somewhat lower in the upper part of the core and hot leg due to thermal expansion of the carrier fluid, assumed here as salt FLiBe.

Conclusion

In conclusion, both methods presented above gave the same results. **Method 2** is simpler and therefore this method is recommended for analyzing fission product behavior in circulating fuel.

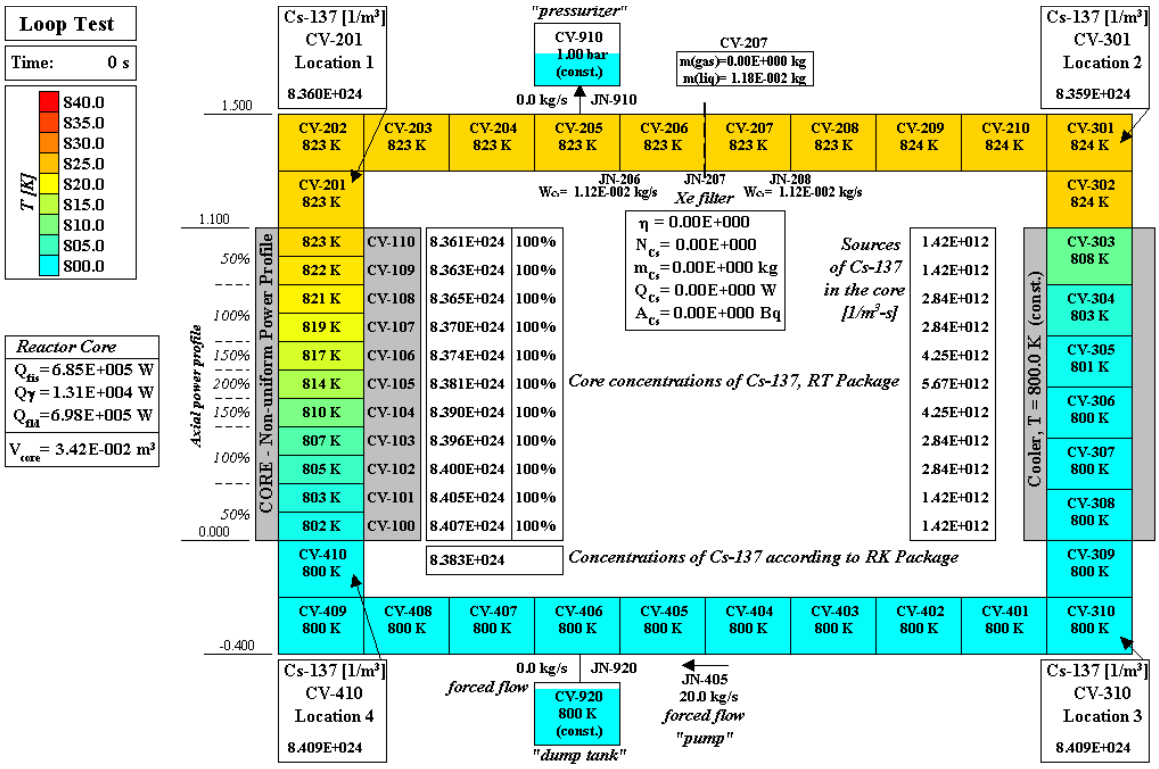

Figure 3-485 Analysis of chain 137, non-uniform power, concentrations of Cs-137, method 1

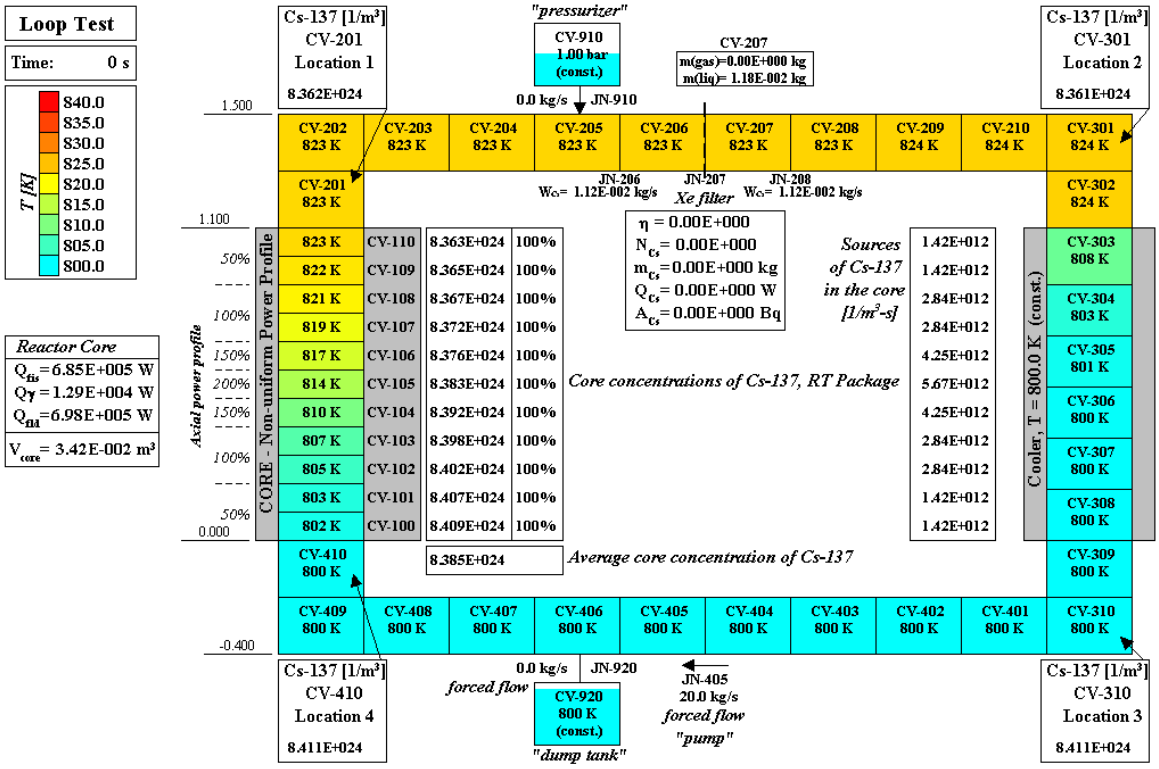

Figure 3-486 Analysis of Chain 137, non-uniform power, concentrations of Cs-137, method 2

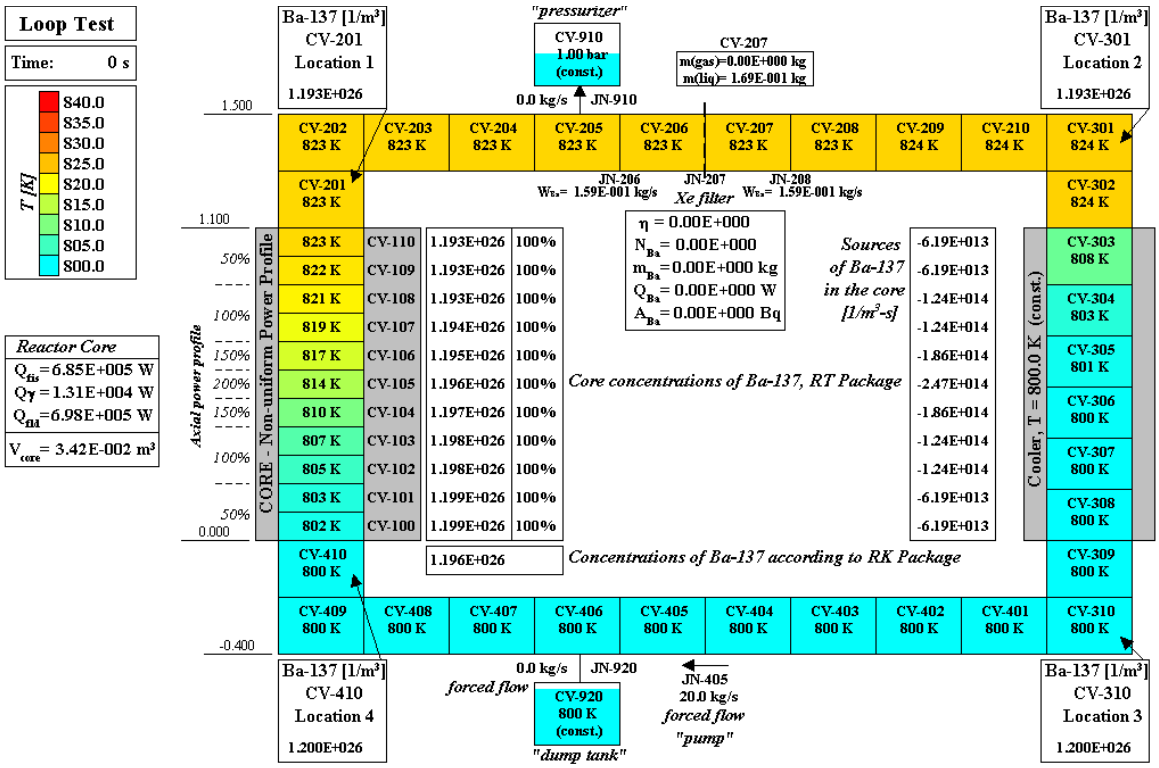

Figure 3-487 Analysis of Chain 137, non-uniform power, concentrations of Ba-137, method 1

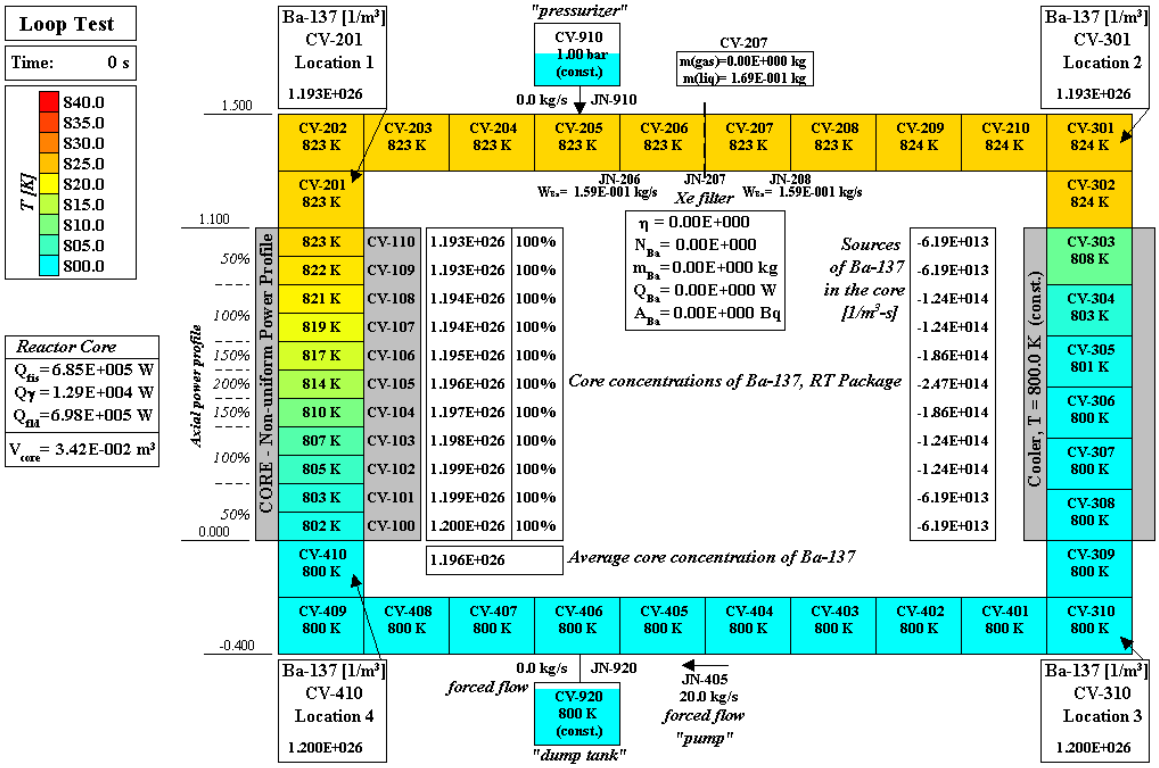

Figure 3-488 Analysis of Chain 137, non-uniform power, concentrations of Ba-137, method 2

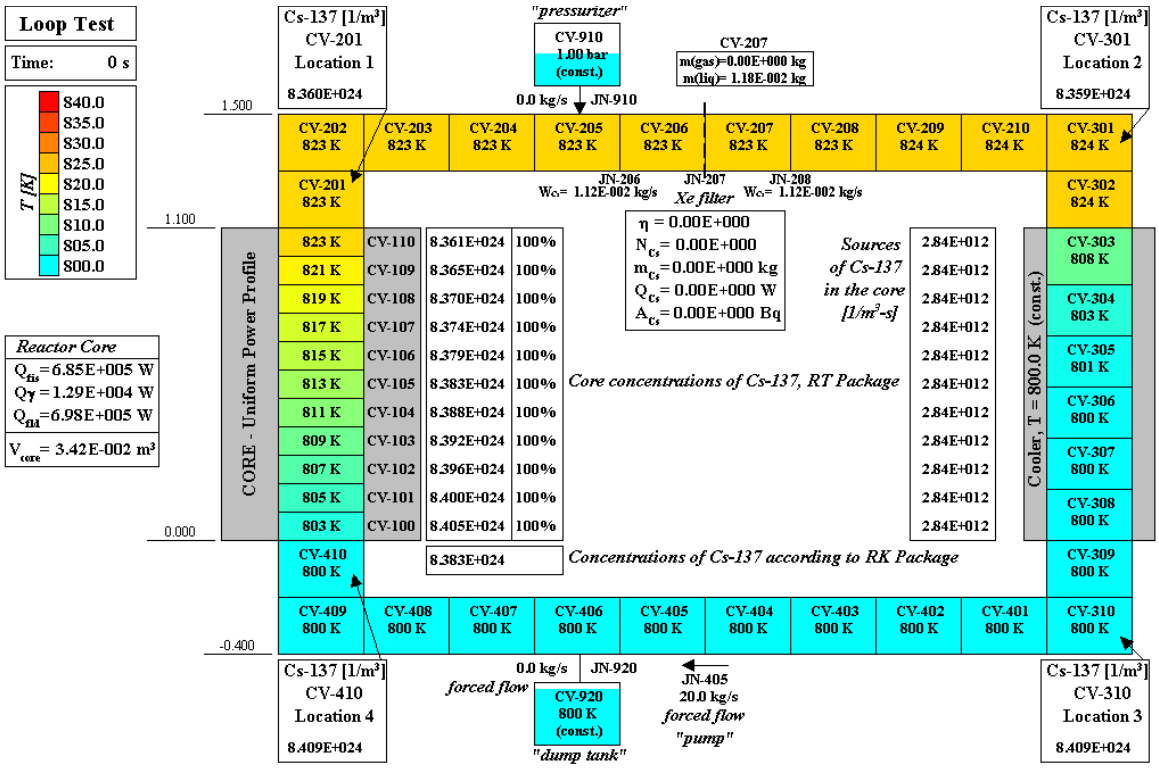

Figure 3-489 Analysis of chain 137, uniform power, concentrations of Cs-137, method 1

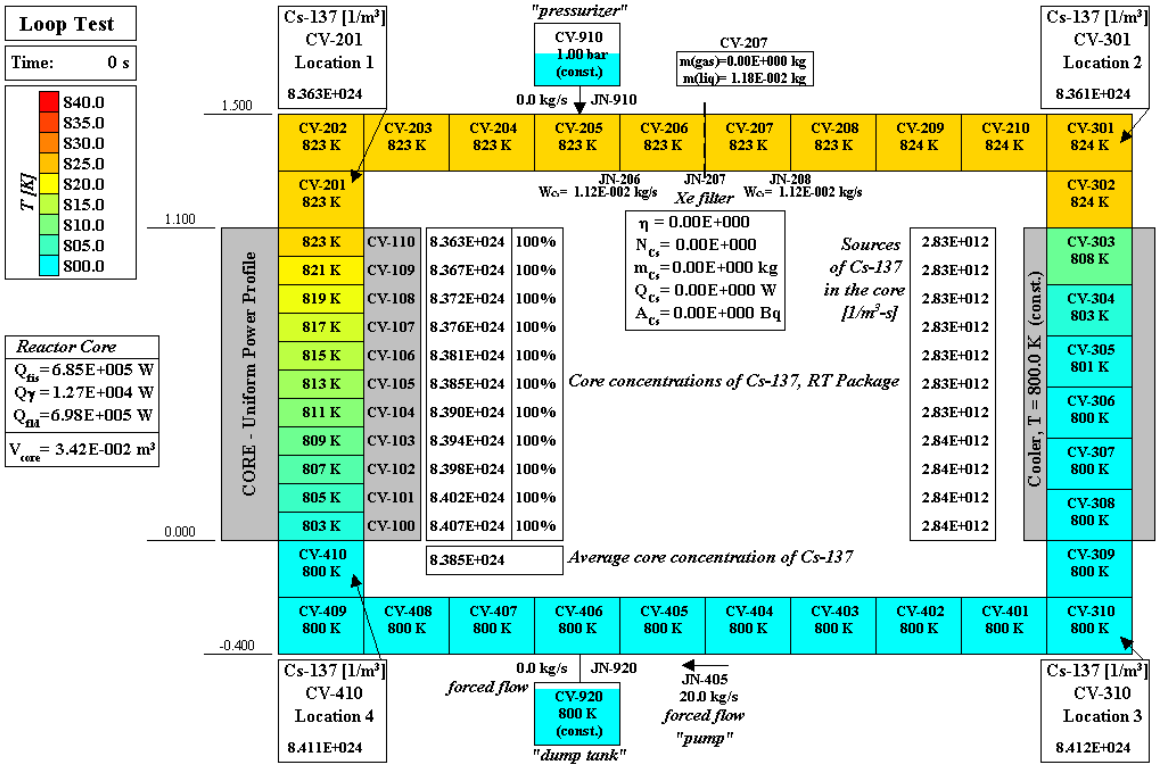

Figure 3-490 Analysis of Chain 137, uniform power, concentrations of Cs-137, method 2

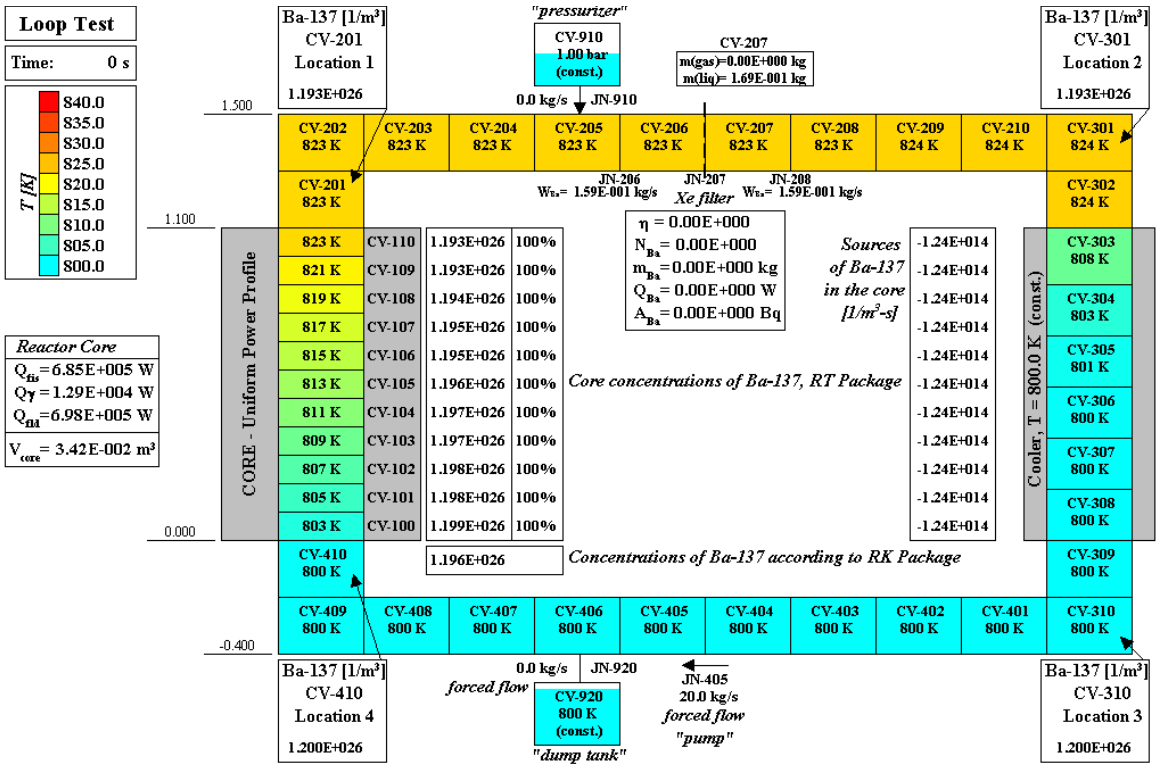

Figure 3-491 Analysis of Chain 137, uniform power, concentrations of Ba-137, method 1

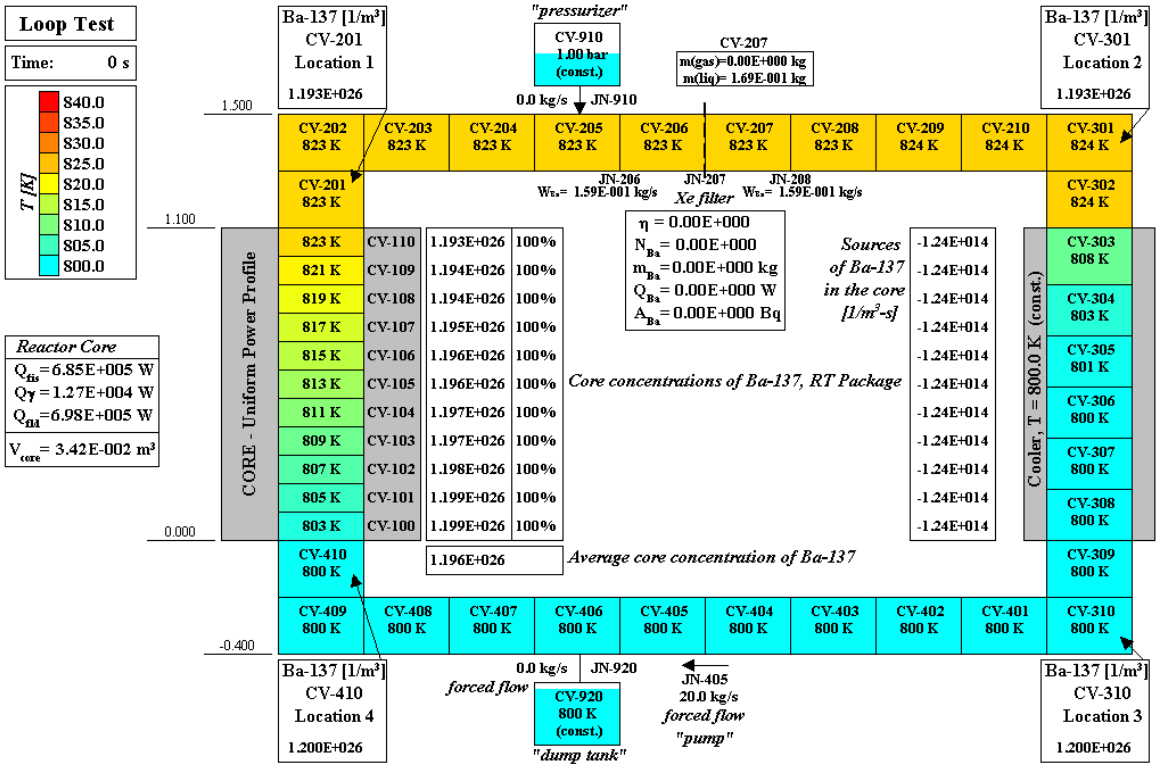

Figure 3-492 Analysis of Chain 137, uniform power, concentrations of Ba-137, method 2

3.9.3.13 Circulating Fuels - Influence of Reactor Volume

Typically, the reactor core of a molten salt reactor consists of liquid (with dissolved fuel) and solid (for example graphite moderator in MSRE). In the case of MSRE, the liquid volume fraction is 0.225; the graphite volume fraction is 0.775.

When preparing an input deck, the user may define the reactor as just liquid volume or the total volume of liquid and solid. The results will be the same, as is shown below, however, the user must enter consistently all relevant parameters. The main input parameters involved are:

- Reactor core volume (m^3): RVOLRK (record 751000)
- Liquid volume fraction in the reactor with circulating fuel: RLTVRK (record 748000)
- Macroscopic fission cross section, Σ_f, (1/m), SIGFRK (record 750000)
- Prompt neutron generation time, Λ, (s), PNGTRK (record 750000)

The example discussed below shows both ways of defining the reactor volume and shows that results are identical. The input decks are located in:

```
\Z-INPUTS\RT\Cir-fuel\Loop\Xe-Cs-Uniform
\Z-INPUTS\RT\Cir-fuel\Loop\Xe-Cs-Nonuniform
```

Two cases are considered. In the base case, the reactor volume is defined as just the fluid volume. These are the two cases discussed in the previous section:

- XE-CS-CIR-RK.SPE (RLTVRK=1.0, RVOLRK=0.0342, SIGFRK=1.0)
- XE-CS-CIR-RT.SPE (RLTVRK=1.0, RVOLRK=0.0342, SIGFRK=1.0)

The reactor volume is in this case the sum of liquid volumes in all core volumes (CV-100 through CV-110), which is equal to $(1 - \alpha)\ (L\ \pi\ D^2 / 4) = 0.99 \times 1.10 \times \pi \times 0.2^2/4 = 0.0342\ m^3$. The macroscopic fission cross section is assumed as $\Sigma_f = 1.0$ (1/m). The core power is assumed to be 0.685 MW. This leads to average neutron density of 2.54E+14 ($1/m^3$) - Figure 3-495, left.

For the next two cases, the liquid volume fraction was assumed as 0.25. These cases are:

- XE-CS-CIR-RK-025.SPE (RLTVRK=0.25, RVOLRK=0.1368, SIGFRK=0.25)
- XE-CS-CIR-RT-025.SPE (RLTVRK=0.25, RVOLRK=0.1368, SIGFRK=0.25)

The liquid fraction is for these cases equal to RLTVRK = 0.25. The reactor volume is set to the fluid volume divided by 0.25: RVOLRK = 0.0342 / 0.25 = 0.1368 m^3. Finally the macroscopic fission cross section is set to SIGFRK = 1.0×0.25 = 0.25 1/m. In short, when the reactor volume is increased, the average concentrations of fuel has to be decreased by the same factor. Consequently, the average neutron density is the same: 2.54E+14 ($1/m^3$) - Figure 3-495, right. Note that the default value of PNGTRK was used in all cases, which means PNGTRK increases by a factor of 4 when SIGFRK is reduced by a factor of 4 ($\Lambda \sim 1 / \Sigma_f$).

Results of the cases XE-SC-RK and XE-CS-RK-025 are compared in Figure 3-493 through Figure 3-497. It is seen that the stationary state values are practically identical (Figure 3-493, Figure 3-494, Figure 3-495).

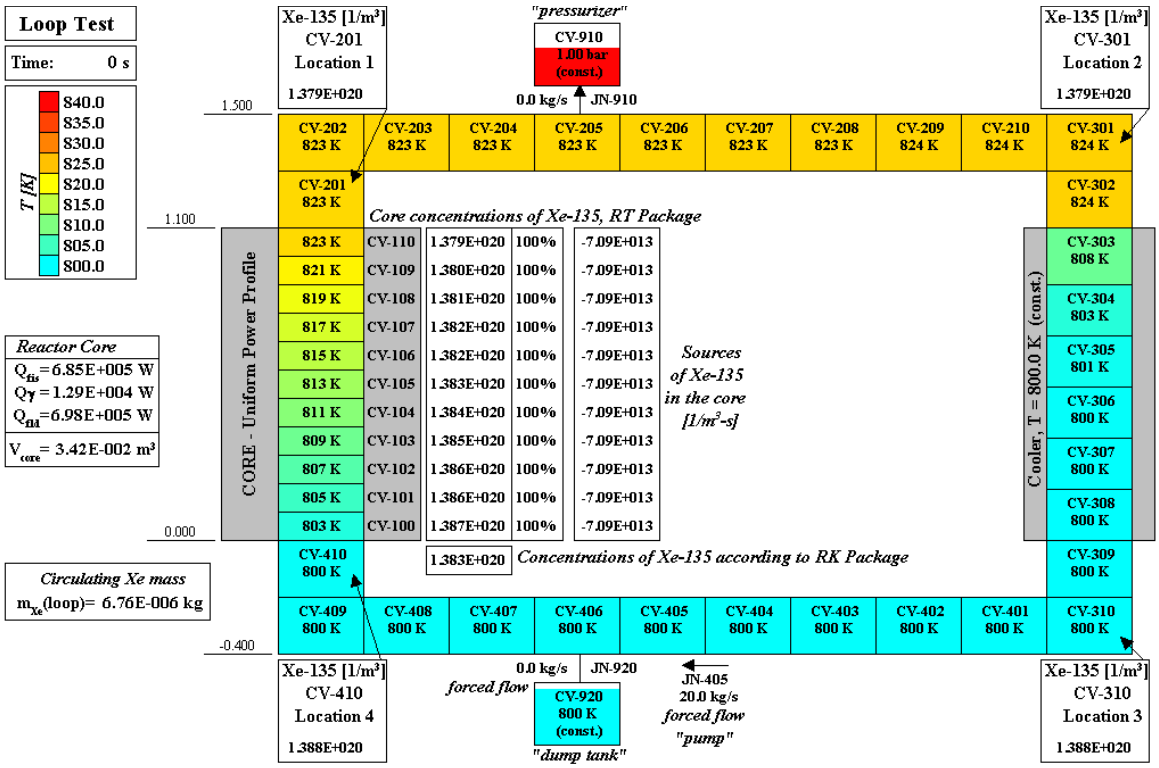

Figure 3-493 Xe-CS-CIR-RK test, steady state, reactor volume = fluid volume

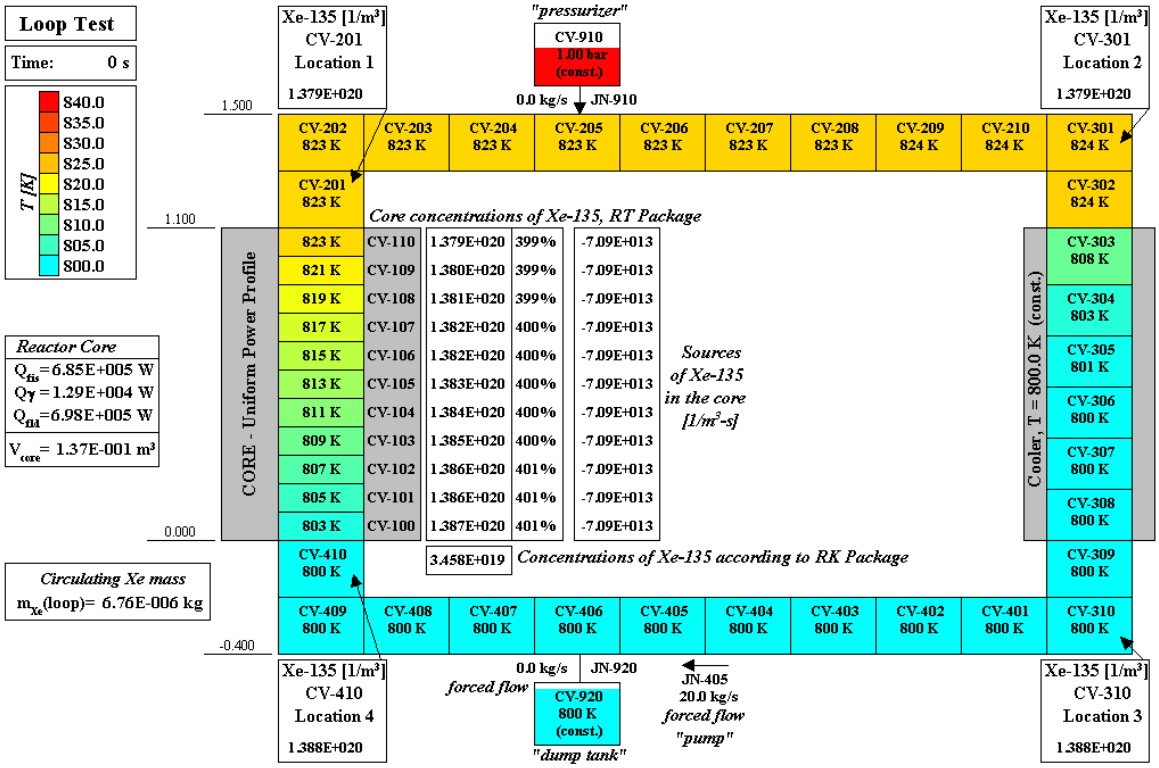

Figure 3-494 Xe-CS-CIR-RK-025 test, steady state, reactor volume = fluid volume / 0.25

Reactor Kinetics | Time: 0.2 s 0.00 hr

=RK= Data

Neutron Data

Neutron density, n, 1/m³	2.54E+014
Neutron flux, Φ, 1/m²-s	6.50E+017
Neutron source, S, 1/s	

Reactivity Data

Toatal reactivity, $	5.47E-001
Control rod, $	-0.165
Fuel+mod feedback, $	1.872
Isotope feedback, $	35.998
Volume change feedback, $	0.000

Reactor Core Power Data, RK

Fission power, W	6.850E+005
Decay power, W	1.290E+004
Total core power, W	6.979E+005

Core, RK

Active core volume, m³	3.42E-002

Delayed Neutron Precursors - RK

Group 1, [1/m³]	4.67E+015
Group 2, [1/m³]	1.33E+016
Group 3, [1/m³]	5.43E+015
Group 4, [1/m³]	7.53E+015
Group 5, [1/m³]	9.09E+014
Group 6, [1/m³]	1.37E+014

Decay Heat Isotope Data - RK

	N, [1/m³]	q, [W/m³]
Group 1	7.91E+016	5.37E+004
Group 2	5.09E+017	1.13E+005
Group 3	2.19E+018	5.67E+004
Group 4	2.49E+019	5.93E+004
Group 5	2.00E+020	3.64E+004
Group 6	1.08E+021	1.99E+004
Group 7	3.46E+021	7.09E+003
Group 8	2.29E+022	5.03E+003
Group 9	8.82E+022	3.52E+003
Group 10	1.57E+023	1.78E+003
Group 11	6.12E+023	1.78E+002

Poison Data - RK

	N, [1/m³]	R, [$]	ΔR, [$]
I-135	2.16E+020	0.00	0.00
Xe-135	1.38E+020	-2.41	0.01
Sm-149	1.70E+021	-0.67	0.00

Fuel Data - RK

	N, [1/m³]	R, [$]	ΔR, [$]
U-233	0.00E+000	0.00	0.00
U-235	1.97E+025	78.54	-0.25
U-238	9.67E+026	-35.53	0.11
Pu-239	6.57E+018	0.00	0.00
Pu-241	1.93E+009	0.00	0.00

=RT= Data

Reactor Core Power Data, RT

Decay power, W	1.290E+004

Core, RT

Active core volume, m³	3.42E-002

Delayed Neutron Precursors - RT

Group 1, [1/m³]	4.67E+015
Group 2, [1/m³]	1.33E+016
Group 3, [1/m³]	5.43E+015
Group 4, [1/m³]	7.53E+015
Group 5, [1/m³]	9.09E+014
Group 6, [1/m³]	1.37E+014

Decay Heat Isotope Data - RT

	N, [1/m³]	q, [W/m³]
Group 1	7.91E+016	5.37E+004
Group 2	5.09E+017	1.13E+005
Group 3	2.19E+018	5.67E+004
Group 4	2.49E+019	5.92E+004
Group 5	2.00E+020	3.64E+004
Group 6	1.08E+021	1.99E+004
Group 7	3.46E+021	7.08E+003
Group 8	2.29E+022	5.03E+003
Group 9	8.82E+022	3.52E+003
Group 10	1.57E+023	1.78E+003
Group 11	6.11E+023	1.78E+002

Poison Data - RT

	N, [1/m³]
I-135	2.16E+020
Xe-135	1.38E+020
Sm-149	1.69E+021

Fuel Data - RT

	N, [1/m³]
U-233	0.00E+000
U-235	1.97E+025
U-238	9.67E+026
Pu-239	6.57E+018
Pu-241	1.93E+009

Reactor Kinetics | Time: 0.2 s 0.00 hr

=RK= Data

Neutron Data

Neutron density, n, 1/m³	2.54E+014
Neutron flux, Φ, 1/m²-s	6.50E+017
Neutron source, S, 1/s	

Reactivity Data

Toatal reactivity, $	5.47E-001
Control rod, $	-0.165
Fuel+mod feedback, $	1.872
Isotope feedback, $	35.998
Volume change feedback, $	0.000

Reactor Core Power Data, RK

Fission power, W	6.850E+005
Decay power, W	1.290E+004
Total core power, W	6.979E+005

Core, RK

Active core volume, m³	1.37E-001

Delayed Neutron Precursors - RK

Group 1, [1/m³]	1.17E+015
Group 2, [1/m³]	3.33E+015
Group 3, [1/m³]	1.36E+015
Group 4, [1/m³]	1.88E+015
Group 5, [1/m³]	2.27E+014
Group 6, [1/m³]	3.44E+013

Decay Heat Isotope Data - RK

	N, [1/m³]	q, [W/m³]
Group 1	1.98E+016	1.34E+004
Group 2	1.27E+017	2.82E+004
Group 3	5.48E+017	1.42E+004
Group 4	6.21E+018	1.48E+004
Group 5	5.00E+019	9.10E+003
Group 6	2.70E+020	4.98E+003
Group 7	8.64E+020	1.77E+003
Group 8	5.72E+021	1.26E+003
Group 9	2.20E+022	8.81E+002
Group 10	3.92E+022	4.46E+002
Group 11	1.53E+023	4.46E+001

Poison Data - RK

	N, [1/m³]	R, [$]	ΔR, [$]
I-135	5.41E+019	0.00	0.00
Xe-135	3.46E+019	-2.41	0.01
Sm-149	4.24E+020	-0.67	0.00

Fuel Data - RK

	N, [1/m³]	R, [$]	ΔR, [$]
U-233	0.00E+000	0.00	0.00
U-235	4.93E+024	78.54	-0.25
U-238	2.42E+026	-35.53	0.11
Pu-239	1.64E+018	0.00	0.00
Pu-241	4.82E+008	0.00	0.00

=RT= Data

Reactor Core Power Data, RT

Decay power, W	1.290E+004

Core, RT

Active core volume, m³	1.37E-001

Delayed Neutron Precursors - RT

Group 1, [1/m³]	1.17E+015
Group 2, [1/m³]	3.33E+015
Group 3, [1/m³]	1.36E+015
Group 4, [1/m³]	1.88E+015
Group 5, [1/m³]	2.27E+014
Group 6, [1/m³]	3.43E+013

Decay Heat Isotope Data - RT

	N, [1/m³]	q, [W/m³]
Group 1	7.90E+016	5.37E+004
Group 2	5.09E+017	1.13E+005
Group 3	2.19E+018	5.67E+004
Group 4	2.49E+019	5.92E+004
Group 5	2.00E+020	3.64E+004
Group 6	1.08E+021	1.99E+004
Group 7	3.46E+021	7.08E+003
Group 8	2.29E+022	5.03E+003
Group 9	8.82E+022	3.52E+003
Group 10	1.57E+023	1.78E+003
Group 11	6.11E+023	1.78E+002

Poison Data - RT

	N, [1/m³]
I-135	2.16E+020
Xe-135	1.38E+020
Sm-149	1.69E+021

Fuel Data - RT

	N, [1/m³]
U-233	0.00E+000
U-235	1.97E+025
U-238	9.67E+026
Pu-239	6.57E+018
Pu-241	1.93E+009

Figure 3-495 Left: Xe-CS-CIR-RK test, steady state, reactor volume = fluid volume
Right: Xe-CS-CIR-RK-025 test, steady state, reactor volume = fluid volume / 0.25

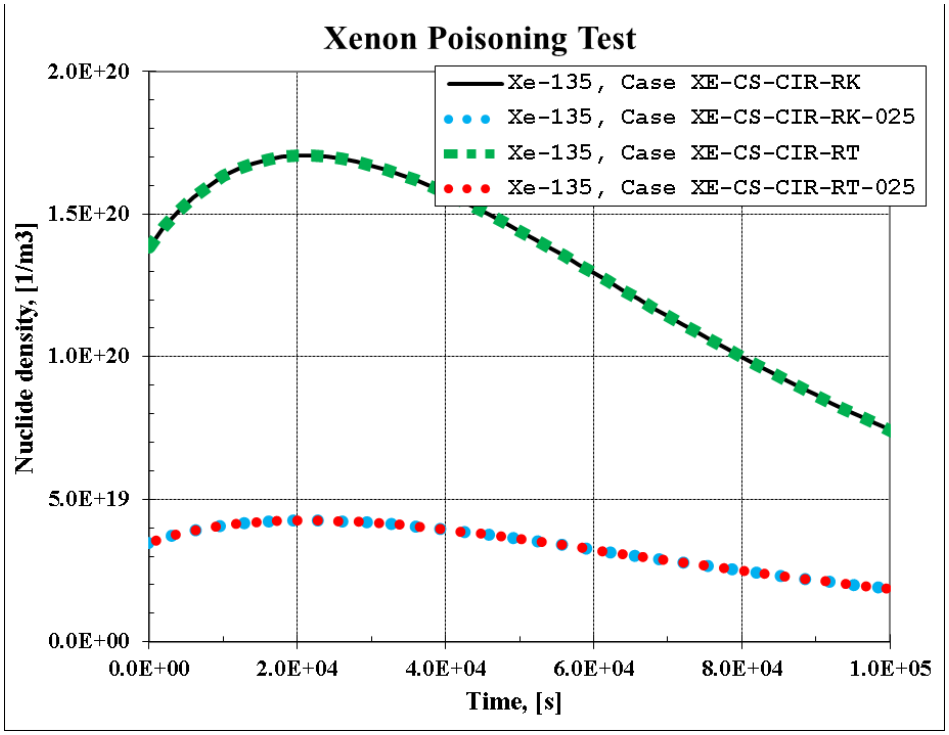

Figure 3-496 Xe-135 density, influence of reactor volume

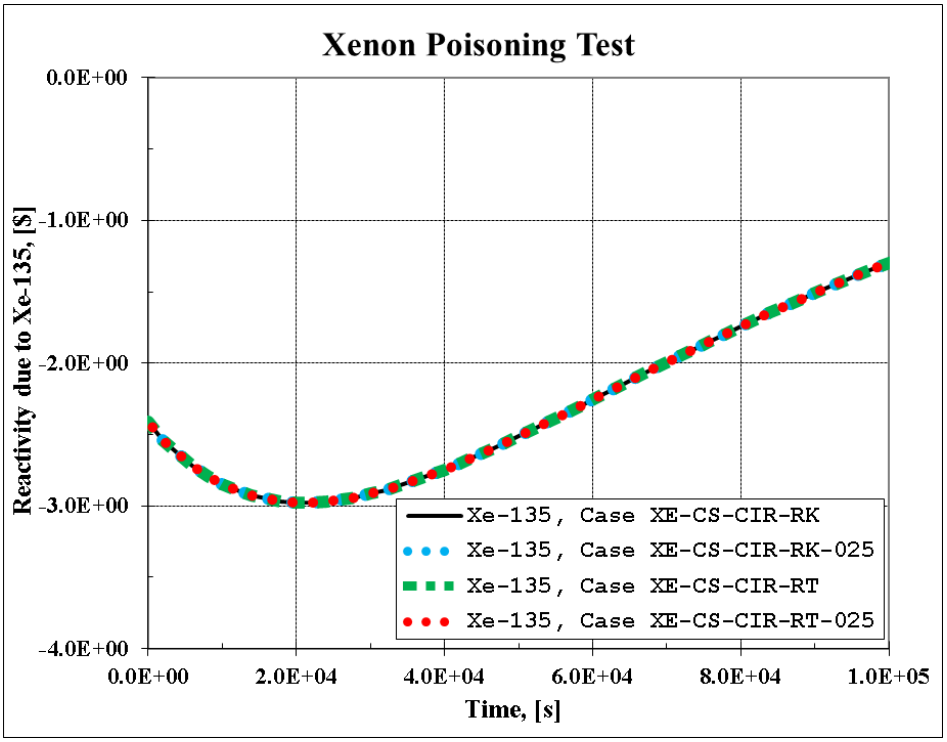

Figure 3-497 Xe-135 reactivity, influence of reactor volume

The concentrations shown in Figure 3-493 and Figure 3-494 are the RT concentrations, which are always the true concentrations in a liquid of CV and as such identical for both cases. The concentrations of isotopes, shown in Figure 3-495 are the RK values and in the "025" case these are 4 times lower, because they are considered as concentrations over the whole core (liquid+solid) which is 4 times larger in the "025" case. For example in case of Xe-135, the steady state values are:

- XE-CS-RK 1.38×10^{20} (1/m^3) (Figure 3-495, left)
- XE-SC-RK-025 3.46×10^{19} (1/m^3) (Figure 3-495, right)

These are concentrations per unit volume of the reactor (smeared liquid and solid). The RT values are meanwhile 1.38×10^{20} (1/m^3) for both cases (Figure 3-493, Figure 3-494) as they always represent the concentrations per unit volume of fluid.

Furthermore, the transient results are the same, which is seen as the Xe-135 poisoning values after shutdown are the same. The Xenon concentrations are of 4 times lower in the "025" cases (Figure 3-496), but the Xenon reactivity effects are exactly the same (Figure 3-497).

Note that in contrast to RVOLRK, which is a constant, user-defined value, the actual reactor volume for a reactor with circulating fuel (plot parameter RK-000-RVol-0000) is a time-dependent parameter and is defined as:

$$V_{core} = \frac{V_{liq}}{RLTVRK} = \frac{1}{RLTVRK} \times \sum_{i=1}^{NTFWRK} V_{pool}(i)$$

Here V_{liq} is the total liquid volume in the core, $V_{pool}(i)$ is the pool volume in the Control Volume i, belonging to the core (with positive power fraction, WTCFRK).

Solid fuel

As an additional check, the same effect is shown for a solid fuel. The input decks are is located:

`\Z-INPUTS\RT\Cir-fuel\Loop\Xe-Cs-Uniform-SOLID`

- XE-CS-CIR-RK.SPE RVOLRK=0.0342, SIGFRK=1.0
- XE-SC-CIR-RK-025.SPE RVOLRK=0.0342/0.25=0.1368, SIGFRK=1.0×0.25= 0.25

Results are shown in Figure 3-498 and Figure 3-499. The concentrations differ by a factor of 4 but the reactivity effect remains the same. The concentrations are of course higher than in case of circulating fuel, for reasons explained in section 3.9.3.7.

Conclusion

The examples presented in this section may seem trivial, but they are shown here mainly as an illustration of how to define the reactor kinetics parameters, such as RVOLRK, SIGFRK, PNGTRK.

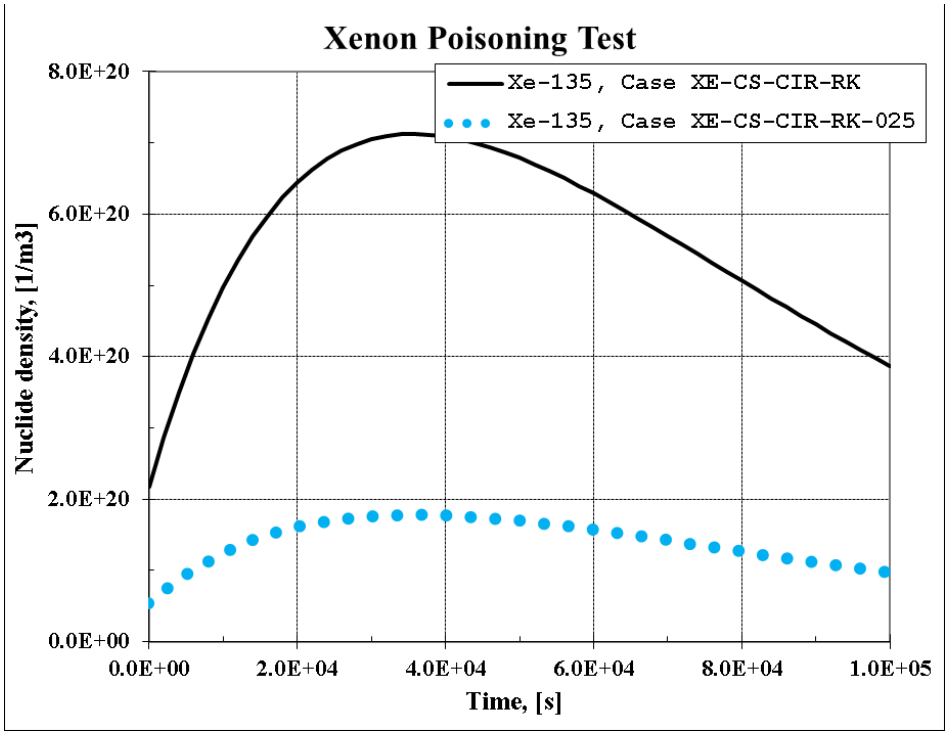

Figure 3-498 Xe-135 density, influence of reactor volume, solid fuel

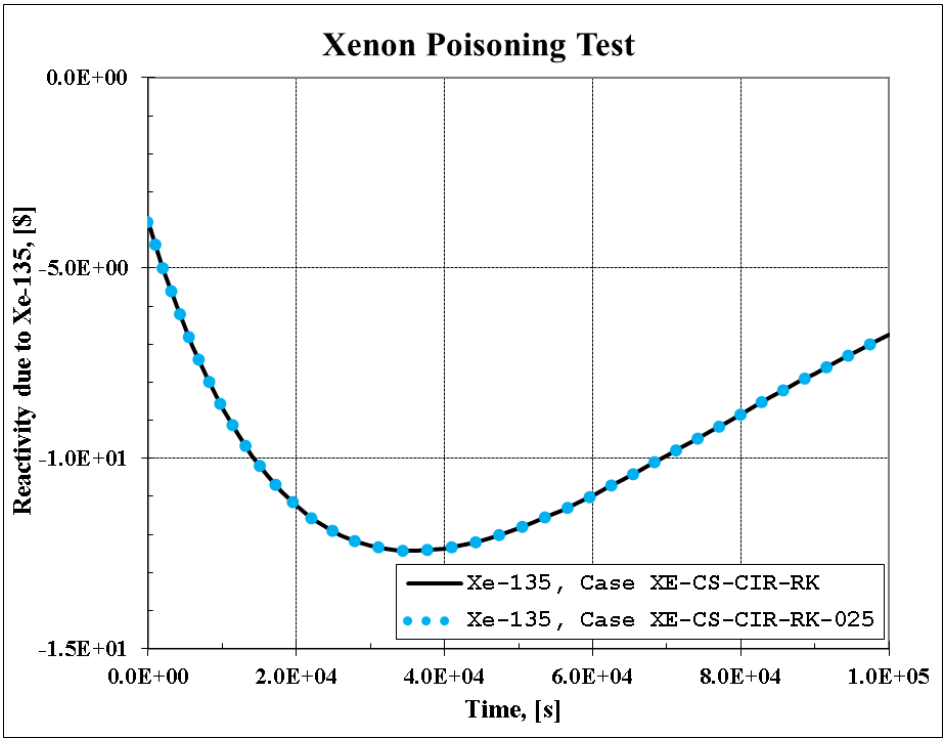

Figure 3-499 Xe-135 reactivity, influence of reactor volume, solid fuel

3.9.3.14 Circulating Fuels - Reactor Volume and DNP Concentrations

This section presents a very simple test case illustrating the difference in the isotope concentrations in the RK Package and in the RT Package. The model consists of two Control Volumes:

- Core salt volume: $V_{c\text{-}s}$ = 1.0 m^3, CV-100
- Non-core salt volume: $V_{n\text{-}s}$ = 3.0 m^3, CV-200

The core is assumed to be composed of the salt and the graphite moderator. The volume of graphite in the core is assumed to be:

- Core graphite volume: $V_{c\text{-}g}$ = 9.0 m^3, SC-100

The total core volume is therefore equal to 10.0 m^3. The ratio of the core salt volume to the total core volume (input parameter RLTVRK) is equal to 0.1. Consequently, the isotope concentrations, as seen by the RK Package, will be 10 times smaller than the concentrations in the core salt volume, which are given by the RT Package.

The input deck is located in: **\Z-INPUTS\RT\Cir-fuel\Loop\DNP\DNP-Test-Case.SPE**. Calculations are performed until stable concentrations of all isotopes are obtained (1000 s). The results are shown in Figure 3-500 and Figure 3-501.

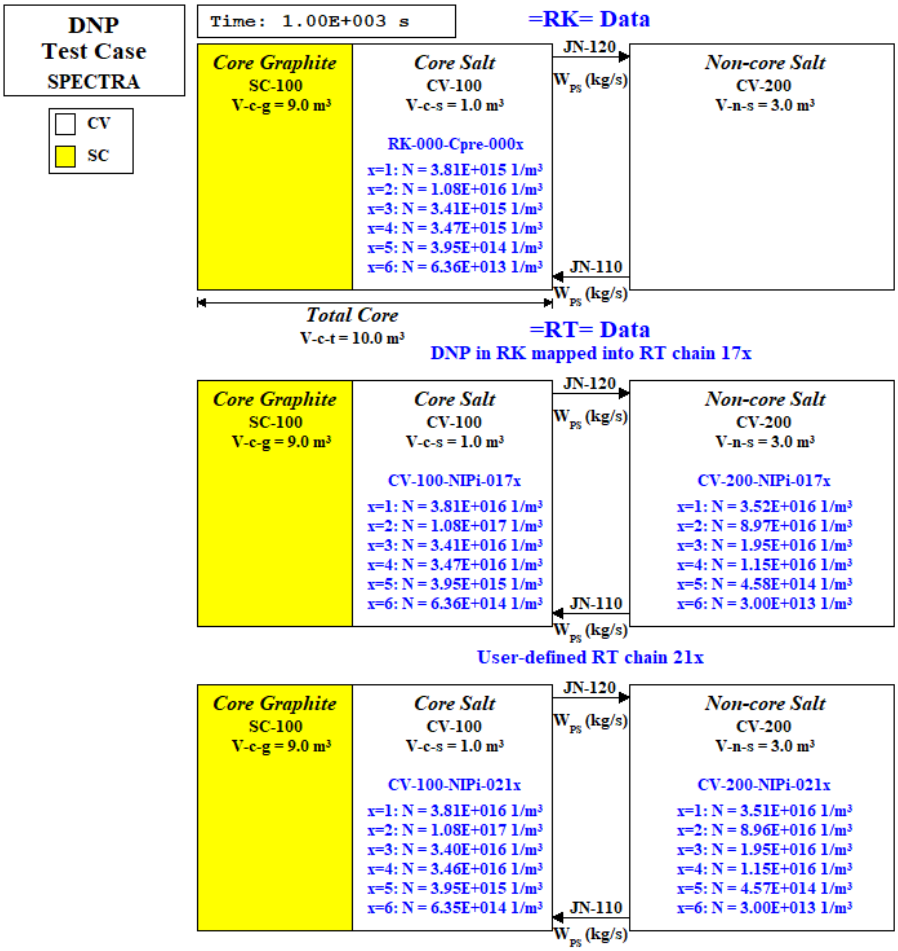

Figure 3-500 Test DNP - isotope concentrations at steady-state conditions

Figure 3-500 shows the delayed neutron precursor (DNP) concentrations in the reactor. Default DNP data is used; six groups with the values of decay constant, λ (1/s) and yield fractions β (-) shown in Table 3-54.

Table 3-54 Delayed neutron precursor data (default values of λ and β)

Group	λ (1/s)	β (-)	γ (-)
1	1.240E-02	2.200E-04	5.500E-04
2	3.050E-02	1.420E-03	3.550E-03
3	1.110E-01	1.270E-03	3.175E-03
4	3.010E-01	2.570E-03	6.425E-03
5	1.140E+00	7.500E-04	1.875E-03
6	3.010E+00	2.700E-04	6.750E-04
	total:	6.500E-03	

The DNP is mapped into RT as chain FP-17x, isotopes FP-171, through FP-176. This may be seen in the output file (*.OUT):

```
 =RT=  DETAILED MAPPING OF ISOTOPES FROM RK TO RT :

         RK Isotope          RT Isotope
         -----------         -------------
       - 101 Th-232   <->  FP-111 Th-232
       - 102 Th-233   <->  FP-112 Th-233
       - 103 Th-234   <->  FP-113 Th-234
       - 104 Pa-233   <->  FP-114 Pa-233
       - 105 Pa-234   <->  FP-115 Pa-234
       - 106  U-233   <->  FP-116  U-233
       - 107  U-234   <->  FP-117  U-234
       - 108  U-235   <->  FP-118  U-235
       - 301  I-135   <->  FP-131  I-135
       - 302 Xe-135   <->  FP-132 Xe-135
       - D.N.PREC.01  <->  FP-171 DNP-01
       - D.N.PREC.02  <->  FP-172 DNP-02
       - D.N.PREC.03  <->  FP-173 DNP-03
       - D.N.PREC.04  <->  FP-174 DNP-04
       - D.N.PREC.05  <->  FP-175 DNP-05
       - D.N.PREC.06  <->  FP-176 DNP-06
```

As may be seen in Figure 3-500, the DNP concentrations in the RK package are exactly an order of magnitude lower than the concentrations in the RT Package (chain 17x), in the core volume, CV-100. Of course, the concentrations in the non-core volume, CV-200, are different and depend on the relative size of the core and the non-core salt volumes, salt flow, decay constant, etc.

Figure 3-501 shows the main parameters of the RK package, the isotope data in the RT package, and the ratio between the RT concentration in CV-100 (the core salt) and the RK concentrations. The concentration ratio is equal to 10.0, as expected.

Figure 3-501 shows also the core volume, as defined by the user in the RK input parameter: RVOLRK and the RT plot parameter RT-000-RVol-0000. The latter is defined as the total core salt volume (in this case CV-100) divide by RLTVRK (=0.1), so it includes the graphite volume.

Another interesting value that may be observed is the reactivity value obtained in the stationary state, equal to 0.536 $ (=0.536×6.5E-3 = 3.48E-3 = 348 pcm). Physically, this means that the DNP fraction of (1 – 0.536 = 0.464) decays outside the core, so an external reactivity must be added to compensate for this loss. A reactivity of 0.0 corresponds to a non-flow situation, where all DNP-s decay inside the core. When the pump is started, forcing the salt circulation, some DNP-s decay outside the core and reactivity has to be added to keep the power constant.

=RK= Data

DNP Test Case

Time: 1.00E+003 s

Neutron Data

Neutron density, n, 1/m^3	4.05E+014
Neutron flux, Φ, 1/m^2-s	1.04E+018
Σ_f Φ, 1/m^3-s	7.15E+017
V_R Σ_f Φ, 1/s	3.44E+019
Toatal reactivity, $	5.36E-001

=RT= Data

Reactor Core Power Data, RK

Fission power, W	1.00E+008
Decay power, W	2.39E+004
Total core power, W	1.00E+008

Reactor Core Power Data, RT

Decay power, W	2.43E+004

Core Volume, RK

Input par.: RVOLRK	1.00E+001

Core Volume, RT

Plot:. RT-000-RVol-0000	1.00E+001

RT/RK

Delayed Neutron Precursors - RK

Group 1, [1/m^3]	3.81E+015
Group 2, [1/m^3]	1.08E+016
Group 3, [1/m^3]	3.41E+015
Group 4, [1/m^3]	3.47E+015
Group 5, [1/m^3]	3.95E+014
Group 6, [1/m^3]	6.36E+013

Delayed Neutron Precursors - RT

Group 1, [1/m^3]	3.81E+016
Group 2, [1/m^3]	1.08E+017
Group 3, [1/m^3]	3.41E+016
Group 4, [1/m^3]	3.47E+016
Group 5, [1/m^3]	3.95E+015
Group 6, [1/m^3]	6.36E+014

Ratio

10.00
10.00
10.00
10.00
10.00
10.00

Poison Data - RK

	N, [1/m^3]	R, [$]	ΔR, [$]
I-135	1.74E+020	0.00	0.00
Xe-135	5.81E+019	-3.24	0.00

Poison Data - RT

	N, [1/m^3] CV-100	N, [1/m^3] CV-200
I-135	1.74E+021	1.74E+021
Xe-135	5.81E+020	5.81E+020

N(CV-100) Ratio

10.00
10.00

Fuel Data - RK

	N, [1/m^3]	R, [$]	ΔR, [$]
U-235	6.18E+024	78.72	-0.07

Fuel Data - RT

	N, [1/m^3] CV-100	N, [1/m^3] CV-200
U-235	6.18E+025	6.18E+025

N(CV-100) Ratio

10.00

Figure 3-501 Test DNP - main parameters

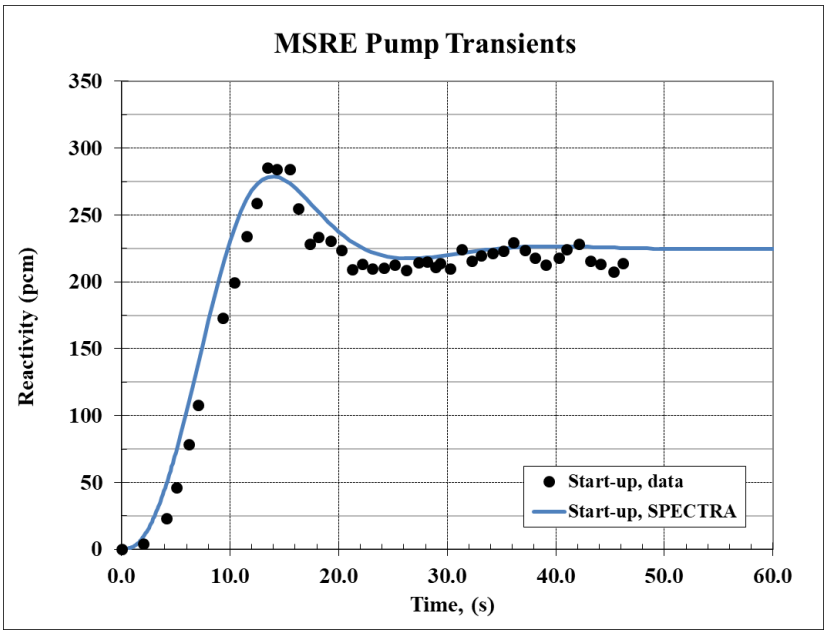

Figure 3-502 Reactivity insertion during pump start-up, SPECTRA versus MSRE data

This is a well-known behavior of the molten salt reactors and it has been observed and measured in MSRE. The reactivity changes required to keep the power constant during pump start-up and shut-down calculated by SPECTRA was compared to the MSRE measured data and a good agreement was observed [206]. The reactivity insertion is about 225 pcm - Figure 3-502.

Finally, the question may arise whether it is possible to define a user-defined fission product chain within the RT Package that will behave in the same way as the DNP chain that is mapped into the RT Package from the RK Package. Definition of such chain is discussed below.

The decay constants λ (1/s) must be of course the same as in the DNP data (Table 3-54). However, the definition of the yield fractions is not that simple and is therefore discussed below in more detail. One needs to bear in mind how the source is defined for the DNP-s and for all other fission products. The equations defining sources are (see Volume 1, section: "Point Kinetics Model Equations - Circulating Fuel").

- DNP-s:

$$S_i = \frac{\beta_i}{\Lambda} n = \frac{\beta_i}{\Lambda v_n} \Phi$$

- Other fission products:

$$S_i = -\Sigma_f \Phi \gamma_i = \sum_{j \neq i} \sigma_{f,j} N_j \Phi \gamma_{f,j \to i}$$

Here:

S	source rate, (1/m^3-s)
n	neutron concentration, (1/m^3)
Φ	neutron flux (one-group) (1/m^2-s)
v_n	the thermal neutron velocity (m/s)
β_i	yield fraction of delayed neutron precursor group i, (-)
Λ	prompt neutron generation time, (s)
$\sigma_{f,j}$	microscopic cross section for fission, (m^2), for isotope j
$\gamma_{f,j \to i}$	yield fraction of isotope i from fission of isotope j
Σ_f	macroscopic cross section for fission, (m^2)
γ_i	average yield fraction of isotope i from fission
N_j	concentration of fissile isotope j in the core, (1/m^3)

Since the sources must be equivalent, we have:

$$\frac{\beta_i}{\Lambda v_n} \Phi = \Sigma_f \Phi \gamma_i$$

or:

$$\gamma_i = \frac{\nu \beta_i}{\Lambda \nu \Sigma_f v_n}$$

The default relationship between the prompt neutron generation time, Λ (PNGTRK), and the macroscopic fission cross section Σ_f (SIGFRK) is (see Volume 2, description of input parameters PNGTRK and SIGFRK):

$$\Lambda = \frac{1}{\nu \Sigma_f v_n}$$

Here ν is the average number of neutrons generated per fission (input parameter XNPFRK, default value = 2.5). Therefore we have:

$$\frac{1}{\Lambda \nu \Sigma_f v_n} = 1$$

If we take this equation into account, the relation and the above relation between γ_i and β_i becomes:

$$\gamma_i = \frac{\nu \beta_i}{\Lambda \nu \Sigma_f v_n} = \nu \beta_i$$

This is quite understandable, considering that ν neutrons are generated per single fission. The values of γ_i obtained from the above relation are shown in the last column of Table 3-54 for the value of ν = 2.5. The fission product chain FP-21x was defined using the above fraction. The concentrations are shown in Figure 3-500 (bottom part). It is seen that the concentrations of this chain are almost identical to the concentrations of the DNP chain 17x.

One last remark has to be made. The relation $\gamma_i = \nu \beta_i$ is true only if the relationship between Λ and Σ_f is: $\Lambda = 1 / (\nu \Sigma_f v_n)$. In general this may not be the case;. the user defines both Λ (PBGTRK) and Σ_f (SIGFRK) in the input deck and those do not necessarily fulfill this condition. In the current example, the following values were used:

- $\Lambda = 5 \times 10^{-4}$ (s)
- $\Sigma_f = 0.3125$ (1/m)
- $\nu = 2.5$
- $v_n = 2560$ (m/s)

Those values fulfill the relation: $\Lambda = 1 / (\nu \Sigma_f v_n)$. If different Σ_f was applied, then the yield fraction has to be corrected accordingly. For example, if Σ_f is twice larger than shown above, then the yield fraction has to be twice smaller to keep the behavior of chain FP-21x equivalent to the DNP chain. Such input deck is located in: **\Z-INPUTS\RT\Cir-fuel\Loop\DNP\DNP-Test-Case-2.SPE**.

Conclusion

As in the previous section, the examples presented here are quite simple and are shown mainly as an illustration of how to define the input parameters, as well as how to interpret the results obtained for reactors with circulating fuel.

3.9.3.15 Isotope Averaging Scheme

The isotope averaging scheme is illustrated in Figure 3-504 and Figure 3-505. Without averaging, the concentration of isotopes, e.g. delayed neutron precursors (DNP), in the core is obtained by summing up concentrations is all Control Volumes belonging to the core. This situation is illustrated in Figure 3-504. With the averaging scheme, an average value of the concentration in the CV and the inlet concentration is used. This situation is illustrated in Figure 3-505. More details are provided in Volume 1.

Standard MSR System test, defined by ANL for the purpose of SPECTRA/SAM comparisons, was selected to test the method. This model is a very simple theoretical molten salt loop that was set up for the purpose of comparisons between SPECTRA and the SAM code, developed by Argonne National Laboratory, specifically for DNP behavior. The model is schematically shown in Figure 3-503. Sixteen tests were performed. In most cases a very good agreement was observed. In four cases some discrepancies were observed. These tests were selected for the present analysis:

- Test 1: step change in the primary flow from 82.95 kg/s to 58.53 kg/s.
- Test 2: step change in the primary flow from 82.95 kg/s to 69.33 kg/s.

The tests 1 and 2 were performed without reactivity feedback (thermal feedback was disabled). The same tests with the thermal reactivity included were defined as tests 7 and 8.

SPECTRA input files for these runs are provided in `\Z-INPUTS\RT\KOVACS`. The results are shown in Figure 3-504 through Figure 3-509.

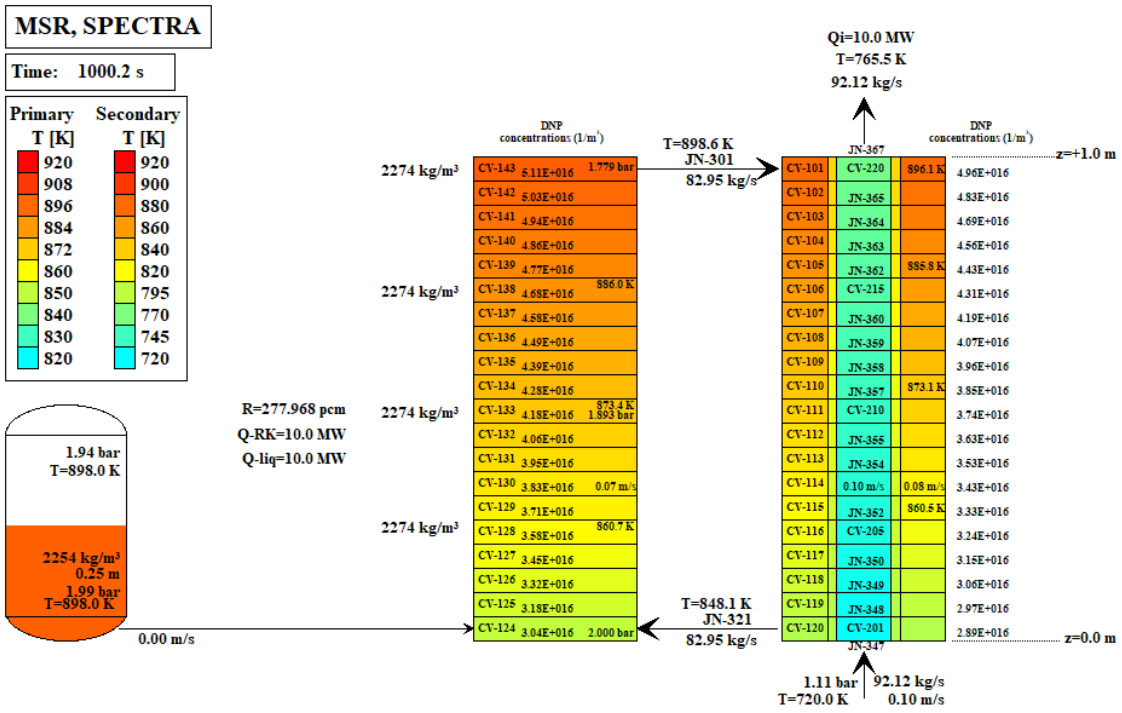

Figure 3-503 Scheme of the Standard MSR System model

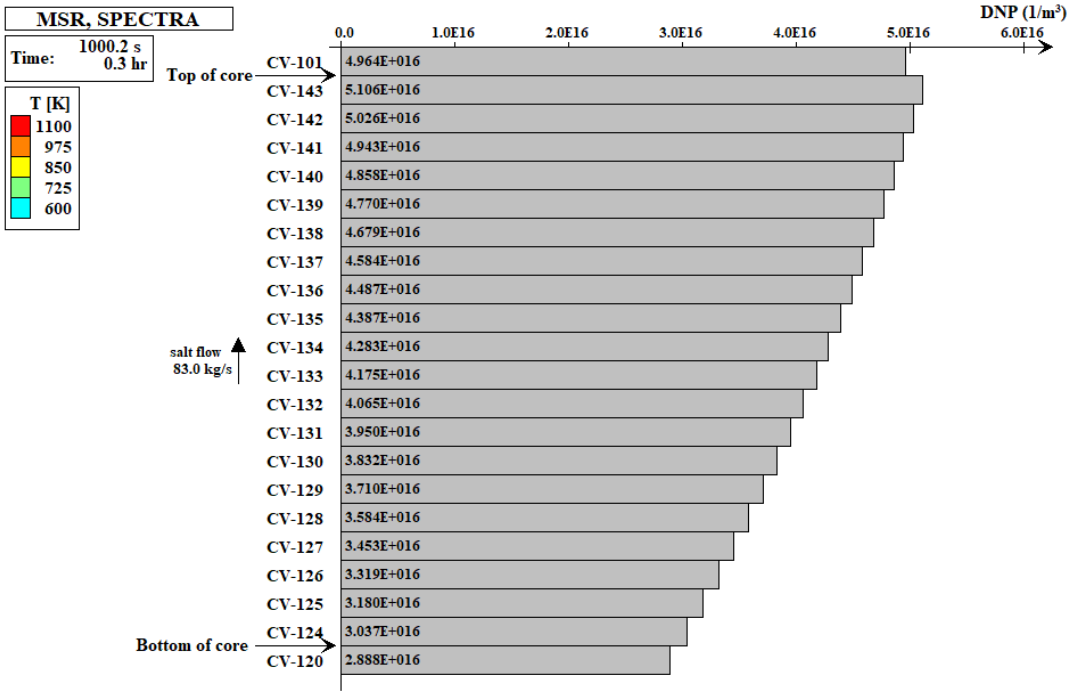

Figure 3-504 Delayed neutron concentrations, no isotope averaging

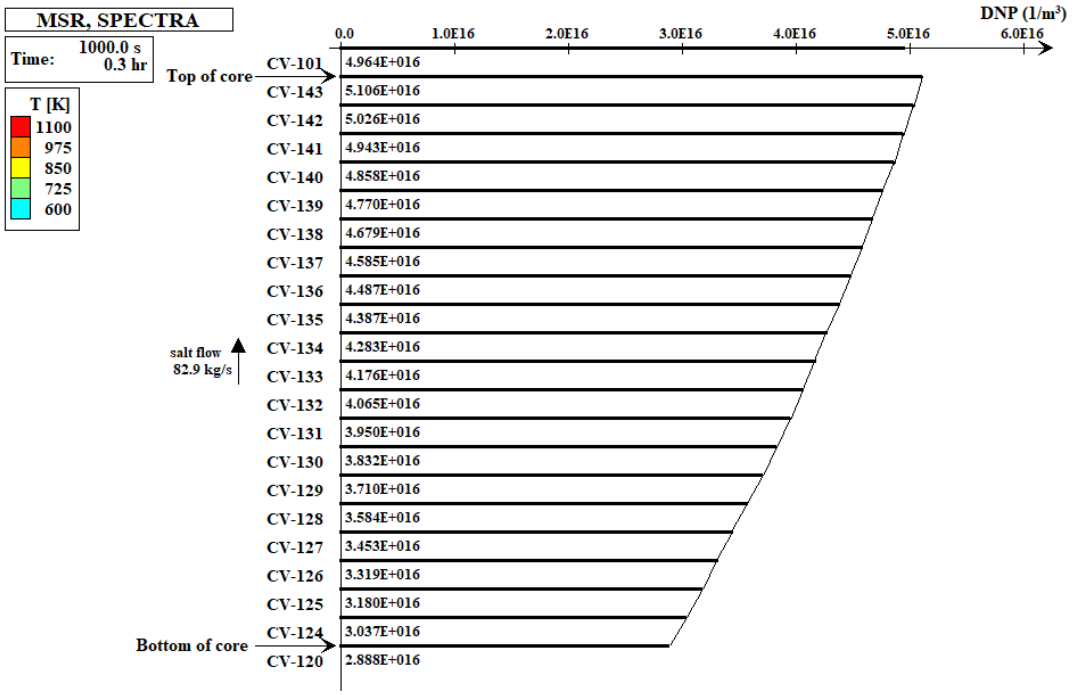

Figure 3-505 Delayed neutron concentrations, isotope averaging, ITAISC=1

Figure 3-506 shows the results of Test 1 obtained with SAM and SPECTRA with and without isotope averaging. When the flow is decreased (t = 0.0 s), fewer DNPs are lost from the core which leads to an increase of the reactivity. Without thermal feedback there is no mechanism to stabilize the power.

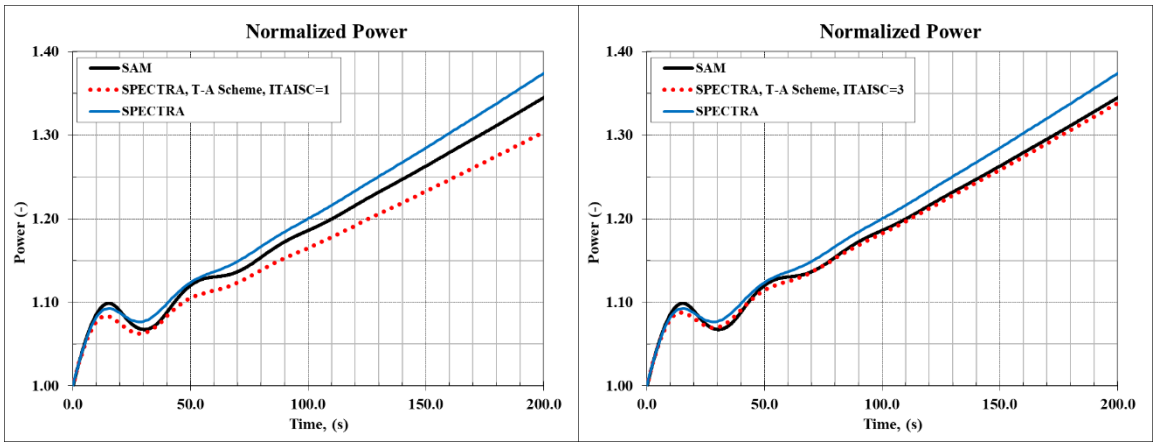

(a) averaging with ITAISC=1 (b) averaging with ITAISC=3

Figure 3-506 Standard MSR System Test 1, SPECTRA versus SAM

The results obtained with full averaging (ITAISC=1, Figure 3-505) are expected to be most accurate, since the DNP concentrations show approximately linear increase along the core and in such case the assumption that the DNP concentration varies linearly within the CV is most accurate. It is seen that a good agreement with SAM is obtained using the averaging scheme with ITAISC = 3, where the average value is taken as 0.75 × CV value + 0.25 × inlet value (see Volume 1), so the outlet value has w weight of 3/4 and the inlet value the weight of 1/4. The physical interpretation of this method is illustrated in Figure 3-507.

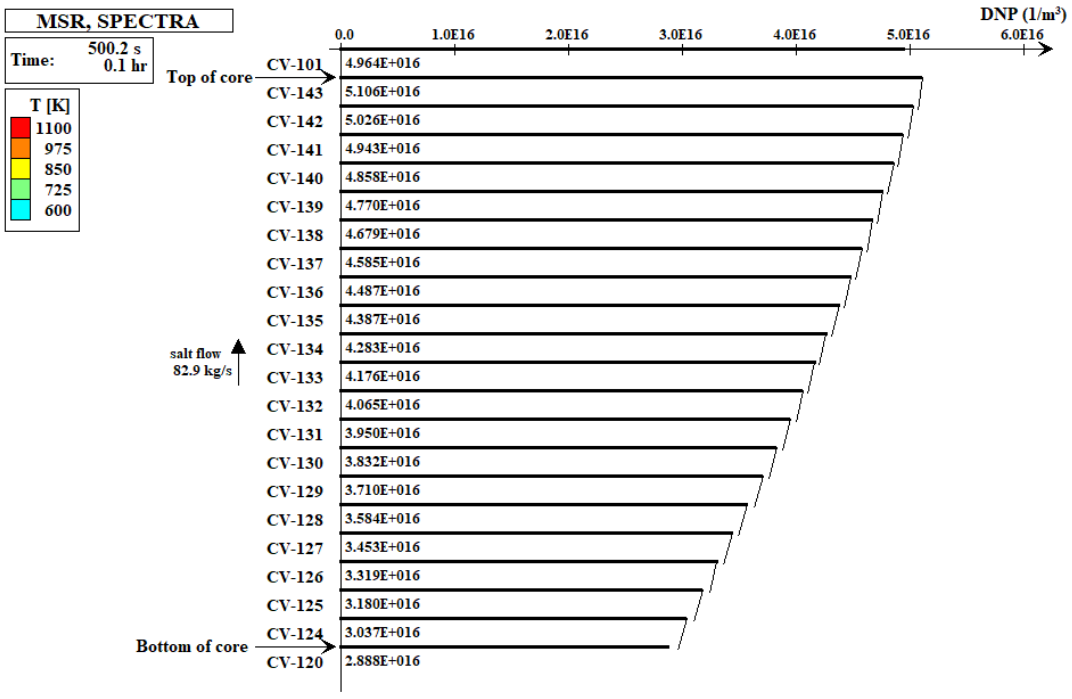

Figure 3-507 Delayed neutron concentrations, isotope averaging, ITAISC=3

Figure 3-508 shows the results for the Test 2. Similar behavior is observed with the best agreement obtained for ITAISC = 3. It is therefore concluded that the best agreement with SAM is obtained with ITAISC = 3. The reader should note that using ITAISC=3 does necessarily yield the most accurate physical solution; it merely leads to the best agreement with another code.

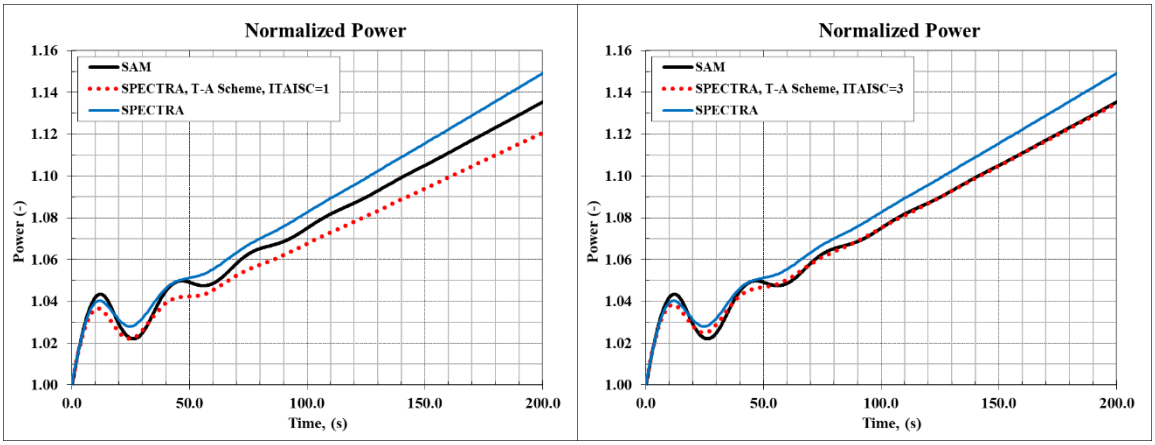

(a) averaging with ITAISC=1 (b) averaging with ITAISC=3

Figure 3-508 Standard MSR System Test 2, SPECTRA versus SAM

Figure 3-509 and Figure 3-510 show the results for the same tests but with reactivity feedback. Again, when the flow is decreased, fewer DNPs are lost from the core which leads to an increase of the reactivity. In this case however there is a negative thermal feedback that quickly stabilizes the core power. It is seen that for those tests the effect of isotope averaging is rather minor. This is because the effect of reactivity feedback is stronger than the inaccuracies in calculating the total concentration of DNP in the core.

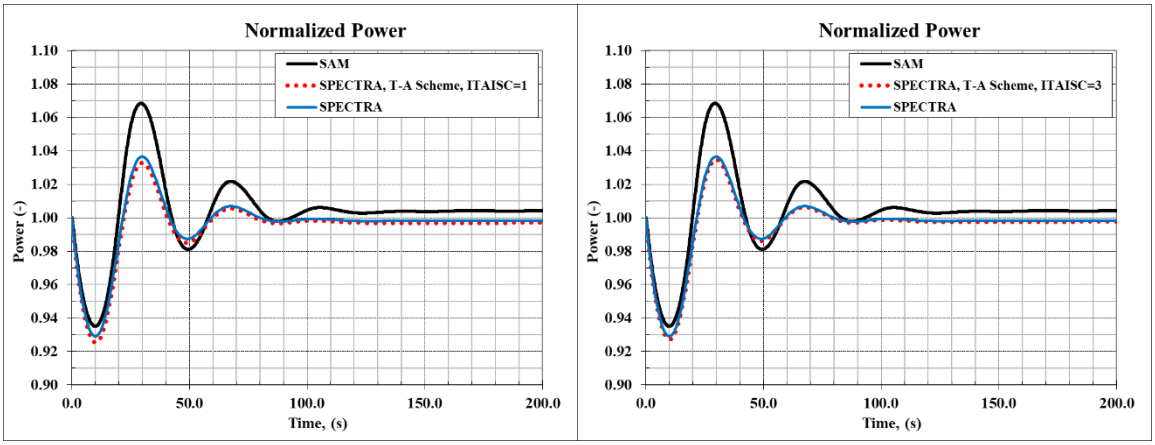

(a) averaging with ITAISC=1 (b) averaging with ITAISC=3

Figure 3-509 Standard MSR System Test 7, SPECTRA versus SAM

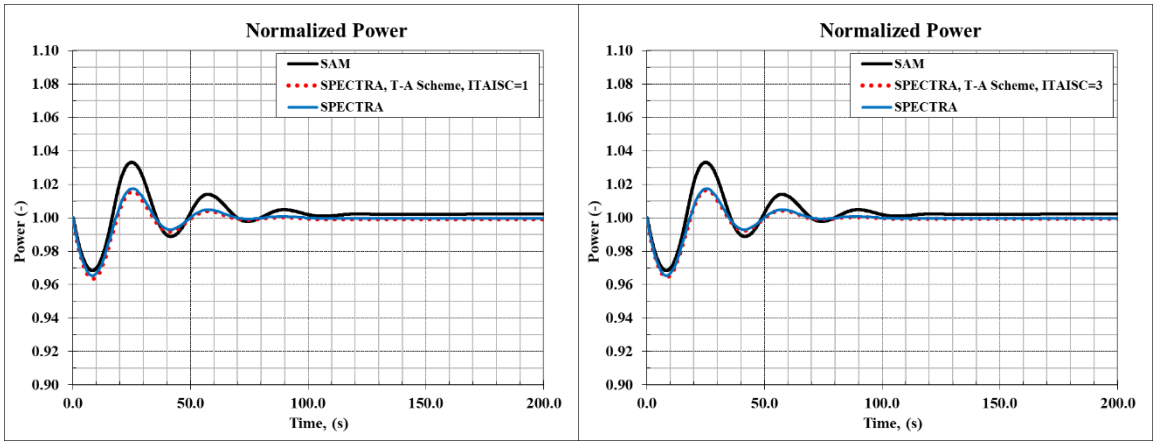

(a) averaging with ITAISC=1 (b) averaging with ITAISC=3

Figure 3-510 Standard MSR System Test 8, SPECTRA versus SAM

3.9.3.16 Summary of Tests for Circulating Fuel

Below all tests performed for circulating fuel are listed, including location of files, a short description and reference to the section containing detailed description of the test, if available. The total number of verification tests for circulating fuel is 159.

Location	Description / reference	No.of tests
\RK\	Comparisons with solid fuel, non-flow cases (1 flow case)	
~\STEP\CIR	Step change of reactivity, sec. 3.9.3.1	3
~\START-UP\CIR	Start-up, sec. 3.9.3.2	1
~\TDOPP\CIR-NonFlow	Doppler effect, non-flow case, sec. 3.9.3.3	2
~\TDOPP\CIR-Flow	Doppler effect, flow case, sec. 3.9.3.4	2
~\XE\CIR	Xenon behavior, non-flow case, sec. 3.9.3.6	2
~\DH\CIR	Decay heat of U-235 and Pu-239, sec. 3.9.3.8, 3.9.3.9	4
\RT\Cir-fuel\	Specific phenomena	
~\Single	Correctness of isotope mapping between RK and RT	8
~\Dump	Reduction of power during fuel dump, sec. 3.9.3.11	10
\RT\Cir-fuel\Multiple\	Multiple CV, open loop (core+inlet+outlet), sec. 3.9.3.5	
~\Multiple-NonFlow	pure kinetics (6 groups DNP), non-flow case	3
~\Multiple-Flow	pure kinetics (6 groups DNP), flow case	3
~\Multiple-DH-NonFlow	includes isotope decay heat, non-flow case	4
~\Multiple-DH-Flow	includes isotope decay heat, flow case	5
\RT\Cir-fuel\Loop\	Loop tests (closed loop, core, HX, pump)	
~\Loop-NonFlow	start-up, pure kinetics (6 groups DNP), non-flow case	3
~\Loop-Flow	start-up, pure kinetics (6 groups DNP), flow case	3
~\Loop-DH-NonFlow	start up, includes isotope decay heat, non-flow case	4
~\Loop-DH-Flow	start-up, includes isotope decay heat, flow case	8
~\Loop-Low-Power	DNP drift, non-uniform core power generation.	6
~\Loop-Low-Power-Uniform	DNP drift, uniform power, comparison with CFD,sec.3.9.3.10	6
~\Xe	Transport of Xe-135, sec. 3.9.3.7	10
~\Xe-Cs-Uniform	Two ways of analyzing FP (sec. 3.9.3.12) and the effect of reactor volume (sec.	5
~\Xe-Cs-Nonuniform	3.9.3.13) for both uniform and non-uniform power, as well as comparison with	2
~\Xe-Cs-Uniform-SOLID	sold fuel	4
\RT\DNP	Delayed neutron precursor concentrations (sec. 3.9.3.14)	2
\RT\Cir-fuel\Sorption\	Sorption of FP liquid-to-walls / dust / gas	
~\Sorption-SC	Sorption of FP on 1-D structures (SC), sec. 3.12.53.1	1
~\Sorption-TC	Sorption of FP on 2-D structures (TC), sec. 3.12.53.1	1
~\Sorption-Part	Sorption of FP on dust particles, sec. 3.12.53.2	3
~\Sorption-Atms	Transport to liquid-gas interface: pool, sec. 3.12.53.3	3
~\Sorption-Bubble	Transport to liquid-gas interface: bubbles, sec. 3.12.53.4	3
~\Sorption-Droplet	Transport to liquid-gas interface: droplets, sec. 3.12.53.5	36
\RT\KOVACS	Isotope concentration averaging (sec. 3.9.3.15)	
~\RUNS	Tests without averaging	4
~\RUNS-N-A	Tests with averaging, ITAISC=1	4
~\RUNS-N-A-3	Tests with averaging, ITAISC=3	4

3.9.4 Nodal Point Reactor Kinetics

Verification of the nodal point reactor kinetics model is performed as follows:

- It is shown that the nodal kinetics model gives exactly the same solution as the point kinetics model, if there is no neutron diffusion (all diffusion coefficients are equal to zero). This is done for two tests:
  - Full reactivity feedback test (section 3.9.4.1)
  - Xe poisoning test (section 3.9.4.2)
- The stationary state power distribution is compared to the power distributions obtained from 3D neutronic codes. This is done for the GEMINI+ plant, a 180 MW prismatic block HTR (section 3.9.4.4).
- Furthermore, a qualitative verification of the transient behavior is performed by comparing the transient results obtained from the nodal kinetics and the point kinetics models for the GEMINI+ plant (section 3.9.4.4).

3.9.4.1 Full Reactivity Feedback - Comparison with Point Kinetics

The FRF test is described in section 3.9.1.4. This test involves reactivity insertion of 0.15 $ in three steps:

- 0.05 $ at t = 0.0
- 0.05 $ at t = 100.0 s
- 0.05 $ at t = 200.0 s

The point kinetics model is shown in Figure 3-511. For the current test, the model shown in Figure 3-512 was created. The nodal kinetics input was defined with all parameters exactly the same as in the point kinetics model. The additional inputs, required for the nodal kinetics include:

- Diffusion coefficients. These were set to a very small number: $D_1 = D_2 = 10^{-30}$ (m), to eliminate the node-to-node diffusion.
- Reflection factors. These were set to $F_{R1} = F_{RN} = 1.0$, to eliminate the neutron escape.

SPECTRA input is provided in `\Z-INPUTS\RK\FRF\FRF-2.SPE`. The results are shown in Figure 3-513. The results show that the nodal kinetics give identical results as the point kinetics when the node-to-node diffusion and the diffusion to the reflectors are eliminated.

An additional run was performed to test the initialization option. The input is provided in `\Z-INPUTS\RK\FRF\FRF-2-I.SPE`. The initialization option INONRK = 1 is defined. With this option the power control system is trying to keep the power constant. Additionally the convergence criterion XCNNRK is set to zero, to prevent the code from stopping when the stationary state is reached. The results are shown in Figure 3-514. It is seen that the control system is able to keep the power practically constant (1000 W in each node). Small power jumps are observed at the moments of the reactivity insertions but are quickly dumped to the requested value. This test illustrates the effectiveness of the automatic power control, in particular the default values of the proportional and integration constants (CPCVRK and CICVRK).

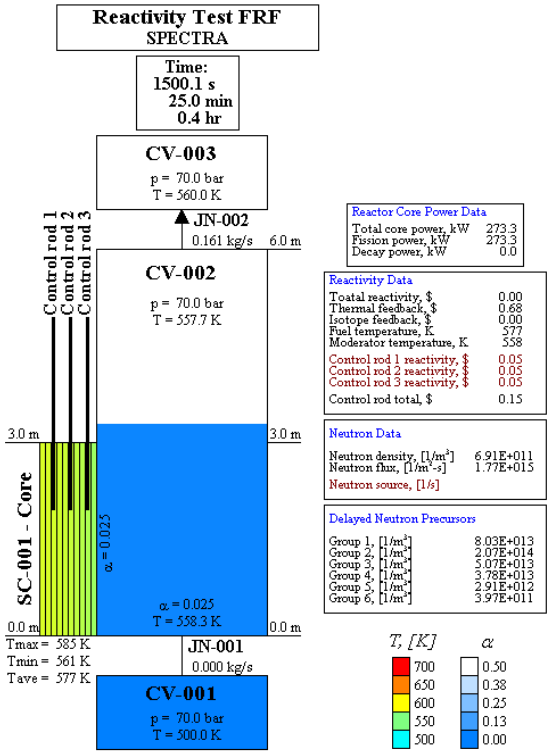

Figure 3-511 Full reactivity feedback test, point kinetics

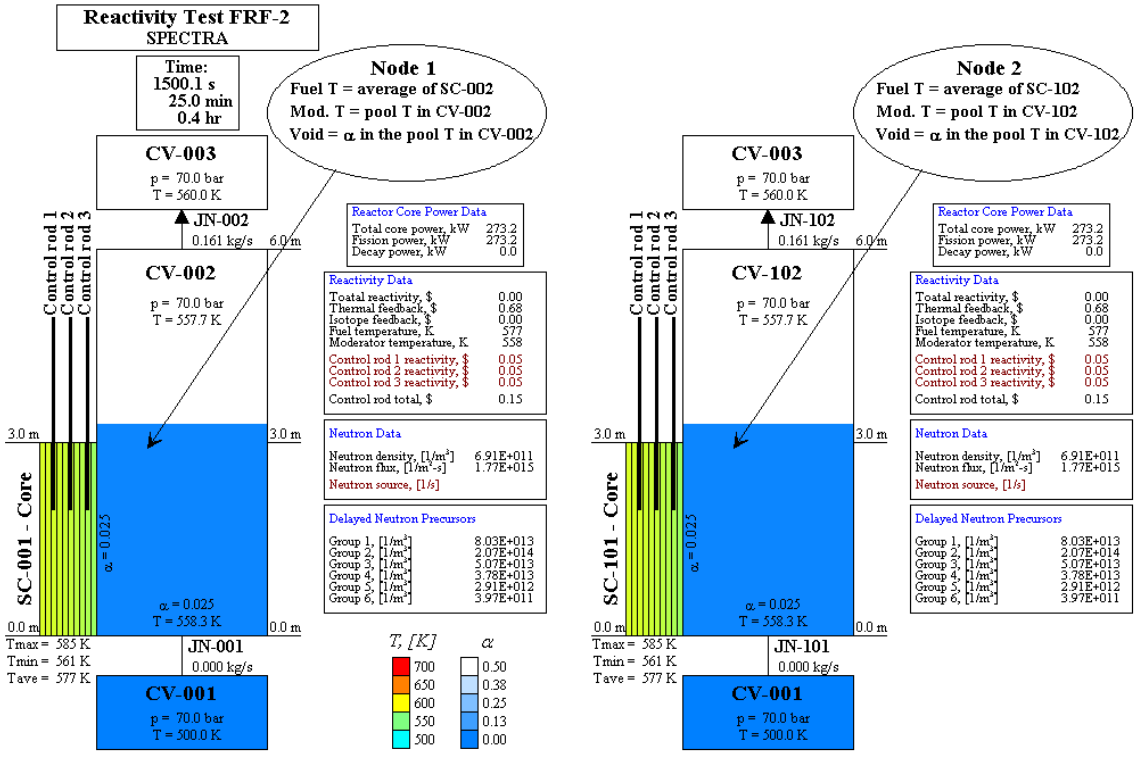

Figure 3-512 Full reactivity feedback test, nodal kinetics

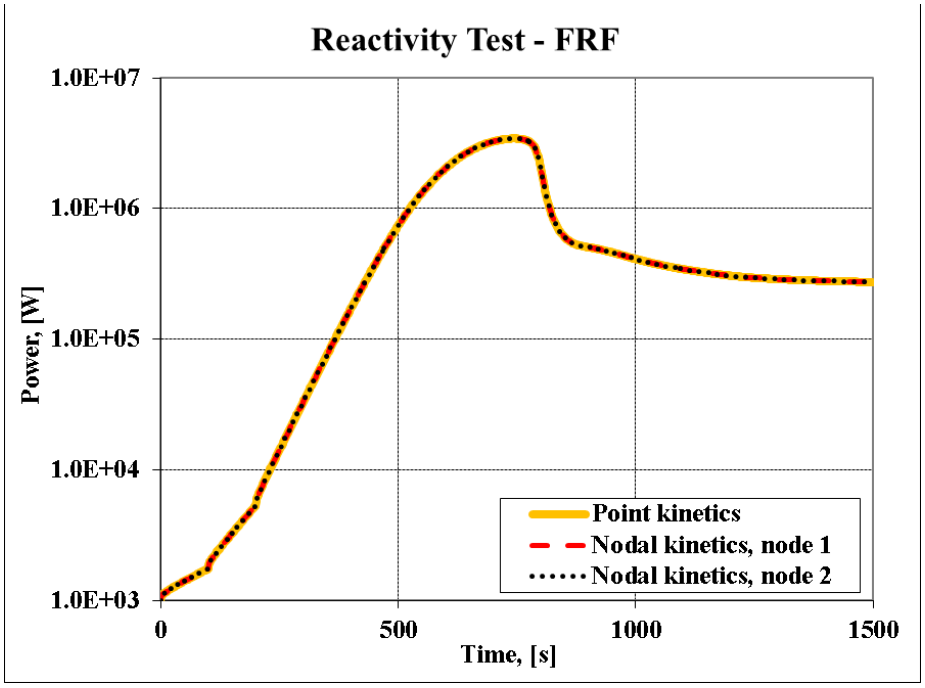

Figure 3-513 Full reactivity feedback test, nodal versus point kinetics

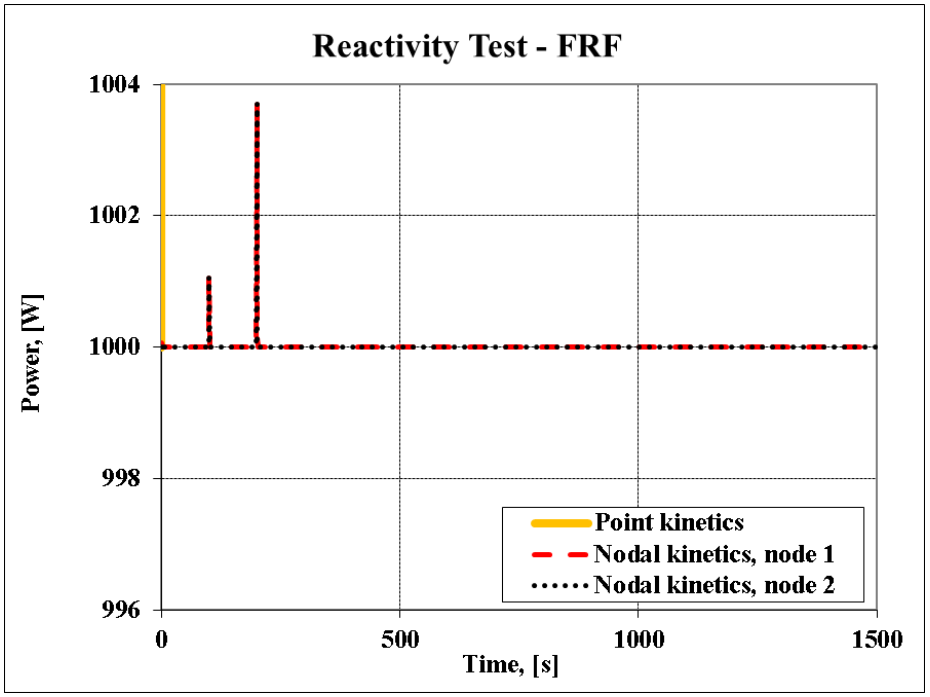

Figure 3-514 Full reactivity feedback test, test of the initialization option

3.9.4.2 Xenon Poisoning Test - Comparison with Point Kinetics

The Xe test is described in section 3.9.2.1. This test shows was designed to verify the Xenon reactivity behavior after the reactor shutdown (Figure 3-385).

For the current test, the nodal kinetics input was defined with all parameters exactly the same as in the point kinetics model. The additional inputs, required for the nodal kinetics include:

- Diffusion coefficients. These were set to a very small number: $D_1 = D_2 = 10^{-30}$ (m), to eliminate the node-to-node diffusion.
- Reflection factors. These were set to $F_{R1} = F_{RN} = 1.0$, to eliminate the neutron escape.

SPECTRA input is provided in `\Z-INPUTS\RK\XE\XE-2.SPE`. The results are shown in Figure 3-515 and Figure 3-516. Figure 3-515 show the end-state values obtained with the point kinetics and the nodal kinetics models. It is seen that the values obtained with the nodal kinetics are identical to the values obtained from the point kinetics model. Figure 3-516 shows the time-dependent graph of the Xe-135 reactivity. The results show that the nodal kinetics give identical results concerning the isotopes as the point kinetics model when the node-to-node diffusion and the diffusion to the reflectors are eliminated.

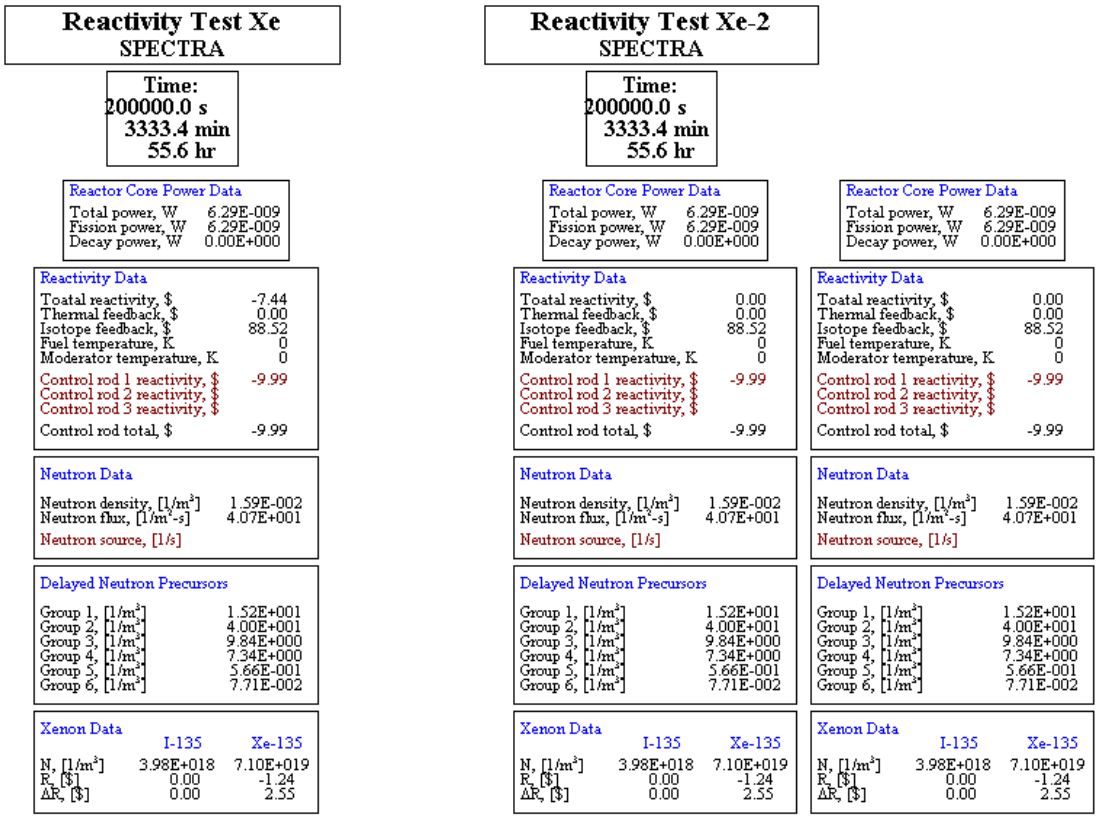

Reactivity Test Xe
SPECTRA

Time:
200000.0 s
3333.4 min
55.6 hr

Reactor Core Power Data

Total power, W	6.29E-009
Fission power, W	6.29E-009
Decay power, W	0.00E+000

Reactivity Data

Toatal reactivity, $	-7.44
Thermal feedback, $	0.00
Isotope feedback, $	88.52
Fuel temperature, K	0
Moderator temperature, K	0
Control rod 1 reactivity, $	-9.99
Control rod 2 reactivity, $	
Control rod 3 reactivity, $	
Control rod total, $	-9.99

Neutron Data

Neutron density, [1/m³]	1.59E-002
Neutron flux, [1/m²-s]	4.07E+001
Neutron source, [1/s]	

Delayed Neutron Precursors

Group 1, [1/m³]	1.52E+001
Group 2, [1/m³]	4.00E+001
Group 3, [1/m³]	9.84E+000
Group 4, [1/m³]	7.34E+000
Group 5, [1/m³]	5.66E-001
Group 6, [1/m³]	7.71E-002

Xenon Data

	I-135	Xe-135
N, [1/m³]	3.98E+018	7.10E+019
R, [$]	0.00	-1.24
ΔR, [$]	0.00	2.55

Reactivity Test Xe-2
SPECTRA

Time:
200000.0 s
3333.4 min
55.6 hr

Reactor Core Power Data

Total power, W	6.29E-009
Fission power, W	6.29E-009
Decay power, W	0.00E+000

Reactivity Data

Toatal reactivity, $	0.00
Thermal feedback, $	0.00
Isotope feedback, $	88.52
Fuel temperature, K	0
Moderator temperature, K	0
Control rod 1 reactivity, $	-9.99
Control rod 2 reactivity, $	
Control rod 3 reactivity, $	
Control rod total, $	-9.99

Neutron Data

Neutron density, [1/m³]	1.59E-002
Neutron flux, [1/m²-s]	4.07E+001
Neutron source, [1/s]	

Delayed Neutron Precursors

Group 1, [1/m³]	1.52E+001
Group 2, [1/m³]	4.00E+001
Group 3, [1/m³]	9.84E+000
Group 4, [1/m³]	7.34E+000
Group 5, [1/m³]	5.66E-001
Group 6, [1/m³]	7.71E-002

Xenon Data

	I-135	Xe-135
N, [1/m³]	3.98E+018	7.10E+019
R, [$]	0.00	-1.24
ΔR, [$]	0.00	2.55

Figure 3-515 Xe poisoning test, left: point kinetics, right: nodal kinetics

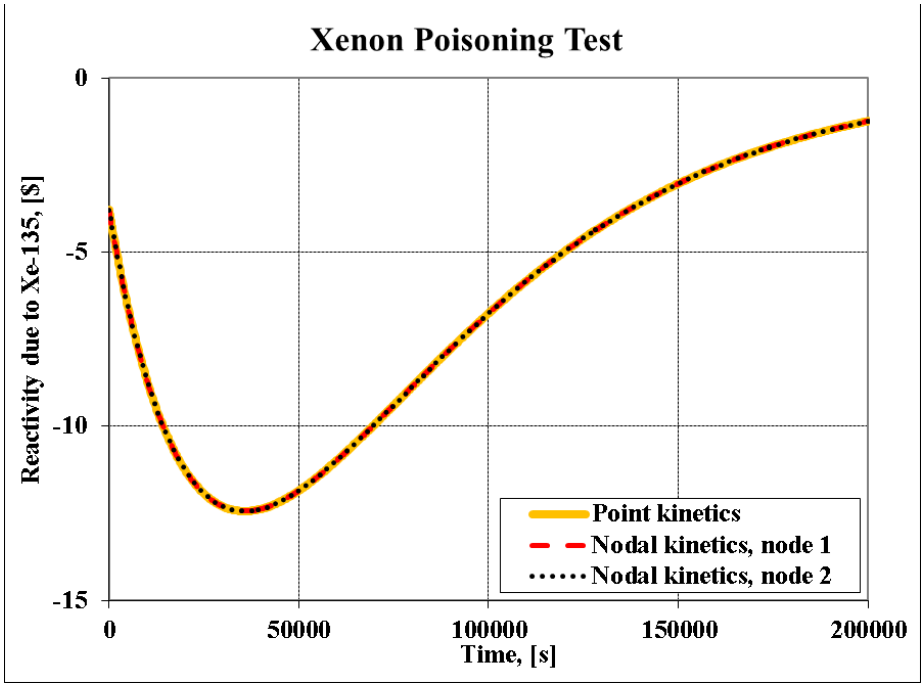

Figure 3-516 Xe poisoning test, nodal kinetics

3.9.4.3 Verification against Analytical Solutions

The nodal kinetics solution is compared to the analytical solutions for three selected cases, described below. The discussion is based on theoretical solutions presented in [203], [204].

❖ **Rectangular Geometry**

Stationary state in a rectangular geometry is considered. The diffusion equation (Volume 1):

$$\frac{1}{v}\frac{d\Phi}{dt} = (1-\beta)\nu\Sigma_f\Phi - \Sigma_a\Phi + \sum_k \lambda_k C_k + D\nabla^2\Phi$$

is written for stationary state. In the stationary state: $d\Phi/dt = 0$ and $\beta\nu\Sigma_f\Phi = \sum_k \lambda_k C_k$.

Therefore:

$$0 = \nu\Sigma_f\Phi - \Sigma_a\Phi + D\nabla^2\Phi$$

We consider a 1-dimentional, rectangular geometry, where $\nabla^2\Phi = d^2\Phi/dx^2$. Therefore:

$$\frac{d^2\Phi}{dx^2} + B^2\Phi = 0$$

where:

$$B^2 = \frac{\nu\Sigma_f - \Sigma_a}{D}$$

The solution is (compare [203], sec. 4.3.1):

$$\Phi = A\cos(Bx)$$

The boundary condition is: $\Phi = 0$ at $x = d_{ex}$, which means:

$$\Phi = A\cos\left(\frac{\pi}{a_{ex}}x\right)$$

Here a_{ex} is the extrapolated width, equal to the true reactor width plus the d_{ex} [204]:

$$d_{ex} = 0.71 \times \lambda_{tr} = 0.71 \times (3 \times D) = 2.13 \times D$$

Here D is the diffusion coefficient. In practice d_{ex} « reactor size [204] and therefore $a_{ex} \approx a$. The boundary condition means that:

$$B^2 = \left(\frac{\pi}{a_{ex}}\right)^2$$

Consequently:

$$\frac{\nu\Sigma_f - \Sigma_a}{D} = \left(\frac{\pi}{a_{ex}}\right)^2$$

Since:

$$k = \frac{\nu\Sigma_f}{\Sigma_a}$$

Therefore:

$$\frac{D}{\nu\Sigma_f}\left(\frac{\pi}{a_{ex}}\right)^2 = \frac{k-1}{k} = \rho$$

As a test case, the GEMINI+ model is used. The GEMINI+ plant and the model are described in more detail in the next section. Here the only important parameters are mentioned. The core height is 8.8 m. 22 axial nodes are used with uniform node size of 0.4 m. The diffusion coefficient is D = 0.0131 m. The macroscopic fission cross section is Σ_f = 0.07 (1/m). The number of neutrons per fission is assumed as ν = 2.5.

Compared to the GEMINI+ model, described in the next section, two modifications are made:

- The thermal feedback coefficients are eliminated.
- The reflection factors are set to zero.

The input deck is located in: \Z-INPUTS\RK\NPK\GEMINI\RUNS\GEMINI-N0.SPE.
The results are shown in Figure 3-517 and Figure 3-518. The agreement is very good; however, the calculated numbers are not identical. The average difference between the calculated and the theoretical values is **δ = 0.17%**. The reason for this discrepancy is the presence of the isotope model, which calculates the decay heat and the poisoning due to Xe-136 and Sm-149.

The SPECTRA-calculated whole-core reactivity is equal to 1.417 $. The theoretical value is equal to:

$$\frac{D}{\nu\Sigma_f}\left(\frac{\pi}{a}\right)^2 = \frac{0.131}{2.5\times 0.07}\left(\frac{\pi}{8.8}\right)^2 = 9.54\times 10^{-3} = 1.407\ \$$$$

Conversion to ($) was done using the delayed neutron fraction of 6.783×10^{-3}. The difference between the calculated and the theoretical value is 0.74%.

As a next step, the isotope model was disabled. The input deck is located in:
\Z-INPUTS\RK\NPK\GEMINI\RUNS\GEMINI-N00.SPE.
The results are shown in Figure 3-519. The values are practically identical. The average difference between the calculated and the theoretical values is **δ = 0.0002%**. The SPECTRA-calculated whole-core reactivity is equal to 1.404 $. The difference between the calculated and the theoretical value is 0.18%.

The results presented above were obtained with a = 8.8 m. The equations for the boundary nodes are formulated in such a way that the reflection factor of zero corresponds to the zero flux at the boundary, $a_{ex} = a$. In order to account for the extrapolation distance, two ways are possible.

- a small positive reflection factor may be used (using the trial and error method), or
- the width of the boundary nodes may be extended to account for the extrapolation distance, d_{ex} .

The second method is easier and was used here. The extrapolation distance is equal to:

$$d_{ex} = 2.13\times D = 2.13\times 0.0131 = 0.0279$$

The node size is 0.4 m. Therefore width of the boundary nodes was increased to 0.4279. The input deck is located in: \Z-INPUTS\RK\NPK\GEMINI\RUNS\GEMINI-N00-ex.SPE.
The results are shown in Figure 3-520. The values are practically identical. The average difference between the calculated and the theoretical values is **δ = 0.007%**. The SPECTRA-calculated whole-core reactivity is equal to 1.387 $. The theoretical value is 1.389 $. The difference between the calculated and the theoretical value is 0.14%.

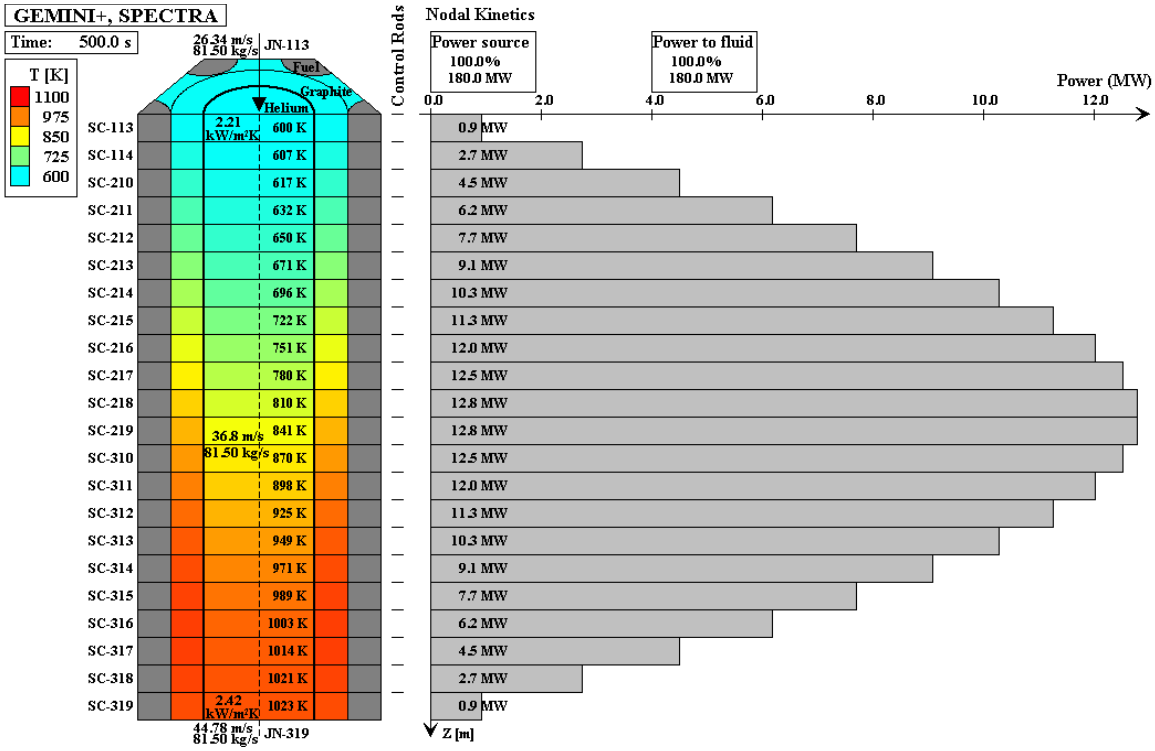

Figure 3-517 Rectangular geometry, case GEMINI-N0: with isotopes

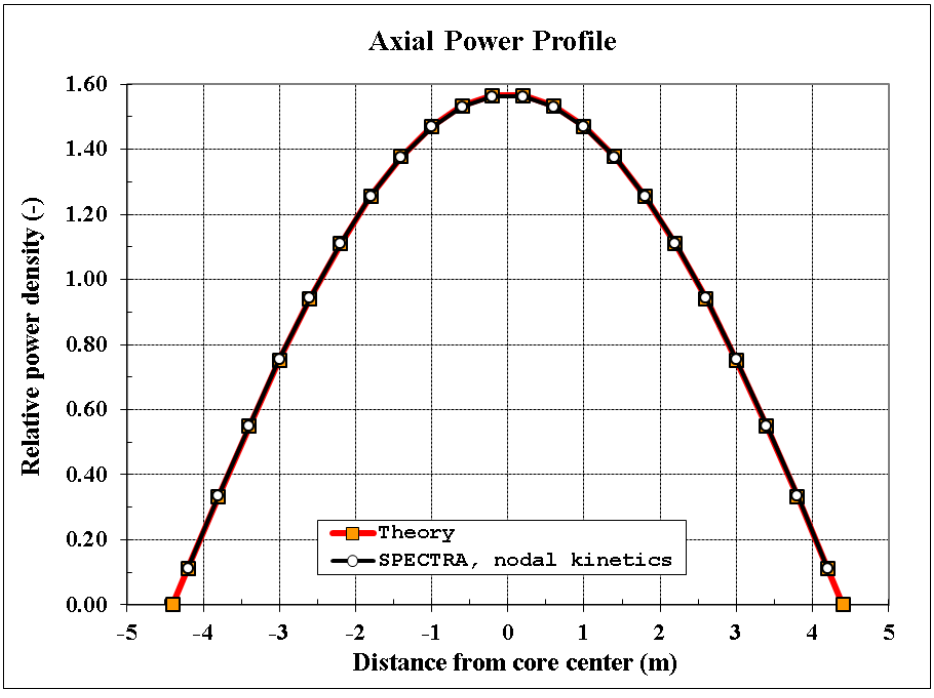

Figure 3-518 Rectangular geometry, case GEMINI-N0: with isotopes

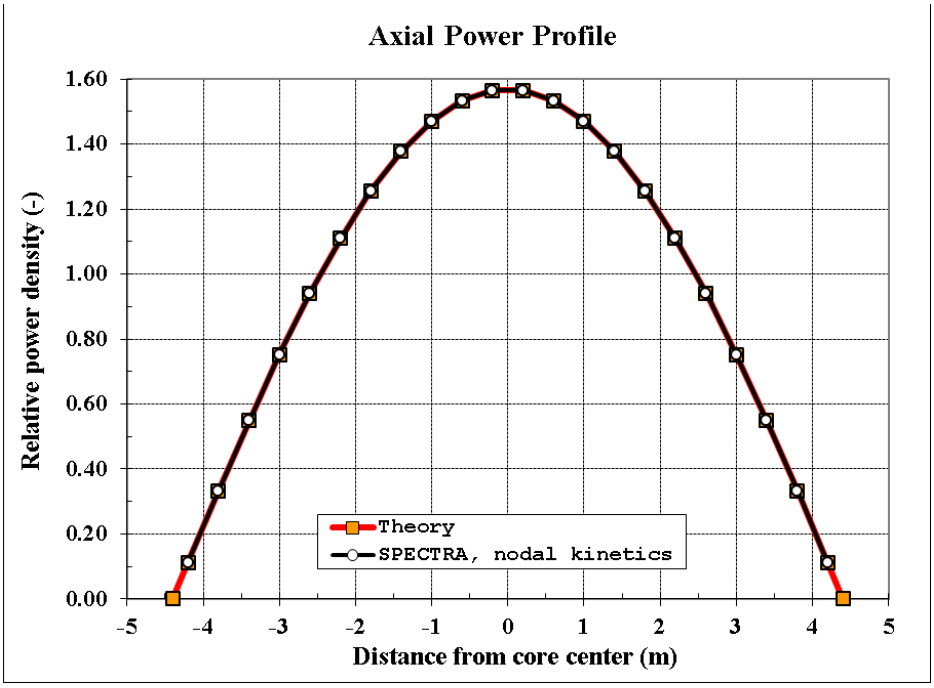

Figure 3-519 Rectangular geometry, case GEMINI-N00: no isotopes

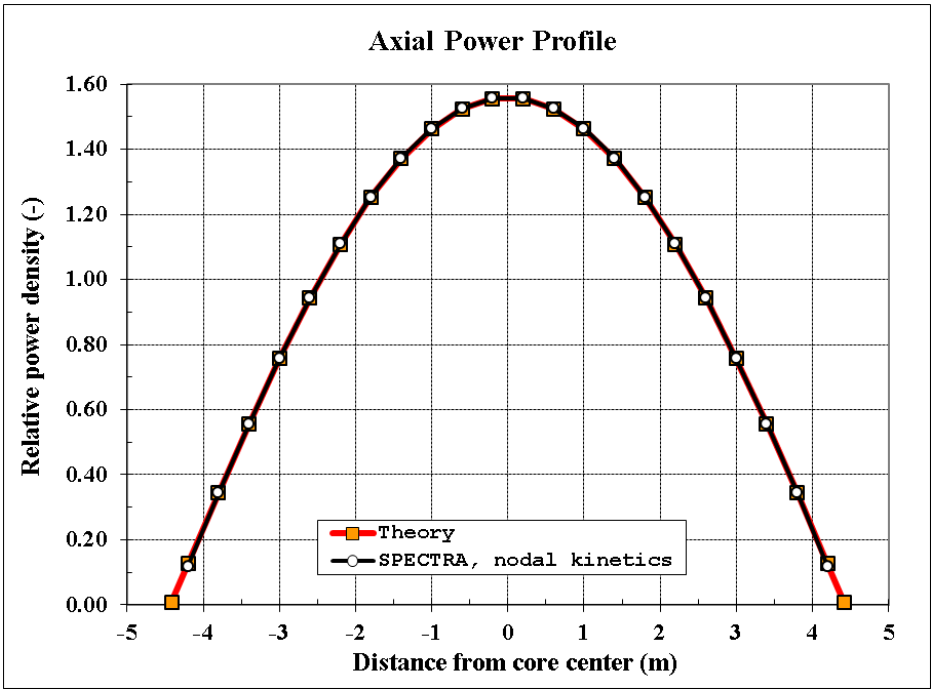

Figure 3-520 Rectangular geometry, case GEMINI-N00-ex: no isotopes, extrapolated length

❖ **Cylindrical Geometry**

The equation presented in the previous section:

$$\nabla^2\Phi + B^2\Phi = 0$$

written in the cylindrical coordinates is (see [203], section 4.3.2):

$$\frac{d^2\Phi}{dr^2} + \frac{1}{r}\frac{d\Phi}{dr} + B^2\Phi = 0$$

The solution is:

$$\Phi = AJ_0(Br) = AJ_0\left(\frac{2.405}{R_{ex}}r\right)$$

where:

$$B^2 = \left(\frac{2.405}{R_{ex}}\right)^2$$

Therefore:

$$\frac{D}{\nu\Sigma_f}\left(\frac{2.405}{R_{ex}}\right)^2 = \frac{k-1}{k} = \rho$$

A simple cylindrical geometry model was created. Twenty radial nodes were used. The size of each node was assumed as 0.1 m. The total radius of the reactor is 2.0 m. All the neutronic data (diffusion coefficients etc.) were the same as in the previous example. The power was selected arbitrarily as 1.257 MW (the value gives the average power density of 10^5 W/m^3). The reflection factor was set to 0.0 for the node 20 (the outer node). The value for the first node is irrelevant because the area is zero for this geometry (solid cylinder); therefore there is no neutron loss from this node regardless of the reflection factor.

The input deck is located in: \Z-INPUTS\RK\NPK\CYLINDER\RUNS\CYLINDER-N0.SPE.
The results are shown in Figure 3-521 and Figure 3-522. The agreement is very good; however, the calculated numbers are not identical. The average difference between the calculated and the theoretical values is **δ = 0.61%**. The reason for this discrepancy is the isotope model, which calculates the decay heat and the poisoning due to Xe-136 and Sm-149.

As a next step, the isotope model was disabled. The input deck is located in:
\Z-INPUTS\RK\NPK\CYLINDER\RUNS\CYLINDER-N00.SPE.
The results are shown in Figure 3-523 and Figure 3-524. The values are practically identical. The average difference between the calculated and the theoretical values is **δ = 0.02%**.

Finally, the case with extrapolated distance was calculated. As previously, this was done by extending the width of the boundary node to account for the extrapolation distance, d_{ex}. The agreement is very good. The average difference between the calculated and the theoretical values is **δ = 0.08%**.

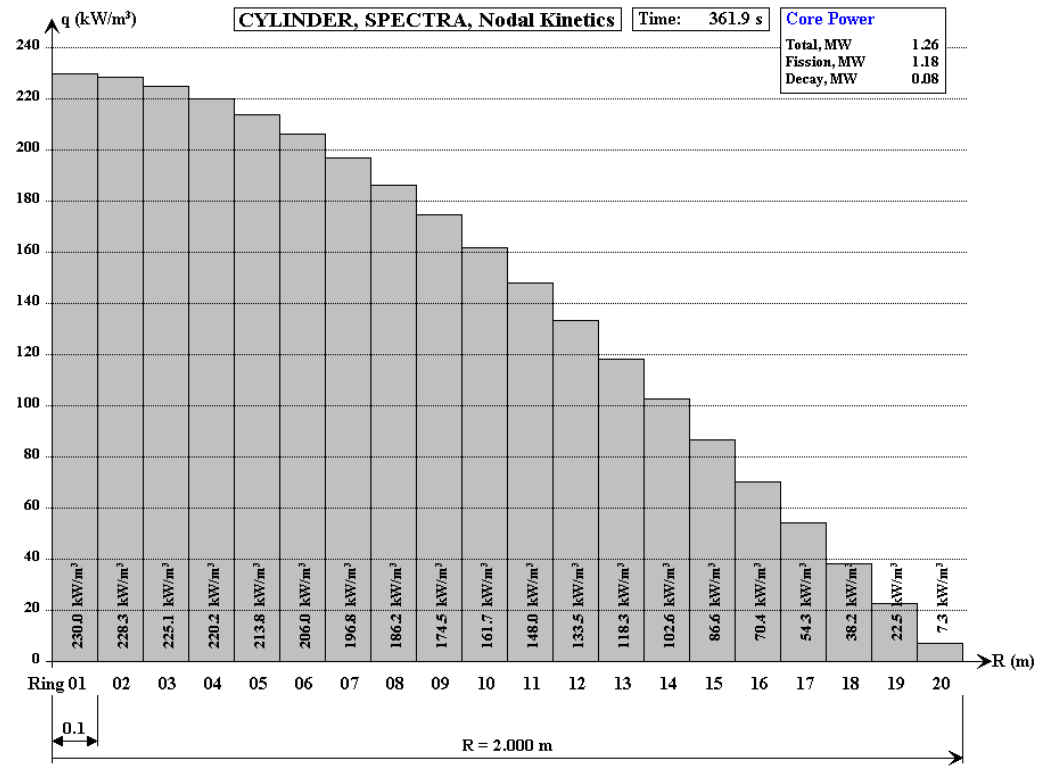

Figure 3-521 Cylindrical geometry, case CYLINDER-N0, with isotopes

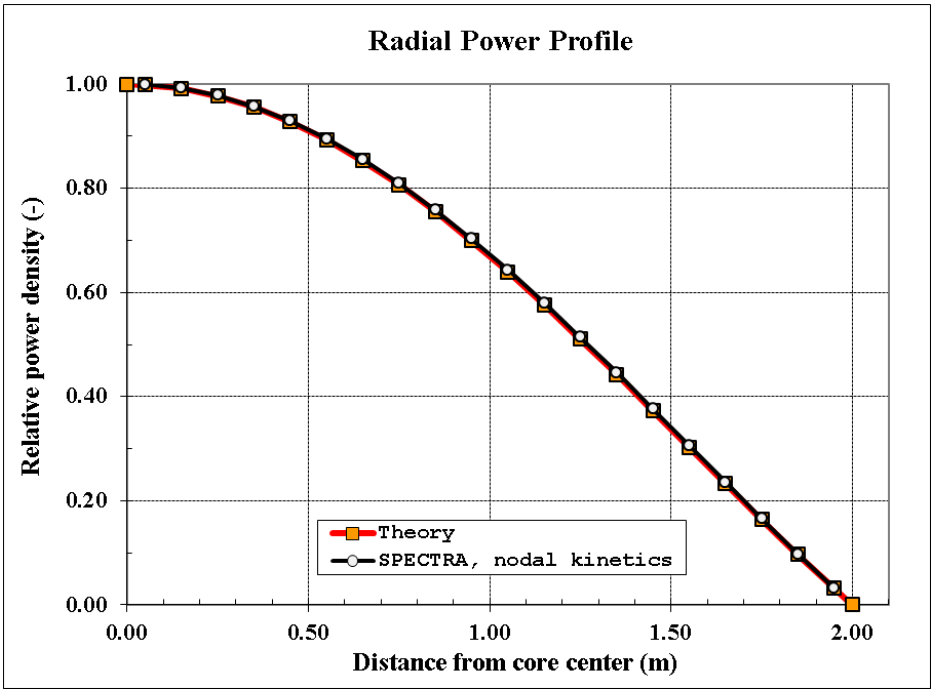

Figure 3-522 Cylindrical geometry, case CYLINDER-N0, with isotopes

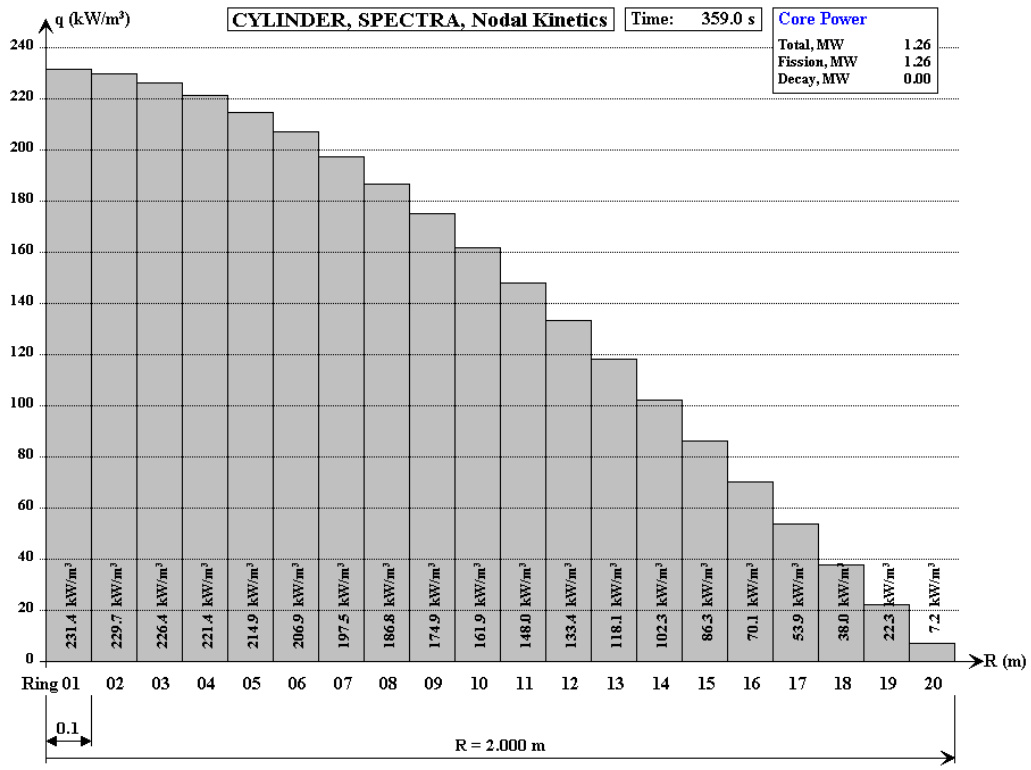

Figure 3-523 Cylindrical geometry, case CYLINDER-N00, no isotopes

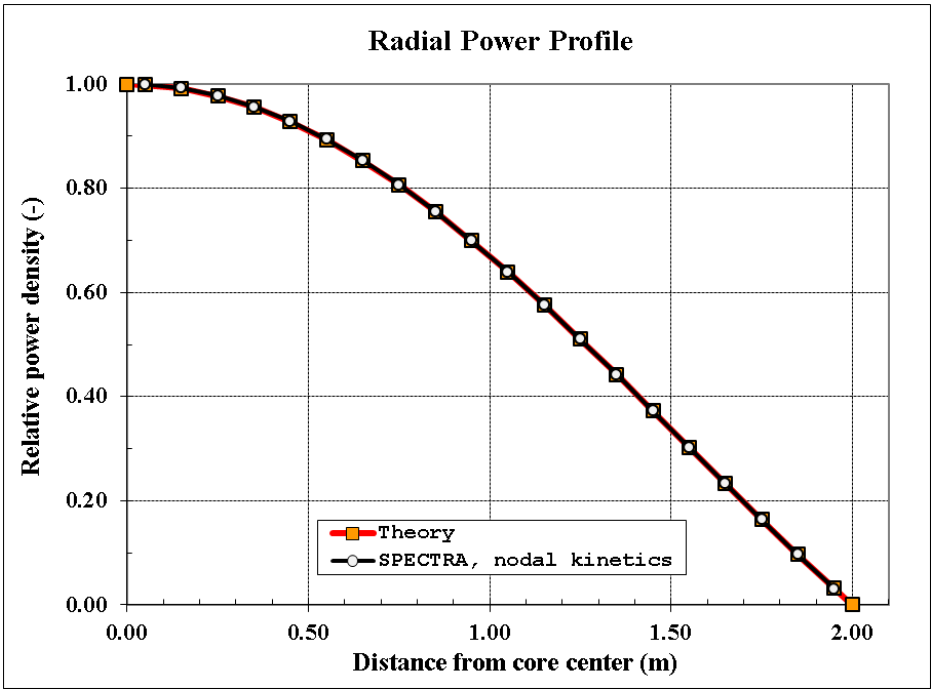

Figure 3-524 Cylindrical geometry, case CYLINDER-N00, no isotopes

❖ **Variable Diffusion Coefficient**

In this test, a variable diffusion coefficient is considered. The rectangular geometry (GEMINI+ core) is considered. The total core height (8.8 m) is divided into two zones.

- **Zone (1)**. The central zone, 4.0 m long (–2.0 m < x < +2.0 m), where the diffusion coefficient is reduced by the factor of 10: D = 0.00131 m.
- **Zone (2)**. The outer zones, 4.8 m long (–4.4 m < x < –2.0 m and +2.0 m < x < +4.4 m), where the original value is kept: D = 0.0131 m.

The equation presented earlier is:

$$\frac{d^2\Phi}{dx^2} + B^2\Phi = 0$$

The solution, written for both zones is:

$$\Phi_1 = A_1 \cos(B_1 x) \qquad \Phi_2 = A_2 \cos(B_2 x)$$

The boundary conditions are:

$$\Phi_1(a_1/2) = \Phi_2(a_1/2) \qquad \Phi_2(a_2/2) = 0$$

Here a_1 is the width of the zone 1, a_1 = 4.0 m, and a_2 is the width of the full core, a_2 = 8.8 m. The values of B_1 and B_2 are given by:

$$B_1^2 = \frac{\nu\Sigma_f\rho}{D_1} \qquad B_2^2 = \frac{\nu\Sigma_f\rho}{D_2}$$

Therefore:

$$B_1 = B_2\sqrt{\frac{D_1}{D_2}}$$

The B_2^2 is calculated from:

$$B_2^2 = \left(\frac{\pi}{a_2}\right)^2$$

The ratio A_1/A_2 is calculated from the continuity at $x = a_1/2$. The values are normalized to obtain the power relative to the average power. All the equations are solved analytically in excel (\Z-INPUTS\RK\NPK\GEMINI\VISOR\Data-GEMINI-N00-D10.xlsx).

The input deck is located in: \Z-INPUTS\RK\NPK\GEMINI\RUNS\GEMINI-N00-D10.SPE.
The results are shown in Figure 3-525 and Figure 3-526. The calculated and the theoretical values are in very good agreement. The average difference between the calculated and the theoretical values is **δ = 0.29%**.

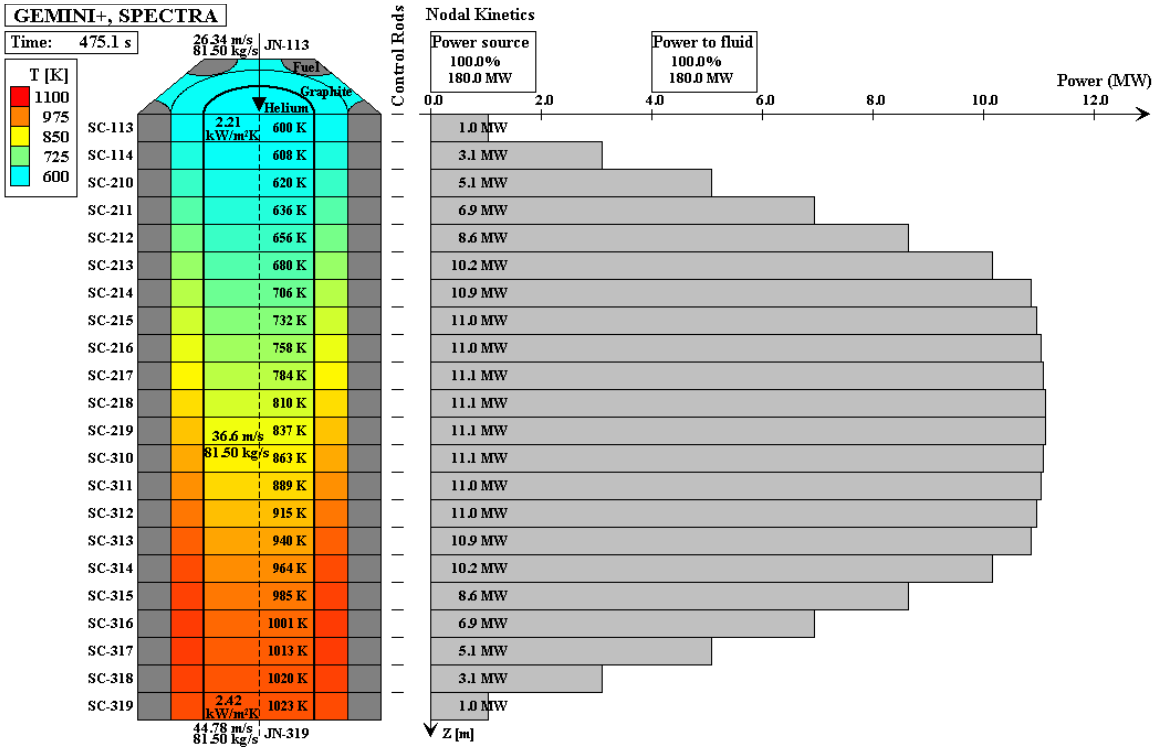

Figure 3-525 Variable diffusion coefficient (GEMINI+ plant)

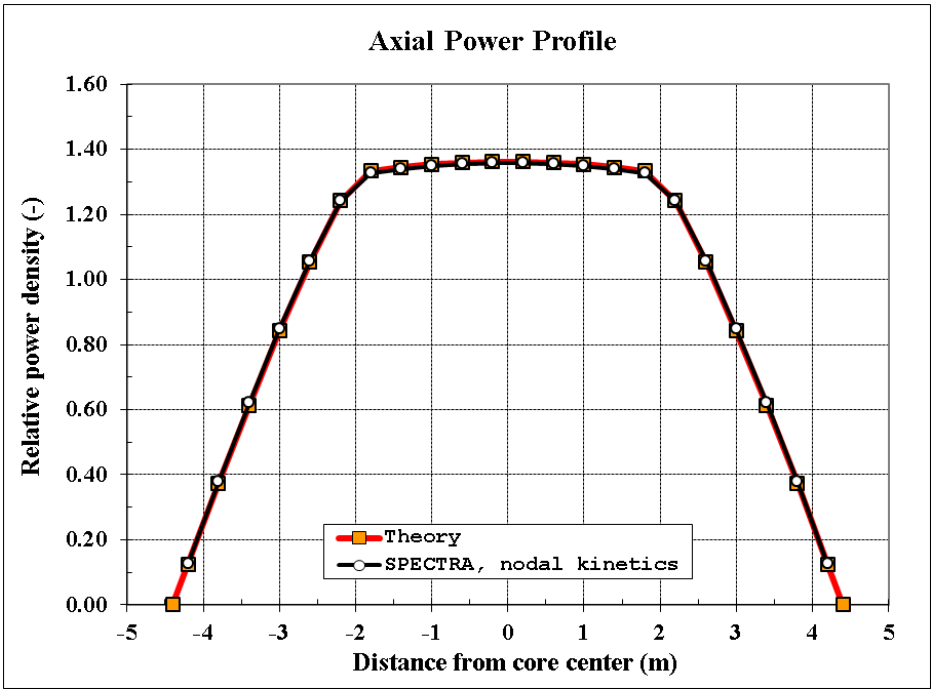

Figure 3-526 Variable diffusion coefficient (GEMINI+ plant)

3.9.4.4 GEMINI+ Plant Model - Comparisons with 3D Neutronics Code SERPENT

❖ **Introduction**

The Euratom Horizon 2020 project GEMINI+ was aimed at designing a reactor system with a net power output of 165 MW (gross thermal power of 180 MW including house load). The GEMINI+ system was designed to provide steam (230 t/h at 540°C and 13.8 MPa) to industrial end users.

The GEMINI+ reactor is a relatively small (180 MW thermal power) prismatic block type reactor HTGR. The reactor vessel is shown in Figure 3-527. The reactor components (fuel blocks, reflector blocks, compacts, coated fuel particles) are very similar to those of existing designs (General Atomics GT-MHR and MHTGR, Framatome SC-HTGR).

The GEMINI+ fuel consists of prismatic graphite blocks, with fuel "rods" and coolant "holes". The fuel block and the fuel model in SPECTRA are shown in Figure 3-528. Within the GEMINI+ project, SPECTRA was used for:

- design support analyses, together with 3D neutronic code SERPENT (used at NUCLIC),
- safety analyses, including DLOFC, PLOFC and air ingress accidents. Results are available in GEMINI+ project reports and several publications, e.g. [201], [202].

Within the design support analyses, the power distribution obtained by SERPENT was used in SPECTRA. A short iteration between SPECTRA and SERPENT was needed, where the temperature distribution calculated by SPECTRA was passed to SERPENT and the updated power distribution obtained in SERPENT was passed on to SPECTRA.

Within the accident analyses, several accident scenarios were analyzed using the point kinetics model. Within the point kinetics model, the reactor parameters, such as fuel and moderator temperature, are averaged over the whole core. The point kinetics model determines the reactivity feedbacks and calculates the reactor power. One of the analyzed scenarios was the unprotected (without SCRAM) Pressurized Loss of Forced Circulation (PLOFC). Due to loss of forced circulation, the core temperature increases and the reactor shuts down due to negative thermal feedback. Subsequently, the reactivity further decreases due to buildup of Xe-135. After many hours, the Xe-135 decays and the reactor becomes critical again (this is possible because the normal shutdown system is assumed unavailable in this scenario).

When criticality is reached, the core temperatures increase. The reactor power stabilizes at the level where there is a sufficient negative thermal feedback to compensate the reactivity increase due to the decay of Xe-135. The point kinetics model uses the average core temperature to calculate the reactor power. As will be shown below, during PLOFC a very large temperature difference is obtained between the top and bottom of the core. Consequently, there is a large difference between the maximum fuel temperature and the average fuel temperature.

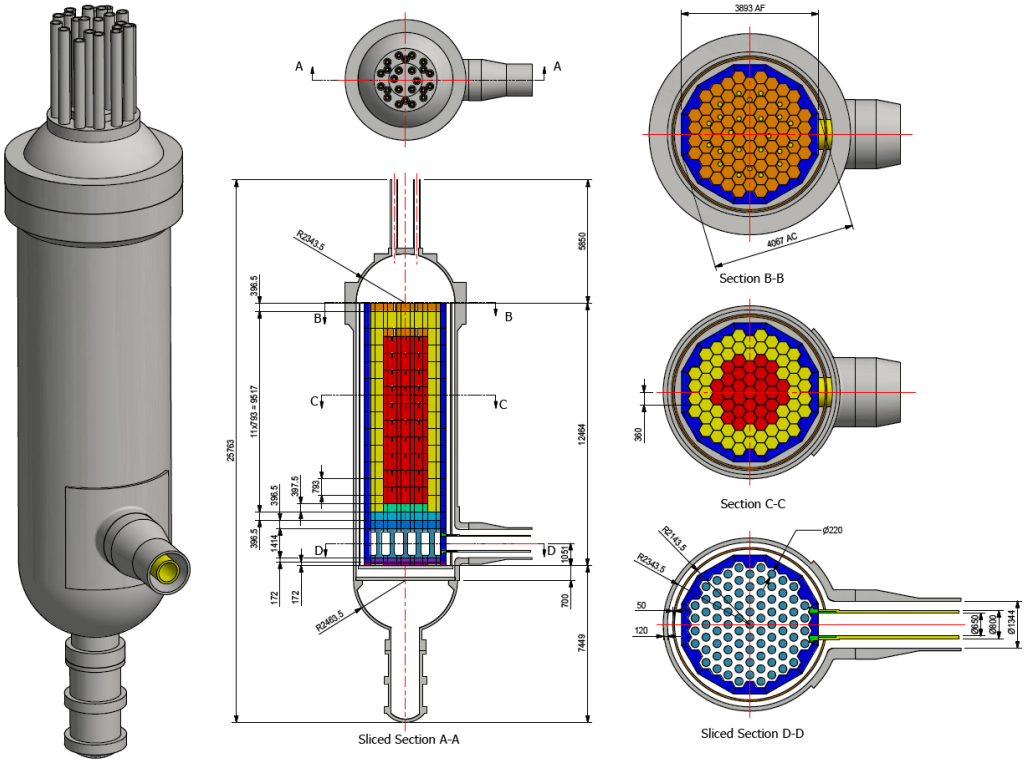

Figure 3-527 GEMINI+ reactor vessel

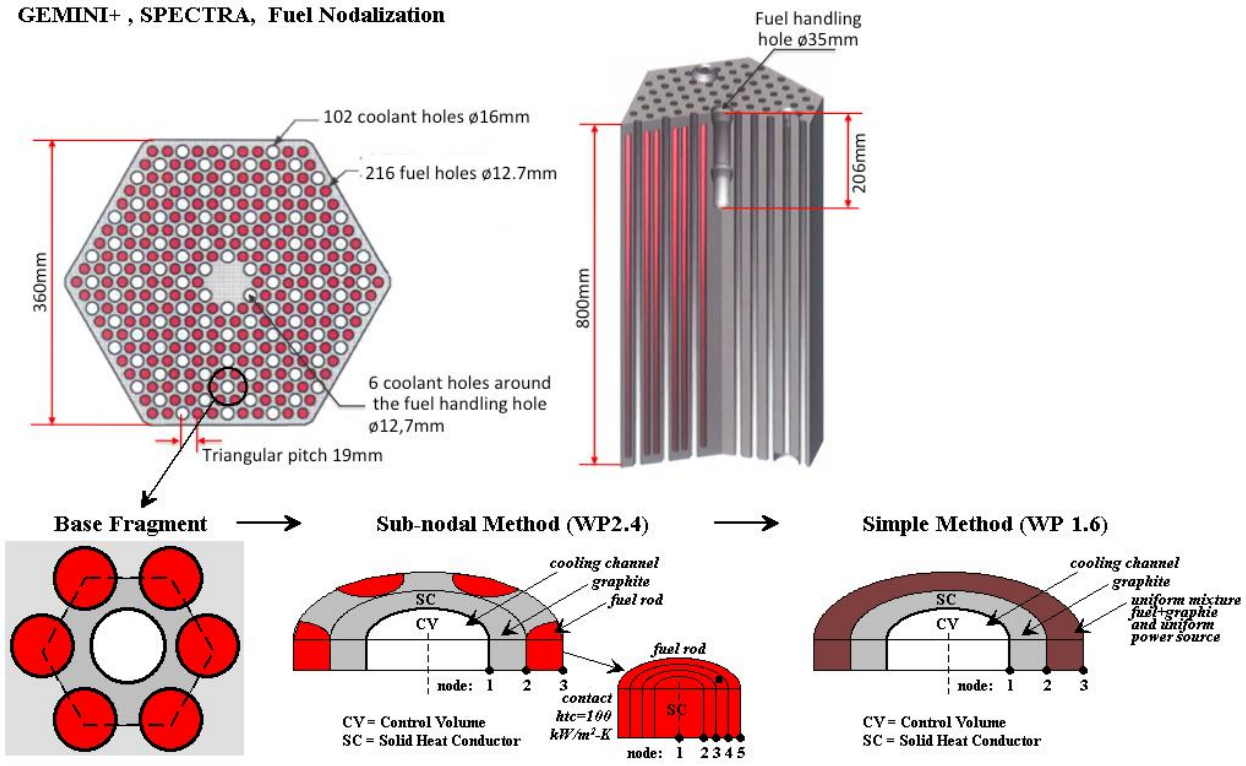

Figure 3-528 GEMINI+ fuel assemblies and the model in SPECTRA

With the point kinetics model, the power distribution after re-criticality remains (by definition) the same throughout the whole transient. In reality, with a large temperature at the core top, one expects a lower power density in this region, due to negative feedback from the fuel and the moderator temperatures. Therefore it is expected that the point kinetics give very conservative results and the conclusion from the PLOFC scenario analyzed within GEMINI+ was: "*the temperature behavior calculated by the point kinetics model is unrealistic and a 3D reactor kinetics model is needed to calculate this case more realistically*".

The use of a full 3-D, multi-group model is possible by coupling the SPECTRA code to one of the available 3-D neutronic codes. Work is ongoing in the direction of such multi-physics coupling. As a practical alternative, the nodal point kinetics model is used. The nodal point kinetics is a 1-D, one-group model, which is using basically the same input as is required by the point kinetics. The computational time is also not very different than that required by the point kinetics. The advantage of this model is the possibility of extending the point kinetics model into a 1-D representation without the need of supplying a significant amount of data required by 3D neutronic codes.

This section describes the analysis of an unprotected PLOFC scenario for the GEMINI+ reactor. In the first part the additional model parameters, needed for the nodal kinetics model, are discussed. Results of steady state simulation are compared to the results obtained with SERPENT. In the second part, the results of unprotected PLOFC obtained by nodal kinetics are compared to the results obtained with the point kinetics model, obtained within the GEMINI+ project.

❖ Model Parameters and Verification

The nodal kinetics model uses the same data as the point kinetics model with only a few additional parameters, including:

- Additional geometrical parameters, such as node thickness d_i, cross section area, A_i, (see Volume 2), which are easily obtained from the core geometry and basic nodalization applied (22 axial nodes, 0.4 m each).
- The neutron diffusion coefficients, which were calculated independently using two different methods. The values were computed at NRG, using the SERPENT code. The following values were obtained:
  - D = 1.035 cm in the horizontal direction,
  - D = 1.310 cm in the vertical direction.

  In addition, theoretical values for graphite and helium from open literature were used and a similar value (1.17 cm) was obtained using simple hand calculations. Details are shown in: \Z-INPUTS\RK\NPK\GEMINI\Doc\Doc-Source\Diffusion-coefficients\Diffusion.xls.
  For the current model the value obtained in SERPENT for the vertical direction was used: D = 0.0131 m.
- The reflection factors at the lower and the upper reflector, which determine the boundary conditions and therefore the loss of neutrons through the lower and upper boundary. These values were obtained by trial and error, as the values that give best agreement of the power distribution with the values calculated by SERPENT. The values are $F_{R1} = F_{RN} = 0.8$.

A simplified model of the GEMINI+ core was created, with all fuel assemblies represented as a single channel. As the base case, the power distribution corresponding to all control rods out of the core was considered. The power distribution was calculated by NUCLIC using SERPENT [202], and passed on to the thermal-hydraulic simulations within the GEMINI+ project.

The steady state calculations were performed using the initialization option (INONRK = 1), described in Volume 1. A uniform power distribution was assumed as a starting point. The target power was set at 180 MW. The default value of the convergence criterion was used (XCNNRK = 10^{-7}). Convergence was reached after 562 seconds of model time. The resulting temperature and power distribution is shown in Figure 3-529. The power profile is compared to the values calculated with SERPENT in Figure 3-530. A very good agreement is observed. The average relative difference is 0.5%.

As a second case, the situation with control rods partly inserted is considered. The control rod insertion is 2.0 m, which means 5 nodes (each node is 0.4 m high). The power data was obtained within the GEMINI+ project. The control rod worth is obtained from [202]: $(1/0.914812 - 1/1.0017)\times10^5$ = 9482 pcm = 13.98 \$ (β=678 pcm). Again, the initialization option with the same target power is used and calculations are started with a uniform power distribution. The desired accuracy was reached after 566 seconds of model time. The resulting temperature and power distribution is shown in Figure 3-531. The power profile is compared to the values calculated with SERPENT in Figure 3-532. The peak power is somewhat lower but the overall agreement is satisfactory. The average relative difference is 11.4%, with the largest relative differences at the top (nodes 1 - 3).

The agreement could be improved by modifying the reflection factors. A better agreement of the axial power distribution was obtained when the reflection factor of the upper reflector was reduced from F_{R1} = 0.8 to F_{R1} = 0.2, while the lower reflection factor was kept at F_{RN} = 0.8. The results are shown in Figure 3-533. The average relative difference is 3.5%; the improvement is mainly in the upper nodes (1 - 3). The reduction of the upper reflection factor may be related to the absorption of neutrons by the control rods.

- **Results of Unprotected PLOFC**

The nodal kinetics input, tested as described in the previous section, was applied for the full GEMINI+ model. The full model consists of 5 different groups of fuel assemblies. The same power was assumed in each assembly (uniform radial power distribution), which is consistent with the original model applied in the GEMINI+ project.

Steady state power distribution was obtained as before, using the initialization option. The resulting axial power distribution was very similar to that shown in Figure 3-529. Some small differences are caused by the bypass flows, the radial conduction, etc. applied in the large model.

Calculations of the unprotected PLOFC scenario were performed using the nodal and the point kinetics models. At the same time the point kinetics model was improved compared to the model originally used in GEMINI+ project because a mistake in the input model (weighting factors) was discovered. Therefore the point kinetics results presented here are slightly different from the results presented in the GEMINI+ project report, but the difference is small.

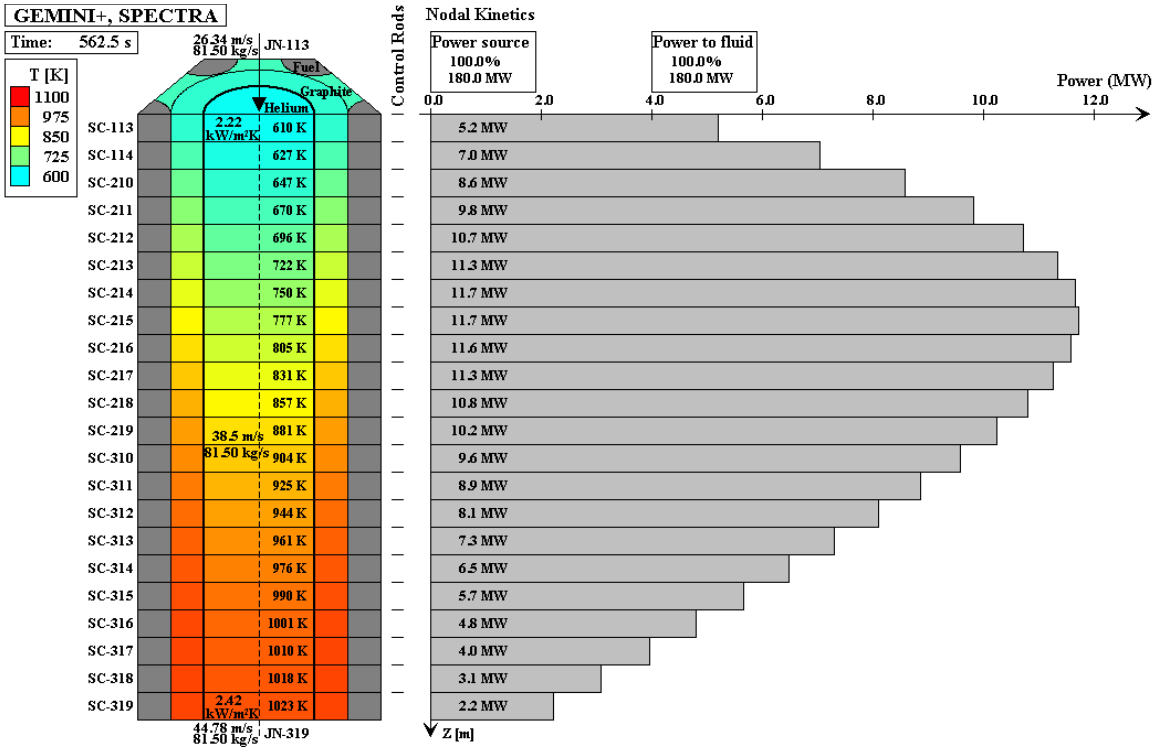

Figure 3-529 GEMINI+, nodal kinetics, base case

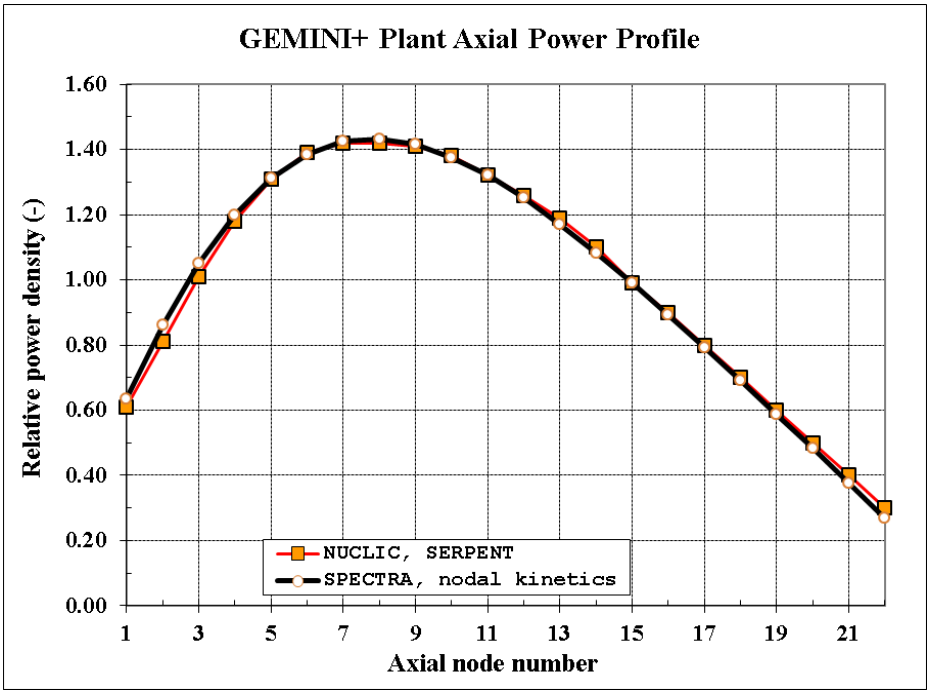

Figure 3-530 GEMINI+, nodal kinetics, base case

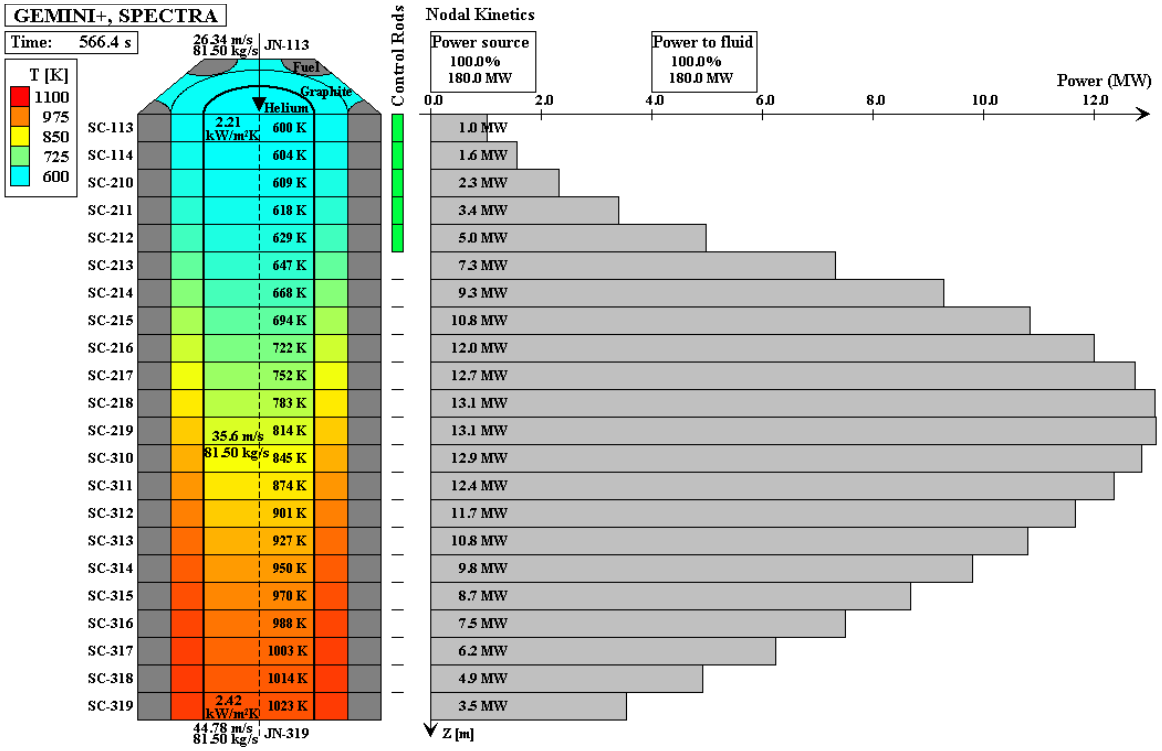

Figure 3-531 GEMINI+, nodal kinetics, control rod insertion, 2.0 m

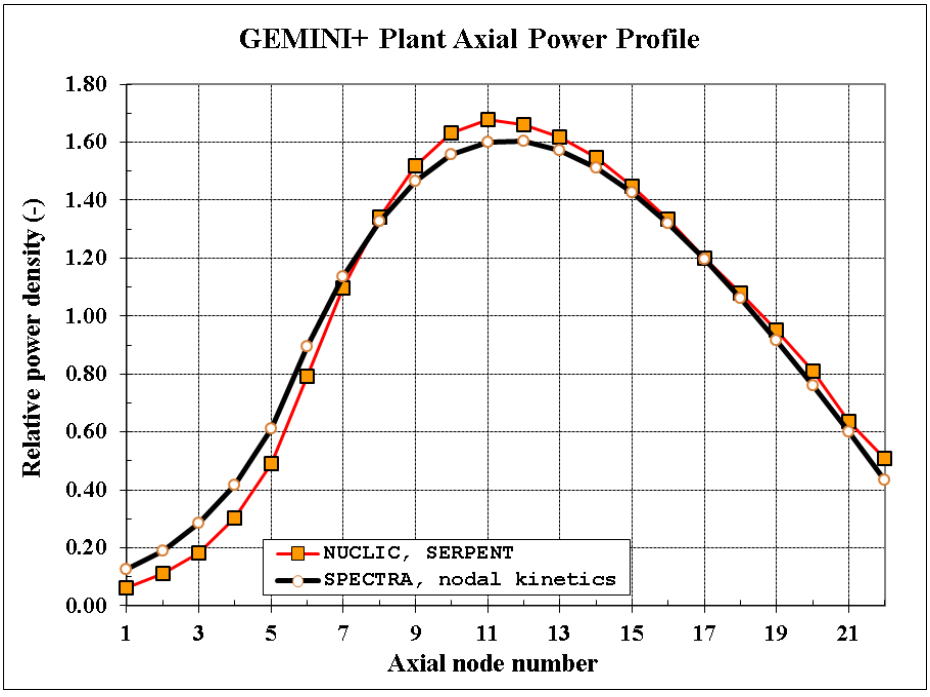

Figure 3-532 GEMINI+, nodal kinetics, control rod insertion, 2.0 m

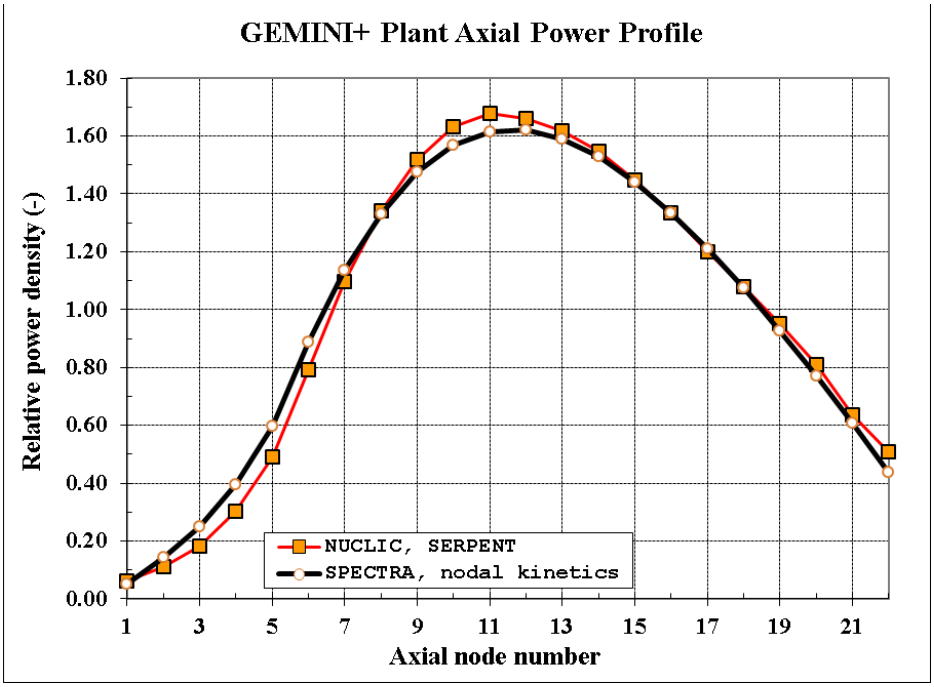

Figure 3-533 GEMINI+, nodal kinetics, control rod insertion, 2.0 m, F_{R1} = 0.2

Calculations were performed for the best estimate case (BE), with the core thermal power of 180 MW. The results are shown in Figure 3-534 through Figure 3-539. The axial temperature distribution in the hottest assembly and the axial power profile at the end of the calculations (t = 500,000 s) are shown in Figure 3-534 and Figure 3-535. Figure 3-534 shows the results obtained with the point kinetics; Figure 3-535 shows the results obtained with the nodal kinetics. With the point kinetics the axial power distribution is the same throughout the transient - it is simply defined by the user. The temperature in the upper part of the core is higher than in the lower part of the core by almost 1000 K - Figure 3-534. In the nodal kinetics the power distribution is different - the power peak is shifted towards the bottom of the core, the maximum temperature is lower than in the point kinetics by about 150°C at this time.

The time dependent graphs are shown in Figure 3-536 through Figure 3-539. Figure 3-536 shows the maximum fuel temperature. The peak value is observed at about 250,000 s and is about 1540°C in the point kinetics and about 1400°C in the nodal kinetics. The difference is approximately 140°C at this time. Figure 3-537 shows the average fuel temperature. The average temperature is higher in the nodal kinetics, which is related to the fact that criticality is reached somewhat earlier.

Figure 3-538 shows the reactor power. It is seen that the criticality is reached earlier in the nodal kinetics model. In the long term, the reactor power is practically the same in both models. A more detailed investigation shows that the criticality is achieved first in the lower part of the core. Firstly, because the temperatures are low, secondly, because the Xe-135 concentrations are low.

Figure 3-539 shows the reactivity of Xe-135 in the uppermost core node (1), the node with maximum power (07), and the lowermost core node (22). For comparison, the point kinetics model results are shown. The Xe-135 reactivities in the lower part of the core are the smallest. The reason is the lowest power and thus neutron flux in this region. The power is approximately 2 MW, while in the node with maximum power it as almost 12 MW - Figure 3-529. The power ratio is about a factor of five. The same ratio is observed for the precursor of Xe-135, Iodine-135. In the case of Xe-135, the ratio is clearly smaller because Xe-135 is "burned" faster in the high flux region, but it is still about a factor of two, as can be seen in the printout of concentrations below.

GEMINI+ Nodal Kinetics
SPECTRA

Nuclide concentrations, N, [1/m³]

Node	I-135	Xe-135
01	2.5E+020	2.0E+020
02	3.4E+020	2.2E+020
03	4.0E+020	2.4E+020
04	4.6E+020	2.5E+020
05	5.0E+020	2.6E+020
06	5.2E+020	2.6E+020
07	5.3E+020	2.7E+020
08	5.3E+020	2.7E+020
09	5.3E+020	2.7E+020
10	5.1E+020	2.6E+020
11	4.9E+020	2.6E+020
12	4.7E+020	2.6E+020
13	4.5E+020	2.5E+020
14	4.2E+020	2.4E+020
15	3.9E+020	2.4E+020
16	3.6E+020	2.3E+020
17	3.2E+020	2.2E+020
18	2.9E+020	2.1E+020
19	2.5E+020	1.9E+020
20	2.1E+020	1.8E+020
21	1.7E+020	1.6E+020
22	1.2E+020	1.3E+020

Steady state concentrations of I-135 and Xe-135

Because of the Xe-135 concentration differences, the depth of the "Xe reactivity well" is smaller in the lower part of the core - Figure 3-539. In combination with the lowest temperature and consequently the highest thermal reactivity feedback, those effects are the reason for earlier criticality in the nodal kinetics than in the point kinetics. The earlier criticality leads to higher core average temperature. In spite of the higher average temperature, the maximum fuel temperature is clearly smaller when the nodal kinetics is used. This is due to different power distribution that is established in the core after the criticality is reached following the Xe-135 decay.

❖ Conclusions

The following main conclusions are reached from the current work.

- Successful verification of the nodal kinetics model was shown for the stationary state conditions - a very good agreement with the power distribution obtained with SERPENT was obtained.
- Transient analysis shows a large effect on the unprotected PLOFC. The results are as expected and therefore serve as a qualitative verification of the current model. A more detailed calculation should be performed in the future with 3D kinetics model.
- A more detailed analysis will be possible using multi-physics interactive coupling with a 3D kinetics code. However, the code to be coupled must be carefully selected. SERPENT or other codes based on a probabilistic approach are not suitable for analyses of extremely long transients (approximately 6 days of transient were analyzed for the GEMINI+ reactor). Therefore a fast running code should be sought.

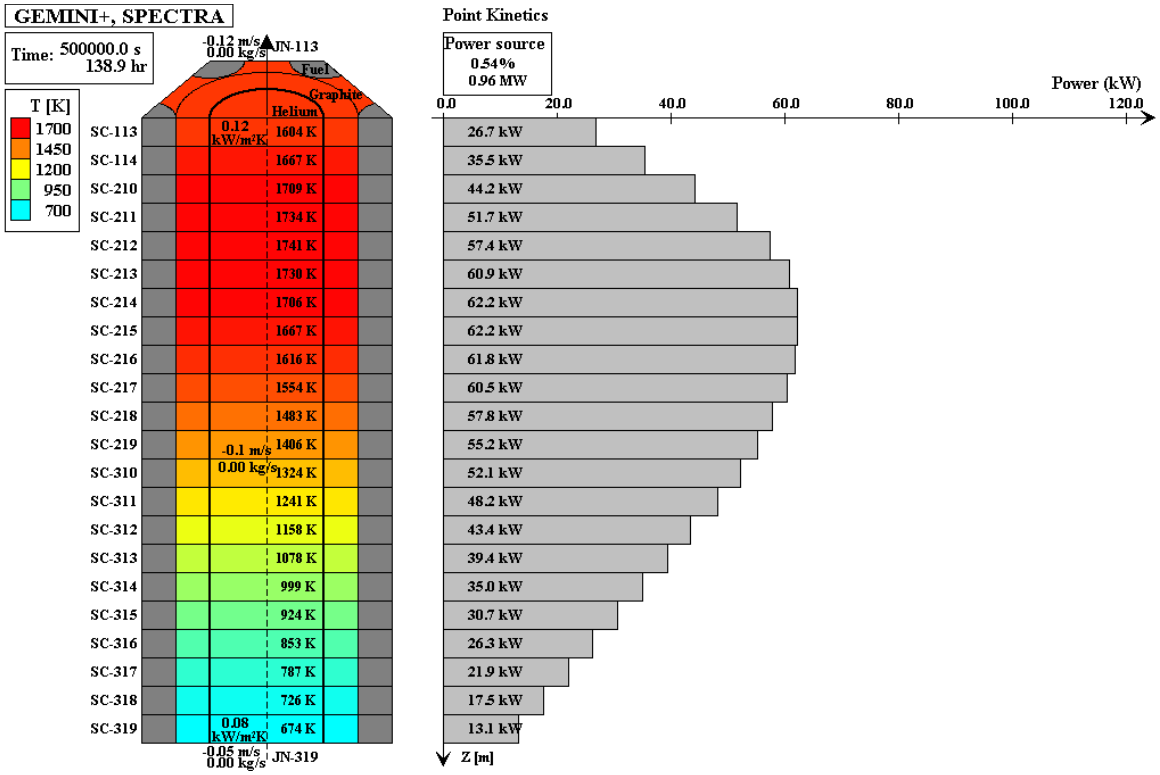

Figure 3-534 GEMINI+, PLOFC, point kinetics

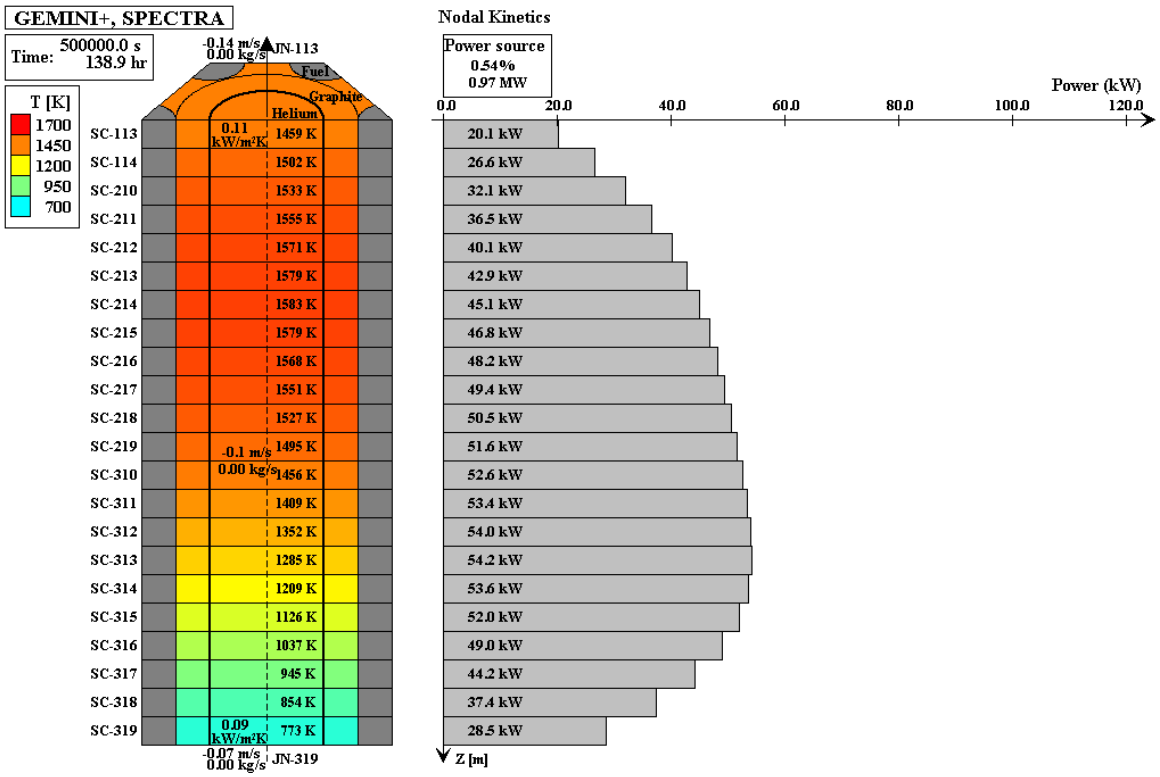

Figure 3-535 GEMINI+, PLOFC, nodal kinetics

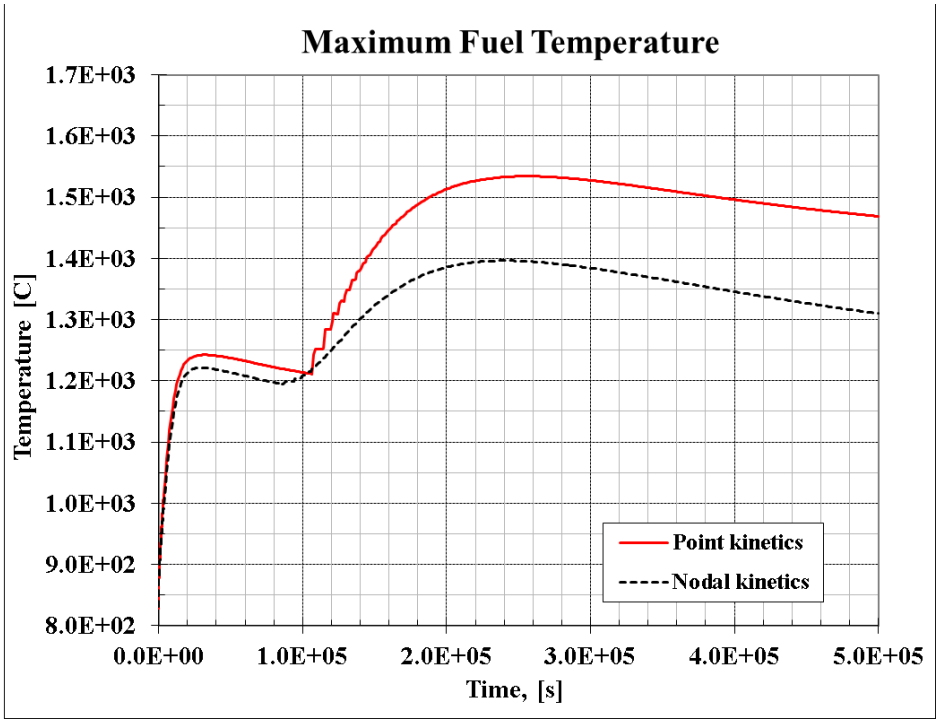

Figure 3-536 GEMINI+, maximum fuel temperatures (BE)

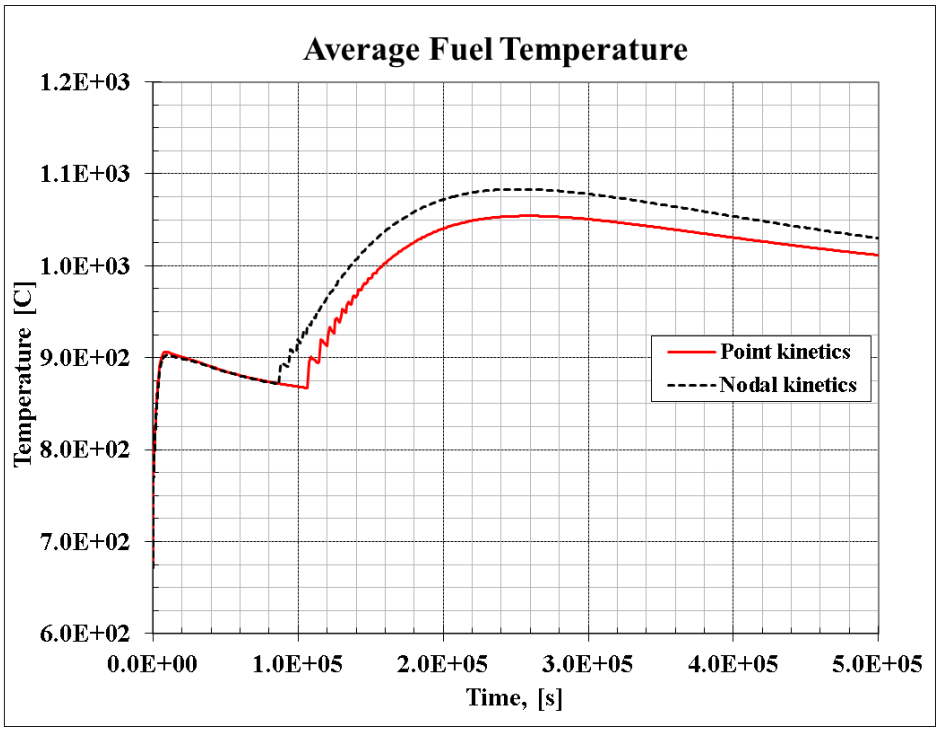

Figure 3-537 GEMINI+, average fuel temperatures (BE)

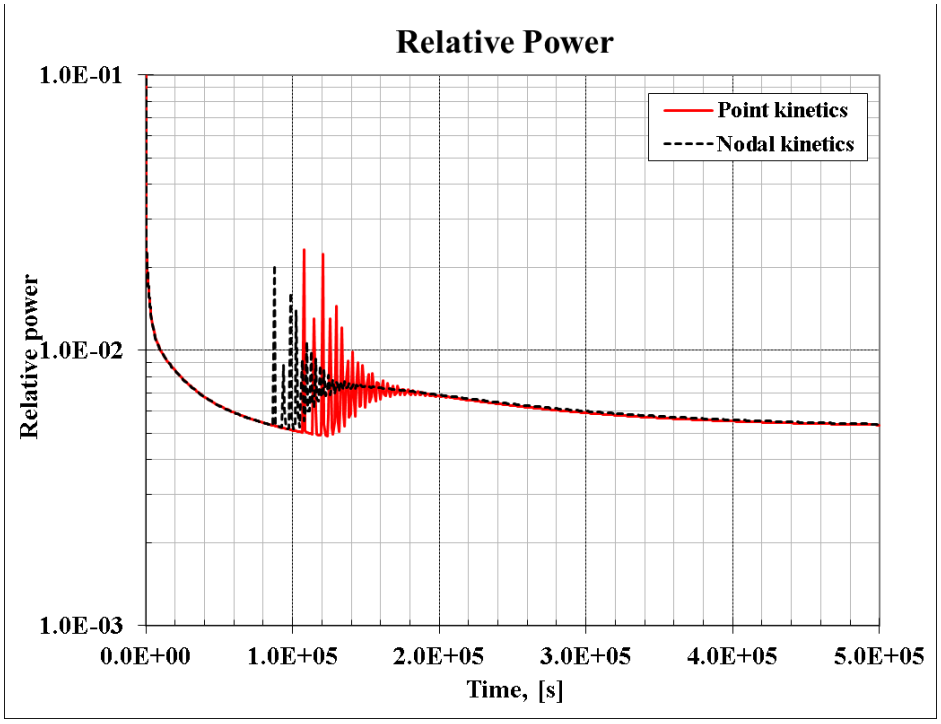

Figure 3-538 GEMINI+, total reactor power (BE)

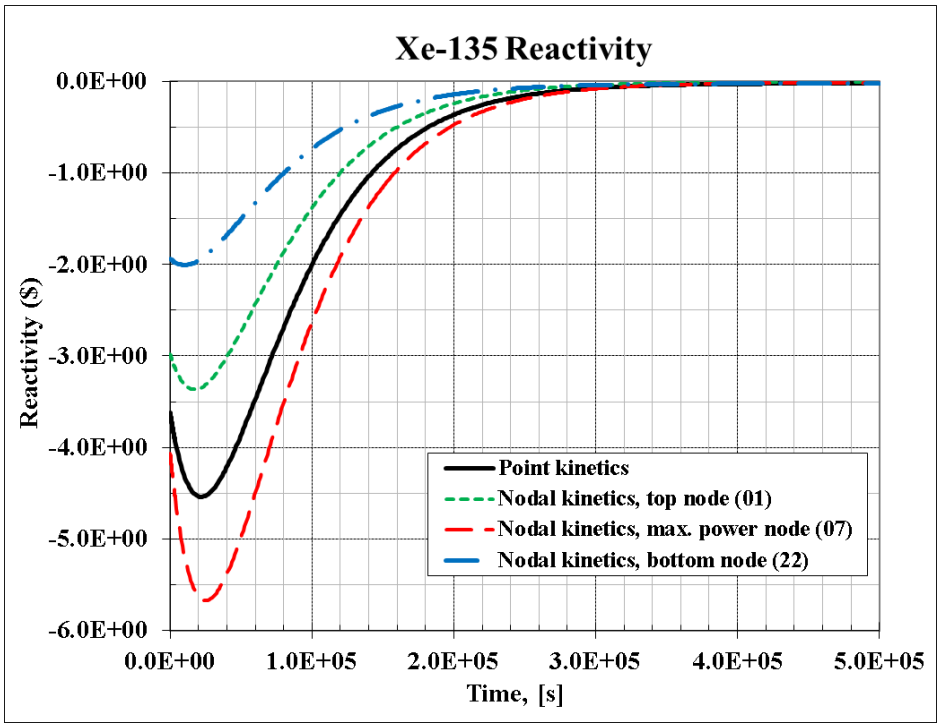

Figure 3-539 GEMINI+, Xe-135 reactivity (BE)

3.10 Oxidation

3.10.1 Zr Oxidation by H_2O

Verification of the Zr oxidation by steam is performed using the same data as was used for independent subroutine testing, shown in section 2.6.1. The present verification was performed from the full SPECTRA code level. An input deck was prepared and a SPECTRA run was performed. The input deck for this test case is described below.

The input deck defines six Control Volumes, CV-101 through CV-106, each with "frozen" conditions. The volumes are filled with steam at 1.0×10^5 Pa pressure and different temperatures:

- CV-101: T = 1273.15 K
- CV-102: T = 1373.15 K
- CV-103: T = 1473.15 K
- CV-104: T = 1573.15 K
- CV-105: T = 1673.15 K
- CV-106: T = 1773.15 K

Six identical 1-D Solid Heat Conductors, SC-101 through SC-106, are defined. Each SC is a rectangular structure, with 1.0 m^2 surface area and two nodes, 0.001 m each. The left surface of each SC is kept at desired temperature using a fixed heat transfer coefficient, defined by the tabular function TF-100, equal to 10^6 ($W/m^2/K$) and appropriate temperature specified by TF-101 through TF-106. The right surface is in contact with the appropriate CV.

Oxidation is defined for the right surface. Built-in model number –1 is used for the first test case (input file "OX-CP.SPE"), and –2 for the second test case (input file "OX-UH.SPE"). In order to keep the SC temperatures approximately constant a large heat transfer coefficient, given by TF-100, is specified also on the right surface. If this were not done, the right surface would significantly heat up in the high temperature cases, in spite of the fixed left boundary temperature. The input decks are located in:

- `\Z-INPUTS\OX\OX-CP.SPE`
- `\Z-INPUTS\OX\OX-UH.SPE`

The calculated oxide thickness is converted to the units used in the source data (μm), using the conversion factor of 1.0×10^6. The square root of time is used, rather than the time itself, for plotting. Results of the run OX-CP and OX-UH are shown in Figure 3-541 and Figure 3-542, respectively. Experimental data from [56] are shown in Figure 3-540.

The calculated results are identical to those obtained during the separate subroutine testing (section 2.6.1). The calculated results show somewhat higher oxide thickness than the data. This discrepancy is discussed in section 2.6.1.

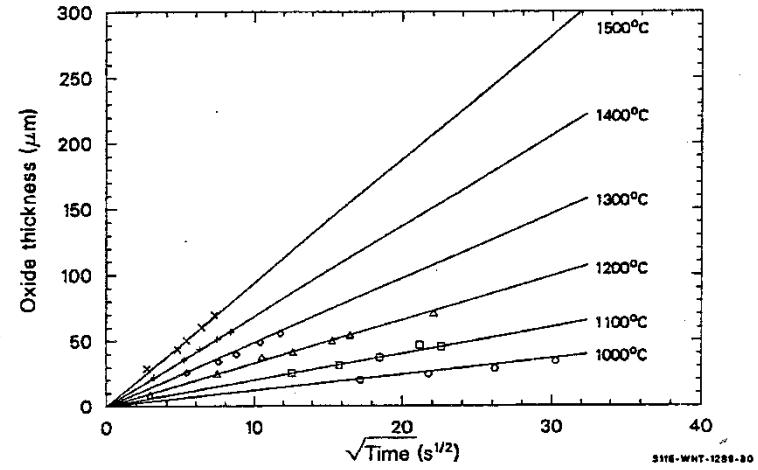

Figure 3-540 Zr oxidation by H_2O – reproduced from [56] (figure 4-66).

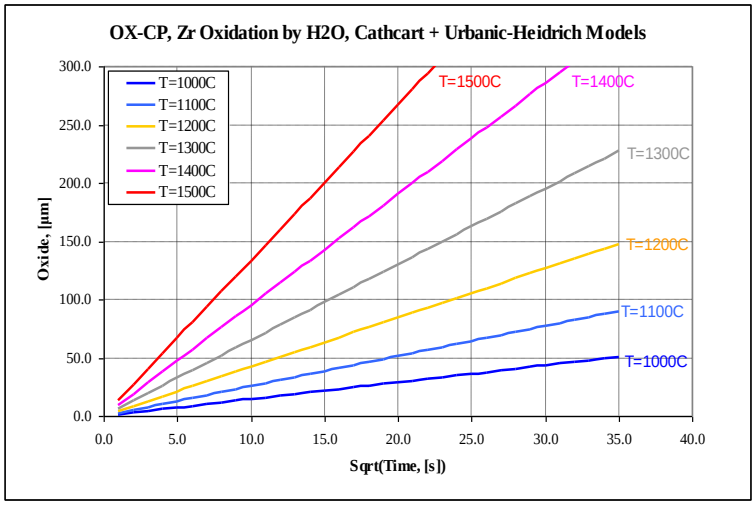

Figure 3-541 Zr oxidation by H_2O – SPECTRA model 1 (Cathcart + Urbanic-Heidrich).

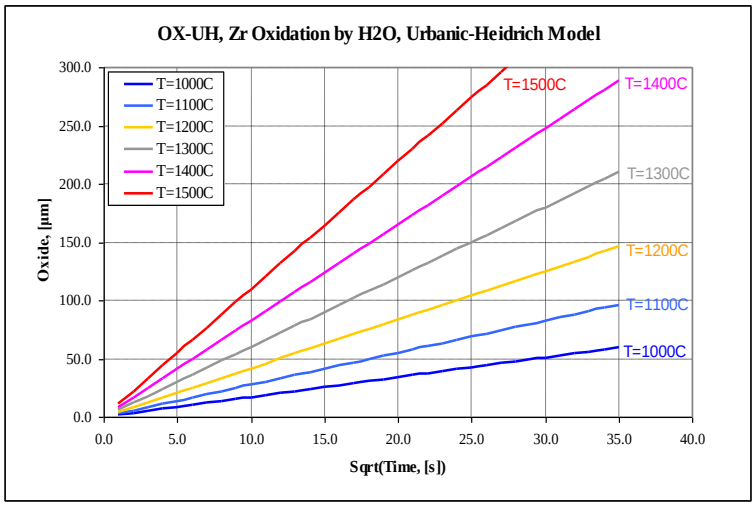

Figure 3-542 Zr oxidation by H_2O – SPECTRA model 2 (Urbanic-Heidrich)

3.10.2 Steel Oxidation by O_2 - Model of Nanni et al.

There is no built-in model for steel oxidation by O_2. A user-defined oxidation model was applied. Data from Nanni et al., reference [60], was used to estimate the reaction coefficients, *A* and *B* (see Volume 1). The reaction kinetics is:

$$\frac{dm^2}{dt} = A \exp\left[-\frac{B}{T}\right] = 2.3\times10^{10} \exp\left[-\frac{45350}{T}\right]$$

The input model for the present test consists of three Control Volumes, CV-101 through CV-103, and three 1-D Solid Heat Conductors, SC-101 through SC-103. The temperatures are: (a) 1073 K, (b) 1273 K, and (c) 1473 K. Isothermal conditions are assured by specifying boundary conditions in the same way as in the Zr tests, see previous section. The initial thickness of material that can be oxidized was set to 1.0×10^{-3} m for SC-102 and SC-103, while for the reason shown below it was limited to 1.0×10^{-6} m for SC-101.

Three Control Functions, CF-101 through CF-103, are used to calculate cumulative weight gain. The SPECTRA parameter: total gas consumption rate at SC surface, is integrated for each SC. The result is therefore equal to the mass of oxygen consumed. In order to obtain output in the same units as the original data the scaling factor of 100.0 is used for all functions (conversion from kg/m^2 to mg/cm^2).

The input deck is located in: `\Z-INPUTS\OX\NANNI.SPE`. Results are shown in Figure 3-544. The measured data is shown in Figure 3-543. Good agreement for T = 1273 K and T = 1473 K is observed. For T = 1073 K the reaction rate is reasonably close to experimentally observed values during about 100 minutes, when the oxide layer grows to about 0.2 μm. Soon afterwards the reaction slowed down and finally stopped, due to crystallographic changes in the oxidized material (see [60]).

In the calculations the initial thickness of the material that can be oxidized was set to 1.0×10^{-6} m. With this value the reaction stopped at approximately the same time as in experiment. It is clear that if the reaction weren't stopped, the weight growth would significantly exceed the measured value. This could be remedied by using different sets of coefficients for lower and higher temperatures. This means, instead of the single-set formula, shown above, a full formula could be used:

$$\frac{dm^x}{dt} = K_T(T) = \begin{cases} A_1 \exp\left[-B_1/T\right] & for\ T < T_1 \\ A_2 \exp\left[-B_2/T\right] & for\ T > T_2 \end{cases}$$

However, since the reaction practically stopped at 1073 K, it would be very difficult to find a set of coefficients that would well represent the reaction rate in the low temperature range. Therefore it was decided not to attempt to develop a different set of coefficients for the low temperatures, but simply to limit the oxidizable layer thickness for the first SC. This of course could not be done in a general plant model, so the user would simply have to accept the fact that at low temperatures the oxidation rate is overestimated.

This is not a big problem since at low temperatures the oxidation is very slow anyway. Moreover the small overestimation during an early (low temperature) stage of an accident will to a certain degree be compensated in the later (high temperature) stage of the accident due to larger oxide thickness.

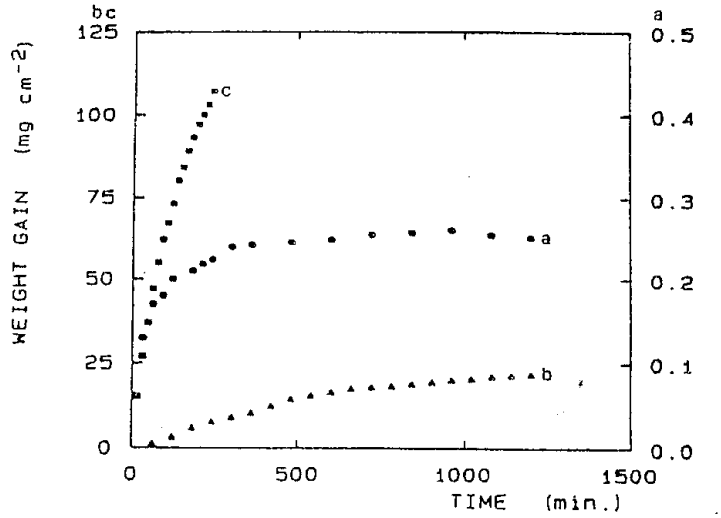

Figure 3-543 Steel oxidation by O_2, reproduced from [60].

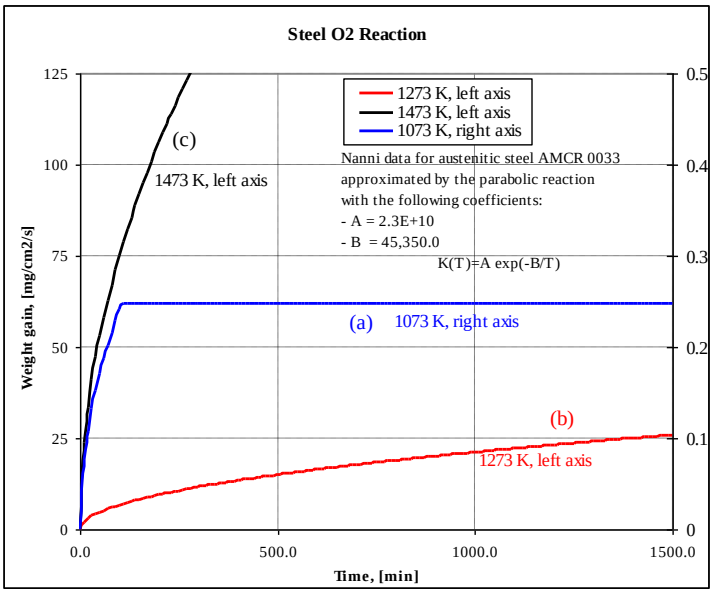

Figure 3-544 Steel oxidation by O_2, SPECTRA results.

3.10.3 Low Temperature Zr Oxidation – Comparison with EPRI Model

The low-temperatures Zr oxidation by water (corrosion) is a very slow process. There are models appropriate for BWR and PWR conditions, for example EPRI model [63]. The model distinguishes two stages of oxidation: pre-transition and post-transition. Results of such model for PWR corrosion are reproduced in Figure 3-545 and Figure 3-547. Using a trial and error method the data shown in these figures was approximated in SPECTRA by the user-defined model, as:

$$\frac{dm^{1/2}}{dt} = A\exp\left[-\frac{B}{T}\right] = 1.9\times10^{-7}\ \exp\left[-\frac{2320}{T}\right]$$

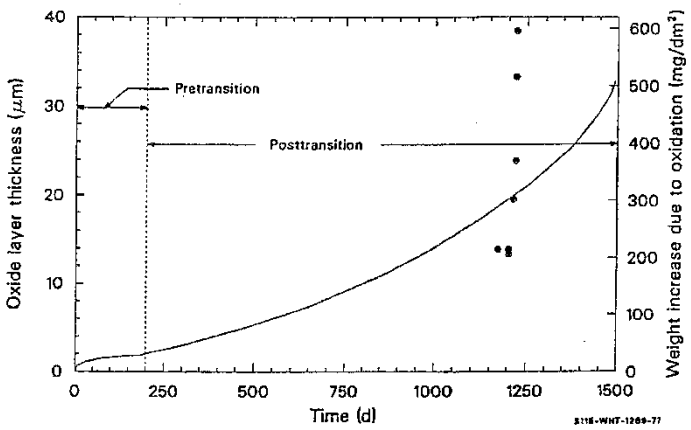

Figure 3-545 Zr oxidation by water, T = 550 K, reproduced from [56] (fig. 4-63).

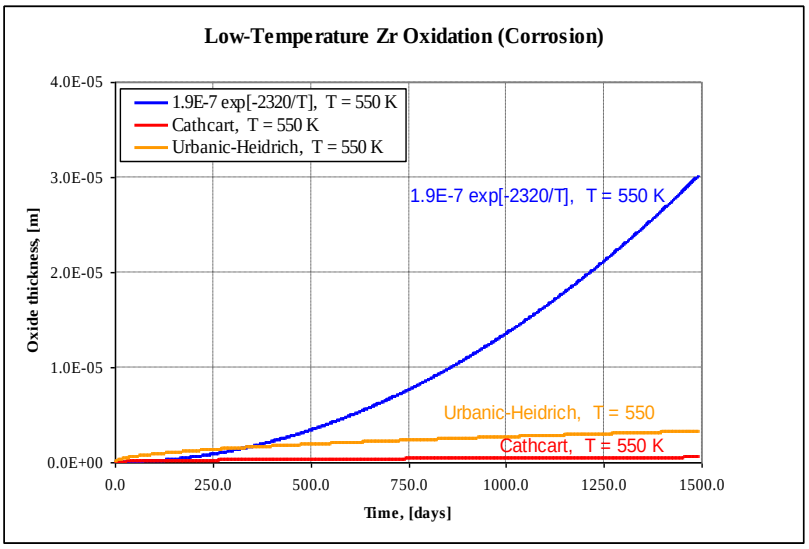

Figure 3-546 Zr oxidation by water, T = 550 K, SPECTRA results.

SPECTRA input deck is located in: `\Z-INPUTS\OX\EPRI-1.SPE`. Results of this formula are shown in Figure 3-546 and Figure 3-548. Note that the power of 0.5 is used in the present reaction rate, rather than 2.0 (as in the high temperature oxidation, Cathcart or Urbanic-Heidrich models). Different reaction kinetics in the pre- and post-transition region cannot be modelled within the SPECTRA oxidation model; therefore the pre-transition kinetics is ignored here. For comparison results of Catchcart and Urbanic-Heidrich models are included in the figures. It is important to note that the built-in Catchcart and Urbanic-Heidrich models work only for steam and for $T > 600$ K. In order to apply the models for water oxidation at temperatures below 600 K, user-defined models were created, with the reaction kinetics coefficients equal to the built-in Catchcart and Urbaic-Heidrich values, but with low temperature limit, TMINOX, set to 300 K and the water option, XWATOX, set to a negative value, to allow water reaction (see Volume 2).

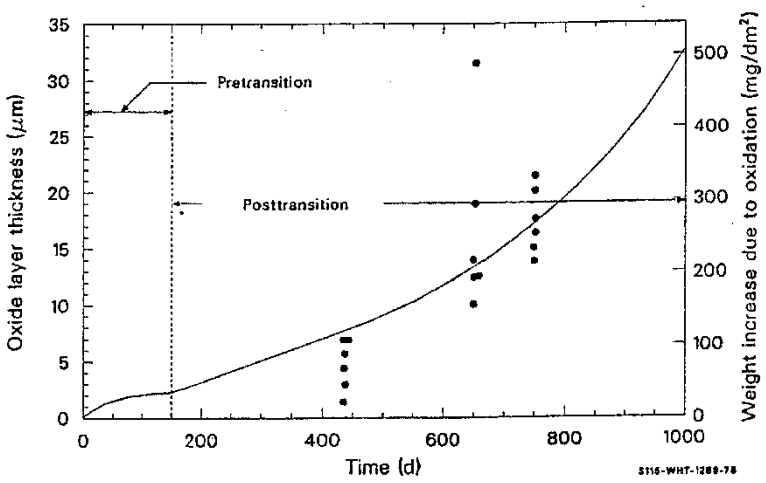

Figure 3-547 Zr oxidation by water, T = 613 K, reproduced from [56] (fig. 4-64)

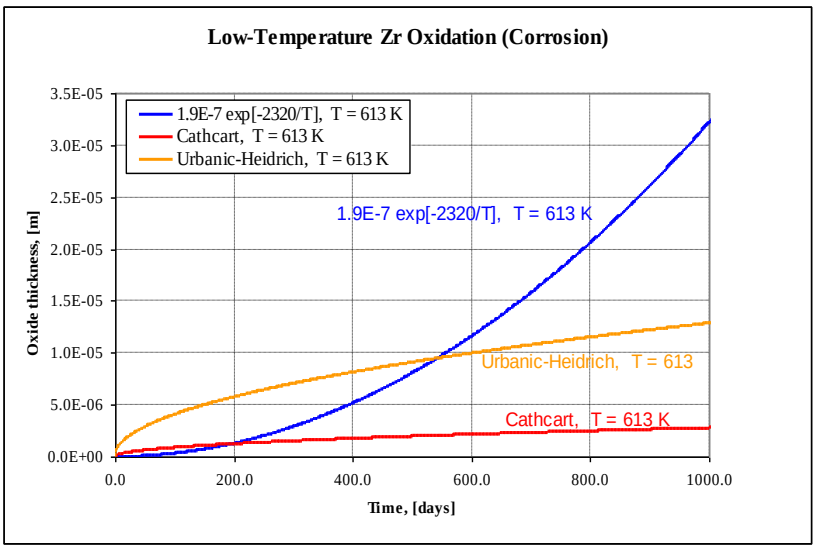

Figure 3-548 Zr oxidation by water, T = 613 K, SPECTRA results.

3.10.4 Low Temperature Zr Oxidation – Breakaway included

The same test case as discussed in the previous section. In the present case, breakaway model is used. The pre-breakaway regime, the Urbanic-Heidrich correlation is used. In the post-breakaway, the correlation shown in the previous section is used:

$$\frac{dm^{1/2}}{dt} = A\exp\left[-\frac{B}{T}\right] = 1.9\times10^{-7}\ \exp\left[-\frac{2320}{T}\right]$$

SPECTRA input deck is located in: `\Z-INPUTS\OX\EPRI-1.SPE`. Results of this formula are shown in Figure 3-549 and Figure 3-550. The results are in better agreement with the EPRI model.

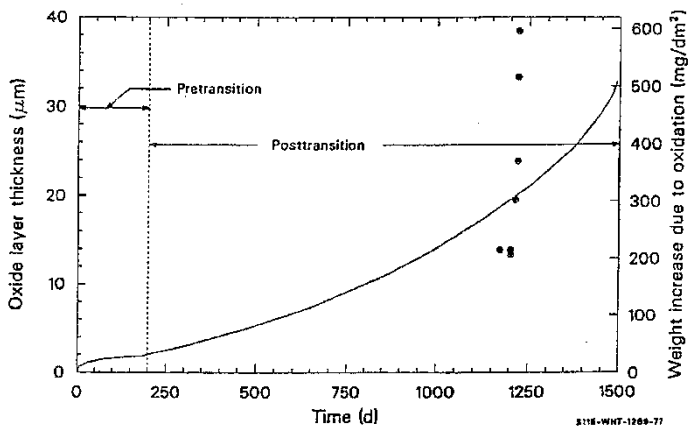

Figure 3-549 Zr oxidation by water, T = 550 K, reproduced from [56] (fig. 4-63).

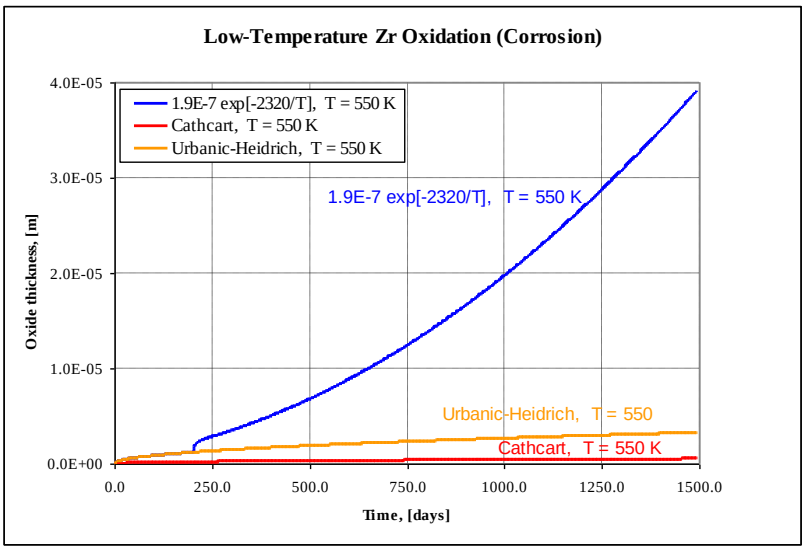

Figure 3-550 Zr oxidation by water, T = 550 K, SPECTRA pre- and post-breakaway model

3.10.5 User-Defined Oxidation Model

If a user wishes to perform sensitivity studies with some of the built-in models, he must do that with the user-defined oxidation model. It is good to first build the user-defined model with exactly the same coefficients as the built-in model and check that the same results are obtained, before performing the sensitivity study. The test shown in this section is provided as an example of how to build a user-defined model which behaves as one of the built-in models.

A model for Zr - steam reaction is built, using the Cathcart coefficients (built-in model 1). The coefficients are taken from Volume 1. Two structures, SC-001 and SC-002, are defined. The structures are 2 mm thick and consist of 2 nodes, 1 mm each. The temperature of these structures is kept at the desired level by specifying a large (10^6 W/m^2-K) heat transfer coefficient on both surfaces. On the left surface a tabular function is used to define the boundary temperature. On the right surface convection to a CV is used (this must be the case to be able to use the oxidation models). The boundary CV is kept at constant temperature. The temperature selected for this test is 2500 K. The oxidation models are selected as follows:

- SC-101 - built-in Zr - H_2O oxidation, Cathcart model
- SC-102 - user-defined Zr - H_2O oxidation with coefficients from the Cathcart model

SPECTRA input for this test is provided in `\Z-INPUTS\OX\OX-COMP.SPE`. Results are shown in Figure 3-551. As expected, the structures SC-101 and SC-102 show identical behavior.

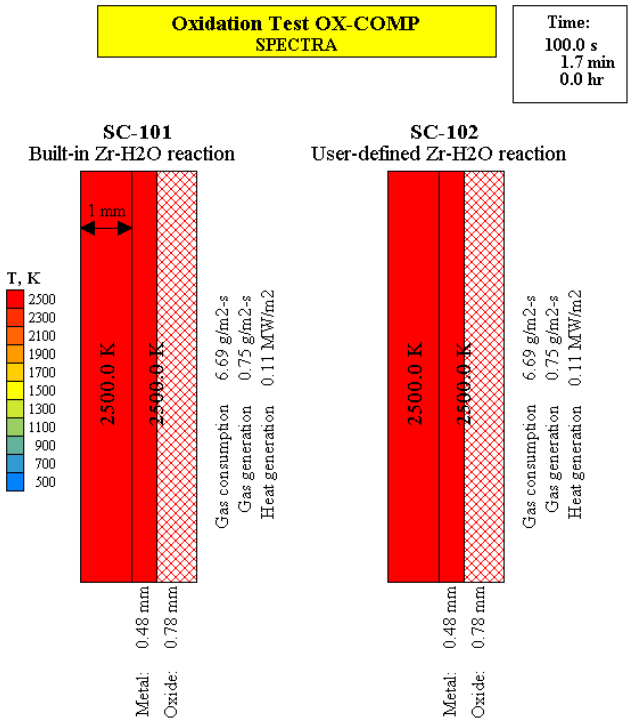

Figure 3-551 Comparison of built-in and user-defined Zr oxidation by steam

3.10.6 Multiple Oxidation Reactions - Zr Oxidation by H_2O and O_2

The present example shows multiple oxidation reactions. The oxidation of Zr by H_2O and O_2 is considered. The input deck is very similar to the one used in the previous section. The temperature was again set to 2500 K for this test. The gas composition is such that both steam and oxygen are available for oxidation. The oxidation models are selected as follows:

- SC-101 - Zr - H_2O oxidation, built-in model of Cathcart and Urbanic-Heidrich
- SC-102 - Zr - O_2 oxidation, built-in model of Benjamin
- SC-103 - both models

SPECTRA input for this test is provided in `\Z-INPUTS\OX\Zr-H2O-O2.SPE`. Results are shown in Figure 3-552 and Figure 3-555. The oxygen reaction is faster and more exothermic than the steam reaction. When both models are active, the reaction proceeds faster, but not as would be obtained by summing up the two individual reactions. This is a result of the parabolic reaction rate - the reaction slows down with increasing oxide thickness. Two more cases were calculated for qualitative verification of the oxidation model:

- Lack of oxygen - input deck in: `\Z-INPUTS\OX\Zr-H2O-O2-a.SPE`
- Lack of steam - input deck in: `\Z-INPUTS\OX\Zr-H2O-O2-b.SPE`

Results are shown in Figure 3-553 and Figure 3-554. As expected, the results of SC-101 and SC-103 are identical in the (a) case, Figure 3-553, while the results of SC-102 and SC-103 are identical in the (b) case, Figure 3-554.

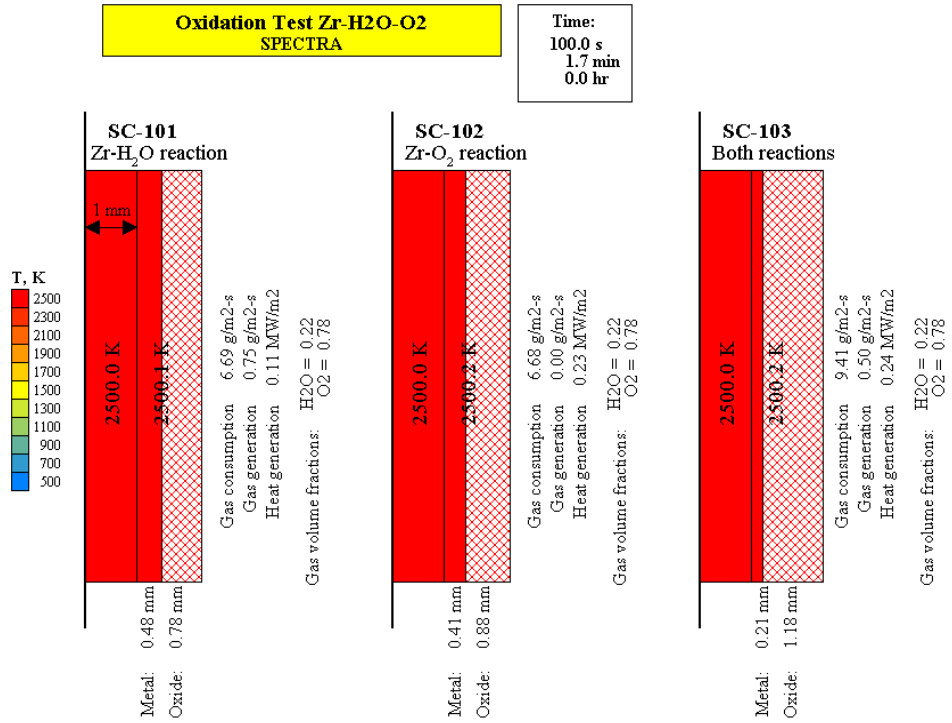

Figure 3-552 Multiple oxidations reactions - Zr oxidation by H_2O and O_2

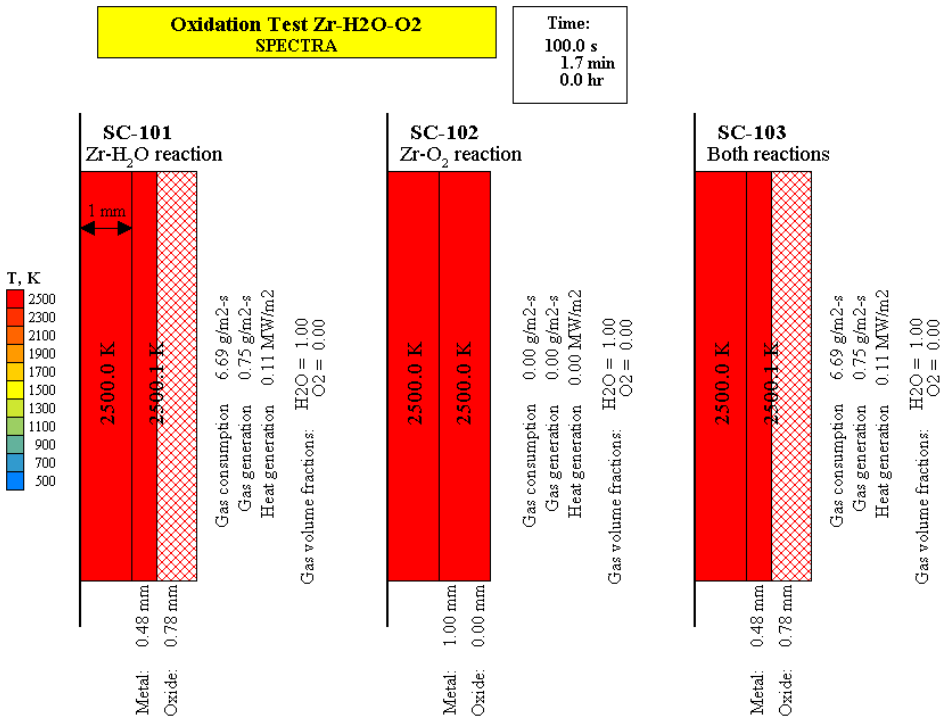

Figure 3-553 Multiple oxidations reactions - lack of O_2 in the atmosphere

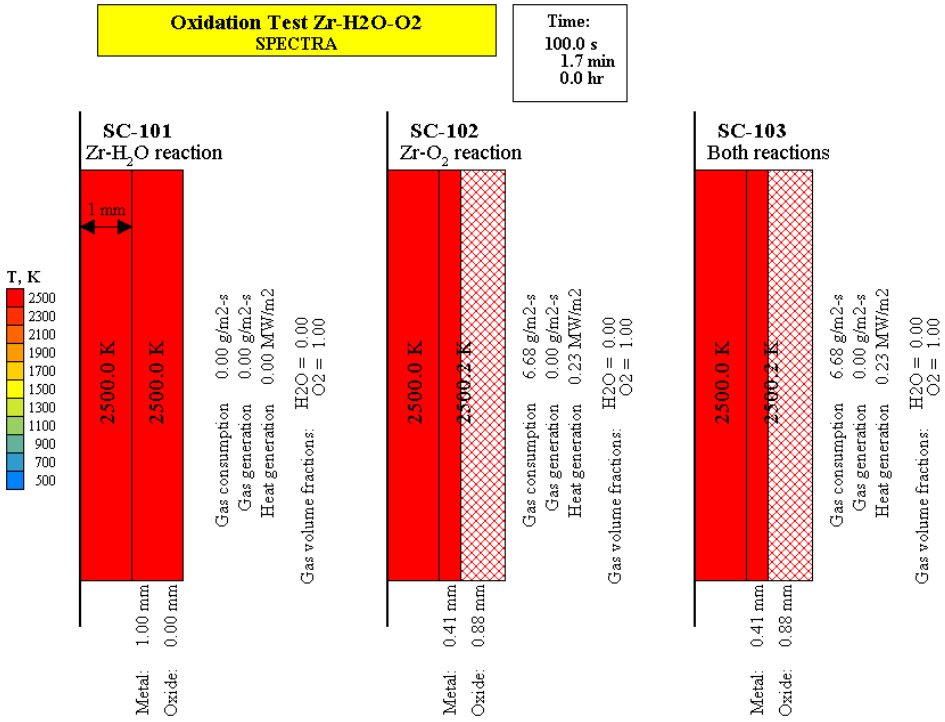

Figure 3-554 Multiple oxidations reactions - lack of H_2O in the atmosphere

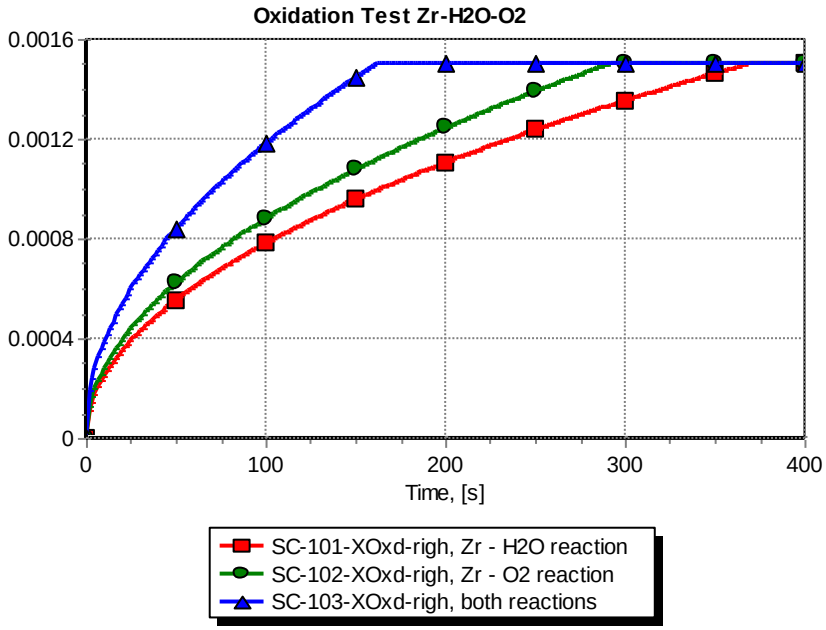

Figure 3-555 Oxide layer thickness - Zr oxidation by H_2O and O_2

Verification is performed by hand calculations, shown below.

- Zr - H_2O reaction

  At 2500 K the reaction is governed by Urbanic-Heidrich constants (see Volume 1):

$$\frac{dm^2}{dt} = A\exp\left[-\frac{B}{T}\right] = 87.9\exp\left[-\frac{16{,}610}{2500}\right] = 0.114$$

  At t = 100 s m^2 = 11.4 and $m = 11.4^{1/2} = 3.38$ kg/m^2. The oxide thickness is:

$$t_{ox} = \frac{m}{\rho_{Zr}}\cdot\sigma_{ox} = \frac{3.38}{6490}\cdot 1.5 = 0.78\times 10^{-3}$$

  The calculated values at t = 100 s are shown in Figure 3-552. The value for Zr-H_2O reaction (SC-101) is 0.78 mm, in agreement with the hand calculations.

- Zr - O_2 reaction

  The reaction is coefficients of Benjamin are used (see Volume 1):

$$\frac{dm^2}{dt} = A\exp\left[-\frac{B}{T}\right] = 50.4\exp\left[-\frac{14{,}630}{2500}\right] = 0.145$$

At t = 100 s m^2 = 14.5 and m = $14.4^{1/2}$ = 3.81 kg/m^2. The oxide thickness is:

$$t_{ox} = \frac{m}{\rho_{Zr}} \cdot \sigma_{ox} = \frac{3.81}{6490} \cdot 1.5 = 0.88 \times 10^{-3}$$

The calculated values at t = 100 s are shown in Figure 3-552. The value for Zr-H_2O reaction (SC-102) is 0.88 mm, in agreement with the hand calculations.

- Simultaneous reactions

  In case of simultaneous parabolic reactions, the total reaction thickness should be equal to the square root of the individual reactions squared:

$$t_{ox} = \sqrt{t_{ox,1}^2 + t_{ox,2}^2} = \sqrt{(0.78 \times 10^{-3})^2 + (0.88 \times 10^{-3})^2} = 1.18 \times 10^{-3}$$

  The calculated values at t = 100 s are shown in Figure 3-552. The value for both reactions (SC-103) is 1.18 mm, in agreement with the hand calculations.

3.10.7 Multiple Oxidation Reactions - Steel Oxidation by H_2O and O_2

The present example shows multiple oxidation reactions. The oxidation of steel by H_2O and O_2 is considered. The input deck is very similar to the one used in the previous section. The temperature was set to 1500 K for this test. The gas composition is such that both steam and oxygen are available for oxidation. The oxidation models are selected as follows:

- SC-101 - Steel - H_2O oxidation, built-in model of White
- SC-102 - Steel - O_2 oxidation, user-defined model of Nanni et al. (see section 3.10.2)
- SC-103 - both models

SPECTRA input for this test is provided in `\Z-INPUTS\OX\Steel-H2O-O2.SPE`. Results are shown in Figure 3-556 and Figure 3-557. The oxygen reaction is faster and more exothermic than the steam reaction. When both models are active then the reaction proceeds faster, but not as would be obtained by summing up the two individual reactions. This is a result of the parabolic reaction rate - the reaction slows down with increasing oxide thickness.

In case of oxygen reaction there is of course no gas generation. Only the steam reaction produces gas, namely hydrogen. The oxygen reaction is a simple synthesis of the oxygen molecules with these of Fe or Cr (see Volume 1). The same behavior was observed in the previous test, where the oxygen reacts with Zr.

Verification is performed by hand calculations, shown below.

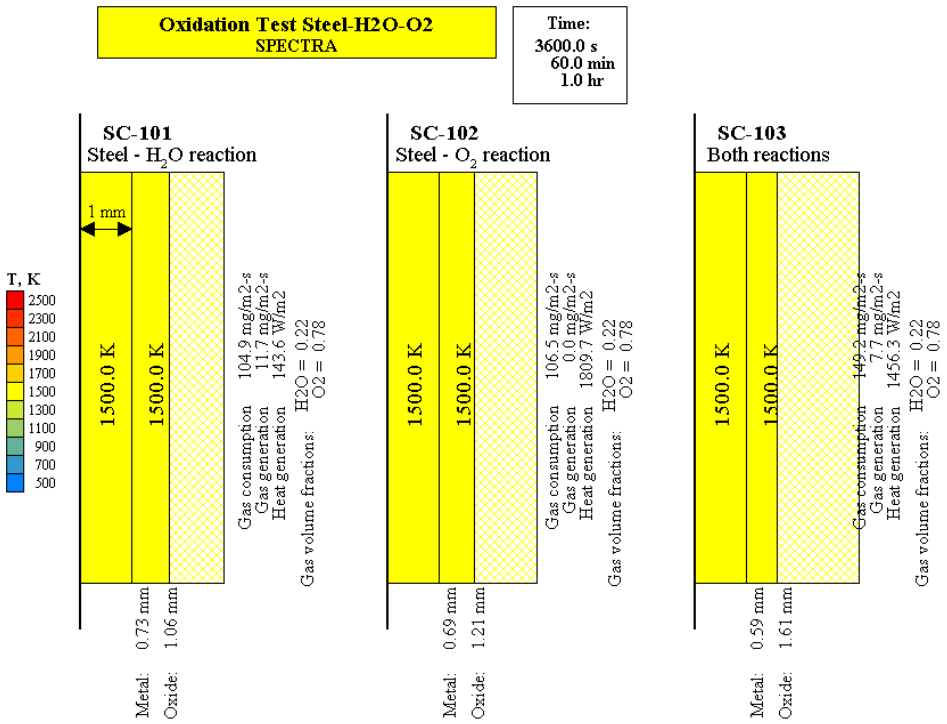

Figure 3-556 Multiple oxidations reactions - steel oxidation by H_2O and O_2

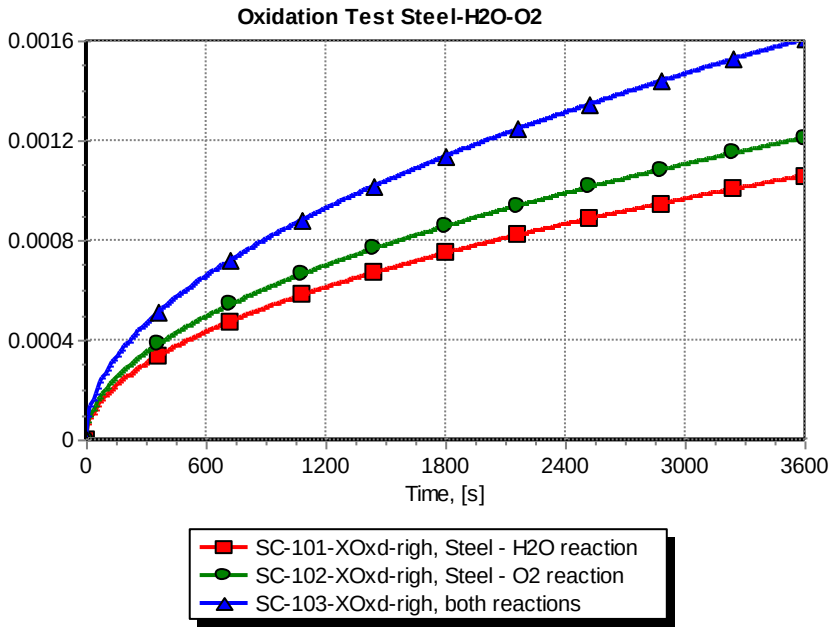

Figure 3-557 Oxide layer thickness - steel oxidation by H_2O and O_2

- Steel - H_2O reaction

  Model of White (see Volume 1):

$$\frac{dm^2}{dt} = A\exp\left[-\frac{B}{T}\right] = 2.51\times10^{9}\ \exp\left[-\frac{42{,}428}{1500}\right] = 1.305\times10^{-3}$$

  At t = 3600 s m^2 = 4.7 and $m = 4.7^{1/2}$ = 2.17 kg/m^2. The oxide thickness is:

$$t_{ox} = \frac{m}{\rho_{St}}\cdot\sigma_{ox} = \frac{2.17}{8020}\cdot 3.92 = 1.06\times10^{-3}$$

  The calculated values at t = 3600 s are shown in Figure 3-556. The value for Zr-H_2O reaction (SC-101) is 1.06 mm, in agreement with the hand calculations.

- Zr - O_2 reaction

  The user-defined coefficients are used (see section 3.10.2):

$$\frac{dm^2}{dt} = A\exp\left[-\frac{B}{T}\right] = 2.3\times10^{10}\ \exp\left[-\frac{45{,}350}{1500}\right] = 1.704\times10^{-3}$$

  At t = 3600 s m^2 = 6.13 and $m = 6.13^{1/2}$ = 2.48 kg/m^2. The oxide thickness is:

$$t_{ox} = \frac{m}{\rho_{St}}\cdot\sigma_{ox} = \frac{2.48}{8020}\cdot 3.92 = 1.21\times10^{-3}$$

  The calculated values at t = 3600 s are shown in Figure 3-556. The value for Zr-H_2O reaction (SC-102) is 1.21 mm, in agreement with the hand calculations.

- Simultaneous reactions

  In case of simultaneous parabolic reactions, the total reaction thickness should be equal to the square root of the individual reactions squared:

$$t_{ox} = \sqrt{t_{ox,1}^2 + t_{ox,2}^2} = \sqrt{(1.06\times10^{-3})^2 + (1.21\times10^{-3})^2} = 1.61\times10^{-3}$$

  The calculated values at t = 3600 s are shown in Figure 3-556. The value for both reactions (SC-103) is 1.61 mm, in agreement with the hand calculations.

3.10.8 Linear Reactions

In the previous two sections multiple reactions were discussed. The parabolic reaction rate slows down with increasing oxide thickness, therefore when two reactions are present the reaction rate is slower than the sum of individual reactions.

The reaction rate of two reactions is equal to the sum of the individual reactions only for linear reactions. The present example shows this case. The input deck is very similar to the one used in the previous section. The temperature was set to 1500 K for this test.

- SC-101 - Linear model 1
- SC-102 - Linear model 2
- SC-103 - both models

The linear models were obtained by using Cathcart coefficients for Zr steam reaction, with two modifications: x = 1.0 instead of 2.0 (linear reaction), A = 1000 rather than 273 (compare Cathcart model in the file OX-COMP.SPE - section 3.10.5).

SPECTRA input for this test is provided in `\Z-INPUTS\OX\Linear.SPE`. Results are shown in Figure 3-558 and Figure 3-559. Both reactions 1 and 2 are the same, therefore SC-101 and SC-102 show the same behavior. Oxidation on SC-103 is equal to the sum of SC-101 and SC-102, at for the times t < ~2000 s when all material is oxidized in SC-103 - see Figure 3-559.

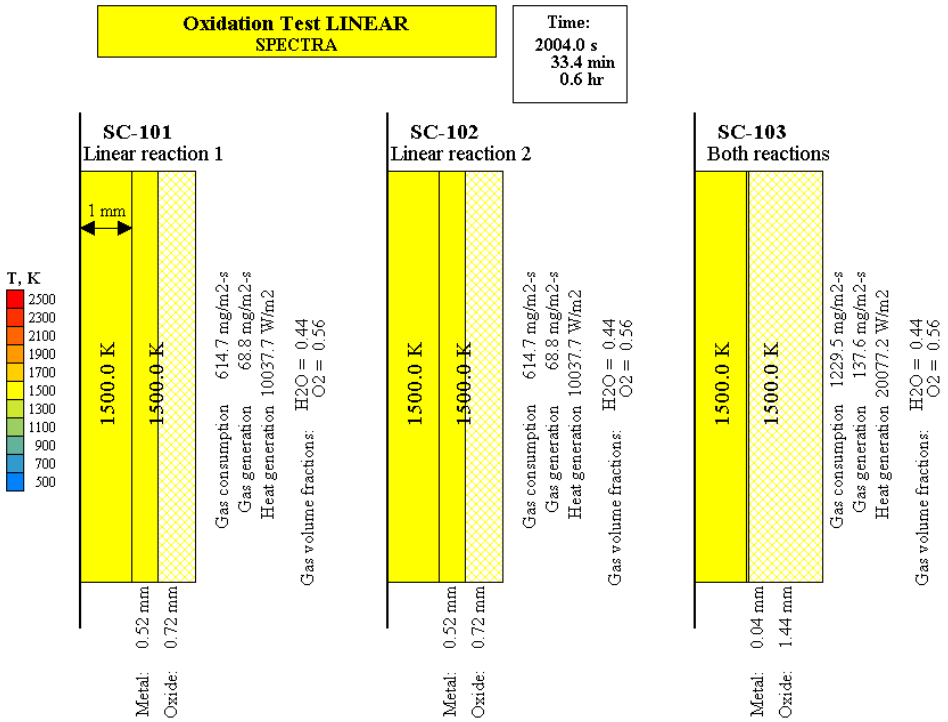

Figure 3-558 Multiple oxidations reactions - linear reactions

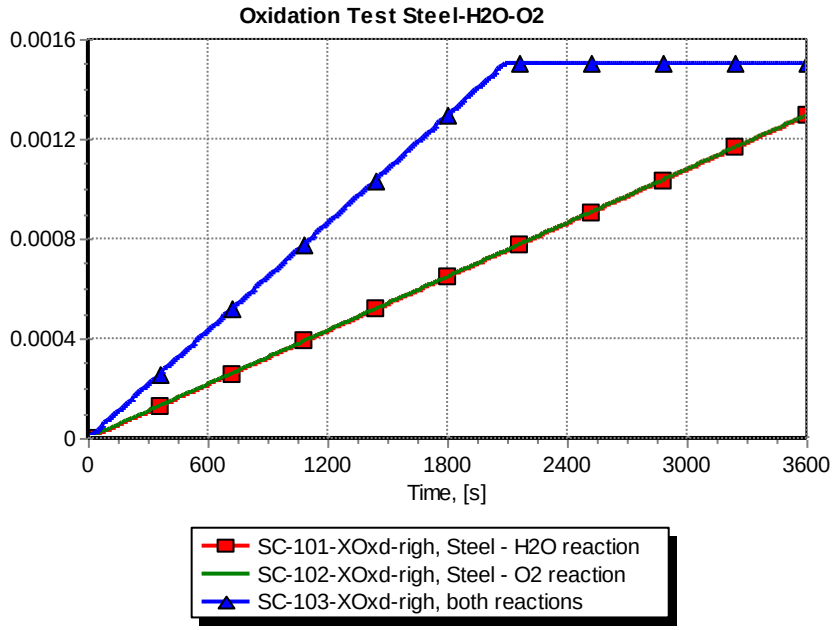

Figure 3-559 Oxide layer thickness - linear reactions

Verification is performed by hand calculations, shown below.

- Individual reactions

  At 2500 K the reaction is goverened by Urbanic-Heidrich constants (see Volume 1):

$$\frac{dm}{dt} = A\exp\left[-\frac{B}{T}\right] = 1000\exp\left[-\frac{20{,}060}{1500}\right] = 1.556\times10^{-3}$$

  At t = 2004 s m = 3.12 kg/m^2. The oxide thickness is:

$$t_{ox} = \frac{m}{\rho_{Zr}}\cdot\sigma_{ox} = \frac{3.12}{6490}\cdot1.5 = 0.72\times10^{-3}$$

  The calculated values at t = 2004 s are shown in Figure 3-558. The value for individual reactions (SC-101, SC-102) is 0.72 mm, in agreement with the hand calculations.

- Total reaction

  In case of linear reaction rate the reaction depth in case of the two simultaneous reactions is simply equal to the sum of the individual reactions: $t_{ox} = 2\times(0.72\times10^{-3}) = 1.44\times10^{-3}$ m. The calculated values at t = 2004 s are shown in Figure 3-558. The value for both reactions (SC-103) is 1.44 mm, in agreement with the hand calculations.

3.10.9 Graphite Oxidation by Steam - Verification Calculations

This section provides verification of the graphite oxidation by steam. The reaction is

$$C + H_2O \rightarrow H_2 + CO$$

The reaction kinetics taken from the report of Kubaschewski and Heinrich [64] (converted to SI units, see Volume 2 - Examples of user-defined oxidation models):

$$\frac{dm}{dt} = \frac{1.12 \cdot 10^4 \cdot \exp\left[-\frac{30788}{T}\right] \cdot \left(p_{H2O}\right)^{0.44}}{1 + 2.37 \cdot 10^{-7} \cdot \exp\left[\frac{14552}{T}\right] \cdot \left(p_{H2}\right)^{0.9} \cdot \left(p_{H2O}\right)^{-0.4}}$$

Three test cases were chosen (arbitrarily) to perform verification:

- Case 1 - H_2O at p_{H2O} = 70.00 bar (pure steam)
- Case 2 - H_2O at p_{H2O} = 66.09 bar, H_2 at p_{H2} = 3.914 bar
- Case 3 - H_2O at p_{H2O} = 22.03 bar, H_2 at p_{H2} = 47.97 bar

In all cases constant temperature, T = 1000˚C = 1273 K was used. SPECTRA input for this test is provided in the directory: `\Z-INPUTS\OX\Graphite-Steam` as the following files:

- `C-H2O-Case-1.SPE`
- `C-H2O-Case-2.SPE`
- `C-H2O-Case-3.SPE`

Results of SPECTRA calculations are compared below to hand calculation obtained using Excel file (C-H2O.xls). The SPECTRA values were obtained from the time-dependent graphs, as time at which the initially 1 mm thick layer of graphite disappears. There is a good agreement between the hand calculation and the SPECTRA-calculated values.

V&V of Test Case C-H2O - Verification Run					
		Case 1	Case 2	Case 3	
	T=	1273.0	1273.0	1273.0	K
	p(H2O)=	70.00	66.09	22.03	bar
	p(H2)=	0.000	3.914	47.970	bar
	M(B,P)=	1.000	1.000	1.000	-
Correlation:	dm/dt=	130.2	23.4	1.2	mg/cm2-hr
converted to SI:	dm/dt=	3.62E-04	6.51E-05	3.28E-06	kg/m2-s
directly in SI:	dm/dt=	3.61E-04	6.50E-05	3.27E-06	kg/m2-s
	ρ=	1740.0	1740.0	1740.0	kg/m3
	dx/dt=	2.1E-07	3.7E-08	1.9E-09	m/s
	dx/dt=	2.1E-04	3.7E-05	1.9E-06	mm/s
	τ=	4820	2.675E+04	5.315E+05	s/mm
SPECTRA:	τ=	4820	2.680E+04	5.315E+05	s/mm

3.10.10 Graphite Oxidation by Steam - Validation Calculations

This section provides validation calculations for the graphite-steam reaction kinetics, as calculated by the correlation of Kubaschewski and Heinrich [64] (converted to SI units, see Volume 2 - Examples of user-defined oxidation models):

$$\frac{dm}{dt} = \frac{1.12 \cdot 10^{4} \cdot \exp\left[-\frac{30788}{T}\right] \cdot \left(p_{H2O}\right)^{0.44}}{1 + 2.37 \cdot 10^{-7} \cdot \exp\left[\frac{14552}{T}\right] \cdot \left(p_{H2}\right)^{0.9} \left(p_{H2O}\right)^{-0.4}}$$

Validation is performed by comparing results of correlation with available experimental data, obtained from references [65], [67] and in one case from an analytical model, reference [66].

- Oxidation at different steam pressures - validation against data of Loenißen [65]

  Experiments were performed at 2.9 bar total pressure and 1000˚C. Page 95 of reference [65] gives oxidation results for several steam pressures. The results obtained from the correlation are compared to the experimental data below.

Test Case Loenissen 1 - Data from Leonissen (1987) page 95, material: graphite A3-3							
		1000	1000	1000	1000	˚C	
	T=	1273.0	1273.0	1273.0	1273.0	K	
	p(H2O)=	0.066	0.243	0.394	0.973	bar	
	p(H2)=	0.000	0.000	0.000	0.000	bar	
	M(B,P)=	1.00E+00	1.00E+00	1.00E+00	1.00E+00	-	P=2.9 bar
Correlation:	dm/dt=	6.07E+00	1.08E+01	1.33E+01	1.98E+01	mg/cm2-hr	
converted to SI:	dm/dt=	1.69E-05	2.99E-05	3.70E-05	5.51E-05	kg/m2-s	
directly in SI:	dm/dt=	1.69E-05	3.00E-05	3.71E-05	5.52E-05	kg/m2-s	
Data, p. 95:	dm/dt=	1.78E-03	4.17E-03	4.39E-03	9.72E-03	mg/cm2-s	
	dm/dt=	1.78E-05	4.17E-05	4.39E-05	9.72E-05	kg/m2-s	
Ratio:		1.05	1.39	1.18	1.76		
Conclusion:							
Values obtained from the investigated correlation							
need to be multiplied by a factor of 1.05 - 1.76 to match the considered data							

It is concluded that the correlation gives reaction rates lower than the experimental data. In order to best represent the measured data, the values obtained from the correlation should be multiplied by:

$$Data = (1.05 \div 1.76) \times Correlation$$

- Electrode graphite oxidation - validation against data of Abel-Holden [67]

Reference [67] shows data for graphite steam reaction. Page 7 shows reaction rate of 0.0126 g/min measured for a rectangular prism, 7.9×7.9×31.7 mm specimen, placed in steam at 1900˚F. The value converted to SI units is 1.86×10^{-4} kg/m^2-s. The correlation gives for this case 1.12×10^{-4} kg/m^2-s. Results of calculations are shown below.

Test Case Abel-Holden - Data for non-nuclear graphite (thermic type electrode in He/steam mixture)								
		1900	1900	1900	˚F			
		2359.67	2359.67	2359.67	˚R	Dimensions:		
	T=	1310.9	1310.9	1310.9	K	A=	1.13E-03	m2
	p(H2O)=	1.00	1.00	1.00	bar	L=	0.0317	m
	p(H2)=	0.000	0.000	0.000	bar	a=	0.0079	m
	M(B,P)=	1.00E+00	1.67E+00	1.80E+00	-	b=	0.0079	m
			(best est.)	(conserv.)		Measured:		
Correlation:	dm/dt=	40.4	67.5	72.8	mg/cm2-hr	dM/dt=	0.0126	g/min
converted to SI:	dm/dt=	1.12E-04	1.87E-04	2.02E-04	kg/m2-s	dM/dt=	2.10E-07	kg/s
directly in SI:	dm/dt=	1.12E-04	1.87E-04	2.02E-04	kg/m2-s	dm/dt=	1.86E-04	kg/m2-s
	ρ=	1740.0	1740.0	1740.0	kg/m3			
	dx/dt=	6.4E-08	1.1E-07	1.2E-07	m/s			
	dx/dt=	6.4E-05	1.1E-04	1.2E-04	mm/s			
	τ=	15525	9296	8625	s/mm			
SPECTRA:	τ=	15530	9300	8630	s/mm			
	Ratio:	1.66	1.00	0.92				
Conclusion:								
Values obtained from the investigated correlation								
need to be multiplied by a factor of 1.66 to match the considered data								

It is concluded that the correlation gives reaction rate lower than the experimental data. In order to best represent the measured data, the values obtained from the correlation should be multiplied by:

$$Data = (1.66) \times Correlation$$

The values of best estimate and conservative multiplier $M(B,P)$, will be explained below. One has to keep in mind that experiments reported in [67] were performed for electrode graphite, not nuclear graphite.

- Oxidation at low steam pressure - validation (code-to-code) against data of Xinli Yu, Suyuan Yu [66]

Reference [66] provides an analytical estimation of the amount of oxidation that can occur at low steam pressures. This may occur in the HTR system if helium is not sufficiently purified. Also humidity of air can be absorbed and stored in the outer part of the graphite spheres, since the pebbles are not always stored under exclusion of air. The value mentioned is 280 kg of graphite oxidized per year at steam partial pressure of 14 Pa. Considering that the number of pebbles is 420,000 and the fuel-free zone of pebbles is 5 mm [66], this corresponds to oxidation of 0.62% of the fuel-free zone, or oxidation depth of 3.1×10^{-5} m. The value obtained from the correlation is 0.73 year. Results of calculations are shown below.

Test Case Xinli Yu, Suyuan Yu - analytical model							
		750	750	750	˚C		HTR=PM
	T=	1023.0	1023.0	1023.0	K	N=	420000
	p(H2O)=	1.40E-04	1.40E-04	1.40E-04	bar	D=	0.06
	p(H2)=	0.000	0.000	0.000	bar	d-free=	0.005
	M(B,P)=	1.00E+00	6.30E-01	1.80E+00	-	rho=	1740
			(best est.)	(conserv.)		V-free=	4.76E-05
Correlation:	dm/dt=	1.10E-03	6.91E-04	1.97E-03	mg/cm2-hr	V=	2.00E+01
converted to SI:	dm/dt=	3.05E-09	1.92E-09	5.48E-09	kg/m2-s	M=	3.48E+04
directly in SI:	dm/dt=	3.04E-09	1.92E-09	5.47E-09	kg/m2-s	V-pebb=	1.13E-04
	ρ=	1740.0	1740.0	1740.0	kg/m3	M-pebb=	1.97E-01
	dx/dt=	1.8E-12	1.1E-12	3.2E-12	m/s		
	dx/dt=	1.8E-09	1.1E-09	3.2E-09	mm/s		
	τ=	5.71E+08	9.06E+08	3.17E+08	s/mm		
		158635	251801	88130	hr/mm		
		18.11	28.74	10.06	years		
To oxidize:	d-OX=	4.021E-05	4.021E-05	4.021E-05	m	Data:	
of:	d-free=	5.0E-03	5.0E-03	5.0E-03	m	280	kg per year
	Oxidized=	0.80	0.80	0.80	%	280 kg is:	
Correlation:	τ=	2.30E+07	3.64E+07	1.28E+07	s	0.80	%
SPECTRA:	τ=	2.30E+07	3.64E+07	1.28E+07	s	of the fuel-free zone	
	τ=	0.73	1.16	0.40	years	oxidized per:	
multiplier needed to get τ=1 year		0.73	1.16	0.40		1.00	year
Conclusion:							
Values obtained from the investigated correlation							
need to be multiplied by a factor of 0.73 to match the considered data							

It is concluded that:

- The correlation can be applied at very low steam pressure.
- The correlation gives reaction rate higher than the reference data. In order to best represent the measured data, the values obtained from the correlation should be multiplied by:

$$Data = (0.73) \times Correlation$$

The values of best estimate and conservative multiplier $M(B,P)$, will be explained below.

- Effect of burn-off

Burn-off increases reaction rate because the surface area accessible for oxidation reaction increases by formation of geometrically regular pits, which seems to be an inherent feature of graphite oxidation [69]. The surface area increases until a certain value, at which the whole surface is covered by pits, upon which there is no further effect of burn-off - see Figure 3-560. A detailed discussion of the subject is provided in [69].

There are two main parameters of interest here:

- Oxidation depth (burn-off), B_{max}, at which the area increase reaches maximum.
- Maximum area increase factor, $f_{max} = f(B_{max})$

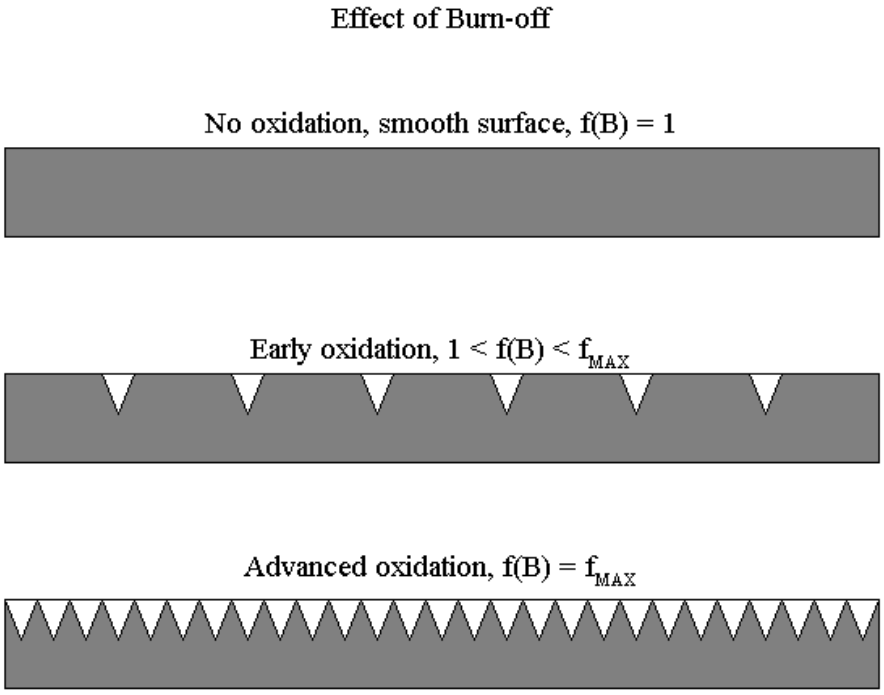

Figure 3-560 Increase of effective oxidation area due to graphite burn-off

Several correlations were proposed to calculate the burn-off factor, $f(B)$. Reference [66] gives:

$$f(B) = (1-B)\cdot(1-\xi_0 \cdot \ln(1-B))^{0.5}$$

Here B is burn-off (-) and ξ_0 is a constant, equal to 45. The results of the correlation is shown in Figure 3-561. Reference [68] gives another correlation:

$$f(B) = 0.477 + 0.8094 \cdot B - 0.3221 \cdot B^2 + 0.0681 \cdot B^3 - \\ - 0.00613 \cdot B^4 + 12.32 \cdot 10^{-6} \cdot B^5 + 2.89 \cdot 10^{-5} \cdot B^6 - 1.15 \cdot 10^{-6} \cdot B^7$$

Here B is in % and is valid from 1 to 13%, beyond which the 13% value should be used. The results of the correlation is shown in Figure 3-562.

Summarizing, both correlations give $f(B)$ increasing from 1.0 (at $B = 0.0$) to a maximum of $f_{max} = 3.0$ (at $B = B_{max}$). The discussion above is only to introduce the problem of burn-off and show a qualitative behavior. Neither of these correlations is used, but a fit to available data is developed, which is shown below.

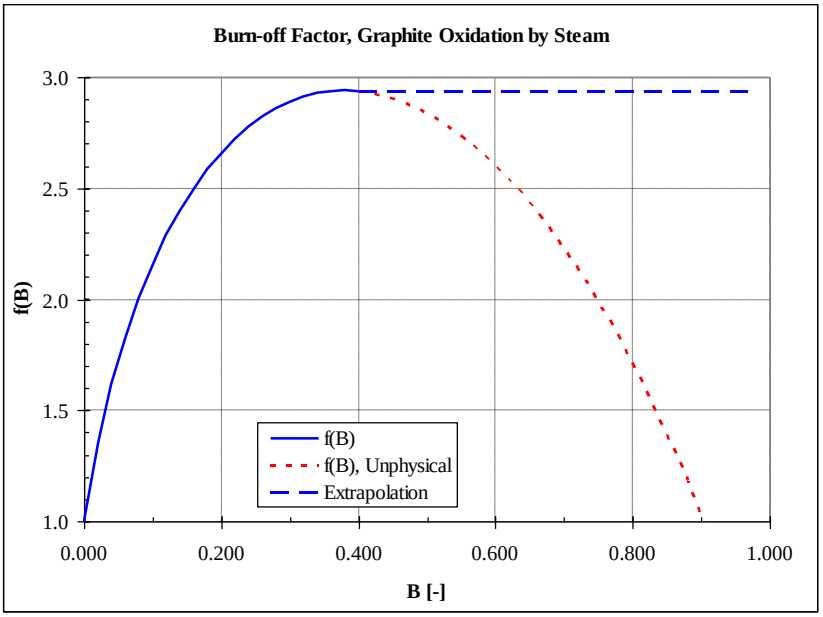

Figure 3-561 Burn-off correlation from [66]

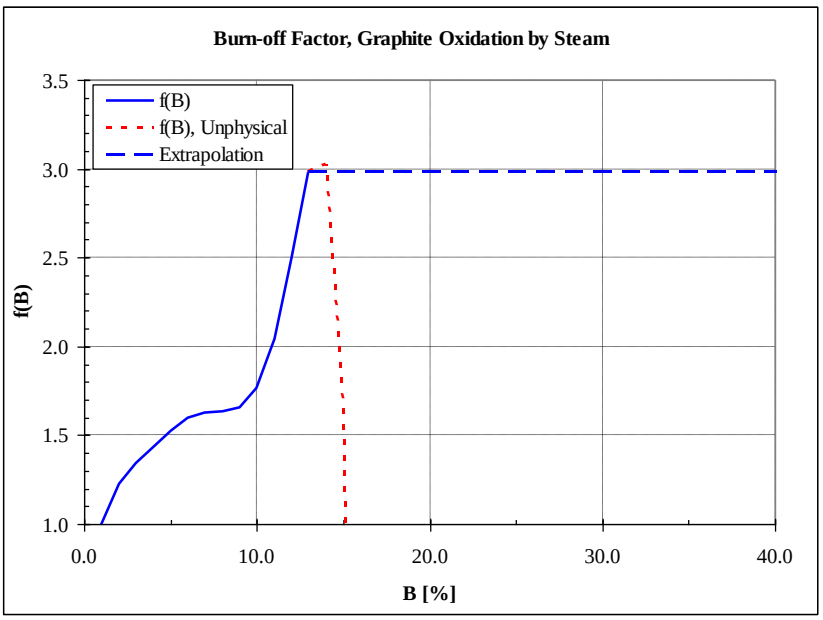

Figure 3-562 Burn-off correlation from Graphite Design Handbook [68]

- Oxidation at different burn-offs - validation against data of Loenißen [65]

  Experiments were performed at 0.474 bar steam pressure and 1000˚C. Reference [65] gives oxidation results for different burn-off values. The results obtained from the correlation are compared to the experimental data below. It should be noted that the burn-off, as well as the total pressure, are not taken into account in the correlation.

Test Case Loenissen 2 - Data from Leonissen (1987), material: graphite A3-27						
	Burn-off:	1	40	60	80	mg/cm2
	Burn-off:	5.75E-06	2.30E-04	3.45E-04	4.60E-04	m
		1000	1000	1000	1000	˚C
	T=	1273.0	1273.0	1273.0	1273.0	K
	p(H2O)=	0.474	0.474	0.474	0.474	bar
	p(H2)=	0.000	0.000	0.000	0.000	bar
	M(B,P)=	1.00E+00	1.00E+00	1.00E+00	1.00E+00	-
Correlation:	dm/dt=	1.45E+01	1.45E+01	1.45E+01	1.45E+01	mg/cm2-hr
converted to SI:	dm/dt=	4.02E-05	4.02E-05	4.02E-05	4.02E-05	kg/m2-s
directly in SI:	dm/dt=	4.01E-05	4.01E-05	4.01E-05	4.01E-05	kg/m2-s
	ρ=	1740.0	1740.0	1740.0	1740.0	kg/m3
	Data from Leonissen (1987) Table 5					
	Burn-off:	~1	~40	~60	~80	mg/cm2
at 3 bar:	dm/dt=	1.33E-03	6.13E-03	6.54E-03	6.45E-03	mg/cm2-s
at 4 bar:	dm/dt=	1.49E-03	-	-	-	mg/cm2-s
at 7 bar:	dm/dt=	1.20E-03	5.14E-03	5.54E-03	-	mg/cm2-s
at 15 bar:	dm/dt=	1.11E-03	-	5.16E-03	4.81E-03	mg/cm2-s
at 40 bar:	dm/dt=	-	2.36E-03	2.75E-03	3.12E-03	mg/cm2-s
at 55 bar:	dm/dt=	-	2.14E-03	2.51E-03	-	mg/cm2-s
	Converted to SI:					
	Burn-off:	~0.0	~2E-4	~3E-4	~4E-4	m
at 3 bar:	dm/dt=	1.33E-05	6.13E-05	6.54E-05	6.45E-05	kg/m2-s
at 4 bar:	dm/dt=	1.49E-05	-	-	-	kg/m2-s
at 7 bar:	dm/dt=	1.20E-05	5.14E-05	5.54E-05	-	kg/m2-s
at 15 bar:	dm/dt=	1.11E-05	-	5.16E-05	4.81E-05	kg/m2-s
at 40 bar:	dm/dt=	-	2.36E-05	2.75E-05	3.12E-05	kg/m2-s
at 55 bar:	dm/dt=	-	2.14E-05	2.51E-05	-	kg/m2-s
	Ratio (Experiment/Correlation):					
	Burn-off:	~0.0	~2E-4	~3E-4	~4E-4	m
at 3 bar:	exp/corr=	0.33	1.53	1.63	1.61	-
at 4 bar:	exp/corr=	0.37	-	-	-	-
at 7 bar:	exp/corr=	0.30	1.28	1.38	-	-
at 15 bar:	exp/corr=	0.28	-	1.29	1.20	-
at 40 bar:	exp/corr=	-	0.59	0.69	0.78	-
at 55 bar:	exp/corr=	-	0.53	0.63	-	-
				Min=	0.28	-72%
Conclusion:				Max=	1.63	63%
Values obtained from the investigated correlation						
need to be multiplied by a factor of 0.28 - 1.63 to match the considered data						

It is concluded that in order to best represent the measured data, the values obtained from the correlation should be multiplied by:

$$Data = (0.28 \div 1.63) \times Correlation$$

This is quite a large spread of measured data compared to the results of the correlation. This fact was a motivation to develop an extension to the existing correlation. This extension, as well as the resulting improvement in the obtained accuracy, are described below.

- Extension of the Kubaschewski-Heinrich correlation

Based on the results of Loenißen, the following observations are made:

- At low burn-off, $B = 0.0$ (clean surface) the correlation should be multiplied by 0.28 - 0.37. The value decreases slightly with total pressure.
- At high burn-offs, B_{max}, the correlation should be multiplied by 1.5 - 1.6 at low pressures and 0.7 - 0.8 at high pressures.
- A surface can be considered as "high burn-off", B_∞, for 0.3 mm oxidation depth.

Based on the above observations, a multiplier, $M_{BE}(B,P)$, dependent on burn-off, B, and total pressure, P, is proposed:

$$M_{BE}(B,P) = f_B(B)\cdot[f_{P,\infty}(P) - f_{P,0}(P)] + f_{P,0}(P)$$

Here $f_B(B)$ is the burn-off dependent factor, $f_{P,\infty}(P)$ is the pressure-dependent factor for high burn-off, $f_{p,0}(P)$ is the pressure-dependent factor for no burn-off.

The following correlations were developed for the pressure-dependent factors $f_{P,0}(P)$ and $f_{P,\infty}(P)$:

$$f_{P,0}(P) = 0.35\cdot\exp(-7.0\times10^{-8}P)$$
$$f_{P,\infty}(P) = 1.70\cdot\exp(-1.8\times10^{-7}P)$$

Here pressure P is in (Pa). The correlations are shown in Figure 3-563 as solid lines. Since no data was found for total pressure of 55×10^5 Pa, the pressure range for the correlations is limited to $P<55\times10^5$ Pa. For the burn-off dependent factor, the following correlation is used:

$$f_B(B) = \begin{cases} 1-\left(\dfrac{B}{B_\infty}-1\right)^2 & if\ B < B_\infty \\ 1 & if\ B > B_\infty \end{cases}$$

The correlation is shown in Figure 3-564. The burn-off B is the average depth of the oxidized material (m). Based on comparison with data of Loenißen, the value of B_∞ is taken as 0.3×10^{-3} m.

The values of $M_{BE}(B,P)$ are tabulated in Table 3-55. The end-point values should be kept outside the tabulated area.

Table 3-55 Tabulated values of $M_{BE}(B,P)$

	B [m]:	0.00E+00	6.00E-05	1.20E-04	1.80E-04	2.40E-04	3.00E-04
	B/B∞ [-]:	0.00	0.20	0.40	0.60	0.80	1.00
	f(B/B∞) [-]:	0.00	0.36	0.64	0.84	0.96	1.00
P [Pa]	1.00E+05	0.35	0.82	1.19	1.46	1.62	1.67
	5.00E+05	0.34	0.78	1.12	1.36	1.51	1.55
	1.00E+06	0.33	0.72	1.03	1.24	1.38	1.42
	1.50E+06	0.32	0.67	0.94	1.14	1.26	1.30
	2.00E+06	0.30	0.62	0.87	1.04	1.15	1.19
	2.50E+06	0.29	0.58	0.80	0.96	1.05	1.08
	3.00E+06	0.28	0.54	0.74	0.88	0.96	0.99
	3.50E+06	0.27	0.50	0.68	0.80	0.88	0.91
	4.00E+06	0.26	0.47	0.62	0.74	0.80	0.83
	4.50E+06	0.26	0.44	0.58	0.68	0.74	0.76
	5.00E+06	0.25	0.41	0.53	0.62	0.67	0.69
	5.50E+06	0.24	0.38	0.49	0.57	0.62	0.63

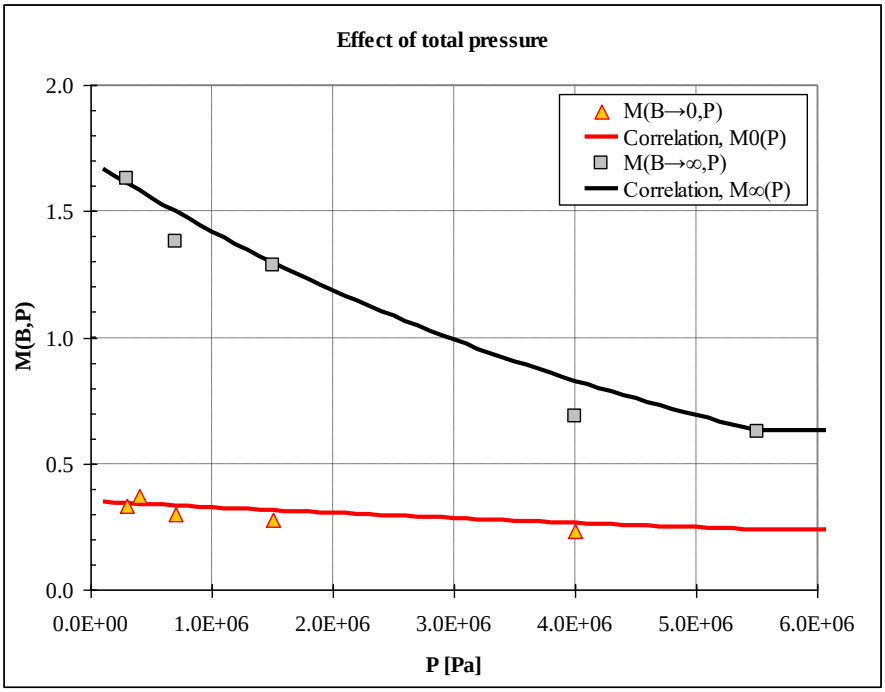

Figure 3-563 Burn-off and pressure dependent multiplier, $M_{BE}(B,P)$

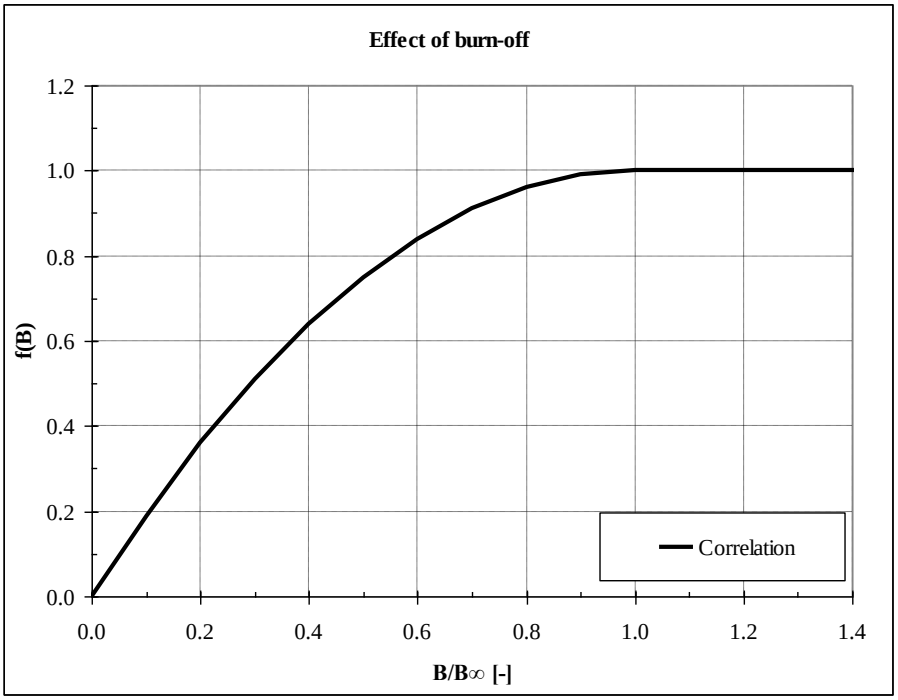

Figure 3-564 Burn-off factor, $f(B)$

One important fact is that there is a limited amount of experimental data and the data scatter is significant. Therefore, in order to cover all uncertainties one should use a conservative correlation. Based on the considered experimental data, for conservative calculations the Kubaschewski-Heinrich correlation should be used with a constant multiplier of:

$$M_C = 1.8$$

This value of multiplier gives higher oxidation rate than all measurement data considered here.

Figure 3-565 shows results of the verification Case 1 (T=1273 K, $p = p_{H2O}$ = 70 bar): Three cases: correlation of Kubaschewski-Heinrich, correlation of Kubaschewski-Heinrich × $M_{BE}(B,P)$ (Best-Estimate), correlation of Kubaschewski-Heinrich × M_C (Conservative). The times to oxidize the considered layer of graphite (1 mm) are:

- Kubaschewski-Heinrich: τ = 6233 s (see 3.10.9)
- Kubaschewski-Heinrich × $M_{BE}(B,P)$ (best-estimate): τ = 10,920 s
- Kubaschewski-Heinrich × M_C (conservative): τ = 3450 s

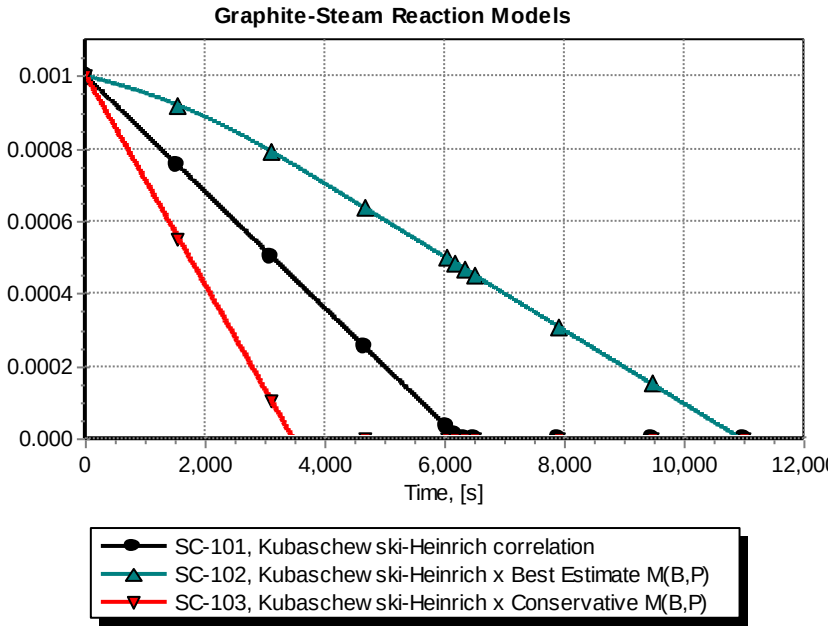

Figure 3-565 Comparison of correlations - verification test “Case 1”

- Validation of the extended correlation

The results obtained from the correlation of Kubaschewski-Heinrich together with the pressure and burn-off dependent multiplier, $M_{BE}(B,P)$, is compared to the measured data of Loenißen for the 0.474 bar steam pressure cases.

Test Case Loenissen 2, influence of M(B,p) - Data from Leonissen (1987), material: graphite A3-27						
	Burn-off:	1	40	60	80	mg/cm2
	Burn-off:	5.75E-06	2.30E-04	3.45E-04	4.60E-04	m
		1000	1000	1000	1000	˚C
	T=	1273.0	1273.0	1273.0	1273.0	K
	p(H2O)=	0.474	0.474	0.474	0.474	bar
	p(H2)=	0.000	0.000	0.000	0.000	bar
	M(B,P)=	1.00E+00	1.00E+00	1.00E+00	1.00E+00	-
Correlation:	dm/dt=	1.45E+01	1.45E+01	1.45E+01	1.45E+01	mg/cm2-hr
converted to SI:	dm/dt=	4.02E-05	4.02E-05	4.02E-05	4.02E-05	kg/m2-s
directly in SI:	dm/dt=	4.01E-05	4.01E-05	4.01E-05	4.01E-05	kg/m2-s
	ρ=	1740.0	1740.0	1740.0	1740.0	kg/m3
	Data from Leonissen (1987) Table 5					
	Burn-off:	~1	~40	~60	~80	mg/cm2
at 3 bar:	dm/dt=	1.33E-03	6.13E-03	6.54E-03	6.45E-03	mg/cm2-s
at 4 bar:	dm/dt=	1.49E-03	-	-	-	mg/cm2-s
at 7 bar:	dm/dt=	1.20E-03	5.14E-03	5.54E-03	-	mg/cm2-s
at 15 bar:	dm/dt=	1.11E-03	-	5.16E-03	4.81E-03	mg/cm2-s
at 40 bar:	dm/dt=	9.44E-04	2.36E-03	2.75E-03	3.12E-03	mg/cm2-s
at 55 bar:	dm/dt=	-	2.14E-03	2.51E-03	-	mg/cm2-s
	Converted to SI:					
	Burn-off:	~0.0	~2E-4	~3E-4	~4E-4	m
at 3 bar:	dm/dt=	1.33E-05	6.13E-05	6.54E-05	6.45E-05	kg/m2-s
at 4 bar:	dm/dt=	1.49E-05	-	-	-	kg/m2-s
at 7 bar:	dm/dt=	1.20E-05	5.14E-05	5.54E-05	-	kg/m2-s
at 15 bar:	dm/dt=	1.11E-05	-	5.16E-05	4.81E-05	kg/m2-s
at 40 bar:	dm/dt=	9.44E-06	2.36E-05	2.75E-05	3.12E-05	kg/m2-s
at 55 bar:	dm/dt=	-	2.14E-05	2.51E-05	-	kg/m2-s
	M(B,P)		B∞	3.00E-04		
	Burn-off:	0.00E+00	2.00E-04	3.00E-04	4.00E-04	m
P, [Pa]	Burn-off:	0.00E+00	6.67E-01	1.00E+00	1.33E+00	B∞
3.00E+05	M(B,P)=	3.43E-01	1.47E+00	1.61E+00	1.61E+00	-
4.00E+05	M(B,P)=	3.40E-01	1.44E+00	1.58E+00	1.58E+00	-
7.00E+05	M(B,P)=	3.33E-01	1.37E+00	1.50E+00	1.50E+00	-
1.50E+06	M(B,P)=	3.15E-01	1.19E+00	1.30E+00	1.30E+00	-
4.00E+06	M(B,P)=	2.65E-01	7.65E-01	8.27E-01	8.27E-01	-
5.50E+06	M(B,P)=	2.38E-01	5.88E-01	6.32E-01	6.32E-01	-
	Correlation * M(B,P)					
	Burn-off:	~0.0	~2E-4	~3E-4	~4E-4	m
at 3 bar:	dm/dt=	1.37E-05	5.89E-05	6.46E-05	6.46E-05	kg/m2-s
at 4 bar:	dm/dt=	1.36E-05	-	-	-	kg/m2-s
at 7 bar:	dm/dt=	1.34E-05	5.49E-05	6.01E-05	-	kg/m2-s
at 15 bar:	dm/dt=	1.26E-05	-	5.20E-05	5.20E-05	kg/m2-s
at 40 bar:	dm/dt=	1.06E-05	3.07E-05	3.32E-05	3.32E-05	kg/m2-s
at 55 bar:	dm/dt=	-	2.36E-05	2.53E-05	-	kg/m2-s
	Ratio (Experiment/Correlation):					
	Burn-off:	~0.0	~2E-4	~3E-4	~4E-4	m
at 3 bar:	exp/corr=	0.97	1.04	1.01	1.00	-
at 4 bar:	exp/corr=	1.09	-	-	-	-
at 7 bar:	exp/corr=	0.90	0.94	0.92	-	-
at 15 bar:	exp/corr=	0.88	-	0.99	0.92	-
at 40 bar:	exp/corr=	0.89	0.77	0.83	0.94	-
at 55 bar:	exp/corr=	-	0.91	0.99	-	-
				Min=	0.77	-23%
Conclusion:				Max=	1.09	9%
Values obtained from the correlation × M(B,P)						
need to be multiplied by a factor of 0.77 - 1.09 to match the considered data						

It is concluded that:

$$Data = (0.77 \div 1.09) \times Correlation \times M_{BE}(B,P)$$

In other words it represents the data with maximum deviations of –23% and +9%. For comparison, the original correlation had to be multiplied by (0.28 ÷ 1.63), as shown above. That means the maximum deviations were –72% and +63%.

Next, the new correlation is compared to the measured data of Loenißen for the 2.9 bar total pressure cases. The burn-off values are reported on page 95 of reference (3) as 0.7 - 2.5%. Calculations are shown below.

P [Pa]	Correlatio	Correlation, M∞(P)
2.90E+05	0.34	1.61

B [%]	B [mm]	B/B∞ [-]	Correlation	M(B,P)
0.7	1.40E-01	0.47	0.72	1.25
1.3	2.60E-01	0.87	0.98	1.59
1.9	3.80E-01	1.00	1.00	1.61
2.5	5.00E-01	1.00	1.00	1.61

based on Lohnert: 0.8% corresponds to 0.16 mm

0.8	0.16

Test Case Loenissen 1 - Data from Leonissen (1987) page 95, material: graphite A3-3							
		1000	1000	1000	1000	˚C	
	T=	1273.0	1273.0	1273.0	1273.0	K	
	p(H2O)=	0.066	0.243	0.394	0.973	bar	
	p(H2)=	0.000	0.000	0.000	0.000	bar	
	M(B,P)=	1.25E+00	1.59E+00	1.61E+00	1.61E+00	-	P=2.9 bar
Correlation:	dm/dt=	7.60E+00	1.71E+01	2.15E+01	3.20E+01	mg/cm2-hr	
converted to SI:	dm/dt=	2.11E-05	4.76E-05	5.97E-05	8.89E-05	kg/m2-s	
directly in SI:	dm/dt=	2.11E-05	4.77E-05	5.98E-05	8.90E-05	kg/m2-s	
Data, p. 95:	dm/dt=	1.78E-03	4.17E-03	4.39E-03	9.72E-03	mg/cm2-s	
	dm/dt=	1.78E-05	4.17E-05	4.39E-05	9.72E-05	kg/m2-s	
Ratio:		0.84	0.87	0.73	1.09		
Conclusion:							
Values obtained from the investigated correlation							
need to be multiplied by a factor of 0.73 - 1.09 to match the considered data							

It is concluded that:

$$Data = (0.73 \div 1.09) \times Correlation$$

In other words it represents the data with maximum deviations of –27% and +9%. For comparison, the original correlation had to be multiplied by (1.05 ÷ 1.76), as shown above. That means the maximum deviations were +5% and +76%.

Next, the new correlation is compared to the measured data of Abel Holden earlier in this section, next to the original correlation in the column marked "best est.". The value at high burn-off and 1 bar pressure (1.67 - see Table 3-55) is taken. The multiplier is 1.00, compared to 1.66 in the original correlation. That means the error is reduced from 66% to 0%.

Finally, the new correlation is compared to the measured data of Xinli Yu, Suyuan Yu earlier in this section, next to the original correlation in the column marked "best est.". The value at high burn-off and high pressure (0.63 - see Table 3-55) is taken. The multiplier is 1.16, compared to 0.73 in the original correlation. That means the error is reduced from 27% to 16%.

It is shown that the new correlation gives better agreement with all considered experimental data. Therefore this correlation may be recommendable for best estimate calculations.

- Summary of graphite-steam reaction validation

Comparison of the results obtained using the Kubaschewski-Heinrich correlation against available measurement data, showed that:

$$Data = (0.28 \div 1.76) \times Correlation$$

The correlation does not include the burn-off factor and total pressure. Based on the performed comparisons, a multiplier dependent on burn-off and total pressure, $M_{BE}(B,P)$, is proposed. When the correlation of Kubaschewski-Heinrich is applied together with $M_{BE}(B,P)$, the calculated results are in agreement with the available data with maximum deviations of –27% and +15%.

$$Data = (0.73 \div 1.15) \times Correlation \times M_{BE}(B,P)$$

The improvement of accuracy, as well as experimental conditions for each case are shown in Table 3-56. Based on the experimental conditions, the range of application of the new correlation is:

○ temperatures:	T	1000 K ÷1300 K	(750˚C ÷ 1100˚C)
○ pressures:	p	10^5 Pa ÷ 55×10^5 Pa	(1 ÷ 55 bar)
○ steam pressures	p_{H2O}	14 Pa ÷ 10^5 Pa	(0.00014 ÷ 1.0 bar)

The recommendations are:

- ○ For best estimate results the Kubaschewski-Heinrich correlations should be used with the Best-Estimate multiplier, $M_{BE}(B,P)$, proposed here.

- ○ For conservative results the Kubaschewski-Heinrich correlations should be used with a constant multiplier of M_C=1.8, which gives higher oxidation rate than all measurement data considered here.

Table 3-56 Graphite-steam oxidation - experimental condition and correlation accuracy

Test	Temperature	Pressure	Steam pressure	Maximum deviation	
				Original corr. $M(B,P)$=1.0	New corr. $M(B,P)$=B.E.
Leonißen 1	1273 K (1000˚C)	2.9 bar	0.066 ÷ 0.0973 bar	+5% ÷ +76%	–27% ÷ +9%
Leonißen 2	1273 K (1000˚C)	3 ÷ 55 bar	0.474 bar	–72% ÷ +23%	–23% ÷ +9%
Abel-Holden	1311 K (1038˚C)	1.0 bar	1.0 bar	+66%	0%
Yu (code-to-code)	1023 K (750˚C)	0.00014	-	+27%	+16%

3.11 Hydrogen Burn

This section describes verification of the burn model in the SPECTRA code. SPECTRA input models were set up for several test cases, selected to cover most possible conditions and modelling options. Results of SPECTRA calculations for these tests are compared to the results of MELCOR calculations. Comparisons are presented by plotting time behavior of several more important parameters (pressures, temperatures, etc.). The MELCOR code was used as a verification tool, rather than experimental data, because it is difficult to find measurement data detailed enough to allow time-dependent comparisons.

A number of different test cases were analyzed. Seven most representative cases are described here. These tests are listed below.

- Test H2-1, Single CV adiabatic deflagration test
- Test H2-2, Single CV adiabatic deflagration test, alternative models for the flame velocity and the combustion completeness
- Test H2-3, Deflagration test with multiple volumes and structures
- Test H2-4, Detonation test with multiple volumes and structures
- Test H2-5, Deflagration, detonation, and flame propagation test, with multiple volumes and structures.

The above five tests are described in sections 3.11.1 through 3.11.5.

3.11.1 Test H2-1, Single CV Adiabatic Deflagration Test

The model consists of a single, 10 m^3 Control Volume, CV-001, filled initially with air (30% humidity), at 315 K and atmospheric pressure - see Figure 3-566. An igniter is present in the Control Volume. The igniter temperature, assumed to be equal to 900 K, is set by Tabular Function TF-001. For simplicity adiabatic conditions are assumed - there are no structures connected to CV-001.

A mass source injects hydrogen at 315 K. The injection rate is constant and equal to 0.01 kg/s for the first 5.0 seconds, and then it decreases linearly to zero at 6.0 s. The test duration is 10.0 s. SPECTRA input deck for this case is provided in `\Z-INPUTS\H2\H2-1\H2-1.SPE`.

For comparison calculation the same model was set up for MELCOR. Two modifications were made in MELCOR modelling parameters, to make MELCOR burn models similar to the SPECTRA default models. These include:

- The value of the ignition limit with igniters was changed from 7.0% H_2 (MELCOR default) to 4.5% H_2. In SPECTRA this limit is temperature dependent. The value appropriate for the gas temperature in the present test is about 4.5% (see Volume 1).

- The combustion completeness correlation from HECTR 1.5 (default correlation in MELCOR) was replaced by a constant combustion completeness, equal to 0.99 (default setting in SPECTRA - see Volume 1). The influence of the combustion completeness model is further discussed in the next section.

MELCOR input decks for this case are provided in:
`\Z-INPUTS\H2\H2-1\MELCOR\H2-1.GEN and H2-1.COR`

Results are shown as visualization pictures in Figure 3-566, Figure 3-567, Figure 3-568, and time dependent graphs in Figure 3-569 through Figure 3-575. The visualization pictures show the state of the system at the start of the calculations (*t*= 0.0 s) - Figure 3-566, and just after the burn is initiated, at 3.9 s - Figure 3-567 and Figure 3-568. Similar behavior is observed in both SPECTRA and MELCOR.

Figure 3-569 and Figure 3-570 show the hydrogen and oxygen concentrations. Ignition occurs at about 3.6 s and the burn continues until about 4.2 s. In MELCOR the burn is a little shorter.

Figure 3-573 and Figure 3-574 show the pressure behavior. In MELCOR the pressure rise during the burn is nearly linear. This is a consequence of using different flame speed correlations in MELCOR and SPECTRA (see Volume 1). The gas temperatures are plotted in Figure 3-571 and Figure 3-572. The calculated values are very similar in both codes.

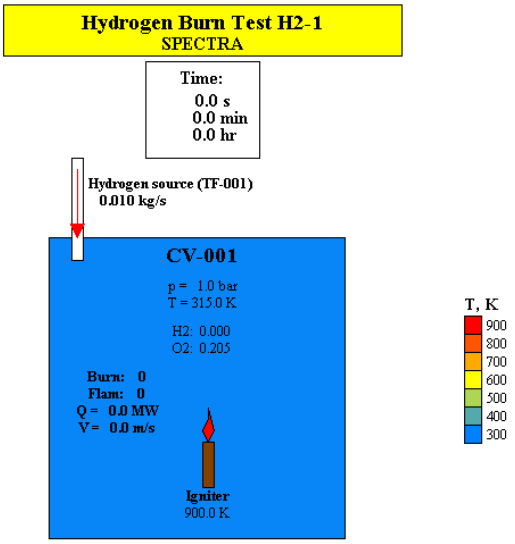

Figure 3-566 Single volume adiabatic deflagration test, *t*= 0.0 s

In MELCOR the heat of burn is somewhat higher than in SPECTRA (Figure 3-567 and Figure 3-568). The difference comes mainly from different flame velocity. Flame velocity calculated by SPECTRA is shown in Figure 3-575. In MELCOR the flame velocity is not a plottable parameter, but comparison of the correlations applied in both codes, shown in Volume 1, indicates somewhat higher flame velocity is obtained from the MELCOR model. This issue is discussed further in the next section.

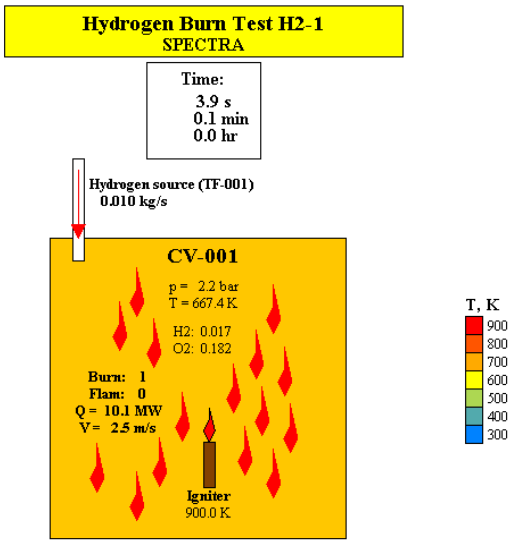

Figure 3-567 Single volume adiabatic deflagration test H2-1, *t* = 3.9 s, SPECTRA

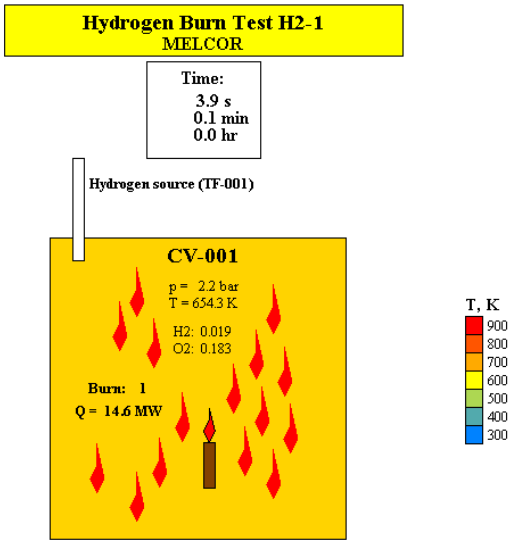

Figure 3-568 Single volume adiabatic deflagration test H2-1, *t* = 3.9 s, MELCOR

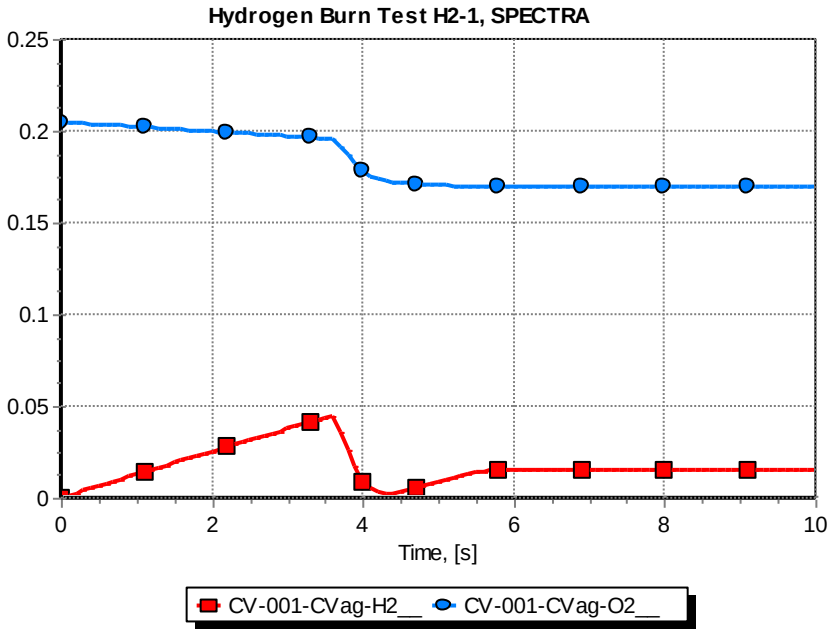

Figure 3-569 H_2 and O_2 mole fractions, test H2-1, SPECTRA

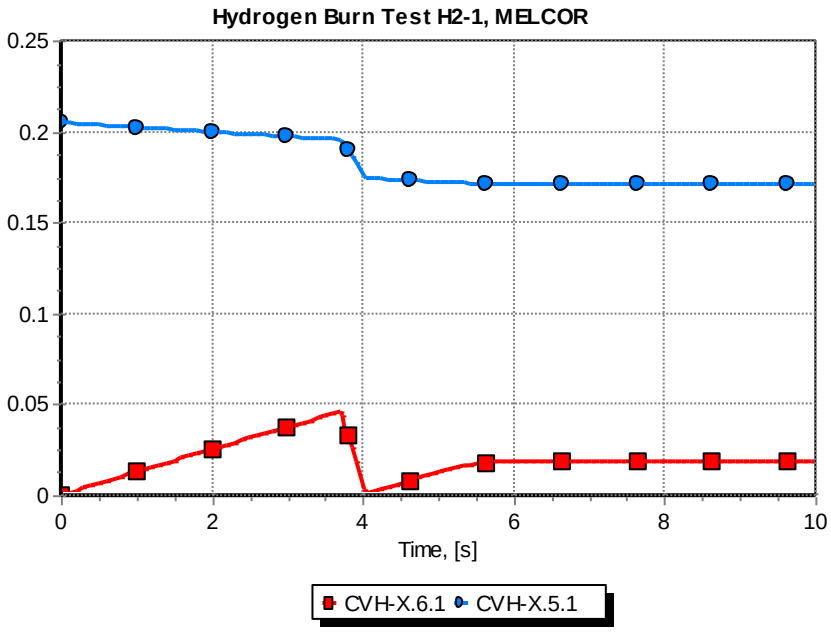

Figure 3-570 H_2 and O_2 mole fractions, test H2-1, MELCOR

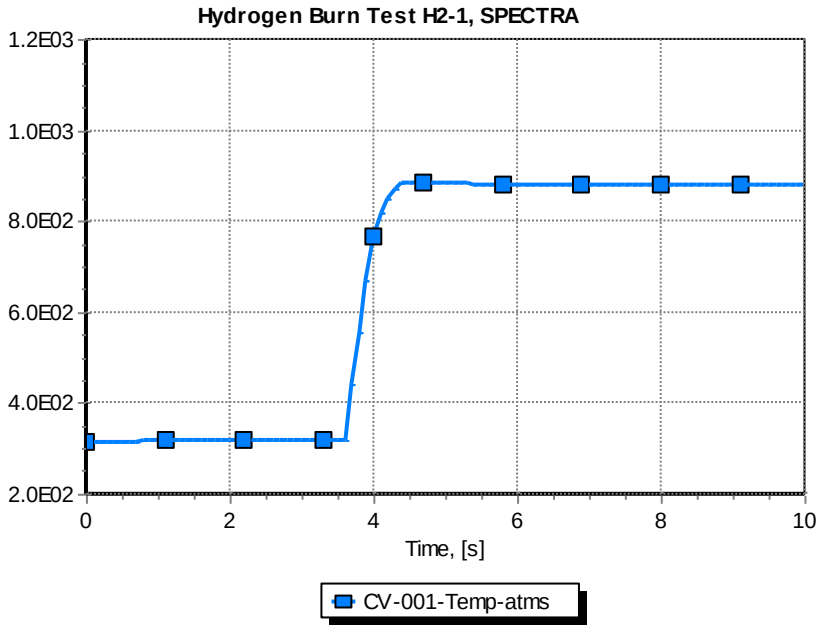

Figure 3-571 Gas temperature in CV-001, test H2-1, SPECTRA

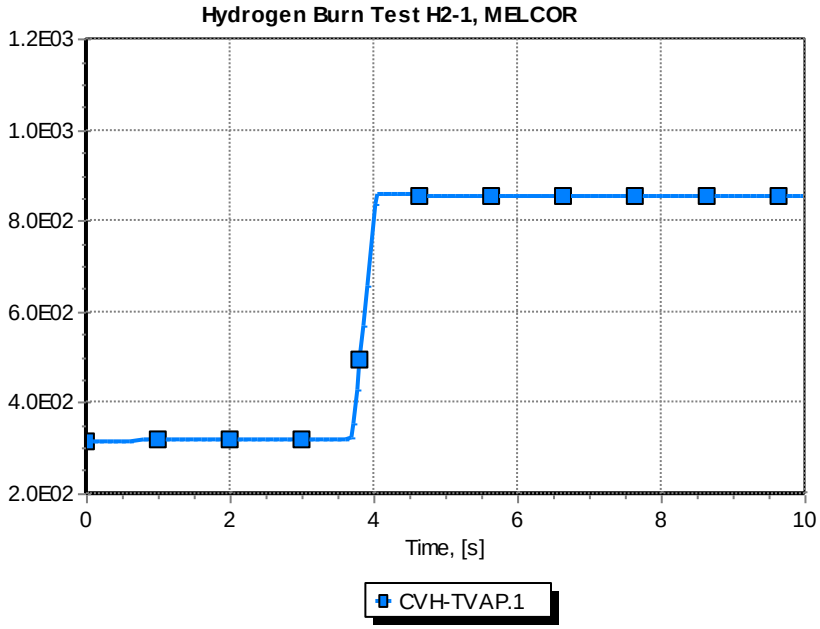

Figure 3-572 Gas temperature in CV-001, test H2-1, MELCOR

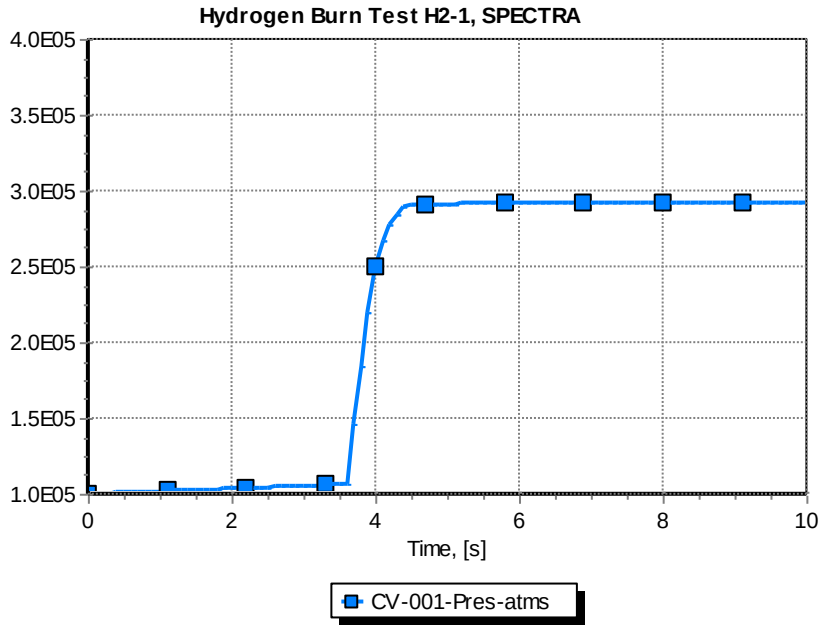

Figure 3-573 Pressure in CV-001, test H2-1, SPECTRA

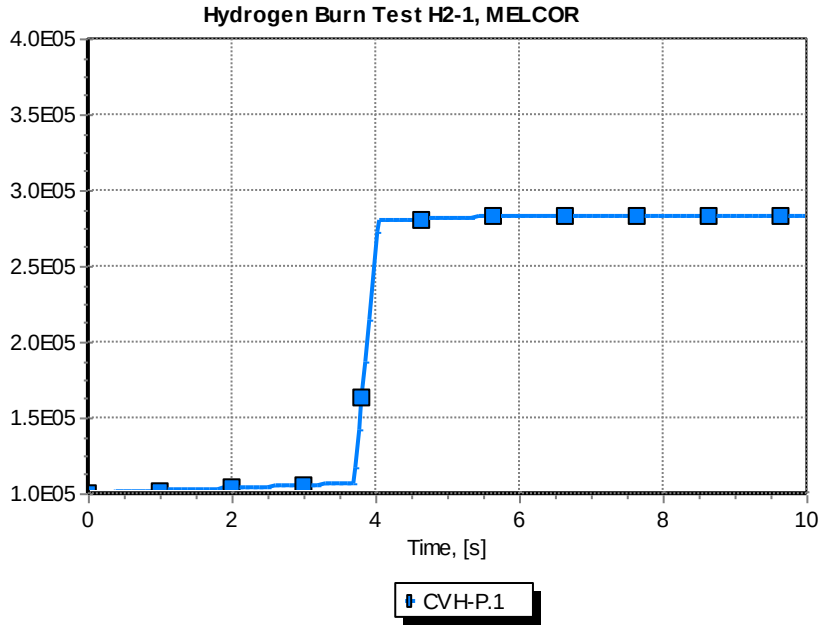

Figure 3-574 Pressure in CV-001, test H2-1, MELCOR

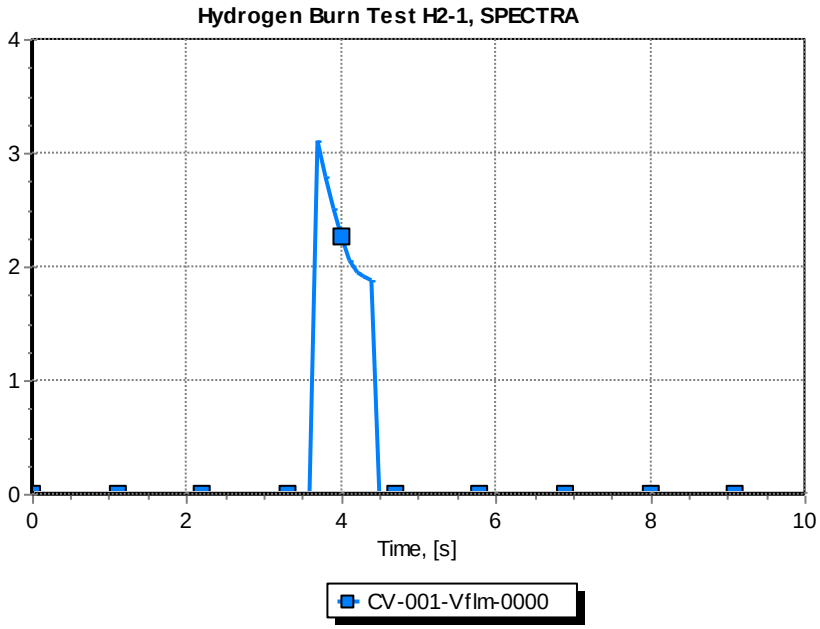

Figure 3-575 Flame velocity, test H2-1, SPECTRA

3.11.2 Test H2-2, Single CV, Alternative Flame Velocity and CC Models

This section presents two tests that are almost identical to the test described in the previous section. There are two differences:

- The flame velocity is calculated using the gas temperature in a Control Volume rather than the default value of 1150 K. To obtain similar flame velocity in MELCOR, the default correlation in MELCOR was replaced by a constant, user defined flame velocity. The velocity was set at 0.7 m/s, approximately the average value calculated by SPECTRA for this case.
  SPECTRA input deck is provided in `\Z-INPUTS\H2\H2-2\H2-2a.SPE`
  MELCOR input decks are provided in `\Z-INPUTS\H2\H2-2\MELCOR\H2-2a.GEN` and `H2-2a.COR`.

- In previous section the Combustion Completeness (CC) was set to a constant value of 0.99. In the present case the combustion completeness is set to a low value (0.1).
  SPECTRA input deck is provided in `\Z-INPUTS\H2\H2-2\H2-2b.SPE`
  MELCOR input decks are provided in `\Z-INPUTS\H2\H2-2\MELCOR\H2-2b.GEN` and `H2-2b.COR`.

Results are shown in Figure 3-576 through Figure 3-583. H_2 and O_2 concentrations for the test H2-2a are shown in Figure 3-576 and Figure 3-577. Good agreement between MELCOR and SPECTRA is observed.

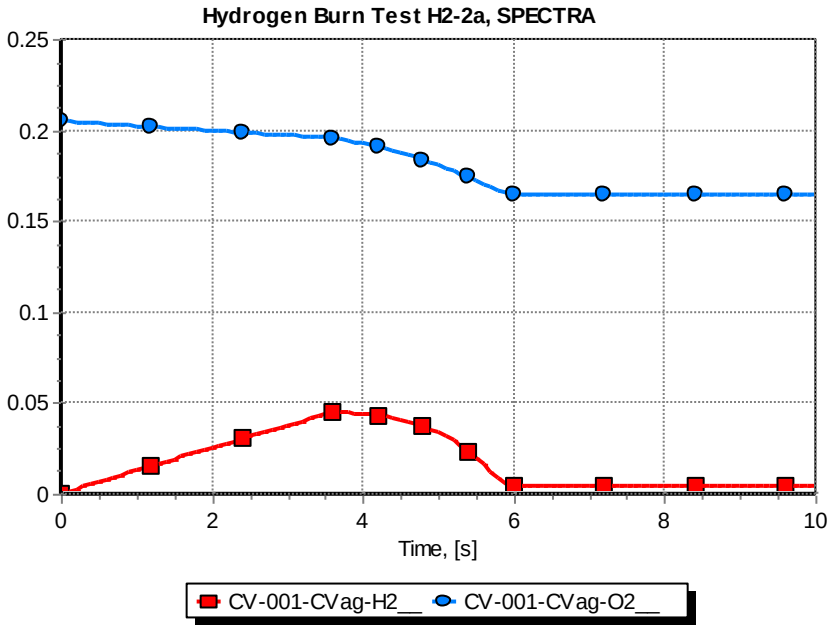

Figure 3-576 H_2 and O_2 mole fractions, test H2-2a, SPECTRA

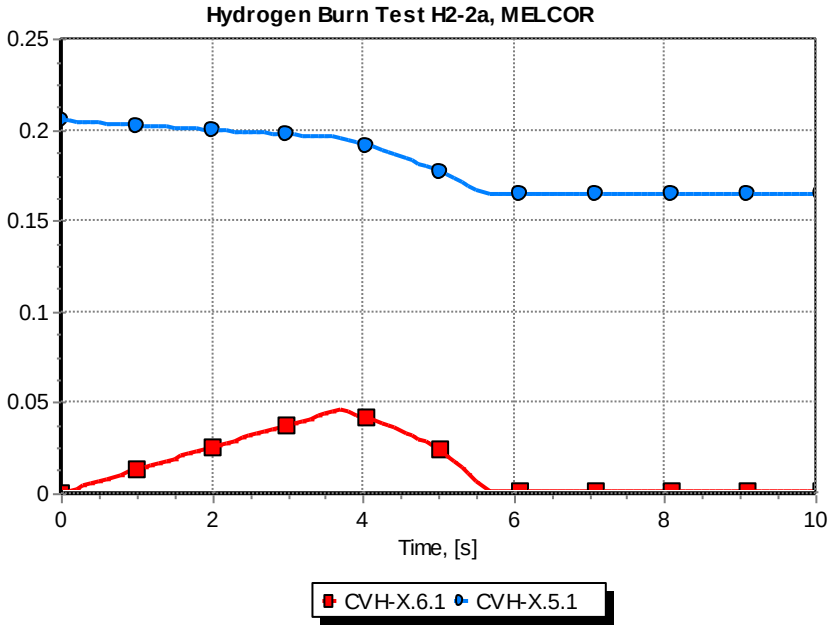

Figure 3-577 H_2 and O_2 mole fractions, test H2-2a, MELCOR

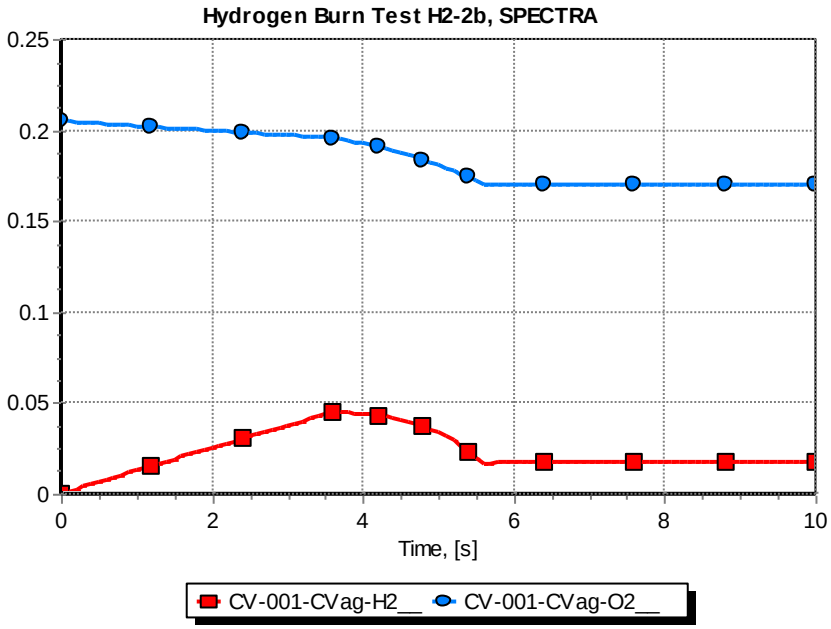

Figure 3-578 H_2 and O_2 mole fractions, test H2-2b, SPECTRA

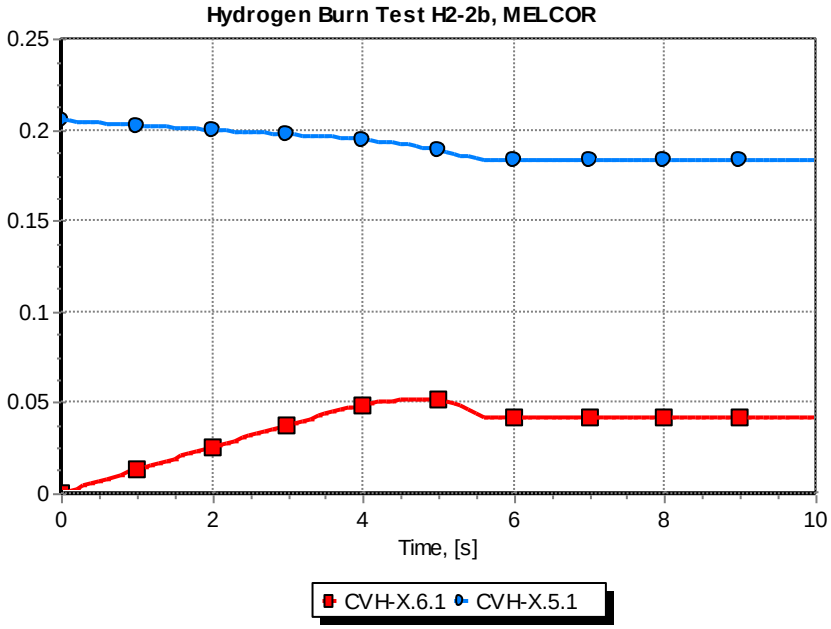

Figure 3-579 H_2 and O_2 mole fractions, test H2-2b, MELCOR

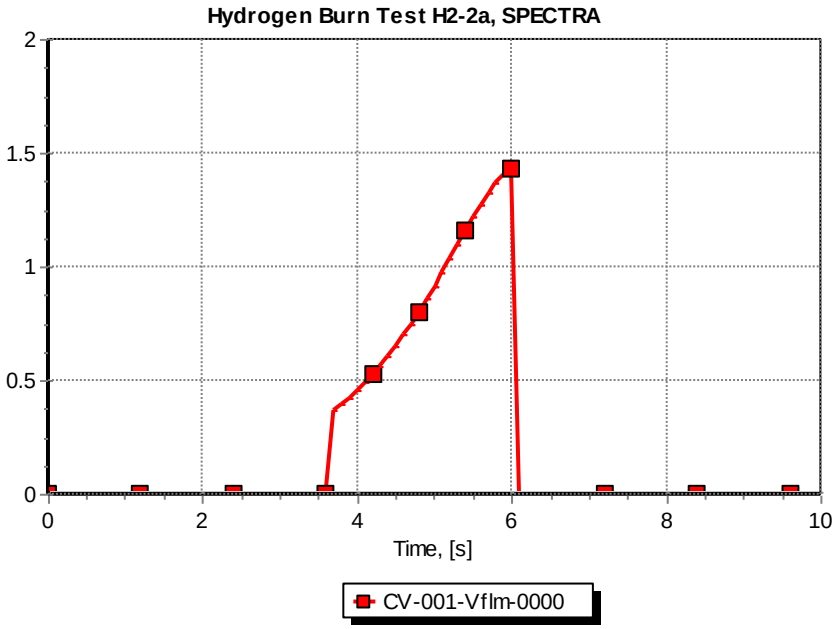

Figure 3-580 Flame velocity, test H2-2a, SPECTRA

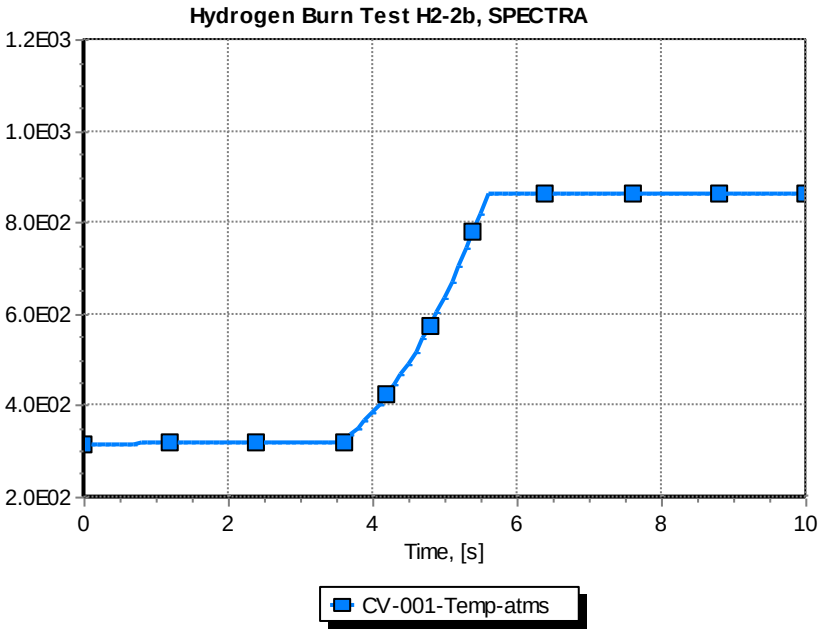

Figure 3-581 Gas temperature, test H2-2b, SPECTRA

The burn is slower than in the case H2-1, discussed in the previous section. This is clearly seen as the hydrogen concentration decrease is slower (compare Figure 3-576 and Figure 3-569). The flame velocity is 0.5 - 1.5 m/s (Figure 3-580), while with the default flame speed model the values were 2 - 3 m/s (Figure 3-575). Therefore the default model, with the flame speed calculated using a constant gas temperature of:

- T = 1150 K

gives more conservative (higher) flame speed than the alternative flame method, with the flame speed being calculated based on the average gas temperature in a Control Volume:

- $T = T_{atms}$(CV)

This is one of the reasons for selecting the default flame speed calculation - see Volume 1.

Figure 3-582 shows gas flammability status and burn status, as calculated by SPECTRA for the case H2-2a. Burn is initiated as soon as the gas becomes flammable (about 3.6 s), and continues till about 6 s, although the gas mixture becomes inflammable already at about 5.6 s due to hydrogen depletion. This fact is caused by using a large value of combustion completeness (0.99). Burn continues until the hydrogen concentration falls below 1% of the hydrogen concentration at the start of burn, independently of the gas flammability status.

If the user should like to terminate burn as soon as the gas mixture becomes inflammable, then he should use a small value of combustion completeness, for example 0.1. This is done in the test H2-2b, where the CC of 0.1 is used.

A CC of 0.1 means that the burn is terminated when the hydrogen fraction decreases by 10% compared to the initial value, it means about 4% hydrogen volume fraction. Results are shown in Figure 3-578, Figure 3-579, Figure 3-581, and Figure 3-583. The results are similar to the results of the test H2-2a, except that the burn is terminated earlier. In MELCOR the burn is terminated very soon; in SPECTRA the burn is a little longer. This is because in SPECTRA hydrogen burn continues if the gas mixture is flammable (see Volume 1). In the present case the gas mixture is still flammable when the hydrogen concentration decreases to ~4%, because the gas temperature has meanwhile significantly increased (Figure 3-581). If the burn was terminated at ~4% hydrogen fraction, then it would immediately start again in the following time step. To avoid an unphysical situation, with burn being turned off and on again, the SPECTRA burn model does not terminate burn in case of a flammable gas mixture - see Volume 1. Note that in MELCOR the flammability limits are not temperature dependent and this behavior would not take place.

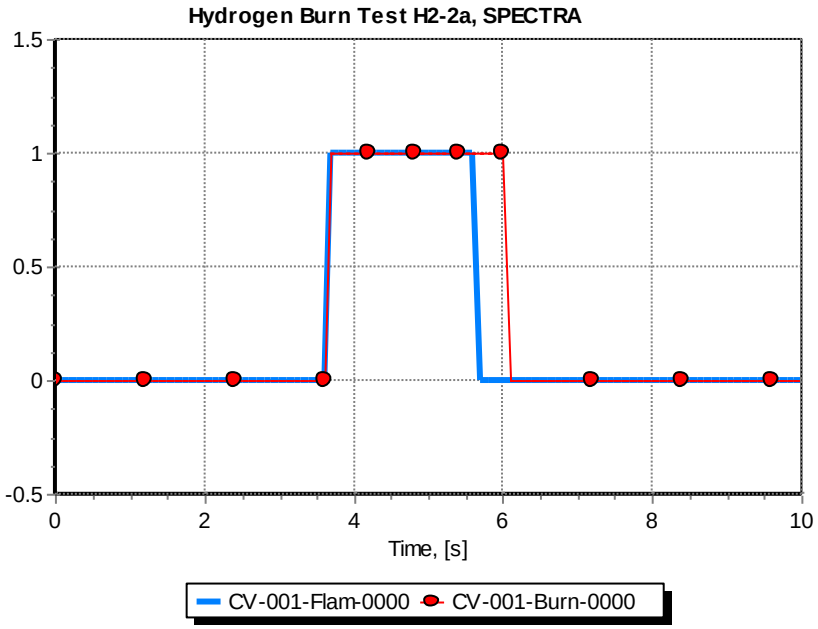

Figure 3-582 Gas flammability status and burn status, test H2-2a, SPECTRA

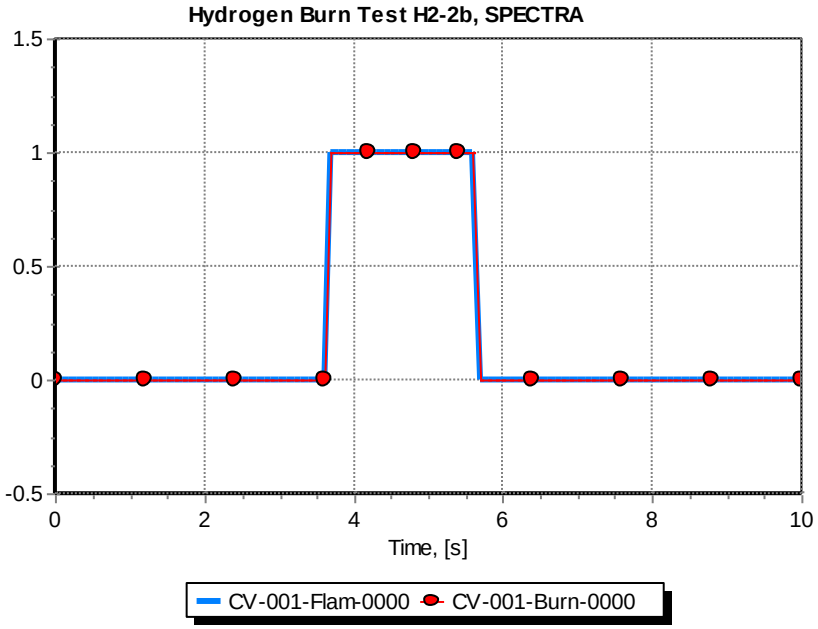

Figure 3-583 Gas flammability status and burn status, test H2-2b, SPECTRA

3.11.3 Test H2-3, Deflagration Test - Multiple Volumes and Structures

The "test section" consists of six Control Volumes of 1.0 m^3, connected by six junctions, as shown in Figure 3-584. The system considered is symmetrical, to verify whether identical conditions will be calculated in CV-002, CV-003, as in their "mirror images" - CV-004, CV-005. The initial conditions in all Control Volumes were set to 300 K, 1 bar pressure. The relative humidity is 0.3. There are six Solid Heat Conductors (Heat Structures). The heat transfer area of each of them is equal to 6 m^2. The wall emissivities, ε_{wall}, were set to 0.9. The gas was assumed to be opaque (ε_{gas} = 1.0). A valve is present on CV-006 which leads to environment (CV-900 with constant pressure of 1 bar). For the present test the valve is closed. This allows to observe pressure increase in the system caused by the hydrogen burn.

An igniter is present in CV-001. The igniter temperature is assumed to be equal to 900 K. A mass source injects hydrogen at 315 K into CV-001. The injection rate is constant and equal to 0.0004 kg /s for the first 10.0 seconds, and then decreases linearly to zero at 10.1 s. The test duration is 20.0 s. SPECTRA input deck is provided in `\Z-INPUTS\H2\H2-3\H2-3.SPE`.

For comparison calculation the same model was set up for MELCOR. Similarly as in the previous cases, three modifications were made in MELCOR modelling parameters, to make MELCOR burn models similar to the SPECTRA models (see section 3.11.1). These include:

- The value of the ignition limit with igniters was changed from 7.0% H2 to 4.5% H2.
- The combustion completeness was set to a constant value, equal to 0.99.

The MELCOR input decks are provided in `\Z-INPUTS\H2\H2-3\MELCOR\H2-3.GEN` and `H2-3.COR`. Results are shown in visualization pictures in Figure 3-585 and Figure 3-586, as well as time dependent graphs in figures Figure 3-587 through Figure 3-593.

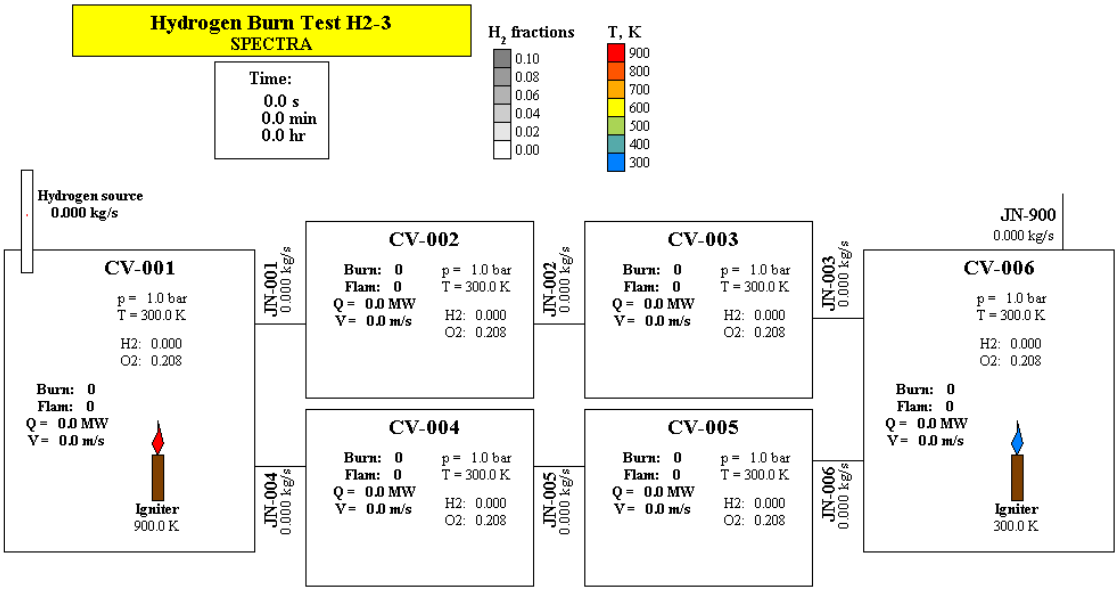

Figure 3-584 Multiple volume and structure test - nodalization scheme

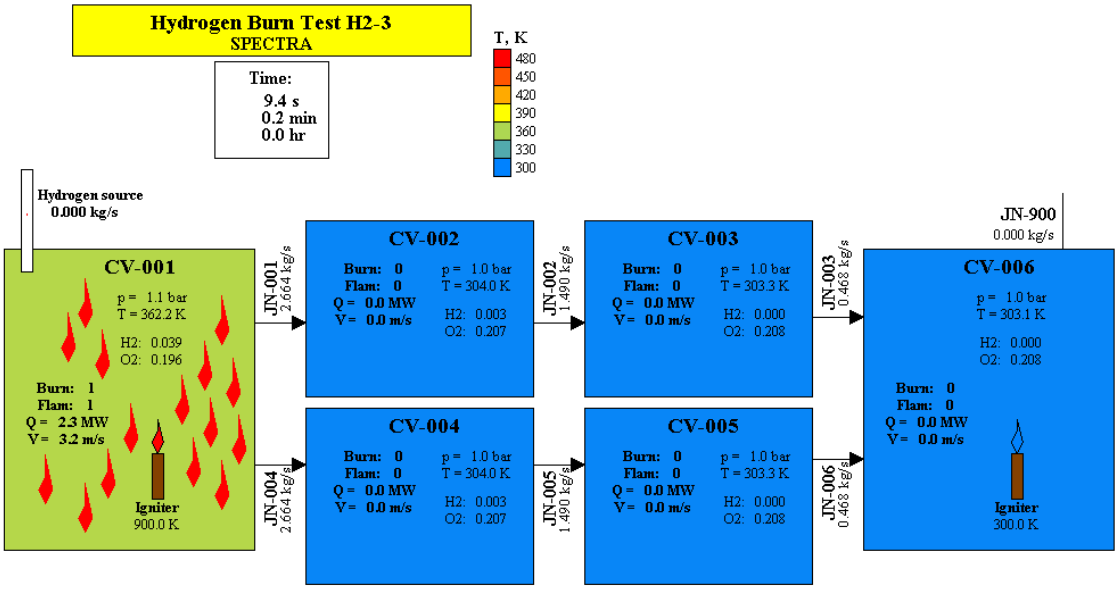

Figure 3-585 Test H2-3, visualization at t = 9.4 s, SPECTRA

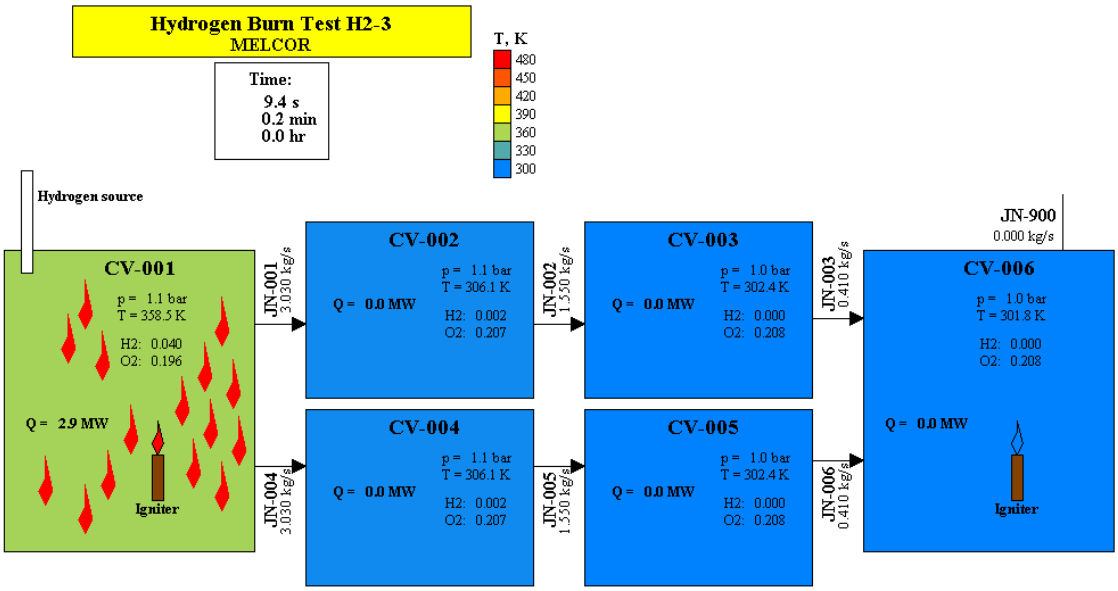

Figure 3-586 Test H2-3, visualization at t = 9.4 s, MELCOR

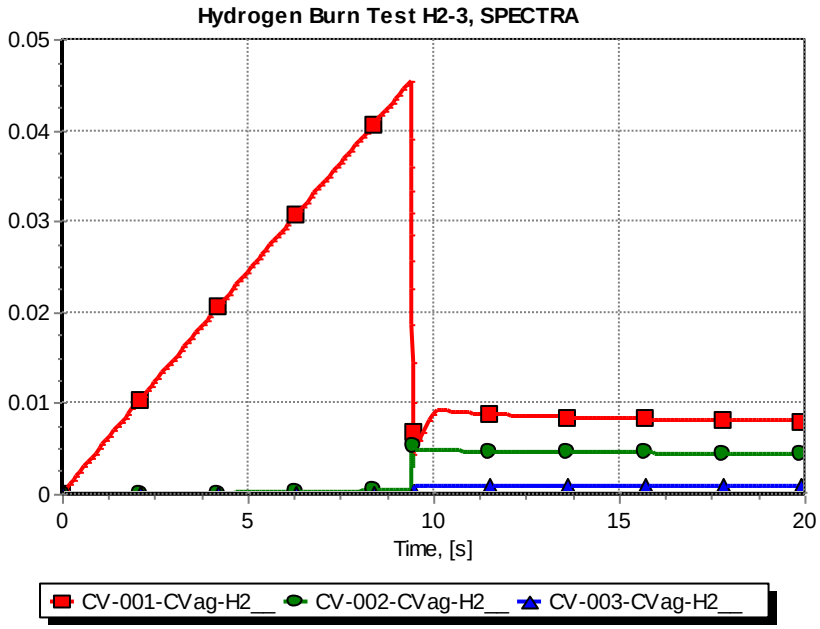

Figure 3-587 Hydrogen volume fractions, Test H2-3, SPECTRA

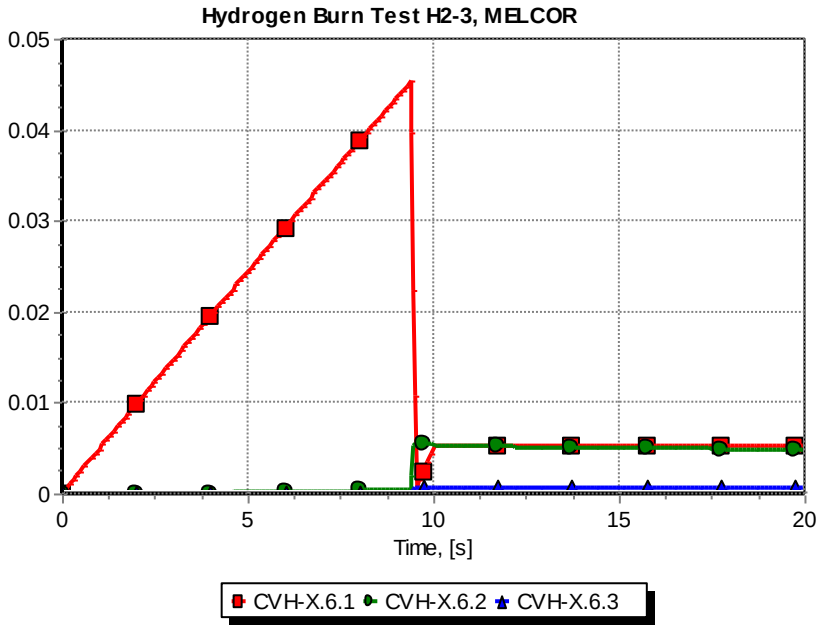

Figure 3-588 Hydrogen volume fractions, Test H2-3, MELCOR

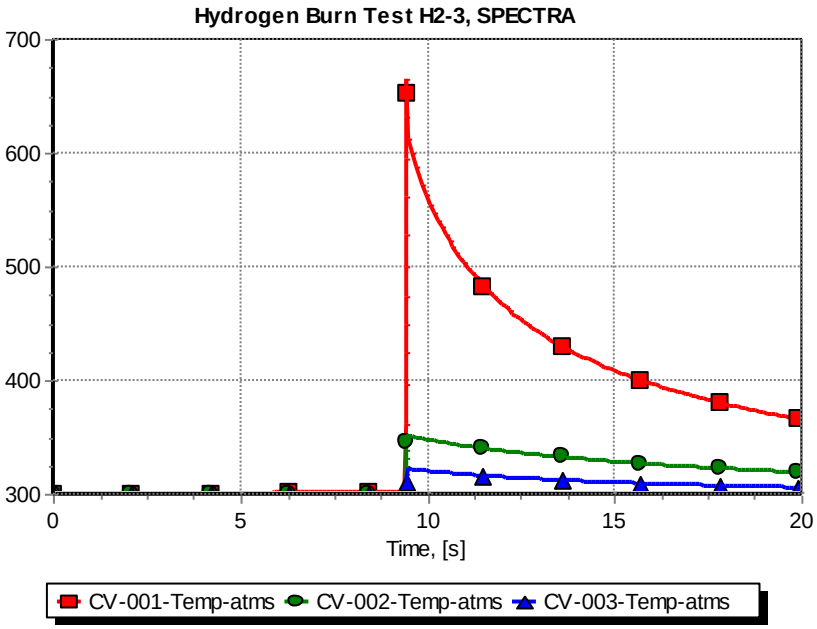

Figure 3-589 Temperatures, Test H2-3, SPECTRA

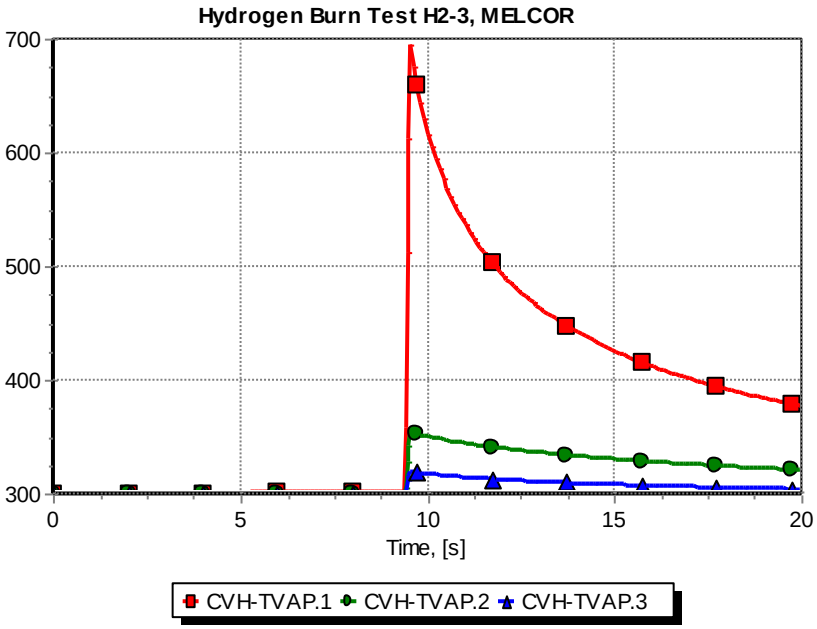

Figure 3-590 Temperatures, Test H2-3, MELCOR

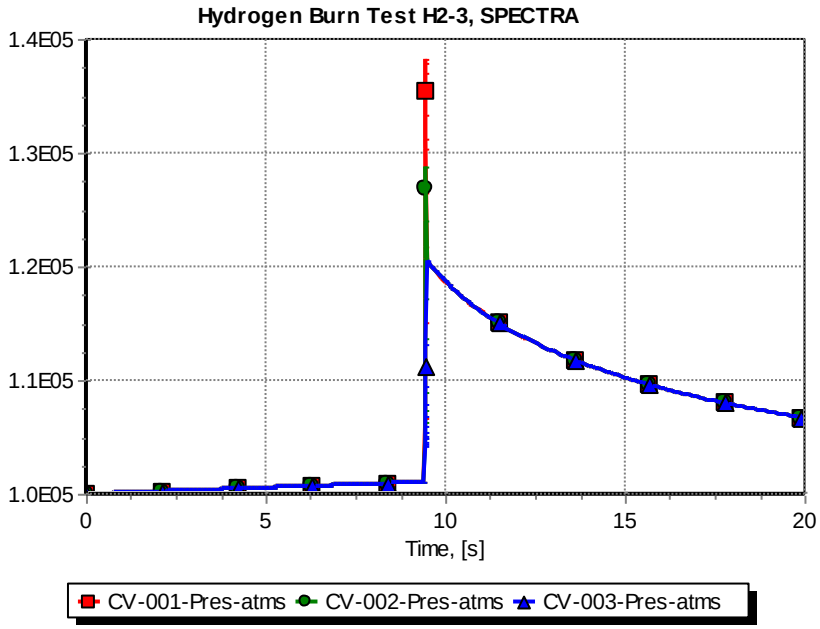

Figure 3-591 Pressures, Test H2-3, SPECTRA

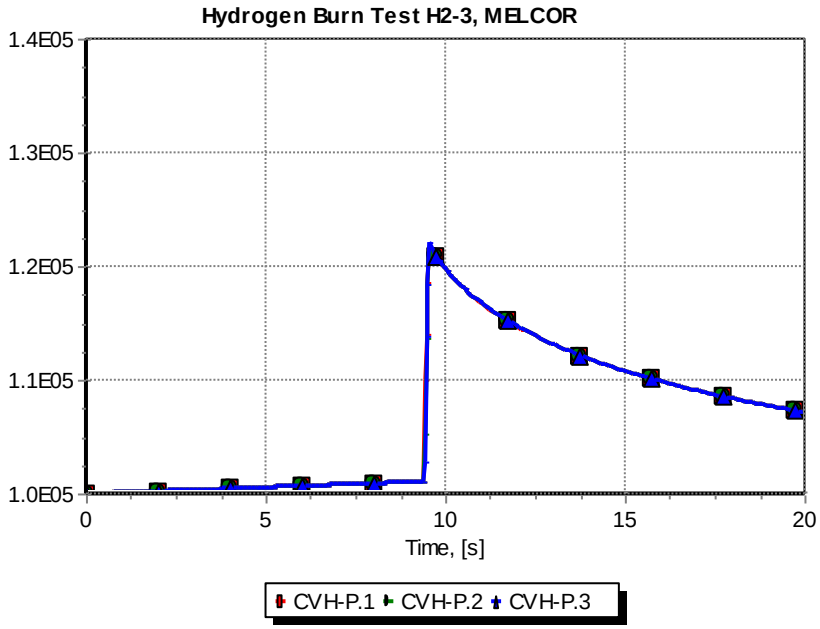

Figure 3-592 Pressures, Test H2-3, MELCOR

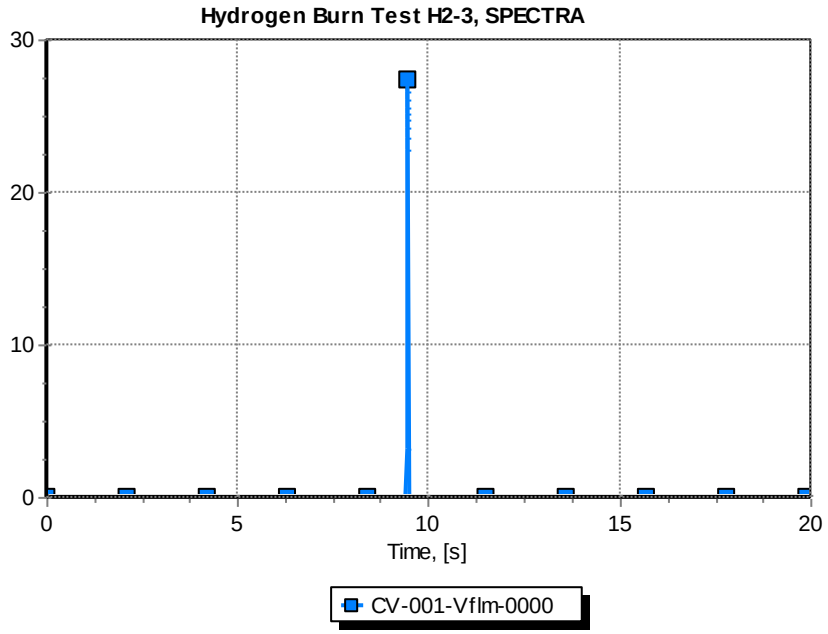

Figure 3-593 Flame velocity, Test H2-3, SPECTRA

The hydrogen fraction in CV-001 increases till about 9.4 s (Figure 3-587, Figure 3-588). At about 9.4 s burn is initiated. Pressure rapidly increases in CV-001 (Figure 3-591, Figure 3-592), and then in other volumes. The visualization pictures show the results at 9.4 s, when the burn is initiated. Detailed investigation of the results showed that the parameters in CV-004, CV-005 are indeed identical to the corresponding values in CV-002, CV-003 (Figure 3-585 and Figure 3-586).

The pressure peak calculated by SPECTRA is higher than in MELCOR. This indicates that in MELCOR the inertia of gas is somewhat smaller, although the same value of inertial length (1.0 m) has been specified for all junctions in both SPECTRA and MELCOR inputs. Another possible reason for higher peak in SPECTRA is more frequent plot points. During burn SPECTRA makes a plot point every time step (see Volume 2), while in MELCOR additional plot points are made only at the start and at the end of each burn (see [20], BUR-UG-9).

Figure 3-593 shows flame velocity calculated by SPECTRA. The velocity increases during burn to about 30 m/s. This is significantly larger than in tests H2-1, H2-2. The velocity is larger mainly because of turbulence. In the present case relatively large velocities between Control Volumes are encountered. Consequently SPECTRA calculates large turbulent velocity and finally large flame velocity (see Volume 1).

3.11.4 Test H2-4, Detonation Test - Multiple Volumes and Structures

This case is very similar to the previous case (Figure 3-584). The hydrogen source is in this case equal to 0.001 kg/s for 15 s; afterwards it is stopped. The only other difference concerns the igniter in CV-001. In the previous test the igniter was active during the whole test. In the present test the igniter is activated at 15 s. This is achieved by setting the igniter temperature (value of TF-004) to a low value (300.0 K) for the first 15.0 s, and to a high value (900.0 K) at 15.1 s.

During the 15 s a large amount of hydrogen is accumulated in CV-001. When the igniter is finally activated and causes hydrogen to burn, a detonation is observed. SPECTRA input deck is provided in `\Z-INPUTS\H2\H2-4\H2-4.SPE`.

For comparison calculation the same model was set up for MELCOR. MELCOR does not model detonations. The only action that is taken by MELCOR when a detonation is encountered is to write a warning message. For the present calculation a detonation was modelled as a fast deflagration, with user specified flame velocity. Three modifications were made in MELCOR modelling parameters:

- The value of the ignition limit with igniters was set at 16.7% H_2. This is the value of hydrogen concentration in CV-001 at the time of ignition in SPECTRA. This was done because in MELCOR one cannot change the igniter temperature during calculations. The igniter is either on or off during the whole calculation.
- The combustion completeness was set to a constant value, equal to 0.99.
- The flame velocity was set to 1500 m/s, based on the value calculated by SPECTRA for this detonation (Figure 3-594).

MELCOR input decks are provided in `\Z-INPUTS\H2\H2-4\MELCOR\H2-4.GEN` and `H2-4.COR`. Results are shown in visualization pictures in Figure 3-594 and Figure 3-595 and time dependent graphs in Figure 3-596 through Figure 3-602.

When detonation occurs the pressure in CV-001 rapidly increases (Figure 3-600 and Figure 3-601), and the hydrogen is quickly consumed (Figure 3-596 and Figure 3-597). The gas temperature in CV-001 rises to almost 2000 K and then slowly decreases, as the heat is radiated and convected to the walls (Figure 3-598 and Figure 3-599).

The CV pressures, shown in Figure 3-600 and Figure 3-601, are calculated by SPECTRA and MELCOR using a lumped parameter Control Volume approach. Therefore the values shown in Figure 3-600 and Figure 3-601 are the average CV pressures, and do not reflect the local pressures at the detonation front. During detonations (as well as fast turbulent deflagrations) the flame propagates with supersonic velocity and a shock wave is created. Detailed analysis requires CFD calculation with a small mesh size. In SPECTRA the shock wave pressure is estimated using a simplified method. The shock wave pressure is calculated using the equation derived for ideal gas (see Volume 1). The pressure behind the shock wave is assumed to be equal to the current average CV pressure, calculated by the code. Figure 3-602 shows the calculated shock wave pressure, as well as the average CV pressure. While the average CV pressure rises only to about 5 bars, the shock wave pressure peak is about 30 bars.

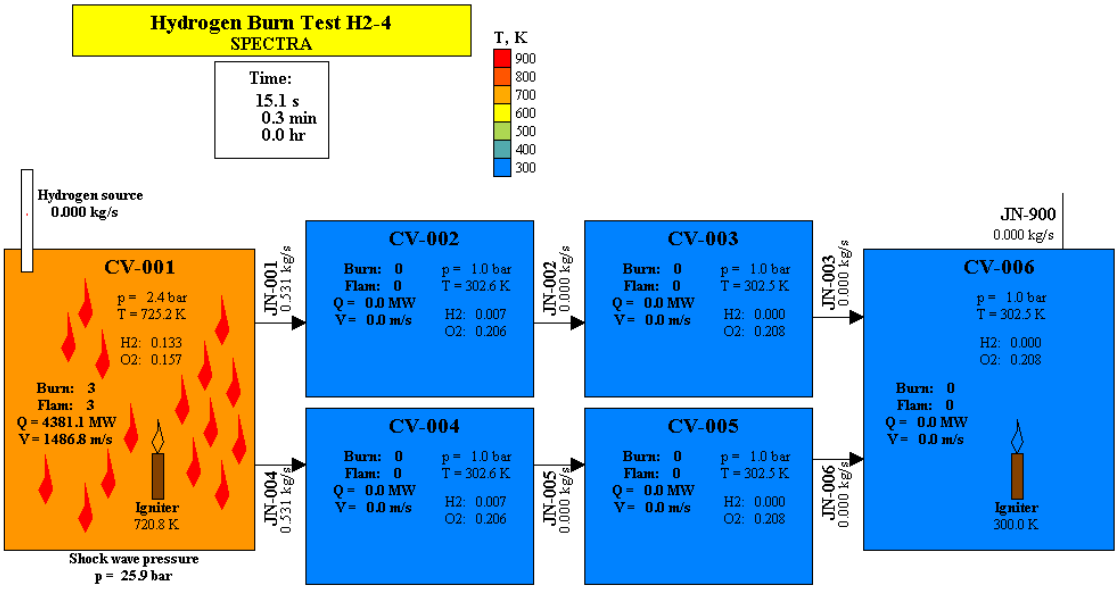

Figure 3-594 Test H2-4, visualization at *t* = 15.1 s, SPECTRA

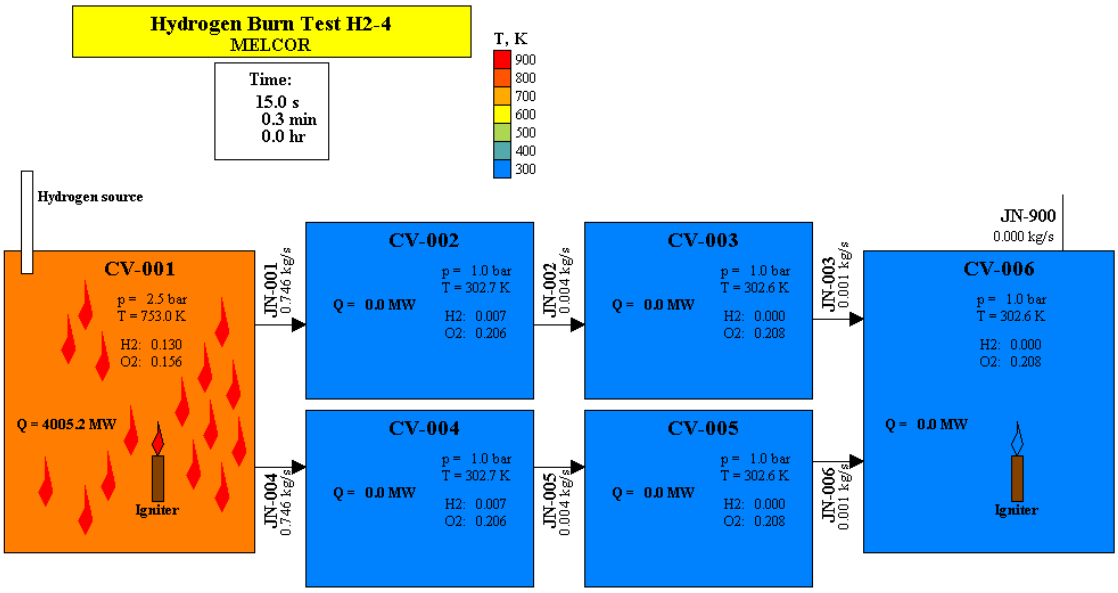

Figure 3-595 Test H2-4, visualization at *t* = 15.0 s, MELCOR

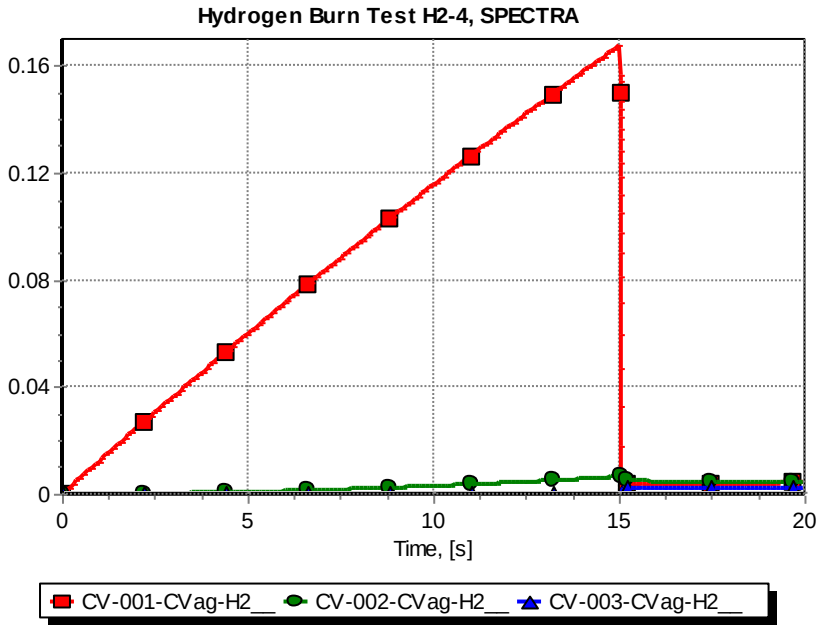

Figure 3-596 Hydrogen volume fractions, Test H2-4, SPECTRA

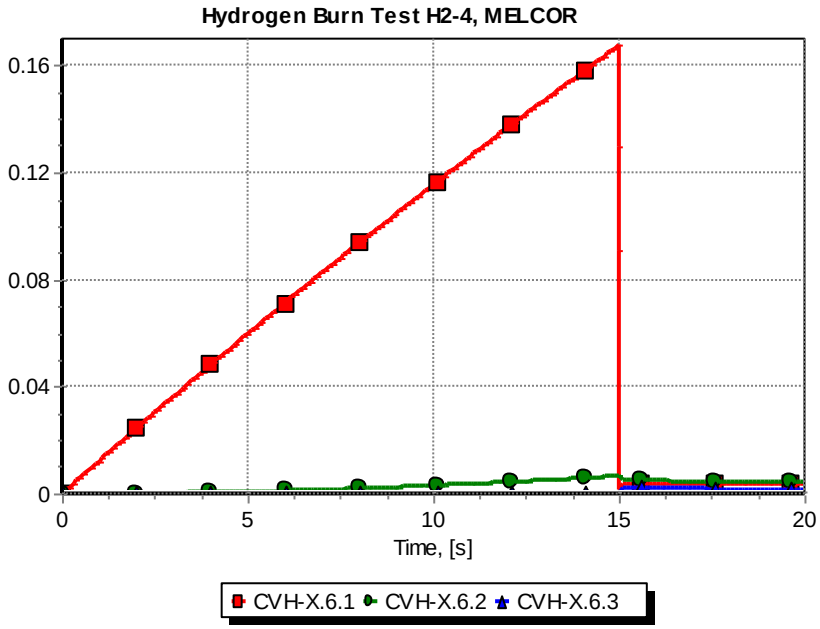

Figure 3-597 Hydrogen volume fractions, Test H2-4, MELCOR

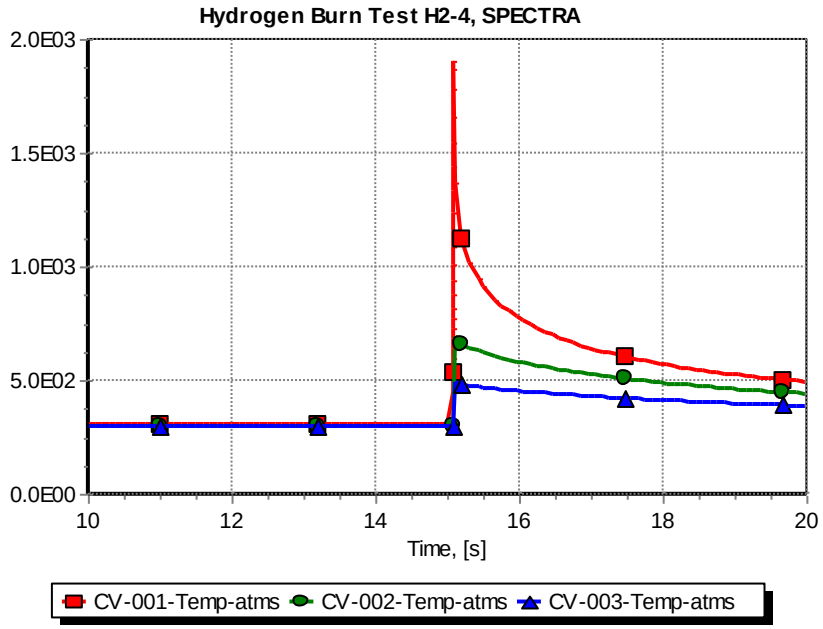

Figure 3-598 Temperatures, Test H2-4, SPECTRA

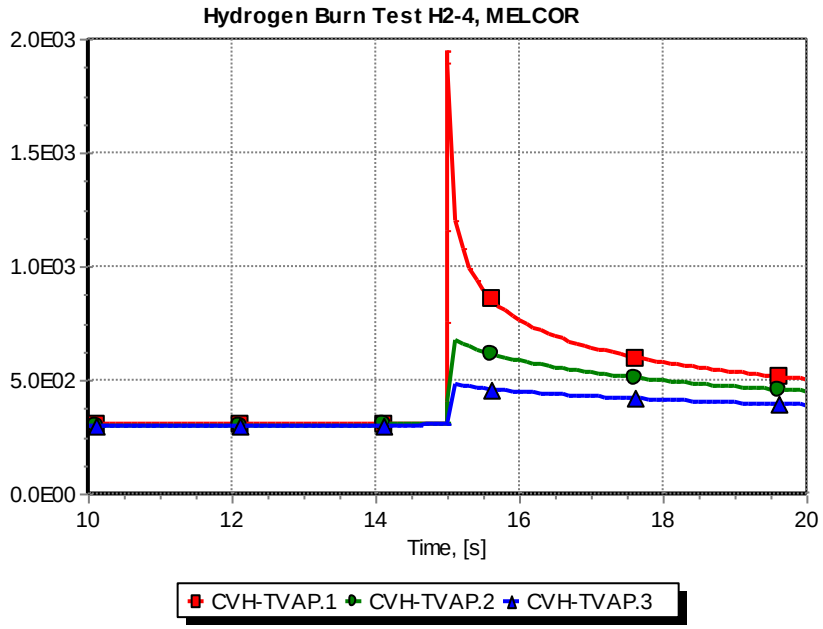

Figure 3-599 Temperatures, Test H2-4, MELCOR

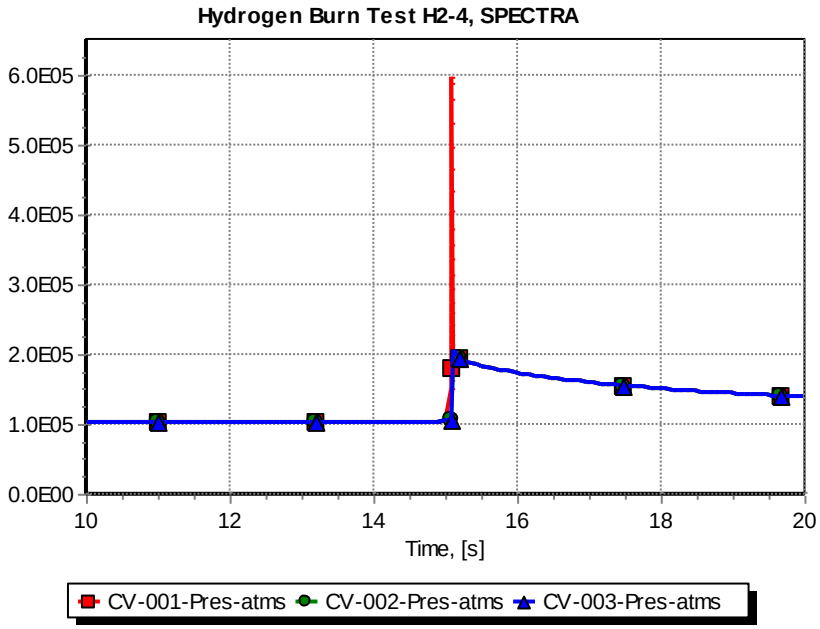

Figure 3-600 Pressures, Test H2-4, SPECTRA

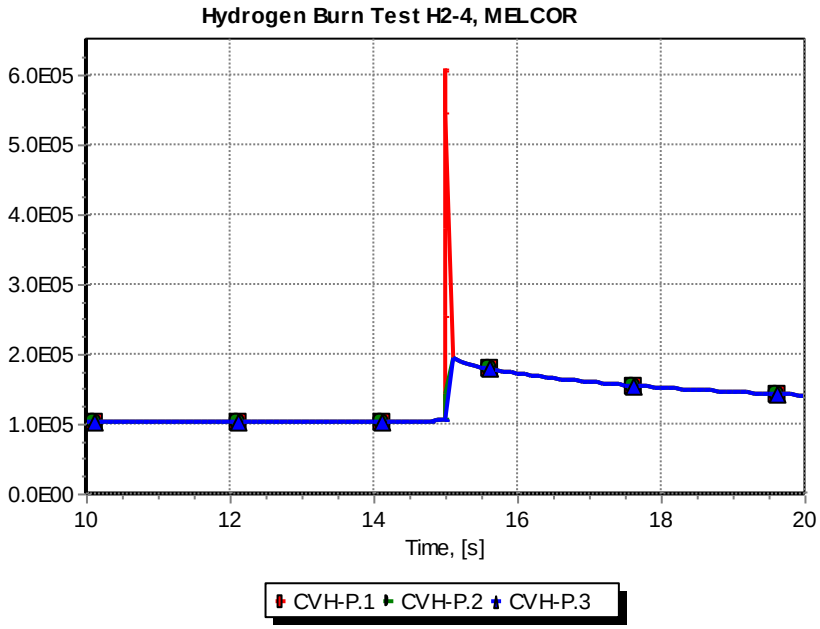

Figure 3-601 Pressures, Test H2-4, MELCOR

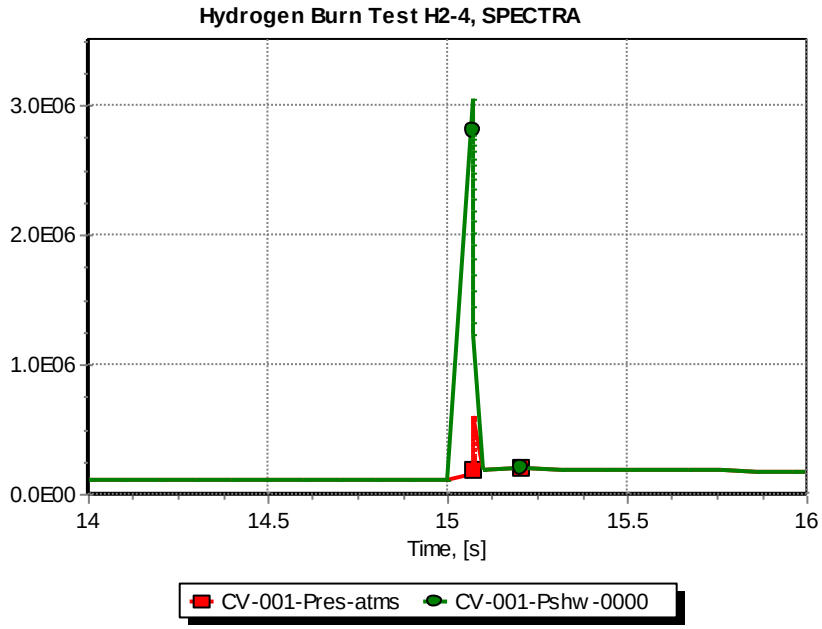

Figure 3-602 Average pressure and shock wave pressure, Test H2-4, SPECTRA

3.11.5 Test H2-5, Deflagration, Detonation, and Flame Propagation Test

The model used for this test is the same as the model used for the previous two cases (Figure 3-584). The hydrogen source is in this case equal to 0.01 kg/s. The igniter is present in CV-006. The vent line to the environment (JN-900) is open. The burn is initiated in the volume with the igniter, CV-006. By the time the H_2 concentration in CV-006 is high enough to burn (about 4.5%), the concentrations in other volumes, closer to the H_2 source, are much higher. Therefore when the flame propagates to these volumes, detonation is expected. SPECTRA input deck is provided in `\Z-INPUTS\H2\H2-5\H2-5.SPE`.

For comparison calculation the same model was set up for MELCOR. MELCOR does not model detonations. The only action that is taken by MELCOR when a detonation is encountered is to write a warning message. For the present calculation a detonation was modelled as a fast deflagration, with user specified (large) flame velocity.

In this test a slow deflagration is expected in CV-006 and detonations in other volumes. In MELCOR one needs to specify one flame velocity for all Control Volumes. The detonation velocity calculated by SPECTRA (~2000 m/s) was applied in all volumes. The fact that the burn is initiated by a slow deflagration in CV-006 has a small influence on the results. Three modifications were made in MELCOR modelling parameters:

- The value of the ignition limit with igniters was set at 4.5% H_2. This is the value of hydrogen concentration in CV-006 at the time of ignition in SPECTRA. In MELCOR one cannot change the igniter temperature during calculations. The igniter is either on or off during the whole calculations.
- The combustion completeness was set to a constant value, equal to 0.99.
- The flame velocity was set to 2000 m/s, based on the value calculated by SPECTRA.

MELCOR input decks are provided in `\Z-INPUTS\H2\H2-5\MELCOR\H2-5.GEN` and `H2-5.COR`. Results are shown in visualization pictures in Figure 3-603 and Figure 3-604 and time dependent graphs in Figure 3-605 through Figure 3-608.

Hydrogen burn is initiated in CV-006 at about 15 s. In SPECTRA and MELCOR the burn is initiated at almost the same time - 15.1 s in SPECTRA (Figure 3-607) and 15.0 s in MELCOR (Figure 3-608). This shows that the gas flow and mixing is very similar in both codes.

The flame propagates quickly to the other volumes, where FTD and detonation occurs. Results of SPECTRA and MELCOR are very similar. Differences are caused by the use of a constant flame velocity in MELCOR and variable flame velocities in SPECTRA. Another important difference is the fact that the flammability limits are temperature-dependent in SPECTRA while in MELCOR the limits are constant. As a consequence in MELCOR only a single burn is observed, except for CV-006, where two burns occurred. In SPECTRA several burns are observed in all Control Volumes. In MELCOR the burn did propagate to all volumes except for CV-001, while in SPECTRA the burn propagated to all volumes.

In summary, although several differences exists between the MELCOR and the SPECTRA results, the general picture and the main parameters are quite similar. The differences are understandable in view of the different modelling assumptions in the two codes.

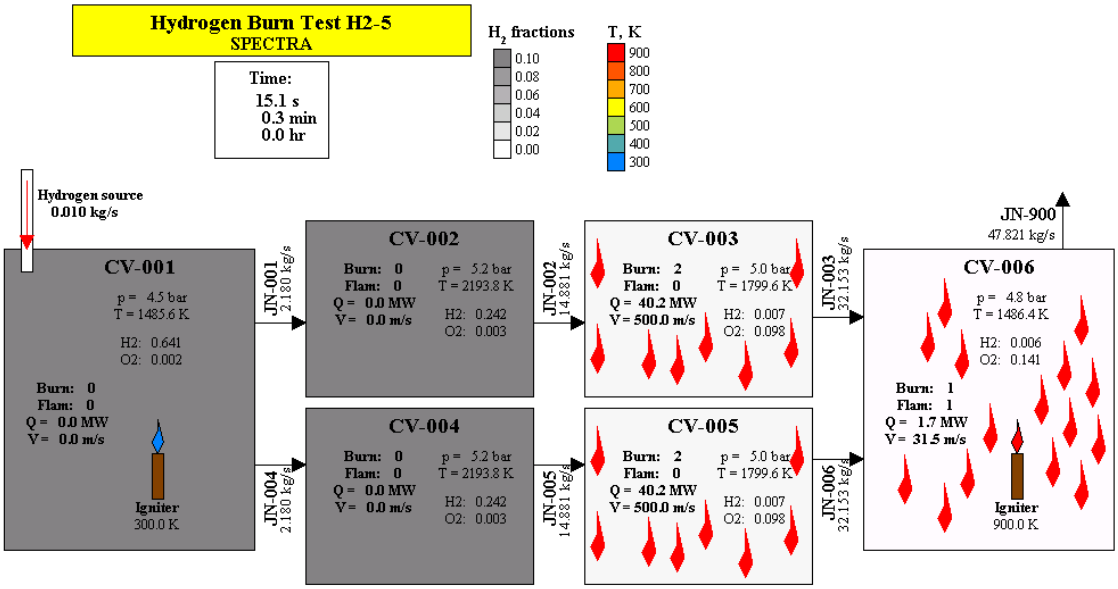

Figure 3-603 Test H2-5, visualization at t = 15.1 s, SPECTRA

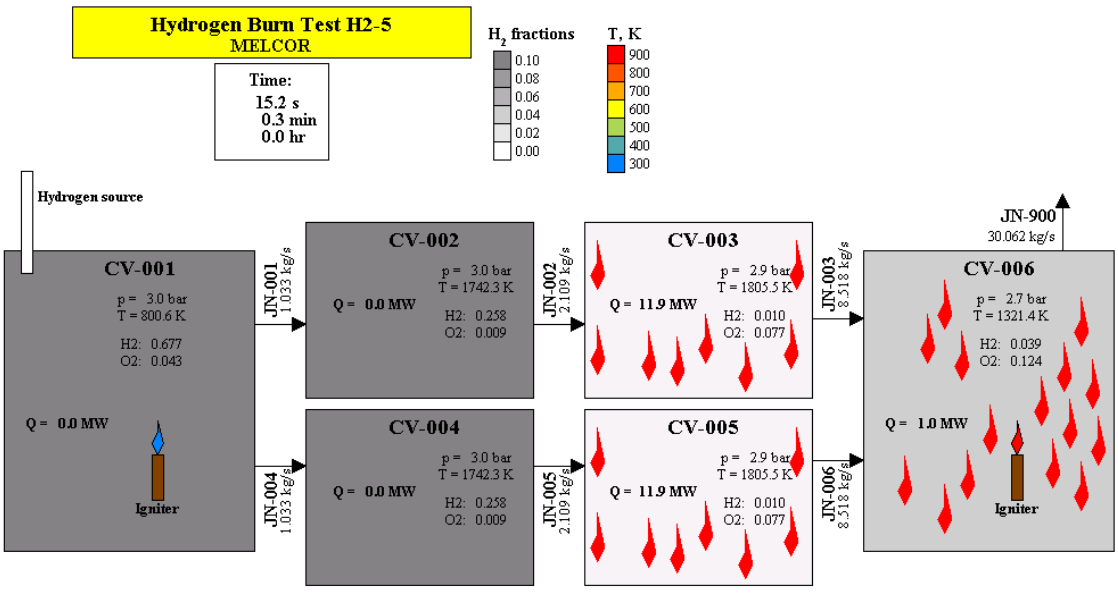

Figure 3-604 Test H2-5, visualization at t = 15.1 s, MELCOR

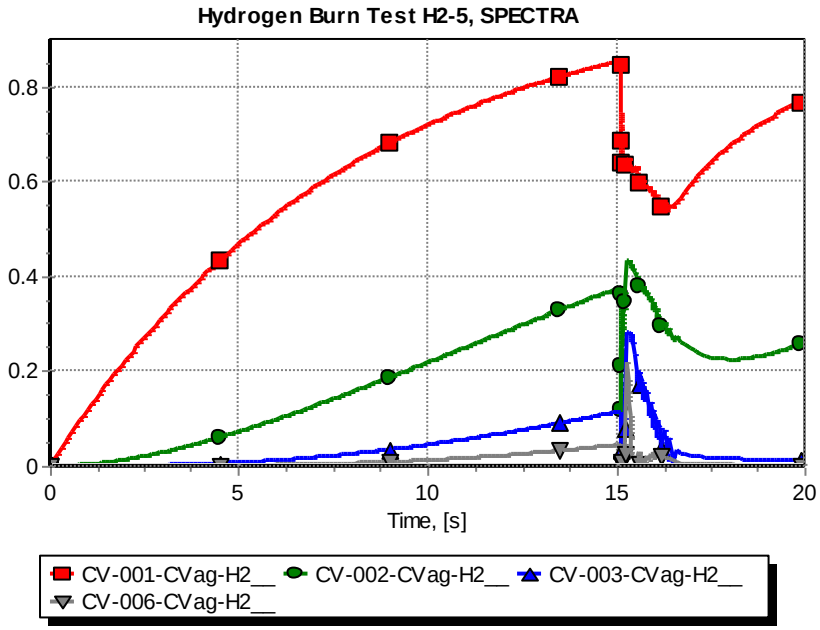

Figure 3-605 Hydrogen volume fractions, Test H2-5, SPECTRA

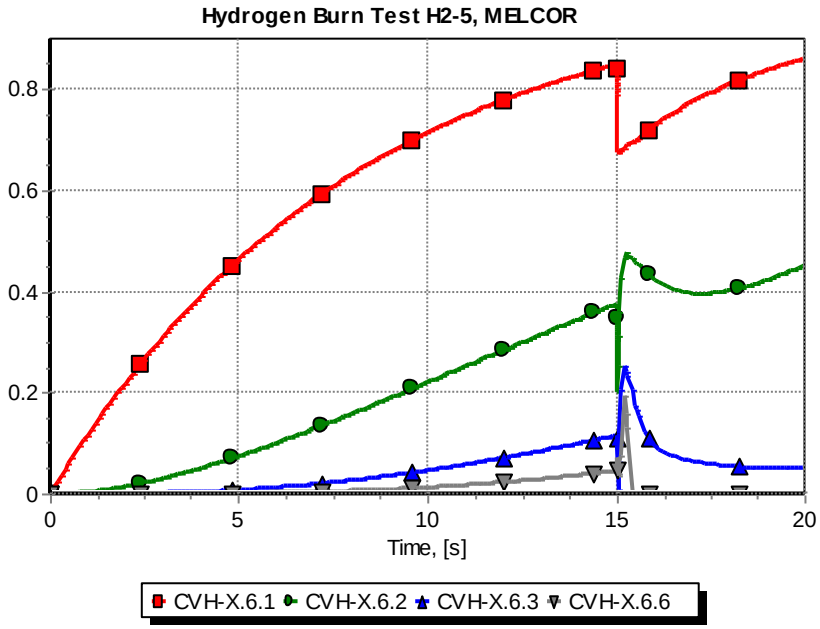

Figure 3-606 Hydrogen volume fractions, Test H2-5, MELCOR

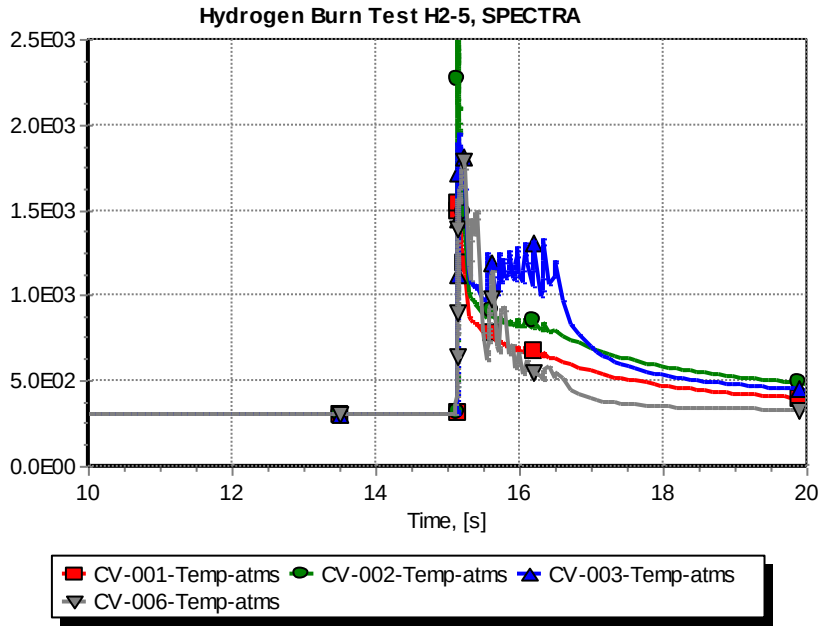

Figure 3-607 Temperatures, Test H2-5, SPECTRA

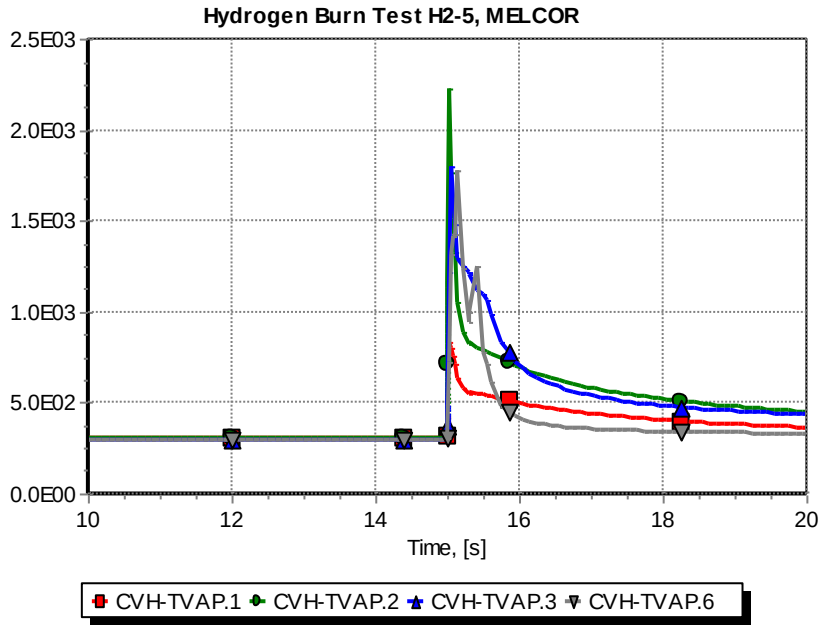

Figure 3-608 Temperatures, Test H2-5, MELCOR

3.12 Radioactive Particles Transport

3.12.1 Single Volume Deposition Test

A simple test model has been used to test the aerosol deposition in a single Control Volume. The model consists of CV-101, with atmospheric conditions (300 K, 1.0 bar, dry air). Verification was performed by comparison with MELCOR [20].

The aerosol size section boundaries were chosen as shown in Table 3-57. MELCOR uses the section boundaries – minimum and maximum diameter for each size section. SPECTRA on the other hand, requires representative diameters for each size section (the aerosol equations are formulated for these representative diameters and therefore the section boundary diameters are not being used). MELCOR assumes logarithmic size distribution within each section [20]. Therefore the representative section diameters for SPECTRA were calculated from:

$$D_r = \frac{\int_{D1}^{D2} D \log D \, dD}{\int_{D1}^{D2} \log D \, dD}$$

The values are shown in the table below. MELCOR prints the average aerosol diameter. When only a single size section is used, then the average diameter is a constant number. Using a quick MELCOR run with a single section (1 – 2 μm) it was verified that the average diameter was in this case indeed about 1.4 μm.

Table 3-57 Size section boundaries, (MELCOR) and representative diameters (SPECTRA)

	Section 1	Section 2	Section 3	Section 4	Section 5
Low D, μm	1.0	2.0	4.0	8.0	16.0
High D, μm	2.0	4.0	8.0	16.0	32.0
Repr. D_r, μm	1.44	2.87	5.73	11.4	22.8

An initial mass of 0.1 kg of the smallest section aerosols has been placed in CV-101. Two cases were considered:

- Case 1: spherical particles, the dynamic shape factors are equal to 1.0, and the agglomeration shape factors are equal to 1.0. The input deck is provided in: `\Z-TESTS\RT\DEP-GRAV\GRAV.SPE`

- Case 2: Linear chains of 8 beads – see [72], dynamic shape factors are equal to 2.22, and the agglomeration shape factors are equal to 2.66. The input deck is provided in: `\Z-TESTS\RT\DEP-GRAV\GRAV2.SPE`

Calculations were performed for 5000 s, using the maximum time step of 1.0 s. Both codes were using the maximum time step.

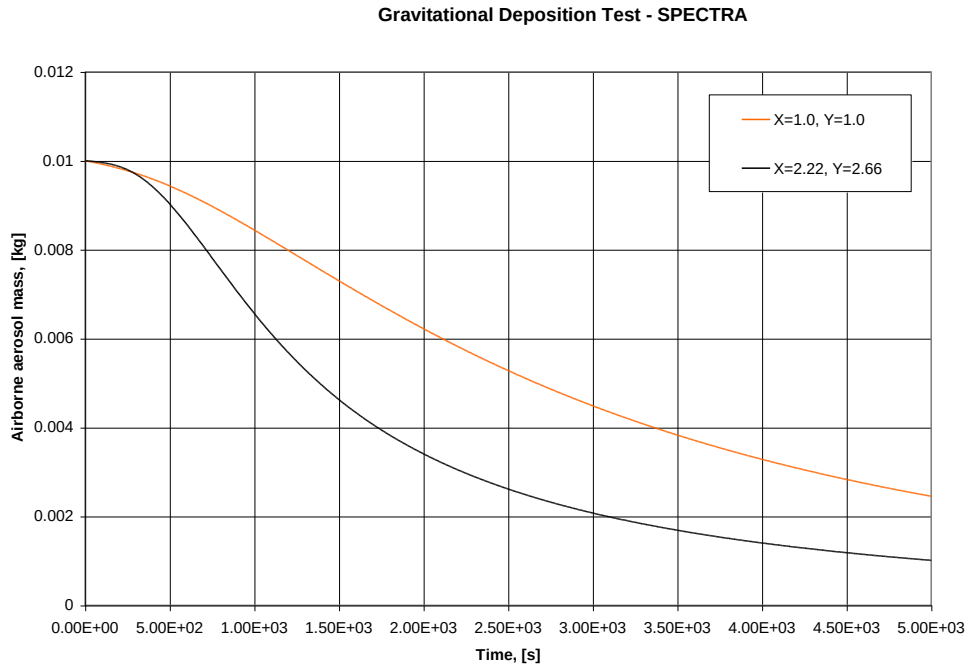

Figure 3-609 Single volume deposition test – SPECTRA.

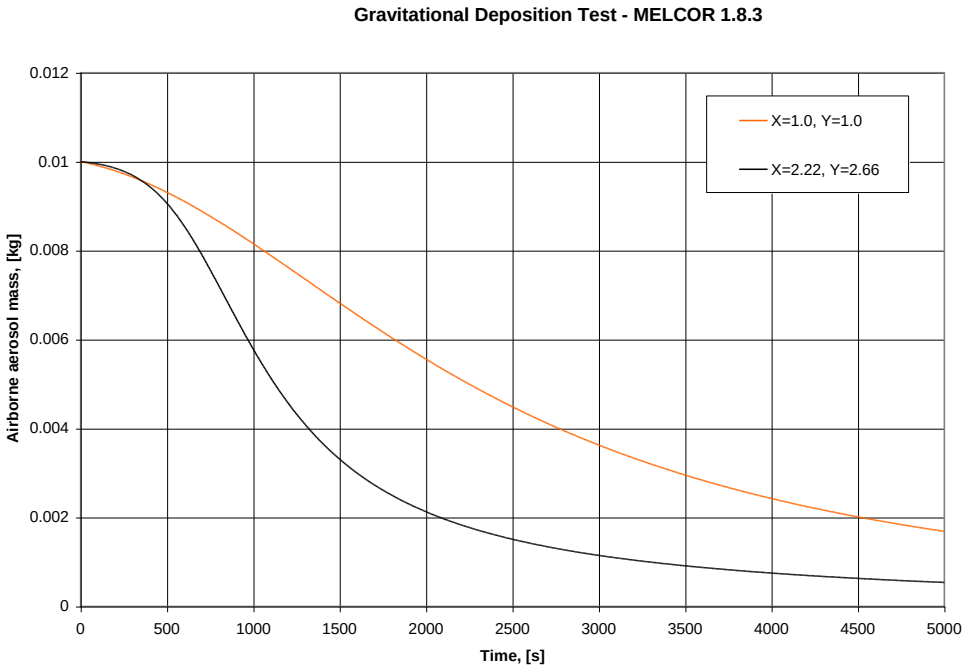

Figure 3-610 Single volume deposition test – MELCOR 1.8.3.

The calculated airborne aerosol masses are shown in Figure 3-609 and Figure 3-610. The deposition is governed by the coagulation process. The particles coagulate to form larger particles and those deposit quickly, mainly due to the gravitational deposition. Since the 8-bead chains from Case 2 coagulate faster than the spherical particles from Case 1, a faster deposition is observed for this case.

It is seen that in MELCOR the deposition is somewhat faster. This fact is a consequence of somewhat faster coagulation rate observed in the MELCOR calculations for this case (compare sections 3.12.9, 3.12.10 and 3.12.12).

The shape factors have strong influence on the particle coagulation and settling. In MELCOR the shape factors are the same for all size sections (only a single value is entered for the dynamic shape factor as well as the agglomeration shape factor). One would expect that the shape factors would vary from size section to size section, as the small particles coagulate to form larger particles with more complex shapes. Therefore in SPECTRA the shape factors are defined for each size section independently (see Volume 1 and 2).

3.12.2 Simple Coagulation Test

A simple test was set up to verify the coagulation rates. The set consists of a single Control Volume, CV-101 with two aerosol size sections. The section sizes were set up in such way that the section 2 volume is exactly twice larger than the volume of section 1 particles. Therefore every collision should result in transfer of particles from the size section 1 to the size section 2.

Verification was performed by comparison with MELCOR. The size section boundaries for MELCOR were defined as:

- Section 1: 1.00 – 1.26 μm.
- Section 2: 1.26 – 1.59 μm.

For SPECTRA the representative values were obtained using logarithmic average of the MELCOR boundaries:

- Section 1: 1.11 μm.
- Section 2: 1.40 μm.

Initially there is 1.0 kg of aerosols of section 1 present. To avoid deposition no structures are present in the SPECTRA model and in MELCOR the deposition area of the single (required) structure was set to 10^{-6} m^2. The input deck is provided in **\Z-TESTS\RT\COAG\COAG.SPE**.

In the present test the coagulation occurs mainly due to Brownian diffusion. The turbulent coagulation model is somewhat different in both codes. In order to provide clearer comparison the turbulent coagulation was eliminated by setting the turbulent energy dissipation density, ε_T, to a small value: 10^{-10}.

The results are shown in Figure 3-611 and Figure 3-612. The figures show the mass of airborne particles in section 1. The results are in good agreement.

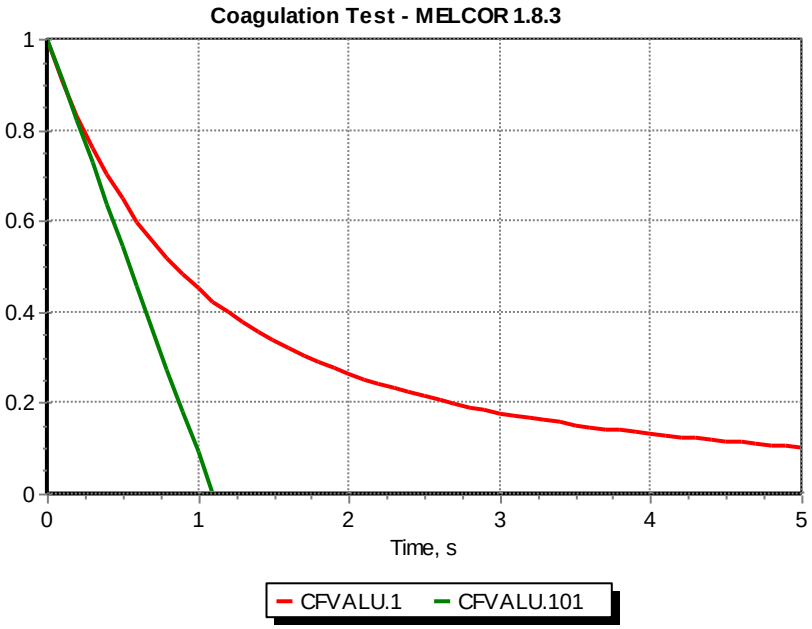

Figure 3-611 Coagulation test – MELCOR 1.8.3.

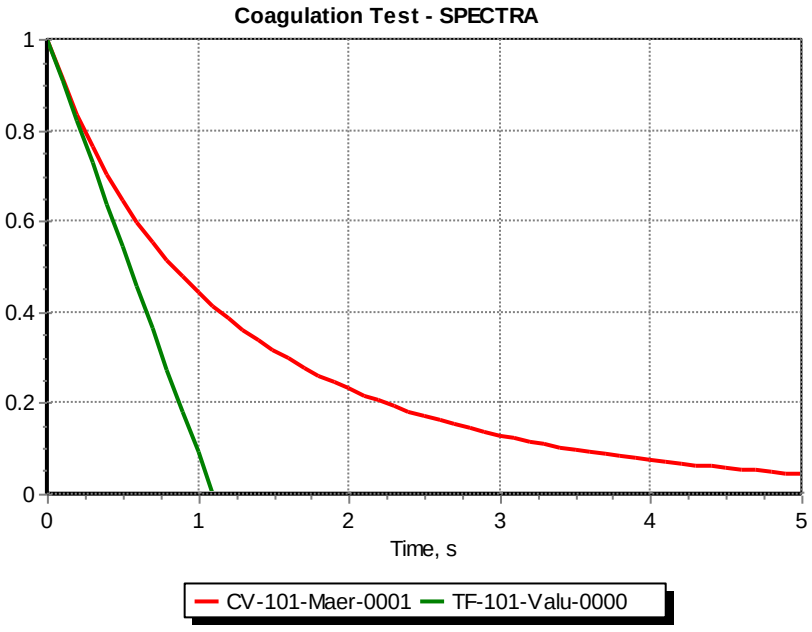

Figure 3-612 Coagulation test – SPECTRA.

As an extra verification of the coagulation model the initial rate of change of particle density in section 1 is calculated by hand. The rate of change of the section 1 particles due to coagulation is (see [79], equation 12.7, or Volume 1):

$$\frac{dn_1}{dt} = \frac{1}{2} K_{11} \cdot n_1^2 \cdot 2 = K_{11} \cdot n_1^2$$

The coagulation kernel, K_{11}, is equal to the Brownian coagulation and is taken from SPECTRA as about 7×10^{-16}. The number cannot be verified in the MELCOR output, nevertheless it is considered to be quite certain that this is the correct number, because SPECTRA contains three different models for calculating the coagulation kernels and they all give the value of between 6×10^{-16} and 7×10^{-16} for the particle size of about 1 μm (see Figure 2-148). The diffusion model gives the smallest values, and the validity of this model may be questioned for such small particles. Therefore the values obtained from the two other models: the slip flow and the Fuchs model (also used by MELCOR), were used to performed quick hand calculations. The slip flow model gives coagulation kernel of about 7.0×10^{-16}, the Fuchs model about 6.9×10^{-16}.

The particle density depends on the chosen diameter and is calculated below for the average and the minimum diameter:

$$n_1 = \frac{m_1}{\rho \pi d^3 / 6} = \frac{1.0}{1000 \cdot \pi (1.11\times10^{-6})^3 / 6} = 1.39\times10^{15}$$

The slope is calculated from:

$$\left(\frac{1}{n_1}\right)\frac{dn_1}{dt} = K_{11} \cdot n_1 = 6.9\times10^{-16} \cdot 1.39\times10^{15} = 0.96$$

If the slope was kept the same, then the time required to decrease the mass to zero would be equal to:

$$\Delta t = \frac{1}{0.96} = 1.1$$

The calculated slope was drawn in the figures showing SPECTRA and MELCOR calculations (green lines in Figure 3-611 and Figure 3-612). It is seen that the initial rate of change calculated by the codes is in good agreement with the value calculated by hand.

3.12.3 Aerosol Flow and Deposition Test 1

The aerosol flow and deposition test consists of six Control Volumes: CV-101, 102, 103, 104, 105, and CV-200. The last volume is held at constant conditions and it serves as a boundary condition. The volumes are connected with junctions JN-101, 102, 103, 104, and JN-105. Each CV has a horizontal structure (floor) for deposition. The floors are represented by The Solid Heat Conductors SC-101 through SC-105. In order to maximize the deposition a large area (100 m^2) was selected for each of these structures. The MELCOR model was set up in the same way.

According to the MELCOR convention FL (Flow Path) replaces JN and HS (Heat Structure) replaces SC. The SPECTRA and MELCOR models are visualized in Figure 3-613 and Figure 3-614 (the time-independent volume CV-200 is not shown in the picture).

The aerosol size section boundaries were chosen as in the previous test. The values are shown in Table 3-57. A source of gas and aerosols is present in volume CV-101. The source provides 0.11236 kg/s of gas (the mass source rate was selected to give the velocities of 1.0 m/s) and 1.0×10^{-4} kg/s of aerosols. The aerosol source provides aerosols of size section 1 (the smallest size) only.

The input deck is provided in **\Z-TESTS\RT\FLOW1\FLOW1.SPE**. Calculations were performed for 200 s, using the maximum time step of 1.0 s. Both codes were using the maximum time step.

Results of MELCOR and SPECTRA calculations are shown in Figure 3-613 through Figure 3-618. The state of the analyzed system at the end of the analyzed period is shown in Figure 3-613 and Figure 3-614. The figures show the masses and densities (only available in SPECTRA) of airborne aerosols, as well as deposited masses.

In the present test the gas velocities are low (~1.0 m/s - Figure 3-613 and Figure 3-614). The deposition occurs mainly due to gravitational settling – see the SPECTRA output for SC-105 at the end of the analyzed period:

```
SC-105 Left surface data at time :  2.00376E+02 (s)

 Deposition velocities
 Sec.     V-grav.      V-Brown      V-ther.      V-diff.      V-turb.      V-total
  No.       (m/s)        (m/s)        (m/s)        (m/s)        (m/s)        (m/s)
   1   7.1047E-05  1.9182E-06  0.0000E+00  0.0000E+00  2.3457E-07  7.3200E-05
   2   2.6766E-04  9.1278E-07  0.0000E+00  0.0000E+00  1.4294E-07  2.6872E-04
   3   1.0378E-03  4.4469E-07  0.0000E+00  0.0000E+00  8.8480E-08  1.0383E-03
   4   4.0500E-03  2.2038E-07  0.0000E+00  0.0000E+00  2.1964E-07  4.0505E-03
   5   1.6084E-02  1.0940E-07  0.0000E+00  0.0000E+00  3.4640E-06  1.6087E-02
```

The time evolutions of the airborne aerosol masses are shown in Figure 3-615 and Figure 3-616. The time evolutions of the deposited masses are shown in Figure 3-617 and Figure 3-618. It is concluded that MELCOR and SPECTRA results are in very good agreement.

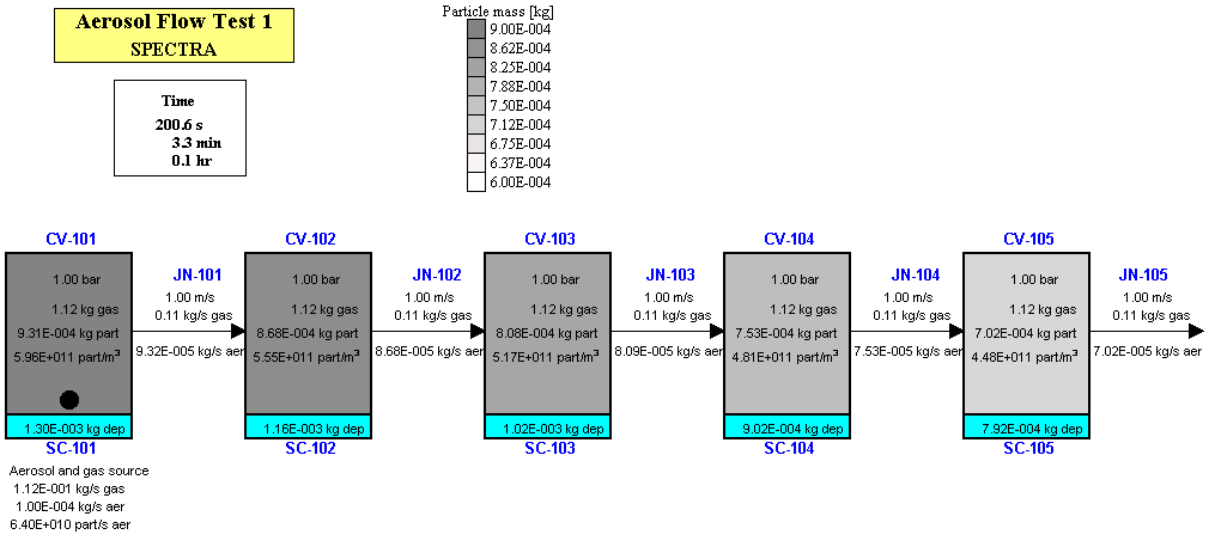

Figure 3-613 Aerosol flow and deposition test 1, SPECTRA.

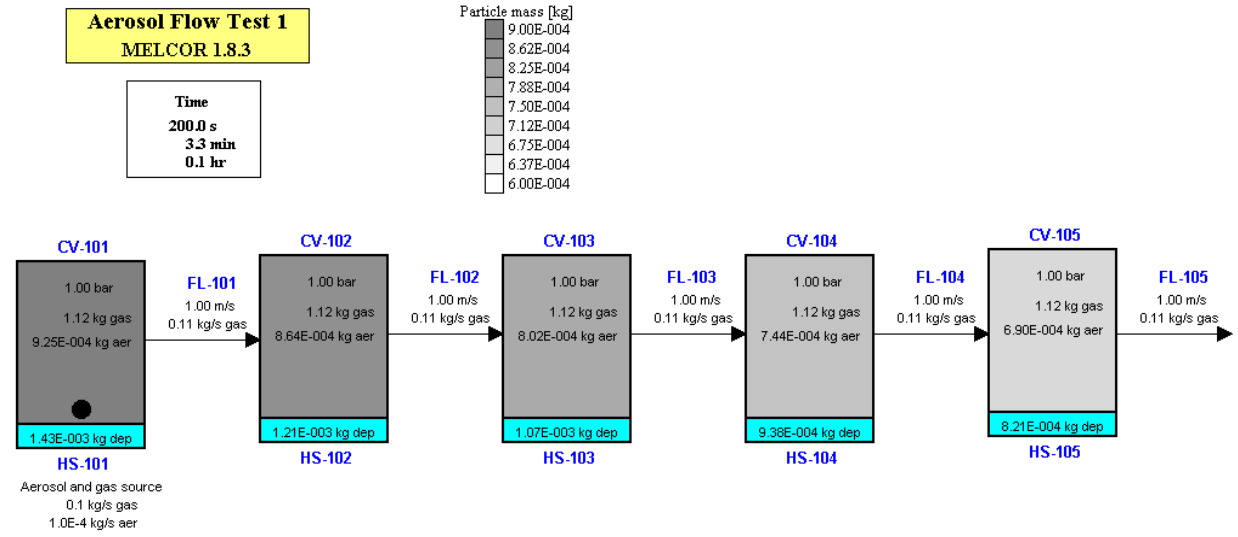

Figure 3-614 Aerosol flow and deposition test 1, MELCOR 1.8.3.

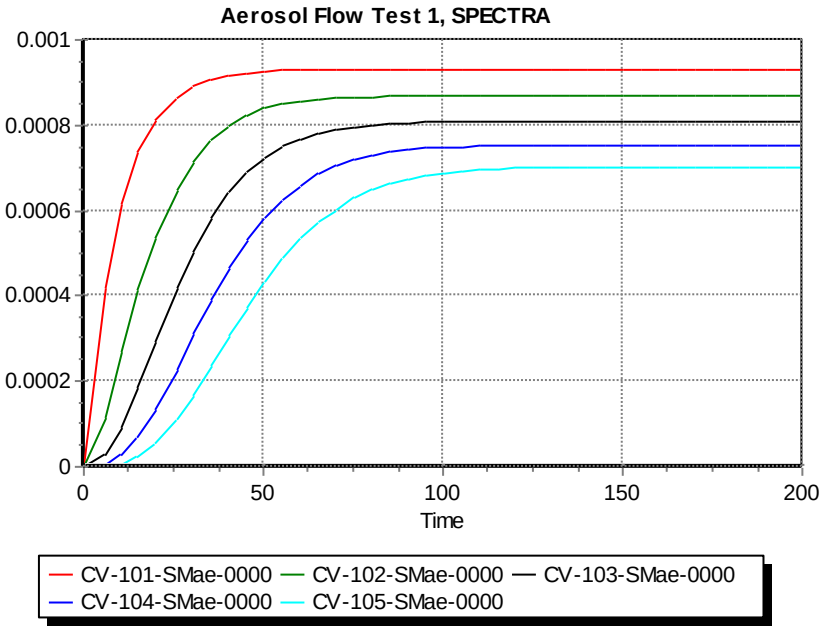

Figure 3-615 Aerosol flow and deposition test 1, airborne masses, SPECTRA.

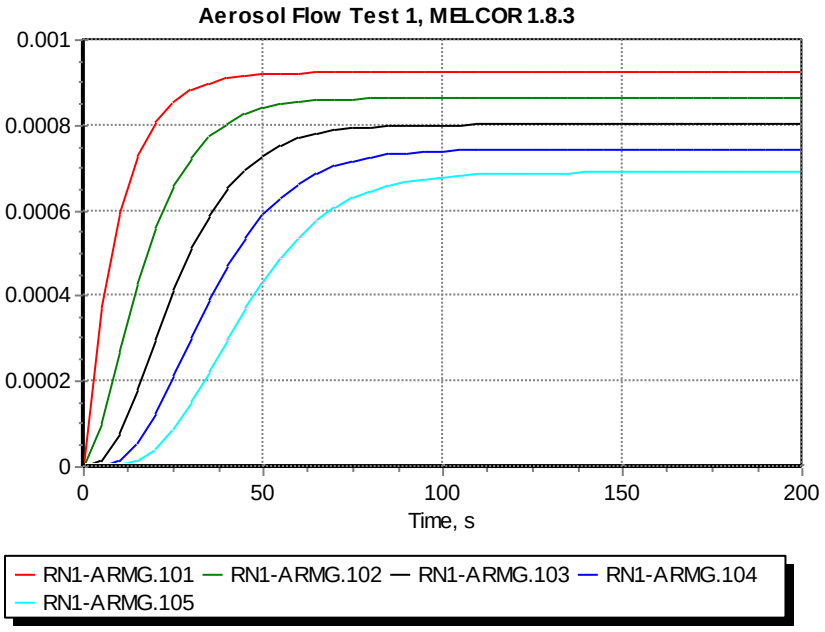

Figure 3-616 Aerosol flow and deposition test 1, airborne masses, MELCOR 1.8.3.

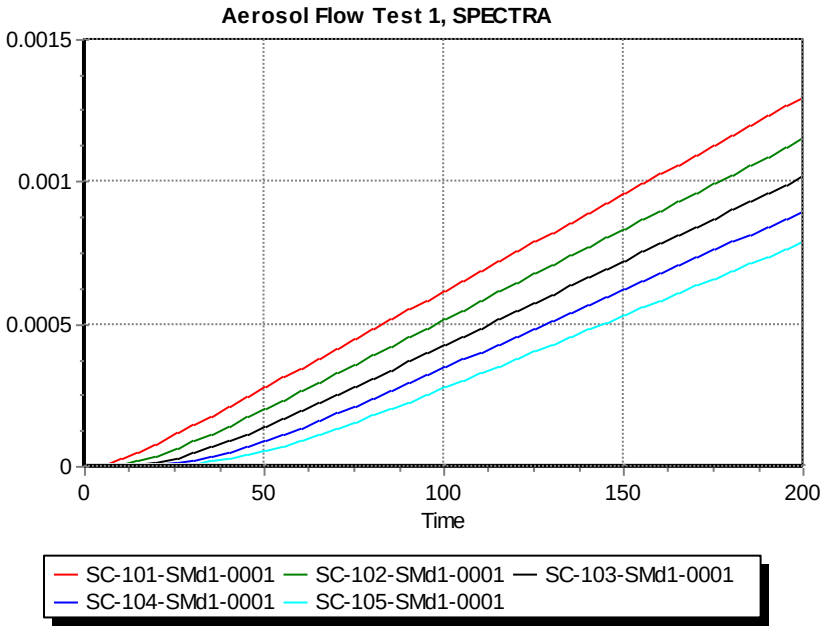

Figure 3-617 Aerosol flow and deposition test 1, deposited masses, SPECTRA.

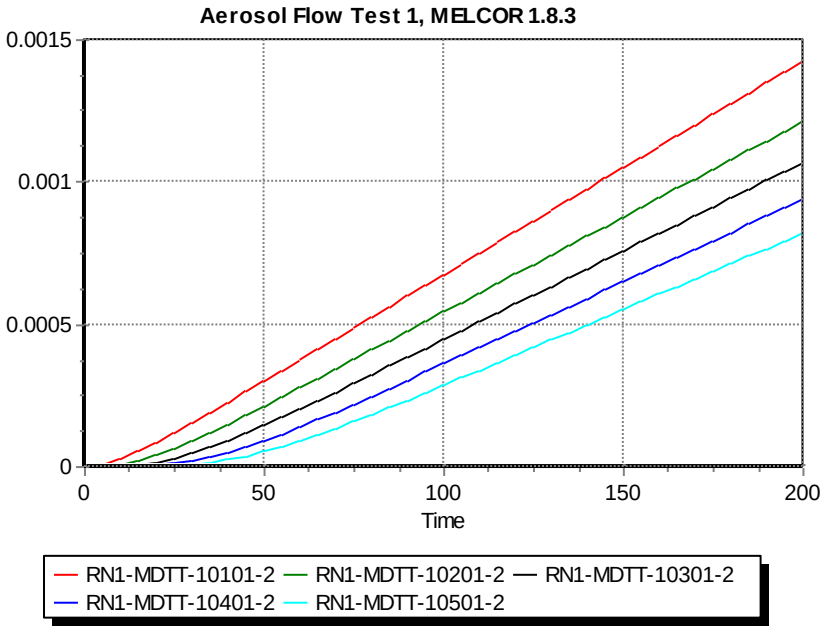

Figure 3-618 Aerosol flow and deposition test 1, deposited masses, MELCOR 1.8.3.

3.12.4 Aerosol Flow and Deposition Test 2

The aerosol flow and deposition test 2 is very similar to Test 1, described in the previous section. The only difference being the flow area changed from 0.1 m^2 to 0.005 m^2 for all Junctions and Control Volumes. The input deck is provided in **\Z-TESTS\RT\FLOW2\FLOW2.SPE**.

The gas velocities are about 20.0 m/s, instead of about 1.0 m/s in the previous test. As a consequence the turbulent deposition becomes important. The printout below shows the deposition velocities for SC-105:

```
SC-105 Left surface data at time :  2.00281E+02 (s)

 Deposition velocities
 Sec.     V-grav.      V-Brown      V-ther.      V-diff.      V-turb.      V-total
  No.       (m/s)        (m/s)        (m/s)        (m/s)        (m/s)        (m/s)
   1   7.1064E-05  1.9186E-06  0.0000E+00  0.0000E+00  6.1447E-05  1.3443E-04
   2   2.6769E-04  9.1289E-07  0.0000E+00  0.0000E+00  8.7194E-04  1.1405E-03
   3   1.0378E-03  4.4471E-07  0.0000E+00  0.0000E+00  1.3105E-02  1.4144E-02
   4   4.0502E-03  2.2039E-07  0.0000E+00  0.0000E+00  1.6131E-01  1.6536E-01
   5   1.6084E-02  1.0940E-07  0.0000E+00  0.0000E+00  1.5056E-01  1.6664E-01
```

The turbulent deposition is now of the same importance as the gravitational settling. The results are shown in Figure 3-619 and Figure 3-620. The deposition is clearly higher than in the previous case (compare Figure 3-617 and Figure 3-620 – note that the *y*-scale is different in those graphs). Consequently the stable airborne aerosol concentrations are somewhat lower (compare Figure 3-613 and Figure 3-619).

The MELCOR code does not model turbulent deposition – see [20]. The MELCOR Peer Review placed the omission of the turbulent deposition and the inertial deposition on the list of the most important models missing in MELCOR 1.8.3, as well as MELCOR 1.8.4 (see [20], RN Reference Manual, section 3.1).

In order to compare results of the test 2 with MELCOR, the SPECTRA calculation was repeated with the turbulent deposition disabled (the input parameter IJNART was set to –1, see Volume 2). The run was assigned a code name Test 2A. The input deck is provided in **\Z-TESTS\RT\FLOW2\FLOW2A.SPE**. The printout of the deposition velocities for SC-105 is shown below.

```
SC-105 Left surface data at time :  2.00567E+02 (s)

 Deposition velocities
 Sec.     V-grav.      V-Brown      V-ther.      V-diff.      V-turb.      V-total
  No.       (m/s)        (m/s)        (m/s)        (m/s)        (m/s)        (m/s)
   1   7.1064E-05  1.9186E-06  0.0000E+00  0.0000E+00  0.0000E+00  7.2982E-05
   2   2.6769E-04  9.1289E-07  0.0000E+00  0.0000E+00  0.0000E+00  2.6861E-04
   3   1.0378E-03  4.4471E-07  0.0000E+00  0.0000E+00  0.0000E+00  1.0383E-03
   4   4.0502E-03  2.2039E-07  0.0000E+00  0.0000E+00  0.0000E+00  4.0504E-03
   5   1.6084E-02  1.0940E-07  0.0000E+00  0.0000E+00  0.0000E+00  1.6084E-02
```

The MELCOR results of Test 2 and the SPECTRA results of Test 2A are shown in Figure 3-621 through Figure 3-624. It is seen that when the turbulent deposition is disabled, the results are in very good agreement.

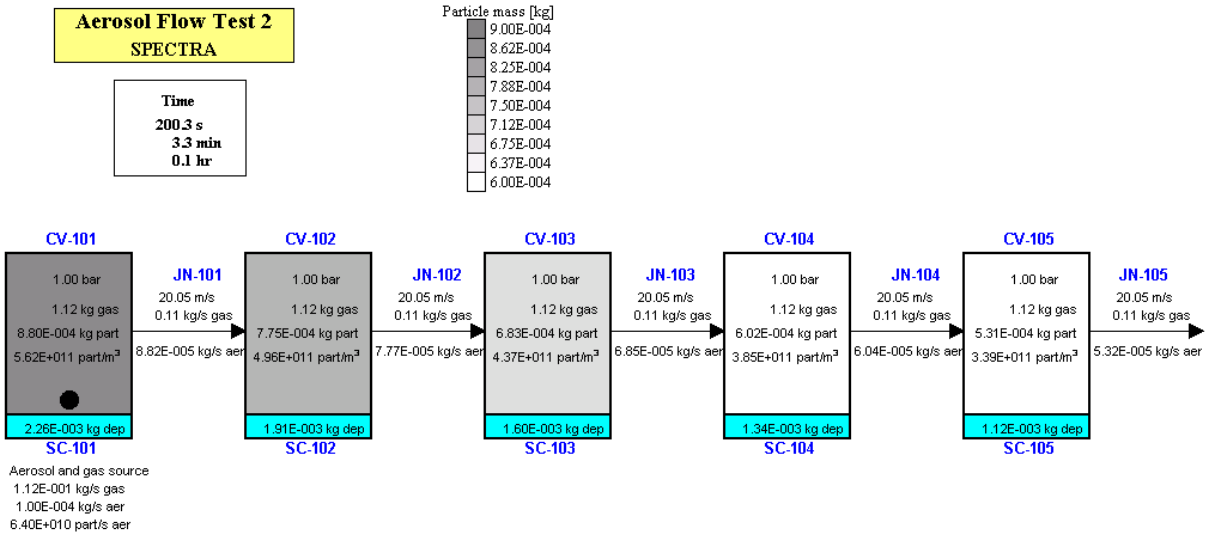

Figure 3-619 Aerosol flow and deposition test 2, SPECTRA.

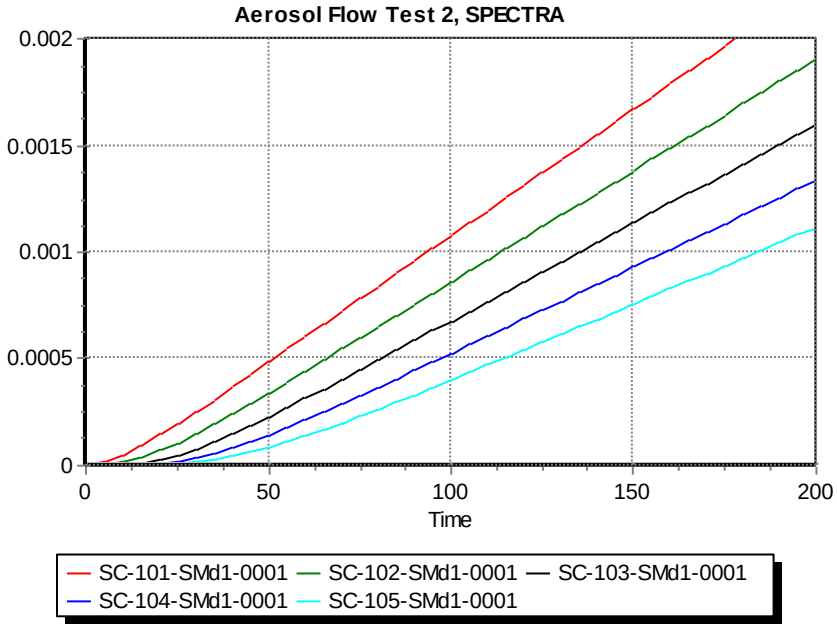

Figure 3-620 Aerosol flow and deposition test 2, deposited masses, SPECTRA.

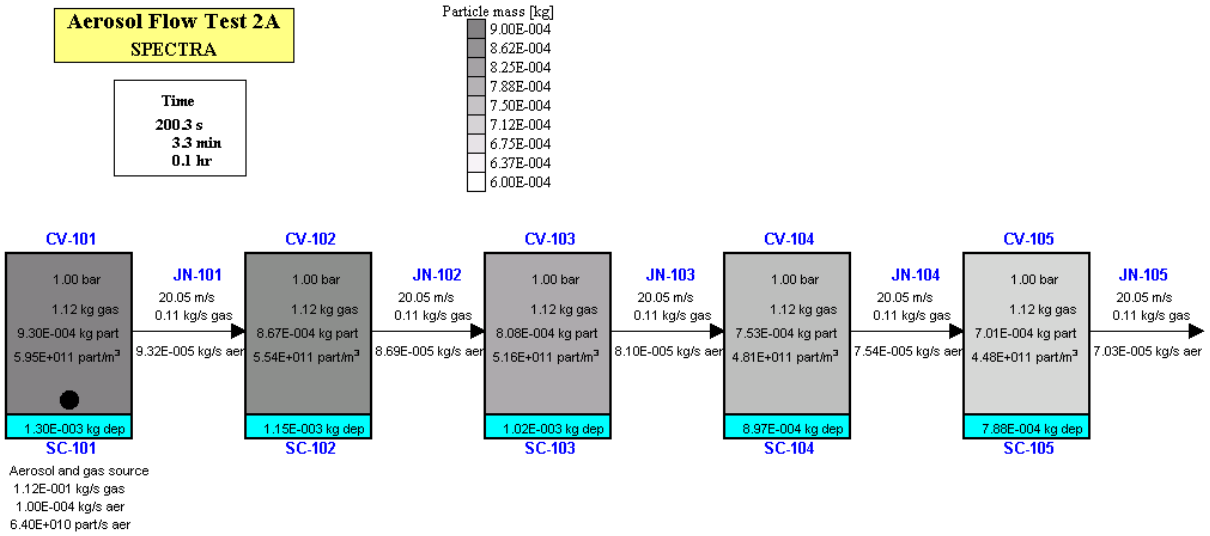

Figure 3-621 Aerosol flow and deposition test 2A (disabled turbulent deposition), SPECTRA.

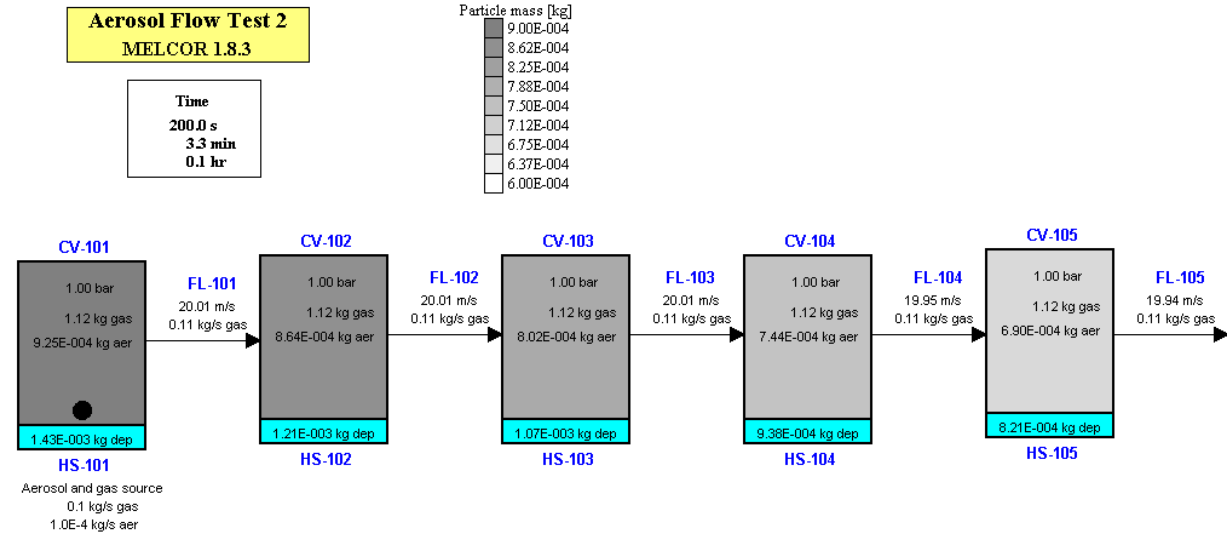

Figure 3-622 Aerosol flow and deposition test 2, MELCOR 1.8.3.

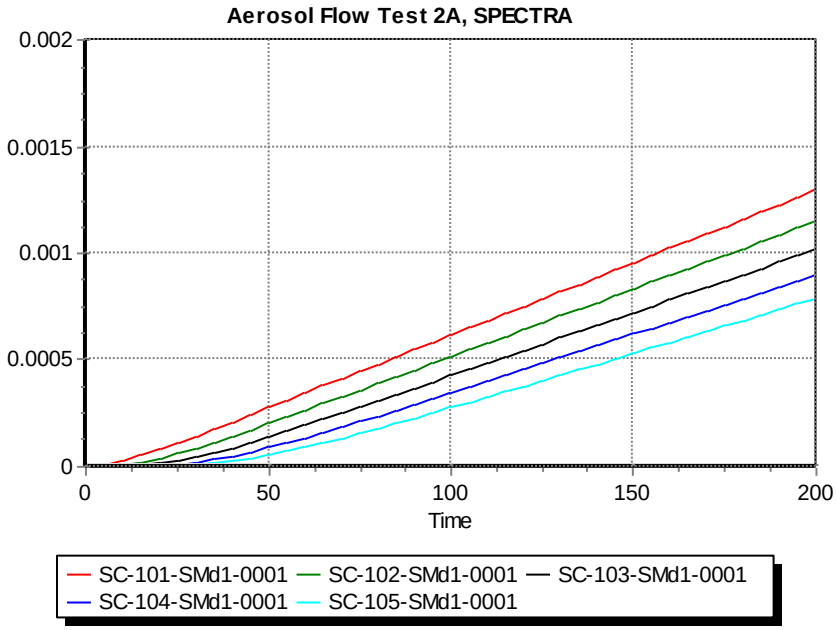

Figure 3-623 Deposited masses, Test 2A (disabled turbulent deposition), SPECTRA.

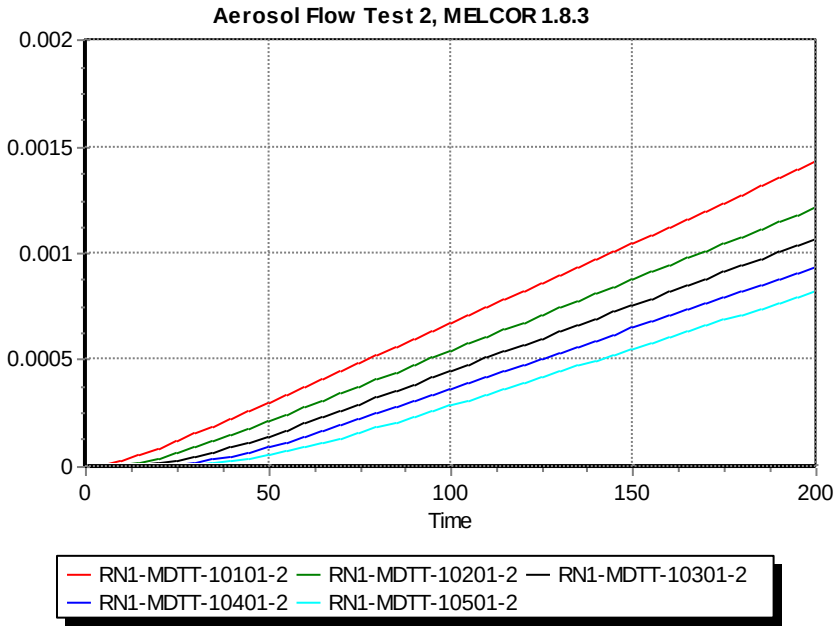

Figure 3-624 Deposited masses, Test 2, MELCOR 1.8.3.

3.12.5 Thermophoresis Test 1

The thermophoresis test is very similar to the flow and deposition test, described in section 3.12.3 and 3.12.4. The present test is aiming at investigating thermophoresis, so the conditions are set in such way that thermophoresis is maximized and other deposition mechanisms are minimized. To achieve this goal, the following changes were made:

- The walls are vertical, to eliminate gravitational deposition.
- The walls are kept at 300 K (external cooling) while the gas source is at 500 K, to maximize thermophoretic deposition.
- The walls have smaller area (1.0 m^2) in order to limit total heat exchange and the decrease of gas temperature along the flow.
- To provide good comparison between SPECTRA and MELCOR, the Brock correlation is used in the SPECTRA run.

The input deck is provided in **\Z-TESTS\RT\THERMO\THERMO.SPE**. The calculated deposition was checked that indeed thermophoresis had a dominant effect. For example, the printout below shows the deposition velocities for SC-105:

```
SC-105 Left surface data at time :  2.00228E+02 (s)

 Deposition velocities
 Sec.     V-grav.      V-Brown      V-ther.      V-diff.      V-turb.      V-total
  No.       (m/s)        (m/s)        (m/s)        (m/s)        (m/s)        (m/s)
   1   0.0000E+00  2.3031E-06  6.5631E-04  0.0000E+00  1.0550E-08  6.5862E-04
   2   0.0000E+00  1.0613E-06  4.7792E-04  0.0000E+00  6.2924E-09  4.7899E-04
   3   0.0000E+00  5.0788E-07  3.0523E-04  0.0000E+00  3.8487E-09  3.0574E-04
   4   0.0000E+00  2.4933E-07  1.8032E-04  0.0000E+00  2.3945E-09  1.8057E-04
   5   0.0000E+00  1.2316E-07  1.0319E-04  0.0000E+00  1.4960E-09  1.0331E-04
```

SPECTRA results are shown in Figure 3-625 and Figure 3-626. The MELCOR results for this case are shown in Figure 3-627, Figure 3-629, and Figure 3-631. Comparison of deposited masses shows that in SPECTRA the deposition rates are clearly higher. This should be expected because the coefficients in Brock correlation are different in SPECTRA than in MELCOR (see section 2.8.3).

	SPECTRA	MELCOR
C_s =	1.17	0.75
C_t =	2.50	2.25

To compare SPECTRA and MELCOR results using the same coefficients, the test was re-calculated by SPECTRA using the coefficients from MELCOR. The results are shown in Figure 3-628, Figure 3-630, and Figure 3-632. The results are in very good agreement; the deposition is slightly higher in SPECTRA than in MELCOR.

An interesting effect in this test is the increase of aerosol concentrations along the flow. This fact is related to the gas density increase, caused by the decrease of gas temperature along the flow. The effect is clearly visible in both codes (see Figure 3-625, Figure 3-627, Figure 3-628, Figure 3-631, and Figure 3-632. In absence of deposition, the stable concentrations would increase in such way that the products of the particle velocity (decreasing along the flow), and the particle concentrations (increasing along the flow) would be everywhere the same.

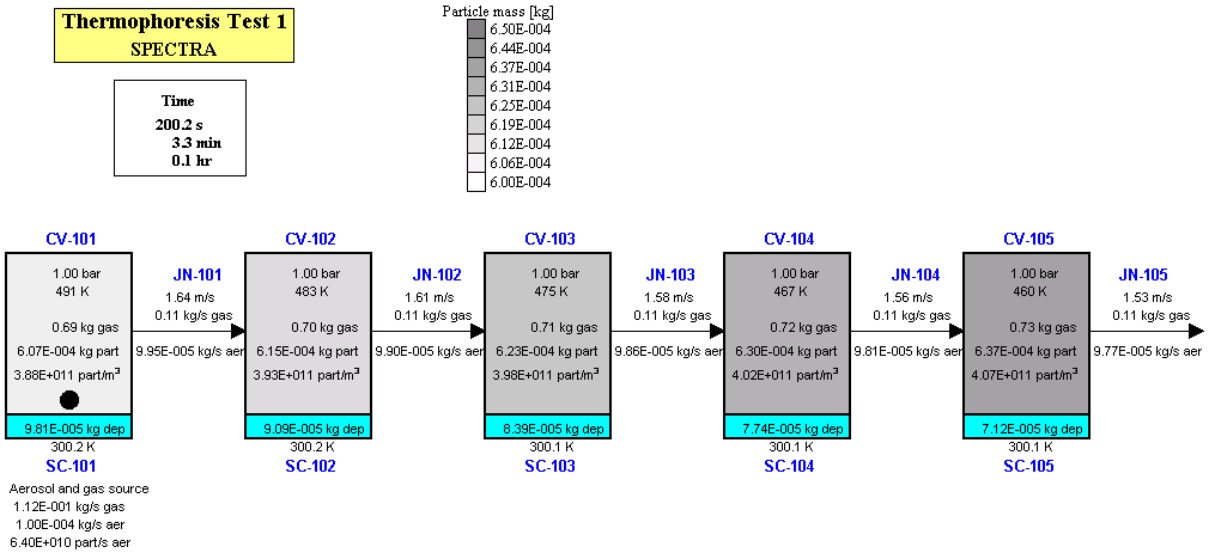

Figure 3-625 Thermophoresis Test 1, SPECTRA, default constants (C_s = 1.17, C_t = 2.5).

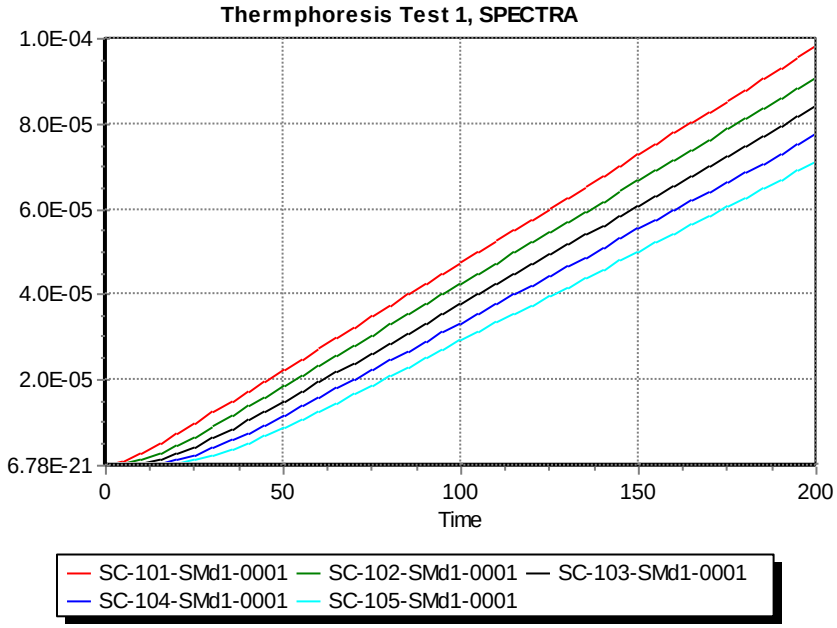

Figure 3-626 Deposited masses, SPECTRA, default constants (C_s = 1.17, C_t = 2.5).

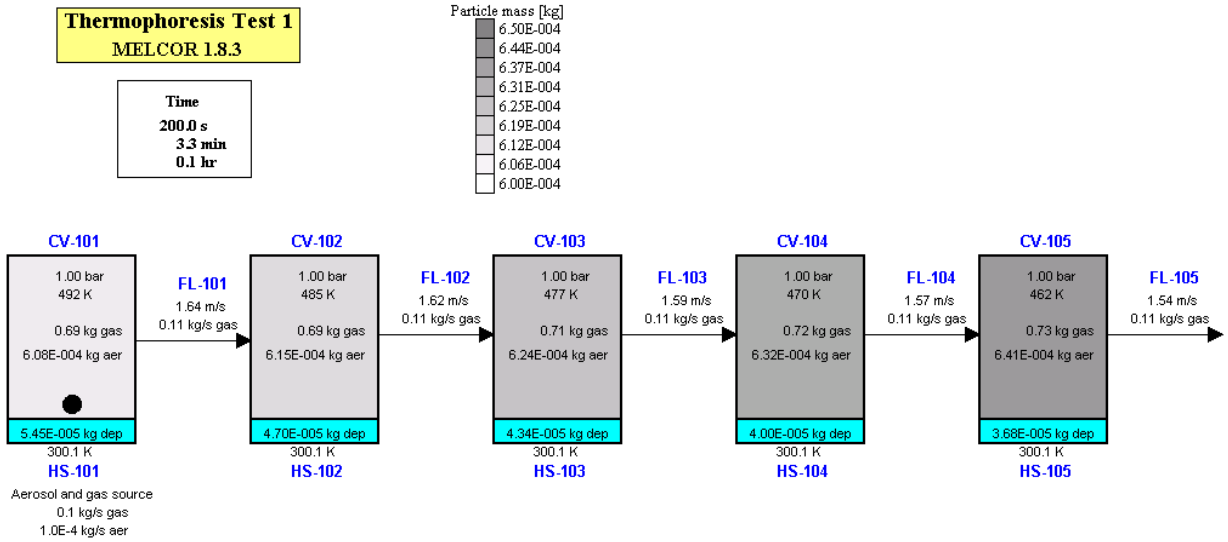

Figure 3-627 Thermophoresis Test 1, MELCOR 1.8.3 (C_s = 0.75, C_t = 2.25).

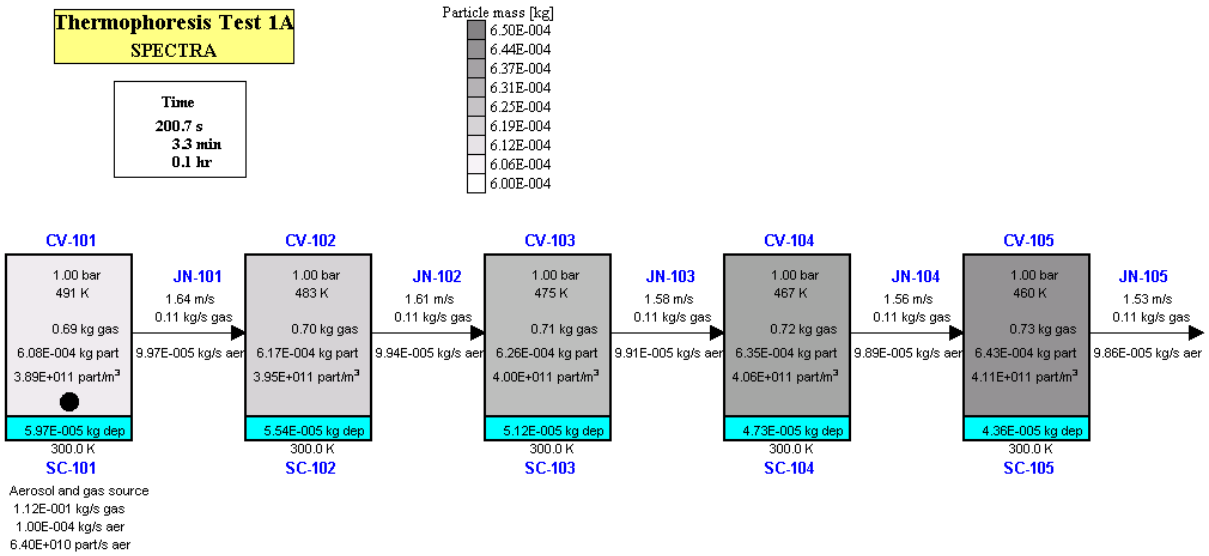

Figure 3-628 Thermophoresis Test 1A (C_s = 0.75, C_t = 2.25), SPECTRA.

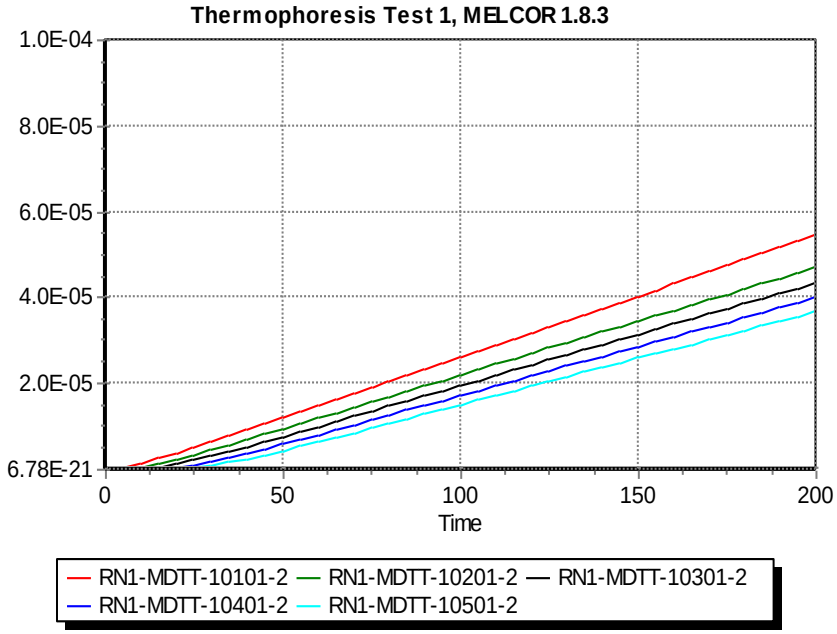

Figure 3-629 Deposited masses, Test 1, MELCOR 1.8.3 (C_s = 0.75, C_t = 2.25)

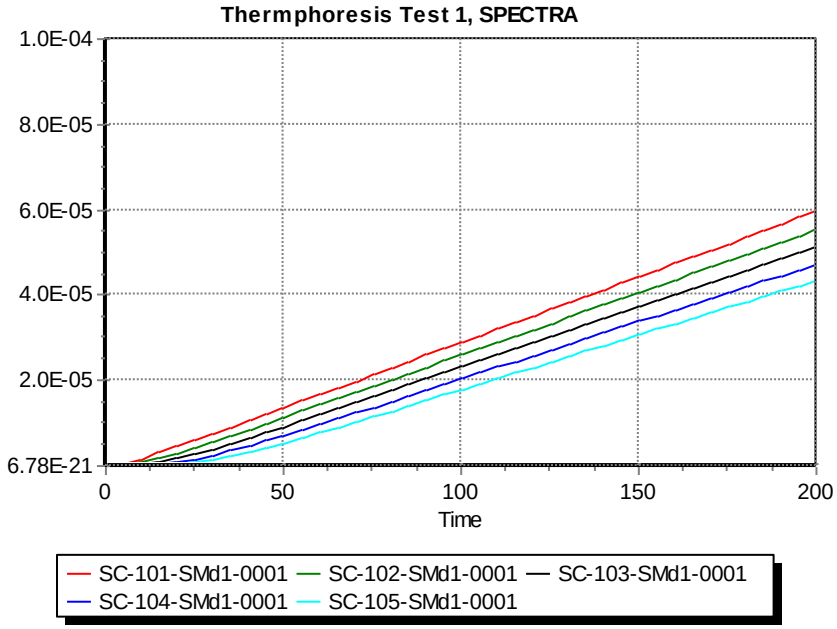

Figure 3-630 Deposited masses, Test 1A (C_s = 0.75, C_t = 2.25), SPECTRA.

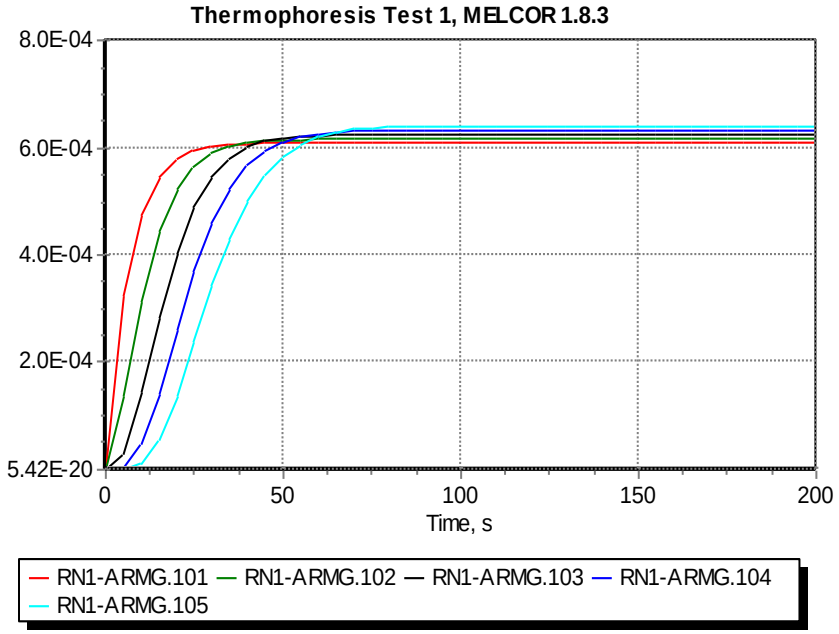

Figure 3-631 Airborne masses, Test 1, MELCOR 1.8.3 (C_s = 0.75, C_t = 2.25)

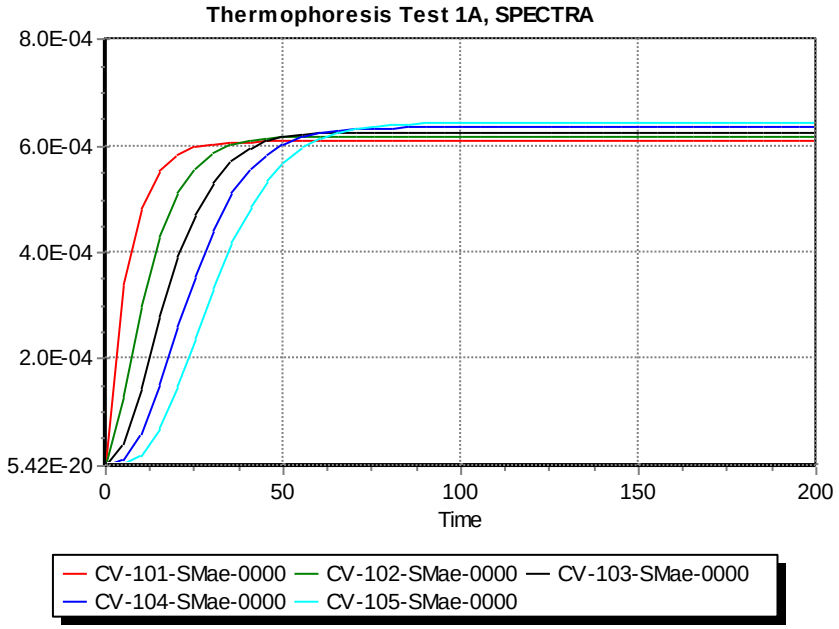

Figure 3-632 Airborne masses, Test 1A (C_s = 0.75, C_t = 2.25), SPECTRA.

3.12.6 Inertial Impaction in Pipe Bends

Inertial impaction in pipe bends was investigated by Pui et al. [117]. Table 2 in this reference shows data for:

- stainless steel tubes with inner diameter of 5.03 mm and 8.51 mm
- glass tubes with inner diameter of 0.93 mm and 3.95 mm

For the present comparison the cases with 3.95 mm and 5.03 mm are considered. These results are presented in sections 3.12.6.1 and 3.12.6.2 respectively.

3.12.6.1 Pui et al. Tests, *D* = 3.95 mm

A simple model of a 3.95 mm pipe with a bend has been prepared. Calculations were performed using the correlations of Pui and McFarland (see section 3.12.6.3 for an overview of correlations). The input decks are provided in:

- `\Z-TESTS\RT\IN-IM\Bend-Pui\Bend-Pui-395.Pui.SPE` Pui correlation
- `\Z-TESTS\RT\IN-IM\Bend-Pui\Bend-Pui-395.McF.SPE` McFarland correlation

Results are provided in Figure 3-633, Figure 3-634, and Figure 3-635. It is seen that the Pui correlation provides more conservative (higher) collection efficiency and gives better agreement with the considered data.

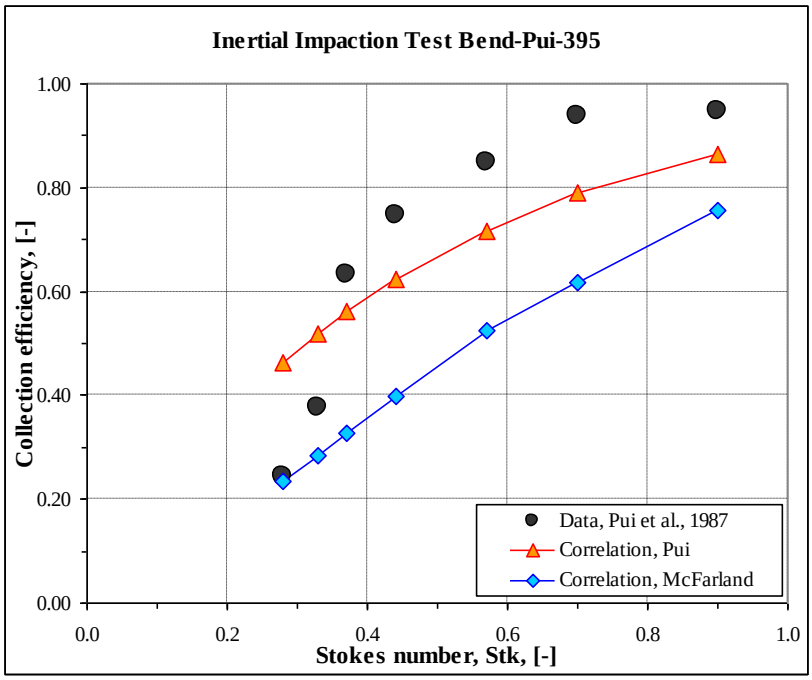

Figure 3-633 Pui et al. tests, *D* = 3.95 mm

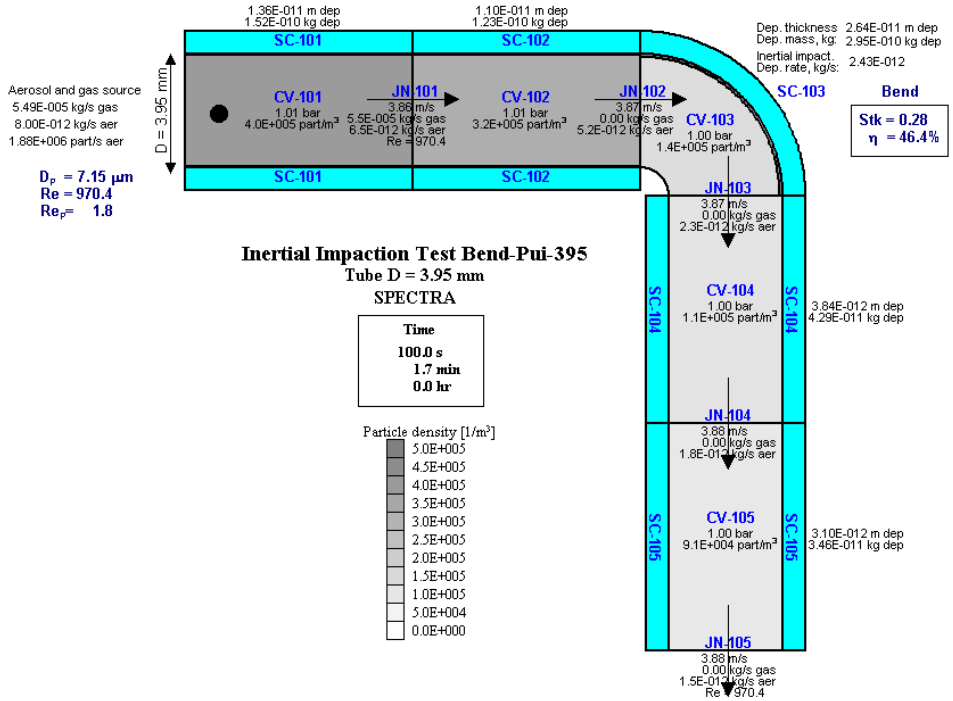

Figure 3-634 Pui et al. tests, *D* = 3.95 mm - results obtained with Pui et al. correlation

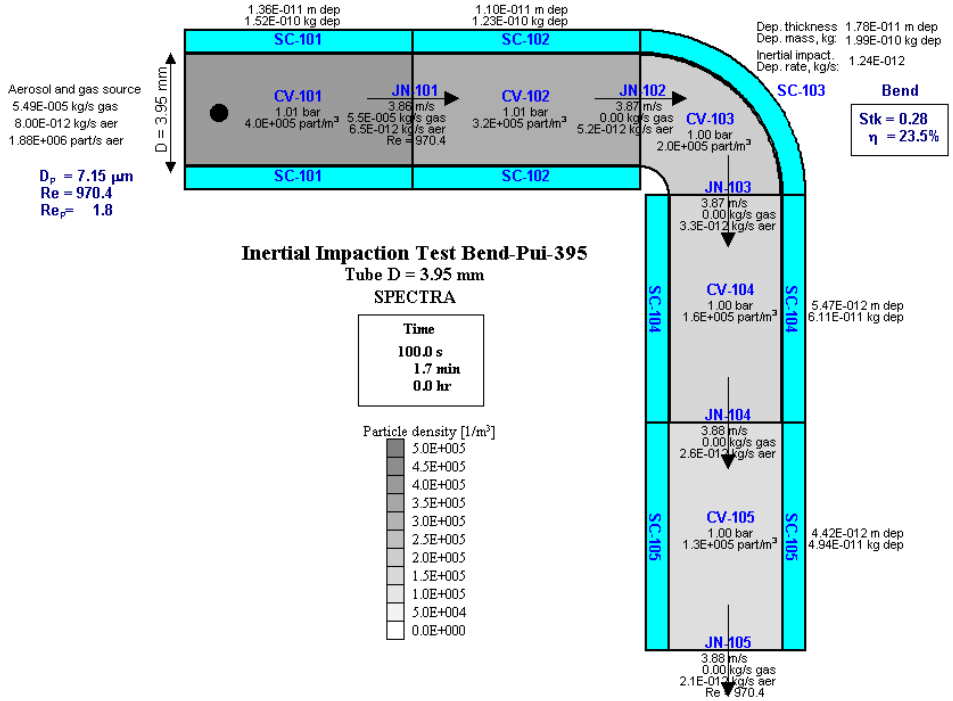

Figure 3-635 Pui et al. tests, *D* = 3.95 mm - results obtained with McFarland correlation

3.12.6.2 Pui et al. Tests, *D* = 5.03 mm

A simple model of a 5.03 mm pipe with a bend has been prepared. Calculations were performed using the correlations of Pui and McFarland (see section 3.12.6.3 for an overview of correlations). The input decks are provided in:

- `\Z-TESTS\RT\IN-IM\Bend-Pui\Bend-Pui-503.Pui.SPE` Pui correlation
- `\Z-TESTS\RT\IN-IM\Bend-Pui\Bend-Pui-503.McF.SPE` McFarland correlation

Results are provided in Figure 3-636, Figure 3-637, and Figure 3-638. It is seen that the Pui correlation provides more conservative (higher) collection efficiency and gives better agreement with the considered data.

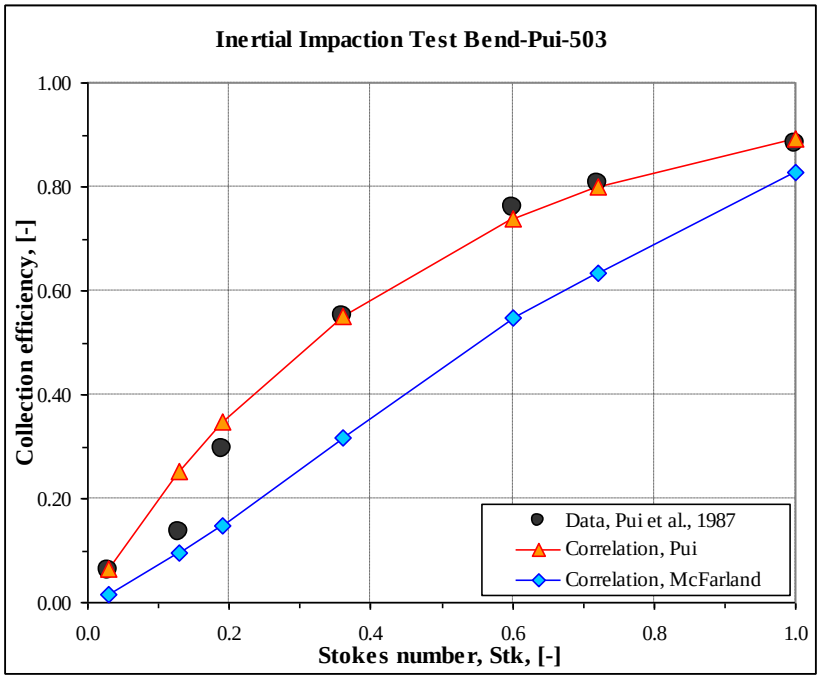

Figure 3-636 Pui et al. tests, *D* = 5.03 mm

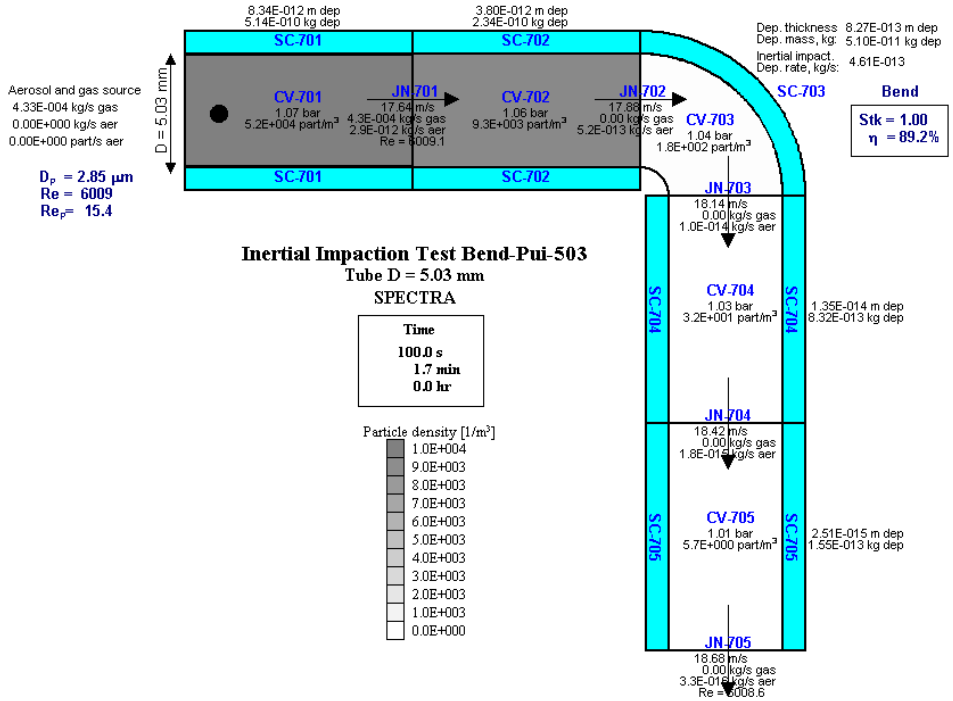

Figure 3-637 Pui et al. tests, *D* = 5.03 mm - results obtained with Pui et al. correlation

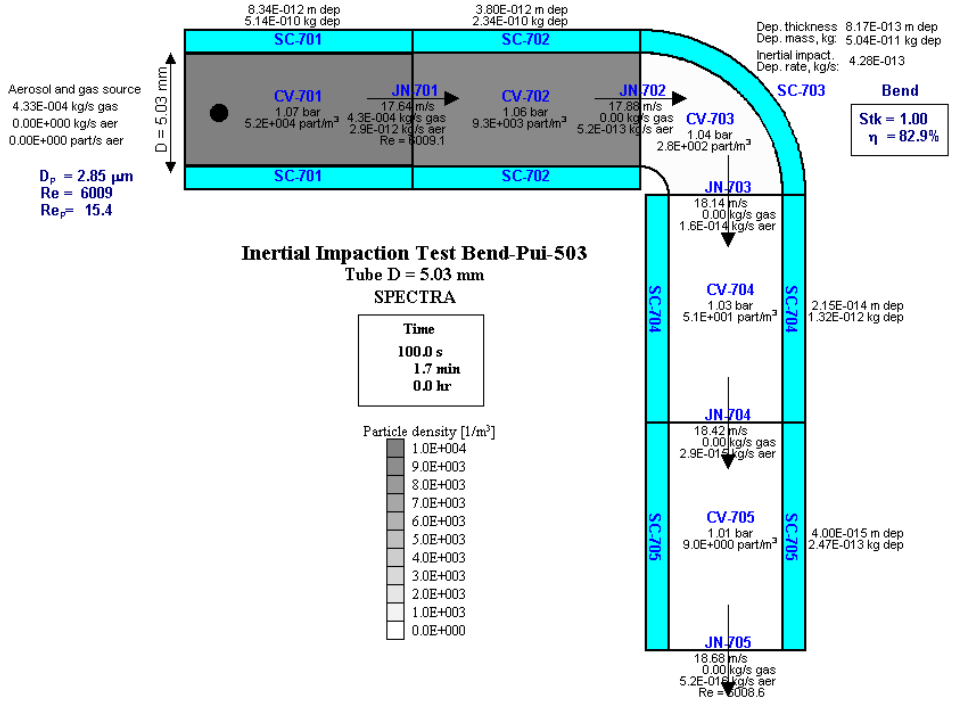

Figure 3-638 Pui et al. tests, *D* = 5.03 mm - results obtained with McFarland correlation

3.12.6.3 Overview of Pipe Bend Correlations

This section provides an overview of several correlations and comparison with experimental data of Pui et al. [117]. The following correlations are considered.

- Pui et al. correlation [117]:

$$\eta = 1 - 10^{-0.963 Stk}$$

- McFarland correlation [118]:

$$\eta = 0.01 \cdot \exp\left(\frac{4.61 + a \cdot \theta \cdot Stk}{1 + b \cdot \theta \cdot Stk + c \cdot \theta \cdot Stk^2 + d \cdot \theta^2 \cdot Stk} \right)$$

with:

$$a = -0.9526 - 0.05686 \cdot R_0$$

$$b = \frac{-0.297 - 0.0174 \cdot R_0}{1 - 0.07 \cdot R_0 + 0.01717 \cdot R_0^2}$$

$$c = -0.306 + \frac{1.895}{\sqrt{R_0}} - \frac{2.0}{R_0}$$

$$d = \frac{0.131 - 0.0132 \cdot R_0 + 0.000383 \cdot R_0^2}{1 - 0.129 \cdot R_0 + 0.136 \cdot R_0^2}$$

- Langmuir and Blodgett correlation (see [119], eq. 3):

$$\eta = \frac{Stk^2}{(Stk + 0.25)^2}$$

- Stempniewicz-Komen (S-K) correlation:

$$\eta = \eta_{\max} \cdot \left(1 - \exp\left[-A \cdot Stk^B \right] \right)$$

with:

$$\eta_{\max} = 0.95$$

$$A = 7.0$$

$$B = 2.0$$

This correlation was recently developed at NRG, to provide a good match with the data of Pui et al. [117].

SPECTRA input files are located in **\Z-INPUTS\RT\IN-IM\Bemd-Pui**. Results are provided in Figure 3-639 and Figure 3-640. It is seen that the S-K correlation provides more conservative (higher) collection efficiency and gives better agreement with the considered data.

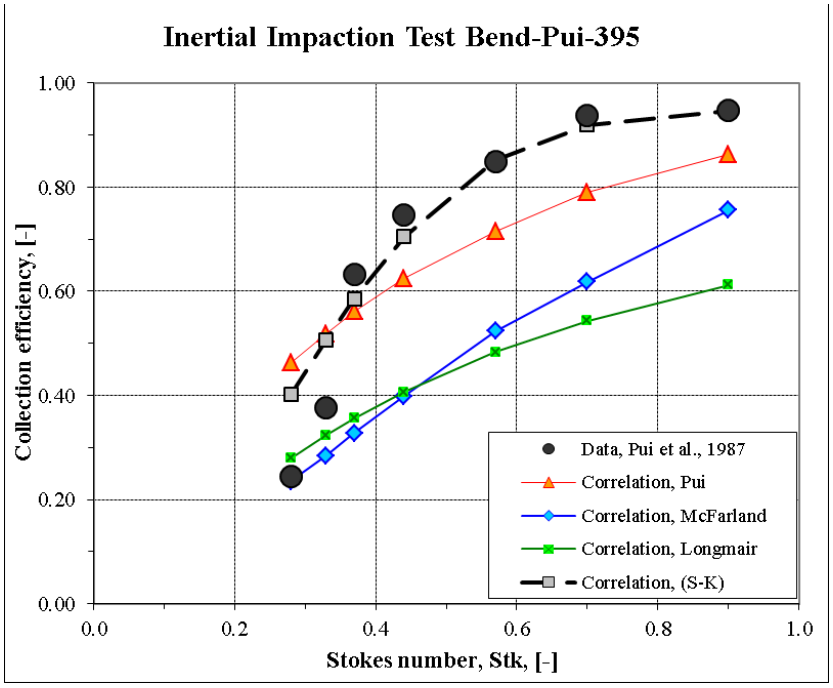

Figure 3-639 Pui et al. tests, D = 3.95 mm - comparison of correlations with data

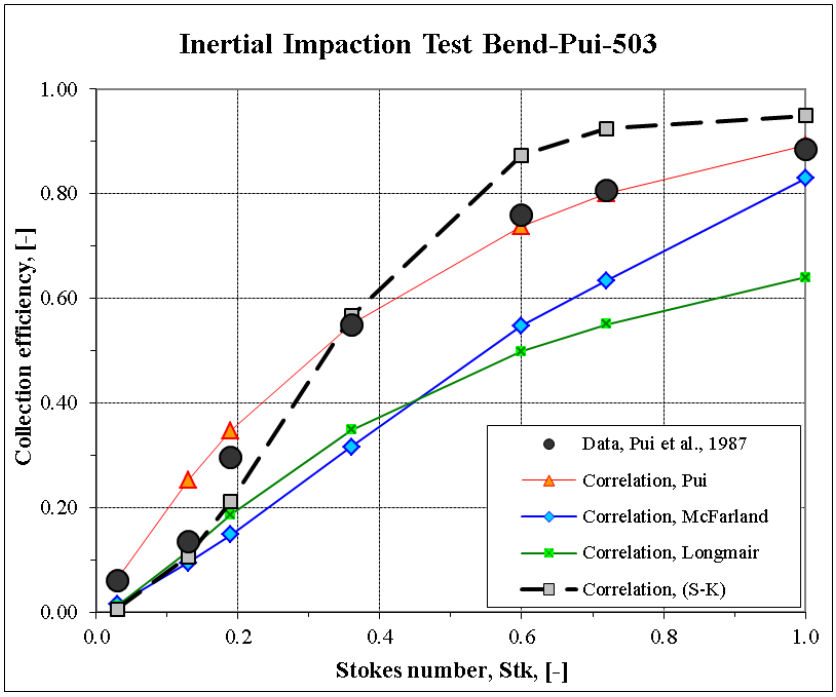

Figure 3-640 Pui et al. tests, D = 5.03 mm - comparison of correlations with data

3.12.7 Inertial Impaction in Tube Bundles

In the past, the inertial impaction on tube bundles has been studied for refrigerant tubes and finned tube heat exchangers [120]. Recently, the inertial impaction has been investigated both experimentally and theoretically for the geometry of a typical steam generator of a PWR [121]. A correlation has been developed at Ciemat, based on the obtained experimental data.

This section shows tests of the inertial impaction models for tube bundle geometry. First, a short overview of available correlations is presented in section 3.12.7.1. Next, results of the test calculations are presented in section 3.12.7.2.

3.12.7.1 Overview of Tube Bundle Correlations

This section provides an overview of several correlations and comparison with experimental data for deposition on the tube, rows of tubes, and tube bundles.

- Ilias & Douglas correlation [122] ([121] Table III):

$$\eta = \frac{Stk^3 + 1.622 \times 10^{-4} / Stk}{1.031 \cdot Stk^3 + [1.140 + 4.044 \times 10^{-2} \cdot \ln(Re)] \cdot Stk^3 + 1.479 \times 10^{-2} \cdot \ln(Re) + 0.3013}$$

  The applicability range is: $30 < Re < 40{,}000$, $0.07 < Stk < 5.0$.

- Wessel correlation [123] ([121] Table III). For small Stokes numbers, $0.125 < Stk < 0.5$:

$$\eta = 0.0198 \cdot \ln(8 \cdot Stk) + 0.514 \cdot (Stk - 0.125) - 0.0483 \cdot (Stk - 0.125)^2$$

  For large Stokes numbers, $0.125 < Stk < 0.5$:

$$\eta = \left(1 + \frac{1.544}{Stk - 0.125} - \frac{0.538}{(Stk - 0.125)^2} + \frac{0.202}{(Stk - 0.125)^2}\right)^{-1}$$

  The applicability range is: $30 < Re^2/Stk < 50{,}000$ $Stk > 0.125$.

- Wang correlation [124]:

$$\eta = \frac{2}{\pi} \cdot \arctan[0.8 \cdot (Stk - 0.125)^{0.8}]$$

  The applicability range is: $Stk > 0.125$

Wang developed a correlation for particle impact on refrigerant tubes. The correlation as presented above is valid for a single row of tubes. Reference [124] gives also an effect of multiple rows of offset tubes. This effect is taken into account by considering the probability of particle passing a given tube row, $1 - \eta$. The expression involves the tube diameter-to-pitch ratio (D_{tube}/P_{tube}), the number of tube rows in the direction of flow (N), and the number of offset rows (N_{offset}), i.e. rows not in line with the stream of gas - see Figure 3-641. The expression is:

$$P = 1 - \eta = \left(1 - \eta_{single} \cdot \frac{D_{tube}}{P_{tube}} \cdot N_{offset}\right)^{N / N_{offset}}$$

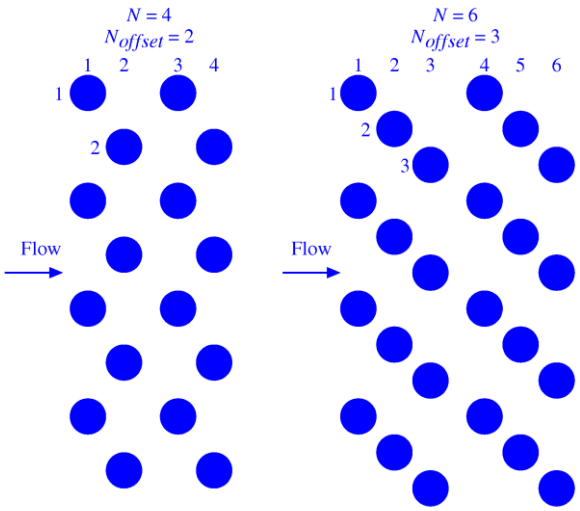

Figure 3-641 Tube bundle examples, left: N=4, N_{offset}=2, right: N=6, N_{offset}=3

- Ciemat correlation [121]:

$$\eta = \frac{\eta_{\max}}{1 + c_1 \cdot \exp(-c_2 \cdot Stk^{c_3})}$$

Here $\eta_{\max}$, c_1, c_2, c_3 are user defined coefficients with the default values of 0.75, 29.31, 3.85, and 0.5 respectively, based on [121]. Stk is the Stokes number, defined as:

$$Stk = \frac{C_m \cdot \rho_p \cdot d_p^2 \cdot v_g}{18 \cdot \mu_g \cdot D}$$

C_m	Cunningham correction factor, (-)
ρ_p	particle density, (kg/m^3)
d_p	particle diameter, (m)
v_g	gas velocity, (m/s)
μ_g	gas viscosity, (kg/m/s)
D	impactor dimension, (m)

The above correlation has been developed for impaction on a single tube. A model for the collection efficiency in a tube bundle has been derived in [126]. This model for the bundle efficiency is based on the product of a factor which is dependent upon the topology, i.e., the diameter of the tubes, *D*, clearance between the tubes, and a factor which is a function of the individual efficiency of the single tubes. The clearance (spacing) between the tubes, *s*, is equal to the tube pitch minus the tube diameter. In order to obtain this model, it was assumed that the particles escaping particle retention onto a tube become the particle source to the next one in the row. Under this assumption, the following model for the bundle efficiency as a function of the single tube efficiencies was obtained in [126]:

$$\eta = 1 - \exp\left(- \frac{4D(s+D)}{\pi s(s+D)} \cdot \left(1 + (-1)^{N+1} \cdot \prod_{i=1}^{N} (\eta_{single} - 1) \right) \right)$$

where *N* is the total number of tubes in the row in flow direction up to the distance the particle-loaded gas flow penetrates into the bundle.

Results of the single tube correlations are compared to data of Wong & Johnstone and of Ranz & Wong in Figure 3-642 (reproduced from [121]). Results of tube bundle correlations are compared to the results of tube bundle data from ARTIST [127] in Figure 3-643.

The tube bundle correlations shown in Figure 3-643 were obtained using $N = 3$ rows. The value was estimated based on photograph presenting ARTIST results [127]. The offset rows, N_{offset}, is 1.0 for the rectangular tube arrangement in ARTIST.

Results of multiple tubes correlations are below the experimental data of ARTIST. This is consistent with the interpretation of the ARTIST data, which, according to the experimentalists, “The deposition is the combination of inertial impaction (...) and turbulent deposition.”.

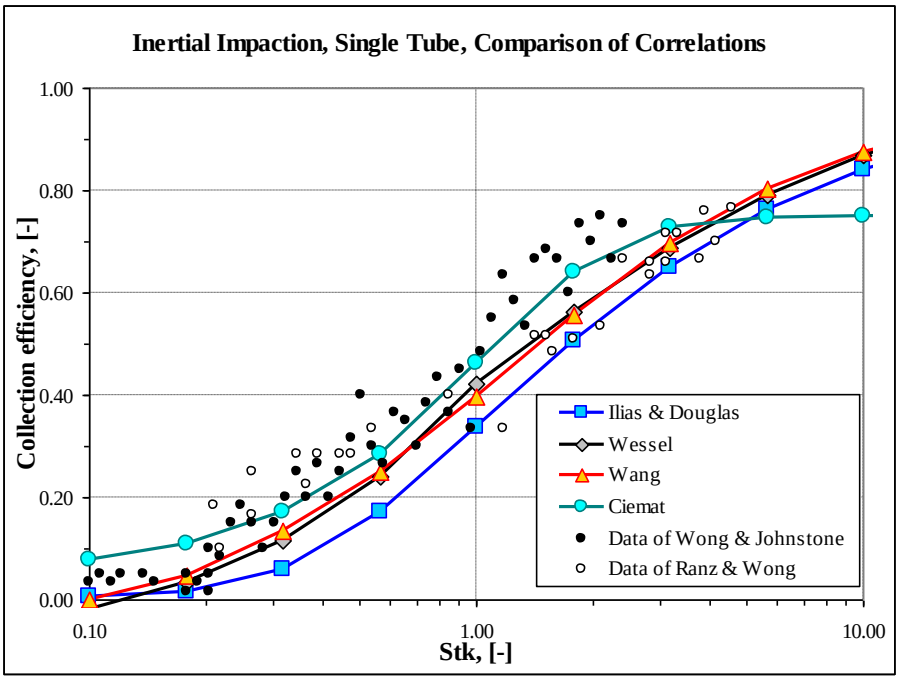

Figure 3-642 Inertial impaction - comparison of single tube correlations and data

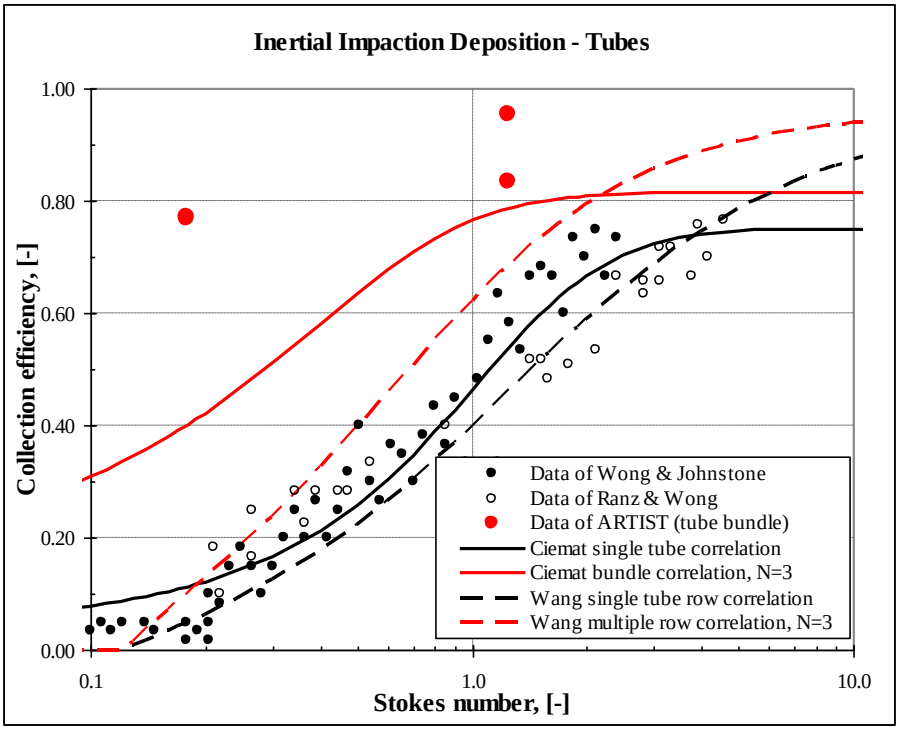

Figure 3-643 Inertial impaction - single tube and tube bundles

3.12.7.2 Tests Calculations

A simple test case has been set up consisting of four tubes (CV-x01 through CV-x04, where x is the Case number). The tube inner/outer diameter is 0.02/0.03 m. The tubes are located in the volume CV-x20, representing the secondary side of the SG. This volume is connected to the outlet, CV-x90. Tube x01 is assumed to be broken; the break diameter is 0.01 m (small break). The particles flowing through the break impact on the neighboring three tubes (x02, x03, and x04) with relative fractions of 0.25, 0.50, and 0.25 respectively. The primary pressure is kept constant at 140 bar. The secondary pressure is kept constant at 70 bar. The aerosol particles are 5 microns in diameter. Two cases were analyzed:

- Bundle correlation of Wang
- Bundle correlations of Ciemat

The input decks are provided in: `\Z-TESTS\RT\IN-IM\Bundle\Bundle.SPE`. Results are shown in Figure 3-644 and Figure 3-645. The calculated impaction efficiencies are:

- 32.5 + 16.2 + 16.2 = 64.9% in case of Wang correlation
- 38.8 + 19.4 + 19.4 = 77.6% in case of Ciemat correlation

For this value of *Stk* the correlations give 64.9% and 77.5% - Figure 3-643 (the exact values are calculated in the Excel file, stored as: `\Z-TESTS\RT\IN-IM\Bundle\Bundle.xls)`. The SPECTRA-calculated values are in agreement with hand calculations.

A similar test case has been set up for impaction on single tube. Two cases were analyzed:

- Single tube correlation of Wang
- Single tube correlations of Ciemat

The input decks are provided in: `\Z-TESTS\RT\IN-IM\Bundle\Tube.SPE`. Results are shown in Figure 3-646 and Figure 3-647. The calculated impaction efficiencies are:

- 42.3% in case of Wang correlation
- 49.5% in case of Ciemat correlation

For this value of *Stk* the correlations give 42.3% and 49.4% - Figure 3-643 (the exact values are calculated in the Excel file, stored as: `\Z-TESTS\RT\IN-IM\Bundle\Bundle.xls)`. The SPECTRA-calculated values are in agreement with hand calculations.

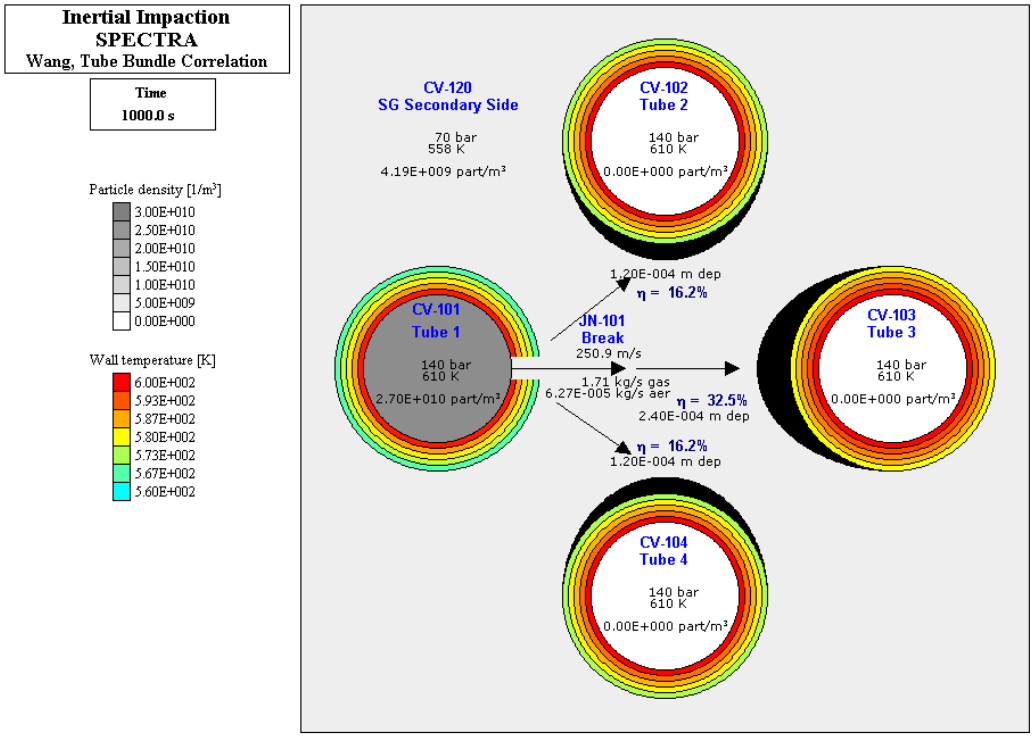

Figure 3-644 Test of inertial impaction in tube bundle - Wang tube bundle correlation

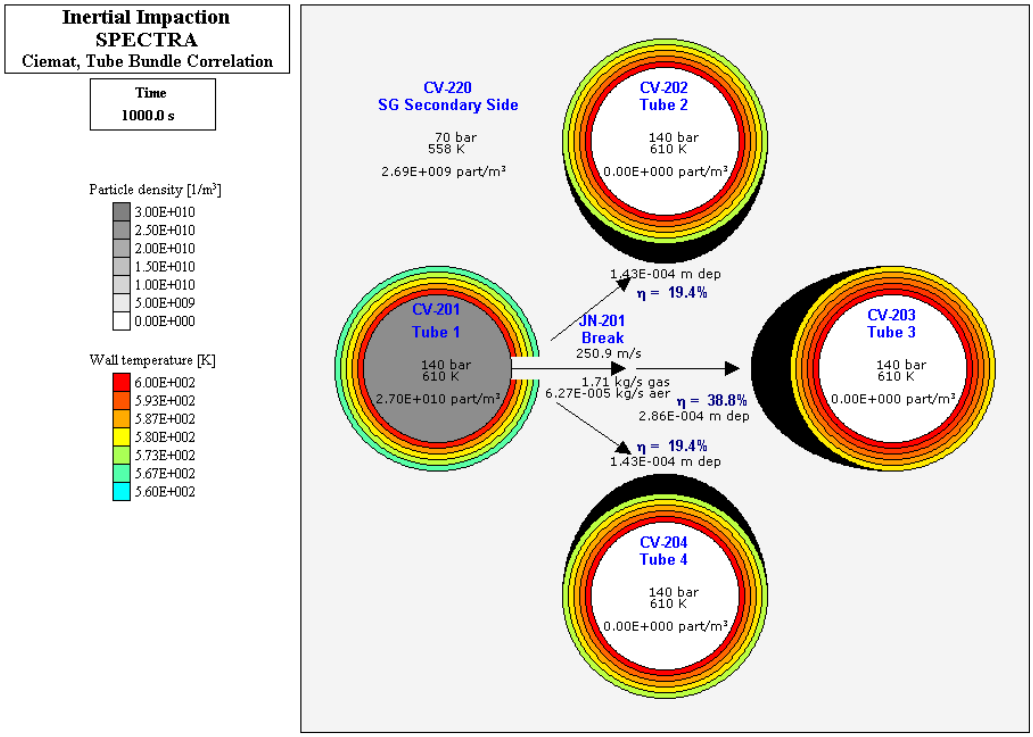

Figure 3-645 Test of inertial impaction in tube bundle - Ciemat tube bundle correlation

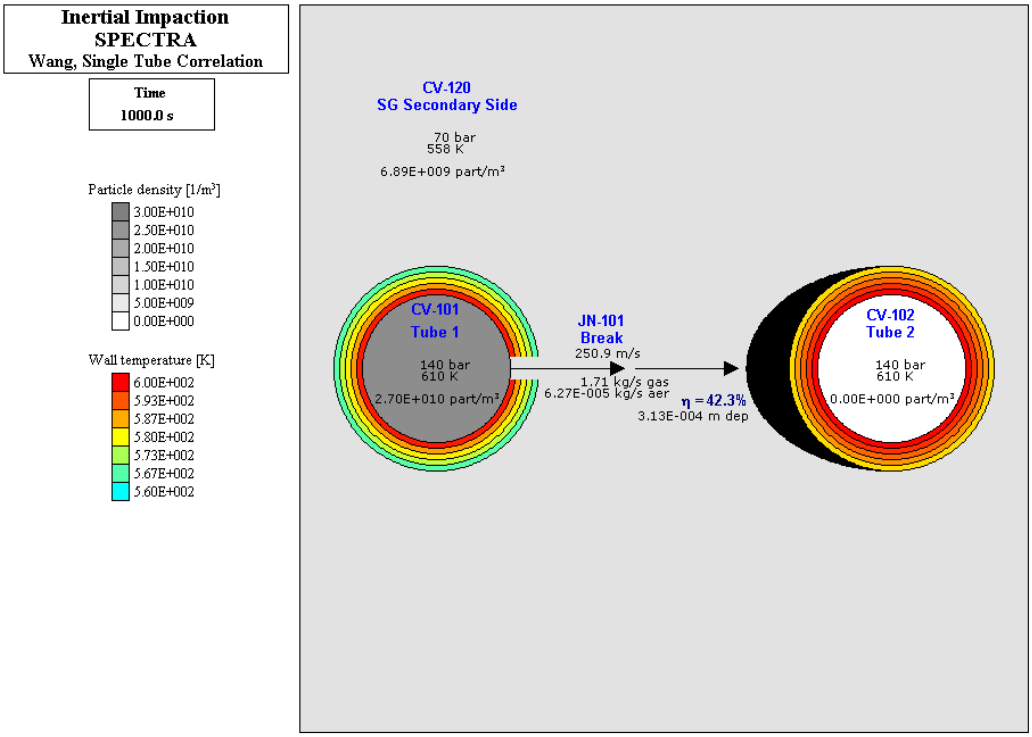

Figure 3-646 Test of inertial impaction in tube bundle - Wang single tube correlation

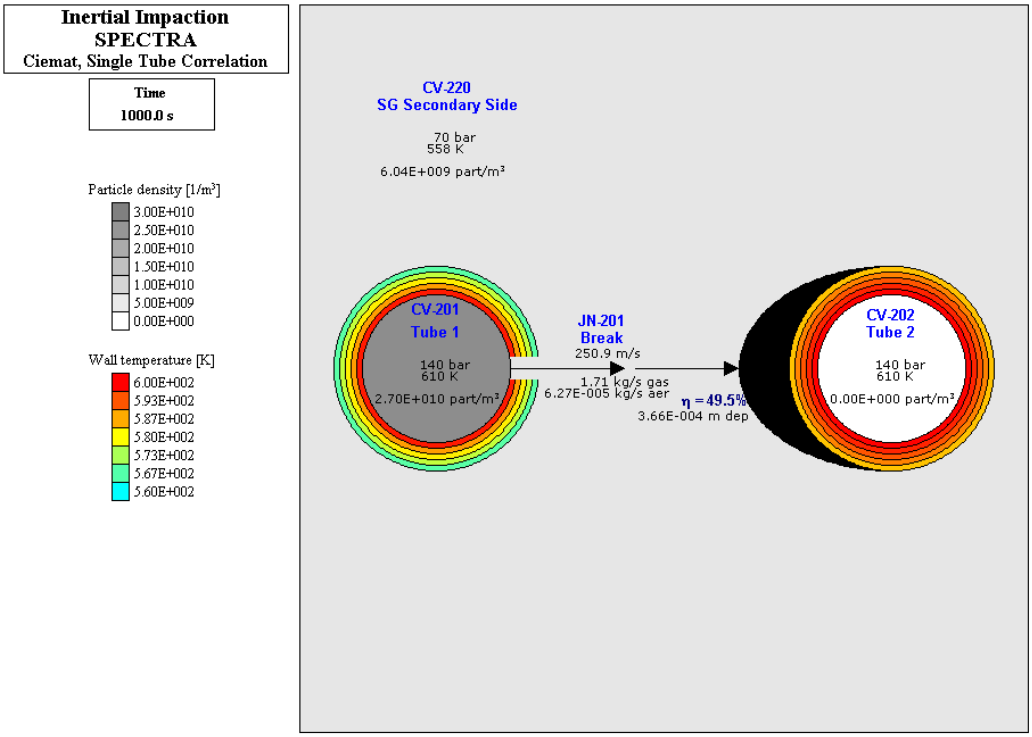

Figure 3-647 Test of inertial impaction in tube bundle - Ciemat single tube correlation

3.12.8 Electrophoretic Deposition Test

A simple test model has been used to test the electrophoretic deposition. The model is the same as the single volume deposition test, described in section 3.12.1. The model consists of CV-101, with atmospheric conditions (300 K, 1.0 bar, dry air). Verification was performed by comparison with hand calculations.

Five aerosol size sections were used, with size definitions as described in section 3.12.1. The dynamic shape factors are equal to 1.0. An initial mass of 0.1 kg of the smallest section aerosols has been placed in CV-101. An electrical field was applied at the vicinity of the SC surfaces, with the strength of:

$$E = 10.0 \text{ (V/m)}$$

The following three cases were considered:

- Case 1: No electrical charge on aerosol particles. The input deck is provided in:
  `\Z-INPUTS\RT\ELEC-DEP\Elec-Dep-No-Charge.SPE`

- Case 2: Minimum (equilibrium) charge on aerosol particles. The input deck is provided in:
  `\Z-INPUTS\RT\ELEC-DEP\Elec-Dep-Min-Charge.SPE`
  The equilibrium charge is defined as (see Volume 1):

  $$q = 3.8\times10^{-19}\cdot\sqrt{D_p\times10^6}$$

  Here D_p is the particle diameter (m).

- Case 3: Maximum charge on aerosol particles. The input deck is provided in:
  `\Z-INPUTS\RT\ELEC-DEP\Elec-Dep-Max-Charge.SPE`
  The equilibrium charge is defined as (see Volume 1):

  $$q = 4.5\times10^{-14}\cdot(D_p\times10^6)^2$$

- Case 4: Additionally the Case 3 was re-run with the electric field strength changed to 0.1 V/m. Maximum charge on aerosol particles, E=0.1 V/m. The input deck is provided in:
  `\Z-INPUTS\RT\ELEC-DEP\Elec-Dep-Max-Charge-01.SPE`

Calculations were performed for 5000 s, using the maximum time step of 1.0 s. Results are shown in Figure 3-648 through Figure 3-651. In case of equilibrium charge there is practically no effect of the electric field of the strength of 10 V/m on the particle behavior (Figure 3-649). In the third case the particles carry maximum charge and the electric field causes fast deposition (Figure 3-650). It was found out that a minimum field strength that causes visible effect on particles is about 0.1 V/m (Figure 3-651). In order to obtain approximately the same effect with the equilibrium charge, the electric field would have to be stronger by 5 orders of magnitude (for 1 micron particles this ratio is $4.5\times10^{-14}/3.8\times10^{-19} = 1.2\times10^5$). Thus, electrical field becomes important in determining the behavior of aerosol particles if:

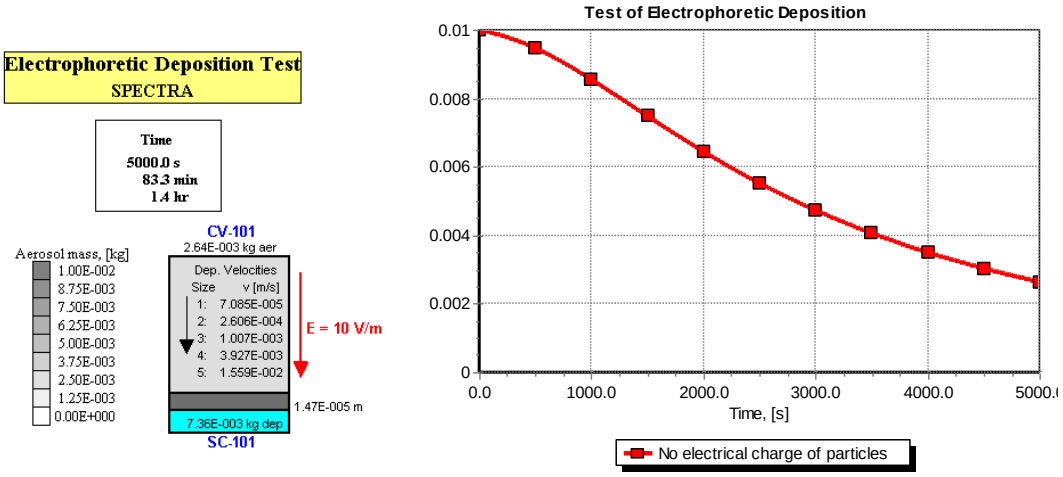

Figure 3-648 Electrophoresis test – no charge on particles

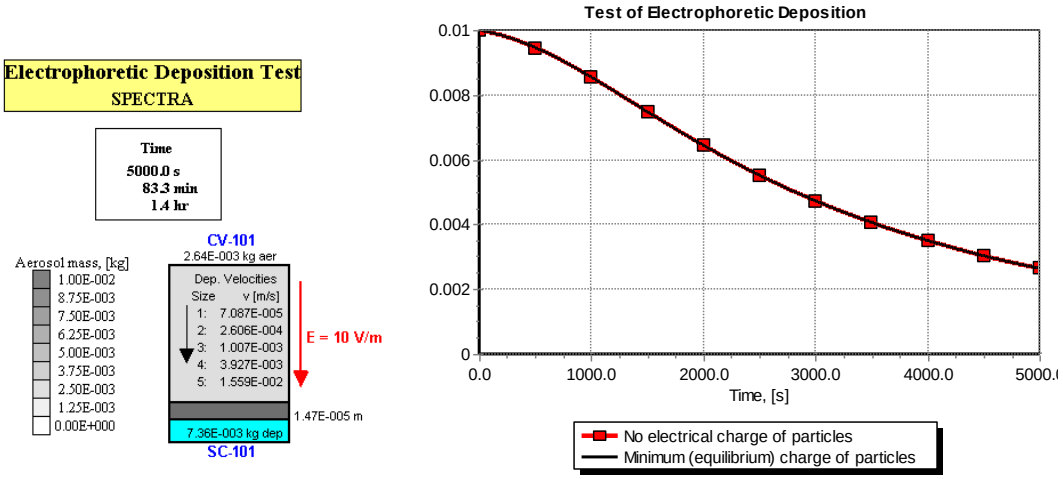

Figure 3-649 Electrophoresis test – minimum (equilibrium) charge on particles, *E*=10 V/m

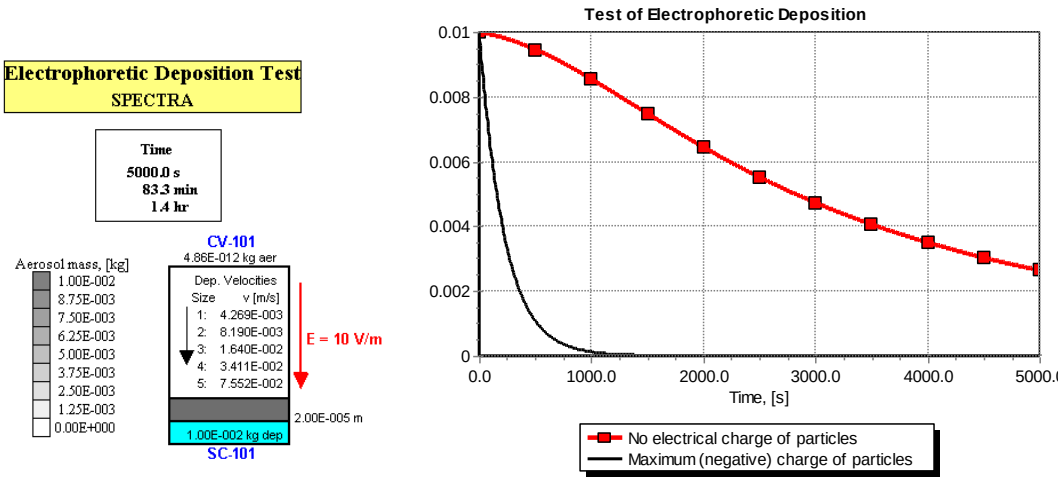

Figure 3-650 Electrophoresis test – maximum charge on particles, *E*=10 V/m

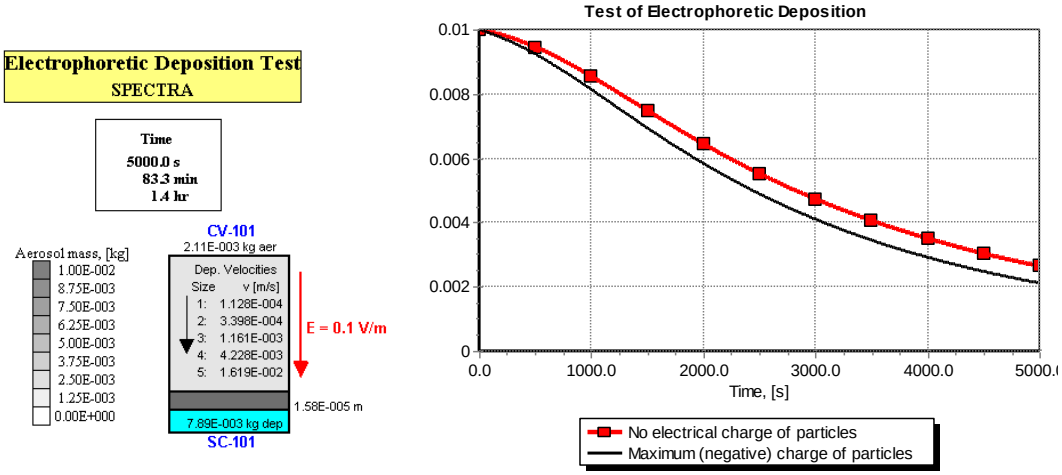

Figure 3-651 Electrophoresis test – maximum charge on particles, *E*=0.1 V/m

- $E > \sim 10^{-1}$ V/m for large (maximum) charge of aerosol particles
- $E > \sim 10^{4}$ V/m for small (equilibrium) charge of aerosol particles

Verification of the deposition velocity is performed by hand calculation. For the case 3, size section 1, the electrophoretic deposition velocity is 4.1983×10^{-3} m/s (see code output below):

Deposition velocities

Sec. No.	V-grav. (m/s)	V-Brown (m/s)	V-ther. (m/s)	V-diff. (m/s)	V-turb. (m/s)	**V-elec. (m/s)**	V-total (m/s)
1	6.8983E-05	1.8624E-06	0.0000E+00	0.0000E+00	0.0000E+00	**4.1983E-03**	4.2691E-03

The formulae (see Volume 1) give:

$$l = 1.25 \cdot \frac{\mu_g}{\rho_g} \cdot \frac{1}{\sqrt{RT}} = 1.25 \cdot \frac{1.83\times10^{-5}}{1.155} \cdot \frac{1}{\sqrt{288.6\times300}} = 6.73\times10^{-8}$$

$$Kn = 2l / D_p = 2\times6.73\times10^{-8} / 1.44\times10^{-6} = 0.0935$$

$$C_m = 1 + Kn \cdot \left(A_1 + A_2 \cdot \exp\left[-\frac{A_3}{Kn} \right] \right) = 1 + 0.0935 \times \left(1.257 + 0.4 \cdot \exp\left[-\frac{1.1}{0.0935} \right] \right) = 1.118$$

$$q = C_q \cdot (D_p \times 10^6)^{x_q} = 4.5\times10^{-14} \cdot 1.44^2 = 9.33\times10^{-14}$$

$$v_{D,e} = \frac{1}{3\pi} \frac{C_m}{D_p \mu_g \chi} qE = \frac{1}{3\pi} \frac{1.118}{1.44\times10^{-6} \times 1.83\times10^{-5} \times 1.0} 9.33\times10^{-14} \times 10.0 = 4.20\times10^{-3}$$

The gas viscosity, 1.83×10^{-5} kg/(m·s), and density, 1.155 kg/m^3, were obtained from the code output. The final result is in agreement with the printed value. The calculations are stored in:

\Z-INPUTS\RT\ELEC-DEP\Elec-Dep-Verification.xls

3.12.9 Aerosol Loop Flow and Deposition Test

The aerosol loop flow and deposition test consists of five Control Volumes: CV-101, 102, 103, 104, and 105. The volumes are connected with junctions JN-101, 102, 103, 104, and JN-105. Each CV has a horizontal structure (floor) for deposition. The floors are represented by SC-101 through SC-105. The deposition area is 1.0 m^2. The MELCOR model was set up in the same way. According to the MELCOR convention FL (Flow Path) replaces JN and HS (Heat Structure) replaces SC.

A source of gas and aerosols is present in volume CV-101. The source provides 0.1 kg/s of gas and 1.0×10^{-4} kg/s of aerosols. The aerosol source provides aerosols of size section 1 (the smallest size) only.

In contrast to the previous tests, which all were performed using an open loop with fixed boundary conditions at the exit, the present test is a closed loop test, with a flow forced by a simple flow circulator present in JN-101 (FL-101). With the closed loop the time needed to reach equilibrium between the source rate and deposition rate is relatively large. The present test was run for 5000 s, with the requested time step of 5.0 s. The actual time step was governed by an internal courant limit, and it was equal to 4.99 s in both SPECTRA and MELCOR. The input deck is provided in **\Z-TESTS\RT\LOOP\LOOP.SPE**.

Results of SPECTRA and MELCOR calculations are shown in Figure 3-652 and Figure 3-653. A good agreement between those codes is observed. The aerosol mass in the source volume (CV-101) is too low in case of MELCOR. This is caused by the implicit aerosol flow solution scheme, which seems to have some deficiency in a vicinity of a flow path with a constant (forced flow) and an aerosol source. This was confirmed in a separate MELCOR run, performed with the maximum time step of 0.5 s. The results are shown in Figure 3-654; the “strangely low” aerosol concentration in the source volume, CV-101 has disappeared.

The time behavior of airborne and deposited aerosol masses is shown in Figure 3-655 through Figure 3-658. Because of continuous circulation flow the gas and particles are well mixed in the test volumes, and the results are very similar in all control volumes. The deposition is somewhat higher in MELCOR, and consequently the aerosol concentrations are somewhat lower. The reason for this is explained below.

Because the present test was “slower”, the aerosols had more time to coagulate. In the previous tests the flow through the “test tube” was so fast that very little coagulation occurred. In the present test, a quite significant growth of aerosols is observed. Detailed comparison of individual size section aerosol masses are presented in Figure 3-659 and Figure 3-660. The mass of the size section 1 (the smallest aerosols) is clearly higher in SPECTRA. This indicates that, in general, the coagulation process proceeds somewhat faster in MELCOR than in SPECTRA (compare sections 3.12.1, 3.12.10 and 3.12.12). A straightforward consequence of the faster coagulation is faster deposition, simply because large particles deposit faster than small.

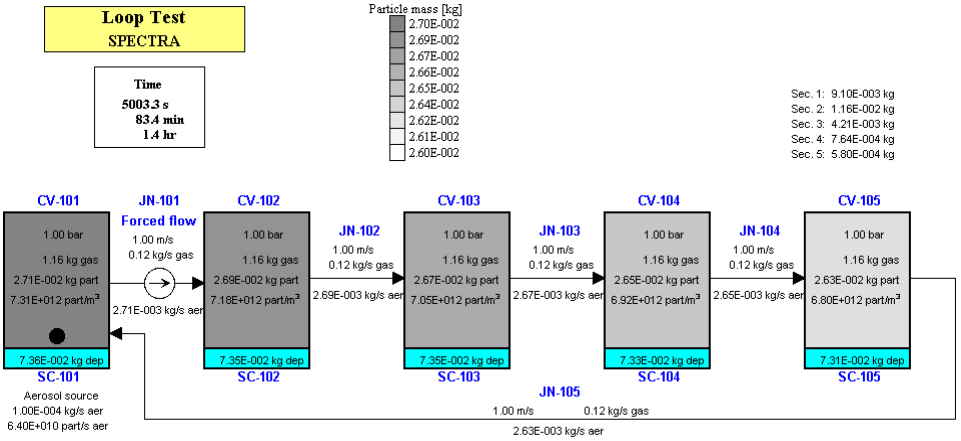

Figure 3-652 Loop test – SPECTRA

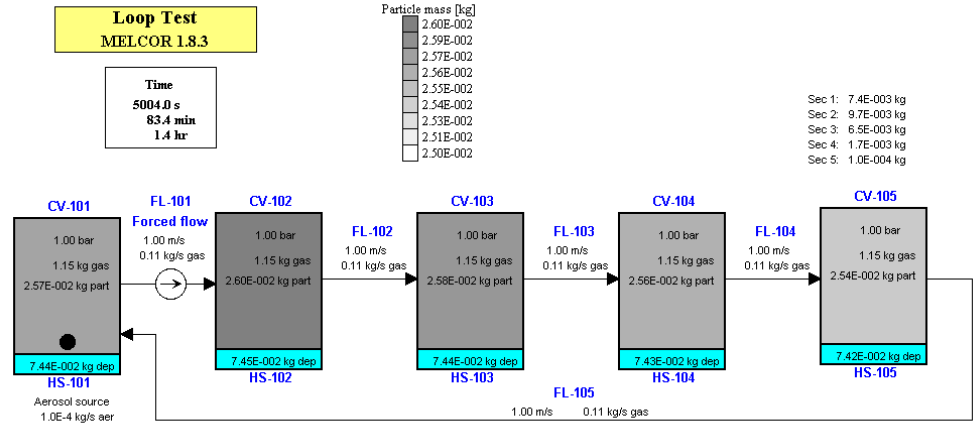

Figure 3-653 Loop test – MELCOR 1.8.3

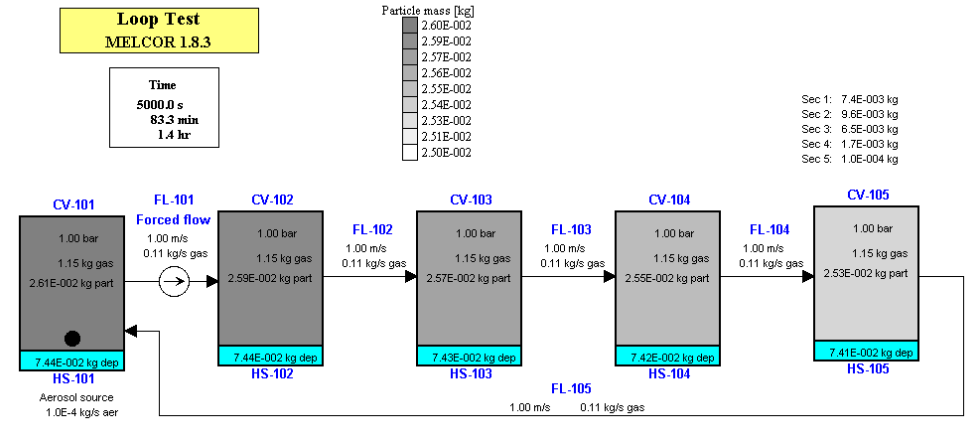

Figure 3-654 Loop test (small time step) – MELCOR 1.8.3

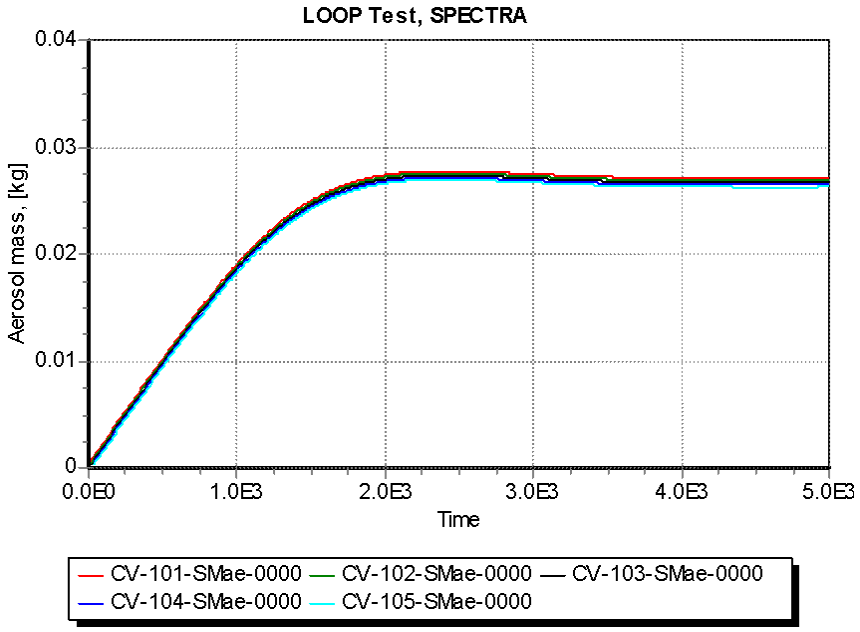

Figure 3-655 Loop test - airborne masses, SPECTRA

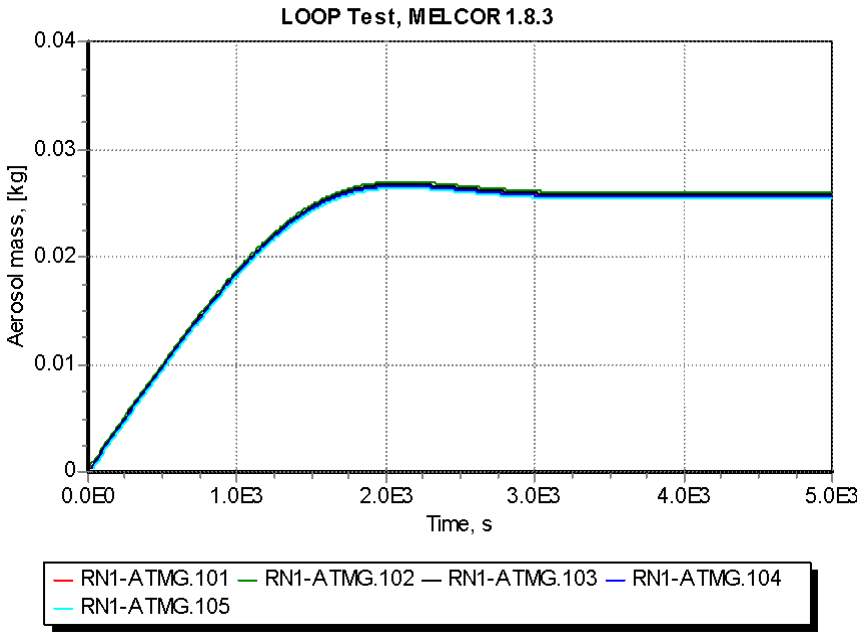

Figure 3-656 Loop test - airborne masses, MELCOR 1.8.3

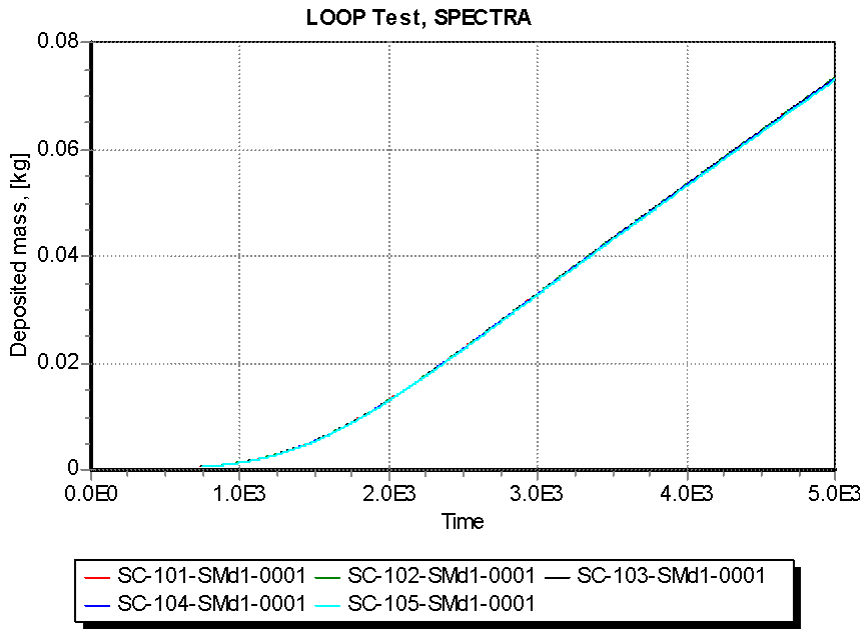

Figure 3-657 Loop test, deposited masses, SPECTRA.

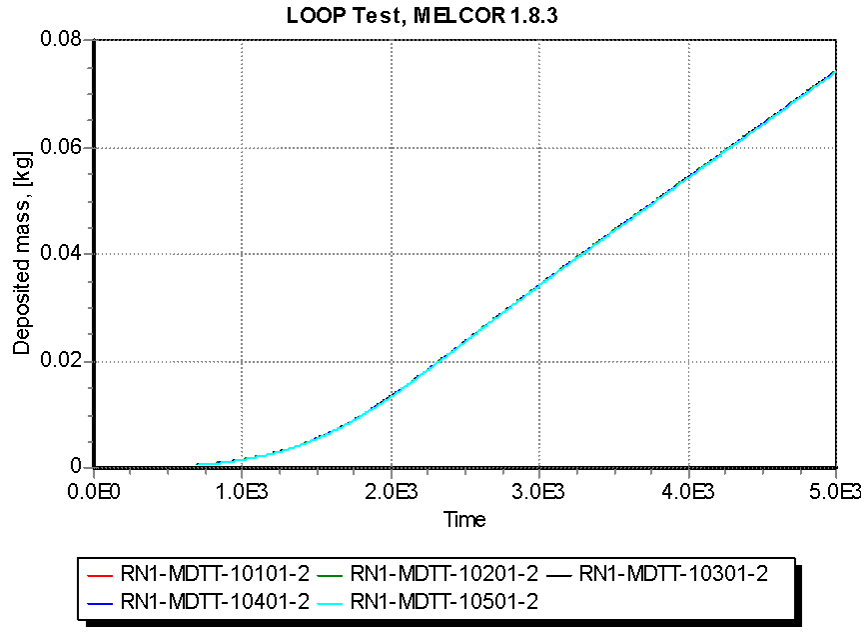

Figure 3-658 Loop test, deposited masses, MELCOR 1.8.3.

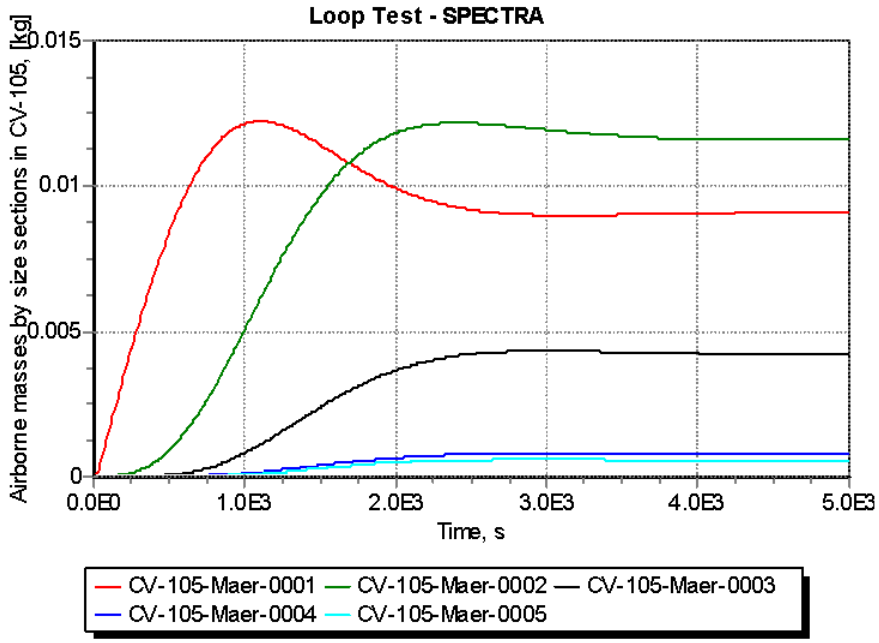

Figure 3-659 Loop test - airborne masses by size sections, SPECTRA

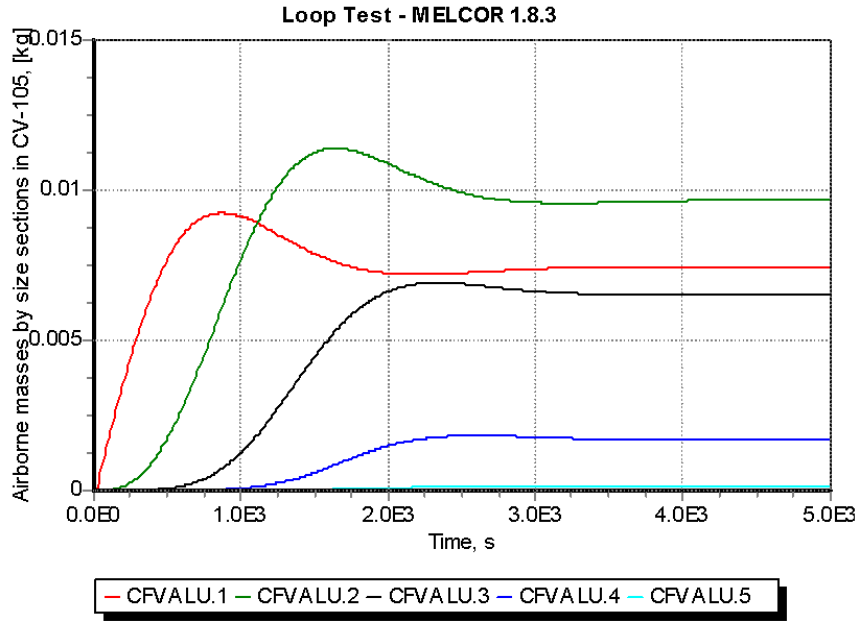

Figure 3-660 Loop test - airborne masses by size sections, MELCOR 1.8.3

3.12.10 Particle Flow with Pool - Test 1

The nodalization applied for the particle flow with pool test is the same as that for the aerosol flow test, described in section 3.12.3. For the present test the water levels in all Control Volumes were set at 0.8 m (80% of the volume height). The aerosol source is located at the top of CV-101. The source provides 0.1 kg/s of gas and 1.0×10^{-4} kg/s of aerosols. The aerosol source provides aerosols of size section 1 (the smallest size) only. The liquid source of 100.0 kg/s is present in CV-101.

The input deck is provided in **\Z-TESTS\RT\POOL1\POOL1.SPE**. Calculations were performed for 1000 s, using the maximum time step of 1.0 s. Both codes were using the maximum time step.

SPECTRA results of the Pool Test 1 are shown in Figure 3-661 and Figure 3-663. Because the junctions are located at the centers of the volumes (elevation of 0.5 m, opening height of 0.1 m), the gas does not flow through and the aerosol particles have to settle on the pool of CV-101 before they can be transported to the subsequent Control Volumes. Figure 3-663 shows the time history of aerosol concentrations in CV-101 and the concentrations of particles in the pool. The pool concentrations are quite similar in all Control Volumes. The aerosol concentration in CV-101 stabilizes at about 0.029 kg (Figure 3-663, right scale).

MELCOR results of the Pool Test 1 are shown in Figure 3-662 and Figure 3-664. The concentrations in the water are very similar to those obtained by SPECTRA, but the airborne aerosol mass in CV-101 is somewhat lower (stable value of about 0.026 kg). This fact indicates somewhat faster deposition of aerosols in MELCOR, and is a consequence of somewhat faster coagulation (compare sections 3.12.1, 3.12.9, and 3.12.12).

3.12.11 Particle Flow with Pool - Test 2

The particle flow with pool Test 2 is very similar to the Test 1, described in the previous section. The only difference is the location of the particle source. In SPECTRA the particle source is located at the bottom of CV-101. In MELCOR it is defined as the source for the liquid phase.

The input deck is provided in **\Z-TESTS\RT\POOL2\POOL2.SPE**. Calculations were performed for 120 s, using the maximum time step of 1.0 s. Both codes were using the maximum time step.

Results are shown in Figure 3-665 through Figure 3-668. Results of both MELCOR and SPECTRA code are in very good agreement. Note that in the present test coagulation does not occur, so in contrast to the previous test the size section diameters are not important.

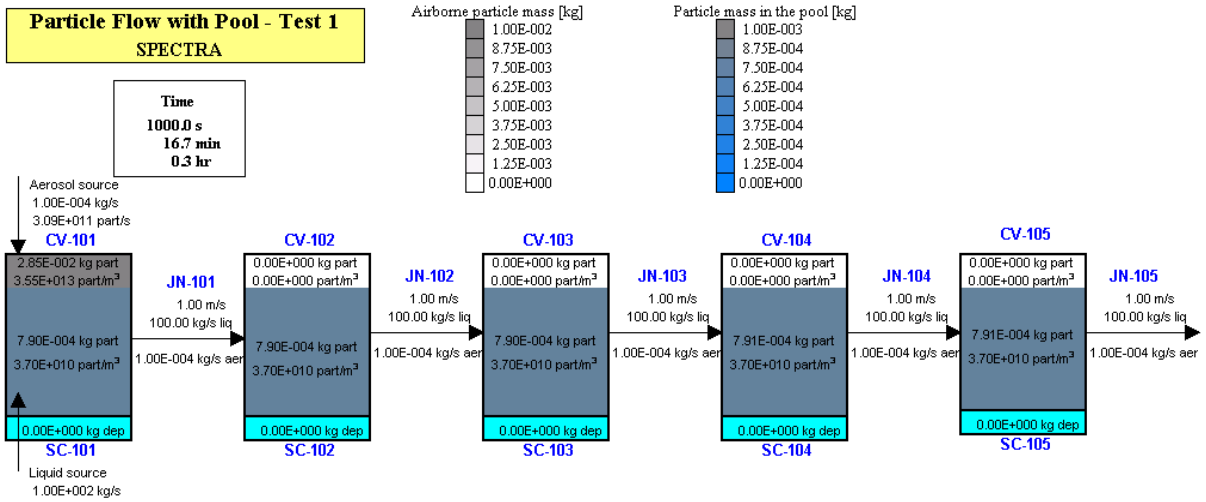

Figure 3-661 Particle flow with pool, Test 1, SPECTRA

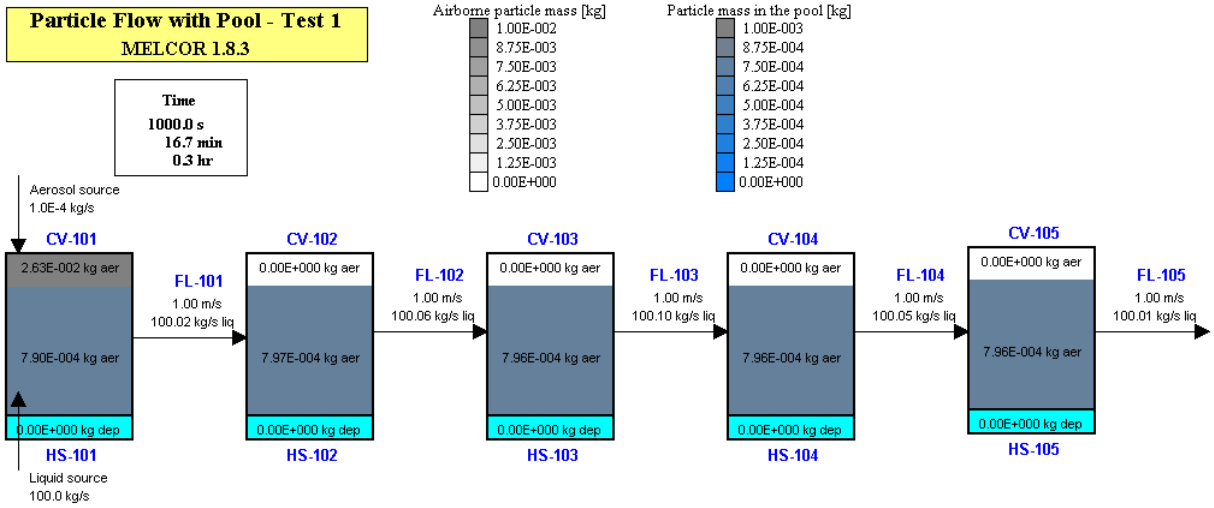

Figure 3-662 Particle flow with pool, Test 1, MELCOR 1.8.3

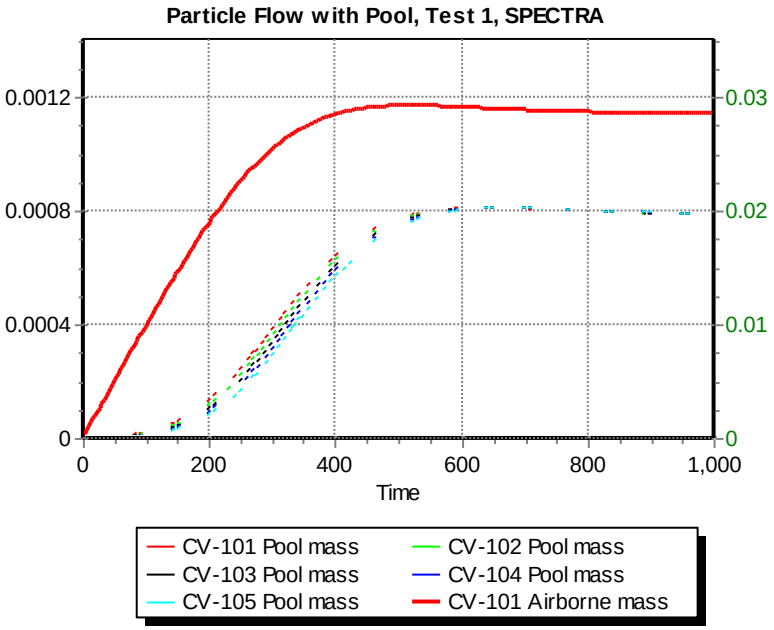

Figure 3-663 Particle flow with pool, Test 1, deposited and airborne masses, SPECTRA

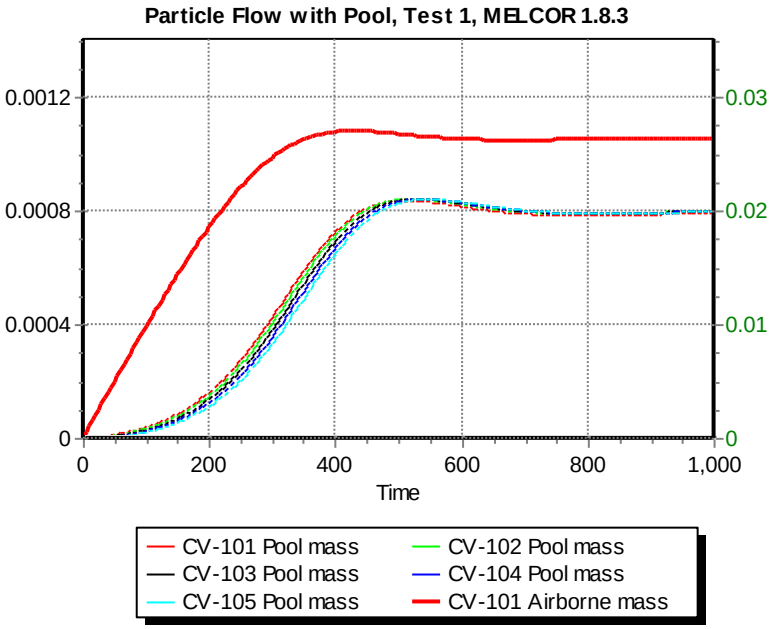

Figure 3-664 Particle flow with pool, Test 1, deposited and airborne masses, MELCOR 1.8.3

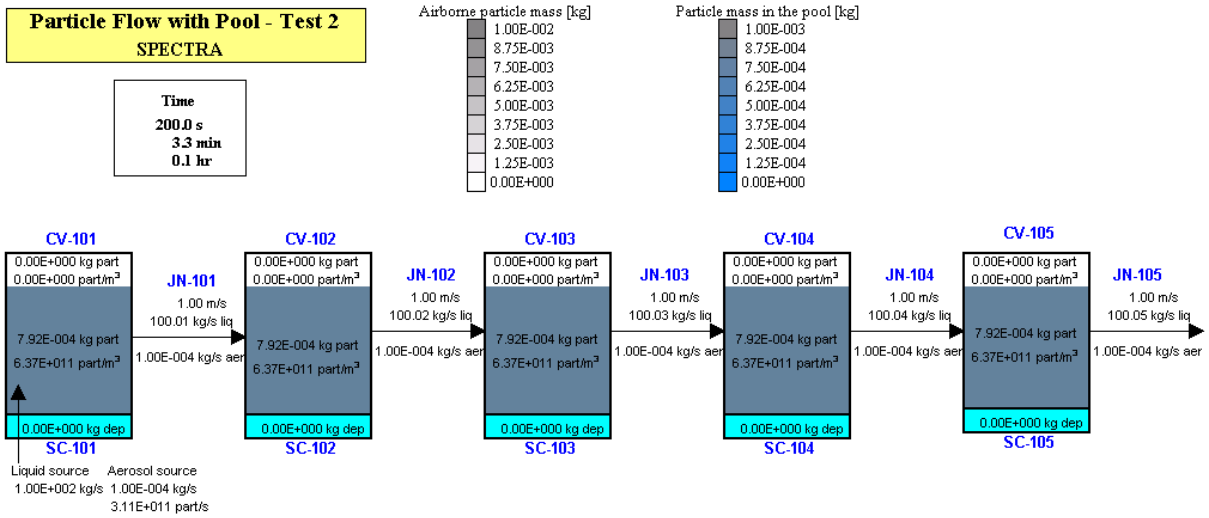

Figure 3-665 Particle flow with pool, Test 2, SPECTRA

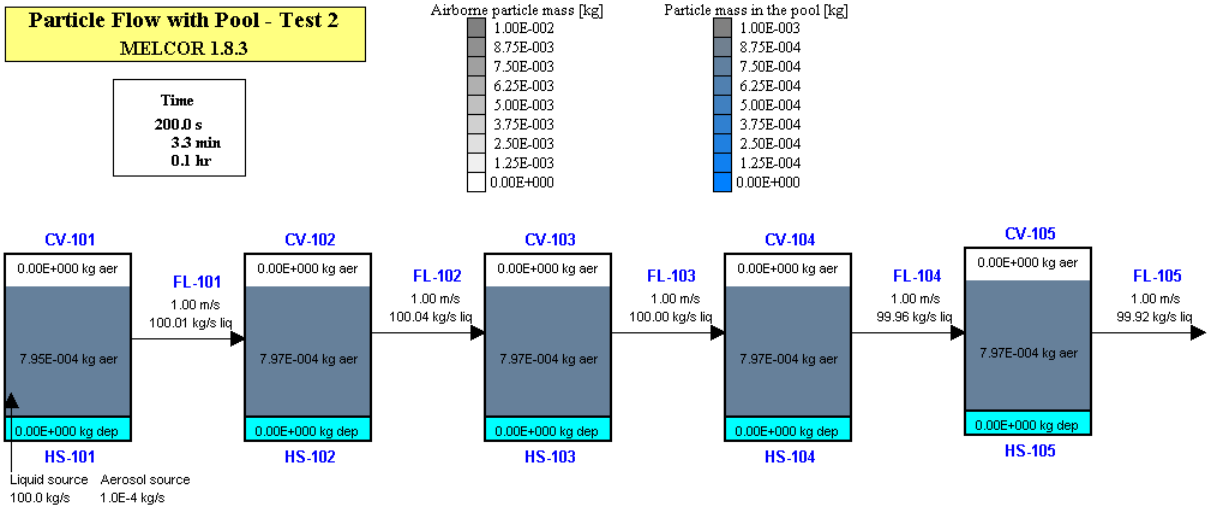

Figure 3-666 Particle flow with pool, Test 2, MELCOR 1.8.3

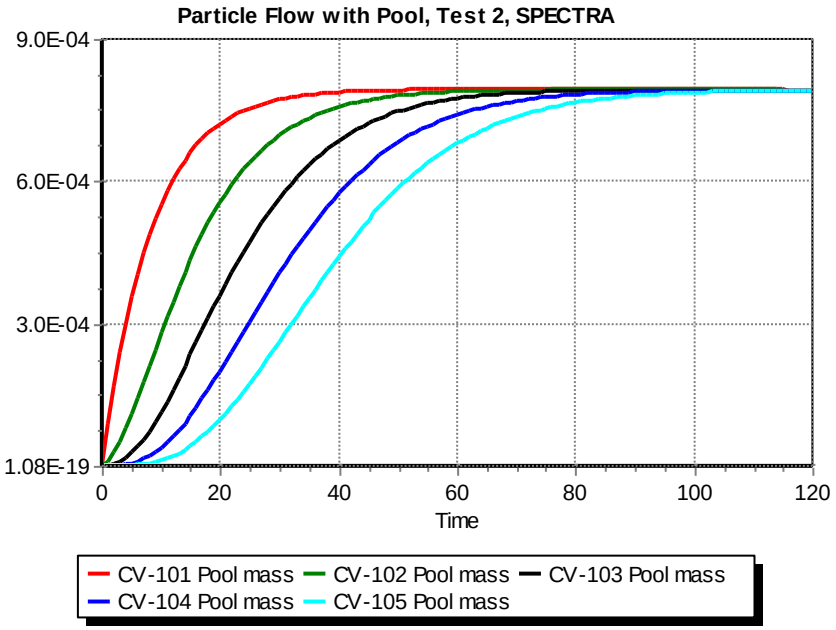

Figure 3-667 Particle flow with pool, Test 2, particle mass in the pool, SPECTRA

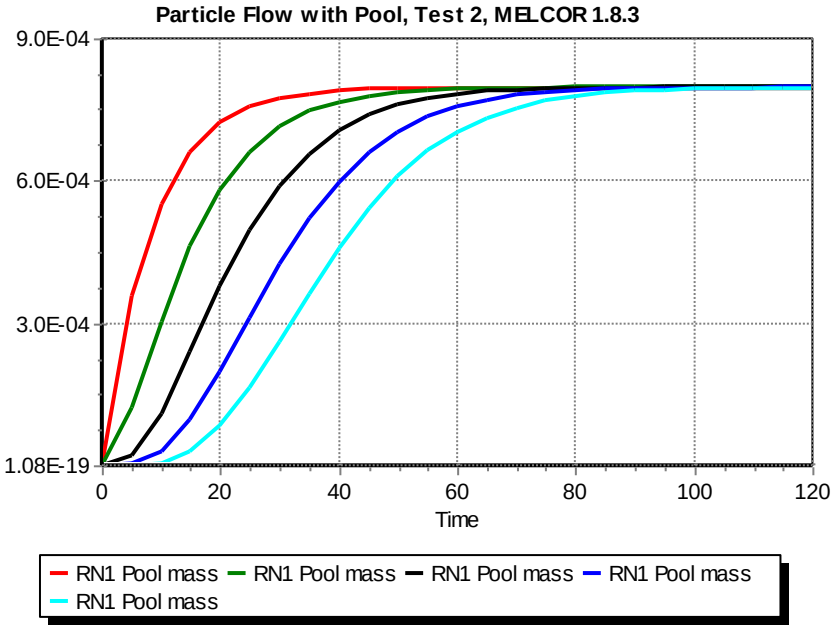

Figure 3-668 Particle flow with pool, Test 2, particle mass in the pool, MELCOR 1.8.3

3.12.12 Particle Flow with Pool - Test 3

The particle flow with pool Test 3 is very similar to the two tests described in the previous sections. In case of Test 3 the water level is set in the middle of the Control Volumes (0.5 m), and the aerosol source is at the top of CV-100. Consequently the aerosols flow with the gas and simultaneously deposit on the pool surface and are transported with the pool. In the stable conditions the airborne aerosol concentration decreases along the flow, as some of the aerosols deposit on the pool. At the same time the concentration in the pool increases, for the very same reason.

The input deck is provided in **\Z-TESTS\RT\POOL3\POOL3.SPE**. The calculations were performed for 4000 s, using the maximum time step of 1.0 s. Both codes were using the maximum time step.

Results are shown in Figure 3-669 through Figure 3-674. Results of both MELCOR and SPECTRA code are in good agreement. Airborne concentrations are somewhat lower in MELCOR, which is a result of somewhat faster coagulation (compare sections 3.12.1, 3.12.9, and 3.12.10)

It is interesting to observe that in order to obtain good thermal-hydraulic results in MELCOR, it was necessary to increase artificially the junction flow areas. In the original model set-up the flow areas are equal to 0.1 m^2, and the opening heights are 0.1 m. With this configuration there is (according to SPECTRA results) very little change of water level in all volumes (see Figure 3-669). The water level is 0.5 m at the exit (fixed value) and is about 0.52 in the first volume, CV-101. Since the opening heights are 0.5 m, the top of the junction openings are at 0.55 m. Thus all water levels (0.52 - 0.5 m) are clearly below the top of the junctions, allowing free flow of gas along with the liquid. The pressures were practically the same in all Control Volumes. The SPECTRA calculated pressures, pool levels, and junction velocities are shown in the printout below.

SPECTRA results for the run Pool 3:

CV	ATMS-PRES	ATMS-TEMP	POOL-LEVEL	POOL-TEMP
101	9.99925665E+04	3.00187590E+02	5.21813326E-01	3.00004719E+02
102	9.99934724E+04	3.00128787E+02	5.18140136E-01	3.00004694E+02
103	9.99947075E+04	3.00077234E+02	5.14132393E-01	3.00004683E+02
104	9.99966513E+04	3.00044716E+02	5.09705555E-01	3.00004678E+02
105	9.99980504E+04	3.00025800E+02	5.04720584E-01	3.00004676E+02
200	1.00000000E+05	3.00000000E+02	5.00000000E-01	3.00000000E+02

JN	ATMS-VELOCITY	POOL-VELOCITY
101	2.83319744E-02	1.39735524E+00
102	2.52715177E-02	1.47267185E+00
103	2.25240374E-02	1.56470694E+00
104	2.00721363E-02	1.68072921E+00
105	1.78774081E-02	1.83383522E+00

In MELCOR the water levels in all junctions stabilized nearly the top of the flow paths (0.549 m). The stable results are printed below:

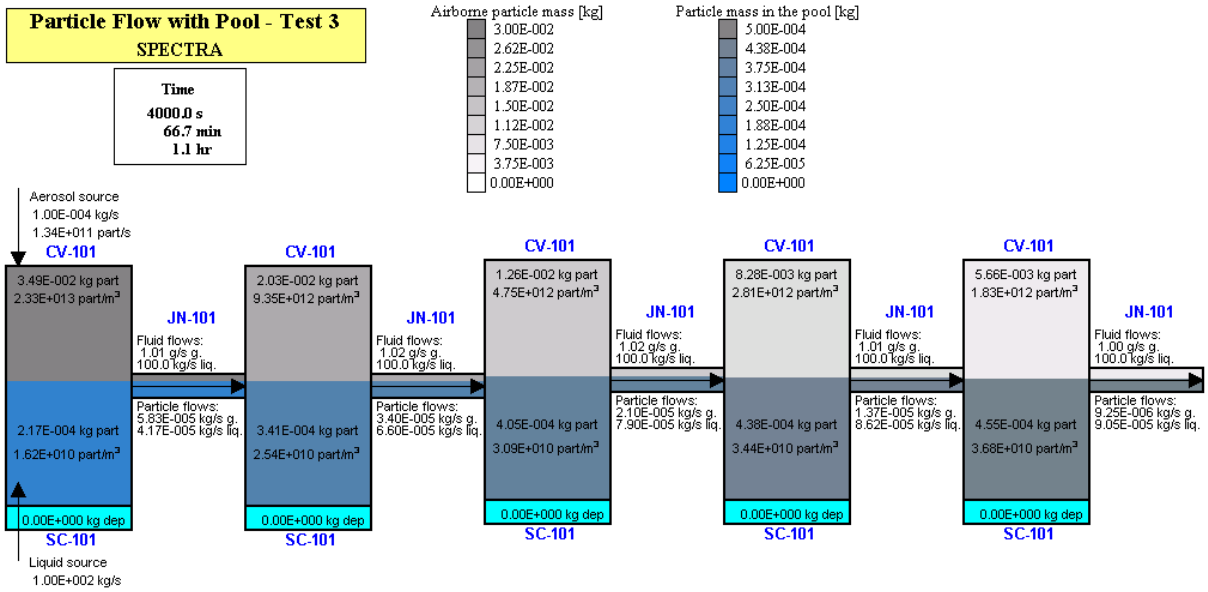

Figure 3-669 Particle flow with pool, Test 3, SPECTRA.

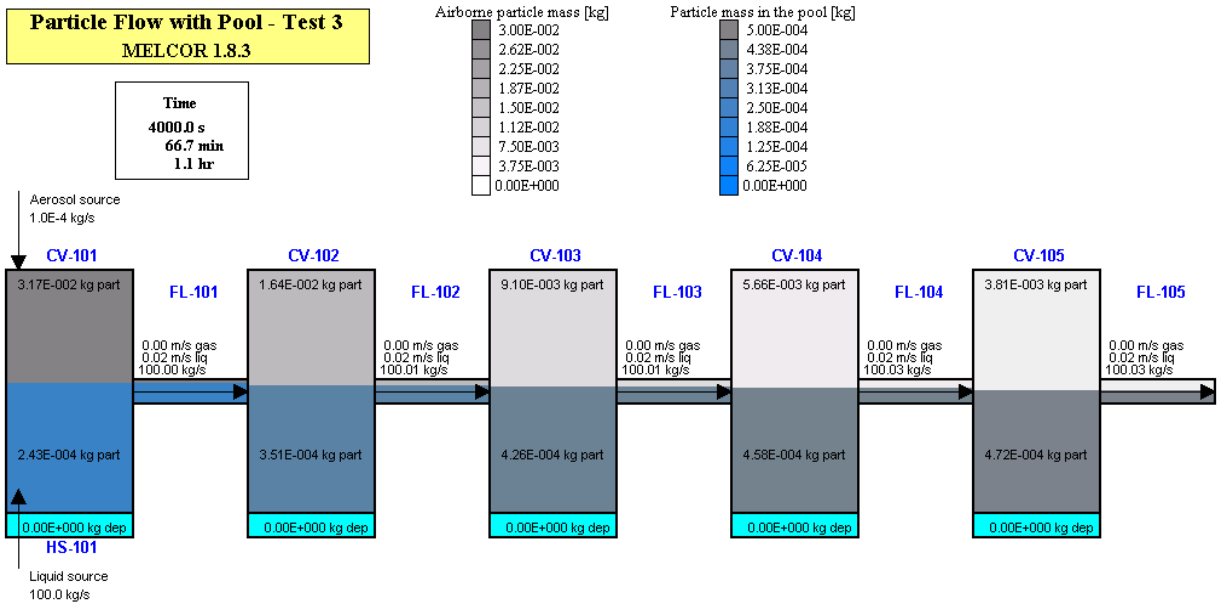

Figure 3-670 Particle flow with pool, Test 3, MELCOR 1.8.3.

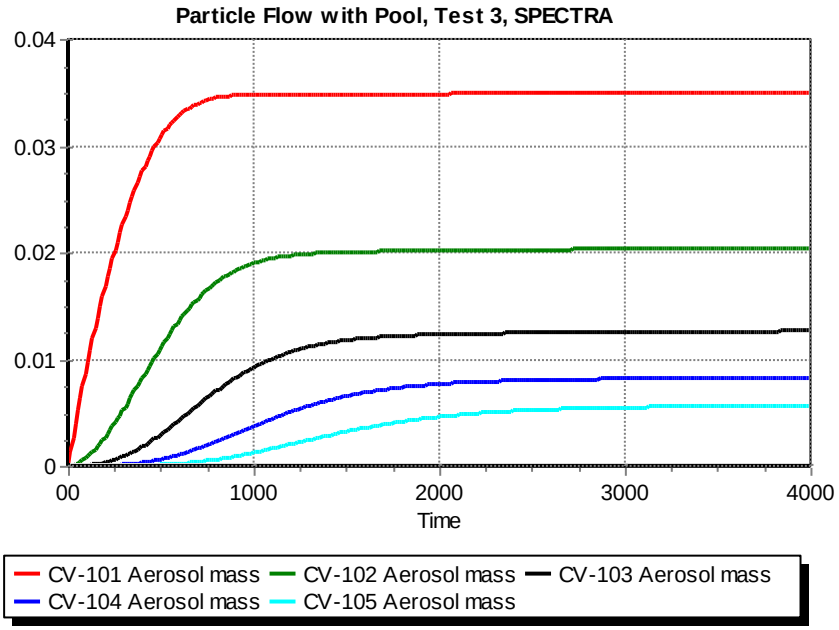

Figure 3-671 Particle flow with pool, Test 3, airborne masses, SPECTRA.

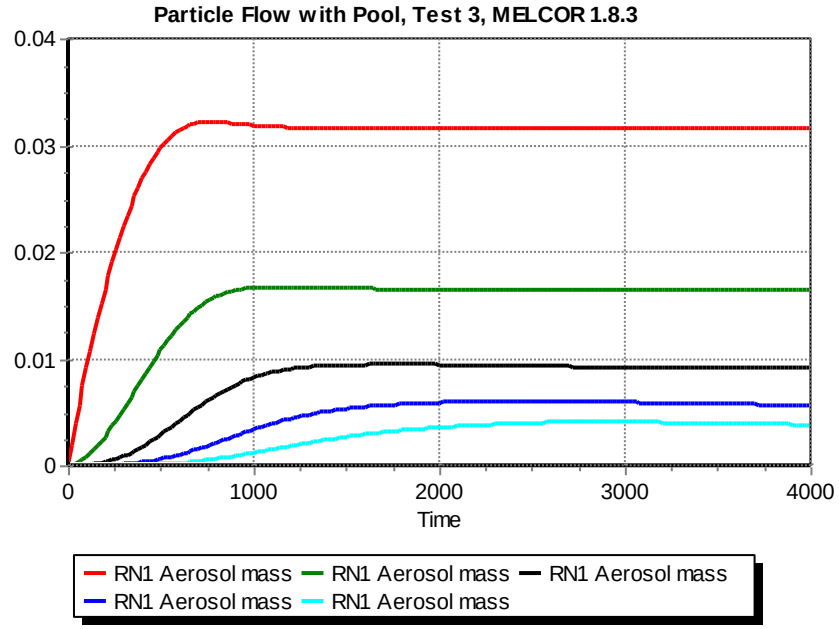

Figure 3-672 Particle flow with pool, Test 3, airborne masses, MELCOR 1.8.3.

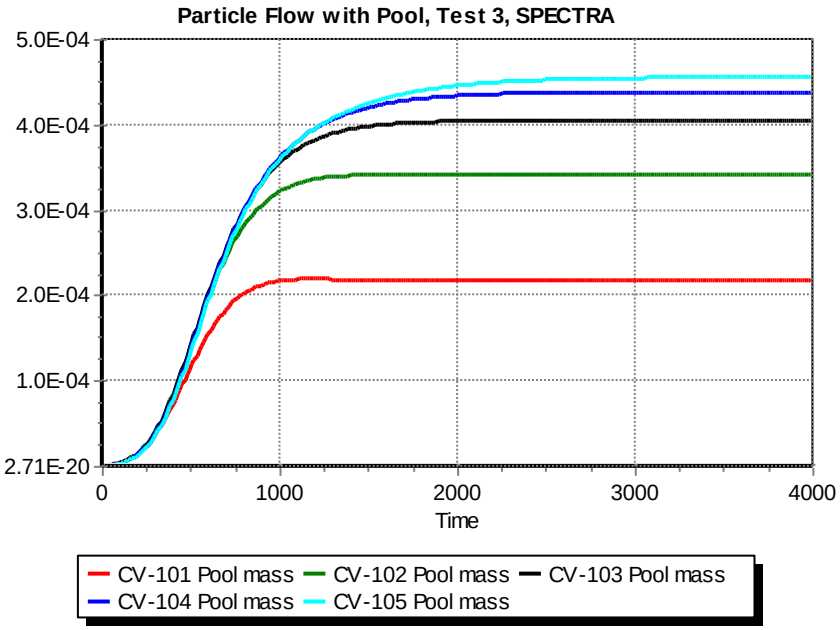

Figure 3-673 Particle flow with pool, Test 3, particle mass in the pool, SPECTRA.

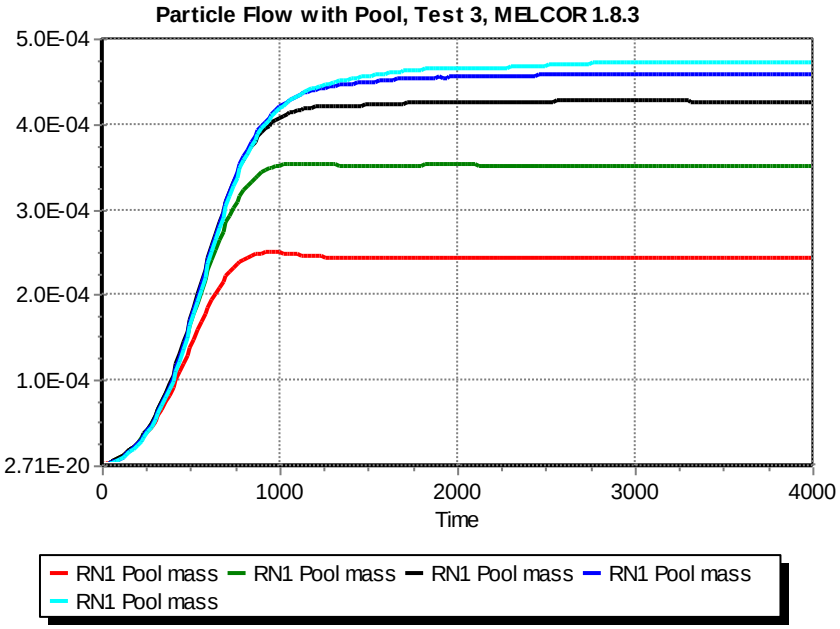

Figure 3-674 Particle flow with pool, Test 3, particle mass in the pool, MELCOR 1.8.3.

MELCOR results of the run Pool 3 with original FL areas and opening heights:

VOLUME NUMB	PRESSURE PA	TLIQ K	TVAP K	MASS KG	ENERGY J/KG	DENSITY KG/M**3
101	9.9564E+04	299.9788	300.0581	5.4792E+02	1.3089E+05	5.4792E+02
102	9.9541E+04	299.9788	300.0077	5.4909E+02	1.3034E+05	5.4909E+02
103	9.9550E+04	299.9787	299.9984	5.4825E+02	1.3012E+05	5.4825E+02
104	9.9500E+04	299.9787	299.9709	5.4983E+02	1.2933E+05	5.4983E+02
105	9.9526E+04	299.9787	299.9716	5.4814E+02	1.2824E+05	5.4814E+02
200	1.0000E+05	299.9998	299.9999	4.9889E+02	1.1696E+05	4.9889E+02

VOLUME NUMB	S-Z-POOL M	C-Z-POOL M	ENERGY J	AREA M**2	NAME
101	5.4920E-01	5.4920E-01	7.1715E+07	1.0000E+00	INLET BOUNDARY
102	5.5038E-01	5.5038E-01	7.1570E+07	1.0000E+00	CV-102
103	5.4953E-01	5.4953E-01	7.1338E+07	1.0000E+00	CV-103
104	5.5113E-01	5.5113E-01	7.1109E+07	1.0000E+00	CV-104
105	5.4942E-01	5.4942E-01	7.0293E+07	1.0000E+00	CV-105
200	5.0000E-01	5.0000E-01	5.8352E+07	1.0000E+00	DOWNSTREAM BOUND

It is seen that the water levels are at about the top of the junctions (0.55 m) and because of that the pressure in CV-101 through CV-104 is 0.05 bar lower than in CV-200 (5 cm water column). The gas flowing into CV-200 is therefore flowing against the pressure change.

As a first attempt to correct this problem, the opening heights of all junctions were increased. It was found out however, that even with the opening heights of 0.9 the problem still persisted. The results of 0.9 case are shown below.

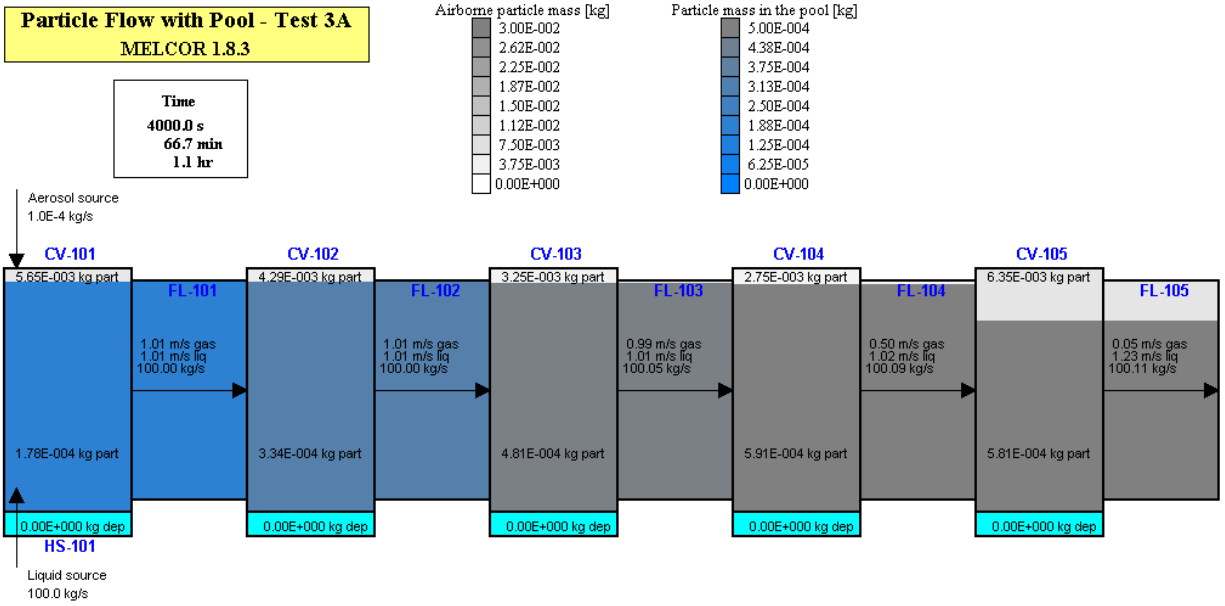

Figure 3-675 Particle flow with pool, Test 3A, Large opening heights, MELCOR 1.8.3.

The pressures, water levels, and velocities are shown in the printout below.

MELCOR results of the run Pool 3A (increased opening heights):

VOLUME NUMB	PRESSURE PA	TLIQ K	TVAP K	MASS KG	ENERGY J/KG	DENSITY KG/M**3
101	9.6258E+04	299.9795	299.9692	9.3962E+02	1.1384E+05	9.3962E+02
102	9.6249E+04	299.9795	299.9651	9.3943E+02	1.1381E+05	9.3943E+02
103	9.6243E+04	299.9794	300.1099	9.3923E+02	1.1382E+05	9.3923E+02
104	9.6303E+04	299.9793	300.0776	9.3179E+02	1.1400E+05	9.3179E+02
105	9.7737E+04	299.9792	299.9922	7.8260E+02	1.1842E+05	7.8260E+02
200	1.0000E+05	299.9998	299.9999	4.9889E+02	1.1696E+05	4.9889E+02

VOLUME NUMB	S-Z-POOL M	C-Z-POOL M	ENERGY J	AREA M**2	NAME
101	9.4271E-01	9.4271E-01	1.0696E+08	1.0000E+00	INLET BOUNDARY
102	9.4253E-01	9.4253E-01	1.0692E+08	1.0000E+00	CV-102
103	9.4233E-01	9.4233E-01	1.0690E+08	1.0000E+00	CV-103
104	9.3486E-01	9.3486E-01	1.0622E+08	1.0000E+00	CV-104
105	7.8498E-01	7.8498E-01	9.2675E+07	1.0000E+00	CV-105
200	5.0000E-01	5.0000E-01	5.8352E+07	1.0000E+00	DOWNSTREAM BOUND

FLOW PATH	FROM VOL.	TO VOL.	VELLIQ M/S	VELVAP M/S	MFLOW KG/S	AREA M**2	TYP	ACT
101	101	102	1.0116E+00	1.0142E+00	1.0000E+02	1.0000E-01	3	0
102	102	103	1.0118E+00	1.0144E+00	1.0000E+02	1.0000E-01	3	0
103	103	104	1.0124E+00	9.8990E-01	1.0005E+02	1.0000E-01	3	0
104	104	105	1.0214E+00	5.0149E-01	1.0009E+02	1.0000E-01	3	0
105	105	200	1.2300E+00	4.6625E-02	1.0011E+02	1.0000E-01	3	0

In this case the water level in CV-100 was nearly half a meter higher (0.46 m) than in the receiving volume! The pressure stabilized at about 0.96 bar (corresponding to about half a meter water column). The gas flow has now to overcome the pressure difference of about 0.4 bar, the only available force being the interfacial friction. With velocities of about 1.0 m/s it is practically impossible that the gas will be dragged along with liquid against such pressure difference. It is therefore concluded that the two-phase flow solution may need looking into be the code development team.

In order to obtain physical results with MELCOR the junction flow areas were artificially increased. Increasing area to 1.0 m^2 (velocities of about 0.1 m/s) did not cure the problem. The flow areas were further increased to 10 m^2 (velocities of about 0.01 m/s). Finally the problem disappeared, and results of this run are presented above, as the MELCOR results of the run Pool 3 (Figure 3-670). It should be noted that in the final run the large flow path opening heights were kept, so the visualization shown in Figure 3-670 may be somewhat misleading. Since it is felt quite certain that the flow results with the original opening heights would look very much like the results shown in Figure 3-670, if MELCOR solved the two-phase flow equations correctly, therefore the visualization picture was left unmodified (while in fact it should look more like the picture shown in Figure 3-675).

3.12.13 Vertical Flow of Aerosol Particles in the Pool

This section provides verification of the model used for vertical transport of particles in the pool. The correlation used to calculate the terminal velocity (i.e. vertical velocity of particles in a stagnant pool) is described in detail in Volume 1 (section: Alternative Correlation Terminal Velocity of Particles) and also discussed in this Volume in section 2.2.3. The correlation is:

$$v_\infty = \left(\frac{4/3}{C_D} \cdot \frac{D_p g(\rho_f - \rho_p)}{\rho_f} \right)^{0.5}$$

Here g is the gravity acceleration (m/s^2), ρ is density (kg/m^3), η is viscosity, (kg/m-s), D is diameter. Subscripts p refers to particle, while f to fluid. The alternative correlation for particle terminal velocity may be applied in two ways:

- Drag coefficient, C_D, calculated using five correlations, valid for different Re.
- Drag coefficient, C_D, defined by the user.

The correlation is applied in the following situations:

- Within a single CV, to calculate particle terminal velocity in the CV pool (that is added to the liquid vertical velocity in the pool). Two situations are possible:
  - downflow towards a solid structure (if present) - the process referred to as sedimentation of pool particles,
  - upflow towards the pool surface and further to atmosphere of CV - the process referred to as resuspension of pool particles.

  The flow direction is determined as follows.
  - If the terminal velocity is defined by the user - positive value means the particles will flow up, towards the pool surface.
  - If the correlation is used, the flow direction depends on the density of particles (ρ_p = DENART - Volume 2) compared to the density of the liquid, ρ_f. The flow is positive when $\rho_p < \rho_f$. (light particles, for example representing gas bubbles). The flow is negative when $\rho_p > \rho_f$. (heavy particles).
- In vertical junctions connecting different CVs, to calculate the terminal velocity of particles in a junction (that is added to the liquid velocity multiplied by a slip ratio). The remarks above concerning the flow direction apply here as well.

The verification tests are performed for all above mentioned situations are described below:

- sedimentation of heavy particles in a single CV - section 3.12.13.1,
- flow to pool surface of light particles in a single CV - section 3.12.13.2,
- downflow of heavy particles through multiple CVs - section 3.12.13.3,
- upflow of light particles through multiple CVs - section 3.12.13.4.

3.12.13.1 Sedimentation of Heavy Particles in a Single CV

The test case consists of a single CV, half-filled with water at 1 bar, 300 K (density of ρ_f = 996.5 kg/m^3). The volume of water is V_{pool} = 1.0 m^3 (A = 1.0 m^2, H_{pool} = 1.0 m). An initial mass of 10^{-3} kg of 100 micron particles ($D_p = 10^{-4}$ m) is initially suspended in the pool. "Heavy" particles ($\rho_p > \rho_f$) are used. Particle density is equal to ρ_p = 2000 kg/m^3. A solid structure, SC-101, provides the surface for sedimentation. Three cases are considered:

- Case 1: Particles have a constant, user-defined velocity of v_∞ = –0.01 m/s
- Case 2: Correlation for v_∞ is used with $C_{D,Re\to\infty}$ = 0.47
- Case 3: Correlation for v_∞ is used with C_D = 0.47 = const.

The particle mass balance is:

$$\frac{dm}{dt} = -A \cdot v_\infty \cdot \frac{m}{V_{pool}}$$

solution:

$$m = m_0 \cdot \exp\left(-\frac{A \cdot v_\infty}{V_{pool}} \cdot t \right)$$

Here m is the mass of particles in the pool, m_0 is the initial mass: m_0 = 0.001 (kg), A is the horizontal cross-section of the CV pool (m^2), V_{pool} is the pool volume (m^3), and t is time (s). In order to perform verification of the computed values, an automated verification was set-up using Tabular Functions and Control Functions, defined as follows:

- TF-201 = A = 1.0
- CF-111 = $v_\infty = W \times V_{pool} / m / A$
  = SC-101-DR03-0001 × CV-101-Volm-pool / CV-101-SMaP-0000 / 1.0
- CF-201 = $A\ v_\infty\ t / V_{pool}$ =
  = TF-201-Valu-0000 × CF-111-Valu-0000 × SL-000-Time-0000 /
  / CV-101-Volm-pool
- CF-202 = $m = \exp(-A\ v_\infty\ t / V_{pool})$ =
  = exp (– CF-101-Valu-0000)

The particle terminal velocity is not available as a plot/CF parameter, therefore it is obtained in CF-111 as particle mass transfer rate W (kg/s), divided by the particle density in the pool (m/V_{pool}) (kg/m^3), multiplied by the deposition area A = 1.0 m^2. The parameter SC-101-DR03-0001 is the deposition mass transfer rate W (kg/s) for size section 3 (size section of $D = 10^{-4}$ m, used in the present test). Furthermore, correctness of the v_∞ is verified by hand calculation as will be shown below.

The SPECTRA input files are located in: **`\Z-INPUTS\RT\Pool-Vinf\CV-Down`**

Results for the three cases are discussed below.

- **Case 1: Constant velocity, v_∞ = –0.01 m/s**

In this case a constant velocity v_∞ = –0.01 m/s is defined in the input deck. The input file is located in: **`\Z-INPUTS\RT\Pool-Vinf\CV-Down\Pool-Vinf-1.SPE`**

Results are shown in Figure 3-676 and Figure 3-677. Figure 3-676 shows the state of the system at t = 100 s, when approximately 1/3 of the particles remain suspended in the pool. Figure 3-677 shows the mass of particles in the pool and the theoretical solution, obtained with CF-202. The calculated results are in good agreement with the theoretical solution.

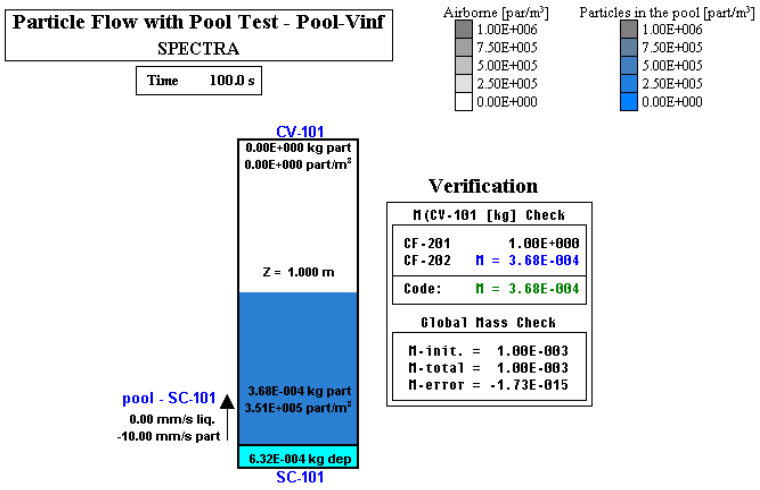

Figure 3-676 Sedimentation in a single CV pool, Case 1

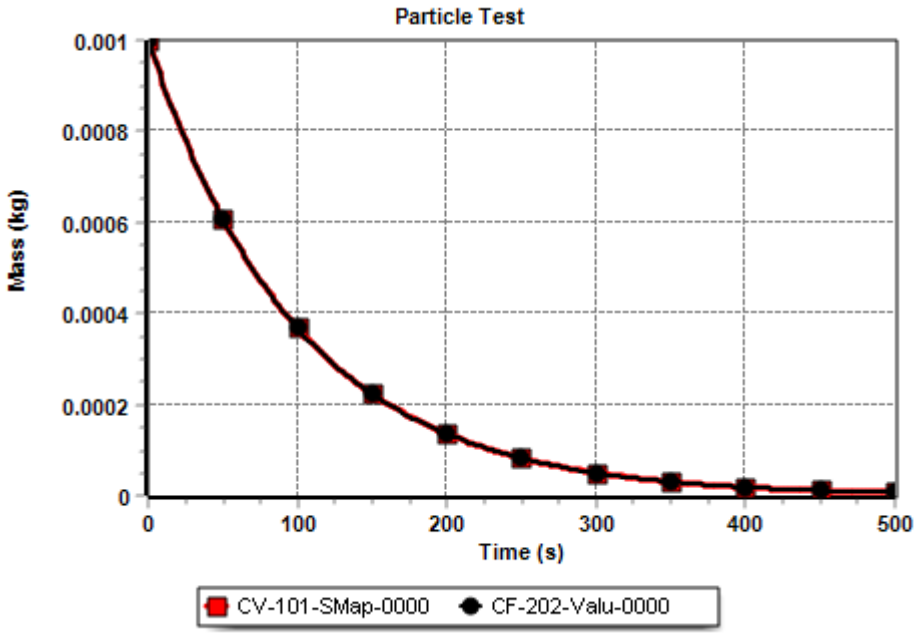

Figure 3-677 Calculated and theoretical (CF-202) mass in the pool, Case 1

- **Case 2: Correlation for v_∞ with $C_{D,Re\to\infty}$ = 0.47**

In this case the terminal velocity correlation is used with $C_{D,Re\to\infty}$ = 0.47. The input file is located in: **`\Z-INPUTS\RT\Pool-Vinf\CV-Down\Pool-Vinf-2.SPE`**

Results are shown in Figure 3-678 and Figure 3-679. Figure 3-678 shows the state of the system at t = 100 s, when approximately 1/2 of the particles remain suspended in the pool. Figure 3-679 shows the mass of particles in the pool and the theoretical solution, obtained with CF-202. The calculated results are in good agreement with the theoretical solution.

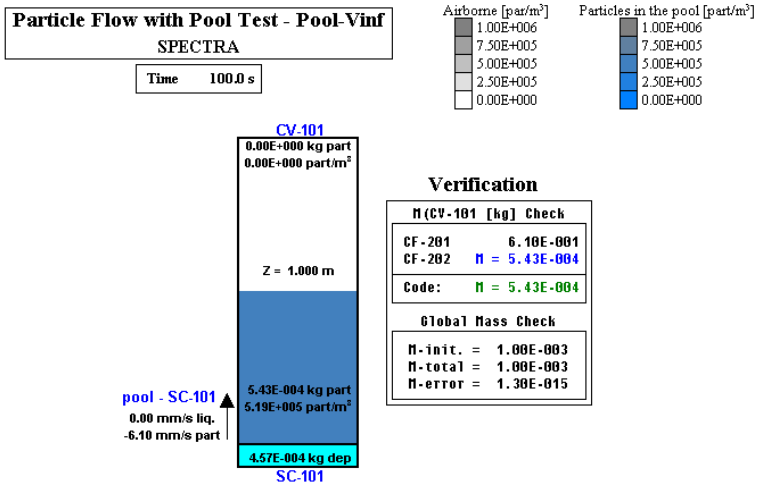

Figure 3-678 Sedimentation in a single CV pool, Case 2

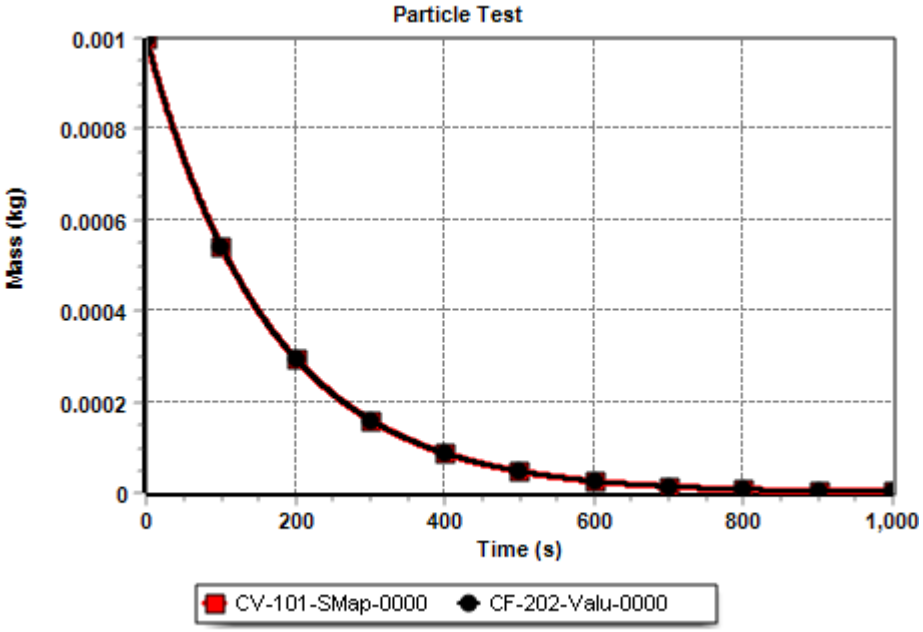

Figure 3-679 Calculated and theoretical (CF-202) mass in the pool, Case 2

- **Case 3: Correlation for v_∞ with C_D = 0.47 = const.**

In this case the terminal velocity correlation is used with constant C_D = 0.47. To see the effect of drag coefficient, the correlation for small particles was eliminated by setting CSMLCV to zero, otherwise this correlation would affect the results here. The input file is located in:
\Z-INPUTS\RT\Pool-Vinf\CV-Down\Pool-Vinf-3.SPE

Results are shown in Figure 3-680 and Figure 3-681. Figure 3-680 shows the state of the system at t = 20 s, when approximately 1/3 of the particles remain suspended in the pool. Figure 3-681 shows the mass of particles in the pool and the theoretical solution, obtained with CF-202. The calculated results are in good agreement with the theoretical solution.

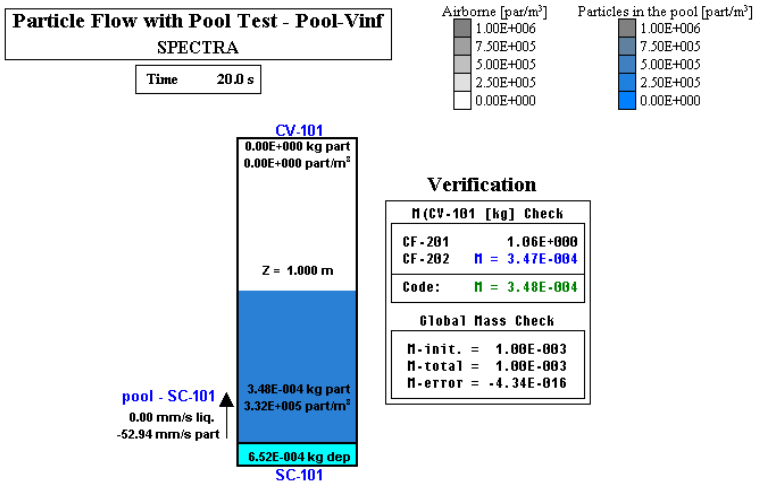

Figure 3-680 Sedimentation in a single CV pool, Case 3

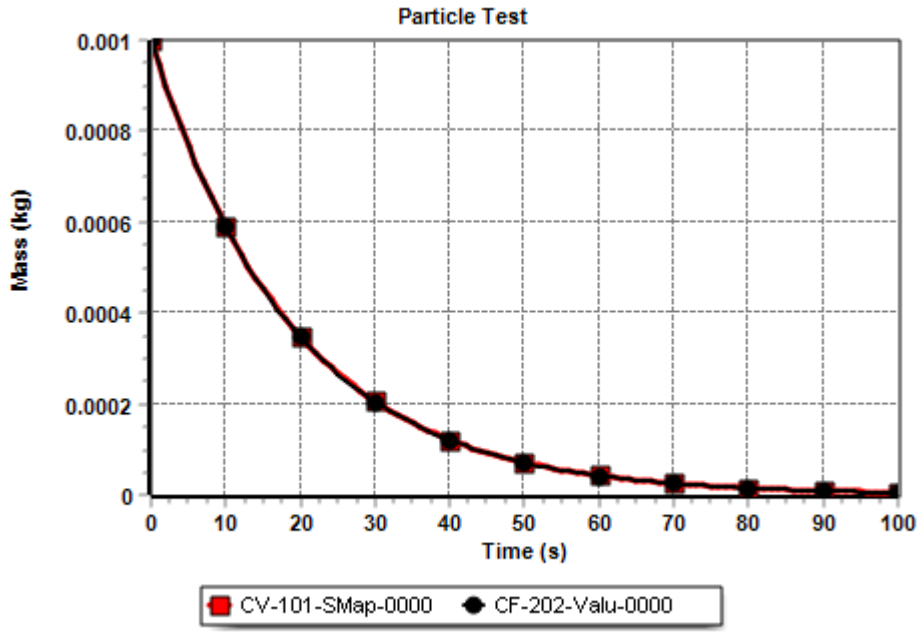

Figure 3-681 Calculated and theoretical (CF-202) mass in the pool, Case 3

As an additional verification, the terminal velocity was checked by hand calculations:

$$v_\infty = \left(\frac{4/3}{C_D} \cdot \frac{D_p g(\rho_p - \rho_f)}{\rho_f} \right)^{0.5} = \left(\frac{4/3}{0.47} \cdot \frac{10^{-4} \times 9.81 \times (2000 - 996.5)}{996.5} \right)^{0.5} = 0.05294$$

The value calculated by the code (not directly plottable, it is obtained here by Control Function CF-111, using particle mass transfer rate from the pool to SC) is equal to 0.05294 (Figure 3-680), in very good agreement with the theoretical value.

It should be noted that the total time of sedimentation is very different in the case 2 and 3:

- Case 2, $C_{D,Re\to\infty} = 0.47$, $\tau \sim 1000$ s
- Case 3, $C_D = 0.47$, $\tau \sim 100$ s

The reason for this difference is that the drag coefficient is much larger at low Reynolds numbers - Figure 3-682. In the current test particles have diameter of 10^{-4} m and the Reynolds number is very small.

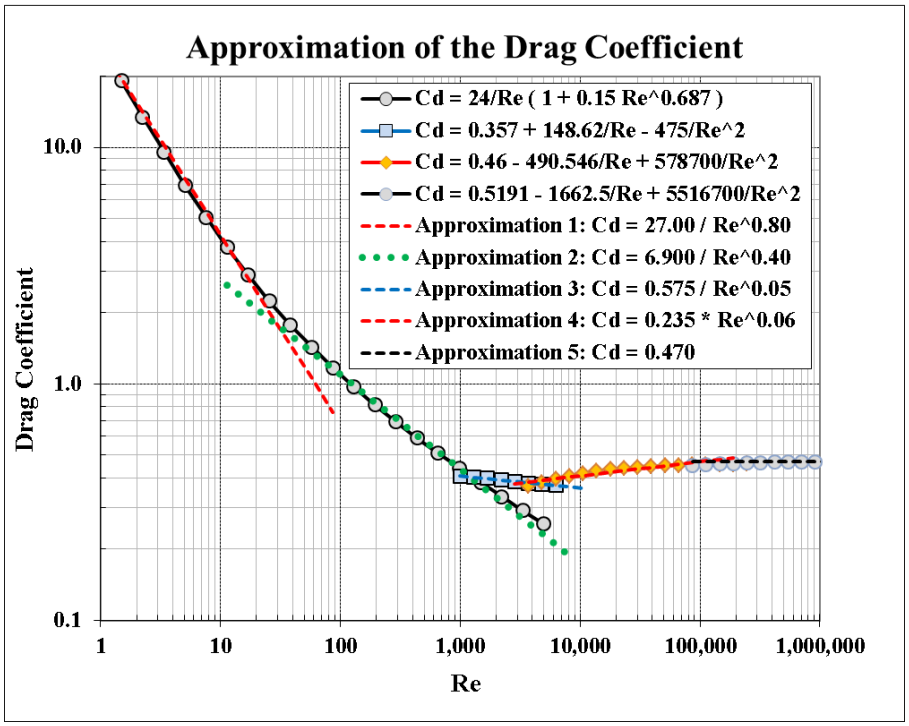

Figure 3-682 Drag coefficient correlation
(Volume 1, section: Alternative Correlation for Terminal Velocity of Particles)

In Case 2:

$$\mathrm{Re} = \frac{v_\infty \cdot D_p \cdot \rho_f}{\eta_f} = \frac{0.0061 \cdot 10^{-4} \cdot 996.5}{8.55 \cdot 10^{-4}} \approx 0.7$$

The drag coefficient in this region is about 30, which is nearly two orders of magnitude larger than in the second case, where the user-defined coefficient is constant and equal to 0.47 independently of the Reynolds number. Since the deposition velocity is proportional to square root of C_D, the velocity ratio is one order of magnitude larger and so is the ratio of the deposition times.

3.12.13.2 Flow to Pool Surface of Light Particles in a Single CV

This test is very similar to the previous one. This time the particle flow is upwards, which is obtained by:

- In Case 1 simply by changing the velocity sign, from $v_\infty = -0.01$ m/s to $v_\infty = +0.01$ m/s
- In Case 2 and 3 by changing the particle density from "heavy" (ρ_p =2000.0 kg/s > ρ_f) to "light" (ρ_p = 1.0 kg/s < ρ_f).

One important modeling option needs to be used here:

- Aerosol deposition on the pool surface must be disabled (IDEPRT(1)=–1, record 865002), otherwise some of the particles released to the atmosphere of CV-101 will be depositing back on the pool surface due to deposition mechanisms (gravitational settling, Brownian motion, thermophoresis, turbulent deposition, etc.).

Furthermore, the automated verification function needs to be modified. In the present case, the mass transfer rate W (kg/s) in CF-111 has to be the pool-atmosphere transfer, parameter CV-101-RRPL-0003 (the value for size section number 3, which is the size section of $D = 10^{-4}$ m, used in the present test). The automatic verification functions for this case are:

- TF-201 = A = 1.0
- CF-111 = $v_\infty = W \times V_{pool} / m / A$
  = CV-101-RRPL-0003 × CV-101-Volm-pool / CV-101-SMaP-0000 / 1.0
- CF-201 = $A\, v_\infty\ t / V_{pool}$ =
  = TF-201-Valu-0000 × CF-111-Valu-0000 × SL-000-Time-0000 /
  / CV-101-Volm-pool
- CF-202 = $m = \exp(-A\, v_\infty\ t / V_{pool})$ =
  = exp (– CF-101-Valu-0000)

The SPECTRA input files are located in: **\Z-INPUTS\RT\Pool-Vinf\CV-Up**

Results for the three cases are discussed below.

- **Case 1: Constant velocity, v_∞ = –0.01 m/s**

In this case a constant velocity v_∞ = –0.01 m/s is defined in the input deck. The input file is located in: **`\Z-INPUTS\RT\Pool-Vinf\CV-Up\Pool-Vinf-1.SPE`**

Results are shown in Figure 3-683 and Figure 3-684. Figure 3-683 shows the state of the system at t = 100 s, when approximately 1/3 of the particles remain suspended in the pool. Figure 3-684 shows the mass of particles in the pool and the theoretical solution, obtained with CF-202. The calculated results are in good agreement with the theoretical solution.

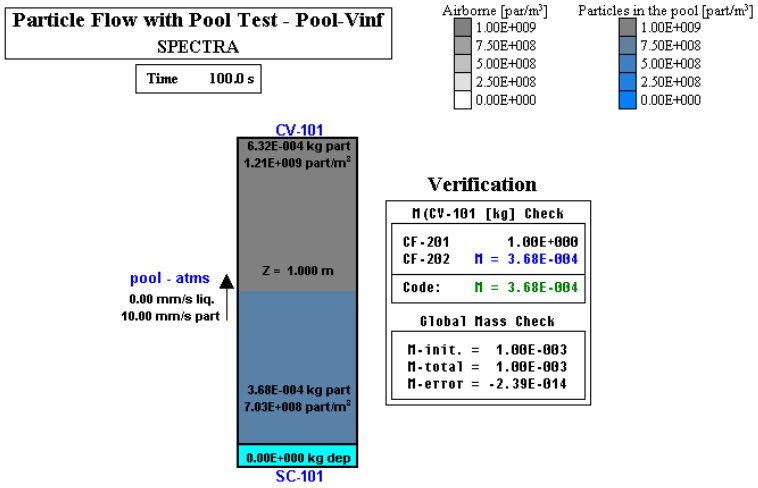

Figure 3-683 Particle flow to pool surface in a single CV, Case 1

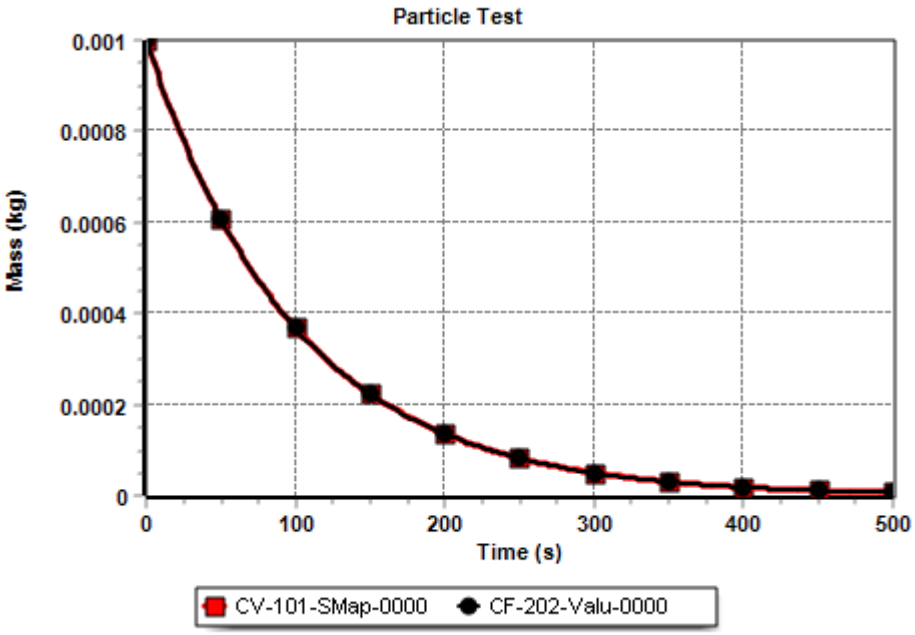

Figure 3-684 Calculated and theoretical (CF-202) mass in the pool, Case 1

- **Case 2: Correlation for v_∞ with $C_{D,Re\to\infty}$ = 0.47**

In this case the terminal velocity correlation is used with $C_{D,Re\to\infty}$ = 0.47. The input file is located in: **`\Z-INPUTS\RT\Pool-Vinf\CV-Up\Pool-Vinf-2.SPE`**

Results are shown in Figure 3-685 and Figure 3-686. Figure 3-685 shows the state of the system at t = 100 s, when approximately 1/2 of the particles remain suspended in the pool. Figure 3-686 shows the mass of particles in the pool and the theoretical solution, obtained with CF-202. The calculated results are in good agreement with the theoretical solution.

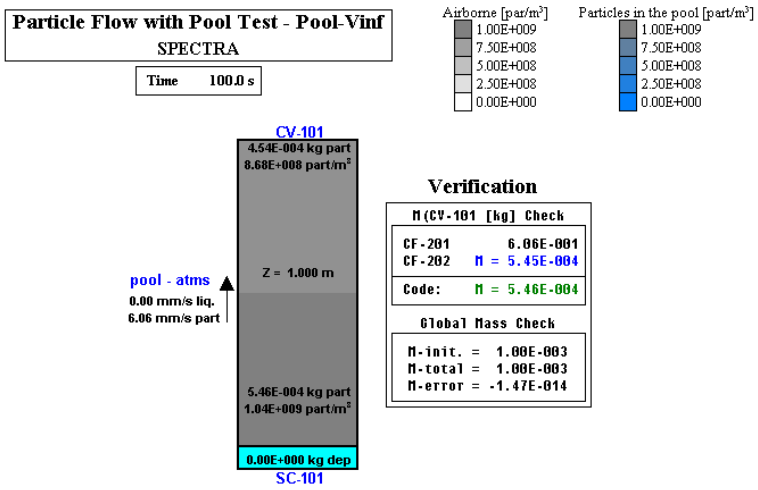

Figure 3-685 Particle flow to pool surface in a single CV, Case 2

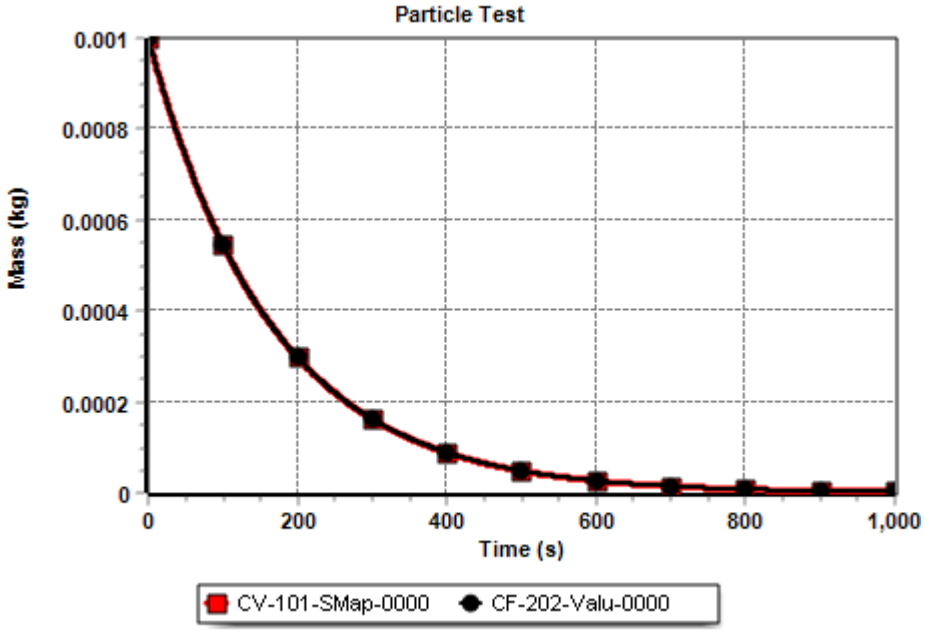

Figure 3-686 Calculated and theoretical (CF-202) mass in the pool, Case 2

- **Case 3: Correlation for v_∞ with C_D = 0.47 = const.**

In this case the terminal velocity correlation is used with constant C_D = 0.47. To see the effect of drag coefficient, the correlation for small particles was eliminated by setting CSMLCV to zero, otherwise this correlation would affect the results here. The input file is located in:
\Z-INPUTS\RT\Pool-Vinf\CV-Up\Pool-Vinf-3.SPE

Results are shown in Figure 3-687 and Figure 3-688. Figure 3-687 shows the state of the system at t = 20 s, when approximately 1/3 of the particles remain suspended in the pool. Figure 3-688 shows the mass of particles in the pool and the theoretical solution, obtained with CF-202. The calculated results are in very good agreement with theoretical solution.

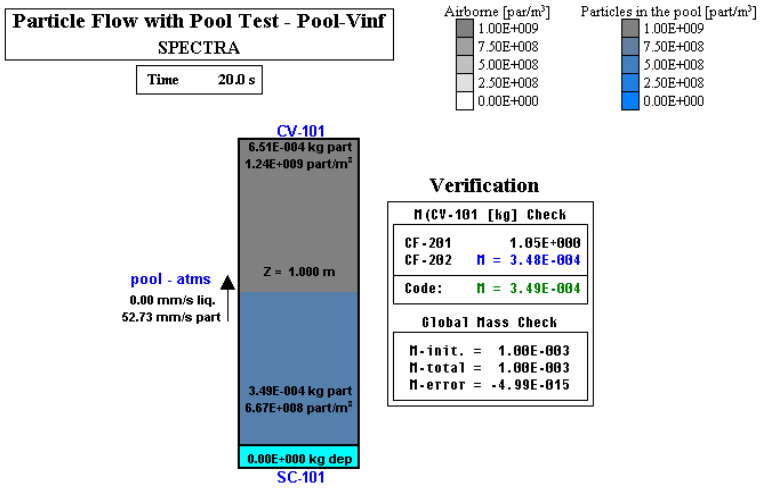

Figure 3-687 Particle flow to pool surface in a single CV, Case 3

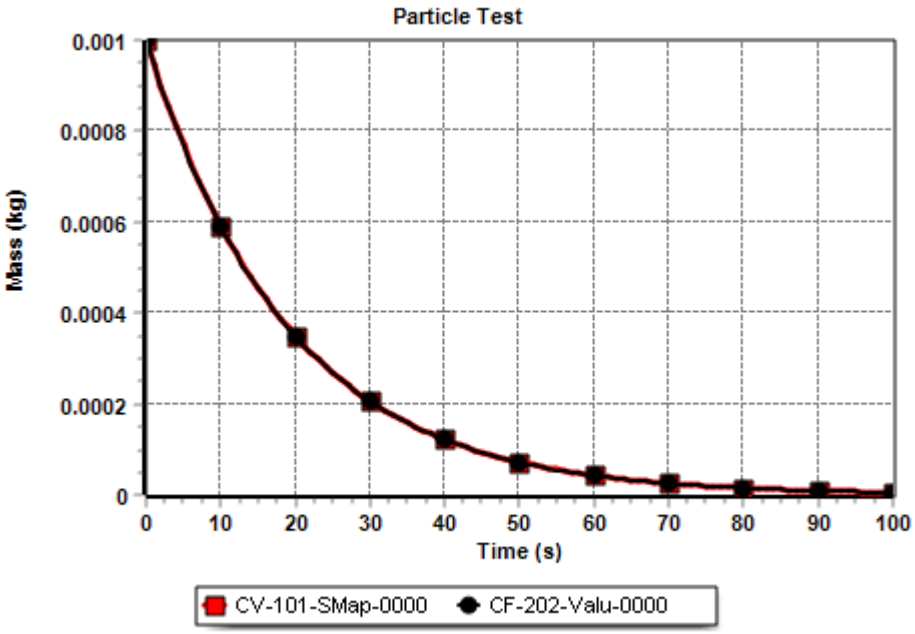

Figure 3-688 Calculated and theoretical (CF-202) mass in the pool, Case 3

The current set of tests is very similar to the one presented in the previous section. While in the previous section heavy particles were depositing on SC-101, in the present cases they are transferred to the atmosphere of CV-101. The velocity in Case 2 and 3 is slightly different because the density difference is not the same:

- heavy particles: $\Delta\rho = (\rho_p - \rho_f) = 2000 - 996.5 = 1003.5$ kg/m^3, $v_{\infty,2} = 6.10$, $v_{\infty,3} = 52.9$
- light particles: $\Delta\rho = (\rho_f - \rho_p) = 996.5 - 1.0 = 995.5$ kg/m^3, $v_{\infty,2} = 6.06$, $v_{\infty,3} = 52.7$

3.12.13.3 Downflow of Heavy Particles through Multiple CVs

The test is aimed at verification of particle velocity in junctions and consists of multiple Control Volumes connected by junctions, including:

- JN-101: $A = 0.5$ m^2, vertical up
- JN-102: $A = 0.5$ m^2, vertical down
- JN-103: $A = 0.5$ m^2, horizontal

The initial conditions are shown in Figure 3-689 (A). CV-101 and CV-102 are filled with water at 1 bar, 300 K (density of $\rho_f = 996.5$ kg/m^3). The volume of water is:

- CV-101: $V_{pool} = 1.0$ m^3 ($A = 1.0$ m^2, $H_{pool} = 1.0$ m).
- CV-102: $V_{pool} = 0.5$ m^3 ($A = 1.0$ m^2, $H_{pool} = 0.5$ m).
- CV-103: $V_{pool} = 1.5$ m^3 ($A = 1.0$ m^2, $H_{pool} = 1.5$ m).

An initial mass of 0.5×10^{-3} kg of 100 micron particles ($D_p = 10^{-4}$ m) is initially suspended in the pool of CV-102. "Heavy" particles ($\rho_p > \rho_f$) are used. Particle density is equal to $\rho_p = 2000$ kg/m^3. A solid structure, SC-101, provides the surface for sedimentation in CV-101. The particles are transported from CV-102 down to CV-101 through the two vertical junctions and then deposited on SC-101. No flow is expected through JN-103, because the terminal particle velocity in the horizontal direction is zero and the liquid velocity is practically zero all the time. Three cases are considered:

- Case 1: Particles have a constant, user-defined velocity of $v_\infty = -0.01$ m/s
- Case 2: Correlation for v_∞ is used with $C_{D,Re\to\infty} = 0.47$
- Case 3: Correlation for v_∞ is used with $C_D = 0.47$ = const.

The particle mass balance in CV-102 is:

$$\frac{dm}{dt} = -A \cdot v_\infty \cdot \frac{m}{V_{pool}}$$

solution:

$$m = m_0 \cdot \exp\left(-\frac{A \cdot v_\infty}{V_{pool}} \cdot t \right)$$

Here m is the mass of particles in the pool, m_0 is the initial mass: m_0 = 0.0005 (kg), A is the total horizontal cross-section of the vertical junctions JN-101 and JN-102 (m^2), V_{pool} is the pool volume (m^3), and t is time (s).

The particle terminal velocities are not available as a plot/CF parameters, therefore they are obtained using Control Functions, as the particle mass transfer rate W (kg/s), divided by the particle density in the pool (m/V_{pool}) (kg/m^3), and multiplied by the deposition area A (m^2). The values are shown in visualization pictures (e.g.: Figure 3-691). Correctness of the values may be checked by looking up the velocities in the main ouput file (*.OUT):

```
=RT=  JN POOL, VELOCITIES OF PARTICLES [m/s]

                Size sec.:   1          2          3          4          5
JN-101, CV-101 -> CV-102,  0.000E+00  0.000E+00 -6.102E-03  0.000E+00  0.000E+00
JN-102, CV-102 -> CV-101,  0.000E+00  0.000E+00  6.101E-03  0.000E+00  0.000E+00
JN-103, CV-101 -> CV-103,  0.000E+00  0.000E+00  0.000E+00  0.000E+00  0.000E+00
```

In order to perform verification of the computed values, an automated verification was set-up using Tabular Functions and Control Functions, defined as follows:

- TF-201 = $A = A_{101} + A_{102} = 1.0$
- CF-101 = v_∞ (JN-101) = $W_{101} \times V_{pool} / m / A_{101}$
  = JN-101-WmPf-0000 × CV-102-Volm-pool / CV-102-SMaP-0000 / 0.5
- CF-102 = v_∞ (JN-102) = $W_{102} \times V_{pool} / m / A_{102}$
  = JN-102-WmPf-0000 × CV-102-Volm-pool / CV-102-SMaP-0000 / 0.5
- CF-111 = v_∞ (CV-101) = $W \times V_{pool} / m / A$
  = SC-101-DR03-0001 × CV-101-Volm-pool / CV-101-SMaP-0000 / 1.0
- CF-201 = $A\, v_\infty\, t / V_{pool}$ =
  = TF-201-Valu-0000 × CF-102-Valu-0000 × SL-000-Time-0000 /
  / CV-102-Volm-pool
- CF-202 = $m = \exp(-A\, v_\infty\, t / V_{pool})$ =
  = exp (– CF-201-Valu-0000)

The SPECTRA input files are located in: **\Z-INPUTS\RT\Pool-Vinf\JN-Down**

Results for the three cases are discussed below.

- **Case 1: Constant velocity, v_∞ = –0.01 m/s**

In this case a constant velocity v_∞ = –0.01 m/s is defined in the input deck. The input file is located in: **\Z-INPUTS\RT\Pool-Vinf\JN-Down\Pool-Vinf-1.SPE**

Results are shown in Figure 3-689 and Figure 3-690. Figure 3-689 (A) shows the initial state of the system. Figure 3-689 (B) shows the state of the system at t = 100 s, when about 7×10^{-5} kg (14%) is in the pool of CV-102, 23×10^{-5} kg (46%) is in the pool of CV-101, and 20×10^{-5} kg (40%) is deposited on SC-101. Figure 3-690 shows the time-dependent masses of particles in CV-101 and CV-102, deposited on SC-101, as well as the theoretical solution obtained for CV-102. The calculated results are in good agreement with the theoretical solution.

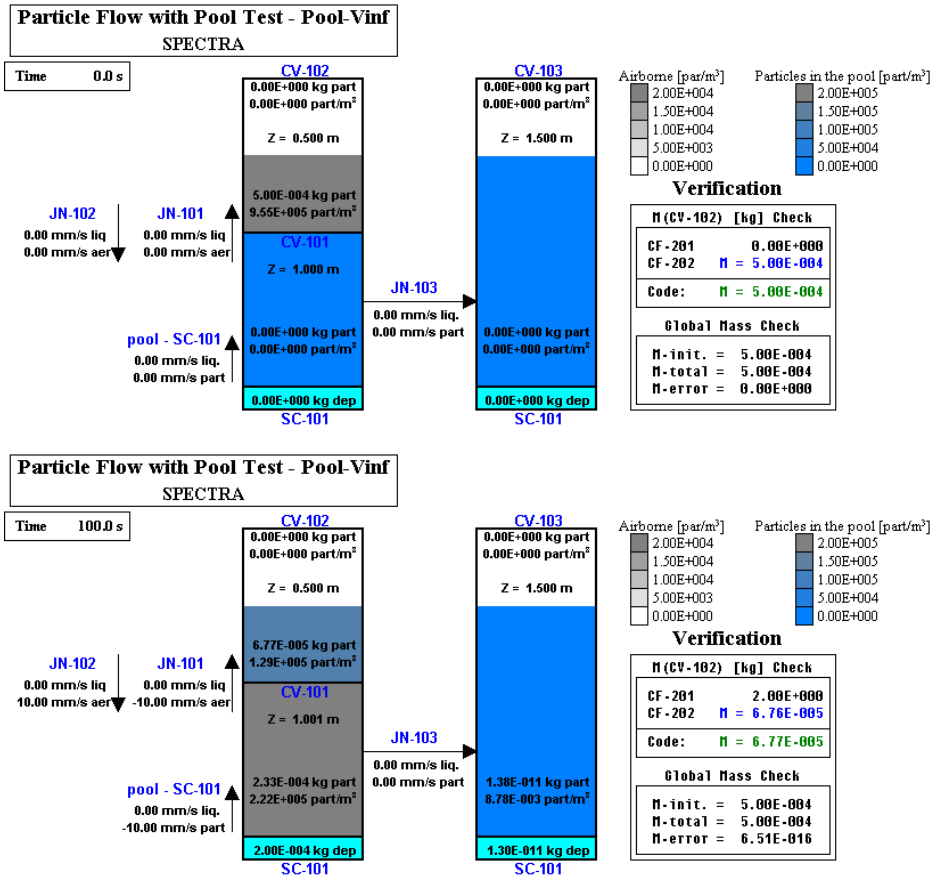

(A)

(B)

Figure 3-689 Downflow of particles, Case 1 (A) initial state, (B) state at t = 100 s

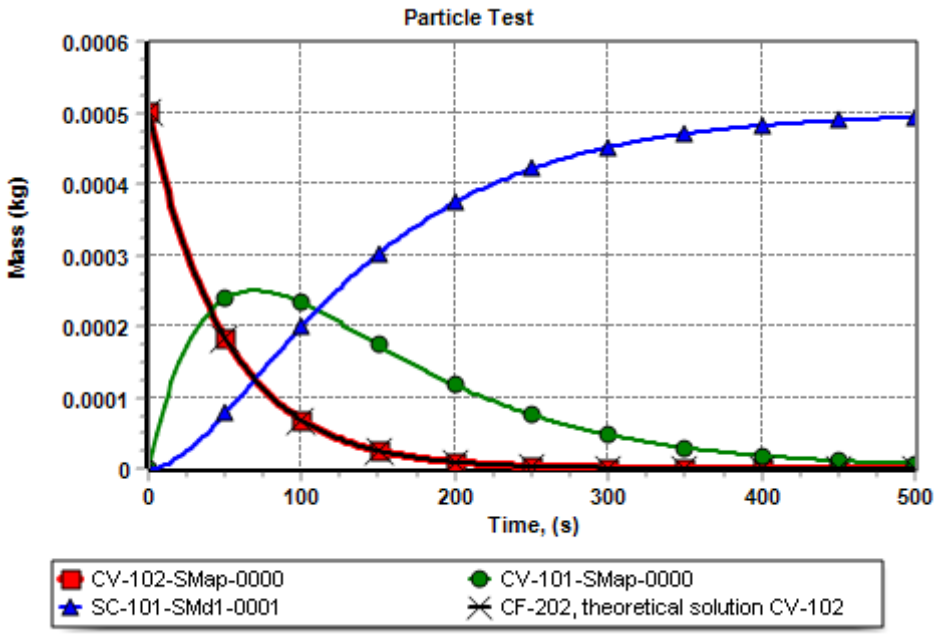

Figure 3-690 Mass distribution, Case 1

- **Case 2: Correlation for v_∞ with $C_{D,Re\to\infty}$ = 0.47**

In this case the terminal velocity correlation is used with $C_{D,Re\to\infty}$ = 0.47. The input file is located in: **`\Z-INPUTS\RT\Pool-Vinf\JN-Down\Pool-Vinf-2.SPE`**

Results are shown in Figure 3-691 and Figure 3-692. Figure 3-691 shows the state of the system at t = 100 s, when about 15×10^{-5} kg (30%) is in the pool of CV-102, 25×10^{-5} kg (50%) is in the pool of CV-101, and 10×10^{-5} kg (20%) is deposited on SC-10l. Figure 3-692 shows the time-dependent masses of particles in CV-101 and CV-102, deposited on SC-101, as well as the theoretical solution obtained for CV-102. The calculated results are in good agreement with the theoretical solution.

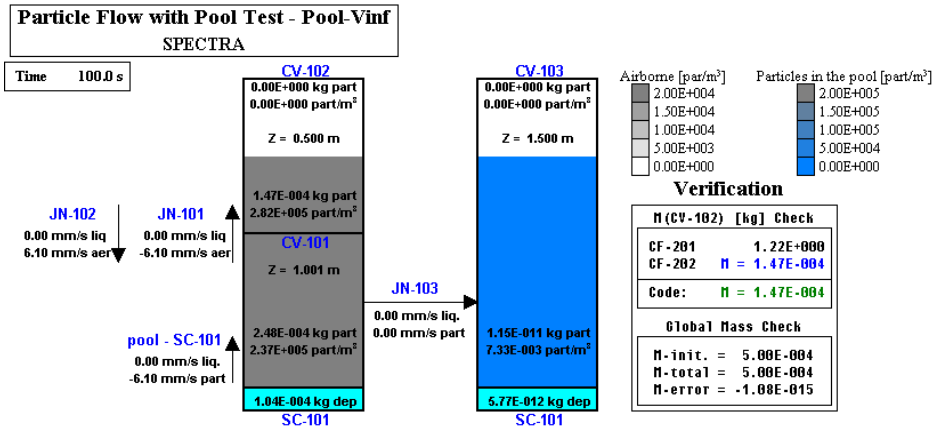

Figure 3-691 Downflow of particles, Case 2 state at t = 100 s

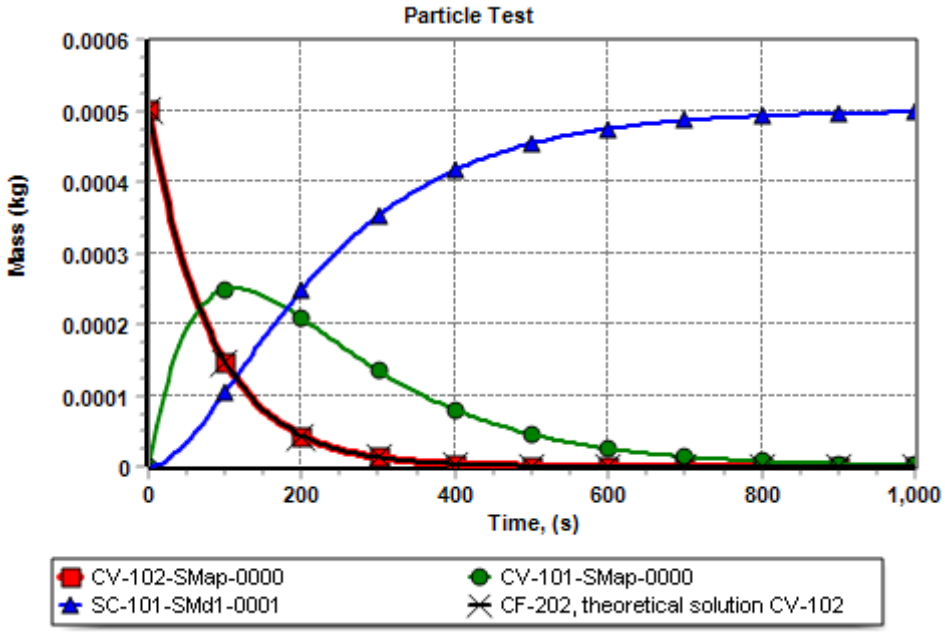

Figure 3-692 Mass distribution, Case 2

- **Case 3: Correlation for v_∞ with C_D = 0.47 = const.**

In this case the terminal velocity correlation is used with constant C_D = 0.47. To see the effect of drag coefficient, the correlation for small particles was eliminated by setting CSMLCV to zero, otherwise this correlation would affect the results here. The input file is located in:
\Z-INPUTS\RT\Pool-Vinf\JN-Down\Pool-Vinf-3.SPE

Results are shown in Figure 3-693 and Figure 3-694. Figure 3-693 shows the state of the system at t = 20 s, when about 6×10^{-5} kg (12%) is in the pool of CV-102, 23×10^{-5} kg (46%) is in the pool of CV-101, and 21×10^{-5} kg (42%) is deposited on SC-10l. Figure 3-694 shows the time-dependent masses of particles in CV-101 and CV-102, deposited on SC-101, as well as the theoretical solution obtained for CV-102. The calculated results are in good agreement with the theoretical solution.

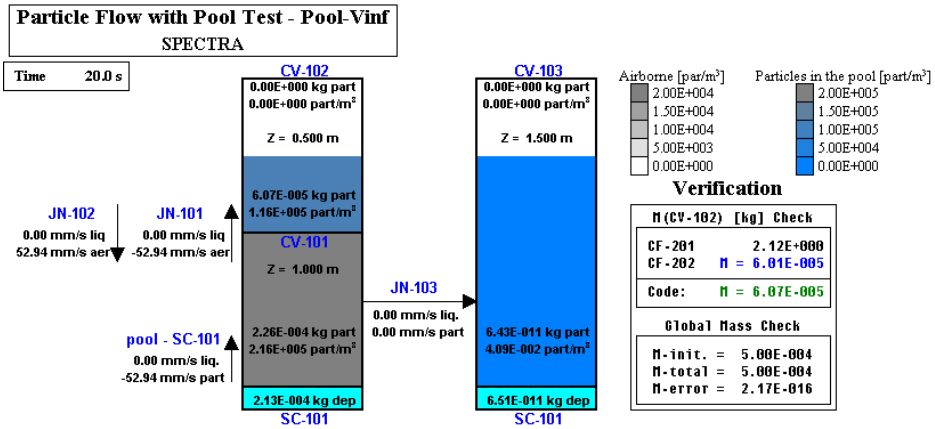

Figure 3-693 Downflow of particles, Case 3 Sate at t = 20 s

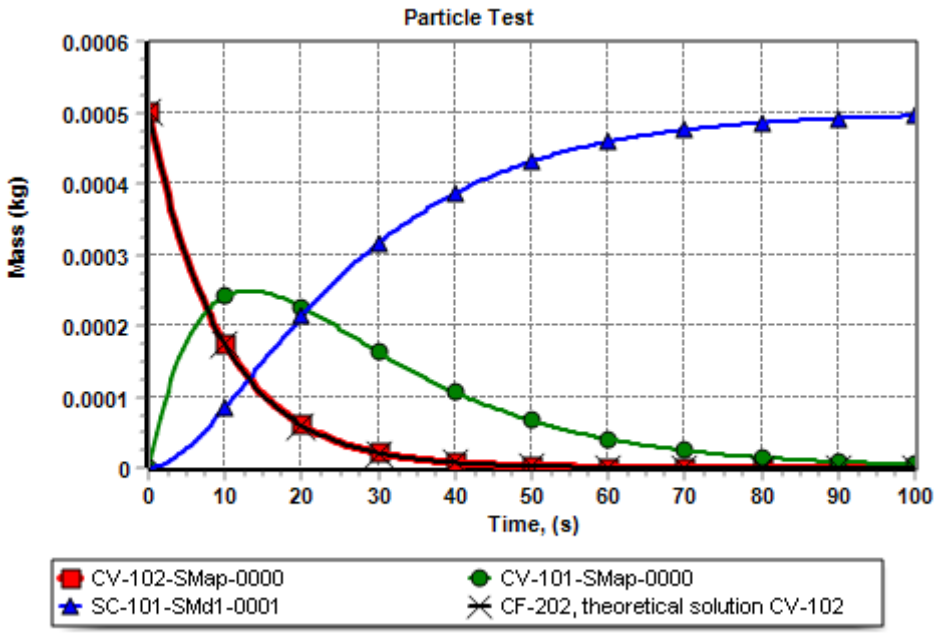

Figure 3-694 Mass distribution, Case 3

3.12.13.4 Upflow of Light Particles through Multiple CVs

Compared to the previous test, the particle flow is upwards, which is obtained by:

- In Case 1 simply by changing the velocity sign, from $v_\infty = -0.01$ m/s to $v_\infty = +0.01$ m/s
- In Case 2 and 3 by changing the particle density from "heavy" (ρ_p =2000.0 kg/s > ρ_f) to "light" (ρ_p = 1.0 kg/s < ρ_f).

The initial conditions are shown in Figure 3-695 (A). An initial mass of 10^{-3} kg of 100 micron particles ($D_p = 10^{-4}$ m) is suspended in the pool of CV-101. The particles are transported from CV-101 up to CV-102 through flow through the two vertical junctions and then released to the atmosphere of CV-102. Two important modeling options need to be used here:

- Aerosol deposition on the pool surface must be disabled (IDEPRT(1)=–1, record 865002), otherwise some of the particles released to the atmosphere of CV-102 will be depositing back on the pool surface due to deposition mechanisms (gravitational settling, Brownian motion, thermophoresis, turbulent deposition, etc.).
- Flow to the pool surface of CV almost filled with liquid must be disabled for CV-101 (a limit of 90% is set by ISVBCV=90 in the record 150XXX), otherwise some of the particles would be transported to the (very small) atmosphere volume of CV-101 rather than through JN-101 and JN-102.

Furthermore, the automated verification function needs to be modified. In the present case, the following functions are used:

- TF-201 = $A = A_{101} + A_{102} = 1.0$
- CF-101 = v_∞ (JN-101) = $W_{101} \times V_{pool} / m / A_{101}$
  = JN-101-WmPf-0000 × CV-101-Volm-pool / CV-101-SMaP-0000 / 0.5
- CF-102 = v_∞ (JN-102) = $W_{102} \times V_{pool} / m / A_{102}$
  = JN-102-WmPf-0000 × CV-101-Volm-pool / CV-101-SMaP-0000 / 0.5
- CF-111 = v_∞ (CV-102) = $W \times V_{pool} / m / A$
  = CV-102-RRPL-0003 × CV-102-Volm-pool / CV-102-SMaP-0000 / 1.0
- CF-201 = $A\, v_\infty\, t / V_{pool}$ =
  = TF-201-Valu-0000 × CF-102-Valu-0000 × SL-000-Time-0000 /
  / CV-101-Volm-pool
- CF-202 = $m = \exp(-A\, v_\infty\, t / V_{pool})$ = exp (– CF-201-Valu-0000)

The SPECTRA input files are located in: **\Z-INPUTS\RT\Pool-Vinf\JN-Up**
Results for the three cases are discussed below.

- **Case 1: Constant velocity, v_∞ = +0.01 m/s**

In this case a constant velocity v_∞ = +0.01 m/s is defined in the input deck. The input file is located in: **\Z-INPUTS\RT\Pool-Vinf\JN-Up\Pool-Vinf-1.SPE**

Results are shown in Figure 3-695 and Figure 3-696. Figure 3-695 (A) shows the initial state of the system. Figure 3-695 (B) shows the state of the system at t = 100 s, when about 37×10^{-5} kg (37%) is in the pool of CV-101, 23×10^{-5} kg (23%) is in the pool of CV-102, and 40×10^{-5} kg (40%) is released to the atmosphere of CV-102. Figure 3-696 shows the time-dependent masses of particles in the pool of CV-101 and CV-102, released to the atmosphere of CV-102, as well as the theoretical solution obtained for CV-101. The calculated results are in good agreement with the theoretical solution.

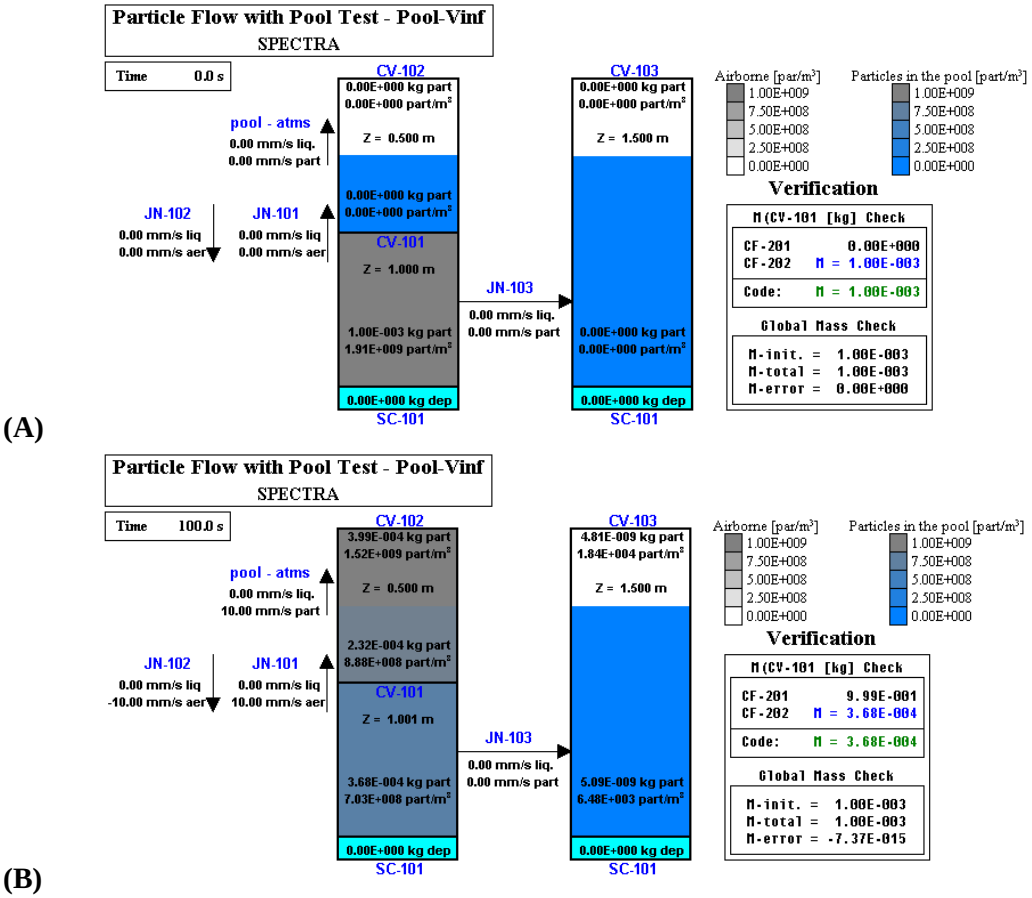

(A)

(B)

Figure 3-695 Downflow of particles, Case 1 (A) initial state, (B) state at t = 100 s

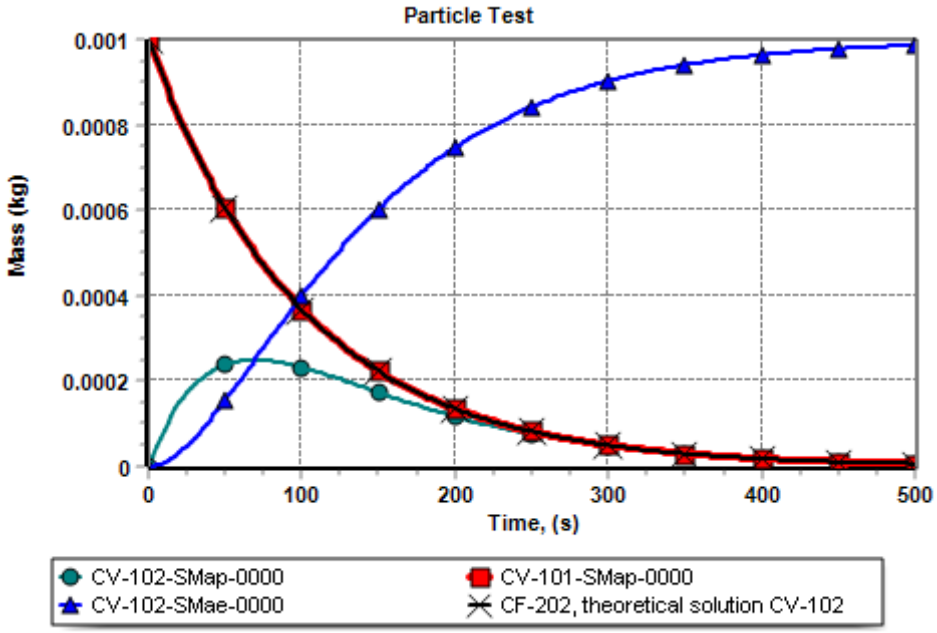

Figure 3-696 Mass distribution, Case 1

- **Case 2: Correlation for v_∞ with $C_{D,Re\to\infty}$ = 0.47**

In this case the terminal velocity correlation is used with $C_{D,Re\to\infty}$ = 0.47. The input file is located in: **`\Z-INPUTS\RT\Pool-Vinf\JN-Up\Pool-Vinf-2.SPE`**

Results are shown in Figure 3-697 and Figure 3-698. Figure 3-697 shows the state of the system at t = 100 s, when about 55×10^{-5} kg (55%) is in the pool of CV-101, 25×10^{-5} kg (25%) is in the pool of CV-102, and 21×10^{-5} kg (21%) is released to the atmosphere of CV-101. Figure 3-698 shows the time-dependent masses of particles in CV-101 and CV-102, released to the atmosphere of CV-102, as well as the theoretical solution obtained for CV-102. The calculated results are in good agreement with the theoretical solution.

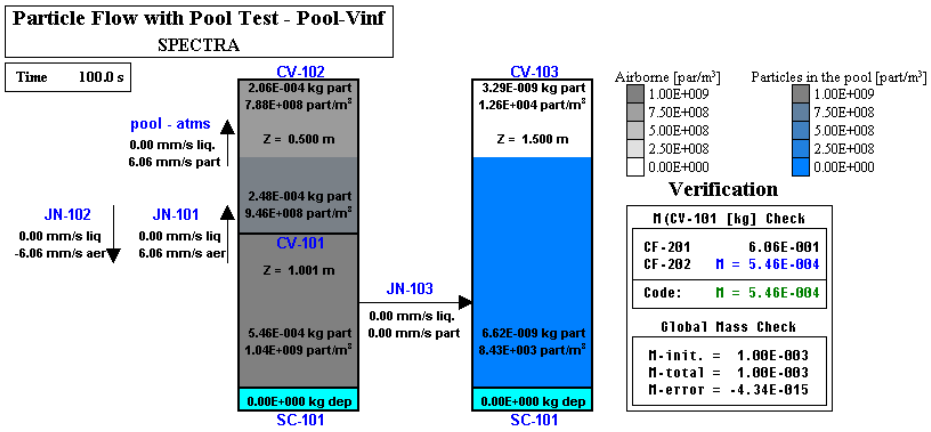

Figure 3-697 Downflow of particles, Case 2 state at t = 100 s

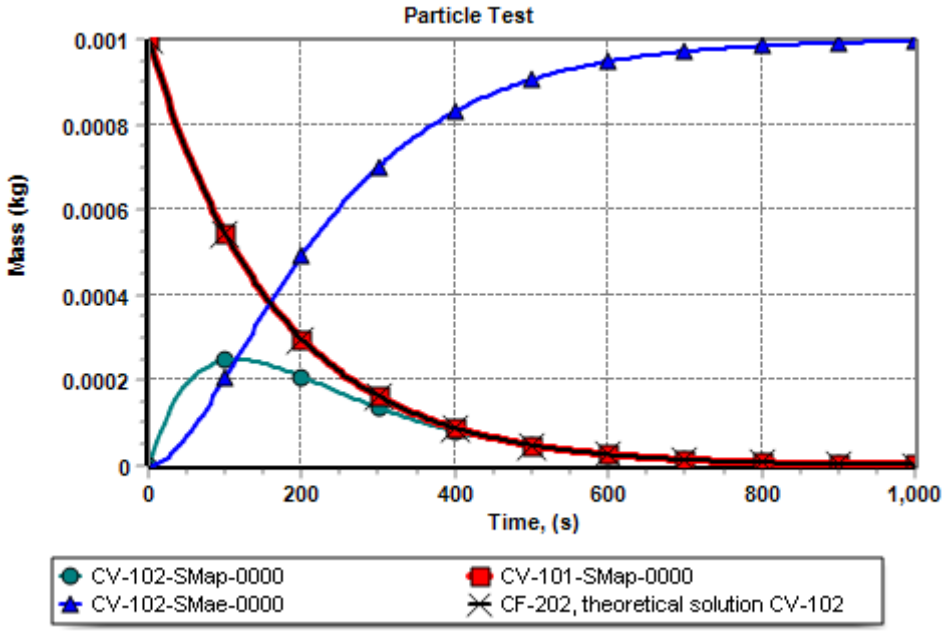

Figure 3-698 Mass distribution, Case 2

- **Case 3: Correlation for v_∞ with C_D = 0.47 = const.**

In this case the terminal velocity correlation is used with constant C_D = 0.47. To see the effect of drag coefficient, the correlation for small particles was eliminated by setting CSMLCV to zero, otherwise this correlation would affect the results here. The input file is located in:
\Z-INPUTS\RT\Pool-Vinf\JN-Up\Pool-Vinf-3.SPE

Results are shown in Figure 3-699 and Figure 3-700. Figure 3-699 shows the state of the system at t = 20 s, when about 35×10^{-5} kg (35%) is in the pool of CV-101, 23×10^{-5} kg (23%) is in the pool of CV-102, and 42×10^{-5} kg (42%) is released to the atmosphere of CV-102. Figure 3-700 shows the time-dependent masses of particles in CV-101 and CV-102, released to the atmosphere of CV-102, as well as the theoretical solution obtained for CV-102. The calculated results are in good agreement with the theoretical solution.

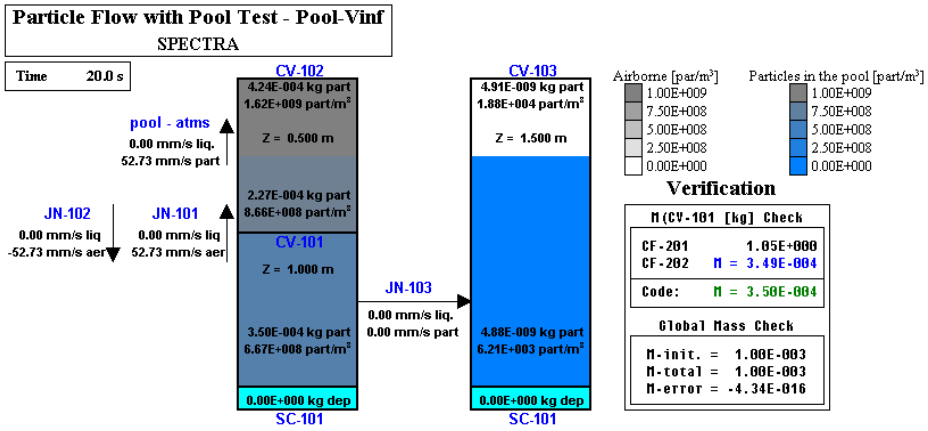

Figure 3-699 Downflow of particles, Case 3 Sate at t = 100 s

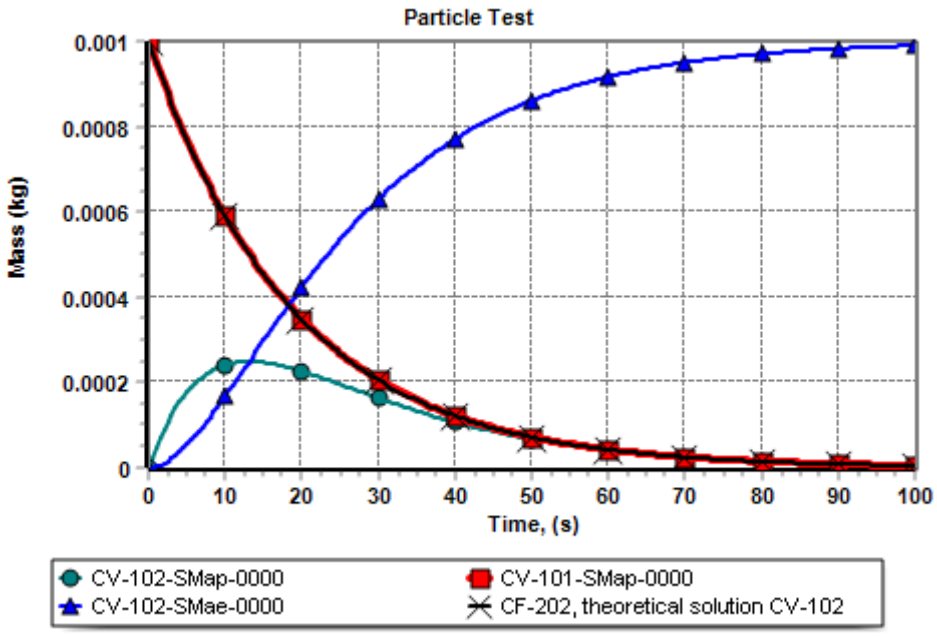

Figure 3-700 Mass distribution, Case 3

3.12.14 Vertical Flow of FP Particles in the Pool

By default, the fission product isotopes are transported in molecular form, until they are attached to aerosol particles (typical size of aerosol particles is $>10^{-6}$ m). Fission products are transported with atmosphere or pool using the velocity of gas or liquid. An alternative way of fission product transport is available; they may be transported as small particles (typical size $<10^{-6}$ m). The main difference is the possibility of sedimentation of particles in the pool and different models for transport to bubbles and aerosol particles (use of Brownian force and inertial impaction rather than use of a Sherwood number correlation - see Volume 1)

This section provides verification of the model used for vertical transport of fission product particles in the pool. The structure of this section is very similar to the previous section. The only difference is that here an isotope is considered rather than an aerosol particle.

The considered isotope is Mo-96, stable isotope, member of vapor class 7. In order to allow sedimentation, the particle size and density of Mo-96 particles are defined in the record 8932XX as.

- $D_p = 10^{-6}$ m
- ρ_p = 10,280 kg/m^3 (density of Molybdenum)

The correlation used for sedimentation velocity is the same as for particles (see previous section). For large particles the drag coefficient correlation is:

$$v_\infty = \left(\frac{4/3}{C_D} \cdot \frac{D_p g(\rho_f - \rho_p)}{\rho_f} \right)^{0.5}$$

However, for very small particles the following correlation is used:

$$v_\infty = \frac{1}{18} \cdot \frac{D_p{}^2 g(\rho_f - \rho_p)}{\eta_f} \cdot C_{small}$$

Here g is the gravity acceleration (m/s^2), ρ is density (kg/m^3), η is viscosity, (kg/m/s), D is diameter. Subscripts p refers to particle, while f to fluid. Again, the verification tests are performed for all possible situations:

- sedimentation of heavy particles in a single CV - section 3.12.14.1,
- flow to pool surface of light particles in a single CV - section 3.12.14.2,
- downflow of heavy particles through multiple CVs - section 3.12.14.3,
- upflow of light particles through multiple CVs - section 3.12.14.4.

In case of light particles, the Molybdenum particles are replaced by Argon particles with the same diameter. The values defined in the record 8932XX are:

- $D_p = 10^{-6}$ m
- ρ_p = 1.6 kg/m^3 (density of Argon at 1 bar, 300 K)

Strictly speaking, the isotope data (such as name, molar weight, and vapor class number) should also be changed (to Ar-40, 40.0, 1), but these parameters are meaningless for the current tests and therefore were not modified.

3.12.14.1 Sedimentation of Heavy Particles in a Single CV

The test case consists of a single CV, half-filled with water at 1 bar, 300 K (density of ρ_f = 996.5 kg/m^3). The volume of water is V_{pool} = 1.0 m^3 (A = 1.0 m^2, H_{pool} = 1.0 m). An initial mass of 10^{-10} kg of 1 micron particles ($D_p = 10^{-6}$ m) is initially suspended in the pool. "Heavy" particles ($\rho_p > \rho_f$) are used. Particle density is equal to ρ_p = 10,280 kg/m^3. Three cases are considered: A solid structure, SC-101, provides the surface for sedimentation.

- Case 1: Particles have a constant, user-defined velocity of $v_\infty = -0.01$ m/s
- Case 2: Correlation for v_∞ is used with $C_{D,Re\to\infty} = 0.47$
- Case 3: Correlation for v_∞ is used with $C_D = 0.47$ = const.

The particle mass balance is:

$$\frac{dm}{dt} = -A \cdot v_\infty \cdot \frac{m}{V_{pool}}$$

Solution:

$$m = m_0 \cdot \exp\left(-\frac{A \cdot v_\infty}{V_{pool}} \cdot t \right)$$

Here m is the mass of particles in the pool, m_0 is the initial mass: $m_0 = 10^{-10}$ (kg), A is the horizontal cross-section of the CV pool (m^2), V_{pool} is the pool volume (m^3), and t is time (s). In order to perform verification of the computed values, an automated verification was set up using Tabular Functions and Control Functions, defined as follows:

- TF-201 = A = 1.0
- CF-111 = $v_\infty = W \times V_{pool} / m / A$
  = SC-101-SF07-0001 × CV-101-Volm-pool / CV-101-MIPi-0191 / 1.0
- CF-201 = $A\ v_\infty\ t / V_{pool}$ =
  = TF-201-Valu-0000 × CF-111-Valu-0000 × SL-000-Time-0000 /
  / CV-101-Volm-pool
- CF-202 = m = exp($-A\ v_\infty\ t / V_{pool}$) =
  = exp (– CF-201-Valu-0000)

The particle terminal velocity is not available as a plot/CF parameter, therefore it is obtained in CF-111 as particle mass transfer rate W (kg/s), divided by the particle density in the pool (m/V_{pool}) (kg/m^3), multiplied by the deposition area A = 1.0 m^2. The parameter SC-101-SF07-0001 is the sedimentation mass transfer rate W (kg/s) for vapor class 7, used in the present test. Furthermore, the correctness of v_∞ is verified by hand calculation as will be shown below.

The SPECTRA input files are located in: **`\Z-INPUTS\RT\Pool-Vinf-FP\CV-Down`**

Results for the three cases are discussed below.

- **Case 1: Constant velocity, v_∞ = –0.01 m/s**

In this case a constant velocity v_∞ = –0.01 m/s is defined in he record 8932XX. The input file is located in: **`\Z-INPUTS\RT\Pool-Vinf-FP\CV-Down\Pool-Vinf-1.SPE`**

Results are shown in Figure 3-701 and Figure 3-702. Figure 3-701 shows the state of the system at t = 100 s, when approximately 1/3 of the particles remain suspended in the pool. Figure 3-702 shows the mass of particles in the pool and the theoretical solution, obtained with CF-202. The calculated results are in good agreement with the theoretical solution.

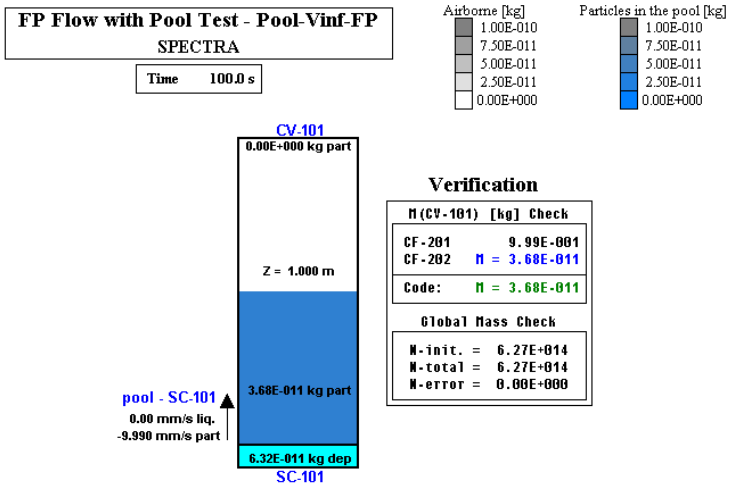

Figure 3-701 Sedimentation in a single CV pool, Case 1

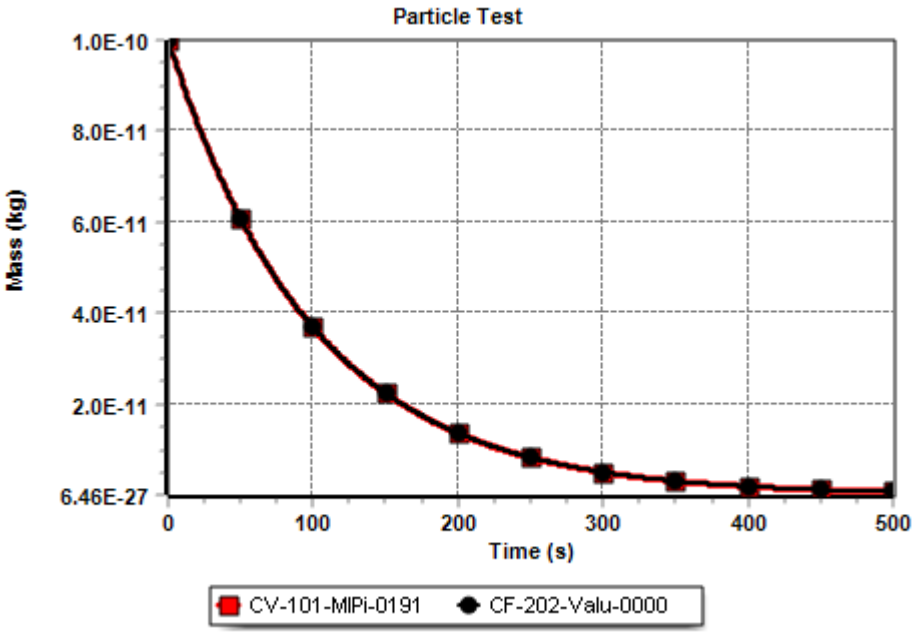

Figure 3-702 Calculated and theoretical (CF-202) mass in the pool, Case 1

- **Case 2: Correlation for v_∞ with $C_{D,Re\to\infty}$ = 0.47**

In this case the terminal velocity correlation is used with $C_{D,Re\to\infty}$ = 0.47, C_{small} = 1.0 (the latter determines the particle behavior). The input file is located in:
\Z-INPUTS\RT\Pool-Vinf-FP\CV-Down\Pool-Vinf-2.SPE

Results are shown in Figure 3-703 and Figure 3-704. Figure 3-703 shows the state of the system at t = 200,000 s, when approximately 1/3 of the particles remain suspended in the pool. Figure 3-704 shows the mass of particles in the pool and the theoretical solution, obtained with CF-202. The calculated results are in good agreement with the theoretical solution.

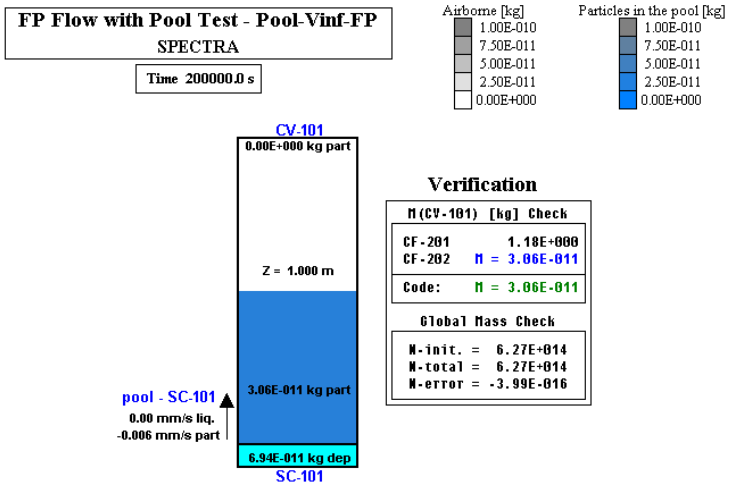

Figure 3-703 Sedimentation in a single CV pool, Case 2

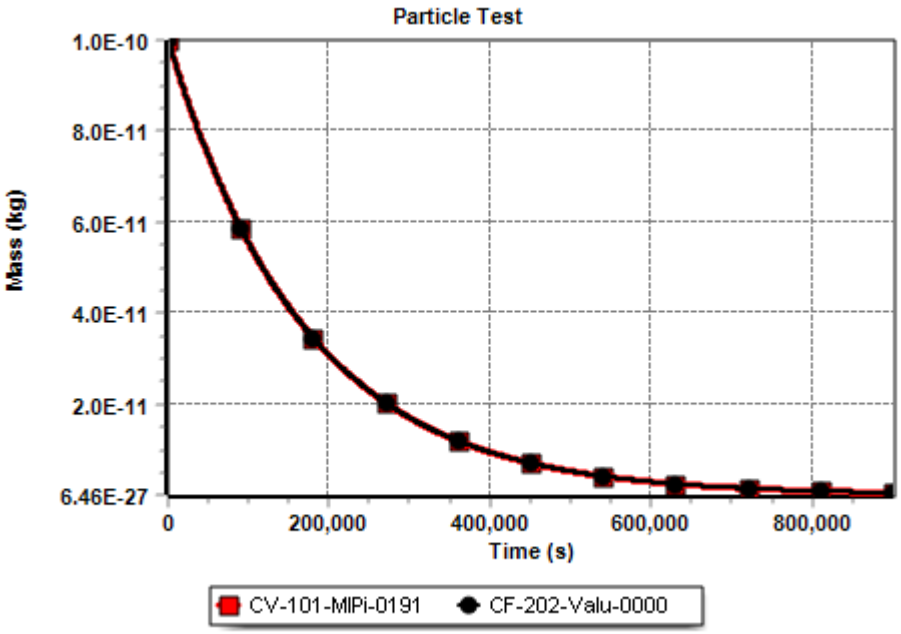

Figure 3-704 Calculated and theoretical (CF-202) mass in the pool, Case 2

- **Case 3: Correlation for v_∞ with C_D = 0.47 = const.**

In this case the terminal velocity correlation is used with constant C_D = 0.47. The correlation for small particles was disabled by setting C_{small} = 0.0 (if this was not done, the results would be identical to the previous case results; for 10^{-6} m particles the velocity is determined by the correlation for small particles). The input file is located in:
\Z-INPUTS\RT\Pool-Vinf-FP\CV-Down\Pool-Vinf-3.SPE

Results are shown in Figure 3-705 and Figure 3-706. Figure 3-705 shows the state of the system at t = 100 s, when approximately 1/5 of the particles remain suspended in the pool. Figure 3-706 shows the mass of particles in the pool and the theoretical solution, obtained with CF-202. The calculated results are in good agreement with the theoretical solution.

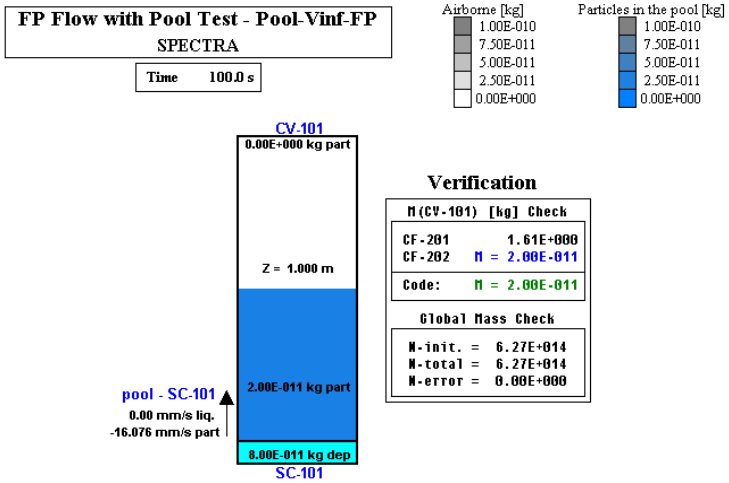

Figure 3-705 Sedimentation in a single CV pool, Case 3

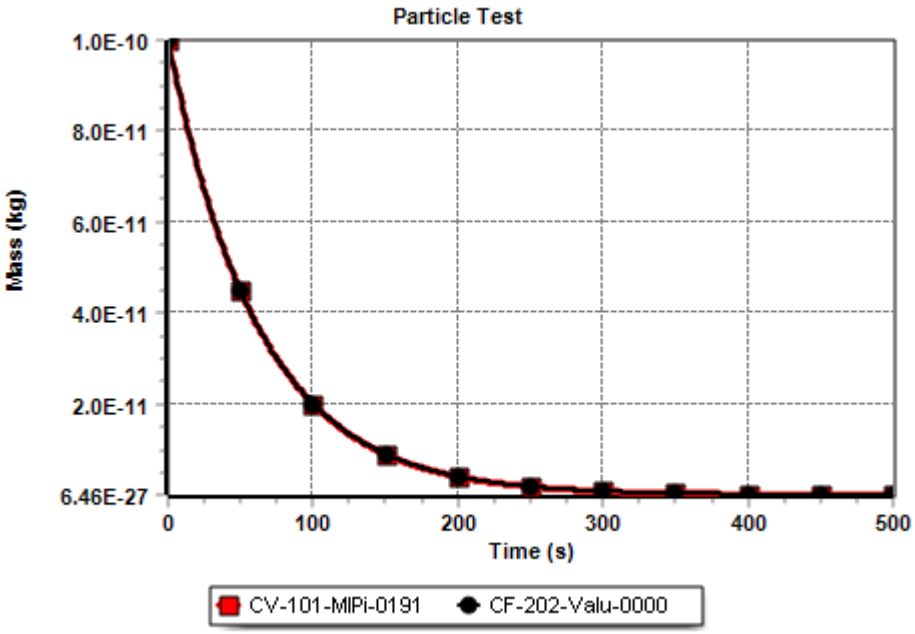

Figure 3-706 Calculated and theoretical (CF-202) mass in the pool, Case 3

As an additional verification, the terminal velocity was checked by hand calculations:

$$v_\infty = \left(\frac{4/3}{C_D} \cdot \frac{D_p g(\rho_p - \rho_f)}{\rho_f} \right)^{0.5} = \left(\frac{4/3}{0.47} \cdot \frac{10^{-6} \times 9.81 \times (10{,}280 - 996.5)}{996.5} \right)^{0.5} = 0.0161$$

The value calculated by the code (not directly plottable, it is obtained here by Control Function CF-111, using particle mass transfer rate from the pool to SC) is equal to 16.076 mm/s = 0.0161 m/s (Figure 3-705), in very good agreement with the theoretical value.

3.12.14.2 Flow to Pool Surface of Light Particles in a Single CV

This test is very similar to the previous one. This time the particle flow is upwards, which is obtained by:

- In Case 1 simply by changing the velocity sign, from v_∞ = –0.01 m/s to v_∞ = +0.01 m/s
- In Case 2 and 3 by changing the particle density from "heavy" (ρ_p =10,280 kg/s > ρ_f) to "light" (ρ_p = 1.6 kg/s < ρ_f).

Furthermore, few other additions are needs for this test:

- Transport of isotopes to the pool surface is activated (record 196000, IPAGRT=1).
- Aerosol deposition on the pool surface is disabled (record 865002, IDEPRT(1)=–1. This is needed because the isotope data was not modified for light particles. If the isotope was defined as Argon, member of class 1 (noble gases), then once transported to the CV atmosphere it would stay there. However, since the isotope is still a member of class 7, it cannot stay in the atmosphere as a vapor at low temperature. Therefore it will condense to form aerosol particles that will subsequently deposit on the pool surface and eventual walls. The aerosol transport back to the pool would create an equilibrium state with some fraction of the isotope in the atmosphere and some in the pool. As it is modeled, the final situation for this test is with practically all isotopes released to the atmosphere.

Finally, the automated verification function needs to be modified. In the present case, the mass transfer rate W (kg/s) in CF-111 has to be the pool-atmosphere transfer, parameter CV-101-FmPA-0191 (the value for isotope 191, used in the present test). The automatic verification functions for this case are

- TF-201 = A = 1.0
- CF-111 = $v_\infty = W \times V_{pool} / m / A$
  = CV-101-FmPA-0191 × CV-101-Volm-pool / CV-101-MIPi-0191 / 1.0
- CF-201 = $A\, v_\infty\ t / V_{pool}$ =
  = TF-201-Valu-0000 × CF-111-Valu-0000 × SL-000-Time-0000 /
  / CV-101-Volm-pool
- CF-202 = $m = \exp(-A\, v_\infty\ t / V_{pool}\ )$ =
  = exp (– CF-201-Valu-0000)

The SPECTRA input files are located in: **\Z-INPUTS\RT\Pool-Vinf-FP\CV-Up**
Results for the three cases are discussed below.

- **Case 1: Constant velocity, v_∞ = +0.01 m/s**

In this case a constant velocity v_∞ = –0.01 m/s is defined in the input deck. The input file is located in: **\Z-INPUTS\RT\Pool-Vinf-FP\CV-Up\Pool-Vinf-1.SPE**

Results are shown in Figure 3-707 and Figure 3-708. Figure 3-707 shows the state of the system at t = 100 s, when approximately 1/3 of the particles remain suspended in the pool. Figure 3-708 shows the mass of particles in the pool and the theoretical solution, obtained with CF-202. The calculated results are in good agreement with the theoretical solution.

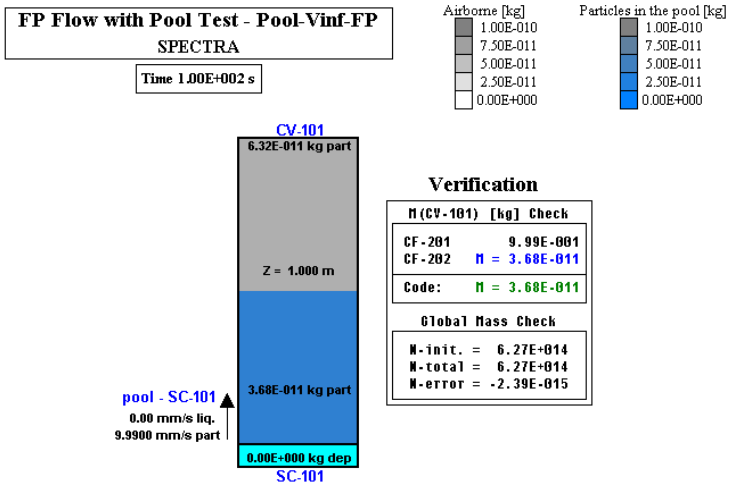

Figure 3-707 Particle flow to pool surface in a single CV, Case 1

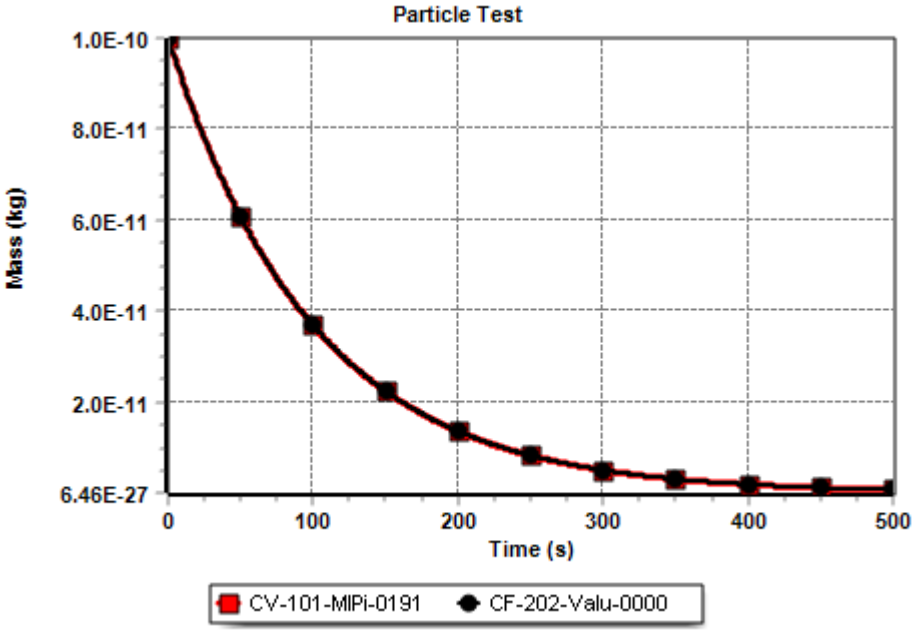

Figure 3-708 Calculated and theoretical (CF-202) mass in the pool, Case 1

- **Case 2: Correlation for v_∞ with $C_{D,Re\to\infty}$ = 0.47**

In this case the terminal velocity correlation is used with $C_{D,Re\to\infty}$ = 0.47, C_{small} = 1.0 (the latter determines the particle behavior). The input file is located in:
\Z-INPUTS\RT\Pool-Vinf-FP\CV-Up\Pool-Vinf-2.SPE

Results are shown in Figure 3-709 and Figure 3-710. Figure 3-709 shows the state of the system at t = 1,000,000 s, when approximately 1/2 of the particles remain suspended in the pool. Figure 3-710 shows the mass of particles in the pool and the theoretical solution, obtained with CF-202. The calculated results are in good agreement with the theoretical solution.

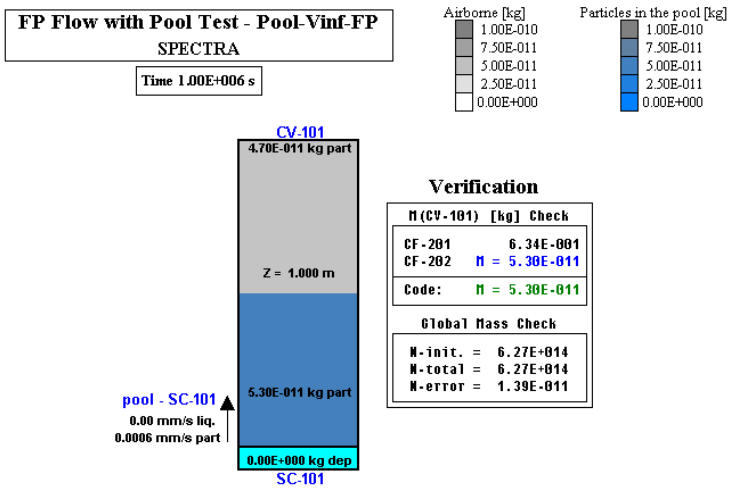

Figure 3-709 Particle flow to pool surface in a single CV, Case 2

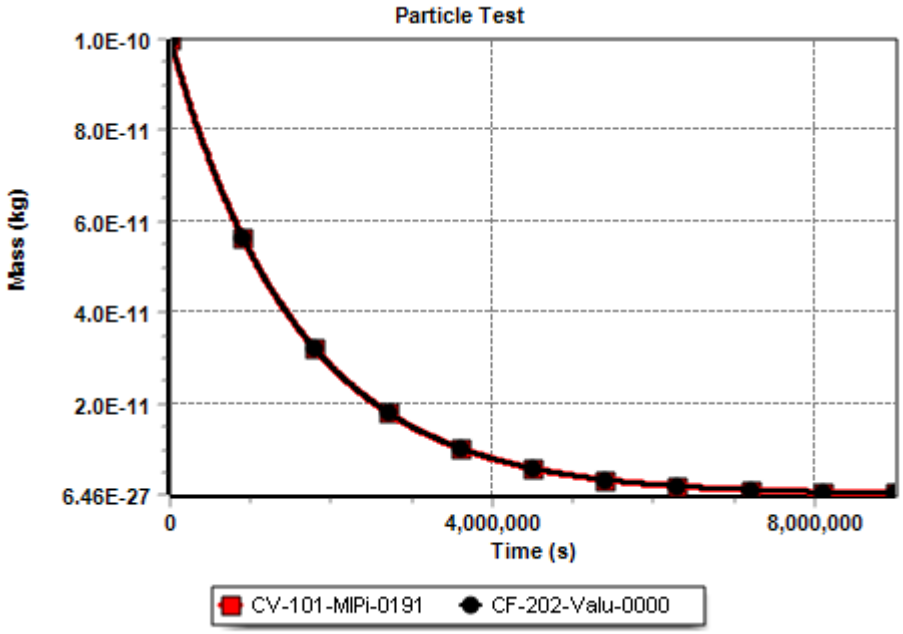

Figure 3-710 Calculated and theoretical (CF-202) mass in the pool, Case 2

- **Case 3: Correlation for v_∞ with C_D = 0.47 = const.**

In this case the terminal velocity correlation is used with constant C_D = 0.47. The correlation for small particles was disabled by setting C_{small} = 0.0 (if this was not done, the results would be identical to the previous case results; for 10^{-6} m particles the velocity is determined by the correlation for small particles). The input file is located in:
\Z-INPUTS\RT\Pool-Vinf-FP\CV-Up\Pool-Vinf-3.SPE

Results are shown in Figure 3-711 and Figure 3-712. Figure 3-711 shows the state of the system at t = 100 s, when approximately 1/2 of the particles remain suspended in the pool. Figure 3-712 shows the mass of particles in the pool and the theoretical solution, obtained with CF-202. The calculated results are in very good agreement with theoretical solution.

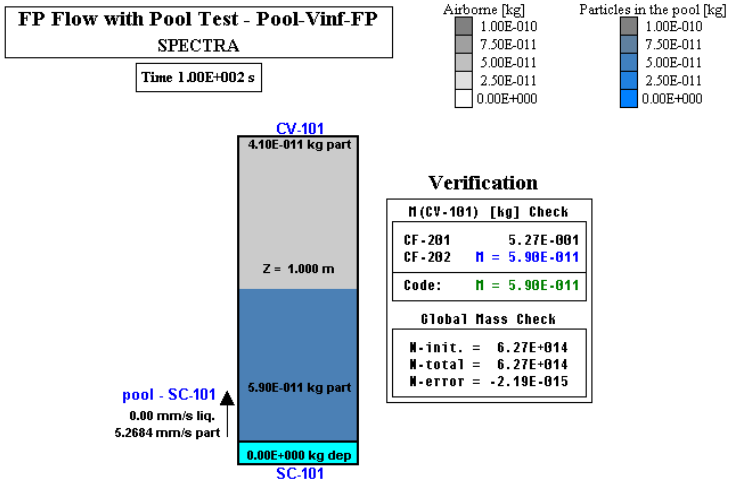

Figure 3-711 Particle flow to pool surface in a single CV, Case 3

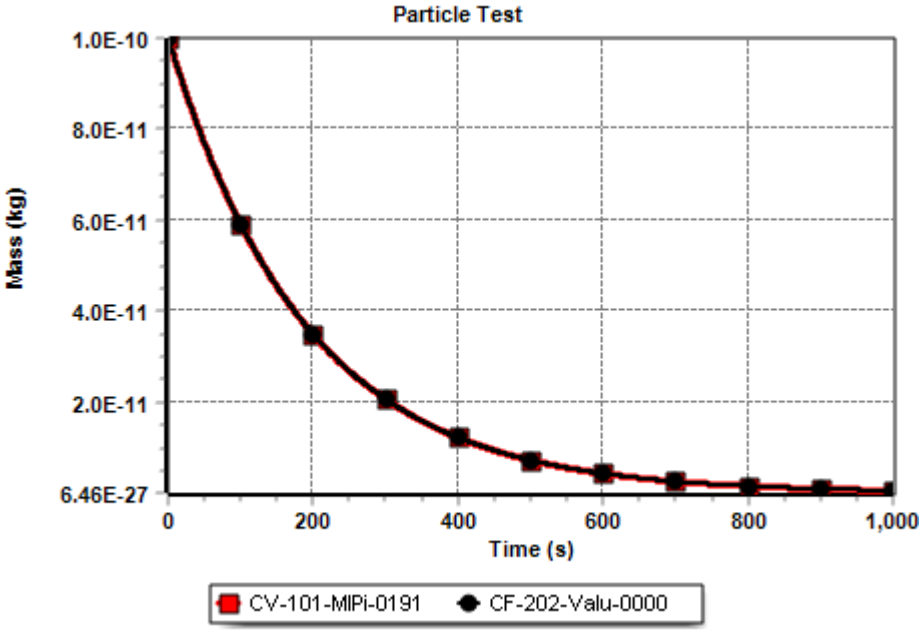

Figure 3-712 Calculated and theoretical (CF-202) mass in the pool, Case 3

The current set of test is very similar to the one presented in the previous section. While in the previous section heavy particles were depositing on SC-101, in the present cases they are transferred to the atmosphere of CV-101. The velocity in Case 2 and 3 is different because the density difference is not the same:

- heavy particles: $\Delta\rho = (\rho_p - \rho_f) = 10280–996.5 = 9283.5$ kg/m^3, $v_{\infty,2} = 0.006$, $v_{\infty,3} = 16.1$
- light particles: $\Delta\rho = (\rho_f - \rho_p) = 996.5 - 1.6 = 994.9$ kg/m^3, $v_{\infty,2} = 0.0006$, $v_{\infty,3} = 5.27$

3.12.14.3 Downflow of Heavy Particles through Multiple CVs

The test is aimed at verification of particle velocity in junctions and consists of multiple Control Volumes connected by junctions, including:

- JN-101: $A = 0.5$ m^2, vertical up
- JN-102: $A = 0.5$ m^2, vertical down
- JN-103: $A = 0.5$ m^2, horizontal

The initial conditions are shown in Figure 3-689 (A). CV-101 and CV-102 are filled with water at 1 bar, 300 K (density of $\rho_f = 996.5$ kg/m^3). The volume of water is:

- CV-101: $V_{pool} = 1.0$ m^3 ($A = 1.0$ m^2, $H_{pool} = 1.0$ m).
- CV-102: $V_{pool} = 0.5$ m^3 ($A = 1.0$ m^2, $H_{pool} = 0.5$ m).
- CV-103: $V_{pool} = 1.5$ m^3 ($A = 1.0$ m^2, $H_{pool} = 1.5$ m).

An initial mass of 10^{-10} kg of 1 micron particles ($D_p = 10^{-6}$ m) is initially suspended in the pool of CV-102. "Heavy" particles ($\rho_p > \rho_f$) are used. Particle density is equal to $\rho_p = 10{,}820$ kg/m^3. A solid structure, SC-101, provides the surface for sedimentation in CV-101. The particles are transported from CV-102 down to CV-101 through the two vertical junctions and then deposited on SC-101. No flow is expected through JN-103, because the terminal particle velocity in the horizontal direction is zero and the liquid velocity is practically zero all the time. Three cases are considered:

- Case 1: Particles have a constant, user-defined velocity of $v_\infty = -0.01$ m/s
- Case 2: Correlation for v_∞ is used with $C_{D,Re\to\infty} = 0.47$
- Case 3: Correlation for v_∞ is used with $C_D = 0.47$ = const.

The particle mass balance in CV-102 is:

$$\frac{dm}{dt} = -A \cdot v_\infty \cdot \frac{m}{V_{pool}}$$

solution:

$$m = m_0 \cdot \exp\left(-\frac{A \cdot v_\infty}{V_{pool}} \cdot t \right)$$

Here m is the mass of particles in the pool, m_0 is the initial mass: $m_0 = 10^{-10}$ (kg), A is the total horizontal cross-section of the vertical junctions JN-101 and JN-102 (m^2), V_{pool} is the pool volume (m^3), and t is time (s).

The particle terminal velocities are not available as a plot/CF parameters, therefore they are obtained using Control Functions, as the particle mass transfer rate W (kg/s), divided by the particle density in the pool (m/V_{pool}) (kg/m^3), and multiplied by the deposition area A (m^2). The values are shown in visualization pictures (e.g.: Figure 3-717). Correctness of the values may be checked by looking up the velocities in the main output file (*.OUT):

```
=RT=  JN POOL FLOW DATA, FP VAPOR VELOCITIES [m/s]

Chain No.: 19, Isotopes:    Mo-96
------------------------  ---------
JN-101, CV-101 -> CV-102, -1.607E-02
JN-102, CV-102 -> CV-101,  1.607E-02
JN-103, CV-101 -> CV-103, -5.672E-05
```

In order to perform verification of the computed values, an automated verification was set up using Tabular Functions and Control Functions, defined as follows:

- TF-201 = $A = A_{101} + A_{102} = 1.0$
- CF-101 = v_∞ (JN-101) = $W_{101} \times V_{pool} / m / A_{101}$
  = JN-101-WIsP-0191 × CV-102-Volm-pool / CV-102-MIPi-0191 / 0.5
- CF-102 = v_∞ (JN-102) = $W_{102} \times V_{pool} / m / A_{102}$
  =JN-102-WIsP-0191 × CV-102-Volm-pool / CV-102-MIPi-0191 / 0.5
- CF-111 = v_∞ (CV-101) = $W \times V_{pool} / m / A$
  = SC-101-SF07-0001 × CV-101-Volm-pool / CV-101-MIPi-0191 / 1.0
- CF-201 = $A\, v_\infty\, t / V_{pool}$ =
  = TF-201-Valu-0000 × CF-102-Valu-0000 × SL-000-Time-0000 /
  / CV-102-Volm-pool
- CF-202 = $m = \exp(-A\, v_\infty\, t / V_{pool})$ =
  = exp (– CF-201-Valu-0000)

The SPECTRA input files are located in: **\Z-INPUTS\RT\Pool-Vinf-FP\JN-Down**

Results for the three cases are discussed below.

- **Case 1: Constant velocity, v_∞ = –0.01 m/s**

In this case a constant velocity v_∞ = –0.01 m/s is defined in the input deck. The input file is located in: **\Z-INPUTS\RT\Pool-Vinf-FP\JN-Down\Pool-Vinf-1.SPE**

Results are shown in Figure 3-713 and Figure 3-714. Figure 3-713 (A) shows the initial state of the system. Figure 3-713 (B) shows the state of the system at t = 100 s, when about 1.4×10^{-11} kg (14%) is in the pool of CV-102, 4.6×10^{-11} kg (46%) is in the pool of CV-101, and 4.0×10^{-11} kg (40%) is deposited on SC-101. Figure 3-714 shows the time-dependent masses of particles in CV-101 and CV-102, deposited on SC-101, as well as the theoretical solution obtained for CV-102. The calculated results are in good agreement with the theoretical solution.

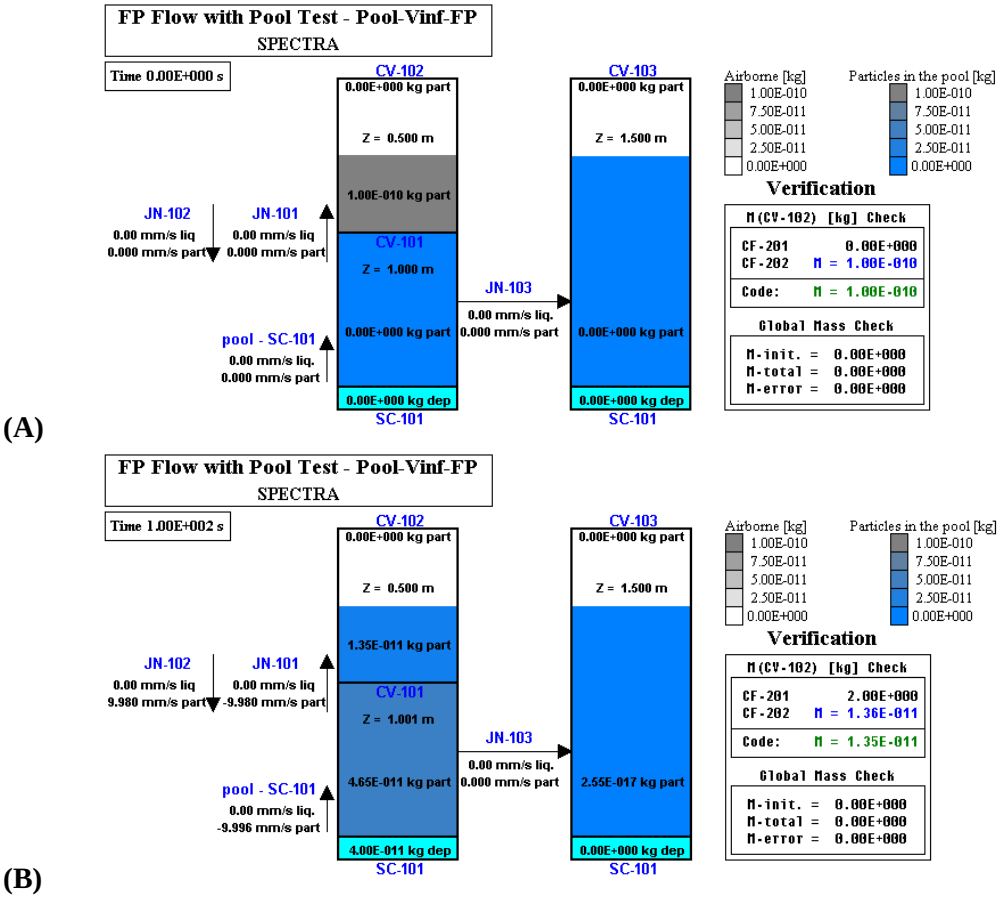

Figure 3-713 Downflow of particles, Case 1 (A) initial state, (B) state at t = 100 s

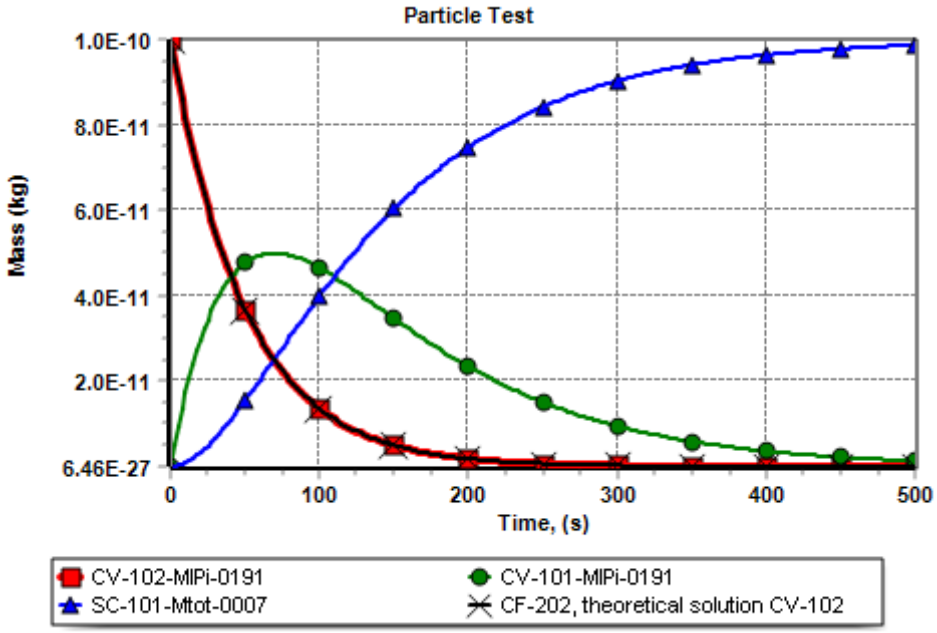

Figure 3-714 Mass distribution, Case 1

- **Case 2: Correlation for v_∞ with $C_{D,Re\to\infty}$ = 0.47**

In this case the terminal velocity correlation is used with $C_{D,Re\to\infty}$ = 0.47, C_{small} = 1.0 (the latter determines the particle behavior). The correlation gives v_∞=0.006 mm/s - Figure 3-715. This is below the limit for transport through a junction, which is VMINRT=10^{-5} m/s. This limit had to be set at lower number, VMINRT=10^{-6}, otherwise no particle flow would occur. The input file is located in: **\Z-INPUTS\RT\Pool-Vinf-FP\JN-Down\Pool-Vinf-2.SPE**

Results are shown in Figure 3-715 and Figure 3-716. Figure 3-715 shows the state of the system at t = 100,000 s, when about 3.0.6×10^{-11} kg (30%) is in the pool of CV-102, 5.0×10^{-11} kg (50%) is in the pool of CV-101, and 2.0×10^{-11} kg (20%) is deposited on SC-10l. Figure 3-716 shows the time-dependent masses in CV-101 and CV-102, deposited on SC-101, as well as the theoretical solution obtained for CV-102. The calculated results are in good agreement with the theoretical solution.

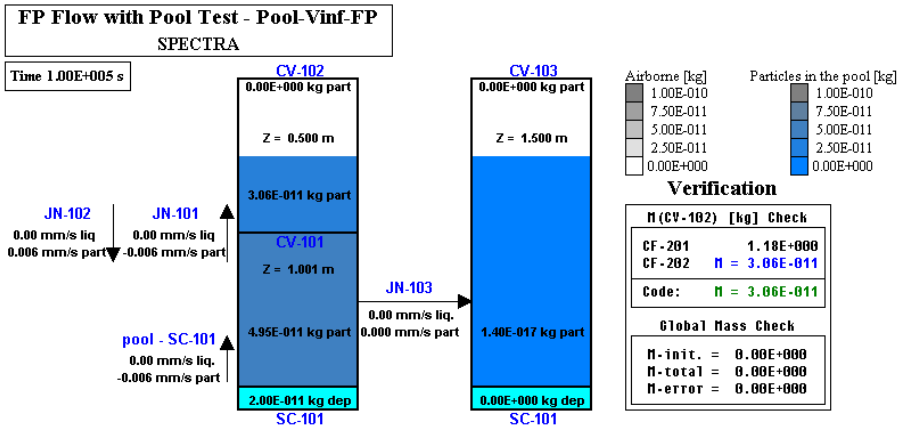

Figure 3-715 Downflow of particles, Case 2 at t = 10,000 s

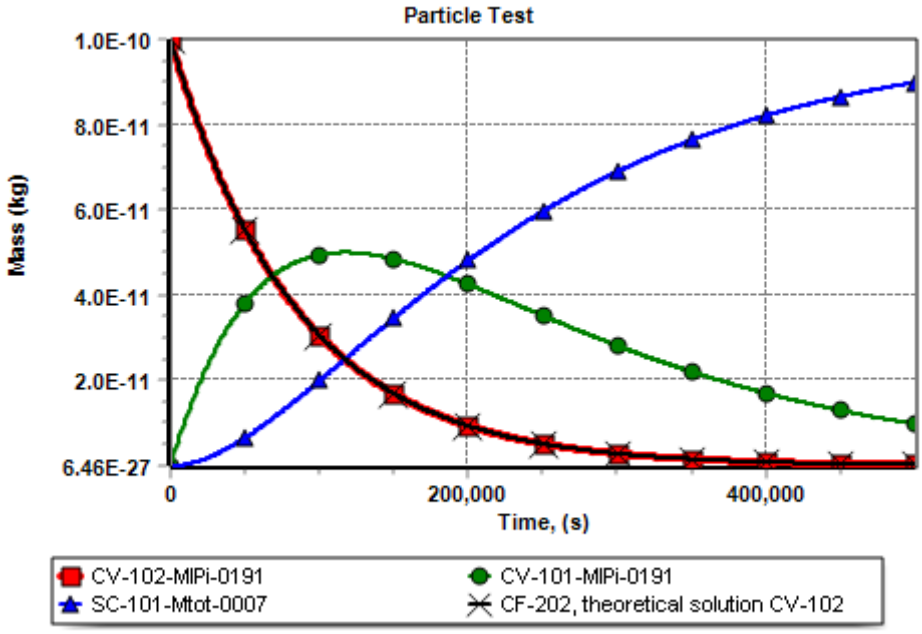

Figure 3-716 Mass distribution, Case 2

- **Case 3: Correlation for v_∞ with C_D = 0.47 = const.**

In this case the terminal velocity correlation is used with constant C_D = 0.47. The correlation for small particles was disabled by setting C_{small} = 0.0 (if this was not done, the results would be identical to the previous case results; for 10^{-6} m particles the velocity is determined by the correlation for small particles). The input file is located in: **\Z-INPUTS\RT\Pool-Vinf-FP\JN-Down\Pool-Vinf-3.SPE**

Results are shown in Figure 3-717 and Figure 3-718. Figure 3-717 shows the state of the system at t = 100 s, when about 0.4×10^{-11} kg (4%) is in the pool of CV-102, 3.2×10^{-11} kg (32%) is in the pool of CV-101, and 6.4×10^{-11} kg (64%) is deposited on SC-10l. Figure 3-718 shows the time-dependent masses in CV-101 and CV-102, deposited on SC-101, as well as the theoretical solution obtained for CV-102. The calculated results are in good agreement with the theoretical solution.

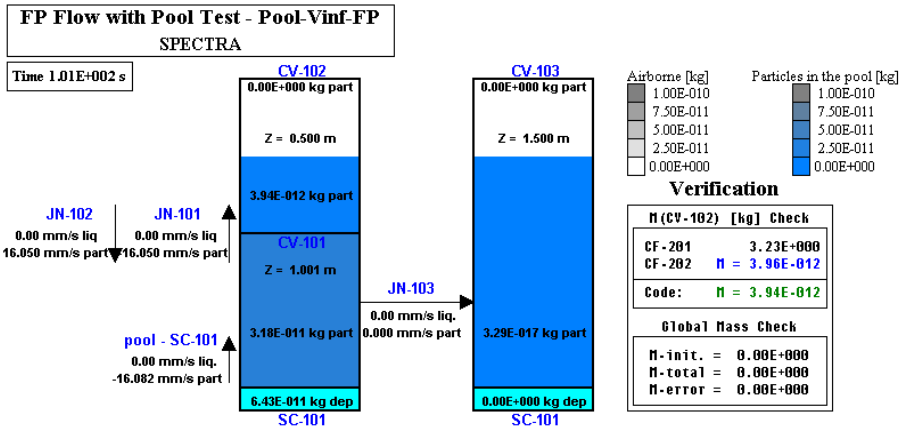

Figure 3-717 Downflow of particles, Case 3 at t = 100 s

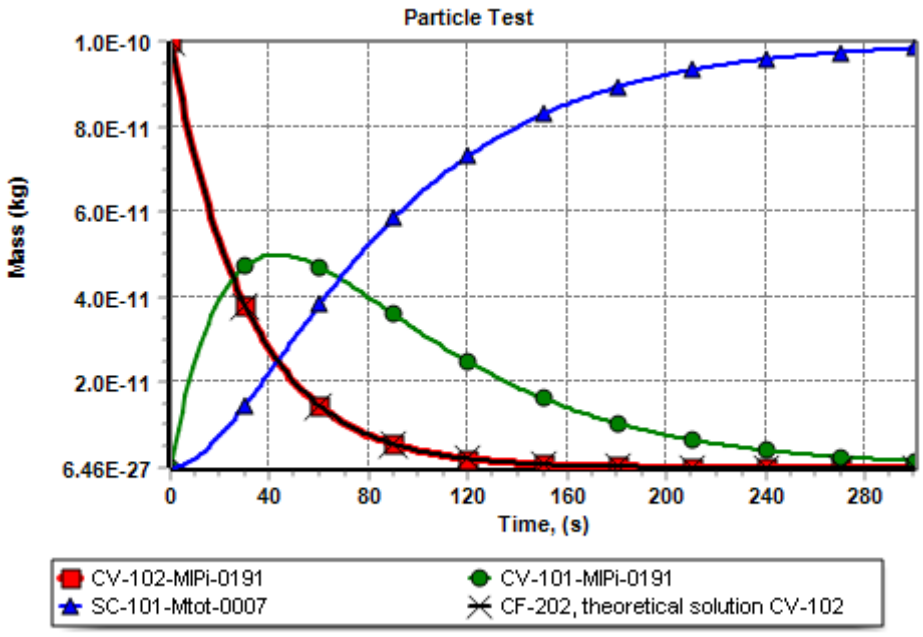

Figure 3-718 Mass distribution, Case 3

3.12.14.4 Upflow of Light Particles through Multiple CVs

Compared to the previous test, the particle flow is upwards, which is obtained by:

- In Case 1 simply by changing the velocity sign, from $v_\infty = -0.01$ m/s to $v_\infty = +0.01$ m/s
- In Case 2 and 3 by changing the particle density from "heavy" (ρ_p =10,280.0 kg/m^3 > ρ_f) to "light" (ρ_p = 1.6 kg/m^3 < ρ_f).

The initial conditions are shown in Figure 3-719 (A). An initial mass of 10^{-10} kg of 100 micron particles ($D_p = 10^{-4}$ m) is suspended in the pool of CV-101. The particles are transported from CV-101 up to CV-102 through flow through the two vertical junctions and then released to the atmosphere of CV-102. Two important modeling options need to be used here:

- Aerosol deposition on the pool surface must be disabled (IDEPRT(1)=–1, record 865002), otherwise some of the particles released to the atmosphere of CV-102 will be depositing back on the pool surface due to deposition mechanisms (gravitational settling, Brownian motion, thermophoresis, turbulent deposition, etc.).
- Flow to the pool surface of CV almost filled with liquid must be disabled for CV-101 (a limit of 90% is set by ISVBCV=90 in the record 150XXX), otherwise some of the particles would be transported to the (very small) atmosphere volume of CV-101 rather than through JN-101 and JN-102.

Furthermore, the automated verification function needs to be modified. In the present case, the following functions are used:

- TF-201 = $A = A_{101} + A_{102} = 1.0$
- CF-101 = v_∞ (JN-101) = $W_{101} \times V_{pool} / m / A_{101}$
  = JN-101-WIsP-0191 × CV-101-Volm-pool / CV-101-MIPi-0191 / 0.5
- CF-102 = v_∞ (JN-102) = $W_{102} \times V_{pool} / m / A_{102}$
  = JN-102-WIsP-0191 × CV-101-Volm-pool / CV-101-MIPi-0191 / 0.5
- CF-111 = v_∞ (CV-101) = $W \times V_{pool} / m / A$
  = CV-102-FmPA-0191 × CV-102-Volm-pool / CV-102-MIPi-0191 / 1.0
- CF-201 = $A\, v_\infty\, t / V_{pool}$ =
  = TF-201-Valu-0000 × CF-101-Valu-0000 × SL-000-Time-0000 /
  / CV-101-Volm-pool
- CF-202 = $m = \exp(-A\, v_\infty\, t / V_{pool})$ = exp (– CF-201-Valu-0000)

The SPECTRA input files are located in: **\Z-INPUTS\RT\Pool-Vinf-FP\JN-Up**
Results for the three cases are discussed below.

- **Case 1: Constant velocity, v_∞ = +0.01 m/s**

In this case a constant velocity v_∞ = +0.01 m/s is defined in the input deck. The input file is located in: **\Z-INPUTS\RT\Pool-Vinf-FP\JN-Up\Pool-Vinf-1.SPE**

Results are shown in Figure 3-719 and Figure 3-720. Figure 3-719 (A) shows the initial state of the system. Figure 3-719 (B) shows the state of the system at t = 100 s, when about 3.7×10^{-11} kg (37%) is in the pool of CV-101, 2.3×10^{-11} kg (23%) is in the pool of CV-102, and 4.0×10^{-5} kg (40%) is released to the atmosphere of CV-102. Figure 3-720 shows the time-dependent masses of particles in the pool of CV-101 and CV-102, released to the atmosphere of CV-102, as well as the theoretical solution obtained for CV-101. The calculated results are in good agreement with the theoretical solution.

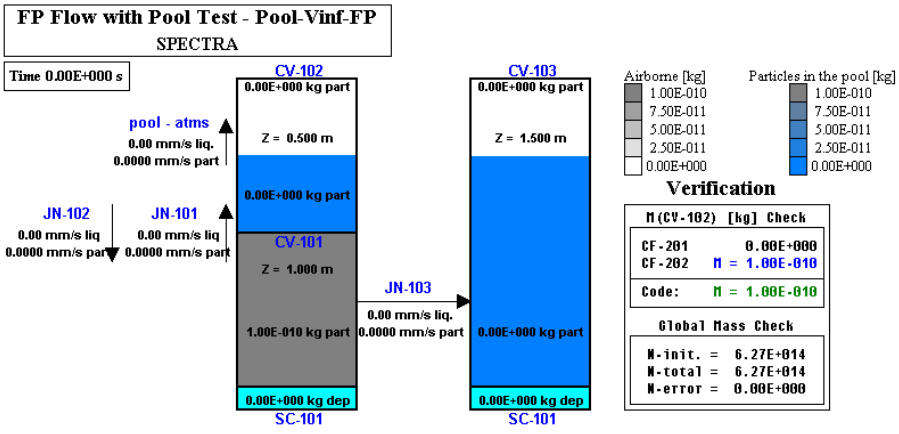

(A)

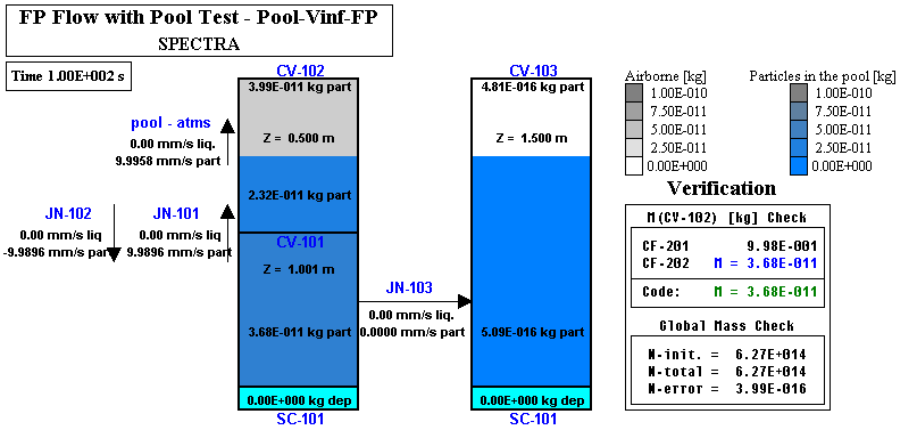

(B)

Figure 3-719 Upflow of particles, Case 1 (A) initial state, (B) state at t = 100 s

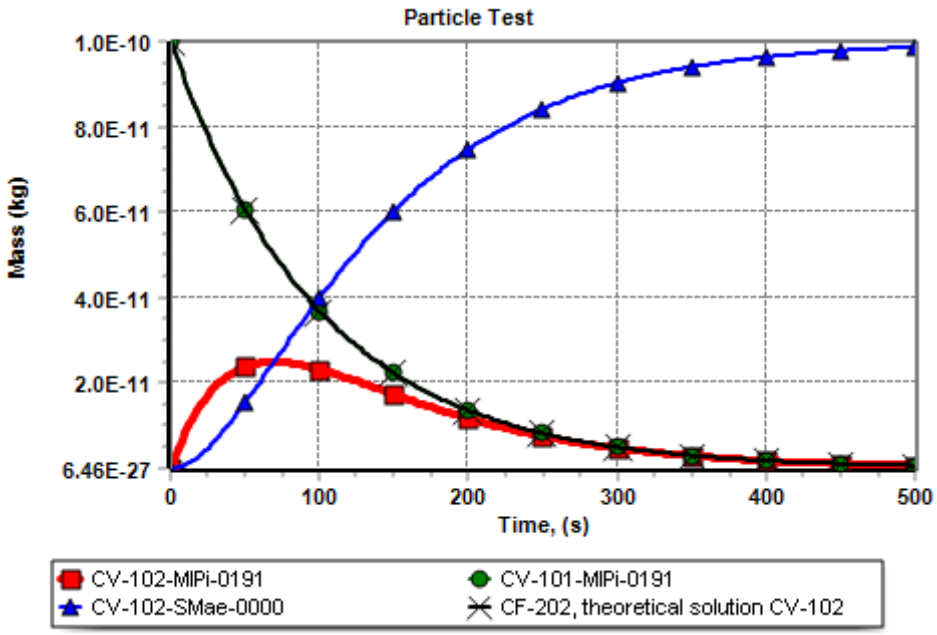

Figure 3-720 Mass distribution, Case 1

- **Case 2: Correlation for v_∞ with $C_{D,Re\to\infty}$ = 0.47**

In this case the terminal velocity correlation is used with $C_{D,Re\to\infty}$ = 0.47, C_{small} = 1.0 (the latter determines the particle behavior). The correlation gives v_∞=0.0006 mm/s - Figure 3-721. This is below the limit for transport through a junction, which is VMINRT=10^{-5} m/s. This limit had to be set at lower number, VMINRT=10^{-7}, otherwise no particle flow would occur. The input file is located in: **\Z-INPUTS\RT\Pool-Vinf-FP\JN-Up\Pool-Vinf-2.SPE**

Results are shown in Figure 3-721 and Figure 3-722. Figure 3-721 shows the state of the system at t = 2,000,000 s, when about 2.8×10^{-11} kg (28%) is in the pool of CV-101, 2.0×10^{-11} kg (20%) is in the pool of CV-102, and 5.2×10^{-11} kg (52%) is in the atmosphere of CV-101. Figure 3-722 shows the time-dependent masses in CV-101 and CV-102, as well as the theoretical solution obtained for CV-102. The calculated results are in good agreement with the theoretical solution.

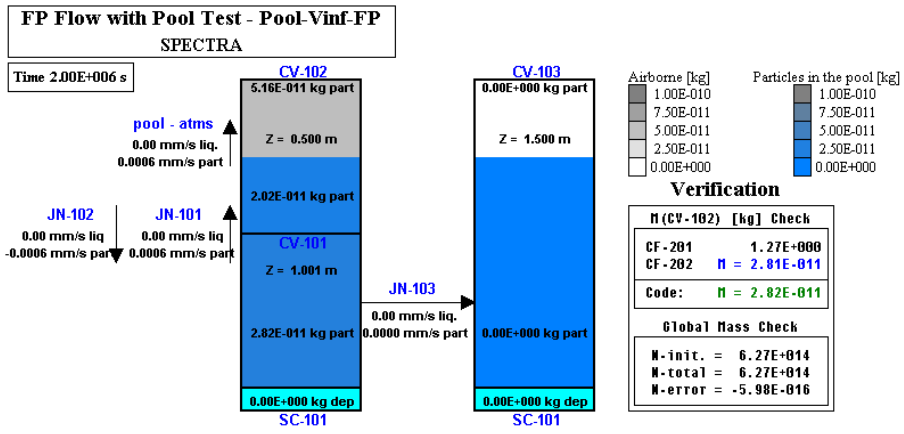

Figure 3-721 Upflow of particles, Case 2 at t = 100,000 s

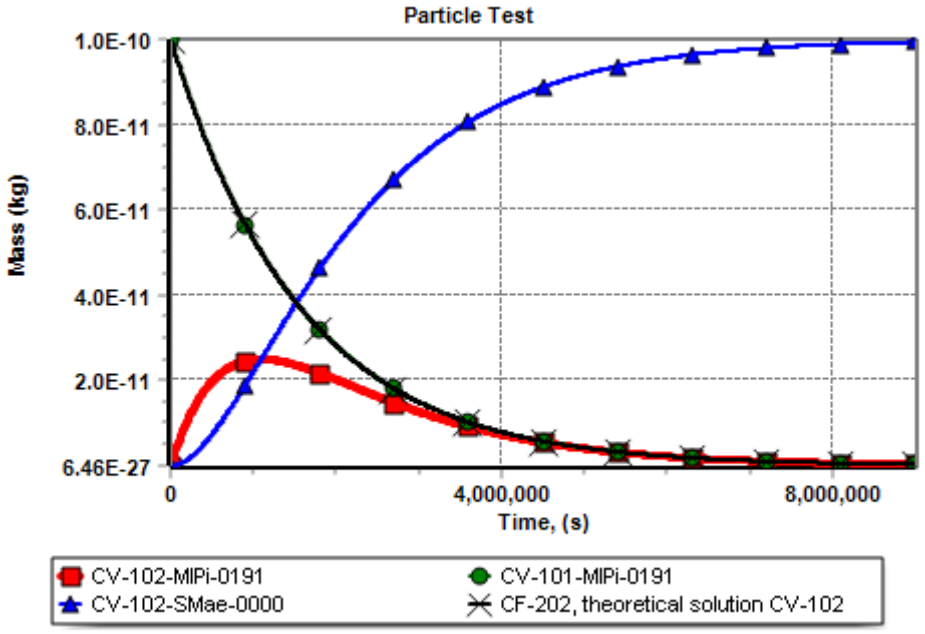

Figure 3-722 Mass distribution, Case 2

- **Case 3: Correlation for v_∞ with C_D = 0.47 = const.**

In this case the terminal velocity correlation is used with constant C_D = 0.47. The correlation for small particles was disabled by setting C_{small} = 0.0 (if this was not done, the results would be identical to the previous case results; for 10^{-6} m particles the velocity is determined by the correlation for small particles). The input file is located in:
\Z-INPUTS\RT\Pool-Vinf-FP\JN-Up\Pool-Vinf-3.SPE

Results are shown in Figure 3-723 and Figure 3-724. Figure 3-723 shows the state of the system at t = 200 s, when about 35×10^{-5} kg (35%) is in the pool of CV-101, 23×10^{-5} kg (23%) is in the pool of CV-102, and 42×10^{-5} kg (42%) is released to the atmosphere of CV-102. Figure 3-724 shows the time-dependent masses of particles in CV-101 and CV-102, as well as the theoretical solution obtained for CV-102. The calculated results are in good agreement with the theoretical solution.

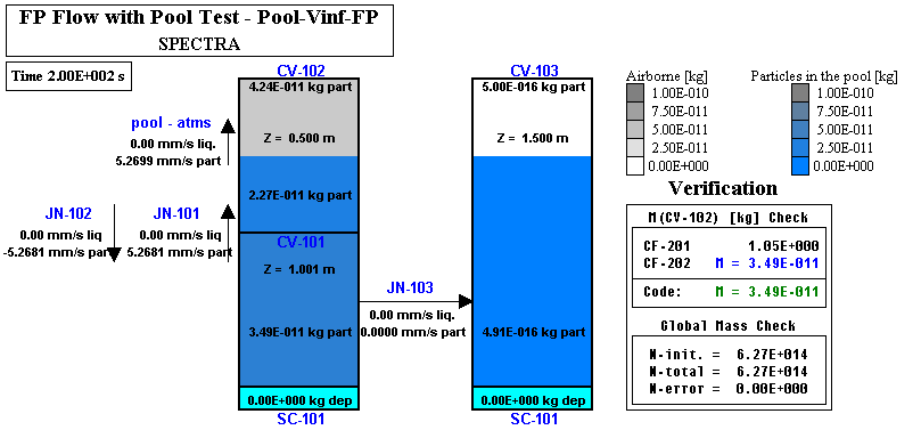

Figure 3-723 Upflow of particles, Case 3 at t = 200 s

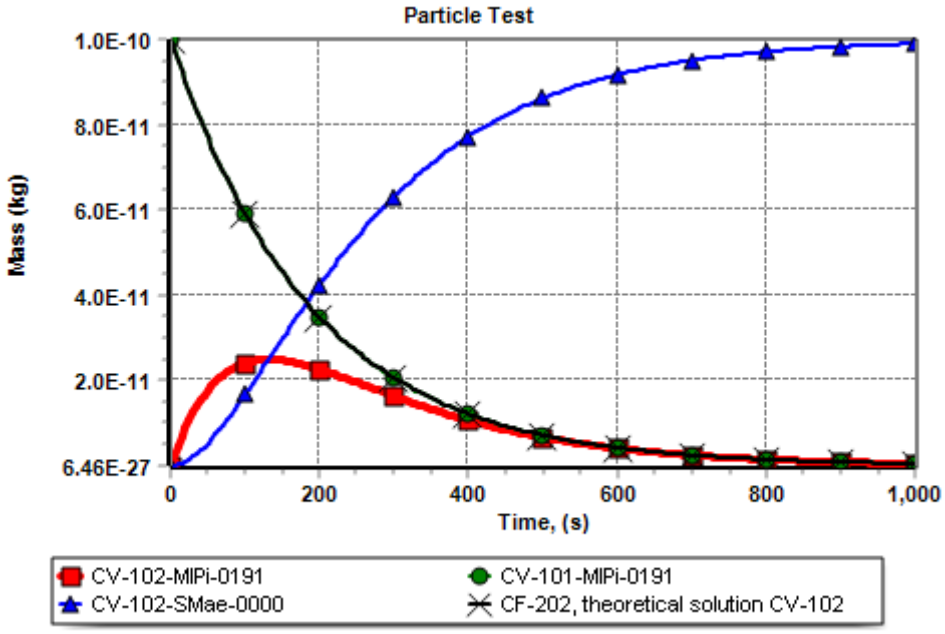

Figure 3-724 Mass distribution, Case 3

3.12.15 Vent Test (Pool Scrubbing)

The Vent test (pool scrubbing test) consists of three Control Volumes: CV-100 "Drywell", 200 "Wetwell", and CV-300 "Vent pipe". The initial temperatures are 300 K, the initial pressures are 1.0 bar. A source of hot (420 K) steam is present at the top of the Drywell. The source provides 0.5 kg/s of steam during the period 30 ÷ 300 s. Additionally a source of aerosol particles is present in this volume. The source provides 1.0×10^{-4} kg/s of aerosols during the entire test. The aerosol source provides aerosols of size section 1 (the smallest size) and 5 (the largest size). The aerosol size section boundaries were chosen as in the earlier tests (see Table 3-57).

Calculations were performed for 350 s, using the maximum time step of 0.1 s in SPECTRA and 0.02 s in MELCOR (application of a time step of 0.1 s in MELCOR resulted in an oscillatory flow in the vent pipe, which clearly affected the particle flow solution).

In this test an important parameter is the pool scrubbing efficiency, E_{PS}. Certain fraction of aerosols that enter the wetwell pool is transported through the pool with the gas bubbles and enters the wetwell gas space. This fraction is equal to (see Volume 1):

$$\frac{W_G(1-E_{PS})}{W_L+W_G}$$

where: W_G - mass flow rate, uncondensed steam + gas, end of bubble collapse, (kg/s),
W_L - mass flow rate, condensed steam, end of bubble collapse, (kg/s),
E_{PS} - pool scrubbing efficiency, (-).

Thus if E_{PS} = 1.0, then all particles are deposited in the pool. If E_{PS} = 0.0, then the fraction of particles deposited in the pool is equal to the fraction of condensed gas. MELCOR contains a model for pool scrubbing efficiency, which is based on the SPARC (Suppression Pool Aerosol Removal Code) - see [20]. In SPECTRA a correlation is used:

$$E_{PS} = A\cdot(1-\exp[-BD_p])$$

where the default values of the coefficients A and B are 0.9 and 0.5×10^6 respectively. These values provide a conservative (low) estimate - see section 2.8.11.

Two SPECTRA calculations were performed.

- Vent 1, "small" aerosols, injected aerosols are of the smallest size section (1.44 μm)
- Vent 5, "large" aerosols, injected aerosols are of the largest size section (22.8 μm)

The input decks are provided in **\Z-TESTS\RT\VENT\VENT1.SPE** and **VENT5.SPE**. Results of both runs Vent 1 and Vent 5 are compared to the MELCOR results in Figure 3-725 through Figure 3-740. In terms of thermal-hydraulic behavior both SPECTRA and MELCOR give similar results except for the cooling of gas in the wetwell. MELCOR predicts relatively fast decrease of the wetwell gas temperature to nearly the level of the pool temperature (Figure 3-726) during the injection phase (50 - 300 s).

In SPECTRA on the other hand the gas temperature remains higher (Figure 3-725). This is a consequence of a very low heat transfer coefficient for heat transfer at the pool surface (~2 W/m^2K). This low heat transfer coefficient was calculated by SPECTRA for a thermally stratified layer, with warm gas on top of the colder pool. The difference in the calculated wetwell gas temperature is not very important for the aerosol behavior predictions.

The aerosol particles are transported to wetwell between about 40 s and 100 s (Figure 3-727 and Figure 3-728). At about 40 s the vent is cleared and the gas present in the vent pipe start flowing through the pool. At about 100 s the drywell and the vent pipe are practically filled with steam. The steam condenses upon entering the cold water in the wetwell, and therefore after about 100 s practically all aerosols are deposited in the pool independently of what is the pool scrubbing efficiency. At 300 s the steam injection is stopped. The steam filling the drywell and the vent pipe slowly condenses on the water surfaces during the next 50 s, which leads to a decrease of the drywell pressure and increase of the water level in the vent pipe. The visualization pictures are shown at 340.0 s, when a significant amount of water is present in the vent pipe. The aerosol behavior is discussed below for the two analyzed cases.

- **Vent 1 "small" aerosols**

  SPECTRA and MELCOR transported similar amount of aerosols to the wetwell gas space (airborne mass of about 1.1×10^{-3} kg in SPECTRA and 1.3×10^{-3} kg in MELCOR - Figure 3-729 and Figure 3-730). As mentioned above the aerosols are transported to the wetwell gas space only during the first 100 s. In spite of the lack of source, the airborne masses remain practically the same. This is a result of a repelling diffusiophoretic force, caused by evaporation of water from the pool surface. Below a printout of SPECTRA output for airborne masses and deposition velocities in CV-200 at 350 s, is shown. It is seen that for the size section 1 (which contains most aerosol particles in this case) the diffusiophoretic velocity (-60×10^{-6} m/s) practically balances the other deposition velocities ($58+2+4)\times10^{-6}$, and the net deposition velocity is only about 3×10^{-6} m/s. Therefore the airborne aerosol mass remains practically the same after about 100 s (Figure 3-731, Figure 3-732)

```
CV-200 Airborne aerosols
Sec.      Mass          Density      Heat source     Activity
 No.      (kg)         (part/m3)         (W)           (Bq)
  1   1.11602E-03   3.71503E+11   0.00000E+00   0.00000E+00
  2   1.30314E-05   5.47929E+08   0.00000E+00   0.00000E+00
  3   7.24481E-08   3.82774E+05   0.00000E+00   0.00000E+00
  4   4.88539E-10   3.27766E+02   0.00000E+00   0.00000E+00
  5   5.12992E-12   4.30214E-01   0.00000E+00   0.00000E+00
     ------------  ------------  ------------  ------------
      1.12912E-03   3.72052E+11   0.00000E+00   0.00000E+00

Deposition velocities
Sec.     V-grav.      V-Brown      V-ther.      V-diff.      V-turb.      V-total
 No.      (m/s)        (m/s)        (m/s)        (m/s)        (m/s)        (m/s)
  1   5.7579E-05  1.8325E-06  3.8944E-06 -5.9815E-05  0.0000E+00  3.4907E-06
  2   2.2427E-04  9.0155E-07  2.2526E-06 -5.9815E-05  0.0000E+00  1.6761E-04
  3   8.8503E-04  4.4706E-07  1.2761E-06 -5.9815E-05  0.0000E+00  8.2694E-04
  4   3.4855E-03  2.2357E-07  7.4417E-07 -5.9815E-05  0.0000E+00  3.4267E-03
  5   1.3907E-02  1.1150E-07  4.6309E-07 -5.9815E-05  0.0000E+00  1.3847E-02
```

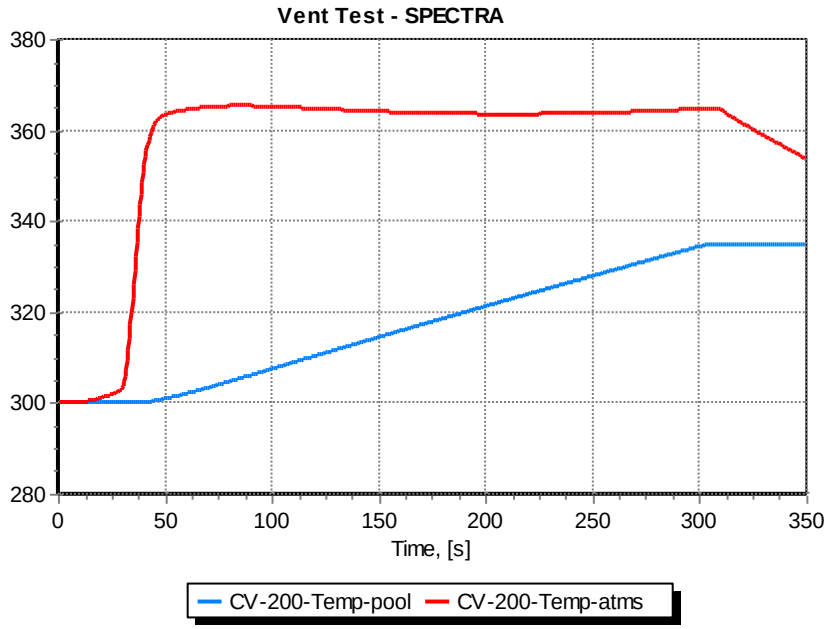

Figure 3-725 Wetwell temperatures - SPECTRA.

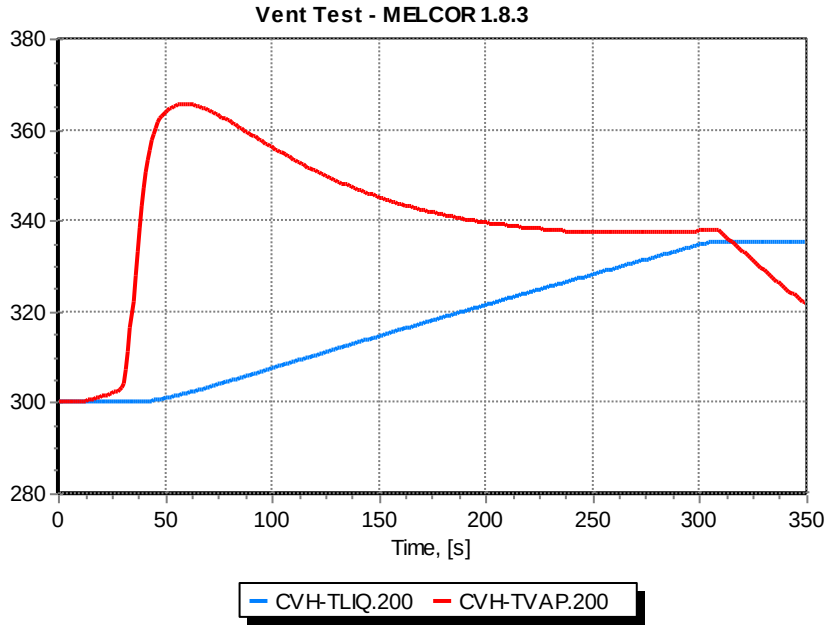

Figure 3-726 Wetwell temperatures - MELCOR.

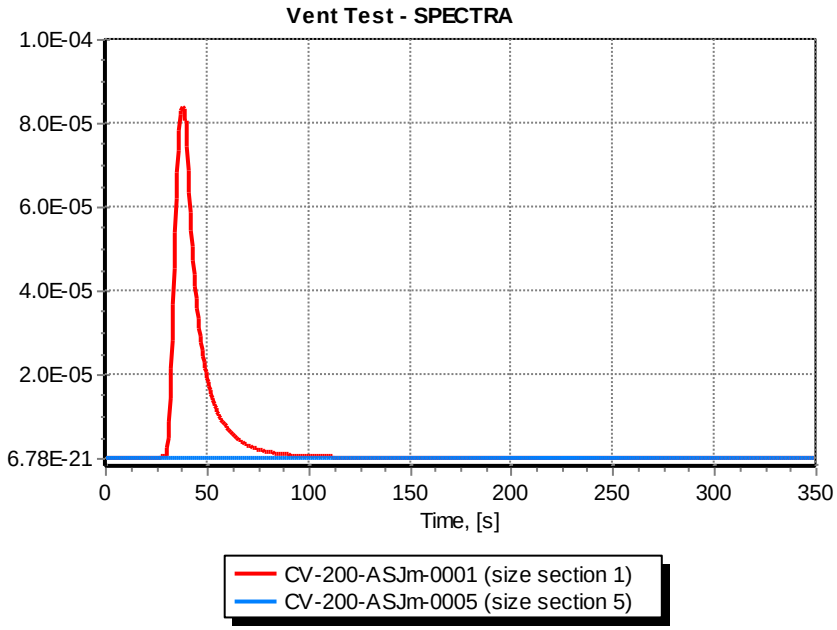

Figure 3-727 Source of aerosols for the wetwell gas space, Vent 1, SPECTRA.

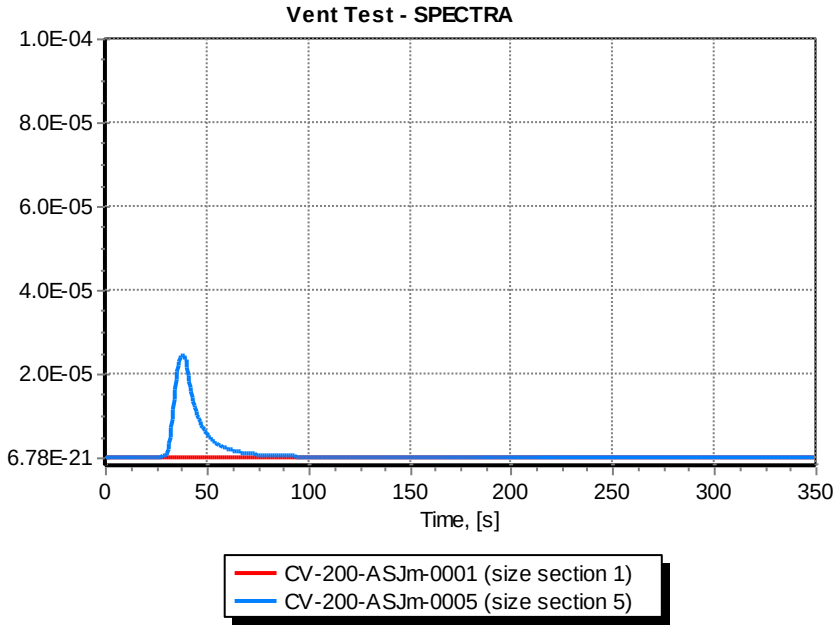

Figure 3-728 Source of aerosols for the wetwell gas space, Vent 5, SPECTRA.

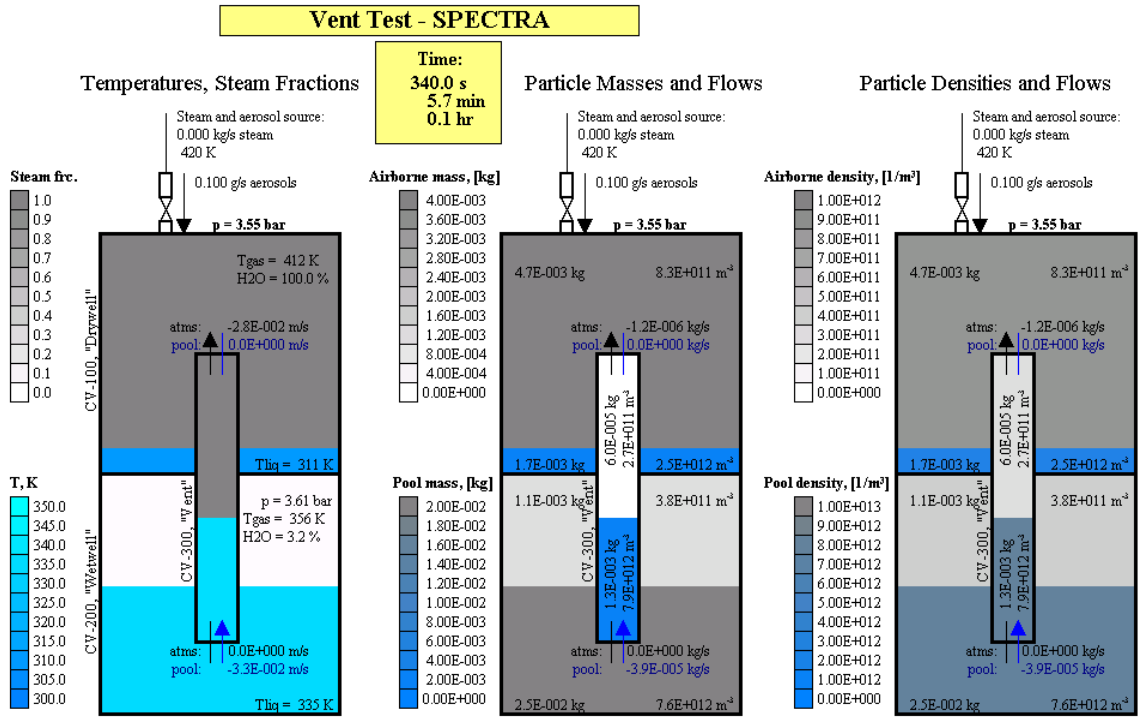

Figure 3-729 Vent 1 test (“small” aerosols), SPECTRA.

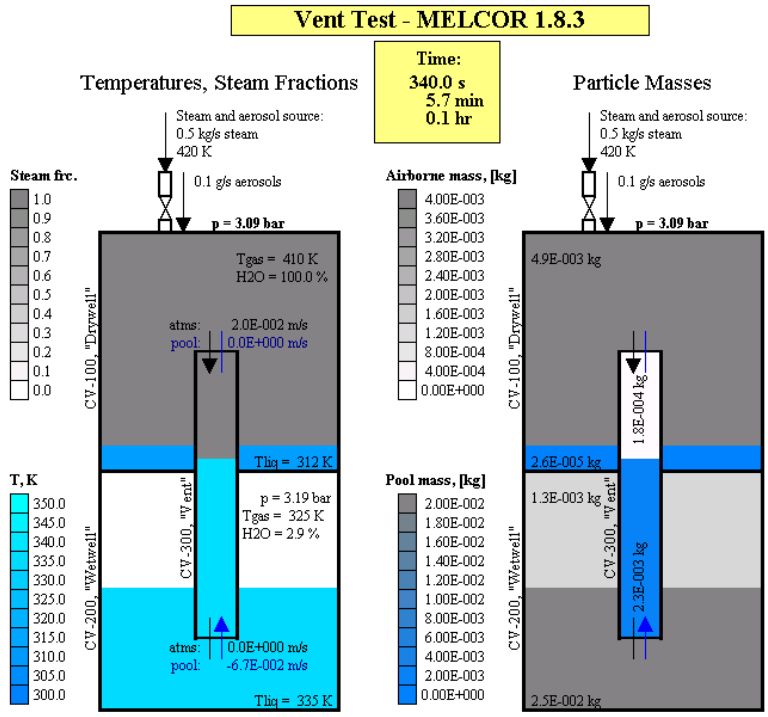

Figure 3-730 Vent 1 test (“small” aerosols), MELCOR 1.8.3.

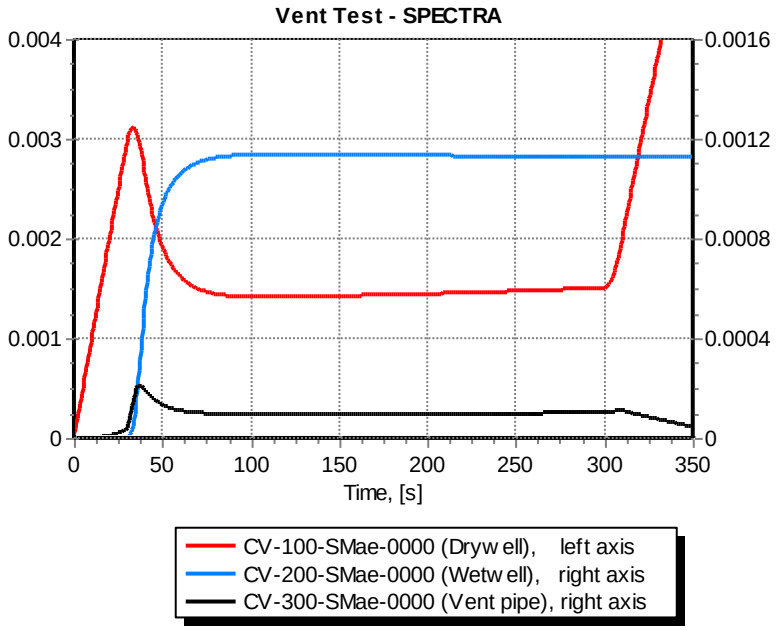

Figure 3-731 Vent 1 test (“small” aerosols), airborne masses, SPECTRA.

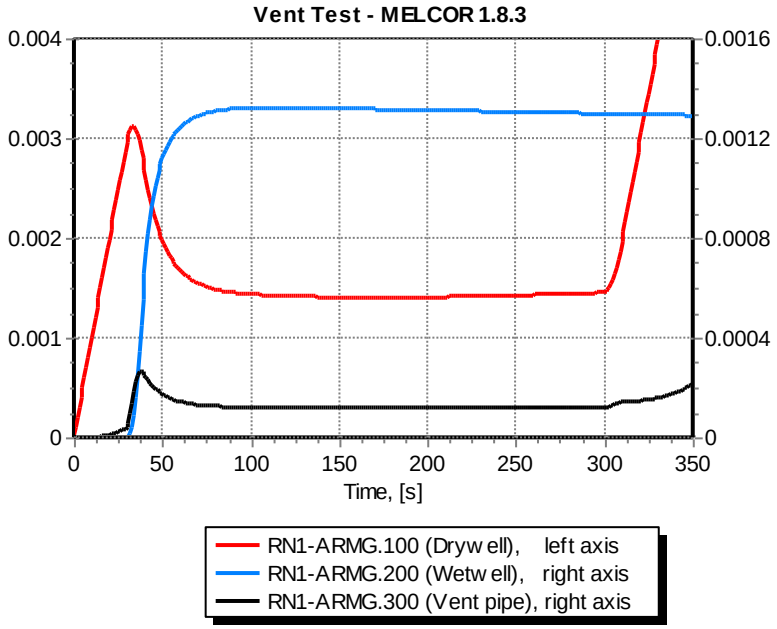

Figure 3-732 Vent 1 test (“small” aerosols), airborne masses, MELCOR 1.8.3.

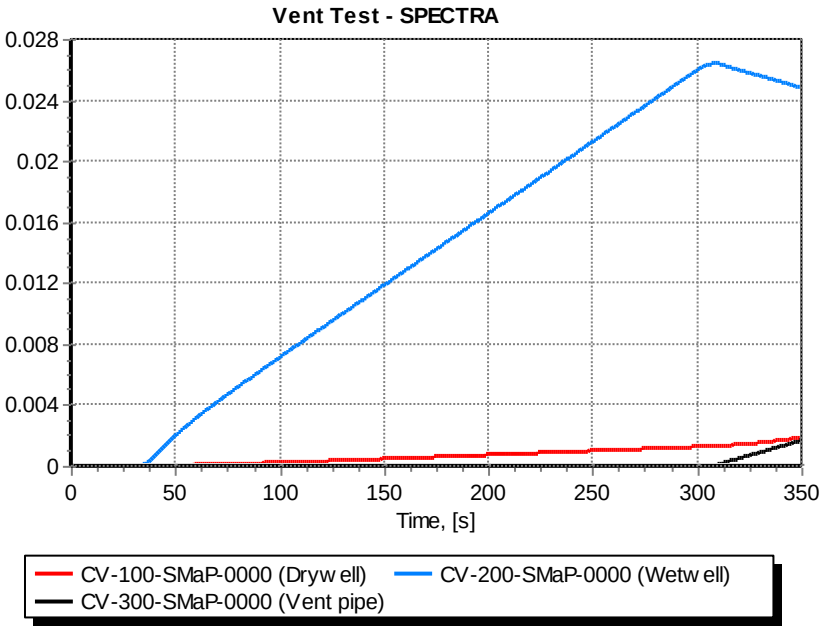

Figure 3-733 Vent 1 test (“small” aerosols), deposited masses, SPECTRA.

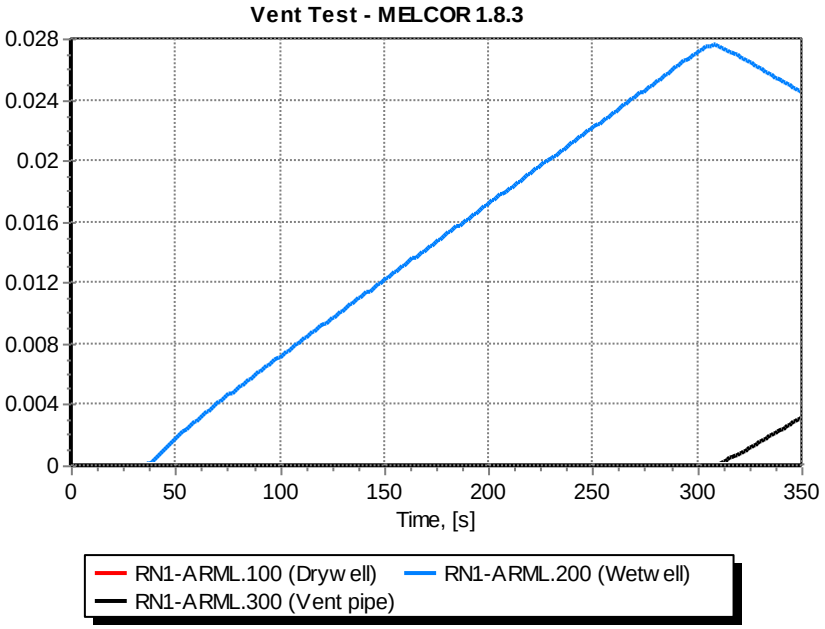

Figure 3-734 Vent 1 test (“small” aerosols), deposited masses, MELCOR 1.8.3.

A small deposition on the drywell pool surface, visible in Figure 3-733, is only observed in SPECTRA. Investigation of the deposition mechanism showed that the deposition is caused mainly by diffusiophoresis, caused by steam condensation on the pool surface. This deposition is not observed in MELCOR - Figure 3-734.

- **Vent 5 "large" aerosols**

In this case the amount of aerosols transported into the wetwell gas space is much smaller than in the previous case, because the pool scrubbing efficiency is very large for large particles (see section 2.8.11). The maximum amount of the airborne aerosols is about 2.4×10^{-4} kg in both SPECTRA (Figure 3-737) and MELCOR (Figure 3-738). In SPECTRA however the airborne aerosols deposit slowly on the pool surface and the airborne mass decreases. This behavior is different than in the previous case, because now particles are much larger and they deposit due to gravity force. The gravitational settling velocity is about 10^{-2} m/s (see the printout below) and the repelling thermophoretic force (deposition velocity of about 6×10^{-5} m/s) is way too small to compensate for the gravity in this case. The reason why this effect is not observed in MELCOR calculations (wetwell airborne mass remains constant - Figure 3-738) is unclear.

CV-200 Airborne aerosols

Sec. No.	Mass (kg)	Density (part/m3)	Heat source (W)	Activity (Bq)
1	0.00000E+00	0.00000E+00	0.00000E+00	0.00000E+00
2	0.00000E+00	0.00000E+00	0.00000E+00	0.00000E+00
3	0.00000E+00	0.00000E+00	0.00000E+00	0.00000E+00
4	0.00000E+00	0.00000E+00	0.00000E+00	0.00000E+00
5	3.80194E-06	3.18845E+05	0.00000E+00	0.00000E+00
	3.80194E-06	3.18845E+05	0.00000E+00	0.00000E+00

Deposition velocities

Sec. No.	V-grav. (m/s)	V-Brown (m/s)	V-ther. (m/s)	V-diff. (m/s)	V-turb. (m/s)	V-total (m/s)
1	5.7579E-05	1.8325E-06	3.8944E-06	-5.9815E-05	0.0000E+00	3.4907E-06
2	2.2427E-04	9.0155E-07	2.2526E-06	-5.9815E-05	0.0000E+00	1.6761E-04
3	8.8503E-04	4.4706E-07	1.2761E-06	-5.9815E-05	0.0000E+00	8.2694E-04
4	3.4855E-03	2.2357E-07	7.4417E-07	-5.9815E-05	0.0000E+00	3.4267E-03
5	1.3907E-02	1.1150E-07	4.6309E-07	-5.9815E-05	0.0000E+00	1.3847E-02

- **Summary**

  - Similar maximum concentrations of aerosol masses in the wetwell gas space were calculated by SPECTRA and MELCOR. Therefore the pool scrubbing model is considered as validated based on comparisons with the MELCOR results.
  - The "small" aerosols in the wetwell gas space do not deposit on the pool surface because evaporation from the pool surface creates a repelling diffusiophoretic force that approximately counterbalance the other deposition forces.
  - The "large" aerosols in the wetwell gas space deposit on the pool surface. The gravitational settling velocity is large and the repelling thermophoretic force is way too small to compensate for the gravity in this case. It is unclear why MELCOR does not confirm this deposition.

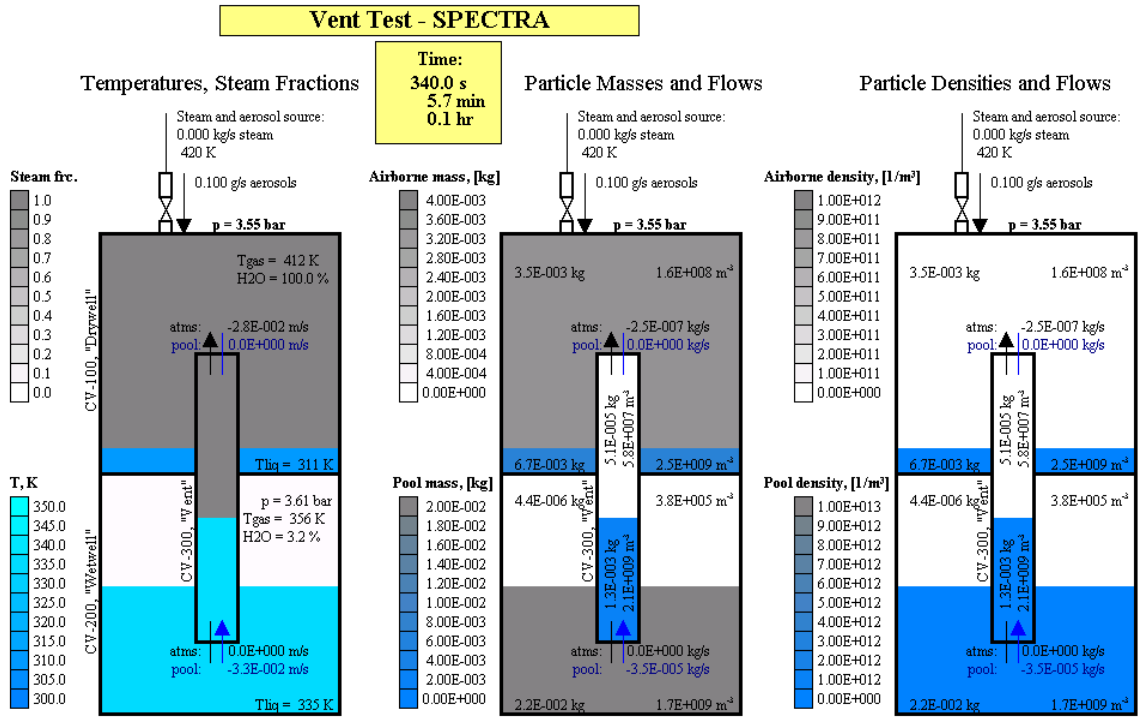

Figure 3-735 Vent 5 test, (“large” aerosols), SPECTRA.

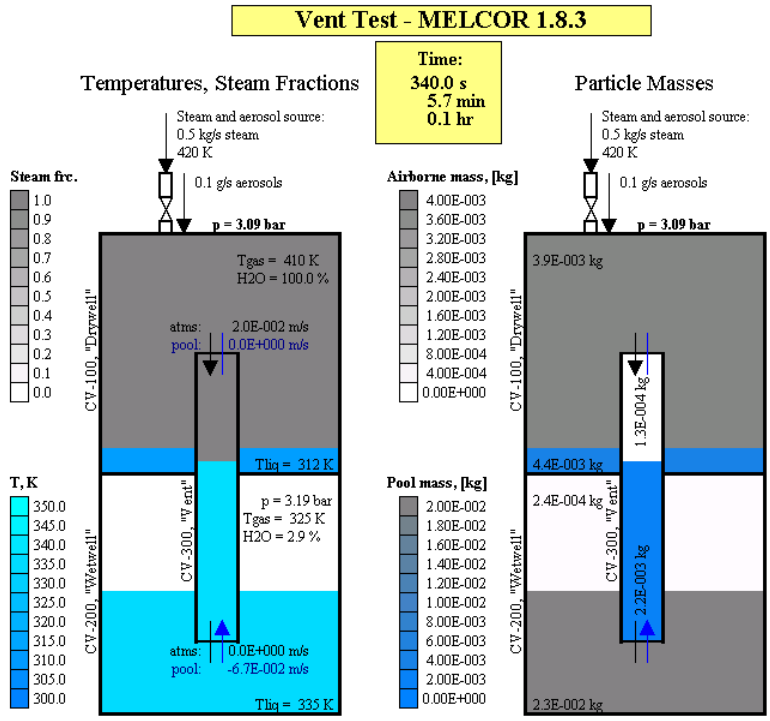

Figure 3-736 Vent 5 test (“large” aerosols”), MELCOR 1.8.3.

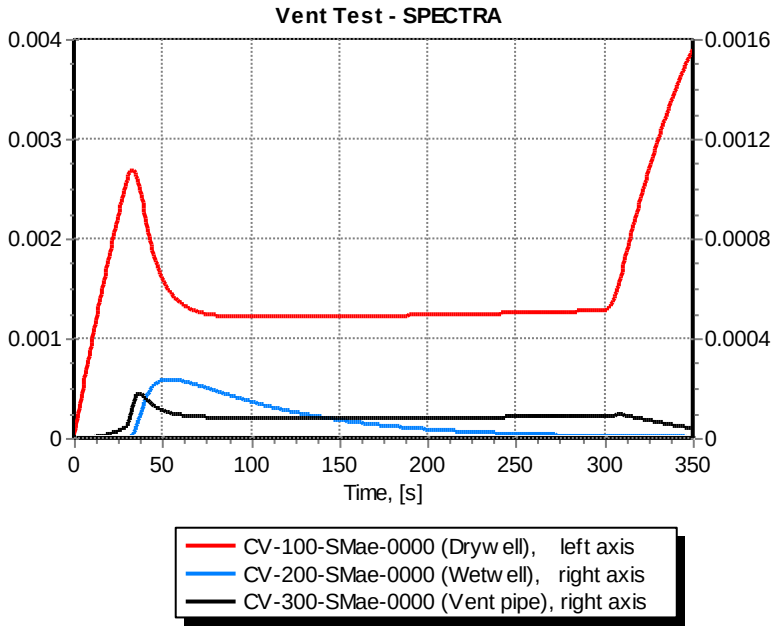

Figure 3-737 Vent 5 test, (“large” aerosols), airborne masses, SPECTRA.

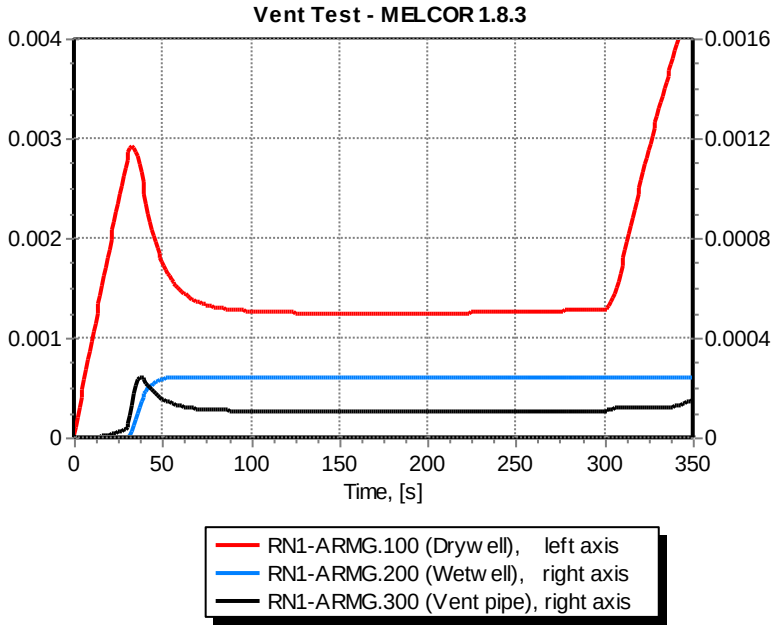

Figure 3-738 Vent 5 test, (“large” aerosols), airborne masses, MELCOR 1.8.3.

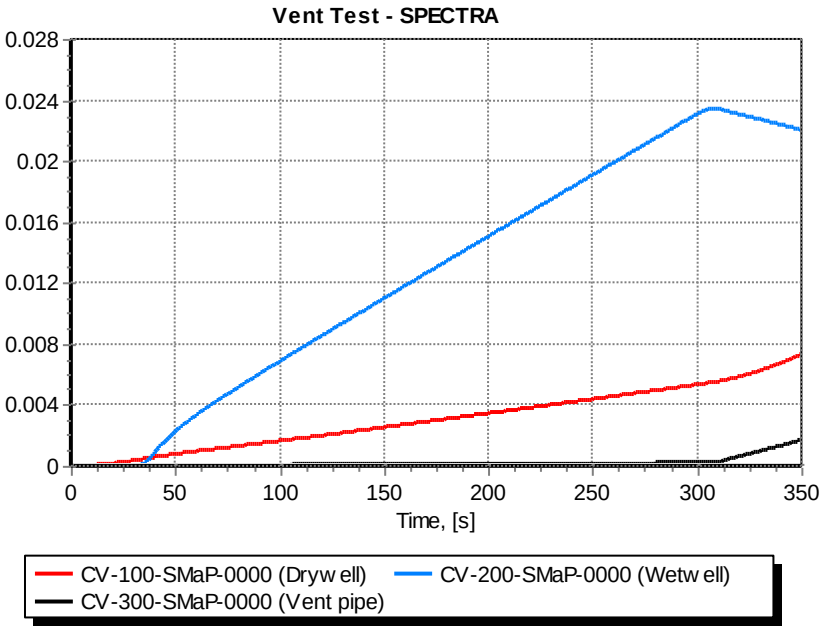

Figure 3-739 Vent 5 test, (“large” aerosols), deposited masses, SPECTRA.

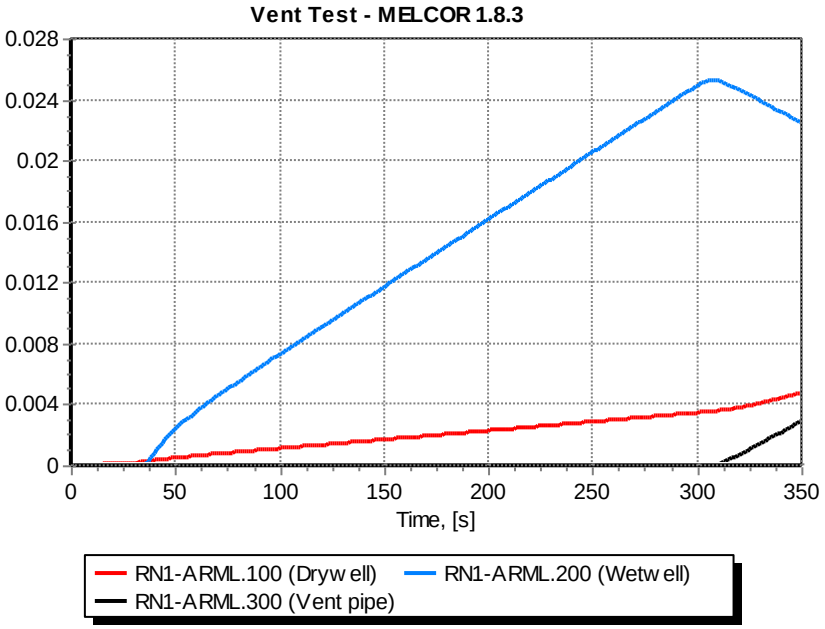

Figure 3-740 Vent 5 test, (“large” aerosols), deposited masses, MELCOR 1.8.3.

3.12.16 Filter Test – Constant Efficiency Filter

A model that has been set up for testing the aerosol filter is very similar to the aerosol model test 1, described in section 3.12.3. The test consists of six Control Volumes: CV-101, 102, 103, 104, 105, and CV-200. The last volume is held at constant conditions and it serves as a boundary condition. The volumes are connected with junctions JN-101, 102, 103, 104, and JN-105. The filter is present in JN-103. The structures SC-101 through SC-105 were removed from the model in order to have a single effect (filter) test. (The MELCOR code requires at least one structure in a CV where the deposition can occur. Therefore the structures HS-101 through HS-105 were preserved in the MELCOR model, but the areas of these structures were set to a very small number, 10^{-5} m^2, to minimize the deposition.)

The filter was placed in JN-103. A simple filter model, with a constant, user-defined efficiency was used in the test because the models, which are available in the codes to compute the filter efficiency, are valid for different kind of filters. The filter efficiency, ε_F, was assumed to be 0.5. The corresponding filter decontamination factor, DF_F, used by MELCOR as an input parameter, is equal to:

$$DF_F = \frac{1}{1-\varepsilon_F} = \frac{1}{1-0.5} = 2.0$$

As in Test 1, a source of gas and aerosols is present in volume CV-101. The source provides 0.1 kg/s of gas and 1.0×10^{-6} kg/s of aerosols. The input deck is provided in **\Z-TESTS\RT\FILTER\FILTER.SPE**.

The results are shown in Figure 3-741 through Figure 3-746 (the time-independent volume CV-200 is not shown in the visualization pictures). The stable aerosol concentrations in the volumes downstream the filter (CV-104, CV-105) are equal to one half of the stable aerosol concentrations in the volumes upstream the filter (CV-101, CV-102, CV-103). This is simply a consequence of the assumed filter efficiency of 0.5.

The calculated aerosol concentrations and the amount of aerosols deposited in the filter are in very good agreement.

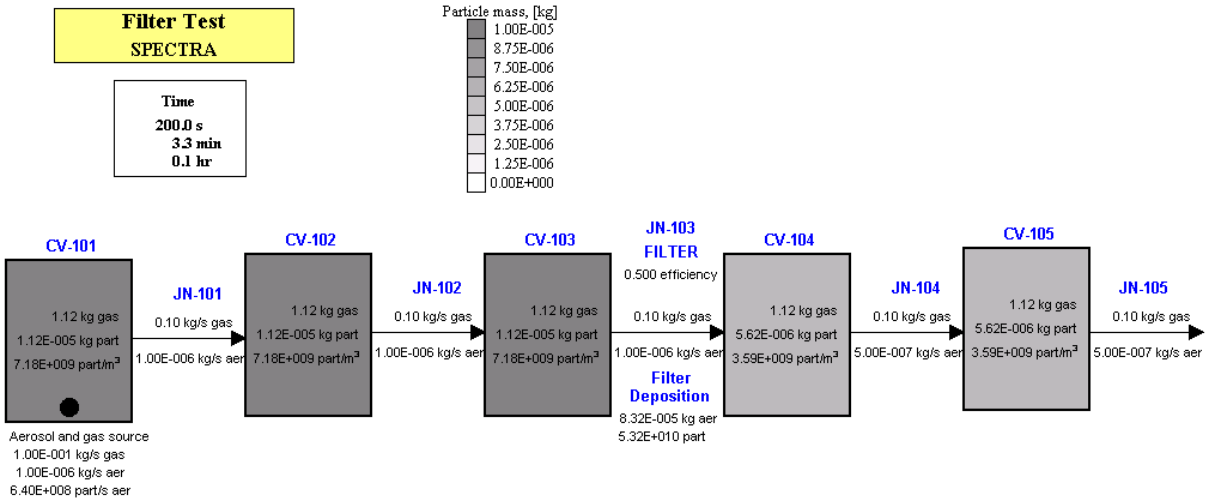

Figure 3-741 Filter test – SPECTRA.

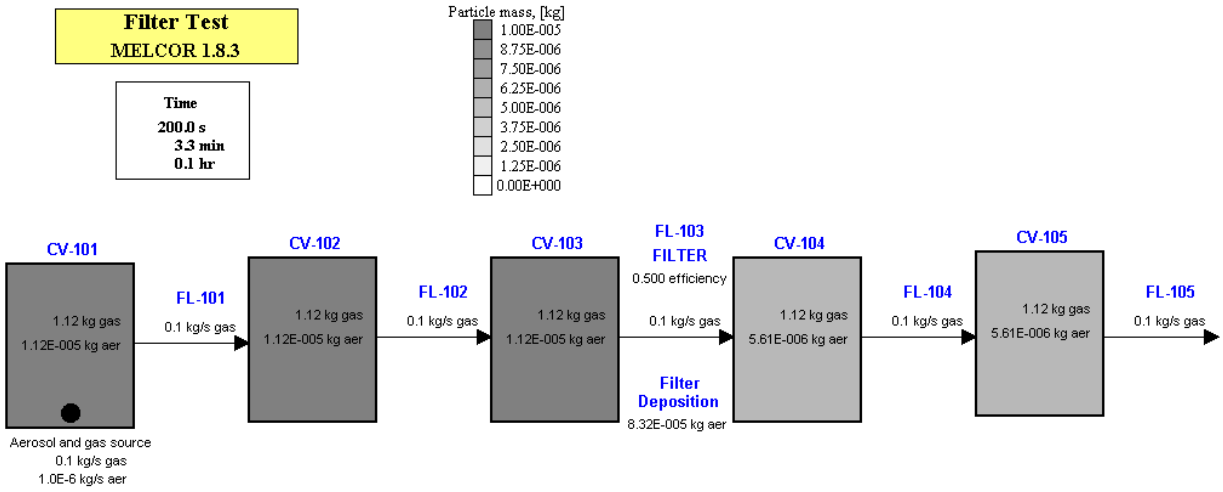

Figure 3-742 Filter test – MELCOR 1.8.3.

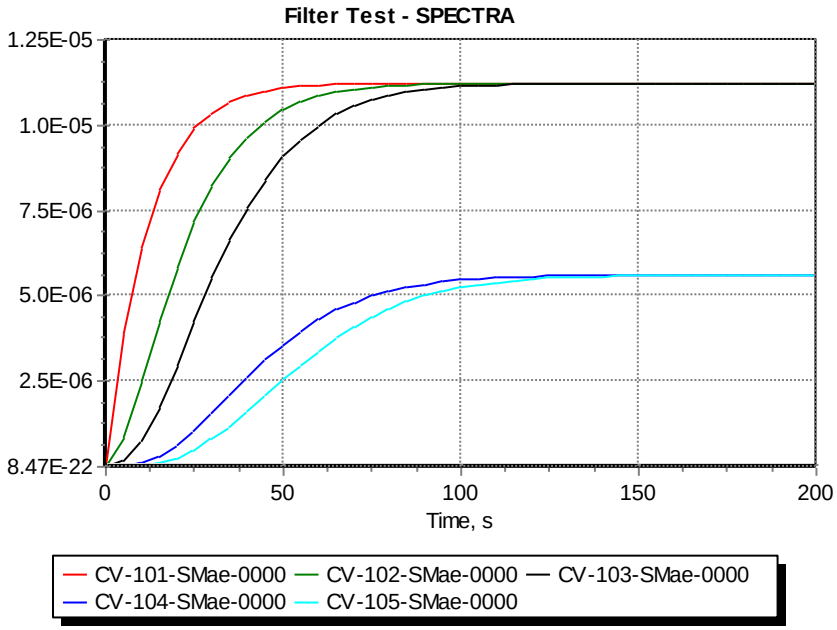

Figure 3-743 Filter test, airborne masses, SPECTRA.

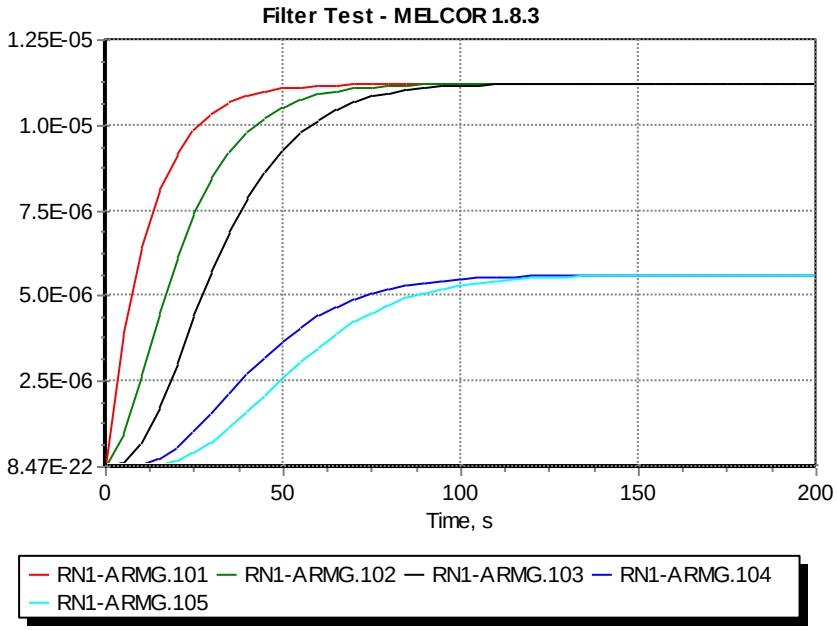

Figure 3-744 Filter test, airborne masses, MELCOR 1.8.3.

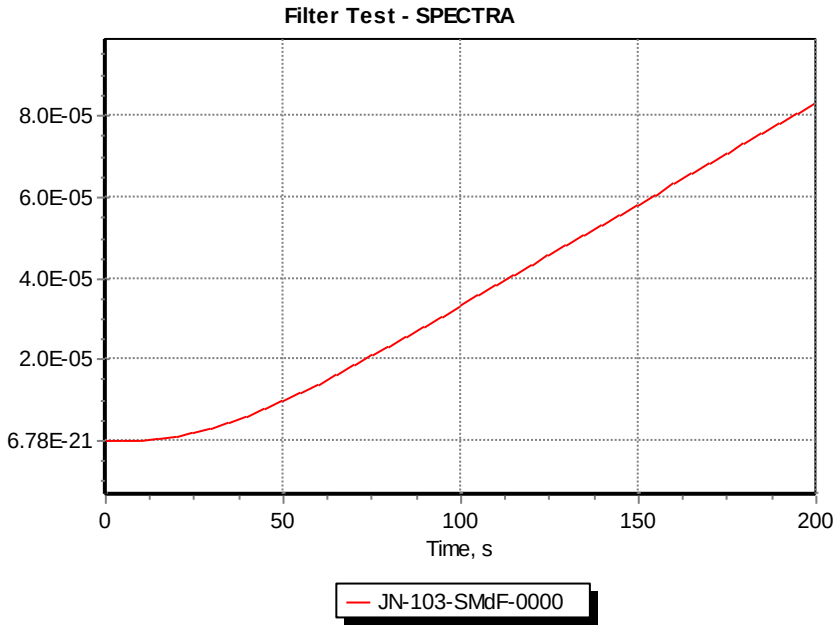

Figure 3-745 Filter test, mass deposited on the filter, SPECTRA.

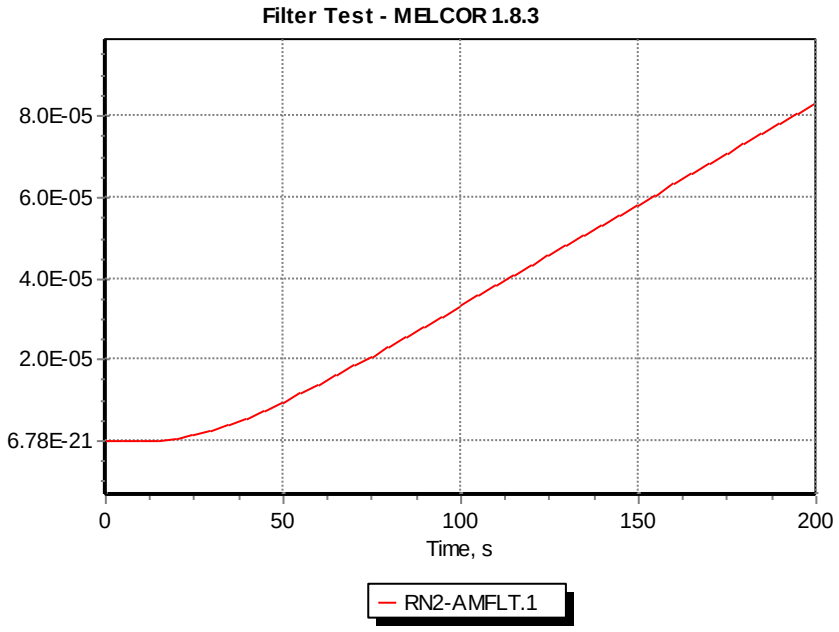

Figure 3-746 Filter test, mass deposited on the filter, MELCOR 1.8.3.

3.12.17 Filter Test – Glass Fiber Filter

A simple model has been set up for testing the fiber filter with SPECTRA. The comparison is made with the data shown in [79]. The model consists of three Control Volumes: CV-101, 102, 103, and two Junctions: JN-101, JN-102. The Volumes CV-101 and CV-103 are kept at constant conditions. The filter is located in JN-101. The junction JN-101 direction is vertical – down (the fiber filter efficiency depends on the downwards velocity).

The flow through JN-101 is forced by a tabular function. This is done in such way as to cover the velocity range shown in [79]. Four aerosol size sections were used (as in [79]):

- Section 1: $d = 0.2$ μm.
- Section 2: $d = 0.4$ μm.
- Section 2: $d = 0.5$ μm.
- Section 2: $d = 1.0$ μm.

The mass flow in JN-101 was varied according to the following table:

- $t = 0.0$ s v = 0.0001 kg/s
- $t = 50.0$ s v = 0.001 kg/s
- $t = 100.0$ s v = 0.01 kg/s
- $t = 150.0$ s v = 0.1 kg/s
- $t = 200.0$ s v = 0.3 kg/s

The input deck is provided in **\Z-TESTS\RT\FILTER-F\FILTRT-F.SPE**. Results are shown in Figure 3-747, Figure 3-748, and Figure 3-749. Figure 3-747 shows the state of the test system, at 100 s, when the velocity is approximately 0.09 m/s. Figure 3-748 shows efficiencies for each size section, as well as the gas velocity in JN-101. Finally, Figure 3-749 presents the filter efficiencies plotted versus the gas velocity in JN-101. The gas velocity for filter junction is defined in SPECTRA as the face velocity – that is a velocity that the gas would have in absence of the filter. The JN loss factor is related to that velocity and is calculated based on filter data (see Volume 2).

The data shown in Figure 3-749 is compared to the literature data, shown in Figure 3-750, reproduced from [79]. A very good agreement is observed.

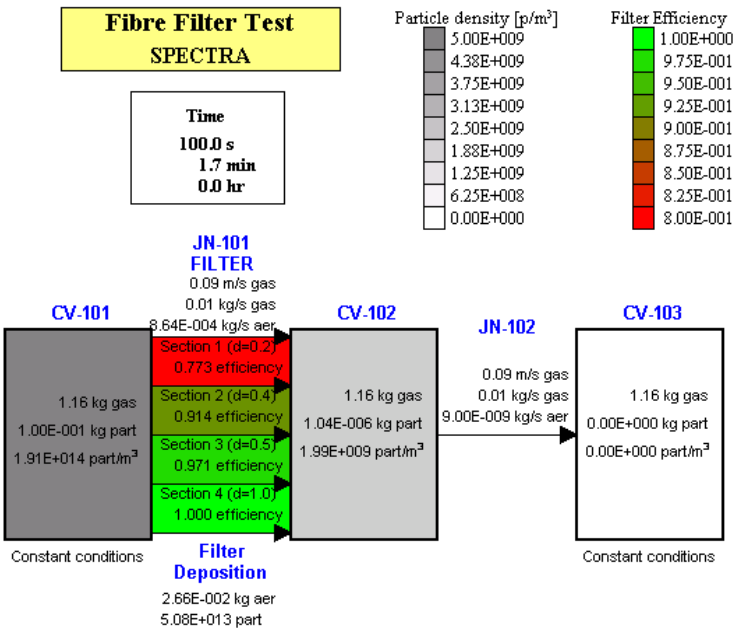

Figure 3-747 Fiber filter test – SPECTRA.

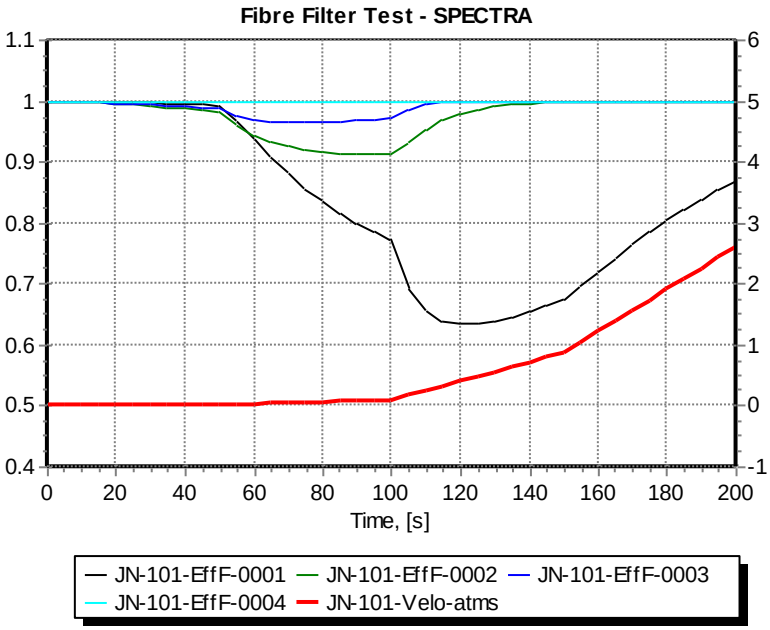

Figure 3-748 Fiber filter test, filter efficiencies and gas velocity – SPECTRA.

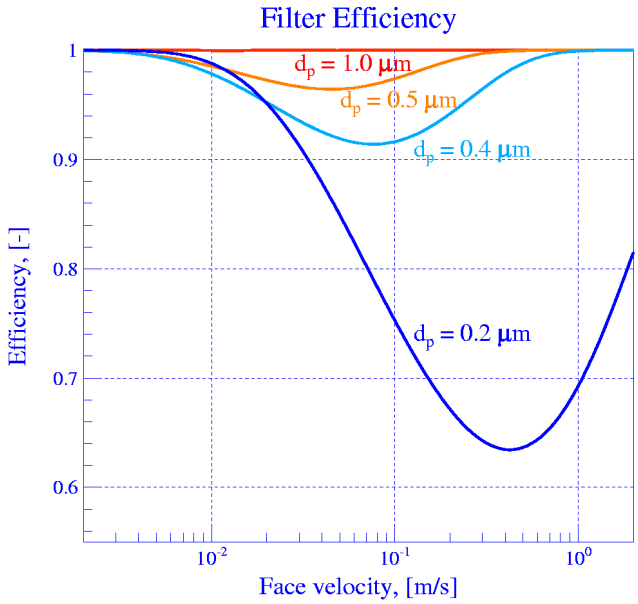

Figure 3-749 Fiber filter test, filter efficiencies versus gas velocity – SPECTRA.

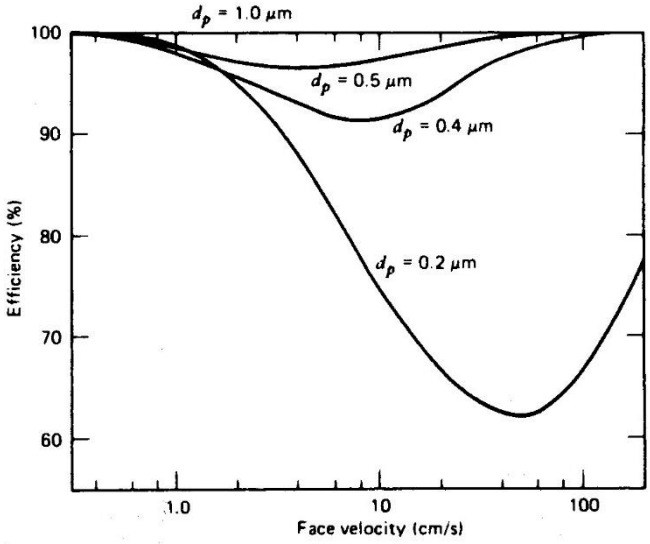

Figure 3-750 Filter efficiency data (reproduced from [79]).

3.12.18 Parametric Resuspension Model Test - Corn and Stein Data

Resuspension may occur as a result of air jets, mechanical forces, impaction of other particles, or electrostatic forces [79]. Re-entrainment, or blow-off, a more specific term, refers to resuspension by a jet of gas. Re-entrainment is a stochastic process in which a given condition of gas velocity permits one to estimate the fraction of particles of a given size that will be removed from a surface ([79], section 6.3). Representative data from Corn and Stein [80] for the bulk air velocity required to re-entrain different sizes of glass beads are shown in [79], and reproduced in Figure 3-751.

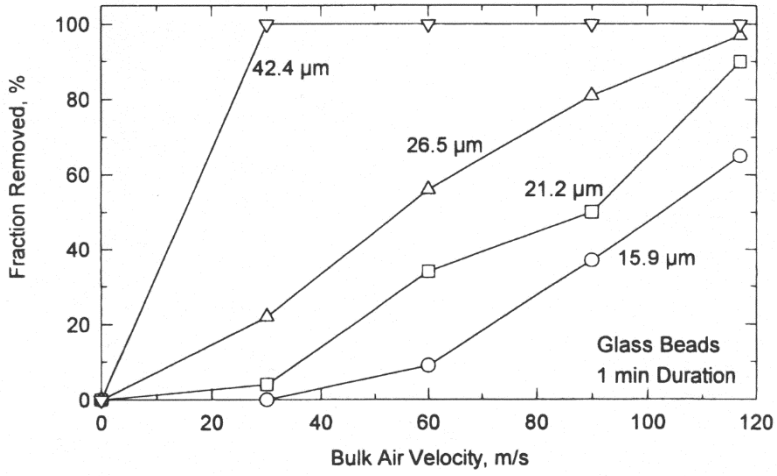

Figure 3-751 Resuspension data, removed fractions, reproduced from [79].

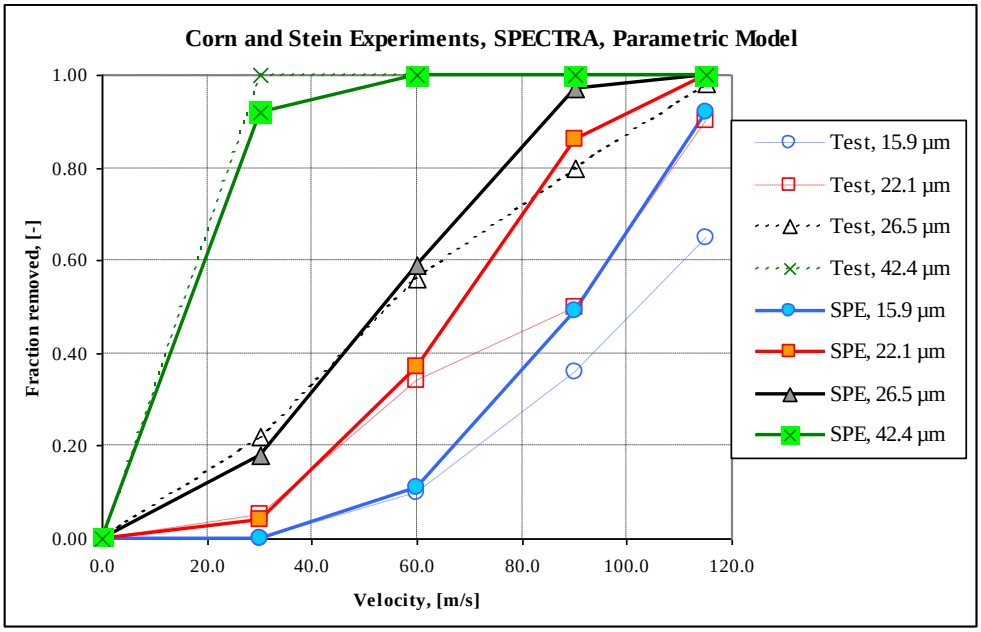

Figure 3-752 Removed fractions, data from [79], and results of the parametric model.

The velocity-dependent parametric model is used (see Volume 1):

$$R_v(t) = C_1(v - v_0) + C_2(v - v_0)^x$$

The resuspension coefficients were selected using a trial and error method. The resuspension rates are calculated using the following formulae:

- For 15.9 μm beads: $R = 1.0\times10^{-3} \cdot (v - 50.0) + 5.0\times10^{-9} \cdot (v - 50.0)^4$
- For 21.2 μm beads: $R = 1.0\times10^{-3} \cdot (v - 25.0) + 5.0\times10^{-9} \cdot (v - 25.0)^4$
- For 26.5 μm beads: $R = 1.0\times10^{-3} \cdot (v - 5.0) + 5.0\times10^{-9} \cdot (v - 5.0)^4$
- For 42.4 μm beads: $R = 5.0\times10^{-2} \cdot (v - 0.0) + 5.0\times10^{-8} \cdot (v - 0.0)^4$

Default time dependent term is used (Model 1, $B = 0.1$). Calculations were run for 60 s. The input deck is provided in **\Z-TESTS\RT\Res-Corn\Results\Corn-P.SPE**.The results obtained at 60 s are shown in Figure 3-752 and Figure 3-753. Results of the source data are included in this figure for comparison. It is seen that the selected formulae represent well the resuspension data from [79],

For comparison the Corn experiments were recalculated using the mechanistic resuspension models of Vainshtein (file: **Corn-V.SPE**) and Rock'n Roll (file: **Corn-R.SPE**). The model constants were the same as for the Reeks and Hall experiments, "all default" cases (see section 3.12.29). Smooth wall was assumed.

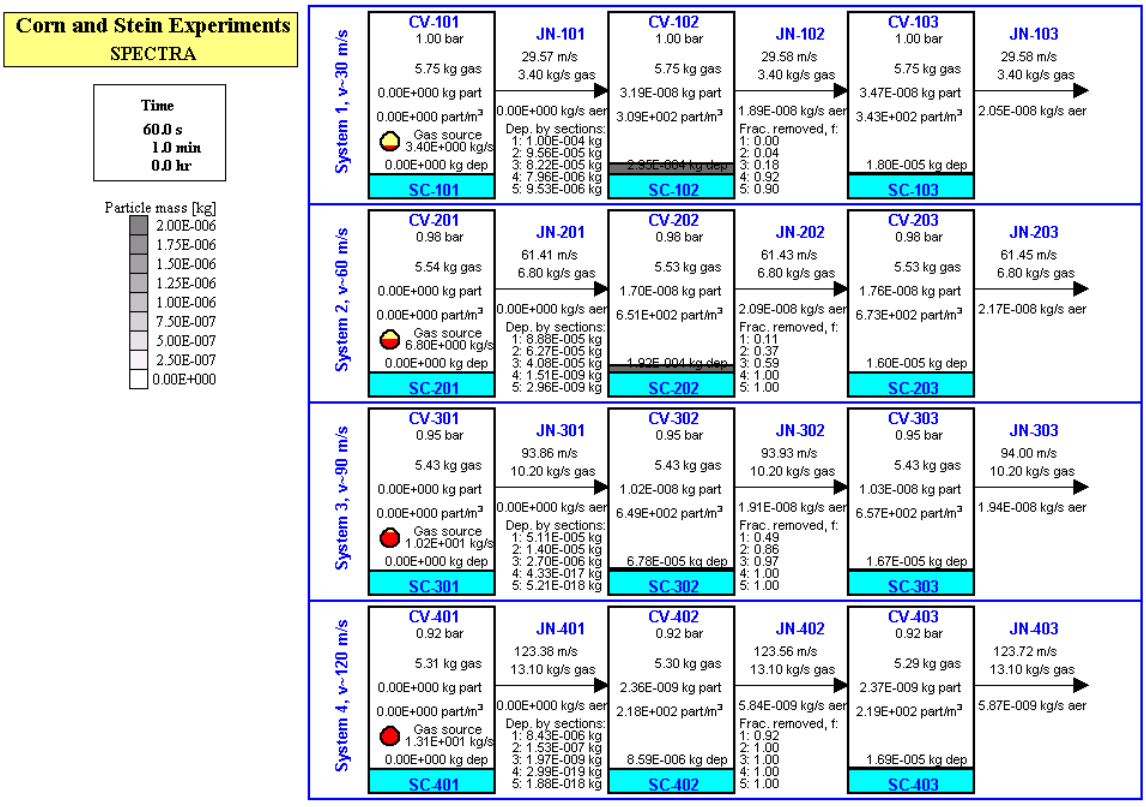

Figure 3-753 Calculation of Corn and Stain test – final state (t = 60 s).

Results are shown in Figure 3-754 and Figure 3-755. Both models give higher resuspension than the experimentally reported values. The Rock'n Roll gives higher resuspension than the Vainshtein model, which marks a general trend, observed also in other calculations (sections 3.12.29 and 3.12.30).

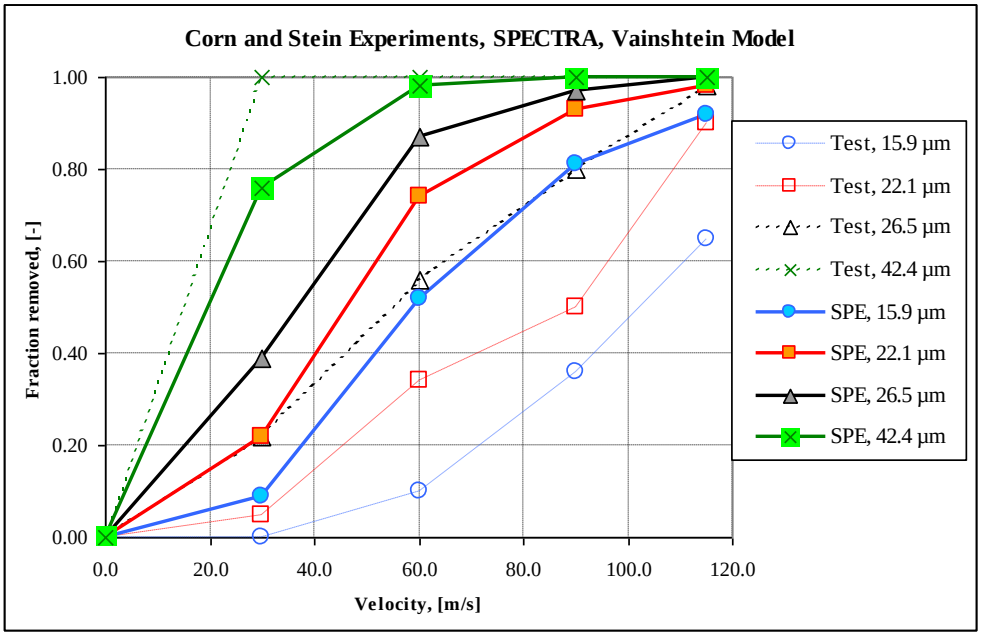

Figure 3-754 Removed fractions, data from [79], and results of the Vainshtein model.

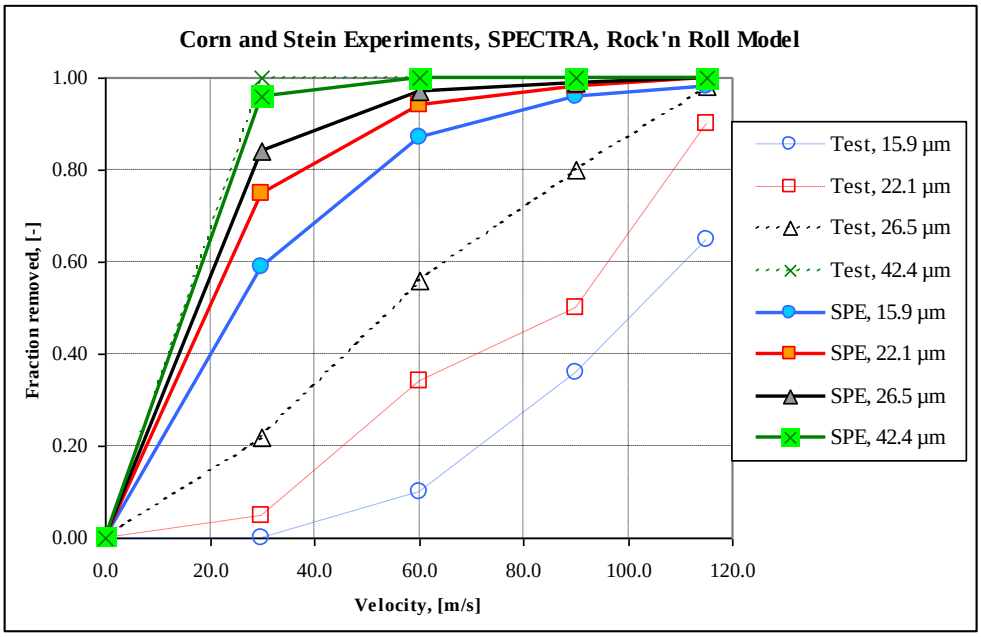

Figure 3-755 Removed fractions, data from [79], and results of the Rock'n Roll model.

3.12.19 Parametric Resuspension Model Test – STORM Experiment SR11

The resuspension test 5 is a model of the STORM experiment SR11 (ISP-40) [84]. The STORM test SR11 was performed in April 1997 at the Joint Research Center of the European Commission (JRC). The test included two distinct phases, the first concentrating on aerosol deposition, mostly by thermophoresis and eddy impaction, and the second on aerosol resuspension under a stepwise increasing gas flow.

The test facility consisted of a 5.0 m long straight pipe with 63 mm internal diameter [84]. In the deposition section a mixture the carrier gas and aerosols was injected into the test section. The mass flows of gases are shown in Table 3-58. In the SPECTRA calculations carbon dioxide was used instead of argon, because of lack of gas properties for argon in the Fluid Property Package.

Table 3-58 Carrier gas mass flows during the deposition phase [84].

Gas	Mass flow, (kg/s)
Steam	1.106×10^{-2}
Nitrogen	5.467×10^{-3}
Air	5.728×10^{-3}
Argon	7.194×10^{-3}
Helium	0.119×10^{-3}

A constant mass flow, 3.83×10^{-4} kg/s [84] of SnO_2 aerosols was supplied during the deposition phase. The aerosol density was 4000 kg/m^3; the conductivity was 11 W/(m·K) [84]. The following size distribution data was supplied:

- mean diameter: 0.43 μm
- standard deviation 1.7

For SPECTRA calculations 5 size sections were used, with diameters of:

- 0.25 μm,
- 0.50 μm
- 1.00 μm
- 2.00 μm
- 4.00 μm

The mass source for each particular section was calculated using the lognormal distribution with the mean diameter and the standard deviation shown above. The results are shown in Table 3-59 and Figure 3-756.

The gas inlet temperature was equal to 640 K [84]. The wall temperature was between 520 and 480 K [84], as shown in Table 3-60. The wall temperatures were estimated based on figure 4, presented in [84]. These temperatures were supplied as boundary values for the five Solid Heat Conductors (SC-101 through SC-105) representing the test section.

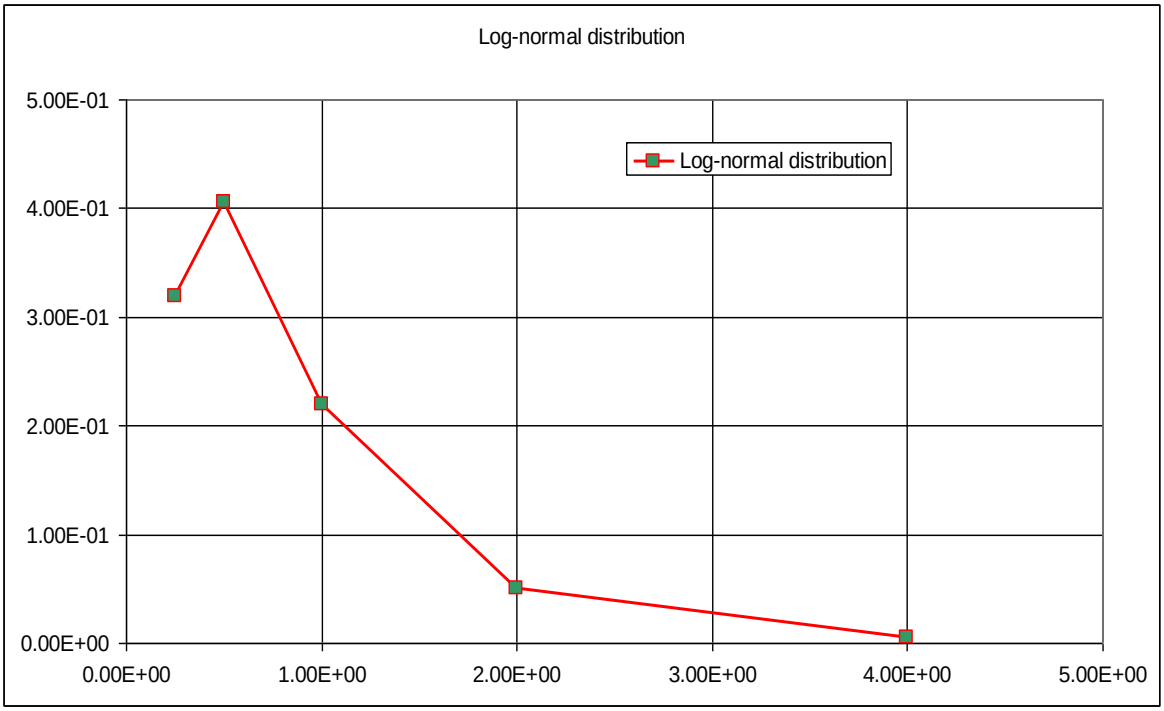

Figure 3-756 Aerosol fractions (frequency) per size section.

Table 3-59 Aerosol source per section.

Size section	Mass source (kg/s)	Fraction, (%)
1	1.22×10^{-4}	31.9
2	1.55×10^{-4}	40.6
3	8.42×10^{-5}	22.0
4	1.95×10^{-5}	5.1
5	1.91×10^{-6}	0.5
Total	3.83×10^{-4}	100.0

Table 3-60 Tube wall temperatures [84] (figure 4).

No.	Tube length, (m)	Temperature, (K)
SC-101	0.0 – 1.0	520.0
SC-102	1.0 – 2.0	510.0
SC-103	2.0 – 3.0	500.0
SC-104	3.0 – 4.0	490.0
SC-105	4.0 – 5.0	480.0

In SPECTRA calculations the test section was represented by five Control Volumes (CV-101 through CV-105) connected by Junctions, and five 1-D Solid Heat Conductors (SC-101 through SC-105). Each CV and SC represent 1.0 m of the test section length. Two extra volumes (CV-100 at the inlet and CV-200 at the exit) were used to provide boundary conditions. Detailed data on the flanges present in the test section (visible in Figure 3-758, Figure 3-760, Figure 3-764, and Figure 3-766) was not available in [84]; therefore the flanges were not included in the present model.

The deposition phase took two and a half hour (12:00 – 14:30 [84]), which means 9000 seconds. Calculations of the resuspension phase were performed for 9000 s, starting at 0.0 s (12:00:00) and ending at 9,000 s (14:30:00).

The resuspension phase was performed on the following day, after equalizing the gas and wall temperature to avoid thermophoretic deposition. The gas inlet temperature was 640 K; the wall temperatures were about 630 K ([84], figure 6).

In SPECTRA calculations the resuspension phase directly followed the deposition phase, and was preceded by 1000 s (from 9,000 to 10,000 s) of simulation during which the wall temperatures were brought up to 630 K by changing the boundary temperatures and venting small amount of aerosol-free nitrogen through the test section. The resuspension phase started at 10,000 s. This phase consisted of six steps of increasing gas velocity through the test section. The carrier gas was pure nitrogen; the mass flows during each step are shown in Table 3-61.

Table 3-61 Mass flows during the resuspension phase.

Step number	Start time, experiment	Start time, simulation	Mass flow (kg/s)
1	12:13:00	10,780 s	0.102
2	12:20:00	11,200 s	0.126
3	12:50:00	13,000 s	0.152
4	13:06:40	14,000 s	0.175
5	13:23:20	15,000 s	0.199
6	13:40:00	16,000 s	0.224

The SPECTRA velocity-dependent resuspension model was applied. The model coefficients were specified based on the data of Corn and Stein [80] (see section 3.12.18). The coefficients for the smallest size section of the Corn and Stein data were applied for all size sections of this test. Therefore (see section 3.12.18) the velocity-dependent resuspension rate is given by:

$$R = 1.0\times10^{-4} \cdot (v - 50.0) + 5.0\times10^{-9} \cdot (v - 50.0)^4$$

The default value of the exponent B in the time-dependent resuspension formula was applied: B=BRMTRT=0.1 (see Volume 2). The default value of the coefficient for agglomeration of deposited particles was used X=XCD1RT=1.0 (see Volume 2).

The resuspension phase took two hours (12:00 – 14:00, on the following day [84]), which means 7200.0 seconds. The times of gas velocity steps were obtained from reference [84] figure 8, and are shown in Table 3-61. Calculations of the resuspension phase were performed for 7200 s, starting at 10,000 s (12:00:00) and ending at 17,200 s (14:00:00).

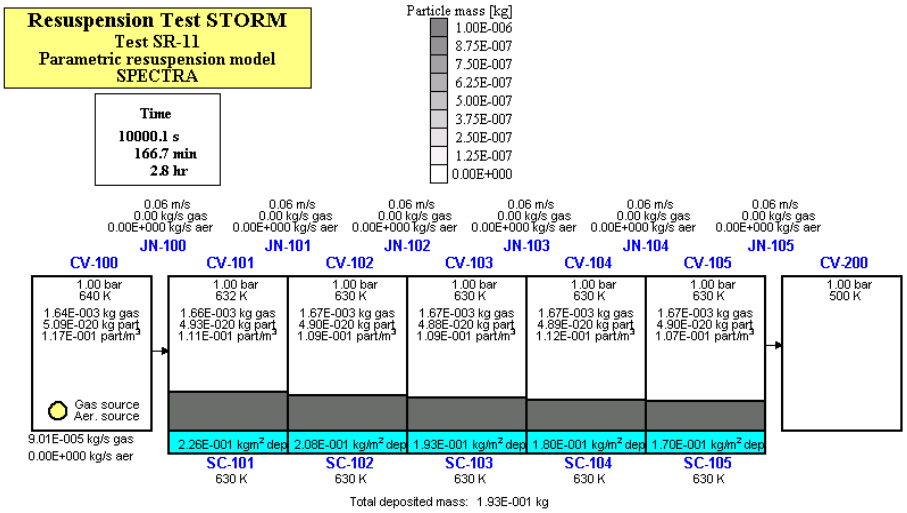

Figure 3-757 SPECTRA results, run STORM-P, end of the deposition phase.

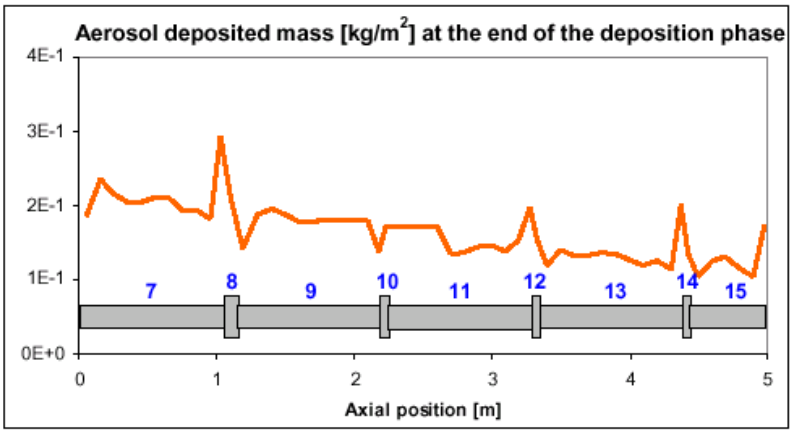

Figure 3-758 Deposited masses, end of the deposition phase, SR11 test data [84].

Two calculations were performed. For the first calculation all default parameters were applied. Results of this run (run STORM-P, file: **\Z-INPUTS\RT\Res-STORM\Parametric\STORM-P**) are compared to the test data in Figure 3-757 through Figure 3-762. The total deposition during the deposition phase is 0.194 kg (Figure 3-757) a little more than the measured value of 0.162 kg [84]. The distribution of deposited aerosols along the test section is in quite good agreement with the test data (compare Figure 3-757 and Figure 3-758).

The airborne concentrations are shown in Figure 3-761 and Figure 3-762. The units are different, so only qualitative comparison is made. Comparison of these values is not very important because measurements are not very accurate. The mass measurement is more reliable than the airborne concentrations measurement. As mentioned in [84], the airborne measurement could not pick larger particles that might have been rolling near the bottom. Qualitatively the results look correct; the calculated peaks are short, which means that the default value of the exponent *B* is reasonably good time decay.

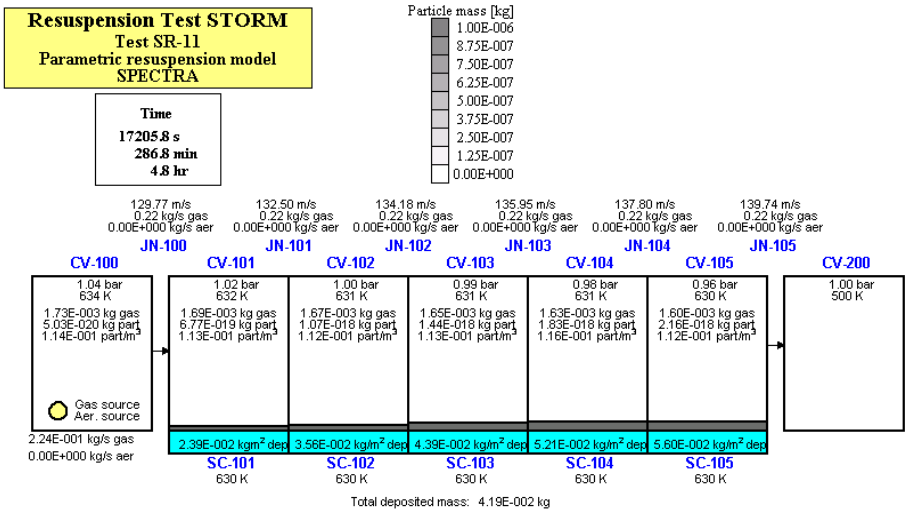

Figure 3-759 SPECTRA results, run STORM-P, end of the resuspension phase.

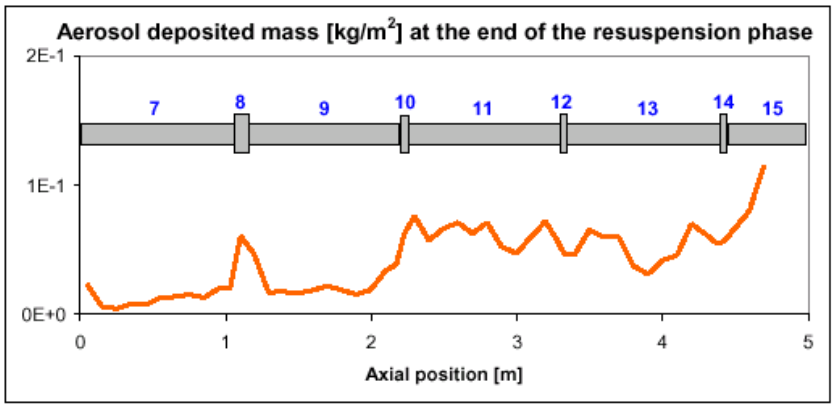

Figure 3-760 Deposited masses, end of the resuspension phase, SR11 test data [84].

In order to eliminate the discrepancy in the calculated deposition of aerosols, and provide a better starting point for the resuspension calculation, the second run (STORM-PA, file: **\Z-INPUTS\RT\Res-STORM\Parametric\STORM-PA**) has been performed. In the test SR11 deposition occurs mainly due to thermophoresis. The thermophoresis model, as implemented in SPECTRA, contains the parameter C_s The default value of C_s is 1.17 (see Volume 2). For the run STORM-PA the value has been set to 0.97. With this value a very good match was obtained with the deposited mass (0.162 kg in the experiment, 0.163 kg in the run STORM-PA - see Table 3-62, values at the end of the deposition phase are printed in blue). The default value of C_s may be changed in the future. Further investigation and confirmatory experimental data is needed before such change is made. It should be noted that the value of C_s applied for STORM-PA is larger than the default value applied in the MELCOR code, which is equal to 0.75 – see section 2.8.3. Therefore MELCOR is expected to give deposition lower than measured. This fact has been observed in MELCOR calculations of ISP-40 [84]. The University of Bohum performed several sensitivity calculations with the MELCOR 1.8.3 code, and found the deposition to be between 0.121 and 0.135 kg ([84], table 6).

Results of the run STORM-PA are compared to the test data in Figure 3-763 through Figure 3-766 and in Table 3-62.

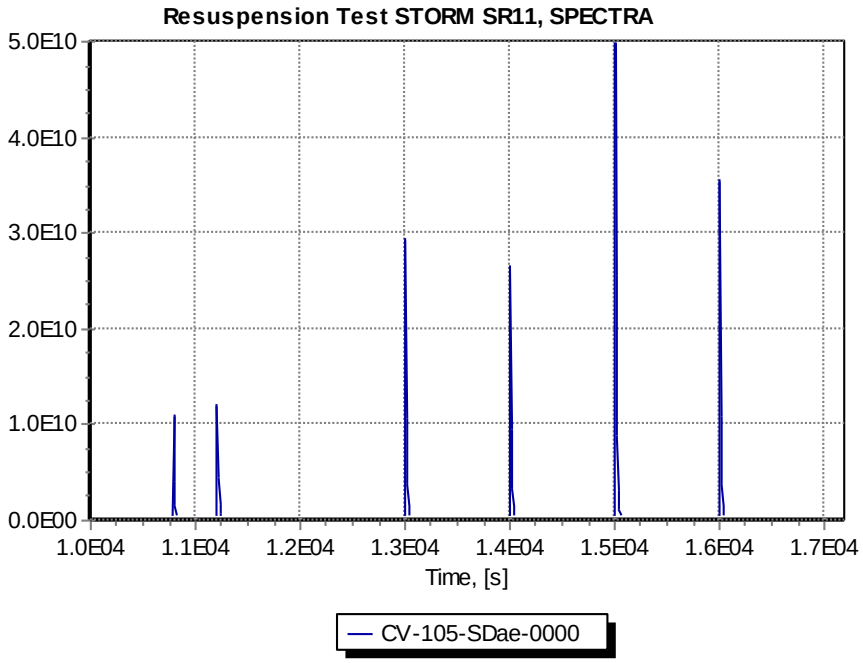

Figure 3-761 Airborne concentrations, run STORM-P, resuspension phase.

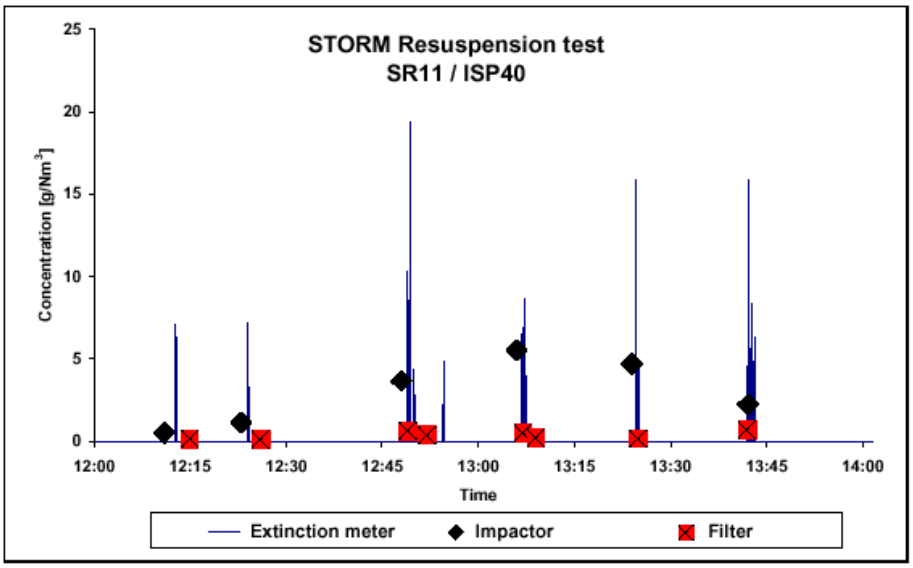

Figure 3-762 Airborne concentrations, resuspension phase, SR11 test data [84].

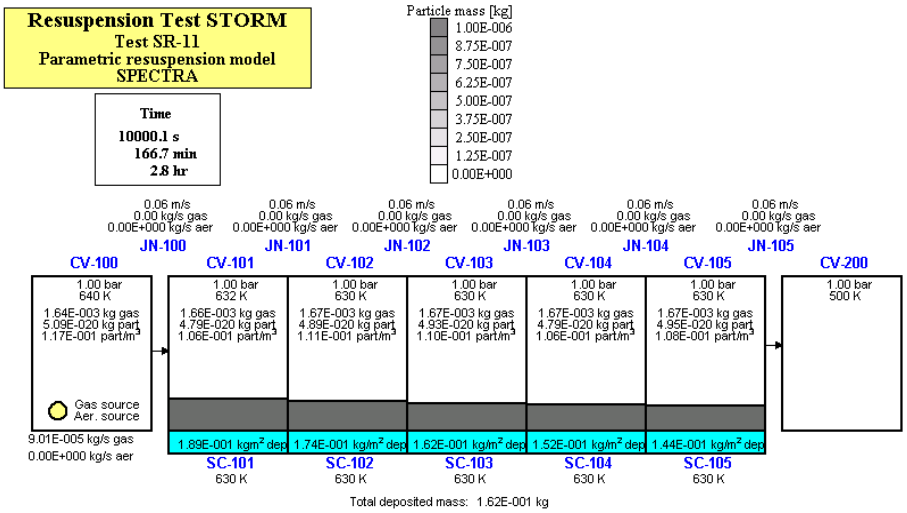

Figure 3-763 SPECTRA results, run STORM-PA, end of the deposition phase

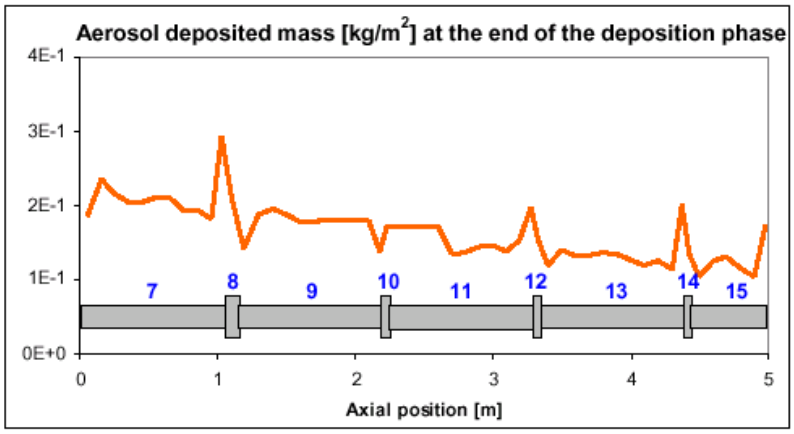

Figure 3-764 Deposited masses, end of the deposition phase, SR11 test data [84]

Since the SPECTRA default value of C_s (1.17) gave the deposition of 0.194 kg, and C_s =0.97 gave the deposition of 0.163 kg, a simple extrapolation indicates that the MELCOR value of C_s = 0.75 should lead to the deposition of about 0.125 kg. In fact the expected MELCOR results should be even lower because MELCOR neglects the turbulent deposition (eddy impaction). However, investigation of SPECTRA output shows that compared to thermophoresis the turbulent deposition is only important for the largest particle size, which contains only about 0.5% of the total amount of aerosols – see Table 3-59. Therefore lack of the turbulent deposition model in MELCOR can be safely neglected, and the expected "MELCOR value" is about 0.125 kg. This is almost exactly in the middle of the values obtained by the University of Bohum.

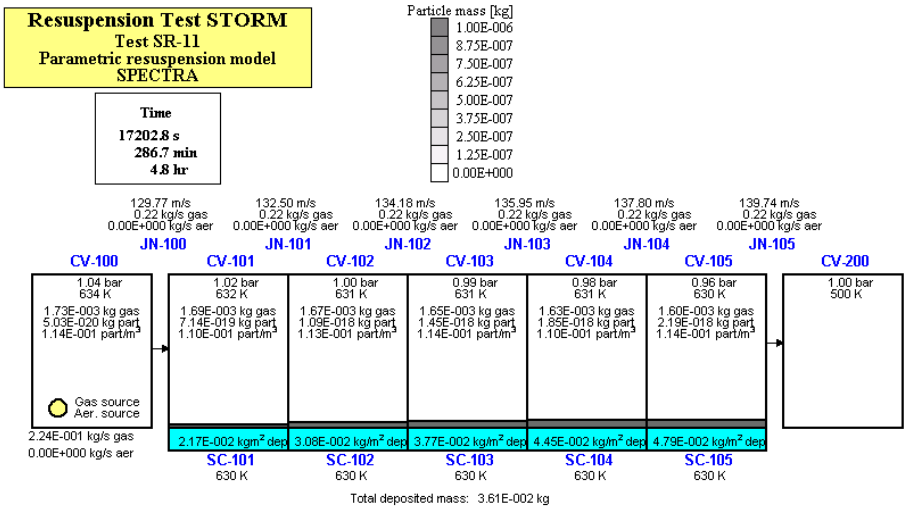

Figure 3-765 SPECTRA results, run STORM-PA, end of the resuspension phase

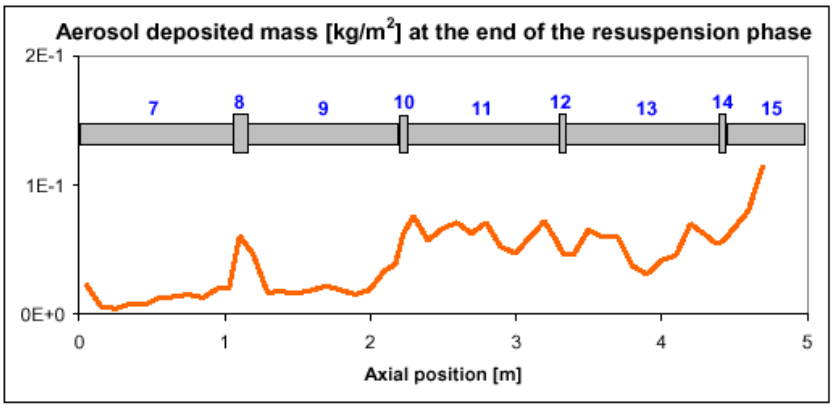

Figure 3-766 Deposited masses, end of the resuspension phase, SR11 test data [84]

Other MELCOR users reported even smaller deposition values. For example, the Kurchatov Institute obtained in the blind calculation the deposition of only 0.014 kg. However, as mentioned in [84], this was simply due to too small temperature difference between walls and gas, resulting from wrong wall temperatures in the model. In the open phase the recalculated deposition was already increased to about 0.080 kg.

The particle distribution at the end of the resuspension phase is different than at the start of this phase; the deposited layer is thinner at the first part of the tube. This is a consequence of agglomeration of deposited particles. If the deposited particle agglomeration model is disabled than the distribution of the deposit would be approximately the same at the end as at the start of the resuspension phase.

Results of both runs, STORM-P and STORM-PA, are compared to the test data in Figure 3-767 and Table 3-62. The resuspension rates are very similar in both cases, as the remaining fractions expressed in percent are very similar in both runs (Table 3-62). The modified C_s value has only provided a better starting point for the resuspension phase.

Table 3-62 Deposited masses at the end of each step (step **0** = end of deposition phase).

Resuspension Step Number	Deposited Mass					
	Test Data		STORM-P (C_s=1.17)		STORM-PA (C_s=0.97)	
	Mass, kg	Fraction %	Mass, kg	Fraction %	Mass, kg	Fraction %
0	0.162	100	0.193	100	0.163	100
1	0.156	96	0.186	96	0.156	96
2	0.151	93	0.177	92	0.148	91
3	0.124	77	0.159	82	0.134	82
4	0.096	59	0.130	67	0.111	68
5	0.070	43	0.089	46	0.077	47
6	0.042	26	0.042	22	0.036	22

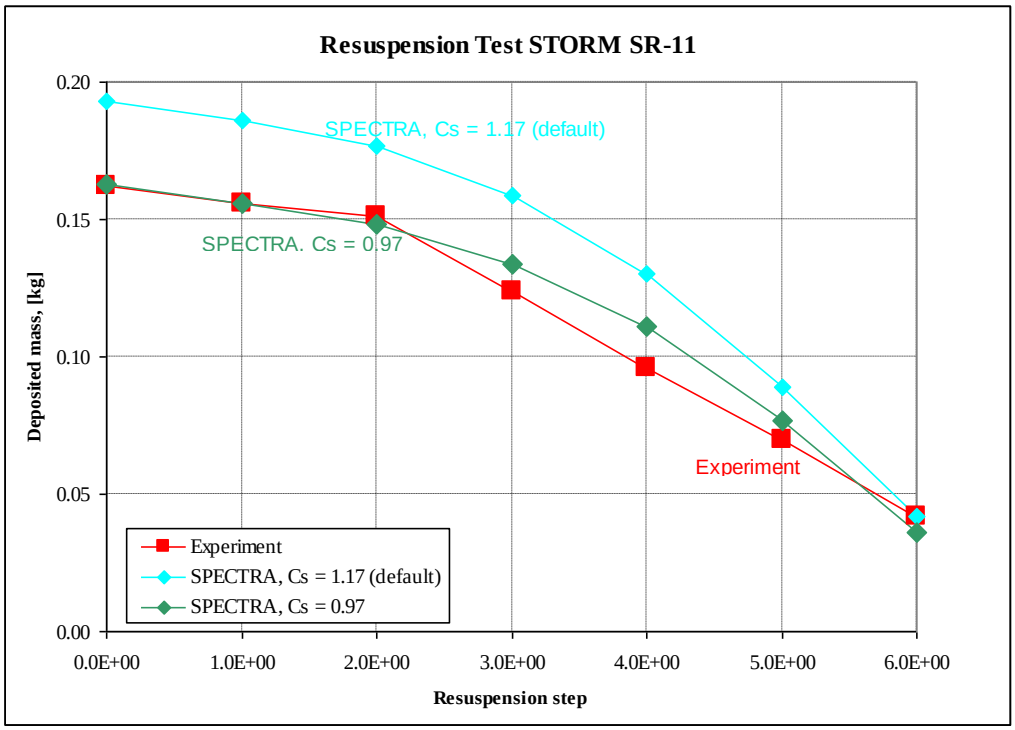

Figure 3-767 Deposited masses at the end of each step (step 0 = end of deposition phase).

3.12.20 Mechanistic Resuspension Model - Comparisons with Analytical Solutions

The mechanistic resuspension model is based on work of Vainshtein et al. (see Volume 1). As a first set of tests the model results are compared to "analytical solutions", obtained with help of the MathCAD program.

The SPECTRA model consists of three Control Volumes, CV-101, CV-102, and CV-103, each of 1.0 m^3. Fixed conditions are used for the exit volume (CV-103) in order to provide constant pressure in the analyzed system. The volumes are filled with helium at 5.0 MPa and 700 K. The volumes are connected with Junctions JN-101, JN-102, with flow areas equal to 0.1 m^2.

A mass source is present in CV-101. The source provides constant mass flow during calculations. The mass flow was tuned to provide appropriate friction velocity for each of the analyzed cases. The friction velocity is calculated by Control Functions CF-111 and CF-101, as:

$$CF-111 = \sqrt{f/8}$$
$$CF-101 = CF-111 \times V_g = \sqrt{f/8} \times V_g$$

where f is the friction factor, (-), and V_g is the gas velocity, (m/s). The selected friction velocities were 5.0, 10.0, and 15.0 m/s. The corresponding gas mass flows, W_g, and source gas temperature, T_g, that is needed to compensate for the kinetic energy when the fluid accelerates in CV-101 (and therefore obtain 700 K in CV-101), were found by trial and error. The mass flows, the corresponding gas velocities, V_g, and the gas temperatures are:

- Friction velocity 5.0 m/s W_g = 52.0 kg/s, V_g = 153 m/s T_g = 701.7 K
- Friction velocity 10.0 m/s W_g = 105.0 kg/s, V_g = 309 m/s T_g = 706.9 K
- Friction velocity 15.0 m/s W_g = 156.3 kg/s, V_g = 459 m/s T_g = 715.3 K

The deposition surface is modeled using a 1-D Solid Heat Conductor, SC-102, with the surface area of 100 m^2. The material of SC-103 is assumed to be stainless steel SS-304. Three aerosol size sections are defined, with the following particle diameters:

- Size section 1: $D_p = 0.4\times10^{-6}$ m
- Size section 2: $D_p = 1.5\times10^{-6}$ m
- Size section 3: $D_p = 4.0\times10^{-6}$ m

The initial mass of deposited aerosols is assumed to be 0.05 kg for each of the three size sections. Thus the total amount of aerosols initially deposited on the SC-102 is equal to 0.15 kg.

The resuspension model of Vainshtein was used, which means:

- The adhesion force distribution is given through the asperity distribution (IAFRRT = 2, Volume 2, record 8700XX).

- The default option of balancing each F_a-section separately is selected.

- The Young modulus for the particles and the surface are set to 2.0×10^{10} and 2.1×10^{11} (Pa) respectively.
- The Poisson's ratio for the particles and the surface are set to 0.3 and 0.29 respectively.

- The cut-off of the slowly resuspending sections is avoided by setting the cut-off parameter CUTRRT (see Volume 2, record 8700XX) to 20. This means the resuspension rates are set to zero only for those sections for which it is very low anyway $\exp(-20) = \sim10^{-9}$. (Influence of the cut-off parameter on the results is shown in section 3.12.23.)

- The lognormal asperity size distribution was selected, with the mean asperity radius is set to 0.1 of the particle radius: $\langle r_{as}\rangle = 0.1(D_p/2)$. This means the following asperity radii are assumed:

    - Size section 1 ($D_p = 0.4\times10^{-6}$ m): $\langle r_{as}\rangle = 0.20\times10^{-7}$ m
    - Size section 2 ($D_p = 1.5\times10^{-6}$ m): $\langle r_{as}\rangle = 0.75\times10^{-7}$ m
    - Size section 3 ($D_p = 4.0\times10^{-6}$ m): $\langle r_{as}\rangle = 2.00\times10^{-7}$ m

  It should be noted that the mean asperity radius, $\langle r_{as}\rangle$, is a parameter that characterizes the surface and not the particle. Therefore use of different asperity radii for different particle size sections is, strictly speaking, inconsistent. Nevertheless this value is given in the original article of Vainshtein et al. It comes from the fact that the asperity radius is treated as a "scaling factor" or a "reduction factor" (f_{red}) for the rough surface compared to the smooth surface. In other words, use of the relation $\langle r_{as}\rangle = 0.1(D_p/2)$ means that the adhesion force for rough surface is assumed to be equal to one tenth of the adhesion force on a smooth surface (f_{red}=0.1). Influence of this assumption is further discussed in section 3.12.24, and in the analysis of STORM experiment (section 3.12.30), where the cases with the original Vainshtein reduction factor, $\langle r_{as}\rangle = 0.1(D_p/2)$, is compared to a case with $\langle r_{as}\rangle$ being fixed and independent of the particle size.

- The adhesive spread factor, σ_a, was set to 4.0.

- The surface roughness, R, is set to zero (the input parameter RGHRRT is set to a negative number) and the constant A_1 (input parameter A1ARRT) is set to 3.53×10^{-6}. Note that in SPECTRA the value of R has an internal limit of a minimum of 10^{-9}. Thus the "smooth surface" line is obtained for R=10^{-9}. With the value of $A_1 = 3.53\times10^{-10}$ the proportionality coefficient in the adhesion force is equal to:

$$C = \frac{A_1}{R^{x_1}} = \frac{3.53\times10^{-10}}{(1\times10^{-9})^1} = 0.353$$

  This value is in agreement with the "Vainshtein value": $3/2\pi\Delta\gamma/2 = 0.353$ with $\Delta\gamma$=0.15, [86]. Furthermore, the effective diameter:

$$D_{eff} = \frac{1}{\frac{1}{x_{p,1}D_p} + \frac{1}{x_{as,1}2r_{as}}}$$

must be equal to twice the asperity radius, $2r_{as}$. This is achieved by setting $x_{as,1}$ to 1.0, and $x_{p,1}$ to a large value (10^{10}).

Therefore:

$$D_{eff} = \frac{1}{\frac{1}{10^{10} D_p} + \frac{1}{2r_{as}}} = 2r_{as}$$

and the adhesion force is equal to:

$$F_a = C \cdot D_{eff} = 0.353 \cdot (2r_{as})$$

which is in agreement with the adhesion force definition in the Vainshtein model (see [86], discussion of rough surfaces, on page 553).

Other adhesion forces, namely:

- The force arising from the surface tension of adsorbed liquid
- The electrostatic force
- The gravity force

are eliminated by setting the relative humidity to zero (H=0.0), the electric charge constant to zero (C_q = 0.0), and the gravity vector to zero.

The MathCAD calculations provide remaining fractions of aerosols for times between 1.0×10^{-5} s and 1.0×10^{3} s. In order to reproduce these results the SPECTRA calculations were performed using different maximum time steps and plot time steps. Seven time step domains were defined, with different time steps, as shown below.

- $\Delta t_{Max} = 1.0\times10^{-5}$ s, $\Delta t_{Plot} = 1.0\times10^{-5}$ s, $t \le 1.0\times10^{-4}$ s
- $\Delta t_{Max} = 1.0\times10^{-4}$ s, $\Delta t_{Plot} = 1.0\times10^{-4}$ s, $t \le 1.0\times10^{-3}$ s
- $\Delta t_{Max} = 1.0\times10^{-3}$ s, $\Delta t_{Plot} = 1.0\times10^{-3}$ s, $t \le 1.0\times10^{-2}$ s
- $\Delta t_{Max} = 1.0\times10^{-2}$ s, $\Delta t_{Plot} = 1.0\times10^{-2}$ s, $t \le 1.0\times10^{-1}$ s
- $\Delta t_{Max} = 1.0\times10^{-1}$ s, $\Delta t_{Plot} = 1.0\times10^{-1}$ s, $t \le 1.0$ s
- $\Delta t_{Max} = 1.0$ s, $\Delta t_{Plot} = 1.0$ s, $t \le 100.0$ s
- $\Delta t_{Max} = 1.0$ s, $\Delta t_{Plot} = 5.0$ s, $t \le 1000.0$ s

In the last two time step domains the option for frozen flow solutions was used, in order to avoid the time step limitations set by the Courant limit.

Additionally the following procedure was applied in order to provide accurate solution at the initial steps.

- A preliminary calculation was performed for each case. Results were stored as the Initial Condition Files (*.ICF).

- The real calculations were performed starting from the conditions in the appropriate ICF files. In this way an initial flow transient was avoided, i.e. the calculations were always starting with a fully developed flow. If this hadn't been not done, the initial resuspension would have been be altered by changing gas flow.
- It has to be remembered that resuspension has occurred in the pre-calculations. Therefore the masses of deposited aerosols in the ICF files had in each case to be manually re-set to their original values (0.05 kg for each of the three size sections). Additionally the airborne aerosol masses (although very small) were reset to zero.

SPECTRA input decks, as well as MathCAD files are provided in **\Z-INPUTS\RT\Res-Ed**

- **Res-Ed1.SPE** friction velocity of 5.0 m/s
- **Res-Ed2.SPE** friction velocity of 10.0 m/s
- **Res-Ed3.SPE** friction velocity of 15.0 m/s.

SPECTRA results are shown in Figure 3-768 through Figure 3-775. Comparisons with MathCAD are shown in Figure 3-776 through Figure 3-781. The figures show that an excellent agreement with the "analytical", i.e. the MathCAD solution.

It should be remembered that the agreement was achieved using the default option of balancing each F_a-section separately. In the "analytical" (MathCAD) solution numerical evaluation of the following integral is used to calculate the relative remaining mass, m/m_0, where m is the deposited mass at time t, and m_0 is the initial deposited mass.

$$\left(\frac{m}{m_0}\right) = \int_0^\infty \exp\left[-R_m t\right]\cdot\varphi(F_a)\cdot dF_a = \int_0^\infty \exp\left\{-f_0 \exp\left[-\left(\frac{F_{a\tau}}{F_d}\right)^{4/3} t\right]\right\}\cdot\varphi(F_a)\cdot dF_a$$

where $\varphi(F_a)$ is the distribution function per unit adhesion force, (1/N). A lognormal distribution is used. In SPECTRA on the other hand the resuspension is calculated by solving numerically the set of differential equations:

$$\left.\frac{dm}{dt}\right|_{resusp} = \sum_i \frac{dm(i)}{dt} = \sum_i R_m(i)\cdot m(i)$$

$$\left.\frac{dm(i)}{dt}\right|_{resusp} = -R_m(i)\cdot m(i) = -f_0 \exp\left[-\left(\frac{F_{a\tau}(i)}{F_d}\right)^{4/3}\right]\cdot m(i)$$

for the finite number of 51 (by default) F_a-sections. The advantage of SPECTRA solution is its validity for the time-dependent (changing in time) drag force, while the analytical solution is valid only for a constant (time-independent) drag force. Moreover the full particle balance SPECTRA includes eventual simultaneous deposition (see Volume 1).

On the other hand, the limited number of F_a-sections is a disadvantage of the SPECTRA solution. This has been remedied by selecting the default number of the F_a-sections after multiple test calculations as the value providing good agreement with theoretical solution and making the solution insensitive to variations (increase) of the number of sections. The default number of the F_a-sections is 51. The number of sections may be increased to a maximum of 99. The user is warned against decreasing the number of sections below the default value (see Volume 2), as this would reduce the accuracy of the solution as well as the quality of the solution (make it sensitive to the number of F_a-sections). Influence of the number of F_a-sections on results is discussed in the next section.

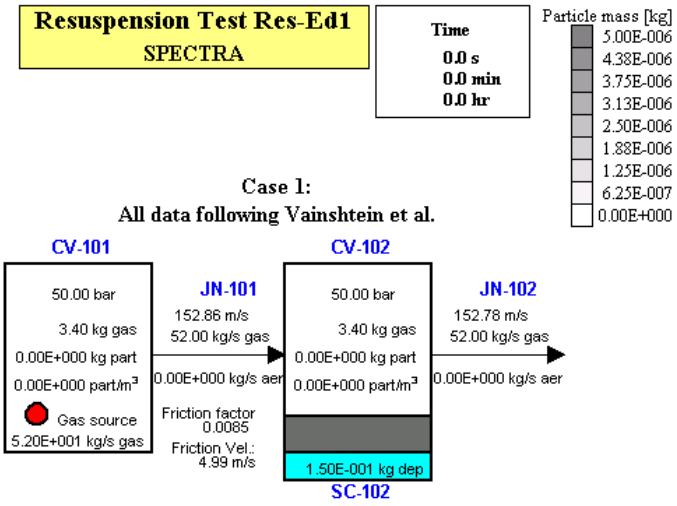

Figure 3-768 Resuspension test Res-Ed1, t = 0.0 s.

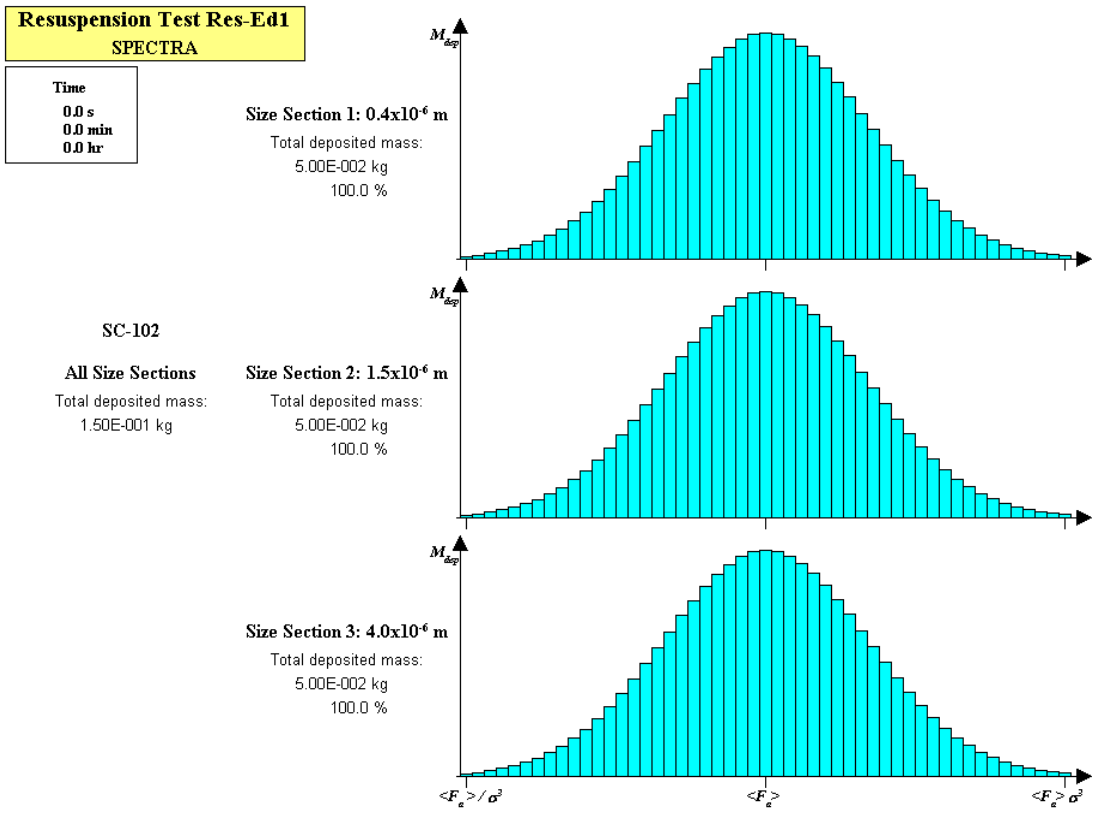

Figure 3-769 Resuspension test Res-Ed1, t = 0.0 s - adhesion force-sections.

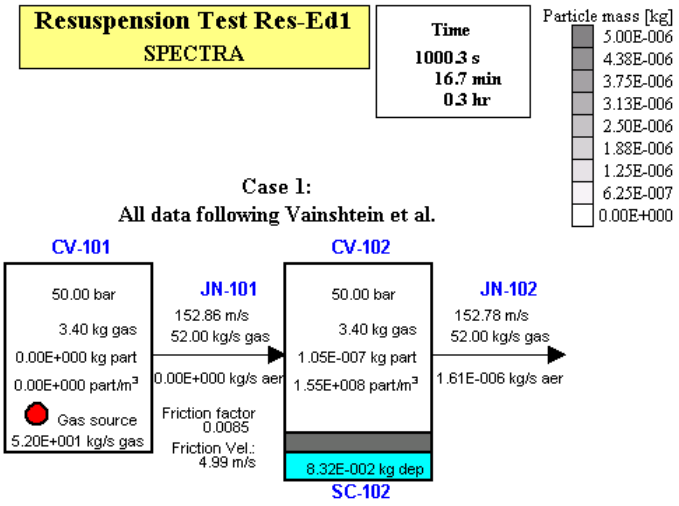

Figure 3-770 Resuspension test Res-Ed1, *t* = 1000 s.

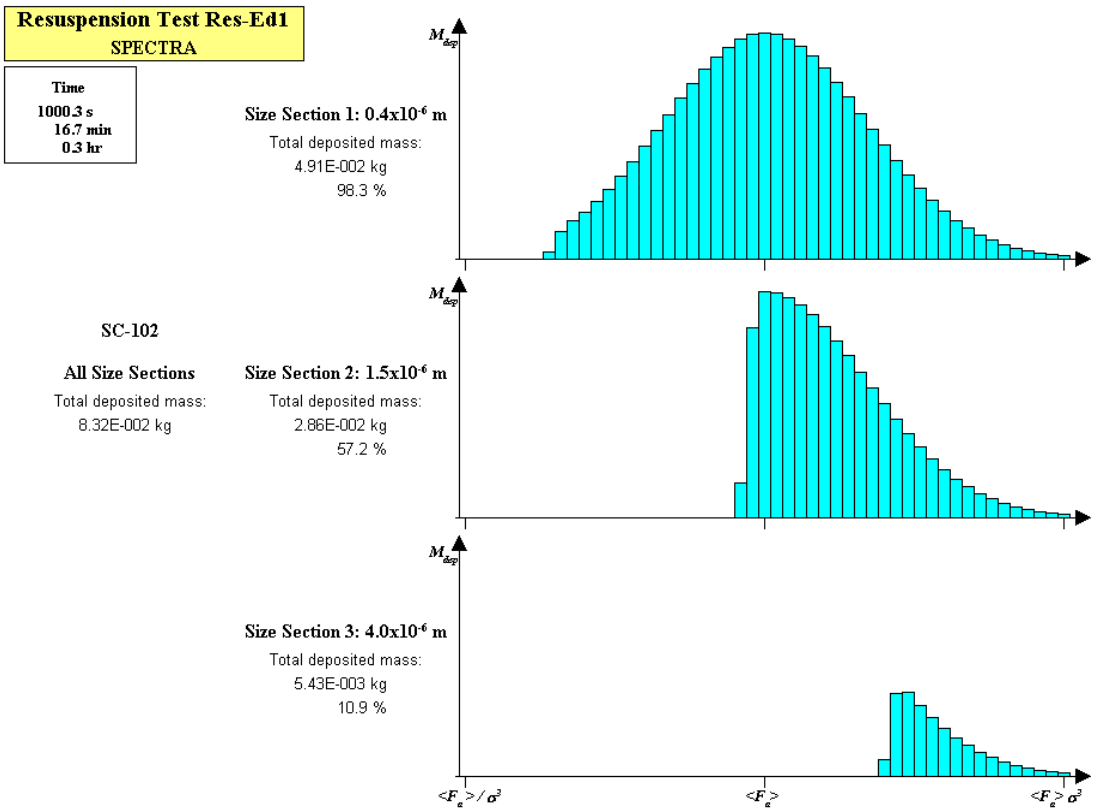

Figure 3-771 Resuspension test Res-Ed1, *t* = 1000 s - adhesion force-sections.

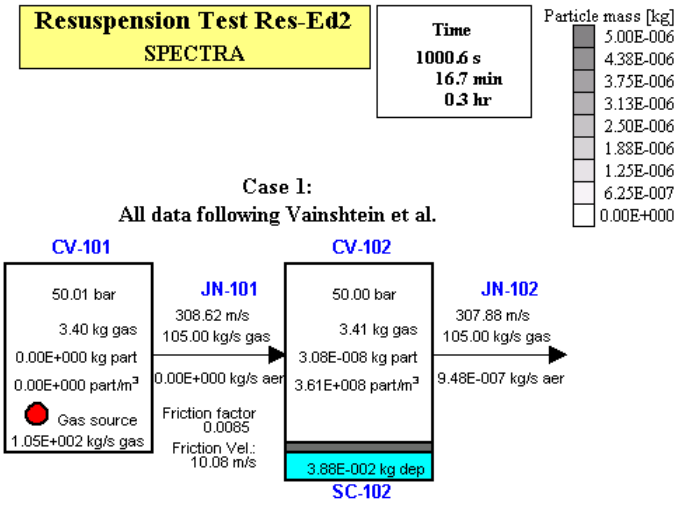

Figure 3-772 Resuspension test Res-Ed2, *t* = 1000 s.

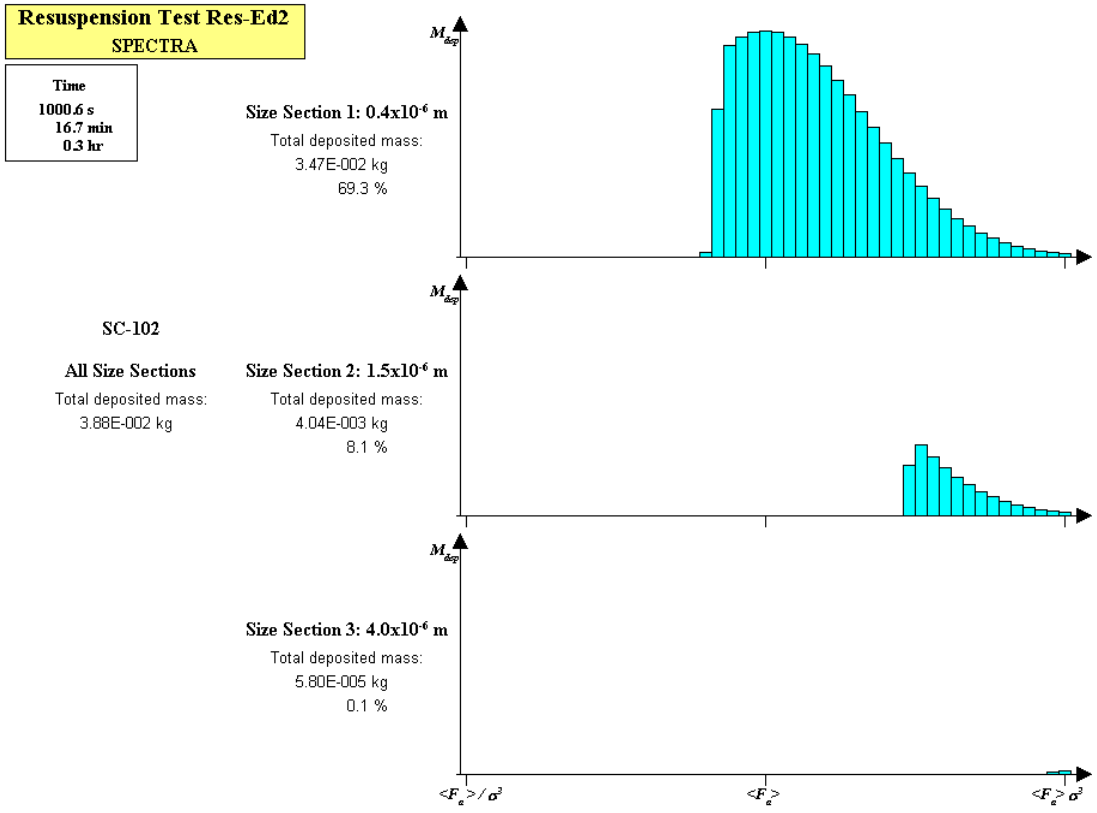

Figure 3-773 Resuspension test Res-Ed2, *t* = 1000 s - adhesion force-sections.

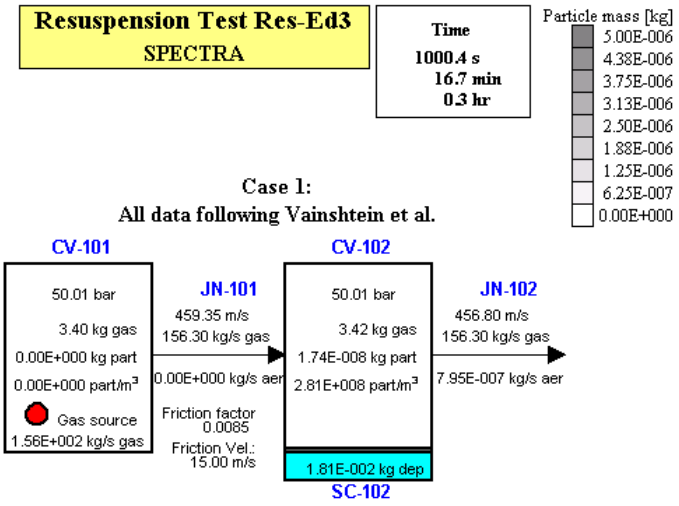

Figure 3-774 Resuspension test Res-Ed3, *t* = 1000 s.

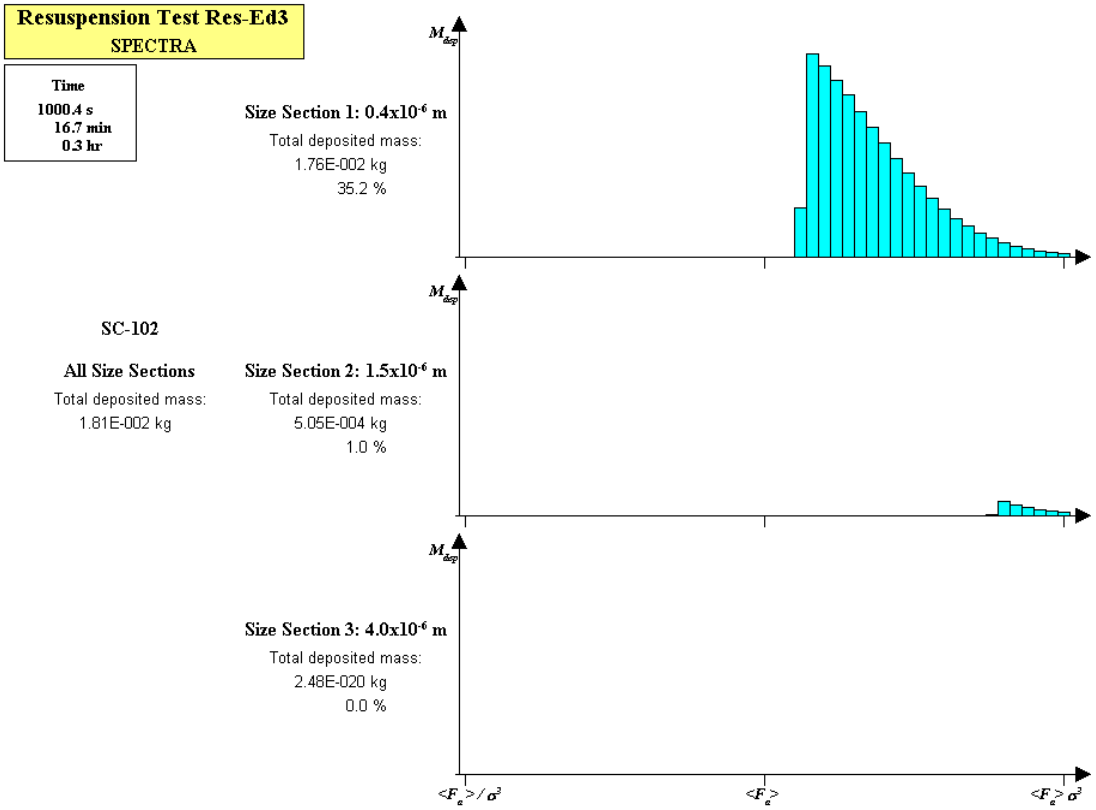

Figure 3-775 Resuspension test Res-Ed3, *t* = 1000 s - adhesion force-sections.

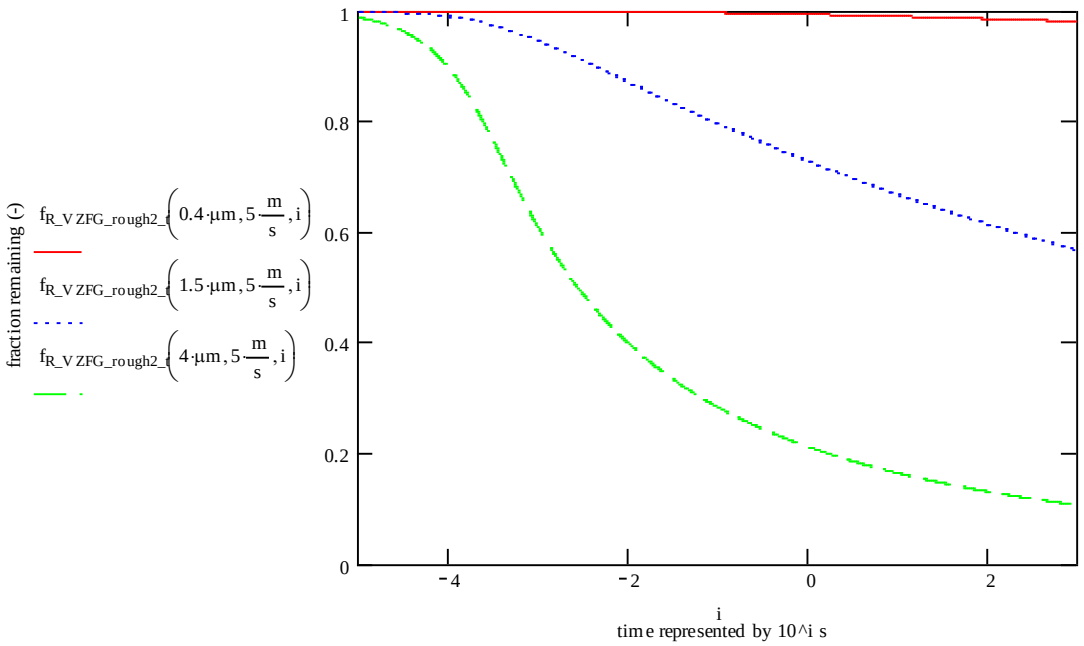

Figure 3-776 Particle resuspension, friction velocity 5 m/s, MathCAD

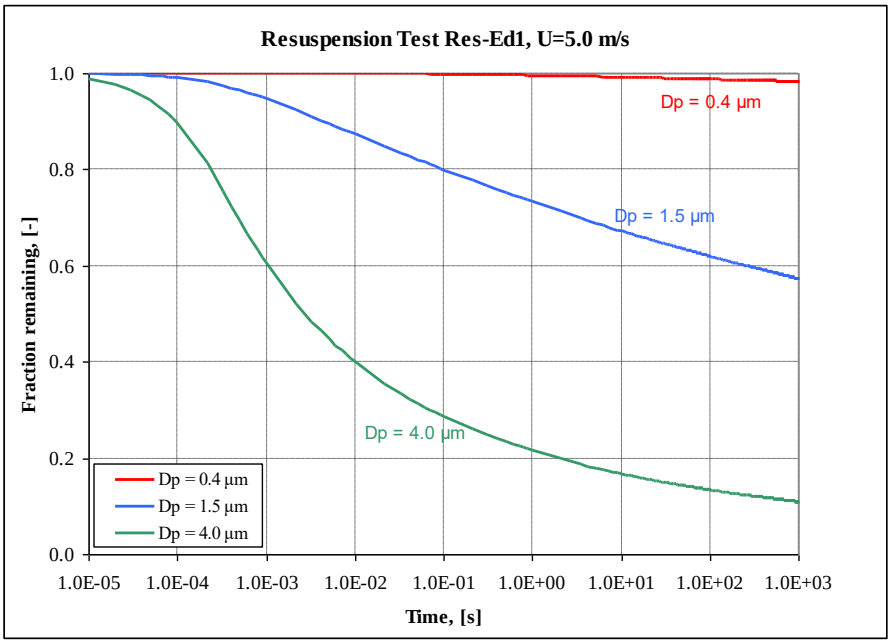

Figure 3-777 Particle resuspension, friction velocity 5 m/s, SPECTRA run Res-Ed1

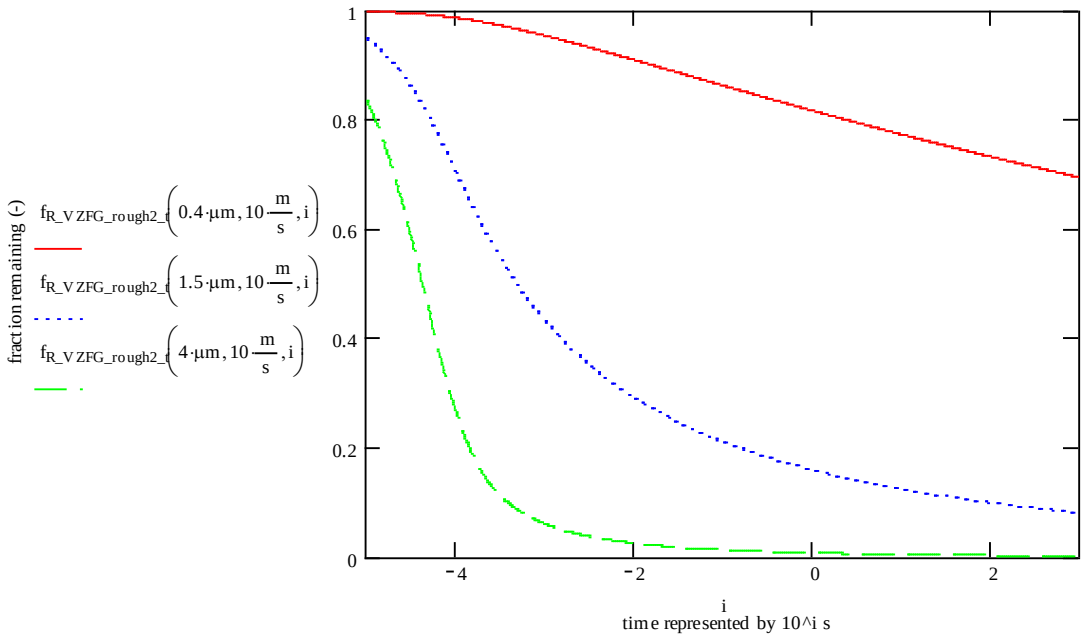

Figure 3-778 Particle resuspension, friction velocity 10 m/s, MathCAD

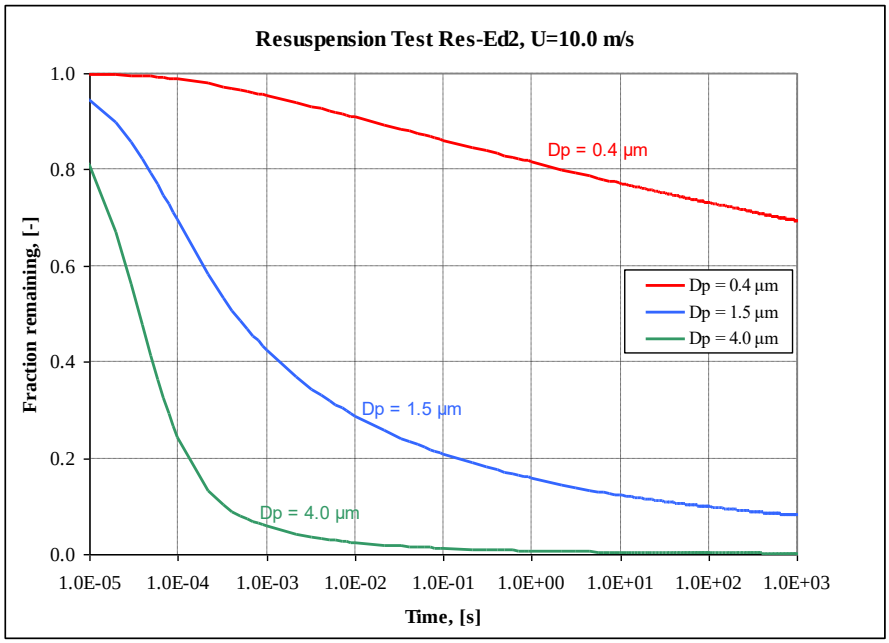

Figure 3-779 Particle resuspension, friction velocity 10 m/s, SPECTRA run Res-Ed2

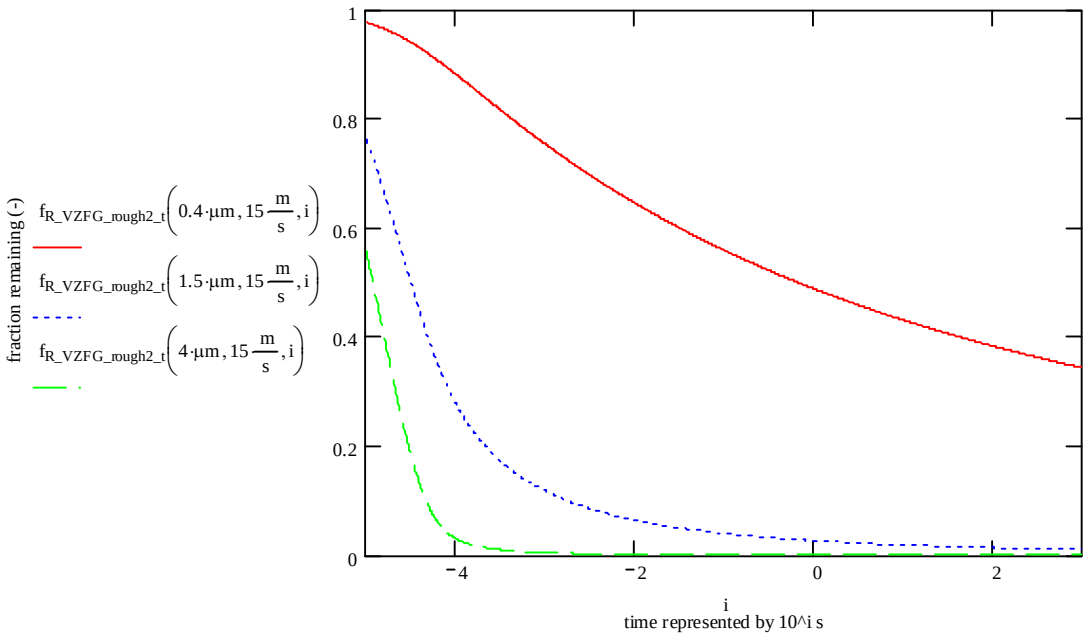

Figure 3-780 Particle resuspension, friction velocity 15 m/s, MathCAD

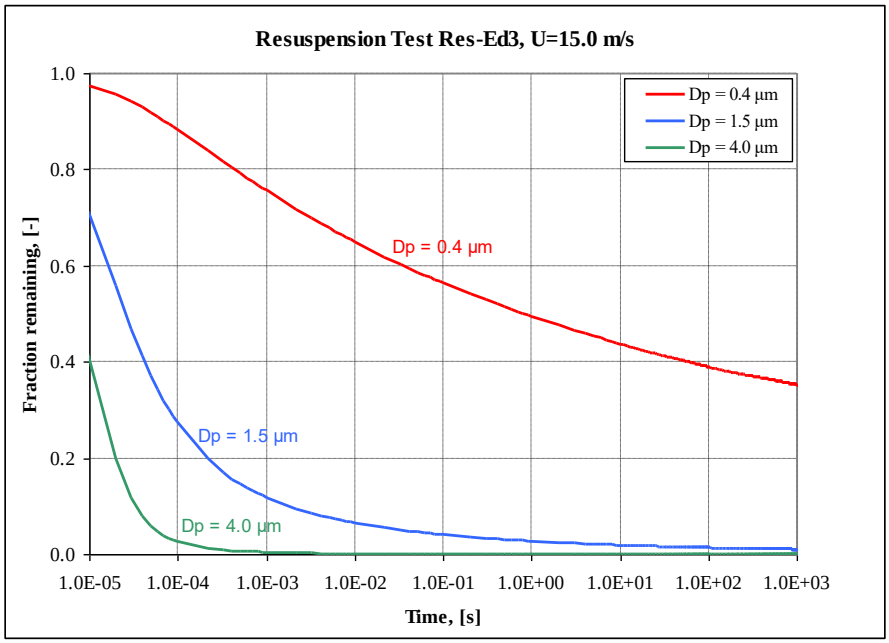

Figure 3-781 Particle resuspension, friction velocity 15 m/s, SPECTRA run Res-Ed3

3.12.21 Mechanistic Resuspension Model - Influence of the Number of F_a-sections

Influence of the number of F_a-sections is investigated based on the test run shown in previous section, the case with friction velocity of 5.0 m/s. Three cases are considered:

- 51 sections (default), input deck: **\Z-INPUTS\RT\Res-Ed\Res-Ed1.SPE**
- 99 sections (maximum), **\Z-INPUTS\RT\Res-Ed\N-sec\Res-Ed1-Nsec.SPE**
- 25 sections, input deck: **\Z-INPUTS\RT\Res-Ed\N-sec-10\Res-Ed1-Nsec10.SPE**

For the first set of calculations the adhesive spread factor, σ_a, was set to 4.0, the same as in previous section. Results are shown in Figure 3-783 through Figure 3-788. Figure 3-783 shows the end state, at t = 1000 s. The deposited masses are very similar in all three cases and equal to 8.3×10^{-2} kg. Figure 3-784, Figure 3-785, and Figure 3-786 show F_a-distributions for the three analyzed cases at the end time, t = 1000.0 s. The shapes of the distributions are similar in all cases. Finally Figure 3-782, Figure 3-787, and Figure 3-788 show time-dependent graphs. The first two cases give very similar curves. The lines are smooth. In the third case (Figure 3-788) the lines are somewhat wavy. This is an effect of having relatively few sections.

In conclusion, 51 sections provide accurate and smooth solution for the present test case, since no differences in the results are observed when changing from 51 to 99 F_a-sections. The model with 25 F_a-sections still produces accurate results, but the time-dependent curves are not as smooth. It must be remembered that the influence of the number of F_a-sections becomes more important with increasing adhesive spread factor, σ_a. The results presented here were obtained with σ_a = 4.0. Results obtained with σ_a = 10.0, with the number of F_a-sections of 99 and 25 are compared in Figure 3-789 and Figure 3-790. The lines obtained with 25 sections are not smooth, although there is no significant loss of accuracy. For the adhesive spreads above 10 the recommended number of F_a-sections is 99 (see Volume 2).

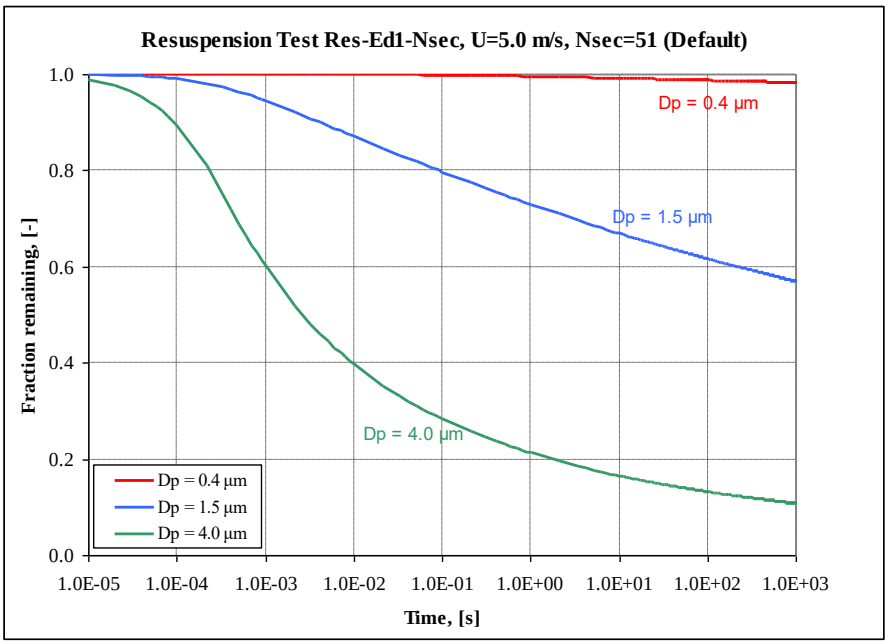

Figure 3-782 Deposited mass fractions, 51 sections (default).

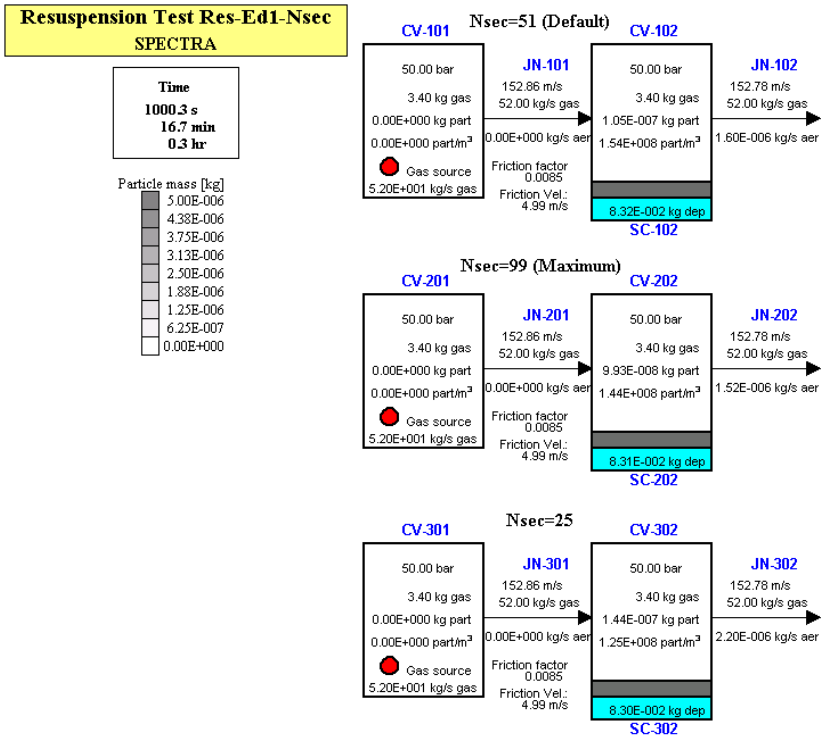

Figure 3-783 Influence of the number of F_a-sections, end results, t=1000 s.

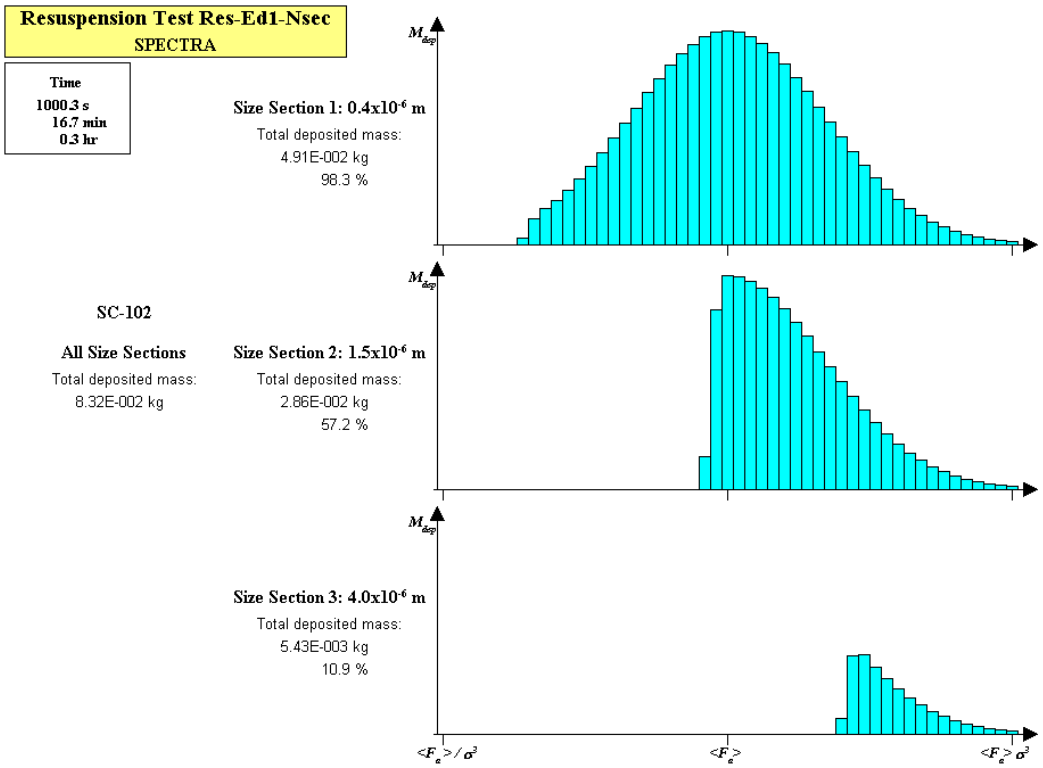

Figure 3-784 F_a-distributions, 51 sections (default), end results, t=1000 s.

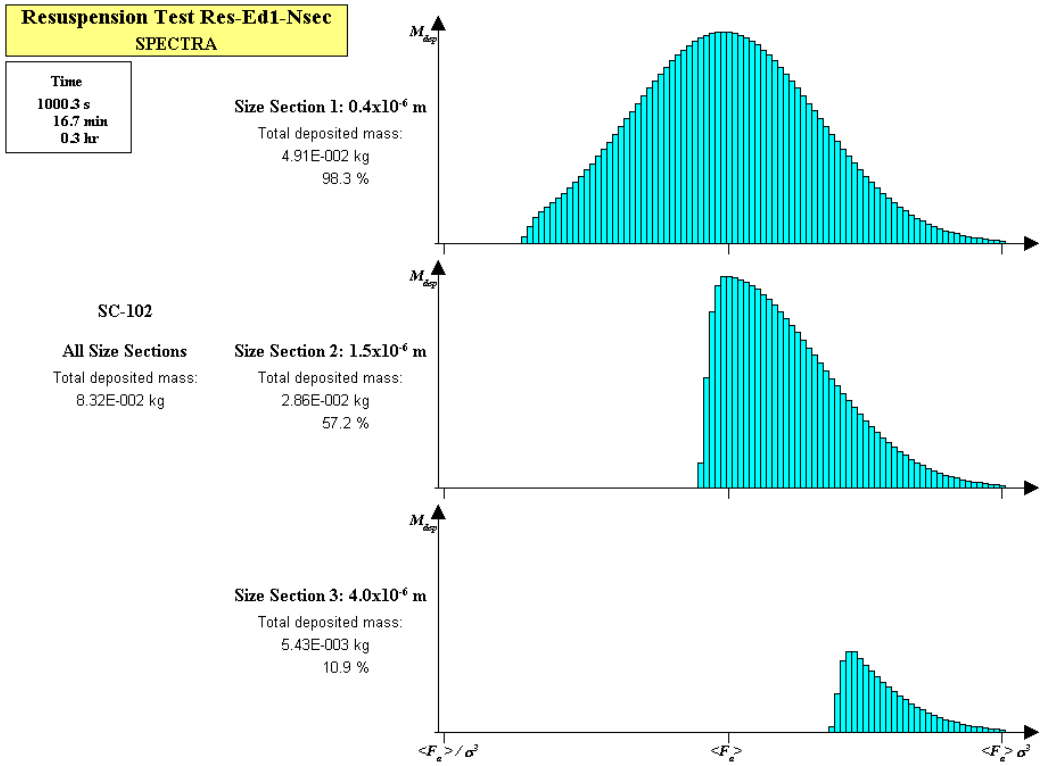

Figure 3-785 F_a-distributions, 99 sections (maximum), end results, t=1000 s.

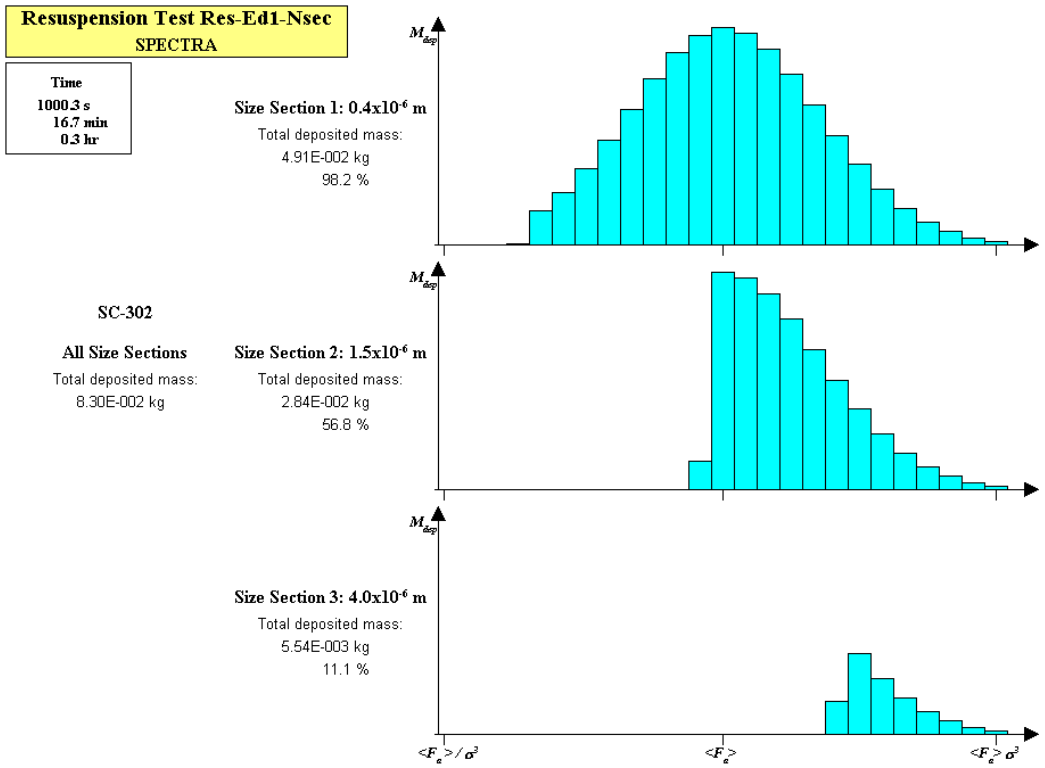

Figure 3-786 F_a-distributions, 25 sections, end results, t=1000 s.

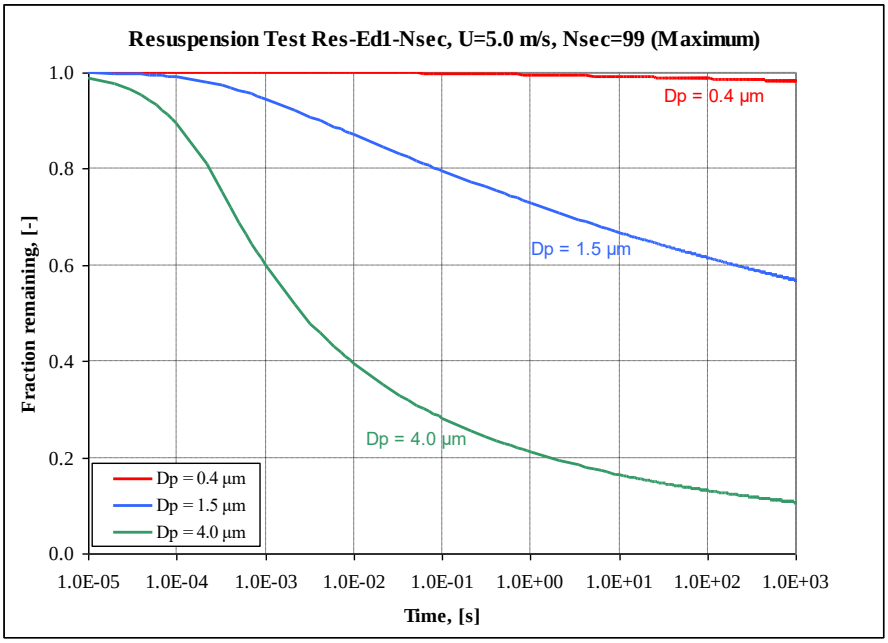

Figure 3-787 Deposited mass fractions, 99 sections (maximum).

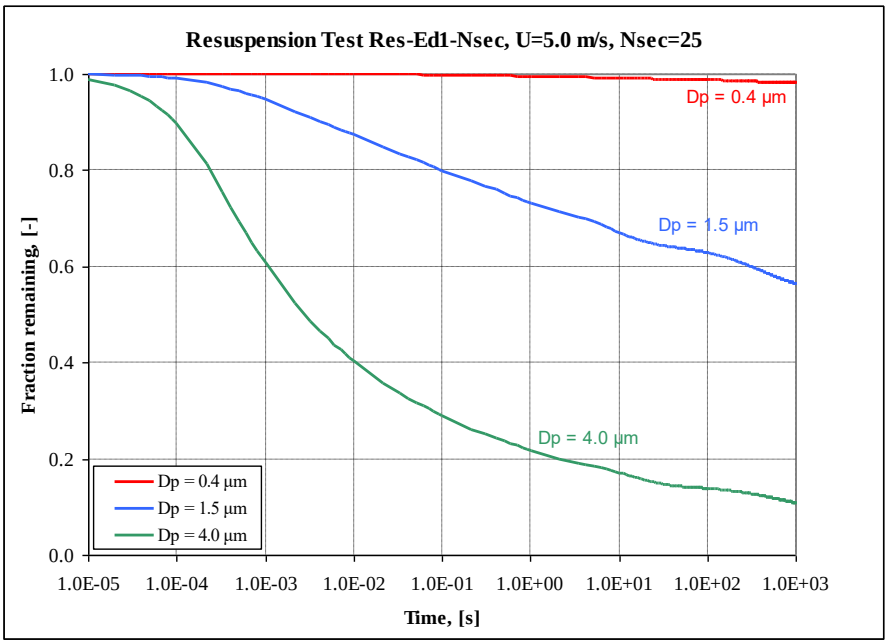

Figure 3-788 Deposited mass fractions, 25 sections.

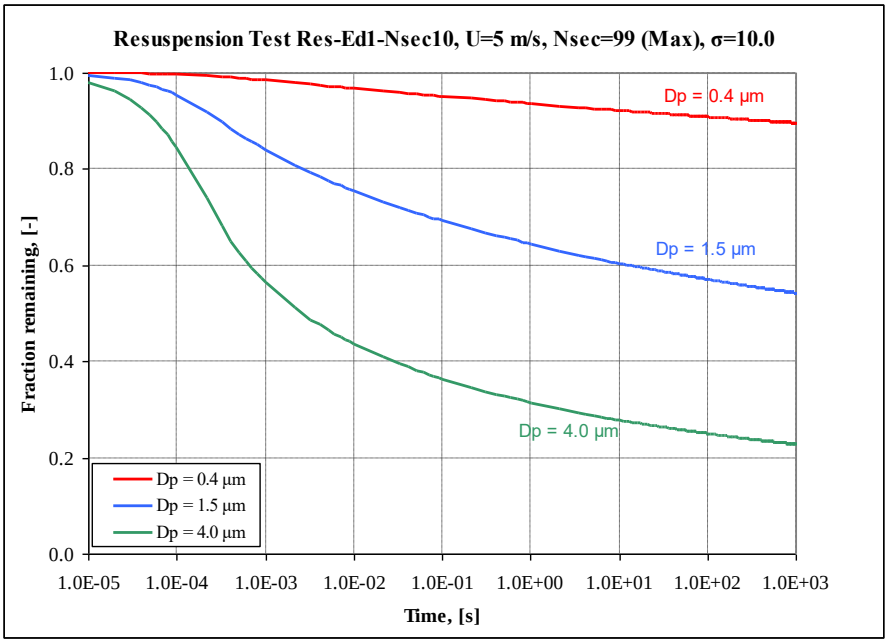

Figure 3-789 Deposited mass fractions, large spread (σ_a=10.0), 99 sections.

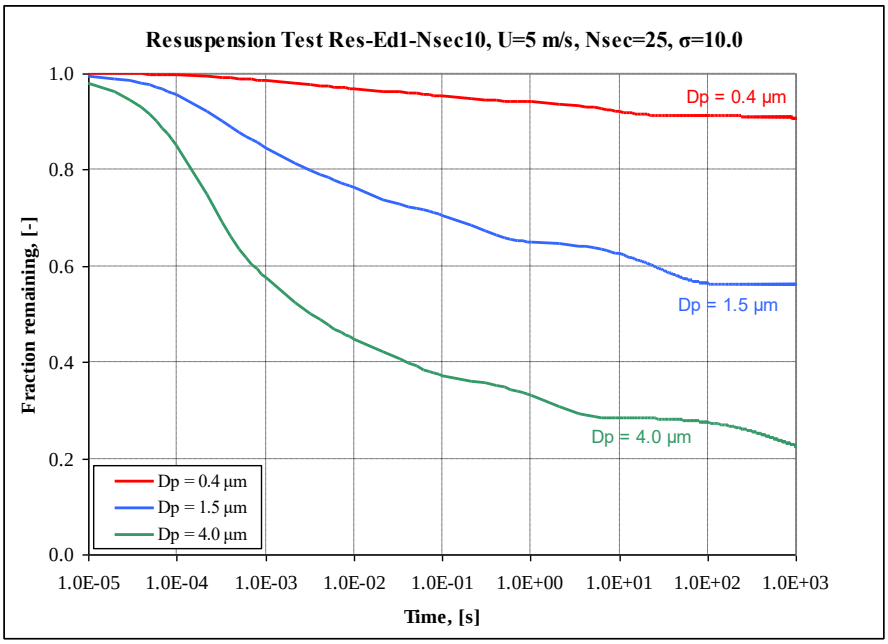

Figure 3-790 Deposited mass fractions, large spread (σ_a=10.0), 25 sections.

3.12.22 Mechanistic Resuspension Model - Influence of C_χ

Default value of the model coefficient C_χ is based on maximum "spring" stiffness - see Volume 1. This approach leads to the value of C_χ equal to 1.13. Other values may be applied; for example average spring stiffness may be used, which is achieved by setting C_χ to the value of about 0.56. The influence of the parameter C_χ on the calculated resuspension rates is shown below.

Influence of the number of C_χ is investigated based on the test run shown in 3.12.20, the case with friction velocity of 5.0 m/s. Three cases are considered:

- C_χ = 1.13 (default, based on maximum "spring" stiffness),
  input deck: **\Z-INPUTS\RT\Res-Ed\Res-Ed1.SPE**
- C_χ = 0.56 (1/2 of the default, average "spring" stiffness)
  input deck: **\Z-INPUTS\RT\Res-Ed\C-hi\Res-Ed1-Chi.SPE**

Results are shown in Figure 3-791, Figure 3-792, and Figure 3-793. A some effect is clearly visible but, based on this figures, it may be concluded that the results are not drastically changed by the change of C_χ by a factor of 2. The default value of C_χ is also the maximum theoretical value (maximum spring" stiffness). With the value of C_χ equal to 0.56 the resuspension rates are somewhat lower, which means less conservative. This effect is quite obvious because the tangential pull-off force, $F_{a\tau}$, is inversely proportional to χ and therefore to C_χ (see Volume 1):

$$F_{a\tau} \sim \frac{1}{\chi^{1/2}} \sim \frac{1}{C_\chi^{1/2}}$$

The default value of C_χ is also the maximum theoretical value. Thus the default value gives most conservative result. It is therefore not recommended to change this value.

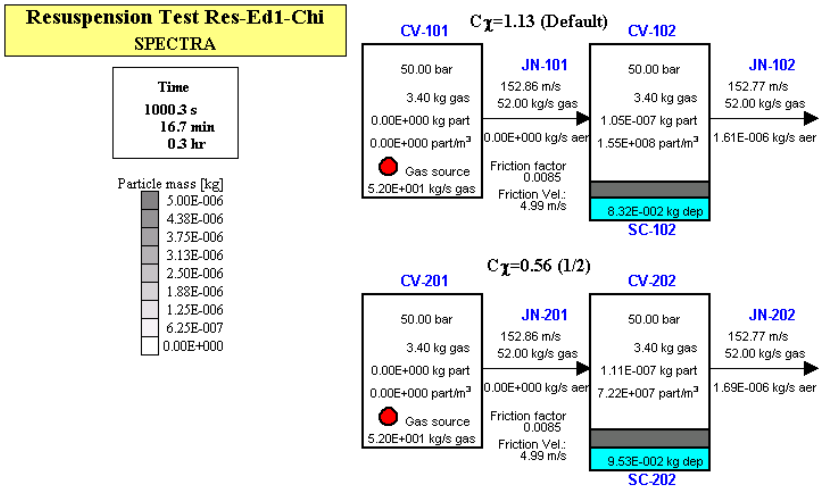

Figure 3-791 Influence of C_χ, end results, t=1000 s.

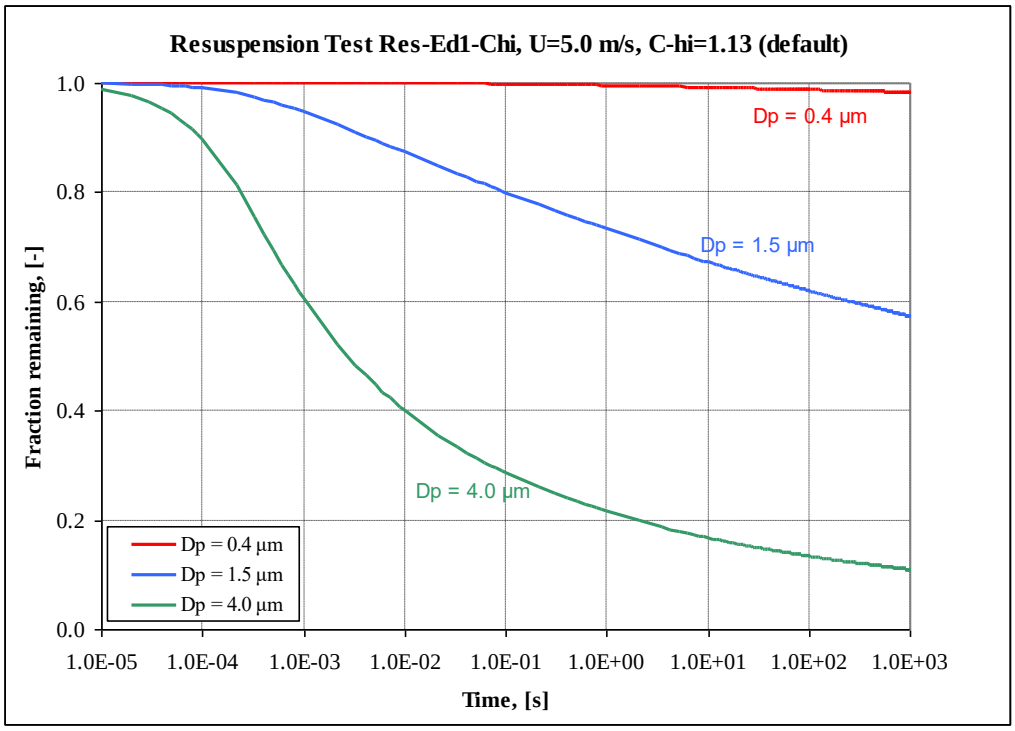

Figure 3-792 Deposited mass fractions, C_χ = 1.13 (default).

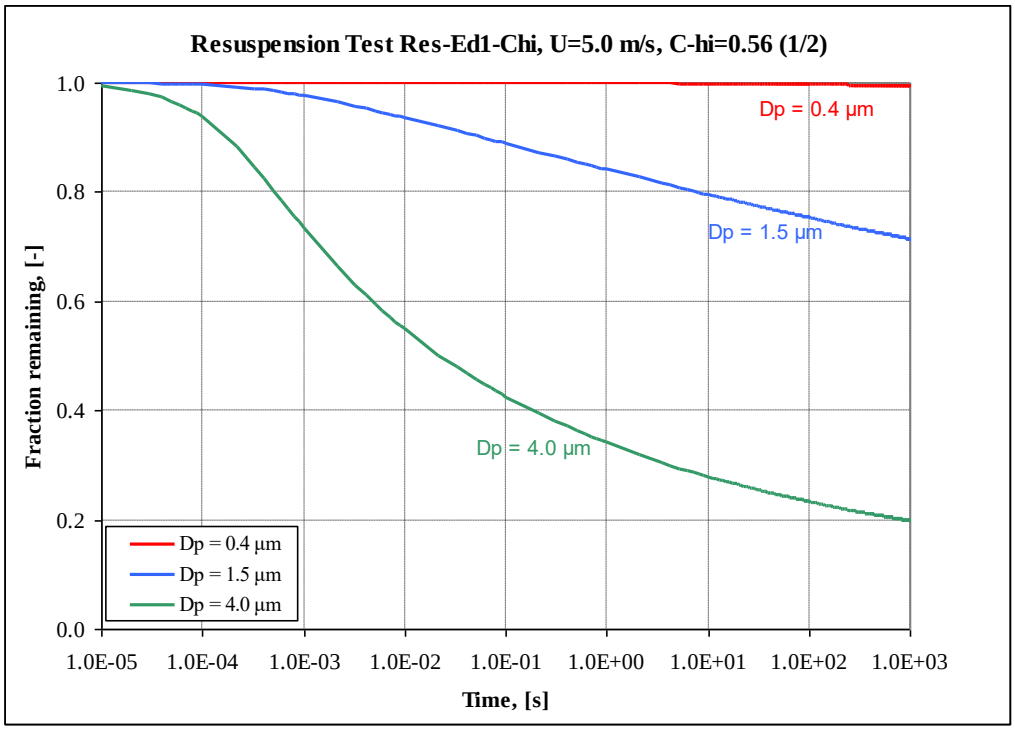

Figure 3-793 Deposited mass fractions, C_χ = 0.56 (1/2 of the default value).

3.12.23 Mechanistic Resuspension Model - Sensitivity to the Cut-off Parameter

The resuspension rate is calculated for each F_a-section from the following formula:

$$R_m(i) = f_0 \exp\left[-\left(\frac{F_{a\tau}(i)}{F_d(i)} \right)^{x_F} \right]$$

In other words:

$$R_m(i) = f_0 \exp\left[-Y(i) \right]$$

where $Y(i)$ is an exponent, characteristic for the given F_a-section. In SPECTRA a limit is provided for the maximum value of $Y(i)$. This limit (an input parameter CUTRRT, see Volume 2, record 8700XX) is an important parameter, therefore a short discussion is provided here.

Applying the limit, means that the resuspension rate is calculated from:

$$R_m(i) = \begin{cases} f_0 \exp\left[-Y(i) \right] & if \quad Y(i) < CUTRRT \\ 0.0 & if \quad Y(i) > CUTRRT \end{cases}$$

The cut-off values are between 5 and 20, with a default value of 10 (see Volume 2). Therefore the cut-off limits are:

- Minimum: CUTTRT = 10.0, $\exp(-Y(i)) > 4.5\times10^{-5}$ (-)
- Default: CUTTRT = 15.0, $\exp(-Y(i)) > 3.1\times10^{-7}$ (-)
- Maximum: CUTTRT = 20.0, $\exp(-Y(i)) > 2.1\times10^{-9}$ (-)

The input model for the test shown in this figure is identical to the input described in detail in the previous section. The case of friction velocity of 5.0 m/s was selected, which means gas velocity of 153 m/s (test Res-Ed1). The cut-off parameter, which was equal to 20 in the test Res-Ed1, was in this test varied. Three values were applied, namely 20, 15, and 10. The input deck is provided in **\Z-INPUTS\RT\Res-Sen\Res-Sen1.SPE**. Results obtained for all three values are compared in Figure 3-794.

With CUTOFF = 20.0 the resuspension rates are set to zero only for those sections for which it is very low anyway ~10^{-9}. This means that there is practically no cut-off, and the results are representing the model of Vainshtein et al. This is shown as the first line in Figure 3-794.

With the cut-off limit of 20 most resuspension (~35%) occurs during the first second. During the slow resuspension that follows (1000 s) another ~10 % is resuspended. During this and later times the resuspension is governed by the size sections for which $\exp(-Y(i)) \sim 10^{-5}$ (resuspension time of order of 10^5 s. While in theory this resuspension rates are possible, the experimental evidence (see discussion of the STORM experiment, section 3.12.30) shows that resuspension is typically much more rapid and occurs in a matter of seconds rather than thousands of seconds. Therefore it is surmised that applying the Vainshtein formula to the sections for which $\exp(-Y(i)) \sim 10^{-7}$ is simply applying the model beyond it's range of validity.

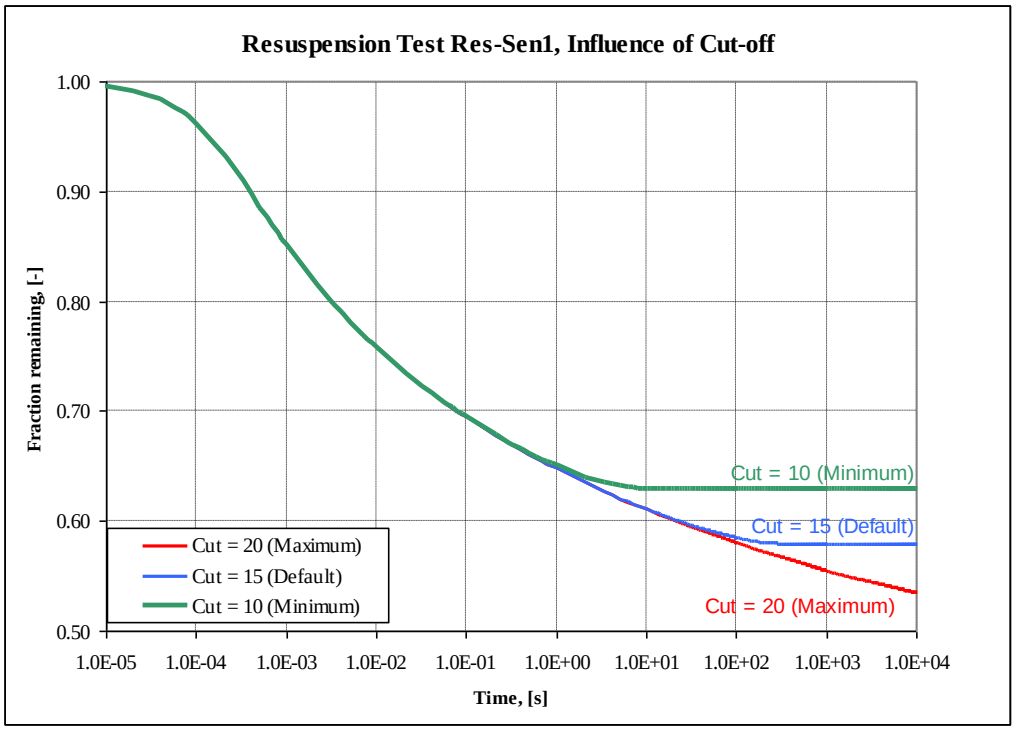

Figure 3-794 Influence of the cut-off limit on resuspension rates.

With the cut-off limit of 20 most resuspension (~35%) occurs during the first second. During the slow resuspension that follows (1000 s) another ~10 % is resuspended. During this and later times the resuspension is governed by the size sections for which $\exp(-Y(i)) \sim 10^{-5}$ (resuspension time of order of 10^5 s. While in theory this resuspension rates are possible, the experimental evidence (see discussion of the STORM experiment, section 3.12.30) shows that resuspension is typically much more rapid and occurs in a matter of seconds rather than thousands of seconds. Therefore it is surmised that applying the Vainshtein formula to the sections for which $\exp(-Y(i)) \sim 10^{-7}$ is simply applying the model beyond it's range of validity.

Therefore CUTRRT of 15 is applied as a default value. This cut-off value will remove all the lower rate resuspension terms. This means in practice that the resuspension will stop after the time of order of 100 s (Figure 3-794, second line). It is shown in section 3.12.30 (STORM experiment) that results obtained with this cut-off were in better agreement with experimental data than the results obtained without the cut-off (CUTRRT=20). Therefore this value was selected as a defaults value for SPECTRA.

3.12.24 Mechanistic Resuspension Model - Sensitivity to the Asperity Size

The test presented in this section shows the influence of the asperity size definition on the resuspension result. The input model is identical to the input described in detail in section 3.12.23. The case of friction velocity of 5.0 m/s was selected, which means gas velocity of 153 m/s (test Res-Ed1).

As shown in section 3.12.23, when the SPECTRA model is set to represent exactly the original "Vainshtein", the asperity size is defined as:

The lognormal asperity size distribution was selected, with the mean asperity radius is set to 0.1 of the particle radius: $<r_{as}> = 0.1(D_p/2)$. This means the following asperity radii are assumed:

- Size section 1 ($D_p = 0.4\times10^{-6}$ m): $<r_{as}> = 0.20\times10^{-7}$ m
- Size section 2 ($D_p = 1.5\times10^{-6}$ m): $<r_{as}> = 0.75\times10^{-7}$ m
- Size section 3 ($D_p = 4.0\times10^{-6}$ m): $<r_{as}> = 2.00\times10^{-7}$ m

The mean asperity radius, $<r_{as}>$, is a parameter that characterizes the surface and not the particle. Therefore use of different asperity radii for different particle size sections is, strictly speaking, inconsistent. Nevertheless this value is given in the original article of Vainshtein et al. It comes from the fact that the asperity radius is treated as a "scaling factor" for rough surface compared to the smooth surface. In other words, use of the relation $<r_{as}> = 0.1(D_p/2)$ means that the adhesion force for rough surface is assumed to be equal to one tenth of the adhesion force on a smooth surface. Influence of this assumption is further discussed in the analysis of STORM experiment.

For the present sensitivity runs three cases were selected, with different mean asperity radii, $<r_{as}>$, and the same adhesive spread factor, σ, (equal to 4.0). These cases are shortly described below.

- Case 1: $<r_{as}> = 0.1(D_p/2)$, the "Vainshtein" case. The mean asperity size definitions for the three applied particle sizes (0.4, 1.5, 4.0 μm) are shown below.

```
*     Asperity radius distribution
*
*      <Ras>   sigma
870101 0.20E-7  4.0   * size section 1, Dp = 0.40E-6
870201 0.75E-7  4.0   * size section 2, Dp = 1.50E-6
870301 2.00E-7  4.0   * size section 3, Dp = 4.00E-6
*
```

- Case 2: $<r_{as}> = 0.20\times10^{-7}$ m, a constant value, equal to the minimum value from the Case 1 is used.

```
*
*     Asperity radius distribution
*
*      <Ras>  sigma
870102 0.20E-7 4.0   * size section 1
870202 0.20E-7 4.0   * size section 2
870302 0.20E-7 4.0   * size section 3
*
```

- Case 2: $<r_{as}> = 2.0\times10^{-7}$ m, a constant value, equal to the maximuma value from the Case 1 is used.

```
*     Asperity radius distribution
*
*      <Ras>  sigma
870103 2.00E-7 4.0   * size section 1
870203 2.00E-7 4.0   * size section 2
870303 2.00E-7 4.0   * size section 3
```

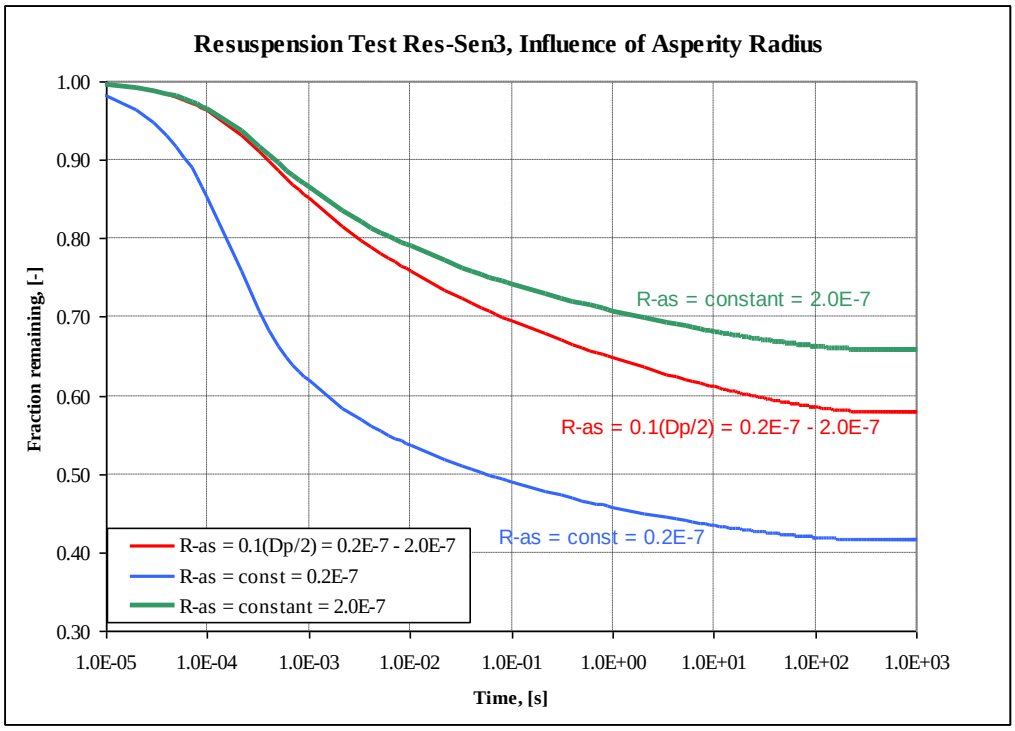

Figure 3-795 Influence of the mean asperity radius, test Res-Sen3.

The input deck is provided in **\Z-INPUTS\RT\Res-Sen\Res-Sen3.SPE**. Results are shown in Figure 3-795. The figure shows deposited mass divided by the initial deposited mass (remaining fraction) for all three analyzed cases for times between 10^{-5} s and 10^{+3} s.

In the case 2 the mean asperity size is the smallest, 0.2 μm for all particle size sections. This fact results in smallest adhesion forces are fastest resuspension for this case. Note that in SPECTRA the adhesion force is proportional to the "effective diameter", given by (see Volume 1):

$$D_{eff} = \frac{1}{\frac{1}{x_{p,1} D_p} + \frac{1}{x_{as,1} 2r_{as}}}$$

For the present test ($x_{as,1}$ to 1.0, and $x_{p,1} = 10^{10}$ - see section 3.12.23). Therefore:

$$D_{eff} = \frac{1}{\frac{1}{10^{10} D_p} + \frac{1}{2r_{as}}} = 2r_{as}$$

It is interesting to compare the adhesive forces for these cases. The values extracted from SPECTRA output are presented below.

- Adhesion forces, SPECTRA output, Case 1: $\langle r_{as} \rangle = 0.1(D_p/2)$, the "Vainshtein" case.

```
 Mean asperity radius, <Ras> (m), and spread factor, Sigma (-), per size section
 Sec.  :      1          2          3
 -----    ---------  ---------  ---------
 <Ras> =  2.000E-08  7.500E-08  2.000E-07
 Sigma =  4.000E+00  4.000E+00  4.000E+00

- ADHESION FORCE DISTRIBUTIONS:

 Adhesion force distribution per size section and Fa-section
 Representative adhesion forces, Fa (N), for Nsec = 51 Fa-sections

   \ Size :   1          2          3
 Fa-sec.  ---------  ---------  ---------
     1    2.394E-10  8.976E-10  2.394E-09
     2    2.818E-10  1.057E-09  2.818E-09
     3    3.317E-10  1.244E-09  3.317E-09
     4    3.904E-10  1.464E-09  3.904E-09
     5    4.596E-10  1.724E-09  4.596E-09
     6    5.410E-10  2.029E-09  5.410E-09
     7    6.369E-10  2.388E-09  6.369E-09
     8    7.497E-10  2.811E-09  7.497E-09
     9    8.825E-10  3.309E-09  8.825E-09
    10    1.039E-09  3.896E-09  1.039E-08
    11    1.223E-09  4.586E-09  1.223E-08
    12    1.439E-09  5.398E-09  1.439E-08
    13    1.694E-09  6.354E-09  1.694E-08
    14    1.995E-09  7.480E-09  1.995E-08
    15    2.348E-09  8.805E-09  2.348E-08
    16    2.764E-09  1.036E-08  2.764E-08
    17    3.254E-09  1.220E-08  3.254E-08
    18    3.830E-09  1.436E-08  3.830E-08
    19    4.508E-09  1.691E-08  4.508E-08
    20    5.307E-09  1.990E-08  5.307E-08
    21    6.247E-09  2.343E-08  6.247E-08
    22    7.354E-09  2.758E-08  7.354E-08
    23    8.657E-09  3.246E-08  8.657E-08
    24    1.019E-08  3.821E-08  1.019E-07
    25    1.200E-08  4.498E-08  1.200E-07
    26    1.412E-08  5.295E-08  1.412E-07
    27    1.662E-08  6.233E-08  1.662E-07
    28    1.957E-08  7.337E-08  1.957E-07
    29    2.303E-08  8.637E-08  2.303E-07
    30    2.711E-08  1.017E-07  2.711E-07
    31    3.191E-08  1.197E-07  3.191E-07
    32    3.757E-08  1.409E-07  3.757E-07
    33    4.422E-08  1.658E-07  4.422E-07
    34    5.206E-08  1.952E-07  5.206E-07
    35    6.128E-08  2.298E-07  6.128E-07
    36    7.213E-08  2.705E-07  7.213E-07
    37    8.491E-08  3.184E-07  8.491E-07
    38    9.995E-08  3.748E-07  9.995E-07
    39    1.177E-07  4.412E-07  1.177E-06
    40    1.385E-07  5.194E-07  1.385E-06
    41    1.630E-07  6.114E-07  1.630E-06
    42    1.919E-07  7.197E-07  1.919E-06
    43    2.259E-07  8.472E-07  2.259E-06
    44    2.659E-07  9.973E-07  2.659E-06
    45    3.131E-07  1.174E-06  3.131E-06
    46    3.685E-07  1.382E-06  3.685E-06
    47    4.338E-07  1.627E-06  4.338E-06
    48    5.106E-07  1.915E-06  5.106E-06
    49    6.011E-07  2.254E-06  6.011E-06
    50    7.076E-07  2.653E-06  7.076E-06
    51    8.329E-07  3.123E-06  8.329E-06
```

- Adhesion forces, SPECTRA output, Case 2: $\langle r_{as} \rangle = 0.20 \times 10^{-7}$ m, minimum value.

```
 Mean asperity radius, <Ras> (m), and spread factor, Sigma (-), per size section
 Sec.  :      1          2          3
 -----    ---------  ---------  ---------
 <Ras> =  2.000E-08  2.000E-08  2.000E-08
 Sigma =  4.000E+00  4.000E+00  4.000E+00

- ADHESION FORCE DISTRIBUTIONS:

 Adhesion force distribution per size section and Fa-section
 Representative adhesion forces, Fa (N), for Nsec = 51 Fa-sections

   \ Size :   1          2          3
 Fa-sec.  ---------  ---------  ---------
     1    2.394E-10  2.394E-10  2.394E-10
     2    2.818E-10  2.818E-10  2.818E-10
     3    3.317E-10  3.317E-10  3.317E-10
     4    3.904E-10  3.904E-10  3.904E-10
     5    4.596E-10  4.596E-10  4.596E-10
     6    5.410E-10  5.410E-10  5.410E-10
     7    6.369E-10  6.369E-10  6.369E-10
     8    7.497E-10  7.497E-10  7.497E-10
     9    8.825E-10  8.825E-10  8.825E-10
    10    1.039E-09  1.039E-09  1.039E-09
```

```
  11    1.223E-09  1.223E-09  1.223E-09
  12    1.439E-09  1.439E-09  1.439E-09
  13    1.694E-09  1.694E-09  1.694E-09
  14    1.995E-09  1.995E-09  1.995E-09
  15    2.348E-09  2.348E-09  2.348E-09
  16    2.764E-09  2.764E-09  2.764E-09
  17    3.254E-09  3.254E-09  3.254E-09
  18    3.830E-09  3.830E-09  3.830E-09
  19    4.508E-09  4.508E-09  4.508E-09
  20    5.307E-09  5.307E-09  5.307E-09
  21    6.247E-09  6.247E-09  6.247E-09
  22    7.354E-09  7.354E-09  7.354E-09
  23    8.657E-09  8.657E-09  8.657E-09
  24    1.019E-08  1.019E-08  1.019E-08
  25    1.200E-08  1.200E-08  1.200E-08
  26    1.412E-08  1.412E-08  1.412E-08
  27    1.662E-08  1.662E-08  1.662E-08
  28    1.957E-08  1.957E-08  1.957E-08
  29    2.303E-08  2.303E-08  2.303E-08
  30    2.711E-08  2.711E-08  2.711E-08
  31    3.191E-08  3.191E-08  3.191E-08
  32    3.757E-08  3.757E-08  3.757E-08
  33    4.422E-08  4.422E-08  4.422E-08
  34    5.206E-08  5.206E-08  5.206E-08
  35    6.128E-08  6.128E-08  6.128E-08
  36    7.213E-08  7.213E-08  7.213E-08
  37    8.491E-08  8.491E-08  8.491E-08
  38    9.995E-08  9.995E-08  9.995E-08
  39    1.177E-07  1.177E-07  1.177E-07
  40    1.385E-07  1.385E-07  1.385E-07
  41    1.630E-07  1.630E-07  1.630E-07
  42    1.919E-07  1.919E-07  1.919E-07
  43    2.259E-07  2.259E-07  2.259E-07
  44    2.659E-07  2.659E-07  2.659E-07
  45    3.131E-07  3.131E-07  3.131E-07
  46    3.685E-07  3.685E-07  3.685E-07
  47    4.338E-07  4.338E-07  4.338E-07
  48    5.106E-07  5.106E-07  5.106E-07
  49    6.011E-07  6.011E-07  6.011E-07
  50    7.076E-07  7.076E-07  7.076E-07
  51    8.329E-07  8.329E-07  8.329E-07
```

- Adhesion forces, SPECTRA output, Case 3: $<r_{as}>$ = 2.00×10^{-7} m, maximum value.

```
 Mean asperity radius, <Ras> (m), and spread factor, Sigma (-), per size section
 Sec.  :      1          2          3
 -----    ---------  ---------  ---------
 <Ras> =  2.000E-07  2.000E-07  2.000E-07
 Sigma =  4.000E+00  4.000E+00  4.000E+00

- ADHESION FORCE DISTRIBUTIONS:

 Adhesion force distribution per size section and Fa-section
 Representative adhesion forces, Fa (N), for Nsec = 51 Fa-sections

   \ Size :   1          2          3
 Fa-sec.  ---------  ---------  ---------
     1    2.394E-09  2.394E-09  2.394E-09
     2    2.818E-09  2.818E-09  2.818E-09
     3    3.317E-09  3.317E-09  3.317E-09
     4    3.904E-09  3.904E-09  3.904E-09
     5    4.596E-09  4.596E-09  4.596E-09
     6    5.410E-09  5.410E-09  5.410E-09
     7    6.369E-09  6.369E-09  6.369E-09
     8    7.497E-09  7.497E-09  7.497E-09
     9    8.825E-09  8.825E-09  8.825E-09
    10    1.039E-08  1.039E-08  1.039E-08
    11    1.223E-08  1.223E-08  1.223E-08
    12    1.439E-08  1.439E-08  1.439E-08
    13    1.694E-08  1.694E-08  1.694E-08
    14    1.995E-08  1.995E-08  1.995E-08
    15    2.348E-08  2.348E-08  2.348E-08
    16    2.764E-08  2.764E-08  2.764E-08
    17    3.254E-08  3.254E-08  3.254E-08
    18    3.830E-08  3.830E-08  3.830E-08
    19    4.508E-08  4.508E-08  4.508E-08
    20    5.307E-08  5.307E-08  5.307E-08
    21    6.247E-08  6.247E-08  6.247E-08
    22    7.354E-08  7.354E-08  7.354E-08
    23    8.657E-08  8.657E-08  8.657E-08
    24    1.019E-07  1.019E-07  1.019E-07
    25    1.200E-07  1.200E-07  1.200E-07
    26    1.412E-07  1.412E-07  1.412E-07
    27    1.662E-07  1.662E-07  1.662E-07
    28    1.957E-07  1.957E-07  1.957E-07
    29    2.303E-07  2.303E-07  2.303E-07
    30    2.711E-07  2.711E-07  2.711E-07
    31    3.191E-07  3.191E-07  3.191E-07
    32    3.757E-07  3.757E-07  3.757E-07
    33    4.422E-07  4.422E-07  4.422E-07
    34    5.206E-07  5.206E-07  5.206E-07
    35    6.128E-07  6.128E-07  6.128E-07
    36    7.213E-07  7.213E-07  7.213E-07
    37    8.491E-07  8.491E-07  8.491E-07
```

```
38    9.995E-07  9.995E-07  9.995E-07
39    1.177E-06  1.177E-06  1.177E-06
40    1.385E-06  1.385E-06  1.385E-06
41    1.630E-06  1.630E-06  1.630E-06
42    1.919E-06  1.919E-06  1.919E-06
43    2.259E-06  2.259E-06  2.259E-06
44    2.659E-06  2.659E-06  2.659E-06
45    3.131E-06  3.131E-06  3.131E-06
46    3.685E-06  3.685E-06  3.685E-06
47    4.338E-06  4.338E-06  4.338E-06
48    5.106E-06  5.106E-06  5.106E-06
49    6.011E-06  6.011E-06  6.011E-06
50    7.076E-06  7.076E-06  7.076E-06
51    8.329E-06  8.329E-06  8.329E-06
```

It is seen that the adhesion forces for the first and second case are identical for the size section 1 $10^{-10} \div 10^{-10}$ N), while for the second and third case they are identical for the size section 3. For the cases 2 and 3 the adhesion forces are independent of the particle size. This is a consequence of using a large value for $x_{p,1}$ (10^{10}). Physically it means that the adhesion force is assumed to be governed by the curvatures of the asperities rather that those of the particles, that means the asperity radii are assumed to be much smaller than the particle diameter, $r_{as} \ll (D_p/2)$. If such assumption is made, then to be consistent one should use a single asperity size for calculation for adhesion forces for all particle sizes. This fact, together with the fact that the asperity radius is a surface-related parameter, is a reason why the original Vainshtein recommendation of using, $r_{as} = 0.1\times(D_p/2)$ is considered as an inconsistency. Further discussion of this issue is provided in the STORM experiment - section 3.12.30.

3.12.25 Mechanistic Resuspension Model - Equivalence of F_a Calculation Options

Two options are available to calculate the adhesion force, F_a. With the first option (IAFRRT=1, Volume 2), the mean adhesion force, $\langle F_a \rangle$, and a spread factor, σ_a, are defined by the user independently for each particle size section. Additionally, the user defines a mean asperity radius, $\langle r_{as} \rangle$, applied for all particle size sections. With the second option (IAFRRT=2), a mean asperity radius, $\langle r_{as} \rangle$, and a spread factor, σ_{as}, are defined by the user independently for each particle size section. If the mean asperity radius is the same for all sections then identical results may be obtained through both options. First, a resuspension model using the option 1 is shown:

```
*      MECHANISTIC RESUSPENSION MODEL 1, Option 1: Fa distribution
*                                                  Distribution
*      Cf0  XF   Chi  Vp  Ep  Vs   Es   CFa  Ivel  Xvel  Fa Log Opt Nsec Nj    Cut-off
870001  0   0     0   0   0   0    0     0     0   0.0   1   1   1   0   0       0.0  *
*
*     Asperity radius distribution
*
*      <Fs>   sigma
870101 0.0    0.0  * size section 1  (use default values)
870201 0.0    0.0  * size section 2  (use default values)
870301 0.0    0.0  * size section 3  (use default values)
870401 0.0    0.0  * size section 4  (use default values)
870501 0.0    0.0  * size section 5  (use default values)
*
*      <Ras>  sigma    xp0   xa0
879101 1.e-7  0.0      0.0   0.0
*
*        Adhesion force mean value <Fa> calculation - model constants
*        van der Waals
*        A1    x1   R    xp1    xa1
879201  0.0   0.0  -1  1.0e10   0.0
```

Exactly the same results will be obtained using the asperity size distribution, $\varphi_{as}(r_{as})$, option, if the mean asperity size is specified as the same as above, i.e. 1.0×10^{-7} m for all size sections (in this case the mean asperity radius defined in the record 8791101 is not used):

```
*      MECHANISTIC RESUSPENSION MODEL 2, Option 2: Asperity distribution, <R-as> = 1.0E-7
*                                                  Distribution
*      Cf0  XF   Chi  Vp  Ep  Vs   Es   CFa  Ivel  Xvel  Fa Log Opt Nsec Nj    Cut-off
870002  0   0     0   0   0   0    0     0     0   0.0   2   1   1   0   0       0.0  *
*
*     Asperity radius distribution
*
*     <Ras>   sigma
870102 1.e-7  0.0  * size section 1
870202 1.e-7  0.0  * size section 2
870302 1.e-7  0.0  * size section 3
```

```
870402 1.e-7  0.0  * size section 4
870502 1.e-7  0.0  * size section 5
*
*      <Ras>  sigma    xp0   xa0
879102 0.0    0.0      0.0   0.0
*
*        Adhesion force mean value <Fa> calculation - model constants
*        van der Waals
*        A1    x1   R    xp1    xa1
879202  0.0   0.0  -1  1.0E10   0.0
```

The results are identical provided that the adhesive force is proportional to the asperity size, $D_{eff,1} \propto r_{as}$ ($x_{p,1}$ is set to a large number). If this is not the case there will be some differences in the calculated adhesion force. In contrast to $x_{p,1}$, $x_{p,0}$ does not need to be set to a large number. This value is used only for the spring stiffness calculation and identical results will be obtained if the same value is used consistently in both models. The input deck is provided in **\Z-INPUTS\RT\Res-Sen\Res-Sen5.SPE**.

3.12.26 Mechanistic Resuspension Model - Sensitivity to the Distribution Option

Influence of balancing separately all size sections is illustrated in Figure 3-796 through Figure 3-800. In this test gas mass source linearly increases from zero to 10 kg/s in fifty seconds. This corresponds to an increase of the gas velocity from V_g = 0.0 m/s at time t=0.0, to V_g ~ 88 m/s at time t = 50.0. For t > 50.0 s the gas velocity is kept constant at V_g ~ 88 m/s.

The input deck is provided in **\Z-INPUTS\RT\Res-Sen\Res-Sen4.SPE**. Two options were used:

- Option 1 - particle balance separately for each F_a-section.
- Option 2 - the same (lognormal) particle distribution is kept.

The figures show calculations performed with the default option (Option 1) and keeping fixed distribution (Option 2). With the first option, only the particles from the "left" F_a-sections (i.e. the particles which are weakly attached to the surface) are resuspended. Once these weakly attached particles are removed from the surface, there is practically no more resuspension until the gas velocity and thus the drag force increases.

On the other hand, if the Option 2 is selected, particle resuspension is much faster. Physically this option means that particles from all sections are resuspended, with the resuspension rate equal to the average for all F_a-sections. Figure 3-796 shows the total deposited mass divided by the initial mass for both options. With Option 2 all particles are resuspended after about 50 s, while with the Option 1 more than 50% of particles remain on the surface (Figure 3-796). These are only the strongly bound particles from the "right" sections (Figure 3-800).

The Option 2 is included only for some testing calculations and the results shown in this section are the only results obtained with this option. All other test runs were performed using the default Option 1 (particle balance separately for each F_a-section).

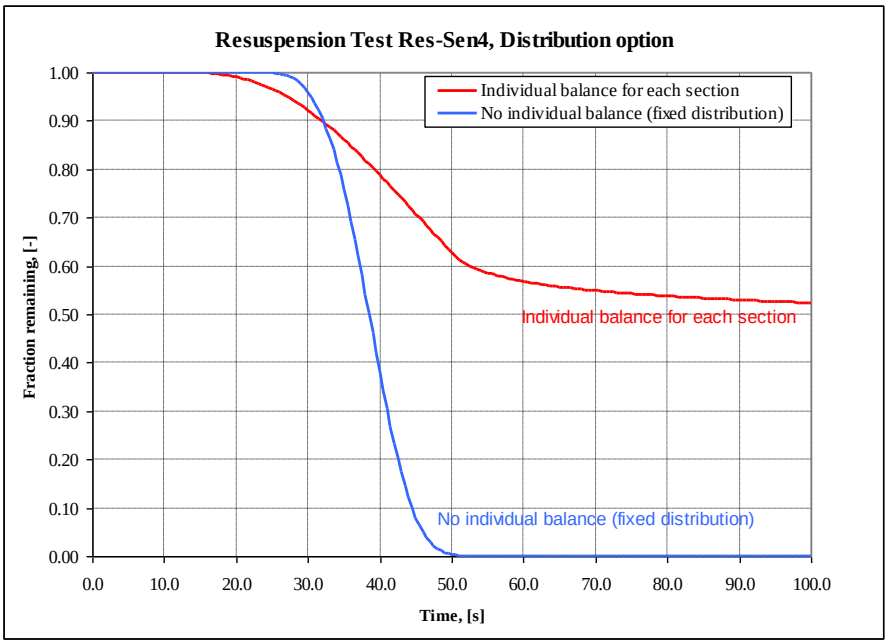

Figure 3-796 Resuspension test Res-Sen4, influence of balancing each F_a-section.

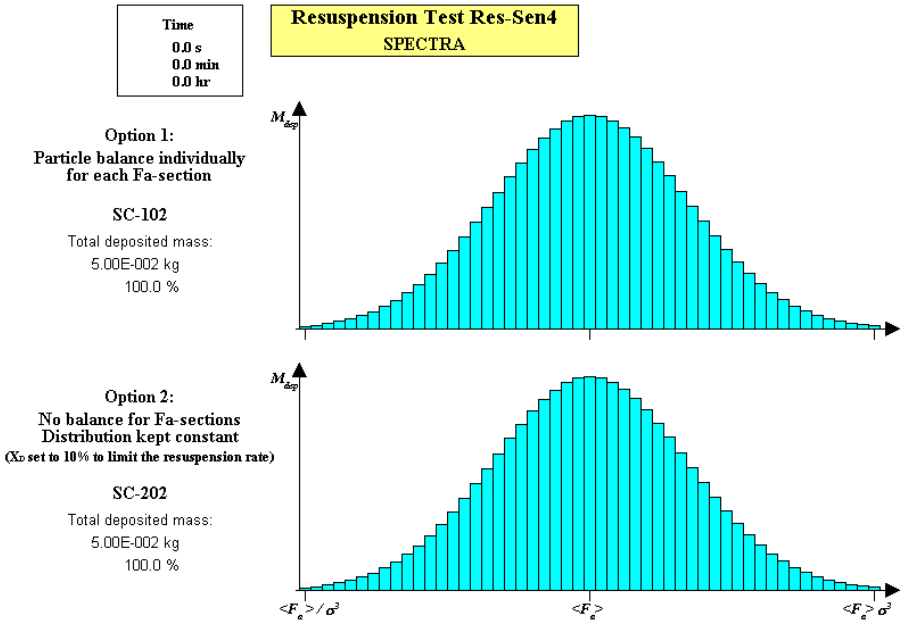

Figure 3-797 Resuspension test Res-Sen4, influence of balancing each F_a-section, t = 0.0 s.

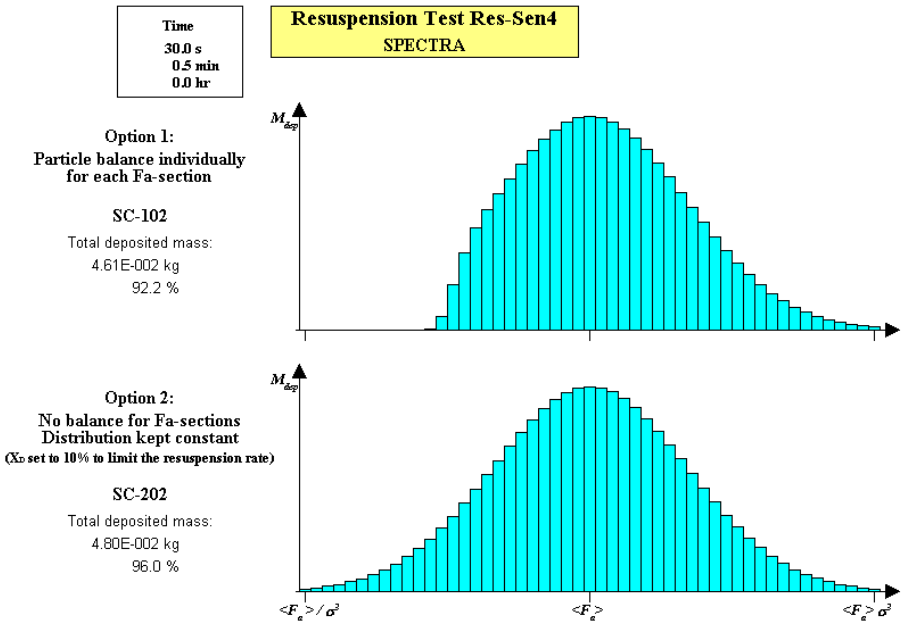

Figure 3-798 Resuspension test Res-Sen4, influence of balancing each F_a-section, t = 30.0 s.

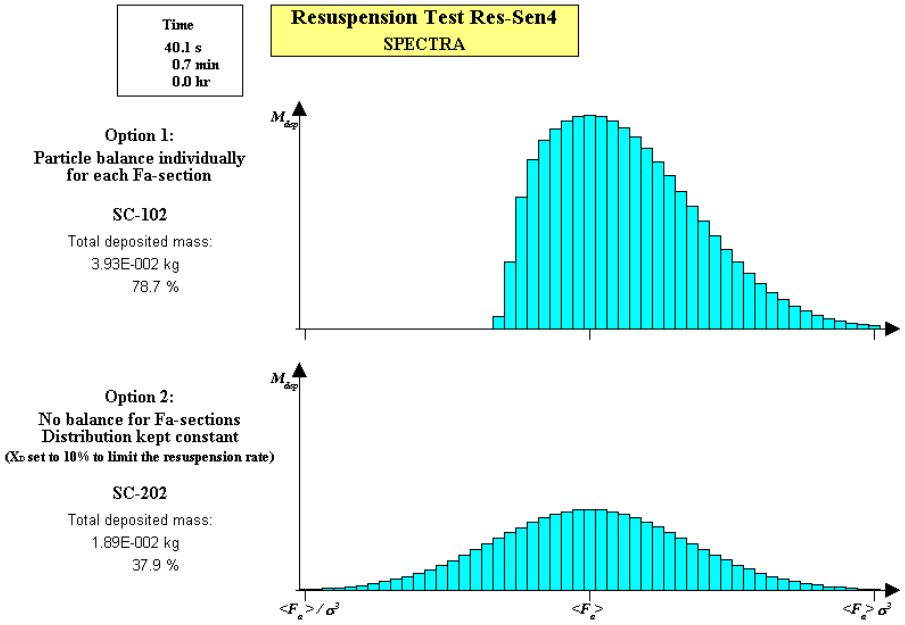

Figure 3-799 Resuspension test Res-Sen4, influence of balancing each F_a-section, t = 40.0 s.

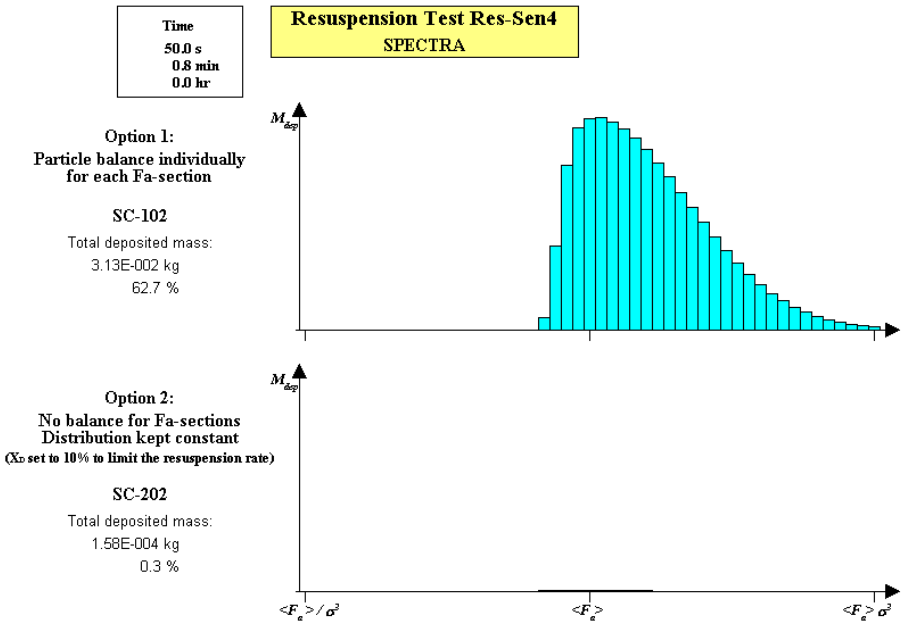

Figure 3-800 Resuspension test Res-Sen4, influence of balancing each F_a-section, t = 50.0 s.

3.12.27 Mechanistic Resuspension Model - Alternative Formulation, "On/Off"

An advantage of the resuspension model, as built in SPECTRA is its flexibility and possibilities to apply formulations other than that of Vainshtein. This fact is quite important in view of huge uncertainties (orders of magnitude) that exist in the knowledge of the main parameters involved, such as the adhesion force.

The example given in this section shows how to build an on-off resuspension model, for which a fast resuspension ($R_m \sim 1.0\ s^{-1}$) will be occurring above a certain drag force limit, and practically no resuspension ($R_m \sim 0.0\ s^{-1}$) will occur otherwise. Such are the resuspension models NRG3 and NRG4, that were formulated and described in [167] and [168] (NRG4 is referred to as KS-MB model in [168]). This section shows comparison of such models with the Vainshtein model. Further discussion and verification of the NRG3 and NRG4 (KS-MB) model, as built in SPECTRA, is provided in the following section.

The "on/off" behavior is obtained by using the extended formulation:

$$R_m = f_0 \exp\left[-C_1 \left(\frac{F_{a\tau} - C_2 F_d}{F_d} \right)^{x_F} \right]$$

In SPECTRA a limit is imposed on the difference, such that the difference never becomes negative ($F_{a\tau} - C_2\ F_d \geq 0.0$). Suppose the user wishes to build a resuspension model in which there is no resuspension when the drag force is smaller than the tangential pull-off force, and a very fast resuspension otherwise. In other words, the model should provide:

$$R_m = \begin{cases} very\ small & if \quad F_{a\tau} > F_d \\ very\ large & if \quad F_{a\tau} < F_d \end{cases}$$

This may be achieved by setting C_1 to a large value, and $C_2 = 1.0$. When the difference $F_{a\tau} - F_d$ is positive, it is multiplied by a large number (C_1) and the exponent function is practically zero. When the difference $F_{a\tau} - F_d$ is negative, the exponent is equal to 1.0; therefore the resuspension rate is equal to f_0. In order to make sure that the resuspension rate is large in this region, it is convenient to use a large constant value for f_0. This is obtained by specifying a negative value of the coefficient C_{f0}, equal to the absolute value of the desired (constant) f_0 (input parameter CF0RRT, see Volume 2). For example, a constant value of $f_0 = 10^3$ is obtained by setting CF0RRT to -10^3.

Furthermore, if the drag force, F_d, must be applied, therefore the selector IDRRT must be set to 1 (1=use the drag force only, do not use the lift force), and multiplier on the drag force, X_d, must be set to 1.0. Note that the default value of the multiplier X_d (input parameter XDRRT) is not 1.0 but 0.3 (see Volume 2, records 8793XX)

Therefore the "On/Off" resuspension model for the drag/tangential pull off forces is built using the following coefficients:

- $C_1 = 10^6$ (input parameter C1ERRT)
- $C_2 = 1.0$ (input parameter C2ERRT)
- $C_{f0} = -10^3$ (input parameter CF0RRT)
- $X_d = 1.0$ (input parameter XDRRT)
- $I_d = 1$ (input parameter IDRRT)

Similarly an "On/Off" model may be defined for the adhesion force, i.e. particle resuspension when the drag force is larger than the adhesion force. To do that one must use the adhesion force, F_a, instead of the tangential pull-off force, F_{at}. This is obtained by setting the value of the coefficient C_{Fa} to –1.0 (input parameter CFARRT, see Volume 2).

Alternatively the "On/Off" resuspension model may be built for the drag/adhesion moments. The adhesion moment, M_a, and the drag moment, M_d, are:

$$M_a \sim F_a \cdot r_a \qquad M_d \sim F_d \cdot \left(\frac{D_p}{2}\right)$$

Here D_p is the particle diameter, r_a is the contact radius. The proportionality constants are may in general be different for different particle shapes, surface asperity shapes. In the present calculations it is assumed for simplicity that the proportionality constant is 1 for both cases:

$$M_a = F_a \cdot r_a \qquad M_d = F_d \cdot \left(\frac{D_p}{2}\right)$$

Equilibrium of moments means that:

$$F_a \cdot r_a = F_d \cdot \left(\frac{D_p}{2}\right)$$

or:

$$F_a = \left(\frac{D_p}{2r_a}\right) \cdot F_d$$

The main difficulty here is to establish the value of the contact radius, r_a. For the JKR adhesion model [87], the resulting moment for a smooth surface can be expressed in the form [86]:

$$r_a = \left(\frac{3\pi \cdot \Delta\gamma \cdot D_p^2}{4K}\right)^{1/3}$$

The ratio: $(D_p/2r_a)$ is therefore given by:

$$\left(\frac{D_p}{2r_a}\right) = \left(\frac{4K \cdot D_p}{24\pi \cdot \Delta\gamma}\right)^{1/3} = 0.38 \cdot \left(\frac{K}{\Delta\gamma}\right)^{1/3} \cdot D_p^{\,1/3}$$

The value of K is given by [86]:

$$K = \frac{4}{3}\left(\frac{1-\nu_p^2}{E_p} + \frac{1-\nu_s^2}{E_s}\right)^{-1}$$

ν_i and E_i are Poisson's ratio and Young modulus respectively. It is printed by SPECTRA for each resuspension model. For the present calculations the values of $\nu_p = 0.3$, $E_p = 2.0\times10^{10}$, $\nu_s = 0.29$, $E_s = 2.1\times10^{11}$, were assumed, which means $K = 2.67\times10^{10}$.

The value of $\Delta\gamma$ (adhesive surface energy, J/m^2) is related to the input parameter A_1 by (see Volume 2, input parameter A1ARRT):

$$\Delta\gamma = \frac{A_1}{2.356\times10^{-9}}$$

In the present model A_1 of 3.53×10^{-10} was applied, with the corresponding value of $\Delta\gamma$ of 0.15. The ratio $(D_p/2r_a)$ is therefore equal to:

$$\left(\frac{D_p}{2r_a}\right) = 0.38\cdot\left(\frac{K}{\Delta\gamma}\right)^{1/3}\cdot D_p{}^{1/3} = 0.38\cdot\left(\frac{2.67\times10^{10}}{0.15}\right)^{1/3}\cdot D_p^{1/3}$$

The value of course depends on the particle size. For the present test three particle size sections were applied, with diameters of $D_p = 0.4$, 1.5, and 4.0 micrometers:

- Size section 1, $D_p = 0.4\times10^{-6}$ m, $(D_p/2r_a) = 15.7$
- Size section 2, $D_p = 1.5\times10^{-6}$ m, $(D_p/2r_a) = 24.4$
- Size section 3, $D_p = 4.0\times10^{-6}$ m, $(D_p/2r_a) = 33.8$

To define the drag/adhesion moments in SPECTRA one should use the term $(F_{a\tau} - C_2\,F_d)$, and set $(F_{a\tau} = F_a)$ and $C_2 = (D_p/2r_a)$. The first is achieved by setting $C_{Fa} = -1.0$, the second by setting an appropriate value for C_2:

$$C_2 = \left(\frac{D_p}{2r_a}\right) = 0.38\cdot\left(\frac{K}{\Delta\gamma}\right)^{1/3}\cdot D_p{}^{1/3}$$

Therefore the "On/Off" resuspension model for the drag/adhesion moments is built using the following coefficients:

- $C_1 = 10^6$ (input parameter C1ERRT)
- $C_2 = (D_p/2r_a)$ (input parameter C2ERRT, depends on particle size, D_p)
- $C_{f0} = -10^3$ (input parameter CF0RRT)
- $C_{Fa} = -1$ (input parameter CFARRT)
- $X_d = 1.0$ (input parameter XDRRT)
- $I_d = 1$ (input parameter IDRRT)

Finally a lift force (or a combination of the drag and lift forces) may be used instead of the drag force by specifying the coefficients X_L, X_d (input parameters XLRRT, XDRRT). As shown above an "On/Off" model may be built using a variety of force combinations. Below the results of Vainshtein model are compared to:

- "On/Off" model for the drag/tangential pull off forces
- "On/Off" model for the drag/adhesion moments

The input deck is provided in **\Z-INPUTS\RT\Res-Sen\Res-Sen2.SPE**. Results are shown in Figure 3-801. The results obtained with the drag/tangential forces give too low resuspension and therefore NRG3 model should be used with care. shouldn't be used. The drag/adhesion moment balance gives similar end resuspension as the Vainshtein model, but of course the resuspension process is faster with this "On/Off" formulation. In theory the resuspension is instantaneous, as in this model $R_m = \infty$, but in practice R_m is a large but finite number. The resuspension takes a few milliseconds (Figure 3-801). Note that in the Vainshtein model the resuspension takes a few hundred seconds.

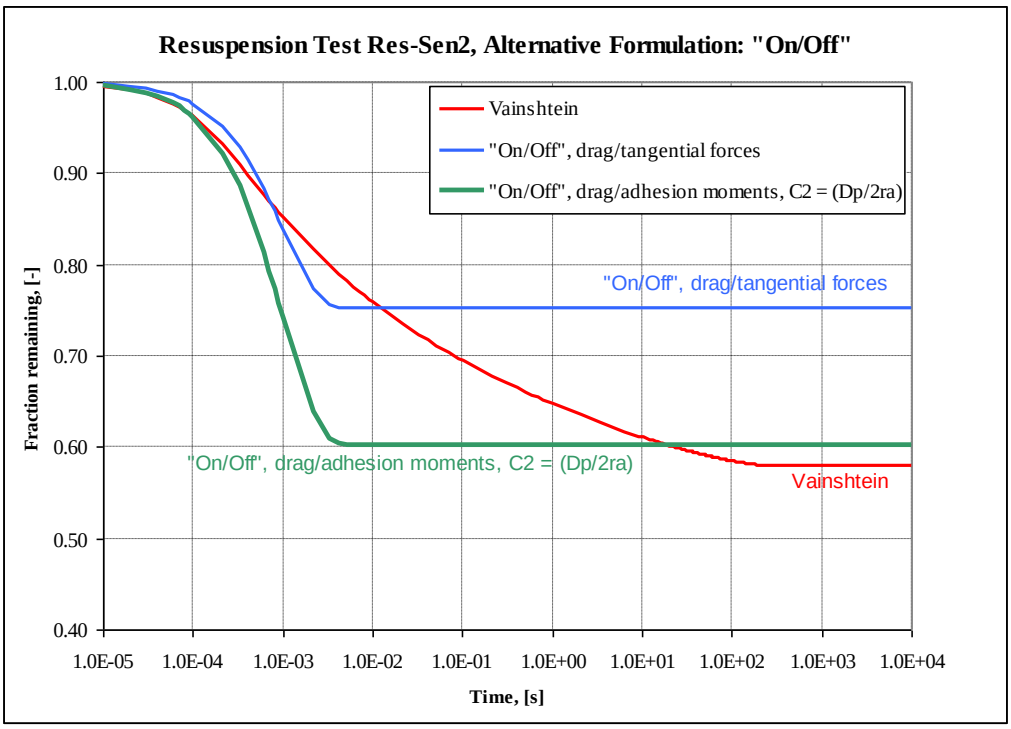

Figure 3-801 Alternative formulation: "On/Off" resuspension.

3.12.28 Verification of the "On/Off" Resuspension Model against MathCAD Calculations

The resuspension models called NRG3 and NRG4 were formulated and documented in reference [167], [168] (NRG4 is referred to as KS-MB model in [168]). Generally speaking, the models are the On/Off models discussed in the previous section.

- NRG3 model - the "On/Off" resuspension model for the drag/tangential pull off forces
- NRG4 model - the "On/Off" resuspension model for the drag/adhesion moments

While the previous section gives a general overview of this type of models and comparison with the Vainshtein model, this section presents the NRG3 and NRG4 (KS-MB) and compares the SPECTRA results with results obtained by MathCAD.

For comparisons with MathCAD the two models were set up as described in the previous section. In the "On/Off" formulation based on the drag / adhesion moments, slightly different constant C_2 was used, for the reasons described below.

- NRG3 model - the "On/Off" resuspension model for the drag/tangential pull-off forces

  The model is built using the following coefficients (see section 3.12.27):

  - $C_1 = 10^6$ (input parameter C1ERRT)
  - $C_2 = 1.0$ (input parameter C2ERRT)
  - $C_{f0} = -10^3$ (input parameter CF0RRT)
  - $X_d = 1.0$ (input parameter XDRRT)
  - $I_d = 1$ (input parameter IDRRT)

- NRG4 model - the "On/Off" resuspension model for the drag/adhesion moments

  The model is built using the following coefficients (see section 3.12.27):

  - $C_1 = 10^6$ (input parameter C1ERRT)
  - $C_2 = 2.1 \cdot (D_p/2r_a)$ (input parameter C2ERRT, depends on particle size, D_p)
  - $C_{f0} = -10^3$ (input parameter CF0RRT)
  - $C_{Fa} = -1$ (input parameter CFARRT)
  - $X_d = 1.0$ (input parameter XDRRT)
  - $I_d = 1$ (input parameter IDRRT)

  Compared to the values used in the section 3.12.27, different value of the constant C_2 is applied. This is because of the definitions of moments applied in MathCAD are somewhat different than those applied in the previous section. The adhesion moment is obtained from the JKR model [87] (proportionality constant of 2/3 - MathCAD eq. 2.181), while the drag moment (proportionality constant of 1.399 - MathCAD eq. 2.156):

$$M_a = \frac{2}{3} \cdot F_a \cdot r_a \qquad M_d = 1.399 \cdot F_d \cdot \left(\frac{D_p}{2} \right)$$

The balance of moments, $M_a = M_d$, gives:

$$\frac{2}{3} \cdot F_a \cdot r_a = 1.399 \cdot F_d \cdot \left(\frac{D_p}{2} \right)$$

or:

$$F_a = 2.1 \cdot \left(\frac{D_p}{2r_a} \right) \cdot F_d$$

As shown in the previous section, the value of $(D_p/2r_a)$ may be estimated as:

$$\left(\frac{D_p}{2r_a} \right) = 0.38 \cdot \left(\frac{K}{\Delta\gamma} \right)^{1/3} \cdot D_p{}^{1/3}$$

Therefore:

$$F_a = 2.1 \cdot 0.38 \cdot \left(\frac{K}{\Delta\gamma} \right)^{1/3} \cdot D_p^{1/3} \cdot F_d = 0.798 \cdot \left(\frac{K}{\Delta\gamma} \right)^{1/3} \cdot D_p^{1/3} \cdot F_d$$

or:

$$F_a = C_2 \cdot F_d$$

$$C_2 = 0.798 \cdot \left(\frac{K}{\Delta\gamma} \right)^{1/3} \cdot D_p^{1/3}$$

The values of $K = 2.67 \times 10^{10}$ and $\Delta\gamma$ of 0.15 were applied. Two particle size sections were applied, with diameters of $D_p = 0.4$ and 1.5 micrometers:

- Size section 1, $D_p = 0.4 \times 10^{-6}$ m, $C_2 = 33.1$
- Size section 2, $D_p = 1.5 \times 10^{-6}$ m, $C_2 = 51.4$

For the SPECTRA calculations the above values were specified using the section-by-section C_2 input (record 8796XX, Volume 2).

Both NRG3 and NRG4 models were used with the adhesion force calculated through the asperity size distribution, with reduction factor of $f' = 0.1$ and spread factor of $\sigma = 4.0$. The input parameter A_1 is related to the value of $\Delta\gamma$ (adhesive surface energy, J/m^2):

$$A_1 = 2.356 \times 10^{-9} \Delta\gamma$$

For the present calculation $\Delta\gamma = 0.15$ was used, which corresponds to $A_1 = 3.53 \times 10^{-10}$. The thermal-hydraulic conditions were assumed:

- fluid: He
- $T = 700$ K
- $p = 5.0 \times 10^6$ Pa

The input decks as well as the MathCAD files are provided in **\Z-INPUTS\RT\Res-Ed\NRG**. The MathCAD results are provided in the same location. Results are shown in Figure 3-802 and Figure 3-803. Results are in very good agreement. The SPECTRA and MathCAD results are quite close, so it is concluded that the method presented here to build the NRG3 and NRG4 models in SPECTRA has been successfully verified.

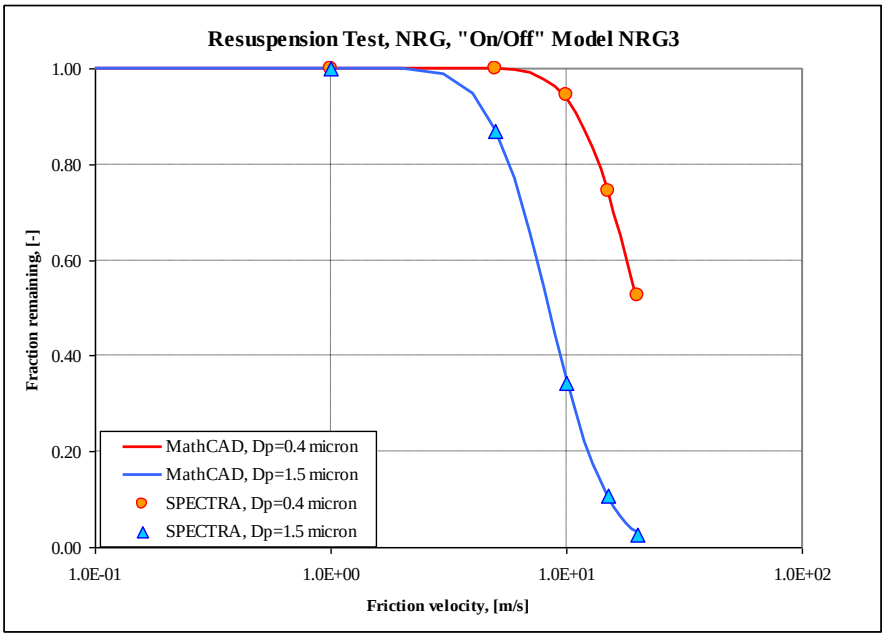

Figure 3-802 Verification of the NRG models against MathCAD - NRG3 model

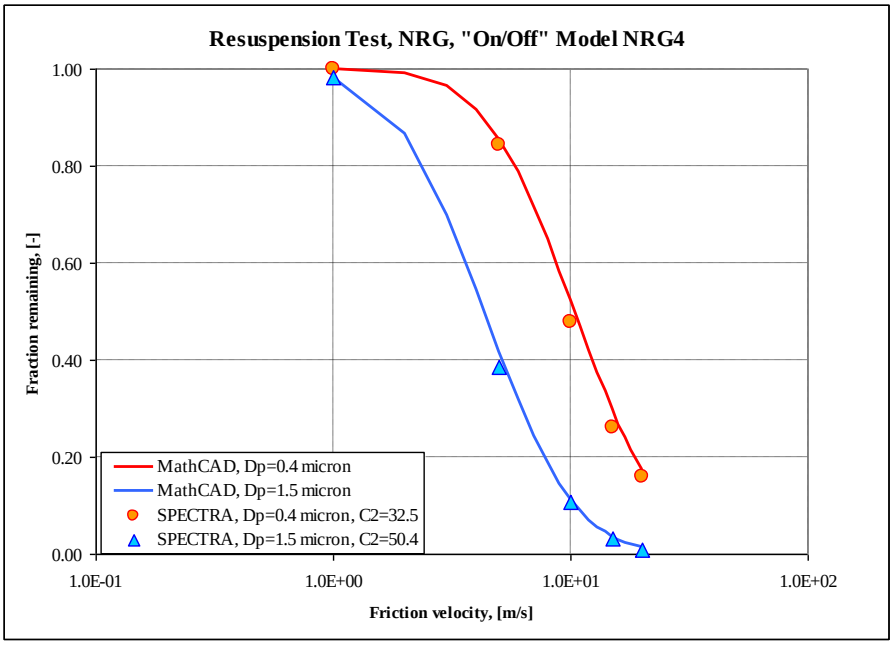

Figure 3-803 Verification of the NRG models against MathCAD - NRG4 model

3.12.29 Mechanistic Resuspension Model - Reeks and Hall Experiments

The article of Reeks and Hall [88] reports measurements of the short-term resuspension of nominal 10 and 20 μm alumina spheres and graphite particles from a polished stainless-steel flat plate in fully developed turbulent channel flow. Below SPECTRA results are compared to the experimental data for the 10 and the 20 μm particles.

Input decks, as well as the MathCAD files are located in: \Z-INPUTS\RT\Res-Reeks-Hall\

"10 μm" particles

The nominal "10-μm" particles had the mean diameter of 12.2 μm ([88], Table 1); the minimum and maximum diameters were 6 and 18 μm respectively. SPECTRA calculations were performed using a single size section with the mean diameter (12.2 μm).

Geometrical Models

The SPECTRA model of the test facility is very simple and consists of a Control Volume with a gas source (CV-101), the test section (CV-102) with the structure (SC-102) on which the particles are initially deposited (Figure 3-804), and the outlet boundary volume with fixed parameters (CV-103) Two versions of the SPECTRA input were used:

- *"Single-facility" model*
  In the first version, called the "single-facility" model the calculations were performed in a way similar to the way the experiments were done; gas velocity was simply increased in steps (total of 9 steps were made) and the remaining mass of aerosols were observed after every step. The model is shown in Figure 3-804.

- *"Multiple-facility" model*
  In the second version, called the "multiple-facility" model there are nine identical "test facilities"; each of them performing a single step of the velocity. The model is shown in Figure 3-805. The second method is more convenient in practice because it is faster and the results are readily available in a single picture, such as that shown in Figure 3-805.

It was checked that both methods give practically the same results. Good agreement was obtained provided that sufficient time was given for each step to achieve stable conditions (with practically no-resuspension) prior to the next step. The required time was about 1000 s for each step. This time was selected to run each step in the "single facility" model, and as the total run time for the "multiple-facility" model. Comparison of both methods is shown in Figure 3-804 and Figure 3-805. Results of the "multiple-facility" model are shown at the end-time, t=1000 s - Figure 3-805. Results of the "single-facility" model are shown at the end of the step 4 (t = 3990 s - Figure 3-804). Those results compare well with the results visible for the "test facility 4" in Figure 3-805.

Since it was proven that both methods give the same results, the "multiple-facility" model, as the one that is more convenient, was used for all calculations presented here.

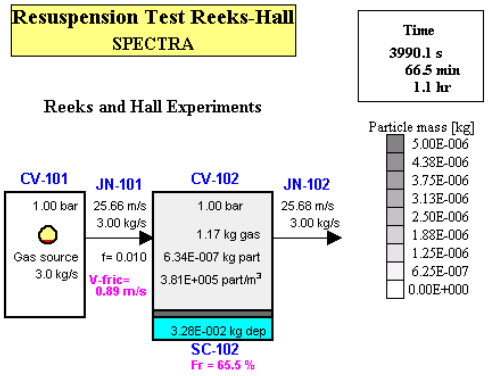

Figure 3-804 Reeks and Hall experiment, SPECTRA “single facility”, end of step 4.

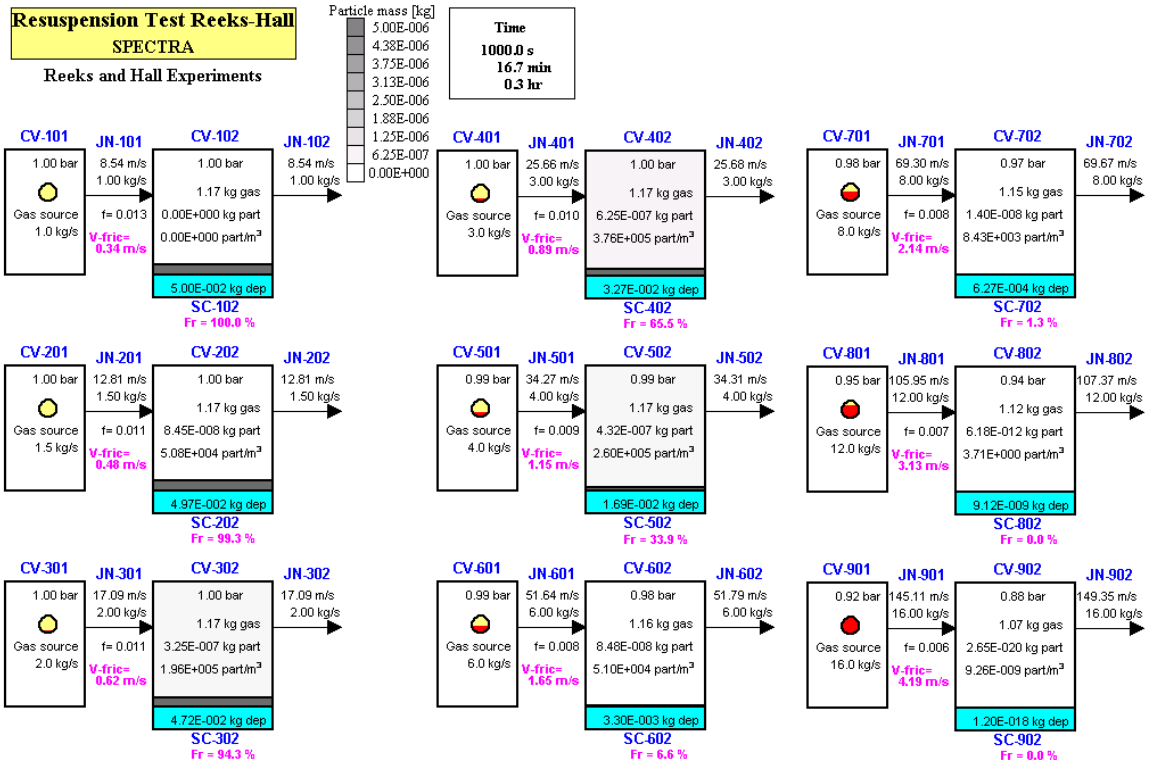

Figure 3-805 Reeks and Hall experiment, SPECTRA “multiple facility”.

Resuspension Models

Two resuspension models were used:

- Vainshtein model, with the resuspension rate, R_m (s^{-1}), given by (see Volume 1):

$$R_m = f_0 \exp\left[-\left(\frac{F_{a\tau}}{F_d} \right)^{x_F} \right]$$

- Rock'n Roll model (built using the "extended mechanistic model" - see Volume 1), with the resuspension rate, R_m (s^{-1}), given by:

$$R_m = f_0 \cdot \exp\left[-\frac{1}{2}\left(\frac{F_a - F_{aero}}{0.2 \cdot F_{aero}} \right)^2 \right]$$

where:

$$F_{aero} = \left(\frac{r}{a} F_d' \right) + \left(\frac{1}{2} F_L' \right)$$

F_d' and F_L' are the drag force and the lift force respectively (see Volume 1). The ratio (r/a) is assumed to be 100.

Adhesion Forces, F_a

Two options were used for the adhesion force, F_a, calculation:

- Mean adhesion force, $<F_a>$, calculated using the default, built-in correlations (see Volume 1), assuming the surface roughness of 1.0×10^{-6} and the relative humidity of 1.0. The mean asperity radius (needed in such case only for conversion of the adhesion force, F_a, to the tangential pull-off force, $F_{a\tau}$) is equal to:

$$\langle r_{as} \rangle = 1.0 \times 10^{-7} \text{ m}$$

This is the default value (see Volume 2) and it was used with the spread factor, σ_a, as described below.

- Adhesion forces calculated from the asperity distribution. This is the original approach of Vainshtein et al. (see Volume 1). The adhesion force, F_a, is proportional to the particle diameter, D_p: $F_a \sim D_p$ (see Volume 1). Next a reduction factor is applied by arguing that for relatively small asperity radii, $r_{as} \ll D_p$, the small asperity may play a role of a particle deposited on a relatively flat surface of the real particle. The resulting reduction factor is equal to $(r_{as}/R_p)=(2r_{as}/D_p)$ and the adhesion force becomes proportional to the asperity radius, $F_a \sim r_{as}$. The original article gives the reduction factor of 1/37=0.027 for the "10-μm" particles ([88], Table 4). Therefore the mean asperity radius was defined as:

$$\langle r_{as} \rangle = 0.027 \times \frac{1}{2} \times 12.2 \times 10^{-6} = 1.6 \times 10^{-7} \text{ m}$$

The value of 12.2×10^{-6} is the mean diameter $<D_p>$ of the "10-μm" particles. The value of $A_1 = 1.32\times10^{-9}$ was applied, based on alumina value $\Delta\gamma=0.56$ [88] ($3/2\pi\Delta\gamma D_p/2=1.32$).

Adhesive Spread Factors, σ_a

Considering the adhesive spread factors, σ_a, the original article [88] (Table 4) mentions two different values, namely 2.55 and 10.4. The first value is mentioned in relation to the RRH model (Reeks, Reed, and Hall model - which was the basis for the Vainshtein model), while the second is mentioned in relation with the Rock'n Roll model. Since the spread factors determine the range of adhesion forces, so in a sense the adhesion forces themselves, it is felt that comparing different resuspension models that are using different adhesion forces doesn't make much sense, specifically when the adhesive spreads are so different. It should be remembered that the range of adhesion forces is: $<F_a>/\sigma_a^3 \div <F_a>\times\sigma_a^3$ (see Volume 1). Therefore the ranges of relative adhesion forces are:

- $\sigma_a = 2.55$ $\quad 6.0\times10^{-2} < (F_a/<F_a>) < 1.7\times10^{1}$
- $\sigma_a = 10.4$ $\quad 8.2\times10^{-4} < (F_a/<F_a>) < 1.1\times10^{3}$

Therefore both models were run with both adhesive spreads. The value of 10.4 seems somewhat large. With this value of σ_a the ratio of the maximum and the minimum force is about 10^6, thus the adhesive force spreads over six orders of magnitude. With the value of 2.55 the ratio of the maximum and the minimum force is about 300.

Results

All analyzed cases are summarized in Table 3-63. Results are shown in Figure 3-806 through Figure 3-809. The following observation can be made:

- Results close to experimental measurement are obtained with the Vainshtein mode with default adhesion force $<F_a>$ calculation. Results obtained with the F_a calculation through asperity size calculation with the reduction factor of $f_{red} = 0.027$ give too large fraction of remaining particles. This means the resuspension rate is underestimated.
- Results obtained with the adhesive spread of $\sigma_a = 2.55$ give closer match to experimental data than the results of $\sigma_a = 10.4$. The large spread results in less steep line than that observed in the experiments. The value of $\sigma_a = 2.55$ give somewhat too steep lines, which is visible when the remaining fractions decrease quickly to zero with increasing friction velocities. A value of adhesive spread in between the two used values is expected to give best results. Default value in SPECTRA is 4.0. Results for this value are shown below.
- The Rock'n Roll model with the mean adhesion force $<F_a>$ calculated from the default correlations and $\sigma_a = 2.55$ predicted the remaining fractions that are somewhat lower than in experiments (Figure 3-808, blue square markers). The Vainshtein model with the same assumptions predicted somewhat higher fractions (Figure 3-806, blue square markers). With these assumptions results of both models are quite close to the measured data.

Table 3-63 Reeks and Hall experiments, "10-μm" particles - summary of analyzed cases.

Model	Vainshtein	Rock'n Roll
F_a	Default models for $<F_a>$, $<r_{as}>=1.0\times10^{-7}$ "Vainshtein", $f_{red}=0.027$, $<r_{as}>=1.6\times10^{-7}$	Default models for $<F_a>$, $<r_{as}>=1.0\times10^{-7}$ "Vainshtein", $f_{red}=0.027$, $<r_{as}>=1.6\times10^{-7}$
σ_a	2.55 10.4	2.55 10.4

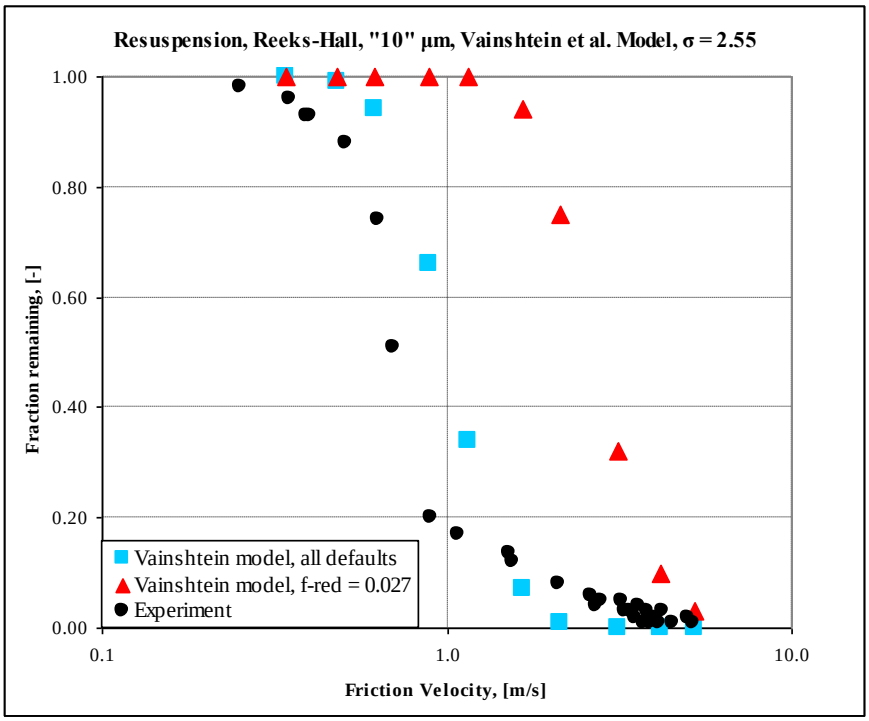

Figure 3-806 Reeks and Hall experiment, “10-µm”, SPECTRA, Vainshtein model, $\sigma = 2.55$.

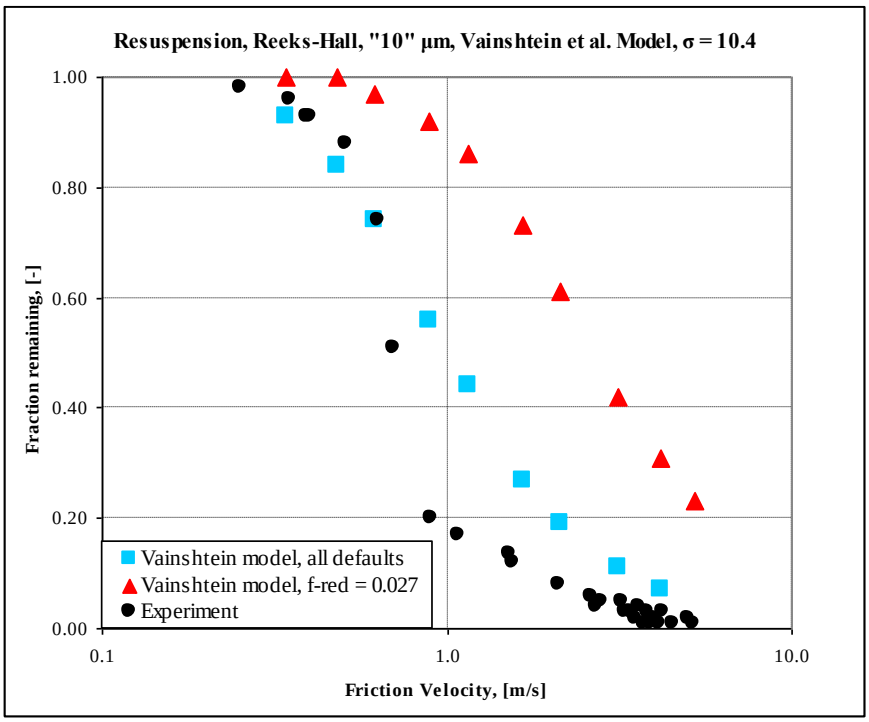

Figure 3-807 Reeks and Hall experiment, “10-µm”, SPECTRA, Vainshtein model, $\sigma = 10.4$.

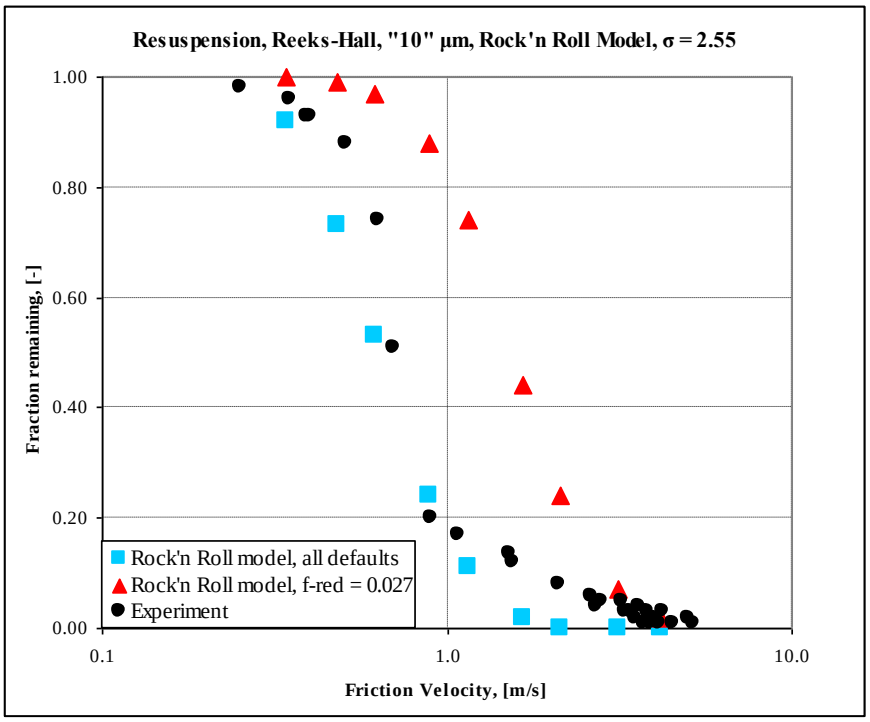

Figure 3-808 Reeks and Hall experiment, “10-µm”, SPECTRA, Rock’n Roll model, $\sigma = 2.55$.

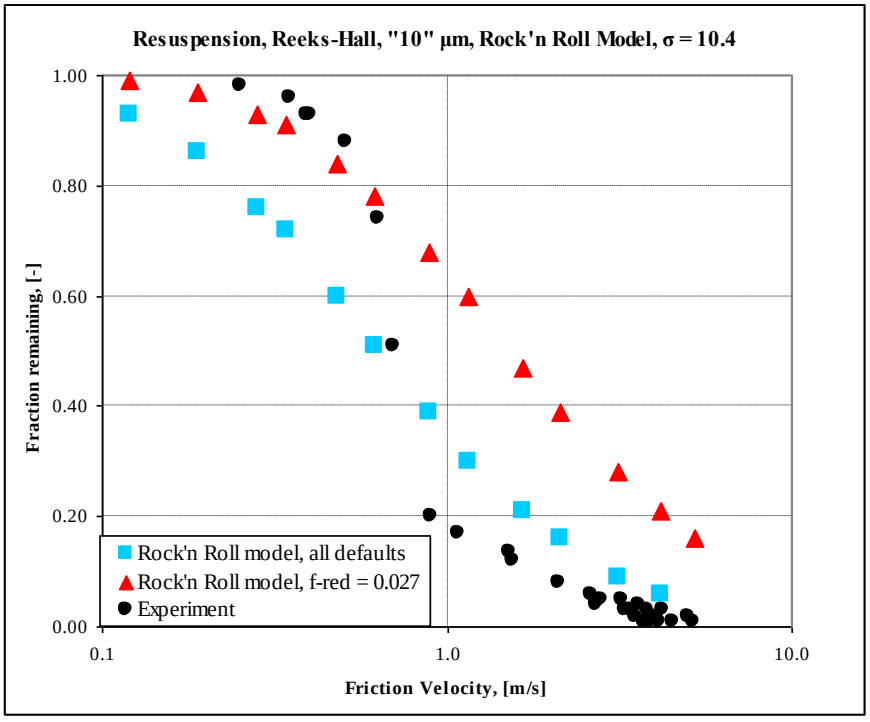

Figure 3-809 Reeks and Hall experiment, “10-µm”, SPECTRA, Rock’n Roll model, $\sigma = 10.4$.

Comparison of the Rock'n Roll model in SPECTRA with the article [88]

The results of the Rock'n Roll model, as calculated by SPECTRA are compared to the Rock'n Roll model, as presented in the original article of Reeks and Hall in Figure 3-810 and Figure 3-811. The case with σ_a = 10.4 and the Vainshtein et al. approach with the reduction factor of f_{red} = 0.027 is presented in the article (a copy is shown in Figure 3-810), therefore the same case is shown in Figure 3-811. It is clear that the SPECTRA results for this case (red triangles in Figure 3-811) agree well with the Rock'n Roll model data presented in [88]. It is also clear that the slope of calculated results is too small compared to the experiment. This is a consequence of applying a large value of σ_a and has been discussed above.

In the Rock'n Roll model the R_m is divided by a term with error function (see Volume 1):

$$\frac{1}{2}\left[1+errf\left(\frac{F_a-F_{aero}}{\sqrt{2\cdot(0.2\cdot F_{aero})^2}}\right)\right]$$

This term has been neglected. This term gives the values between 1/2 ($errf(0)=0$) and 1.0 ($errf(\infty)=1$), which can be accommodated by dividing f_0 by 1/2. This is achieved by dividing the input parameter C_{f0} by 1/2. The value of C_{f0} appropriate for the Rock'n Roll model is 6.58×10^{-3} (see Volume 1). Division by 1/2 gives $C_{f0} = 13.2\times10^{-3}$ Sensitivity calculations were performed with this value. Results of such sensitivity calculations are shown in Figure 3-812. It is clearly seen that the effect of this term is very small, in any case negligible compared to the discrepancy between the model prediction and the measured data. This small effect may at first seem surprising, since a factor of up to 2.0 is neglected in the resuspension formula. Explanation of this surprisingly small effect is given below.

The Rock'n Roll model the resuspension is quite rapid, more rapid than in the Vainshtein model. This is seen in Figure 3-813, where time-dependent values of the deposited mass are shown for the "single-facility" model. After a short resuspension period the lines become practically flat, which means that the resuspension stops until the next velocity increase step is made. In other words, the F_a-sections that are being resuspended are gone very quickly (which means that R_m is very large for these sections), while the others stay (which means that $R_m \sim 0.0$). If an "error" of a factor of 2 in the R_m calculations is made, it won't affect the sections for which $R_m \sim 0.0$. Similarly for the sections for which R_m is large there will be no visible effect; the particles from these sections will simply be swept away fraction of a second sooner or later.

An effect may be observed only in the section, which is at the "edge" of a resuspension ($0.0 < R_m < 1.0$). Thus at the worst an error of a single F_a-section resuspension is made. In the SPECTRA modeling the number of F_a-sections is typically between 51 and 99 (see Volume 2). Thus an error made by resuspending or not a single section is on the average 1÷2%, which is very small compared to the accuracy of the model against the experimental data.

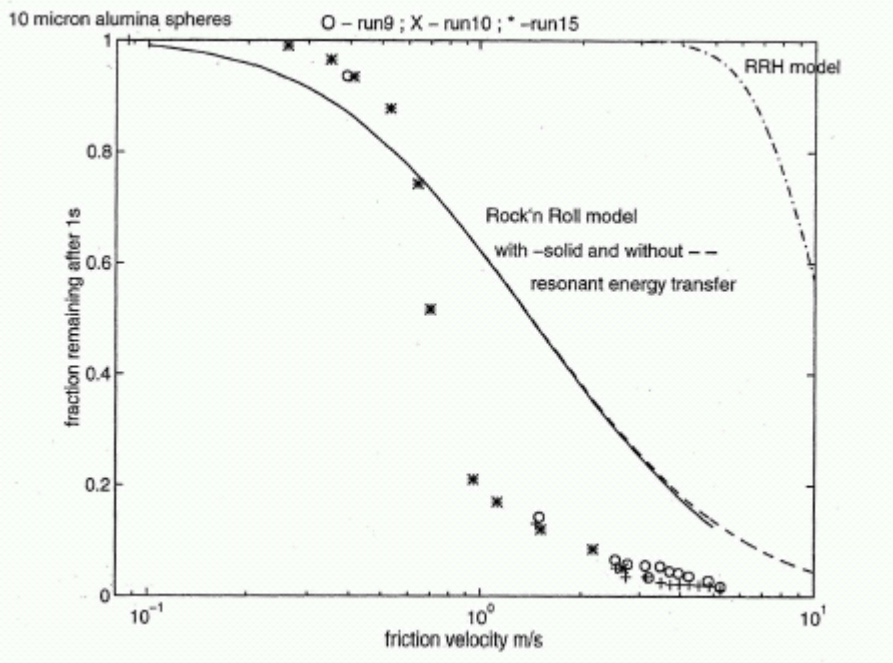

Figure 3-810 Reeks and Hall experiment, “10-µm” [88].

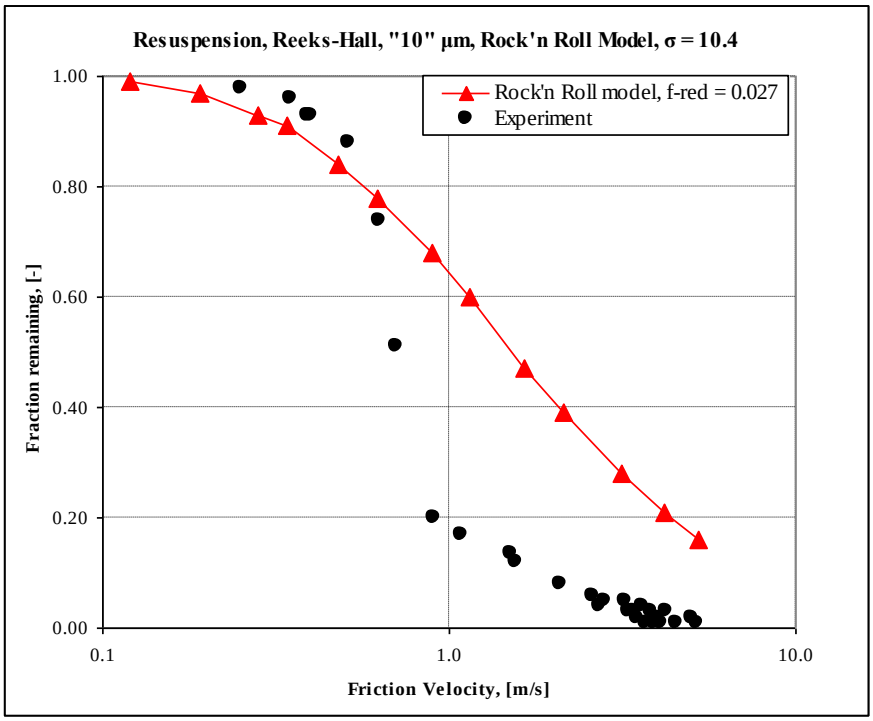

Figure 3-811 Reeks and Hall experiment, “10-µm”, SPECTRA, Rock’n Roll model, $\sigma = 10.4$.

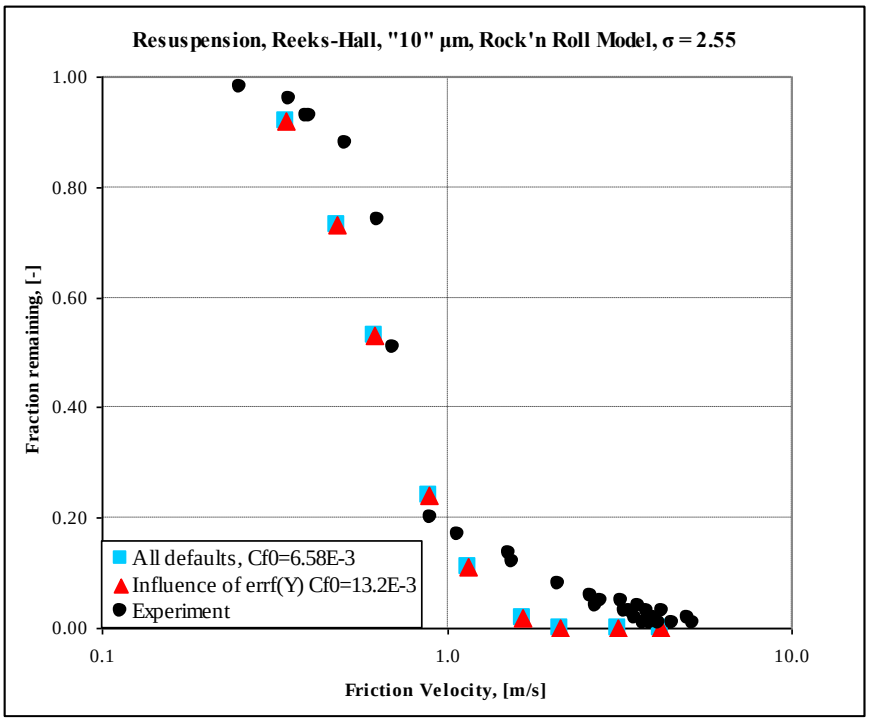

Figure 3-812 Influence of neglecting the errf(*Y*) in the Rock'n Roll model.

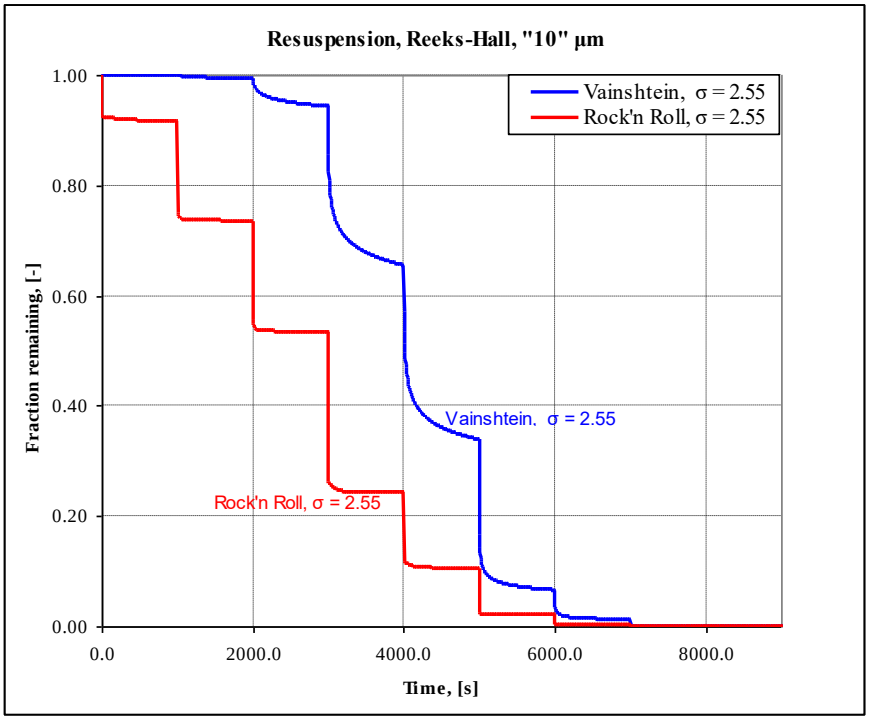

Figure 3-813 Reeks and Hall experiment, "10-µm", SPECTRA, time-dependent curves.

Comparison of the Vainshtein model in SPECTRA with MathCAD analytical results

The results of the Vainshtein model, as calculated by SPECTRA are compared to the analytical solutions obtained by means of MathCAD in Figure 3-814 through Figure 3-817. The case with σ_a = 10.4 and the Vainshtein et al. approach with the reduction factor of f_{red} = 0.027 is considered. MathCAD results are presented in Figure 3-814 and Figure 3-816. SPECTRA results are shown in Figure 3-815 and Figure 3-817. It is seen that the SPECTRA results for this case agree well with the Rock'n Roll model results from MathCAD.

It is also clear that the calculated remaining fractions are in most cases (except for the "20-μm" particles with very small friction velocities) too large, which means that the calculated resuspension rates are too small compared to the experiment.

The SPECTRA results shown in Figure 3-815 and Figure 3-817 are obtained after 1000 s after a velocity step (the velocity step was assumed to occur within 1 second in SPECTRA simulations). It has been observed that the results practically do not change after that time. MathCAD results on the other hand are those obtained for 1.0 second (Figure 3-814, Figure 3-816) after an ideal (instantaneous) step change of velocity. It has been observed that the values after 1000 s are smaller than the 1-second value by about 5 - 10%. Because of that, SPECTRA results in Figure 3-815 and Figure 3-817 are somewhat lower than those in Figure 3-814 and Figure 3-816.

Particle distributions

Figure 3-818 and Figure 3-819 show a section-by-section distribution of the deposited particles at the start of the calculations (t = 0.0 s) and after 1000 s for the "multiple-facility" model for the case:

- Vainshtein resuspension model
- Adhesion force $<F_a>$ calculation using "all defaults"
- Adhesive spread of σ_a = 2.55

Initially the particle distribution follows the assumed lognormal distribution (Figure 3-818). Figure 3-819 shows how the weakly bound particles (particles left hand side in these figures) are gradually swept away with the increasing gas velocity.

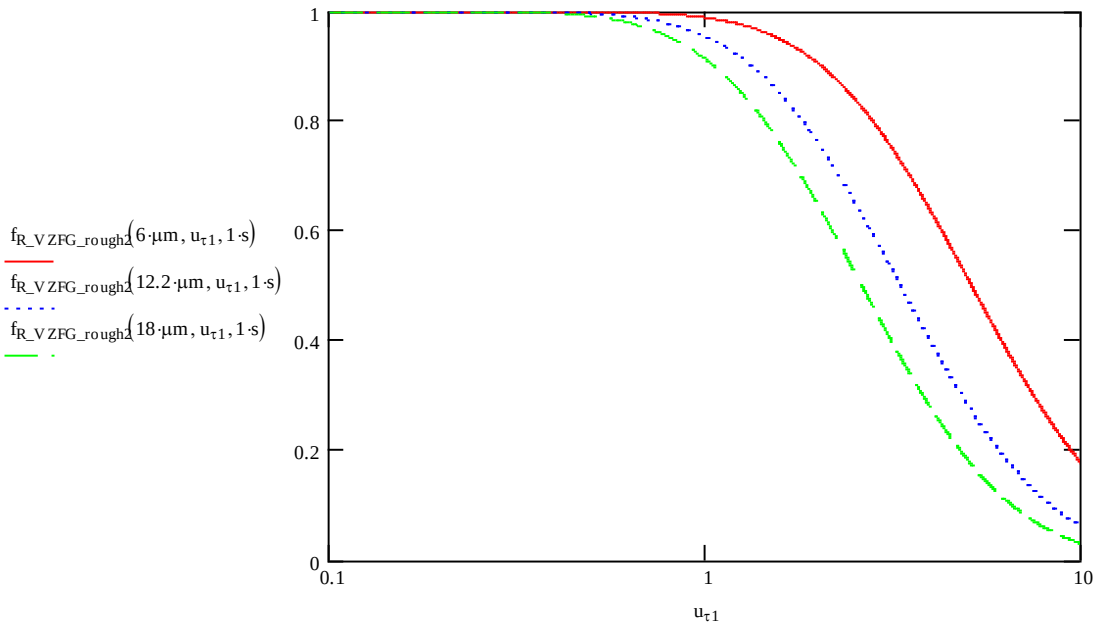

Figure 3-814 Reeks and Hall experiment, “10-µm”, MathCAD, Vainshtein model, σ = 10.4

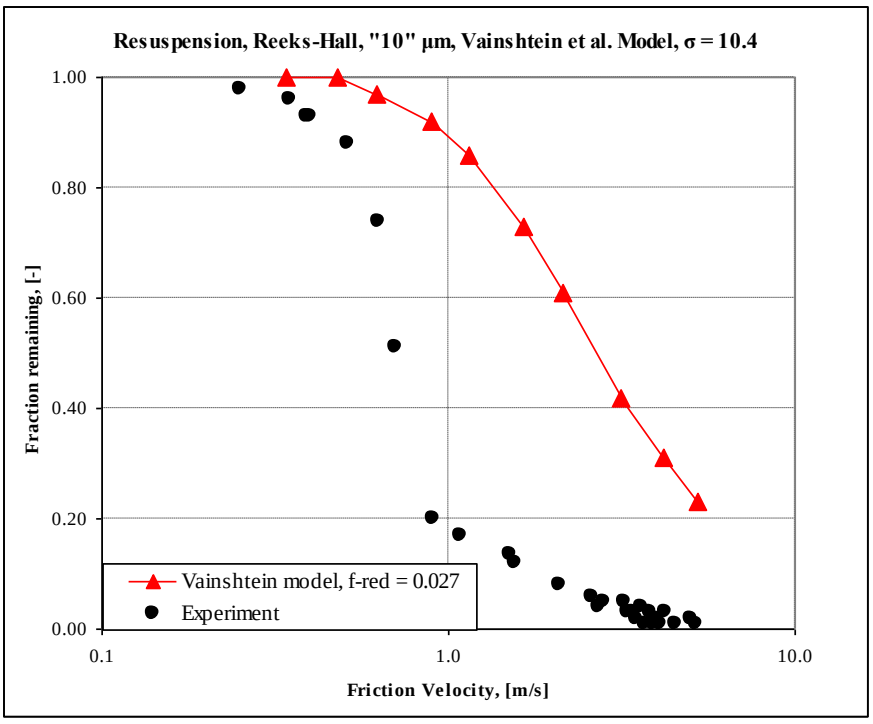

Figure 3-815 Reeks and Hall experiment, “10-µm”, SPECTRA, Vainshtein model, σ = 10.4

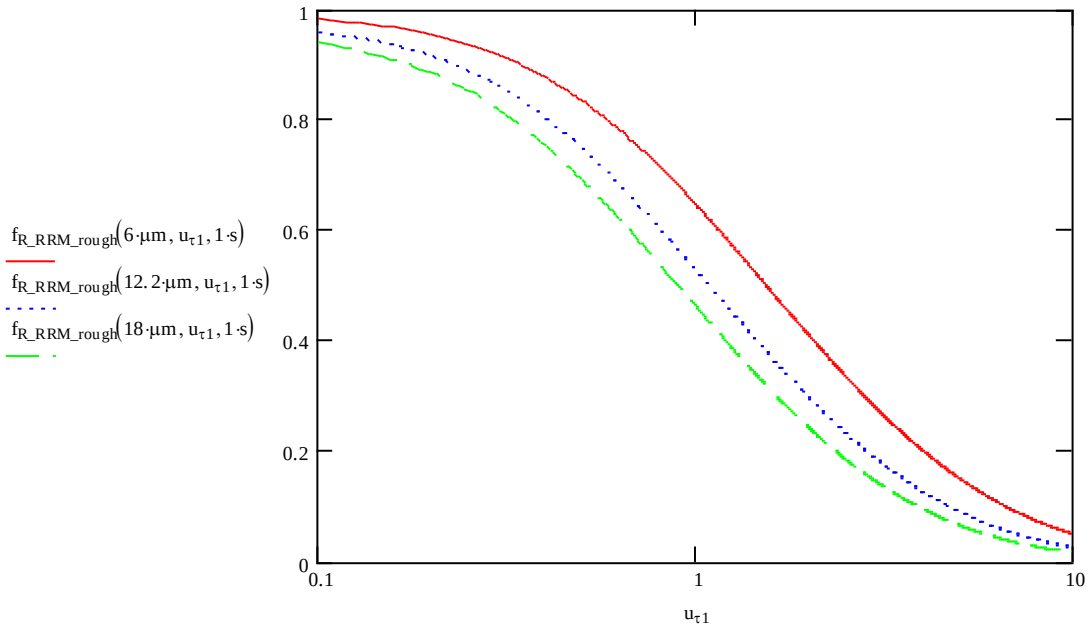

Figure 3-816 Reeks and Hall experiment, “10-µm”, MathCAD, Rock’n Roll model, σ = 10.4

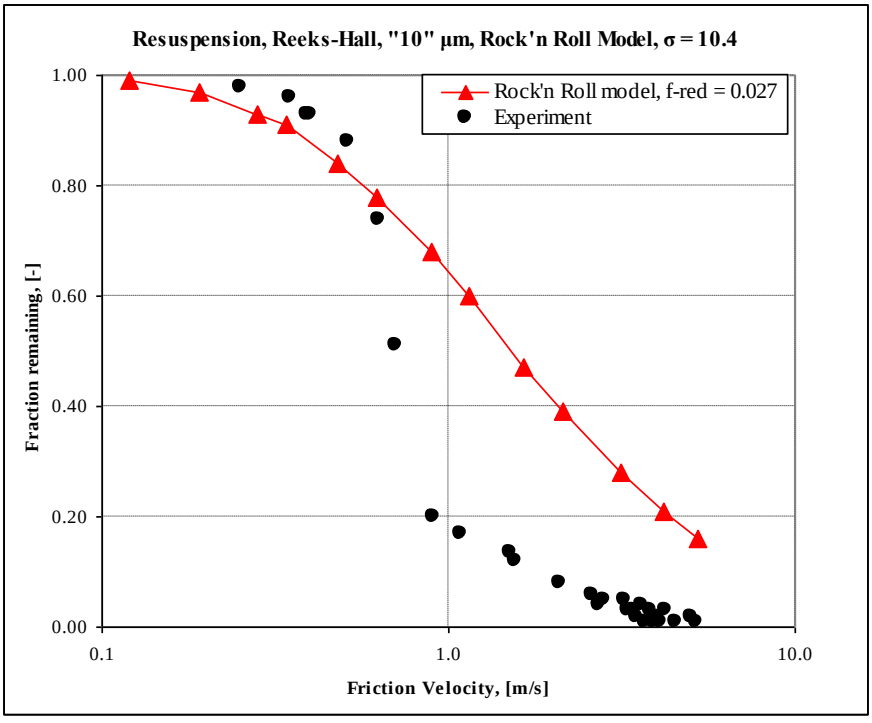

Figure 3-817 Reeks and Hall experiment, “10-µm”, SPECTRA, Rock’n Roll model, σ = 10.4

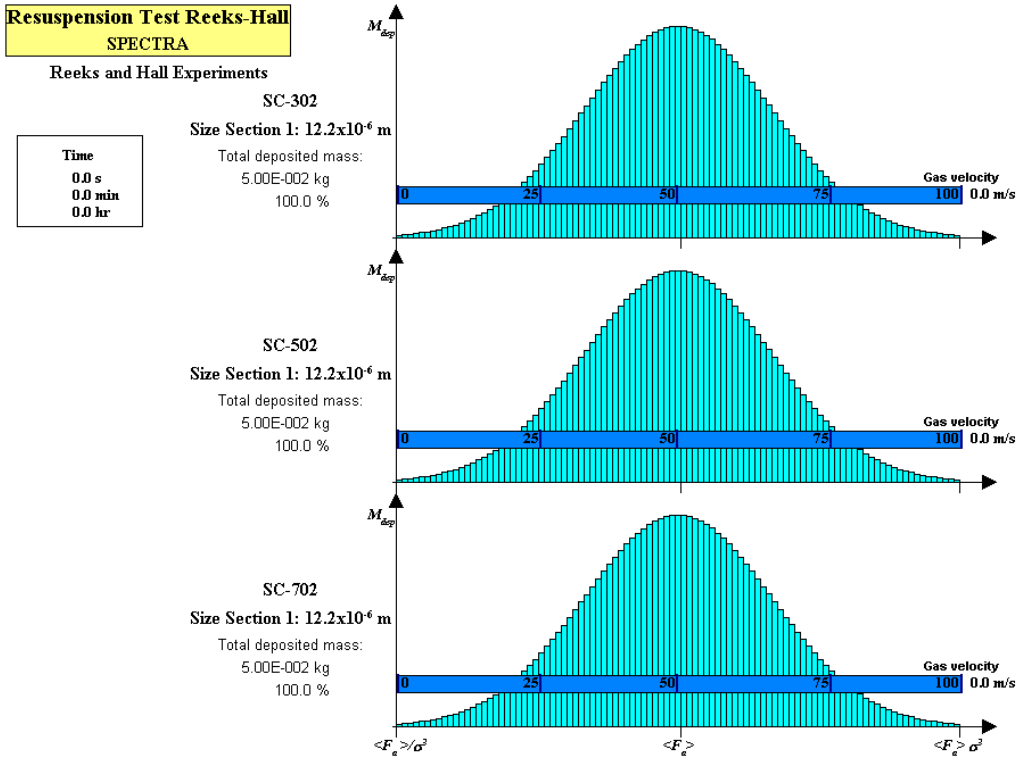

Figure 3-818 Reeks and Hall experiment, "10-µm", F_a-distributions, SPECTRA t=0.0 s.

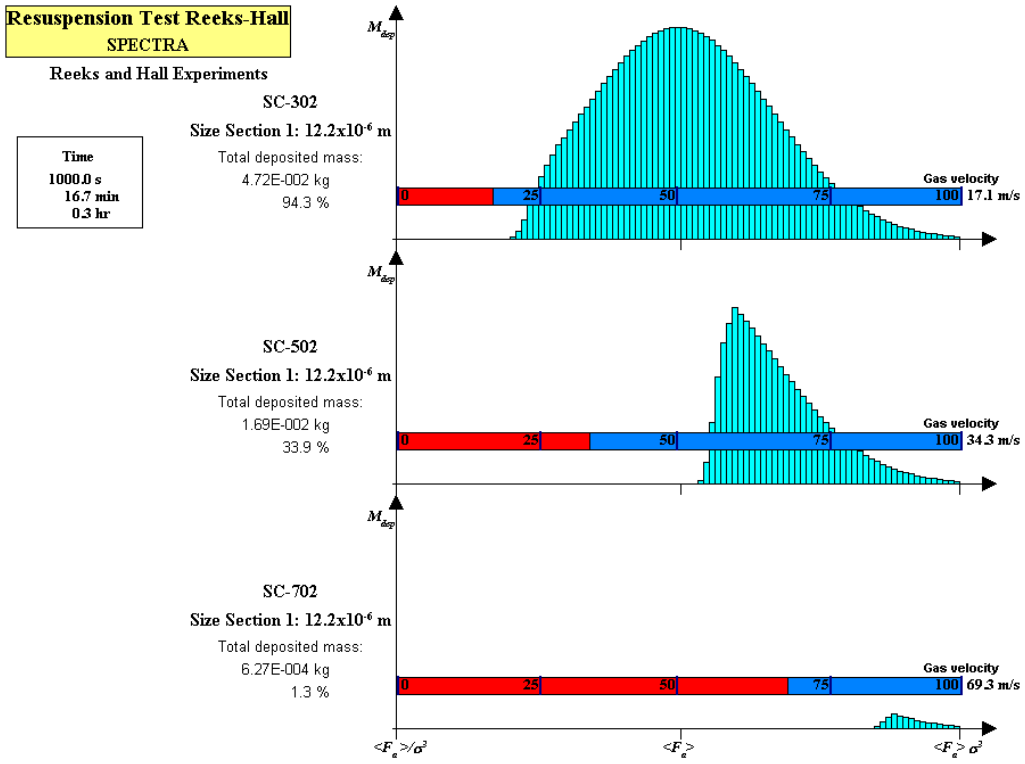

Figure 3-819 Reeks and Hall experiment, "10-µm", F_a-distributions, SPECTRA t=1000 s.

"20-μm" particles

The nominal "20-μm" particles had the mean diameter of 23 μm ([88], Table 1); the minimum and maximum diameters were 16 and 30 μm respectively. SPECTRA calculations were performed using a single size section with the mean diameter (23 μm).

Geometrical Model

The "multiple-facility" model, described above at the "10-μm" particles, was used.

Resuspension Models

The same as for the "10-μm" particles, two models were used:

- Vainshtein model:

$$R_m = f_0 \exp\left[-\left(\frac{F_{a\tau}}{F_d}\right)^{x_F}\right]$$

- Rock'n Roll model:

$$R_m = f_0 \cdot \exp\left[-\frac{1}{2}\left(\frac{F_a - F_{aero}}{0.2 \cdot F_{aero}}\right)^2\right]$$

Adhesion Forces, F_a

Similarly as for the "10-μm" particles, two options were used for the adhesion force, F_a, calculation.

- Mean adhesion force, $\langle F_a \rangle$, calculated using the default, built-in correlations (see Volume 1), assuming the surface roughness of 1.0×10^{-6} and the relative humidity of 1.0. The mean asperity radius (needed in such case only for conversion of the adhesion force, F_a, to the tangential pull-off force, $F_{a\tau}$) is equal to:

$$\langle r_{as} \rangle = 1.0\times10^{-7} \text{ m}$$

  This is the default value (see Volume 2) and it was used with the spread factor, σ_a, as described below.

- Adhesion forces calculated from the asperity size distribution. The original article gives the reduction factor of 1/56=0.018 for the "20-μm" particles ([88], Table 4). Therefore the mean asperity radius was defined as:

$$\langle r_{as} \rangle = 0.018 \times \frac{1}{2} \times 23\times10^{-6} = 2.1\times10^{-7} \text{ m}$$

  The value of 23×10^{-6} is the mean diameter $\langle D_p \rangle$ of the "20-μm" particles.

Adhesive Spread Factors, σ_a

The same as for the "10-µm" particles, two values of the adhesive spread factors were used:

- $\sigma_a = 2.55$
- $\sigma_a = 10.4$

Results

Results are shown in Figure 3-820 through Figure 3-823. The following observation can be made:

- Results close to experimental measurement are obtained with the Vainshtein mode with default adhesion force $<F_a>$ calculation. Results obtained with the F_a calculation through asperity size calculation with the reduction factor of $f_{red} = 0.018$ give too large fraction of remaining particles. This means the resuspension rate is underestimated.
- Results obtained with the adhesive spread of $\sigma_a = 2.55$ give somewhat closer match to the experimental data than the results of $\sigma_a = 10.4$. The large spread results in less steep line than that observed in the experiments. The value of $\sigma_a = 2.55$ gives somewhat too steep lines, which is visible when the remaining fractions decrease quickly to zero with increasing friction velocities. A value of adhesive spread in between the two used values is expected to give best results. Default value in SPECTRA is 4.0. Results for this value are shown below.
- The Rock'n Roll model with the mean adhesion force $<F_a>$ calculated from the default correlations and $\sigma_a = 2.55$ predicted remaining fractions that are somewhat lower than in experiments (Figure 3-822, blue square markers). The Vainshtein model with the same assumptions gives results that are quite close to the experiment (Figure 3-820, blue square markers). With these assumptions results of both models are close to the measured data.

Comparison of the Rock'n Roll model in SPECTRA with the article [88]

The results of the Rock'n Roll model, as calculated by SPECTRA are compared to the Rock'n Roll model, as presented in the original article of Reeks and Hall in Figure 3-824 and Figure 3-825. The case with $\sigma_a = 10.4$ and the Vainshtein et al. approach with the reduction factor of $f_{red} = 0.018$ is presented in the article (a copy is shown in Figure 3-824), therefore the same case is shown in Figure 3-825. It is clear that the SPECTRA results for this case (red triangles in Figure 3-825) agree well with the Rock'n Roll model data presented in [88]. It is also clear that the slope of the calculated results is too small compared to the experiment. This is a consequence of applying a large value of σ_a and has been discussed above.

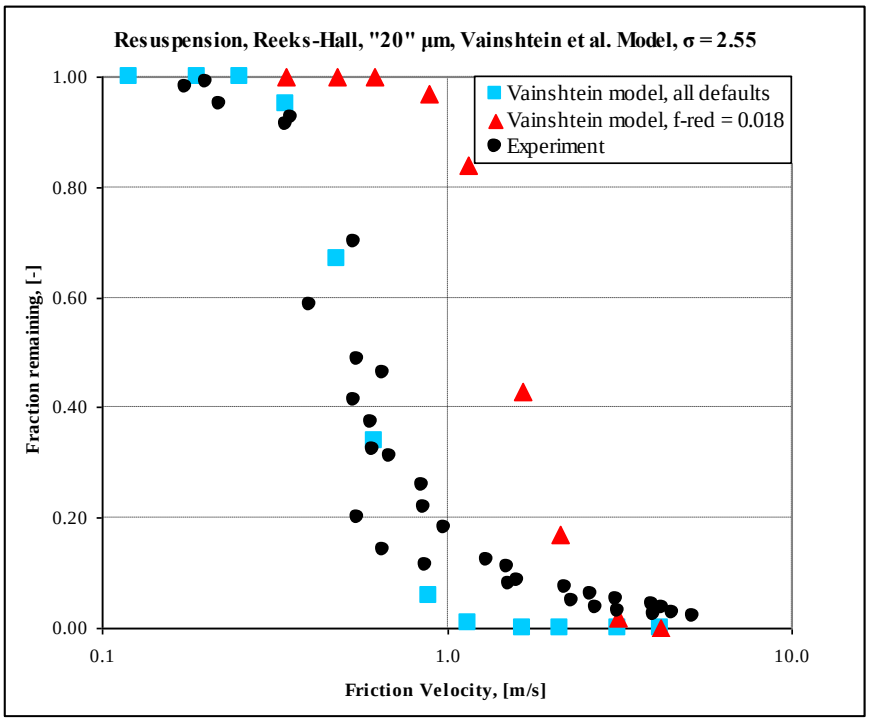

Figure 3-820 Reeks and Hall experiment, “20-µm”, SPECTRA, Vainshtein model, σ = 2.55.

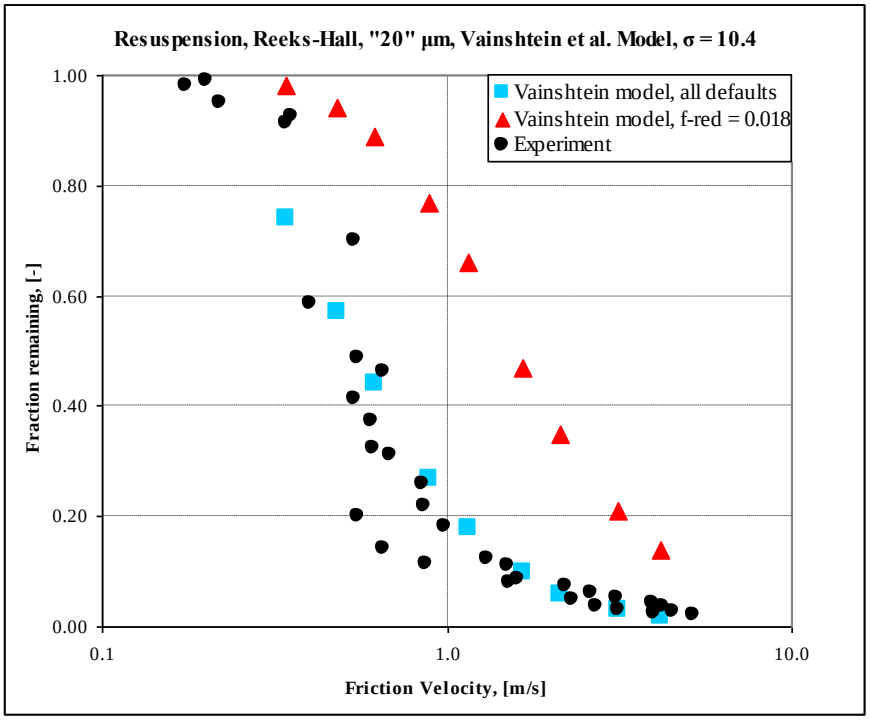

Figure 3-821 Reeks and Hall experiment, “20-µm”, SPECTRA, Vainshtein model, σ = 10.4.

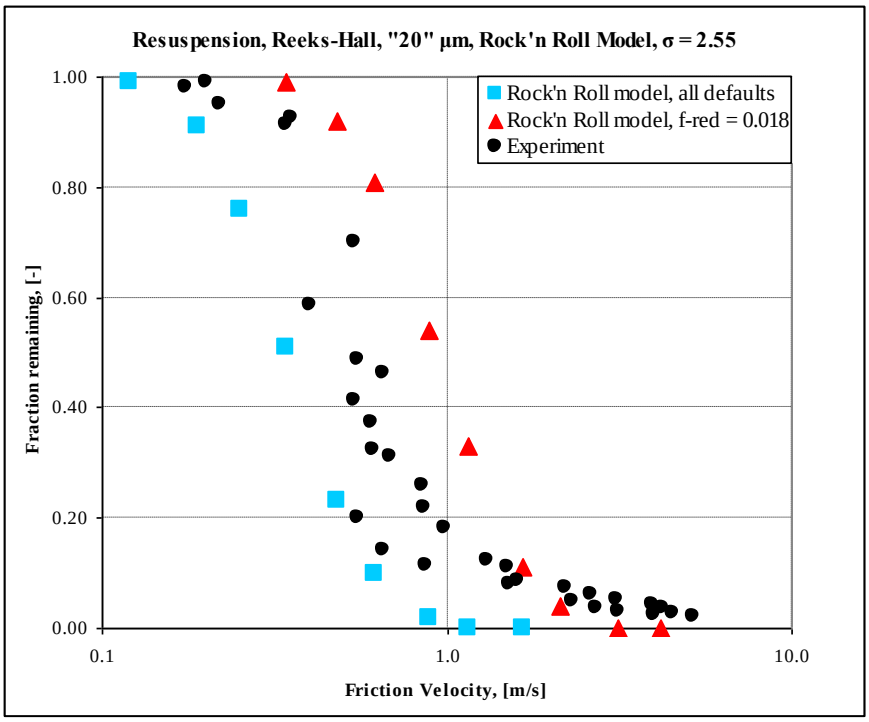

Figure 3-822 Reeks and Hall experiment, “20-µm”, SPECTRA, Rock’n Roll model, σ = 2.55.

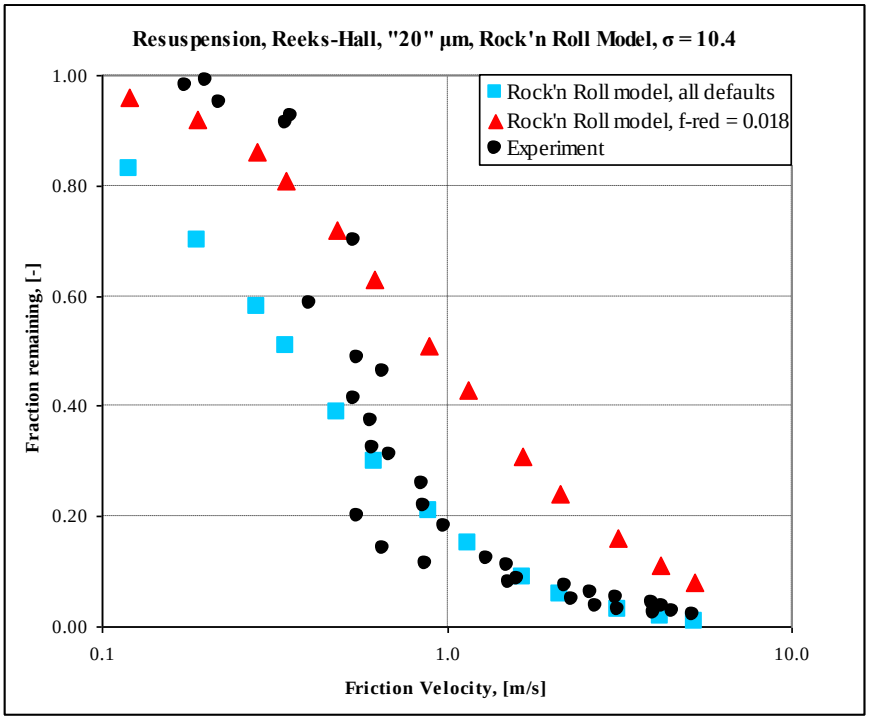

Figure 3-823 Reeks and Hall experiment, “20-µm”, SPECTRA, Rock’n Roll model, σ = 10.4.

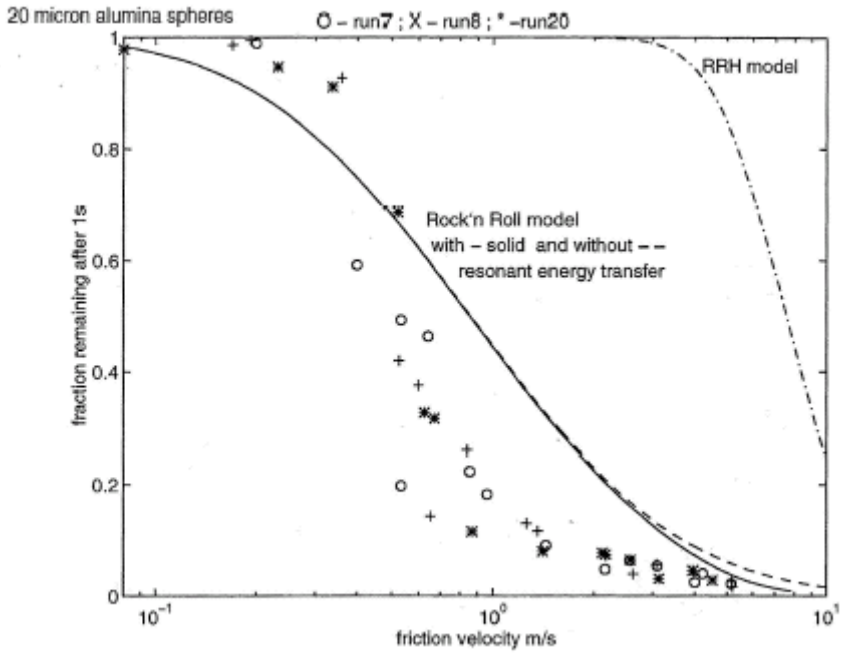

Figure 3-824 Reeks and Hall experiment, “20-µm” particles [88].

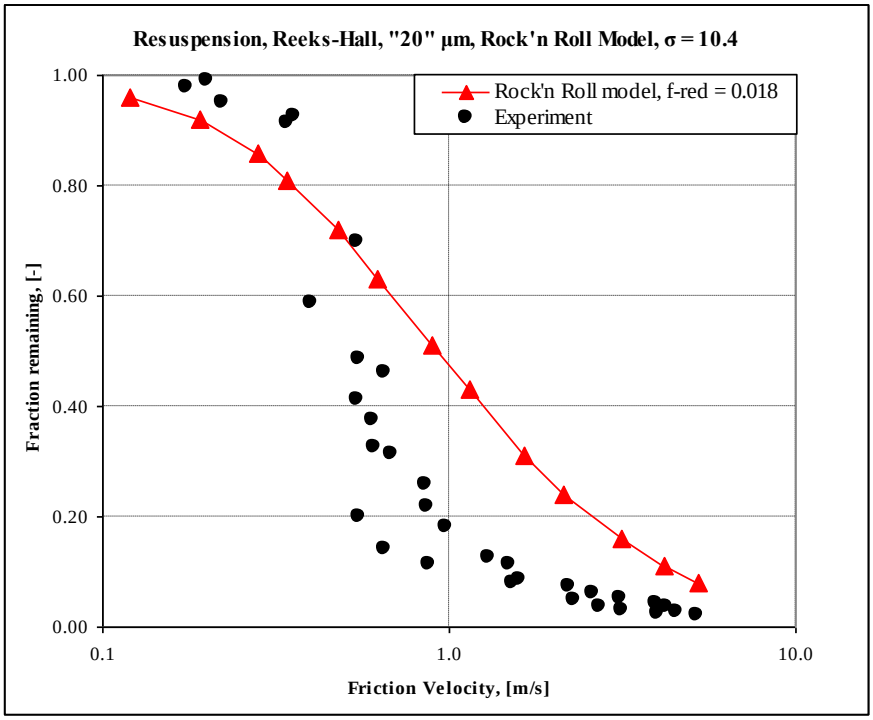

Figure 3-825 Reeks and Hall experiment, “20-µm”, SPECTRA, Rock’n Roll model, $\sigma = 10.4$

Comparison of the Vainshtein model in SPECTRA with MathCAD analytical results

The results of the Vainshtein model, as calculated by SPECTRA are compared to the analytical solutions obtained by means of MathCAD in Figure 3-826 and Figure 3-827. The case with $\sigma_a = 10.4$ and the Vainshtein et al. approach with the reduction factor of $f_{red} = 0.018$ is considered. MathCAD results are presented in Figure 3-826). SPECTRA results are shown in Figure 3-827. It is clear that the SPECTRA results for this case (red triangles in Figure 3-827) agree well with the Rock'n Roll model results of MathCAD. It is also clear that the calculated remaining fractions are too large, which means that the calculated resuspension rates are too small compared to the experiment.

Particle distributions

Figure 3-829 shows a section-by-section distribution of the deposited particles at the start of the calculations ($t = 0.0$ s) and after 1000 s for the "multiple-facility" model (Figure 3-828) for the case:

- Vainshtein resuspension model
- Adhesion force $<F_a>$ calculation using "all defaults"
- Adhesive spread of $\sigma_a = 2.55$

Initially the particle distribution follows the assumed lognormal distribution (the same as shown in Figure 3-818). Figure 3-829 shows how the weakly bound particles (particles left hand side in these figures) are gradually swept away with the increasing gas velocity. In the present case particles are relatively large so they are swept easier, i.e. with smaller gas velocities, which is visible by comparing Figure 3-829 with Figure 3-819.

"10-µm" and "20-µm" particles - "all defaults" resuspension model

Results shown above for both "10-µm" and "20-µm" particles the indicated that the considered adhesive spread factors of 2.55 and 10.4 bounded the expected value. The default value of the adhesive spread in SPECTRA is 4.0 (see Volume 2). It is therefore interesting to compare the results calculated with this value. For the comparison selected below, the "all default" model parameters were selected. Two resuspension models were used, the Vainshtein and the Rock'n Roll model. The analyzed cases are summarized in Table 3-64.

Results are shown in Figure 3-830 and Figure 3-831. The results obtained with both models are in good agreement with the experiment. Rock'n Roll model gives somewhat too fast resuspension (too low remaining fractions) in the low friction velocity region. Therefore it is concluded that the Vainshtein model with "all defaults" model coefficients may be considered as a "best estimate" resuspension model, while the Rock'n Roll model with "all defaults" model coefficients may be considered as a "conservative" resuspension model.

Table 3-64 Reeks and Hall experiments, "All defaults" - summary of analyzed cases.

Model	Vainshtein	Rock'n Roll
F_a	Default models for $<F_a>$, $<r_{as}>=1.0\times10^{-7}$	Default models for $<F_a>$, $<r_{as}>=1.0\times10^{-7}$
σ_a	Default value, $\sigma_a = 4.0$	Default value, $\sigma_a = 4.0$

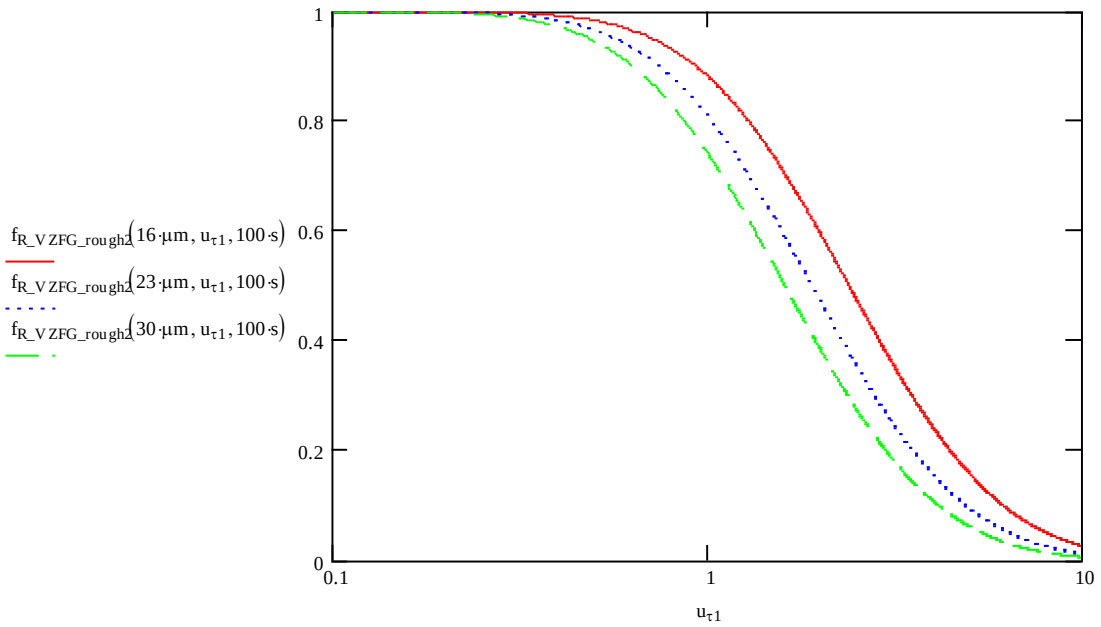

Figure 3-826 Reeks and Hall experiment, “20-µm”, MathCAD, Vainshtein model, σ = 10.4

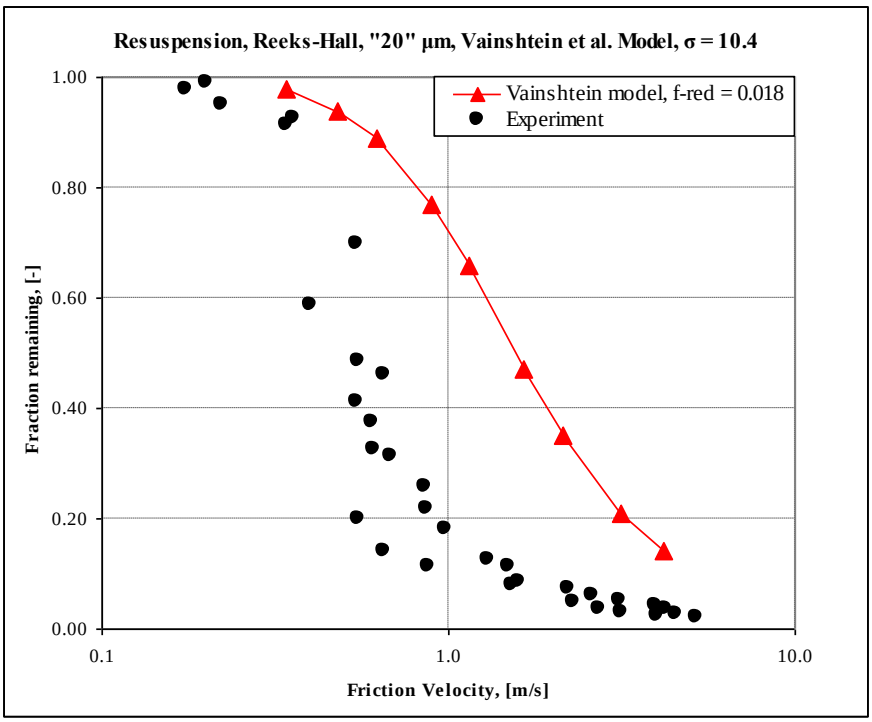

Figure 3-827 Reeks and Hall experiment, “20-µm”, SPECTRA, Vainshtein model, σ = 10.4

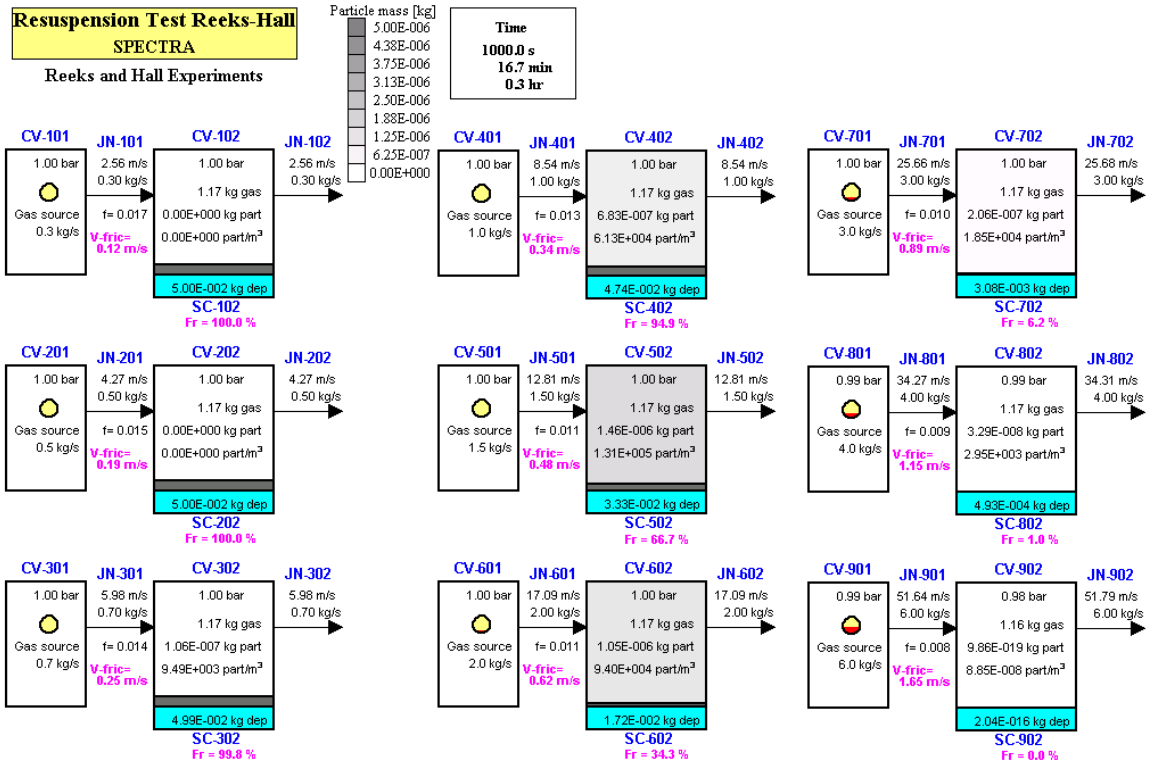

Figure 3-828 Reeks and Hall experiment, “20-μm” particles, SPECTRA *t*=1000 s.

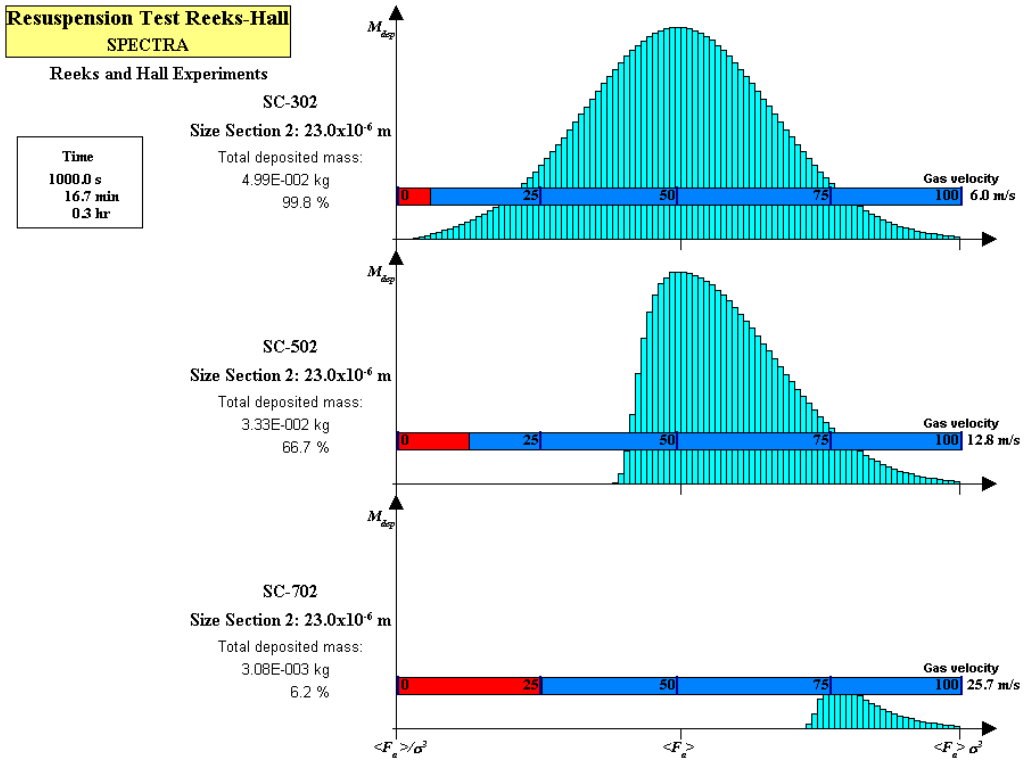

Figure 3-829 Reeks and Hall, “20-μm” particles, F_a-distributions, SPECTRA *t*=1000 s.

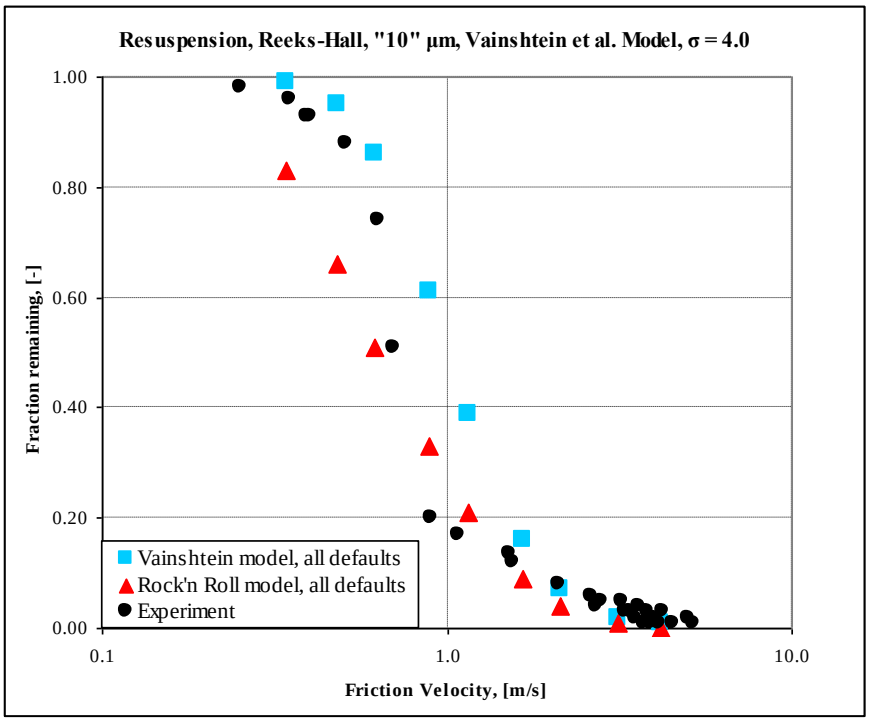

Figure 3-830 Reeks and Hall, “10-µm”, SPECTRA “all defaults”.

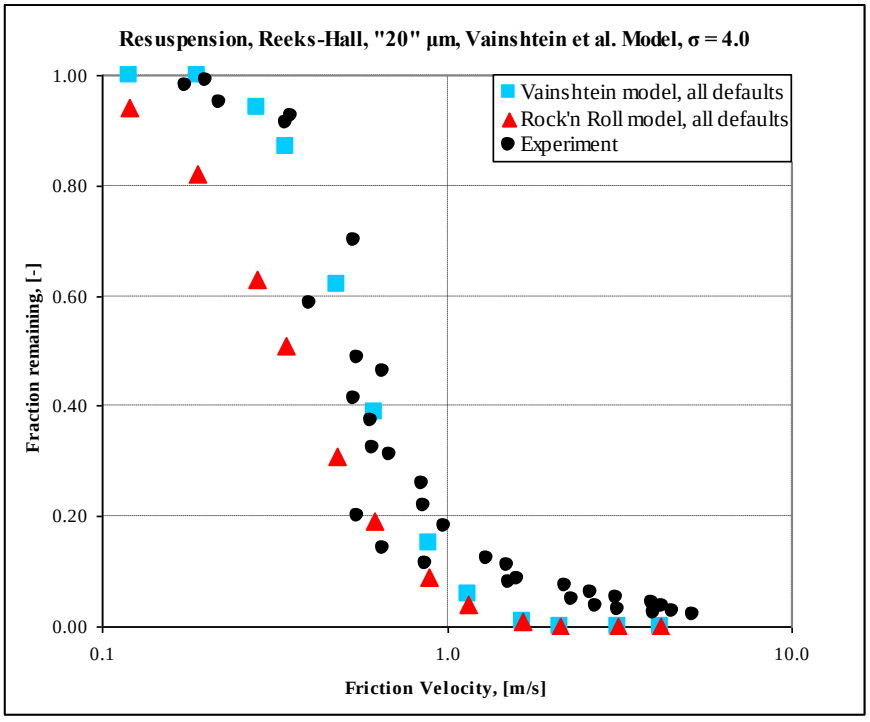

Figure 3-831 Reeks and Hall, “20-µm”, SPECTRA “all defaults”.

"Vainshtein" with $\langle r_{as} \rangle = 10^{-8}$ m

Results shown above for both "10-μm" and "20-μm" particles the indicated that the Vainshtein model with certain the reduction factors did not give a very good results. Firstly, the obtained numbers were quite far from the measured ones. Secondly, the obtained values were not conservative, i.e. the resuspended fractions were too small compared to the experimental data. This fact is important if the models are to be applied for safety analyses of a Nuclear Power Plant.

A short sensitivity study has been performed with the model in order to investigate what values of the mean asperity radius would provide a more reasonable fit to the experiment. A single value of the mean asperity radius was chosen for both "10-μm" and "20-μm" particles. It is explained in Volume 1 why the use of a single asperity radius is preferred over the use of different asperity radii for different particle sizes, as recommended in the original article.

It was found out that the mean asperity radius of $\langle r_{as} \rangle = 10^{-8}$ m gives quite a good match to the experimental data. Results are shown in Figure 3-832 and Figure 3-833.

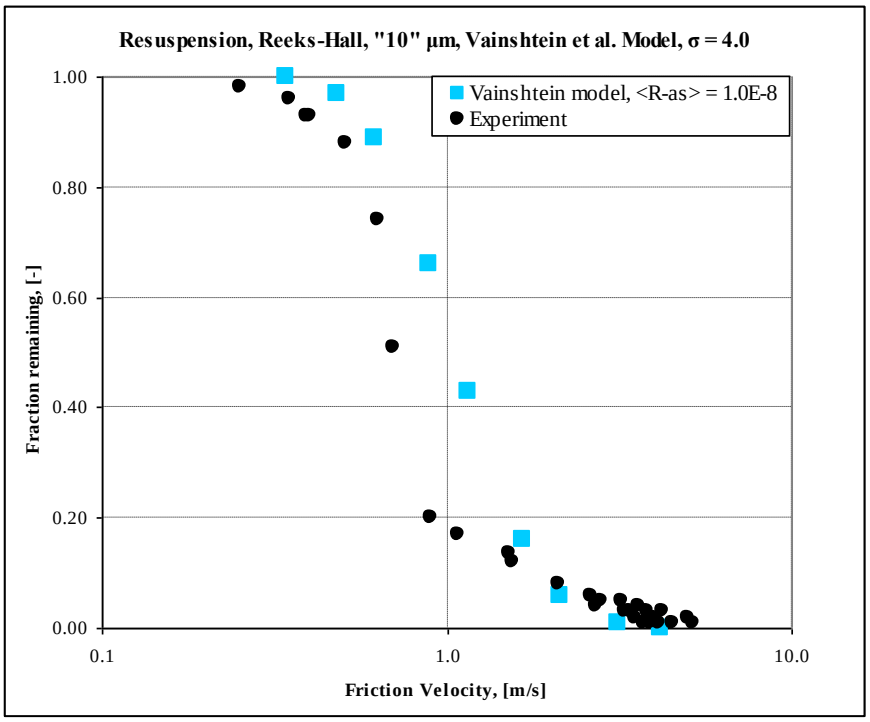

Figure 3-832 Reeks and Hall, “10-µm”, SPECTRA, “Vainshtein” with $<r_{as}>=10^{-8}$ m.

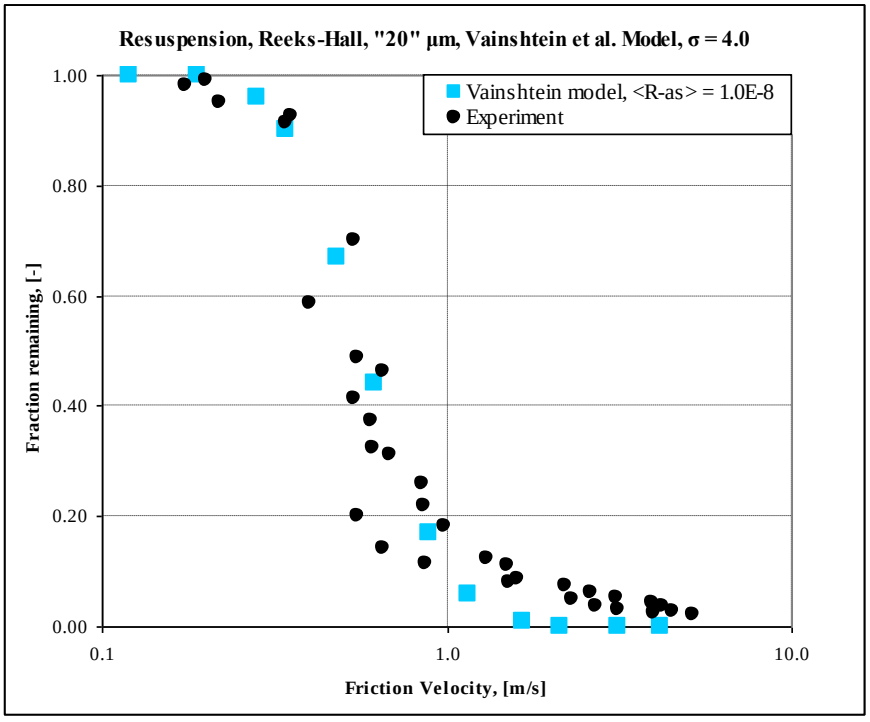

Figure 3-833 Reeks and Hall, “20-µm”, SPECTRA, “Vainshtein” with $<r_{as}>=10^{-8}$ m.

3.12.30 Mechanistic Resuspension Model - STORM SR11 Test

Model

The STORM experiment SR11 (ISP-40) [84] and the SPECTRA model is described in section 3.12.19. The same model is used for the calculations presented in this section, with the parametric resuspension model replaced by the mechanistic model. All calculations were performed with C_s = 0.97, which gives best thermophoretic deposition prediction (see section 3.12.19, Table 3-62 and Figure 3-767) Three sets of calculations were performed with the present resuspension model:

- Mean adhesion force, $<F_a>$, calculated using the default, built-in correlations (see Volume 1), assuming the surface roughness of 1.0×10^{-5} and the relative humidity of 1.0. The mean asperity radius (needed in such case only for conversion of the adhesion force, F_a, to the tangential pull-off force, $F_{a\tau}$) is equal to:

$$\langle r_{as} \rangle = 1.0\times10^{-7} \text{ m}$$

  This is the default value (see Volume 2) and it was used with the spread factor, σ_a, as described below.

- Adhesion forces calculated from the asperity size distribution. Two cases were considered.
  - The "Vainshtein" case, with the reduction factor equal to f_{red} = 0.1, based on the article of Vainshtein et al. [86]. The mean asperity size equal to:

$$\langle r_{as} \rangle = 0.1\times\left(D_p/2\right)$$

    This means the mean asperity size of: $<r_{as}>$ = 0.0125, 0.025, 0.05, 0.1, 0.2 μm
    for the particle diameters of: D_p, = 0.25, 0.5, 1.0, 2.0, 4.0 μm
  - Mean asperity size independent of the particle size and equal to 10^{-8} m.

$$\langle r_{as} \rangle = 1.0\times10^{-8} \text{ m}$$

    This value provided a good match to experimental data for the Reeks and Hall experiments (see section 3.12.29, Figure 3-832 and Figure 3-833).
    It is important to keep in mind that apart from the fact that $<r_{as}>$ is an order of magnitude smaller, there is another important difference between this case and the very first case. In the first case the mean adhesion force, $<F_a>$, is calculated using the built-in correlations. The adhesion forces for each F_a-section are determined based on this value and the adhesive spread factor, σ_a. The mean asperity radius is needed only for the conversion of the adhesion force, F_a, to the tangential pull-off force, $F_{a\tau}$. In the present case on the other hand the asperity radius, r_{as}, is determined for each F_a-section based on the $<r_{as}>$ and the adhesive spread factor, σ_a. The adhesion forces are calculated using the effective diameter, which depends on the asperity radius and the particle diameter (see Volume 1):

$$D_{eff,1} = \frac{1}{1/D_p + 1/3(2r_{as})}$$

- Rock'n Roll model (built using the "extended mechanistic model" - see Volume 1), with the resuspension rate, R_m (s^{-1}), given by:

$$R_m = f_0 \cdot \exp\left[-\frac{1}{2}\left(\frac{F_a - F_{aero}}{0.2 \cdot F_{aero}} \right)^2 \right]$$

where:

$$F_{aero} = \left(\frac{r}{a} F_d' \right) + \left(\frac{1}{2} F_L' \right)$$

F_d' and F_L' are the drag force and the lift force respectively (see Volume 1). The ratio (r/a) is assumed to be 100. The mean adhesion force, $<F_a>$ was calculated from the default correlations.

Results

Results are shown in Figure 3-834, Figure 3-835, Figure 3-836, and Figure 3-837. The following observation can be made.

- When the mean adhesion force $<F_a>$ is calculated using the built-in correlations, the resuspension is somewhat overestimated in the early resuspension steps, i.e. the deposited masses are below the measured ones (Figure 3-834, circles). When the adhesive spread of $\sigma_a = 2.5$ is used the resuspension is overestimated during all steps (Figure 3-834, triangles). These results indicate that the adhesion force distribution is shifted to the right (higher adhesion forces), compared to the distributions assumed here. A more detailed discussion of the adhesion force distributions and the tangential pull-off force distributions is presented later in this section.

- The results obtained with the asperity size distribution and the Vainshtein value: $f_{red} = 0.1$, which means the mean asperity size equal to $<r_{as}> = 0.1 \times (D_p/2)$, give clearly too low resuspension (Figure 3-835). This is consistent with the observation already made at the Reeks and Hall experiments, where an underestimation of the resuspension rates was observed in spite of using even lower reduction factors (0.027 ÷ 0.018 - see section 3.12.29, Figure 3-806, Figure 3-807, Figure 3-820, and Figure 3-821).

- Relatively good results were obtained when the adhesion forces are calculated from the asperity size, with the mean asperity radius of $<r_{as}> = 1.0 \times 10^{-8}$ m, applied for all particle size sections (Figure 3-835). It is interesting to observe that the same conclusion was reached from the Reeks and Hall experiments. This fact would indicate that when the method of Vainshtein is used, the mean asperity radius of order of 10^{-8} m is a better number than 10^{-7} m, which is being used with the default correlations. More experiments and measurement data are needed in order to clarify whether this is just a coincidence or can this be considered a generally applicable.

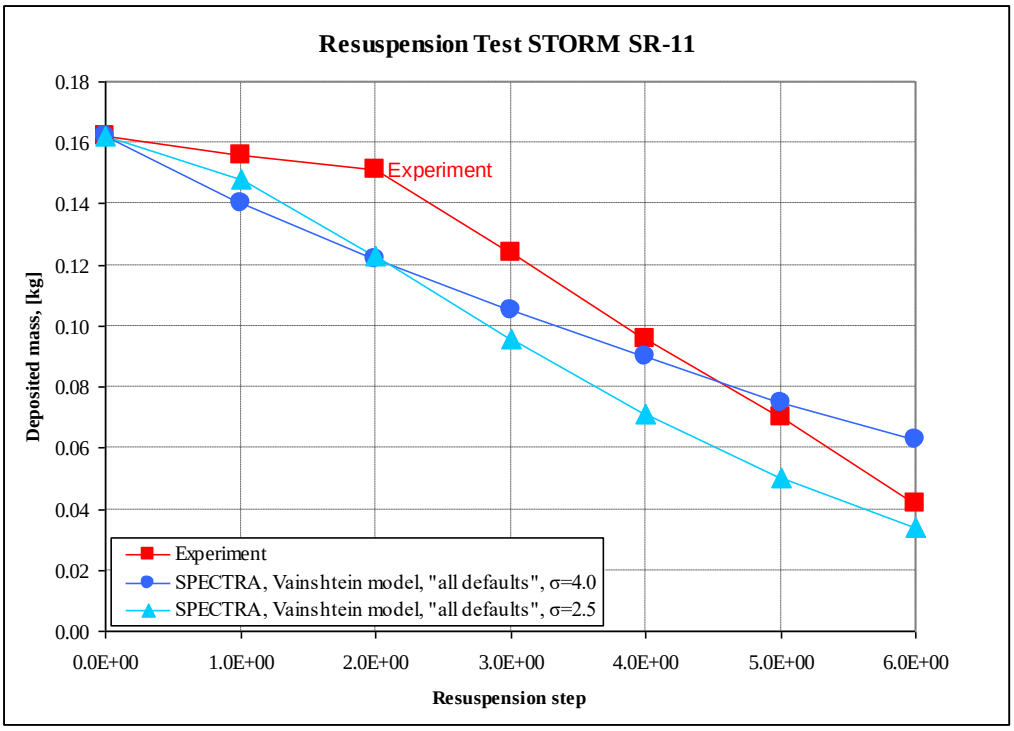

Figure 3-834 STORM experiment SR11, resuspension with default F_a calculation.

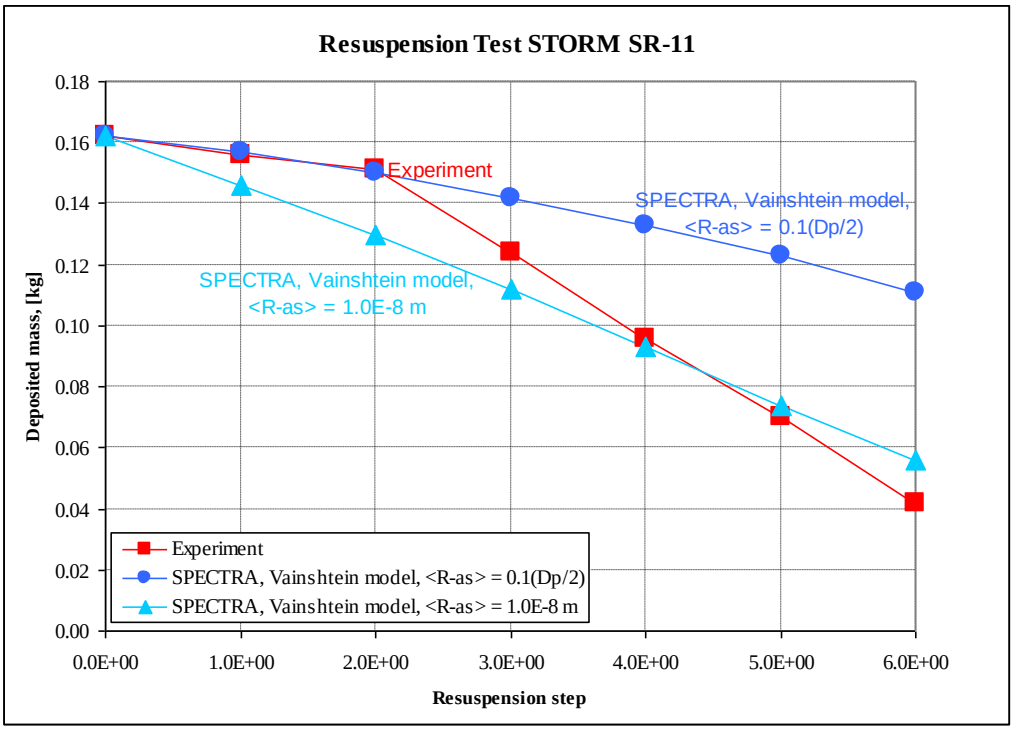

Figure 3-835 STORM SR11, F_a calculation through asperity size (“Vainshtein”).

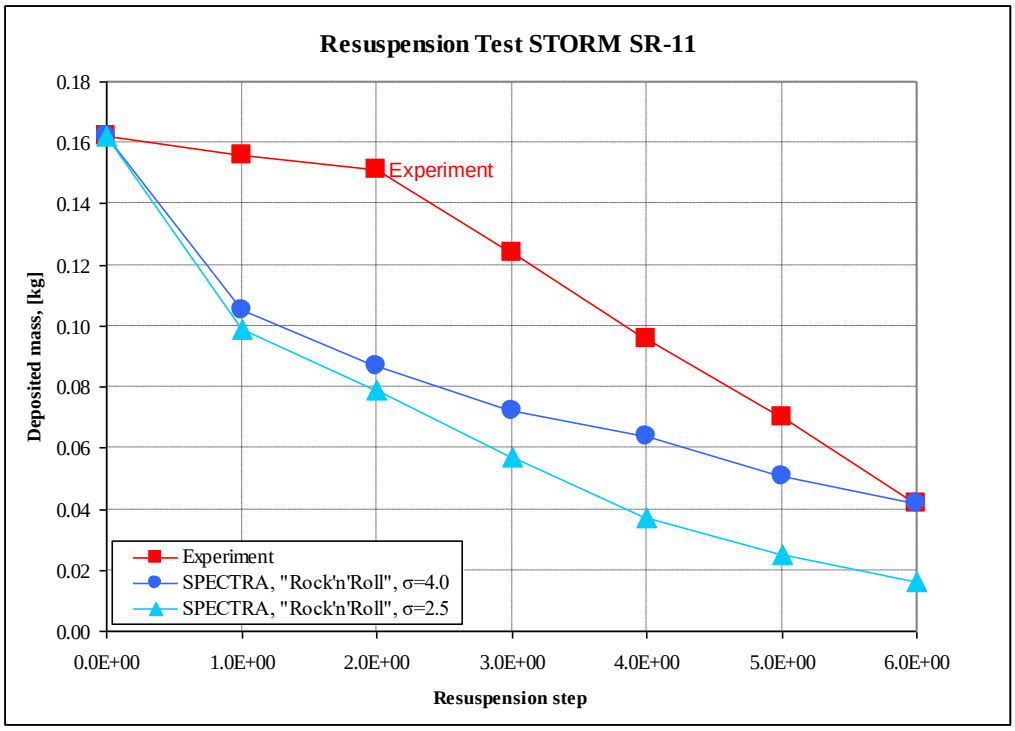

Figure 3-836 STORM experiment SR11, Rock'n Roll model.

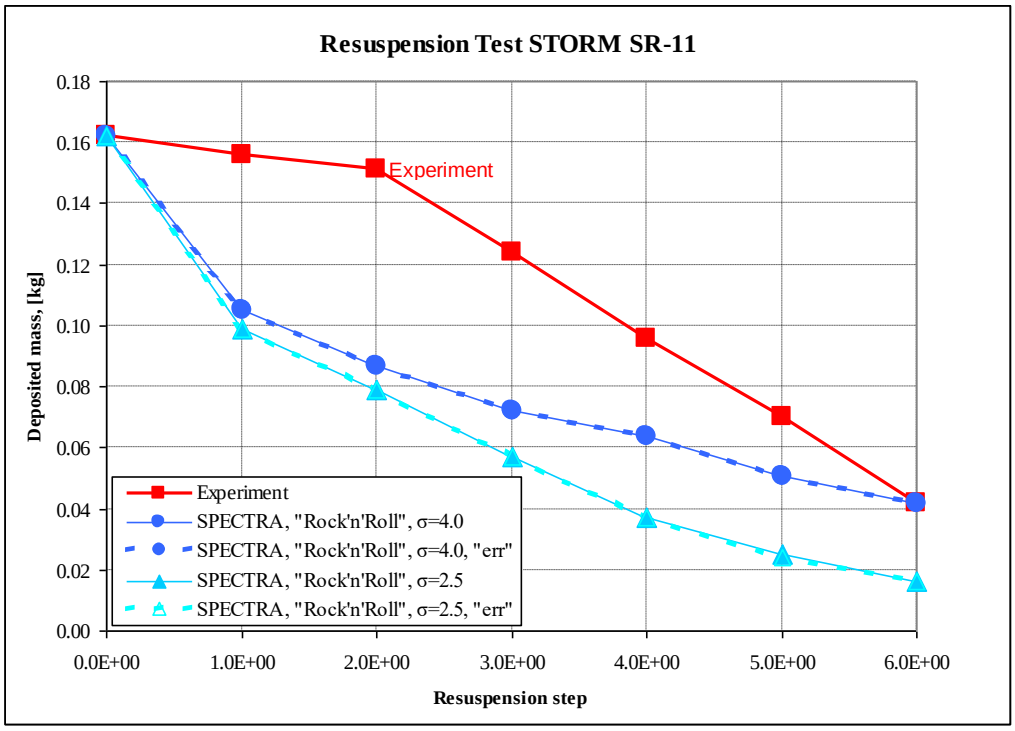

Figure 3-837 STORM experiment SR11, Rock'n Roll model, influence of error function.

- The Rock'n Roll model gives too high resuspension rates (Figure 3-836). This is consistent with the observation already made at the Reeks and Hall experiments, where it was concluded that the Rock'n Roll model with $<F_a>$ calculated from the default correlations gives conservative results (see section 3.12.29, Figure 3-830 and Figure 3-831).

- The term with error function has been neglected in the Rock'n Roll model. Influence of this term on the results is investigated in the same way as in case of Reeks and Hall experiments. Bounding calculations are performed with the limiting values of the error function: $errf(0)=0$ and $errf(\infty)=1$. Results are shown in Figure 3-837. As in case of the Reeks and Hall experiments very small difference is found between the two bounding values of the error function. Explanation of such small influence of this term is given in the discussion of the Reeks and Hall experiments (section 3.12.29). Based on the calculations of the Reeks and Hall experiments and this calculation it is concluded that the term with error function may be safely neglected in the Rock'n Roll model.

F_a-distributions and $F_{a\tau}$-distributions

Comparison of the adhesion force, $F_{a,}$ distributions and the tangential pull-off force, $F_{a\tau}$, distributions are shown in Figure 3-838 and Figure 3-839. The following cases are compared:

- Vainshtein model, default models for the $<F_a>$ calculation, $<r_{as}> = 10^{-7}$ m (default)
- Vainshtein model, F_a calculated from the asperity distribution, $<r_{as}> = 10^{-8}$ m
- Vainshtein model, F_a calculated from the asperity distribution, $<r_{as}> = 0.1\times(D_p/2)$

Only the cases with the Vainshtein model are shown. In case of the Rock'n Roll model the default adhesion force models were used, therefore the adhesion force distribution is exactly the same as the first line shown in Figure 3-838. The tangential pull-off force is not used by the Rock'n Roll model, so there are no values to be shown in Figure 3-839.

It is seen in Figure 3-838 that the largest adhesion forces are observed in the case of the Vainshtein reduction factor of 0.1: $<r_{as}> = 0.1\times(D_p/2)$. The smallest forces are observed in the case with $<r_{as}> = 1.0\times10^{-8}$ m. The default models for $<F_a>$ give the values roughly in the middle between the previous two.

The Vainshtein resuspension model does not use the adhesion force, F_a, directly, but the tangential pull-off force, $F_{a\tau}$, which is calculated from the F_a. The tangential pull-off force, $F_{a\tau}$, distributions are shown in Figure 3-839 for the same cases for which F_a-distributions were shown. The largest pull-off forces are observed for the case with $<r_{as}> = 0.1\times(D_p/2)$. The default $<F_a>$ correlations with $<r_{as}> = 10^{-7}$ m give very similar results as the use of the asperity size distribution with $<r_{as}> = 10^{-8}$ m. Both these cases give good agreement with experiment (Figure 3-834 and Figure 3-835).

It may seem surprising that the case with $<r_{as}> = 10^{-8}$ m exhibits similar values of $F_{a\tau}$, as the default case, while it gives the smallest adhesion force, F_a. It is explained as follows. $F_{a\tau}$, is proportional to $(F_a)^{3/2}$ and inversely proportional to $(D_{eff,0})^{2/3}$ (see Volume 1):

$$F_{a\tau} \sim \frac{F_a^{3/2}}{D_{eff,0}^{2/3}}$$

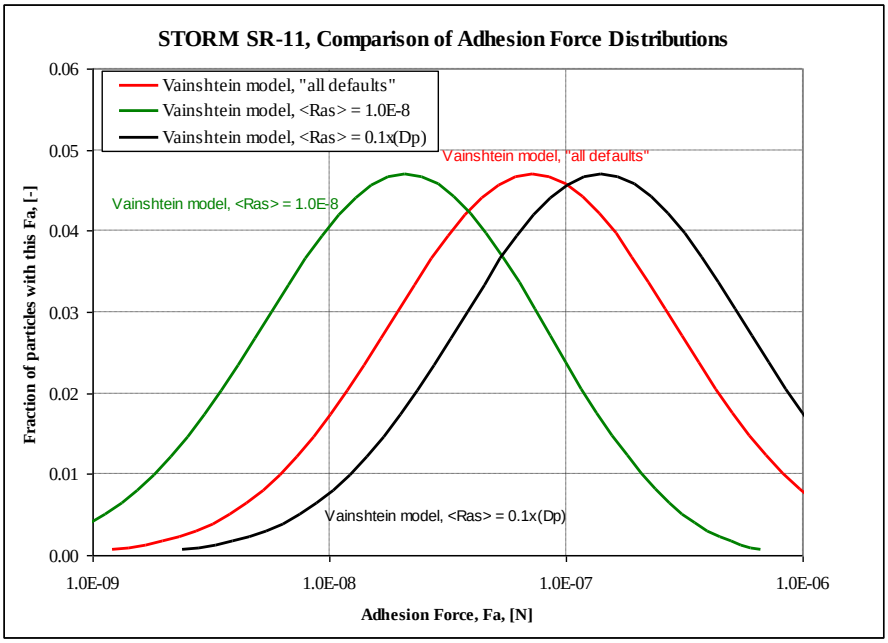

Figure 3-838 STORM SR11, F_a distributions.

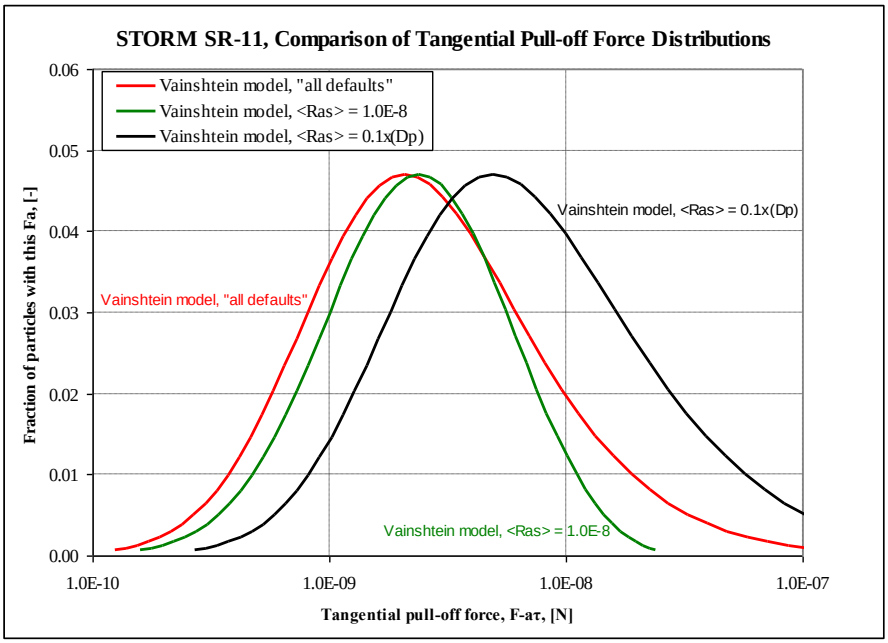

Figure 3-839 STORM SR11, F_{ar} distributions.

The effective diameter is equal to:

$$D_{eff,0} = \frac{1}{1/D_p + 1/(2r_{as})}$$

For small asperities, $r_{as} \ll D_p$, it is practically equal to twice the asperity radius:

$$D_{eff,0} \approx 2r_{as}$$

Therefore:

$$F_{a\tau} \sim \frac{F_a^{3/2}}{r_{as}^{2/3}}$$

When the asperity radius is made smaller, then with the same value of F_a, a larger value of $F_{a\tau}$, is obtained. Therefore the $F_{a\tau}$ is in the third case similar to the one obtained in the second case, while the F_a is much smaller in the third case compared to the second case.

Finally, it is interesting to compare the time-dependent behavior of the deposited masses in case of different resuspension models. Figure 3-840 compares the results of the Vainshtein model with the Rock'n Roll model. Both models were run using the default correlations for $<F_a>$. It is seen that in the case of the Rock'n Roll model the lines are more flat between the velocity increase steps. This means that with this model, whatever F_a-sections are to be resuspended at a given step, are being resuspended very quickly (in a matter of seconds). The deposited masses in the other F_a-sections are practically constant.

In the Vainshtein model there are always some slowly resuspending F_a-sections, which contribute to a longer time resuspension (of order of hundreds of seconds). Theoretically there are even sections which resuspension times are of order of thousands of seconds or more, but these low resuspension rates are set to zero in the calculation procedure. This is done by the cut-off parameter (CUTRRT, see Volume 2). Applying the limit, means that the resuspension rate is calculated from:

$$R_m(i) = \begin{cases} f_0 \exp[-Y(i)] & if \quad Y(i) < CUTRRT \\ 0.0 & if \quad Y(i) > CUTRRT \end{cases}$$

The cut-off values are between 5 and 20, with a default value of 10 (see Volume 2). Here three calculations are shown for the STORM experiment. The cut-off limits for these three cases are:

- Default cut-off: $Y(i) < 15.0$, $\exp(-Y(i)) > 3.1\times10^{-7}$ (-)
- Moderate cut-off: $Y(i) < 13.0$, $\exp(-Y(i)) > 2.3\times10^{-6}$ (-)
- Large cut-off: $Y(i) < 10.0$, $\exp(-Y(i)) > 4.5\times10^{-5}$ (-)

Results are shown in Figure 3-841. It is seen that with the large cut-off the lines between the velocity increase steps are very flat. However, the total resuspension becomes significantly different (smaller) and moreover it becomes sensitive to the choice of the total number of the F_a-sections used in the calculations. In the moderate and large cut-off cases a maximum value of 99 F_a-sections was used. Therefore the user should not apply large cut-offs. If a moderate cut-off is applied, the calculation should be run with the maximum number of the F_a-sections.

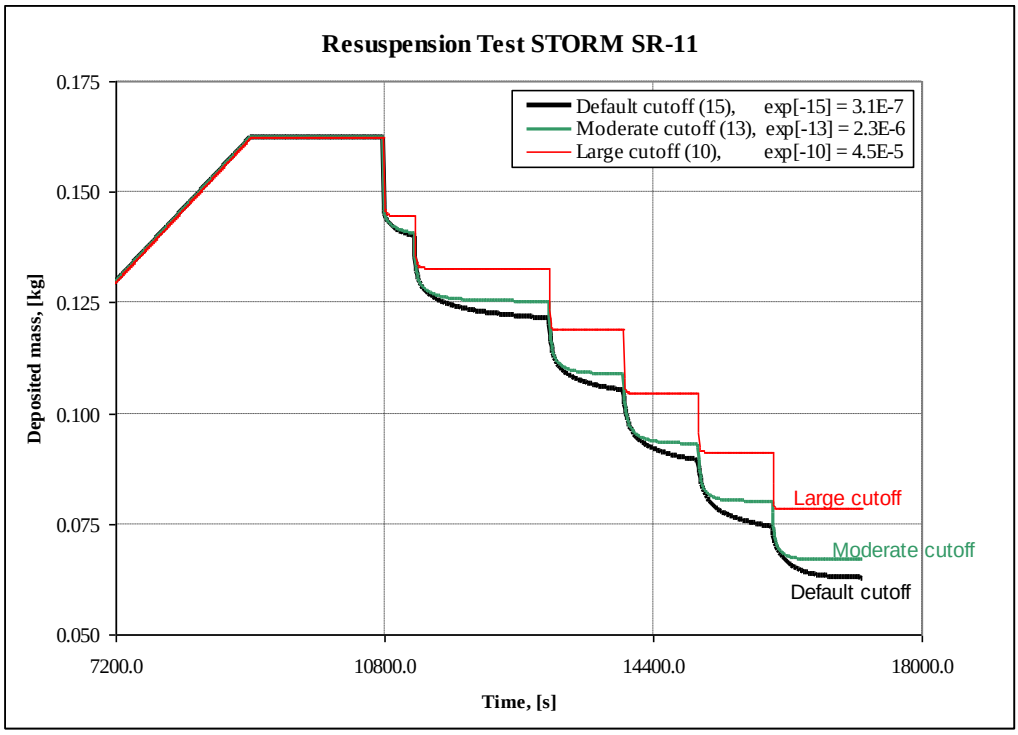

Figure 3-840 STORM SR11, influence of the model on a long-term resuspension.

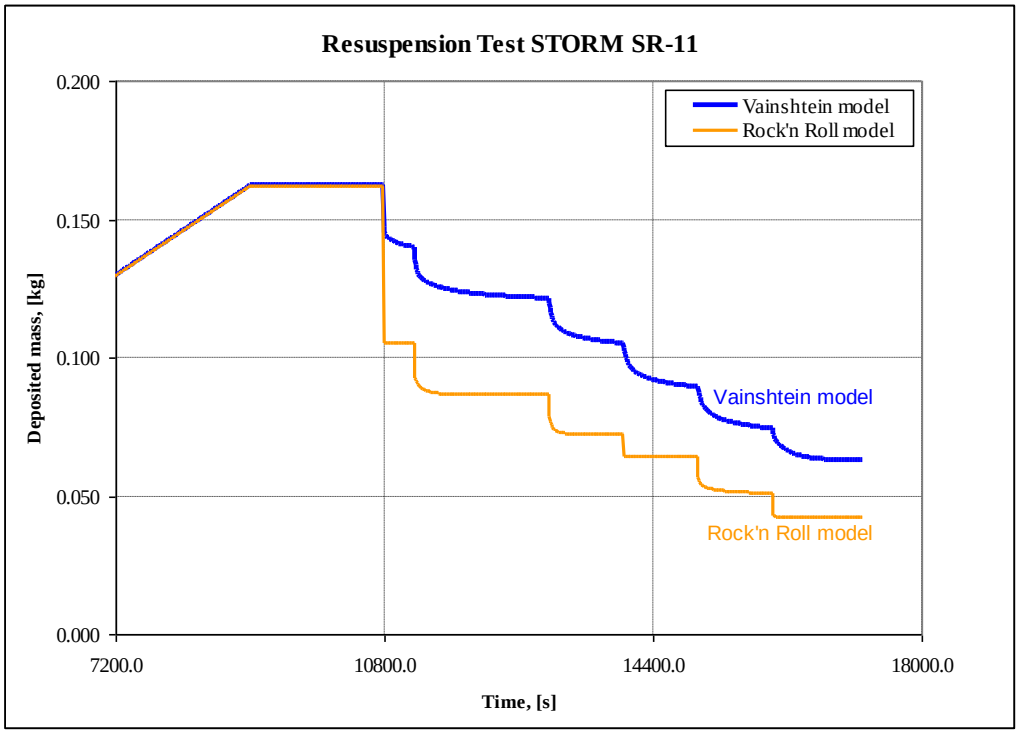

Figure 3-841 STORM SR11, influence of the cut-off on a long-term resuspension.

3.12.31 Influence of Humidity and Roughness on STORM Results

This section presents results of sensitivity studies performed to investigate the importance of two parameters: humidity and wall roughness. The case selected for this sensitivity study is the STORM experiment, Vainshtein model, all defaults, with σ = 4.0. This case gives the best agreement with experiment - see Figure 3-834. The adhesion forces for this model were calculated using the following values:

- Humidity $H = 1.0$
- Wall roughness $R = 5\times10^{-5}$ m

In the sensitivity runs the following values were used:

- Humidity:
  - $H = 0.75$
  - $H = 0.50$
  - $H = 0.25$
  - $H = 0.00$
- Wall roughness,
  - $R = 1\times10^{-6}$ m
  - smooth walls

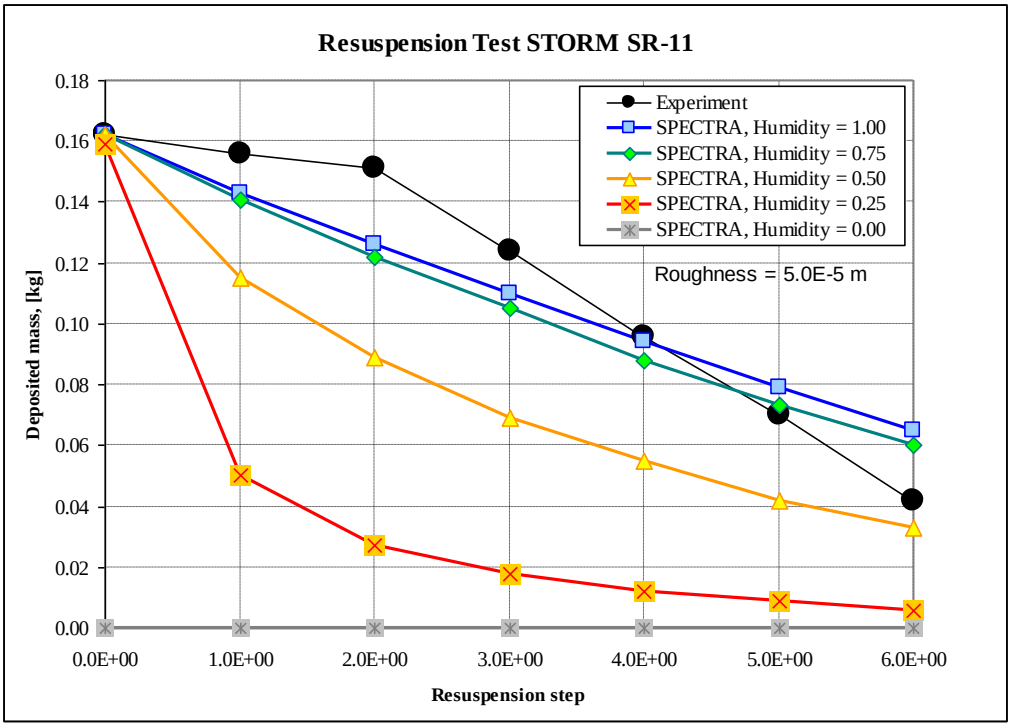

Figure 3-842 STORM experiment SR11, influence of humidity

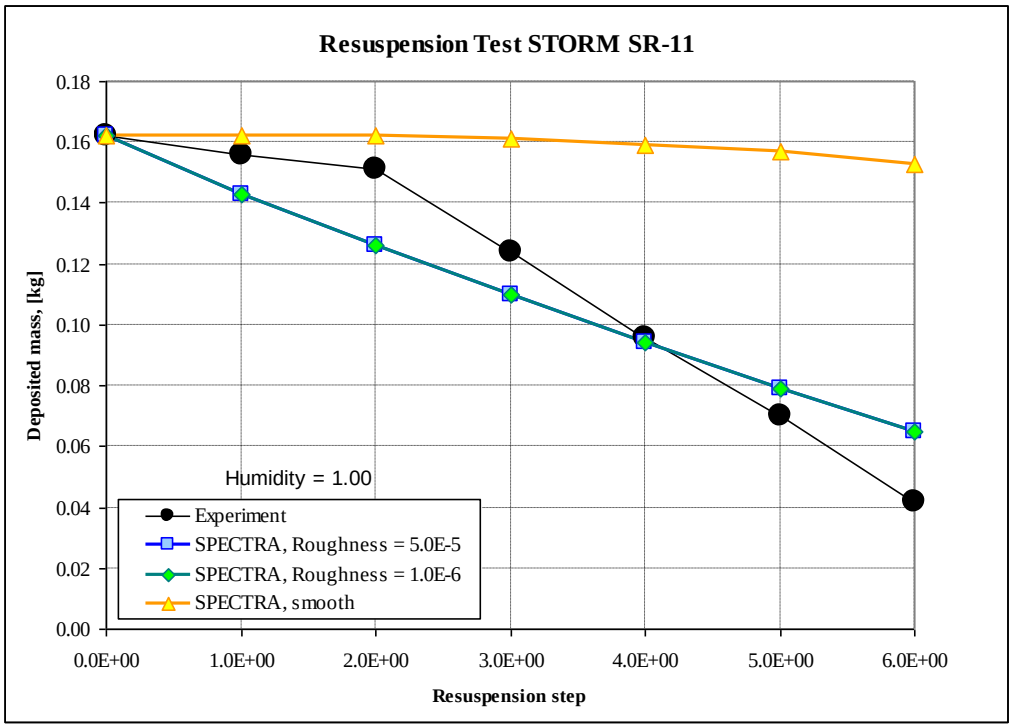

Figure 3-843 STORM experiment SR11, influence of roughness - humidity = 1.0

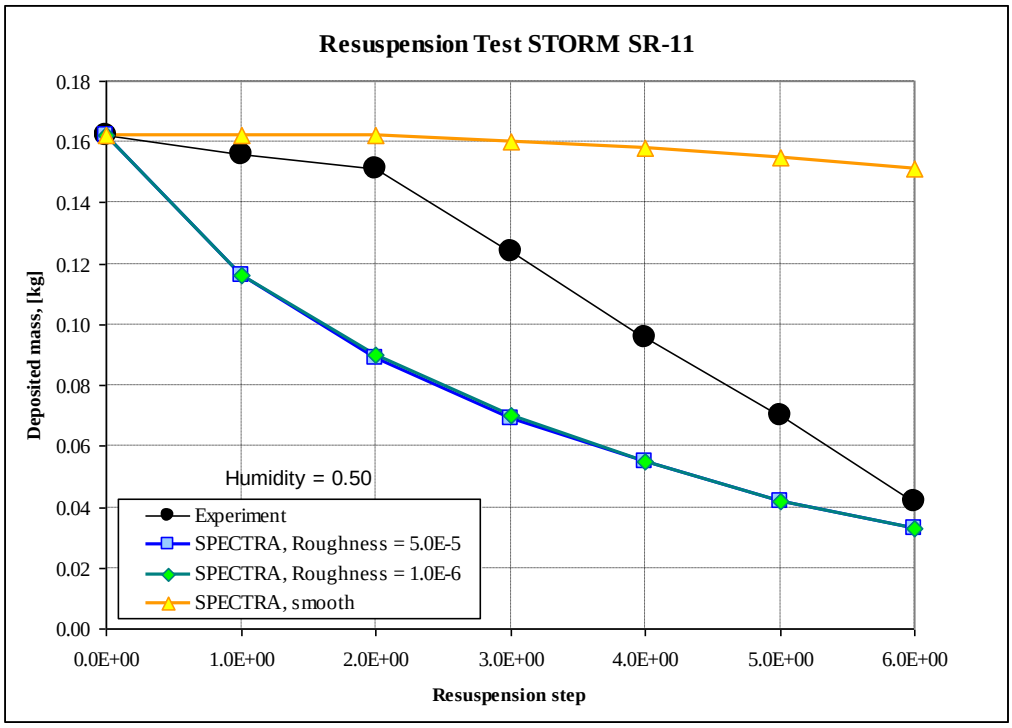

Figure 3-844 STORM experiment SR11, influence of roughness - humidity = 0.5

Results are shown in Figure 3-842, Figure 3-843, and Figure 3-844. The effect of humidity is shown in Figure 3-842. Results close to experiment are obtained with H = 1.0 and 0.75. Results obtained with H = 0.50 and 0.25 are clearly below the experimental data. In the case of H = 0.0 the adhesion forces are solely due to van der Waals forces and are so small that the particles are being blown off the surface already during the deposition phase. Therefore the line shows practically zero deposition at all times Figure 3-842.

The effect of surface roughness is shown in Figure 3-843 and Figure 3-844. There is no visible change in results when the roughness is changed from 5×10^{-5} to 1×10^{-6}. This is because the adhesion forces due to humidity are dominant. If a smooth surface is assumed, the van der Waals forces become dominant. The overall adhesion force is so large in such cases that very little resuspension occurs.

3.12.32 Summary of Resuspension Model Results

The runs performed with the mechanistic resuspension model, described in sections 3.12.20 through 3.12.30 are summarized as follows.

- Agreement between the MathCAD results and SPECTRA results is very good, even for very short times when a careful calculation procedure is applied to match closely the instantaneous velocity step in MathCAD. This agreement proves that the equations were correctly coded in SPECTRA; therefore the model is verified.

- The validation includes comparisons with the experimental results of the Reeks and Hall and STORM experiments.

- Analysis of the Reeks and Hall experiments has shown that:
    - Vainshtein model with the built-in correlations for the adhesion force and adhesive spread of 4.0 gives very good agreement with the experiments.
    - Rock'n Roll model with the built-in correlations for the adhesion force and an adhesive spread of 4.0 gives somewhat too fast resuspension.
    - Vainshtein model with the adhesion force calculated through the asperity size and an adhesive spread of 4.0 gives good agreement with the experiments for the mean asperity size of:

$$\langle r_{as} \rangle = 10^{-8} \text{ m}$$

    - Vainshtein model with the reduction factor of 0.018÷0.027 (recommended in [88]), which means:

$$\langle r_{as} \rangle = 1.6\times10^{-7} - 2.1\times10^{-7} \text{ m}$$

      leads to too low resuspension.

- Analysis of the STORM experiment SR11 has shown that:
    - Vainshtein model with the built-in correlations for the adhesion force and adhesive spread of 4.0 gives very good agreement with the STORM experiment.
    - Rock'n Roll model with the built-in correlations for the adhesion force and adhesive spread of 4.0 gives somewhat too fast resuspension.

- Vainshtein model with the adhesion force calculated through the asperity size and an adhesive spread of 4.0 gives good agreement with the STORM experiment for the mean asperity size of:

$$\langle r_{as} \rangle = 10^{-8} \text{ m}$$

- Vainshtein model with the reduction factor of 0.1 (recommended in [86]), which means:

$$\langle r_{as} \rangle = 0.125 \times 10^{-7} - 2.0 \times 10^{-7} \text{ m}$$

  leads to too low resuspension.

- The observations are very similar for both Reeks and Hall, and STORM experiments. More experiments and measurement data are needed to confirm if those observations can be considered as generally applicable.

3.12.33 Conclusions from the Resuspension Model Tests

- Both the Vainshtein the Rock'n Roll model, applied with "all defaults" model coefficients, give good results of the analyzed Reeks and Hall and STORM experiments. The Rock'n Roll model gives somewhat more conservative results (higher resuspension).

- The Vainshtein model with the mean reduction factor of 0.1, which means $<r_{as}> = 0.1 \times D_p$, leads to too optimistic results (too low resuspension). Since the obtained values are not conservative the model should not be applied for safety analyses of a Nuclear Power Plant. Better results are obtained with the mean asperity size of $<r_{as}> = 10^{-8}$ m, independently of the particle size. More experiments and measurement data are needed to confirm this observation.

- A key factor in successful resuspension predictions is a good knowledge of the adhesion force and its distribution for dust particles deposited on rough surfaces. Theoretical considerations may lead to helpful expressions for the adhesive forces under a variety of conditions. However they cannot be reliably used yet for the assessment of the safety of a Nuclear Power Plant. Therefore, experimental data is needed that will allow to obtain adhesion force distribution for the materials and corresponding surfaces roughness of the components in the analyzed Nuclear Power Plant.

3.12.34 Comparison of Several Resuspension Models for STORM Test

Results of several resuspension models for STORM SR11 test are compared in this section. The following resuspension models are investigated

- KS-MB (former name NRG4)
- KS-RnR (combination of KS-MB and Rock'n Roll model)
- KS-MB-Mod
- KS-RnR-Mod

The model names and explanations are given in Table 3-65. The definitions of models are shortly discussed below.

Table 3-65 Naming convention of the resuspension models

Abbreviation	Full name	Comment
RnR	Rock'n Roll	
KS-FB	Komen-Stempniewicz model based on Force Balance	Former name: NRG3
KS-MB	Komen-Stempniewicz model based on Moment Balance	Former name: NRG4
KS-RnR	Combination of KS and RnR models	KS-MB with moments defined as in the RnR model
KS-MB-Mod	Modified KS model	KS-MB model with Gaussian distribution of drag force
KS-RnR-Mod	Modified KS-RnR model	KS-RnR model with Gaussian distribution of aerodynamic forces (drag and lift)

- Definition of the resuspension models
  - KS-FB:

$$R = \begin{cases} 0.0 & if \quad F_d < F_a \\ \infty & if \quad F_d > F_a \end{cases}$$

  - KS-MB, KS-RnR, KS-MB-Mod, KS-RnR-Mod:

$$R = \begin{cases} 0.0 & if \quad M_d < M_a \\ \infty & if \quad M_d > M_a \end{cases}$$

F_a adhesion force, (N)
F_d drag force, (N)
M_a adhesion moment, (Nm)
M_d drag moment, (Nm)

- Definition of the drag moments
  - KS-MB, KS-MB-Mod:

$$M_d = 1.399 \cdot F_d \cdot R_p$$

  - KS-RnR, KS-RnR-Mod:

$$M_d = \left[\left(\frac{R_p}{r_{as}} \right) \cdot F_d + \left(\frac{1}{2} \right) \cdot F_L \right] \cdot R_p$$

R_p particle radius, (m)
r_{as} asperity radius, (m)
F_d drag force, (N)
F_L lift force, (N)

Calculations were performed for two different adhesion force distributions:

- f' = 0.01, σ' =4.0.
- f' and σ' obtained from Biasi correlations [133]:

$$f' = 0.016 - 0.0023 \cdot (1.0 \times 10^6 \times D_p / 2)^{0.545}$$
$$\sigma' = 1.8 + 0.136 \cdot (1.0 \times 10^6 \times D_p / 2)^{1.4}$$

Here D_p is the particle diameter, (m). The values obtained from the Biasi correlations are shown in Figure 3-845.

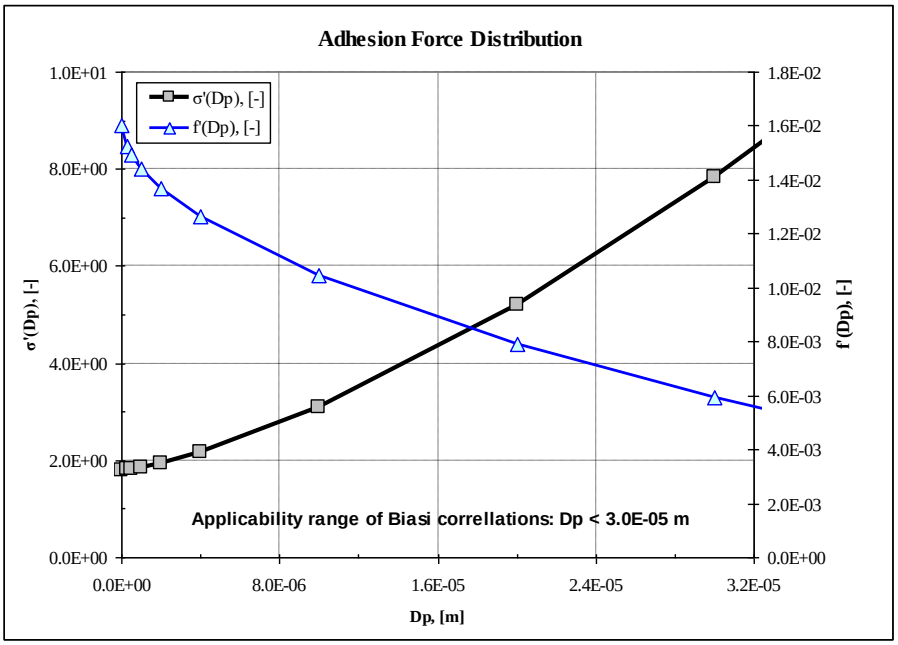

Figure 3-845 Results of Biasi correlations

Results are shown in Figure 3-846 and Figure 3-847. The following remarks can be made:

- The applied models have a tendency to predict too high resuspension rates.
- The results of the KS-MB models are slightly closer to the experiment than the results of the KS-RnR models

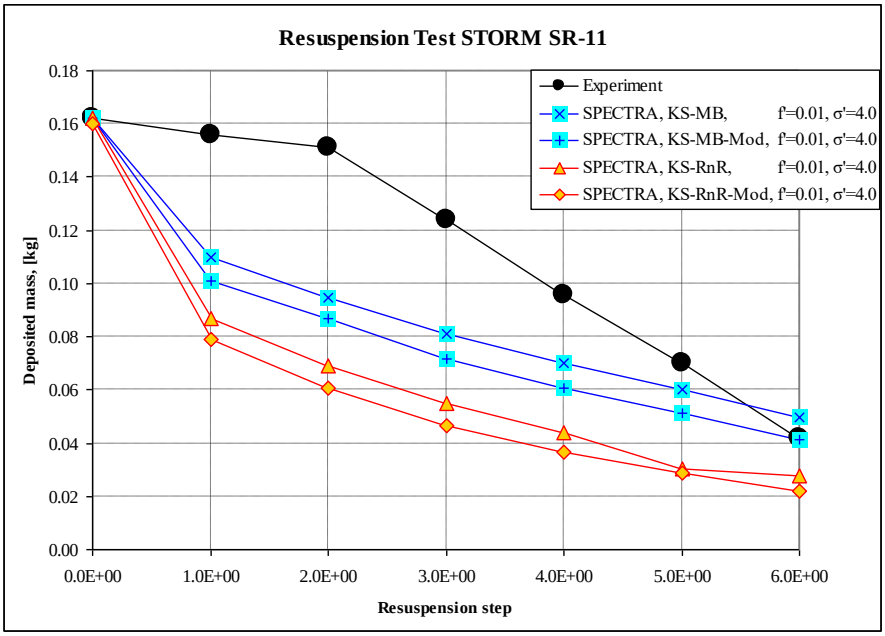

Figure 3-846 Results of resuspension models, f' = 0.01 and σ' =4.0,

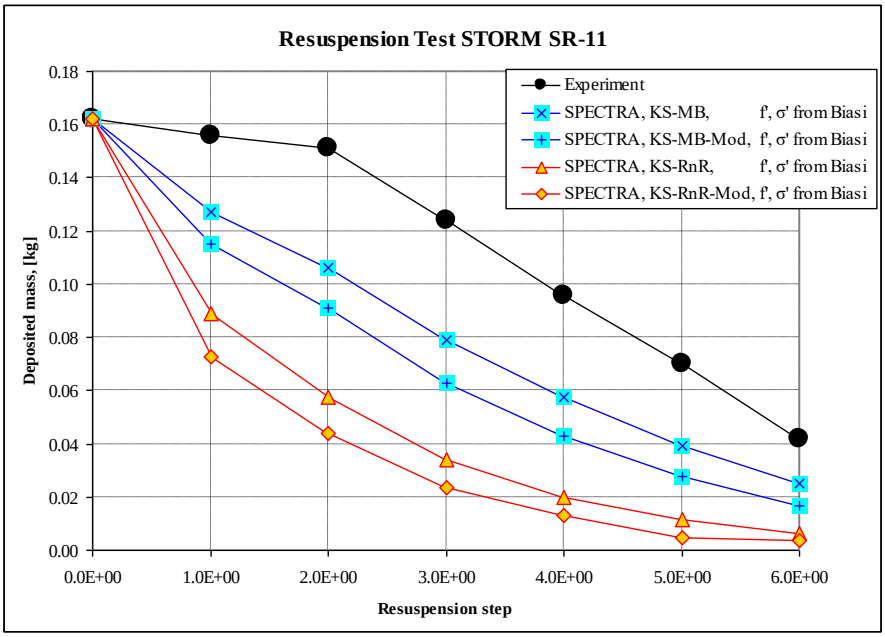

Figure 3-847 Results of resuspension models, f' and σ' from the Biasi correlation

3.12.35 Dust Release During Pipe Break - FTD Test

The objective of the present test is to investigate what is the amount of deposited dust that can be released during a pipe break at high pressure.

Test section dimensions: length: L_T = 10.0 m, five CV with 2 m each
diameter: D_T = 1.0 m
flow area: A_T = 0.785 m2

Initial conditions: fluid: He, p = 90 bar, T = 900 K

Particle size sections: 5 sections covering range of 1 - 32 micron, see table Table 3-57. The initial distribution of the deposited particles is assumed to be uniform according to mass, one gram (10^{-3} kg) of dust per size section, per CV:

```
Deposited aerosols
Sec.      Mass          Density      Heat source     Activity
 No.      (kg)         (part/m2)         (W)           (Bq)
  1   1.00000E-03   1.01797E+11   0.00000E+00   0.00000E+00
  2   1.00000E-03   1.28581E+10   0.00000E+00   0.00000E+00
  3   1.00000E-03   1.61569E+09   0.00000E+00   0.00000E+00
  4   1.00000E-03   2.05167E+08   0.00000E+00   0.00000E+00
  5   1.00000E-03   2.56458E+07   0.00000E+00   0.00000E+00
     ------------  ------------  ------------  ------------
      5.00000E-03   1.16501E+11   0.00000E+00   0.00000E+00
```

The deposited layer thickness is about 1.5 micrometer. Break sizes from 0.25% to 100% of the pipe flow area are considered. Resuspension models of Vainshtein and Rock'n Roll are applied, with adhesion forces calculated for *RH* =1.0 and *RH*=0.0.

Input decks are located in: `\Z-TESTS\RT\FDT`

Results are shown in Figure 3-848 through Figure 3-853 and summarized in Table 3-66. It is concluded that for a large break (100%) most of the deposited particles are expected to be released.

Table 3-66 Fractions of initial deposit released during pipe break

Break Size		*RH* = 1.0		*RH* = 0.0	
D (m)	*A* (%)	Vainshtein	Rock'n Roll	Vainshtein	Rock'n Roll
0.05	0.25	0.00	0.01	0.37	0.47
0.10	1.0	0.01	0.15	0.68	0.77
0.20	4.0	0.21	0.52	0.91	0.96
0.30	9.0	0.45	0.74	0.98	1.00
0.40	16.0	0.62	0.86	1.00	
0.50	25.0	0.75	0.92		
0.80	64.0	0.89	0.97		
1.00	100.0	0.92	0.98		

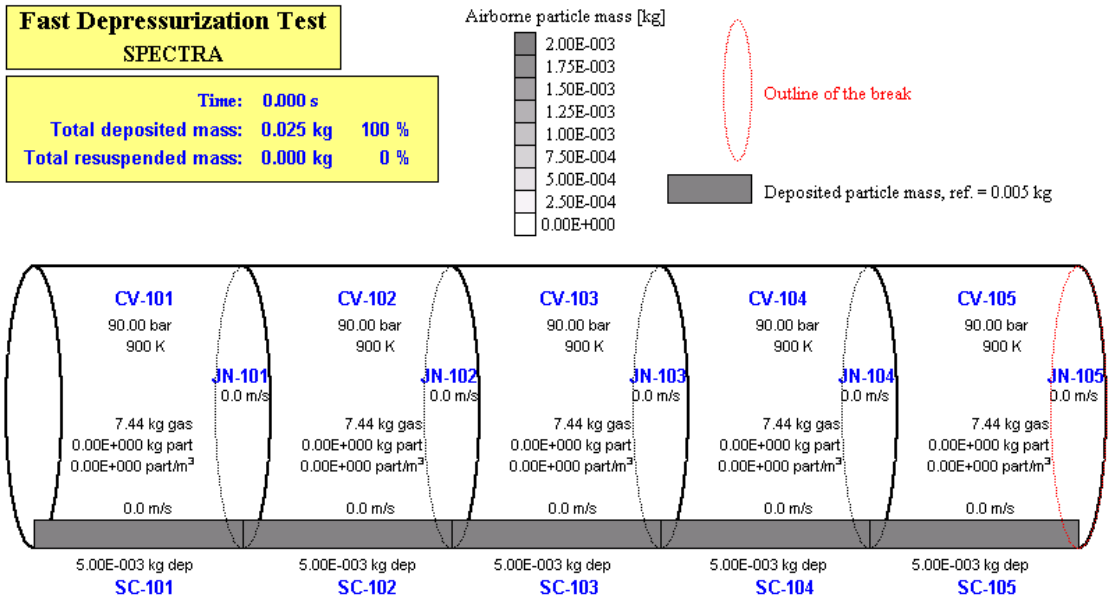

Figure 3-848 100% break, t = 0.0 s

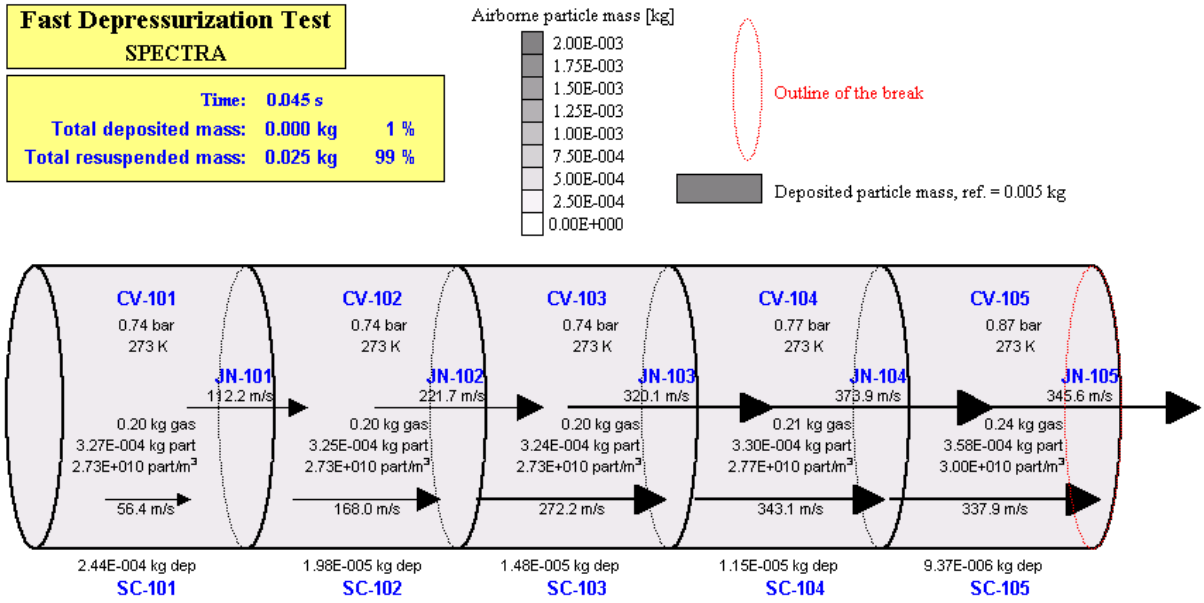

Figure 3-849 100% break, t = 0.025 s

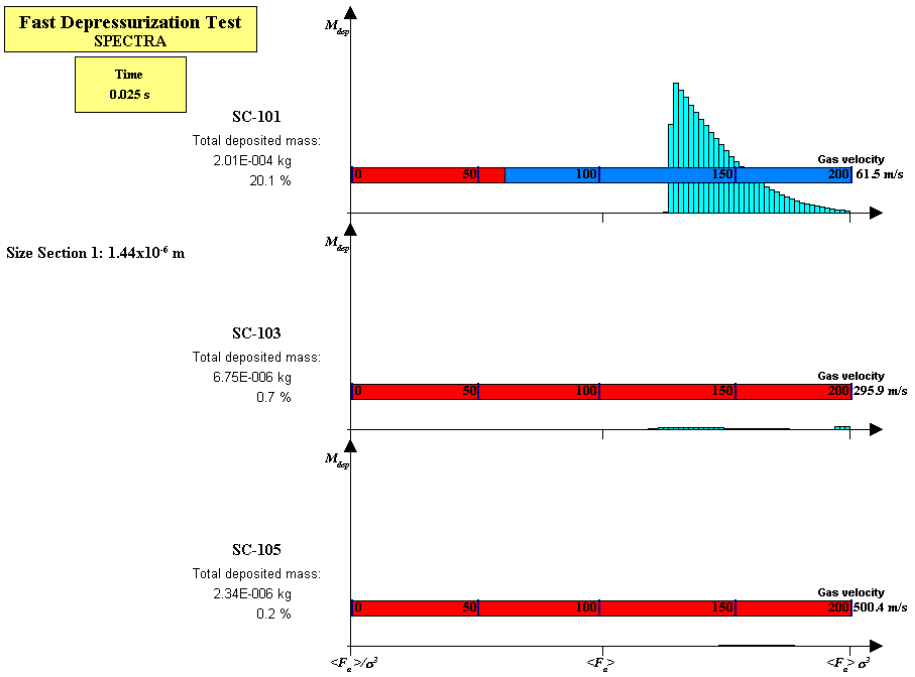

Figure 3-850 F_a-distributions, size section 1, 100% break, t = 0.025 s

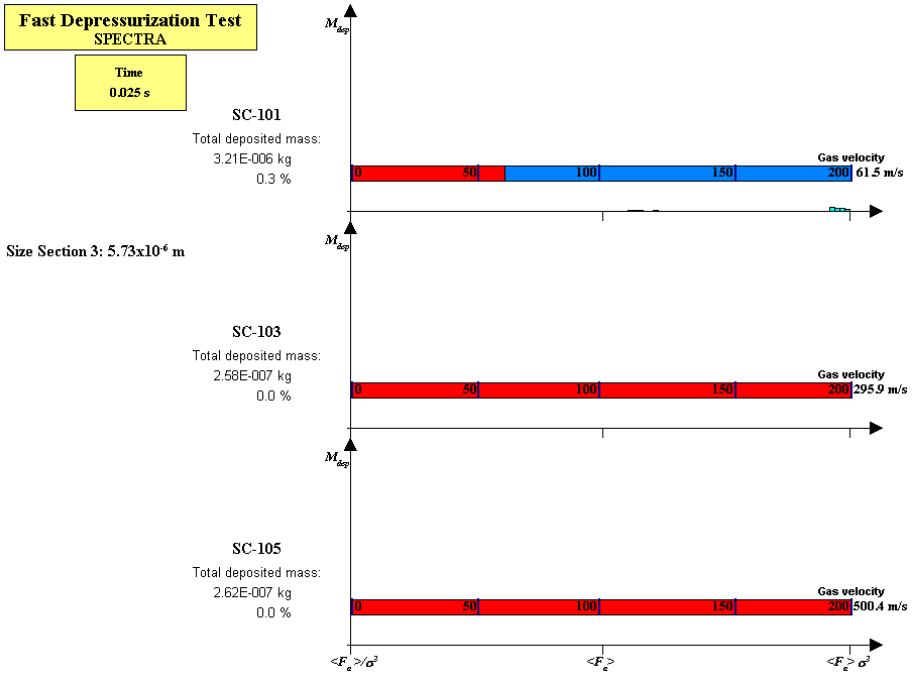

Figure 3-851 F_a-distributions, size section 3, 100% break, t = 0.025 s

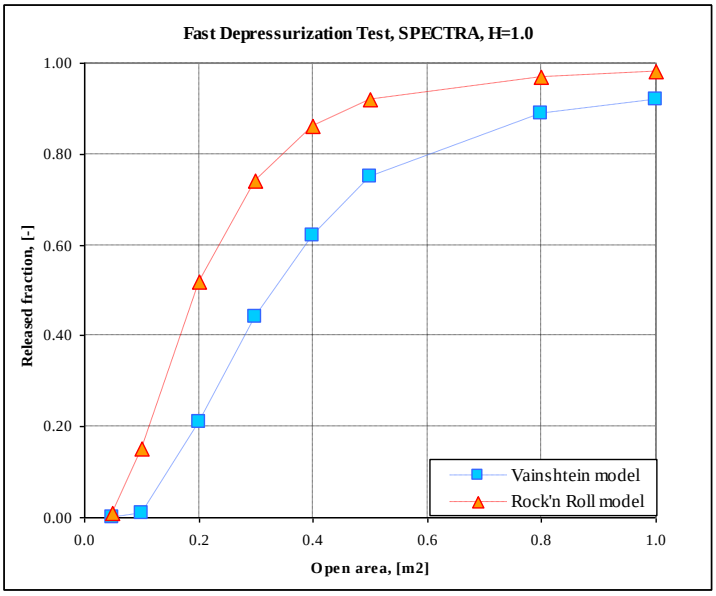

Figure 3-852 Released fraction, humid conditions

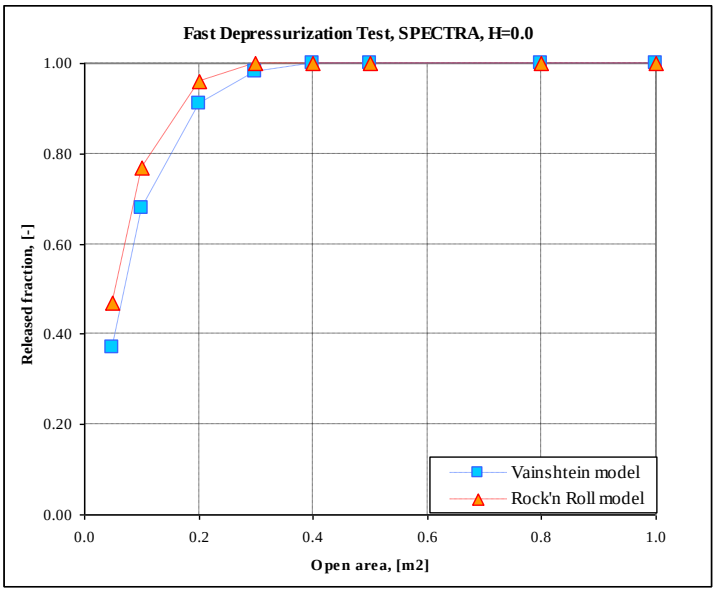

Figure 3-853 Released fraction, dry conditions

3.12.36 Dust Release During Pipe Break - Influence of Electrical Charge

The influence of electrical charge is studied for the Fast Depressurization Test. There are two different phenomena to be considered for electrically charged particles, external electric field and field induced on the surface

- Effect of external electric field

  In case of electrically charged airborne particles, an external electric field will affect (increase or diminish) the deposition rate (see section 3.12.8). In case of electrically charged deposited particles, an external electric field will affect (increase or diminish) the adhesion forces and therefore affect the resuspension rates.

- Effect of the surface

  In case of electrically charged deposited particles, an electric charge may be induced on the surface. Such induced charge will affect (increase) the adhesion forces and therefore affect the resuspension rates. The constant A_3 (A3ARRT, Volume 2) characterizes the ability of the surface to induce electric charge. $A_3 = 0.0$ means that electric charge is not induced on the surface and therefore an electric charge of particles does not affect the adhesion force. $A_3 = 1.0$ means that a charge q placed at the surface induces the same opposite sign charge on the surface. In this case the adhesion force of the charged particles is larger than that for non-charged particles. The constant A_3 of a given material may be calculated from

$$A_3 = \left(\frac{\varepsilon_r - 1}{\varepsilon_r} \right)$$

  Here ε_r is the relative permittivity (dielectric constant) of the surface material.

The analyzed case is the Fast Depressurization Test, described in section 3.12.35. The following case was taken for the present analysis:

- Break diameter of 0.3 m (break size of 9%)
- Resuspension model of Vainshtein., adhesion force calculated with $RH = 1.0$

The calculations were performed for the case of non-inductive surface and inductive surface. The input decks are provided in:

`\Z-TESTS\RT\ELEC-RES\A3=0`	no induction on the surface
`\Z-TESTS\RT\ELEC-RES\A3=1`	large induction on the surface

For each case five different electrostatic strengths of the external field are considered, namely $E = -10^6$, $E = -10^3$ =, $E = 0.0$, $E = +10^3$, and $E = +10^6$ (V/m). The inputs are located in the subdirectories:
`\E=-1E6` `\E=-1E3` `\E=0` `\E=1E3` `\E=1E6`

Finally, there are three different cases of electric charge on particles, no charge, minimum (equilibrium) charge, and maximum charge. The input files are:

```
\FTD-No-Charge.SPE
\FTD-Min-Charge.SPE
\FTD-Max-Charge.SPE
```

Results, expressed as fraction of particles that are released (resuspended) during the Fast Depressurization Test, are summarized in Table 3-67 and Table 3-68. The case with E = 0.0 and no charge on particles corresponds to the case shown in section 3.12.35 (Table 3-66, D=0.3 m, RH = 1.0, Vainshtein). The following observations can be made:

- Particles with equilibrium (minimum) charge behave the same as non-charged particles. Therefore equilibrium charge may be neglected in the calculations.
- Charged particles experience a very large attractive force on materials with large permittivity ($\varepsilon \to \infty$, A_3 = 1.0). For particles with maximum charge the adhesion force is so large that there is no resuspension in the present test - Table 3-67
- If the surface does not induce an electric charge (ε = 1.0, A_3 = 0.0), then only strong external fields have a significant impact on resuspension. Fields of E ~10^3 V/m do not significantly affect the resuspension behavior. The effect is clearly visible for fields of E ~10^6 V/m - Table 3-68. If the field is directed towards the surface, then there is no resuspension from that surface (just as in case $\varepsilon \to \infty$). If the field is away from the surface and thus decreases the adhesion force, the resuspension is enhanced (in the present case to 90%).

In summary:

- Equilibrium charge has no practical effect on the results and can be neglected.
- Particles that have a charge significantly larger than the equilibrium charge will see a strong adhesion force on materials for which $\varepsilon \to \infty$ ($A_3 \to 1.0$). In such case external electric fields are meaningless compared to the induced field and can safely be neglected for fields smaller than 10^6 V/m. Note that this conclusion is valid for resuspension only. For deposition, fields of 10 V/m are already becoming important - see section 3.12.8.

Table 3-67 Release fractions, induction on the surface ($\varepsilon \to \infty$, A_3 = 1.0)

	External electrical field strength, E (V/m)				
Particle charge	-10^6	-10^3	0.0	$+10^3$	$+10^6$
No charge	0.45	0.45	0.45	0.45	0.45
Minimum	0.45	0.45	0.45	0.45	0.45
Maximum	0.00	0.00	0.00	0.00	0.00

Table 3-68 Release fractions, no induction on the surface (ε = 1.0, A_3 = 0.0)

	External electrical field strength, E (V/m)				
Particle charge	-10^6	-10^3	0.0	$+10^3$	$+10^6$
No charge	0.45	0.45	0.45	0.45	0.45
Minimum	0.45	0.45	0.45	0.45	0.45
Maximum	0.90	0.47	0.45	0.36	0.00

3.12.37 LWR Fission Product Release Model Verification and Validation

This section shows the results of verification and validation tests of the LWR fission product release models: CORSOR-M and ARSAP.

3.12.37.1 Verification

Verification of the CORSOR-M and ARSAP model is discussed in this section. The verification is performed by comparing the calculated release with analytical solutions.

- **CORSOR-M Model**

An isothermal test is set up. The tested fuel rod is represented by SC-619. The fuel pellet is represented by 8 nodes, 0.0006 m each (fuel radius of R_{fuel} = 0.0048 m). The cladding is represented by a single node, 0.0007 m thick. The fuel is kept at a constant temperature of 2000 K (using appropriate boundary conditions). The cladding failure criterion is set to 1173 K, which means that the cladding failure is occurring immediately at the start of the calculations. An initial mass of I-136 (built-in isotope 061) of 10^{-10} kg is defined in the fuel region. Calculations are performed for 10,000 seconds. The release is compared to the theoretical solution for Iodine (vapor 4) which in case of the CORSOR-M model is (Volume 1):

$$R_{CORSOR\text{-}M} = A \cdot \exp\left(-\frac{B}{T}\right) = 3.333 \times 10^{3} \cdot \exp\left(-\frac{32108.7}{T}\right)$$

The effect of surface-to-volume ratio is taken into account as follows.

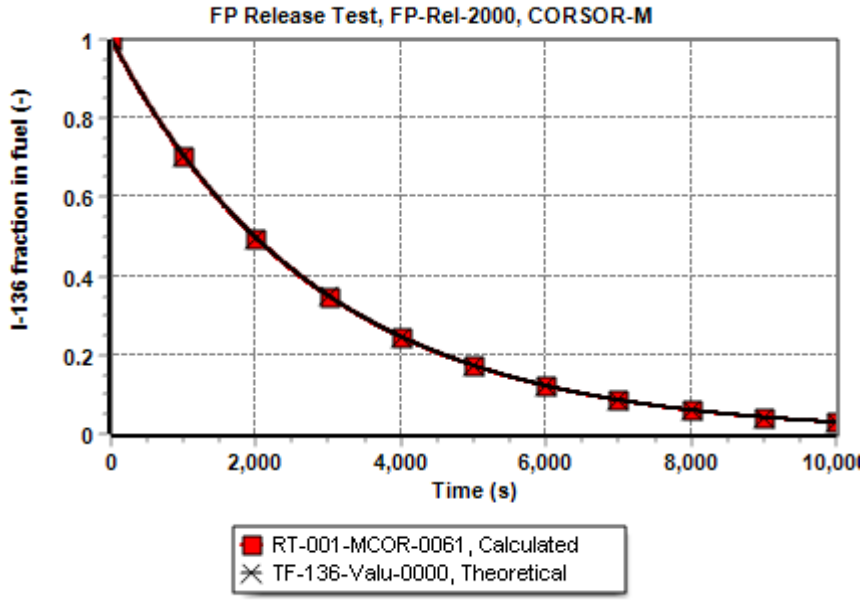

Figure 3-854 Test FP-Rel-2000, CORSOR-M model

$$R = R_{CORSOR\text{-}M} \times (S/V) / (S/V)_{CORSOR\text{-}M}$$

(S/V) is the current surface-to-volume ratio, $=2/R_{fuel} = 416.667$
$(S/V)_{CORSOR\text{-}M}$ reference surface-to-volume ratio, $=2/R_{fuel} = 422.5$

The theoretical mass of the fission product remaining in the fuel is obtained from:

$$M_{FP} = M_{FP,0} \cdot \exp(-R \cdot t)$$

The input file is located in: \Z-INPUTS\RT\FP-Release\LWR\Verification\I-136\CORSOR-M. The theoretical mass was calculated in Excel file I-136-theory.xlsx, stored in this folder. The results are shown in Figure 3-854. The calculated masses agree very well with the theoretical values.

- **ARSAP Model**

The same test as before is studied using the ARSAP fission product release model. The theoretical solution for Iodine (vapor 4) is in this case (Volume 1):

$$R_{ARSAP} = \left(\frac{C}{R_g}\right) \cdot \exp\left(-\frac{c_1}{T}\right) = \left(\frac{2.55}{R_g}\right) \cdot \exp\left(-\frac{42100.0}{T}\right)$$

Here R_g is the grain size, assumed as 10^{-5} m. The effect of surface-to-volume ratio is the same as in case of the CORSOR-M model. The input file is located in: \Z-INPUTS\RT\FP-Release\LWR\Verification\I-136\ARSAP. The theoretical mass was calculated in Excel file I-136-theory.xlsx, stored in this folder. The results are shown in Figure 3-855. The calculated masses agree very well with the theoretical values.

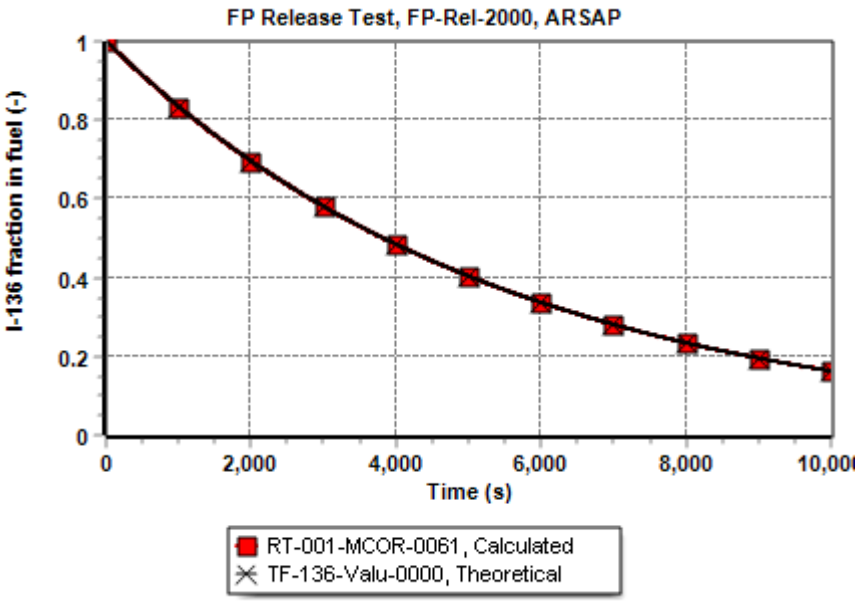

Figure 3-855 Test FP-Rel-2000, ARSAP model

3.12.37.2 Validation

Two validation tests are discussed in this chapter:

- ORNL VI Tests
- VECTORS Tests

These tests are discussed below.

- **ORNL VI Tests**

The data of ORNL VI tests were obtained from [199]. Three tests were considered:

- ORNL VI-2 maximum temperature: 2300 K
- ORNL VI-3 maximum temperature: 2700 K
- ORNL VI-5 maximum temperature: 2740 K

The tests were simulated using both LWR fission product release models available:

- ***CORSOR-M***
- ***ARSAP***. In this case the effect of input parameters: the grain size (R_g, RGARRT) and the fuel-cladding interaction temperature (T_{FCI}, TFCIRT) was studied. The best agreement with experiments was obtained using R_g, = 3.0×10^{-5} m and T_{FCI} = 2500 K, therefore these values are selected as default (Volume 2).

The input files are located in: \Z-INPUTS\RT\FP-Release\LWR\Validation\VI-2, \VI-3, and \VI-5. Results are shown in Figure 3-856.

In test ORNL VI-2, run under steam-rich conditions, the peak temperature attained was ~2300 K. Both models overpredicted the Cs release for this test, with the ARSAP model performing slightly better - Figure 3-856 (a). Test VI-3 was similar to VI-2, except that higher temperatures were attained. In analyses of this test, both models yielded predictions closer to the data. Again the ARSAP model performed somewhat better Figure 3-856 (b). These two tests were run under oxidizing conditions (steam flow). Test VI-5 was conducted under reducing conditions (H_2 flow). This test was well predicted by both models, as shown in Figure 3-856 (c). Table 3-69, Table 3-70, and Table 3-71 provide total releases predicted by CORSOR-M and ARSAP compared with totals reported for the ORNL VI tests 2, 3, and 5, respectively.

Table 3-69 ORNL VI-2 test - measured [199] and calculated release

Isotope	Data [199]	CORSOR-M	ARSAP
Kr-85	-	100%	97%
Cs-137	67%	100%	99%
Ba-134	18%	25%	4%
I-131	40%	100%	99%
Te-132	-	100%	91%
Mo-99	86%	82%	28%
Sb-131	68%	62%	56%

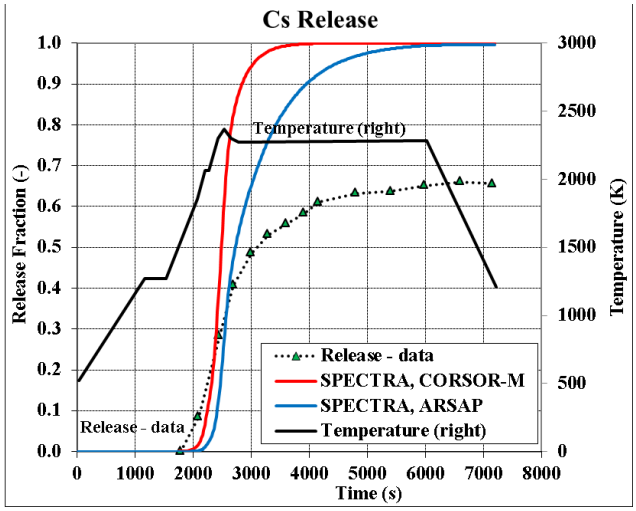

(a) ORNL VI-2

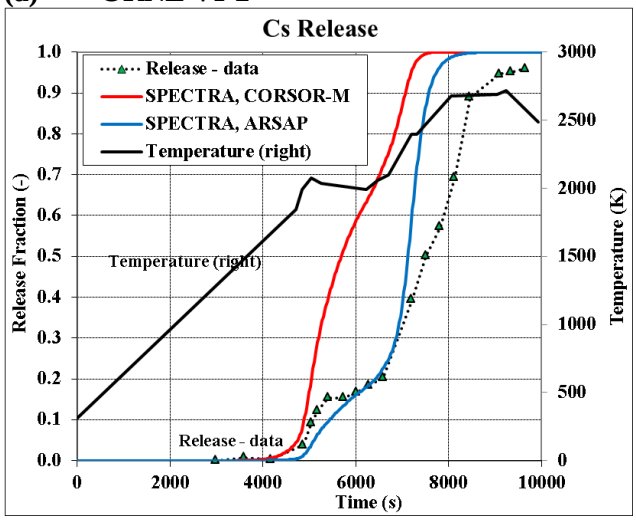

(b) ORNL VI-3

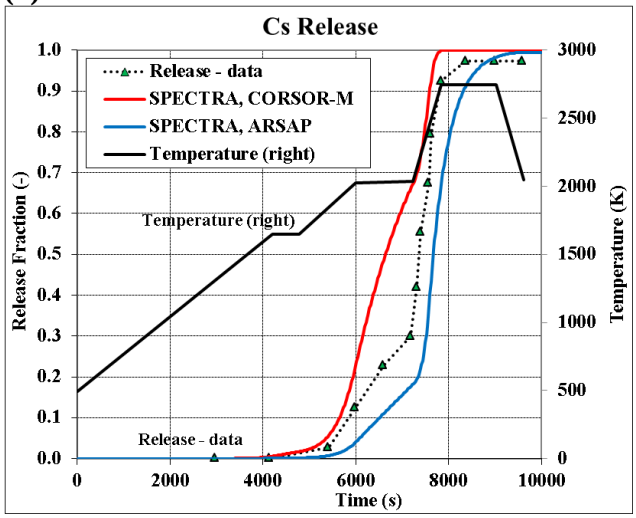

(c) ORNL VI-5

Figure 3-856 ORNL VI tests - measured [199] and calculated release of Cs

Table 3-70 ORNL VI-3 test - measured [199] and calculated release

Isotope	Data [199]	CORSOR-M	ARSAP
Kr-85	100%	100%	100%
Cs-137	100%	100%	100%
Ba-134	30%	97%	11%
I-131	80%	100%	100%
Te-132	99%	100%	100%
Mo-99	77%	100%	47%
Sb-131	99%	98%	85%

Table 3-71 ORNL VI-5 test - measured [199] and calculated release

Isotope	Data [199]	CORSOR-M	ARSAP
Kr-85	100%	100%	99%
Cs-137	100%	100%	100%
Ba-134	76%	98%	7%
I-131	70%	100%	100%
Te-132	82%	100%	98%
Mo-99	2%	100%	35%
Sb-131	18%	97%	72%

- **VECTORS Tests**

The data of the VECTORS tests were obtained from [199]. The test VECTORS-4 was considered. The test was simulated using both LWR fission product release models available:

- ***CORSOR-M***
- ***ARSAP***. In this case the effect of input parameters: the grain size (R_g, RGARRT) and the fuel-cladding interaction temperature (T_{FCI}, TFCIRT) were studied. The best agreement with experiments was obtained using R_g, = 3.0×10^{-5} m and T_{FCI} = 2500 K, therefore these values are selected as default (Volume 2).

The input files are located in: \Z-INPUTS\RT\FP-Release\LWR\Validation\VECTORS. Results are shown in Figure 3-857. Test VERCORS 4 was performed under completely reducing conditions during the release phase. In case of Xenon, Iodine, Tellurium, and Cesium both models provide reasonably good agreement with the data. In case of Barium, the ARSAP model underpredicted release, whereas the CORSOR-M model captured the release behavior very well. In case of Molybdenum, the CORSOR-M model overpredicted release, whereas the ARSAP model captured the release behavior quite well.

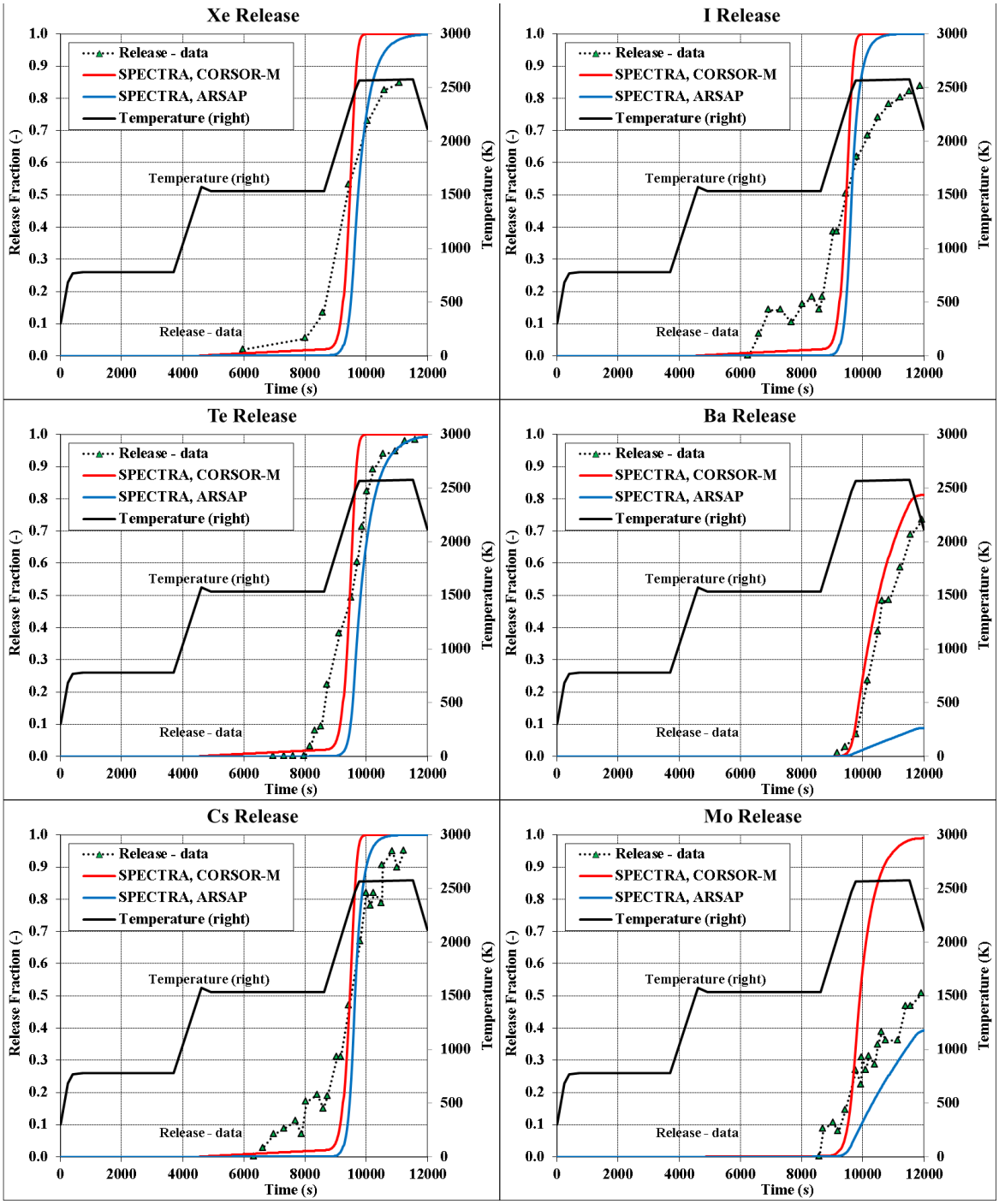

Figure 3-857 VECTORS-4 test - measured [199] and calculated release; Xe, I, Te, Ba, Cs, Mo

3.12.38 HTR Fission Product Release Model Verification and Validation

This section shows the results of verification and validation tests of the fission product release model HTR-FPR.

3.12.38.1 Verification

The following verification tests were performed on the HTR-FPR model:

- Test TRISO-Cs
- Test TRISO-Xe
- Test TRISO-Sr
- Test Fail-0-5-const
- Test Fail-0-5
- Test Diff-const
- Test Diff
- Test Cs-1900
- Test Cs-1600
- Test Ba-135 (release of isotope produced due to decay)
- Test Te-132 (release of isotope produced due to fission)
- Tests Cs-137-Sorp and Sr-90-Sorp (sorption isotherms)

These tests are discussed below.

- **Test TRISO-Cs**

In order to calculate diffusion, a diffusion equation may be applied directly for a TRISO particle. However in practical application to large reactors this would be rather time consuming. Therefore a simplified approach is available; the diffusion is calculated using an approximation formula, rather than solving a diffusion equation inside TRISO particles. The following formula is used to calculate release by diffusion through the coating layers (see Volume 1):

$$\left(\frac{dM_{FP}}{dt}\right)_{diff} = -\frac{3}{R_{TRISO}} \cdot \frac{M_{FP}}{R_{diff}}$$

$$R_{diff} = \frac{X_{\ker}}{D_{\ker}} + \frac{X_{SiC}}{D_{SiC}} + \frac{X_{PyC}}{D_{PyC}}$$

In the present test, the results of this formula are compared to the exact solution of the diffusion equation. A model of a TRISO particle with a UO_2 kernel and two coating layers is made. The diffusion coefficients are as follows:

UO_2	$D = 5.6\times10^{-8} \times \exp(-25{,}137/T) = 5.3050\times10^{-13}$ at T=2173.14 K =1900°C
SiC	$D = 2.8\times10^{-4} \times \exp(-50{,}514/T) = 2.2495\times10^{-14}$ at T=2173.14 K =1900°C
PyC	$D = 6.3\times10^{-8} \times \exp(-26{,}700/T) = 2.9065\times10^{-13}$ at T=2173.14 K =1900°C

The diffusion coefficients are those appropriate for Cesium - see Volume 1. The thickness of the coating layers are assumed to be:

UO_2 X_{ker} = 250/4 =62.5 μm
SiC X_{SiC} = 35 μm
PyC X_{PyC} = 175 (95 buffer + 40 inner PyC + 40 outer PyC) μm

Since no diffusion data was found for the buffer material, the buffer and the inner PyC layer are treated as one material - Figure 3-858. An initial mass of Cs-137 (long-life isotope number 0072) of 10^{-9} kg is defined as initially present in the kernel nodes (nodes 1 - 10, Figure 3-858-a). The sorption model is defined on the surface, with maximum desorption coefficient (B_S = 1.0) and minimum adsorption coefficient (A_S = 0.0), to obtain maximum release. Consequently, the resistance on the surface is negligible and the diffusion resistance of the coating is dominant. The solution of the theoretical formula for isothermal conditions is:

$$M_{FP} = M_{FP,0} \cdot \exp(-X \cdot t)$$

where:

$$X = \frac{3}{R_{TRISO} \cdot R_{diff}}$$

(a) initial state (t = 0.0 s)

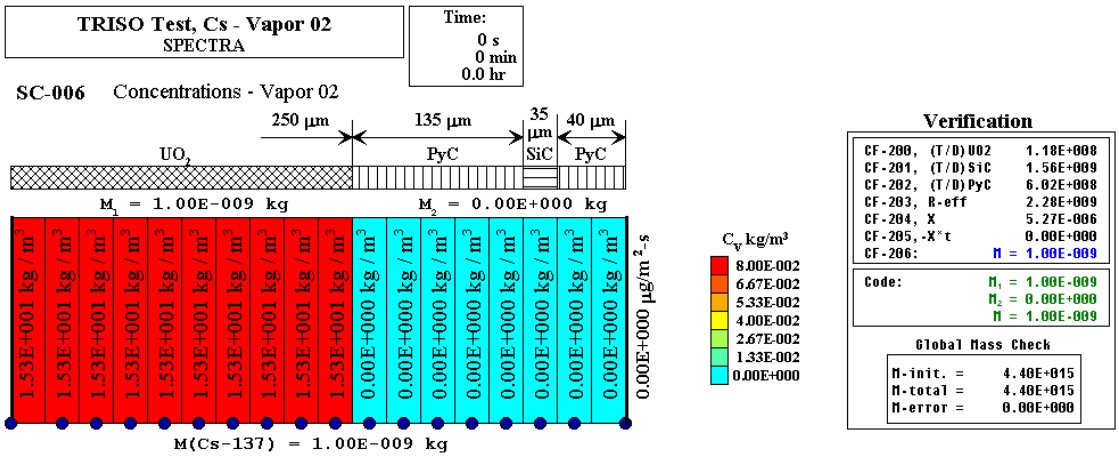

(b) final state (t = 100,000 s)

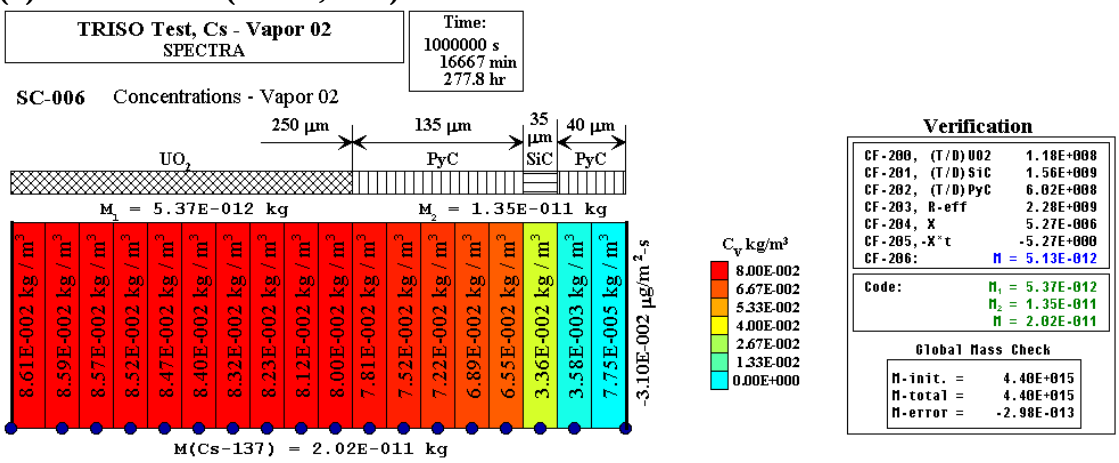

Figure 3-858 TRISO-Cs test, the initial and the final state

The above formula is defined in the input deck using Control Functions, CF-201 through CF-206, defined as follows:

CF-200 = X_{UO2} / D_{UO2}
CF-201 = X_{SiC} / D_{SiC}
CF-202 = X_{PyC} / D_{PyC}
CF-203 = $R_{eff} = X_{UO2} / D_{UO2} + X_{SiC} / D_{SiC} + X_{PyC} / D_{PyC}$
CF-204 = $X = 3 / R_{TRISO} / R_{diff}$
CF-205 = $- X \cdot t$
CF-206 = $M_{FP,0} \cdot \exp (- X \cdot t)$

The input file is located in: \Z-INPUTS\RT\FP-Release\HTR\Verification\TRISO-Cs. Results are shown in Figure 3-858 and Figure 3-859. As seen in Figure 3-859 (a) the diffusion solution gives slightly higher mass than the theoretical solution.

(a) approximation formula: $X = 3/(R_{TRISO} \cdot R_{diff})$

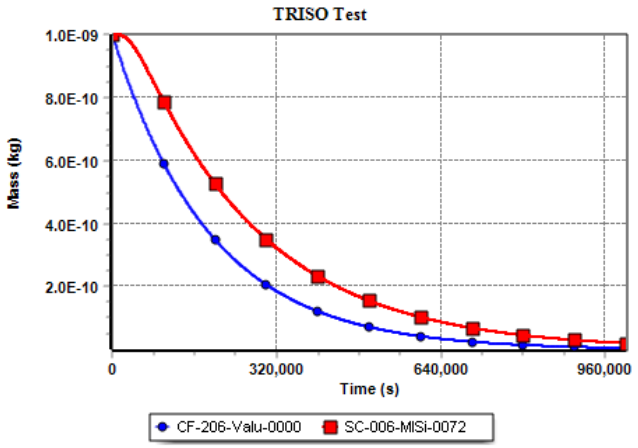

(b) approximation formula: $X = 2/(R_{TRISO} \cdot R_{diff})$

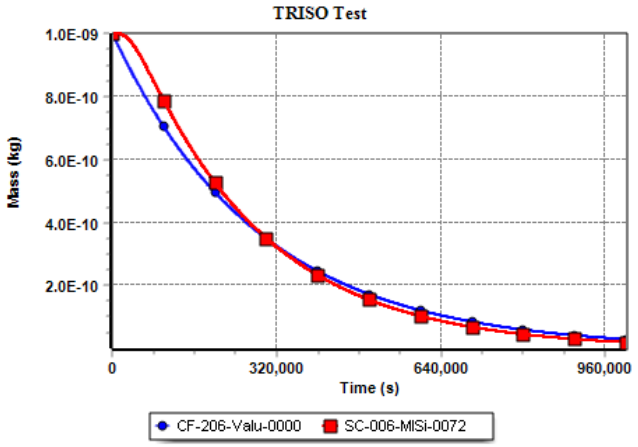

Figure 3-859 TRISO-Cs test, comparison of diffusion solution with approximation formula

The coating layers accumulate the diffusing isotope and therefore the mass released from the surface is somewhat smaller than in the approximation formula. The approximation gives a somewhat lower mass inside the TRISO particle and therefore a conservative estimation of the release by diffusion. Because of this observation, the approximation formula contains a user-defined constant C_{FPR} :

$$\left(\frac{dM_{FP}}{dt}\right)_{diff} = -\frac{C_{FPR}}{R_{TRISO}} \cdot \frac{M_{FP}}{R_{diff}}$$

The default value is C_{FPR} = 3.0 but it can be varied between 1.0 and 5.0 (Volume 2). A smaller value of C_{FPR} means a smaller resistance. Figure 3-859 shows that results obtained with C_{FPR} = 2.0 provide quite a good match with results of the detailed diffusion model.

- **Test TRISO-Xe**

This test is very similar to the previous one. The only difference is that the isotope Xe-131 (vapor class 01) is used. The diffusion coefficients are as follows (see Volume 1):

UO_2 $D = 1.3\times10^{-12}\times \exp(-15{,}154/T) = 1.2174\times10^{-15}$ at T=2173.14 K =1900°C
SiC $D = 5.0\times10^{-5} \times \exp(-50{,}514/T) = 4.0169\times10^{-15}$ at T=2173.14 K =1900°C
PyC $D = 2.9\times10^{-8} \times \exp(-34{,}999/T) = 2.9373\times10^{-15}$ at T=2173.14 K =1900°C

The input files for this test are located in: \Z-INPUTS\RT\FP-Release\HTR\Verification\TRISO-Xe. Results are shown in Figure 3-860 and Figure 3-861. In this case the approximation formula with C_{FPR} = 3.0 (Figure 3-861) gives results very similar to the results obtained with the diffusion model.

- **Test TRISO-Sr**

This test is very similar to the previous tests. The only difference is that the isotope Sr-90 (vapor class 03) is used. The diffusion coefficients are as follows (see Volume 1):

UO_2 $D = 2.2\times10^{-3} \times \exp(-58{,}693/T) = 4.1011\times10^{-15}$ at T=2173.14 K =1900°C
SiC $D = 5.0\times10^{-5} \times \exp(-50{,}514/T) = 4.0169\times10^{-15}$ at T=2173.14 K =1900°C
PyC $D = 2.3\times10^{-6} \times \exp(-23{,}694/T) = 4.2331\times10^{-11}$ at T=2173.14 K =1900°C

The input files for this test are located in: \Z-INPUTS\RT\FP-Release\HTR\Verification\TRISO-Xe. Results are shown in Figure 3-862 and Figure 3-863. In this case the approximation formula with C_{FPR} = 3.0 (Figure 3-863) gives results very similar to the results obtained with the diffusion model.

Summarizing, the tests TRISO-Cs, TRISO-Xe, and TRISO-Sr, demonstrate the correctness of the approximation used to model the fission product release, in particular the effective length of diffusion through UO_2 kernel being equal to ¼ of the kernel radius (see Volume 1). The approximation allows modeling the release from TRISO without a necessity to physically model diffusion through TRISO particles, which would be too time consuming in practical models involving large reactor cores. Further comparison of the approximation and the diffusion model is shown in the validation runs JMTR Isothermal Tests, section 3.12.38.2.

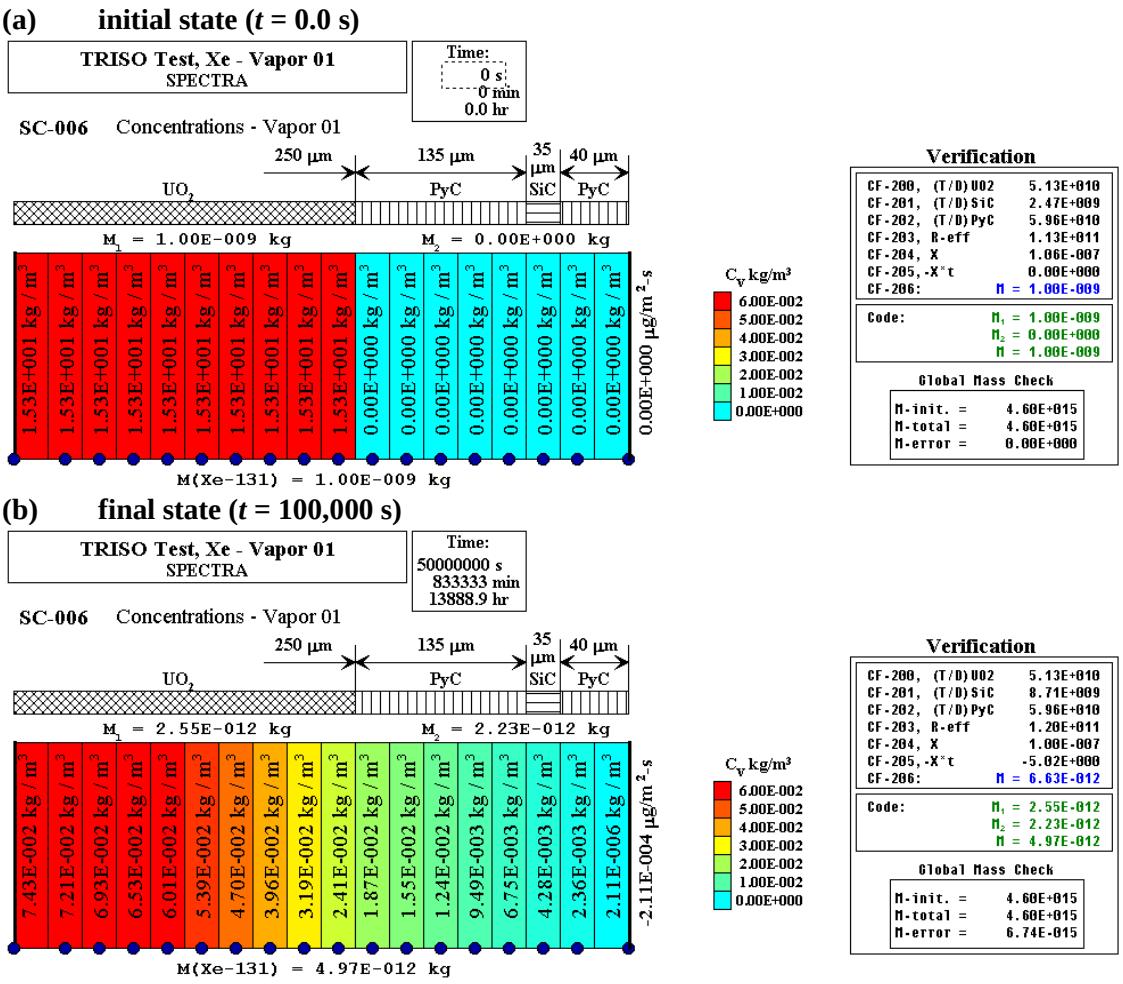

Figure 3-860 TRISO-Xe test, the initial and the final state

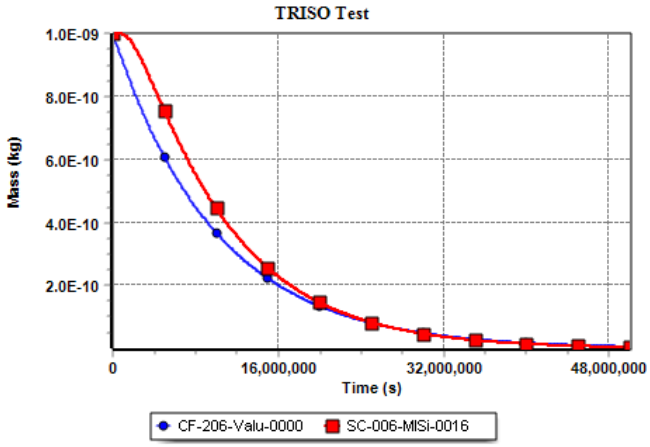

Figure 3-861 TRISO-Xe test, comparison of diffusion solution with approximation formula

(a) initial state (t = 0.0 s)

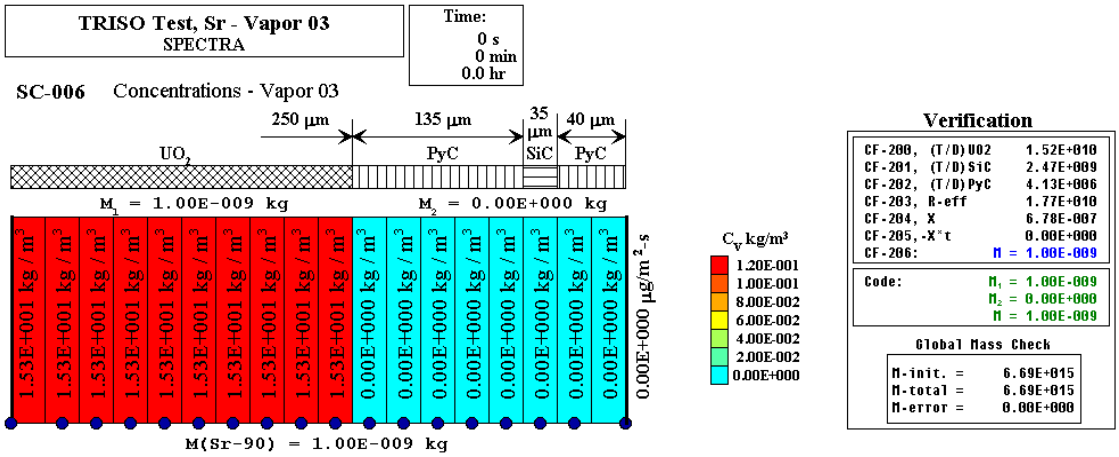

(b) final state (t = 100,000 s)

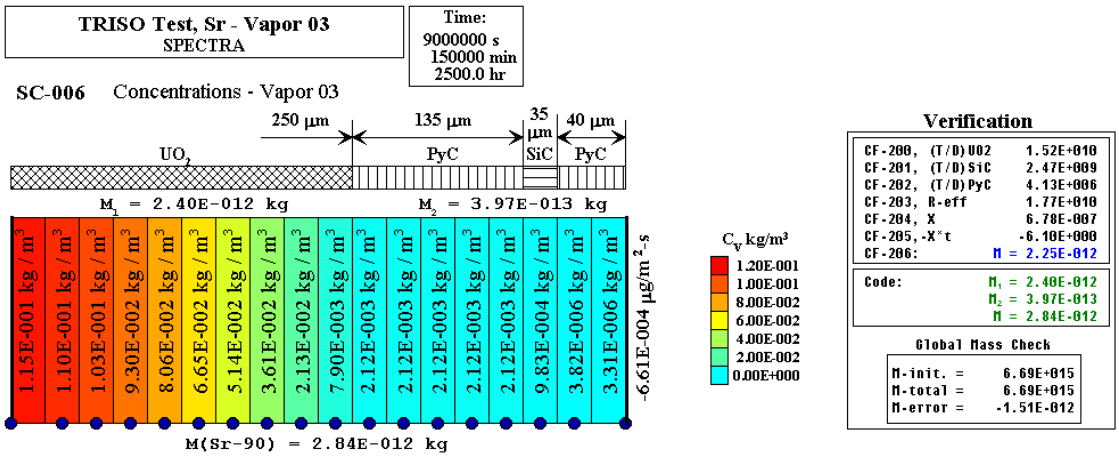

Figure 3-862 TRISO-Sr test, the initial and the final state

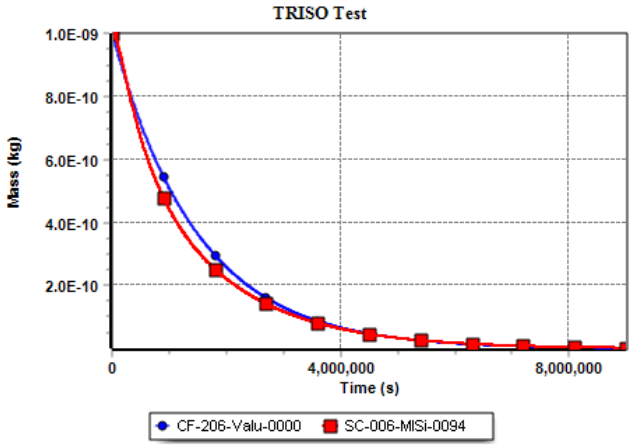

Figure 3-863 TRISO-Sr test, comparison of diffusion solution with approximation formula

- **Test Fail-0-5-const**

In this test a single pebble is modeled by a spherical SC-006 which is linked to fuel region 1. The outer radius is 6 cm (30 nodes, 0.2 mm each), the radius of fuel/graphite matrix is 5 cm. An initial mass of Xe-131 (stable isotope number 0016) of 10^{-9} kg is defined in the fuel region. For simplicity, the failure fraction is defined by a Control Function (CF-100) instead of the correlation. CF-100 defines $F = 0.0$ for $T < 2000.0$ K and $F = 0.5$ for $T > 2000.1$ K. Diffusion inside SC-006 is disabled (diffusion coefficients are set to zero). The input file is located in: \Z-INPUTS\RT\FP-Release\HTR\Verification\Fail\Fail-05-const.SPE. Results are shown in Figure 3-864. The pebble is slowly heated up from 1900 K. When the temperature exceeds 2000 K ($t \approx 430$ s), 50% of TRISO particles fail and 50% of Xe-131 is deposited in the nodes 1 - 25 (non-zero power density). Since there is no diffusion, Xe-131 remains in those nodes; no Xe-131 is released to gas - Figure 3-864.

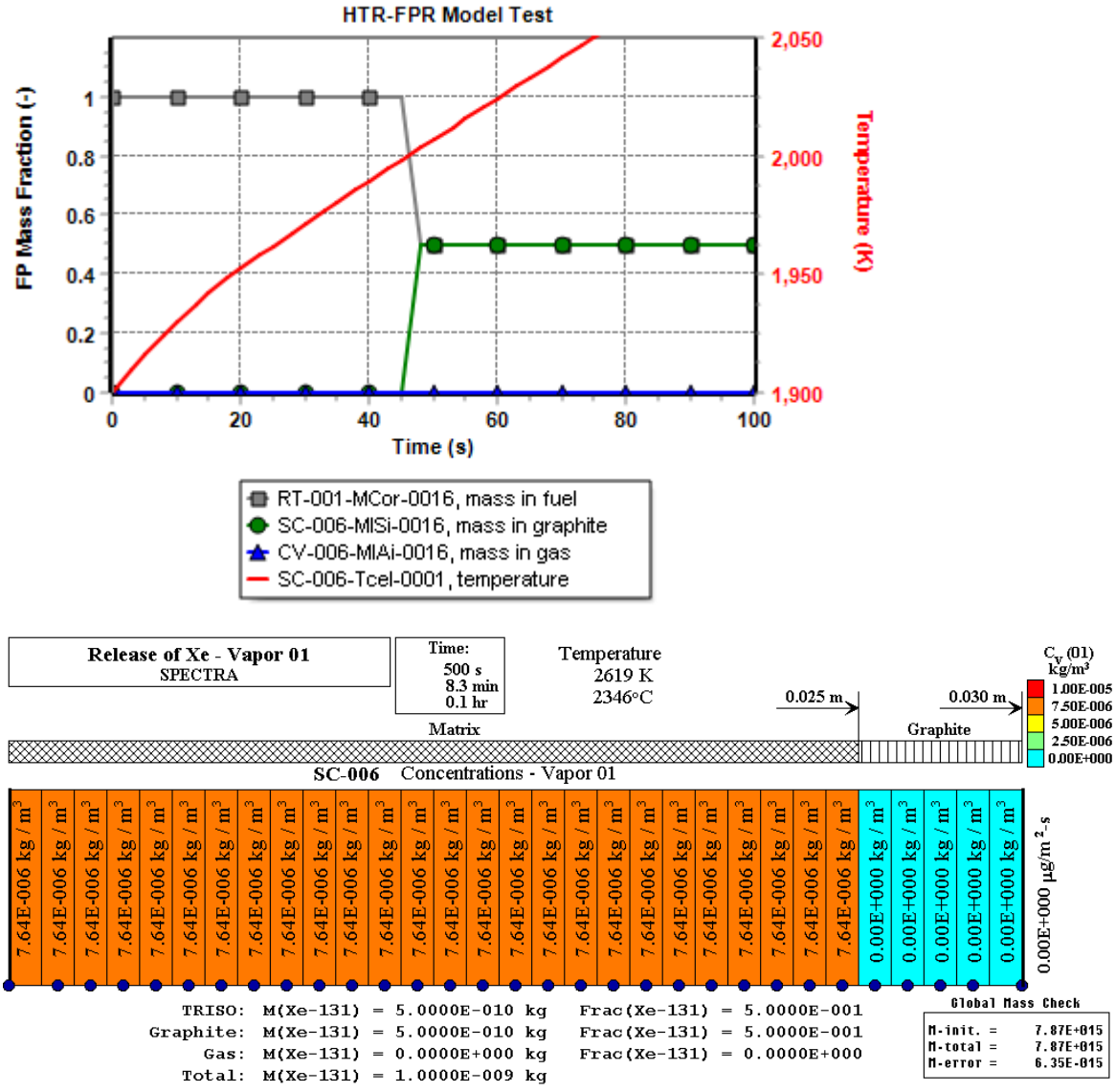

Figure 3-864 Test Fail-0-5-const

Clearly, these results are correct. They are also independent of the applied time step, which was checked in calculations by varying time step between 0.1 s and 5.0 s.

- **Test Fail-0-5**

This test is the same as before but now diffusion in SC-006 is possible. The input file is located in: \Z-INPUTS\RT\FP-Release\HTR\Verification\Fail\Fail-05.SPE. Results are shown in Figure 3-865. Calculations are performed for a longer time, 1,000,000 s. The 50% failure is occurring practically at the start of the test but diffusion from the pebble to gas is very slow. Clearly, the fission product release results are correct. The diffusion results are qualitatively correct and are not checked here in detail since the correctness of the diffusion model is shown by comparing results to theoretical solutions in sections 3.12.42, 3.12.43, and 3.12.44. The results are independent of the applied time step, which was checked in calculations by varying time step between 1.0 s and 10.0 s.

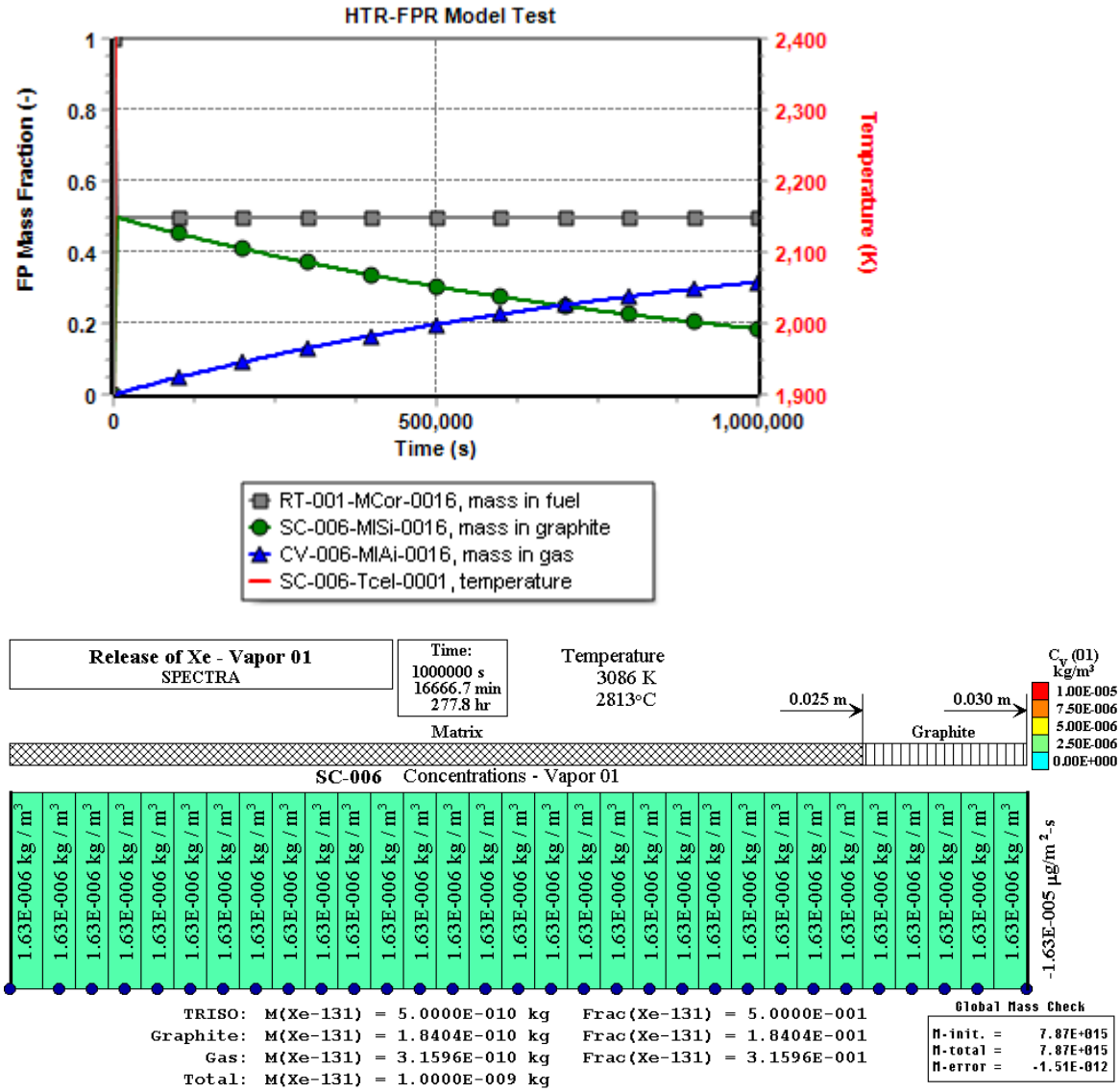

Figure 3-865 Failure test 2 - release of Xe-131

- **Test Diff-Xe-const**

This test is very similar to the test Fail-0-5-const. In contrast to Fail-0-5-const, in the present case release is caused by diffusion only. Failure is disabled by using a Control Function which gives failure fraction of 0.0, independently of temperature. The pebble is heated up quickly to 1900°C and kept at this temperature. Release of Xe-131 is monitored by plotting the following parameters:

- mass of Xe-131 in the TRISO particles (fuel region 1): RT-001-MCor-0016,
- mass of Xe-131 released that is present in graphite: SC-006-MISi-0016,
- mass of Xe-131 released from graphite to the gas: CV-006-MIAi-0016.

The theoretical value of Xe-131 remaining inside the fuel is in this case:

$$M_{FP} = M_{FP,0} \cdot \exp(-X \cdot t)$$

$$X = \frac{3}{R_{TRISO} \cdot R_{diff}}$$

In order to perform verification of the computed values, an automated verification was set up using Control Functions, defined as follows:

CF-200 = X_{UO2} / D_{UO2}
CF-201 = X_{SiC} / D_{SiC}
CF-202 = X_{PyC} / D_{PyC}
CF-203 = $R_{eff} = X_{UO2} / D_{UO2} + X_{SiC} / D_{SiC} + X_{PyC} / D_{PyC}$
CF-204 = $X = 3 / R_{TRISO} / R_{diff}$
CF-205 = $-X \cdot t$
CF-206 = $M_{FP,0} \cdot \exp(-X \cdot t)$

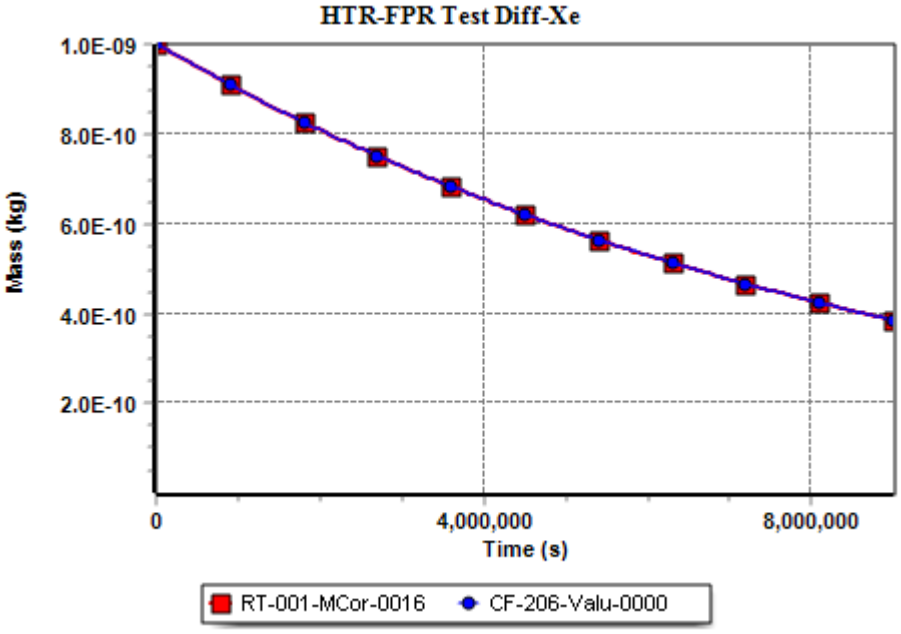

Figure 3-866 Verification of Xe-131 mass in fuel - test Diff-Xe-const

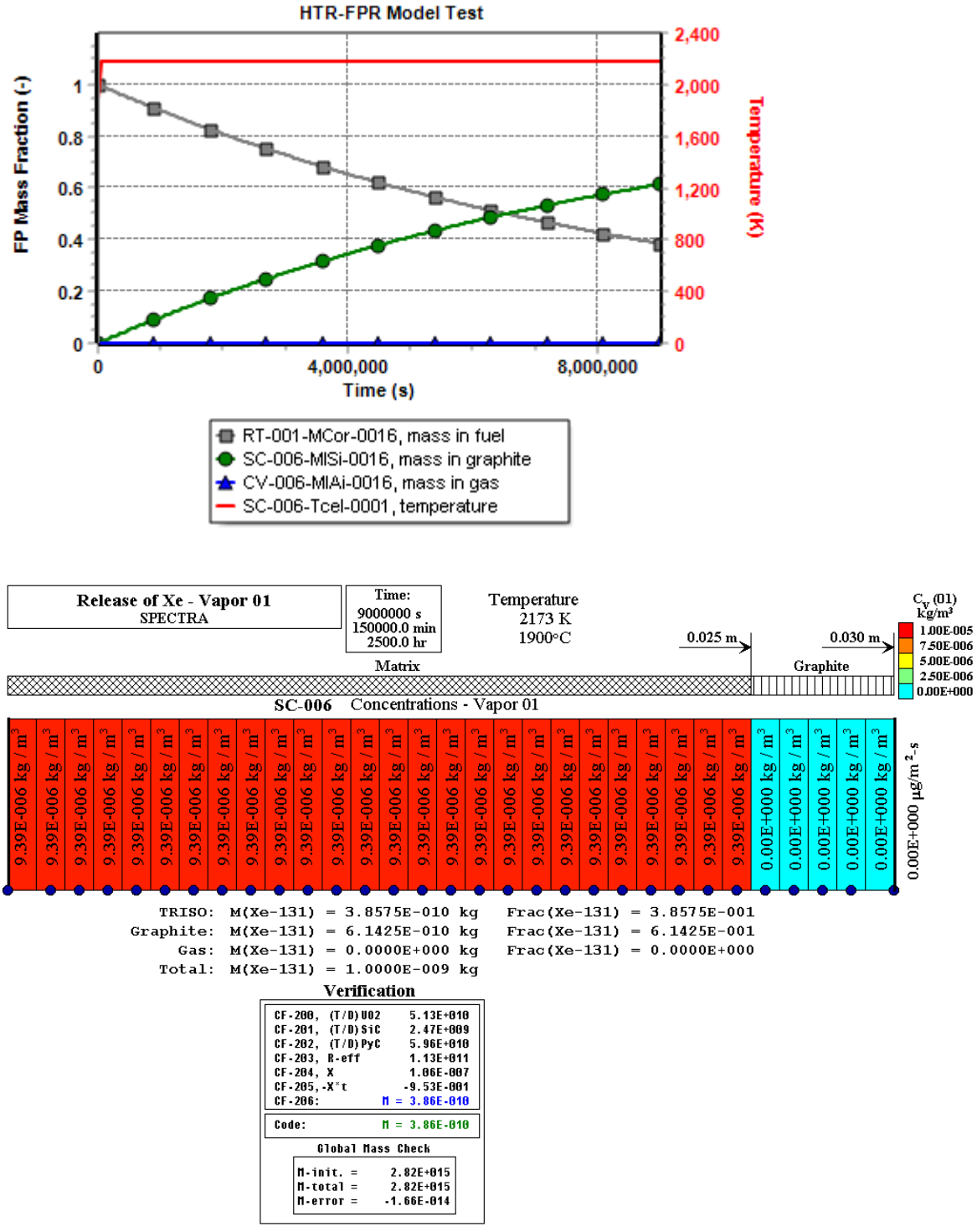

Figure 3-867 Test Diff-Xe-const

The input file is located in: \Z-INPUTS\RT\FP-Release\HTR\Verification\Diff\Diff-Xe-const.SPE. Results are shown in Figure 3-866 and Figure 3-867. Verification is shown in Figure 3-866 and the bottom of Figure 3-867, by comparing the mass of Xe-131 in the core with the theoretical value obtained as CF-206. A very good agreement is obtained. The results are independent of the applied time step, which was checked in calculations varying time step between 1.0 s and 10.0 s.

In this case the diffusion of Xe in the graphite is not possible (the diffusion coefficients in the matrix and in the graphite are set to zero). Therefore all the released Xe-131 remains in the fuel nodes: 25 nodes of SC-006 - Figure 3-867. For the same reason there is no release to the gas, which is clear in Figure 3-867.

- **Test Diff-Xe**

This test is very similar to the test Diff-Xe-const. Again, release is caused by diffusion only. The release of Xe-131 is monitored by plotting the following parameters:

- mass of Xe-131 in the TRISO particles (fuel region 1): RT-001-MCor-0016,
- mass of Xe-131 released that is present in graphite SC-006-MISi-0016,
- mass of Xe-131 released from graphite to the gas CV-006-MIAi-0016.

The theoretical value of Xe-131 remaining inside the fuel is obtained by CF-206, defined in the same way as in the previous test. The input file is located in: \Z-INPUTS\RT\FP-Release\HTR\Verification\Diff\Diff-Xe.SPE. Results are shown in Figure 3-868 and Figure 3-869. Verification is shown in Figure 3-868 and the bottom of Figure 3-869, by comparing the mass of Xe-131 in the core with the theoretical value obtained as CF-206. A very good agreement is obtained. The results are independent of the applied time step, which was checked in calculations varying time step between 1.0 s and 10.0 s.

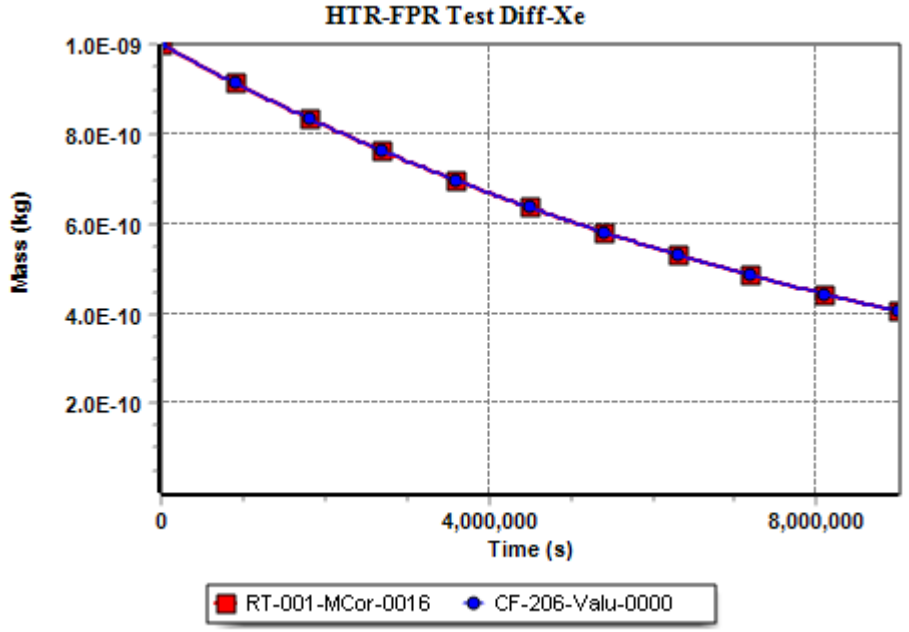

Figure 3-868 Verification of Xe-131 mass in fuel - test Diff-Xe

In this case diffusion of Xe in the graphite is possible. Xe-131 is slowly diffusing through the matrix and the graphite and is finally released to the gas space - Figure 3-869. The diffusion results are qualitatively correct and are not checked here in detail since the correctness of the diffusion model is shown by comparing results to theoretical solutions in sections 3.12.42, 3.12.43, and 3.12.44.

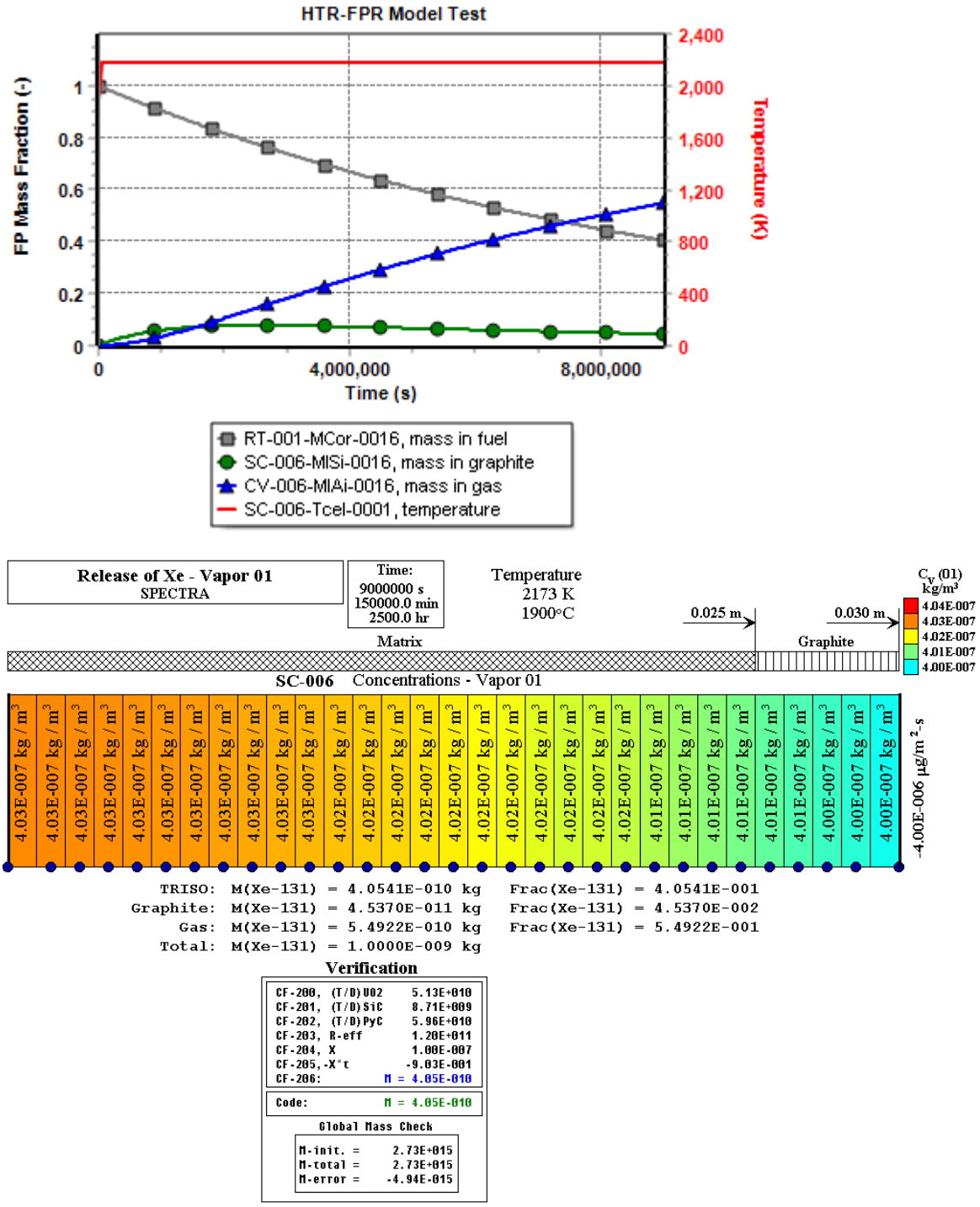

Figure 3-869 Test Diff-Xe

- **Test Cs-1900**

This test compares the results of the full fission product release model HTR-FPR and separate elements. A single pebble is modeled. The initial mass of 10^{-9} kg of Cs-137 is defined in the fuel region. The SC is quickly heated to 1900°C and kept at that temperature. The input file is located in: \Z-INPUTS\RT\FP-Release\HTR\Verification\Cs-1900. Three cases are analyzed:

(a) No diffusion - release only due to failure of TRISO particles
(b) No failure - release only due to diffusion through the coating layers
(c) Full model

Results are shown in Figure 3-870 through Figure 3-874. Each case is shortly discussed below.

(a) Figure 3-870 and Figure 3-874 (a) show results obtained for the case where release is assumed to occur due to failure only. The default failure correlation is used. For T=1900°C the correlation gives failure fraction of $F = 2.257\times10^{-3}$ (for maximum burn-up, B=1.0). This is the "theoretical value" calculated by CF-206 for this case. It is seen that this mass of Cs-137 is released to graphite at the start of the test (when the temperature rises 1900°C). Due to slow diffusion, practically all of this mass is released to the gas by the end of the test, phase: 108,000 s or 300 h.

(b) Figure 3-871 and Figure 3-874 (b) show results obtained for the case where release is assumed to occur due to diffusion only. The "theoretical value" of Cs-137 mass in fuel is calculated by CF-206, defined as follows:

CF-200 = X_{UO2} / D_{UO2}
CF-201 = X_{SiC} / D_{SiC}
CF-202 = X_{PyC} / D_{PyC}
CF-203 = $R_{eff} = X_{UO2} / D_{UO2} + X_{SiC} / D_{SiC} + X_{SiC} / D_{SiC}$
CF-204 = $X = 3 / R_{TRISO} / R_{diff}$
CF-205 = $- X \cdot t$
CF-206 = $M_{FP,0} \cdot \exp (- X \cdot t)$

The mass of Cs-137 in the fuel agrees very well with the theoretical solution. The Cs-137 that is released from the fuel starts diffusing through the matrix and graphite nodes, which is seen in Figure 3-871. Due to slow diffusion, practically all of this mass is released to the gas by the end of the test, phase: 1,080,000 s or 300 h. The diffusion results are qualitatively correct and are not checked here in detail since the correctness of the diffusion model is shown by comparing results to theoretical solutions in sections 3.12.42, 3.12.43, and 3.12.44.

(c) Figure 3-872 and Figure 3-874 (c) show results obtained for the full release model, failure + diffusion. It is clear that the results are very similar to the test (b). This means that in cases where the fuel is kept at elevated temperature for an extended period of time (in this case 500 h) the release is caused mainly by diffusion. Note that analyses of accident sequences in HTR reactors indicate periods when fuel may be exposed to elevated temperature are clearly shorter than that.

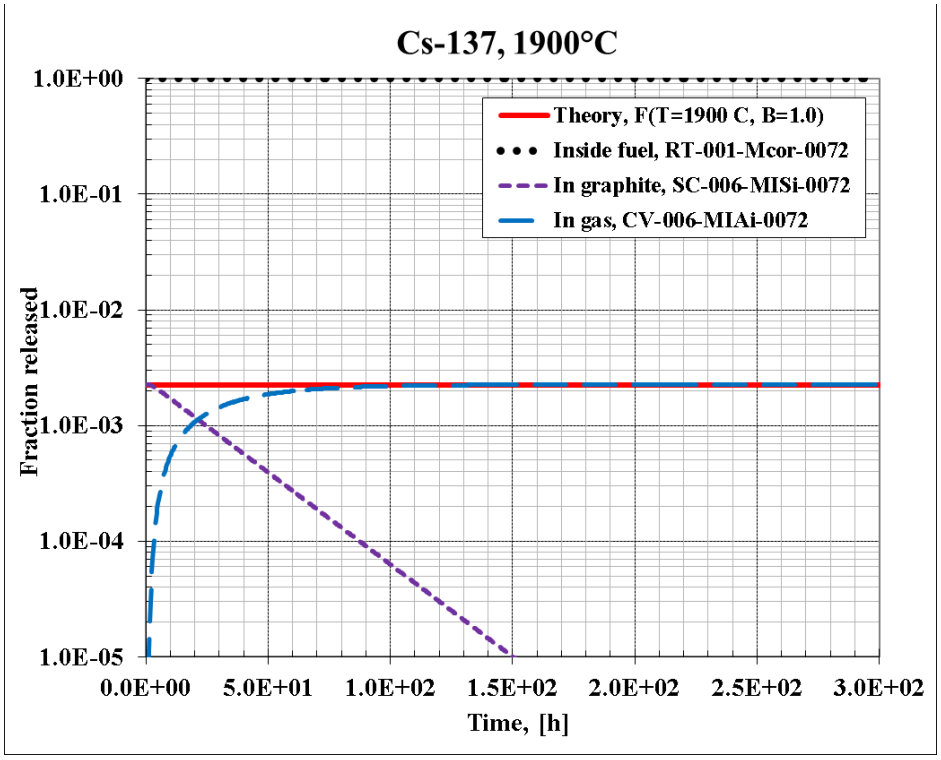

Figure 3-870 Results of test Cs-1900, failure only, no diffusion

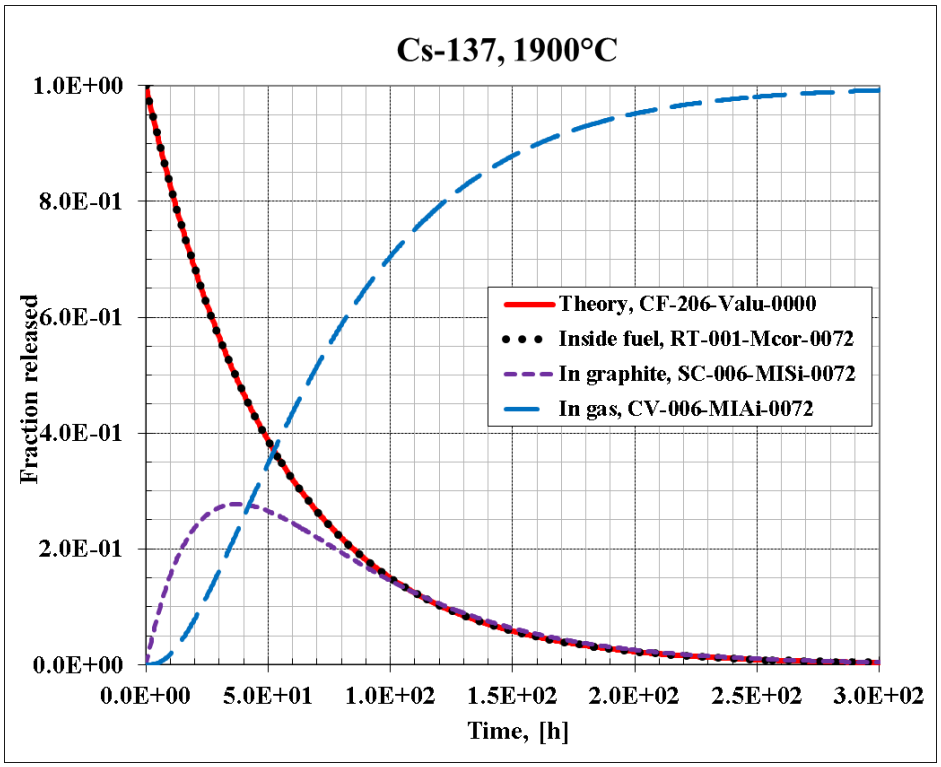

Figure 3-871 Results of test Cs-1900, diffusion only, no failure

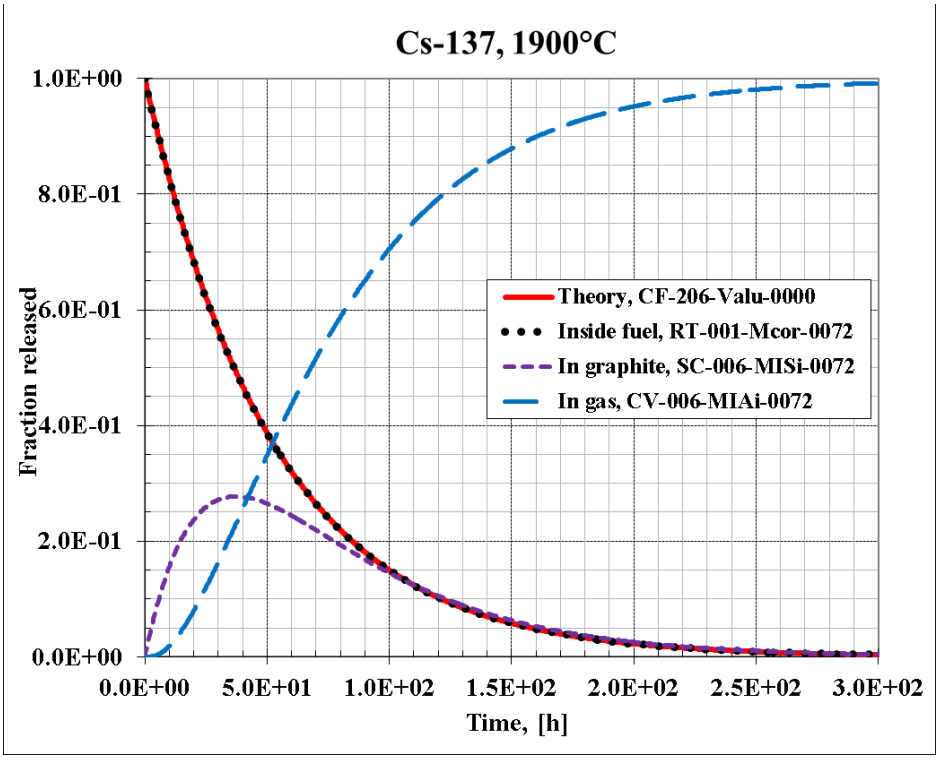

Figure 3-872 Results of test Cs-1900, full model

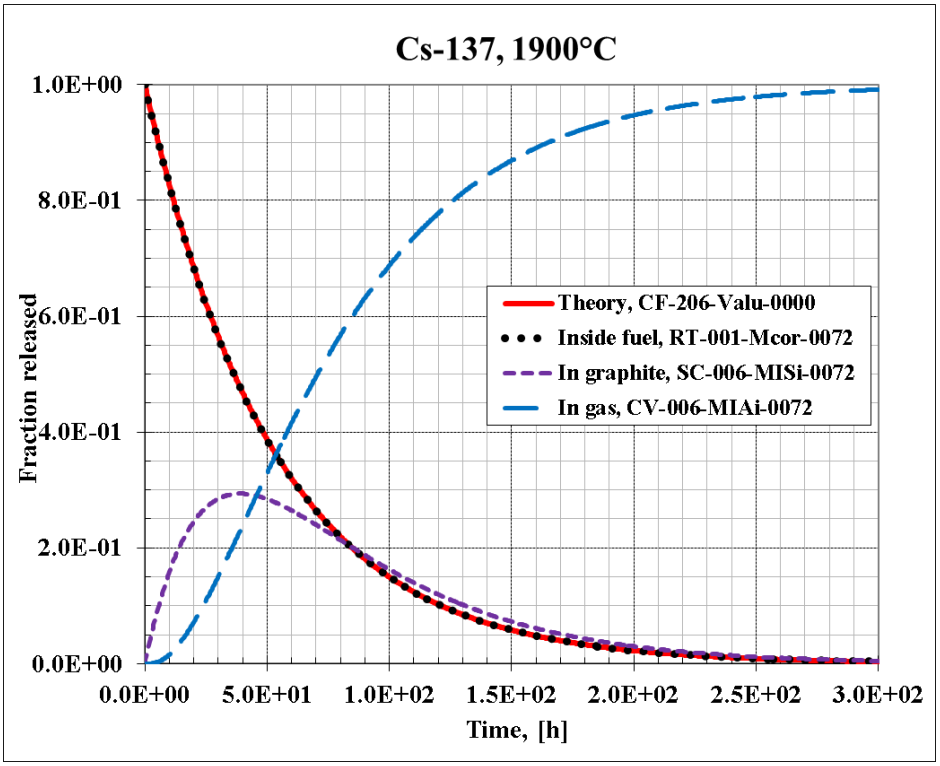

Figure 3-873 Results of test Cs-1900, full model, desorption constant $B_S = 10^{-6}$

(a) no diffusion

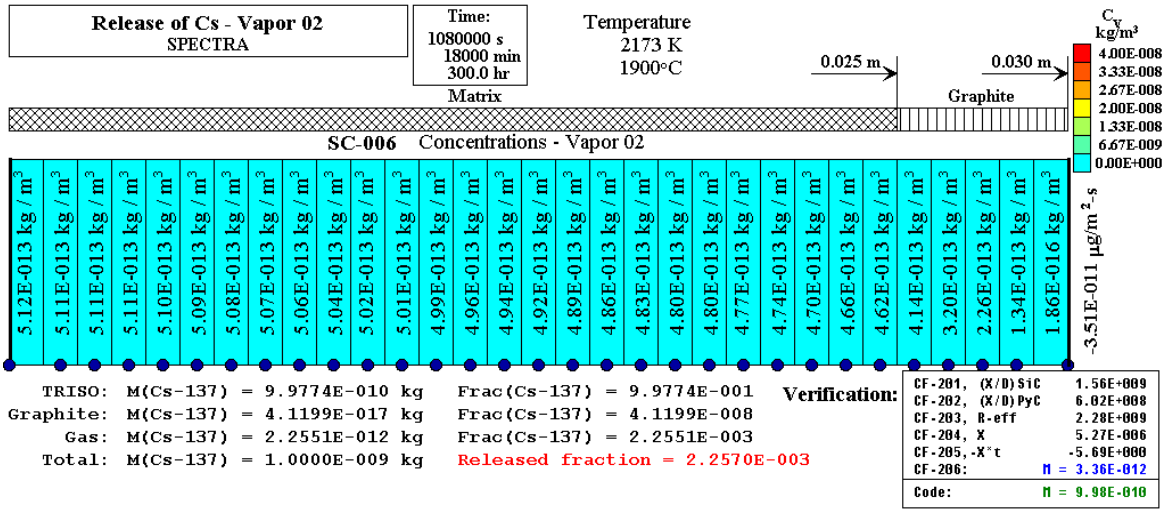

(b) no failure

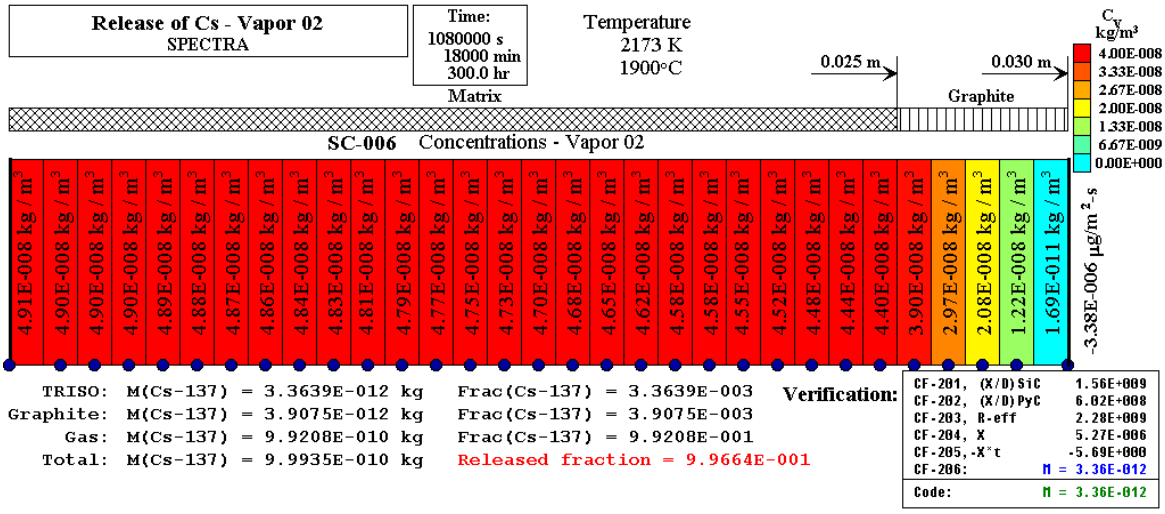

(c) full model

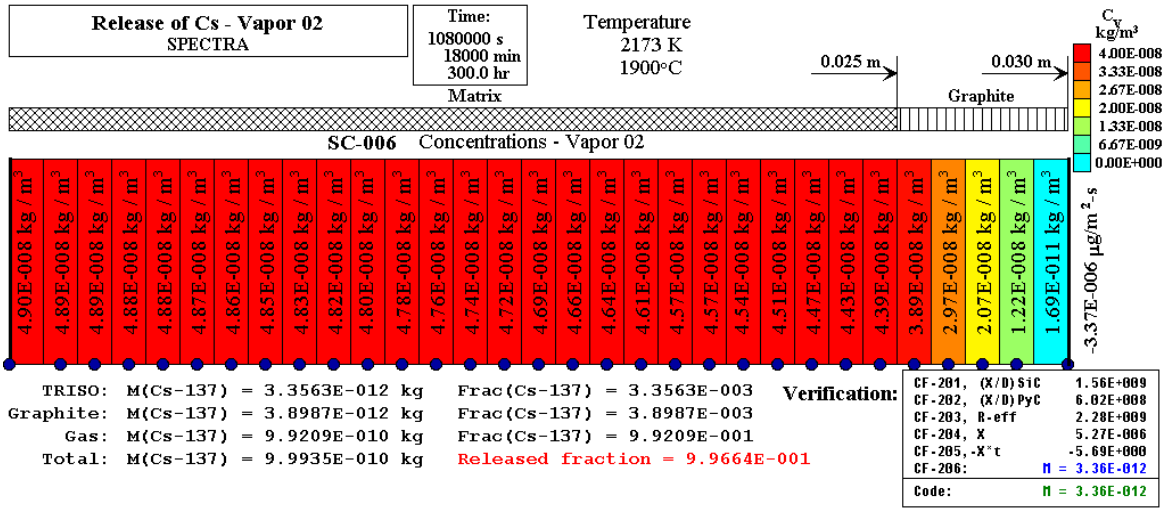

Figure 3-874 Results of test Cs-1900

Figure 3-873 shows the results of the sensitivity calculations studying the effect of the desorption coefficient. In most cases B_S=1.0 (maximum desorption) is used to maximize the release. Data show that a realistic value is $B_S \sim 10^{-6}$ [95]. Results obtained with this value are shown in Figure 3-873. This figure is very similar to Figure 3-872, which shows that the selection of B_S is not very important, as long as large enough value is used.

In the considered examples the released fission products are assumed to be removed immediately by the gas. Consequently, the effect of isotope vapor pressure in the gas (and sorption isotherms) is not important. The sorption isotherms are discussed shortly in the last verification test, Cs-137-Sorp, discussed later in this section.

- **Test Cs-1600**

This test is very similar to the previous test. The only difference is the lower temperature: 1600°C. This temperature is considered as an upper limit for HTRs during accidents. Results are shown in Figure 3-875, Figure 3-876, and Figure 3-877. Generally the results are very similar. Diffusion is dominant, but now it takes significantly longer; after 1000 h (3,600,000 s) about 50% of Cs-137 is released. The failure fraction at this temperature (and maximum burnup, B = 1.0) is 8.013×10^{-4}, which is in agreement with the calculated value shown in Figure 3-875 (a).

(a) no diffusion

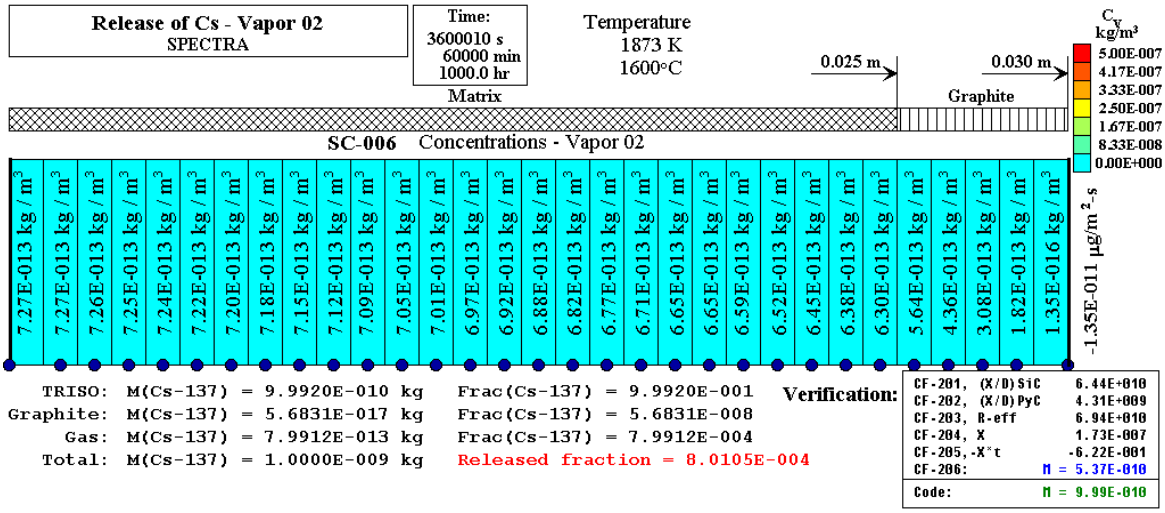

(b) no failure

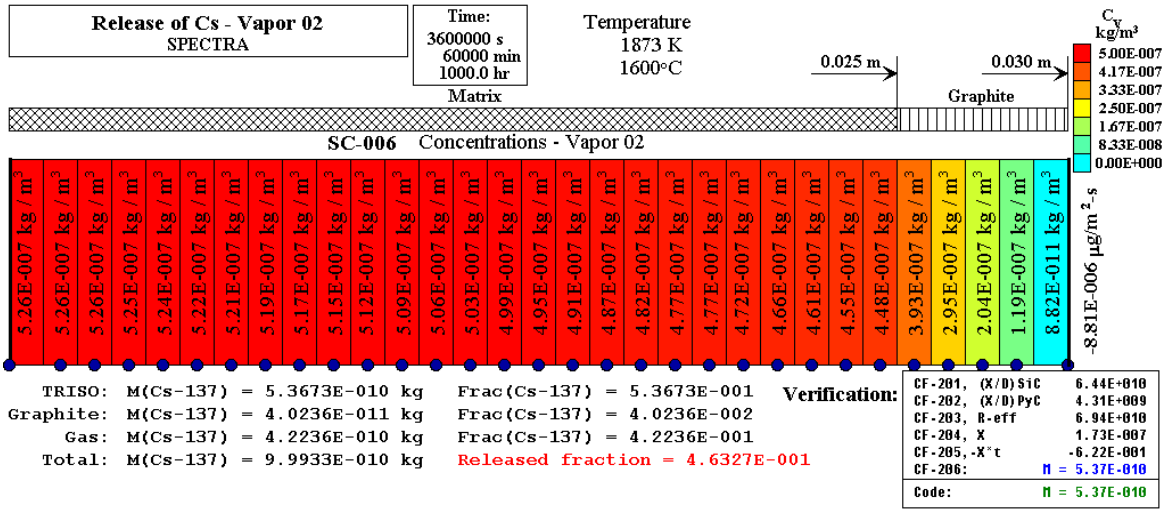

(c) full model

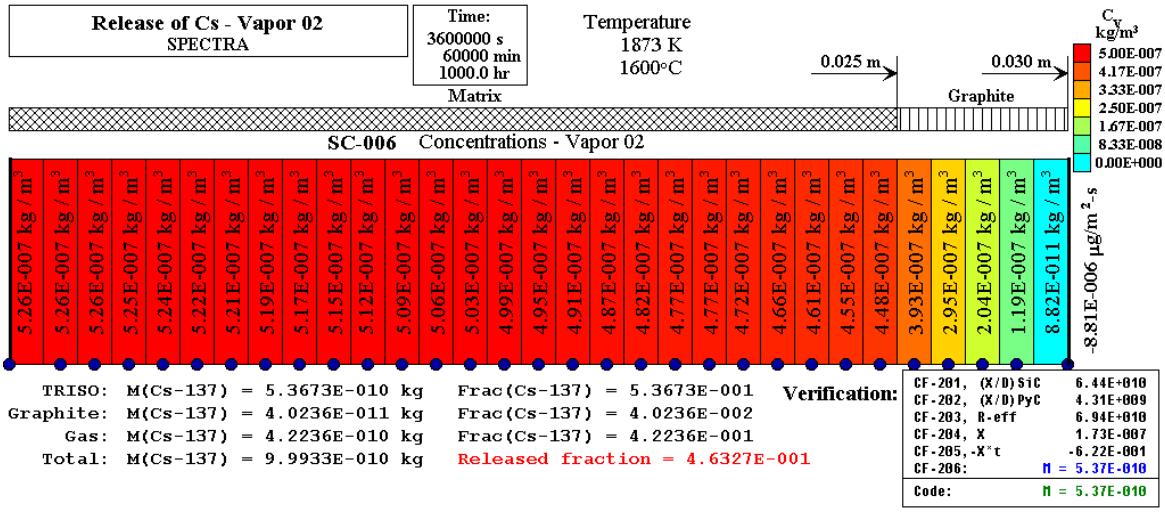

Figure 3-875 Results of test Cs-1600

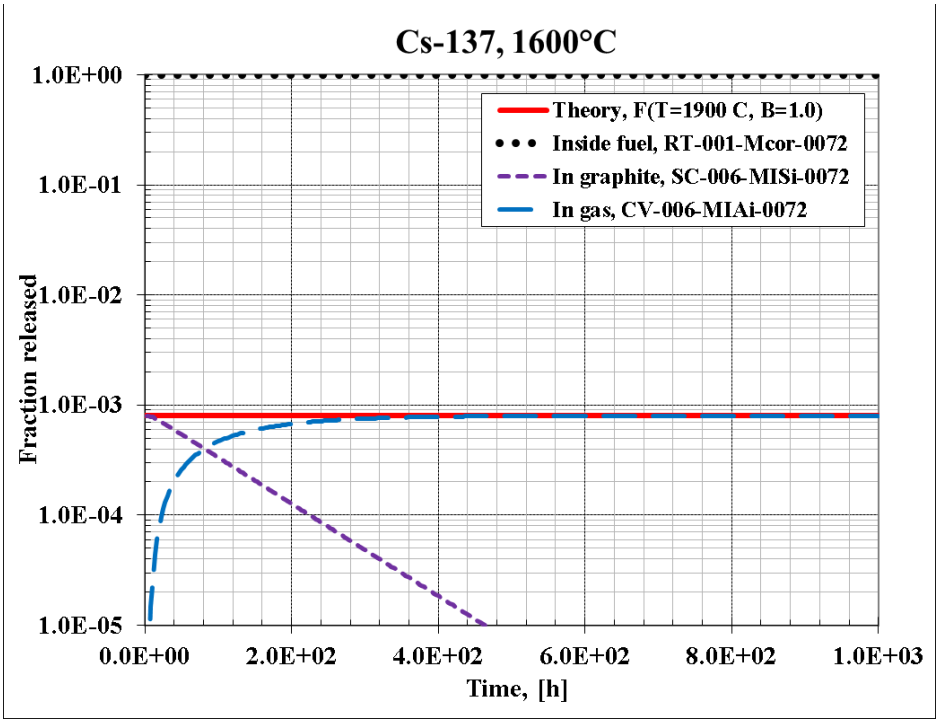

Figure 3-876 Results of test Cs-1600, failure only, no diffusion

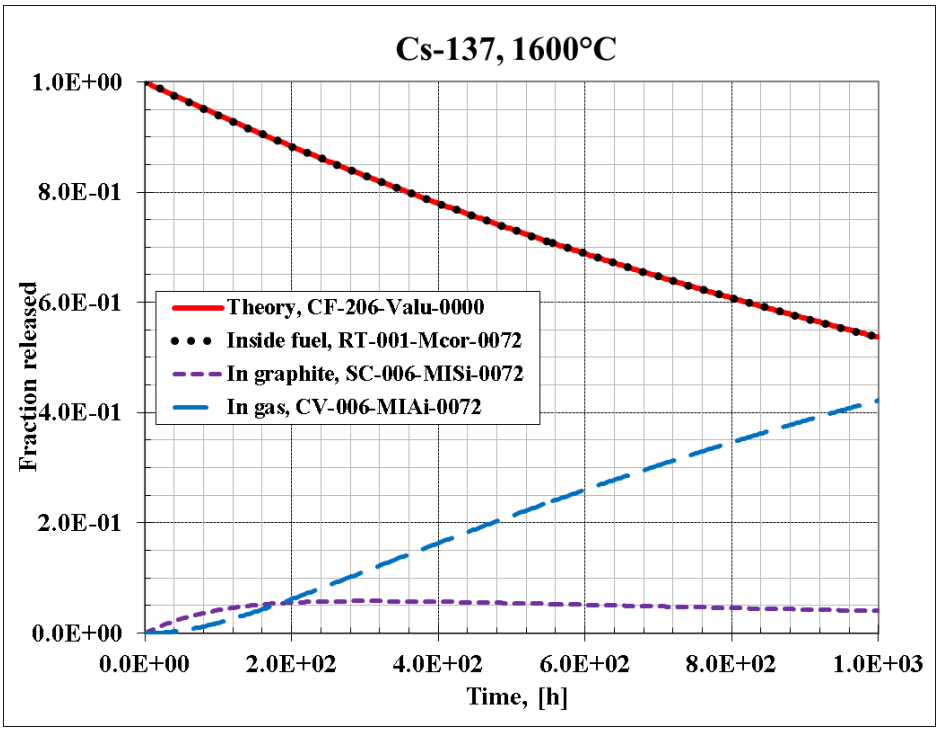

Figure 3-877 Results of test Cs-1600, diffusion only, no failure

- **Test Ba-135 (release of isotope produced due to decay)**

As shown in Volume 1, release due to failure is obtained from:

$$\left(\frac{dM_{FP}}{dt}\right)_{fail} = -\left(\frac{M_{FP}\cdot\Delta F}{(1-F_0)} + F_0\cdot\Delta M_{FP,f}\right)\cdot\frac{1}{\Delta t}$$

The present test is designed to provide a numerical verification of the case when the failure fraction is constant and there is a continuous production of an isotope by decay. In such case the second term is zero, since $\Delta M_{FP,f}$ is source due to fission. Therefore the release is calculated in this case from:

$$\left(\frac{dM_{FP}}{dt}\right)_{fail} = -\left(\frac{M_{FP}\cdot\Delta F}{(1-F_0)}\right)\cdot\frac{1}{\Delta t}$$

For this purpose, the isotope chain 135 (Figure 3-878) was selected. In this chain, the long-life isotope Cs-135 is slowly decaying into Ba-135.

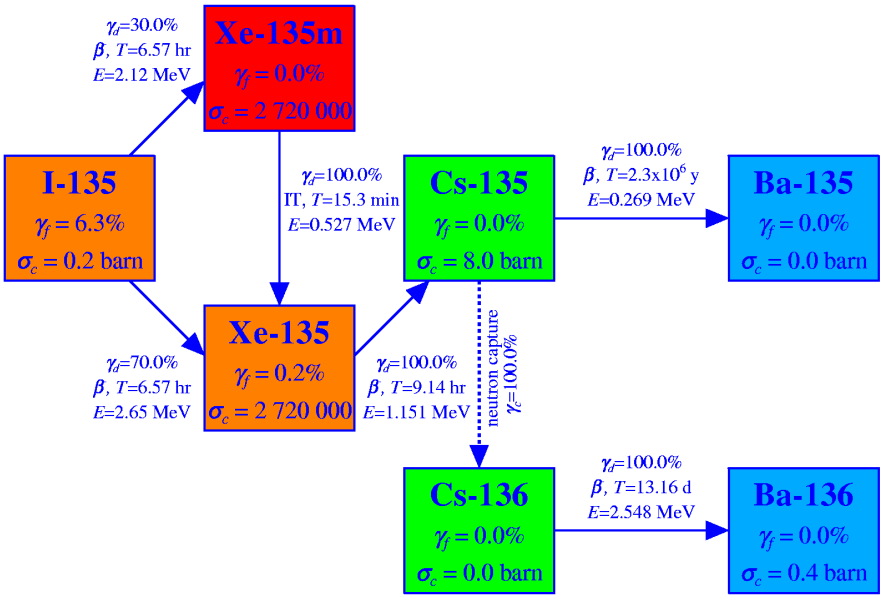

Figure 3-878 Decay chain 135, long-life Cs-135 slowly producing Ba-135

The test case is very similar to the previous tests. An initial mass of Cs-135 (isotope 0054) of 10^{-9} kg is placed in the tested pebble. Release by diffusion is disabled; release is only assumed to occur due to failure of TRISO particles. The failure fraction is defined by a Control Function (CF-100) rather than a correlation. Three cases are considered with failure fractions of 0.0, 0.5, and 1.0 respectively. Release from pebble surface to gas is disabled to make this case easier to interpret.

The input files are located in: \Z-INPUTS\RT\FP-Release\HTR\Verification\Ba-135-Decay. Results are shown in Figure 3-880 (Cs-135) and Figure 3-881 (Ba-135). The following observations can be made:

- The mass of Cs-135 is remaining practically constant (10^{-9} kg) because the decay is very slow (furthermore the reactor is assumed to be shut down, therefore there is no Cs-136 production by neutron capture).
- The mass of Ba-135 is linearly increasing due to decay of Cs-135 (Ba-135 does not decay).

The results of three cases are discussed below.

- ***F* = 0.0**: There is no release. All Cs-135 (10^{-9} kg) remains in fuel - Figure 3-880 (a). All Ba-135 (1.223×10^{-17} kg) that is produced within the analyzed time frame (1,280,000 s) remains in the fuel - Figure 3-881 (a). This is what is expected for this case.
- ***F* = 0.5**: In this case 50% of TRISO particles fail practically at the start of the test. Half of Cs-135 (0.5×10^{-9} kg) remains in fuel and half is outside of the fuel - Figure 3-880 (b). All Ba-135 (1.223×10^{-17} kg) that is produced within the analyzed time frame (1,280,000 s) is divided as follows: one half (6.116×10^{-18} kg) is inside the fuel and one half (6.116×10^{-18} kg) is outside of the fuel. This is what is expected for this case. The equal fractions throughout the analyzed test are shown in the time-dependent graph Figure 3-879.
- ***F* = 1.0**: In this case 100% of TRISO particles fail practically at the start of the test. Practically all (a minimum fraction of 10^{-4} remains in fuel for numerical reasons, explained below) of the Cs-135 mass (10^{-9} kg) is released - Figure 3-880 (c). All Ba-135 (1.223×10^{-17} kg) that is produced within the analyzed time frame (1,280,000 s) is also released - Figure 3-881 (c). This is what is expected for this case because the Ba-135 production took place after the failure of 100% of the TRISO particles.

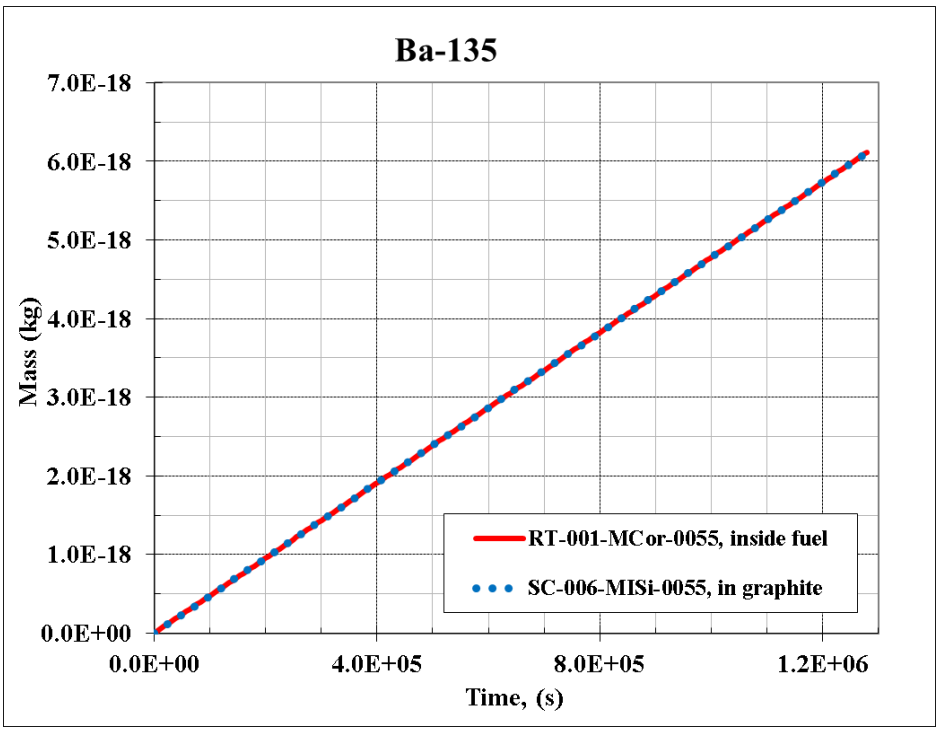

Figure 3-879 Test Ba-135, masses of stable Ba-135 in fuel and graphite

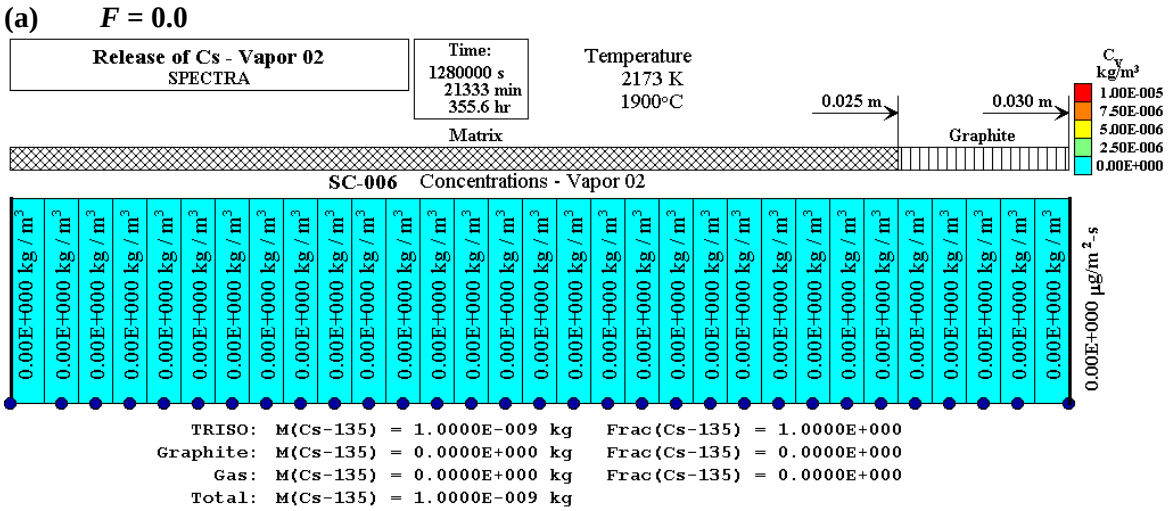

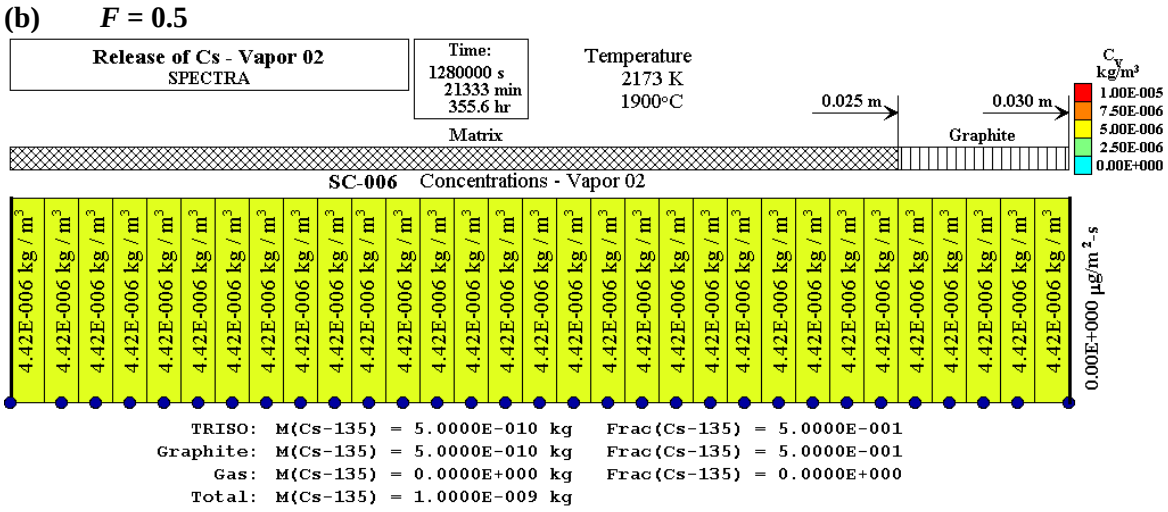

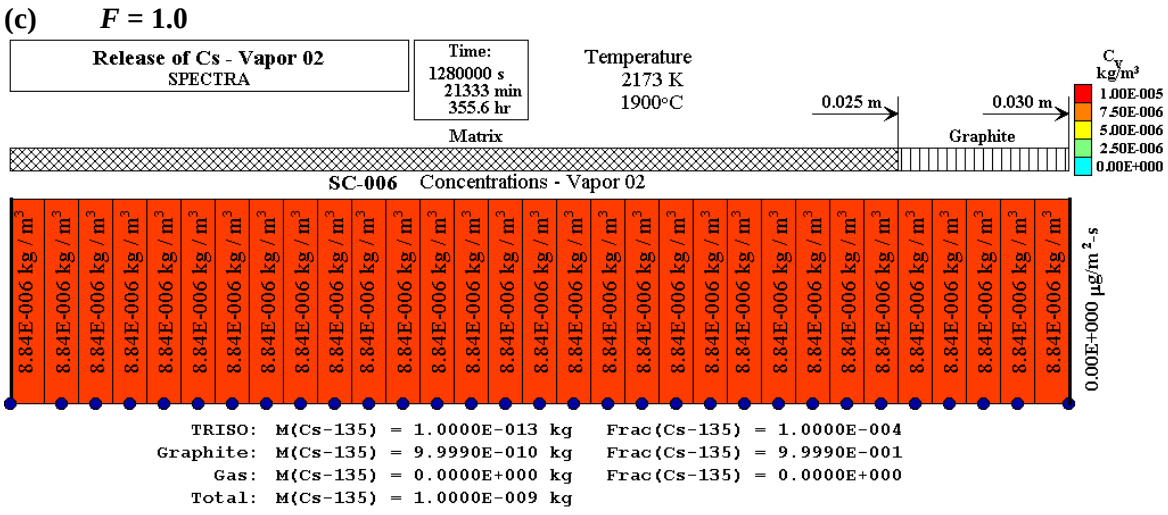

Figure 3-880 Test Ba-135, masses of long-life Cs-135

(a) ***F*** **= 0.0**

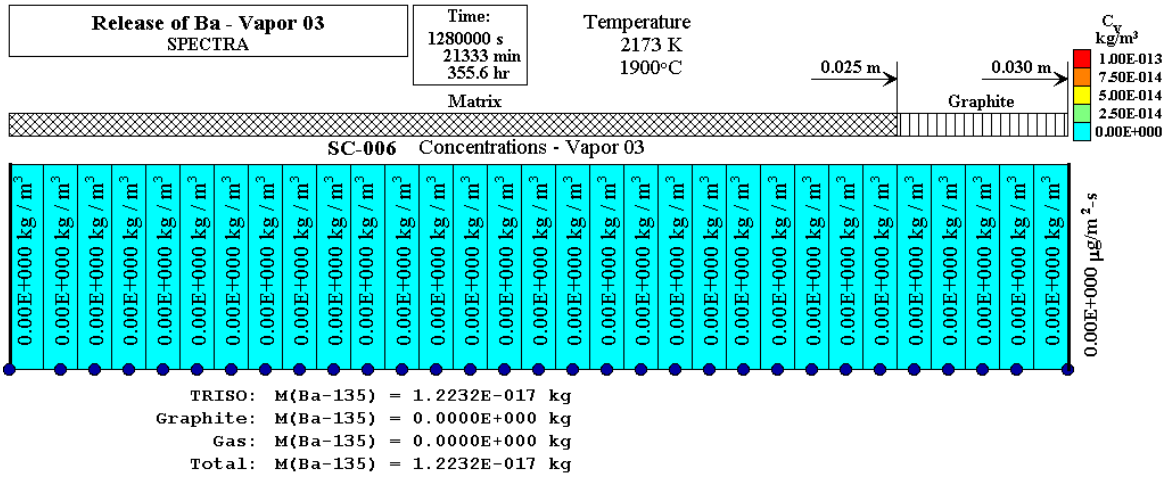


```
TRISO:  M(Ba-135) = 1.2232E-017 kg
Graphite:  M(Ba-135) = 0.0000E+000 kg
    Gas:  M(Ba-135) = 0.0000E+000 kg
  Total:  M(Ba-135) = 1.2232E-017 kg
```

(b) ***F*** **= 0.5**

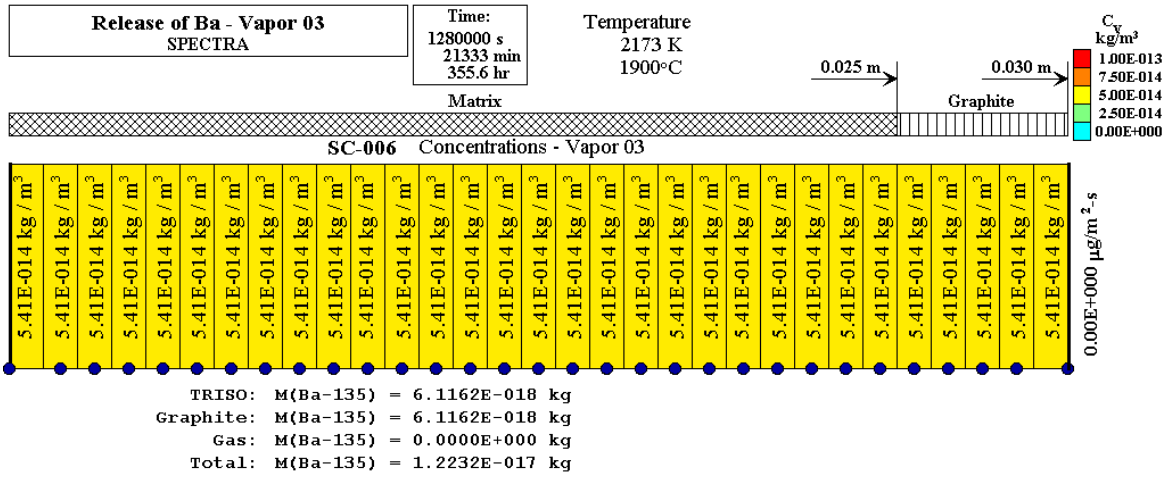


```
TRISO:  M(Ba-135) = 6.1162E-018 kg
Graphite:  M(Ba-135) = 6.1162E-018 kg
    Gas:  M(Ba-135) = 0.0000E+000 kg
  Total:  M(Ba-135) = 1.2232E-017 kg
```

(c) ***F*** **= 1.0**

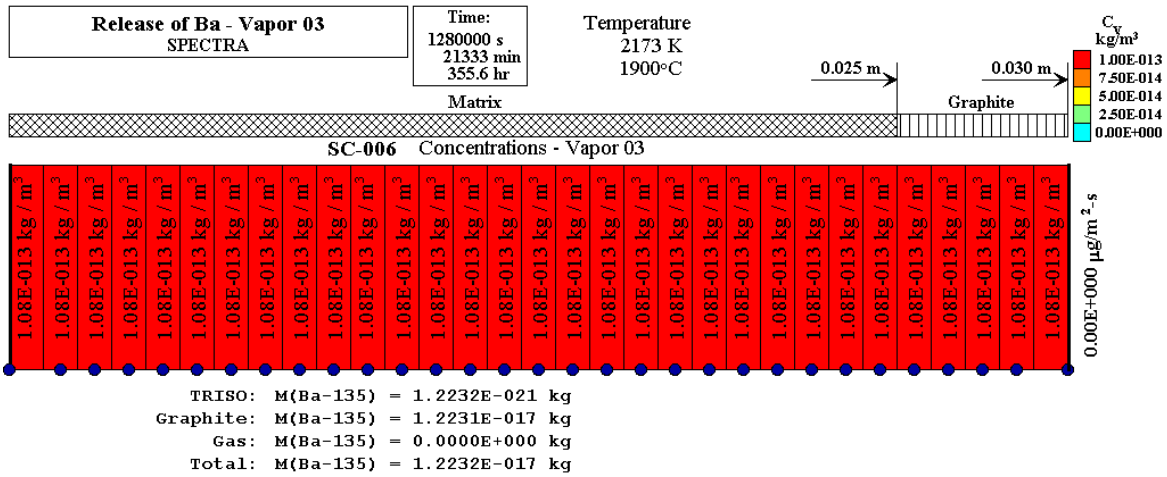


```
TRISO:  M(Ba-135) = 1.2232E-021 kg
Graphite:  M(Ba-135) = 1.2231E-017 kg
    Gas:  M(Ba-135) = 0.0000E+000 kg
  Total:  M(Ba-135) = 1.2232E-017 kg
```

Figure 3-881 Test Ba-135, masses of stable Ba-135

One additional explanation is needed, namely the use of $(1 - F_0)$ in the denominator of the release formula. This is easiest explained using a simple example. Suppose that the failure fraction increases from 0.0 to 1.0 in a single (large) time step, $\Delta F = 1.0$. The released mass during this time step is $M_{FP} \times \Delta F = M_{FP}$, which is correct. Now, let's assume that we use smaller time steps and the failure fraction increases from 0.0 to 0.5 in the first time step and from 0.5 to 1.0 in the second time step. In such case we have:

- release during the first time step (initial mass in fuel M_{FP}):

$$M_{FP} \times \Delta F = M_{FP} \times 0.5 = 0.5\ M_{FP}$$

- release during the second time step (initial mass in fuel $0.5\ M_{FP}$):

$$0.5\ M_{FP} \times \Delta F/(1 - F_0) = 0.5\ M_{FP} \times 0.5 / (1–0.5) = 0.5\ M_{FP}$$

Therefore after the second step the total mass released is equal to M_{FP}, so 100%. Without the term $(1 - F_0)$, the mass released during the second step would be equal to:

$$0.5\ M_{FP} \times \Delta F = 0.5\ M_{FP} \times 0.5 = 0.25\ M_{FP}$$

Consequently, the total mass released after the two time steps would be 75% instead of 100%. The term $\Delta F / (1 - F_0)$ gives the particles that fail during the time step compared to the particles that are intact at the start of time step. Test calculations show that with this formula the results are correct and independent of the time step used. In order to avoid division by zero when $F_0 = 1.0$, a maximum value of 0.9999 is set internally by the code. Consequently a very small fraction of fission products (10^{-4}) remains in the fuel even if the calculated failure fraction is 1.0.

- **Test Te-132 (release of isotope produced due to fission)**

As shown in Volume 1, release due to failure is obtained from:

$$\left(\frac{dM_{FP}}{dt}\right)_{fail} = -\left(\frac{M_{FP} \cdot \Delta F}{(1-F_0)} + F_0 \cdot \Delta M_{FP,f}\right) \cdot \frac{1}{\Delta t}$$

The present test is designed to provide a numerical verification of the case when the failure fraction is constant and there is a continuous production of a given isotope due to fission. In such case the first term is only active during the initial period and release during the long-term slow production is calculated from:

$$\left(\frac{dM_{FP}}{dt}\right)_{fail} = -\left(F_0 \cdot \Delta M_{FP,f}\right) \cdot \frac{1}{\Delta t}$$

This term is needed because in case of fission the fission products are being produced in all TRISO particles, intact and damaged as well.

For the purpose of testing, the isotope chain 132 (Figure 3-882) was selected. In this chain, the long-life isotope Te-132 is created by fission with yield fraction of 4.7%. A simple point kinetics model was set up, with approximately constant power of 1000 W (roughly equal to the power per pebble in a typical pebble reactor) set in SC-006, which represents a single pebble. In order to simplify the test for analytical verification, the decay is minimized by setting the decay constant to 10^{-20} 1/s (half-life of 6.9×10^{19} s). This means there is practically no decay and the change of Te-132 in time is only due to fission.

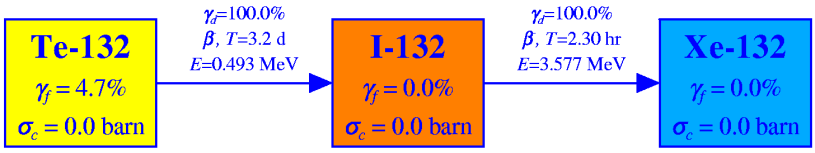

Figure 3-882 Decay chain 132, Te-132 produced by fission and very slowly decaying

The test case is very similar to the previous tests. Te-132 (isotope no. 0021) is constantly being produced in the core. The initial (equilibrium) mass at the considered conditions is 3.22×10^{-4} kg. This mass remains approximately constant during the considered period (1,280,000 s = 356 h). Release by diffusion is disabled; release is only assumed to occur due to failure of TRISO particles. The failure fraction is defined by a Control Function (CF-100) rather than a correlation. Three cases are considered with failure fractions of 0.0, 0.5, and 1.0 respectively. Release from the pebble surface to the gas is disabled to make this case easier to interpret.

The input files are located in: \Z-INPUTS\RT\FP-Release\HTR\Verification\Te-132-Fission. Results are shown in Figure 3-883, Figure 3-884, and Figure 3-885. The results of three cases are discussed below.

- ***F* = 0.0**: There is no release. All Te-132 (1.152×10^{-5} kg) remains in the fuel - Figure 3-885 (a). This is what is expected for this case.
- ***F* = 0.5**: In this case 50% of TRISO particles fail practically at the start of the test (the failure temperature, 2000 K, is reached at about 11 seconds). Half of Te-132 (5.76×10^{-6} kg) remains in the fuel and half is outside of the fuel - Figure 3-885 (b). This is what is expected for this case. The equal fractions throughout the analyzed test are shown in the time-dependent graph Figure 3-883.
- ***F* = 1.0**: In this case 100% of TRISO particles fail practically at the start of the test (the failure temperature, 2000 K, is reached at about 11 seconds). Practically all of the Te-132 mass (1.152×10^{-5} kg) is released - Figure 3-885 (c). This is what is expected for this case.

Finally, Figure 3-884 shows results that would be obtained if the term $F_0\ \Delta M_{FP,f}$ was not included. For this test calculation a specific code version was created in which this term was eliminated. In such case the released mass ("mass in graphite") is only increasing at the moment of failure of 50% of the particles at approximately the initial moment of the test. All the Te-132 produced during the test is in the fuel, which is clearly incorrect.

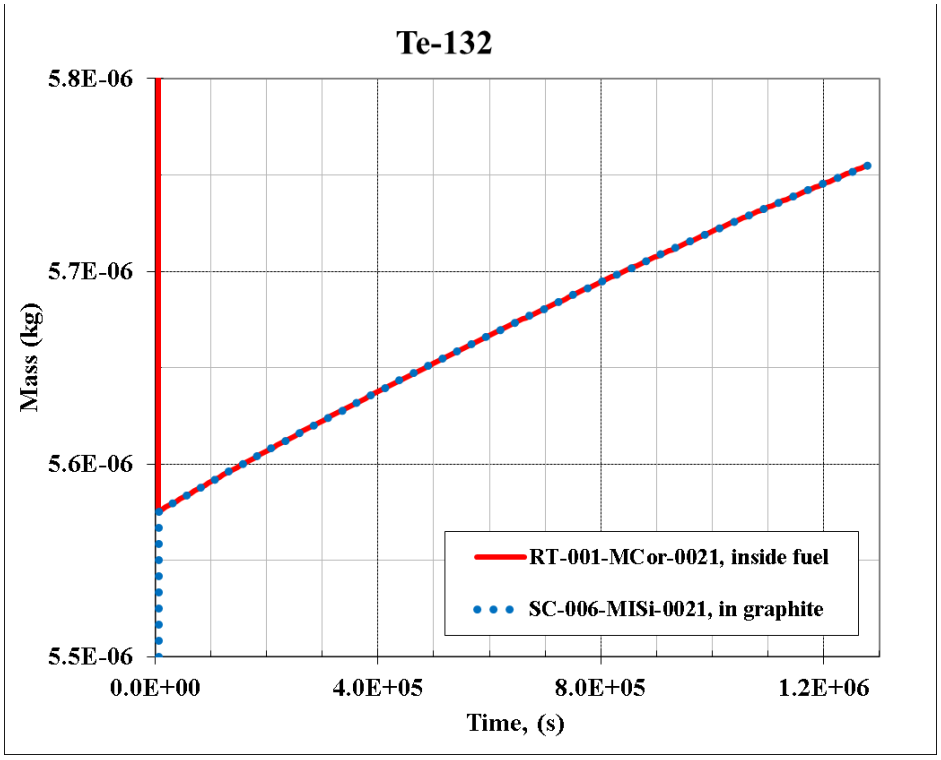

Figure 3-883 Test Te-132, masses of Te-132 in fuel and graphite

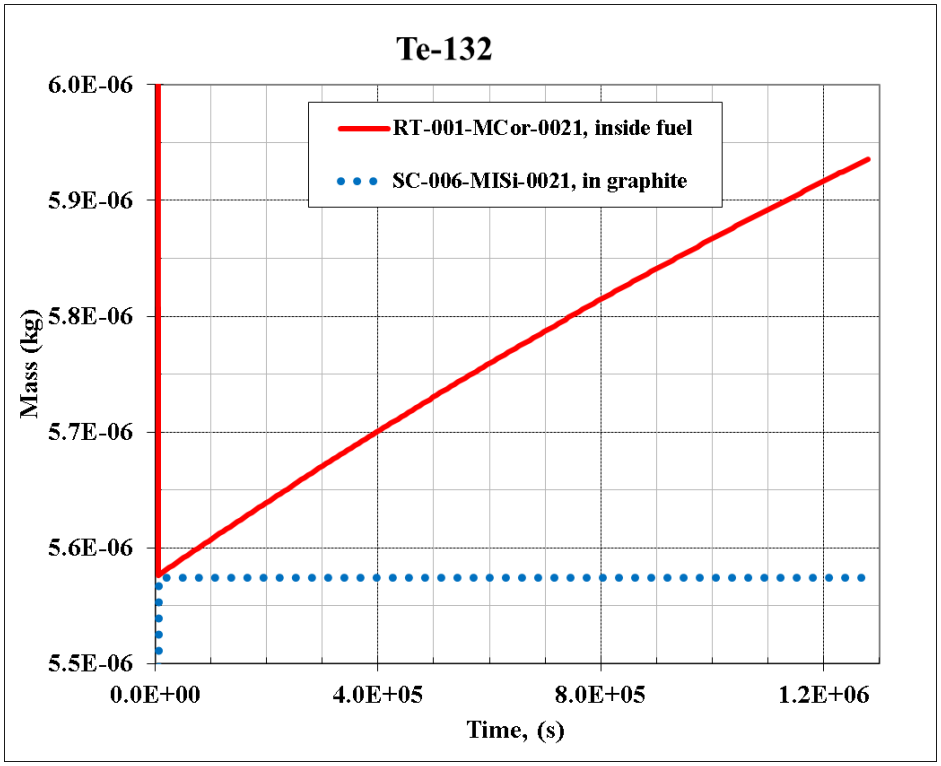

Figure 3-884 Test Te-132, results obtained without the term: $F_0 \times \Delta M_{FP,f}$

(a) $F = 0.0$

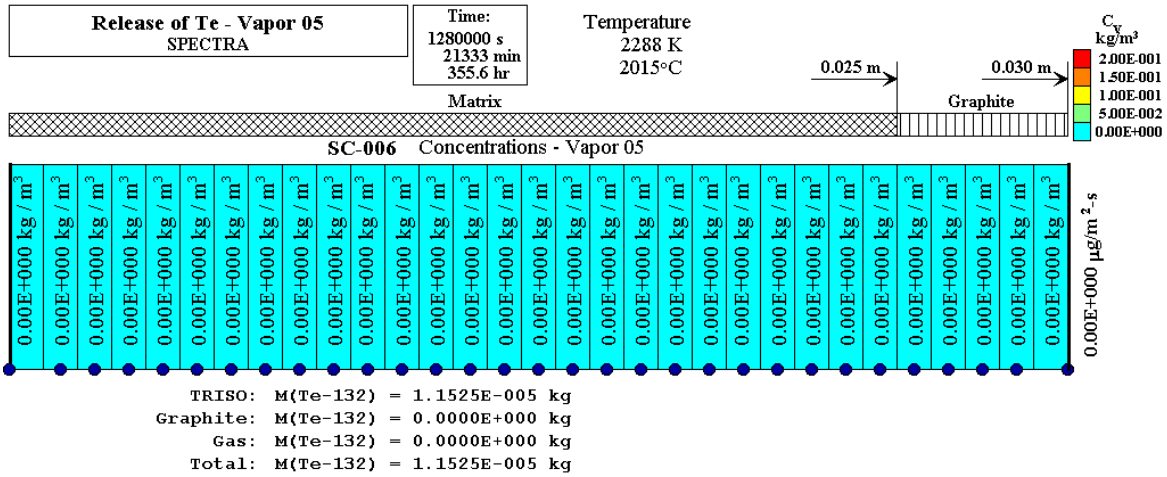


```
TRISO:  M(Te-132) = 1.1525E-005 kg
Graphite:  M(Te-132) = 0.0000E+000 kg
Gas:  M(Te-132) = 0.0000E+000 kg
Total:  M(Te-132) = 1.1525E-005 kg
```

(b) $F = 0.5$

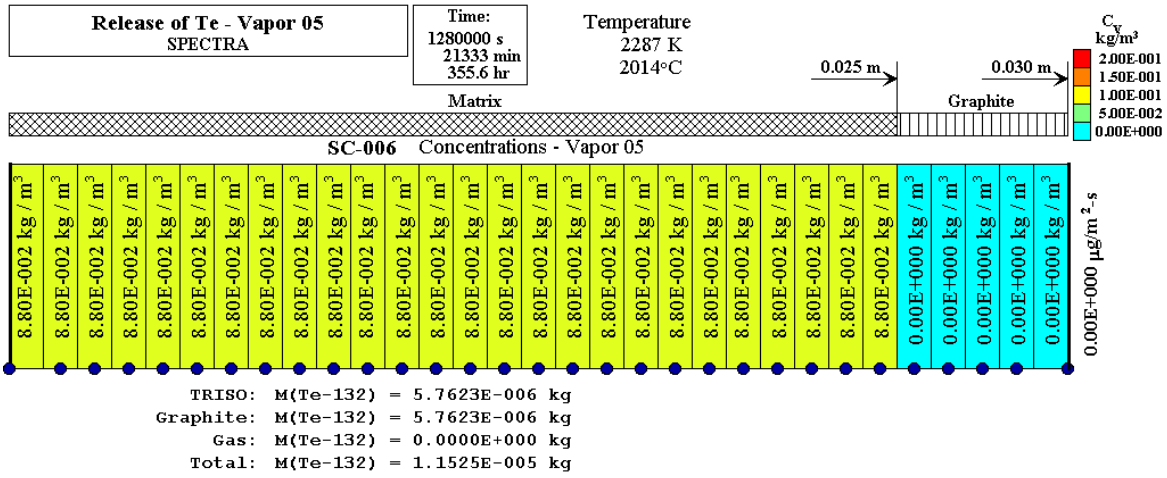


```
TRISO:  M(Te-132) = 5.7623E-006 kg
Graphite:  M(Te-132) = 5.7623E-006 kg
Gas:  M(Te-132) = 0.0000E+000 kg
Total:  M(Te-132) = 1.1525E-005 kg
```

(c) $F = 1.0$

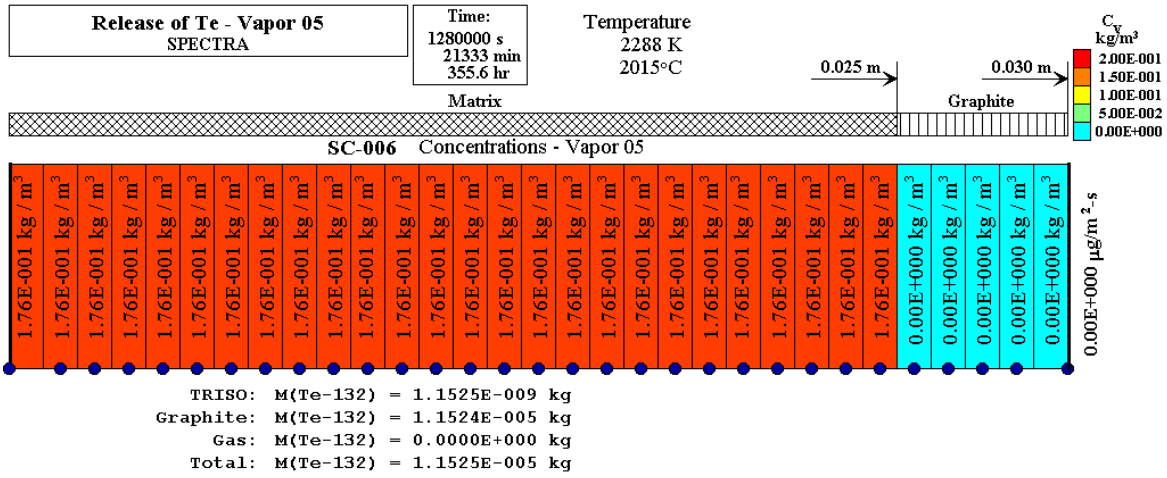


```
TRISO:  M(Te-132) = 1.1525E-009 kg
Graphite:  M(Te-132) = 1.1524E-005 kg
Gas:  M(Te-132) = 0.0000E+000 kg
Total:  M(Te-132) = 1.1525E-005 kg
```

Figure 3-885 Test Te-132

- **Tests Cs-137-Sorp and Sr-90-Sorp (sorption isotherms)**

This section illustrates the use of the sorption isotherms with the HTR-FPR model and presents verification of numerical results. All previous calculations were performed using only desorption (B_S>0.0, A_S=0.0). This approach will result in conservative (maximum) release to gas. The present tests were performed using A_S>0.0. As shown in Volume 1, a general modeling of sorption is available, including Henrian (linear) and Freundlich (non-linear) isotherms (see Volume 1 - "Sorption of Fission Product Vapors on Surfaces").

As a first step, the sorption coefficients are determined based on data from [195]. The sorption isotherms for Cs and Sr on matrix graphite are shown in Figure 3-886 (a) and Figure 3-887 (a) respectively. The Henrian isotherm is used (exponent x_A = XASRRT = 1.0). In such case the sorption flux is obtained from (Volume 1):

$$\left(\frac{dC_S}{dt}\right)_{total} = -A_S \cdot C_{gas} - B_S \cdot C_{wall}$$

$(dC_S/dt)_{total}$	mass transfer rate due to sorption, (kg/m^2-s)
C_{gas}	concentration of the vapor in the gas, (kg/m^3)
A_S	adsorption coefficient, (m/s)
C_{wall}	concentration of the vapor in the wall material, (kg/m^3)
B_S	desorption coefficient, (m/s)

In equilibrium conditions:

$$A_S \cdot C_{gas} = B_S \cdot C_{wall}$$

or:

$$C_{gas} = B_S \cdot C_{wall} / A_S$$

Values of A_S were selected by trial and error for five isotherms:

Cs: 1400°C, 1600°C, 1800°C, 2000°C, 2400°C, - Figure 3-886 (a)
Sr: 1600°C, 1800°C, 2000°C, 2200°C, 2400°C, - Figure 3-887 (a)

In order to do that, the values are converted to the units used in [195]:

C'_{wall} (mmol / kg) = $M_w \times 10^{-6} \times \rho_{graphite} \times C_{wall}$ (kg/m^3)
P_{gas} (Pa) = $C_{gas} \times R_{gas} / M_w \times T$

M_w	molar weight (=137 kJ/kmol for Cs and 90 kJ/kmol for Sr)
$\rho_{graphite}$	density of graphite (=1780 kg / m^3)
R_{gas}	universal gas constant (=8314.5 J/kg-K)
T	temperature (K)

The values of P_{gas} (Pa) versus C'_{wall} (mmol/kg) for the five isotherms were superimposed on the graphs from [195]. All calculations and graphs are shown in the excel sheets located in:

\Z-INPUTS\RT\FP-Release\HTR\Verification\Sorption\Cs-137-Sorp\Cs-137-Sorption.xlsx
\Z-INPUTS\RT\FP-Release\HTR\Verification\Sorption\Sr-90-Sorp\Sr-90-Sorption.xlsx

(a) sorption isotherms: source data [195] and lines obtained with best fit A_S

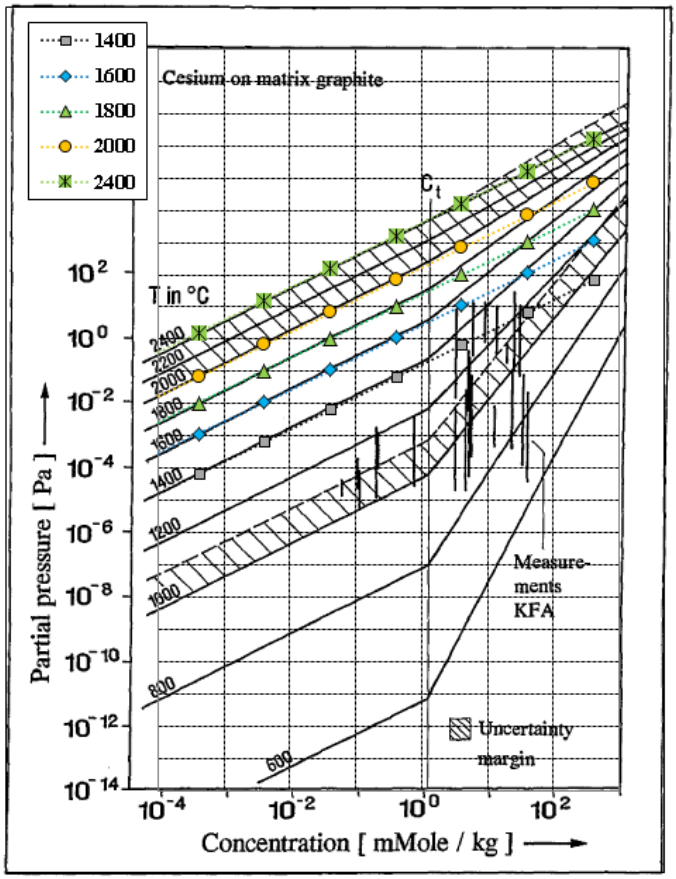

(b) adsorption coefficients A_S and correlation: $A_S = 1.04\times10^{-12} \times \exp(43{,}000/T)$

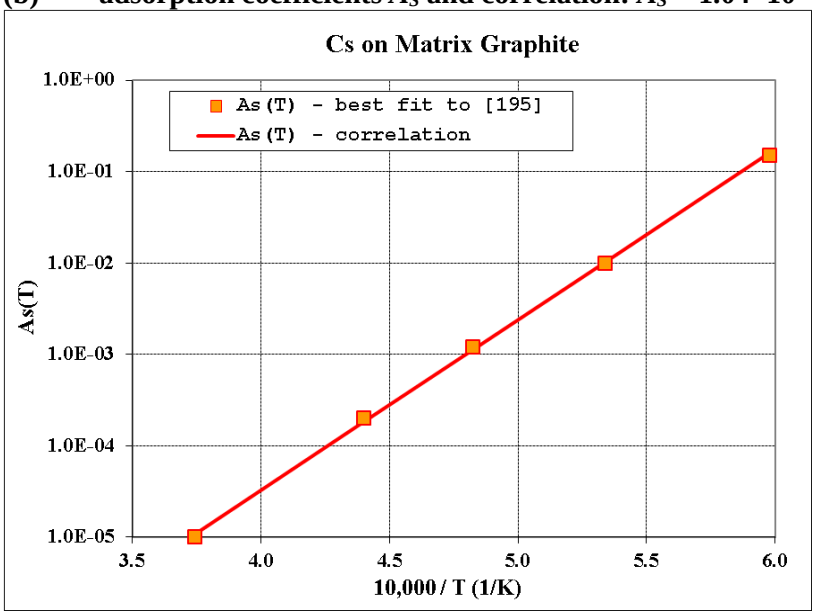

Figure 3-886 Cs sorption isotherms, source data [195] and approximation

(a) sorption isotherms: source data [195] and lines obtained with best fit A_S

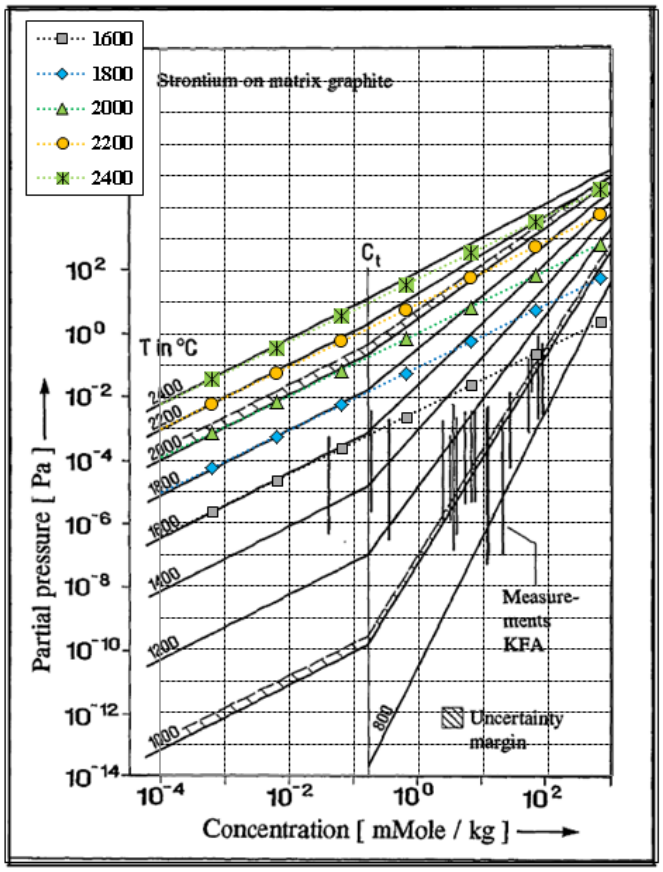

(b) adsorption coefficients A_S and correlation: $A_S = 2.60\times10^{-13} \times \exp(58{,}000/T)$

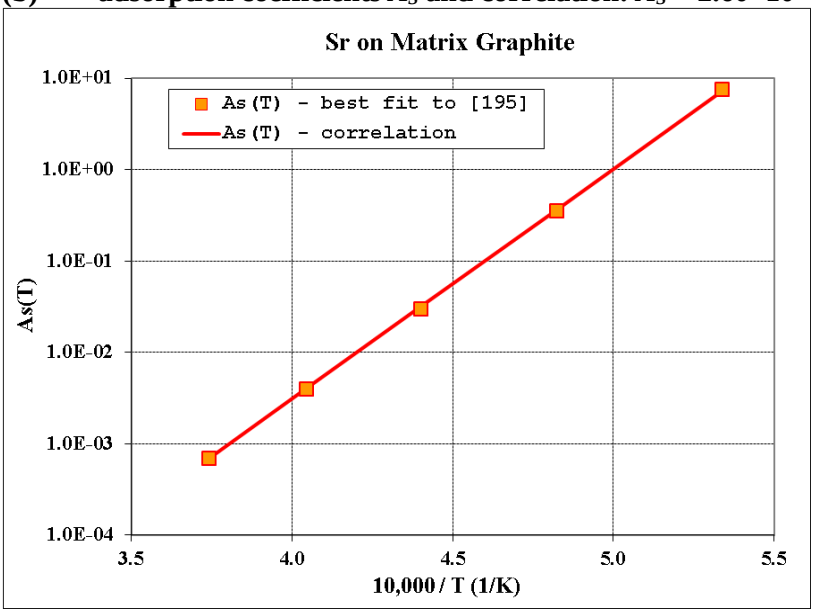

Figure 3-887 Sr sorption isotherms, source data [195] and approximation

Next, the values of A_S, selected by fit to the data, were plotted against (10,000/T) and the temperature-dependent correlations were developed. The general form of such correlation is (Volume 1):

$$A_S(T) = A_0 \cdot \exp\left(-\frac{A_A}{T}\right)$$

The correlations for Cs and Sr on matrix graphite are:

- Cs: $A_S(T) = 1.04\times10^{-12} \cdot \exp\left(\frac{43{,}000}{T}\right)$ error 6.2% for 1400°C<T<2400°C
- Sr: $A_S(T) = 2.60\times10^{-13} \cdot \exp\left(\frac{58{,}000}{T}\right)$ error 2.9% for 1600°C<T<2400°C

Similar correlations were developed for H-451 graphite (the data [195] is limited to 1400°C):

- Cs: $A_S(T) = 4.40\times10^{-13} \cdot \exp\left(\frac{38{,}000}{T}\right)$ error 3.0% for 1000°C<T<1400°C
- Sr: $A_S(T) = 8.77\times10^{-12} \cdot \exp\left(\frac{48{,}000}{T}\right)$ error 5.6% for 1000°C<T<1400°C

Note that Henrian isotherms are used here which are valid until the transition point (marked as C_t on the graphs). In the current code version it is also possible to use Freundlich isotherm but it is not possible to use both, with a transition point.

As verification, a number of isothermal tests were performed. A single pebble was modeled surrounded by a closed gas space (CV-006) with the volume of 1.0 m^3. An initial mass of 10^{-3} kg of Cs-137 or Sr-90 was placed in the tested pebble. Calculations were performed for the same temperatures for which isotherms were drawn in Figure 3-886 (a) and Figure 3-887 (a). A failure fraction of 1.0 was assumed when the temperature exceeds 1000 K, which occurs very soon after the start of each test. The fission products (Cs-137, Sr-90) are therefore quickly released to the graphite and start diffusing towards the surface. Calculations are performed until stationary conditions are reached. The input files are located in:

\Z-INPUTS\RT\FP-Release\HTR\Verification\Sorption\Cs-137-Sorp
\Z-INPUTS\RT\FP-Release\HTR\Verification\Sorption\Sr-90-Sorp

The results are shown in Figure 3-888 through Figure 3-891. In order to have an easy reference case, comparable to the results discussed earlier, one case was defined with desorption only (A_S = 0.0). Figure 3-888 shows results obtained for this case. The desorption process proceeds until practically all fission products are released from the graphite to the gas (see also dotted line in Figure 3-890).

Figure 3-889 shows stationary state results for the case with T = 2400°C. Table 3-72 shows the theoretical values (calculated in Cs-137-Sorption.xlsx) for a wall concentration of 10^{-2} kg, which approximately corresponds to the equilibrium at 2400°C. The theoretical ratio of C_{wall} / C_{gas} is 10.0. The value obtained in SPECTRA is 10.1 (Figure 3-889) because SPECTRA uses the correlation, which for 2400°C gives A_S about 1% higher than the best fit - Table 3-73.

When the correlation is used, the ratio of (A_S/B_S) is for T=2673 K (2400°C) equal to 1.01×10^{-5} / 1.0×10^{-6} = 10.1, exactly the number obtained from the code. The agreement was checked for all considered temperatures and both Cs-137 as well as Sr-90.

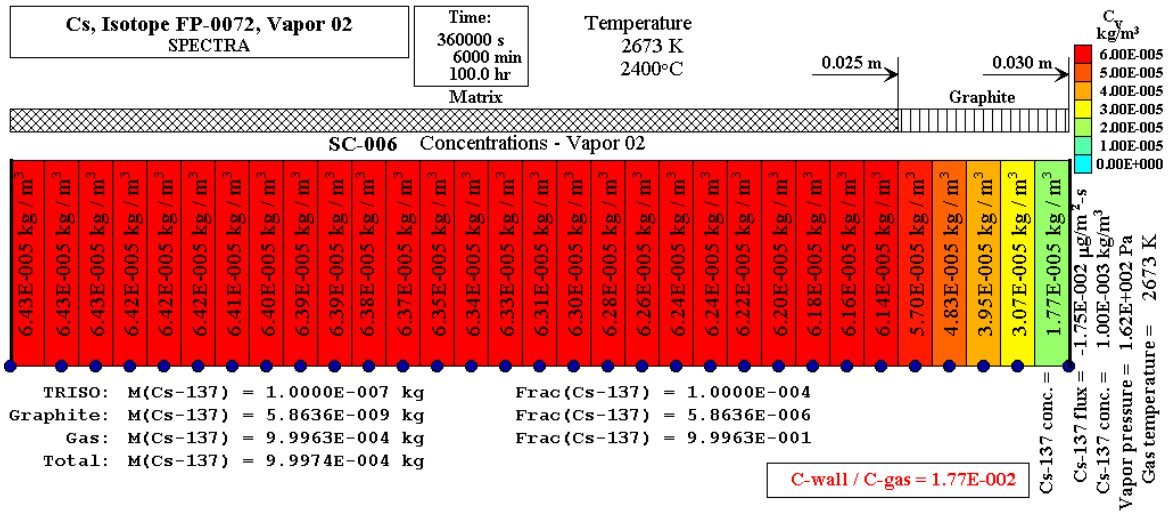

Figure 3-888 Test Cs-137-Des, T = 2400°C, A_S = 0.0

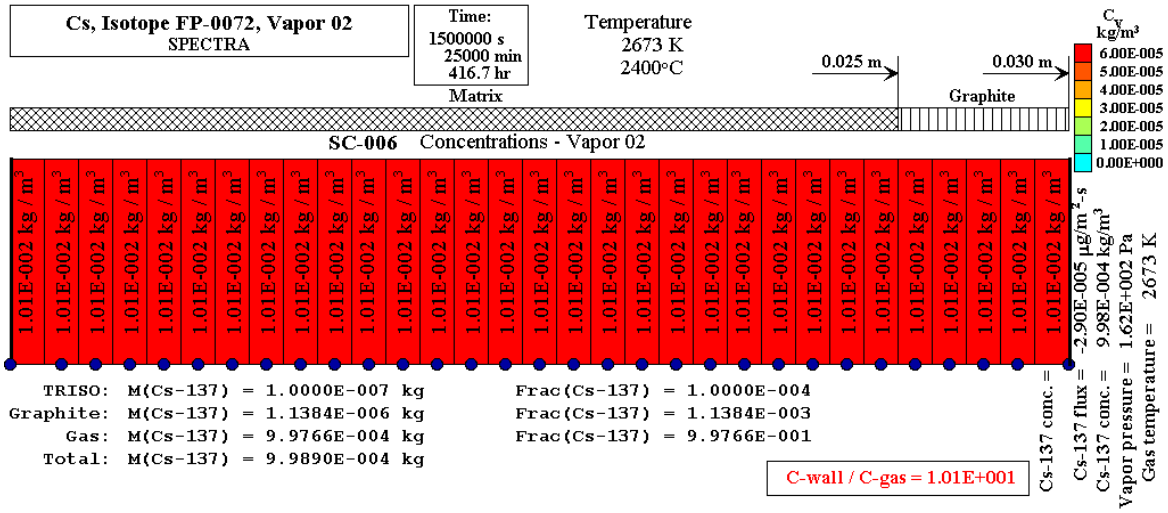

Figure 3-889 Test Cs-137-2400, T = 2400°C, $A_S = 1.04\times10^{-12} \times \exp(43{,}000/T)$

Table 3-72 Theoretical values for Cs-137-Sorp test

C-wall kg/m3	C'-wall mmol/kg	C-gas kg/m3	P-gas Pa	C-wall / / C-gas
1.00E-02	4.10E-02	1.00E-03	1.62E+02	1.00E+01

Table 3-73 Values of A_S from best fit and correlation $A_S = 1.04\times10^{-12} \times \exp(43{,}000/T)$

T (K)	10,000/T	*As(T)* best fit	*As(T)* correl.	Error $\lvert\Delta As\rvert/As$
1673	5.977	1.50E-01	1.51E-01	0.8%
1873	5.339	1.00E-02	9.72E-03	2.8%
2073	4.824	1.20E-03	1.06E-03	11.6%
2273	4.399	2.00E-04	1.71E-04	14.5%
2673	3.741	1.00E-05	1.01E-05	0.8%
			average:	**6.1%**

Figure 3-890 shows the mass of Cs-137 in graphite, while Figure 3-891 shows the mass of Cs-137 released to the gas space. In the cases with $A_S > 0$ a stationary state is reached where the concentrations in the gas space and in the graphite are in equilibrium. In the case with $A_S = 0.0$ the release is continuous, which is seen in Figure 3-890.

The calculations and results shown here may be summarized as follows. Maximizing the release by using desorption only (B_S>0.0, A_S=0.0), as was done in case (a) and in all previous examples, leads to a clearly too conservative release for low temperatures. The release fractions for each case (based on Figure 3-891) are shown below:

Case	T (°C)	T (K)	Release mass (kg)	Release fraction (%)
1	1400	1673	5.47E-5	5.47
2	1600	1873	4.75E-4	47.5
3	1800	2073	8.92E-4	89.2
4	2000	2323	9.80E-4	98.0
5	2400	2673	9.98E-4	99.8

In the case A_S=0.0 the total release will reach 100%, it is just a question how long it takes. Note that the example considered here is a 100% failure fraction and release of ALL fission product mass into the graphite at the start of the test. At 1600°C or lower the overestimation of the case A_S=0.0 is clear, so one might be tempted to consider this case as over conservative. However, it has to be remembered that the accuracy of the presented calculation depends on the accuracy with which the vapor pressure is known. In the considered example, a single gas volume of 1.0 m^3 (well mixed) was applied. The question is whether system codes such as SPECTRA, where fluid modeling is based on large and well-mixed control volumes, are accurate enough in calculating concentrations of fission product vapors in the vicinity of the graphite (pebbles or prismatic block) surfaces. Since it is doubtful if this is really the case, the use of A_S=0.0 seems to offer a reasonable conservative approach. The value of the desorption coefficient B_S is not very important, as long as it is not smaller than 10^{-6}, as was shown in the test Cs-1900.

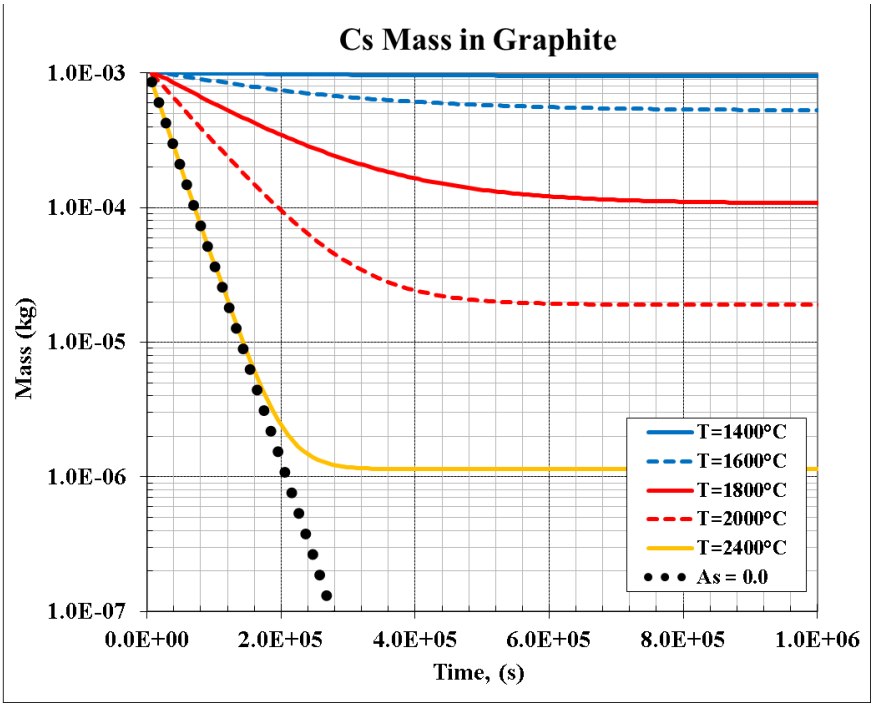

Figure 3-890 Test Cs-137-Sorp, masses of Cs in graphite

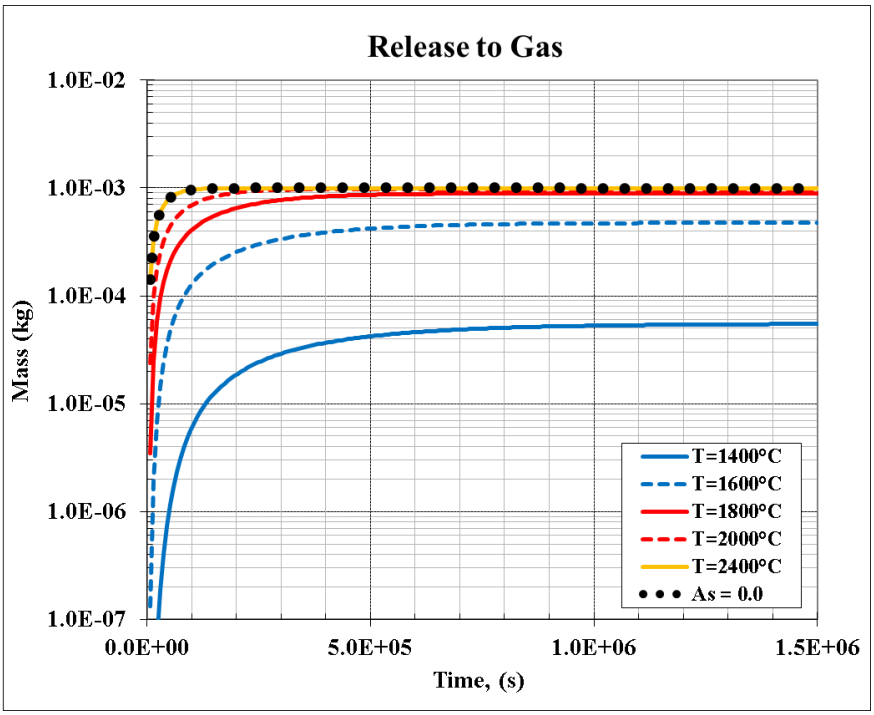

Figure 3-891 Test Cs-137-Sorp, masses of Cs released to gas

- **Summary of Verification Tests**

The results of verification tests are summarized in Table 3-74.

Table 3-74 Summary of HTR-FPR verification tests

Test	Description
TRISO -Cs, -Xe, -Sr	Verification of the effective diffusion resistance for multiple coating layers (approximation formula for diffusion through coating layers)
Fail-0-5-const	Verification of release due to failure of TRISO particles - constant failure fraction (0.5) - no diffusion through the graphite
Fail-0-5	Verification of release due to failure of TRISO particles - constant failure fraction (0.5) - diffusion through the graphite to the gas
Diff-Xe-const	Verification of a release due to diffusion through intact coating layers - diffusion through multiple coating, - no diffusion through the graphite
Diff-Xe -Cs -Sr	Verification of a release due to diffusion through intact coating layers - diffusion through multiple coating, - no diffusion through the graphite
Cs-1900	Comparison of different elements of the release model for T = 1900°C - full model - no diffusion - release only due to failure of TRISO particles - no failure - release only due to diffusion through the coating layers
Cs-1900	Comparison of different elements of the release model for T = 1600°C - full model - no diffusion - release only due to failure of TRISO particles - no failure - release only due to diffusion through the coating layers
Ba-135-0-0 Ba-135-0-5 Ba-135-1-0	Slow release of isotope created by decay, upon failure of TRISO - constant failure fraction (0.5) - slow production of Ba-135 from decay of Cs-135 - three cases: F = 0.0, F = 0.5, F = 1.0
Te-132-0-0 Te-132-0-5 Te-132-1-0	Slow release of isotope created by fission in failed TRISO - constant failure fraction (0.5) - slow production of Te-132 from fission - three cases: F = 0.0, F = 0.5, F = 1.0
Cs-132-Sorp Sr-90-Sorp	Sorption isotherms

3.12.38.2 Validation

Three validation tests are discussed in this chapter:

- JMTR Isothermal Tests
- JMTR Temperature Ramp Tests
- KÜFA Tests

These tests are discussed below.

- **JMTR Isothermal Tests**

The tests were performed at Japan Material Testing reactor (JMTR). The TRISO coated UO_2 particles used in the test were taken from irradiated fuel compacts by electrolytic deconsolidation ([93], sec. 4.1.2). The thickness of coating layers were ([93], Table 4-7):

Kernel	596/2 = 298 μm
Buffer:	59 μm
Inner PyC	29 μm
SiC	24 μm
Inner PyC	44 μm

Two samples, A and B were irradiated at different temperatures: sample A at 1250°C, sample B at 1510°C. The post irradiation heating tests were carried out at 1600°C to 1900°C. About 100 particles were heated in each test. In all heating tests, no coating failure was detected. The measured fractional release of Cs-137 is shown in Figure 3-893 ([93], Fig. 4-21).

A simple model was built, with an initial mass of 10^{-9} kg of Cs-137 placed in the fuel. The temperature Calculations were performed using three release models:

failure only model,
diffusion only model,
direct application of the diffusion model to a TRISO particle.

The input files are located in: \Z-INPUTS\RT\FP-Release\HTR\Validation\JMTR-Iso\Cs-137. The results are shown in Figure 3-892. Only the mass that is released from fuel is plotted here because these tests investigated TRISO particles only and not fuel elements like pebbles or blocks. Therefore only the release from TRISO is tested here, so the failure curve and the approximation formula for diffusion through the coating layers.

Calculations showed that the release by diffusion was by far dominant and consequently the full model results are practically the same as the results obtained in the diffusion only case. Figure 3-892 (a) shows results of the failure-only model. The release due to failure is determined by the failure fraction at given temperature. The calculated results are clearly below the experimental values. The calculated numbers are verified by comparing the observed released fraction by the failure fraction obtained from the built-in correlation (Volume 1):

T (°C)	T (K)	Release (Figure 3-892-a)	Built-in correlation (for *B*=1.0)
1600	1873	8.011×10^{-4}	8.013×10^{-4}
1800	2073	1.591×10^{-3}	1.591×10^{-3}
1900	2173	2.257×10^{-3}	2.257×10^{-3}

The results obtained with the diffusion model are shown in Figure 3-892 (b). The agreement is good. The biggest discrepancy is observed in the early phase. This is a consequence of the model

simplification (neglecting the accumulation of fission products in the coating layers, see section 3.12.38.1, test TRISO-Cs). When the diffusion model is applied directly for TRISO particles, the agreement with experiment is better. Figure 3-892 (c) shows results obtained with the diffusion model. The input files are located in: \Z-INPUTS\RT\FP-Release\HTR\Validation\JMTR-Iso\Cs-137-diff.

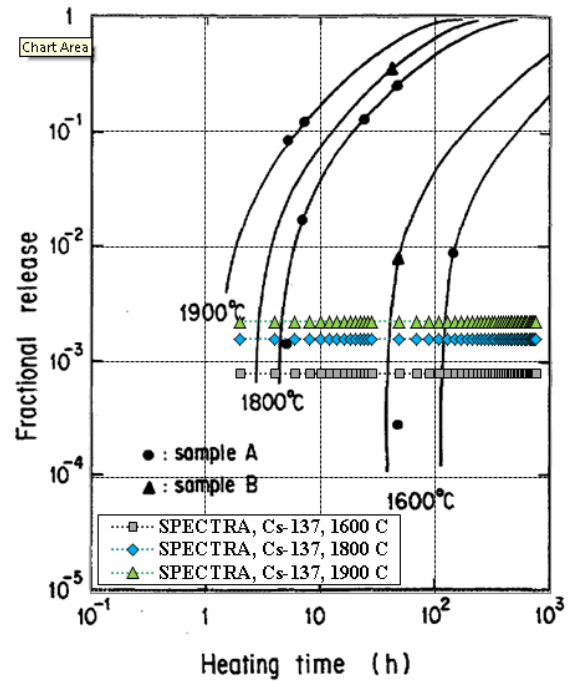

(a) failure only

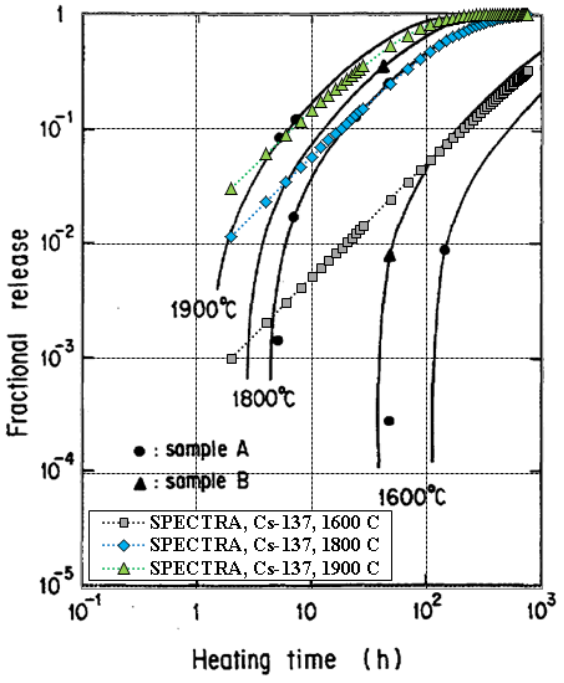

(b) diffusion only, C_{FPR} = 3.0 (default)

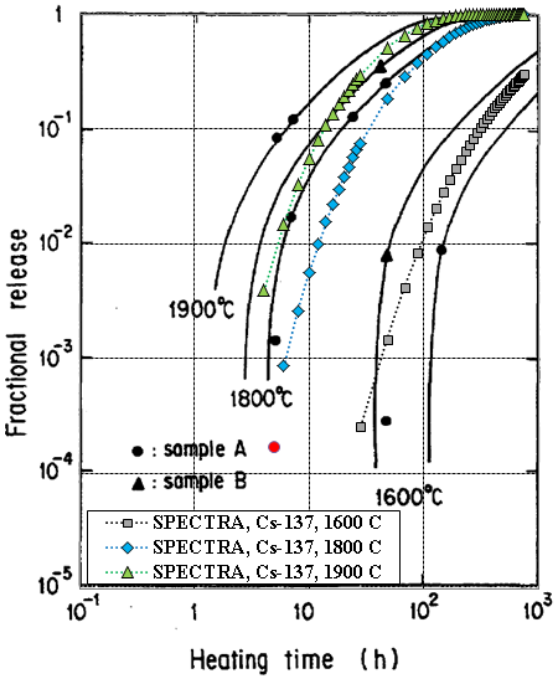

(c) diffusion model (exact diffusion solution)

Note:

Table 4-9 of TECDOC-978 [93] *shows additional data point: t = 5 h, Cs-137 release fraction of 1.7×10^{-4} for sample A. This value however, does not appear in the TECDOC diagram. If it was inserted, the curve for Cs release would look different. This point is not depicted on the graph. If it were, the shape of the curve would look different. The missing data point was inserted in the figure (c) as a red circle.*

Furthermore, the extrapolation of the last data point, which is at 144 h, to 1000 h can also ne questionable.

Figure 3-892 Release of Cs, JMTR data [93] and HTR-FPR model

- **JMTR Temperature Ramp Tests**

The post irradiation temperature ramp tests were performed at ramp rates of 1°C/min and 5°C/min. Figure 3-893 (a) shows the result of a ten-particle run up to 100% failure at the ramp rate of 1 °C/min ([93], Fig. 4-23). Figure 3-893 (b) shows the results of ramp tests at 5°C/min ([93], Fig. 4-23). As in the case of the previous test, only the release from TRISO is tested here. In particular, the failure curve is investigated.

The model built here is for a single TRISO particle with boundary conditions provided by a boundary CV with properties (temperature) defined as a function of time. The temperature was changed from 2100 K to 2800 K in 42,000 s (1°C/min). An initial mass of 10^{-9} kg of Cs-137 was placed in the fuel. Calculations were performed using the failure model, including:

the built-in failure curve,
a failure curve tabulated versus temperature using the data from [93]. The 5°C/min data was used below 2150°C, while the 1°C/min data was used above 2150°C.

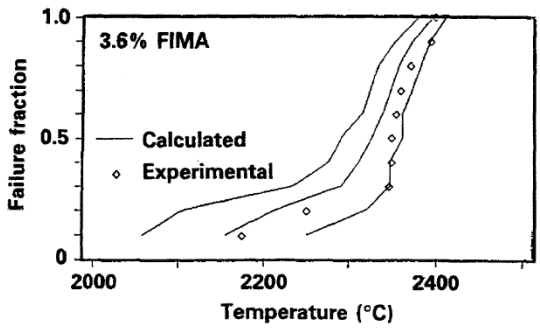

(a) source data 1°C/min ([93], Fig. 4-23)

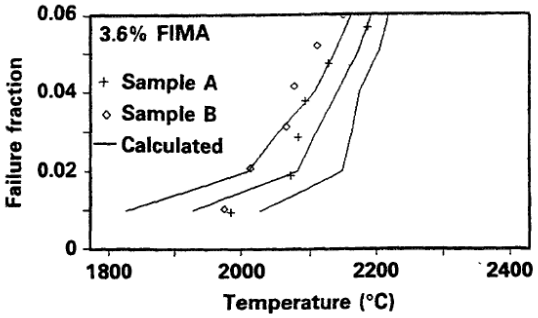

(b) source data 5°C/min ([93], Fig. 4-24)

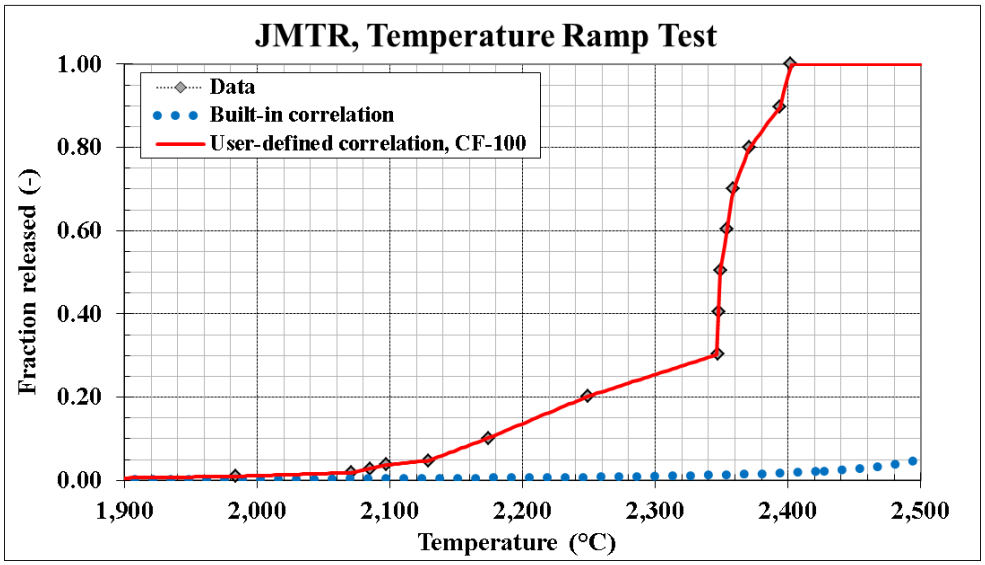

(c) Results of calculations

Figure 3-893 JMTR temperature ramp test [93], data and HTR-FPR model

The input files are located in: \Z-INPUTS\RT\FP-Release\HTR\Validation\JMTR-TRamp. The results are shown in:

built-in failure curve, Figure 3-894 (a),
user-defined curve, Figure 3-894 (b).

Both results are shown in Figure 3-893 (c) where the released fractions are plotted against the temperature. Two observations can be made here:

(1) The built-in correlation gives clearly lower failure fractions than the JHTR test data. Therefore the built-in correlation should be used with care. The correlation is based on a large number of data and is recommended by AREVA [196] but does not provide conservative results for all measurement data that can be found in literature.

(2) In view of the observation (1), the option to define the failure curve by a tabulated function is very convenient for the user (the same is done in MELCOR 2.2). Any available data can be easily incorporated using this option. However, applicability of the model for each particular case and its validation is the responsibility of the user.

(a) built-in correlation (test JMTR-TRamp-1)

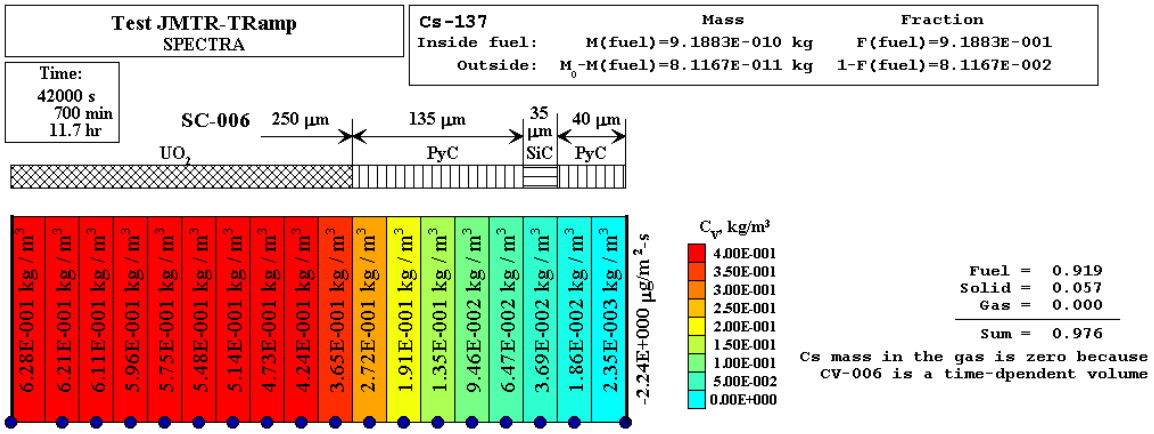

(b) user-defined failure fraction (test JMTR-TRamp-2)

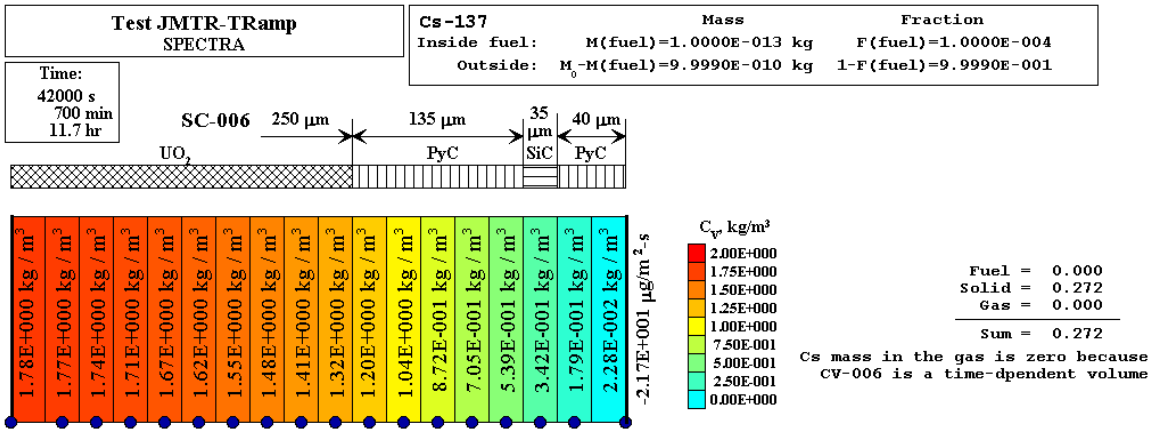

Figure 3-894 JMTR temperature ramp test, model and results

- **HFR-K3/1 Tests and KÜFA Tests**

The HFR-K3/1 test results are discussed in [93] (Fig. 4-1). The (KÜFA=KÜhlFinger-Anlage) tests are discussed in [197], [198]. Figure 3-895 (a) shows a schematic of the heating furnace. The model consists of the tested spherical element (SC-006) with 30 nodes (1 mm each), the gas space (CV-006), and the cylindrical walls (SC-009) that provide the desired temperature. The tested fuel element is initially cold and is being quickly heated up by the surrounding gas. The gas temperature is kept practically constant by the walls. The model and initial conditions are shown in Figure 3-895 (b). Dimensions of the heating chamber were estimated based on Figure 3-895 (a).

Four isotopes, Cs-137, Kr-85, Sr-90, and Ag-110m, are initially placed in the fuel (fuel region 1, located in SC-006). The initial masses were assumed based on the activity data from [198] (shown in Figure 3-896 and Figure 3-897). The initial masses are not important for the conservative case ($A_S = 0.0$, $B_S = 10^{-6}$), however it does play a role for cases where sorption isotherms are used ($A_S > 0.0$). The initial masses and activities are shown below.

Isotope	Mass (kg)	Activity (Bq)	Data (Bq / fraction) Figure 3-896
Cs-137 :	3.2×10^{-5}	1.03×10^{11}	$\sim 1\times10^{7} / 1\times10^{-4} = 1\times10^{11}$
Kr-85 :	7.1×10^{-7}	1.02×10^{10}	$\sim 2\times10^{4} / 2\times10^{-6} = 1\times10^{10}$
Sr-90 :	1.2×10^{-5}	6.13×10^{10}	$\sim 6\times10^{5} / 1\times10^{-5} = 6\times10^{10}$
Ag-110m:	5.7×10^{-9}	1.00×10^{09}	$\sim 2\times10^{7} / 2\times10^{-2} = 1\times10^{09}$

Two sets of calculations were performed:

(0) Conservative, using only the desorption coefficient $B_S = 10^{-6}$, while $A_S = 0.0$.
(1) Use was made of sorption coefficients developed in the verification tests Cs-137-Sorp and Sr-90-Sorp, described in section 3.12.38.1. For Cs-137 and Sr-90 the values developed there were used. For Kr-85 and Ag-110m no data was found. For Kr-85 the values for Cs-137 were used. For Ag-110m no adsorption model, $A_S = 0.0$ was used, with the desorption coefficient reduced from 10^{-6} to 10^{-8}. The coefficients are shown below.

Cs-137 : $A_S(T) = 1.04\times10^{-12} \times \exp(43{,}000 / T)$
Kr-85 : $A_S(T) = 1.04\times10^{-12} \times \exp(43{,}000 / T)$
Sr-90 : $A_S(T) = 2.60\times10^{-13} \times \exp(58{,}000 / T)$
Ag-110m: $A_S(T) = 0.0$

The input files are located in: \Z-INPUTS\RT\FP-Release\HTR\Validation\KUFA. The results for case (0) are provided in the subdirectory KUFA-0. The results for case (1) are provided in the subdirectory KUFA-1. The results are shown in Figure 3-896 through Figure 3-899. In each case the calculated results were superimposed on the source data graphs copied from [93] and [198].

Figure 3-896 shows the release of Kr, Cs, Sr, and Ag at 1600°C. The measured data are compared to the results of case (0), i.e.: $A_S = 0.0$. All calculated results show releases that are higher than measured.

Figure 3-897 shows the same experimental results, but this time the measured data are compared to the results of case (1), i.e.: $A_S > 0.0$. The calculated results show better agreement with the experiment than in the previous case.

(a) KÜFA test facility [197], [198]

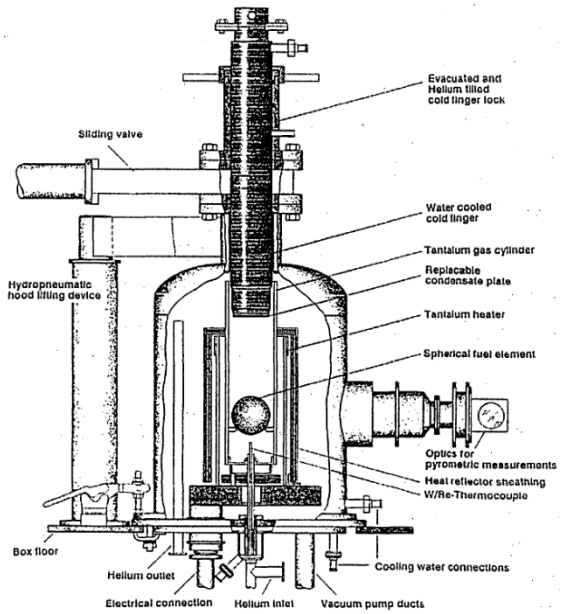

Heating furnace used in accident simulation tests with irradiated spherical fuel elements (KÜFA).

(b) Model and initial conditions

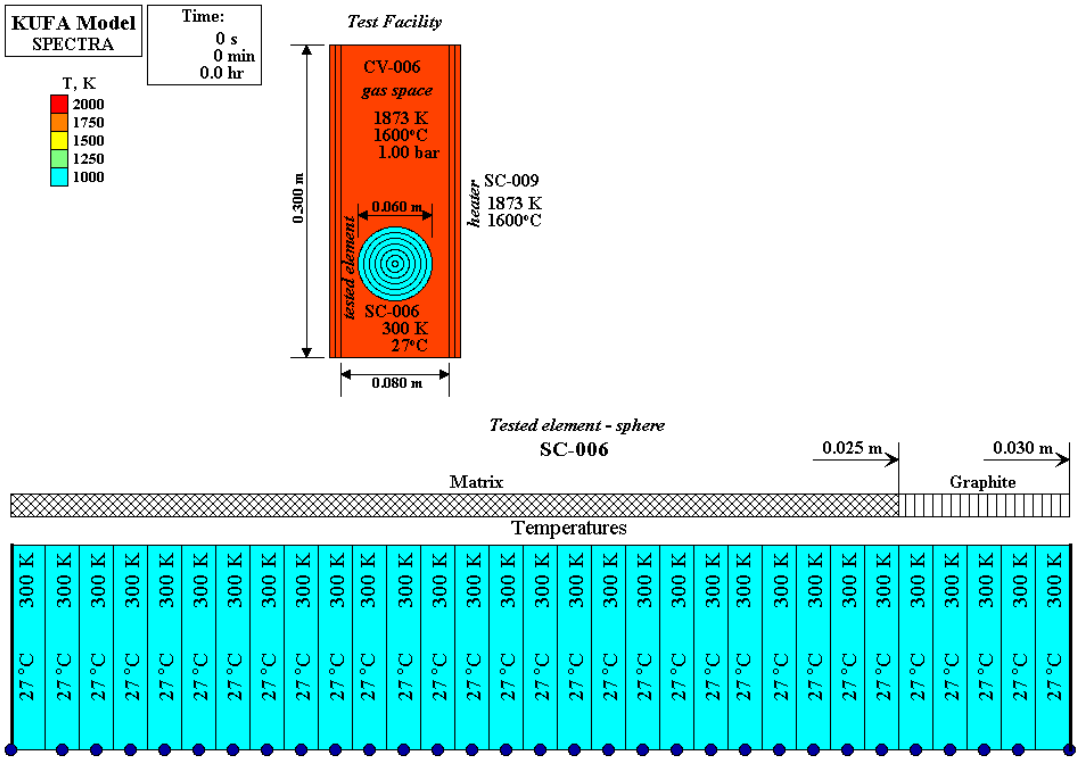

Figure 3-895 KÜFA test facility [197], [198] and model.

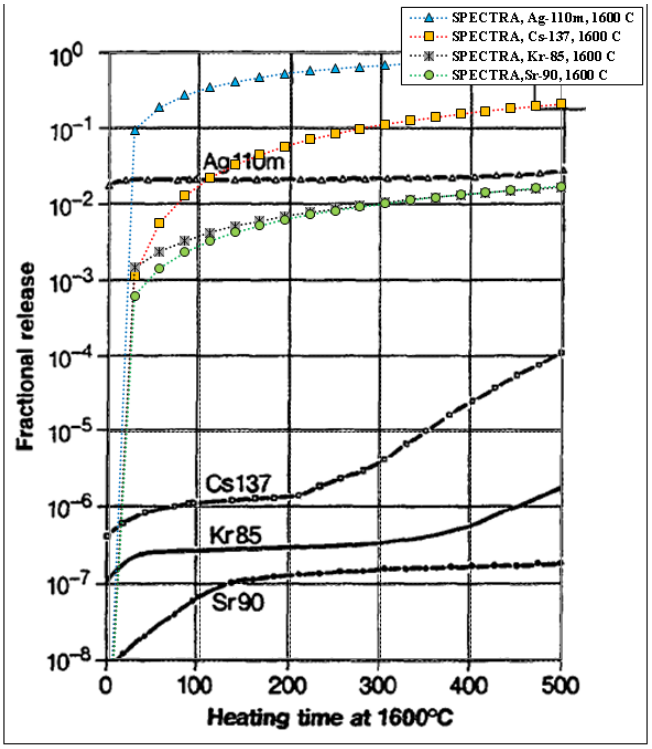

Figure 3-896 HFR K3/1 tests, data [93] and calculations, A_S = 0.0, case (0)

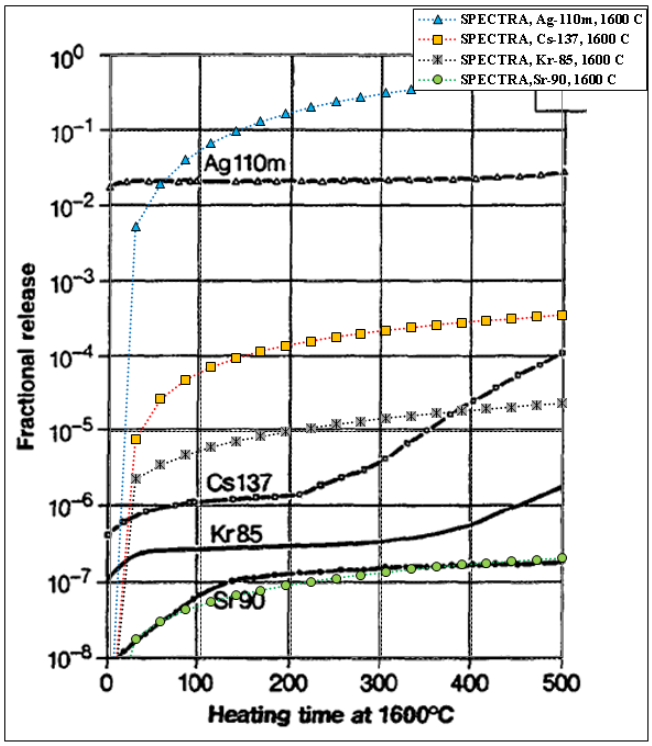

Figure 3-897 HFR K3/1 tests, data [93] and calculations, $A_S = A_0 \times \exp(-A_A/T)$, case (1)

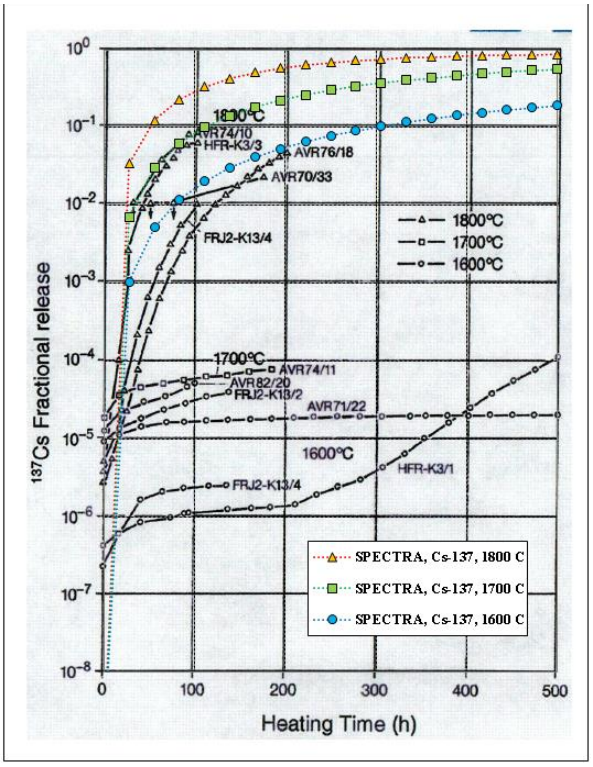

Figure 3-898 KÜFA tests, Cs-137 data [198] and calculations, A_S = 0.0, case (0)

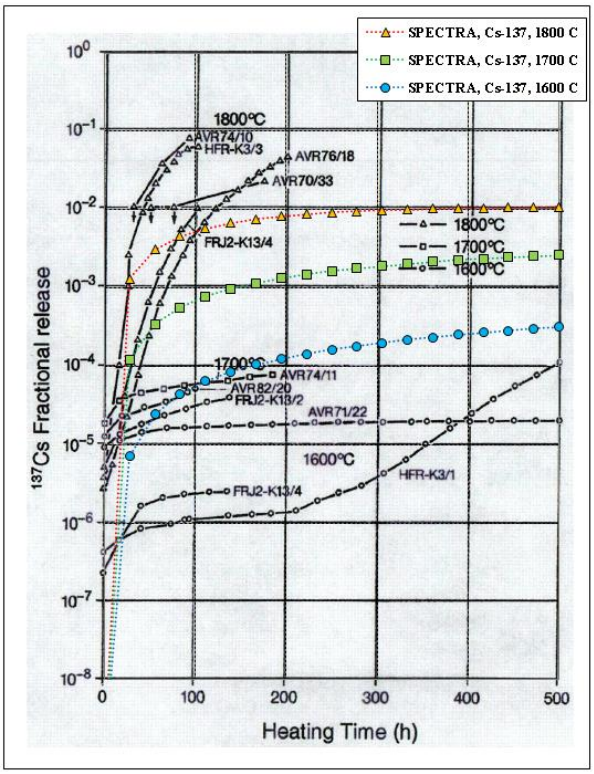

Figure 3-899 KÜFA tests, Cs-137 data [198] and calculations, $A_S = A_0 \times \exp(-A_A/T)$, case (1)

Figure 3-898 shows the release of Cs-137 at 1600°C, 1700°C, and 1800°C. The measured data are compared to the results of case (0), i.e.: $A_S = 0.0$. All calculated results show releases that are higher than measured.

Figure 3-899 shows the same experimental results, but this time the measured data are compared to the results of case (1), i.e.: $A_S > 0.0$. The calculated results show better agreement with the experiment than in the previous case.

The overall conclusions from the present tests are as follows:

- The case (0) ($A_S = 0.0$) gives conservative results by several orders of magnitude.
- If the sorption isotherms are used ($A_S > 0.0$) the results generally agree better with experiments (they are still off by about one order of magnitude, but this is similar to the spread of the measured data). It has to be remembered that the accuracy of the presented calculation depends on the accuracy with which the vapor pressure is known. This is difficult because details of the furnace are not described in detail. Furthermore, the question is whether system codes such as SPECTRA, where fluid modeling is based on large and well-mixed control volumes, are accurate enough in calculating concentrations of fission product vapors in the vicinity of the graphite (pebbles or prismatic block) surfaces. Since it is doubtful if this is really the case, the use of A_S=0.0 seems to offer a reasonable conservative approach.

- **Discussion and additional verification of HFR-K3/1 Tests results**

The amount of fission product that is released to the gas is significantly smaller when the realistic desorption model is used, compared to the situation when a conservative model is used. The release is smaller by 3 orders of magnitude in case of Cs-137 and by 5 orders of magnitude in case of Sr-90. This is quite large for comfort. Therefore an in-depth analysis of the calculated results and additional verification was performed for Cs-137 and Sr-90. The results are discussed below.

Cs-137 release at 1600°C

The fraction remaining inside TRISO particles, calculated by SPECTRA is equal to 0.73 at 500 h. This is of course independent of the desorption model, which is seen in Figure 3-900 and Figure 3-901. This number was verified by hand calculations, shown in Table 3-75. It is seen that the fraction remaining is 0.73 or 73%, the same as calculated by SPECTRA.

This result shows that after 500 h the fraction that is released from the coated particles is equal to 0.27 or 27%. This amount will slowly diffuse towards the surface of the pebble and will eventually be released from to gas. The amount that is released to the gas depends on the sorption model.

With the conservative sorption model, the concentration of Cs-137 in the pebble is decreasing to zero at the pebble surface. This is seen in Figure 3-900 and Figure 3-902. In such case only a small amount of fission product is present in the pebble at all times, most of it is released. The time-dependent values are shown in Figure 3-903. At the end of the test, 500 h, the fraction that is released to the gas is (Figure 3-900) 0.21 or 21%. The mass that remains in the graphite is (Figure 3-900) 0.056 or 5.6%.

With the realistic sorption model, the desorption is much slower. The concentration of Cs-137 at the pebble surface is quite high and is gradually increasing in time - Figure 3-901, Figure 3-902. A relatively large amount of fission product is trapped in the pebble and is slowly released, therefore the release to gas is seemingly much smaller. The time-dependent values are shown in Figure 3-904. At the end of the test, 500 h, the fraction that is released to the gas is (Figure 3-901) 3.5×10^{-4} or 0.035%. The mass that remains in the graphite is (Figure 3-901) 0.27 or 27%.

Table 3-75 Verification of the release of Cs-137 at 1600°C

Cs-137	*Temperature*	
T =	1600 C	
T =	1873 K	
	Diffusion coefficients	
UO2	$D = 5.6\times10^{-8} \times \exp(-25{,}137/T)$	8.31E-14
SiC	$D = 2.8\times10^{-4} \times \exp(-50{,}514/T)$	5.43E-16
PyC	$D = 6.3\times10^{-8} \times \exp(-26{,}700/T)$	4.06E-14
	Layer thickness	
UO2	$X_{ker} = 250/4 = 62.5$ µm	6.25E-05
SiC	$X_{SiC} = 35$ µm	3.50E-05
PyC	$X_{PyC} = 175$ µm	1.75E-04
	Diffusion Resistance	
	$R_{diff} = \frac{X_{\ker}}{D_{\ker}} + \frac{X_{SiC}}{D_{SiC}} + \frac{X_{PyC}}{D_{PyC}}$	6.96E+10
	Exponent	
	$R_{TRISO} = 250$ µm	2.50E-04
	$X = \frac{3}{R_{TRISO} \cdot R_{diff}}$	1.72E-07
	Time	
	t = 500 h	1.80E+06
	Fraction remaining	
	$f_{rem} = \exp(-X \cdot t)$	**0.73**
	Fraction released	
	$f_{rel} = 1 - \exp(-X \cdot t)$	**0.27**

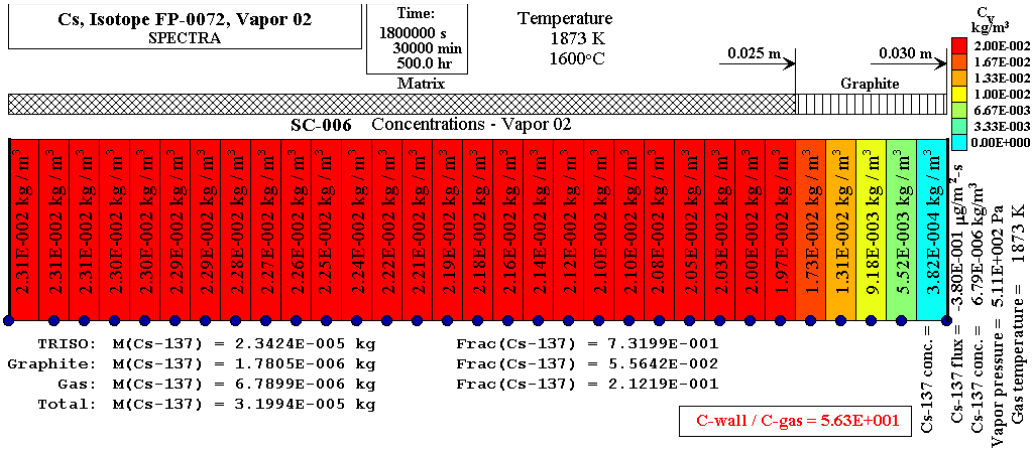

Figure 3-900 Cs-137, T=1600°C, t = 500 h, maximum desorption model

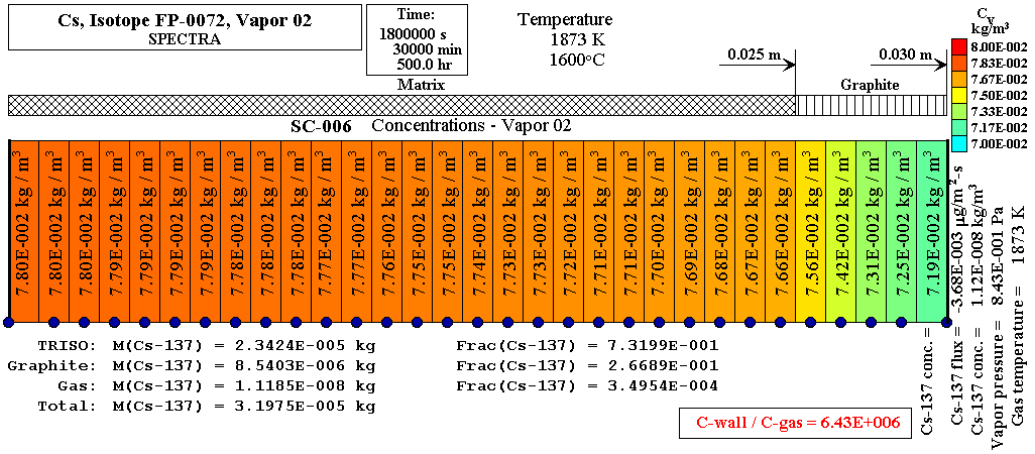

Figure 3-901 Cs-137, T=1600°C, t = 500 h, realistic desorption model

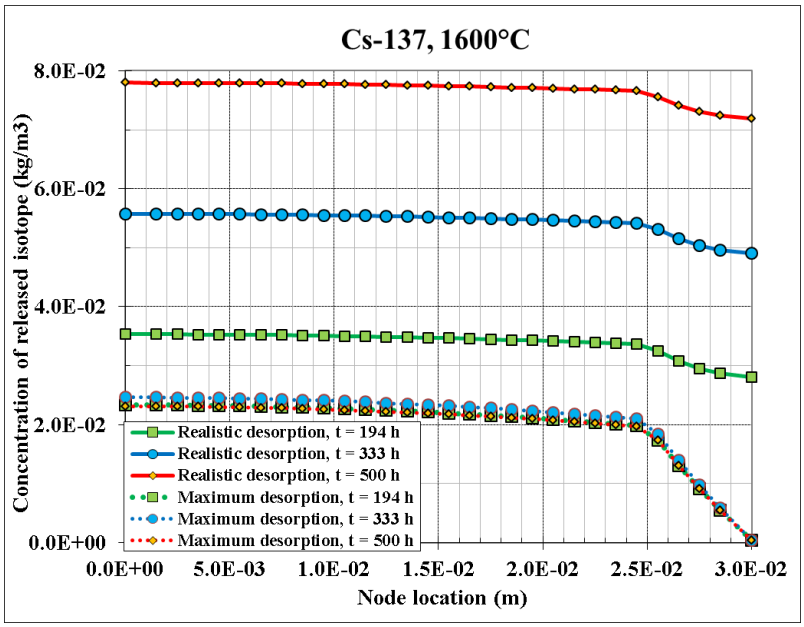

Figure 3-902 Cs-137, T=1600°C, t = 500 h, radial concentration profiles

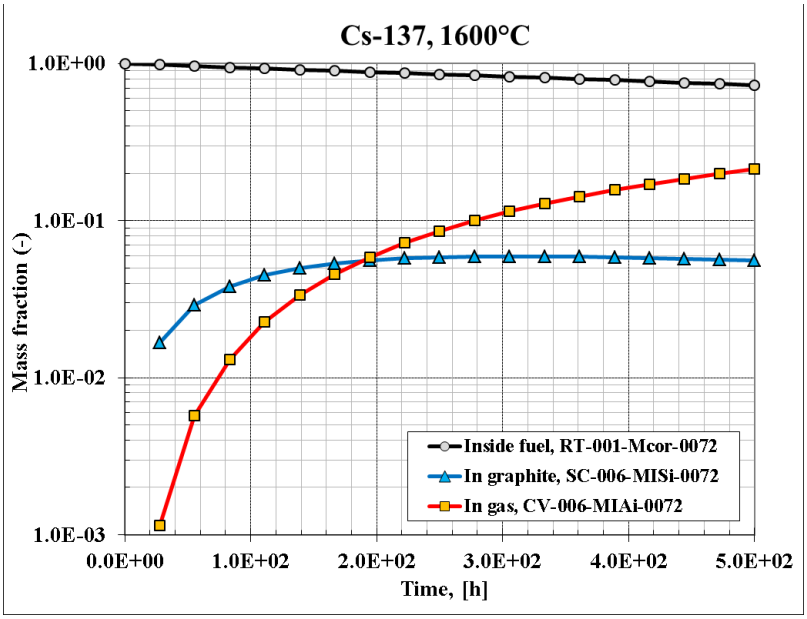

Figure 3-903 Cs-137, T=1600°C, maximum desorption model

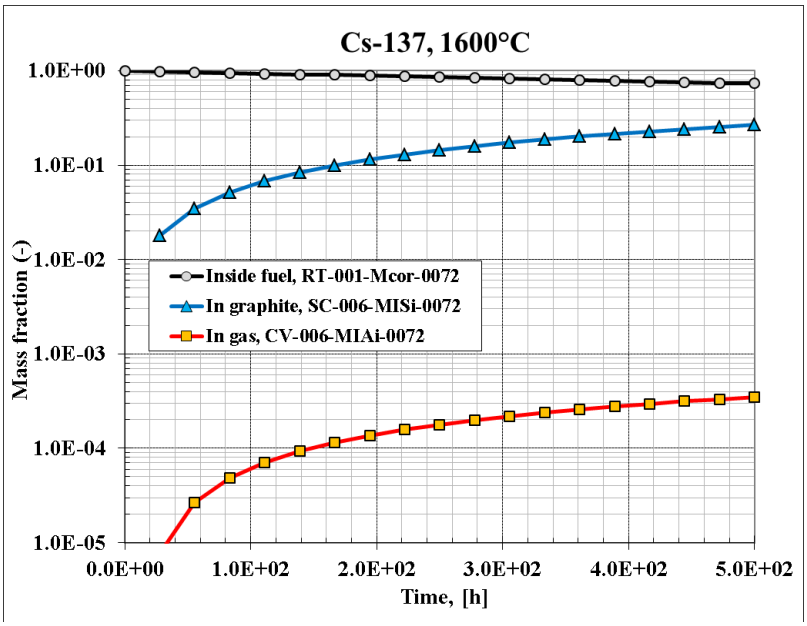

Figure 3-904 Cs-137, T=1600°C, realistic desorption model

Sr-90 release at 1600°C

The fraction remaining inside TRISO calculated by SPECTRA is equal to 0.98 at 500 h. This is of course independent of the desorption model, which is seen in Figure 3-905 and Figure 3-906. This number was verified by hand calculations, shown in Table 3-76. It is seen that the fraction remaining is 0.98 or 98%, the same as calculated by SPECTRA.

This result shows that after 500 h the fraction that is released from the coated particles is equal to 0.02 or 2%. This amount will slowly diffuse towards the surface of the pebble and will eventually be released from to gas. The amount that is released to the gas depends on the sorption model.

With the conservative sorption model, the concentration of Sr-90 in the pebble is decreasing to zero at the pebble surface. This is seen in Figure 3-905 and Figure 3-907. In such case only a small amount of fission product is present in the pebble at all times, most of it is released. The time-dependent values are shown in Figure 3-908. At the end of the test, 500 h, the fraction that is released to the gas is (Figure 3-905) 0.017 or 1.7%. The mass that remains in the graphite is (Figure 3-905) 1.6×10^{-3} or 0.016%.

Table 3-76 Verification of the release of Sr-90 at 1600°C

Sr-90	*Temperature*	
T =	1600 C	
T =	1873 K	
	Diffusion coefficients	
UO2	$D = 2.2\times10^{-3} \times \exp(-58{,}693/T)$	5.41E-17
SiC	$D = 1.2\times10^{-9} \times \exp(-24{,}656/T)$	2.30E-15
PyC	$D = 2.3\times10^{-6} \times \exp(-23{,}694/T)$	7.38E-12
	Layer thickness	
UO2	$X_{ker} = 250/4 = 62.5$ μm	6.25E-05
SiC	$X_{SiC} = 35$ μm	3.50E-05
PyC	$X_{PyC} = 175$ μm	1.75E-04
	Diffusion Resistance	
	$R_{diff} = \frac{X_{\ker}}{D_{\ker}} + \frac{X_{SiC}}{D_{SiC}} + \frac{X_{PyC}}{D_{PyC}}$	1.17E+12
	Exponent	
	$R_{TRISO} = 250$ μm	2.50E-04
	$X = \frac{3}{R_{TRISO} \cdot R_{diff}}$	1.03E-08
	Time	
	t = 500 h	1.80E+06
	Fraction remaining	
	$f_{rem} = \exp(-X \cdot t)$	**0.98**
	Fraction released	
	$f_{rel} = 1 - \exp(-X \cdot t)$	**0.02**

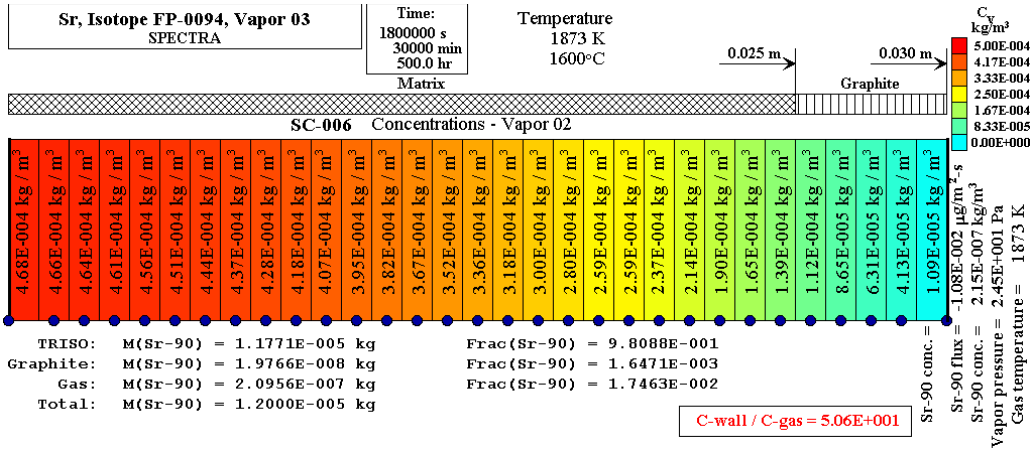

Figure 3-905 Sr-90, T=1600°C, t = 500 h, maximum desorption model

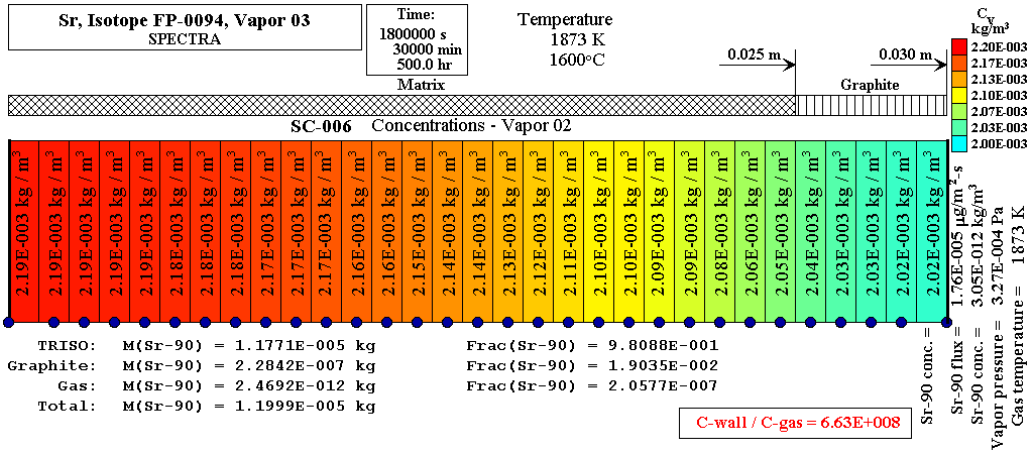

Figure 3-906 Sr-90, T=1600°C, t = 500 h, realistic desorption model

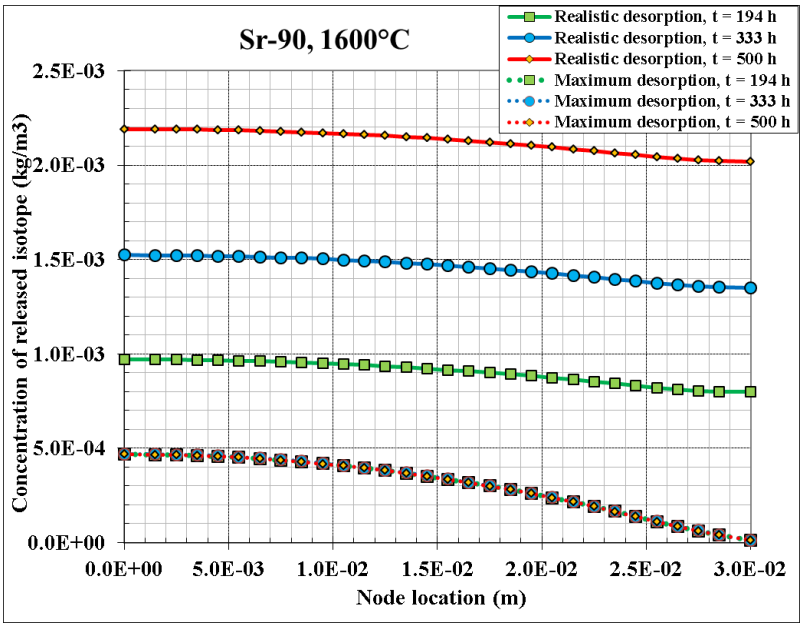

Figure 3-907 Sr-90, T=1600°C, t = 500 h, radial concentration profiles

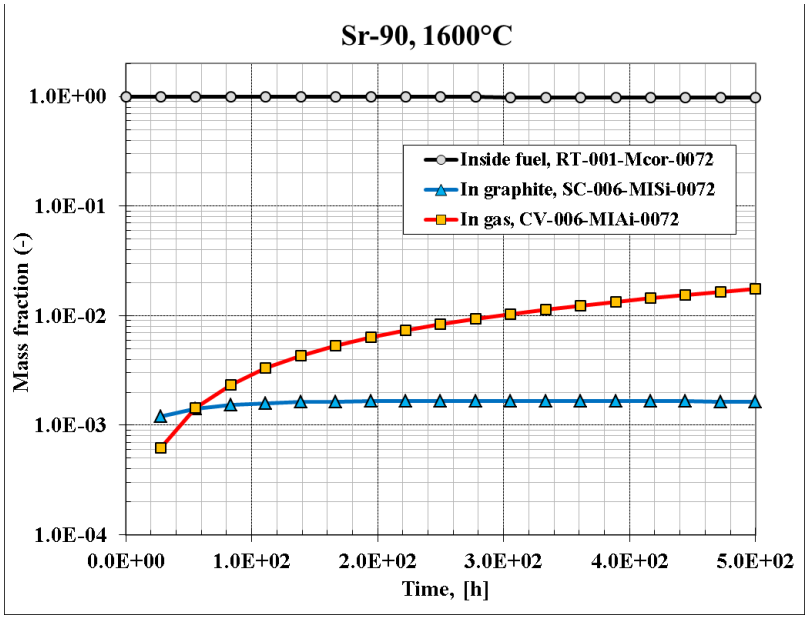

Figure 3-908 Sr-90, T=1600°C, maximum desorption model

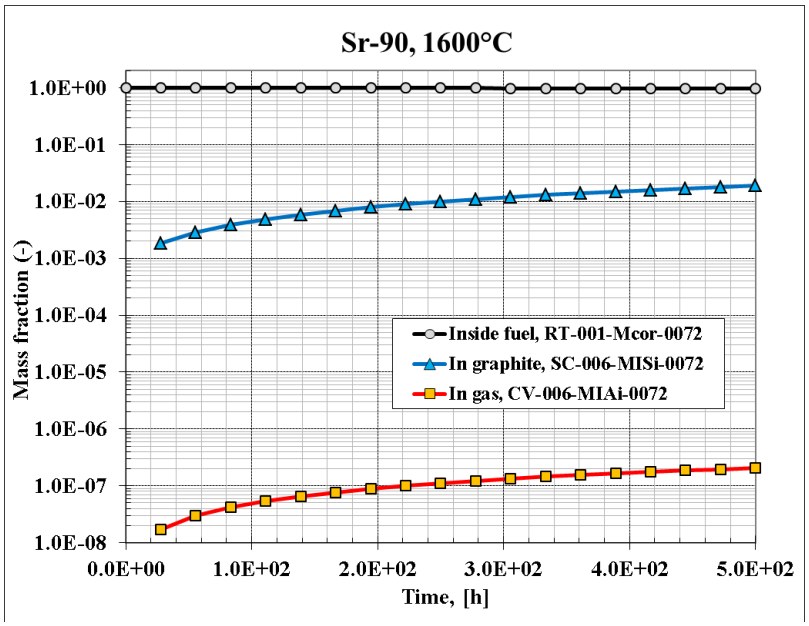

Figure 3-909 Sr-90, T=1600°C, realistic desorption model

With the realistic sorption model, the desorption is much slower. The concentration of Sr-90 at the pebble surface is quite high and is gradually increasing in time - Figure 3-906, Figure 3-907. A relatively large amount of fission product is trapped in the pebble and is slowly released, therefore the release to gas is seemingly much smaller. The time-dependent values are shown in Figure 3-909. At the end of the test, 500 h, the fraction that is released to the gas is (Figure 3-906) 2.1×10^{-7} or 2.1×10^{-5}%. The mass that remains in the graphite is (Figure 3-906) 0.019 or 1.9%.

Conclusions:

The main conclusions are:

- Qualitative and quantitative correctness of the calculated results have been confirmed. Release from TRISO was confirmed by hand calculations. Correctness of the desorption boundary condition was confirmed by plotting the radial concentration profiles at different times.
- The desorption model does not affect the release from coated particles. As was shown above, the release from TRISO is 23% in case of Cs-137 and 2% in case of Sr-90. It is commonly accepted that the layers of coated particles have a very good retention capability and are considered as a main barrier against the fission product release. If, based on the current verified calculations, we know that 23% of Cs-137 and 2% of Sr-90 will be released, it may be argued that all this mass will eventually find its way into the atmosphere. Therefore the use of the conservative desorption model seems justified.
- Realistic sorption model is very uncertain. Therefore the conservative model is a safer estimation of fission product release, although it is clear that in some cases it may overestimate the release by several orders of magnitude.

3.12.39 Test Kr-88-SOL

The test Kr-88-SOL provides verification of the concentration of a short-living isotope Kr-88 in the solid (LWR, HTR) fuel, in particular the case where the yield fractions depend on the fissile isotope. SPECTRA input decks and support files are provided in \Z-INPUTS\RT\Kr-88\SOL\.

The Kr-88 chain is shown in Figure 3-910. The fission yields, γ_f, are those for U-235. The individual fission yields are shown in Table 3-77. The current test is very similar to the DNP-2 test, described in section 3.9.2.9. A long term behavior (10 years) is analyzed. The initial fuel composition (Σ_f, U-235 enrichment) is assumed in such a way that the consumption of U-235 is approximately compensated by the production of Pu-239 from U-238, and therefore a long term operation is possible without fuel reload. Two input decks are defined:

- Kr-88-SOL-1: fission yields of Kr-88 and Rb-88 for U-235,
- Kr-88-SOL-2: individual fission yields, data shown in Table 3-77.

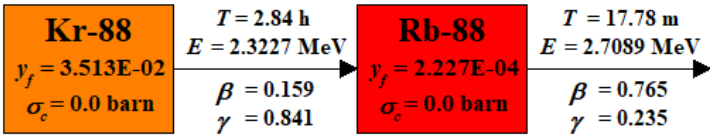

Figure 3-910 Kr-88 chain

Table 3-77 Individual fission yields

Isotope	Fission yields, γi		
	U-235	Pu-239	Pu-241
Kr-88	3.513E-02	1.272E-02	3.259E-02
Rb-88	2.227E-04	5.730E-04	2.625E-04

The results are shown in Figure 3-911 through Figure 3-915 and Table 3-78. Figure 3-911 shows the concentrations of U-235 and Pu-239. Figure 3-912 shows the macroscopic fission cross section, equal to (see Volume 1):

$$\Sigma_f = \sum_i \sigma_{f,i} N_i(t)$$

where $\sigma_{f,i}$ is a microscopic cross section for fission, (m^2), for isotope i. and $N_i(t)$ is a concentration ($1/m^3$) of the fissile isotope i. The initial value of Σ_f is assumed to be 10.0 (1/m). The value is approximately constant because U-235 is in time being replaced by Pu-239. Figure 3-913 shows the neutron flux. The value is approximately constant because the macroscopic fission cross section is constant.

Figure 3-914 shows the concentrations of Kr-88. In the case Kr-88-SOL-1, the yield is constant (3.513E-2) and therefore the Kr-88 concentration is practically constant with constant neutron flux/concentration. In the case Kr-88-SOL-2, the Kr-88 concentrations are slowly decreasing in time as more fission is caused by Pu-239, which has about three time smaller Kr-88 yield than U-235.

Figure 3-915 shows the values of Kr-88-SOL-1 and Kr-88-SOL-2 cases at the end of the calculations. The Kr-88 concentration is clearly smaller in the case of Kr-88-SOL-2. The results are compared to the theoretical solutions in Table 3-78. Theoretical calculations are provided in the Excel file Kr-88-

SOL.xlsx. Since the fuel concentration changes are very slow, stationary-state values of isotope concentrations are used.

- Kr-88: removal due to decay is equal to the production from fission

$$\lambda_{Kr-88} \cdot N_{Kr-88} = \gamma_{Kr-88}(t) \cdot \Sigma_f \cdot \Phi$$

- Rb-88: removal due to decay is equal to the production from fission and from the decay of Kr-88

$$\lambda_{Rb-88} \cdot N_{Rb-88} = \gamma_{Rb-88}(t) \cdot \Sigma_f \cdot \Phi + \lambda_{Kr-88} N_{Kr-88}$$

The total number of atoms in the core is obtained from:

$$n_{Kr-88} = V_{tot} \cdot \gamma_{Kr-88}(t) \cdot \Sigma_f \cdot \Phi / \lambda_{Kr-88}$$
$$n_{Rb-88} = V_{tot} \cdot [\gamma_{Rb-88}(t) \cdot \Sigma_f \cdot \Phi + \lambda_{Kr-88} \cdot N_{Kr-88}] / \lambda_{Rb-88}$$

Here V_{tot} is the total volume of the core. The current fission yields are given by (see Volume 1, individual fission yields):

$$\gamma_i(t) = \frac{\sum_{j \in fis} \sigma_{f,j} \, N_j(t) \, \gamma_{f,j \to i}}{\sum_{j \in fis} \sigma_{f,j} \, N_j(t)}$$

All theoretical calculations from the above formulae are shown in the Excel file Kr-88-SOL.xlsx. The concentrations of fissile isotopes, N_j, for U-235 and Pu-239 are taken from SPECTRA output files. The other fissile isotopes have negligible effect. The theoretical results, shown in Table 3-78, are in very good agreement with the SPECTRA results. The yield fractions are not plottable, therefore could not be included in the visor picture in Figure 3-915, but can be seen in the output files. Below the printouts of the 10-year values for Kr-88-SOL-2:

- current fission yields:

```
Total mass of all isotopes in the system and all sources

                          Total      External sources      Release     Total     Current
                           mass     Aerosols     Vapors     Vapors    Sources    fission
   No.       Isotope       [kg]       [kg/s]     [kg/s]     [kg/s]    [kg/s]   yield [-]
---------  -----------  ---------  ---------  ---------  ---------  ---------  ---------
  371        Kr-88       0.000E+00  0.000E+00  0.000E+00  0.000E+00  0.000E+00  3.259E-02
  372        Rb-88       0.000E+00  0.000E+00  0.000E+00  0.000E+00  0.000E+00  2.624E-04
```

- isotope atomic number of iotopes in the reactor core:

```
=RT=  IN-CORE FISSION PRODUCT MASSES

=RT=  Location   1: SC-101  Reactor

              In-Core      In-Core       Decay
               Mass        Nuclides      Heat       Activity
 i  Isotope     [kg]          [-]         [W]         [Bq]
--- -------  -----------  -----------  -----------  -----------
371 Kr-88    2.27268E-04  1.55523E+21  3.92361E+04  1.05445E+17
372 Rb-88    2.39078E-05  1.63605E+20  4.61317E+04  1.06294E+17
```

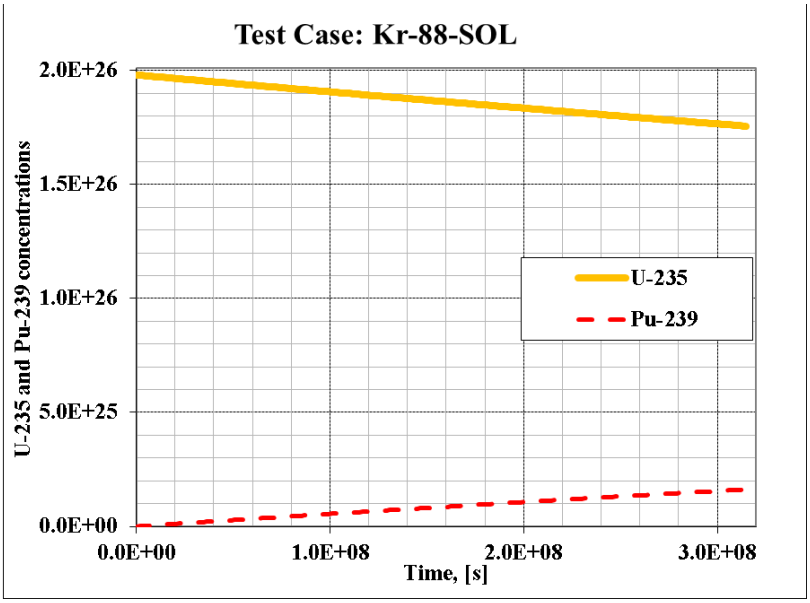

Figure 3-911 Test Kr-88-SOL, concentrations of U-235 and Pu-239

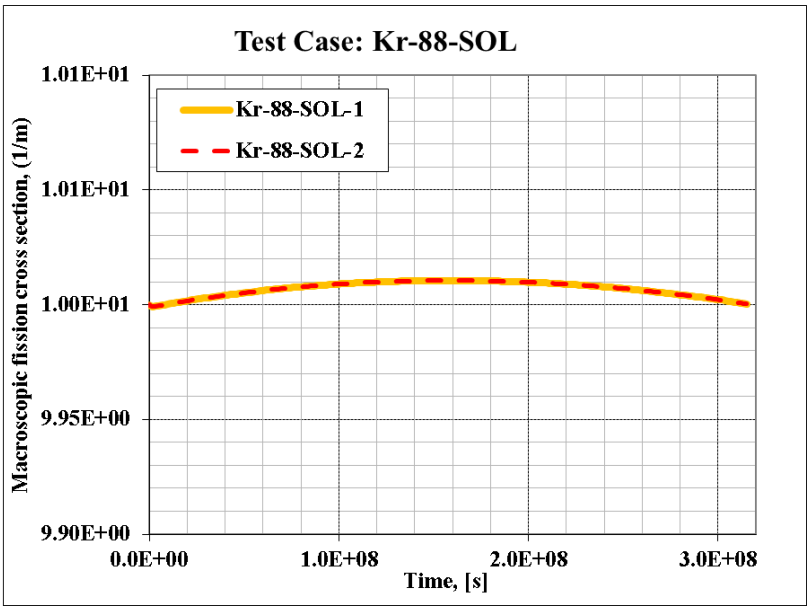

Figure 3-912 Test Kr-88-SOL, macroscopic fission cross-section

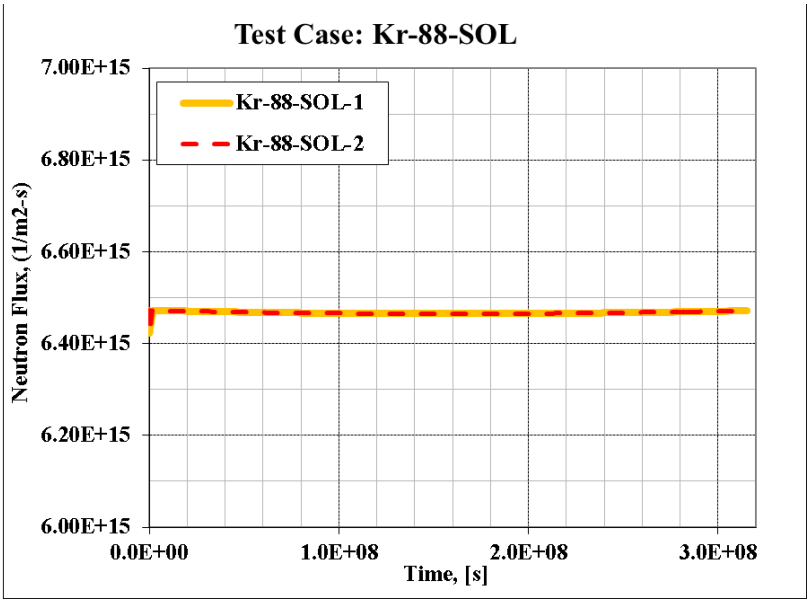

Figure 3-913 Test Kr-88-SOL, neutron flux

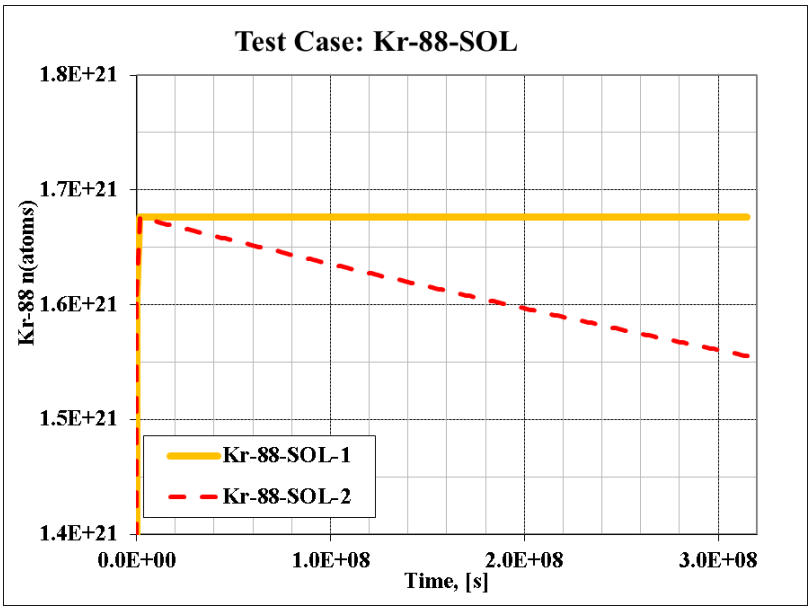

Figure 3-914 Test Kr-88-SOL, number of atoms of Kr-88 in the core

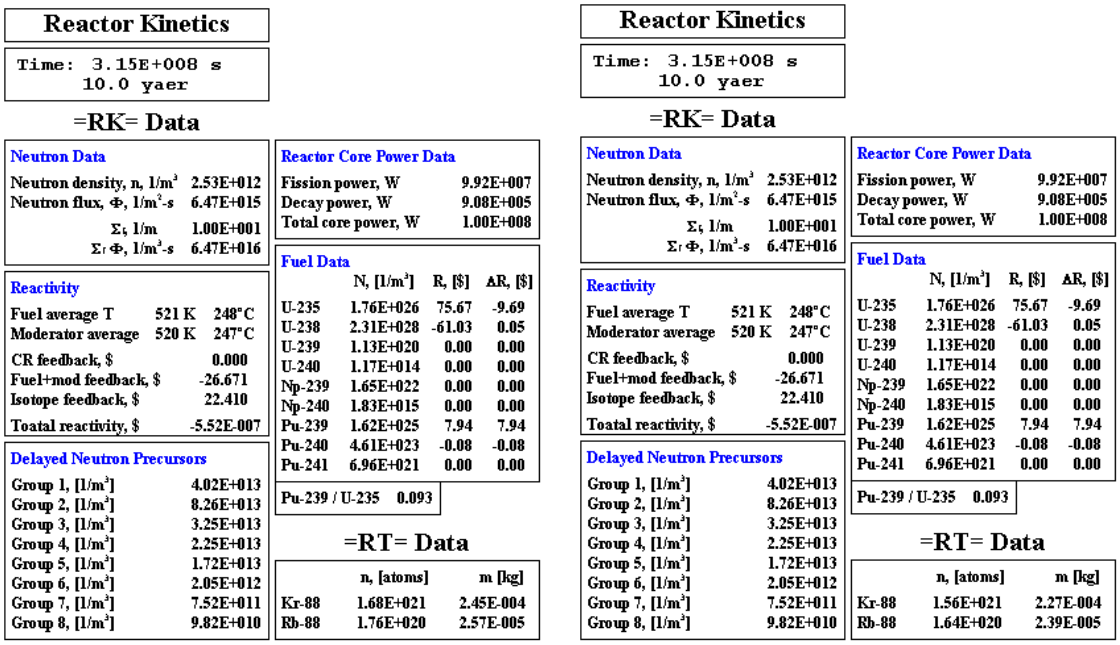

Reactor Kinetics

Time: 3.15E+008 s
10.0 yaer

=RK= Data

Neutron Data

Neutron density, n, 1/m³	2.53E+012
Neutron flux, Φ, 1/m²-s	6.47E+015
Σ, 1/m	1.00E+001
Σf Φ, 1/m³-s	6.47E+016

Reactivity

Fuel average T	521 K	248°C
Moderator average	520 K	247°C
CR feedback, $		0.000
Fuel+mod feedback, $		-26.671
Isotope feedback, $		22.410
Toatal reactivity, $		-5.52E-007

Delayed Neutron Precursors

Group 1, [1/m³]	4.02E+013
Group 2, [1/m³]	8.26E+013
Group 3, [1/m³]	3.25E+013
Group 4, [1/m³]	2.25E+013
Group 5, [1/m³]	1.72E+013
Group 6, [1/m³]	2.05E+012
Group 7, [1/m³]	7.52E+011
Group 8, [1/m³]	9.82E+010

Reactor Core Power Data

Fission power, W	9.92E+007
Decay power, W	9.08E+005
Total core power, W	1.00E+008

Fuel Data

	N, [1/m³]	R, [$]	ΔR, [$]
U-235	1.76E+026	75.67	-9.69
U-238	2.31E+028	-61.03	0.05
U-239	1.13E+020	0.00	0.00
U-240	1.17E+014	0.00	0.00
Np-239	1.65E+022	0.00	0.00
Np-240	1.83E+015	0.00	0.00
Pu-239	1.62E+025	7.94	7.94
Pu-240	4.61E+023	-0.08	-0.08
Pu-241	6.96E+021	0.00	0.00

Pu-239 / U-235 0.093

=RT= Data

	n, [atoms]	m [kg]
Kr-88	1.68E+021	2.45E-004
Rb-88	1.76E+020	2.57E-005

Reactor Kinetics

Time: 3.15E+008 s
10.0 yaer

=RK= Data

Neutron Data

Neutron density, n, 1/m³	2.53E+012
Neutron flux, Φ, 1/m²-s	6.47E+015
Σ, 1/m	1.00E+001
Σf Φ, 1/m³-s	6.47E+016

Reactivity

Fuel average T	521 K	248°C
Moderator average	520 K	247°C
CR feedback, $		0.000
Fuel+mod feedback, $		-26.671
Isotope feedback, $		22.410
Toatal reactivity, $		-5.52E-007

Delayed Neutron Precursors

Group 1, [1/m³]	4.02E+013
Group 2, [1/m³]	8.26E+013
Group 3, [1/m³]	3.25E+013
Group 4, [1/m³]	2.25E+013
Group 5, [1/m³]	1.72E+013
Group 6, [1/m³]	2.05E+012
Group 7, [1/m³]	7.52E+011
Group 8, [1/m³]	9.82E+010

Reactor Core Power Data

Fission power, W	9.92E+007
Decay power, W	9.08E+005
Total core power, W	1.00E+008

Fuel Data

	N, [1/m³]	R, [$]	ΔR, [$]
U-235	1.76E+026	75.67	-9.69
U-238	2.31E+028	-61.03	0.05
U-239	1.13E+020	0.00	0.00
U-240	1.17E+014	0.00	0.00
Np-239	1.65E+022	0.00	0.00
Np-240	1.83E+015	0.00	0.00
Pu-239	1.62E+025	7.94	7.94
Pu-240	4.61E+023	-0.08	-0.08
Pu-241	6.96E+021	0.00	0.00

Pu-239 / U-235 0.093

=RT= Data

	n, [atoms]	m [kg]
Kr-88	1.56E+021	2.27E-004
Rb-88	1.64E+020	2.39E-005

Figure 3-915 Test Kr-88-SOL, end-results (t=10 years), left: SOL-1, right: SOL-2

Table 3-78 Test Kr-88-SOL, theoretical solution and SPECTRA end-results

Kr-88-SOL					SPECTRA n (atoms)	
Φ = 6.4717E+15 1/m2-s					SOL-1	SOL-2
Σf = 1.00E+01 1/m					1.68E+21	1.56E+21
V-tot = 5.00E+01 m3					1.76E+20	1.64E+20
Isotope	λi (1/s)	SOL-1 γi	SOL-2 γi	Isotope	Equilibrium n (atoms) SOL-1	SOL-2
Kr-88	6.78000E-05	3.513E-02	3.259E-02	Kr-88	1.68E+21	1.56E+21
Rb-88	6.49700E-04	2.227E-04	2.625E-04	Rb-88	1.76E+20	1.64E+20

Kr-88-SOL, Theoretical calculation of the γi				SPECTRA γi	
Isotope	U-235 γi	Pu-239 γi	10-year γi	SOL-1	SOL-2
Kr-88	3.513E-02	1.272E-02	3.259E-02	3.513E-02	3.259E-02
Rb-88	2.227E-04	5.730E-04	2.625E-04	2.227E-04	2.624E-04

3.12.40 Test Kr-88-LIQ

The test Kr-88-LIQ provides verification of the concentration of a short-living isotope Kr-88 in the liquid (MSR) fuel, in particular the case where the yield fractions depend on the fissile isotope. SPECTRA input decks and support files are provided in \Z-INPUTS\RT\Kr-88\LIQ\.

The Kr-88 chain is shown in Figure 3-916. The fission yields, γ_f, are those for U-235. The individual fission yields are shown in Table 3-79. The current test is very similar to the DNP-2 and Kr-88-SOL tests, described in sections 3.9.2.9 and 3.12.39, respectively. A long term behavior (10 years) is analyzed. The reactor power is kept constant at 100 MW. The initial fuel composition (Σ_f, U-235 enrichment) is assumed in such a way that the consumption of U-235 is approximately compensated by the production of Pu-239 from U-238, and therefore a long term operation is possible without fuel reload. Two input decks are defined:

- Kr-88-LIQ-1: fission yields of Kr-88 and Rb-88 for U-235,
- Kr-88-LIQ-2: individual fission yields, data shown in Table 3-79.

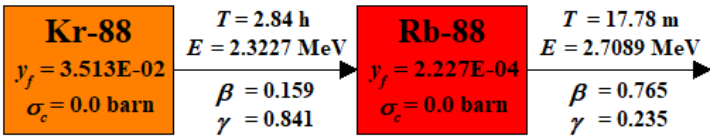

Figure 3-916 Kr-88 chain

Table 3-79 Individual fission yields

Isotope	Fission yields, γi		
	U-235	Pu-239	Pu-241
Kr-88	3.513E-02	1.272E-02	3.259E-02
Rb-88	2.227E-04	5.730E-04	2.625E-04

The results are shown in Figure 3-917 through Figure 3-921 and Table 3-80. Figure 3-917 shows the concentrations of U-235 and Pu-239. Figure 3-918 shows the macroscopic fission cross section, equal to (see Volume 1):

$$\Sigma_f = \sum_i \sigma_{f,i} N_i(t)$$

where $\sigma_{f,i}$ is a microscopic cross section for fission, (m^2), for isotope i. and $N_i(t)$ is a concentration ($1/m^3$) of the fissile isotope i. The initial value of Σ_f is assumed to be 10.0 (1/m). The value is approximately constant because U-235 is in time being replaced by Pu-239. Figure 3-919 shows the neutron flux. The value is approximately constant because the macroscopic fission cross section is constant.

Figure 3-920 shows the concentrations of Kr-88. In the case Kr-88-LIQ-1, the yield is constant (3.513E-2) and therefore the Kr-88 concentration is practically constant. In the case Kr-88-LIQ-2, the Kr-88 concentrations are slowly decreasing in time as more fission is caused by Pu-239, which has about three time smaller Kr-88 yield than U-235.

Figure 3-921 shows the values of Kr-88-LIQ-1 and Kr-88-LIQ-2 cases at the end of the calculations. The Kr-88 concentration is clearly smaller in the case of Kr-88-LIQ-2. The results are compared to

the theoretical solutions in Table 3-80. The theoretical calculations are provided in the Excel file Kr-88-LIQ.xlsx. Since the fuel concentration changes are very slow, stationary-state values of isotope concentrations are used.

- Kr-88: removal due to decay in the salt volume, V_{liq}, is equal to the production from fission in the core volume, V_{tot}:

$$\lambda_{Kr-88} \cdot N_{Kr-88} \cdot V_{liq} = \gamma_{Kr-88}(t) \cdot \Sigma_f \cdot \Phi \cdot V_{tot}$$

- Rb-88: removal due to decay is equal to the production from fission and from the decay of Kr-88

$$\lambda_{Rb-88} \cdot N_{Rb-88} \cdot V_{liq} = \gamma_{Rb-88}(t) \cdot \Sigma_f \cdot \Phi \cdot V_{tot} + \lambda_{Kr-88} N_{Kr-88} \cdot V_{liq}$$

The concentrations of isotopes in the salt are obtained from:

$$N_{Kr-88} = \gamma_{Kr-88}(t) \cdot \Sigma_f \cdot \Phi \cdot (V_{tot}/V_{liq}) / \lambda_{Kr-88}$$
$$N_{Rb-88} = [\gamma_{Rb-88}(t) \cdot \Sigma_f \cdot \Phi \cdot (V_{tot}/V_{liq}) + \lambda_{Kr-88} N_{Kr-88}] / \lambda_{Rb-88}$$

The current fission yields are given by (see Volume 1, individual fission yields):

$$\gamma_i(t) = \frac{\sum_{j \in fis} \sigma_{f,j} \, N_j(t) \, \gamma_{f,j \to i}}{\sum_{j \in fis} \sigma_{f,j} \, N_j(t)}$$

All theoretical calculations from the above formulae are shown in the Excel file Kr-88-LIQ.xlsx. The concentrations of fissile isotopes, N_j, for U-235 and U-239 are taken from SPECTRA output files. The other fissile isotopes have negligible effect. The theoretical results, shown in Table 3-80, are in very good agreement with the SPECTRA results. The yield fractions are not plottable, therefore could not be included in the visor picture in Figure 3-921, but can be seen in the output files. Below the printouts of the 10-year values for Kr-88-LIQ-2:

- current fission yields:

No.	Isotope	Total mass [kg]	External sources Aerosols [kg/s]	External sources Vapors [kg/s]	Release Vapors [kg/s]	Total Sources [kg/s]	Current fission yield [-]
[...]							
371	Kr-88	2.727E-04	0.000E+00	0.000E+00	0.000E+00	0.000E+00	**3.259E-02**
372	Rb-88	2.868E-05	0.000E+00	0.000E+00	0.000E+00	0.000E+00	**2.624E-04**

- isotope concentrations in the pool (salt) of the reactor (CV-101):

CV-101 Isotopes present in the pool at t = 3.15000E+08 (Vpool = 9.99933E+00 [m3])

i	Isotope	Class	Mass [kg]	Nuclides [1/m3]	Heat [W]	Activity [Bq]
[...]						
371	Kr-88	C-01	2.27254E-04	**1.55524E+20**	3.92336E+04	1.05438E+17
372	Rb-88	C-00	2.39063E-05	**1.63606E+19**	4.61288E+04	1.06288E+17

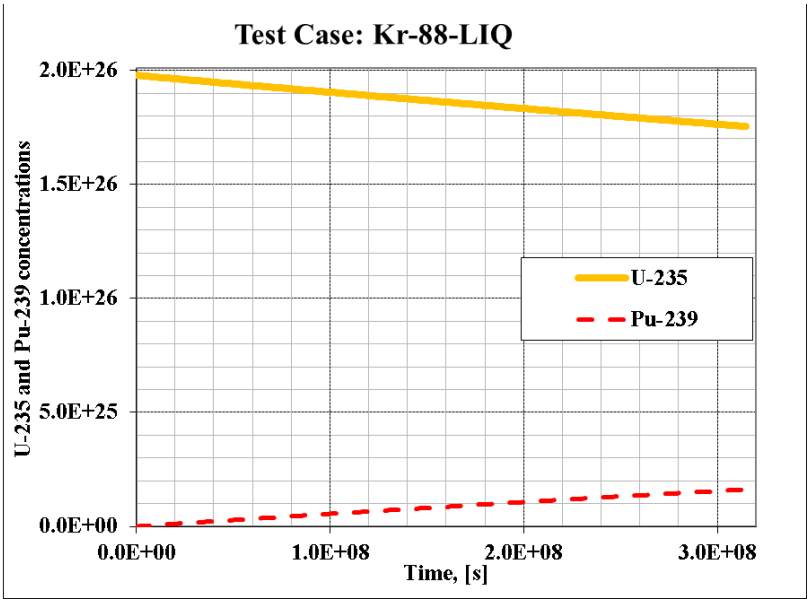

Figure 3-917 Test Kr-88-LIQ, concentrations of U-235 and Pu-239

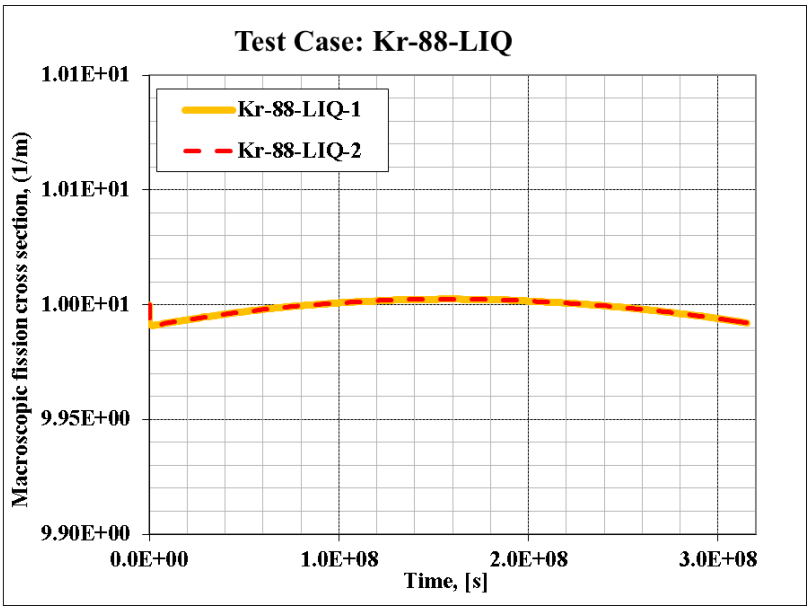

Figure 3-918 Test Kr-88-LIQ, macroscopic fission cross-section

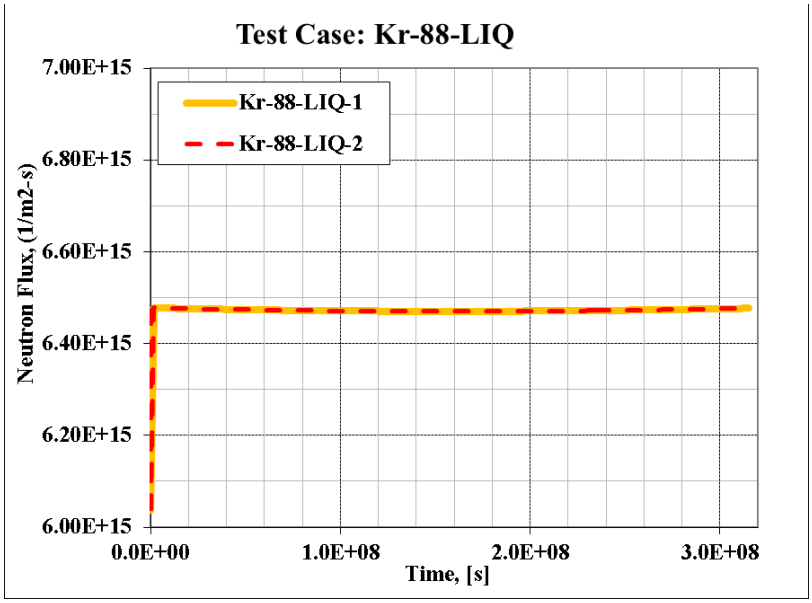

Figure 3-919 Test Kr-88-LIQ, neutron flux

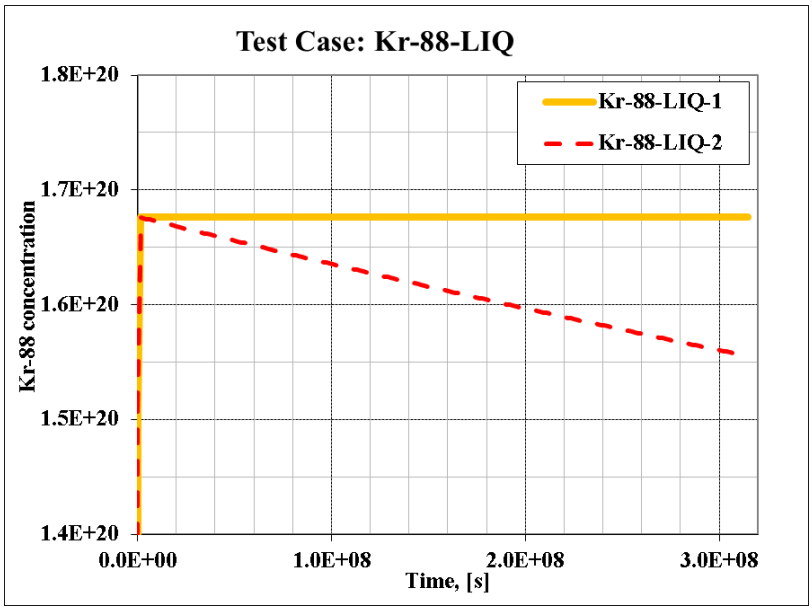

Figure 3-920 Test Kr-88-LIQ, concentrations of Kr-88

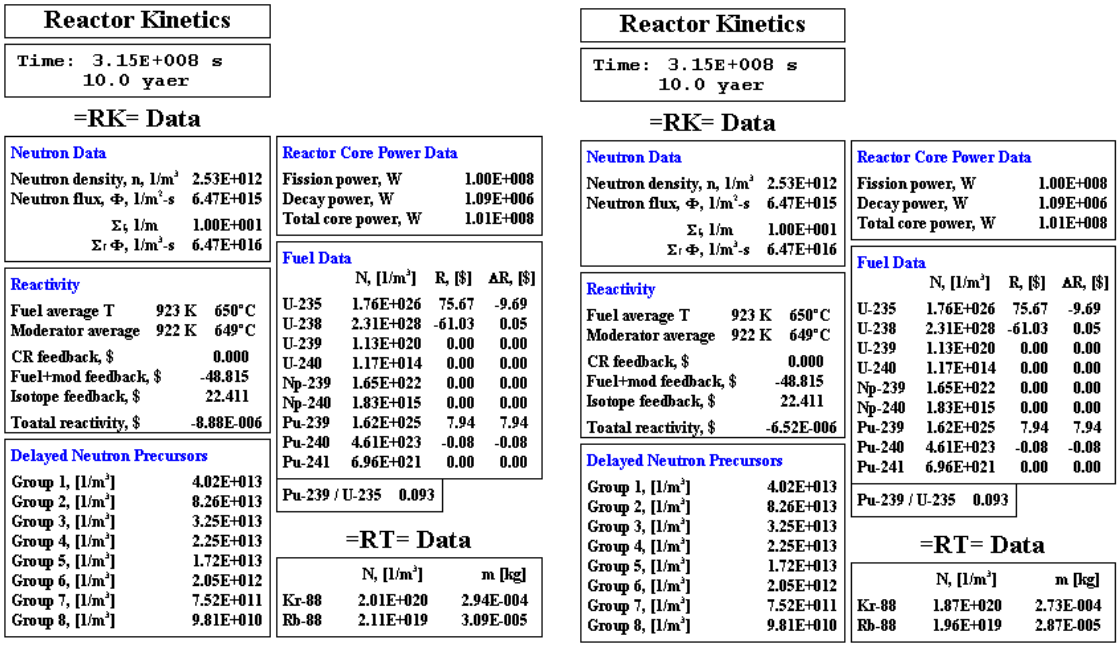

Reactor Kinetics

Time: 3.15E+008 s
10.0 yaer

=RK= Data

Neutron Data

Neutron density, n, 1/m³	2.53E+012
Neutron flux, Φ, 1/m²-s	6.47E+015
Σt, 1/m	1.00E+001
Σr Φ, 1/m³-s	6.47E+016

Reactivity

Fuel average T	923 K	650°C
Moderator average	922 K	649°C
CR feedback, $		0.000
Fuel+mod feedback, $		-48.815
Isotope feedback, $		22.411
Toatal reactivity, $		-8.88E-006

Delayed Neutron Precursors

Group 1, [1/m³]	4.02E+013
Group 2, [1/m³]	8.26E+013
Group 3, [1/m³]	3.25E+013
Group 4, [1/m³]	2.25E+013
Group 5, [1/m³]	1.72E+013
Group 6, [1/m³]	2.05E+012
Group 7, [1/m³]	7.52E+011
Group 8, [1/m³]	9.81E+010

Reactor Core Power Data

Fission power, W	1.00E+008
Decay power, W	1.09E+006
Total core power, W	1.01E+008

Fuel Data

	N, [1/m³]	R, [$]	ΔR, [$]
U-235	1.76E+026	75.67	-9.69
U-238	2.31E+028	-61.03	0.05
U-239	1.13E+020	0.00	0.00
U-240	1.17E+014	0.00	0.00
Np-239	1.65E+022	0.00	0.00
Np-240	1.83E+015	0.00	0.00
Pu-239	1.62E+025	7.94	7.94
Pu-240	4.61E+023	-0.08	-0.08
Pu-241	6.96E+021	0.00	0.00

Pu-239 / U-235 0.093

=RT= Data

	N, [1/m³]	m [kg]
Kr-88	2.01E+020	2.94E-004
Rb-88	2.11E+019	3.09E-005

Reactor Kinetics

Time: 3.15E+008 s
10.0 yaer

=RK= Data

Neutron Data

Neutron density, n, 1/m³	2.53E+012
Neutron flux, Φ, 1/m²-s	6.47E+015
Σt, 1/m	1.00E+001
Σr Φ, 1/m³-s	6.47E+016

Reactivity

Fuel average T	923 K	650°C
Moderator average	922 K	649°C
CR feedback, $		0.000
Fuel+mod feedback, $		-48.815
Isotope feedback, $		22.411
Toatal reactivity, $		-6.52E-006

Delayed Neutron Precursors

Group 1, [1/m³]	4.02E+013
Group 2, [1/m³]	8.26E+013
Group 3, [1/m³]	3.25E+013
Group 4, [1/m³]	2.25E+013
Group 5, [1/m³]	1.72E+013
Group 6, [1/m³]	2.05E+012
Group 7, [1/m³]	7.52E+011
Group 8, [1/m³]	9.81E+010

Reactor Core Power Data

Fission power, W	1.00E+008
Decay power, W	1.09E+006
Total core power, W	1.01E+008

Fuel Data

	N, [1/m³]	R, [$]	ΔR, [$]
U-235	1.76E+026	75.67	-9.69
U-238	2.31E+028	-61.03	0.05
U-239	1.13E+020	0.00	0.00
U-240	1.17E+014	0.00	0.00
Np-239	1.65E+022	0.00	0.00
Np-240	1.83E+015	0.00	0.00
Pu-239	1.62E+025	7.94	7.94
Pu-240	4.61E+023	-0.08	-0.08
Pu-241	6.96E+021	0.00	0.00

Pu-239 / U-235 0.093

=RT= Data

	N, [1/m³]	m [kg]
Kr-88	1.87E+020	2.73E-004
Rb-88	1.96E+019	2.87E-005

Figure 3-921 Test Kr-88-LIQ, end-results (t=10 years), left: LIQ-1, right: LIQ-2

Table 3-80 Test Kr-88-LIQ, theoretical solution and SPECTRA end-results

Kr-88-LIQ		
Φ =	6.4770E+15	1/m2-s
Σf =	1.00E+01	1/m
V-liq =	1.00E+01	m3
V-tot =	5.00E+01	m3

SPECTRA N (1/m3)	
LIQ-1	LIQ-2
1.68E+20	1.56E+20
1.76E+19	1.64E+19

Isotope	λi (1/s)	LIQ-1 yi	LIQ-2 yi	Isotope	Equilibrium N (1/m3) LIQ-1	LIQ-2
Kr-88	6.78000E-05	3.513E-02	3.259E-02	Kr-88	1.68E+20	1.56E+20
Rb-88	6.49700E-04	2.227E-04	2.625E-04	Rb-88	1.76E+19	1.64E+19

Kr-88-LIQ, Theoretical calculation of the γi

Isotope	U-235 γi	Pu-239 γi	10-year γi
Kr-88	3.513E-02	1.272E-02	3.259E-02
Rb-88	2.227E-04	5.730E-04	2.625E-04

SPECTRA γi	
LIQ-1	LIQ-2
3.513E-02	3.259E-02
2.227E-04	2.624E-04

3.12.41 Test Xe-136

Since Xe-136 is one of the major contributors to the pressurization of the primary system of molten salt reactors, an accurate prediction of the Xe-136 production is important for designing the reactor. It is interesting to analyze the production of Xe-136 in different reactor types. The present section contains a short analysis of Xe-136 in solid fuel reactors and circulating fuel reactors and an analytical verification of the calculated results. SPECTRA input decks and support files are provided in \Z-INPUTS\RT\Xe-136\.

The Xe-135 / 136 chain is shown in Figure 3-922. The fission yields of Xe-135 and Xe-136 from different fuel isotopes is shown in Table 3-81. In the case of Xe-135, the cumulative yields are given. Xe-135 itself has rather low yield; it is created mainly by the decay of I-135. Roughly speaking, the cumulative yield of Xe-135 is approximately equal to the yield of Xe-136, 6% - 7%.

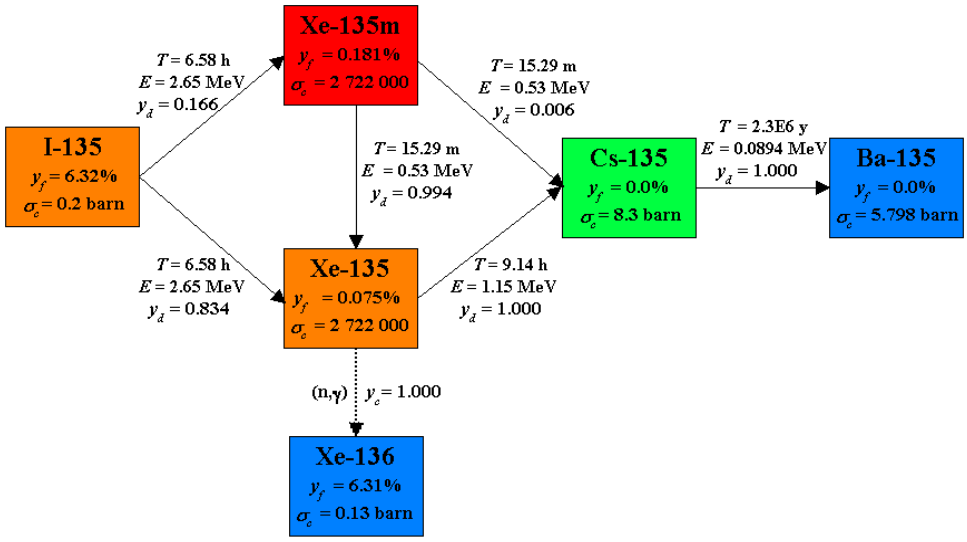

Figure 3-922 Xe-135 / 136 chain

Table 3-81 Individual fission yields

	Fission yields, γi		
Isotope	U-235	Pu-239	Pu-241
Xe-135	6.58E-02	7.23E-02	7.28E-02
Xe-136	6.31E-02	7.05E-02	7.10E-02

Xe-135 has an extremely large cross section for neutron absorption, about 2.7×10^6 barn. Upon the neutron capture, Xe-136 is created. Consequently a large amount of Xe-135 is converted to Xe-136 before it can decay to produce Cs-135. The ratio of capture to decay depends on the neutron flux. For a typical reactor, the neutron flux is of order of 10^{13} n/cm^2-s, for example in MSRE the thermal flux was about 4×10^{13} n/cm^2-s = 4×10^{17} n/m^2-s ([182], fig. 9.5, page 63).

Considering that the capture cross section is equal to: $\sigma = 2.7\times10^{6}$ barn $= 2.7\times10^{-22}$ m^2, the absorption term is equal to:

$$N_{Xe\text{–}135} \cdot \sigma \cdot \Phi = N_{Xe\text{–}135} \cdot 2.7 \cdot 10^{-22} \cdot 4 \cdot 10^{17} = N_{Xe\text{–}135} \cdot 1.1 \cdot 10^{-4}$$

On the other hand, the decay term is equal to:

$$N_{Xe\text{–}135} \cdot \lambda = N_{Xe\text{–}135} \cdot 2.1 \cdot 10^{-5}$$

Here λ is the decay constant of Xe-135, approximately equal to 2.1×10^{-5} (1/s). Therefore, with this neutron flux, the fraction of Xe-135 that captures neutron and is converted to Xe-136 will be equal to:

$$\frac{1.1 \cdot 10^{-4}}{1.1 \cdot 10^{-4} + 2.1 \cdot 10^{-5}} = 0.84$$

Since the fission yields are nearly equal, the total production of Xe-136 will be in this case equal to 1.84 of the value that would be obtained if Xe-136 was only created by fission:

$$X = \frac{N_{Xe\text{–}136}}{N_{Xe\text{–}136,\,fission}} \approx 1.84$$

With higher flux the ratio will be higher and will approach the limiting value where all Xe-135 is converted to Xe-136 (for example, for U-235 it will be (6.31+6.58)/6.31 = 2.04). With lower neutron flux, the ratio will be lower; the limiting value is of course 1.0 (for an extremely small neutron flux). Generally the fraction of Xe-135 that is converted to Xe-136 is given by:

$$\frac{\sigma \cdot \Phi}{\sigma \cdot \Phi + \lambda}$$

This is the case for a typical reactor with solid fuel (LWR, HTR, etc.). In the case of reactors with circulating liquid fuel, such as Molten Salt Reactors (MSR), this will be quite different. The present analysis shows the production of Xe-136 in different reactor types and shows verification of the SPECTRA results by comparison with analytical equations. The following cases were analyzed:

- Solid fuel (LWR, HTR, etc.) - section 3.12.41.1.
  - Xe-136-SOL-U-Pu: U-235 and Pu-239, Pu 241 present in the core.
  - Xe-136-SOL-U: only one fuel isotope, U-235, present in the core.
- Liquid fuel (MSR) - section 3.12.41.2.
  - Xe-136-LIQ-V00: Ratio of non-core salt volume to core salt volume = 0.
  - Xe-136-LIQ-V01: Ratio of non-core salt volume to core salt volume = 1.
  - Xe-136-LIQ-V04: Ratio of non-core salt volume to core salt volume = 4.
  - Xe-136-LIQ-V10: Ratio of non-core salt volume to core salt volume = 10.

3.12.41.1 Xe-136-SOL

Xe-136-SOL-U-Pu: U-235 and Pu-239, Pu 241 present in the core

In this case a reactor with solid fuel is considered. The fuel is initially composed of 2.5% enriched Uranium (ratio of U-238-to-U-235 of 40). Ten years of continuous reactor operation at full power (assumed as 400 MW) is considered. A slow loading rate of U-235 is assumed, equal to 1.4E-8 (1/s). SPECTRA input decks are provided in \Z-INPUTS\RT\Xe-136\SOL-U-Pu. Two cases are considered:

- Xe-136-SOL-1 base case
- Xe-136-SOL-2 production of Xe-136 from the neutron capture by Xe-135 is disabled.

The results are shown in Figure 3-923 and Figure 3-924. Figure 3-923 shows the changes of the concentration of fuel isotopes, U-235, Pu-239, and Pu-241, in time. Figure 3-924 shows the mass of Xe-136 produced in the reactor in the two cases, Xe-136-SOL-1 and Xe-136-SOL-2. The 10-year values are:

- Xe-136-SOL-1: 114.3 kg of Xe-136
- Xe-136-SOL-2: 60.61 kg of Xe-136

The ratio is equal to, R_X = **1.88**.

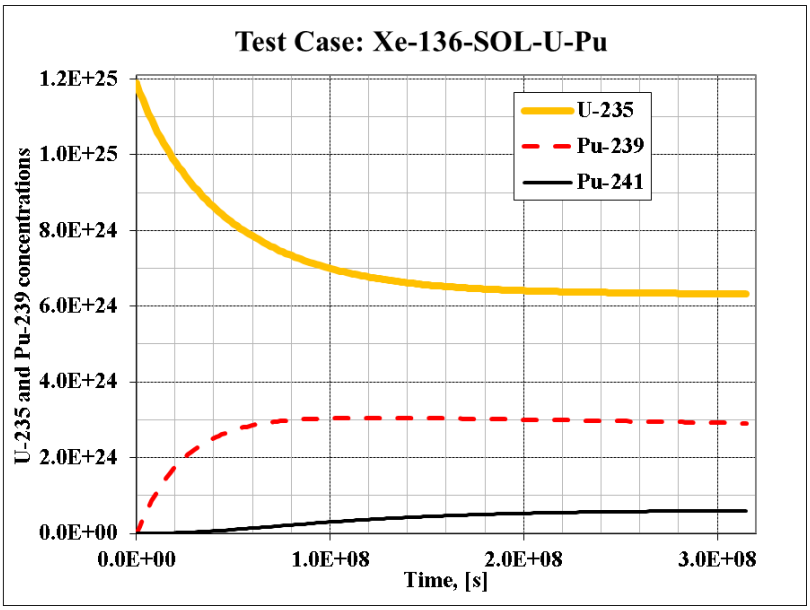

Figure 3-923 Test Xe-136-SOL-U-Pu, fuel concentrations

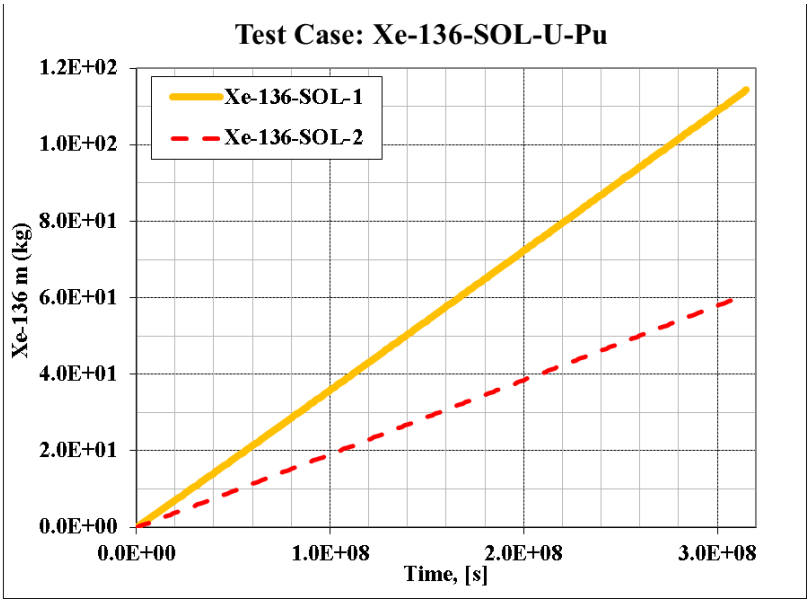

Figure 3-924 Test Xe-136-SOL-U-Pu, Xe-136 masses

Verification by analytical solution is described below. First, the fission yields are calculated analytically, from the following equations.

$$\gamma_i(t) = \frac{\sum_{j \neq i} \sigma_{f,j} \; N_j(t) \; \gamma_{f,j \to i}}{\sum_{j \neq i} \sigma_{f,j} \; N_j(t)}$$

All calculations are stored in the Excel file, Xe-136-SOL.xlsx, located in \Z-INPUTS\RT\Xe-136\SOL-U-Pu. The analytical results are shown below in the column "Theory".

Xe-136-SOL-U-Pu, Theoretical calculation of the γi, 10-year values						SPECTRA
	U-235	Pu-239	Pu-241		Theory	values
Isotope	γi	γi	γi		γi	γi
Xe-135	6.580E-02	7.230E-02	7.280E-02	→	6.877E-02	6.877E-02
Xe-136	6.310E-02	7.050E-02	7.100E-02	→	6.647E-02	6.647E-02

The SPECTRA values are taken from the output files:

No.	Isotope	Total mass [kg]	External sources Aerosols [kg/s]	Vapors [kg/s]	Release Vapors [kg/s]	Total Sources [kg/s]	Current fission yield [-]
[...]							
131	I-135	0.000E+00	0.000E+00	0.000E+00	0.000E+00	0.000E+00	**6.348E-02**
132	Xe-135	0.000E+00	0.000E+00	0.000E+00	0.000E+00	0.000E+00	**5.292E-03**
133	Xe-136	0.000E+00	0.000E+00	0.000E+00	0.000E+00	0.000E+00	**6.647E-02**

The cumulative values are shown in the last column of the table above. The values are in agreement with the theoretical values.

Next, the masses of Xe-135 and Xe-136 are checked by using analytical formulations. For Xe-135 an equilibrium concentration is calculated by equating the production from fission with the removal from radioactive decay and neutron capture:

$$\gamma_{Xe\text{–}135}(t) \cdot \Sigma_f \cdot \Phi = \lambda_{Xe\text{–}135} \cdot N_{Xe\text{–}135} + \sigma_{Xe\text{–}135} \cdot N_{Xe\text{–}135} \cdot \Phi$$

which leads to:

$$N_{Xe\text{–}135} = \frac{\gamma_{Xe\text{–}135}(t) \cdot \Sigma_f \cdot \Phi}{\lambda_{Xe\text{–}135} + \sigma_{Xe\text{–}135} \cdot \Phi}$$

Calculation of Xe-136 mass is done differently. Since Xe-136 does not decay and does not absorb neutrons, there is no equilibrium concentration for this isotope. The concentrations increase in time, as shown in Figure 3-924. The total mass is equal to the source rates integrated over the reactor operation period (10 years = 3.15×10^8 s). The source rate due to fission is equal to:

$$\Sigma_f \cdot \Phi \cdot \gamma_{Xe\text{–}136}$$

The concentration after the reactor operating time of $\Delta t = 3.15\times10^8$ s is equal to:

$$N_{Xe\text{–}136,\,f} = \Sigma_f \cdot \Phi \cdot \gamma_{Xe\text{–}136} \cdot \Delta t$$

Here Δt is the reactor operation period ($\Delta t = 3.15\times10^8$ s). The source rate due to neutron capture in Xe-135 is equal to:

$$\Sigma_f \cdot \Phi \cdot \gamma_{Xe\text{–}135} \cdot \frac{\sigma_{Xe\text{–}135} \cdot \Phi}{\sigma_{Xe\text{–}135} \cdot \Phi + \lambda_{Xe\text{–}135}}$$

The quotient gives the fraction of Xe-135 that captures neutrons (number of neutron captures divided by the number of neutron captures plus the number of decays). The concentration after the reactor operating time of $\Delta t = 3.15\times10^8$ s is equal to:

$$N_{Xe\text{–}136,\,c} = \Sigma_f \cdot \Phi \cdot \gamma_{Xe\text{–}135} \cdot \frac{\sigma_{Xe\text{–}135} \cdot \Phi}{\sigma_{Xe\text{–}135} \cdot \Phi + \lambda_{Xe\text{–}135}} \cdot \Delta t$$

The total Xe-136 is:

$$N_{Xe\text{–}136,\,t} = N_{Xe\text{–}136,\,f} + N_{Xe\text{–}136,\,c}$$

The corresponding masses are obtained from:

$$m_i = \left(\frac{dN}{dt}\right)_i \cdot V_{tot} \cdot \frac{M_w}{A_v}$$

Here V_{tot} is the reactor volume, A_v is the Avogadro number and M_w is the molar weight. All calculations are stored in the Excel file, Xe-136-SOL.xlsx, located in \Z-INPUTS\RT\Xe-136\SOL-U-Pu. The results are shown below.

Xe-136-SOL-U-Pu						
Φ =	4.4727E+17	1/m^2-s			SPECTRA values, m (kg)	
Σf =	5.79E-01	1/m		Isotope	SOL-1	SOL-2
V-tot =	5.00E+01	m^3		Xe-135	1.40E-03	1.40E-03
				Xe-136	1.14E+02	6.08E+01
					Theoretical values	
Isotope	λi (1/s)	σi (barn)	γi	Isotope	N (1/m3)	m (kg)
Xe-135	2.10700E-05	2.722E+06	6.877E-02	Xe-135	1.25E+20	1.40E-03
Xe-136	0.00000E+00	0.000E+00	6.647E-02	Xe-136-f	5.42E+24	6.12E+01
				Xe-136-c	4.78E+24	5.40E+01
				Xe-136-t	1.02E+25	1.15E+02

The analytical results are shown in the column "Theoretical values". The Xe-135 mass is marked using the blue color. The Xe-136 mass originating from fission only is marked by the red color. The total Xe-136 mass (fission + capture) is marked by the orange color.

The SPECTRA results, extracted from the output files, are shown under "SPECTRA values, m (kg)". The Xe-135 values are marked by the blue color. There is of course no difference between SOL-1 and SOL-2 result for this isotope. The value is in agreement with the theoretical value.

The Xe-136 value for the base case (SOL-1) is marked by the orange color and it corresponds to the theoretical total value the total Xe-136 mass. The Xe-136 values for the case SOL-2 are marked by the red color and it corresponds to the theoretical value of the Xe-136 mass originating from fission only.

The SPECTRA values for Xe-136 are in somewhat different form the theoretical values because in this case the fission yield varies slightly over the 10-years period as the fuel composition changes (Figure 3-923). In the theoretical calculation, the end-value (1t 10 years) of the fission yields were taken. To avoid this problem, the next test case is analyzed, where the fuel is composed of U-235 only.

Xe-136-SOL-U: Only U-235 present in the core

This test is very similar to the previous test. There are two differences:

- There us no U-238 in the core (ratio of U-238-to-U-235 changed from 40 to 0)
- U-235 loading rate was set to 2.5518E-8 (1/s), a value found by trial and error that compensates the fuel depletion at the assumed power.

With this assumption the analytical verification is easier. The yield fractions are constant and equal to those for U-235 all through the 10-year operation. SPECTRA input decks are provided in \Z-INPUTS\RT\Xe-136\SOL-U-Pu. Two cases are considered:

- Xe-136-SOL-1 base case
- Xe-136-SOL-2 production of Xe-136 from the neutron capture by Xe-135 is disabled.

The results are shown in Figure 3-925, which shows the mass of Xe-136 produced in the reactor in the two cases, Xe-136-SOL-1 and Xe-136-SOL-2. The 10-year values are:

- Xe-136-SOL-1: 109.5 kg of Xe-136
- Xe-136-SOL-2: 58.1 kg of Xe-136

The ratio is equal to, $\boldsymbol{R_X}$ **= 1.88**.

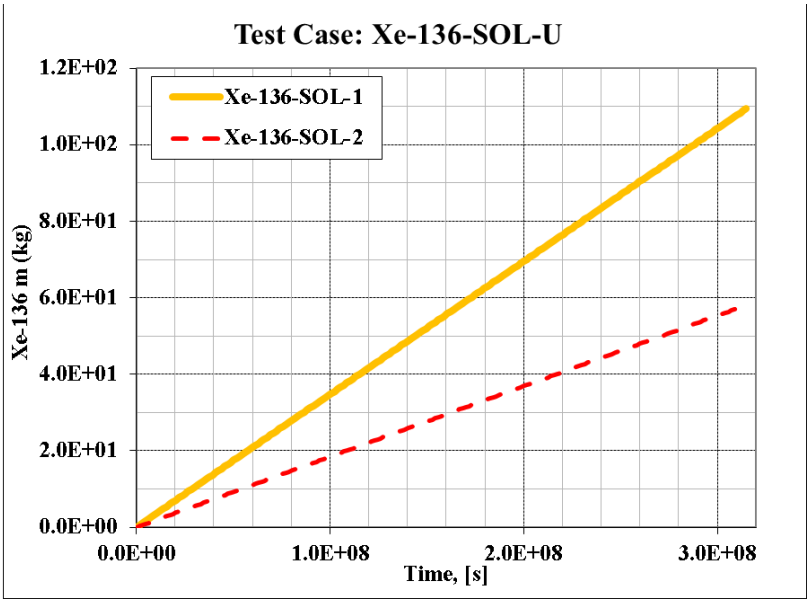

Figure 3-925 Test Xe-136-SOL-U, Xe-136 masses

Verification by analytical solution is described below. All calculations are stored in the Excel file, Xe-136-SOL.xlsx, located in \Z-INPUTS\RT\Xe-136\SOL-U. Verification of fission yields is quite trivial (actual yields = U-235 yields) and therefore not shown here. The masses of Xe-135 and Xe-136 are checked by using analytical formulations shown in the previous section. The results are shown below.

Test Xe-136-SOL-U			
Φ =	4.3153E+17	1/m^2-s	
Σf =	6.00E-01	1/m	
V-tot =	5.00E+01	m^3	
Isotope	λi (1/s)	σi (barn)	γi
Xe-135	2.10700E-05	2.722E+06	6.580E-02
Xe-136	0.00000E+00	0.000E+00	6.310E-02

	SPECTRA values, m (kg)	
Isotope	SOL-1	SOL-2
Xe-135	1.378E-03	1.378E-03
Xe-136	1.095E+02	5.810E+01

	Theoretical values	
Isotope	N (1/m3)	m (kg)
Xe-135	1.230E+20	1.378E-03
Xe-136-f	5.146E+24	5.811E+01
Xe-136-c	4.550E+24	5.138E+01
Xe-136-t	9.697E+24	1.095E+02

The analytical results are shown in the column "Theoretical values". The Xe-135 mass is marked using the blue color. The Xe-136 mass originating from fission only is marked by the red color. The total Xe-136 mass (fission + capture) is marked by the orange color.

The SPECTRA results, extracted from the output files, are shown under "SPECTRA values, m (kg)". The Xe-135 values are marked by the blue color. There is of course no difference between SOL-1 and SOL-2 result for this isotope. The value is in agreement with the theoretical value.

The Xe-136 value for the base case (SOL-1) is marked by the orange color and it corresponds to the theoretical total value the total Xe-136 mass. The Xe-136 values for the case SOL-2 are marked by the red color and it corresponds to the theoretical value of the Xe-136 mass originating from fission only. Both values are in agreement with the theoretical solution.

3.12.41.2 Xe-136-LIQ

This section discusses the results obtained for a similar reactor but with circulating liquid fuel (Molten Salt Reactor). The reactor parameters (power core volume, Σ_f) are the same as in previous section. A very simple model was set up, consisting of one solid structure (SC-101), representing the graphite and two fluid volumes (CV-101 and CV-102), representing the core salt volume (V_{cs}) and the non-core salt volume (V_{ns}), respectively. The model is shown in Figure 3-926. Several cases were analyzed, assuming different ratio of the non-core salt to the core salt volumes:

- Xe-136-LIQ-V00 $(V_{ns}/V_{cs}) = 0$ $V_{ns} = 0.0$ m^3
- Xe-136-LIQ-V01 $(V_{ns}/V_{cs}) = 1$ $V_{ns} = 10.0$ m^3
- Xe-136-LIQ-V04 $(V_{ns}/V_{cs}) = 4$ $V_{ns} = 40.0$ m^3
- Xe-136-LIQ-V10 $(V_{ns}/V_{cs}) = 10$ $V_{ns} = 100.0$ m^3
- Xe-136-LIQ-V15 $(V_{ns}/V_{cs}) = 15$ $V_{ns} = 150.0$ m^3

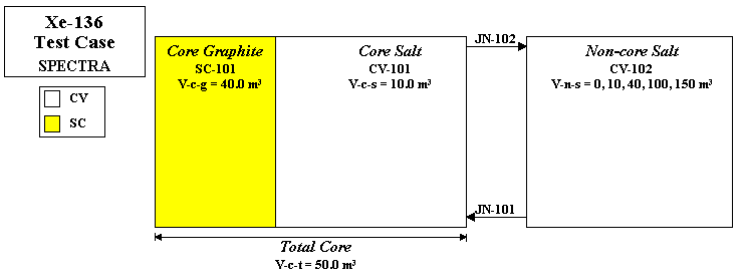

Figure 3-926 Test Xe-136-LIQ, nodalization

In order to have a simple verification the pure U-235 is used as fuel. This gives constant yield fractions over the whole 10 year period.

Xe-136-LIQ-V00: All salt in the core

In this case all salt is assumed to be present in the core. Therefore only CV-101 (Figure 3-926) is present in the model. SPECTRA input decks are provided in \Z-INPUTS\RT\Xe-136\LIQ-V00. Two cases are considered:

- Xe-136-LIQ-1 base case
- Xe-136-LIQ-2 production of Xe-136 from the neutron capture by Xe-135 is disabled.

The results are shown in Figure 3-927, which shows the mass of Xe-136 produced in the reactor in the two cases, Xe-136-LIQ-1 and Xe-136-LIQ-2. The 10-year values are:

- Xe-136-SOL-1: 109.5 kg of Xe-136
- Xe-136-SOL-2: 58.1 kg of Xe-136

The ratio is equal to, $\boldsymbol{R_X}$ **= 1.88**.

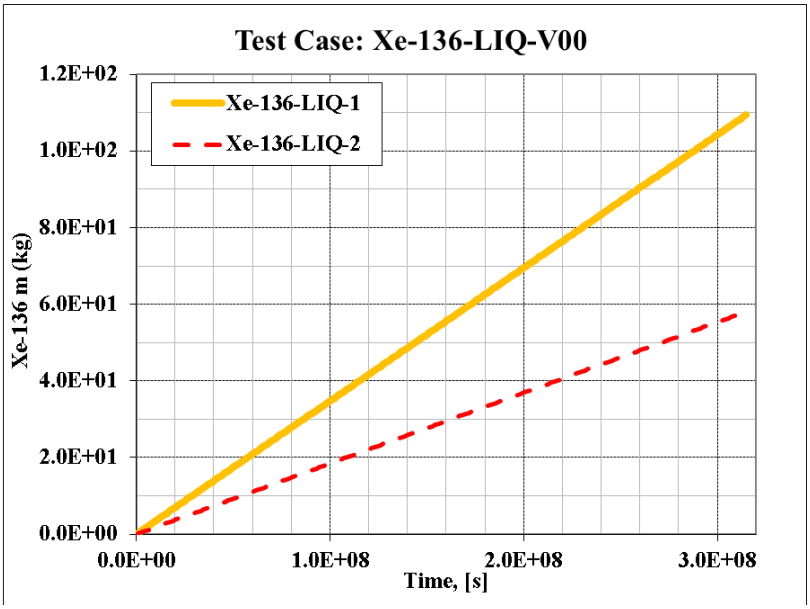

Figure 3-927 Test Xe-136-LIQ-V00, Xe-136 masses

The values are exactly the same as in the case of the solid fuel, Xe-136-SOL-U, because there is no fuel circulation (all salt stays in the core) and therefore no reason for differences in Xenon production.

Verification by analytical solution is described below. The theoretical solution is obtained from:

$$\left(\gamma_{Xe\text{–}135}(t)\cdot\Sigma_f\cdot\Phi\right)\cdot V_{ct}=\left(\lambda_{Xe\text{–}135}\cdot N_{Xe\text{–}135}\right)\cdot\left(V_{cs}+V_{ns}\right)+\left(\sigma_{Xe\text{–}135}\cdot N_{Xe\text{–}135}\cdot\Phi\right)\cdot V_{cs}$$

The first term gives production from fission, which occurs in the core volume, V_{ct} (50 m^3). The second term gives radioactive decay, which occurs in the whole salt volume, V_{cs} + V_{ns}. The last term gives removal due to neutron capture, which occurs in the core salt volume, V_{cs}. Therefore the theoretical concentration of Xe-135 is obtained from:

$$N_{Xe\text{–}135}=\frac{\gamma_{Xe\text{–}135}(t)\cdot\Sigma_f\cdot\Phi\cdot V_{ct}}{\lambda_{Xe\text{–}135}\cdot\left(V_{cs}+V_{ns}\right)+\sigma_{Xe\text{–}135}\cdot\Phi\cdot V_{cs}}$$

Note: the concentrations are defined here per unit volume of salt. In SPECTRA those are the concentrations in Control Volumes and are reported by the RT Package. The concentration of Xe-135 that are seen by the reactor kinetics RT Package are different. The ratio is equal to V_{ct}/V_{cs}, in this case 5.0, which is seen in the picture below.

Xe-135 / 136 Chain

=RK= Data

	N, [1/m³]	R, [$]	ΔR, [$]
I-135	5.58E+020	0.00	0.00
Xe-135	1.23E+020	-3.58	0.00
Xe-136	5.15E+024	0.00	0.00

=RT= Data

	N, [1/m³]	Ratio	m, [kg]
I-135	2.79E+021	5.00	6.26E-003
Xe-135	6.15E+020	5.00	1.38E-003
Xe-136	2.57E+025	5.00	5.81E+001

The mass of Xe-136 is obtained as before, calculating, the fission source and the source from neutron capture in Xe-135. The total production of Xe-136 from fission is given by:

$$V_{ct} \cdot \Sigma_f \cdot \Phi \cdot \gamma_{Xe\text{–}136}$$

The concentration in the salt volume (V_{cs}+V_{ns}) after the reactor operating time of $\Delta t = 3.15\times10^8$ s is equal to:

$$N_{Xe\text{–}136,\,f} = \Sigma_f \cdot \Phi \cdot \gamma_{Xe\text{–}136} \cdot \frac{V_{ct}}{V_{cs}+V_{ns}} \cdot \Delta t$$

The total production of Xe-136 from neutron capture in Xe-135 is given by:

$$V_{ct} \cdot \Sigma_f \cdot \Phi \cdot \gamma_{Xe\text{–}135} \cdot \frac{\sigma_{Xe\text{–}135} \cdot \Phi \cdot V_{cs}}{\sigma_{Xe\text{–}135} \cdot \Phi \cdot V_{cs} + \lambda_{Xe\text{–}135}(V_{cs}+V_{ns})}$$

The quotient gives the fraction of Xe-135 that captures neutrons (number of neutron captures divided by the number of neutron captures plus the number of decays). The concentration in the salt volume (V_{cs}+V_{ns}) after the reactor operating time of $\Delta t = 3.15\times10^8$ s is equal to:

$$N_{Xe\text{–}136,\,c} = \Sigma_f \cdot \Phi \cdot \gamma_{Xe\text{–}135} \cdot \frac{V_{ct}}{V_{cs}+V_{ns}} \cdot \frac{\sigma_{Xe\text{–}135} \cdot \Phi}{\sigma_{Xe\text{–}135} \cdot \Phi + \lambda_{Xe\text{–}135}(V_{cs}+V_{ns})/V_{cs}} \cdot \Delta t$$

The total Xe-136 is:

$$N_{Xe\text{–}136,\,t} = N_{Xe\text{–}136,\,f} + N_{Xe\text{–}136,\,c}$$

The corresponding masses are obtained from:

$$m_i = \left(\frac{dN}{dt}\right)_i \cdot (V_{cs}+V_{ns}) \cdot \frac{A_v}{M_w} \cdot \Delta t$$

All calculations are stored in the Excel file, Xe-136-LIQ.xlsx, located in \Z-INPUTS\RT\Xe-136\LIQ-V00. The results are shown below.

Xe-136-LIQ-V00		
Φ =	4.3148E+17	1/m²-s
Σf =	6.00E-01	1/m
V-c-t =	5.00E+01	m³
V-c-s =	1.00E+01	m³
V-n-s =	0.00E+00	m³

Isotope	λi (1/s)	σi (barn)	γi
Xe-135	2.10700E-05	2.722E+06	6.580E-02
Xe-136	0.00000E+00	0.000E+00	6.310E-02

	SPECTRA m (kg)	
Isotope	LIQ-1	LIQ-2
Xe-135	1.38E-03	1.38E-03
Xe-136	1.09E+02	5.81E+01

	Theoretical values	
Isotope	N (1/m3)	m (kg)
Xe-135	6.15E+20	1.38E-03
Xe-136-f	2.57E+25	5.81E+01
Xe-136-c	2.27E+25	5.14E+01
Xe-136-t	4.85E+25	1.09E+02

The analytical results are shown in the column "Theoretical values". The Xe-135 mass is marked using the blue color. The Xe-136 mass originating from fission only is marked by the red color. The total Xe-136 mass (fission + capture) is marked by the orange color.

The SPECTRA results, extracted from the output files, are shown under "SPECTRA values, m (kg)". The Xe-135 values are marked by the blue color. There is of course no difference between SOL-1 and SOL-2 result for this isotope. The value is in agreement with the theoretical value.

The Xe-136 value for the base case (SOL-1) is marked by the orange color and it corresponds to the theoretical total value the total Xe-136 mass. The Xe-136 values for the case SOL-2 are marked by the red color and it corresponds to the theoretical value of the Xe-136 mass originating from fission only. Both values are in agreement with the theoretical solution.

Xe-136-LIQ-V01, -V04, V10, V15: Non-core salt / core salt ratio of 1, 4, 10, and 15

In this case there is core salt and non-core salt volumes. Both CV-101 and CV-102 (Figure 3-926) are present in the model. A forced flow is provided to ensure continuous mixing of the core salt and the non-core salt. The results of all cases are shown in Figure 3-928.

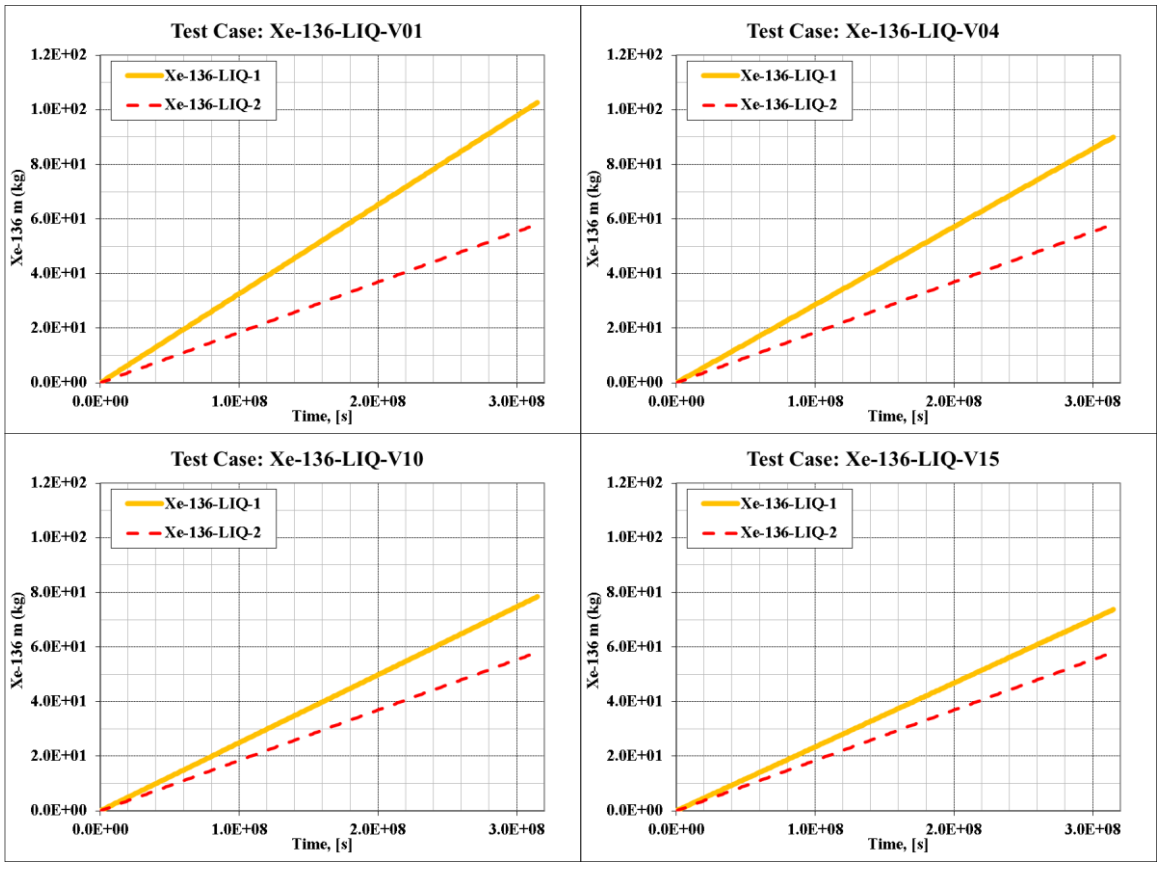

Figure 3-928 Tests Xe-136-LIQ-V01, -V04, -V10, and -V15, Xe-136 masses

The Xe-136 ratio is equal to:

Volume ratio	Xe-136 ratio
$R_V = 1$	$R_X = 1.77$
$R_V = 4$	$R_X = 1.55$
$R_V = 10$	$R_X = 1.35$
$R_V = 15$	$R_X = 1.27$

The analytical solution is performed using the equations shown in the case Xe-136-LIQ-V00. All calculations are stored in the Excel files located in appropriate folders \Z-INPUTS\RT\Xe-136\LIQ-Vxx. The results are shown below

Xe-136-LIQ-V01

Φ =	4.3134E+17	1/m²-s
Σf =	6.00E-01	1/m
V-c-t =	5.00E+01	m³
V-c-s =	1.00E+01	m³
V-n-s =	1.00E+01	m³

Isotope	λi (1/s)	σi (barn)	γi
Xe-135	2.10700E-05	2.722E+06	6.580E-02
Xe-136	0.00000E+00	0.000E+00	6.310E-02

Isotope	SPECTRA m (kg) LIQ-1	SPECTRA m (kg) LIQ-2
Xe-135	2.39E-03	2.39E-03
Xe-136	1.03E+02	5.81E+01

Isotope	Theoretical values N (1/m3)	Theoretical values m (kg)
Xe-135	5.34E+20	2.39E-03
Xe-136-f	1.29E+25	5.81E+01
Xe-136-c	9.87E+24	4.46E+01
Xe-136-t	2.27E+25	1.03E+02

Xe-136-LIQ-V04

Φ =	4.3138E+17	1/m²-s
Σf =	6.00E-01	1/m
V-c-t =	5.00E+01	m³
V-c-s =	1.00E+01	m³
V-n-s =	4.00E+01	m³

Isotope	λi (1/s)	σi (barn)	γi
Xe-135	2.10700E-05	2.722E+06	6.580E-02
Xe-136	0.00000E+00	0.000E+00	6.310E-02

Isotope	SPECTRA m (kg) LIQ-1	SPECTRA m (kg) LIQ-2
Xe-135	4.29E-03	4.29E-03
Xe-136	9.00E+01	5.81E+01

Isotope	Theoretical values N (1/m3)	Theoretical values m (kg)
Xe-135	3.82E+20	4.29E-03
Xe-136-f	5.15E+24	5.81E+01
Xe-136-c	2.83E+24	3.19E+01
Xe-136-t	7.97E+24	9.00E+01

Xe-136-LIQ-V10

Φ =	4.3140E+17	1/m²-s
Σf =	6.00E-01	1/m
V-c-t =	5.00E+01	m³
V-c-s =	1.00E+01	m³
V-n-s =	1.00E+02	m³

Isotope	λi (1/s)	σi (barn)	γi
Xe-135	2.10700E-05	2.722E+06	6.580E-02
Xe-136	0.00000E+00	0.000E+00	6.310E-02

Isotope	SPECTRA m (kg) LIQ-1	SPECTRA m (kg) LIQ-2
Xe-135	6.02E-03	6.02E-03
Xe-136	7.85E+01	5.81E+01

Isotope	Theoretical values N (1/m3)	Theoretical values m (kg)
Xe-135	2.44E+20	6.01E-03
Xe-136-f	2.34E+24	5.81E+01
Xe-136-c	8.20E+23	2.04E+01
Xe-136-t	3.16E+24	7.85E+01

Xe-136-LIQ-V10

Φ =	4.3140E+17	1/m²-s
Σf =	6.00E-01	1/m
V-c-t =	5.00E+01	m³
V-c-s =	1.00E+01	m³
V-n-s =	1.50E+02	m³

Isotope	λi (1/s)	σi (barn)	γi
Xe-135	2.10700E-05	2.722E+06	6.580E-02
Xe-136	0.00000E+00	0.000E+00	6.310E-02

Isotope	SPECTRA m (kg) LIQ-1	SPECTRA m (kg) LIQ-2
Xe-135	6.72E-03	6.72E-03
Xe-136	7.37E+01	5.81E+01

Isotope	Theoretical values N (1/m3)	Theoretical values m (kg)
Xe-135	1.87E+20	6.72E-03
Xe-136-f	1.61E+24	5.81E+01
Xe-136-c	4.33E+23	1.57E+01
Xe-136-t	2.04E+24	7.38E+01

All results agree well with theoretical values. To allow easy comparison the corresponding values are marked using the same color.

Summary and Conclusions

All results are summarized in Figure 3-929, showing the "Xe-136 curve", defined as the ratio of total mass of Xe-136 produced in a reactor divided by the mass of Xe-136 produced by fission only. As may be seen, the production of Xe-136 decreases with increasing ratio of non-core salt volume to the core salt volume. In a molten salt reactor with the ratio of $\boldsymbol{R_V}$ = 15, the amount of Xe-136 produced is expected to be only about 30% larger than produced directly by fission.

Since Xe-136 is one of the major contributors to the pressurization of the primary system, an accurate prediction of the Xe-136 production is important for designing the reactor. It is concluded that the amount of Xe-136 produced in MSR is significantly smaller than that in for example LWR. The reason is that with salt (and thus Xe-135) spending a significant fraction of time in the volume outside the core, more Xe-135 has a chance to decay before it can return to the core where it can capture neutron and be converted to Xe-136.

The calculations presented here were performed assuming that all Xenon remains in the salt. In reality some part of Xenon will be removed by engineering features. For example, in the case of MSRE, presence of the Helium bubbler and the Xenon stripper allowed to remove efficiently most of the Xenon. In such case the ratio of Xe-136 production will be very close to 1.0, meaning that the Xe-136 is basically produced from fission only and not from neutron capture in Xe-135.

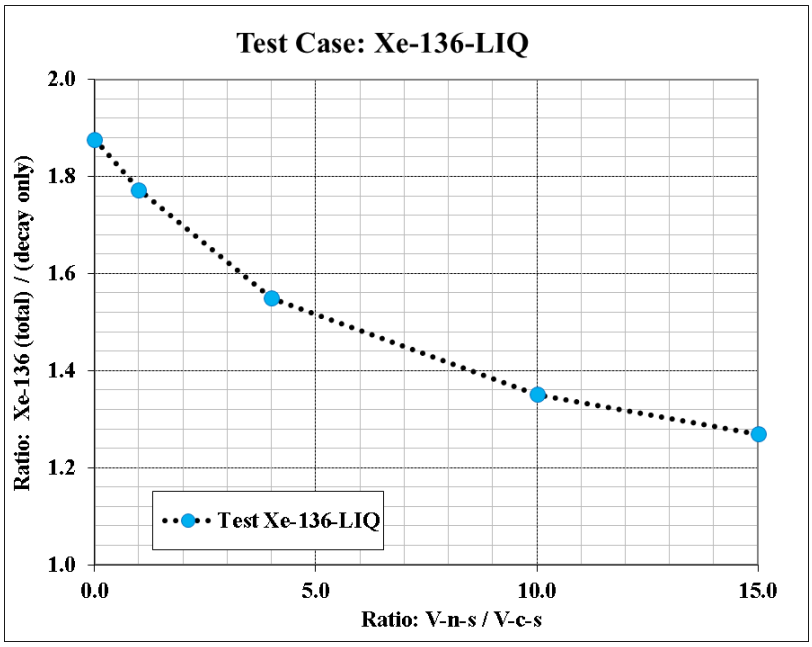

Figure 3-929 Xe-136 curve

3.12.42 FP Vapor Diffusion Test 1 - Constant Boundary Concentration

The geometry chosen for the diffusion tests described in this, as well as the following sections, is the same as the geometry used for the transient conduction test (section 3.5.4). A rectangular structure (SC-006) is considered with a unit surface area (A=1.0 m^2). The thickness is 0.01 m, divided into 21 cells. The thickness of cells is:

- 5.0×10^{-4} m for the internal cells
- 2.5×10^{-4} m for the boundary cells

A stable isotope, Xe-136, is used in the calculations. Xe-136 is a member of the Vapor Class 01 (noble gases). A stable isotope must be used to compare results of the present test with an analytical solution.

A constant concentration at the boundary surface is obtained using the adsorption model, linked to a user-defined Control Function (CF-100). The Control Function determining the sorption flux for the vapor class 1 is defined as:

$$S = A \cdot (C_{d,1} - C_{d,tar})$$

$C_{d,1}$ concentration in the node 1 (left boundary node), (kg/m^3)
$C_{d,tar}$ target concentration in the node 1, assumed equal to 10^{-3}, (kg/m^3)
A proportionality constant, assumed equal to 10.0 (m/s)
S sorption flux, ((kg/s)/m^2)

The value of the constant A needs to be large enough to keep the boundary node concentration at almost exactly the desired value of 10^{-3} kg/m^3. Of course, with increasing value of A the numerical solution becomes more difficult which may lead to reduction of time step because of oscillations of the Control Function. It was found in several test calculations that the value of 10.0 allows to keep the boundary concentration practically constant with only short time step reductions at the start of the calculations. These time step reductions were caused by negative masses in SC-006 (encountered when the Control Function becomes temporarily negative) and may be avoided by putting limits on the Control Function that prevent the function from becoming negative. The lower limit of zero (input entry: 10^{-90}) and the upper limit of 10^{-3} were applied for CF-100.

A corresponding model was built for a 2-D Solid Heat Conductor (TC-006). TC-006 is nodalized the same as SC-006 in the x-direction. This means the cell half-thickness of 2.5×10^{-4} m, which means the total cell thickness of:

- 5.0×10^{-4} m for the x-direction internal cells
- 2.5×10^{-4} m for the x-direction boundary cells

In the y-direction it is divided into 11 cells with the cell half-thickness of 0.05 m, which means the total cell thickness of:

- 0.10 m for the y-direction internal cells
- 0.05 m for the y-direction boundary cells

Therefore the total size of TC-006 in the *y*-direction is 1.0 m. The length of TC-006 was set to 1.0 m, so that the total area of heat transfer as well as sorption is 1.0 m^2, the same as for SC-006.

The boundary conditions are specified in such a way that this 2-D structure should behave exactly the same as the 1-D structure, SC-006.

Results are compared to the analytical solution of the diffusion equation obtained for a semi-infinite slab. Transient diffusion in a semi-infinite slab with a step change concentration of the diffusive molecules at the surface is considered. The initial concentrations are C_0 = 0.0 kg/m^3. At time equal to zero the surface concentration is set to 0.001 kg/m^3. The theoretical solution of the diffusion equation is analogous to the heat conduction equation, with the thermal diffusivity replaced by the diffusion coefficient. This means:

- $a = k/(\rho c_p)$, thermal diffusivity, (m^2/s) → D, diffusion coefficient, (m^2/s)

The result is based on the solution presented in [15] (chapter 3, eq. 55, see section 3.5.4):

$$C(x,t) = C_w \cdot erfc\left(\frac{x}{2\sqrt{Dt}}\right)$$

$C(x,t)$	concentration at location x from the left boundary, at time t, (kg/m^3)
C_w	concentration at the boundary surface, (=0.001 kg/m^3)
D	diffusion coefficient, (assumed equal to 1×10^{-6} m^2/s)

The input file for this run is stored in: `\Z-INPUTS\RT\DIFF\DIFF1.SPE`

Results are shown in Figure 3-930 through Figure 3-938. Figure 3-930 through Figure 3-933 show visualization pictures of SPECTRA results at times 1.0, 5.0, 10.0, and 20.0 s.

Figure 3-934 shows comparisons of SPECTRA results to the analytical solution obtained for a semi-infinite slab. The calculated values are in good agreement with the theoretical values, except near the right boundary, at t = 20 s. At that time the diffusive isotope has penetrated into the right side of the conductor and the analytical solution, obtained for a semi-infinite slab, becomes a bad approximation of the real geometry in the region close to the right boundary.

Figure 3-935 and Figure 3-936 show time-dependent graphs of vapor concentrations and sorption flux. These graphs are included for qualitative verification of the obtained results.

Results of the 2-D model are compared to the results of the 1-D model in Figure 3-937 and Figure 3-938 s. It is seen that the 2-D results are identical to the 1-D results for this test.

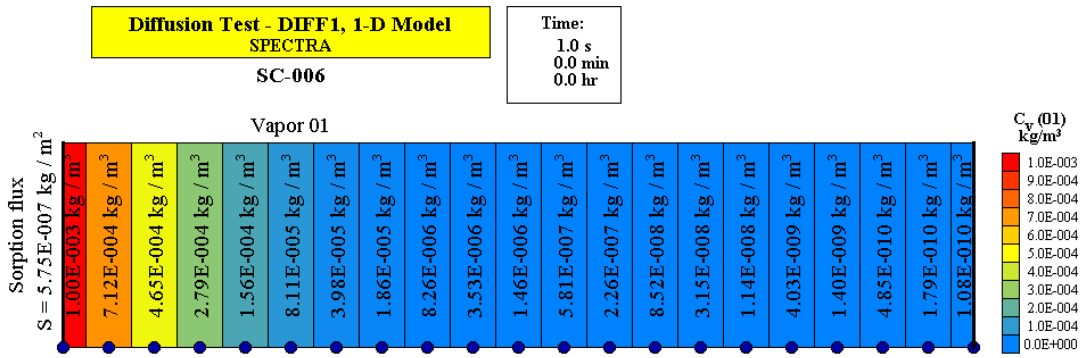

Figure 3-930 Diffusion test, constant boundary concentration, SPECTRA, t=1.0 s.

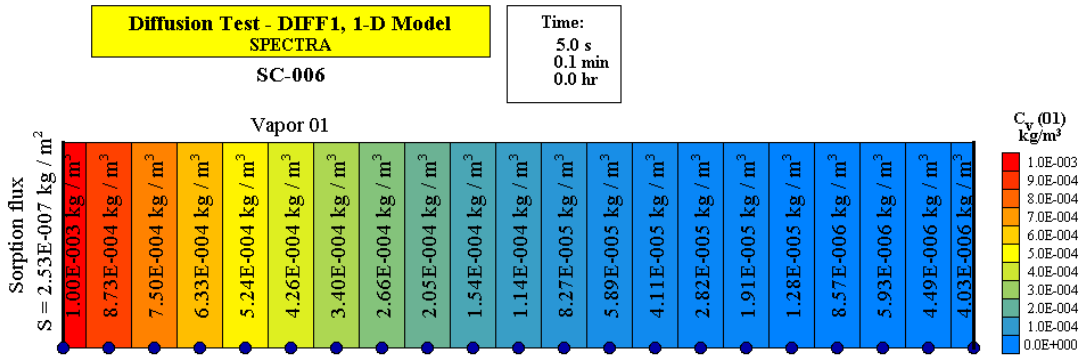

Figure 3-931 Diffusion test, constant boundary concentration, SPECTRA, t=5.0 s.

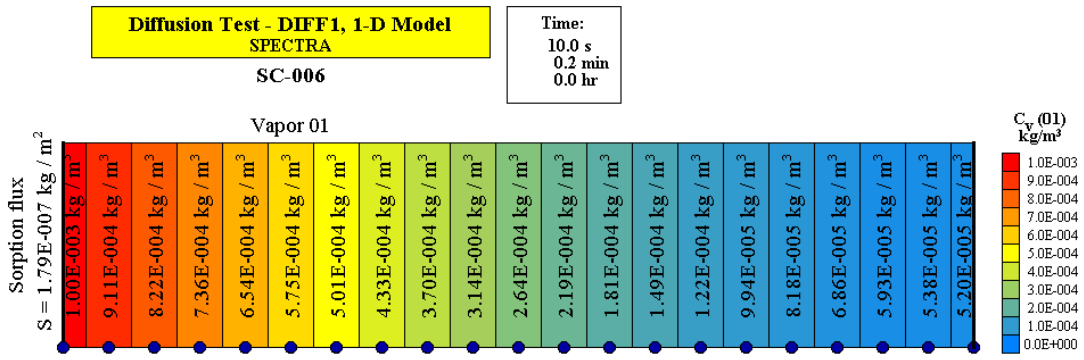

Figure 3-932 Diffusion test, constant boundary concentration, SPECTRA, t=10.0 s.

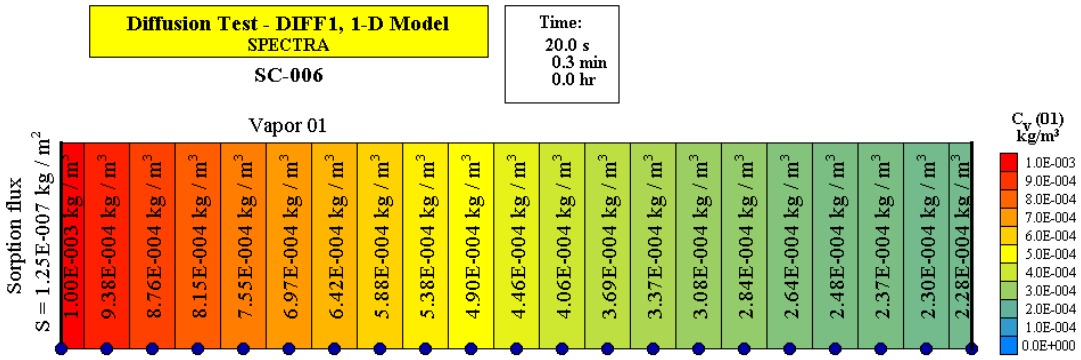

Figure 3-933 Diffusion test, constant boundary concentration, SPECTRA, t=20.0 s.

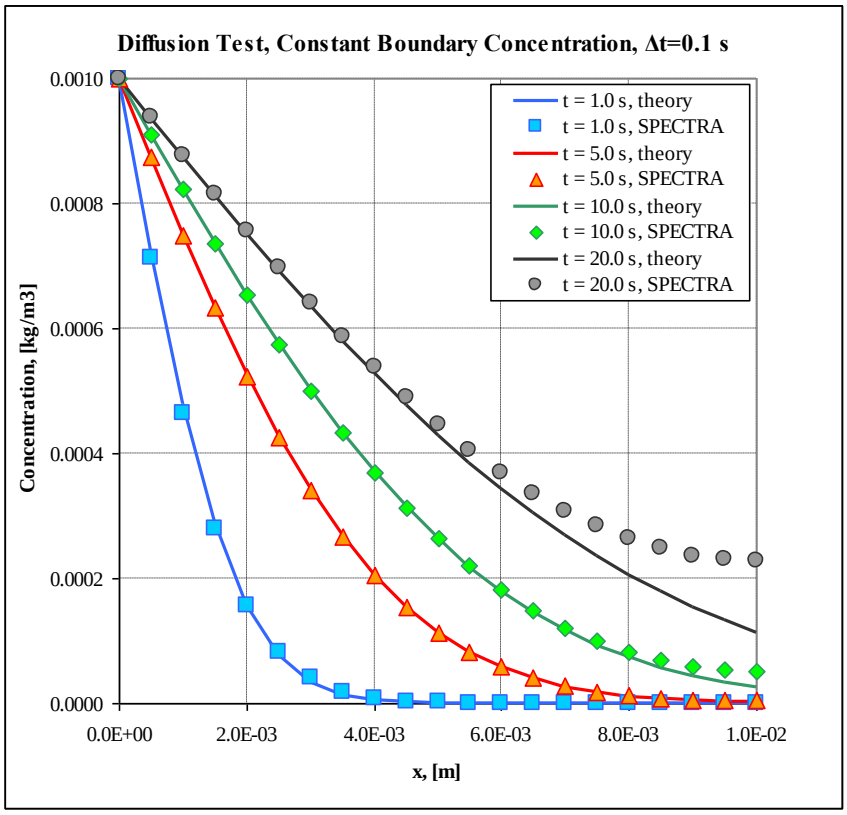

Figure 3-934 Diffusion test, constant boundary concentration, theory and SPECTRA.

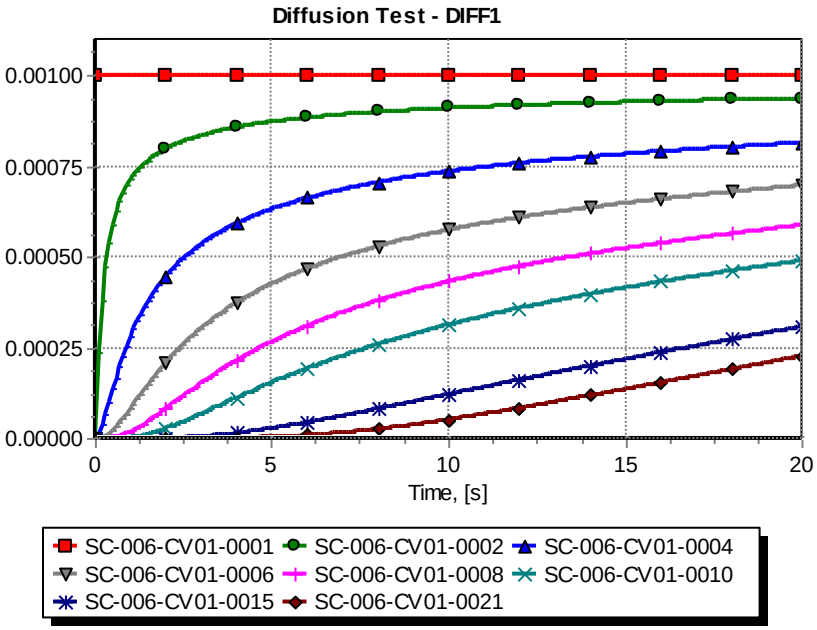

Figure 3-935 Concentrations of vapor 01 (CV01) in different nodes (0001=left, 0021=right).

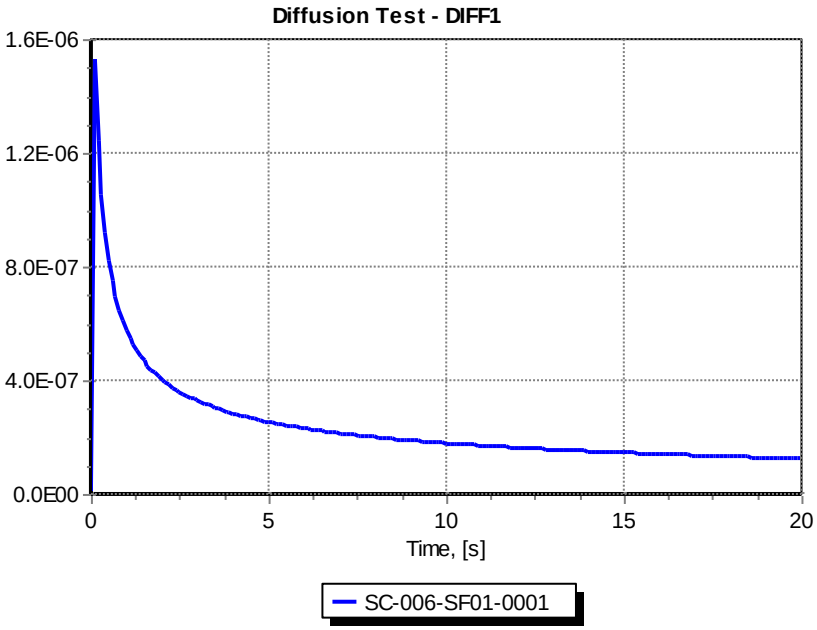

Figure 3-936 Sorption flux of vapor 01 (SV01) at the left surface (0001) of SC-006.

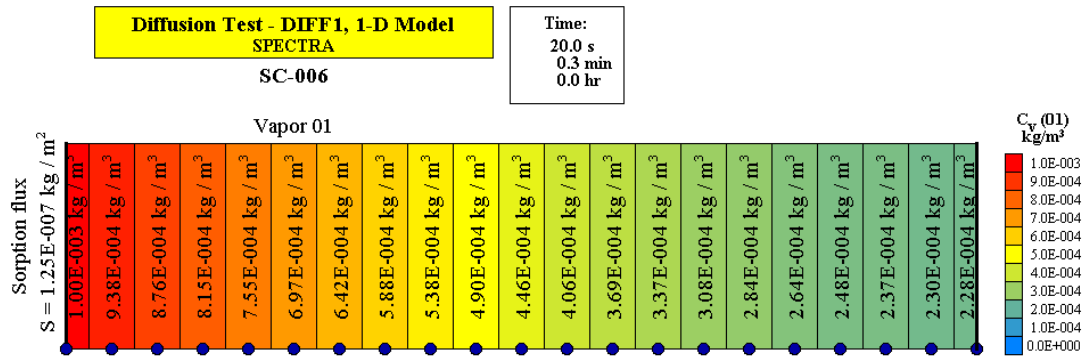

Figure 3-937 Diffusion test, constant boundary concentration, 1-D model, t=20.0 s.

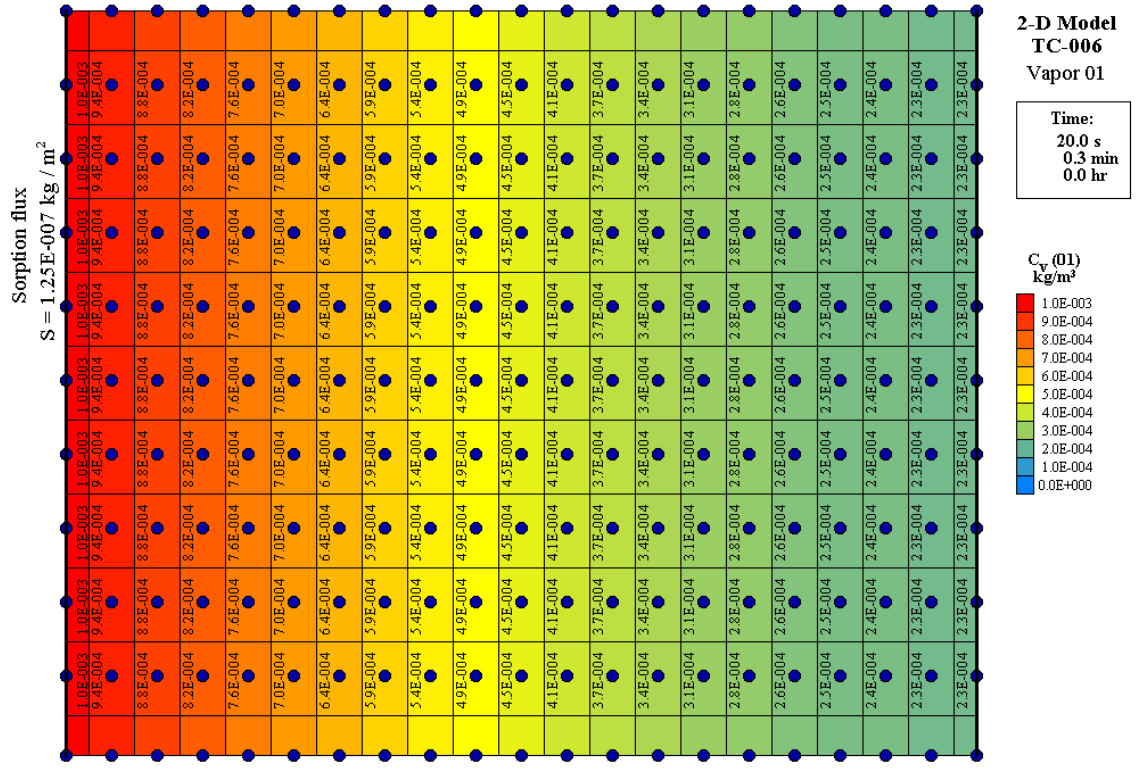

Figure 3-938 Diffusion test, constant boundary concentration, 2-D model, t=20.0 s.

3.12.43 FP Vapor Diffusion Test 2 - Constant Boundary Flux

The geometry chosen for the diffusion test described in this section is the same as the geometry used for the FP vapor diffusion test 1 (section 3.12.42). Again a stable isotope, Xe-136, is used in the calculations. Xe-136 is a member of the Vapor Class 01 (noble gases). A stable isotope must be used to compare results of the present test with an analytical solution.

In the present test a constant sorption flux is applied, assumed equal to 2.0×10^{-7} ((kg/s)/m^2) (approximately the average value of the sorption flux calculated for the previous test - Figure 3-936):

$$S = 2.0\times10^{-7}$$

As in the diffusion test 1, a corresponding model was built for a 2-D Solid Heat Conductor (TC-006). The boundary conditions are specified in such a way that this 2-D structure should behave exactly the same as the 1-D structure SC-006.

Results are compared to the analytical solution of the diffusion equation obtained for a semi-infinite slab. Transient diffusion in a semi-infinite slab with a constant boundary flux (q) is considered. The initial concentrations are C_0 = 0.0 kg/m^3. At time equal to zero the sorption flux is set to 2.0×10^{-7} (kg/s)/m^2. The theoretical solution of the diffusion equation is analogous to the heat conduction equation, with the thermal diffusivity replaced by the diffusion coefficient. This means:

- $a = k/(\rho c_p)$, thermal diffusivity, (m^2/s) → D, diffusion coefficient, (m^2/s)
- q, surface heat flux ((J/s)/m^2) → S, sorption flux ((kg/s)/m^2)

Furthermore, in order to obtain the diffusion equation of exactly the same form as the conduction equation, the volumetric heat capacity (ρc_p) in the conduction equation must be equal to 1.0. Consequently the thermal conductivity is equal to D:

- (ρc_p) = 1.0
- k = D

The result is based on the solution presented in [15], chapter 3, equation 60:

$$C(x,t) = \frac{S}{D}\cdot\left[\sqrt{\frac{4Dt}{\pi}}\cdot\exp\left(-\frac{x^2}{4Dt}\right) - x\cdot erfc\left(\frac{x}{4\sqrt{Dt}}\right)\right]$$

$C(x,t)$	concentration at location x from the left boundary, at time t, (kg/m^3)
S	sorption flux, equal to 2.0×10^{-7} ((kg/s)/m^2)
D	diffusion coefficient, (assumed equal to 1×10^{-6} m^2/s)

The input file for this run is stored in: `\Z-INPUTS\RT\DIFF\DIFF2.SPE`

Results are shown in Figure 3-939 through Figure 3-947. Figure 3-939 through Figure 3-943 show visualization pictures of SPECTRA results at times 0.0 (start time), 1.0, 5.0, 10.0, and 20.0 s.

Figure 3-944 shows comparisons of SPECTRA results to the analytical solution obtained for a semi-infinite slab. The calculated values are in good agreement with the theoretical values, except near the right boundary, at t = 20 s). At that time the diffusive isotope has penetrated into the right side of the conductor and the analytical solution, obtained for a semi-infinite slab, becomes a bad approximation of the real geometry in the region close to the right boundary.

Figure 3-945 show a time-dependent behavior of vapor concentrations. This graph is included for qualitative verification of the obtained results.

Results of the 2-D model are compared to the results of the 1-D model in Figure 3-946 and Figure 3-947 s. It is seen that the 2-D results are identical to the 1-D results for this test.

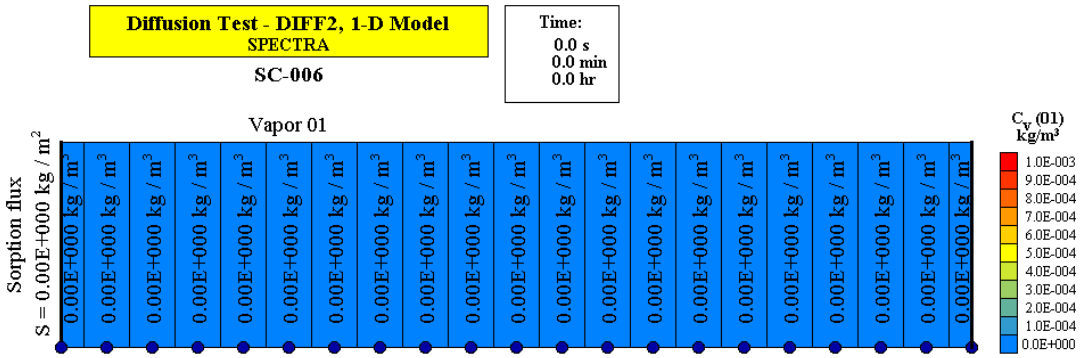

Figure 3-939 Diffusion test, constant boundary flux, SPECTRA, t=0.0 s.

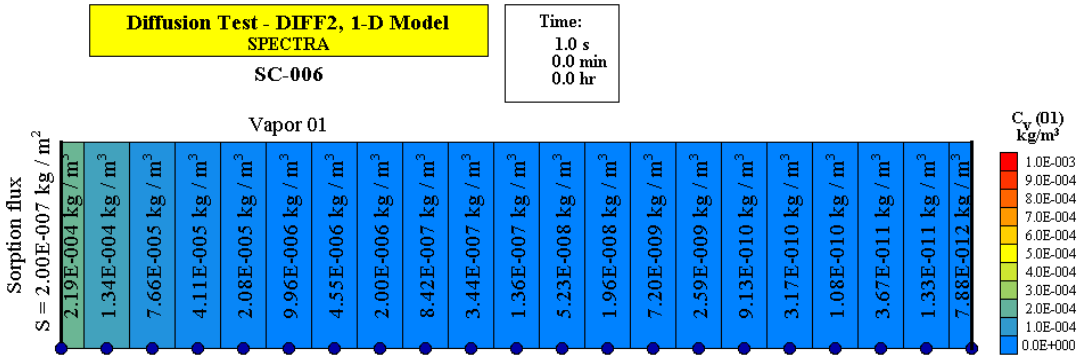

Figure 3-940 Diffusion test, constant boundary flux, SPECTRA, t=1.0 s.

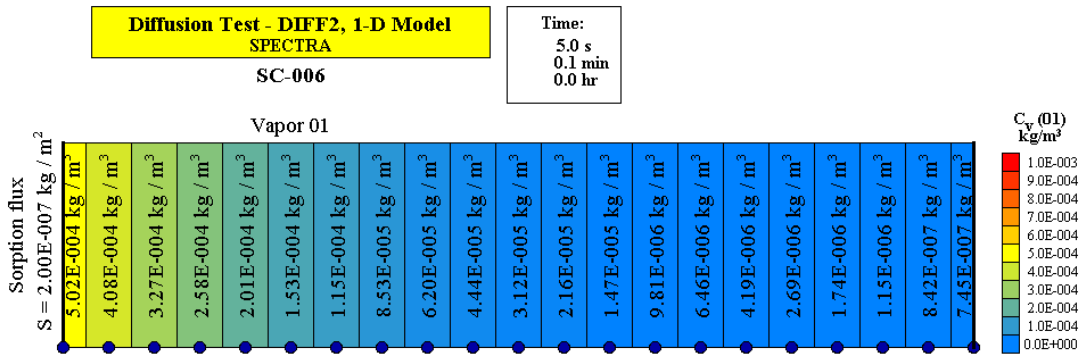

Figure 3-941 Diffusion test, constant boundary flux, SPECTRA, t=5.0 s.

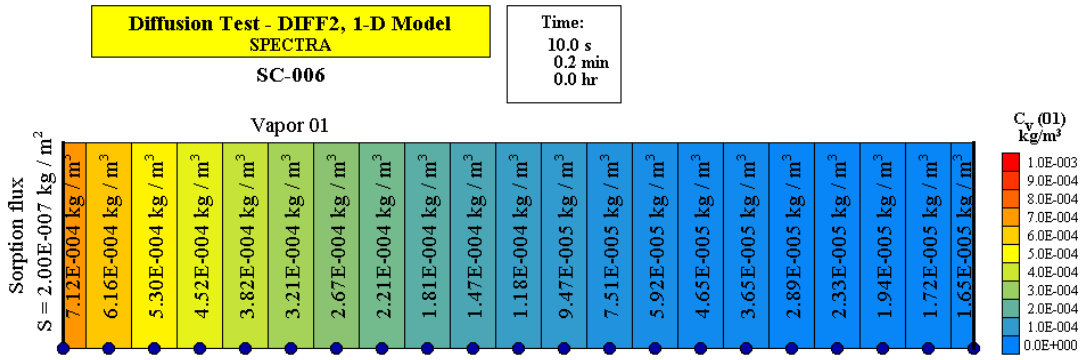

Figure 3-942 Diffusion test, constant boundary flux, SPECTRA, t=10.0 s.

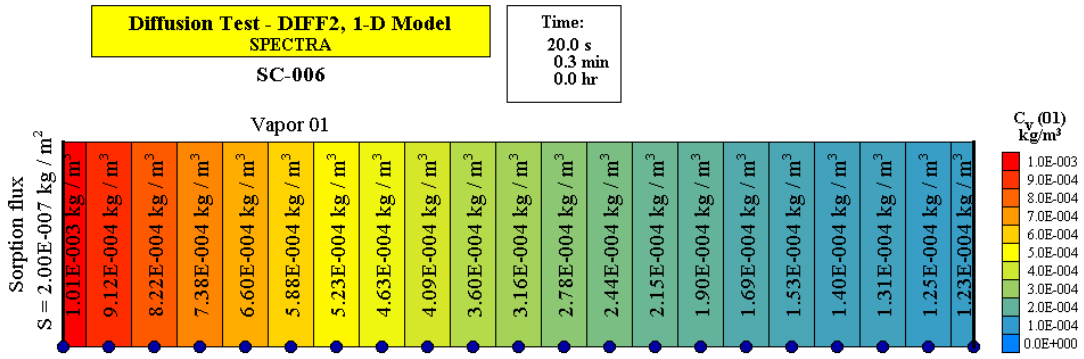

Figure 3-943 Diffusion test, constant boundary flux, SPECTRA, t=20.0 s.

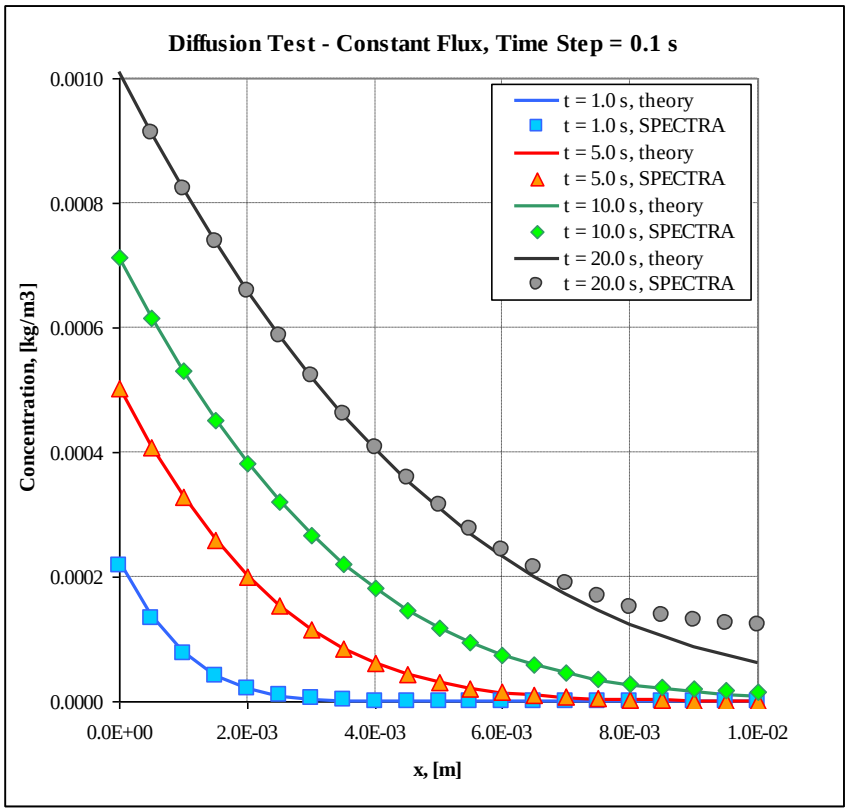

Figure 3-944 Diffusion test, constant boundary flux, theory and SPECTRA.

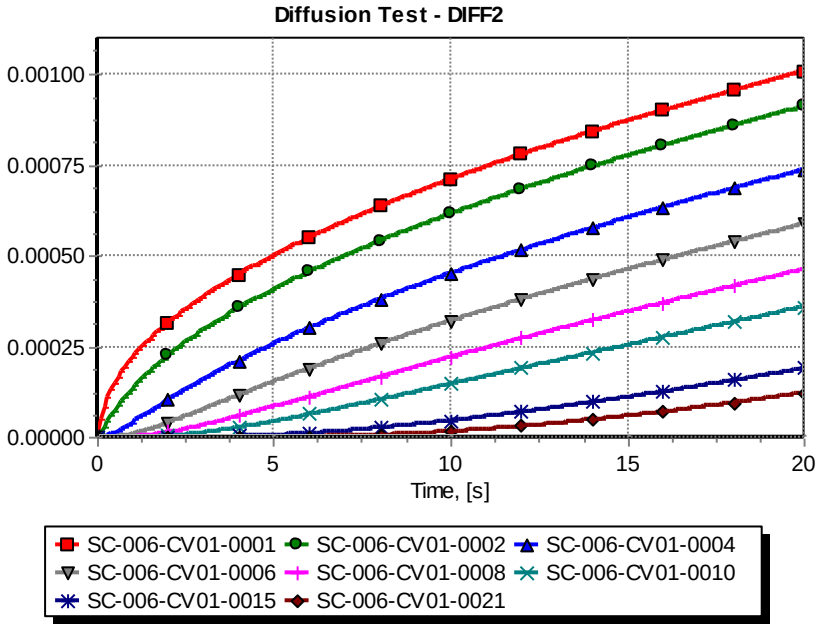

Figure 3-945 Concentrations of vapor 01 (CV01) in different nodes (0001=left, 0021=right).

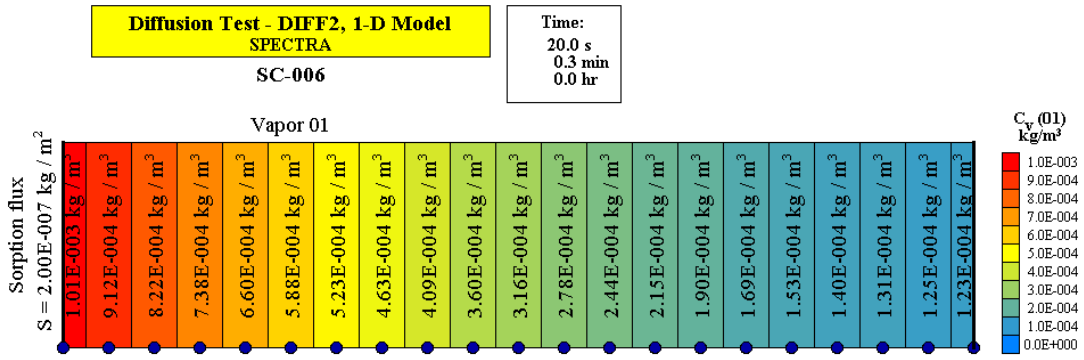

Figure 3-946 Diffusion test, constant boundary flux, 1-D model, t=20.0 s.

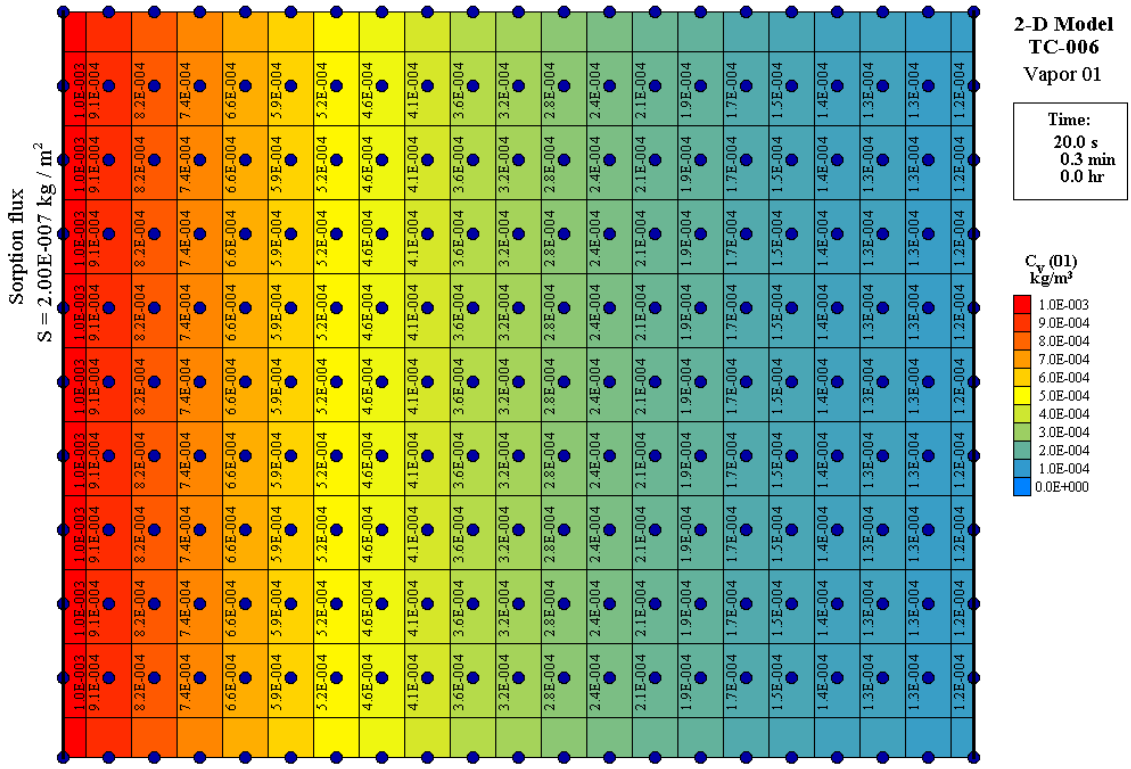

Figure 3-947 Diffusion test, constant boundary flux, 2-D model, t=20.0 s.

3.12.44 FP Vapor Diffusion Test 3 - Decay of a Non-Diffusive into a Diffusive Isotope

The geometry chosen for the decay of a non-diffusive into a diffusive isotope test described in this section is the same as the geometry used for the FP vapor diffusion test 1 (section 3.12.42).

As in the previous two tests, a corresponding model was built for a 2-D Solid Heat Conductor (TC-006). The boundary conditions are specified in such a way that this 2-D structure should behave exactly the same as the 1-D structure SC-006.

In the present case there are two isotopes:

- Isotope A, a non-diffusive, long life isotope decaying into B
- Isotope B, a diffusive, non-radioactive isotope

The isotope A is present in the left surface node of SC-006. Here it provides a continuous source of the isotope B, due to radioactive decay. Since the isotope A is a long life (half-life of 1 month was assumed, $\lambda_A = \ln(2)/(1\times31\times24\times3600) = 2.59\times10^{-7}$ (s^{-1})), the source of isotope B is practically constant during the calculated period of 20 s, and equal to $N_A\lambda_A$, where N_A is the concentration of the isotope A.

The initial mass of isotope A was set to $m_A = 0.01$ kg. Both isotopes A and B are assumed to have the same molar weight. Therefore the source of the isotope B may be written as $m_A\lambda_A$ (in general the mass source for the isotope B is equal to: $m_A\times M_{w,B}/M_{w,A}$, where $M_{w,B}$, $M_{w,A}$ are the molar weights of B and A respectively). The diffusion coefficients were assumed in the calculations as: $D_A = 10^{-20}$ (m^2/s) for the non-diffusive isotope A (zero could be used as well to eliminate completely diffusion of the isotope A) and $D_B = 10^{-6}$ (m^2/s) for the diffusive isotope B.

From the point of view of the diffusive isotope B, this case represents a constant source in the left surface node, very similar to the test described in the previous section (3.12.43). Solution of the analogous heat transfer case, with constant heat flux at the surface is presented in [15] (section 3.4.2, equation 3.60).

Using an analogy between the heat conduction and the diffusion, the solution is written here by replacing the thermal diffusivity by the diffusion coefficient and the surface heat flux by the source due to decay of the isotope A:

- $a = k/(\rho c_p)$, thermal diffusivity, (m^2/s) $\rightarrow D_B$, diffusion coefficient, (m^2/s)
- q, boundary heat flux, (W/m^2) $\rightarrow (m_A\lambda_A)/A$ mass source, ($(kg/s)/m^2$)

A is the surface area (equal to 1.0 in this test case - see section 3.12.42). Furthermore, in order to obtain the diffusion equation of exactly the same form as the conduction equation, the volumetric heat capacity (ρc_p) in the conduction equation must be equal to 1.0. Consequently the thermal conductivity is equal to D_B:

- $(\rho c_p) = 1.0$
- $k = D_B$

The analytical solution is (see [15], section 3.4.2, equation 3.60):

$$C_B(x,t) = \frac{(m_A\lambda)/A}{D_B} \cdot \left[\sqrt{\frac{4D_B t}{\pi}} \cdot \exp\left(-\frac{x^2}{4D_B t} \right) - x \cdot erfc\left(\frac{x}{\sqrt{4D_B t}} \right) \right]$$

Note that this is the same as the solution obtained in the previous section, with the source due to sorption, S, replaced by the source due to radioactive decay of the isotope A, $(m_A\lambda_A)/A$.

The input file for this run is stored in: `\Z-INPUTS\RT\DIFF\DIFF3.SPE`. Results are shown in Figure 3-948 through Figure 3-956. Figure 3-948 through Figure 3-952 show visualization pictures of SPECTRA results at times 0.0 s (start time), 1.0, 5.0, 10.0, and 20.0 s.

Figure 3-953 shows comparisons of SPECTRA results to the analytical solution obtained for a semi-infinite slab. The calculated values are in good agreement with the theoretical values, except near the right boundary, at t = 20 s). At that time the diffusive isotope has penetrated into the right side of the conductor and the analytical solution, obtained for a semi-infinite slab, becomes a bad approximation of the real geometry in the region close to the right boundary.

Figure 3-954 show time-dependent behavior of vapor concentrations. This graph is included for qualitative verification of the obtained results.

Results of the 2-D model are compared to the results of the 1-D model in Figure 3-955 and Figure 3-956 s. It is seen that the 2-D results are identical to the 1-D results for this test.

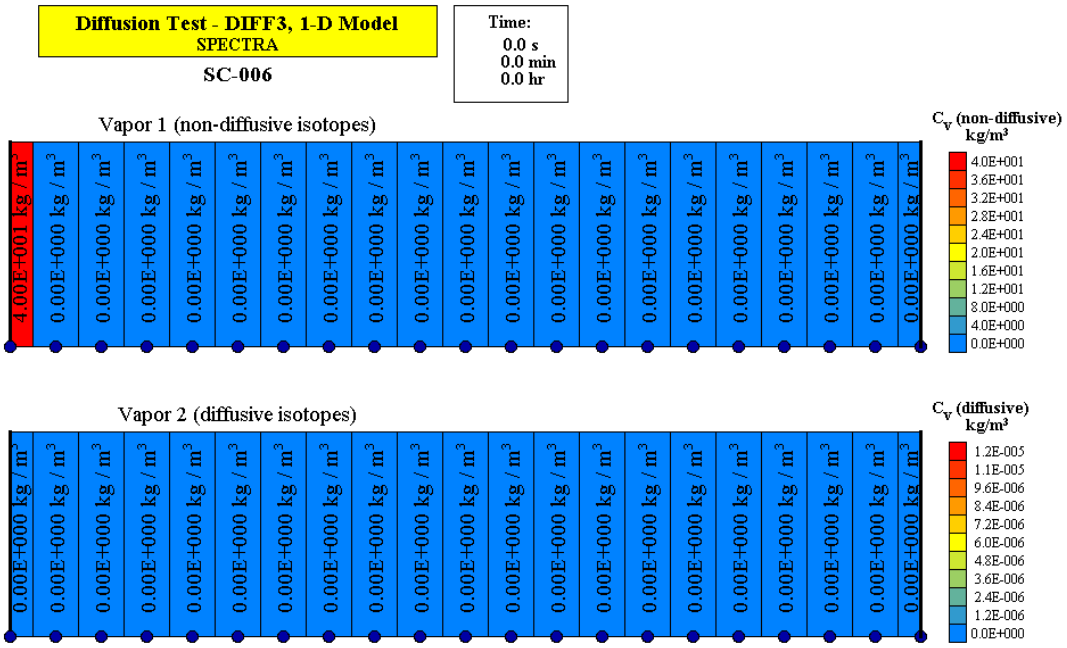

Figure 3-948 Decay of a non-diffusive into a diffusive isotope, SPECTRA, t=0.0 s.

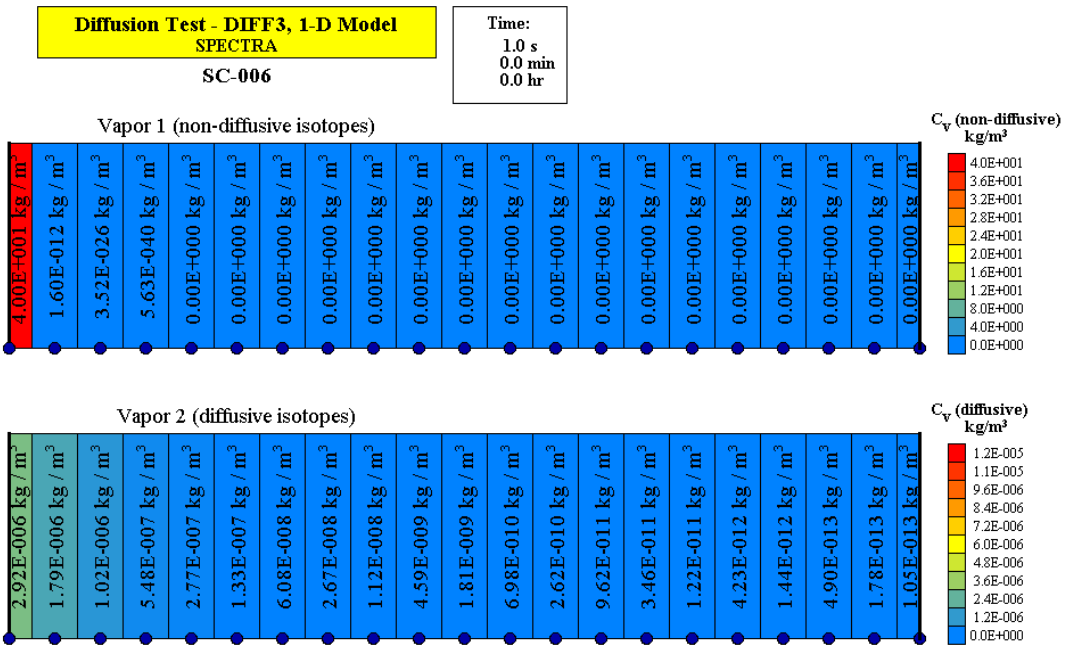

Figure 3-949 Decay of a non-diffusive into a diffusive isotope, SPECTRA, *t*=1.0 s.

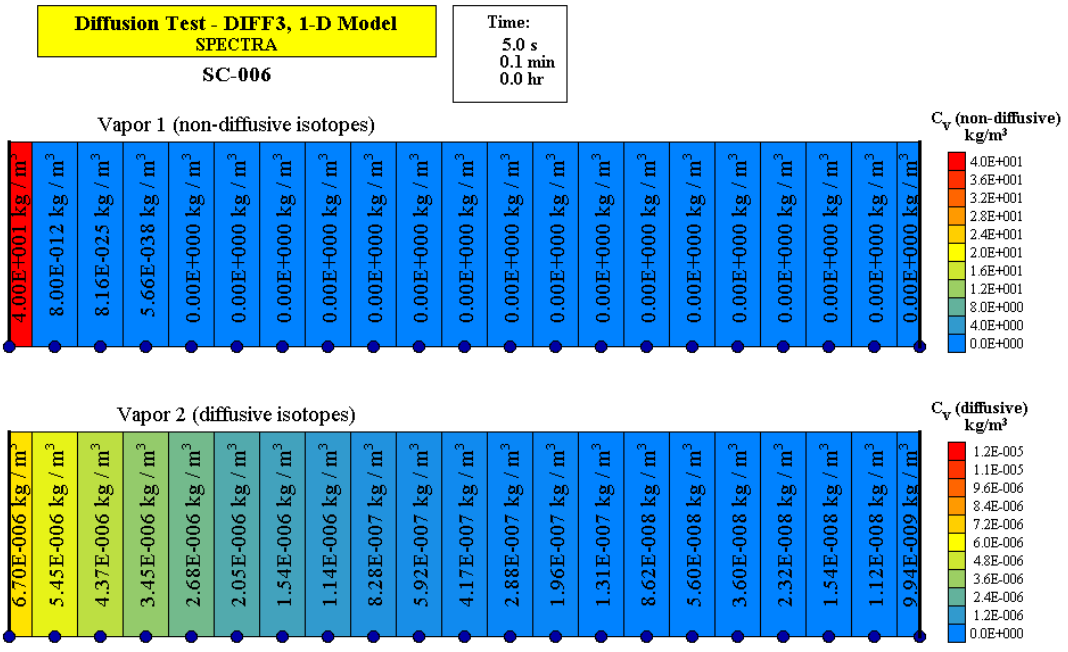

Figure 3-950 Decay of a non-diffusive into a diffusive isotope, SPECTRA, *t*=5.0 s.

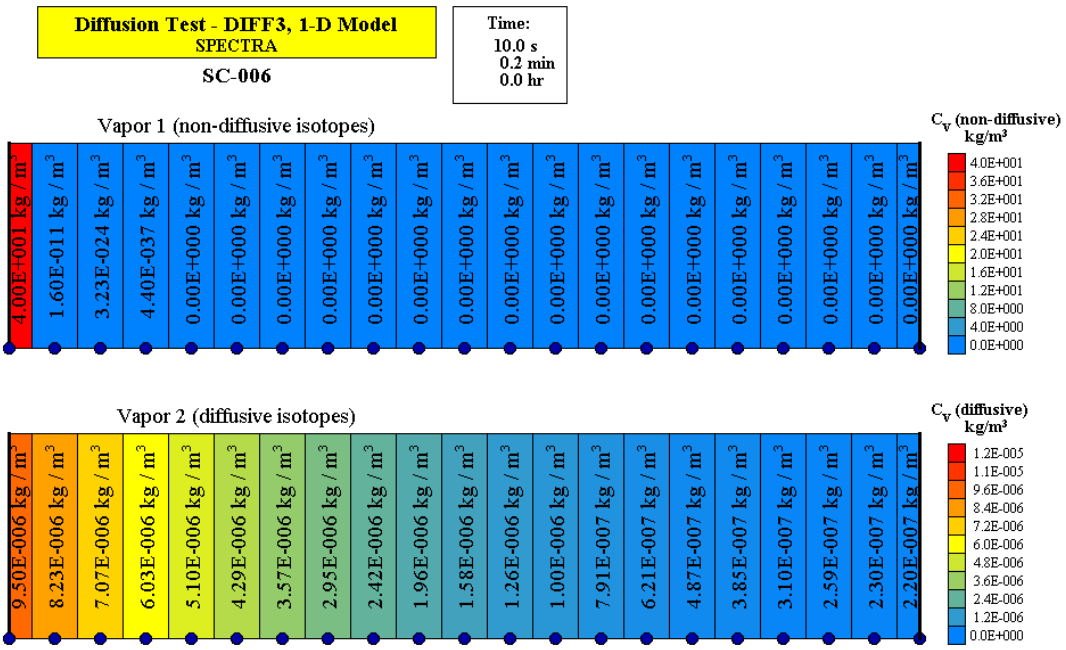

Figure 3-951 Decay of a non-diffusive into a diffusive isotope, SPECTRA, *t*=10.0 s.

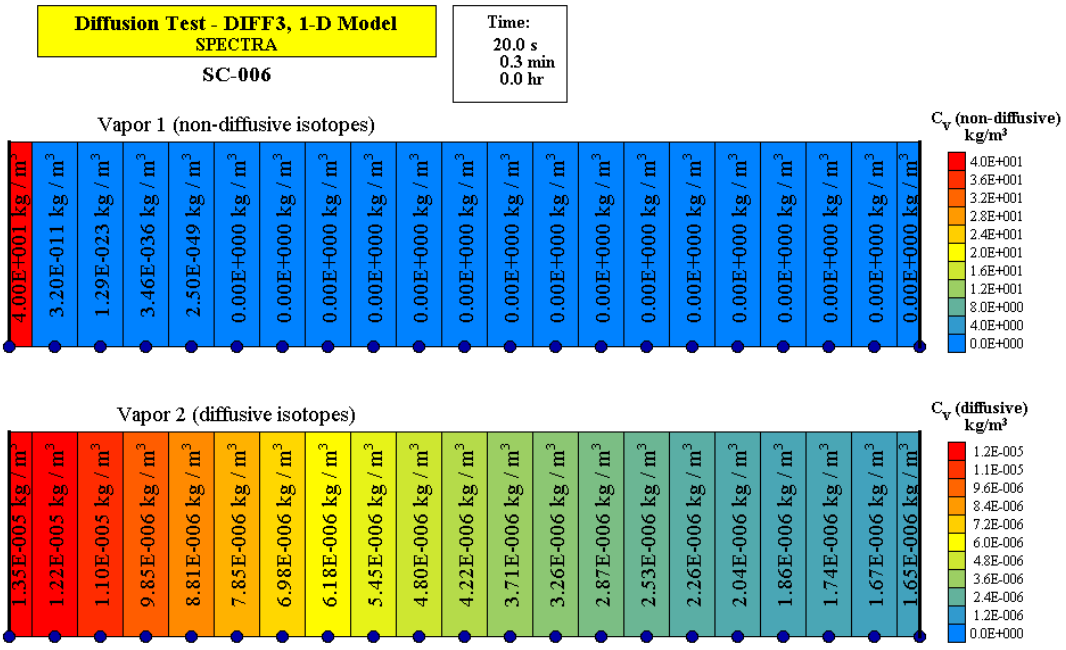

Figure 3-952 Decay of a non-diffusive into a diffusive isotope, SPECTRA, *t*=20.0 s.

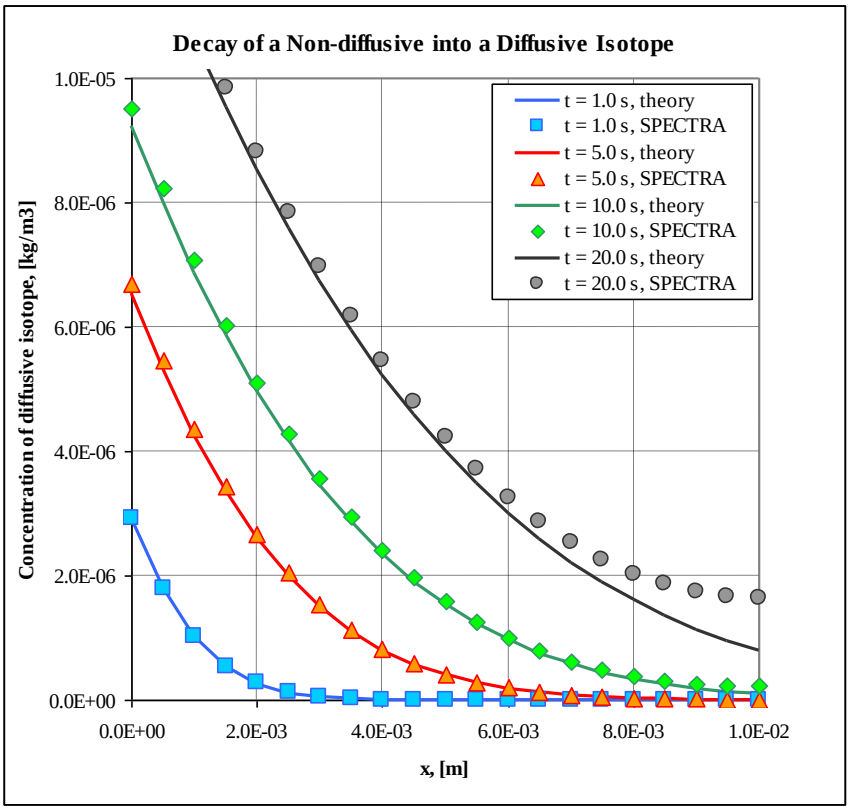

Figure 3-953 Decay of a non-diffusive into a diffusive isotope, theory and SPECTRA.

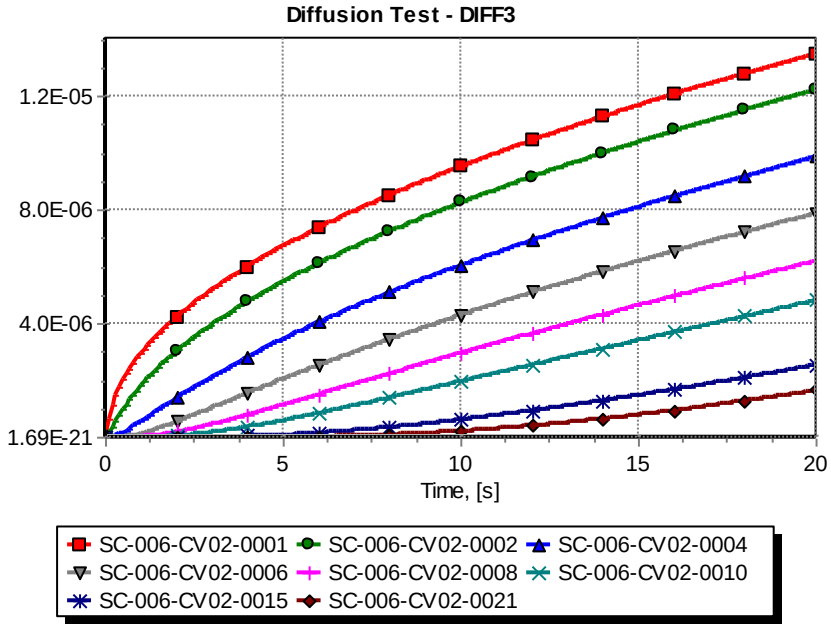

Figure 3-954 Concentrations of vapor 02 (CV02) in different nodes (0001=left, 0021=right).

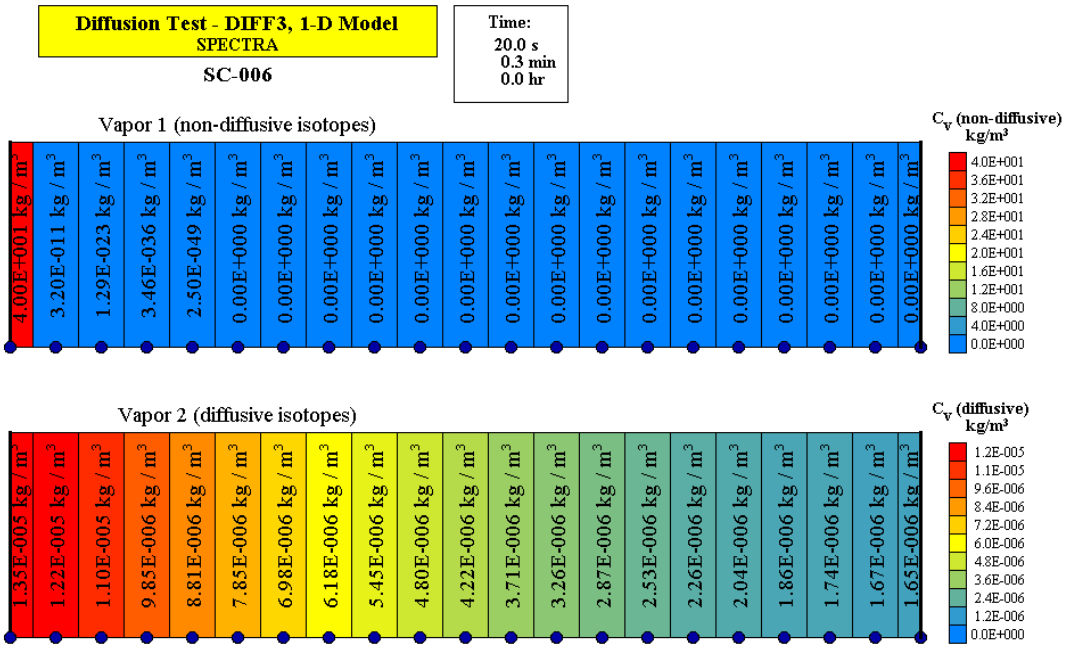

Figure 3-955 Decay of a non-diffusive into a diffusive isotope, 1-D model, SPECTRA, t=20.0 s.

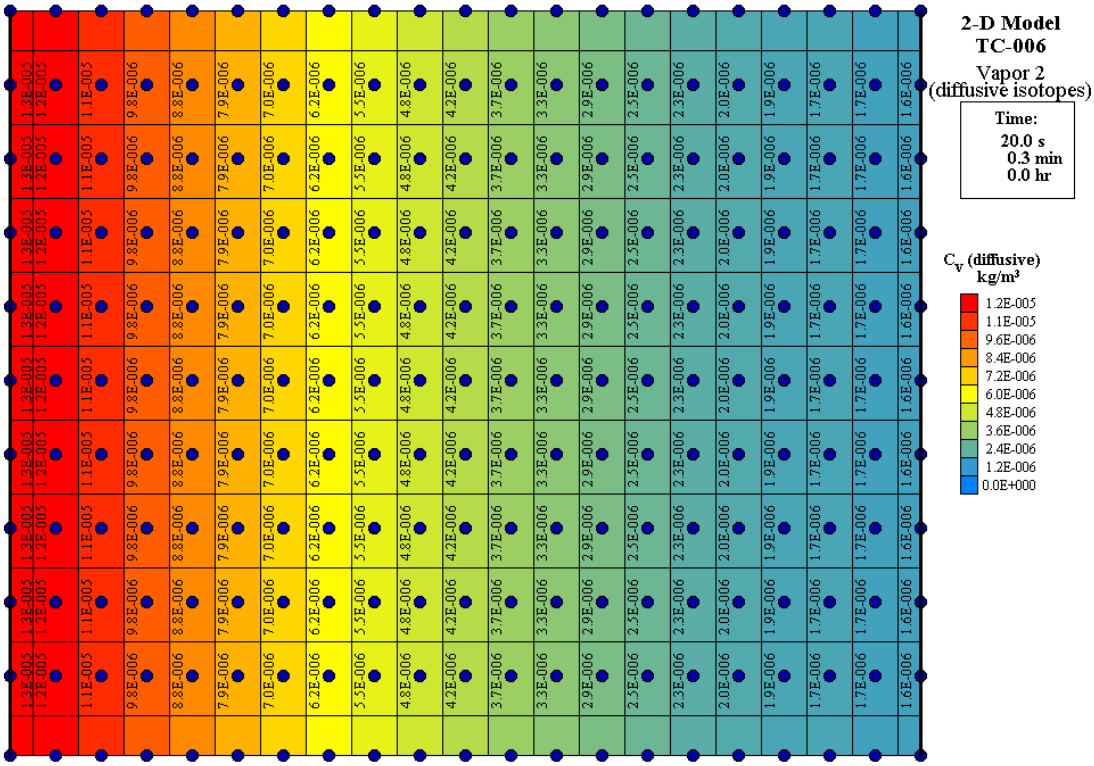

Figure 3-956 Decay of a non-diffusive into a diffusive isotope, 2-D model, SPECTRA, t=20.0 s.

3.12.45 FP Vapor Flow and Sorption Test ATMS-CF

The geometry chosen for this test is very similar to the geometry used for the aerosol flow and deposition test (section 3.12.3). The model consists of six Control Volumes: CV-101, 102, 103, 104, 105, and CV-200. The last volume is held at constant conditions and it serves as a boundary condition. The volumes are connected with junctions JN-101, 102, 103, 104, and JN-105. Each CV has a horizontal structure (floor) available for deposition or sorption. The floors are represented by The Solid Heat Conductors SC-101 through SC-105, with the area of 1.0 m^2 and thickness of 2 mm (2 nodes, 1 mm each).

As in the test described in section 3.12.3, a source of gas is present in the volume CV-101. The source provides 0.11236 kg/s of gas. The mass source rate was selected to give the velocities of 3.0 m/s at the applied temperature of 900 K and pressure of 1.0 bar. The temperature of 900 K was selected in order to have Cs in vapor form. At the room temperature the Cs would condense.

Additionally a source of Cs-133 (isotope number 37) is placed in CV-101. The mass source strength is defined by Tabular Function TF-870. The value of this function is constant and equal to 10^{-7} kg/s. The sorption model defined by a Control Function was used. The sorption rate is defined by CF-101, which was set to a constant value of 2.5×10^{-8} ((kg/s)/m^2). No diffusion is modelled (diffusion coefficient is zero). Therefore the sorbed molecules remain in the boundary node (node thickness of 10^{-3} m, area of 1.0 m^2, volume of 10^{-3} m^3). Note that with this sorption model there are no surface molecules (i.e. the adsorbed mass is the same as the penetrated mass).

The input file for this run is stored in: `\Z-INPUTS\RT\FLOW-FP\ATMS-CF.SPE`. Results are shown in Figure 3-957, Figure 3-958, and Figure 3-959. The visualization picture, shown in Figure 3-957, provides a quick check of the mass transport. Out of the 1.0×10^{-7} kg/s of Cs-133 that is coming from the source into CV-101, one quarter, i.e. 2.5×10^{-8} kg/s is adsorbed on SC-101 (sorption flux of $S = 2.5\times10^{-8}$ (kg/s)/m^2 times the surface area of $A = 1.0$ m^2).

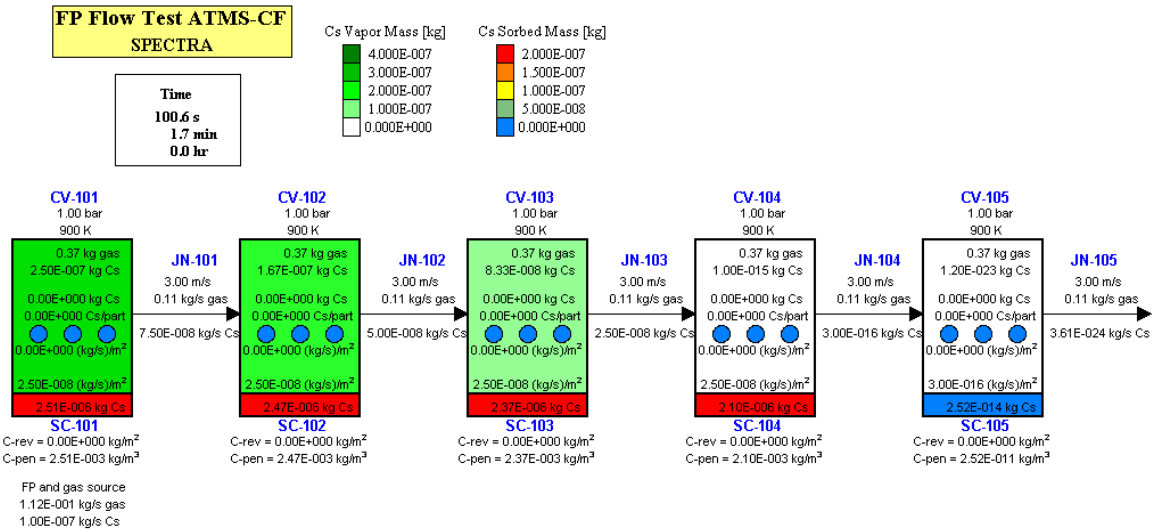

Figure 3-957 Test ATMS-CF, quasi-stationary results, t = 100 s.

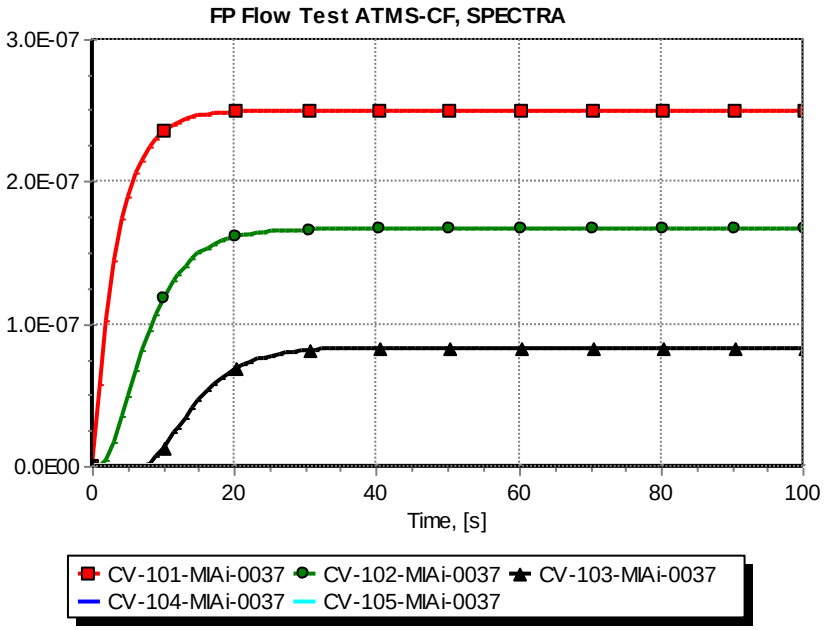

Figure 3-958 Mass of Cs-133 (isotope 0037), test ATMS-CF.

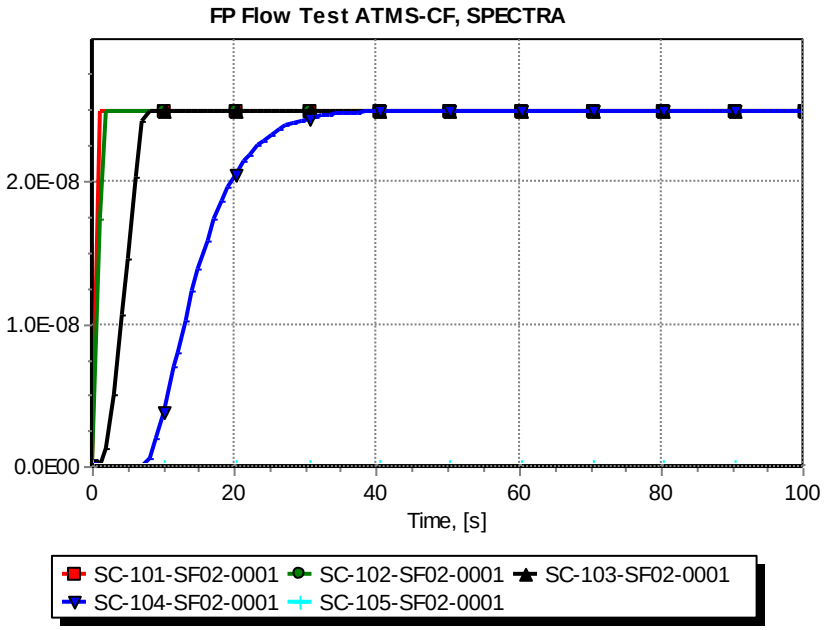

Figure 3-959 Sorption flux vapor class 02 (Cs), node 0001 (left surface).

The rest, i.e. 7.5×10^{-8} kg/s flows with the stream of atmosphere gas into CV-102. There another 2.5×10^{-8} kg/s is adsorbed on the surface of SC-102, leaving 5.0×10^{-8} kg/s which exits this volume. Similar behavior is observed in the next two volumes. Practically all Cs that is coming from the source is adsorbed in the first four volumes. Therefore there is practically no Cs in CV-105. Consequently there is practically no sorption on SC-105. Although the "prescribed" sorption flux, i.e. the value of CF-101, is all the time equal to 2.5×10^{-8} kg/s, the code identifies lack of the adsorbed material and reduces the sorption flux accordingly (this is called a "source starvation scheme").

3.12.46 FP Vapor Flow and Sorption Test ATMS-S2

The geometry chosen for this test is very similar to the geometry used for the aerosol flow and deposition test (section 3.12.3). The model consists of six Control Volumes: CV-101, 102, 103, 104, 105, and CV-200. The last volume is held at constant conditions and it serves as a boundary condition. The volumes are connected with junctions JN-101, 102, 103, 104, and JN-105. Each CV has a horizontal structure (floor) available for deposition or sorption. The floors are represented by The Solid Heat Conductors SC-101 through SC-105, with the area of 1.0 m^2.

As in the test described in section 3.12.3, a source of gas is present in the volume CV-101. The source provides 0.11236 kg/s of gas. The mass source rate was selected to give the velocities of 3.0 m/s at the applied temperature of 900 K and pressure of 1.0 bar. The temperature of 900 K was selected in order to have Cs in vapor form. At the room temperature the Cs would condense.

Additionally a source of Cs-133 (isotope number 37) is placed in CV-101. The mass source strength is defined by Tabular Function TF-870. The value of this function is constant and equal to 10^{-7} kg/s. The full sorption model (Sorption Model 2), with the coefficients appropriate for Cs sorption on Incoloy 800 (shown in Volume 1) was used. The penetrated fraction ($1–\beta$) was set to 10^{-1} rather than 10^{-5} for the reason explained below. Therefore the penetration is overestimated in this test. No diffusion is modelled (diffusion coefficient is zero). Therefore the penetrated molecules remain in the boundary node (V=10^{-3} m^3). The adsorption flux was maximized by selecting a large value for the Sherwood number correlation, A_{Sh} = 1000 (maximum acceptable value).

The input file for this run is stored in: `\Z-INPUTS\RT\FLOW-FP\ATMS-S2.SPE`. Results are shown in Figure 3-960 through Figure 3-966. Figure 3-960, Figure 3-961, and Figure 3-962 show visualization pictures at the times 50, 70, and 100 s, respectively. The next four figures show time behavior of the Cs vapor mass (Figure 3-963), the sorption fluxes (Figure 3-964), the sorbed masses (Figure 3-965), as well as the surface density and penetrated density on SC-101 (Figure 3-966).

The following remarks can be made:

- Sorption on the structures is very fast until the surfaces become "saturated" with the adsorbed molecules (all adsorption sites are occupied). During this time a large amount of Cs entering a Control Volume is being sorbed on the structure and a small amount flows out of the volume.

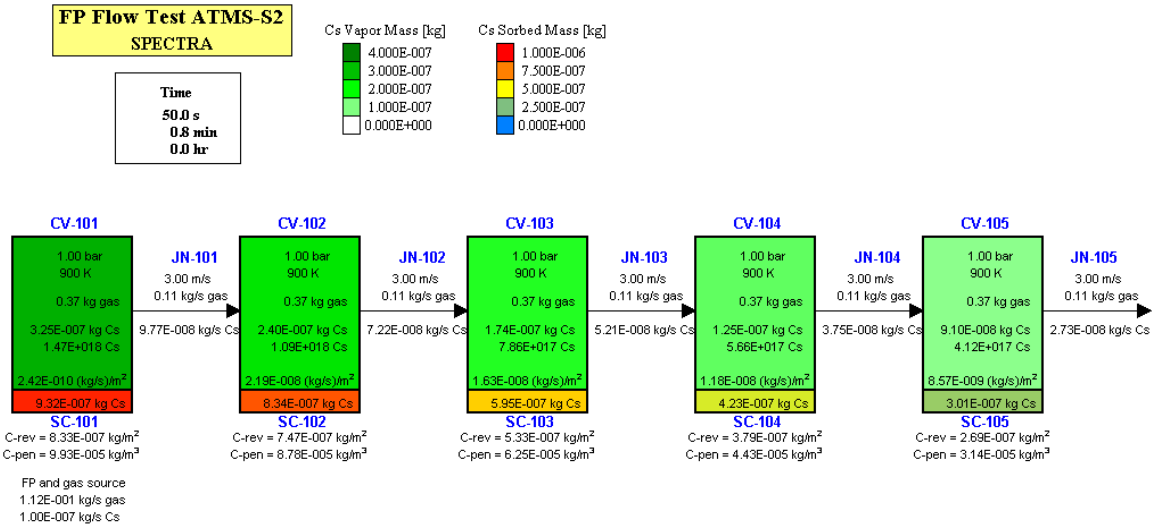

Figure 3-960 Test ATMS-S2, *t* = 50.0 s.

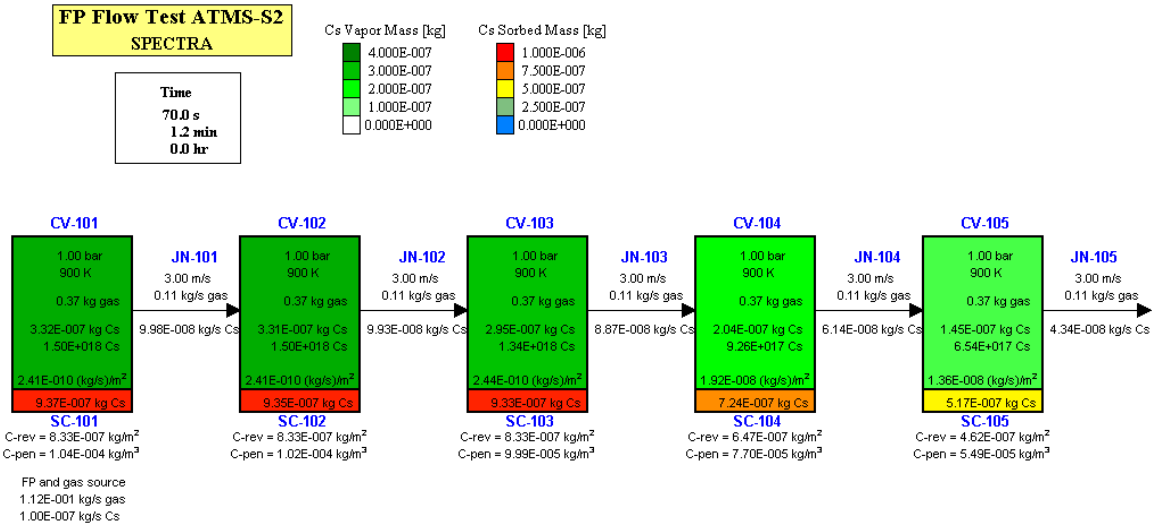

Figure 3-961 Test ATMS-S2, *t* = 70.0 s.

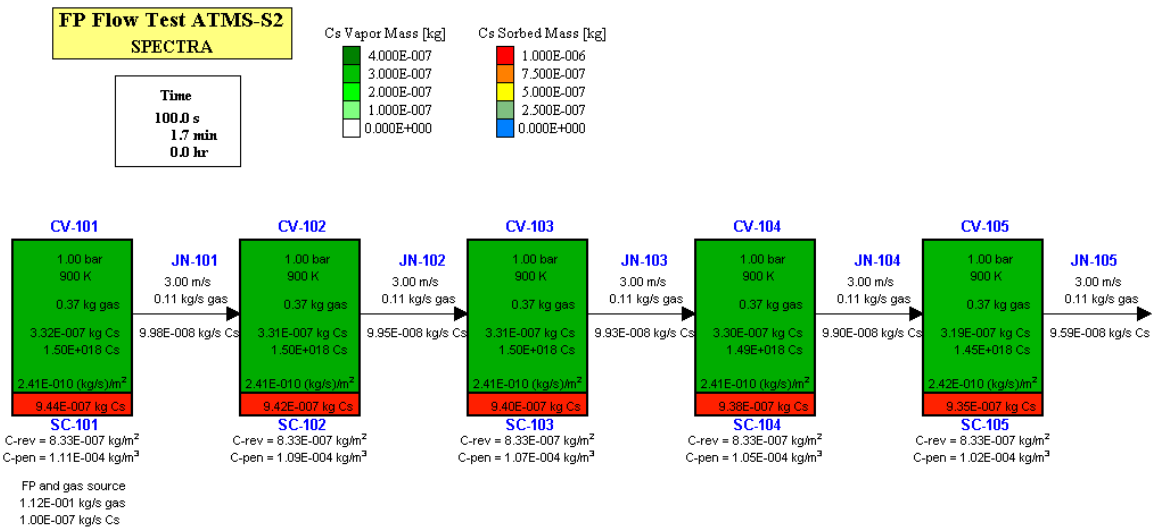

Figure 3-962 Test ATMS-S2, *t* = 100.0 s.

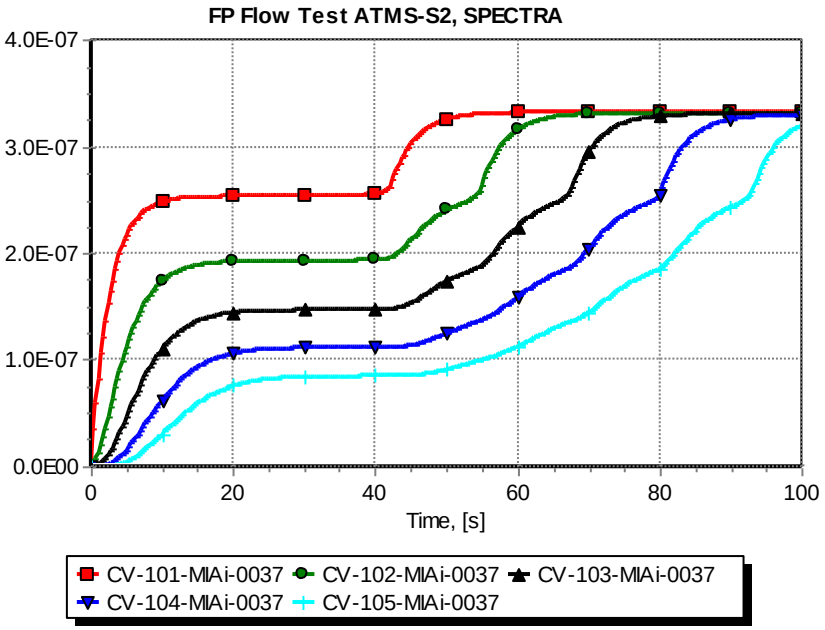

Figure 3-963 Mass of Cs-133 (isotope 0037), test ATMS-S2

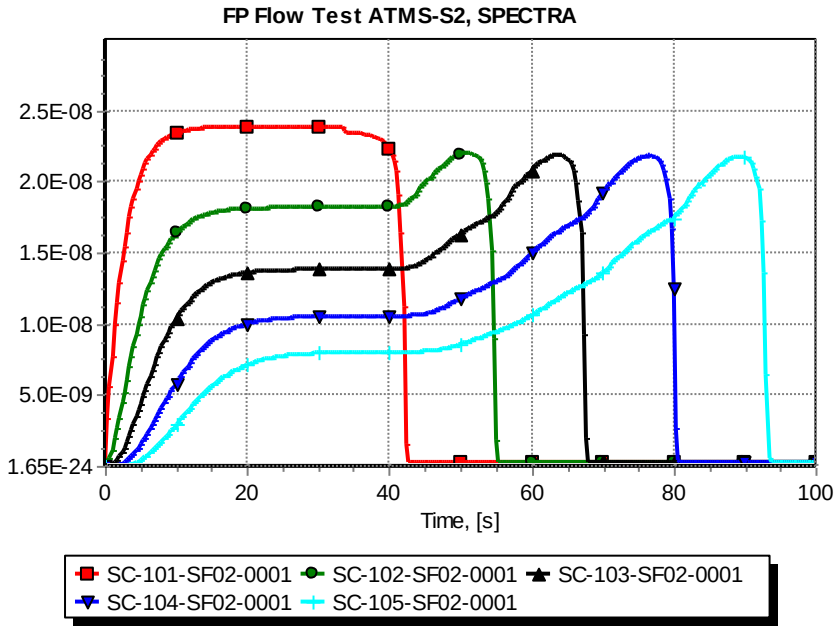

Figure 3-964 Sorption flux vapor class 02 (Cs), node 0001 (left surface).

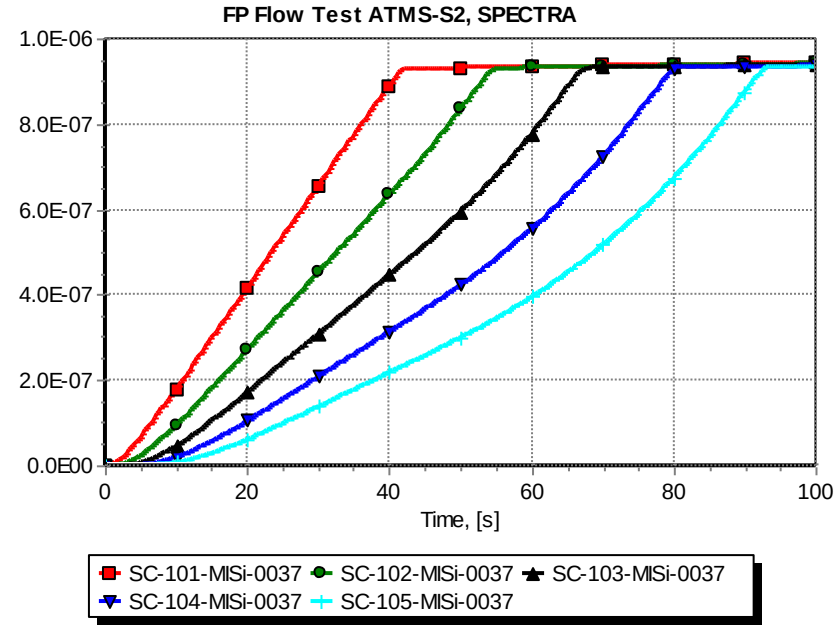

Figure 3-965 Sorbed mass of Cs-133 (isotope 0037).

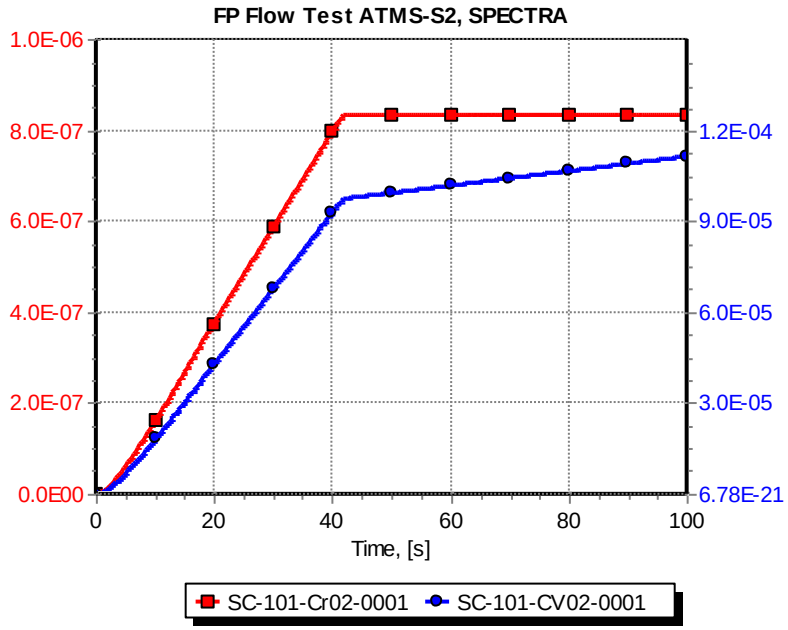

Figure 3-966 Surface density of vapor 02 (Cr02) and penetrated density (CV02).

- When the surface becomes saturated the net sorption flux is practically zero. In fact there is a small desorption flux, which results in "freeing" some adsorption sites and make the adsorption possible. The adsorption flux is practically equal to the desorption flux. Since some of the adsorbed molecules penetrate into the structure, there is a net positive flux which results in an increase of the penetrated Cs mass, while the surface (reversibly-bound) Cs mass remains practically constant (see Figure 3-966). The increase of the penetrated mass is responsible for the slow increase visible in Figure 3-965. It should be noted that the penetrated fraction ($1–\beta$) was set to 10^{-1} rather than 10^{-5}. Therefore the penetration is overestimated in this test. This was done in order to make the increase of the penetrated mass visible on the graphs. With the default value (10^{-5}) the lines would be practically flat in the saturated regime.

- When the surface becomes saturated, then a large amount of Cs is transported with the gas stream to the next CV, where it is being adsorbed and the process repeats in the subsequent CVs until the surfaces are saturated in all CVs (Figure 3-962).

3.12.47 FP Vapor Flow and Condensation Test COND-S2

The geometry chosen for this test is the same as the geometry used for the previous test (section 3.12.46). Again a source of gas (air at 900 K) is present in the volume CV-101 A source of Cs-133 (isotope number 37) provides a constant source if 10^{-7} kg/s for CV-101.

The only difference compared to the previous test is the presence of a negative heat source (modelled using a Tabular Function TF-004). The heat source is located in CV-104. The tabular function TF-004 gives a constant value of -50×10^{3}, which means that there is a constant heat removal from CV-004, equal to 50 kW. This heat sink is able to decrease the temperature of the incoming gas from the initial 900 K to about 500 K. At 500 K the Cs saturation pressure is close to zero (~10^{-5} Pa - see Figure 2-183, section 2.8.15). Therefore Cs condenses, forming aerosol particles in CV-104. The full sorption model (Sorption Model 2), the same as in the previous test was applied. The penetrated fraction ($1-\beta$) was set again to 10^{-1} to make penetration visible on the graphs. No diffusion is modelled (diffusion coefficient is zero). Therefore the penetrated molecules remain in the boundary node (V=10^{-3} m^3). The adsorption flux was maximized by selecting a large value for the Sherwood number correlation, A_{Sh} = 1000 (maximum acceptable value).

The input file for this run is stored in: `\Z-INPUTS\RT\FLOW-FP\COND-S2.SPE`. Results are shown in Figure 3-967 through Figure 3-976. Figure 3-967, Figure 3-968, and Figure 3-969 show visualization pictures at the times 30, 50, and 100 s, respectively. The visualization pictures include aerosol particles, marked as circles. The size of the circles is proportional to the mass of the aerosol particles in a given CV.

The next figures show time behavior of the Cs vapor mass (Figure 3-970), the sorption fluxes (Figure 3-971), the sorbed masses (Figure 3-972), the Cs vapor pressures and saturation pressures (Figure 3-973 and Figure 3-974), the aerosol masses (Figure 3-975), as well as the Cs condensation rate in CV-104 (Figure 3-976).

The following remarks can be made:

- Results are the same as in previous vase for the first 3 volumes. In CV-104 a major part of the Cs vapor condenses; the vapor pressure decreases from ~1.9×10^{-2} Pa to the saturation pressure of ~3×10^{-5} Pa (Figure 3-968).

- The Cs condensation starts at about 15 s (Figure 3-976), when the surfaces SC-101, SC-102, and SC-103 approach saturation of the adsorbed Cs, and significant amount of Cs starts flowing into the CV-104. After about 70 s the condensation rate is close to 0.9×10^{-7} kg/s (Figure 3-976), which is close to the source strength. Thus very little Cs may flow into the following volume - CV-105.

- Very little Cs is present in CV-005. The vapor pressure is below 10^{-7} Pa - Figure 3-974. The sorption rate is slow (Figure 3-971).

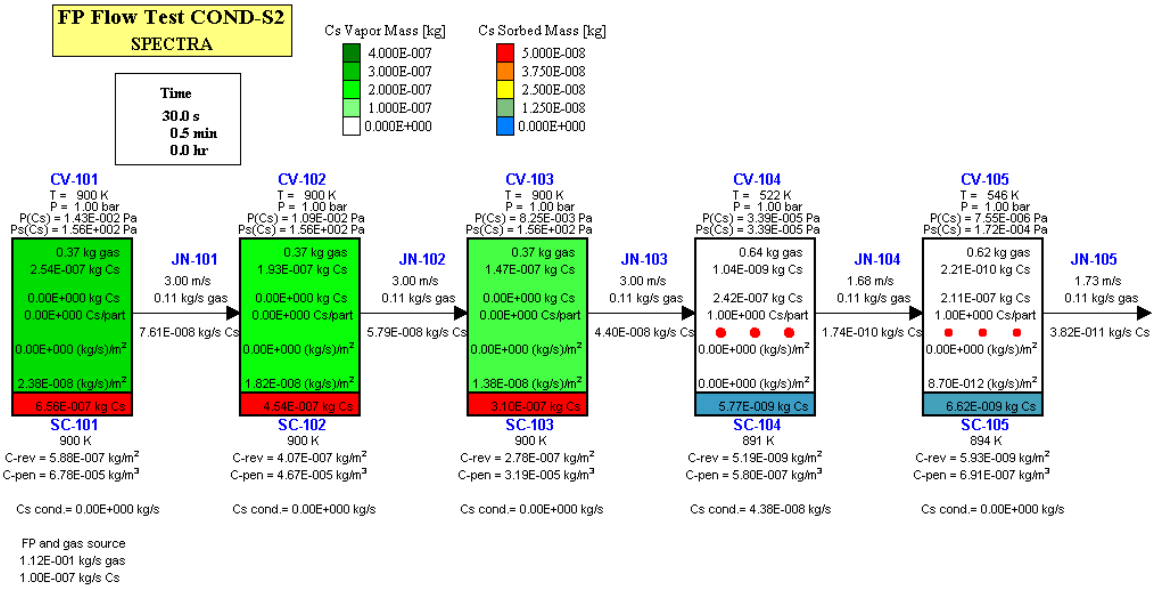

Figure 3-967 Test COND-S2, t = 30.0 s.

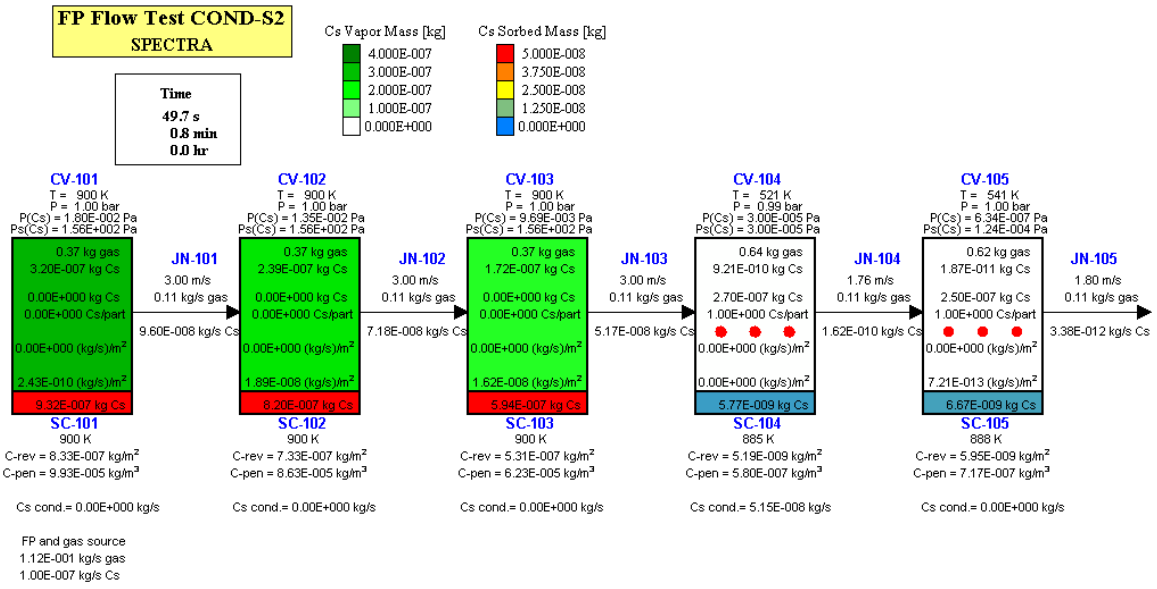

Figure 3-968 Test COND-S2, t = 50.0 s.

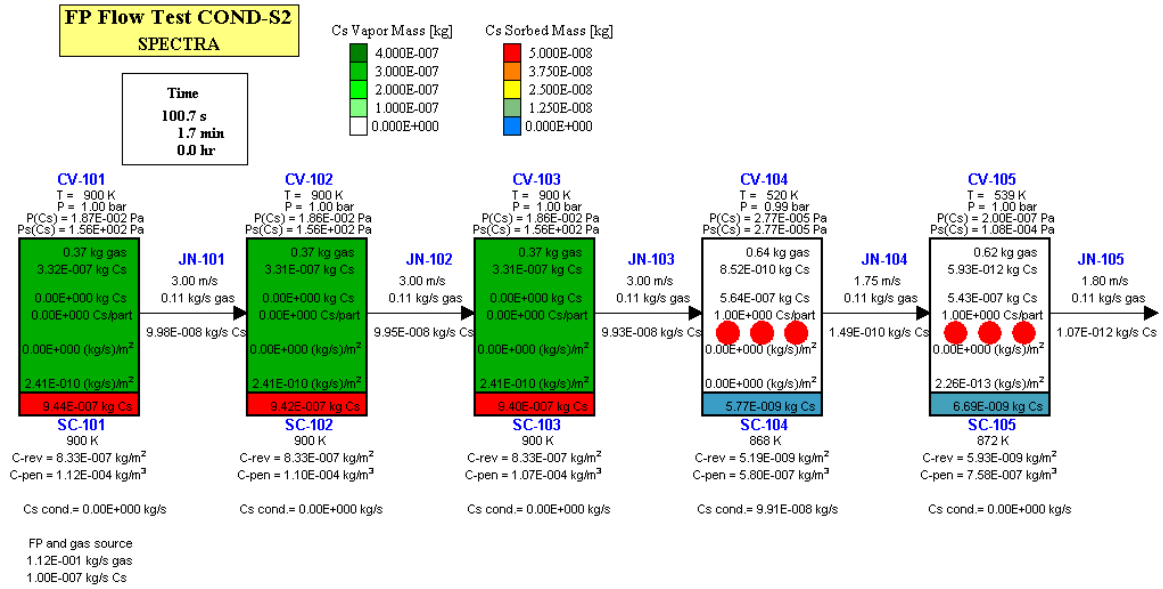

Figure 3-969 Test COND-S2, t = 100.0 s.

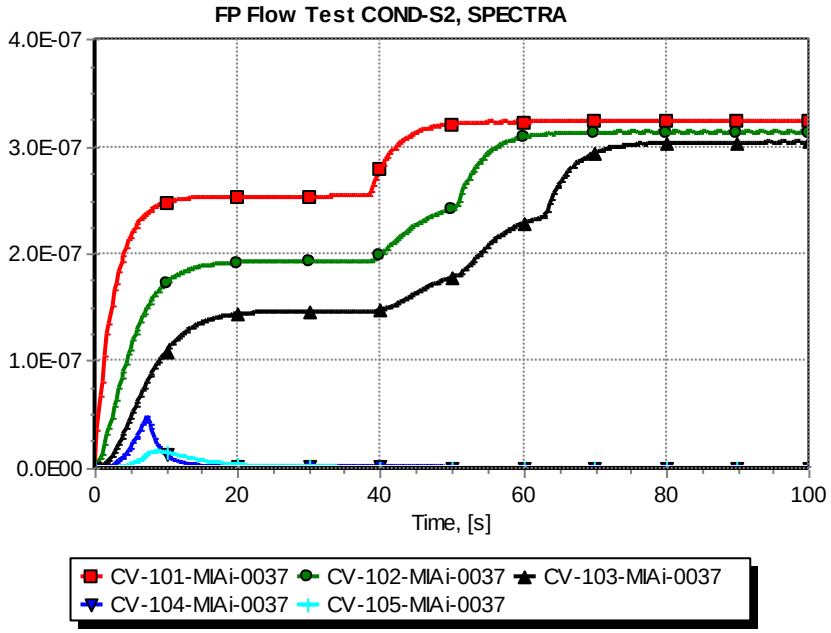

Figure 3-970 Mass of Cs-133 (isotope 0037), test COND-S2

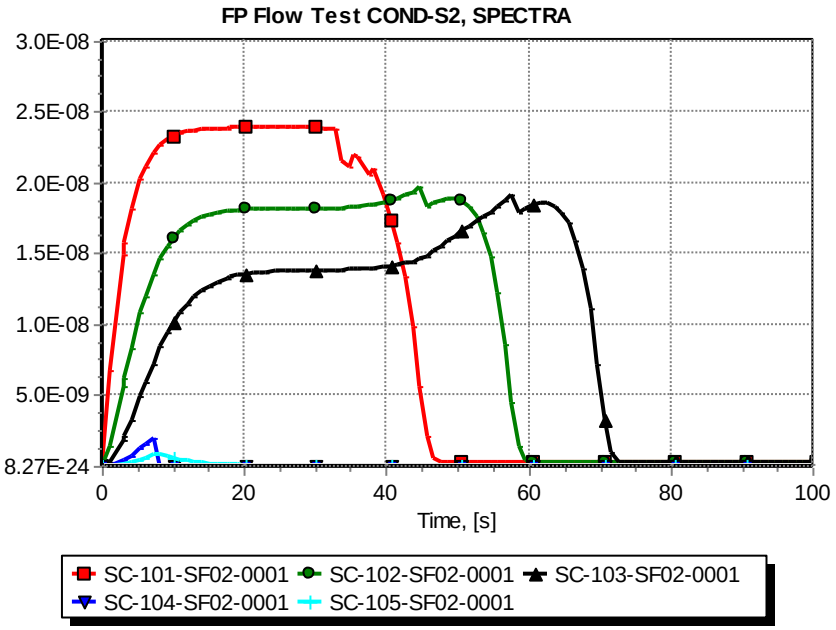

Figure 3-971 Sorption flux vapor class 02 (Cs), node 0001 (left surface).

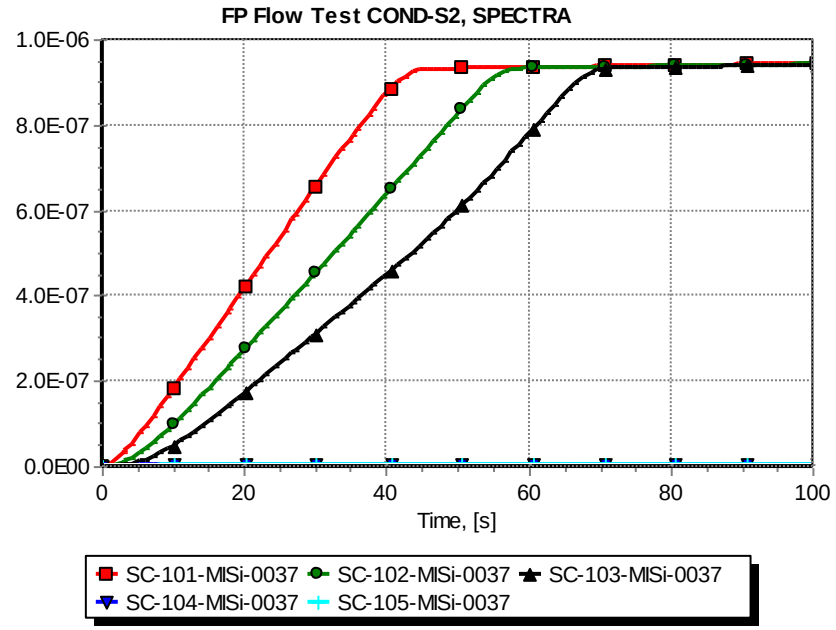

Figure 3-972 Sorbed mass of Cs-133 (isotope 0037).

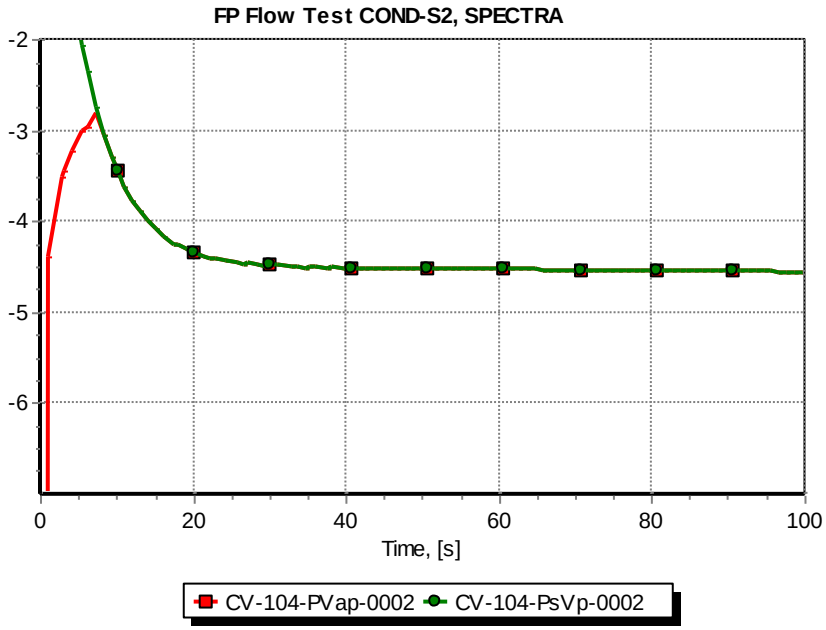

Figure 3-973 Cs vapor pressure and saturation pressure in CV-104.

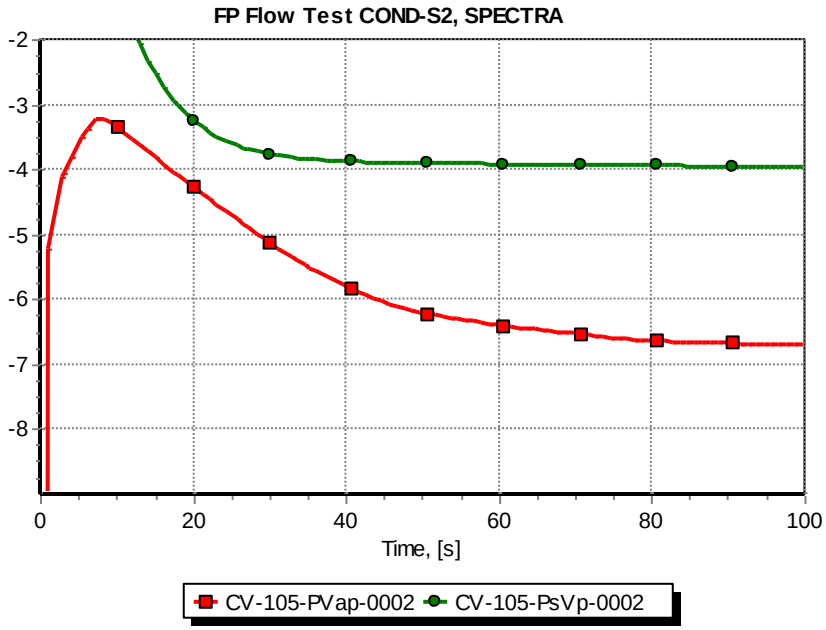

Figure 3-974 Cs vapor pressure and saturation pressure in CV-105.

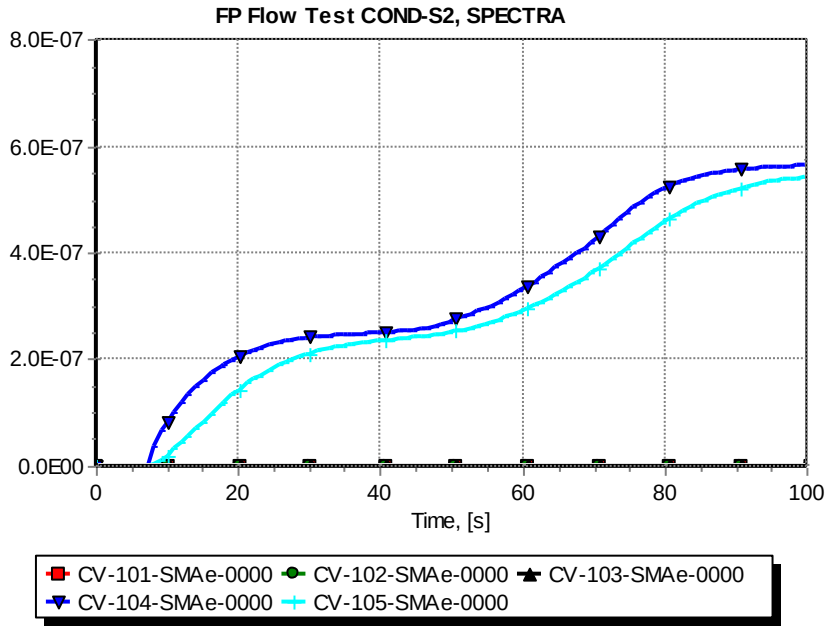

Figure 3-975 Aerosol masses.

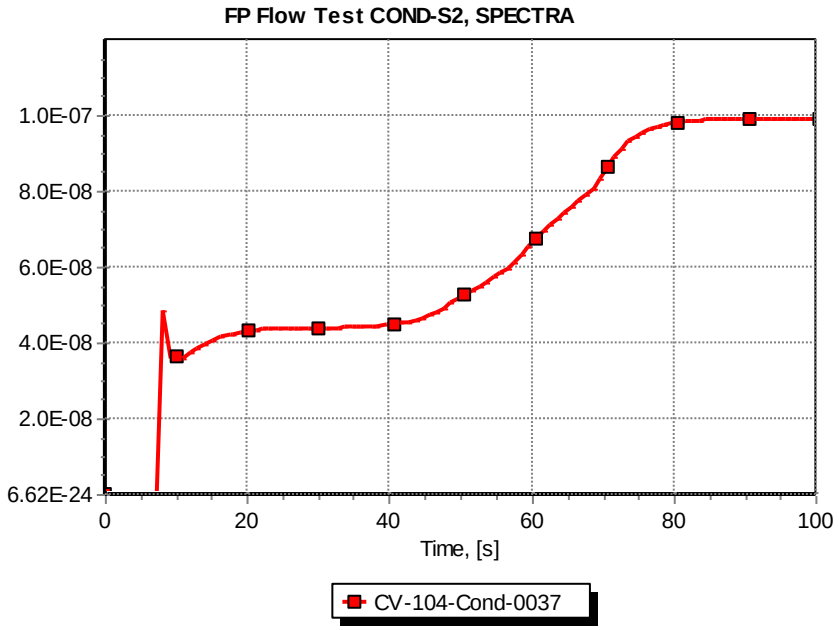

Figure 3-976 Cs-133 (isotope 0037) condensation rate in CV-104.

3.12.48 FP Sorption Tests - Sorption Model 2

This section presents results of the sorption validation tests:

- Laminar Loop experiments (sections 3.12.48.1 and 3.12.48.2)
- Vampyr experiments (section 3.12.48.3)
- Dragon experiments (section 3.12.48.4)

Calculations presented in this section were performed with the Sorption Model 2 (PATRAS/SPATRA model). Results are compared to the experimentally measured values.

3.12.48.1 FP Sorption Tests - Laminar Loop Experiment 4 (Run-4)

The data for the Laminar Loop experiments was obtained from [90], [91], and [94]. The test section for the experiment No. 4 (Run-4) consists of a tube, made of Incoloy 800. The tube dimensions are:

- Inner diameter, D = 0.020 m
- Length, L = 2.4 m

The tube was divided into 16 sections, following [94]. The section lengths and the gas and wall temperatures in each section are shown in Table 3-82. The gas and wall temperatures for each section were entered as the arithmetic average of the values given in [94] for the edges of each section. The gas pressure is 3.0 bar.

Table 3-82 Laminar Loop, Run-4 (Cs on Incoloy 800), geometry and temperatures

No.	Section length (m)	Position, (m)	T_{wall}, (K)	T_{gas}, (K)
		0.000		
1	0.085	0.085	966.4	992.8
2	0.150	0.235	966.9	991.7
3	0.145	0.380	967.6	990.3
4	0.155	0.535	968.3	989.0
5	0.150	0.685	969.0	987.6
6	0.150	0.835	969.6	986.2
7	0.135	0.970	970.3	984.9
8	0.155	1.125	971.0	983.6
9	0.140	1.265	971.7	982.2
10	0.145	1.410	972.3	980.9
11	0.160	1.570	973.0	979.5
12	0.140	1.710	973.7	978.1
13	0.140	1.850	974.3	976.8
14	0.150	2.000	975.0	975.5
15	0.150	2.150	975.7	974.2
16	0.250	2.400	976.6	972.3

The thermal-hydraulic solution was disabled. Therefore, the temperatures shown in the table are kept throughout the whole transient, in order to allow using large time steps. For the present run the time step of 1000 s was used. (A sensitivity calculation was performed with the time step of 100 s. There were no differences observed in the results of the 1000 s and the 100 s runs). The total calculation time was 50 days, which is the same as the experimental time.

A constant source of Helium, equal to 5×10^{-3} kg/s, was present during the test. Sources of Cs-133 and Cs-134 were present during the test. The source of Cs-134 was entered following [94], as shown in Table 3-83. The values obtained from [94] are atoms/s. The SPECTRA input is in kg/s. The values were converted as:

$$S_{kg/s} = S_{atoms/s} \cdot \frac{M_w}{N_{Av}} = S_{atoms/s}$$

Here M_w is the molar weight in kg/kmol, and N_{Av} is the Avogadro number, equal to 6.022×10^{26} atoms/kmol. The full sorption model was used. For the base calculations the sorption coefficients were assumed following [93]. As sensitivity runs the same experiment was re-run with the coefficients that were used in [94] to analyze the Laminar Loop (L-L) experiments as well as the ones used to analyze the Vampyr II (V-II) experiment. The base case values and the alternative values of the sorption coefficients are given in Table 3-84. The desorption coefficients, E_ϑ in kJ/mol, are converted into the value used by SPECTRA, A_ϑ in K, using the universal gas constant of $R = 8314.51$ J/(kmol K).

Table 3-83 Laminar Loop, Run-4 (Cs on Incoloy 800), source of Cs-134

Test	Material	*S*(Cs-133) (atoms/s)	*S*(Cs-134) (atoms/s)	*S*(Cs-133) (kg/s)	*S*(Cs-134) (kg/s)
4	Incoloy 800	3.26×10^{12}	3.26×10^{8}	7.20×10^{-13}	7.25×10^{-17}
7	Inconel 617	3.51×10^{12}	4.13×10^{9}	7.75×10^{-13}	9.19×10^{-16}
10	Inconel 617	2.51×10^{12}	2.51×10^{8}	5.54×10^{-13}	5.58×10^{-17}

Table 3-84 Sorption coefficients for the base case calculation and the alternative calculations

Material	Base Case	Alternative L	Alternative V
Sorption coefficients	IAEA-TECDOC-978 [93], Table A-13	Used for L-L tests [94], Fig.2,3, Tab.23	Used for V-II test [94], Fig.9,12
Cs on Incoloy 800:			
E_ϑ	235	234	180
$A_\vartheta = E_\vartheta / R$	28,263	28,144	21,649
$1-\beta$	10^{-5}	10^{-5}	10^{-5}
Cs on Inconel 617:			
E_ϑ	250	230	165
$A_\vartheta = E_\vartheta / R$	30,067	27,662	19,844
$1-\beta$	10^{-5}	10^{-6}	10^{-5}

The input file for the base case and the alternative sorption coefficients are stored in:
`Z-INPUTS\RT\Sorption-Tests\LAMINAR\Run-4\`

The input files are:

- `Run-4.SPE` Sorption coefficients based on IAEA-TECDOC-978 [93]
- `Run-4-A-L.SPE` Coefficients as used in [94] for the Laminar Loop tests
- `Run-4-A-V.SPE` Coefficients as used in [94] for the Vampyr II/V01 test

Results are shown in Figure 3-977, Figure 3-978, and Figure 3-979. Figure 3-977 show visualization picture obtained for the Base Case at the end of the test. Time dependent activities at the beginning and at the end of the test tube, obtained for the same case are shown in Figure 3-978.

Results of the three analyzed cases are compared to experimental results in Figure 3-979. It is seen that the sorption coefficients found in IAEA-TECDOC-978 [93] provide somewhat too high activity for this test. Similar result was obtained by Radax (see reference [94], Figure 2). The alternative coefficients, used in [94] to analyze the Laminar Loop experiments, give very similar results. The alternative coefficients, used in [94] to analyze the Vampyr II experiment, give lower activity and quite different qualitative behavior.

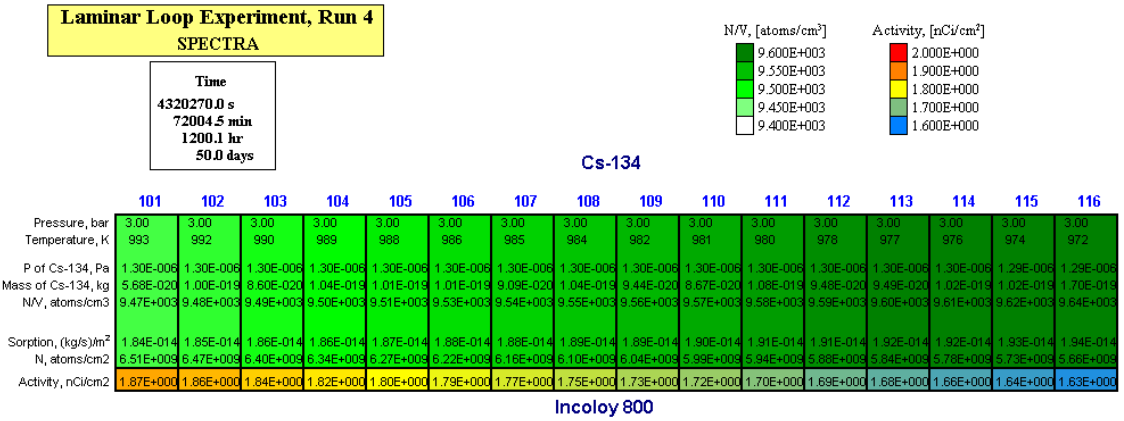

Figure 3-977 Laminar Loop Tests - Run 4, Cs-134 on Incoloy 800.

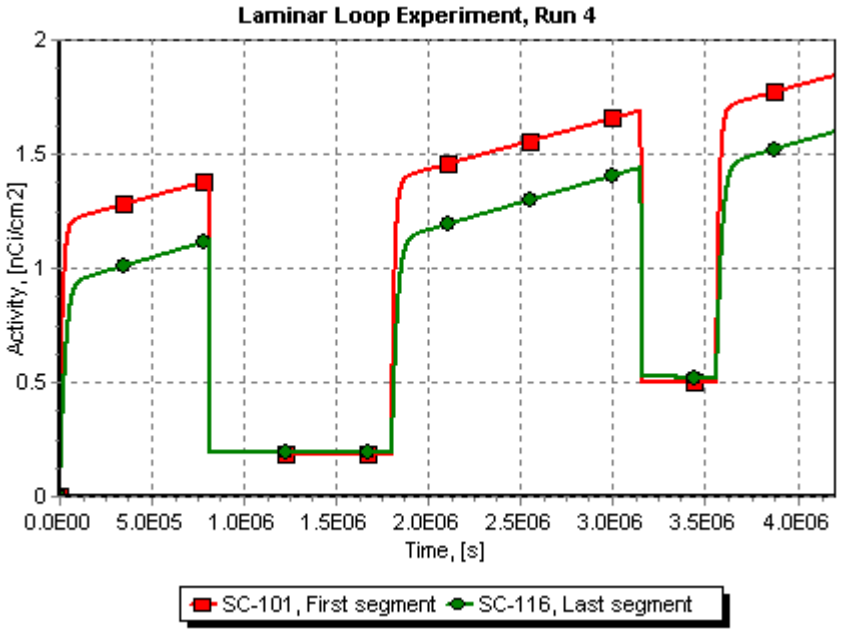

Figure 3-978 Laminar Loop Tests - Run 4, Cs-134 on Incoloy 800.

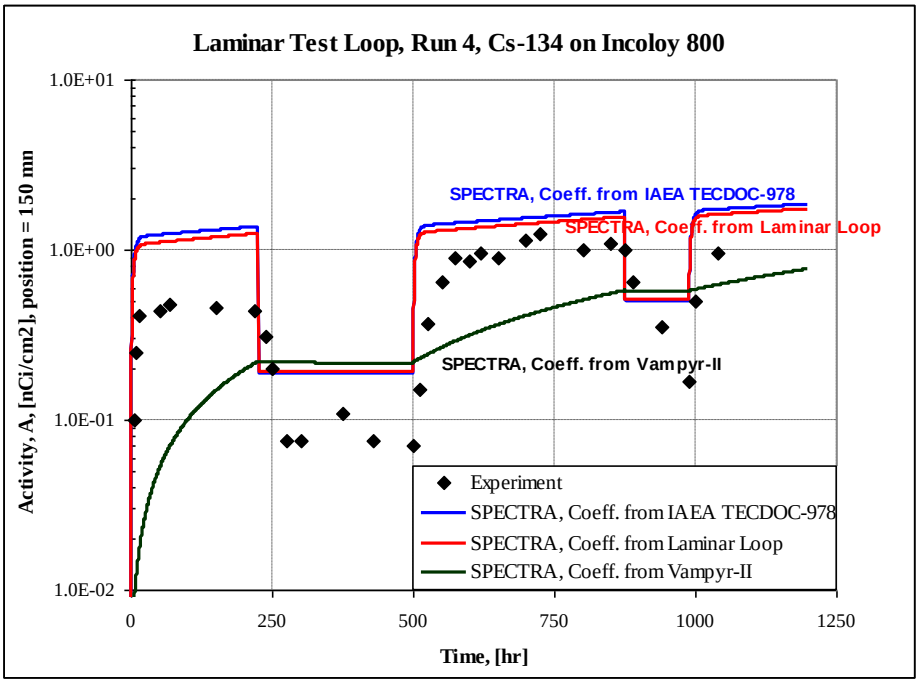

Figure 3-979 Laminar Loop Tests - Run 4, Cs-134 on Incoloy 800.

3.12.48.2 FP Sorption Tests - Laminar Loop Experiment 4 (Run-7)

The data for the Laminar Loop experiments was obtained from [90], [91], and [94]. The test section for the experiment No. 7 (Run-7) consists of a tube, made of Inconel 617. The tube dimensions are:

- Inner diameter, D = 0.020 m
- Length, L = 2.4 m

The tube was divided into 16 sections, following [94]. The section lengths and the gas and wall temperatures in each section are shown in Table 3-85. The gas and wall temperatures for each section were entered as the arithmetic average of the values given in [94] for the edges of each section. The gas pressure is 3.0 bar.

The thermal-hydraulic solution was disabled. Therefore, the temperatures shown in the table are kept throughout the whole transient, in order to allow using large time steps. For the present run the time step of 1000 s was used. (A sensitivity calculation was performed with the time step of 100 s. There were no differences observed in the results of the 1000 s and the 100 s runs). The total calculation time was 50 days, which is the same as the experimental time.

Table 3-85 Laminar Loop, Run-4 (Cs on Incoloy 800), geometry and temperatures

No.	Section length (m)	Position, (m)	T_{wall}, (K)	T_{gas}, (K)
		0.000		
1	0.095	0.095	982.8	982.9
2	0.155	0.250	981.9	982.0
3	0.140	0.390	980.8	981.0
4	0.160	0.550	979.7	980.0
5	0.165	0.715	978.4	978.9
6	0.150	0.865	977.2	977.9
7	0.135	1.000	976.2	976.9
8	0.160	1.160	975.1	976.0
9	0.140	1.300	974.0	975.0
10	0.145	1.445	972.9	974.0
11	0.165	1.610	971.7	973.0
12	0.150	1.760	970.5	972.0
13	0.150	1.910	969.4	971.0
14	0.155	2.065	968.3	969.9
15	0.165	2.230	967.1	968.8
16	0.170	2.400	965.8	967.7

A constant source of Helium, equal to 5×10^{-3} kg/s, was present during the test. Sources of Cs-133 and Cs-134 were present during the test. The source of Cs-134 was entered following [94], as shown in Table 3-83. The values obtained from [94] are atoms/s. The SPECTRA input is in kg/s.

The full sorption model was used. For the base calculations the sorption coefficients were assumed following [93]. As sensitivity runs the same experiment was we-run with the coefficients that were used in [94] to analyze the Laminar Loop (L-L) experiments as well as the ones used to analyze the Vampyr II (V-II) experiment. The base case values and the alternative values of the sorption coefficients are given in Table 3-84.

The input file for the base case and the alternative sorption coefficients are stored in:
`Z-INPUTS\RT\Sorption-Tests\LAMINAR\Run-7\`

The input files are:

- `Run-7.SPE` Sorption coefficients based on IAEA-TECDOC-978 [93]
- `Run-7-A-L.SPE` Coefficients as used in [94] for the Laminar Loop tests
- `Run-7-A-V.SPE` Coefficients as used in [94] for the Vampyr II/V01 test

Results are shown in Figure 3-980, Figure 3-981, and Figure 3-982. Figure 3-980 shows visualization picture obtained for the Base Case at the end of the test. Time dependent activities at the beginning and at the end of the test tube, obtained for the same case are shown in Figure 3-981.

Results of the three analyzed cases are compared to experimental results in Figure 3-982. It is seen that the sorption coefficients found in IAEA-TECDOC-978 [93] gives clearly too high activity for this test. The alternative coefficients, used in [94] to analyze the Laminar Loop experiments, give good results. Similar result was obtained by Radax (see reference [94], Figure 4). The alternative coefficients, used in [94] to analyze the Vampyr II experiment, give lower activity and a different qualitative behavior.

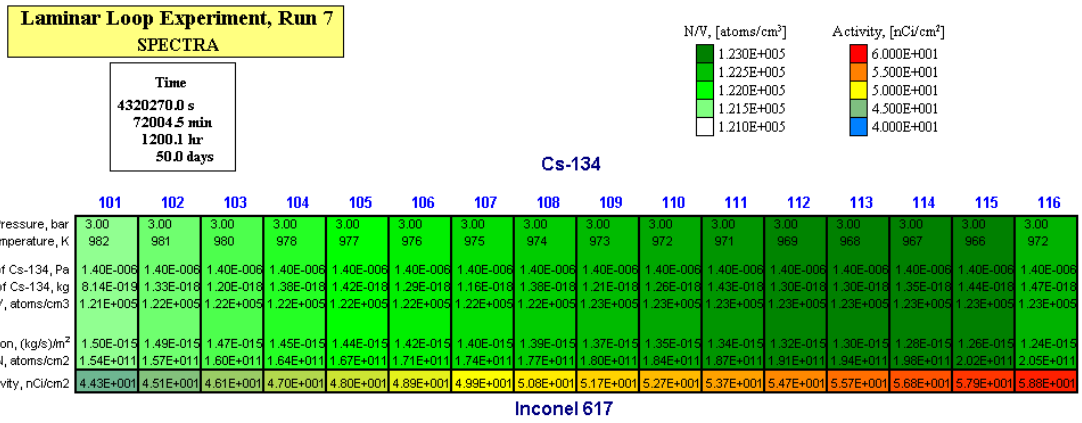

Figure 3-980 Laminar Loop Tests - Run 7, Cs-134 on Inconel 617.

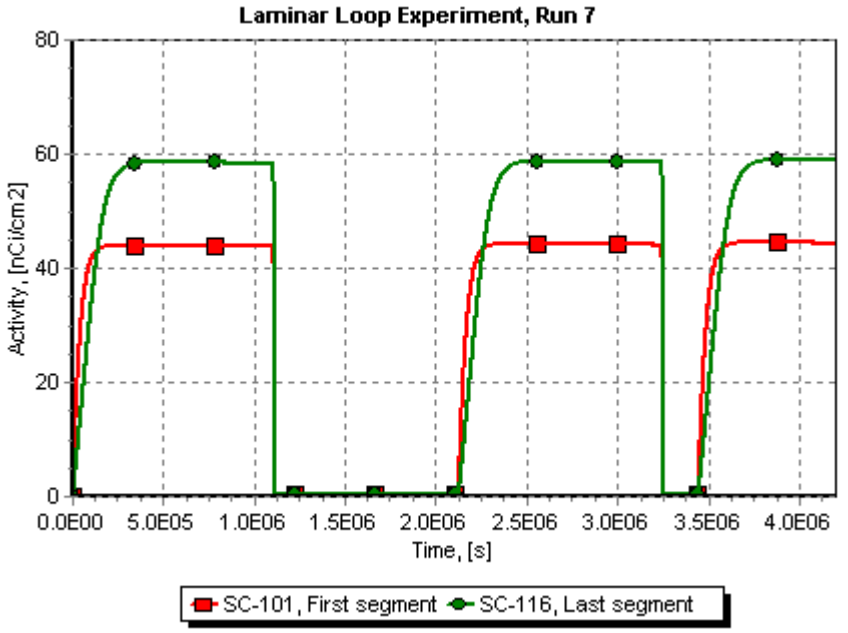

Figure 3-981 Laminar Loop Tests - Run 7, Cs-134 on Inconel 617.

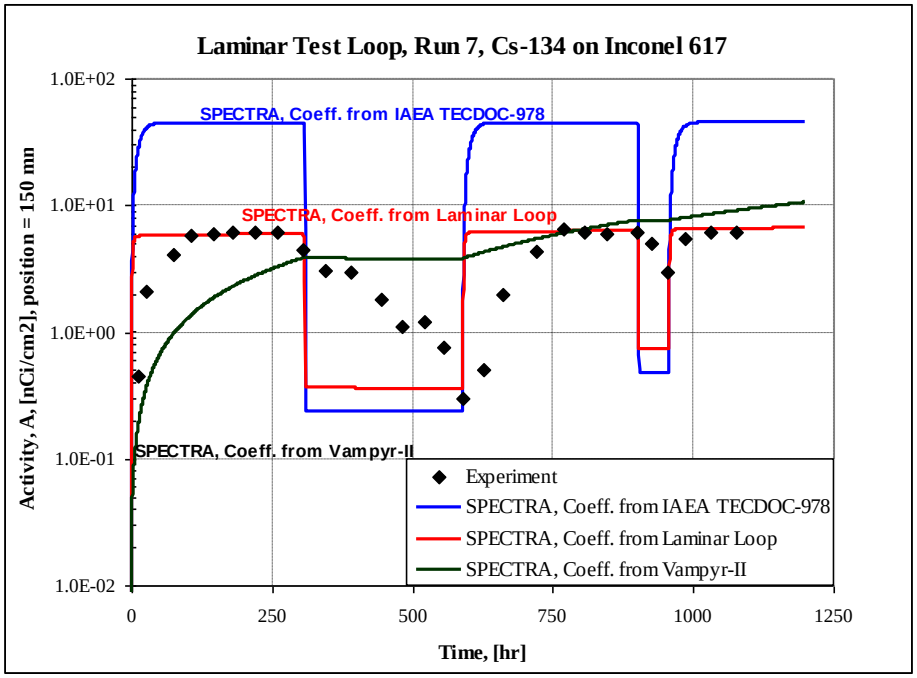

Figure 3-982 Laminar Loop Tests - Run 7, Cs-134 on Inconel 617.

3.12.48.3 FP Sorption Tests - Vampyr II/V01 Experiment

The data for the Vampyr II/V01 experiment was obtained from [92] and [94]. The test section consists of a tube, made of Incoloy 800, and a central rod, made of Inconel 617. The dimensions are:

- Tube inner diameter, D = 0.014 m
- Tube thickness, t = 0.020 m
- Central rod outer diameter, D_r = 0.009 m
- Length, L = 3.52 m

The tube was divided into 11 sections, following [94]. The section lengths and the gas and wall temperatures in each section are shown in Table 3-86. The gas and wall temperatures for each section were entered as the values given in [94] for the given section. The gas pressure is 10.8 bar.

The thermal-hydraulic solution was disabled. Therefore, the temperatures shown in the table are kept throughout the whole transient, in order to allow using large time steps. For the present run the time step of 1000 s was used. The total calculation time was 60 days (the same as the experimental time).

A constant source of Helium, equal to 2.48×10^{-3} kg/s, was present during the test. A source of Cs-137 and Ag-110 was present during the test. The source of Cs-137 and Ag-110 were entered following [94], as shown in Table 3-87. The values obtained from [94] are atoms/s. The SPECTRA input is in kg/s. The values were converted as:

$$S_{kg/s} = S_{atoms/s} \cdot \frac{M_w}{N_{Av}} = S_{atoms/s}$$

Table 3-86 Vampyr II/V01, geometry and temperatures

No.	Section length (m)	Position, (m)	T_{wall}, (K)	T_{gas}, (K)
		0.000		
1	0.257	0.257	1006.15	1064.15
2	0.306	0.563	981.15	1026.15
3	0.306	0.869	941.15	989.15
4	0.306	1.175	902.15	949.15
5	0.306	1.481	863.15	911.15
6	0.306	1.787	831.15	875.15
7	0.306	2.093	802.15	841.15
8	0.306	2.399	768.15	798.15
9	0.306	2.705	741.15	777.15
10	0.306	3.011	716.15	749.15
11	0.509	3.520	667.15	691.15

Here M_w is the molar weight, in kg/kmol, and N_{Av} is the Avogadro number, equal to 6.022×10^{26} atoms/kmol.

Table 3-87 Vampyr II/V01 sources of Cs-137 and Ag-110

Test	*S*(Cs-137) (atoms/s)	*S*(Ag-110) (atoms/s)	*S*(Cs-137) (kg/s)	*S*(Ag-110) (kg/s)
Vampyr II/V01	1.041×10^{10}	5.430×10^{7}	2.36×10^{-15}	9.92×10^{-18}

The full sorption model was used. For the base calculations the sorption coefficients were assumed following [93]. As sensitivity runs the same experiment was we-run with the coefficients that were used in [94] to analyze the Laminar Loop (L-L) experiments as well as the ones used to analyze the Vampyr II (V-II) experiment. The base case values and the alternative values of the sorption coefficients are given in Table 3-88. The desorption coefficients, E_ϑ in kJ/mol, are converted into the value used by SPECTRA, A_ϑ in K, using the universal gas constant of $R = 8314.51$ J/(kmol K).

Table 3-88 Sorption coefficients for the base case calculation and the alternative calculations

Material	Base Case	Alternative L	Alternative V
Sorption coefficients	IAEA-TECDOC-978 [93], Table A-13	Used for L-L tests [94], Fig.2,3, Tab.23	Used for V-II test [94], Fig.9,12
Cs on Incoloy 800:			
E_ϑ	235	234	180
$A_\vartheta = E_\vartheta / R$	28,263	28,144	21,649
$1-\beta$	10^{-5}	10^{-5}	10^{-5}
Ag on Incoloy 800:			
E_ϑ	200	-	255
$A_\vartheta = E_\vartheta / R$	24,054		30,669
$1-\beta$	10^{-6}		10^{-5}
Cs on Inconel 617:			
E_ϑ	250	230	165
$A_\vartheta = E_\vartheta / R$	30,067	27,662	19,844
$1-\beta$	10^{-5}	10^{-6}	10^{-5}
Ag on Inconel 617:			
E_ϑ	215	-	240
$A_\vartheta = E_\vartheta / R$	25,858		28,865
$1-\beta$	10^{-6}		10^{-6}

The input file for the base case and the alternative sorption coefficients are stored in:
`Z-INPUTS\RT\Sorption-Tests\VAMPYRE\`

The input files are:

- `VampyrII-V01.SPE` Sorption coefficients from IAEA-TECDOC-978 [93]
- `VampyrII-V01-A-L.SPE`. Coefficients as used in [94] for the Laminar Loop tests
- `VampyrII-V01-A-V.SPE` Coefficients as used in [94] for the Vampyr II/V01 test

Results are shown in Figure 3-984 through Figure 3-989. Figure 3-984 and Figure 3-985 show visualization picture obtained for the Base Case at the end of the test. It is seen in Figure 3-985 that SPECTRA calculates condensation of Ag-110 in the last part of the tube. The gas temperature in CV-111 is 691 K. Figure 3-983 shows that at this temperature the saturation pressure of Vapor 12 (to which silver belongs) is 0.0. Therefore any vapor of silver entering this volume is immediately condensing to form aerosols. Some condensation is observed already in CV-110 where the saturation pressure is positive, although very small (10^{-10} Pa - Figure 3-985).

Results of the three analyzed cases are compared to experimental results in Figure 3-986, Figure 3-987, Figure 3-988, and Figure 3-989. It is seen that the sorption coefficients found in IAEA-TECDOC-978 [93] provide too high activity and qualitatively incorrect results for this test. The alternative coefficients that were used in [94] to analyze the Laminar Loop experiments, again give too high activity and qualitatively incorrect results. The alternative coefficients, used in [94] to analyze the Vampyr II experiment, give very good agreement with experiment. Similar result was obtained by Radax (see reference [94], Figure 9, Figure 12, Figure 14, and Figure 17).

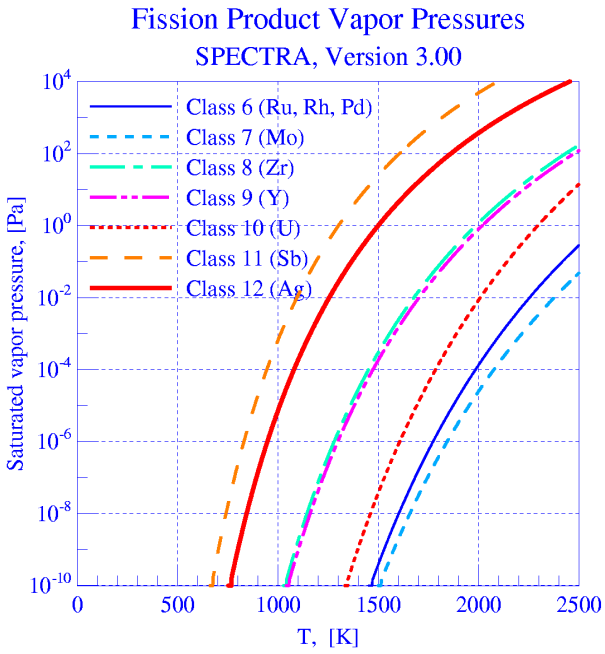

Figure 3-983 Saturation pressures for built-in vapor classes 6 – 12 (reproduced from Vol. 1)

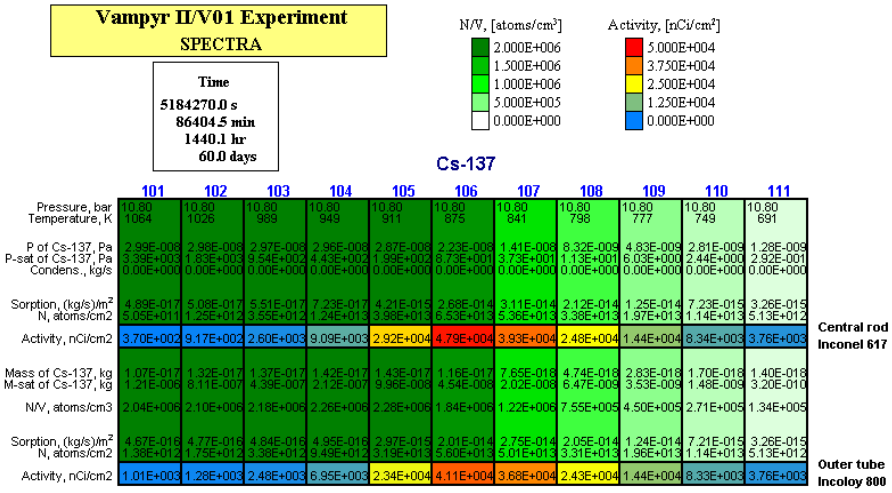

Figure 3-984 Vampyr II/V01 experiment, Cs-137 on Incoloy 800 and Inconel 617

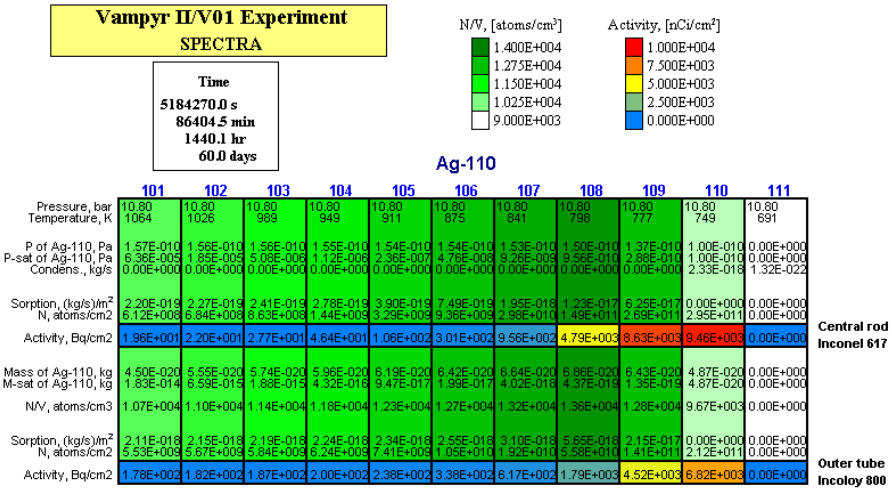

Figure 3-985 Vampyr II/V01 experiment, Ag-110 on Incoloy 800 and Inconel 617

Note that the alternative coefficients from the Laminar Loop give different coefficients only for Cs. For Ag the same (base case) coefficients are used. Therefore the values of IAEA-TECDOC-978 and L-L for Ag, shown in Figure 3-988 and Figure 3-989 are obtained from the same set of coefficients. Although the values are very similar, they are not exactly identical. This is because the different behavior of Cs to a small extend affects the behavior of Ag.

The condensation of silver in the last node (CV-111) results in zero activity on SC-111 (no value is plotted in the logarithmic graphs). Note that this is only the activity of adsorbed vapor and does not show the activity of deposited silver aerosols, which is in fact quite large but cannot be compared to experimental data. Since the experimental measurement show a positive activity at the last part of the tube, it is concluded that the saturation pressure of silver is somewhat higher than the value used in SPECTRA for the Vapor 12 and the condensation was not so intensive in reality.

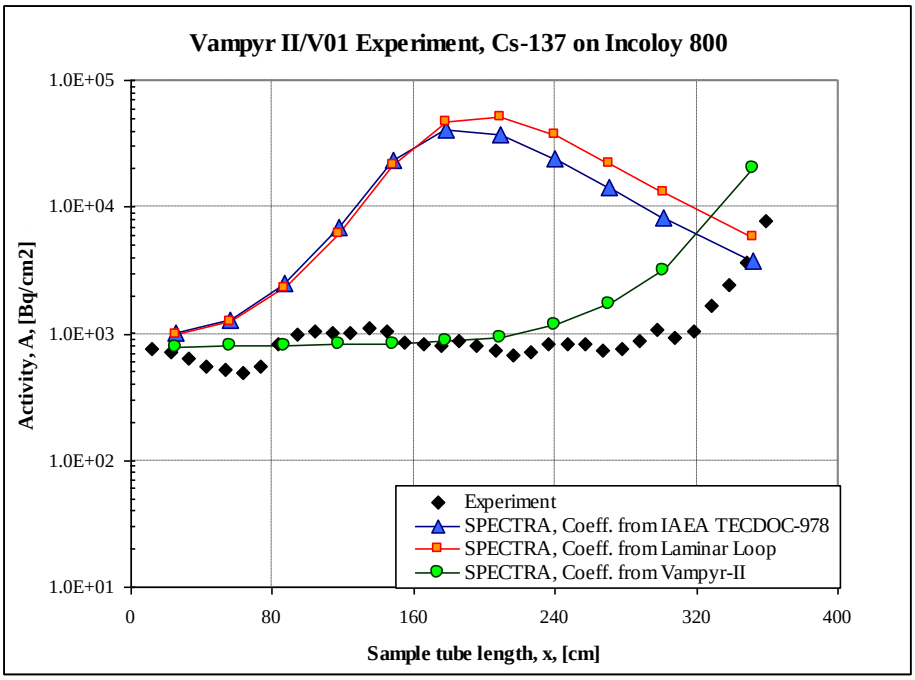

Figure 3-986 Vampyr II/V01 experiment, Cs-137 on Incoloy 800

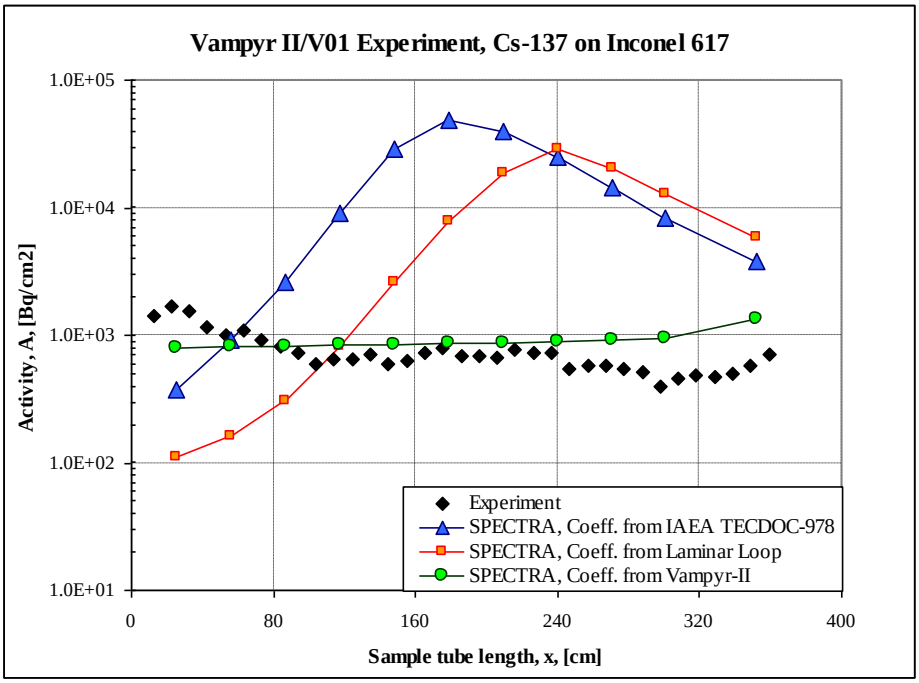

Figure 3-987 Vampyr II/V01 experiment, Cs-137 on Inconel 617

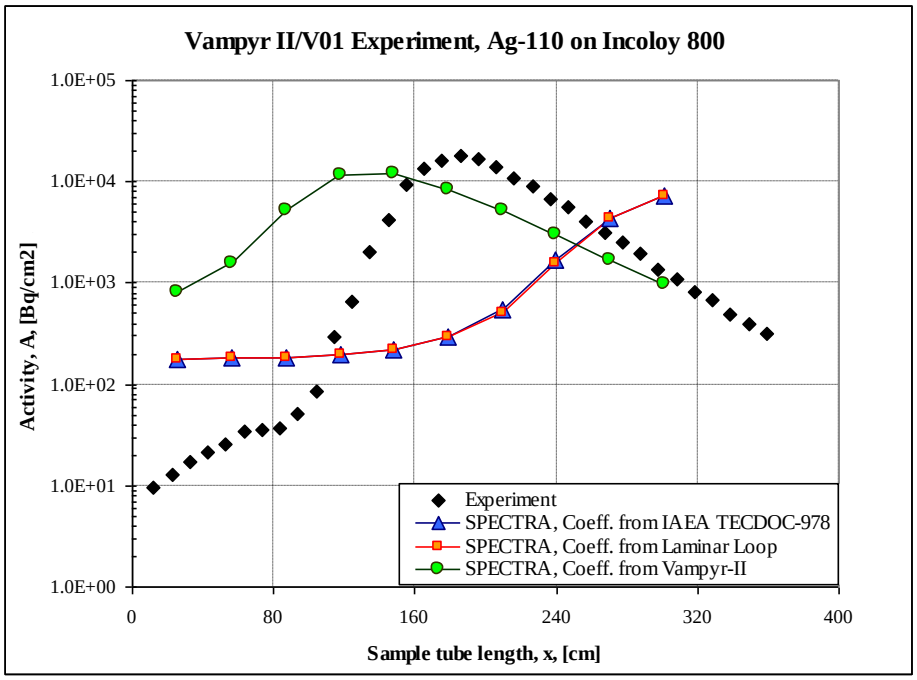

Figure 3-988 Vampyr II/V01 experiment, Ag-110 on Incoloy 800

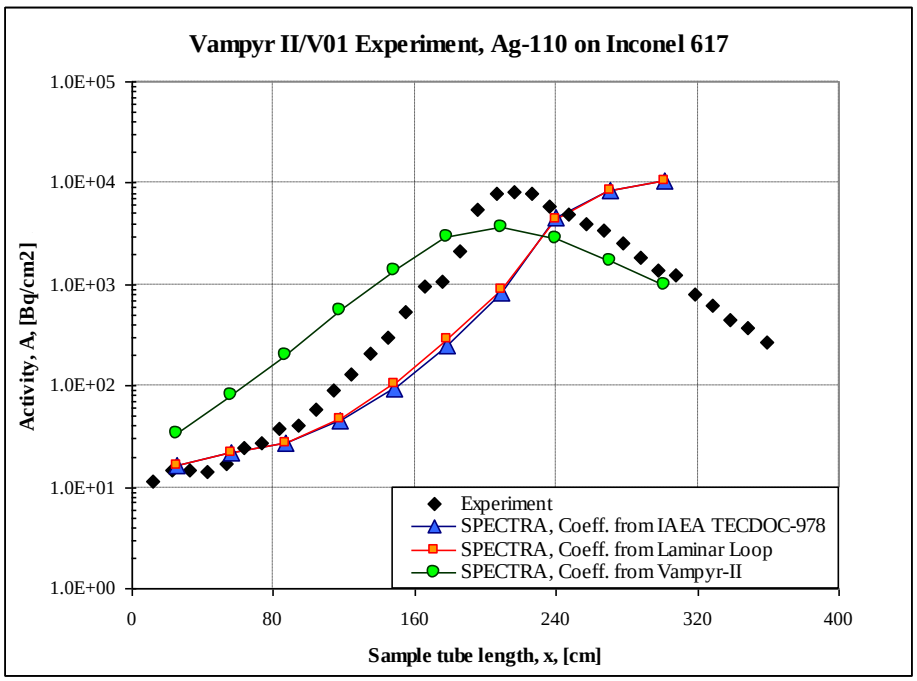

Figure 3-989 Vampyr II/V01 experiment, Ag-110 on Inconel 617

3.12.48.4 FP Sorption Tests - Dragon Experiment

The data for the Dragon experiment was obtained from [94]. The test section consists of a tube made of Incoloy 800. The dimensions of the tube are:

- Tube inner diameter, D = 0.1937 m
- Length, L = 0.6 m

The tube was divided into 12 sections, following [94]. The section lengths and the gas and wall temperatures in each section are shown in Table 3-89. The gas and wall temperatures for each section were entered as the values given in [94] for the given section. The gas pressure is 20.0 bar.

The thermal-hydraulic solution was disabled. Therefore, the temperatures shown in the table are kept throughout the whole transient, in order to allow using large time steps. For the present run the time step of 1000 s was used. The total calculation time was 487 days (the same as the experimental time).

A constant source of Helium, equal to 1.6 kg/s, was present during the test. Sources of Cs-137 and Ag-110 were present during the test. The source of Cs-137 and Ag-110 were entered following [94], as shown in Table 3-90. The values obtained from [94] are atoms/s. The SPECTRA input is in kg/s. The values were converted as:

$$S_{kg/s} = S_{atoms/s} \cdot \frac{M_w}{N_{Av}} = S_{atoms/s}$$

Here M_w is the molar weight, in kg/kmol, and N_{Av} is the Avogadro number, equal to 6.022×10^{26} atoms/kmol.

Table 3-89 Vampyr II/V01, geometry and temperatures

No.	Section length (m)	Position, (m)	T_{wall}, (K)	T_{gas}, (K)
		0.000		
1	0.050	0.050	973.15	973.15
2	0.050	0.100	973.15	973.15
3	0.050	0.150	973.15	973.15
4	0.050	0.200	973.15	973.15
5	0.050	0.250	973.15	973.15
6	0.050	0.300	973.15	973.15
7	0.050	0.350	973.15	973.15
8	0.050	0.400	973.15	973.15
9	0.050	0.450	973.15	973.15
10	0.050	0.500	973.15	973.15
11	0.050	0.550	973.15	973.15
12	0.050	0.600	973.15	973.15

Table 3-90 Dragon sources of Cs-137

Start-time (s)	End-time (s)	*S*(Cs-137) (atoms/s)	*S*(Cs-137) (kg/s)
0.0	5.44×10^{6}	1.70×10^{12}	3.87×10^{-13}
5.45×10^{6}	10.5×10^{6}	2.80×10^{12}	6.37×10^{-13}
10.6×10^{6}	15.6×10^{6}	4.80×10^{12}	1.09×10^{-13}
15.7×10^{6}	21.3×10^{6}	1.40×10^{12}	3.18×10^{-13}
21.4×10^{6}	26.5×10^{6}	1.40×10^{12}	3.18×10^{-13}
26.6×10^{6}	31.8×10^{6}	2.80×10^{12}	6.37×10^{-13}
31.9×10^{6}	36.5×10^{6}	1.60×10^{12}	3.64×10^{-13}
36.6×10^{6}	38.9×10^{6}	1.10×10^{12}	2.50×10^{-13}
39.0×10^{6}	42.1×10^{6}	4.80×10^{12}	1.09×10^{-13}

The full sorption model was used. For the base calculations the sorption coefficients were assumed following [93]. As sensitivity runs the same experiment was we-run with the coefficients that were used in [94] to analyze the Laminar Loop (L-L) experiments as well as the ones used to analyze the Vampyr II (V-II) experiment. The base case values and the alternative values of the sorption coefficients are given in Table 3-88.

The input file for the base case and the alternative sorption coefficients are stored in:
`Z-INPUTS\RT\Sorption-Tests\DRAGON\`

The input files are:

- `Dragon.SPE` Sorption coefficients based on IAEA-TECDOC-978 [93]
- `Dragon-A-L.SPE` Coefficients as used in [94] for the Laminar Loop tests
- `Dragon-A-V.SPE` Coefficients as used in [94] for the Vampyr II/V01 test

Results are shown in Figure 3-990, Figure 3-991, and Figure 3-992. Figure 3-990 show visualization picture obtained for the Base Case at the end of the test. Time dependent activities at the beginning (inlet) of the test tube, obtained for the same case, are shown in Figure 3-991. Activities obtained at different locations are practically the same.

Results of the three analyzed cases are compared to experimental results in Figure 3-992. It is seen that all sorption coefficients provide very similar results, with slightly too low activity. The results are qualitatively correct for this test.

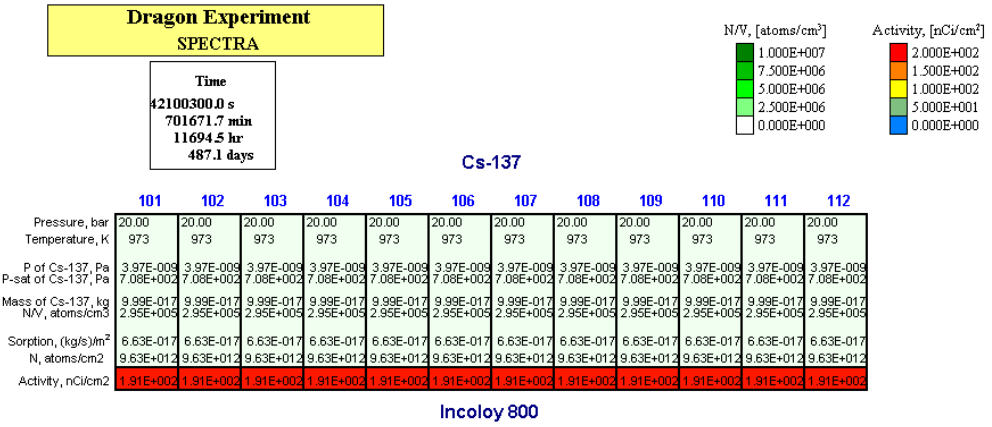

Figure 3-990 Dragon experiment, Cs-137 on Incoloy 800

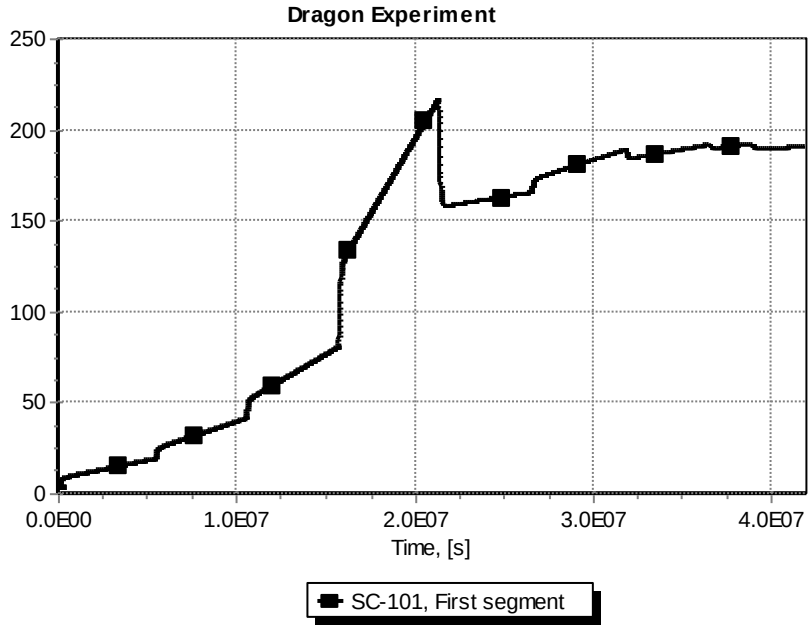

Figure 3-991 Dragon experiment, Cs-137 on Incoloy 800

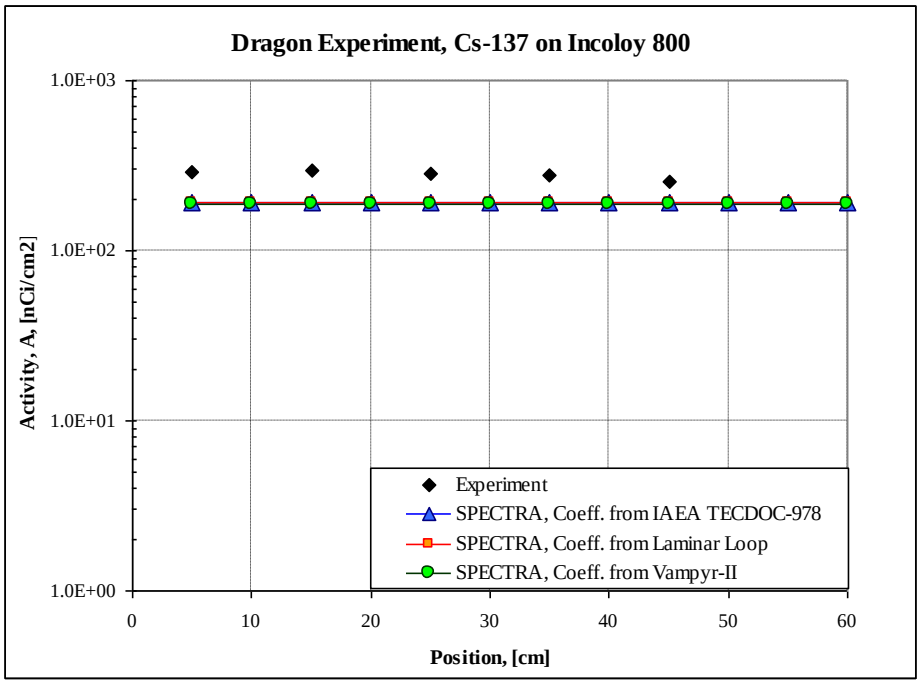

Figure 3-992 Dragon experiment, Cs-137 on Incoloy

3.12.48.5 Summary of the Sorption Validation Tests

Three experiments have been analyzed to perform code validation on sorption model. These are:

- Laminar Loop (L-L) experiments (Run-4 and Run-7)
- Vampyr II/V01 (V-II) experiment
- Dragon (D) experiment.

The results are summarized as follows:

- The sorption coefficients from IAEA-TECDOC-978 provide somewhat too high activity for the L-L tests. The alternative coefficients, used for the L-L experiments, give very similar results. The alternative coefficients, used for the V-II experiment, give lower activity and qualitatively incorrect behavior.
- The sorption coefficients from IAEA-TECDOC-978 provide too high activity and qualitatively incorrect results for the V-II test. The alternative coefficients, used for the L-L experiments give again too high activity and qualitatively incorrect results. The alternative coefficients, used for the V-II experiment, give very good agreement with experiment.
- All sorption coefficients provide very similar results for the Dragon test, with slightly too low activity. All results are qualitatively correct for this test.

3.12.48.6 Conclusion and Recommendation from the Sorption Validation Tests

The Laminar Loop results are well reproduced by the code using the coefficients derived for these tests. Also the Vampyr-II results are well reproduced by the coefficients derived for the corresponding Vampyr test. Unfortunately, when the Laminar Loop coefficients are applied to the Vampyr-II test, or vice versa, the results are inadequate, occasionally displaying the wrong trends. The coefficients from IAEA-TECDOC-978 occasionally give good predictions, but do not seem to be generally applicable. In short, the problem of generally applicable sorption coefficients remains unsolved.

It is therefore recommended to use the existing coefficients with caution. Furthermore, a set of coefficient more generally applicable for various conditions should be found. The set should than be tested in order to derive the corresponding applicability range. A preliminary search for a common sorption coefficients has been performed using the Sorption Model 1. The results are described in the next section.

3.12.49 FP Sorption Tests - Sorption Model 1

This section presents results of the sorption validation tests:

- Laminar Test Loop (sections 3.12.49.1 and 3.12.49.2)
- Vampyr experiments (section 3.12.49.3)
- Dragon experiments (section 3.12.49.4)

Calculations presented in this section were performed with the Sorption Model 1 (SPECTRA model). Results are compared to the experimentally measured values. For the purpose of the present calculations the adsorption and desorption coefficients used by the Model 1 were derived to match the experimentally measured values.

A drawback of the sorption test analyses described in the previous section was the necessity of using different sorption coefficients for different experiments. In the present task a single set of coefficients was developed for the Model 1 and all experiments were recalculated with the same coefficients. The applied sorption coefficients $A_S(T)$ and $B_S(T)$ are presented below. The maximum concentration $C_{sat}(T)$ was not used (the value was set to a large number - 1.0).

- Cs on Incoloy 800 (Figure 3-993):

$$A_S(T_w) = 3.6\times10^{-17}\cdot\exp\left(\frac{23{,}000}{T_w}\right) \qquad 10^{-2} \le A_S(T_w) \le 10^{-1}$$

$$B_S(T_w) = 1.0\times10^{-10}$$

- Ag on Incoloy 800 (Figure 3-994):

$$A_S(T_w) = 2.0\times10^{-21}\cdot\exp\left(\frac{39{,}000}{T_w}\right) \qquad 10^{-5} \le A_S(T_w) \le 10^{-1}$$

$$B_S(T_w) = 1.0\times10^{-10}$$

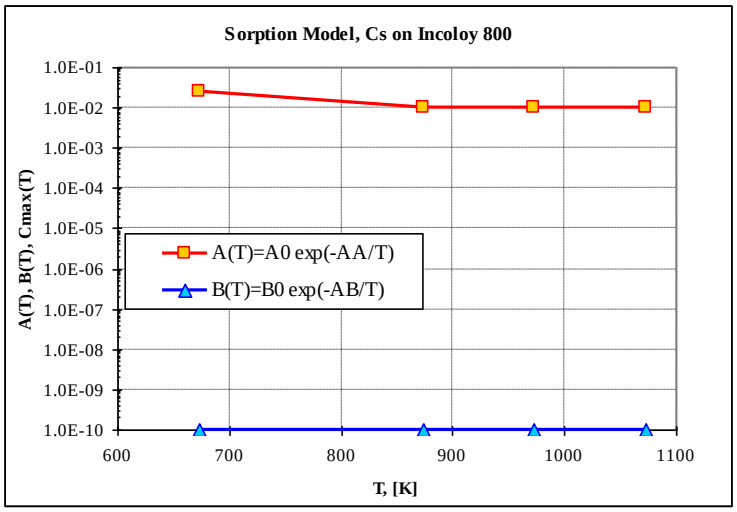

Figure 3-993 Sorption coefficients for Cs on Incoloy 800

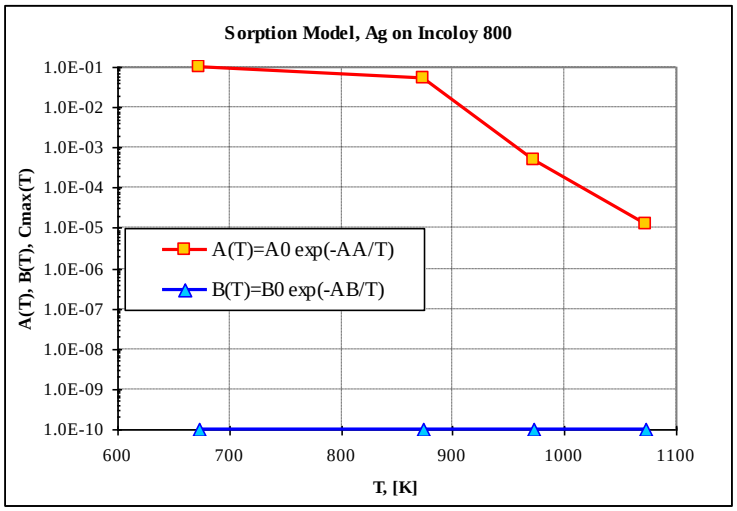

Figure 3-994 Sorption coefficients for Ag on Incoloy 800

- Cs on Inconel 617 (Figure 3-995):

$$A_S(T_w) = 1.0 \times 10^{-2} \cdot \exp\left(-\frac{1{,}400}{T_w}\right) \qquad 10^{-5} \le A_S(T_w) \le 10^{-1}$$

$$B_S(T_w) = 1.0 \times 10^{-10}$$

- Ag on Inconel 617 (Figure 3-996):

$$A_S(T_w) = 1.2 \times 10^{-16} \cdot \exp\left(\frac{29{,}000}{T_w}\right) \qquad 10^{-5} \le A_S(T_w) \le 10^{-1}$$

$$B_S(T_w) = 1.0 \times 10^{-10}$$

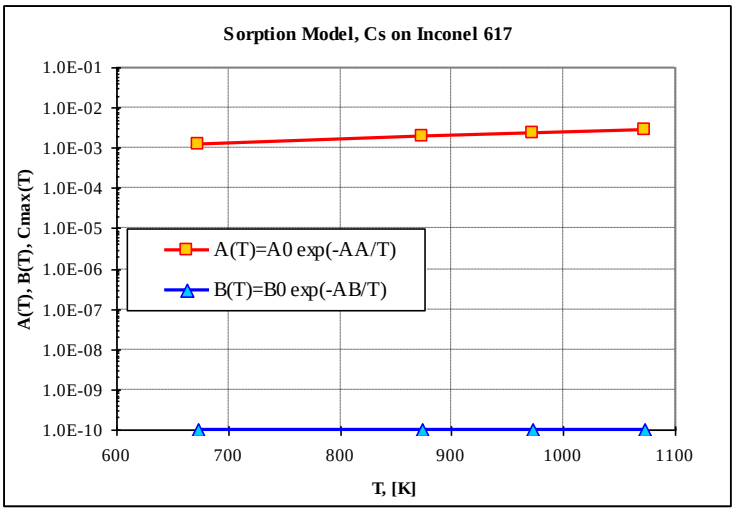

Figure 3-995 Sorption coefficients for Cs on Inconel 617

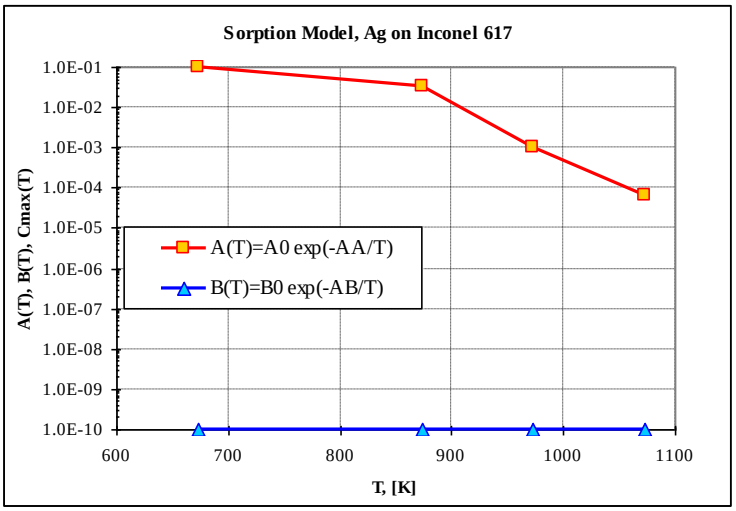

Figure 3-996 Sorption coefficients for Ag on Inconel 617

The total sorption flux is equal to:

$$\left(\frac{dC_S}{dt}\right)_{total} = A_S(T_w)\cdot C_V - B_S(T_w)\cdot C_d$$

$(dC_S/dt)_{total}$	total sorption mass transfer rate, (kg/(m^2-s))
C_V	concentration of the vapor in the gas space (kg/m^3)
C_d	concentration of the vapor in the material (kg/m^3)

Two cases are considered:

- Case 1 Negative values permitted for total sorption flux $(dC_S/dt)_{total} <> 0$
- Case 2 Negative values of the total sorption flux not permitted $(dC_S/dt)_{total} \geq 0$

3.12.49.1 FP Sorption Tests - Laminar Loop Experiment 4 (Run-4)

The input file for the base case and the alternative sorption coefficients are stored in:
`Z-INPUTS\RT\Sorption-Tests\LAMINAR\Run-4\Sorption-Model-1`

- `Run-4.SPE` Negative values permitted for total sorption flux
- `Run-4-2.SPE` Negative total sorption flux not permitted

Results are shown in Figure 3-997 and Figure 3-998. Figure 3-997 show visualization picture obtained at the end of the Run-4. Figure 3-998 shows comparison with measured data. Results obtained with the negative sorption flux (Run-4.SPE) are closer to the experimental data. The results of Run-5-2.SPE give of course higher activities. Both results are in reasonably good agreement with experiment. The sorption model applied in Run-4-2 is recommended for conservative analyses.

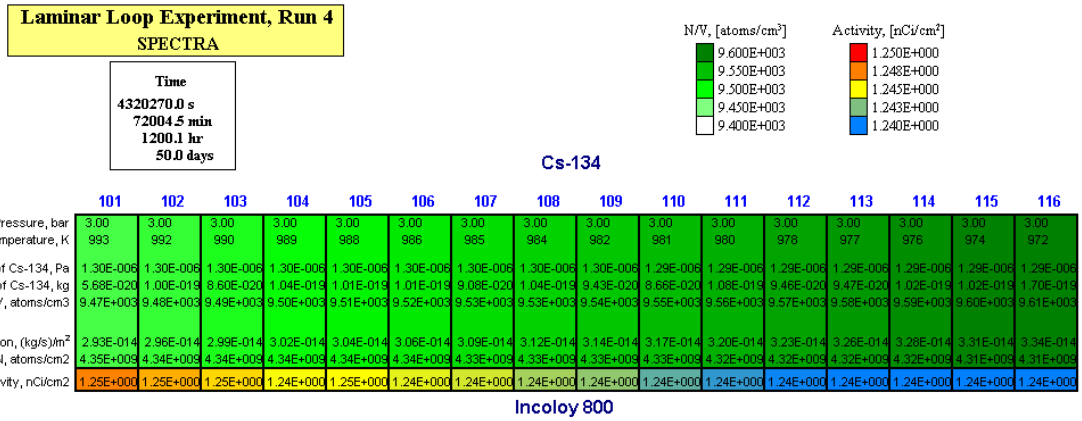

Figure 3-997 Laminar Loop Tests - Run 4, Cs-134 on Incoloy 800 (Run-4-B-1)

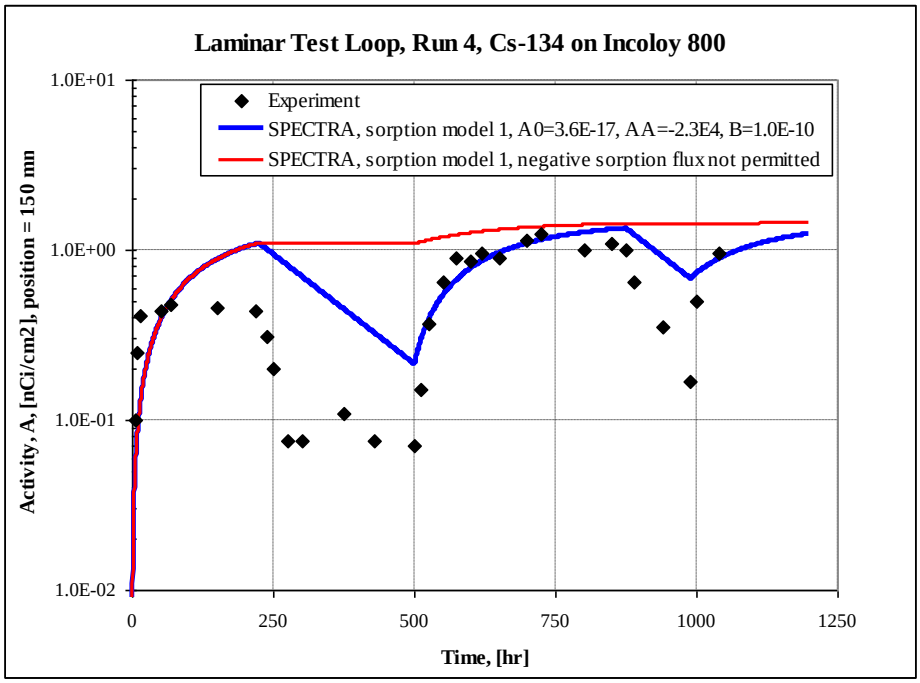

Figure 3-998 Laminar Loop Tests - Run 4, Cs-134 on Incoloy 800 [95]

3.12.49.2 FP Sorption Tests - Laminar Loop Experiment 4 (Run-7)

The input file for the base case and the alternative sorption coefficients are stored in:
`Z-INPUTS\RT\Sorption-Tests\LAMINAR\Run-7\Sorption-Model-1`

- `Run-7.SPE` Negative values permitted for total sorption flux
- `Run-7-2.SPE` Negative total sorption flux not permitted

Results are shown in Figure 3-999 and Figure 3-1000. Figure 3-999 shows visualization picture obtained at the end of the Run-7. Figure 3-1000 shows comparison with measured data. Both results give reasonably good agreement with experiment. The calculated values are somewhat below the measured data. To obtain a conservative bounding case the adsorption coefficient was increased to $A_S(T_w) = A_0 = 2.0\times10^{-2}$.

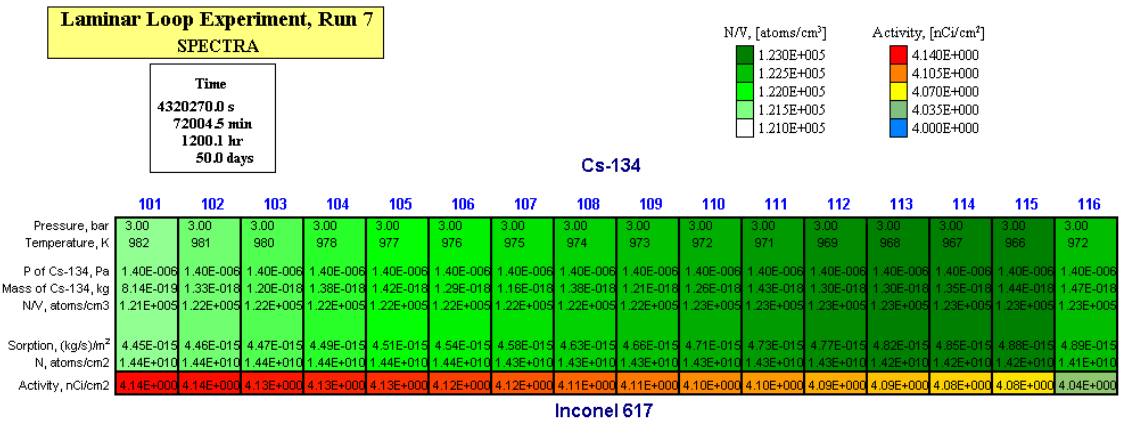

Figure 3-999 Laminar Loop Tests - Run 7, Cs-134 on Inconel 617 (Run-7-B-1)

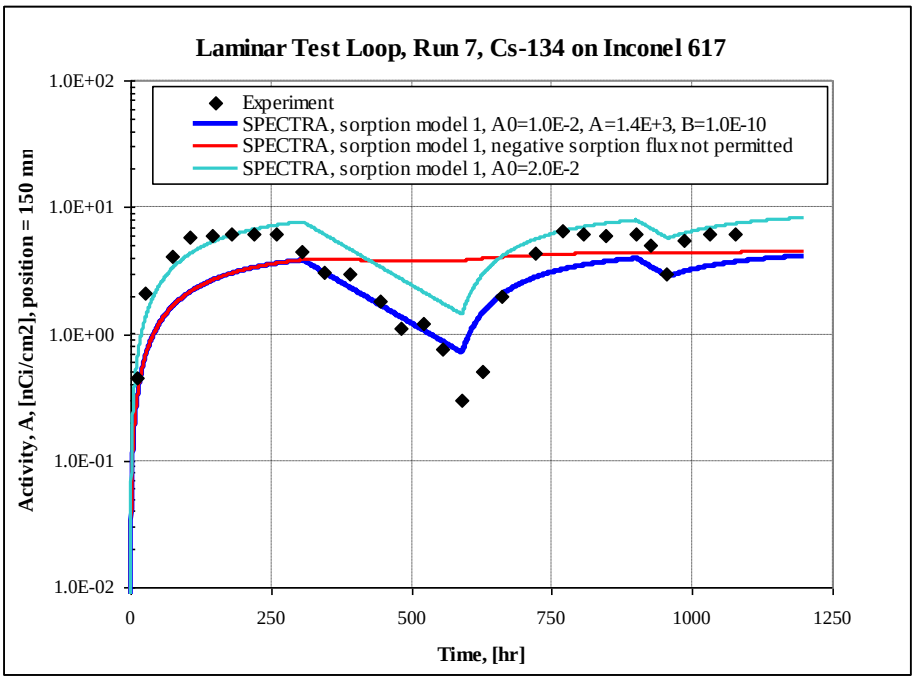

Figure 3-1000 Laminar Loop Tests - Run 7, Cs-134 on Inconel 617 [95]

3.12.49.3 FP Sorption Tests - Vampyr II/V01 Experiment

The input file for the base case and the alternative sorption coefficients are stored in:
`Z-INPUTS\RT\Sorption-Tests\VAMPYRE\Sorption-Model-1`

- `VampyrII-V01.SPE` Negative values permitted for total sorption flux
- `VampyrII-V01-2.SPE` Negative total sorption flux not permitted

Results are shown in Figure 3-1001 through Figure 3-1006. Figure 3-1001 and Figure 3-1002 show visualization pictures obtained for the VampyrII-V01 run at the end of the test.

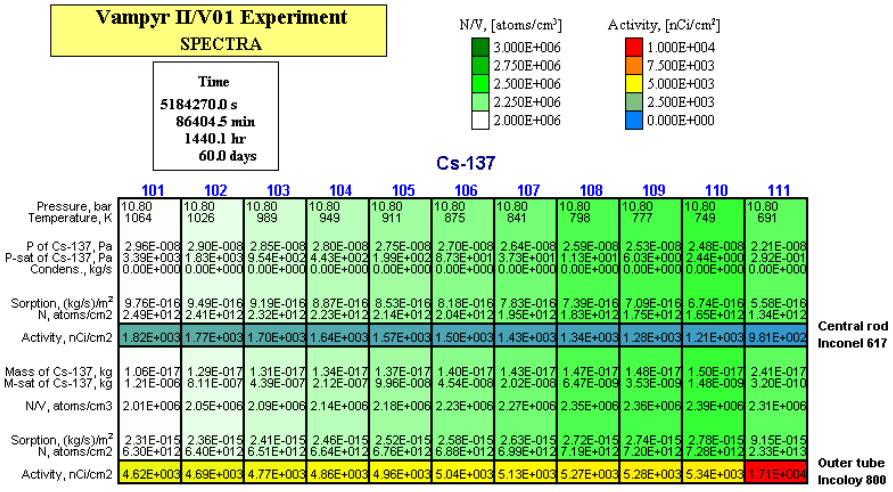

Figure 3-1001 Vampyr II/V01 experiment, Cs-137 on Incoloy 800 and Inconel 617

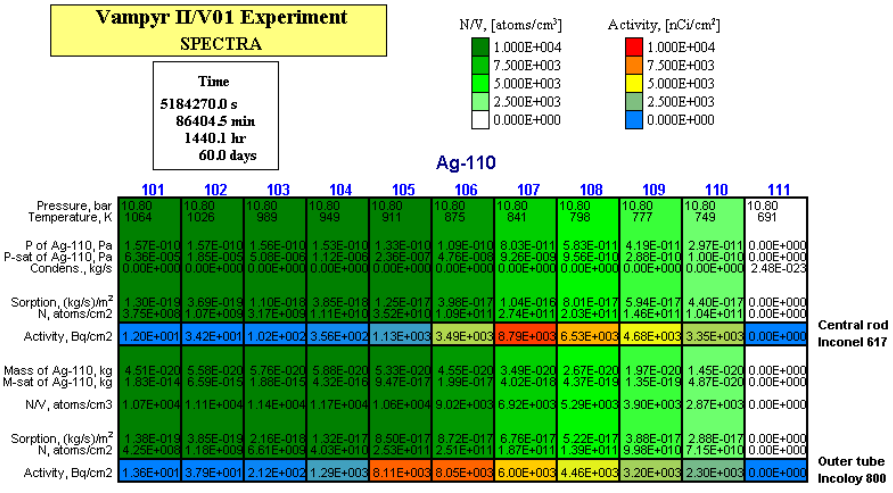

Figure 3-1002 Vampyr II/V01 experiment, Ag-110 on Incoloy 800 and Inconel 617

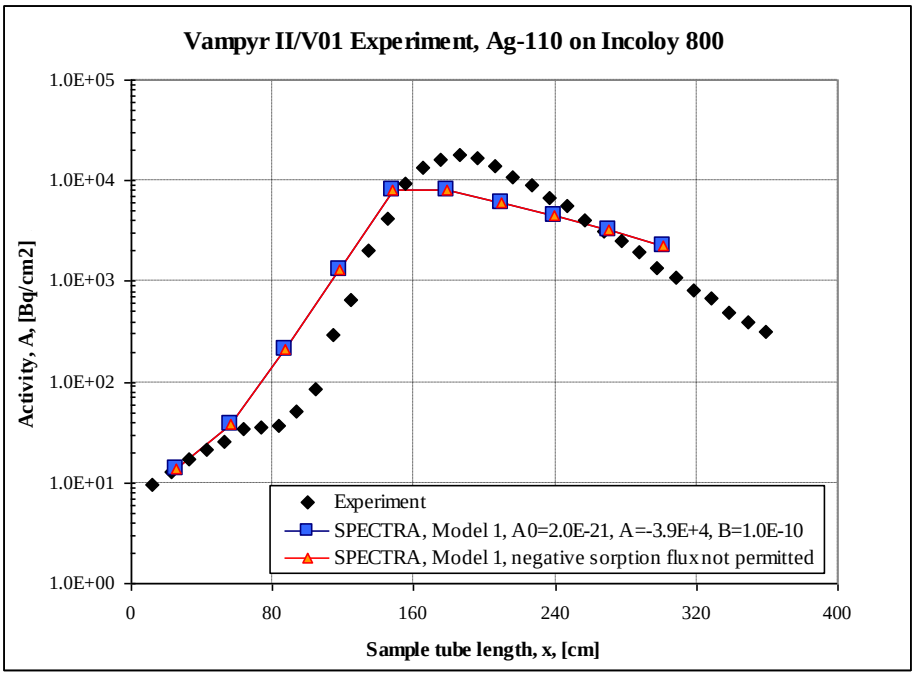

Figure 3-1003 Vampyr II/V01 experiment, Ag-110 on Incoloy 800

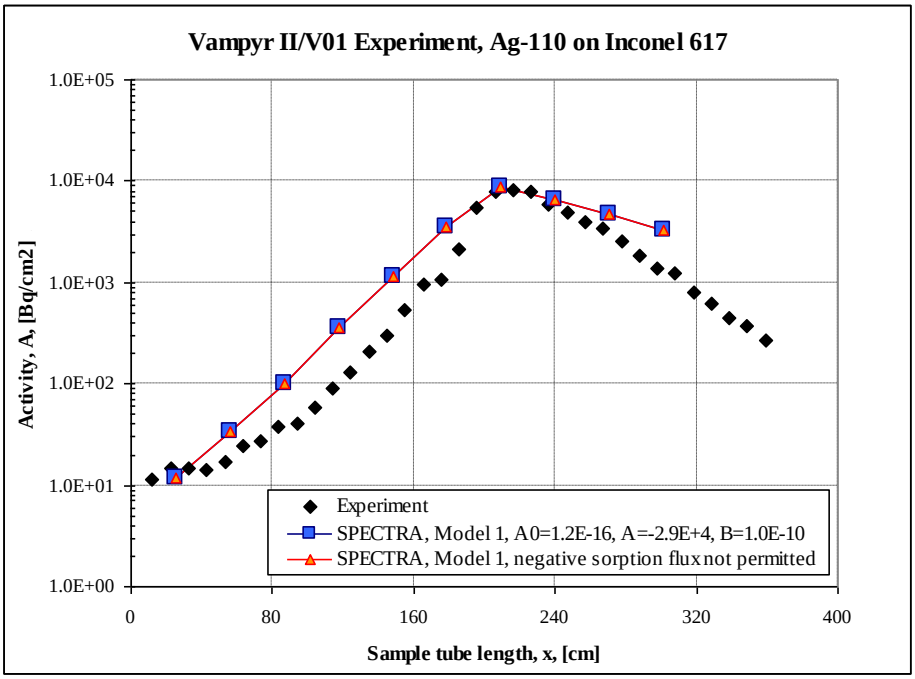

Figure 3-1004 Vampyr II/V01 experiment, Ag-110 on Inconel 617

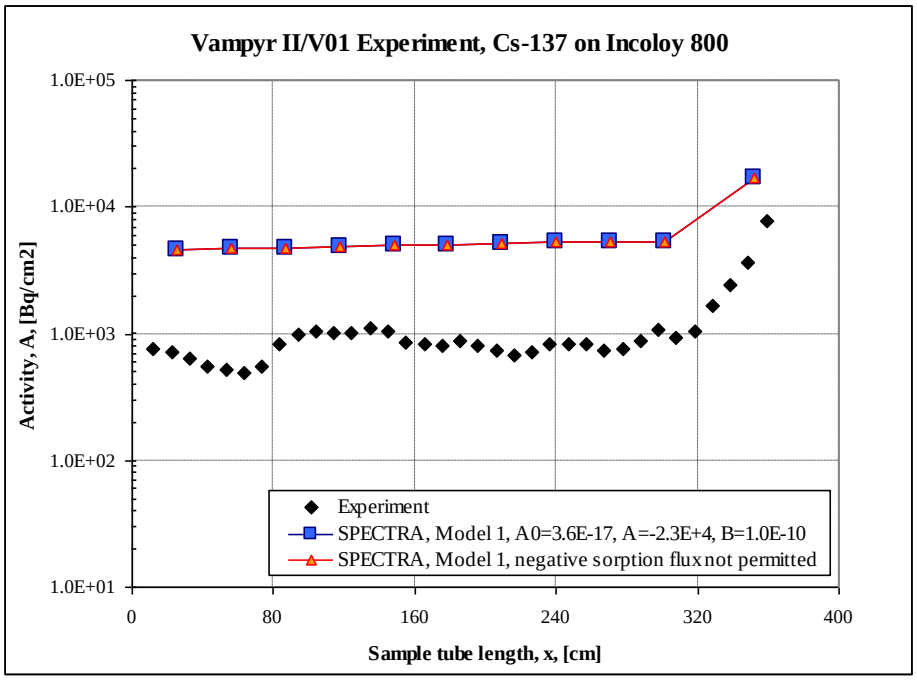

Figure 3-1005 Vampyr II/V01 experiment, Cs-137 on Incoloy 800

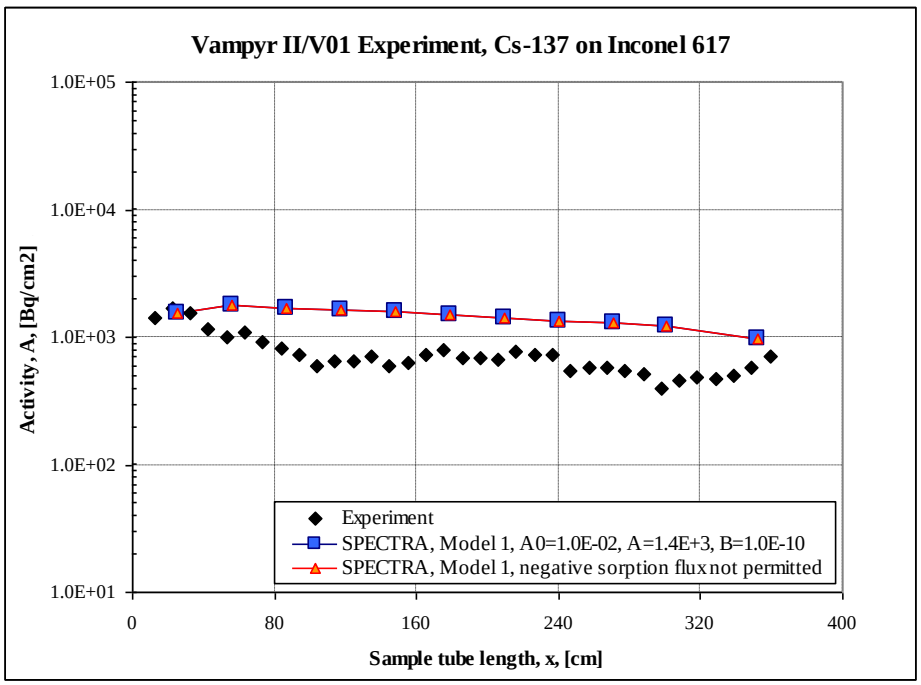

Figure 3-1006 Vampyr II/V01 experiment, Cs-137 on Inconel 617

The following four figures show comparisons with measured data for:

- Ag-110 on Incoloy 800 - Figure 3-1003
- Ag-110 on Inconel 617 - Figure 3-1004
- Cs-137 on Incoloy 800 - Figure 3-1005
- Cs-137 on Inconel 617 - Figure 3-1006

The results are in quite good agreement with measurement.

3.12.49.4 FP Sorption Tests - Dragon Experiment

The input file for the base case and the alternative sorption coefficients are stored in:
`Z-INPUTS\RT\Sorption-Tests\DRAGON\Sorption-Model-1`

The input files are:

- `Dragon.SPE` Negative values permitted for total sorption flux
- `Dragon-2.SPE` Negative total sorption flux not permitted

Results are shown in Figure 3-1007 through Figure 3-1014. Results obtained with the first run are shown in Figure 3-1008 through Figure 3-1011. Comparison of the FP vapor pressure history (Figure 3-1009) with the surface activity (Figure 3-1010) shows that a significant desorption is observed when the vapor concentration decreases (see the sorption flux in Figure 3-1011). As a consequence the final activity is very low - about 3 nCi/cm^2 - Figure 3-1008. This is two orders of magnitude smaller than the measured value, which is about 300 nCi/cm^2.

Results obtained with the second run are shown in Figure 3-1012 through Figure 3-1014. This In this case there is no desorption. The sorption flux is always positive of zero (Figure 3-1014). The surface activity is almost constant after the decrease of vapor concentration at about 2.1×10^7 s - Figure 3-1013. A slow decrease of the activity visible in Figure 3-1013 is due to radioactive decay of Cs-137. Note that Cs-137 is a long-life isotope with a decay constant of $\lambda = 7.33.\times10^{10}$ s^{-1}. The final activity is about 100 nCi/cm^2 (Figure 3-1012) which is still a factor of 3 smaller than measured but is much closer than the first case.

Summarizing it is to be said that the search for a single set of coefficients that would be capable of reproducing the three sets of experiments (Laminar Loop, Vampyr, Dragon) has failed because of a difficulty in correct representation of the Dragon test. This work should be continued in the future.

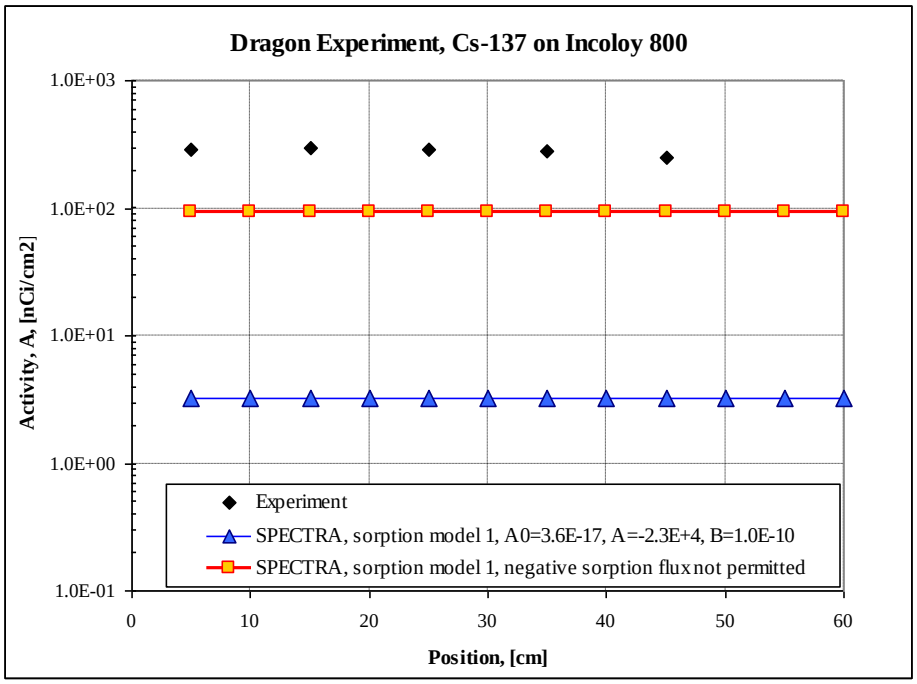

Figure 3-1007 Dragon experiment, Cs-137 on Incoloy

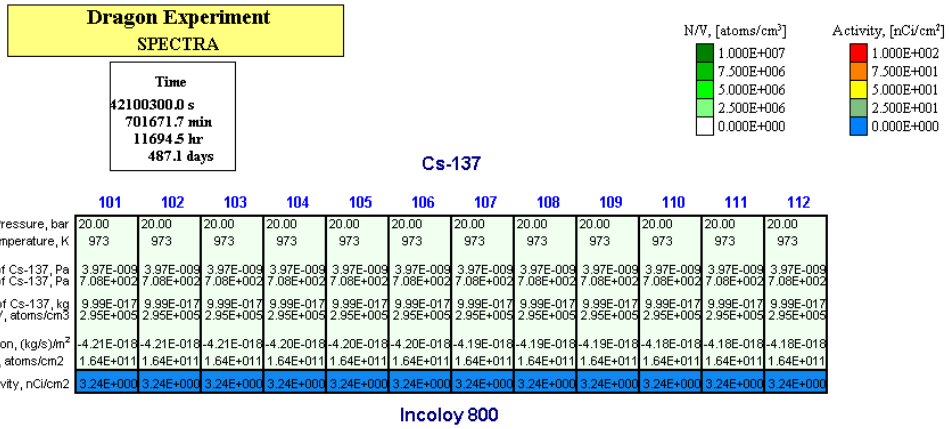

Figure 3-1008 Dragon experiment, base model

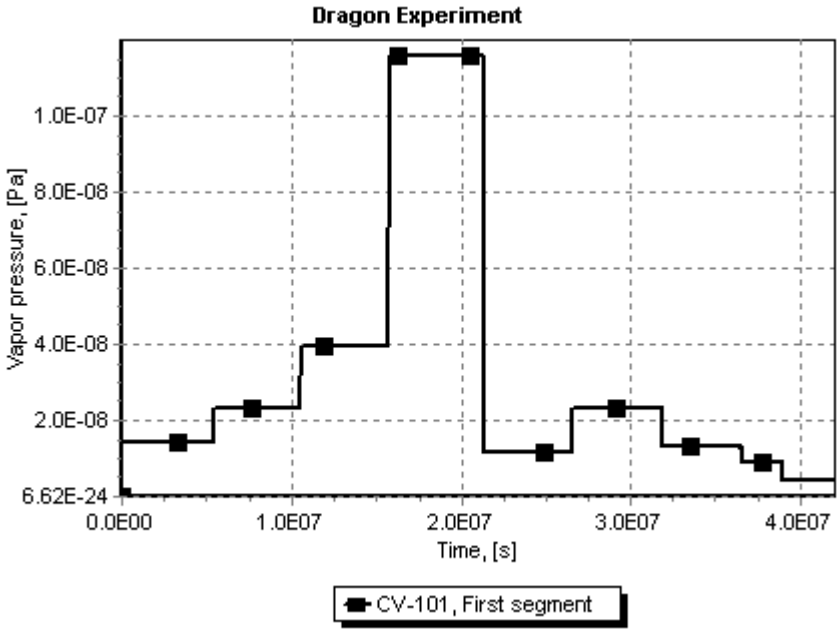

Figure 3-1009 Cs vapor pressure, Dragon experiment, base model

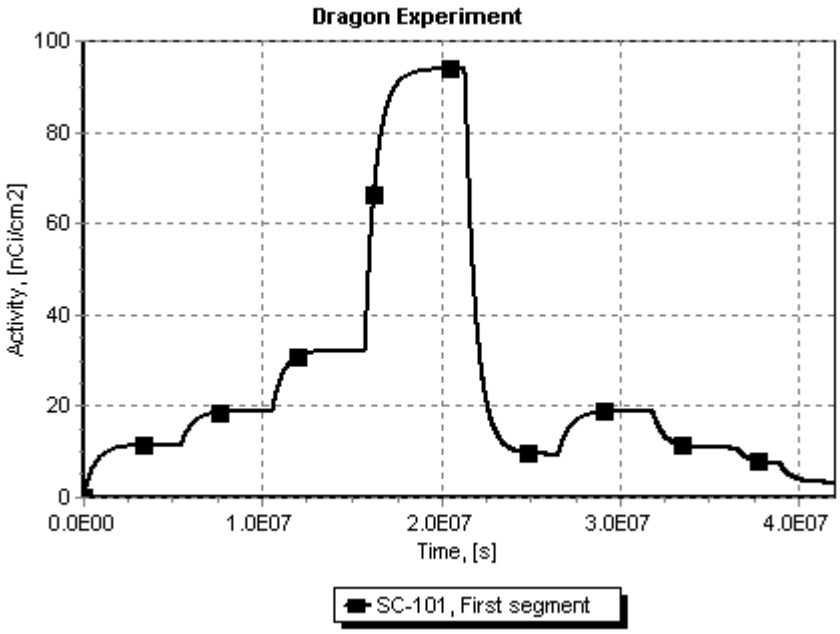

Figure 3-1010 Cs activity, Dragon experiment, base model

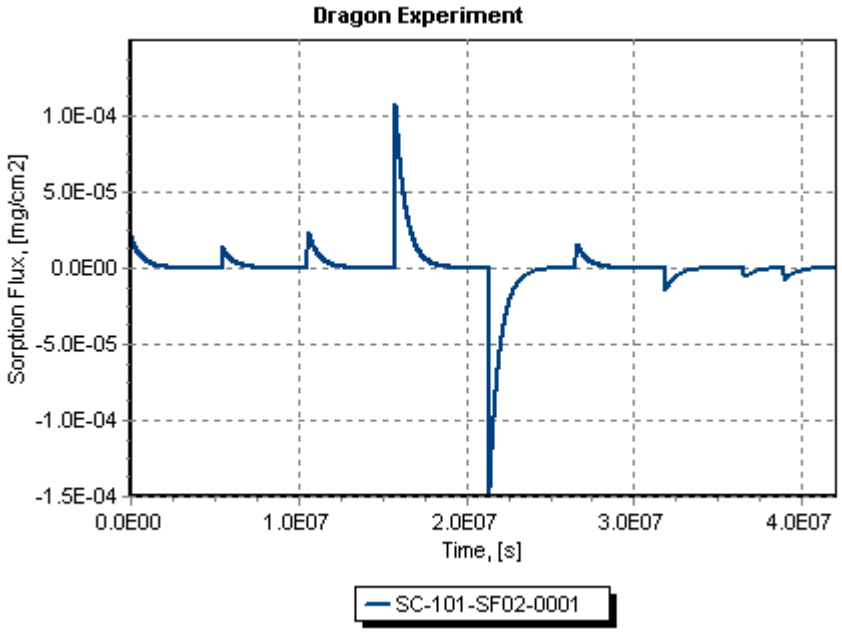

Figure 3-1011 Cs sorption flux, Dragon experiment, base model

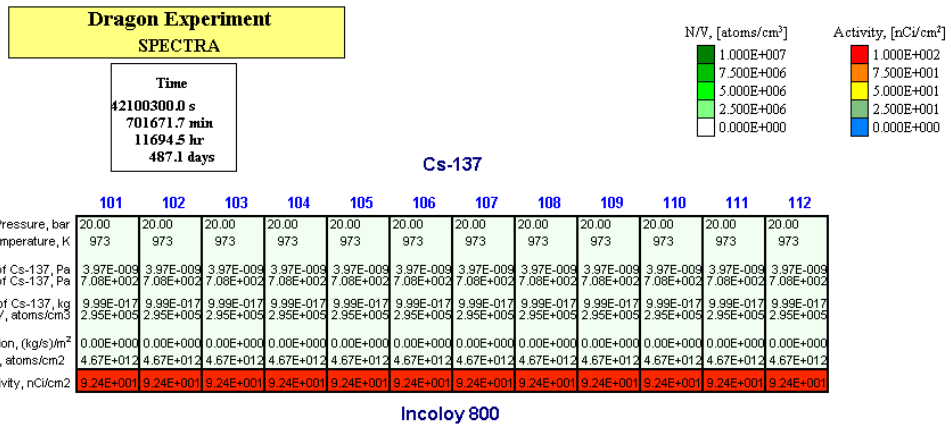

Figure 3-1012 Dragon experiment, negative sorption flux not permitted

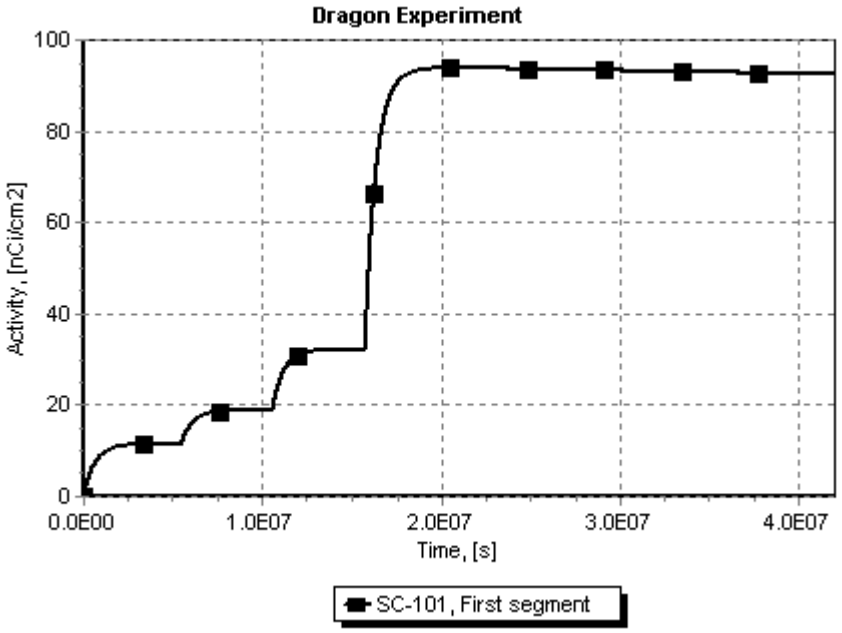

Figure 3-1013 Activity, Dragon experiment, negative sorption flux not permitted

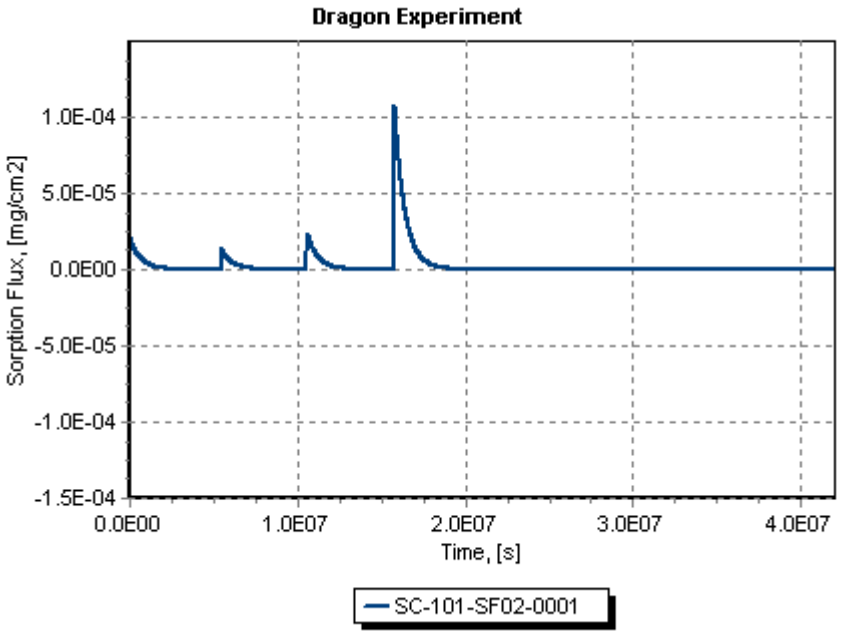

Figure 3-1014 Sorption flux, Dragon experiment, negative sorption flux not permitted

3.12.49.5 Summary of the Sorption Validation Tests

Three experiments have been analyzed to perform code validation on sorption model. These are:

- Laminar Loop (L-L) experiments (Run-4 and Run-7)
- Vampyr II/V01 (V-II) experiment
- Dragon (D) experiment.

The results are summarized as follows:

- The selected sorption coefficients provide a good agreement with the L-L tests and the V-II experiment.
- In case of D experiment the selected sorption coefficients result in activities too low by 2 orders of magnitude compared to experimental data. Results indicate that the desorption is responsible for this discrepancy. Results are much closer to experiment if desorption is prevented (by selecting an appropriate option).
- The present search for a single set of coefficients that would be capable of reproducing the three sets of experiments (L-L, V-II, D) has failed because of a difficulty in correct representation of the Dragon test. This work should be continued in the future.

3.12.50 Transport of FP Vapors Adsorbed on Aerosol Particles

The STORM test (section 3.12.30) was used to test the transport of the isotopes attached to the aerosol particles. The experimental setup is described in section 3.12.30. The case with the mechanistic resuspension model with all resuspension parameters equal to their default values and relative humidity of 1.0 was used - see section 3.12.30. For the present calculation it was assumed that the aerosol particles contain a non-radioactive isotope Xe-131 (isotope number 016). The mass fraction of this isotope in the incoming particles is 0.1. Transport of this aerosol-bound isotope during deposition and resuspension phase of the STORM test is investigated.

Since Xe-131 is non-radioactive, the correct solution of the mass fractions of this isotope in the deposited and the resuspended aerosol particles must be constant and equal to 0.1. The input file for this run is provided in:
`\Z-INPUTS\RT\Res-STORM-FP\Mechanistic 1\STORM-M1A1-FP1.SPE.`

Results are shown in Figure 3-1015, Figure 3-1016, and Figure 3-1017. The mass fractions of Xe-131 are everywhere the same as seen in Figure 3-1015 and Figure 3-1016. The mass fraction does not change in time, as seen in Figure 3-1017. In the time period when there are no aerosols at all (~10,000 to ~11,000 s) the isotope fraction cannot be calculated and zeroes are plotted in Figure 3-1017.

Results shown above were obtained using a normal solution procedure (with Courant limit) during the resuspension steps and larger time steps (10.0 s) "far" from the resuspension steps. During the resuspension steps the time step was limited by the Courant Limit of order of 10^{-2} s. An advantage of the RT Package is the possibility of obtaining solution even with extremely large time steps are permitted (10^3 s ÷ 10^5 s) when the thermal-hydraulic conditions do not change.

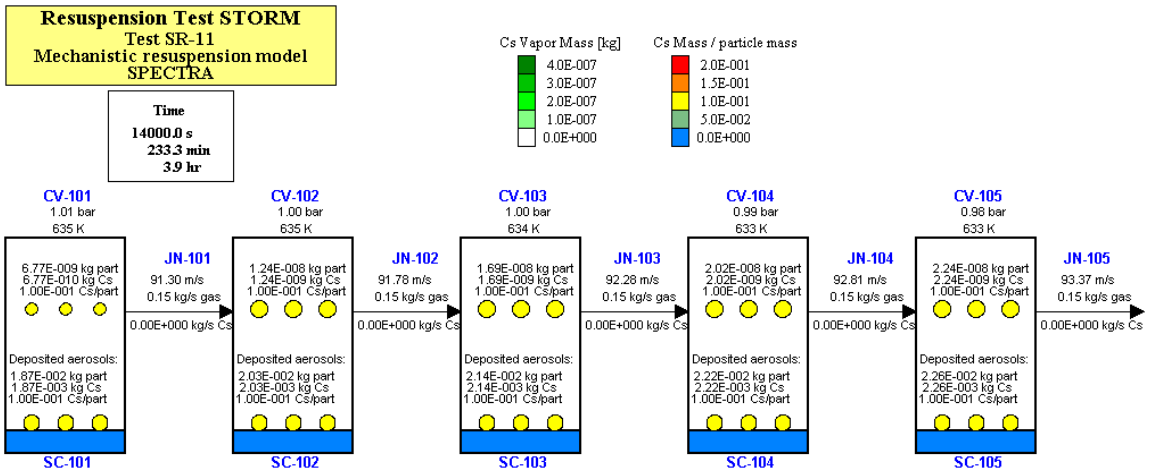

Figure 3-1015 STORM SR11 test, Xe-131 on aerosol particles, *t* = 14,000 s

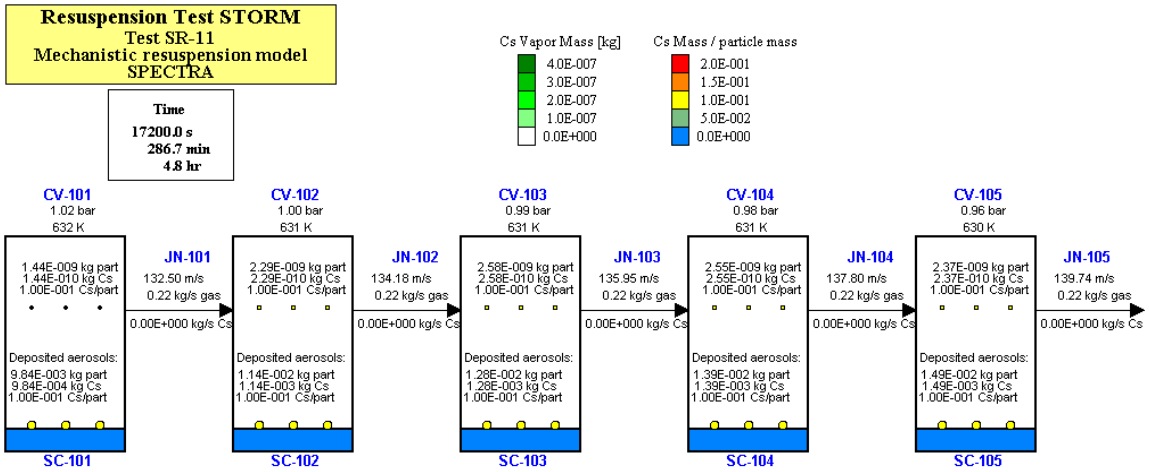

Figure 3-1016 STORM SR11 test, Xe-131 on aerosol particles, *t* = 17,200 s

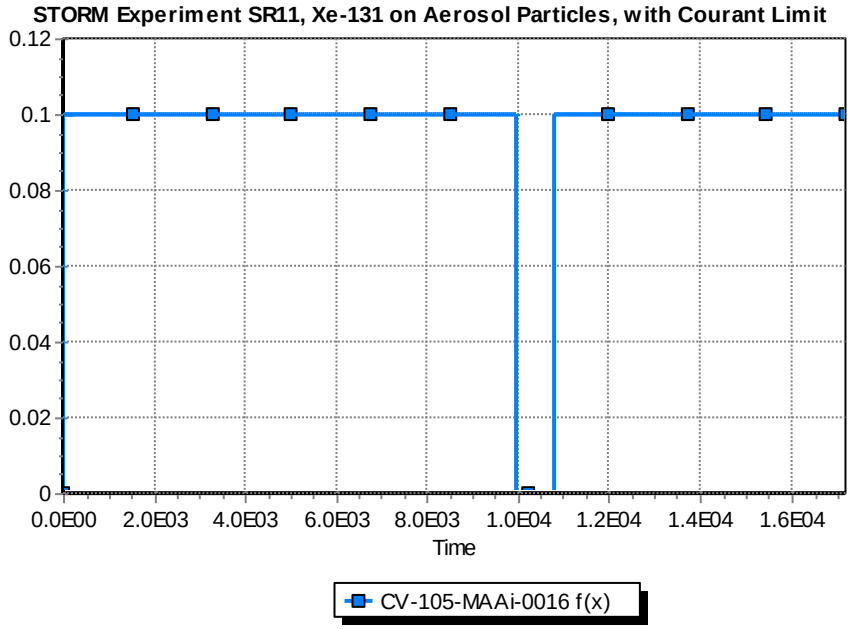

Figure 3-1017 STORM SR11 test, Xe-131 fractions on aerosol particles

Further testing of transport of fission products on aerosols is performed based on the Oak Ridge data and the AVR data. These calculations are described in the following sections.

3.12.51 Oak Ridge Data

Sorption data for Iodine I-131 on different surfaces is available in the review of fission product plateout and liftoff in MHTGR systems, performed at Oak Ridge and documented in reference [114]. The data available there include:

- Sorption of I-131 on graphite
- Sorption of I-131 on steel
- Sorption of I-131 on dust

The results are presented below. First the Langmuir isotherm is discussed. Next, SPECTRA calculations for the graphite, steel, and dust, are described in the following three sub-sections.

3.12.51.1 Langmuir Isotherm

The sorption process is described in reference [114] by making use of the Langmuir isotherm. Written for an *i*-th isotope out of a total of *N* isotopes, it has the form:

$$C_{S,i} = \frac{LKP_i}{1 + K\sum_{i=1}^{N} P_i}$$

$C_{S,i}$ surface concentration of the sorbed isotope *i*, (mol/m^2)
P_i partial pressure of the isotope *i* in equilibrium with $C_{S,i}$, (Pa)
L concentration of the sorption sites, (kg/m^2)
K sorption equilibrium constant, (Pa^{-1})

The term $\sum P_i$ is the element partial pressure summed for all isotopes. Therefore, whenever $\sum P_i$ is significant compared with unity, the sorbed concentration of the isotope *i* is coupled with sorbed concentrators of all other isotopes. In such case the transport behavior of, say, I-131, must be solved simultaneously with other isotopes. It has been shown in [114] that for iodine in the MHTGR primary system: $K\sum P_i \ll 1$, which results in simplification:

$$C_{S,i} = LKP_i$$

The above equation applies in the so-called Henrian regime. The surface coverage, $C_{S,i}$, is in this regime proportional to the partial pressure P_i, and independent of other isotopes, which provides a considerable computational simplification.

Construction of a Langmuir isotherm is quite simple, and is illustrated in Figure 3-1018. For pressures above $1/K$ the surface concentration (surface load) is equal to L. For pressures lower than $1/K$, the load increases linearly with pressure. Figure 3-1018 shows a Langmuir isotherm for $L=10^{-5}$, $K=10^4$.

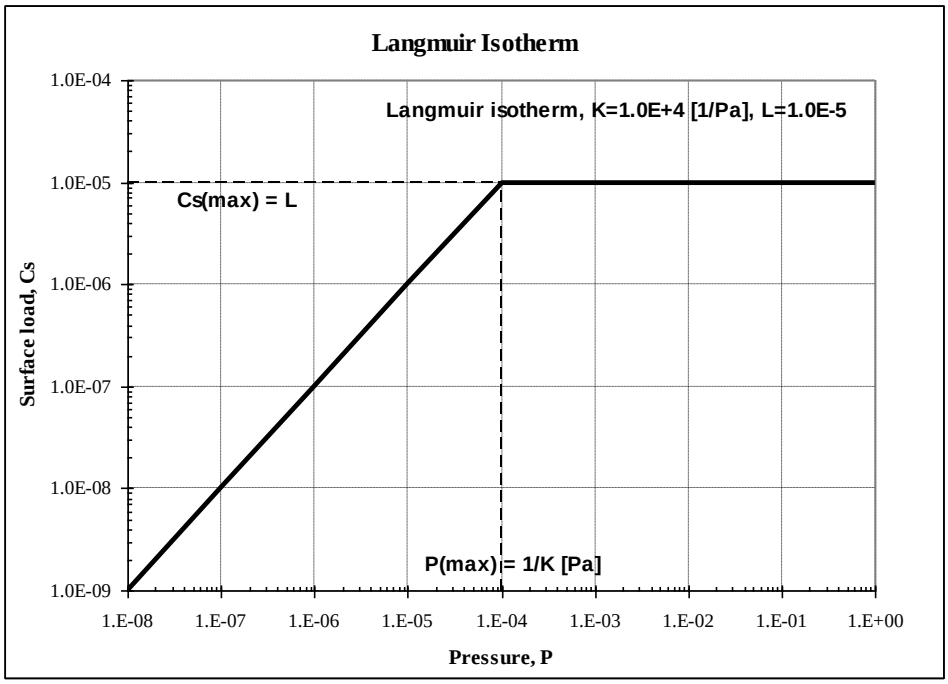

Figure 3-1018 Langmuir isotherm

There are several key features of the Langmuir isotherm, worth remembering:

- Pressure at which line becomes flat is given by:

$$P_{\max} = \frac{1}{K}$$

- Maximum surface concentration:

$$C_{S,\max} = L$$

- The ratio between the surface concentration and the vapor concentration (the slope) of the left part of the curve is given by:

$$\frac{C_S}{P} = KL$$

Of course the Langmuir isotherm gives only an equilibrium value, so there is no information about the time dependency of the sorption process. For example, suppose the vapor pressure is constant and equal to 10^{-5}. The Langmuir isotherm shown in Figure 3-1018 (L=10^{-5}, K=10^{4}) predicts the equilibrium surface load of $C_S = 10^{-6}$. When a surface is subjected to a constant vapor pressure, the sorbed concentration will reach that equilibrium with a certain time constant, as illustrated in Figure 3-1019.

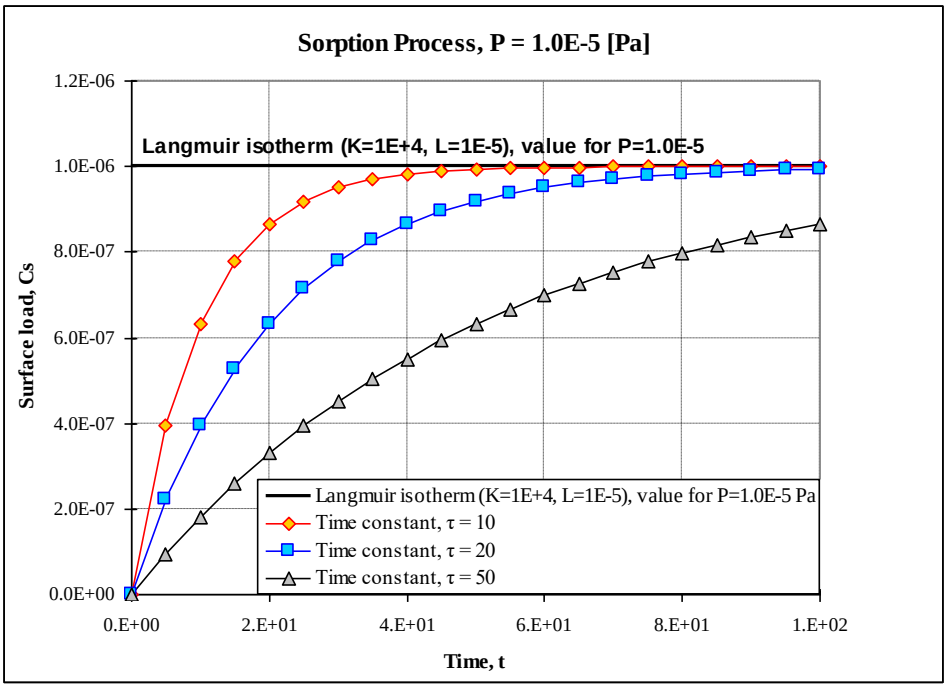

Figure 3-1019 Time-dependent surface concentrations.

The information which line adequately represents reality is not available from the Langmuir isotherm and therefore the user has a certain degree of freedom in choosing the coefficients in the sorption model equation. This problem is further discussed in the next section.

3.12.51.2 Sorption of I-131 on Graphite

Out of the two sorption models available in SPECTRA, the simpler Sorption Model 1 was used. The available data is provided as equilibrium data - see the discussion of the Langmuir isotherm above. This means the data gives a relation between the isotope concentration in the gas and on the surface in the equilibrium conditions. There is no information as to how quickly the equilibrium condition is reached, in other words, what is the time constant of the process. Therefore even the simpler sorption model requires more data than is available and one of the model constants has to be assumed based on an engineering judgment, as will be shown below.

The equation of the Sorption Model 1 is (see Volume 1):

$$S = A(T) \cdot C_V - B(T) \cdot C_d$$

C_V isotope concentration in the gas (kg/m^3), with a maximum limit of C_{sat}, $C_V \leq C_{sat}$.
C_d surface concentration (kg/m^2)
S sorption flux (kg/m^{2}s)
A, B temperature-dependent coefficients

Note that for C_d the user may choose either the surface concentration in kg/m^2 or the penetrated concentration in kg/m^3 (see Volume 2). To represent the available data the option with kg/m^2 is obviously a better choice. In the literature the Langmuir isotherm is populated with pressure (Pa) and equilibrium load in (mol/m^2). Therefore the first step is to convert these parameters into the parameters used by SPECTRA, i.e. (kg/m^3) and (kg/m^2) respectively:

- Pressure, P (Pa) → vapor concentration (density), C_V (kg/m^3)
- Surface load, C_S, (mol/m^2) → surface concentration, C_d (kg/m^2)

Conversion from the pressure to the vapor density is:

$$C_V = \left(\frac{1}{RT}\right) \cdot P$$

Here T is temperature and R is the gas constant, equal to R_u/M, where R_u is the universal gas constant, equal to 8314.5 (J/kmol K), and M is the molar weight. For I-131 $M_{I\text{-}131}$ = 131 (kg/kmol) and R = 63.4 (J/kg K).

Conversion of the surface concentration from C_S in (mol/m^2) to C_d in (kg/m^2) is done using the molar weight, M:

$$C_d = \left(\frac{M}{1000}\right) \cdot C_S$$

The Langmuir isotherm for graphite is available for T = 400˚C = 673 K [114]. The coefficients are:

L = 6.9×10^{-7} mol/m^2	×(131/1000)	= 9.04×10^{-8} kg/m^2
K = 1.2 Pa^{-1}	×(63.5×673)	= 5.13×10^4 m^3 /kg

The Langmuir isotherm for graphite is drawn in Figure 3-1020. As a next step the sorption model coefficients needed by SPECTRA must be selected. As mentioned in the section above, the model requires more data than can be derived from the Langmuir isotherm. The characteristic time for the process cannot be deduced from the equilibrium data. The user has therefore a certain degree of freedom in selecting the coefficients. The discussion below illustrates how the coefficients may be chosen.

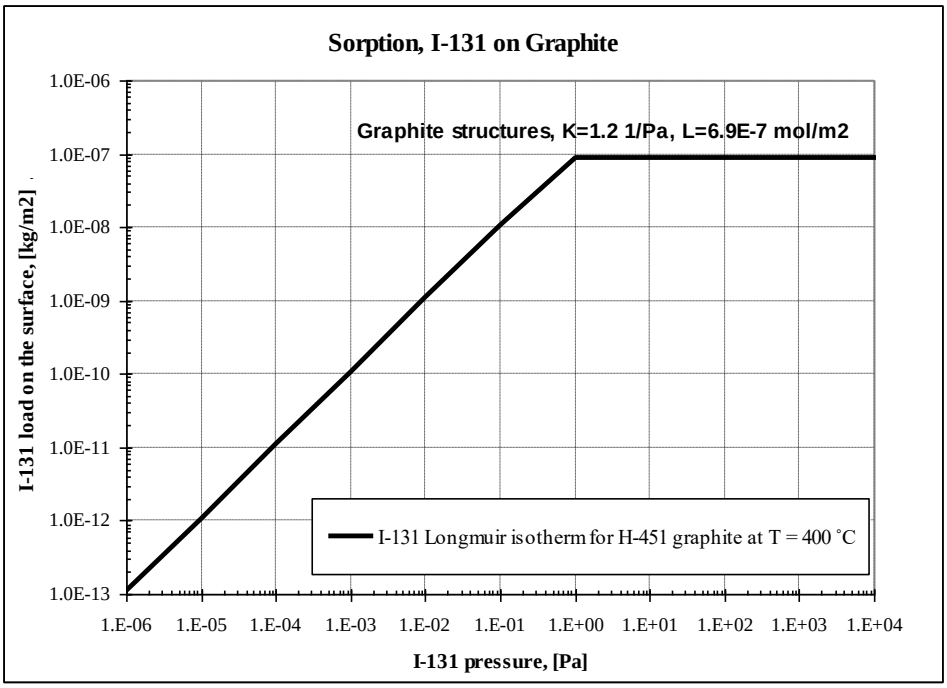

Figure 3-1020 Sorption isotherm for graphite

Equilibrium means that the source due to adsorption and removal due to desorption as well as radioactive decay are equal. Suppose that the radioactive decay is very small (the half-life of say thousands of years). In such case of the radioactive decay may be neglected and the source due to adsorption equals the removal due to desorption:

$$A(T) \cdot C_V = B(T) \cdot C_d$$

This leads to the following relation between the surface concentration and the vapor concentration:

$$\frac{C_d}{C_V} = \frac{A(T)}{B(T)}$$

The Langmuir isotherm gives (see section 3.12.51.1):

$$\frac{C_S}{P} = KL$$

Therefore the ratio of *A* and *B* should be equal to:

$$\frac{A(T)}{B(T)} = KL$$

The user may select one of the coefficients, *A* or *B*. The other coefficient must be obtained from the above relation. With increasing value of both coefficients the process becomes faster, that means the characteristic time to reach equilibrium, τ, becomes shorter - Figure 3-1019

This above discussion concerns cases when the radioactive decay is very slow. For short lived isotopes the radioactive decay has a significant contribution and may be as strong or even stronger than desorption. In case of I-131 the half-life is about 8 days, which is relatively short. Therefore, as a first step the desorption is neglected, by setting:

$$B(T) = 0.0$$

In such case the adsorption is balanced mainly by the radioactive decay, and:

$$A(T) \cdot C_V = \lambda N \cdot \left(\frac{M}{N_A} \right)$$

λ decay constant (1/s)
N number of molecules of the radioactive isotope per unit surface area (1/m^2)
N_A Avogadro number, equal 6.02×10^{26} (1/kmol)
M molar weight, (kg/kmol)

Therefore:

$$A(T) \cdot C_V = \lambda \cdot C_d$$

and

$$\frac{C_d}{C_V} = \frac{A(T)}{\lambda}$$

Since the ratio of surface concentration to volume concentration is equal to *KL* (see discussion of the Langmuir isotherm - section 3.12.51.1), this means:

$$A(T) = \lambda KL$$

For I-131 $\lambda = 1.0\times10^{-6}$ (s^{-1}). Therefore: $A(T) = (1.0\times10^{-6})\ (9.04\times10^{-8})\ (5.13\times10^{4}) = 4.63\times10^{-9}$.

Since the available data is known for one temperature only ($T = 400^{\circ}$C), the temperature dependence of *A* cannot be obtained. Therefore a constant value of *A* is used. In SPECTRA $A(T)$ is given by:

$$A(T) = A_0 \cdot \exp\left(-\frac{A_A}{T} \right)$$

In order to obtain a constant value one needs to set A_A to zero and A_0 to the desired constant value, in this case 4.6×10^{-9}. Finally the value of C_{sat} is needed. The value is equal to $1/K$ in the appropriate units:

$$C_{sat} = 1/K$$

Therefore C_{sat} =1/(5.13×10^4) = 1.95×10^{-5} (kg/m^3). The following values were used for the calculations:

- A_0 = 4.6×10^{-9} m/s
- C_{sat} = 2.0×10^{-5} kg/m^3

All other sorption model parameters were set to zero. A simple test run has been set up with a tabulated source of I-131. The source strength increases in steps to cover the whole range of interest. Each step lasted 10^7 s. A large plot frequency was used (10^7 s) to make sure that the system is already at equilibrium when a plot point is made. The input files for this test are provided in:
`\Z-INPUTS\RT\Sorption-Tests\Oak-Ridge\Iodine-on-Graphite\I-131-Graphite-Ver-1.SPE`

The results are provided in Figure 3-1021. For comparison Figure 3-1022 is included. This figure shows experimental data and is copied from reference [114]. It is seen in Figure 3-1021 that the sorption model with the applied coefficients perfectly represents the Langmuir isotherm. The adequacy of the isotherm itself may be judged by comparing with experimental data shown in Figure 3-1022. It is clear that the accuracy of the Langmuir isotherm is at best within an order of magnitude.

A question may be asked what is the rationale for neglecting the desorption and setting B to zero. The answer is with the lack of data any value may be used and the value of zero is just a convenient first approximation. Once the value of B is chosen then the A must follow from the Langmuir isotherm.

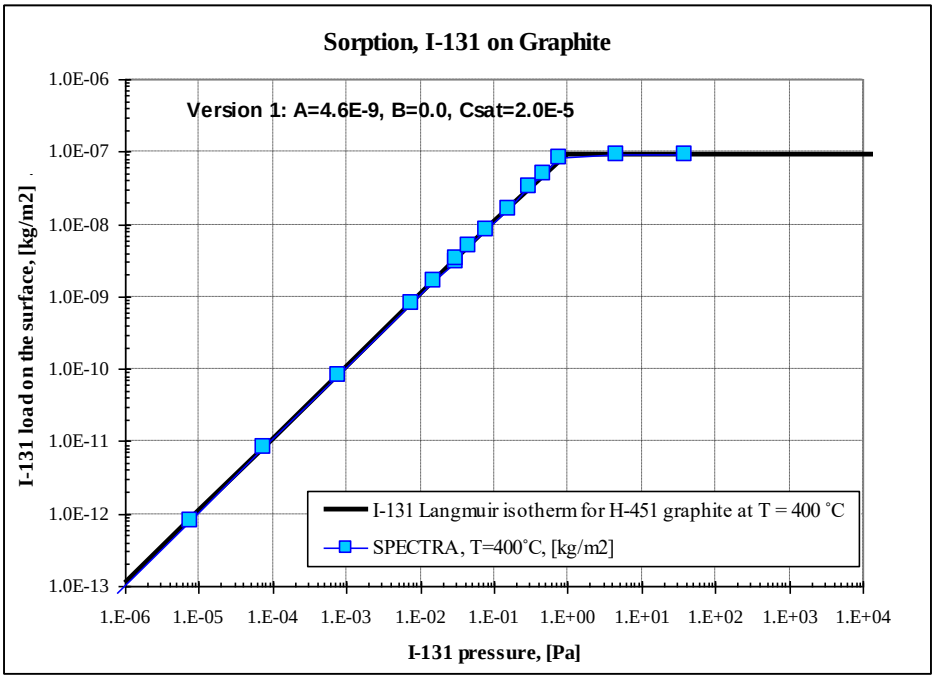

Figure 3-1021 Sorption of I-131 on graphite, A = 4.6×10^{-9}, B = 0.0, C_{sat} = 2.0×10^{-5}

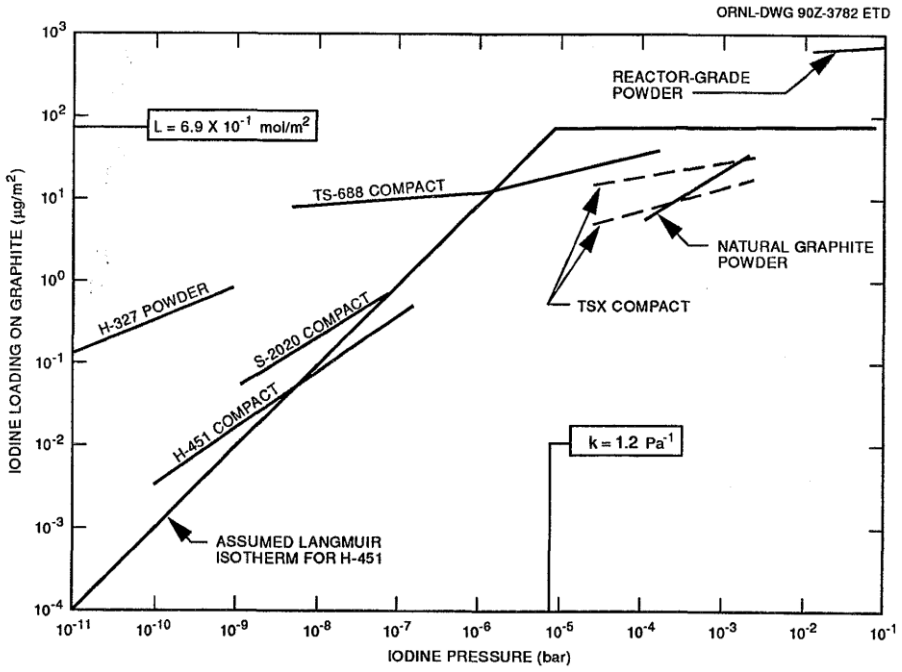

Figure 3-1022 Sorption of I-131 on graphite - reference [114].

If the desorption is not neglected and a non-zero value is selected for *B*, then the coefficient *A* is obtained from the following reasoning. In equilibrium, the source due to adsorption and removal due to both desorption and the radioactive decay are equal:

$$A(T)\cdot C_V = B(T)\cdot C_d + \lambda N\cdot\left(\frac{M}{N_A}\right)$$

or:

$$A(T) = [B(T)+\lambda]\cdot\frac{C_d}{C_V}$$

Finally:

$$A(T) = [B(T)+\lambda]\cdot KL$$

The decay constant, λ, for I-131 is equal to 10^{-6} s^{-1}, which corresponds to the half-life of about 8 days. Let's now assume the desorption coefficient of $B = 1\times10^{-6}$ (the value was based on the Laminar Loop experiments - section 3.12.48.1). In such case:

$A(T) = (1.0\times10^{-6} + 1.0\times10^{-6})\ (9.04\times10^{-8})\ (5.13\times10^{4}) = 9.27\times10^{-9}$.

The value of C_{sat} is the same as above, 2.0×10^{-5} (kg/m^3).

The following values were used for the second calculation:

- A_0 = 9.3×10^{-9} m/s
- B_0 = 1.0×10^{-6} 1/s
- C_{sat} = 2.0×10^{-5} kg/m^3

All other sorption model parameters were set to zero. The input files for this test are provided in:
`\Z-INPUTS\RT\Sorption-Tests\Oak-Ridge\Iodine-on-Graphite\I-131-Graphite-Ver-2.SPE`

Results are provided in Figure 3-1023. It is seen in Figure 3-1023 that the sorption model with the applied coefficients represents very well the Langmuir isotherm.

Finally, let's assume a "large" value of B, 1.0×10^{-5} 1/s, which is a maximum value accepted by the code for B - see Volume 2. In such case the characteristic time is roughly 1 day. The value of A is obtained as before: $A(T) = (1.0\times10^{-5} + 1.0\times10^{-6})\ (9.04\times10^{-8})\ (5.13\times10^{4}) = 5.10\times10^{-8}$. The following values were used for the second calculation:

- A_0 = 5.1×10^{-8} m/s
- B_0 = 1.0×10^{-5} 1/s
- $C_{V,max}$ = 2.0×10^{-5} kg/m^3

All other sorption model parameters were set to zero. The input files for this test are provided in:
`\Z-INPUTS\RT\Sorption-Tests\Oak-Ridge\Iodine-on-Graphite\I-131-Graphite-Ver-3.SPE`

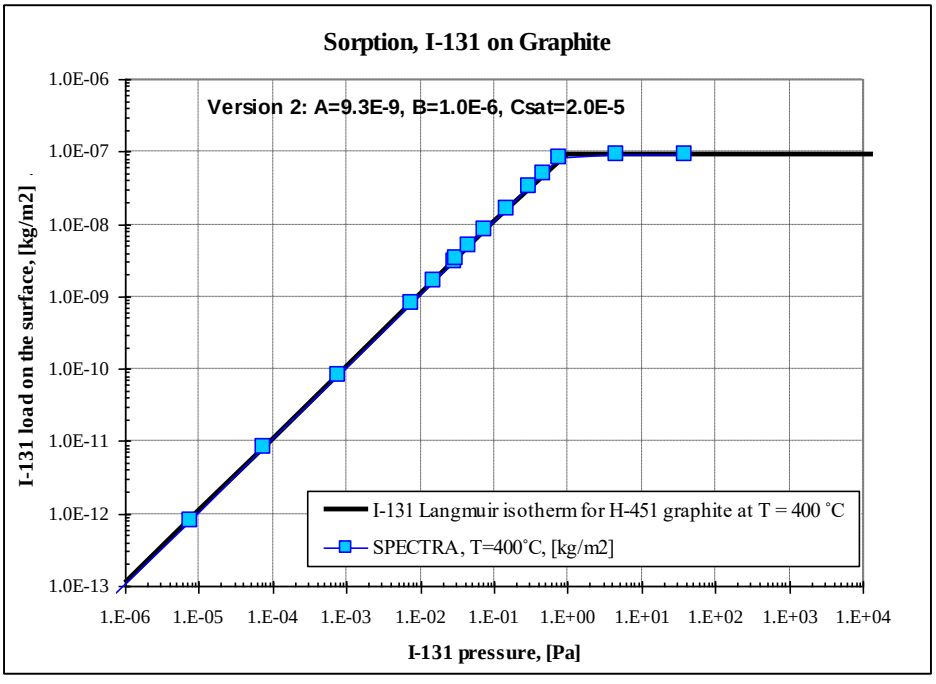

Figure 3-1023 Sorption of I-131 on graphite, $A = 9.3\times10^{-9}$, $B = 1.0\times10^{-6}$, $C_{sat} = 2.0\times10^{-5}$

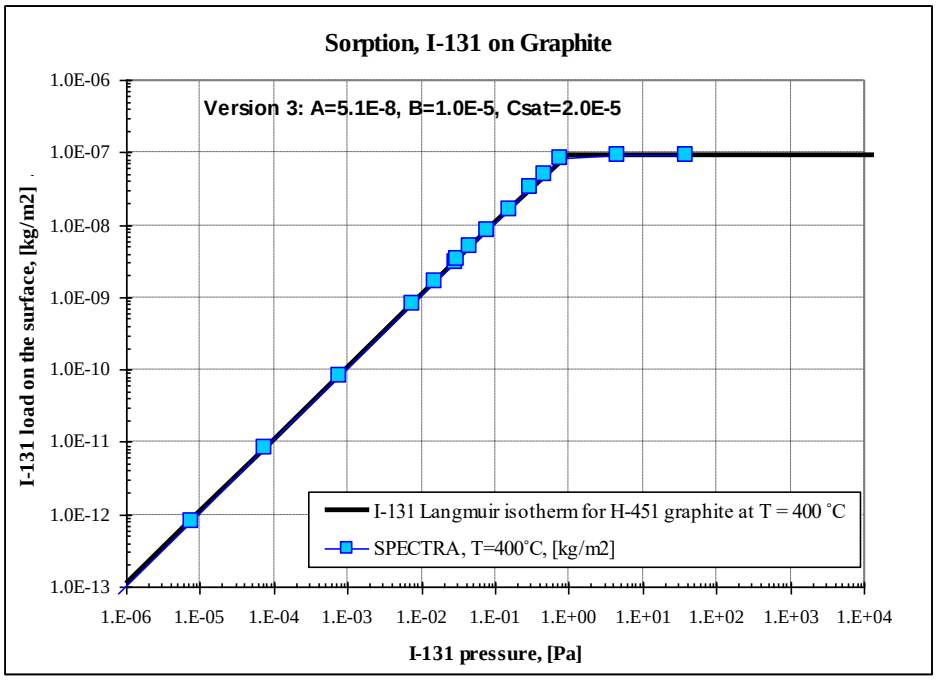

Figure 3-1024 Sorption of I-131 on graphite, A = 5.1×10^{-8}, B = 1.0×10^{-5}, C_{sat} = 2.0×10^{-5}

Results are shown in Figure 3-1024. Again a good representation of the Langmuir isotherm is obtained. It should be remembered that in each case the time behavior is different. This is illustrated in Figure 3-1025, showing the surface concentrations plotted versus time for a single step of the vapor pressure increase.

Figure 3-1025 shows that the difference between the three different versions of the sorption model is surprisingly small, considering that the adsorption constants were varied by three orders of magnitude. The reason is a feedback of the sorption mechanism on the vapor concentration, which is explained below.

- With small sorption coefficients, a small amount of vapor is sorbed. Consequently the concentration of vapor in the gas becomes relatively large and this in the end causes faster sorption.
- With large sorption coefficients, a large amount of vapor is sorbed. Consequently the concentration of vapor in the gas becomes relatively small and this in the end causes smaller sorption.

The differences in the vapor pressures causes the sorbed mass to be very similar in each case. The vapor pressures are shown in Figure 3-1026. It is therefore concluded that due to the self-stabilizing feedback described above, the sorption coefficients do not need to be known with very good accuracy. It is only important that the ratio between the adsorption on one hand and the desorption plus the decay on the other hand, is correctly captured. This ratio can easily be derived from the Langmuir isotherm, as has been shown in above. If this ratio was wrong then the stable values would be different i.e. the flat lines in Figure 3-1025 and Figure 3-1026 would be located at different levels. Consequently the calculated level of radioactivity from the surfaces would be wrong.

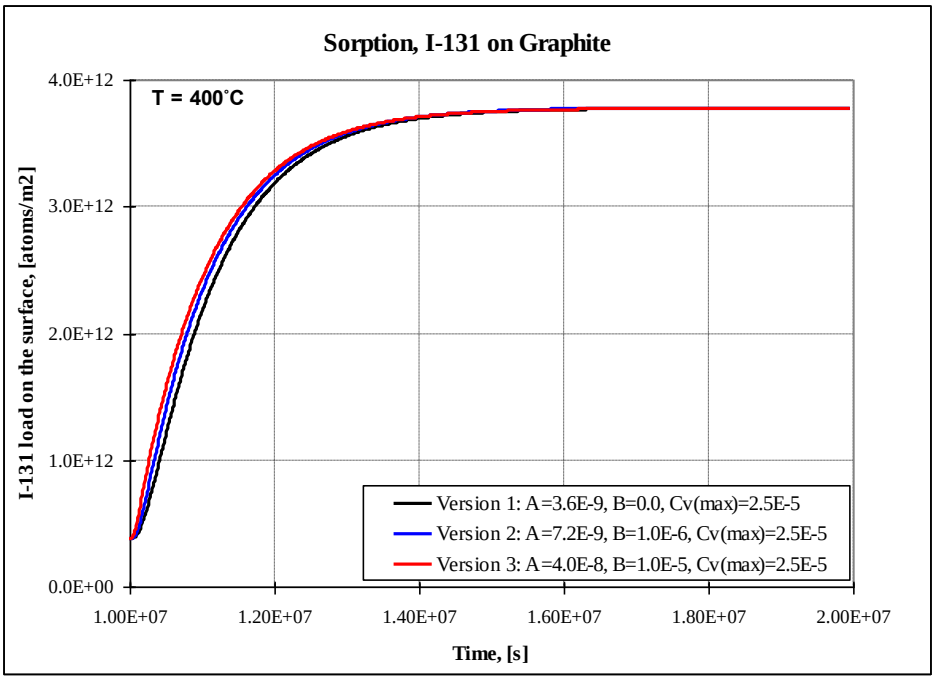

Figure 3-1025 I-131 concentration on graphite, time-dependent graph

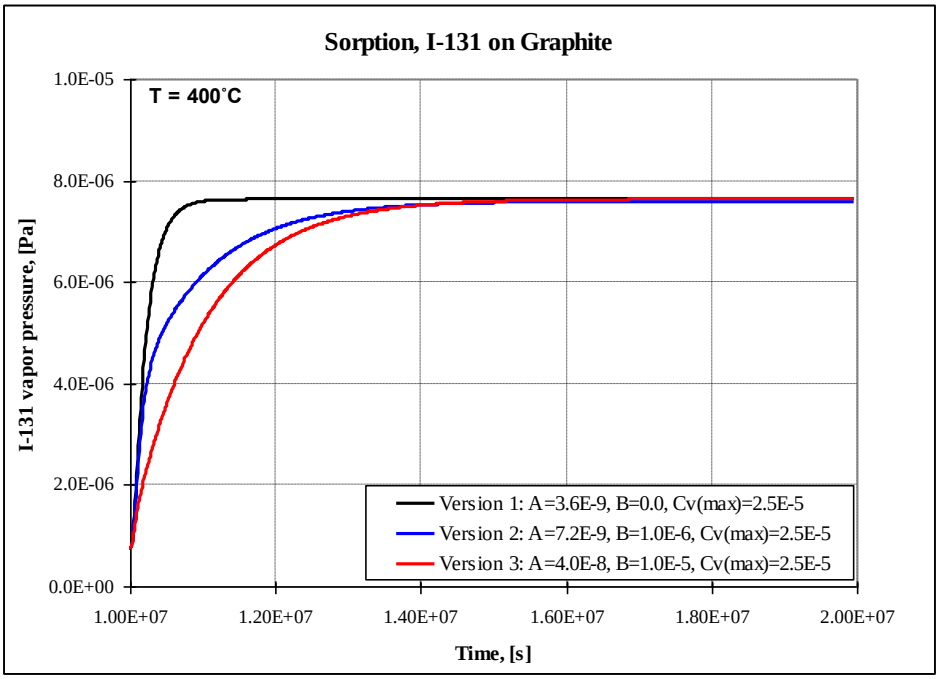

Figure 3-1026 I-131 vapor pressure, time-dependent graph

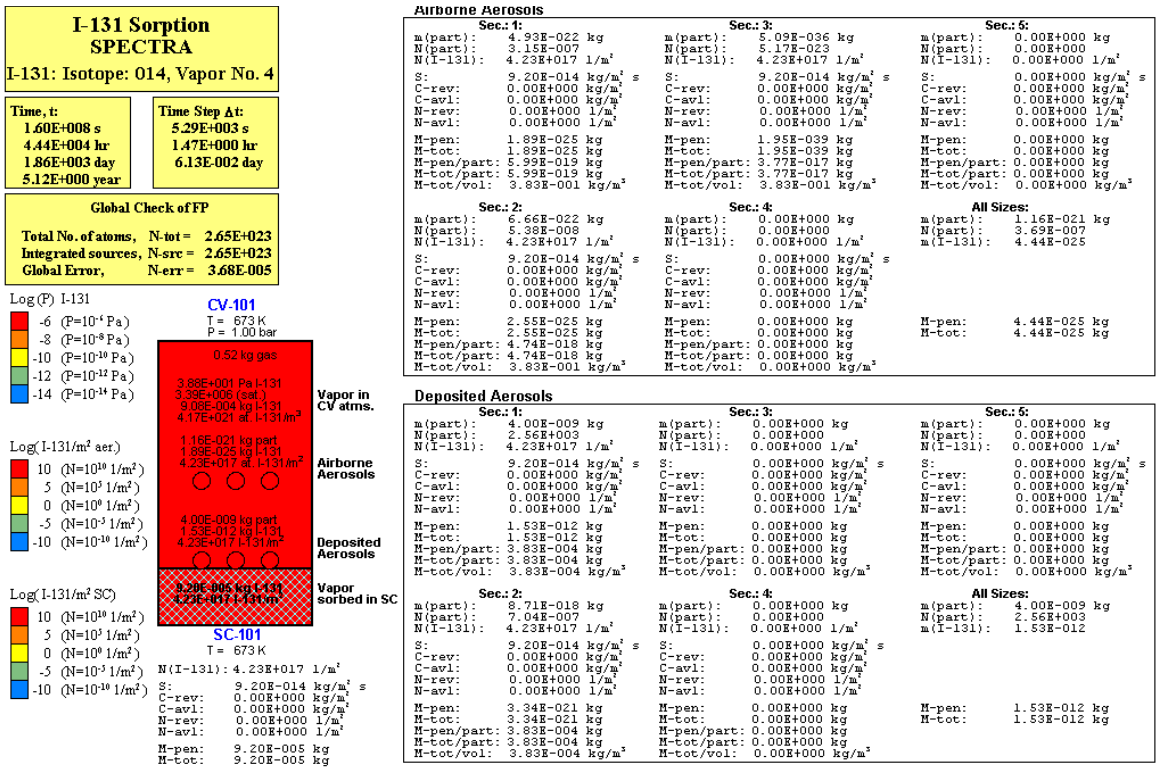

Figure 3-1027 I-131 on graphite surfaces, test I-131-Graphite-Ver-1, end of calculations

Figure 3-1027 shows the end-results obtained for the sorption coefficients used for Version 1. The same sorption model has been applied on the surface as well as the aerosol particles. Consequently the resulting surface concentrations of I-131, N(I-131) are the same for the SC-101, the airborne aerosols in CV-101, as well as the aerosols deposited on SC-101, and equal to:

$$N(I-131) = 4.23\times10^{17} \ (\text{atoms/m}^2)$$

3.12.51.3 Sorption of I-131 on Steel

In case of steel, the Langmuir isotherms are given in [114] for four temperatures: $T = 400$˚C, 600˚C, 700˚C, and 800˚C. The data is shown in Figure 3-1030 (reproduced from [114]). The values of K and L has been read from this graph and are given in Table 3-91.

Table 3-91 I-131 isotherms for steel.

Parameter	$T = 400$˚C $T = 673$ K	$T = 600$˚C $T = 873$ K	$T = 700$˚C $T = 973$ K	$T = 800$˚C $T = 1073$ K
K, (Pa^{-1}) L, (μg/cm²)	$1\times10^{+4}$ 4	$1\times10^{+3}$ 2	$2\times10^{+2}$ 1	$5\times10^{+1}$ 0.5

As shown in the previous sections, the conversion of Langmuir isotherms to SPECTRA input requires assuming one of the sorption parameters. For simplicity let's assume $B = 0.0$. In such case $A(T)$ is given by (see discussion in the previous section):

$$A(T) = \lambda KL$$

The values of $C_{sat}(T)$ are obtained from:

$$C_{sat}(T) = 1/K$$

The values of $A(T)$ and $C_{sat}(T)$ are given in Table 3-92 together with the values of K and L converted into appropriate units.

Table 3-92 I-131 isotherms for steel - SPECTRA parameters

Parameter	T = 400˚C T = 673 K	T = 600˚C T = 873 K	T = 700˚C T = 973 K	T = 800˚C T = 1073 K
K, (m^3/kg)	$4.27\times10^{+8}$	$5.54\times10^{+7}$	$1.24\times10^{+7}$	$3.41\times10^{+6}$
L, (kg/m^2)	4.00×10^{-5}	2.00×10^{-5}	1.00×10^{-5}	5.00×10^{-6}
$A=\lambda KL$, (m/s)	1.71×10^{-2}	1.11×10^{-3}	1.24×10^{-4}	1.70×10^{-5}
$C_{sat}=1/K$, (kg/m^3)	2.34×10^{-9}	1.80×10^{-8}	8.10×10^{-8}	2.94×10^{-7}

There are two possible ways of preparing data for SPECTRA:

- Correlations for $A(T)$, $B(T)$, and $C_{sat}(T)$
- Tabulated $A(T)$, $B(T)$, and $C_{sat}(T)$

Use of both methods is made for the present data. The use of tabulated data option is obviously an easier and more accurate choice. Nevertheless it is sometimes convenient to use the equations, for example for comparison with other codes that are using such equations. Therefore both methods are discussed subsequently below.

- Correlations for $A(T)$, $B(T)$, and $C_{sat}(T)$

  With this option the A, B, and C_{sat} are calculated from the following correlations:

$$A(T) = A_0 \cdot \exp\left(-\frac{A_A}{T}\right)$$

$$B(T) = B_0 \cdot \exp\left(-\frac{A_B}{T}\right)$$

$$C_{sat}(T) = C_0 \cdot \exp\left(-\frac{A_C}{T}\right)$$

  The model coefficients: A_0, A_A, B_0, A_B, C_0, A_C, must be defined by the user. In the present case $B(T)$ is assumed to be zero, therefore only $A(T)$ and $C_{sat}(T)$ need to be determined. The values of $A(T)$ and $C_{sat}(T)$ are plotted in Figure 3-1028 and Figure 3-1029.

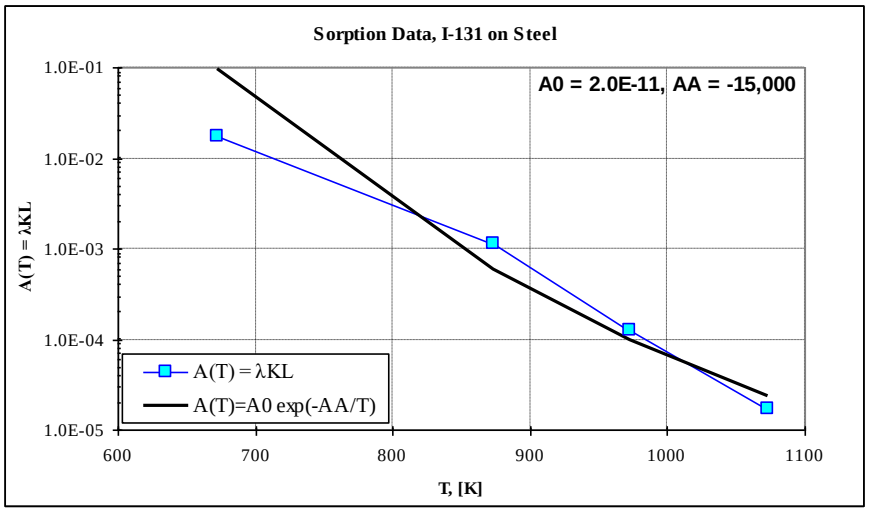

Figure 3-1028 Values of $A(T)$ and data fit equation

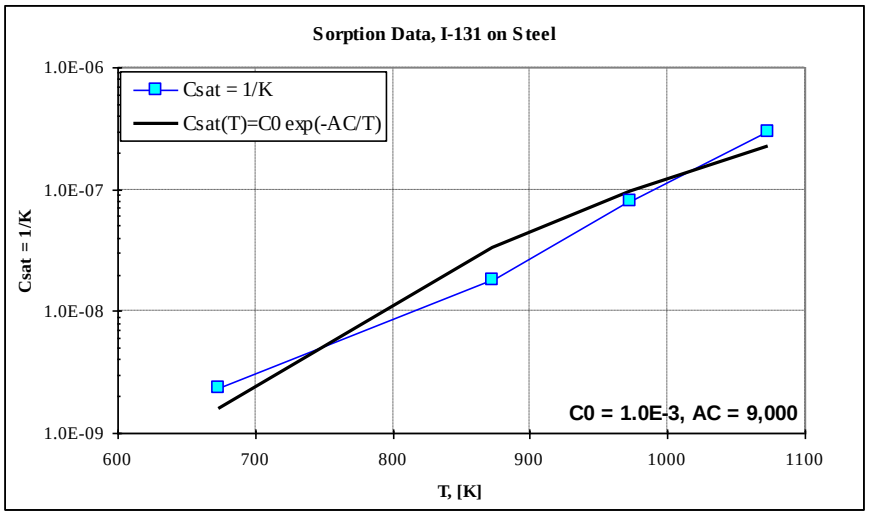

Figure 3-1029 Values of $C_{sat}(T)$ and data fit equation

The coefficients could be established by some more sophisticated method, such as for example the least squares method, but for the present case the coefficients were found by using a simple trial and error method and comparing the plotted lines representing the fit equations with the tabulated data. The obtained values are: $A_0 = 3.0\times10^{-13}$, $A_A = -1.5\times10^{4}$, $B_0 = 0.0$, $C_0 = 0.1$, $A_C = -1.0\times10^{4}$. The fit lines for $A(T)$ and $C_{sat}(T)$ are shown in Figure 3-1028 and Figure 3-1029. The final formula for the sorption model applied on steel surfaces becomes:

$$A(T) = 2.0\times10^{-11}\exp\left(\frac{15{,}000}{T}\right) \qquad B(T) = 0.0$$

$$C_{sat}(T) = 1.0\times10^{-3}\exp\left(-\frac{9{,}000}{T}\right)$$

The input deck for this case is provided in:
`\Z-INPUTS\RT\Sorption-Tests\Oak-Ridge\Iodine-on-Steel\I-131-Steel-Ver-1.SPE`

Results are provided in Figure 3-1031. The source data is provided in Figure 3-1030, copied from reference [114]. The fit equations give somewhat different values of $A(T)$ and $C_{sat}(T)$ than the source. Because of these differences, the calculated isotherms in Figure 3-1031 are somewhat different from the isotherms in the source data Figure 3-1030. However, the experimental data scatter is still larger therefore the use of the fit equations is justified.

- Tabulated $A(T)$, $B(T)$, and $C_{sat}(T)$
  With this option the data given in Table 3-92 is directly used in SPECTRA. The input deck for this case is provided in:
  `\Z-INPUTS\RT\Sorption-Tests\Oak-Ridge\Iodine-on-Steel\I-131-Steel-Ver-2.SPE`

  Results are provided in Figure 3-1032. The isotherms are now much closer to those provided in the source data. In fact they can be as close as the values of K and L can be read from the Figure 3-1030. The decrease of sorption sites ("saturation concentration") from about 4 μg/cm^2 (4×10^{-5} kg/m^2) at 400˚C (strictly speaking reference [114] gives 3.6 but it is here rounded up) down to 0.5 μg/cm^2 (5×10^{-6} kg/m^2) at 800˚C is obtained exactly by the use of the tables.

The results presented above show that with the tabulated coefficients one can obtain a very close match to the desired isotherms. The source data show a slight increase of the saturated values with vapor pressure. This effect can be achieved by using the "reduced exponent" x_{red} - see Volume 1. All previous calculations were performed with $x_{red} = 0.0$ (note that the adsorption exponent is equal to $x_A = 1.0$). The final calculations were performed with the same tabulated coefficient but this time using a positive reduced exponent, $x_{red} = 0.05$. The input deck for this case is provided in:
`\Z-INPUTS\RT\Sorption-Tests\Oak-Ridge\Iodine-on-Steel\I-131-Steel-Ver-2-05.SPE`

Results are provided in Figure 3-1033. This figure provides the closest match to the isotherms from the source data. The end-results for this run are presented in Figure 3-1034 and Figure 3-1035, for 400˚C and 800˚C respectively. The same sorption model has been applied on the surface as well as the aerosol particles. For given temperature, the surface concentrations of I-131, N(I-137), are the same for the SC surfaces, the airborne aerosols in CVs, as well as the aerosols deposited on SC-s, and equal to:

$$N(I-131) = 5.57\times10^{20} \qquad at\ T = 400^0 C$$
$$N(I-131) = 5.47\times10^{19} \qquad at\ T = 800^0 C$$

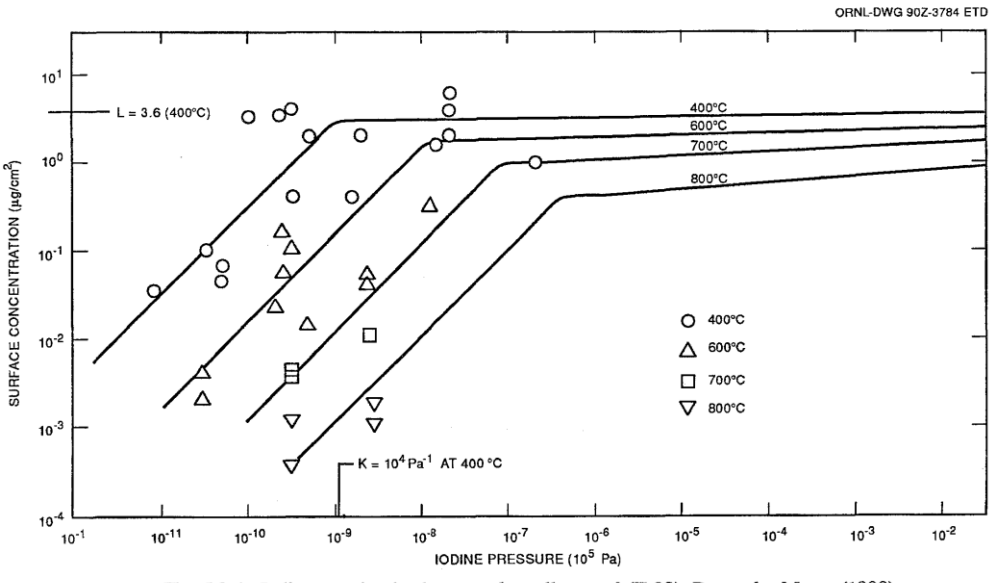

Figure 3-1030 Sorption of I-131 on steel - reference [114].

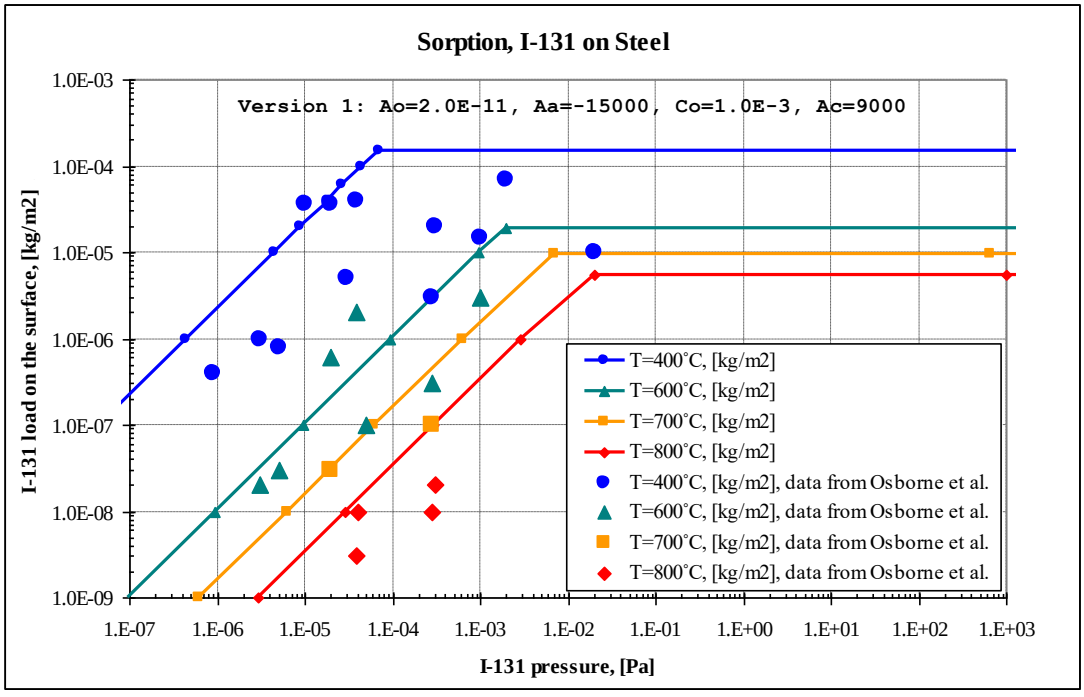

Figure 3-1031 Sorption of I-131 on steel, $A_0 = 2\times10^{-11}$, $A_A = -15000$, $C_0 = 10^{-3}$, $A_C = -9000$

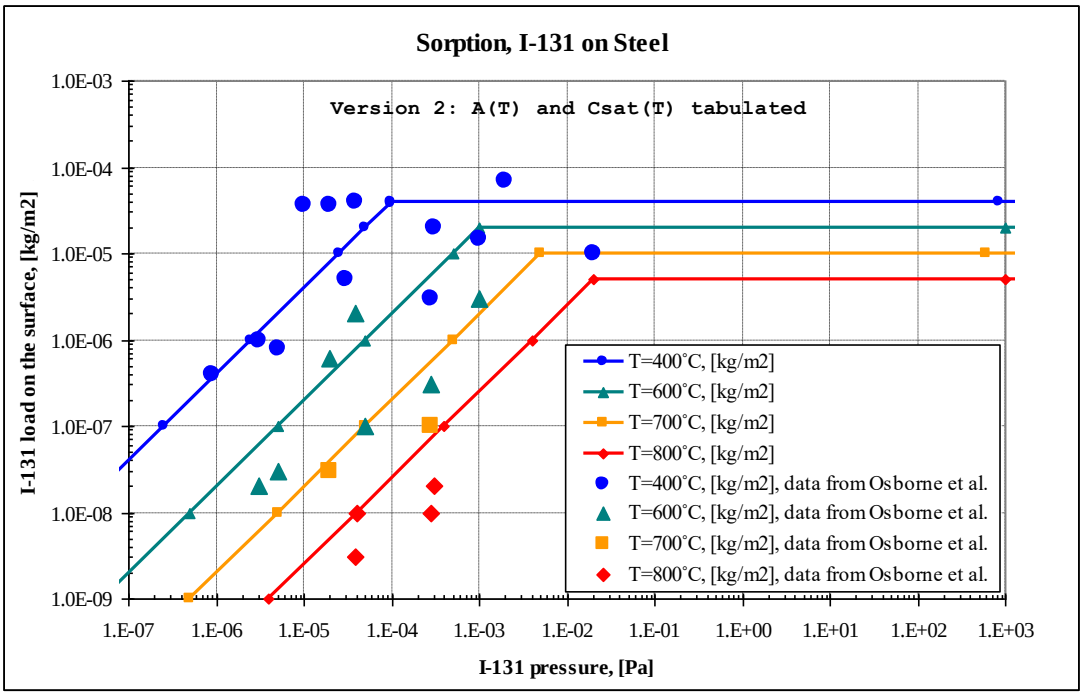

Figure 3-1032 Sorption of I-131 on steel - SPECTRA, tabulated $A(T)$ and $C_{sat}(T)$

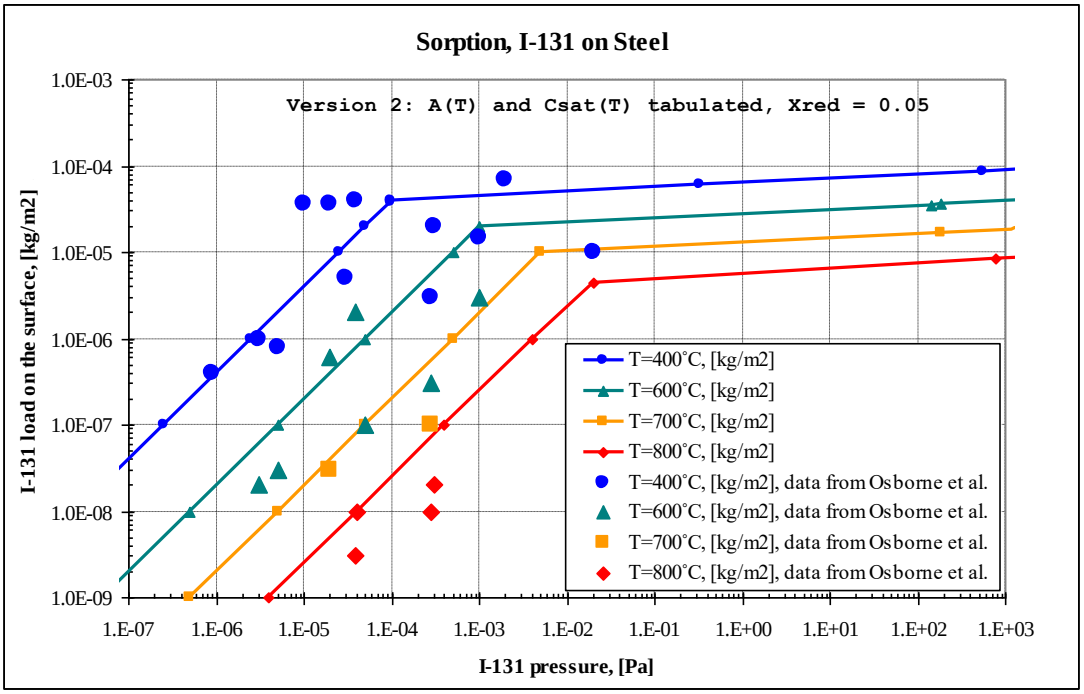

Figure 3-1033 Sorption of I-131 on steel - SPECTRA, tabulated $A(T)$ and $C_{sat}(T)$, x_{red} = 0.1

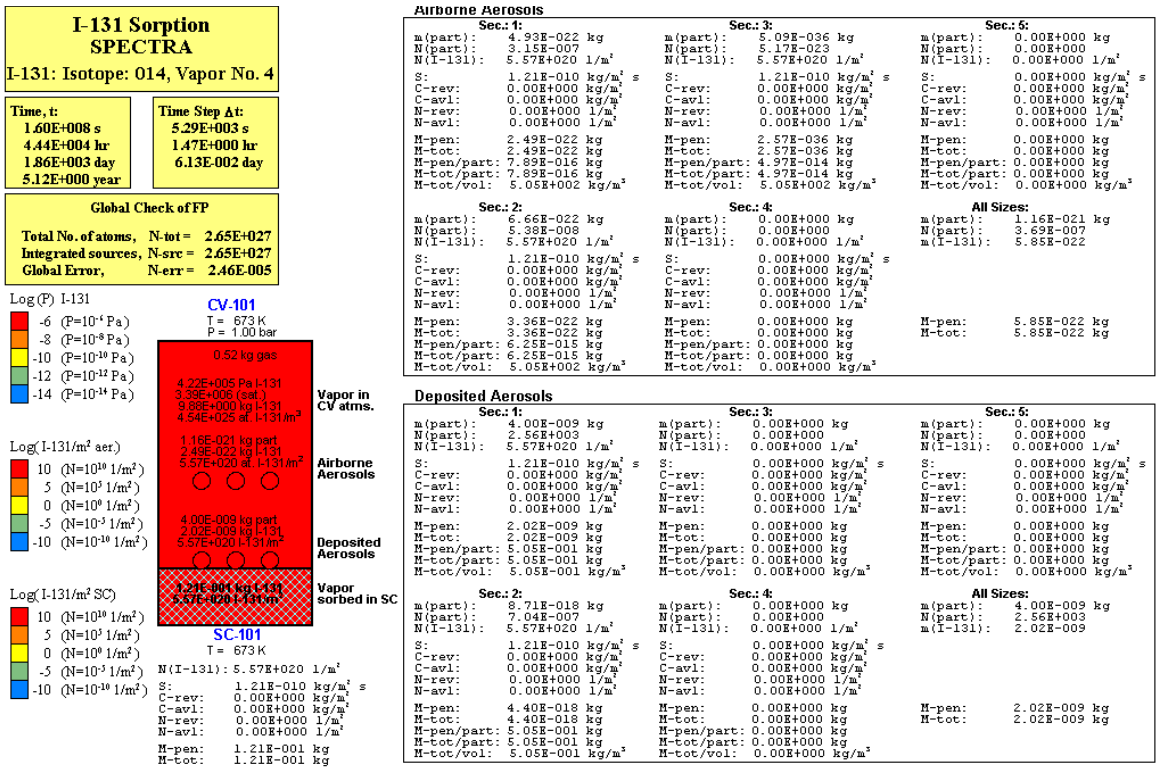

Figure 3-1034 I-131 on steel surfaces, test I-131-Steel-Ver-2-05, end state in CV-101 (400˚C)

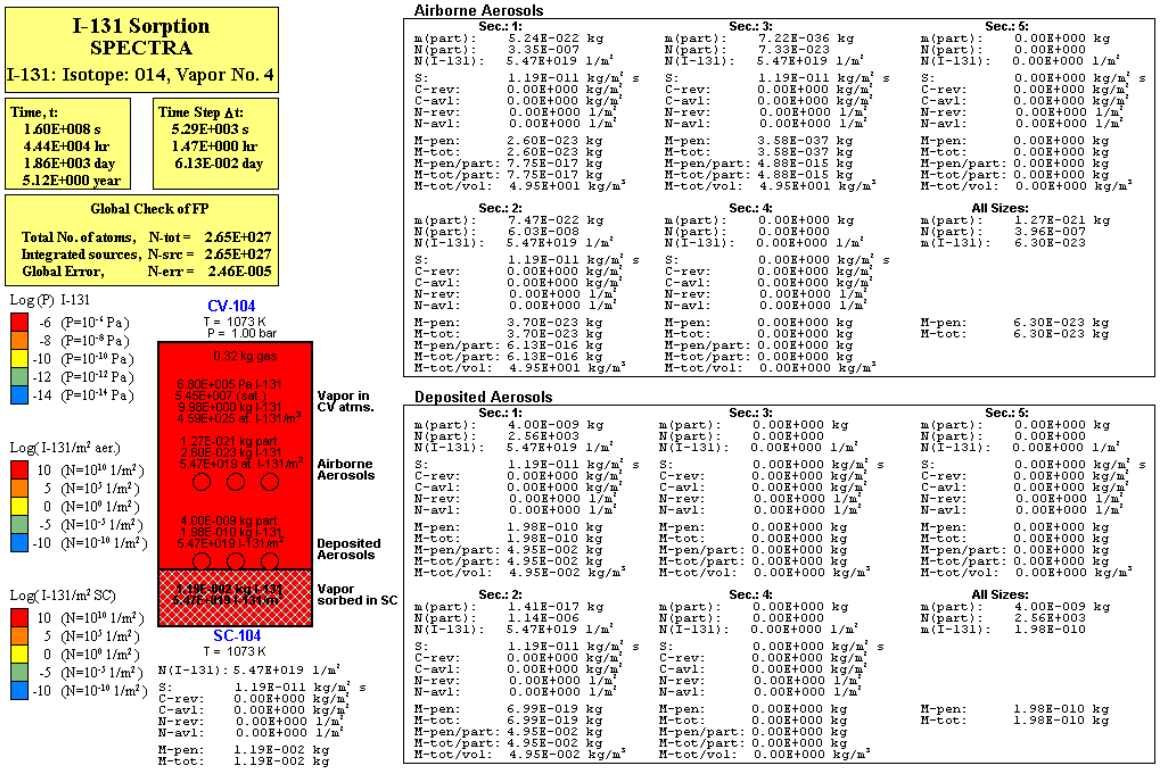

Figure 3-1035 I-131 on steel surfaces, test I-131-Steel-Ver-2-05, end state in CV-104 (800˚C)

3.12.51.4 Sorption of I-131 on Dust

For sorption of I-131 on dust reference the [114] (section 5.2.3) following data of Osborne [115], provides the following isotherm:

- $K = 10^3$ (Pa^{-1})
- $L = 4\times10^{-6}$ (mol/m^2)

The data is presumably valid for 400˚C. This is concluded from the context, but it is not clearly stated in the text. The procedure to use Langmuir isotherm to produce SPECTRA input has been well-established and discussed in the previous two sections, therefore it is given here without any further explanations.

- Step 1 - conversion to SPECTRA units:
  - $K = 10^3$ Pa^{-1} $\times(RT) = (63.5\times673)$ $\rightarrow 4.27\times10^7$ m^3/kg
  - $L = 4\times10^{-6}$ mol/m^2 $\times(M_{I\text{-}131}/1000) = 0.131$ $\rightarrow 5.24\times10^{-7}$ kg/m^2
- Step 2 - assume the desorption coefficient: (1) small, (2) equal, and (3) large, compared to the decay constant, $\lambda=10^{-6}$ 1/s.
  - Version 1: $B = 0.0$
  - Version 2: $B = 1\times10^{-6}$
  - Version 2: $B = 1\times10^{-5}$
- Step 3 - calculate A and C_{sat}
  - $C_{sat} = 1/K = 1/1.05\times10^4 = 2.34\times10^{-8}$ kg/m^3
  - $A = (B + \lambda)KL$, where $KL = 4.27\times10^7\times5.24\times10^{-7} = 22.4$ m
    Version 1: $A = (\ 0 + 10^{-6}) \times 22.4 = 2.24\times10^{-5}$ m/s
    Version 2: $A = (1\times10^{-6} + 10^{-6}) \times 22.4 = 4.48\times10^{-5}$ m/s
    Version 3: $A = (1\times10^{-5} + 10^{-6}) \times 22.4 = 2.46\times10^{-4}$ m/s

The input files for the three calculations are provided in:

```
\Z-INPUTS\RT\Sorption-Tests\Oak-Ridge\Iodine-on-Dust\I-131-Dust-Ver-1.SPE
\Z-INPUTS\RT\Sorption-Tests\Oak-Ridge\Iodine-on-Dust\I-131-Dust-Ver-2.SPE
\Z-INPUTS\RT\Sorption-Tests\Oak-Ridge\Iodine-on-Dust\I-131-Dust-Ver-3.SPE
```

Results obtained for the Version 1, 2, and 3, are shown in Figure 3-1036, Figure 3-1037, and Figure 3-1038 respectively. It is seen that in all cases the sorption model is capable to reproduce the Langmuir isotherm. The fastest sorption is of course obtained with larger coefficients, however as shown in section 3.12.51.2, the surface concentrations are quite insensitive to the choice of the sorption parameters.

The end-results for this run are presented in Figure 3-1039. The same sorption model has been applied on the surface as well as the aerosol particles. Consequently the surface concentrations of I-131, N(I-137), are the same for the SC surfaces, the airborne aerosols in CVs, as well as the aerosols deposited on SC-s, and equal to:

$$N(I-131) = 2.33 \times 10^{18} \text{ (atoms/m}^2\text{)}$$

Figure 3-1040 shows comparison of Langmuir isotherms for dust, graphite, and steel. The highest activity (I-131 concentration) is observed on the steel surface; the lowest on the graphite surfaces.

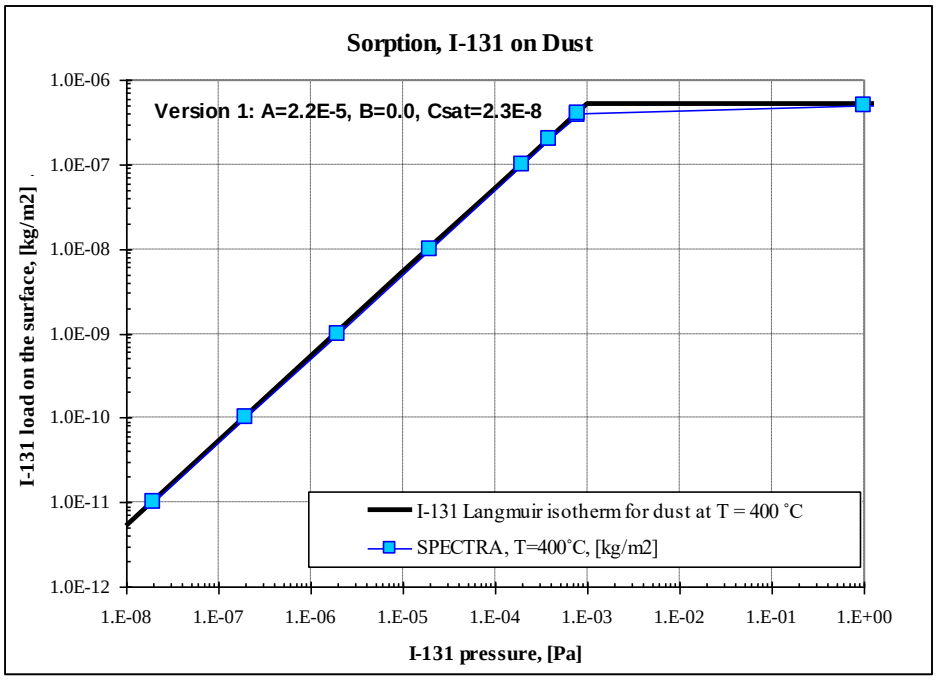

Figure 3-1036 Sorption of I-131 on dust, A = 2.2×10^{-5}, B = 0.0, C_{sat} = 2.3×10^{-8}

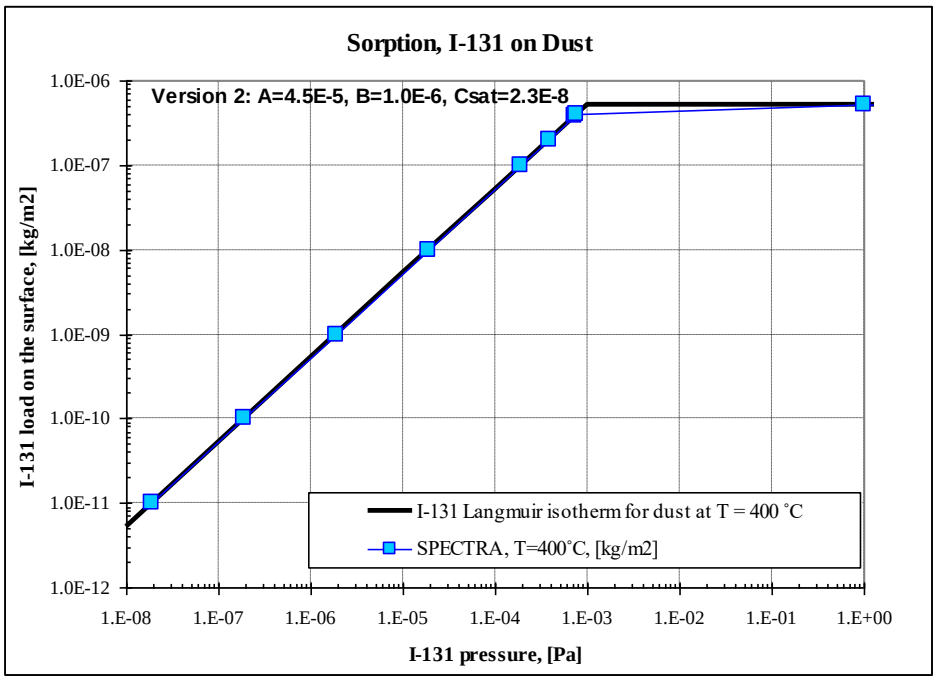

Figure 3-1037 Sorption of I-131 on dust, A = 4.5×10^{-5}, B = 1.0×10^{-6}, C_{sat} = 2.3×10^{-8}

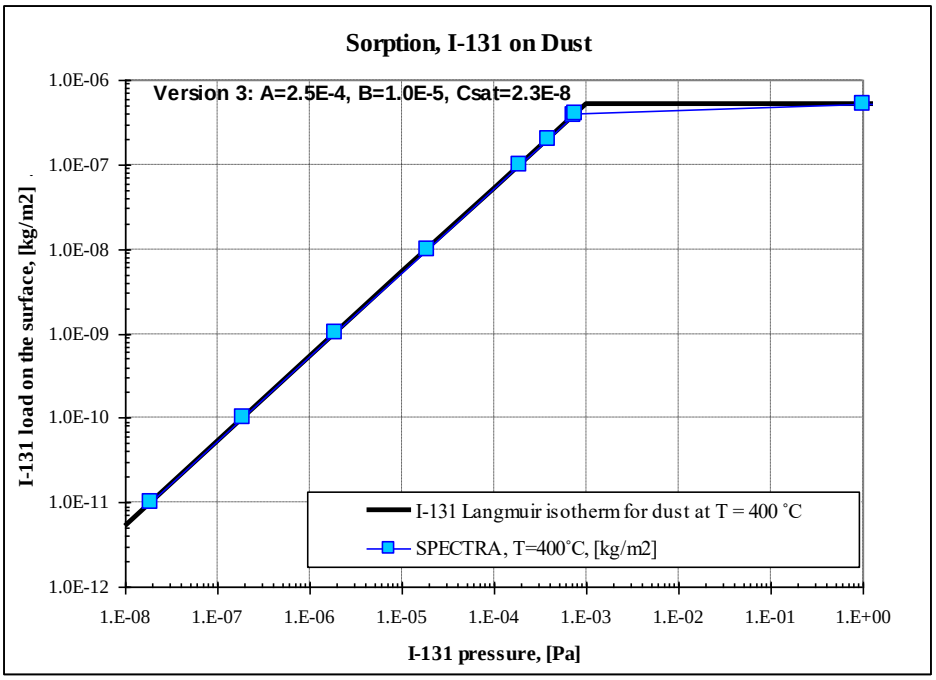

Figure 3-1038 Sorption of I-131 on dust, A = 2.5×10^{-4}, B = 1.0×10^{-5}, C_{sat} = 2.3×10^{-8}

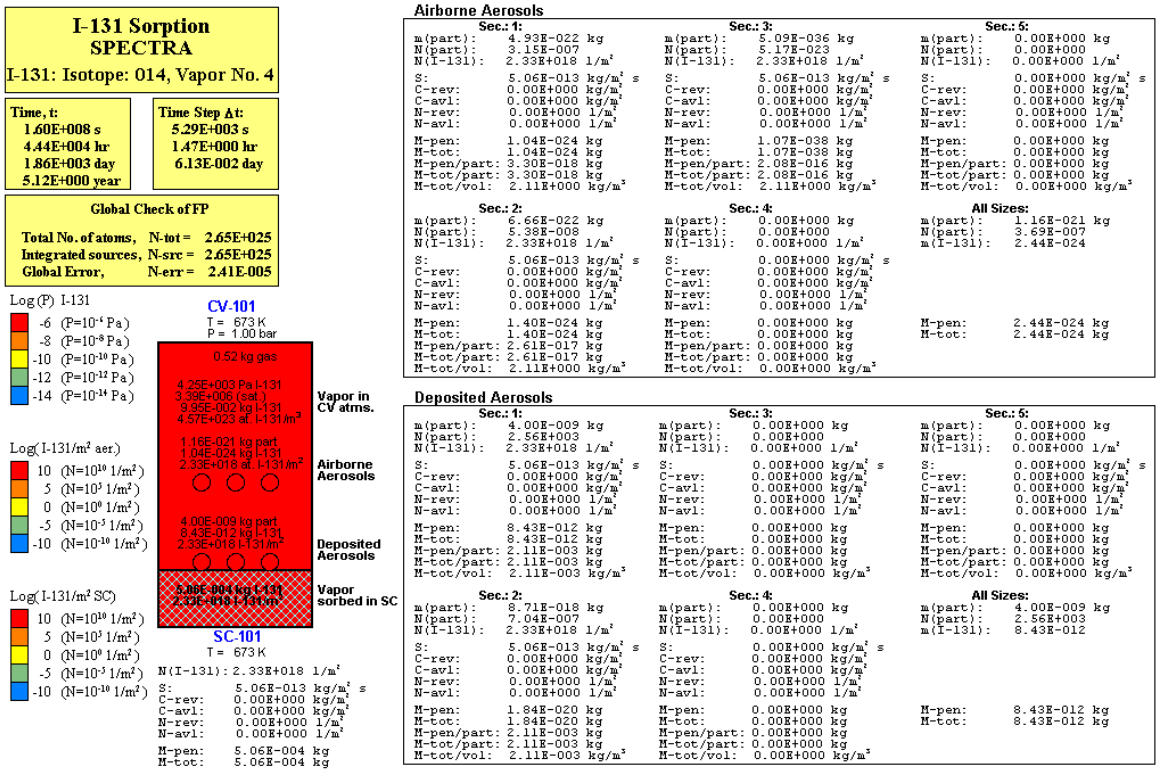

Figure 3-1039 I-131 on dust, test I-131-Dust-Ver-1, end state in CV-101 (400˚C)

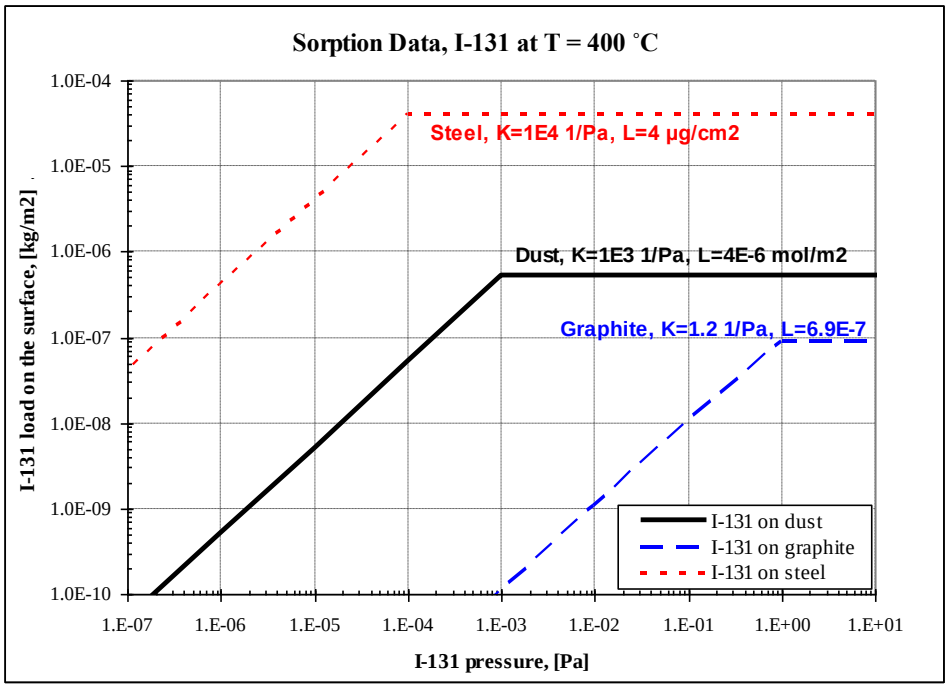

Figure 3-1040 Sorption on structures and dust

3.12.51.5 Summary of the Sorption Validation Tests

Calculations were performed for the following data:

- Sorption of I-131 on graphite
- Sorption of I-131 on steel
- Sorption of I-131 on dust

Calculations of the validation tests described in this section were performed using the Sorption Model 1, with the following alternative sets of coefficients:

- Sorption of I-131 on graphite:
  - $A = 4.6\times10^{-9}$, $B = 0.0$, $C_{sat} = 2.0\times10^{-5}$
  - $A = 9.3\times10^{-9}$, $B = 1.0\times10^{-6}$, $C_{sat} = 2.0\times10^{-5}$
  - $A = 5.1\times10^{-8}$, $B = 1.0\times10^{-5}$, $C_{sat} = 2.0\times10^{-5}$

- Sorption of I-131 on steel:
  - $A = 2.0\times10^{-11}\times\exp(15{,}000/T)$, $B = 0.0$, $C_{sat} = 10^{-3}\times\exp(-9{,}000/T)$
  - A tabulated versus T, $B = 0.0$, C_{sat} tabulated versus T
  - As above but with a non-zero reduced exponent, x_{red}.

- Sorption of I-131 on dust:
  - $A = 2.24\times10^{-5}$, $B = 0.0$, $C_{sat} = 2.34\times10^{-8}$
  - $A = 4.48\times10^{-5}$, $B = 1.0\times10^{-6}$, $C_{sat} = 2.34\times10^{-8}$
  - $A = 2.46\times10^{-4}$, $B = 1.0\times10^{-5}$, $C_{sat} = 2.34\times10^{-8}$

The results are summarized as follows:

- The available data is provided in form of Langmuir isotherms.
- The Langmuir isotherms do not provide sufficient data to define all coefficients of the Sorption Model 1. The Langmuir isotherm provide equilibrium data; the relaxation time (to get to equilibrium) needs to be guessed. In practice this means that one of the coefficients of the Model 1 must be guessed. In the present calculations the desorption coefficient, $B(T)$, was being guessed and then varied in sensitivity calculations. The calculations showed that surface concentration is not sensitive to the choice of the parameter.
- The Sorption Model 1 is capable to correctly reproduce the sorption behavior given by the Langmuir isotherms.
- Out of the calculated cases, the highest activity (surface concentration) is observed on the steel surface; the lowest on the graphite surfaces.

3.12.52 AVR Data

Sorption on dust particles based on AVR data is described in a separate report [116]. Results are shown in Figure 3-1041, Figure 3-1042, and Figure 3-1043. The following conclusions and recommendations were obtained:

- The available data can be correlated. The data scatter is about four orders of magnitude. Therefore the coefficients of the Langmuir isotherms vary by four orders of magnitude.

- Sorption rates are higher at low temperatures and lower at high temperatures. This tendency has been observed in the data compiled at Oak Ridge - reference [114] - see section 3.12.51.3. It is therefore surmised that the highest value of the sorption coefficients are appropriate for the low temperatures and the lowest value of the sorption coefficients are appropriate for the high temperatures. The recommended sorption coefficients are:

    - Iodine on dust.

$$A_S(T_w) = \begin{cases} 4.5\times10^{-1} & low\ T\ (T \sim 400-500\ K) \\ 4.5\times10^{-3} & middle\ T\ (T \sim 700-800\ K) \\ 4.5\times10^{-5} & high\ T\ (T \sim 1000-1100\ K) \end{cases}$$

$$B_S(T_w) = 1.0\times10^{-6}$$

$$C_{sat}(T_w) = \begin{cases} 4.0\times10^{-12} & low\ T\ (T \sim 400-500\ K) \\ 4.0\times10^{-10} & middle\ T\ (T \sim 700-800\ K) \\ 4.0\times10^{-8} & high\ T\ (T \sim 1000-1100\ K) \end{cases}$$

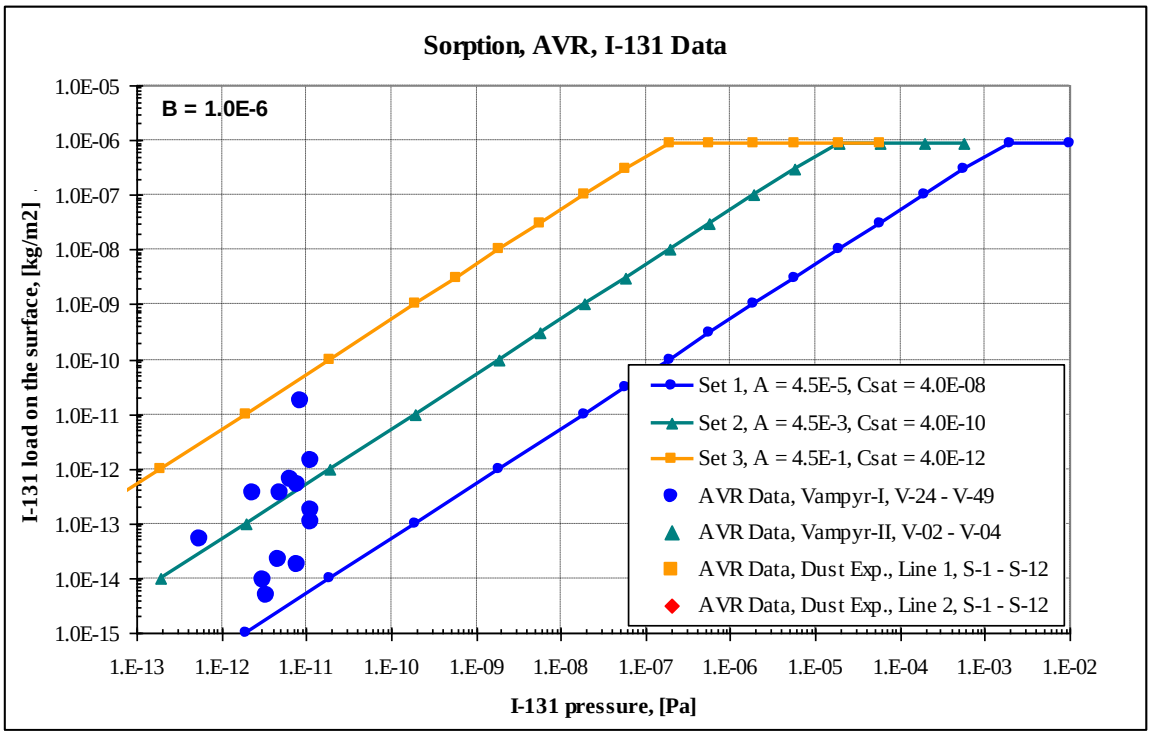

Figure 3-1041 I-131 - AVR data and Langmuir isotherms

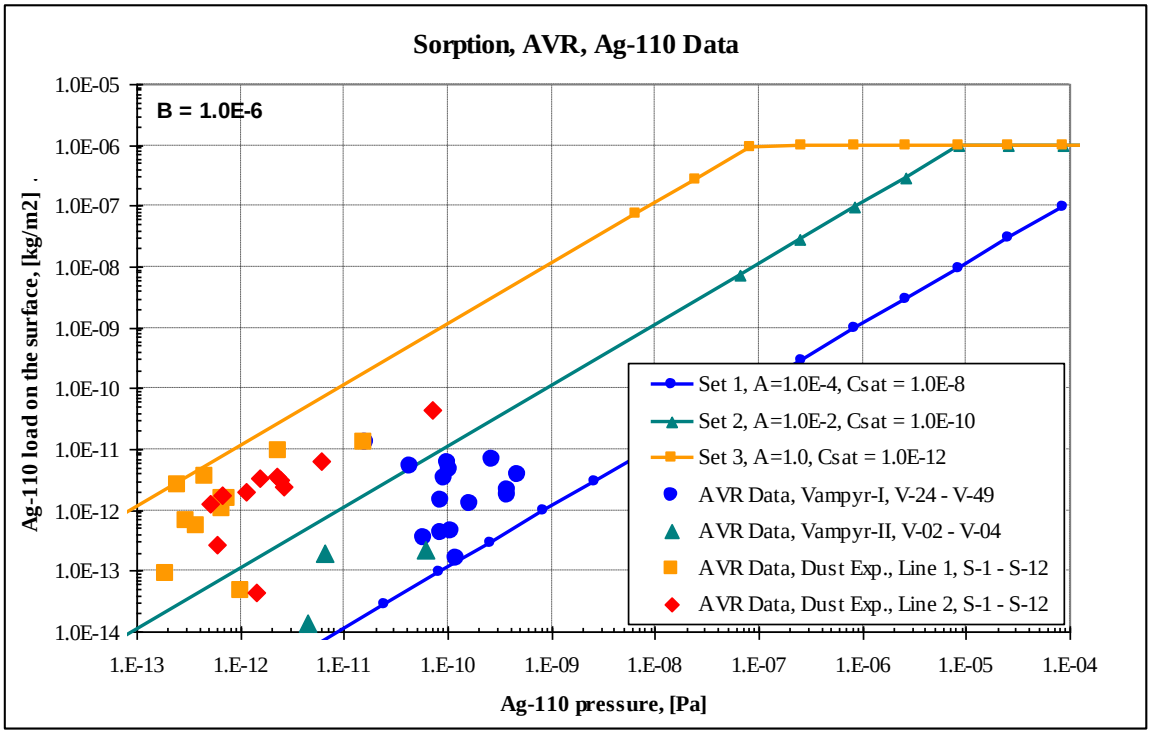

Figure 3-1042 Ag-110m - AVR data and Langmuir isotherms

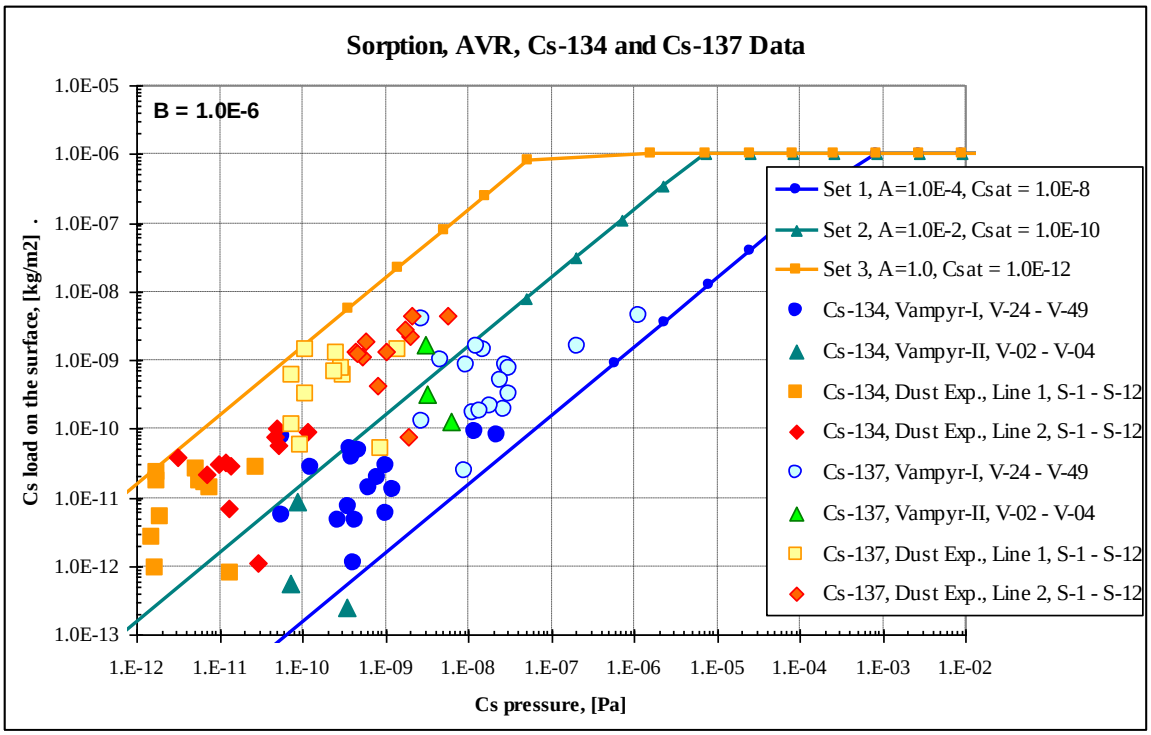

Figure 3-1043 Cs-134 and Cs-137 - AVR data and Langmuir isotherms

- Silver on dust:

$$A_S(T_w) = \begin{cases} 1.0 & low\ T\ (T \sim 400-500\ K) \\ 1.0\times10^{-2} & middle\ T\ (T \sim 700-800\ K) \\ 1.0\times10^{-4} & high\ T\ (T \sim 1000-1100\ K) \end{cases}$$

$$B_S(T_w) = 1.0\times10^{-6}$$

$$C_{sat}(T_w) = \begin{cases} 1.0\times10^{-12} & low\ T\ (T \sim 400-500\ K) \\ 1.0\times10^{-10} & middle\ T\ (T \sim 700-800\ K) \\ 1.0\times10^{-8} & high\ T\ (T \sim 1000-1100\ K) \end{cases}$$

- Cesium on dust.

$$A_S(T_w) = \begin{cases} 1.0 & low\ T\ (T \sim 400-500\ K) \\ 1.0\times10^{-2} & middle\ T\ (T \sim 700-800\ K) \\ 1.0\times10^{-4} & high\ T\ (T \sim 1000-1100\ K) \end{cases}$$

$$B_S(T_w) = 1.0\times10^{-6}$$

$$C_{sat}(T_w) = \begin{cases} 1.0\times10^{-12} & low\ T\ (T \sim 400-500\ K) \\ 1.0\times10^{-10} & middle\ T\ (T \sim 700-800\ K) \\ 1.0\times10^{-8} & high\ T\ (T \sim 1000-1100\ K) \end{cases}$$

3.12.53 Sorption in Liquids

Sorption of fission products dissolved in liquids is important for example in molten salt reactors, where a group of fission products, referred to as noble metals, exists in the fuel salt deposits on surfaces exposed to salt.

Generally fission products in molten fuel salt can be grouped into three principal types where the mechanics of migration is the distinguishing feature (l) salt seekers, (2) noble gases, and (3) noble metals [135]. The salt-seeking fission products (which include Sr, Y, Zr, I, Cs, Ba, and Ce) are soluble in a fuel salt and remain with the fuel salt in inventory amounts. The noble gases are Kr and Xe. A great deal of work has been done at ORNL to understand noble gas migration particularly Xe-135 because of its thermal neutron cross section of over 10^6 barns. The third group, the so-called "noble metals", Nb, Mo, Ru, Sb, and Te, is specifically important in molten salt reactors. The noble metals are reduced by the UF_3 in the fuel salt, and therefore exist in salt in the metallic state. They are insoluble in fuel salt and are unwet by it. Because of their incompatibility with salt, they migrate to various surfaces (in MSRE graphite moderator, Hastelloy N piping) and adhere to them. They apparently also migrate to gas-liquid interfaces and adhere to these in a stable manner [135].

In SPECTRA sorption models are present for the following situations:

- Sorption of fission products on solid surfaces covered by liquid (for example the graphite moderator of the MSRE core).
- Sorption of fission products on dust particles deposited in the liquid pool.
- Transport of fission products from the pool to the pool-atmosphere surface or pool-bubble surface, or droplet-atmosphere surface. This mechanism is included as a part of sorption verification because it is based on very similar equations as the other two, although, strictly speaking, this is not a sorption phenomenon.

Verification runs performed for the above mentioned three situations are described in the following sections.

3.12.53.1 Sorption on Solid Surfaces (SC / TC)

Sorption on solid surfaces is tested using a simple input model described below. Results are compared to the results of hand calculations. In order to simplify the verification, the “hand calculations” were programmed using a set of Control Functions. Input decks for the 1D and 2D versions of this test are provided in:

```
\Z-INPUTS\RT\Cir-fuel\Sorption\Sorption-SC\Sorption-SC.SPE
\Z-INPUTS\RT\Cir-fuel\Sorption\Sorption-TC\Sorption-TC.SPE
```

The analyzed model consists of a pipe (ID = 127 mm) represented by 5 Control Volumes (CV-101 through CV-105) connected to the environment (CV-200) at the outlet. The volumes are filled with salt (salt composition: LiF 65.0%, BeF_2 29.1%, ZrF_4 5.0%, UF4 0.9%; salt properties based on data in [135]). A constant source of salt and a noble metal Pd-106 (Vapor class 6, part of the built-in chain 106 - Figure 3-1044) is located in the first CV, with a constant salt source rate of 1300 kg/s and Pd-106 source rate of 10^{-7} kg/s.

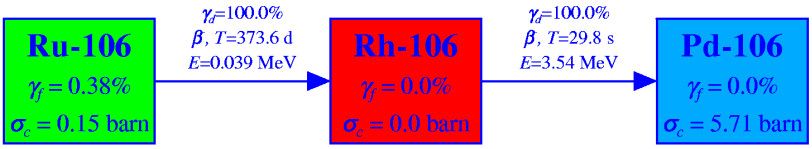

Figure 3-1044 Decay chain 106 used in the verification test run

It is assumed that the transport from salt to surfaces may be represented using a heat and mass transfer analogy. For a forced convective flow, we have:

$$Sh = 0.023\ Re^{0.8}\ Sc^{0.4}$$

Here *Re* is the Reynolds number, *Sc* is the Schmidt number, *and Sh* is the Sherwood number. The mass transfer coefficient (m/s) is obtained as: $Sh \times D_C / D_{FC}$, where D_{FC} is the characteristic dimension for forced convection (hydraulic diameter = 0.127 m), D_C, is the diffusion coefficient, equal to 1.32×10^{-9} (based on [135]).

In order to perform verification of the computed values, an automated verification was set-up using Tabular Functions and Control Functions, defined as follows:

- TF-100 = $D_C = 1.32\times10^{-9}$
- TF-101 = D_{FC} = 0.127 m
- CF-101 = $Re = v \times D_{FC} \times \rho / \eta$ =
  = SC-101-Vfld-l-pl × TF-101 × CV-101-Dens-pool / CV-101-Visc-pool
- CF-102 = $Sc = v / \rho / D_C$ =
  = CV-101-Visc-pool / CV-101-Dens-pool / TF-100
- CF-103 = $Re^{0.8}$ = CF-101$^{0.8}$
- CF-104 = $Sc^{0.4}$ = CF-102$^{0.4}$
- CF-105 = $Sh = 0.023\ Re^{0.8}\ Sc^{0.4}$ =
  = 0.023 × CF-103 × CF-104
- CF-106 = mass transfer coefficient, *MTC* (m/s) = $Sh \times D_C / D_{FC}$ =
  = CF-105 × TF-100 / TF-101
- CF-107 = Sorption mass transfer rate (kg/m^2-s) = $MTC \times M_{Pd\text{-}106} / V_{pool}$ =
  = CF-106 × CV-101-MIPi-0103 / CV-101-Volm-pool

Here $M_{Pd\text{-}106} / V_{pool}$ is the average density of Pd-106 in the pool, $M_{Pd\text{-}106}$ is the mass of Pd-106 in the pool (kg), and V_{pool} is the pool volume (m^3).

Figure 3-1045 shows the calculated values at 400 s, when stationary state is reached. The mass transfer coefficient is not directly available from SPECTRA plot parameters, however it can be constructed from the following plot parameters:

- Sorption flux (kg/m^2-s) of vapor class 6 on left (inner) surface of SC-101:
  SC-101-SF06-0001 (plot pointers: 8 / 101 / 222 / 1 / 6)
- No. of nuclides of isotope 103 (Pd-106) in the pool of CV-101, (nucl/m^3)
  CV-101-NIPi-0103 (plot pointers: 8 / 101 / 167 / 103)

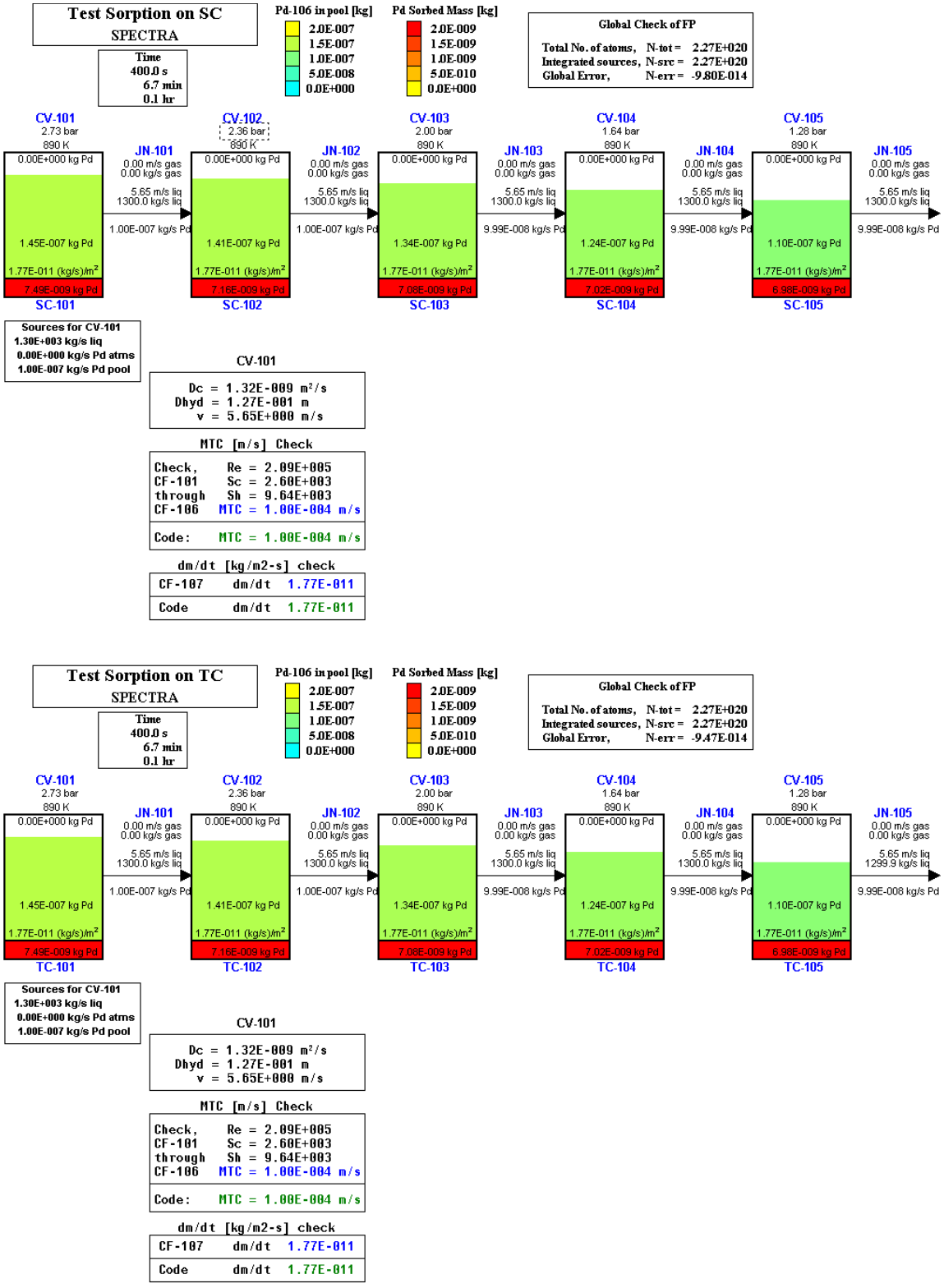

Figure 3-1045 Sorption of noble metals on solid surface (above: SC, below: TC)

The ratio of the above parameters must be multiplied by (Avogadro/Molar weight), which may be taken from the SPECTRA output file for Pd-106:

i	Isotope	Mass in the core (kg)	Molar weight (kg/kmol)	Beta- -fraction (-)	Gamma- -fraction (-)	Fission Yield (-)	Avogadro / / Molar w. (1/kg)
...							
103	Pd-106	0.00000E+00	1.06000E+02	5.00000E-01	5.00000E-01	0.00000E+00	**5.68113E+24**

The value obtained in such a way is given in Figure 3-1045 as "Code: MTC = 1.00E-4 m/s". The value obtained from the automated check is shown in Figure 3-1045 as "CF-106: MTC = 1.00E-4 m/s". Both values are in agreement.

The mass transfer rate (kg/m^2-s) is available as plot parameter: SC-101-SF06-0001 (plot pointers: 8 / 101 / 222 / 0001 / 6). The value is given in Figure 3-1045 as "Code: dm/dt = 1.77E-11". The value obtained from the automated check is shown in Figure 3-1045 as "CF-107: dm/dt = 1.77E-11". Both values are in agreement.

As an additional verification, the fission product relative mass error is shown in Figure 3-1045 (in the block Global Check of FP). As can be seen the relative mass error is of order of 10^{-14}, which is similar to the round-off errors for double precision arithmetics.

3.12.53.2 Sorption on Dust Particles in the Pool of a CV

Sorption on dust particles is tested using a simple input model described below. Results are compared to the results of hand calculations. In order to simplify the verification, the "hand calculations" were programmed using a set of Control Functions. Input deck is provided in:

```
\Z-INPUTS\RT\Cir-fuel\Sorption\Sorption-Part\Sorption-Part-1.SPE
```

The analyzed model consists of a single Control Volume (CV-101) connected to the environment above (CV-200). The volume is filled with salt (salt composition: LiF 65.0%, BeF_2 29.1%, ZrF_4 5.0%, UF4 0.9%; salt properties based on data in [135]). An initial mass of 10^{-6} kg of noble metal Pd-106 (Vapor class 6, part of the built-in chain 106 - Figure 3-1044) is assumed to be present in the CV. Furthermore, a constant source of Pd-106 is located in the CV, with a source rate 10^{-7} kg/s. An initial mass of dust particles in the pool is assumed as equal to 1.0 kg. The particle diameter is assumed to be 10^{-4} m.

It is assumed that the transport from salt to particle surface can be represented using a heat and mass transfer analogy. The particles are suspended in the salt with practically no relative movement between particles and salt. For such case a laminar flow around dust particles is expected, with the laminar correlation:

$$Sh = 3.656$$

The mass transfer coefficient (m/s) is obtained as: $Sh \times D_C / D_{FC}$, where D_{FC} is the characteristic dimension for forced convection (hydraulic diameter), D_C, is the diffusion coefficient, equal to 1.32×10^{-9} (based on [135]).

In order to perform verification of the computed values, an automated verification was set-up using Tabular Functions and Control Functions, defined as follows:

- TF-100 = $D_C = 1.32\times10^{-9}$
- TF-101 = D_{FC} = 0.0001 m (diameter of dust particles)
- CF-105 = Sh = 3.656
- CF-106 = mass transfer coefficient, MTC (m/s) = $Sh \times D_C / D_{FC}$ =
  = CF-105 × TF-100 / TF-101
- CF-107 = Sorption mass transfer rate (kg/m^2-s) = $MTC \times N / V_{pool}$ =
  = CF-106 × CV-101-MIPi-0103 / CV-101-Volm-pool

Figure 3-1046 shows the calculated values at 3600 s, when stationary state is reached. The mass transfer coefficient is not directly available from SPECTRA plot parameters, however it can be constructed from the following plot parameters:

- Sorption flux (kg/m^2-s) of vapor class 6 on dust particles size 1 in the pool of CV-101: CV-101-SF01-1006 (plot pointers: 8 / 101 / 186 / 6 / 1)
- No. of nuclides of isotope 103 (Pd-106) in the pool of CV-101, (nucl/m^3) CV-101-NIPi-0103 (plot pointers: 8 / 101 / 167 / 103)

The ratio of the above parameters must be multiplied by (Avogadro/Molar weight), which may be taken from the SPECTRA output for Pd-106:

i	Isotope	Mass in the core (kg)	Molar weight (kg/kmol)	Beta- -fraction (-)	Gamma- -fraction (-)	Fission Yield (-)	Avogadro / / Molar w. (1/kg)
...							
103	Pd-106	0.00000E+00	1.06000E+02	5.00000E-01	5.00000E-01	0.00000E+00	**5.68113E+24**

The value obtained in such a way is given in Figure 3-1046 as "Code: MTC = 4.83E-5". The value obtained from the automated check is shown in Figure 3-1046 as "CF-106: MTC = 4.83E-5". Both values are in agreement.

The mass transfer rate is available as plot parameter: CV-101-SF01-1006 (plot pointers: 8 / 101 / 186 / 6 / 1). The value is given in Figure 3-1046 as "Code: dm/dt = 1.67E-9". The value obtained from the automated check (CF-107) is shown in Figure 3-1046 as "CF-107: dm/dt = 1.67E-9". Both values are in agreement.

Figure 3-1047 shows time-dependent mass of Pd-106 in the pool and adsorbed on dust particles. The mass of Pd-106 in the pool of CV-101 reaches equilibrium at 3.45E-5 kg. At that value the mass source (1.0E-7 kg/s) is balanced by the sorption rate, which is 1.67E-9 kg/m^2-s times the number of particles (CV-101-DaeP-0001×V_{pool} = 1.91E9×1.0) times the surface area of a single particle, obtained from the code output:

Sec. No.	Average Diameter (m)	Relative Diameter (-)	Average Area (m2)	Relative Area (-)	Average Volume (m3)	Relative Volume (-)
1	1.00000E-04	1.00E+00	**3.14159E-08**	1.00E+00	5.23599E-13	1.00E+00

As an additional verification, the fission product relative mass error is shown in Figure 3-1046 (in the block Global Check of FP). As can be seen the relative mass error is of the order of 10^{-13}, which is similar to the round-off errors for double precision arithmentics.

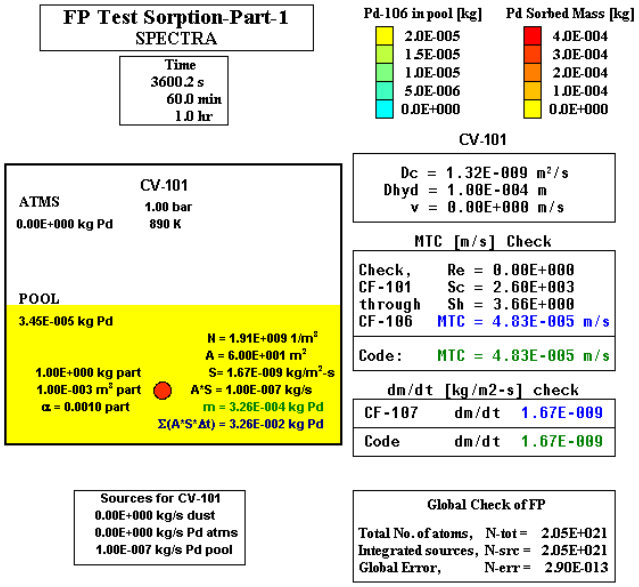

Figure 3-1046 Sorption of noble metals on dust surface, case Part-1

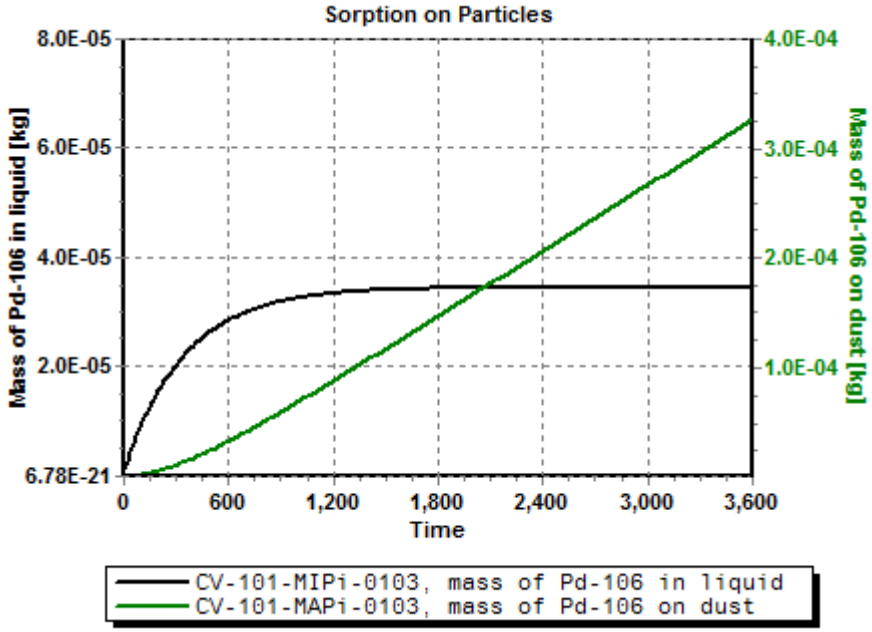

Figure 3-1047 Mass of noble metals in the liquid and on dust surface

In the above check, the surface area of single particles was taken from the code output. In the present case, only one size section was defined, with diameter of 10^{-4} m. In this case the area of a single particle is equal to the $\pi D^2 = \pi \times (10^{-4})^2$ = 3.14159E-8 m^2. However, if several size sections are defined, the larger particles is assumed to be conglomerates of smaller size particles and the surface area of the conglomerate and the area of the larger particles is different from the area of a sphere with given diameter. This is necessary to conserve surface area available for sorption during coagulation of dust particles. This is further explained in Volume 2, in the input record 861001.

For example, suppose we define 7 size sections, with the smallest size section of 1 micron and the largest size section 7 of 100 microns. Input deck is provided in:

`\Cir-fuel\Sorption\Sorption-Part\7-size-sections\Sorption-Part-7.SPE`

The surface areas (code output) are copied below.

Sec. No.	Average Diameter (m)	Relative Diameter (-)	Average Area (m2)	Relative Area (-)	Average Volume (m3)	Relative Volume (-)
1	1.00000E-06	1.00E+00	3.14159E-12	1.00E+00	5.23599E-19	1.00E+00
2	2.00000E-06	2.00E+00	2.51327E-11	8.00E+00	4.18879E-18	8.00E+00
3	5.00000E-06	5.00E+00	3.92699E-10	1.25E+02	6.54499E-17	1.25E+02
4	1.00000E-05	1.00E+01	3.14159E-09	1.00E+03	5.23599E-16	1.00E+03
5	2.00000E-05	2.00E+01	2.51327E-08	8.00E+03	4.18879E-15	8.00E+03
6	5.00000E-05	5.00E+01	3.92699E-07	1.25E+05	6.54499E-14	1.25E+05
7	1.00000E-04	1.00E+02	**3.14159E-06**	1.00E+06	5.23599E-13	1.00E+06

It is seen that the surface area of size 7 is 100 times larger than the surface area of a sphere with $D = 10^{-4}$ m. This is because in this case the size section particle, with effective diameter of 10^{-4} m, is assumed to be a conglomerate of a 10^6 particles of size section 1, with diameter of 10^{-6} m.

Results obtained for such case are shown in Figure 3-1048, left. Here the sorption flux needs to be taken for the size section 7, not 1, therefore the parameter CV-101-SF01-1006 is replaced by CV-101-SF07-1006 (plot pointers: 8 / 101 / 186 / 6 / 7). It is seen that now the stable value of mass transfer rate is 1.67E-11, two orders of magnitude smaller than in the previous case. This is a consequence of a 100 times larger surface area available for sorption. In order to obtain results identical to case Part-1, the base area (input parameter XBASRT) is set to 1.0E-2. The input deck is located in:

`\Cir-fuel\Sorption\Sorption-Part\7-size-sections\Sorption-Part-7-corr.SPE`

Results are obtained for this case are shown in Figure 3-1048, right. The results are identical to the results of case Part-1, shown in Figure 3-1046.

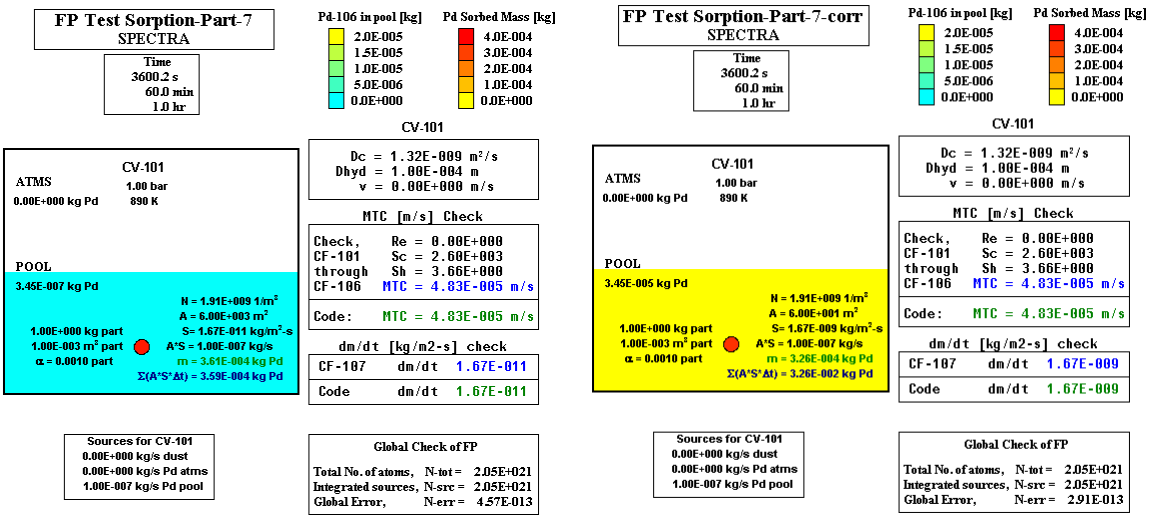

Figure 3-1048 Sorption of noble metals on dust surface, cases: Part-7 and Part-7-corr

3.12.53.3 Transport to Liquid-Gas Interfaces - Pool Surface

Transport to pool-atmosphere surface is tested using a simple input model described below. Results are compared to the results of hand calculations. In order to simplify the verification, the "hand calculations" were programmed using a set of Control Functions. Input deck is provided in:

```
\Z-INPUTS\RT\Cir-fuel\Sorption\Sorption-Atms\Sorption-Atms-1.SPE
```

The analyzed model consists of a single Control Volume (CV-101) connected to the environment above (CV-200). The volume is half-filled with salt (salt composition: LiF 65.0%, BeF_2 29.1%, ZrF_4 5.0%, UF4 0.9%; salt properties based on data in [135]). An initial mass of 10^{-6} kg of the noble metal Pd-106 (Vapor class 6, part of the built-in chain 106 - Figure 3-1044) is assumed to be present in the CV. A constant source of Pd-106 is located in the CV, with a source rate 10^{-7} kg/s.

It is assumed that the transport from salt to atmosphere surface can be represented using a heat and mass transfer analogy. There is practically no movement of salt and gas in this test. Therefore the laminar correlation is used:

$$Sh = 3.656$$

The mass transfer coefficient (m/s) is obtained as: $Sh \times D_C / D_{FC}$, where D_{FC} is the characteristic dimension for forced convection (hydraulic diameter, assumed equal to 0.1 m), D_C, is the diffusion coefficient, equal to 1.32×10^{-9} (based on [135]).

In order to perform verification of the computed values, an automated verification was set-up using Tabular Functions and Control Functions, defined as follows:

- TF-100 = $D_C = 1.32\times10^{-9}$
- TF-101 = D_{FC} = 0.1 m (= hydraulic diameter in CV-101)
- CF-105 = Sh = 3.656
- CF-106 = mass transfer coefficient, MTC (m/s) = $Sh \times D_C / D_{FC}$ =
  = CF-105 × TF-100 / TF-101
- CF-107 = Sorption mass transfer rate (kg/m^2-s) = $MTC \times N / V_{pool}$ =
  = CF-106 × CV-101-MIPi-0103 / CV-101-Volm-pool

Figure 3-1049 shows the calculated values at 2000 s, when a stationary state is reached. The mass transfer coefficient is not directly available from SPECTRA plot parameters, however it can be constructed from the following plot parameters:

- Pool-atmosphere mass transfer (kg/s) of isotope 103 (Pd-106):
  CV-101-FmPA-0103 (plot pointers: 8 / 101 / 164 / 103)
- Pool-atmosphere surface area, (m^2)
  CV-101-A_IN-pl>a (plot pointers: 1 / 101 / 68 / 1)
- No. of nuclides of isotope 103 (Pd-106) in the pool of CV-101, (nucl/m^3)
  CV-101-NIPi-0103 (plot pointers: 8 / 101 / 167 / 103)

The mass transfer divided by interface surface area and by nuclide density must be multiplied by (Avogadro/Molar weight), which may be taken from the SPECTRA output for Pd-106:

i	Isotope	Mass in the core (kg)	Molar weight (kg/kmol)	Beta- -fraction (-)	Gamma- -fraction (-)	Fission Yield (-)	Avogadro / / Molar w. (1/kg)
...							
103	Pd-106	0.00000E+00	1.06000E+02	5.00000E-01	5.00000E-01	0.00000E+00	**5.68113E+24**

The value obtained in such a way is given in Figure 3-1049 as "Code: MTC = 4.83E-8". The value obtained from the automated check is shown in Figure 3-1049 as "CF-106: MTC = 4.83E-8". Both values are in agreement.

The mass transfer rate (kg/m^2-s) is not available as plot parameter; however it may be constructed as a ratio of the following parameters:

- Pool-atmosphere mass transfer (kg/s) of isotope 103 (Pd-106):
  CV-101-FmPA-0103 (plot pointers: 8 / 101 / 164 / 103)
- Pool-atmosphere surface area, (m^2)
  CV-101-A_IN-pl>a (plot pointers: 1 / 101 / 68 / 1)

Ratio of the above parameters is given in Figure 3-1049 as "Code: dm/dt = 9.65E-12". The value obtained from the automated check (CF-107) is shown in Figure 3-1049 as "CF-107: dm/dt = 9.65E-12". Both values are in agreement. Furthermore, the area, A, times the transport rate, S, is equal to $A \times S = 1.0 \times 10^{-7}$ kg/s (Figure 3-1049), the same as the source rate, and the time-integrated value $\Sigma A \times S = 9.65 \times 10^{-9}$ kg is the same as the mass of Pd in the atmosphere.

Figure 3-1049 shows relative mass error of 10^{-16} (in the block Global Check of FP). This was obtained using a default error correction scheme (AMFPRT=0). If the mass error correction is disabled (AMFPRT=–1) the mass error at the end of calculations is of order of 10^{-12}.

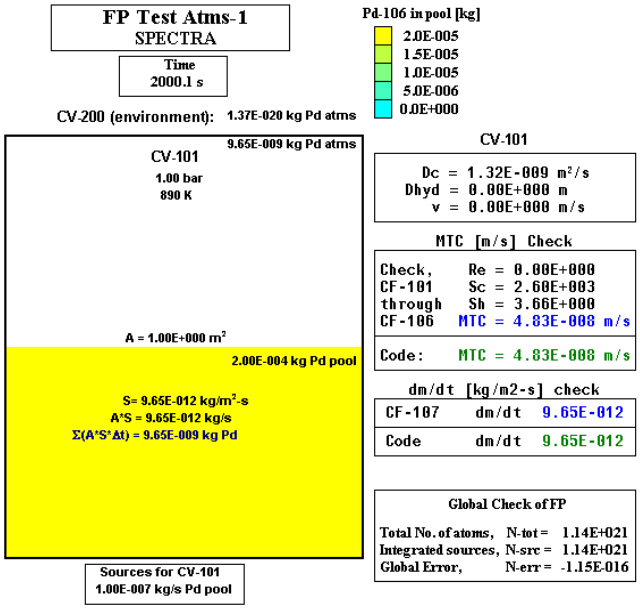

Figure 3-1049 Transport of noble metals to pool-atmosphere surface, case Atms-1

The test above was made using the default volume type: heterogeneous (MELCOR-type) Control Volume. The next test is identical, but with the volume type changed to homogeneous (RELAP-type) Control Volume. Input deck is provided in:

```
\Z-INPUTS\RT\Cir-fuel\Sorption\Sorption-Atms\Sorption-Atms-2.SPE
```

The results are shown in Figure 3-1050. The flow regime predicted for this CV is "stratified", which is seen in the CV output:

```
=CV=  CV-101,   HOMOGENEOUS CV DATA AT TIME :  2.00010E+03 (s)
Quantity                 Value
-----------------------  -----------
Flow regime              Stratified
Void fraction            5.00000E-01
Interface area       m2  1.00000E+00
Interf.area/unit V  1/m  5.00000E-01
Bubble/drop diameter m   0.00000E+00
```

The fission product mass transfer results, shown in Figure 3-1050, are practically identical to the results obtained for the heterogeneous volume, Figure 3-1049. This is because the interface area is in both cases the same, equal to the horizontal cross section area of CV-101 (1.0 m^2). As will be shown in the subsequent sections this is not the case for bubbly and droplet flow regimes.

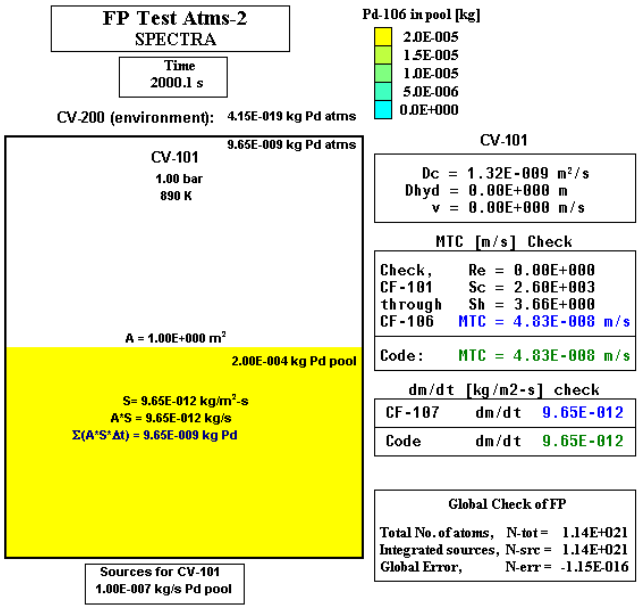

Figure 3-1050 Transport of noble metals to pool-atmosphere surface, case Atms-2

3.12.53.4 Transport to Liquid-Gas Interfaces - Bubble Surface

Transport to bubble surface is tested using a simple input model described below. Results are compared to the results of hand calculations. In order to simplify the verification, the "hand calculations" were programmed using a set of Control Functions. Input deck is provided in:

```
\Z-INPUTS\RT\Cir-fuel\Sorption\Sorption-Bubble\Sorption-Bubble-1.SPE
```

The analyzed model consists of a single Control Volume (CV-101) connected to the environment above (CV-200). The volume is filled with salt (salt composition: LiF 65.0%, BeF_2 29.1%, ZrF_4 5.0%, UF4 0.9%; salt properties based on data in [135]). An initial mass of 10^{-6} kg of the noble metal Pd-106 (Vapor class 6, part of the built-in chain 106 - Figure 3-1044) is assumed to be present in the CV. A constant source of Pd-106 is located in the CV, with a source rate 10^{-7} kg/s. A constant source of Helium is located at the bottom of CV-101, to create gas bubbles. The Helium source strength is 10^{-3} kg/s. The source injection parameters (diameter, area) were selected in order to obtain approximately 1 mm diameter bubbles. The actual diameter of the obtained bubbles was 0.959 mm.

It is assumed that the transport from salt to bubble surface can be represented using a heat and mass transfer analogy. The bubbles are moving relatively slowly (0.0639 m/s). The Reynolds number is low: 17.9. Therefore the flow around the bubbles is laminar, and the laminar correlation is used:

$$Sh = 3.656$$

The mass transfer coefficient (m/s) is obtained as: $Sh \times D_C / D_{FC}$, where D_{FC} is the characteristic dimension for forced convection (hydraulic diameter), D_C, is the diffusion coefficient, equal to 1.32×10^{-9} (based on [135]).

In order to perform verification of the computed values, an automated verification was set-up using Tabular Functions and Control Functions, defined as follows:

- TF-100 = $D_C = 1.32\times10^{-9}$
- CF-105 = $Sh = 3.656$
- CF-106 = mass transfer coefficient, MTC (m/s) = $Sh \times D_C / D_{bubb}$ =
  = CF-105 × TF-100 / CV-101-P_Di-bubb
- CF-107 = Sorption mass transfer rate (kg/m^2-s) = $MTC \times N / V_{pool}$ =
  = CF-106 × CV-101-MIPi-0103 / CV-101-Volm-pool

Figure 3-1051 shows the calculated values at 2000 s, when a stationary state is reached. The mass transfer coefficient is not directly available from SPECTRA plot parameters, however it can be constructed from the following plot parameters:

- Pool-atmosphere mass transfer (kg/s) of isotope 103 (Pd-106):
  CV-101-FmPA-0103 (plot pointers: 8 / 101 / 164 / 103)
- Pool-bubble surface area, (m^2)
  CV-101-A_IN-pl>b (plot pointers: 1 / 101 / 68 / 3)
- No. of nuclides of isotope 103 (Pd-106) in the pool of CV-101, (nucl/m^3)
  CV-101-NIPi-0103 (plot pointers: 8 / 101 / 167 / 103)

The mass transfer divided by interface surface area and by nuclide density must be multiplied by (Avogadro/Molar weight), which may be taken from the SPECTRA output for Pd-106:

Mass in the core	Molar weight	Beta--fraction	Gamma--fraction	Fission Yield	Avogadro / / Molar w.

i	Isotope	(kg)	(kg/kmol)	(-)	(-)	(-)	(1/kg)
...							
103	Pd-106	0.00000E+00	1.06000E+02	5.00000E-01	5.00000E-01	0.00000E+00	**5.68113E+24**

The value obtained in such a way is given in Figure 3-1051 as "Code: MTC = 5.03E-6". The value obtained from the automated check is shown in Figure 3-1051 as "CF-106: MTC = 5.03E-6". Both values are in agreement.

The mass transfer rate (kg/m^2-s) is not available as plot parameter; however it may be constructed as a ratio of the following parameters:

- Pool-atmosphere mass transfer (kg/s) of isotope 103 (Pd-106):
  CV-101-FmPA-0103 (plot pointers: 8 / 101 / 164 / 103)
- Pool-bubble surface area, (m^2)
  CV-101-A_IN-pl>b (plot pointers: 1 / 101 / 68 / 3)

The value is given in Figure 3-1051 as "Code: dm/dt = 4.24E-11". The value obtained from the automated check (CF-107) is shown in Figure 3-1051 as "CF-107: dm/dt = 4.24E-11". Both values are in agreement. Furthermore, the area, A, times the transport rate, S, is equal to $A{\times}S{=}1.0{\times}10^{-7}$ kg/s (Figure 3-1051), the same as the source rate, and the time-integrated value $\Sigma A{\times}S{=}1.79{\times}10^{-4}$ kg is the same as the mass of Pd in the atmosphere.

Mass errors are somewhat larger in the test problems involving bubbles. Figure 3-1051 shows relative mass error of 10^{-9} (in the block Global Check of FP). This was obtained using a default error correction scheme (AMFPRT=0). If the mass error correction is disabled (AMFPRT=–1) the mass error at the end of calculations is of order of 10^{-5}.

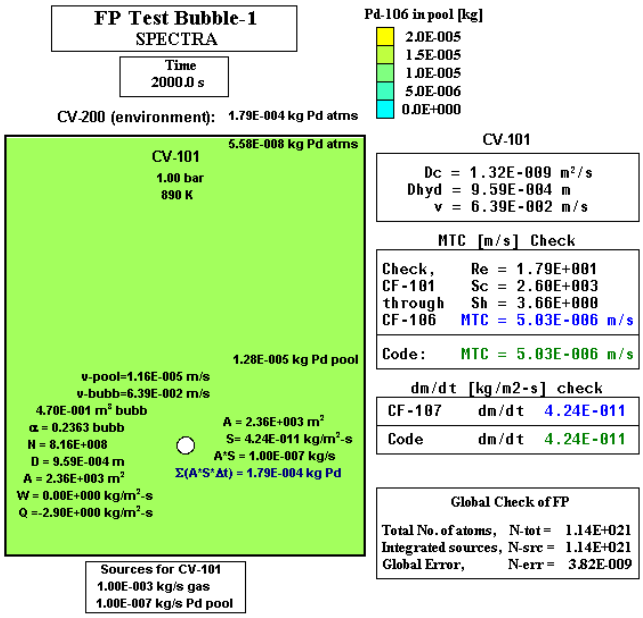

Figure 3-1051 Transport of noble metals to bubble surface, case Bubble-1

The test above was made using the default volume type: heterogeneous (MELCOR-type) Control Volume. The next test is identical, but with the volume type changed to homogeneous (RELAP-type) Control Volume. Input deck is provided in:

\Z-INPUTS\RT\Cir-fuel\Sorption\Sorption-Bubble\Sorption-Bubble-2.SPE

The results are shown in Figure 3-1052 (note that for homogeneous volumes the plot parameters pl>b must be replaced by pl>a). The flow regime predicted for this CV is “bubbly flow”, which is seen in the CV output:

```
=CV=  CV-101,   HOMOGENEOUS CV DATA AT TIME :  2.00009E+03 (s)
Quantity                  Value
------------------------  -----------
Flow regime               Bubbly Flow
Void fraction             1.92324E-02
Interface area       m2   2.81917E+02
Interf.area/unit V  1/m   1.40958E+02
Bubble/drop diameter m    8.18640E-04
```

The fission product mass transfer results, shown in Figure 3-1052, are quite different from the results obtained for the heterogeneous CV. The mass transfer coefficient is the same because it is obtained from the same correlation: *Sh* = 3.565. The mass transfer rate is however very different. This is caused by different bubble behavior. Due to higher velocity, the void fraction and therefore the number of bubbles is much smaller in the homogeneous CV than in the heterogeneous CV, Figure 3-1051. Because of smaller surface area, less Pd-106 is migrating to the gas. Consequently the Pd-106 concentrations in the liquid are much larger than in the heterogeneous CV. The following conclusion can be made here. *Migration of fission products from liquid to bubbles depend not only on the fission product mass transfer rate but also on the bubble parameters, such as bubble velocity, diameter, etc. The accuracy of these parameters will heavily affect the accuracy with which the migration of fission products is predicted.*

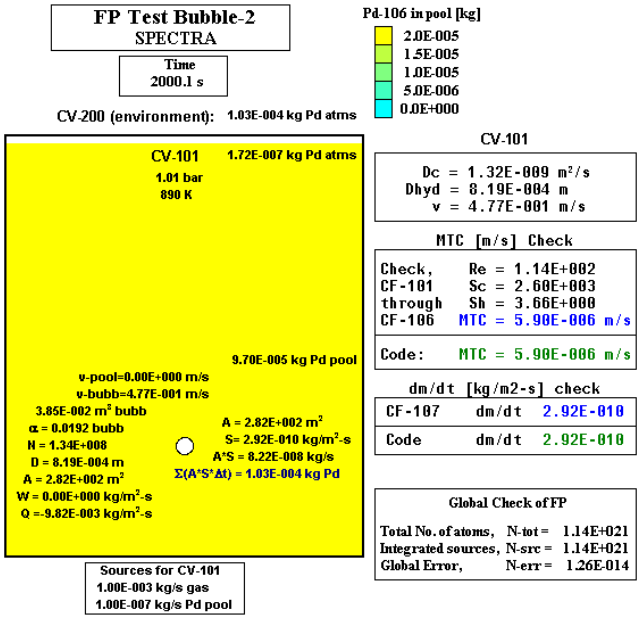

Figure 3-1052 Transport of noble metals to bubble surface, case Bubble-2

3.12.53.5 Transport to Liquid-Gas Interfaces - Droplet Surface

Transport to droplet surface is tested using a simple input model described below. Results are compared to the results of hand calculations. In order to simplify the verification, the "hand calculations" were programmed using a set of Control Functions. Input deck is provided in:

```
\Z-INPUTS\RT\Cir-fuel\Sorption\Sorption-Droplet\Sh-6\
Sorption-droplet-D02-2.SPE
```

The analyzed model consists of three Control Volumes: source volume: CV-100, volume where spray is located, CV-101, and the environment, CV-200. The source volume is filled with salt (salt composition: LiF 65.0%, BeF_2 29.1%, ZrF_4 5.0%, UF4 0.9%; salt properties based on data in [135]). During the first 1000 s a constant source (10^{-4} kg/s) of the noble metal Pd-106 (Vapor class 6, part of the built-in chain 106 - Figure 3-1044) in CV-100 is used to slowly build up the concentration of Pd-106. At 1000 s the mass is 0.1 kg, which means relative mass of 4.35×10^{-6}%. After 1000 s, the liquid present in CV-100 sprayed using JN-190, with a small flow area (10^{-4} m^2) and diameter (10^{-3} m). The source volume is large enough (A=1000.0 m^2), so that the conditions (liquid level) does not change significantly during the spraying period.

It is assumed that the transport from droplet surface can be represented using a heat and mass transfer analogy. Reference [180] shows that for mass transfer inside a bubble $6 < Sh < 18$. It is expected that mass transfer inside a droplet will be very similar. The lower value $Sh = 6$ was selected for the present test case:

$$Sh = 6.0$$

The mass transfer coefficient (m/s) is obtained as: $Sh \times D_C / D_{FC}$, where D_{FC} is the characteristic dimension for forced convection (hydraulic diameter), D_C, is the diffusion coefficient, equal to 1.32×10^{-9} (based on [135]).

In order to perform verification of the computed values, an automated verification was set-up using Tabular Functions and Control Functions, defined as follows:

- TF-100 = $D_C = 1.32\times10^{-9}$
- CF-105 = $Sh = 6.0$
- CF-106 = mass transfer coefficient, MTC (m/s) = $Sh \times D_C / D_{FC}$ =
  = CF-105 × TF-100 / CV-101-P_Di-drop
- CF-107 = Sorption mass transfer rate (kg/m^2-s) = $MTC \times N / V_{pool}$ =
  = CF-106 × CV-101-MIPi-0103 / CV-101-Volm-pool

Figure 3-1053 shows the calculated values at 7200 s, when a stationary state is reached. The mass transfer coefficient is not directly available from SPECTRA plot parameters, however it can be constructed from the following plot parameters:

- Pool-atmosphere mass transfer (kg/s) of isotope 103 (Pd-106):
  CV-101-FmPA-0103 (plot pointers: 8 / 101 / 164 / 103)
- Droplet surface area, (m^2)
  CV-101-A_IN-dp>a (plot pointers: 1 / 101 / 68 / 2)
- No. of nuclides of isotope 103 (Pd-106) in the pool of CV-101, (nucl/m^3)
  CV-101-NIPi-0103 (plot pointers: 8 / 101 / 167 / 103)

The mass transfer divided by interface surface area and by nuclide density must be multiplied by (Avogadro/Molar weight), which may be taken from the SPECTRA output for Pd-106:

i	Isotope	Mass in the core (kg)	Molar weight (kg/kmol)	Beta- -fraction (-)	Gamma- -fraction (-)	Fission Yield (-)	Avogadro / / Molar w. (1/kg)
...							
103	Pd-106	0.00000E+00	1.06000E+02	5.00000E-01	5.00000E-01	0.00000E+00	**5.68113E+24**

The value obtained in such a way is given in Figure 3-1053 as “Code: MTC = 3.96E-5”. The value obtained from the automated check is shown in Figure 3-1053 as “CF-106: MTC = 3.95E-5”. Both values are in agreement.

The mass transfer rate (kg/m^2-s) is not available as plot parameter; however it may be constructed as a ratio of the following parameters:

- Pool-atmosphere mass transfer (kg/s) of isotope 103 (Pd-106):
  CV-101-FmPA-0103 (plot pointers: 8 / 101 / 164 / 103)
- Droplet surface area, (m^2)
  CV-101-A_IN-dp>a (plot pointers: 1 / 101 / 68 / 2)

The value is given in Figure 3-1053 as “Code: dm/dt = 1.21E-9”. The value obtained from the automated check (CF-107) is shown in Figure 3-1053 as “CF-107: dm/dt = 1.21E-9”. Both values are in agreement. A “stripping efficiency” of the spray system may be defined as the decrease of Pd-106 in the liquid due to spray:

stripping efficiency: $$\eta = 1 - \frac{fraction\,of\ Pd-106\,in\,the\,pool\,of\ CV-101}{fraction\,of\ Pd-106\,in\,the\,pool\,of\ CV-100}$$

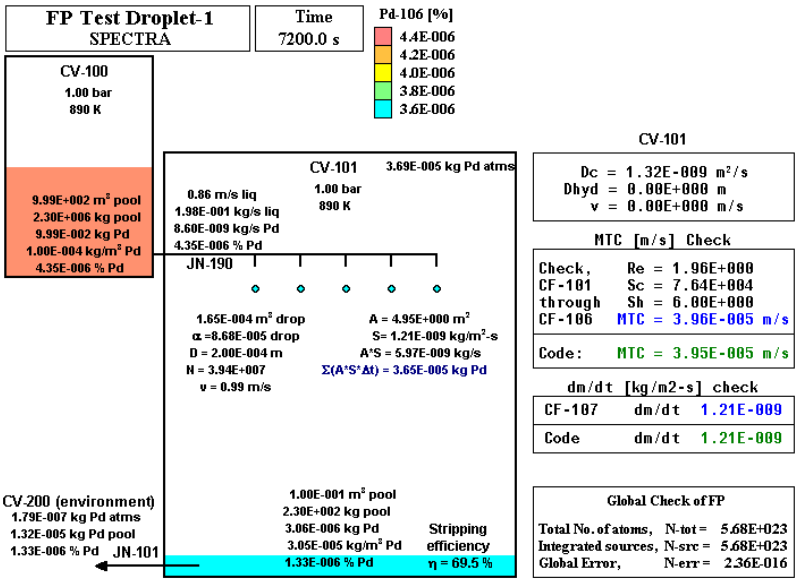

Figure 3-1053 Transport of noble metals from droplet surface, case Droplet-1

The stripping efficiency is 69.5% in the present test. The above definition is strictly valid only for a non-decaying isotope. For a decaying isotope it is better to use the ratio of mass transfer to droplets, CV-101-FmPA-0103 divided by the inlet flow rate JN-190-WIsP-0103.

Relative mass error is of order of 10^{-16} (block Global Check of FP). This was obtained using a default error correction scheme (AMFPRT=0). If the mass error correction is disabled (AMFPRT=–1) the mass error at the end of the run is of order of 10^{-11}.

The test above was made using the default volume type: heterogeneous (MELCOR-type) Control Volume. The next test is identical, but with the volume type changed to homogeneous (RELAP-type) Control Volume. Input deck is provided in:

```
\Z-INPUTS\RT\Cir-fuel\Sorption\Sorption-Droplet\Sh-6\
Sorption-droplet-D02-2.SPE
```

The results are shown in Figure 3-1054. The flow regime predicted for this CV is “mist flow”, which is seen in the CV output:

```
=CV=  CV-101,    HOMOGENEOUS CV DATA AT TIME :  7.20000E+03 (s)
Quantity                  Value
------------------------  -----------
Flow regime               Mist flow
Void fraction             9.99423E-01
Interface area       m2   3.45912E+01
Interf.area/unit V  1/m   1.72956E+01
Bubble/drop diameter m    2.00000E-04
```

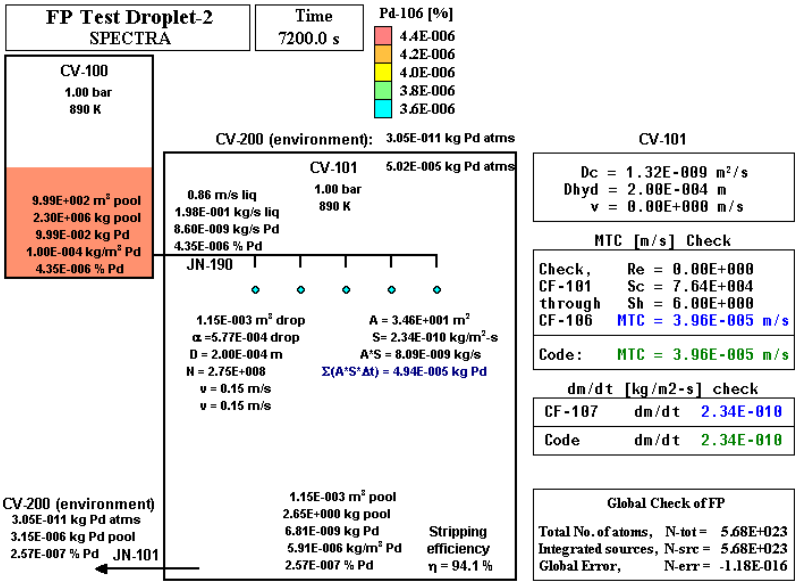

Figure 3-1054 Transport of noble metals from droplet surface, case Droplet-2

The fission product mass transfer results, shown in Figure 3-1054, are quite different from the results obtained for the heterogeneous CV. The mass transfer coefficient is the same because it is obtained from the same correlation: *Sh* = 6.0. The mass transfer rate is however quite different, 3.48E-10 versus 4.79E-10 kg/m^2-s. This is caused by different droplet behavior. The droplet velocity is obtained from different correlations and is quite different (0.15 versus 0.99 m/s) and therefore the number of droplets is much larger in the homogeneous CV (2.8×10^8) than in the heterogeneous CV (3.5×10^7, Figure 3-1053). Because of larger surface area, more Pd-106 is migrating to the gas and the stripping efficiency is larger (94.1%) than in the heterogeneous CV (69.5%). It is expected that for this case the heterogeneous CV is more accurate than the homogeneous CV.

In order to investigate further the effect of droplet diameter, calculations were performed using droplet diameters between 0.2 mm and 2.0 mm (the input parameter DDWFCV was used to set the droplet diameter to a desired value). Results are shown in Figure 3-1055 and Table 3-93. It is clear that the droplet diameter has an important effect. If the droplets are larger, then the stripping efficiency become smaller because of two reasons:

- with a large droplet diameter the overall surface area is small and
- the droplet velocity is large, so the droplet falling time is short - Table 3-94.

The following general conclusion can be drawn. *Migration of fission products from droplets to gas depend not only on the fission product mass transfer rate but also on the droplet parameters, such as droplet velocity, diameter, etc. The accuracy of these parameters will heavily affect the accuracy with which the migration of fission products is predicted.*

In the above examples the correlation *Sh* = 6.0 was used to calculate the mass transport within a droplet. Literature provides correlations for mass transfer in bubbles. The correlation recommended in [180] is:

$$Sh = \frac{1}{1+\exp(-a\cdot[\ln(Pe)-b)}\cdot(Sh_{\max}-Sh_{\min})+Sh_{\min}$$

The constants are: Sh_{min} = 6.58, Sh_{max} = 18.0, a = 1.89, b = 3.3, 3.8, 4.2. Results are shown in Figure 3-1056.

It may be expected that the mass transfer in droplets is similar as in bubbles and the same formula may be apply. This means that Sherwood number between 6 and 18 would be reasonable. One can also use a correlation. The correlation shown above cannot be directly applied in SPECTRA. The correlation that is available in SPECTRA has the following form (see Volume 2, record 895YXX):

$$Sh = A + B\,\frac{Re^C\ Sc^D}{1+E\ Re^F\ Sc^G}$$

The coefficients for this correlation were fit to provide a good match with the correlation from [180], as follows. Since $Pe = Re\times Sc$, this implies $C=D$ and $F=G$.

In order to be consistent with the correlation from [180], the coefficients C and D were set to zero. The correlation is:

$$Sh = A + \frac{B}{1 + E\ Re^{F}\ Sc^{G}}$$

The other constants were obtained by trial and error. The values that provide a good fit to the data are: A = 6.58, B = 11.4, F = G = –2, E = 800, 1900, 4200. Results are shown in Figure 3-1057 (correlation is shown by red lines and yellow markers, original data [180] in black).

Table 3-93 Transport from droplet surface

Dp	Sh = 6.0	Sh = 18.0
0.20	69.5	87.2
0.50	8.4	21.7
1.0	1.1	3.3
2.0	0.2	0.5

Table 3-94 Droplet velocity

D [mm]	v [m/s]
0.2	1.0
0.5	3.9
1.0	8.0
2.0	14.7

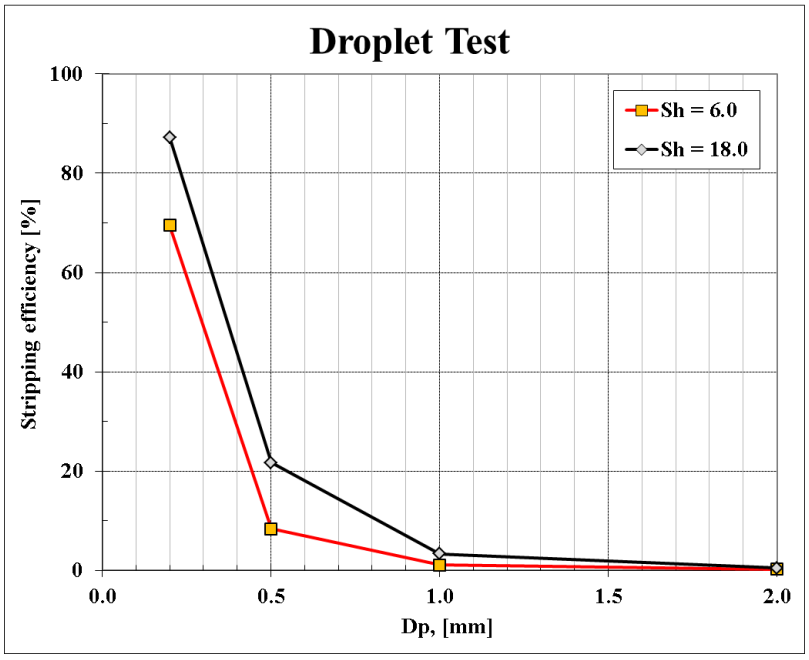

Figure 3-1055 Transport from droplet surface - effect of droplet size

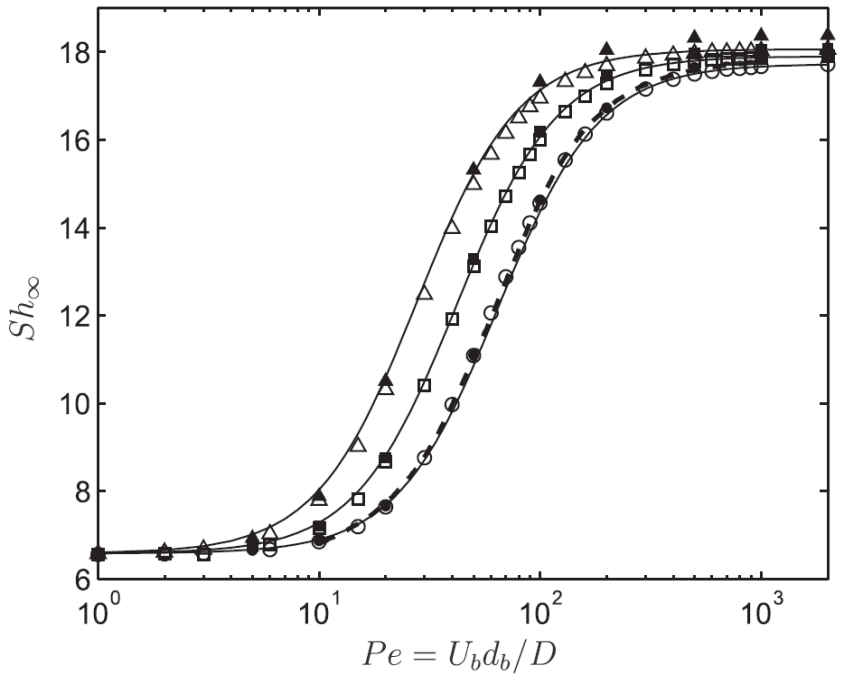

Figure 3-1056 Transport from droplet surface - correlations from [180]

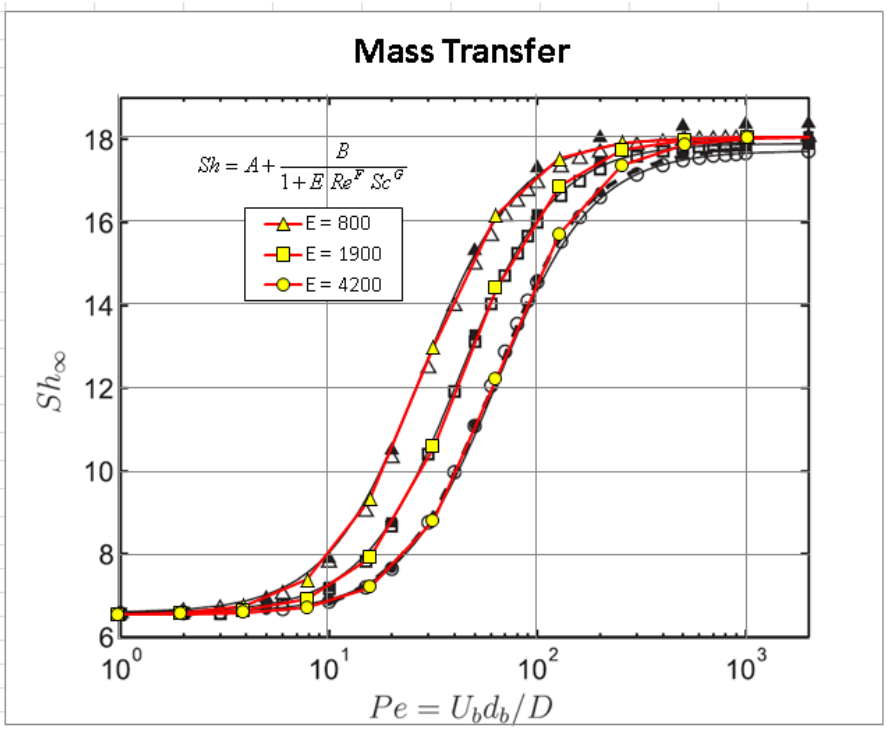

Figure 3-1057 Transport from droplet surface - SPECTRA correlation

3.12.54 Transport of Fission Product Isotopes to Bubbles - Single CV

This section provides verification of the model used for transport of fission products as well as aerosol particles suspended in the pool to bubbles. The tests consider a single Control Volume. Similar tests involving flow through multiple Control Volumes are shown in the following section.

The test case consists of a single Control Volume (CV-101) filled up to 1.0 m with water pool at 1 bar, 310 K. A large gas space is provided in the upper part, to keep the conditions approximately constant. A mass of 10^{-10} kg of the stable isotope Mo-96 is initially suspended in the pool. A source of air, located at the bottom of CV, provides a source of bubbles. The bubbles rise up to the pool surface and collect some mass of the isotope Mo-96 (density of ρ_p = 10,280 kg/m^3). Two methods are used to calculate the mass transfer rate of Mo-96 to bubbles:

- Sherwood number correlation, *Sh* = 41.7 (correlation applied in MSRE). Mo-96 is assumed to be transported in molecular form (sedimentation velocity is zero).
- Brownian diffusion + inertial impaction. This model is available if Mo-96 is assumed to be transported as small particles. The particle size and density are set to: DPFPRT = 0.1×10^{-6} m, RHFPRT = 10,280 kg/m^3. The diffusion boundary layer thickness is assumed as 10^{-5} m. The constant in the inerial impaction correlation is set to 0.25 (original value of Langmuir and Blodgett (see Volume 1).

No sticking coefficient was defined in the analyzed cases (which means that the sticking coefficient is 1.0). The diffusion coefficient of water was obtained from [171]. The values obtained from the references and tabulated for SPECTRA are shown in Figure 3-1058.

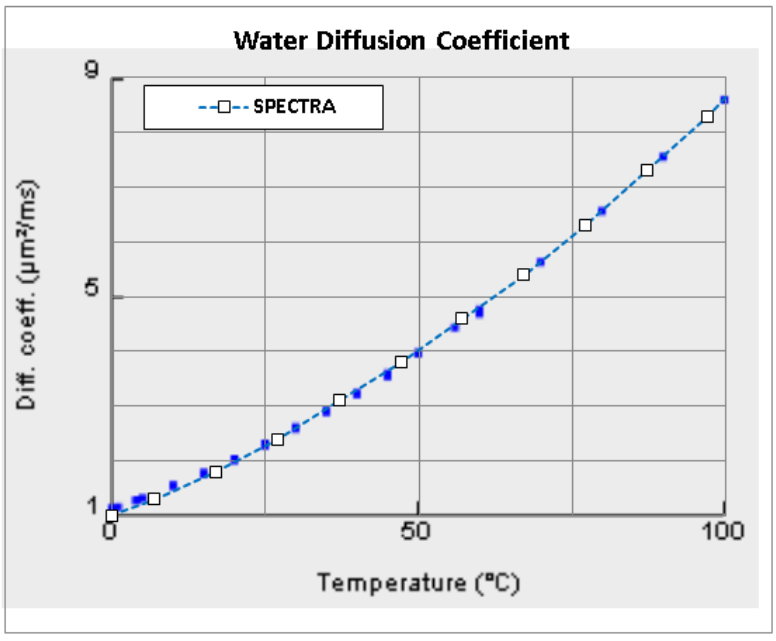

Figure 3-1058 Water diffusion coefficient, data (blue markers) [171] and SPECTRA values

Three cases are considered:

- Transport of fission product isotope to bubbles in a pool of a single CV
- Transport of fission product isotope to aerosol particles suspended in a pool of CV
- Transport of aerosol particles to bubbles in a pool of a single CV

The present test shows that exactly the same results are obtained for the three above mentioned situations, if the same mass transfer correlation is used.

3.12.54.1 Fission Product Transport to Bubbles

The following assumptions are made:

- ***Bubble rise velocity.***
  - Correlation for v_∞ with user-defined $C_{D,Re\to\infty}$=0.443 (record 161000, CDRGCV=0.443).
- ***Pool-bubble transport of FP.***
  - Active (IPATRT=2, record 196XXX)
  - Correlations used (record 8960XX):
    - Sh=41.7
    - Brownian diffusion + inertial impaction (TBL1RT=10^{-5}, CBL1RT=0.25)

The SPECTRA input files are located in: **`\Z-INPUTS\RT\Pool-Bubb\FP-on-Bubb`**

Figure 3-1059 and Figure 3-1060 show results obtained using the Brownian diffusion and inertial impaction models. The mass transfer velocity, (v_{mt} in Figure 3-1059) is not available as a plot/CF parameter, therefore it is obtained in CF-101 as the mass transfer rate W (kg/s) (CV-101-FmPA-0191), divided by the particle density in the pool (CV-101-MIPi-0191/CV-101-Volm-pool) (kg/m^3), multiplied by the mass transfer area (equal to number of bubbles time the surface area of a single bubble πD^2=$\pi\times5.01079\times10^{-3}$ = 7.8879E-05: CV-101-P_No-bubb × 7.8879E-05), $v_{mt} = W / (m/V_{pool}) / A$.

An automated verification of the obtained values is performed as follows. The particle mass balance is:

$$\frac{dm}{dt} = -A \cdot v_{mt} \cdot \frac{m}{V_{pool}}$$

solution:

$$m = m_0 \cdot \exp\left(-\frac{A \cdot v_{mt}}{V_{pool}} \cdot t \right)$$

Here m is the mass of particles in the pool, m_0 is the initial mass: $m_0 = 10^{-10}$ kg, A is the total surface area of bubbles (m^2), V_{pool} is the pool volume (m^3), and t is time (s). The following Control Functions were defined in order to perform automated verification of the computed values:

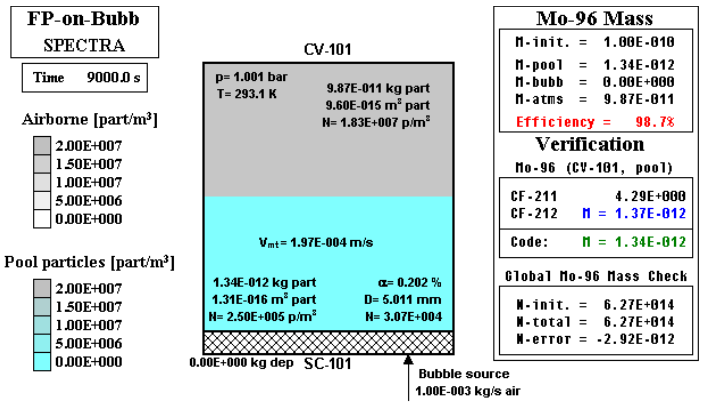

Figure 3-1059 Fission product transport to bubbles, *t* = 9,000 s, diffusion + impaction

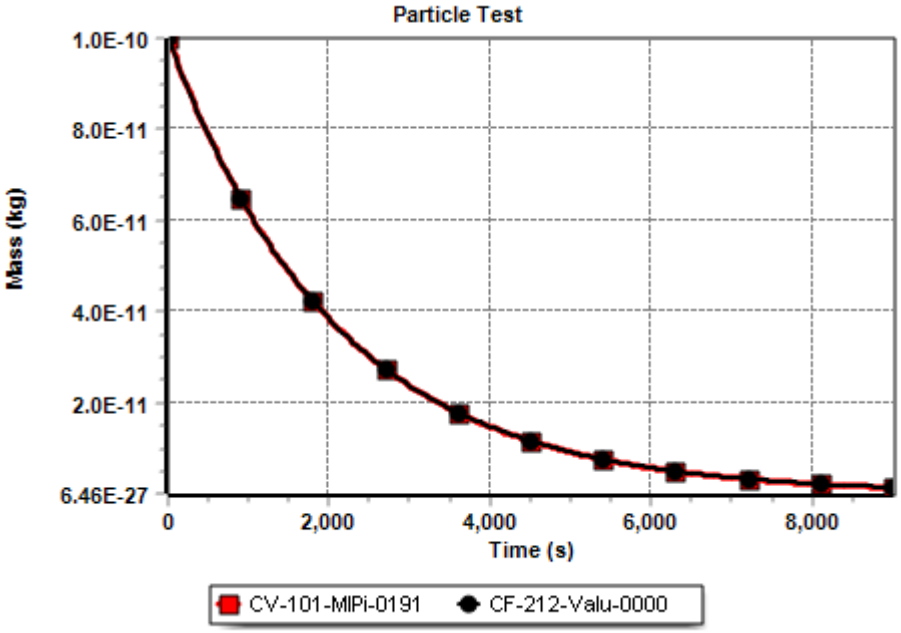

Figure 3-1060 Calculated and theoretical (CF-212) mass in the pool, diffusion + impaction

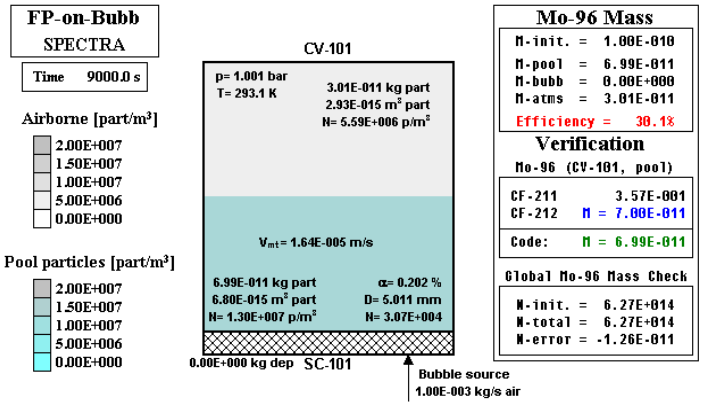

Figure 3-1061 Fission product transport to bubbles, *t* = 9,000 s, Sh = 41.7

- CF-101 = $v_{mt} = W \times V_{pool} / m / A$
  = CV-101-FmPA-0191 / (CV-101-P_No-bubb × 7.88790E-05) × CV-101-Volm-pool / CV-101-MIPi-0191
- CF-211 = $A\, v_{mt}\, t / V_{pool}$ =
  = (CV-101-P_No-bubb × 7.88790E-05) × CF-101-Valu-0000 × SL-000-Time-0000 / CV-101-Volm-pool
- CF-212 = $m = \exp(-A\, v_{mt}\, t / V_{pool})$ =
  = exp (– CF-211-Valu-0000)

Figure 3-1059 shows the state of the system at 9000 s. Almost all of Mo-96 (98.7%) has been collected by bubbles and moved to the atmosphere. The calculated mass transfer velocity is equal to $v_{mt} = 1.97\times10^{-4}$ m/s. Figure 3-1060 shows the mass of particles in the pool and the theoretical solution, obtained with CF-212. The calculated results are in good agreement with the theoretical solution.

Figure 3-1061 shows results obtained using the correlation Sh=41.7. Figure shows state of the system at 9000 s. The calculated mass transfer velocity is much smaller than in previous case, $v_{mt} = 1.64\times10^{-5}$ m/s. Consequently much less Mo-96 (30.1%) has been collected by bubbles and moved to the atmosphere by the end of the analyzed period. The calculated results are in very good agreement with theoretical solution, which is seen in Figure 3-1061 (values shown as "CF-212" and "Code").

3.12.54.2 Fission Product Transport to Aerosol Particles

In this case aerosol particles in the pool are used to simulate bubbles. The mass source of bubbles is replaced by the mass source of particles. The particle density is set to 1.23 kg/m^3 (= density of bubbles in the previous test). The particle diameter is set to: 5.01079 mm (= diameter of bubbles in the previous test). The same assumptions are made as in the previous case:

- ***Bubble rise velocity.***
  - Correlation for v_∞ with user-defined $C_{D,Re\to\infty}$=0.443 (record 171000, VINPRT=100.443).
- ***Pool-bubble transport of FP.***
  - Active, sorption model 1 is used (record 898000)
  - Correlations used (record 895107):
    - Sh=41.7
    - Brownian diffusion + inertial impaction (TBL1RT=10^{-5}, CBL1RT=0.25)

The SPECTRA input files are located in: **`\Z-INPUTS\RT\Pool-Bubb\FP-on-Aer`**

Figure 3-1062 and Figure 3-1063 shows results obtained using the Brownian diffusion and inertial impaction models. The mass transfer velocity, (v_{mt} in Figure 3-1063) is not available as a plot/CF parameter, therefore it is obtained in CF-101 as the mass transfer flux (mass per unit area) F (kg/m^2-s) (CV-101-SF01-1007), divided by the particle density in the pool (CV-101-MIPi-0191/CV-101-Volm-pool) (kg/m^3), $v_{mt} = F / (m/V_{pool})$.

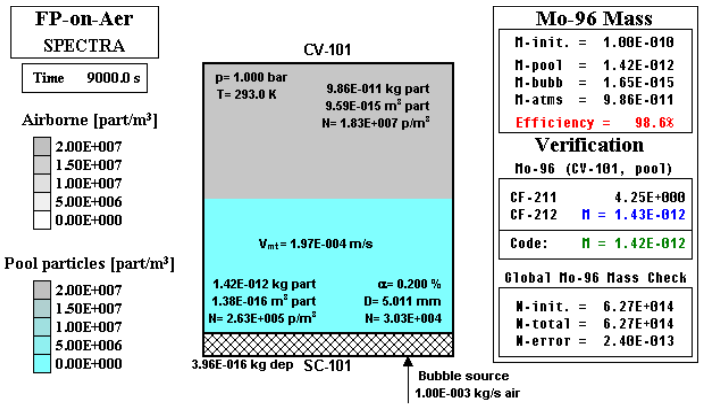

Figure 3-1062 Fission product transport to aerosol particles, *t* = 9,000 s, diffusion + impaction

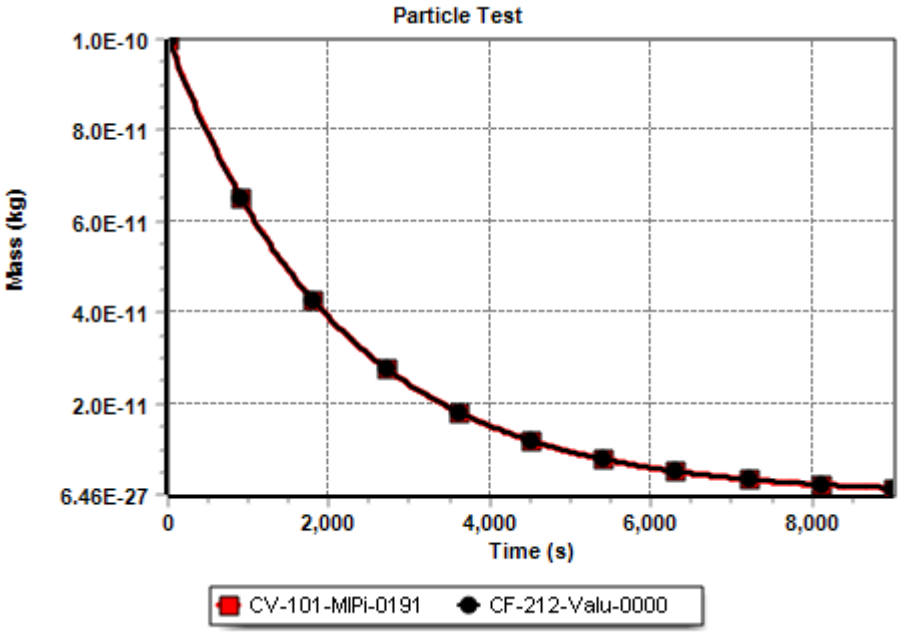

Figure 3-1063 Calculated and theoretical (CF-212) mass in the pool, diffusion + impaction

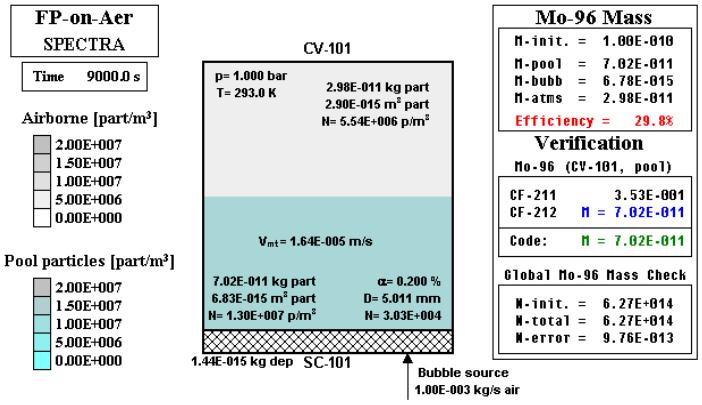

Figure 3-1064 Fission product transport to aerosol particles, *t* = 9,000 s, Sh = 41.7

An automated verification of the obtained values is performed as follows. The particle mass balance is:

$$\frac{dm}{dt} = -A \cdot v_{mt} \cdot \frac{m}{V_{pool}}$$

solution:

$$m = m_0 \cdot \exp\left(-\frac{A \cdot v_{mt}}{V_{pool}} \cdot t \right)$$

Here m is the mass of particles in the pool, m_0 is the initial mass: $m_0 = 10^{-10}$ kg, A is the total surface area of aerosol particles (m^2), V_{pool} is the pool volume (m^3), and t is time (s). The following Control Functions were defined in order to perform automated verification of the computed values:

- CF-101 = $v_{mt} = F / (m / V_{pool})$
  = CV-101-SF01-1007 * CV-101-Volm-pool / CV-101-MIPi-0191
- CF-211 = $A\ v_{mt}\ t / V_{pool}$ =
  = (CV-101-DaeP-0001 × 7.88790E-05) × CF-101-Valu-0000 ×
  SL-000-Time-0000
- CF-212 = $m = \exp(-A\ v_{mt}\ t / V_{pool})$ =
  = exp (– CF-211-Valu-0000)

Figure 3-1062 shows the state of the system at 9000 s. Almost all Mo-96 (98.6%) has been collected by bubbles and moved to the atmosphere. The calculated mass transfer velocity is equal to v_{mt} = 1.97×10^{-4} m/s. Figure 3-1063 shows the mass of particles in the pool and the theoretical solution, obtained with CF-212. The calculated results are in good agreement with the theoretical solution.

Figure 3-1064 shows results obtained using the correlation Sh=41.7. The figure shows the state of the system at 9000 s. The calculated mass transfer velocity is much smaller than in previous case, v_{mt} = 1.64×10^{-5} m/s. Consequently much less Mo-96 (29.8%) has been collected by bubbles and moved to the atmosphere by the end of the analyzed period. The calculated results are in very good agreement with theoretical solution, which is seen in Figure 3-1061 (values shown as “CF-212” and “Code”).

The results are practically identical to the results of previous test, where “physical” bubbles are used. This shows that one may in certain situations use aerosol field instead of bubbles. This adds to code flexibility and user convenience.

3.12.54.3 Aerosol Particle Transport to Bubbles

In this case the isotope is modeled using the aerosol field. Aerosols suspended in the pool of CV can be transported to bubbles, however the mechanistic correlations are not available in this case. Exactly the same mass source of bubbles is present as in section 3.12.54.1. The aerosol particle density is set to Mo-96 density, 10,280 kg/m^3. The particle diameter is set to 0.1×10–6 m (= isotope diameter in section 3.12.54.2). The assumptions are:

- ***Bubble rise velocity.***
  - Correlation for v_∞ with user-defined $C_{D,Re\to\infty}$=0.443 (record 161000, CDRGCV=0.443).
- ***Pool-bubble transport of FP.***
  - Active (KPATRT=2, record 172XXX)
  - The "migration correlations" are not available here (only the drag coefficient correlation can be used. Therefore constant, user-defined transport velocities (record 171XXX, VINPRT) are specified based on results of the previous test:
    - $v_{mt} = 1.97\times10^{-4}$ m/s (the "diffusion + impaction" case)
    - $v_{mt} = 1.64\times10^{-5}$ m/s (the "Sh=41.7" case)

The SPECTRA input files are located in: **`\Z-INPUTS\RT\Pool-Bubb\Aer-on-Bubb`**

Figure 3-1065 and Figure 3-1066 shows results obtained using the "diffusion + impaction" model. The mass transfer velocity, (v_{mt} in Figure 3-1065) is not available as a plot/CF parameter, therefore it is obtained in CF-101 as the mass transfer rate W (kg/s) (CV-101-Resm-0001), divided by the particle density in the pool (CV-101-SMaP-0000/CV-101-Volm-pool) (kg/m^3), divided by the mass transfer area A (equal to number of bubbles times the surface area of a single bubble, CV-101-P_No-bubb × 7.88790E-05), $v_{mt} = W / (m/V_{pool}) / A$.

An automated verification of the obtained values is performed as follows. The particle mass balance is:

$$\frac{dm}{dt} = -A \cdot v_{mt} \cdot \frac{m}{V_{pool}}$$

solution:

$$m = m_0 \cdot \exp\left(-\frac{A \cdot v_{mt}}{V_{pool}} \cdot t \right)$$

Here m is the mass of particles in the pool, m_0 is the initial mass: $m_0 = 10^{-10}$ kg, A is the total bubble surface area (m^2), V_{pool} is the pool volume (m^3), and t is time (s). The following Control Functions were defined in order to perform automated verification of the computed values:

- CF-101 = $v_{mt} = W \times V_{pool} / m / A$
  = CV-101-Resm-0001 / (CV-101-P_No-bubb × 7.88790E-05) ×
  CV-101-Volm-pool / CV-101-SMaP-0000
- CF-211 = $A\ v_{mt}\ t / V_{pool}$ =
  = (CV-101-P_No-bubb × 7.88790E-05) × CF-101-Valu-0000 ×
  SL-000-Time-0000 / CV-101-Volm-pool
- CF-212 = $m = \exp(-A\ v_{mt}\ t / V_{pool})$ =
  = exp (– CF-211-Valu-0000)

Figure 3-1065 shows the state of the system at 9000 s. Almost all Mo-96 (98.6%) has been collected by bubbles and moved to the atmosphere. The mass transfer velocity is $v_{mt} = 1.97\times10^{-4}$ m/s (defined in input). Figure 3-1066 shows the mass of particles in the pool and the theoretical solution, obtained with CF-212. The calculated results are in good agreement with the theoretical solution.

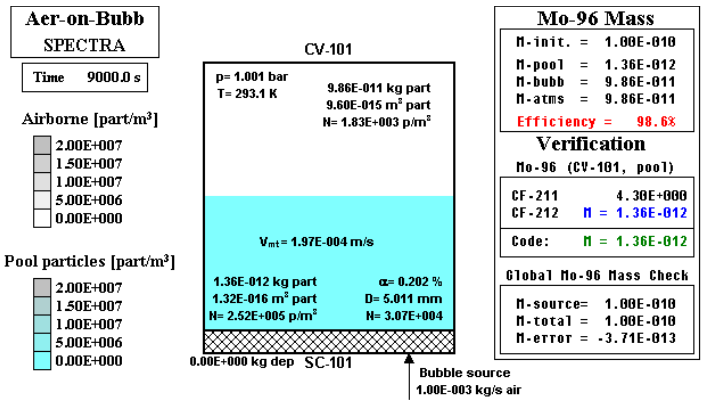

Figure 3-1065 Aerosol particle transport to bubbles, *t* = 9,000 s, “diffusion + impaction”

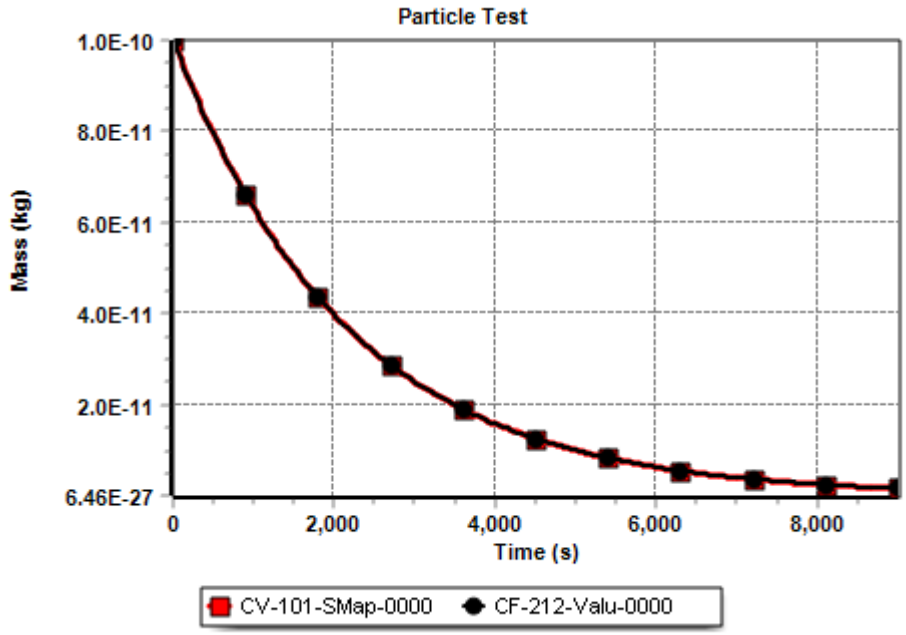

Figure 3-1066 Calculated and theoretical (CF-212) mass in the pool, “diffusion + impaction”

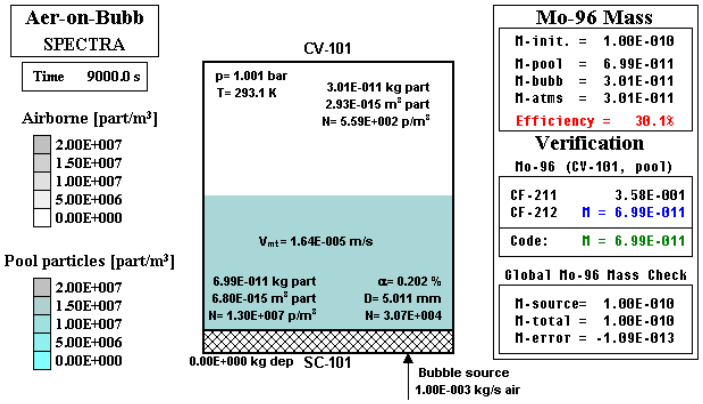

Figure 3-1067 Aerosol particle transport to bubbles, *t* = 9,000 s, “Sh = 41.7”

Figure 3-1067 shows results obtained using the "Sh=41.7" correlation. The figure shows the state of the system at 9000 s. The mass transfer velocity is v_{mt} = 1.64×10^{-5} m/s (defined in input). Consequently much less Mo-96 (30.1%) has been collected by bubbles and moved to the atmosphere by the end of the analyzed period. The calculated results are in very good agreement with theoretical solution, which is seen in Figure 3-1061 (values shown as "CF-212" and "Code").

Results are practically identical to the results of previous two tests, which shows that one may model this third method, although the mass transfer velocity cannot be calculated and must be provided by the user.

3.12.55 Transport of Particles and Fission Product Isotopes - Multiple CVs

This section provides tests very similar to the tests described in the previous section. The main difference is that here we consider transport through Control Volumes.

The test case consists of a two Control Volumes (CV-101, CV-102). The bottom CV is filled to the top (1.0 m) with water pool at 1 bar, 310 K. The top CV is filled up to 1.0 m with water pool at 1 bar, 310 K. A large gas space is provided in the upper part of CV-102, to keep the conditions approximately constant. A mass of 10^{-10} kg of the stable isotope Mo-96 is initially suspended in the pool of CV-101. A source of air, located at the bottom of CV, provides a source of bubbles. The bubbles rise up to the pool surface and collect some mass of the isotope Mo-96 (density of ρ_p = 10,280 kg/m^3).

As in the previous section, two methods are used to calculate the mass transfer rate of Mo-96 to bubbles:

- Sherwood number correlation, *Sh* = 41.7.
- Brownian diffusion + inertial impaction, with particle size and density of 0.1×10^{-6} m, and 10,280 kg/m^3 respectively.

The same three cases are considered:

- Transport of fission product isotope to bubbles in a pool
- Transport of fission product isotope to aerosol particles suspended in a pool
- Transport of aerosol particles to bubbles in a pool

Again, it is demonstrated that exactly the same results are obtained for the three above mentioned situations, if the same mass transfer correlation is used.

A modeling option, used in the present tests, is shortly discussed below. The option defined by ISVBCV is illustrated in Figure 3-1068 (see Volume 2, record 150XXX). As shown in the right figure, if this option is used, the user defines the water level limit (in %) above which the bubbles will not be transported to the pool surface. Without this option at least part of the bubbles will be hitting the pool surface and transported through the junction as an atmosphere flow. In the stationary situation there will be simultaneous flow of pool + bubbles + atmosphere. It is better for numerical stability and also more realistic to have there flow of pool +bubbles. This is achieved by using the ISVBCV option.

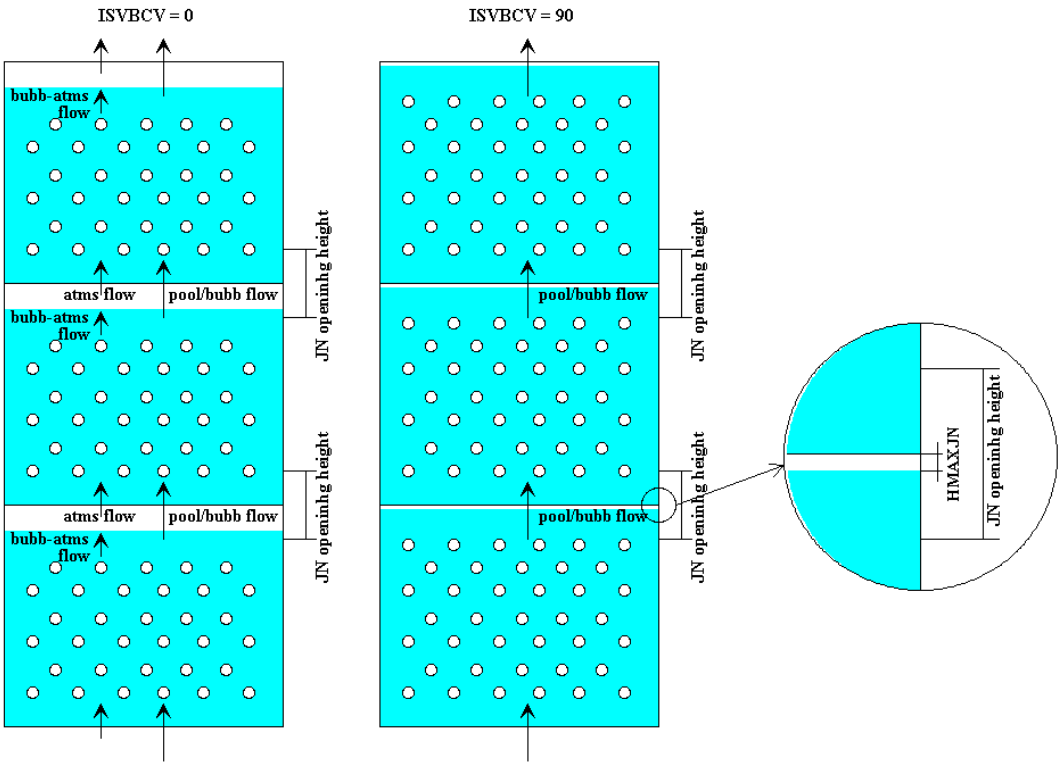

Figure 3-1068 Use of ISVBCV to define vertical pool / bubble flow

3.12.55.1 Fission Product Transport to Bubbles

The same assumptions as in the previous section are used, namely:

- ***Bubble rise velocity.***
  - Correlation for v_∞ with user-defined $C_{D,Re\to\infty}$=0.443 (record 161000, CDRGCV=0.443).
- ***Pool-bubble transport of FP.***
  - Active (IPATRT=2, record 196XXX)
  - Correlations used (record 8960XX):
    - Sh=41.7
    - Brownian diffusion + inertial impaction (TBL1RT=10^{-5}, CBL1RT=0.25)

Additionally, the option ISVBCV (ISVBCV=90), described above, is used in this test. Furthermore, the isotope Mo-96, which is a member of vapor class 7, was defined to be a member of vapor class 1 (noble gases) for reasons explained below. The SPECTRA input files are located in: **`\Z-INPUTS\RT\Pool-Bubb-Flow\FP-on-Bubb`**

Results are shown in Figure 3-1069 and Figure 3-1070. Figure 3-1069 show results obtained using the Brownian diffusion and inertial impaction models. The bubbles collect the isotope Mo-96 from pool of CV-101 and carry it up to CV-102 where they finally deposit it in the atmosphere of CV-102. The calculated mass transfer velocity is equal to v_{mt} = 1.97×10^{-4} - 1.98×10^{-4} m/s. At 10,000 s 98.8% of Mo-96 has been collected and moved to the atmosphere of CV-102.

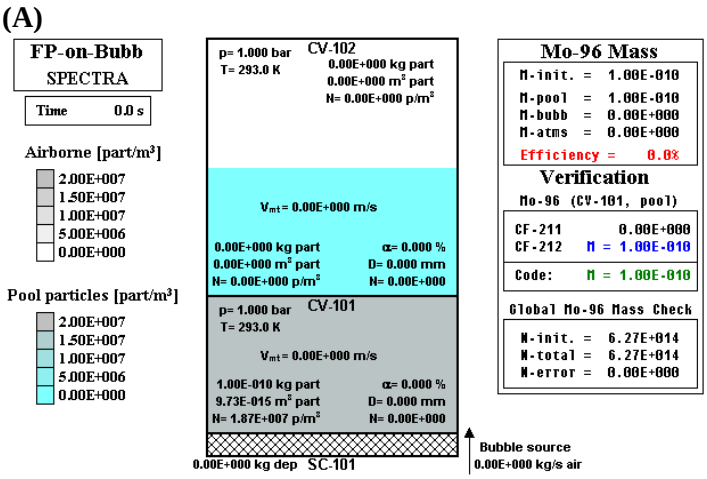

Figure 3-1069 FP on bubbles, diffusion+impaction, (A) initial state, (B) state at *t* = 10,000 s

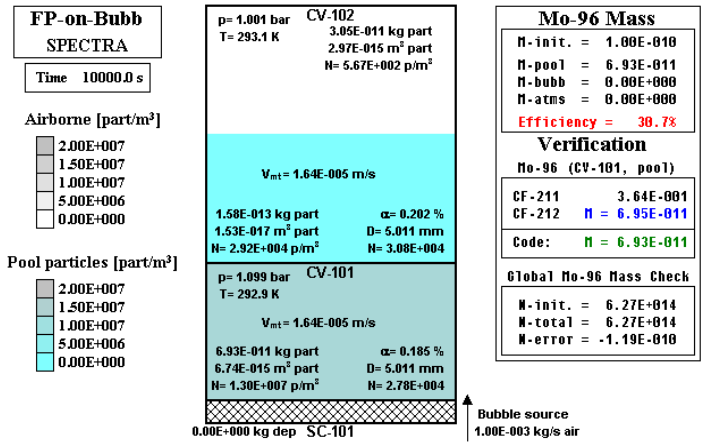

Figure 3-1070 FP on bubbles, Sh=41.7, state at *t* = 10,000 s

Figure 3-1070 shows results obtained using the "Sh=41.7" correlation. The bubbles collect the isotope Mo-96 from pool of CV-101 and carry it up to CV-102 where they finally deposit it in the atmosphere of CV-102. The calculated mass transfer velocity is equal to $v_{mt} = 1.64 \times 10^{-5}$ m/s. At 10,000 s 30.7% of Mo-96 has been collected and moved to the atmosphere of CV-102.

The mass transfer velocities and the automated verification are computed from the same functions as described in the previous section. The calculated results are in very good agreement with the theoretical solution, which is seen in Figure 3-1069 and Figure 3-1070 (values shown as "CF-212" and "Code").

The vapor class 1 (noble gases) was used for the following reason. Members of this class (noble gases) once released to the atmosphere, always stay as gas. In contrast, if Mo-96 is a member of Vapor class 7, then it cannot be in gaseous form in the atmosphere (saturated vapor pressure is practically zero for temperatures below 1500 K - Figure 3-1071). In that case the code assumes that the Mo-96 released to the atmosphere condenses to form small aerosol particles. In order to obtain correct results for this situation, one needs to activate the following additional options.

- KPATRT=2 (record 172XXX) to allow aerosol transport through JN (otherwise Mo-96 will be staying as aerosols in gas phase of CV-101)
- IDEPRT(1) = –1 (record 865002) to disable deposition of aerosols in the gas phase on the pool surface (otherwise Mo-96 present on the aerosol particles would re-deposit on the pool surface, which would change the mass distribution).

Additionally, to plot the mass of Mo-96 in the atmosphere one has to use:

- CV-102-MIAi-0191 mass of Mo-96 as vapor in CV-102, if vapor class 1 is used.
- CV-102-MAAi-0191 mass of Mo-96 on airborne aerosols (Mo-96 vapor condensed in the atmosphere of CV-102), if vapor class 7 is used.

If those assumptions are made, the case may be run and identical results are obtained (see input file **\Z-INPUTS\RT\Pool-Bubb-Flow\FP-on-Bubb\FP-on-Bubb-In-7**).

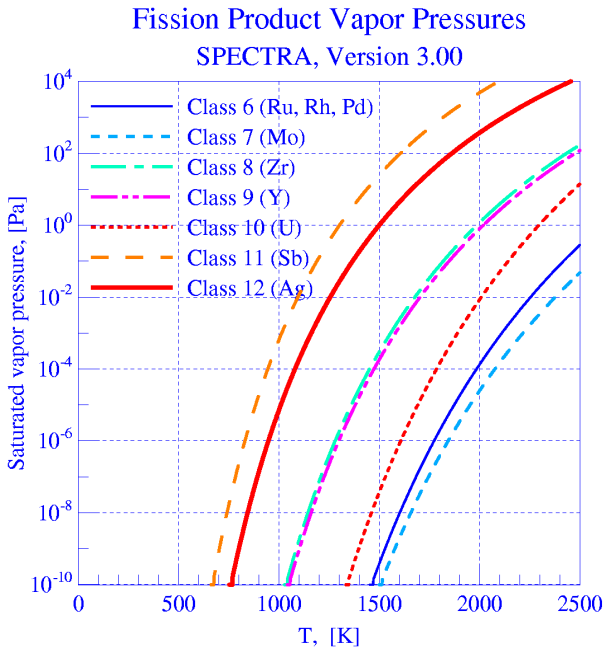

Figure 3-1071 Vapor pressure of Mo (class 7)

3.12.55.2 Fission Product Transport to Aerosol Particles

The same assumptions as in the previous section are used, namely:

- ***Bubble rise velocity.***
  - Correlation for v_∞ with user-defined $C_{D,Re\to\infty}$=0.443 (record 171000, VINPRT=100.443).
- ***Pool-bubble transport of FP.***
  - Active, sorption model 1 is used (record 898000)
  - Correlations used (record 895107):
    - Sh=41.7
    - Brownian diffusion + inertial impaction (TBL1RT=10^{-5}, CBL1RT=0.25)

Additionally, the option ISVBCV (ISVBCV=90), described above, is used in this test. This option is needed because it works not only for bubbles but also aerosol particles. If the option was not set, some of the aerosol particles would be transferred to the pool surface of CV-101 and remain in the (very small) gas space of CV-101. The particle density is set to 1.34 kg/m^3 (= density of bubbles in CV-101 the previous test), somewhat larger than in section 3.12.54, because the pool is twice deeper here. The SPECTRA input files are located in:
\Z-INPUTS\RT\Pool-Bubb-Flow\FP-on-Aer

Results are shown in Figure 3-1072 and Figure 3-1073. Figure 3-1072 show results obtained using the Brownian diffusion and inertial impaction models. The bubbles collect the isotope Mo-96 from pool of CV-101 and carry it up to CV-102 where they finally deposit it in the atmosphere of CV-102. The calculated mass transfer velocity is equal to v_{mt} = 1.97×10^{-4} - 1.98×10^{-4} m/s. At 10,000 s 98.7% of Mo-96 has been collected and moved to the atmosphere of CV-102.

Figure 3-1073 shows results obtained using the "Sh=41.7" correlation. The "bubbles" (strictly speaking: the low-density aerosol particles, representing here the bubbles) collect the isotope Mo-96 from pool of CV-101 and carry it up to CV-102 where they finally deposit it in the atmosphere of CV-102. The calculated mass transfer velocity is equal to v_{mt} = 1.64×10^{-5} - 1.65×10^{-5} m/s. At 10,000 s 30.4% of Mo-96 has been collected and moved to the atmosphere of CV-102.

The mass transfer velocities and the automated verification are computed from the same functions as described in the previous section. The calculated results are in very good agreement with theoretical solution, which is seen in Figure 3-1072 and Figure 3-1073 (values shown as "CF-212" and "Code").

The results are practically identical to the results of the previous test, where "physical" bubbles are used. This shows that one may in certain situations use aerosol field instead of bubbles. This adds to code flexibility and user convenience.

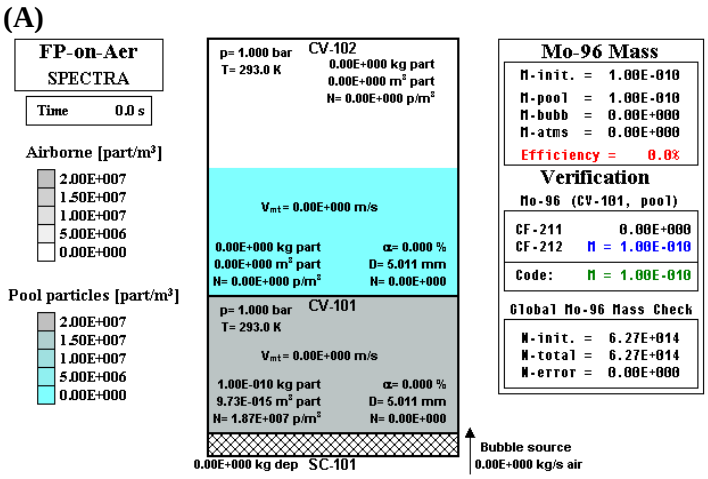

Figure 3-1072 FP on aerosols, diffusion+impaction, (A) initial state, (B) state at *t* = 10,000 s

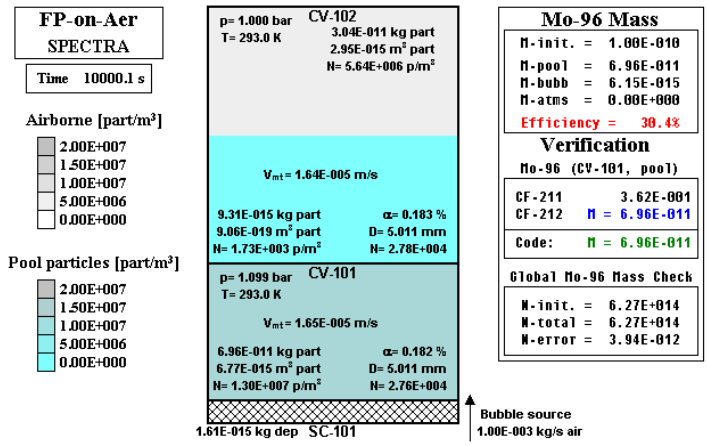

Figure 3-1073 FP on aerosols, Sh=41.7, state at *t* = 10,000 s

3.12.55.3 Aerosol Particle Transport to Bubbles

The same assumptions as in the previous section are used, namely:

- ***Bubble rise velocity.***
  - Correlation for v_∞ with user-defined $C_{D,Re\to\infty}$=0.443 (record 161000, CDRGCV=0.443).

- ***Pool-bubble transport of FP.***
  - Active (KPATRT=2, record 172XXX)
  - The "migration correlations are not available here (only the drag coefficient correlation can be used. Therefore constant, user-defined transport velocities (record 171XXX, VINPRT) are specified based on results of the previous test:
    - $v_{mt} = 1.97\times10^{-4}$ m/s (the "diffusion + impaction" case)
    - $v_{mt} = 1.64\times10^{-6}$ m/s (the "Sh=4.17" case)

Additionally, the option ISVBCV (ISVBCV=90), described above, is used in this test. The SPECTRA input files are located in: **`\Z-INPUTS\RT\Pool-Bubb-Flow\Aer-on-Bubb`**

Results are shown in Figure 3-1074 and Figure 3-1075. Figure 3-1074 shows results obtained using the "diffusion + impaction" model. The bubbles collect the isotope Mo-96 from the pool of CV-101 and carry it up to CV-102 where they finally deposit it in the atmosphere of CV-102. The calculated mass transfer velocity is equal to $v_{mt} = 1.97\times10^{-4}$ m/s. At 10,000 s 98.7% of Mo-96 has been and moved to the atmosphere of CV-102.

Figure 3-1075 shows results obtained using the "Sh=41.7" correlation. The bubbles collect the isotope Mo-96 from pool of CV-101 and carry it up to CV-102 where they finally deposit it in the atmosphere of CV-102. The calculated mass transfer velocity is equal to $v_{mt} = 1.64\times10^{-5}$ m/s. At 10,000 s 30.6% of Mo-96 has been collected and moved to the atmosphere of CV-102.

The mass transfer velocities and the automated verification are computed from the same functions as described in the previous section. The calculated results are in very good agreement with theoretical solution, which is seen in Figure 3-1074 and Figure 3-1075 (values shown as "CF-212" and "Code").

Results are practically identical to the results of previous two tests, which shows that one may model this third method, although the mass transfer velocity cannot be calculated and must be provided by the user.

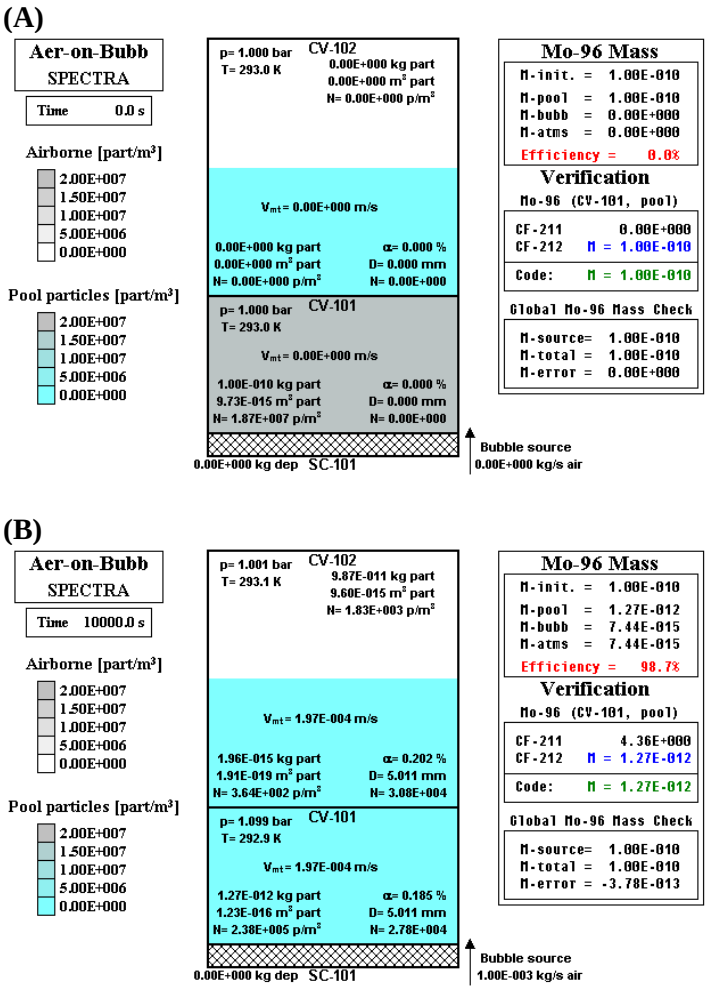

Figure 3-1074 Aerosols on bubbles, diffusion+impaction, (A) initial state, (B) state at t = 10,000 s

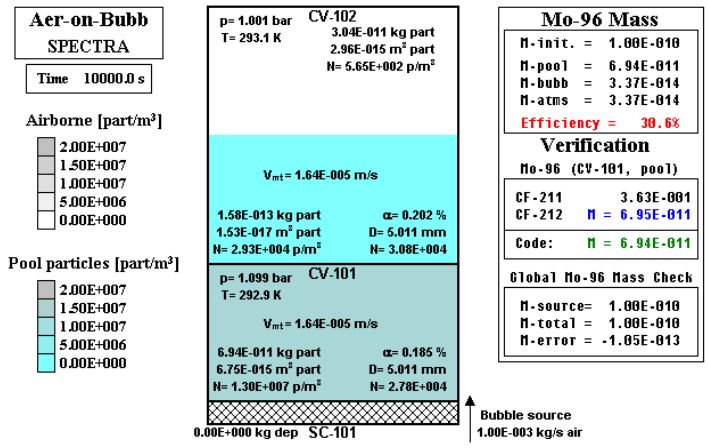

Figure 3-1075 Aerosols on bubbles, Sh=41.17, state at t = 10,000 s

3.12.56 Static Column Experiments

Static Column experiments were performed at the Delft University of Technology. The main goal of the experiments was to determine the flotation extraction efficiency as a function of particle size and bubble size. This section presents results of SPECTRA simulation of the Static Column experiments. The main motivation for this work was to gain experience in modeling particle-to-bubble transport, which will be applicable to analyses of fission product transport in MSRE and other molten salt reactors. Section 3.12.56.1 provides a short description of the Static Column experiments. Description of the SPECTRA model is provided in section 3.12.56.2. Sections 3.12.56.3 and 3.12.56.4 present comparison of the calculated values with the measured data. Finally, section 3.12.56.5 gives summary and conclusions.

3.12.56.1 Description of Experiments

The Static Column experiments [175] were performed at Delft University of Technology. The experimental setup consists of a glass column, shown in Figure 3-1076, of diameter D = 0.026 m, height H = 0.5 m. The column was filled with glycerol aqueous solution (41.6%). The fluid properties at the applied (room) temperature are:

- density: 1090 kg/m^3,
- viscosity: 3.275×10^{-3} kg/m-s,
- surface tension: 0.068 N/m.

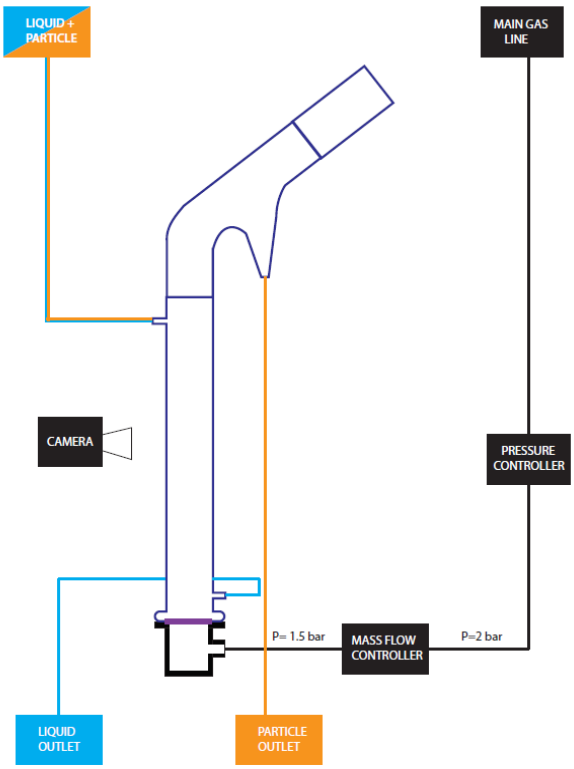

Figure 3-1076 Static Column experiments [175]

Table 3-95 Static Column experimental conditions

Air flow rate		Bubble		
sccm	kg/s	D (mm)	v (m/s)	void
5.0	1.025E-07	0.481	0.029	0.0054
10.0	2.050E-07	0.550	0.035	0.0089
15.0	3.075E-07	0.597	0.039	0.012
25.0	5.125E-07	0.657	0.045	0.018
40.0	8.200E-07	0.725	0.051	0.025
50.0	1.025E-06	0.761	0.054	0.029
60.0	1.230E-06	0.789	0.056	0.034
70.0	1.435E-06	0.811	0.058	0.038

Air bubbles and molybdenum metallic particles were used. An initial particle mass of about 0.2 g is added to the column. Five different particle sizes were used, with mean diameters of: 0.1 μm, 1.5 μm, 5.0 μm, 88.0 μm, 149.0 μm. The particle-bubble separation was performed using a Hallimond tube at the top of the column. When the particle-bubble aggregate reached the liquid interface at the top, the bubble collapsed and the falling particles were collected in the reservoir of the Hallimond tube. Experiments were performed at eight different gas flow rates, ranging from 5 to 70 sccm (standard cubic centimeters per minute). The corresponding air mass flows are shown in Table 3-95. The bubble parameters, shown in Table 3-95, were estimated by the supporting CFD analyses.

The following experimental procedure was applied. The column was partially filled with a water-glycerol mixture and the gas volumetric flow rate was set to the desired value to start the bubbling. The particles of the selected size were mixed with the remaining liquid solution in a glass funnel and added to the static column by opening the valve at the top of the column. The reservoir of the Hallimond tube is drained at fixed time steps and the samples are analyzed to determine the collection efficiency as function of time. At the end of the experiment (1.0 hour), the reservoir of the Hallimond tube was completely drained and the sample is analyzed to determine the total extraction efficiency. The total efficiency obtained for different particle sizes and gas flow rates is tabulated in Table 3-96.

Table 3-96 Static Column experimental results

Gas flow rate	Extraction efficiency (%)				
sccm	0.1 μm	1.5 μm	5.0 μm	88 μm	149 μm
5	13.53	18.12	32.11	32.67	16.79
10	10.05	19.27	42.49	32.96	22.78
25	16.81	18.18	45.04	35.73	25.08
40	10.69	18.74	47.05	32.94	22.82
50	23.50	27.84	50.70	42.38	15.30
70	-	-	42.43	42.43	22.59

3.12.56.2 Model

Description of the Model

The applied nodalization is shown in Figure 3-1077. The model consists of 10 Control Volumes (CV-101 through CV-110) with a cross section area of $\pi D^2/4 = 5.309\times10^{-4}$ m^2 and a height of 0.05 m. The volumes are connected with Junctions (JN-101 through JN-109). A large gas space (10^6 m^3) is provided at the top volume (CV-110) to keep the pressure approximately constant. A 1-D Solid Heat Conductor (SC-101) at the bottom of the column is defined to provide a surface for sedimentation of particles.

An alternative fluid is used, with user-defined properties. The properties of glycerol solution, shown in section 3.12.56.1, were defined in the input file GLYCEROL-WATER. For all other properties, the properties of pure water (copied from the built-in SPECTRA properties) were applied. The diffusion coefficient for glycerol-water solution was obtained from [176] and tabulated as a function of temperature. The source values and the tabulated values are shown in Figure 3-1078. The values for $X_{glycerol} = 0.5$ were used.

Molybdenum particles are modeled using the fission product isotope chains. A stable isotope Mo-96 was defined. Mo-96 is a member of the vapor class 7. Two versions of inputs were prepared:

- **Model 1**, isotope on bubbles. In this model bubbles are created by injecting air as a mass source at the bottom of the static column (CV-101).
- **Model 2**, isotope on aerosol particles. The bubble source is replaced by an aerosol source. The aerosol density is set to the bubble density (1.23 kg/m^3). This method was applied to model circulating bubbles in MSRE. The main advantage is the computational speed; tracking of aerosols is much faster than tracking of bubbles.

Both methods should give very similar results. The main difference between the two methods lies in the liquid volume. In Model 1 the liquid level increases somewhat due presence of bubbles. In model 2 the liquid level does not change because aerosol particles are assumed to be trace species that does not occupy any volume. Therefore the Model 2 results are not identical to Model 1 but if the void fractions are small, the difference is not important.

The duration of each experiment was 1.0 hour (section 3.12.56.1). Therefore the run time is 1.0 hour = 3600 s for every analyzed test.

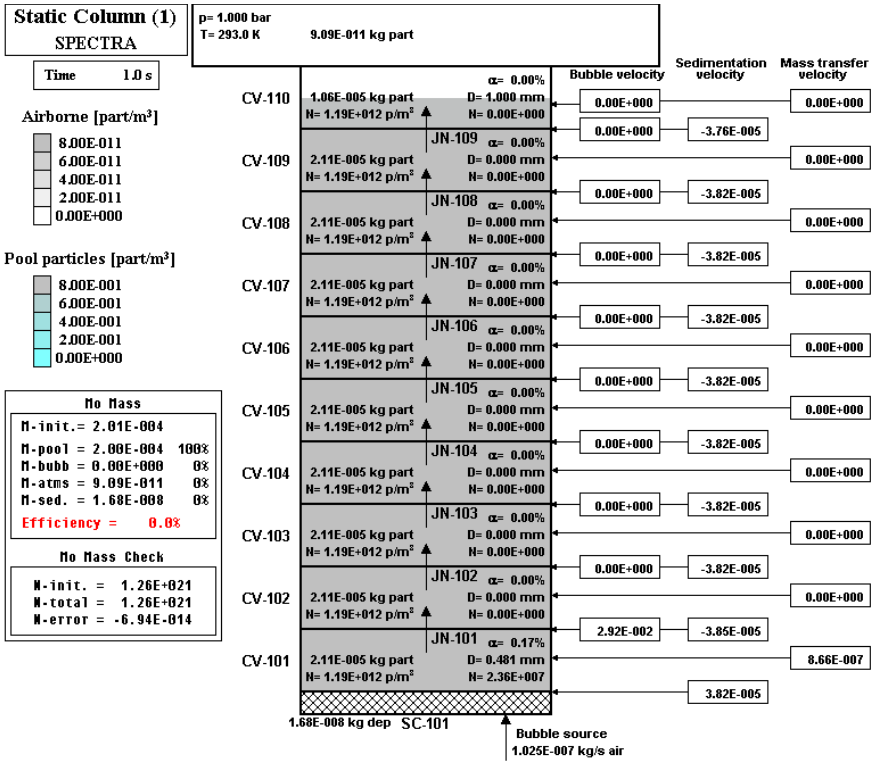

Figure 3-1077 Static Column experiments - model

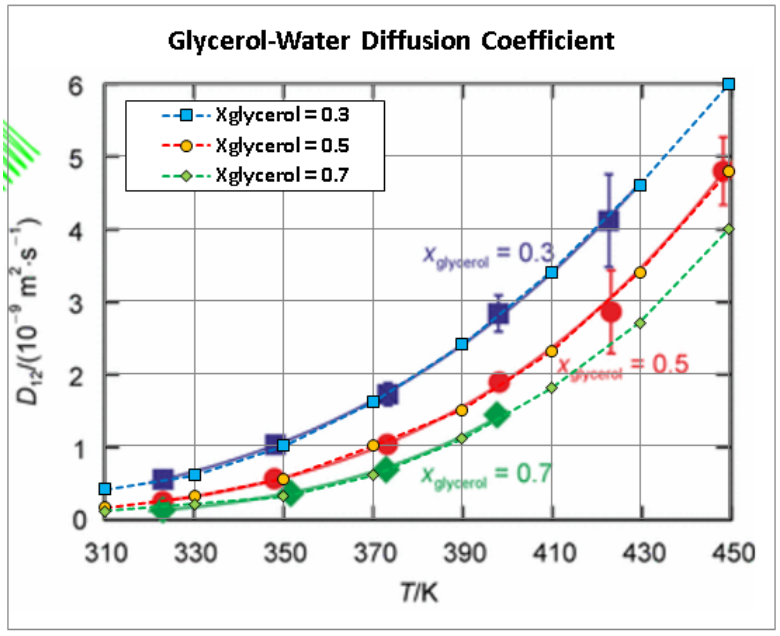

Figure 3-1078 Diffusion coefficient in glycerol solution [176]

Assumptions

The main assumptions are listed below

- Bubble size. The bubble diameter, D_p, can be calculated by the code or entered as a user-defined parameter. The bubble size was set based on the supporting CFD analyses shown in Table 3-95. In Model 1 the bubble size is set by DBWFCV (record 158XXX). In Model 2 the bubble size is equal to the aerosol particle size set by DASCRT (record 861000).

- Bubble rise velocity: The alternative correlation is used, with the user-defined drag coefficient $C_{D,\mathrm{Re}\to\infty} = 0.443$. The value is slightly smaller than the default $C_{D,\mathrm{Re}\to\infty} = 0.47$, and was obtained in trial and error runs to match approximately the bubble rise velocities estimated in the supporting CFD analyses, shown in Table 3-95.

$$v_\infty = \left(\frac{4/3}{C_D} \cdot \frac{D_p g(\rho_f - \rho_p)}{\rho_f} \right)^{0.5}$$

  Here g is the gravity acceleration (m/s^2), ρ is density (kg/m^3), η is viscosity, (kg/m/s), D is diameter. Subscripts p refers to particle (bubble), while f to fluid.

- Particle sedimentation velocity: The same correlation is used. The particle density was set to 10,280 kg/m^3 (Mo density), the same as in the supporting CFD analysis. Five different particle sizes used in the experiments were defined, with mean diameters of: 0.1 μm, 1.5 μm, 5.0 μm, 88.0 μm, 149.0 μm. The user-defined coefficient of $C_{D,\mathrm{Re}\to\infty} = 0.47$ was used.

  Since particles are much smaller than bubbles, the correlation valid for small particles is used for most particles, except for the largest ones. The correlation is:

$$v_\infty = \frac{1}{18} \cdot \frac{{D_p}^2 g(\rho_f - \rho_p)}{\eta_f} \cdot C_{small}$$

  The default value of the user-defined constant $C_{small} = 1.0$ was used.

- Mass transfer coefficient.
  - As a first step, the Sherwood number correlation was used, exactly the same that was recommended in ORNL reports for MSRE and used in the analyses of MSRE. The correlation is:

$$Sh = 41.7$$
$$Sh_{eff} = C_s \cdot Sh$$

    Here C_s is the sticking fraction, equal to 0.1. The mass transfer velocity is equal to:

$$v = Sh \cdot \frac{D_C}{D_p}$$

    Here D_C is the diffusion coefficient (m^2/s) and D_p is the particle diameter (m). Results obtained with this model are marked in the figures as "**Sh**".

- In the second step the, Brownian diffusion and inertial impaction correlations are used. For this method the particle density and particle size must be defined.

  The Brownian diffusion is obtained from:

$$v_{Brown} = \frac{D_C}{\delta_{BL}}$$

  Here D_C is the diffusion coefficient (m^2/s) and δ_{BL} is diffusion boundary layer thickness, (m). The default value of $\delta_{BL} = 5\times10^{-5}$ m is used.

  The inertial impaction velocity is obtained from (Volume 1):

$$v_{inertial} = v_\infty \cdot \eta / 4$$

  Here v_∞ is the relative particle-to-bubble velocity (m/s), η is the collection efficiency, calculated from the modified Langmuir and Blodgett correlation (section 2.8.17.1) and the correlation based on the data of Yoon & Lutrell [172] and Afruns & Kitchener [173] (section 2.8.17.2).

  The modified Langmuir and Blodgett correlation is:

$$\eta = \eta_{\max} \cdot \begin{cases} \dfrac{0.25}{C_{LB}} \cdot Stk & for \quad Stk < C_{LB} \\ \dfrac{Stk^2}{(Stk + C_{LB})^2} & for \quad Stk > C_{LB} \end{cases}$$

  Here Stk is the Stokes number, C_{LB} and $\eta_{\max}$ are constants (equal to 0.25 and 1.0 respectively). Comparison of the modified L-M correlation with the original L-M correlation [119]:

$$\eta = \frac{Stk^2}{(Stk + C_{LB})^2}$$

  is shown in Figure 2-190, section 2.8.17.1. In the low Stk range the modified correlation gives somewhat higher collection efficiency than the original L-B correlation. The difference is quite small, smaller than the scatter of the source data ([119], figure 1). The difference is important only for small values of the Stokes number. For example, for Stk=0.03, the L-B correlation gives η=0.01 and the modified correlation η=0.03, so the relative difference is quite large in this region. The modified correlation gives better agreement with the experimental data for the Static Column experiments, as will be shown below. Calculations were performed with the user-defined constants of C_{LB}=0.25 and $\eta_{\max}$=1.0. Results obtained with this model are marked in the figures as "**L-B**".

  The correlation developed based on the data of Yoon & Lutrell [172] for coal particles and Afruns & Kitchener [173] for quartz particles is:

$$\eta = Min\left(\eta_{\max}, A \cdot \frac{d_p^{\,2}}{D_b}\right)$$

Here D_p is the particle diameter, D_b is the bubble diameter and A is a constant. The data, (copied from [174], figure 9.5) is shown in Figure 2-191, section 2.8.17.2. It was found that, due to the scatter of data, values between $9{,}000 \le A \le 17{,}000$ can be justified (section 2.8.17.2) Calculations were performed with the user-defined constants of A=17,000. Results obtained with this model are marked in the figures as "**YLAK**".

Visualization of Results and Plotting Parameters

The following parameters are shown in the visualization pictures at every level:

- *Bubble velocity*. The bubble velocity is a plottable parameter so this is used in Model 1. In Model 2 the aerosol particles movement is not plottable, therefore it is calculated by Control Functions as: $v = W / A\rho$, where W is the mass flow of particles through a junction (kg/s), A is the cross section area (=5.309×10^{-4} m^2), and ρ is the particle density, equal to: m/V, m = mass of aerosol particles in the upstream CV, V = pool volume in the upstream CV.
- *Sedimentation velocity*. The sedimentation velocity of Mo-96 isotope is not plottable, therefore it is calculated by Control Functions as: $v = W / A\rho$, where W is the mass flow of isotope through a junction (kg/s), A is the cross section area (m^2), and ρ is the particle density, equal to: m/V, m = mass of isotope in the upstream CV, V is the pool volume in the upstream CV.
- *Mass transfer velocity*. The mass transfer velocity of Mo-96 isotope to the bubbles is not plottable, therefore it is calculated by Control Functions as: $v = w / \rho$, where w is the mass flux (mass transfer rate per unit volume, kg/m^2-s) in CV, and ρ is the particle density, equal to: m/V, m = mass of isotope in CV, V is the pool volume in CV.

Furthermore, the following parameters are calculated using Control Functions:

- CF-201: mass of Mo-96 in the pool (sum of Mo-96 masses in the pool of all Control Volumes).
- CF-202: mass of Mo-96 in the bubbles (Model 1: sum of Mo-196 masses in the gas phase of CV-101 through CV-109, Model 2: sum of aerosol-bound masses of Mo-96 in the pool of all Control Volumes).
- CF-203: mass of Mo-96 in the atmosphere (Model 1: Mo-196 mass in the gas phase of CV-110, Model 2: aerosol-bound mass of Mo-96 in the atmosphere of CV-110).
- CF-204: mass of Mo-96 deposited at the bottom due to sedimentation (Mo-96 mass deposited on SC-101).
- CF-210: total mass of CF-201 through CF-204.
- CF-211 through CF-214 calculate the relative values, equal to CF-201 through CF-204 respectively, divided by CF-210 and multiplied by 100 (%).

The extraction efficiency is defined as the ratio of CF-203 and the total mass of Mo-96:

Extraction efficiency = CF-213 = CF-203 / CF-210

Initial Conditions

The experimental procedure is defined clearly - see section 3.12.56.1. It is not clear what was the volume of the mixture that was added at the top. Even if this was known, the method of adding the mixture to the column would still play a role; if added rapidly, the mixture would mix with the fluid already present in the column; if added slowly, the particle-rich mixture would remain at the top. In the supporting CFD analysis it was assumed that the particles were initially uniformly mixed in the entire column. The same assumption was taken here. The effect of this assumption is discussed in section 3.12.56.3.

3.12.56.3 Results - Effect of Particle Size

As a first step, the effect of particle size is discussed. The experimental results obtained for a certain gas mass flow are plotted against the particle size. The gas mass flows are:

- V_{gas} = 5 sccm, Figure 3-1079,
- V_{gas} = 10 sccm, Figure 3-1080,
- V_{gas} = 25 sccm, Figure 3-1081,
- V_{gas} = 40 sccm, Figure 3-1082,
- V_{gas} = 50 sccm, Figure 3-1083,
- V_{gas} = 70 sccm, Figure 3-1084.

When the Sherwood number correlation is used, the particle size is irrelevant. A single value of collection efficiency is obtained, independently of the particle size. The value is shown in Figure 3-1079 in a dashed line and is marked as "**Sh**". It is seen that the Sherwood number correlation applied in the MSRE analyses gives a reasonable value for the static column experiments. In order to investigate the effect of particle size, the model based on Brownian diffusion and inertial impaction is used. Two inertial impaction correlations are used: modified Langmuir-Blodgett ("**L-B"**) and the correlation based on Yoon & Lutrell and Afruns & Kitchener data ("**YLAK**").

For small particles (0.1 - 1.0 μm) the Brownian diffusion is dominant and the results of both L-B and YLAK are practically identical. For larger particles the inertial impaction becomes important. The extraction efficiency becomes larger. In case of the largest particles, the extraction efficiency becomes smaller due to fast sedimentation. This is shown in Figure 3-1085 and Figure 3-1086.

Figure 3-1085 shows the relative masses in case of the relatively small particles - 1.5 μm. The sedimentation velocities are very small (3.4×10^{-6} m/s). The extraction efficiency (CF-213) increases practically linearly during the whole experiment (1.0 hour). The extraction efficiency at t = 3600 s is 24.6%.

Figure 3-1086 shows the relative masses in case of the largest particles - 149 μm. The sedimentation velocities are quite large (2.8×10^{-2} m/s - Figure 3-1088). Due to fast sedimentation, the particles are deposited on SC-101 already within the first 60 s. There is no particle removal by bubbles and the extraction efficiency (CF-213) remains constant after that time. The extraction efficiency is 30.2% at t = 60 s as well as at t = 3600 s.

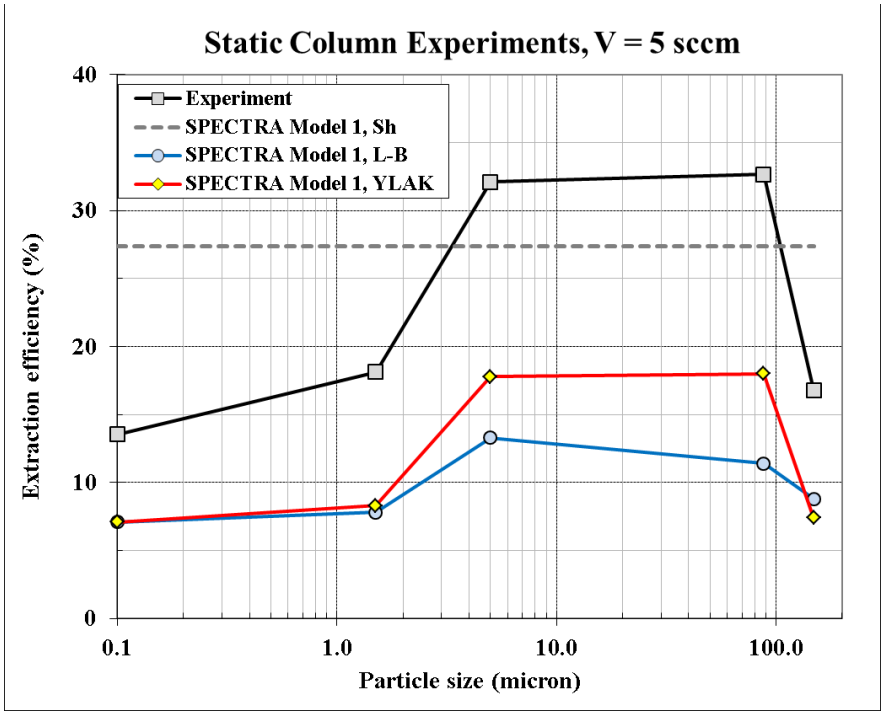

(A) Model 1 (isotopes on bubbles)

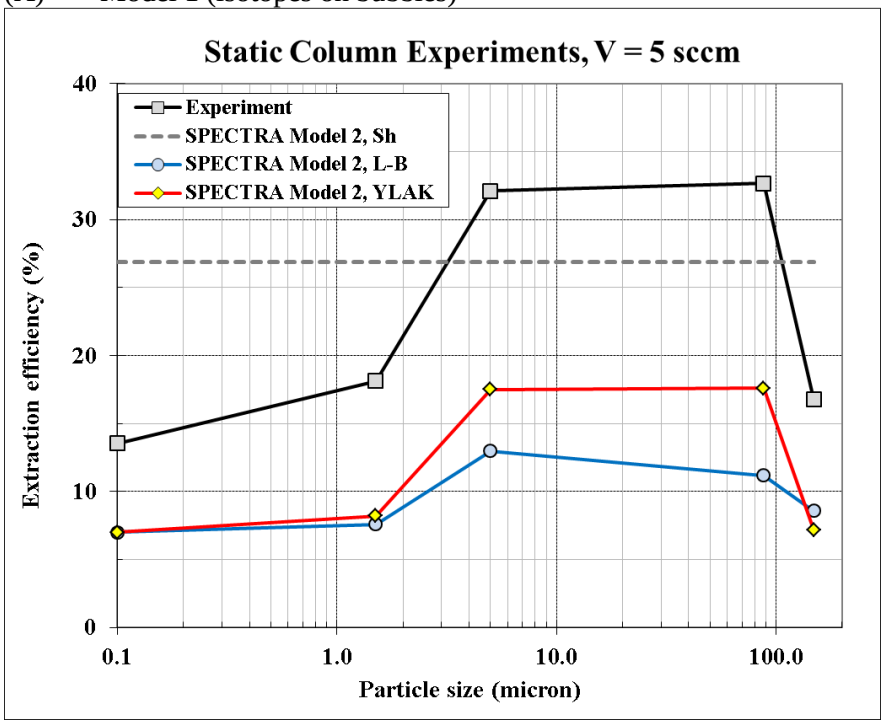

(B) Model 2 (isotopes on aerosols)

Figure 3-1079 Static Column experiments - gas flow of 5 sccm

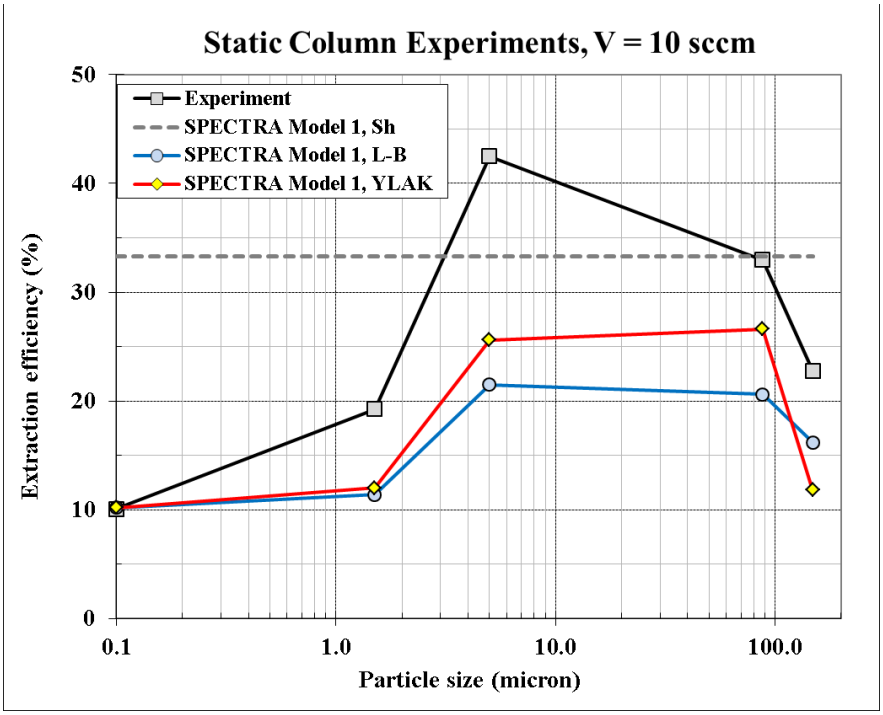

(A) Model 1 (isotopes on bubbles)

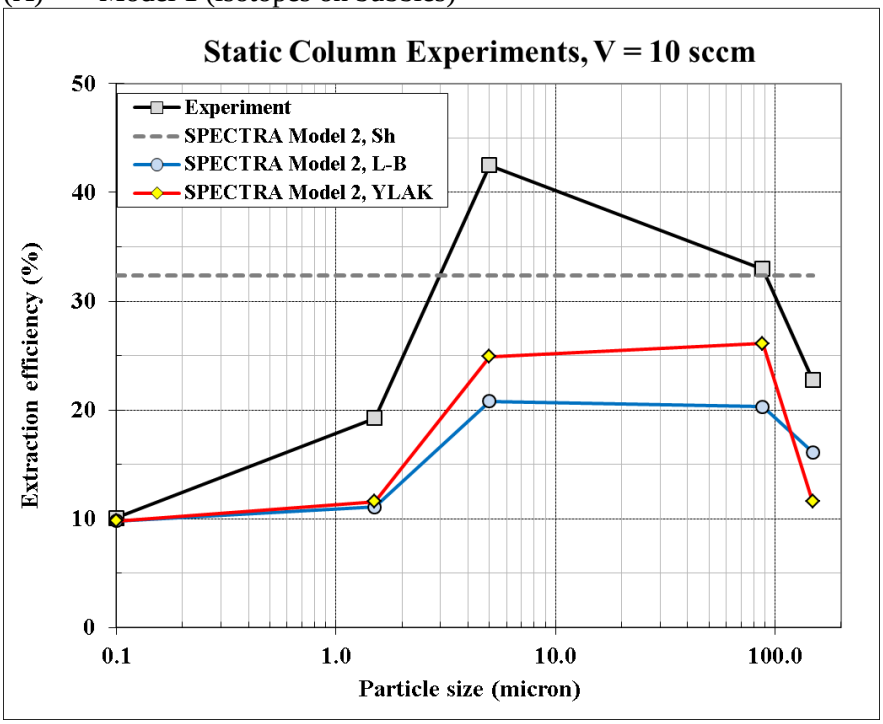

(B) Model 2 (isotopes on aerosols)

Figure 3-1080 Static Column experiments - gas flow of 10 sccm

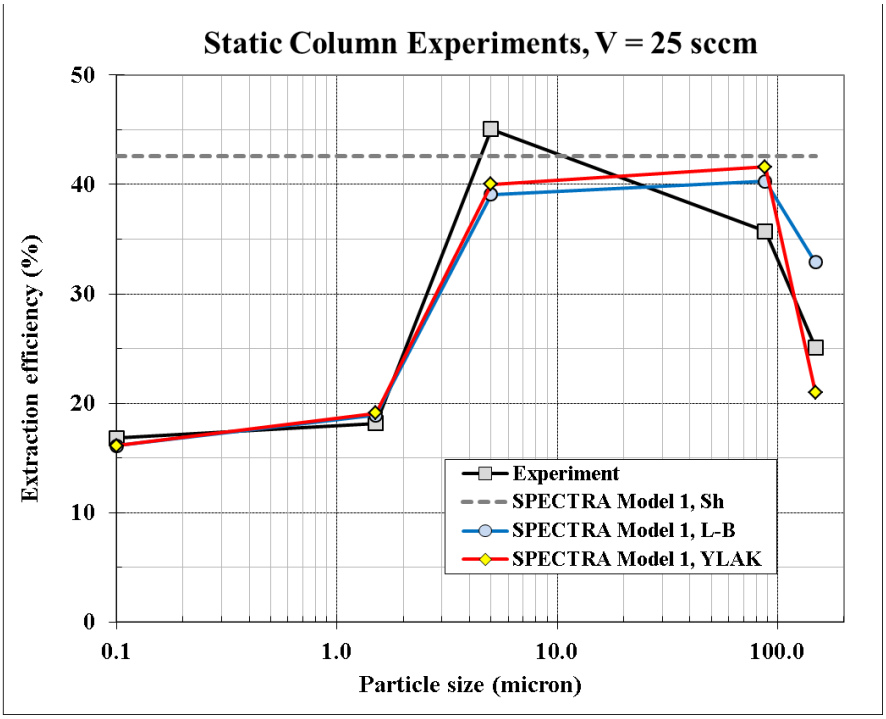

(A) Model 1 (isotopes on bubbles)

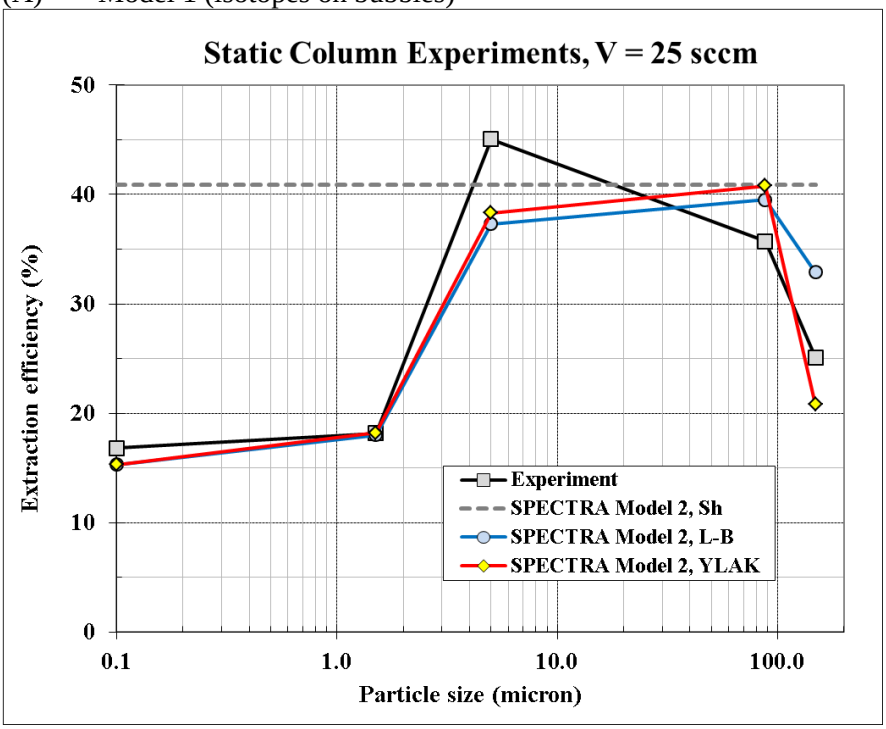

(B) Model 2 (isotopes on aerosols)

Figure 3-1081 Static Column experiments - gas flow of 25 sccm

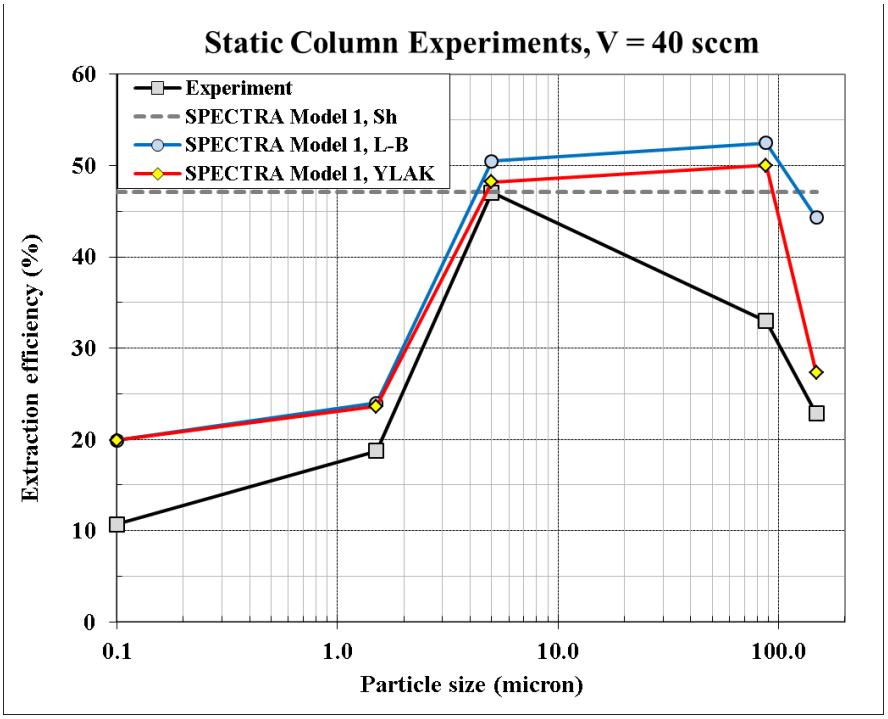

(A) Model 1 (isotopes on bubbles)

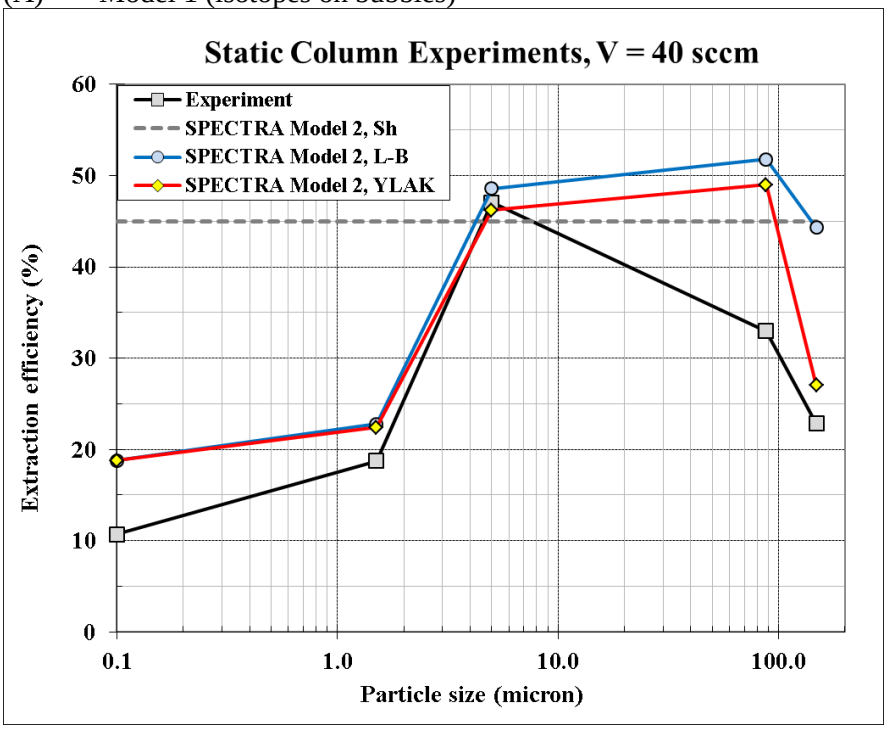

(B) Model 2 (isotopes on aerosols)

Figure 3-1082 Static Column experiments - gas flow of 40 sccm

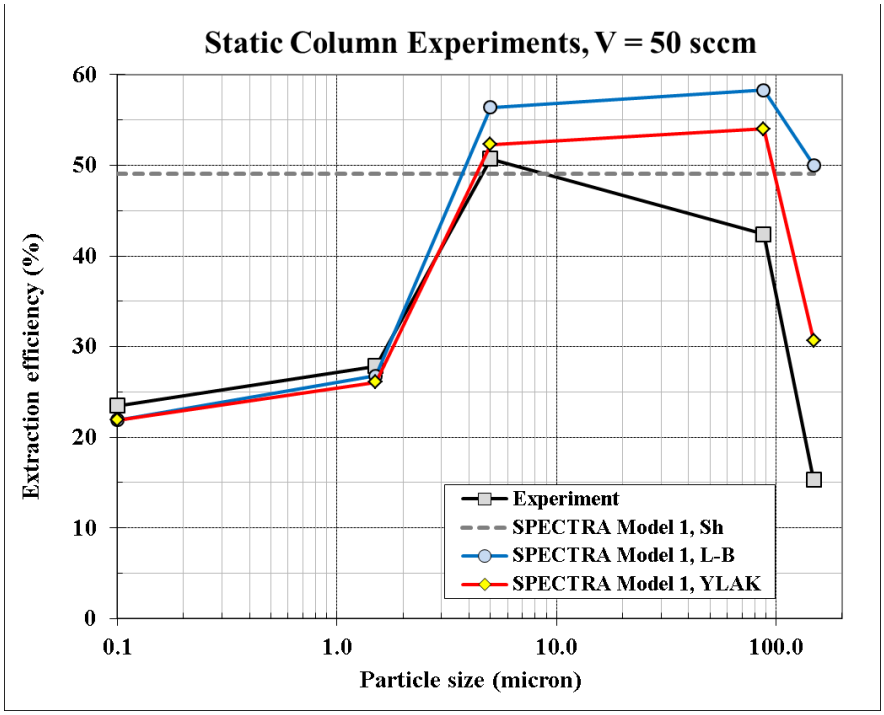

(A) Model 1 (isotopes on bubbles)

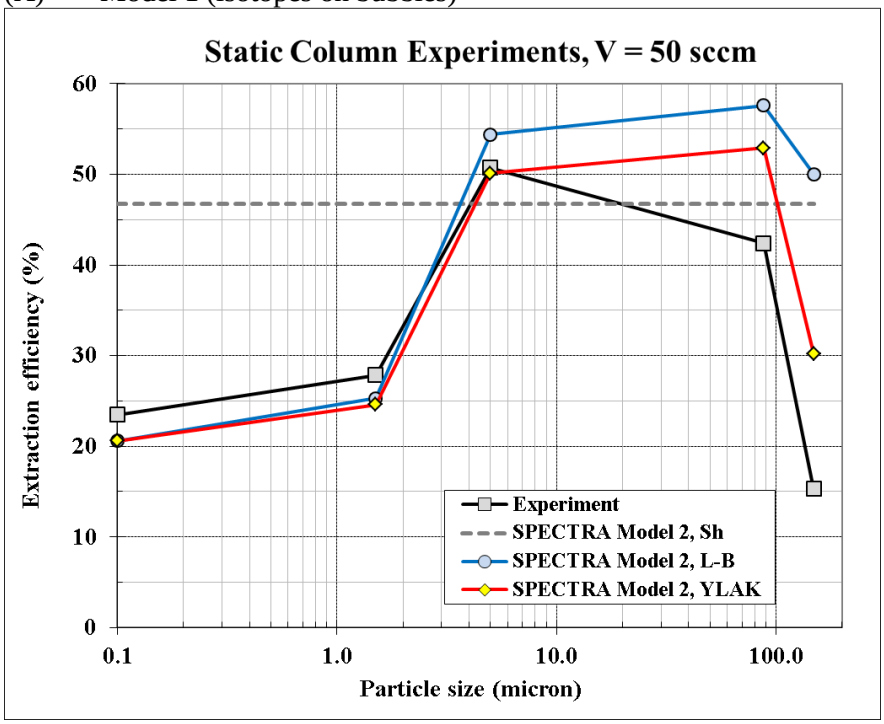

(B) Model 2 (isotopes on aerosols)

Figure 3-1083 Static Column experiments - gas flow of 50 sccm

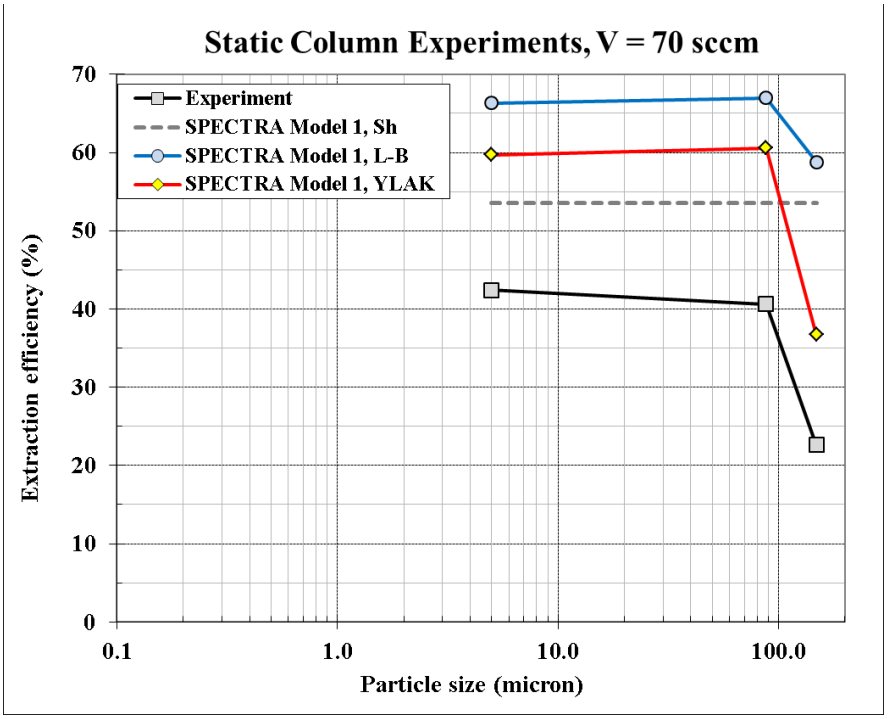

(A) Model 1 (isotopes on bubbles)

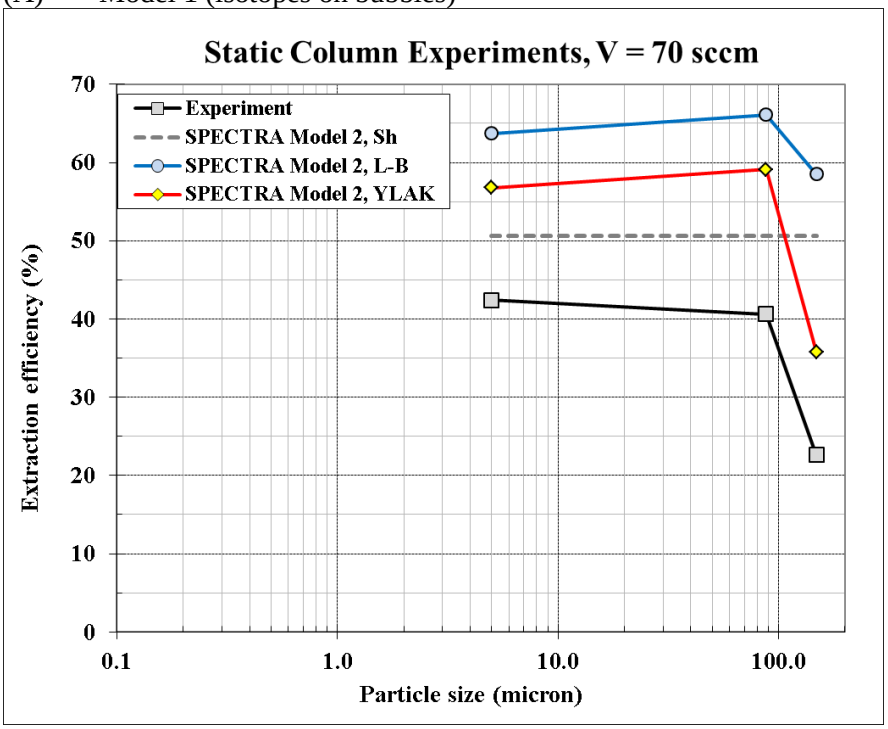

(B) Model 2 (isotopes on aerosols)

Figure 3-1084 Static Column experiments - gas flow of 70 sccm

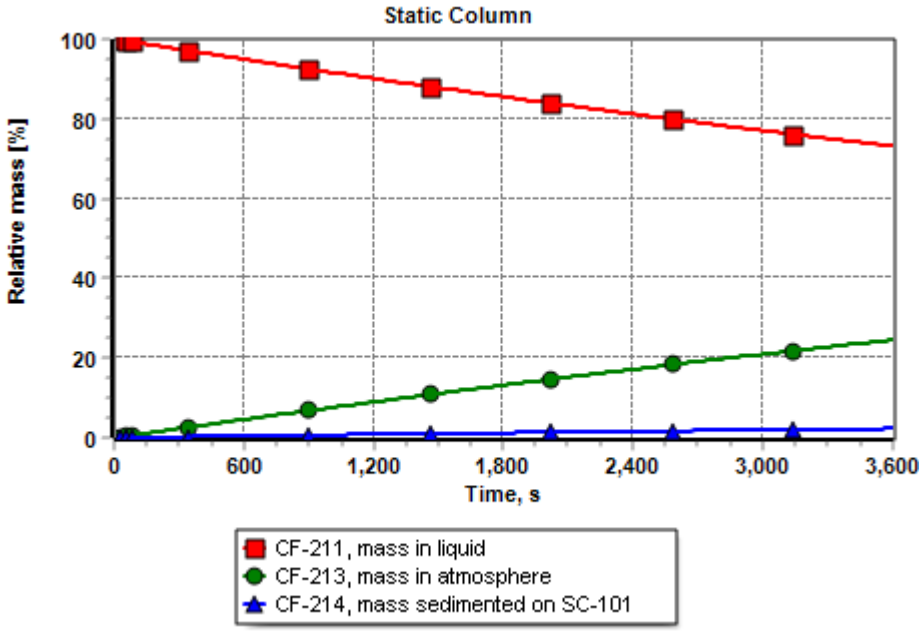

Figure 3-1085 Mass fractions vs. time - Model 2, YLAK, V_{gas} = 50 sccm, D_p = 1.5 µm

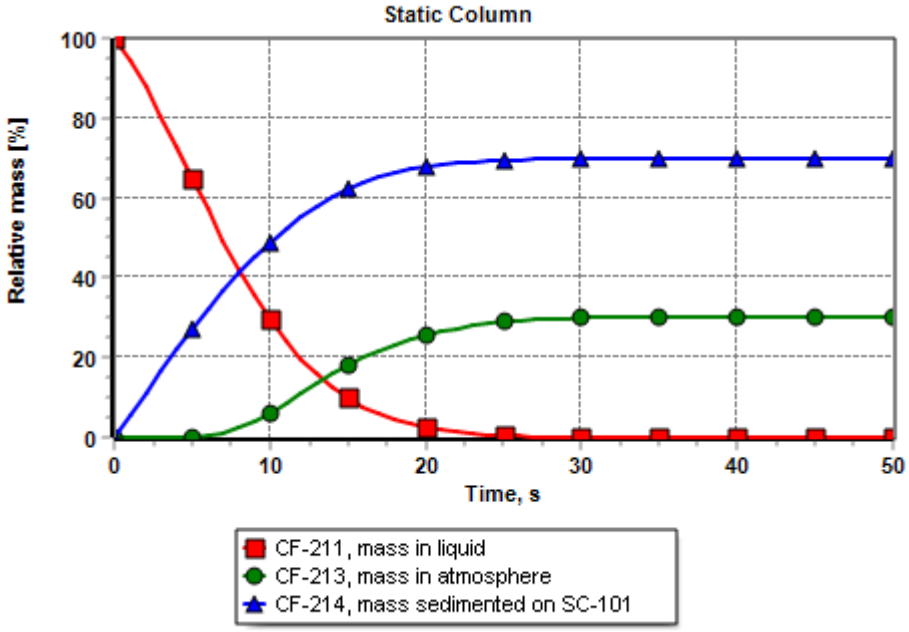

Figure 3-1086 Mass fractions vs. time - Model 2, YLAK, V_{gas} = 50 sccm, D_p = 149 µm

The sedimentation velocities calculated by SPECTRA were compared to the values obtained from the supporting CFD analysis. The values are shown in Table 3-97. There is a good agreement between the SPECTRA-calculated velocities and the source data.

The bubble rise velocities calculated by SPECTRA were compared to the values obtained from the supporting CFD analysis. The values are shown in Table 3-98. There is a good agreement between the SPECTRA-calculated velocities and the source data.

Fast sedimentation in case of large particles makes it very difficult to correctly model the experiment. Firstly, there is a complicated behavior of particles near the bottom, where the bubble source is located. Secondly, the unclear definition of initial conditions, described in section 3.12.56.2 (Initial Conditions), possibly plays a role. A sensitivity calculation was performed for the case: Model 2, YLAK, V_{gas} = 5 sccm, D_p = 149 μm. It was assumed that the particles are initially located only in the upper half of the column. The same mass of particles was used. The initial situation is shown in Figure 3-1089. For comparison, the initial situation for the base case (uniform initial concentrations) is shown in Figure 3-1087. The situation at time t = 5.0 s is shown in Figure 3-1090 for the sensitivity case and Figure 3-1088 for the base case. The mass fractions versus time are shown in Figure 3-1092 for the sensitivity case and Figure 3-1091 for the base case. In the sensitivity run, the sedimentation takes longer and therefore more particles are captured and removed by the bubbles. The final results are:

	Base case	Sensitivity	Measured
V_{gas} = 5 sccm, D_p = 149 μm:	7.2%	10.4%	16.8%

Table 3-97 Sedimentation velocities

Particle	Sedimentation, (m/s)	
μm	Source	SPECTRA
0.1	1.53E-08	1.53E-08
1.5	3.44E-06	3.44E-06
5.0	3.82E-05	3.82E-05
88.0	1.11E-02	1.17E-02
149.0	2.85E-02	2.82E-02

Table 3-98 Bubble rise velocities

Gas flow	Bubble velocity, (m/s)		
		SPECTRA	
sccm	Source	Model 1	Model 2
5.0	0.0291	0.0292	0.0291
10.0	0.0353	0.0355	0.0356
25.0	0.0447	0.0447	0.0465
40.0	0.0506	0.0511	0.0539
50.0	0.0536	0.0564	0.0579
70.0	0.0576	0.0615	0.0637

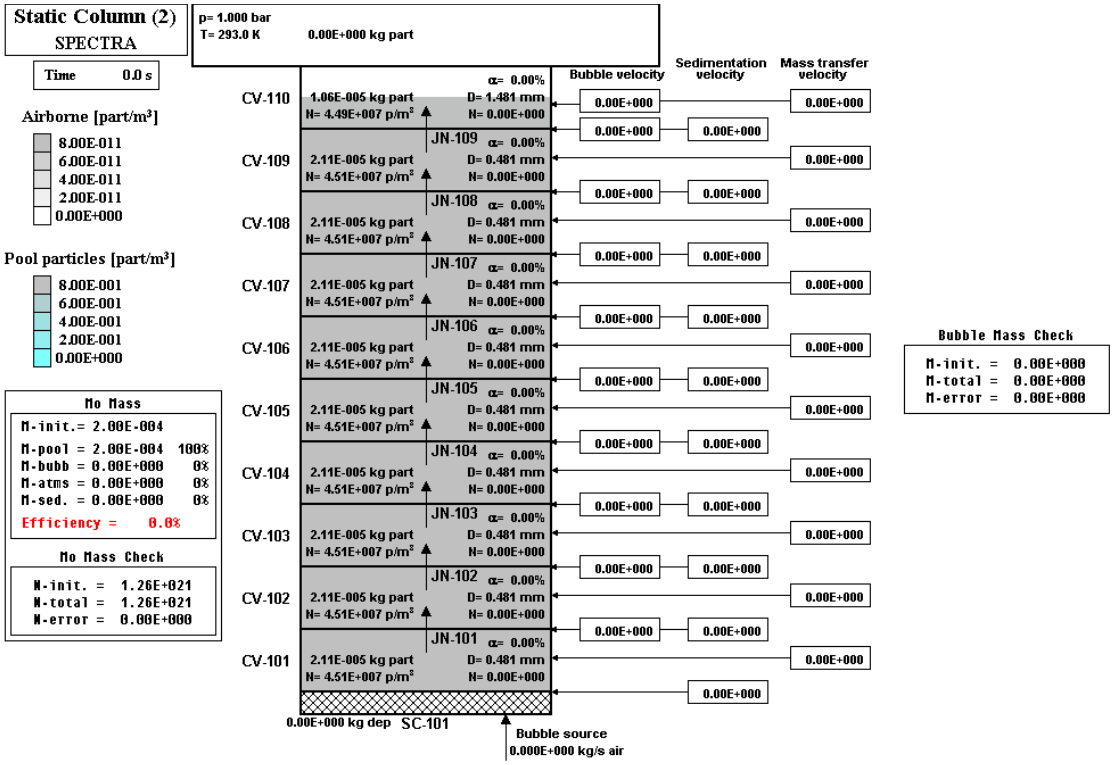

Figure 3-1087 Model 2 YLAK, V_{gas} = 5 sccm, D_p = 149 μm, initial state, t = 0.0 s

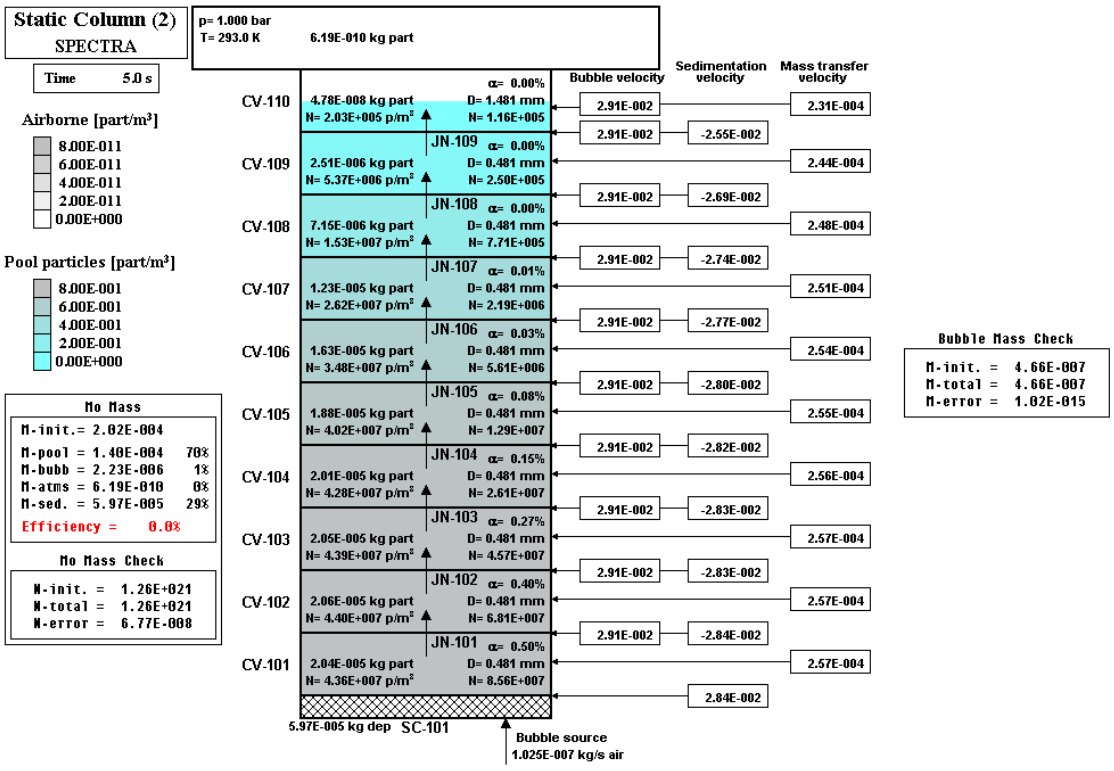

Figure 3-1088 Model 2, YLAK, V_{gas} = 5 sccm, D_p = 149 μm, state at t = 5.0 s

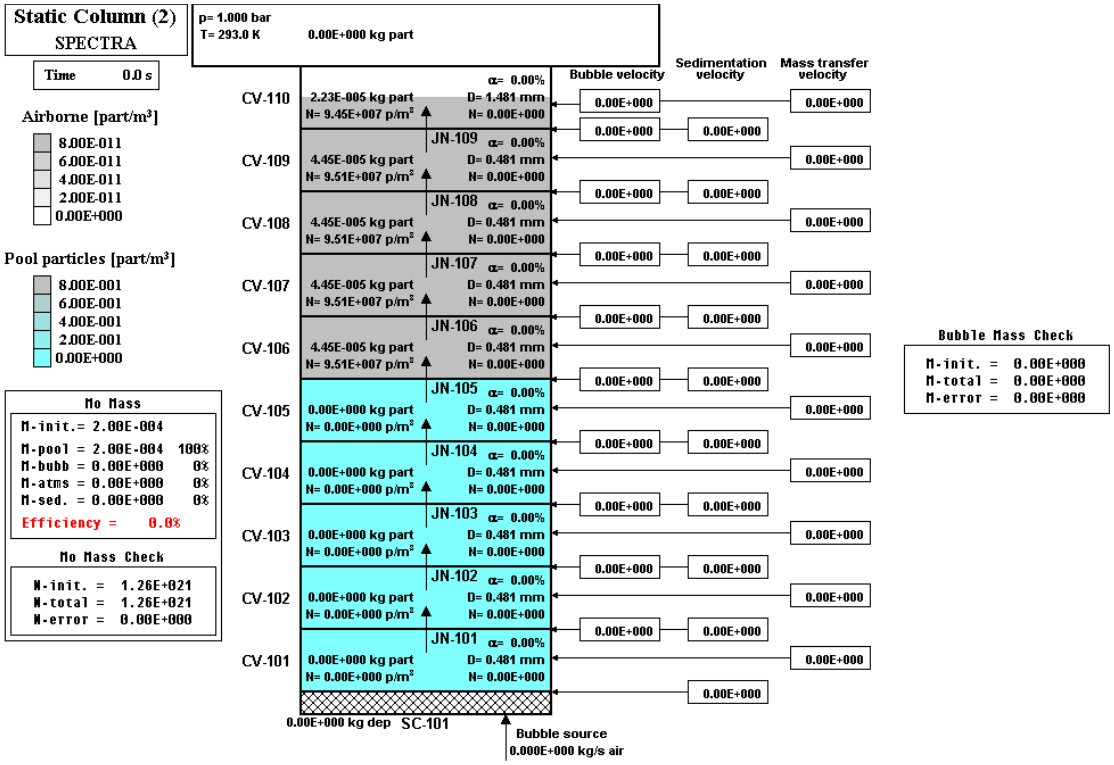

Figure 3-1089 Sensitivity, Model 2 YLAK, V_{gas} = 5 sccm, D_p = 149 μm, initial state, t = 0.0 s

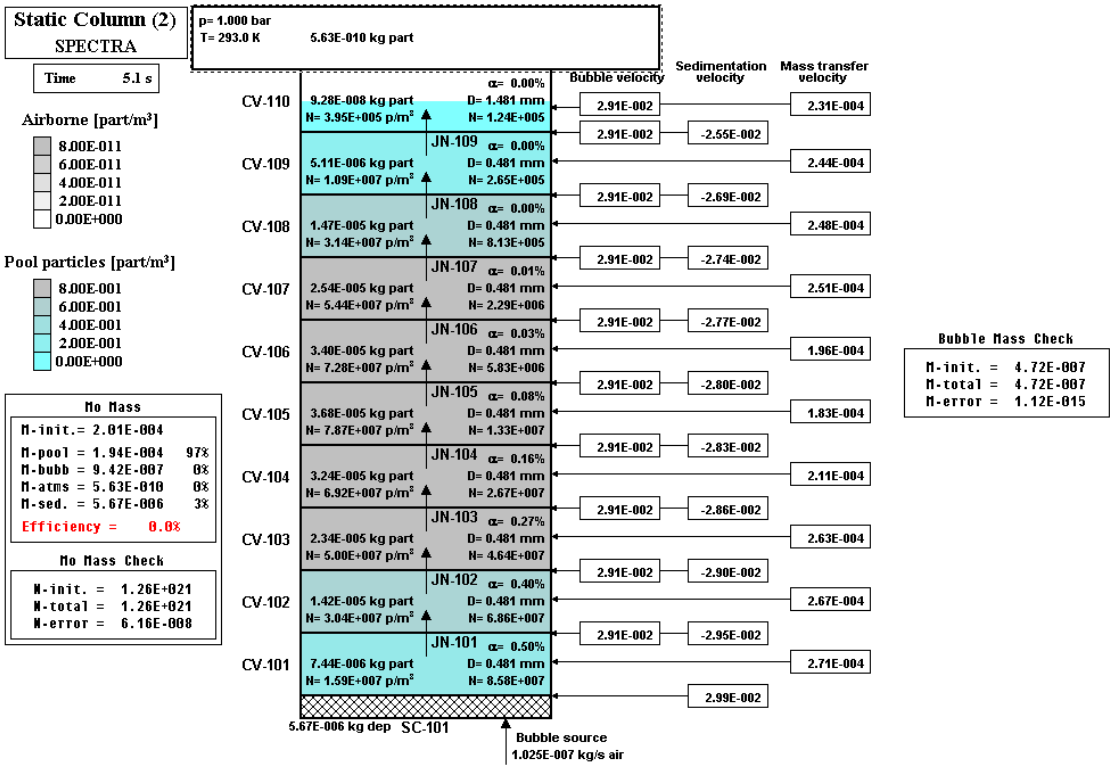

Figure 3-1090 Sensitivity, Model 2, YLAK, V_{gas} = 5 sccm, D_p = 149 μm, state at t = 5.0 s

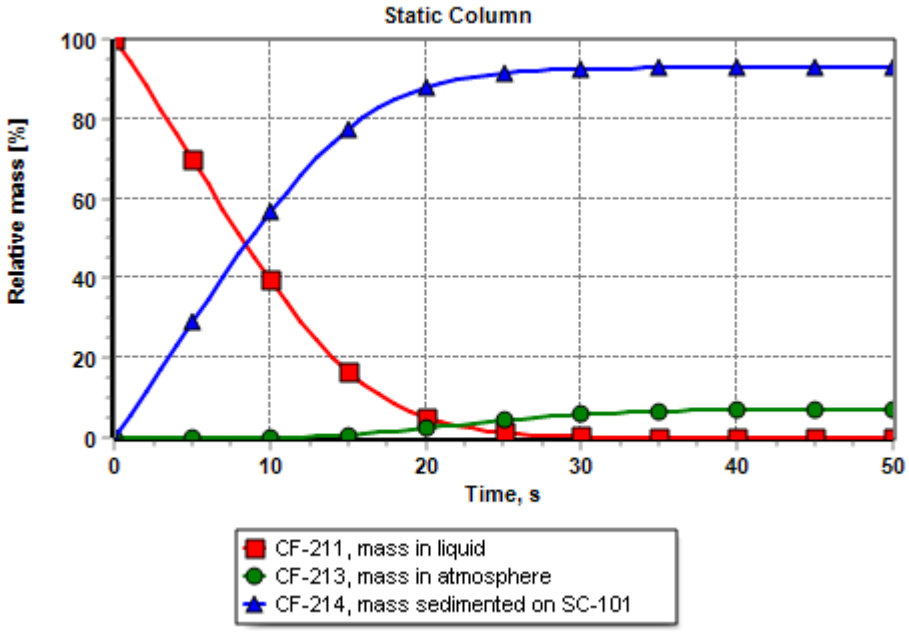

Figure 3-1091 Mass fractions vs. time - Model 2, YLAK, V_{gas} = 5 sccm, D_p = 149 µm

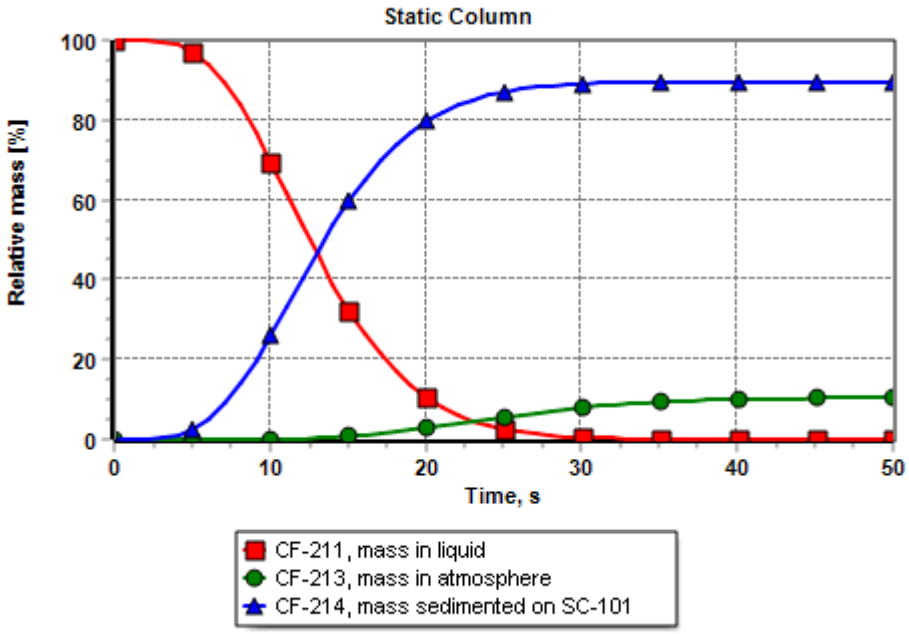

Figure 3-1092 Mass fractions vs. time - Sensitivity Model 2, YLAK, V_{gas} = 5 sccm, D_p = 149 µm

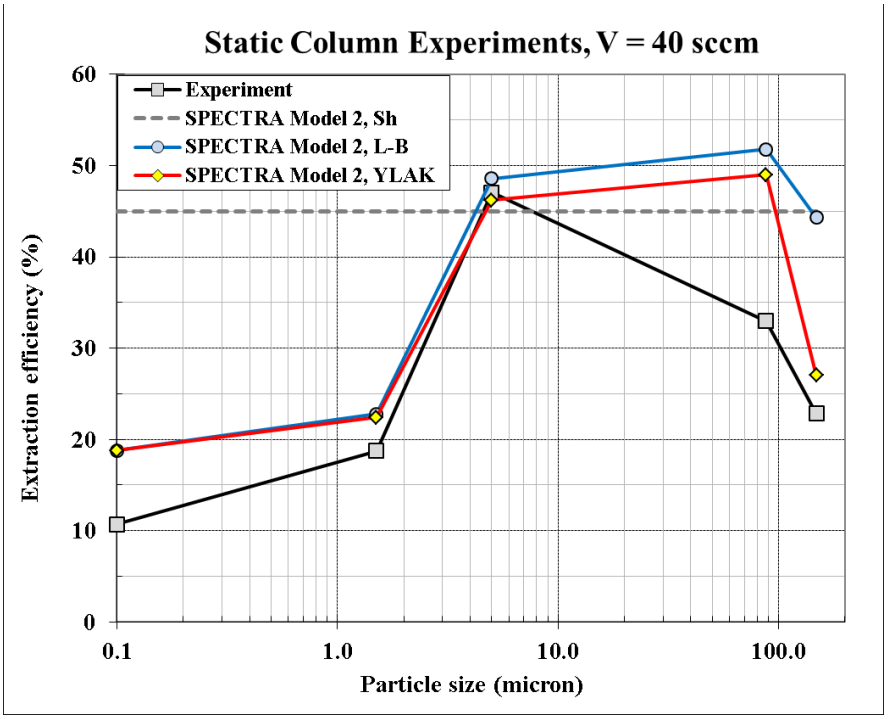

(A) Modified Langmuir and Blodgett correlation

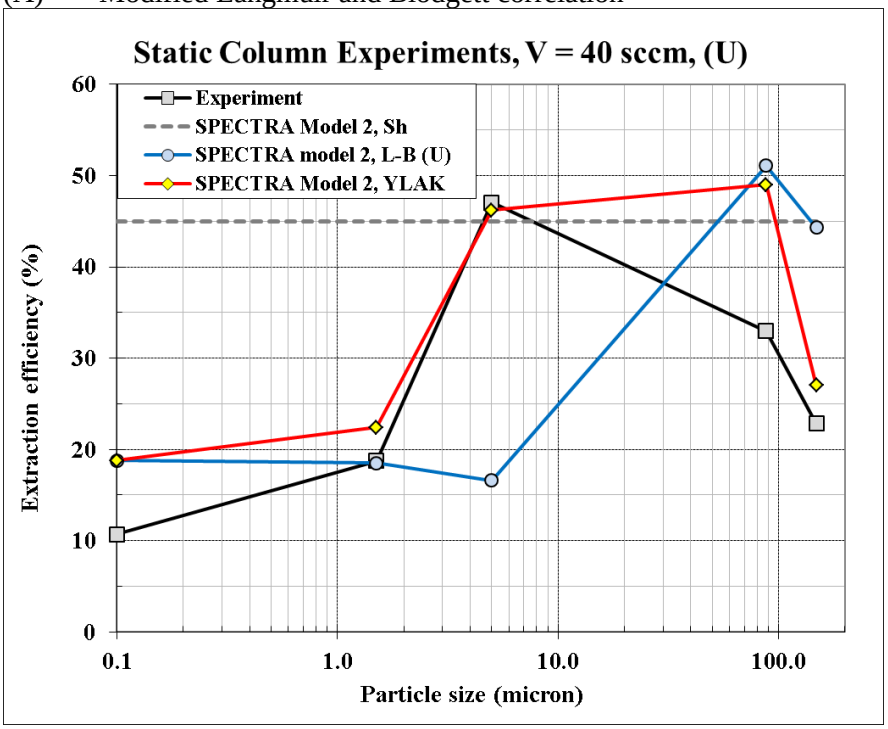

(B) Original Langmuir and Blodgett correlation

Figure 3-1093 Effect of modified L-B correlation - gas flow of 40 sccm, model 2

As mentioned in section 3.12.56.2, the modified Langmuir-Blodgett correlation was used. Both the original and modified correlations are available in SPECTRA; the choice is made by the user in input data (parameter ILBORT, record 860000). The difference between the original and the modified correlation is quite small - Figure 2-190. This difference has however quite a significant effect on the results of the Static Column tests. The results of the original correlation obtained for the case of V_{gas} = 40 sccm, are shown in Figure 3-1093 (B). For comparison, the results obtained with the modified correlation are shown in Figure 3-1093 (A). The difference is clear in case of 1.5 μm and 5.0 μm particles.

3.12.56.4 Results - Effect of Gas Flow

This section presents the same results as those discussed in the previous section. In contrast to the previous section, where results for a given gas flow were plotted versus particle size, in this section results for a given particle size are plotted versus gas flow. This allows to see the effect of gas flow.

As a first step, the total surface area of bubbles is plotted versus gas flow in Figure 3-1094. The value was obtained using the bubble size and density, which were in a good agreement with the supporting CFD analysis. The mass transfer to bubbles should be, roughly speaking, proportional to the bubble surface area, so the collection efficiency should exhibit similar trend.

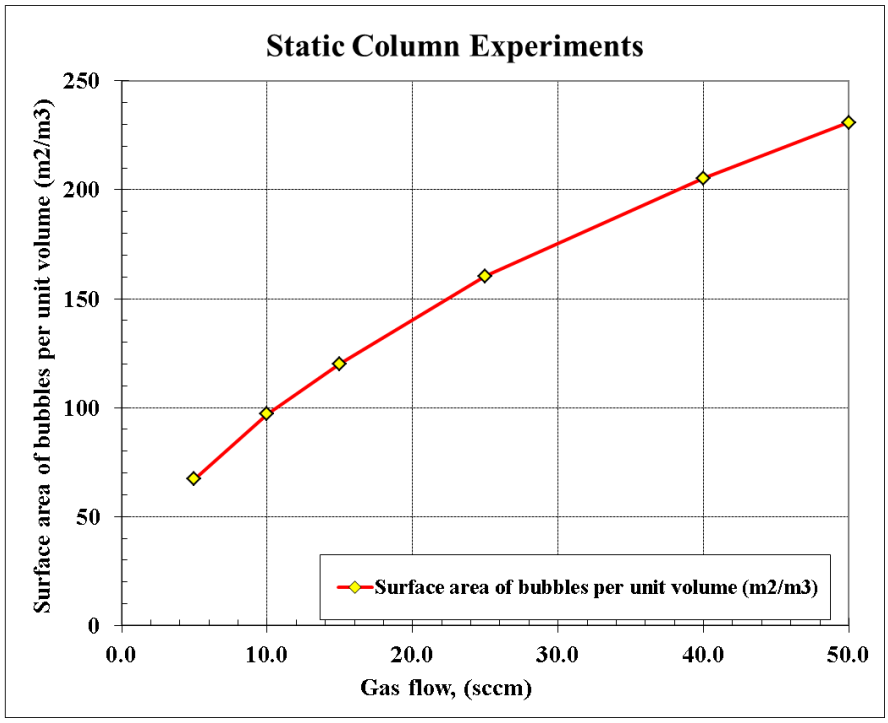

Figure 3-1094 Surface area of bubbles for different gas flows

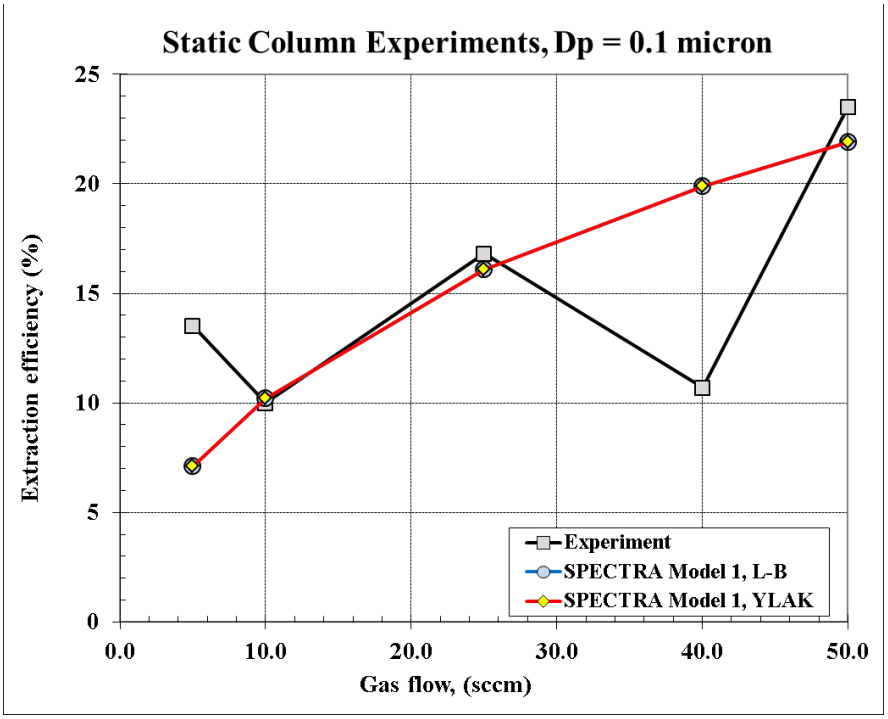

(A) Model 1 (isotopes on bubbles)

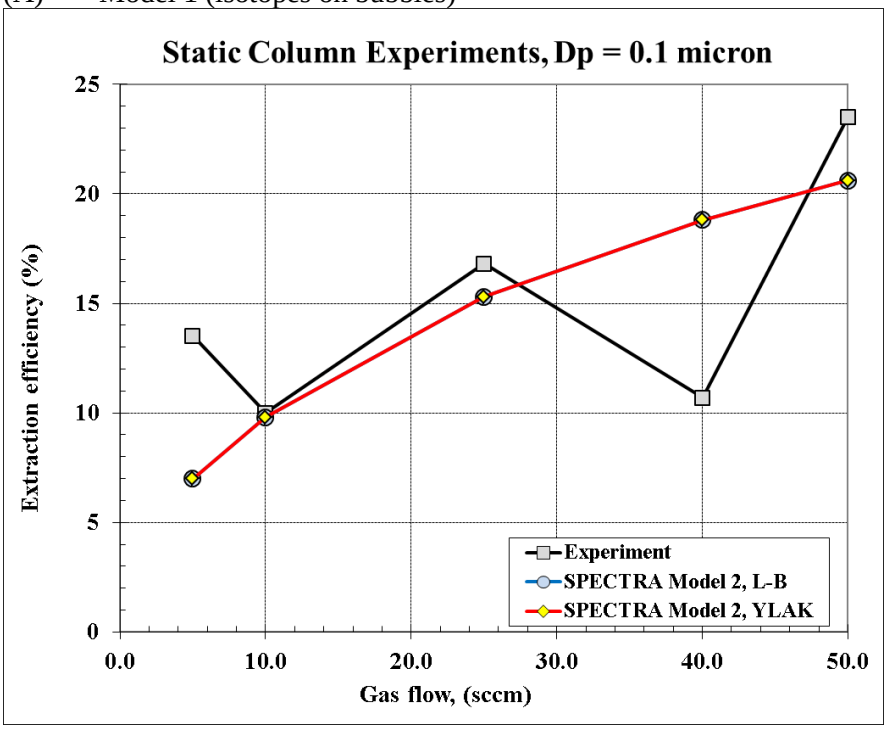

(B) Model 2 (isotopes on aerosols)

Figure 3-1095 Static Column experiments - particle size of 0.1 μm

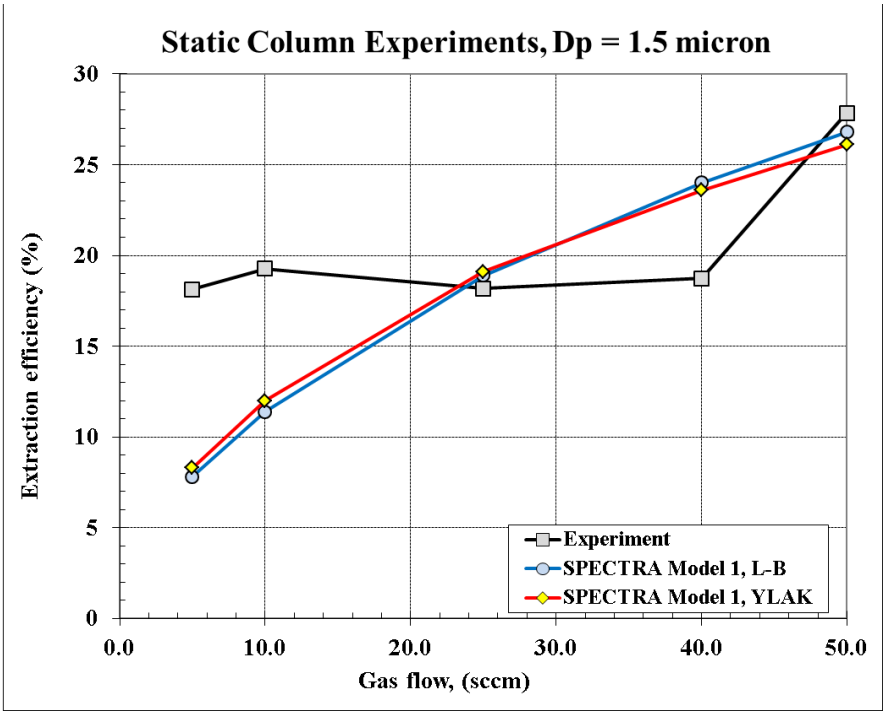

(A) Model 1 (isotopes on bubbles)

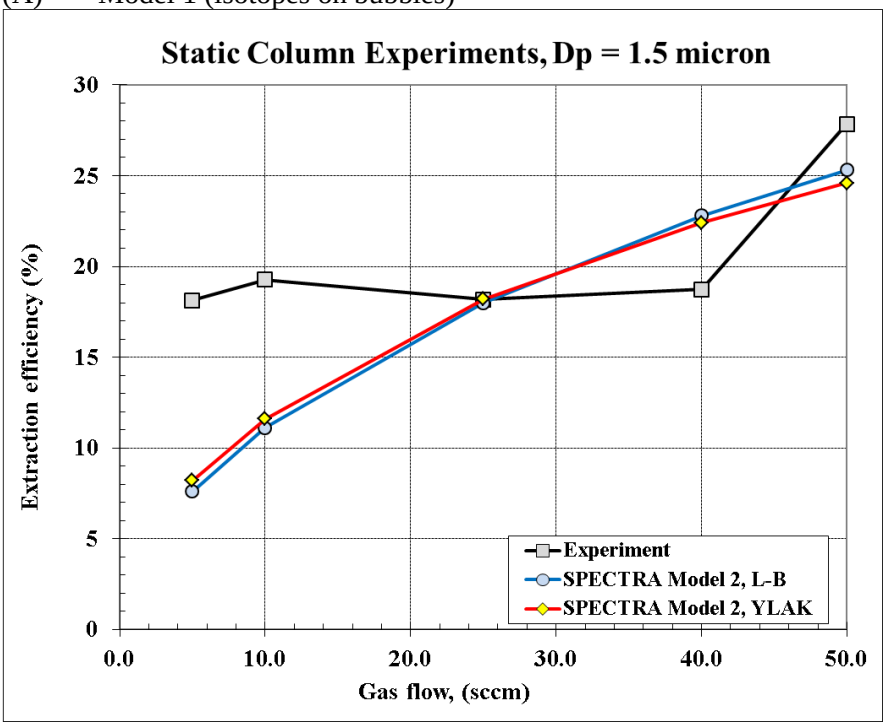

(B) Model 2 (isotopes on aerosols)

Figure 3-1096 Static Column experiments - particle size of 1.5 μm

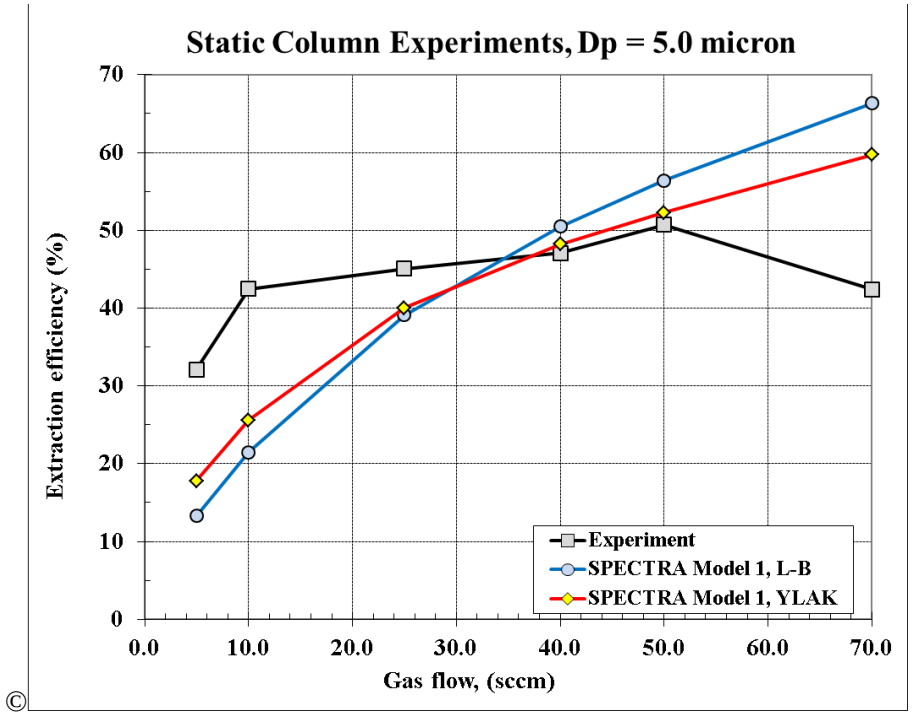

(A) Model 1 (isotopes on bubbles)

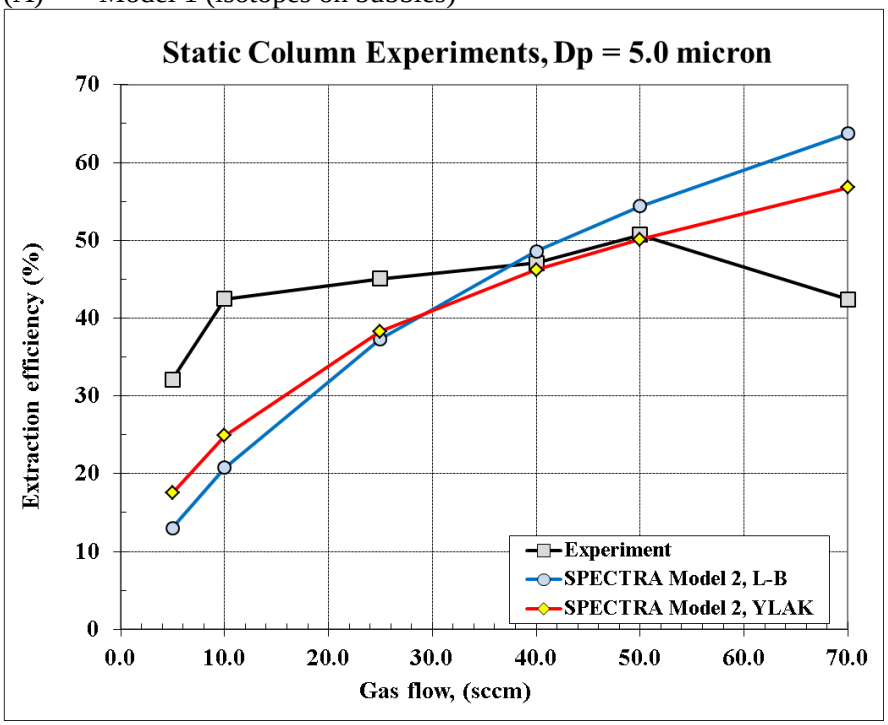

(B) Model 2 (isotopes on aerosols)

Figure 3-1097 Static Column experiments - particle size of 5.0 μm

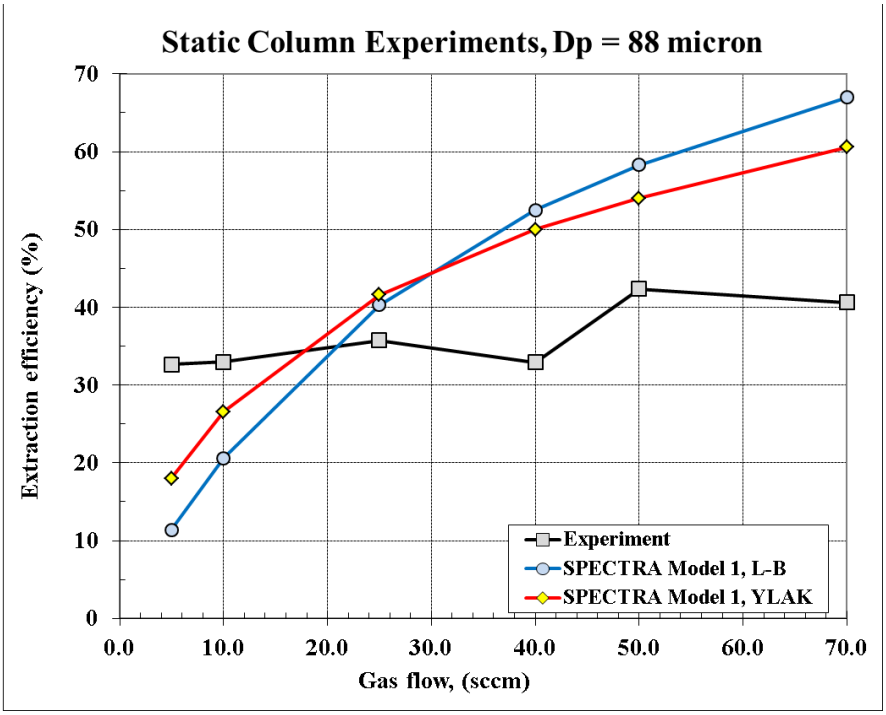

(A) Model 1 (isotopes on bubbles)

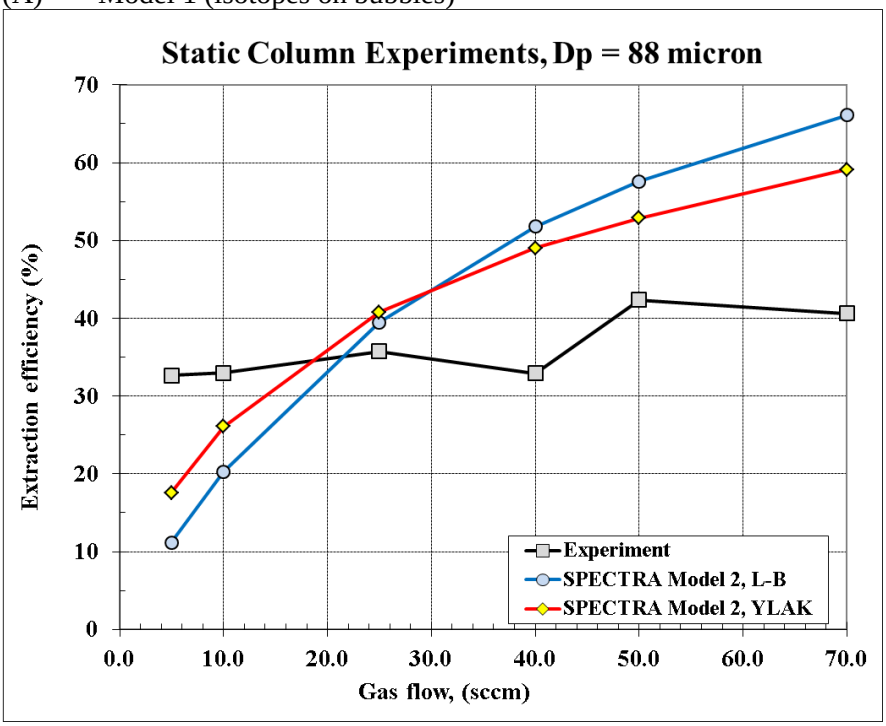

(B) Model 2 (isotopes on aerosols)

Figure 3-1098 Static Column experiments - particle size of 88.0 μm

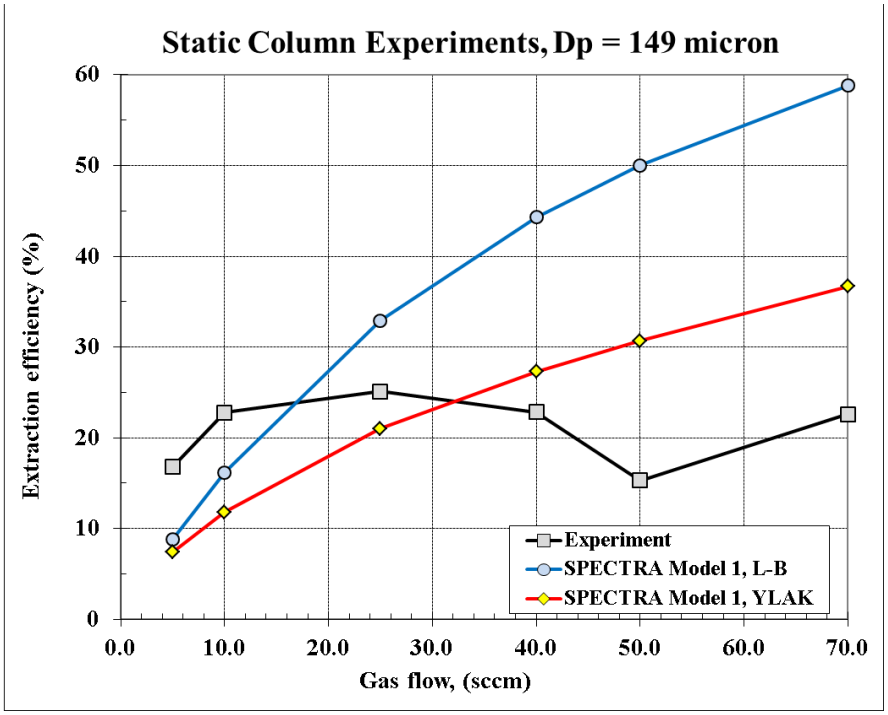

(A) Model 1 (isotopes on bubbles)

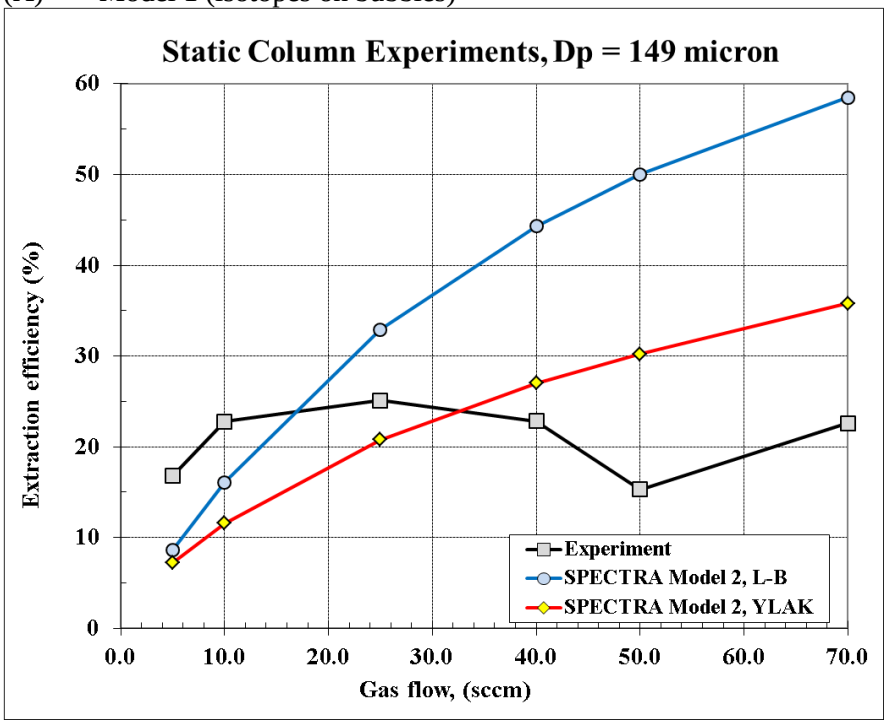

(B) Model 2 (isotopes on aerosols)

Figure 3-1099 Static Column experiments - particle size of 149.0 μm

The collection efficiency obtained for different particle sizes are shown in:

- D_p = 0.1 μm - Figure 3-1095,
- D_p = 1.5 μm - Figure 3-1096,
- D_p = 5.0 μm - Figure 3-1097,
- D_p = 88.0 μm - Figure 3-1098,
- D_p = 149.0 μm - Figure 3-1099.

In case of calculated values, the correct trend is observed. The trend of experimental values is somewhat more difficult to explain, specifically in case of small particles - Figure 3-1095. Possibly the bubble size was somewhat different that in the supporting CFD analysis that has been taken over in SPECTRA analysis. Different bubble size means different rise velocity and finally different surface area.

3.12.56.5 Summary and Conclusions

The agreement between calculated values and experiment is rather good in case of small particles and becomes worse in case of larger particles. The difficulty with large particles lies in very fast sedimentation and difficulty in modeling particle bubble interactions at the bottom, near the bubble injection point. Furthermore, uncertainties related to the initial experimental conditions may have an important effect. Considering all the difficulties in modeling the experiments, the obtained results are considered as satisfactory. The main reason for modeling the present experiment was to apply lessons learned to the analyses of MSRE, where interactions of fission products such as noble metals and noble gases with bubbles are very important. In case of MSRE, the particles are very small, as they are created by the fission process. The ability to model sedimentation of heavier particles is an advantage but is not important for MSRE analyses.

The main conclusions from the Static Column experiments are as follows.

- The results obtained with Model 1 and Model 2 are almost identical. This justifies the use of the faster Model 2 in MSRE analyses.
- The alternative correlation for particles / bubbles / droplets terminal velocity allows to model accurately the particle velocities. The accuracy was checked against the supporting CFD analysis and very good agreement was found for both the bubble velocity as well as the particle sedimentation velocity. The main advantage of the correlation is its flexibility (user-defined coefficients $C_{D,\mathrm{Re}\to\infty}$, C_{small}, C_D tabulated for the entire Reynolds number). This is important for analyses of fission product transport in MSRE.

3.12.57 Chromium Leaching Test

Reference [177] presents experimental results and a mathematical model based on the assumption of diffusion-controlled corrosion for UNS N10003 in a nonfuel bearing FLiBe salt. The removal of Cr is through an outward diffusion in the alloy. The effective diffusion coefficient was calculated to be 8.72×10^{-19} m^2/s at 700°C, which is lower than for UNS N10003 in fueled molten fluoride salt (containing 1%UF_4), ~2.9×10^{-18} m^2/s [177]. This indicated that the corrosion in nonfuel bearing FLiBe is significantly slower than in UF_4 dissolved FLiBe. Cr concentration profiles obtained with this model for 1,000 hours and 365 days are shown in Figure 3-1100.

This section presents verification results of the diffusion-controlled leaching model. The model was tested using the values calculated in [177]. The stable element Cr-52 was defined (isotope 191). The wall is represented by SC-006; the fluid volume by CV-006. The wall material is Hastelloy N (UNS N10003). The diffusion coefficient was defined as: $D_C = 8.72\times10^{-19}$ m^2/s. The wall temperature and the fluid temperature are set to 973 K (700°C). The SPECTRA input files are located in:
`\Z-INPUTS\RT\Leaching`

Results are shown in Figure 3-1101 through Figure 3-1108. Figure 3-1101 shows the visualization of the Cr-52 concentrations at the end of the calculation period (365 days). Figure 3-1102 shows the calculated concentration profiles at the times of 1000 hours and 365 days. The values calculated by SPECTRA were superimposed on the graph obtained from [177]. A very good agreement is observed between the SPECTRA values and the source data.

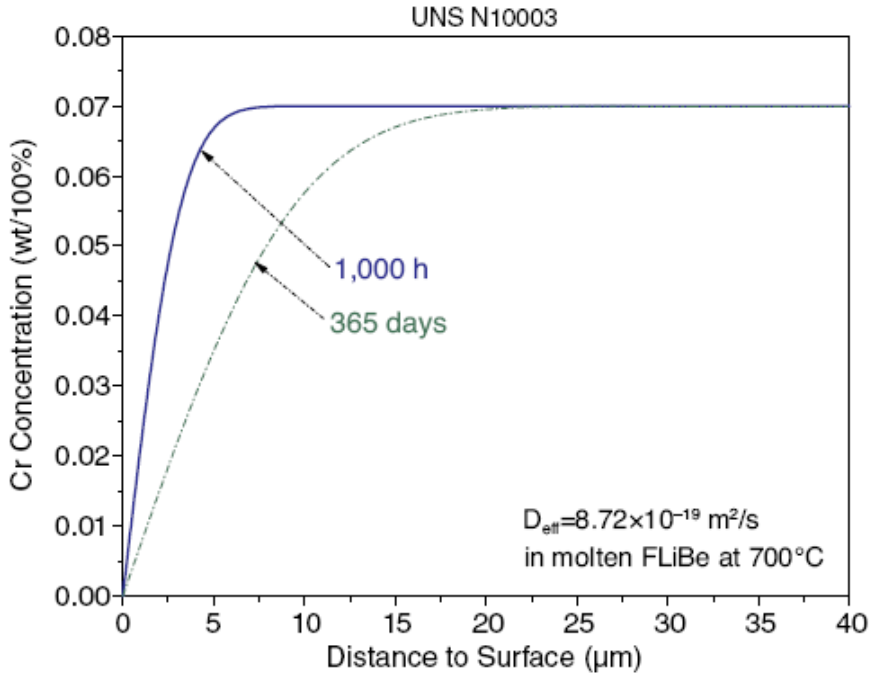

Figure 3-1100 Cr concentration profiles, Hastelloy N (UNS N10003) in FLiBe at 700°C [177]

Effect of node size

Lack of nodalization sensitivity was demonstrated by varying the size of the base node size between 1 μm and 10 μm. For each case SPECTRA results are compared to the mathematical model from [177].

- Node size of 1.0 μm, input deck: Leaching-01.SPE - Figure 3-1102
- Node size of 2.0 μm, input deck: Leaching-02.SPE - Figure 3-1103
- Node size of 5.0 μm, input deck: Leaching-05.SPE - Figure 3-1104
- Node size of 10.0 μm, input deck: Leaching-10.SPE - Figure 3-1105

The results are in good agreement with the reference results even when a relatively large nodes (10 μm) are used. 10 μm is the maximum allowed node size when the diffusion-limited leaching model is used (see Volume 1).

Effect of time step size

Δt = 10.0 s was used as a base time step. All results shown in this section were obtained using this time step. For comparison, time steps of Δt = 5.0 s and Δt = 100.0 s were used. The input decks are Leaching-02-dt-5.SPE and Leaching-02-dt-100.SPE respectively. Results were very similar. The graphs are practically identical to Figure 3-1103, therefore no separate graphs are presented.

Effect of T_0

Figure 3-1106 shows the concentration profiles in the two stages. The results were obtained using the default value of the Stage I characteristic time T_0 = 1000 s and node size of 2 μm. During Stage I the concentrations on the surface decrease to zero. During Stage II the concentration at the surface remains as ≈0.0 and the mass transfer is limited by the diffusion from the inner nodes.

The end of Stage I is at approximately 10,000 s. This is also seen in Figure 3-1107, showing the comparison of two cases:

- T_0 = 1000 s (default), input deck: Leaching-02.SPE
- T_0 = 100 s (minimum), input deck: Leaching-02-T0-Min.SPE

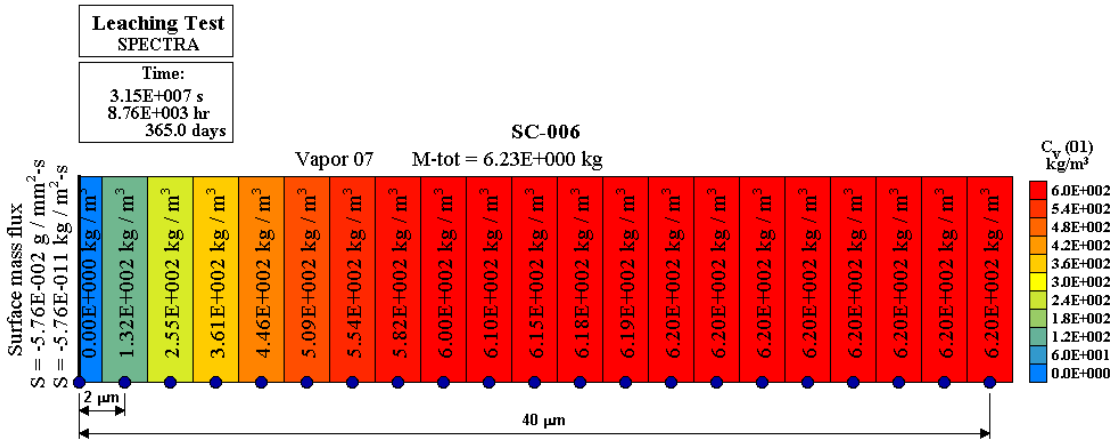

Figure 3-1101 Cr concentrations, Hastelloy N in FLiBe at 700°C, SPECTRA model, t = 365 days

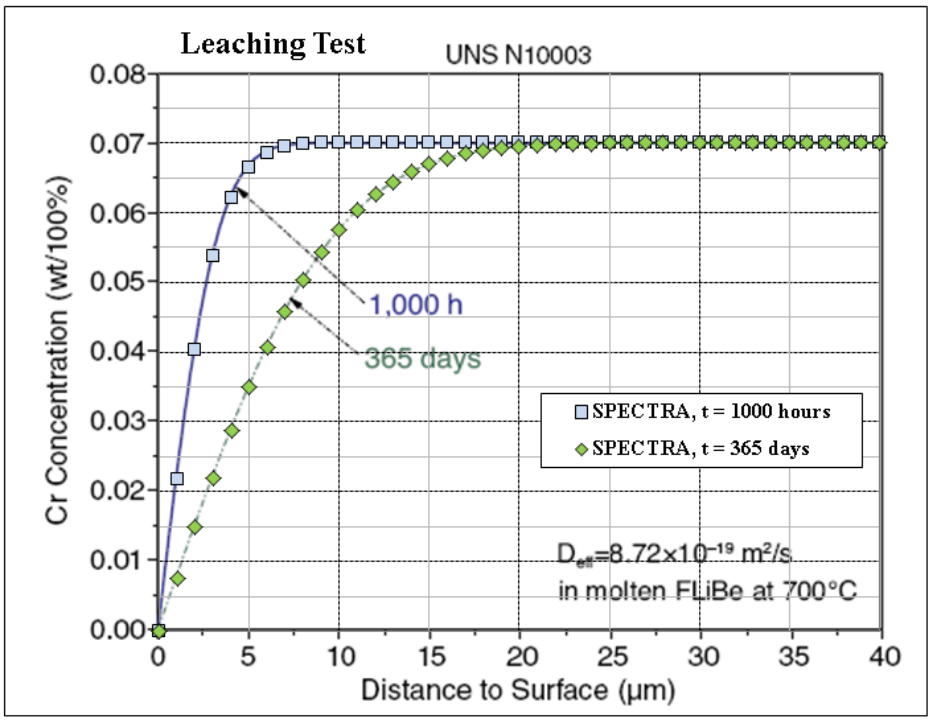

Figure 3-1102 Cr concentration profiles, Hastelloy N in FLiBe at 700°C SPECTRA, node size = 1.0 μm versus model of [177]

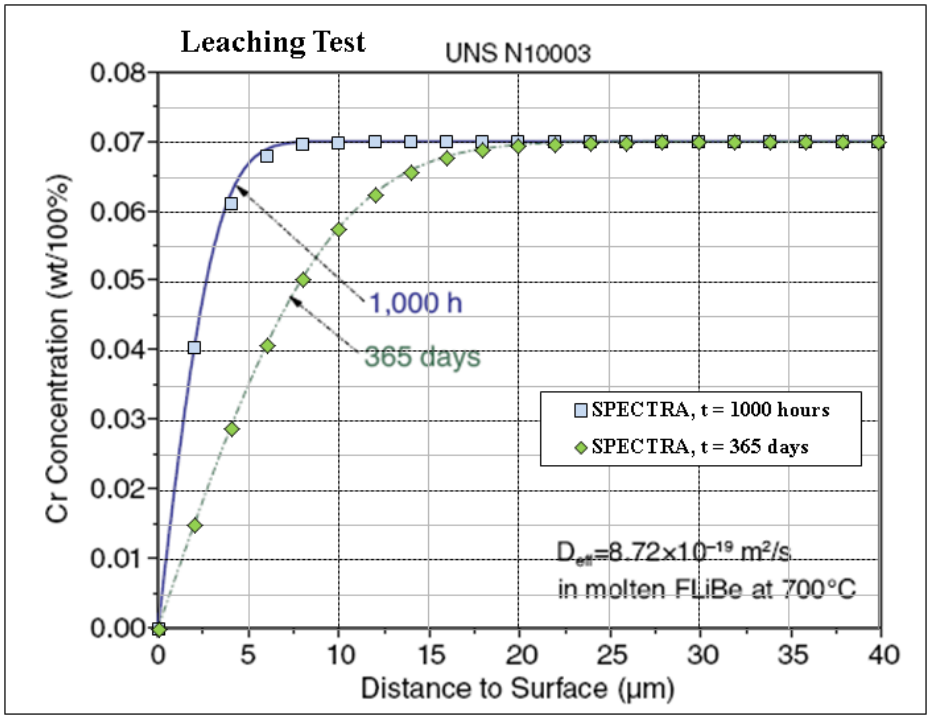

Figure 3-1103 Cr concentration profiles, Hastelloy N in FLiBe at 700°C SPECTRA, node size = 2.0 μm versus model of [177]

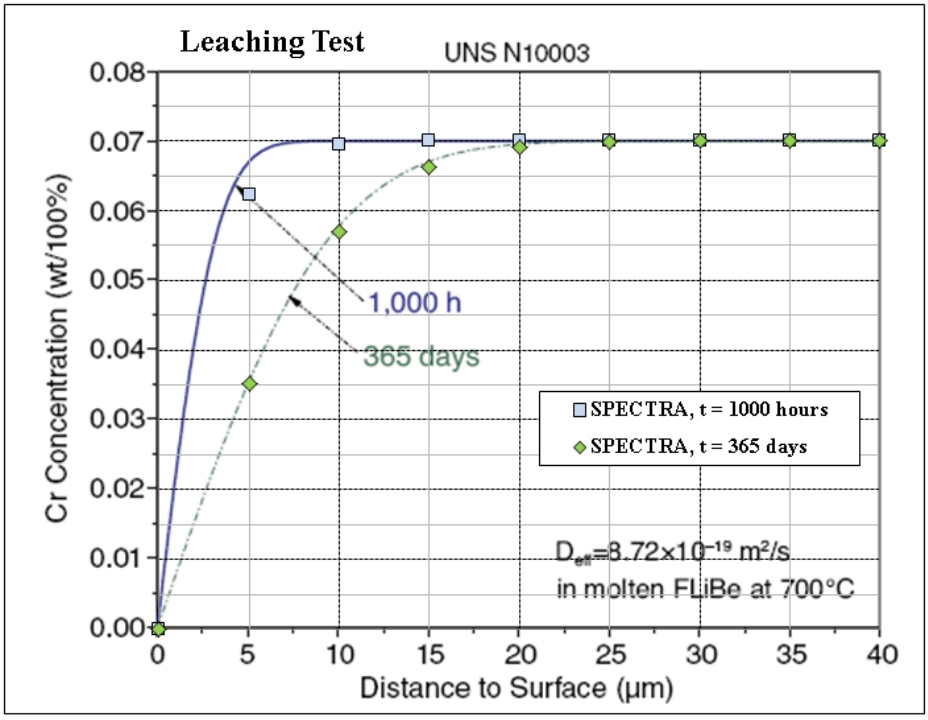

Figure 3-1104 Cr concentration profiles, Hastelloy N in FLiBe at 700°C SPECTRA, node size = 5.0 μm versus model of [177]

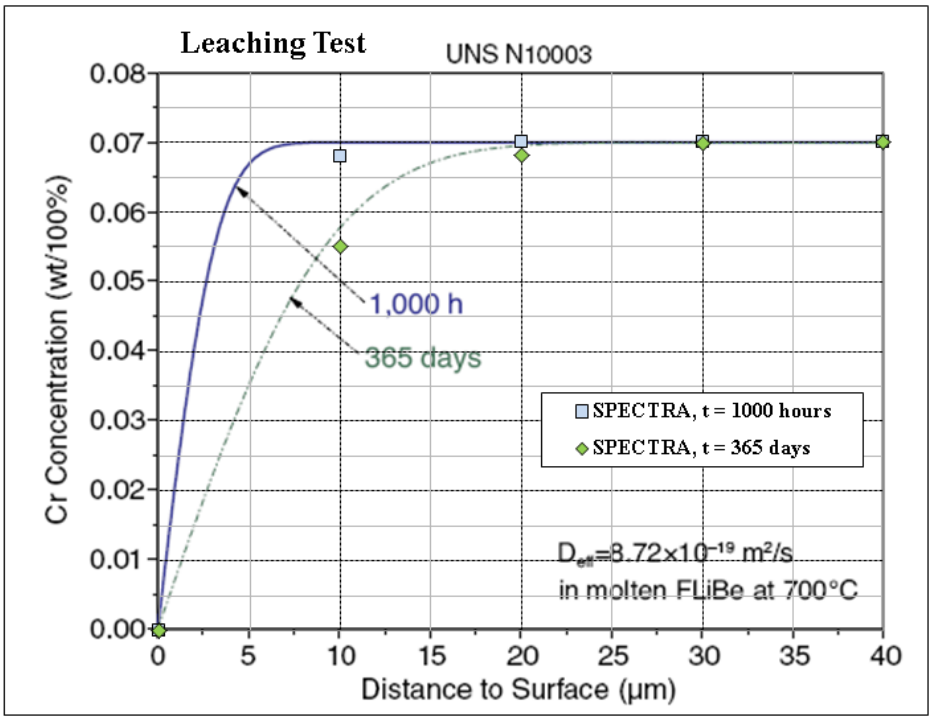

Figure 3-1105 Cr concentration profiles, Hastelloy N in FLiBe at 700°C SPECTRA, node size = 10.0 μm versus model of [177]

It is seen that with smaller value of T_0 the initial mass transfer rate is larger and the diffusion-limited value of the surface mass flux (~2×10^{-10} kg/m^2-s) is reached sooner. Figure 3-1108 shows the long-term (Stage II) values of the surface mass flux. The values are of order of 10^{-10} kg/m^2-s and slowly decreasing. (The values shown in Figure 3-1107 and Figure 3-1108 are plotted with reversed sign, as the convention in SPECTRA is that the mass flux from the surface is negative.)

A smaller value of T_0 provides theoretically a better agreement with the model from [177], where the initial surface concentration is taken as zero (the corresponding T_0 is infinitely short). Calculations performed for 2 µm nodes showed that the concentration profiles at 1000 h and 365 days are practically identical with both T_0 = 1000 s and T_0 = 100 s. The graphs from the run with T_0 = 100 s are practically identical to Figure 3-1103, therefore no separate graphs are presented.

CF Model

On top of the diffusion model discussed above, a simple CF model is available. With this model the user can define the surface mass flux using a Control Function. One advantage of using this method is that there is no need to use very small nodes next to the surface. In the case of the diffusion model, the recommended node size is 1 - 10 µm (see Volume 1). In the case of the CF model, the node size may and should be large (>0.1 mm, see Volume 1).

A simple CF was defined, which gives a constant surface mass flux of 10^{-9} kg/m^2-s. The remaining data is the same as in the diffusion model. The input deck is: Leaching-CF.SPE. Figure 3-1109 shows the results of this run at 365 days.

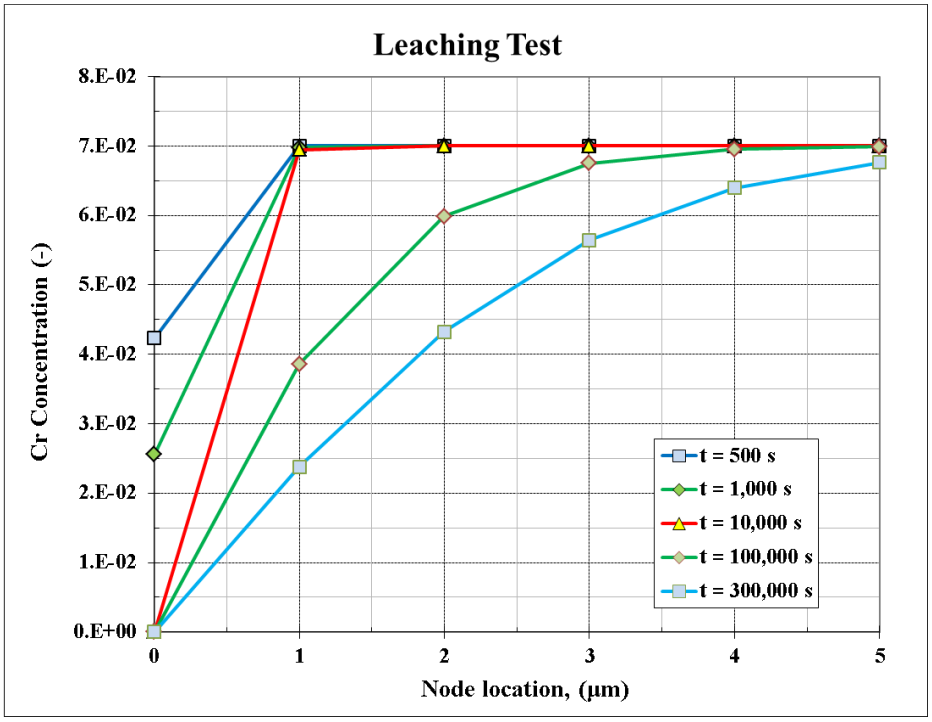

Figure 3-1106 Cr concentration profiles, T_0=1000 s,
Stage I: t <~10,000 s, Stage II: t > ~10,000 s

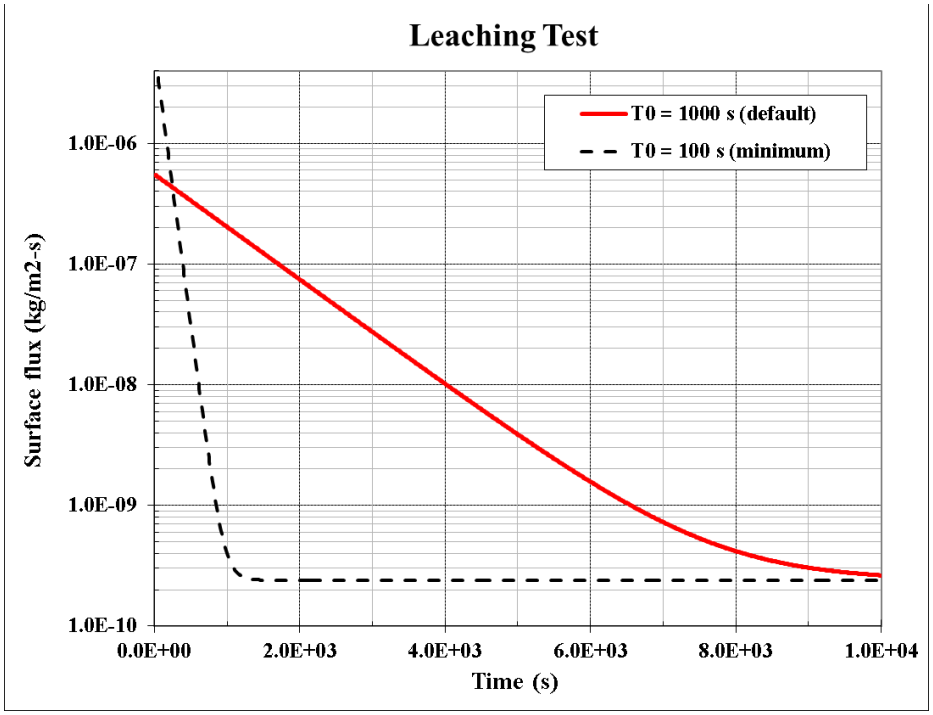

Figure 3-1107 Surface mass fluxes during Stage I (<~10,000 s)

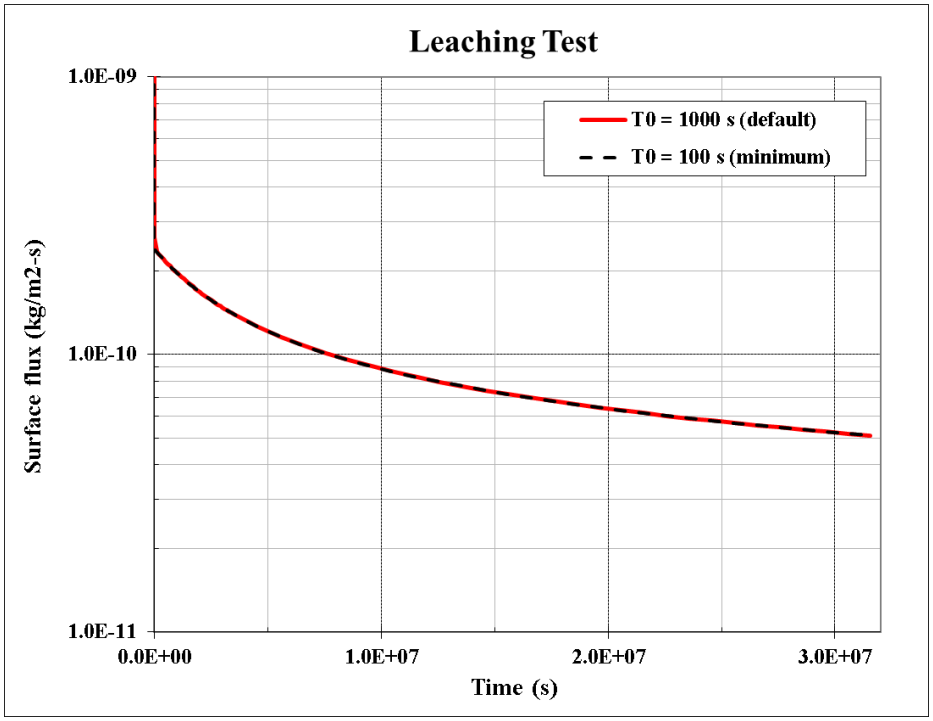

Figure 3-1108 Surface mass fluxes during Stage II (> ~10,000 s)

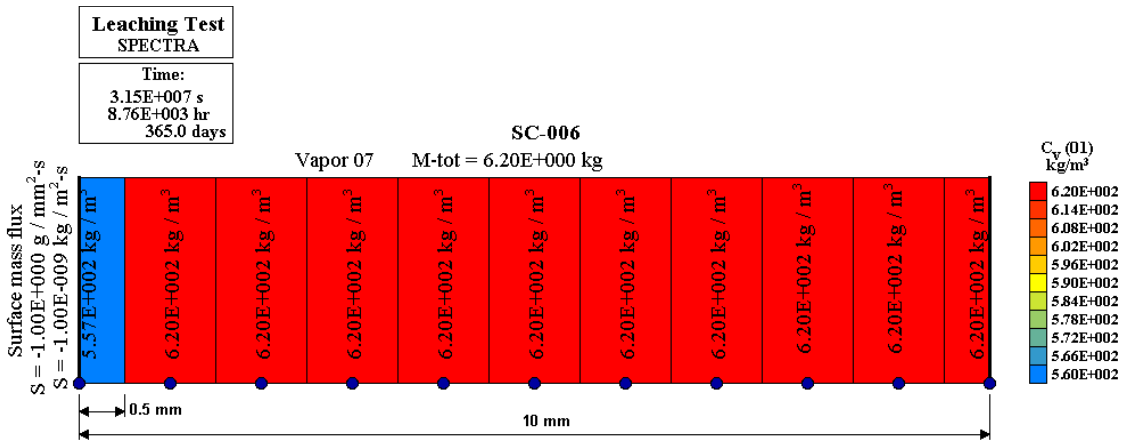

Figure 3-1109 Results of the CF model, CF= 10^{-9} = const.

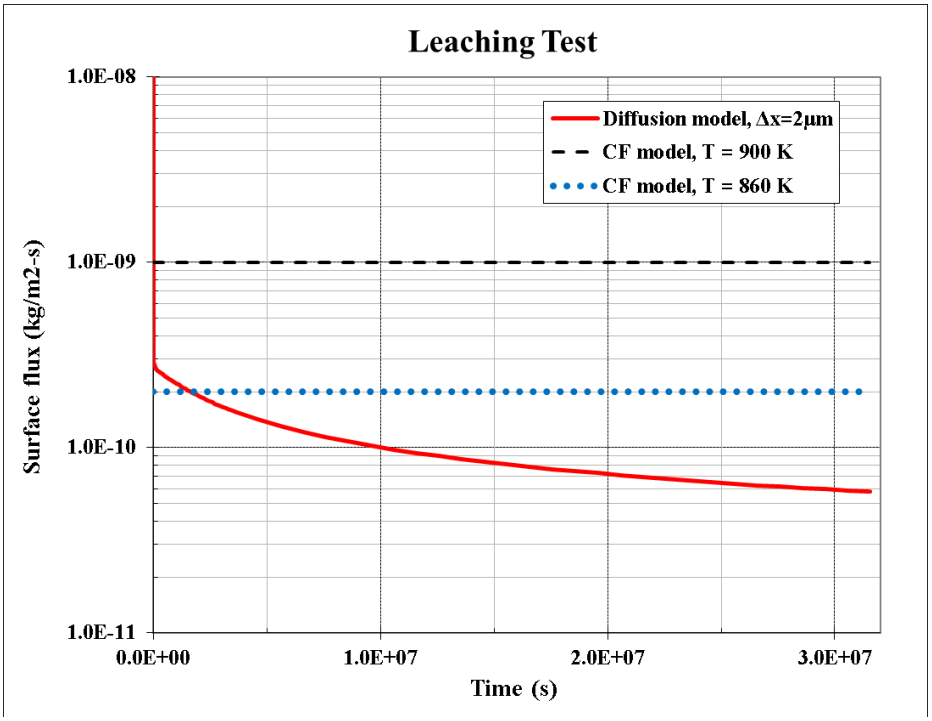

Figure 3-1110 Comparison of the diffusion model with the CF model

Figure 3-1110 shows comparison of the surface mass flux from the CF model and the diffusion model (this very simple CF was used here for illustration purposes; of course a more complicated CF may be defined, e.g. flux may be tabulated versus time).

Figure 3-1110 shows also the temperature effect. The surface mass flux is interpolated between zero and the full value in the temperature range $T_{min} < T < T_{min} + \Delta T_{int}$ (default: $850 < T < 900$ K) - see Volume 1. The input deck for the 860 K is: Leaching-CF-860.SPE. The value obtained at 860 K is 20% of the full value.

3.13 MCCI

This section presents results of the MCCI test. The current results are compared to the results of a severe accident scenario, loss of feedwater with failure of all safety systems, analyzed with MELCOR. The scenario leads to vessel failure at about 20,000 s and relocation of about 70 tons of corium to the concrete cavity.

3.13.1 MCCI Test - Model

The MCCI test considered consists of a cylindrical cavity with inner radius of 2.4 m filled with corium. The concrete type 2 is assumed (limestone common sand concrete - see Volume 1). The mass of corium initially present in the cavity is assumed based on reference MELCOR calculations. The corium composition masses of metals were estimated based on MELCOR results as follows: overall metal fraction of 0.3, Zr fraction of 0.0, Cr fraction of 0.18, Ni fraction of 0.08, and Fe fraction of 0.74. The model parameters were, as far as possible kept at their default values (exceptions are the metal fractions). A sensitivity study was performed for several modeling parameters (section 3.13.3).

3.13.2 MCCI Test - Results

The analysis starts at the time of vessel failure, assumed equal to 20,000 s, based on reference MELCOR calculations. The results are shown in Figure 3-1112 trough Figure 3-1117. First, visualization pictures are shown in Figure 3-1112 and Figure 3-1113. Next, time-dependent graphs are shown and compared to the MELCOR results.

Visualization pictures show the state of the system at 40,000 s (Figure 3-1112) and at 90,000 s (Figure 3-1113). Note that Figure 3-1112 shows only a part of the entire model and is cut few cells below the current level of ablated concrete (the lower part of concrete not shown). Figure 3-1113 shows the entire model (all vertical cells). The visualization pictures show that the behavior is similar to the theoretical behavior described in [208] and shown in Figure 3-1111. The solid concrete and the molten corium pool may be separated by a thin layer of corium crust and molten concrete. The gas bubbles, rising from the decomposing concrete, are in the model assumed to pass through the layer of solid corium crust; the crust is probably porous and permeable to gases from the concrete [208].

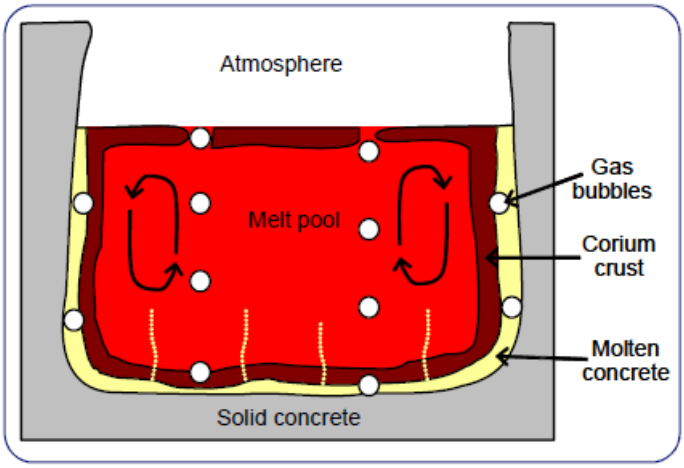

Figure 3-1111 Qualitative picture of MCCI phenomena [208]

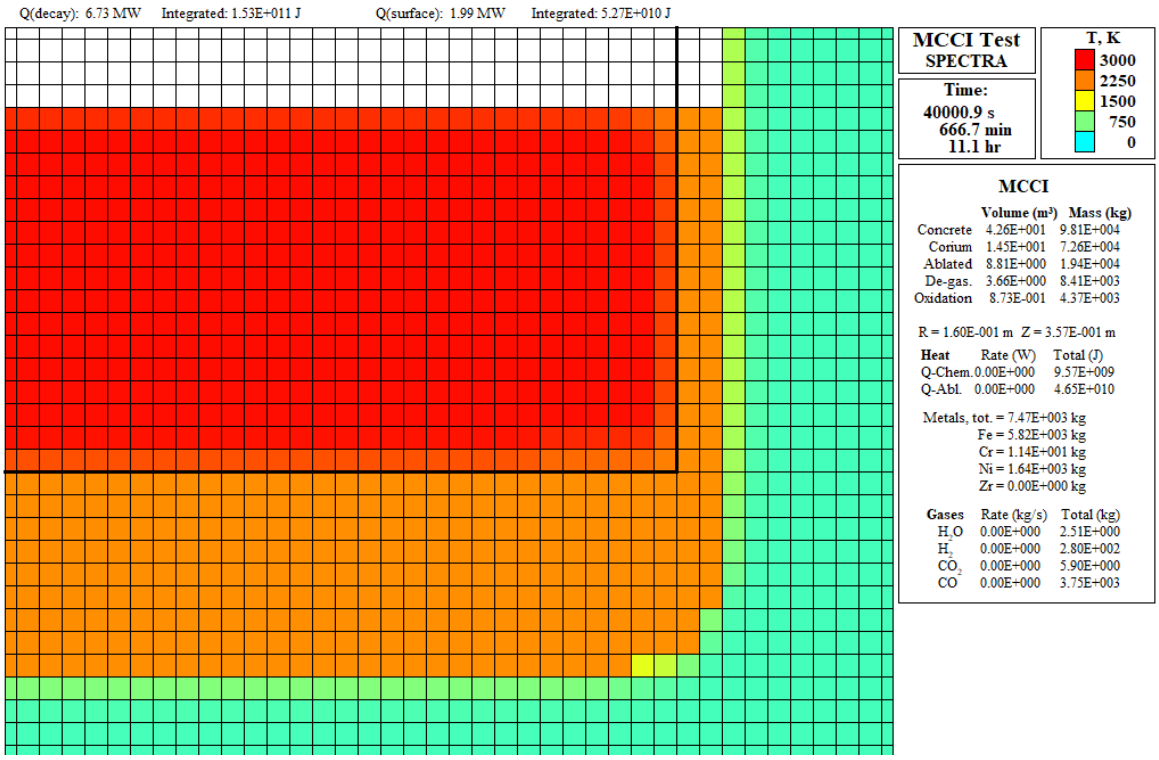

(a) temperatures

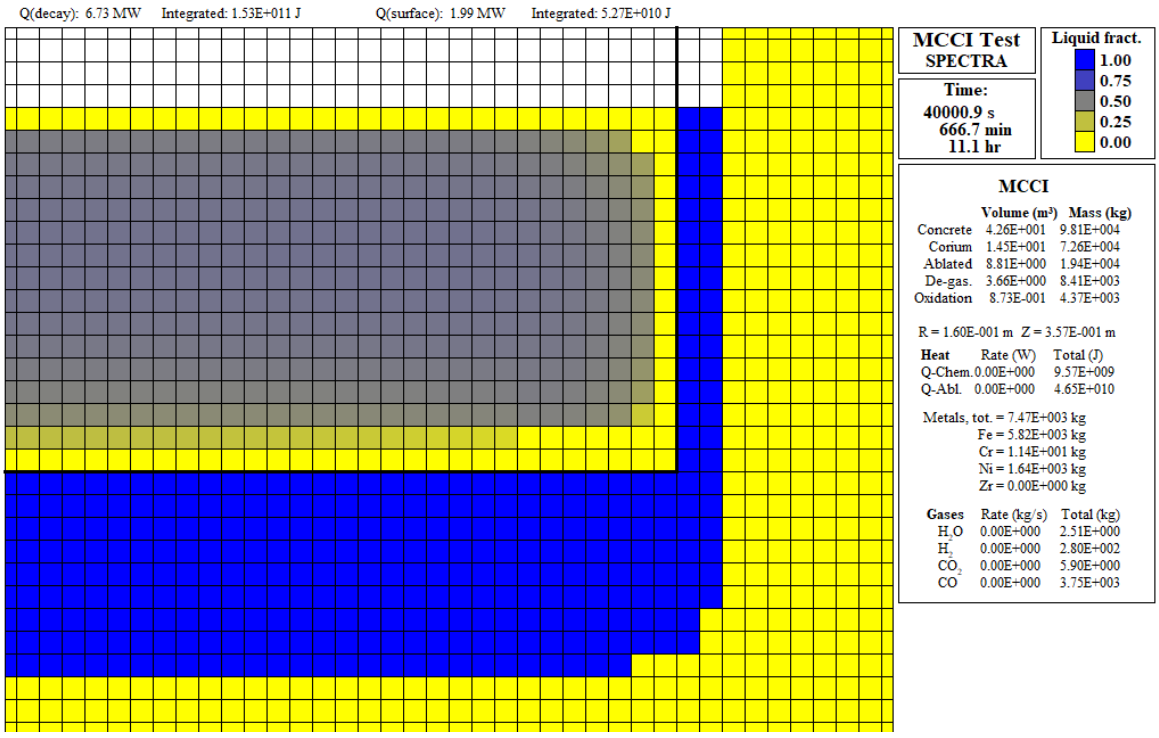

(b) liquid fractions

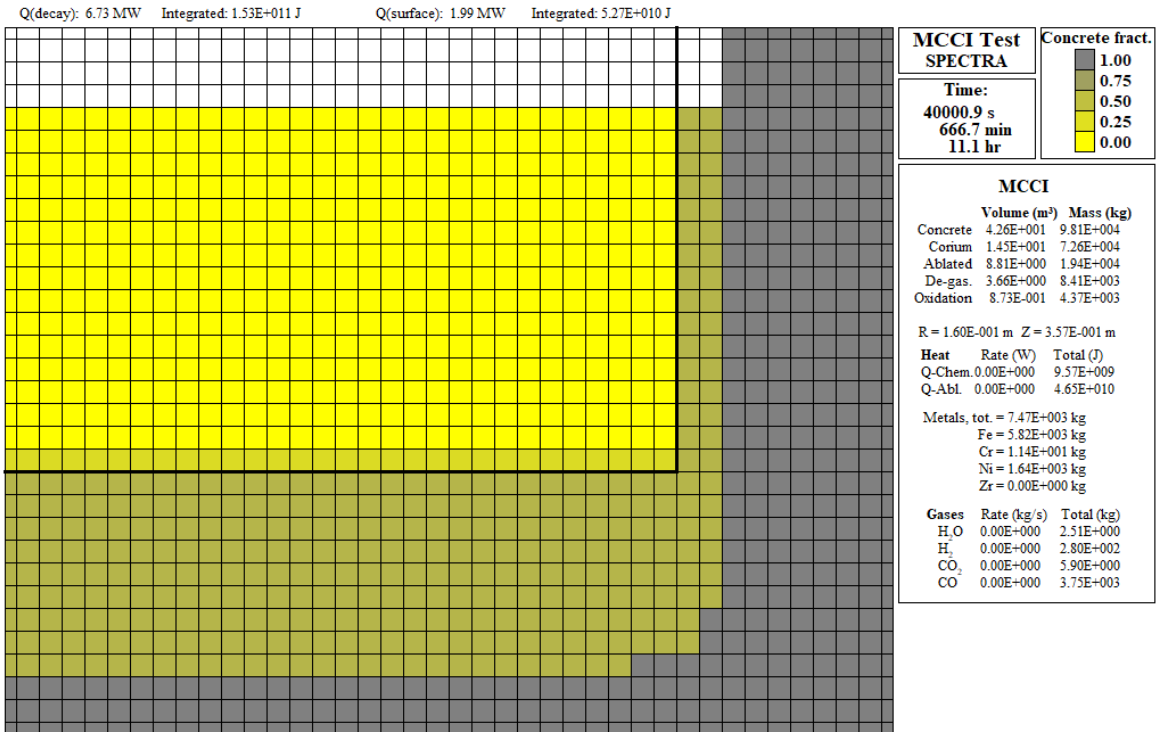

(c) concrete fractions

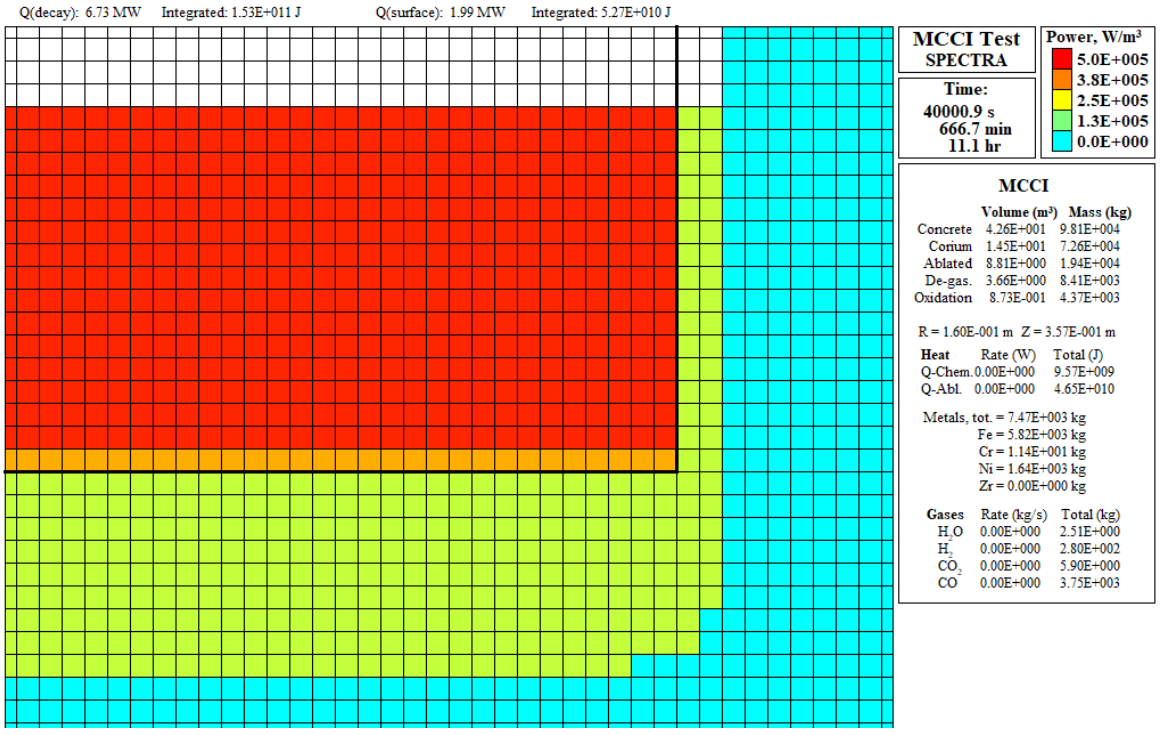

(d) power density

Figure 3-1112 MCCI test, t = 40,000 s.

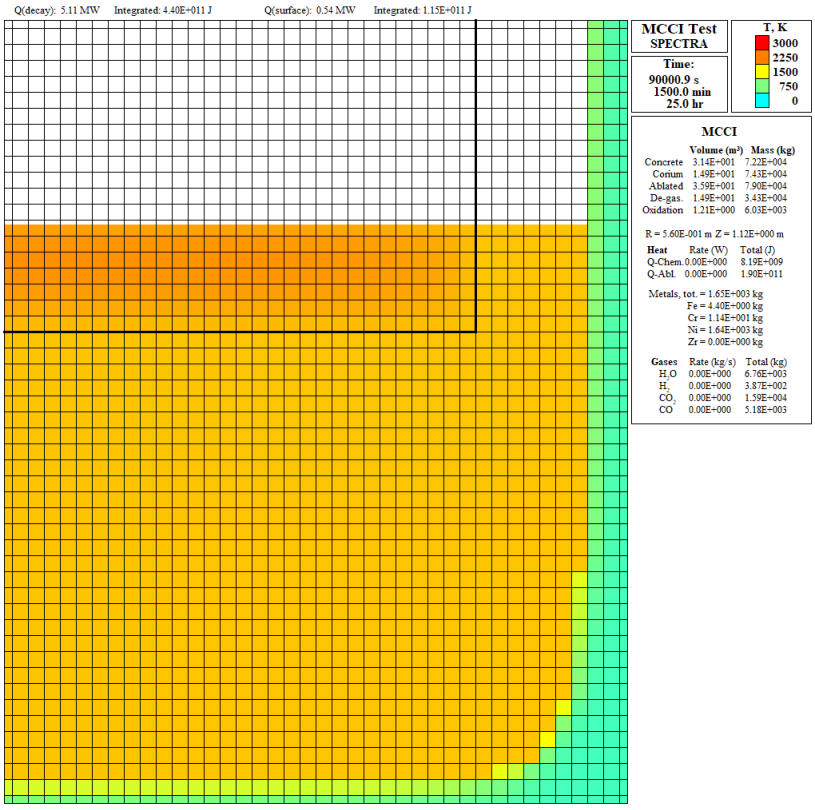

(a) temperatures

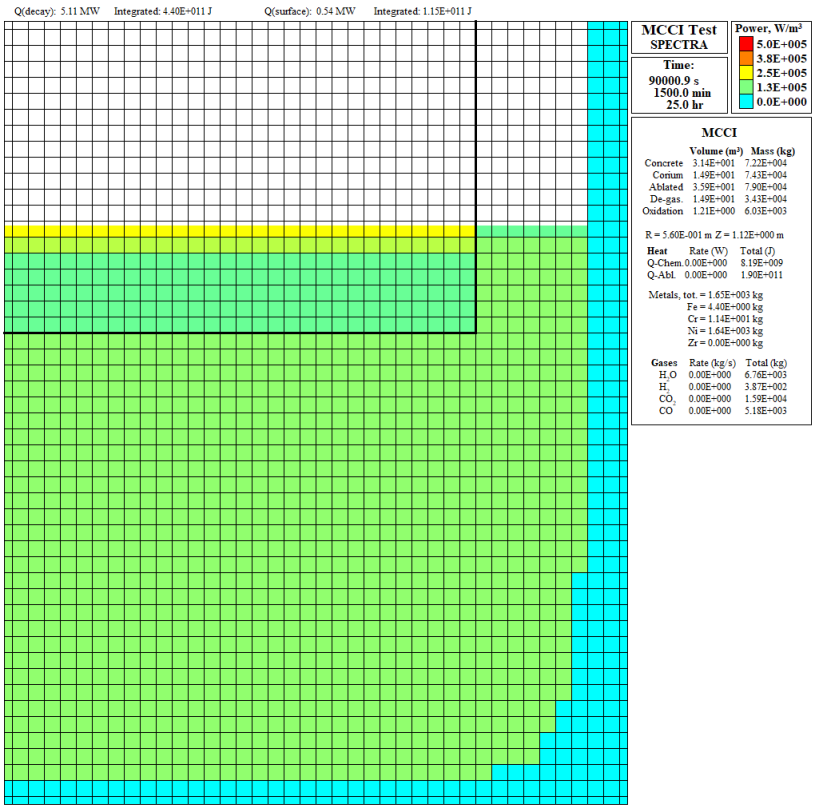

(b) power density

Figure 3-1113 MCCI test, t = 90,000 s.

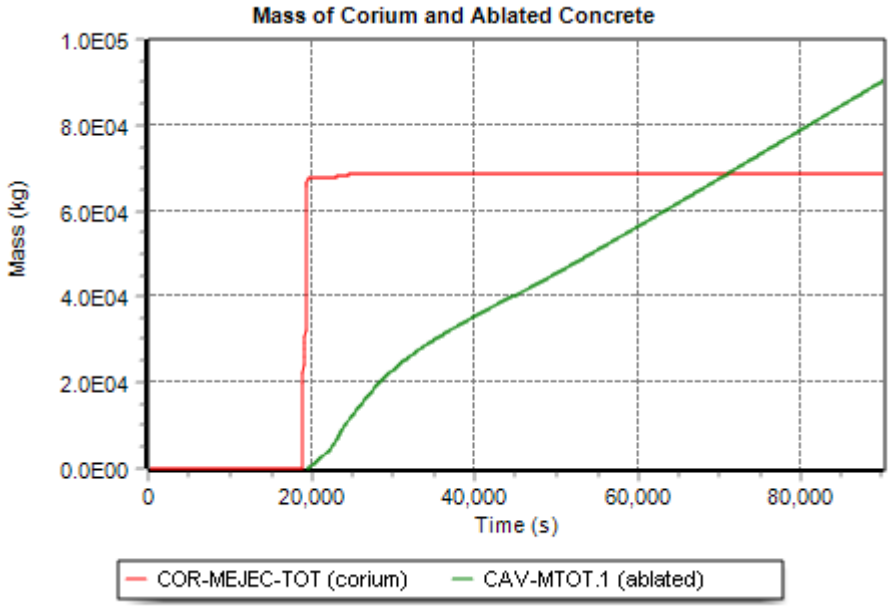

(a) MELCOR

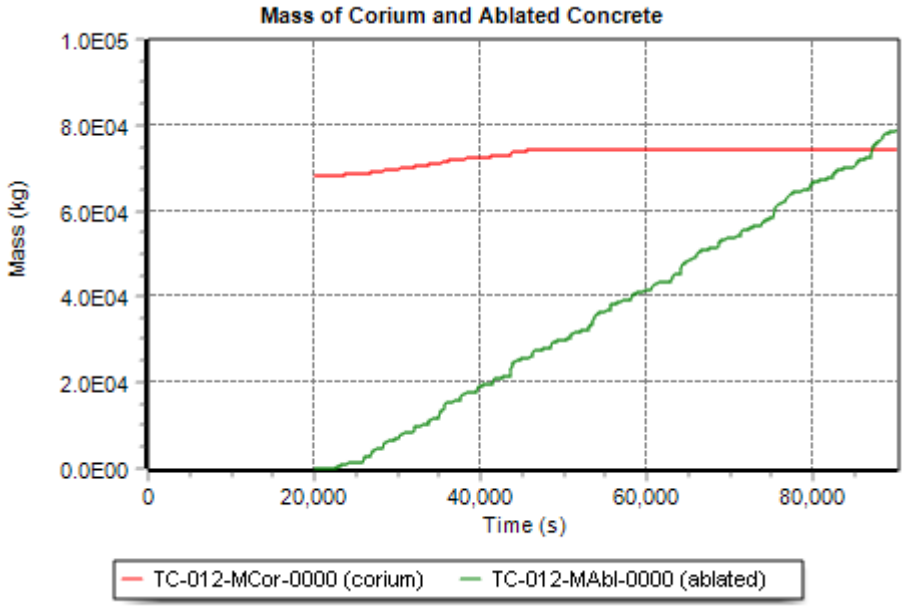

(b) SPECTRA

Figure 3-1114 MCCI test, mass of corium and ablated concrete

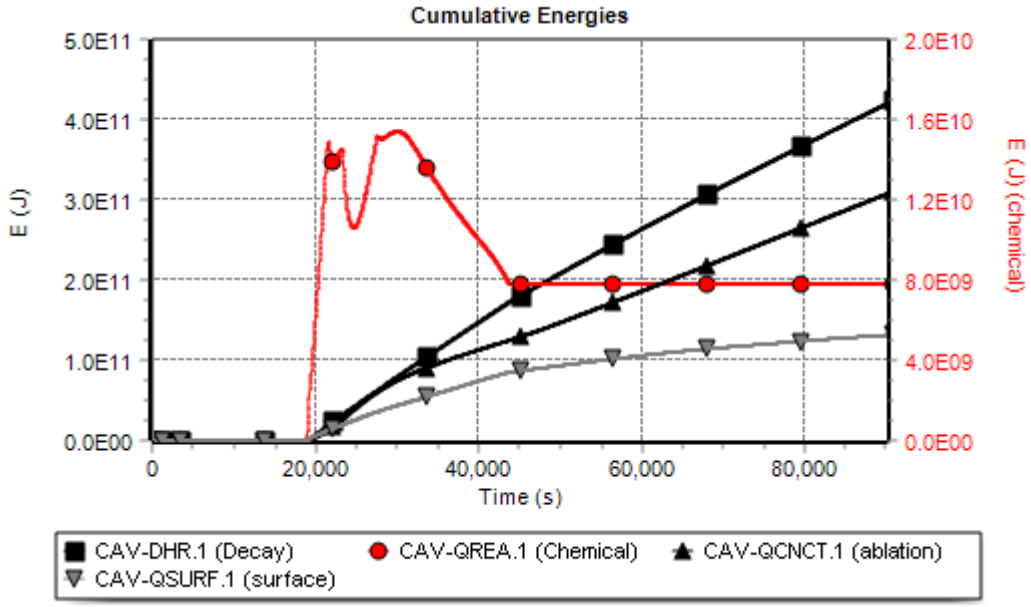

(a) MELCOR

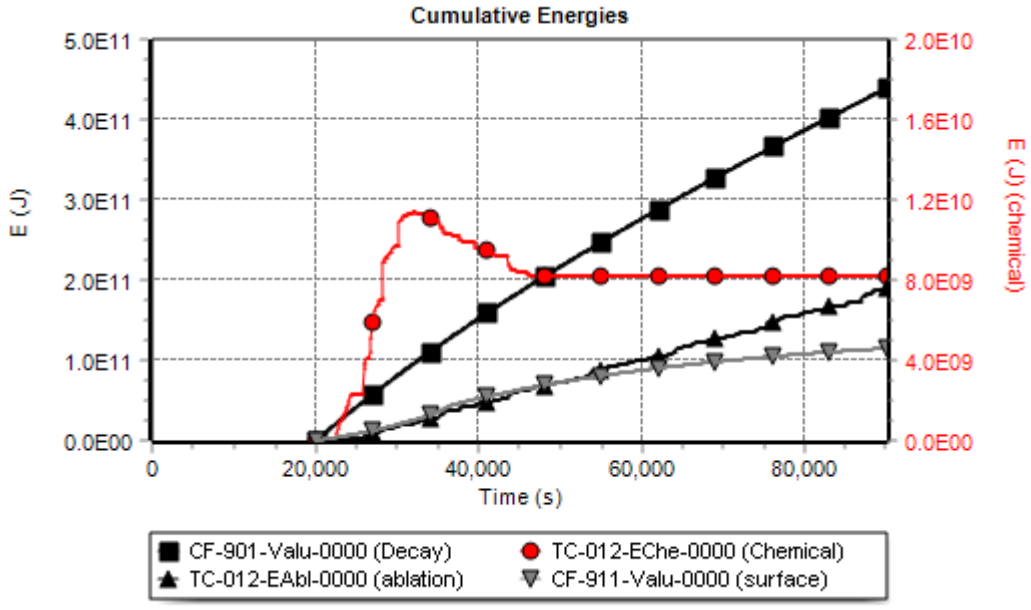

(b) SPECTRA

Figure 3-1115 MCCI test, cumulative energies

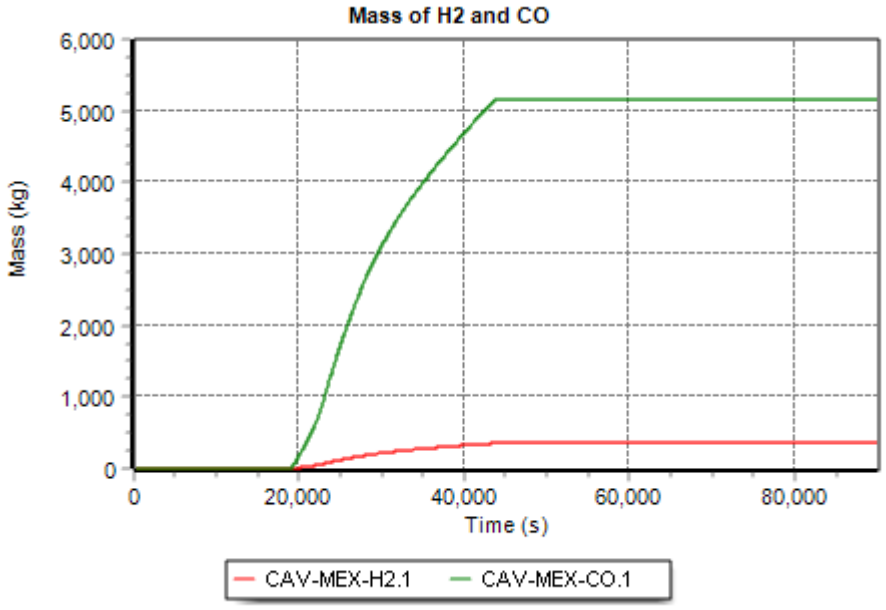

(a) MELCOR

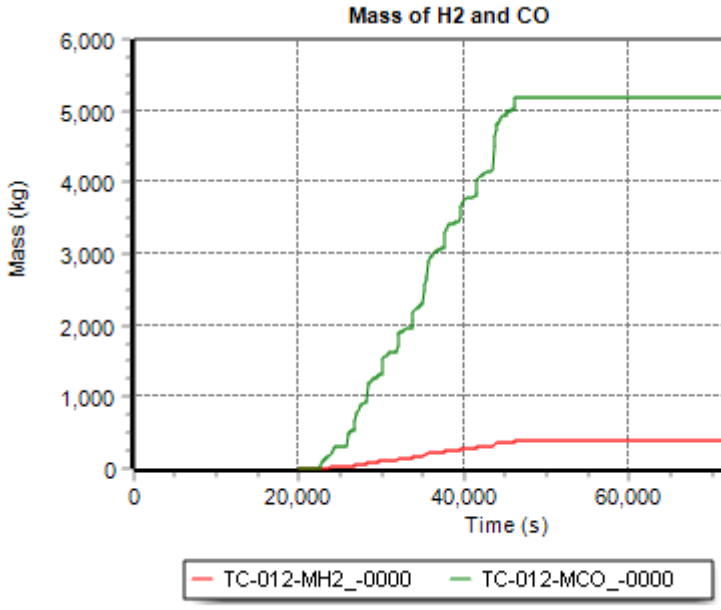

(b) SPECTRA

Figure 3-1116 MCCI test, masses of H_2 and CO

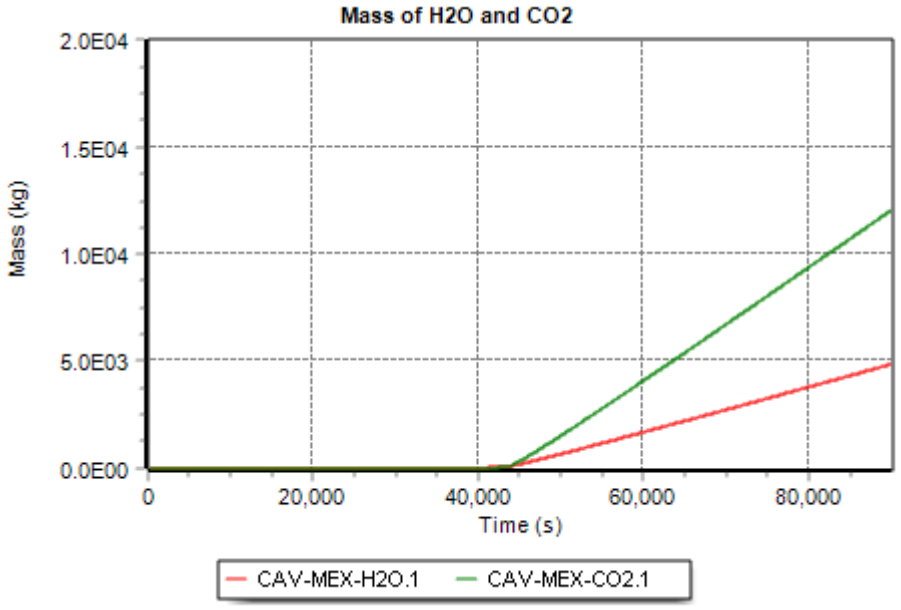

(a) MELCOR

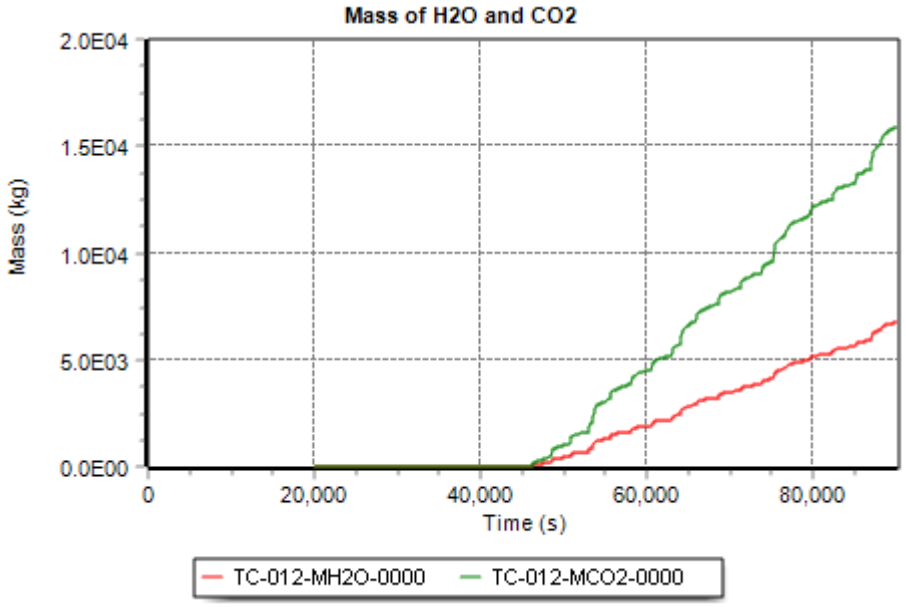

(b) SPECTRA

Figure 3-1117 MCCI test, masses of H_2O and CO_2

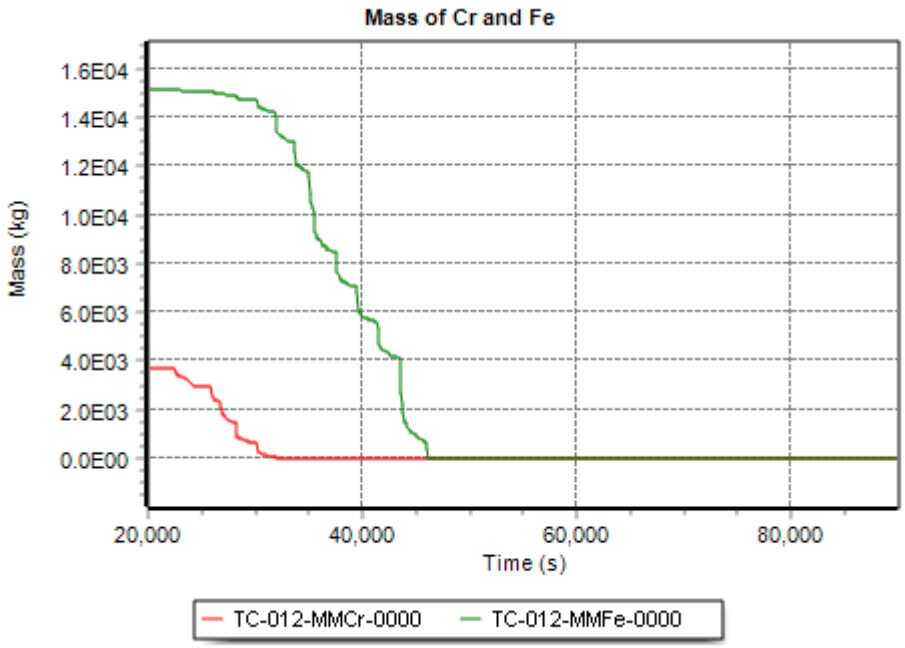

Figure 3-1118 MCCI test, masses of Fe and Cr (SPECTRA)

Figure 3-1114 shows the mass of corium and the mass of ablated concrete. A small increase of the corium mass (~ 20,000 – ~40,000 s) is due to chemical reactions (oxygen uptake during oxidation of metals). The ablated concrete mass is somewhat lower in SPECTRA: ~80 tons, compared to MELCOR: ~90 tons.

Figure 3-1115 shows the cumulative energies, including:

- decay power,
- chemical energy (see Volume 1, Chapter 13, section “Chemical Reactions”); the values are shown using the right axis,
- ablation energy,
- integrated heat flux from the surface.

As may be seen, the decay heat is in this case dominating. The heat from chemical reactions is by far the smallest and is shown on a separate (right-hand side) axis. The heat lost from the surface is the depends on the surface conditions. In the current case a dry cavity was assumed with convection and radiation to surrounding structures.

Qualitative behavior is very similar in both codes. The decay power was estimated based on the decay heat curve and is slightly higher in SPECTRA than in MELCOR. The heat lost from the surface due to radiation and convection was calculated assuming the parameters such as heat transfer coefficient and emissivity. The heat lost is very similar in both codes. First (~20,000 – ~30,000 s), the integrated chemical energy is increasing, as the Cr is consumed in the melt because Cr reactions are exothermic (see Volume 1). Next (~30,000 – ~46,000 s), the integrated chemical energy is decreasing, as the Fe is consumed in the melt because Fe reactions are endothermic (see Volume 1). The masses of Cr and Fe are shown in Figure 3-1118 (the values are not plottable from MELCOR).

Figure 3-1116 shows the masses of H_2 and CO. Figure 3-1117 shows the masses of H_2O and CO_2. A significant release of those gases begins when the metals are fully oxidized (~46,000 s). The releases of those gases is somewhat higher in SPECTRA than in MELCOR.

In general, a higher content of metals in the melt would lead to higher masses of H_2 and CO and lower masses of H_2O and CO_2. The current results are considered as sufficiently close, considering all the uncertainties involved in a severe accident. The main results are summarized in Table 3-99, showing values for t = 90,000 s..

Table 3-99 Summary of MCCI test results

Parameter	SPECTRA	MELCOR
Mass of ablated concrete (kg)	79,000	90,400
Cumulative decay heat (J)	4.40×10^{11}	4.20×10^{11}
Cumulative chemical energy (J)	8.19×10^{9}	7.76×10^{9}
Cumulative ablation energy (J)	1.90×10^{11}	3.08×10^{11}
Cumulative surface heat (J)	1.13×10^{11}	1.31×10^{11}
Mass of generated H_2O (kg)	6,760	4,860
Mass of generated H_2 (kg)	387	353
Mass of generated CO_2 (kg)	15,900	12,000
Mass of generated CO (kg)	5,180	5,150

3.13.3 Sensitivity Results

Several sensitivity calculations were performed, including:

- Nodalization,
- Axial/radial erosion (input parameters XZAPTC/XRAPTC),
- Sequential oxidation reaction (input parameter IRSQTC),
- Operating system.

Nodalization study

Analyzed cases:

- **Case 10/20:** Vertical cell size: 8.2 cm.
  10 cells representing corium in vertical direction,
  20 cells representing concrete below corium,
- **Case 15/15:** Vertical cell size: 5.4 cm.
  15 cells representing corium in vertical direction,
  15 cells representing concrete below corium,
- **Case 20/20:** Vertical cell size: 4.0 cm.
  20 cells representing corium in vertical direction,
  20 cells representing concrete below corium,
- **Case 20/30 (base case):** Vertical cell size: 4.0 cm.
  20 cells representing corium in vertical direction,
  30 cells representing concrete below corium,

It needs to be remembered that the number of nodes should be sufficiently large, otherwise the ablation front reaches the bottom of the cavity. In such case calculations are continued but it is questionable if the results may still be trusted. This may be illustrated based on the case 20/20. Ablation reaches the bottom of cavity at time close to 70,000 s. At 60,000 s both results are very similar; the ablated concrete mass is equal to 4.16 tons and 4.27 tons for the cases 20/20 and 20/30 respectively. However, at t = 90,000 s the ablated concrete mass is 69.6 tons and 79.0 tons for the cases 20/20 and 20/30 respectively.

The main results are shown in Table 3-100. In the case 20/20 the erosion depth reached the bottom of the modelled space, so this case is excluded from comparison. Generally the results are similar, although ablation increases with decreasing the node size.

Table 3-100 Nodalization sensitivity results, values at 90,000 s

Parameter	10/20	15/15	20/30	MELCOR
Mass of ablated concrete (t)	62.5	69.7	79.0	90.4
Mass of generated H_2O (kg)	4,620	5,550	6,760	4,860
Mass of generated H_2 (kg)	387	389	387	353
Mass of generated CO_2 (kg)	10,900	13,100	15,900	12,000
Mass of generated CO (kg)	5,180	5,200	5,180	5,150

Axial/radial erosion.

Analyzed cases:

- **Case MCCI-1-05:** Vertical erosion parameter of XZAPTC = 0.5
- **Case MCCI-1-08:** Vertical erosion parameter of XZAPTC = 0.8
- **Case MCCI-1 (base case):** erosion parameters calculated internally

The main results are shown in Table 3-101. The internally calculated value (specific for a given concrete type) is 0.415. The axial erosion parameter was increased to 0.5 and 0.8 (the radial parameter was kept as in the base case). Consequently the vertical ablation is faster. The results are becoming more conservative and also closer to the MELCOR results.

Table 3-101 Erosion parameters sensitivity results, values at 90,000 s

Parameter	MCCI-1-05	MCCI-1-08	MCCI-1	MELCOR
Mass of ablated concrete (t)	82.5	83.1	79.0	90.4
Mass of generated H_2O (kg)	7,210	7,280	6,760	4,860
Mass of generated H_2 (kg)	387	388	387	353
Mass of generated CO_2 (kg)	17,000	17,100	15,900	12,000
Mass of generated CO (kg)	5,190	5.190	5,180	5,150

Sequential oxidation reactions

Equilibrium constants for the reactions tell that Zr is oxidized first, and Si, Cr, and Fe follow in this order (see Volume 1). In the current case, there is no Zr in corium; there is Cr, Fe, and Ni. The oxidation sequence is therefore Cr, then Fe (no reactions with Ni are present). Analyzed cases:

- **Case RSEQ1:** Sequential parameter IRSQTC =1 (simultaneous reactions)
- **Case RSEQ2:** Sequential parameter IRSQTC =2
- **Case MCCI-1 (default):** Sequential parameter IRSQTC =3
- **Case RSEQ4:** Sequential parameter IRSQTC =4

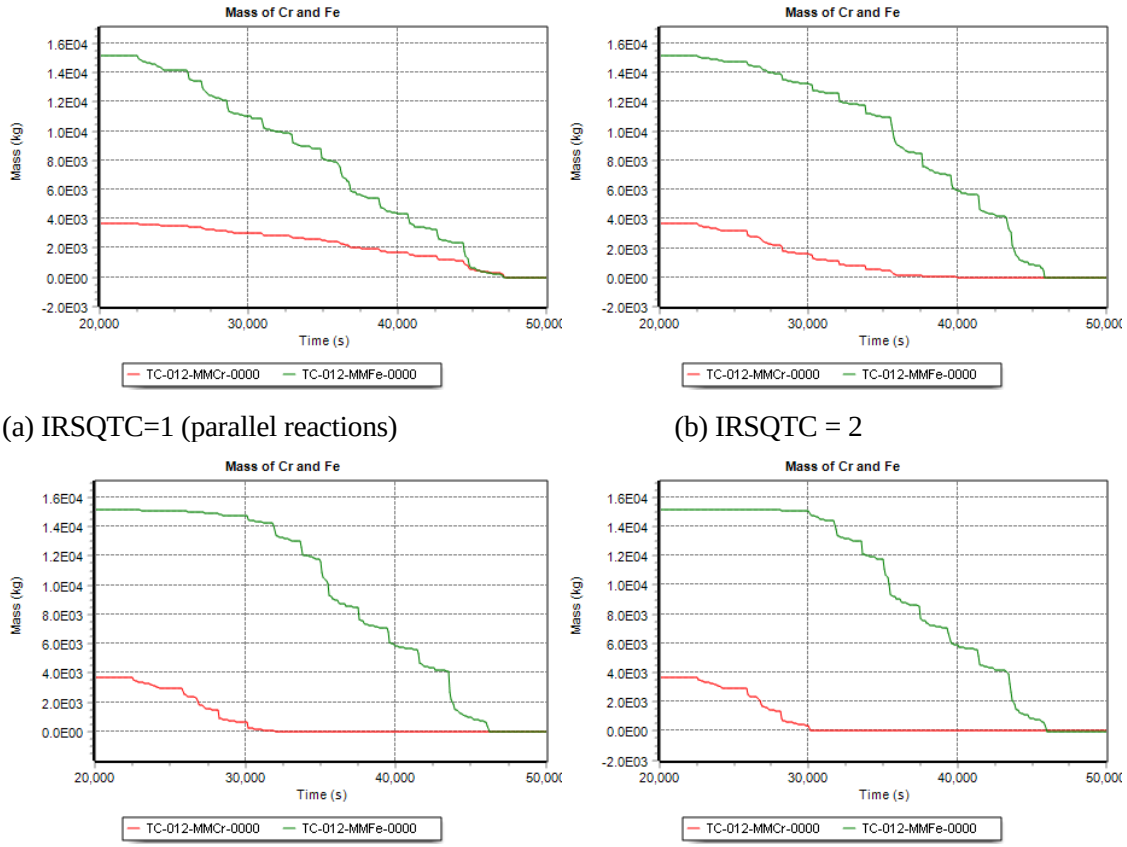

(a) IRSQTC=1 (parallel reactions) (b) IRSQTC = 2

(c) IRSQTC = 3 (default) (d) IRSQTC = 4

Figure 3-1119 Masses of Fe and Cr, influence of IRSQTC

The main results are shown in Figure 3-1119. With IRSQTC=1 all reactions are simultaneous. With IRSQTC =2, the ratio of the stronger reaction (Cr) to the weaker reaction (Fe) is $10^{1-\mathrm{IRSQTC}} = 10^{-1}$ (Volume 2). Cr is consumed faster than Fe. With IRSQTC =3, the ratio is 10^{-2}. Here most of Ce is consumed before significant reaction with Fe occurs. With IRSQTC =4, the ratio is 10^{-3}. Practically all Cr is consumed before reaction with Fe starts. The main results, such as ablated mass, generated gases are practically no different in all the cases presented here. Therefore it is concluded that the results are not sensitive to the value of IRSQTC.

Operating system

Calculations were performed on both Linux and Windows operating systems. The results described above are those obtained under Linux. The main results are shown in Table 3-102. The results are somewhat different but the differences are very small.

Table 3-102 Influence of the operating system

Parameter	Linux	Windows
Mass of ablated concrete (t)	79.0	78.7
Mass of generated H_2O (kg)	6,760	6,720
Mass of generated H_2 (kg)	387	388
Mass of generated CO_2 (kg)	15,900	15,800
Mass of generated CO (kg)	5,180	5,190

3.13.4 Summary and Conclusion

The current verification of the MCCI model is limited to a code-to-code (MELCOR) comparison for one scenario only. In the future this should be extended to more scenarios, different concrete types, and comparisons with experimental data. Furthermore, the deficiencies identified in the current model (see Volume 1) should be improved:

- Reactions such as melting of quartz, decomposition of hematite into magnetite, melting of magnetite) are currently not modeled.
- Reduction of SiO_2 and Fe_2O_3 by Zr is not taken into account.

3.14 Material Properties

3.14.1 Materials Composed of Several Materials

As described in Volume 1, the user may define a material that is a composition of different basic materials. In such case the properties are obtained from:

$$\overline{\rho \cdot c_p} = \sum_i x_i \cdot \rho_i \cdot c_{p,i} \qquad \bar{k} = \sum_i x_i \cdot k_i \qquad or \qquad \overline{1/k} = \sum_i x_i / k_i$$

x_i = volumetric fraction of the material *i* in the mixture, (-)
ρ_i = density of the material *i*, (kg/m^3)
$c_{p,i}$ = specific heat of the material *i*, (J/kg-K)
k_i = conductivity of the material *i*, (W/m^2-K)

Verification of the material definition is performed using as a test case the TRISO fuel designed for the GEMINI+ reactor, discussed in section 3.9.4.4). The TRISO particles are imbedded in graphite matrix. The properties of the fuel matrix is composed of the following materials:

- Material 502 - graphite
- Material 111 - fuel kernel
- Material 122 - PyC (buffer)
- Material 123 - iPyC
- Material 121 - SiC
- Material 124 - oPyC

Volume fractions of the fuel and coatings in a single TRISO particle were calculated assuming the following dimensions: fuel kernel diameter 500 μm, buffer 95 μm, iPyC 40 μm, SiC 35 μm, oPyC 40 μm. The volume fractions are:

- Material 502 - graphite 0.8897
- Material 111 - fuel kernel 0.01771
- Material 122 - PyC (buffer) 0.02883
- Material 123 - iPyC 0.01814
- Material 121 - SiC 0.01929
- Material 124 - oPyC 0.02635

The input deck defining such material is shown below.

```
805572  Graphite-Fuel
*          Graphite       Fuel          buffer       iPyC           SiC           oPyC
*       c  Mat. Vol.fr.  Mat. Vol.fr.  Mat. Vol.fr.  Mat. Vol.fr.  Mat. Vol.fr.  Mat. Vol.fr.
806572 0.0  502 8.897E-01 111 1.771E-02 122 2.883E-02 123 1.814E-02 121 1.929E-02 124 2.635E-02
```

The output generated during the processing of input data is shown below.

```
=MP=  =======MP-572=======  Graphite-Fuel

      MULTIPLIERS
      - THERMAL CONDUCTIVITY: TCMLMP = 1.00000E+00
      - DENSITY             : RHMLMP = 1.00000E+00
      - SPECIFIC HEAT       : CPMLMP = 1.00000E+00

      COMPOSITION:

      MATERIAL     VOLUME FRACTION
       ------    -----------
       MP-502    8.89682E-01
       MP-111    1.77096E-02
       MP-122    2.88294E-02
       MP-123    1.81396E-02
       MP-121    1.92896E-02
       MP-124    2.63495E-02
                 -----------
                 1.00000E+00

      MATERIAL  MASS FRACTION
       ------     -----------
       MP-502    7.89985E-01
       MP-111    8.30504E-02
       MP-122    3.95249E-02
       MP-123    2.48693E-02
       MP-121    2.64459E-02
       MP-124    3.61249E-02
                 -----------
                 1.00000E+00

      CONDUCTIVITY CALCULATION, CCOMMP = 2.00000E+00

 MP-CON    [K]              [W/M/K ]
       2.95000E+02        2.99728E+01
       3.00000E+02        2.99864E+01
       4.73000E+02        3.04277E+01
       5.00000E+02        3.01371E+01
       6.00000E+02        2.88119E+01
       6.73000E+02        2.78562E+01
       8.73000E+02        2.53237E+01
       9.00000E+02        2.50446E+01
       1.00000E+03        2.39945E+01
       1.07300E+03        2.34235E+01
       1.20000E+03        2.32409E+01
       1.50000E+03        2.27545E+01
       1.80000E+03        2.22348E+01
       2.00000E+03        2.18217E+01
       2.10000E+03        2.17343E+01
       2.40000E+03        2.14644E+01
       2.50000E+03        2.13714E+01
       2.70000E+03        2.13414E+01
       3.00000E+03        2.12993E+01

 MP-RHO    [K]              [KG/M3 ]
       3.00000E+02        2.34137E+03

 MP-CP     [K]              [J/KG/K]
       2.73000E+02        8.16511E+02
       3.00000E+02        8.57550E+02
       7.73000E+02        1.57648E+03
       1.20000E+03        1.79811E+03
       1.27300E+03        1.83602E+03
       1.60000E+03        1.93305E+03
       1.77300E+03        1.98465E+03
       1.80000E+03        1.98870E+03
       2.00000E+03        2.01886E+03
       2.20000E+03        2.04925E+03
       2.27300E+03        2.06043E+03
       2.40000E+03        2.07044E+03
       2.77300E+03        2.09805E+03
```

For comparison the values for a selected (minimum) temperature were calculated by "hand" calculations in the Excel file: Z-INPUTS\RK\NPK\GEMINI\VISOR\GEMINI-MATRIX.xls. The results are shown in Table 3-103. It is seen that a very good agreement between the SPECTRA-calculated values and the theoretically computed values is observed.

Table 3-103 Results of "hand calculations" (file: GEMINI-model-support.xls)

	Graphite	UO2	Buffer	IPyC	SiC	OPyC	Average
fraction	**8.897E-01**	**1.771E-02**	**2.883E-02**	**1.814E-02**	**1.929E-02**	**2.635E-02**	**Value**
ρ	**2079**	**10980**	**3210**	**3210**	**3210**	**3210**	**2341.4**
	1.850E+03	*1.945E+02*	*9.254E+01*	*5.823E+01*	*6.192E+01*	*8.458E+01*	
mass frc.	*7.89985E-01*	*8.30504E-02*	*3.95249E-02*	*2.48693E-02*	*2.64459E-02*	*3.61249E-02*	
Cp	**833.3**	**320.9**	**750.0**	**750.0**	**750.0**	**750.0**	**816.53**
at 273 K	*7.414E+02*	*5.683E+00*	*2.162E+01*	*1.361E+01*	*1.447E+01*	*1.976E+01*	
ρ Cp	**1.732E+06**	**3.523E+06**	**2.408E+06**	**2.408E+06**	**2.408E+06**	**2.408E+06**	**1.8267E+06**
at 273 K	*1.541E+06*	*6.240E+04*	*6.941E+04*	*4.367E+04*	*4.644E+04*	*6.344E+04*	
k (opt.1)	**31.4**	**6.0**	**36.3**	**36.3**	**330.3**	**36.3**	**37.08**
at 295 K	*2.794E+01*	*1.063E-01*	*1.047E+00*	*6.585E-01*	*6.371E+00*	*9.565E-01*	
k (opt.2)	**31.4**	**6.0**	**36.3**	**36.3**	**330.3**	**36.3**	**29.97**
at 295 K	*2.833E-02*	*2.952E-03*	*7.942E-04*	*4.997E-04*	*5.840E-05*	*7.259E-04*	

In order to verify the use of mass fractions, the input deck GEMINI-0-M.SPE was prepared. The mass fractions were defined in the input as follows:

```
*  USE MASS FRACTIONS FOR GRAPHITE FUEL
*             Graphite          Fuel            buffer          iPyC             SiC             oPyC
*       c  Mat.  Vol.fr.   Mat. Vol.fr.    Mat. Vol.fr.    Mat. Vol.fr.    Mat. Vol.fr.    Mat. Vol.fr.
806572 -2  502 7.89985E-01 111 8.30504E-02 122 3.95249E-02 123 2.48693E-02 121 2.64459E-02 124 3.61249E-02
```

The results were compared to the results of the base model (GEMINI-0.SPE). Practically the same results were obtained:

```
=MP=  =======MP-572=======  Graphite-Fuel

      MULTIPLIERS
      - THERMAL CONDUCTIVITY: TCMLMP = 1.00000E+00
      - DENSITY             : RHMLMP = 1.00000E+00
      - SPECIFIC HEAT       : CPMLMP = 1.00000E+00

      COMPOSITION:

      MATERIAL     VOLUME FRACTION
       ------    -----------
       MP-502    8.89682E-01
       MP-111    1.77096E-02
       MP-122    2.88294E-02
       MP-123    1.81396E-02
       MP-121    1.92896E-02
       MP-124    2.63495E-02
                 -----------
                 1.00000E+00

      MATERIAL   MASS FRACTION
       ------     -----------
       MP-502    7.89985E-01
       MP-111    8.30504E-02
       MP-122    3.95249E-02
       MP-123    2.48693E-02
       MP-121    2.64459E-02
       MP-124    3.61249E-02
                 -----------
                 1.00000E+00
```

```
2437:
2438: =MP=  =======MP-572=======  Graphite-Fuel
2439:
2440:       MULTIPLIERS
2441:       - THERMAL CONDUCTIVITY: TCMLMP = 1.00000E+00
2442:       - DENSITY             : RHMLMP = 1.00000E+00
2443:       - SPECIFIC HEAT       : CPMLMP = 1.00000E+00
2444:
2445:       COMPOSITION:
2446:
2447:       MATERIAL     VOLUME FRACTION
2448:        ------    -----------
2449:        MP-502    8.89682E-01
2450:        MP-111    1.77096E-02
2451:        MP-122    2.88294E-02
2452:        MP-123    1.81397E-02
2453:        MP-121    1.92896E-02
2454:        MP-124    2.63495E-02
2455:                  -----------
2456:                  1.00000E+00
2457:
2458:       MATERIAL   MASS FRACTION
2459:        ------     -----------
2460:        MP-502    7.89985E-01
2461:        MP-111    8.30504E-02
2462:        MP-122    3.95249E-02
2463:        MP-123    2.48693E-02
2464:        MP-121    2.64459E-02
2465:        MP-124    3.61249E-02
2466:                  -----------
2467:                  1.00000E+00
2468:
```

The differences are caused by round-off errors in conversion from volume fractions to mass fractions. In order to minimize the round off errors, six significant places were used in definition of mass fractions.

3.15 Tabular Functions

3.15.1 Simple Tabular Function Test

An input deck defining examples of Tabular Functions is provided in **\Z-INPUTS\TF\TF.SPE**. Two functions are defined:

- TF-001, linear interpolation type
- TF-002, cubic interpolation type

The tabulated data points for TF-001 and TF-002 are shown in Table 3-104. Note that the end-values were entered twice (for the times of 35.0 and 45.0 s). For a linear type function the last point is not needed and exactly the same values would be obtained if it was skipped. For the cubic function this definition allows to obtain smooth function (continuous derivative) at the end point.

Table 3-104 Data for the TF example

Point No.	Time value	TF-001	TF-002
1	5.0	0.10	2.10
2	10.0	1.10	3.10
3	15.0	1.10	3.10
4	25.0	0.20	2.20
5	30.0	2.50	4.50
6	35.0	1.00	3.00
7	45.0	1.00	3.00

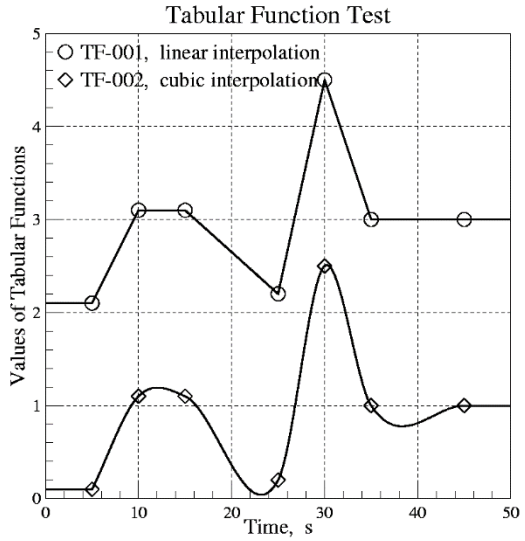

Figure 3-1120 Results for TF example

Results are shown in Figure 3-1120. The influence of the last point on the cubic function is shown in Figure 3-1121. If the last point (t =35.0 s) is repeated, then the function goes smoothly down and then stabilizes at the repeated point (t = 45.0 s). If the last point is not repeated, the function becomes abruptly flat at the last point (t = 35.0 s), resulting in discontinuity in the TF derivative.

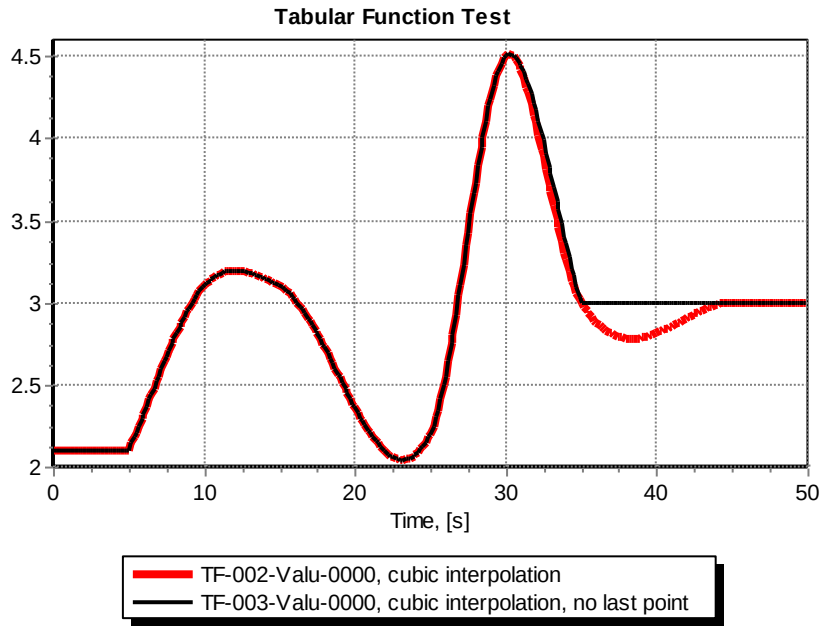

Figure 3-1121 Cubic interpolation - influence of doubling the last point

3.15.2 Interactive Tabular Function

An input deck is provided in **\Z-INPUTS\TF\TF-interactive.SPE**. Two functions, TF-001 and TF-002 are defined. The tabulated data consists of a single point per function, defining a value of zero. The following limits are applied:

$$TF_{\min} = 0.0$$

$$TF_{\max} = 5.0$$

$$-\left.\frac{d(TF)}{dt}\right|_{\min} = \left.\frac{d(TF)}{dt}\right|_{\max} = 1.0$$

To perform an interactive run, the user should start the SPECTRA run first (double-click on the file TF-interactive.SPE), then open the corresponding Visor screen (double-click on the file TF-interactive.VSD), and start the interactive simulation by pressing the “Play” button on the Visor screen.

The Visor screen looks as shown below. The TF values are marked by the red and blue circular markers, with a flat bar indicating the current value.

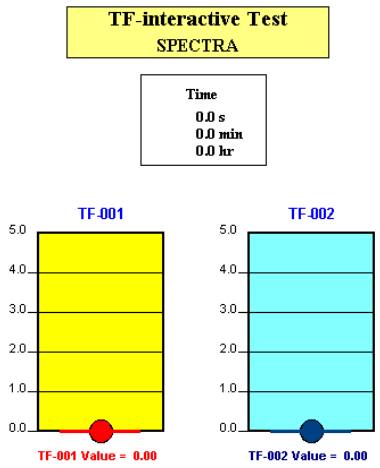

The values indicated in the box "Time" are of course changing as the simulation is running. For the current test the 1:1 (real time) simulation is used (the value is defined in the right-most button in the Visor tool bar).

In order to change the value of a function one needs to:

- Pause the simulation by pressing the "Pause" button in the Visor screen.
- Right-click on one of the circles indicating a TF. The box "Set TF value" appears on the screen, as shown below.

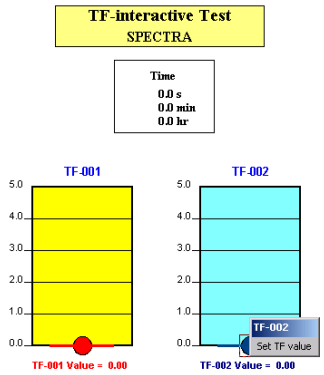

- Left-click on the field “Set TF value”. A new window appears titled “Value of TF-002”, where the TF value should be typed. In the example shown below a value of 5 has been typed.

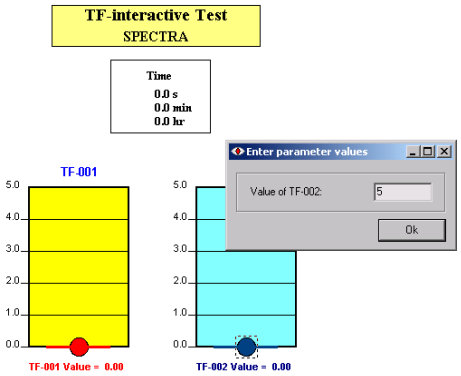

- Resume the simulation by pressing the “Play” button. The value of the Tabular Function is slowly changing (a limit of 1.0 s^{-1} is applied on the rate of change for the TF-s in the present example) until the prescribed value is reached. The final screen looks as shown below.

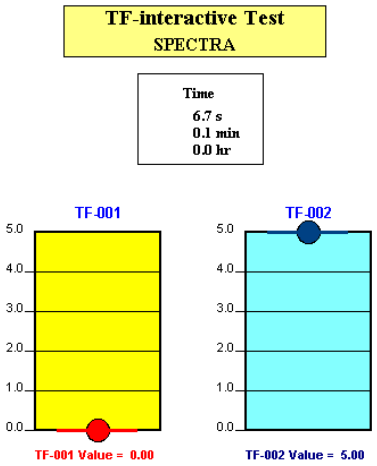

The example shown above illustrates the interactive procedure with the Visor program. One does not need Visor to perform interactive actions. All Visor does is writing a message to a TF Data file, *.TFD. The same may be done using just a text editor. The example below shows how this may be done.

The following procedure allows to perform interactive actions using just a text editor.

- Start again the SPECTRA run (double-click on the file TF-interactive.SPE - of course the previous calculation, described above, must be terminated first).
- Start the Visor screen (double-click on the file TF-interactive.VSD), and start the interactive simulation by pressing the “Play” button on the Visor screen. Here Visor is used just as a tool to observe what is happening in SPECTRA, but is not needed to perform the interactive action described below.

- Open the TF Data file (TF-interactive.TFD) using an available text editor (for example notepad). Place all three windows conveniently on the screen, so they are all visible at the same time. Select some values for the Tabular Functions, for example:

  TF-001 = 3.5, TF-002 = 2.5

  Type the values in the *.TFD file, remembering that the first number must be the TF number and the second number the TF value. Therefore one needs to type:

```
001    3.5
002    2.5
```

- Save the *.TFD file, using the normal save option within your editor. Once the TFD file with the entered numbers is saved, SPECTRA "sees" the values and performs appropriate actions. The screen looks as shown below.

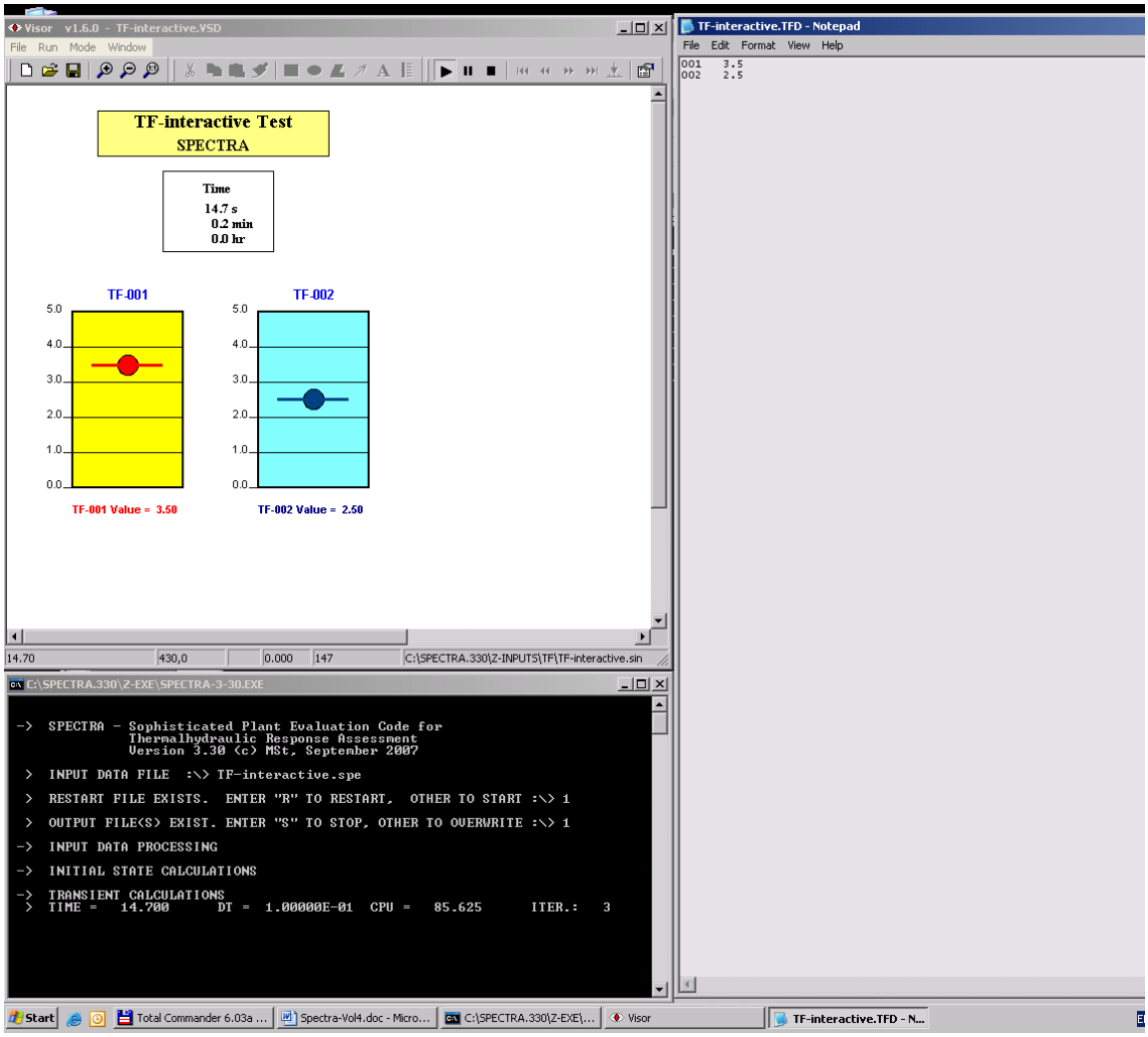

3.16 Control Functions

3.16.1 Control Function Test

An input deck is provided in **\Z-INPUTS\CF\CF.SPE**. The example integrates the function:

$$x_1(t) = 1.0 - t$$

The integration gives:

$$f(x_1) = \int_0^t x_1 dt' = t - \frac{t^2}{2}$$

A scaling factor of $S = -2.0$ and an additive constant of $A = 1.0$ are applied, so the final value of CF becomes:

$$CF(t) = \int_0^t x_1 dt' \cdot S + A = 1 - 2t + t^2$$

The values are tabulated for several points in Table 3-105 and Figure 3-1122.

When SPECTRA calculations are performed, one needs to remember that the initial value of the integral function is by default equal to zero. Since one needs to obtain the function shown above, the initial value must be set equal to 1.0. Therefore the initial value of CF-108 was set to 1.0 in the input.

SPECTRA results are shown in Figure 3-1123. It may easily be checked that the values are in agreement with the theoretical values shown in Table 3-105.

Table 3-105 CF test - theoretical values

t, (s)	$x_1(t)$	$f(x_1)$	CF(t)
0.0	1.0	0.000	1.00
0.5	0.5	0.375	0.25
1.0	0.0	0.500	0.00
1.5	–0.5	0.375	0.25
2.0	–1.0	0.000	1.00
2.5	–1.5	–0.625	2.25
3.0	–2.0	–1.500	4.00

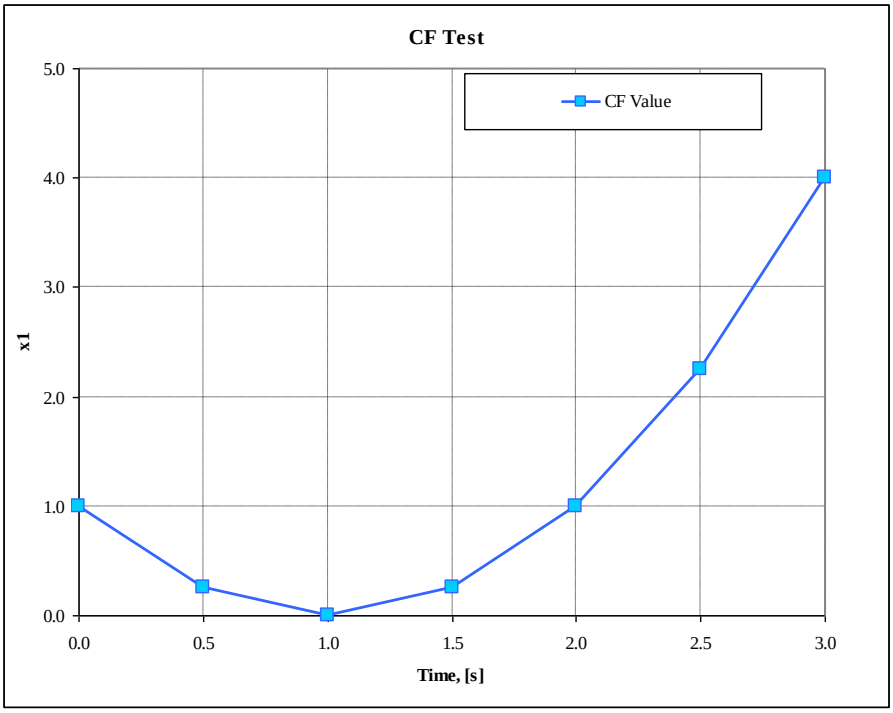

Figure 3-1122 CF test - theoretical values

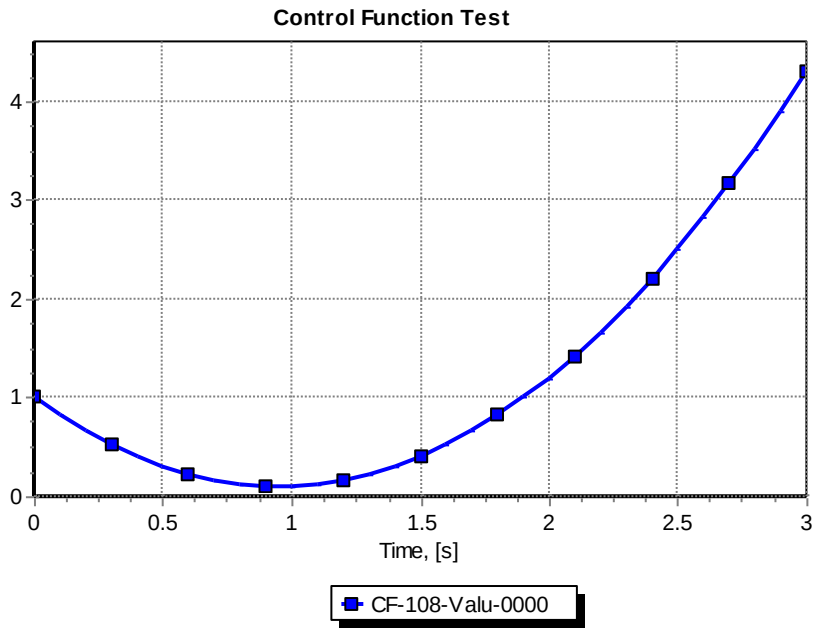

Figure 3-1123 CF test - SPECTRA values

3.16.2 Random Control Function Test

An input deck is provided in **\Z-INPUTS\CF\CF-rnd.SPE**. The example shows the application of random functions. Two random functions are defined, CF-108 and CF-109. The scaling factor and the additive constants for the dummy argument of each of these functions are 1.0 and –0.5 respectively:

$$CF_{108}(t) = rnd() \cdot 0.5 - 0.5$$
$$CF_{208}(t) = rnd() \cdot 0.5 - 0.5$$

This means that the functions give random numbers from the range –0.5 < CF < 0.5. Results are shown in Figure 3-1124.

Random functions can be used for example to simulate random changes of environment pressure, temperature, etc.. This can be done by using integrals of random functions with certain limits, to prevent too fast changes and keep the values in acceptable limits. Two functions were defined, CF-109 and CF-209, that calculate integrals of the random functions defined above:

$$CF_{109}(t) = \int_0^t CF_{108} dt'$$
$$CF_{209}(t) = \int_0^t CF_{208} dt'$$

The following limits were imposed on the functions:

CF-109:	0.0 < CF <5.0	–0.01 < dCF / dt < +0.01
CF-209:	0.0 < CF <5.0	–0.1 < dCF / dt < +0.1

Results are shown in Figure 3-1125. It is seen that a very rapid changes of the function can be avoided by choosing a sufficiently small scaling limit on the rate of change.

The functions CF-109 and CF-209 have a neutral general tendency because the random functions are from the range –0.5, +0.5. A general increasing or decreasing tendency can be achieved by changing the additive constant in the random functions.

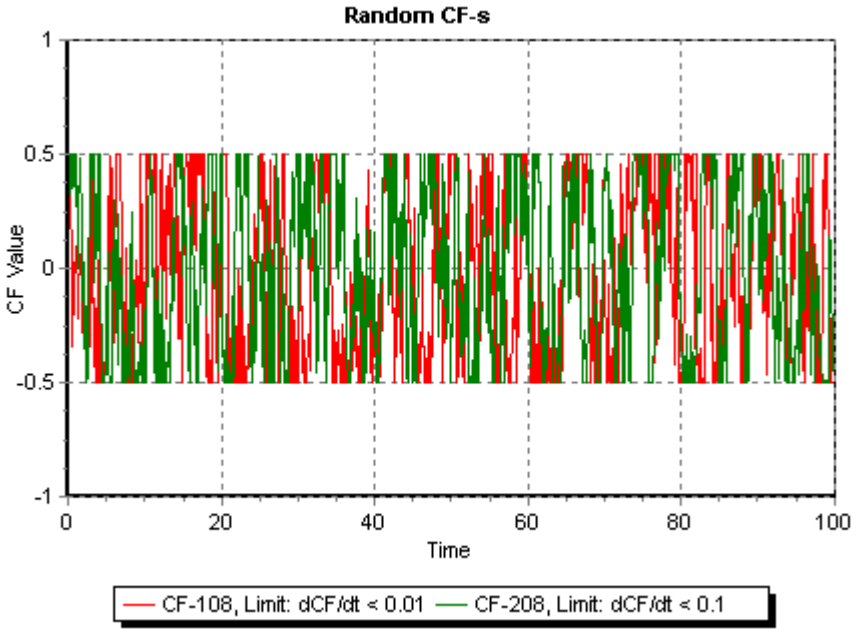

Figure 3-1124 CF test - random functions

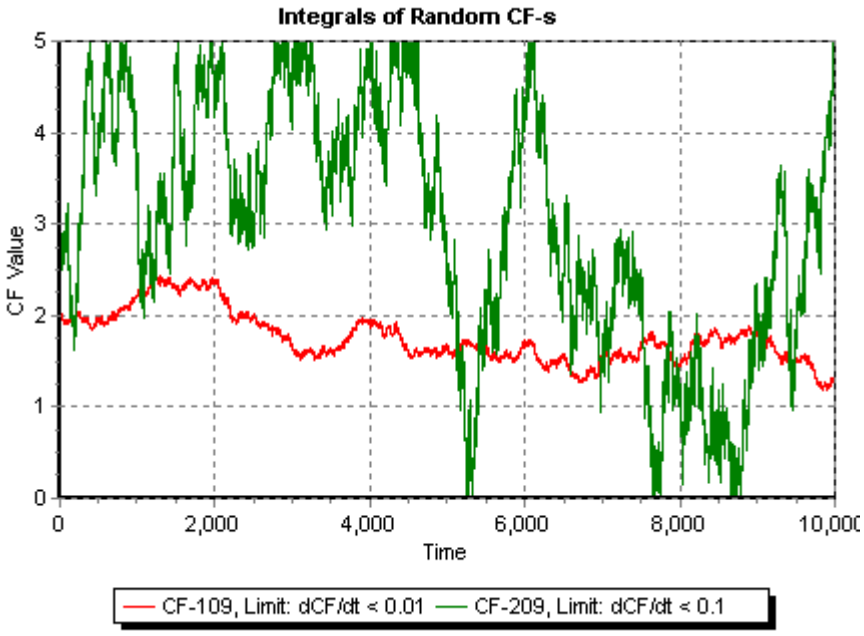

Figure 3-1125 CF test - integrals of random functions

3.16.3 Stiff Set of Ordinary Differential Equations (ODE)

A "stiff" set of differential equation was selected, taken from [97]. Stiff equation sets are particularly difficult to solve. The equation set is:

$$(1)\quad \frac{dy_1}{dt} = -0.013 \cdot y_1 - 1000 \cdot y_1 \cdot y_3$$

$$(2)\quad \frac{dy_2}{dt} = -2500 \cdot y_2 \cdot y_3$$

$$(3)\quad \frac{dy_3}{dt} = -0.013 \cdot y_1 - 1000 \cdot y_1 \cdot y_3 - 2500 \cdot y_2 \cdot y_3$$

The initial conditions are:

$$y_1(0) = 1$$
$$y_2(0) = 1$$
$$y_3(0) = 0$$

The above set of differential equations was solved using two methods, with appropriate subroutines taken from [97]:

- Runge-Kutta method,
- Rosenbrock method.

Finally the SPECTRA code was used to solve the equation system, defined using Control Functions. Thus the third solution was obtained by:

- SPECTRA Solver.

All three solutions are shortly discussed below.

Runge-Kutta

As a first method of solution a general purpose ODE solver was used: the fifth order Runge-Kutta method with adaptive step size (subroutine RKQX, with the driver ODEINT [97], section 16.6). The requested accuracy was $\varepsilon=10^{-4}$. A FORTRAN program to perform calculations is provided in:

\Z-INPUTS\CF\STIFF\Runge-Kutta\SRKQS.FOR.

Results were compared to the solution of the Rosenbrock method, shown in Figure 3-1126 (the comparison is not shown in this figure). Good accuracy of the solution was achieved. The expense is the computational effort. To obtain the solution about 9,500 steps were made. The average step size was 1.1×10^{-3}. The integrated functions had to be evaluated more than **50,000 times**.

Rosenbrock

A method specifically recommended for stiff equation systems is the fourth order Rosenbrock method (see [97] section 16.6). This method (subroutine STIFF - [97], section 16.6) has been used next to solve the example problem. A FORTRAN program to perform calculations is provided in:

`\Z-INPUTS\CF\STIFF\Rosenbrock\SSTIFF.FOR`

The results are shown in Figure 3-1126, as the "theoretical" solution. The requested accuracy was 10^{-4}. Subroutine STIFF obtained the solution in 29 steps (average step size of 0.34), with the necessity of calculating the functions **120 times**. The shortest steps were taken in the initial period. Later the steps were increased. Thus for this test problem the Rosenbrock method is far more effective than the Runge-Kutta method. The Rosenbrock method uses the Jacobian, consisting of the second order mixed derivatives of the analyzed equations. In the presented case it is of course very easy to calculate the Jacobian and provide the appropriate derivatives. However in case of equations being solved by the SPECTRA code it would be practically impossible to create the Jacobian, because of both the complex nature of the equations, and because of the very large number of equations being solved in case of practical applications.

SPECTRA

The equation set was modeled using Control Functions. Nine Control Functions were used to define the analyzed equation set. The definitions of the Control Function definitions are shown in Table 3-106. For the first three functions initial values are specified. These are the integral-type functions, and for such functions SPECTRA requires the user to enter the initial values. For other Control Functions the initial values were left to be calculated by the code. The input deck is quite self explanatory and no more comments are needed

SPECTRA input file for this test is provided in `\Z-INPUTS\CF\STIFF\STIFF.SPE`. Calculations were performed using the time step of 1.0 (s). The run was completed in 10 advancements, without any time step reductions, with a small number of iterations per time step (on the average about 12). Therefore the functions had to be evaluated about **120 times**. Results are shown in Figure 3-1126. It is seen that the results are very accurate.

The results show that for stiff set of differential equations the SPECTRA Solver was much more effective than the Runge-Kutta method. It turned out to be competitive even with the Rosenbrock method, developed specifically for stiff systems. The Rosenbrock method is not applicable for relatively complex problems, like that solved by SPECTRA, because of the need to calculate the Jacobian. The SPECTRA ability of solving the present test is a result of a fully implicit solution scheme for all problem variables, including control functions. In the MELCOR code [20] control functions are calculated explicitly, and the present test problem could be solved correctly only with time step of 10^{-4}. Application of time steps of 10^{-3}, or larger, resulted in a diverging solution and finally a floating exception. The MELCOR input decks for this case are provided in:
`\Z-INPUTS\CF\STIFF\MELCOR\STIFF.GEN` and `STIFF.COR`.

Table 3-106 Definition of Control Functions for the Stiff ODE test

CF No. and type		Value	Definition of CF	Initial Value
CF	Type			
CF-001	Integral	y_1	∫ (CF-007) dt	1.0
CF-002	Integral	y_2	∫ (CF-008) dt	1.0
CF-003	Integral	y_3	∫ (CF-009) dt	0.0
CF-004	Multiply	$0.013 \times y_1$	0.013×CF-001	
CF-005	Multiply	$1000 \times y_1 \times y_3$	1000×CF-001×CF-003	
CF-006	Multiply	$2500 \times y_2 \times y_3$	2500×CF-002×CF-003	
CF-007	Add	dy_1/dt	– CF-004 – CF-005	
CF-008	Add	dy_2/dt	– CF-006	
CF-009	Add	dy_3/dt	– CF-004 – CF-005 – CF-006	

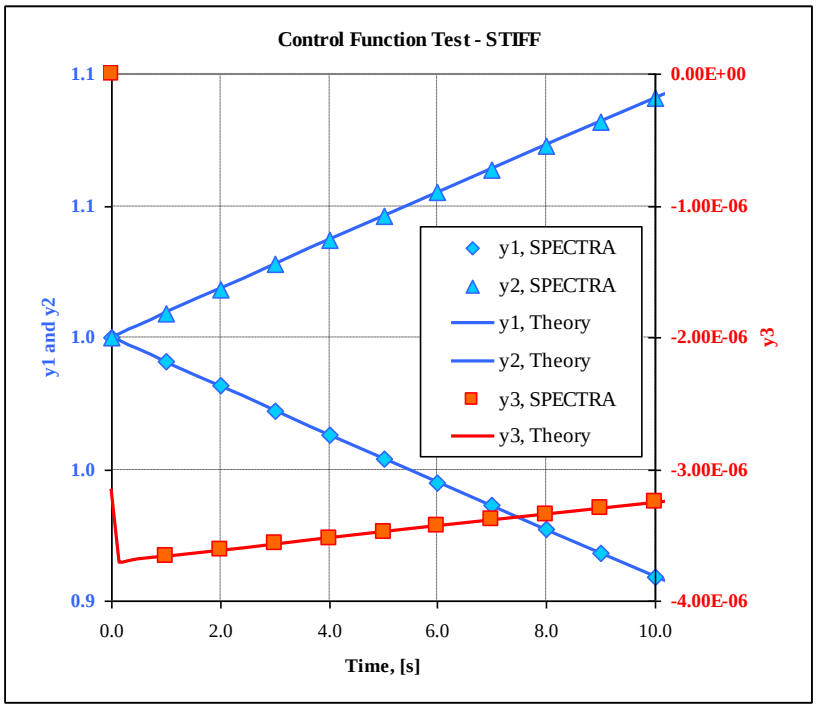

Figure 3-1126 Stiff equation set - SPECTRA with Δt=1.0 s and Rosenbrock “theoretical” solution.

3.17 External Data Files

The External Data File (EDF) Package serves as a utility in SPECTRA to communicate with external data files. SPECTRA has two external data files:

- "Write-EDF", and
- "Read-EDF"

There are two main options of using EDF:

- Normal run with EDF
- Synchronized run with EDF

Verification of normal runs with write and read EDF is described in sections 3.17.1, 3.17.2, and 3.17.3. Verification of synchronized runs with write and read EDF is described in sections 3.17.4 and 3.17.5.

3.17.1 Test of Write-EDF

A simple test with Write-EDF is provided in **\Z-INPUTS\ED\WRITE\ED-W.SPE**. The test run writes pressures and temperatures of CV-001 and CV-002 to the Write-EDF file: ED-W.EDF. The input diagnostics related to the EDF, copied from the output file ED-W.OUT, is shown below.

```
================================================================================
 =ED=  EXTERNAL DATA FILE
================================================================================

 =ED=  OPTION: NORMAL RUN, WITH WRITE EXTERNAL DATA FILE (IEDFED=2)
       EDF READ OPTION :  STOP IN CASE OF ERRORS IN DATA
       EDF WRITE FORMAT:  5 DATA FIELDS PER LINE (NNFMED =  5)
       ACCEPTABLE ERROR IN SYNCHRONISM = 2.00000E-01 * DTEXED
       DATA EXCHANGE TIME STEP, DTEXED = 2.50000E-01 [s]
       MESSAGE OPTION,          IMESED =    0
       INITIALIZATION OPTION,   INITED =    2
       RELATIVE ERROR, IMPLICIT,EMICED = 1.00000E-03
       MAX. NO. ITERATIONNS,    MIICED =   50
       IMPLICIT FACTOR,         XIMPED =-1.00000E+00

 =ED=  ======= INPUT DATA FOR   1 EDF PROCESSES

 =ED=  =======ED-000=======  EDF PROCESS, Sequential No.:  1

 =ED=  WRITE-EDF FILE NAME:  ED-W

       No. OF VARIABLES IN THE WRITE EDF:   4

       No.    EDF Variable
       --- -------------------
        1. CV-001-Pres-atms-Pa
        2. CV-002-Pres-atms-Pa
        3. CV-001-Temp-atms-K
        4. CV-002-Temp-atms-K

================================================================================
 =ED=  END OF EDF DATA
================================================================================
```

The four values are written into the EDF file with the frequency of 0.25 s, while the maximum time step, equal to 0.1 s for this test. The run time is 2.0 s. The file ED-W.EDF is printed below. The first column contains time, the next columns contain values of the EDF four parameters.

```
   4
 0.000000000E+00  1.000000000E+05  1.000000000E+05  3.000000000E+02  3.000000000E+02
 0.000000000E+00  1.000000000E+05  1.000000000E+05  3.000000000E+02  3.000000000E+02
 2.500000000E-01  1.000000000E+05  9.992426803E+04  3.000000000E+02  2.999357897E+02
 5.000000000E-01  1.000000000E+05  9.994005954E+04  3.000000000E+02  2.999493401E+02
 7.500000000E-01  1.000000000E+05  9.994143395E+04  3.000000000E+02  2.999506238E+02
 1.000000000E+00  1.000000000E+05  9.994131741E+04  3.000000000E+02  2.999506404E+02
 1.250000000E+00  1.000000000E+05  9.994143180E+04  3.000000000E+02  2.999508498E+02
 1.500000000E+00  1.000000000E+05  9.994161960E+04  3.000000000E+02  2.999511192E+02
 1.750000000E+00  1.000000000E+05  9.994176889E+04  3.000000000E+02  2.999513584E+02
 2.000000000E+00  1.000000000E+05  9.994195749E+04  3.000000000E+02  2.999516296E+02
```

Verification was performed by checking that the values at t = 2.0 s are in agreement with the corresponding values printed in the ICF file, ED-W.ICF:

```
 CV  ATMS-PRES       ATMS-TEMP       POOL-LEVEL      POOL-TEMP
001  1.00000000E+05  3.00000000E+02  0.00000000E+00  0.00000000E+00
002  9.99419575E+04  2.99951630E+02  0.00000000E+00  0.00000000E+00
```

It is seen that the first two parameters in the ED-W.EDF give the pressures in the CV-001 and CV-002, while the next two give the temperatures in these volumes. Therefore it is concluded that the values are correctly written to the EDF file.

3.17.2 Test of Read-EDF

A simple test with Read-EDF is provided in **\Z-INPUTS\ED\READ\ED-R.SPE**. The test run reads the data file written by the run described in the previous section, and assigns the read values to the following Tabular Functions:

- TF-202
- TF-110
- TF-200
- TF-201

The input diagnostics related to the EDF, copied from the output file ED-R.OUT, is shown below.

```
================================================================================
 =ED=  EXTERNAL DATA FILE
================================================================================

 =ED=  OPTION: NORMAL RUN, WITH READ EXTERNAL DATA FILE (IEDFED=3)
       EDF READ OPTION :  STOP IN CASE OF ERRORS IN DATA
       EDF WRITE FORMAT:  5 DATA FIELDS PER LINE (NNFMED =  5)
       ACCEPTABLE ERROR IN SYNCHRONISM = 2.00000E-01 * DTEXED
       DATA EXCHANGE TIME STEP, DTEXED = 2.50000E-01 [s]
       MESSAGE OPTION,          IMESED =    0
       INITIALIZATION OPTION,   INITED =    2
       RELATIVE ERROR, IMPLICIT,EMICED = 1.00000E-03
       MAX. NO. ITERATIONNS,    MIICED =   50
       IMPLICIT FACTOR,         XIMPED =-1.00000E+00

 =ED=  ======= INPUT DATA FOR   1 EDF PROCESSES

 =ED=  =======ED-000=======  EDF PROCESS, Sequential No.:  1

 =ED=  READ-EDF FILE NAME :  ED-R.EDF
```

```
       No. OF VARIABLES IN THE READ-EDF:   4

       No.    EDF Variable
       --- -------------------
        1. TF-202-Valu-0000-
        2. TF-110-Valu-0000-
        3. TF-200-Valu-0000-
        4. TF-201-Valu-0000-
```

Results obtained at the end of calculations (t = 2.0 s) are shown below. It is seen that the printed values are in agreement with the values in the ED-W.EDF file at t = 1.9 s (explicit data transfer), presented in section 3.17.1. Therefore it is concluded that the values are correctly read from the EDF file.

```
================================================================================
 =TF=  OUTPUT DATA FOR   5 TABULAR FUNCTIONS, AT TIME :  2.00000E+00 [s]
================================================================================

       Function     Value     Name
       =TF-100   1.00000E+05  Downstream boundary pressure versus time, p(t)
       =TF-110   9.99424E+04  TF-110 to read from EDF, data column No. 2
       =TF-200   3.00000E+02  TF-200 to read from EDF, data column No. 3
       =TF-201   2.99952E+02  TF-201 to read from EDF, data column No. 4
       =TF-202   1.00000E+05  TF-202 to read from EDF, data column No. 1

================================================================================
```

3.17.3 Test of Read and Write EDF

A simple test with Write-EDF and Read-EDF is provided in **\Z-INPUTS\ED\RW\ED-RW.SPE**. The test run reads the data file written by the run described in section 3.17.1, and assigns the Tabular Functions as in the test shown in section 3.17.2. The input diagnostics related to the EDF, copied from the output file ED-RW.OUT, is shown below.

```
================================================================================
 =ED=  EXTERNAL DATA FILE
================================================================================

 =ED=  OPTION: NORMAL RUN, WITH WRITE AND READ EXTERNAL DATA FILES (IEDFED=4)
       EDF READ OPTION :  STOP IN CASE OF ERRORS IN DATA
       EDF WRITE FORMAT:  5 DATA FIELDS PER LINE (NNFMED =  5)
       ACCEPTABLE ERROR IN SYNCHRONISM = 2.00000E-01 * DTEXED
       DATA EXCHANGE TIME STEP, DTEXED = 2.50000E-01 [s]
       MESSAGE OPTION,          IMESED =    0
       INITIALIZATION OPTION,   INITED =    2
       RELATIVE ERROR, IMPLICIT,EMICED = 1.00000E-03
       MAX. NO. ITERATIONNS,    MIICED =   50
       IMPLICIT FACTOR,         XIMPED =-1.00000E+00

 =ED=  ======= INPUT DATA FOR   1 EDF PROCESSES

 =ED=  =======ED-000=======  EDF PROCESS, Sequential No.:  1

 =ED=  WRITE-EDF FILE NAME:  ED-W.EDF

       No. OF VARIABLES IN THE WRITE EDF:   4

       No.    EDF Variable
       --- -------------------
        1. CV-001-Pres-atms-Pa
        2. CV-002-Pres-atms-Pa
        3. CV-001-Temp-atms-K
        4. CV-002-Temp-atms-K
```

```
 =ED=  READ-EDF FILE NAME :  ED-R.EDF

       No. OF VARIABLES IN THE READ-EDF:   4

       No.    EDF Variable
       --- --------------------
        1. TF-202-Valu-0000-
        2. TF-110-Valu-0000-
        3. TF-200-Valu-0000-
        4. TF-201-Valu-0000-

================================================================================
```

Results obtained at the end of calculations (t = 2.0 s) are shown below. It is seen that the printed values are in agreement with the values in the ED-W.EDF file, presented in section 3.17.1. Therefore it is concluded that the values are correctly written to and read from the EDF file.

```
================================================================================
 =TF=  OUTPUT DATA FOR   5 TABULAR FUNCTIONS, AT TIME :  2.00000E+00 (s)
================================================================================

       Function    Value     Name
       TF-100   1.00000E+05  Downstream boundary pressure versus time, p(t)
       TF-110   9.99424E+04  TF-110 to read from EDF, data column No. 2
       TF-200   3.00000E+02  TF-200 to read from EDF, data column No. 3
       TF-201   2.99952E+02  Efficiency, normal flow
       TF-202   1.00000E+05  TF-202 to read from EDF, data column No. 1

================================================================================
```

3.17.4 Test of a Simple Synchronized Run

A synchronized run allows to interactively read/write EDF. With this option SPECTRA may run in parallel with another program (or another model run by the SPECTRA code itself) and exchange information at the intervals of 0.25 s (maximum time step is 0.1 s).

A synchronized run may be used for example to couple thermal hydraulic calculations done with SPECTRA with a more complex reactor kinetics (3-D kinetics) calculations done by some other code.

As a first test of a synchronized run a simple test has been prepared in which SPECTRA runs in parallel with a simple code, built just for this case. The program name is "PANTHER.EXE". SPECTRA input file is `ED-S.SPE`. The files are located in: **`\Z-INPUTS\ED\SYNCH\`**
Two versions were tested with different initialization option:

- Single data exchange during initialization (INITED=1), **`\SYNCH\INIT-1\`**
- Double data exchange during initialization (INITED=2), **`\SYNCH\INIT-2\`**

The parameters that are being send from SPECTRA to "PANTHER" are:

```
 =ED=  WRITE-EDF FILE NAME:  SPECTRA.DAT

       No. OF VARIABLES IN THE WRITE EDF:   4

       No.    EDF Variable
       --- --------------------
        1. CV-001-Pres-atms-Pa
        2. CV-002-Pres-atms-Pa
        3. CV-001-Temp-atms-K
        4. CV-002-Temp-atms-K
```

The parameters that are read from the "PANTHER" code are assigned to the following Tabular Functions:

```
 =ED=  READ-EDF FILE NAME :  PANTHER.DAT

       No. OF VARIABLES IN THE READ-EDF:   4

       No.    EDF Variable
       --- -------------------
        1. TF-202-Valu-0000-
        2. TF-110-Valu-0000-
        3. TF-200-Valu-0000-
        4. TF-201-Valu-0000-
```

The program "PANTHER" is assigning the following values to the data that is send to EDF:

Data number 1: Value = 10.0
Data number 2: Value = 20.0
Data number 3: Value = 30.0
Data number 4: Value = 40.0

The values Tabular Functions copied from the SPECTRA output, ED-S.OUT, are shown below.

```
================================================================================
 =TF=  OUTPUT DATA FOR   5 TABULAR FUNCTIONS, AT TIME :  1.00000E+02 (s)
================================================================================

       Function    Value     Name
       TF-100   1.00000E+05  Downstream boundary pressure versus time, p(t)
       TF-110   2.00000E+01  Flow
       TF-200   3.00000E+01  Power
       TF-201   4.00000E+01  Efficiency, normal flow
       TF-202   1.00000E+01  Efficiency, reverse flow
```

It is seen that the values of the functions that are read from the EDF are:

TF-202 = 10.0
TF-110 = 20.0
TF-200 = 30.0
TF-201 = 40.0

Therefore it is concluded that the values obtained by SPECTRA from the "PANTHER" code are correct. The values that are being send from SPECTRA to PANTHER are given in the PATHER output file PANTHER.DIA. The last line in this file is:

```
  1.00000E+02  1.00000E+05  9.99786E+04  3.00000E+02  2.99998E+02
```

The first value represents the time; the next values are the values obtained from the EDF. The SPECTRA values obtained at the time of 100 s may be checked in the output file ED-S.EDF, or more easily in the file ED-S.ICF:

```
 CV  ATMS-PRES       ATMS-TEMP       POOL-LEVEL      POOL-TEMP
001  1.00000000E+05  3.00000000E+02  0.00000000E+00  0.00000000E+00
002  9.99786228E+04  2.99997717E+02  0.00000000E+00  0.00000000E+00
```

It is seen that the first two values in the PATHER.DIA give the pressures in the CV-001 and CV-002, while the next two give the temperatures in these volumes. Therefore it is concluded that the values are correctly send from SPECTRA to the "PANTHER" code.

The difference between option INITED=1 and INITED=2 is that in the first case there is sigle data exchange for the initial time, t = 0.0 s, while in the second there is a double data exchange for the initial time. The first part of the PANTHER.DIA file is:

- Single data exchange during initialization (INITED=1)

```
  0.00000E+00  1.00000E+05  1.00000E+05  3.00000E+02  3.00000E+02
  2.50000E-01  1.00000E+05  9.99242E+04  3.00000E+02  2.99936E+02
  5.00000E-01  1.00000E+05  9.99399E+04  3.00000E+02  2.99949E+02
  7.50000E-01  1.00000E+05  9.99413E+04  3.00000E+02  2.99950E+02
  . . .
```

- Double data exchange during initialization (INITED=1)

```
  0.00000E+00  1.00000E+05  1.00000E+05  3.00000E+02  3.00000E+02
  0.00000E+00  1.00000E+05  1.00000E+05  3.00000E+02  3.00000E+02
  2.50000E-01  1.00000E+05  9.99242E+04  3.00000E+02  2.99936E+02
  5.00000E-01  1.00000E+05  9.99399E+04  3.00000E+02  2.99949E+02
  7.50000E-01  1.00000E+05  9.99413E+04  3.00000E+02  2.99950E+02
  . . .
```

The first part of the SPECTRA message file, ED-S.MES, is:

- Single data exchange during initialization (INITED=1)

```
================================================================================
=SPE=  SPECTRA Version 23-04, Apr. 2023, Windows

 Sophisticated
   Plant
     Evaluation
       Code for
         Thermal-hydraulic
           Response
             Assessment
--------------------------------------------------------------------------------
 Validity: 12/2025,   Applicability:  AppC = 0000
--------------------------------------------------------------------------------

--------------------------------------------------------------------------------
 Message file for the problem:
--------------------------------------------------------------------------------
  SYNCHRONIC EDF test
================================================================================


  t [s] =  0.0000     :  EDF EXPLICIT DATA TRANSFER NO.:       1 (Initialization, final stage)
                         DESIGNATED TRANSFER TIME:  0.00000E+00 ,  MISMATCH:  0.00

  t [s] = 0.25000     :  EDF EXPLICIT DATA TRANSFER NO.:       2
                         DESIGNATED TRANSFER TIME:  2.50000E-01 ,  MISMATCH:  0.00

  t [s] = 0.50000     :  EDF EXPLICIT DATA TRANSFER NO.:       3
                         DESIGNATED TRANSFER TIME:  5.00000E-01 ,  MISMATCH:  0.00

  t [s] = 0.75000     :  EDF EXPLICIT DATA TRANSFER NO.:       4
                         DESIGNATED TRANSFER TIME:  7.50000E-01 ,  MISMATCH:  0.00
  . . .
```

- Double data exchange during initialization (INITED=1)

```
================================================================================
 =SPE=  SPECTRA Version 23-04, Apr. 2023, Windows

 Sophisticated
   Plant
     Evaluation
       Code for
         Thermal-hydraulic
           Response
             Assessment
--------------------------------------------------------------------------------
 Validity: 12/2025,   Applicability:  AppC = 0000
--------------------------------------------------------------------------------

--------------------------------------------------------------------------------
 Message file for the problem:
--------------------------------------------------------------------------------
  SYNCHRONIC EDF test
================================================================================


  t [s] =  0.0000     :  EDF EXPLICIT DATA TRANSFER NO.:       0 (Initialization, preliminary stage)
                         DESIGNATED TRANSFER TIME:  0.00000E+00 ,  MISMATCH:  0.00

  t [s] =  0.0000     :  EDF EXPLICIT DATA TRANSFER NO.:       1 (Initialization, final stage)
                         DESIGNATED TRANSFER TIME:  0.00000E+00 ,  MISMATCH:  0.00

  t [s] = 0.25000     :  EDF EXPLICIT DATA TRANSFER NO.:       2
                         DESIGNATED TRANSFER TIME:  2.50000E-01 ,  MISMATCH:  0.00

  t [s] = 0.50000     :  EDF EXPLICIT DATA TRANSFER NO.:       3
                         DESIGNATED TRANSFER TIME:  5.00000E-01 ,  MISMATCH:  0.00

  t [s] = 0.75000     :  EDF EXPLICIT DATA TRANSFER NO.:       4
                         DESIGNATED TRANSFER TIME:  7.50000E-01 ,  MISMATCH:  0.00
   . . .
```

3.17.5 Complex Synchronized Run - GCFR Model

As a test of the synchronized run, the SPECTRA model of the GCFR reactor is used [100]. The aim of this test is to show that EDF may be used to perform a combined run with a reactor kinetics model running separately and exchanging data with the thermal hydraulic model in SPECTRA and to estimate what is the necessary frequency of the data exchange in order to provide accurate results. For the present test the calculations are performed with the SPECTRA code only. The following calculation procedure is applied:

- First an integrated model is run.
- Second, the reactor kinetics is separated from the rest of the model and run in parallel exchanging data using the EDF. Different data exchange frequencies are applied in order to check what frequency assures accurate results. The accuracy of the obtained results are judged by comparison of the results of the synchronized run with the results of the integrated run.

For the present test only the GCFR reactor vessel model was used, together with the reactor kinetics. The model is shown in Figure 3-1127 and Figure 3-1128. A detailed description of the model is provided in reference [100] and is not repeated here. A single test run was selected, R-165-2, described in [100], in section 4.2.1. This is a reactivity insertion test. A reactivity of 165 pcm/s (0.90411 $) is inserted over a time period of 2.0 seconds.

As a first step an integrated SPECTRA run is performed. SPECTRA input file for this run is provided in `\Z-INPUTS\ED\GCFR\INTEGRATED\R-165-2.SPE`.

As a second step synchronized runs are performed using the data exchange frequencies of:

Δt =0.1 seconds, the files are located in `\Z-INPUTS\ED\GCFR\SYNCHRONIZED-01`
Δt =0.01 seconds, the files are located in `\Z-INPUTS\ED\GCFR\SYNCHRONIZED-001`

To perform the synchronized runs the model is split in two parts, the Reactor Pressure Vessel part (RPV) and the Reactor Kinetics part (RK).

- Part I - the RPV model is used without the Reactor Kinetics model. The input file name is `R-165-2(RPV).SPE`. Only one parameter is read from the EDF (i.e. is obtained from the Reactor Kinetics model):
    - Relative reactor power, TF-100. The relative power is defined in the base model as CF-100 (reactor kinetics function). For the synchronized run this definition is overwritten in the scenario file: R-165-2(RPV).SPE by setting CF-100 equal to TF-100.

  The parameters that are written to the EDF (i.e. that are passed on to the Reactor Kinetics model) include:
    - Gas pressures in core volumes (CV-151 through CV-173)
    - Gas temperatures in core volumes (CV-151 through CV-173)

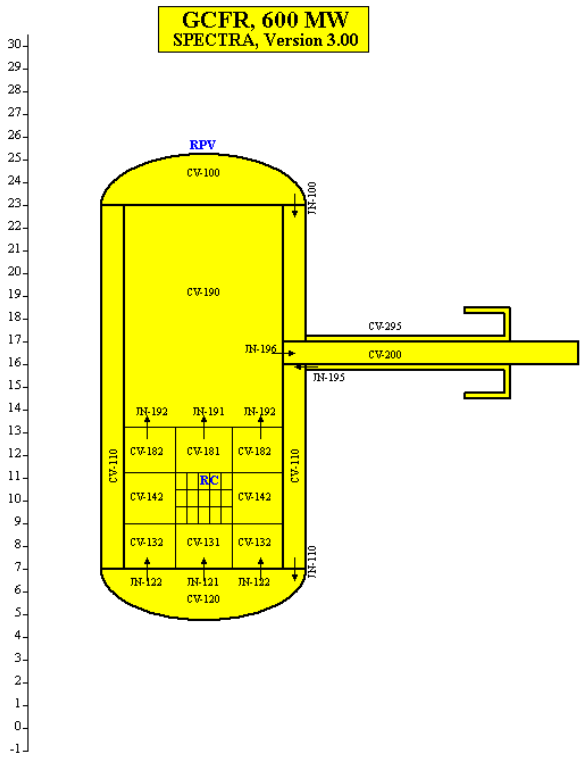

Figure 3-1127 GCFR model - reactor vessel nodalization

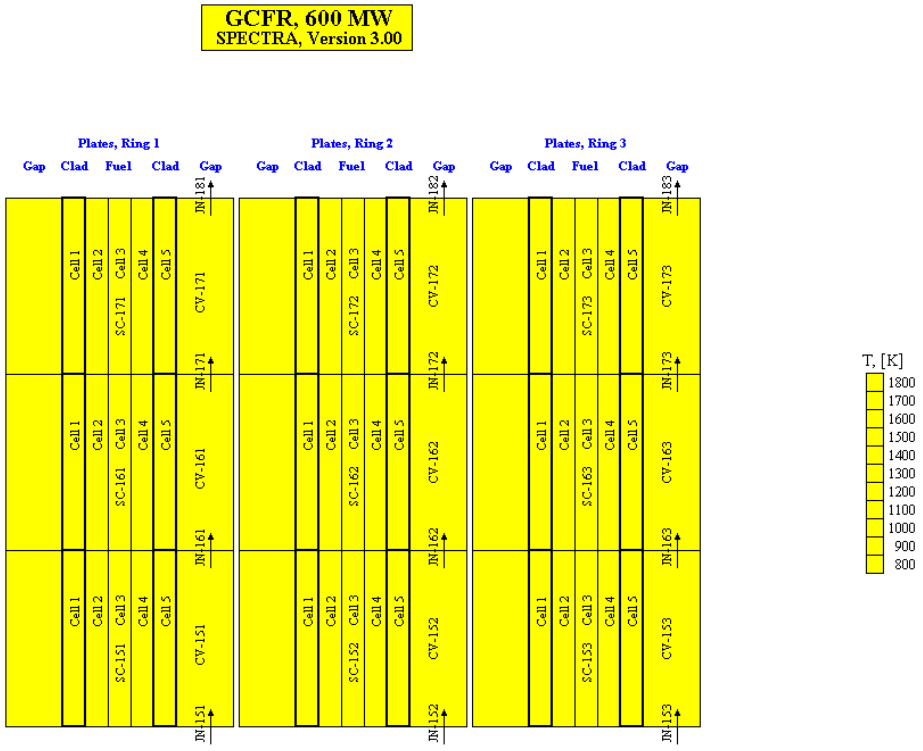

Figure 3-1128 GCFR model - reactor core nodalization

  - Fuel average temperatures, (CF-951 through CF-973). These temperatures are calculated by Control Functions that are created specifically for this purpose in the scenario file R-165-2(RPV).SPE. For the reason explained below (see description of the Part II - Reactor Kinetics model) the values that are passed on to the Reactor Kinetics Part must represent the average temperatures of the fuel plates, computed with the same weighting factors that are used in the Reactor Kinetics model. In the GCFR model the weighting factors are all equal to one (uniform weighting factors) for all fuel nodes (3 nodes per fuel plate). Therefore the Control Functions are defined to give average temperatures of the three nodes for each fuel plate. Note that this was necessary because SPECTRA is used presently as the counterpart that calculates the reactor kinetics. If a 3-D kinetics model was used, then one would simply have to transfer all temperatures in all fuel nodes.
  - Power transferred to the fluid in the reactor core, CF-181 (this Control Function is being used by the power control system inside the Reactor Kinetics model).

- Part II - the Reactor Kinetics model is used. The input file includes all Control Volumes and structures in the core. The input file name is `R-165-2(RK).SPE`. Only one parameter is written to the EDF (i.e. is passed on to the Reactor Pressure Vessel model):
  - Relative reactor power, CF-100. This Control Function gives relative core power calculated by the Reactor Kinetics model.

  The parameters that are read from the EDF (i.e. are obtained from the Reactor Pressure Vessel model) include:
  - Gas pressures in core volumes (TF-751 through TF-773). These values are used to define pressures for CV-151 through CV-173, using the "CV time dependent parameter definition", (record 125XXX - Volume 2).
  - Gas temperatures in core volumes (TF-851 through TF-873). These values are used to define temperatures for CV-151 through CV-173, using the "CV time dependent parameter definition", (record 125XXX - Volume 2).
  - Fuel average temperatures (TF-951 through TF-973). Defining time-dependent structure temperatures is more difficult than for a Control Volume and may only be done by using boundary conditions. The Tabular Functions TF 951 - TF-973 were used to define boundary fluid temperatures for the structures SC-151 - SC-173. A very large convective heat transfer coefficient (CF-999 = 10^{10} W/m^{2}K) and a very small material conductivity (true value$\times 10^{-6}$) were used to assure that the temperature of all nodes are the same as the boundary temperatures. Because of this approach the temperatures that are obtained from the RPV part must represent the average temperatures of the fuel plates, computed with the same weighting factors that are used in the Reactor Kinetics model
  - Power transferred to the fluid in the reactor core, CF-181.

  Additionally the input file contains the accident scenario data - i.e. the reactivity insertion data, as well as data overruling reactor power control and scram signals, necessary for the present scenario.

Results are shown in time dependent graphs in Figure 3-1129 through Figure 3-1134 and as visualization pictures in Figure 3-1135 through Figure 3-1139. Figure 3-1129, Figure 3-1130, and Figure 3-1131 show the reactor power computed in the integrated run (Figure 3-1129) and the synchronized run with the data exchange every 0.01 s (Figure 3-1130) and 0.1 s (Figure 3-1131).

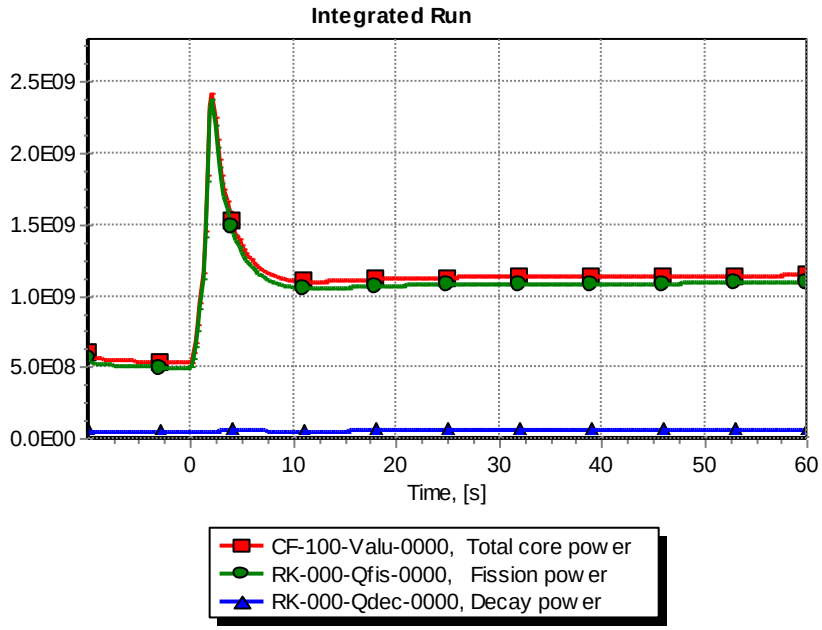

Figure 3-1129 Core power - integrated run

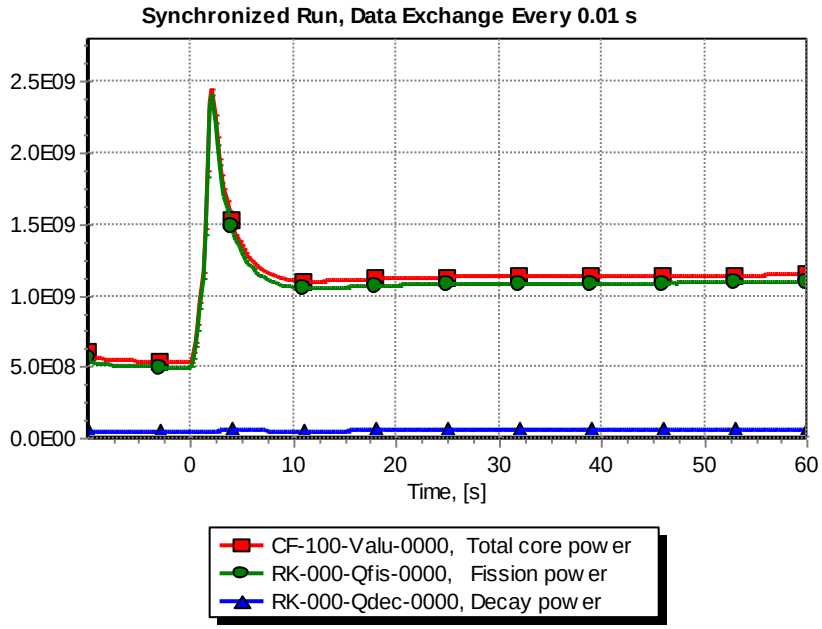

Figure 3-1130 Core power - synchronized run, data exchange every 0.01 s

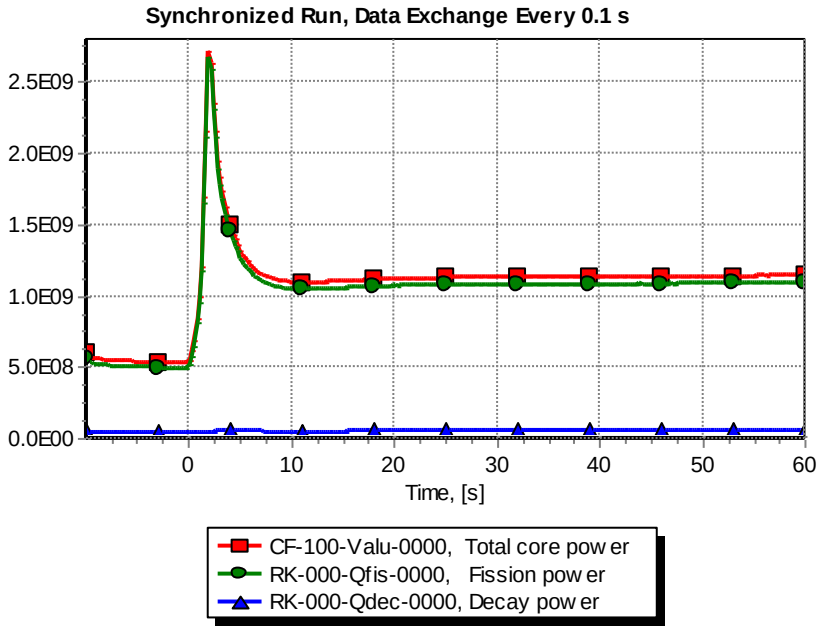

Figure 3-1131 Core power - synchronized run, data exchange every 0.1 s

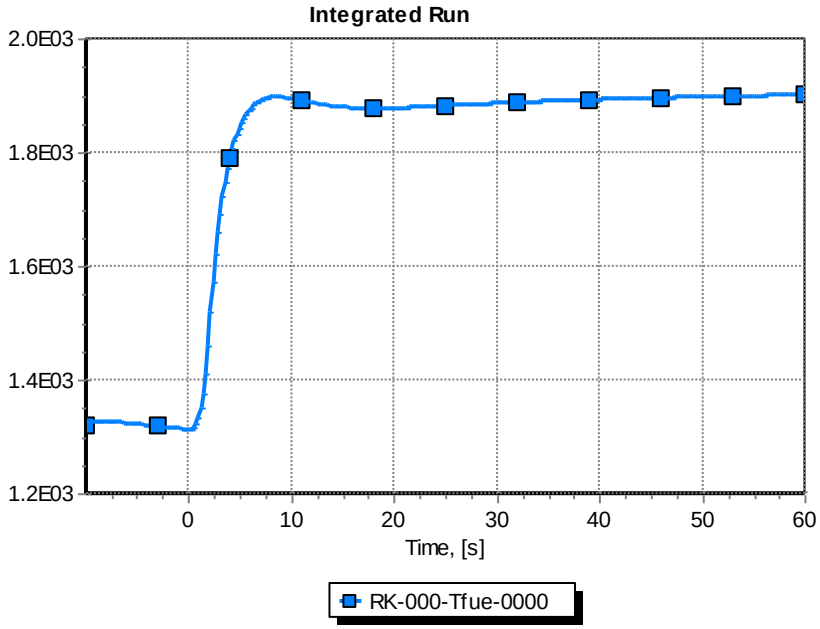

Figure 3-1132 Fuel average temperature - integrated run

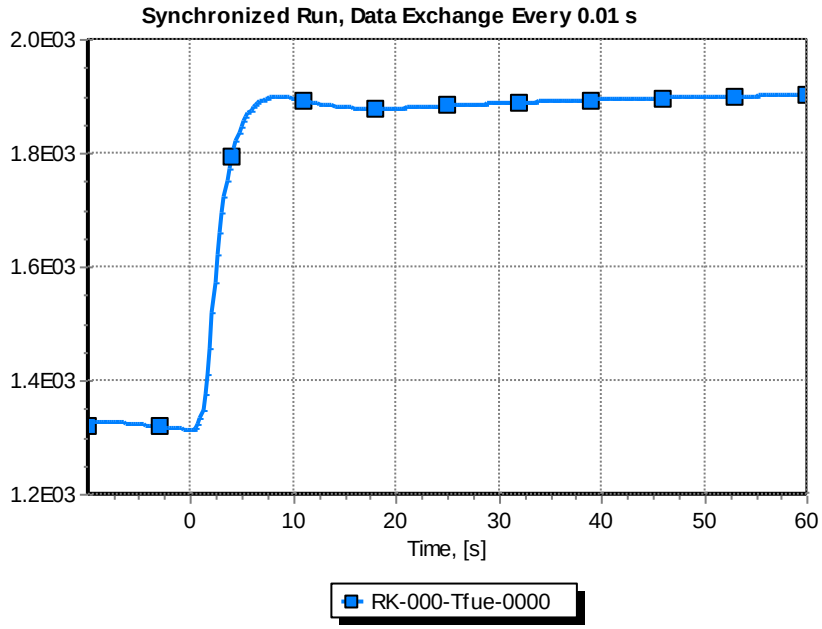

Figure 3-1133 Fuel average temperature, data exchange every 0.01 s

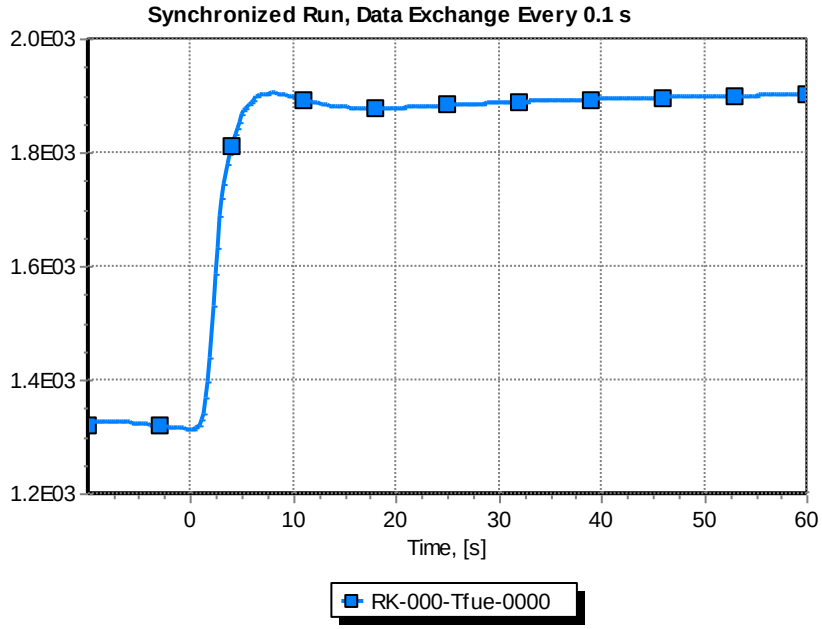

Figure 3-1134 Fuel average temperature, data exchange every 0.1 s

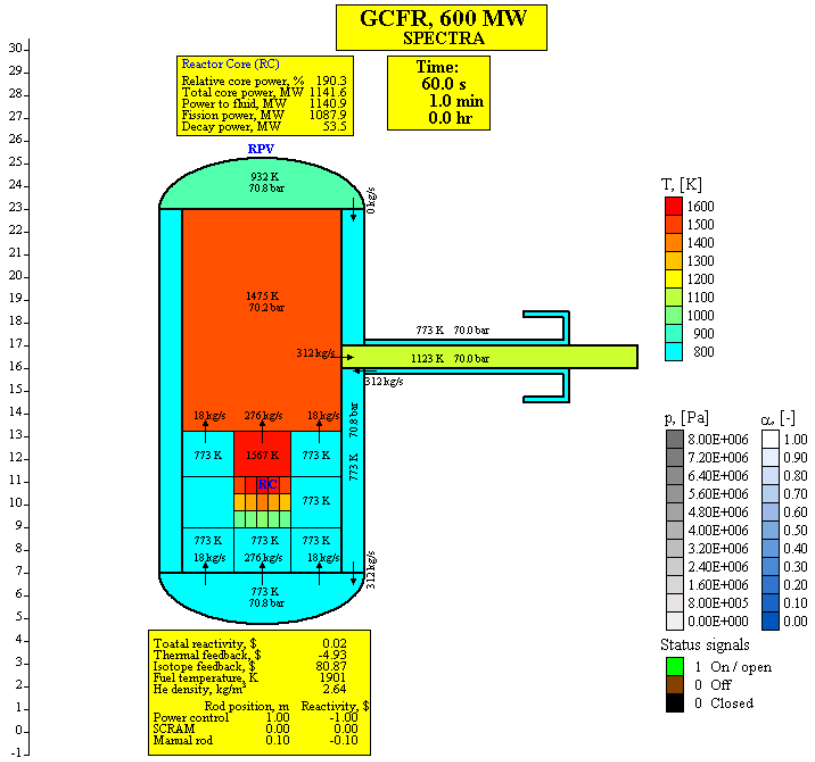

Figure 3-1135 Reactor vessel at *t* = 60.0 s, integrated run

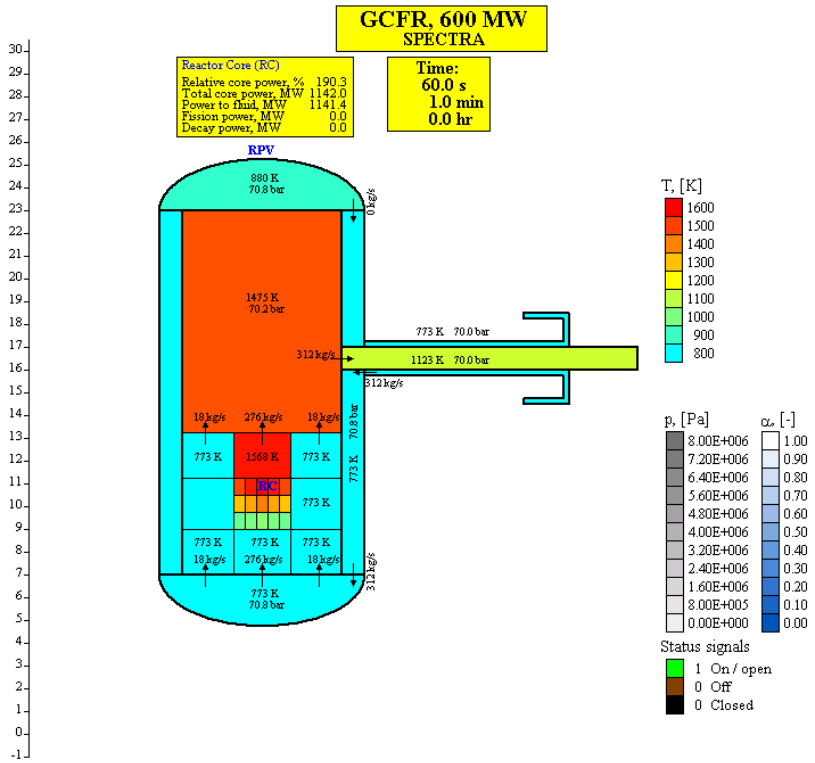

Figure 3-1136 Reactor vessel at *t* = 60.0 s, RPV model, data exchange every 0.01 s

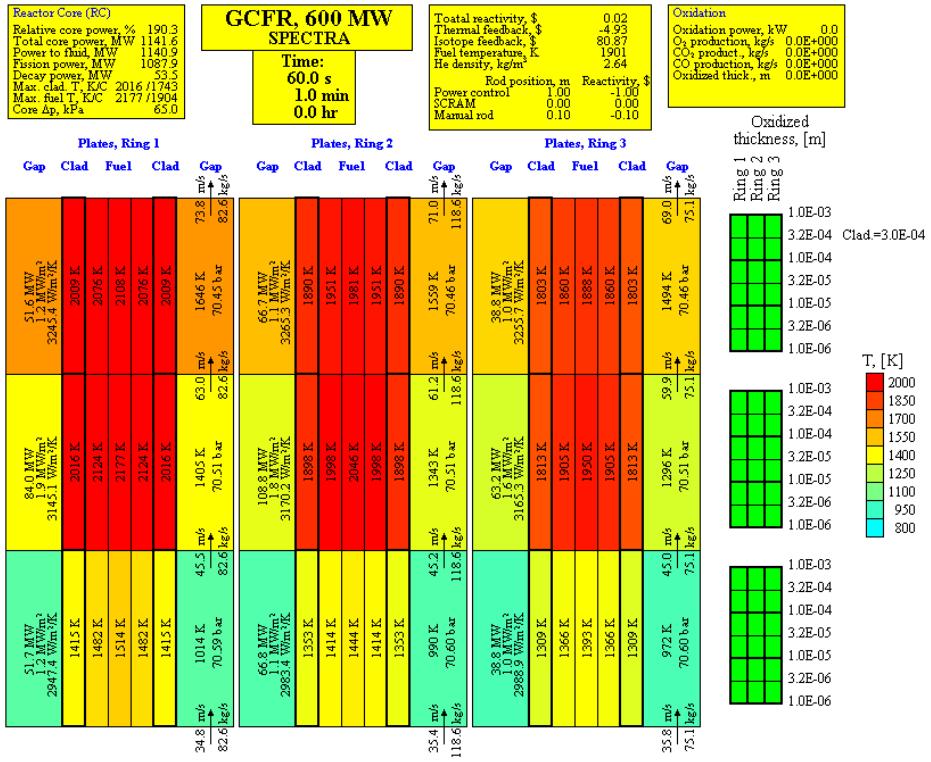

Figure 3-1137 Core at *t* = 60.0 s, integrated run

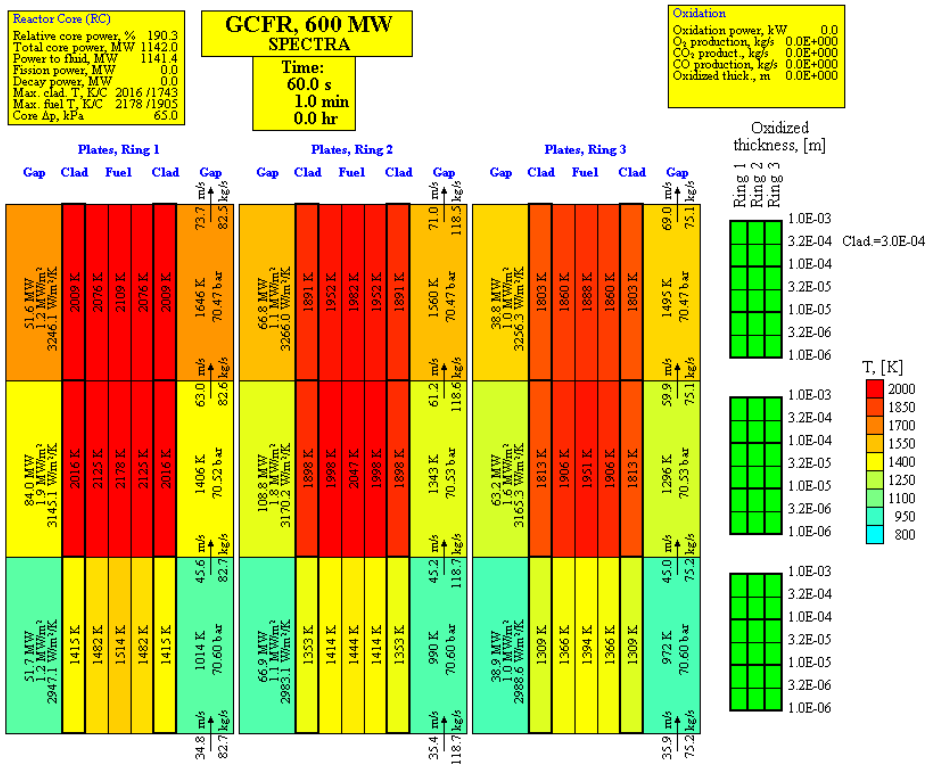

Figure 3-1138 Core at *t* = 60.0 s, RPV model, data exchange every 0.01 s

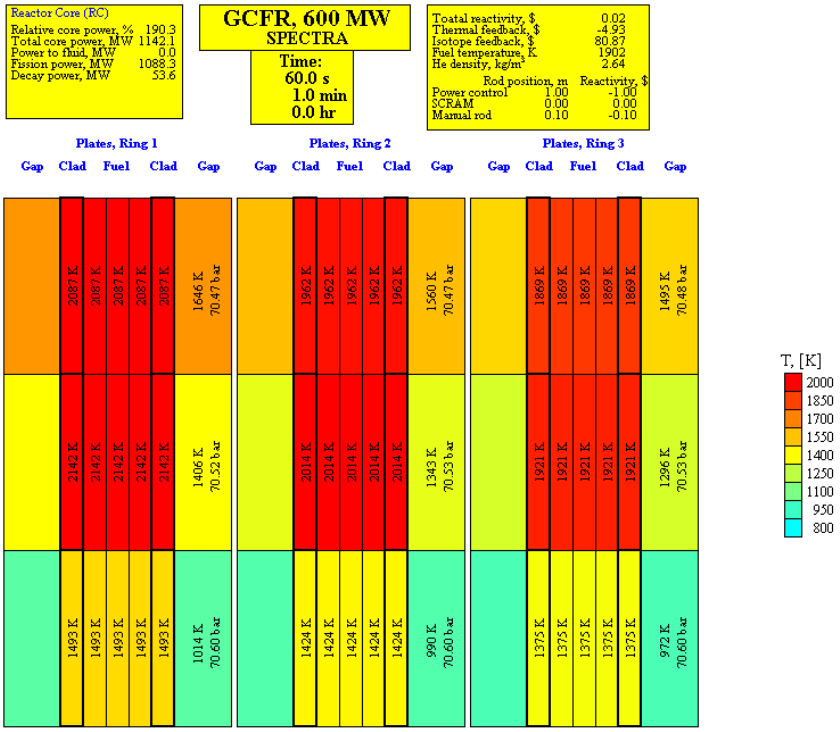

Figure 3-1139 Core at t = 60.0 s, Reactor Kinetics model, data exchange every 0.01 s

It is seen that a good agreement with the results of the integrated run is observed in case of data exchange every 0.01 s. With the data exchange of 0.1 s the power peak is somewhat higher. Apart from the short peak the results are in good agreement with the results of the synchronized run.

Figure 3-1132, Figure 3-1133, and Figure 3-1134 show the fuel average temperature. The results of both synchronized runs are in good agreement with the results of the integrated run. The difference in the short power peak in did not influence the average core temperature.

Visualization pictures shown in Figure 3-1135 and Figure 3-1136 are shown to compare RPV results of the integrated run and the synchronized run with data exchange every 0.01 s, for the end-time, t = 60 s. It is seen that the results are nearly identical.

Visualization pictures shown in Figure 3-1137, Figure 3-1138, and Figure 3-1139 are shown to compare core results of the integrated run and the synchronized run with data exchange every 0.01 s, for the end-time, t = 60 s. The results shown in Figure 3-1137, Figure 3-1138 are nearly identical. The RK results show fuel temperatures which are equal to the average temperatures, for the reason explained at the beginning of this section.

In conclusion, the synchronized run with data exchange every 0.01 s gives results very similar to the results of the integrated model for this rapid power transient. SPECTRA results obtained with the integrated model have been verified in [100] by comparison with the results of MAT4DYN.

3.17.6 Implicit Coupling

Implicit coupling is intended for cases where explicit coupling is insufficient and cannot provide stable results, such as domain decomposition with fluid flow from one domain to the other. Verification of the implicit coupling is performed with three tests, described below.

3.17.6.1 Test SYNCH-IMPL-1

The first test is intended to verify correctness of the coupling procedure. A very simple test is set up, where the values obtained from the other code are only read and are not affecting the results (no feedback from the other code). The inputs consist of a single Control Volume (CV-004) with pressure and temperature determined by user-defined Tabular Functions, TF-110 and TF-120, respectively. The functions define linear increase of pressure and temperature, as follows.

- Pressure, TF-110 : linear increase from 1.0×10^5 to 1.1×10^5 in 10.0 s.
- Temperature, TF-120 : linear increase from 300.0 to 400.0 in 10.0 s.

A synchronized EDF run is defined, where each job sends out the pressure and the temperature of CV-004 to the other job. The values that are read from EDF are assigned to TF-210 and TF-220 and can be plotted by plotting these functions.

The run time is 10.0 s. The minimum time step, the maximum time step, and the data exchange time step are equal to 1.0 s (implicit coupling requires that all these values are the same - see Volume 2). The following five cases were analyzed:

- Explicit coupling
- Implicit coupling, implicit factor XIMPED = 0.0
- Implicit coupling, implicit factor XIMPED = 0.5
- Implicit coupling, implicit factor XIMPED = 1.0
- Implicit coupling, implicit factor XIMPED = –1.0 (Solver)

The implicit factor, XIMPED determines the value that is written to the EDF:

$$V_{EDF} = V \times \text{XIMPED} + V_0 \times (1.0 - \text{XIMPED})$$

Here V is the current (end of time step) value and V_0 is the start of time value. SPECTRA input files for these runs are provided in `\Z-INPUTS\ED\SYNCH-IMPL-1`. The model is schematically shown in Figure 3-1140. The results are shown in Figure 3-1141 and Figure 3-1142.

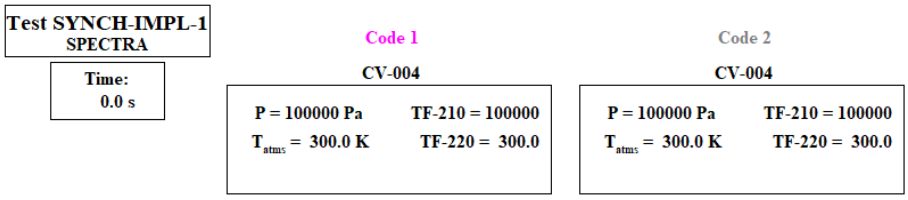

Figure 3-1140 Test SYNCH-IMPL-1, model

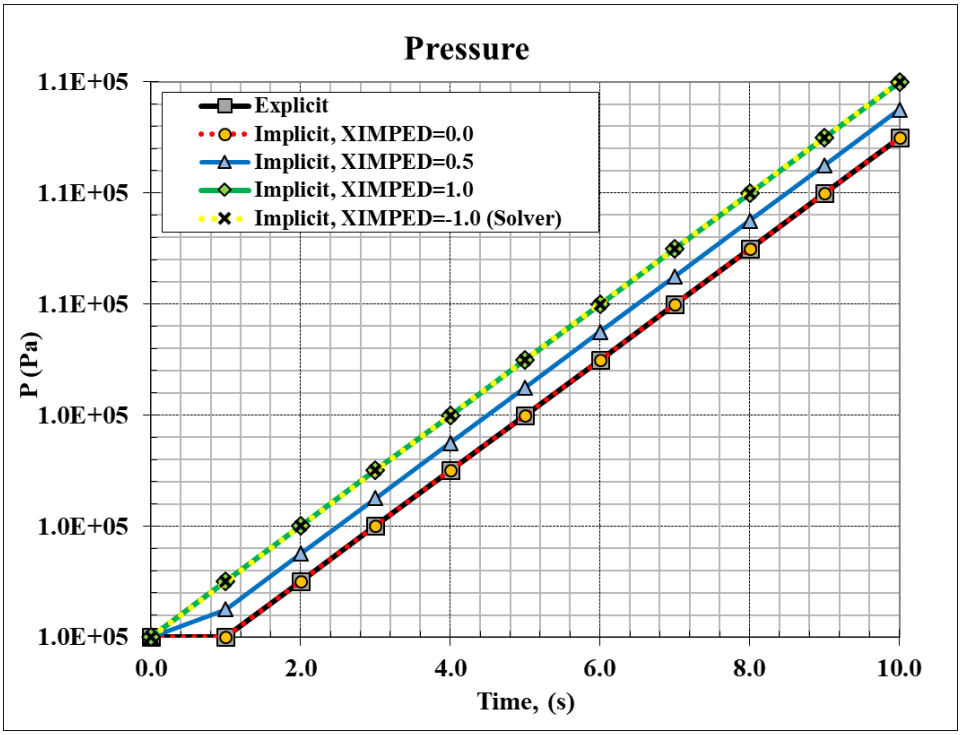

Figure 3-1141 Test SYNCH-IMPL-1, results: pressures

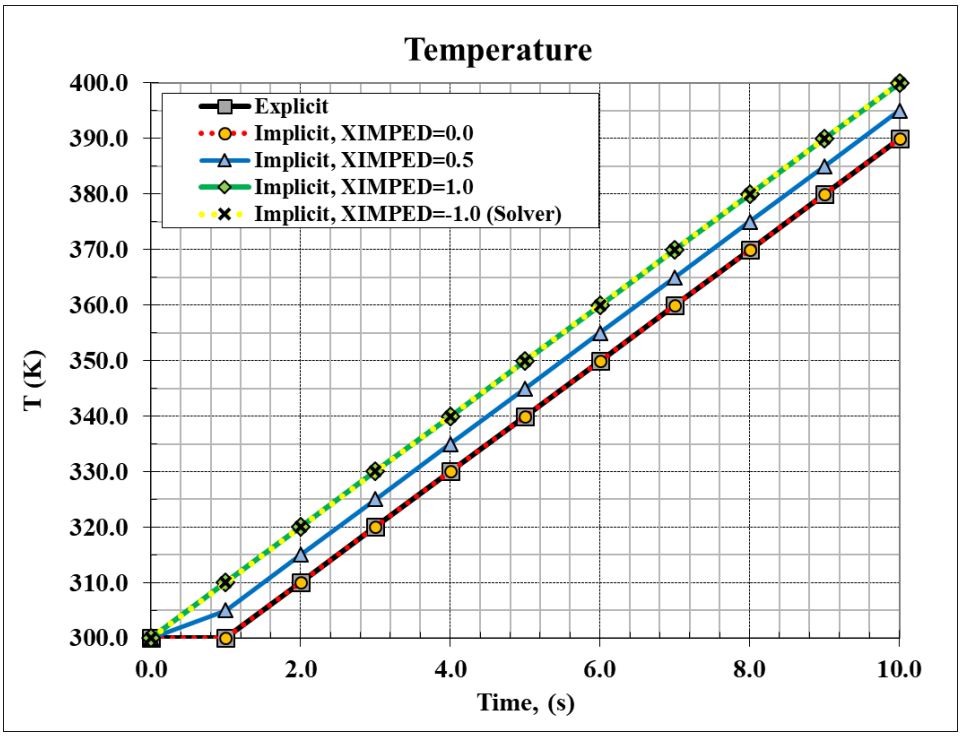

Figure 3-1142 Test SYNCH-IMPL-1, results: temperatures

Figure 3-1141 shows the values of TF-210 (pressure) read from the other code. Figure 3-1142 shows the values of TF-220 (temperature) read from the other code. The figures shows the following.

- With explicit coupling, the values read are lagging by one time step (to be more precise by one data exchange step, but in this case the data exchange step is equal to the maximum as well as the minimum time step).
- With XIMPED =0.5, the values are in the middle between the explicit and the implicit values.
- With implicit coupling, the read values are identical to the current values of pressure and temperature, as the data is exchanged in several iterations until sufficient convergence is reached. Iterations proceed differently for XIMPED = 1.0 and –1.0 (Solver) but since in this case there is no feedback, the end results are identical. Printouts of messages from both explicit and implicit couplings are shown below.

- Explicit coupling, EDF messages from the last time step

```
 t [s] =  9.0000     :  EDF EXPLICIT DATA TRANSFER NO.:      10
                        DESIGNATED TRANSFER TIME:  9.00000E+00 ,  MISMATCH:  0.00
WRITTEN:    2  9.000E+00  1.090E+05  3.900E+02
READ   :    2  9.000E+00  1.090E+05  3.900E+02
```

- Implicit coupling, XIMPED = 1.0, EDF messages from the last time step

```
 t [s] =  9.0000     :  EDF EXPLICIT DATA TRANSFER NO.:      10
                        DESIGNATED TRANSFER TIME:  9.00000E+00 ,  MISMATCH:  0.00
WRITTEN:    2  9.000E+00  1.090E+05  3.900E+02
READ   :    2  9.000E+00  1.090E+05  3.900E+02

 t [s] =  10.000     :  EDF IMPLICIT DATA TRANSFER NO.  1
WRITTEN:   -2  1.000E+01  1.100E+05  4.000E+02
READ   :   -2  1.000E+01  1.100E+05  4.000E+02

 t [s] =  10.000     :  EDF IMPLICIT DATA TRANSFER NO.  2
WRITTEN:    2  1.000E+01  1.100E+05  4.000E+02
READ   :    2  1.000E+01  1.100E+05  4.000E+02
```

- Implicit coupling, XIMPED = –1.0, EDF messages from the last time step

```
 t [s] =  9.0000     :  EDF EXPLICIT DATA TRANSFER NO.:      10
                        DESIGNATED TRANSFER TIME:  9.00000E+00 ,  MISMATCH:  0.00
WRITTEN:    2  9.000E+00  1.090E+05  3.900E+02
READ   :    2  9.000E+00  1.090E+05  3.900E+02

 t [s] =  10.000     :  EDF IMPLICIT DATA TRANSFER NO.  1
WRITTEN:   -2  1.000E+01  1.091E+05  3.904E+02
READ   :   -2  1.000E+01  1.091E+05  3.904E+02

 t [s] =  10.000     :  EDF IMPLICIT DATA TRANSFER NO.  2
WRITTEN:   -2  1.000E+01  1.100E+05  3.942E+02
READ   :   -2  1.000E+01  1.100E+05  3.942E+02

 t [s] =  10.000     :  EDF IMPLICIT DATA TRANSFER NO.  3
WRITTEN:   -2  1.000E+01  1.100E+05  4.000E+02
READ   :   -2  1.000E+01  1.100E+05  4.000E+02

 t [s] =  10.000     :  EDF IMPLICIT DATA TRANSFER NO.  4
WRITTEN:   -2  1.000E+01  1.100E+05  4.000E+02
READ   :   -2  1.000E+01  1.100E+05  4.000E+02

 t [s] =  10.000     :  EDF IMPLICIT DATA TRANSFER NO.  5
WRITTEN:    2  1.000E+01  1.100E+05  4.000E+02
READ   :    2  1.000E+01  1.100E+05  4.000E+02
```

3.17.6.2 Test SYNCH-IMPL-2

The second test is a single pipe model with domain decomposition, shown in Figure 3-1143. All volumes are filled with Nitrogen. The boundary volumes (CV-100 and CV-110) are kept at user-prescribed values:

- CV-100
  - Temperature: 900 K (const.)
  - Pressure: $t = 0.0$ $p = 9.5\times10^5$
    $t = 1.0$ $p = 9.6\times10^5$
    $t = 2.0$ $p = 9.5\times10^5$
    $t = 3.0$ $p = 9.4\times10^5$
    $t = 4.0$ $p = 9.5\times10^5$
    $t = 5.0$ $p = 9.5\times10^5$
- CV-110
  - Temperature: 70 K (const.)
  - Pressure: $p = 9.5\times10^5$ (const.)

The data that is being transferred through EDF include the following pressures (p), temperatures (T) and gas mass flow (W_{gas}):

- Domain 1 → 2: p(CV-104), T(CV-104), W_{gas}(JN-104).
- Domain 2 → 1: p(CV-105), T(CV-105).

The run time is 5.0 s. The minimum time step, the maximum time step, and the data exchange time step are equal to 0.01 s (since with implicit coupling no time step cut is allowed, the maximum time step must be selected small enough to avoid time step cuts during calculations). The following five cases were analyzed:

- Full mode. No domain decomposition. This is the reference case.
- Explicit coupling
- Implicit coupling, implicit factor XIMPED = 0.0
- Implicit coupling, implicit factor XIMPED = 0.5
- Implicit coupling, implicit factor XIMPED = 1.0
- Implicit coupling, implicit factor XIMPED = –1.0 (Solver)

SPECTRA input files for these runs are provided in `\Z-INPUTS\ED\SYNCH-IMPL-2`. The results are shown in Figure 3-1144. The coupled code results are plotted against the reference (full model) results.

It is seen that for the present test all coupling procedures are able to reproduce the full model results with a good accuracy. This is because in the present test the gas is used as a fluid. Consequently, although this is the domain decomposition case with fluid flow from one domain to the other, the solution is relatively easy and implicit coupling is not necessary. A more difficult case to solve is presented in the next section, where the same pipe is filled with liquid sodium, a nearly incompressible fluid. For such case the explicit solution fails completely.

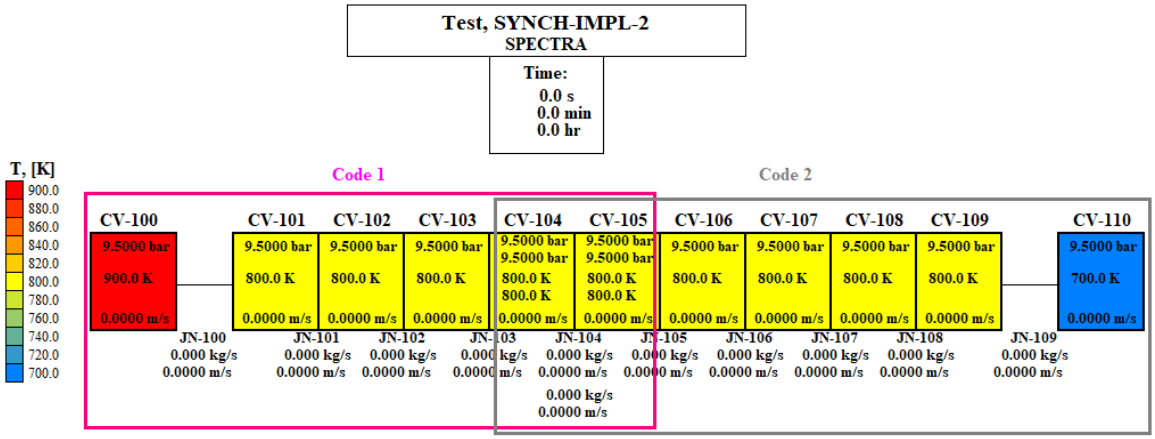

Figure 3-1143 Test SYNCH-IMPL-2, model

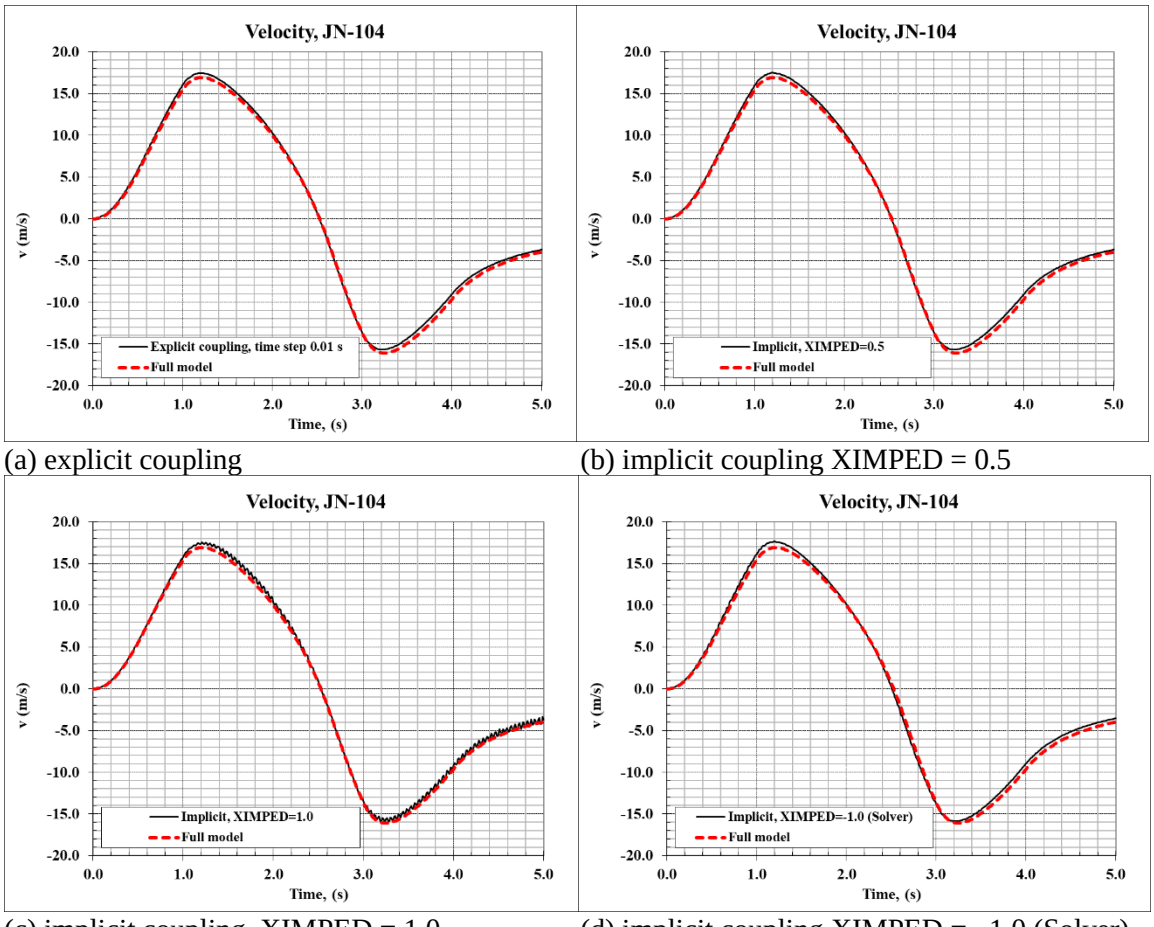

(a) explicit coupling (b) implicit coupling XIMPED = 0.5

(c) implicit coupling, XIMPED = 1.0 (d) implicit coupling XIMPED = –1.0 (Solver)

Figure 3-1144 Test SYNCH-IMPL-2, results: gas velocity at the coupling interface

3.17.6.3 Test SYNCH-IMPL-3

The third test is again a single pipe model with domain decomposition, shown in Figure 3-1145. All volumes are filled with liquid Sodium. The boundary volumes (CV-100 and CV-110) are kept at user-prescribed values:

- CV-100
  - Temperature: 900 K (const.)
  - Pressure: $t = 0.0$ $p = 9.5\times10^5$
    $t = 1.0$ $p = 9.6\times10^5$
    $t = 2.0$ $p = 9.5\times10^5$
    $t = 3.0$ $p = 9.4\times10^5$
    $t = 4.0$ $p = 9.5\times10^5$
    $t = 5.0$ $p = 9.5\times10^5$
- CV-110
  - Temperature: 70 K (const.)
  - Pressure: $p = 9.5\times10^5$ (const.)

The data that is being transferred through EDF include the following pressures (p), temperatures (T) and liquid mass flow (W_{liq}):

- Domain 1 → 2: p(CV-104), T(CV-104), W_{liq}(JN-104)
- Domain 2 → 1: p(CV-105), T(CV-105)

The run time is 5.0 s. The minimum time step, the maximum time step, and the data exchange time step are equal to 0.01 s (again the maximum time step must be selected small enough to avoid time step cuts during calculations). The following five cases were analyzed:

- Full mode, no domain decomposition. This is the reference case.
- Explicit coupling
- Implicit coupling, implicit factor XIMPED = 0.0
- Implicit coupling, implicit factor XIMPED = 0.5
- Implicit coupling, implicit factor XIMPED = 1.0
- Implicit coupling, implicit factor XIMPED = –1.0 (Solver)

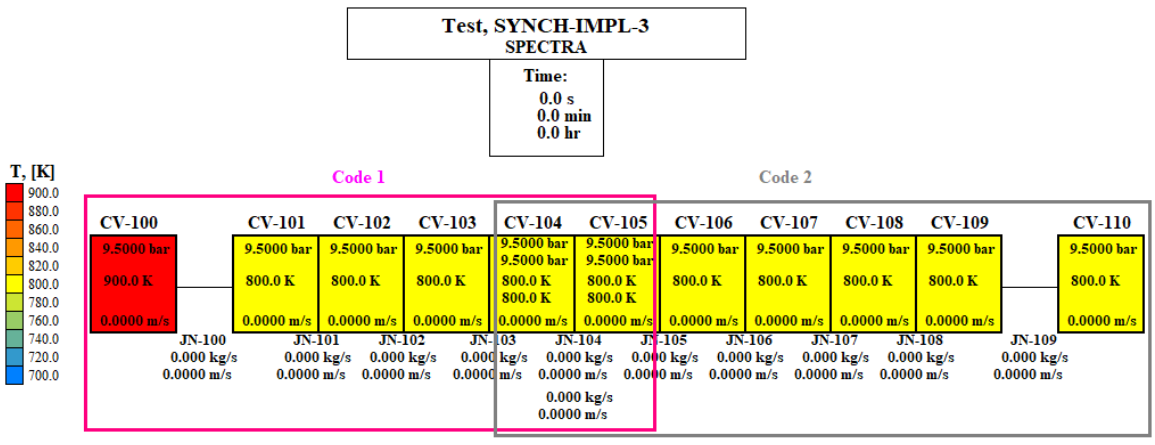

Figure 3-1145 Test SYNCH-IMPL-3, model

SPECTRA input files for these runs are provided in `\Z-INPUTS\ED\SYNCH-IMPL-3`. The results are shown in Figure 3-1146 and Figure 3-1147. The coupled code results are plotted against the reference (full model) results.

Figure 3-1146 and Figure 3-1147 (a) show the results obtained with explicit coupling (input files: SYNCH-IMPL-00-00X.SPE, X=1 and 2). The results show heavy oscillations of pressures and flows. Clearly the explicit coupling is insufficient to solve this case, with a nearly incompressible fluid flowing across the domain boundary.

Figure 3-1146 and Figure 3-1147 (b) show the results obtained with implicit coupling, XIMPED = 0.5 (input files: SYNCH-IMPL-05-00X.SPE, X=1 and 2). The results are improved but significant oscillations still occur at later times.

Figure 3-1146 and Figure 3-1147 (c) show the results obtained with implicit coupling, XIMPED = 1.0 (input files: SYNCH-IMPL-10-00X.SPE, X=1 and 2). Oscillations are still present, although much smaller than in the explicit coupling.

A few test runs performed with different values of XIMPED showed that the best results were obtained with XIMPED of 0.9. The results obtained with XIMPED = 0.8 and 0.9 are shown in Figures (d) and (e) respectively.

Figure 3-1146 and Figure 3-1147 (f) show the results obtained with implicit coupling, XIMPED = –1.0 (input files: SYNCH-IMPL-1-00X.SPE, X=1 and 2) applying SPECTRA Solver to control the iterations in implicit solution. This method provides the best results and is therefore recommended for general use (default value of XIMPED is –1.0 - see Volume 2).

Finally, the last two sets of calculations were investigated for the following reason. SPECTRA Solver is available in only in SPECTRA. In above test, two SPECTRA jobs were coupled; i.e. the option XIMPED = –1.0 was used in both jobs. The question arise, if it is sufficient to use the Solver option on one job only, for cases SPECTRA is coupled to another code. It is assumed that the "other code" has the capability to use an "implicit factor", similar to XIMPED in SPECTRA. Two cases were considered:

(1) Solver is used in the Code 1 (left domain in Figure 3-1145). The Code 2 (right domain in Figure 3-1145) uses XIMPED of 0.9. The input files are: SYNCH-IMPL-1a-00X.SPE, X=1 and 2. The results are shown in Figure 3-1148.

(2) Solver is used in the Code 2 (right domain in Figure 3-1145). The Code 1 (left domain in Figure 3-1145) uses XIMPED of 0.9. The input files are: SYNCH-IMPL-1b-00X.SPE, X=1 and 2. The results are shown in Figure 3-1149.

It is seen that the results are similar to the results shown in Figure 3-1147 (f). Therefore it is concluded that it is sufficient to apply the Solver on one of the coupled jobs.

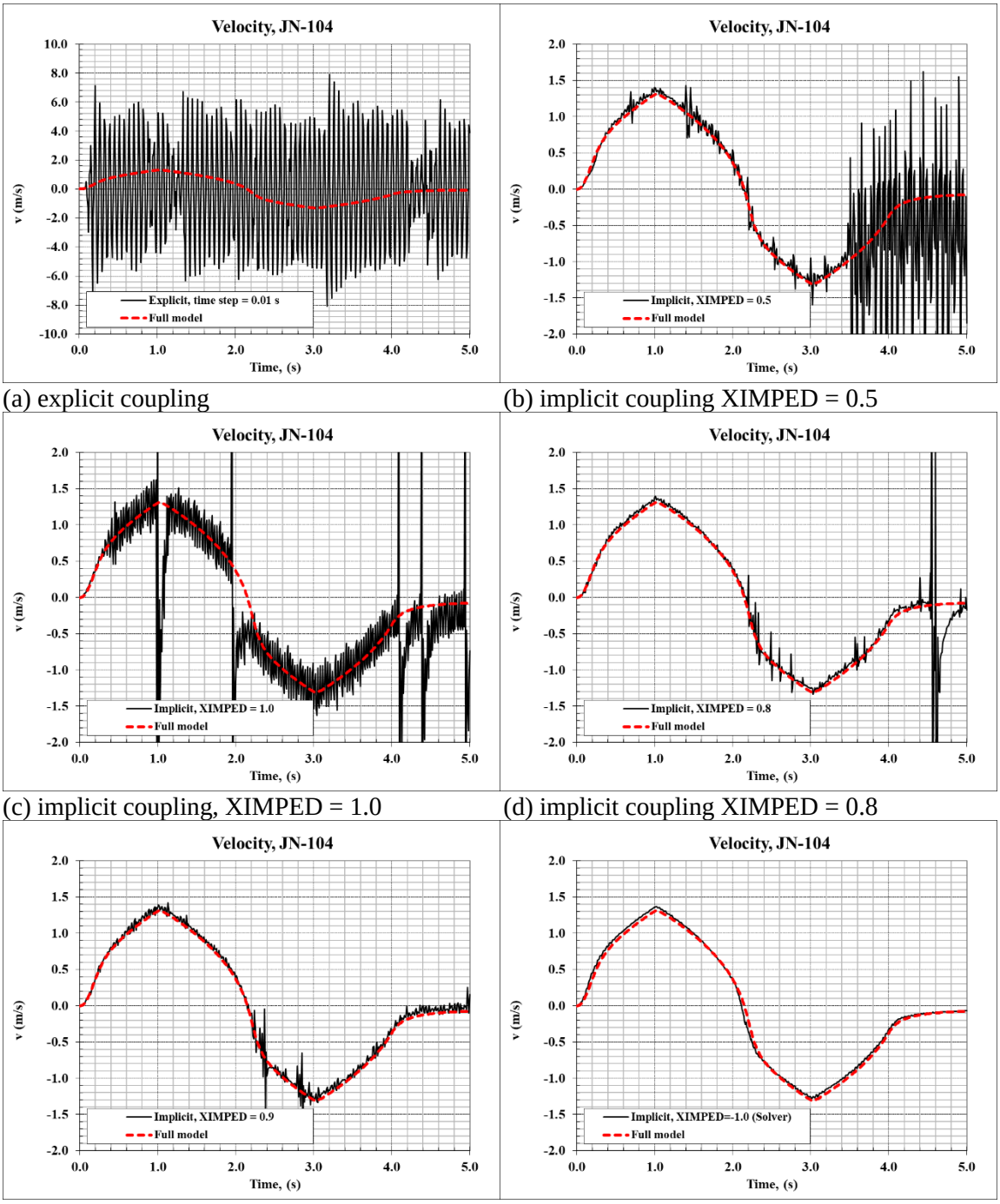

(a) explicit coupling (b) implicit coupling XIMPED = 0.5

(c) implicit coupling, XIMPED = 1.0 (d) implicit coupling XIMPED = 0.8

(e) implicit coupling, XIMPED = 0.9 (f) implicit coupling XIMPED = –1.0 (Solver)

Figure 3-1146 Test SYNCH-IMPL-3, results: liquid velocity at the coupling interface

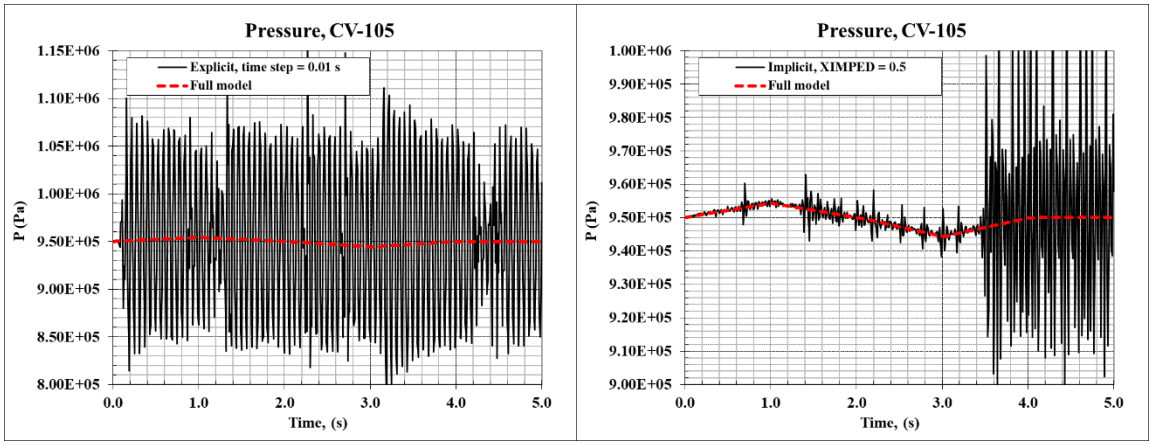

(a) explicit coupling

(b) implicit coupling XIMPED = 0.5

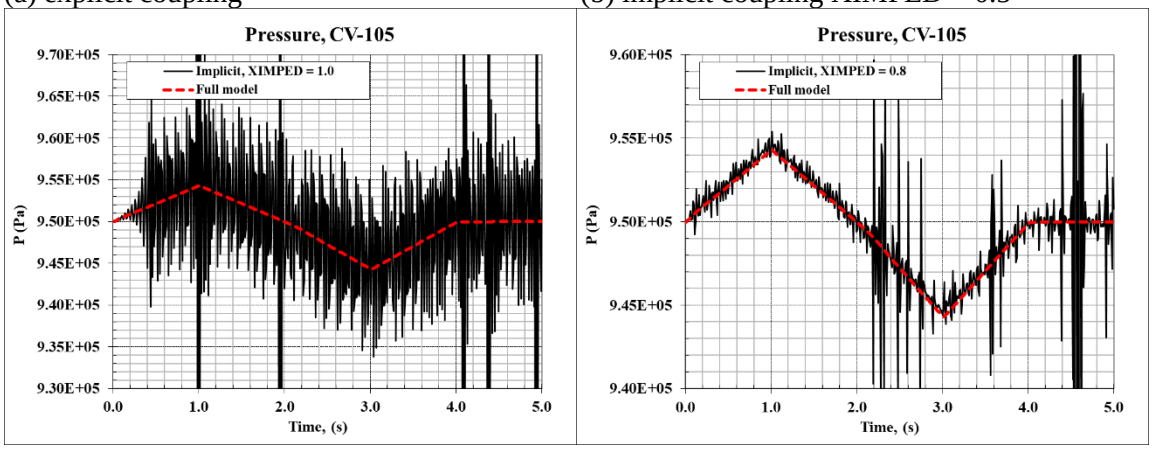

(c) implicit coupling, XIMPED = 1.0

(d) implicit coupling XIMPED = 0.8

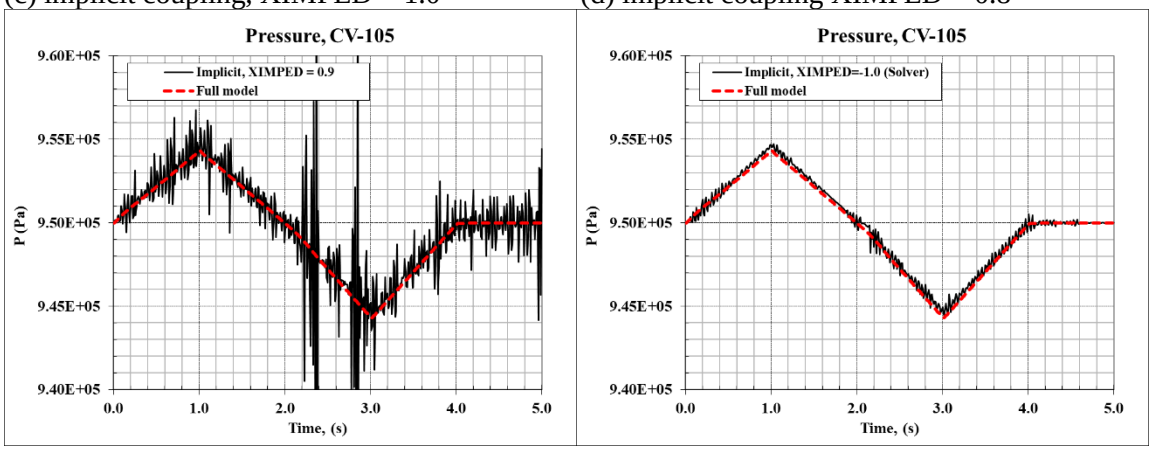

(e) implicit coupling, XIMPED = 0.9

(f) implicit coupling XIMPED = –1.0 (Solver)

Figure 3-1147 Test SYNCH-IMPL-3, results: pressures at the coupling interface

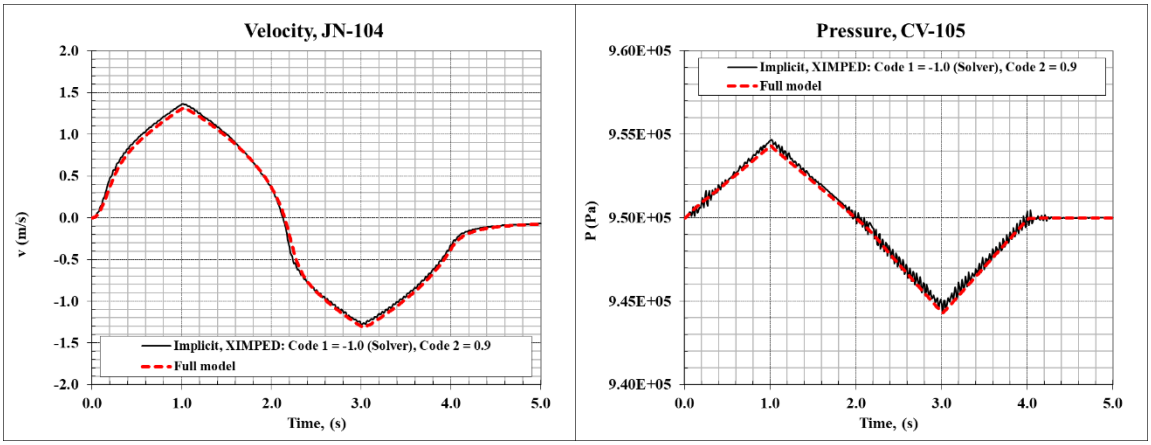

Figure 3-1148 Test SYNCH-IMPL-3, XIMPED: Code 1 = -1.0 (Solver), Code 2 = 0.9

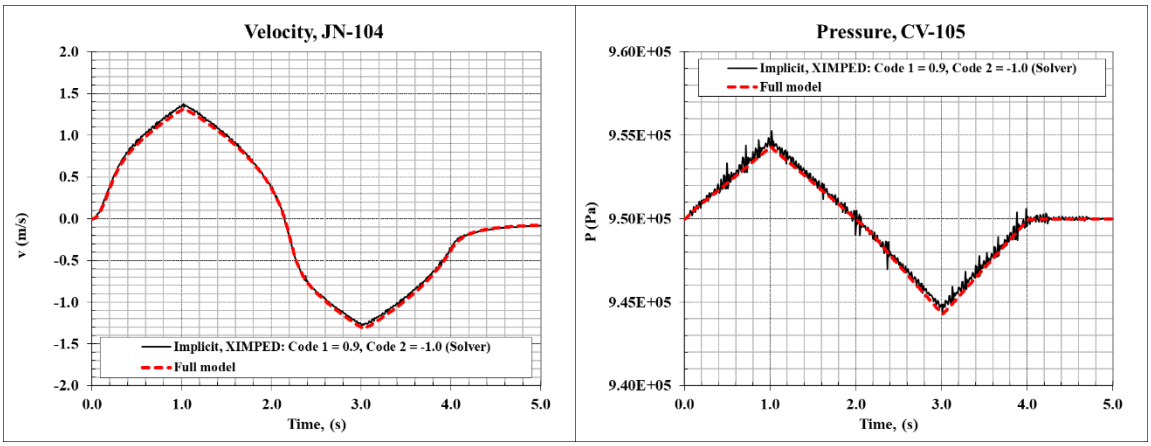

Figure 3-1149 Test SYNCH-IMPL-3, XIMPED: Code 1 = 0.9, Code 2 = -1.0 (Solver)

3.17.6.4 Test SYNCH-IMPL-3-LFM

The tests described in the previous two sections were repeated using Limited Flow Matrix (MSFMJN = 2), for the following reason. If only the Full Flow Matrix (MSFMJN = 1) is used, then the junction flows are computed using the pressures at the beginning of time step (see Volume 1, section: Flow Solution for Continuous Components - Method 1 - FFM). Therefore the pressure in CV-105 that is updated by Code 2 during iterations is not taken into account by Code 1 to calculate the flow in JN-104, that is passed on to Code-2. Consequently the flow practically does not change from iteration to iteration. This fact makes the convergence slower. This may be changed by activating the Limited Flow Matrix, which uses the end of time step pressures (see Volume 1, section: Flow Solution for Continuous Components - Method 1 - LFM).

Calculations using LFM were performed for both tests discussed in the previous sections, namely SYNCH-IMPL-2 and SYNCH-IMPL-3. Input files for the test SYNCH-IMPL-2 are provided in `\Z-INPUTS\ED\SYNCH-IMPL-2-LFM`. These are very similar to the results shown in section 3.17.6.2 and are not discussed here.

Input files for the test SYNCH-IMPL-3 are provided in `\Z-INPUTS\ED\SYNCH-IMPL-3-LFM`. The results are shown in Figure 3-1150 and Figure 3-1151. As may be seen, a good solution is obtained implicit coupling in all cases. Therefore, it may be concluded that the use of LFM significantly improves convergence in the present test.

The results presented here were obtained using the LFM within the Code 1, in order to allow the Code 1 to use the updated pressures, received from Code 2 during the iterations. A separate test was performed applying LMF on both sides (booth Code 1 and 2). In this case the convergence was even better in most cases.

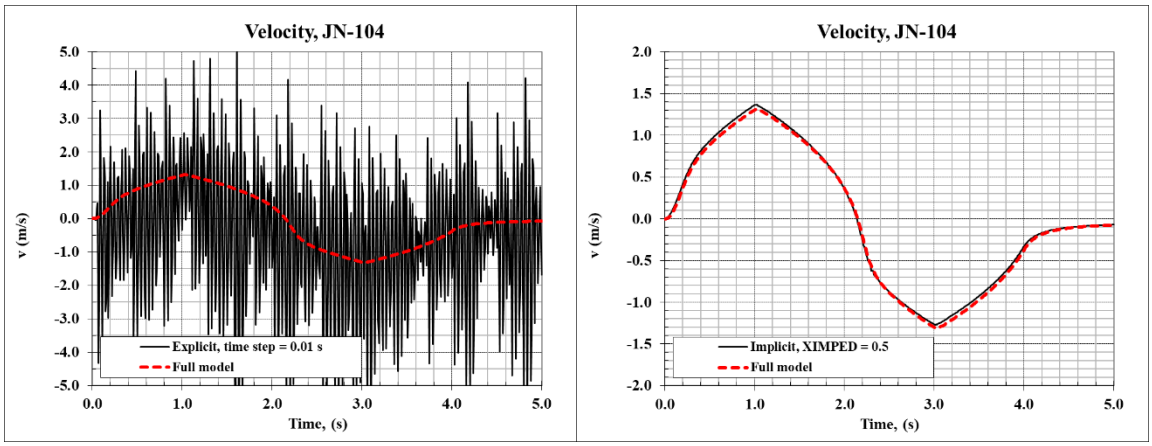

(a) explicit coupling (b) implicit coupling, XIMPED = 0.5

(c) implicit coupling, XIMPED = 1.0 (d) implicit coupling XIMPED = –1.0 (Solver)

Figure 3-1150 Test SYNCH-IMPL-3-LFM, results: liquid velocity at the coupling interface

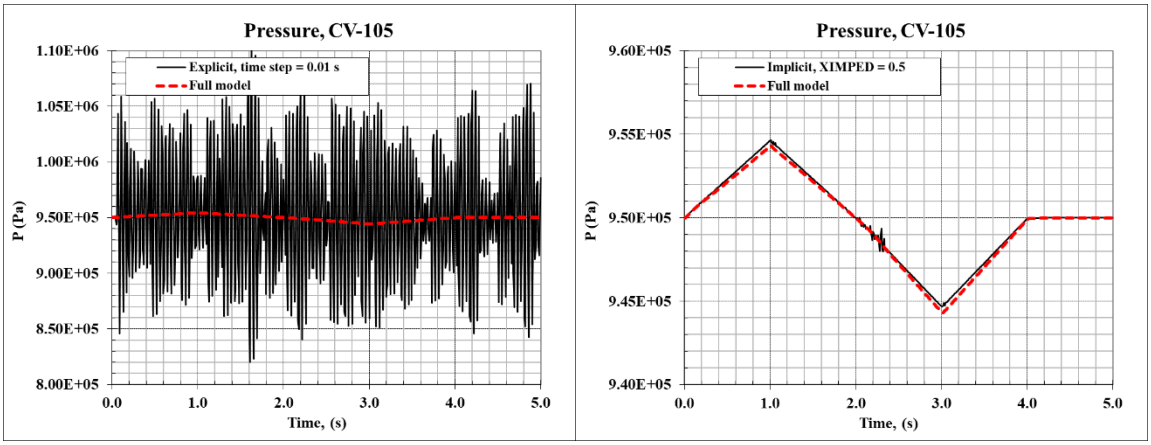

(a) explicit coupling (b) implicit coupling XIMPED = 0.5

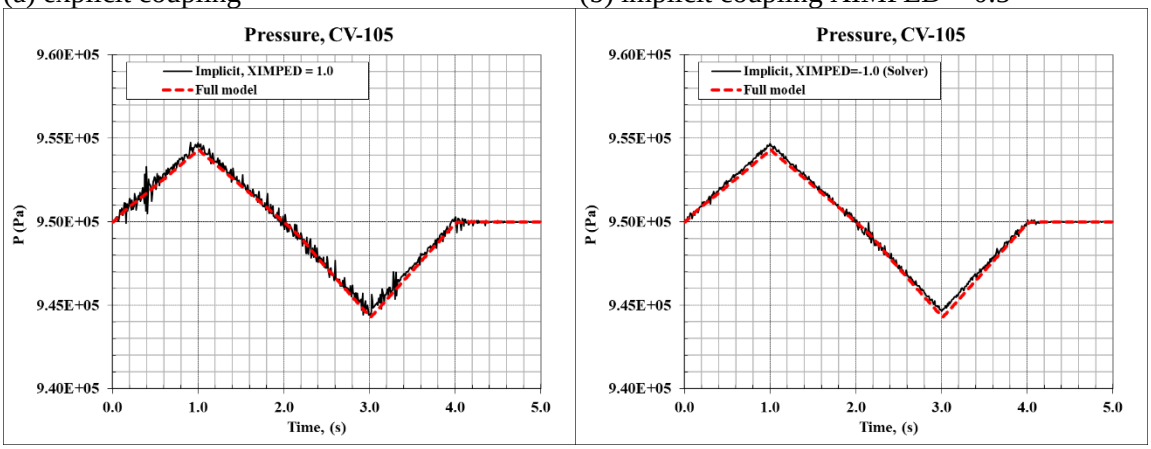

(c) implicit coupling, XIMPED = 1.0 (d) implicit coupling XIMPED = –1.0 (Solver)

Figure 3-1151 Test SYNCH-IMPL-3-LFM, results: pressures at the coupling interface

3.18 Numerical Solver

This section gives verification of the SPECTRA Numerical Solver Package, referred to shortly as the Solver. Basically all tests presented in this chapter and in chapter 4 can be considered as verification tests of the Solver. Therefore only two test problems are presented here.

As the first test problem a "stiff" set of equations is solved. The solution obtained by the Solver is compared to the solution obtained with Runge-Kutta method and Rosenbrock method, which is specifically useful for stiff systems and using the integrated code MELCOR. This test is described in section 3.18.1. As the second test problem a simple case with two radiating slabs is considered. The solution of SOLVER is compared to the solution obtained with Runge-Kutta method and using the integrated code MELCOR 1.8.3. This test is described in section 3.18.2. Finally, a summary of the Numerical Solver testing is provided in section 3.18.3

3.18.1 Stiff Set of Ordinary Differential Equations

This test is described in detail in section 3.16.3. Here only the main results are shown. A “stiff” set of differential equation was selected, taken from [97]. Stiff equation sets are particularly difficult to solve. The equation set is:

$$(1)\quad \frac{dy_1}{dt} = -0.013 \cdot y_1 - 1000 \cdot y_1 \cdot y_3$$

$$(2)\quad \frac{dy_2}{dt} = -2500 \cdot y_2 \cdot y_3$$

$$(3)\quad \frac{dy_3}{dt} = -0.013 \cdot y_1 - 1000 \cdot y_1 \cdot y_3 - 2500 \cdot y_2 \cdot y_3$$

The initial conditions are:

$$y_1(0) = 1$$
$$y_2(0) = 1$$
$$y_3(0) = 0$$

Results obtained with SPECTRA are compared here to the results obtained with the MELCOR code [20]. SPECTRA calculations were performed using a large time step (1.0 s). The run was completed with this time step without any time step reductions. Results are shown in Figure 3-1152. In the MELCOR code the present test problem could be solved correctly only with time step of 10^{-4}. Application of time steps of 10^{-3}, or larger, resulted in a diverging solution and finally a floating exception. With the small time steps MELCOR results are in good agreement with the SPECTRA results, see Figure 3-1152 and Figure 3-1153.

SPECTRA input for this test is provided in `\Z-INPUTS\CF\STIFF\STIFF.SPE`. MELCOR input decks for this case are provided in: `\Z-INPUTS\CF\STIFF\MELCOR\STIFF.GEN` and `STIFF.COR`.

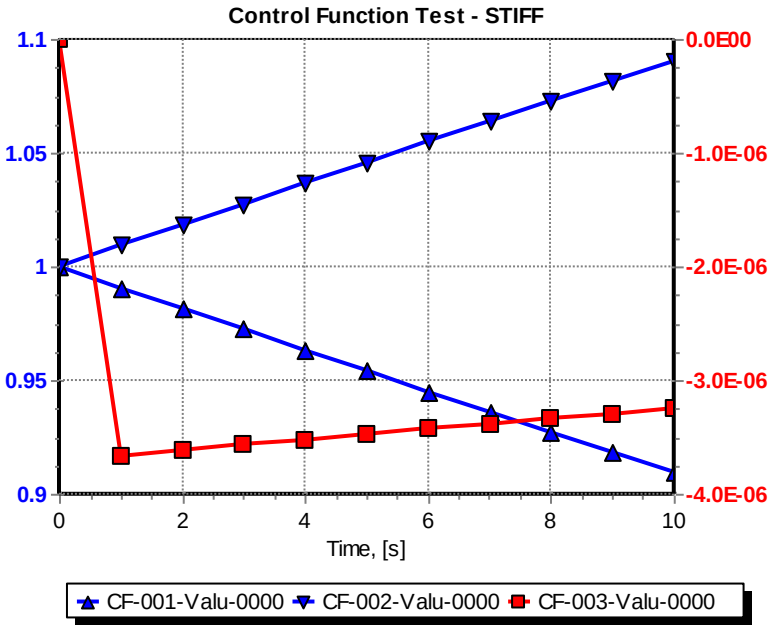

Figure 3-1152 Stiff set of ODE, SPECTRA, Δt = 1.0 s

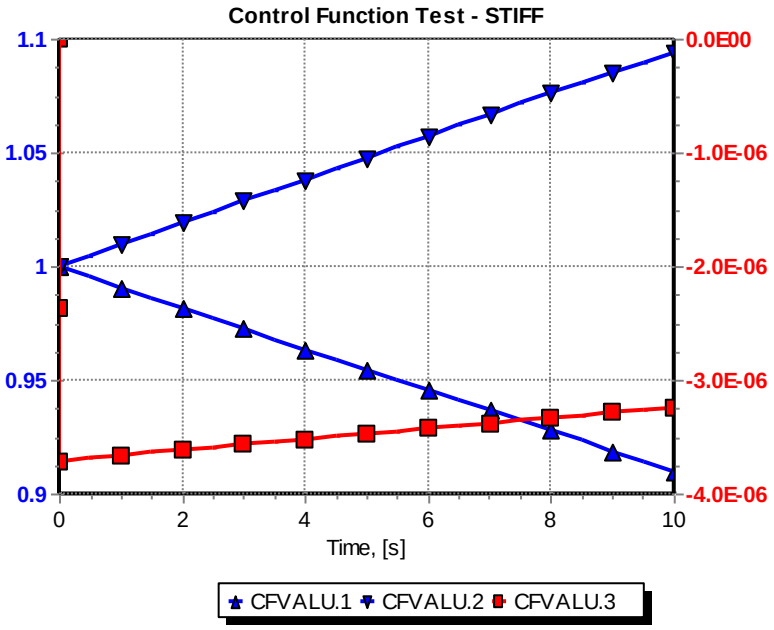

Figure 3-1153 Stiff set of ODE, MELCOR, $\Delta t = 1.0 \times 10^{-4}$ s

3.18.2 Two Radiating Surfaces - Test R2

The test problem R2 is used to verify the ability of SOLVER to obtain stable solution regardless of the time step. In the test problem R2 two parallel thin (1 mm) slabs exchange heat by means of thermal radiation. The surface area of the slabs is: A = 1.0 m^2. The first slab is heated by an internal source (2.0 MW power). The second slab is cooled down externally by a coolant with temperature: T_{cool} = 300 K. A large heat transfer coefficient (10^9 W/m^2-K) is assumed to keep the cooled slab at the desired temperature. Both slabs are initially cold (300 K). Due to the internal source in the slab 1 it is quickly heated up, until the heat radiated from its surface is equal to the internal source power.

Theoretical solution

The slabs are considered thin enough so that temperature may be assumed constant across the slab. The internal energy of a slab is equal to: $U_1 = V\rho c_p T_1$, where V is the volume of the slab 1, (equal to 10^{-3} m^3), ρ is the material density (assumed equal to 1000.0 kg/m^3), c_p is the specific heat, (assumed equal to 1000.0 J/kg-K), and T_1 is the slab 1 temperature (K). In case of the first slab the increase of the internal energy, dU_1/dt, is equal to the heat supplied from the internal source, Q_{source}, minus the energy radiated away from the surface, Q_{rad}:

$$V\rho c_p \frac{dT_1}{dt} = Q_{source} - Q_{rad}$$

In case of the second slab the temperature is kept constant:

$$T_2 = 300 = const$$

The radiative heat exchange is equal to [21]:

$$Q_{rad} = A\sigma\varepsilon_{12} \cdot \left(T_1^4 - T_2^4\right)$$

Here A is the surface area, σ is the Stefan-Boltzman constant (equal to 5.67×10^{-8} W/m^2-K^4), T_1 and T_2 are temperatures of the surfaces 1 and 2. The effective emissivity for radiant heat exchange between surfaces 1 and 2, ε_{12}, is given by ([21], section 7.1):

$$\varepsilon_{1-2} = \left(\frac{1}{\varepsilon_1} + \frac{1}{\varepsilon_2}\right)^{-1}$$

The ε_1, ε_2, are the emissivities of the surfaces 1 and 2. For the present calculations the emissivities were set to one. Therefore the effective emissivity is equal to ε_{12} = 0.5.

Substituting the formula for Q_{rad} one obtains the following equation:

$$V\rho c_p \frac{dT_1}{dt} = Q_{source} - A\sigma\varepsilon_{12}\left(T_1^4 - T_2^4\right)$$

or:

$$\frac{dT_1}{dt} = \frac{Q_{source}}{V\rho c_p} - \frac{A\sigma\varepsilon_{12}}{V\rho c_p}\cdot\left(T_1^4 - T_2^4\right)$$

A finite difference form is written explicitly:

$$T_1 = \overline{T_1} + \Delta t \cdot \left[\frac{Q_{source}}{V\rho c_p} - \frac{A\sigma\varepsilon_{12}}{V\rho c_p}\cdot\left(\overline{T_1}^4 - T_2^4\right)\right] =$$

$$= \overline{T_1} + \Delta t \cdot \left[\frac{2\times10^6}{10^{-3}\times1000\times1000} - \frac{1\times5.67\times10^{-8}\times0.5}{10^{-3}\times1000\times1000}\cdot\left(\overline{T_1}^4 - 300^4\right)\right]$$

Finally:

$$T_1 = \overline{T_1} + \Delta t \cdot \left(2.0\times10^3 - 2.835\times10^{-11}\times\overline{T_1}^4\right)$$

Here $\overline{T_1}$ is the previous time step value of T_1. This equation is solved using a small time step (equal to 10^{-2} s) using Excel. Results are shown in Figure 3-1155.

Calculations with SPECTRA

Two versions are considered for SPECTRA calculations:

- The radiation model in non-absorbing/non-emitting medium is used. No gas volume is modelled. Only the radiative heat transfer occurs. The model consists of two Solid Heat Conductors - Figure 3-1154, left. The input deck for this test problem is provided in **\Z-INPUTS\TR\R2\R2.SPE**.

- The radiation model with participating gas is used. The gas space is modelled using a single Control Volume. Both radiative and convective heat transfer occurs, but the convective part is minor compared to the radiative. The model consists of two Solid Heat Conductors, SC-001, SC-002, and a single Control Volume - CV-001 - Figure 3-1154, middle. The input deck for this test problem is provided in **\Z-INPUTS\TR\R2\R2-A.SPE**.

  In case of participating gas, the effective emissivity between surfaces 1 and 2 is given by ([21], section 7.1):

$$\varepsilon_{1-2} = \left(\frac{1}{\varepsilon_1} + \frac{1}{\varepsilon_2} - 1 + \frac{\varepsilon_g}{2-\varepsilon_g}\right)^{-1}$$

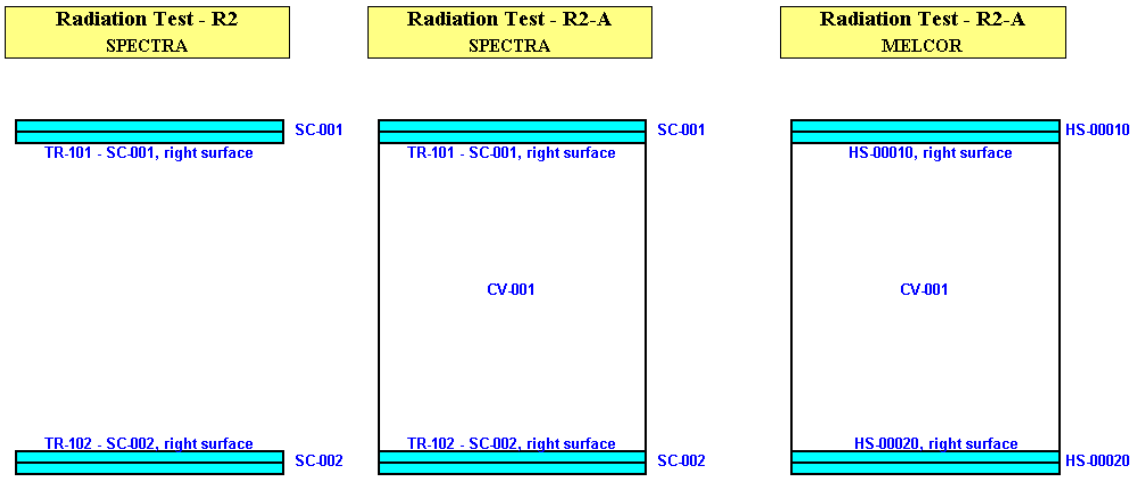

Figure 3-1154 SPECTRA case R2 (left), R2-A (middle), MELCOR case R2-A (right)

Here ε_1 and ε_2 are the emissivities of the surfaces 1 and 2, ε_g is the gas emissivity. In order to make this case comparable with the previous case, the following values were assumed:

- Gas emissivity, ε_g = 1.0. This particular gas emissivity was used to allow comparison with MELCOR for this case, as described below. The radiating gas CO_2 was used. The gas emissivity of 1.0 was achieved by specifying a large radiation path (100.0 m) and overruling the default correlations for the maximum emissivity (see Volume 1).
- Wall surface emissivities, $\varepsilon_1 = \varepsilon_2 = 2/3$.

With the above values of ε_1, ε_2, snd ε_g, the effective emissivity is equal to $\varepsilon_{12} = 0.5$, the same as in the test case R2, above.

Calculations with MELCOR

For MELCOR [20] calculations a simplified radiation model was used. With this model a surface radiates to gas only (no direct surface-to-surface radiation). Therefore the case R2 cannot be analyzed; only the case R2-A was analyzed. As explained in section 3.5.6, when the simplified radiation model is used correct results are obtained only in case of opaque atmosphere (ε_g = 1). If the gas emissivity is lower (ε_g < 1), the radiative flux calculated from the simplified radiation model becomes lower. In reality the radiative flux increases because of the direct radiation between surfaces. Therefore the gas emissivity of 1.0 was selected for the case R2-A. The radiating gas CO_2 was used. The gas emissivity of 1.0 was achieved by specifying a large radiation path (100.0 m)

Again the surface emissivities of 2/3 were used, to obtain the same effective emissivity, ε_{12}, as in the R2 case. The MELCOR input deck for this case is provided in **\Z-INPUTS\TR\R2\MELCOR\R2-A.GEN** and **R2-A.COR**. Basically the MELCOR input (geometry, properties etc.) is the same as the input for SPECTRA. The MELCOR nodalization is shown in Figure 3-1154, right.

Results of SPECTRA and MELCOR calculations are shown in Figure 3-1156 through Figure 3-1160. The following remarks can be made.

- Comparison of Figure 3-1155 and Figure 3-1156 shows that a good agreement with the theoretical solution is obtained for the run R2, for which the theoretical solution was obtained. SPECTRA could solve the R2 test with large step size. The maximum time step of 2.0 s was used. No time step reductions were observed.
- The case R2-A is somewhat different because of gas participation. In this test there is some convective heat transfer, although it is minor compared to radiation (see Figure 3-1160, left). The heat up is somewhat slower because of the additional heat capacity of the gas. Both SPECTRA and MELCOR results are similar for this case. The transient behavior is slightly different (Figure 3-1157 and Figure 3-1158), but the stationary end-results are very similar (Figure 3-1160). The differences come from using different models for radiation and convection. SPECTRA could solve the R2-A test with large step size. The maximum time step of 2.0 s was used. No time step reductions were observed. In MELCOR time step reductions down to slightly below 0.1 s were observed. The time step was limited by the Heat Structure (HS) Package.

The aim of this test was to show the capability of the Solver from SPECTRA to obtain a solution for rapidly changing parameters ("stiff" equation sets) using large time steps. The test shows that a time step larger than a factor of 10 could be used, compared to the MELCOR code.

3.18.3 Summary of the Numerical Solver Performance

In case of a stiff set of differential equations the Solver was much more effective than the fifth order Runge-Kutta method. From the point of view of the computational effort it turned out to be competitive even with the Rosenbrock method, which is specifically useful for the stiff systems. In case of large steps the accuracy of the Solver was somewhat better than the accuracy of Rosenbrock. When the same test case was calculated with MELCOR very small time steps (equal to 10^{-4} s) had to be used.

In case of the radiation test R2, the Solver can obtain a stable solution even with a relatively large time step (2.0 s). MELCOR had to run this problem with the average time step of about 0.1 s.

Basically all tests presented in this chapter can be considered as verification tests of the SPECTRA numerical solver. Therefore only two tests, described in sections 3.18.1 and 3.18.2 above, were selected here as a verification of the numerical solver. Based on the results shown in this section it is concluded that the Solver Package is very useful for providing an implicit solution of complex sets of equations.

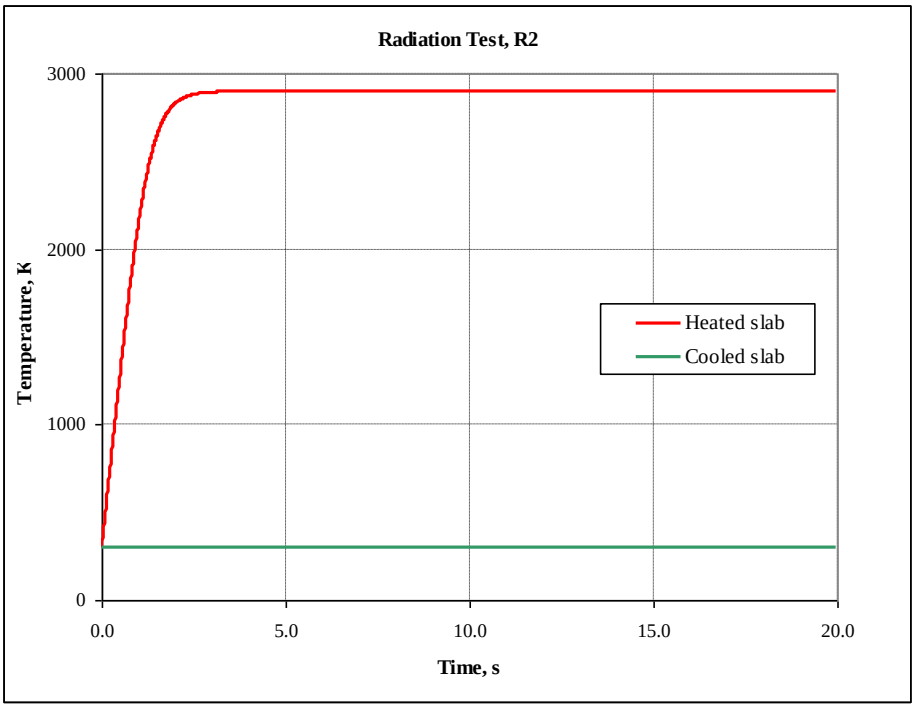

Figure 3-1155 Test R2, theoretical solution, explicit integration with small time step.

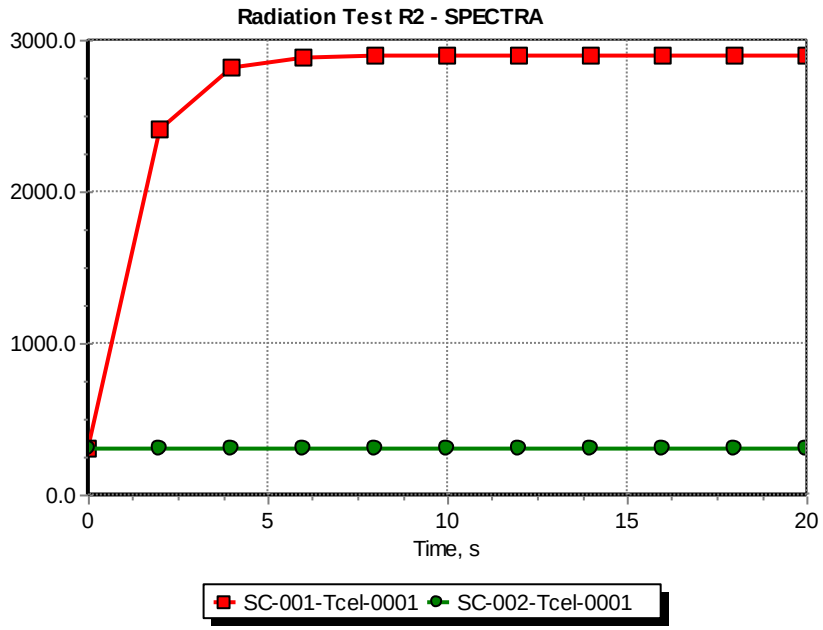

Figure 3-1156 Temperatures, Test R2, SPECTRA, Δt = 2.0 s

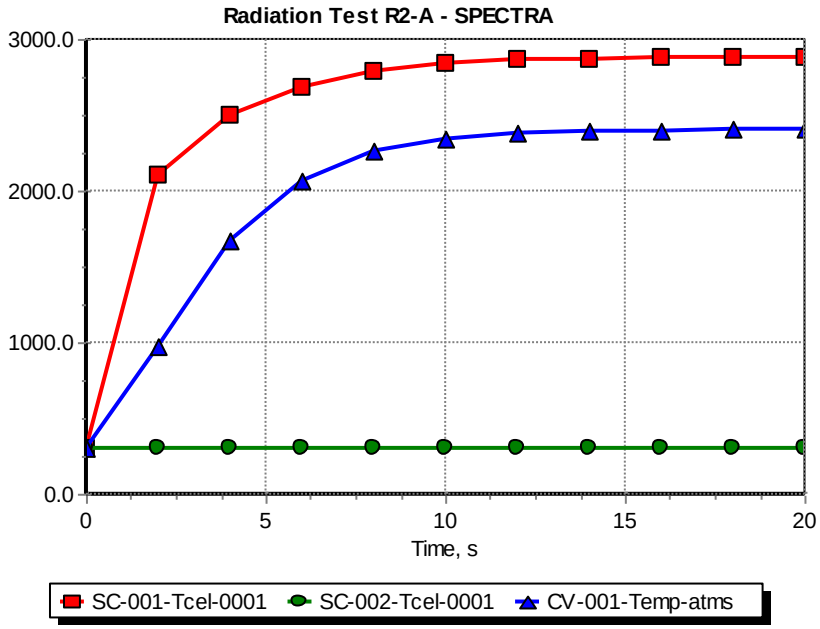

Figure 3-1157 Temperatures, Test R2-A, SPECTRA, Δt = 2.0 s

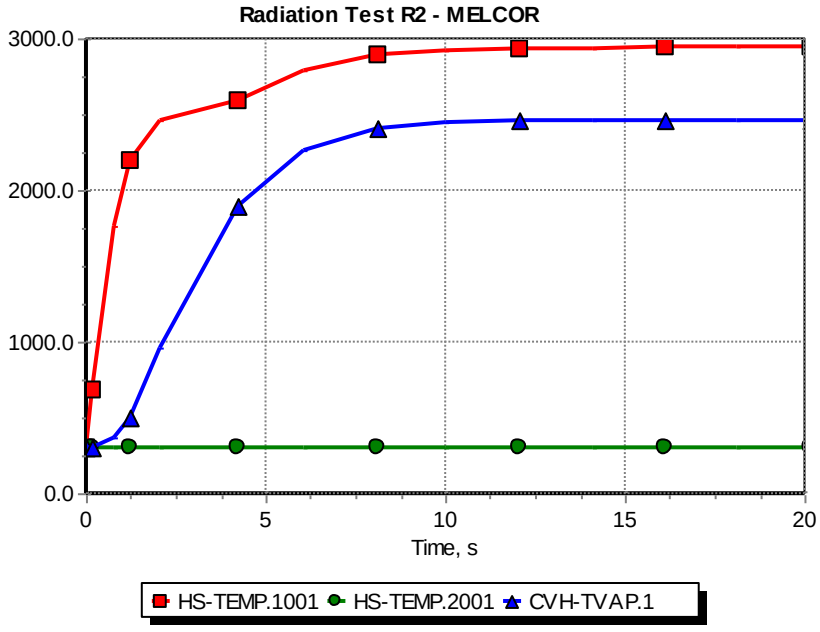

Figure 3-1158 Temperatures, Test R2-A, MELCOR, $\Delta t \sim 10^{-2}$ s

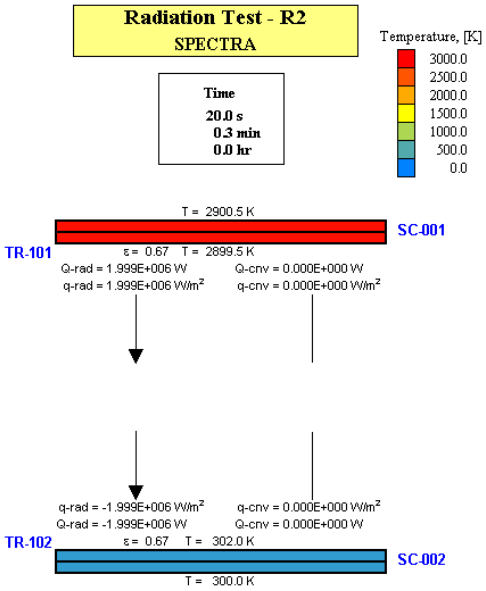

Figure 3-1159 Stationary results, SPECTRA, Δt = 2.0 s

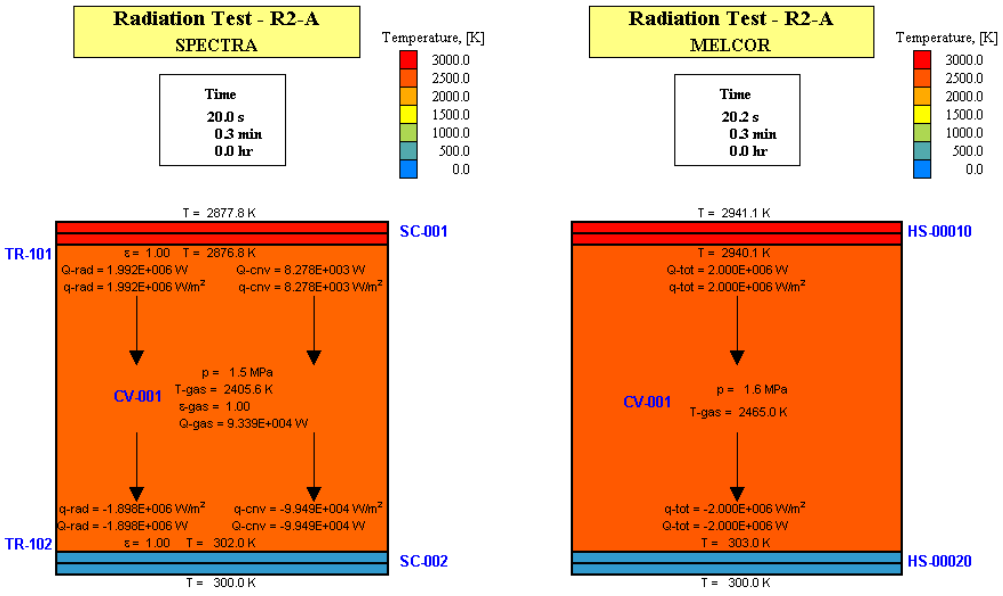

Figure 3-1160 Stationary results, left: SPECTRA, Δt = 2.0 s, right: MELCOR, $\Delta t \sim 10^{-1}$ s

3.18.4 Acceleration of Steady State by Reducing Heat Capacity

Calculations are often started with an approach to steady state. Such approach may be significantly accelerated by reducing the volumetric heal capacity ($\rho \times c_p$) of materials present in the model. The user may reduce the volumetric heat capacity of all solid materials (used by SC and TC). The fluid properties in Control Volumes remain unaltered. The reduction factor is defined in input (see Volume 2, input parameter CREDSL).

This section presents results of test calculations performed to show the effect of heat capacity reduction. The test case is very similar to the transient conduction test described in section 3.5.4. The heat capacity was increased by setting ρ = 9000 kg/m^3 and c_p = 5000 J/kg-K, ($\rho \times c_p = 4.5 \times 10^7$ J/m^3-K). Calculations were performed using the full heat capacity and reduction factors of 0.1, 0.01, and 0.001. Input decks are located in `\Z-INPUTS\SC\T-CON\`. Results are shown in Figure 3-1161. The timing to reach stationary state by the rightmost node (node 21 - Figure 3-124) is given below.

- Full heat capacity: stationary temperature is reached at ~10,000 s,
- Reduction factor od 0.1: stationary temperature is reached at ~1,000 s,
- Reduction factor od 0.01: stationary temperature is reached at ~100 s,
- Reduction factor od 0.001: stationary temperature is reached at ~10 s.

The above results illustrate the use of the reduction factor CREDSL, and confirm the correctness of the implementation of the reduction factor.

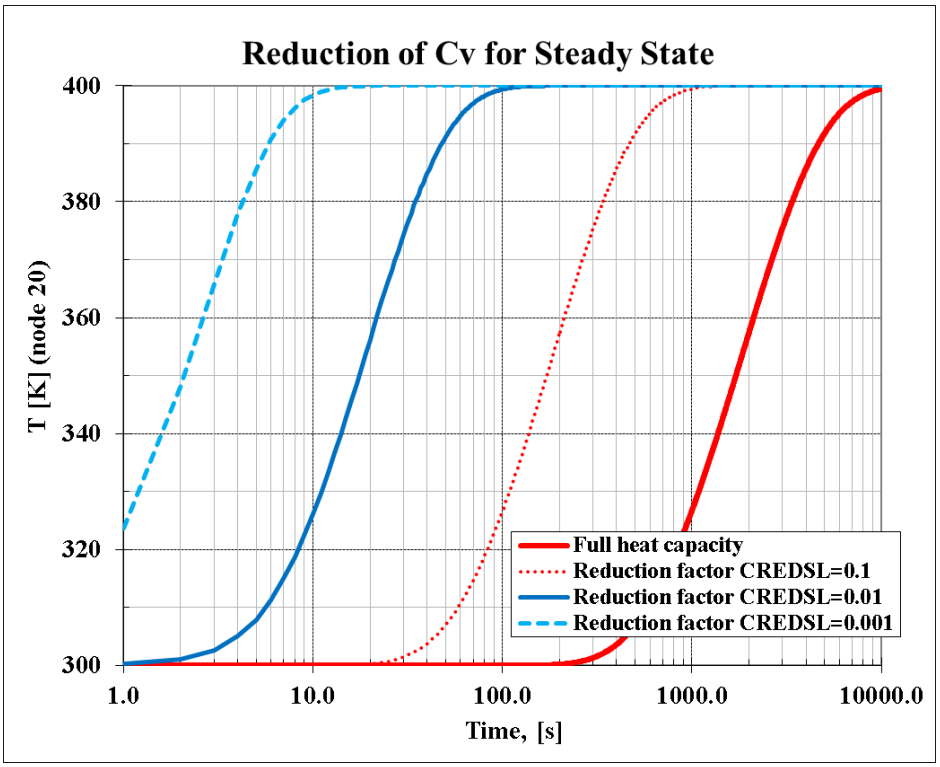

Figure 3-1161 Test of steady state acceleration by reduction of heat capacity

4 V&V of the Program - Integral System Tests

Analysis of integral system tests is the main part of code validation. While analyses of the separate effect tests allow to build up confidence in specific models in the code, analyses of the integral system tests allow to build up confidence in the code itself.

4.1 Application of SPECTRA to PWR Reactors

4.1.1 HDR E11.2 Test (ISP-29)

In 1992 Germany formally submitted the experiment E11.2 as a basis for an "open" Standard Problem to the Principal Working Group No. 4. The experiment E11.2 was run to study the distribution of hydrogen inside a pressurized water reactor (PWR) containment. The objectives of the experiment E11.2 were the following [147]:

- determine the temperature distribution during the entire transient,
- study the distribution of energy during and after the SBLOCA-phase,
- measure the steam/air/hydrogen distribution within the containment atmosphere under severe accident conditions initiated by a SBLOCA.

Post-test calculations were performed with SPECTRA. The main conclusions were:

- Stratification models were investigated based on the experimental results.
- With the available parametric stratification model, one can bound the results and therefore provide a conservative estimation of the containment pressure during accidents

Detailed description of the ISP-29 simulation, including comparison of SPECTRA results with experimental data, as well with MELCOR results [148], is currently provided only in an internal NRG report. The results will be published in open literature in the future.

4.1.2 NUPEC, M-7-1 Test (ISP-35)

NUPEC hydrogen mixing and distribution test performed in Japan had been selected by CSNI as International Standard Problem No. 35 [149]. The purpose of this ISP was to verify the predictive capabilities of computer codes with respect to simulation of light gas (helium) mixing and distribution in a containment. NRG (at that time KEMA Nuclear) participated in ISP-35 with MAAP-4, including blind and open calculations. Later a SPECTRA model was created and open analysis was performed. The conclusions from MAAP4 and SPECTRA calculations:

- Good results were obtained with both codes.
- Multidimensional effects of spray were important.
- Modeling of spray in the MAAP and SPECTRA codes was adjusted to mimic the multi-dimensional effects in the open phase. This adjustments improved containment pressure prediction; helium concentrations were practically unaffected.

Detailed description of the ISP-35 simulation, including comparison of SPECTRA results with experimental data, as well as the MAAP and MELCOR results [150], is currently provided only in an internal NRG report. The results will be published in open literature in the future.

4.1.3 Generic Containment - Code-to-Code Benchmark

One outcome of the OECD/NEA ISP-47 activity was the recommendation to elaborate a 'Generic Containment' in order to allow comparing and rating the results obtained by different lumped-parameter models on plant scale. Within the European SARNET2 project such a Generic Containment nodalization, based on a German PWR (1300 MWe), was defined.

The methodology applied in order to compare the different code predictions consisted of a series of three benchmark steps with increasing complexity as well as a systematic comparison of characteristic variables and observations:

- Run 0 – initial step
- Run 1 – detailed comparisons
- Run 2 – application to PAR (hydrogen recombiners) modeling

The participants used codes APROS, ASTEC, COCOSYS, CONTAIN, ECART, GOTHIC, MELCOR, SPECTRA. NRG participated in Generic Containment using MELCOR and SPECTRA codes. Both codes provided very similar results in all three steps.

A significant user effect was observed among the participants; even results obtained with the same code (e.g. MELCOR) by different participants differed significantly. It was concluded that, even though the problem was well defined, the uncertainty of calculated results due to different modelling approaches and users may be much higher than expected [151].

4.1.4 AIR-SFP - Code-to-Code Benchmark

The Fukushima Dai-chi nuclear accident has renewed international interest in the safety of SFPs. In the frame of the SARNET2 FP7 project, several partners performed simulations of accident scenarios in SFP using different Severe Accident (SA) codes (ASTEC, MELCOR, ATHLET-CD, RELAP/SCDAPSIM, ICARE/CATHARE, SPECTRA) [152]. The studies have raised questions about the reliability of the results obtained since these codes were developed for reactor applications. The code to code comparison of the Air-SFP benchmark project showed not only differences from the different severe accident codes but also user differences by using the same code.

NRG participated in AIR-SFP using MELCOR and SPECTRA codes. Quite similar results were obtained with both MELCOR and SPECTRA codes. Detailed description of MELCOR and SPECTRA modeling and results are currently provided only in internal NRG reports. The results will be published in open literature in the future.

4.2 Application of SPECTRA to BWR Reactors

4.2.1 PANDA BC Tests

4.2.1.1 Combined SPECTRA / CFD Analysis of the PANDA BC Test

The TEMPEST project was devoted to studying passive decay heat removal systems for advanced BWR systems. The SWR-1000 configuration, designed by Siemens, was investigated. The passive decay heat removal system for SWR-1000 consists of the Building Condenser (BC) - a finned tube heat exchanger placed at the top of the drywell. Experimental investigation of the BC performance was performed at the PANDA test facility. The PANDA experiments consisted of a series of tests, called "PANDA BC Tests". One of the experiments, namely the BC4 Test [153], was designed to study the BC performance under severe accident conditions, with hydrogen being generated in the core, and released to the containment (in the experiment helium was used instead of hydrogen). This test was selected for analytical investigation within the TEMPEST project.

The present analytical investigation is aiming not only at simulation of the BC4 test, but is also a demonstration of using a coupled System Thermal-Hydraulic (STH) code and CFD code. Currently an interactive ("on-line") coupling with CFD is available using the EDF Package [159]. The analysis of PANDA BC4 test, presented in this chapter, was done when the interactive coupling was not available yet and therefore it was performed using the "off-line" coupling. The parametric stratification model was used, with the stratification parameters defined based on the observations from the CFD code. The following codes are used for the combined analysis:

- STH code: SPECTRA
- CFD code: ANSYS CFX

SPECTRA is used to model the whole PANDA facility, and perform preliminary simulation of the BC4 test. Nodalization of the SPECTRA model is shown in Figure 4-1. CFX is used to model selected parts of the test facility, namely the Building Condenser (BC) pool, and the drywells.

4.2.1.2 Step 1 - Stand-Alone SPECTRA Analysis of the BC Test

As a first step the stand-alone SPECTRA analysis of PANDA BC4 test was performed. The calculated maximum containment pressure was higher (5.0 bar) than measured (4.7 bar).

4.2.1.3 Step 2 - CFD Analysis of Selected Parts of the Test Facility

CFX simulation of the PANDA drywells was performed using the boundary conditions obtained from experiment (if data were not available, the system code results from Step 1 could be used here). The results show clearly that a strong stratification developed in Drywell-2 (the drywell without the BC unit), while Drywell-1 remain quite well mixed during the whole test. This is visible in Figure 4-2. Simulation of the BC pools was also performed with CFX and it showed some thermal stratification of the pools (Wetwell-1 and Wetwell-2).

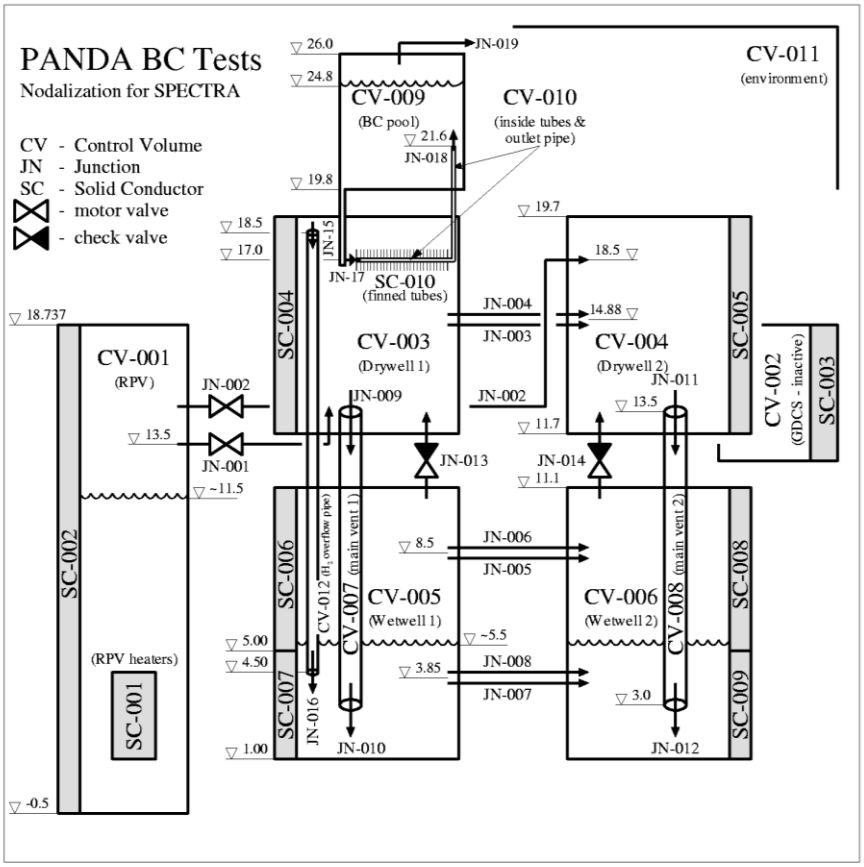

Figure 4-1 SPECTRA model of the PANDA facility configured for the BC tests

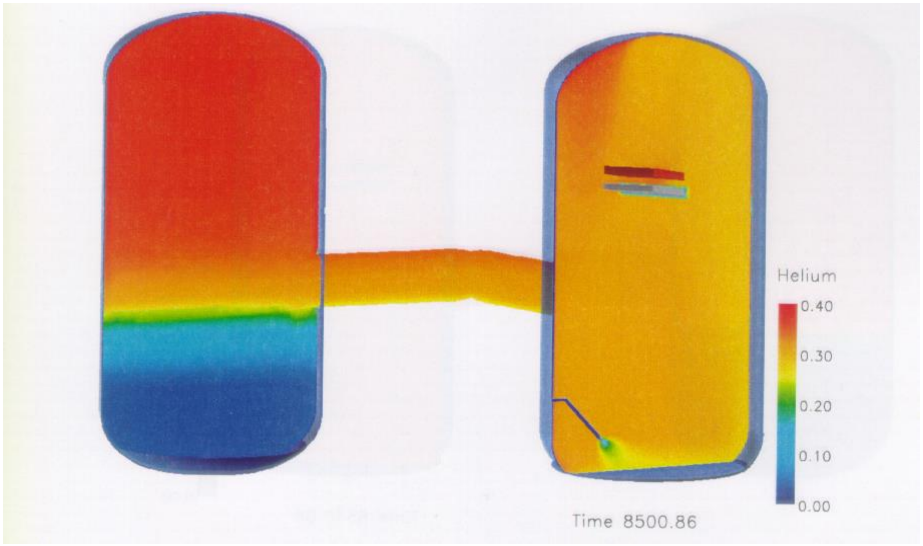

Figure 4-2 Helium concentrations in the drywells - CFX results
(note: drywel location is reversed: DW1 is on the right)

4.2.1.4 Step 3 - Final SPECTRA Analysis - Stratification from CFD Results

Based on the observations from CFD analysis, the following assumptions were made, concerning the stratification of gases:

- Drywell-1 is assumed to be well mixed: Density Stratification Parameter, DSP = 0.0.
- In Drywell-2 a strong stratification is assumed: DSP = 0.9.
- In RPV also a large stratification is expected, therefore DSP = 0.9 was used.

The thermal stratification of the wetwell pool was also studied but it was concluded that it has very little effect on the main results of the BC4 and therefore is not discussed here.

The containment pressures at the end of the test are shown in Table 4-1. In the Step 1, the containment pressure was overestimated. This overestimation of pressure was characteristic to all calculations of the BC4 tests, performed with variety of computer codes [154]. This fact temporarily gave reason for a doubt in the accuracy of the experimental measurement. In the Step 3, the containment pressure is very close to experimentally measured value. Therefore with the combined SPECTRA/CFX codes it has been demonstrated that the stratification of helium is the explanation for the earlier observed discrepancy between the measured and computed containment pressure.

Table 4-1 Containment pressure at the end of the BC4 test

Case	Pressure, (Pa)
Step 1	5.0×10^5
Step 3	4.7×10^5
Experiment	4.7×10^5

4.2.1.5 Summary and Conclusions

SPECTRA / CFD, multi-step analysis of the BC4 test was performed, as follows:

- Step 1 Full scope analysis using the system code SPECTRA
- Step 2 CFX analyses of the selected parts of the system including BC pool and drywells.
- Step 3 Updated full scope analyses with the system code SPECTRA, using CFD results.

In Step 1, the SPECTRA calculated containment pressure was overestimated. This overestimation of pressure was characteristic to all calculations of the BC4 tests, performed with variety of computer codes. In Step 2, CFX simulation of the PANDA drywells showed clearly a strong stratification in Drywell-2 and well mixed gases in Drywell-1. In Step 3, the SPECTRA-calculated containment pressure is very close to experimentally measured value. Therefore, with the combined SPECTRA/CFX codes, it has been demonstrated that the stratification of helium is the explanation for the earlier observed discrepancy between the measured and computed containment pressure. The main conclusions are:

- There is a significant influence of the gas stratification on the containment pressure.
- There is very small influence of BC pool stratification on the results.

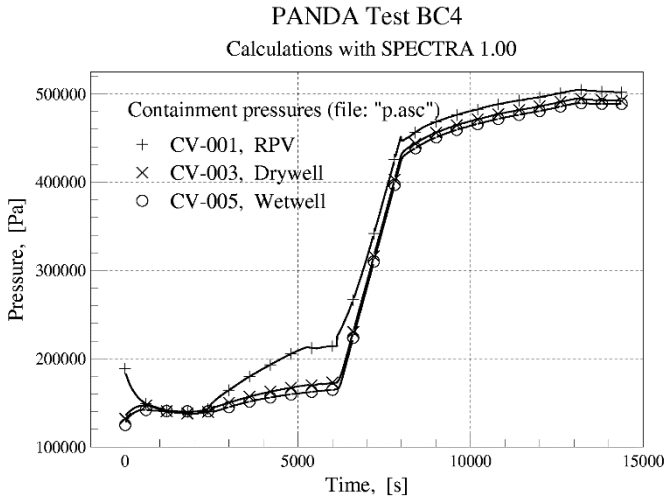

(a) Step 1 results

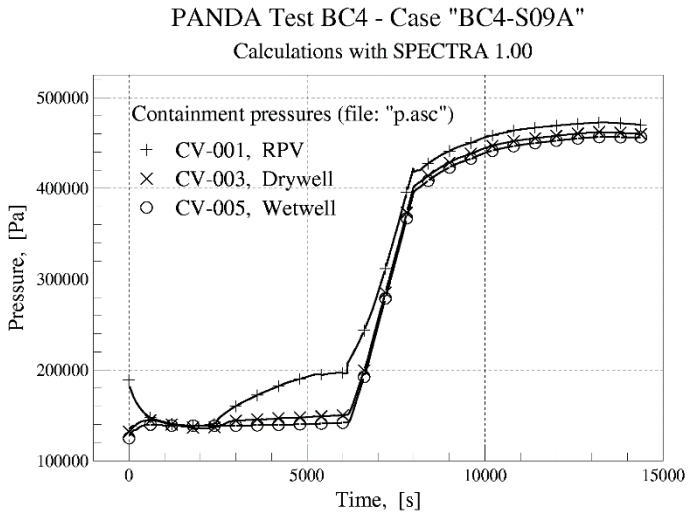

(b) Step 3 results

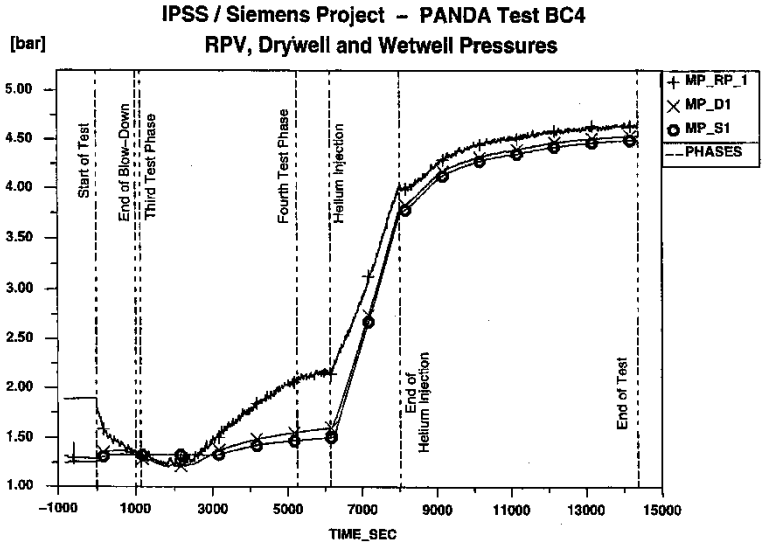

(c) Experiment

Figure 4-3 Containment pressures

4.2.2 PANDA PCC Steady State Tests

4.2.2.1 Introduction

The PANDA test facility - "Passive Nachwärmeabfuhr- und Druckabbau- Testanlage" ("Passive Decay Heat Removal and Depressurization Test Facility"), has been constructed at Paul Scherrer Institute (PSI) in Switzerland to study long term performance of the Simplified Boiling Water Reactor (SBWR) passive containment cooling system [105]. The first experiments, conducted at the beginning of 1995, were the so-called S-series tests, performed to investigate the steady state operation of the Passive Containment Cooling (PCC) condenser unit at different fractions of noncondensables.

A PCC unit is a heat exchanger, which consists of several vertical tubes, the upper (inlet) and the lower (outlet) headers. The PANDA PCC unit is a scaled down (1/25) model of the SBWR unit. In the SBWR design the PCC units should provide the long term decay heat removal from the containment. The main goal of the PANDA experiments was to demonstrate that the PCC units are able to perform this task at different conditions (non-condensable fractions).

4.2.2.2 Description of the PANDA PCC Steady State Tests

The PANDA facility [106] is shown in Figure 4-4. It consists of six large vessels: RPV (Reactor Pressure Vessel), GDCS (Gravity Driven Cooling System), two Drywells and two Wetwells. RPV contains a 1.5 MW electrical heat source. In the upper part of the test facility there are four pools. One of the pools contains the IC (Isolation Condenser) unit, three others contain the PCC (Passive Containment Cooling) units. While the IC is connected to the RPV, the three PCC units are connected to the two drywell volumes. Two units are connected to one drywell, the third unit is connected to the other drywell.

A PCC unit is a heat exchanger with vertical tubes (Figure 4-5). The unit consists of cylindrical upper drum, called also the steam box, 20 vertical tubes which are slightly bent at the bottom and at the top, and cylindrical lower drum, called also the water box. The inlet pipe is connected at the top of the steam box. Two outlet connections are present in the water box: vent pipe, connected at the upper part of the side wall, and drain pipe, connected at the bottom of the water box. The drain pipe allows quick drainage of any water from the lower drum thus, in spite of its name, the water box is never filled with water.

The first series of PANDA experiments, conducted at the beginning of 1995, were steady state PCC condenser performance tests [106]. In this first series the effect of non-condensable gases on the condenser performance was investigated. Most of the tests were performed at the same steam flow rate and different non-condensable mass fractions.

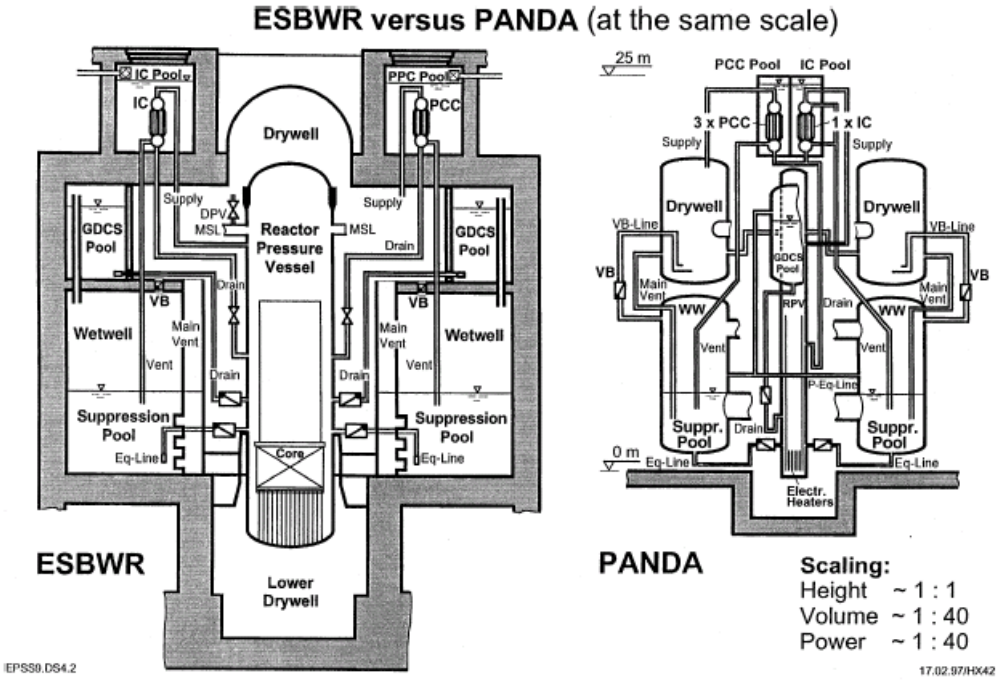

Figure 4-4 PANDA test facility

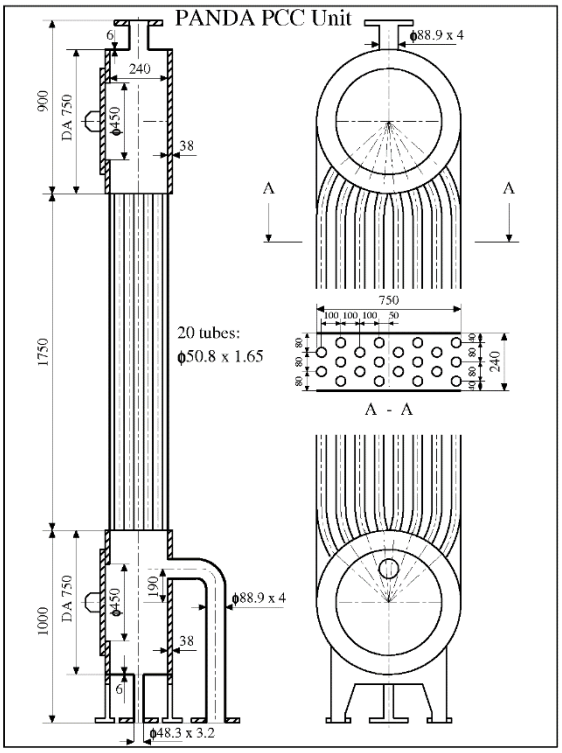

Figure 4-5 PANDA PCC unit

In these tests one of the PCC condenser units (the most extensively instrumented one) was connected directly to RPV by a specially built line. RPV heaters provided the required steam flow rate. The required non-condensable gas flow rate was achieved by injection of air into the same pipe, sufficiently above the inlet of the condenser, to ensure adequate mixing. The liquid drain flow was discharged via the PCC drain line to the GDCS pool, and from there it was returned to RPV. The vent flow was directed to an empty wetwell. The drywells were isolated. The GDCS pool and the wetwells were connected and preheated to avoid subcooling of condensate and condensation of any steam vented from the condensers.

In the steam-air tests the pressure downstream the condenser (and hence also the condenser pressure) was kept at the desired level (~3 bar for the S-series tests) by venting to the atmosphere. For the pure steam tests the condenser vent line was closed and the pressure in the PCC condenser was allowed to find its own equilibrium value; this pressure corresponds to full condensation.

After achieving stable operation at the required condenser pressure conditions, the test data were recorded for at least 10 minutes. The test was judged to be successfully completed when the specified conditions had been maintained within a given tolerance and for a given time period, for example ±5% for 10 minutes, for the steam flow. Repeatability tests showed differences in condenser performance of only a few percent.

The PANDA S-series tests consisted of two groups of tests. The first group: tests S1, S2, S3, S4, S5, and S6. The second group consisted of tests S10, S11, S12, and S13. The tests from the second group are mainly repetitions of some tests from the first group, made to verify repeatability of the results. In this group only the test S13 is a new test. Therefore, for the purpose of the present comparison, the tests S1 through S6, and S13 were selected. Three of those tests (S1, S6, S13) are pure steam tests. The remaining four tests (S2, S3, S4, S5) are steam/air tests.

The test conditions are shown in Table 4-2. The steam/air tests were performed at the nominal pressure of 3 bar (at this pressure the PCC units are expected to operate under typical accident conditions). It is seen in Table 4-2 that the actual values only slightly deviate from the nominal pressure.

Table 4-2 Test conditions, PANDA PCC Tests

Test	Pressure (Pa)	Steam flow (kg/s)	Air flow (kg/s)	Air fraction (-)
S1	2.744	0.1893	0.00000	0.0000
S2	3.018	0.1933	0.00302	0.0154
S3	3.011	0.1927	0.00599	0.0301
S4	3.006	0.1942	0.01596	0.0759
S5	3.023	0.1960	0.02786	0.1245
S6	3.354	0.2610	0.00000	0.0000
S13	3.050	0.2628	0.00000	0.0000

Three pure steam tests were analyzed. Test S1 is the nominal steam injection case (0.19 kg/s nominal flow). Test S6 is the large steam injection case (0.26 kg/s flow). Test S13 is the same as test S6, except that the liquid level in the secondary side pool was decreased. In this test the upper header was uncovered, the liquid level was located at the connection of upper header and the PCC tubes. This test was performed to estimate the influence of the heat transferred through the header on the overall PCC performance. This point was important for the applicability of data for the SBWR, since the PCC headers in PANDA have relatively large heat transfer areas, compared to the PCC units in the SBWR.

A characteristic parameter, which is often used to summarize the PCC Steady State Test results, is the "PCC efficiency". The efficiency of the PCC unit is defined as the fraction of incoming steam that is condensed in the unit, and is therefore calculated as:

$$\eta = \frac{W_{drain}}{W_{steam}} \cdot 100\%$$

W_{steam} inlet steam mass flow rate, (kg/s)
W_{drain} water flow in the drain line, (kg/s)

4.2.2.3 SPECTRA Model

The base model used to perform SPECTRA calculations of the PCC tests is shown in Figure 4-6. The PCC primary side is represented by CV-002 (representing the steam box), CV-003 through CV-007 (representing the tubes), and CV-008 (representing the water box). CV-009 provides back-pressure (constant during calculations) for the PCC primary side.

The secondary side is represented by CV-010, connected to the atmosphere: CV-011, where the pressure is constant and equal to 1.0 bar. The gas source is provided in the "inlet line": CV-001. There are two outlet Junctions: the "drain line JN" - JN-008, and the "vent line JN" - JN-009.

The secondary side is represented by a single Control Volume, which means that the natural circulation in the pool is not calculated. This approach is sufficient when the external boiling correlation (Rohsenow) is used.

Heat is transferred from the primary side of the PCC unit to the pool through the walls of the PCC tubes, the walls of the steam and water boxes, as well as the walls of the part of inlet pipe which is immersed in the pool. All these walls are modelled using 10 Solid Heat Conductors (SC) described below.

SC-001: Vertical side walls of the steam box
- Geometry: rectangular, vertical
- Thickness: 38 mm
- Nodes: 5 nodes: 7.6 mm/node
- Area: 0.88 m2

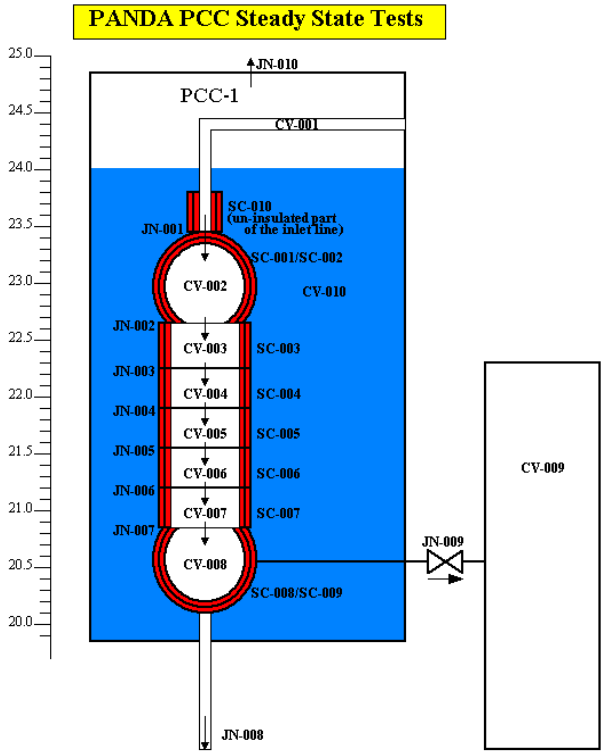

Figure 4-6 SPECTRA model of the PANDA PCC

SC-002: Cylindrical wall of the steam box

Geometry:	cylindrical, horizontal
Thickness:	6 mm
Nodes:	3 nodes: 2 mm/node
Length:	0.24 m
Diameter:	ID=0.75 m, OD=0.762

SC-003: Tube walls, part 1

Geometry:	cylindrical, vertical
Thickness:	1.65 mm
Nodes:	3 nodes: 0.55 mm/node
Length:	0.35 m
Diameter:	ID=0.0475 m, OD=0.0508 m
Multiplier:	20.0 × 1.21 = 24.2

The geometry of SC-004 trough SC-007 is the same as SC-003. A total of five sections are used to represent the tubes; the length of each is 0.35 m, therefore the total length is 1.75 m (in agreement with elevations). In reality the lower and the parts of the tubes are not vertical (Figure 4-5). Because of that the average length of the tubes is equal to 1.8975 m [108]. The length increase in the lower and upper parts is (1.8975 – 1.75)/2 = 0.07375. To account for the length increase a multiplier of (0.35 + 0.07375)/0.35 = 1.21 was used for SC-003 and SC-007. Therefore the total multiplier for SC-003 and SC-007 was set to 1.21×20 = 24.2. For the other SC-s the multiplier was set equal to the number of tubes (20).

The geometry of SC-008 (vertical side walls of the water box) is the same as SC-002. The geometry of SC-009 (cylindrical wall of the water box) is the same as SC-002.

SC-010: Inlet pipe wall, un-insulated part.
Geometry: cylindrical, vertical.
Thickness: 2.3 mm.
Nodes: 3 nodes: 0.8, 0.8, 0.7 mm.
Length: 0.15 m.
Diameter: ID=0.0843 m, OD=0.0889 m.

The material of all the walls is stainless steel.

Two phenomena are specifically important for simulation of the PANDA PCC Steady State tests: condensation in presence of noncondensables, and nucleate boiling. SPECTRA modelling related to these phenomena are discussed below

- Condensation in presence of noncondensables
  Based on the earlier experience [108] the KSP correlation for the non-condensable degradation factor has been applied (see Berkeley tests and MIT tests, sections 3.7.1, 3.7.2). Note that by default SPECTRA selects the Modified Ogg correlation, which gives the most conservative results. The KSP correlation is activated in the input deck for the condensing side of all SC-s.

- Boiling
  Based on the earlier experience [108] the external flow model (with the Rohsenow correlation for the nucleate boiling) has been applied. Note that by default SPECTRA selects the internal flow model (with the Chen correlation for the nucleate boiling). The Chen correlation is very sensitive to the fluid flow. Therefore in order to apply the Chen correlation one needs to have a more realistic model of the PCC pool, capable of estimating the fluid velocities in the space among the PCC tubes. The present model (a single CV, practically no liquid flow) is sufficient for the Rohsenow correlation, which does not depend on the fluid flows. Results obtained with the Chen correlation are discussed in [108].

4.2.2.4 Procedure for Test Simulations

Four steam/air tests (S2, S3, S4, S5), and three pure steam tests (S1, S6, S13), were simulated. In all simulations steam and air sources were modelled using the "tabular mass sources". The mass flow rates of steam and air were entered following the experimental measurement (Table 4-2). For the steam-air tests the source gas pressure was set to 3 bar, and the source gas temperature was set to 407 K [108]. For the pure steam tests the source pressure and temperature were set to the final stable pressure and the corresponding saturation temperature (the values obtained during pre-runs with 3 bar source pressure). The air source temperature is 305 K [108]

In all steam/air tests the valve on JN-009, was kept open. The noncondensables and the uncondensed steam were vented into CV-009. In all pure steam tests the valve on JN-009 was closed. The pressure inside the PCC unit was allowed to change until a stable pressure level was reached, for which the rate of steam condensed in the PCC unit matched exactly the mass flow rate of the incoming steam.

In the test S13 the initial liquid level in the secondary side pool was set to a value a little lower than the bottom elevation of the steam box. This has been done to compensate for the initial water level increase, when the water starts boiling. The initial water level was found by trial-and-error. With the selected initial value the level increases to about 2.81 m when the boiling starts, and then decreases slowly to the desired elevation, as the water evaporates.

All tests were run for times sufficient to obtain stable conditions in all parts of the analyzed model. The steam/air tests were stabilizing somewhat faster and those tests were run for 100 s. The pure steam tests, S1, S6, needed more time to stabilize, because pressure was changing in the PCC unit. Those two tests were run for 200 s. The S13 test was run for 300 s.

4.2.2.5 Results

4.2.2.6 Results of Base Model

Results of the base model are shown in visualization pictures, in Figure 4-7 through Figure 4-13. The results show stationary state for each test. Results of the pure steam tests, S1, S6, and S13, are shown in Figure 4-7, Figure 4-8, and Figure 4-9. The steam-air tests, S2, S3, S4, and S5, are shown in Figure 4-10, Figure 4-11, Figure 4-12, Figure 4-13.

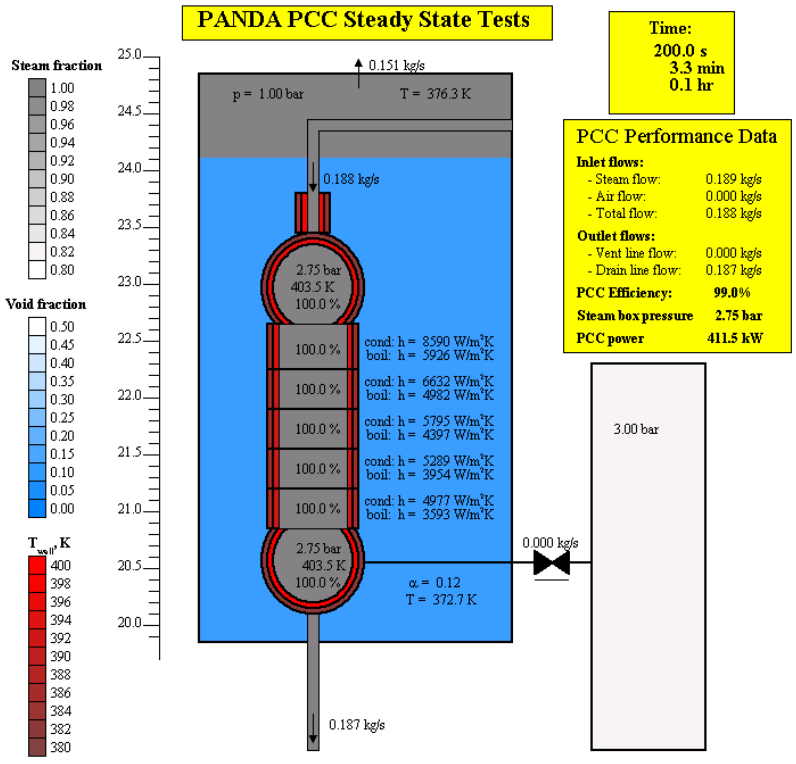

Figure 4-7 Pure steam test S1 - stationary state results, run “PCC-S1”

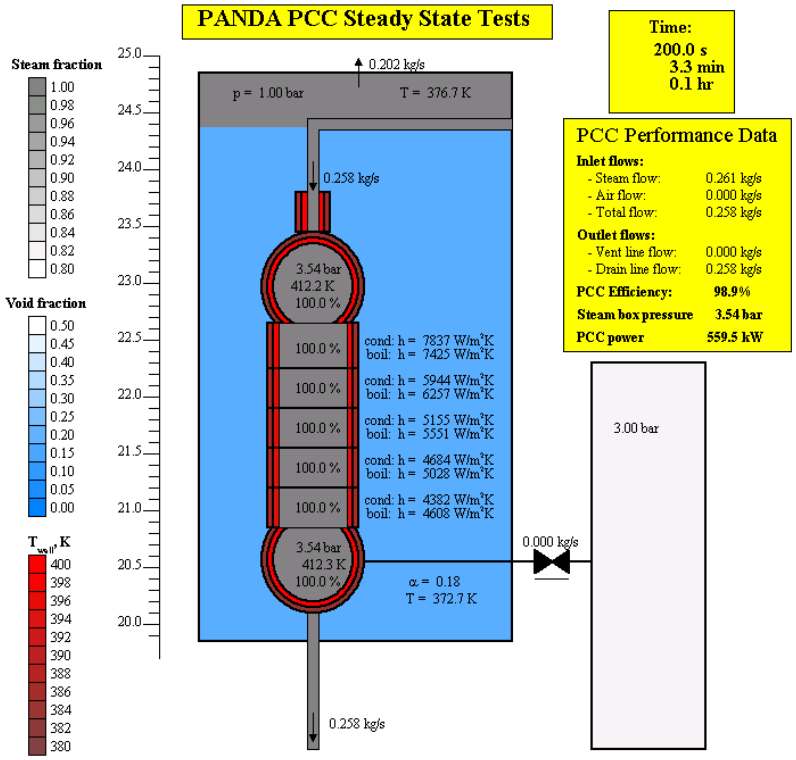

Figure 4-8 Pure steam test S6 - stationary state results, run “PCC-S6”

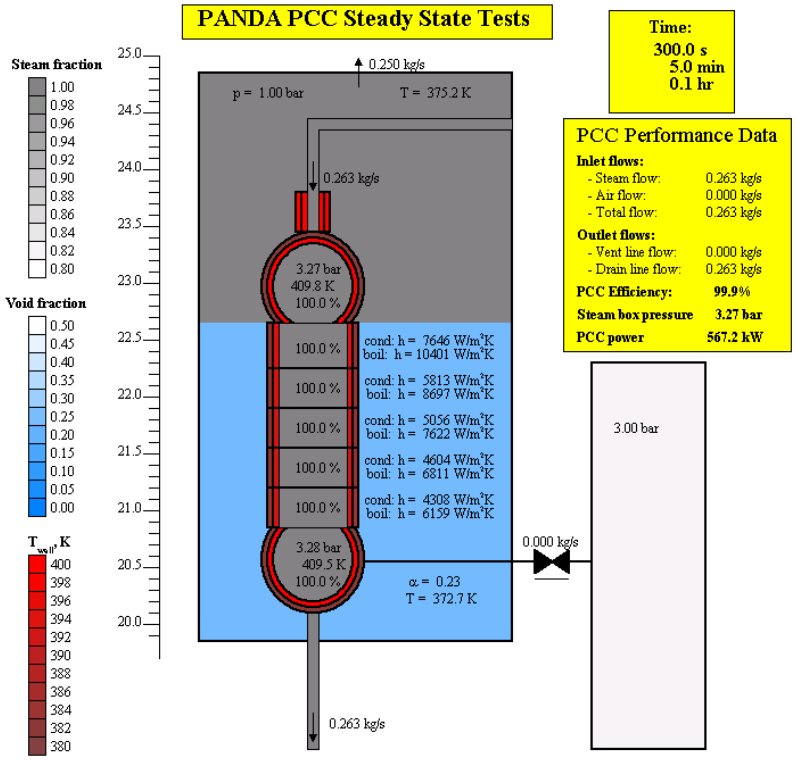

Figure 4-9 Pure steam test S13 - stationary state results, run “PCC-S13”

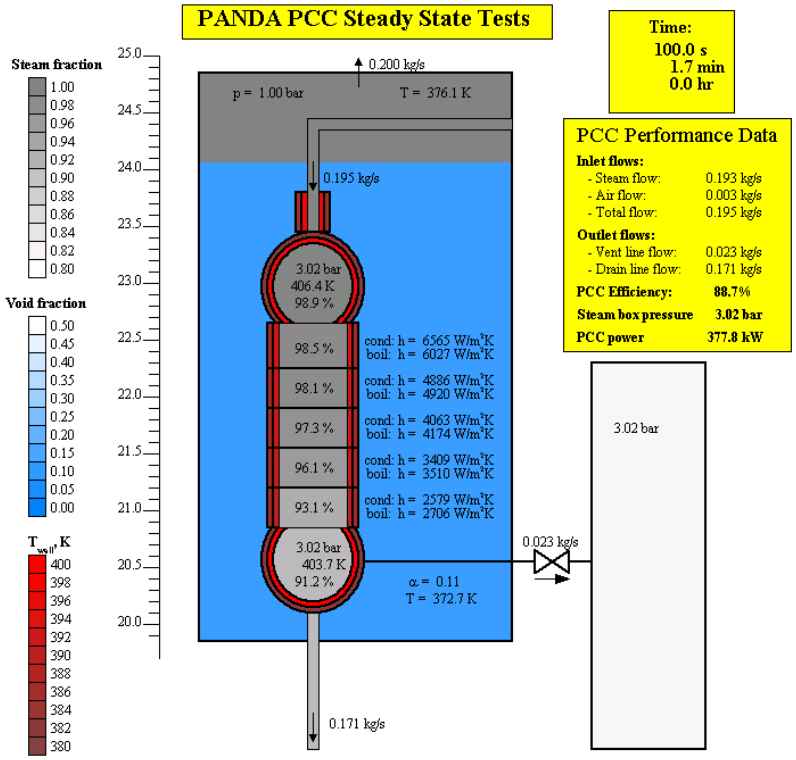

Figure 4-10 Steam-air test S2 - stationary state results, run “PCC-S2”

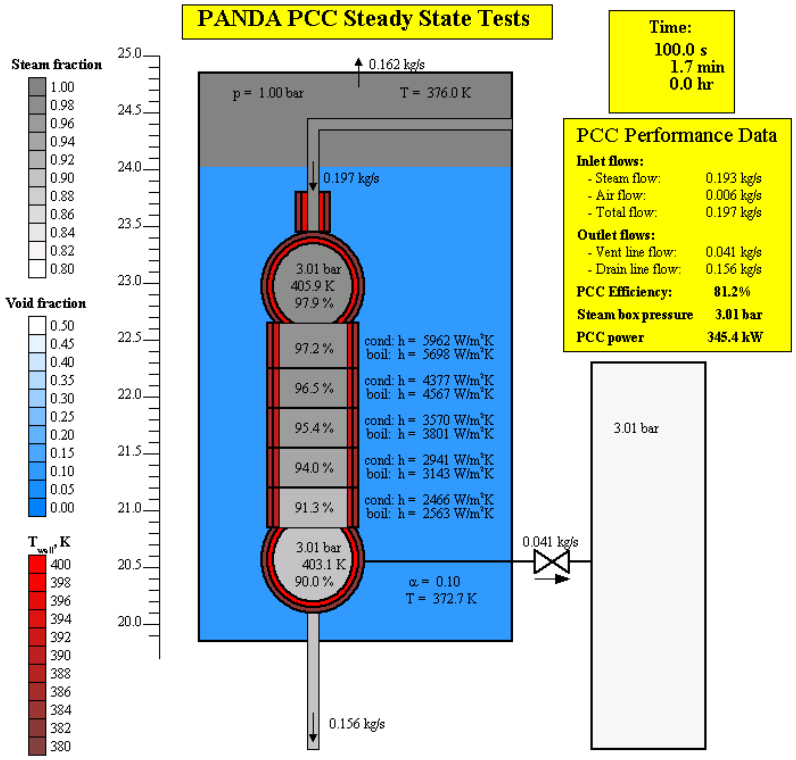

Figure 4-11 Steam-air test S3 - stationary state results, run “PCC-S3”

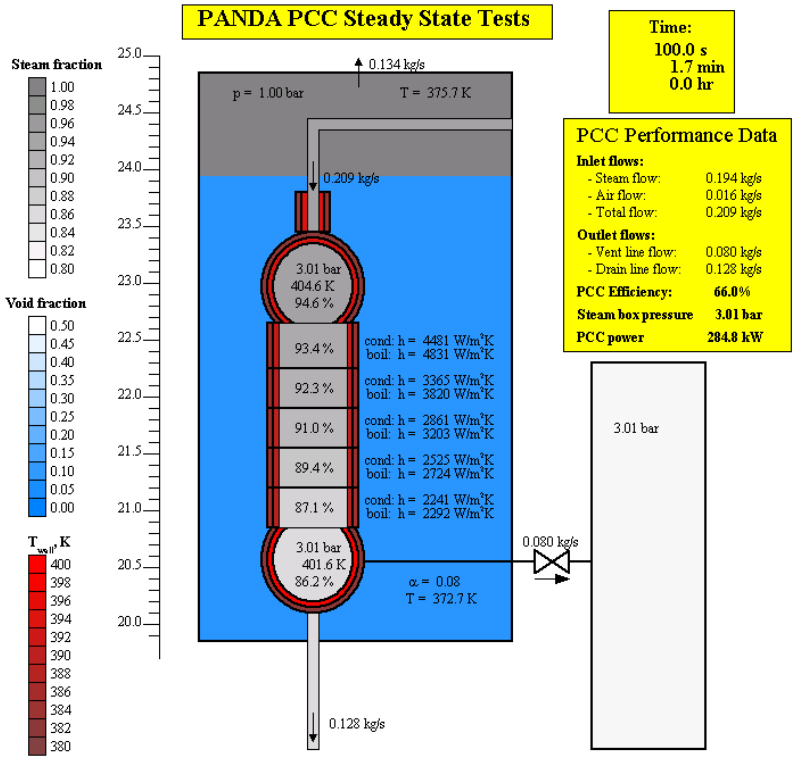

Figure 4-12 Steam-air test S4 - stationary state results, run “PCC-S4”

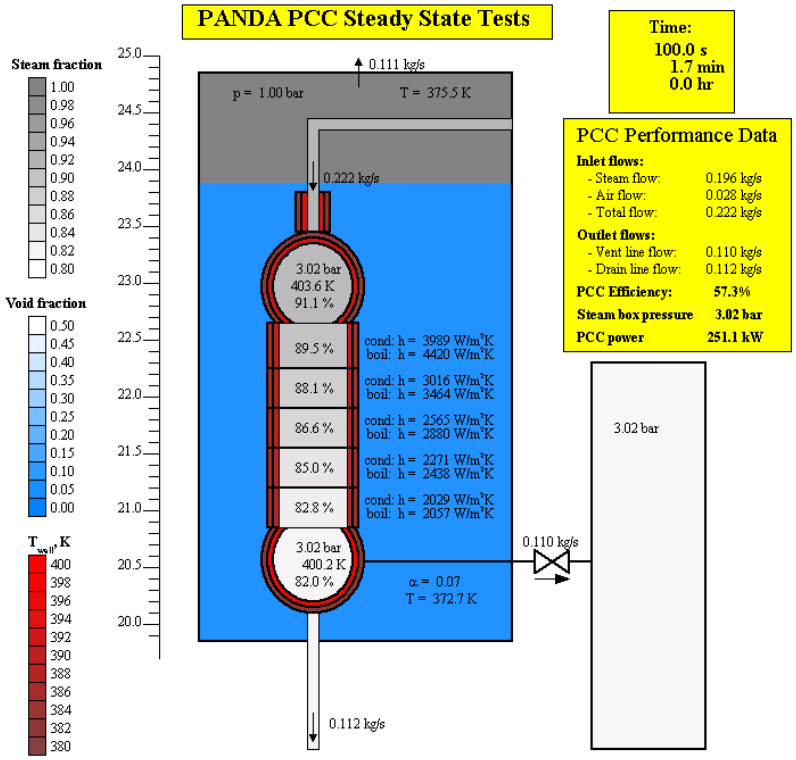

Figure 4-13 Steam-air test S5 - stationary state results, run “PCC-S5”

The PCC efficiencies calculated with the base model are compared to the experimental data in Table 4-3 (see also Table 4-5 and Figure 4-22). The calculated efficiencies are smaller, therefore it is concluded that the PCC performance (measured by the fraction of steam that is condensed) is underestimated in these calculations. For the pure steam tests the calculated pressures were higher than the measured pressures (Table 4-6, Figure 4-23). This again mean an underestimation of the PCC performance (higher pressures are needed to condense all steam).

Similar underestimation of the PCC performance was observed in the past in calculations performed with the codes TRACG, TRAC-BF1, and MELCOR. These results are shown in Table 4-4 [108]. Results of an earlier SPECTRA version are included in this table.

Table 4-3 Results of the steam-air tests

Test	PCC efficiency, (%)	
	SPECTRA	**Experiment**
S2	88.7	**99.0**
S3	81.2	**87.6**
S4	66.0	**73.4**
S5	57.3	**63.1**

Table 4-4 Results of the steam-air tests obtained in the past with other codes, [108]

Test	SPECTRA Version 1.00	TRACG	TRAC-BF1/ MOD1	MELCOR 1.8.2	**Experiment**
S2	89.1	83.2	85.6	88.2	**99.0**
S3	81.9	75.4	76.9	82.6	**87.6**
S4	66.5	64.2	67.2	72.3	**73.4**
S5	58.2	58.2	58.5	61.0	**63.1**

4.2.2.7 Results of with Alternative Drainage in the Water Box

In the calculations presented above the condensate was assumed to flow down from top to bottom of PCC on the surface of all Solid Heat Conductors. As a consequence the film thickness becomes larger for the lower Conductors. This approach of liquid film flowing down on the surfaces of stacked Heat Conductors is the most natural, and has been used in most analyses of PCC behavior. In case of PCC tubes (SC-003 - SC-007) there is no doubt that this approach should be used. The question is whether the condensate film in the tubes should be affected by the condensate produced in the steam box, and whether the condensate film in the water box should be affected by the condensate produced above in the steam box and the tubes. It is presently assumed that the answer to both these questions is no, which is justified as follows. Condensate coming into the tubes is assumed to flow down as a stream in one or two tubes connected in the lower part of steam box, leaving most of the tubes unaffected. For the condensate entering the water box it is assumed that the condensate does not flow down on the walls (as shown in Figure 4-14.a), but falls in form of droplets, as shown in Figure 4-14.b.

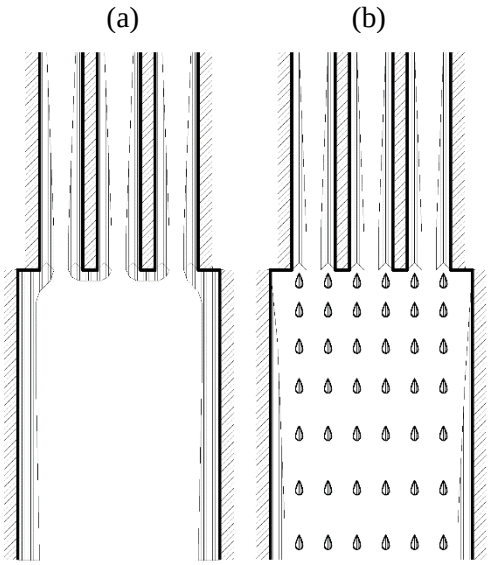

Figure 4-14 Condensate drainage in the water box, (a) base model, (b) alternative

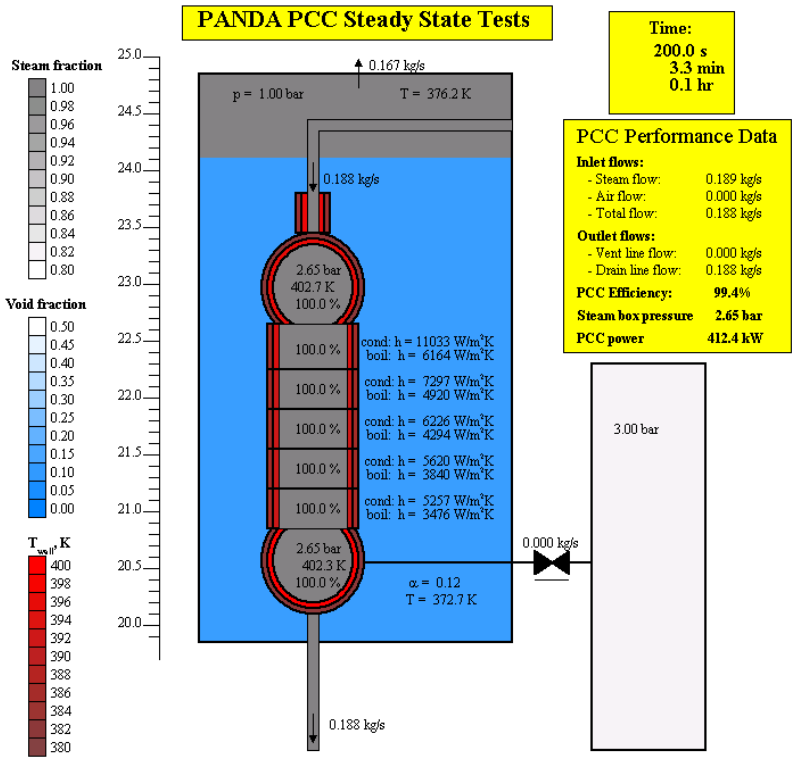

Figure 4-15 Pure steam test S1 - stationary state results, run “PCC-S1-D”

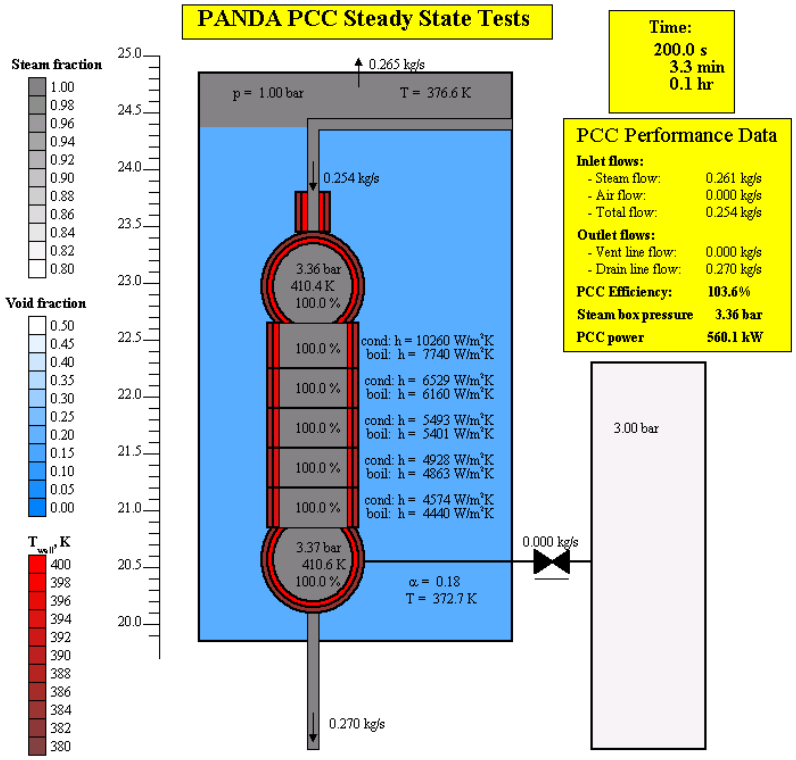

Figure 4-16 Pure steam test S6 - stationary state results, run “PCC-S6-D”

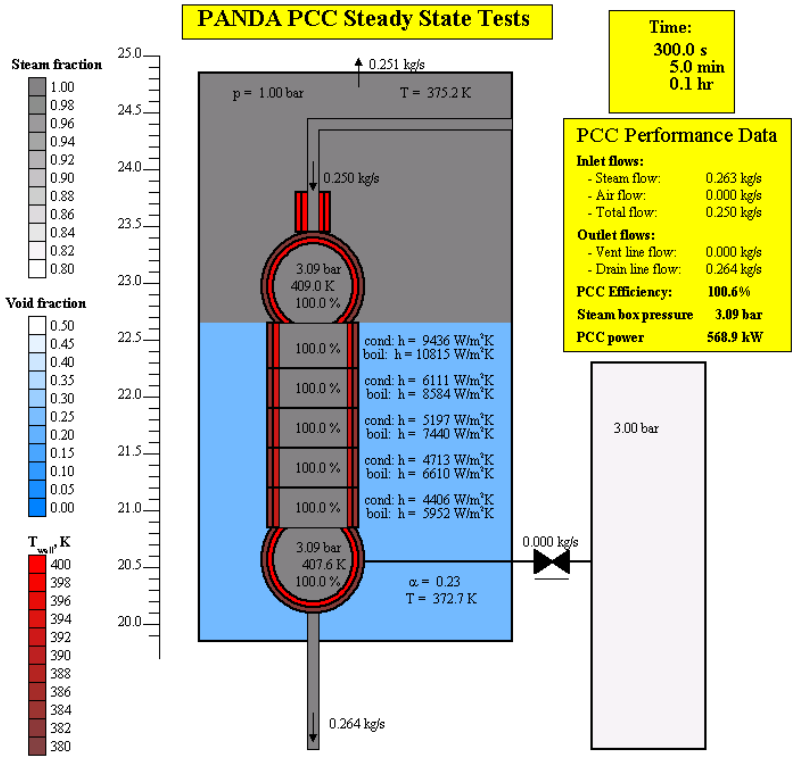

Figure 4-17 Pure steam test S13 - stationary state results, run “PCC-S13-D”

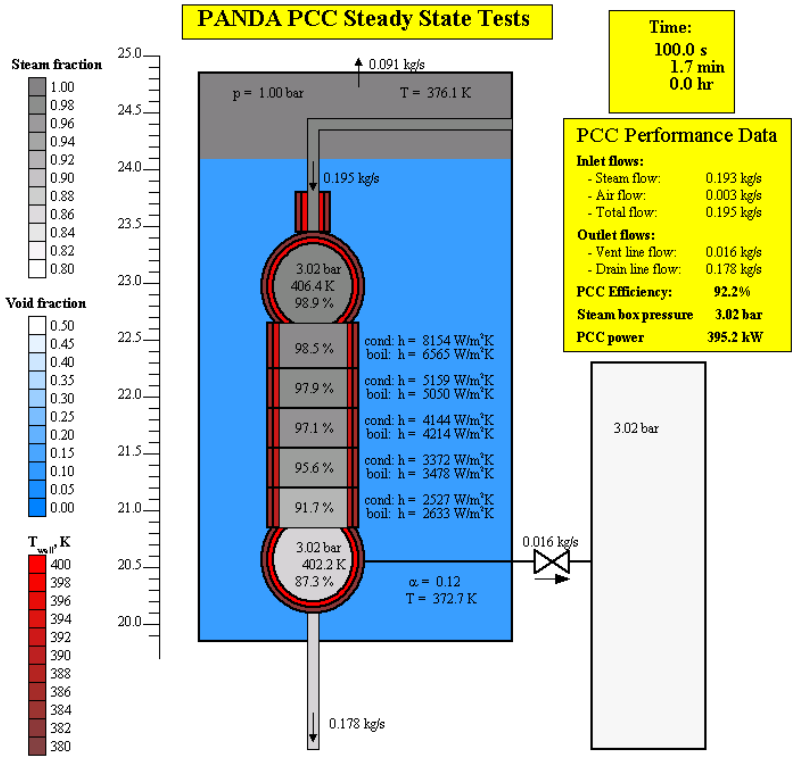

Figure 4-18 Steam-air test S2 - stationary state results, run “PCC-S2-D”

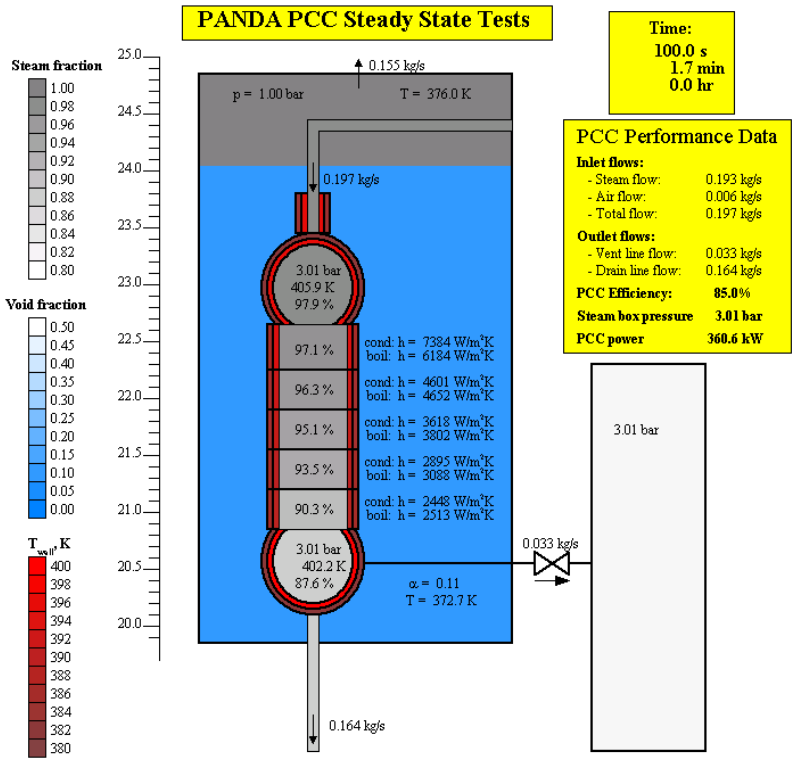

Figure 4-19 Steam-air test S3 - stationary state results, run “PCC-S3-D”

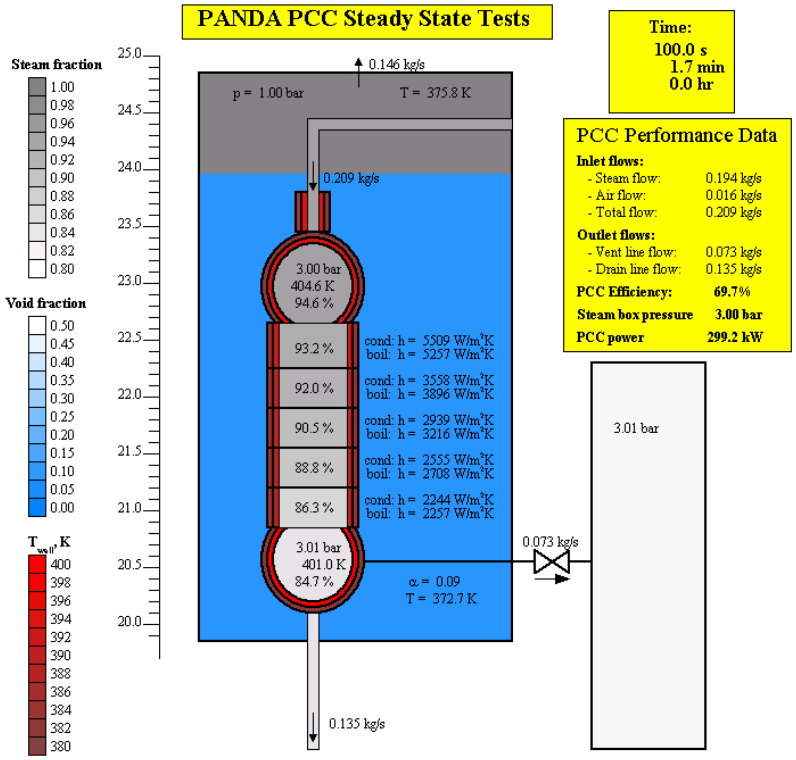

Figure 4-20 Steam-air test S4 - stationary state results, run “PCC-S4-D”

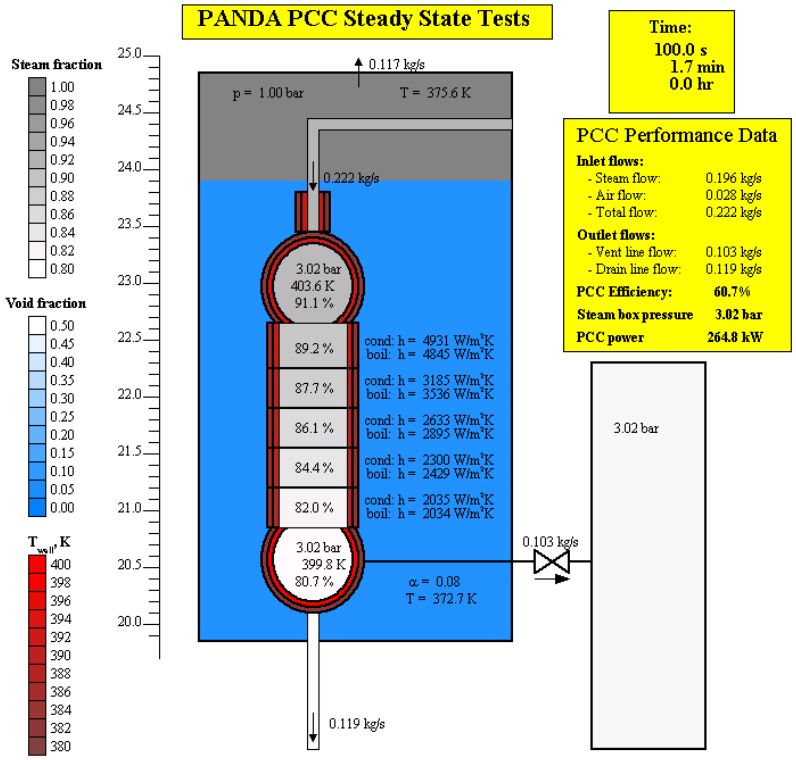

Figure 4-21 Steam-air test S5 - stationary state results, run “PCC-S5-D”

Those two assumptions will result in increased condensation rate, caused by reduced condensate film thickness in the tubes and in the water box. Formation of droplets in the lower drum will additionally increase the PCC efficiency because of condensation of steam on the surface of droplets. Since the droplets are close to saturation this effect will be rather small.

Results of the alternative drainage model are shown in visualization pictures, in Figure 4-15 through Figure 4-21. The results show stationary state for each test. Results of the pure steam tests, S1, S6, and S13, are shown in Figure 4-15, Figure 4-16, and Figure 4-17. The pure steam tests, S2, S3, S4, and S5, are shown in Figure 4-18, Figure 4-19, Figure 4-20, and Figure 4-21. The results are summarized in Table 4-5, Table 4-6, Figure 4-22, and Figure 4-23. The results obtained with the alternative drainage model are closer to the experimental results.

4.2.2.8 Summary and Conclusions

- The PCC efficiencies calculated for the steam-air tests are compared to the experimental data in Table 4-5 and Figure 4-22. The calculated efficiencies are smaller, therefore it is concluded that the PCC performance (measured by the fraction of steam that is condensed) is underestimated in these calculations. For the pure steam tests the calculated pressures were higher than the measured pressures (Table 4-6, Figure 4-23). This again mean an underestimation of the PCC performance (higher pressures are needed to condense all steam).
- Similar underestimation of the PCC performance was observed in the past in calculations performed with the codes TRACG, TRAC-BF1, and MELCOR.
- Results obtained with the alternative drainage model are very close to the experimental results for the pure steam tests. For the steam-air tests a small underprediction of the PCC performance is still visible, but it is much smaller than in the base model.

Table 4-5 Results of the steam-air tests

Test	PCC efficiency, (%)		
	SPECTRA base model	SPECTRA alternative drainage	**Experiment**
S2	88.7	92.2	**99.0**
S3	81.2	85.0	**87.6**
S4	66.0	69.7	**73.4**
S5	57.3	60.7	**63.1**

Table 4-6 Results of the pure steam tests

Test	Steam Box Pressure, (Pa)		
	SPECTRA base model	SPECTRA alternative drainage	**Experiment**
S1	2.75×10^5	2.65×10^5	$\mathbf{2.74\times10^5}$
S6	3.54×10^5	3.36×10^5	$\mathbf{3.35\times10^5}$
S13	3.27×10^5	3.09×10^5	$\mathbf{3.05\times10^5}$

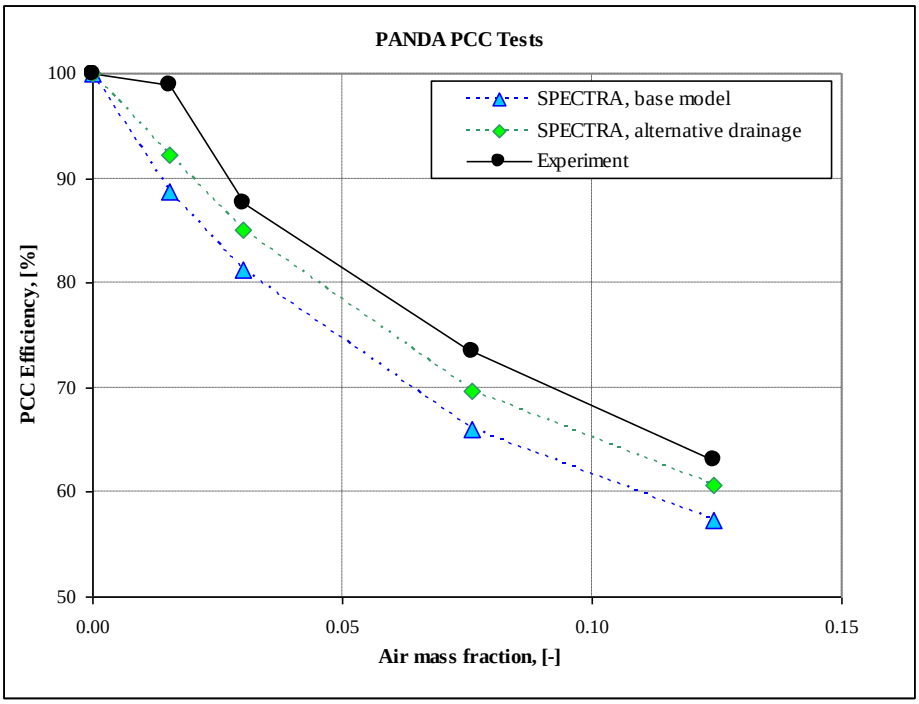

Figure 4-22 Results of the PANDA PCC tests

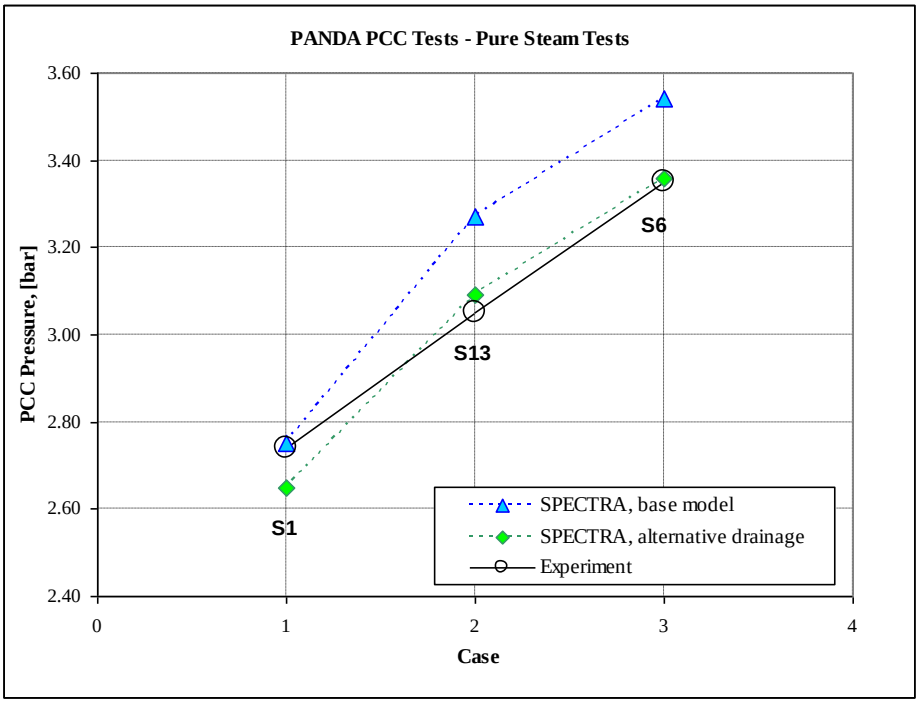

Figure 4-23 Results of the PANDA PCC pure steam tests

4.2.3 PANDA ESBWR Configuration Tests (ISP-42)

4.2.3.1 Introduction

The ISP-42 test was performed at Paul Scherrer Institute (PSI) on April 21/22, 1998. This ISP was run under auspices of the OECD NEA Committee for the Safety of Nuclear Installations (CSNI) and was financially supported by the research foundation of the Swiss Utilities.

ISP-42 was performed at the PANDA test facility - "Passive Nachwärmeabfuhr- und Druckabbau-Testanlage" ("Passive Decay Heat Removal and Depressurization Test Facility"), which had been constructed in Paul Scherrer Institute (PSI), Switzerland. The facility, as configured for the ISP-42 test, is a scaled down model of the ESBWR containment and passive decay heat removal systems, with 1:40 volumetric and power scale, and is at full scale for elevations and time. The ISP-42 test was performed as a sequence of Phases A through F, representing typical passive safety system operating modes under standard or challenging conditions.

Results of blind and open calculations of ISP-42 performed with the SPECTRA computer code are presented in [109]. This section presents results recalculated with the current code version. The present results are very similar to the results of the open calculations presented in [109].

4.2.3.2 PANDA Test Facility

PANDA is a large scale facility, which has been constructed at Paul Scherrer Institute (PSI) for the investigation of both dynamic response and the key phenomena of passive containment systems during the long term heat removal phase for Advanced Light Water Reactors. The facility is a scaled down model of ESBWR containment and safety systems (Figure 4-24), with 1:40 volumetric and power scale, and is at full scale for time and thermodynamic state.

The test facility consists of six large vessels: one representing RPV, two representing drywell, two representing wetwell, and one representing Gravity Driven Cooling System (GDCS) tank. The RPV contains a 1.5 MW electrical heat source. In the upper part of the facility there are four pools. One of the pools contains the Isolation Condenser (IC) unit, three others contain the Passive Containment Cooling (PCC) units. A PCC unit is a heat exchanger with vertical tubes. The unit consists of cylindrical upper drum, called also the steam box, twenty vertical tubes, and cylindrical lower drum, called also the water box. While the IC is connected to the RPV, the three PCC units are connected to the two drywell volumes. Two units are connected to one drywell, the third unit is connected to the other drywell.

4.2.3.3 ISP-42 Tests

The ISP-42 test, performed in the PANDA facility, consists of six different phases, called Phase A, through F. Each of those phases is in fact a separate experiment, with its own initial and boundary conditions. ISP-42 consists of the following test phases:

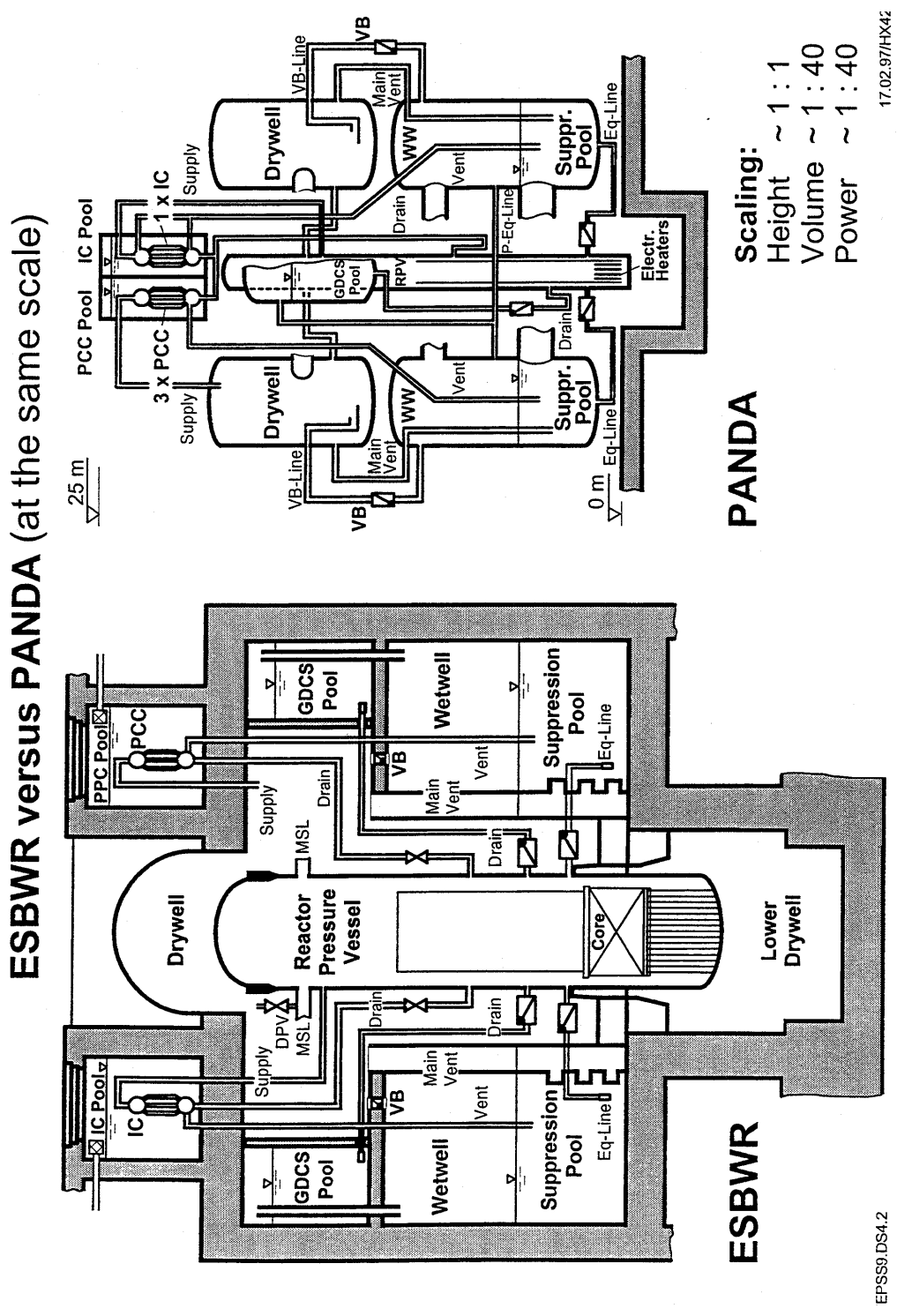

Figure 4-24 ESBWR versus PANDA test facility.

- *Phase A: Passive Containment Cooling System Start-up*
- *Phase B: Gravity Driven Cooling System Discharge*
- *Phase C: Long Term Passive Decay Heat Removal*
- *Phase D: Overload at Pure Steam Conditions*
- *Phase E: Release of Hidden Air*
- *Phase F: Release of Light Gas in Reactor Pressure Vessel*

Descriptions of different phases of the PANDA tests may be found in [7], [8], [9].

4.2.3.4 SPECTRA Model

The model of PANDA facility is shortly described in this section. A more detailed description is given in [109]. Since the facility configuration for the Phase F was much simpler than for all other phases, also a simpler SPECTRA model has been used for this case. The model used for simulation of Phases A through E is discussed first. The model used for simulation of Phase F is discussed next. The SPECTRA model as well as the input files for all phases A through F are provided in:
\Z-ANALYSES\BWR\ISP-42\CALCULATIONS.

- **Model Applied for Phases A Through E**

  The SPECTRA model is shown in Figure 4-25. The input file name is:
  \Z-ANALYSES\BWR\ISP-42\CALCULATIONS\PANDA
  For convenience from now on the path is omitted, therefore the location is shortly **\PANDA**. The model was first built for blind calculations and then updated for open calculations. For the present calculations (done with the recent code version) the latest model (the model used for the open phase) was applied. The modifications performed for open calculations include [109].

  - *Division of air lines into lower and upper halves*
    The most important modification involves the relatively large pipes connecting drywells and wetwells (Figure 4-24). In these pipes counter-current flow and mixing of fluid may occur. This effect may be captured in calculations by using two parallel junctions, representing for example the lower half and the upper half of the pipe. In the blind calculations these pipes were represented by single junctions. In the open calculations, as well as the present calculations all three connections were represented by double junctions (Figure 4-25):

    - Drywell air line: JN-003 and JN-103
    - Wetwell air line JN-004 and JN-104
    - Wetwell water line: JN-005 and JN-105

  - *Division of RPV walls into lower (water) and upper (steam) parts*
    In the model applied for blind calculations, RPV vertical walls were represented by a single 1-D heat conductor. Consequently, both water and steam in RPV were in contact with the same SC surface. In Phase B cold water injected from GDCS quickly cooled down the RPV walls. In such circumstance steam condensation, occurring on the part of SC-002 above water surface, was significantly overpredicted in the blind calculations [109]. For the open calculations and the present calculations SC-002 has been divided into two parts; the lower part, in contact with water, SC-002, and the upper part, in contact with atmosphere, SC-003, see Figure 4-25).

- *Division of PCC primary side tube space into five CV's*
  In blind calculations PCC tube space was represented by a single CV. A better representation is obtained by dividing PCC tubes into a number of connected CVs. For open analysis the PCC tubes were divided into five CVs (Figure 4-26). For the present analysis the KSP correlation for the noncondensable gases and the Rohsenow boiling correlation (external flow) were applied, to be consistent with the model used for the PCC steady state tests (section 4.2.2).

- *Correction of error in loss factor for PCC feed lines*
  The loss factor for PCC feed lines was incorrectly specified in blind calculation. While the overall loss factor in these lines is about 30 [112], the values used in the input resulted in overall factor of about 2 (*K*-factor of 1.0 in JN-012 and JN-013). This was corrected in open analysis.

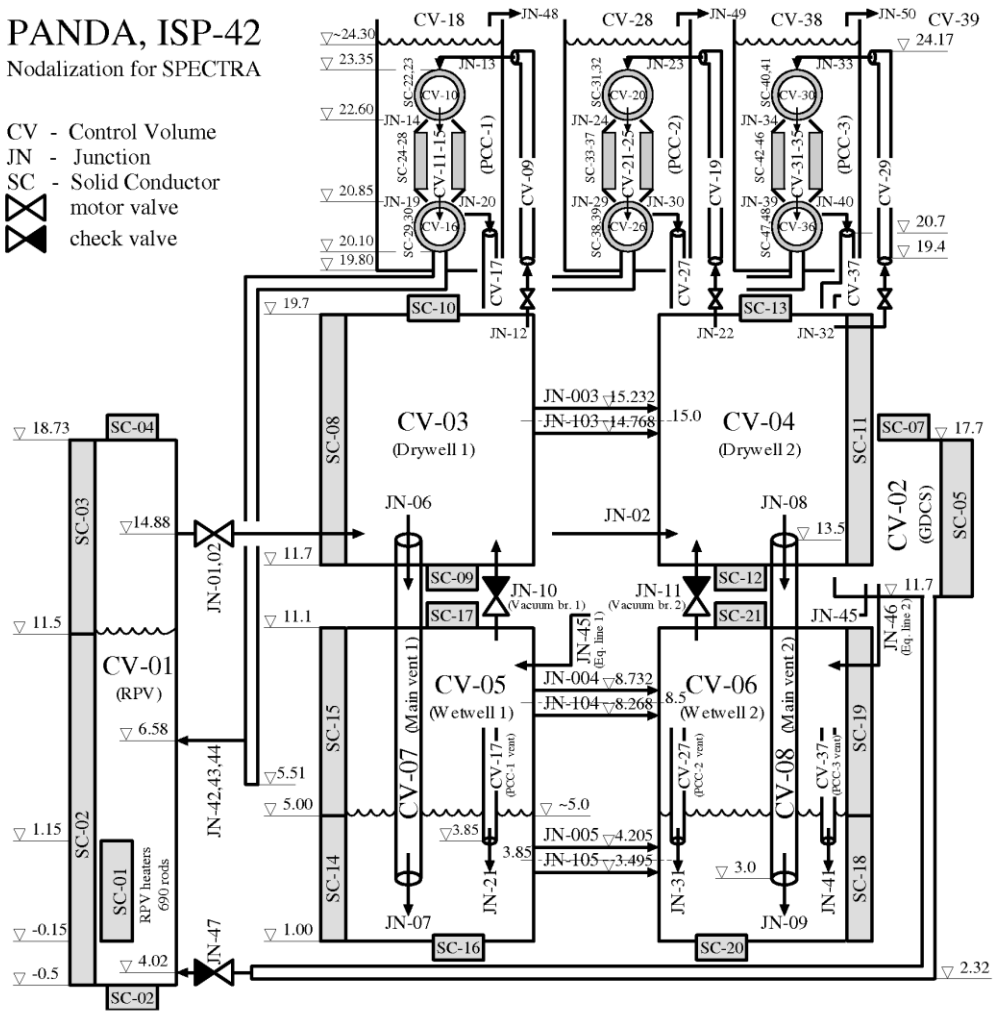

Figure 4-25 SPECTRA model of PANDA test facility applied for test phases A through E

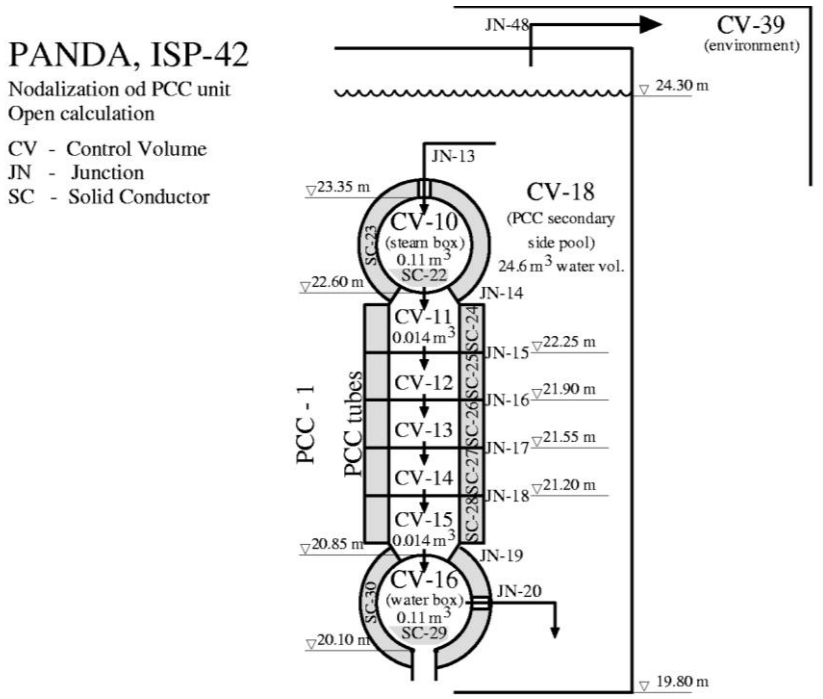

Figure 4-26 Nodalization of PCC unit applied (PCC-1)

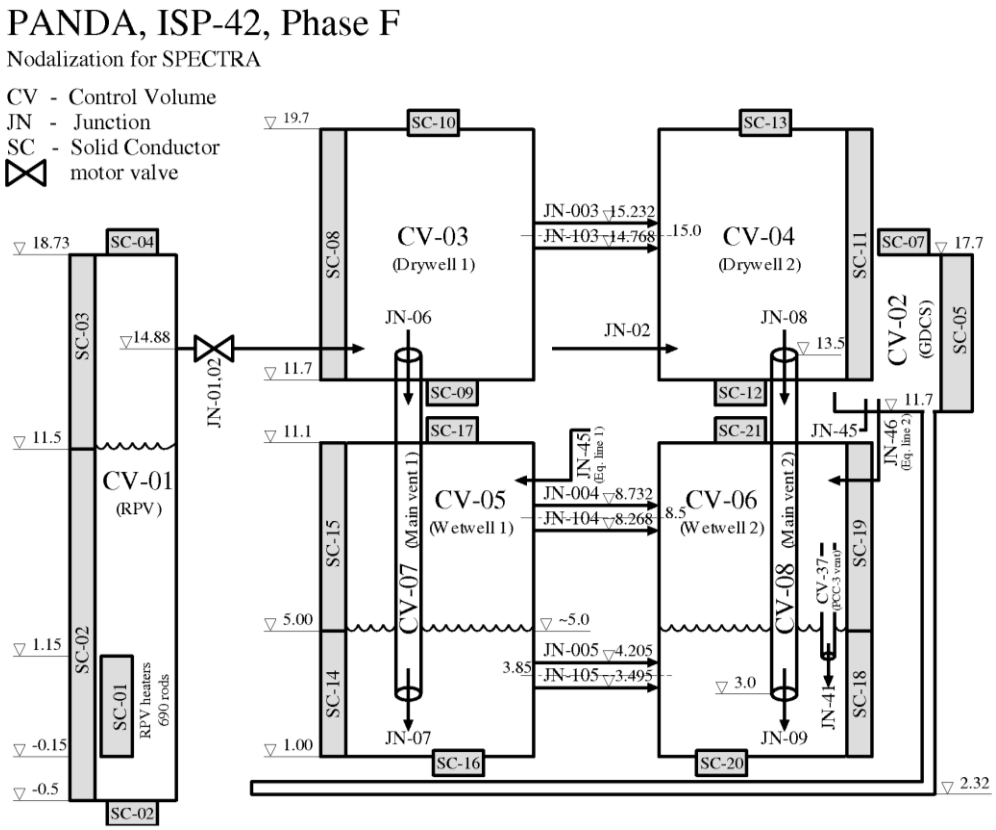

Figure 4-27 SPECTRA model of PANDA test facility applied for test phase F

- *Correction of initial conditions in PCC units*
  The initial conditions inside the PCC tubes, drums and piping system, were not given in the test specification. In absence of data the relative humidity was assumed equal to 0.9. Investigation of the test results showed that for most phases an initial humidity of 1.0 was a better value. This value was applied in the open (and the present) analyses.

- *Correction of the initial air pressures in drywells*
  In some cases the initial air pressures given in test specification were not consistent with the initial gas temperatures. SPECTRA requires gas relative humidity as input parameter. The lowest possible noncondensable gas pressure in a Control Volume is obtained by setting the relative humidity to 1.0. In several cases even with humidity equal to 1.0 the initial air pressure in SPECTRA was higher than that given in the test specification. For the open analysis it was decided to adjust the initial gas temperatures, in order to obtain correct initial air pressures.

- **Model Applied for Phase F**

  The model applied for calculation of Phases F is shown in Figure 4-27. SPECTRA input file name is `\PANDA-F`. Only the main vessels: RPV, DW1, DW2, GDCS, WW1, WW2, and only one vent pipe (from DW1 to WW1) were included in the model. For the present calculations (done with the recent code version) the latest model (the model used for the open phase) was applied. The modifications performed for open calculations include (see [109]).

  - *Division of air lines into lower and upper halves*
    This modification is described above, at the discussion of the model applied for phases A through E.

  - *Gas stratification model in the drywells*
    The gas density stratification model was activated in both drywells. In the blind calculations the stratification model was applied only in the RPV. Comparison of blind results with the experimental results showed that stratification was important also in the drywell. Therefore in the open calculations (as well as the present calculations) the stratification model was applied for the drywells

  - *Initial thermal stratification of wetwell pools*
    In the blind calculations the wetwell pool temperatures were initialized at constant temperatures, equal to the average pool temperature. In Phase F there was a small initial thermal stratification, which resulted in the fact that pool surface temperature was about 2 K higher than in SPECTRA. For the open analysis (as well as the present analysis) the initial pool stratification has been taken into account, and the initial pool surface temperature was closer to the test data.

4.2.3.5 Results

Results presented here are very similar to the open calculation results presented in [109]. Therefore the number of plots presented here was minimized - comparisons with experiment are shown only for the containment pressure plots. The containment pressure is the most important parameter in the PANDA tests. Comparison of other parameters is shown in [109], [110], and [111]. Although the results shown there were obtained with an earlier SPECTRA version, the present recalculation showed that there are practically no differences between the current version and the earlier version.

- **Phase A: Passive Containment Cooling System Start Up**

  SPECTRA input file for this run is: **\A\Phase-A.SPE**. Results obtained for Phase A are shown in Figure 4-28, Figure 4-29, and Figure 4-30. During Phase A there is a continuous boiling in the RPV; the steam produced in RPV enters the drywells through the steam lines. The air is slowly purged from the drywells to the wetwells. Some air was trapped in the lower part of Drywell 2. This couldn't be captured in calculations, in which the drywells were represented by a well-mixed CVs.

  During the first 30 minutes of the test air pressure in the drywells is large. As a consequence PCC units cannot operate properly. Some steam is condensed on the drywell walls. There is almost no condensation in the PCC units. After about half an hour steam starts to condense in the PCC units; the PCC power is relatively low (0.02 MW - Figure 4-29). Out of the total amount of steam entering the containment through the two steam lines (~0.17×2 = 0.34 kg/s - Figure 4-29), very small amount of steam is condensed and returned to the RPV (~0.01×3 = 0.03 kg/s - Figure 4-29). A really effective PCC operation is observed at the end of the test; the PCC power is 0.32 MW (Figure 4-30). Almost all steam entering the PCCs (~0.15×3 = 0.45 kg/s) is condensed in the PCC units and returned to the RPV (~0.14×3 = 0.42 kg/s - Figure 4-30).

  A very good agreement between the calculations and experiment are observed (Figure 4-28). There are almost no difference between the results of the blind and the open calculations [109]. According to the FFT (Fast Fourier Transform) error evaluation, presented in [110] and [111], the blind results from SPECTRA turned out to be the closed to the experiment out of all participants of the ISP-42, involving the computer codes RELAP5, CONTAIN, CATHARE, RALOC, COCOSYS, RBIC.

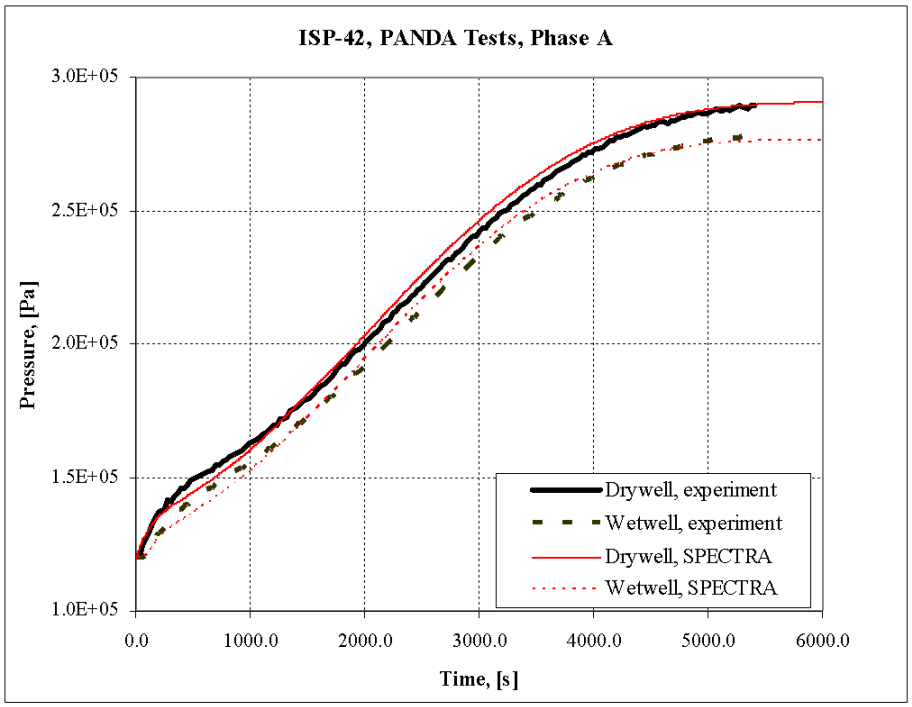

Figure 4-28 ISP-42, Phase A, containment pressures, experiment and SPECTRA

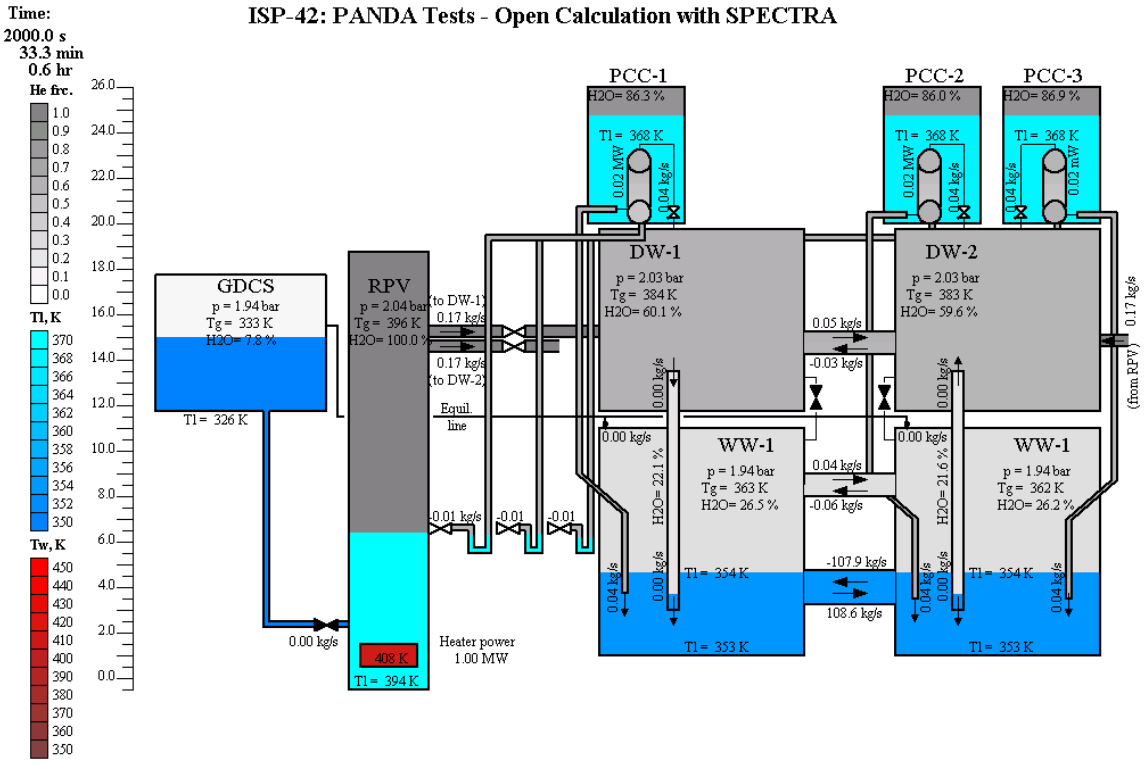

Figure 4-29 ISP-42, Phase A, SPECTRA, *t* = 2,000.0 s

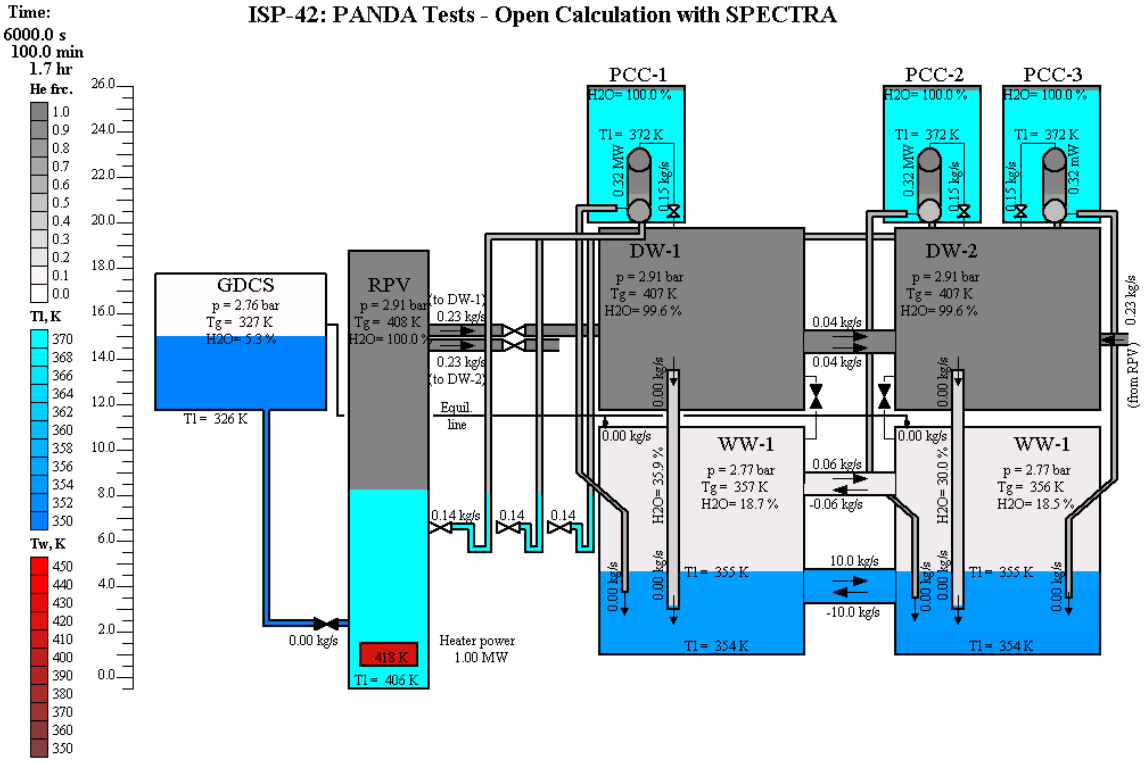

Figure 4-30 ISP-42, Phase A, SPECTRA, *t* = 6,000.0 s (end of the test)

- **Phase B: Gravity Driven Cooling System Discharge**

  SPECTRA input file for this run is: **\B\Phase-B.SPE**. Results obtained for Phase B are shown in Figure 4-31 and Figure 4-32. GDCS injection starts at the beginning of the phase and lasts for about 1000 s. Due to the GDCS injection containment pressure decreases. In the blind calculation this pressure decrease was overestimated [109] because the RPV walls were modelled by a single 1-D Solid Heat Conductor (SC-002), which was in contact with both pool and atmosphere of CV. The temperature of the surface of SC-002 was very close to the temperature of RPV water (large heat transfer coefficient for liquid heat transfer), and intensive condensation took place on the part of SC-002 in contact with the CV atmosphere. In other words, use of a single SC meant no resistance for heat flow in the axial direction. The energy flow was from the steam to the uncovered part of SC-002, and then from the SC to the water, through the covered part. For the open calculation (as well as the present calculation) the RPV walls were represented by two SCs - see section 4.2.3.4, Figure 4-25. As a result of this change, the calculated pressures are in much better agreement with experiment during the GDCS injection phase.

  When the GDCS injection was terminated, RPV water was heated up and, at ~2500 s, boiling in the RPV was resumed. Steam began to flow to the drywells through steam lines, and then to the PCC units. The PCC units started to operate. At the end of the test the calculated flow through the two steam lines is ~0.18×2 = 0.36 kg/s (Figure 4-32). The flow into the PCC units is ~0.12×3 = 0.36 kg/s (Figure 4-32). The amount of condensate returned to the RPV is practically the same (~0.12×3 = 0.36 kg/s - Figure 4-32). Those results agree very well with the experimental measurements (see [109]).

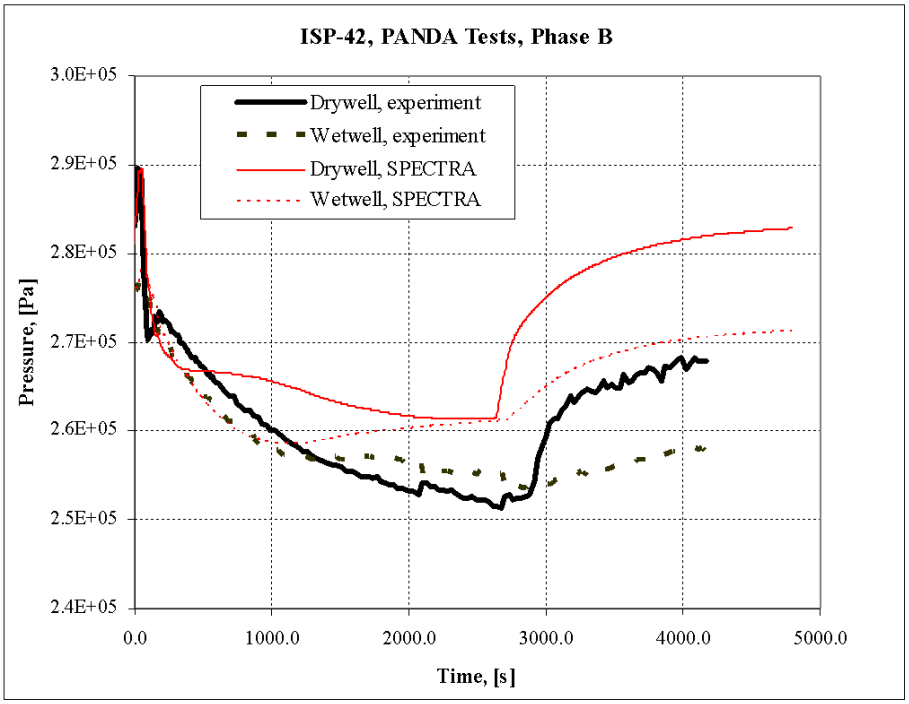

Figure 4-31 ISP-42, Phase B, containment pressures, experiment and SPECTRA

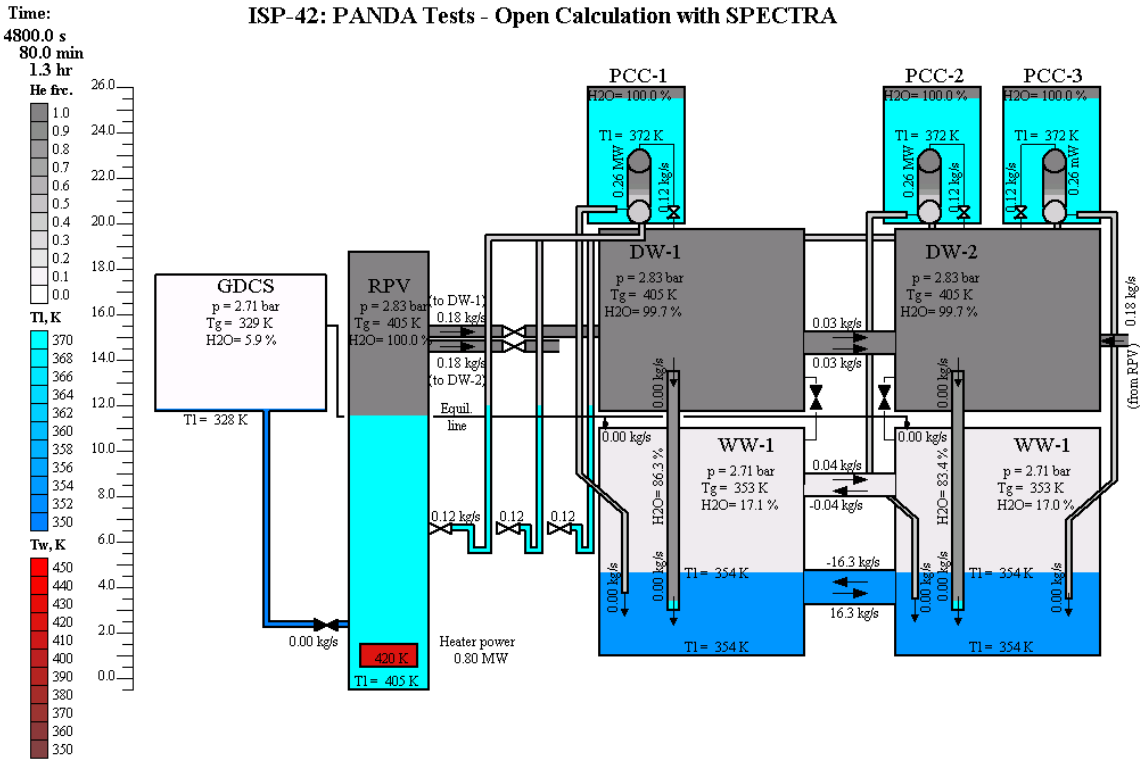

Figure 4-32 ISP-42, Phase B, SPECTRA, *t* = 4,800.0 s (end of the test)

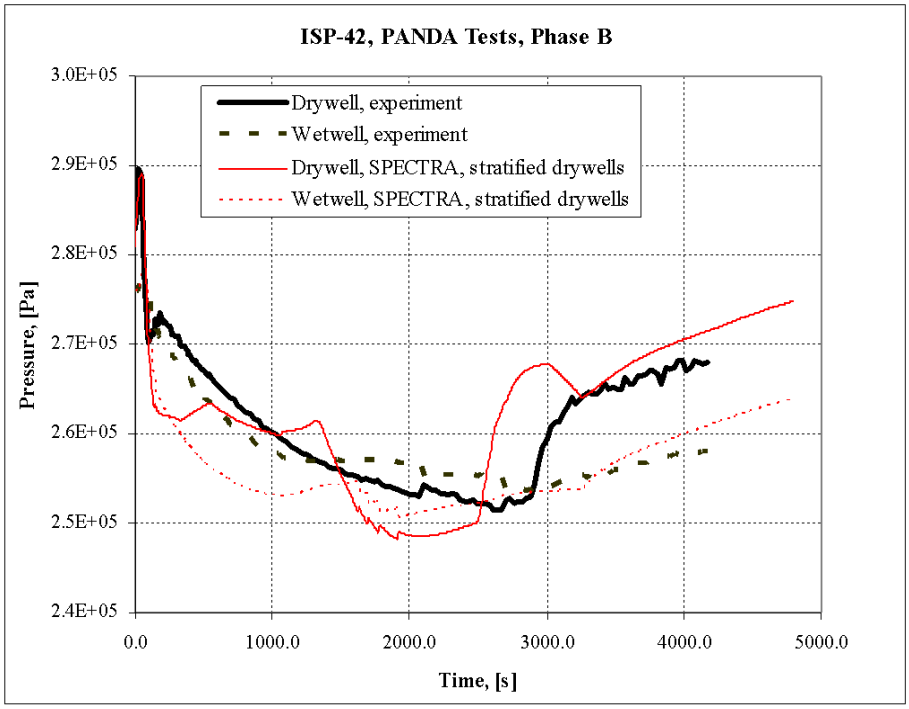

Figure 4-33 ISP-42, Phase B pressures, experiment and SPECTRA drywell stratifications

The containment pressure is overpredicted (Figure 4-31). This is caused by the fact that in the experiment some air remained in the drywells (trapped in the lower part of the vessel), while in calculations nearly all air was purged to the wetwells. This was verified in a separate run with the stratification model activated in the drywells. SPECTRA input file for this run is: **\B\Phase-B-S.SPE**. Results are shown in Figure 4-33. The containment pressure is in better agreement with the experiment.

- **Phase C: Long Term Passive Decay Heat Removal**

SPECTRA input file for this run is: **\C\Phase-C.SPE**. Results are shown in Figure 4-34 and Figure 4-35. Generally quite good agreement is obtained for this phase. At the end of the test the drywell pressure was 2.84×10^5 Pa in the experiment and 2.86×10^5 Pa in the calculations (Figure 4-34). A good agreement was obtained already in the blind calculation. The containment pressure was overpredicted in the blind calculations (at the end of the test the drywell pressure was 2.90×10^5 Pa [109]. For the open analysis (as well as the present analysis) two modifications of the model, discussed below, had an important effect on the Phase C results.

Firstly, in the open analysis the PCC tubes were modelled by five connected CVs, instead of one CV - see section 4.2.3.4. This modification allowed to represent better the gas composition change in the tubes, namely the accumulation of air in the lower part of the PCC tubes. This accumulation is clearly visible in Figure 4-35 (the steam fractions in the PCC units are shown using different shades of grey). The division of PCC tubes into five CVs allowed to improve the agreement of the PCC performance, but had almost no effect on the overall parameters, for example the containment pressure, which with this modification alone, were almost the same as in the blind analysis. To improve the pressure prediction, the second modification, described below, was needed.

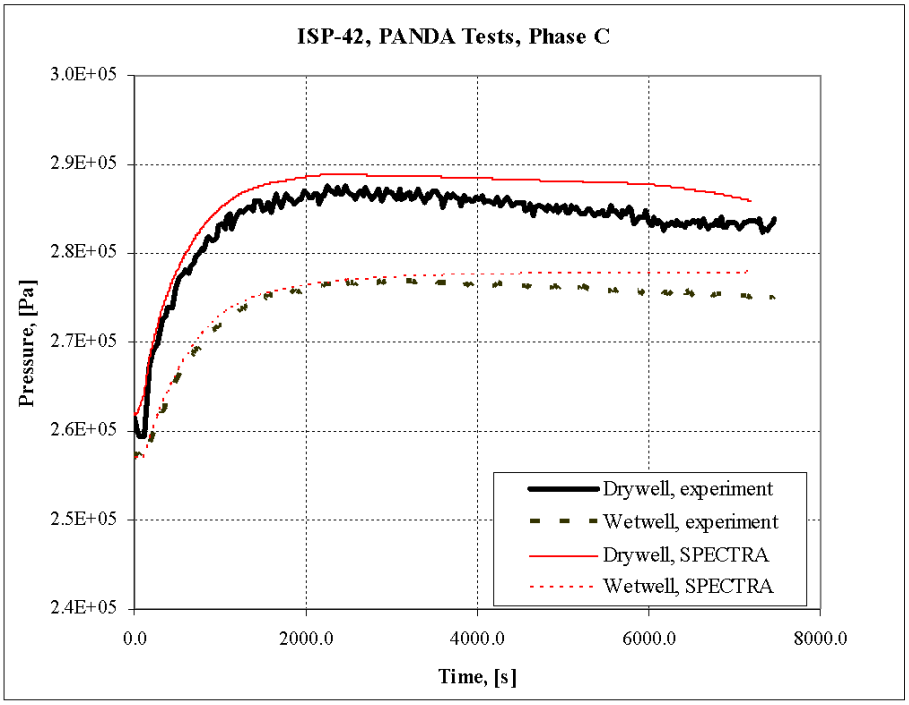

Figure 4-34 ISP-42, Phase C, containment pressures, experiment and SPECTRA

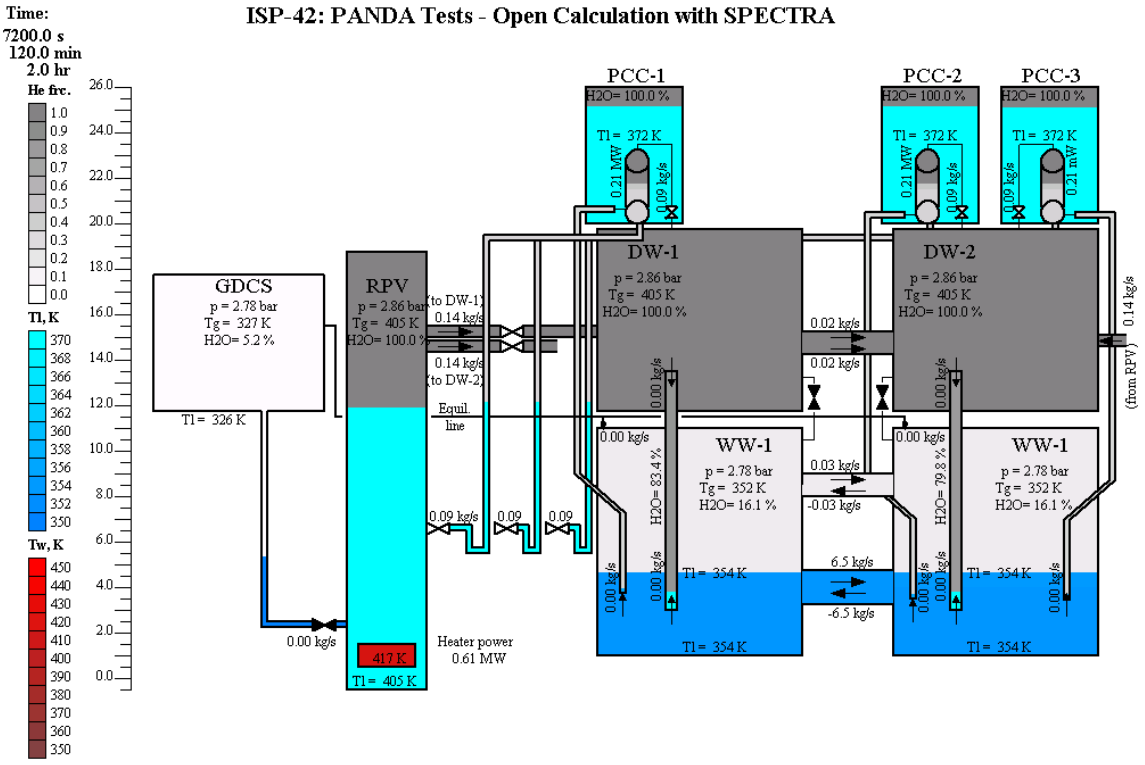

Figure 4-35 ISP-42, Phase C, SPECTRA, t = 7,200.0 s (end of the test)

Secondly, the initial air pressures in the drywells were corrected by increasing slightly the initial gas temperatures - see section 4.2.3.4. This improved the containment pressure prediction compared to the blind calculations.

- **Phase D: Overload at Pure Steam Conditions**

SPECTRA input file for this run is: **\D\Phase-D.SPE**. Results obtained for Phase D are shown in Figure 4-36 and Figure 4-37. The containment pressure is somewhat overpredicted. At the end of the test the drywell pressure was 2.99×10^5 Pa in the experiment and 3.06×10^5 Pa in the calculations (Figure 4-37). A better pressure agreement was obtained in the blind calculation [109] - at the end of the test the drywell pressure was 2.98×10^5 Pa. This fact is explained below.

During Phase D the two operating PCC units (both on drywell 2) were overloaded. The excess of steam, which couldn't be condensed in PCCs, was vented to the wetwell pools, rising the pool surface temperature. This caused an increase of the steam partial pressure in the wetwells (usually close to the saturation pressure at the pool surface temperature), and consequently an increase of the total containment pressures.

For Phase D, the most important modification made for the open analysis was the correction of the PCC feed lines loss factor - section 4.2.3.4. In the blind calculation the resistance of the PCC feed lines was too low (loss factor of ~2 instead of ~30). As a consequence, the uncondensed steam was vented through the PCC vents, rather than the main vents. Due to too low loss factor, the pressure difference between the drywells and the wetwells could not build up sufficiently to clear the main vents. In the open (as well as the present) calculation the loss factor was correct, and the calculated mass flow through PCC units was in very good agreement with the experiment. The excess of steam was vented through the main vent pipes.

Because in the open (and the present) calculation the main vents are cleared, the gas is flowing through the drywell 1, which in the blind analysis remained a "dead-end" volume with approximately constant air content. In the open analysis the gas flow through drywell 1 slowly pushes the air from this vessel to the wetwells. This fact causes an increased wetwell pressure in the open calculation, and worse pressure prediction, compared to the blind calculation.

On top of the fact that the wetwell pressure was higher in the open than in the blind calculation, the drywell-to-wetwell pressure difference increased, because of the larger resistance of the PCC feed lines. This further worsened the agreement in the drywell pressure prediction. However, the drywell-to-wetwell pressure difference is almost exactly correct:

- ~0.16×10^5 Pa - in the experiment - Figure 4-36
- ~0.16×10^5 Pa - in the open and present calculation - Figure 4-37
- ~0.12×10^5 Pa - in the blind calculation [109]

This proves that the PCC resistance was correctly entered in the open (and present) analysis. Since the model improvements made for the open analysis, specifically the correction of the PCC feed lines resistance, cannot be questioned, the problem remains why the open results gave too high wetwell pressure. To explain that fact one needs to take a closer look at the wetwell parameters.

At the end of the Phase D, the parameters calculated for wetwell 1 (CV-005) were equal to: p=2.88 bar, p_{air}=2.40 bar, p_{steam}=0.48 bar, RH=88.9%. The experimental values were: p=2.84 bar, p_{air}=2.40 bar, which means that the steam pressure was equal to: p_{steam}=0.44 bar, and the relative humidity RH=~80%. The calculated relative humidity was about 9% too high. This indicates that possibly the evaporation from the pool surface was overestimated in SPECTRA. The code has a mechanistic evaporation model, very carefully selected and verified, and it is not believed that the model itself could be seriously improved.

The accuracy of the model depends however on the accuracy with which the steam partial pressure above the pool is known. In the analysis wetwells were represented by well-mixed volumes. It is possible that in reality the steam concentration near the pools was higher than the average steam concentration (due to intensive evaporation). To include this effect in the computations, a CFD-type code would be needed.

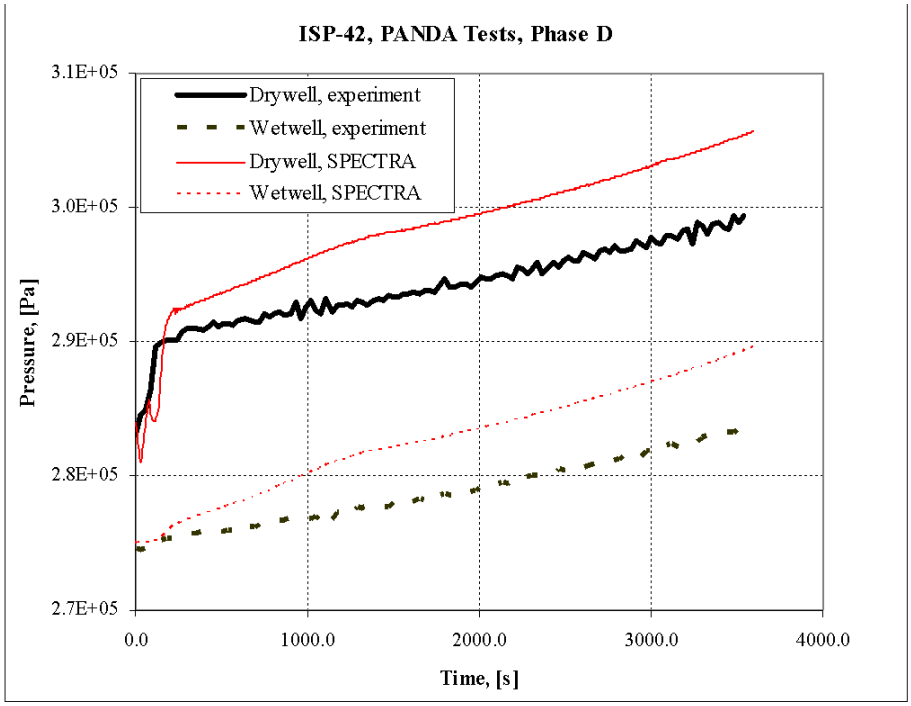

Figure 4-36 ISP-42, Phase D, containment pressures, experiment and SPECTRA

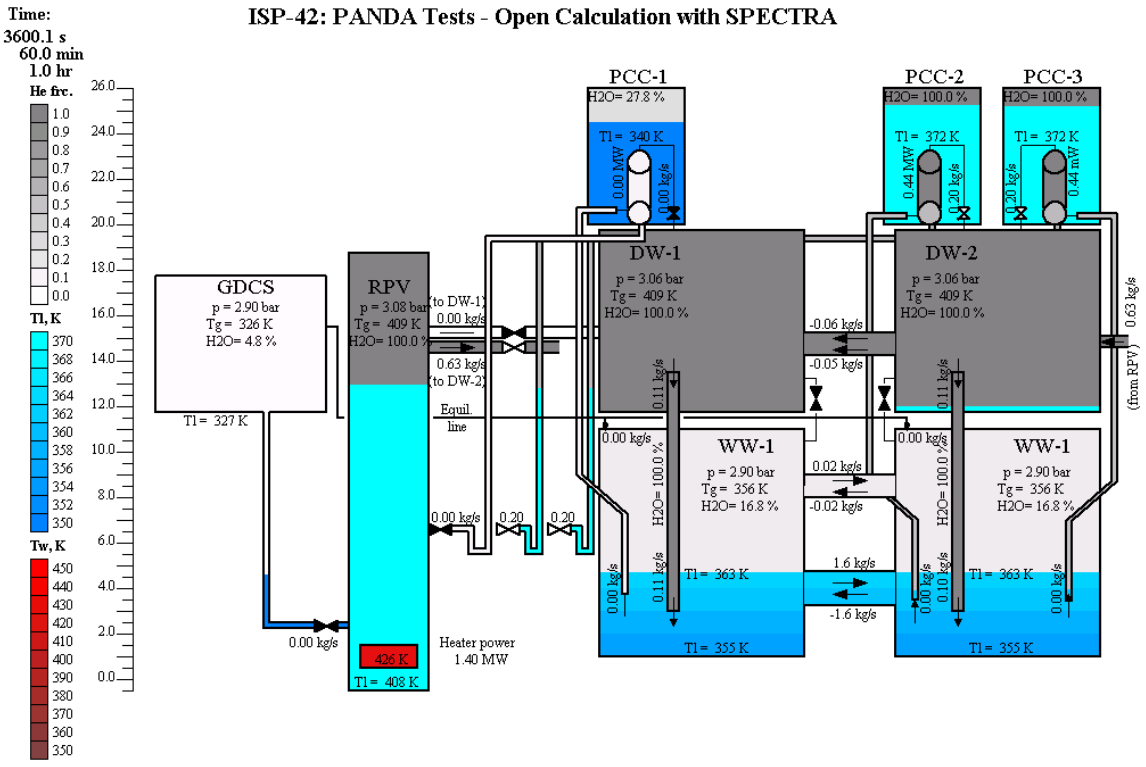

Figure 4-37 ISP-42, Phase D, SPECTRA, t = 3,600.0 s (end of the test)

- **Phase E: Release of Hidden Air**

SPECTRA input file for this run is: **\E\Phase-E.SPE**. Results obtained for Phase E are shown in Figure 4-38 and Figure 4-39. During the first half hour of the test air was injected into the drywell 1. Since the PCC connected to the drywell 1 was isolated in this phase, then, as long as the main vent is not cleared, the drywell 1 may be viewed as a "dead-end" volume. The blind simulation resulted in a clear underestimation of the containment pressure (end-pressure in the drywells of 3.29×10^5 Pa in the experiment and 3.10×10^5 Pa in the calculations [109]). This underestimation was caused by the fact that in the calculations the injected air remained inside the "dead-end" drywell 1 vessel during the whole test. In the experiment however, the air from the drywell 1 was entering the rest of the system. The reason for this discrepancy between the experiment and the blind calculation is twofold.

Firstly, in the experiment air-rich gas from the drywell 1 was constantly mixing with steam-rich gas from the drywell 2. As a result some small amounts of air were constantly entering the drywell 2, and the two operating PCC units, where they were degrading the PCC performance. This phenomenon could not be captured in the blind calculation, because the line connecting drywells was represented by a single junction (JN-003). For the open (as well as the present) analysis the air line was divided into a lower and upper halves (JN-003 and JN-103 - see section 4.2.3.4, Figure 4-25). With this division, the gas mixing in the drywells was calculated quite well. Figure 4-39 shows that the steam fractions in both drywells are very similar. The counter-current flow in the drywell air line is visible in Figure 4-39.

Secondly, the mistake in the resistance of the PCC feed line resulted in the fact that the main vents were never cleared. The venting was performed through the vent lines of the two operating PCCs (both on wetwell 2), rather than through the main vents (one on each wetwell). This had an additional contribution to the isolation of air in drywell 1 in the blind analysis.

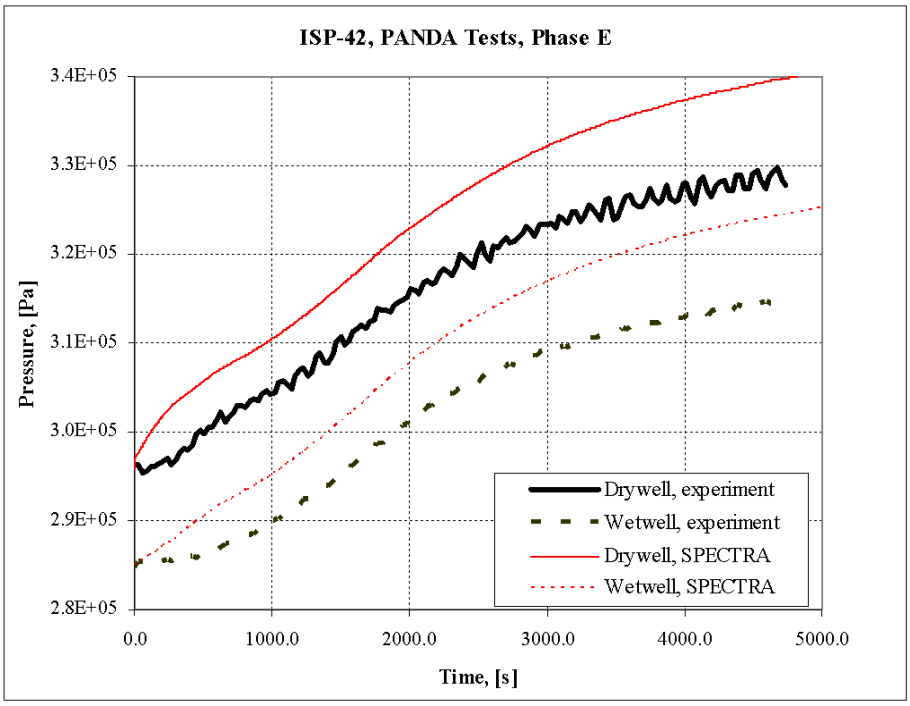

Figure 4-38 ISP-42, Phase E, containment pressures, experiment and SPECTRA

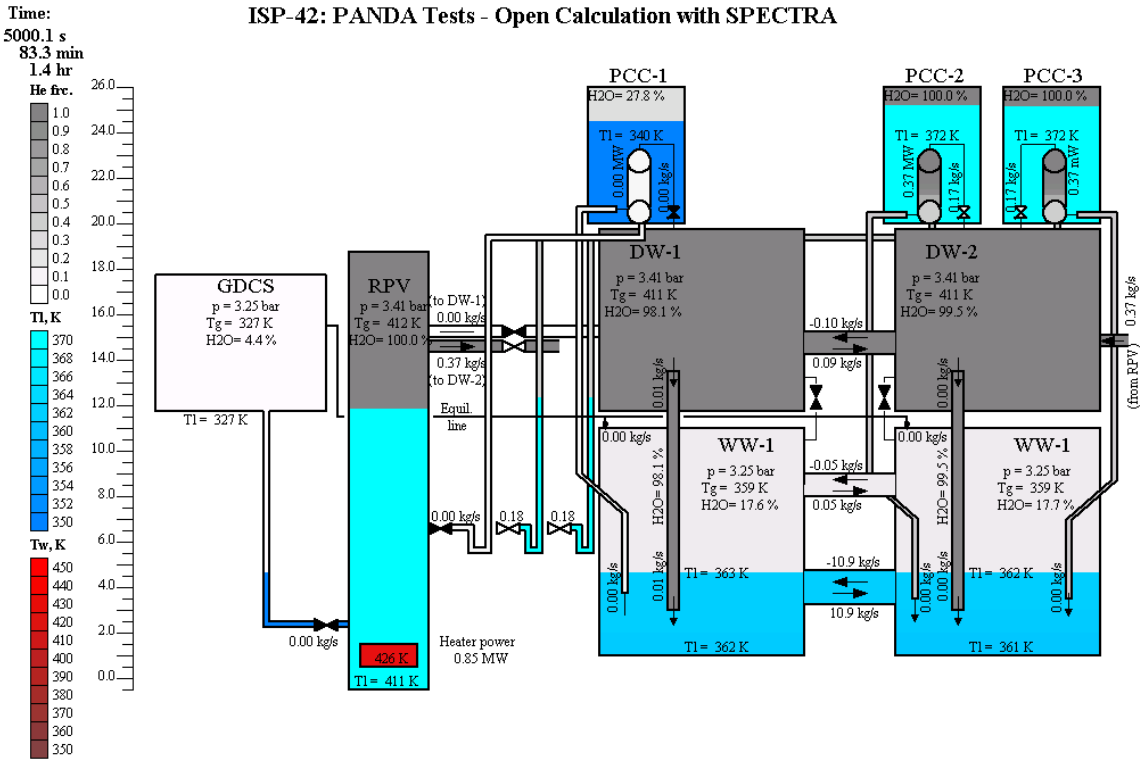

Figure 4-39 ISP-42, Phase E, SPECTRA, *t* = 5,000.0 s (end of the test)

- **Phase F: Release of Light Gas in Reactor Pressure Vessel**

  SPECTRA input file for this run is: **\F\Phase-F.SPE**. During Phase F helium was injected into the RPV during the time period between 900 s and 2700 s. Only one steam line (from RPV to drywell 2) and only one main vent pipe (from drywell 1 to wetwell 1) were open. All PCC units were isolated. The helium injected into RPV was flowing first into drywell 2, next to drywell 1, then it was vented into wetwell 1, and finally it mixed with the gas of wetwell 2. Results obtained for Phase F are shown in Figure 4-40 and Figure 4-41.

  In the blind analysis the containment pressure was overestimated (the end-pressure in the drywells of 5.0×10^5 Pa in the experiment and 5.56×10^5 Pa in the calculations [109]). The main reason for this overestimation was the lack of gas density stratification model in the drywells. When the stratification model was activated in the drywells - see section 4.2.3.4 - the calculated containment pressures were in very good agreement with experiment (Figure 4-40). The air is trapped in the lower part of the drywells, which is visible in Figure 4-41.

  Summarizing, the results of open calculation are quite satisfactory for this phase. With the gas density stratification model in the drywells, the calculated containment pressures are nearly identical as the measured pressure. Note that these results were obtained with a very simple stratification model present in the SPECTRA code. A better prediction of stratification and related phenomena is possible by coupling to CFD, as has been demonstrated in numerous applications (EBR-II SHRT, SESAME CIRCE-HERO, SESAME-Phenix).

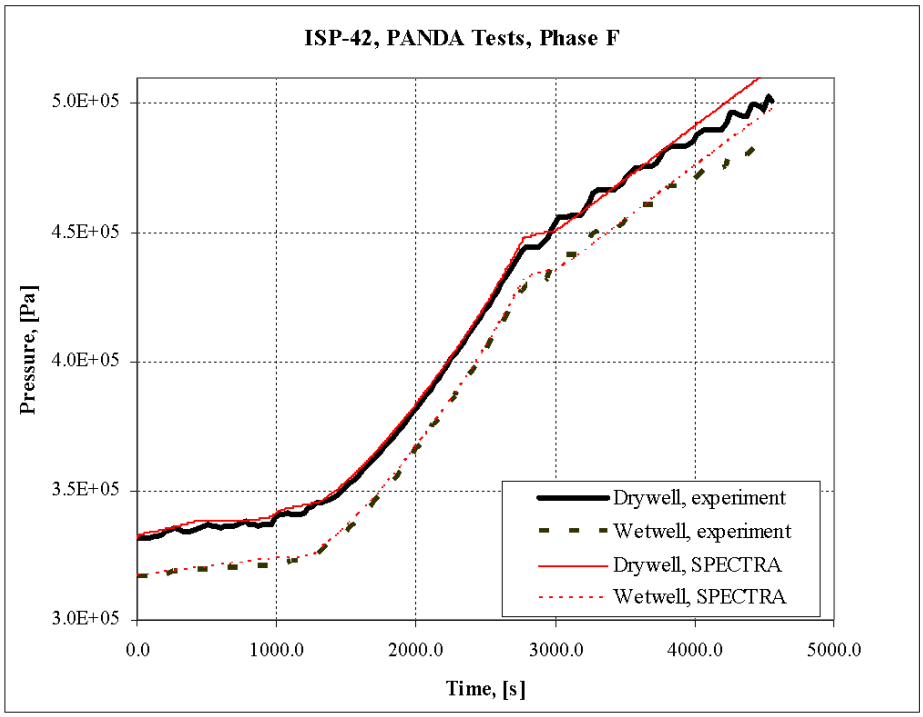

Figure 4-40 ISP-42, Phase F, containment pressures, experiment and SPECTRA

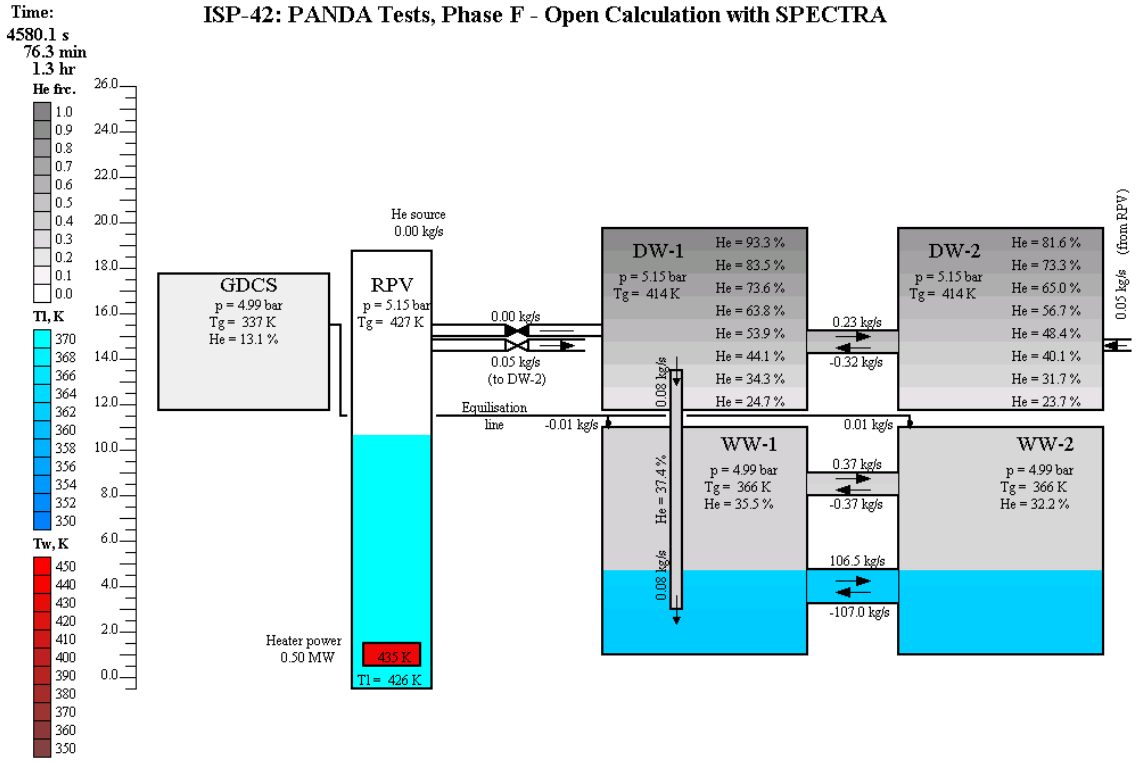

Figure 4-41 ISP-42, Phase F, SPECTRA, *t* = 4,580.0 s (end of the test)

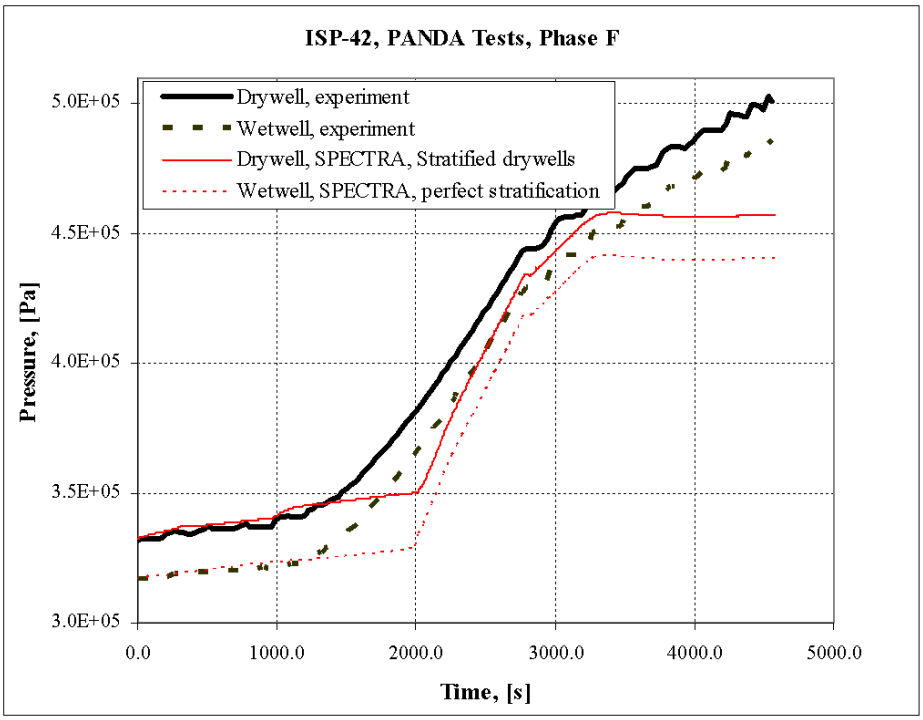

Figure 4-42 ISP-42, Phase F pressures, experiment and SPECTRA maximum stratification

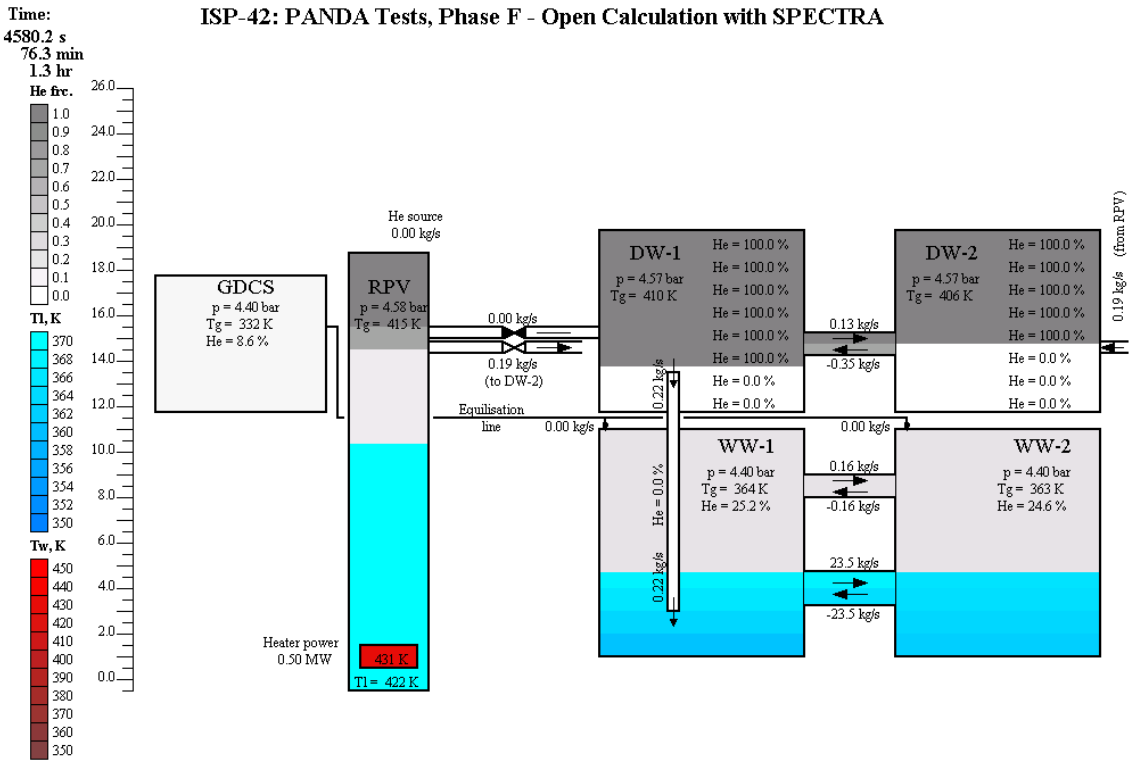

Figure 4-43 ISP-42, Phase F, SPECTRA maximum stratification in the drywells, *t* = 4,580.0 s

Without coupling to CFD or implementing a mechanistic stratification model, the stratification models available in the present code version allow to perform bounding analysis to obtain a conservative estimation of the containment pressure. As an example, the Phase F was recalculated using maximum stratification (helium creates perfectly stratified layers at the top of RPV and drywells). SPECTRA input file for this run is: **\F\Phase-F-S.SPE**. Results are shown in Figure 4-43 and Figure 4-42. The containment pressure at the end of the test is 4.57×10^5 Pa (Figure 4-42). Recalling that the blind calculations with perfect mixing volumes gave 4.57×10^5 Pa [109], one may write:

- Perfect mixing: 5.6×10^5 Pa
- Best estimate stratification: 5.2×10^5 Pa
- Experiment: 5.0×10^5 Pa
- Maximum stratification: 4.6×10^5 Pa

The experimental pressure is within the pressures calculated with different stratification models. Therefore one may conclude that the present stratification models allow to perform bounding calculations in order to obtain a conservative estimation of the containment pressure.

4.2.3.6 Conclusions

ISP-42 PANDA Tests were recalculated using the current SPECTRA version. Results are very similar to the open results, reported in [109]. Based on the results of the calculations of ISP-42, PANDA Tests, the following conclusions are drawn:

- A user should avoid using long 1-D heat conducting structures, that may be in contact with both pool and atmosphere of a Control Volume. This observation is expected to be valid not only for SPECTRA, but for all codes with similar concept of Control Volumes (relatively large CVs, with defined pool surface), that is CONTAIN, MELCOR, MAAP, RELAP4.
- A good representation of the PCC tubes is obtained if they are divided into a number of Control Volumes. This is again expected to be valid for codes like CONTAIN, MELCOR, etc. With this representation a SPECTRA (CONTAIN, MELCOR) model of a PCC unit becomes more similar to a model used by RELAP5 or TRAC, where it is natural to divide tubes into a relatively large number of Control Volumes. There are no adverse effects caused by the fact that the code "thinks" that there are multiple pool surfaces inside the tubes. Care should be taken that the drainage of condensate from one heat conductor to another is properly modelled. MELCOR offers mechanistic film tracking model. In SPECTRA, one can use the characteristic dimension for condensation to define the condensate behavior. A mechanistic film tracking model should be implemented in the future.
- Care should be taken that appropriate input parameters, for example loss coefficients, etc., are used in an analysis.
- In cases when light gas is present in the analyzed system, the simple stratification models offered by SPECTRA provide a way to obtain bounding calculations in order to obtain a conservative estimation of the containment pressure. If stratification is specifically important in a selected part of the system, a complementary SPECTRA-CFD analysis may be performed, with a full system modelled with SPECTRA part of the system modelled with the CFD code - see sections 4.2.1, 4.4.1.

4.3 Application of SPECTRA to HTR/PBMR Reactors

4.3.1 ACACIA - Code-to-Code Comparison

For markets other than large-scale electricity production, a 60 MWth (23 MWel) nuclear plant design with an indirect Brayton cycle was proposed in the past [155]. The reactor is cooled by helium, whereas for the secondary cycle nitrogen was proposed as a heat carrier. In this way, a conventional air based gas turbine could be applied, while at the same time excluding the scenario of air ingress in the reactor core through a heat exchanger leak.

The reactor core geometry was annular with a central graphite reflector region, creating an optimal location for burnable poison. Optimization calculations on burnable poison distribution show that burnup of fuel and poison are balancing each other into a fairly constant reactivity behavior during the entire core lifetime. The main parameters of the plant are shown in Table 4-7.

The plant layout is shown in Figure 4-44. Nodalization applied for the SPECTRA model is shown in Figure 4-45. Steady state design parameters are shown in Figure 4-46, while Figure 4-47 shows the SPECTRA-calculated steady state, in good agreement with the design data. Analyses of Pressurized and Depressurized Loss Of Forced Cooling (PLOFC, DLOFC) were performed and results were compared to the results of the PANTHERMIX code [155]. It was shown that the maximum fuel temperatures will at all times stay below the level where fuel damage starts.

One of possible applications of such system is to couple it to a model for a multi-stage flash desalination system (MSF) - Figure 4-48. The system consists of a main heat exchanger and three stages, each operating at different pressures and temperatures. In the heat exchanger steam is condensed in order to provide energy needed for the process. In each stage sea water is evaporated and then condensed on the tubes of a stage condenser. The energy gained from condensation is used to pre-heat the sea water before it enters the main heat exchanger. Figure 4-49 shows SPECTRA model and steady state results.

Detailed description of SPECTRA calculations are currently provided only in an internal NRG reports. The results will be published in open literature in the future.

Table 4-7 Main features of ACACIA indirect cycle plant [155]

	Baseline cogeneration	Combined cycle
Reactor power (MWt)	60	
Core inlet/outlet temperatures (°C) ((K))	352/900 (625/1173)	
Helium inlet pressure (MPa)	4.1	
Helium mass flow (kg/s)	21	
Net electrical power output (MWe)	18.1	23.2
Gas turbine output (MWe)	18.8	18.8
Steam turbine output (MWe)	-	5.2
Process steam production (tons/h, 425°C/ 4.14 MPa)	27.8	-
Net power generation efficiency (% max.)	30.1	38.7
Net total thermal efficiency (%)	70.0	38.7

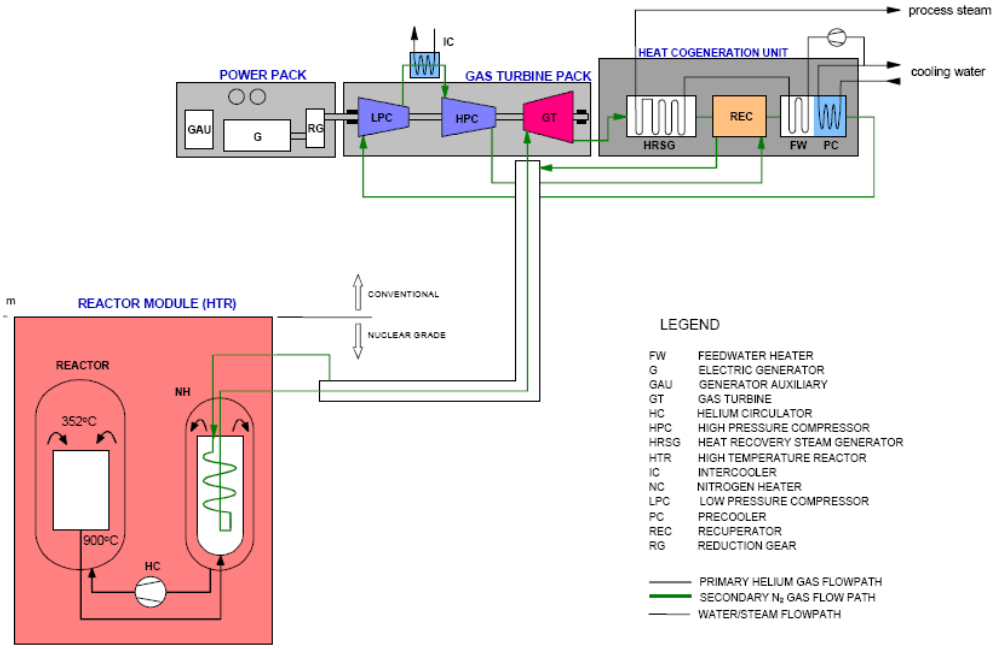

Figure 4-44 ACACIA general plant layout [155]

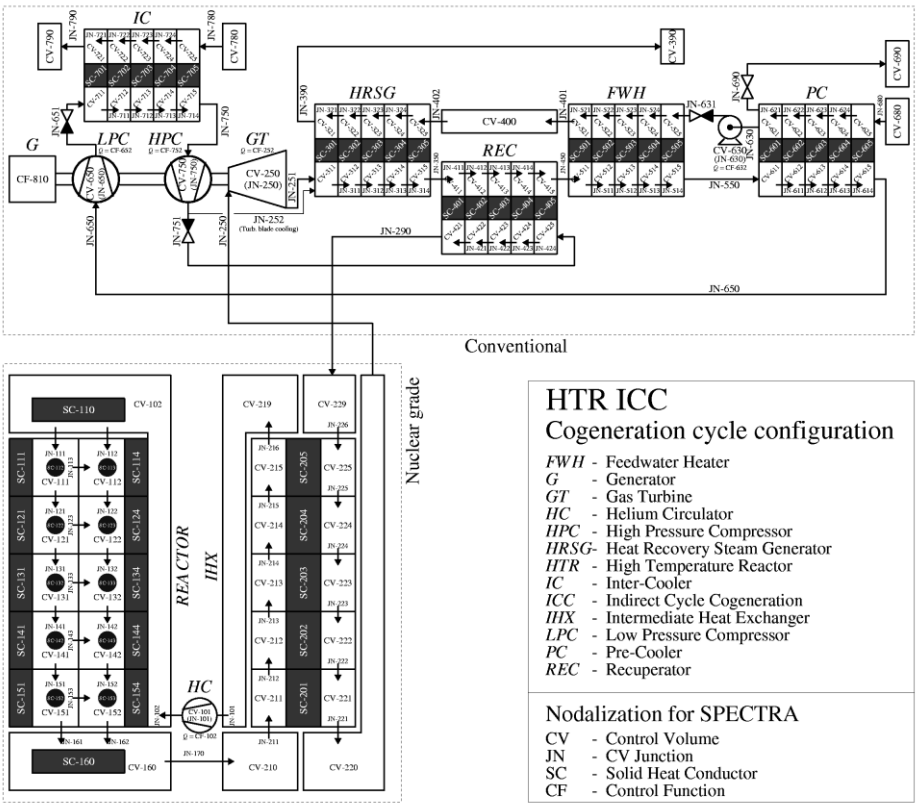

Figure 4-45 ACACIA model - nodalization

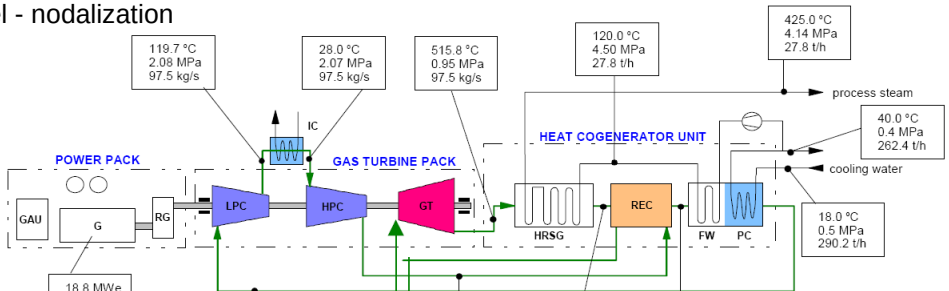

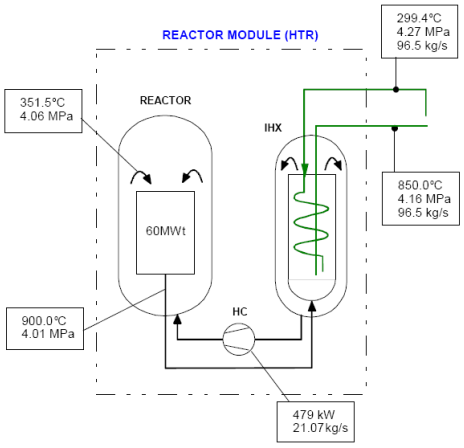

Figure 4-46 ACACIA design data [155]

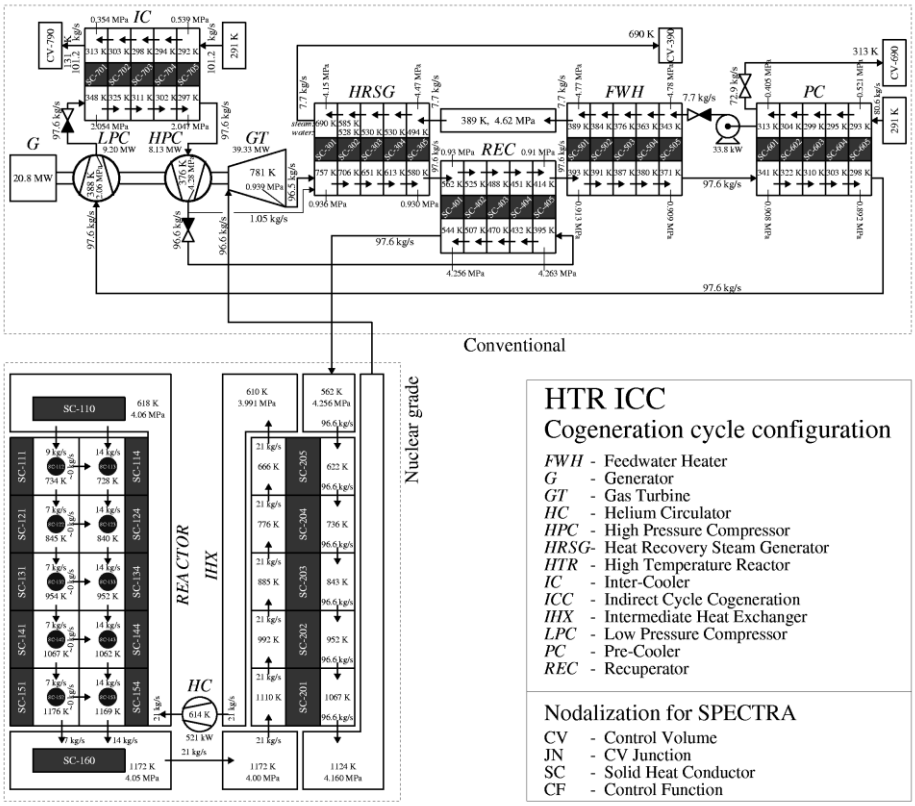

Figure 4-47 ACACIA model -steady state results

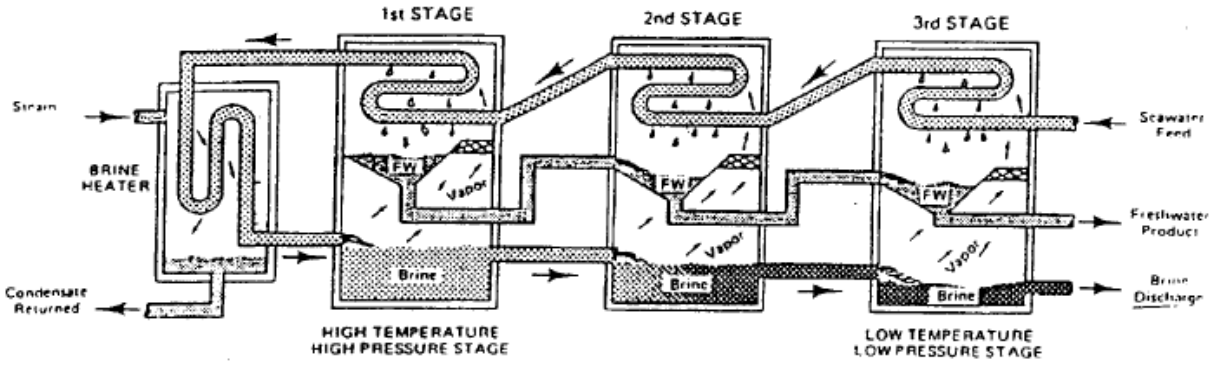

Figure 4-48 Schematic diagram of a multi-stage flash (MSF) desalination system

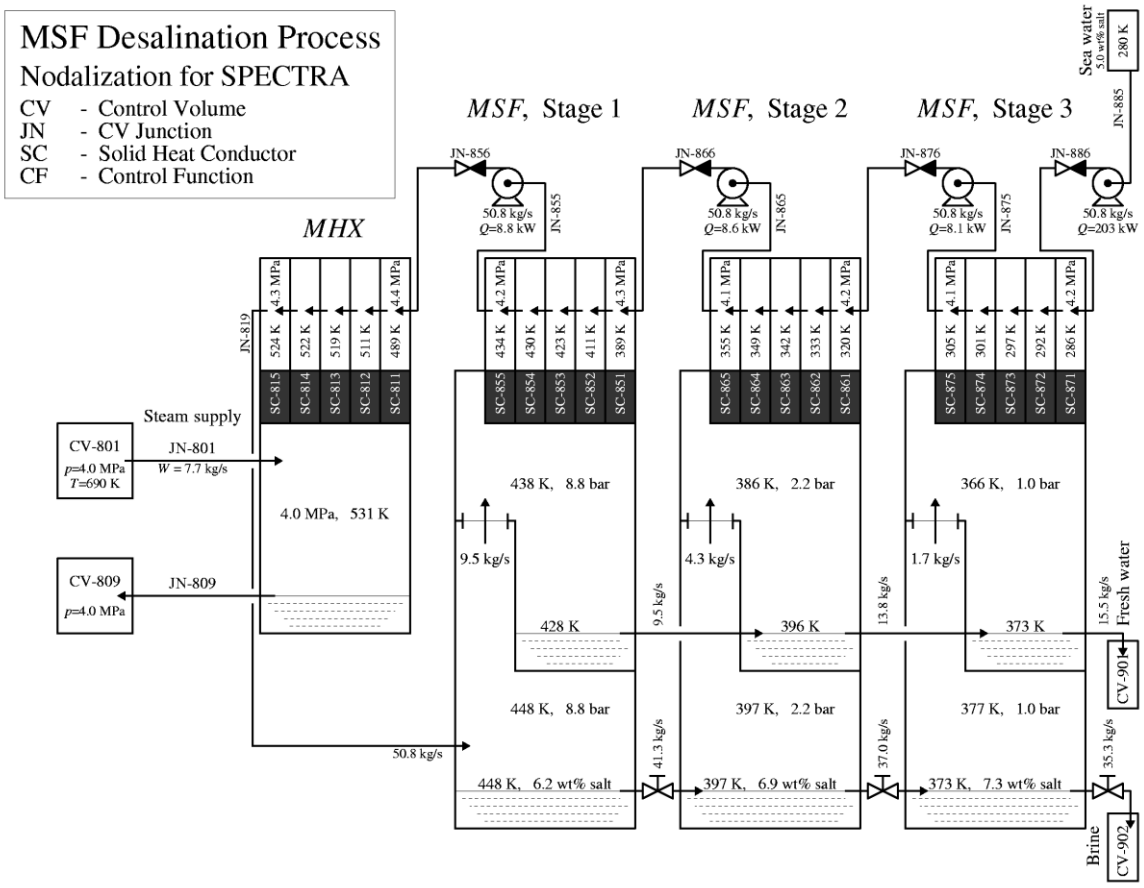

Figure 4-49 SPECTRA model and stationary state results of the MSF desalination system

4.3.2 NACOK - Comparison with Experiment

Air ingress into to the core after the primary circuit depressurization due to large breaks of the pressure boundary is considered as one of the severe hypothetical accidents for the High Temperature gas-cooled Reactor (HTR). The NACOK (Naturzug im Core mit Korrosion) facility was built at Jülich Research Center in Germany to study the effects of air flow driven by natural convection as well as to investigate the corrosion of graphite.

The NACOK air ingress experiment carried out on October 23, 2008 to simulate the chimney effect, was analyzed at NRG with the SPECTRA code (Figure 4-50), as well as at INET, Tsinghua University of China with the TINTE and THERMIX/REACT codes [156]. The calculated results of air flow rate by natural convection, time-dependent graphite corrosion, and temperature distribution were compared with the NACOK test results. The code-to-experiment and code-to-code comparisons show good agreement - Table 4-8. The validation efforts successfully proved the codes capability to simulate graphite corrosion during air-ingress accidents.

Table 4-8 Comparison of SPECTRA, TINTE and THERMIX results with NACOK data [156]

	Mass loss (average all blocks)
Experiment	8.4%
SPECTRA, Roes correlation	9.0%
SPECTRA, CEA correlations	9.4%
SPECTRA, NKL correlation	9.7%
TINTE	9.9%
THERMIX/REACT	10.9%

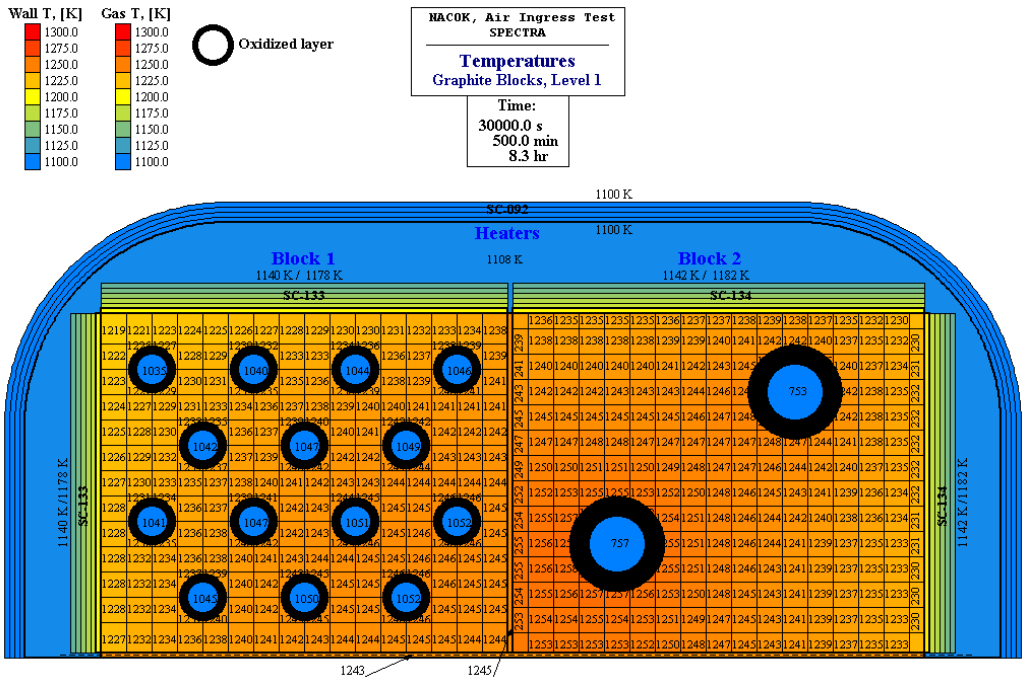

Figure 4-50 SPECTRA results of NACOK oxidation test [156]

4.3.3 HTR-PM - Code-to-Code Comparison

The modular high temperature gas-cooled reactor (HTR), recognized as a candidate for the Generation IV nuclear energy system technology, has well-known inherent safety features. After the successful design, construction and operation of the 10 MW high temperature gas-cooled test reactor (HTR-10); a commercial-scale 200 MWe High Temperature gas-cooled Reactor Pebble-bed Module project (HTR-PM) was designed and recently constructed in China.

A code to code benchmark was performed for depressurized loss of forced cooling (DLOFC) and pressurized loss of forced cooling (PLOFC) accident scenarios of the HTR-PM. A detailed simulation model of the HTR-PM was developed at NRG with the SPECTRA code and at INET, Tsinghua University of China, with the TINTE code.

Three typical accident scenarios were studied [157]:

- DLOFC DN65 mm : break of a tube with diameter of 65 mm
- DLOFC DN10 mm : break of a tube with diameter of 10 mm
- PLOFC : primary circuit helium flow rate decrease to zero in 30 s

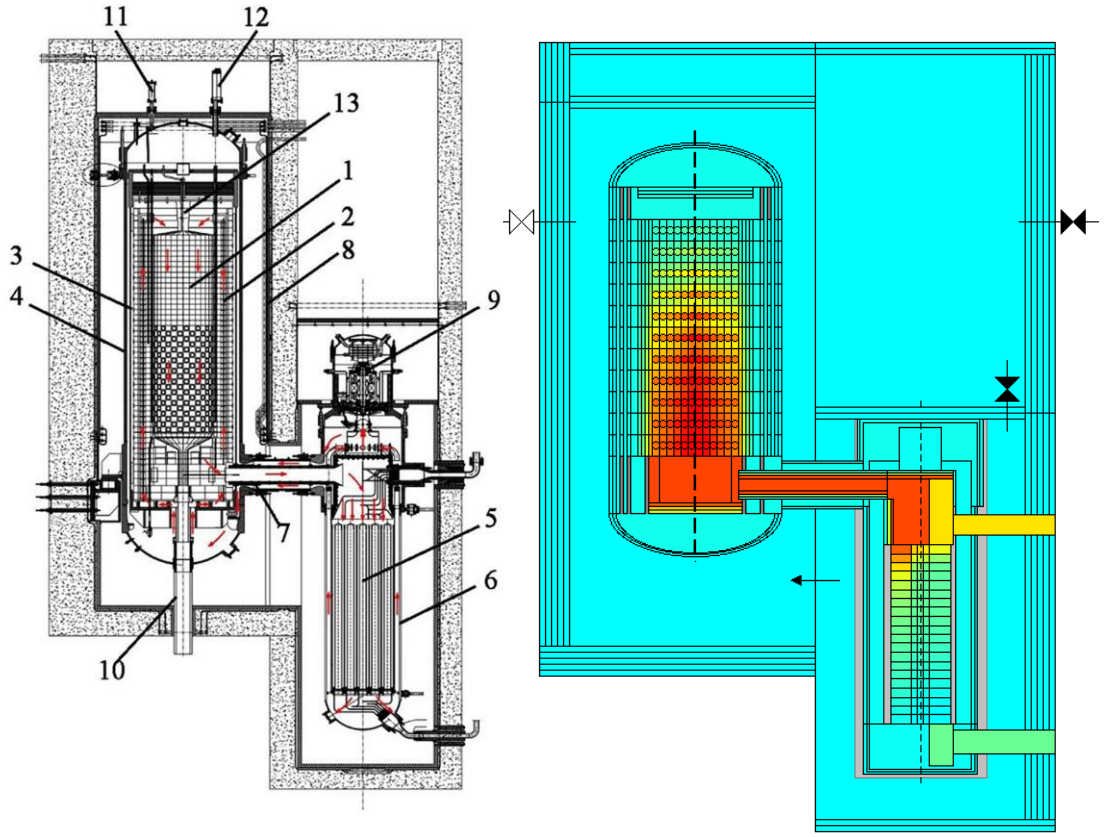

1 reactor core; 2 side reflector and carbon thermal shield; 3 core barrel; 4 reactor pressure vessel;
5 steam generator; 6 steam generator vessel; 7 coaxial hot-gas duct; 8 water-cooling panel; 9 blower;
10 fuel discharging tube; 11 control rod driving system; 12 small absorber sphere unit; 13 fuel charging tube

Figure 4-51 HTR-PM (left) plant layout (right) SPECTRA model and steady state

All three accidents can be detected by the protective system due to the signal of 'low ratio of primary mass flow to secondary mass flow'. The calculated results are shortly described below. A more detailed description is provided in [157].

- **DN65 mm DLOFC: break of a tube with diameter of 65 mm**

  A DN65 mm DLOFC accident is a typical DBA and receives high attention, because it results in the higher maximum fuel temperature compared to other DBAs. Compared to the results of the TINTE model, the maximal fuel temperature of the SPECTRA model in the first 30 h, as well as the peak value of the maximal fuel temperature, is a little higher as shown in Figure 4-52. The peak fuel temperature is 1485°C in TINTE model and 1502°C in SPECTRA; the difference is 17°C or 1.1%.

  Above the top carbon brick, metal internals are designed to serve as the thermal barrier and protect the components installed in the top of the RPV. In the present SPECTRA model these metal internals are not modeled accurately, since the detailed design parameters were not known at the time the model was built. This is one of the reasons why the temperatures are higher in SPECTRA than in TINTE. Another reason is explained below, at the discussion of PLOFC.

- **DN10 mm DLOFC: break of a tube with diameter of 10 mm**

  The accident scenario and the calculation results are similar to those from the DN65 mm case. With the smaller pipe break, the critical flow rate is smaller expected to take about 8–10 h for the coolant to depressurize to ambient pressure. So, during the early stage of the accident, the natural convection of the helium still plays a significant role for the heat transfer, while the fuel temperature is somewhat lower than that for the DN65 mm DLOFC. SPECTRA and TINTE results are shown in Figure 4-53. The peak fuel temperature is 1477°C in TINTE model and 1491°C in SPECTRA; the difference is 14°C or 0.9%.

- **PLOFC: the primary circuit the helium flow rate decreases to zero in 30 s.**

  In the PLOFC accident, the high temperature difference in the core and the high pressure helium in the primary circuit will cause a strong natural convection, which can effectively enhance the heat transfer and cooling of the core. Maximal fuel temperatures and average fuel temperatures during the accident are much lower compared to those in the DLOFC accidents. The peak value of the maximal fuel temperature is less than 1100°C. The peak fuel temperature is 1036°C in TINTE model and 1066°C in SPECTRA; the difference is 30°C or 2.9%.

  Differences between the results of the two codes are most clear in the PLOFC case - Figure 4-54. Therefore this case was selected to perform some sensitivity calculations. One modeling difference identified was the heat transfer from the RPV to the cooling panel: in the TINTE code simulation, only radiation and an insignificant air heat conduction are considered, while in the SPECTRA code simulation, air convection is also included. Additional calculations were performed with the convection from the RPV walls disabled in the SPECTRA simulation. The agreement between two codes became much better. The maximum fuel temperatures are quite similar - Figure 4-55.

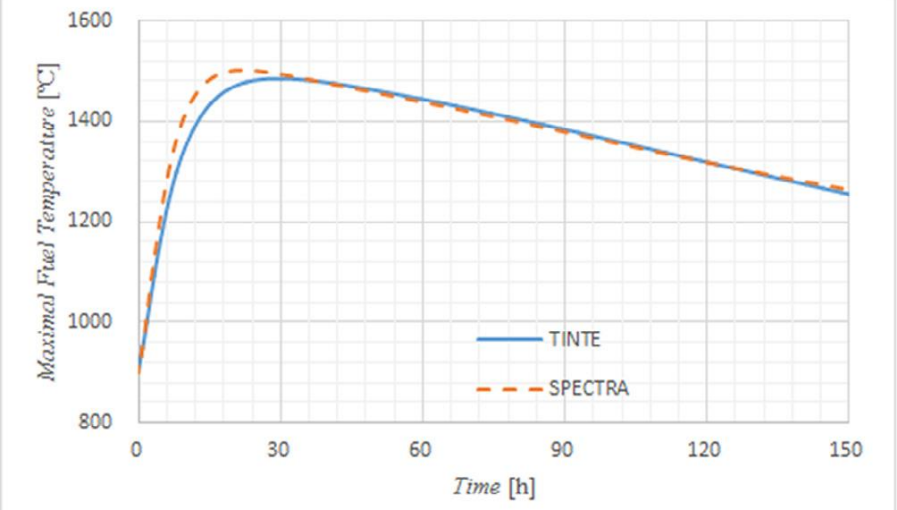

Figure 4-52 HTR-PM Fuel temperature during DLOFC accident (DN 65 mm)

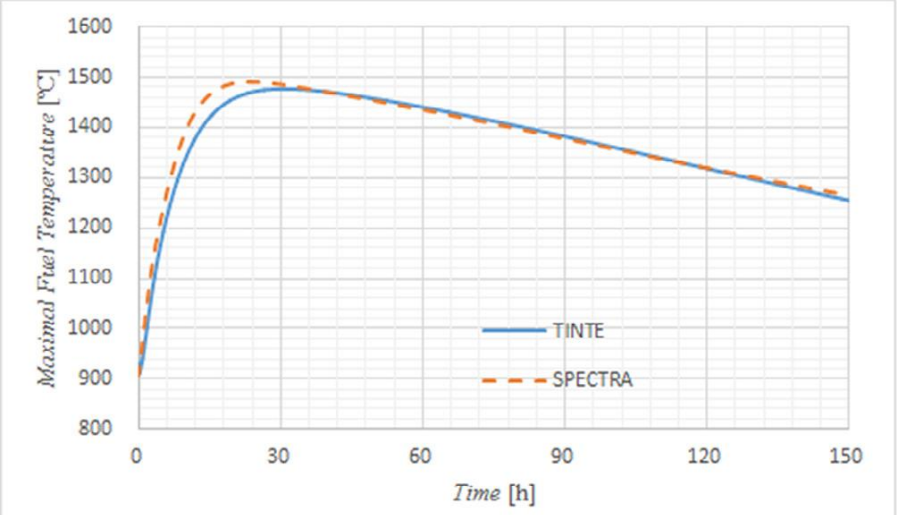

Figure 4-53 HTR-PM Fuel temperature during DLOFC accident (DN 10 mm)

- **Summary**

  Within a project between the NRG and the INET, the SPECTRA code was selected for code to code verification against the TINTE code, which has been approved by the Chinese authorities as the design and analysis tool to be applied to the HTR-PM. The calculation results of these two codes for two typical DLOFC accident scenarios and one PLOFC accident scenario are introduced and compared.

  Both codes are in good agreement, in particular:

  ✓ In the DLOFC accident, the peak fuel temperature is about 1500°C, with a large margin to the design limit of 1620°C.

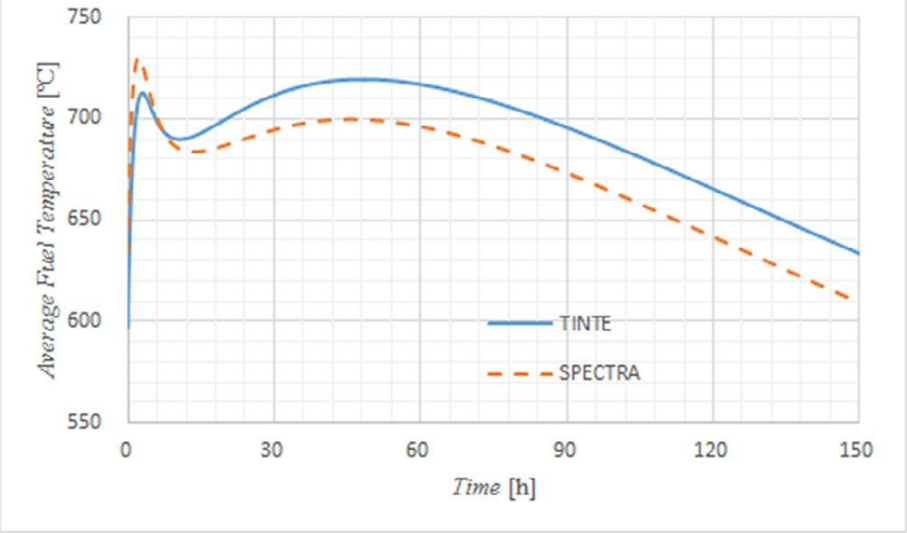

Figure 4-54 HTR-PM Fuel temperature during PLOFC accident

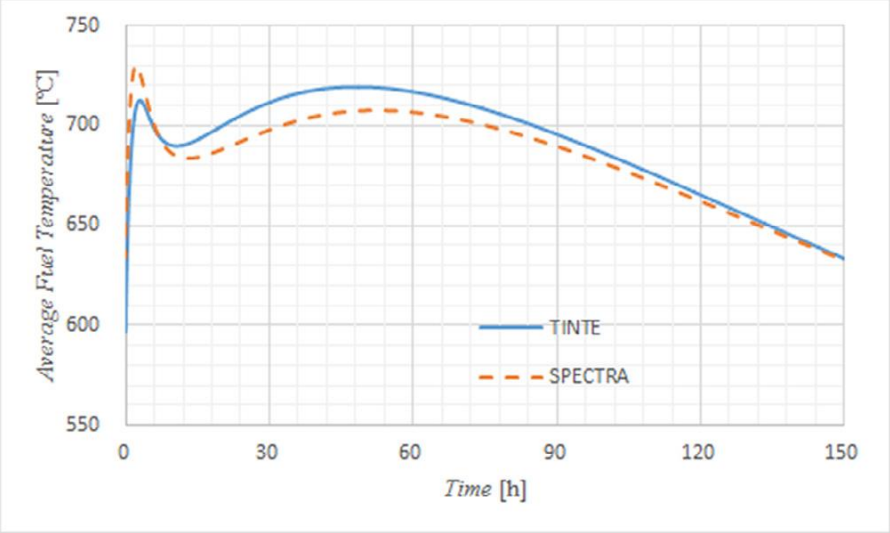

Figure 4-55 HTR-PM Fuel temperature during PLOFC accident - convection model disabled in SPECTRA

- ✓ In the PLOFC accident, the high temperature difference in the core and the high pressure helium in the primary circuit will cause the strong natural convection, which can effectively enhance the heat transfer and cooling the core. The peak fuel temperature is below 1100°C, far below the limit of 1620°C.
- ✓ Results of both codes show good agreement, especially in the DLOFC accident scenarios. Differences can be explained by :
  - differences in geometry: e.g. SPECTRA model of upper plenum is simplified due to lack of detailed design information at the time the model was built,
  - differences in modeling: e.g. heat transfer in cavity radiation + convection in SPECTRA versus radiation on TINTE.

4.4 Application of SPECTRA to Liquid Metal Reactors

4.4.1 EBR-II (IAEA CRP) - Comparison with Experiment

The International Atomic Energy Agency (IAEA) Coordinated Research Project (CRP) "Benchmark Analyses of EBR-II Shutdown Heat Removal Tests" [158] was initiated in 2012 with the objective of improving state-of-the-art SFR codes by extending code validation to include comparisons against whole-plant data recorded during landmark shutdown heat removal tests (SHRT) that were conducted at Argonne's Experimental Breeder Reactor II (EBR-II) in the 1980's.

The shutdown heat removal tests were simulated by participants using system codes in combination with CFD codes: SASSYS-1/SAS4A, SAC-CFR, THACS, CATHARE, SIMMER-III, FRENTIC, NETFLOW++, RELAP5-3D, MARS-LMR, SOCRAT-BN, TRACE, ANSYS-CFX [160]. At NRG the multi-scale thermal hydraulic simulation platform, consisting of the system thermal-hydraulic (STH) code SPECTRA and the CFD code ANSYS CFX (Figure 4-56), was used for transient simulations. This means the codes are coupled interactively ("on-line") and are exchanging data every time step. Based on comparisons of the main parameters, such as:

- pump flow,
- core inlet/outlet coolant temperatures,
- intermediate heat exchanger (IHX) primary inlet temperatures,
- IHX secondary outlet temperatures,
- primary coolant flow rates,

with the measured data provided by Argonne National Laboratory (ANL), the SPECTRA stand-alone model and the multi-scale thermal hydraulic coupled SPECTRA/CFX model proved to be able to provide satisfactory results for both tests SHRT-17 (Figure 4-57) and SHRT-45R (Figure 4-58). More details are provided in the internal NRG reports and open publication [159].

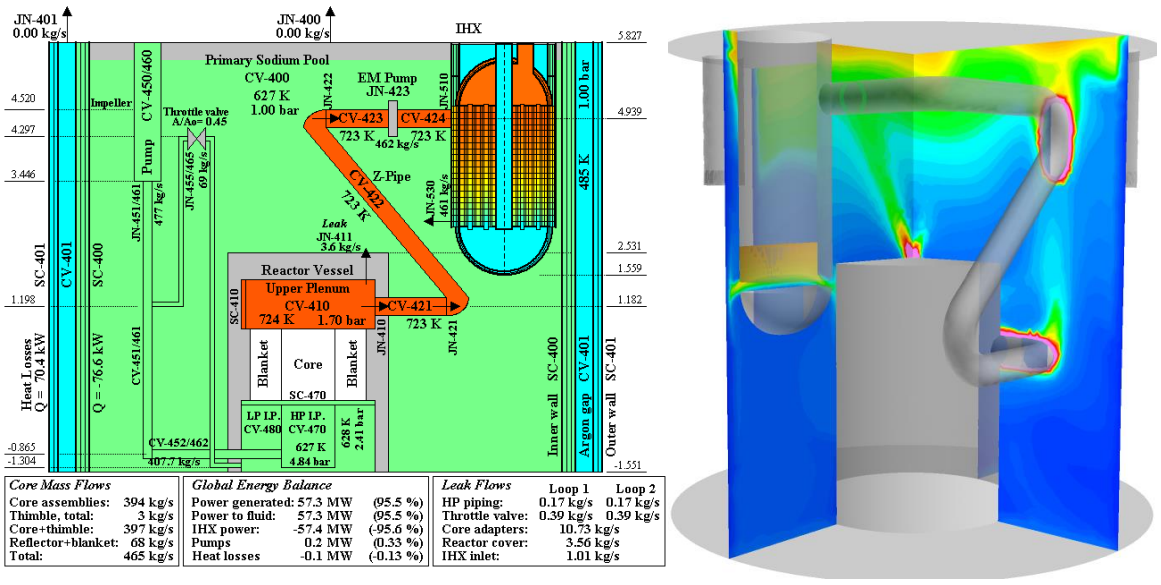

Figure 4-56 SPECTRA / CFX model of EBR-II, steady state results [159]

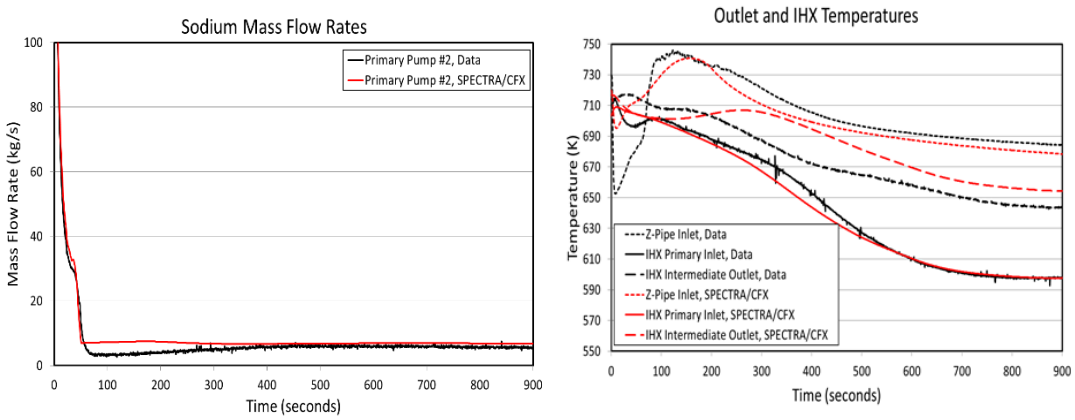

Figure 4-57 SHRT-17 final results: (a): pump flow, (b): coolant temperatures, [159]

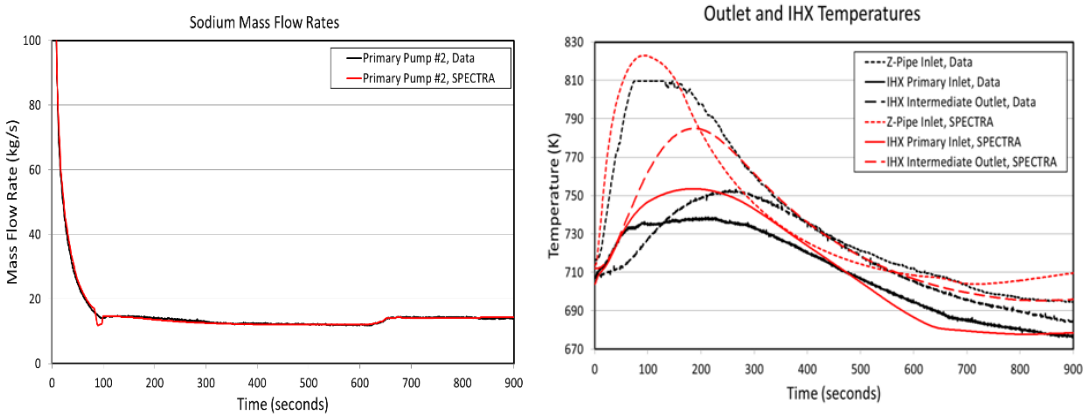

Figure 4-58 SHRT-45R final results: (a): pump flow, (b): coolant temperatures, [159]

4.4.2 ASTRID - Code-to-Code Comparison

In the frame of the ESNII+ FP7 EU Project, participants of the benchmark, using the ASTRID-like core neutronic and thermal-hydraulic specification (including reactivity feedback coefficients), developed the core models with their system codes and point (0D) neutron kinetics models. Calculations were performed on the most representative design basis accident: the unprotected loss of flow accident (ULOF) up to the initiation of sodium boiling. Steady-state and dynamic simulation of the ULOF transient was simulated by participants using system codes in combination with neutron point kinetics: TRACE, CATHARE, SIM-SFR, SAS-SFR, ATHLET, SPECTRA, SAS4A [160]. NRG participated with the SPECTRA code [161]. The NRG results agreed well with the results obtained by other participants and were roughly in the middle of the results of all codes (Figure 4-59).

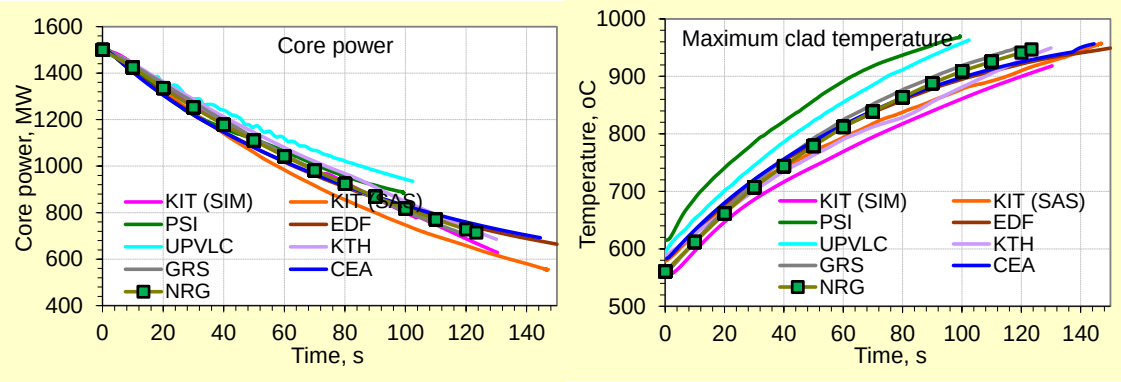

Figure 4-59 ASTRID ULOF results
(a) core power, (b) maximum cladding temperature, [161]

NRG sensitivity analysis concentrated on the gap modeling. In the base calculations, a constant gap conductance was used. The (time-independent) values were provided by CEA as a function of fissile height. As a sensitivity, the dynamic gap expansion model was used, with a rough guess for the EOC parameters [161]. When the dynamic gap expansion model is used, the gap size, and consequently the gap conductance, decreases during the transient. The maximum value at the start of the transient is about 7000 W/m^2-K. At t = 100 s it is only about 2500 W/m^2-K - Figure 4-60 (a). Those results are in agreement with the KIT SAS results - Figure 4-60 (b), with maximum value of $h \approx$ 7000 W/m^2-K at t = 0.0 s and $h \approx$ 2500 W/m^2-K at t = 100 s.

Figure 4-61 and Figure 4-62 show comparison of the results obtained for the base case and the dynamic expansion model case. During the analyzed transient, the gap conductance decreases by almost a factor of three. As a consequence, the maximum fuel temperature is higher than in the base case - Figure 4-61. A relative scale is used in Figure 4-61 (b), to show more clearly the rate of change of the temperature in time. As can be seen, at 120 s the maximum fuel temperature is about 0.75 of the initial value in the base case, while it is about 0.83 of the initial value in the case where the dynamic gap conductance model was used.

The consequence of different fuel temperature decrease rate is different behavior of the Doppler reactivity - Figure 4-62 (a). The Doppler reactivity increase is slower when the dynamic gap expansion is used. As a consequence, the reactor power decrease is faster - Figure 4-62 (b). Finally, due to lower power, the timing when boiling starts is delayed. The onset of boiling was calculated by SPECTRA as 123 s in the base case and 159 s in the sensitivity case.

Figure 4-61 (b) and Figure 4-62 show SPECTRA results together with two other participants:

- CEA results, obtained using constant gap conductance,
- KIT (SAS) results, obtained for the dynamic gap expansion model.

It is seen that the trend predicted by CEA and KIT agree well with the NRG base case and sensitivity case respectively. Based on the above results it is concluded that the modelling of dynamic gap expansion is important. The gap conductance changes by roughly a factor of three during the present transient, which has an important effect on fuel temperature and thus the Doppler effect and finally the core power and timing to reach the sodium boiling point. Due to the difference in the gap modelling alone, the sodium boiling is reached nearly 40 seconds later.

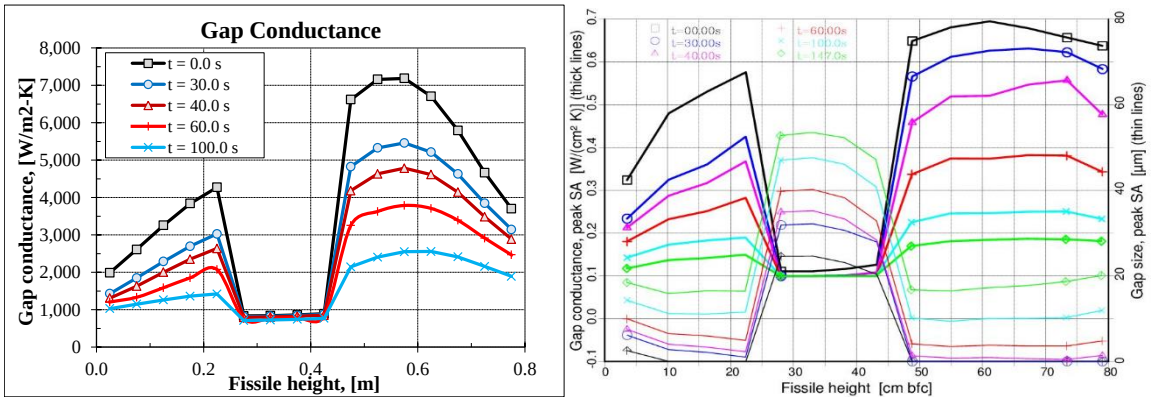

Figure 4-60 ASTRID ULOF, dynamic gap expansion model
(a) NRG SPECTRA results, (b) KIT SAS results, [161]

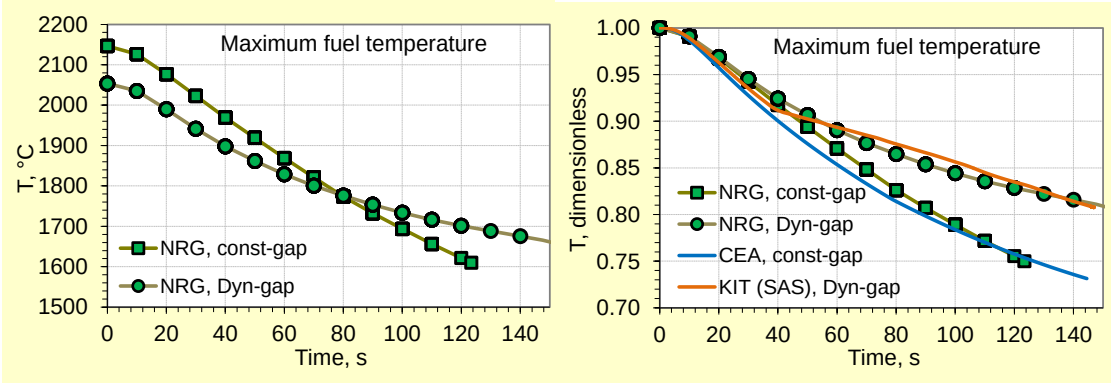

Figure 4-61 ASTRID ULOF, base case versus dynamic gap expansion model,
(a) maximum fuel temperature, T_{MAX}, (b) dimensionless T_{MAX}, [161]

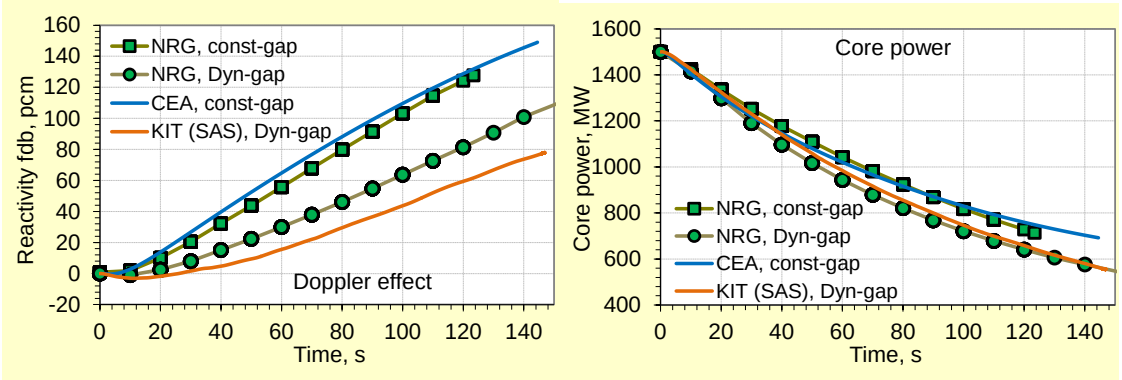

Figure 4-62 ASTRID ULOF, base case versus dynamic gap expansion model
(a) Doppler effect, (b) core power, [161]

4.4.3 ESFR - Code-to-Code Comparison

The new reactor concepts proposed in the Generation IV International Forum (GIF) are conceived to improve the use of natural resources, reduce the amount of high-level radioactive waste and excel in their reliability and safe operation. Among these novel designs Sodium Fast Reactors (SFRs) stand out due to their technological feasibility as demonstrated in several countries during the last decades. As part of the contribution of EURATOM to GIF the CP-ESFR is a collaborative project with the objective, among others, to perform extensive analysis on safety issues involving renewed SFR demonstrator designs. The verification of computational tools able to simulate the plant behavior under postulated accidental conditions by code-to-code comparison was identified as a key point to ensure the reactor safety level. In this line, several organizations developed models able to simulate the complex and specific phenomena involving multi-physics studies that this fast reactor technology requires. The participant used codes CATHARE, RELAP5, TRACE, SIM-SFR, SAS-SFR, MAT4-DYN, SPECTRA [162], [163]. NRG participated in the ESFR benchmark using the SPECTRA code.

The main outcome of this study is that all codes used are able to analyze the transient behavior of the ESFR plant design. In general terms the benchmark demonstrated good agreement among the various codes in the various parameters calculated that are relevant for safety, considering the complexity of the different codes, their different origin, and quite different modelling approach. The participants of the benchmark comparison case have consistently calculated the main parameters of the transient and have thus demonstrated to be able to simulate the transient behavior of SFR reactors [163].

Results of SPECTRA were compared to the results obtained at ENEA with RELAP5. SPECTRA and RELAP results were in good agreement. Detailed results of SPECTRA nad comparison to RELAP results are currently provided only in an internal NRG report and the presentations made at the project meetings. The results will be published in open literature in the future.

4.4.4 LEADER - Code-to-Code Comparison

Lead-cooled European Advanced DEmonstration Reactor (LEADER) is an EU design of liquid lead-cooled fast reactor. Within WP5, several computer codes (SAS-LFR, RELAP, TRACE, CFX, SIMMER, SPECTRA) were applied to evaluate consequences of selected unprotected accident scenarios such as Loss of Flow, Loss of Heat Sink, and reactivity-initiated accidents [164]. NRG participated with the SPECTRA code (Figure 4-63). Eight accident scenarios were analyzed [165]:

- TR-4 Unprotected Transient Overpower: reactivity insertion
- T-DEC1 Unprotected Loss of Flow: loss of all primary pumps.
- T-DEC3 Unprotected Loss of Heat Sink: loss of SCS
- T-DEC4 Loss of off-site power.
- TO-3 Loss of FW pre-heater
- TO-6 20% increase of FW flow
- T-DEC6 SCS failure
- T-DEC5 Partial blockage of hottest assembly

Results of SPECTRA were compared to the results obtained at ENEA with RELAP5. SPECTRA and RELAP results were in good agreement - Figure 4-64. Furthermore the calculations of all participants showed very good intrinsic safety features of ALFRED design, which are due to:

- good natural circulation characteristics,
- large thermal inertia,
- dominant negative reactivity feedbacks.

It was found that in all analyzed transients there was no risk for significant core damage or risk for lead freezing. Consequently a large grace time is left to the operator to take the appropriate corrective actions and bring the plant in safe conditions in the medium and long term [165].

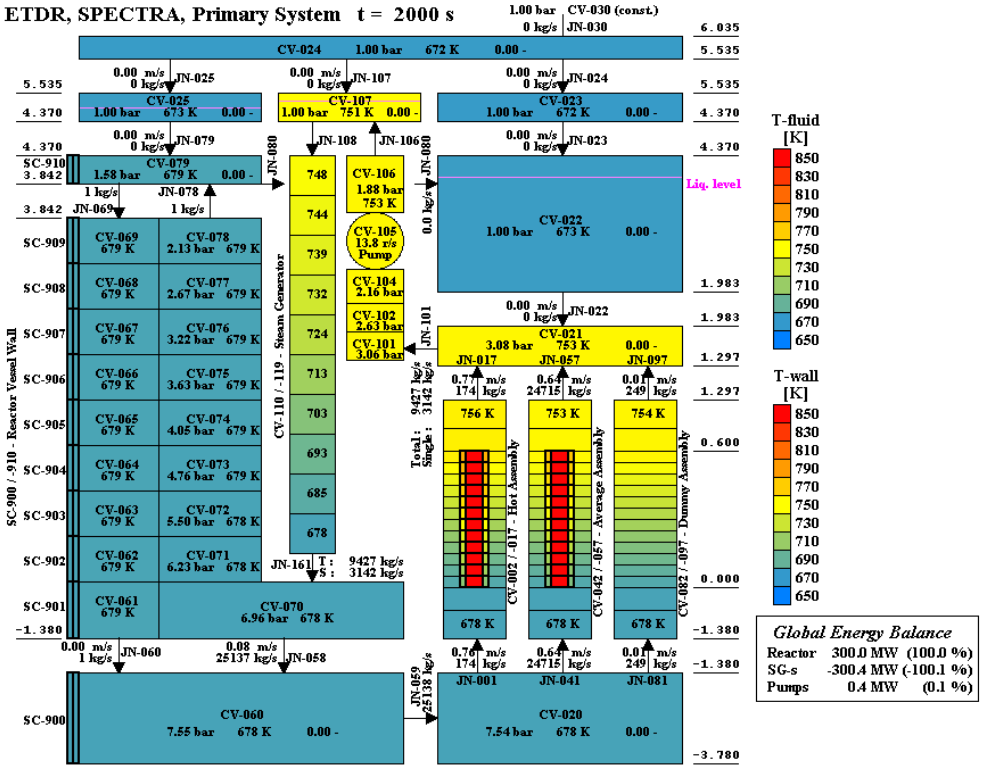

Figure 4-63 LEADER, NRG SPECTRA model and steady state results, [165]

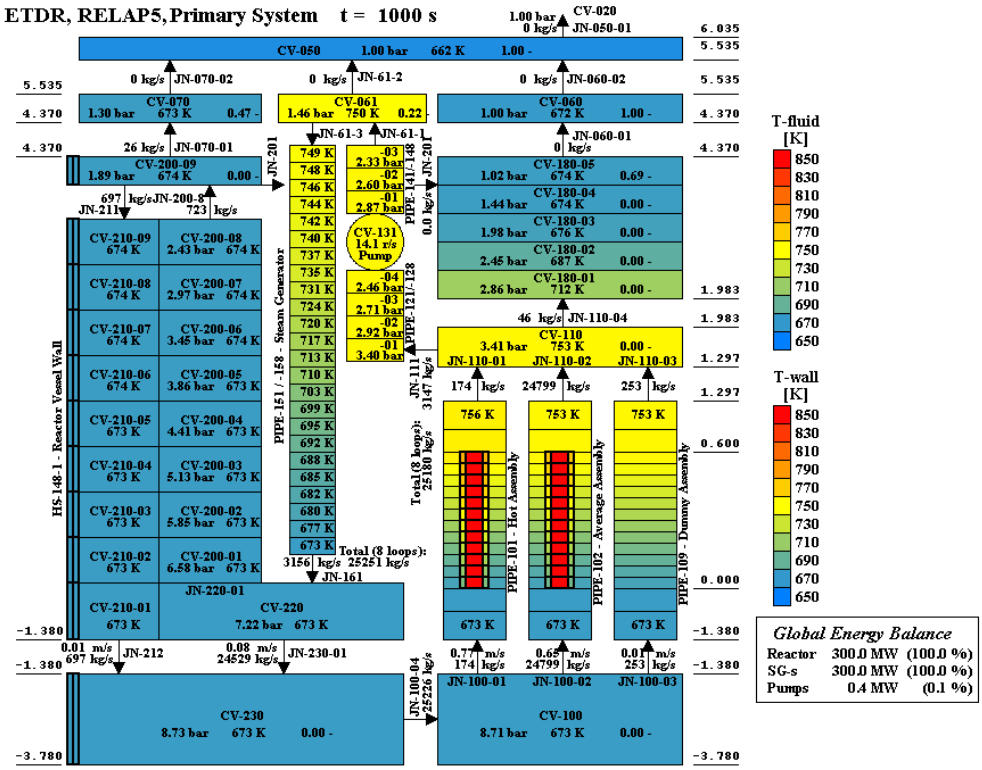

Figure 4-64 LEADER, ENEA RELAP5 model and steady state results, [165]

4.5 Application of SPECTRA to Molten Salt Reactors

The main capabilities of the current code version with respect to Molten Salt Reactors are given below.

- The fluid properties and heat transfer correlations are defined by the user. This enables analysis of various types of salts (fuel salts as well as coolant salts) without any code modifications.
- The thermal-hydraulic part is coupled to the reactor physics part (currently point kinetics) In ongoing work the code will be interactively coupled to 3D kinetics program or will incorporate a 3D kinetics module.
- For fluids other than water, the user has to provide heat transfer correlations and fluid properties using general functions. Applications to high Prandtl number fluids like molten salts are demonstrated by comparisons to measured data [166] as well as code-to-code benchmarks [181].
- Reactor control logic is easily modelled via control and tabular function packages.

The thermal radiation model includes the net enclosure with and without participating gas. The radiation properties of gases are dependent on temperature. Currently the model works only for gas-covered surfaces. Extension of the model to radiation in liquids is planned in future versions of the code.

4.5.1 MSRE - Comparison with Measured Data and Analytical Models

4.5.1.1 MSRE Description

Figure 1 (a) shows a schematic of the Molten Salt Reactor Experiment (MSRE). The reactor was designed for a power of 10 MWt, and the values shown in this section are for this power. The primary loop with the molten salt circulating with a pump at a flow of 75.7 l/s enters the reactor vessel at a temperature of 908 K and leaves at a temperature of 936 K [194]. The primary loop salt was LiF-BeF_2-ZrF_4, with the fuel dissolved as UF_4. The heat generated in the core was removed in a heat exchanger (HX). The core was made of graphite blocks - Figure 1 (b) with the molten salt circulating upwards inside vertical channels. The reactor vessel and piping were made of Hastelloy-N, a nickel-molybdenum-chromium alloy compatible with molten fluoride salts.

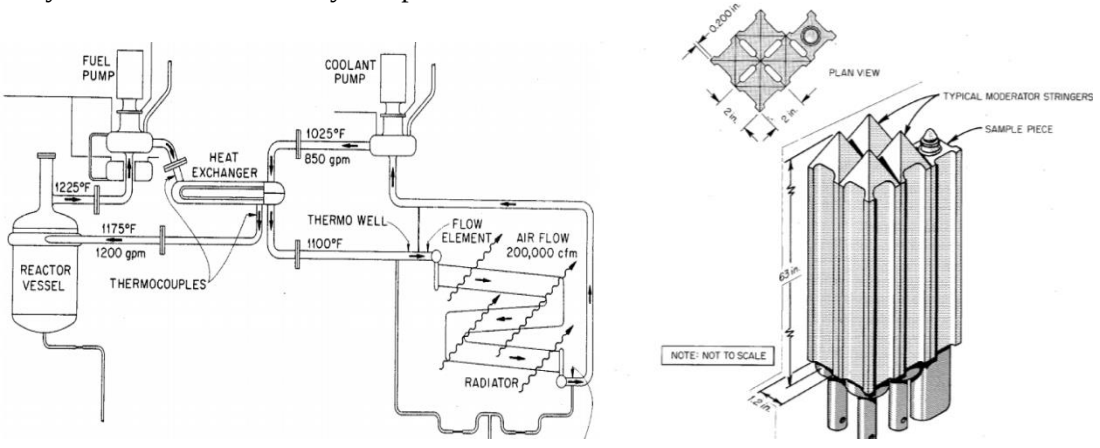

Figure 4-65 MSRE, MSRE (a) loop [182], (b) graphite blocks [183]

4.5.1.2 Thermal Hydraulic Model

A model of MSRE was built for SPECTRA, using data from the ORNL reports [182], [183], [184], [185], [186], [187], [188], [189], [190], [191], [192], [193], and [194]. The molten salt properties were defined following [182]. The dimensions were obtained from: core [183], [190], reactor vessel [187], [188], loop [182], HX [186], [194], pump [187], [188]. The delayed neutron precursor (DNP) data for six DNP groups was obtained from [184]. The heat transfer correlations were obtained from [191]. The model includes the primary loop and secondary side of the HX, with inlet and outlet boundary conditions. Steady state operation was simulated for the design conditions (10 MW reactor power) and compared to available data [166].

Results are shown in Figure 4-66, Figure 4-67, and Figure 4-68. The steady state results are compared to the reference data in Table 4-9. A good agreement is observed. It has to be remembered that the source data are design data and not measured values. MSRE was never operated at design power. The typical operational power was 7.5 - 8.0 MW.

For the purpose of analyzing migration of noble gases and noble metals to the graphite and metallic surfaces, it is important to model all surface areas of structures where the fission product can deposit. The MSRE model was built including all structures with the best possible accuracy. The structures were modeled using the drawings and available data (pipe length, diameters, etc.) and then the overall data of certain groups of structures were checked against the MSRE data. However, different ORNL reports provide different values concerning the overall surface areas. The numbers based on two ORNL reports are shown in Table 4-10. The structures present in the SPECTRA input, arranged by SC groups, are shown in Table 4-11.

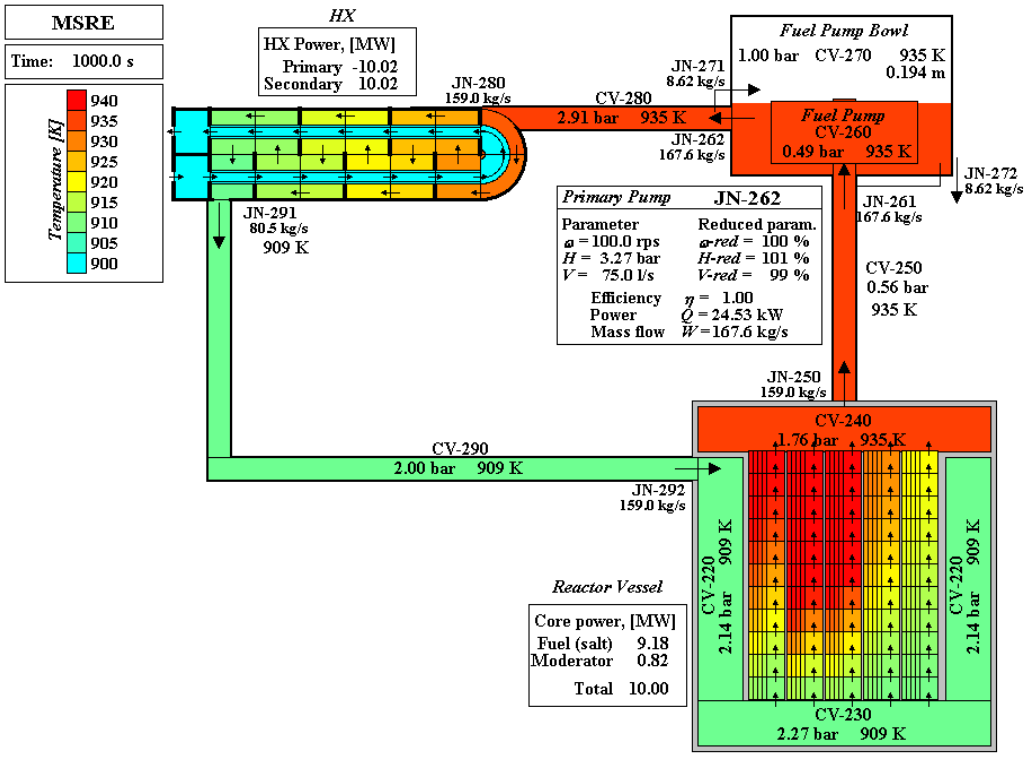

Figure 4-66 MSRE, steady state results at 10 MW

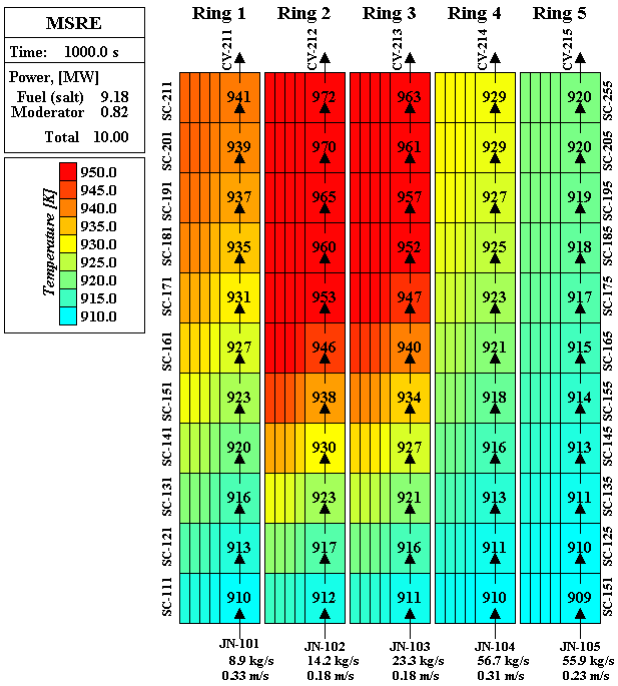

Figure 4-67 MSRE core, steady state results at 10 MW

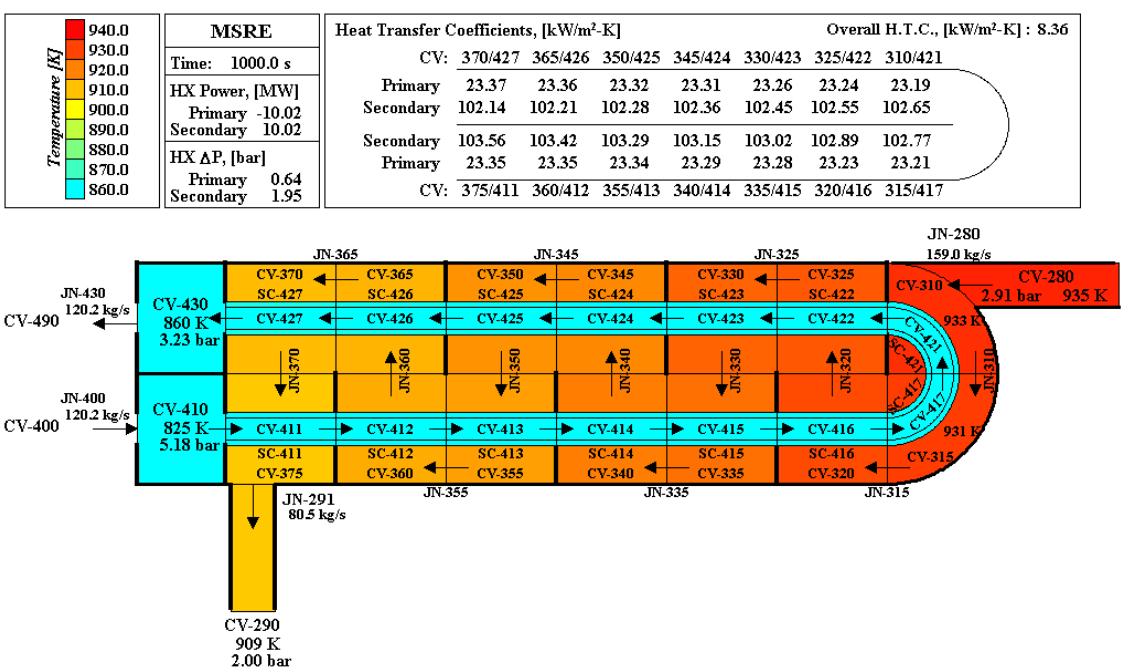

Figure 4-68 MSRE HX, steady state results at 10 MW

Table 4-9 Comparison of MSRE steady state parameters

Parameter	SPECTRA	MSRE [186], [187], [190], [194]
Power [MW_t]	10.0	10.0
Primary T_{IN} [K]	909	908
Primary T_{OUT} [K]	935	936
Coolant flow [l/s]	75.0	75.7
Coolant flow [kg/s]	168	171
ρ [kg/m^3] at 920 K	2,241	2,258
T_{MAX} fuel [K]	972	956
T_{MAX} graphite [K]	974	975
Graphite power [%]	8	6
V core [m/s]	0.18 – 0.33	0.18 – 0.61
Secondary T_{IN} [K]	825	825
Secondary T_{OUT} [K]	860	866

Table 4-10 Surface areas of all structures, source data from [135] (left) and [182] (right)

ORNL-TM-3884	**A [ft2]**	**A [m2]**
Hastelloy N surfaces		
Misc	54	5.02
Piping, pump volute	71	6.60
HX, shell side	315	29.26
Core wall cooling a.	154	14.31
	Σ	**55.18**
Graphite surfaces		
Core graphite	1465	136.10
Misc	146.5	13.61
	Σ	**149.7**

ORNL-4865	**A [ft2]**	**A [m2]**
Hastelloy N surfaces		
Pump	30	2.79
Piping	45	4.18
HX	346	32.14
Reactor vessel	431	40.04
	Σ	**79.15**
Graphite surfaces		
Fuel channels		132.35
Tops and bottoms		3.42
Contact edges		*80.25*
Support lattice bars		8.95
Σ(*excluding C.e.***)**		**144.7**

Table 4-11 Surface areas of all structures, SPECTRA model

Group	**Surface**	**A [m2]**	
Hastelloy N surfaces			
3	Pump bowl	2.56	**Σ**
6	Piping	3.37	5.93
2	HX walls	29.93	**Σ(HX)**
4	HX shell	2.84	32.77
5	Reactor vessel walls	33.50	
	Σ	**72.20**	
Graphite surfaces			
1	Core	135.87	
7	Support lattice bars	8.95	
	Σ	**144.8**	

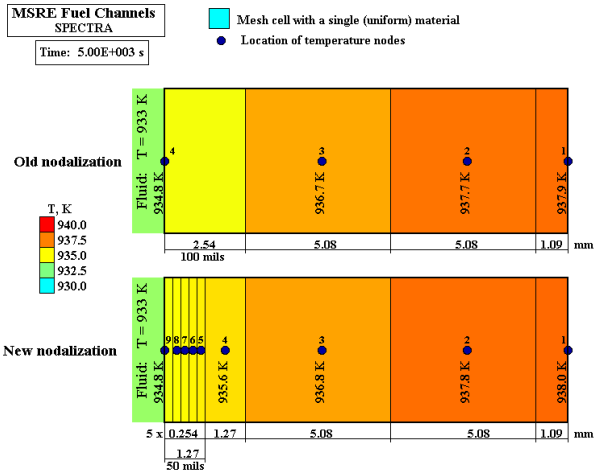

Figure 4-69 Re-nodalization of the near-surface region, to calculate diffusion of FP

Furthermore, in order to calculate diffusion of fission products into materials with a reasonable accuracy, a fine nodalization was applied in the region near the surface. Nodalization used in initial, pure thermal-hydraulic, analysis [166] is shown in Figure 4-69 (top). The nodalization applied for fission product analyses is shown in Figure 4-69 (bottom). The first node (the node at the boundary surface), which had a thickness of 2.54 mm (100 mils), was divided into six nodes: the first five nodes from the surface have thickness of 0.254 mm, the sixth node has thickness of 1.27 mm.

4.5.1.3 Delayed Neutron Precursor Drift

As a first application to fission product behavior, the model was used to calculate the drift of Delayed Neutron Precursors (DNP). First, as a verification SPECTRA results were compared to the results obtained with CFD calculations for a simple loop test case. In the CFD calculations the source of DNPs was provided based on SPECTRA results. The model and calculations are described in section 3.9.3.10. A good agreement was obtained (Figure 3-456).

Next, the behavior of DNPs was calculated using the MSRE model and compared to the values calculated at ORNL. Figure 4-70 shows DNP concentrations in the core. The SPECTRA-calculated values are superimposed on the graph with the values obtained from reference [184]. The lines marked as "stationary" represent the DNP generation rates and are proportional to the axial reactor power profile (defined as user input). The lines marked as "circulating" represent the sum of DNP concentrations multiplied by the decay constant [184]:

$$\sum_{i=1}^{6} C_i(z) \cdot \lambda_i$$

These values represent the total local rate of emission of delayed neutrons along the flow path through the reactor core. The source data include here circulating critical state (ω = 0.0 s^{-1}) as well as supercritical with 10 s reactor period (ω = 0.1 s^{-1}). Only the stationary state results are compared. The results vary slightly from ring to ring. The values shown in Figure 4-70 are those for Ring 2, which has the most representative characteristics. The results show very good agreement. In the MSRE, the time it takes to make a full circle through the primary loop is about 25 s [182], [184]. The DNPs half-life is between 0.23 and 55.9 s [184]. Thus the long-life DNPs will flow through the complete loop one or more times before they decay and release neutrons. Consequently, the DNP concentrations at the core inlet are not negligible and the capability to accurately model the DNPs transport in the entire loop is important.

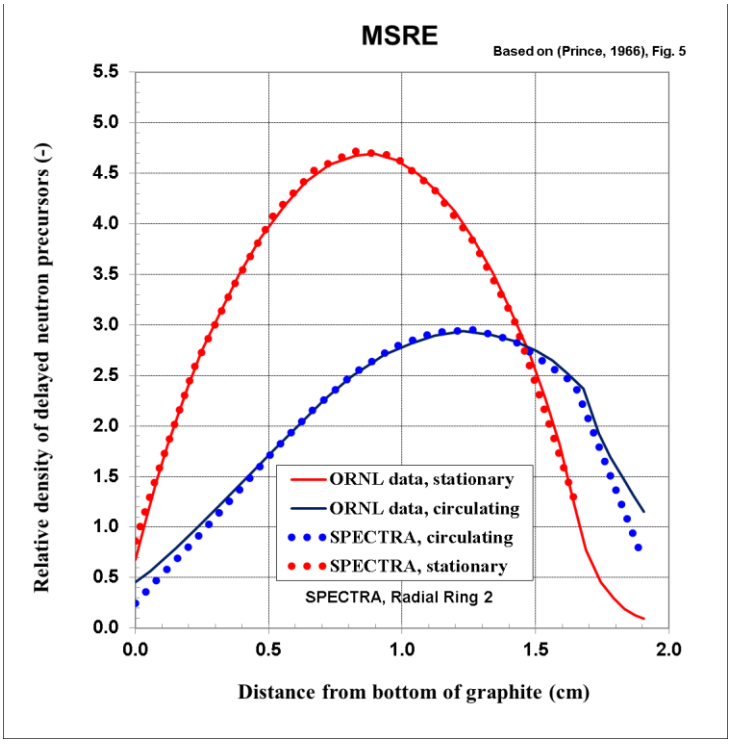

Figure 4-70 MSRE, concentrations of delayed neutron precursors

4.5.1.4 Fission Product Behavior in Salt

For the purpose of fission product release, each isotope present in the core is associated with one of the fission product release classes. Twelve default vapor classes are built-into the SPECTRA code (Volume 1). The discussion below is based on MSRE observations, presented in [135]. Based on their migrational characteristics the fission products are classified as follows:

- ***Salt seekers***. Unless affected by migrational characteristics of their precursors, they remain dissolved in the fuel.
- ***Noble gases***. There are only two noble gas fission products, Kr and Xe. They appear, however, in over 30 mass number decay chains and therefore significantly affect the general fission product disposition. The noble gases, particularly xenon, are very insoluble in fuel salt; therefore, they are readily transported into any available gas phase such as the circulating bubbles, the gas space in the pump bowl, and the pores of the moderator graphite.
- ***Noble metals***. Similarly to noble gases, the noble metals migrate to surfaces such as graphite, metallic walls, as well as gas. In MSRE noble metals have been found throughout the entire reactor fuel salt loop. They have been found in fuel salt and gas phase samples from the pump bowl. They have been found on the Hastelloy-N and graphite core surveillance samples, and on the primary heat exchanger tube surfaces and loop piping surfaces. They have been found at various locations in the off-gas system.

Based on the data presented in [135], all the default fission product classes in SPECTRA were divided into three categories, as shown in Table 4-12. The modeling assumptions made for each category are discussed in the next section.

Table 4-12 Fission product classes in SPECTRA

Class	Member elements	Behavior in salt
1	**Xe**, He, Ne, Ar, Kr, Rn, H, N	Noble Gas
2	**Cs**, Li, Na, K, Rb, Fr, Cu	Salt Seeker
3	**Ba**, Be, Mg, Ca, Sr, Ra, Es, Fm	Salt Seeker
4	**I**, F, Cl, Br, At	Salt Seeker
5	**Te**, O, S, Se, Po	Noble Metals
6	**Ru**, Rh, Pd, Re, Os, Ir, Pt, Au, Ni	Noble Metals
7	**Mo**, V, Cr, Fe, Co, Mn, Nb(*), Tc, Ta, W	Noble Metals
8	**Ce**, Ti, Zr, Hf, Th, Pa, Np, Pu, C	Salt Seeker
9	**La**, Al, Sc, Y, Ac, Pr, Nd, Pm, Sm, Eu, Gd, Tb, Dy, Ho, Er, Tm, Yb, Lu, Am, Cm, Bk, Cf	Salt Seeker
10	**U**	-
11	**Cd**(*), Hg, Zn, As, Sb, Pb, Tl, Bi	Noble Metals
12	**Sn**, Ga, Ge, In, Ag	Noble Metals

(*) A salt-seeker in an oxidizing environment.

4.5.1.5 Modeling Assumptions

The main observations from the MSRE operation that are basis for the fission product modeling assumptions are listed below. First, general observations are shown that are used to select the forms of equations. Next, specific observations are listed, that are used to determine coefficients applied in the model. The general observations are listed below.

- Each noble metal migrates as a function of its own concentration in salt and is not influenced by other elemental species, or even isotopic species of the same element [135] (sec. 5.2).
- Noble metals migrate according to the simplest form of mass transfer theory [135] (sec. 5.2).
- Deposition on liquid-gas interfaces (bubbles) must be included in the calculation [135] (sec. 5.2).
- Noble metals found in the gas samples owe their existence to a salt mist generated by bursting bubbles [135] (sec. 5.5).

The specific observations are listed below.

- MSRE observations showed that if the sticking fraction (defined as that fraction of atoms that contact the interface and adhere to it) of noble metals to solid surfaces is close to unity, then the sticking fraction to liquid-gas interfaces is 0.1 – 0.2 [135] (sec. 5.2).
- A sticking fraction of noble metals to a liquid-gas interface considerably smaller than 1.0 was not expected. A rationalization of this apparent paradox is as follows. An observation from the reactor is that many of the smaller bubbles circulating with the fuel salt completely dissolve in the higher pressure part of the loop [135] (sec. 5.2).
- "*It appears that the sticking fraction of noble metals to graphite is less than unity*" [135] (sec. 5.3).

- "*The sticking fraction of noble metals to graphite is apparently less than the sticking fraction to Hastelloy N. Because of scatter in the data, it was difficult to draw a firm value, but something in the range of 0.1 - 0.6 would be in order*" [135] (sec. 5.7.1).

The fission product modeling parameters were selected based on the MSRE observations. The following correlations were used for transport of fission products (noble gases and noble metals) to the surfaces:

- Core surfaces, Sieder-Tate:

$$Sh = 1.86 \cdot Re^{0.33} \cdot Sc^{0.33} \cdot (D/L)^{0.33} = 0.575 \cdot Re^{0.33} \cdot Sc^{0.33}$$

- Other surfaces, turbulent forced convection:

$$Sh = 0.023 \cdot Re^{0.8} \cdot Sc^{0.4}$$

- Bubble surfaces: the mass transfer coefficient is estimated in [135] as *mtc* = 5.0 ft/h = 4.23×10^{-4} m/s. The corresponding *Sh* number was obtained for an average bubble diameter of D_{bubb} = 0.005 in. = 1.27×10^{-4} m [135] and the diffusion coefficient in liquid of D_L = 5.0×10^{-4} ft^2/h = 1.29×10^{-9} m^2/s [136]:

$$Sh = mtc \cdot D_{bubb} / D_L = 41.7$$

The following diffusion coefficients are used for diffusion in the liquid (salt):

- Noble gases: D_L = 1.35×10^{-9} m^2/s (average of Xe: 1.29×10^{-9}, Kr: 1.42×10^{-9} [136])
- Noble metals: D_L = 1.32×10^{-9} m^2/s [135]

The following sticking factors are used for solid surfaces:

	graphite surfaces	metallic surfaces	liquid-gas interfaces
• Noble gases:	C_G = 1.0	C_H = 1.0	C_I = 0.1
• Noble metals:	C_G = 0.1	C_H = 1.0	C_I = 0.1

In SPECTRA the dissolving of small bubbles in the higher pressure parts of the loop, described above, is not modeled. Therefore the sticking fraction of 0.1 is used.

The following diffusion coefficients are used for diffusion of noble gases in graphite:

- core top and middle graphite samples: D_G = 4.65×10^{-9} m^2/s
- core bottom graphite samples: D_G = 1.78×10^{-8} m^2/s

The values were obtained from [136], converted to SI units and divided by porosity (ε=0.1) for reasons explained in Appendix A.1. The diffusion coefficients of noble gases in Hastelloy N are not available and these values were assumed as zero, D_H = 0.0. Isotopes other than noble gases practically do not diffuse in solid materials. Therefore, for all fission product classes other than noble gases, it was assumed that: $D_G = D_H = 0.0$.

4.5.1.6 Noble Gases

The behavior of noble gases was investigated using available data for Xe-135, Xe-140, and Xe-137.

Steady State Xe-135 Poisoning - Comparison with Other Calculation

An analysis of the behavior of Xe-135 was performed in the past at Oak Ridge and is described in [185]. The model includes all main sources and sinks of Xe-135:

- Generation from fission (cumulative rate of 6.4% per fission)
- Decay in salt
- Burnup in salt
- Stripping in the pump bowl stripper
- Migration to graphite
- Migration to circulating bubbles

All the phenomena taken into account in the ORNL analysis are also taken into account in the present analysis. The main parameters used in the analysis of Xe behavior are discussed below.

- ***Migration to circulating bubbles.*** Because migration to bubbles is of primary importance, the value of the mass transfer coefficient to bubbles needs to be known with fair accuracy. Based on reference [135] (see section 4.5.1.5): $Sh = 41.7$.
- ***Migration to bubbles in He bubbler.*** The He bubbler is located in the pump bowl. The bubbles are injected at a constant rate. The migration to the bubbles is calculated from the same correlation as the migration to circulating bubbles: $Sh = 41.7$.
- ***Migration from droplets.*** Mass transfer from droplets in the Xenon stripper (spray ring) to the cover gas has relatively small effect because of small residence time of droplets. A more important effect on Xe-135 removal is the stripping of bubbles (described below). Nonetheless the effect is included in the model. The mass transfer coefficient is obtained from the Sherwood number correlation, which for the spherical droplets is $6 < Sh < 18$ (see Appendix A.2). In the current analysis the lower value was applied: $Sh = 6.0$.
- ***Bubble stripping.*** A parameter that was introduced at ORNL is the bubble stripping efficiency [185]. This is defined as the percentage of Xe-135 enriched bubbles that burst in passing through the spray ring and are replaced with pure helium bubbles. In the current model this is achieved by using a filter model. The filter removes a prescribed fraction (= stripping efficiency) of bubbles passing through the stripper). At the same time the same amount of fresh bubbles (free of Xe-135) are placed in the pump bowl.

Calculations were performed for the same combinations of parameters as in [185], namely:

Parameter	Values considered				
Mean circulating void volume, %	0.0	0.125	0.25	0.50	1.0
Mean bubble diameter, in	0.005	0.01	0.020		
Mean bubble mass transfer coefficient, ft/hr	0.5	2.0	4.0		
Mean bubble stripping efficiency, %	10	50	100		

Figure 4-71 shows the Xe-135 poisoning. The SPECTRA results are superimposed on the original graph from ORNL. The graph shows the effect of bubble stripping efficiency. Results from both ORNL and SPECTRA show that the bubble stripping efficiency has a strong effect on the Xe-135 poisoning. The agreement between SPECTRA and ORNL calculations is good.

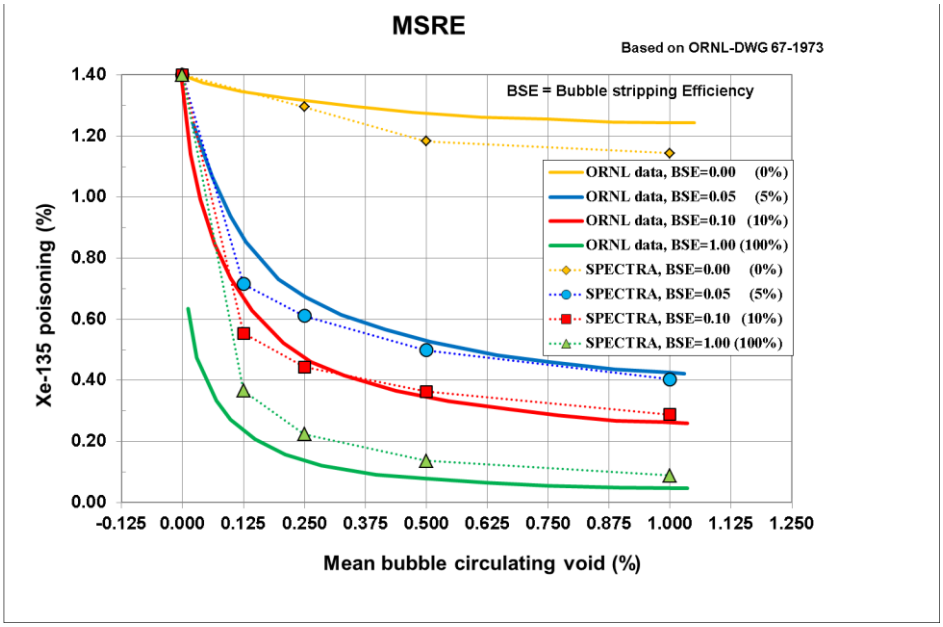

Figure 4-71 Effect of bubble stripping efficiency on Xe-135 poisoning, source data [185] and SPECTRA

Xe-135 Poisoning at Shutdown - Comparison with Data

Reference [189] shows the Xenon reactivity, measured during the MSRE Run 10, with a step decrease in power level from 7.4 MW to 0. The circulating bubbles void fraction was 0.15%. Also results obtained with the ORNL analytical model are shown.

The SPECTRA model was applied to analyze this transient. Figure 4-72 shows the Xenon poisoning data as well as calculated results. Three cases are considered:

- Bubble Stripping Efficiency of: BSE = 0.10
- Bubble Stripping Efficiency of: BSE = 0.50
- Bubble Stripping Efficiency of: BSE = 1.00

It is seen that the best agreement is obtained using a stripping efficiency of 0.1. Although this does not agree with calculations from [189], where the best value of bubble stripping efficiency was found to be 0.5, it is in better agreement with another estimation, saying: "*In magnitude it* (the stripping efficiency) *turns out to be between 8 and 15%*" [185].

The main purpose of the present calculation is to check which value of stripping efficiency gives best results in our model. Admittedly, there is a disagreement between the best stripping efficiency in our model and in the theoretical model applied by Engel and Steffy [189], however the agreement with the estimation provided by Kedl and Houtzeel, [185] is quite good.

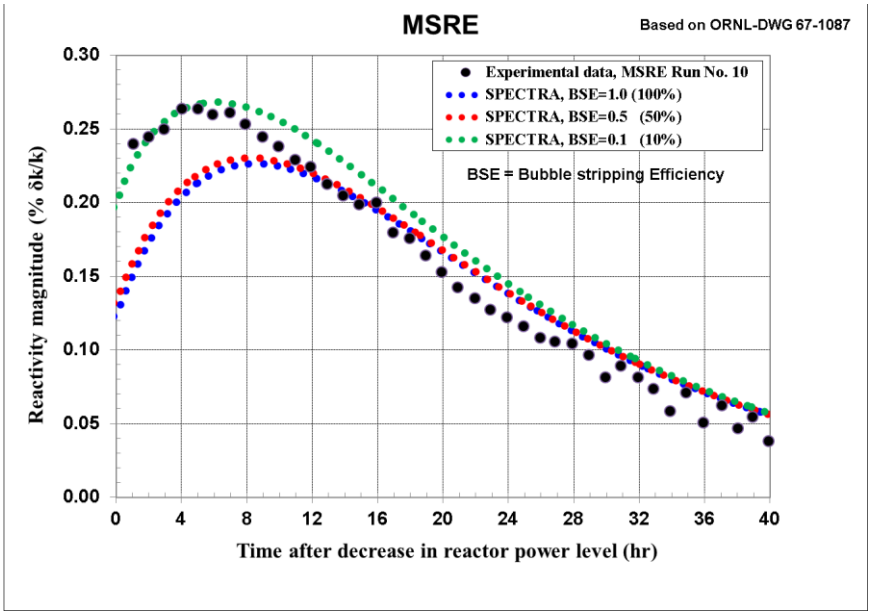

Figure 4-72 Results for Run 10 [189] and calculated values

Table 4-13 Stationary state distribution of Xe-135 in the core, U-235 run, 7.40 MW, α =0.15%

Mass of Xe-135 in the core	(at BSE= 100%)		(at BSE= 50%)		(at BSE= 10%)	
Core graphite surfaces	1.51E-006 kg	81.1%	1.50E-006 kg	71.5%	1.43E-006 kg	38.1%
Salt in the core	8.74E-008 kg	4.7%	8.68E-008 kg	4.1%	8.30E-008 kg	2.2%
Circulating bubbles in the core	2.64E-007 kg	14.2%	5.11E-007 kg	24.4%	2.24E-006 kg	59.7%
Total	1.86E-006 kg	100.0%	2.09E-006 kg	100.0%	3.76E-006 kg	100.0%

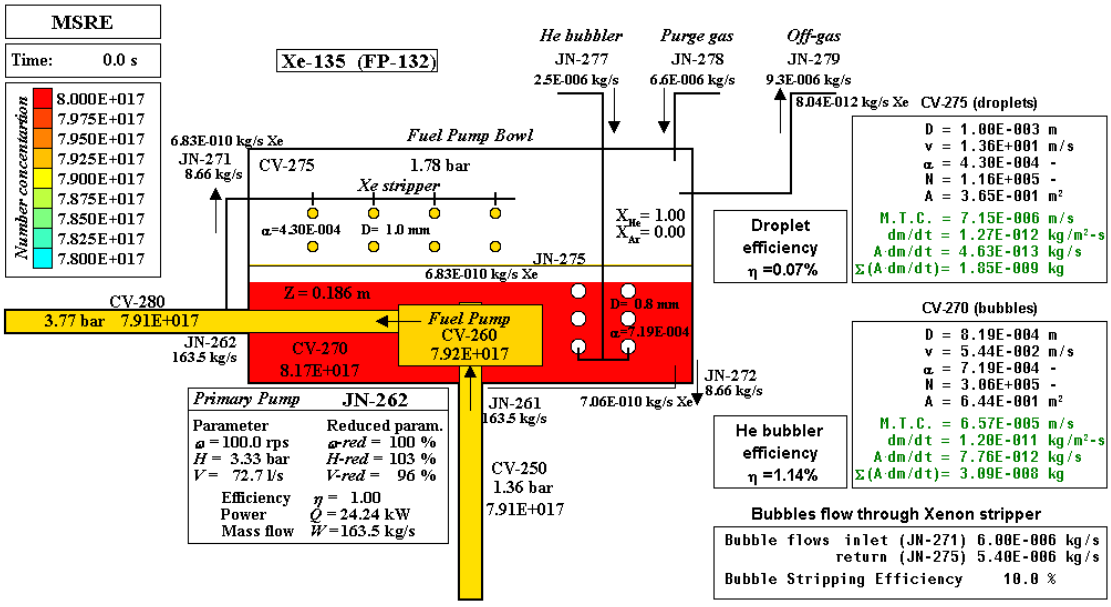

Figure 4-73 Steady state distribution of Xe-135 in the pump bowl

Table 4-13 shows the Xenon data in the core. For high bubble stripping efficiency the majority of Xe is on the bubbles. For low bubble stripping efficiency the majority of Xe is on the graphite. This is consistent with the ORNL observations: "*When the void fraction was high, a major part of the poisoning was due to xenon in the bubbles but, at low void fractions, the xenon in the graphite was the major contributor*" [189].

Figure 4-73 shows the pump bowl, including the Xenon stripper and the Helium bubbler. The droplet stripping efficiency is defined as the percentage of dissolved gas transferred from the salt droplets to the gas phase in passing through the xenon stripper spray system.

$$\eta = \frac{A_d \cdot (dm/dt)_d}{W_{in}}$$

A_d total surface area [m^2] of all droplets in the pump bowl gas space,
$(dm/dt)_d$ mass transfer rate [kg/m^2-s] of Xe-135 to droplets in the pump bowl gas space,
W_{in} mass flow rate [kg/s] of Xe-135 at the inlet to the pump bowl gas space.

The calculated droplet stripping efficiency is very small, only about 0.07% (Figure 4-73). A similar definition is applied to the bubbles produced by the Helium bubbler:

$$\eta = \frac{A_b \cdot (dm/dt)_b}{W_{in}}$$

A_b total surface area [m^2] of all bubbles in the pump bowl liquid space,
$(dm/dt)_b$ mass transfer rate [kg/m^2-s] of Xe-135 to bubbles in the pump bowl liquid space,
W_{in} mass flow rate [kg/s] of Xe-135 at the inlet to the pump bowl liquid space.

The He bubbler stripping efficiency is 1.14% (Figure 4-73).

Short-Lived Isotope Behavior, Xe-140 / Ba-140 - Comparison with Data

In 1966 some graphite samples were removed from the MSRE core after 7800 MWh of power operation [136]. While in the reactor, these samples were exposed to flowing fuel salt, and as a result they absorbed fission products. After removal from the reactor, the concentrations of several of these fission product isotopes were measured as a function of depth in the samples. Among others, measured data for the decay chain 140 is shown, with noble gas precursor Xe-140. Results include measured concentrations as a function of depth.

In order to perform a realistic simulation, first the reactor operating history had to be established as accurately as possible. The operational history of MSRE was taken from [188]. During the period of June - July 1966 MSRE was operating with a power of 8.00 MW, with a short break approximately in the middle. Taken that the total irradiation period was 7800 MWd and the irradiation time was 1100 h [136], the operational history during that period was reconstructed as follows:

- Full power operation at 8.00 MW for 487.5 h, (0.0 h - 487.5 h)
- Reactor shutdown for 125.0 h, (487.5 h - 612.5 h)
- Full power operation at 8.00 MW for 487.5 h, (612.5 h - 1100 h)

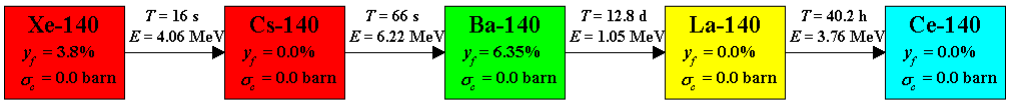

Figure 4-74 Decay chain for Xe-140 / Ba-140

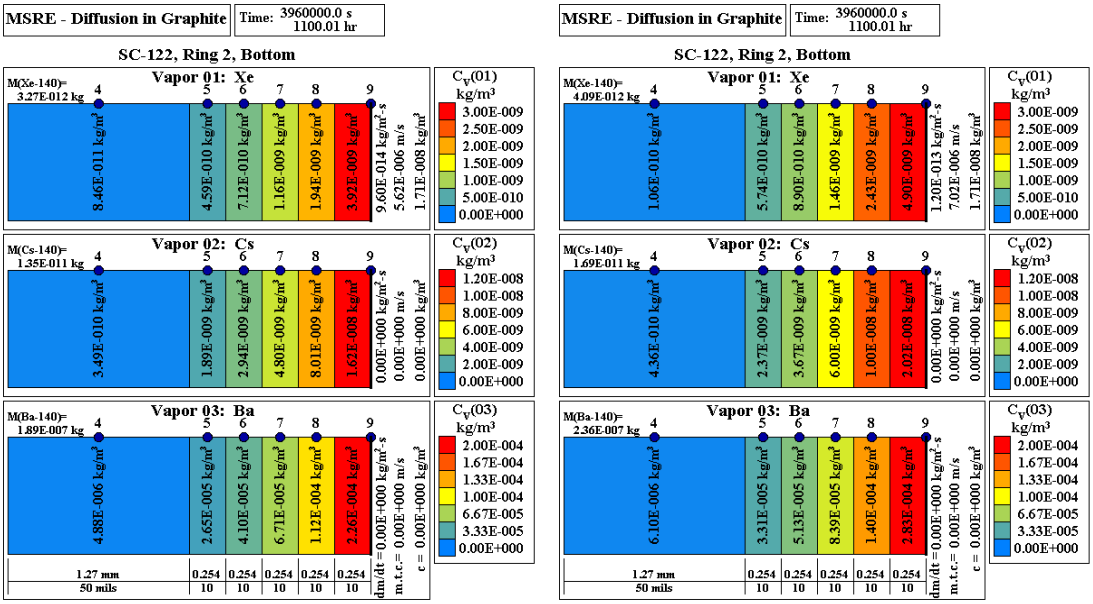

Figure 4-75 Concentration at 7800 MWh, core bottom
left: without tuning, right: with tuning of the mass transfer coefficients

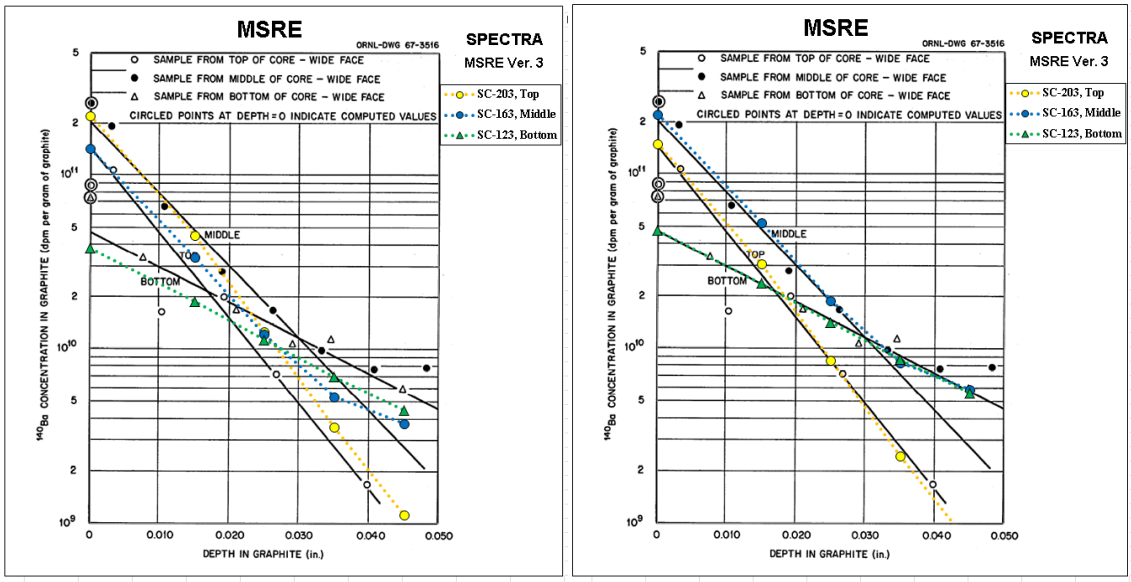

Figure 4-76 Ba-140 distribution in graphite - comparison with data [136]
left: without tuning, right: with tuning of the mass transfer coefficients

The chain 140 is shown in Figure 4-74. For the present calculations, a version limited to the first three isotopes was applied. La-140 and Ce-140 are therefore not tracked, which allows to speed up the calculations.

Calculations were performed for the total operating time of 1100 h. Generally, the behavior of the isotopes is the following. The short-lived noble gas Xe-140 is migrating towards the graphite and diffusing within it. The depth it can diffuse is limited because of its short life. Since the half-life is 16 s, after about one minute 98% of Xe-140 would be decayed. The daughter-product, Cs-140, is not diffusing, so the distribution of Cs-140 follows the distribution of Xe-140. Cs-140 is decaying fast (half-life of 66 seconds - Figure 4-74) into Ba-140 which concentrations were measured in the experiment.

Visualization pictures, showing the end-state (after 7800 MWh) are shown in Figure 4-75. Figure 4-76 shows calculated and measured distributions of Ba-140. The left figure shows results obtained using the best guess of the mass transfer coefficient, described in section 4.5.1.5. The main challenge for the simulation was the lack of experimental details on fluid velocities and hydraulic diameters in the test section. Therefore the mass transfer coefficients may be not very accurate. The right figure shows results after tuning the mass transfer coefficients. The value of mass transfer coefficients in the base model and tuned model are shown below.

	mass transfer coefficient (m/s)	
	base model	tuned model
top:	5.64×10^{-6}	3.83×10^{-6}
middle	5.63×10^{-6}	8.75×10^{-6}
bottom	5.62×10^{-6}	7.02×10^{-6}

Short-Lived Isotope Behavior, Xe-137 / Ba-137 - Comparison with Observation

A very general description of Cs-137 is provided in [135]: "[...] *consider the salt seeker Cs-137 with a cumulative yield of 6.15 percent. Most of its yield comes from the decay of Xe-137 that has a yield of about 6.0 percent and a half-life of 3.9 min. Xenon can be transferred to the off-gas system and also can diffuse into the porous structure of the graphite. Accordingly, only 80 to 90 percent of the Cs-137 inventory was found in the fuel salt and significant quantities were found deep inside the graphite where it deposited upon decay of its precursor.*"

In order to verify this qualitative statement, the chain Xe-137 / Cs-137 was considered. The chain is shown in Figure 4-77. Calculations were performed for a reactor power of 8.0 MW. Stationary state was reached within 10,000 s. Calculations were performed for two cases:

- U-233 runs - circulating void fractions of approximately $\alpha = 0.55\%$ [135]
- U-235 runs - circulating void fractions of approximately $\alpha = 0.033\%$ [135]

The calculated global distribution of Cs-137 is shown in Table 4-14 and Table 4-15. The concentrations of Cs-137 increase in time, therefore the derivative of the concentrations is shown, which is approximately constant. The concentrations in fuel salt are 66% and 77% in case of U-235 runs and U-233 respectively. A significant amount of Cs-137 is found in graphite and HX tubes where it is created by the decay of Xe-137. This is qualitatively in agreement with the general description in [135].

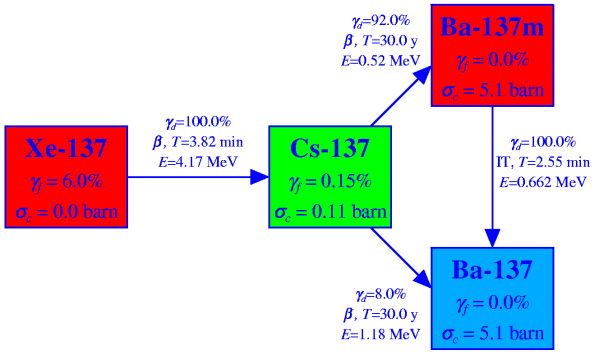

Figure 4-77 Decay chain for Xe-137 / Ba-137

Table 4-14 Global distribution of Cs-137, U-235 run

Distribution of Cs-137 (Isotope No. 072)

CV pool (salt)	8.20E-010 kg/s	66.0%
SC (solid: graphite + steel)	4.23E-010 kg/s	34.0%
Total	1.24E-009 kg/s	100.0%

1.) Core graphite	1.32E-010 kg/s	10.6%
2.) HX tubes	1.30E-010 kg/s	10.4%
3.) Pump bowl walls	5.20E-014 kg/s	0.0%
4.) HX shell	1.23E-011 kg/s	1.0%
5.) Vessel walls	1.05E-010 kg/s	8.5%
6.) Pipe walls	4.40E-011 kg/s	3.5%

Table 4-15 Global distribution of Cs-137, U-233 run

Distribution of Cs-137 (Isotope No. 072)

CV pool (salt)	1.45E-010 kg/s	76.7%
SC (solid: graphite + steel)	4.39E-011 kg/s	23.3%
Total	1.88E-010 kg/s	100.0%

1.) Core graphite	1.78E-011 kg/s	9.5%
2.) HX tubes	1.24E-011 kg/s	6.6%
3.) Pump bowl walls	1.67E-015 kg/s	0.0%
4.) HX shell	1.15E-012 kg/s	0.6%
5.) Vessel walls	8.37E-012 kg/s	4.4%
6.) Pipe walls	4.15E-012 kg/s	2.2%

4.5.1.7 Noble Metals

The principal observation from ORNL is that the sticking fraction to graphite is apparently less than the sticking fraction to Hastelloy-N. “Because of scatter in the data, it is difficult to draw a firm value, but something in the range of 0.1 - 0.6 would be in order” [135] (sec. 5.7.1). It appears that the sticking factor of tellurium on metal is relatively high [182] (sec. 9.2.8). For the current calculations the following sticking factors were assumed:

- C = 0.1 for noble metals on graphite surfaces as well as the bubbles,
- C = 1.0 for noble metals on metallic surfaces.

This section discusses behavior of noble metals, using three arbitrarily selected isotopes, Te-131 - Figure 4-78, Te-132 - Figure 4-79, and Te-134 - Figure 4-80. Noble metal calculations are performed until stationary state is reached (total time of the runs with fission products was selected as 14,000 s). The reactor power was assumed as 8.0 MW. The results are compared to the available measured data.

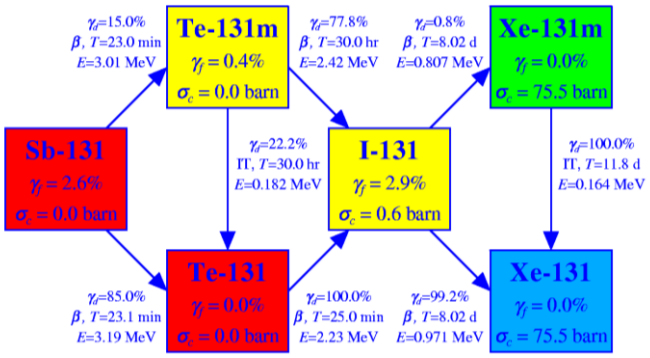

Figure 4-78 Decay chain for Te-131 (see Volume 1)

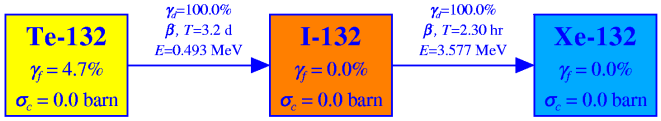

Figure 4-79 Decay chain for Te-132 (see Volume 1)

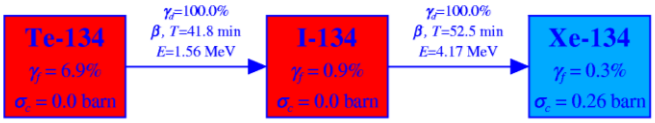

Figure 4-80 Decay chain for Te-134 (see Volume 1)

Calculations were performed for the reactor power of 8.0 MW. Stationary state was reached within 10,000 s. Calculations were performed for two cases:

- U-233 runs - circulating void fractions of α = 0.55% ([135] reports 0.5 - 0.6%),
- U-235 runs - circulating void fractions of α = 0.033% ([135] reports 0.02 - 0.045%).

The mass transfer coefficients to various surfaces as well as the circulating bubbles are shown in Table 4-16 (the calculated mass transfer coefficients to graphite and bubbles were multiplied here by 10 because the sticking factor of 0.1 was used). As seen in Table 4-16, the calculated values agree well with the estimations from ORNL.

The global distribution of noble metals, as estimated in [135], is shown in Table 4-17. Calculated values are shown in Table 4-18. Here data for Te-134 was used. For U-235 runs a good agreement with ORNL estimations were obtained using the circulating bubble size of 0.01 in (= 2.54×10^{-4} m), which is given in [135] (page 82) as a maximum bubble diameter. For U-233 runs a good agreement with ORNL estimations was obtained using the circulating bubble size of 0.005 in (= 1.27×10^{-4} m), which is the given in [135] (page 82) as an average bubble diameter. The results show how important it is to accurately predict the bubble size.

Table 4-16 Mass transfer coefficients reported in [135] and calculated

	MSRE values		ORNL-TM-3884		SPECTRA values				calculated
	mtc	A	mtc	A	SC / CV	A	D-hyd	V-liq	mtc
	ft/hr	ft2	m/s	m2	group No.	m2	m	m/s	m/s
HX (shell side)	0.55	315	4.7E-05	29.3	SC g. 2	29.9	2.74E-02	1.0	3.2E-05
Piping	1.23	71	1.0E-04	6.6	SC g. 3	4.6	1.27E-01	5.7	1.0E-04
Core graphite	0.063	1465	5.3E-06	136.1	SC g. 1	136.0	1.25E-02	0.17	5.8E-06
Vessel walls	0.51	154	4.3E-05	14.3	SC g. 5	19.3	5.10E-02	0.6 - 1.4	4.7E-05
Circ. bubbles, U-235	5.0	345	4.2E-04	32.1	CV g. 1	30.0	D-bubb		4.3E-04
Circ. bubbles, U-233	5.0	5581	4.2E-04	518.5	CV g. 1	492.0	D-bubb		4.3E-04

Table 4-17 Noble metal distribution [135]

Noble Metal Distribution in the MSRE*

	During ^{235}U Runs	During ^{233}U Runs
Noble Metals on Heat Exchanger Surfaces	40%	6%
Noble Metals on Other Hastelloy-N Surfaces in Fuel Loop	50	8
Noble Metals on Graphite Surfaces in Core	1	0.4
Noble Metals in Pump Bowl, Overflow Tank, Off-Gas System, etc. (by Difference)	9	86
	100%	100%

Table 4-18 Noble metal distribution, SPECTRA, Te-134

U-235 Runs ($D = 2.54\times10^{-4}$ m)

MSRE, SPECTRA t = 10000 s

Distribution of Te-134 (Isotope No. 041)

HX surfaces	9.75E-010 kg/s	37.5%
Other Hastelloy-N surfaces	1.24E-009 kg/s	47.8%
Core graphite surfaces	1.00E-010 kg/s	3.9%
Pump bowl, off-gas, etc .	2.82E-010 kg/s	10.9%
Total	2.60E-009 kg/s	100.0%

U-233 Runs ($D = 1.27\times10^{-4}$ m)

MSRE, SPECTRA t = 10000 s

Distribution of Te-134 (Isotope No. 041)

HX surfaces	1.32E-010 kg/s	4.8%
Other Hastelloy-N surfaces	1.64E-010 kg/s	5.9%
Core graphite surfaces	1.36E-011 kg/s	0.5%
Pump bowl, off-gas, etc .	2.45E-009 kg/s	88.8%
Total	2.76E-009 kg/s	100.0%

4.5.2 Summary and Conclusion

The purpose of the presented analyses was to demonstrate that the SPECTRA code is able to model the main phenomena concerning the fission product transport in molten salt reactors, including noble gases and noble metals.

- ***Noble gases***. The behavior of noble gases was investigated using available data for Xe-135, Xe-140, and Xe-137. The agreement of the calculated parameters and the measured data was satisfactory.
- ***Noble metals***. The behavior of noble metals was investigated using available data for Te-131, Te-132, Te-134. The results show satisfactory agreement.

The purpose of the current analysis was to verify that the SPECTRA code is able to model the main phenomena concerning the fission product transport in molten salt reactors, including noble gases and noble metals. A satisfactory agreement between the calculated values and the measured data was obtained for noble gases and noble metals. Of course it would be good to have a stronger statement with a more quantitative result, stating percentage difference compared to the measured data. However it is felt that it is not possible to do so at this stage. This is because MSRE is a large integrated system test, with all phenomena interlinked, so it is difficult to estimate the accuracy of the individual models involved. Furthermore, it was not possible to obtain exact data for each analyzed experiment. In some cases circulating voids were just rough estimations, in some cases (Xe/Ba-140) void fractions as well as fluid velocities were unknown. The purpose of the present work was to make sure that all relevant phenomena that play role in fission product transport are available in the code, even if some of the models have to rely on user-defined coefficients that must be delivered in input. In the next stages the models will be validated using separate effect tests, where clear test definition and relatively few phenomena involved will allow to quantify the accuracy of models.

4.6 Application of SPECTRA to Chemical Reactors

In the past, SPECTRA was used to perform analysis of cooling systems of several non-nuclear systems, among others the chemical reacotrs designed by Shell Oil, including:

- Design-support analyses of the cooling system of a multi-tubular reactor for heavy paraffin synthesis at Ras Laffan Industrial City in the State of Qatar (PEARL project), using two independent system codes: RELAP5 and SPECTRA.
- Design-support analyses for the upscaling of PEARL design, using two independent system codes: RELAP5 and SPECTRA.

Results of these analyses are proprietary and the owner is Shell Oil. Therefore the results cannot be shown here, although they could serve as code V&V by code-to-code benchmark, since a very good agreement between SPECTRA and RELAP was obtained.

4.6.1 Emergency Shutdown Scenario in a Hypothetical Multi-Tubular Reactor

In order to avoid the confidentiality problem, a completely hypothetical design was developed. All the applied dimensions including tube diameters, length, number of tubes, etc. were set up to an arbitrary (round) numbers. Also the power density that is generated in the tubes is very different from the real value. In this way a Hypothetical Multi-Tubular Reactor (HMTR) was designed with no reference to any real data. However, the general layout of the cooling system is preserved, i.e.:

- vertical tubes,
- cooling by natural circulation,
- steam separation using a dedicated vessel (steam drum).

It is therefore expected that the qualitative behavior of HMTR will be similar to the real reactors.

Figure 4-81 shows the cooling system of HMTR at steady state operation. Figure 4-82 shows tube temperature behavior of the upper part of the tubes during an emergency shutdown scenario. A short heat up of the tubes due to collapse of liquid level is observed, which is qualitatively correct for this event.

For comparison, a model for RELAP5 was generated using the automated export option (IEXPSL=3). SPECTRA results obtained for HMTR were compared to RELAP5. A good agreement was obtained.

Detailed results of the emergency shutdown scenario in HMTR are currently provided only in an internal NRG report. The results will be published in open literature in the future.

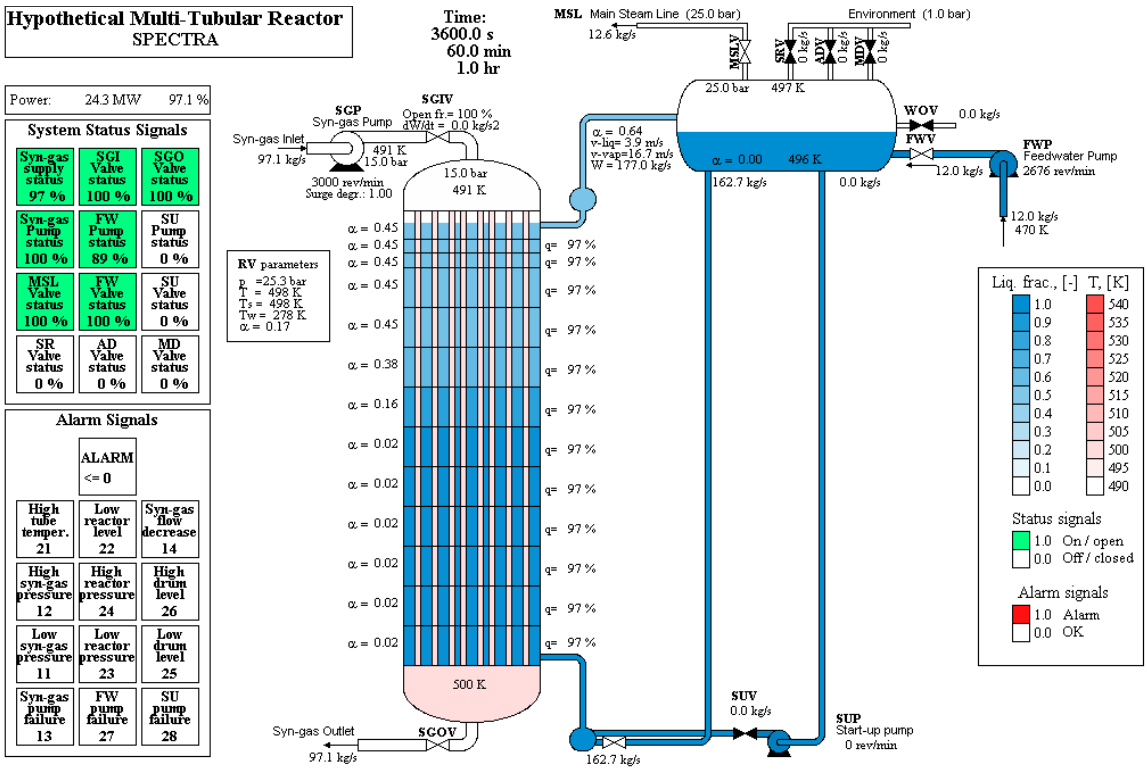

Figure 4-81 HMTR - steady state operation

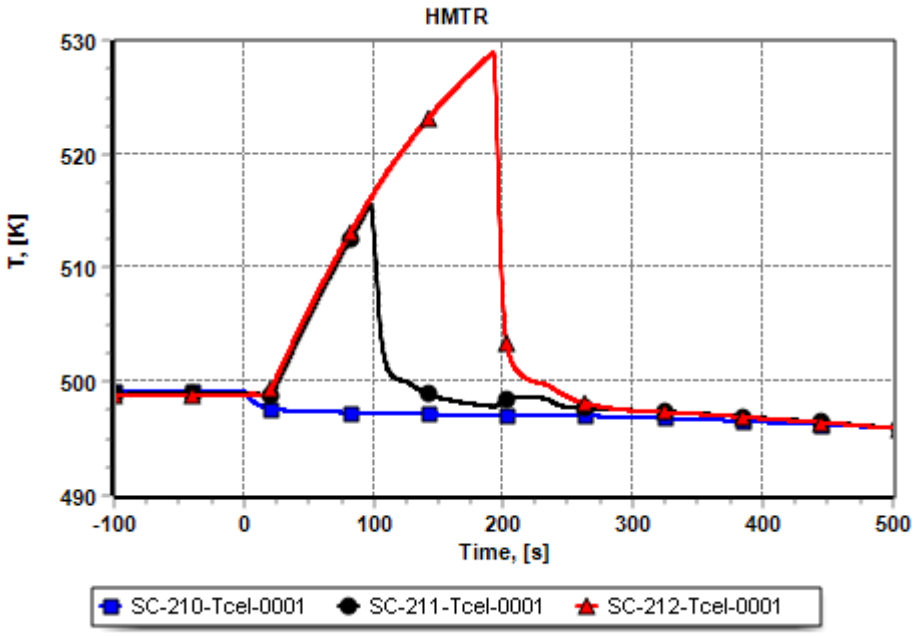

Figure 4-82 HMTR - temperatures in the upper part of the tubes during emergency shutdown.

Literature

[1] "Guidelines for the Verification and Validation of Scientific and Engineering Computer Programs for the Nuclear Industry", ANSI/ANS-10.4-1987, Prepared by the American Nuclear Society Standards Committee Working Group 10.4, Published by the American Nuclear Society, 555 North Kensington Avenue, La Grange Park, Illinois 60525 USA, May 1987.

[2] "Documentation of Computer Software, an American National Standard", ANSI/ANS-10.3-1995, Prepared by the American Nuclear Society Standards Committee Working Group 10.3, Published by the American Nuclear Society, 555 North Kensington Avenue, La Grange Park, Illinois 60525 USA, April 1995.

[3] "Recommended Programming Practices to Facilitate the Portability of Scientific and Engineering Computer Programs", ANSI/ANS-10.2-1988, Revision of ANSI/ANS-10.2-1982, Prepared by the American Nuclear Society Standards Committee Working Group 10.2, Published by the American Nuclear Society, 555 North Kensington Avenue, La Grange Park, Illinois 60525 USA, April 1988.

[4] Anklam T. M. et al., "Experimental investigations of uncovered-bundle heat transfer and two-phase mixture level swell under high pressure low heat flux conditions", NUREG/CR-2456, USNRC, April 1982.

[5] Anklam T. M. and Miller R. F., "Void fraction under high pressure, low flow conditions in rod bundle geometry", *Nuclear Engineering and Design*, **75**, pp. 99-108, 1982.

[6] M.M. Stempniewicz, "Simulation of Containment Transient Response During Accidents in Advanced Reactor Types - The Computer Code SPECTRA", PhD Thesis at Silesian Technical University, May 2000.

[7] D. Lűbbesmeyer, S.N. Aksan, "Comparison of Blind Phase Calculations for International Standard Problem 42 (ISP42) PANDA Test Phases -A- and -B-", *Proceedings of ICONE9*, Nice, Acropolis, France, April 8-12, 2001.

[8] D. Lűbbesmeyer, S.N. Aksan, "Comparison of Blind Phase Calculations for International Standard Problem 42 (ISP42) PANDA Test Phases -C- and -D-", *Proceedings of ICONE9*, Nice, Acropolis, France, April 8-12, 2001.

[9] D. Lűbbesmeyer, S.N. Aksan, "Comparison of Blind Phase Calculations for International Standard Problem 42 (ISP42) PANDA Test Phases -E- and -F-", *Proceedings of ICONE9*, Nice, Acropolis, France, April 8-12, 2001.

[10] J. Hilsenrath, et al., "Tables of Thermal Properties of Gases", National Bureau of Standards, Washington D.C., National Bureau of Standards Circular 564, November 1, 1955.

[11] Vargaftik, "Handbook of Physical Properties of Liquids and Gases: Pure Substances and Mixtures", ISBN 0-89116-356-5, Hemisphere Publishing Co., 1975.

[12] V.D. Arp, R.D. McCarty, "Thermophysical Properties of Helium-4 from 0.8 to 1500 K with pressures to 2000 MPa", US Department of Commence, National Institute of Standards and Technology, TN 1334, November 1989.

[13] L. Haar, J.S. Gallagher, G.S. Kell, "NBS/NRC Wasserdampftafeln", ("NBS/NRC Steam Tables"), Springer-Verlag, Berlin, ISBN 3-540-18039-7, Springer-Verlag, New York, ISBN 0-387-18039-7, 1988.

[14] C.R. Wilke, "A viscosity equation for a gas mixture", *J. Chem. Phys.*, Vol. **18**, p. 517-519, 1950.

[15] W.M. Rohsenow, J.P. Harnett, "Handbook of Heat Transfer", McGraw Hill, ISBN 0-07-053576-0, 1973.

[16] A.F. Mills, "Heat and Mass Transfer", Richard D. Irwin, Inc., ISBN 0-256-11443-9, Chicago, 1995.

[17] H.C. Hottel, "Radiant Heat Transmission", Chapter 4 in W.H. McAdams, "Heat Transmission", ISBN-13: 978-0898748765, Robert E. Krieger Publishing Company, Third Edition, Malabar, Florida, 1985.

[18] A. Wassiljewa, "Heat conduction in gaseous mixtures", *Physik. Z.*, Vol. **5**, p. 737, 1904.

[19] E.A. Mason, S.C. Saxena, "Approximate formula for the thermal conductivity of gas mixtures", *Phys. Fluids*, Vol. **1**, p. 361, 1958.

[20] R.O. Gauntt, et.al., "MELCOR Computer Code Manuals, Reference Manuals, Version 1.8.6, September 2005", NUREG/CR-6119, Vol. 2, Rev. 3, SAND 2005-5713, published: September 2005.

[21] E. Kostowski, "Promieniowanie cieplne" ("Thermal Radiation"), ISBN 83-01-10847-9, Warsaw, PWN 1993.

[22] A. Sala, "Radiacyjna Wymiana Ciepła" ("Radiation Heat Transfer"), ISBN 83-204-0367-7, WNT, Warsaw 1982.

[23] B. Leckner, "Spectral and Total Emissivity of Water Vapor and Carbon Dioxide", *Combustion and Flame*, Vol. **19**, pp. 13-48, 1972.

[24] R.C. Wheast, et al., "CRC Handbook of Chemistry and Physics", ISBN-0-8493-0472-5, CRC Press Inc., 59-th edition, 1978-1979.

[25] R. Reid, J.M. Prausnitz, B.E. Poling, "The Properties of Gases and Liquids", Fourth Edition, ISBN 0-07-051799-1, McGraw Hill, New York, 1989.

[26] C.C.M. Luijten, K.J. Bosschaart, M.E.H. van Dongen, "A new method for determining binary diffusion coefficients in dilute condensable vapors", *Int. J. Heat Mass Transfer*, Vol. **40**, No. 15, pp. 3497-3502, 1997.

[27] J.J. Ginoux, "Two-Phase Flows and Heat Transfer, with Application to Nuclear Reactor Design Problems", ISBN 0-07-023305-5, Hemisphere Publishing Corporation, 1978.

[28] Y.Y. Hsu, R.W. Graham, "Transport Process in Boiling and Two-Phase Systems", ISBN 0-07-030637-0, McGraw Hill, 1976.

[29] K.H. Ardron, R.A. Furness, "A study of the critical flow models used in reactor blowdown analysis", *Nuclear Engineering and Design*, Vol. **39**, pp. 257-266, 1976.

[30] D.J. Maneely, "A study of the expansion process of low-quality steam through a de Laval nozzle", University of California, Livermore report UCRL 6230, 1962.

[31] F.J. Moody, "Maximum flow rate of a single component two-phase mixture", *Trans. ASME, J. Heat Transfer*, Vol. **87c**, p. 134, 1965.

[32] Starkman, V.E. Schrock, K.F. Neusen, D.J. Maneely, "Expansion of a very low quality two-phase fluid through a convergent-divergent nozzle", *Trans. ASME, J. Basic Eng.* Vol. **86D**, pp. 247-256, 1964.

[33] R.E. Henry, H.K. Fauske, "The two-phase critical flow of one-component mixtures in nozzles, orifices and short tubes", ASME paper, 70-WA/HT-5, 1971.

[34] H.Friedrich, "Flow through single-stage nozzles with different thermodynamic states" *Energie* **12**, 3, 1960.

[35] G.L. Sozzi, W.A. Sutherland, "Critical flow of saturated and subcooled flow at high pressures, General Electric Company, Report NEDO-13418, 1975.

[36] H.K. Fauske, "The discharge of saturated water through tubes", *Chem. Eng. Progr. Symp. Ser.*, 61, **59**, 210-216, 1965.

[37] H. Uchida, H. Nariari, "Discharge of saturated water through pipes and orifices", Proc. of Third International Heat Trans. Conf. Vol. 5, 1, 1966.

[38] F.R. Zaloudek, "The critical flow of hot water through short tubes", General Electric Company, Report HW-77594, Hanford Works, 1963.

[39] R.T. Lahey, F.J. Moody, "The Thermal-Hydraulics of a Boling Water Reactor", ISBN 0-89448-010-3, American Nuclear Society, 1977.

[40] I.E. Idelchik, "Handbook of Hydraulic Resistance", Second Edition, ISBN 3-540-15962-2, Hemisphere Publishing Corporation, 1986.

[41] W.T. Hancox, W.B. Nicoll, "Prediction of Time Dependent Diabatic Two-phase Flows", *Progress in Heat and Mass Transfer*, Vol. **6**, pp. 119-135, 1972.

[42] S. Levy, “Steam Slip – Theoretical Prediction from Momentum Model”, *Journal of Heat Transfer*, **82C** (1), pp. 113-124, 1960.

[43] R.W. Lockhart, R.C. Martinelli, "Proposed Correlation of Data for Isothermal Two-Phase, Two-Component Flow in Pipes", *Chem. Eng. Prog.*, Vol. **45**, No. 1, pp. 39-48, 1949.

[44] Martinelli, D.B. Nelson, "Prediction of Pressure Drop during Forced-Convection Boiling of Water", *Trans. ASME*, Vol. **70**, pp. 695-702, 1948.

[45] C.J. Baroczy, "A Systematic Correlation for Two-Phase Pressure Drop", *Chem. Eng. Prog. Symp. Ser.*, Vol. **62**, no. 64, pp. 232-249, 1966.

[46] Chisholm, "The influence of mass velocity on friction pressure gradients during steam-water flow", paper 35 presented at 1968 Thermodynamics and Fluid Mechanics Convention, Institute of Mechanical Engineers, Bristol, March 1968.

[47] J.A., Borkowski, N.L. Wade, "TRAC-BF1/MOD1 Models and Correlations" NUREG/CR-4391, EGG-2680, R4, August 1992.

[48] J.M. Delhaye, M. Giot, M.L. Rietmuller, "Thermohydraulics of Two-Phase Systems for Industrial Design and Nuclear Engineering", ISBN 0-07-016268-9, McGraw Hill Book Company, New York 1981.

[49] L. Friedel, "Mean Void fraction and Friction Pressure Drop: Comparison of Some Correlations with Experimental Data", European Two-Phase Flow Group Meeting, Grenoble, paper A7, 1977.

[50] R.A. Dimenna, J.R. Larson, R.W. Johnson, T.K. Larson, C.S. Miller, J.E. Streit, R,G, Hanson, D.M. Kiser, "RELAP5/MOD2 Models and Correlations", NUREG/CR-5194, EGG-2531, August 1988.

[51] A.E. Bergles, W.M. Rohsenow, "The determination of forced convection surface boiling heat transfer", Paper 63-HT-22 presented at 6-th National Heat Transfer Conference of the ASME-AIChE, Boston, 11-14 August, 1963.

[52] J.G. Collier, Convective Boiling and Condensation", ISBN 0-19-856296-9, McGraw Hill International Book Company, First Edition: 1972, Second Edition: 1981.

[53] W.M. Rohsenow, J.A. Clark, "Heat transfer and pressure drop data for high heat flux densities to water at high subcritical pressure", 1951 Heat Transfer and Fluid Mechanics Institute, Stanford University Press, Stanford, California, 1951.

[54] S.S. Hsieh, P.T. Hsu, "Nucleate boiling characteristics of R-114, distilled water (H_2O) and R134a on plain and rib-roughened tube geometries", *Int. J. Heat Mass Transfer*, Vol. **37**, No. 10, pp.1423-1432, 1994.

[55] L.J. Siefken, E.W. Coryell, E.A. Harvego, J.K Hohorst, "SCDAP/RELAP5/MOD3.3 Code Manual", NUREG/CR-6150, Rev.2, INEL-96/0422, January 2001.

[56] L.J. Siefken, et al., "MATPRO - A Library of Material Properties for Light Water Reactor Accident Analysis", NUREG/CR-6150, Vol. 4, Rev. 2, INEL-96/0422, January 2001.

[57] J.J. Duderstad, L.J. Hamilton, "Nuclear Reactor Analysis", ISBN 0-471-22363-8, John Wiley & Sons, Inc., New York, 1976.

[58] A.F. Henry, "Nuclear Reactor Analysis", ISBN 0-262-08081-8, Massachusetts Institute of Technology, Cambridge, 1975.

[59] C.J. Dean, R.J. Perry, "The 1995 WIMS Nuclear Data Library", AEA Technology, Technical Service Division, AEA-TSD-0630, March 1995.

[60] P. Nanni, V. Buscaglia, G. Battilana, "E. Reudl, "Air Oxidation of a Mn-Cr austenitic steel of potential use for fusion reactor structural applications between 1073 and 1473 K at 10^5 Pa", *Journal of Nuclear Materials*, Vol. **182**, pp. 118-127, 1991.

[61] J.Roes, "Experimentelle Untersuchungen zur Graphitkorrosion und Aerosolentstehung beim Lufteinbruch in das Core eines Kugelhaufen-Hochtemperaturreaktors", Jul-2956, KfA, 1994.

[62] D.L. Hargman, et al., "MATPRO Version 11 (Revision 2), A Handbook of Material Properties for Use in the Analysis of Light Water Reactor Fuel Rod Behavior" NUREG/CR-0479, TREE-1280, Rev. 2, August, 1981.

[63] "ESCORE: The EPRI Steady-State Core Reload Evaluator Code, Volume 1: Theory Manual", EPRI NP-4492-CCMP, August 1986.

[64] R. Nieder et al., "Chemie des Hochtemperaturreaktors", Jülich, November 1981, Jül-Conf-43, ISSN 0344-5798, pp. 30- 42: P. Kubaschewski, B. Heinrich: "Graphitkorrosion durch Wasserdampf", PhD, Hochtemperaturreaktorbau GmbH".

[65] K.-J. Loenißen, "Untersuchungen zur Druckabhängigkeit der Graphit/Wasserdampf-reaktion im Porendiffusionsbereich im Zusammenhang mit Wassereinbruchsstörfällen in Hochtemperatur-Reaktoren, Juel-2159, ISSN 0366-0885, September 1987.

[66] Xinli Yu, Suyuan Yu, "Analysis of fuel element matrix graphite corrosion in HTR-PM for normal operating conditions", *Nuclear Engineering and Design*, Vol. **240**, pp. 738-743, 2010.

[67] W.T. Abel, J.H. Holden, "The Suspended Specimen Method for Determining the Rate of Steam-Carbon Oxidation", RI Bureau of Mines, 1962.

[68] F.H. Ho, "Graphite Design Handbook", DOE-HTGR-88111, Revision 0, September 1988.

[69] W.A. Stark, "Surface Area - Burn-off Correlation for the Steam-Graphite Reaction", Los Alamos Scientific Laboratory, LA-UR-77-1956, 1977. *Proceedings of the Japan-US Seminar on HTGR Safety Technology*, Brookhaven National Lab., September 15-16, 1977.

[70] J.R. Brock, "On the theory of thermal forces acting on aerosol particles", *J. of Colloid Science*, No. **17**, p. 768, 1962.

[71] C. He, G. Ahmadi, "Particle deposition with thermophoresis in laminar and turbulent duct flows", *Aerosol Science and Technology*, **29**(6), pp. 525-546, 1998.

[72] M.M.R. Williams, S.K. Loyalka, "Aerosol Science Theory and Practice - with Special Application to the Nuclear Industry", ISBN 0-08-037209, Pergamon Press, First Edition, Oxford, 1991.

[73] S.K. Kær, "Numerical investigation of deposit formation in straw-fired boilers – Using CFD as the framework for slagging and fouling predictions", PhD Thesis, Aalborg University, Institute of Energy Technology, October 2001.

[74] J.Young and A. Leeming, "A theory of particle deposition in turbulent pipe flow", *Journal of Fluid Mechanics* **340**, 129-159, 1997.

[75] N.A. Fuchs, "The Mechanics of Aerosols", ISBN 10: 0486660559, Pergamon, New York, 1964.

[76] H.R. Pruppacher, J.D. Klett, "Microphysics of Clouds and Precipitation", ISBN-13: 978-90-277-1106-9, Reidel, New York, 1978.

[77] K.W. Tu, D.T. Shaw, "Experimental Determination of Interception Collection Efficiencies for Small Cloud Droplets", *J. Colloid Interface Sci.*, **62**, 1977.

[78] G.A. Pertmer, S.K. Loyalka, "Gravitational Collision Efficiency of Post Hypothetical Core Disruptive Accident Liquid Metal Fast Breeder Reactor Aerosols: Spherical Particles", *Nuclear Technology*, **47**, p. 70, January 1980.

[79] W.C. Hinds, "Aerosol Technology – Properties, Behavior, and Measurement of Airborne Particles", John Wiley & Sons, Inc., ISBN 0-471-19410-7, New York, 1999.

[80] M. Corn, F. Stein, "Re-entrainment of Particles from a Plane Surface", *Am. Ind. Hyg. Assoc. J.*, Vol. **26**, pp. 325-336, 1965.

[81] M.R. Kuhlman, D.J. Lemicke, R.O Meyer, "CORSOR User's Manual", NUREG/CR-4173, BMI-2122, March 1985.

[82] K.Y. Suh, R.J. Hammersley, "Modelling of Fission Product Release and Transport for Severe Fuel Damage Analyses", *Nuclear Science and Engineering*, Vol. **109**, pp.26-38, 1991.

[83] R.A. Lorenz,, M.F. Osborne, "A Summary of ORNL Fission Product Release Tests with Recommended Release Rates and Diffusion Coefficients", NUREG/CR-6261, ORNL/TM-12801, July 1995.

[84] A.R. Costelo, J.A. Capitao, G.D. Santi, "International Standard Problem 40 – Aerosol Deposition and Resuspension, Final Comparison Report", OECD NEA/CSNI/R(99)4, February 1999.

[85] E.Hontanon, A. de los Reyes, J.A. Capitao, "The Caesar Code for Aerosol Resuspension in Turbulent Pipe Flows. Assessment Against the STORM Experiments", *J. Aerosol Sci.* Vol. **31**, No. 9, pp. 1061-1076, 2000.

[86] P. Vainshtein, G. Ziskind, M. Fichman, C. Gutfinger, "Kinetic Model of Particle Resuspension by Drag Force", *Physical Review Letters*, Vol. **78**, No. 3, pp. 551 - 554, 1997.

[87] K.L. Johnson, K. Kendall, and A.D. Roberts, "Surface energy and the contact of elastic solids", *Proceedings of the Royal Society A*, **324**, pp. 301-313, 1971

[88] M.W. Reeks, D. Hall, "Kinetic models for particle resuspension in turbulent flows: theory and measurement", *Aerosol Science*, **32**, 1-31, 2001.

[89] M.E. Berzal, et al., "State of the art review on fission products aerosol pool scrubbing under severe accident conditions", European Commission, Contract No. FI3S-CT93-0009, EUR 16241, 1995.

[90] K. Röllig, “Cesium Deposition on HTR Primary Circuit Materials”, IAEA Specialists Meeting on Fission Product Release and Transport in Gas Cooled Reactors, Gloucester, UK, IWGGCR 13, p.329, 22 - 25 October 1985.

[91] Dr. Wiedmann, “Data Set for Cs Plateout on Incoloy 800”, PNP-5137-BF-GHRA 001241, October 24, 1984.

[92] P. Biedermann, B. Sackmann, “Laboratory and Reactor Experiments on Deposition of Fission Products in HTR Primary Cuircuits”, Jül-Conf-64 (Ed. F. Scholz), 1988.

[93] “Fuel performance and fission product behaviour in gas cooled reactors”, IAEA-TECDOC-978, International Atomic Energy Agency, November 1997.

[94] L. Stassen, “Validation of the Plate-out Model in the RADAX code used for Plate-out and Dust Activity Calculations at PBMR”, PHYSOR-2006, ANS Topical Meeting on Reactor Physics, Canadian Nuclear Society. Vancouver, September 10 - 14, 2006.

[95] M.M. Stempniewicz, P. Goede, “Recommended coefficients for sorption of iodine, silver, and cesium on graphite dust particles”, *Nuclear Engineering and Design* **306** pp. 69–76, 2016

[96] V. Gnielinski, “Neue Gleichungen fur den Warmte- und den Stoffubergang in turbulent durchstromten Rohren und Kanalen”, *Forschung im Ing. Wes.* **41**, No. 1, p. 8-16, 1975.

[97] W.H. Press, S.A. Teukolsky, W.T. Wetterling, B.P. Flannery, "Numerical Recipes in FORTRAN. The Art of Scientific Programming", Second edition, ISBN 0-521-43064-X, Cambridge University Press, 1992.

[98] Szmelter, "Metody Komputerowe w Mechanice" ("Computing Methods in Mechanics"), ISBN 83-01-00686 2, PWN, Warsaw 1980.

[99] Bjorck, G. Dahlquist, "Metody Numeryczne" ("Numerical Methods" - Polish translation), ISBN 83-01-04276 1, PWN, Warsaw 1987.

[100] M.M. Stempniewicz, A. de With, “Passive Safety Design Optimization for 600 MWth GCFR”, *The 13th International Topical Meeting on Nuclear Reactor Thermal Hydraulics* (NURETH-13), Kanazawa City, Ishikawa Prefecture, Japan, September 27-October 2, 2009

[101] J.L. Rempe, et al., “Light Water Reactor Lower Head Failure Analysis”, NUREG/CR-5642, EGG-2618,October 1993.

[102] J.P. Holman, "Heat Transfer", Fourth edition, ISBN 0-07-029598-0, McGraw Hill, Inc., Tokyo 1976.

[103] Kuhn S.Z., Schrock V. E., Peterson P.F., "An investigation of condensation from steam-gas mixtures flowing downward inside a vertical tube", *Nuclear Engineering and Design* **177** (1997) 53-69.

[104] A.A. Dehbi, M.W. Golay, M.S. Kazimi, "Condensation experiments in steam-air and steam-air-helium mixtures under turbulent natural convection", AIChE Symposium Series, No 283, Vol. 87, Minneapolis 1991.

[105] A. S. Rao, "Simplifying the BWR", *ATOM*, **430** (September/October 1993).

[106] J. Dreier, M. Huggenberger, C. Aubert, T. Bandurski, O. Fisher, J. Healzer, S. Lomperski, H.-J. Strassberger, G. Varadi, G. Yadigaroglu, "The PANDA facility and first test results", *Kerntechnik* **61**, 5-6, pp. 214 - 222, (1996).

[107] R.O. Gauntt, "MELCOR Computer Code Manuals, Volume 1: User's Guide; Volume 2: Reference Manuals, Version 1.8.6, September 2005", NUREG/CR-6119, Vol. 1, Rev. 3, SAND 2005-5713.

[108] M.M Stempniewicz, "Analysis of PANDA PCC Steady State Tests with the SPECTRA Code", *Nuclear Technology*, **131**, pp. 82-101, July 2000.

[109] M.M Stempniewicz, "Analysis of ISP-42 PANDA Tests with the SPECTRA Code", *ICONE9, Nineth International Conference on Nuclear Engineering*, Nice, France, 8-12 April 2001.

[110] D. Lübbesmeyer, N.S. Aksan, "ISP-42 (PANDA) Blind Phase Comparison Report", NEA/CSNI/R(2003)6, May 2003. https://inis.iaea.org/collection/NCLCollectionStore/_Public/41/041/41041109.pdf

[111] N. Aksan, "Overview on the Panda Test Facility and ISP-42 PANDA Tests Data Base", Joint ICTP-IAEA Course on Natural Circulation Phenomena and Passive Safety Systems in Advanced Water Cooled Reactors, 2152-4, 17 - 21 May 2010, http://indico.ictp.it/event/a09155/session/31/contribution/26/material/0/0.pdf.

[112] C. Aubert, J. Dreier, "ISP-42, PANDA Test Phases, History of Events, Boundary and Initial Conditions, Calculational Parameters", PSI report, TM-42-98-40, ALPHA-835-1, January 1999.

[113] "Handbook on Lead-bismuth Eutectic Alloy and Lead Properties, Materials Compatibility, Thermal-hydraulics and Technologies", OECD/NEA Nuclear Science Committee. ISBN 978-92-64-99002-9, 2007.

[114] R.P. Wichner, "Fission Product Plateout and Liftoff in the MGHTR Primary System: A Review", NUREG/CR-5647, ORNL/TM-11685, April 1991.

[115] M.F. Osborne, et al., "Iodine Sorption on Low Chromium Alloy Steel", ORNL/TM-7755, 1982.

[116] M.M. Stempniewicz, "Sorption Coefficients for Iodine, Silver, and Cesium on Dust Particles", *Nuclear Engineering and Design*, **306**, (2016) 69-76

[117] D.Y.H. Pui, F. Romay-Novas, B.Y.H. Liu, "Experimental Study of Particle Deposition in Bends of Circular Cross-Section", *Aerosol Science and Technology*, **7**, pp. 301-315, 1987.

[118] McFarland, A.R., Gong, H., Muyshondt, A., Wente, W.B. and Anand, N.K. (1997) Aerosol deposition in bends with turbulent flow. *Environmental Science and Technology*, **31**: 3371-3377, 1997.

[119] D.E. Jacober, M.J. Matteson, "The Collection of Aerosols from Gas Streams by Impaction on Multiple Spherical Targets", *Aerosol Science and Technology* **4**, pp.:433-443, 1985

[120] J.A. Siegel, W.W. Nazaroff, "Predicting particle deposition on HVAC heat exchangers", *Atmospheric Environment*, **37**, pp. 5587 - 5596, 2003.

[121] L.E. Herranz, C.L. Del Pra, A. Dehbi, "Major Challanges to Modelling Aerosol Retention Near a Tube Breach During Steam Generator Tube Rupture Sequences", *Nuclear Technology*, Vol. **158**, pp. 83 - 93, April 2007.

[122] S. Ilias, P.L. Douglas, "Inertial Impaction of Aerosol particles on Cylinders at Intermediate and High Reynolds Numbers", *Chem. Eng. Sci.*, **44**, p. 81, 1989.

[123] R.A. Wessel, J. Righi, "Generalized Correlations for Inertial Impaction of Particles in a Cylinder", *Aerosol Sci. Tech.*, **9**, p. 29, 1988

[124] H.C. Wang, "Theroetical adhesion efficiency for particles impacting a cylinder at high Reynolds numbers", *Journal of Aerosol Science*, **17**, pp 827-837, 1986.

[125] D.R. Lide, et al., ""CRC Handbook of Chemistry and Physics, A Ready-Reference Book of Chemical and Physical Data", 72-nd edition, ISBN-0-8493-0472-5, CRC Press Inc., 1991-1992.

[126] L.E. Herranz, "Modelling aerosol retention in the secondary side of a vertical steam generator." FIKS-CT1999-00007, April 2003.

[127] T. Lind, S. Güntay, L.E. Herranz, S. Jayaraju, "The results of the ARTIST projects – aerosol retention in a steam generator during SGTR", 5th European Review meeting on Severe Accident Research (ERMSAR-2012) Cologne (Germany), March 21-23, 2012.

[128] P. Gruner, H. Schulz, "Investigation on the Primary Pressure Boundary Within Risk Analyses of German PWR's", Transactions of the 10th International Conference on Structural Mechanics in Reactor Technology, SMIRT-10/M, 1989

[129] D. Azodi, P. Gruner, “Numerical simulation of a BWR lower head with penetration subjected to a postulated core damage accident”, Transactions of the 14th International Conference on Structural Mechanics in Reactor Technology, SMiRT 14, Lyon, France, 1977.

[130] “Special Metals, Incoloy alloy 800H & 800HT”, www.specialmetals.com

[131] “Special Metals, Incoloy alloy 800”, www.specialmetals.com

[132] P. Wangyao, J. Zrnik, V. Vrchovinsky, Z. Novy, B. Kosanicka, “The Analysis of Creep Behavior in an Annealed Nickel-Based Alloy”, *Journal of Metals, Materials and Minerals*, **Vol. 12**, No. 2, pp. 67-73, 2003.

[133] L. Biasi, A. de los Reyes, M.W. Reeks, and G.F. Santi, "Use of a simple model for the interpretation of experimental data on particle resuspension in turbulent lows*", J. of Aerosol Sci*., **32**, pp. 1175-1200, 2001

[134] O. Benes, R.J.M. Konings, “Molten Salt Reactor Fuel and Coolant”, *Comprehensive Nuclear Materials*, Volume **3**, 2012, pp. 359-389

[135] R.J. Kedl, “The Migration of Fission Products (Noble Metals) in the Molten Salt Reactor Experiment”, ORNL-TM-3884, December 1972

[136] R.J. Kedl, "A Model for Computing the Migration of Very Short-lived Nobel Gases into MSRE Graphite", ORNL-TM-1810, July 1967.

[137] Kerntechnischer Ausschuss, SAFETY STANDARDS of the Nuclear Safety Standards Commission (KTA), “KTA 3102.1, Reactor Core Design for High-temperature Gas-Cooled Reactor, Part 1: Calculations of the Material Properties of Helium”, Carl Heymanns Verlag KG (1978).

[138] "RELAP5/MOD33 Code Manual Volume IV: Models and Correlations", NUREG/CR-5535/Rev P4-Vol IV, October 2010.

[139] J. Garnier, S. Begej, "Ex-Reactor Determination of Thermal Gap Conductance Between Uranium Dioxide and Zircaloy-4 Stage II: High Gas Pressure", NUREG/CR-0330, PNL-3232 Vol. 2, July 1980.

[140] J. R. Larson, et al. PBF-LOCA Test Series Test LOC-11 Test Results Report. NUREG/CR-0618, TREE-1329. Idaho National Engineering Laboratory. April 1979. https://inis.iaea.org/search/searchsinglerecord.aspx?recordsFor=SingleRecord&RN=11499829

[141] D.D. Lanning, C.R. Hann, "Review of Methods Applicable to the Calculation of Gap Conductance in Zircaloy-Clad UO_2 Fuel Rods", BNWL-1894, UC-78b, Battelle, April 1975.

[142] L.L. Humphries, et al., "MELCOR Computer Code Manuals, Vol. 3: MELCOR Assessment Problems, Version 2.1.7347 2015", SAND2015-6693 R, August 2015.

[143] M.J. Loftus, et al., "PWR FLECHT SEASET Unblocked Bundle, Forced and Gravity Reflood Task Data Report", NUREG/CR-1532, June 1980.

[144] "RELAP5/MOD3.3 code manuals – Volume III: Developmental Assessment Problems", https://www.nrc.gov/docs/ML1103/ML110330201.pdf

[145] A. Woudstra, J.P.A. van de Bogaard, P.M. Stoop, "Assessment of RELAP5/MOD2 Against ECN Reflood Experiments", NUREG/IA-0112, ECN-C-92-008, July 1993.

[146] M.M. Stempniewicz, "RMV - Reflood Model Validation, Analysis of ECN Reflood Tests with SPECTRA", NRG report 26187/22.246224, September 2022.

[147] H. Karwat, "Distribution of Hydrogen within the HDR-Containment under Severe Accident Conditions - Final Comparison Report -", OECD-CSNI-ISP 29, August 1992.

[148] J. Phillips, "HDR Test Analyses with MELCOR", SAND2017-3409 C, 2017.

[149] "Final Comparison Report on ISP-35: NUPEC Hydrogen Mixing and Distribution Test (Test M-7-1), NEA/CSNI/R(94)29, December 1994.

[150] M.A. Jimenez Garcia, F. Martin-Fuertes, J.M. Martin-Valdepenas, "MELCOR 1.8.3 Application to NUPEC M-7-1 Test (ISP-35) and Two Hydrogen Severe Accident Scenarios in a Typical PWR Plant", AECL-11762, NEA/CSNI/R(96)8, 1996.

[151] S. Kelm, et al., "Generic Containment: Detailed comparison of containment simulations performed on plant scale", *Annals of Nuclear Energy*, **74**, December 2014, Pages 165-172

[152] Coindreau et al., "Severe accident code to code comparison for two accident scenarios in a spent fuel pool", *The 8th European Review Meeting on Severe Accident Research – ERMSAR 2017*, Warsaw, Poland, 16-18 May 2017

[153] J. Dreier, C. Aubert, M. Huggenberger, H.J. Strassberger, G. Yadigaroglu, "The PANDA Tests for the SWR 1000 Passive Containment Cooling System", https://inis.iaea.org/collection/NCLCollectionStore/_Public/30/035/30035877.pdf

[154] W.Vichers, et al., "Testing and Enhanced Modelling of Passive Evolutionary Systems Technology for Containment Cooling - TEMPEST, Final Synthesis Report", 5th Euratom Framework Programme 1998-2003, CONTRACT N°: FIKS-CT-2000-00095, https://cordis.europa.eu/docs/projects/files/FIKS/FIKS-CT-2000-00095/tempest_projrep_en.pdf

[155] D.F. da Cruz, J.B.M. de Haas, A.I. van Heek, M.M. Stempniewicz, "ACACIA: a Small Scale Power Plant With Pebble Bed Cartridge Reactor and Indirect Brayton Cycle", GENES4/ANP2003, Kyoto, Japan, Sep. 15-19, 2003

[156] Zheng Y., Stempniewicz, M.M., "Investigation of NACOK Air Ingress Experiment Using Different System Analysis Codes", *Nuclear Engineering and Design*, **251** (2012) 423– 432

[157] Zheng Yanhua, Marek M. Stempniewicz, Chen Zhipeng, Shi Lei, "Study on the DLOFC and PLOFC accidents of the 200 MWe pebble-bed modular high temperature gas-cooled reactor with TINTE and SPECTRA codes", *Annals of Nuclear Energy* **120** (2018) 763–777

[158] Briggs, et al., "Benchmark Analyses of EBR-II Shutdown Heat Removal Tests", IAEA-TECDOC-1819; ISBN:978-92-0-105517-0; Vienna 2017.

[159] M.M. Stempniewicz, P.A. Breijder, H.J. Doolaard, F. Roelofs, "Multi-Scale Thermal Hydraulic Analysis of the EBR-II Loss of Flow Tests SHRT-17 And SHRT-45R", NURETH-17 (paper 21062), Xi'an, China, 3-8 September 2017.

[160] Bubelis et al., "System codes benchmarking on a low sodium void effect SFR heterogeneous core under ULOF conditions", *Nuclear Engineering and Design* **320** (2017) 325–345.

[161] M.M. Stempniewicz, E.A.R. de Geus, F. Roelofs, "NRG analysis of SFR heterogeneous core under ULOF conditions", *Nuclear Engineering and Design* **339** (2018) 65–74.

[162] A. Lazaro et al., "Code assessment and modelling for Design Basis Accident Analysis of the European Sodium Fast Reactor Design, Part I: System description, modelling and benchmarking", *Nuclear Engineering and Design*, **266**, (2014), pp. 1-16.

[163] A. Lazaro et al., "Code assessment and modelling for Design Basis Accident Analysis of the European Sodium Fast Reactor Design, Part II: Optimised core andrepresentative transients analysis", *Nuclear Engineering and Design* **277** (2014), pp. 265–276

[164] "ETDR, DEL022: Work Schedule", LEADER 5th WP5 Meeting, Petten, February 2013, (https://www.slideserve.com/wilma-mathis/leader-project-task-5-5)

[165] M.M. Stempniewicz, "LEADER, Task 5.5 ETDR Transient Analyses with the SPECTRA Code", LEADER Project meeting, JRC, Petten, February 26, 2013, https://slideplayer.com/slide/7055779/

[166] M.M. Stempniewicz, E.A.R. de Geus, B. Mikuž, F. Roelofs, "A New Model to Simulate Molten Fuel Systems with the SPECTRA Code", NURETH-17 (paper 21065), Xi'an, China, September 3 - 8, 2017.

[167] M.M. Stempniewicz, E.M.J. Komen, "Comparison of several resuspension models against measured data", *Nuclear Engineering and Design* **240**, pp. 1657–1670, 2010.

[168] M.M. Stempniewicz, Chen Zhipeng, Zheng Yanhua, E.M.J. Komen, "Resuspension models for monolayer and multilayer deposits of graphite dust", *Annals of Nuclear Energy* **120**, pp. 186–197, 2018.

[169] G.B. Wallis, "One-Dimensional Two-Phase Flow", ISBN-13: 978-0070679429, McGraw Hill, Inc., New York, 1969.

[170] R.J. Andreini, J.S. Foster, R.W. Callen, "Characterization of Gas Bubbles Injected into Molten Metals Under Laminar Flow Conditions", *Metallurgical Transactions,* Vol. **88**, pp. 625 - 631, 1977.

[171] https://dtrx.de/od/diff/

[172] Yoon, R. H. and Luttrell, G. H. (1989), "The effect of bubble size on fine particle flotation", *Mineral Processing and Extractive Metallurgy Review,* **Vol 5**. pp. 101-122.

[173] Afruns, J. P. and Kitchener, J. A. (1976), "The absolute rate of capture of single particles by single bubbles", *Flotation. Gaudin Memorial Volume*, M. C. Fuerstenau Editor. SME pp. 625-637.

[174] http://www.mineraltech.com/MODSIM/ModsimTraining/Module5/TechnicalNotes9.pdf

[175] E. Capelli, E.M.A. Frederix, A. Mathur, R. P. Hania, J.L. Kloosterman, R.J.M. Konings, "Noble metal behaviour and extraction in molten salt reactor", Thorium Energy Conference 2018 - ThEC18, Brussels, Belgium, October 29-31, 2018.

[176] https://pubs.acs.org/doi/abs/10.1021/acs.jced.7b00717

[177] Guiqiu Zheng, Brian Kelleher, Lingfeng He, Guoping Cao, Mark Anderson, Todd Allen, Kumar Sridharan, "High-Temperature Corrosion of UNS N10003 in Molten Li2BeF4 (FLiBe) Salt", *Corrosion*, Vol. **71**, No. 10, October 2015.

[178] Zheng Yanhua, Marek M. Stempniewicz, Chen Zhipeng, Shi Lei, "Study on the DLOFC and PLOFC accidents of the 200 MWe pebble-bed modular high temperature gas-cooled reactor with TINTE and SPECTRA codes", *Annals of Nuclear Energy* **120** (2018) 763–777.

[179] Tanaka M, Chisaka F (1990), "Effective thermal conductivity of discontinuous and continuous solid systems", *Kagaku-Kougaku* **16**:1688–173, 1990.

[180] D. Colombet, D. Legendre, A. Cockx, P. Guiraud, "Mass or heat transfer inside a spherical gas bubble at low to moderate Reynolds number", http://oatao.univ-toulouse.fr/10540/1/colombet_10540.pdf

[181] M.M. Stempniewicz, E.A.R. de Geus, F. Roelofs, "Benchmark on Natural Circulation with Salt Working Fluid - Mark1 Pebble Bed FHR (Mk1 PB-FHR) Benchmark Analysis with

SPECTRA", *Thorium Energy Conference 2018*, **ThEC18**, October 29-31, 2018, Brussels, Belgium.

[182] E.L. Compere, S.S. Kirslis, E.G. Bohlmann, F.F. Blankenship, W.R. Grimes, "Fission Product Behavior in the Molten Salt Reactor Experiment", ORNL-4865, October 1975.

[183] R.J. Kedl, "Fluid Dynamic Studies of The Molten-Salt Reactor Experiment (MSRE) Core", ORNL-TM-3229, November 1970.

[184] B.E. Prince, "Period Measurement on the Molten salt Experiment during Fuel Circulation: Theory and Experiment", ORNL-TM-1626, October 1966.

[185] R.J. Kedl, A. Houtzeel, "Development of a Model for Computing Xe-135 Migration in MSRE", ORNL-4069, June 1967.

[186] C.H. Gabbard, "Reactor Power Measurement and Heat Transfer Performance in the Molten Salt Reactor Experiment", ORNL-TM-3002, May 1970.

[187] W.C. Ulrich, "An Extended Hydraulic Model of the MSRE Circulating Fuel System", ORNL-TM-3007, June 1970.

[188] R.H. Guymon et al., "MSRE Systems and Components Performance", ORNL-TM-3039, June 1973.

[189] J.R. Engel, R.C. Steffy, "Xenon Behavior in Molten Salt Reactor Experiment", ORNL-TM-3464, October 1971.

[190] J.R. Engel, P.N. Haubenreich, "Temperatures in the MSRE Core During Steady -State Power Operation", ORNL-TM-378, November 1962.

[191] J. W. Cooke, B. Cox, "Forced-Convection Heat-Transfer Measurements with a Molten Fluoride Salt Mixture Flowing in a Smooth Tube", ORNL-TM-4079, March 1793.

[192] J.R. Engel, P.N. Haubenreich, S.J. Ball, "Analysis of Filling Accidents in MSRE", ORNL-TM-497, August 1966.

[193] S.J. Ball, T.W. Kerlin, "Stability Analysis of the Molten Salt Reactor Experiment", ORNL-TM-1070, December 1965.

[194] J.J. Carbajo, D. De Wet, N.R. Brown, "Modelling the Molten Salt Reactor Experiment with the RELAP5-3D Code", 2017 ANS Annual Meeting, San Francisco, CA, June 11-15, 2017.

[195] K. Verfondern, R. C. Martin, R. Moormann, "Methods and Data for HTGR Fuel Performance and Radionuclide Release Modeling during Normal operation and Accidents for Safety Analysis", Jüllich - 2721 January 1993.

[196] N. Hottle, "Pebble Bed Reactor Plant Design Description", AREVA NP Inc. Technical Data Record, Document No.: 12-9149697-000, 20004-018 (10/18/2010), https://art.inl.gov/NGNP/NEAC%202010/Pebble%20Bed%20Reactor%20Plant%20Design%20Description%20-%20AREVA.pdf

[197] "Performance Analysis Review of Thorium TRISO Coated Particles during Manufacture, Irradiation and Accident Condition Heating Tests" IAEA-TECDOC-1761, Vienna 2015.

[198] Heinz Nabielek, Forschungszentrum Jülich, D, Presented at the 2nd Planning Workshop of the Task Force "Zero Emissions Technologies- Strategy" lEA Working Party on Fossil Fuels, Washington D.C., 20 March 2002.

[199] R.O. Gauntt, "MELCOR 1.8.5 Modeling Aspects of Fission Product Release, Transport and Deposition - an Assessment with Recommendations", SAND 2010-1635, April, 2010.

[200] P.G. Rousseau, C.G. du Toit, W. van Antwerpen, H.J. van Antwerpen, "Separate effects tests to determine the effective thermal conductivity in the PBMR HTTU test facility", *Nuclear Engineering and Design* **271** (2014) 444–458.

[201] M.M. Stempniewicz, E.A.R. de Geus, E.Y. Garcia Servantes, F. Roelofs, J. Kuijper, M. Skrzypek, E. Skrzypek, J. Malesa, D. Muszyński, C. Pohl, N. Kohtz, "Unprotected PLOFC Scenario In GEMINI+ Plant", The 19th International Topical Meeting on Nuclear Reactor Thermal Hydraulics (NURETH-19), Brussels, Belgium, March 6 - 11, 2022.

[202] J.C. Kuijper, D. Muszynski, "Neutronics for the GEMINI+ HTGR", *Proceedings of HTR 2020*, Yogyakarta, Indonesia, October 6-8, 2020.

[203] Benjamin Rouben, Eleodor Nichita, "Reactor Statics", (Chapter 4 of The Essential CANDU), http://nuceng.ca/candu/pdf/4%20-%20Reactor%20Statics.pdf

[204] Wm. J. Garland, "Reactor Physics: The Diffusion of Neutrons", (Based on Chapter 5 of Lamarsh), http://nuceng.ca/ep4d3/text/3-diffusion-r1.pdf

[205] A. Beluco, E.B. Camano Schettini, "An Improved Expression for a Classical Type of Explicit Approximation of the Colebrook White Equation with Only One Internal Iteration", International Journal of Hydraulic Engineering 2016, 5(1): 19-23.

[206] T. Hua, T. Fei, B. Feng, R. Hu, M.M. Stempniewicz, F. Roelofs, "Benchmarking MSRE Transient Tests Using SPECTRA and SAM", The 19th International Topical Meeting on Nuclear Reactor Thermal Hydraulics (NURETH-19), Brussels, Belgium, March 6 - 11, 2022.

[207] https://www.nuclear-power.com/nuclear-power/fission/delayed-neutrons/

[208] T. Sevón, "Molten Core - Concrete Interactions in Nuclear Accidents, Theory and Design of an Experimental Facility", VTT Research Notes 2311, ESPOO 2005 https://publications.vtt.fi/pdf/tiedotteet/2005/T2311.pdf

Appendix A Fission Product Modeling Parameters

The parameters affecting fission product transport are given in this appendix.

A.1 Diffusion Coefficients in Solids

The diffusion equation in solids in SPECTRA (in 1-D Solid Conductors) is (see Volume 1: "Diffusion Inside Solid Materials"):

$$\frac{\partial C}{\partial t} = \frac{\partial}{\partial x}\left(D \cdot \frac{\partial C}{\partial x} \right) + S_V$$

Here C is the concentration of an isotope in the solid material [kg/m^3], D is the diffusion coefficient [m^2/s] and S_V is the local volumetric source rate [kg/m^3-s] due to various reasons, such as radioactive decay (negative), precursor decay (positive), neutron capture in core regions, as well as migration from the fluid (either gas or liquid) to the solid surface. In a steady state condition, with a constant value of D, this reduces to:

$$D \cdot \frac{\partial^2 C}{\partial x^2} = -S_V$$

Reference [136] uses the steady-state diffusion equation:

$$\frac{\partial^2 C}{\partial x^2} + \frac{\partial^2 C}{\partial y^2} + \frac{\partial^2 C}{\partial z^2} = \frac{\varepsilon}{D} \cdot \lambda C$$

In 1-D this reduces to:

$$\frac{\partial^2 C}{\partial x^2} = \frac{\varepsilon}{D} \cdot \lambda C$$

Here the term λC represents the (negative) source due to radioactive decay, in SPECTRA included as one of the volumetric sources present in the diffusion equation. Comparing the above equation to the equation applied in SPECTRA, it is seen that the diffusion coefficient that needs to be used in SPECTRA is equal to D/ε in [136]. The values of D reported in [136] are:

- middle and top of core: $D = 1.6\times10^{-5} – 2.0\times10^{-5}$ ft^2/h,
  average = 1.8×10^{-5} ft^2/h = 4.65×10^{-10} m^2/s
- bottom of core: $D = 6.9\times10^{-5}$ ft^2/h = 1.78×10^{-9} m^2/s

Since $\varepsilon = 0.1$ [136], the values that need to be applied in SPECTRA are an order of magnitude larger:

- middle and top core : $D = 4.65\times10^{-9}$ m^2/s
- bottom of core: $D = 1.78\times10^{-8}$ m^2/s

A.2 FP Transport to Bubble/Droplet Surface

Literature provides correlations for mass transfer in bubbles. The correlation recommended in [180] is:

$$Sh = \frac{1}{1+\exp(-a\cdot[\ln(Pe)-b)}\cdot(Sh_{\max}-Sh_{\min})+Sh_{\min}$$

The constants are: $Sh_{\min}$ = 6.58, $Sh_{\max}$ = 18.0, a = 1.89, b = 3.3, 3.8, 4.2. Results are shown in Figure A.1. It may be expected that the mass transfer in droplets is similar as in bubbles and the same formula may be apply. This means that Sherwood number between 6 and 18 would be reasonable. Alternatively a correlation can be applied. The correlation shown above cannot be directly applied in SPECTRA. The correlation that is available in SPECTRA has the following form (see Volume 2, record 895YXX):

$$Sh = A + B\,\frac{Re^{C}\;Sc^{D}}{1+E\;Re^{F}\;Sc^{G}}$$

The coefficients for this correlation were fit to provide a good match with the correlation from [C-3], as follows. Since $Pe = Re \times Sc$, this implies $C=D$ and $F=G$. In order to be consistent with the correlation from [180], the coefficients C and D were set to zero. The correlation is:

$$Sh = A + \frac{B}{1+E\;Re^{F}\;Sc^{G}}$$

The other constants were obtained by trial and error. The values that provide a good fit to the data are: A = 6.58, B = 11.4, $F = G = -2$, E = 800, 1900, 4200. Results are shown in Figure A-2 (correlation is shown by red lines and yellow markers, original data [180] in black).

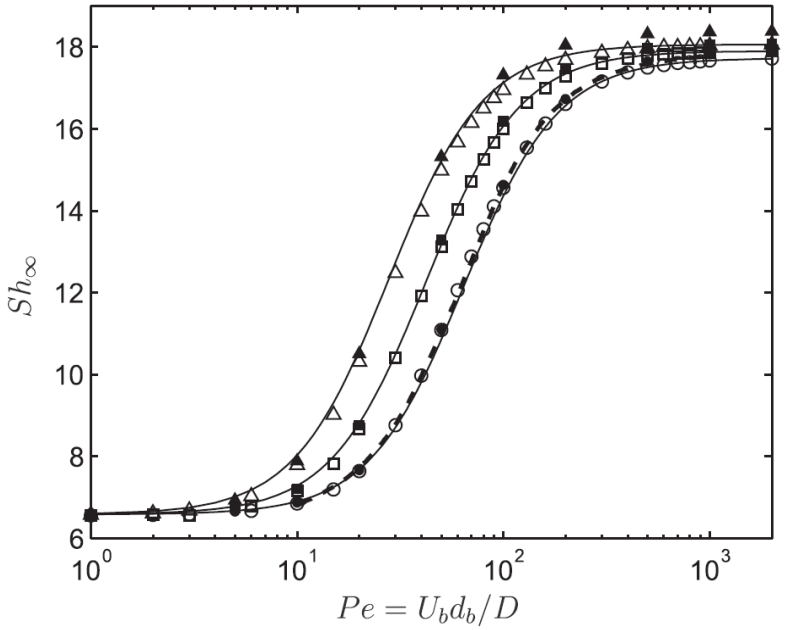

Figure A.1 Transport to bubble/droplet surface - correlations from [180]

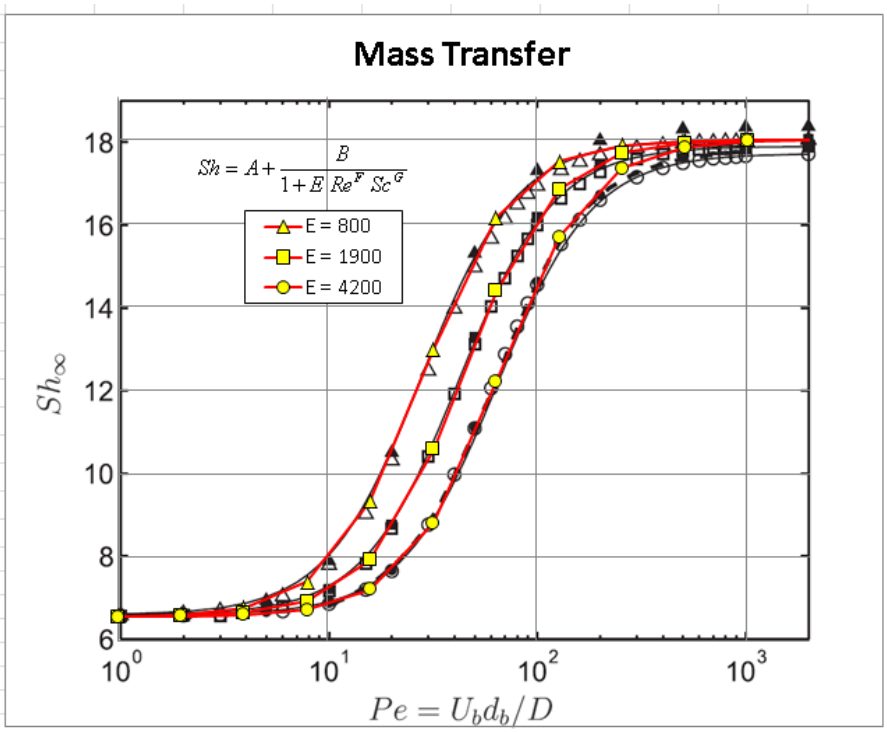

Figure A.2 Transport to bubble/droplet surface - SPECTRA correlation